SECOND EDITION

TREATISE ON GEOPHYSICS

Volume 1

DEEP EARTH SEISMOLOGY

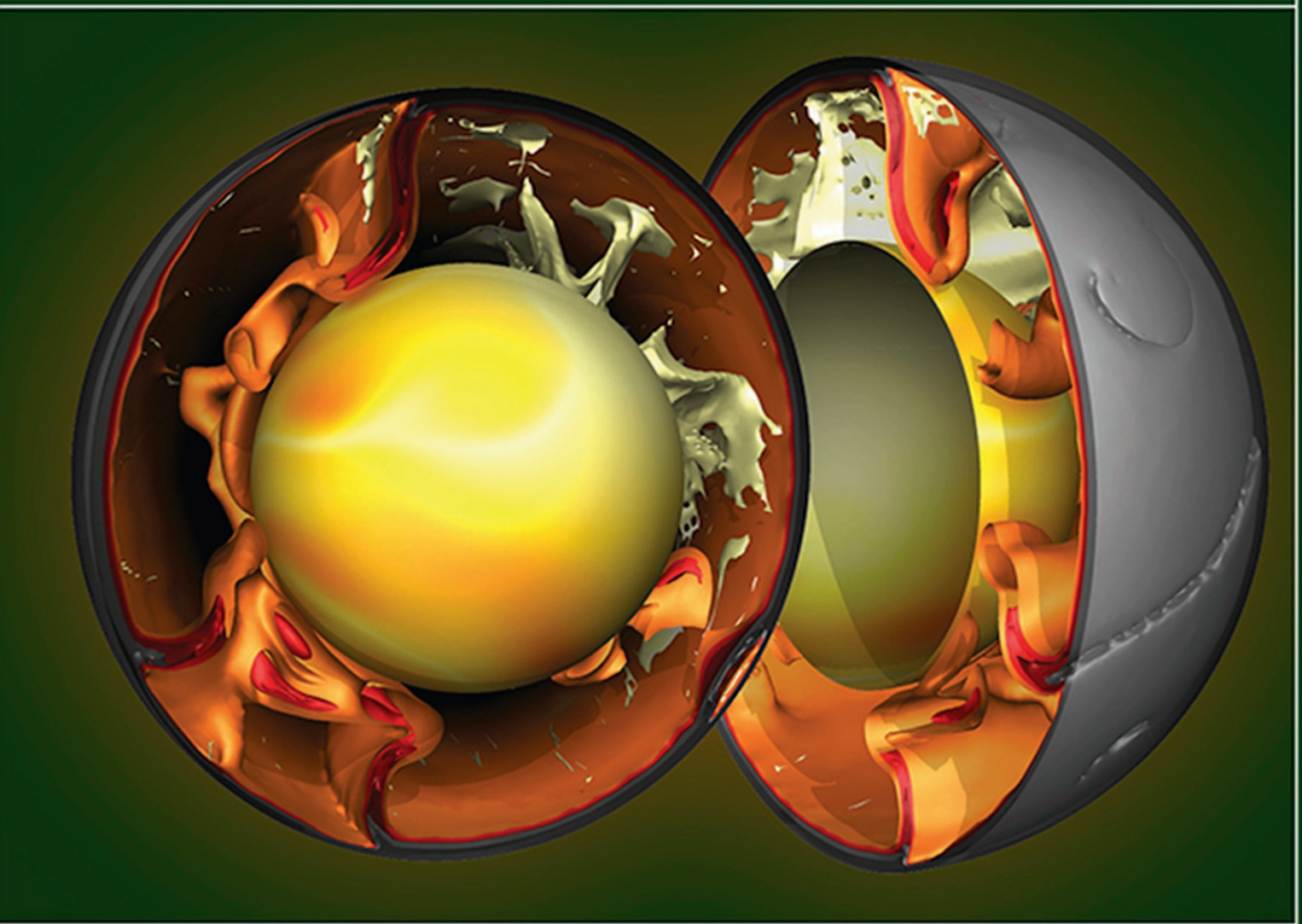

VOLUME EDITORS: BARBARA ROMANOWICZ AND ADAM DZIEWONSKI

EDITOR-IN-CHIEF: GERALD SCHUBERT

TREATISE ON GEOPHYSICS

SECOND EDITION

This page intentionally left blank

TREATISE ON GEOPHYSICS

SECOND EDITION

EDITOR-IN-CHIEF

Gerald Schubert

Distinguished Professor Emeritus, Department of Earth, Planetary and Space Sciences, University of California, Los Angeles

VOLUME 1

DEEP EARTH SEISMOLOGY

VOLUME EDITORS

Professor Barbara Romanowicz

Berkeley Seismological Laboratory, University of California at Berkeley and Collège de France, Paris

And

Professor Adam Dziewonski

Department of Earth and Planetary Sciences, Harvard University

ELSEVIER AMSTERDAM • BOSTON • HEIDELBERG • LONDON • NEW YORK • OXFORD
PARIS • SAN DIEGO • SAN FRANCISCO • SINGAPORE • SYDNEY • TOKYO

Elsevier
Radarweg 29, PO Box 211, 1000 AE Amsterdam, The Netherlands
The Boulevard, Langford Lane, Kidlington, Oxford OX5 1GB, UK
30 Corporate Drive, Suite 400, Burlington MA 01803, USA

Copyright © 2015 Elsevier B.V. unless otherwise stated. All rights reserved.

Cover image created for this work by Fabio Crameri, University College London.
The figure depicts the temperature field from a convection calculation using the code STAG-YY, written by Paul Tackley.

The following chapters are US Government works in the public domain and not subject to copyright:

1.11 Crust and Lithospheric Structure - Global Crustal Structure; 3.09 Earth Rotation Variations – Long Period; 4.07 The Role of Fault-Zone Drilling; 5.11 The Time-Averaged Field and Paleosecular Variation; 10.21 Exoplanetary Geophysics: An Emerging Discipline; 11.12 Tools and Techniques: Gravitational Method.

No part of this publication may be reproduced or transmitted in any form or by any means, electronic or mechanical, including photocopying, recording, or any information storage and retrieval system, without permission in writing from the publisher. Details on how to seek permission, further information about the Publisher's permissions policies and our arrangements with organizations such as the Copyright Clearance Center and the Copyright Licensing Agency, can be found at our website: www.elsevier.com/permissions.

This book and the individual contributions contained in it are protected under copyright by the Publisher (other than as may be noted herein).

Notices
Knowledge and best practice in this field are constantly changing. As new research and experience broaden our understanding, changes in research methods, professional practices, or medical treatment may become necessary.

Practitioners and researchers may always rely on their own experience and knowledge in evaluating and using any information, methods, compounds, or experiments described herein. In using such information or methods they should be mindful of their own safety and the safety of others, including parties for whom they have a professional responsibility.

To the fullest extent of the law, neither the Publisher nor the authors, contributors, or editors, assume any liability for any injury and/or damage to persons or property as a matter of products liability, negligence or otherwise, or from any use or operation of any methods, products, instructions, or ideas contained in the material herein.

Library of Congress Cataloging-in-Publication Data
A catalog record for this book is available from the Library of Congress

British Library Cataloguing-in-Publication Data
A catalogue record for this book is available from the British Library

ISBN (print): 978-0-444-53802-4

For information on all Elsevier publications
visit our website at http://store.elsevier.com/

Editorial & Production: Gemma Tomalin, Richard Berryman, Marise Willis, Michael Nicholls, Ellen Bishop
Cover design: Matthew Limbert

Printed and bound in the United Kingdom

15 16 17 18 19 10 9 8 7 6 5 4 3 2 1

CONTENTS

Preface *vii*

Editor-in-Chief *ix*

Contributors *xi*

Contents of all Volumes *xiii*

1.01 Deep Earth Seismology: An Introduction and Overview 1
AM Dziewonski and BA Romanowicz

1.02 Theory and Observations - Instrumentation for Global and Regional Seismology 29
JM Steim

1.03 Theory and Observations - Earth's Free Oscillations 79
JH Woodhouse and A Deuss

1.04 Theory and Observations: Normal Mode and Surface Wave Observations 117
G Laske and R Widmer-Schnidrig

1.05 Theory and Observations: Body Waves, Ray Methods, and Finite-Frequency Effects 169
J Virieux and G Lambaré

1.06 Theory and Observations: Forward Modeling: Synthetic Body Wave Seismograms 201
VF Cormier

1.07 Theory and Obeservations - Forward Modeling and Synthetic Seismograms, 3D Numerical Methods 231
J Tromp

1.08 Theory and Observations - Seismology and the Structure of the Earth: Teleseismic Body-Wave Scattering and Receiver-Side Structure 253
MG Bostock

1.09 Theory and Observations - Seismic Anisotropy 277
V Maupin and J Park

1.10 Theory and Observations - Seismic Tomography and Inverse Methods 307
C Thurber and J Ritsema

1.11 Crust and Lithospheric Structure - Global Crustal Structure 339
WD Mooney

1.12 Crust and Lithospheric Structure - Seismic Imaging and Monitoring with Ambient Noise Correlations 391
M Campillo and P Roux

1.13 Crust and Lithospheric Structure - Seismic Structure of Mid-Ocean Ridges 419
RA Dunn

1.14 Crust and Lithospheric Structure - Hot Spots and Hot-Spot Swells 453
M McNutt and DW Caress

1.15 Crust and Lithospheric Structure - Active Source Studies of Crust and Lithospheric Structure 479
A Levander, CA Zelt, and WW Symes

1.16 Crust and Lithospheric Structure - Natural Source Portable Array Studies of the Continental Lithosphere 513
DE James

1.17 Crustal and Lithospheric Structures Between the Alps and East European Craton from Long-Range Controlled Source Seismic Experiments 557
A Guterch, M Grad, G Randy Keller, and E Brückl

1.18 Crust and Lithospheric Structure - Seismological Constraints on the Lithosphere-Asthenosphere Boundary 587
KM Fischer

1.19 Deep Earth Structure - Upper Mantle Structure: Global Isotropic and Anisotropic Elastic Tomography 613
J-P Montagner

1.20 Deep Earth Structure - Subduction Zone Structure in the Mantle Transition Zone 641
Y Fukao and M Obayashi

1.21 Deep Earth Structure - Transition Zone and Mantle Discontinuities 655
R Kind and X Li

1.22 Deep Earth Structure: Lower Mantle and D″ 683
T Lay

1.23 Deep Earth Structure: The Earth's Cores 725
A Souriau and M Calvet

1.24 Deep Earth Structure: Seismic Scattering in the Deep Earth 759
PM Shearer

1.25 Deep Earth Structure: *Q* of the Earth from Crust to Core 789
BA Romanowicz and BJ Mitchell

1.26 Constraints on Seismic Models from Other Disciplines - Constraints from Mineral Physics on Seismological Models 829
L Stixrude and R Jeanloz

1.27 Constraints on Seismic Models from Other Disciplines - Constraints on 3-D Seismic Models from Global Geodynamic Observables: Implications for the Global Mantle Convective Flow 853
AM Forte, NA Simmons, and SP Grand

PREFACE

The *Treatise on Geophysics* is a comprehensive and in-depth study of the physics of the Earth and of terrestrial-like planets residing both within and outside our solar system. Its breadth and detail of coverage are beyond what any single geophysics text can provide. The first edition of the *Treatise on Geophysics* was published in 2007, nearly a decade ago. Of course, there is much progress in science in that length of time and the field of geophysics has grown rapidly and developed new lines of inquiry. Accordingly, we have brought the *Treatise on Geophysics* up-to-date with this second edition. The new edition will continue to provide students and professionals with fundamental and state-of-the-art discussion of all aspects of geophysics. In this new edition, the reader will find updates to all the chapters contained in the first edition and new chapters that discuss topics missing from the first edition. In a few instances, chapters from the first edition have simply been reprinted in order to avoid gaps in coverage. Chapters that emphasized fundamental physics often required little updating.

A highlight of the second edition is a new volume on Resources in the Near-Surface Earth. The new volume discusses the role of geophysics in the exploitation and conservation of natural resources and the assessment of degradation of natural systems by pollution. The near surface is a zone where humans and natural systems interact. Understanding the effects of human impacts is a challenge particularly for the long term.

There are four new chapters in the volume on Deep Earth Seismology. One of them describes progress in seismic instrumentation in the last 30 years in the era of broadband digital sensor and recording systems. Another one addresses a new approach for the determination of crust and uppermost mantle structure, based on ambient noise cross-correlations. This has revolutionized the field, since it allows the study of regional structure at high resolution in areas where there are no earthquakes. The third new chapter is devoted to recent advances in characterizing the lithosphere–asthenosphere boundary under both oceans and continents. Finally, the last new chapter discusses the morphology of subducted slabs in the Earth's transition zone.

The Mineral Physics volume has new chapters on dynamic (shock-wave) compression methods, and on the mineralogy of the upper mantle and the D″ layer focusing on post-perovskite, and extrasolar super-Earths.

New material in the Geodesy volume expands the temporal resolution and latency of geodetic measurements to high-rate, real-time measurements and increases the spatial resolution to meter size pixels with optical and radar imaging systems. Application areas are extended with new material on the uses of Earth gravity measurements.

The Earthquake Seismology volume has a new chapter on rock mechanics that is a comprehensive account of modern rock mechanics with emphasis on the variation of frictional properties of rocks during an earthquake cycle. Many chapters have considerable updates reflecting the lessons from significant recent earthquakes (e.g., the 2011 Tohoku-Oki earthquake and the 2013 Okhotsk deep earthquake), new observations on slow slips and triggered earthquakes, and developments of new methods (e.g., back projection method). Some chapters are updated (e.g., paleoseismology and strong ground motion) with substantial new material.

Chapters in the Geomagnetism volume have been updated to include recent advances in the acquisition of larger data sets and higher quality data and in the construction of more reliable and sophisticated models. Improvements in data have occurred in areas such as magnetic anomalies, paleointensities, and planetary magnetism. Improvements in models of the present day field include so-called comprehensive models and models that incorporate data assimilation.

The Crustal and Lithosphere Dynamics volume has new contributions on mountain building and landscape evolution.

The Mantle Dynamics volume contains new chapters on the generation of plate tectonics from mantle convection and the core–mantle boundary region.

The Core Dynamics volume features a comprehensive update of this rapidly changing subject, including new chapters on turbulence and waves in the fluid outer core.

The volume on the Evolution of the Earth presents a new assessment on the role of volatiles in Earth evolution.

There are new chapters in the Physics of Terrestrial Planets and Moons volume on planetary atmospheres, planetary tectonics, extrasolar planets and asteroids and comets. The study of extrasolar planets has had explosive growth in the last decade and new spacecraft missions have significantly enhanced our knowledge of solar system planets and moons.

Finally, this is an opportunity for me to thank and acknowledge the editors of the individual volumes for their hard work, patience, dedication, and commitment in bringing this new edition of the Treatise to fruition. I am also indebted to Gemma Tomalin of Elsevier for her care and attention to the organization and production of the Treatise and to Deepa Arumugam for her careful coordination of the proofs from the copyeditor and typesetter. Of course, the authors of the individual chapters are the ones who are responsible for the excellence of the Treatise. We have all had some ups and downs in the process of producing the second edition of the Treatise but the final product is one that we can all view with pride.

Gerald Schubert
Editor-in-Chief

EDITOR-IN-CHIEF

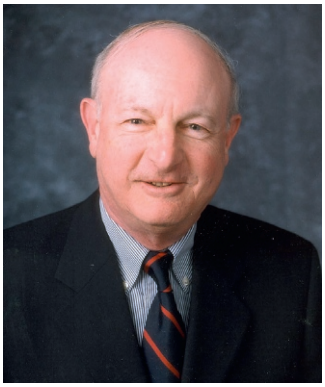

Gerald Schubert is Distinguished Professor Emeritus in the Department of Earth, Planetary and Space Sciences at the University of California, Los Angeles. His research interests encompass the physics of the interiors and atmospheres of the Earth, the Moon, and the other moons and planets of the solar system. He is co-author with Donald Turcotte of *Geodynamics* (ed. 3, Cambridge University Press, 2014) and with Turcotte and Peter Olson of *Mantle Convection in the Earth and Planets* (Cambridge University Press, 2001). He is the author of over 540 research papers. He has participated in a number of NASA's planetary missions, including Apollo, Pioneer Venus, Magellan, and Galileo, and has been editor and editorial board member of many journals, including *Icarus*, *Journal of Geophysical Research*, *Geophysical Research Letters*, and *Annual Reviews of Earth and Planetary Sciences*. Professor Schubert is a Fellow of the American Geophysical Union and a recipient of the Union's James B. MacElwane medal and the Harry H. Hess medal. He is a member of the National Academy of Sciences and the American Academy of Arts and Sciences.

This page intentionally left blank

CONTRIBUTORS

MG Bostock
The University of British Columbia, Vancouver, BC, Canada

E Brückl
Vienna University of Technology, Vienna, Austria

M Calvet
CNRS and Université Paul Sabatier, Toulouse, France

M Campillo
Isterre, Université Joseph Fourier and CNRS, Grenoble, France

DW Caress
Monterey Bay Aquarium Research Institute, Moss Landing, CA, USA

VF Cormier
University of Connecticut, Storrs, CT, USA

A Deuss
University of Oxford, Oxford, UK; Utrecht University, Utrecht, The Netherlands

RA Dunn
University of Hawaii at Manoa, Honolulu, HI, USA

AM Dziewonski
Harvard University, Cambridge, MA, USA

KM Fischer
Brown University, Providence, RI, USA

AM Forte
Université du Québec à Montréal, Montréal, QC, Canada

Y Fukao
Japan Agency for Marine-Earth Science and Technology, Kanagawa, Japan

M Grad
University of Warsaw, Warsaw, Poland

SP Grand
University of Texas, Austin, TX, USA

A Guterch
Institute of Geophysics, Polish Academy of Sciences, Warsaw, Poland

DE James
Carnegie Institution of Washington, Washington, DC, USA

R Jeanloz
University of California at Berkeley, Berkeley, CA, USA

R Kind
Deutsches GeoForschungsZentrum GFZ, Potsdam, Germany

G Lambaré
CGG, Massy, France

G Laske
Scripps Institution of Oceanography, University of California San Diego, La Jolla, CA, USA

T Lay
University of California Santa Cruz, Santa Cruz, CA, USA

A Levander
Rice University, Houston, TX, USA

X Li
Deutsches GeoForschungsZentrum GFZ, Potsdam, Germany

V Maupin
University of Oslo, Oslo, Norway

M McNutt
Monterey Bay Aquarium Research Institute, Moss Landing, CA, USA

BJ Mitchell
Saint Louis University, St. Louis, MO, USA

J-P Montagner
Université paris-Diderot, Paris, France

WD Mooney
USGS, Menlo Park, CA, USA

M Obayashi
Japan Agency for Marine-Earth Science and Technology, Kanagawa, Japan

J Park
Yale University, New Haven, CT, USA

G Randy Keller
University of Oklahoma, Norman, OK, USA

J Ritsema
University of Michigan, Ann Arbor, MI, USA

BA Romanowicz
University of California, Berkeley, CA, USA; Collège de France, Paris, France

P Roux
Isterre, Université Joseph Fourier and CNRS, Grenoble, France

PM Shearer
University of California, San Diego, La Jolla, CA, USA

NA Simmons
Lawrence Livermore National Laboratory, Livermore, CA, USA

A Souriau
CNRS and Université Paul Sabatier, Toulouse, France

JM Steim
Quanterra Inc., Shirley, MA, USA; Harvard University, Cambridge, MA, USA

L Stixrude
University College London, London, UK

WW Symes
Rice University, Houston, TX, USA

C Thurber
University of Wisconsin–Madison, Madison, WI, USA

J Tromp
Princeton University, Princeton, NJ, USA

J Virieux
ISTerre, Université Joseph Fourier, Grenoble, France

R Widmer-Schnidrig
Black Forest Observatory, Wolfach, Germany

JH Woodhouse
University of Oxford, Oxford, UK; University of Cambridge, Cambridge, UK

CA Zelt
Rice University, Houston, TX, USA

1.01 Deep Earth Seismology: An Introduction and Overview

AM Dziewonski, Harvard University, Cambridge, MA, USA
BA Romanowicz, University of California, Berkeley, CA, USA; Collège de France, Paris, France

© 2015 Elsevier B.V. All rights reserved.

1.01.1	**Developments from the Late Nineteenth Century until the Early 1950s**	2
1.01.2	**Developments from 1950s to the Early 1980s**	4
1.01.3	**From 1980 to Present: The Era of Tomography and Broadband Digital Seismic Networks**	9
1.01.4	**Current Issues in Global Tomography**	14
1.01.4.1	Resolving Power of Datasets Used for Constructing Models	16
1.01.4.2	Theoretical Assumptions	17
1.01.4.3	Robust Features of Current Global Mantle Models and Their Implications	19
1.01.4.4	Stability of the Planetary-Scale Heterogeneities	23
1.01.4.5	The Need for Consideration of More Complete Modeling of Mantle Flow	24
References		25

Applications of seismology to the study of the Earth's interior are only a little over 100 years old. Its tools in determining the properties of inaccessible Earth are the most powerful among all geophysical methods. The principal reasons are the availability of natural (earthquakes) or controlled (explosions and vibrators) sources of elastic waves and their relatively low attenuation with distance. Seismological methods span some six orders of magnitude in frequency, and the depth of an investigated structure may range from a few meters in engineering applications to the center of the Earth. Progress in seismology has been achieved through developments on several fronts: theory, instrumentation, and its deployment, as well as computational resources.

Even though the studies of earthquakes and the Earth's structure are closely related, the two subjects are often discussed separately. This volume is devoted to the Earth's structure and Volume 4 to studies of earthquakes. Nevertheless, the relationship is intimate. For example, it is possible to formulate an inverse problem in which earthquake locations are sought simultaneously with the parameters of the Earth's structure, including three-dimensional (3-D) models (see Chapter 1.10).

In the past 25 years, important progress has been made on several fronts: (1) the development of broadband digital instrumentation (see Chapter 1.02), which has allowed the construction of digital seismic databases of unprecedented quality at both the global and the regional scales; (2) the development of powerful data analysis tools, made possible by ever more efficient computer technology; and (3) theoretical progress in the forward and inverse computation of the effects of strong lateral heterogeneity on seismic-wave propagation. The combination of these factors has led to much improved images of structure at the global and regional scale, often helped by the inclusion of constraints from other types of data, primarily from the fields of mineral physics and geodynamics. This volume is thus divided into four parts. The first part principally covers seismic instrumentation, theoretical developments, and seismic data analysis techniques. Chapter 1.03 discusses the state of the art in the computation of the Earth's normal modes, while Chapter 1.04 describes progress in the measurements of normal-mode and long-period surface waves. Two chapters are devoted to the computation of synthetic seismograms in the presence of lateral heterogeneity, suitable for the case of body waves (see Chapters 1.05 and 1.06). Significant progress has recently been made in the computation of synthetic seismograms in a 3-D Earth using numerical methods. A review is given in Chapter 1.07. With the deployment of dense regional arrays of broadband seismometers, another area of rapid progress has been that of the adaptation of methodologies first developed in exploration seismology to the case of fine structure imaging of the crust and upper mantle at larger scale. These approaches are described in Chapter 1.08 for passive-source applications and in Chapter 1.15 for the case of active sources. The realization of the importance of anisotropy in the Earth has led to theoretical and methodological developments (see Chapters 1.09 and 1.18). Note that the issue of anisotropy is also discussed in Chapter 1.19 in the context of the inversion of surface-wave data. Inverse methods, in particular in the context of global and regional tomography, are discussed in Chapter 1.10.

In the second part of Volume 1, reviews of the status of our knowledge on the structure of the Earth's shallow layers are presented, starting with a global review of the Earth's crustal structure (see Chapter 1.11). During the last decade, there has been rapid development in using the Earth's noise as a source of the signal. A review of these developments is presented in Chapter 1.12. Two chapters discuss regional structure in the oceans: Chapter 1.13 for mid-ocean ridges and Chapter 1.14 for hot-spot swells. Chapter 1.18 presents results of studying anisotropy in subduction zones with particular attention devoted to the flow-induced preferential orientation of olivine crystals. Finally, two chapters are devoted to the results of regional experiments: upper-mantle studies using data from portable broadband experiments (see Chapter 1.16) and crustal studies, specifically in Europe, from high-resolution long-range active-source experiments (see Chapter 1.17).

The third part of this volume concerns the Earth's deep structure, divided into its main units: the upper mantle (see Chapter 1.19); the transition zone and upper-mantle discontinuities (see Chapter 1.21); regional tomography of

subducted slabs, with particular attention given their stagnation at the bottom of the transition zone (Chapter 1.20); the lower mantle; and the highly complex D″ region at the base of the mantle (Chapter 1.22) as well as the Earth's core (see Chapter 1.23). Chapter 1.24 is devoted to the subject of scattering in the Earth and Chapter 1.25 to that of attenuation. Finally, the fourth part of this volume comprises two chapters, in which constraints on the Earth's structure from fields other than seismology, mineral physics (see Chapter 1.26) and geodynamics (see Chapter 1.27), are discussed.

This volume addresses various aspects of 'structural seismology' and its applications to other fields of Earth sciences. Not all the subjects are covered in comparable detail, even though the completeness of the coverage was the initial objective of the editors. Compared to the 2007 edition of Volume 1 of *Treatise on Geophysics*, this edition contains four new (Chapters 1.02, 1.12, 1.18, and 1.20). Most of the other chapters have been significantly updated, except Chapters 1.14, 1.15, and 1.16, which are reprinted 'as is' from the 2007 edition.

In what follows, we briefly describe the developments in seismology from the end of the nineteenth century until the present, with the main emphasis on the development of instrumentation and its deployment, because seismology is a data-driven science. An account of the history of seismology can be found, among others, in Agnew et al. (2002). We also present our point of view, which some may consider controversial, specifically on current issues in global tomography and interpretation of the 3-D models not discussed in any of the chapters. We justify bringing these issues forward because of our belief that interpretation of tomographic results in terms of mantle dynamics does not match the robustness of models built using data that have good resolution at all depths in the mantle.

1.01.1 Developments from the Late Nineteenth Century until the Early 1950s

The theoretical beginnings of seismology may be traced to the eighteenth- and nineteenth-century studies of elasticity and propagation of elastic waves in solids. Lord Kelvin provided the first numerical estimate of the period of the fundamental vibrational mode ($_0S_2$) in 1863, but the development of the proper theory for a homogeneous sphere had to wait nearly 50 years (Love, 1911). Lord Rayleigh solved the problem of propagation of surface waves in an elastic half-space in 1877.

This preceded the first mechanical seismographs, which were developed in the 1880s. Originally, the seismographs had very low sensitivity and were used for the recording of local earthquakes. The history of global seismology begins with the recording of an earthquake in Japan on 19 April 1889 by von Rebeur-Paschwitz. He associated a disturbance recorded on a tiltmeter, used to study the Earth's tides, with the reports of a great earthquake in Japan. Figure 1 shows a copy of this recording as published in *Nature* (von Rebeur-Paschwitz, 1889, 1895).

The early seismographs were mechanical pendulums with no damping, other than friction. Their magnifications (the ratio of the amplitude on a seismogram to the actual ground motion) were very low, and because of the lack of damping, the records were very oscillatory and it was difficult to distinguish the arrivals of different phases. An improved mechanical

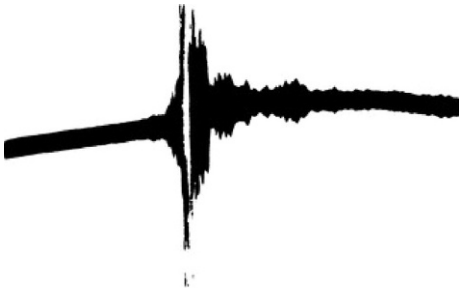

Figure 1 The historical first recording of a teleseismic event: an earthquake in Japan recorded in Potsdam on a tiltmeter designed by von Rebeur-Paschwitz. The early seismograms had difficulty with damping the pendulum motion and made phase identification difficult. Reproduced from von Rebeur-Paschwitz (1895) Horizontalpendal-Beobachtungen auf der Kaiserlichen Universitats-Sternwarte zu Strassburg 1892–1894. *Gerlands Beiträge zur Geophysik* 2: 211–536.

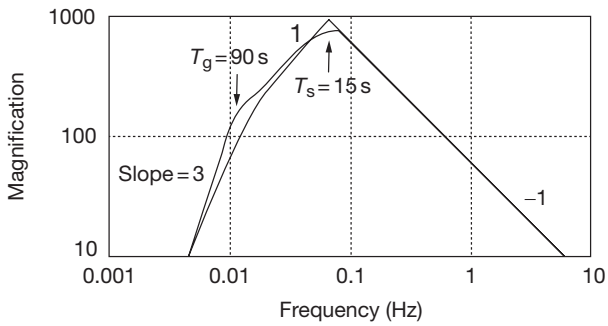

Figure 2 Plot of the ground-motion (amplitude) response of a World-Wide Standardized Seismograph Network (WWSSN) station with a seismograph free period (T_s) of 15 s and galvanometer with a free period (T_g) of 90 s. The segment between these two periods has a flat velocity response, characteristic of broadband seismometers. The response in modern instruments is shaped electronically; a typical FDSN station has a flat velocity response from 5 Hz to 360 s. Reproduced from Wielandt E (2002) Seismic sensors and their calibration. In: Bormann IP (ed.) *IASPEI New Manual of Seismological Observatory Practice*, vol. I, pp. 1–46. Potsdam: GeoForschungsZentrum Potsdam, Chapter 1.06.

seismograph with controlled damping was built by Wiechert in 1904. Soon afterward, Galitzin (1914) developed an electromagnetic seismograph system, where the motion of the seismometer's pendulum generated an electric current by motion of a coil in the magnetic field. This current was, in turn, carried to a galvanometer; the rotation of the galvanometer's coil in a magnetic field was recorded on photographic paper by a beam of light reflected from a mirror attached to the coil. The response of the system depended on the sensitivity and free period of the seismometer and of the galvanometer and their damping. While the system was more complex, it allowed for much more flexibility in selecting a desired response. Figure 2 shows the response of the seismograph–galvanometer system and gives an idea of the way it could be shaped by the choice of different free periods of the system's components. With gradual improvements, the seismometer–galvanometer system, recording on photographic paper, was commonly used during the following 60–70 years, when it was gradually replaced by digital systems (see Chapter 1.02).

With the improvement of the recording systems technology, phase identification became easier, and it was possible to identify P-arrivals (primary) corresponding to compressional waves, S-arrivals (secondary) corresponding to shear waves, and L-arrivals, sometimes called 'the main phase,' corresponding to surface waves. The surface waves caused some confusion because there was also a transverse motion, not predicted by Rayleigh. It was not until 1911 that Love showed that transversely polarized surface waves can propagate in a layered Earth.

Progress in the first decade of the twentieth century was rapid. Some classical problems such as computation and inversion of travel times for the velocity structure were solved by (Benndorf, 1905, 1906; Herglotz, 1907; Knott, 1899; Wiechert, 1907; Zöppritz, 1907) independently developed equations for the amplitude of reflected and transmitted waves at the boundary between two elastic media.

As regards the Earth's structure, there was a paper by Oldham (1906), in which he proposed the existence of the Earth's core, although there has been some confusion in identification of phases: what he thought to be a delayed S-wave was actually an SS (e.g., Schweitzer, 2007). Gutenberg (1913) properly identified reflections from the core–mantle boundary (CMB) and determined the radius of the core quite accurately, and Jeffreys (1926) showed that the core is liquid. Mohorovičić (1910) discovered the boundary between the crust and the upper mantle, thus beginning the era of studies of the crust and lithosphere, which greatly accelerated after World War II.

The first global seismographic networks (GSNs) were established in the early years of the twentieth century. The first one was deployed by John Milne in various countries of the British Commonwealth with the support of the British Association for the Advancement of Science and eventually consisted of 30 stations (Adams et al., 2002). The Jesuit Network was established soon afterward, with a particularly large number of instruments in the United States, but also including stations on all continents (Udias and Stauder, 2002). With a global coverage sufficient to locate large earthquakes, informal bulletins were published using the location method developed by Geiger (1910, 1912), which (with many modifications) is still used today. In 1922, the International Seismological Summary (ISS), with international governance, was established under Professor Turner of the University of Oxford with the charge to produce 'definitive global catalogs' from 1918 onward.

The slow progress in unraveling the Earth's structure culminated in the 1930s with the discovery of the inner core by Lehmann (1936) and the compressional velocity, shear velocity, and density models by Gutenberg (1913), Jeffreys (1926), and Bullen (1940). The Gutenberg and Jeffreys velocity models are shown in **Figure 3**; except for the details of the upper-mantle structure, these models are very similar to the modern ones. The low-velocity zone above the inner–outer core boundary in the model of Jeffreys illustrates the sometimes unfortunate tendency of seismologists to introduce physically implausible features in the model in order to match the data; Jeffreys needed to add a 2 s delay to match the inner-core travel times and accomplished it by inserting this feature, which is impossible to reconcile with the chemical and physical properties of materials in this depth range (Birch, 1952). The other important difference between the models of Jeffreys and Gutenberg was the existence of a low-velocity zone in the depth range 100–200 km in the upper mantle. There were very hot debates on this issue; it can now be explained by the fact that they used data from tectonically different regions; there is a pronounced low-velocity zone in the western United States, but not under the Eurasian shield regions.

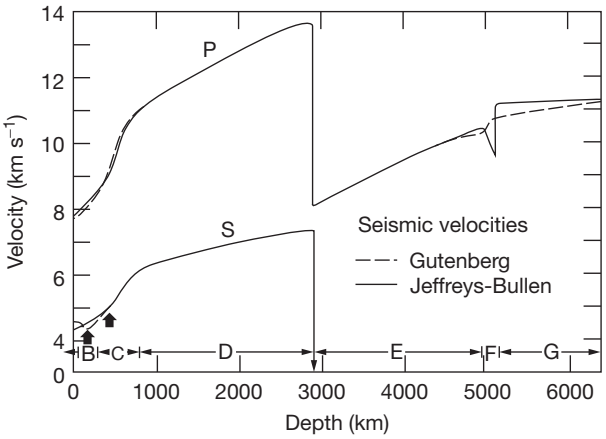

Figure 3 Comparison of the seismic velocity models of Gutenberg and Jeffreys, both built in the 1930s. The principal difference between the models is the presence of the low-velocity zone in the Gutenberg model and the structure near the inner–outer core boundary where the low-velocity zone in the Jeffreys model is erroneous and the velocity increase in the inner core is larger than in the Gutenberg model. With the exception of the transition zone (400–650 km depth), the modern models are not very different. Reproduced from Anderson DL (1963) Recent evidence concerning the structure and composition of the Earth's mantle. *Physics and Chemistry of the Earth* 6: 1–129.

With internal reflections and conversions of waves at the boundaries, seismologists developed a system of phase identification that reflects a combination of the types of waves (P or S), the region in which they propagate (K and I for the P-waves in the outer and inner core, respectively; PKIKP designates a phase that travels as P in the mantle, P in the outer core, and P in the inner core) and the boundary at which they were reflected (c for CMB and i for the inner–outer core boundary). A shear wave reflected once from the free surface at the midpoint of its path is designated by SS; higher multiple reflections, like SSS or SSSSS, can be observed by sampling a large volume of the Earth along their paths. For earthquakes with a finite focal depth, the P- and S-waves traveling upward from the source have designation of p or s; following reflection at the surface, they represent the so-called depth phases (e.g., pP and sP); the travel-time difference between the arrival of pP and P strongly depends on focal depth.

Figure 4 shows examples of various seismic phases, and **Figure 5** is the graphic representation of the travel times as a function of distance computed by Jeffreys and Bullen (1940) for the model of Jeffreys (1939). It is remarkable that this set of tables, including predictions for different focal depths, was calculated using a manual mechanical calculator! The data used by Jeffreys were extracted from the ISS, the precursor of the International Seismological Centre (ISC), which (with international financial support and governance) resumed the ISS role in 1964 and continues until today.

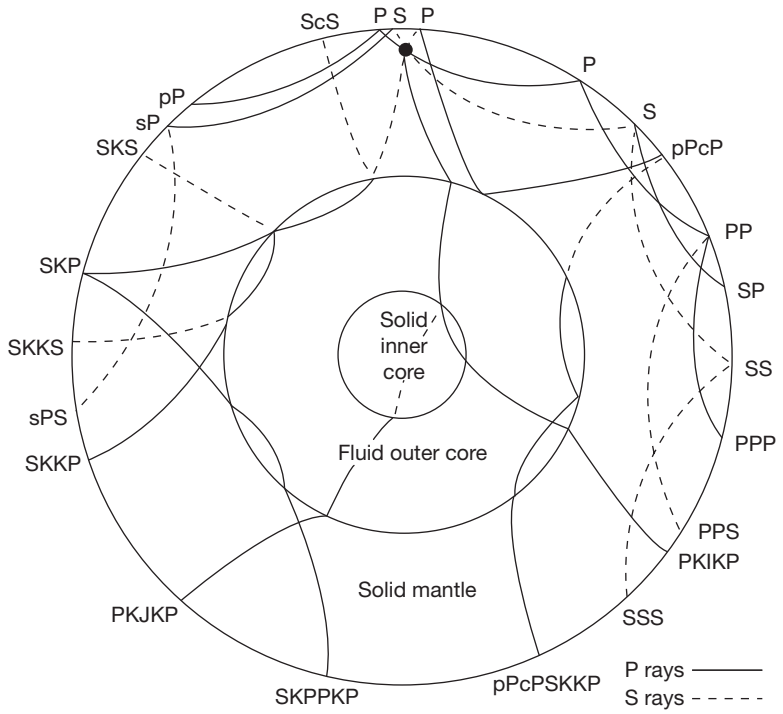

Figure 4 Examples of seismic rays and their nomenclature. The most commonly identified phases used in earthquake location are the first arriving phases: P and PKIKP. Reproduced from Stein S and Wysession M (2003) *An Introduction to Seismology, Earthquakes and Earth Structure*. Oxford: Blackwell, ISBN: 0865420785.

Bullen (1949) divided the Earth into a number of concentric shells, designated by letters from A to F; in this division, the lower mantle was designated by the letter D″. when Bullen recognized that the deepest 150 km of the lower mantle had an anomalously flat velocity gradient, he divided the region D into D′ and D″. More recently, and not entirely correctly, D″ came to signify the structure in the deepest 300 km, or so, of the lower mantle, which is characterized by a still-growing collection of structural and compositional complexities (see **Chapter 1.22**).

It was recognized relatively early that the dispersion of surface waves was different in the continents than in the oceans, with an indication that the oceanic crust was significantly thinner. Computing the dispersion of surface waves was algebraically and numerically difficult; the correct formulas for the dispersion of Rayleigh waves in a layer over a half-space were formulated by Stoneley (1928), and the case of the two layers over a half-space could be solved only for a very specific set of parameters.

1.01.2 Developments from 1950s to the Early 1980s

It must have been frustrating for seismologists not to be able to use information about the Earth's structure contained in the most prominent features of the seismograms: the dispersed surface waves. This changed when Haskell (1953) adapted to the case of elastic media the method first proposed by Thomson (1950) in the acoustics case. The approach made it possible to compute dispersion of surface waves (Rayleigh and Love) in a layered medium with an arbitrary number of layers over a half-space. It involved multiplication of matrices, one for each layer, changing the wave number for a fixed frequency such as to match the boundary conditions (vanishing of stresses) at the free surface. Because of the enormous amount of calculations to be performed, it required application of an electronic computer, and its application opened yet a new era in seismology. The Haskell's matrix method has been adapted to other problems in seismology, such as calculation of synthetic seismograms using the 'reflectivity method' (Fuchs and Müller, 1971). Electronic computers were at first very expensive and rare, and it was not until the 1960s that they became generally available at universities (Haskell worked at the Air Force Cambridge Research Laboratories).

Surface-wave dispersion began to be studied intensively in the 1950s principally at the Lamont Geological Observatory of Columbia University, primarily by Ewing and Press, who observed mantle waves in the 1952 Kamchatka earthquake, identifying arrivals from R6 to R15 (see **Chapter 1.04**) and measuring their group velocities up to a period of 500 s (Ewing and Press, 1954). Regional measurements of surface-wave dispersion were initiated by Press (1956). A monograph by Ewing et al. (1957) summarizes the state of the knowledge on seismic-wave propagation in layered media at that time. Ewing and Press also developed a true long-period seismograph, which was capable of recording mantle waves even for moderately sized earthquakes. This instrument was deployed at 10 globally distributed International Geophysical Year network stations operated by Lamont.

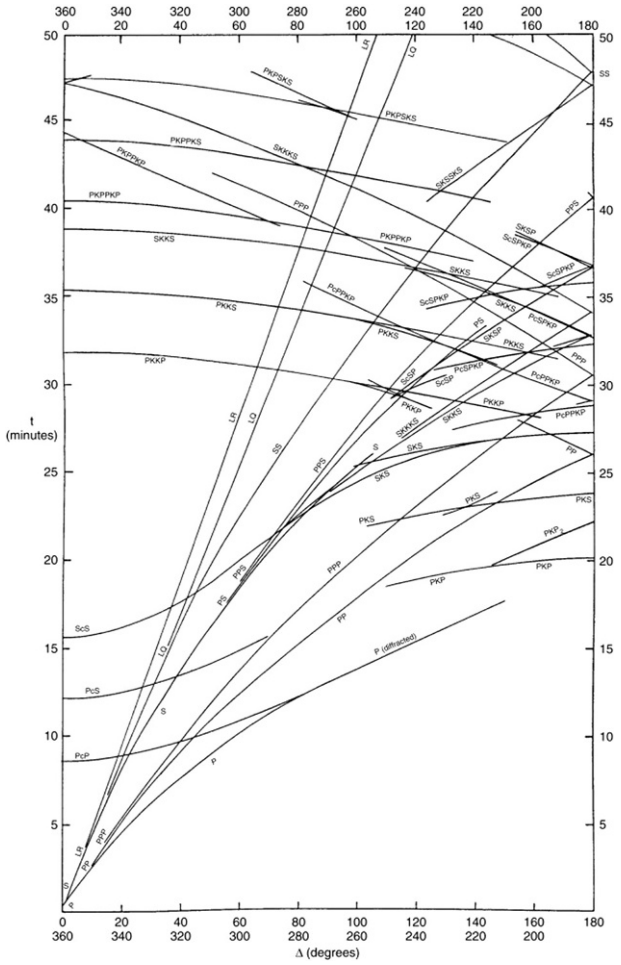

Figure 5 Travel times of seismic phases for the surface focus as computed by Jeffreys and Bullen (1940). Reproduced from Jeffreys H and Bullen KE (1940) *Seismological Tables*, p. 50. London: British Association for the Advancement of Science.

It is not often that a mistake leads to favorable results, but this was the case with the free oscillations of the Earth. Benioff (1958) reported an oscillation with a period of 57 min seen in the record of the 1952 Kamchatka earthquake. Even though this observation was eventually attributed to an artifact in the functioning of the instrument, it stimulated the theoretical and computational research needed to calculate eigenfrequencies for a realistic Earth model. Some of the calculations preceded Benioff's report (Jobert, 1956, 1957), but the efforts of Pekeris and Jarosch (1958) and Takeyuchi (1959) were clearly motivated to explain the observed period. These calculations, using the variational approach and the Jeffreys–Bullen Earth model, predicted the period of ${}_0S_2$ to be 52 min and that of ${}_0T_2$ 43.5 min. Neither was close enough to Benioff's 'observation.' The modern approach was developed by Alterman et al. (1959), who recast the system of three second-order partial differential equations into a system of six first-order differential equations, thus removing the need for differentiation of the elastic constants, and allowed the use of standard numerical methods to obtain the solution. Tests using the Gutenberg and the Jeffreys–Bullen models showed that they predict very similar free oscillation periods for the gravest modes but differ at shorter periods by 1–2%.

When the greatest instrumentally recorded earthquake of 20 May 1960 occurred in Chile, seismologists had all the tools (theory, computers, and instrumentation) needed to measure and interpret its recordings. Three back-to-back papers in a 1961 issue of the *Journal of Geophysical Research* reported the first correct measurements of free oscillation periods: Benioff et al., Ness et al. (1961), and Alsop et al. (1961). The observations were made on strainmeters in Isabella, Ñaña, and Ogdensburg; seismographs at Pasadena; and a gravimeter at the University of California, Los Angeles (UCLA). All three studies agreed in mode identification and found that their periods were very close to those predicted by the existing Earth models (Pekeris et al., 1961a). More detailed studies of the spectra revealed that they are split; the effect of the Earth's rotation was shown to explain this effect (Backus and Gilbert, 1961; Pekeris et al., 1961b). Thus, normal-mode seismology was born. Progress in the theory, particularly considering the effect of lateral heterogeneities and mode coupling, would extend over decades to come. First attempts at inversion of normal-mode data were not particularly successful; the density model of Landisman et al. (1965) was flat throughout the lower mantle, implying either a strong radial heterogeneity or an immensely superadiabatic temperature gradient.

Backus and Gilbert (1967), Backus and Gilbert (1968), and Backus and Gilbert (1970) provided the formal background for consideration of geophysical inverse problems, and even though their own experiments with inversion of normal-mode periods for the velocities and density, using a subset of normal-mode data, were discouraging (two very different models were found fitting the data nearly exactly; Backus and Gilbert, 1968), the idea of resolving kernels and trade-offs became part of the geophysical terminology.

Because seismic methods were considered essential in discriminating between earthquakes and nuclear explosions (Berkner et al., 1959), an intensive observational program, called Vela Uniform, was initiated. One of its components of great significance to studies of the Earth's interior was the World-Wide Standardized Seismograph Network (WWSSN), consisting of a set of three-component short-period and three-component long-period seismographs, with identical responses, except for magnification, which depended on local noise levels. At its peak, the WWSSN consisted of 125 stations (**Figure 6**), with distribution limited by geography and politics: there were no stations in the Soviet Union, China, and poorly developed areas in Africa and South America. The novel aspect of WWSSN was its standardized response and centralized system of distribution of copies of seismograms. Individual stations were sending the original seismograms to a central location, where they were microfilmed, using a very high-resolution camera, and then returned to the stations. A seismologist could request copies of seismograms for a particular date and receive them as either microfilm chips or photographic enlargements to the original size. Several larger institutions had a blanket order on all the records. This data accessibility represented major progress with respect to the earlier procedures, where one had to request copies of seismograms from individual stations, which greatly limited and delayed the research. WWSSN functioned for 20–25 years,

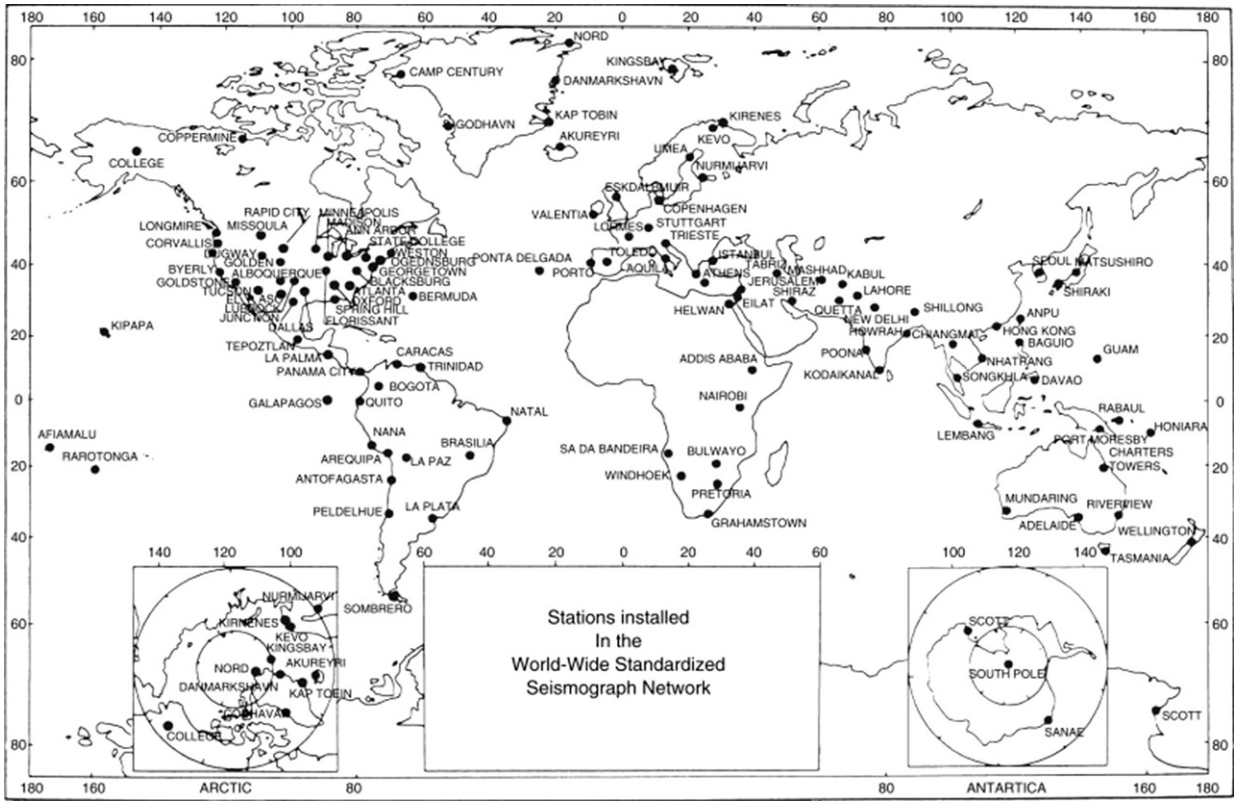

Figure 6 Map of the stations of WWSSN established in the early 1960s, following recommendations of Berkner et al. (1959). Courtesy of US Geological Survey.

slowly declining in the quality and number of stations; it ceased functioning in the late 1980s when data from new digital stations became available.

Another development of the 1960s was the introduction to seismology of digital recording, greatly facilitating research and the development of massive, computerized data-processing methods. One such facility, the large aperture seismic array (LASA), shown in Figure 7, was built in the mid-1960s in Montana. It consisted of six 'rings,' for a total of 21 subarrays, each with 25 short-period seismometers emplaced in boreholes, to improve the signal-to-noise ratio. The data were telemetered in real time to a central location in Billings, Montana, where they were processed for detection of a signal. Major scientific discoveries were made with this tool, particularly when weak signals were involved, for example, observations of reflections from the inner core. In practical terms, the array did not meet the expectations; the site response across this 200 km aperture array varied so much that the signals had limited coherency and signal enhancement by stacking was not as effective as expected. A somewhat smaller array was installed a few years later in Norway (NORSAR); elements of this array are still active and have been upgraded recently to modern, high-dynamic-range band–band response. Most of the arrays of the International Monitoring System (IMS) used for seismic discrimination purposes have an aperture of only several kilometers; because on that scale, the coherency at 1 Hz frequency can be achieved.

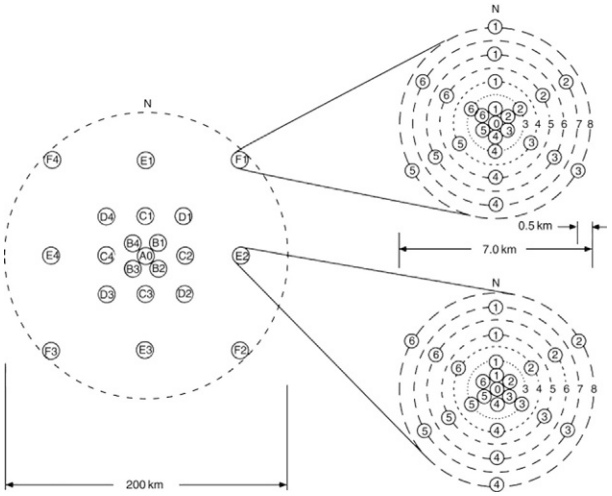

Figure 7 Configuration of the large aperture seismic array (LASA) and an expanded view of two of its subarrays. Reproduced from Stein S and Wysession M (2003) *An Introduction to Seismology, Earthquakes and Earth Structure*. Oxford: Blackwell, ISBN: 0865420785.

One of the important results obtained from the analysis of array data was the detection of upper-mantle discontinuities (Johnson, 1967), confirming the result predicted by experimental petrology that there should be two discontinuities at

pressures and temperatures corresponding to depths of about 400 and 650 km, respectively (Birch, 1952).

Surface-wave studies blossomed in the 1960s. At first, measurements of dispersion involved rather simple 'analog' methods, such as the peak-and-trough approach to measuring phase and group velocities. Some very important results were obtained in this way, such as the Canadian Shield study of Brune and Dorman (1963). Digital analysis, however, was soon to take over. Manual digitization of analogue recordings, WWSSN data in particular, became easier, and with increasing availability of computers and decreasing cost of computations, various techniques were developed, for the most part involving applications of the Fourier transform. With the development of the fast Fourier transform (FFT) algorithm (Cooley and Tukey, 1965), the cost of time-series analysis declined dramatically; a review by Dziewonski and Hales (1972) summarizes the state of the art at the beginning of the 1970s. Some of these methods, such as the multiple filtration technique to measure group velocity dispersion, residual dispersion measurements, and time-variable filtration, are still in use today. The 1960s have also seen the first studies of intrinsic attenuation by Anderson and Archambeau (1964), who developed partial derivatives (kernels) for Q from mantle-wave attenuation. Also, the first studies of lateral heterogeneity were conducted using the 'pure path' approach (Toksöz and Anderson, 1966).

Seismic experiments with controlled sources were conducted in a multi-institutional mode. One of the largest experiments was 'Early Rise' carried out in the July of 1966. A series of 38 explosions in Lake Superior of up to 5 tons of outdated torpedoes were used as the source of signals recorded by hundreds of seismometers – deployed by 12 governmental and academic groups – spreading radially in all directions. Signals were recorded as far as 2500 km, reaching teleseismic distances and providing a detailed profile of P velocity under a continental upper mantle (Green and Hales, 1968). A detailed review of crustal and upper-mantle studies with controlled sources is provided in **Chapter 1.11**.

With a large new data set, particularly measurements of previously unreported periods of long-period overtones provided by the analysis of free oscillations generated by the 1964 Alaskan earthquake and recorded at WWSSN stations (Dziewonski and Gilbert, 1972, 1973), studies of 1-D structure entered a new era. The resolution of this data set was sufficient to constrain the density profile in the mantle and the core; this turned out to be quite consistent with the behavior, in the lower mantle and outer core, of a homogeneous material under adiabatic compression. Jordan and Anderson (1974) were the first to combine the normal-mode and travel-time data, including differential travel-time data.

Numerous additional overtone data were obtained by Mendiguren (1973) and Gilbert and Dziewonski (1975) by introducing phase equalization techniques, such as 'stacking' and 'stripping.' These methods require the knowledge of the source mechanism to predict the proper phase for each seismogram to be considered; this in itself turned out to be a challenging inverse problem. Dziewonski and Gilbert (1974) derived the spectrum of all six components of the moment-rate tensor as a function of time for two deep earthquakes (Brazil, 1963; Colombia, 1970). For both events, they detected a precursive isotropic component. Eventually, this turned out to be an artifact of coupling between toroidal and spheroidal (Russakoff et al., 1998) modes, but the requisite theory to consider this effect was not available until 1984. Gilbert and Dziewonski (1975) presented two models based on measurements of eigenfrequencies of 1064 modes and mass and moment of inertia for a total of 1066 data. They derived two models 1066A and 1066B, with the first being smooth through the transition zone and the latter including the 400 and 660 km discontinuities; both models fit the data equally well.

At the 1971 General Assembly of the International Union of Geodesy and Geophysics (IUGG) in Moscow, the need for a reference Earth model was stated, and a Standard Earth Model Committee formed under the chairmanship of Keith Bullen. The Committee appointed several subcommittees, including one for the radius of the CMB: there were discrepancies on the order of 10 km at the time. The value recommended by the subcommittee was 3484 km (Dziewonski and Haddon, 1974), which – within 1 km – withstood the trial of time. Hales et al. (1974) proposed that the seismic velocities and density in the standard Earth model should be described by a low-order polynomial, with discontinuities at the appropriate depths. Dziewonski et al. (1975) constructed such a model, named parametric Earth model (PEM), which satisfied the normal-mode, travel-time, and surface-wave data. The novelty of this model was that, in a single inversion, different structures were obtained for the continental and oceanic crust and upper mantle. The normal-mode periods predicted by these two models (PEM-O and PEM-C) averaged in 2/3 and 1/3 proportion were constrained to match the observed periods and teleseismic travel times but separate data sets for continental and oceanic surface-wave dispersion. The differences between these two models ceased at the 400 km discontinuity, at which depth they became identical with the average Earth model, PEM-A.

The drawback of the PEM and all the previous models was that they did not consider the physical dispersion due to anelastic attenuation. For a signal propagating in an attenuating medium to be causal, the wave with higher frequencies must propagate with higher velocities. Thus, waves with a frequency of 1 Hz will propagate more rapidly than waves at a frequency of 1 mHz. In order to reconcile the seismic data that span 3.5 orders of magnitude, it is necessary to consider the frequency dependence of elastic parameters. This was pointed out by Liu et al. (1976). The Preliminary Reference Earth Model (PREM) constructed by Dziewonski and Anderson (1981), following the idea of parametric representation, considered the frequency dependence using the assumption that Q is constant in the band from 0.3 mHz to 1 Hz.

This necessitated obtaining the radial profiles of Q_μ and Q_κ; fortunately, there were new measurements available of normal-mode and surface-wave Q (Sailor and Dziewonski, 1978) such that a formal inversion for Q could be conducted simultaneously with the inversion for the velocities and density. It was recognized earlier that to explain the observed attenuation of radial modes, which contain a very high percentage of compressional energy (97.5% for ${}_0S_0$), it was necessary to introduce a finite bulk attenuation; Anderson and Hart (1978) preferred to place it in the inner core, and Sailor and

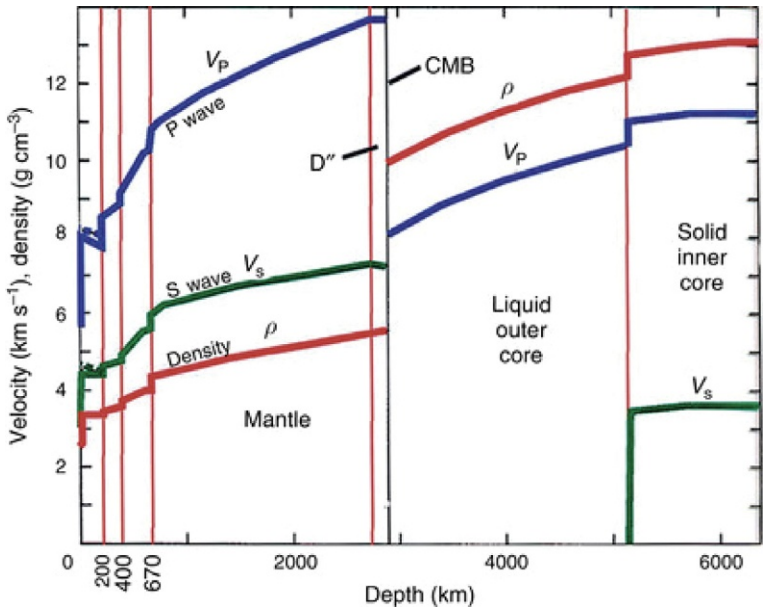

Figure 8 The Preliminary Reference Earth Model (PREM) of Dziewonski and Anderson (1981). In addition to the distribution of seismic velocities and density, PREM contains also the distribution of attenuation of the shear and compressional energy. From the website of Ed Garnero.

Dziewonski (1978) thought that Q_κ is finite in the upper mantle; unfortunately, the radial modes do not have the requisite depth resolution. **Figure 8** shows the seismic velocities and density as a function of radius; the attenuation in PREM is discussed in **Chapter 1.25**. Another novel aspect of PREM was its radial anisotropy between the Moho and 220 km depth. This feature, at first suspected to be an artifact of the nonlinearity of the inverse problem, has been confirmed by global tomographic studies (e.g., Ekström and Dziewonski, 1998). The PREM model remains to this day a widely used 1D reference model for seismological studies based on long period data. For P wave studies, especially those concerning core sensitive phases, model AK135 (Kennett et al., 1995), which was built to constrain a global dataset of travel times from the ISC bulletins, is often preferred as a 1D reference model. It is to be noted, however, that this model includes a 36 km continental crust, and cannot be used for waveform modeling outside of continental areas.

The 1970s have also seen the beginning of seismic tomography; two studies published simultaneously (Aki et al., 1977; Dziewonski et al., 1977) addressed the problem on different scales: regional and global. Aki et al. solved for 3-D velocity structure under the NORSAR array, while Dziewonski et al. obtained a very low-resolution model of 3-D velocity perturbations in the entire mantle and showed significant correlation between velocity anomalies in the lowermost mantle and the gravest harmonics of the gravity field. The study of Dziewonski et al. (1977) was motivated by a paper by Julian and Sengupta (1973) who noticed that travel times for rays bottoming in the same region of the mantle tend to show similar residuals. They interpreted this result qualitatively as the evidence of lateral velocity variations; no modeling was presented in that paper. The first continental-scale 3-D model of the upper mantle, under North America, was published by Romanowicz (1979).

Two digital seismographic networks were established in the mid-1970s. One was the International Deployment of Accelerometers (IDA; Agnew et al., 1976, 1986), consisting of 18 globally distributed LaCoste–Romberg gravimeters with a feedback system that allowed digitization of the signal. It was designed to record very long-period waves, including the gravest modes of free oscillations of the Earth: one sample was taken every 20 s (later changed to 10 s). Only the vertical component of acceleration was recorded and the word length was 12 bits; the dynamic range was, therefore, rather limited but still considerably greater than that of analogue recordings. The sensitivity was set such that the scale was saturated for the first surface-wave arrivals for events with magnitude 7.0, or so, depending on the station's distance from the source and radiation pattern. The IDA network was operated by the Scripps Institution of Oceanography, and the centrally collected data were freely distributed to the academic community. This later became the future standard in global seismology. An early illustration of the power of such a global array was the analysis of the splitting of the gravest modes of free oscillations generated by the 1977 Sumbawa earthquake (Buland et al., 1979; M_w only 8.4).

The other network consisted originally of nine installations called Seismic Research Observatories (SROs) and five Abbreviated Seismic Research Observatories (ASROs). The SROs used borehole instruments, with significantly suppressed wind-generated noise levels, particularly on horizontal components. The ASROs were placed in underground tunnels or mine shafts and the seismographs were protected from the effects of changing pressure and temperature. The instrumentation is described by Peterson et al. (1976). This network was designed for monitoring the Nuclear Test Ban Treaty and high sensitivity was the main objective. In order to increase the dynamic range, the signal was sharply band-pass-filtered, so that at very long periods (>200 s), the response to acceleration was falling as ω^{-3}, while it was flat for the IDA instruments.

Even so, the SRO and ASRO stations were able to produce useful mantle-wave records for events with magnitude greater than about 6.5. Later, the network was augmented by 10 WWSSN stations, with the analogue output amplified and digitized at 16-bit analog to digital converters. The entire system was called Global Digital Seismographic Network (GDSN). There was no general data distribution system, but data for selected dates were available upon request from the Albuquerque Seismological Laboratory.

Until then, a seismic station typically comprised a set of seismometers with either 'long-period' or 'short-period' responses, or sometimes, as was the case for the WWSSN, one of each. This setup was designed at the time of analogue recording to avoid the microseismic noise peak around 6–7 s period, which would have made it impossible to digitize all but the largest earthquake signals. With digital recording, and the possibility of filtering out the microseismic noise by post-processing, this traditional instrument design became unnecessary.

A very important development in seismic instrumentation took place in Germany in the mid-1970s. An array of a new kind of instruments with digital recording was deployed near Gräfenberg (Harjes and Seidl, 1978). It used a novel feedback seismograph (Wielandt and Streckeisen, 1982). The system was rapidly recognized for its linearity and large dynamic range within a wide band of frequencies – hence the name 'broadband.' The Gräfenberg array's central station had been colocated with the SRO borehole station GRFO, and the comparisons were very favorable for the broadband instruments, which were capable of reproducing different narrowband responses using a single data stream. This type of instrumentation became the pattern for future developments (e.g., **Chapter 1.02**).

In addition to the developments in instrumentation, the late 1970s saw important theoretical developments, related to the asymptotic properties and coupling of the normal modes. Examples of such developments are papers by Woodhouse and Dahlen (1978), Jordan (1978), and Woodhouse and Girnius (1982).

1.01.3 From 1980 to Present: The Era of Tomography and Broadband Digital Seismic Networks

The data from both global networks of the 1970s led to results that demonstrated the need for development of a global network that would better satisfy the needs of basic research in seismology; three studies are noteworthy. A robust method, which uses entire segments of (digital) seismograms, was developed to obtain reliable mechanisms of earthquakes with magnitude 5.0 and above (Dziewonski et al., 1981; Ekström et al., 2005). In addition, the method refines the location of the source, which for an event of finite size need not be identical with the hypocenter determined from the first arrivals of the P-waves. This topic is discussed at length in **Chapter 4.16**. The reason why the subject is brought up here is that in most aspects of using waveform analysis for the purpose of drawing inferences about the Earth's structure, it is necessary to know the source mechanism. The so-called 'centroid moment tensor' method has now been applied to over 40 000 earthquakes from 1976 till present, and this catalog is available online (http://www.globalcmt.org).

Masters et al. (1982) measured center frequencies of spectral peaks of the fundamental spheroidal mode from hundreds of IDA records and discovered that there are spatially distinct patterns in the frequency shifts when plotted at locations of the poles of the great circles corresponding to the paths between the source and the receiver. By fitting spherical harmonics (even degrees only, because of the symmetry), these authors realized that the pattern is dominated by spherical harmonics of degree 2, an observation also made from great-circling surface waves by Souriau and Souriau (1983). **Figure 9** shows the pattern of the shifts of spectral peaks and zero line of the best-fitting spherical harmonics of degree 2 for four groups of ${}_0S_\ell$ modes with different ranges of degree ℓ. Note that the modes with the lowest ℓ show a different pattern than the remaining three groups. Our current understanding of this fact is that the low-ℓ modes sample deeper structure (lower mantle) than the higher-ℓ groups that predominantly sample the upper mantle. The authors performed a parameter search, in which they changed the radii of a shell in which the anomaly is located. The best variance reduction was for the anomaly placed in the transition zone. The lasting importance of this chapter is that it demonstrated that heterogeneity of very large wavelength and sizeable amplitude ($\pm 1.5\%$) exists in the Earth's interior.

Following the development of a waveform-fitting technique that allowed the simultaneous measurement of phase velocity and attenuation along a great-circle path (Dziewonski and Steim, 1982), Woodhouse and Dziewonski (1984) developed an approach to the interpretation of waveforms that could extract both the even and the odd harmonic coefficients of lateral heterogeneity as a function of depth. This method involves the 'path average approximation,' sometimes called PAVA. The seismograms are represented as a sum of all normal modes (spheroidal and toroidal) up to a certain frequency ω_{max}. For a given great circle, each mode is assumed to be affected by the average deviation from reference structure along the great-circle path (which is sensitive only to even-order harmonics) and along the minor-circle path (sensitive to both even and odd harmonics). The effect of the great-circle path can be modeled by a shift in eigenfrequency of the mode; the effect of the minor-arc structure is modeled by a fictitious shift of the epicentral distance for that mode; this shift depends on both even and odd parts of the structure. Woodhouse and Dziewonski (1984) processed about 2000 mantle-wave seismograms from the GDSN and IDA networks and obtained a model of the upper mantle (Moho – 670 km), M84C, using as basis functions spherical harmonics up to degree 8 for horizontal variations and Legendre polynomials as a function of radius up to degree 3. **Figure 10** shows a map of shear velocity anomalies at a depth of 100 km; there was no a priori information used on the location of the plate boundaries. Corrections were made for crustal thickness, recognizing only the continental and oceanic structure. An experimental model, M84A, obtained without applying crustal corrections, showed that not taking crustal thickness into account may result in mapping artificial anomalies at depths as large as 300 km. Model M84C had a strong degree-2 anomaly in the transition zone, confirming the results of Masters et al. (1982).

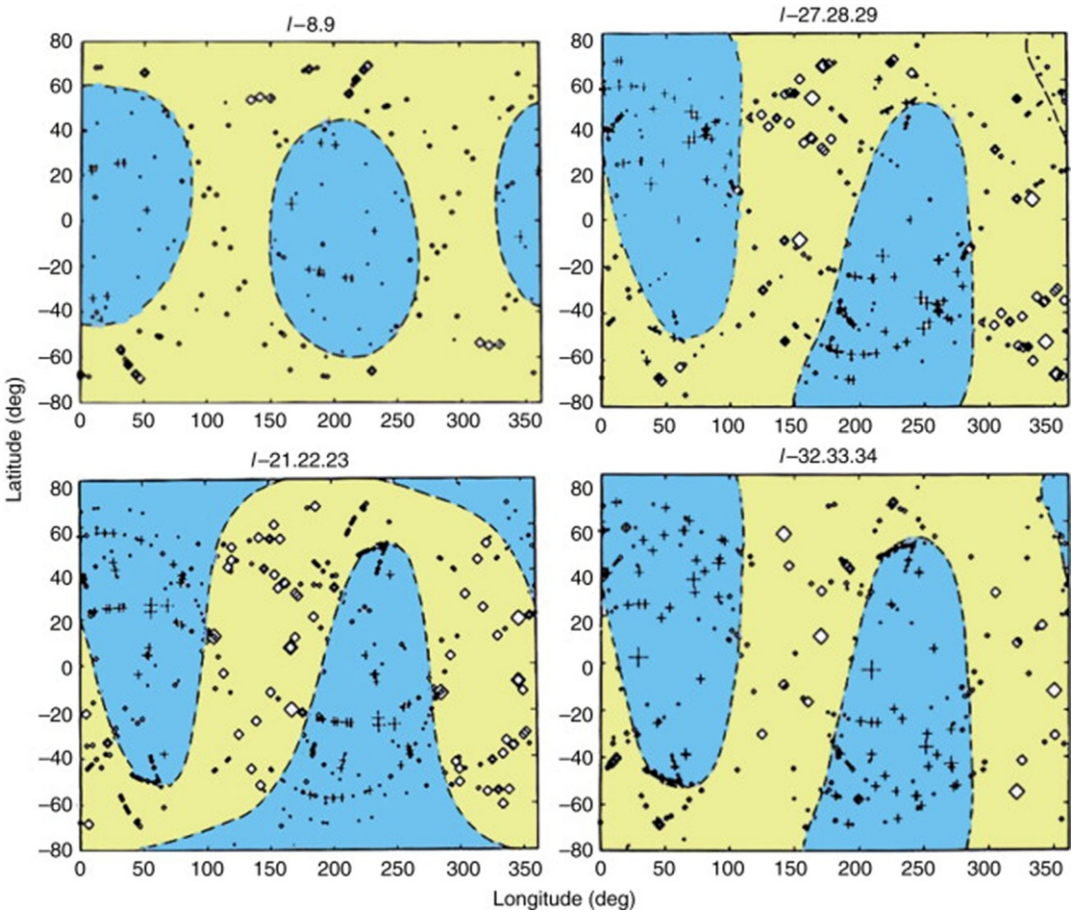

Figure 9 Maps of the observed frequency shifts of the fundamental spheroidal modes for four ranges of the order numbers as reported by Masters et al. (1982). The frequency shifts are plotted at the poles of the individual great-circle paths. It indicates the presence of very large wavelength–velocity anomalies in the Earth's interior; the preferred location of the source of the anomaly shown in the figure is the transition zone. However, the frequency shifts for the largest wavelength panel (top left; modes ${}_0S_8$ and ${}_0S_9$) show a different pattern than in the other three panels (modes from ${}_0S_{27}$ to ${}_0S_{34}$); the low-ℓ data have the greatest sensitivity in the lower mantle. Modified from Masters G, Jordan TH, Silver PG, and Gilbert F (1982) Aspherical Earth structure from fundamental spheroidal mode data. *Nature* 298: 609–613.

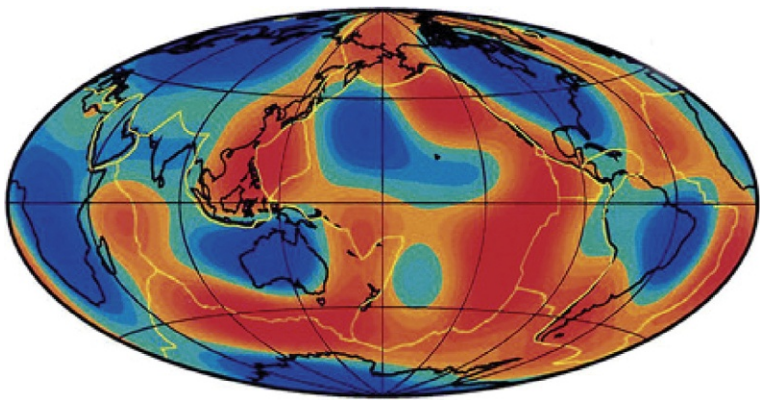

Figure 10 Shear velocity anomalies at a depth of 100 km in the model M84C of Woodhouse and Dziewonski (1984). The scale range is $\pm$5% and the resolving half-wavelength is 2500 km. Plate boundaries are shown as thin yellow lines. Except for the correction for crustal thickness, there was no other a priori information included in the inversion. Thus, the result demonstrates that the waveform inversion approach is able to distinguish the slow velocities under the mid-ocean ridges and ancient cratons, for example.

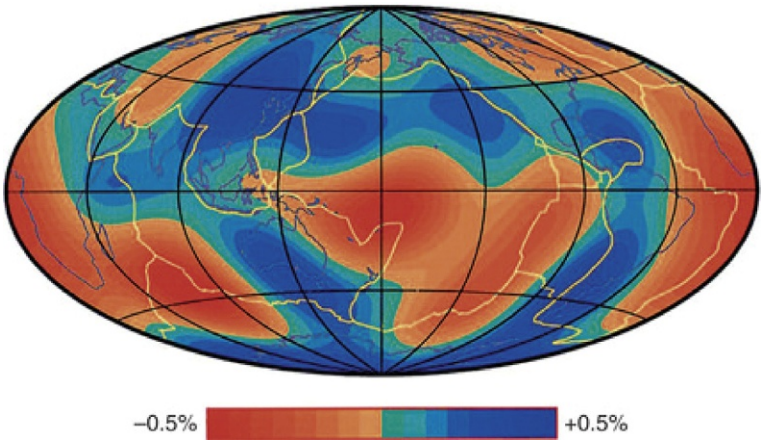

Figure 11 Map of P-velocity anomalies at a depth of 2500 km in model of Dziewonski (1984) derived from inversion of travel-time anomalies from ISC Bulletins. The resolving half-wavelength of the model is about 3500 km (at the surface). The model, dominated by the harmonics 2 and 3, clearly shows two large superplumes (African and Pacific) and the ring of fast velocities circumscribing the Pacific Rim. The scale is ±0.5%.

Another result also affected future developments, even though this study was not based on waveform analysis, but on the ISC bulletin data. With greater computational resources, it was possible to cast the inverse problem for lateral heterogeneities in the lower mantle on a larger scale using a substantially greater body of data than in Dziewonski et al. (1977). Unlike in this earlier study, in which blocks were used, Dziewonski (1984) used global basis functions: spherical harmonics representing horizontal variations and Legendre polynomials for radial variations. The degree of expansion was modest: only degree 6 in harmonics and degree 4 in radius, with the inversion limited to lower-mantle structure. In many ways, this new study confirmed the earlier one – including the correlation of lower-mantle structure with the gravity field (Dziewonski et al., 1977) – but it showed resolution of a truly remarkable concentration of the power of heterogeneity in low-order harmonics. **Figure 11** shows a map of P-velocity anomalies at a depth of 2500 km. The structure, dominated by degree 2 (and, to a lesser extent, degree 3), shows two large slow regions, which came to be known as the African and Pacific 'superplumes', and a ring of fast velocities around the Pacific.

Why does global tomography work? Some suspected that truncation of the expansion at relatively low harmonic order may lead to aliasing and structures dominated by degrees 2 and 3, such as the one shown in **Figure 11**, are an artifact. The short answer is that global mantle heterogeneity has a 'red' spectrum. That is, the power spectrum of the spherical harmonic expansion begins to drop rapidly above a certain wave number ('corner wave number'). Su and Dziewonski (1991, 1992) showed that it is clearly visible even in data, such as maps of travel-time anomalies of SS-S or ScS-S. The concept is illustrated in **Figure 12**, using the continent–ocean variations of crustal thickness.

Figure 12 illustrates the point that for functions with a 'red' spectrum that is flat for small wave numbers but rapidly decreasing for larger wave numbers, it is possible to extract most of the signal using the 'red' part of the spectrum. Panel (a) shows the power spectrum of the continent–ocean function. It is flat for degrees from 1 to 5, and then, the power is offset at degree 6 and begins to decrease rapidly, roughly as ℓ^{-2}; the 'corner wave number' is in this case $\ell = 5$. Part (b) is the synthesis of this function using degrees from 1 to 8 (81 coefficients). The shapes of the continents are clearly recognizable, but details of the coastlines or islands are missing. Panel (c) shows the result of a synthesis using harmonics from 1 to 32 (1089 coefficients or 15 times more). There is an obvious improvement: Madagascar, New Zealand, Japanese Islands, Gulf of Mexico, can be identified, but the principal information on the outline of continental masses is already contained in panel (b).

Another point is that power at degree 32 is two orders of magnitude less than at degree 3. Actually, it is lower by three orders for the individual $Y_{\ell m}$ coefficients, since we define the power as the sum of all squared coefficients of degree ℓ. It is impractical to think that such a large range of values could be resolved in an inverse problem, particularly because the strength of the kernels commonly decreases with increasing wave number (see Figure 3 a–d in Dziewonski, 1984). However, if the continents were broken up into many smaller 'islands,' then a synthesis of the spherical harmonic coefficients up to degree 8 might be misleading and provide an aliased picture.

The 'corner wave number' seems to be a feature of many geophysically important functions: Su and Dziewonski (1992) showed that it occurs in spectra of several global functions, such as free air gravity, SS-S travel-time residuals, phase velocity, and 3-D models, which have a power spectrum that is relatively flat up to degrees from 6 to 8, after which it begins to decrease as ℓ^{-2}. This seems typical of the spectra of two-dimensional functions that are characterized by a set of large 'patches,' such as the large land masses in the continent–ocean function. If the spherical harmonic expansion is truncated at an order number beyond the corner wave number, the synthesis of such truncated series retains the main character of the original function (e.g., **Figure 12**). Similarly, an inversion for a truncated series of spherical harmonic coefficients does not introduce aliasing if truncation occurs in the steeply decreasing part of the power spectrum. Of course, there are some geophysically important functions

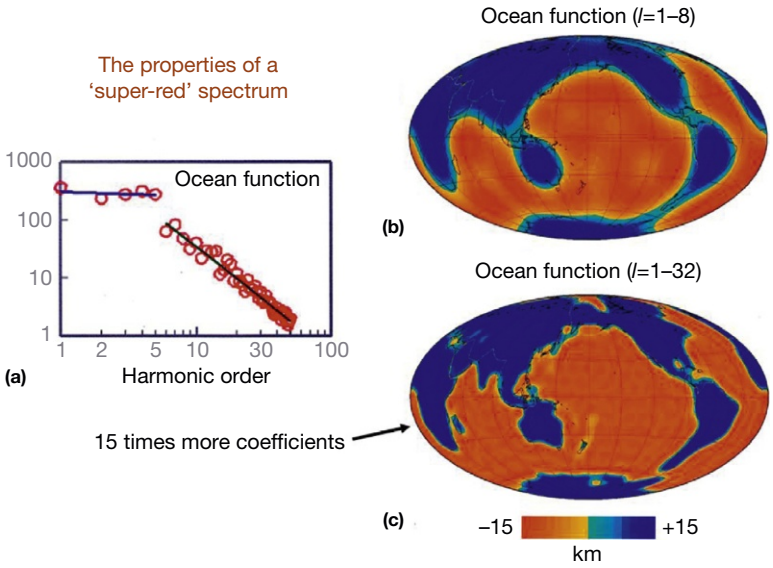

Figure 12 An example of a global function with a 'super red' spectrum. Crustal thickness under the oceans and continents, with a constant crust thickness for a given type, is expanded in spherical harmonics and then synthesized using a different cutoff wave number. Panel (a) shows the power spectrum of the continent–ocean function. Note the nearly flat spectrum for orders from 1 to 5 and then nearly linear decrease (in the log–log scale) for orders 6 and higher. The slope of that line is about ℓ^{-2}; the corner wave number is $\ell = 5$ in this case. Panel (b) shows the synthesized continent–ocean function for $\ell_{max} = 8$. All contours of continents are delineated and much of the variance is explained by this low-order model; this expansion has been used by Woodhouse and Dziewonski (1984) to introduce corrections for crustal structure. Panel (c) shows the result of a synthesis using $\ell_{max} = 32$. The details such as coastline and recovery of larger islands are clear, but they are achieved by using about 15 times more coefficients than those used to obtain panel (b). Also, the coefficients at higher wave numbers are very small, and it would be unlikely to be correctly derived through an inversion of observations with errors.

whose spectra have distinctly different characters, for example, linear features (slabs) have power spectra that are flat with harmonic order; point-like features (plumes?) have power spectra whose values increase with ℓ. In these cases, truncation would result in significantly lower amplitudes in the low-pass-filtered image.

This could also happen if the truncation of the spectrum occurred before the corner wave number. An example of the consequences of such an action is given by Mégnin et al. (1997). In a synthetic test, they limited to degree-6 inversion of waveform data calculated for a degree-12 model and showed that the results are aliased by the missing part of the structure (degrees 7 through 12). But in their test, the power spectrum had a maximum at degrees 6 and 7, and truncation at the maximum power is bound to cause aliasing. Boschi and Dziewonski (1999) demonstrated that there is no aliasing when travel times computed for a degree 40 model are inverted for a synthetic model limited to degree 12 (their plate 6), but the truncation was applied at the corner wave number.

Thus, in the 1980s, seismologists demonstrated that they can resolve 3-D structure within the Earth interior, giving the promise of an unprecedented ability to look at a present-day snapshot of mantle dynamics. Yet, the observing networks were in decline, with the support for the GDSN likely to be discontinued altogether and the original IDA network (limited to recording of vertical-component mantle waves and free oscillations) not meeting the needs of the broader community. In 1983, a plan was put forward to create a GSN of some 100 broadband, three-component seismographic stations sending the data in nearly real time to a central collection facility. The expectation was that this network would be supported by the National Science Foundation (NSF), in analogy to NSF supporting astronomy facilities. At the same time, seismologists using portable instrumentation came to the realization that they needed a centralized and standardized instrument pool. This led to the formation of a project called Portable Array for Seismic Studies of the Continental Lithosphere – PASSCAL. The GSN and PASSCAL groups merged and formed a consortium known as Incorporated Research Institutions for Seismology (IRIS), which incorporated in 1984.

At the same time, Steim (1986) was developing at Harvard his very broadband (VBB) instrument, based on the STS-1 broadband seismograph (Wielandt and Steim, 1986), and a very high-resolution (24-bit) digitizer. The response of a VBB instrument is designed to have a flat response to ground velocity between 5 Hz and 3 mHz, that is, over more than three orders of magnitude. Such an instrument had to have a very large dynamic range, of about 140 dB to span the range of ground velocities from the minimum Earth noise to a magnitude 9.4 earthquake at 30° epicentral distance. All these requirements were met, and Steim's VBB system became the design goal for the GSN and other networks. **Figure 13** shows the operating range of the system, and **Figure 14** illustrates the dynamic range of the GSN station in Albuquerque. The high-pass-filtered (75 s) record of the Sumatra–Andaman $M_w = 9.3$ earthquake shows surface waves with an amplitude of several millimeters and a record of a local microearthquake ($M < 1$) extracted from the same record; the ratio of the amplitudes is about 10 000 000! **Chapter 1.02** describes in detail the concept and history of the modern broadband

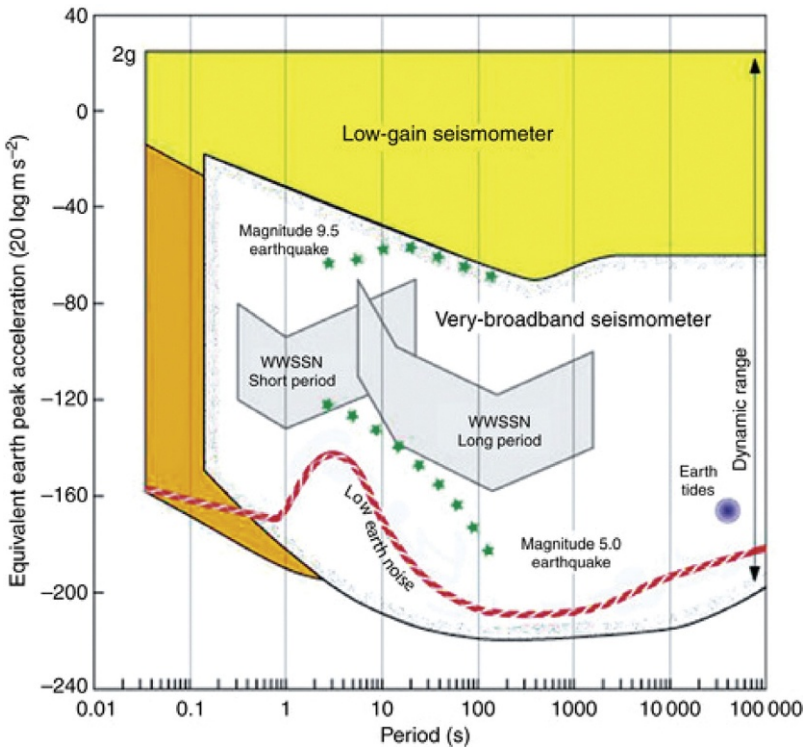

Figure 13 The dynamic range of the VBB channels of a Global Seismographic Network station. The range of the WWSSN short- and long-period channels are shown for comparison. At some GSN stations, the VBB channels are augmented by very short-period channels and accelerometers. The response was designed to resolve the ground noise from 5 Hz to tidal frequencies and to record on scale a magnitude 9 earthquake at a distance of 30°. Courtesy of IRIS.

digital seismograph that has now been implemented in stations of the global international network as well as many regional seismic networks.

Meanwhile, as the US seismologists were organizing themselves, a French effort named GEOSCOPE had already began taking shape. The objective of GEOSCOPE was the establishment of a global network of some 20–25 broadband digital seismographic stations utilizing the STS-1 seismometer, and destined in priority for locations around the world that filled gaps in the distribution of seismic stations. The project had officially begun in 1982, and in 1984, there were already five operational stations (Romanowicz et al., 1984), and 13 in 1986, (e.g., Romanowicz et al., 1991; Roult et al., 2010a,b).

While telemetry of the data was established later (in 1987), the state of health of the remote stations was monitored from early on using the satellite system Argos, which greatly facilitated their maintenance. As it was clear that it was inefficient to have two competing global networks, the need for a framework for international cooperation arose. Also, many countries were interested in deploying broadband instrumentation for their national or regional purposes and were agreeable to share these data. The international Federation of Digital Seismographic Networks (FDSN) was formed in 1986 (Romanowicz and Dziewonski, 1986), with the purpose of coordinating site selection, data exchange, and standardizing instrument responses. The FDSN has been very successful in achieving these goals, despite the fact that it is a purely voluntary, zero-budget organization. **Figure 15** shows a map of the FDSN network as of January 2014 (after some 25 years of development); there are over 200 participating VBB stations, most of which now send data in nearly real time.

Similarly impressive progress was made in the area of field seismology, where progress in electronics led to overall improvement of the portability of the equipment and, in particular, reduction of power requirements, which makes operations much easier. In parallel with the development of the PASSCAL program of IRIS in the United States (see **Chapter 1.16**), other portable arrays were developed in other countries in the last 20 years, such as the LITHOPROBE cross continental project in Canada (Hammer et al., 2010), Lithoscope program in France (Poupinet et al., 1989), or the SKIPPY array in Australia (van der Hilst et al., 1994). Most recently, an ambitious program, USArray, was launched in the United States in 2007 as part of the EarthScope project. USArray is aimed at a systematic investigation of the structure under the contiguous United States with uniform resolution. It consists of three parts: a Permanent Array of 100 stations (the 'backbone' or 'reference array'), a Transportable Array (TA), and a Flexible Array (FA). The FA provides some 300 broadband seismographs and over 1000 active-source instruments, for experiments proposed by individual research groups, aimed at elaborating detailed local structure. The TA is the largest component of the program, and it consists of 400 broadband seismograph systems that, starting from the West Coast of the United States, have been moving gradually across the continental United States to cover the entire area with, roughly,

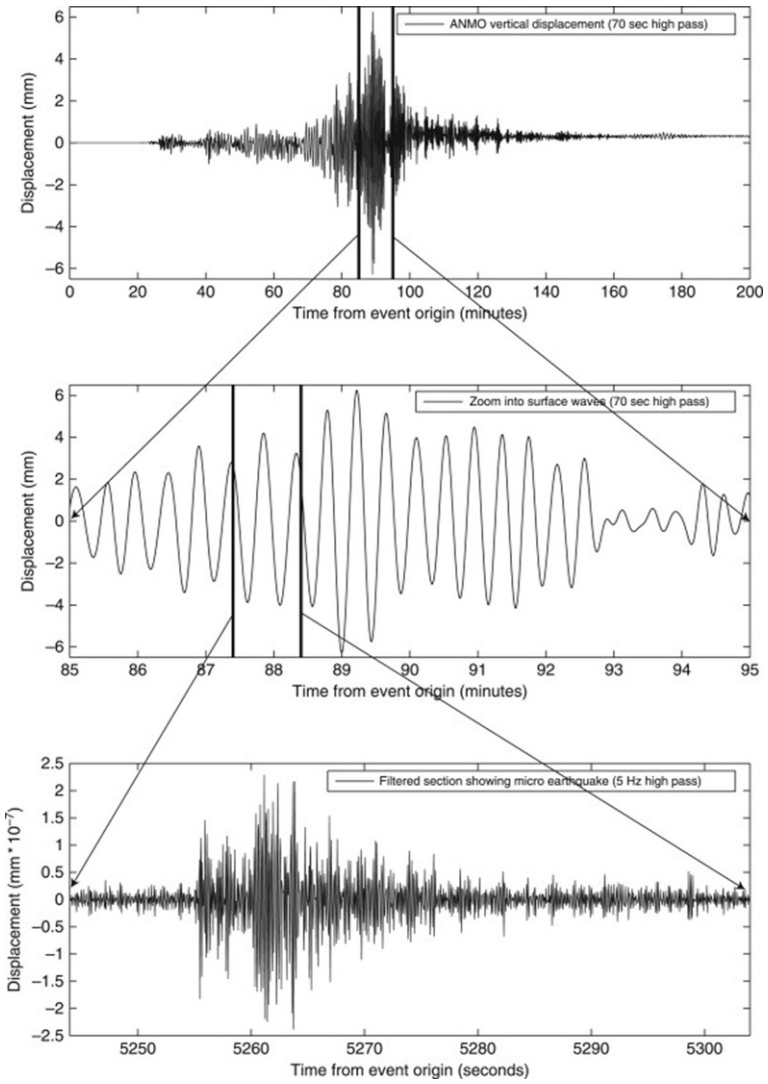
ANMO vertical displacement (70 sec high pass)
Displacement (mm)
Time from event origin (minutes)
Zoom into surface waves (70 sec high pass)
Displacement (mm)
Time from event origin (minutes)
Filtered section showing micro earthquake (5 Hz high pass)
Displacement (mm * 10⁻⁷)
Time from event origin (seconds)

Figure 14 Illustration of the dynamic range of a VBB station (ANMO). A recording of a local microearthquake with magnitude below 1 is extracted from the record dominated by the minor-arc surface waves generated by the 2004 Sumatra–Andaman magnitude 9.3 event. Reproduced from Park J, Butler R, Anderson K, et al. (2005) Performance review of the global seismographic network for the Sumatra–Andaman megathrust earthquake. *Seismological Research Letters* 76 (3): 331–343.

2000 deployments for up to 2 years in a given location; the average instrument spacing is 70 km. In 2013, it has reached the East Coast and preparations are under way to redeploy about half of the instruments in Alaska. The 'reference array' provides the means to relate the waveforms recorded at different stages of TA deployment. Many other portable networks for regional studies of the crust and lithosphere using passive and active sources have been developed and deployed in the last 20 years (see Chapters 1.11, 1.16, and 1.17).

1.01.4 Current Issues in Global Tomography

In parallel with instrument development, scientific progress in seismic tomography has been rapid during the last 20 years, and most of the accomplishments are summarized in two reviews by Romanowicz (1991) and Romanowicz (2003), as well as in Chapters 1.10 and 1.19. However, there are still issues that remain unresolved or controversial. Certainly, there are confusing observations related, for example, to anisotropic properties or differential rotation of the inner core, the core–mantle topography, anticorrelation of density and shear velocity near the bottom of the mantle, the strength and depth distribution of anisotropy in the Earth's mantle, the presence of the postperovskite phase at the base of the mantle, and its role in mantle dynamics.

But the foremost issue in our view relates to the derivation and interpretation of 3-D Earth models. We will mention three issues in particular: parameterization, datasets used for model construction, and theoretical assumptions.

Ever since it was discovered that inversion of ill-conditioned matrices can be dealt with by requiring minimization of the norm or roughness of the model, we have been obtaining models whose reliability is difficult to assess.

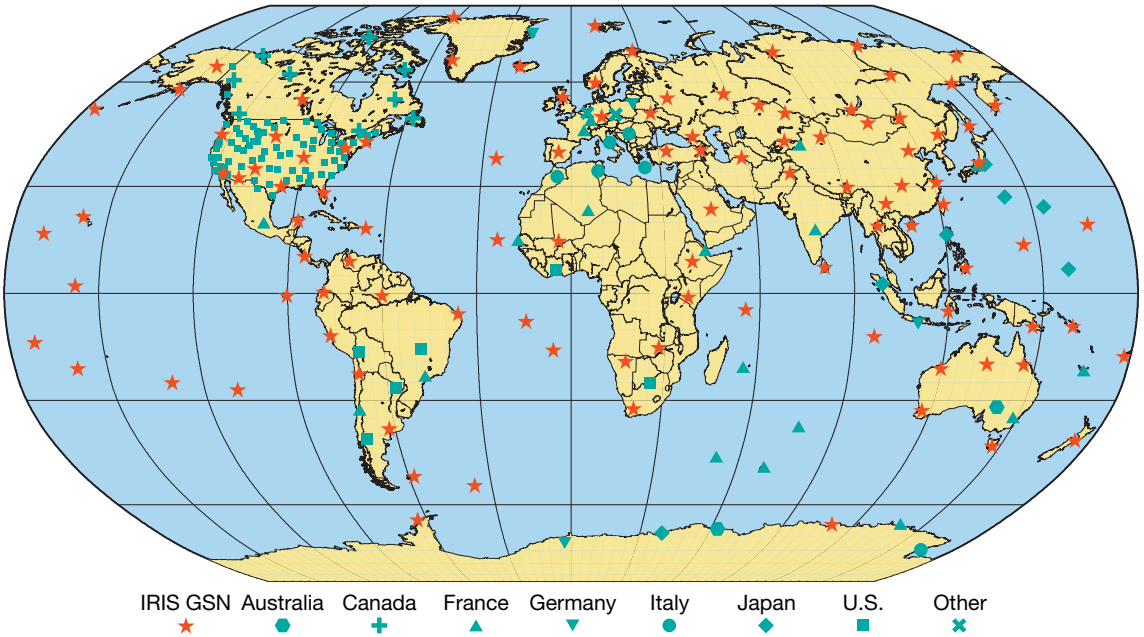

Figure 15 Current (January 2014) map of the stations of the Federation of Digital Seismographic Networks. Stations of different member networks are identified by symbols shown at the bottom. Courtesy of Andy Frassetto (IRIS Instrumentation Services).

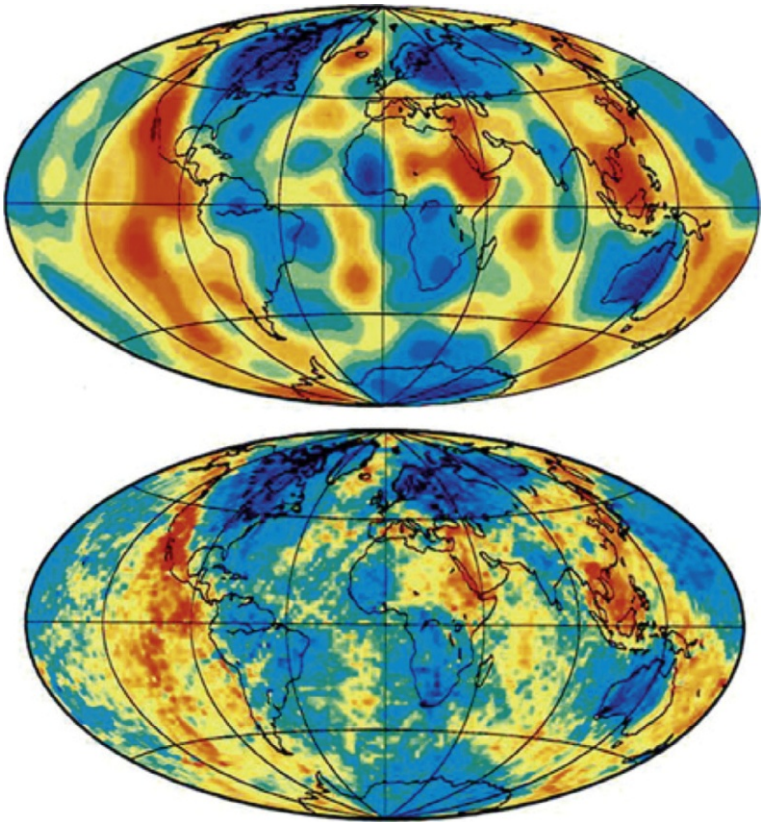

Figure 16 Demonstration of the results of inversion of the same data set (40 000 phase-delay data for 75 s Rayleigh waves measured by Ekström et al., 1997) for different numbers of parameters. The top map shows inversion for spherical harmonic coefficients up to degree 16 (289 parameters). The bottom map shows the results of inversion for about 10 000 equal-area blocks; in this case, matrix conditioning is necessary. The amplitude of the anomalies is lower, artifacts of an uneven path distribution are visible (e.g., across the central Atlantic), and it is difficult to find features that have not been resolved by the top map. The conclusion is that there is a price for unduly increasing the number of unknowns. Courtesy of L. Boschi.

Figure 16 illustrates an example of how the results can be altered with the change of parameterization. A set of about 40 000 phase-delay data for Rayleigh waves with 75 s period (Ekström et al., 1997) are inverted for 'local' phase velocities. The top panel of Figure 16 shows the result in which the data were inverted for a set of basis functions represented by spherical harmonics up to degree 16; this requires solving for 289 unknown coefficients. Because the data set is so large and the global coverage is good, the solution was obtained by an exact matrix inversion. The results look reasonable, without any indication of instability. The lower panel of Figure 16 shows the result obtained using a $2^\circ \times 2^\circ$ block expansion, which requires solving for approximately 10 000 unknown values. Matrix conditioning was required in this case, and it was accomplished by applying combined norm and roughness damping. What is clear from the 'high-resolution' solution is that the amplitudes are generally lower and there are 'streaks' indicating artifacts caused by uneven sampling of the area. What is difficult to find, however, are any features that appear to be significant that are not present in the solution with 30 times fewer parameters. Thus, sometimes, less is better. There is no absolute rule; as discussed in the previous section, the answer depends on the character of power spectra of a particular function.

The issue of parameterization is an important one, particularly if the global behavior of the solution is to be preserved. Figure 17 illustrates cross sections of four global P-velocity models – derived from the same data source (ISC Bulletins) – that span three orders of magnitude in the number of parameters. Clearly, there is not a simple relationship between the number of parameters and information contained in the model. It is so, partly, because the lower-mantle spectrum is dominated by the very low degrees that are well recovered by the degree-6 model.

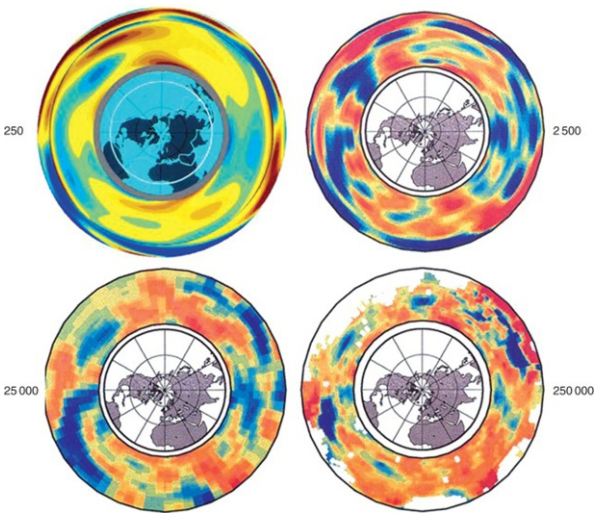

Figure 17 Comparison of the equatorial cross sections of four P-velocity models obtained by inversion of travel-time residuals from ISC Bulletins using a number of unknown parameters that span three orders of magnitude. The image of the African and Pacific superplumes is clearly seen in the model derived by using 250 parameters, while it could not be readily inferred from the model that used 250 000 parameters. The models obtained using 2500 and 25 000 parameters support the conclusion drawn from discussion of Figure 16. Modified from Boschi L and Dziewonski AM (1999) 'High' and 'low' resolution images of the Earth's mantle – Implications of different approaches to tomographic modeling. *Journal of Geophysical Research* 104: 25567–25594.

1.01.4.1 Resolving Power of Datasets Used for Constructing Models

Another important issue in assessing global, as well as regional, tomographic models is the data set (or subsets) and the resolving properties that were used to derive them. The mantle models derived using only teleseismic travel times, for example, have very little radial resolution in the upper mantle, because the ray paths do not bottom there. The teleseismic travel times are sensitive to velocity perturbations in the upper mantle, but the variations with radius cannot be satisfactorily resolved above the lower mantle. For example, all maps of upper-mantle velocity anomalies in Figure 18 show that a model derived using only teleseismic travel times has slow velocities under mid-ocean ridges at all upper-mantle depths, simply from the smearing with depth of the large slow anomalies occurring near the surface. This is a result of norm damping in a situation where sampling is inadequate: a compromise between fitting the data and having a low norm (low sum, or integral, of squared model perturbations). The spreading centers and cratons have largest signal in the uppermost 250 km of the upper mantle; the variance in the next

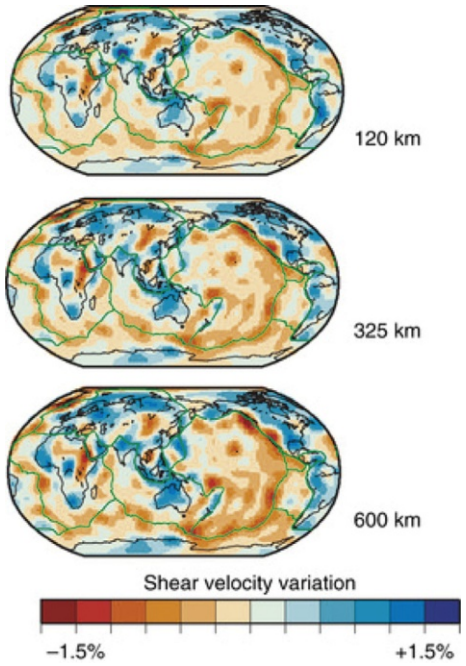

Figure 18 A fragment of a figure from Ritsema et al. (2004) illustrating a typical result of an upper-mantle structure obtained using teleseismic travel times, whose rays do not bottom in the upper mantle. The three maps show smeared-out structure from near the top of the mantle (mid-ocean ridge anomalies). The conclusion drawn from the full figure (see Chapter 1.10) is that, to obtain a whole-mantle model, one should use diverse types of data. Modified from Ritsema J, van Heijst HJ, and Woodhouse JH (2004) Global transition zone tomography. *Journal of Geophysical Research* 109: B02302, http://dx.doi.org/10.1029/2003JB002610.

400 km is an order of magnitude less. Thus, the minimum norm compromise leads to the smearing of the shallow structure over the entire upper mantle (for positive integers, $l+m+n=3$ has the minimum norm solution (1, 1, 1) with the norm of 3, the 'true' solution (3, 0, 0) has a norm of 9, and an intermediate solution (2, 1, 0) has a norm of 5). Another way to accommodate the minimum norm compromise is to make the upper-mantle model small; there are published models derived using only teleseismic travel times that have heterogeneous structure in the upper mantle with very small amplitude.

Models built using teleseismic travel times and fundamental-mode dispersion data do not have sufficient resolution in the transition zone to distinguish its unique properties. So far, only three research groups involved in whole-mantle modeling (Michigan/Oxford, Berkeley, and Harvard) use data allowing sufficient resolution in this region; it is interesting that they obtain these models using different kinds of data and theories, therefore adding to the credibility to the results. The use of waveforms in deriving 3-D models was pioneered by Woodhouse and Dziewonski (1984), but in the original paper, only data with periods longer than 135 s were used. Long-period body waves were used in inversions by Woodhouse and Dziewonski (1986) and Woodhouse and Dziewonski (1989). Dziewonski and Woodward (1991) combined waveforms and teleseismic travel times measured by Woodward and Masters (1991). The immediate result was that the two models they derived showed a sudden change in the pattern of heterogeneities across the 670 km boundary, and this was pointed out and discussed by Woodward et al. (1994). Later inversions by the Harvard group included also surface-wave dispersion data reported by Ekström et al. (1997). This increased resolution near the surface but did not alter the behavior across the upper–lower mantle boundary (Gu et al., 2001, 2003; Kustowski et al., 2008). All these models were obtained using the path average approximation (PAVA), which assumes constant average structure along the great-circle path connecting the source and the receiver. The Berkeley group pioneered use of a more advanced theory called nonlinear asymptotic coupling theory (NACT) first described by Li and Romanowicz (1995) and based on the across-branch coupling asymptotic development of Li and Tanimoto (1993). This theory allowed them to construct body-wave kernels that give good representation of the sensitivity along and around the ray path as shown in **Figure 19** and therefore opened the way to tomographic inversions for whole-mantle structure based entirely on waveform data and thus exploit more information in the seismograms than can be achieved with only those phases that are well separated from others in teleseismic records. In applying NACT to the development of several generations of global mantle models (Li and Romanowicz, 1996; Mégnin and Romanowicz, 2000), most recently including attenuation (Gung and Romanowicz, 2004) and radial anisotropy (Panning and Romanowicz, 2006), the Berkeley group divided the seismograms into wave packets containing one or several body waves or surface-wave overtones, which allowed them to weigh different phases differently in order to obtain uniform sensitivity with depth. The Berkeley group does not use travel times explicitly, but information on structure is included in the phase of a waveform of, for example, an SS-arrival. Thus, a large collection of waveforms containing

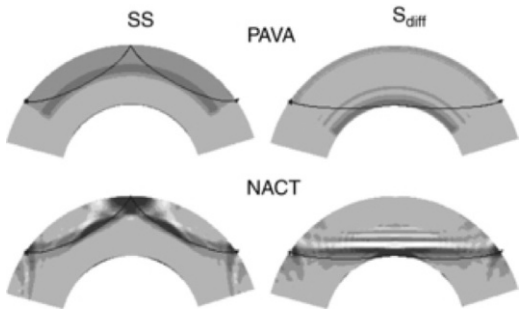

Figure 19 Comparison of sensitivity kernels in the vertical plane containing the source and the receiver for SS waves (left) and S_{diff} waves (right), using the path average approximation (PAVA, top) and the nonlinear asymptotic coupling theory (NACT, bottom). PAVA produces 1-D kernels, which do not represent well the ray character of body waves. NACT, which includes across-branch mode coupling, produces 2-D finite-frequency kernels that more accurately represent the sensitivity along and around the ray path as well as its variations with position along the ray. Because this is a time domain formalism, the NACT kernels are time-dependent and are here represented at a particular point in the waveform, with positive maxima in black and negative ones in white. Shadows beyond the source and receiver are due to the truncation in the coupling series. Adapted from Li XD and Romanowicz B (1995) Comparison of global waveform inversions with and without considering cross branch coupling. *Geophysical Journal International* 121: 695–709.

images of phases such as S, SKS, S_{diff}, Love, and Rayleigh fundamental and overtone waves will represent similar information as the combination of teleseismic travel times and surface-wave phase velocities in the Caltech/Oxford or Harvard models. In addition, unlike travel-time analysis, wave packets containing several phases with close arrival times but different sampling of mantle structure can be included, improving resolution. An important element of the data set used by Ritsema et al. (1999) is a set of maps of Rayleigh wave overtone dispersion from the first to the fifth overtones. These were obtained by 'stripping' the seismograms of subsequent overtones, thus providing the data on the average phase velocity of a particular overtone between the source and the receiver (van Heijst and Woodhouse, 1997). Since body waves represent superposition of overtones, use of complete waveforms is, to a large extent, equivalent; however, the separation of data for individual overtones allows assignment of different weights to different overtones, while direct waveform methods use them with the weight that is determined by their excitation; generally, the amplitude of overtones decreases with the overtone number. On the other hand, waveforms contain information about all the overtones. The importance of the overtones (body-wave waveforms) was shown implicitly by Gu et al. (2001) and explicitly by Ritsema et al. (2004). The importance of using adequate kernels for overtone and body waveforms was illustrated by Mégnin and Romanowicz (1999) in a comparison of the PAVA and NACT inversion approaches.

1.01.4.2 Theoretical Assumptions

Ray theory vs. finite-frequency theory has been the subject of a lively debate within the seismological community during the last decade. Much of it has revolved around the

'banana–doughnut' kernels (Dahlen et al., 2000) and its application to mantle modeling (Montelli et al., 2004a,b). The implication conveyed by those authors was that the results obtained using finite-frequency theory were distinctly superior to those obtained using ray theory. The serious implication of this was that all tomographic studies to date were deficient. Yet, a direct comparison of the finite-frequency and ray theory models published by Montelli et al. (2004b, Figure 9) demonstrates that the two models are nearly identical, save for a scaling factor of 1.14 (van der Hilst and deHoop, 2005). This is because these authors introduced finite volume parameterization by tetrahedra with unknown velocity perturbations at the vertices (with linear interpolation within each tetrahedron) without acknowledging that this is equivalent to a low-pass filtration.

There have been quite a few papers published on this subject (e.g., Peter et al., 2007). While it is obviously desirable to use a more accurate theory, it is worthwhile to investigate why the ray theory and finite-frequency theory yield nearly identical results. A particularly clear explanation of this effect is presented by Dalton (2007) who used the orthogonal basis functions (spherical harmonics) for both the kernels and velocity perturbation, with the phase velocity model truncated at degree $\boldsymbol{L}$. A perturbation in phase travel time between source located at s and receiver at **r** can be calculated by integration over the surface of the sphere Ω:

$$\delta t_{\mathrm{s,r}} = \int_{\Omega} \frac{\delta v}{v_0}(\theta, \varphi) K^{\mathrm{s,r}}(\theta, \varphi) \mathrm{d}\Omega \qquad [1]$$

where v_0 is the reference velocity and $K^{\mathrm{s,r}}(\theta,\phi)$ is the kernel calculated for a particular location of the source and the receiver. Expanding δv and $K^{\mathrm{s,r}}(\theta,\phi)$ in spherical harmonics and truncating expansion of δv at $l = L$, we have

$$\delta t_{\mathrm{s,r}} = \int_{\Omega} \left(\sum_{l=0}^{l=L} \sum_{m=-l}^{m=+l} \delta v_{l,m}/v_0 Y_{l,m}(\theta, \varphi) \mathrm{x} \right) \cdot \left(\sum_{l'=0}^{l'=\infty} \sum_{m=-l'}^{m'=+l'} K^{s,r}_{l',m'} Y_{l',m'}{}^{*}(\theta, \varphi) \right) \mathrm{d}\Omega \qquad [2]$$

However, because of the orthogonality of spherical harmonics, this reduces to

$$\delta t_{\mathrm{s,r}} = \sum_{l=0}^{l=L} \sum_{m=-l}^{m=+l} \delta v_{l,m}/v_0 K^{\mathrm{s,r}}_{l,m} \qquad [3]$$

with the terms in expansion of the kernel function for $l' > L$ having no effect.

Figure 20 (*top*) shows the frequency-dependent kernels for Love waves at 35 and 200 s period. In the *middle*, there is the frequency-dependent kernel expanded to degree 18. At the bottom is the spherical harmonic expansion of a line ('ray theory') along the equator $K = \delta(\theta - \pi/2)$ for $\phi > 0$ and $\phi < \Phi$ and zero elsewhere. At the period of 35 s, it is difficult to tell the difference between the *middle* and the *bottom* 'effective' kernel functions. The difference is still quite small at 200 s period. Thus, finite parameterization can imitate the finite-frequency effect, and for relatively low L, the advantage of using the finite-frequency kernels vanishes. Dalton showed that differences are more pronounced at larger L, but the earlier discussion indicates that there is very little power in the higher degrees of $\delta v_{l,m}$ and the effect on the observed, or computed, $\delta t_{\mathrm{s,r}}$ will be insignificant because of 'natural truncation.' Thus, under the circumstances presented here, the effect of using finite-frequency kernels is very small. In general, the ratio of the width of the finite-frequency kernel to the path length

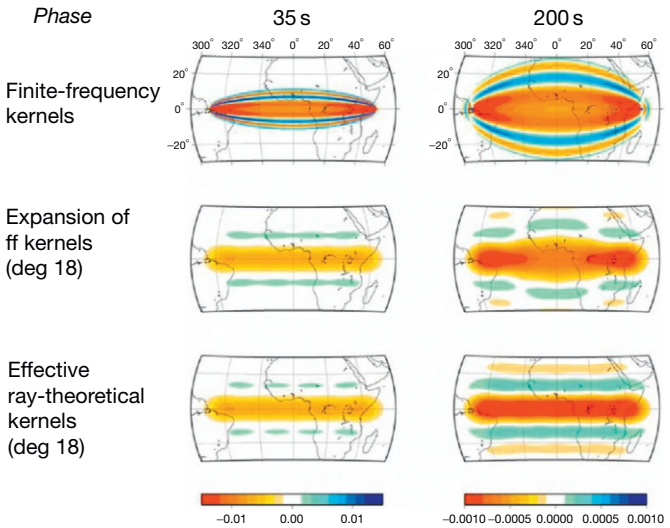

Figure 20 Demonstration of the perhaps counterintuitive fact that 'finite-frequency' kernels and 'ray theory' kernels may lead to very similar models if the model to be obtained using 'ray theory' is parameterized. Parameterization using spherical harmonic expansion up to a maximum order L is used here, because the result is exact. *Top*: Born (finite-frequency) kernels for the phase travel-time delay for Love waves at 35 s (left) and 200 s (right). *Middle*: Synthesis of the Born kernels above obtained by synthesis of spherical harmonic coefficients up to degree $L = 18$. The spherical harmonic coefficients for $l > 18$ are irrelevant because of the orthogonality of the basis functions. *Bottom*: Expansion of a 90° long ray up to the same $L = 18$. The effective kernels for 35 s waves are difficult to distinguish from the expanded finite-frequency kernels; the differences are more noticeable at 200 s period but they are still minor.

determines how good the ray theory approximation is; finite-frequency kernels can be important in regional-scale studies.

Indeed, as discussed earlier, the possibility of inverting complete seismograms (i.e., seismic waveforms) without selecting individual phases for travel-time measurements opens the way for exploiting more of the information contained in the recorded wavefield, thereby achieving better sampling of the mantle. In particular, we note that models based entirely on the inversion of time domain waveforms are able to achieve comparable results, with an order of magnitude fewer records (e.g., a total of 20 000 records in Panning and Romanowicz, 2006) as models based on the standard combination of surface-wave dispersion and body-wave travel times, which typically use tens to hundreds of thousands of measurements. This is because the smaller number of source-station paths considered is compensated by the inclusion of waves that sample mantle structure in a richer variety of ways.

Since our ability to improve the global distribution of sources and receivers is limited, once it is recognized that waveform inversion represents potential for better sampling of the Earth's mantle, the attention then shifts to improving the methods of computation of synthetic seismograms in a 3-D Earth.

NACT (Li and Romanowicz, 1995) provided a successful theoretical approach for this purpose and has led to several generations of whole-mantle shear velocity models in the last 20 years. However, asymptotic normal-mode perturbation theory is only valid for Earth models for which the wavelength of the structure is large compared to that of the seismic waves considered (i.e., smooth models) and heterogeneity is weak (nominally, lateral variations of up to ~10%). Yet, in the Earth's boundary layers, that is, in the upper mantle and in the D″ region, there is ample evidence for the presence of stronger heterogeneity, whereas throughout the mantle, heterogeneity at many different scales may be present. First-order mode perturbation theory is not appropriate in this case. While higher-order perturbation theory has been worked out (e.g., Lognonné and Romanowicz, 1990; Lognonné, 1991), it is cumbersome for use in practice, in particular because it always requires a 1-D reference model.

In the last decade, advances in numerical methods for the computation of the seismic wavefield in arbitrary 3-D structures, and increased computational power, have made it possible to replace normal mode-based synthetics by more accurate ones, based on the spectral element method (SEM), first introduced in global seismology by Komatitsch and Vilotte (1998) and later perfected by Komatitsch and Tromp (2002). The use of SEM has now been implemented in tomographic inversions for crustal structure at the local scale (e.g., Tape et al., 2010) and upper-mantle structure at regional scales (e.g., Fichtner et al., 2009; Rickers et al., 2013; Zhu et al., 2012). The forward numerical computation is generally combined with an 'adjoint' numerical computation of the kernels for inversion (e.g., Tromp et al., 2005; see **Chapter 1.07**) or, alternatively, with a 'scattering integral formalism' (e.g., Chen et al., 2007). Still, computational time increases as the third power of frequency, so the computational challenge limits the frequency range of computations to relatively long periods (typically longer than 40 or 50 s), especially when using the adjoint framework, which requires many iterations (sometimes 20–30) due to the slow convergence of the conjugate-gradient method.

Because the teleseismic wavefield needs to be computed for a long time interval, in order to include all seismic phases of interest (up to and including second orbit fundamental-mode Love and Rayleigh waves), the use of the SEM for global tomography is particularly challenging computationally. The first global shear velocity models developed using SEM (French et al., 2013; Lekic and Romanowicz, 2011) are limited to the upper mantle due to the use of relatively long periods (longer than 60 s) for computational efficiency. To reduce further computation time, they take advantage of efficiencies gained, in the forward step of the computation, by restricting the numerical computation to the mantle through coupling with 1-D mode computations in the core (CSEM, Capdeville et al., 2003) and replacing the finely layered crust by an equivalent smooth crust constrained by surface-wave dispersion data. In the inverse step, the kernels, which do not need to be as accurate as the forward predictions (e.g., Lekic and Romanowicz, 2011; Tarantola, 2005), are calculated using a mode-based approximation. The use of a Gauss–Newton formulation of the inverse problem leads to much more rapid convergence than the adjoint approach. The use of accurate wavefield computations, such as afforded by SEM, is particularly important to improve resolution of low-velocity regions, which tend to be hidden from observation, when ray theory is used, due to wave front healing effects (e.g., Nolet and Dahlen, 2000). For example, the new-generation tomographic models based on the use of SEM resolve the minimum amplitude of the upper-mantle low-velocity zone better than previously, even in areas far away from sources and stations, as illustrated in **Figure 21**, and are starting to resolve finer details of the 'plumbing' system in the oceanic upper mantle (e.g., Colli et al., 2013; French et al., 2013; Rickers et al., 2013).

1.01.4.3 Robust Features of Current Global Mantle Models and Their Implications

The full impact of the completed FDSN network, progress in automatic processing of data – measurements of travel times from waveforms or selection of time windows for waveform inversion, for example – improved the database by an order of magnitude in comparison with earlier models. This has been accompanied by better recognition of what is required to obtain a stable 3-D model of shear velocity anomalies in the mantle. Among these are as follows:

(i) Assembly of data that are sensitive to structure from the Moho to CMB; usually, this calls for a combination of surface-wave dispersion, overtones, and teleseismic travel times.
(ii) Proper weighting of the subsets of data to assure comparable radial resolution.
(iii) Careful selection of matrix stabilization parameters.
(iv) Even though gaps in coverage due to the uneven distribution of sources and receivers are unavoidable, it is desirable to minimize the impact of this inequality. For example, Dziewonski (1984) used a form of a 'summary ray' approach, counting the number of rays connecting a particular 'receiver cell' and 'source cell' (each $5° \times 5°$ at the equator) and then counterweighed individual

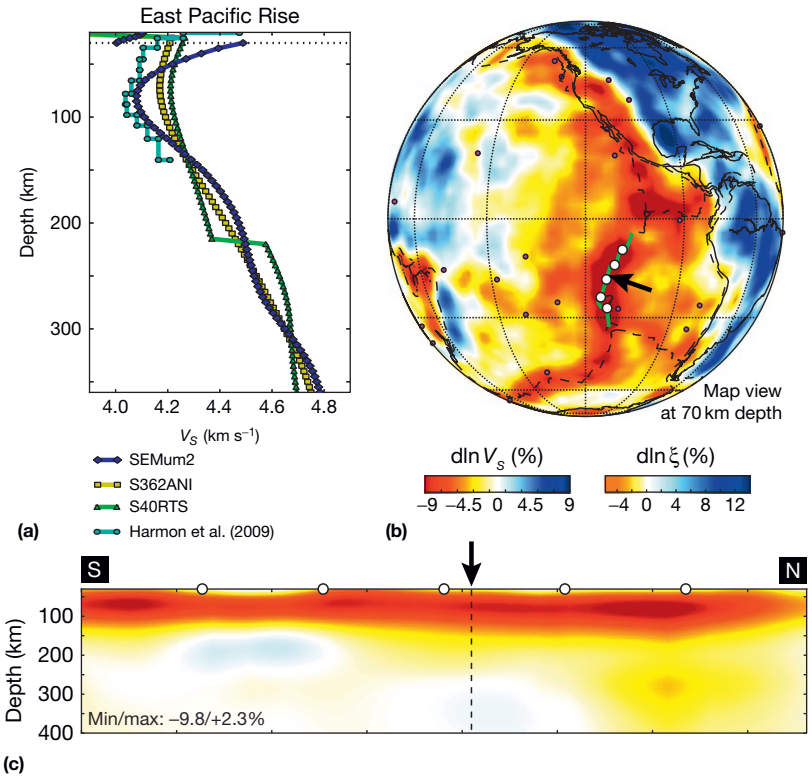

Figure 21 Isotropic V_S structure beneath the East Pacific Rise (EPR). (a) A comparison between the mean 1-D V_S profile obtained from the high-resolution OBS-based tomographic study of EPR structure by Harmon et al. (2009) and that sampled from global models SEMum2 (French et al., 2013), S362ANI (Kustowski et al., 2008), and S40RTS (Ritsema et al., 2011), in the same location. The 1-D profile of the Harmon et al. study was obtained from a harmonic mean of the central portion of their model over length scales consistent with the a priori correlation lengths employed in the SEMum2 inversion (~400 km). SEMum2 more closely recovers the strength and depth of the low-velocity zone (LVZ) beneath the EPR inferred from the local study than either of the other global models. (b) Relative variations in isotropic V_S structure at 70 km depth in SEMum2, focused on the EPR, showing both the location of the comparison in (a) (black arrow) and the extent of the ~3750 km line of section in (c) (portion of EPR highlighted in green). (c) A cross section along the EPR, following the green line and white dots shown in (b), illustrating the strength and extent of the strong low-velocity anomaly imaged beneath the EPR in SEMum2 (c), nearly −10%. Black arrow and dashed line indicate approximate location of profiles in (a). Reproduced from Figure S6 of French S, Lekic V, and Romanowicz B (2013) Waveform tomography reveals channeled flow at the base of the oceanic asthenosphere. *Science* 342: 227–230.

observations such that impact of a given pair of cells was equal regardless of the number of connections. Since there were about 25% of pairs with only one connection and only 25% had more than ten connections, the variance reduction was very modest.

Figure 22 compares model S40RTS (Ritsema et al., 2011) at seven different depths with four other relatively recent models: S362ANI (Kustowski et al., 2008), SAW642AN (Panning and Romanowicz, 2006), TX2008 (Simmons et al., 2009), and HMSL-S (Houser et al., 2008). The data sets used to derive each of these models were different; even the theories used were different. Therefore, their overall similarity (with one exception) indicates congruence of the global 3-D models of the whole mantle. There are differences, of course, and some of them should be resolved, but the 'big picture' is robust and its implications should be considered in modeling the global mantle flow. Such modeling is necessary to understand mantle dynamics and evolution, since tomography can retrieve only the present-day picture. What makes the work of Ritsema et al. (2011) particularly important is that the data set used in this inversion is an order of magnitude greater than in their earlier model S20RTS (Ritsema et al., 1999) and, yet, the differences between the two models are small, especially at larger wavelengths. This means that the features within the 'red' part of the spectrum are well resolved and further increase in the data set will not change the image appreciably at long wavelengths.

There is a fundamental similarity among the models; all show an order of magnitude decrease in power between 100 and 400 km depth (the scale for the top row of maps is ±7%, or 3.5 times larger than at other depths). While the dramatic difference between the maps at 600 and 800 km is distinct for the first three models, it is less so for the last two; the explanation is that models TX2008 and, especially, HMSL-S did not use enough data with resolution in this depth range to map properly this critically important feature. The rms amplitude is the lowest between 650 and 1800 km depth but then increases again to reach the maximum at the CMB.

The power spectrum as a function of depth and wave number is a robust feature (see Figure 9 in Kustowski et al., 2008). On this basis, it is possible to distinguish several depth regions with different spectral characteristics; Dziewonski et al. (2010)

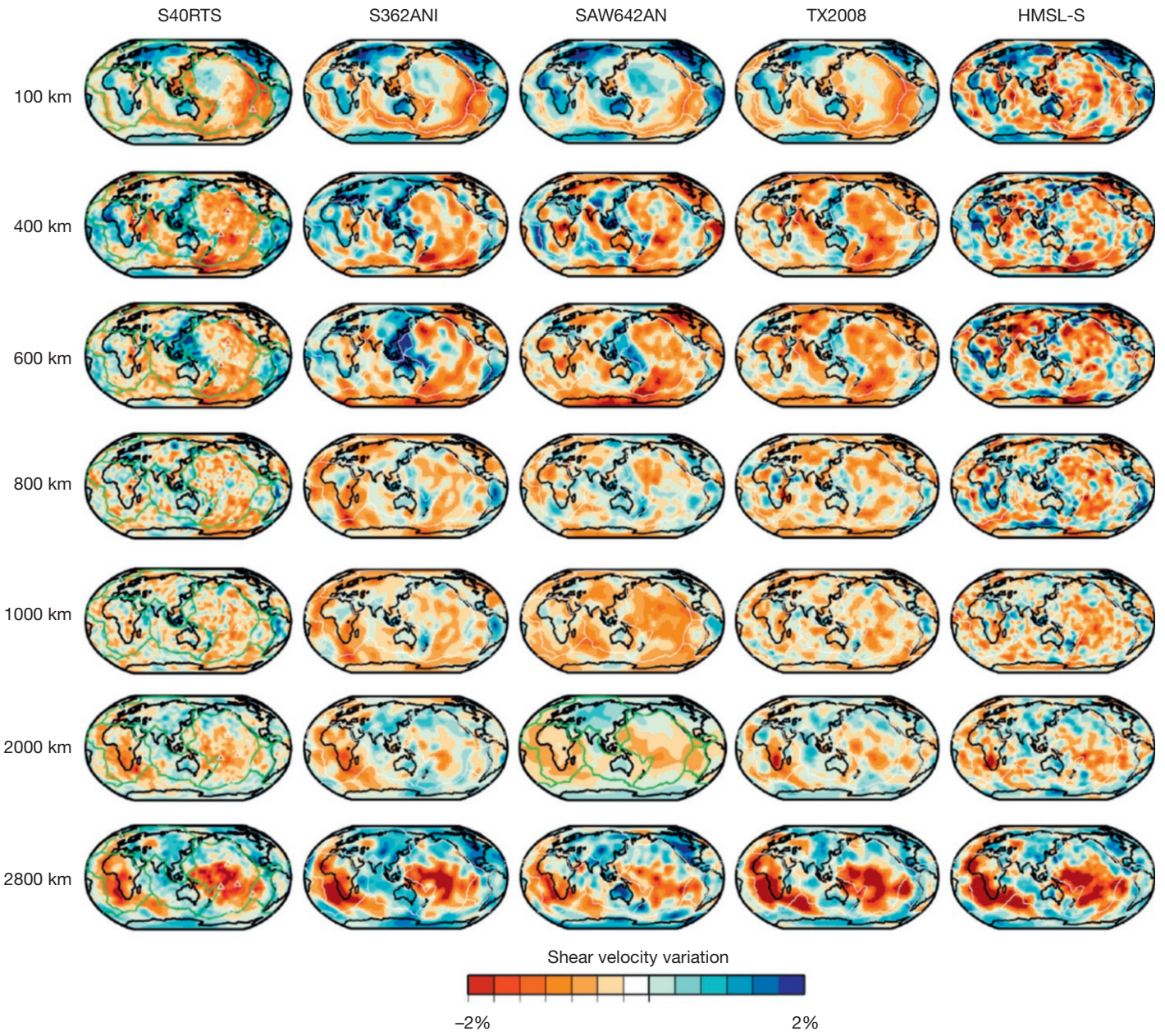

Figure 22 Comparison of shear velocity maps at depths of (from top to bottom) 100, 400, 600, 800, 1000, 2000, and 2800 km for models (from left to right) S40RTS (Ritsema et al., 2011), S362ANI (Kustowski et al., 2008), SAW642AN (Panning and Romanowicz, 2006), TX2008 (Simmons et al., 2009), and HMSL-S (Houser et al., 2008). The velocity varies from −2% to +2% from the average value. Shear velocity perturbations are between −7% and +7% from the average value for the map at 100 km depth. Reproduced from Ritsema J, Deuss A, van Hejst HJ, and Woodhouse JH (2011) S40RTS: A degree-40 shear-velocity model for the mantle from new Raleigh wave dispersion, teleseismic traveltime and normal-mode splitting function measurements. *Geophysical Journal International* 184: 1223–1236, http://dx.doi.org/10.1111/j.1365-246X.2010.04884.x.

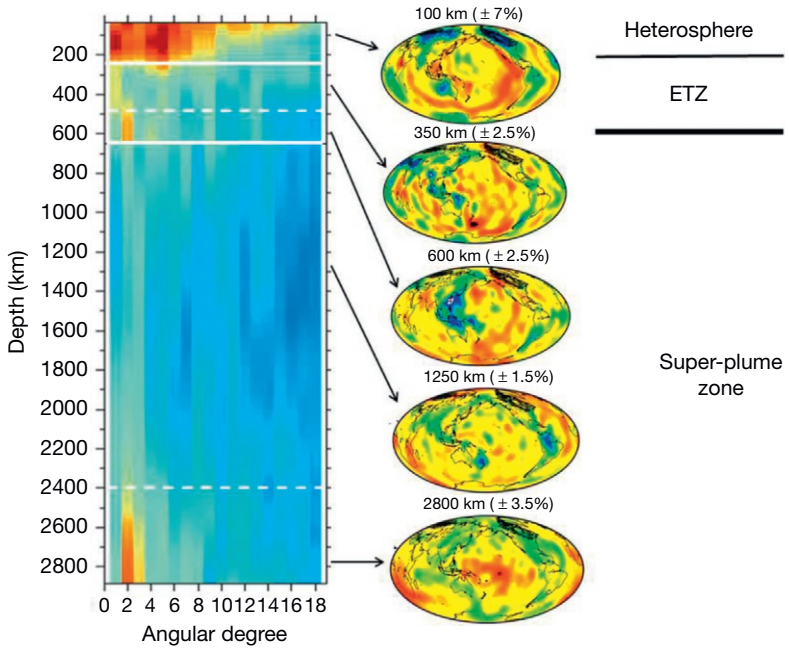

Figure 23 *Left:* Power spectrum of model S362ANI of Kustowski et al. (2008) as a function of harmonic degree and depth. Continuous white lines indicate inferred major divisions in spectral characteristics; broken white lines show additional subdivisions. *Center*: Maps of shear velocity anomalies at depths 100 km (±7%), 350 km (±2.5%), 600 km (±2.5%), 1250 km (±1.5%), and 2800 km (±3.5%). *Right*: Schematic division of the mantle into three zones with profound changes at their boundaries: 'heterosphere' with a very high level of heterogeneity; 'extended transition zone,' with a weak, white spectrum at the top and power shifting to degree 2 above the 650 km discontinuity; and 'superplume zone' dominated by degrees 2 and 3, which is strongest at the CMB but continuing with decreasing amplitude throughout the entire lower mantle.

proposed five such regions; more recent analysis (Dziewonski et al., 2013) finds that these can be combined into three principal zones.

Figure 23 shows the power spectrum of model S362ANI with maps of shear velocity anomalies at five different depths. The principal divisions are between the 'heterosphere' (HS, Moho – 250 km depth), the 'extended transition zone' (ETZ; 250–650 km), and the lower mantle or 'superplume zone' (SPZ). The spectrum changes gradually within the ETZ from white to being dominated by degree 2, but this change is not sudden and is not associated with the 410 km discontinuity. In the SPZ, there is a change in the gradient of heterogeneity at about 2400 km depth (e.g., Lekic et al., 2012), but the pattern does not change. These two more subtle spectral changes are shown with broken lines; the fundamental ones - with continuous lines.

Comparison of the five maps shows that the heterogeneity is distinctly different in each zone or subzone. 'Heterosphere' is dominated by surface tectonic features: slow ridges, cooling plates, and fast cratons. Between 150 and 250 km depth, the power of heterogeneity decreases by an order of magnitude, hence the name.

Below 250 km, the upper part of the ETZ is characterized by a nearly white spectrum. Oceans, particularly Pacific, are slow but do not show the age signature; continental structure tends to be faster than average, but the location of the anomalies is not as closely associated with the cratons as at 100 km depth. Between 450 and 650 km depth, the degree-2 anomalies become dominant. Regional-scale studies such as Fukao et al. (1992, 2001, 2009), Fukao and Obayashi (2013), and **Chapter 1.20** as well as global scale of Gu et al. (2001, 2003) explain this by stagnation above the 650 km discontinuity of the recently subducted slab, which appears to lay flat at the bottom of the transition zone for sometimes as far as 2000 km. This is consistent with the already discussed pattern of abrupt change of shear velocity anomalies at depths of 600 and 800 km for the first three models in Figure 22.

At the top of the 'superplume planet' in the mid-mantle, the signal is weak and has a somewhat flat spectrum, even though the degrees 2 and 3 have the largest power. The amplitude of anomalies begins to increase below 1800 km depth. In the 'abyssal layer' (2400 km – CMB), degrees 2 and 3 are clearly dominant and show the pattern of two superplumes (African and Pacific) separated by a wide circumpolar ring of higher than average velocities. This pattern of zero line is very robust, as shown by Lekic et al. (2012).

Figure 24 shows the result of cluster analysis of the deepest 1000 km of the mantle of the five models shown in Figure 22. On a constant area $2^\circ \times 2^\circ$ grid, the average velocity anomaly for a particular model is classified as either 'slow' or 'fast'; if it is slow, integer 1 is added to the voting map and 0 if it is fast. If all models are 'slow' at a given grid point, the corresponding color is deep red; if all models are fast, then deep blue. The robustness of this classification is demonstrated by the fact that over 95% of the area is either deep red or dark blue. The other important inference is that even though the individual models show variations in amplitude, these do not lead to the change in sign of the anomaly: the dark red and dark blue regions are contiguous. One exception is a distinctly separated 'slow' anomaly, which Lekic et al. (2012) named the 'Perm anomaly' because of the proximity of its surface projection to the city of Perm (Russia). Another possible exception is a larger area beneath the East Pacific Rise, but the models are not

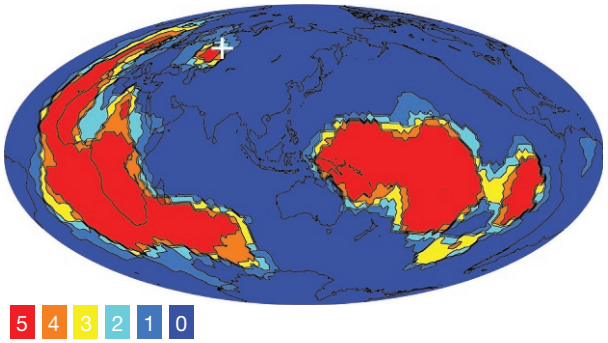

Figure 24 Cluster analysis of shear velocity (V_s) profiles (1000–2800 km depth range) from five recent global tomographic models (Houser et al., 2008; Kustowski et al., 2008; Mégnin and Romanowicz, 2000; Simmons et al., 2010; Ritsema et al., 2011) in the lower mantle defines two regions whose geographic extents are consistent across models, tracing out the African and Pacific superplumes, as well as a single, globally contiguous faster-than-average region. Pixels that make up this map are color-coded according to how many models assign the V_s profile beneath that point to the slow cluster. The models are spatially filtered to exclude power at spherical harmonic degrees $\ell > 18$. Reconstructed location (Torsvik et al., 2008) of the center of Siberian Trap eruptions is indicated by the white cross. Reproduced from Lekic V, Cottaar S, Dziewonski A, and Romanowicz B (2012) Cluster analysis of global lower mantle tomography: A new class of structure and implications for chemical heterogeneity. *Earth and Planetary Science Letters* 357–358: 68–77.

unanimous here. The white cross indicates the location of the Siberian Traps 250 Ma ago by Torsvik et al. (2008).

In order to put the Perm Anomaly on the map, it is necessary to synthesize the first 12 harmonics of the expansion of the map shown in **Figure 24** (see Figure 7 in Lekic et al., 2012). The significance of the unanimity of all five models is that we can resolve the structure near the CMB to about 1000 km half-wavelength. This confirms the conclusion that degree-2 and degree-3 anomalies are real features rather than a result of insufficient data to resolve smaller-scale structures. Another conclusion is that there is a dichotomy between the planetary-scale structures (superplumes) and smaller-scale anomalies, such as ULVZs or hypothetical narrow plumes. It is not clear, therefore, that the latter structures play a predominant role in whole-mantle dynamics. On the other hand, the superplume pattern continues upward to the middle mantle. Figure 3 in Lekic et al. (2012) shows that the voting pattern of **Figure 24** continues into the middle mantle; even though the signal-to-noise ratio is considerably lower in the 800–1800 km depth range. The superplume pattern is distinct and contains all the surface locations of hot spots; also, the band of faster-than-average velocities continues to maintain its width, indicating that the fundamental pattern of velocity anomalies continues throughout the lower mantle, although with decreasing amplitude.

A by-product of the voting procedure is the derivation of average fast and slow velocity anomalies for each of the all five models (see Figure 5 of Lekic et al., 2012). There are two important conclusions that can be drawn from this comparison. First, the slow anomalies are about three times stronger than the fast ones; this is consistent with the fact that in **Figure 24**, the area of 'blue' is much larger than that of 'red.' Second, there is a sharp change in the gradient of the velocity anomalies at about 500 km from the CMB, above which it becomes much shallower. It is possible to speculate that the steep gradient in the lowermost mantle is due to a chemical heterogeneity whose strength decreases with radius to reach that of the ambient mantle 500 km above the CMB. Further, it would be possible to modify the 'average' Earth model by adding a small 1-D linear increase of velocities between 1600 km depth and the CMB, where it would amount to 0.5%. If this were then subtracted from the 3-D model, the map of anomalies in the abyssal zone region would be mostly limited to slow anomalies, such that with this modification, the principal anomalies would be limited to superplumes. Thus, the chemical heterogeneity and the abyssal layer could be limited to the base of the superplumes.

1.01.4.4 Stability of the Planetary-Scale Heterogeneities

Richards and Engebretson (1992) mapped four geophysical functions (their Figure 1): geoid, hot-spot locations, velocity anomalies near the CMB, and a sum of the mass of all slabs subducted during the last 120 Ma. Correlation is significant only for degrees 2 and 3. Of the four functions, the first three are surface observables; only the seismic velocity anomalies correspond to a particular depth – the lowermost mantle. Even though Ricard et al. (1993) and Lithgow-Bertelloni and Richards (1998) proposed a model with the sinking slabs distributed at different depths according to their age, correlation between the velocity and the density anomalies (sinking slabs) is poor in the lowermost mantle. This may be called the 'slab sinking paradox': how the velocity anomalies near the CMB may "know" about slabs that are still suspended higher in the mantle? Dziewonski et al. (2010) proposed that this paradox could be explained if the long-term (~100 Ma) slab subduction cyclically repeats itself and the anomalies in the lowermost mantle reflect a long-term average of these cycles. The important degrees are 2 and 3; for each of these degrees, the correlation is very high, but the relative power of degree 2 of seismic anomalies is three times greater than that of degree 3; in integrated slab expansion, degree 3 has higher power than degree 2. This may mean that degree 2 may be more stable in time than degree 3. Because of its apparent longevity, Dziewonski et al. (2010) named the degrees 2 and 3 the 'mantle anchor structure' (MAS).

The degree-2 anomaly, which dominates the abyssal layer, has geometric properties that have led Dziewonski et al. (2010) to a speculation – which some thought 'outrageous' – that degree-2 anomalies may be stable over very long times. What is special about degree-2 is that when translated into density anomalies, it may affect the Earth's nonhydrostatic moment of inertia tensor. **Figure 25** shows a comparison of the degree-2 anomaly at 2800 km depth in 3-D models S362ANI (Kustowski et al., 2008), SAW24B16 (Mégnin and Romanowicz, 2000) and S20RTS (Ritsema et al., 1999). It shows nearly identical images that are very close to the harmonic Y_{20} rotated so that its symmetry axis lies in the equatorial plane. The random test shows that to obtain such a result by chance is less than 1 in 1000. If the negative velocity anomalies are associated with higher effective density, then the minimum moment of inertia axis would be crossing the equator at the center of the red anomalies (about 10° east or 170° west) as required by the rotation dynamics. The solution is degenerate for the other two principal components: any axis

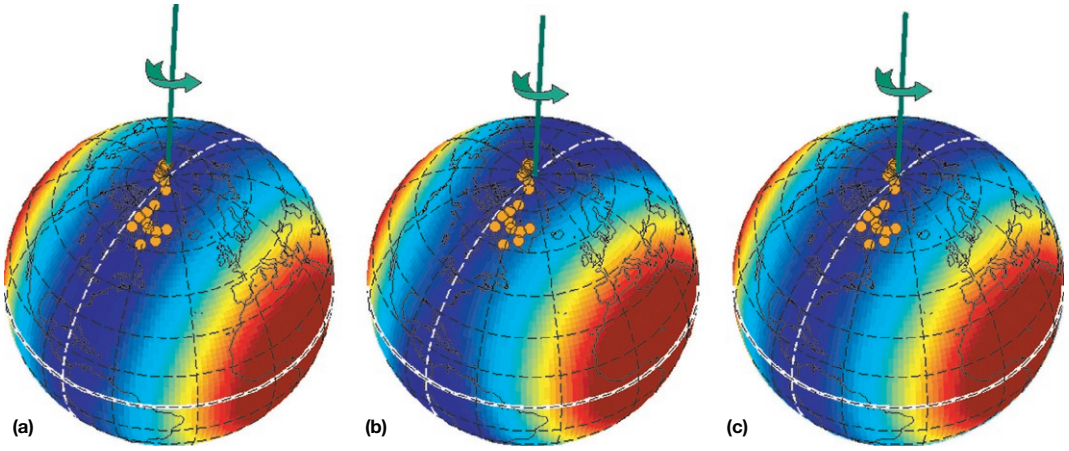

Figure 25 The nearly indistinguishable degree-2 structures at 2800 km depth of three global tomographic S-velocity models: (a) S362ANI (Kustowski et al., 2008), (b) SAW24B16 (Mégnin and Romanowicz, 2000), (c) S20RTS (Ritsema et al., 1999). Pink circles indicate paleopole locations from the true polar wander reconstructions of Besse and Courtillot (2002). Reproduced from Dziewonski A, Lekic, and Romanowicz A (2010) Mantle anchor structure; an argument for bottom up tectonics. *Earth and Planetary Science Letters* 299: 69–79.

passing through the polar great circle crossing the equator at 100° east or 80° west will have the maximum moment of inertia. Thus, this great circle would be the preferred direction of 'true polar wonder' (TPW) due to mass redistribution. The orange dots in Figure 25 are the TPW positions during the last 200 Ma as determined by Besse and Courtillot (2002); the agreement is good even though no TWP observations were included in building the seismic models. Modeling of TPW using geodynamic data was initiated by Steinberger and O-'Connell (1997) and continues till the present (c.f. Conrad et al., 2013; Rouby et al., 2010; Steinberger and Torsvik, 2010). The TPW is increasingly difficult to determine for times before the magnetic stripes on the oceanic floor have been destroyed. Some paleomagnetic evidence exists that the MAS hypothesis is consistent with the data as old as 1.3 Ga (Jean Besse, 2013, personal communication). If this is correct, then there is no reason not to test an assumption that it was formed not long after the Earth's accretion.

1.01.4.5 The Need for Consideration of More Complete Modeling of Mantle Flow

A quadrupole convection essentially identical to the pattern in Figure 25 has been proposed by Busse (1983) and its stability implications pointed out by Le Pichon and Huchon (1984) on the basis of correlation of the degree-2 geoid with velocity anomalies in the lowermost mantle (Dziewonski et al., 1977). With the incomparably higher quality of current global models of heterogeneity, we do not have a mantle flow model that reproduces large-scale features revealed by mantle tomography.

The concepts of 'top-down' or 'bottom-up' tectonics are not contradictory, but rather complementary. The heterosphere of Figure 23 is highly energetic – it contains above 80% of the volume integrated power of mantle heterogeneity – and acts on a relatively short timescale: the pattern of subductions has changed considerably during the last 200 Ma (Lithgow-Bertelloni and Richards, 1998, Figure 6). The lower-mantle heterogeneity structure (superplume zone) shows great stability, as indicated by the 'slab paradox' and TPW results, and may impose the long time influence on the heterosphere's behavior. The 'ETZ' is the critical region in which the communication between the heterosphere and the superplume zone is taking place. It is clear that some slabs become stagnant above the 650 km discontinuity, but the degree-2 velocity anomaly is well correlated with the integrated slabs during the last 15–20 Ma and does not show evidence of earlier accumulation. Thus, it is not clear what happens with the material subducted earlier. It is also not clear how the superplumes interact with the transition zone. The Pacific is slow both below and above the 650 km discontinuity, but this is not as obvious for the African superplume. Romanowicz and Gung (2002) argued that attenuation in the transition zone better reflects its thermal state than the velocity anomalies and that the Q anomalies in the transition zone are well correlated with the velocity anomalies at the CMB.

The paradigm of three-layer mantle dynamics, each of which acts on a different spatial and temporal scale and has been derived mostly from seismic data providing a present-day snapshot of 3-D velocity anomalies, must be tested by geodynamic modeling. From the published results of numerical modeling of mantle flow, it is clear that such a structure with three boundary layers has yet to be realized and match the observations.

With the recent advances in numerical modeling, a clearer picture of the connection between lower-mantle and transition zone structure on the one hand and structure in the asthenosphere on the other hand is starting to emerge. Figure 26 shows a 3-D rendering of the central Pacific portion of upper-mantle model SEMum2 (French et al., 2013), viewed from the east to the west, which shows a number of vertically elongated low-velocity columns (plumes?), many of them rooted in the lower mantle and extending up to about 350 km depth. At shallower depths, this structure is replaced by a series of horizontally elongated low-velocity channels or 'fingers,' aligned parallel to the absolute plate motion and extending into the low-velocity zone right below the lithosphere. These low-velocity channels, which are present in all major ocean basins, are spaced regularly with a wavelength of about 1800–2000 km and manifest the dynamic interaction in the 'heterosphere' between the upwellings from the 'superplume zone' and ETZ (e.g., Figure 23) and the tectonic plates.

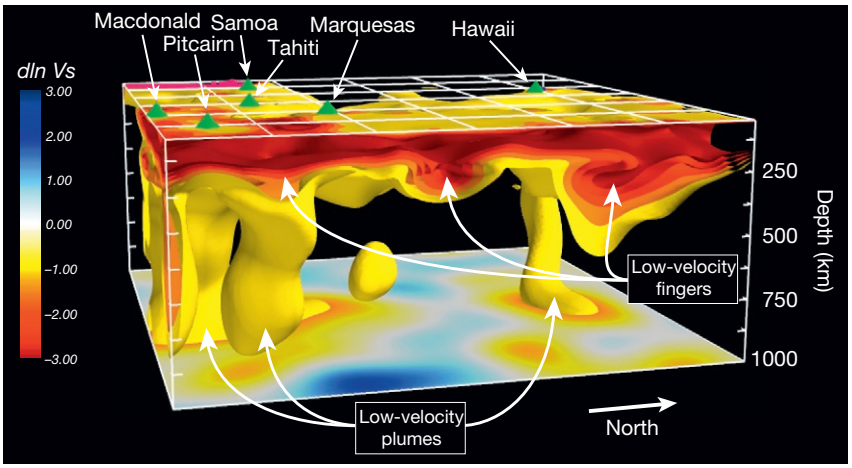

Figure 26 3-D rendering of the low-velocity parts of a portion of model SEMum2 (French et al., 2013) in the central Pacific, shown down to 1000 km depth. The range of velocity anomalies shown is −1% to −3%. The view is from the east, standing in the vicinity of the East Pacific Rise and looking towards the west. Green cones indicate major hot spots. Note the regularly spaced low-velocity fingers right below the very slow low-velocity zone. These fingers extend for several thousand kilometers into the Pacific basin, in the direction of the Pacific Plate absolute plate motion. Similar structures are seen in the south and North Atlantic Ocean and in the Indian Ocean.

We expect that, in the next 5–10 years, these images, as well as those of the lower mantle, will become even sharper, as the frequency range accessible to global tomography based on numerical methods increases, providing definitive clues on such fundamental questions as the relation of hot spots to plumes, and plumes to superplumes, and the role of superplumes in the global mantle circulation and the fate of subducted slabs.

References

Adams RD, et al. (2002) International seismology. In: Lee WHK, Kanamori H, Jennings PC, and Kisslinger C (eds.) *International Handbook of Earthquake and Engineering Seismology Part A*, pp. 29–37. San Diego, CA: Academic Press.

Agnew D, Berger J, Buland R, Farrell W, and Gilbert F (1976) International deployment of accelerometers: A network for very long period seismology. *EOS. Transactions of the American Geophysical Union* 57: 180–188.

Agnew DC, Berger J, Farrell WE, Gilbert JF, Masters G, and Miller D (1986) Project IDA; a decade in review. *EOS. Transactions of the American Geophysical Union* 67: 203–212.

Agnew DC, et al. (2002) History of seismology. In: Lee WHK, Kanamori H, Jennins PC, and Kisslinger C (eds.) *International Handbook of Earthquake and Engineering Seismology*, pp. 3–12. San Diego, CA: Academic Press.

Aki K, Christofferson A, and Husebye E (1977) Determination of the three-dimensional structure of the lithosphere. *Journal of Geophysical Research* 82: 277–296.

Alsop LE, Sutton GH, and Ewing M (1961) Free oscillations of the Earth observed on strain and pendulum seismographs. *Journal of Geophysical Research* 66: 631–641.

Alterman Z, Jarosch H, and Pekeris CL (1959) Oscillations of the Earth. *Proceedings of the Royal Society of London, Series A* 259: 80–95.

Anderson DL (1963) Recent evidence concerning the structure and composition of the Earth's mantle. *Physics and Chemistry of the Earth* 6: 1–129.

Anderson DL and Archambeau CB (1964) The anelasticity of the Earth. *Journal of Geophysical Research* 69: 2071–2084.

Anderson DL and Hart RS (1978) Q of the Earth. *Journal of Geophysical Research* 83: 5869–5882.

Backus GE and Gilbert F (1961) The rotational splitting of free oscillations of the Earth. *Proceedings of the National Academy of Sciences of the United States of America* 47: 362–371.

Backus GE and Gilbert F (1967) Numerical applications of formalism for geophysical inverse problems. *Geophysical Journal of the Royal Astronomical Society* 13: 247–276.

Backus GE and Gilbert F (1968) The resolving power of gross Earth data. *Geophysical Journal of the Royal Astronomical Society* 16: 169–205.

Backus GE and Gilbert F (1970) Uniqueness in the inversion of gross Earth data. *Philosophical Transactions of the Royal Society of London, Series A* 266: 169–205.

Benioff H (1958) Long waves observed in the Kamchatka earthquake of November 2, 1952. *Journal of Geophysical Research* 63: 589–593.

Benndorf H (1905) Über die Art der Fortpflanzung der Erdbebenwellen im Erdinneren. 1. Mitteilung. Sitzungsberichte der Kaiserlichen Akademie in Wien. Mathematisch-Naturwissenschaftliche Klasse 114, Mitteilungen der Erdbebenkommission. *Neue Folge* 29: 1–42.

Benndorf H (1906) Über die Art der Fortpflanzung der Erdbebenwellen im Erdinneren. 2. Mitteilung. Sitzungsberichte der Kaiserlichen Akademie in Wien. Mathematisch-Naturwissenschaftliche Klasse 115, Mitteilungen der Erdbebenkommission. *Neue Folge* 31: 1–24.

Berkner LV and Members of the panel (1959) *Report of the Panel on Seismic Improvement. The Need for Fundamental Research in Seismology*, p. 212. Washington, DC: Department of State.

Besse J and Courtillot V (2002) Apparent and true polar wander and the geometry of the geomagnetic field over the last 200 Myr. *Journal of Geophysical Research* 107: 2300. http://dx.doi.org/10.1029/2000JB000050.

Birch AF (1952) Elasticity and constitution of the Earth's interior. *Journal of Geophysical Research* 57: 227–286.

Boschi L and Dziewonski AM (1999) High' and 'low' resolution images of the Earth's mantle – Implications of different approaches to tomographic modeling. *Journal of Geophysical Research* 104: 25567–25594.

Brune J and Dorman J (1963) *Seismic Waves and the Structure of the Crust and Mantle in the Canadian Shield*: Geological Society of America, pp. 28–29, Special Paper.

Buland R, Berger J, and Gilbert F (1979) Observations from the IDA network of attenuation and splitting during a recent earthquake. *Nature* 277: 358–362.

Bullen KE (1940) The problem of the Earth's density variation. *Bulletin of the Seismological Society of America* 30: 235–250.

Bullen KE (1949) Compressibility-pressure hypothesis and the Earth's interior. *Geophysical Journal of the Royal Astronomical Society* 5: 355–368.

Busse F (1983) Quadrupole convection in the lower mantle. *Geophysical Research Letters* 10: 285–288.

Capdeville Y, Chaljub E, Vilotte JP, and Montagner JP (2003) Coupling the spectral element method with a modal solution for elastic wave propagation in global earth models. *Geophysical Journal International* 152: 34–67. http://dx.doi.org/10.1046/j.1365-246X.2003.01808.x.

Chen P, Jordan TH, and Zhao L (2007) Full three-dimensional tomography: A comparison between the scattering-integral and adjoint-wavefield methods. *Geophysical Journal International* 170: 175–181.

Colli L, Fichtner A, and Bunge H-P (2013) Full waveform tomography of the upper mantle in the south Atlantic region: Imaging a westward fluxing shallow asthenosphere? *Tectonophysics* 604: 26–40.

Conrad CP, Steinberger B, and Torsvik TH (2013) Stability of active mantle upwelling revealed by net characteristics of plate tectonics. *Nature* 498: 479–482.

Cooley JW and Tukey JW (1965) An algorithm for machine computation of complex Fourier series. *Mathematics of Computation* 19: 297–301.

Dahlen F, Hung S-H, and Nolet G (2000) Fréchet kernels for finite-frequency traveltimes – I. Theory. *Geophysical Journal International* 141: 157–174.

Dalton CA (2007) *The global attenuation structure of the upper mantle*. Ph.D. thesis. Harvard University.

Dziewonski AM (1984) Mapping the lower mantle: Determination of lateral heterogeneity in *P*-velocity up to degree and order 6. *Journal of Geophysical Research* 89: 5929–5952.

Dziewonski AM and Anderson DL (1981) Preliminary Earth model (PREM). *Physics of the Earth and Planetary Interiors* 25: 297–356.

Dziewonski AM, Chou T-A, and Woodhouse JH (1981) Determination of earthquake source parameters from waveform data for studies of global and regional seismicity. *Journal of Geophysical Research* 86: 2825–2852.

Dziewonski AM and Gilbert F (1972) Observations of normal modes from 84 recordings of the Alaskan earthquake of 28 March 1964. *Geophysical Journal of Royal Astronomical Society* 27: 393–446.

Dziewonski AM and Gilbert F (1973) Observations of normal modes from 84 recordings of the Alaskan earthquake of 28 March 1964, Part II: Spheroidal overtones from 285–100 seconds. *Geophysical Journal of the Royal Astronomical Society* 35: 401–437.

Dziewonski AM and Gilbert F (1974) Temporal variation of the seismic moment tensor and the evidence of precursive compression for two deep earthquakes. *Nature* 247: 185–188.

Dziewonski AM and Haddon RAW (1974) The radius of the core–mantle boundary inferred from travel time and free oscillation data: A critical review. *Physics of the Earth and Planetary Interiors* 9: 28–35.

Dziewonski AM, Hager BH, and O'Connell RJ (1977) Large scale heterogeneities in the lower mantle. *Journal of Geophysical Research* 82: 239–255.

Dziewonski AM and Hales AL (1972) Numerical analysis of dispersed seismic waves. In: Adler B, Fernbach S, and Bolt BA (eds.) *Methods in Computational Physics*, vol. 11, pp. 39–85. New York: Academic Press.

Dziewonski AM, Hales AL, and Lapwood ER (1975) Parametrically simple Earth models consistent with geophysical data. *Physics of the Earth and Planetary Interiors* 10: 12–48.

Dziewonski AM, Lekic V, and Romanowicz B (2010) Mantle anchor structure: An argument for bottom up tectonics. *Earth and Planetary Science Letters* 299(2010): 69–79.

Dziewonski AM, Lekic V, and Romanowicz B (2013) Planet within a planet: Implications of principal component analysis of global tomographic models. *EOS. Transactions of the American Geophysical Union* 94(Fall Meeting Supplement), Abstract DI32-01.

Dziewonski AM and Steim JM (1982) Dispersion and attenuation of mantle waves through waveform inversion. *Geophysical Journal of the Royal Astronomical Society* 70: 503–527.

Dziewonski A, Su W-J, and Woodward R (1991) Global structures of the Earth's interior. *EOS, Transactions American Geophysical Union, fall meeting:* 72: 451.

Ekström G, Dziewonski AM, Maternovskaya NN, and Nettles M (2005) Global seismicity of 2003: Centroid-moment-tensor solutions for 1087 earthquakes. *Physics of the Earth and Planetary Interiors* 148: 327–351.

Ekström G and Dziewoski AM (1998) The unique anisotropy of the Pacific upper mantle. *Nature* 394: 168–172.

Ekström G, Tromp J, and Larson EW (1997) Measurements and models of global surface wave propagation. *Journal of Geophysical Research* 102: 8137–8157.

Ewing M, Jardetzky WS, and Press F (1957) *Elastic Waves in Layered Media*. New York: McGraw-Hill.

Ewing M and Press F (1954) An investigation of mantle Rayleigh waves. *Bulletin of the Seismological Society of America* 44: 127–148.

Fichtner A, Kennett B, Igel H, and Bunge H (2009) Full seismic waveform tomography for upper mantle structure in the Australasian region using adjoint methods. *Geophysical Journal International* 179: 1703–1725.

French S, Lekic V, and Romanowicz B (2013) Waveform tomography reveals channeled flow at the base of the oceanic asthenosphere. *Science* 342: 227–230.

Fuchs K and Müller G (1971) Computation of synthetic seismograms and comparison with observations. *Geophysical Journal of the Royal Astronomical Society* 23: 417–433.

Fukao Y and Obayashi M (2013) Subducted stagnant slabs above, penetrating through and trapped below the 660 km discontinuity. *Journal of Geophysical Research* 118: 1–19.

Fukao Y, Obayashi M, Inoue H, and Nenbai M (1992) Subducting slabs stagnant in the mantle transition zone. *Journal of Geophysical Research* 97: 4809–4822.

Fukao Y, Obayashi M, and Nakakuki T (2009) the Deep Slab Project Group. *Annual Review of Earth and Planetary Sciences* 37: 19–46. http://dx.doi.org/10.1146/annurev.earth.36.031207.124224.

Fukao Y, Widiyantoro S, and Obayashi M (2001) Stagnant slabs in the upper and lower mantle transition region. *Reviews of Geophysics* 39: 291–323.

Galitzin BB (1914) Vorlesungen über Seismometrie, deutsche Bearbeitung unter Mitwirkung von Clara Reinfeldt (also Golicyn). *Herausgegeben von Oskar Hecker*, vol. VIII, p. 538. Berlin: Verlag Teubner.

Geiger L (1910) Herdbestimmung bei Erdbeben aus den Ankunftszeiten. Nachrichten von der Königlichen Gesellschaft der Wissenschaften zu Göttingen. *Mathematisch-physikalische Klasse*. pp. 331–349 (Translated into English by Peebles FWL, Anthony H, Corey SJ).

Geiger L (1912) Probability method for the determination of earthquake epicenters from the arrival time only. *Bulletin of St. Louis University* 8: 60–71.

Gilbert F and Dziewonski AM (1975) An application of normal mode theory to the retrieval of structural parameters and source mechanisms from seismic spectra. *Philosophical Transactions of the Royal Society of London, Series A* 278: 187–269.

Green RWE and Hales AL (1968) Travel times of P waves to 30 degrees in central United States and upper mantle structure. *Bulletin of the Seismological Society of America* 58: 267–289.

Gu YJ, Dziewonski AM, and Ekström G (2003) Simultaneous inversion for mantle shear velocity and topography of transition zone discontinuities. *Geophysical Journal International* 154: 559–583.

Gu JY, Dziewonski AM, Su W-J, and Ekström G (2001) Shear velocity model of the mantle and discontinuities in the pattern of lateral heterogeneities. *Journal of Geophysical Research* 106: 11169–11199.

Gung Y, Panning M, and Romanowicz B (2003) Global anisotropy and the thickness of continents. *Nature* 422: 707–711.

Gung Y and Romanowicz B (2004) Q tomography of the upper mantle using three component long period waveforms. *Geophysical Journal International* 157: 813–830.

Gutenberg B (1913) Über die Konstitution des Erdinnern, erschlossen aus Erdbebenbeobachtungen. *Physikalische Zeitschrift* 14: 1217–1218.

Hales AL, Lapwood ER, and Dziewonski AM (1974) Parameterization of a spherically symmetrical Earth model with special references to the upper mantle. *Physics of the Earth and Planetary Interiors* 9: 9–12.

Hammer PTC, Clowes RM, Cook FA, van der Velden AJ, and Vosudevan K (2010) The Lithoprobe trans-continental lithospheric cross-sections imaging the internal structure of the North American continent. *Canadian Journal of Earth Sciences* 47: 821–857.

Harjes H-P and Seidl D (1978) Digital recording and analysis of broad-band seismic data at the Gräfenberg (GRF) array. *Journal of Geophysics* 44: 511–523.

Harmon N, Forsyth D, and Weeraratne DS (2009) Thickening of young Pacific lithosphere from high-resolution Rayleigh wave tomography: A test of the conductive cooling model. *Earth and Planetary Science Letters* 278: 96–106.

Haskell NA (1953) The dispersion of surface waves on multilayered media. *Bulletin of the Seismological Society of America* 43: 17–43.

Herglotz G (1907) Über das Benndorfsche Problem der Fortpflanzungsgeschwindigkeit der Erdbebenwellen. *Physikalische Zeitschrift* 8: 145–147.

Houser C, Masters G, Shearer P, and Laske G (2008) Shear and compressional velocity models of the mantle from cluster analysis of long-period waveforms. *Geophysical Journal International* 174: 195–212. http://dx.doi.org/10.1111/j.1365-246X.2008.03763.x.

Jeffreys H (1926) The rigidity of the Earth's central core. *Monthly Notices of the Royal Astronomical Society* 1(Geophysical Supplement): 371–383.

Jeffreys H (1939) The times of P, S and SKS, and the velocities of P and S, month not. *Royal Astronomical Society, Geophysical Supplement* 4: 498–533.

Jeffreys H and Bullen KE (1940) *Seismological Tables*, p. 50. London: British Association for the Advancement of Science.

Jobert N (1956) Évaluation de la période d'oscillation d'une sphere hétérogène, par application du principe de Rayleigh. *Comptes Rendus De L Academie Des Sciences, Paris* 243: 1230–1232.

Jobert N (1957) Sur la période propre des oscillations sphèroïdales de la Terre. *Comptes Rendus De L Academie Des Sciences, Paris* 244: 242–258.

Johnson LR (1967) Array measurements of P velocity in the upper mantle. *Journal of Geophysical Research* 72: 6309–6325.

Jordan TH (1978) A procedure for estimating lateral variations from low-frequency eigenspectra data. *Geophysical Journal of the Royal Astronomical Society* 52: 441–455.

Jordan TH and Anderson DL (1974) Earth structure from free oscillations and travel times. *Geophysical Journal of the Royal Astronomical Society* 36: 411–459.

Julian BR and Sengupta MK (1973) Seismic travel time evidence for lateral inhomogeneity in the deep mantle. *Nature* 242: 443–447.

Kennett BLN, Engdahl ER, and Buland R (1995) Constraints on seismic velocities in the Earth from traveltimes. *Geophysical Journal International* 122: 108–124.
Knott CG (1899) Reflection and refraction of elastic waves, with seismological applications. *The London, Edinburgh, and Dublin Philosophical Magazine and Journal of Science, Series 5* 48, 64–97, 567–569.
Komatitsch D and Tromp J (2002) Spectral-element simulations of global seismic wave propagation: I. Validation. *Geophysical Journal International* 149: 390–412.
Komatitsch D and Vilotte J-P (1998) The spectral element method: An efficient tool to simulate the seismic response of 2D and 3D geological structures. *Bulletin of the Seismological Society of America* 88: 368–392.
Kustowski B, Ekström G, and Dziewonski AM (2008) The shear-wave velocity structure in the upper mantle beneath Eurasia. *Geophysical Journal International* 174: 978–992.
Landisman M, Sato Y, and Nafe JE (1965) Free vibrations of the Earth and the properties of its deep interior regions: Part 1. Density. *Geophysical Journal of the Royal Astronomical Society* 9: 439–502.
Le Pichon X and Huchon P (1984) Geoid, Pangea and convection. *Earth and Planetary Science Letters* 67: 123–135.
Lehmann I (1936) P'. *Publ. Bureau Cent. Sëism. Inter., Série A, Trav. Scient* 14: 87–115.
Lekic V, Cottaar S, Dziewonski AM, and Romanowicz B (2012) Cluster analysis of global lower mantle tomography: A new class of structure and implications for chemical heterogeneity. *Earth and Planetary Science Letters* 357–358: 68–77.
Lekic V and Romanowicz B (2011) Inferring upper-mantle structure by full waveform tomography with the spectral element method. *Geophysical Journal International* 185: 799–831.
Li XD and Romanowicz B (1995) Comparison of global waveform inversions with and without considering cross branch coupling. *Geophysical Journal International* 121: 695–709.
Li X-D and Romanowicz B (1996) Global mantle shear velocity model developed using nonlinear asymptotic coupling theory. *Journal of Geophysical Research* 101: 22245–22272.
Li XD and Tanimoto T (1993) Waveforms of long-period body waves in a slightly aspherical Earth model. *Geophysical Journal International* 112: 92–102.
Lithgow-Bertelloni C and Richards MA (1998) The dynamics of Cenozoic and Mesozoic plate motions. *Reviews of Geophysics* 36: 27–78.
Liu H-P, Anderson DL, and Kanamori H (1976) Velocity dispersion due to anelasticity: Implications for seismology and mantle composition. *Geophysical Journal of the Royal Astronomical Society* 47: 41–58.
Lognonné P (1991) Normal modes and seismograms in an anelastic rotating Earth. *Journal of Geophysical Research* 96: 20309–20319.
Lognonné P and Romanowicz B (1990) Modelling of coupled normal modes of the Earth: The spectral method. *Geophysical Journal International* 102(2): 365–395.
Love AEH (1911) *Some Problems of Geodynamics*. Cambridge: Cambridge University Press.
Masters G, Jordan TH, Silver PG, and Gilbert F (1982) Aspherical earth structure from fundamental spheroidal mode data. *Nature* 298: 609–613.
Mégnin C, Bunge HP, Romanowicz B, and Richards MA (1997) Imaging 3-D spherical convection models: What can seismic tomography tell us about mantle dynamics? *Geophysical Research Letters* 24(11): 1299–1302.
Mégnin C and Romanowicz B (1999) The effects of the theoretical formalism and data selection on mantle models derived from waveform tomography. *Geophysical Journal International* 138: 366–380.
Mégnin C and Romanowicz B (2000) The three-dimensional shear velocity structure of the mantle from the inversion of body, surface and higher-mode waveforms. *Geophysical Journal International* 143(3): 709–728.
Mendiguren J (1973) Identification of free oscillation spectral peaks for 1970 July 31, Colombian deep shock using the excitation criterion. *Geophysical Journal of the Royal Astronomical Society* 33: 281–321.
Mohorovičić A (1910) Potres od 8. X 1909. God. Izvjesće Zagr. met. Ops. Zag. 1909, Zagreb (Das Beben vom 8. X 1909. Jahrbuch des meteorologischen Observatoriums in Zagreb f ür das Jahr 1909), 9, Part 4, 1–63.
Montelli R, Nolet G, Dahlen F, Masters G, Engdahl E, and Hung SH (2004a) Global P and PP travel time tomography: Rays vs. waves. *Geophysical Journal International* 158: 637–654.
Montelli R, Nolet G, Dahlen F, Masters G, Engdahl E, and Hung SH (2004b) Finite-frequency tomography reveals a variety of plumes in the mantle. *Science* 303: 338–343.
Ness NF, Harrison JC, and Slichter LB (1961) Observations of the free oscillations of the Earth. *Journal of Geophysical Research* 66: 621–629.
Nolet G and Dahlen FA (2000) Wave front healing and the evolution of seismic delay times. *Journal of Geophysical Research* 105: 19043–19054.
Oldham RD (1906) The constitution of the interior of the Earth, as revealed by earthquakes. *Quarterly Journal of the Geological Society* 62(1–4): 456–475.
Panning M and Romanowicz B (2006) A three dimensional radially anisotropic model of shear velocity in the whole mantle. *Geophysical Journal International* 167: 361–379.
Park J, Butler R, Anderson K, et al. (2005) Performance review of the global seismographic network for the Sumatra–Andaman megathrust earthquake. *Seismological Research Letters* 76(3): 331–343.
Pekeris CL, Alterman Z, and Jarosch H (1961a) Comparison of theoretical with observed values of the periods of the free oscillations of the Earth. *Proceedings of the National Academy of Sciences of the United States of America* 47: 91–98.
Pekeris CL, Alterman Z, and Jarosh H (1961b) Rotational multiplets in the spectrum of the Earth. *Physical Review* 122: 1692–1700.
Pekeris CL and Jarosch H (1958) The free oscillations of the Earth. In: Benioff H, Ewing M, HowellJun BF, and Press K (eds.) *Contributions in Geophysics in Honor of Beno Gutenberg*, pp. 171–192. New York: Pergamon.
Peter D, Tape C, Boschi L, and Woodhouse JH (2007) Surface wave tomography: Global membrane waves and adjoint methods. *Geophysical Journal International* 171: 1098–1117. http://dx.doi.org/10.1111/j.1365-246X.2007.03554.x.
Peterson J, Butler HM, Holcomb LT, and Hutt C (1976) The seismic research observatory. *Bulletin of the Seismological Society of America* 66: 2049–2068.
Poupinet G, Frechet J, and Thouvenot F (1989) Portable short period vertical seismic stations transmitting via telephone or satellite. In: Cassinis R and Nolet G (eds.) *Digital Seismology and Fine Modelling of the Lithosphere*, pp. 9–26. London: Plenum.
Press F (1956) Determination of crustal structure from phase velocity of Rayleigh waves – Part I. Southern California. *Bulletin of Geological Society of America* 67: 1647–1658.
Ricard Y, Richards M, Lithgow-Bertelloni C, and LeStunff YL (1993) A geodynamic model of mantle density heterogeneity. *Journal of Geophysical Research* 98: 21895–21910.
Richards M and Engebretson D (1992) Large-scale mantle convection and the history of subduction. *Nature* 355: 437–440.
Rickers F, Fichtner A, and Trampert J (2013) The Iceland–Jan Mayen plume system and its impact on mantle dynamics in the North Atlantic region: Evidence from full-waveform inversion. *Earth and Planetary Science Letters* 367: 39–51.
Ritsema J, Deuss A, van Heijst HJ, and Woodhouse J (2011) HS40RTS: A degree-40 shear-velocity model for the mantle from new Rayleigh wave dispersion, teleseismic traveltime and normal-mode splitting function measurements. *Geophysical Journal International* 184: 1223–1236.
Ritsema J, van Heijst HH, and Woodhouse JH (1999) Complex shear wave velocity structure imaged beneath Africa and Iceland. *Science* 286: 1925–1928.
Ritsema J, van Heijst HJ, and Woodhouse JH (2004) Global transition zone tomography. *Journal of Geophysical Research* 109. B02302: http://dx.doi.org/10.1029/2003JB002610.
Romanowicz B (1979) Seismic structure of the upper mantle beneath the United States by three-dimensional inversion of body wave arrival times. *Geophysical Journal of the Royal Astronomical Society* 57: 479–506.
Romanowicz B (1991) Seismic tomography of the Earth's mantle. *Annual Review of Earth and Planetary Science* 19: 77–99.
Romanowicz B (2003) Global mantle tomography: Progress status in the last 10 years. *Annual Review of Geophysics and Space Physics* 31: 303–328.
Romanowicz BA, Cara M, Fels JF, and Rouland D (1984) Geoscope: A French initiative in long-period three-component seismic networks. *EOS. Transactions of the American Geophysical Union* 65: 753–754.
Romanowicz BA and Dziewonski AM (1986) Towards a federation of broadband seismic networks. *EOS. Transactions of the American Geophysical Union* 67: 541–542.
Romanowicz B and Gung Y (2002) Superplumes from the core–mantle boundary to the lithosphere: Implications for heat flux. *Science* 296(2002): 513–516.
Romanowicz B, Karczewski J-F, et al. (1991) The GEOSCOPE program: Present status and perspectives. *Bulletin of the Seismological Society of America* 81: 243–264.
Rouby H, Greff-Lefftz M, and Besse J (2010) Mantle dynamics, geoid, inertia and TPW since 120 Myr. *Earth and Planetary Science Letters* 292: 301–311.
Roult G, Montagner JP, Romanowicz B, et al. (2010a) The GEOSCOPE program: Progress, and challenges during the past 30 years. *Seismological Research Letters* 81: 428–452.
Roult G, Montagner J-P, Romanowicz B, et al. (2010b) The GEOSCOPE Program: Progress and challenges during the past 30 years. *Seismological Research Letter* 81: 429–452.
Russakoff D, Ekström G, and Tromp J (1998) A new analysis of the great 1970 Colombia earthquake and its isotropic component. *Journal of Geophysical Research* 102: 20423–20434.
Sailor RV and Dziewonski AM (1978) Observations and interpretation of attenuation of normal modes. *Geophysical Journal of the Royal Astronomical Society* 53: 559–581.

Schweitzer J (2007) In: Gubbins D and Herrero-Bervera E (eds.) *Encyclopedia of Geomagnetism and Paleomagnetism*: Kluwer-Springer, ISBN:1-4020-3992-1 (in print).

Simmons NA, Forte AM, and Grand SP (2009) Joint seismic, geodynamic and mineral physical constraints on three-dimensional mantle heterogeneity: Implications for the relative importance of thermal versus compositional heterogeneity. *Geophysical Journal International* 177: 1284–1304.

Simmons NA, Forte A, Boschi L, and Grand S (2010) GyPSuM: a joint tomographic model of mantle density and seismic wave speeds. *Journal of Geophysical Research* 115(B12310). http://dx.doi.org/10.1029/2010JB007631.

Souriau A and Souriau M (1983) Test of tectonic models by great-circle Rayleigh waves. *Geophysical Journal of the Royal Astronomical Society* 73: 533–551.

Steim JM (1986) *The very-broad-band seismograph*. Doctoral Thesis, Cambridge, MA: Department of Geological Sciences, Harvard University, p. 184.

Stein S and Wysession M (2003) *An Introduction to Seismology, Earthquakes and Earth Structure*. Oxford: Blackwell, ISBN: 0865420785.

Steinberger B and O'Connell RJ (1997) Changes of the Earth's rotation axis owing to advection of mantle density heterogeneities. *Nature* 387: 169–173.

Steinberger B and Torsvik TH (2010) Toward an explanation for the present and past locations of the poles. *Geochemistry, Geophysics, Geosystems*. http://dx.doi.org/10.1029/2009GC002889.

Stoneley R (1928) A Rayleigh wave problem. *Proceedings of the Leeds Philosophical and Literary Society (Science Section)* 1: 217–225.

Su W-J and Dziewonski AM (1991) Predominance of long-wavelength heterogeneity in the mantle. *Nature* 352: 121–126.

Su W-J and Dziewonski AM (1992) On the scale of mantle heterogeneity. *Physics of the Earth and Planetary Interiors* 74: 29–54.

Takeyuchi H (1959) Torsional oscillations of the Earth and some related problems. *Geophysical Journal of the Royal Astronomical Society* 2: 89–100.

Tape C, Liu Q, Maggi A, and Tromp J (2010) Seismic tomography of the southern California crust based on spectral-element and adjoint methods. *Geophysical Journal International* 160: 195–216.

Tarantola A (2005) *Inverse Problem Theory and Methods for Model Parameter Estimation*. Philadelphia, PA: Society for Industrial and Applied Mathematics.

Thomson ST (1950) Transmission of elastic waves through a stratified solid medium. *Journal of Applied Physics* 21: 89–93.

Toksöz MN and Anderson DL (1966) Phase velocities of long-period surface waves and structure of the upper mantle. *Journal of Geophysical Research* 71: 1649–1658.

Torsvik TH, Steinberger B, Cocks LRM, and Burke K (2008) Longitude: Linking Earth's ancient surface to its deep interior. *Earth and Planetary Science Letters* 276: 273–282.

Tromp J, Tape C, and Liu Q (2005) Seismic tomography, adjoint methods, time reversal and banana doughnut kernels. *Geophysical Journal International* 160: 195–216.

Udias A and Stauder W (2002) The Jesuit contribution to seismology. In: Lee WHK, Kanamori H, Jennins PC, and Kisslinger C (eds.) *International Handbook of Earthquake and Engineering Seismology*, pp. 19–27. San Diego, CA: Academic Press.

van der Hilst RD and deHoop MV (2005) Banana-doughnut kernels and mantle tomography. *Geophysical Journal International* 163: 956–961.

van der Hilst R, Kennett B, Christie D, and Grant J (1994) Project Skippy explores the lithosphere and upper mantle below Australia. *EOS. Transactions of the American Geophysical Union* 75(177): 180–181.

van Heijst HJ and Woodhouse JH (1997) Measuring surface-wave overtone phase velocities using a mode-branch stripping technique. *Geophysical Journal International* 131: 209–230.

von Rebeur-Paschwitz E (1889) The earthquake of Tokyo, April 18, 1889. *Nature* 40: 294–295.

von Rebeur-Paschwitz E (1895) Horizontalpendal-Beobachtungen auf der Kaiserlichen Universitats-Sternwarte zu Strassburg 1892–1894. *Gerlands Beiträge zur Geophysik* 2: 211–536.

Wiechert E (1907) Über Erdbebenwellen. Theoretisches über die Ausbreitung der Erdbebenwellen. *Nachrichten von der Königlichen Gesellschaft der Wissenschaften zu Göttingen, Mathematisch-physikalische Klasse*, pp. 413–529.

Wielandt E (2002) Seismic sensors and their calibration. In: Bormann IP (ed.) *IASPEI New Manual of Seismological Observatory Practice*, vol. 1, pp. 1–46. Potsdam: GeoForschungsZentrum Potsdam, Chapter 5.

Wielandt E and Steim JM (1986) A digital very-broad-band seismograph. *Annales Geophysicae* 4: 227–232.

Wielandt E and Streckeisen G (1982) The leaf-spring seismometer: Design and performance. *Bulletin of the Seismological Society of America* 72: 2349–2367.

Woodhouse JH and Dahlen FA (1978) The effect of a general aspherical perturbation on the free oscillations of the Earth. *Geophysical Journal of the Royal Astronomical Society* 53: 335–354.

Woodhouse JH and Dziewonski AM (1984) Mapping the upper mantle: Three dimensional modeling of earth structure by inversion of seismic waveforms. *Journal of Geophysical Research* 89: 5953–5986.

Woodhouse J and Dziewonski A (1986) Three dimensional mantle models based on mantle wave and long period body wave data. *EOS. Transactions of the American Geophysical Union* 67: 307.

Woodhouse JH and Dziewonski AM (1989) Seismic modelling of the Earth's large-scale three dimensional structure. *Philosophical Transactions of the Royal Society of London, Series A* 328: 291–308.

Woodhouse JH and Girnius TP (1982) Surface waves and free oscillations in a regionalized Earth model. *Geophysical Journal International* 68: 653–673.

Woodward RL, Dziewonski AM, and Peltier WR (1994) Comparisons of seismic heterogeneity models and convective flow calculations. *Geophysical Research Letters* 21: 325–328.

Woodward RL and Masters G (1991) Lower-mantle structure from *ScS-S* differential travel times. *Nature* 352: 231–233.

Zhu H, Bozdag E, Peter D, and Tromp J (2012) Structure of the European upper mantle revealed by adjoint tomography. *Nature Geoscience* 5: 493–498.

Zöppritz K (1907) Über Erdbebenwellen. II: Laufzeitkurven. *Nachrichten von der Königlichen Gesellschaft der Wissenschaften zu Göttingen, Mathematisch-physikalische Klasse:* 529–549.

Relevant Website

http://www.globalcmt.org – Global CMT Web Page.

1.02 Theory and Observations - Instrumentation for Global and Regional Seismology

JM Steim, Quanterra Inc., Shirley, MA, USA; Harvard University, Cambridge, MA, USA

© 2015 Elsevier B.V. All rights reserved.

1.02.1	**Introduction**	29
1.02.2	**Seismic Signals and Noise**	31
1.02.2.1	Representations: Time Series and Spectra	31
1.02.2.1.1	Spectral analysis	31
1.02.2.1.2	Power spectral density: power and amplitude	32
1.02.2.1.3	Bandwidth	32
1.02.2.1.4	Minimum earth noise	33
1.02.2.1.5	Measuring signal amplitudes	35
1.02.2.1.6	Observed signal amplitudes and noise	35
1.02.2.1.7	Saturation (clip) level	36
1.02.2.1.8	Operating range	36
1.02.2.2	Representations: Instrumentation Systems	37
1.02.2.2.1	Seismograph systems	38
1.02.2.2.2	Noise, signals, and sensor response	39
1.02.2.3	Actual GSN Operating Range	41
1.02.2.4	Dynamic Range and Bandwidth	42
1.02.3	**Seismometers and Systems**	42
1.02.3.1	Mechanical Pendulum	42
1.02.3.2	Electronic Force Feedback	42
1.02.3.2.1	Limits on seismometer resolution and operating range	46
1.02.3.3	Systems	51
1.02.3.3.1	A/D conversion	51
1.02.3.3.2	Digital filters	56
1.02.3.3.3	Timing	59
1.02.3.3.4	Ancillary data	61
1.02.3.3.5	Archival methods: impact on quality and longevity of data set	63
1.02.3.4	Calibration	64
1.02.3.4.1	Sensor	64
1.02.3.4.2	Orientation and location	66
1.02.3.4.3	Network calibration	67
1.02.3.5	Quality Assessment and System Characterization	67
1.02.3.5.1	Noise	67
1.02.3.5.2	Signals	68
1.02.3.5.3	Instrument nonidealities	69
1.02.3.6	Instruments in Global and Regional Networks	70
1.02.3.7	Instrumentation Directions	73
1.02.3.7.1	Renewed interest in boreholes	73
1.02.3.7.2	Lower gain and greater bandwidth	74
1.02.3.7.3	Downhole digitization: integrated with a sensor	74
1.02.3.7.4	Complementary technologies	74
Acknowledgments		74
References		74

1.02.1 Introduction

Dewey and Byerly (1969) explained that by 1900, the first global network of observatories equipped with seismographs designed by the British seismologist John Milne regularly sent records to Milne's laboratory (Hoover, 1912) and contributed to the development of the first global travel-time tables. Milne's broadband seismograph photographically recorded ground displacement with low mechanical magnification. By 1903, Galiztin's seismographs incorporated the important features of instrumentation used for global and regional observation for much of the twentieth century (Reid, 1912). Galiztin's design used an inertial pendulum having an electrodynamic transducer and damping, with photographic recording of ground velocity over a broad range of frequencies using a beam of light deflected by a sensitive galvanometer. Such

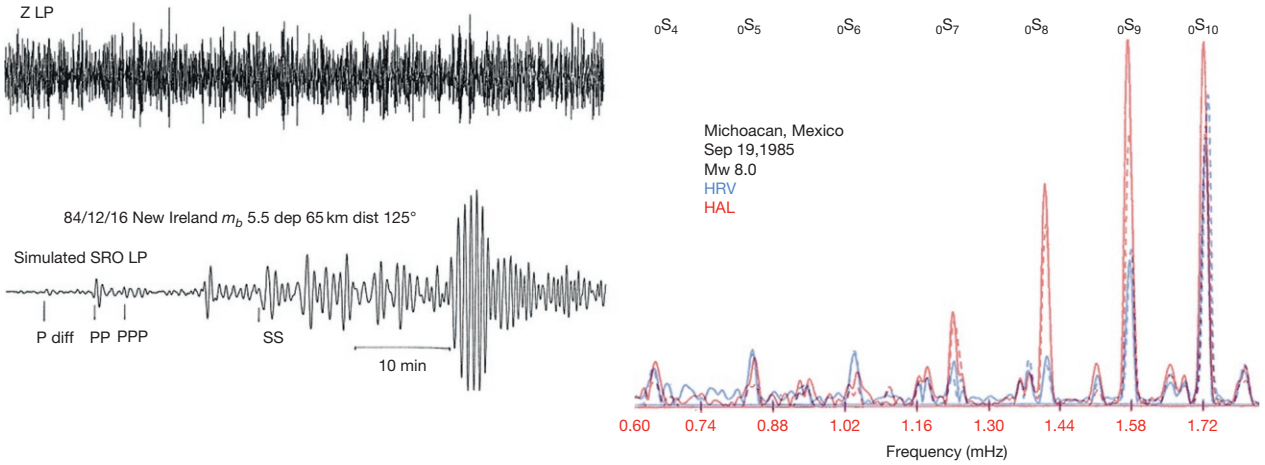

Figure 1 Two examples showing low-frequency information obtained from very broadband (VBB) recordings. Resolution of signals such as these previously required instrumentation specialized for low-frequency measurement. The left panel shows extraction of a long-period seismogram from VBB data that appears to contain only noise. The upper trace is dominated by 3–4 s microseisms. The trace below has been digitally filtered to reveal a small, distant event. The right panel shows observed (solid) and synthetic (dashed) free-oscillation amplitude spectra from the Michoacan, Mexico, Mw 8.0 event on 19 September 1985 recorded on the prototype VBB system at HRV (blue) and very long-period IDA station HAL (red) in Halifax, Nova Scotia. Signal-to-noise and synthetic agreements are comparable at the two sites located at similar distances and azimuths from the event. Horizontal axis is frequency from 0.60 to 1.8 mHz. Adapted from Steim, J., 1986. The very broadband seismograph, PhD Thesis, Harvard University.

instrumentation evolved during the early twentieth century (Benioff, 1932; Press et al., 1958) and remained a standard for sensitive observation of long-period and short-period signals well into the 1980s in the World-Wide Standard Seismograph Network (WWSSN) (Oliver and Murphy, 1971).

Early studies using hand-digitized photographic records (e.g., Bloch and Hales, 1968; Dziewonski et al., 1969; Iyer, 1964; Satô, 1958) showed the information that could be harvested through digital processing of seismograms. At the same time, the need to detect and quantify the yield of nuclear explosions began to shape much of the development of instrumentation for global observation. The resulting focus for several decades during the second half of the twentieth century was on the detection of the smallest signals. Because of the limitations of recording technology then available, instrument designers were driven to shape the frequency response of seismographs to amplify, selectively, segments of the seismic spectrum where ambient Earth noise is least, above and below the frequencies of marine microseisms (Longuet-Higgins, 1950), roughly 0.02–0.04 Hz, and in a narrowband around 1 Hz.

The potential advantages of a seismograph having a broad, flat frequency response with direct digital recording in a computer were recognized as early as 1961 in Caltech's broadband digital seismograph project (Miller, 1963):

> The broad-band system can be used to simulate any desired standard seismograph and provides greater dynamic range and more flexibility than most existing seismographs. (Smith, 1965)

Some efforts during the 1970s concentrated on idealized wideband accelerometers (e.g., Usher et al., 1977, 1978, 1979), including the venerable Teledyne–Geotech KS-36000-01 – an anachronistic combination of new electronic force-feedback (EFFB) and narrowband filtration – used in the Seismic Research Observatory (SRO) stations (Peterson et al., 1976). Evolution of the broadband seismographs of the early twentieth century was delayed by the detection mission. The Graefenberg (GRF) array project (Harjes and Seidl, 1978) during the 1970s, however, illustrated the unrealized potential of digital broadband data.

Although the available digitally recorded low-frequency data (Agnew et al., 1976; Peterson et al., 1976) were limited in the early 1980s, the use of whole waveforms (Dziewonski and Steim, 1982) began to elucidate features of global earth structure, culminating in derivation of the first Earth models (Woodhouse and Dziewonski, 1984) using information contained in the entire waveform. This type of analysis was not possible before the availability of substantial amounts of high-quality digital data made possible by the pioneering digital networks. Both the great potential and considerable limitations of the digital instrumentation deployed during the 1970s became apparent (Dziewonski et al., 1981; Peterson, 1982).

Desire for better, higher dynamic range broadband instrumentation as well as simultaneous rapid development in electronics finally enabled the realization of an instrumentation technique that could embody in a practical way most of the requirements of global seismological research. Building upon the works of Plešinger and Horalek (1976) and Wielandt and Streckeisen (1982) and the first broadband array at GRF (Harjes and Seidl, 1978), the very broadband, or VBB, system was developed at ETH, Zürich, and Harvard University in the early 1980s (Steim, 1986; Steim and Wielandt, 1985; Wielandt and Steim, 1985, 1986). The objective was a single high-quality digital broadband data stream that included low frequencies previously measured only with specialized instrumentation that tended to saturate on large earthquakes (Agnew et al., 1976). Results from experimental VBB systems (**Figure 1**) showed that the objective was achievable.

Except for implementation, the technology now in global and regional networks is largely unchanged from the system

design developed at Harvard in the early 1980s (Peterson and Hutt, 1989; Steim, 1986; Steim and Wielandt, 1985), using a single sensor (Wielandt and Steim, 1986) to acquire the seismic spectrum from tidal frequencies to about 10 Hz, a high-linearity analog-to-digital (A/D) converter, contemporaneous digital data reduction with compact data streams at several sampling rates, and remote data access (Steim, 1987). The initial goals of instrumentation for new global and regional networks (Lay et al., 2002, after IRIS, 1985) had been achieved in the Harvard system, enabling rapid establishment and growth of broadband networks during the past 25 years:

(1) On-scale broadband recordings of earthquakes as large as Mw = 9.5 (equivalent to the 1960 Chile earthquake) at 30°. On-scale low-gain recordings of all earthquakes at 1 sps (samples per second)
(2) Noise below ambient Earth noise
(3) Bandwidth spanning all solid Earth free oscillations and regional body waves (up to 15 Hz or higher as regional wave propagation considerations dictate)
(4) Linearity sufficient to record signals near ambient noise in the presence of signals near clipping at well-separated frequencies
(5) Response known to 1% across the bandwidth
(6) Sensor cross axis coupling less than about 1%
(7) Timing adequate to measure teleseismic body wave arrivals to 0.01 s

In 1987, the addition to the data system of strong motion for the first time in a station of the global network, Caltech's PAS (Pasadena, CA) station (Kanamori, 1990; Kanamori et al., 1990), achieved the goal of measurement at a single station of more than 220 dB dynamic range in ground acceleration. This chapter will focus on the technology of global and regional teleseismic observation as currently practiced in the widely used facilities comprising the continuously recording research networks typical of contributors to the International Federation of Digital Seismic Networks (Dziewonski, 1994).

This instrumentation comprises sensitive inertial broadband seismometers and associated recording equipment and provides the majority of data for studies of earthquakes and deep earth structure. Complementary instrumentations, including, 'strong motion,' arrays, strainmeters (Barbour and Agnew, 2012), or rotational (Forbriger, 2009) sensors, are not treated here. The 'broadband revolution' was approached in the 1980s mainly from the perspective of standards appropriate for global science-driven seismology. Over the past 30 years, VBB design elements have diffused throughout most aspects of modern earthquake instrumentation for regional and global-scale observation and will continue to influence new instrumentation developed over the next decade.

1.02.2 Seismic Signals and Noise

Seismologists are primarily interested in seismic signals. Seismic signals may appear as transient wavelets lasting seconds to minutes or oscillatory wave trains lasting as long as days or months and, in terms of acceleration, span eleven orders of magnitude. Signals occur in the presence of background activity that also spans a wide range in frequencies and amplitudes and exhibits a variety of characteristics, appearing as impulses, steps, transient wavelets, quasioscillatory wave trains, or apparently random waveforms, and may originate as ground motion or artifacts of instrumentation. Some continuous background activity, for example, marine microseisms, may be considered noise in many contexts, however, may contain significant information (Shapiro and Campillo, 2004). Noise for an instrument designer is the background level of actual or instrument-generated equivalent ground motion observed at the output of a seismograph. Instrument designers, sometimes to the consternation of seismologists, devote considerable effort to the study and minimization of noise. Noise defines the smallest detectable signal in an instrumentation system and, therefore, its usefulness for many requirements. Studies, for example, of small, low-frequency signals, such as normal modes from moderate earthquakes or 'hum' (Kurrle and Widmer-Schnidrig, 2008; Tanimoto et al., 1998), require instrumental resolution at the level of minimum Earth noise. Understanding instrument behavior requires some representations appropriate to describe simultaneously the amplitude and frequency of signals and noise to be measured.

1.02.2.1 Representations: Time Series and Spectra

1.02.2.1.1 Spectral analysis

Spectral analysis (e.g., Bracewell, 1978; Oppenheim and Schafer, 2009; Scherbaum, 2001) is a primary tool for characterization of ambient seismic noise and instrument behavior and is possible because the Earth and seismographic instrumentation systems can be considered within some range of input to be linear time-invariant, or LTI (Oppenheim and Schafer, 2009). Although spectral analysis is an essential tool for instrumentation, seismic signals occur and are measured in the time domain. Some phenomena – for example, 'clipping' – can be described adequately only in the time domain, since these violate the LTI assumption. This chapter therefore develops a representation to characterize the range of amplitudes and frequencies measured by instrumentation from the perspective of behavior in the time domain.

Let a real sequence $\{x_m\}$ represent M samples at discrete times $m\Delta t$ of a continuous function of time $x(t)$ containing seismic noise or signals. Define a sequence $\{X_\kappa\}$ of length M:

$$\mathcal{D}\{x_m\} = X_\kappa = \frac{1}{\sqrt{M}} \sum_{m=0}^{M-1} x_m e^{-i2\pi\kappa m/M} \qquad [1]$$

as the discrete Fourier transform (DFT) of the sequence $\{x_m\}$. The corresponding inverse DFT represents a sequence in time as the sum of its DFT spectral coefficients X_κ:

$$\mathcal{D}^{-1}\{X_k\} = x_m = \frac{1}{\sqrt{M}} \sum_{k=0}^{M-1} X_k e^{i2\pi km/M} \qquad [2]$$

In practice, the DFT is computed by one of many fast Fourier transform (FFT) (Cooley and Tukey, 1965) algorithms for efficiency. We assume familiarity with operations with the DFT but will review some topics relevant to the description of seismic signal and noise spectra.

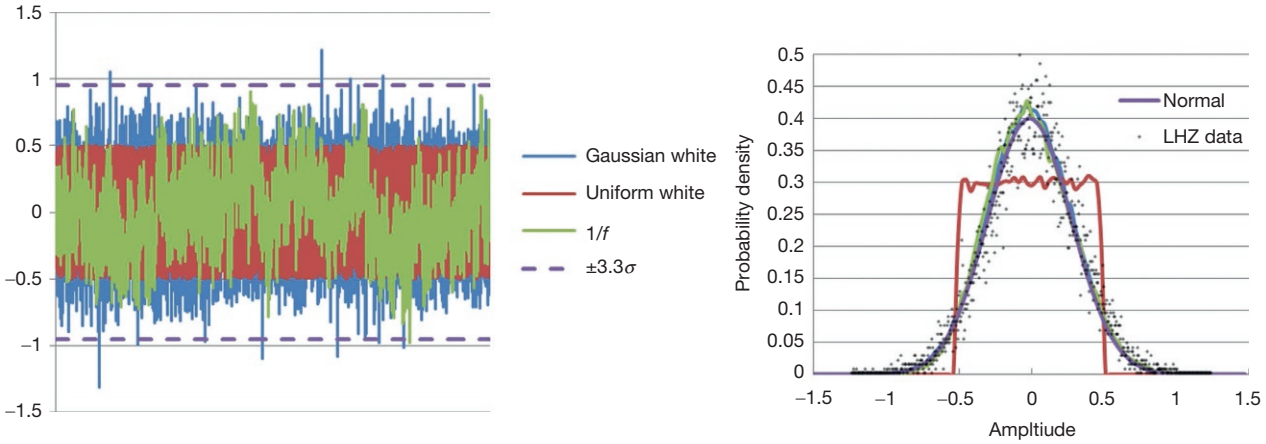

Figure 2 Left: Three types of noise, all with identical variance = $\text{rms}^2 = \sigma^2 = 1/12$: white noise having a normal distribution (blue), white noise with uniform distribution (red), and 1/*f* noise (green). The crest factor for 1/*f* and normally distributed white noise is ~3–4, while the crest factor for uniform white noise is $\sqrt{3}$. The crest factor 3.3 includes most peaks for normally distributed noise. The noise of quantization in digital instrumentation (Bennett, 1948) is uniformly distributed and can be minimized by design. Right: Amplitude probability density distributions for the three noise sources at left. The scattered dots show actual (scaled) amplitudes of a broadband velocity seismic noise sample with a bandwidth of ~0.4 Hz, having a normal distribution. Stationary seismic noise not of cultural origin typically is normally distributed; the time-domain amplitude can be estimated with a crest factor 3.3.

1.02.2.1.2 Power spectral density: power and amplitude

Power spectral density (PSD) is defined as power per unit of bandwidth. This can be written for the discrete series X_κ as

$$\text{PSD}_\kappa = \frac{|X_\kappa|^2/M}{\text{width of frequency bin}\,\kappa} = \frac{|X_\kappa|^2/M}{1/M\Delta t} = \Delta t|X_\kappa|^2 = \frac{|X_\kappa|^2}{\rho} \quad [3]$$

where $\rho = 1/\Delta t =$ the sample rate in samples per second. PSD has units *amplitude*^{2}/Hz or *power*/Hz. PSD contains no phase information – only the distribution of power over frequency – and therefore cannot be inverted to infer time-domain amplitudes for arbitrary waveforms. For a real sequence $\{x_m\}$, X_κ is conjugate-symmetric about $M/2$. PSD may therefore be reported as twice the value for $0 < \kappa \leq M/2$; the value for $\kappa = 0$ is the mean of $\{x_m\}$. Spectra are often represented as $dB(P) = 10\log(P)$, where P represents power density PSD_κ, or power $\text{PSD}_k\Delta f$. $\Delta f = 1/M\Delta t = \rho/M$ is the frequency bin width.

The types of stationary noise typically encountered in seismic systems comprise both *white* and *1/f* noise with amplitudes having uniform or normal (Gaussian) probability density functions (PDFs). White noise is defined as noise in which $|X_\kappa| \cong$ constant in eqns [1] and [2]. 1/*f* noise typically includes a large class of physical behaviors in which $|X_\kappa|^2$ grows with inverse frequency raised to some power, often as f^{-1}.

The *crest factor* for a waveform is defined as the ratio of peak amplitude to rms (root mean squared). For a sine wave, this is $\sqrt{2}$. For a sequence of normally distributed noise of reasonable length for analysis, the crest factor is typically ~3–4. The crest factor 4 corresponds to a statistical confidence level of ~99.99% that the maximum amplitude in a sequence is contained within four standard deviations from the mean of the sequence. PSD is a correct measure of stationary noise power as a function of frequency, but not transient signals, and can be used to approximate the amplitude in the time domain of stationary noise with a known crest factor. Minimum ambient seismic noise has been shown to behave as normally distributed random noise (Peterson, 1993). The time-domain amplitude of seismic noise can be estimated by the product of the crest factor for normally distributed noise times the rms amplitude within a defined bandwidth. Figure 2 shows the time-domain amplitudes of several noise sources and their amplitude probability density distributions compared with the (scaled) distribution for a sample of broadband velocity data representing marine microseisms. The choice of crest factor is arbitrary. A peak will typically be distinguishable above noise using a crest factor of 3.3.

1.02.2.1.3 Bandwidth

Signal and noise amplitudes are measured in the time domain over a finite bandwidth. Bandwidth is important when considering seismic signals that span more than five decades in frequency. The integrated power of a constant PSD over the decade from 10 to 100 Hz contains 10 000 times the power in a decade from 1 to 10 mHz. Development of a representation to describe, simultaneously, large transient signals and small stationary noise therefore requires an appropriate consideration of bandwidth.

A seismograph responds to both signals and noise in a band of frequencies in which the signals are contained. An objective in instrument design is to maximize the signal-to-noise (SNR) ratio in the band of frequencies of interest. Seismic signals – body and surface waves at frequencies higher than a few mHz – comprise wave groups of widely varying amplitude (more than 11 orders of magnitude) recognized in frequency bands of constant relative width (width proportional to frequency) spanning perhaps a small fraction to several octaves. Below several mHz, seismic noise represented as any typical function of ground motion (e.g., acceleration, velocity, or displacement) increases. Over the large bandwidth of more than four decades in frequency from ~0.3 mHz to 10 Hz or above, SNR can be maximized by a sensor with an output having roughly equal noise (and large signal) power in bands of constant relative width across the entire frequency range of

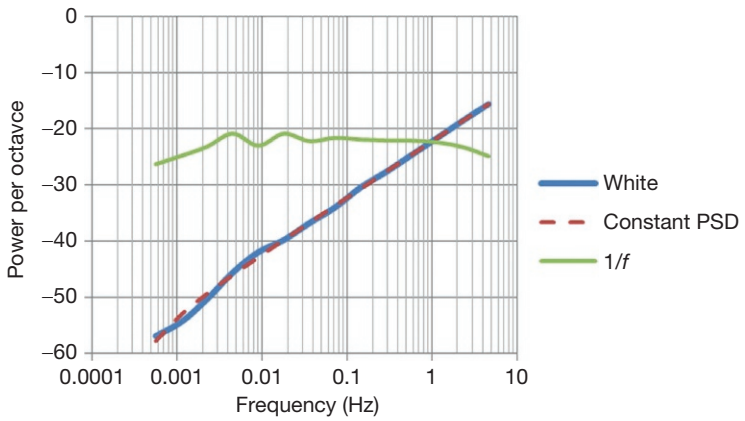

Figure 3 Power spectra of synthetic random noise representing white noise (blue) and 1/*f* noise (green) sampled at 20 sps (samples per second) having identical variance 1/12, summed over bands of constant relative width of one octave. For reference, an isoline of PSD = variance/sample rate is also shown (dashed red). Constant PSD produces increasing power with increasing frequency in bands of constant relative width, as appropriate for signal measurement. 1/*f* noise produces constant power when summed over bands of constant relative width. 1/*f* noise in bands of constant relative width cannot be reduced by filtering to reduce bandwidth. 1/*f* noise is typical of physical systems below some corner frequency.

interest. Under this condition, at the sensor output, the band, for example, from 0.005 to 0.01 Hz, would contain the same noise and signal power as the band from 5 to 10 Hz. While this cannot be exactly achieved, it is approximated with VBB seismograph systems.

Discrete PSD spectra represent power density in bands of constant, finite, width, for example, the bin width equal to ρ/M in previous examples. The power in a band of constant relative width centered at frequency f is computed by integrating (summing) PSD over bands from frequency f_1 to f_2 that are proportional to f. For example, the band limits for a one-octave band where $f_2 = 2f_1$ may be defined as $f_1 = f/\sqrt{2}$ and $f_2 = f\sqrt{2}$. The bandwidth, therefore, is $f_2 - f_1 = f(\sqrt{2} - 1/\sqrt{2}) = f/\sqrt{2}$. Constant PSD in bands of constant relative width produces power increasing proportional to f. Processes, including many instrumentation and physical noise sources, characterized by 1/*f* noise produce constant power in bands of constant relative width (**Figure 3**).

To appreciate the contrast in consideration of power in bands of constant width or constant relative width, the particular relative band size, for example, 1/3 octave or one octave, is not important. The important aspect is the dependence on f of the power over a large range of frequencies. The choice of bandwidth for signals to determine the frequency dependence of their time-domain amplitudes is more significant.

1.02.2.1.4 Minimum earth noise

A number of parametric models of ambient seismic noise have been constructed over the past 50 years (Agnew and Berger, 1978; Berger et al., 2004; Brune and Oliver, 1959; Fix, 1972; Melton, 1976; Murphy and Savino, 1975; Peterson, 1980, 1993; Peterson and Tilgner, 1985; Wielandt and Streckeisen, 1982). All models are based on a collection of observations and hence limited by instrumentation of the era and represent minimum noise levels in observed spectra. The minimum level observed at any particular frequency is not necessarily observed simultaneously at another frequency. Although obvious instrumental disturbances and earthquakes were omitted, the intrinsic noise and the sensitivity of the instruments to environmental inputs are included in these models. These models, therefore, tend to be biased toward high estimates of actual Earth noise. The models could be interpreted as a behavioral model of the performance expected from a well-installed, properly running instrument of similar technology. Generally, the progression of models has been toward lower minimum noise over a wider frequency range, although recent estimates of noise >1 Hz based on actual global and regional stations are somewhat higher than some earlier, perhaps optimistic, models. The general rise in observed levels >1 Hz may reflect the encroachment of man-made noise sources on many of the observation sites that comprise existing networks. **Figure 4** compares several important vertical models. The GSNtypZ trace is the visually estimated low percentile of the most often observed quiet levels in the Global Seismographic Network (GSN) low-noise model (Berger et al., 2004). At low frequencies, GSNtypZ is roughly equivalent to the Peterson (1993) new low-noise model (NLNM). From the perspective of instrument design, low vertical noise levels present a greater challenge than higher horizontal noise levels. Horizontal noise levels between 100 and 250 s period in the GSN and GEOSCOPE (Roult et al., 2010) networks typically are between −160 and −165 dB acceleration PSD, more than 20 dB above vertical levels.

Heightened cold-war detection work during the 1980s drove efforts to find unusually quiet sites at frequencies >1 Hz, remote from man-made noise sources (Bache et al., 1986; Berger et al., 1988; Bungum et al., 1985; Herrin, 1982; Li et al., 1984; Rodgers et al., 1987; Gurrola et al., 1990). More recent efforts have found quiet sites in Antarctica (Anderson et al., 2006) and Central Asia (Hutt, personal communication). High-frequency levels at exceptionally quiet sites can be as low as 30–40 dB below typical levels at many global and regional stations, although these low levels are observed infrequently during no-wind periods and at culturally quiet time times (nights and weekends). Resolution of the lowest high-frequency levels constitutes a weak goal for general broadband

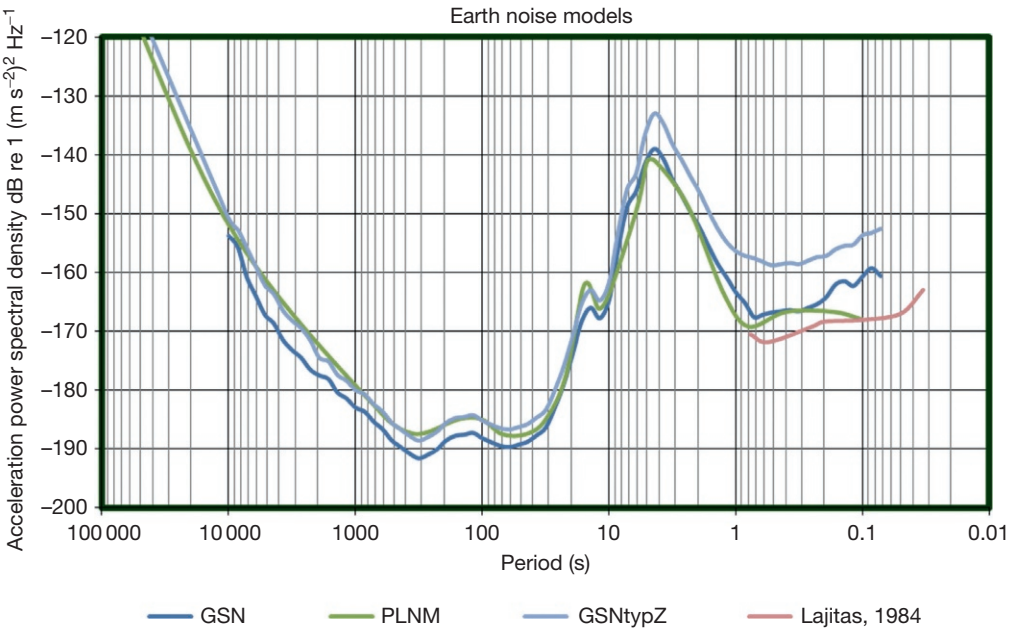

Figure 4 The two most commonly used vertical minimum Earth noise models: the Peterson model (Peterson, 1993; green) and the global seismographic network (GSN) noise model (Berger et al., 2004; blue) as acceleration PSD. The trace-labeled GSNtypZ (light blue) is the visually estimated lower limit of the most dense areas (not the lowest percentile) of the probability distribution in the GSN model, representing typical observations at quiet sites. The Lajitas, 1984 trace (Li et al., 1984; pink) shows the low-percentile, no-wind measurements in boreholes at a then-quiet remote site in Lajitas, TX, United States. Current levels at that site are above the levels seen three decades ago. The Peterson (trace-labeled PLNM) model represents a reasonable estimate of achievable minimum noise at the quietest sites at frequencies near 10 Hz (Hutt, personal communications) and is not typically observed at current operating sites of global and regional networks. Above ~1 Hz, seismic noise is mainly man-made and wind-generated (Carder, 1963). The range from ~0.05 Hz to 1 Hz is dominated by marine microseisms. Minimum levels below 0.01 Hz are observable only on lowest-noise instruments in thermally stable installations.

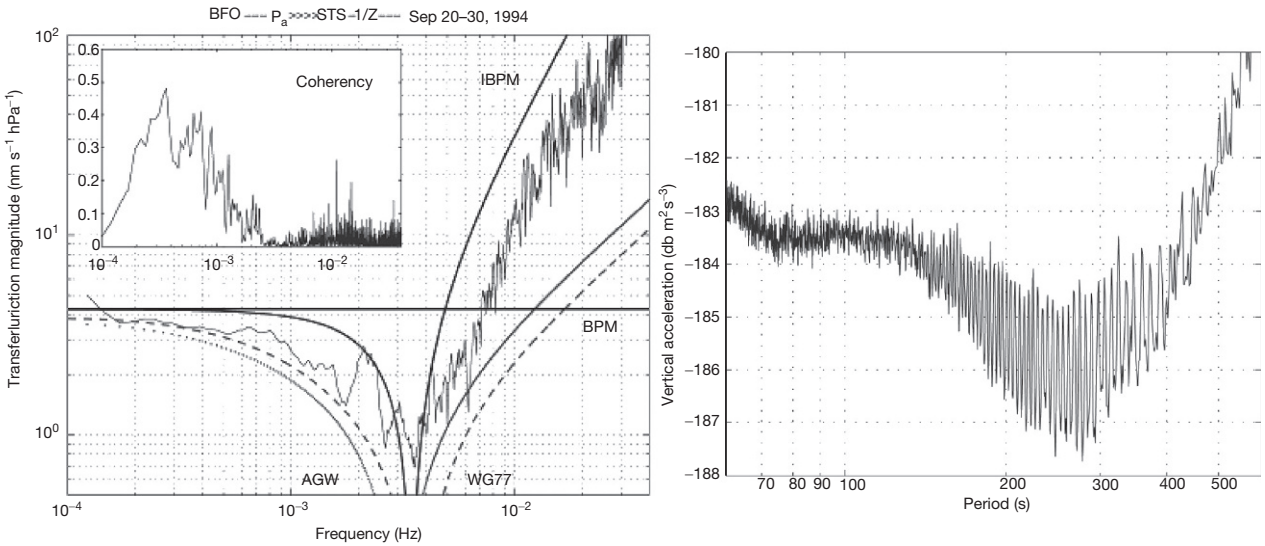

Figure 5 Left: Admittance of several models between local atmospheric pressure and vertical acceleration versus frequency for 10 days data from September 1994. The models show minima near 3 mHz where effects of Newtonian attraction and surface loading approximately cancel. Reprinted by permission from W. Zürn and E. Wielandt. On the minimum of vertical seismic noise near 3 mHz *Geophysical Journal International* (2007) 168 (2): 647–658, Figure 8. Right: Stack of quiet-time noise spectra from 32 of the lowest-noise GSN stations, showing 'hum' (Nawa et al., 1998) in the frequency range of the Earth noise minimum near 3 mHz. With permission from Berger et al. (2004).

instrumentation for earthquake studies where low gain is required to acquire large signals on-scale. Instrumentation for detection purposes may require very low intrinsic sensor noise and may also exchange dynamic range for increased gain to overcome A/D noise.

The vertical noise minimum at frequencies less than several mHz may not be fully described by existing models. Figure 5 shows that the low levels frequently observed near 3 mHz comprise clear signals ('hum') above the background minimum (Zürn and Wielandt, 2007) in atmospherically generated noise.

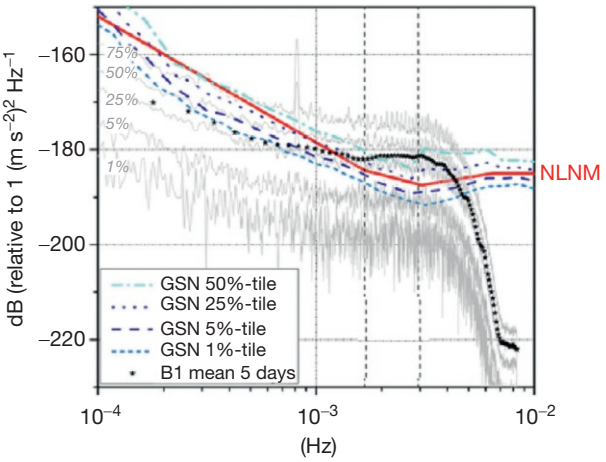

Figure 6 Observed gravity residuals (1st, 5th, 25th, 50th, and 75th percentiles, gray lines) from the OSG-056 (B1) superconducting gravimeter (SG) at BFO (Schiltach, Germany), compared with the 1st, 5th, 25th, and 50th percentiles for the vertical GSN noise model (Berger et al., 2004 – dashed blue lines) and USGS NLNM (red). The 75th percentile of the mean PSD of the five most quiet SG days (small black stars) is also plotted. The GSN noise model is derived from STS-1/VBB sensors and is not corrected for barometric pressure. Adapted from Rosat S and Hinderer J (2011). Noise levels of superconducting gravimeters: updated comparison and time stability. *Bulletin of the Seismological Society of America* 101(3), 1233–1241.

Hum (Nawa et al., 1998) is at the current limit of instrumental resolution (Widmer-Schnidrig, 2003) and can be observed only in spectra stacked to reduce uncorrelated noise. Observation on horizontal sensors is unusual (Kurrle and Widmer-Schnidrig, 2008). Minimum ambient seismic noise may be below current models at frequencies <1 mHz. Spectra (**Figure 6**) from superconducting gravimeters (SG) show levels (Rosat and Hinderer, 2011; Widmer-Schnidrig, 2003) below the current noise models at frequencies <1 mHz when the SG data are corrected for barometric pressure (see later this chapter), suggesting future model revisions. Recent increased availability to seismologists of SG data (Van Camp et al., 2008; Xu et al., 2008; GWR-Instruments, 2011) may encourage re-examination of the low-noise models for frequencies <1 mHz. With the deployment of digital networks over the last 25 years, long observation times and millions of observations are now possible.

1.02.2.1.5 Measuring signal amplitudes

Signals generated by earthquakes span a range of 11 orders of magnitude in amplitude from the level of minimum Earth noise, roughly 10^{-10} m s^{-2}, to greater than 10 m s^{-2} near a significant earthquake. The goal for instrumentation is to sense and record the largest possible range of amplitudes across the broadest frequency range. The peak time-domain amplitude of signals defines the ability to measure the largest signals linearly. Every instrumentation system has a maximum amplitude limit, its *saturation* or *clip* level, above which the LTI assumption is invalid, and all frequencies are affected. Clip level expressed as ground motion is dependent on the frequency of signals comprising a transient wave group. Peak time-domain signal amplitude, with an estimated frequency content, therefore appropriately describes the largest signals encountered by instrumentation.

Like noise, signals span a broad range of frequencies, and their time-domain amplitudes depend on their bandwidth and frequency content. Definition of a bandwidth over which to consider, simultaneously, signals and noise enables description of the dependence on frequency of the largest and smallest signals observed and measurable by a system. The particular choice of bandwidth is arbitrary; however, the bandwidth should be sufficiently wide to make a reasonable estimate of the peak time-domain amplitude of coherent signals within the band while not so wide as to obscure the dependence on frequency. Wave groups tend to be dominated by a small range of frequencies comprising, for example, often on the order of an octave or two (Steim, 1986). Clinton and Heaton (2002) chose one-octave bands to estimate the frequency dependence of time-domain amplitudes using ~1000 recordings. One octave may be appropriate for most dispersed waveforms, that is, typically for events beyond 100 km. One octave is not adequate for nondispersed waveforms, for example, from nearby events, potentially containing high frequencies in phase, and hence tightly grouped in time, creating brief peaks considerably higher than would be observed in an arbitrarily limited band. **Figure 7** (Clinton and Heaton, 2002), for example, shows that the one-octave filtered acceleration of a large close-by event has ~20% of the actual peak amplitude of the signal energy over a wide bandwidth.

The peak time-domain amplitude of signals is used here without arbitrary bandwidth restriction. To estimate the band of frequencies comprising a signal peak, a band-pass filter is used that is sufficiently wide to retain, say, at least 80% of the peak amplitude. This may require two or more octaves, depending on frequency content. Such an approach is roughly equivalent to estimation of frequency based on measuring the reciprocal time of zero crossings of a peak oscillatory signal cycle. This approach to represent the frequency dependence of peak signal amplitudes differs from some previous analyses (Bormann and Wielandt, 2013; Clinton and Heaton, 2002; Evans et al., 2010; Steim, 1986) in which signal amplitudes may be somewhat underestimated by arbitrary band limiting. A seismometer never 'sees' a peak signal limited to an arbitrary band such as 1/3 octave. The seismometer sees all frequencies comprising a wave group. We seek an approximation of the frequency content of signal peaks in order to localize, on a plot of amplitude versus frequency, a data point that may be compared with the saturation level of instrumentation.

1.02.2.1.6 Observed signal amplitudes and noise

Figure 8 shows noise models and selected signals, represented as measured peak amplitudes (for signals) and equivalent peak amplitudes for the GSN LNM (Berger et al., 2004) and new high-noise model (Peterson, 1993). Some peak signal measurements are shown as one-octave-wide bars, although the actual measurement bandwidth may be wider. Spectra extending from <0.1 Hz to >10 Hz are based on one-octave filtered seismograms of large events from Clinton and Heaton (2002). In addition, the amplitude of solid Earth tides and the amplitude of free mode $_0S_0$ during the first days following the Mw 8.8 Chile earthquake of 2010 are shown. The range in measured peak accelerations exceeds 230 dB, which no wideband accelerometer has ever come close to resolving.

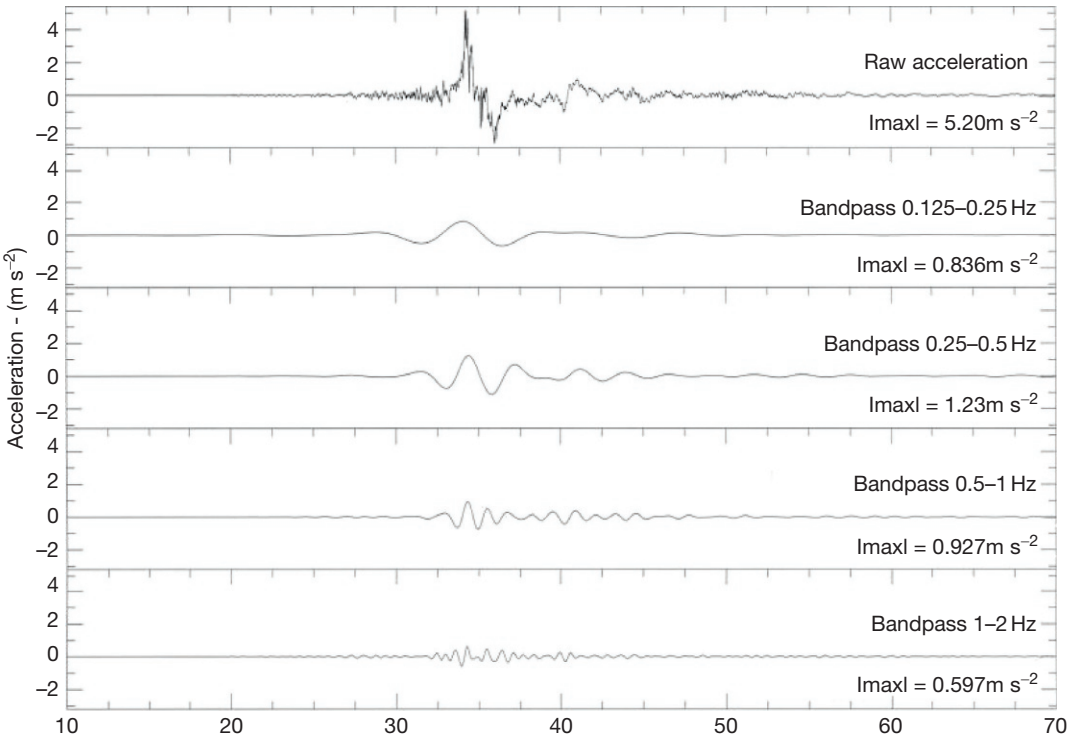

Figure 7 Sample of vertical acceleration data band-passed for M7.5 earthquake at 10 km distance (from Clinton and Heaton, 2002). The actual peak acceleration is approximately five times higher than viewed in one-octave bands.

1.02.2.1.7 Saturation (clip) level

Within some defined band of frequencies, the saturation level of a sensor in terms of ground motion in principle is the maximum output (voltage or digital representation) divided by the transfer function relating the output to ground motion. For an EFFB sensor, the power supply voltage and maximum feedback force define the actual saturation level across some range of frequencies. There may be additional design-dependent physical mechanical or electrical limits that reduce the actual input-equivalent saturation level. For example, the saturation level of a Streckeisen STS-2 seismometer is specified as ± 13 mm s^{-1} velocity at 20 Hz, decreasing linearly to ± 5.3 mm s^{-1} at 50 Hz. This is because the maximum input acceleration that can be balanced by the feedback system is ± 1.67 m s^{-2}. Outside the nominal signal passband, there may be additional limitations.

1.02.2.1.8 Operating range

Hutt et al. (2009b) defined operating range as

> The portion of the ground motion spectrum between the clip level and the self noise of a seismometer, [where the latter is represented as the root mean square (rms) of a sliding half-octave window.] Operating range depends on the bandwidth in which the noise is measured.

The present analysis considers peak amplitudes; however, this results in small differences compared with appropriate use of rms values. The overall dependence on frequency of operating range as the interval between noise and clip level describes the important aspect of a sensor's ability to measure signals. The most striking feature is the extent in amplitude and frequency of the operating range required of a broadband system meeting the goals for global network operation. *Dynamic range*, like operating range, is frequency-dependent and can be considered to be the frequency- and bandwidth-dependent ratio of maximum/minimum operating range limits. One may also consider definition of a companion *useful dynamic range* for a seismometer, as the interval between a seismometer's clip level and the level of ambient seismic noise at the seismometer output. The difference in definition can be quite large. The KS36000-01 seismometer used in the SRO system (Herrin, 1982), for example, was described as having 120 dB dynamic range, whereas the useful dynamic range was typically only about 50 dB at 6 s period, because high gain caused much of the operating range to be occupied with microseismic noise. Using peak or rms descriptions of amplitudes, the required useful dynamic range for broadband systems reaches a maximum of order 10^7, or 140 dB.

The frequency dependence of a system's operating range is readily visualized as a bounded area in a two-dimensional amplitude–frequency plot. Steim (1986) introduced such a representation as a readily interpretable method to visualize the dependence of seismograph operating range on frequency and to describe the optimum approach to realize design goals established for new networks. Such a representation is approximate because of the arbitrary choices necessary to represent simultaneously the amplitude of stationary noise and transient signals as a function of frequency. The approach, however, has become frequently used in the past three decades (Hutt et al., 2009a). Evans et al. (2010) recently proposed this approach to represent the operating range of instrumentation in a standardized way.

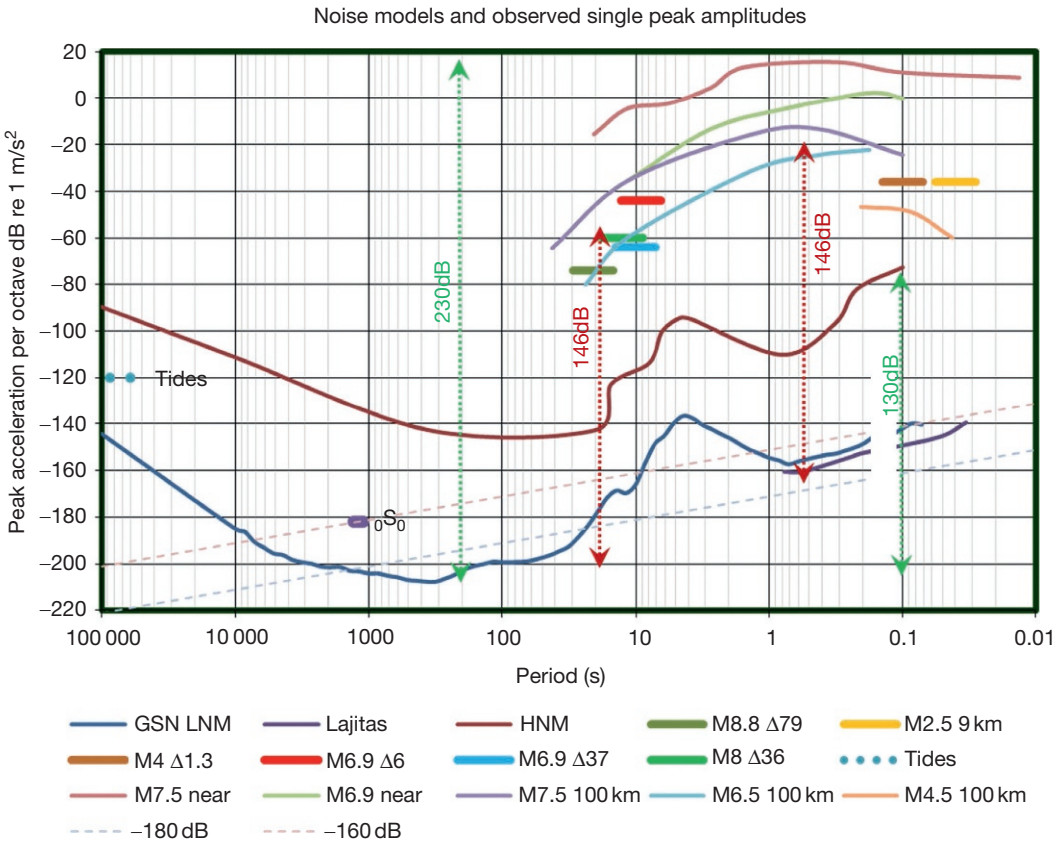

Figure 8 Noise models and signals as equivalent peak acceleration in a one-octave bandwidth. The peak amplitude of transient signals and stationary noise cannot be represented exactly in a common representation. The equivalent peak amplitude of stationary noise is approximated as 3.3 times the rms value in a one-octave band in order to compare with peak earthquake signal amplitudes. Peak levels (GSN stations HRV and PFO, 1985–2010) of six events, for example, M6.9Δ37 (an earthquake of undifferentiated magnitude 6.9 at epicentral distance 37°; thick blue), are represented as a one-octave wide bar at the estimated frequency of the wave group having the maximum peak amplitude. The peak amplitude of these signals is not band-limited. Four spectra spanning the frequency range ~0.1–10 Hz, for example, M6.5 100 km (light blue), are peak amplitudes measured in one-octave wide bands (from Clinton and Heaton, 2002). The GSN (dark blue) and Lajitas (violet) noise models from **Figure 4** are included along with the Peterson (1993) new high-noise model (HNM; brown). Additionally, the amplitude of solid Earth tides and mode ${}_0S_0$ (0.8 nm s^{-2} peak) following the 2010 Chile Mw 8.8 earthquake are shown. The ratio of maximum acceleration to minimum noise level exceeds 230 dB, while the amplitude range from just below the LNM to the amplitudes of moderate events at global and regional distances exceeds 140 dB. Relatively small nearby events produce accelerations exceeding that of the greatest earthquakes seen at distances >30°. Isolines of constant acceleration PSD appear with increasing power per octave. Power of the HNM near 10 Hz exceeds minimum Earth noise at 3 mHz by ~130 dB. The octave-filtered (M4.5 100 km; tan) spectra are much lower than the peak amplitude (M4 Δ1.3; thick brown) over a larger bandwidth.

While the bandwidth used to estimate the frequency content of signal peaks may be variable, the choice of an arbitrary bandwidth for the estimation of the time-domain amplitude of stationary noise affects only the interval between signals and noise. Various noise contributions are compared exactly to each other, when the conversion to time-domain amplitude for all noise sources is consistent. Signal peaks also compare with instrument clip level.

Clinton and Heaton (2002) partially compensated for bandwidth limitation in peak signal estimation by reducing the representation of instrumental clip level by a bandwidth-dependent factor. The approach here is simply to plot actual peak signal amplitudes at an estimated frequency, along with instrument peak clip level and an empirically justified representation of noise as an equivalent peak amplitude in the time domain.

1.02.2.2 Representations: Instrumentation Systems

The problem of optimization over a large operating range of SNR of a seismograph system requires a consideration of seismograph system frequency response. The *transfer function* of a continuous-time LTI system, such as a seismometer, is typically described using Laplace transforms (e.g., Bracewell, 1978). The Laplace transform $F(s)$ of the function $f(t)$ is given by

$$F(s) = L\{f(t)\} = \int_0^\infty e^{-st} f(t)dt \qquad [4]$$

where $F(s)$ is defined as the Laplace transform of $f(t)$, a function of time $t \geq 0$, and s is complex. In the case of $s = i\omega = i2\pi f$, the Fourier transform results. $f(t)$ and $F(s)$ define a Laplace transform pair. When $f(t)$ is convolved with the *impulse* response $h(t)$ of a system assumed to be LTI, such as a

seismometer, the resultant output $y(t)$ may be represented in the time domain as the convolution $f(t)*h(t)$ or in the frequency domain as $Y(s)$, the product of $F(s)\bullet H(s)$, where $H(s)$ is the transfer function describing the LTI system with impulse response $h(t)$. The transfer function $H(s)$ of an LTI system is defined as the ratio of the Laplace transforms of the system output $Y(s)$ divided by the system input $F(s)$.

An analogous *Z-transform* is defined for discrete-time causal systems (which all digital seismographs can be considered):

$$X(z) = Z\{x_m\} = \sum_{m=0}^{\infty} x_m z^{-m} \qquad [5]$$

where $\{x_m\}$ is a real sequence and z is complex. A particularly useful feature of the Z-transform is that a unit delay in the time domain is represented by multiplication by z^{-1} in the z-domain, that is,

$$Z\{x_{m-n}\} = z^{-n}X(z) \qquad [6]$$

A *digital filter* may be described by

$$y_m = \sum_{n=0}^{N} d_n x_{m-n} \qquad [7]$$

where a sequence $\{d_n\}$ of N real constant coefficients is convolved with the input sequence $\{x_m\}$ to produce an output sequence $\{y_m\}$. The operation may be expressed as multiplication of rational polynomials in the z-domain using the transfer function $D(z)$ of the filter:

$$D(z) = \sum_{n=0}^{N} d_n z^{-n} \qquad [8]$$

and

$$Y(z) = Z\{y_m\} = D(z) \cdot X(z) \qquad [9]$$

Equation [7] represents a class of digital filter called a finite impulse response (FIR) filter used universally in the digitizing and processing systems of broadband seismographs. FIR filters have the desirable property of unconditional stability, since their evaluation depends solely on current and prior samples of an input sequence, and not on the output of the filter. Low-pass FIR filters are typically used as digital anti-alias filters because of the ability to construct very sharp filters of high rejection of unwanted frequencies while preserving a maximum passband.

The general topic of discrete-time signal processing is beyond the scope of this section. The reader is referred to the general literature on discrete signal processing (e.g., Welch, 1967; Bracewell, 1978; Cooley et al., 1970; Oppenheim and Schafer, 2009; Rabiner et al., 1972; Rader and Gold, 1967) and specific seismological applications (e.g., Haney et al., 2012; Harjes and Seidl, 1978; IRIS, 2012; Scherbaum, 2001; Seidl, 1980). This chapter will use Laplace and z-transforms, however, to describe important aspects of seismometer and system behavior.

1.02.2.2.1 Seismograph systems

The seismograph systems providing global and regional data comprise one or more sensors with a voltage output that is digitized in an A/D converter. Additional digital processing follows to record and transmit digitized data. Other approaches to convert ground motion to numbers are in principle possible, but until now, and likely during at least the next decade, sensors having a voltage output followed by an A/D will continue to be dominant.

The major elements of a system are represented in Figure 9: a sensor with transfer function $H(s) = E(s)/V(s)$ relating the transforms of, say, input ground velocity $v(t)$ to output voltage $e(t)$; a digitizer converting samples of voltage $e(m\Delta\tau)$ at

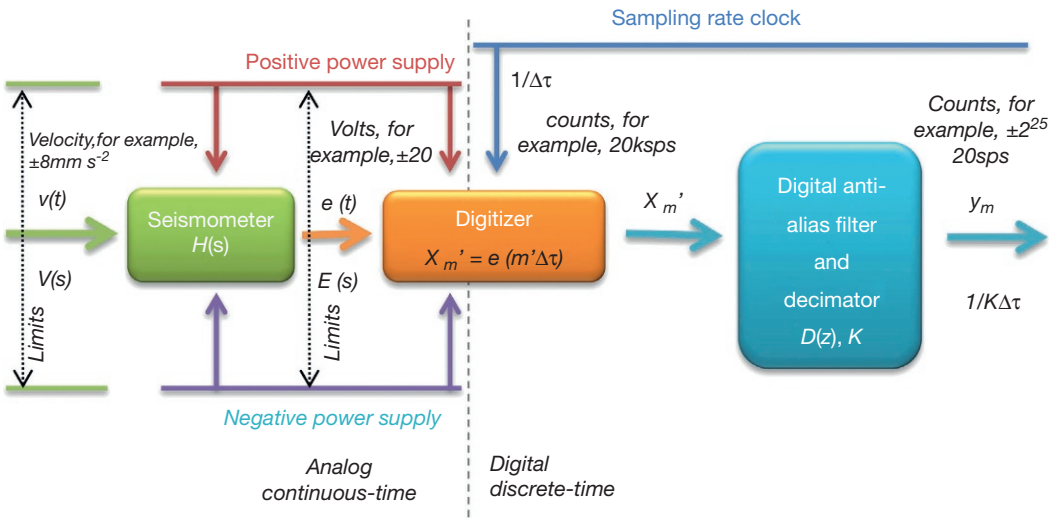

Figure 9 A simplified digital seismograph. The elements include a sensor with Laplace transfer function $H(s)$ to produce a voltage, a digitizer to sample the voltage, and low-pass digital filters to produce a digital sequence $\{y_m\}$ representing the physical ground motion input, for example, ground velocity $v(t)$. The transfer function $H(s)$ maps the strong frequency dependence of ground motion amplitude, in terms of ground acceleration, onto a weaker frequency dependence of voltage measured by the digitizer. The transfer function $H(s)$ is designed to maximize SNR (signal-to-noise) across the frequency range of operation, not to enhance specific signals. The system saturation (clip) level is limited partially by power supply voltages, although additional limits may exist.

discrete times $m'\Delta\tau$ to an output digital sequence $x_{m'}$ at a rate $1/\Delta\tau$ much higher than the highest signal frequency of interest; and a digital anti-alias filter with transfer function $D(z)$ and decimator of factor K. The final stage decimates the filtered sequence

$$y'_{m'} = \sum_{n=0}^{N} d_n x_{m'-n} \quad [10]$$

at a high rate $1/\Delta\tau$ to the reduced-bandwidth output sequence $\{y_m\}$ delivered for analysis at a lower sample rate $1/\Delta t = 1/K\Delta\tau$:

$$y_m = y'_{Km} \quad [11]$$

This description is greatly simplified to focus on the effect of sensor frequency response on system operating range and omits important features: noise in the sensor and digitizer, analog anti-alias filtration in the digitizer, time labeling, and additional stages of digital filtration and decimation. Although anti-alias filtration in the digitizer is an essential element, its impact on the overall system behavior seen at seismic frequencies is generally only a small time delay that can be compensated in a time label, since *oversampling* A/D converters operate with a high rate $1/\Delta\tau$.

1.02.2.2.2 Noise, signals, and sensor response

The central issue for broadband system design is the choice of response $H(s)$ that both optimizes SNR in the output voltage of the sensor $E(s)$ and allows the greatest operating range to be 'mapped' onto the available capability of the digitizer, defined by its intrinsic noise and maximum signal limits. The limits may be mechanical and electrical in the seismometer and are electrical in the A/D. Power supply voltages partially define these limits.

1.02.2.2.2.1 Significance of frequency response

The question of an 'optimum' frequency response for a broadband seismic sensor was not frequently considered before the 1980s (e.g., Berckhemer, 1970; Lake, 1964). Because of the limitations of photographic recording and then-current A/D and digital data storage technology, considerable efforts in networks such as the WWSSN, high-gain long-period (HGLP), and SRO programs were devoted to shaping the frequency response of instruments to enhance signals suitable for detection of small nuclear explosions and reject frequencies considered to be dominated by noise (Murphy and Savino, 1975; Oliver and Murphy, 1971; Peterson et al., 1976; Sutton and Oliver, 1959).

The objectives for sensor frequency response in a broadband system instead are to include many frequencies, to maximize SNR, and to minimize gain. It is not surprising that such a system was not the focus of attention and in fact was considered cumbersome (Smith, 1964) until digital computing and storage became widely available during the 1980s.

Digital VBB instrumentation shapes sensor frequency response $H(s)$ to include most signals seen at teleseismic distances at the sensor output in a manner approximately optimally matched with the A/D. Matching means that the noise voltage at the sensor's output is only slightly larger than the noise voltage of the A/D as a function of frequency and that the maximum voltage produced by a large signal roughly corresponds to the maximum voltage measurable by the A/D. The frequency response of the sensor maps the sensor's operating range as a function of frequency onto the operating range of the A/D and ideally preserves maximum SNR. While a variety of sensor frequency responses are possible, particularly in an EFFB seismometer, only a small class of frequency responses and gains similar to VBB are useful in optimally delivering a voltage representing seismic signals from <1 mHz to >10 Hz so matched to a digitizer.

Frequency response and gain are not strictly related to a seismometer's SNR. For example, although a strong-motion accelerometer has a frequency response extending to zero frequency, its SNR is many orders of magnitude less than a modern broadband seismometer at frequencies of, say, 1 mHz, despite the fact that such a seismometer has a high-pass response to acceleration. It is also possible to design an electronic seismometer with very high sensitivity resulting from high gain and a flat frequency response extending from 10 s to 100 Hz, but this could result in having an SNR and dynamic range worse than a simple geophone.

1.02.2.2.2.2 Synthesis of a VBB system response

Figure 10 shows spectra of the seismic noise models on land shown in Figure 8 represented as ground velocity. The amplitude in bands of constant relative width from ~3 mHz to >10 Hz is roughly constant and increases approximately 40 dB/decade at frequencies <3 mHz. Let $V(s)$ represent ground velocity, $E(s)$ the voltage output of a seismometer, and G a *generator constant*, having units volts/velocity, for example, V m^{-1} s. A second-order high-pass transfer function $H(s)$ relating $E(s)$ to $V(s)$ of the form

$$\frac{E(s)}{V(s)} = H(s) = G\frac{s^2}{s^2 + 2\xi\omega_0 s + \omega_0{}^2} \quad [12]$$

where ξ is the fraction of critical damping, is proportional to velocity above a corner at angular frequency ω_0. The choice of $\omega_0 \cong 2\pi/360$ tends to equalize noise and, coincidentally, signal power in bands of constant relative width from 0.01 mHz to 10 Hz. $H(s)$ can be considered the frequency response of a VBB seismometer. An aside: on the sea floor surface, the seismic noise distribution is different, resulting in a better match over 0.02–10 Hz to the higher overall noise level there with a response proportional to acceleration (Webb, 2002; Webb et al., 2001). Sea floor low-frequency noise levels are high relative to sea floor high-frequency levels, although all sea floor levels are above quiet levels on land (Webb and Crawford, 2010).

Figure 11 shows the match between seismic noise levels at the output of a VBB seismometer described by eqn [12] and actual representative noise of a high-resolution A/D converter (Quanterra Q330HR) used in global and regional networks. The constant $G \cong 2200$ V m^{-1} s has been chosen to adequately resolve minimum noise without loss of large signals. In such a system, both seismic noise and A/D noise are described by roughly flat noise amplitude in frequency bands of constant relative width from <0.1 mHz to >10 Hz. The noise of 24-bit quantization (Bennett, 1948) at 100 sps with a range of ± 20 V is also shown for comparison. The typical vertical noise levels observed at quiet GSN sites are well above actual A/D noise. Only high-frequency noise during the quietest

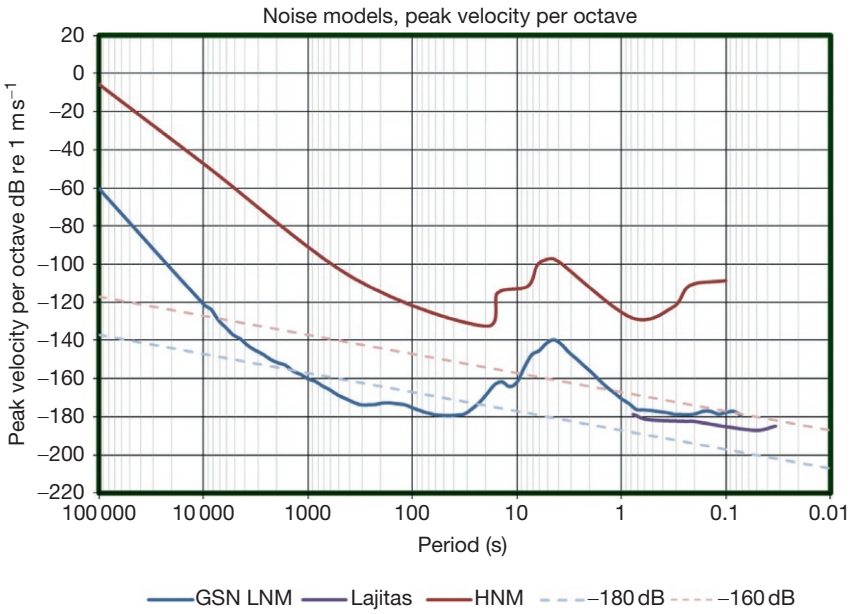

Figure 10 This figure shows the noise models of **Figure 8** represented as peak ground velocity (crest factor 3.3) in one-octave bands. The noise models are approximately 'rotated' clockwise compared to acceleration per octave, reducing the ratio of maximum to minimum amplitude over the frequency range from ~3 mHz to >10 Hz. Noise levels at frequencies below ~3 mHz increase ~40 dB per decade. The amplitude in bands of constant relative width from 0.01 mHz to 10 Hz or higher can be roughly equalized with a second-order high pass at ~3 mHz. −180 dB (dashed light blue) and −160 dB (dashed violet) are acceleration PSD isolines.

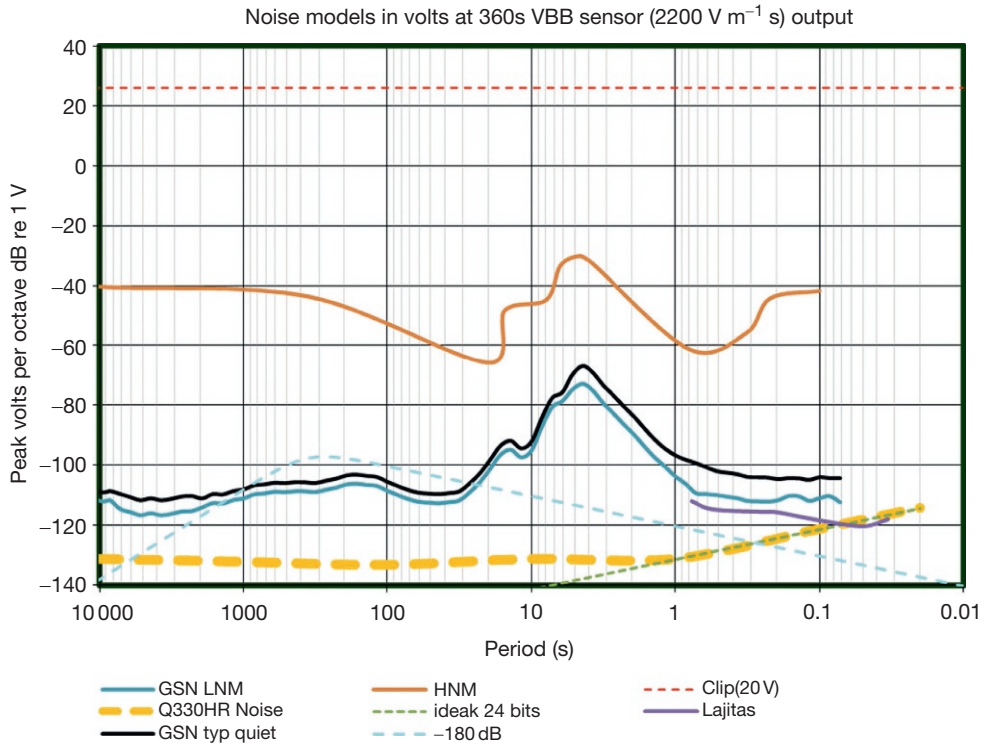

Figure 11 The noise models of **Figure 10** represented as peak voltage (crest factor 3.3) at the output of a very broadband (VBB) seismometer having a response flat to ground velocity with a two-pole high-pass corner at 360 s period and gain 2200 V m^{-1} s. The noise models are compared with the actual noise of A/D systems (thick yellow dashed line) used in global network stations. Except for the peak containing marine microseisms, the amplitude of the noise models as a function of frequency is nearly equalized with this frequency response. The amplitude variation of minimum Earth noise with frequency is ~50 dB over the entire frequency range. The margin between low Earth noise and A/D noise is positive and roughly uniform. The interval from noise to 20 V clip level (red dotted line) is similarly nearly constant. 24-bit, 100 sps quantization noise is also shown (dashed green). The isoline −180 dB acceleration PSD is 'bent' and 'tilted' by this approach showing VBB's frequency-dependent map of constant acceleration PSD to voltage at the A/D converter (dashed blue). The frequency response described is VBB, originally implemented in the STS-1/VBB seismometer for frequencies <10 Hz.

periods at exceptional sites, such as Lajitas, TX, during the 1980s (current levels; there are higher), is not well resolved by such a system.

A system as represented in Figure 11 with flat response to velocity extending from 360 s to arbitrarily high frequency does not quite exist. Existing Streckeisen STS-1/VBB and Geotech KS54000I sensors used in global networks, however, provide an approximation, with an upper second-order corner frequency at 5–10 Hz. A number of existing broadband sensors with a lower corner period of 120 s or more have nearly flat frequency responses extending well above 10–40 Hz or higher but do not typically resolve minimum Earth noise at frequencies <4–5 mHz. The development of sensors better approximating the wide response depicted in Figure 11 with lowest noise is an area of current research.

1.02.2.3 Actual GSN Operating Range

Figure 12 shows the signals and noise of Figure 8 and includes the actual saturation and estimated noise level of the STS-1/VBB seismometer to represent the frequency dependence of the operating range of global network systems. A similar figure would result with other types of velocity broadband sensors, such as the Geotech KS54000I, the Streckeisen STS-2, and the Nanometrics T240, with differences in the clip level and low-frequency noise level (discussed later). With the STS-1/VBB, such a system is capable of high-SNR recording of free oscillations and on-scale recordings of most events to at least M8 at 30° distance. Moderately large events at regional distances, illustrated by the M6.9, 6°, are at the maximum signal-handling limit. Small, nearby, felt events, illustrated by M4, 1.3°, are well within the capability. Large events nearby and at regional distances are well above the maximum signal-handling capability and require a lower-gain sensor to measure on scale. Although the interval between the sensor's intrinsic noise and saturation level is ~146 dB, this range is never fully exercised, since Earth noise defines the minimum output level. Figure 11 or 12, based on peak levels as described earlier, shows that a maximum observed dynamic range of ~135–140 dB defined as $20\log\left[\frac{\text{clip level}}{\text{noise level}}\right]$ using peak amplitudes (the more often defined rms ratio is $20\log(3.3/\sqrt{2}) = \sim 7$ dB higher) is achieved in an octave band of frequencies near 30 s period, where surface wave signals may be large and seismic noise low.

Such an operating range representation helps illustrate the difference between a sensitive instrument and a low-gain or strong-motion instrument. Strong-motion instruments designed for large signals as seen in the near field of an earthquake are defined from the 'top down' by their maximum peak signal levels, usually 2 g; their noise level is subordinate, defined by their electronics and mechanical system at a level somewhere below their defined maximum signal level. Strong-motion sensors in current use achieve a typical useful dynamic range approaching 150 dB, diminishing at frequencies <1 Hz. Instruments intended for the most sensitive low-frequency measurements, however, are designed from the 'bottom up' for a target noise level and achieve some maximum signal level dependent on electronics.

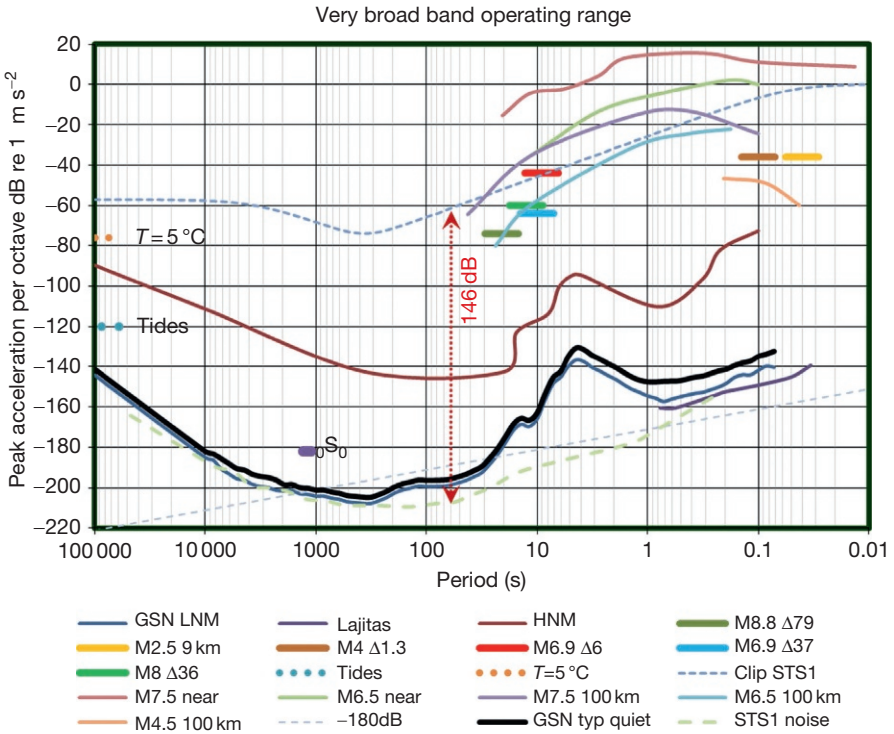

Figure 12 The frequency-dependent operating range of a VBB system. The seismic noise models and signals of Figure 8 are combined with the instrumentation noise (dashed green) and clip level (dashed blue) of a VBB system using the frequency response illustrated in Figure 11. Many large signals at regional and teleseismic distances are within the operating range. The largest signals at regional and near distances are above the maximum capability. The actual maximum useful dynamic range of a VBB system exceeds 140 dB at some frequencies. Also shown is the approximate acceleration equivalent of a 5 °C temperature change on the effective mass position. Thermal stability in the installation is required.

1.02.2.4 Dynamic Range and Bandwidth

Dynamic range is a number often used to describe the ratio of the largest to smallest time-domain signal handled by an instrumentation system. Dynamic range, however, is meaningless without specification of the frequency band over which the measurement is made. In the case of a broadband seismic system spanning nearly seven decades in frequency, the particular choice of band limits greatly affects the resulting ratio. A few examples illustrate this point.

The useful dynamic range observed over the full bandwidth of the GSN VBB sensors is not particularly impressive when deployed at a noisy site. The interval between short-period ambient noise and clipping may be only 80 dB or less: this is the ratio of clip level to the voltage produced by the sensor that one would measure with a voltmeter at such a site. The maximum dynamic range defined as an rms ratio, say in one octave near 30 s, on the other hand, exceeds 140 dB. Dynamic range is usually specified in instrumentation as the rms ratio of a maximum amplitude sine wave to the noise within a specified band of frequencies. For the system shown in Figure 11 where actual A/D noise is ~75 nV rms/octave and the A/D maximum rms level for a sine wave is 14.14 V, actual A/D rms dynamic range is roughly a constant 164 dB in one-octave bands below the $1/f$ corner and ~147 dB in a one-octave band at 50 Hz.

1.02.3 Seismometers and Systems

Measurement conventions, models of Earth noise and signals, and a system matching frequency response to noise and signals to achieve design goals of global and regional networks have been introduced. This section will discuss the design and operation of sensors and systems to achieve the result depicted in Figure 12. The discussion partially follows Steim (1986).

1.02.3.1 Mechanical Pendulum

An inertial seismometer sensitive to vertical motion consists of a mass suspended elastically against gravity from a frame that rests on the Earth's surface. The inertial mass and viscoelastic suspension create a mechanical oscillator that for small motions can be described by a second-order linear differential equation:

$$\ddot{x}(t) + \frac{b}{m}\dot{x}(t) + \frac{k}{m}x(t) = a(t) \qquad [13]$$

where m is the inertial mass, $x(t)$ is the displacement of the mass as a function of time in a fixed coordinate system, b describes frictional damping of the mass motion and has units force/velocity, k is the spring constant of the elastic suspension and has units force/displacement, and $a(t)$ is the acceleration of the seismometer frame as a function of time. If the seismometer frame is coupled firmly to the ground, $a(t)$ also represents ground acceleration. Laplace transformation of eqn [13] gives

$$s^2X(s) + s\frac{b}{m}X(s) + \frac{k}{m}X(s) = A(s) \qquad [14]$$

where s is the complex frequency variable and $X(s)$ and $A(s)$ represent Laplace-transformed mass displacement and ground acceleration. The transfer function of the mechanical system $M(s)$ is defined as

$$M(s) = \frac{X(s)}{A(s)} = \frac{1}{s^2 + s\frac{b}{m} + \frac{k}{m}} \qquad [15]$$

Equation [15] can be written as

$$M(s) = \frac{X(s)}{A(s)} = \frac{1}{s^2 + 2\xi\omega_0 s + {\omega_0}^2} \qquad [16]$$

where ξ represents the fraction of critical damping of the oscillator and $\omega_0 = 2\pi/T_0 = \sqrt{k/m}$ is the (angular) resonant frequency of the undamped mechanical oscillator having period T_0. Above resonance ω_0, the displacement $X(s)$ of the mass relative to the frame represents ground displacement $D(s)$:

$$X(s) \approx \frac{A(s)}{s^2} = D(s) \qquad [17]$$

Below resonance, $X(s)$ is proportional to ground acceleration:

$$X(s) \approx \frac{A(s)}{{\omega_0}^2} \qquad [18]$$

The addition of an electrodynamic transducer, that is, a coil of wire moving through a magnetic field, with generator constant G to measure $X(s)$ creates the familiar seismometer producing a voltage $E(s)$ proportional to mass velocity:

$$E(s) = G \cdot sX(s) = G\frac{sA(s)}{s^2 + 2\xi\omega_0 s + {\omega_0}^2} = G\frac{s^2V(s)}{s^2 + 2\xi\omega_0 s + {\omega_0}^2} \qquad [19]$$

Well above resonance ω_0, $E(s)$ is proportional to ground velocity $V(s)$. This is the form of response of a conventional electrodynamic geophone:

$$E(s) \approx G \cdot V(s) \qquad [20]$$

The frequency response of eqn [19] is simulated by a force-feedback broadband velocity sensor. Compare eqn [12]. Traditional seismographs such as the WWSSN with photographic recording are described by eqn [19] with an additional second-order low-pass function describing the galvanometer (Hagiwara, 1958; Wielandt and Mitronovas, 1976).

1.02.3.2 Electronic Force Feedback

EFFB has been used in seismometry since at least the mid-1950s (Benioff, 1955). EFFB was originally used primarily to generate a restoring force to maintain the inertial pendulum within its mechanical operating limits, typically under variation of position caused by temperature change, tilt change, and mechanical creep (Sutton and Latham, 1964). At least one early effort (DeBremaecker et al., 1962) included direct digitization having a claimed dynamic range of 100 dB, and a system with EFFB featuring laser displacement sensing of the inertial pendulum and a dynamic range up to 140 dB (Hemelrick, 1964) was proposed, but apparently not constructed.

EFFB sensors first reached wide deployment in the International Deployment of Accelerometers (IDA) network (Agnew et al., 1976) with the Block and Moore (1966) conversion of gravimeters (LaCoste, 1934) by the addition of capacitive displacement sensing. The weak electrostatic feedback limited the

saturation level. The low-frequency noise, however, was quite low and these systems provided valuable data.

The present era of high-dynamic-range EFFB sensors began with the deployment of relatively small sensors having strong feedback to shape response using electromagnetic transducers. The SRO (Melton, 1976; Peterson et al., 1976) program using the Geotech KS36000 and the GRF array (Harjes and Seidl, 1978) using the newly developed Streckeisen STS-1 (Wielandt and Streckeisen, 1982) provided the first significant volumes of high-quality digital data from broadband EFFB sensors. The KS36000 operated as an accelerometer, which unnecessarily restricted its potential operating range (Peterson, 1982; Steim, 1986). The STS-1's application of EFFB for the first time enabled a dynamic range of 140 dB in a broadband sensor. The STS-1/VBB version with a 360 s corner period enabled by 1986 (Wielandt and Steim, 1986) the first realization of digital VBB seismometry in global and regional networks. At the same time, miniaturized versions of EFFB sensors (Usher et al., 1977, 1978, 1979) were developed throughout the 1980s and 1990s. The use of EFFB allows a relatively compact sensor that is comparatively easy to isolate against environmental inputs to achieve the response of a much larger equivalent open-loop sensor. The stable 360 s corner period of the STS-1/VBB, in fact, is not practically achievable in an open-loop sensor. For a review of EFFB seismometers during this period of rapid development, see Steim (1986).

Figure 13 shows the mechanical seismometer of eqn [16], with response $M(s)$ converting ground acceleration $A(s)$ into inertial mass displacement $X(s)$. EFFB requires an electrical transducer that converts the inertial mass displacement $X(s)$ into an electrical voltage $E(s)$. The electrical transducer may, in general, have any frequency response $R(s)$, although the primary types of transducer would be an electromagnetic velocity transducer, as in a geophone, or a displacement transducer, in which $R(s)$ would equal a constant, say, r having units volts/displacement. The choice of a displacement transducer is most appropriate for resolution of the inertial mass motion at very low frequencies. The combined frequency response of the mechanical seismometer and electrical transducer is given by $O(s) = M(s)R(s)$, the *open-loop* response, that is, without feedback.

In the model of **Figure 13**, a feedback force is generated by an electrical frequency response – shaping network that drives a force transducer acting on the inertial mass. The network is described as an admittance, or inverse impedance, network that converts a voltage to a current $I(s)$ for driving a transducer that generates a feedback force proportional to applied current. The force operates on the sensor's suspension to produce an input to the mechanical sensor that is equivalent to an acceleration acting on the mass of the sensor.

The admittance network contains the electrical components or subcircuits that determine the overall response of the seismometer in the *closed loop*, that is, with feedback applied. An admittance network to convert a voltage to a current for the force transducer may consist simply of resistors and capacitors, or it may include active circuits. An electromagnetic force transducer is typically a coil of wire in a magnetic field, equivalent to an electromagnetic velocity transducer used to sense motion in, for example, a geophone. The coil produces a force proportional to the current flowing through it. The admittance network has response $N(s)$ having units current/voltage $= 1\ \Omega^{-1}$. The force transducer and inertial mass may be considered together to have a response $G(s)$ that can be simply a constant, say, g (not to be confused with the acceleration of gravity), having units acceleration/current. In this formulation, a current applied to the force transducer produces an equivalent acceleration of the mass of the mechanical seismometer. The combined response of the feedback from voltage to ground acceleration is then $F(s) = N(s)G(s)$.

The voltage $E(s)$ may be written as the sum of ground and (negative) feedback accelerations acted upon by the open-loop transfer function $O(s)$:

$$E(s) = (A(s) - E(s)F(s))O(s) = A(s)O(s) - E(s)F(s)O(s) \quad [21]$$

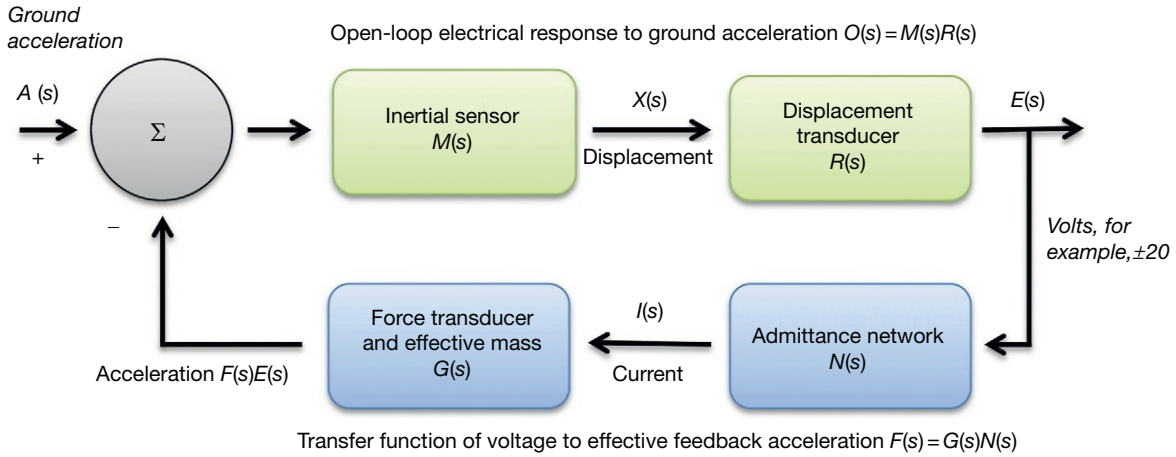

Figure 13 A generalized Laplace-transformed description of an electronic force-feedback (EFFB) seismometer, with acceleration input $A(s)$, and voltage output $E(s)$. Feedback reduces the displacement of the inertial mass $X(s)$ by a frequency-dependent factor $O(s)F(s)$ (the loop gain) compared to the open-loop case. Smaller physical displacement improves linearity in the closed loop. Useful dynamic range can be very high in terms of acceleration over a wide frequency range if the feedback path $F(s)$ is controlled by passive electrical components. Active components in the feedback path introduce noise that appear in the output signal $E(s)$. At frequencies where $O(s)F(s) \gg 1$, the frequency response $E(s)/A(s)$ of the closed loop is $\sim 1/F(s)$, controlled mainly by the feedback network.

which may be rewritten to give the output voltage $E(s)$ as a function of ground acceleration or the closed-loop transfer function:

$$\frac{E(s)}{A(s)} = \frac{O(s)}{1 + O(s)F(s)} \quad [22]$$

At frequencies where $O(s)F(s) \gg 1$ (true for frequencies up to about 5 Hz in the STS-1/VBB), the closed-loop response is approximately

$$\frac{E(s)}{A(s)} \approx \frac{1}{F(s)} \quad [23]$$

In this case, the closed-loop response of the seismometer is controlled entirely by the feedback network and force transducer and is independent of the mechanical response of the seismometer without feedback. The quantity $O(s)F(s)$ is called the *loop gain* and is a measure of the effectiveness of feedback in determining the seismometer response. Loop gain is a fundamental descriptor of any feedback system.

In a high-dynamic-range VBB sensor, such as the STS-1/VBB, the admittance network has the form illustrated in Figure 14. The three feedback paths describe a system with proportional, integral, and derivative (PID) feedback. This architecture is common in many feedback control systems (Ang et al., 2007). At frequencies where the feedback force is strong (loop gain $\gg 1$), the feedback current delivered to the force transducer by the admittance network balances ground acceleration. Each of the three parallel paths has the highest admittance over different frequency ranges. The voltage $E(s)$ is proportional to the integral of ground acceleration, or ground velocity in the broad range where the path across C is dominant, and to the derivative of ground acceleration or the second derivative of ground velocity where the path through the integrator is dominant.

The open-loop $O(s)$ and feedback $F(s)$ transfer functions can be generalized to better model a typical sensor:

$$O(s) = R(s)M(s) = \left[\frac{r}{sT_D + 1}\frac{M'(s)}{M_{eq}(s)}\right]M(s) = \left[\frac{r}{sT_D + 1}\right]M'(s) \quad [24]$$

$$F(s) = G(s)N(s) = \frac{g\left(sC + 1/R_p + 1/s\tau R\right)}{sCR_C + 1} \quad [25]$$

where R_C is the resistance of the feedback transducer coil and the transfer function $R(s)$ of the displacement transducer includes a single-pole time delay T_D and the response of an *inverse filter* (Wielandt and Steim, 1986). The inverse filter has response $M'(s)/M_{eq}(s)$. If $M_{eq}(s) \approx M(s)$, the inverse filter converts the second-order mechanical response $M(s)$ into a response of the same form $M'(s)$ describing an effective mechanical sensor with a much longer free period $T_0' = 2\pi/\omega_0'$ than the actual sensor. The purpose is to boost the loop gain at frequencies where the condition $O(s)F(s) \gg 1$ is not otherwise met. The identical match $M_{eq}(s) = M(s)$ is not required, and the exact choice of parameters of the inverse filter has little effect on the overall closed-loop response. Higher loop gain enforces the approximation in eqn [23] and desensitizes the closed-loop response to variations in the free period and damping of the mechanical suspension.

Substitution of eqns [24] and [25] into eqn [22], and some approximations, gives the closed-loop response to acceleration explicitly including the effects of finite $R_{C'}T_{D'}$ and ω_0':

$$\frac{E(s)}{A(s)} = \frac{1}{gC} \times \frac{s(sCR_C+1)}{s^5\frac{R_C T_D}{rg} + s^4 K + s^3\frac{1}{rgC} + s^2\left[K\omega_0'^2 + \frac{2\xi}{rgC}\omega_0' + 1\right] + s\left[\frac{1}{CR_p} + \frac{\omega_0'^2}{rgC}\right] + \frac{1}{\tau RC}} \quad [26]$$

where $K = (R_C + T_D/C)/rg$

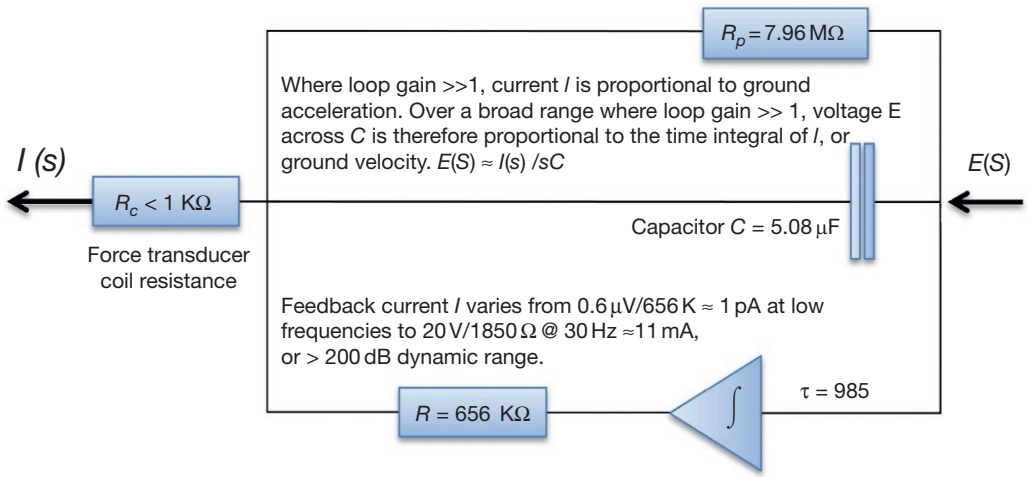

Figure 14 An admittance network in an EFFB seismometer converts an output voltage to a frequency-dependent current applied to a force transducer. The feedback force is equivalent to ground acceleration with a maximum useful dynamic range exceeding 200 dB. The feedback path controlling closed-loop response is frequency-dependent and dominated by the capacitive path over a broad range. Feedback current is limited at high frequency by force transducer internal resistance. The network is a simplified version of the network used in the STS-1/VBB. In the actual sensor, two force transducers are used: one for the R_p and C path, and one with a smaller transducer constant and opposite polarity for the integral path, which is inverted. The values of feedback components are representative of the median of a population of ~200 vertical and horizontal sensors, and hence do not represent a specific instrument.

Consider first the case where $R_C = T_D = 0$, that is, there is no feedback transducer coil resistance or time delay in the displacement transducer. Even for relatively large values of ω_0', the term $\frac{2\xi}{rgC}\omega_0' \ll 1$, allowing eqn [26] to be written:

$$\frac{E(s)}{A(s)} = \frac{1}{gC}\frac{s}{s^3\frac{1}{rgC} + s^2 + s\left[\frac{1}{CR_p} + \frac{\omega_0'^2}{rgC}\right] + \frac{1}{\tau RC}} \quad [27]$$

The coefficient of s^3 affects frequencies >1 Hz. The remaining second-order polynomial defines the low-frequency behavior of the transfer function, with closed-loop free period $T_C = 2\pi\sqrt{\tau RC}$, and the fraction of critical damping:

$$\xi_c = \frac{1}{2}\left[\frac{1}{R_p} + \frac{\omega_0'^2}{rg}\right]\left[\frac{\tau R}{C}\right]^{0.5} \quad [28]$$

Equation [28] shows the importance of the inverse filter in desensitizing the closed-loop damping to changes in the mechanical period of the inertial suspension. With the inverse filter, $\omega_0' \ll \omega_0$, and $\omega_0'^2/rg \ll 1/R_p$, allowing damping to be set by R_p. Having made this approximation, the closed-loop response including the effects of R_C, T_D can be considered:

$$\frac{E(s)}{A(s)} = \frac{1}{gC}\frac{s(sCR_C + 1)}{s^5\frac{R_C T_D}{rg} + s^4\left[\frac{R_C + T_D/C}{rg}\right] + s^3\frac{1}{rgC} + s^2 + s\frac{1}{CR_p} + \frac{1}{\tau RC}} \quad [29]$$

For $R_C = 800$, $T_D = 10^{-2}$, $r = 100\,000$ V m^{-1}, $g = 82$ m s^{-2} A^{-1}, and other values as in Figure 14, eqn [29] gives the nominal response of the STS-1/VBB, flat in ground velocity with closed-loop generator constant:

$$G_c = 1/gC \quad [30]$$

where with the nominal parameters, $G_c = 2400$ V m^{-1}s from 360 s to ~10 Hz. The behavior above 10 Hz is strongly dependent on the loop gain, defined by r, g, and C, and the poles created by $R_C \neq 0$ and $T_D \neq 0$. While a flat response to higher frequency is possible in principle by increasing r alone with electronic gain, increasing r alone creates a sharply peaked response. A flat response to higher frequency without peaking is possible only if T_D is minimized, and the loop gain is increased using a higher value of r and g/R_C. This is the approach taken in later-generation sensors such as the STS-2, STS-2.5, and T240. Table 1 lists a few parameter variations whose effect on amplitude response is shown in Figure 15. Increasing displacement transducer gain r has no effect on the closed-loop gain,

Table 1 Parameters of the STS-1/VBB closed-loop transfer function, varied to produce the five cases shown in Figure 15

Param\case	*Nominal STS-1*	*r↑*	*g↑*	*g↑, r↑, T_D↓, R_C↓*	*No inverse filter*
r (V m^{-1})	100 000	400 000	100 000	400 000	100 000
R_C (Ω)	800	800	800	100	800
T_D (s)	0.01	0.01	0.01	0.0001	0.01
g (m s^{-2}A^{-1})	82	82	328	328	82
T_0 (s)	30	30	30	30	3

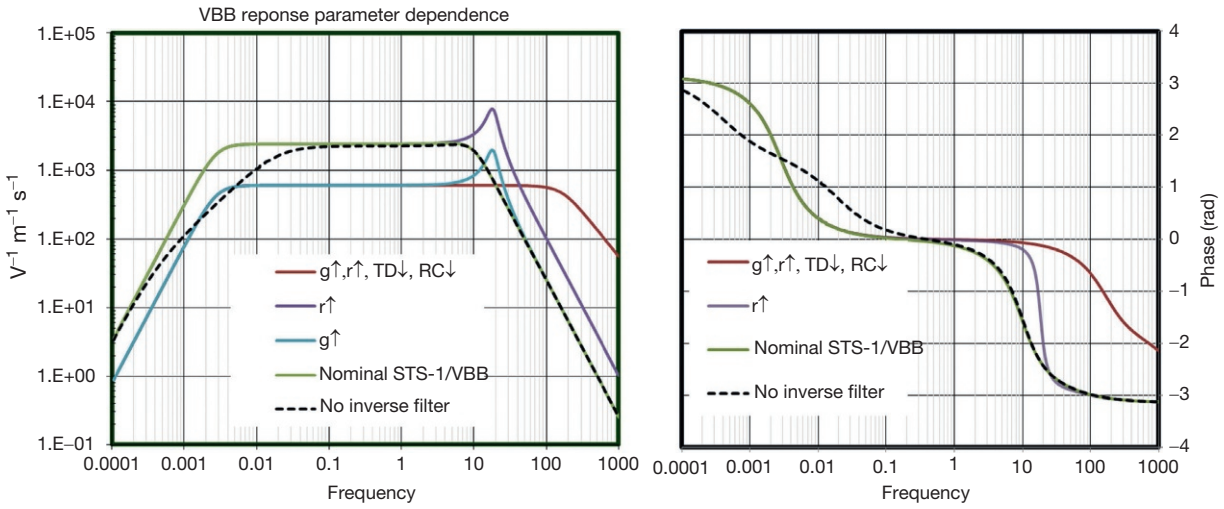

Figure 15 The effect on the closed-loop bandwidth, flatness, gain, and phase of the STS-1/VBB for various parameter changes in Table 1. Other parameter values as in Figure 14. The up and down arrows indicate changes in the parameters relative to the nominal response. Bandwidth may be extended by increasing r or gain reduced by increasing g, but peaking occurs at the upper corner unless T_D and R_C are minimized. The closed-loop gain is controlled by the force transducer constant g and feedback capacitor C. The inverse filter reduces dependence of the low-frequency corner on parameters of the mechanical suspension. The actual sensor uses a smaller T_D, and includes a single-pole low-pass filter external to the feedback network to define the two-pole asymptotic response above 10 Hz. In addition, the effective R_C is higher and is adjusted at the time of manufacture to control uniformity of the response at the 10 Hz corner. These parameter values are representative of the median of a population of ~200 horizontal and vertical sensors. Actual vertical sensors have lower g; horizontal sensors have higher g, resulting in corresponding differences in other feedback components in actual sensors to achieve the nominal response. Actual feedback component values are trimmed to produce a uniform response on all instruments.

which is controlled in the flat portion of the velocity response by the force transducer constant g and value of the feedback capacitor C. Increasing g (or C) reduces gain of the closed-loop transfer function. This flattens frequency response and increases the possible dynamic range of the sensor but places additional demand on the digitizer, since the amplitude of signals (and seismic noise) is reduced. Reduction of closed-loop gain has no effect on the sensor noise level referred to ground motion. At low frequencies, without the inverse filter, the damping at the 360 s corner is strongly dependent on ω_0.

A feedback system that produces a force proportional to applied current using a frequency-dependent admittance allows the generation of a feedback force having a large dynamic range over the operating frequency range. Because seismic noise and signal acceleration amplitude increases with frequency (**Figure 8**), the required feedback force also increases with frequency. A capacitor provides this function over most of the frequency range. The current through the force transducer, producing feedback acceleration, varies over a range of the order of 200 dB. This is roughly two orders of magnitude greater than could be achieved with frequency-independent feedback, such as provided by a resistor. Feedback across a resistor defines an accelerometer in the closed loop.

Noise present at the input of the feedback path $F(s)$ appears in the output signal. Generally, the use of only passive components is preferred in this path, because they tend to operate with minimum noise and, at seismic frequencies, can behave nearly ideally. The integral feedback path, however, although it introduces noise, is required to obtain the desired second-order high-pass to ground velocity discussed earlier.

1.02.3.2.1 Limits on seismometer resolution and operating range

1.02.3.2.1.1 Intrinsic noise

A fundamental limit of resolution of an inertial sensor is defined by the Brownian motion of the inertial mass (Byrne, 1961; Wolf, 1942). The well-known MT_0Q criterion (Melton, 1976; Usher, 1973) can be shown to define the minimum product of inertial mass M (kg), period T_0 (s) of the inertial suspension, and quality factor Q of the suspension. The Brownian noise of the inertial suspension creates a noise-equivalent acceleration power

$$\ddot{x}_{\mathrm{ne}}{}^2 = \frac{8\pi kT\Delta f}{MT_0Q} \qquad [31]$$

in a bandwidth Δf. k is the Boltzmann constant and T is the absolute temperature (minimized in superconducting gravimeters). $Q = 1/2\xi$ in eqn [16]. The resulting acceleration PSD at room temperature is independent of frequency with value

$$\frac{\ddot{x}_{\mathrm{ne}}{}^2}{\Delta f} = \frac{8\pi kT}{MT_0Q} \approx \frac{10^{-19}\left(\mathrm{m\,s^{-2}}\right)^2\mathrm{Hz^{-1}}}{MT_0Q} \qquad [32]$$

Therefore, a sensor with $MT_0Q \geq 1$ will achieve a Brownian noise-equivalent acceleration PSD of -190 dB or less relative to 1 $(\mathrm{m\,s^{-2}})^2\,\mathrm{Hz^{-1}}$. $MT_0Q \geq 1$ is achieved for most broadband sensors in current use having relatively large mass, moderately long period, and moderate subcritical damping. Although not a limitation in these sensors, Brownian motion may limit the potential to miniaturize sensors capable of resolution of minimum Earth noise, which is coincidentally roughly -190 dB acceleration PSD at several mHz. Resolution of seismic noise at the level -190 dB requires on the order of -200 dB intrinsic thermal sensor noise. Few sensors achieve this.

1.02.3.2.1.2 Thermal sensitivity

The sensitivity of a seismometer's mechanical structure to temperature changes presents a challenge to resolving minimum seismic noise levels at frequencies below about 100 mHz. The coefficients of thermal expansion for many of the metals used in typical sensor construction are of order $10^{-5}\,\mathrm{K^{-1}}$. A vertical seismometer must operate in the presence of the Earth's static gravity of $\sim 10\,\mathrm{m\,s^{-2}}$ while simultaneously resolving accelerations corresponding to minimum ambient levels, ~ 11 orders of magnitude less than gravity at, say, 3 mHz (see **Figure 8**). Since a displacement of the inertial mass relative to the frame is proportional to ground acceleration, the change in temperature of the sensor must be maintained within $\sim 10^{-6}$ K over the timescale of minutes to hours in order to resolve the acceleration levels of minimum Earth noise. This level of temperature stability and uniformity throughout the sensor mechanics cannot be achieved through active control and is achieved instead by thermally coupling the sensor to the ground as a heat sink and isolating the sensor through evacuation and insulation against external heat sources. Wielandt and Streckeisen (1982) called this type of passive thermal control the 'cold thermostat.' Burial can provide a thermally stable environment if fluid or air mobility, such as in a borehole casing, does not transport heat over relevant timescales. The 'cold thermostat' is achieved by maximization of the thermal time constant for heat transfer between the sensor mechanics and the ambient environment. A large thermal mass surrounding the sensor and efficient insulation is more effective than insulation alone. The $\sim$2000 installations (http://www.passcal.nmt.edu/taweb) of the EarthScope Transportable Array (http://www.usarray.org/researchers/obs/transportable), for example, achieve the 'cold thermostat' for periods at least to 100 s using a combination of ~ 2 m burial and thermal insulation to stratify air temperature and attenuate large daily surface temperature variations of tens of degrees (**Figure 16**).

Heat sources internal to the sensor can create internal convection, as well as thermal gradients within the sensor structure. The STS-1/VBB sensor (and its replacement M2166-VBB) contains no active heat-producing electronics within the sensor vessel. It is essential for low-frequency observation that the sensor be shielded against the force and heat transport of air motion. Several studies (Berger, 2009; Forbriger, 2011; Holcomb and Hutt, 1992; Trnkoczy et al., 2011; Uhrhammer et al., 1998; Wielandt, 2011a; Widmer-Schnidrig and Kurrle, 2006) have described installation techniques to achieve adequate thermal and physical stability. Despite the best efforts to effectively and uniformly install instruments for low-frequency use, variability of noise performance remains in part because of the variation from sensor to sensor in their intrinsic thermal sensitivity.

1.02.3.2.1.3 Displacement transducer resolution

For an inertial suspension with displacement sensor and a defined minimum observable acceleration on the order of $10^{-10}\,\mathrm{m\,s^{-2}}$, eqn [18] relates the mass displacement at low

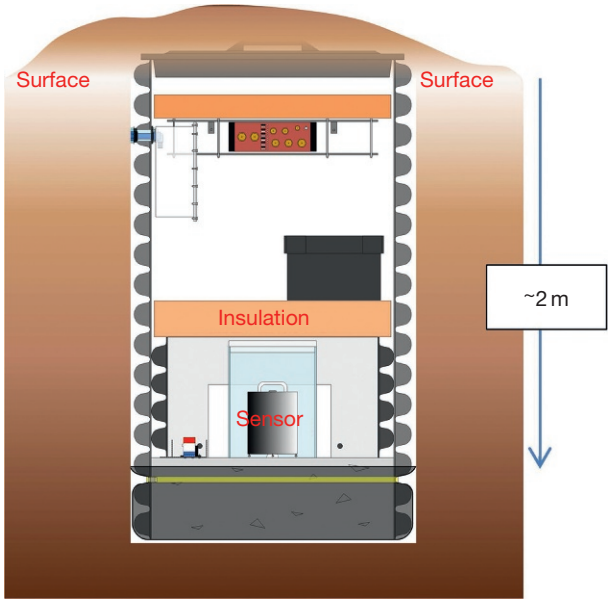

Figure 16 The installation method to achieve thermal isolation in near surface installations of the EarthScope Transportable Array (TA) stations. Approximately 2000 such installations have been made over the past decade, achieving consistent low-frequency vertical noise levels throughout much of the continental United States. Such an installation is not adequate for resolution of minimum Earth noise levels at frequencies <5 mHz; however, near-LNM vertical resolution is possible above these frequencies. Adapted from figure provided by R. Busby.

frequencies to the resonant frequency of the suspension (Melton and Kirkpatrick, 1970; Wielandt and Streckeisen, 1982). The required displacement resolution varies inversely with the square of the suspension natural frequency. The resolution of a suspension with natural frequency >1 Hz must be less than 10^{-12} m. This resolution is achievable with capacitive displacement sensing (Jones and Richards, 1973; Usher et al., 1977). The linear variable differential transformer displacement sensor in the STS-1/VBB with displacement resolution of the order of 10^{-10} m requires a mechanical resonant period of at least 6 s to resolve minimum low-frequency ground acceleration. EFFB broadband sensors used in global and regional networks are not typically limited at low frequencies by resolution of their displacement transducer. Equation [17], however, shows that at high frequencies, the displacement of the inertial mass equals ground displacement. Minimum seismic noise expressed as displacement decreases with increasing frequency. The input-equivalent noise of broadband displacement-sensing EFFB sensors typically exceeds minimum, infrequently observed Earth noise at tens of hertz and above. A displacement transducer with resolution sufficient to resolve minimum ambient Earth noise on the order of 10^{-12} m rms in a 30 Hz bandwidth has proven difficult to realize simultaneously with constraints to achieve high dynamic range and low noise at low frequencies. An electrodynamic transducer can have an SNR advantage (Rodgers, 1992a,b) at frequencies of tens of hertz and above, although in typical installations, commonly used EFFB sensors are not limited by displacement transducer noise. From a low-frequency perspective, a longer mechanical resonant period is preferred, since the requirements on noise and stability of the displacement transducer and dimensional stability of the sensor are relaxed. Wielandt and Streckeisen (1982) note that integrator noise can also be a significant contributor in an EFFB sensor at low frequencies.

1.02.3.2.1.4 Environmental and ambient seismic noise

Local ambient seismic noise defines the minimum observable signal. In addition, the effect of environmental inputs to a sensor may further increase the apparent noise level. Ambient seismic noise divides into three main bands, say, >1 Hz, 0.03–1 Hz, and <0.03 Hz. The range 0.03–1 Hz is dominated by microseisms and presents no challenge to instrumental resolution. Above 1 Hz, two major contributors to ambient noise at most sites are 'cultural,' that is, the result of human activity, including traffic and machinery, and wind-generated. Peterson (1993) showed dependence of noise >1 Hz on local time of day at GSN stations. A recent unpublished study (Coughlin and Harms, 2012) of ~3500 stations including GSN and regional networks during the past 5 years shows noise levels relative to a local reference as a function of time of day and frequency (**Figure 17**). Noise above 1 Hz rises significantly during daytime hours, when both cultural activity and wind velocity typically increase. The same study shows a strong temporal correlation with wind speed and observed noise in stations of the transportable array, uniformly installed at roughly 2 m depth. Few if any typical surface-installed global and regional network broadband sites (see **Figure 12**) are limited by intrinsic sensor noise at frequencies 0.1–5 Hz. In rare, exceptionally quiet locations, and at quiet times, minimum levels observable on broadband sensors may be limited by both sensor intrinsic noise (of the displacement transducer) and input-equivalent digitizer noise, defined by the low gain of broadband systems. A consistent feature in a number of studies of dependence of noise >1 Hz on depth (Carter and Barstow, 1991; Young et al., 1996; Withers et al., 1996) is rapid noise reduction generally within 100 m depth, although a reduction in the variability of noise as a function of surface wind speed is seen down to 2000 m. Douze (1964) examined both signal and noise level as a function of depth for frequencies >1 Hz. Levels of both noise and signals >1 Hz are reduced at depth, with significant SNR improvement only at 1000 m or greater. None of the studies of high-frequency noise in boreholes, nor research on high-frequency noise models discussed earlier, used displacement-sensing seismometers.

A combination of intrinsic sensor noise and site and instrument response to environmental inputs, particularly variation in temperature and barometric pressure, often limits vertical sensor resolution at frequencies <0.03 Hz. Forbriger et al. (2010) suggest that susceptibility to magnetic field variation may also limit many broadband seismometers in current use. The effect of barometric pressure variation is particularly important and plays predominantly different roles in vertical and horizontal low-frequency measurements.

Barometric pressure changes affect a vertical seismometer in four principal ways:

1. Buoyancy variation of the mass producing an equivalent change in ground acceleration (Block and Moore, 1966; Crary and Ewing, 1952; Press et al., 1958; Sorrells, 1971; Wielandt and Streckeisen, 1982)

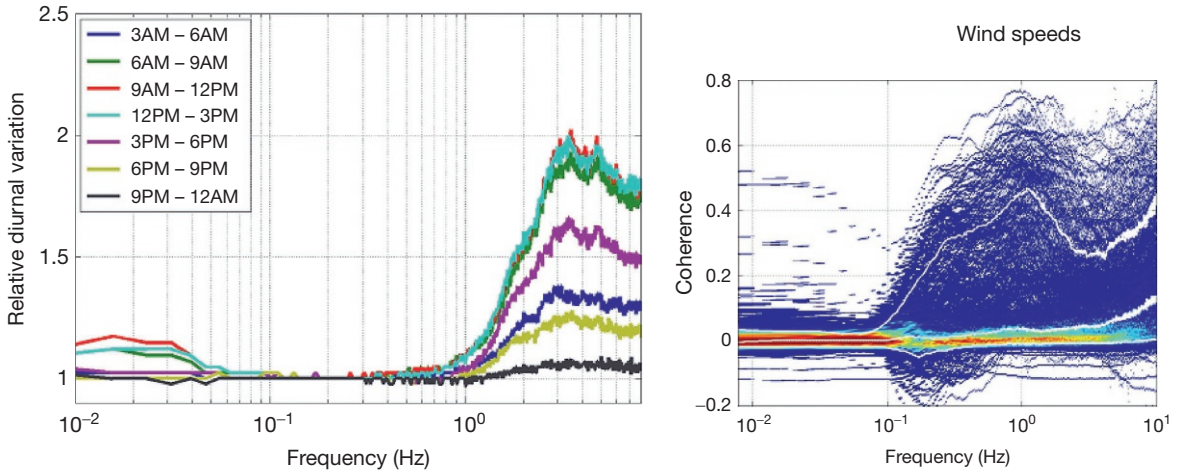

Figure 17 The plot at left shows global noise medians as a function of frequency within seven ranges of local station time divided by the midnight median 12–3 am. Seismic noise is stronger during the day. Only the frequency band of oceanic microseisms does not show significant diurnal variation. At right, noise level as a function of frequency is correlated with local wind speed showing strong dependence above 0.1 Hz. Approximately 3500 stations are used over a period of 5 years. Adapted from Coughlin MW and Harms J (2012) Global characterization of seismic noise with broadband seismometers. arXiv, preprint arXiv:1202. 4826.

2. Variation in Newtonian gravitational attraction of the seismometer mass by the atmosphere (Beauduin et al., 1996; Block and Moore, 1966; Warburton and Goodkind, 1977; Zürn and Widmer, 1995)
3. Deformation, including the instrument housing itself; the local instrument setting, such as the vault; and the Earth's surface (Sorrells and Goforth, 1973; Sorrells et al., 1971; Zürn and Wielandt, 2007)
4. Adiabatic temperature changes accompanying barometric pressure change

Buoyancy is addressed by enclosing the suspension in a sealed vessel such as in the HGLP/ASRO systems (Pomeroy et al., 1969) and STS-1 (Wielandt and Streckeisen, 1982). Evacuation is not necessary, but helps purge the vessel of humidity, which can activate noise-generating chemical processes over years of operation. All broadband sensors developed during the last 40 years are sealed against barometric pressure changes. One source of deformation of the instrument housing has been mitigated using a construction that minimizes the presence of large areas exposed to asymmetrical pressure loading. The so-called *warpless* (Holcomb and Hutt, 1992) construction has replaced the use of large flat mounting bases, such as in the STS-1 and HGLP/ASRO instruments, with mounting systems symmetrically loaded to reduce bending. Careful design and testing is required to reduce the effect of distortion of the housing. This is particularly challenging for horizontal instruments that are very sensitive to tilt. This will be discussed further later. Adiabatic temperature changes are generally suppressed in instruments with multiple isolation methods, such as evacuation, heat sinking, and thermal insulation, as in STS-1 or gravimeter installations.

There are two effects of barometric pressure against which an inertial instrument cannot be shielded: gravitational attraction of the atmosphere on the sensor mass and loading of the Earth's surface under local pressure variation. These effects act with opposite signs (Zürn and Wielandt, 2007) as an equivalent net

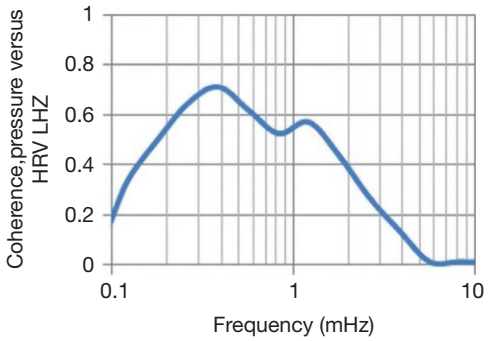

Figure 18 Coherence between barometric pressure and the vertical STS-1/VBB seismometer during a representative 12-day period at GSN station HRV. Significant coherence is common at frequencies from several tenths of 1 mHz to several mHz – the normal mode band. Coherence is rare at frequencies >4 mHz.

ground acceleration proportional to local air pressure. The effect on vertical low-frequency data may be removed (Beauduin et al., 1996; Zürn and Widmer, 1995) from an observed seismogram using an arbitrary scaling constant in the subtraction:

$$z_{\text{corr}}(t) = z(t) - \alpha \cdot h(t) * p(t) \qquad [33]$$

where $z(t)$ represents an observed seismogram, $p(t)$ local observed pressure, $h(t)$ the response of the seismometer to an impulse in ground acceleration, and α an empirically determined constant (often in the range of $\sim 3.5\ \text{nm s}^{-2}\ \text{hPa}^{-1}$) to reduce the resulting variance of $z_{\text{corr}}(t)$. The $*$ denotes convolution. $h(t) * p(t)$ can be calculated quickly on arbitrarily long sequences of sampled data with the application of a suitably derived equivalent recursive digital filter. Zürn and Widmer (1995) stated that this approach is effective up to frequencies of 1–2 mHz. Low-frequency vertical land data and pressure typically exhibit little coherence above 4 mHz (see **Figure 18**).

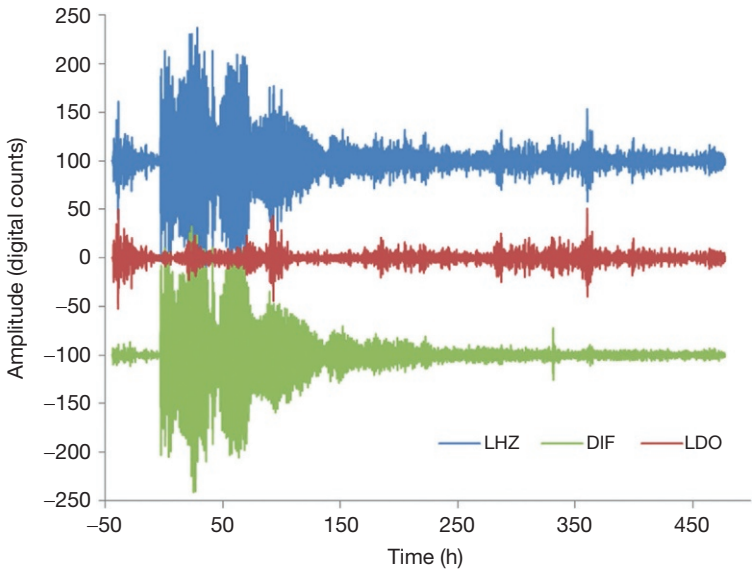

Figure 19 Removal of the effect of barometric pressure on low-frequency vertical data. ~3 weeks of vertical STS-1/VBB data from GSN station HRV for the 2010 Mw 8.8 Chile event, band-pass-filtered 0.25–0.7 mHz. LHZ is the observed data. LDO (red) is barometric pressure with a time-domain filter applied representing the seismometer transfer function to ground acceleration, arbitrarily scaled. Obvious visual correlation exists with the LHZ (blue) envelope. DIF=LHZ – LDO, showing variance reduction (green).

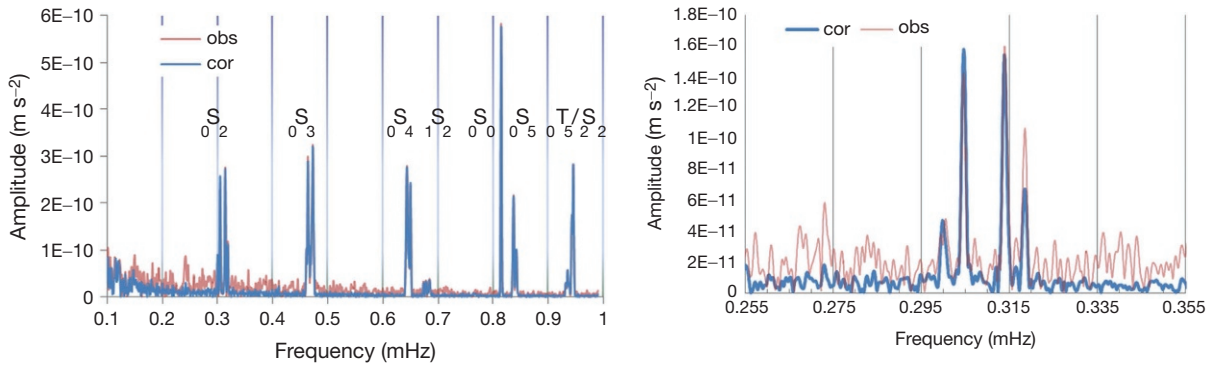

Figure 20 Left: The observed (red) and pressure-corrected (blue) spectra from the data in **Figure 19** spanning 0.1–1 mHz showing improvement in the corrected data. Right: ${}_0S_2$ showing resolution of all singlets present. The apparent frequency of one singlet is slightly shifted in the corrected data.

Figure 19 shows the application of pressure correction to vertical data from the 2010 Mw 8.8 Chile earthquake recorded at GSN station HRV. The reduction in variance in the time domain is clear. Figure 20 shows the observed and corrected spectrum, including a close-up of ${}_0S_2$ with substantial background reduction and a small shift in one singlet. Similarly, Figure 21 shows ${}_0S_3$ with resolution of all seven singlets, one of which is significantly moved. The result is comparable with gravimeter records (Rosat and Hinderer, 2011). Figure 22 shows the result of barometric correction on a measurement of the decay envelope of ${}_0S_0$. The ratio of smoothed envelope amplitude to the decay calculated with various Q values from 5400 to 5700 is shown. With correction, the SNR is improved and the variance of the ratio over 2 weeks is reduced by a factor of three, producing an estimate of $Q=5500–5600$, consistent with recent estimates (Rosat et al., 2007).

The effect of atmospheric pressure changes on the resolution of low-frequency signals observable on horizontal sensors is generally greater and more complex. Pressure changes induce deformation of the Earth's surface resulting in tilts. Horizontal inertial sensors are sensitive to tilt-induced acceleration of the order of the change in tilt angle times the acceleration of gravity (Rodgers, 1968). Hence, a very small tilt change can produce acceleration far above minimum seismically generated signal levels. A tilt angle α of 10^{-10} radians, or 10^{-6} m over a baseline of 10 km, produces an acceleration of $\alpha \bullet g \cong 10^{-9} \mathrm{m\ s^{-2}}$, which is an order of magnitude larger than the amplitude of the gravest free modes from large earthquakes. As Holcomb et al. (1998) point out, this tilt is roughly equivalent to the thickness of a piece of paper inserted under one end of the North American continent. This analogy allows one to appreciate the problem of tilt minimization in instrumentation, where

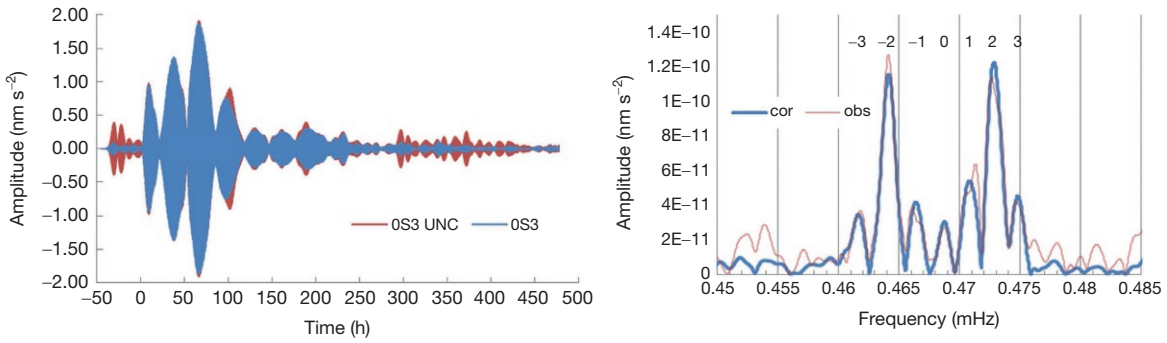

Figure 21 Left: Data of **Figure 19** band-pass-filtered 0.45–0.5 mHz to show the time-domain beating of the multiplet comprising ${}_0S_3$ and variance reduction with barometric correction. Right: All seven singlets in the corrected data with SNR similar to gravimeter records. The frequency of $m=1$ singlet is shifted significantly in the corrected data.

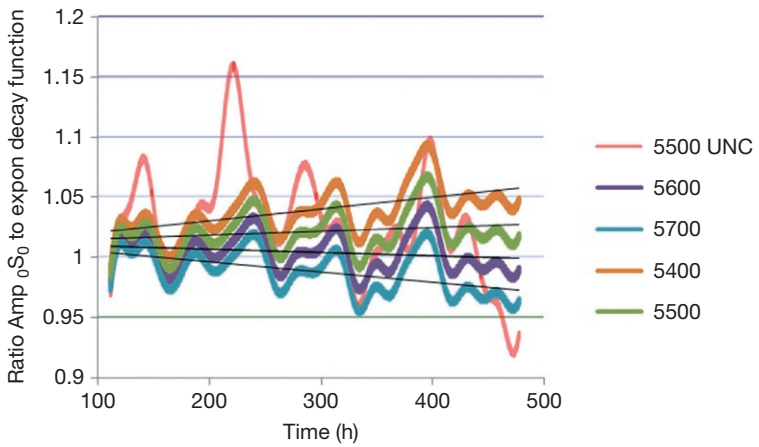

Figure 22 Pressure correction improves estimate of Q of ${}_0S_0$ from the 2010 Mw 8.8 Chile event. The ratio of decay envelopes and trend lines for various Q values compared to the smoothed, band-pass-filtered time-domain record are calculated using observed, uncorrected (trace-labeled 5500 UNC; red), and pressure-corrected data. The variance in the ratio is reduced by a factor of three for the corrected data, leading to an estimated Q 5500–5600, consistent with recent estimates.

the baseline is as little as 0.1 m. Tilts may be induced by barometric pressure variation operating to deform the Earth's surface or the instrument itself. Tilts may also be the result of air convection, ground water mobility, diurnal temperature changes, seasonal freezing and thawing, or mechanical defects in the local installation environment. Typically, several tilt sources combine. Zürn et al. (2007) have demonstrated that the effect of pressure variation on horizontal data can be reduced, although the approach generally requires 'customization' for each time segment analyzed and more complex models than the correction of vertical data.

Figure 23 shows an example of pressure-induced local tilt accompanying the passage of a weather system on the horizontals of EarthScope TA station K62A on 11 September 2013. The E axis is virtually identical to the pressure signal scaled with an apparent coefficient of 2.5×10^{-9} m s^{-2} Pa^{-1} and convolved with the seismometer response to acceleration. If the entire signal is tilt-generated, this is equivalent to a tilt sensitivity to pressure of 2.5×10^{-10} rad Pa^{-1}. The vertical axis is essentially unaffected. The peak acceleration of the pressure-induced signal is $\sim10^{-7}$ m s^{-2} at ~500 s period. The peak pressure signal in this band is ~50 Pa. The entire broadband pressure change accompanying the weather system passage was about 300 Pa. Such effects may be quite localized to the immediate installation environment. It is not uncommon for nearby horizontal sensors to produce significantly different outputs as a result of localized tilt (Hutt et al., 2004). For instrument evaluation purposes, horizontal coherence of adjacent instruments can be increased by placement on a common competent platform, such as a thick granite or metal base.

Crawford and Webb (2000) and Crawford et al. (2006) have shown that on the sea floor, correction of vertical data using locally recorded pressure (Cox et al., 1984) and tilt noise obtained from horizontal sensors can also produce up to 25 dB improvement at low frequency. The relative importance of surface deformation is higher than on land. In addition, because of the large tilts present on the sea floor surface, very slight misalignment of a vertical sensor's sensitive axis with the gravity vector creates tilt-generated noise on the vertical. From an instrumentation perspective, the observed noise levels on the sea floor are high compared with on land and are more easily resolved. Measurement of local pressure and correction

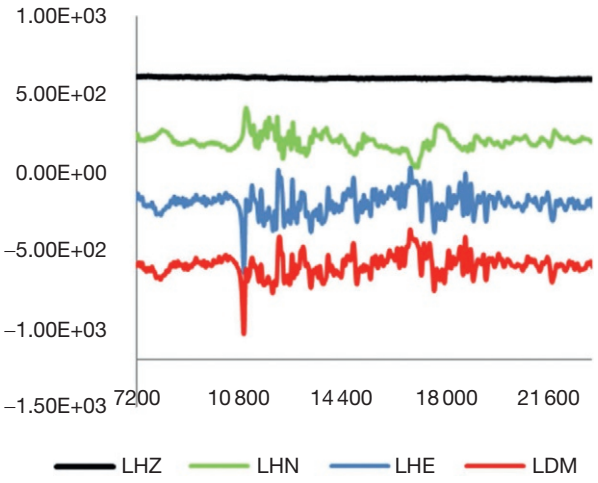

Figure 23 An example of pressure-induced tilt. Station TA-K62A, showing ~3 h, 1 sps, three-axis broadband data, low-pass filtered at 0.01 Hz. Ordinate in digital counts; horizontal axis is time (second). LDM (red) is barometric pressure filtered with the seismometer's response to ground acceleration and scaled with an apparent coefficient of pressure to ground acceleration of 2.5×10^{-9} m s^{-2} Pa^{-1}. The LDM channel records the passage of a weather system. The LHE (blue) and LDM channels are visually nearly identical, while LHZ (black) is undisturbed. The horizontal signal is tilt of the local station environment induced by the air pressure change (see text).

of observed data are necessary, however, to maximize useful SNR (Crawford and Webb, 2000; Taira et al., 2014).

Tilt limits the operating range of a broadband instrument. The low-frequency sensitivity of early mechanical horizontal seismographs was often limited by the maximum allowable tilt or temperature change before hitting mechanical stops. Early efforts at EFFB were mostly directed to maintenance of the sensor mass within its nominal travel range. An EFFB sensor having a PID feedback system (e.g., **Figure 14**) with velocity output can function apparently normally in the presence of static tilts until the electrical limit defined by the maximum static feedback current (the sum of the integral and proportional feedback path) can no longer maintain the equilibrium position of the mass. When this point is reached, the sensor must be 'recentered' to adjust the mechanical portion of restoring force acting on the mass. The 'mass position' signal from broadband EFFB sensors is, in fact, the integrator output voltage. In a frequency band defined by the integrator time constant, a change in mass-position output is proportional to a change in acceleration acting on the sensor's mass. In a broadband sensor designed for the resolution of minimum Earth noise, the strength of the integral feedback path is designed so that the equivalent acceleration noise of the active electronic integrator driving the feedback force transducer is less than minimum Earth noise. Electronic amplifiers, on which integrators are built, typically have of the order of 140–150 dB useful dynamic range at low frequencies, for example, ~0.3–1 μV peak noise and a 10 V peak maximum output. If minimum Earth noise is $\sim 10^{-10}$ m s^{-2}, the maximum equivalent tilt-induced acceleration that the integral feedback can cancel is, say, $3 \times 10^{7} \times 10^{-10} = 3 \times 10^{-3}$ m s^{-2} or $\sim 3 \times 10^{-4}$ rad, or ~0.02 ° tilt. Triaxially symmetric (Melton, 1965; Melton and Kirkpatrick, 1970) seismometers such as the STS-2 or T240 are limited by the maximum tilt of any individual sensor since the outputs are vector sums of all sensors. Integral feedback may be increased to increase the tilt range of the closed loop, although this increases the input-equivalent noise. Some portable instruments use this approach to extend the maximum operational tilt at the expense of small signal resolution. The best usage of data from EFFB sensors requires monitoring that the mass-position limit has not been exceeded. This information is recorded as ancillary data by most data acquisition systems but is frequently overlooked in analysis. A broadband sensor whose mass-position limit is exceeded may appear to produce seismograms until the point where the limit of its displacement transducer is reached, but the transfer function is no longer LTI. If one sensor of a triaxially symmetric seismometer is beyond its mass-position limit, all axes are affected.

The pressure fields associated with wind turbulence induce long-period but comparatively short-wavelength ground motion, resulting in rapid attenuation with depth, so that substantial low-frequency tilt reduction is achieved by installation at least 100 m below the surface (Sorrells, 1971; Sorrells and Goforth, 1973). The absolute decrease in pressure-induced tilt with depth is dependent on the rigidity of the site rock (Sorrells and Goforth, 1973). Underground installations (150 m) have shown tilt reduction by as much as 20 dB (compared to a surface installation) at periods from 30 to 50 s period (Murphy and Savino, 1975). Peterson et al. (1976) showed improvement at 100 m relative to 15 m depth of more than 10 dB at periods to 100 s. Hutt et al. (2002) depict a typical improvement in horizontal noise level as a function of frequency and depth in **Figure 24(a)**. Holcomb et al. (1998), however, point out that the improvement in tilt noise is highly installation-dependent. Current practice favors sand to stabilize the sensor in the borehole and to suppress convection currents acting directly on the package. In other experiments (Hutt, personal communication), partial evacuation of the borehole has reduced tilt noise. The published results at frequencies below a few mHz, however, may be instrumentation limited (**Figure 24(b)**), since instruments with intrinsic noise levels near minimum Earth noise have not been available for operation in a borehole.

1.02.3.3 Systems

1.02.3.3.1 A/D conversion

The early 1960s saw pioneering efforts in digital earthquake data acquisition and recording (Bogert, 1961; DeBremaecker et al., 1962; Haubrich and Iyer, 1962). The large-aperture seismic array project (Green et al., 1965) demonstrated digital recording on a large scale. At Caltech (Miller, 1963; Phinney and Smith, 1963), continuous operation of a seismograph suitable for general studies with a 'library' of digital tapes was envisioned at least a decade before such a system became operational in the SRO (Peterson et al., 1976).

Today, virtually all seismic systems employ 'wide' ($\geq$24 binary bits) data word A/Ds based on oversampling delta–sigma ($\Delta\sum$) architecture (Inose et al., 1962; Steim and Wielandt, 1989). Following the introduction to broadband global seismographic systems of $\Delta\sum$ A/D technology in the original Harvard system (Steim, 1986), 'gain-ranged' A/Ds

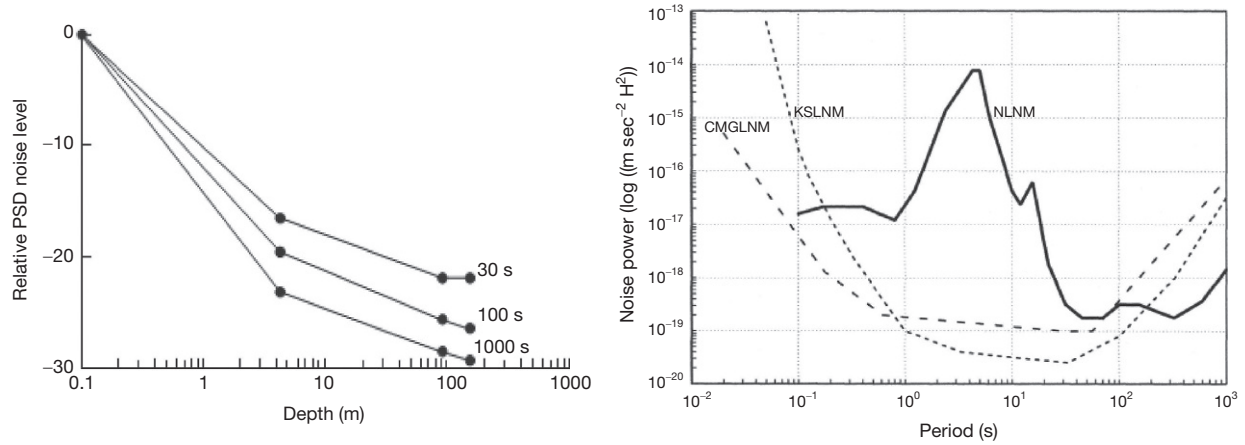

Figure 24 Left: Horizontal noise attenuation in a borehole as a function of depth at three selected periods. Depths 0, 4.3, 89, and 152 m. Reduction of nearly 20 dB is achieved at modest depths. The rate of improvement decreases with depth. The apparent improvement may be affected by changes in temperature variance as a function of depth. Right: Noise models of KS54000 and CMG-3TB borehole seismometers in use at GSN stations during the past decade. These borehole sensors do not resolve minimum low-frequency noise, suggesting that the measurements of borehole noise reduction may be affected by instrument noise. Adapted from Hutt CR, Bolton HF, and Holcomb LG (2002) US contribution to digital global seismograph networks. In: Lee W, et al. (ed.) *International Handbook of Earthquake and Engineering Seismology*. pp. 319–332.

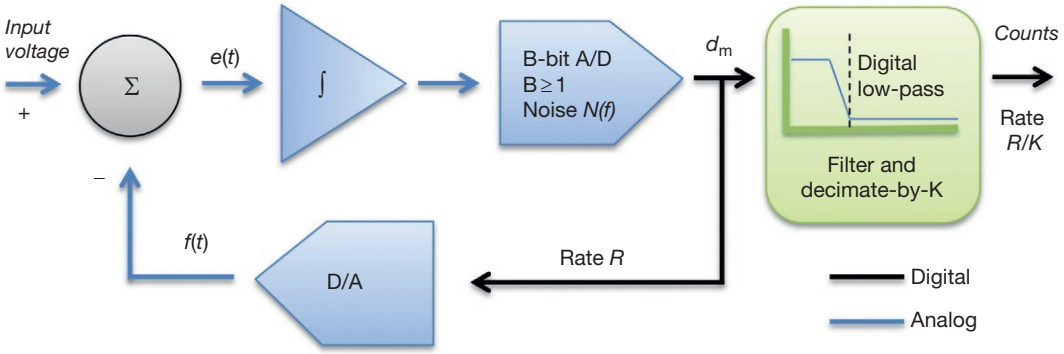

Figure 25 A first-order $\Delta\sum$ A/D converter. The input signal is summed with a feedback signal derived from a D/A converter. The difference signal is integrated and quantized to produce the digital output d_m which is fed back to the D/A converter. The integration boosts the ability of the quantizer to measure deviations in the average of the feedback signal from the input signal. The loop operates at a rate R much higher than the desired information bandwidth in the input voltage. Unwanted quantization noise outside the information passband is removed by the digital filter. Achievable SNR is defined by the noise and linearity of the D/A.

(Harjes and Seidl, 1978; Peterson et al., 1976), once popular in the exploration industry and global seismology, have essentially disappeared. They can be a source of demonstrable distortion in broadband systems (Steim, 1986).

$\Delta\sum$ A/D technology relies on *oversampling* and *noise shaping* to initially acquire digital samples of an analog signal at a sample rate that is highly relative to the information content, pushing the noise inherent in quantization to frequencies above the frequency band of interest. The resulting high-data-rate digital stream is low-pass-filtered and decimated (eqn [11]) to a sampling rate appropriate for the bandwidth delivered for analysis.

A $\Delta\sum$ system comprises a feedback loop containing an internal quantizer, a digital-to-analog (D/A) converter, and one or more integrators, as shown in Figure 25. The feedback tends to cause the time average of the digital output code d_m to represent the input voltage to the loop. The difference $e(t)$ between the input voltage and the D/A output $f(t)$ is integrated to give greater weight to lower frequencies in the comparison. This weighting achieves noise shaping. There are many loop topologies, although all rely on the same general principle. The most important element of a $\Delta\sum$ A/D is the D/A converter. As in the case of the force-feedback seismometer, the performance of the closed-loop system depends upon the linearity and noise of the element(s) that feeds back the output signal to the input. In a seismometer, these feedback elements over much of the frequency range are passive electronic components (resistors and capacitors) with high linearity and low noise. In the $\Delta\sum$ A/D, feedback is through a potentially complex active element, the D/A converter. Although an A/D may have an arbitrary data width (the number of bits in the output signal), the useful SNR of a $\Delta\sum$ A/D is defined by its D/A converter's actual electrical noise.

It can be shown (Aziz et al., 1996) that for a $\Delta\sum$ loop of order L (the number of integrations), setting the loop input voltage to zero leads to a description of the frequency dependence of the shaped noise power $N(f)$ of quantization of the B-bit A/D operating at rate R. For an input voltage range $\pm V$ and frequency f, $N(f)$ can be written:

$$N(f) = \frac{V^2}{3R \cdot 2^{2B-1}} \left(2\sin\left(\frac{\pi f}{R}\right)\right)^L \quad [34]$$

Figure 26 (with $V = R = 1$) shows that the shaped noise is increased beyond some signal passband of interest and decreased within the passband ($f \ll R$). The noise outside the passband is rejected by the low-pass digital filter. Equation [34] suggests that arbitrarily low noise within a defined passband is possible given high R and L; however, actual noise of a physical A/D is dominated by electronic noise, typically $1/f$ below some frequency and at some level. The measured terminated-noise spectrum (e.g., Figures 11, 28, and 29) is the only reliable specification of minimum A/D noise, that is, in the presence of no input signal. Noise may increase with signal applied. Tests discussed later address quantification of such signal-dependent noise.

Noise level, saturation level, linearity, signal bandwidth, and sampling rate define an A/D system. Noise and linearity

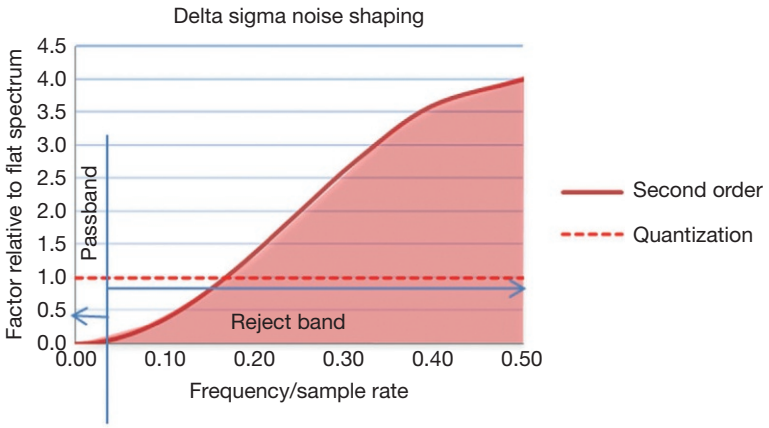

Figure 26 Noise shaping for a second-order $\Delta\sum$ A/D. The noise of quantization without shaping appears as the red-dashed line. Shaping forces quantization noise out of the passband, which is some small fraction of the $\Delta\sum$ loop rate. Quantization noise is increased above the passband of interest. Total quantization noise is actually increased. Noise above the passband is rejected by low-pass digital anti-alias filters. Noise shaping affects only quantization noise, not electronic noise in the shaping circuits, which limits the improvement achievable by a noise-shaped A/D.

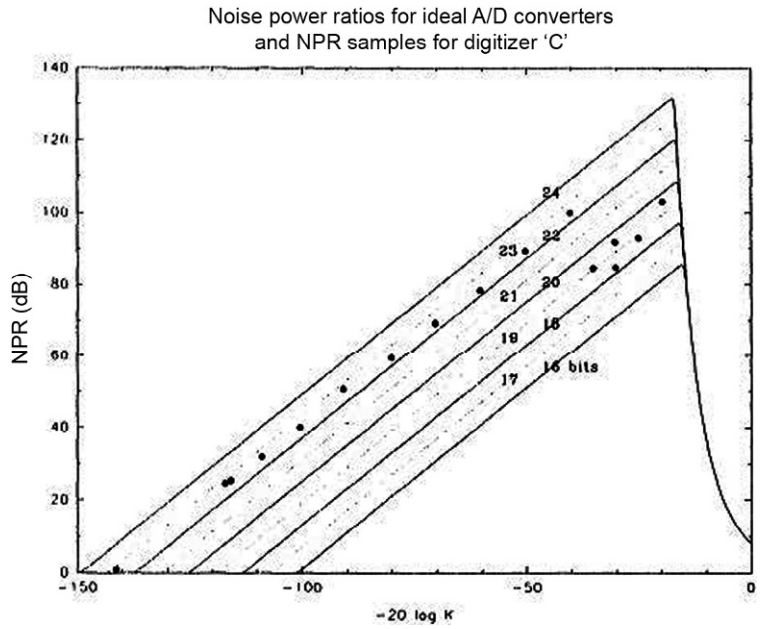

Figure 27 Results of modified noise power ratio (MNPR) test on a high-resolution digitizer. Dots indicate measurement of effective noise of an A/D with a signal applied. Horizontal axis is proportional to the amplitude of applied test signal. Vertical axis is proportional to SNR. In the case of this A/D under test, at a signal level well below its full scale, the effective noise of the A/D suddenly increases, resulting in a reduction of SNR. Adapted from McDonald T (1994) Modified noise power ratio testing of high resolution digitizers. *Sandia Report SAND94-0221*.

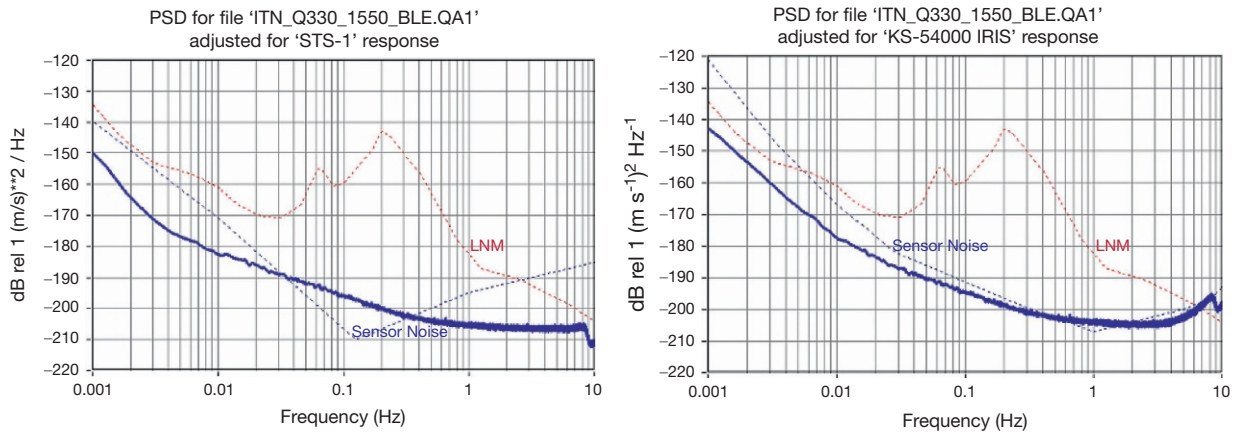

Figure 28 Engineering tests of the terminated-input noise of the A/D system used in global networks, represented as equivalent ground velocity PSD when connected with an STS-1/VBB seismometer, or a KS54000I. The input-equivalent noise is inversely proportional to the frequency-dependent magnitude of the seismometer transfer function. Adapted from Kromer RP (2006) *Technology Report Evaluation of the Kinemetrics/Quanterra Q330HR Remote Seismic System for IRIS/GSN Q330HR/GainX1 Configuration*.

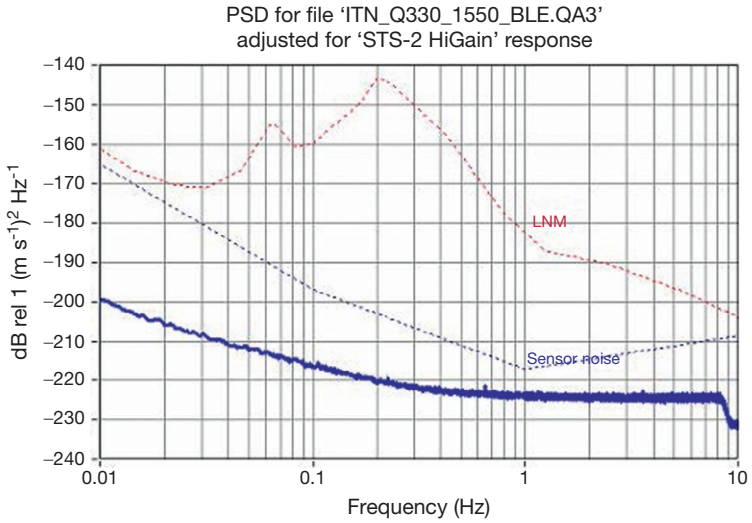

Figure 29 Similar to **Figure 28** for the large gain of the STS-2/high-gain seismometer. The excessive gain of the STS-2/HG wastes useful dynamic range, by reducing system clip level referred to ground acceleration. Digitizer input-equivalent noise is unnecessarily low when combined with a seismometer of such high gain. Adapted from Kromer RP (2006) *Technology Report Evaluation of the Kinemetrics/Quanterra Q330HR Remote Seismic System for IRIS/GSN Q330HR/GainX1 Configuration*.

are related, since if understood broadly, noise includes any digital output generated that is not strictly representative of the analog input signal. Such signal-generated noise may include products of nonlinear distortion in the A/D.

In the engineering literature, A/D behavior is often treated as having an essentially flat noise spectrum, since many applications of A/D converters involve frequencies above the $1/f$ corner of A/D noise. A/Ds with a comparatively small number of bits, say < 20, are typically dominated by quantization noise (white, uniformly distributed), since their quantization steps are large. Quantization noise (Bennett, 1948) is typically insignificant in digitizers for earthquake studies having 24 or more bits of resolution because the quantization steps are small; these systems are limited for small signals by their actual electronic noise. A nearly arbitrary number of bits may be included in the output words, sufficient to suppress quantization noise to an insignificant level. The number of bits in the output word of a $\Delta\sum$ A/D is nearly irrelevant, since that number is defined by the mathematics engines used to digitally low-pass filter the output data. An A/D with 24-bit arithmetic resolution, however, may produce many bits of actual noise.

Like sensors, the actual noise of A/D converters is frequency-dependent. The operating range of an A/D for earthquake seismology can be represented in an operating range diagram or the noise may be specified as a PSD spectrum along with the clip level. **Figure 11**, for example, shows A/D operating range expressed as equivalent peak noise and clip level. Such a representation shows the minimum A/D noise level in the absence of input to the A/D. These noise measurements are taken with a *terminated input*, that is, a resistance bridging the A/D inputs to

simulate the source resistance of a sensor. The A/D noise cannot be less than its terminated-input noise, although it can be higher in the presence of signal-related nonlinear distortion. The maximum potential dynamic range (MPDR) of an A/D is usually quoted in dB as the rms ratio of A/D output for a maximum continuous sine-wave input to its input-terminated noise. As with sensors, specification of bandwidth is required. For example, the A/D noise illustrated in Figure 11 is equivalent to an MPDR of 164 dB in an octave below 1 Hz. As Figure 11 shows, terminated-input noise is white to some $1/f$ corner frequency, below which power is constant in bands of constant relative width. Similar behavior appears to be common to many seismic A/Ds (Sleeman, 2006).

Terminated input noise tests are important for earthquake A/Ds because many signals are small compared to the available operating range. A complete characterization of an A/D, however, also requires measurement of the A/D noise level in the presence of large signals. There are several approaches. The simplest conceptually is to apply a signal of known characteristics, such as a sine wave, and measure the power of harmonics in the A/D output resulting from nonlinear distortion. Such a total harmonic distortion (THD) measurement (Kromer, 2006) is effective because most signal-dependent distortions generate harmonics of a comparatively pure input sine, although the method is difficult to apply for high-resolution seismic digitizers because signal sources with the required THD approaching −140 dB are not widely available. The known THD of the signal source must be significantly less than A/D THD to resolve A/D nonlinearity meaningfully. In addition, a standard A/D capable of verifying the signal source is required for reliable measurements over time.

Another approach to nonlinearity measurement is to inject an arbitrary signal into two nominally identical channels and calculate the incoherent noise power between the resulting digital outputs. Alternatively, one may analyze or model the arithmetic difference of the outputs. The latter approach is slightly less robust, since sample-wise subtraction of two potentially large signals is sensitive to small phase shifts between channels. Measurement of incoherent power is able to simultaneously resolve small phase differences, which can be corrected.

The incoherent power so calculated can be compared with the terminated-input noise or compared to the ideal noise of quantization for a digitizer with the same number of bits in the output word. If the arbitrary signal injected spans a wide range of amplitudes, the behavior of the A/D as a function of amplitude can be characterized. Nonlinear distortion may appear as an elevated ratio of incoherent power between the two channels at low or high amplitudes. McDonald (1994) applied the so-called modified noise power ratio (MNPR) method for the first time to the measure of nonlinearity of several then-current models of 24-bit A/D converter as a function of applied signal amplitude using a white noise source, finding in some A/Ds a strong knee-like dependence on amplitude. Figure 27 shows the result of such an analysis. McDonald described the behavior of this A/D:

> . . .this system has about 22 bits of linearity for low-level signals, but suddenly degrades to an erratic 18-to-20-bit performance level for large signals. The break occurs when the RMS input signal value is approximately 2% of positive full scale. This severe characteristic is typical of gain-ranged systems, which achieve a large dynamic range with limited linearity.

The MNPR test requires no special test equipment. A/D systems capable of generating a signal used for sensor calibration may use the same signal for the A/D. The characteristics of the input signal are unimportant, provided that a sufficient range of frequencies and amplitudes are driven, because the same signal is applied to both input channels. In principle, the method is unable to detect an error in the A/D that would generate identical distortion products for a given input signal input to two channels; however, application of the method has shown that results are generally correlated with THD measurements. THD measurements are preferred where available. IEEE Std-1057 (IEEE, 2001), standard for digitizing waveform recorders, and IEEE Std-1241 (IEEE, 2000), standard for terminology and test methods for A/D converters, define formalized test procedures for quantification of A/D systems.

From a system design perspective, one can today nearly assume that A/D noise will not limit system performance in combination with an active force-feedback sensor. Figure 28, for example, shows that digitizer noise in the GSN is uniformly below sensor noise within the sensor's passband. The positioning of noise of the digitizer relative to sensor noise is defined by sensor or digitizer gain. Generally, only sufficient gain should be used to result in the condition illustrated in Figure 28, where digitizer noise is slightly below sensor noise. Additional gain results in a loss of operating and dynamic range for large signals. The powers of uncorrelated noise sources add.

Figure 29 shows the positioning of digitizer noise relative to sensor noise using a sensor with high gain (the STS-2/HG, having a generator constant of 20 000 V m^{-1} s instead of the usual 1500).

In this case, the digitizer noise is unnecessarily below sensor noise – and farther still below actual ambient seismic noise at most sites. McNamara et al. (2005) concluded that the choice of high-gain sensors is likely to result in saturation on large events in North America. Excess gain in a sensor is generally a historical remnant from the time when A/D dynamic range was 100 times less than now. Present A/D systems typically incorporate the option to use modest additional gain where low sensor output requires better matching, or in applications requiring increased SNR, such as comparative instrument research or high-frequency/low-noise work. Gain within the digitizer is preferred because of the likelihood of a faster recovery time from saturation. A force-feedback sensor having high gain within its feedback loop, for example, may require many minutes to recover from saturation, whereas a digitizer will generally recover within the equivalent time length of its digital anti-alias filters – on the order of a few seconds for data rates on the order of 40 sps. Lower A/D noise permits the use of lower sensor gain, increasing operating and dynamic range. Lower gain in sensors and A/Ds moves the amplitudes of typical signals farther below the saturation level, which reduces the possible effect of power-law or threshold-driven amplitude-dependent nonlinearity, such as illustrated in Figure 27.

The sharp-cutoff frequency response of most low-pass digital anti-alias filters necessarily implies Gibbs-phenomenon (Scherbaum, 2001) overshoot on signals that contain substantial energy at the filter corner frequency, as may arise at regional distances. The response of a typical filter to a unit step is shown in Figure 30. This filter has about 25% overshoot

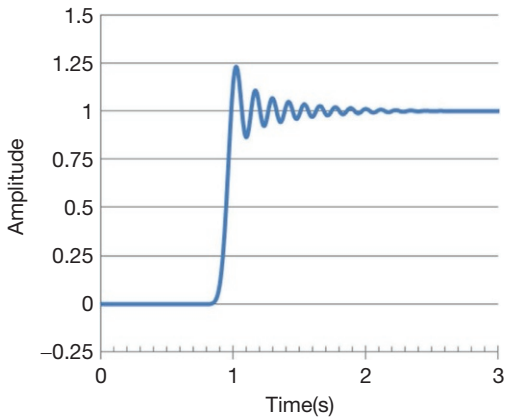

Figure 30 The response to a unit step of a typical high-order minimum-delay digital anti-alias filter used in A/D systems. The horizontal axis is time. The overshoot is ~25% of the step amplitude. Some A/D systems use arithmetic that cannot represent numbers larger than a nominal fixed value representing a full scale of 1.0. When overshoot occurs, such arithmetic may fail, or 'wrap' to a maximum value of opposite sign. This limitation is typically compensated by reducing effective gain so that a static signal can never reach more than, say, 1/1.25 of the nominal fixed value representing full scale. This approach wastes dynamic range. Other A/D systems can generate output codes significantly above the nominal full scale.

for a unit step input. Some integrated A/Ds use numeric accumulators with a fixed word length. In these A/Ds, the overshoot on dynamic signals may exceed the word length, resulting in clipping or amplitude 'wrapping' around the word length. Avoidance requires reduction of the signal level by the inverse of the overshoot factor, say to 80%. Systems so affected have an effective operating range reduction by the overshoot factor.

Another aspect of behavior at and above the nominal saturation level varies among various A/D systems. Each A/D's nominal saturation level is stated usually as a maximum peak bipolar voltage, for example, ±20 V for a specific digital code, say $\pm 2^{23}$ counts. When this value is exceeded, the output of the A/D may limit at the nominal maximum code, or it may wrap from maximum positive to maximum negative within some amplitude range, or it may be undefined if the A/D abruptly fails above the nominal saturation voltage. Another behavior is to continue to output a code representing the input signal exceeding the nominal saturation level by as much as 30%. This is a useful feature because many broadband sensors may produce output signals above their nominal maximum output voltages of, say, ±20 V, being limited only by higher power supply voltages. The linearity of both sensor and digitizer will be degraded in such an *overrange* condition, but these data may be useful if analyzed with caution. Analysts and code writers should be prepared to find signals above the nominal maximum A/D code expected for given systems. Many global and regional network systems operate this way.

1.02.3.3.2 Digital filters

Digital low-pass filters are an important element of digital broadband instrumentation. Many references address the topic of digital filters in general and with specific application to seismology (e.g., Oppenheim and Schafer, 2009; Rabiner and Gold, 1975; Scherbaum, 2001; Seidl, 1980). This section will treat one aspect of digital FIR filters that is important to both the problem of instrumentation and analysis of seismograms.

Whereas early analog systems required extensive use of electronic or electromechanical filters to shape frequency response to enhance small signals and reject 'noise,' filters are used within a broadband data system for only one reason: as anti-alias filters to reduce bandwidth accompanying decimation to a specified sample rate (Bennett, 1948; Blackman and Tukey, 1959; Oppenheim and Schafer, 2009; Shannon, 1949). Typically, a single data source is successively reduced in bandwidth to create compact data streams appropriate for long-duration analyses. For example, the GSN system records data simultaneously at 100, 40, 1, and 0.1 sps from the same sensor, reducing the data volume by as much as 1000 times for analyses requiring only low-bandwidth data. This would be cumbersome to do after the fact if only the highest-rate data were recorded. The required anti-alias FIR filters (eqn [10]) are applied in nearly real time in the time domain on a continuous input data sequence from the A/D.

Other types of digital filters may also be calculated in nearly real time for application-specific data processing. Examples include bandwidth limitation for event detection or simulation of Wood–Anderson seismometers (Anderson and Wood, 1925; Kanamori, 1999). These applications are not considered intrinsically part of the data system.

The principal guiding design of digital anti-alias filters is to pass a maximum band of frequencies for a given sampling rate, using a filter with a 'reasonable' time duration. An ideal filter would pass all frequencies with constant amplitude up to 1/2 the sampling rate at the output of the filter, would have a brief duration, and would contribute no phase distortion. Such a filter is unfortunately impossible, since the sharpness in the frequency domain is necessarily related to the duration of the filter's time-domain response. The filters used for anti-alias filtration, therefore, as in all engineering represent a compromise.

The most common anti-alias filter is a 'linear-phase' filter, which has a symmetrical response in time (zero-phase) shifted by 1/2 the filter duration to make the filter physically realizable. In many cases, this filter can simply be ignored in data analysis. The constant delay is compensated in the time labels of acquired data. The phase response of waveforms is not distorted by such a filter. Where substantial signal energy exists near the corner frequency of the filter, however, the symmetrical filter response introduces *acausal* effects in the filtered data that appear to originate before their associated signal. For many analyses, an appropriate procedure is to simply slightly reduce the bandwidth of observation with an additional causal filter, such as a Butterworth low-pass filter. In general, information near the corner frequency of sharp filters should be treated with caution because of the steep roll-off. Deconvolution of data near the corner frequency is unreliable because of the rapid loss of SNR near and above the corner frequency.

The problem of ex post facto elimination of such acausal effects has been considered (Haney et al., 2012; Scherbaum and Bouin, 1997). As Scherbaum and Bouin (1997) has pointed out, a generalized approach is tedious and error prone – if not impossible – without detailed knowledge of each filtration and decimation step occurring inside a data acquisition system.

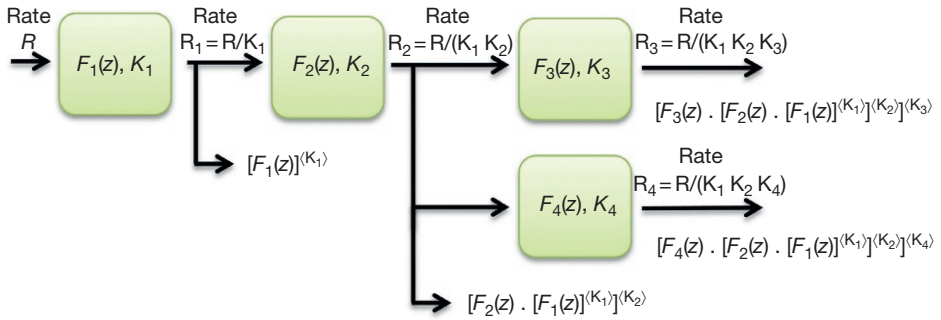

Figure 31 A digital anti-alias filtration and decimation 'chain.' Each filter stage has a Z-transform response $F_n(z)$ and a decimation factor K_n. The output from successive stages combines the effect of each prior stage, including phase shifts corresponding to time intervals less than one sample of the output rate. Such phase shifts result in difficulty modeling the filtration decimation process (Scherbaum, 2001). Consider the case where $K_3 = K_4$, and filters F_3 and F_4 have an identical length and amplitude response. If one filter has a minimum-delay response and the other has a linear-phase response, the resulting decimated filters represent a complementary *composite* pair. Such a pair concisely contains the information necessary to deconvolve acausal effects from data acquired with the linear-phase member of the pair, or to remove the phase from data acquired with the minimum-delay member of the pair (see text).

1.02.3.3.2.1 Composite responses and correction of acausal effects

In an A/D system, digital anti-alias filtration and decimation are successively applied in stages, comprising a chain. The response at the output of each stage builds upon the preceding stage. Figure 31 illustrates a filtration/decimation chain with four simultaneous output sampling rates, R_n. The notation $[F_1(z)]^{\langle K_1 \rangle}$ describes filtration by filter F_1 having Z-transform response $F_1(z)$ followed by decimation by factor K_1. At the output of each stage of filtration and decimation, the effective response incorporates the response and effect of decimation in all preceding stages.

The effective responses corresponding at each filter output are compact, since they are decimated. There is no information in the decimated responses describing the bands of frequencies rejected. Such a response description can be called a *composite* response.

The widely used Standard for the Exchange of Earthquake Data (SEED) format (IRIS, 2012) includes features to describe analog and digital filters within instruments, however, is not well suited to a detailed description of implementation-dependent operations internal to a data logger, such as in a decimation chain. Most of the information contained in the internal filters pertains to frequencies that are filtered out in the data delivered to the seismologist. If the anti-alias rejection is assumed to be adequate by design, the response at frequencies not present in the output has no value in seismological analysis. The response in the remaining passband, represented in the composite response, is of seismological interest.

Consider the example of Figure 31 where filters F_1, F_2, and F_3 have minimum delay, while F_4 has linear phase. In addition, specify that the $|F_3(z)| = |F_4(z)|$, $K_3 = K_4$. The resulting responses from stages 3 and 4 are a complementary pair differing only in phase. The two members of the pair incorporate identical inter-stage fractional-sample phase shifts accompanying decimation described by Scherbaum (2001) that are necessary to understand for accurate deconvolution of acausal effects. An A/D system would not typically actually record data simultaneously with two different phase responses; the choice to record linear-phase or minimum-delay filtered data would be made by a network operator. The availability of complementary composite pairs, however, enables a simple method to remove acausal effects in recorded data.

For example, the Quanterra Q330 defines seven possible selectable sample rates and four possible combinations of filters: all linear-phase filters or minimum-delay filters to reach 100, 40, or 20 sps followed by linear-phase filters for lower sample rates. Higher-rate data using minimum-delay filters may be used, for example, for seismic arrival picking, while lower-rate data, with a simple phase response, may be used for whole-waveform modeling. Twenty-eight possible filters comprise the canonical set of composite responses of the A/D system within the signal passband pertinent to the associated sample rate.

Figure 32 shows one complementary pair from the canonical set of FIR filters for a Q330. In blue is the A filter, having K elements a_k, for 20 sps output with linear-phase response; in red is the minimum-delay filter B, having K elements b_k for 20 sps data. The pair of filters has identical length $K = 67$ and amplitude response that is flat to roughly 80% of the passband and rolls off steeply. A filter C comprising a sequence c_n of arbitrary length N may be defined to filter a sequence $\{x_m\}$ originally acquired using A to the sequence $\{y_m\}$ as if it were acquired with B:

$$y_m = \sum_{n=0}^{N} c_n x_{m-n} \qquad [35]$$

Equation [35] can be recognized as description of a FIR filter, as in eqn [7]. Delay of the result y_m is ignored for the present discussion. The filter C can be derived from only the A, B filter pair and can be considered to be the convolution of B with a filter $\widetilde{A}$, where $\widetilde{A}$ represents a filter with a response inverse to A, such that convolution of $\widetilde{A}$ with the sequence $\{x_m\}$ deconvolves the response of A from $\{x_m\}$. Physically, such a filter $\widetilde{A}$ cannot be realized, since the frequency response of A sharply reduces the SNR in $\{x_m\}$ at frequencies above the filter corner. The application of $\widetilde{A}$ can be viewed as equivalent to the unstable division of the spectrum $\mathcal{D}\{x_m\}$ of $\{x_m\}$ by arbitrarily small numbers as 1/2 the sample rate is approached. However, the amplitude spectrum of A and B

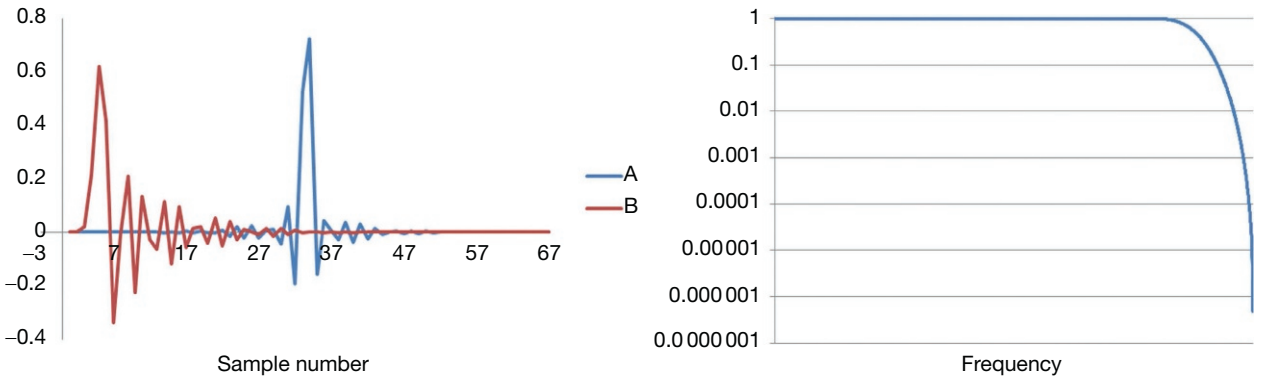

Figure 32 Left: The minimum-delay (B, red) and linear-phase (A, blue) members of a complementary composite pair of digital low-pass filters, each having 67 coefficients. This pair is used to generate 20 sps data in a Quanterra Q330. The apparently slightly asymmetrical appearance results from subsample phase shifts in earlier filtration stages. Right: The identical amplitude response of both filters.

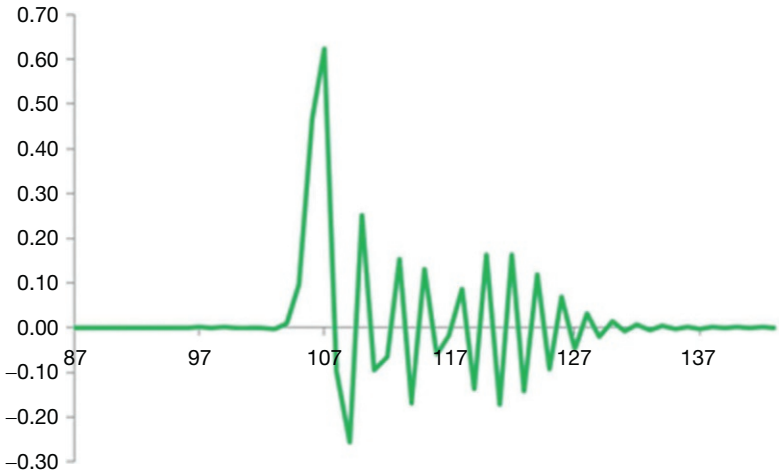

Figure 33 The time-domain filter derived from the complementary composite pair in **Figure 32** used to deconvolve acausal effects from data recorded using the linear-phase member of the pair.

are defined as identical. Therefore, a division of the finite spectra

$$\frac{\mathcal{D}\{b_k\}}{\mathcal{D}\{a_k\}} \qquad [36]$$

is stable and in principle represents the discrete phase-only, unit-amplitude spectrum of C if $N = K$, that is,

$$\mathcal{D}^{-1}\left\{\frac{\mathcal{D}\{b_k\}}{\mathcal{D}\{a_k\}}\right\} = \{c_k\} \qquad [37]$$

The filter $\{c_k\}$ calculated by eqn [37] would exhibit Gibbs-phenomenon oscillations caused by end effects. A numerical procedure to reduce such 'ringing' is to define sequences a'_n and b'_n of length N where $N > K$, for example, $4K$, and the elements $a'_{k+2K} = a_k, b'_{k+2K} = b_k$ with all other elements of $a'_n = b'_n = 0$. The actual sequences a_k and b_k therefore are padded with leading and trailing zeros to reduce wrap-around effects. The amplitude of the spectral ratio in eqn [37] can be set to unify at all frequencies to further suppress ringing at the sample rate.

Figure 33 shows the resulting all-phase FIR filter, arbitrarily shifted for clarity. Figure 34 shows application of the all-phase filter to the removal of acausal precursors in recorded data; the horizontal axis is sample number at 20 sps. The blue trace in the left panel of Figure 34 shows the data from a local magnitude 2.5 earthquake at about 9 km epicentral distance recorded on an STS-2 at 20 sps using the A linear-phase filter shown in Figure 32. The peak amplitude is 1.6×10^{-4} m s^{-1}, dominated by 25 Hz. This was a strong signal with rich high-frequency content. Overlain in the red trace are data simultaneously acquired from a preceding 100 sps output rate in the filter chain. The 100 sps data are casually filtered to the same ~7.5 Hz bandwidth as the 20 sps data. An oscillatory acausal precursor on the 20 sps data is obvious. The right panel of Figure 34, magnified, shows the application of the correction FIR filter in Figure 33, using eqn [35], to the 20 sps data from this event. The trace in black shows the corrected data with no precursor and agreement with the data derived by causal filtration from 100 sps. The trace in black, after application of the correction filter, has the effective response of the B filter in Figure 32.

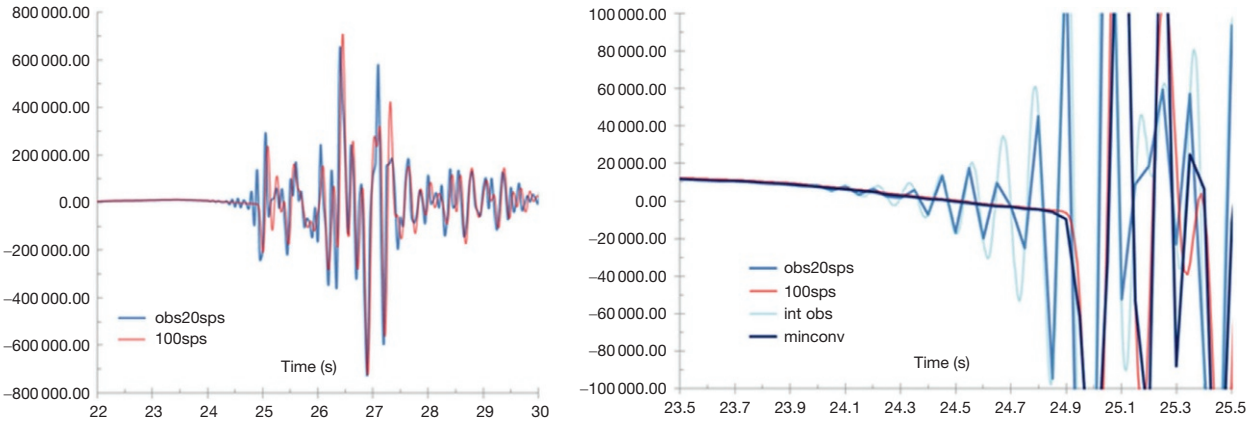

Figure 34 An example of the removal of acausal ringing using the all-phase filter shown in **Figure 33**. Left: The original 20 sps data (blue) for an M2.5 event at about 9 km distance are shown with data simultaneously acquired from an earlier stage in the filtration chain at 100 sps (red). The sharp linear-phase filter used to produce the 20 sps creates a strong acausal effect not present on the 100 sps data. Right: The initial onset is magnified ×8, with two additional traces. The light blue (int obs) is the observed 20 sps data interpolated to a higher sample rate to remove distortion of the plotted waveform. The black trace (minconv) is the observed 20 sps after passing through the filter of **Figure 33**, showing removal of the acausal precursor. The onset of the deconvolved data agrees closely with the data originally acquired at 100 sps using causal filtration.

1.02.3.3.3 Timing

Timing to a seismologist processing digital data is generally understood to describe the accuracy of time labels applied to acquired data sequences. To an instrument designer, timing implies the coordination of several elements necessary to result in the continuous delivery of accurately timed data.

1.02.3.3.3.1 Time reference

A system requires a time reference, traceable to universal time (UT). For most land-based instrumentation over the past 20 years, GPS has become the *de facto* standard time reference, provided through a small receiver. GPS receivers provide three necessary pieces of information to enable their use as a time reference:

1. A fiducial pulse, such as 1 pulse s^{-1}, occurring on transitions of UT. The pulse is derived from a local oscillator inside the receiver that is phase-locked to information derived from the radio signal. Without radio reception, the receiver's oscillator stability is typically fairly poor and the 1 pulse s^{-1} is not UT-synchronous.
2. A digital label identifying the UT represented by each pulse.
3. *State-of-health* (SOH) information on the potential errors that may arise with variations in or loss of radio reception. This information is necessary to provide to users of the reference information provided in points 1 and 2, because when radio reception is degraded, the time reference may rapidly become very inaccurate.

Sites such as those on the ocean bottom or deep underground may be unable to use a radio-based time reference and may depend on a local time reference that is periodically synchronized to UT. Such a local time reference depends on a very stable oscillator and accurate initial (and final) synchronization with a known reference. The accuracy of such a reference depends on minimum and predictable frequency error. Recently, low-power atomic-standard oscillators have become available, making possible the construction of a local time reference that has been shown to accumulate an error that can be much less than 10^{-4} s day^{-1} (Gardner and Collins, 2012). This compares with a typical 10^{-6} s rms time reference stability from common C/A code GPS receivers, independent of duration.

Although GPS receivers have become remarkably reliable, errors in their internal data processing, and possible occasional errors in the signals transmitted from the GPS ground management system, occur with finite probability. Some receivers have been observed to randomly, and persistently, emit erroneous codes for long intervals. In some cases, the errors are immediately obvious, such as incorrect management of 19-year GPS epochs, while in other cases, errors of 1 s are essentially undetectable by equipment dependent on the receiver as a reference source. Because the probability of an error is finite, and the operation of GPS receivers in global and regional seismic networks is continuous, the likelihood of inaccurately timed data is not insignificant. The probability of an error can be reduced to a manageable level by the application of further heuristic qualification of the time reference signals provided by receivers in the A/D system. A common tool, for example, is to ignore the time reference if a phase discontinuity is detected in the sequence of time reference pulses.

1.02.3.3.3.2 Time base purity

Oversampling A/Ds in ubiquitous use require a constant frequency *clock* (not to be confused with a clock giving the time of day) signal, from which the initial high sampling rate is derived. In these types of A/Ds, clock *jitter*, that is, variation in the width of sample periods Δt, can significantly elevate noise of the A/D. The local clock, therefore, must typically be derived from a stable local oscillator. This oscillator may or may not be the same local oscillator used to provide a time reference. For the time reference oscillator, the integrated stability is important: over a long period such as a day, the number of cycles should be constant and predictable. For the A/D clock oscillator, the jitter must be low, although the frequency need not necessarily be precisely known or stable over long times in order to attach an accurate time label.

1.02.3.3.3.3 Static time corrections and time label management

Every system includes fixed, known delays that may depend on physical circuit elements or digital data processing, such as digital filters. Known delays are compensated for in-time labels attached to acquired data or described in some accompanying embedded metadata. Minimum-delay anti-alias filters, in which the group delay is a function of frequency, require an arbitrary definition for delay compensation. One approach is not to compensate at all for delays of minimum-delay filters and require that data consumers calculate the group delay. Another approach is to estimate the filter group delay in the limit of zero frequency (as in the GSN system) or some reference frequency. Ambiguity for data consumers can be reduced by introducing a known waveform such as a step into the input of the A/D system at a defined time, such as a 1 min transition of UT. This approach was used many years ago in the WWSSN and remains a useful check on the management of static time corrections in complex digital systems. Uncertainties arise in each element of a potentially long chain of operations associated with time label management.

1.02.3.3.3.4 Time labels and sampling

Time labeling is defined as the attachment of a UT time label to a specific data sample. An A/D may free run – the samples of the A/D may be taken at any time offset τ with respect to UT and the offset τ measured (case A in Figure 35) – or the samples, taken at intervals Δt_{nom}, may be sampled at fiducial transitions of UT (case B in Figure 35). In Figure 35, the heavy black arrows represent the occurrence of a time reference pulse. The figure depicts, for example, an interval of four samples between time reference pulses. Ideally, the A/D clock oscillates at a frequency resulting in as close as possible to, for example, 86400.0 samples taken at 1 sps during a 24 h period. The green arrow indicates an active *phase lock* process to drive the sampling transitions to coincide with the transitions of UT. The data represented in case A are accurately timed, but do not occur at UT transitions. The time, for example, in case A of sample zero following the reference pulse T_n, is $T_n+\tau_1$. At constant clock frequency, $\tau_1=\tau_2=\tau_3$. A *time tear* is defined as the difference between the time label of a sample and the time of the sample calculated by counting samples from a previously labeled sample. By definition of Δt_{nom}, $T_{n+4}=T_n+4\Delta t_{\text{nom}}$. If the frequency of the clock in case A is such that, for example, $\tau_1\neq\tau_2\neq\tau_3$, there may be small apparent time tears, for example, between the samples taken at time $T_n+\tau_1$ and $T_{n+4}+\tau_2$. If, for example, $|\tau_1-\tau_2|\ll\tau_1$, the time tear can be considered insignificant. Typically, data segments are analyzed using the time label nearest the start of the

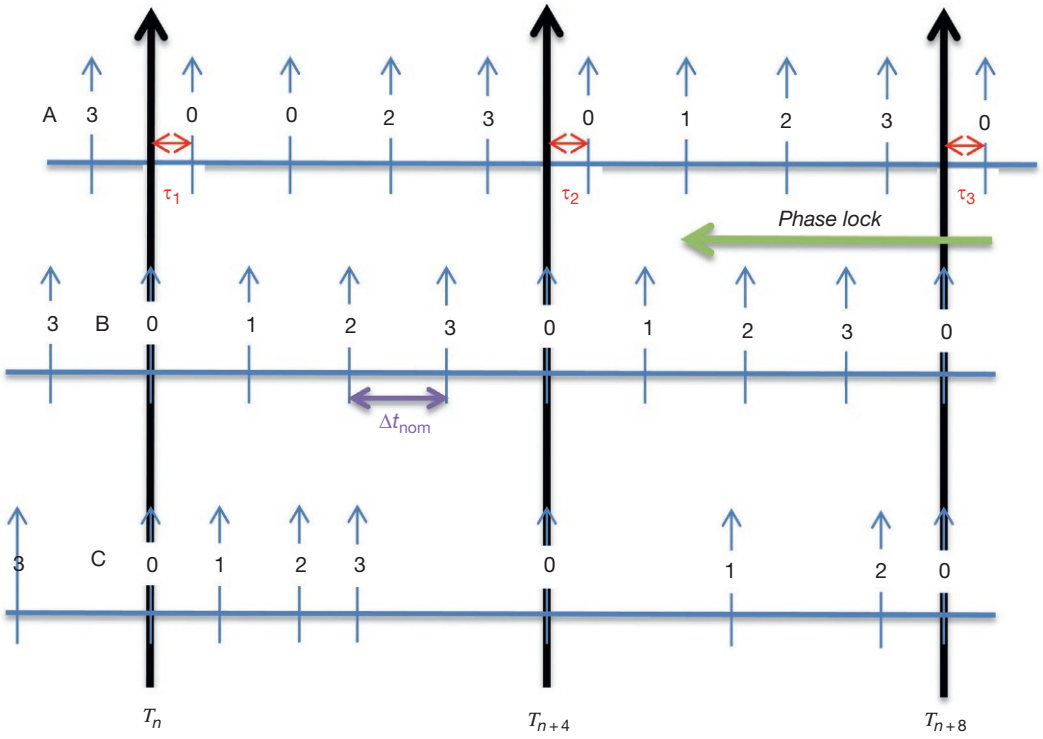

Figure 35 Three cases showing time labeling and sampling. The heavy black lines represent universal time (UT) transitions occurring, for illustration purposes, at intervals of 4 s. The thin blue arrows indicate the times at which samples are taken. Case A shows a system in which the samples are taken at an arbitrary offset τ with respect to UT. At each transition of UT, τ is measured and used to create a time label. For example, the time label of the second sample after UT transition T_n is $T_n+\tau_1+2\bullet\Delta t_{\text{nom}}$ where Δt_{nom} is the nominal sample interval. The accuracy of time labels diminishes with increasing time between measurements of τ. A sampling interval slightly different than Δt_{nom} creates small 'time tears' of magnitude $\tau_{n+1}-\tau_n$. The sampling times may be aligned with transitions of UT, and τ made arbitrarily small by *phase locking* A/D sampling to UT, as shown in case B. All stations in a network sample synchronously in this case. Case C, highly exaggerated, shows an system in which a sampling clock with poor stability is periodically 'jam set' to UT transitions, and actual offset τ is not measured. Such a sampling system can exhibit low-phase purity that can degrade high-resolution A/Ds and accumulate time errors that are unreported.

segment. If no significant time tear occurs within the segment, all samples in the data segment can be considered uniformly sampled and timed as accurately as the first time label.

Case C represents two scenarios using exaggeration: an A/D clock of poor stability and the *jam setting* of an A/D timing system. In this case, the A/D is forcibly resynchronized to the time reference at every reference occurrence. Data samples at the reference times are labeled correctly and are taken at fiducial transitions of UT. As time from the nearest reference pulse increases, however, the accuracy degrades because of variation and error in the sample interval. In extreme cases, samples may even be missing. This approach was frequently used before the appearance of oversampling A/Ds, which cannot tolerate excessive clock phase variance. A system such as C in which sample alignment with the time reference is assumed, but not measured, can lead to a false appearance of accurate timing.

1.02.3.3.5 Phase lock

The A/D sampling clock may be phase-locked (case B **Figure 35**) to a UT reference using a PID feedback loop. **Figure 36** (right) shows the PID loop used in GSN systems to maintain sampling in UT synchrony and to generate time quality information. **Figure 36** (left) shows that the sampling clock frequency control is forced to follow ambient seasonal temperature variation and secular aging of the sampling clock oscillator. In a network of such systems, each data sample throughout the network is taken simultaneously. Array processing is simplified with network-wide UT-synchronous sampling (IRIS, 2012).

1.02.3.3.6 Time quality and the time label vector

The PID control loop used to phase lock the A/D clock generates as a by-product significant amounts of SOH information that describe the *quality* of time labeling. Time quality quantifies in some way confidence in time label accuracy. Time quality uses all available information, including the SOH information available from the time reference, and internal measures, such as the variance of the sequence of phase measurements τ_n of the A/D clock to determine if the oscillator quality and time label accuracy are within defined limits.

With a quality measure available, the time labels applied to data may be considered to be a vector-valued function representing the notion of time in the A/D system. The components of the vector for each time label include one or more measures of time quality and the value of time label. Time labels in an A/D system should not be considered without evaluation of the quality components. The time quality concept was developed in the original Harvard system. Data management facilities make an abbreviated time quality available to users in the SEED *data extension blockette* (IRIS, 2012) as a percentage 0–100 that can help the user detect data that may be unreliably timed. The quality components of the time label vector may also be treated as independent time series synchronous with data. Some data management systems now make available several quality components of the time vector as uniformly sampled time series (e.g., the SEED channels LCE, τ_n, in **Figure 35**; LCQ, time quality; LCL, time since the loss of acceptable time quality; and VCO, the frequency control value used by the A/D sampling clock).

1.02.3.3.4 Ancillary data

Broadband data systems typically have the ability to collect multiple data sources in addition to the output of one or more seismometers. While in principle the measurement of temperature could be used to improve the quality of low-frequency seismic data in post processing, the required resolution of the order of 10^{-6} K is not feasible, although resolution of 10^{-4} K has been reported in some GEOSCOPE (Romanowicz et al., 1985) stations (Roult et al., 2010). A seismometer responds not only to uniform variations in temperature, but also the gradient throughout the structure. A low-frequency seismometer, in fact, is a sensitive and very high-resolution averaging temperature transducer. Contemporaneous recording of quantities such as atmospheric pressure and temperature and other meteorological data, information

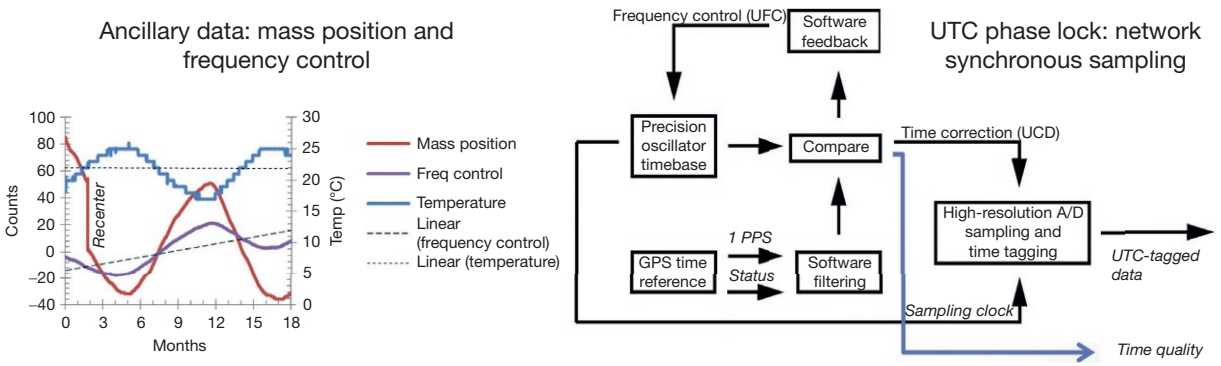

Figure 36 *Right*: The system for sampling clock generation and phase locking in GSN stations. A local sampling clock is derived from a frequency controllable temperature-compensated oscillator. The small time offsets (τ_n in **Figure 35**) between the sample times and UT are driven toward zero by controlling the oscillator frequency. The software-driven phase-locked loop assigns the *quality* of time labeling based on information provided by the UT time reference and variance of the sequence τ_n. When phase-locked, the sample times of stations in a network are simultaneous at UT transitions. Time labels and time quality constitute the *time vector*, fully describing data timing. *Left*: 18 months of ancillary data from GSN station HRV including the phase-locked frequency control (violet) and sensor mass position (brown) as a function of temperature (blue). During this period, the temperature changes seasonally with an amplitude of $\pm 3.5\,^{\circ}$. The 'time correction' (τ_n) during this interval did not exceed 4 μs. The frequency control is adjusted by the PID loop to compensate for seasonal temperature change and aging-induced secular change of the sampling clock. The STS-1/VBB sensor was recentered at month 2 to correspond with seasonal temperature zero-crossing.

on power supply voltages or other states of health, and even quantities such as efficiency of communications, however, can be valuable in analyzing the causes of noise or disturbances in the seismic data. Such analyses are particularly helpful if ancillary data are recorded as a time series with accurate time labels. Systems such as the GSN, for example, typically record 40 or more independent time series including the ancillary data, co-sampled with seismic data.

Atmospheric pressure deserves consideration because of its strong effect on low-frequency measurements (Figures 18–22). Seismographic observatories have long recorded meteorological background data. The value of digital barometric data for low-frequency seismology was recognized early (DeBremaecker and Sitton, 1963). Figure 37 shows the barometric pressure spectrum spanning the frequencies of broadband systems. Various typical and low-level observed spectra

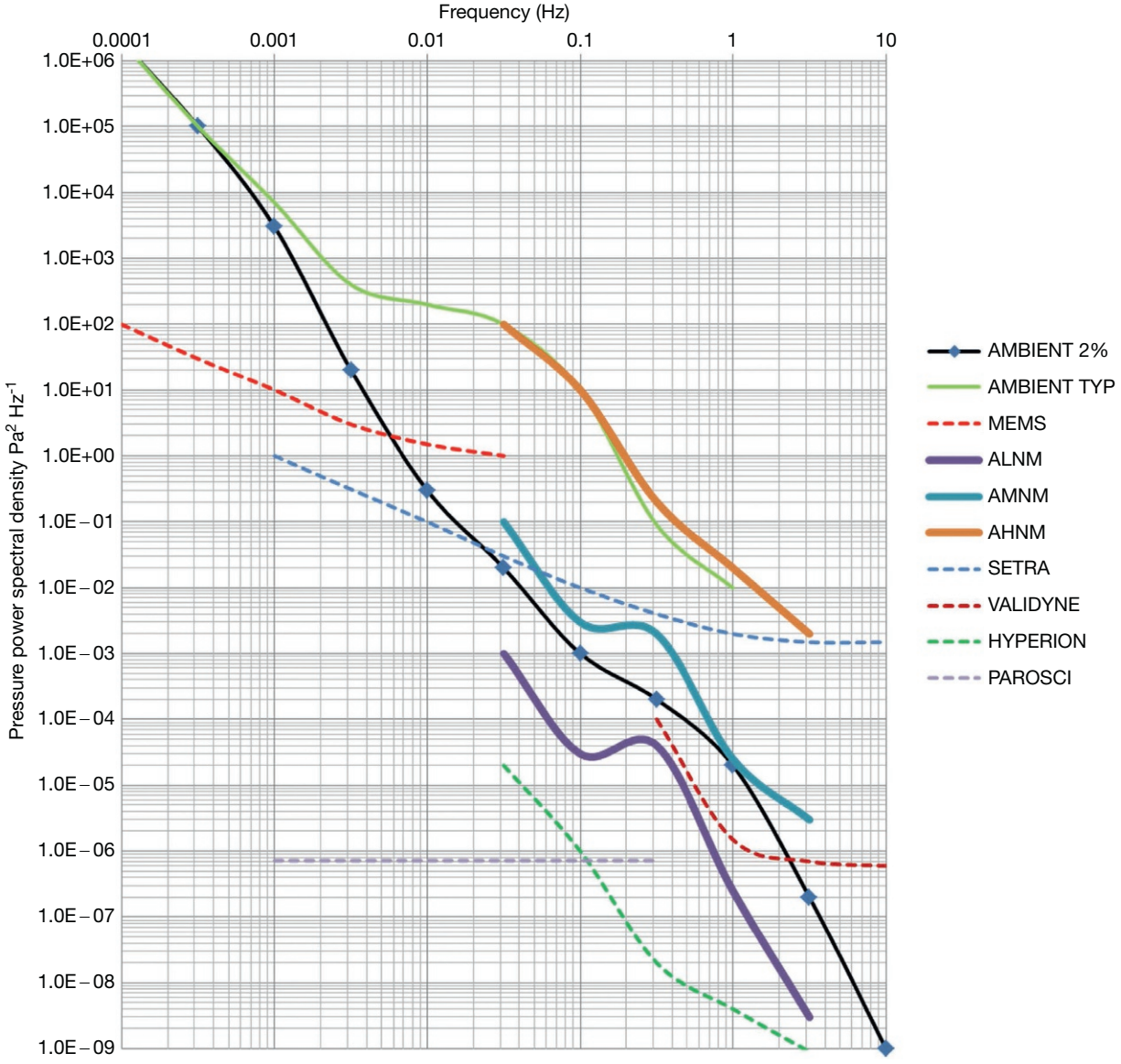

Figure 37 The spectrum of ambient low and typical barometric pressure, the intrinsic noise of several barometric sensors, and the low (ALNM), median (AMNM), and high (AHNM) infrasound noise models of Bowman et al. (2005). The measurements of intrinsic sensor noise are based on incoherent or arithmetically differenced time series using two or more identical instruments of the same type. The instruments compared are pressure sensors manufactured by VTI (now Murata, labeled MEMS), Setra Systems, and Paroscientific, and infrasound sensors, which are high-sensitivity pressure sensors typically with a high-pass frequency response, from Validyne and Hyperion, the latter originally developed by the National Center for Physical Acoustics (NCPA). The MEMS, Setra, and Hyperion sensors are deployed in hundreds of stations of the USArray Transportable Array. Combined, the three sensors are capable of resolution of minimum ambient pressure noise over more than five decades in frequency. Ambient typical and ambient two-percentile measurements were made at GSN station HRV. Noteworthy features of the barometric spectrum are the steep decrease in pressure noise with increasing frequency, and the level at frequencies <4 mHz, resolvable using low-cost MEMS barometers. These data are useful for pressure correction of low-frequency seismograms. See manufacturer's data on barometric pressure sensors (VTI, Setra, Validyne, Hyperion, Paroscientific, not dated).

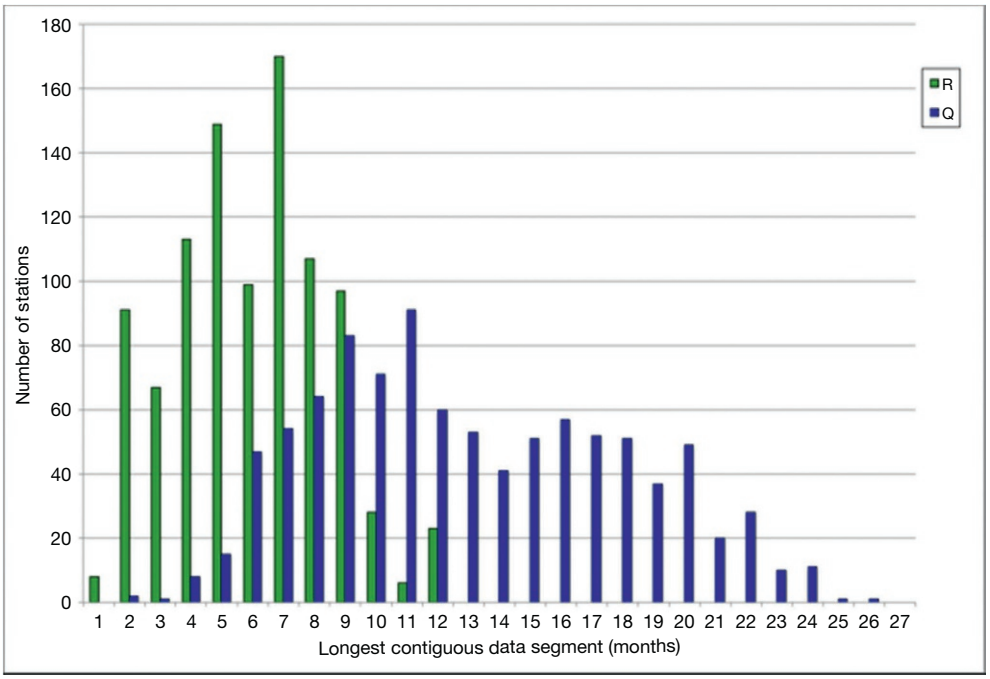

Figure 38 The effect of multiple independent data archives on data completeness over 958 stations of the USArray Transportable Array. The horizontal axis shows one measure of data completeness: the longest *contiguous* data segment (months) acquired during the station's 2-year deployment (nominal maximum 24 months). Contiguous is defined as zero missing data. The ordinate is the number of stations. The green bars represent the SEED 'R' (raw) data obtained via the real-time telemetry path only. The blue bars represent a merged 'Q' (quality-controlled) data set including both real-time telemetered and on-site recorded data. The mean length (on the order of 1 year or more) of contiguous Q data is roughly double the mean R data. No R data exceed 1 contiguous year. (Figure courtesy of R. Busby, unpublished) Some data breaks are planned, such as during firmware upgrades or system reconfiguration.

are shown, along with acoustic noise models (Bowman et al., 2005; Brown et al., 2012) and the intrinsic noise level of a number of barometric sensors. Barometric minimum ambient PSD varies on average over the five decades from 0.1 mHz to 10 Hz as $\sim 1/f^3$, although the slope is steeper at high frequencies. Ambient barometric pressure PSD varies over more than 150 dB over this frequency range. Ambient barometric noise below about 10 mHz, where coherence exists with waveforms observed on seismometers, is high and increases rapidly with period, and so can be measured with relatively simple and low-cost MEMS barometric pressure transducers. Hundreds of stations of the IRIS USArray Transportable Array program use three barometric sensors (VTI, now Murata, MEMS; Setra; and Hyperion, Hart et al., 2011) with overlapping operating ranges capable of resolving minimum ambient background levels over the frequency range of Figure 37. Multiple sensors facilitate cross-checking their calibration and operation *in situ*.

1.02.3.3.5 Archival methods: impact on quality and longevity of data set

A few design aspects developed in the original Harvard VBB system have improved the usefulness and longevity of broadband data. Perhaps, the most important feature is continuous recording rather than event-based. Contemporaneous resampling and reduction of broadband data rates in the A/D system to time series sampled at 1 and 0.1 sps makes more convenient data usage and quality analyses based on low-frequency data. In addition, the likelihood of successful telemetric transmission of complete low-frequency data sets is improved. Resampling to produce lower-rate time series requires 100% complete data at the initial rate, the likelihood of which is diminished as bandwidth, data volume, and time duration are increased.

Recording and telemetry systems fail. Multiple independent data archives, on-site and off-site through telemetry links have improved overall data integrity. Two or more independent and redundant data sets increase the likelihood of recovery of an intact and complete merged data set (Figure 38). The systems of the GSN and many regional networks incorporate this capability. The seismic data and ancillary data can be considered to comprise a 'station data vector' representing a broad view of the physical environment and configuration of the station at the time the seismic data are acquired.

Lossless data compression has reduced the data volume required for storage (essential in the 1980s and 90s) and telemetry (still important through bandwidth or volume-limited radio links or some commercial services such as cellular and satellite). The Steim1 and Steim2 (IRIS, 2012) compression techniques have become a *de facto* standard for many seismic networks and A/D systems, as a reasonable compromise of efficiency and complexity.

The method exploits the high correlation over 1–2 samples in seismic time series by storing differences only in a compact binary representation. Figure 39 shows a typical broadband 1 sps data stream along with the first and second differenced series superimposed, with a reduction in amplitude and whitening. The resulting series of differences can be coded in a tightly packed representation. Such compression is efficient

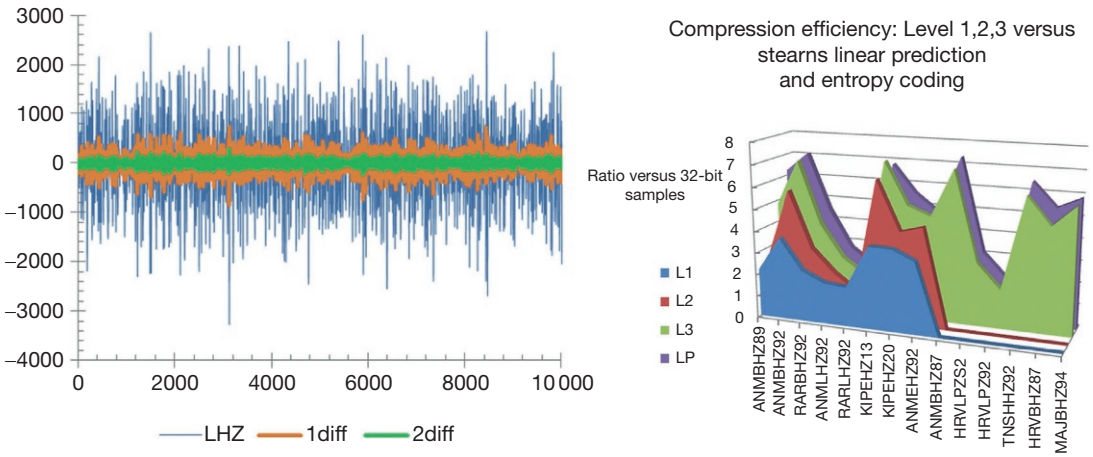

Figure 39 The basis of differencing data compression. *Left*: The reduction in amplitude of 1 sps broadband noise dominated by microseisms (LHZ, blue) when first (brown) and second (green) differenced. The smaller and relatively uniform amplitudes approximate a maximum-entropy residual and are encoded with smaller storage space than the original data. *Right*: The efficiency of three levels of 'Steim' data compression (IRIS, 2012) compared to the linear prediction and entropy coding (LP) method of Stearns (Peterson and Hutt, 1994). The ordinate is the ratio of 32 to the average number of bits required per sample. The data set comprises 14 segments (horizontal axis) representative of various ambient noise and earthquake signal characters; each data segment exhibits a different compression ratio. The stations are ANMO, RAR, KIP, HRV, and MAJO of the GSN and TNS of the German regional seismic network. Level 1 and level 2 results are shown with only eight segments of the complete data set. Level 2 is the most commonly used compromise of efficiency and complexity. Storage efficiency of level 3 is nearly equivalent to the method of Stearns, but is ~50 × more computationally efficient.

on many of the station vector 'state of health' data streams, which are often slowly varying compared to the sample rate, and therefore highly predictable. The SOH data are therefore acquired at little marginal cost in storage or bandwidth.

A further Steim3 extension (Steim, 1994), having additional coding groups and the automatic adaptive usage of first or second differences was defined and implemented in 1993 (Peterson and Hutt, 1994), but not deployed in operational networks. The method compares favorably with the maximum-entropy linear prediction coding developed by Stearns (Stearns et al., 1993), while using only integer arithmetic and about 2% of the computational effort. While potentially much larger compression efficiencies are possible using lossy techniques, these are generally destructive to broadband data because the instantaneous amplitude of the full-bandwidth signal that drives the compressor is not correlated with low-frequency signals. Although ambient noise drives the time-averaged effectiveness of compression of continuous data, earthquake data, particularly at sample rates 40 sps and higher, are generally effectively compressed. Compression is therefore effective in reducing average telemetry rates during both ambient and event conditions.

Because these compression techniques are lossless, that is, all bits of the compressed time series are preserved, the effectiveness depends on the number of bits remaining to be coded after the redundancy has been removed. Therefore, compression efficiency is inversely correlated with gain. System gain in excess of the amount required to overcome seismic noise is generally superfluous and detrimental to storage efficiency.

Small additional marginal storage reduction (10–20%) is often possible with commonly used general lossless compression methods (e.g., 'gzip'), mainly through exploiting redundancies in header information.

1.02.3.4 Calibration

Calibration is usually thought of as a means or process to measure and describe the transfer function of the sensor to ground motion. Calibration can be thought of more broadly to include measurement and verification of several other important aspects of network systems that affect the accuracy of acquired data, including orientation and location, and validation of the data processing that may affect accuracy following acquisition in the A/D system.

1.02.3.4.1 Sensor

Most sensors in current use in global and regional networks are commercially produced and are standardized; units of each make and model have nominally identical transfer functions within typically of the order of 1% accuracy. The transfer functions primarily require verification of conformance to nominal behavior while deployed. Calibration analyses may be considered to divide into 'research,' for characterization of new systems or detailed investigation of behavior using new methods, and 'operational.' Operational calibration analysis is typically used in global and regional networks. Research calibration may require special equipment or test configurations and cannot easily be performed longitudinally. Operational checks should therefore be able not only to verify nominal conformance to known behavior, but also to detect deviations requiring further study.

A sensor transfer function, say, relating output voltage $E(s)$ to ground acceleration $A(s)$ can be written as the product of a constant G_C, the gain or absolute responsivity, and a frequency-dependent $H(s)$. The factors can be identified in eqns [29] and [30]:

$$\frac{E(s)}{A(s)} = G_C H(s) \quad [38]$$

For an EFFB sensor where an electrical calibration signal is applied, either, for example, as a voltage or current summed into the drive of the feedback force transducer, or through a separate *calibration coil* that applies a force to the suspended mass by acting on the force transducer's permanent magnet, the constant G_C cannot be determined. This is because any force so applied to the suspended mass is always countered by an opposite force applied to the mass that is generated against the same magnet. This is expressed in eqn [39] simplified for zero frequency:

$$i_{cal} \cdot B \cdot K_{cal} = i_{fb} \cdot B \cdot K_{fb} \quad [39]$$

where i_{cal} is a current applied to the calibration coil, K_{cal} is a constant for the calibration coil relating the force generated for an applied current through the coil in the field of a magnet with flux density B, and K_{fb} is a similar constant, usually much larger, for the coil through which feedback is applied. On rearrangement, the balancing feedback current i_{fb}, which is proportional to the observed output signal resulting from application of the applied calibration current, can be written

$$i_{fb} = i_{cal} \cdot \frac{K_{cal}}{K_{fb}} \quad [40]$$

and measures only the ratio K_{cal}/K_{fb} in which information related to the sensor's response to ground acceleration is not present. The behavior can be seen to be equivalent if different magnets are used or a voltage is applied to the closed loop. A change from a previously measured ratio is cause for investigation, but measurement of G_C using inputs to the calibration coil is not possible.

Application of a calibration signal to a calibration coil can, however, illuminate $H(s)$, the frequency dependence of the transfer function. Most A/D systems in global and regional network use are capable of generating some type of electrical calibration signal, such as steps, sine waves, or random functions, and various methods have been extensively described (Berger and Agnew, 1979; Farrell and Berger, 1979; Fels and Berger, 1994; Peterson et al., 1980; Wielandt, 2011a,b) to derive $H(s)$ from the response to various electrical stimuli. These methods can be used for the operational determination of $H(s)$. $H(s)$ may be described in terms of a parametric model that may correspond to the physical design of the sensor, or $H(s)$ may be represented as tabulated amplitude and phase measurements as a function of frequency. A system, such as used in global networks, capable of simultaneous A/D sampling on multiple channels and synchronous with the calibration signal source can be used to derive an estimate of $H(s)$ using spectral division (Ringler et al., 2012b; Wielandt, 2011a,b). A requirement is that the calibration signal source must have sufficient energy at the frequencies where the transfer function is to be measured. To reduce variance of the estimate, multiple measurements may be stacked, and the contemporaneous ground motion input may be subtracted if available on another sensor (**Figure 40**).

Measurement of $H(s)$ using electrical inputs tests primarily the feedback system, since forcing inputs are not applied through the sensor's coupling to the ground and the sensor's feet, frame, and mass supports. Such measurements not only quantify $H(s)$, but also can detect some mechanical failures, such as defective elements of the inertial suspension. Maximum allowed electrical calibration input amplitudes and frequencies are often limited by the sensor or calibration generator, and calibration force transducers apply only a uniaxial signal aligned with the sensor's sensitive axis.

The determination of the gain constant G_C, that is, 'absolute' calibration, is more difficult requiring traceability of a stimulus signal to actual ground acceleration. Many

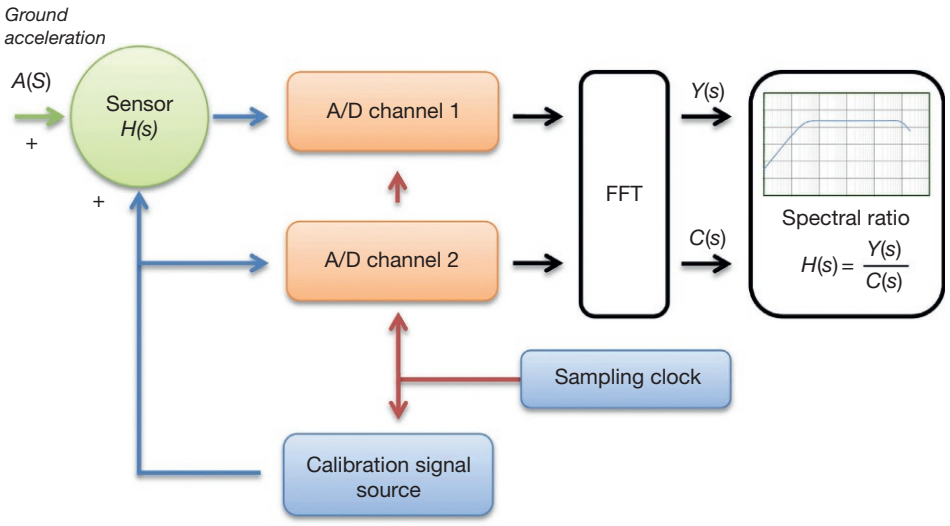

Figure 40 Measurement of the frequency-dependent part of sensor transfer function using spectral division or linear modeling. Synchronous sampling of the A/D and calibration signal source allows stable recovery of sensor transfer function from spectral division. The transfer function of the A/D is identical on both channels and does not affect the ratio $H(s)$. Sufficient SNR must be present in the input signal $C(s)$. The sensor output on channel 1 may also be linearly modeled for a known input signal measured on channel 2. Linear modeling in the time domain can provide insight into possible mechanisms of nonlinearity.

approaches have been developed, including the use of the gravity field of an external nearby rotating mass (Bernard and Karczewski, 1991), comparison against a known reference sensor using ambient seismic noise as a stimulus (Pavlis and Vernon, 1994), measurement on a motion table (Wielandt, 2011a,b; Wielandt and Zumberge, 2013), analysis of signals having well-known amplitudes such as solid Earth tides and the free mode ${}_0S_0$ (Davis and Berger, 2007, 2012), and comparison against expected synthetic signal amplitudes (Ekström et al., 2006).

Global and regional networks have recently adopted systematic programs to regularly compare, using an approach similar to Pavlis and Vernon (1994), the output of installed sensors with that of a portable transfer standard whose calibration has been independently verified (Davis and Berger, 2012). In addition, since most global and many regional network stations are equipped with multiple sensors, the consistency of records from multiple sensors for events with large SNR can be regularly analyzed (Ringler et al., 2012a), including verification against synthetic seismograms.

Both the absolute and frequency-dependent parts of the transfer function are measured by comparison to a calibrated reference sensor. The accuracy of this approach, however, diminishes at frequencies where SNR is low, such as extreme low or high frequencies where signals are small, and temporary installation of the reference sensor may limit SNR. However, the frequency-dependent $H(s)$ may be determined reliably using high-SNR electrical drive signals, and the gain G_C may be determined using the reference sensor at frequencies, such as the microseism band, and at times, such as during large events, where SNR is high.

Acquisition and recording systems are indirectly verified during network operational calibration checks. Some acquisition equipment performs automatic self tests and adjustment of gain within $<1\%$. A/D systems may fail or degrade, however, in ways similar to sensors. Observed failure modes include sudden increases in noise or changes in gain.

1.02.3.4.2 Orientation and location

Two historically difficult aspects of station operation on land, precise timing and location, have been solved nearly universally using GPS. Many global and regional seismic network stations are equipped only with C/A code, single-frequency receivers capable of precise timing and only moderate location accuracy. Multiple-frequency and code receivers capable of higher-precision location measurement are increasingly being colocated with seismic stations and promise to complement seismic data in the rapid measurement of static displacements accompanying large nearby events (Emore et al., 2007; Bock et al., 2011; Houlié et al., 2011). Commercial demands on increased location accuracy and miniaturization will drive high-accuracy global navigation satellite system technology into low-power products suitable for incorporation in seismograph systems.

Another important aspect of station operation is azimuthal orientation of three-axis sensors. This has historically been difficult, requiring astronomical sighting or other geodetic surveys. Surveyed azimuths then require transfer to an underground instrument site, with multiple opportunities to accumulate error. GPS survey instruments have also increasingly replaced historical methods for orientation measurements, although this approach still typically requires the transfer of a measured azimuth to an underground site because GPS reception requires unobstructed sky view. Small fiber-optic gyro (FOG) systems (IXBLUE) have recently enabled measurement of actual instrument orientation to $<1^\circ$. This technology does not depend on a sky view and hence can directly measure the azimuth of an instrument. The EarthScope Transportable Array first used this approach to measure the orientation of sensors directly in their instrument vaults. The known orientations were checked (**Figure 41**, Ekström and Busby, 2008) against orientations derived from polarization of observed surface waves compared with synthetics, finding close agreement. This controlled experiment confirmed the validity of polarization measurements as a routine tool in global and regional network operations.

Polarization analyses of other networks (**Figure 42**) show that the orientations of TA stations generally fall within a somewhat narrower distribution than most other networks, although orientation accuracy remains a challenge. Ringler et al. (2013) show that sensors installed by experienced field engineers can be expected to fall within 2° of an available azimuthal reference.

Just as the transfer function of a sensor may be verified using a transfer standard, the azimuthal orientation of maximum sensitivity of the sensor may be determined by measurement of coherence with a reference sensor having known orientation (Holcomb, 2002). This approach is particularly useful for determination of orientation of borehole sensors,

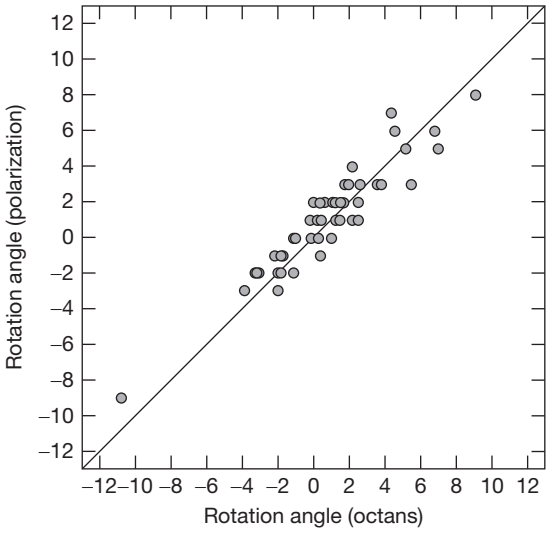

Figure 41 Comparison between two types of measurements of rotation angle. The horizontal axis corresponds to high-precision field measurements of seismometer orientation obtained at 49 TA sites at the time of station removal. The measurements were obtained using an IXSEA Octans IV interferometric fiber-optic gyroscope. The vertical axis corresponds to the rotation angle obtained from surface-wave-polarization measurements. The thin line indicates equal values of the two measurements. The difference between the two measurements is less than 3° for all stations. From Ekström G and Busby RW (2008) Measurements of seismometer orientation at USArray transportable array and backbone stations. *Seismological Research Letters* 79(4): 554–561.

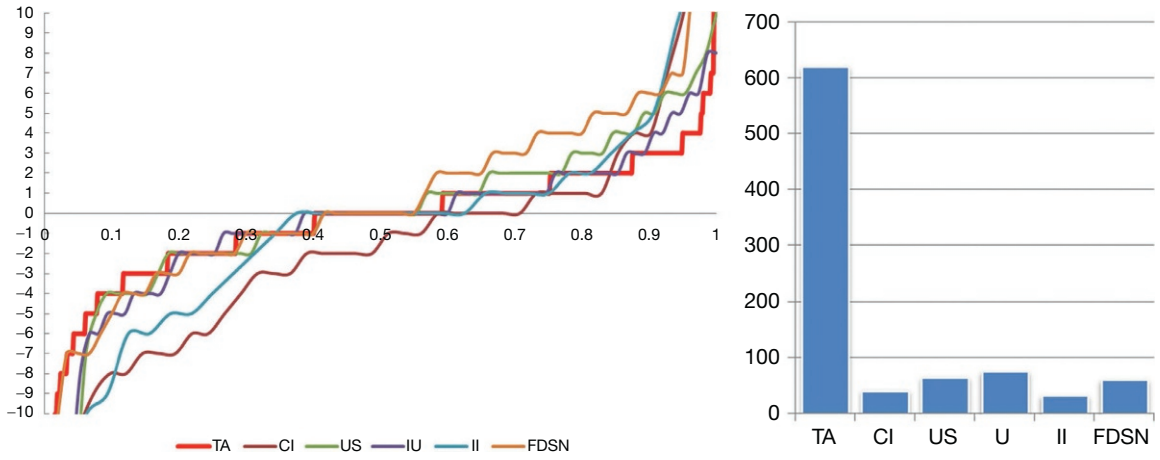

Figure 42 At left, the deviation in degrees of orientations of horizontal axes from reported values based on comparison of data with synthetic seismograms. FDSN network codes identify all networks except 'FDSN' which includes various contributing regional and global stations. The abscissa is the fraction of stations per network code. At right is the total number of stations in the analysis by network code. TA stations have been installed using a fiber-optic gyro. Data from http://www.ldeo.columbia.edu/~ekstrom/Projects/USARRAY/POLARIZATION/index.html.

where physical rotation of the instrument package to a specified azimuth may be impossible. This method can also detect faulty wiring, polarity inversion, or misalignment of the sensor's actual sensitive axis with package markings. Zha et al. (2013) have measured orientations of ocean-bottom sensors using correlations on multiple sensors of ambient noise.

1.02.3.4.3 Network calibration

Although 'calibration' has traditionally been viewed to refer to station equipment, and most specifically seismometers, increasing reliance on automatic processing chains beyond the direct view of researchers creates a need to calibrate not only the sensors, but the entire end-to-end data acquisition and delivery process. Data distributed by data management facilities in general is not identical to that acquired by field equipment, further necessitating the end-to-end verification particularly of potential time delays or errors in data center processing. MiniSEED data routinely distributed by the IRIS data management system, for example, are identified with the SEED data record type 'M' indicating 'data center modified.' Laske (2004, unpublished report), for example, shows a case where data center operations introduce a timing error. McNamara et al. (2009) show the effect of minor errors in instrument response on noise PSD calculation. Quality control analysts associated with most network operators carefully monitor acquired data for indication of timing or response errors, although in some cases, the potential errors may occur after quality control processes are applied.

Many GSN and regional network station A/D systems incorporate the ability to generate a 'network calibration' signal. In some equipment, the electrical sensor stimuli used for transfer function calibration start at precise UTC times, synchronized by the station's GPS time reference. The GSN system also includes the ability to introduce a signal only into the A/D system (and hence the subsequent data path through all data management facilities) at UTC-defined times. Just as regular sensor calibration measurements are necessary, so are 'network calibration' measurements to assure that data collection and distribution do not introduce errors in timing or data completeness. Calibration pulses at known times were used in the WWSSN.

1.02.3.5 Quality Assessment and System Characterization

When broadband instrumentation began to be deployed in the late 1980s, network operators phased out the daily calibration pulses that ruined the ability to acquire long undisturbed time series needed for some analyses (Woodward and Masters, 1989). By the mid-2000s, many sensors that were installed during the initial wave of broadband installations had been in use for nearly two decades. Sufficient data had accumulated to enable critical review of instrumentation performance. Some cases of significant deviation from assumed parametric models became apparent in the mid 2000s (Davis et al., 2005; Ekström et al., 2006). A regular and adequately frequent application of various methods to verify the system transfer function improves the accuracy of instrument models, as well as timeliness to correct a problem.

Systems are initially characterized at design time. Longitudinal analysis helps maintain network quality. Hutt et al. (2009b) and have described laboratory tests to quantify the behavior of seismic sensors. Most manufacturers and instrumentation developers have generally adopted these or equivalent methods. In general during the past three decades, designers, manufacturers, and network operators have converged on meaningful representations of noise and signal over the large potential operating range of brand band systems. Near universal adoption of Peterson's LNM and successors and refinements has facilitated comparison of diverse broadband instrumentation to an absolute reference. The level of noise and signals yield much of the operational quality information in global and regional networks.

1.02.3.5.1 Noise

Where one sensor is available, only total observed noise, including the ambient seismic noise of the site, intrinsic sensor

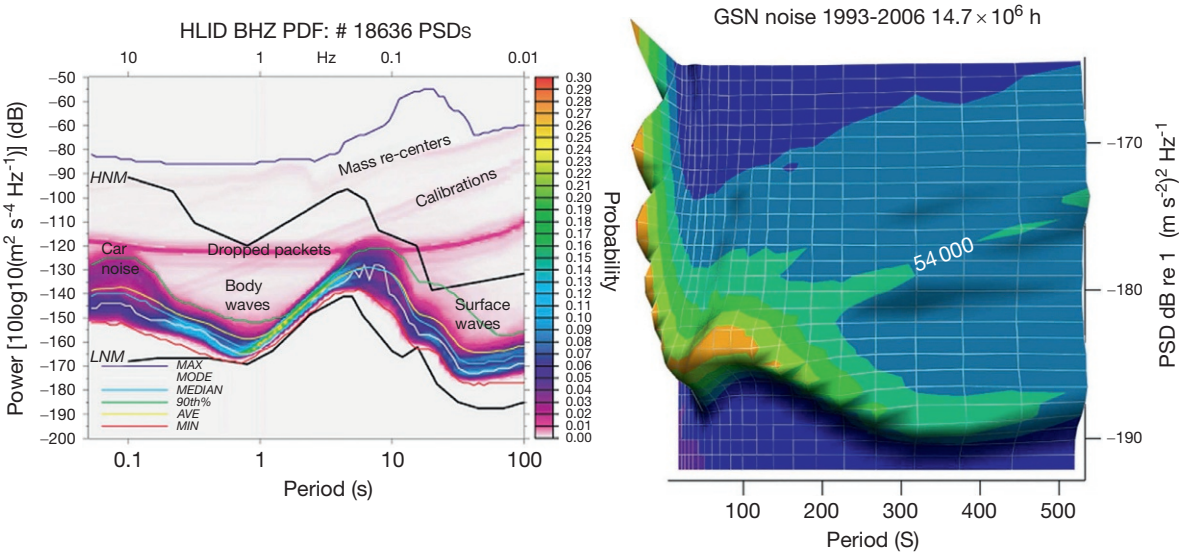

Figure 43 Left: PDF for station HLID using 18236 PSDs from 2000–09 through 2003–09. Recording system transients are observable. From McNamara and Buland (2004). Right: Cumulative noise-only vertical PSDs for GSN 1993–2006 using 1.47×10^7 1 h data segments. The 'surface' may be rotated to view features, such as the 'ridge' produced by KS54000 seismometers. Compare **Figure 50**. The depth/color axis represents number of observations. One-hour spectra to build the image from http://www.ldeo.columbia.edu/~ekstrom/Projects/WQC/MONTHLY_HTML/index_time.html.

and A/D system noise, and the effects of installation and environment is measurable, and is usually presented as PSD compared with an accepted LNM. Low noise models have been based on the lowest observed noise levels in many observations, representing the smallest percentiles of a distribution. McNamara and Buland (2004) and McNamara and Boaz (2005) introduced the routine calculation and color presentation of PSD PDFs, allowing a rapid visual assessment of typical station noise levels. The PDF plots continuously calculated at data management facilities typically extend from ~0.01–10 or 20 Hz, and hence do not cover the lowest frequency range of global instrumentation. Data segments spanning 1 h are used in construction of the routinely generated PDF plots. Features in PDF representations can be associated with scenarios that elevate apparent noise level, including sensor adjustment or missing data (**Figure 43**). McNamara et al. (2009) have proposed development of automated screening of noise PDF results to assist in quality assessment. Because PDF representations of PSD lose phase information, multiple phenomena may degenerate to produce similar spectra. Recognition of common occurrences such as clipping, mass recentering, missing data, etc., may be more effectively done using a time-domain correlation with the signature of such scenarios. Cumulative spectra also reveal persistent features related to specific sites and types of instrumentation.

Where multiple sensors are available on-site, many techniques may be used to separate apparent ambient noise from sensor intrinsic noise or the effect of installation methods on a particular sensor. Some of these approaches were discussed in connection with calibration. Spectral coherence is a common tool in deriving estimates of the PSD of noise that is uncorrelated on multiple colocated sensors (Holcomb, 1989, 1990; Ringler et al., 2011; Sleeman, 2006). **Figure 44** (Sleeman and Melichar, 2012), for example, shows estimates of the intrinsic noise of thermally insulated STS-2s compared with total observed noise. The measurement of intrinsic noise using coherence cannot distinguish between multiple sources of coherent energy, including nonseismic inputs such as thermal, barometric, or magnetic. A combination of low total observed noise, low apparent intrinsic noise derived through coherence measurement, and low correlation with environmental inputs provide reasonable confidence in the measurement of sensor performance. The analysis of arithmetic sample-by-sample differences between the outputs of nominally identical sensors can yield equivalent results. Time-domain analysis of the correlation of transient phenomena can yield physical insight into the origin. Examples include correlation with barometric or magnetic pulses (Forbriger, 2007a,b; Forbriger et al., 2010)

Routine noise PSD calculation by Lamont–Doherty Earth Observatory for global and regional stations (http://www.ldeo.columbia.edu/~ekstrom/Projects/WQC/MONTHLY_HTML/index_time.html) provides a valuable resource for longitudinal and network-wide noise studies and station quality assessment. These data comprise millions of 1-h PSD measurements in 25 frequency bands with center periods of 518–10 s, derived from 1 sps data, spanning up to 20 years of operation. Ringler and Hutt (2010) have examined temporal noise variation in the GSN. Seasonal noise variations in some period bands are common, while very low-frequency noise, particularly vertical, is relatively constant. **Figure 45**, for example, shows seasonal variation at GSN station HRV of several dB in noise PSD at 27 s period, with <1 dB variation at 100 s period. Significant departure from seasonal norms is cause for investigation.

1.02.3.5.2 Signals

Noise measurement is an important component of station quality assessment, but insufficient alone. Noise may appear to diminish over time, for example, if absolute gain decreases, or if the frequency-dependent part of the transfer function changes reducing gain in a specific range of frequencies. Such

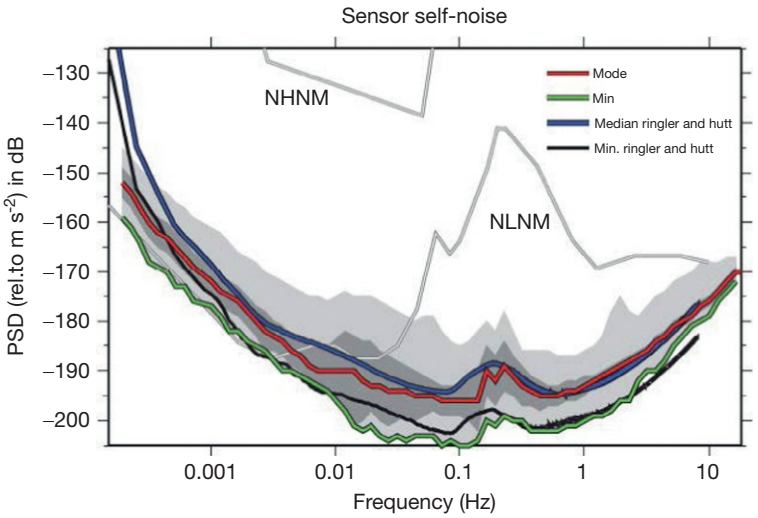

Figure 44 Mode (red) and minimum (green) values of STS2 self-noise PSD from an experiment with insulated sensors compared to results from Ringler and Hutt (2010; blue and black). The light gray and dark gray bands contain 95% and 68% of our PSD estimates. Adapted from Sleeman R and Melichar P (2012) A PDF representation of the STS-2 self-noise obtained from 1 year of data recorded in the Conrad observatory, Austria. *Bulletin of the Seismological Society of America* 102(2): 587–597.

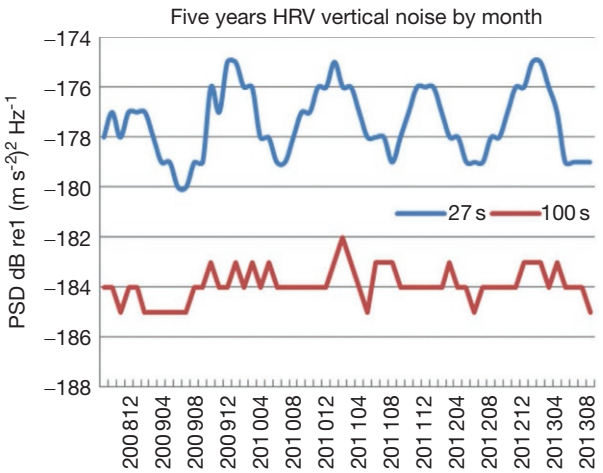

Figure 45 Monthly averaged noise (acceleration PSD) at GSN station HRV over a period of 5 years at 27 s and 100 s period. Noise at 27 s shows seasonal variation of several dB.

changes have been detected in longitudinal studies by comparing signal amplitudes between multiple colocated sensors where available, or with the amplitude of synthetic seismograms (**Figure 46**). In some cases, these problems have been caused by deterioration of electrical connections of broadband sensors after many years in service in humid environments (Hutt and Ringler, 2011; Yuki and Ishihara, 2002).

1.02.3.5.3 Instrument nonidealities

Rotations accompanying seismic signals in the far-field are not significant (Forbriger, 2009; Rodgers, 1969). Low-frequency instrumentation can be plagued by 'glitches' or brief impulses and steps. These may arise from chemical or electrochemical processes, aggravated by the high humidity environments common in seismic observation. Inherent mechanical stresses in instruments may also relax episodically over long periods – days to years. Formerly 'quiet' instruments may slowly or suddenly develop episodic noise, or the opposite. Manufacturers attempt to relieve stress through selection of materials and assembly processes, including accelerated thermal aging, and enclosure of sensitive mechanical systems in hermetic environments.

Linearity of sensors and A/D systems is often cited. Given as a single number without reference to the amplitude or type of applied signals, the type of apparent nonlinear result generated, and the band of frequencies, such a description is not meaningful. A common measure of nonlinearity is the familiar 'two-tone' intermodulation (IMD) test (Peterson et al., 1980) for mixing of the frequencies of applied electrical test signals. This test is applicable for A/D systems; however, the value is unclear as a predictor of the operation of sensors. Sensor gains and transfer functions vary widely, so that an electrical 'full scale' test of one sensor may refer to a very different equivalent ground motion input than the same test with another sensor. Importantly, the application of an electrical stimulus for linearity measurement does not duplicate the actual forces present on the inertial system in an earthquake, particularly when a test signal is uniaxial. Wielandt and Zumberge (2013) have applied uniaxial mechanical test signals on a shake table to broadband sensors, while independently measuring the shake table motion using optical interferometry. The resulting sensor outputs are linearly modeled for the known, measured table input including the table's own nonlinearity. The results show for several different types of EFFB sensor that for input signals in the range 0.25–8 Hz of nearly half the maximum input signal of the sensor, IMD products are, in terms of ground accelerations, of order −90 to −100 dB, but vary over a 30 dB range for various instruments. Expression of low-frequency distortion products as ground velocity or displacement results in an apparent distortion much higher, by the ratio of applied frequency to frequency of the mixing product. Is this 'good enough?' What is an appropriate representation? How is this

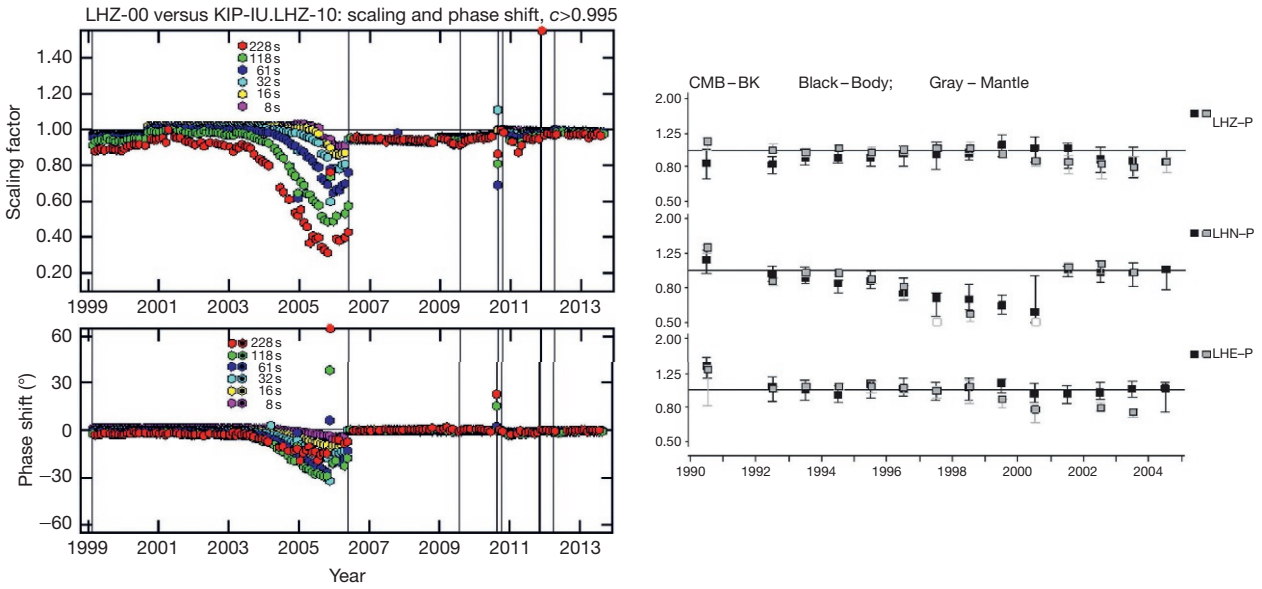

Figure 46 Left: Comparison of amplitude and phase of signals measured on two seismometers at GSN station KIP over a 14-year period. Beginning as early as 2001, low-frequency data from LHZ-00 began to decrease relative to a colocated instrument. The instrument was replaced in 2006. Such longitudinal studies are an important quality assessment tool (http://www.ldeo.columbia.edu/~ekstrom/Projects/WQC/COMB_QC/COH/cohfig.html#KIP-IU.LHZ-10_LHZ-00). Right: The amplitudes of observed and synthetic long-period signals are compared over a period of 14 years at station BK-CMB, showing a gradual deterioration on the LHN sensor beginning in 1996 and ending in 2000 when the sensor was replaced. Adapted from Ekström G, Dalton C, and Nettles M (2006) Observations of time-dependent errors in long-period instrument gain at global seismic stations. *Seismological Research Letters* 77(1).

measurement related to the apparent distortion using only an electrical stimulus to an instrument's calibration coil? Wielandt and Zumberge find that the distortion for inputs on the shake table is much higher than with electrical stimuli. The principal requirement on the type of linearity the 'two-tone' test seeks to measure is that significant high-frequency or microseismic ambient noise should not significantly affect the simultaneous low-frequency resolution of a broadband sensor or system. Apparently, this goal has been achieved with the present generation of global instrumentation, or measurements of minimum seismic noise or long-term observations of very small low-frequency signals such as free modes or hum would not be possible. Despite no obvious quantifiable association with multiaxial ground motion input, the electrical linearity test can detect certain failures (e.g., bent hinges, Hutt, personal communication), and remains a helpful engineering tool. Hutt and Ringler (2011), for example, describe 'amplitude-dependent amplitude' in an instrument sensitive to humidity, which would be expected to produce a high apparent distortion in a two-tone electrical test. Reasonable behavior in the electrical linearity test may be considered a necessary but insufficient indicator of correct operation.

Other nonlinear effects that have been observed may be less deterministic than the distortion measurable in a two-tone test. Phenomena have been observed (Delorey et al., 2008; Zahradník and Plešinger, 2005) where moderately strong high-frequency signals apparently well below the nominal clip level of broadband instruments appear to be correlated with low-frequency transients. In many cases, these signals may be explained by small permanent tilts that may arise in the sensor installation or in the local environment. Figure 47 shows an example of an apparent transient equivalent to a step in acceleration that would arise from a small tilt coincident with signal onset.

Zahradník and Plešinger (2010) suggest that some apparently unexplained nonlinear effects observed during moderately strong signals that are well below nominal clip level may be the result of saturation embedded within sensor feedback systems at frequencies outside the recorded signal passband. Such phenomena may, however, in some cases be explained by exceeding sensor clip level (Egli, 2011). An estimate of the dominant frequency of the full-bandwidth acceleration (as used in estimates of peak signals in this chapter) seen by the sensor is necessary to determine the proximity to the frequency-dependent clip level of broadband sensors. For example, Zahradník and Plešinger (2010) show a signal (their Figure 2) with peak displacement $\sim 1.5 \times 10^{-4}$ m. If this occurs at a dominant frequency ≥ 13.8 Hz, the sensor's published limit of 0.1 g is exceeded, without the need to resort to a more complex explanation. Such large acceleration amplitudes at high frequencies generated from relatively small events support the concept of low-gain velocity sensors (Clinton and Heaton, 2002) for general-purpose use at local and regional distances. New lower-gain sensors may take advantage of current A/Ds that are lower noise than those prevalent when the *de facto* gain near 1500 V m^{-1}s for sensors was chosen for general-purpose broadband sensors two decades ago.

1.02.3.6 Instruments in Global and Regional Networks

A descriptive summary of current sensors grows rapidly out-of-date. After a period of relative stability in the preceding two

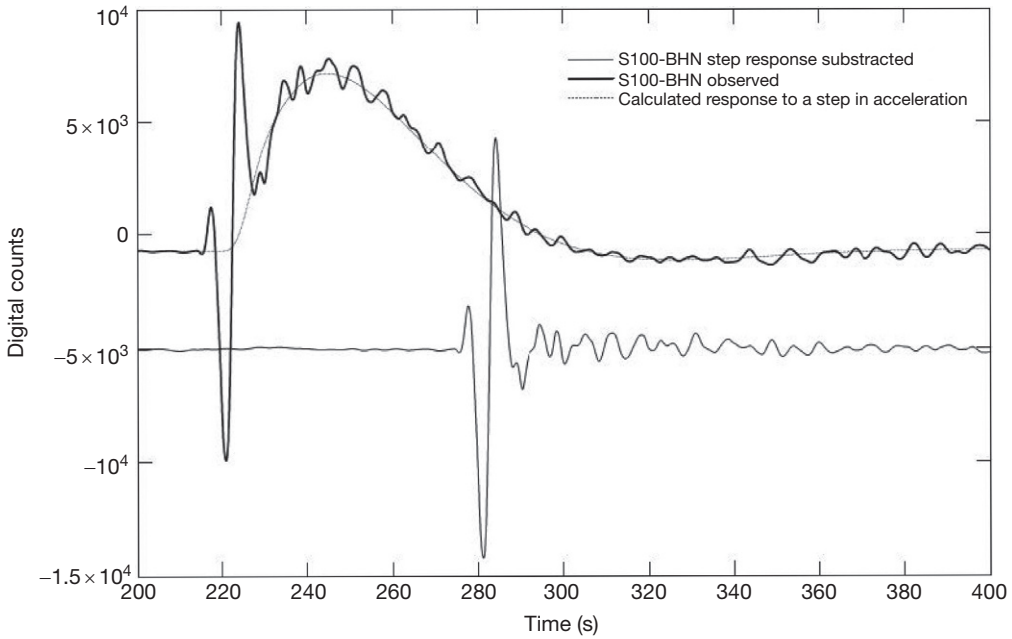

Figure 47 Small tilts on a broadband seismometer seen at regional distances accompanying felt ground shaking. The low-pass filtered signal, well below clip level, recorded on station S100 in NW United States includes an almost ideal acceleration step response that is removed in the lower trace (time shifted for clarity). Adapted from Delorey et al. (2008) Broadband sensor nonlinearity during moderate shaking. *Bulletin of the Seismological Society of America* 98(3): 1595–1601.

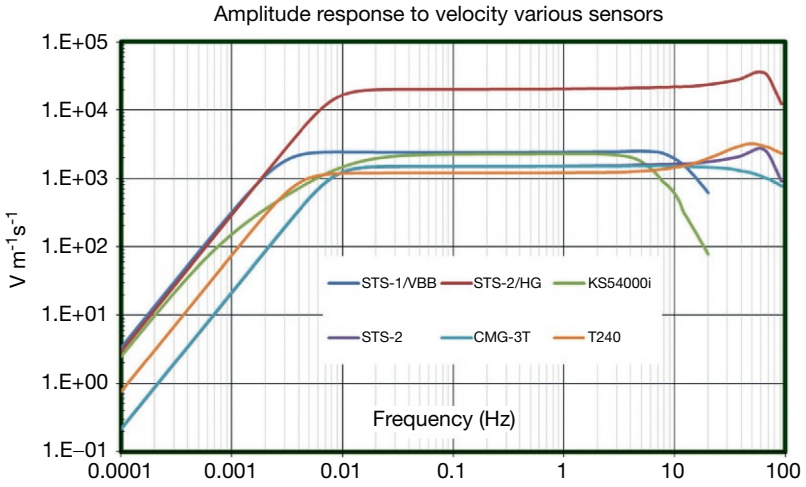

Figure 48 The amplitude response to ground velocity (volts per meter per second at the output) of the sensors providing the majority of data in global and regional networks currently and during the past two decades. These responses are approximately inverse to the spectrum of ambient Earth noise shown in **Figure 10**.

decades, resurgent interest in new instrumentation is driving rapid development. Figure 48 compares the response to ground velocity of the existing sensors responsible for the majority of high-quality data in current global and regional networks over the past two decades:

- Streckeisen, AG STS-1/VBB (replaced by Metrozet, LLC M2166-VBB sensor; Figure 49)
- Streckeisen, AG STS-2 (replaced by Streckeisen GmbH STS-2.5)
- Nanometrics, Inc. T240
- Güralp Systems, Ltd. CMG-3T
- Geotech Instruments, LLC KS54000I

The STS-1/VBB and STS-2 sensors are no longer produced and, however, have been replaced by new sensors with equivalent characteristics and performance, which are included in this brief overview. The standout feature of the frequency responses of all of these sensors, except the STS-2HG and a similar CMG-3T variant with high gain, is the similarity, having

been designed following the development of the original VBB concept (Steim, 1986; Wielandt and Steim, 1986). The STS-2 and CMG3T sensors have been produced in special 'high-gain' models for incorporation in some networks, in principle, to improve the high-frequency (>>1 Hz) match to digitizing equipment. The gain of these variants is excessive in view of actual global surface high-frequency noise levels and presents digitizer capability (McNamara et al., 2005), causing saturation on moderate events at regional distances.

The performance of the sensors in **Figure 51** can be comparable (Ringler and Hutt, 2010). All can provide high-quality broadband data in a wide variety of environments, if careful

Figure 49 Left: The STS-1/VBB vertical seismometer, viewed as it is installed in the original glass vacuum enclosure. A warpless baseplate (Holcomb and Hutt, 1992) is used in current installations. The STS-1/VBB has a response flat to ground velocity from 360 s to 10 Hz and provides the majority of high-quality very low-frequency data in global networks. Center: IRIS (2004) articulated a need to replace the STS-1/VBB, not produced since the 1990s. An industry-academic program (VanZandt et al., 2010) produced an equivalent replacement. The M2166-VBB, manufactured by Metrozet, LLC (Metrozet, 2011), comprises three mutually orthogonal sensors on a common all-metal warpless baseplate. In both the STS-1/VBB and M2166-VBB, heat-producing feedback electronics are external to the sensor vessel. Right: A comparison of free mode ${}_0S_0$ visible in 2 weeks of data following 1 month after the 2011 Tohoku Mw 9.0 earthquake recorded at the USGS Albuquerque Seismological Laboratory on an STS-1/VBB and M2166-VBB. The incoherent noise (green) between the two recordings is below the GSN (solid red line, Berger et al., 2004) low-noise model. The rms amplitude of the mode is 1.6×10^{-10} m s^{-2}, or 6.5 μV at the output of the sensors. The logarithmic scale shows the signal to be about 30 dB above the ambient seismic noise and nearly 50 dB above the noise incoherent between the two sensors. See manufacturer's data (Streckeisen G.; Metrozet, 2011)

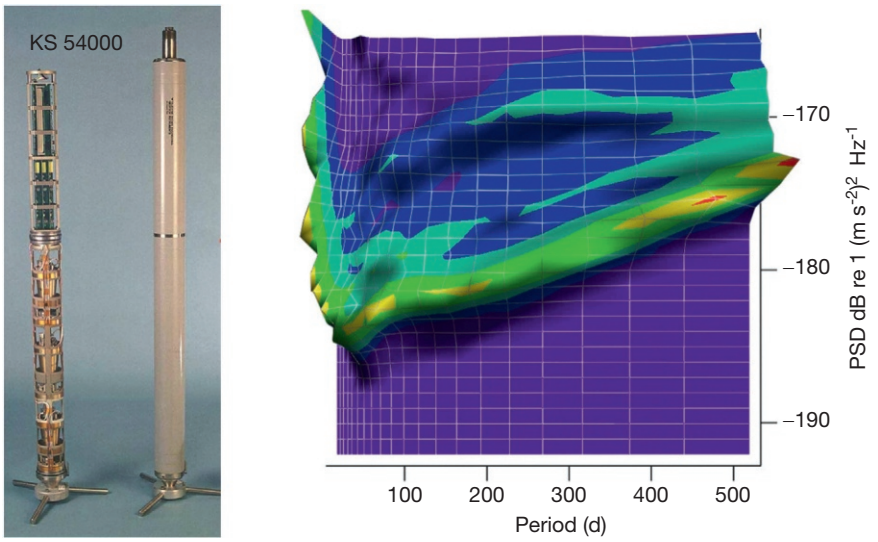

Figure 50 *Left*: The Geotech Instruments KS54000I (http://www.geoinstr.com/ks54000i.htm) very broadband borehole seismometer provides all of the high-quality low-frequency data from borehole installations in the GSN. The frequency response is nearly flat to ground velocity over a broad range from 4 Hz at 100 s, with an asymptotic response at frequencies <1 mHz similar to an STS-1/VBB. *Right*: Cumulative vertical low-frequency acceleration PSD representing about 3×10^6 1-h spectra for stations of the GSN equipped with KS54000I sensors obtained from http://www.ldeo.columbia.edu/~ekstrom/Projects/WQC/MONTHLY_HTML/index_time.html. The depth (color) axis shows number of observations. The KS54000I does not resolve levels of minimum vertical Earth noise at frequencies <5–10 mHz. Most noise observations are tightly grouped along a line roughly −182 dB at 100 s to −174 at 500 s. Several 'ridges' at higher noise levels identify significant atypical modes of operation or behaviors. Compare **Figure 43** including data from all GSN vertical sensors. See manufacturer's data (Geotech Instruments).

Figure 51 Three of the sensors providing the majority of broadband data worldwide during the past two decades. Thousands of these sensors have been produced. All three sensors have similar responses, flat to ground velocity over a broad range, extending to higher frequency (tens of hertz) than the STS-1/VBB. These sensors are typically not used for nor are capable of resolution of minimum signals at frequencies <5–10 mHz. All three sensors house their heat-producing feedback electronics inside the sealed sensor vessel. Left: The Streckeisen, GmbH, STS-2.5 is pictured, the current-production successor to the STS-2. Externally, the STS-2.5 is distinguished from the STS-2 only by the color (gray, not green), and the absence of mechanical controls to lock the sensor for transport, although the internal design is entirely new. The STS-2.5 is locked electrically. Center: The Nanometrics, Inc., T240. The STS-2, STS-2.5, and T240 are triaxially symmetric (Melton and Kirkpatrick, 1970), comprising three identical matched sensors with sensitive axes oriented at 120° azimuths and ~54 ° to the vertical. The familiar XYZ outputs are derived through a coordinate rotation performed electronically in the sensor. Right: The Güralp Systems, Ltd. CMG-3T. The CMG-3T comprises independent vertical and horizontal sensors in a common package. See manufacturers data (Guralp, 2013; Streckeisen, 2013; Nanometrics).

attention is paid to physical stability of the installation and thermal isolation. The EarthScope Transportable Array project over the last decade has deployed all three sensors in over 2000 installations using a uniform model of station construction achieving consistent noise levels within the sensors' design capability (Figure 52).

1.02.3.7 Instrumentation Directions

Hutt et al. (2002) cite some remarkable goals for a hypothetical broadband system. As yet and likely for more than the next decade, this vision of a 'super sensor' will remain unrealized. Some near-term areas in instrumentation development research are currently active, however, and will benefit new initiatives in proposed broadband array deployments (Dziewonski, 2013).

1.02.3.7.1 Renewed interest in boreholes

As cultural noise has encroached on many sites and difficulty in securing siting for installations with a large surface 'footprint' grows, borehole broadband instrumentation is receiving new attention (Busby et al., 2013a,b). Recent developments by several manufacturers will bring capable and cost-effective borehole broadband instruments into service during the next decade. The advantages of burial have been well known, but availability of reliable, cost-effective instruments has limited the deployment of this technology. Borehole systems promise a smaller surface footprint, simpler deployment, a lower-noise environment, and better physical security. New instrumentation preserves three-axis mutual orthogonality and

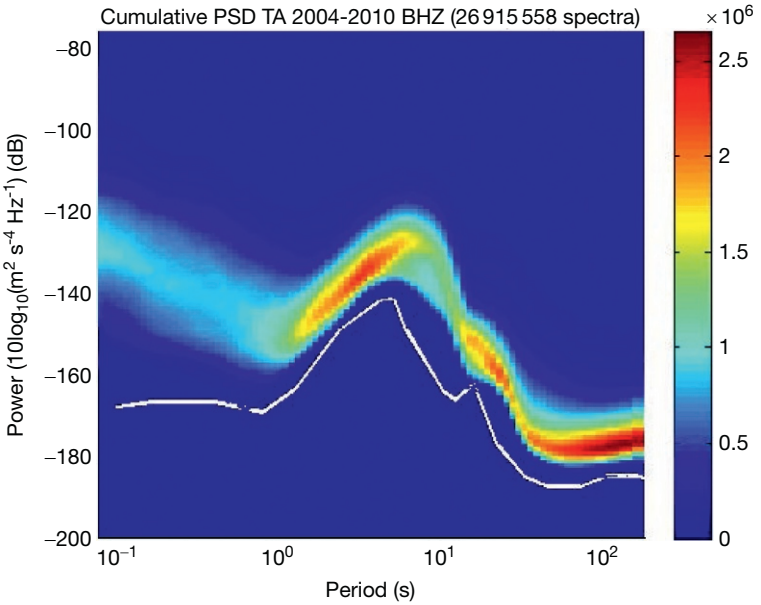

Figure 52 Showing the cumulative vertical acceleration PSD from 6 years (~27 million spectra) representing all installations of the EarthScope Transportable Array spanning the period 2004–10. At frequencies ~5–50 mHz, levels within ~10 dB of the NLNM are consistently resolved. Noise above 1 Hz shows greater variance, with levels typical of non-urban surface sites. Adapted from Busby R, Hafner K, and Woodward B (2013) Transportable array: experience in station design and new prospects. In: *IRIS Seismic Instrumentation Technology Symposium*; Busby R, et al. (2013) Sensor emplacement techniques and seismic noise analysis for USArray transportable array seismic stations. In: *EGU General Assembly Conference Abstracts*, p. 13298.

can self-level in the borehole. Installation methods and siting criteria for the best low-frequency noise, however, are not necessarily mature or standardized and are areas of active research.

1.02.3.7.2 Lower gain and greater bandwidth

New borehole sensors are within reach achieving GSN-goal performance with a response extending to higher frequencies. Future sensors may also be able to increase operating range using lower gain. Lower gain potentially improves signal handling in the presence of strong high-frequency signals.

1.02.3.7.3 Downhole digitization: integrated with a sensor

Digitizing equipment has been incorporated in borehole sensors for decades (Rodgers et al., 1987), but this technique has not been used on a wide scale in present major research broadband networks because no integrated borehole system meeting global network design goals has yet been demonstrated. Potential advantages include the following:

- No analog cabling carrying very low-level signals susceptible to corrosion, noise, or electromagnetic interference.
- Simpler connectors and small flexible cables.
- Tight integration of metadata, since the digital system is coupled to a known sensor.
- Possible digital orientation compensation.
- Thermal stability of both digitizer and sensor in the borehole environment.
- Minimal surface expression.
- Sensor 'fusion.' For example, accelerometer and velocity output data can be digitally merged.
- Possible output in physical units, such as 'nanometer per second.'
- Many fewer and less sensitive lines exposed to lightning.
- Simpler and faster deployment.

The approach also carries some disadvantages compared to current practice:

- Loss of modularity for sensor and system fault isolation.
- Forces affinity of a sensor with a particular manufacturer's acquisition methods, formats, protocols, and 'eccentricities' – especially disparate concepts of time. Current networks achieve uniformity at the level of data acquisition using sensors with a voltage output and network-wide usage of a common A/D system. Diverse digital operating environments can be difficult and time consuming to merge.
- More buried equipment to fail.
- Dynamic power variation creates thermal transients.
- More rapid system obsolescence. Few data loggers installed in 1990 are still operating, while many very good sensors continue to produce high-quality data when well maintained.

1.02.3.7.4 Complementary technologies

Incorporation of additional SG into seismic data sets may improve low-frequency data (Rosat and Hinderer, 2011; Van Camp et al., 2008; Widmer-Schnidrig, 2003). Optically sensed systems (Zumberge et al., 2010, 2012) may improve the ability to deploy instrumentation in unusual environments, such as extreme cold or heat, although such systems will need to overcome dependence on variation of mechanical parameters. MEMS technology will require significant improvement to compete with the performance of sensitive broadband electromechanical sensors. MEMS sensors reporting the lowest noise (Milligan, 2013; Standley and Pike, 2008) achieve −140 dB acceleration PSD at 0.1 Hz and show a $1/f$ noise characteristic. Use as a general-purpose broadband sensor will require noise reduction of several orders of magnitude. MEMS sensors will continue, however, to replace conventional electromechanical sensors in high-signal/high-noise applications (Wu et al., 2013). GPS will continue to be integrated in stations complementing inertial measurements not only in near-source applications (Bock et al., 2011; Guo et al., 2013; Houlié et al., 2011; Zheng et al., 2012).

Acknowledgments

The author would like to thank Charles R. Hutt, Adam Ringler, Tom VanZandt, and the editors for helpful reviews and discussions.

References

Agnew D, Berger J, Buland R, Farrell W, and Gilbert F (1976) International deployment of accelerometers – a network for very long period seismology. *EOS* 57(4): 180–188.

Agnew DC and Berger J (1978) Noise at very low frequencies. *Journal of Geophysical Research* 83(B11): 5420–5424.

Anderson J and Wood H (1925) Description and theory of the torsion seismometer. *Bulletin of the Seismological Society of America* XV(1).

Anderson K, Aster R, Beaudoin B, et al. (2006) Analysis of background seismic noise recorded at the Amundsen-Scott South Pole Station, Antarctica. In: *AGU Fall Meeting Abstracts*, p. A1313.

Ang KH, Chong G, and Li Y (2007) PID control system analysis, design, and technology. *IEEE Transactions on Control Systems Technology* 13(4): 559–576.

Aziz P, Sorensen H, and Spiegel JVd (1996) An overview of sigma-delta converters. *IEEE Signal Processing Magazine* 13(1): 61–84.

Bache T, Marshall P, and Young J (1986) High-frequency seismic noise characteristics at the four United Kingdom-type arrays. *Bulletin of the Seismological Society of America* 76(3): 601–616.

Barbour AJ and Agnew DC (2012) Detection of seismic signals using seismometers and strainmeters. *Bulletin of the Seismological Society of America* 102(6): 2484–2490.

Beauduin R, et al. (1996) The effects of the atmospheric pressure changes on seismic signals or how to improve the quality of a station. *Bulletin of the Seismological Society of America* 86(6): 1760–1769.

Benioff H (1932) A new vertical seismograph. *Bulletin of the Seismological Society of America* 22(2): 155–169.

Benioff H (1955) Earthquake seismographs and associated instruments. *Advances in Geophysics* 2: 219–275.

Bennett W (1948) Spectra of quantized signals. *Bell System Technical Journal* 27(3): 446–472.

Berckhemer H (1970) The concept of wide band seismometry. *Communications Observatoire Royal de Belgique: Geophysics Series* 13(1).

Berger J (2009) Long-period seismometry. In: *IRIS Seismic Instrumentation Technology Symposium*.

Berger J, et al. (1988) Studies of high-frequency seismic noise in eastern Kazakhstan. *Bulletin of the Seismological Society of America* 78(5): 1744–1758.

Berger J and Agnew D (1979) Seismic system calibration 2. Cross-spectral calibration using random binary signals. *Bulletin of the Seismological Society of America* 69: 271–288.

Berger J, Davis P, and Ekström G (2004) Ambient Earth noise: a survey of the global seismographic network. *Journal of Geophysical Research* 109(11): 11307.

Bernard P and Karczewski J (1991) The G-calibration: a new method for an absolute in situ calibration of long-period accelerometers, tested on the Streckeisen instruments of the GEOSCOPE network. *Bulletin of the Seismological Society of America* 81(4): 1360–1372.

Blackman RB and Tukey JW (1959) *The Measurement of Power Spectra: From the Point of View of Communications Engineering*, vol. 190. New York: Dover Publications.
Bloch S and Hales AL (1968) New techniques for the determination of surface wave phase velocities. *Bulletin of the Seismological Society of America* 58(3): 1021–1034.
Block B and Moore R (1966) Measurements in the earth mode frequency range by an electrostatic sensing and feedback gravimeter. *Journal of Geophysical Research* 71(18).
Bock Y, Melgar D, and Crowell BW (2011) Real-time strong-motion broadband displacements from collocated GPS and accelerometers. *Bulletin of the Seismological Society of America* 101(6): 2904–2925.
Bogert B (1961) Seismic data collection, reduction, and digitization. *Bulletin of the Seismological Society of America* 51(4): 515–525.
Bormann P and Wielandt E (2013) Seismic signals and noise. In: Bormann P (ed.) *New Manual of Seismological Observatory Practice (NMSOP-2), IASPEI*. Potsdam: GFZ German Research Centre for Geosciences.
Bowman JR, Baker GE, and Bahavar M (2005) Ambient infrasound noise. *Geophysical Research Letters* 32: L09803.
Bracewell RN (1978) *The Fourier Transformation and Its Applications*, 2nd edn. New York: McGraw-Hill.
Brown D, et al. (2012) The IDC seismic, hydroacoustic and infrasound global low and high noise models. *Pure and Applied Geophysics* 185: 201–209.
Brune J and Oliver J (1959) The seismic noise of the earth's surface. *Bulletin of the Seismological Society of America* 49(4): 349–353.
Bungum H, Mykkeltveit S, and Kvaerna T (1985) Seismic noise in Fennoscandia, with emphasis on high frequencies. *Bulletin of the Seismological Society of America* 75(6).
Busby R, et al. (2013b) Sensor emplacement techniques and seismic noise analysis for USArray transportable array seismic stations. In: *EGU General Assembly Conference Abstracts* 13298.
Busby R, Hafner K, and Woodward B (2013a) Transportable array: experience in station design and new prospects. In: *IRIS Seismic Instrumentation Technology Symposium*.
Byrne C (1961) Instrument noise in seismometers. *Bulletin of the Seismological Society of America* 51: 69–84.
Carder DS (1963) The requirements of a high-sensitivity seismograph station. VESIAC Report 4410-63-X.
Carter J and Barstow N (1991) High-frequency seismic noise as a function of depth. *Bulletin of the Seismological Society of America* 81(4): 1101–1114.
Clinton JF and Heaton TH (2002) Potential advantages of a strong-motion velocity meter over a strong-motion accelerometer. *Seismological Research Letters* 73(3): 332–342.
Cooley J, Lewis P, and Welch P (1970) The fast Fourier transform algorithm: programming considerations in the calculation of sine, cosine and Laplace transforms. *Journal of Sound and Vibration* 12: 315–337.
Cooley J and Tukey J (1965) An algorithm for the machine calculation of complex Fourier series. *Mathematics of Computation* 19: 297–301.
Coughlin MW and Harms J (2012) Global characterization of seismic noise with broadband seismometers. arXiv, preprint arXiv:1202.4826.
Cox C, Deaton T, and Webb S (1984) A deep-sea differential pressure gauge. *Journal of Atmospheric and Oceanic Technology* 1: 237–246.
Crary AP and Ewing M (1952) On a barometric disturbance recorded on a vertical long-period seismograph. *Transactions of the American Geophysical Union* 33: 499–501.
Crawford W and Webb S (2000) Identifying and removing tilt noise from low-frequency (<0.1 Hz) seafloor vertical seismic data. *Bulletin of the Seismological Society of America* 90(4): 952–963.
Crawford WC, Stephen RA, and Bolmer ST (2006) A second look at low-frequency marine vertical seismometer data quality at the OSN-1 site off Hawaii for seafloor, buried, and borehole emplacements. *Bulletin of the Seismological Society of America* 96(5): 1952–1960.
Davis P and Berger J (2007) Calibration of the global seismographic network using tides. *Seismological Research Letters* 78(4): 454–459.
Davis P and Berger J (2012) Initial impact of the global seismographic network quality initiative on metadata accuracy. *Seismological Research Letters* 83(4): 697–703.
Davis P, Ishii M, and Masters G (2005) An assessment of the accuracy of GSN sensor response information. *Seismological Research Letters* 76(6): 678–683.
DeBremaecker J, Donoho P, and Michel JG (1962) A direct digitizing seismograph. *Bulletin of the Seismological Society of America* 52(3): 661–672.
DeBremaecker J and Sitton G (1963) The rice digital seismograph system. *Journal of Geophysical Research* 68(17): 5029–5034.
Delorey A, Vidale J, Steim J, and Bodin P (2008) Broadband sensor nonlinearity during moderate shaking. *Bulletin of the Seismological Society of America* 98(3): 1595–1601.
Dewey J and Byerly P (1969) The early history of seismometry (to 1900). *Bulletin of the Seismological Society of America* 59(1): 183–227.
Douze EJ (1964) Signal and noise in deep wells. *Geophysics* XXIX(5): 721–732.
Dziewonski A, Bloch S, and Landisman M (1969) A technique for the analysis of transient seismic signals. *Bulletin of the Seismological Society of America* 59(1): 427–444.
Dziewonski AM (2013) Global seismic tomography: why we need GSN and GABBA (global array of broadband arrays). In: *IRIS Workshop on Arrays in Global Seismology. Raleigh, NC*.
Dziewonski AM (1994) The FDSN: history and objectives. *Annali di Geofisica* XXXVII(5): 1039–1041.
Dziewonski AM, Chou T-A, and Woodhouse JH (1981) Determination of earthquake source parameters from waveform data for studies of global and regional seismicity. *Journal of Geophysical Research: Solid Earth* 86(B4): 2825–2852.
Dziewonski AM and Steim JM (1982) Dispersion and attenuation of mantle waves through waveform inversion. *Geophysical Journal International* 70(2): 503–527.
Egli F (2011) Comment to: Zahradnik J and Plesinger A (2010), Toward understanding subtle instrumentation effects associated with earthquake peak acceleration related to clip level and D. T. output current, Pfungen, Switzerland.
Ekström G and Busby RW (2008) Measurements of seismometer orientation at USArray Transportable Array and Backbone Stations. *Seismological Research Letters* 79(4): 554–561.
Ekström G, Dalton C, and Nettles M (2006) Observations of time-dependent errors in long-period instrument gain at global seismic stations. *Seismological Research Letters* 77(1).
Emore GL, et al. (2007) Recovering seismic displacements through combined use of 1-Hz GPS and Strong-Motion Accelerometers. *Bulletin of the Seismological Society of America* 97(2): 357–378.
Evans JR, et al. (2010) Method for calculating self-noise spectra and operating ranges for seismographic inertial sensors and recorders. *Seismological Research Letters* 81(4): 640–646.
Farrell W and Berger J (1979) Seismic system calibration: 1. Parametric models. *Bulletin of the Seismological Society of America* 69(1): 251–270.
Fels J and Berger J (1994) Parametric analysis and calibration of the STS-1 seismometer of the IRIS/IDA seismographic network. *Bulletin of the Seismological Society of America* 84(5): 1580–1592.
Fix J (1972) Ambient earth motion in the period range from 0.1 to 2560 sec. *Bulletin of the Seismological Society of America* 62(6): 1753–1760.
Forbriger T (2009) About the nonunique sensitivity of pendulum seismometers to translational, angular, and centripetal acceleration. *Bulletin of the Seismological Society of America* 99(2B): 1343–1351.
Forbriger T (2011) Information Sheet IS 5.4 Recommendations for seismometer deployment and shielding. In: *New Manual of Seismological Observatory Practice (NMSOP-2), IASPEI*, pp. 1–10.
Forbriger T, et al. (2010) Magnetic field background variations can limit the resolution of seismic broad-band sensors. *Geophysical Journal International* 183: 303–312.
Forbriger T, et al. (2007) Magnetic field background variations can limit the sensitivity of seismic broad-band sensors Response of the GSN to a magnetic storm Signal power at 228 s. Available at: http://www.rz.uni-karlsruhe.de/~bi77/public/presentations/oral/akgg2007.pdf.
Forbriger T (2007b) Reducing magnetic field induced noise in broad-band seismic recordings. *Geophysical Journal International* 169(1): 240–258.
Gardner AT and Collins JA (2012) Advancements in high-performance timing for long term underwater experiments: a comparison of chip scale atomic clocks to traditional microprocessor-compensated crystal oscillators. *Oceans* 2012: 1–8.
Geotech-Instruments, Broadband Borehole Seismometer System Model KS-54000 and Model KS-1 Specifications, p. 1. Available at: http://www.geoinstr.com/ds-ks54000.pdf.
Green PE, Frosch RA, and Romney CF (1965) Principles of an experimental large aperture seismic array (LASA). *Proceedings of the IEEE* 53(12): 1821–1833.
Guo A, et al. (2013) Observation of core phase ScS from the Mw 9.0 Tohoku-Oki earthquake with high-rate GPS. *Seismological Research Letters* 84(4): 594–599.
Güralp (2013) CMG-3T Data Sheet. Available at: http://www.guralp.com/datasheets/DAS-030-0001.pdf.
Gurrola H, Minster J, and Given H (1990) Analysis of high-frequency seismic noise in the western United States and eastern Kazakhstan. *Bulletin of the Seismological Society of America* 80(4): 951–970.
GWR-Instruments (2011) Superconducting Gravity Meters for Low Frequency Seismology the World' s Most Stable and Precise Gravity Meter, pp. 1–4.
Hagiwara T (1958) A note on the theory of the electromagnetic seismograph. *Bulletin of the Earthquake Research Institute* 36: 139–164.
Haney MM, et al. (2012) Causal instrument corrections for short-period and broadband seismometers. *Seismological Research Letters* 83(5): 834–845.

Harjes H-P and Seidl D (1978) Digital recording and analysis of broad-band seismic data at the Graefenberg (GRF)-array. *Journal of Geophysics* 44: 511–523.

Hart DM, Jones KR, and Sauter A (2011) Characterization of NCPA infrasound sensors. In: *AGU Fall Meeting Abstracts*, p. A47.

Haubrich R and Iyer H (1962) A digital seismograph system for measuring earth noise. *Bulletin of the Seismological Society of America* 52(1): 87–93.

Hemelrick LV (1964) A lunar long-period seismometer and a laser-transducer seismometer. VESIAC report no 4410–77-X, University of Michigan, pp. 1–17.

Herrin E (1982) The resolution of seismic instruments used in treaty verification research. *Bulletin of the Seismological Society of America* 72(6).

Holcomb GL (1989) A direct method for calculating instrument noise levels in side-by-side seismometer evaluations. U. S. Geological Survey Open-file report 89-214.

Holcomb GL (1990) A numerical study of some potential sources of error in side-by-side seismometer evaluations. U. S. Geological Survey, Open-file report 90-406.

Holcomb GL and Hutt CR (1992) An evaluation of installation methods for STS-1 seismometers. U. S. Geological Survey, Open File Report 92-302.

Holcomb LG (2002) Experiments in seismometer azimuth determination by comparing the sensor signal outputs with the signal output of an oriented sensor. USGS Open File Report 02-0183.

Holcomb LG, Sandoval L, and Hutt B (1998) Experimental investigations regarding the use of sand as an inhibitor of air convection in deep seismic boreholes. USGS Open File Report 98-362.

Hoover L (1912) John Milne, seismologist. *Bulletin of the Seismological Society of America* 2: 2–7.

Houlié N, et al. (2011) New approach to detect seismic surface waves in 1Hz-sampled GPS time series. *Scientific Reports* 1: 44.

Hutt C, Holcomb LG, and Sandoval LD (2004) An inertial rotation meter (tiltmeter). In: *IRIS VBB Workshop. Granlibakken Conference Center*.

Hutt CR, Nigbor RL, and Evans JR (eds.) (2009a) *Proceedings of the Guidelines for Seismometer Testing Workshop, Albuquerque, New Mexico, 9–10 May 2005 ("GST2")* Open File Report 2009-1055.

Hutt C and Ringler A (2011) Some possible causes of and corrections for STS-1 response changes in the global seismographic network. *Seismological Research Letters* 82(4): 560–571.

Hutt CR, Evans JR, Followill F, Nigbor RL, and Wielandt E (2009b) Guidelines for standardized testing of broadband seismometers and accelerometer. USGS Geological Survey, Open File Report 2009-1295.

Hutt CR, Bolton HF, and Holcomb LG (2002) US contribution to digital global seismograph networks. In: Lee W, et al. (eds.) *International Handbook of Earthquake and Engineering Seismology*, pp. 319–332. San Diego: Academic Press.

Hyperion, IFS-4000 Series Analog Infrasound Sensor. Available at: http://mabushost.com/hype/wp-content/uploads/2012/11/IFS4000.pdf.

IEEE (2001) *IEEE Standard for Digitizing Waveform Recorders Std 1057*.

IEEE (2000) IEEE standard for terminology and test methods for analog-to-digital converters Std 1241–2000.

Inose H, Yasuda Y, and Murakami J (1962) A telemetering system by code modulation – Δ– Σ modulation. *IRE Transactions on Space Electronics and Telemetry* SET-8(3): 204–209.

IRIS (2004) Prospects for low-frequency seismometry. In: Ingate S and Berger J (eds.) *A Report of the IRIS Broadband Seismometer Workshop*. California: Granlibakken.

IRIS (2012) SEED Reference Manual, SEED Format Version 2.4, Aug, 2012.

IRIS (1985) *The Design Goals for a New Global Seismographic Network*.

IXBLUE, Octans high-performance surface gyrocompass and motion sensor. Available at: http://www.ixsea.com/pdf/br-octans3000-2012-09-web.pdf.

Iyer H (1964) A frequency-velocity-energy diagram for the study of dispersive surface waves. *Bulletin of the Seismological Society of America* 54(1): 183–190.

Jones RV and Richards JCS (1973) The design and some applications of sensitive capacitance micrometers. *Journal of Physics E: Scientific Instruments* 6: 589–600.

Kanamori H (1999) Continuous monitoring of ground-motion parameters. *Bulletin of the Seismological Society of America* 89(1): 311–316.

Kanamori H (1990) Pasadena very-broad-band system and its use for real-time seismology. In: *Proceedings of Workshop XLVI. The 7th U.S. – Japan Seminar on Earthquake Prediction, September, 1988*. USGS Open File Report 90-98, pp. 135–144.

Kanamori H, Mori J, and Heaton T (1990) The 3 December 1988, Pasadena earthquake (M_L = 4.9) recorded with the very broadband system in Pasadena. *Bulletin of the Seismological Society of America* 80(2): 483–487.

Kromer RP (2006) Technology Report Evaluation of the Kinemetrics/Quanterra Q330HR Remote Seismic System for IRIS/GSN Q330HR/GainX1 Configuration.

Kurrle D and Widmer-Schnidrig R (2008) The horizontal hum of the Earth: a global background of spheroidal and toroidal modes. *Geophysical Research Letters* 35(6): L06304.

LaCoste LJB (1934) A new type long period seismograph. *Physics* 5: 178–180.

Lake HR (1964) Dynamic range of broad-band seismographs. VESIAC report no 4410-77-X, University of Michigan, pp. 19–35.

Laske G (2004) Instrumental effects as seen by a data analyst. In: *IRIS VBB Workshop, Granlibakken Conference Center*, pp. 1–35.

Lay T, et al. (2002) Global seismic network design goals update 2002. *IRIS*, pp. 1–9.

Li T, et al. (1984) High-frequency seismic noise at Lajitas, Texas. *Bulletin of the Seismological Society of America* 74(5): 2015–2033.

Longuet-Higgins M (1950) A theory of the origin of microseisms. *Philosophical Transactions of the Royal Society of London. Series A* 243(857): 1–35.

McDonald T (1994) Modified noise power ratio testing of high resolution digitizers. Sandia Report SAND94-0221.

McNamara D and Buland R (2004) Ambient noise levels in the continental United States. *Bulletin of the Seismological Society of America* 94(4): 1517–1527.

McNamara D, Buland R, and Benz H (2005) *An Assessment of the High-gain Streckeisen STS2 Seismometer for Routine Earthquake Monitoring in the United States*.

McNamara DE, et al. (2009) A method to establish seismic noise baselines for automated station assessment. *Seismological Research Letters* 80(4): 628–637.

Mcnamara DE and Boaz RI (2005) Seismic Noise Analysis System Using Power Spectral Density Probability Density Functions: A Stand-Alone Software Package. USGS Open File Report 2005-1438.

Melton B and Kirkpatrick B (1970) The symmetrical triaxial seismometer—its design for application to long-period seismometry. *Bulletin of the Seismological Society of America* 60(3): 717–739.

Melton BS (1965) Angular Composite Seismometer. US Patent 3222636.

Melton BS (1976) The sensitivity and dynamic range of inertial seismographs. *Reviews of Geophysics* 14(1): 93.

Metrozet (2011) Metrozet M2166-VBB Very Broadband Triaxial Seismometer System. Available at: http://metrozetvbb.com/images/Metrozet_M2166-VBB_Seismometer_Datasheet.pdf.

Miller WF (1963) The Caltech digital seismograph. *Journal of Geophysical Research* 68(3): 841–847.

Milligan D (2013) HP MEMS seismic sensor. In: *IRIS Seismic Instrumentation Technology Symposium*.

Murphy A and Savino J (1975) A comprehensive study of long-period (20 to 200 seconds) earth noise at the high-gain worldwide seismograph stations. *Bulletin of the Seismological Society of America* 6: 1827–1862.

Nanometrics, Trillium Datasheet. Available at: http://www.nanometrics.ca/ckfinder/userfiles/files/NMX-Trillium.pdf.

Nawa K, et al. (1998) Incessant excitation of the Earth's free oscillations frequency-time spectrogram. *Earth, Planets and Space* 50: 3–8.

Oliver J and Murphy L (1971) WWNSS: seismology's global network of observing stations. *Science* 174: 254–261.

Oppenheim A and Schafer R (2009) *Discrete-Time Signal Processing*, 3rd edn. Prentice Hall.

Paroscientific, Oceanic and Atmospheric Pressure Sensors 6000, 1000 & 9000, 8700 (425). Available at: http://www.paroscientific.com/Nano_Resolution_Data_Sheet.pdf.

Pavlis GL and Vernon FL (1994) Calibration of seismometers using ground noise. *Bulletin of the Seismological Society of America* 84(4): 1243–1255.

Peterson CV and Hutt CR (1994) Lossless compression of seismic data. In: *Workshop on the Use of Data Compression in Seismic Data*. Pasadena, CA: JPL.

Peterson J (1982) A note on transients in the SRO and ASRO long-period data. US Geological Survey Open-File Report 82-702.

Peterson J (1993) Observations and modeling of seismic background noise. US Geological Survey Open-File Report 93-322.

Peterson J (1980) Preliminary observations of noise spectra at the SRO and ASRO stations. USGS Open-File report 80-992.

Peterson J, et al. (1976) The seismic research observatory. *Bulletin of the Seismological Society of America* 66(6): 2049–2068.

Peterson J and Hutt CR (1989) IRIS/USGS plans for upgrading the global seismograph network. USGS Open File Report 89-471, p. 46.

Peterson J, Hutt CR, and Holcomb LG (1980) Test and calibration of the seismic research observatory. US Geological Survey, Open-File Report 80-187.

Peterson J and Tilgner EE (1985) Description and preliminary testing of the CDSN seismic sensor systems. USGS Open File Report 85-288.

Phinney R and Smith S (1963) Processing of seismic data from an automatic digital recorder. *Bulletin of the Seismological Society of America* 53(3): 549–562.

Plešinger A and Horalek J (1976) The seismic broadband recording and data processing system FBV/DPS and its seismological applications. *Journal of Geophysics* 42: 201–217.

Pomeroy PW, et al. (1969) Preliminary results from the high-gain, wide-band, long-period electromagnetic seismograph system. *Journal of Geophysical Research* 74: 3295–3298.

Press F, Ewing M, and Lehner F (1958) A long-period seismograph system. *Transactions of the American Geophysical Union* 39(1): 106–108.

Rabiner L and Gold B (1975) *Theory and Application of Digital Signal Processing*. Englewood Cliffs, NJ: Prentice-Hall.

Rabiner LR, et al. (1972) Terminology in digital signal processing. *IEEE Transactions on Audio and Electroacoustics* AU-20(5): 322–337.
Rader CM and Gold B (1967) Digital filter design techniques in the frequency domain. *Proceedings of the IEEE* 55(2): 149–171.
Reid H (1912) On the choice of a seismograph. *Bulletin of the Seismological Society of America* 8–30.
Ringler A, et al. (2013) Seismic station installation orientation errors at ANSS and IRIS/USGS stations. *Seismological Research Letters* 84(6).
Ringler A and Hutt C (2010) Self-noise models of seismic instruments. *Seismological Research Letters* 81(6): 972–983.
Ringler AT, et al. (2011) A comparison of seismic instrument noise coherence analysis techniques. *Bulletin of the Seismological Society of America* 101(2): 558–567.
Ringler AT, Gee LS, et al. (2012a) Data quality of seismic records from the Tohoku, Japan, earthquake as recorded across the Albuquerque Seismological Laboratory Networks. *Seismological Research Letters* 83(3): 575–584.
Ringler AT, Hutt CR, et al. (2012b) Estimating pole-zero errors in GSN-IRIS/USGS network calibration metadata. *Bulletin of the Seismological Society of America* 102(2): 836–841.
Ringler AT, et al. (2010) Temporal variations in global seismic station ambient noise power levels. *Seismological Research Letters* 81(4): 605–613.
Rodgers P (1969) A note on the response of the pendulum seismometer to plane wave rotation. *Bulletin of the Seismological Society of America* 59(5): 2101–2102.
Rodgers P (1992a) Frequency limits for seismometers as determined from signal-to-noise ratios. Part 1. The electromagnetic seismometer. *Bulletin of the Seismological Society of America* 82(2): 1071–1098.
Rodgers P (1992b) Frequency limits for seismometers as determined from signal-to-noise ratios. Part 2. The feedback seismometer. *Bulletin of the Seismological Society of America* 82(2): 1099–1123.
Rodgers P (1968) The response of the horizontal pendulum seismometer to Rayleigh and Love waves, tilt, and free oscillations of the Earth. *Bulletin of the Seismological Society of America* 58(5): 1384–1406.
Rodgers P, Taylor SR, and Nakanishi KK (1987) System and site noise in the regional seismic test network from 0.1 to 20 Hz. *Bulletin of the Seismological Society of America* 77(2): 663–678.
Romanowicz B, et al. (1985) GEOSCOPE—a French initiative in long-period three-component global seismic networks. *EOS Transactions of the American Geophysical Union* 65(42): 753–754.
Rosat S and Hinderer J (2011) Noise levels of superconducting gravimeters: updated comparison and time stability. *Bulletin of the Seismological Society of America* 101(3): 1233–1241.
Rosat S, Watada S, and Sato T (2007) Geographical variations of the ${}_0S_0$ normal mode amplitude: predictions and observations after the Sumatra–Andaman earthquake. *Earth, Planets and Space* 59: 307–311.
Roult G, et al. (2010) The GEOSCOPE program: progress and challenges during the Past 30 years. *Seismological Research Letters* 81(3): 427–452.
Satô Y (1958) Attenuation, dispersion, and the wave guide of the G wave. *Bulletin of Seismological Society of America* 48(1): 231–251.
Scherbaum F (2001) *Of Poles and Zeros: Fundamentals of Digital Seismology*, 2nd edn. Kluwer Academic Publishers.
Scherbaum F and Bouin M-P (1997) FIR filter effects and nucleation phases. *Geophysical Journal International* 130(3): 661–668.
Seidl D (1980) The simulation problem for broad-band seismograms. *Journal of Geophysics* 48: 84–93.
Setra, Model 270 Pressure Sensor Data Sheet, pp. 263–264. Available at: http://www.setra.com/products/pressure/analog-pressure-transducer-model-270/.
Shannon CE (1949) Communication in the presence of noise. *Proceedings of the IRE* 37(1): 10–21.
Shapiro N and Campillo M (2004) Emergence of broadband Rayleigh waves from correlations of the ambient seismic noise. *Geophysical Research Letters* 31(7): L07614.
Sleeman R (2006) Three-channel correlation analysis: a new technique to measure instrumental noise of digitizers and seismic sensors. *Bulletin of the Seismological Society of America* 96(1): 258–271.
Sleeman R and Melichar P (2012) A PDF representation of the STS-2 self-noise obtained from one year of data recorded in the Conrad observatory, Austria. *Bulletin of the Seismological Society of America* 102(2): 587–597.
Smith S (1964) Broadband digital recording. VESIAC report no 4410-77-X, University of Michigan, pp. 87–90.
Smith SW (1965) Seismic digital data acquisition systems. *Reviews of Geophysics* 3(1): 151–156.
Sorrells G (1971) A preliminary investigation into the relationship between long-period seismic noise and local fluctuations in the atmospheric pressure field. *Geophysical Journal International* 26(1–4): 71–82.
Sorrells G and Goforth T (1973) Low-frequency earth motion generated by slowly propagating partially organized pressure fields. *Bulletin of the Seismological Society of America* 63(5): 1583–1601.
Sorrells G, McDonald J, Der Z, and Herrin E (1971) Earth motion caused by local atmospheric pressure changes. *Geophysical Journal of the Royal Astronomical Society* 26(1–4): 83–98.
Standley I and Pike W (2008) *Initial results on rugged low power compact silicon MEMS sensors for use in nuclear explosion monitoring. 2008 Monitoring Research Review: Ground-Based Nuclear Explosion Monitoring Technologies*. pp. 494–503.
Stearns SD, Tan L-Z, and Magotra N (1993) Lossless compression of waveform data for efficient storage and transmission. *IEEE Transactions on Geoscience and Remote Sensing* 31(3): 645–654.
Steim J (1986) The very-broad-band seismograph, PhD Thesis, Harvard University.
Steim J and Wielandt E (1989) Analog to digital converter employing delta-sigma modulation. US Patent 4866442.
Steim JM (1987) Dial-a-broad-band seismogram. *EOS Transactions of the American Geophysical Union* 68(27).
Steim JM (1994) "Steim" compression. In: *Workshop on the Use of Data Compression in Seismic Data, Pasadena, CA: JPL*.
Steim JM and Wielandt E (1985) The very broad band seismograph. Part 2: station processor (abstract). *EOS Transactions of the American Geophysical Union* 66(312).
Streckeisen (2013) STS-2.5 Datasheet. Available at: http://kmi.com/uploads/PDFs/STS-2_5.pdf.
Streckeisen, G. STS-1 Product Specification.
Sutton GH and Latham GV (1964) Analysis of a feedback-controlled seismometer. *Journal of Geophysical Research* 69(18): 3865–3882.
Sutton G and Oliver J (1959) Seismographs of high magnification at long periods. *Annales de Geophysique* T15: 424–433.
Taira T, Zheng Z, and Romanowicz B (2014) On the systematic long period noise reduction on ocean floor broadband seismic sensors collocated with differential pressure gauges. *Bulletin of the Seismological Society of America* 104(1): 247–259.
Tanimoto T, et al. (1998) Earth's continuous oscillations observed on seismically quiet days. *Geophysical Research Letters* 25(10): 1553–1556.
Trnkoczy A, et al. (2011) Site selection, preparation and installation of seismic stations. In: Bormann P (ed.) *New Manual of Seismological Observatory Practice (NMSOP-2)*, pp. 1–143. Potsdam: IASPEI.
Uhrhammer RA, Karavas W, and Romanowicz B (1998) Broadband seismic station installation guidelines. *Seismological Research Letters* 69(1): 15–26.
Usher M, Buckner I, and Burch R (1977) A miniature wideband horizontal-component feedback seismometer. *Journal of Physics E: Scientific Instruments* 10: 1253–1260.
Usher M, Guralp C, and Burch R (1978) The design of miniature wideband seismometers. *Geophysical Journal of the Royal Astronomical Society* 55(3): 605–613.
Usher MJ (1973) Developments in seismometry. *Journal of Physics E: Scientific Instruments* 6(6): 501–507.
Usher MJ, Burch RF, and Guralp C (1979) Wide-band feedback seismometers. *Physics of the Earth and Planetary Interiors* 18: 38–50.
Validyne, DP103 Pressure Transducer. (818). Available at: http://validyne.com/ProductCatalog/16.pdf.
Van Camp M, et al. (2008) Connecting a quanterra data logger Q330 on the GWR C021 superconducting gravimeter. *Seismological Research Letters* 79(6): 785–796.
VanZandt T, Romanowicz B, Karavas B, Friday J, and Wielandt E (2010) STS-1-VBB Sensor Replacement Program: Presentation to GSN Standing Committee, pp. 1–17.
VTI, SCP1000 Pressure Sensor Data Sheet, pp. 1–7. Available at: http://www.muratamems.fi/sites/default/files/uploads/scp1000-d01_-d11_pressure_sensor_datasheet_28-08-2007.pdf.
Warburton RJ and Goodkind JM (1977) The influence of barometric-pressure variations on gravity. *Geophysical Journal International* 48(3): 281–292.
Webb SC (2002) Seismic noise on land and on the sea floor. In: Lee W, et al. (ed.) *International Handbook of Earthquake and Engineering Seismology Part A*, pp. 305–317. San Diego: Academic Press.
Webb SC and Crawford WC (2010) Shallow-water broadband OBS seismology. *Bulletin of the Seismological Society of America* 100(4): 1770–1778.
Webb SC, Deaton TK, and Lemire JC (2001) A broadband ocean-bottom seismometer system based on a 1-Hz natural period geophone. *Bulletin of the Seismological Society of America* 91(2): 304–312.
Welch PD (1967) The use of fast Fourier transform for the estimation of power spectra: a method based on time averaging over short, modified periodograms. *IEEE Transactions on Audio and Electroacoustics* 15(2): 70–73.
Widmer-Schnidrig R (2003) What can superconducting gravimeters contribute to normal-mode seismology? *Bulletin of the Seismological Society of America* 93(3): 1370–1380.
Widmer-Schnidrig R and Kurrle D (2006) Evaluation of installation methods for Streckeisen STS-2 seismometers. Available at: http://www.geophys.uni-stuttgart.de/widmer/DGG2006poster.pdf [accessed July 21, 2013].

Wielandt E (2011a) Chapter 5. Seismic sensors and their calibration. In: Bormann P (ed.) *New Manual of Seismological Observatory Practice (NMSOP-2), IASPEI*, pp. 1–51. Potsdam: GFZ German Research Centre for Geosciences.
Wielandt E (2011b) *Data Sheet 5.1 Common seismic sensors*. *New Manual of Seismological Observatory Practice (NMSOP-2)*. IASPEI pp. 1–26.
Wielandt E and Mitronovas W (1976) An electronic long-period seismograph for surface-wave dispersion studies. *Bulletin of the Seismological Society of America* 66(3): 987–996.
Wielandt E and Steim JM (1985) The very broad band seismograph; Part 1: Sensor (abstract). *EOS Transactions of the American Geophysical Union* 66(312).
Wielandt E and Streckeisen G (1982) The leaf-spring seismometer: design and performance. *Bulletin of the Seismological Society of America* 72(6): 2349–2367.
Wielandt E and Zumberge M (2013) Measuring seismometer nonlinearity on a shake table. *Bulletin of the Seismological Society of America* 103(4): 2247–2256.
Wielandt E and Steim J (1986) A digital very-broad-band seismograph. *Annales Geophysicae* 4(B3): 227–232.
Withers M, et al. (1996) High-frequency analysis of seismic background noise as a function of wind speed and shallow depth. *Bulletin of the Seismological Society of America* 86(5): 1507–1515.
Wolf A (1942) The limiting sensitivity of seismic detectors. *Geophysics* VII: .
Woodhouse JH and Dziewonski AM (1984) Mapping the upper mantle: three-dimensional modeling of earth structure by inversion of seismic waveforms. *Journal of Geophysical Research: Solid Earth* 89(B7): 5953–5986.
Woodward RL and Masters G (1989) Calibration and data quality of the long-period SRA/ASRO networks, 1977 to 1980. *Bulletin of the Seismological Society of America* 79(6): 1972–1983.
Wu Y-M, et al. (2013) A high-density seismic network for earthquake early warning in Taiwan based on low cost sensors. *Seismological Research Letters* 84(6): 1048–1054.
Xu Y, Crossley D, and Herrmann RB (2008) Amplitude and Q of ${}_0S_0$ from the Sumatra earthquake as recorded on superconducting gravimeters and seismometers. *Seismological Research Letters* 79(6): 797–805.
Young C, et al. (1996) A comparison of the high-frequency (>1 Hz) surface and subsurface noise environment at three sites in the United States. *Bulletin of the Seismological Society of America* 86(5): 1516–1528.
Yuki Y and Ishihara Y (2002) Methods for maintaining the performance of STS-1 seismometer. *Frontier Research on Earth Evolution* 2: 1–5.
Zahradník J and Plešinger A (2005) Long-period pulses in broadband records of near earthquakes. *Bulletin of the Seismological Society of America* 95(5): 1928–1939.
Zahradník J and Plešinger A (2010) Toward understanding subtle instrumentation effects associated with weak seismic events in the near field. *Bulletin of the Seismological Society of America* 100(1): 59–73.
Zha Y, Webb SC, and Menke W (2013) Determining the orientations of ocean bottom seismometers using ambient noise correlation. *Geophysical Research Letters* 40(14): 3585–3590.
Zheng Y, et al. (2012) 5Hz GPS seismology of the El Mayor-Cucapah earthquake: estimating the earthquake focal mechanism. *Geophysical Journal International* 190(3): 1723–1732.
Zumberge M, Berger J, Otero J, and Wielandt E (2010) An optical seismometer without force feedback. *Bulletin of the Seismological Society of America* 100(2): 598–605.
Zumberge M, Wielandt E, and Berger J (2012) Optical Seismometer. US Patent Application US 2012/0247213 A1, 00(19).
Zürn W, et al. (2007) On reduction of long-period horizontal seismic noise using local barometric pressure. *Geophysical Journal International* 171(2): 780–796.
Zürn W and Widmer R (1995) On noise reduction in vertical seismic records below 2 mHz using local barometric pressure. *Geophysical Research Letters* 22(24): 3537–3540.
Zürn W and Wielandt E (2007) On the minimum of vertical seismic noise near 3 mHz. *Geophysical Journal International* 168(2): 647–658.

Further Reading

Aki K and Richards P (2002) *Quantitative Seismology: Theory and Methods*, 2nd edn. Sausolito, CA: University Science Books.
Galitzin B (1919) An apparatus for the direct determination of accelerations. *Proceedings of the Royal Society A: Mathematical, Physical and Engineering Sciences* 95(673): 492–507.
Gerner A and Bokelmann G (2012) Self-noise and sensitivity of broadband seismographs. In: *PANGEO Austria 2012*. Salzburg, p. 151.
Havskov BJ and Alguacil G (2010) *Instrumentation in Earthquake Seismology (Modern Approaches in Geophysics)*. Berlin: Springer.
Kinoshita S (2008) Tilt measurement using broadband velocity seismograms. *Bulletin of the Seismological Society of America* 98(4): 1887–1897.
Melton BS (1981a) Earthquake seismograph development: a history – Part 1. *Journal of the European Optical Society* 62(21): 505–510.
Melton BS (1981b) Earthquake seismograph development: a history – Part 2. *Journal of the European Optical Society* 62(25): 545–548.
Melton BS (1971) The LaCoste suspension-principles and practice. *Geophysical Journal International* 22: 521–543.
Michel R, et al. (2013) A geostationary optical seismometer, proof of concept. *IEEE Transactions on Geoscience and Remote Sensing* 51(1): 695–703.
Nijim YW, Stearns SD, and Mikhael WB (2000) Quantitative performance evaluation of the lossless compression approach using pole-zero modeling. *IEEE Transactions on Geoscience and Remote Sensing* 38(1): 39–43.
Nyquist H (1928) Certain topics in telegraph transmission theory. *Transactions of the American Institute of Electrical Engineers* 47(2): 617–644.
Okada Y, Kasahara K, and Hori S (2004) Recent progress of seismic observation networks in Japan-Hi-net, F-net, K-NET and KiK-net. *Earth, Planets and Space* 56: xv–xxviii.
Park J, et al. (2005) Performance review of the global seismographic network for the Sumatra–Andaman megathrust earthquake. *Seismological Research Letters* 76: 331–343.
Riedesel M, Orcutt J, and Moore R (1990) Limits of sensitivity of inertial seismometers with velocity transducers and electronic amplifiers. *Bulletin of the Seismological Society of America* 80(6): 1725–1752.
Rodgers P (1993) Maximizing the signal-to-noise ratio of the electromagnetic seismometer: the optimum coil resistance, amplifier characteristics, and circuit. *Bulletin of the Seismological Society of America* 83(2): 561–582.
Rodgers P (1994) Self-noise spectra for 34 common electromagnetic seismometer/preamplifier pairs. *Bulletin of the Seismological Society of America* 84(1): 222–228.
Rodgers P and Martin A (1995) Signal-coil calibration of electromagnetic seismometers. *Bulletin of the Seismological Society of America* 85(3): 845–850.
Savino J, McCamy K, and Hade G (1972) Structures in earth noise beyond twenty seconds—a window for earthquakes. *Bulletin of the Seismological Society* 62(1): 141–176.
Teupser C and Plešinger A (1979) Design of feedback-controlled wide-band seismographs with respect to undesired side-effects. *Physics of the Earth and Planetary Interiors* 18: 58–63.
Widmer-Schnidrig R and Zürn W (2009) Perspectives for ring laser gyroscopes in low-frequency seismology. *Bulletin of the Seismological Society of America* 99(2B): 1199–1206.
Wielandt E and Forbriger T (1999) Near-field seismic displacement and tilt associated with the explosive activity of Stromboli. *Annali di Geofisica* 42: 407–416.
Yang Z, et al. (2012) The character of seafloor ambient noise recorded offshore New Zealand: results from the MOANA ocean bottom seismic experiment. *Geochemistry, Geophysics Geosystems* 13(10).
Zürn W and Widmer-Schnidrig R (2003) Vertical acceleration noise at seismic frequencies. *Cahiers European Centre for Geodynamics and Seismology* 22: 123–127.

1.03 Theory and Observations - Earth's Free Oscillations

JH Woodhouse, University of Oxford, Oxford, UK; University of Cambridge, Cambridge, UK
A Deuss, University of Oxford, Oxford, UK; Utrecht University, Utrecht, The Netherlands

© 2015 Elsevier B.V. All rights reserved.

1.03.1	**Introduction**	79
1.03.2	**Equations of Motion and Hamilton's Principle**	82
1.03.2.1	Definition of the Earth Model and Lagrangian	82
1.03.2.2	Equations of Motion and Boundary Conditions	83
1.03.2.3	The Seismic Source	84
1.03.2.4	Viscoelasticity and Intrinsic Attenuation	84
1.03.2.5	Final Equation of Motion	85
1.03.3	**Spherical Harmonics and Generalized Spherical Harmonics**	85
1.03.3.1	Spherical Harmonics	85
1.03.3.2	Generalized Spherical Harmonics	85
1.03.3.3	Wigner 3-j Symbols	87
1.03.3.4	Application: Point Force Distribution	88
1.03.4	**The Green's Function for the Spherically Symmetric Earth**	89
1.03.4.1	Reduction of the General Equations to the Spherically Symmetric Case	89
1.03.4.2	Derivation of the Radial Ordinary Differential Equations	89
1.03.5	**Numerical Solution of the Radial Equations**	94
1.03.5.1	Methods of Solution	94
1.03.5.2	Numerical Integration	94
1.03.5.3	Eigenfunctions and Eigenfrequencies	96
1.03.5.4	Minors	97
1.03.5.5	Mode Bracketing and Counting	98
1.03.6	**Elastic Displacement as a Sum Over Modes**	98
1.03.7	**The Normal Mode Spectrum**	100
1.03.7.1	Asymptotic Relations Relating Normal Modes, Body Waves, and Surface Waves	100
1.03.7.2	Differential Kernels for Spherically Symmetric Model Perturbations	101
1.03.7.3	Tour of Frequency-Wavenumber Space	101
1.03.8	**Normal Modes and Theoretical Seismograms in Three-Dimensional Earth Models**	104
1.03.8.1	Theoretical Seismograms	104
1.03.8.2	Splitting of Isolated Modes: The Splitting Function	106
1.03.8.3	Normal Mode Coupling	108
1.03.8.4	Centroid-Moment Tensor Method	111
1.03.8.5	Great Circle Approximation	112
1.03.9	**Concluding Discussion**	112
Acknowledgments		114
References		114

1.03.1 Introduction

Earth's normal modes, or free oscillations, are standing waves along the surface and radius of the Earth. These standing waves only exist at discrete frequencies and are similar to the different 'tones' of musical instruments. The study of the Earth's free oscillations is fundamental to seismology, as it is a key part of the theory of the Earth's dynamic response to external or internal forces. Essentially, the same theory is applicable to phenomena as diverse as post-seismic relaxation, analysis of seismic surface waves and body waves. The study of free oscillations *per se* is concerned with analyzing and extracting information at very long periods (~3000–100 s period) since in this range of periods the intrinsic standing wave modes of oscillation are evident in seismic spectra. Normal mode peaks can be observed in the frequency spectrum of large earthquakes with magnitudes of, say, $M_w > 7.5$, though the best observations are made for large and deep earthquakes such as the $M_w = 8.5$ Bolivia earthquake of 1994. Such spectra contain important information about the large-scale structure of the Earth. For example, the strongest evidence that the inner core is solid (Dziewonski and Gilbert, 1971) and anisotropic (Romanowicz and Breger, 2000; Tromp, 1993; Woodhouse et al., 1986) comes from the study of free oscillations.

Free oscillations provide essential constraints on both the spherically symmetric 'average' Earth, and also on lateral variations in Earth structure due to heterogeneity in temperature, composition, and anisotropy. Modal data are particularly valuable in this regard because, unlike other kinds of seismic data, modal observables depend upon broad averages of the Earth's

structural parameters, and are not nearly so affected by limitations of data coverage due to the uneven distribution of seismic events and stations. There is an enormous wealth of information yet to be extracted from long-period spectra; one has only to examine almost any portion of a seismic spectrum in detail to realize that current models often do not come close to providing adequate predictions. It is only from such very long-period data that it may be possible to obtain direct information on the three-dimensional distribution of density (Ishii and Tromp, 1999; Romanowicz, 2001; Trampert et al., 2004). Even very large scale, information on lateral variations in density has the potential to bring unique information to the study of convection and thermal and compositional evolution.

Very long-period spectra are also an essential element in the study of earthquakes, as it is only by using data at the longest periods that it is possible to determine the overall moment of very large events. For example, estimates of the moment of the great Sumatra earthquake based on mantle waves, even at periods of several hundred seconds, significantly underestimate the true moment, as the length and duration of the rupture make it possible to gauge the true, integrated moment only by using data at the longest seismic periods (e.g., Park et al., 2005).

Figure 1(a) shows an example of data and theoretical amplitude spectra computed for the spherically symmetric nonrotating PREM model (Dziewonski and Anderson, 1981). Modes appear as distinct peaks in the frequency domain. For higher frequencies, the modes are more closely spaced and begin to overlap. The theoretical peaks appear at frequencies very close to the observed peaks. However, the observed peaks are distorted in shape and amplitude due to three-dimensional effects. For example, mode ${}_1S_4$ is split into two peaks in the data spectrum, which is not seen in the theoretical spectrum. When adding the effects of Earth rotation and ellipticity of figure (**Figure 1(b)**), the peaks in the synthetic spectrum start looking more similar to the data; mode ${}_1S_4$ has become broader in the synthetic spectrum. Even better agreement is obtained for a fully three-dimensional Earth model (**Figure 1(c)**), for example, the pair of modes ${}_0S_7$–${}_2S_3$ now looks very similar in the data and synthetic spectra. However, there are also still significant differences demonstrating that a lot can still be learnt from studying long-period normal mode spectra. Not shown here, but equally important in studying both Earth structure and earthquakes, is the *phase spectrum*. Examples illustrating this are shown in later sections.

Normal mode studies represent the quest to reveal and to understand the Earth's intrinsic vibrational spectrum. However, this is a difficult quest, because it is only at the very longest periods ($\geq$100 s, say) that there is the possibility of obtaining data of sufficient duration to make it possible to achieve the necessary spectral resolution. Essentially the modes attenuate before the many cycles necessary to establish a standing wave pattern have elapsed. Thus, in many observational studies, over a wide range of frequencies, the normal mode representation has the role, primarily, of providing a method for the calculation of theoretical seismograms. Although observed spectra contain spectral peaks, the peaks are broadened by the effects of attenuation in a path-dependent way. Thus, rather than making direct measurements

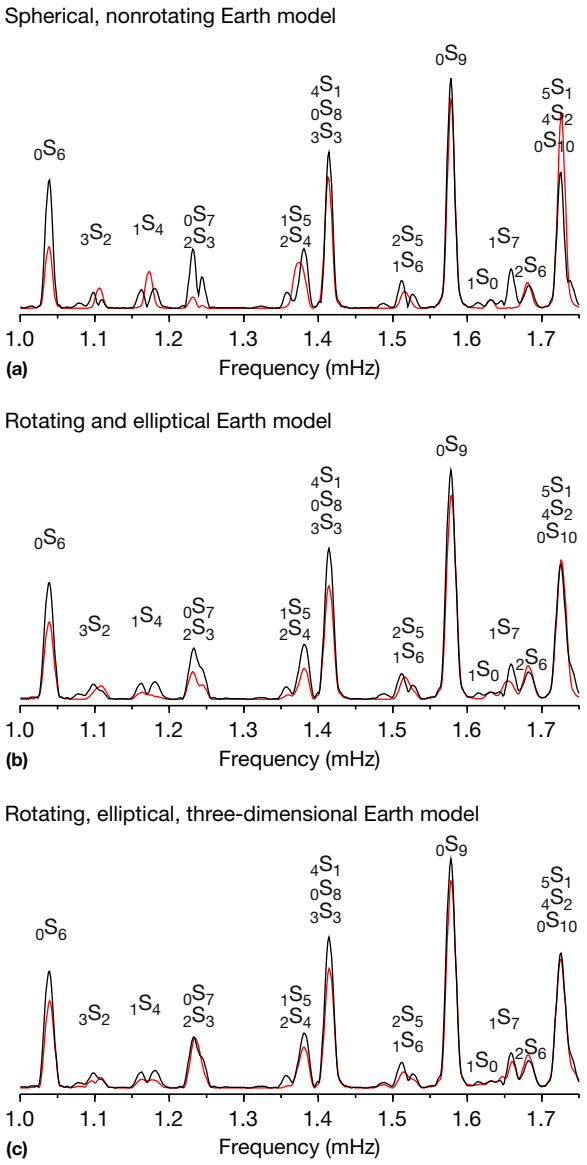

Figure 1 Data (black line) and synthetic spectrum (red line) computed using normal mode summation, for the vertical component recording at station ANMO following the great Sumatra event of 26 December 2004, using three different Earth models: (a) spherical, nonrotating, (b) rotating and elliptical, and (c) rotating, elliptical, three-dimensional structure Earth models. The calculations for rotation, ellipticity, and three-dimensional structure are fully coupled for all 140 modes below 3 mHz.

on observed spectra, the analysis needs to be based on comparisons between data and synthetic spectra, in order to derive models able to give improved agreement between data and synthetics.

The use of normal mode theory as a method of synthesis extends well beyond the realm normally thought of as normal mode studies. For example, it has become commonplace to calculate global body wave theoretical seismograms by mode summation in a spherical model, to frequencies higher than 100 mHz (10 s period). Typically such calculations can be

done in seconds on an ordinary workstation; the time, of course, depending strongly upon the upper limit in frequency and on the number of samples in the time series. The advantage of the method is that all seismic phases are automatically included, with realistic time and amplitude relationships. Although the technique is limited (probably for the foreseeable future) to spherically symmetric models, the comparison of such synthetics with data provides a valuable tool for understanding the nature and potential of the observations and for making measurements such as differences in timing between data and synthetics, for use in tomography. Thus, the period range of applications of the normal mode representation extends from several thousand seconds to ~5 s. In between these ends of the spectrum is an enormous range of applications: studies of modes *per se*, surface wave studies, analysis of overtones and long-period body waves, each having relevance to areas such as source parameter estimation and tomography. **Figure 2** shows an example of synthetic and data traces to illustrate this. The normal mode synthetic is calculated by summing all modes with period ≥6 s. The body waves P, PP, S, and SS are visible in the early part of the synthetic and data seismograms, and the surface waves arrive in the later part. It is important to note that S diffracted waves can also be obtained using normal mode summation, as normal modes form a complete basis set and thus all waves existing in a spherical Earth model are automatically included when all modes are summed up to a certain period. Differences between the synthetic and observed data seismograms can be attributed to unmodeled three-dimensional heterogeneity.

There are a number of excellent sources of information on normal modes theory and applications. The comprehensive monograph by Dahlen and Tromp (1998) provides in-depth coverage of the material and an extensive bibliography. An earlier monograph by Lapwood and Usami (1981) contains much interesting and useful information, treated from a fundamental point of view, as well as historical material about early theoretical work and early observations. A review by Takeuchi and Saito (1972) is a good source for the ordinary differential equations for spherical Earth models and methods of solution. Other reviews are by Gilbert (1980), Dziewonski and Woodhouse (1983b), and Woodhouse (1996). A review of normal mode observations can be found in **Chapter 1.04**. Because of this extensive literature, we tend in this article to expand on some topics that have not found their way into earlier reviews but are nevertheless of fundamental interest and utility. We will first derive the equations of motion using Hamilton's principle, and introduce the concept of generalized spherical harmonics. We will then show how to obtain the

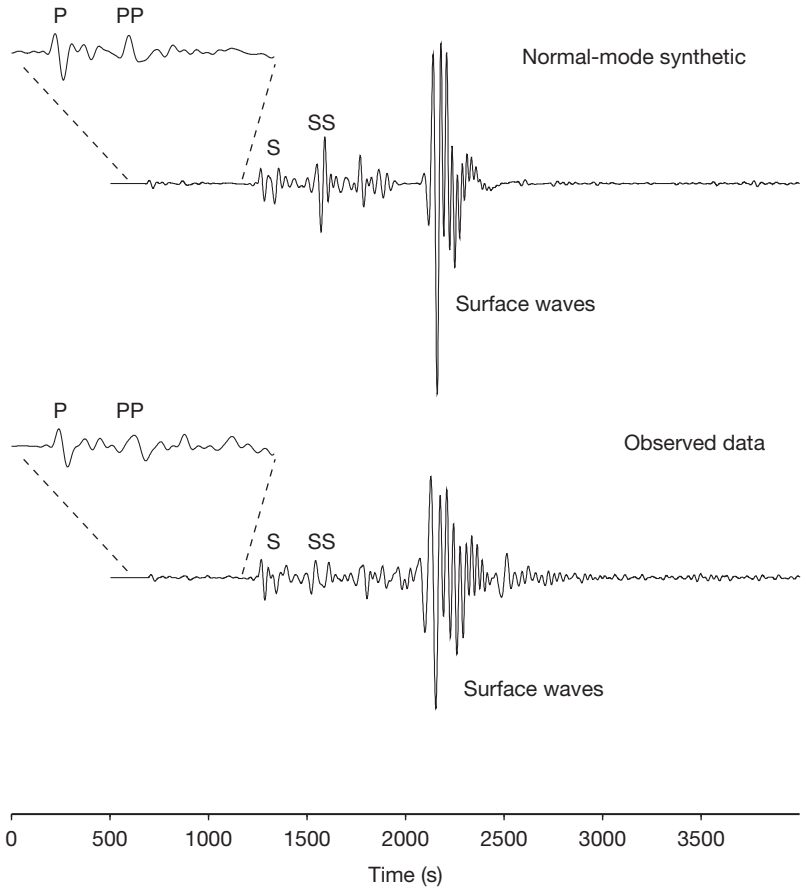

Figure 2 Data and *normal mode* synthetic for a vertical component record at station HRV following an event in Hawaii on 15 October 2006. The epicentral *distance* is 73°. For the calculation of the synthetic seismogram, the Harvard/Lamont quick-CMT centroid location and moment tensor parameters were used (G. Ekström, www.globalcmt.org).

solution for a spherically symmetric Earth and the numerical method used for calculating the modes. Finally, we will explain the calculation of synthetic seismograms in spherical and three-dimensional Earth models and discuss the characteristics of the normal mode spectrum.

1.03.2 Equations of Motion and Hamilton's Principle

To a good approximation, except in the vicinity of an earthquake or explosion, seismic displacements are governed by the equations of elasticity. At long periods self-gravitation also plays an important role. The equations of motion can be derived using conservation laws (e.g., Woodhouse, 1996). Alternatively, they can be derived from a variational principle, which significantly lessens the algebra involved. First, the Lagrangian, which is the total kinetic energy minus the total potential energy, is defined. Then the equations of motion and boundary conditions are obtained by requiring that the Lagrangian be stationary with respect to small variations in displacement and gravitation. There are two alternative ways to use a variational principle, depending on the domain in which the displacement and gravitation are varied. In the frequency domain, Rayleigh's principle has been used (Woodhouse and Dahlen, 1978), and in the time domain Hamilton's principle can be used. Here, we show how the equations of motion arise from Hamilton's principle by first defining the Lagrangian and then varying the Lagrangian with respect to displacement and gravity to get the equations of motion and corresponding boundary conditions.

1.03.2.1 Definition of the Earth Model and Lagrangian

Consider a material which is initially in equilibrium under self-gravitation. Each particle of the material is labeled by Cartesian coordinates x_i ($i=1, 2, 3$), representing its initial position. The material undergoes time-dependent deformation in which the particle initially at x_i moves to $r_i=r_i(\mathbf{x}, t)$ where t is time (Figure 3). A *hyperelastic* material is defined as one in which there exists an internal energy density function which is a function of the Green strain tensor

$$e_{ij}=\frac{1}{2}(r_{k,i}r_{k,j}-\delta_{ij}) \qquad [1]$$

where $r_{k,i}\equiv\partial r_k/\partial x_i$, δ_{ij} is the Krönecker-delta; summation over repeated indices is assumed. Thus, we introduce the internal elastic energy function, per unit mass, $E(\mathbf{x}, \mathbf{e}, s)$, where s is specific entropy. We shall be concerned only with isentropic deformations, and can henceforth omit the dependence on s. Note that E is represented as a function of the coordinates x_i which label a specific material particle. $E(\mathbf{x}, \mathbf{e})$ is regarded as a given function characterizing the elastic properties of the material. This form of the internal energy function, which forms the basis of finite theories of elasticity, as well as the theory of linear elasticity which we need here, arises from the very general consideration that elastic internal energy should not change as a result of rigid rotations of the material.

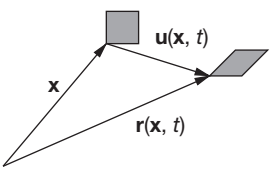

Figure 3 Schematic depiction of the particle at location **x** moving and deforming to location **r**(**x**, t).

The gravitational field is characterized by a potential field $\phi(\mathbf{r})$, which satisfies Poisson's equation

$$\frac{\partial^2\phi}{\partial r_k\partial r_k}=4\pi G\rho(\mathbf{r}) \qquad [2]$$

where ρ is the density. We state this equation in terms of the coordinates r_k, as it represents an equation valid in the current configuration of the material.

The Lagrangian governing motion of the elastic-gravitational system (total kinetic energy minus total potential energy) is

$$L=\int\int\left(\frac{1}{2}\rho\dot{r}_k\dot{r}_k-\rho E(\mathbf{x}, \mathbf{e})-\frac{1}{2}\rho\phi\right)\mathrm{d}^3r\,\mathrm{d}t \qquad [3]$$

where '˙' represents the material time derivative (i.e., the derivative with respect to t at constant $\mathbf{x}$). The three terms of the integrand represent the kinetic energy, (minus) the elastic energy, and (minus) the gravitational energy, respectively, making use of the fact that the gravitational energy released by assembling a body from material dispersed at infinity is $-\int\frac{1}{2}\rho\phi\,\mathrm{d}^3r$. The integral in eqn [3] is over the volume occupied by the Earth, which is taken to consist of a number of subregions with internal interfaces and an external free surface. Hamilton's principle requires that the Lagrangian L be stationary with respect to variations in displacement $\delta r_i(\mathbf{x}, t)$, subject to the constraint that ϕ is determined by eqn [2], and also to the requirement of mass conservation:

$$\rho\mathrm{d}^3r=\rho^0\mathrm{d}^3x \qquad [4]$$

where $\rho^0=\rho^0(\mathbf{x})$ is the initial density. That is

$$\rho=\rho^0/J \qquad [5]$$

where J is the Jacobian

$$J=\frac{\partial(r_1, r_2, r_3)}{\partial(x_1, x_2, x_3)} \qquad [6]$$

The gravitational constraint [2] can be incorporated into the variational principle by introducing a field η which acts as a Lagrange multiplier (e.g., Seliger and Whitham, 1968):

$$L'=\int\int\left\{\frac{1}{2}\rho\dot{r}_k\dot{r}_k-\rho E(\mathbf{x}, \mathbf{e})-\frac{1}{2}\rho\phi+\eta\left(\frac{\partial^2\phi}{\partial r_k\partial r_k}-4\pi G\rho\right)\right\}\mathrm{d}^3r\,\mathrm{d}t \qquad [7]$$

the term involving η vanishes by eqn [2], and therefore, L' is stationary with respect to variations in η. If we also require that L' be stationary under variations in gravitational field $\delta\phi$ we obtain the Euler–Lagrange equation for η:

$$\frac{\partial^2\eta}{\partial r_k\partial r_k}=\frac{1}{2}\rho \qquad [8]$$

which can be satisfied by setting $\eta=\phi/8\pi G$. Thus, we obtain

$$L' = \int\int\left\{\frac{1}{2}\rho\dot{r}_k\dot{r}_k - \rho E(\mathbf{x},\mathbf{e}) - \rho\phi - \frac{1}{8\pi G}\frac{\partial\phi}{\partial r_k}\frac{\partial\phi}{\partial r_k}\right\}\mathrm{d}^3 r\,\mathrm{d}t \qquad [9]$$

Changing the spatial integration variables, making use of eqn [4], we may also write:

$$L' = \int\int\left\{\frac{1}{2}\rho^0\dot{r}_k\dot{r}_k - \rho^0 E(\mathbf{x},\mathbf{e}) - \rho^0\phi - \frac{1}{8\pi G}\phi'_{,k}\phi'_{,k}\right\}\mathrm{d}^3 x\,\mathrm{d}t \quad [10]$$

where ϕ' represents the gravitational potential at the fixed coordinate point $\mathbf{x}$. Notice that the first three terms of the integrand have been transformed by regarding $\mathbf{r}$ to be a function of $\mathbf{x}$ (at each fixed t) through the function $\mathbf{r}(\mathbf{x}, t)$ which defines the deformation. However, the fourth term (which *could* be treated in the same way) has been transformed by renaming the dummy integration variables r_i to x_i. Hence the need to introduce ϕ' since ϕ represents $\phi(\mathbf{r}(\mathrm{x}, \mathrm{t}))$, which is different from $\phi(\mathbf{x}, t)$. The requirement that L' be stationary with respect to variations $\delta\mathbf{r}(\mathbf{x}, t)$, $\delta\phi(\mathbf{r}, t)$ provides a very succinct, complete statement of the elasto-gravitational dynamical equations. In other words, L' will be stationary under variations in $\delta\mathbf{r}(\mathbf{x}, t)$, $\delta\phi(\mathbf{r}, t)$ if and only if $\mathbf{r}$, ϕ are eigenfunctions of the associated Earth model.

1.03.2.2 Equations of Motion and Boundary Conditions

To obtain the partial differential equations for infinitesimal deformations, we approximate L' in the case that $r_k = x_k + \epsilon u_k(\mathbf{x}, t)$ (Figure 3) and $\phi' = \phi^0 + \epsilon\phi^1(\mathbf{x}, t)$ where ϵ is a small parameter. We seek to express the Lagrangian L' in terms of the fields u_i, ϕ^1, to second order in ϵ. We have, to second order in ϵ:

$$\phi = \phi^0 + \epsilon u_i\phi^0_{,i} + \frac{1}{2}\epsilon^2 u_i u_j\phi^0_{,ij} + \epsilon\phi^1 + \epsilon^2 u_i\phi^1_{,i} \qquad [11]$$

We expand $\rho^0 E[\mathbf{x}, \mathbf{e}]$ to second order in strain:

$$\rho^0(\mathbf{x})E(\mathbf{x},\mathbf{e}) = a + t^0_{ij}e_{ij} + \frac{1}{2}c_{ijkl}e_{ij}e_{kl} \qquad [12]$$

As a result of their definitions, as first and second derivatives of $\rho^0(\mathbf{x})E(\mathbf{x}, \mathbf{e})$ with respect to strain, at zero strain, t^0_{ij} and c_{ijkl} possess the symmetries:

$$t^0_{ij} = t^0_{ji} \qquad [13]$$

$$c_{ijkl} = c_{jikl} = c_{ijlk} = c_{klij} \qquad [14]$$

We use the notation t^0_{ij} since these expansion coefficients represent the initial stress field. The strain tensor [1] is

$$e_{ij} = \frac{1}{2}\epsilon\left(u_{i,j} + u_{j,i}\right) + \frac{1}{2}\epsilon^2 u_{k,i}u_{k,j} \qquad [15]$$

Thus, the second order expansion of L' becomes:

$$\begin{aligned} L' = \int\int\Big\{&-a - \rho_0\phi^0 - \frac{1}{8\pi G}\phi^0_{,i}\phi^0_{,i} \\ &-\epsilon\left(t^0_{ij}u_{i,j} + \rho_0 u_i\phi^0_{,i} + \rho_0\phi^1 + \frac{1}{4\pi G}\phi^0_{,i}\phi^1_{,i}\right) \\ &\frac{1}{2}\epsilon^2\Big[\rho^0\dot{u}_k\dot{u}_k - \Lambda_{jilk}u_{i,j}u_{k,l} - \rho^0 u_i u_j\phi^0_{,ij} \\ &-2\rho^0 u_j\phi^1_{,j} - \frac{1}{4\pi G}\phi^1_{,i}\phi^1_{,i}\Big]\Big\}\mathrm{d}^3 x\,\mathrm{d}t \end{aligned} \qquad [16]$$

where we have introduced

$$\Lambda_{jilk} \equiv \delta_{ik}t^0_{jl} + c_{ijkl} \qquad [17]$$

and where the $\Lambda_{jilk}u_{k,l}$ term in eqn [16] is the incremental Piola–Kirchhoff stress tensor. The Euler–Lagrange equations which require that L' be stationary with respect to variations $\delta\mathbf{u}$, $\delta\phi^1$, are given by

$$\frac{\partial L'}{\partial u_i} = \left(\frac{\partial L'}{\partial u_{i,j}}\right)_{,j} \quad \text{and} \quad \frac{\partial L'}{\partial\phi^1} = \left(\frac{\partial L'}{\partial\phi^1_{,i}}\right)_{,i} \qquad [18]$$

They must hold for each power of ϵ. Thus, the first order terms in eqn [16] give the two following equations, which represent the requirement that the initial configuration be (i) in equilibrium and (ii) under self-gravitation:

$$t^0_{ij,j} = \rho^0\phi^0_{,i} \qquad [19]$$

$$\phi^0_{,ii} = 4\pi G\rho^0 \qquad [20]$$

The terms in L' that are independent of ϵ do not contribute to the variation, and thus can be omitted. When eqns [19] and [20] are satisfied, there remain only the second order terms:

$$\begin{aligned} L'' = \int\int\frac{1}{2}\Big[&\rho^0\dot{u}_k\dot{u}_k - \Lambda_{jilk}u_{i,j}u_{k,l} - \rho^0 u_i u_j\phi^0_{,ij} - 2\rho^0 u_i\phi^1_{,i} \\ &-\frac{1}{4\pi G}\phi^1_{,i}\phi^1_{,i}\Big]\mathrm{d}^3 x\,\mathrm{d}t \end{aligned} \qquad [21]$$

In eqn [21] we omit the factor ϵ^2, absorbing the small parameter into the definitions of the fields $\mathbf{u}$, ϕ^1. The Euler–Lagrange equations for L'' (similar to eqn [18]) corresponding to variations $\delta\mathbf{u}$, $\delta\phi^1$ give the equations of motion:

$$\rho^0\left(\ddot{u}_i + \phi^1_{,i} + \phi^0_{,ij}u_j\right) = \left(\Lambda_{jilk}u_{k,l}\right)_{,j} \qquad [22]$$

$$\phi^1_{,jj} = -4\pi G\left(\rho^0 u_i\right)_{,i} \qquad [23]$$

The same equations can alternatively be derived using conservation laws, see for example Woodhouse (1996).

The variational principle also leads to certain natural boundary conditions at the *free* surface (i.e., the ocean surface or the outer surface of the solid Earth in the absence of an ocean) and at internal boundaries in the case that $\mathbf{r}(\mathbf{x}, t)$ is required to be continuous at such boundaries. These internal boundaries are so-called *welded* boundaries, such as the Mohorovicic discontinuity between the crust and mantle and the 660 km discontinuity between the upper and lower mantle. These are as given below. We also wish to include the case that the model contains fluid regions, having free-slip, boundary conditions at their interfaces with solid regions – the so-called *frictionless* boundaries, which exist at the ocean floor, the inner core boundary, and the outer core boundary. The correct treatment of such boundaries introduces complications that, in the interests of giving a concise account, we do not analyze in detail here. Woodhouse and Dahlen (1978) show that it is necessary to include additional terms in the Lagrangian to account for the additional degrees of freedom corresponding to slip (i.e., discontinuous u_i) at such boundaries. The stress boundary conditions are most conveniently stated in terms of the vector t_i defined on the boundary by

$$t_i = \Lambda_{jilk}u_{k,l}n_j - n_i\left(\pi^0 u_k\right)_{;k} + \pi^0 u_{k;i}n_k \quad \text{with } \pi^0 = t^0_{jk}n_j n_k \qquad [24]$$

where n_i is the unit normal to the boundary, and where the semicolon notation, for example, $u_{k;i}$, is used to indicate differentiation *in* the surface: $u_{k;i} = u_{k,i} - n_i n_j u_{k,j}$. We also require the gravitational potential to vanish at *infinity*. The complete set of boundary conditions is

$$\begin{array}{lllll}
\text{Welded}: & \left[t^0_{ij}n_j\right]^+_- = 0, & \overset{-}{[u_i]}^+ = 0, & [t_i]^+_- = 0, & \\
\text{Frictionless}: & \left[t^0_{ij}n_j\right]^+_- = 0, & t^0_{ij}n_j = n_i\pi^0, & [u_k n_k]^+_- = 0, & [t_i]^+_- = 0, \qquad t_i = n_i t_k n_k, \\
\text{Free}: & t^0_{ij}n_j = 0, & & t_i = 0, & \\
\text{All}: & \left[\phi^0\right]^+_- = 0, & \left[\phi^0_{,i}\right]^+_- = 0, & \left[\phi^1\right]^+_- = 0, & \left[\phi^1_i + 4\pi G\rho^0 u_i\right]^+_- = 0, \\
\text{Infinity}: & \phi^0 \to 0, & & \phi^1 \to 0, &
\end{array} \qquad [25]$$

where $[\,]^+_-$ represents the discontinuity of the enclosed quantity across the boundary. Equations [22]–[25] govern the unknown displacement field $u_i(\boldsymbol{x}, t)$ and gravity field $\phi^1(\boldsymbol{x}, t)$ which represent the possible free oscillations of the Earth. All other quantities ρ^0, t^0_{ij}, ϕ^0, Λ_{ijkl} are regarded as given parameters of the Earth model subject to the equilibrium conditions [19] and [20].

1.03.2.3 The Seismic Source

In order to excite the normal modes, we need to apply a force, or seismic source. In the presence of an applied force distribution $f_i = f_i(\mathbf{x}, t)$, per unit volume, the equation of motion [22] becomes

$$\rho^0\left(\ddot{u}_i + \phi^1_{,i} + \phi^0_{,ij}u_j\right) - \left(\Lambda_{jilk}u_{k,l}\right)_{,j} = f_i \qquad [26]$$

Taking the Fourier transform in time, we shall also write

$$\rho^0\left(-\omega^2 u_i + \phi^1_{,i} + \phi^0_{,ij}u_j\right) - \left(\Lambda_{jilk}u_{k,l}\right)_{,j} = f_i \qquad [27]$$

where ω is the frequency. We shall employ the Fourier transform pair:

$$u_i(\mathbf{x}, \omega) = \int_{-\infty}^{\infty} u_i(\mathbf{x}, t)e^{-i\omega t}dt, \quad u_i(\mathbf{x}, t) = \frac{1}{2\pi}\int_{-\infty}^{\infty} u_i(\mathbf{x}, \omega)e^{i\omega t}dt \qquad [28]$$

Here, and in subsequent equations, we rely on the context to distinguish between time-domain and frequency-domain quantities, adopting the convention that if ω appears in an equation then all functions appearing are the Fourier transforms of the original, time-dependent functions.

Earthquake sources can be modeled by choosing particular force distributions f_i. The problem of determining the *equivalent body force distribution* to represent (prescribed) slip on an earthquake fault was originally solved by Burridge and Knopoff (1964) using the elastodynamic representation theorem. A very general and, at the same time, simple approach to the problem of determining body force equivalents is that of Backus and Mulcahy (1976). They argue that an earthquake occurs as a result of the failure of the assumed constitutive law, in the linear case *Hooke's law*, relating stress and strain. This leads them to introduce a symmetric tensor quantity $\Gamma_{ij} = \Gamma_{ij}(\mathbf{x}, t)$, called the *stress glut*, which represents the failure of Hooke's law to be satisfied. Importantly, Γ_{ij} (i) will be zero outside the fault zone, (ii) will be zero at times before the earthquake, and (iii) will have vanishing time derivative at times after slip has ceased. Thus, the *glut rate*, $\dot{\Gamma}_{ij}$, is compact in space and time. The earlier concept of *stress-free strain*, due to Eshelby (1957), is a closely related one. The strain, for slip on a fault, contains δ-function terms at the fault, because the displacement is discontinuous. The stress, on the other hand, is finite on the fault. Thus, there exists a stress glut – a failure of the stress to satisfy Hooke's law, and a stress-free strain, that is, a component of the strain field that is not reflected in the stress. The existence of a nonvanishing stress glut, Γ_{ij}, leads us to replace eqn [22] by

$$\rho^0\left(\ddot{u}_i + \phi^1_{,i} + \phi^0_{,ij}u_j\right) = \left(\Lambda_{jilk}u_{k,l} - \Gamma_{ij}\right)_{,j} \qquad [29]$$

that is

$$\rho^0\left(\ddot{u}_i + \phi^1_{,i} + \phi^0_{,ij}u_j\right) - \left(\Lambda_{jilk}u_{k,l}\right)_{,j} = -\Gamma_{ij,j} \qquad [30]$$

and thus comparing [26] with [30], the equivalent body force distribution is found to be $f_i = -\Gamma_{ij,j}$. Because $\dot{\Gamma}_{ij}(\mathbf{x}, t)$ is compact in space and time, it is appropriate for calculations at long period and long wavelength to replace it by a δ-function in space and time. Defining the *moment tensor*

$$M_{ij} = \int_V \Gamma_{ij}(\mathbf{x}, \infty)d^3x = \int_{-\infty}^{\infty}\int_V \dot{\Gamma}_{ij}(\mathbf{x}, t)d^3x dt \qquad [31]$$

where V is the source volume – the region over which Γ_{ij} is nonzero – a suitable form for Γ_{ij} is $\Gamma(\mathbf{x}, t) \approx M_{ij}\delta^3(\mathbf{x} - \mathbf{x}_s)H(t - t_s)$, where $H(t)$ is the Heaviside step function, and where $\mathbf{x}_s$, t_s are the source coordinates. Thus $f_i \approx -M_{ij}\partial_j\delta^3(\mathbf{x} - \mathbf{x}_s)H(t - t_s)$. In what follows we shall consider the more general point source

$$f_i = \left(F_i - M_{ij}\partial_j\right)\delta^3(\mathbf{x} - \mathbf{x}_s)H(t - t_s) \qquad [32]$$

in which M_{ij} is not necessarily symmetric, recognizing that for sources not involving the action of forces external to the Earth, so-called indigenous sources such as earthquakes, must be symmetric and M_{ij} must be zero. The solution for a point force F_i is of fundamental theoretical interest since the solution in this case is the Green's function for the problem, which can be used to construct solutions for any force distribution f_i. Nonsymmetric M_{ij} corresponds to a source which exerts a net torque or couple on the Earth, such as meteorite impacts.

1.03.2.4 Viscoelasticity and Intrinsic Attenuation

The hyperelastic constitutive law based on the internal energy function $E(\mathbf{x}, \mathbf{e})$ needs to be modified to include the effects of energy loss due to such effects as grain boundary sliding and creep. Such *anelastic* effects lead to dissipation of energy (i.e., conversion of elastic stored energy into heat) and thus to the decay, or *attenuation* of seismic waves. In addition, they are responsible for such effects as post-seismic relaxation, and the theory developed here is in large part applicable to this problem also. A generalization of the constitutive law which retains linearity is the viscoelastic law, which supposes that stress

depends not only on the strain at a given instant, but also on the strain history. This can be written as

$$t_{ij}(t) = \int_{-\infty}^{\infty} c_{ijkl}(t-t')u_{k,l}(t')\mathrm{d}t' \qquad [33]$$

where t_{ij} is incremental stress. (In fact it can be shown that the true increment in stress, at a material particle, includes terms in the initial stress: $t^1_{ij} = c_{ijkl}u_{k,l} + t^0_{ik}u_{j,k} + t^0_{jk}u_{i,k} - t^0_{ij}u_{k,k}$, but this makes no difference to the discussion here.) Thus, the elastic constants become functions of time, relative to a given time t at which the stress is evaluated. Importantly, since stress can depend only upon *past* times, $c_{ijkl}(t)$ must vanish for negative values of t; that is, it must be a *causal* function of time. In order to recover the strict Hooke's law, $t_{ij} = c_{ijkl}u_{k,l}$ we need $c_{ijkl}(t) = c_{ijkl}\delta(t)$ (we are distinguishing here between c_{ijkl} unadorned, which has the units of stress, and $c_{ijkl}(t)$, which has the units of stress/time). In the frequency domain, using the convolution theorem,

$$t_{ij}(\omega) = c_{ijkl}(\omega)u_{i,j}(\omega) \qquad [34]$$

Because $c_{ijkl}(t)$ is a causal function, its Fourier transform

$$c_{ijkl}(\omega) = \int_0^{\infty} c_{ijkl}(t)\mathrm{e}^{-\mathrm{i}\omega t}\,\mathrm{d}t \qquad [35]$$

will be analytic, that is, will have no singularities, in the lower half of the complex ω-plane, as the integral [35] will converge unconditionally in the case that ω possesses a negative imaginary part. From eqn [35] $c_{ijkl}(\omega)^* = c_{ijkl}(-\omega^*)$. For our purposes here, the key conclusion is that *in the frequency domain*, it makes virtually no difference to the theory whether the material is hyperelastic, or viscoelastic, as we have simply everywhere to substitute $c_{ijkl}(\omega)$ for c_{ijkl}. In fact there is even no need to introduce a new notation, but only to remember that now c_{ijkl} can represent a complex quantity depending on ω and analytic in the lower half of the complex ω-plane. When writing equations in the time domain, we have to remember that c_{ijkl} can be a convolution *operator*, acting on the strain. (It may be remarked that the above derivation of the equations of motion, based on Hamilton's principle, is in need of modification if $E(\mathbf{x}, \boldsymbol{\epsilon})$ does not exist. We do not quite know how to do this, but a monograph by Biot (1965) discusses the use of variational principles in the presence of anelastic effects.) Kanamori and Anderson (1977), and references cited therein, is a good source for further information on this topic.

1.03.2.5 Final Equation of Motion

It is often useful to summarize the equations and the boundary conditions by a single simple equation:

$$(\mathcal{H} + \rho^0\partial_t^2)\mathbf{u} = \mathbf{f} \qquad [36]$$

where $\mathcal{H}$ represents the integro-differential operator corresponding to the left side of eqn [26], omitting the term in $\rho^0\ddot{\mathbf{u}}$. Here, ϕ^1 is thought of as a functional of $\mathbf{u}$, that is, as the solution of Poisson's equation [23], corresponding to a given $\mathbf{u}(\mathbf{x}, t)$, together with the boundary conditions relating to ϕ^1 in eqn [25]. Thus, $\mathcal{H}\mathbf{u}$ incorporates the solution of eqn [23]. In the attenuating case, $\mathcal{H}$ also includes the time-domain convolutions arising from the viscoelastic rheology.

1.03.3 Spherical Harmonics and Generalized Spherical Harmonics

Free oscillations involve the motion of the whole Earth, so we need to solve the equations of motion in spherical coordinates. The reduction of these equations in spherical coordinates is most easily accomplished through the use of the generalized spherical harmonic formalism (Phinney and Burridge, 1973). These enable any tensor field to be readily expanded in spherical harmonics, facilitating the derivation of all modal equations in spherical harmonics. Here, we describe how this formalism is used, giving some key results without derivation. We shall use a standard set of Cartesian coordinates (x, y, z) and spherical coordinates (r, θ, ϕ) related by

$$\begin{aligned} x_1 &= x = r\sin\theta\cos\phi, \\ x_2 &= y = r\sin\theta\sin\phi, \\ x_3 &= z = r\cos\theta \end{aligned} \qquad [37]$$

Unit vectors in the coordinate directions are given by

$$\begin{aligned} \hat{\mathbf{r}} &= [\sin\theta\cos\phi, \sin\theta\sin\phi, \cos\theta], \\ \hat{\boldsymbol{\theta}} &= [\cos\theta\cos\phi, \cos\theta\sin\phi, -\sin\theta], \\ \hat{\boldsymbol{\phi}} &= [-\sin\phi, \cos\phi, 0] \end{aligned} \qquad [38]$$

Spherical components of vectors and tensors will be written, for example, $u_\theta = u_k\hat{\theta}_k, t^0_{r\phi} = t^0_{ij}\hat{r}_i\hat{\phi}_j$.

1.03.3.1 Spherical Harmonics

We define the complex spherical harmonics following Edmonds (1960)

$$Y_l^m(\theta,\phi) = (-1)^m\left[\frac{(l-m)!}{(l+m)!}\right]^{(1/2)} P_l^m(\cos\theta)\mathrm{e}^{\mathrm{i}m\phi} \qquad [39]$$

where angular order $l = 0, 1, 2, \cdots$, azimuthal order $m = -l, -l+1, \cdots, l$ and $P_l^m(x)$ are the associated Legendre functions

$$P_l^m(x) = \frac{(1-x^2)^{m/2}}{2^l l!}\frac{\mathrm{d}^{l+m}}{\mathrm{d}x^{l+m}}(x^2-1)^l \qquad [40]$$

The spherical harmonics Y_l^m satisfy the orthogonality relation:

$$\int_{-\pi}^{\pi}\int_0^{\pi} Y_{l'}^{m'}(\theta,\phi)^* Y_l^m(\theta,\phi)\sin\theta\,\mathrm{d}\theta\mathrm{d}\phi = \delta_{l'l}\delta_{m'm} \qquad [41]$$

Figure 4 shows examples of the surface expression of the first few spherical harmonics $Y_l^m(\theta,\phi)$. The number of nodal lines in the θ-direction is given by $l-m$, so for $m=0$ there will be l nodal lines in the θ-direction. The number of nodal lines in the ϕ-direction is given by $2m$, that is, for $m=0$ there are no nodal lines in the ϕ-direction.

1.03.3.2 Generalized Spherical Harmonics

The prescription provided by the generalized spherical harmonic formalism is first to define the *spherical contravariant components* of the vectors and tensors that appear, and then to expand their dependence on (θ,ϕ) in terms of complete sets of functions appropriate to the particular component. For a tensor of rank p, having spherical components $s_{i_1 i_2 \cdots i_p}$, spherical contravariant components are defined by

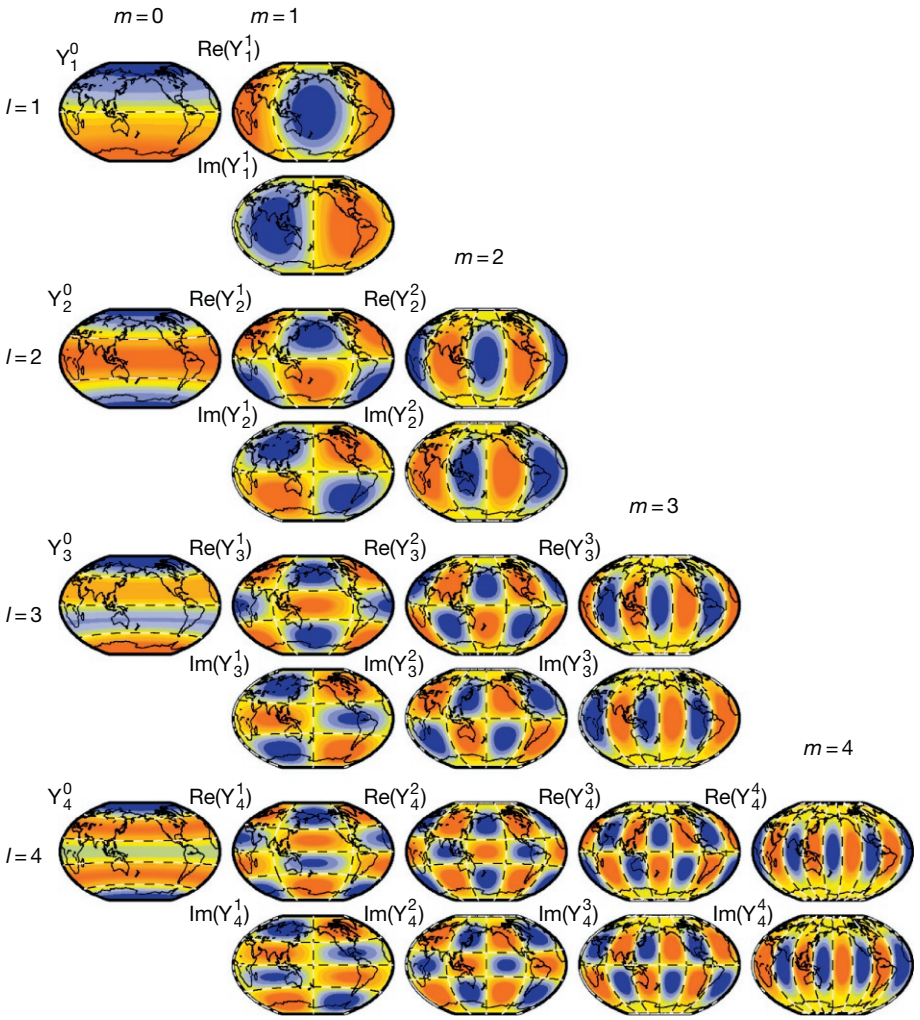

Figure 4 Spherical harmonics Y_l^m, showing real and imaginary parts for $m \geq 1$, for angular order $l = 1 - 4$. Dashed lines indicate the zero value contour, that is, the 'nodal lines' of the spherical harmonic. Blue is positive and red is negative.

$$s^{\alpha_1\alpha_2\cdots\alpha_p} = C^{\dagger\alpha_1 i_1} C^{\dagger\alpha_2 i_2} \times \cdots \times C^{\dagger\alpha_p i_p} s_{i_1 i_2 \cdots i_p} \qquad [42]$$

where indices i_k label the spherical components $i_k \in \{r, \theta, \phi\}$ and where indices α_k take values $\alpha_k \in \{-1, 0, +1\}$; the non-vanishing coefficients $C^{\dagger\alpha i}$ are $C^{\dagger 0r} = 1$, $C^{\dagger\pm 1\theta} = \mp 2^{-1/2}$, $C^{\dagger\pm 1\phi} = 2^{-1/2} i$. The inverse transformation, from spherical contravariant components to spherical components is

$$s_{i_1 i_2 \cdots i_p} = C_{i_1\alpha_1} C_{i_2\alpha_2} \times \cdots \times C_{i_p\alpha_p} s^{\alpha_1\alpha_1\cdots\alpha_p} \qquad [43]$$

with $C_{i\alpha} = (C^{\dagger\alpha i})^*$. The spherical harmonic basis, $Y_l^{Nm}(\theta, \phi)$ appropriate for each contravariant component is determined by the sum $N = \alpha_1 + \alpha_2 \cdots \alpha_p$ of its indices. Thus, we expand

$$s^{\alpha_1\alpha_1\cdots\alpha_p} = \sum_{lm} s_{lm}^{\alpha_1\alpha_1\cdots\alpha_p}(r) Y_l^{Nm}(\theta, \phi) \quad \text{with } N = \alpha_1 + \alpha_1 + \cdots + \alpha_p \qquad [44]$$

where summations over l and m are for integers $l = 0, 1, \ldots, \infty$, $m = -l, -l+1, \ldots, l$. $Y_l^{Nm}(\theta, \phi)$ are the generalized spherical harmonics:

$$Y_l^{Nm}(\theta, \phi) = P_l^{Nm}(\cos\theta) e^{im\phi} = d_{Nm}^{(l)}(\theta) e^{im\phi} \qquad [45]$$

The *real* quantities $d_{Nm}^{(l)}(\theta) = P_l^{Nm}(\cos\theta)$ are rotation matrix elements employed in the quantum mechanical theory of angular momentum (Edmonds, 1960); thus Y_l^{Nm} vanish for N or m outside the range $-l$ to l. The spherical harmonic degree l characterizes a group representation of the rotation group; as a consequence, tensor fields that are spherically symmetric have only the term with $l = 0$, $N = 0$, $m = 0$. The property of the rotation matrix elements

$$d_{Nm}^{(l)}(0) = \begin{cases} 1 & \text{if } m = N \text{ and } l \geq |N| \\ 0 & \text{otherwise} \end{cases} \qquad [46]$$

is a very useful one, for example, for calculations of source excitation coefficients, when it is required to evaluate spherical harmonic expressions for $\theta = 0$ (see the succeeding text). Equation [46] says that regarded as $(2l+1) \times (2l+1)$ matrix, having row index N and column index m, $d_{Nm}^{(l)}(0)$ is the unit matrix. Matrices $d_{Nm}^{(l)}(\theta)$ have symmetries $d_{-N-m}^{(l)}(\theta) = d_{mN}^{(l)}(\theta) = (-1)^{m-N} d_{Nm}^{(l)}(\theta)$, from which follows the relation $Y_l^{Nm}(\theta, \phi)^* = (-1)^{m-N} Y_l^{-N-m}(\theta, \phi)$, where * denotes the complex conjugate.

Y_l^{Nm} satisfy the orthogonality relation

$$\int_{-\pi}^{\pi}\int_{0}^{\pi} Y_{l'}^{Nm'}(\theta,\phi)^* Y_l^{Nm}(\theta,\phi)\sin\theta\,\mathrm{d}\theta\,\mathrm{d}\phi = \frac{4\pi}{2l+1}\delta_{l'l}\delta_{m'm} \quad [47]$$

Other normalizations for the spherical harmonics have frequently been used in the literature. The generalized spherical harmonics can be reduced to completely normalized spherical harmonics using $N=0$ (see eqn [41]), resulting in $Y_l^m(\theta,\phi) = v_l Y_l^{0m}$ where $v_l \equiv \sqrt{(2l+1)/4\pi}$. In this chapter, we shall adopt the same conventions as in the paper by Phinney and Burridge (1973) for the generalized spherical harmonics, using the explicit form $v_l Y_l^{0m}$ when completely normalized spherical harmonics are needed. Thus, the expansion coefficients in eqn [44] can be written

$$s_{lm}^{\alpha_1\alpha_1\cdots\alpha_p}(r) = \frac{2l+1}{4\pi}\int_{-\pi}^{\pi}\int_{0}^{\pi} Y_l^{Nm}(\theta,\phi)^* s^{\alpha_1\alpha_1\cdots\alpha_p}\sin\theta\,\mathrm{d}\theta\,\mathrm{d}\phi \quad \text{with } N=\alpha_1+\alpha_1+\cdots+\alpha_p \quad [48]$$

The following is the key property of the generalized spherical harmonics under differentiation:

$$\left(\pm\partial_\theta + i\csc\theta\,\partial_\phi\right) Y_l^{Nm} = \sqrt{2}\,\Omega_{\pm N}^{l} Y_l^{N\mp 1 m} - N\cot\theta\, Y_l^{Nm} \quad [49]$$

which leads to the following rule for the expansion coefficients of the gradient of a tensor:

$$\left.\begin{aligned} s_{lm}^{\alpha_1\alpha_1\cdots\alpha_p|0} &= \frac{\mathrm{d}}{\mathrm{d}r} s_{lm}^{\alpha_1\alpha_1\cdots\alpha_p} \\ s_{lm}^{\alpha_1\alpha_1\cdots\alpha_p|\pm} &= r^{-1}\Omega_{\mp N}^{l} s_{lm}^{\alpha_1\alpha_1\cdots\alpha_p} - r^{-1}\begin{pmatrix}\text{the sum of the terms}\\ \text{obtained from } s_{lm}^{\alpha_1\alpha_1\cdots\alpha_p}\\ \text{by adding } \pm 1 \text{ to each}\\ \text{of } \alpha_1\alpha_1\cdots\alpha_p \text{ in turn,}\\ \text{omitting any terms for}\\ \text{which the resulting}\\ \text{index } \alpha_k \pm 1 \notin \{-1,0,1\}\end{pmatrix} \end{aligned}\right\} \quad [50]$$

where $\Omega_N^l \equiv [(l+N)(l-N+1)/2]^{1/2}$ and $N \equiv \alpha_1+\alpha_2+\cdots+\alpha_p$. The notation $s_{lm}^{\alpha_1\alpha_2\ldots\alpha_p|\alpha_{p+1}}$ is used to denote the expansion coefficients of the spherical contravariant components of the tensor having Cartesian components $s_{i_1 i_2\cdots i_p, i_{p+1}}$. Contraction over contravariant indices is carried out using the metric tensor $g_{\alpha_1\alpha_2} = C_{i\alpha_1}C_{i\alpha_2}$, which has nonvanishing entries $g_{00}=1$, $g_{-+}=g_{+-}=-1$. Thus, for example, the expansion coefficients of the divergence of a tensor $t_i = s_{ij,j}$, say, is given by

$$t_{lm}^{\alpha} = -s_{lm}^{\alpha+|-} + s_{lm}^{\alpha 0|0} - s_{lm}^{\alpha-|+} = \begin{cases} -s_{lm}^{-+|-} + s_{lm}^{-0|0} - s_{lm}^{--|+} & \alpha=-1 \\ -s_{lm}^{0+|-} + s_{lm}^{00|0} - s_{lm}^{0-|+} & \alpha=0 \\ -s_{lm}^{++|-} + s_{lm}^{+0|0} - s_{lm}^{+-|+} & \alpha=1 \end{cases}$$

$$= \begin{cases} -\frac{1}{r}\left(\Omega_0^l s_{lm}^{-+} - s_{lm}^{-0}\right) + \frac{\mathrm{d}}{\mathrm{d}r}s_{lm}^{-0} - \frac{1}{r}\left(\Omega_2^l s_{lm}^{--} - s_{lm}^{0-} - s_{lm}^{-0}\right) & \alpha=-1 \\ -\frac{1}{r}\left(\Omega_1^l s_{lm}^{0+} - s_{lm}^{-+} - s_{lm}^{00}\right) + \frac{\mathrm{d}}{\mathrm{d}r}s_{lm}^{00} - \frac{1}{r}\left(\Omega_1^l s_{lm}^{0-} - s_{lm}^{+-} - s_{lm}^{00}\right) & \alpha=0 \\ -\frac{1}{r}\left(\Omega_2^l s_{lm}^{++} - s_{lm}^{0+} - s_{lm}^{+0}\right) + \frac{\mathrm{d}}{\mathrm{d}r}s_{lm}^{+0} - \frac{1}{r}\left(\Omega_0^l s_{lm}^{+-} - s_{lm}^{+0}\right) & \alpha=1 \end{cases} \quad [51]$$

The major advantage of this formalism is that, in a spherically symmetric system, it enables vector and tensor relations to be transformed into relations for spherical harmonic coefficients, by the application of a straightforward set of rules. Importantly, the resulting relations (i) are true for each value of l and m separately and (ii) are the same for each spherical harmonic order m.

1.03.3.3 Wigner 3-j Symbols

The treatment of aspherical systems requires results for the products of spherical harmonic expansions. It can be shown that

$$Y_{l_1}^{N_1 m_1} Y_{l_2}^{N_2 m_2} = (-1)^{N_1+N_2-m_1-m_2}\sum_{l=|l_1-l_2|}^{l_1+l_2}(2l+1) \times \begin{pmatrix} l & l_1 & l_2 \\ -N_1-N_2 & N_1 & N_2 \end{pmatrix} \times \begin{pmatrix} l & l_1 & l_2 \\ -m_1-m_2 & m_1 & m_2 \end{pmatrix} Y_l^{N_1+N_2\, m_1+m_2} \quad [52]$$

Where the so-called *Wigner 3-j symbols* are the (real) quantities arising in the theory of the coupling of angular momentum in quantum mechanics (see Edmonds, 1960). These satisfy

$$\begin{pmatrix} l_1 & l_2 & l_3 \\ m_1 & m_2 & m_3 \end{pmatrix} = 0 \quad \text{unless:}$$
$$|l_2-l_3| \le l_1,\ |l_3-l_1| \le l_2,\ |l_1-l_2| \le l_3,$$
any one of which implies the other two
$$|m_1| \le l_1,\ |m_2| \le l_2,\ |m_3| \le l_3,$$
$$m_1+m_2+m_3 = 0 \quad [53]$$

The *3-j* symbol is symmetric under even permutations of its columns, and either symmetric or antisymmetric under odd permutations, depending upon whether $l_1+l_2+l_3$ is even or odd. This has the consequence that if the sum of the l's is odd and if the m's are zero, the *3-j* symbol is 0. Equation [52] leads to the following result for the spherical harmonic coefficients of the product of two tensor fields; suppose that $c_{i_1 i_2\cdots i_p j_1 j_2\cdots j_q} = \alpha_{i_1 i_2\cdots i_p} b_{j_1 j_2\cdots j_q}$; then

$$c_{lm}^{\alpha_1\alpha_2\cdots\alpha_p\beta_1\beta_2\cdots\beta_q} = (-1)^{N_1+N_2-m} \times \sum_{l_1 l_2 m_1}\begin{pmatrix} l & l_1 & l_2 \\ -N_1-N_2 & N_1 & N_2 \end{pmatrix} \times \begin{pmatrix} l & l_1 & l_2 \\ -m & m_1 & m-m_1 \end{pmatrix} a_{l_1 m_1}^{\alpha_1\alpha_2\cdots\alpha_p} b_{l_2 m-m_1}^{\beta_1\beta_2\cdots\beta_q} \quad [54]$$

The summations here are over all values of l, l_1, m_1; however, it is a *finite* sum by virtue of the fact that the terms vanish for values outside the ranges specified in eqn [53].

1.03.3.4 Application: Point Force Distribution

As an application of the spherical harmonic formalism, here we consider the expansion of the point force distribution [32] in spherical harmonics. It will be sufficient to locate the source at time $t_s=0$ and at a point on the positive z-axis, that is, at $x=0$, $y=0, z=r_s$, where r_s is the source radius. Because $\theta=0$ is a singular point in the spherical coordinate system, we shall consider the limit as the source approaches the 'pole,' $\theta_s=0$, along the 'meridian,' $\phi_s=0$. In the frequency domain, eqn [32] becomes

$$f_i=\frac{1}{i\omega}\left(F_i-M_{ij}\partial_j\right)r^{-2}\csc\theta\,\delta(\theta-\theta_s)\,\delta(\phi)\delta(r-r_s) \qquad [55]$$

In the limiting process, $\theta_s\to 0$, we shall take F_i, M_{ij} to have constant spherical components F_ϕ, M_{rr}, $M_{r\theta}$, etc. As $\theta_s\to 0$, the $\hat{\boldsymbol{\theta}}$, $\hat{\phi}$, and $\hat{r}$ directions end up pointing along the x, y, z directions, respectively, of the global Cartesian coordinate system (e.g., see eqn [38]), and thus although $\hat{\boldsymbol{\theta}}, \hat{\phi}$ are undefined at $\theta=0$, we can nevertheless interpret the spherical components F_ϕ, $M_{r\theta}$, etc. as representing the components F_y, M_{zx}, etc. of the point force and moment tensor in the global Cartesian system. Let χ represent the expression $\chi=(i\omega)^{-1}r^{-2}\csc\theta\delta(\theta-\theta_s)\delta(\phi)\delta(r-r_s)$, so that [55] can be written: $f_i=F_i\chi-\partial_i M_{ij}\chi$. The spherical contravariant components of F_i and M_{ij}, using a matrix representation of eqn [43], are given by

$$\begin{bmatrix}F^-\\F^0\\F^+\end{bmatrix}=\begin{pmatrix}\frac{1}{\sqrt{2}}&\frac{i}{\sqrt{2}}&0\\0&0&1\\-\frac{1}{\sqrt{2}}&\frac{i}{\sqrt{2}}&0\end{pmatrix}\begin{bmatrix}F_\theta\\F_\phi\\F_r\end{bmatrix},$$

$$\begin{pmatrix}M^{--}&M^{-0}&M^{-+}\\M^{0-}&M^{00}&M^{0+}\\M^{+-}&M^{+0}&M^{++}\end{pmatrix}=\begin{pmatrix}\frac{1}{\sqrt{2}}&\frac{i}{\sqrt{2}}&0\\0&0&1\\-\frac{1}{\sqrt{2}}&\frac{i}{\sqrt{2}}&0\end{pmatrix}$$

$$\times\begin{pmatrix}M_{\theta\theta}&M_{\theta\phi}&M_{\theta r}\\M_{\phi\theta}&M_{\phi\phi}&M_{\phi r}\\M_{r\theta}&M_{r\phi}&M_{rr}\end{pmatrix}\begin{pmatrix}\frac{1}{\sqrt{2}}&0&-\frac{i}{\sqrt{2}}\\\frac{i}{\sqrt{2}}&0&\frac{i}{\sqrt{2}}\\0&1&0\end{pmatrix} \qquad [56]$$

The spherical harmonic expansion coefficients of $F^\alpha\chi$ and $M^{\alpha_1\alpha_2}\chi$, for which we use the notation $(F^\alpha\chi)_{lm}$, $(M^{\alpha_1\alpha_2}\chi)_{lm}$, are immediate using [48], integrating out the δ-functions contained in χ. We obtain

$$\begin{aligned}(F^\alpha\chi)_{lm}&=\frac{2l+1}{4\pi i\omega}\frac{\delta(r-r_s)}{r^2}Y_l^{\alpha m}(\theta_s,0)^*F^\alpha\\&=\frac{2l+1}{4\pi i\omega}\frac{\delta(r-r_s)}{r^2}d^{(l)}_{\alpha m}(\theta_s)F^\alpha\\&=\begin{cases}\dfrac{2l+1}{4\pi i\omega}\dfrac{\delta(r-r_s)}{r^2}F^\alpha & \text{if } m=\alpha \text{ and } l\ge|\alpha|\\0 & \text{otherwise}\end{cases}\end{aligned} \qquad [57]$$

where θ_s has been set to 0 in the second line, using [46]. Similarly,

$$\begin{aligned}(M^{\alpha_1\alpha_2}\chi)_{lm}&=\frac{2l+1}{4\pi i\omega}\frac{\delta(r-r_s)}{r^2}Y_l^{\alpha_1+\alpha 2m}(\theta_s,0)^*M^{\alpha_1\alpha_2}\\&=\frac{2l+1}{4\pi i\omega}\frac{\delta(r-r_s)}{r^2}d^{(l)}_{\alpha_1\alpha 2m}(\theta_s)M^{\alpha_1\alpha_2}\\&=\begin{cases}\dfrac{2l+1}{4\pi i\omega}\dfrac{\delta(r-r_s)}{r^2}M^{\alpha_1\alpha_2} & \text{if } m=\alpha_1+\alpha_2 \text{ and } l\ge|\alpha_1+\alpha_2|\\0 & \text{otherwise}\end{cases}\end{aligned} \qquad [58]$$

To complete the evaluation of the coefficients f^α_{lm} corresponding to eqn [55], we need to find the spherical harmonic coefficients of the divergence of the field represented in eqn [58], for which we can employ eqn [51]; we find

$$\begin{bmatrix}f^-_{lm}\\f^0_{lm}\\f^+_{lm}\end{bmatrix}=\begin{bmatrix}(F^-\chi)_{lm}+(M^{-+}\chi)^{|-}_{lm}-(M^{-0}\chi)^{|0}_{lm}+(M^{--}\chi)^{|+}_{lm}\\(F^0\chi)_{lm}+(M^{0+}\chi)^{|-}_{lm}-(M^{00}\chi)^{|0}_{lm}+(M^{0-}\chi)^{|+}_{lm}\\(F^+\chi)_{lm}+(M^{++}\chi)^{|-}_{lm}-(M^{+0}\chi)^{|0}_{lm}+(M^{+-}\chi)^{|+}_{lm}\end{bmatrix} \qquad [59]$$

$$=\frac{2l+1}{4\pi i\omega}\times\begin{cases}\begin{bmatrix}M^{--}\Omega_2^l r^{-1}\\0\\0\end{bmatrix}\dfrac{\delta(r-r_s)}{r^2} & m=-2, l\ge 2\\\begin{bmatrix}F^- - M^{-0}\partial_r-2M^{-0}r^{-1}-M^{0-}r^{-1}\\M^{0-}\Omega_1^l r^{-1}\\0\end{bmatrix}\dfrac{\delta(r-r_s)}{r^2} & m=-1, l\ge 1\\\begin{bmatrix}M^{-+}\Omega_0^l r^{-1}\\F_0-M^{00}\partial_r-2M^{00}r^{-1}-M^{-+}r^{-1}-M^{+-}r^{-1}\\M^{+-}\Omega_0^l r^{-1}\end{bmatrix}\dfrac{\delta(r-r_s)}{r^2} & m=0\\\begin{bmatrix}0\\M^{0+}\Omega_1^l r^{-1}\\F^+ - M^{+0}\partial_r-2M^{+0}r^{-1}-M^{0+}r^{-1}\end{bmatrix}\dfrac{\delta(r-r_s)}{r^2} & m=1, l\ge 1\\\begin{bmatrix}0\\0\\M^{++}\Omega_2^l r^{-1}\end{bmatrix}\dfrac{\delta(r-r_s)}{r^2} & m=2, l\ge 2\end{cases} \qquad [60]$$

These are the spherical harmonic coefficients of the force distribution [32] which will be needed in the following sections. The coefficients are zero for $|m|>2$.

1.03.4 The Green's Function for the Spherically Symmetric Earth

1.03.4.1 Reduction of the General Equations to the Spherically Symmetric Case

We consider here the case in which the Earth model is spherically symmetric. In this case the equations of motion are separable in spherical coordinates, and thus can be solved by reduction to ordinary differential equations. Since deviations from spherical symmetry are relatively small in the Earth, they can subsequently be treated by perturbation theory. We assume that in the initial equilibrium configuration the stress is hydrostatic, that is

$$t_{ij}^0 = -p^0\delta_{ij} \qquad [61]$$

Spherical symmetry requires that ρ^0, ϕ^0, p^0 are functions only of r. The gravitational acceleration is $g_i^0 = \phi_{,i}^0 = g^0(r)\hat{r}_i$, and the equilibrium equations [19], [20] and the boundary conditions in eqn [25] have the solutions:

$$\begin{aligned} g^0(r) &= \frac{4\pi G}{r^2}\int_0^r \rho^0(r)\mathrm{d}r,\\ \phi^0(r) &= -\int_r^\infty g^0(r)\mathrm{d}r = \frac{-GM}{a} - \int_r^a g^0(r)\mathrm{d}r,\\ p^0(r) &= \int_r^a \rho^0(r)g^0(r)\mathrm{d}r \end{aligned} \qquad [62]$$

where a is the radius of the Earth and M is the Earth's total mass $M = 4\pi\int_0^a r^2\rho^0(r)\mathrm{d}r$. The equations of motion [26] with [17] and [20] can be put into the form

$$\rho\left[-\omega^2 u_i - u_{k,k}g_i + \varphi_{,i} + (u_k g_k)_{,i}\right] - \left(C_{ijkl}u_{k,l}\right)_{,j} = f_i \qquad [63]$$

$$\left(\varphi_{,k} + 4\pi G\rho u_k\right)_{,k} = 0 \qquad [64]$$

Where we have introduced the effective stiffness tensor

$$C_{ijkl} = c_{ijkl} + p^0\left(\delta_{ij}\delta_{kl} - \delta_{il}\delta_{jk} - \delta_{ik}\delta_{jl}\right) \qquad [65]$$

which has the same symmetries (eqn [14]) as does c_{ijkl}. In eqns [63], [64], and in subsequent equations, we drop the superscripts in ρ^0, g^0, using simply ρ, g for these quantities. We also use the notation φ in place of ϕ^1. The applied force distribution f_i will be taken to be that given in eqns [32] and [55], having the spherical harmonic coefficients [60].

In a spherically symmetric model, the tensor field C_{ijkl} must be a spherically symmetric tensor field, and therefore its spherical harmonic expansion will have terms only of spherical harmonic degree $l=0$. Its spherical contravariant components $C^{\alpha_1\alpha_2\alpha_3\alpha_3} = C_{00}^{\alpha_1\alpha_2\alpha_3\alpha_3}$ must have indices that sum to zero, and must also satisfy the usual elastic tensor symmetries [14]. It is easily seen that there are only five independent components that satisfy these requirements: C^{0000}, C^{+-00}, C^{+0-0}, C^{++--}, C^{+-+-}, which must be real (in the nonattenuating case) in order that the spherical components C_{ijkl} are real. Conventionally, these are designated (Love, 1927; Takeuchi and Saito, 1972)

$$\begin{aligned} C^{0000} &= C(r),\\ C^{+-00} &= -F(r),\\ C^{+0-0} &= -L(r),\\ C^{++--} &= 2N(r),\\ C^{+-+-} &= A(r) - N(r) \end{aligned} \qquad [66]$$

the independent spherical components being (using eqn [43])

$$\begin{aligned} &C_{rrrr} = C(r), \quad C_{rr\theta\theta} = C_{rr\phi\phi} = F(r), \quad C_{r\theta r\theta} = C_{r\phi r\phi} = L(r),\\ &C_{\theta\phi\theta\phi} = N(r), \quad C_{\theta\theta\phi\phi} = A(r) - 2N(r), \quad C_{\theta\theta\theta\theta} = C_{\phi\phi\phi\phi} = A(r) \end{aligned} \qquad [67]$$

The mean *bulk modulus* κ and *shear modulus* μ can be defined by

$$\begin{aligned} \kappa &= \frac{1}{9}C_{iijj} = \frac{1}{9}(4A + C - 4N + 4F),\\ \mu &= \frac{1}{10}C_{ijij} - \frac{1}{30}C_{iijj} = \frac{1}{15}(A + C + 6L + 5N - 2F) \end{aligned} \qquad [68]$$

Other conventional notations are

$$\begin{aligned} \lambda &= \kappa - \frac{2}{3}\mu,\\ \upsilon_{\mathrm{PV}}^2 &= C/\rho,\\ \upsilon_{\mathrm{PH}}^2 &= A/\rho,\\ \upsilon_{\mathrm{SV}}^2 &= L/\rho,\\ \upsilon_{\mathrm{SH}}^2 &= N/\rho,\\ \eta &= F/(A - 2L) \end{aligned} \qquad [69]$$

where λ (and μ) are the Lame parameters, υ_{PV} and υ_{PH} are the vertical and horizontal polarized compressional wave velocities, and υ_{SV} and υ_{SH} are the vertical and horizontal polarized shear wave velocities. Thus, radial anisotropy (also called transverse isotropy) is allowed in a spherically symmetric model. In fact, the PREM model, which is commonly used in normal mode calculations, has radial anisotropy in the top 220 km. This feature is essential to explain the frequencies of Love and Rayleigh waves simultaneously. In the case that the material is *isotropic*, $A = C = \lambda + 2\mu = \kappa + \frac{4}{3}\mu$, $N = L = \mu$, and $\eta = 1$.

1.03.4.2 Derivation of the Radial Ordinary Differential Equations

Now we seek solutions u_i, φ of eqns [63] and [64] in terms of a spherical harmonic expansions. It is convenient to write

$$u_{lm}^- = \upsilon_l\Omega_0^l[V_{lm}(r) - iW_{lm}(r)] \qquad [70]$$

$$u_{lm}^0 = \upsilon_l U_{lm}(r) \qquad [71]$$

$$u_{lm}^+ = \upsilon_l\Omega_0^l[V_{lm}(r) + iW_{lm}(r)] \qquad [72]$$

where $\upsilon_l = \sqrt{(2l+1)/4\pi}$, as the '$U$, V, W' notation is almost universally used in the literature on long-period seismology. $U(r)$, $V(r)$, and $W(r)$ are the radial eigenfunctions which only depend on the radius. $U(r)$ is used to describe motion in the radial direction, while $V(r)$ and $W(r)$ are the tangential scalars. The expansion corresponding to eqn [44] is then equivalent to the vector spherical harmonic representation (e.g., Morse and Feshbach, 1953):

$$
\begin{aligned}
u_r &= \sum\nolimits_{lm} U_{lm}(r) v_1 Y_l^{0m}(\theta,\phi) \\
u_\theta &= \sum\nolimits_{lm} \left[V_{lm}(r)\partial_\theta + W_{lm}(r)\csc\theta\partial_\theta\right] v_1 Y_l^{0m}(\theta,\phi) \\
u_\phi &= \sum\nolimits_{lm} \left[V_{lm}(r)\csc\theta\partial_\phi - W_{lm}(r)\partial_\theta\right] v_1 Y_l^{0m}(\theta,\phi)
\end{aligned}
\qquad [73]
$$

where Y_l^{0m} are the spherical harmonics Y_l^m as defined in eqn [41]. We shall abbreviate such vector spherical armonic expansions using the shorthand

$$
u_i :\rightarrow \begin{bmatrix} U_{lm}(r) \\ V_{lm}(r) \\ W_{lm}(r) \end{bmatrix}
\qquad [74]
$$

meaning that the vector field having Cartesian components u_i is expressible in vector spherical harmonics as in eqn [73]. We shall also suppress the suffices l, m and the explicit dependence upon r, writing simply U, V, W.

The spherical harmonic expansion of f_i can also be converted into this vector spherical harmonic notation. Using eqn [60] with eqn [56] we obtain:

$$
f_i :\rightarrow \frac{v_l}{i\omega}
\begin{cases}
\begin{bmatrix} \left(rF_r + M_{\theta\theta} + M_{\phi\phi}\right)\delta^{(0)}(r) - M_{rr}\delta^{(1)}(r) \\ \frac{1}{2}\left(-M_{\theta\theta} - M_{\phi\phi}\right)\delta^{(0)}(r) \\ \frac{1}{2}\left(-M_{\theta\phi} + M_{\phi\theta}\right)\delta^{(0)}(r) \end{bmatrix} & m = 0 \\
\begin{bmatrix} \frac{\zeta}{2}\left(\mp M_{r\theta} + iM_{r\phi}\right)\delta^{(0)}(r) \\ \frac{1}{2\zeta}\left(\mp rF_\theta + irF_\phi \pm M_{r\theta} - iM_{r\phi}\right)\delta^{(0)}(r) + \left(\mp M_{\theta r} - iM_{\phi r}\right)\delta^{(1)}(r) \\ \mp\frac{i}{2\zeta}\left(\mp rF_\theta + irF_\phi \pm M_{r\theta} - iM_{r\phi}\right)\delta^{(0)}(r) + \left(\mp M_{\theta r} - iM_{\phi r}\right)\delta^{(1)}(r) \end{bmatrix} & m = \pm 1 \\
\begin{bmatrix} 0 \\ \frac{1}{4\zeta}\sqrt{\zeta^2 - 2}\left(M_{\theta\theta} - M_{\phi\phi} \mp iM_{\theta\phi} \mp iM_{\phi\theta}\right)\delta^{(0)}(r) \\ \mp\frac{i}{4\zeta}\sqrt{\zeta^2 - 2}\left(M_{\theta\theta} - M_{\phi\phi} \mp iM_{\theta\phi} \mp iM_{\phi\theta}\right)\delta^{(0)}(r) \end{bmatrix} & m = \pm 2
\end{cases}
\qquad [75]
$$

where $\delta^{(0)}(r) = r^{-3}\delta(r - r_s)$ and $\delta^{(1)}(r) = r^{-2}\delta'(r - r_s)$, and where $\zeta = \sqrt{l(l+1)}$.

Using the spherical harmonic formalism, the vector spherical harmonic representation of the *radial tractions* is given by

$$
C_{ijkl}u_{k,l}\hat{r}_j \rightarrow \begin{cases} P = Fr^{-1}\left(2U - \zeta^2 V\right) + C\partial_r U \\ S = L(\partial_r V - r^{-1}V + r^{-1}U) \\ T = L(\partial_r W - r^{-1}W) \end{cases}
\qquad [76]
$$

where we have introduced traction scalars $P = P_{lm}(r)$, $S = S_{lm}(r)$, and $T = T_{lm}(r)$. Because the radial tractions are required to be continuous at interfaces between different regions of the model (from eqn [25]), it is usual to treat them as a new dependent variables, and to express the derivatives $\partial_r U$, $\partial_r V$, $\partial_r W$ in terms of them:

$$
\begin{aligned}
\partial_r U &= -r^{-1}FC^{-1}\left(2U - \zeta^2 V\right) + C^{-1}P \\
\partial_r V &= r^{-1}(V - U) + L^{-1}S \\
\partial_r W &= r^{-1}W + L^{-1}T
\end{aligned}
\qquad [77]
$$

The vector spherical harmonic expansion of the left side of eqn [63] becomes:

$$
f_i :\rightarrow \begin{cases} -\rho\omega^2 U + 2r^{-2}(A - N)\left(2U - \zeta^2 V\right) + \rho(\partial_r g - 2r^{-1}g)U + \zeta^2 r^{-1}\rho g V - \partial_r P + 2r^{-1}F\partial_r U - 2r^{-1}P + r^{-1}\zeta^2 S + \rho\partial_r\varphi \\ -\rho\omega^2 V - r^{-2}A\left(2U - \zeta^2 V + 2r^{-2}N(U - V)\right) + r^{-1}\rho(gU + \varphi) - \partial_r S - 3r^{-1}S - r^{-1}\partial_r U \\ -\rho\omega^2 W + r^{-2}N\left(\zeta^2 - 2\right)W - \partial_r T - 3r^{-1}T \end{cases}
\qquad [78]
$$

Thus, ordinary differential equations in r for U, V, W, P, S, T are obtained by equating these to the forcing terms in eqn [75]. In addition, the expansion coefficients of the perturbation in gravitational potential, $\varphi = \varphi_{lm}(r)$, are subject to equations derived from eqn [64]. The boundary conditions [25] require that φ and $\partial_r\varphi + 4\pi G\rho U$ are continuous throughout the model, and that φ vanishes at infinity. For a given spherical harmonic degree l the solutions of Laplace's equation tending to zero at infinity are proportional to $r^{-l-1}$and for this reason it is useful to define the new dependent variable $\psi = \partial_r\varphi + (l+1)r^{-1}\varphi + 4\pi G\rho U$, so that ψ is continuous throughout the model and vanishes at the surface. This leads to the following coupled equations for $\varphi_{lm}(r)$, $\psi_{lm}(r)$:

$$
\begin{aligned}
\partial_r\varphi &= \psi - (l+1)r^{-1}\varphi - 4\pi G\rho U \\
\partial_r\psi &= 4\pi G\rho r^{-1}\left(\zeta^2 V - (l+1)U\right) + r^{-1}(l-1)\psi
\end{aligned}
\qquad [79]
$$

Thus, the complete boundary value problem for $\mathbf{u}(\mathbf{x}, \omega)$ is to find, for each l, m, solutions $U_{lm}(r), V_{lm}(r), W_{lm}(r), \phi_{lm}(r)$, $P_{lm}(r)$, $S_{lm}(r)$, $T_{lm}(r)$, $\psi_{lm}(r)$, satisfying (i) equality of the

expressions in eqns [75] and [78], (ii) eqns [77] – in essence definitions of P, S, T, and (iii) eqns [79] governing the self-gravitation.

The equations governing W and T are independent of the others, and so the problem naturally separates into the problems for the six functions U, V, ϕ, P, S, ψ, relating to *spheroidal* motion, and for the two functions W, T, relating to *toroidal* motion. These are related to spheroidal and toroidal modes (see **Figure 5**). Spheroidal modes involve both radial and tangential motion, just like P–SV body waves. Toroidal modes only involve tangential motion. Examples of U, V, W for fundamental spheroidal and toroidal modes are given in **Figure 6**. In a fluid region, shear stresses are required to vanish, resulting in $S=0$ and $L=N=0$, $A=C=F$; the second equation in [76] drops out and the equation arising from the second of eqn [78] can be solved for V, $V=(gU-P/\rho+\varphi)/r\omega^2$, and thus S and V can be eliminated from the equations, resulting in equations for the four remaining variables U, ϕ, P, ψ. The case $l=0$ leads to purely radial motion, $V=0$ with $\psi=\varphi/r$, $\mathrm{d}\varphi/\mathrm{d}r=-4\pi G\rho U$, and the effective equations involve only U, P. Examples of U for radial modes are given in **Figure 7**.

The equations are most conveniently stated as matrix differential equations, by rearranging them to give the radial derivatives of either the six (for spheroidal modes in a solid), four (for spheroidal modes in a fluid), or two functions (for radial and toroidal modes) to be determined in terms of the functions themselves. Here, we define *stress-displacement vectors* as follows:

$$\text{Spheroidal solid}: \ \mathbf{y}^{\mathrm{Ss}}=\begin{bmatrix} rU \\ r\zeta V \\ r\phi \\ rP \\ r\zeta S \\ r\psi/4\pi G \end{bmatrix},$$

$$\text{Spheroidal fluid}: \ \mathbf{y}^{\mathrm{Sf}}=\begin{bmatrix} rU \\ r\phi \\ rp \\ r\psi/4\pi G \end{bmatrix},$$

$$\text{Radial}: \ \mathbf{y}^{\mathrm{R}}=\begin{bmatrix} rU \\ rP \end{bmatrix},$$

$$\text{Toroidal solid}: \ \mathbf{y}^{\mathrm{Ts}}=\begin{bmatrix} r\zeta W \\ r\zeta T \end{bmatrix} \qquad [80]$$

In each case, the resulting equations take the form:

$$\frac{\mathrm{d}\mathbf{y}}{\mathrm{d}r}=\mathbf{A}\mathbf{y}+\mathbf{a}\delta(r-r_s)+\mathbf{b}\delta'(r-r_s) \qquad [81]$$

where the vectors $\mathbf{a}=\mathbf{a}(r, \omega, l, m)$, $\mathbf{b}=\mathbf{b}(r, \omega, l, m)$ represent the forcing or earthquake source and can be readily derived from eqn [75]. The matrices $\mathbf{A}=\mathbf{A}(r, \omega, l)$ can be written in terms of submatrices in the form

$$\mathbf{A}=\begin{pmatrix} \mathbf{T} & \mathbf{K} \\ \mathbf{S} & -\mathbf{T}' \end{pmatrix} \qquad [82]$$

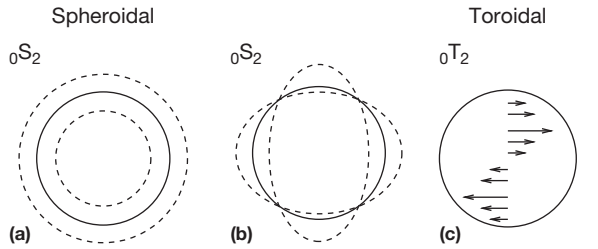

Figure 5 Oscillation patterns for (a) fundamental radial mode $_0S_0$, also called the 'breathing' mode, (b) fundamental spheroidal mode $_0S_2$ ($m=0$), also called the 'football' mode, and (c) fundamental toroidal mode $_0T_2$ ($m=0$).

where $\mathbf{K}$ and $\mathbf{S}$ are symmetric and where $\mathbf{T}'$ is the transpose of $\mathbf{T}$. The fact that the equations have this special form stems from the fact that they arise from a variational principle, and in fact are a case of Hamilton's canonical equations (Chapman and Woodhouse, 1981; Woodhouse, 1974). However, the usual variational derivations of the equations of motion neglect attenuation, and so it is interesting that this symmetry of the equations remains valid in the attenuating case. It plays an important part in methods of calculation normal modes (see the succeeding text), and also enables a complex version of the theory in attenuating media to be developed along the same lines. The specific forms of matrices $\mathbf{T}$, $\mathbf{K}$, $\mathbf{S}$ for spheroidal modes in solid regions are

$$\mathbf{T}^{\mathrm{Ss}}=\begin{pmatrix} (1-2F/C)/r & \zeta F/Cr & 0 \\ -\zeta/r & 2/r & 0 \\ -4\pi G\rho & 0 & -l/r \end{pmatrix}, \quad \mathbf{K}^{\mathrm{Ss}}=\begin{pmatrix} 1/C & 0 & 0 \\ 0 & 1/L & 0 \\ 0 & 0 & 4\pi G \end{pmatrix},$$

$$\mathbf{S}^{\mathrm{Ss}}=\begin{pmatrix} -\rho\omega^2+4(\gamma-\rho gr)/r^2 & \zeta(\rho gr-2\gamma)/r^2 & -\rho(l+1)/r \\ \zeta(\rho gr-2\gamma)/r^2 & -\rho\omega^2+\left[\zeta^2(\gamma+N)-2N\right]/r^2 & \rho\zeta/r \\ -\rho(l+1)/r & \rho\zeta/r & 0 \end{pmatrix} \qquad [83]$$

where $\gamma=A-N-F^2/C$. For spheroidal modes in fluid regions, $V=0$ and $S=0$ and so we have

$$\mathbf{T}^{\mathrm{Sf}}=\begin{pmatrix} \left(g\zeta^2/\omega^2r-1\right)/r & \zeta^2/\omega^2r^2 \\ -4\pi G\rho & -l/r \end{pmatrix}, \quad \mathbf{K}^{\mathrm{Sf}}=\begin{pmatrix} 1/C-\zeta^2/\rho\omega^2r^2 & 0 \\ 0 & 4\pi G \end{pmatrix},$$

$$\mathbf{S}^{\mathrm{Sf}}=\begin{pmatrix} -\rho\omega^2+\rho g\left(g\zeta^2/r\omega^2-4\right)/r & \rho\left(g\zeta^2/r\omega^2-l-1\right)/r \\ \rho\left(g\zeta^2/r\omega^2-l-1\right)/r & \rho\zeta^2/r^2\omega^2 \end{pmatrix} \qquad [84]$$

In the case of radial modes, we also have $\phi=0$ and $\psi=0$, reducing the equations to

$$\mathbf{T}^{\mathrm{R}}=((1-2F/C)/r), \quad \mathbf{K}^{\mathrm{R}}=(1/C), \quad \mathbf{S}^{\mathrm{R}}=\left(-\rho\omega^2+4(\gamma-\rho gr)/r^2\right) \qquad [85]$$

Finally, in the case of toroidal modes, we are only solving for W and T, leading to equations

$$\mathbf{T}^{\mathrm{Ts}}=(2/r), \quad \mathbf{K}^{\mathrm{Ts}}=(1/L), \quad \mathbf{S}^{\mathrm{Ts}}=\left(-\rho\omega^2+\left(\zeta^2-2\right)N/r^2\right) \qquad [86]$$

In the case that there is no forcing f_i, the equations reduce to the homogeneous system $\mathrm{d}\mathbf{y}/\mathrm{d}r=\mathbf{A}\mathbf{y}$, together with the usual

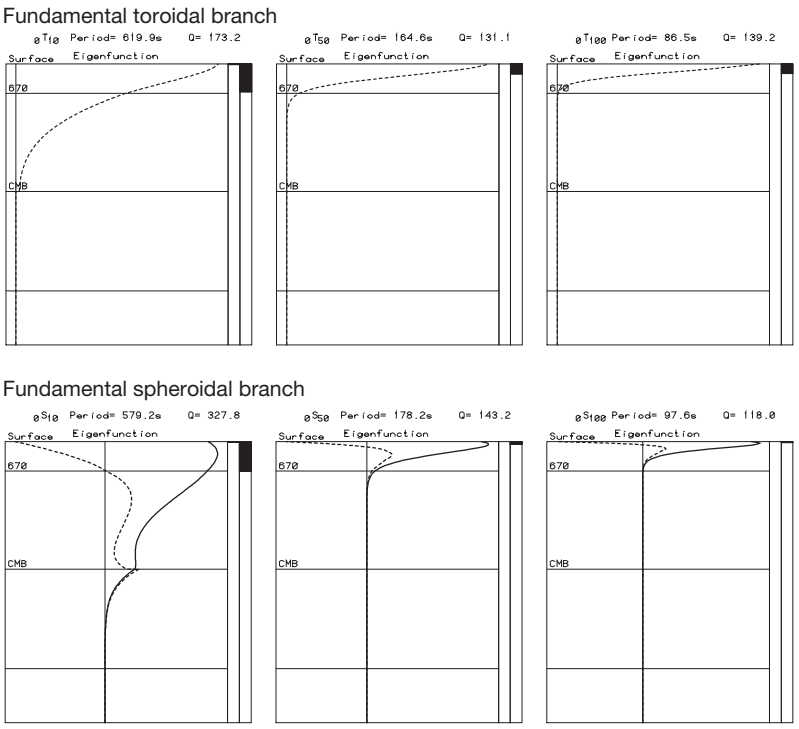

Figure 6 Eigenfunctions of selected toroidal and spheroidal fundamental modes ($n=0$). For the toroidal modes, the dashed lines show $W(r)$, and for spheroidal modes the dashed lines denote $V(r)$ and the solid lines $U(r)$. At high angular order l, the toroidal modes correspond to Love waves and the spheroidal modes to Rayleigh waves.

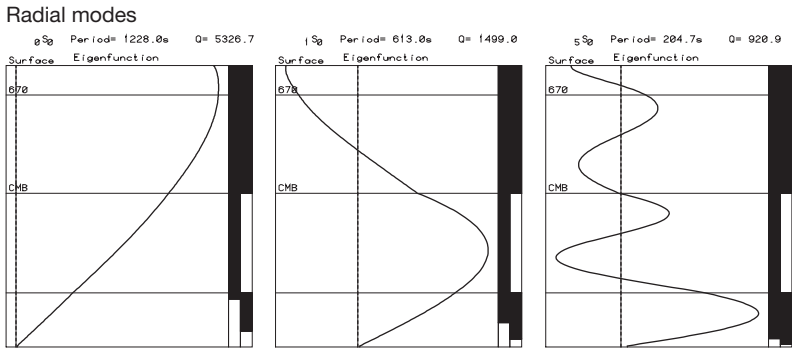

Figure 7 Eigenfunctions of selected radial modes ($l=0$). The solid lines show $U(r)$.

boundary conditions at the center of the Earth and at the surface. This is an eigenvalue problem for ω having solutions corresponding to the modes of *free oscillation*. The eigenvalues will be denoted by ω_k, where k is an index that incorporates the angular order l, the *overtone number* n and the mode type: spheroidal or toroidal. The modal multiplets are conventionally given the names ${}_nS_l$ for spheroidals and ${}_nT_l$ for toroidals. Overtone number is an index labeling the eigenfrequencies for a given l and for a given mode type, in increasing order. For radial modes, the overtone number equals the number of nodal lines along the radius (see Figure 7). Since the spherical harmonic order m does not enter into the equations, the modes are *degenerate*, meaning that there are $2l+1$ different eigenfunctions, $m=-l, -l+1, \ldots, l$ corresponding to the same given eigenvalue ω_k. The eigenfunctions will be denoted by $\mathbf{s}^{(km)}(\mathbf{x})$. These are the solutions $\mathbf{u}(\mathbf{x})$ given by eqn [73], for different values of m, but with the *same* scalar eigenfunctions $U(r)$, $V(r)$, $W(r)$, $\varphi(r)$. The set of $2l+1$ eigenfunctions, $\mathbf{s}^{(km)}(\mathbf{x})$, for a given eigenfrequency ω_k is said to constitute a *multiplet*. The eigenfunctions represent the spatial shape of a mode of free oscillation at frequency ω_k, because $\mathbf{s}^{(km)}(\mathbf{x})e^{i\omega_k t}$ is a solution of the complete dynamical equations in the absence of any forcing. Of course the eigenfunction is defined only up to an overall factor.

If the medium is attenuating, the eigenfrequencies will be complex, their (positive) imaginary parts determining the rate of decay of the mode with time. It is conventional to quantify this decay rate in terms of the 'Q' of the multiplet, Q_k, which is defined in such a way that the mode decays in amplitude by a factor $e^{-\pi/Q_k}$ per cycle. Therefore, $Q_k = \mathrm{Re}\,\omega_k / 2\mathrm{Im}\,\omega_k$, typically

a large number, indicating that the modes decay by a relatively small fraction in each cycle. Q has also been called the *quality factor*.

In the case of forcing, eqn [81] leads to solutions $\mathbf{y}(l, m, r)$ which are discontinuous at the source radius r_s. It can be shown that the discontinuity at r_s is given by (Hudson, 1969; Ward, 1980):

$$[\mathbf{y}]_{r=r_s-}^{r=r_s+} = \mathbf{s} = \mathbf{a} + \mathbf{A}\mathbf{b} - \frac{\mathrm{d}\mathbf{b}}{\mathrm{d}r} \qquad [87]$$

and thus the boundary value problem for $\mathbf{y}$ requires the solution of the homogeneous equation $\mathrm{d}\mathbf{y}/\mathrm{d}r = \mathbf{A}\mathbf{y}$ above and below the source, subject the conditions that the solution (i) is nonsingular at the center of the Earth, (ii) has vanishing traction components at the surface, and (iii) has the prescribed discontinuity $\mathbf{s}$ at the source radius r_s. The specific forms for the discontinuity vector $\mathbf{s}$, using [75] and [87], are (As described earlier, we are here considering the source to be located at $(\theta = \epsilon, \phi = 0)$, for some infinitesimal, positive ϵ; thus (F_θ, F_ϕ, F_r) coincide with (F_x, F_y, F_z) in the global Cartesian frame defined in eqn [37]. Similarly, $(M_{\theta\theta}, M_{\theta\phi}, \text{etc.})$ coincide with $(M_{xx}, M_{xy}, \text{etc.})$. If the source is located at a general colatitude θ_s and longitude ϕ_s, the results can be applied in a rotated frame in which the (θ, ϕ, r) components map into (South, East, Up), coordinate θ is epicentral distance and coordinate ϕ is azimuth of the receiver at the source, measured anticlockwise from South.)

$$\mathbf{s}^{\mathrm{Ss}} = \frac{v_l}{i\omega r_s^2} \times \begin{cases} \begin{bmatrix} r_s M_{rr}/C \\ 0 \\ 0 \\ -r_s F_r - M_{\theta\theta} - M_{\phi\phi} + 2M_{rr}F/C \\ \zeta\left(M_{\theta\theta} + M_{\phi\phi}\right)/2 - \zeta M_{rr}F/C \\ 0 \end{bmatrix} & l \geq 1, m = 0 \\ \begin{bmatrix} 0 \\ r_s\left(\mp M_{\theta r} + iM_{\phi r}\right)/2L \\ 0 \\ \zeta\left(\mp M_{\theta r} + iM_{\phi r} \pm M_{r\theta} - iM_{r\phi}\right)/2 \\ r_s\left(\pm F_\theta - iF_\phi\right)/2 - \left(\mp M_{\theta r} + iM_{\phi r} \pm M_{r\theta} - iM_{r\phi}\right)/2 \\ 0 \end{bmatrix} & l \geq 1, m = \pm 1 \\ \begin{bmatrix} 0 \\ 0 \\ 0 \\ 0 \\ \sqrt{\zeta^2 - 2}\left(-M_{\theta\theta} + M_{\phi\phi} \pm iM_{\theta\phi} \pm iM_{\phi\theta}\right)/4 \\ 0 \end{bmatrix} & l \geq 2, m = \pm 2 \end{cases} \qquad [88]$$

$$\mathbf{s}^{\mathrm{R}} = \frac{v_0}{i\omega r_s^2} \times \begin{bmatrix} r_s M_{rr}/C \\ -r_s F_r - M_{\theta\theta} - M_{\phi\phi} + 2M_{rr}F/C \end{bmatrix} \quad l = m = 0 \qquad [89]$$

$$\mathbf{s}^{\mathrm{Ts}} = \frac{v_l}{i\omega r_s^2} \times \begin{cases} \begin{bmatrix} 0 \\ \zeta\left(M_{\theta\phi} - M_{\phi\theta}\right)/2 \end{bmatrix} & l \geq 1, m = 0 \\ \begin{bmatrix} r_s\left(\pm M_{\phi r} + iM_{\theta r}\right)/2L \\ r_s\left(\mp F_\phi + iF_\theta\right)/2 + \left(\mp M_{\phi r} - iM_{\theta r} \pm M_{r\phi} + iM_{r\theta}\right)/2 \end{bmatrix} & l \geq 1, m = \pm 1 \\ \begin{bmatrix} 0 \\ \sqrt{\zeta^2 - 2}\left(\pm iM_{\theta\theta} \mp iM_{\phi\phi} + M_{\theta\phi} + M_{\phi\theta}\right)/4 \end{bmatrix} & l \geq 2, m = \pm 2 \end{cases} \qquad [90]$$

where the elastic parameters are those evaluated at the source radius r_s. We consider here only the case that the source is located in a continuous, solid region of the model. Equivalent results (in the case that the moment tensor is symmetric and the material is isotropic) are given by Ward (1980).

1.03.5 Numerical Solution of the Radial Equations*

1.03.5.1 Methods of Solution*

The inhomogeneous (i.e., with forcing term f_i) boundary value problem as formulated above gives a unique solution for each value of ω. The solution in the time domain can then be obtained in the form of an integral in ω, using the inverse Fourier transform [28]. This, in essence, is the basis of several practical methods for calculating theoretical seismograms, for example, the *reflectivity method* (Fuchs and Muller, 1971) and the direct solution method of Friederich and Dalkolmo (1995). Alternatively, the inverse transform can be evaluated by completing the integration contour in the upper half of the complex ω plane. Then it is found that the solution can be reduced to a sum over residues, each pole of the integrand corresponding to a particular mode *of free oscillation* of the model. A more usual approach to the normal mode problem is to consider first the free (i.e., unforced) modal solutions of the equations, and then to make use of the orthogonality and completeness properties of the eigenfunctions to obtain solutions of the inhomogeneous (i.e., forced) problem. Here, we have examined first the inhomogenous problem because the demonstration of orthogonality and completeness in the general (attenuating) case is a nontrivial issue, and it is only by virtue of the analysis of the inhomogeneous problem, and the resulting analytic structure of the integrand in the complex ω plane, that orthogonality and completeness can be demonstrated. It is necessary to show (in the nonattenuating case) that the only singularities of the integrand are simple poles on the real ω-axis. Then the modal sum emerges and completeness is demonstrated by the solution itself. In the attenuating case the situation is more complex, and there are other singularities located on the positive imaginary ω axis – let us call them the relaxation singularities, as they are associated with decaying exponential functions in the time domain. Thus, while the solution developed here for the inhomogeneous problem remains valid in this case, arguments based on orthogonality and completeness cannot be made. The solution can nevertheless be derived in the form of a sum over residues, and other singularities. While the contribution from relaxation singularities is the main focus of attention in the analysis of post-seismic relaxation, they are expected to make negligible contributions for the typical seismic application. However, even in the seismic domain it is necessary to know modal excitations in the attenuating case, and these are difficult to determine, other than by a rather complex application of mode-coupling theory (Lognonne, 1991; Tromp and Dahlen, 1990), which will be difficult to carry out to high frequencies. Using the inhomogenous solution, on the other hand, the 'seismic' modes and their excitations emerge naturally as the contributions from the residues of poles near the real axis, and can be calculated exactly and economically.

In both the attenuating and nonattenuating cases and for both the homogenous and inhomogeneous problems, the integration of the ordinary differential equation presents severe numerical difficulties. One problem is that the equations are such that evanescent – exponentially increasing and decreasing – solutions exist on more than one spatial scale. At moderately high frequencies, when the equations are integrated numerically, the solutions are effectively projected onto the solution having the most rapid exponential increase, and thus even though a linearly independent set of solutions is guaranteed, theoretically, to remain a linearly independent set, it becomes, numerically, a one-dimensional projection. The general solution of this difficulty is to reformulate the equations in terms of minors (i.e., subdeterminants) of sets of solutions (Gilbert and Backus, 1966). The standard method for normal mode calculations (Woodhouse, 1988) is based on the minor formulation of the equations, and uses a novel generalization of Sturm–Liouville theory to bracket modal frequencies, itself a nontrivial issue for the spheroidal modes, as the modes are irregularly and sometimes very closely spaced in frequency, making an exhaustive search difficult and computationally expensive. The program MINOS of Guy Masters, developed from earlier programs of Gilbert, and of Woodhouse (also a development of Gilbert's earlier programs), implements this method, and has been generously made available to the community. The direct solution method for the inhomogeneous problem, of Friederich and Dalkolmo (1995) is based on the minor formulation in the non-self-gravitating case, developed for the flat-earth problem by Woodhouse (1980b). Here, we outline some of the key features of the minor approach.

1.03.5.2 Numerical Integration*

Let us be specific by assuming that the model has a solid inner core, a fluid outer core, and a solid mantle. It may or may not have an ocean. Let us also consider the case of spheroidal oscillations, for which the solution vector is six dimensional in solid regions ($\mathbf{y}^{Ss}$) and four dimensional in fluid regions ($\mathbf{y}^{Sf}$). Toroidal and radial modes are much simpler.

The basic method of solution is to start at the center of the Earth, and to specify that the solution should be nonsingular there. By assuming that the medium is homogeneous and isotropic within a small sphere at the center, it is possible to make use of known analytical solutions in terms of the spherical Bessel functions (Love, 1911; Pekeris and Jarosch, 1958; Takeuchi and Saito, 1972). Thus (in the spheroidal case that we are considering), there is a three-dimensional set of solutions to be regarded as candidates for components of the solution at the center. Using these three solutions as starting solutions, the equations can be integrated toward the surface, for example, using Runge–Kutta techniques. We introduce a 6×3 matrix $\mathbf{Y} = \mathbf{Y}^{Ss}(r)$ having colums equal to these three solutions, and which has 3×3 subpartitions $\mathbf{Q} = \mathbf{Q}^{Ss}(r)$ and $\mathbf{P} = \mathbf{P}^{Ss}(r)$, that is, $\mathbf{Y} = \begin{bmatrix} \mathbf{Q} \\ \mathbf{P} \end{bmatrix}$. What is important about $\mathbf{Y}$ is the subspace of six-dimensional space that is spanned by its three columns, a property that is left unchanged if $\mathbf{Y}$ is post-multiplied by any nonsingular 3×3 matrix. Assuming, for the moment, that $\mathbf{Q}$ and $\mathbf{P}$ are nonsingular, and post-multiplying by $\mathbf{Q}^{-1}$ and by $\mathbf{P}^{-1}$ we conclude that both $\begin{bmatrix} \mathbf{1} \\ \mathbf{U} \end{bmatrix}$ and $\begin{bmatrix} \mathbf{V} \\ \mathbf{1} \end{bmatrix}$, where $\mathbf{V}$ and $\mathbf{U}$ are the mutually inverse matrices $\mathbf{V} = \mathbf{Q}\mathbf{P}^{-1}$, $\mathbf{U} = \mathbf{P}\mathbf{Q}^{-1}$ and where $\mathbf{1}$ is the unit matrix, have columns spanning the same three-dimensional space as is spanned by the columns of $\mathbf{Y}$. An unexpected property of $\mathbf{U}$, $\mathbf{V}$, stemming from the self-adjointness property of the equations and boundary conditions, is that

*Starred sections are intended for the more specialist reader, and the chapter can be understood without reading these extra sections.

they are *symmetric*. It is not difficult to show that by virtue of the particular structure of the differential equations noted in eqn [82] that if **U**, and (therefore) **V** are symmetric at a given radius, then they remain symmetric as the equations are integrated to other radii. To demonstrate this, consider:

$$\frac{\mathrm{d}}{\mathrm{d}r}(\mathbf{Q}'\mathbf{P}-\mathbf{P}'\mathbf{Q})=\frac{\mathrm{d}}{\mathrm{d}r}(\mathbf{Y}'\boldsymbol{\Sigma}\mathbf{Y})=\mathbf{Y}'\mathbf{A}'\boldsymbol{\Sigma}\mathbf{Y}+\mathbf{Y}'\boldsymbol{\Sigma}\mathbf{A}\mathbf{Y}=0 \qquad [91]$$

where we have introduced the partitioned matrix

$$\boldsymbol{\Sigma}=\begin{pmatrix}\mathbf{0} & \mathbf{1}\\ -\mathbf{1} & \mathbf{0}\end{pmatrix}$$

where **1** is the unit matrix of appropriate dimension, so that the matrix

$$\boldsymbol{\Sigma}\mathbf{A}=\begin{pmatrix}\mathbf{S} & -\mathbf{T}'\\ -\mathbf{T} & -\mathbf{K}\end{pmatrix}$$

is symmetric. We shall also make use of the fact (Woodhouse, 1988) that in the nonattenuating case, $-\boldsymbol{\Sigma}\mathbf{A}_\lambda$, by which we shall mean the partial derivative of **A** with respect to $\lambda=\omega^2$, is positive semidefinite, that is, that $\gamma'(-\boldsymbol{\Sigma}\mathbf{A}_\lambda)\gamma\geq 0$ for any real column γ, as can be verified using the forms for the submatrices of **A** [83]–[86]. Thus, if $\mathbf{Q}'\mathbf{P}-\mathbf{P}'\mathbf{Q}$ vanishes at a given radius, it vanishes everywhere in the interval over which the equations are being integrated. But we can write $\mathbf{Q}'\mathbf{P}-\mathbf{P}'\mathbf{Q}=\mathbf{Q}'(\mathbf{P}\mathbf{Q}^{-1}-\mathbf{Q}'^{-1}\mathbf{P}')\mathbf{Q}$, which shows that $\mathbf{P}\mathbf{Q}^{-1}$ is symmetric if $\mathbf{Q}'\mathbf{P}-\mathbf{P}'\mathbf{Q}$ vanishes. It is interesting to note that this argument does not rely on **Q** and **P** being nonsingular throughout the interval of integration, since $\mathbf{Q}'\mathbf{P}-\mathbf{P}'\mathbf{Q}$ remains finite and continuous. It is a lengthy algebraic exercise to show that **U** and **V** are symmetric at the center of the Earth (i.e., when the analytic solutions are used), but nevertheless this can be verified (it can be easily checked numerically).

To continue the narrative, the equations for $\mathbf{Y}^{\mathrm{IC}}$ are being integrated in the inner core, and we arrive at the inner core boundary. Here, the component of the solution corresponding to the shear traction on the boundary (the fifth element in our notation) is required to vanish. Thus, at the boundary we need to select from the three-dimensional space spanned by the columns of **Y** the (in general) two-dimensional subspace stress-displacement vectors having vanishing fifth elements. This subspace is most easily identified by considering the basis constituted by $\begin{bmatrix}\mathbf{V}\\ \mathbf{1}\end{bmatrix}$, since its first and third columns have vanishing fifth elements, and thus by deleting the middle column, together with the second and fifth rows, as they correspond to variables not needed on the fluid side, we obtain the following rule for transmitting the basis of allowable solutions from the solid to the fluid side of the boundary:

$$\begin{pmatrix}v_{11} & v_{12} & v_{13}\\ v_{12} & v_{22} & v_{23}\\ v_{13} & v_{23} & v_{33}\\ 1 & 0 & 0\\ 0 & 1 & 0\\ 0 & 0 & 1\end{pmatrix}\rightarrow\begin{pmatrix}v_{11} & v_{13}\\ v_{13} & v_{33}\\ 1 & 0\\ 0 & 1\end{pmatrix} \qquad [92]$$

We can now continue the integration, using the 4×2 matrix $\mathbf{Y}^{\mathrm{OC}}$ in the fluid outer core. We can define **Q**, **P**, **V**, **U** similarly, now 2×2, rather than 3×3 matrices, and again **V**, **U** are symmetric. Continuing the integration, we arrive at the outer core boundary, and again need to consider how to transmit the solution space across the boundary. Elements in rows 1, 2, 3, 4 on the fluid side need to be continuous with elements in rows 1, 3, 4, 6 on the solid side. The fifth element on the solid side, the shear traction component $r\zeta S$, has to vanish. Since the horizontal displacement can be anything on the solid side we have to add to the basis to represent solutions having nonvanishing horizontal displacements on the solid side. The easiest way to satisfy these requirements is to consider the basis represented by $\begin{bmatrix}\mathbf{1}\\ \mathbf{U}\end{bmatrix}$. It can be easily verified that the follwing rule satisfies the requirements:

$$\begin{pmatrix}1 & 0\\ 0 & 1\\ u_{11} & u_{12}\\ u_{12} & u_{22}\end{pmatrix}\rightarrow\begin{pmatrix}1 & 0 & 0\\ 0 & 1 & 0\\ 0 & 0 & 1\\ u_{11} & 0 & u_{12}\\ 0 & 0 & 0\\ u_{12} & 0 & u_{22}\end{pmatrix} \qquad [93]$$

The middle column has been inserted to represent the fact that the solution space has to contain vectors with nonvanishing horizontal displacement scalar $(r\zeta V)$ at the base of the mantle.

We can now continue the integration through the mantle. In the inhomogenous problem, the next interesting event is when we arrive at the source radius r_s. In the homogeneous problem, on the other hand, we can continue the integrations to the ocean floor, applying the same rule as at the inner core boundary to transmit the solution space into the ocean, and then continue to the surface, where the free surface condition needs to be satisfied. The requirement, of course, is that there be a linear combination of the columns of the 4×2 matrix $\mathbf{Y}^{\mathrm{O}}=\begin{bmatrix}\mathbf{Q}^{\mathrm{O}}\\ \mathbf{P}^{\mathrm{O}}\end{bmatrix}$ (where superscript 'O' is for ocean) that have vanishing surface traction scalar rP and vanishing gravity scalar $r\psi/4\pi G$, that is, vanishing elements 3 and 4. This requires $\det(\mathbf{P}^{\mathrm{O}})=0$ at the free surface. In the absence of an ocean, we similarly need $\det(\mathbf{P}^{\mathrm{C}})=0$ where $\mathbf{P}^{\mathrm{C}}$ is the 3×3 matrix in the crust.

In the inhomogeneous case, we need to arrange for there to be a prescribed discontinuity $\mathbf{s}^{\mathrm{Ss}}$ at the source depth. Thus, we need to characterize the solution space above, as well as below the source. At the surface of the ocean the solution must have vanishing elements 3 and 4, and thus we choose $\mathbf{Y}^{\mathrm{O}}$ at the free surface to be, simply $\mathbf{Y}^{\mathrm{O}}=\begin{bmatrix}\mathbf{1}\\ \mathbf{0}\end{bmatrix}$. Now we can integrate the solution downwards, using the same fluid–solid rule at the ocean floor as was employed at the core–mantle boundary, until we reach the source radius r_s from above. If $\begin{bmatrix}\mathbf{1}\\ \mathbf{U}_1^{\mathrm{s}}\end{bmatrix}$ spans the solution space below the source and $\begin{bmatrix}\mathbf{1}\\ \mathbf{U}_2^{\mathrm{s}}\end{bmatrix}$ spans the solution space above the source, we need to solve

$$\begin{bmatrix}\mathbf{1}\\ \mathbf{U}_2^{\mathrm{s}}\end{bmatrix}\mathbf{x}_2-\begin{bmatrix}\mathbf{1}\\ \mathbf{U}_1^{\mathrm{s}}\end{bmatrix}\mathbf{x}_1=\mathbf{s}^{\mathrm{Ss}} \qquad [94]$$

for the two 3-vectors $\mathbf{x}_1$, $\mathbf{x}_2$ which represent the multipliers for the columns of each matrix that are needed to satisfy the

condition that the solution have the prescribed discontinuity. The solution is easily found to be

$$\mathbf{x}_1 = (\mathbf{U}_2 - \mathbf{U}_1)^{-1}\left(\mathbf{s}_{\mathrm{P}}^{\mathrm{Ss}} - \mathbf{U}_2\mathbf{s}_{\mathrm{Q}}^{\mathrm{Ss}}\right),$$
$$\mathbf{x}_2 = (\mathbf{U}_2 - \mathbf{U}_1)^{-1}\left(\mathbf{s}_{\mathrm{P}}^{\mathrm{Ss}} - \mathbf{U}_1\mathbf{s}_{\mathrm{Q}}^{\mathrm{Ss}}\right) \qquad [95]$$

where $\mathbf{s}_{\mathrm{Q}}^{\mathrm{Ss}}$, $\mathbf{s}_{\mathrm{P}}^{\mathrm{Ss}}$ are the upper and lower halves of $\mathbf{s}^{\mathrm{Ss}}$, and the solution vectors below and above the source are given by

$$\mathbf{y}_1^{\mathrm{Ss}} = \begin{bmatrix}\mathbf{x}_1\\ \mathbf{U}_1\mathbf{x}_1\end{bmatrix},\quad \mathbf{y}_2^{\mathrm{Ss}} = \begin{bmatrix}\mathbf{x}_2\\ \mathbf{U}_2\mathbf{x}_2\end{bmatrix} \qquad [96]$$

This determines the linear combination of the basis vectors that are needed to satisfy the source discontinuity condition, and hence to determine the solution at any point of the medium and, in particular, at the surface, where it may be required to calculate some seismograms.

1.03.5.3 Eigenfunctions and Eigenfrequencies*

There will be singularities in the integrand of the inverse Fourier transform when $\mathbf{U}_2 - \mathbf{U}_1$ is singular. This will occur for frequencies ω for which a solution exists to the homogenous (i.e., unforced) problem, that is, at the frequencies of free oscillation. If $\mathbf{U}_2 - \mathbf{U}_1$ is singular at a particular source radius it is, therefore, necessarily singular at all radii. To evaluate the inverse transform as a sum over residues, we can write,

$$\frac{1}{2\pi}\int_{-\infty}^{\infty} I(\omega)\mathrm{e}^{\mathrm{i}\omega t}\,\mathrm{d}\omega \to \sum_k i\frac{\lim_{\omega\to\omega_k}\Delta(\omega)I(\omega)}{\Delta'(\omega_k)} \qquad [97]$$

where ω_k is a mode frequency and where $\Delta(\omega)$ is that factor in the denominator of the integrand $I(\omega)$ that vanishes at ω_k, assuming that it has a simple zero at ω_k. Thus, we can replace the inverse transform by a sum over residues provided that the singular part of the integrand is replaced by the expression corresponding to it on the right side of eqn [97]. From eqn [95], we find that the necessary replacement is

$$(\mathbf{U}_2 - \mathbf{U}_1)^{-1} \to i\frac{\mathrm{adj}(\mathbf{U}_2 - \mathbf{U}_1)}{\partial_\omega \det(\mathbf{U}_2 - \mathbf{U}_1)}\bigg|_{\omega=\omega_k} = \frac{1}{2i\omega_k}\mathbf{z}_k\mathbf{z}_k' \qquad [98]$$

where adj represents matrix adjoint – the matrix of cofactors. The second equality defines the column $\mathbf{z}_k$ and its transpose $\mathbf{z}_k'$, and arises from the fact that the adjoint of a singular matrix, assuming that the rank defect is 1, is expressible as a dyad; the factor $-1/2\omega_k$ is included in the definition for convenience, as with this definition of $\mathbf{z}_k$, it can be shown that the column $\mathbf{y}_k = \begin{bmatrix}\mathbf{z}_k\\ \mathbf{U}_1\mathbf{z}_k\end{bmatrix} = \begin{bmatrix}\mathbf{z}_k\\ \mathbf{U}_2\mathbf{z}_k\end{bmatrix}$ is an eigenfunction (i.e., a solution of $\mathrm{d}\mathbf{y}/\mathrm{d}r = \mathbf{A}\mathbf{y}$) and has normalization

$$\int_0^a \mathbf{y}_k'(-\Sigma\mathbf{A}_\lambda)\mathbf{y}_k\,\mathrm{d}r = 1 \qquad [99]$$

where the notation $-\Sigma\mathrm{A}_\lambda$ is that introduced in the discussion following eqn [82]. The eigenfunctions can be found without needing to calculate the derivatives of solutions with respect to ω, as it can be shown that $\det\mathbf{Q}_1 \det\mathbf{Q}_2\partial_\omega\det(\mathbf{U}_2 - \mathbf{U}_1)$ is independent of r. This is the basis for the construction of the eigenfunctions from solutions of the minor equations, although it was arrived at differently in Woodhouse (1988). We see that it is necessary to integrate both upwards and downwards in order to obtain $\mathbf{U}_1$ and $\mathbf{U}_2$ (or, rather, the minors from which they can be constructed, see below) at all radii r.

In the nonattenuating case, the eigenfunctions $\mathbf{y}_k$ are real, and eqn [99] reduces to the standard normalization conditions for the scalar eigenfunctions U_k, V_k, W_k (defined in terms of $\mathbf{y}_k$ as in eqn [80]),

$$\text{spheroidal}: \int_0^a \rho\left(U_k^2 + \zeta^2 V_k^2\right)r^2\,\mathrm{d}r = 1,$$
$$\text{toroidal}: \int_0^a \rho\zeta^2 W_k^2 r^2\,\mathrm{d}r \qquad [100]$$

In the attenuating case, on the other hand, the eigenfunctions are complex and the normalization condition [99] includes terms arising from the derivatives of the elastic parameters with respect to ω. In this case, eqn [99] determines both the phase and the amplitude of the eigenfunction. Using the replacement [98] in [95], and making use of the definitions of $\mathbf{s}^{\mathrm{Ss}}$, and similarly $\mathbf{s}^{\mathrm{Ts}}$, from eqns [88] to [90] it can be shown that the inhomogeneous solution, now in the time domain, can be written as a sum over residues:

$$\mathbf{y}_{lm}(r,t) = \sum_k -\frac{1}{2\omega_k^2}E_{km}\mathbf{y}_k(r)\mathrm{e}^{\mathrm{i}\omega_k t} \qquad [101]$$

where *modal excitations* E_{km} are given by

$$E_{km} = \begin{cases}\mathbf{y}_k'\boldsymbol{\Sigma}\mathbf{s}^{\mathrm{Ss}} & \text{spheroidal}\\ \mathbf{y}_k'\boldsymbol{\Sigma}\mathbf{s}^{\mathrm{Ts}} & \text{toroidal}\end{cases}$$
$$= \frac{v_l}{r_s}\begin{cases} -r_s U_k F_r - r_s\partial_r U_k M_{rr} - U_k\left(M_{\theta\theta} + M_{\phi\phi}\right) + \frac{1}{2}\zeta^2 V_k\left(M_{\theta\theta} + M_{\phi\phi}\right) + \frac{1}{2}\zeta^2 W_k\left(M_{\theta\phi} - M_{\phi\theta}\right) & m = 0\\ \frac{1}{2}\zeta r_s(V_k \mp iW_k)\left(\pm F_\theta - iF_\phi\right) + \frac{1}{2}\zeta r_s(\partial_r V_k \mp i\partial_r W_k)\left(\mp M_{\theta r} - iM_{\phi r}\right) + \frac{1}{2}\zeta(U_k - V_k \pm iW_k)\left(\pm M_{r\theta} - iM_{r\phi}\right) & l \geq 1, m = \pm 1\\ \frac{1}{4}\zeta\sqrt{\zeta^2 - 2}(V_k \mp iW_k)\left(M_{\phi\phi} - M_{\theta\theta} \pm iM_{\theta\phi} \pm iM_{\phi\theta}\right) & l \geq 2, m = \pm 2\end{cases} \qquad [102]$$

where eqn [76] has been used to express the radial traction components P_k, S_k, T_k in $\mathbf{y}_k$ in terms of U_k, V_k, W_k, and their derivatives. The eigenfunctions are those evaluated at the source radius r_s. In eqn [102], we have combined the results for toroidal and spheroidal modes; of course, for spheroidal modes $W_k = 0$ and for toroidal modes $U_k = V_k = 0$. This result for the modal excitations is equivalent, in the case of a symmetric moment tensor to the forms given in Table 1 of Woodhouse and Girnius (1982).

The sum over residues [101] needs to be carried out over all simple poles in the upper half of the complex ω-plane. It will include the oscillatory 'seismic modes' having $\mathrm{Re}\,\omega_k \neq 0$, and

also, possibly, 'relaxation modes' having Re $\omega_k = 0$, Im $\omega_k > 0$. The seismic modes will occur in pairs, $\omega_k, -\omega_k^*$ because the equations are symmetric under replacement of ω_k by $-\omega_k^*$ followed by complex conjugation (see discussion following eqn [35]). Thus, each seismic mode having Re $\omega_k > 0$ will have a partner, obtained by reflection in the imaginary axis, at $-\omega_k^*$. It is not necessary to consider the modes for which Re $\omega_k < 0$ explicitly, as when the final result for the displacement in the time domain is calculated, it is possible to include them automatically by adding the complex conjugate, in order that the final result should be real. In the attenuating case, the solution is still not necessarily complete, as the constitutive law may introduce a branch cut along the positive imaginary axis, corresponding to a continuous distribution of relaxation mechanisms. In this case the sum over residues needs to be augmented by an integral around any branch-cut singularities on the positive imaginary axis. In order to include the 'static' response of the medium it is necessary to analyze the behavior of the integrand at $\omega = 0$. We do not pursue this in detail here but make some general observations. Because the source that is being considered has, in general, nonvanishing net force and net moment we would obtain secular terms corresponding to translational and rotational rigid motions (degree $l = 1$ spheroidal and toroidal modes having zero frequency). If the force is set to zero and the moment tensor is taken to be symmetric, these modes would not be excited. In this case, the final displacement field, after all seismic modes and relaxation modes have died away can be found from the residue at zero frequency, and will correspond to the static ($\omega = 0$) solution of the equations in which the elastic parameters are replaced by their values at zero frequency – their so-called *relaxed* values. Alternatively, the final displacement can be found by considering the fact that if the static terms are omitted the final displacement is zero, because all modes attenuate with time, whereas, in fact, it is the *initial* displacement that should be zero. Thus, the static terms must be such as to cancel the dynamic terms at zero time. It is not obvious that these two different ways of evaluating the static response will agree (i.e., using the static solution for relaxed values of the moduli, or using the fact that the initial displacement must be zero). We conjecture, but do not claim to prove, that these two methods will give the same result. If this is so, it means that, provided that *all* modes are included in the sum, we can include the static response by substituting $e^{i\omega_k t} - 1$ for $e^{i\omega_k t}$ in eqn [101] – that is, by subtracting the value at zero time.

1.03.5.4 Minors*

A central role is played in the foregoing theory by the symmetric matrices $\mathbf{U}$ and $\mathbf{V}$, notwithstanding that they possess singularities within the domain of integration. From their definitions $\mathbf{V} = \mathbf{Q}\mathbf{P}^{-1}$, $\mathbf{U} = \mathbf{P}\mathbf{Q}^{-1}$, using the following standard formula for the inverse of a matrix in terms of its cofactors and its determinant, they can be expressed in terms of the various 3×3 or (in the fluid case) or 2×2 subdeterminants of $\mathbf{Y}$. Explicitly we have:

$$\mathbf{U} = \frac{m_2}{m_1}, \quad \mathbf{V} = \frac{m_1}{m_2} \quad (n = 1) \qquad [103]$$

$$\mathbf{U} = \frac{1}{m_1}\begin{pmatrix} -m_4 & m_2 \\ m_2 & m_3 \end{pmatrix}, \quad \mathbf{V} = \frac{1}{m_6}\begin{pmatrix} m_3 & -m_2 \\ -m_2 & -m_4 \end{pmatrix},$$

$$m_1 = \det \mathbf{Q}, \qquad m_6 = \det \mathbf{P} \quad (n = 2) \qquad [104]$$

$$\mathbf{U} = \frac{1}{m_1}\begin{pmatrix} m_{11} & -m_5 & m_2 \\ -m_5 & -m_6 & m_3 \\ m_2 & m_3 & m_4 \end{pmatrix}, \quad \mathbf{V} = \frac{1}{m_{20}}\begin{pmatrix} m_{10} & -m_9 & m_8 \\ -m_9 & -m_{15} & m_{14} \\ m_8 & m_{14} & m_{17} \end{pmatrix},$$

$$m_1 = \det \mathbf{Q}, \; m_{20} = \det \mathbf{P} \quad (n = 3) \qquad [105]$$

where m_k are the minors of the relevant 2×1, 4×2, 3×6 ($n = 1$, 2, or 3) solution matrices $\mathbf{Y}$. We are using a standard way of enumerating these (see Gilbert and Backus, 1966; Woodhouse, 1988). We include the $n = 1$ case here, which is relevant to the case of toroidal and radial oscillations, for the sake of completeness. The results still hold in this case, although the matrices $\mathbf{Q}$, $\mathbf{P}$, $\mathbf{V}$, $\mathbf{U}$ reduce in this case to simple numbers, and the minors reduce to the elements of the solution vector itself (the 1×1 subdeterminants of a 2×1 matrix $\mathbf{Y}$). It is well known (Gilbert and Backus, 1966) that differential equations can be derived that are satisfied by the minors, and thus that they can be calculated directly, without the need to integrate the equations for particular solution sets $\mathbf{Y}$. Thus, formulae and results involving $\mathbf{V}$, $\mathbf{U}$ can be readily transcribed into formulae involving the minors. Essentially, any one of $\mathbf{U}$, $\mathbf{V}$, $\mathbf{m}$ provides a way of characterizing a subspace of the $2n$ dimensional space of interest ($n = 1$, 2, or 3), in a way that is independent of any specific basis. However, the minors have the practical advantage that they do not become infinite in the domain of integration.

The matrices $\mathbf{U}$ and $\mathbf{V}$ possess another remarkable property which results from the positive semi-definiteness of $-\boldsymbol{\Sigma}\mathbf{A}_\lambda$ in the nonattenuating case. Using this property, it is possible to show that the derivatives $\mathbf{U}_\lambda$ and $\mathbf{V}_\lambda$ also have definiteness properties. For upward integration $\mathbf{U}_\lambda \leq 0$ and $\mathbf{V}_\lambda \geq 0$ where ≥ 0 and ≤ 0 is used as a shorthand for the relevant semi-definiteness property. To prove this, consider the matrix $\mathbf{P}'\mathbf{Q}_\lambda - \mathbf{Q}'\mathbf{P}_\lambda = -\mathbf{U}'\boldsymbol{\Sigma}\mathbf{U}_\lambda$. The radial derivative of this matrix is given by

$$\begin{aligned} \frac{\mathrm{d}}{\mathrm{d}r}(\mathbf{P}'\mathbf{Q}_\lambda - \mathbf{Q}'\mathbf{P}_\lambda) &= -\frac{\mathrm{d}}{\mathrm{d}r}(\mathbf{Y}'\boldsymbol{\Sigma}\mathbf{Y}_\lambda) \\ &= -(\mathbf{Y}'\mathbf{A}'\boldsymbol{\Sigma}\mathbf{Y}_\lambda) - \mathbf{Y}'\boldsymbol{\Sigma}(\mathbf{A}_\lambda\mathbf{Y} + \mathbf{A}\mathbf{Y}_\lambda) \\ &= -\mathbf{Y}'\boldsymbol{\Sigma}\mathbf{A}_\lambda\mathbf{Y} \geq 0 \end{aligned} \qquad [106]$$

where we have used $\mathrm{d}\mathbf{Y}/\mathrm{d}r = \mathbf{A}\mathbf{Y}$, together with its transpose and its derivative with respect to λ. The cancelation of the terms not involving A_λ is due to the symmetry of $\boldsymbol{\Sigma}\mathbf{A}$ and the antisymmetry of $\boldsymbol{\Sigma}$. We also have

$$\begin{aligned} \mathbf{V}_\lambda &= \left(\mathbf{Q}\mathbf{P}^{-1}\right)_\lambda = \mathbf{Q}_\lambda\mathbf{P}^{-1} - \mathbf{Q}\mathbf{P}^{-1}\mathbf{P}_\lambda\mathbf{P}^{-1} = \mathbf{Q}_\lambda\mathbf{P}^{-1} - \mathbf{P}'^{-1}\mathbf{Q}'\mathbf{P}_\lambda\mathbf{P}^{-1} \\ &= \mathbf{P}'^{-1}(\mathbf{P}'\mathbf{Q}_\lambda - \mathbf{Q}'\mathbf{P}_\lambda)\mathbf{P}^{-1} \end{aligned} \qquad [107]$$

Thus, eqn [106] shows that if $\mathbf{P}'\mathbf{Q}_\lambda - \mathbf{Q}'\mathbf{P}_\lambda \geq 0$ at some initial point, then it remains positive semi-definite during upward integration. Then, from [107], $V_\lambda \geq 0$, as we wished to show. Using the analytic solutions at the center of the Earth, it can be shown that $\mathbf{V}_\lambda$ does have the required properties at the starting point of integration, being independent of frequency at the

center of the Earth. Also, its semidefiniteness property is preserved on passing from solid to fluid and vice versa. Similarly, it can be shown that for upward integration $\mathbf{U}_\lambda \leq 0$.

The diagonal elements of $\mathbf{V}_\lambda$ and $\mathbf{U}_\lambda$, which necessarily share the semi-definiteness properties of the matrices themselves, require, for upward integration, that the diagonal elements of $\mathbf{V}$ and $\mathbf{U}$ are nondecreasing and nonincreasing functions of frequency, respectively. As a function of frequency these diagonal elements behave like the familiar tangent and cotangent function, having monotonic increase or decrease between their singularities. The singularities in $\mathbf{V}$ at the surface are of particular interest, since the frequencies for which $\mathbf{V}$ is singular (i.e., infinite) at the surface are precisely the frequencies of the normal modes. One particular diagonal element, namely υ_{11} in the notation used here, has the additional property, using [92], [93], that it is continuous at solid–fluid and fluid–solid boundaries. In the case of fluid–solid boundaries this is not so obvious, as both m_{10} and m_{20} vanish on the solid side ($\upsilon_{11} = m_{10}/m_{20}$, eqn [105]), but but it can be shown that the limit as the boundary is approached from the solid side is, in fact, equal to υ_{11} on the fluid side.

1.03.5.5 Mode Bracketing and Counting*

The function $\theta_R(r, \lambda) = -\frac{1}{\pi}\cot^{-1}(\upsilon_{11})$, which can be made continuous (as a function of r and as a function of λ) through singularities of υ_{11}, has the properties that (i) it is independent of frequency at the center of the Earth, (ii) it is nondecreasing as a function of λ, and (iii) it takes on integer values at the surface at the frequencies $\omega^2 = \lambda$ corresponding to the normal modes. This makes it an ideal mode counter, since two integrations of the equations, at frequencies ω_1, ω_2, say, can determine the values $\theta_R(a, \omega_1^2)$, $\theta_R(a, \omega_2^2)$ at the Earth's surface and it is necessary only to find how many integers lie between these values to determine how many modal frequencies lie between ω_1 and ω_2. There is a complication associated with fluid–solid boundaries. As discussed above, both m_{10} and m_{20} vanish on the solid side, even though υ_{11} remains continuous. This circumstance leads to singular behavior of θ_R as a function of λ, and we find that it is necessary to increment θ_R by 1 at a fluid–solid boundary when the (2,2) element of $\mathbf{S}^{Ss}$ (eqn [83]) is negative on the solid side, that is, for $\omega^2 > [\zeta^2(A - F^2/C) - 2N]/\rho r^2$, in which the elastic constants are those evaluated at the boundary, on the solid side and r is the radius of the boundary. For upward integration (the usual case), this occurs at the core–mantle boundary.

Figure 8 shows an example of the behavior of $\theta_R(x, \lambda)$ for spheroidal oscillations of degree $l = 10$. The θ_R mode counter can be used to bracket the modal frequencies by a bisection method that seeks values of frequency such that $\theta_R(a, \omega^2)$ takes on values lying between any pair of successive integers in an interval $[\theta_R(a, \omega^2_{\min}), \theta_R(a, \omega^2_{\max})]$.

Having bracketed the modal frequencies (for a given l) it is necessary to converge on the zeros of $\det[\mathbf{P}]|_{r=a}$. This can be done in a variety of standard ways, bisection being the ultimately safe method if all else fails. Figure 9 shows the resulting *dispersion diagram* for spheroidal modes up to 30 mHz. The crowding and irregularity of the distribution in the left side of the diagram demonstrate the need for the mode-counting scheme. For the toroidal modes, the dispersion diagram is much simpler (Figure 10), and so the mode-counting scheme is less critical.

1.03.6 Elastic Displacement as a Sum Over Modes

We shall here assume that a catalog of normal mode eigenfrequencies and scalar eigenfunctions has been calculated, including spheroidal modes (Figure 9) and toroidal modes

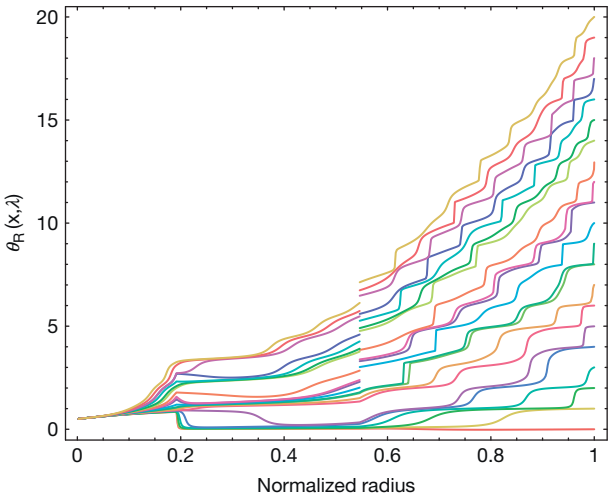

Figure 8 An example of the behavior of $\theta_R(x, \lambda)$ for the spheroidal oscillations of degree $l = 10$. It has been calculated for the true modal frequencies up to ${}_{20}S_{10}$, and thus the surface value of $\theta_R(x, \lambda)$, at normalized radius $x = 1$, takes on successive integer values equal to the overtone number. θ_R can be seen to be independent of frequency at the center of the Earth ($x = 0$) where θ_R $(0, \lambda) = 1/2$. The nondecreasing property of θ_R as a function of $\lambda = \omega^2$ means that successive curves never cross. Notice that θ_R is not a monotonic function of r. The discontinuity in θ_R at the core–mantle boundary, discussed in the text, affects the mode count for modes higher than ${}_9S_{10}$. In a sense, the values of $\theta_R(x, \lambda) = -(1/\pi)\cot^{-1}\upsilon_{11}$ are not of physical significance, since υ_{11} is a dimensional quantity, and thus the value of $\theta_R(x, \lambda)$ depends on the units employed. In any system of units, however, θ_R takes on integer values at the same values of its arguments. In other words, it is the *zero crossings* of υ_{11}, for which θ_R acts as a counter, that are of primary significance. The results shown here are for $\theta_R(x, \lambda) = -(1/\pi)\cot^{-1}\alpha\upsilon_{11}$, with $\alpha = 4 \times 10^4$ N m^{-3}.

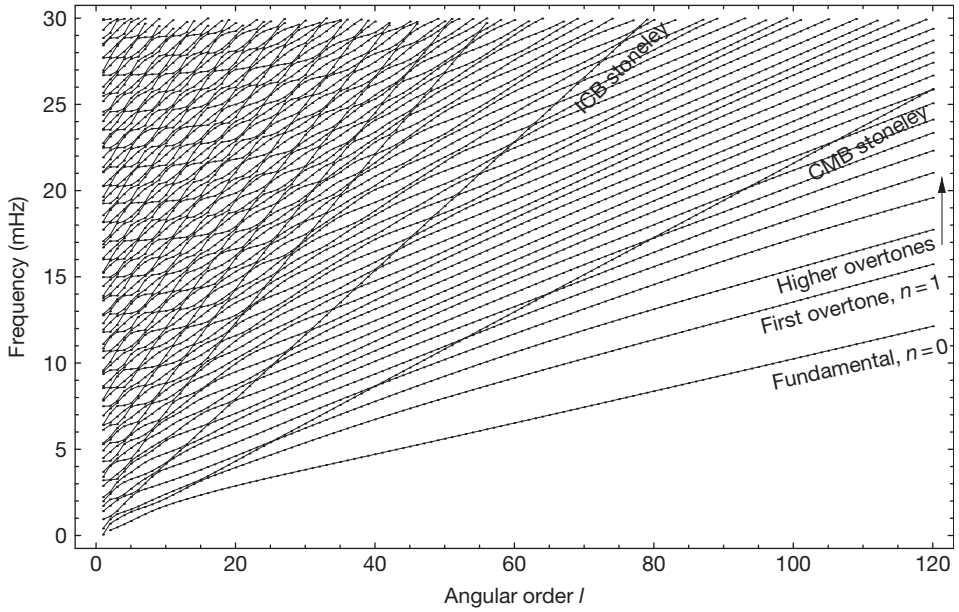

Figure 9 The dispersion diagram for spheroidal modes to 30 mHz. Modes with the same overtone number n are connected by lines, forming branch. The fundamental branch ($n=0$) and the first overtone branch ($n=1$) are indicated. Also shown are the Stoneley branches, which are modes that only exist at solid–fluid interfaces.

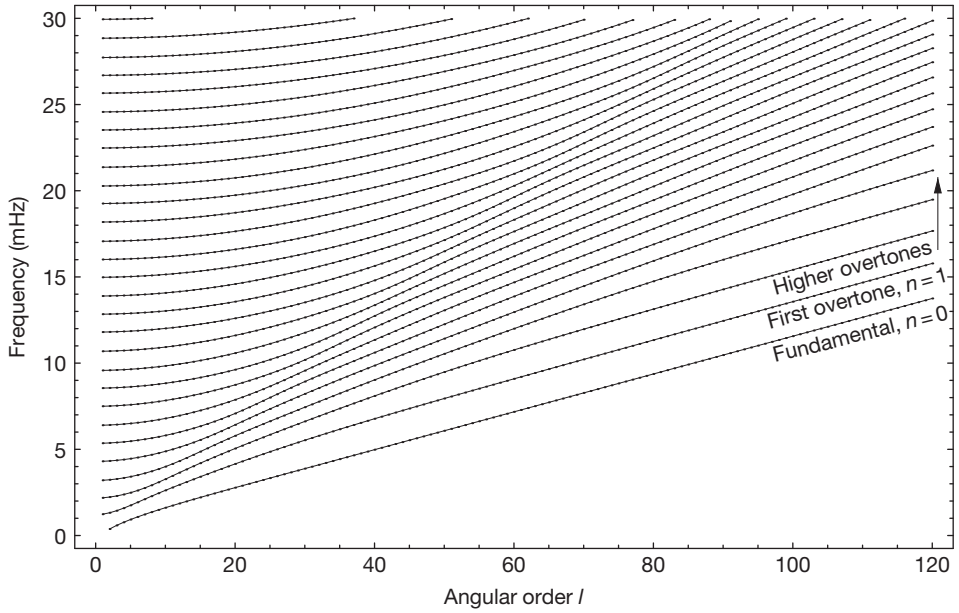

Figure 10 The dispersion diagram for toroidal modes to 30 mHz. Modes with the same overtone number n are connected by lines, forming branch. The fundamental branch ($n=0$) and the first overtone branch ($n=1$) are indicated.

(Figure 10). Rather than pursuing the in-homogenous problem outlined in earlier sections, we shall now adopt the more classical approach, making use of the orthogonality properties of the eigenfunctions to expand the applied force distribution and to find the modal excitations. The argument is strictly valid only in the nonattenuating case. Attenuation is subsequently included by introducing decay constants associated with each mode. Recall that the eigenfrequencies ω_k and the eigenfunctions $\mathbf{s}^{(km)}$ are solutions of the eigenvalue problem

$$\mathcal{H}\mathbf{s}^{(km)} = \rho\omega_k^2\mathbf{s}^{(km)} \qquad [108]$$

where each multiplet is labeled by $k=n, l, q$ with q denoting the modal type (either spheroidal or toroidal), l the angular order and n the overtone number. m is the azimuthal order. The problem is degenerate in the spherical nonrotating case, so for each normal mode multiplet there are $2l+1$ eigenfunctions $\mathbf{s}^{(km)}$ (labeled by m), all with the same eigenfrequency ω_k. It can be shown that the operator $\mathcal{H}$ is self adjoint in the sense

$$\int_V \mathbf{s}' \cdot \mathcal{H}\mathbf{s}\, \mathrm{d}^3x = \int_V \mathbf{s} \cdot \mathcal{H}\mathbf{s}'\, \mathrm{d}^3x \qquad [109]$$

for any differentiable $\mathbf{s}(\mathbf{x})$, $\mathbf{s}'(\mathbf{x})$ satisfying the boundary conditions for $\mathbf{u}$ in eqn [25], where the volume integration is over the entire Earth model. From this it follows that the eigenfunctions $\mathbf{s}^{(km)}(\mathbf{x})$ form a complete set and that the eigenvalues ω_k^2 are real. We can also assume that they are positive, on the grounds that the model should initially be in stable equilibrium. It is not difficult to show that eigenfunctions belonging to different eigenvalues are orthogonal or, in the case of degeneracy, can be orthogonalized, in the sense

$$\int_V \rho \mathbf{s}^{(k'm')*} \cdot \mathbf{s}^{(km)} \mathrm{d}^3x = 0 \quad \text{when } k \neq k' \text{ or } m \neq m' \qquad [110]$$

It is straightforward to obtain a formal solution of the equations of motion [36], that is, $\left(\mathcal{H} + \rho^0 \partial_t^2\right)\mathbf{u} = \mathbf{f}$, in terms of a sum of eigenfunctions $\mathbf{s}^{(km)}$. We expand the displacement field $\mathbf{u}(\mathbf{x}, t)$

$$\mathbf{u}(\mathbf{x}, t) = \sum_{km} a_{km}(t) \mathbf{s}^{(km)}(\mathbf{x}) \qquad [111]$$

where $a_{km}(t)$ are to be found. On substituting into eqn [36], multiplying by $\mathbf{s}^{(k'm')*}$ and integrating, making use of the orthogonality relation [110], we obtain

$$\ddot{a}_{km}(t) + \omega_k^2 a_{km}(t) = \omega_k^2 f_{km}(t) \qquad [112]$$

with

$$f_{km}(t) \equiv \frac{1}{\omega_k^2} \frac{\int_V \mathbf{s}^{(km)*}(\mathbf{x}) \cdot \mathbf{f}(\mathbf{x}, t)\, \mathrm{d}^3x}{\int_V \rho \mathbf{s}^{(km)*}(\mathbf{x}) \cdot \mathbf{s}^{(km)}(\mathbf{x})\, \mathrm{d}^3x} \qquad [113]$$

The ordinary differential equations [112] for each $a_{km}(t)$ may be solved (e.g., using the method of *variation of parameters* or Laplace transformation) to give

$$a_{km}(t) = \int_{-\infty}^{t} h_k(t - t') \dot{f}_{km}(t')\, \mathrm{d}t' \qquad [114]$$

with

$$h_k(t) = 1 - \cos \omega_k t \qquad [115]$$

a result due to Gilbert (1971). As pointed out by Gilbert, this result needs to be modified to account for attenuation by incorporating a decay factor $\exp(-\alpha_k t)$ into the cosine term, and thus in place of eqn [115] we write:

$$h_k(t) = 1 - \mathrm{e}^{-\alpha_k t} \cos \omega_k t \qquad [116]$$

where α_k is given in terms of the *quality factor* Q of the mode by $\alpha_k = \omega_k / 2Q_k$. Inserting the point source defined in eqn [32], we obtain:

$$a_{km}(t) = \frac{1}{\omega_k^2} \left(F_i s_i^{(km)}(\mathbf{x}_s)^* + M_{ij} s_{i,j}^{(km)}(\mathbf{x}_s)^* \right) h_k(t) \qquad [117]$$

assuming that eigenfunctions are normalized such that $\int_V \rho \mathbf{s}^{(km)*}(\mathbf{x}) \cdot \mathbf{s}^{(km)}(\mathbf{x}) \mathrm{d}^3x = 1$. The eigenfunctions are of the form [73], being functions of U, V, and W and the spherical harmonics $Y_l^m(\theta, \phi)$. Thus, it is a further exercise in spherical harmonic analysis to reduce the excitation coefficients, $E_{km} = \left(F_i s_i^{(km)}(\mathbf{x}_s)^* + M_{ij} s_{i,j}^{(km)}(\mathbf{x}_s)^* \right)$, to forms involving the scalar eigenfunctions U_k, V_k, W_k, and their derivatives. The result has already been derived in eqn [102] by a different route. Similar formulae are also to be found in Gilbert and Dziewonski (1975), Woodhouse and Girnius (1982), and Dziewonski and Woodhouse (1983b). Using eqn [117] in eqn [111], we obtain the following expression for a theoretical seismogram:

$$\mathbf{u}(\mathbf{x}, t) = \sum_{km} \frac{1}{\omega_k^2} E_{km} \mathbf{s}^{(km)}(\mathbf{x}) (1 - \mathrm{e}^{-\alpha_k t} \cos \omega_k t) \qquad [118]$$

The argument of the previous section shows that the correct form of this expression in the attenuating case is

$$\mathbf{u}(\mathbf{x}, t) = \sum_{\substack{km \\ \mathrm{Re}\,\omega_k > 0}} \mathrm{Re} \left\{ \frac{1}{\omega_k^2} E_{km} \mathbf{s}^{(km)}(\mathbf{x}) \left(1 - \mathrm{e}^{i\omega_k t}\right) \right\} \qquad [119]$$

where ω_k is now the complex frequency, and $\mathbf{s}^{km}$ is the complex eigenfunction, having normalization [99]. Additional terms need to be added to eqn [119] if it is desired to include relaxation effects. The actual seismogram is obtained by operating an 'instrument vector' in eqn [119].

This rather simple formula is the key ingredient of many seismological studies, as outlined in **Section 1.03.1**. Mode catalogs for PREM (Dziewonski and Anderson, 1981) exist up to 170 mHz (6 s period). **Figure 2** shows an example of such a synthetic seismogram, calculated by summing all modes up to 6 s period. For comparison, the observed seismogram for the same earthquake and station is also shown. The direct P and S and surface reflected PP and SS body waves are visible in both the synthetic and data seismograms. At later times, the surface waves can be observed. Differences between the synthetic and data seismogram can be attributed to 3D structure, which is not included in the calculation.

1.03.7 The Normal Mode Spectrum

1.03.7.1 Asymptotic Relations Relating Normal Modes, Body Waves, and Surface Waves

Here, we illustrate some of the properties of different multiplets in the normal mode spectrum. One way to gain insight into the physical character of modes is by relating them to traveling body waves and surface waves. The essential quantitative connection between modes and traveling waves is made by equating the horizontal wavelength (or wavenumber) of the mode with the corresponding horizontal wavelength (or wavenumber) of a traveling wave. For modes, this wavelength can be derived from the asymptotic properties of the spherical harmonics for large l. A point source at the pole $\theta = 0$ excites only the modes having low azimuthal order $|m| \leq 2$, as we have seen. For fixed m and large l we have (e.g., Abramowitz and Stegun, 1965):

$$Y_l^{0m}(\theta,\phi)\sim\frac{1}{\pi}\sqrt{\frac{2l+1}{4\pi}}(\sin\theta)^{-\frac{1}{2}}\cos\left[\left(l+\tfrac{1}{2}\right)\theta+\tfrac{1}{2}m\pi-\tfrac{1}{4}\pi\right]e^{im\phi} \quad [120]$$

where θ plays the role of epicentral distance. Thus, we can identify the horizontal wavenumber k ($=2\pi/$wavelength) to be

$$k=\left(l+\frac{1}{2}\right)/a \quad [121]$$

The angular order l, therefore, is a proxy for wavenumber k and dispersion diagrams such as those shown in Figures 9 and 10 can be interpreted, for large l, in the same way as are dispersion relations $\omega(k)$ for surface waves. In particular, we can define phase velocity

$$c(\omega)=\frac{\omega}{k} \quad [122]$$

and group velocity

$$U(\omega)=\frac{d\omega}{dk} \quad [123]$$

This defines the relationship between the $\omega-l$ plane and the dispersion properties of Love and Rayleigh waves and their overtones, Love waves corresponding to toroidal modes and Rayleigh waves to spheroidal modes.

In the case of body waves we may, similarly, identify the horizontal wavenumber in terms of frequency and *ray parameter* p (Brune, 1964, 1966). From classical ray theory in the spherical Earth, the horizontal wavenumber at the Earth's surface for a monochromatic signal traveling along a ray with given ray parameter $p=dT/d\Delta$ is

$$k=\frac{\omega p}{a} \quad [124]$$

Therefore, using eqn [121], we write

$$p=\frac{l+\frac{1}{2}}{\omega} \quad [125]$$

Thus, a mode of angular order l and angular frequency ω is associated with rays having the ray parameter given by eqn [125]. For toroidal modes these are S-rays, and for spheroidal modes they are both P- and S-rays. It is well known that rays exist only for ranges of depth for which

$$\frac{r}{v_P(r)}\geq p \quad \text{for P-waves} \quad [126]$$

$$\frac{r}{v_S(r)}\geq p \quad \text{for S-waves} \quad [127]$$

In the diagrams of Figures 6 **and** 11–13, the ranges of depth for which these inequalities are satisfied are indicated in two columns on the right side of each panel. The left column is for P-waves (relevant only for spheroidal multiplets) and the right column for S waves.

1.03.7.2 Differential Kernels for Spherically Symmetric Model Perturbations

Another way to gain understanding of the physical properties is through the use of *differential kernels* $K(r)$. These are, in essence, the derivatives of the eigenfrequency of a given mode with respect to a structural change at any radius. This takes the form of an integral (cf. the chain rule applied to an infinite number of independent variables). Differential kernels can be defined, for example, corresponding to perturbations in shear modulus and bulk modulus, at fixed density, and these are related to the distribution of elastic shear energy and compressional energy with radius. Similarly, kernels can be defined corresponding to anisotropic perturbations (see Chapter 1.19). Theoretical formulae for such kernels can be found in, for example, Backus and Gilbert (1967), and for anisotropic elastic parameters A, C, L, N, F in Dziewonski and Anderson (1981). Such kernels are a special case, in which the perturbation is spherically symmetric, of the kernels that arise when a general aspherical perturbation of the model is considered. This will be further discussed in Section 1.03.8.2. Here, we shall take relative perturbations in (isotropic) P-velocity, v_P, S-velocity, v_S and density ρ (at constant v_P and v_S) as the independent perturbations, and write

$$\delta\omega_k=\int_0^a\left(K_\rho(r)\frac{\delta\rho(r)}{\rho(r)}+K_P(r)\frac{\delta v_P(r)}{v_P(r)}+K_S(r)\frac{\delta v_S(r)}{v_S(r)}\right)dr \quad [128]$$

Our aim here is to use the kernels $K_P(r)$, $K_S(r)$ to give insight into the nature of the mode in terms of its traveling-wave content, and into how the P and S velocity distributions can be constrained by making observations of a given mode. The kernel $K_\rho(r)$ (for constant v_P and v_S) gives information about how the mode probes the density structure, adding to information about v_P and v_S available from modes but also from travel times.

1.03.7.3 Tour of Frequency-Wavenumber Space

Here, we will discuss the characteristics of the spheroidal and toroidal modes. Figure 9 shows the degenerate eigenfrequencies of spheroidal modes as a function of angular order l for the spherical reference model PREM. Lines connect modes of the same overtone number n, and define different *branches* of the dispersion curves. The *fundamental mode branch* ($n=0$) contains the modes with the lowest frequency for each l. Modes with $n>1$ are called *overtones*. The overtone branches cross-cut each other leading to a range of different normal mode classes, which will be discussed in the succeeding text. Figure 10 shows the same for the toroidal modes, which are much simpler and do not have cross-cutting branches. We will make a tour of $\omega-l$ space and use the eigenfunctions and differential kernels defined above to gain insight into the nature of the different types of mode.

Figures 6, 11–13 show eigenfunctions and differential kernels for a number of toroidal and spheroidal modes. By inspecting these diagrams, a few general observations can be made. Moving up along a mode branch (horizontal rows in Figures 11 and 12) will result in eigenfunctions and kernels which are more concentrated toward the surface. This reflects the fact that, for high l, the modes may be interpreted as surface waves as is most obvious for the fundamental branches of the toroidal modes (Figure 11) and spheroidal modes (Figure 12). Moving up in overtone number n, for constant l (vertical columns in Figures 11 and 12), leads to eigenfunctions that

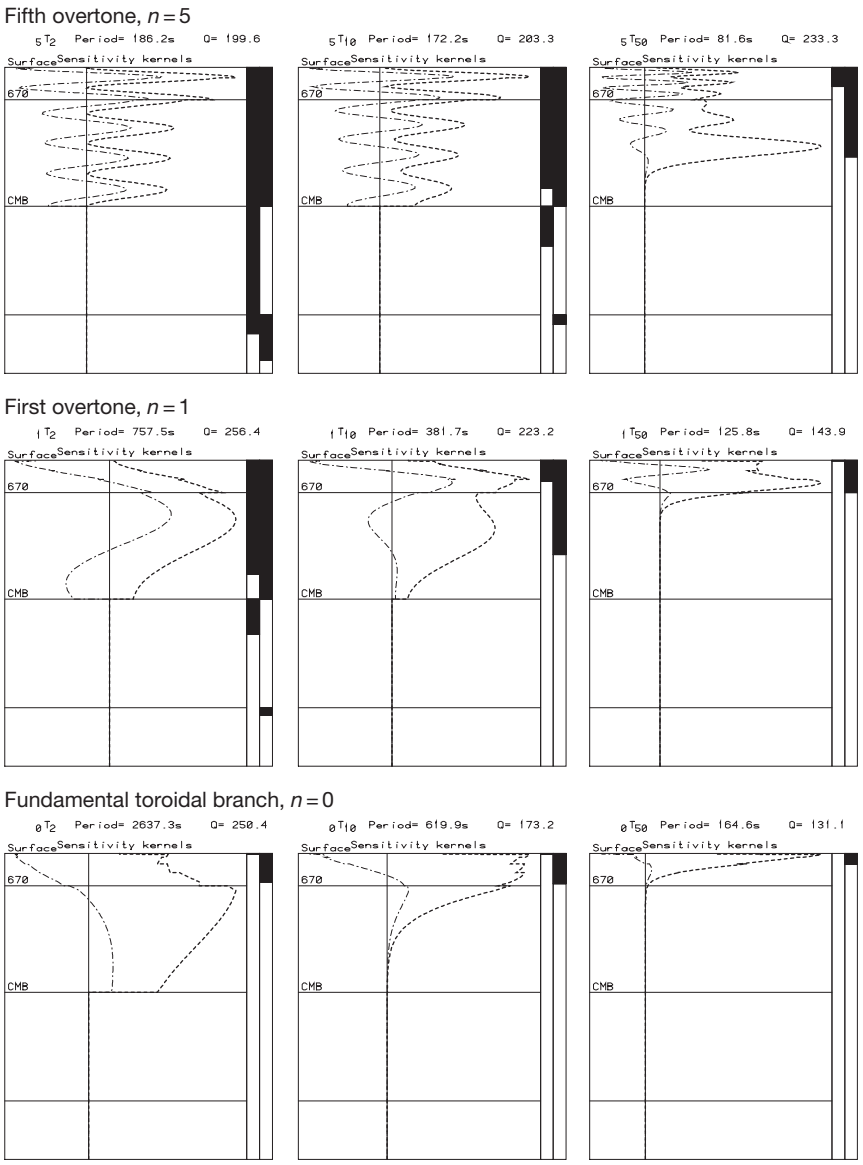
Fifth overtone, n = 5
5T2 Period= 186.2s Q= 199.6
5T10 Period= 172.2s Q= 203.3
5T50 Period= 81.6s Q= 233.3
Surface
Sensitivity kernels
670
CMB
First overtone, n = 1
1T2 Period= 757.5s Q= 256.4
1T10 Period= 381.7s Q= 223.2
1T50 Period= 125.8s Q= 143.9
Fundamental toroidal branch, n = 0
0T2 Period= 2637.3s Q= 250.4
0T10 Period= 619.9s Q= 173.2
0T50 Period= 164.6s Q= 131.1

Figure 11 Sensitivity kernels $K_S(r)$ (dashed lines) and $K_\rho(r)$ (dot-dashed lines) of selected toroidal modes.

are more oscillatory and to sensitivity kernels that penetrate more deeply.

The wave motion of toroidal modes is purely horizontal and only has one eigenfunction W (see Figure 6). Thus, for spherical, nonrotating Earth models, these modes can only be observed on the horizontal components of a theoretical seismogram and not on the vertical component. Toroidal modes are sensitive only to perturbations in S-velocity and density and have no sensitivity to the fluid core (Figure 11). The differential kernels tell us how the frequency of the mode will change if we increase the spherical velocity or density at a certain depth. When inspecting Figure 11, we find that increasing the shear wave velocity at any depth in the mantle will always lead to an increase in toroidal mode frequency as the $K_S(r)$ sensitivity kernel is always positive. For density, however, we find that it depends on the depth of the perturbation. For mode ${}_0T_2$, for example, an increase in density in the upper mantle will lead to a decrease in frequency, while an increase in the lower mantle will increase the frequency. When we move from the fundamentals to the overtones, we find that the density kernel $K_\rho(r)$ becomes oscillatory around zero (see, e.g., the $n=5$ overtones). These modes are almost insensitive to smooth variations in density, as the kernels will average to zero when integrated over depth. The sensitivity to density also becomes smaller for larger l along the same branch, which can clearly be seen when progressing from ${}_0T_2$ to ${}_0T_{10}$ along the fundamental mode branch. This agrees well with the interpretation of shorter period toroidal modes in terms of Love waves, which are also dominated by sensitivity to shear wave velocity and have much smaller sensitivity to density.

Figure 12 shows the examples of sensitivity kernels for the spheroidal modes. The spheroidal modes involve wave motion in both horizontal and vertical directions characterized by eigenfunctions $U(r)$ and $V(r)$ (Figure 6), and so are sensitive to perturbations in density and to both υ_P and υ_S. These modes are observed on both the horizontal and vertical components

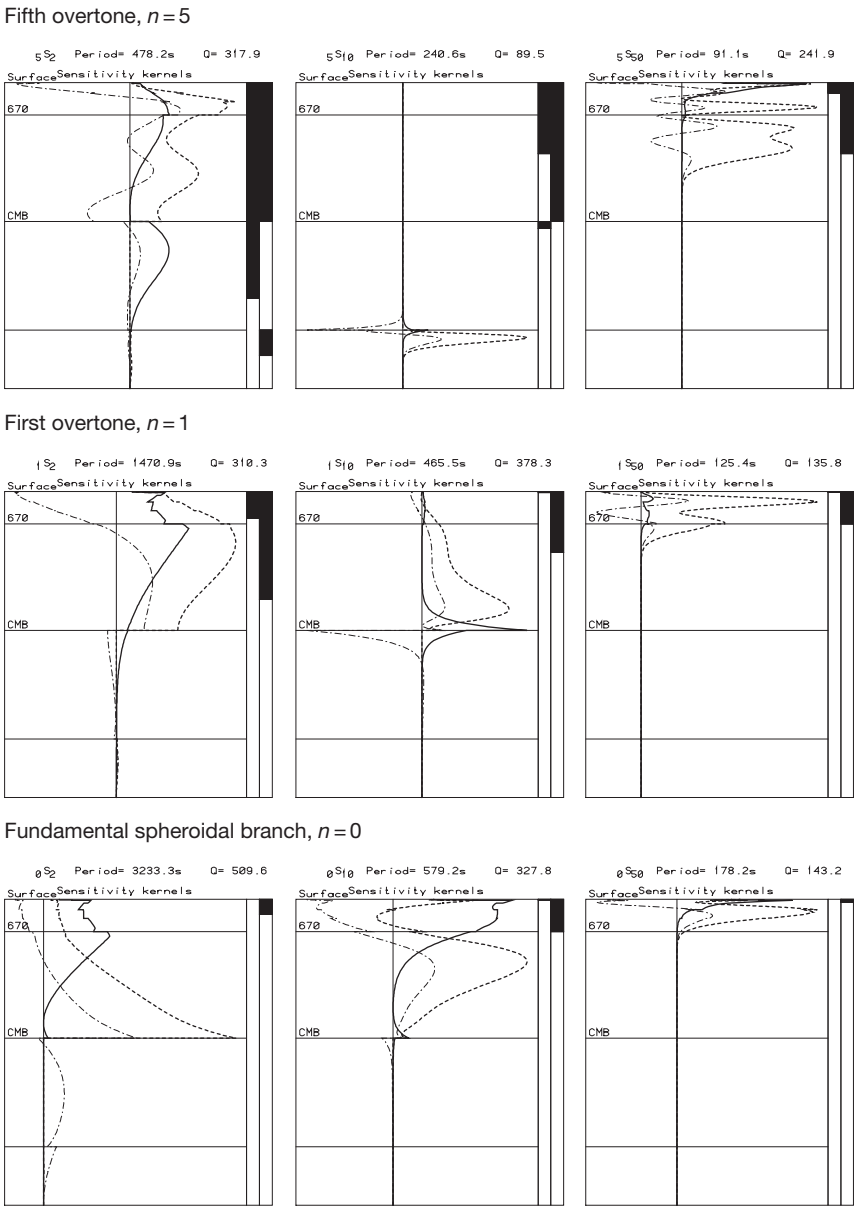
Fifth overtone, n = 5
5S2 Period= 478.2s Q= 317.9
5S10 Period= 240.6s Q= 89.5
5S50 Period= 91.1s Q= 241.9
First overtone, n = 1
1S2 Period= 1470.9s Q= 310.3
1S10 Period= 465.5s Q= 378.3
1S50 Period= 125.4s Q= 135.8
Fundamental spheroidal branch, n = 0
0S2 Period= 3233.3s Q= 509.6
0S10 Period= 579.2s Q= 327.8
0S50 Period= 178.2s Q= 143.2
Surface
Sensitivity kernels
670
CMB

Figure 12 Sensitivity kernels of selected spheroidal modes. $K_S(r)$ dashed, $K_P(r)$ solid, and $K_\rho(r)$ dot-dashed.

of theoretical seismograms for a spherical, nonrotating Earth model. Again, moving to the right along the fundamental mode branch in Figure 12 shows that sensitivities become progressively concentrated closer to the surface. Spheroidal modes correspond to Rayleigh waves and at higher l the largest sensitivity is to shear wave velocity. This is similar to the toroidal modes, except that peak sensitivity is reached at subcrustal depths, making spheroidal modes less sensitive to large variations in shear velocity in the crust than is the case for toroidal modes.

The overtones sample different families of modes which relate to the branch crossings. Mode ${}_5S_{10}$ (Figure 12) corresponds to a Stoneley wave traveling along the inner core boundary. Stoneley waves are the analogue of a Rayleigh wave, but at a fluid–solid interface, rather than at a free surface. They exist both at the inner core boundary and at the core–mantle boundary. These modes follow lines of increasing frequency ω and angular order l in Figure 9, cross-cutting the branches with constant overtone number n. Mode ${}_1S_{10}$ (Figure 12) is a mixture of mantle mode and a Stoneley wave at the core–mantle boundary. The other modes in Figure 12 show a behavior similar to the toroidal modes. Notice that for ${}_5S_{50}$, the υ_P sensitivity decays below the P-wave ray-theoretic turning point (the point at which the shading terminates in the left vertical stripe at the right of the plot), and the υ_S sensitivity decays below the S-wave turning point. The fact that, for a given ray parameter, S-waves turn at greater depth than P-waves means that in modeling there is some potential for shallow P-velocity structure to trade off with deep S-velocity structure.

Figure 13 shows another family of spheroidal modes, which are characterized by low angular order l and high overtone number n. These modes are the PKIKP equivalent modes which

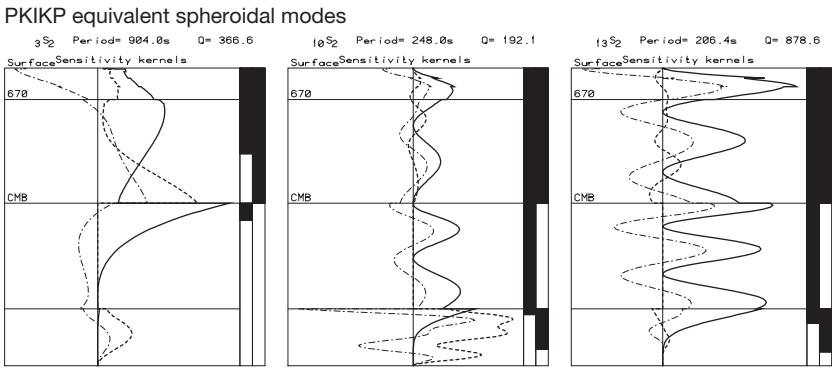

Figure 13 Sensitivity kernels of selected PKIKP equivalent spheroidal modes. $K_S(r)$ dashed, $K_P(r)$ solid, and $K_\rho(r)$ dot-dashed.

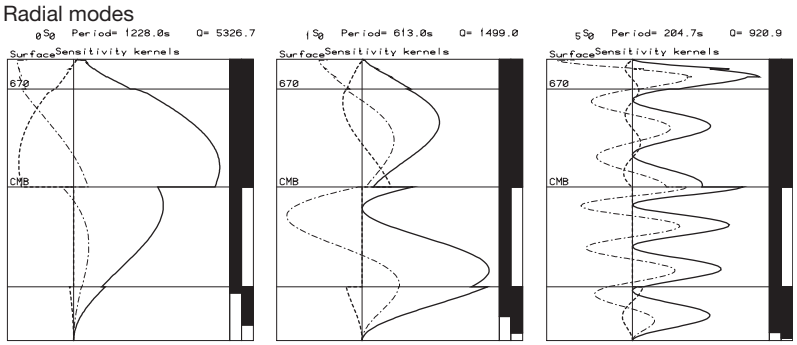

Figure 14 Sensitivity kernels of selected radial modes. $K_S(r)$ dashed, $K_P(r)$ solid, and $K_\rho(r)$ dot-dashed.

have strong sensitivity to core structure. Modes $_3S_2$ and $_{10}S_2$ have strong sensitivity to inner core υ_s, while $_{13}S_2$ is more strongly sensitive to υ_p. These modes display anomalous splitting which has been attributed to inner core anisotropy (Woodhouse et al., 1986) and its hemispherical variation (Deuss et al., 2010).

Finally, Figure 14 shows sensitivity kernels for radial modes, which are yet another subgroup of the spheroidal modes with angular order $l=0$. The radial modes are sensitive to both υ_s and υ_p and also to density. However, the sensitivities to υ_s and density oscillate around zero, while only for υ_p the sensitivity is always positive. This means that radial modes are very useful for obtaining constraints on the one-dimensional compressional structure of the Earth.

1.03.8 Normal Modes and Theoretical Seismograms in Three-Dimensional Earth Models

The previous two sections have dealt with the calculation of normal modes in a spherical symmetric, nonrotating Earth model and discussed the different modes that exist. In the spherical case, the modes are degenerate, that is, all $2l+1$ singlets in one multiplet have the same frequency. Also, toroidal modes will only be visible on the horizontal components of a seismogram, while spheroidal modes will be visible on both horizontal and vertical components. In the real Earth, the modes are split due to heterogeneous structure, rotation, and ellipticity, resulting in all singlets within one multiplet having different frequencies. Splitting effects the singlets within one normal mode multiplet, and is also called *self-coupling*. However, if two (or more) modes are close in frequency, then there will also be *cross-coupling* between the singlets of different modes causing further changes to the singlet frequencies. Cross-coupling also leads to mixing of the singlets of different modes, for example making the toroidal modes become visible on the vertical component of the seismogram. All these effects need to be taken into account when calculating synthetic spectra.

1.03.8.1 Theoretical Seismograms

The problem of calculating theoretical seismograms and spectra for three-dimensional models is a challenging one. A theoretically straightforward formalism exists for such calculations, based on expanding the wave field in terms of a complete set of (vector) functions. The equations that arise from requiring that the equations of motion be satisfied can be regarded as exact matrix equations. However, they are of infinite dimension, and even when truncated to give a practicable method of solution, the calculations require the manipulation and diagonalization of extremely large matrices. This is already problematic in the forward problem, but becomes even more so for the inverse problem, requiring calculations which are equivalent to thousands of forward problems. If the expansion is carried out in terms of the eigenfunctions of a spherical model (that is close to reality), the process is simplified, as the off-diagonal terms in the resulting matrices are small,

allowing some approximate schemes that are much less cumbersome to be developed.

Let us take the equation of motion in operator form (given in eqn [36]) as our starting point in considering the form that this theory takes. In the frequency domain:

$$(\mathcal{H}-\rho\omega^2)\mathbf{u}=\mathbf{f} \qquad [129]$$

The Earth will be considered to be in a state of steady rotation with angular velocity Ω about its center of mass, so that the expression for $\mathcal{H}$ acquires additional terms representing the Coriolis force and the centrifugal potential (Dahlen, 1968):

$$(\mathcal{H}\mathbf{u})_i=\rho\left(\phi^1_{,i}+\left[\phi^0-\tfrac{1}{2}(\Omega_k\Omega_k x_l x_l-\Omega_k\Omega_l x_k x_l)\right]_{,ij}u_j+2i\epsilon_{ijk}\Omega_j u_k\right)-\left(\Lambda_{jilk}u_{k,l}\right)_{,j} \qquad [130]$$

where, as previously, ϕ^1 is regarded as a functional of $\mathbf{u}$, by virtue of Poisson's equation [23]. The terms on the right-hand side of eqn [130] involving $\frac{1}{2}(\Omega_k\Omega_k x_l x_l-\Omega_k\Omega_l x_k x_l)$ relate to the centrifugal potential and the term involving $2i\epsilon_{ijk}\Omega_j u_k$ is the Coriolis force contribution. Let $\mathbf{s}^{(km)}$ represent the eigenfunctions of a spherical, nonrotating, nonattenuating reference model, with eigenfrequencies ω_k, so that

$$\mathcal{H}_0\mathbf{s}^{(km)}=\rho_0\omega_k^2\mathbf{s}^{(km)} \qquad [131]$$

satisfying the orthogonality relation

$$\int_V \rho_0\mathbf{s}^{(k'm')*}\cdot\mathbf{s}^{(km)}\,\mathrm{d}V=\delta_{k'k}\delta_{m'm} \qquad [132]$$

where $\mathcal{H}_0$ and ρ_0 are for the spherical, nonrotating, nonattenuating reference model. Now let us seek a solution of eqn [129] in terms of an expansion

$$\mathbf{u}(\mathbf{x},\omega)=\sum_{km}a_{km}\mathbf{s}^{(km)}(\mathbf{x}) \qquad [133]$$

with coefficients a_{km} to be found. Substituting the expansion for $\mathbf{u}(\mathbf{x},\omega)$ into eqn [129], and then taking the dot product with $\mathbf{s}^{(k'm')*}$ and integrating, we find

$$\sum_{km}\left[(k'm'|\mathcal{H}_1-\rho_1\omega^2|km)-(\omega^2-\omega_k^2)\delta_{k'k}\delta_{m'm}\right]a_{km}=(k'm'|f) \qquad [134]$$

where $\mathcal{H}_1=\mathcal{H}-\mathcal{H}_0,\rho_1=\rho-\rho_0$ and where we have introduced the notations $(k'm'|f)=\int_V \mathbf{s}^{(k'm')*}\cdot\mathbf{f}\,\mathrm{d}V$, $(k'm'|\mathcal{H}_1-\rho_1\omega^2|km)=\int_V \mathbf{s}^{(k'm')*}(\mathcal{H}_1-\rho_1\omega^2)\mathbf{s}^{(km)}\mathrm{d}V$. Equation [134] can be regarded as a matrix equation, albeit of infinite dimension, in which rows and columns of the matrix on the left side are labeled by $(k',\ m')$, $(k,\ m)$, respectively and in which the rows of the column on the right side are labeled by $(k',\ m')$. We can write

$$\mathbf{C}(\omega)\mathbf{a}=\frac{1}{i\omega}\mathbf{E} \qquad [135]$$

where $\mathbf{C}$ is the matrix having matrix elements $(k'm'|C(\omega)|km)=(k'm'|\mathcal{H}_1-\rho_1\omega^2|km)-(\omega^2-\omega_k^2)\delta_{k'k}\delta_{m'm}$ and where $\mathbf{E}/i\omega$ is the column vector having elements $(k'm'|f)$, the factor $1/i\omega$ being inserted to reflect the assumed step-function time dependence of the source, so that $\mathbf{E}$, which has elements E_{km} given in eqn [102], is independent of frequency. Hence, the formal solution is given by

$$\mathbf{a}=\frac{1}{i\omega}\mathbf{C}(\omega)^{-1}\mathbf{E} \qquad [136]$$

Recalling that we are thinking of the index k as incorporating angular order l, overtone number n, and the mode type (spheroidal or toroidal), the matrix $\mathbf{C}(\omega)$ consists of blocks of dimension $(2l'+1)\times(2l+1)$, as row index m' takes on values $-l'$ to l' and column index to takes on values $-l$ to l (**Figure 15**). Thus, each block within $\mathbf{C}(\omega)$ relates two particular multiplets k, k' of the spherical reference model. Because the deviation from the spherical reference model is regarded as small, the matrix elements in $\mathbf{C}$ are small, except for the elements on the diagonal proportional to $\omega^2-\omega_k^2$. These diagonal terms are small for values of ω close to ω_k, for a given multiplet k, but for other diagonal blocks, corresponding to multiplets not close in frequency to multiplet k, they are not small; thus the matrix is, mostly, diagonally dominant, except for diagonal blocks corresponding to multiplets close in frequency to ω. Of course the complete solution is to be obtained by substituting from eqn [136] into eqn [133] and then evaluating the inverse Fourier transform; thus we need to consider the behavior of the solution as a function of complex variable ω. In particular, we are interested in the singularities that occur in the complex ω plane, as these will correspond to the modes of the aspherical model, in much the same way as the modes of the spherical model correspond to singularities, in the frequency domain, of the solution of the inhomogenous problem (eqn [97] and the related discussion). The singularities in the solution [136] will be at the

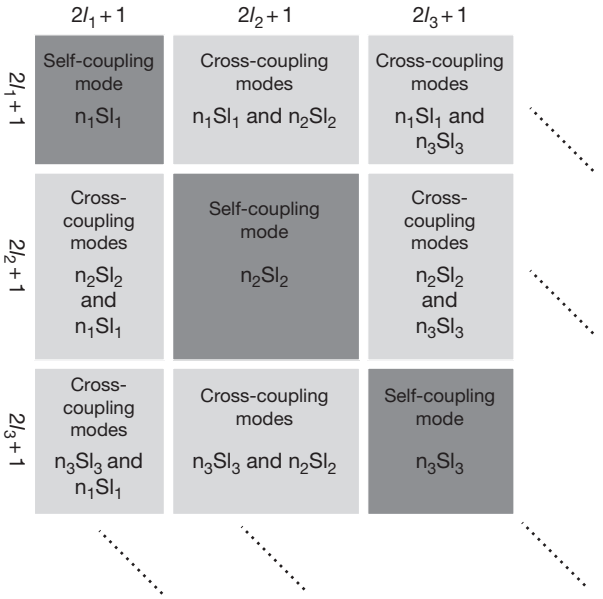

Figure 15 Schematic depiction of the different blocks in the matrix $\mathbf{C}(\omega)$ for the coupling of modes. Self-coupling blocks (dark gray) on the diagonal are of size $(2l_i+1)\times(2l_i+1)$ and one exists for each mode ${}_{ni}S_{li}$. Cross-coupling blocks (light gray) are of size $(2l_i+1)\times(2l_j+1)$ and exists for each pair of modes ${}_{ni}S_{li}$ and ${}_{nj}S_{lj}$.

frequencies $\omega = \omega_h$, say, for which there exists a nontrivial solution to the homogeneous problem

$$\mathbf{C}(\omega_h)\mathbf{r}_h = 0 \qquad [137]$$

This is an eigenvalue problem for ω_h and the corresponding right-eigenvector $\mathbf{r}_h$.

The eigenvalue problem is of a nonstandard form, since the dependence of $\mathbf{C}$ on the eigenvalue parameter $\lambda = \omega^2$, say, is not of the usual form $\mathbf{C}_0 - \lambda\mathbf{1}$. This is because, (i) perturbations in density ρ_1 introduce a more general dependence on ω^2, (ii) by virtue of attenuation, the perturbations in the elastic parameters entering into $\mathcal{H}_1$ are dependent upon ω, (iii) the terms arising from rotation depend upon ω, rather than on ω^2. Thus, the equation for $\mathbf{C}(\omega)$ is of the form

$$\mathbf{C}(\omega) = \mathbf{V}(\omega) + i\omega\mathbf{W} - \omega^2\mathbf{T} - (\omega^2 - \omega_k^2)\mathbf{I} \qquad [138]$$

where $\mathbf{V}(\omega)$ is the potential energy operator which incorporates the contributions from perturbations in the elastic parameters Λ_{ijkl} and the centrifugal potential, $\mathbf{W}$ is the Coriolis rotation operator, $\mathbf{T}$ is the kinetic energy operator which contains the perturbations to density ρ_1 and $\mathbf{I}$ is the identity matrix. (For a spherical, nonrotating model, $\mathbf{V} = \mathbf{W} = \mathbf{T} = 0$ and we find that the eigenvalues are given by $\omega_h = \omega_k$, i.e., the eigenvalues of the spherical, nonrotating reference model.)

The form of the solution as a sum over residues arising from singularities at $\omega = \omega_h$ can be obtained by replacing the inverse Fourier transform by a summation over singularities h, and within the integrand carrying out the replacement (Deuss and Woodhouse, 2004, cf. eqn [98]):

$$\mathbf{C}(\omega)^{-1} \to i\frac{\mathbf{r}_h\mathbf{l}_h}{\mathbf{l}_h\partial_\omega\mathbf{C}(\omega_h)\mathbf{r}_h} \qquad [139]$$

where $\mathbf{l}_h$ is the left-eigenvector (a *row* rather than a column), the solution of

$$\mathbf{l}_h\mathbf{C}(\omega_h) = 0 \qquad [140]$$

We are assuming here that eqns [137] and [140] determine the right and left eigenvectors $\mathbf{r}_h$, $\mathbf{l}_h$ uniquely, up to multiplying factors, such factors being immaterial for the evaluation of the residue contribution [139]. Thus, from eqn [133] the solution in the time domain can be written

$$\mathbf{u}(\mathbf{x}, t) = 2\mathrm{Re}\sum_{hkm}\frac{1}{\omega_h}\frac{\mathbf{l}_h\cdot\mathbf{E}}{\mathbf{l}_h\partial_\omega\mathbf{C}(\omega_h)\mathbf{r}_h}(km|\mathbf{r}_h)\mathbf{s}^{(km)}(\mathbf{x})e^{i\omega_h t} \qquad [141]$$

where the notation $(km/\mathbf{r}_h)$ represents individual elements of the column $\mathbf{r}_h$. As previously, the contribution from singularities in the left half of the complex ω-plane is incorporated by taking twice the real part, the summation in eqn [141] being taken only for ω_k in the right half-plane.

In order to make use of this theory it is necessary to obtain expressions for the matrix elements $(k'm'/\mathbf{C}(\omega)/km)$ in terms of the perturbations in elastic parameters, density, etc. and deviations of surfaces of discontinuity from the spherically symmetric reference model. Fairly complete forms for these are given by Woodhouse (1980a), omitting terms in anisotropic parameters and in initial stress. For anisotropic perturbations, see Chapter 1.19. The basic method is to expand the perturbations in spherical harmonics l'', m'', and then to evaluate the integrals of triples of spherical harmonics using the formula, derivable from eqns [47] and [52],

$$\frac{1}{4\pi}\int_{-\pi}^{\pi}\int_0^{\pi}\left(Y_{l'}^{N'm'}\right)^* Y_{l''}^{N''m''}Y_l^{Nm}\sin\theta\,\mathrm{d}\theta\,\mathrm{d}\phi$$
$$= (-1)^{N'-m'}\begin{pmatrix} l' & l'' & l \\ -N' & N'' & N\end{pmatrix}\begin{pmatrix} l' & l'' & l \\ -m' & m'' & m\end{pmatrix}$$
$$(-N' = N'' + N) \qquad [142]$$

The resulting form for the matrix elements can then be written in the form

$$(k'm'|\mathbf{C}(\omega)|km) = \sum_{l''m''}(-1)^{-m'}\begin{pmatrix} l' & l'' & l \\ -m' & m'' & m\end{pmatrix}\left(k'||\mathbf{C}^{(l''m'')}\right)(\omega)||k) \qquad [143]$$

where the so-called *reduced matrix element* appearing in the right side, itself defined by this equation, is independent of m and m'. This particular form for the dependence of the matrix elements on m and m' is a consequence of the *Wigner–Eckart theorem* (see Edmonds, 1960). The expressions for the reduced matrix elements take the form of radial integrals involving pairs of scalar eigenfunctions, for multiplets k' and k, and on the $(l''m'')$ component of the spherical harmonic expansion of heterogeneity, together with terms evaluated at boundaries corresponding to the $(l''m'')$ components of the deflections of the boundaries.

1.03.8.2 Splitting of Isolated Modes: The Splitting Function

The theory above is fairly complete for the oscillations of a general Earth model. Apart from the treatment of aspherical boundary perturbations, which involves a linearization of the boundary conditions, it is in principal an exact theory (Woodhouse, 1983), provided that coupling between *all* multiplets is take into account – that is, provided that the eigenvalue problem for ω_h includes all the blocks (i.e., all modes) of the full matrix $\mathbf{C}(\omega)$. Of course the theory cannot be applied in its full form, owing to the need to manipulate infinite-dimensional matrices, and so a number of approximate schemes have been developed. The simplest, and up to now most widely applied method is to reduce the eigenvalue problem for ω_h to that for a single diagonal block or mode – the so-called *self-coupling* approximation. In this case, we focus on a single multiplet, k, and reduce $\mathbf{C}(\omega)$ to the $(2l+1)\times(2l+1)$ block matrix corresponding to multiplet k, see Figure 15. This is a justifiable approximation for the calculation of $\mathbf{u}(\mathbf{x}, \omega)$ for frequencies near ω_k if the mode can be considered *isolated*, which is to say that there are no other modes nearby having similar frequency and significant coupling terms. A precise statement of the conditions that need to be satisfied for a mode to be considered isolated has not, to our knowledge, been worked out but, roughly speaking, it is necessary for the ratio $(k'm'|\mathbf{C}(\omega)|km)/(\omega_k^2 - \omega_{k'}^2)$ for all other multiplets k' to be small, for ω near the frequency ω_k of the target multiplet.

In the self-coupling approximation the dependence of $\mathbf{C}(\omega)$ can be linearized for frequencies near ω_k: $\mathbf{C}(\omega) \approx \mathbf{C}(\omega_k) + \mathbf{C}'(\omega_k)\delta\omega$, and a $(2l+1)\times(2l+1)$ matrix eigenvalue problem is obtained for $\delta\omega$:

$$[\mathbf{C}(\omega_k) + \mathbf{C}'(\omega_k)\delta\omega]\mathbf{r} = 0 \qquad [144]$$

having eigenvalues $\delta\omega_h$, say. This can also be written, to zeroth order

$$\mathbf{H}^{(k)}\mathbf{r} = \delta\omega\mathbf{r} \qquad [145]$$

where the $(2l+1)\times(2l+1)$ matrix $\mathbf{H}^{(k)}$, called the *splitting matrix* of the target multiplet, k, has elements $(km'|\mathbf{H}^{(k)}|km) = (km'|\mathbf{C}(\omega_k)|km)/2\omega_k$. This has now become a standard eigenvalue problem, involving diagonalization of the matrix $\mathbf{H}^k = \mathrm{I}\delta\omega\mathrm{r}$, which can easily be performed. The matrix $\mathbf{H}^k$ is given by

$$\mathbf{H}^k = \frac{1}{2\omega_k}\mathbf{C}(\omega_k) = \frac{1}{2\omega_k}\left(\mathbf{V}(\omega_k) + \mathrm{i}\omega_k\mathbf{W} - \omega_k^2\mathbf{T}\right) \qquad [146]$$

The contribution to the right side of eqn [141] can be written (Woodhouse and Girnius, 1982)

$$\mathbf{u}_k(\mathbf{x}, t) = \mathrm{Re}\sum_{m'm} -\frac{1}{\omega_k^2}\left(\exp\left(\mathrm{i}\mathbf{H}^{(k)}t\right)\right)_{mm'} E_{km'}\mathbf{s}^{(km)}(\mathbf{x})\mathrm{e}^{\mathrm{i}\omega_k t} \qquad [147]$$

the matrix exponential arising from the identity

$$\sum_{h=1}^{2l+1}\frac{\mathbf{r}_h\mathbf{l}_h}{\mathbf{l}_h\cdot\mathbf{r}_h}\exp(\mathrm{i}\delta\omega_h t) = \exp(\mathrm{i}\mathbf{H}t) \qquad [148]$$

where $\delta\omega_h$ are the eigenvalues of $\mathbf{H}$ and $\mathbf{r}_h$ and $\mathbf{l}_h$ its right and left eigenvectors; the division by $\mathbf{l}_h\cdot\mathbf{r}_h$ ensures that the eigenvectors are properly normalized. Equation [147], which is directly comparable to the result for the spherical reference model in eqn [119] (The static, time-independent terms are not included, as we are considering an approximation valid only in the spectral neighborhood of ω_k, the frequency of the target multiplet.), has the simple interpretation that at time $t=0$ the modes are excited as they would be in the reference model, as the matrix exponential is initially equal to the unit matrix. With time, the effective excitation $\exp(\mathrm{i}\mathbf{H}^{(k)}t)\mathbf{E}_k$ evolves on a slow time scale characterized by the incremental eigenfrequencies $\delta\omega_h$, the eigenvalues of $\mathbf{H}^{(k)}$. In the frequency domain, this leads to *splitting* of the degenerate eigenfrequency ω_k into $2l+1$ *singlets* – hence the name *splitting matrix* for $\mathbf{H}^{(k)}$.

It is straightforward to set up the inverse problem of estimating the splitting matrix for isolated multiplets using data spectra for many events. This is simplified by recognizing that the $(2l+1)\times(2l+1)$ matrix $\mathbf{H}^{(k)}$ is equivalent to a certain function on the sphere, known as the *splitting function* (Woodhouse and Giardini, 1985). It can be shown that for scalar perturbations from the reference model, such as ρ_1, κ_1, μ_1, $\mathbf{H}^{(k)}$ is expressible in terms of coefficients $c_{l''m''}$ which represent the spherical harmonic expansion coefficients of even degree l'', and up to finite spherical harmonic degree $l'' \le 2l$ by the expression

$$\left(km'|\mathbf{H}^{(k)}|km\right) = \Omega\beta_k m\delta_{m'm} + \omega_k\sum_{\substack{l''=0\\ l'' \text{ even}}}^{2l}\sum_{m''=-l''}^{l''}(-1)m'\left(\frac{2l''+1}{4\pi}\right)^{1/2}$$
$$\times(2l+1)\begin{pmatrix} l & l'' & l\\ 0 & 0 & 0\end{pmatrix}\begin{pmatrix} l & l'' & l\\ -m' & m'' & m\end{pmatrix}c^{(k)}_{l''m''} \qquad [149]$$

where the first term is the effect of Coriolis forces (Dahlen, 1968), β_k being the (known) rotational splitting parameter for the multiplet. Thus, the inverse problem for $\mathbf{H}^{(k)}$ is equivalent to the estimation of $c_{l''m''}$. The function on the sphere

$$\eta(\theta,\phi) = \sum_{\substack{l''=0\\ l'' \text{ even}}}^{2l}\sum_{m''=-l''}^{l''} c^{(k)}_{l''m''}\nu_l Y^{0m''}_{l''}(\theta,\phi) \qquad [150]$$

can be interpreted, at least for high-l modes, as the even degree expansion of $\delta\omega_{\mathrm{local}}/\omega_k$, in which $\delta\omega_{\mathrm{local}}$ is the eigenfrequency that a spherically symmetric model would possess if its radial structure were the same as the structure beneath the point (θ,ϕ) (Jordan, 1978). Only even degrees are present by virtue of the fact that the first 3-j symbol in eqn [149] vanishes for odd values of l''. Thus, self-coupling is only sensitive to even degree structure, that is, the average between pairs of antipodal points. Clearly, this is not the case for traveling waves and represents a shortcoming of splitting theory.

The splitting function leads to a two-stage inversion for three-dimensional structure in which stage 1 is to find the structure coefficients $c^{(k)}_{l''m''}$ that bring data and theoretical spectra into agreement, using as many events and stations as are available. Stage 2 is to determine the structural perturbations to internal heterogeneity of the Earth of degree l'' and m'' needed to match the inferred values of $c^{(k)}_{l''m''}$. Stage 1 of the procedure is nonlinear, owing to the fact that the relation between the synthetics $\mathbf{u}(\mathbf{x}, t)$ and structure coefficients $c^{(k)}_{l''m''}$ involves the exponential $\exp i\mathbf{H}^{(k)}t$. Stage 2, on the other hand, is linear; $c^{(k)}_{l''m''}$ is related to three-dimensional structural perturbations by integrals involving known differential kernels, that is

$$c^{(k)}_{l''m''} = \int_0^a\left(K^{l''}_{\rho}(r)\frac{\delta\rho^{l''m''}(r)}{\rho(r)} + K^{l''}_{\mathrm{P}}(r)\frac{\delta\upsilon_{\mathrm{P}}(r)}{\upsilon_{\mathrm{P}}(r)} + K^{l''}_{\mathrm{S}}(r)\frac{\delta\upsilon^{l''m''}_{\mathrm{S}}(r)}{\upsilon_{\mathrm{S}}(r)}\right)\mathrm{d}r$$
$$+\sum_d \delta h_{l''m''}H^d_{l''} \qquad [151]$$

where $K^{l''}_{\rho}(r)$, $K^{l''}_{\mathrm{P}}(r)$, $K^{l''}_{\mathrm{S}}(r)$ are known kernels for density, compressional velocity, shear wave velocity perturbation and $H^d_{l''}$ for discontinuity perturbations such as crustal thickness and CMB topography. Practical formulas for calculating these kernels are given in Woodhouse (1980a). This is a similar procedure to that commonly employed in surface wave studies, in which one first determines two-dimensional maps of phase velocity, over a range of frequencies, and then uses these to infer the three-dimensional structure perturbations needed to explain the inferred phase velocity maps. The spectral fitting approach using splitting function coefficients $c^{(k)}_{l''m''}$ has been widely applied (e.g., Deuss et al., 2013; Giardini et al., 1987, 1988; He and Tromp, 1996; Masters et al., 2000; Resovsky and Ritzwoller, 1995, 1998; Ritzwoller et al., 1988; Romanowicz and Breger, 2000).

Figure 16 shows an example of data and theoretical spectra using the self-coupling approximation, and including splitting function coefficients estimated from a large collection of data. In the left panel only the splitting effects of rotation and ellipticity are taken into account, whereas in the right panel the estimated splitting function has been used to calculate the synthetic spectra. The effects of ellipticity and rotation can be calculated for the spherical reference model and do not require knowledge of the three-dimensional structure. While rotation and ellipticity lead to some splitting of the singlets (**Figure 16(a)**), further splitting is present which is attributed

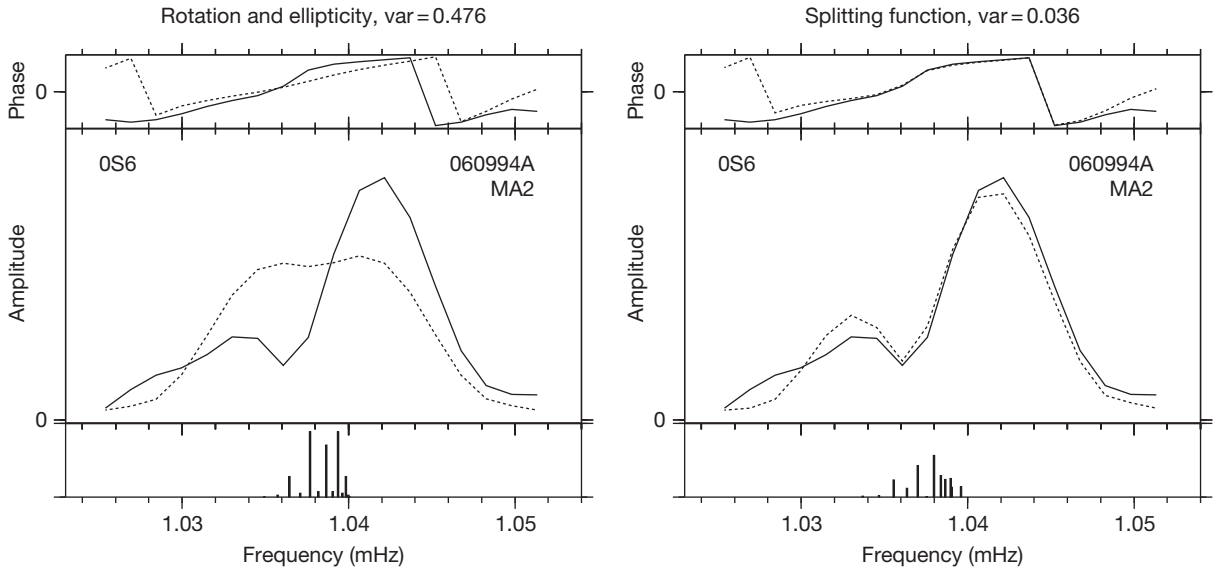

Figure 16 Data and synthetic spectra for ${}_0S_6$ for an earthquake in Bolivia. The time window is 5–70 h. The solid lines are the observed phase (top) and amplitude spectrum (middle), and dashed lines are for the synthetic spectra. In the left diagram, only splitting due to rotation and ellipticity is taken into account, in the right diagram the estimated splitting function is used, reducing the misfit variance ratio for this record from 0.476 to 0.036. The distribution of singlets contributing to the synthetic spectra and their relative excitation amplitudes are indicated at the bottom of each panel. Phase is in the interval $[-\pi, \pi]$. Reproduced from Deuss A, Ritsema J, and van Heijst HJ (2013) A new catalogue of normal-mode splitting function measurements up to 10 mHz. *Geophysical Journal International* 193: 920–937.

to three-dimensional structure and can be accounted for by using the splitting function coefficients in the calculation of the theoretical spectra (**Figure 16(b)**). The distribution of singlets and their excitations is known only by virtue of the inversion itself. There is no possibility here of resolving the singlets in individual spectra, but by modeling a large collection of spectra, for many events and stations, the underlying singlet distribution is unmasked. This example illustrates the fact that there are large differences between data and synthetics prior to estimating the splitting function coefficients, indicating that long-period spectra represent a rich source of information about the Earth's three-dimensional structure.

Figure 17 shows splitting function maps (i.e., using eqn [150]) which are measured by nonlinear inversion of large numbers of spectra such as shown in **Figure 16**. This is stage one of the inversion procedure. The top panel (**Figure 17(a)**) shows mode ${}_1S_{14}$ which is sensitive to shear wave velocity in most of the mantle and peaks in compressional velocity sensitive at the CMB; this mode is almost a Stoneley mode. The observed splitting function for ${}_1S_{14}$ shows higher frequencies in the 'ring around the Pacific,' which is also predicted for the mantle tomographic model S40RTS (Ritsema et al., 2011). These higher frequencies are due to higher velocity anomalies which are found in tomographic models in the regions of the subduction zones around the Pacific. Mode ${}_2S_{12}$ (**Figure 17(b)**) is mainly sensitive to upper mantle shear wave velocity, and is very well predicted by mantle shear wave velocity model S40RTS. Mode ${}_5S_4$ (**Figure 17(c)**) is predominantly sensitive to compressional velocity, and is less well predicted by shear wave velocity model S40RTS. Finally, mode ${}_{13}S_2$ (**Figure 17(d)**) is sensitive to the inner core, and displays strong zonal splitting (i.e., higher frequency anomalies near the poles and low frequency anomaly along the equator). This signature is not predicted by mantle models alone and requires inner core anisotropy (e.g., Woodhouse et al., 1986).

The splitting function approach has been used in inversions for tomographic velocity models (Ishii and Tromp, 1999; Li et al., 1991; Resovsky and Ritzwoller, 1999). Some recent tomographic shear wave velocity models, such as S20RTS and S40RTS (Ritsema et al., 1999, 2011), make use of splitting functions in addition to body wave, surface wave, and overtone data to provide improved constraints on the low degree structure. Splitting functions have also been used in the discovery of inner core anisotropy (Woodhouse et al., 1986), its hemispherical variation (Deuss et al., 2010) and have provided constraints on the possible rotation of the inner core (Laske and Masters, 1999; Sharrock and Woodhouse, 1998).

1.03.8.3 Normal Mode Coupling

The fact that in the self-coupling approximation seismic spectra depend only upon the *even* spherical harmonic degrees of heterogeneity points to a shortcoming of the theory. Since spherical harmonics of even degree are symmetric under point reflection in the center of the Earth, self-coupling theory predicts that the seismic spectra depend only upon the average structure between pairs of antipodal points. Thus, the interaction, or coupling, of modes must be a key effect for understanding wave phenomena that do not have this symmetry property. **Figure 18** shows the combined dispersion diagrams for spheroidal and toroidal modes at low frequencies ($f \leq 3$ MHz), an expanded version of the lower left corner of the dispersion diagrams in **Figures 9** and **10**. Many modes of different branches or even type (e.g., spheroidal or toroidal) have very similar frequencies, which leads to 'resonance' between the singlets of the different modal multiplets; we call

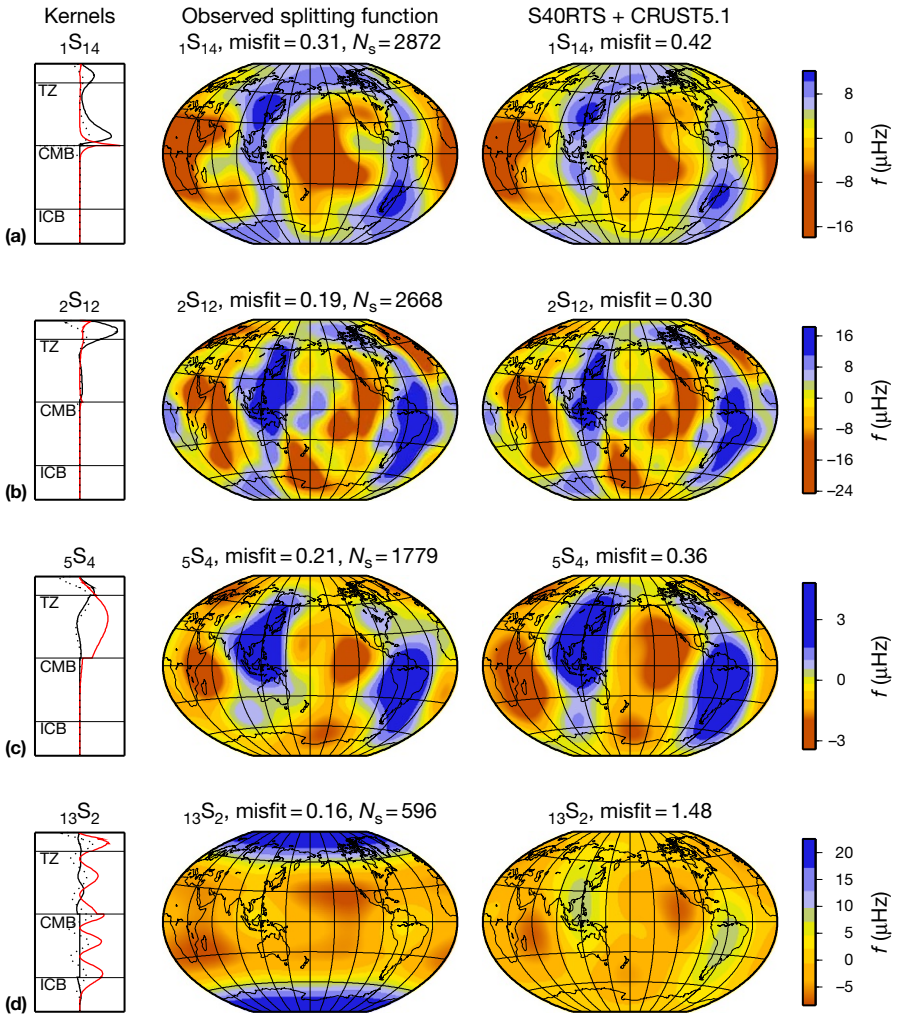

Figure 17 Observed splitting function maps and predictions for mantle model S20RTS. N_s gives the total number of spectra used for the splitting function measurement. The misfit is calculated between the observed spectra and theoretical spectra and is found to be much smaller using the observed splitting functions instead of the predictions for the S40RTS mantle shear wave velocity model (Ritsema et al., 2011) and crustal model CRUST5.1. The left panels show the sensitive kernels for each mode, where red is υ_p, solid black is υ_s, and dashed is density. Reproduced from Deuss A, Ritsema J, and van Heijst HJ (2013) A new catalogue of normal-mode splitting function measurements up to 10 mHz. *Geophysical Journal International* 193: 920–937.

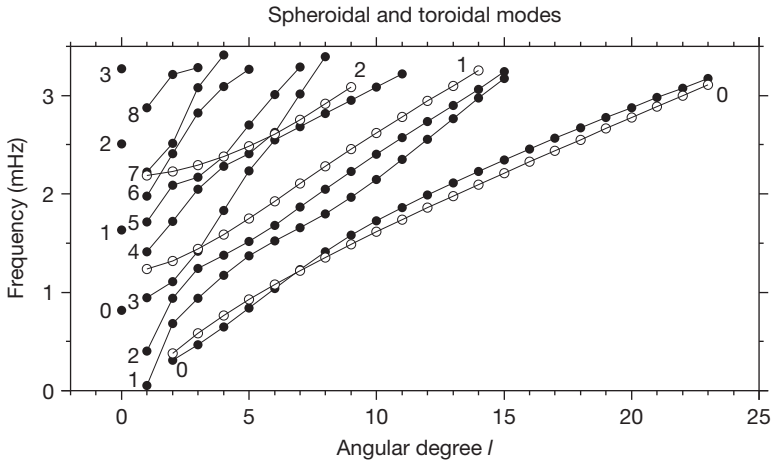

Figure 18 Eigenfrequencies of spheroidal (black circles) and toroidal multiplets (white circles) below 3 mHz for the preliminary reference model (PREM, Dziewonski and Anderson, 1981). A multiplet with angular order l consists of $2l+1$ singlets with azimuthal order $m = -l, -l+1, \cdots, l-1, l$. The branches are labeled by their overtone number n (left spheroidal, right toroidal), the fundamental mode branch is $n = 0$.

this effect *cross-coupling* in seismology. Coupling between modes allows for sensitivity to both even and odd degree structure. Two spheroidal modes ${}_nS_l$, ${}_{n'}S_{l'}$ will be sensitive to structure of degree $|l-l'| \le l'' \le |l+l'|$, and requiring that $l+l'+l''$ is even. So, if $l+l'$ is odd, there will be sensitivity to odd-degree structure. And if $l+l'$ is even (and the special case of self-coupling when $l+l'$), then there will only be sensitivity to even degree structure. The same holds for pairs of toroidal modes. Pairs of spheroidal and toroidal modes also couple due to heterogeneity of degree $|l-l'|+1 \le l'' \le |l+l'|-1$, and requiring that $l+l'+l''$ is odd. Additional coupling exists due to the Coriolis force and ellipticity, which both couple pairs of spheroidal and toroidal modes which differ by one in angular order, that is, ${}_nS_l - {}_{n'}T_{l'\pm1}$. Ellipticity also couples same type modes which differ in angular order by zero or two. Ellipticity coupling can also be seen as special case of $l''=2$ structure.

The theory can be straightforwardly extended to include the coupling of groups of modes. The resulting method is known as *quasi degenerate perturbation theory* (Dahlen, 1969; Luh, 1973, 1974; Woodhouse, 1980a), or *group coupling*. A small group of multiplets $\{k_1, k_2, k_3, \ldots\}$, close in frequency, is selected, and the eigenvalue problem is reduced to that for the matrix obtained from $\mathbf{C}(\omega)$ by selecting only the blocks corresponding to the chosen multiplets. This problem can then be linearized in $\delta\omega$, relative to a fiducial frequency in the chosen band, in much the same way as in the case of self-coupling, outlined above, the resulting matrix eigenvalue problem being of dimension $(2l_1+1)+(2l_2+1)+(2l_3+1)+\cdots$ (**Figure 15**). The selected group of modes is said to form a *super-multiplet*. Resovsky and Ritzwoller (1995) have generalized the notion of the splitting function and structure coefficients to include coupling between pairs of multiplets, so that $c^{(k)}_{l''m''}$ becomes $c^{(k_1k_2)}_{l''m''}$ and estimates have been made of such coefficients from seismic spectra (see, e.g., Deuss et al., 2013; Resovsky and Ritzwoller, 1998). While these have lead to odd-degree splitting function coefficients, they have not yet been included in tomographic inversions. Of particular interest, though, is the observation of hemispherical variations in inner core anisotropy (a type of odd-degree structure) which has been made using cross-coupling between pairs of inner core sensitive and inner core confined modes (Deuss et al., 2010).

The *self-coupling* and *group coupling* techniques depend upon the assumption that further cross-coupling is not needed to approximate the complete solution, which as we have shown, includes coupling between all multiplets. Of course full coupling calculations cannot be done for a truly infinite set of modes, but it is feasible at low frequencies to include coupling between all multiplets below a specified frequency. We shall call this *full coupling*. Deuss and Woodhouse (2001) have compared the different approximations used in computing normal mode spectra, and have found that *self-coupling* and *group coupling* can be a poor approximation to *full coupling*, indicating that a more complete version of the theory will need to be used in the future as it is desired to constrain the three-dimensional distribution of parameters, such as density, attenuation, and mantle anisotropy, on which the spectra depend more subtly.

Figure 19 shows a comparison between data and spectra calculated using *self-coupling* with those resulting from a *full coupling* calculation in which the coupling of all 140 modes up to 3 mHz has been included (see Deuss and Woodhouse, 2001, for details of the calculation). The spheroidal modes are clearly seen, and there is also signal for toroidal mode ${}_0T_{10}$ on the vertical component, which is due to Coriolis coupling. In the self-coupling calculation ${}_0T_{10}$ is not seen, but it appears in the full coupling calculation which includes Coriolis coupling between spheroidal mode ${}_0S_9$ and toroidal mode ${}_0T_{10}$. There is reasonable agreement between the data and full coupling synthetics, but the differences between data and synthetics are comparable to the difference between the *self-coupling* and *full coupling* synthetics. It may be expected that *group coupling* would be justified, and that coupling among wide bands of modes can be ignored. However, coupling on groups still shows significant differences compared to *full-coupling* (see **Figure 20**).

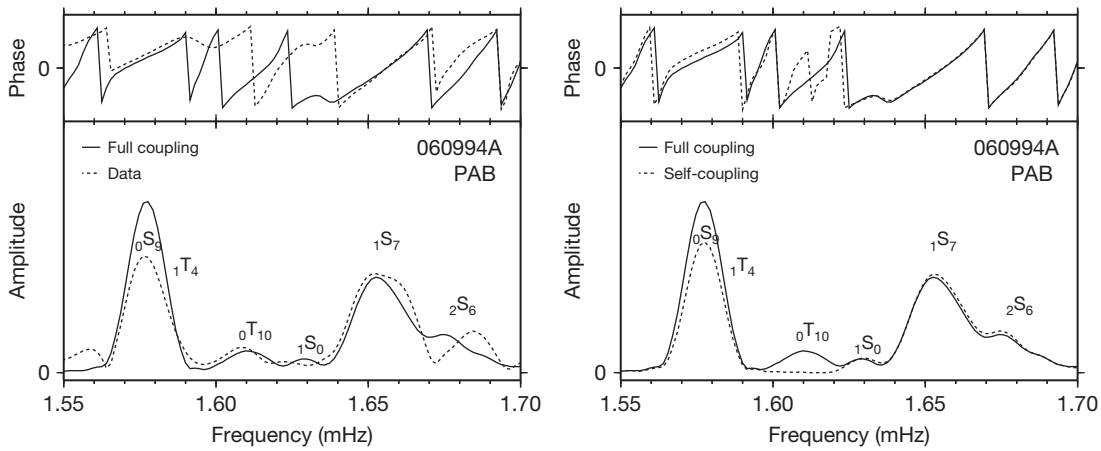

Figure 19 Data and synthetics for modes ${}_0S_9$, ${}_1T_4$, ${}_0T_{10}$, ${}_1S_0$, ${}_1S_7$, and ${}_2S_6$ at station PAB for an earthquake in Bolivia. The time window is 5–45 h. The differences between full coupling and self-coupling are similar to the differences between the data and full coupling and are of the same order as the differences that one would attempt to model. This indicates that full coupling is essential in future attempts to model inhomogeneous structure. Reproduced from Deuss A and Woodhouse JH (2001) Theoretical free oscillation spectra: The importance of wide band coupling. *Geophysical Journal International* 146: 833–842.

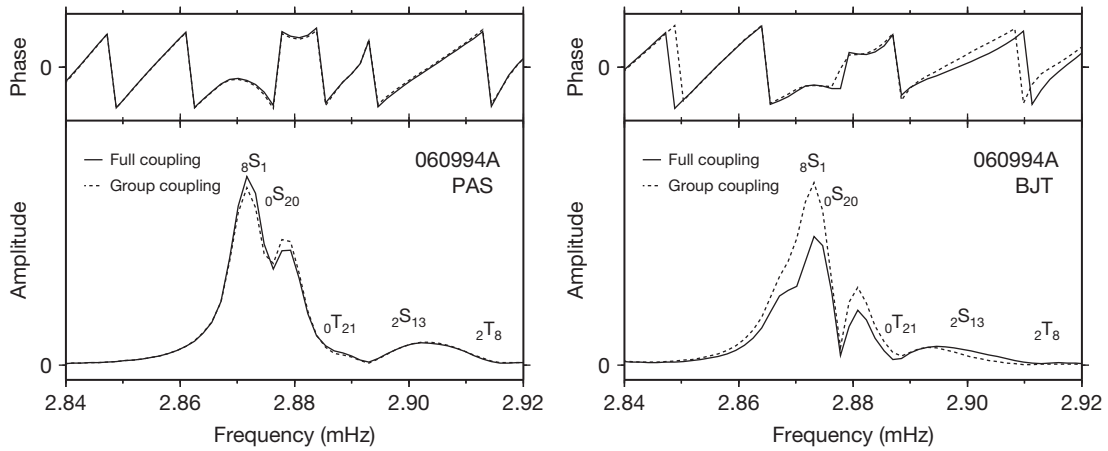

Figure 20 Synthetics for modes $_2S_{13}$, $_0T_{21}$, $_0S_{20}$, $_8S_1$, and $_2T_8$ for stations PAS and BJT of the Bolivia event of 9 June 1994. The time window is 5–80 h. All modes in the frequency interval shown were allowed to couple for the group coupling calculations; the full coupling calculation includes all modes up to 3 mHz. Reproduced from Deuss A and Woodhouse JH (2001) Theoretical free oscillation spectra: the importance of wide band coupling. *Geophysical Journal International* 146: 833–842.

In principle, normal mode spectra can be inverted directly to derive tomographic models, avoiding the intermediate step of estimating the splitting function coefficients (Durek and Romanowicz, 1999; Hara and Geller, 2000; Kuo and Romanowicz, 2002; Li et al., 1991). This leads to a one-step inversion procedure in which model parameter adjustments that enable the data and theoretical spectra to be brought into agreement are sought directly. This scheme has the advantage that the *full coupling* approach can be used for the solution of the forward problem and for calculations of the derivatives needed for formulating the inverse problem. Of course, it has the disadvantage that a nonlinear inverse problem needs to be solved within a large model space, rather than being able to restrict the nonlinear stage of inversion to the much smaller number of parameters represented by splitting functions. The calculations are also much more burdensome in terms of computer time and memory. This means that the splitting function technique is still largely the preferred method in spectral fitting studies; however, to investigate the large regions of the spectrum where wide-band coupling is expected to be significant, a final stage inversion involving full coupling will be needed.

Significant theoretical work has been directed toward developing methods able to give accurate splitting and coupling results using a practicable amount of computer time and memory (e.g., Lognonne, 1991; Lognonne and Romanowicz, 1990; Park, 1990). Deuss and Woodhouse (2004) have developed a technique for solving the *full coupling* generalized eigenvalue problem ([137], [140]) by an iterative technique, not requiring the eigenvalue decomposition of very large matrices, which is well suited to the accurate modeling of small spectral segments. The first iteration of this technique is similar to the *subspace projection method* of Park (1990), which similarly aims to approximate full coupling effects while avoiding the need to find the eigenvectors and eigenvalues of very large matrices. Al-Attar et al. (2012) developed an iterative version of the direct solution method which also does not require the decomposition of very large matrices and has been shown to be very effective in coupling large groups of normal modes.

1.03.8.4 Centroid-Moment Tensor Method

A very useful application of normal mode theory is the centroid moment tensor method, which uses waveform data to derive both the source mechanism of an earthquake and also the hypocentral coordinates of the 'best point source' at a given frequency. This method was introduced by Dziewonski et al. (1981) and applied on a larger scale by Dziewonski and Woodhouse (1983a). Consider the moment tensor as defined in eqn [31]. The moment tensor approach depends on finding the best point source, which is called the *centroid location* and the corresponding *centroid time* for which the first spatial and temporal moments are minimized in the least squares sense. In this case, we can rewrite the synthetic seismogram [119] as

$$u_k(\mathbf{x}, t) = \sum_{i=1}^{6} \psi_{ki}(\mathbf{x}, \mathbf{x}_s, t) * f_i(t) \qquad [152]$$

where $f_i(t)$ represent the six independent components of the moment rate tensor, that is, $f_1 = M_{rr}$, $f_2 = M_{\theta\theta}$, $f_3 = M_{\phi\phi}$, $f_4 = M_{r\theta}$, $f_5 = M_{r\phi}$, $f_6 = M_{\theta\phi}$. The receiver is at position $\mathbf{x}$ and the source at $\mathbf{x}_s = (\theta_S, \phi_s, r_s)$. The excitation kernels ψ_{ik} depend on the properties of the Earth in terms of the eigenfunctions and eigenvalues of the normal modes and represent synthetic seismograms corresponding to the individual components of the moment tensor of unit amplitude. If the earthquake location is fixed, then eqn [152] becomes linear in the six moment tensor components f_i. Hence, the starting solution is obtained by solving eqn [152], for a starting source position $\mathbf{x}_s$ determined from, for example, first P and S arrivals. Having found the initial estimate of the seismic moment tensor $f_i^{(0)}$, the process is then iterated using

$$u_k - u_k^{(0)} = b_k \delta r_s + c_k \delta\theta_s + d_k \delta\phi_s + e_k \delta t_s + \sum_{i=1}^{6} \psi_{ki}^{(0)} * \delta f_i \qquad [153]$$

where b_k, c_k, d_k, e_k are the partial derivatives with respect to the hypocentral coordinates. $u_k^{(0)}$ is the theoretical displacement calculated for the starting source coordinates. The theory so far is standard, but the special point is that the kernels will be

calculated using normal mode summation, see the appendix of Dziewonski et al. (1981) for specific formula. There are ten unknowns to be determined, that is, the centroid time, the three centroid location parameters, and the six moment tensor components. The process keeps on being repeated until convergence is achieved.

Dziewonski et al. (1981) initially developed the method for $45 < T < 60$ s long-period body waves. The method was then extended by Dziewonski and Woodhouse (1983a) to include long-period surface waves with $135 < T < 150$ s. It was modified by Woodhouse and Dziewonski (1984) to include simultaneous inversion for three-dimensional Earth models by using the great circle approximation (see **Section 1.03.8.5**). The method was then enhanced again in 2004 to incorporate intermediate period surface waves (Ekstrom et al., 2012). The CMT mechanisms are now determined on a routine scale for all earthquakes with moments as small as $M_w = 5.0$, with results published on the website: http://www.globalcmt.org.

1.03.8.5 Great Circle Approximation

The development of practical and less time-consuming methods has so far been most successful in the long-period waveform and surface wave approach. Woodhouse and Dziewonski (1984) developed the elegant path-average great circle approximation using phase integrals along the minor and major arcs. Consider the phase ψ of a surface wave with frequency ω. We can then approximate perturbations to the phase because of lateral heterogeneity by

$$\delta\psi = \int_0^t \delta\omega_{\text{local}}\,\mathrm{d}t \qquad [154]$$

where the integration is with respect to the group travel time along the great circle path between the source and receiver. The local perturbation in eigenfrequency $\delta\omega_{\text{local}}$ is defined using the notation of Jordan (1978)

$$\delta\omega_{\text{local}}(\theta, \phi) = k\delta c(\theta, \phi) \qquad [155]$$

where δc is the perturbation to the phase velocity and the wave number k is given by eqn [121]. Woodhouse and Dziewonski (1984) showed that the phase perturbations for both odd and even orbits may be mimicked in terms of a fictitious frequency shift $\delta\hat{\omega}$ and fictitious perturbation in epicentral distance $\delta\theta$, that is

$$\delta\hat{\omega} = \frac{1}{T}\int_0^T \delta\omega_{\text{local}}\,\mathrm{d}t = \text{great circle average} \qquad [156]$$

$$\delta\theta = \frac{t_1}{\left(l + \frac{1}{2}\right)}(\delta\hat{\omega} - \delta\widetilde{\omega}) \qquad [157]$$

where

$$\delta\widetilde{\omega} = \frac{1}{t_1}\int_0^{t_1} \delta\omega_{\text{local}}\,\mathrm{d}t = \text{minor arc average} \qquad [158]$$

and T is the great circle group travel time and t_1 is the minor arc travel time. This result is in agreement with Jordan (1978) that the apparent frequency shift is the great circle average of $\delta\omega_{\text{local}}$, and that the apparent distance shift depends upon the difference between the great circle and minor circle averages. Along branch coupling (i.e., between modes with the same overtone number n) is automatically included by taking the difference between the major and minor arc mode frequency shifts, and thus this method also provides information on odd-degree structure in addition to even-degree structure. It gives a simple way of calculating seismograms, which incorporate the effects of phase delays along incomplete arcs, by replacing the frequency of each mode and the epicentral distance of each path by their perturbed equivalents. It should be noted that this approximation only incorporates an approximation to the phase perturbations and completely omits the consideration of amplitudes. Nevertheless, this simplified version of ray theory is a very useful one for waveform inversion and has been applied in many tomographic studies of mantle structure to both surface wave and long-period body wave data. It is a good approximation for the fundamental mode and low overtones, which constitute a major part of the long-period body wave signal.

Figure 21 illustrates the improvement in phase match after a joint inversion for the CMT source and three-dimensional Earth structure using the great-circle approximation. Performing a combined inversion for sources and structure has great advantages and prevents trade-off between the recovered structure after tomographic inversion and the use of a simplified (i.e., 1D) model for the source inversion. Performing the CMT inversion jointly with a structure inversion leads to a significant improvement in phase match between data and synthetics (**Figure 21**). Procedures for performing a combined inversion are outlined in Woodhouse and Dziewonski (1989) and Valentine and Woodhouse (2010).

The shortcoming of the great circle approximation is that it is not very accurate for direct body wave phases, since it predicts that the observed seismogram depends only upon the horizontally averaged structure. The great circle, or path-average approximation, was extended by Li and Tanimoto (1993) and Li and Romanowicz (1995) to include across branch-coupling (i.e., between modes with different overtone number n), which asymptotically corrects the body wave phases. In practise, nonlinear asymptotic coupling theory splits the synthetic seismogram calculation into two parts. The first part is just the great circle approximation, where the frequency and epicentral distance are replaced by their perturbed equivalents, and then a second part is added which represent the cross-branch mode coupling effects, see Romanowicz et al. (2008) for details. This method has been successfully applied to whole mantle tomography using waveforms.

1.03.9 Concluding Discussion

The normal mode formalism provides a well developed theoretical framework for the calculation of theoretical seismograms in both spherically symmetric and three-dimensional Earth models. For spherically symmetric models the ability to simply and quickly calculate complete theoretical seismograms plays an important role in the formulation and solution of many seismological problems involving both surface waves and long-period body waves. In the three-dimensional case,

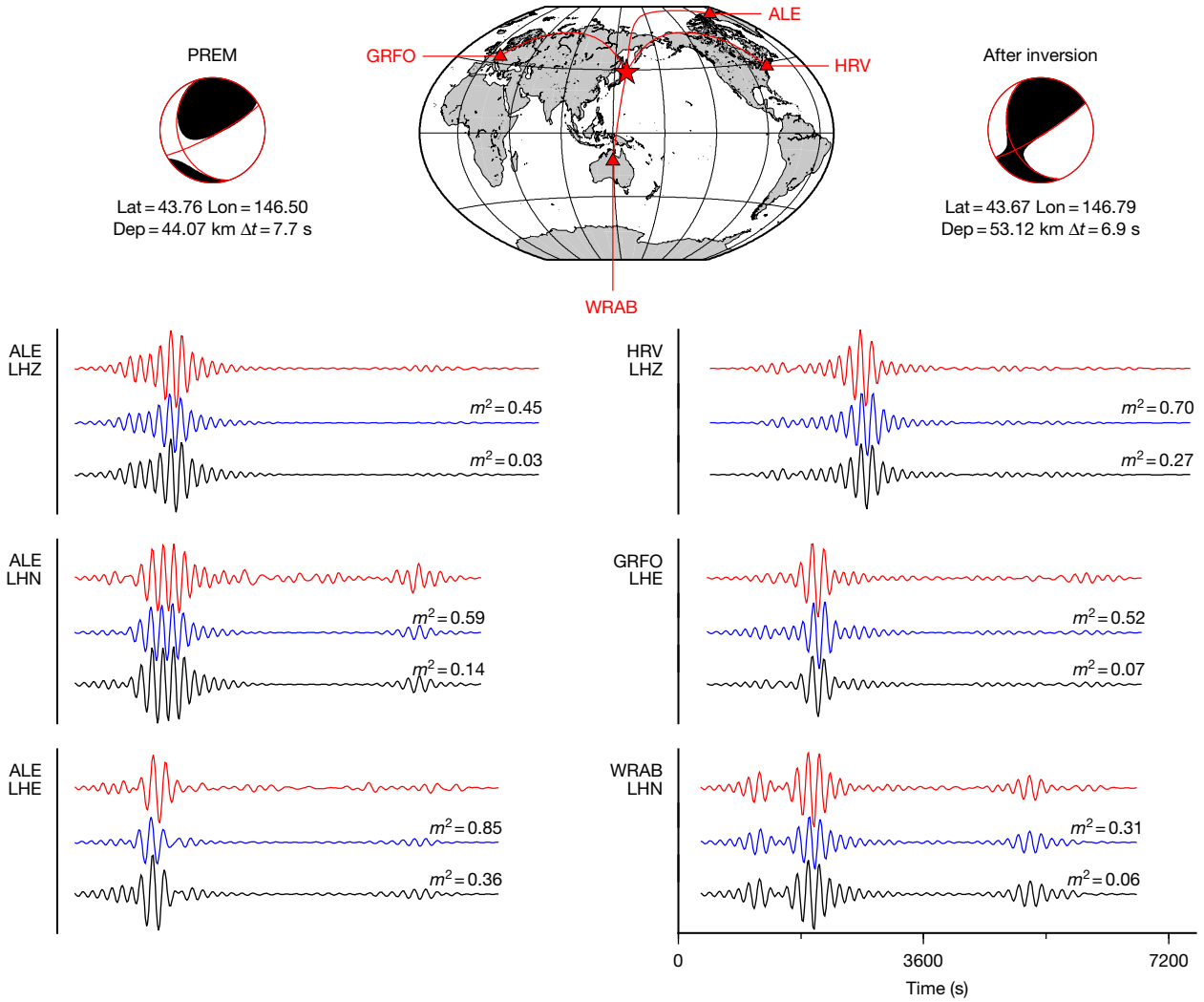

Figure 21 The effects of combining path-average heterogeneity and source determination inversion. One hundred and forty-six long-period surface wave seismograms ($135 < T < 150$) recorded for the 21st January 2000 Kuril Islands event (GCMT code 012800B; star on map) were inverted for the optimal centroid-moment-tensor source description. Six representative data traces are shown, in red, corresponding to stations marked with triangles on map. Inversion in PREM yields best-fitting source shown above left, with overall misfit $m^2 = |d - s|^2/|d|^2 = 0.415$, and waveforms shown in blue. If inversion for path-average structure perturbations is also performed, the source shown above right can be obtained, with $m^2 = 0.272$, and waveforms shown in black. Misfit values for individual paths are given above synthetic traces. We observe that incorporating structural corrections through the path-average approximation allows a significant improvement in agreement between data and synthetics, and that the details of the Earth model affect the results of CMT inversion (see, e.g., Valentine and Woodhouse, 2010; Valentine and Trampert, 2012). Figure courtesy of Andrew Valentine.

the theory of mode coupling is too cumbersome to be applied in full, but it enables a number of useful approximations to be developed and tested. The increasing capacity in high performance computing means that it becomes possible to develop and test increasingly more complete implementations of the fully coupled theory. Progress on fully numerical solutions for seismic wave fields in realistic three-dimensional spherical models (Komatitsch and Tromp, 2002a,b), while it is providing a new and invaluable tool in many areas of global seismology, has not yet made it possible to calculate accurate very long-period spectra. In part this is because a way has not (yet?) been found to fully implement self-gravitation in the spectral element method, and in part because the small time step needed in finite difference and spectral element calculations leads to very long execution times; also, there are very stringent limits on the tolerable amount of numerical dispersion in the solution.

Long-period modal spectra constitute a rich source of information on long wavelength heterogeneity, studies to date, we believe, having only scratched the surface. To realize the potential of this information will require large-scale coupling calculations or, possibly, other methods for calculating very long-period wave fields yet to be developed. This will make it possible to bring modal spectral data increasingly to bear on furthering our understanding of the Earth's three-dimensional structure.

Acknowledgments

We thank Barbara Romanowicz and Adam Dziewonski for thoughtful reviews which helped improve the manuscript. We also thank Andrew Valentine for making Figure 21 illustrating the great circle approximation and CMT method. AD has been funded by the European Research Council under the European Community's Seventh Framework Programme (FP7/2-7-2013)/ERC grant agreement 204995 and a Philip Leverhulme Prize.

References

Abramowitz M and Stegun IA (1965) *Handbook of Mathematical Functions*. New York: Dover.

Al-Attar D, Woodhouse JH, and Deuss A (2012) Calculation of normal mode spectra in laterally heterogeneous earth models using an iterative direct solution method. *Geophysical Journal International* 189: 1038–1046.

Backus GE and Gilbert F (1967) Numerical applications of a formalism for geophysical inverse problems. *Geophysical Journal of the Royal Astronomical Society* 13: 247–276.

Backus GE and Mulcahy M (1976) Moment tensors and other phenomenological descriptions of sesimic sources, i. continuous displacements. *Geophysical Journal of the Royal Astronomical Society* 46: 341–362.

Biot MA (1965) *Mechanics of Incremental Deformation*. New York: John Wiley.

Brune JN (1964) Travel times, body waves and normal modes of the earth. *Bulletin of the Seismological Society of America* 54: 2099–2128.

Brune JN (1966) *p* and *s* wave travel times and spheroidal normal modes of a homogeneous sphere. *Journal of Geophysical Research* 71: 2959–2965.

Burridge R and Knopoff L (1964) Body force equivalents for seismic dislocations. *Bulletin of the Seismological Society of America* 54: 1875–1888.

Chapman CH and Woodhouse JH (1981) Symmetry of the wave equation and excitation of body waves. *Geophysical Journal of the Royal Astronomical Society* 65: 777–782.

Dahlen FA (1968) The normal modes of a rotating, elliptical earth. *Geophysical Journal of the Royal Astronomical Society* 16: 329–367.

Dahlen FA (1969) The normal modes of a rotating, elliptical earth, II, Near resonant multiplet coupling. *Geophysical Journal of the Royal Astronomical Society* 18: 397–436.

Dahlen FA and Tromp J (1998) *Theoretical Global Seismology*. Princeton, NJ: Princeton University Press.

Deuss A, Irving JCE, and Woodhouse JH (2010) Regional variation of inner core anisotropy from seismic normal mode observations. *Science* 328(5981): 1018–1020.

Deuss A, Ritsema J, and van Heijst HJ (2013) A new catalogue of normal-mode splitting function measurements up to 10 mHz. *Geophysical Journal International* 193: 920–937.

Deuss A and Woodhouse JH (2001) Theoretical free oscillation spectra: The importance of wide band coupling. *Geophysical Journal International* 146: 833–842.

Deuss A and Woodhouse JH (2004) Iteration method to determine the eigenvalues and eigenvectors of a target multiplet including full mode coupling. *Geophysical Journal International* 159: 326–332.

Durek JJ and Romanowicz B (1999) Inner core anisotropy inferred by direct inversion of normal mode spectra. *Geophysical Journal International* 139: 599–622.

Dziewonski A and Anderson D (1981) Preliminary reference earth model. *Physics of the Earth and Planetary Interiors* 25: 297–356.

Dziewonski AM, Chou T-A, and Woodhouse JH (1981) Determination of earthquake source parameters from waveform data for studies of global and regional seismicity. *Journal of Geophysical Research* 86(B4): 2825–2852.

Dziewonski AM and Gilbert F (1971) Solidity of the inner core of the earth inferred from normal mode observations. *Nature* 234: 465–466.

Dziewonski AM and Woodhouse JH (1983a) An experiment in systematic study of global seismicity: Centroid-moment tensor solutions for 201 moderate and large earthquakes of 1981. *Journal of Geophysical Research* 88(B4): 3247–3271.

Dziewonski AM and Woodhouse JH (1983b) Studies of the seismic source using normal mode theory. In: Kanamori H and Boschi E (eds.). *Earthquakes: Observation, Theory and Interpretation, Proc. "Enrico Fermi" Int. Sch. Phys*, vol. LXXXV, pp. 45–137. Amsterdam: North Holland.

Edmonds AR (1960) *Angular Momentum and Quantum Mechanics*. Princeton, NJ: Princeton University Press.

Ekstrom G, Nettles M, and Dziewonski A (2012) The global CMT project 2004–2010: Centroid-moment tensors for 13,017 earthquakes. *Physics of the Earth and Planetary Interiors* 200–201: 1–9.

Eshelby JD (1957) The determination of the elastic field of an ellipsoidal inclusion, and related problems. *Proceedings of the Royal Society of London, Series A* 241: 376–396.

Friederich W and Dalkolmo J (1995) Complete synthetic seismograms for a spherically symmetric earth by numerical computation of the green's function in the frequency domain. *Geophysical Journal International* 122: 537–550.

Fuchs K and Muller G (1971) Computation of synthetic seismograms by the reflectivity method and comparison with observations. *Geophysical Journal of the Royal Astronomical Society* 23: 417–433.

Giardini D, Li X-D, and Woodhouse JH (1987) Three dimensional structure of the Earth from splitting in free oscillation spectra. *Nature* 325: 405–411.

Giardini D, Li X-D, and Woodhouse JH (1988) Splitting functions of long-period normal modes of the earth. *Journal of Geophysical Research* 93: 13716–13742.

Gilbert F (1971) Excitation of normal modes of the earth by earthquake sources. *Geophysical Journal of the Royal Astronomical Society* 22: 223–226.

Gilbert F (1980) An introduction to low frequency seismology. In: Dziewonski AM and Boschi E (eds.). *Physics of the Earth's Interior, Proc. "Enrico Fermi" Int. Sch. Phys*, vol. LXXVIII, pp. 41–81. Amsterdam: North Holland.

Gilbert F and Backus GE (1966) Propagator matrices in elastic wave and vibration problems. *Geophysics* 31: 326–333.

Gilbert F and Dziewonski AM (1975) An application of normal mode theory to the retrieval of structural parameters and source mechanisms from seismic spectra. *Philosophical Transactions of the Royal Society of London, Series A* 278: 187–269.

Hara T and Geller R (2000) Simultaneous waveform inversion for three-dimensional earth structure and earthquake source paremeters considering a wide range of modal coupling. *Geophysical Journal International* 142: 539–550.

He X and Tromp J (1996) Normal-mode constraints on the structure of the earth. *Journal of Geophysical Research* 101: 20053–20082.

Hudson JA (1969) A quantitative evaluation of seismic signals at teleseismic distances, i: Radiation from point sources. *Geophysical Journal of the Royal Astronomical Society* 18: 233–249.

Ishii M and Tromp J (1999) Normal-mode and free-air gravity constraints on lateral variations in velocity and density of the Earth's mantle. *Science* 285: 1231–1236.

Jordan TH (1978) A procedure for estimating lateral variations from low-frequency eigenspectra data. *Geophysical Journal of the Royal Astronomical Society* 52: 441–455.

Kanamori H and Anderson DL (1977) Importance of physical dispersion in surface wave and free oscillation problems: Review. *Reviews of Geophysics and Space Physics* 15: 105–112.

Komatitsch D and Tromp J (2002a) Spectral-element simulations of global seismic wave propagation-I. Validation. *Geophysical Journal International* 149: 390–412.

Komatitsch D and Tromp J (2002b) Spectral-element simulations of global seismic wave propagation-II. 3-D models, oceans, rotation, and self-gravitation. *Geophysical Journal International* 150: 303–318.

Kuo C and Romanowicz B (2002) On the resolution of density anomalies in the Earth's mantle using spectral fitting of normal-mode data. *Geophysical Journal International* 150: 162–179.

Lapwood ER and Usami T (1981) *Free Oscillations of the Earth*. Cambridge: Cambridge University Press.

Laske G and Masters G (1999) Limits on differential rotation of the inner core from an analysis of the Earth's free oscillations. *Nature* 402: 66–69.

Li X and Romanowicz B (1995) Comparison of global waveform inversions with and without considering cross-branch modal coupling. *Geophysical Journal International* 121: 695–709.

Li X-D, Giardini D, and Woodhouse JH (1991) Large scale three dimensional even degree structure of the earth from splitting of long period normal modes. *Journal of Geophysical Research* 96: 551–577.

Li X-D and Tanimoto T (1993) Waveforms of long-period body waves in a slightly aspherical earth model. *Geophysical Journal International* 112: 92–102.

Lognonne P (1991) Normal modes and seismograms in an anelastic rotating Earth. *Journal of Geophysical Research* 96: 20309–20319.

Lognonne P and Romanowicz B (1990) Modelling of coupled normal modes of the Earth – The spectral method. *Geophysical Journal International* 102: 365–395.

Love AEH (1911) *Some Problems in Geodynamics*. Cambridge and New York: Cambridge University Press.

Love AEH (1927) *A Treatise on the Theory of Elasticity*. Cambridge and New York: Cambridge University Press.

Luh PC (1973) Free oscillations of the laterally inhomogeneous earth: Quasi-degenerate multiplet coupling. *Geophysical Journal of the Royal Astronomical Society* 32: 187–202.
Luh PC (1974) Normal modes of a rotating, self gravitating inhomogeneous earth. *Geophysical Journal of the Royal Astronomical Society* 38: 187–224.
Masters G, Laske G, and Gilbert F (2000) Matrix autoregressive analysis of free-oscillation coupling and splitting. *Geophysical Journal International* 143: 478–489.
Morse PM and Feshbach H (1953) *Methods of Theoretical Physics*. New York: McGraw Hill.
Park J (1990) The subspace projection method for constructing coupled-mode synthetic seismograms. *Geophysical Journal International* 101: 111–123.
Park J, Song TA, Tromp J, et al. (2005) Earth s free oscillations excited by the 26 December 2004 Sumatra-Andaman earthquake. *Science* 308: 1139–1144.
Pekeris CL and Jarosch H (1958) The free oscillations of the Earth. In: Ewing M, Howell BF Jr., and Press F (eds.) *Contributions in Geophysics in Honor of Beno Gutenberg*, pp. 171–192. New York: Pergamon.
Phinney RA and Burridge R (1973) Representation of the elastic-gravitational excitation of a spherical earth model by generalized spherical harmonics. *Geophysical Journal of the Royal Astronomical Society* 34: 451–487.
Resovsky JS and Ritzwoller MH (1995) Constraining odd-degree earth structure with coupled free-oscillations. *Geophysical Research Letters* 22: 2301–2304.
Resovsky JS and Ritzwoller MH (1998) New and refined constraints on three-dimensional earth structure from normal modes below 3 mHz. *Journal of Geophysical Research* 103: 783–810.
Resovsky JS and Ritzwoller MH (1999) A degree 8 shear velocity model from normal mode observations below 3 mHz. *Journal of Geophysical Research* 104: 993–1014.
Ritsema J, Deuss A, van Heijst HJ, and Woodhouse JH (2011) S40RTS: A degree-40 shear-velocity model for the mantle from new rayleigh wave dispersion, teleseismic traveltime and normal-mode splitting function measurements. *Geophysical Journal International* 184: 1223–1236.
Ritsema J, van Heijst H, and Woodhouse JH (1999) Complex shear wave velocity structure imaged beneath Africa and Iceland. *Science* 286: 1925–1928.
Ritzwoller M, Masters G, and Gilbert F (1988) Constraining aspherical structure with low-degree interaction coefficients: Application to uncoupled multiplets. *Journal of Geophysical Research* 93: 6369–6396.
Romanowicz B (2001) Can we resolve 3D density heterogeneity in the lower mantle? *Geophysical Research Letters* 28: 1107–1110.
Romanowicz B and Breger L (2000) Anomalous splitting of free oscillations: A reevaluation of possible interpretations. *JGR* 105: 21559–21578.
Romanowicz BA, Panning MP, Gung Y, and Capdeville Y (2008) On the computation of long period seismograms in a 3-D earth using normal mode based approximations. *Geophysical Journal International* 175(2): 520–536.
Seliger RL and Whitham GB (1968) Variational principles in continuum mechanics. *Proceedings of the Royal Society of London, Series A* 305: 1–25.
Sharrock DS and Woodhouse JH (1998) Investigation of time dependent inner core structure by analysis of free oscillation spectra. *Earth, Planets and Space* 50: 1013–1018.
Takeuchi H and Saito M (1972) Seismic surface waves. *Methods in Computational Physics* 11: 217–295.
Trampert J, Deschamps F, Resovsky J, and Yuen D (2004) Probabilistic tomography maps chemical heterogeneities throughout the lower mantle. *Science* 306: 853–856.
Tromp J (1993) Support for anisotropy of the Earth's inner core from free oscillations. *Nature* 366: 678–681.
Tromp J and Dahlen FA (1990) Free oscillations of a spherical anelastic earth. *Geophysical Journal International* 103: 707–723.
Valentine AP and Trampert J (2012) Assessing the uncertainties on seismic source parameters: Towards realistic error estimates for centroid-moment-tensor determinations. *Physics of the Earth and Planetary Interiors* 210–211: 36–49.
Valentine AP and Woodhouse JH (2010) Reducing errors in seismic tomography: Combined inversion for sources and structure. *Geophysical Journal International* 180: 847–857.
Ward SN (1980) Body wave calculations using moment tensor sources in spherically symmetric, inhomogeneous media. *Geophysical Journal of the Royal Astronomical Society* 60: 53–66.
Woodhouse JH (1974) Surface waves in a laterally varying layered structure. *Geophysical Journal of the Royal Astronomical Society* 37: 461–490.
Woodhouse JH (1980a) The coupling and attenuation of nearly resonant multiplets in the Earth's free oscillation spectrum. *Geophysical Journal of the Royal Astronomical Society* 61: 261–283.
Woodhouse JH (1980b) Efficient and stable methods for performing seismic calculations in stratified media. In: Dziewonski AM and Boschi E (eds.). *Physics of the Earth's Interior, Proc. "Enrico Fermi" Int. Sch. Phys*, vol. LXXVIII, pp. 127–151. Amsterdam: North Holland.
Woodhouse JH (1983) The joint inversion of seismic waveforms for lateral variations in earth structure and earthquake source parameters. In: Kanamori H and Boschi E (eds.). *Earthquakes: Observation, Theory and Interpretation, Proc. "Enrico Fermi" Int. Sch. Phys*, vol. LXXXV, pp. 366–397. Amsterdam: North Holland.
Woodhouse JH (1988) The calculation of the eigenfrequencies and eigenfunctions of the free oscillations of the Earth and the Sun. In: Doornbos DJ (ed.). *Seismological Algorithms*, pp. 321–370. Academic Press.
Woodhouse JH (1996) Long period seismology and the Earth's free oscillations. In: Boschi E, Ekström G, and Morelli A (eds.) *Seismic Modelling of Earth Structure*, pp. 31–80. Rome: Istituto Nazionale di Geofisica.
Woodhouse JH and Dahlen FA (1978) The effect of a general aspherical perturbation on the free oscillations of the Earth. *Geophysical Journal of the Royal Astronomical Society* 53: 335–354.
Woodhouse JH and Dziewonski AM (1984) Mapping the upper mantle: Three dimensional modelling of earth structure by inversion of seismic waveforms. *Journal of Geophysical Research* 89: 5953–5986.
Woodhouse JH and Dziewonski AM (1989) Seismic modelling of the Earth's large-scale three-dimensional structure. *Philosophical Transactions of the Royal Society A: Mathematical, Physical and Engineering Sciences* 328(1599): 291–308.
Woodhouse JH and Giardini D (1985) Inversion for the splitting function of isolated low order normal mode multiplets. *Eos, Transactions American Geophysical Union* 66: 300.
Woodhouse JH, Giardini D, and Li XD (1986) Evidence for inner core anisotropy from free oscillations. *Geophysical Research Letters* 13: 1549–1552.
Woodhouse JH and Girnius TP (1982) Surface waves and free oscillations in a regionalized earth model. *Geophysical Journal of the Royal Astronomical Society* 68: 653–673.

This page intentionally left blank

1.04 Theory and Observations: Normal Mode and Surface Wave Observations

G Laske, Scripps Institution of Oceanography, University of California San Diego, La Jolla, CA, USA
R Widmer-Schnidrig, Black Forest Observatory, Wolfach, Germany

© 2015 Elsevier B.V. All rights reserved.

1.04.1	**Introduction**	117
1.04.1.1	Free Oscillations	117
1.04.1.2	Surface Waves	118
1.04.1.3	What We See in Seismograms: The Basics	119
1.04.2	**Free Oscillations**	120
1.04.2.1	Modes of a Spherically Symmetric Earth	120
1.04.2.2	Modes of a Heterogeneous Earth	122
1.04.2.2.1	Mode splitting	122
1.04.2.2.2	Mode coupling	126
1.04.2.3	Measuring Mode Observables	128
1.04.2.3.1	Multiplet stripping and degenerate mode frequencies	130
1.04.2.3.2	Singlet stripping and receiver stripping	132
1.04.2.3.3	Retrieving the splitting matrix with the matrix autoregressive technique	133
1.04.2.3.4	Retrieving the splitting matrix with iterative spectral fitting	133
1.04.2.3.5	Observed mode coupling	135
1.04.2.4	Example of a Mode Application: Inner-Core Rotation	136
1.04.2.5	Example of a Mode Application: Earth's Hum	139
1.04.3	**Surface Waves**	141
1.04.3.1	Standing Waves and Traveling Waves	141
1.04.3.2	The Measurement of Fundamental Mode Dispersion	144
1.04.3.2.1	Group velocity	148
1.04.3.2.2	The study of ambient noise	149
1.04.3.2.3	Phase velocity	149
1.04.3.2.4	Time-variable filtering	151
1.04.3.3	Other Surface Wave Observables	152
1.04.3.4	Higher Modes	154
1.04.3.4.1	Higher-mode dispersion and waveform modeling	154
1.04.3.4.2	Love waves and overtones	157
1.04.3.5	Surface Waves and Structure at Depth	157
1.04.3.6	The Validity of the Great-Circle Approximation and Data Accuracy	160
1.04.4	**Concluding Remarks**	160
Acknowledgments		161
References		161

1.04.1 Introduction

1.04.1.1 Free Oscillations

The destructive $M_W = 9.0$, 11 March 2011 Tohoku, Japan, earthquake most certainly raised recent awareness of extremely large earthquakes. And also remembering the $M_W = 9.1$ 26 December 2004 Sumatra–Andaman earthquake and the $M_W = 8.8$ 27 February 2010 Maule, Chile, earthquake, one can easily forget that a seismologist has to wait many years for a great, preferably deep earthquake to occur in order to observe Earth's free oscillations. After all, the last earthquake in this league of 'mega earthquakes' occurred 40 years before the Sumatra–Andaman event: the 'Good Friday' 27 March 1964 Alaska earthquake. It is therefore not surprising that, compared to other seismic studies, free oscillation studies started relatively late last century, after the great $M_W = 9.5$ 22 May 1960 Valdivia, Chile, earthquake. It was not until 1975 – after the analysis of digitized records of the deep, magnitude 8.0 31 July 1970 Colombia earthquake – that enough mode measurements were available to construct the first one-dimensional (1-D), normal-mode derived Earth that could withstand decades of testing as a reference Earth model (REM) (1066A by Gilbert and Dziewonski, 1975). Not much later, great progress was achieved to facilitate the collection of high-quality mode data by installing the global digital seismic network IDA (International Deployment of Accelerometers), a network of LaCoste–Romberg gravimeters that were specifically designed to observe Earth's free oscillations (Agnew et al., 1976, 1986). In the meantime, permanent stations of several other global seismic networks have been upgraded with very broadband seismic sensors – typically Wielandt–Streckeisen STS-1 vault seismometers or Geotech–Teledyne KS-54000 borehole

 http://dx.doi.org/10.1016/B978-0-444-53802-4.00003-8

seismometers – and digital recording units. This includes early networks that were designed to monitor global seismicity and the comprehensive test ban treaty (CTBT), such as the high-gain long-period (HGLP) network (first digitally recording network; Savino et al., 1972), the seismic research observatory (SRO; Peterson et al., 1980), the World-Wide Standardized Seismograph Network (WWSSN; Oliver and Murphy, 1971), and the China Digital Seismograph Network (CDSN; Peterson and Tilgner, 1985). Many of these stations as well as the upgraded IDA network are now part of the US Global Seismic Network (GSN) operated by IRIS (Incorporated Research Institutions for Seismology), but other global networks exist such as the French GEOSCOPE (Romanowicz et al., 1984) and the German GEOFON (Hanka and Kind, 1994). All these and more operate under the umbrella of the international Federation of Digital Seismograph Networks (FDSN; Romanowicz and Dziewonski, 1986). Roughly 25 years into very broadband seismic networks, a normal mode seismologist now can enjoy a more than tenfold increase in high-quality vertical-component long-period seismic records for a given earthquake. But even in the late 1990s – a few years after the deep magnitude 8.2 09 June 1994 Bolivia earthquake provided spectacular spectra – great effort was invested in digitizing the legendary 1970 Colombia records. Before the 26 December 2004 Sumatra–Andaman earthquake, there have been a handful of other great earthquakes since 'Bolivia.' But even the great 23 June 2001 Arequipa, Peru, earthquake, the largest digitally recorded earthquake until then, did not excite the relatively few normal mode observers whose interest lies in unraveling the deep secrets of the inner core (IC). 'Peru' was simply not deep (or great) enough to make some of the modes ring that the observers are interested in. On the other hand, since normal modes involve the vibration of the whole planet, mode observations at a single station readily reveal a wealth of information about Earth structure that no other seismic techniques can provide. Modes are intrinsic low-pass filters of Earth structure. It is relatively easy to collect unbiased estimates of mode observables that constrain the spherical average of Earth as well as long-wavelength perturbations to it. It is therefore not surprising that in the current efforts to remove the more than three-decade-old 'preliminary' from PREM (preliminary reference Earth model, Dziewonski and Anderson, 1981) – the currently still most widely accepted REM of the spherical average – a suitable mode data set for an updated model exists (a 'best-estimate' data set can be obtained from the REM website), while we still struggle to obtain an unbiased body-wave data set.

Normal mode seismology has facilitated other great achievements that we can proudly look back to. For example, the analysis of modes provided the ultimate proof that the IC is solid (Dziewonski and Gilbert, 1971). Normal mode studies were at the forefront to assess Earth's attenuation (Smith, 1972) and to retrieve earthquake moment tensors (Gilbert and Dziewonski, 1975), which has been continued in the faithful delivery of the Harvard centroid moment tensors (CMTs) (Dziewonski et al., 1981) now continued as the 'global CMT project' led by Göran Ekström at Lamont Doherty Earth Observatory (LDEO) (Ekström et al., 2012; www.globalcmt.org) that many colleagues depend on for their own studies. Normal mode studies also were at the forefront to assess Earth's 3-D structure. For example, Jobert and Roult (1978) found early evidence for large-scale lateral variations from free oscillations and surface waves, and Masters et al. (1982) discovered harmonic degree 2 variations in the transition zone that are associated with subducting slabs. The first widely used 3-D models of Earth's upper mantle, M84A and M84C (Woodhouse and Dziewonski, 1984), were obtained using mode theory. Still today, careful analysis of high-precision mode measurements provides crucial clues to answer some of the most fundamental geodynamical questions that remain elusive to other seismic techniques. For example, the analysis of Masters and Gubbins (2003) provided updated estimates of the density jump across the IC boundary, which is relevant to the discussion of the growth rate and the age of the IC. They also argue against a significant overall excess density in the lowermost mantle that was proposed by Kellogg et al. (1999) for locally varying hot abyssal layers for which seismic evidence was presented by Ishii and Tromp (1999). Earth's density structure and the solidity of the IC are best constrained by mode data. Similarly, modes help determine Earth's internal anelastic and anisotropic structure. There are many more aspects where mode data can help out to understand how our planet works. One example is the differential rotation of the IC. Evidence for this was first observed using body-wave data and was initially reported to be between 1° and 3° per year (Song and Richards, 1996; Su et al., 1996) but hotly debated (e.g., Souriau, 1998). As subsequent studies accumulated, this number decreased dramatically and is currently estimated at 1/10 of the initial rate. Mode observations in particular (Laske and Masters, 1999, 2003; Sharrock and Woodhouse, 1998) provided the conclusive constraints to correct the rotation estimates downward.

In the first part of this chapter, the reader gets acquainted with the jargon used in normal mode seismology, some of which requires to summarize the theoretical background that is described in **Chapter 1.02**. We then introduce some of the most commonly used measurement techniques that we have been involved in. Mode analysis involves more than simply reading the peak frequencies and amplitudes from a spectrum. In fact, in most cases, such an approach leads to biased estimates. One also has to bear in mind that the most basic analysis techniques treat modes as being isolated from their neighbors in which case only Earth structure of even-degree symmetry can be retrieved. Earth's rotation and lateral variations cause modes to couple with each other. This complicates mode analysis but also facilitates the assessment of odd-degree structure. This is briefly described.

1.04.1.2 Surface Waves

Surface waves can be understood as a superposition of free oscillations. It is therefore not surprising that many long-period surface wave seismologists analyzed normal modes at some time in their career. With a few exceptions, including very deep earthquakes, fundamental mode surface waves are the largest signal in a seismogram. First-arriving surface wave packets are relatively short and do not require the consistently high signal levels, over several days, as normal modes do. Nor do they require the wait for very large earthquakes. The analysis of surface waves essentially involves the analysis of fundamental modes and the first few overtones, at high frequencies. Surface waves are therefore a natural choice to explore Earth's

crust, upper mantle, and transition zone. Much like in a body-wave study, the analyst collects travel times, but the complication is that these depend on frequency. Rather than a sharp onset, a wave packet is observed that is often likened to a Gaussian packet. The two travel time-equivalent observables of dispersed surface waves are phase velocity, the speed at which a certain point in the waveform travels, and group velocity, the speed at which wave energy or a point on the envelope of the waveform travels. Though both observables constrain structure at depth, they have different dependencies, and ideally one would want to measure both. Group velocity tends to change more significantly with structure at depth, but its measurement errors are also larger than those of phase velocity. On the other hand, source effects on group velocity are relatively small and are usually ignored. Details on earthquake source processes therefore do not have to be known to measure group velocity.

The analysis of surface waves has a major advantage over that of body waves. In the upper mantle, imaging capabilities using body waves are dictated by the distribution of earthquakes and seismic stations. Surface waves travel along the surface between sources and receivers, crossing remote areas and thereby picking up invaluable information about along-path upper-mantle structure that remains elusive to body waves. Like a body-wave arrival, group velocity can be measured on a single wave train recorded at a single station without having to resort to calculating synthetic seismograms that are necessary to measure phase travel times. For this reason, group velocity analysis has seen a wide range of applications in regional seismology, especially in the CTBT community, even before the advent of sophisticated signal processing.

In the second part of this chapter, we first summarize the relationship between normal modes and surface waves. Some of the surface wave observables are described and how they are measured. We touch on the observation of higher modes and discuss the relationship between dispersion and structure at depth, but the reader interested in Earth structure is referred to other contributions in this volume.

1.04.1.3 What We See in Seismograms: The Basics

For moderately large earthquakes, seismograms exhibit a number of wave trains, some of which circled the globe completely before arriving at a station. Figure 1 shows the nomenclature for these wave trains. We distinguish between minor and major arc wave trains that arrive at a station from the source directly or took the long path in the opposite direction. Figure 2 shows an example of a vertical seismic record collected at a station of the GEOSCOPE network. Rayleigh wave trains are usually labeled R, while overtones are often labeled X (e.g., Roult et al., 1986). Love wave trains carry the label G and are observed on the transverse component only, unless Earth's rotation and/or heterogeneity causes strong lateral refraction or, to use the mode analogy, toroidal–spheroidal mode coupling. For large earthquakes with magnitudes typically larger than $M_S = 6.5$, surface waves may be observed as they circle the globe multiple times. At group velocities of about 3.7 km s^{-1}, long-period Rayleigh waves take about 3 h to complete one orbit.

Very large earthquakes can be observed at many global seismic stations with fidelity high enough to discern many

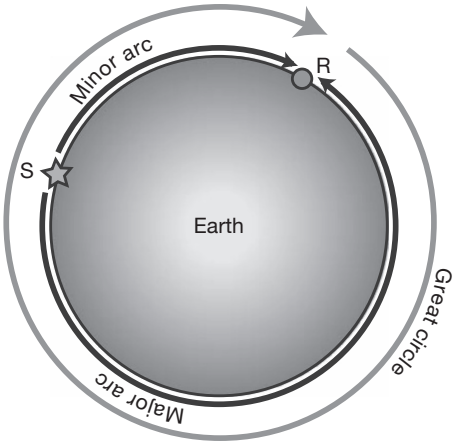

Figure 1 Surface wave paths from source S to receiver R. Paths associated with the shorter distance from the source are minor arc paths (R_1); paths associated with the larger distance are major arc paths (R_2). The number following R is the wave orbit number. The wave orbit number advances by two when successive wave trains include a complete great circle (e.g., R_3 and R_5 for minor arc paths).

wave trains in a record section. Figure 3 shows the tsunami-generating 2001 Arequipa, Peru, earthquake. We can follow R_1 across the globe from the source toward its antipode where the wave train merges with R_2. Near the source, R_2 and R_3 overlap. A similar collapse of waveforms can be observed for later wave trains. Gray lines mark some of the body-wave phases that combine to form the overtones X wave trains as shown in Figure 2. For earthquakes as large as the Arequipa event, multiple body-wave reflections off the surface, or globe-circling overtones, are also discernible. Very nicely displayed for the Arequipa event, we can follow these overtones at significant signal levels between the fundamental modes, and later, overtone packets also merge near the source and its antipode. If we consider these overtone packets as modes, some of them have very low attenuation rates and can persist well after the fundamental modes have decayed into the noise. To observe these modes with high fidelity, the collected records typically have to be at least 5 days long.

Figure 4 shows the spectrum of a large earthquake observed at the Black Forest Observatory (BFO) in Germany. Since Earth is a finite body, transient waves propagating away from a localized source eventually interfere. For paths whose orbital length is an integer multiple of the wavelength, the two signals interfere constructively while destructive interference occurs otherwise. The spectrum of the several-day-long coda therefore yields discrete lines that correspond to Earth's normal modes, while destructive interference is responsible for the gaps separating the peaks.

We distinguish between observably split and not observably split modes. A spectral line of the former type has more than one peak in a typical spectrum (Figure 5). This 'splitting' of a mode is caused by the fact that individual singlets, the different 'vibrational states' of a certain mode (multiplet), are no longer degenerate in a nonspherical Earth. Observably split modes are typically of low angular order, that is, the

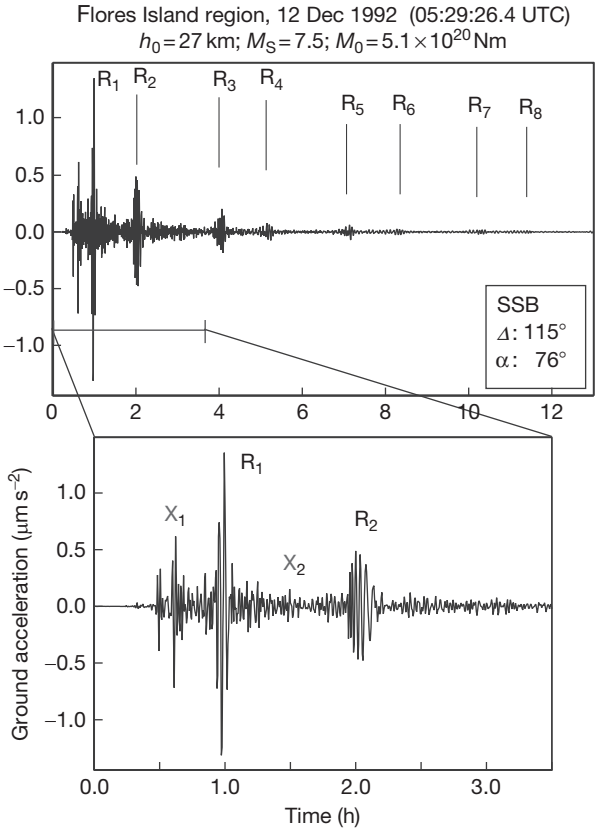

Figure 2 The 1992 Flores Island earthquake, recorded at GEOSCOPE station SSB (Saint Sauveur Badole, France). Marked are eight fundamental mode Rayleigh wave trains (R_n) and the first two overtone groups (X_n). Δ and α are the epicentral distance and the back azimuth to the event. Since the earthquake was more than 90° away, R_1 and R_2 are closer together than R_2 and R_3. At group velocities of about 3.7 km s^{-1}, it takes 3 h for Rayleigh waves to circle the globe. Hence, R_3 arrives at a station 3 h after R_1. The seismogram was low-pass-filtered with a convolution filter to suppress signal above 20 mHz.

geographic pattern of surface displacement is simple and the mode has few singlets. In the case of not observably split modes (Figure 4), there are so many singlets of a mode or the singlets are so close together that a standard spectral analysis is not able to resolve them. Another limiting factor to resolve a mode's splitting is its attenuation rate. The rather complex superposition of all the singlets causes an 'apparent frequency shift' of an otherwise ordinary-looking spectral peak where the shift depends on lateral variations in Earth structure (Jordan, 1978).

Having long wavelengths compared to transient seismic waves, such as body waves and surface waves, free oscillations inherently average over large volumes, which leads to comparatively poor resolution of Earth's heterogeneous structure. On the other hand, free oscillation studies are much less likely biased by the uneven global distribution of earthquake sources and seismic receivers. Mode observables are relatively weakly sensitive to structure with odd-degree symmetry because waves traveling on a sphere lose their sensitivity to this structure as time goes on. With every completed great circle, an observable accumulates information about the average structure over the entire great-circle path. This information is symmetric with respect to Earth's center and thus reflects only even-degree structure. We will revisit this problem in the surface wave section.

1.04.2 Free Oscillations

1.04.2.1 Modes of a Spherically Symmetric Earth

The elastic-gravitational response of Earth to localized, transient excitations consists of impulsive disturbances followed by dispersed wave trains and long-lasting standing waves, as seen in Figures 2–4. As long as an earthquake rupture is ongoing, Earth responds with forced vibrations. Once the rupture has ceased, Earth undergoes free oscillations around its new equilibrium state. The rupture duration of the largest earthquakes is on the order of a few minutes and thus very much shorter than the typical decay time of modes, which is a few tens of hours. A study of the source based on low-frequency seismic records reduces to the estimation of the initial amplitude and phase of the modes, while studies of Earth's internal mechanical structure concentrate on the frequency, ω, and attenuation, α, of the mode, where $\alpha = \omega/2Q$ and Q the quality factor.

The deviations of Earth structure from a spherically symmetric reference state are quite small. It is therefore convenient to discuss free oscillations of a spherically averaged Earth and treat any deviation away from this state with perturbation theory. On a spherically symmetric Earth, three integer quantum numbers, n, ℓ, and m, fully specify the set of normal modes. The azimuthal order, $|m|$, counts the number of nodal surfaces in the longitudinal direction $\hat{\phi}$. The number of nodal surfaces in the colatitudinal direction, $\hat{\theta}$, is $|\ell - m|$, where ℓ is the angular order. For fixed ℓ and m, the overtone number n indexes the modes with increasing frequency.

Solutions of the linearized, homogeneous equations of motion for a self-gravitating elastic Earth can be written as (Aki and Richards, 1980, 2002; Backus, 1967; Dahlen and Tromp, 1998; **Chapter 1.02**)

$$ {}_n u_\ell^m(\mathrm{r}, t) = \mathrm{Re}\left[\left(\hat{\mathrm{r}}_n U_\ell(r) Y_\ell^m(\theta, \phi) + {}_n V_\ell(r) \nabla_1 Y_\ell^m(\theta, \phi) \right.\right. $$
$$ \left.\left. - {}_n W_\ell(r) \hat{\mathrm{r}} \times \nabla_1 Y_\ell^m(\theta, \phi) \right) e^{i\, {}_n \omega_\ell^m t} \right] \quad [1] $$

where ${}_n u_\ell^m$ is the displacement eigenfunction of the mode singlet identified by the (n, ℓ, m)-triplet and ${}_n\omega_\ell^m$ is its eigenfrequency. Y_ℓ^m are surface spherical harmonic functions and ∇_1 is the surface gradient operator. While n and ℓ can be any non-negative number ($n \geq 0$, $\ell \geq 0$), the azimuthal order is limited to the interval $-\ell \leq m \leq \ell$. The spherical harmonics describe the angular shape of the eigenfunction. An example for some low-order spherical harmonics is shown in Figure 6.

The three scalar radial eigenfunctions, ${}_n U_\ell(r)$, ${}_n V_\ell(r)$, and ${}_n W_\ell(r)$, describe the way the modes sample Earth with depth. As n increases, they become more oscillatory with depth, leading to an increased number of nodal spheres. For toroidal modes, n is the number of nodes in W, while for radial modes, n is the number of nodes in U. For spheroidal modes, both U and V can have nodes, but the number of nodes is not as easily related to n. The radial eigenfunctions do not depend on the azimuthal order m and are thus identical for all singlets within a multiplet. Eigenfunctions for some mode examples are shown in Figures 7 and 8. The relevant quantity for the

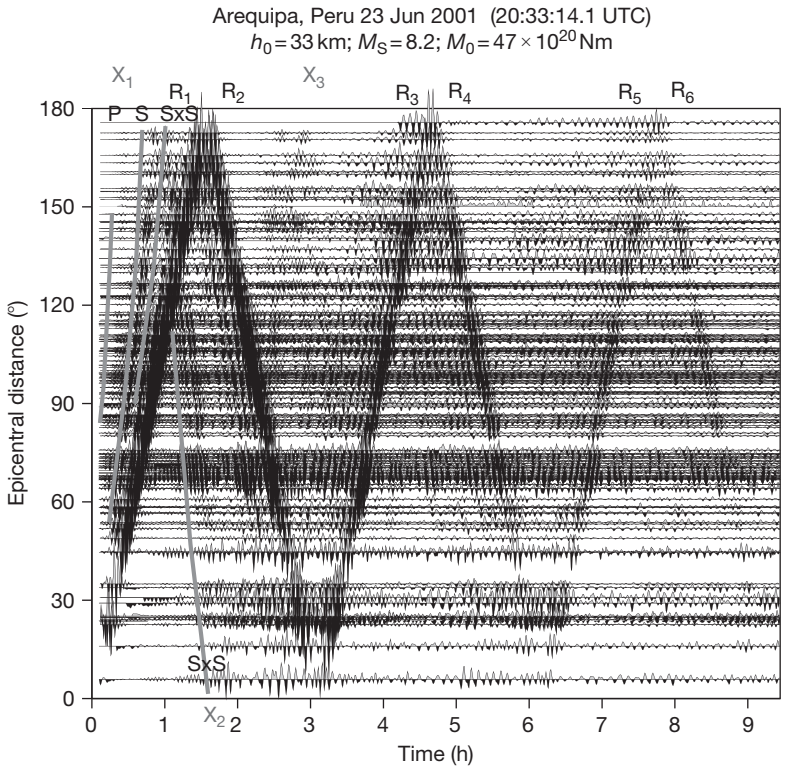

Figure 3 Record section of the 2001 Arequipa, Peru, earthquake, the largest digitally recorded earthquake before the 2004 Sumatra–Andaman earthquake. Marked are six fundamental mode Rayleigh wave trains (R_n) and early compressional (P) and shear (S) body-wave arrivals. Also marked are S multiples that bounced off the surface (S×S). Such phases are contributors to the major arc overtone phases X_n. At 90° epicentral distance, surface wave trains traveling in opposite directions arrive at a station at equidistant time intervals, while wave trains overlap at the antipode and near the source.

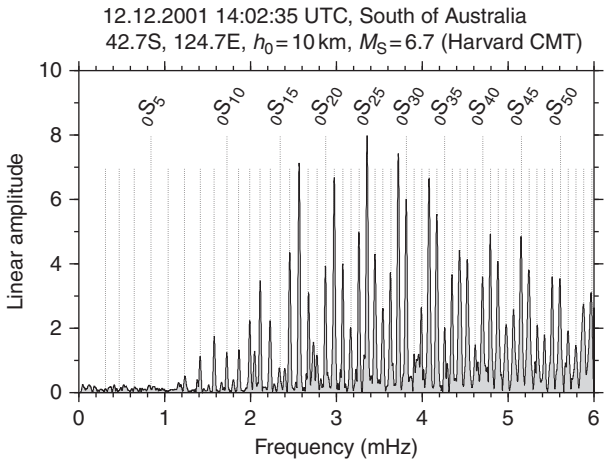

Figure 4 Spectrum of a magnitude $M_S = 6.7$ earthquake south of Australia that was recorded at station BFO (Black Forest Observatory, Germany). The succession of globe-circling Rayleigh wave packets in roughly 3 h intervals manifests itself in the spectrum through the regular spacing between adjacent fundamental spheroidal modes $_0S_\ell$ of about $(3\text{ h})^{-1} \cong 0.1$ mHz. The underlying time series is 18 h long.

sensitivity of a mode to structure with depth is actually not the eigenfunction but the energy density. This is because the modes are stationary solutions to the Lagrangian energy functional (Gilbert, 1980). A mode can store elastic energy in shear and in compression, and it can store gravitational potential energy. Significant amounts of the latter can be stored only by spheroidal modes below 1 mHz. For most other modes, their sensitivity to structure can be discussed based solely on their shear and compressional energy densities.

For the spherically symmetric reference state, the structure of the spectrum of a mode (fixed n and ℓ) exhibits a high degree of degeneracy in that all of its $2\ell+1$ singlets have the same frequency and the same radial eigenfunction. This degeneracy in m is a consequence of the fact that the singlet eigenfrequencies cannot depend on the choice of the coordinate system. The ensemble of $2\ell+1$ singlets comprises the mode multiplet. Further classification into spheroidal and toroidal modes is possible in the spherically symmetric case. The displacement field of toroidal modes, $_nT_\ell^m$, is purely horizontal and divergence-free with $_nU_\ell(r) = {}_nV_\ell(r) = 0$. Thus, it involves only shearing and does not lead to any deformation of the radial interfaces. Spheroidal modes, $_nS_\ell^m$, for which $_nW_\ell(r) = 0$, involve volumetric changes as they are composed of both horizontal and vertical displacements. They deform interfaces and also perturb the gravity field. A third subclass of modes are the radial modes, $_nS_0$, for which $\ell = 0$ and the displacement is purely radial, so that $_nV_\ell(r) = {}_nW_\ell(r) = 0$.

The formulation of computational methods for the practical calculation of normal-mode seismograms reaches back to the early 1970s. Takeuchi and Saito (1972) first formulated a Runge–Kutta matrix integration scheme to solve the ordinary

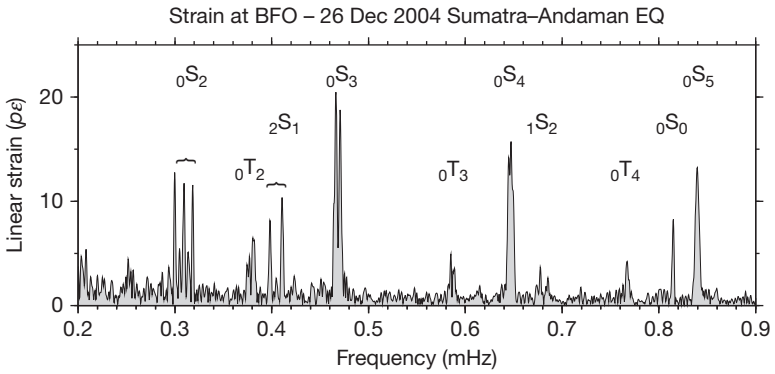

Figure 5 Linear Fourier amplitude spectrum of strain from the 2004 Sumatra–Andaman earthquake recorded by the invar wire strainmeter at station BFO with azimuth N2°E. The time-domain amplitude of ${}_0S_0$ at 0.814 mHz is $8 \times 10^{-12}\epsilon$. This is a rare spectrum showing evidence of Zeeman-type splitting due to Earth's rotation of not only to the lowest-order spheroidal modes ${}_0S_2$, ${}_2S_1$, ${}_0S_3$, and ${}_0S_4$ but also to the two lowest-order toroidal modes ${}_0T_2$ and ${}_0T_3$. The strainmeter array at BFO is described in Widmer et al. (1992a). A barometric correction similar to that of Zürn and Widmer (1995) has been applied to this spectrum. With an empirically determined strain pressure compliance of 0.8 nε hPa^{-1}, a lowering of the noise floor by a factor 4 was achieved. The first 240 h after the event was used for the spectrum.

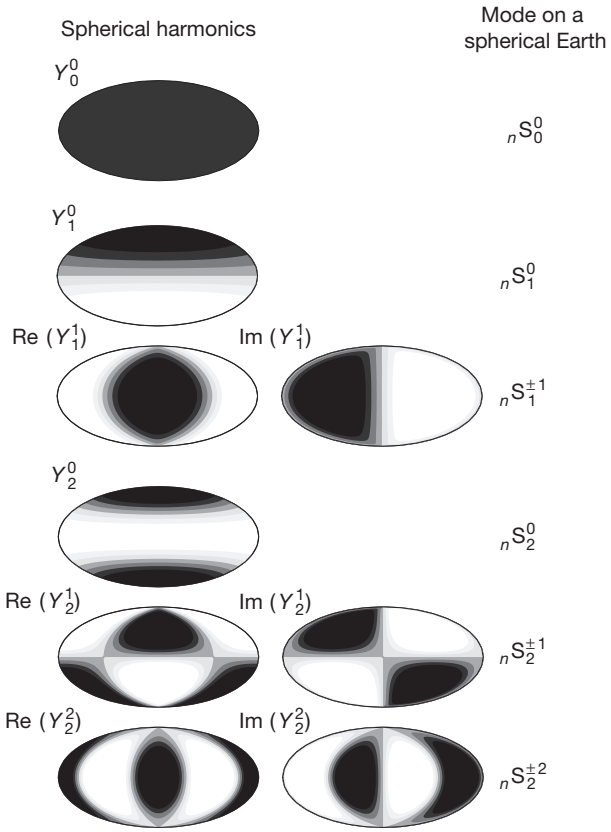

Figure 6 Surface spherical harmonics $Y_\ell^m = X_\ell^m(\theta)e^{im\phi}$ that compose the basis set for radial modes (e.g., ${}_0S_0$, ${}_1S_0$) and $\ell = 0$, 1, and 2 spheroidal modes (e.g., ${}_1S_1$, ${}_2S_1$, ${}_0S_2$, and ${}_3S_2$), plotted in Hammer–Aitoff projection. The singlets of modes have these shapes on the $\hat{\mathbf{r}}$ component of recordings on a spherical, nonrotating Earth. Modified from Masters TG, Laske G, and Gilbert F (2000c) Large-scale Earth structure from analyses of free oscillation splitting and coupling. In: Boschi E, Ekström G, and Morelli A (eds.) *Problems in Geophysics for the New Millennium*, pp. 255–288. Bologna: Editrice Compositori.

differential equations governing free oscillations. This method is still used today. Freeman Gilbert implemented a propagator matrix approach in his computer program EOS, and various descendants of this code have also been circulating informally since that time. We mention two versions here: OBANI by John Woodhouse and MINOS by Guy Masters. Woodhouse advanced the code by allowing to compute the eigenfunctions through the method of minors. He also introduced a mode counter for spheroidal modes, while Masters added one for toroidal and radial, Stoneley, and IC modes. A description of OBANI can be found in Woodhouse (1988). MINOS can be downloaded from the REM website.

1.04.2.2 Modes of a Heterogeneous Earth

1.04.2.2.1 Mode splitting

As an Earth model becomes successively more realistic and complex, the spherical symmetry is broken and a mode spectrum becomes more complex. The principal deviations from the spherically symmetric reference state are Earth's daily rotation, its hydrostatic ellipticity in response to the rotation, and its general aspherical structure. The latter includes the topography of interfaces and lateral variations in isotropic and anisotropic volumetric parameters. The distribution of singlets within a multiplet on a rotating Earth in hydrostatic equilibrium is given by Dahlen (1968). If the (n, ℓ)-tuple denotes the kth spheroidal or toroidal multiplet, then the eigenfrequency of the mth singlet of an isolated multiplet is

$$\omega_k^m = \bar{\omega}_k\left(1 + a + mb + m^2 c\right) \text{ with } -\ell \le m \le \ell \qquad [2]$$

where $\bar{\omega}_k$ is the multiplet degenerate frequency, a and c the ellipticity splitting coefficients (to first order), and b the rotational splitting coefficient (Dahlen, 1968). The ellipticity of figure removes the degeneracy of a mode only partially, with ${}_n\omega_k^m = {}_n\omega_k^{-m}$. This splitting is asymmetric with respect to the degenerate frequency. On the other hand, the rotational splitting is symmetric, or of Zeeman type, and removes the

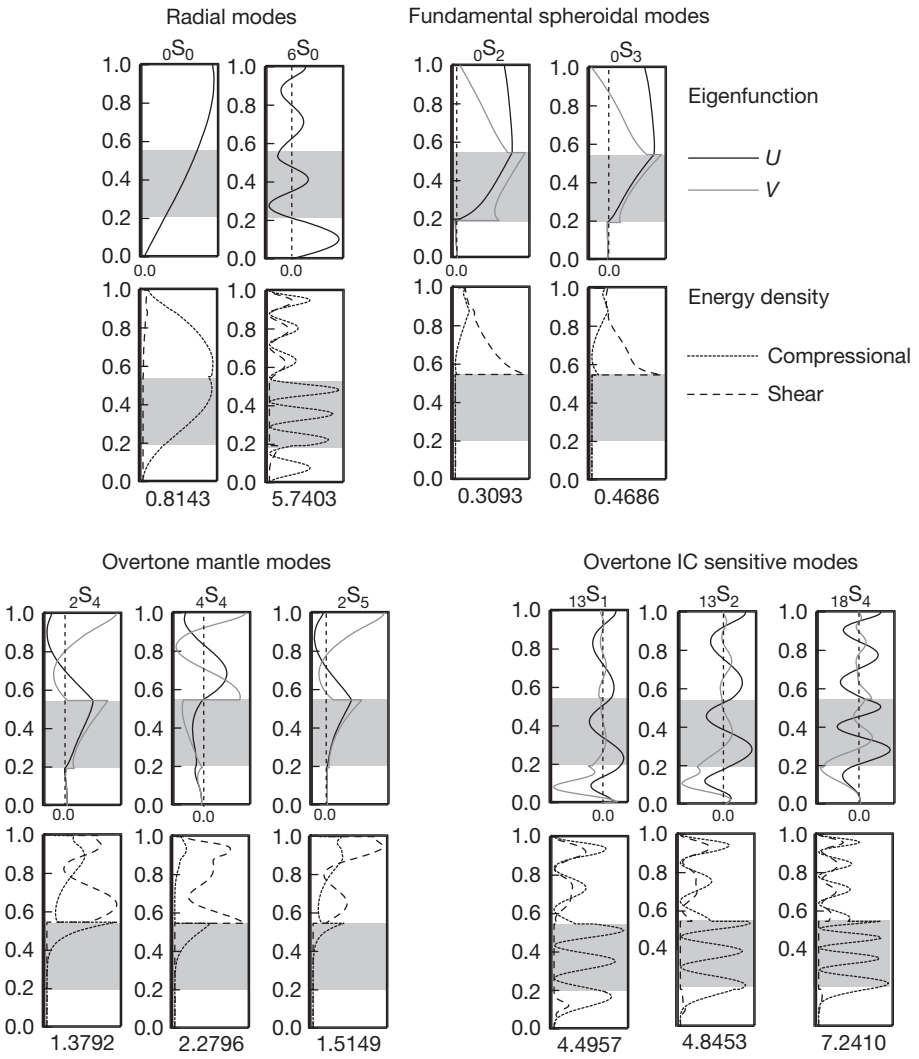

Figure 7 Radial eigenfunctions U and V and compressional and shear energy densities for some modes described in this chapter, displayed as function of normalized radius (0 is at the center; 1 is at the surface). Gray areas mark the outer core. Numbers at the bottom of the panels are PREM mode frequencies in mHz (Dziewonski and Anderson, 1981). Radial modes are very sensitive to core structure, while spheroidal fundamental modes are not very sensitive to κ and μ in the core. On the other hand, overtone mantle modes that are primarily sensitive to mantle structure are also influenced by κ in the core. IC-sensitive modes that can be observed at Earth's surface are typically quite sensitive to mantle structure.

degeneracy completely. Splitting due to rotation dominates at low frequencies ($b \gg c$) so that the spacing between adjacent singlets is nearly constant (see **Figures 5** and **9**). Other examples of modes whose splitting is dominated by rotation are modes $_0S_5$ and $_1S_4$ (**Figure 10**). At higher frequencies, ellipticity and heterogeneous structure become the dominant cause and frequencies become partially degenerate when $b \ll c$. Examples of such modes are $_{13}S_2$ and $_{18}S_4$. IC-sensitive modes $_3S_2$, $_{13}S_2$, and $_{18}S_4$ are anomalously split, as first observed by Masters and Gilbert (1981). In these cases, the splitting width, the range of singlet frequencies, is significantly larger than that predicted by rotation and ellipticity. In fact, the extreme splitting of $_{10}S_2$ led Gilbert and Dziewonski (1975) to misidentify the $m=0$ line of $_{10}S_2$ as mode $_{11}S_2$. Based on their observations, Masters and Gilbert (1981) argued for high Q in the IC but did not interpret the anomalous splitting. Ritzwoller et al. (1986) speculated that the anomalous splitting is due to axisymmetric structure in the outer core (see also Romanowicz and Bréger, 2000). Woodhouse et al. (1986) were the first to attribute this splitting to the anisotropic IC, which now appears to be widely accepted (see, e.g., Tromp, 1993).

Gilbert (1971) investigated how small structural perturbations to a spherically symmetric Earth affect the spectrum of a multiplet. He formulated the 'diagonal sum rule,' which states that, to first order, the arithmetic mean of the $2\ell+1$ singlet frequencies is the multiplet degenerate frequency $\bar{\omega}_k$:

$$\bar{\omega}_k = \frac{1}{2\ell+1} \sum_{m=-\ell}^{\ell} \omega_k^m \qquad [3]$$

Any first-order perturbation in structure leaves the degenerate frequencies of the spherical Earth unchanged. On the other hand, the second-order effects of the Coriolis force may cause a frequency shift. Dahlen (1968) showed that the singlet

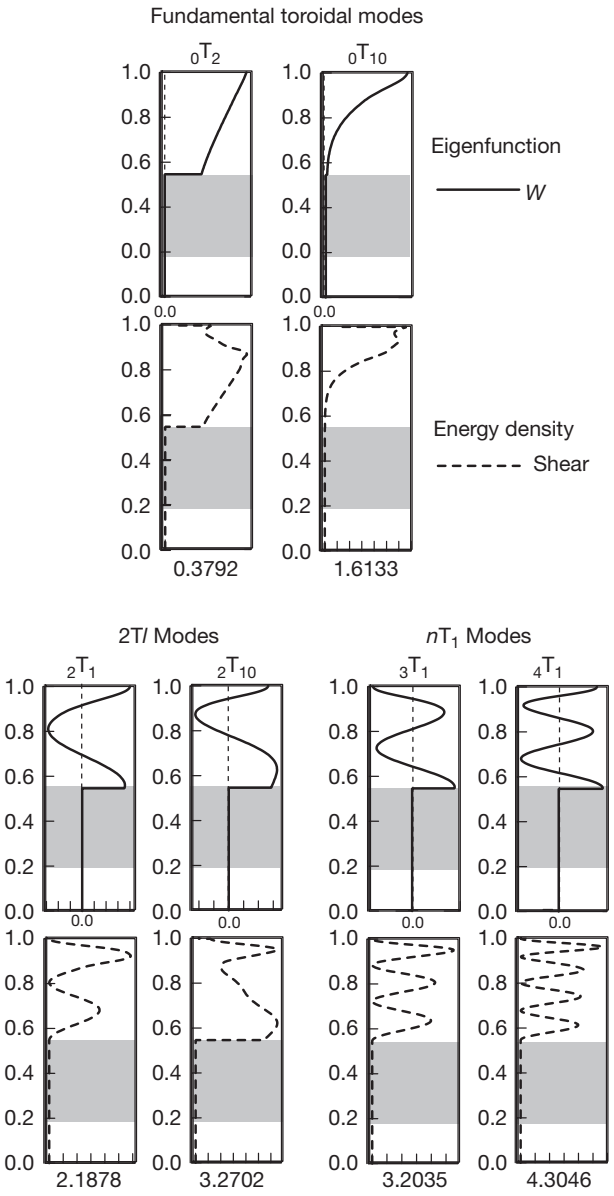

Figure 8 Radial eigenfunction W and shear energy densities for some toroidal modes. Toroidal modes are sensitive only to the shear modulus, μ. For details, see **Figure 7**.

distribution within a multiplet still follows the parabolic distribution of eqn [2], but second-order terms contribute to factors a and c, and the diagonal sum rule is no longer valid. Dahlen (1968) and Dahlen and Sailor (1979) provided the splitting parameters for modes below 2 mHz for a variety of Earth models. Since the splitting parameters caused by rotation and Earth's hydrostatic ellipticity are well understood, their effects are usually corrected for before mode parameters are interpreted in terms of Earth structure.

Once the eigenfrequencies and eigenfunctions of a 1-D Earth model have been computed, the synthesis of seismograms based on free oscillations is rather straightforward as it involves only the summation over all multiplets in a desired frequency band. The representation of the time series of an

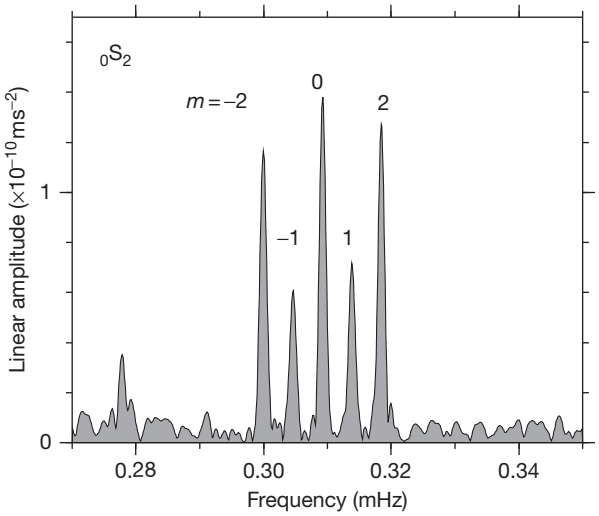

Figure 9 Zeeman splitting of the 'football mode' $_0S_2$. This is a Fourier spectrum of a 500 h long record of the 2004 Sumatra–Andaman earthquake by the superconducting gravimeter at Strasbourg, France (Rosat et al., 2005). A scaled version of the locally recorded barometric pressure was subtracted from the gravity record to achieve a noise reduction by a factor 2. The time-domain acceleration amplitude of the singlets is close to 10^{-10} ms^{-2}. Zeeman-type splitting of a mode is caused by Earth's rotation.

isolated split multiplet with degenerate frequency $\bar{\omega}_k$ at station j is given by

$$u_j(t) = \sum_{m=1}^{2\ell+1} R_{jm} a_m(t) e^{i\bar{\omega}_k t} \quad \text{or} \quad \mathbf{u}(t) = \mathbf{R}\cdot\mathbf{a}(t) e^{i\bar{\omega}_k t} \qquad [4]$$

where the real part is understood (e.g., Landau and Lifshitz, 1958, section 40; Woodhouse, 1983; Woodhouse and Girnius, 1982). The jth row of $\mathbf{R}$ is a $2\ell+1$ vector of spherical harmonics, which describes the motion of the spherical-Earth singlets at the jth receiver and is readily calculated. $\mathbf{a}(t)$ is a slowly varying function of time given by

$$\mathbf{a}(t) = \exp(i\mathbf{H}t)\cdot\mathbf{a}(0) \qquad [5]$$

where $\mathbf{a}(0)$ is a $2\ell+1$ vector of spherical-Earth singlet excitation coefficients, which can be computed if the source mechanism of the event is known. $\mathbf{H}$ is the complex 'splitting matrix' of the multiplet and incorporates all the information about elastic and anelastic 3-D structure to which the mode is sensitive, that is,

$$H_{mm'} = \bar{\omega}_k \left[(a + mb + m^2 c)\delta_{mm'} + \sum \gamma_s^{mm'} c_s^t + i \sum \gamma_s^{mm'} d_s^t \right] \qquad [6]$$

where $-\ell \le m \le \ell$, $-\ell \le m' \le \ell$, and $t = m - m'$. The first term describes the splitting due to Earth's rotation and ellipticity (eqn [2]), and the second and third terms describe the effects from elastic and anelastic structures through the 'structure coefficients,' c_s^t and d_s^t (e.g., Ritzwoller et al., 1986; Smith and Masters, 1989b). Equation [6] changes to equation (14.84) of Dahlen and Tromp (1998) if real instead of complex basis eigenfunctions and spherical harmonics are considered in eqn [1]. $\mathbf{H}$ and consequently $\exp(i\mathbf{H}t)$ are $(2\ell+1)\times(2\ell+1)$-dimensional square matrices. The $\gamma_s^{mm'}$ are integrals over three

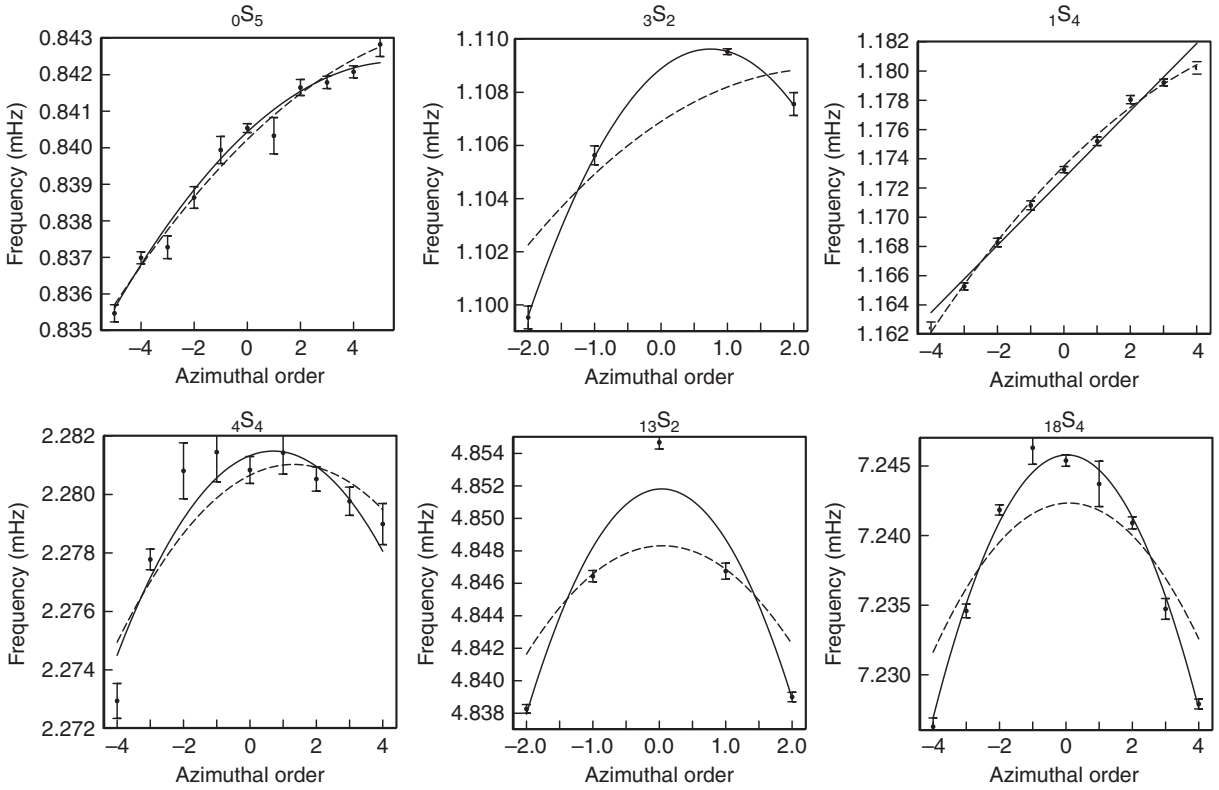

Figure 10 Observed singlet frequencies as a function of azimuthal order, m, for six modes. The dashed lines mark the splitting predicted for Earth's rotation and hydrostatic ellipticity. Solid lines mark the best-fitting parabolas. The splitting of low-frequency modes $_0S_5$ and $_1S_4$ is dominated by rotation, while that of IC-sensitive modes $_{13}S_2$ and $_{18}S_4$ is dominated by ellipticity. The splitting of mantle mode $_4S_4$ and low-frequency IC-sensitive mode $_3S_2$ is mixed. The $m=0$ singlet of $_3S_2$ has not yet been observed reliably. IC-sensitive modes are anomalously split, that is, the observed splitting is significantly larger than that predicted for rotation and ellipticity alone.

spherical harmonics (e.g., Dahlen and Tromp, 1998). These integrals are often zero, and the 'selection rules' summarize the nonzero conditions:

$$\begin{aligned} &1.\ m-m'=t \\ &2.\ \ell+s+\ell \text{ must be even; i.e., } s \text{ must be even} \\ &3.\ 0\le s\le 2\ell \text{ (triangle rule)} \end{aligned} \qquad [7]$$

Rule (1) implies that axisymmetric structure ($t=0$) gives nonzero contributions to the splitting matrix only if $m=m'$, so that $\mathbf{H}$ is diagonal. Rule (2) implies that an isolated mode is sensitive only to structure of even degree. The rule can be extended to two coupled modes in which case $\ell+s+\ell'$ must be even (for same-type coupling; see **Section 1.04.2.2.2** for details). In order to retrieve structure of odd harmonic degree, $\ell+\ell'$ must therefore be odd. Rule (3) implies that a mode cannot be sensitive to structure of arbitrarily high degree. The rule can also be extended to the case of two coupled modes where $|\ell-\ell'|\le s\le \ell+\ell'$. The structure coefficients for elastic structure, c_s^t, are given by

$$c_s^t=\int_0^a \mathbf{M}_s(r)\cdot\delta\mathbf{m}_s^t(r)r^2\,\mathrm{d}r \qquad [8]$$

and a similar expression exists for the anelastic structure coefficients, d_s^t. The coefficients $\delta\mathbf{m}_s^t$ are the expansion coefficients of the 3-D aspherical Earth structure: $\delta\mathbf{m}(r,\theta,\phi)=\sum\delta\mathbf{m}_s^t(r)Y_s^t(\theta,\phi)$ and $\mathbf{M}_s$ are integral kernels, which can be computed (Henson, 1989; Li et al., 1991a; Woodhouse, 1980; Woodhouse and Dahlen, 1978). Equation [8] and its counterpart for the d_s^ts can be regarded as a pair of linear inverse problems for $\mathbf{c}$ and $\mathbf{d}$. Strictly speaking, eqn [4] is not quite correct since both $\mathbf{R}$ and $\mathbf{a}(0)$ should include small renormalization terms (see equations 14.87 and 14.88 in Dahlen and Tromp, 1998). The renormalization requires the knowledge of the splitting matrix, which we ultimately want to determine in a mode analysis. While the renormalization terms are expected to be small for isolated modes, we may have to iterate the retrieval of the splitting matrix for coupled modes.

It is convenient to visualize the geographic distribution of structure as sensed by a mode by forming the elastic and anelastic 'splitting functions' (Woodhouse and Giardini, 1985):

$$\begin{aligned} f_{\mathrm{E}}(\theta,\phi)&=\sum_{s,t}c_s^tY_s^t(\theta,\phi) \\ f_{\mathrm{A}}(\theta,\phi)&=\sum_{s,t}d_s^tY_s^t(\theta,\phi) \end{aligned} \qquad [9]$$

The $Y_s^t=X_s^t(\theta)\mathrm{e}^{\mathrm{i}t\phi}$ is a spherical harmonic of harmonic degree s and azimuthal order number t. An example is shown in **Figure 11**. The elastic splitting function shows local peak shift variations caused by the local structure beneath a geographic location, as 'seen' by an isolated mode. Recall that isolated modes are not sensitive to odd-degree structure. In a similar way, the anelastic splitting function shows attenuation.

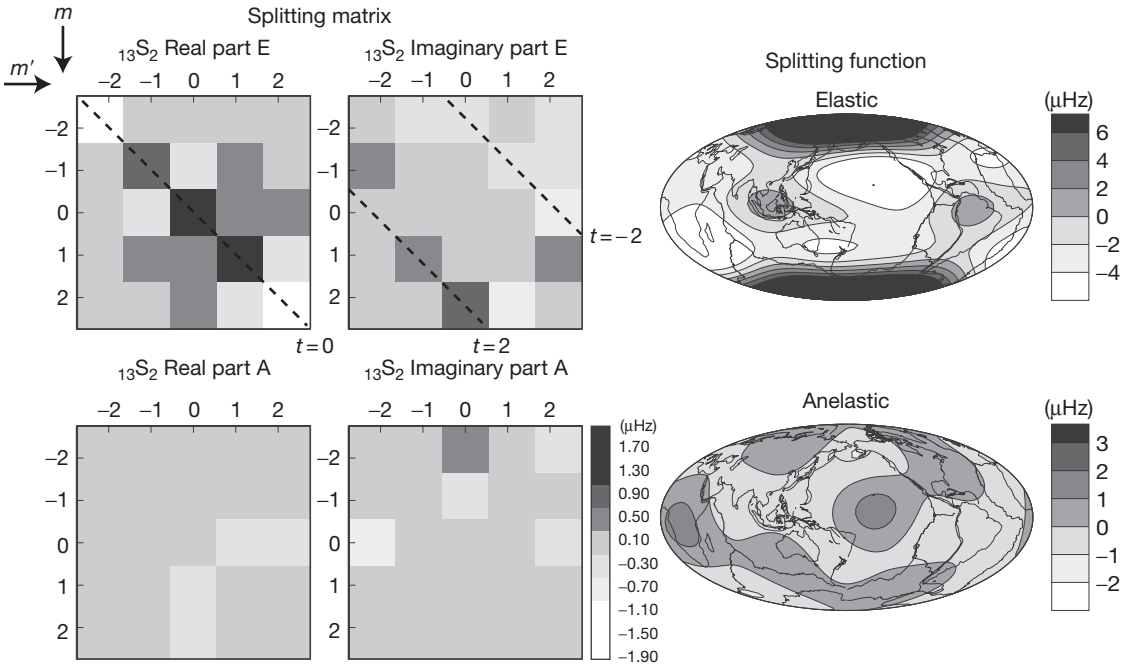

Figure 11 Left: Observed complete splitting matrix for mode $_{13}S_2$, decomposed into its elastic (E) and anelastic (A) parts, both of which are Hermitian. The data from 13 earthquakes were used to determine this matrix. The signal down the diagonal of the matrices is caused by zonal (axisymmetric) structure ($t=0$), as constrained by the selection rules for a mode. Also indicated are the contributions from $t=\pm 2$–structure (which is sectoral for $s=2$). Right: Splitting functions obtained from the splitting matrix on the left. The signal from anelastic structure is typically much smaller than that from elastic structure.

Bearing this restriction in mind, a splitting function can be understood as the mode equivalent of a surface wave phase velocity map.

To summarize, an isolated mode of harmonic degree ℓ is sensitive to even-degree structure only, up to harmonic degree $s=2\ell$. If the structure within Earth is axisymmetric, then the splitting matrix is diagonal, the individual singlets can be identified by the index m, and the only singlet visible at a station at Earth's poles is the $m=0$ singlet.

1.04.2.2.2 Mode coupling

While the treatment of isolated modes is appealing because of its simplicity, it is insufficient to describe free oscillations of the real Earth. The coupling between modes has two fundamental effects: (1) varying coupling effects on individual singlets causes a shift of the mode's degenerate frequency and Q, and (2) coupling to certain other modes gives a mode sensitivity to odd-degree structure. We distinguish between along-branch (same mode type and n but different ℓ) and cross-branch coupling (any other mode combination). The coupling between two modes is particularly strong if their frequencies are close and the radial and geographic shape of their displacement field is similar. Numerically, the complex frequencies must be close, but in fact, the real part (frequency) is more dominant than the imaginary part (attenuation). As in the case of isolated modes, selection rules dictate through which mechanism and in which way two modes couple:

- Coriolis force causes spheroidal–toroidal mode coupling for mode pairs of the form $_nS_\ell - _{n'}T_{\ell\pm1}$, that is, between multiplets that differ by a single angular degree ($|\ell-\ell'|=1$), for example, $_0S_4$–$_0T_3$, $_0S_8$–$_0T_9$, and $_1S_4$–$_0T_3$.
- Earth's ellipticity also causes spheroidal–toroidal mode coupling for $|\ell-\ell'|=1$.
- Earth's ellipticity causes same-type (spheroidal or toroidal) mode coupling for $|\ell-\ell'|=0$ and for $|\ell-\ell'|=2$, for example, $_0S_4$–$_1S_4$ and $_0S_3$–$_0S_5$.
- Rotation causes spheroidal–spheroidal mode coupling for $|\ell-\ell'|=0$, for example, $_0S_4$–$_1S_4$.
- Lateral heterogeneity of degree s causes spheroidal–toroidal mode coupling under the condition that $|\ell-\ell'|+1\le s\le \ell'+\ell-1$ and $\ell'+\ell+s$ is odd, for example, $_0S_4$–$_0T_3$ are coupled through structure of degrees 2, 4, and 6; as a consequence, if $|\ell-\ell'|$ is even, then modes can couple through odd-harmonic degree structure, for example, $_0S_5$–$_0T_3$ are coupled through structure of degrees 3, 5, and 7.
- Lateral heterogeneity of degree s causes same-type mode coupling under the conditions that (1) $m+t-m'=0$; (2) $\ell'+\ell+s$ is even; (3) $|\ell-\ell'|\le s\le \ell'+\ell$, for example, $_0S_2$–$_0S_3$ are coupled through structure of degrees 1, 3, and 5.

Coriolis coupling between fundamental spheroidal and toroidal modes was first observed and modeled by Masters et al. (1983). Coupling spheroidal–toroidal mode pairs form hybrid modes that share some of the characteristics of both modes. Toroidal modes can then be observed on vertical-component seismic spectra in the form of additional peaks, which Masters et al. nicely showed. For angular orders $7\le\ell\le26$, $_0T_{\ell+1}$ modes are closer neighbors to $_0S_\ell$ modes than $_0T_{\ell-1}$ modes are. The strongest coupling occurs between pairs $_0S_{11}$–$_0T_{12}$ whose PREM degenerate frequencies are about

4.5 μHz apart (1 μHz for 1066A) and ${}_0S_{19}$–${}_0T_{20}$ whose PREM frequencies are within 0.5 μHz of each other (2.5 μHz apart in 1066A). Figure 12 shows that predicted frequency shifts for Coriolis-coupled modes can be up to 5 μHz, which is significant with respect to measurement errors (see Figure 24; regard a 'strip' as a spectral line of a mode for now). Figure 12 also indicates that coupling modes 'repel' each other. For example, while the frequency of ${}_0S_{10}$ gets pulled downward, the frequency of ${}_0T_{11}$ gets pushed upward. The coupling between two multiplets actually has a different effect on each singlet of the modes, as is shown in Figure 13. As discussed in the preceding text, for uncoupled modes, rotation and Earth's hydrostatic ellipticity remove the frequency degeneracy. The coupling of the mode pairs causes the sets of mode singlets to rearrange. Strongly coupled modes form a hybrid pair in which the sets of singlet frequencies repel each other but the attenuation is 'shared.' As shown by Masters et al. (1983), Earth's aspherical structure causes further rearrangement of the singlets.

Coupling between two modes also manifests itself in the splitting matrix. Instead of two matrices with ranks $2\ell+1$ and $2\ell'+1$ that describe the effects of rotation, ellipticity, and

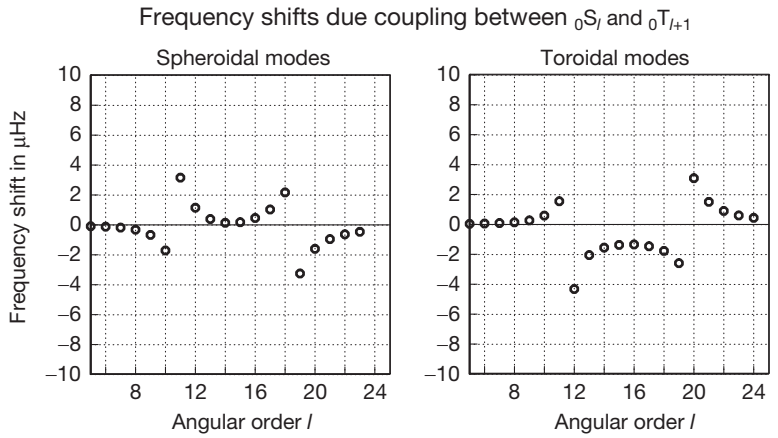

Figure 12 Predicted frequency shifts for mode pairs ${}_0S_\ell - {}_0T_{\ell+1}$ caused by Coriolis coupling. Predictions are for Earth model 1066A (Gilbert and Dziewonski, 1975). The strongest coupling occurs between pairs ${}_0S_{11} - {}_0T_{12}$ and ${}_0S_{19} - {}_0T_{20}$.

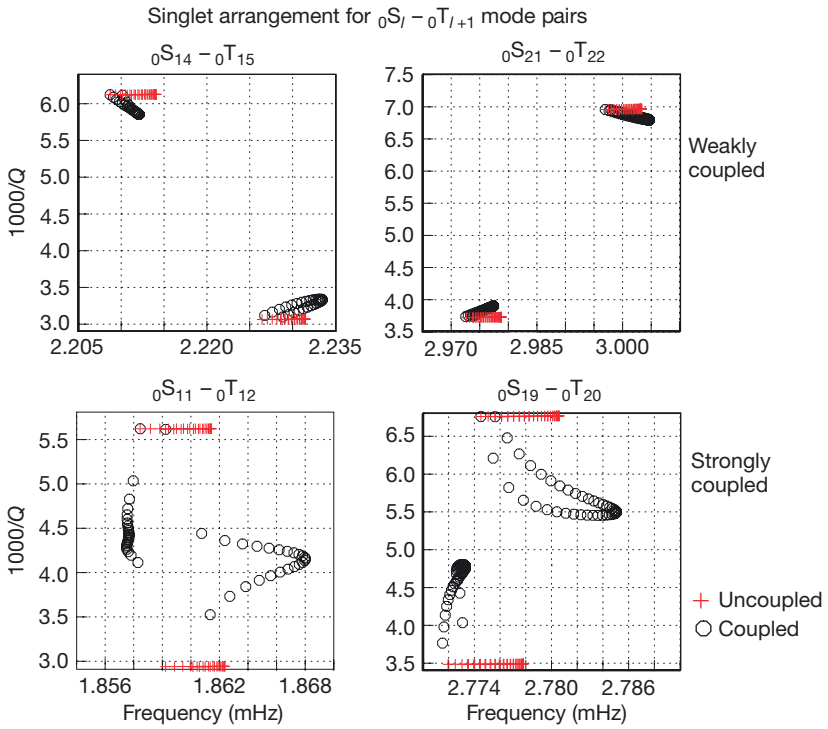

Figure 13 Predicted rearrangement of singlet frequencies and quality factor Q for weakly coupled-mode pairs ${}_0S_{14} - {}_0T_{15}$ and ${}_0S_{11} - {}_0T_{12}$ and for strongly coupled pairs ${}_0S_{21} - {}_0T_{22}$ and ${}_0S_{19} - {}_0T_{20}$. The coupling calculations included effects from both rotation and ellipticity, but for the modes discussed here, Coriolis coupling is the dominant cause. Strongly coupled modes form a hybrid pair in which the sets of singlet frequencies repel each other but the attenuation is 'shared.'

structure for two modes, we now deal with a larger matrix with rank $2(\ell+\ell'+1)$ that has four subblocks: the two original matrices that are now the two self-coupling blocks in the upper-left and lower-right corners, and two cross coupling blocks of dimensions $(2\ell+1)\times(2\ell'+1)$ and $(2\ell'+1)\times(2\ell+1)$. As an example of spheroidal–toroidal mode coupling, Figure 14 shows how Earth's rotation and ellipticity affect the four coupling blocks in the splitting matrix for modes ${}_0S_4$ and ${}_0T_3$.

Earth structure can complicate the splitting matrix substantially, which we show in a schematic example for a $\ell=2$ mode coupling with a $\ell'=3$ mode of the same type (i.e., either spheroidal or toroidal). Figure 15 compares the structure of the splitting matrix in the case of the self-coupling of an isolated $\ell=2$ mode and the upper-right cross coupling block with a $\ell'=3$ mode. According to the selection rules, structure of certain symmetries affects certain elements in the splitting matrix. As already discussed, the effects from axisymmetric structure are found down the diagonal, while non-axisymmetric, even-degree structure affects off-diagonal elements (Figure 11). Depending on ℓ and ℓ' of the coupling modes, some elements in the cross coupling blocks are now affected by structure of odd-harmonic degree. An example of an observed splitting matrix is discussed in Section 1.04.2.3.5.

We should mention that the coupling calculations presented here were done with a code based on the work of Jeff Park (Park and Gilbert, 1986). His method uses a Galerkin procedure that allows the assessment of mode coupling in a dissipating Earth. To reduce the computational burden, the method applies a trick. The exact representation of interaction on a rotating Earth requires a matrix equation that is quadratic in eigenfrequency ω. Coriolis interaction terms are grouped in a matrix linear in ω. This linear dependence is removed by replacing ω with a fixed fiducial frequency (reference frequency) $\hat{\omega}_0$. Park's numerical experiments showed that this approximation is adequate for modes above 1 mHz as long as the relative frequency spread, $\Delta\omega/\hat{\omega}_0$, is not large. Modes in a certain frequency band all couple through various mechanisms. When modeling the interaction in a group of modes, all these have to be taken into account simultaneously. The examples of coupling mode pairs shown here are only to illustrate how mode coupling works and where Park and Gilbert's method is appropriate. A treatment of coupling modes in a wider frequency band requires more general procedures. Some are discussed in Section 1.04.2.3.5, but the interested reader is also referred to Chapter 1.02.

1.04.2.3 Measuring Mode Observables

The most basic approach to extract mode observables from a seismogram is to calculate the spectrum of a tapered seismogram. The finiteness of the underlying time series prohibits a

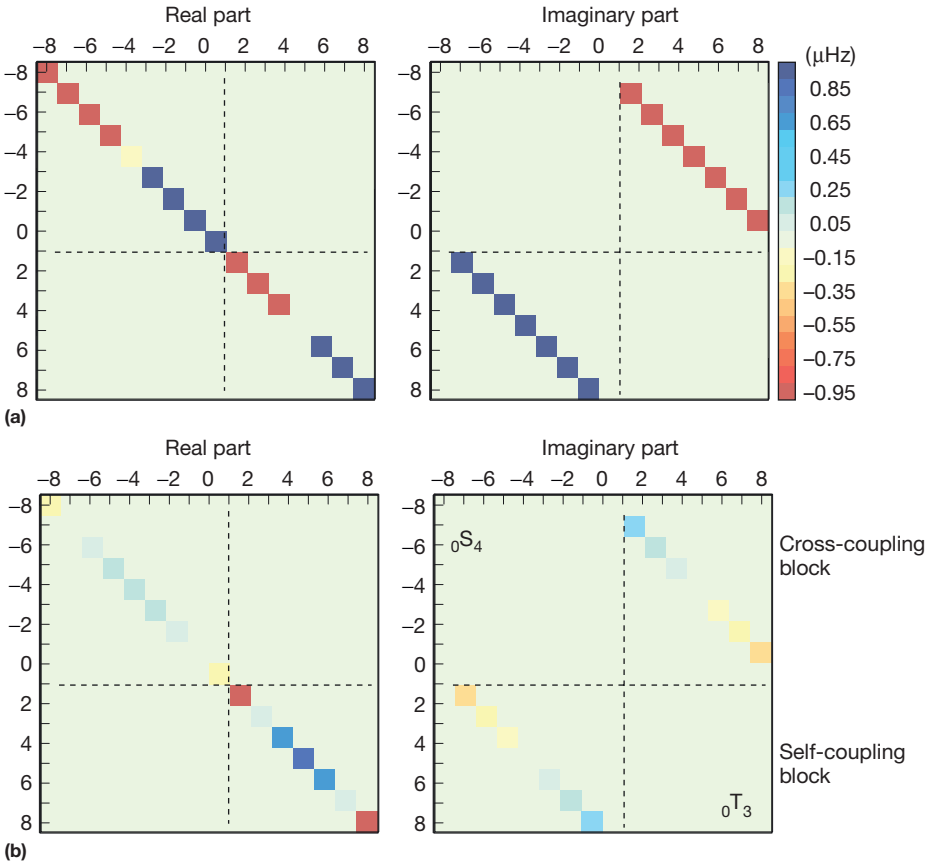

Figure 14 Synthetic splitting matrices to illustrate the coupling effect of Earth's (a) rotation and (b) ellipticity on the mode pair ${}_0S_4 - {}_0T_3$. Self-coupling fills the diagonals of the self-coupling blocks, while multiplet–multiplet coupling fills the cross coupling blocks. For this pair, the effect of rotation is ten times larger than that of ellipticity.

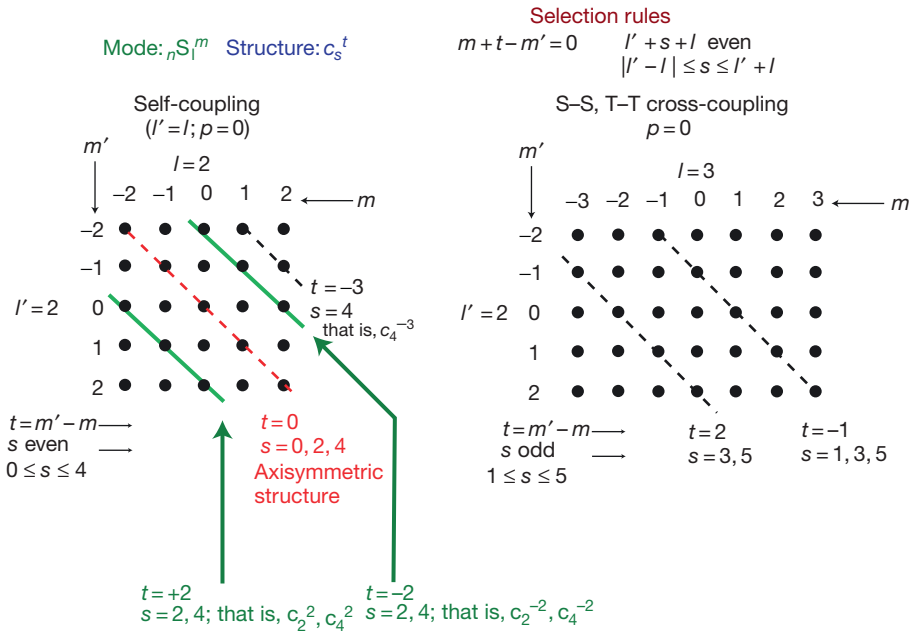

Figure 15 Elements in the splitting matrix that are affected by coupling. Left panel: An isolated $\ell=2$ mode experiences self-coupling through the Earth's rotation and ellipticity. Together with axisymmetric structure, this manifests itself in the diagonal. Other even-degree structure (s even) affects off-diagonal elements. When two modes couple, the splitting matrix has four blocks: two self-coupling blocks (one for each mode) and two cross coupling blocks. The right panel shows how elements in a cross coupling block with an $\ell'=3$ mode are affected for same-type coupling ($p=0$). Some of the elements are now affected by odd-degree structure (s odd).

parameter estimation with arbitrary precision (e.g., see Jenkins, 1961 for an early assessment of the Blackman and Tukey, 1958 approach). Modal decay rates, the vicinity of other modes, and the presence of noise necessitate the application of spectral optimization procedures, which involve the choice of a proper set of time windows. Harris (1978) presented a comprehensive overview on the use of windows in discrete Fourier analysis. Based on this, Dahlen (1982) first provided formal expressions for the variances and covariances of free oscillation parameters when using arbitrary data windows. He also showed that the optimum- or minimum-variance record length for measuring frequencies and decay rates (to determine Earth structure) using a Hanning taper is 1.1 Q cycles but only 0.5 Q-cycles for measuring amplitudes and phases (to determine the earthquake source). Park et al. (1987b) and Lindberg and Park (1987) adapted and applied Thomson's (1982) multitaper technique to optimize the bias from ambient noise and spectral leakage of decaying sinusoids in the free oscillation spectrum. Though we have not used this technique ourselves, they found that their approach provides a much improved detector for modes in a time series contaminated by white noise. Properly tapering free oscillation spectra is particularly important for measuring attenuation rates, which is discussed in Masters and Gilbert (1983). Complicating direct spectral estimation is the fact that, even today, it is not as trivial as it may appear to find continuous undisturbed seismic records that stretch over more than a week or so. A proper analysis of Earth's breathing mode ${}_0S_0$ requires records of more than two and half months! A somewhat disturbing fact is also that some continuous records that were available at the IRIS data management center (DMC) or other DMCs less than 10 years ago now have data gaps due to data storage failures. It is therefore essential to understand how data gaps cause additional distortions in a complex spectrum. The best way to address this is by comparing a real data spectrum with a synthetic one that uses the same windowing and data gap structure, provided the source mechanism is known.

An obvious approach to assess Earth's 1-D and 3-D structure is to measure the apparent frequency of a certain mode for many stations and many earthquakes. Each of these 'peak shift data' can be plotted at the two poles of its source–receiver great circle. We make use of Backus' (1964) discovery that such data represent the great-circle integrals over surface spherical harmonics:

$$P_s(0)Y_s^t(\Theta, \Phi) = \frac{1}{2\pi}\oint_C Y_s^t(\theta, \phi)\mathrm{d}\Delta \qquad [10]$$

where (Θ, Φ) is the positive pole of the source–receiver great-circle C and $P_s(0)$ is a Legendre polynomial. This representation can be used for peak shift data as long as the structural wavelength along the great circle is much longer than the modal wavelength (Jordan, 1978). Thus, we can extract the effects of Earth structure on a particular mode in an inversion for the structure coefficients of a splitting function (see eqn [9]). Examples of using this technique are the work of Masters et al. (1982), who found evidence for subducting slabs in the transition zone and Romanowicz et al. (1987) discussion of the degree 2 pattern of structure in the upper mantle. In principle, the c_0^0 term in the splitting function gives the degenerate mode frequency. In practice, an unbiased estimation of c_0^0 requires a large data set of peak shift measurements. More efficient tools to measure degenerate mode frequencies are based on mode stripping, which is laid out in the next section. Peak shift measurements to extract the effects of 3-D structure

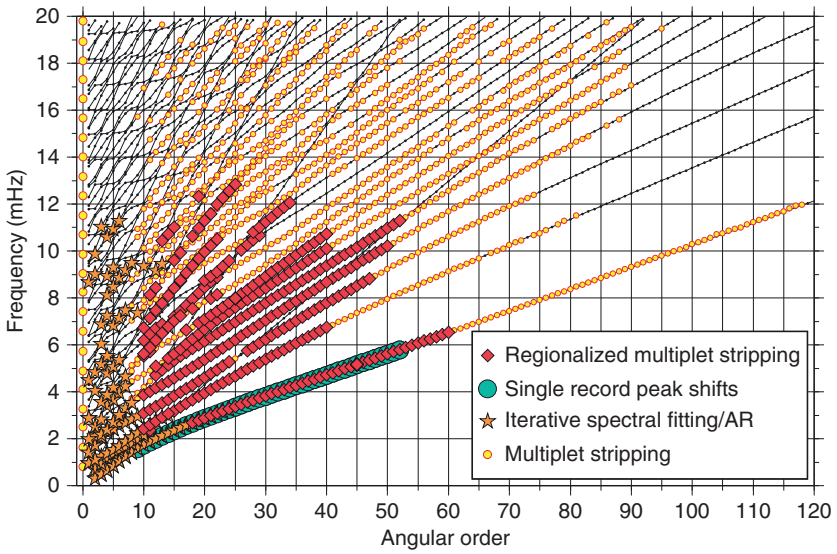

Figure 16 Spheroidal mode dispersion diagram (ω–ℓ plot) for spherical Earth model PREM. Different symbols indicate by which method a particular mode has been observed. Black dots are predicted modes that still await observation. The mode frequencies are published on the REM website except for the multiplet stripping results. Single record peak shifts refer primarily to the work of Smith and Masters (1989b). The first comprehensive ω–ℓ diagram showing observed modes was presented by Dziewonski and Gilbert (1972).

are only possible in spectra with high signal levels and at relatively high frequencies, where asymptotic theory is valid, which is typically the case only for fundamental modes. For other modes, this technique has been superseded by the regionalized stripping technique. The use of the different methods is summarized in **Figure 16** that includes only methods that we have used ourselves. Other methods include the time-lapse spectra approach used by Dratler et al. (1971) to measure attenuation rates of high-Q overtone modes. This method was also used by Roult (1974) and Jobert and Roult (1976) and others to determine attenuation rates for fundamental spheroidal and toroidal modes and the first few overtones. In this method, a sliding window of several hours (e.g., 6 h) is moved over a time series. An attenuation rate is then fitted to the collected amplitude values of a certain mode in a least-squares procedure. Our own (limited) experiments have shown that this technique gives accurate estimates as long as the spectral peaks are large and the frequency picked for the estimation is close to the observed peak shift frequency. Otherwise, oscillating amplitudes hamper the least-squares fitting procedure. For a discussion on mode attenuation rates, the interested reader is referred to **Chapter 1.21**. Roult and colleagues made use of the time-variable filtering technique to extract individual mode branches from a seismogram prior to analysis. This technique is laid out in the surface wave section. Romanowicz and Roult (1986) showed in a later intriguing study that information on lateral heterogeneity can be obtained from records of a single station by modeling the fluctuations of frequency shifts along a mode branch, for different earthquakes, as explained theoretically by Romanowicz (1987).

1.04.2.3.1 Multiplet stripping and degenerate mode frequencies

In the multiplet stripping procedure, we 'strip' an overtone from a 'stack' of spectra. This process requires a large set of recordings from different stations and events. The average location of a multiplet coincides with the multiplet degenerate frequency as long as the set of seismograms samples the globe evenly (condition 1) and as long as the distribution of singlets within a multiplet is relatively even (condition 2). Spectral stacking using a phase equalization procedure to extract free oscillation parameters was first used by Mendiguren (1973). Mode or multiplet 'stripping' was first introduced in the seminal paper of Gilbert and Dziewonski (1975) who used hand-digitized WWSSN recordings of the 1970 Colombian event and the 15 August 1963 Peru–Bolivia event. The set of mode frequencies they obtained constituted the bulk information in the construction of spherical Earth models 1066A, PEM-O/PEM-C/PEM-A (Dziewonski et al., 1975), and, finally, PREM (Dziewonski and Anderson, 1981) that is used as a REM still today.

In the multiplet stripping approach, we measure mode degenerate frequencies by linearly estimating multiplet resonance functions. In a second nonlinear step, a complex synthetic resonance function is fitted to the estimated resonance function to obtain the mode frequency and attenuation rate. With given starting models for the 1-D Earth and the earthquake source, the acceleration spectrum at the jth station, $u_j(\omega)$, can be computed as a weighted sum of multiplet resonance functions $c_k(\omega)$ (see eqn [4]):

$$u_j(\omega) = A_{jk} c_k(\omega) \qquad [11]$$

Within narrow frequency bands, the multiplet excitation, A, can be considered constant and frequency-independent. Multiplet stripping consists in estimating the 'multiplet strips' $\hat{c}_k(\omega) = A_{jk}{}^{-1} u_j(\omega)$ in a least-squares sense, given observed spectra $u_j(\omega)$ and given the predicted multiplet excitations A_{jk}.

By applying multiplet stripping to large sets of seismograms, we can isolate individual multiplets even at frequencies where the spectrum of modes is dense compared to the line width. **Figures 17** and **18** show the result of multiplet

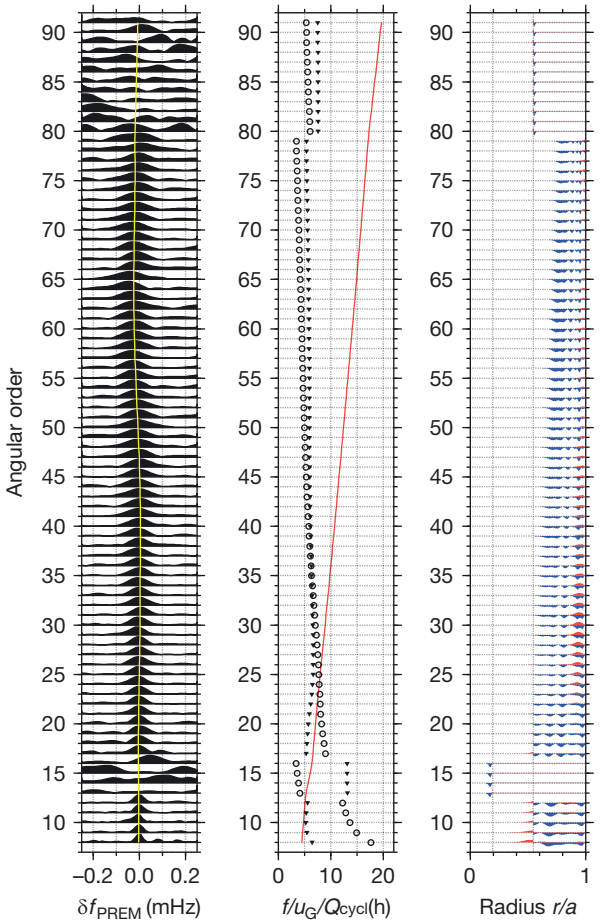

Figure 17 Multiplet strips for mode branch ${}_7S_\ell$, obtained from a data set of 12 000 records of 260 events between 1991 and 1998. The left panel shows the strips for the individual modes centered on the predicted PREM frequencies. The middle panel shows the predicted degenerate frequencies (red line, mHz), group velocity (triangles, km s^{-1}), and Q cycles (circles, h). The right panel shows compressional (red) and shear (blue) energy densities. Multiplet stripping works well up to 17 mHz or angular order $\ell = 79$ where the ${}_7S_\ell$ modes become Stoneley modes. Systematic deviations from PREM are evident in the left panel. The yellow line in that panel shows the predicted frequencies of MEMO0 (Valette and Lesage, 1992). This model seems to go a long way toward explaining the new observations even though it was constructed from a data set of modes below 5.4 mHz.

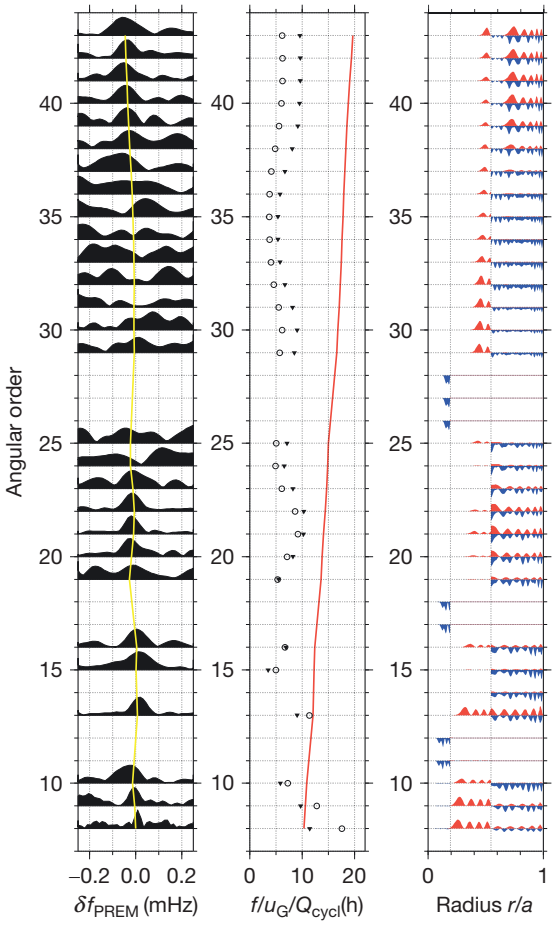

Figure 18 Multiplet strips for mode branch ${}_{23}S_\ell$, obtained from a data set of 12 000 records of 260 events between 1991 and 1998. For well-excited multiplets with intermediate to high-quality factors, Q, and sensitivity to lower mantle and core structure, multiplet stripping works well up to 20 mHz. Systematic deviations from PREM are evident in the left panel, particularly between ${}_{23}S_{39}$ and ${}_{23}S_{43}$. For details, see Figure 17.

stripping for the two spheroidal mode branches ${}_7S_\ell$ and ${}_{23}S_\ell$. The frequency band covered by the strips is 0.5 mHz and contains as many as 200 toroidal and 300 spheroidal modes. Nevertheless, the good sampling of the globe provided by 12 000 seismograms of 260 different events allows us to separate one mode from the others based solely on the shape of its eigenfunction and its excitation. The along-branch consistency such as exhibited by the mode group ${}_{23}S_{39} - {}_{23}S_{44}$ is a strong indication of the success of the method.

With the same large data set, we have tried to extract the radial modes ${}_nS_0$, which consist of only one singlet and hence cannot get split by aspherical structure. They are of particular interest because of their high sensitivity to density structure and to structure of the IC. Figure 19 shows the multiplet strips that we obtain for modes ${}_{10}S_0$ at 9 mHz through ${}_{23}S_0$ at 19.8 mHz. While for the two branches shown in Figures 17 and 18, the prediction of MEMO0 (Mean Earth MOdel) (Valette and Lesage, 1992) is in good agreement with the stripping results, neither PREM nor MEMO0 provides a satisfactory fit to our radial mode observations. The data set used for the construction of MEMO0 consisted of 617 mode degenerate frequencies in the period band 185–3230 s and included 198 toroidal, 10 radial, and 409 spheroidal modes from Masters and Widmer (1995). Whether the inability to fit radial mode observations requires new structure in the IC or whether it is due to coupling with nearby high-Q modes is still an open question.

As stated in the preceding text, one of the conditions for unbiased results is an even data coverage. In the long-wavelength limit of Jordan (1978), the sampling of the globe can be quantified by the density of great-circle poles. A scheme to optimize the selection of high signal-to-noise spectra that provide best possible sampling could minimize a possible bias. Unfortunately, large-size earthquakes and high-quality stations

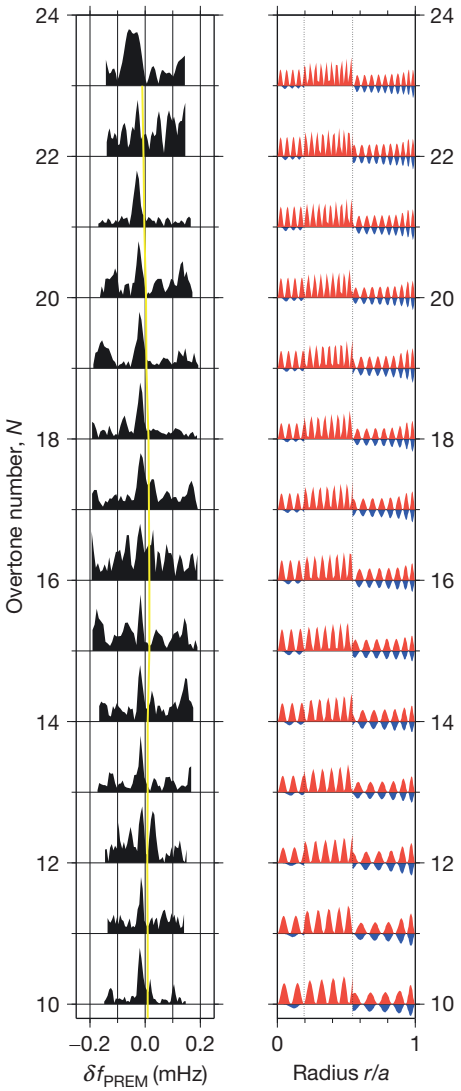

Figure 19 Multiplet stripping results for radial modes between 10 and 20 mHz. Strips with multiple peaks are likely due to coupling to nearby high-Q spheroidal overtones (Laske et al., 2001). The yellow line shows the predictions of MEMO0. Neither PREM nor MEMO0 gives a satisfactory fit to these modes. While a model with an additional first-order discontinuity in the inner core can explain the new radial mode frequencies, such a model leads to degradation of the fit of other IC-sensitive modes (B. Valette, personal communication, 2002). For details, see **Figure 17**.

are very unevenly distributed. These issues have been addressed with regionalized multiplet stripping by Widmer-Schnidrig (2002), where regular multiplet stripping is carried out for subsets of seismograms that sample only a particular great circle. While there is no substitute for missing data, regionalized multiplet stripping has at least allowed us to minimize the bias from long-wavelength structure. To date, about 30 years of high-quality digital seismic data enable us to successfully isolate individual modes to frequencies as high as 20 mHz. However, only the regionalized multiplet stripping results presented by Widmer-Schnidrig (2002), which stop at 12 mHz, are largely free of bias from 3-D structure because the data were selected and weighted to specifically minimize this bias. The multiplet strips presented here maximize the signal-to-noise ratio at the expense of some geographic bias (i.e., some source–receiver great circles may dominate the coverage).

Condition 2 at the beginning of this section addresses pathological cases when one or more singlets are located far away from their neighbors. Isolated singlets with low spectral amplitudes are likely missed and omitted from the stripping. Examples are anomalously split IC-sensitive modes such as ${}_{13}S_2$ for which the $m=0$ singlet lies anomalously far away from the mode's degenerate frequency (see **Figure 10**). Multiplet stripping for such a mode can produce strips with two peaks: a large peak near the four singlets $m=\pm1,2$ and a small peak near the $m=0$ singlet. Estimating the multiplet frequency by fitting only a single resonance function to the large peak produces a biased degenerate frequency estimate. A still elusive mode is ${}_3S_2$ for which no reliable observations of the $m=0$ line exist, not even after the Sumatra–Andaman event. The reason for this is not fully understood, but possible causes include weak excitation, peculiar anelastic structure, and coupling to other modes. Fortunately, the splitting of many low-ℓ modes can be resolved fully so that their degenerate frequency can be estimated using other techniques. For high-ℓ overtones, which are analyzed exclusively with the multiplet stripping technique, this kind of extreme singlet distribution does not appear to be a problem.

1.04.2.3.2 Singlet stripping and receiver stripping

Historically, singlet stripping was the first method to dissect a multiplet into its singlets (Buland et al., 1979). While it is a robust technique, it has been superseded by the AR receiver stripping technique (Masters et al., 2000b). This is because the latter makes less assumptions about the shape of Earth's heterogeneity and also needs no accurate earthquake source model. Singlet stripping assumes that the dominant structure leading to splitting is axisymmetric. In this case, the splitting matrix $\mathbf{H}$ (eqn [6]) remains diagonal. For the vertical component, one singlet frequency is then associated with a single Y_ℓ^m, as on the spherically symmetric Earth. The spectrum of a multiplet with angular order ℓ at the jth station, $u_j\ (\omega)$, can then be written as a weighted sum of singlet resonance functions $c_m(\omega)$:

$$u_j(\omega) = A_{jm} c_m(\omega) \quad \text{with} \quad -\ell \le m \le \ell \qquad [12]$$

where the singlet excitations, A_{jm}, have been computed based on eqn [4]. Equation [12] is an overdetermined system that can be solved for the 'singlet strips,' $\hat{c}_m(\omega) = A_{jm}{}^{-1} u_j(\omega)$. This procedure typically includes the records of many earthquakes.

In the receiver stripping approach, we treat each earthquake individually. Using eqns [4] and [5], we 'collapse' the set of spectra into a set of $2\ell+1$ 'receiver strips,' for each earthquake and each mode:

$$\mathbf{b}(t) = \mathbf{R}^{-1} \cdot \mathbf{u}(t) = \exp[\mathrm{i}(\mathbf{H} + \mathbf{I}\bar{\omega})t] \cdot \mathbf{a}(0) \qquad [13]$$

We actually work in the frequency domain using spectra of Hanning-tapered records in a small frequency band about a multiplet of interest. Examples are found in **Figure 20**. The spectral lines in these diagrams are proportional to the spectra of individual singlets, if axisymmetric structure dominates the

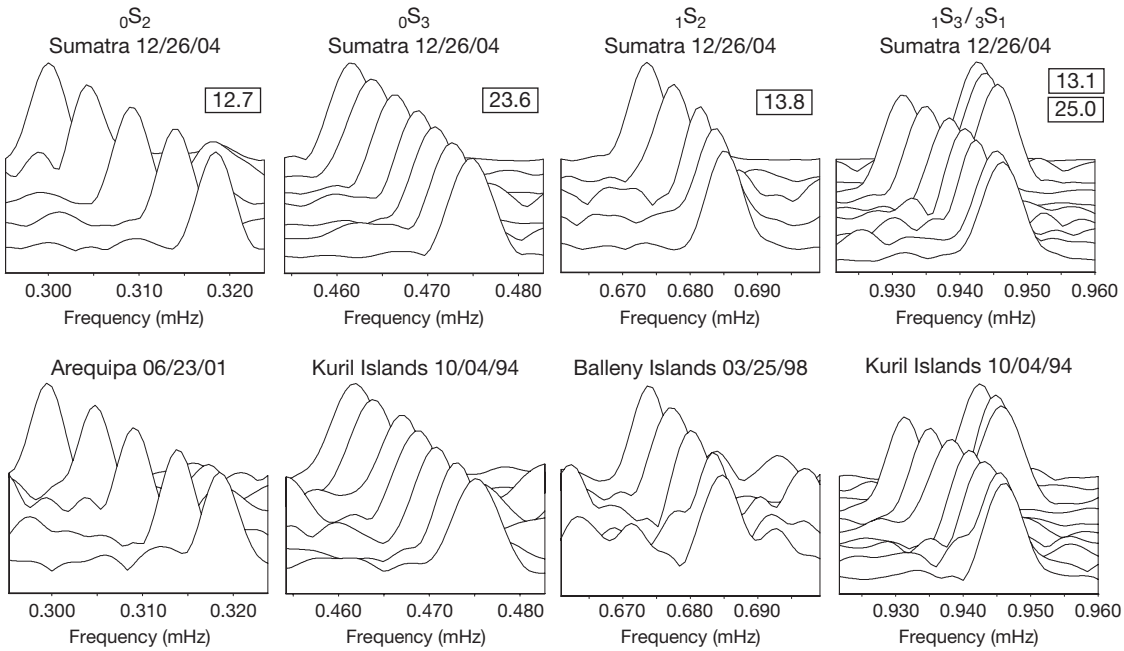

Figure 20 Normalized receiver strips for very low-frequency modes. For these modes, the splitting is dominated by axisymmetric structure, and the $2\ell+1$ strips closely resemble the spectral lines of each singlet. The upper row shows the strips for the 2004 Sumatra–Andaman earthquake, while the lower row shows the best set of strips that we have had so far. The boxed numbers indicate how much larger the amplitudes of the Andaman strips are with respect to the best other earthquake.

splitting matrix. Modes $_1S_3$ and $_3S_1$ are so close together in frequency that their receiver strips overlap. A joint analysis prevents bias introduced when ignoring one of the modes.

1.04.2.3.3 Retrieving the splitting matrix with the matrix autoregressive technique

Figure 21 shows typical examples of spectra for IC-sensitive mode $_{13}S_2$, and the steps involved going from seismograms (or spectra) to retrieve Earth's internal structure. We use the autoregressive nature of the receiver strips to make our analysis technique for the splitting matrix independent of earthquake location and source mechanism. The receiver strips satisfy a recurrence in time. Using eqn [13], we obtain $\mathbf{b}(t)$ after the time increment δt:

$$\begin{aligned}\mathbf{b}(t+\delta t) &= \mathbf{R}^{-1}\cdot\mathbf{u}(t+\delta t)\\ &= \exp[\mathrm{i}(\mathbf{H}+\mathbf{I}\bar{\omega})(t+\delta t)]\cdot\mathbf{a}(0)\\ &= \mathbf{P}(\delta t)\mathbf{b}(t)\end{aligned}$$

so

$$\mathbf{b}(t+\delta t)=\mathbf{P}(\delta t)\mathbf{b}(t),\ \mathbf{P}(\delta t)=\exp[\mathrm{i}\delta t(\mathbf{H}+\mathbf{I}\bar{\omega})] \qquad [14]$$

which describes the autoregressive nature of $\mathbf{b}(t)$. Equation [14] has no term that depends on the seismic source. An inverse problem is set up for the propagator matrix $\mathbf{P}$, using the strips of many events simultaneously. The splitting matrix $\mathbf{H}$ is determined from $\mathbf{P}$ using the eigenvalue decomposition of $\mathbf{P}$ (Masters et al., 2000b). The complex matrix $\mathbf{H}$ we retrieve in this process is non-Hermitian (no symmetry) and includes elastic and anelastic structure. We use the unique representation

$$\mathbf{H}=\mathbf{E}+\mathrm{i}\mathbf{A} \qquad [15]$$

to decompose $\mathbf{H}$ into its elastic, $\mathbf{E}={}^1/_2(\mathbf{H}+\mathbf{H}^{\mathbf{H}})$, and anelastic, $\mathrm{i}\mathbf{A}={}^1/_2[\mathbf{H}-\mathbf{H}^{\mathbf{H}}]$, components where superscript $\mathbf{H}$ indicates Hermitian transpose. Both $\mathbf{E}$ and $\mathbf{A}$ are Hermitian and are the matrices for eqn [6] (where the effects of rotation and ellipticity are included in $\mathbf{E}$). Examples of splitting matrices retrieved with this technique are shown in Figures 11 and 25 in Section 1.04.2.3.5. A discussion on retrieving Earth's density from splitting functions that were obtained using this method can be found in Masters et al. (2000c). An application to investigate the IC differential rotation is described Section 1.04.2.4.

1.04.2.3.4 Retrieving the splitting matrix with iterative spectral fitting

The first technique to retrieve all elements of the splitting matrix of an isolated multiplet was iterative spectral fitting (ISF) introduced by Ritzwoller et al. (1986), Ritzwoller et al. (1988), and Giardini et al. (1987). It has been refined and applied in a number of studies, including Li et al. (1991a), Li et al. (1991b), Widmer et al. (1992b), He and Tromp (1996), and Resovsky and Ritzwoller (1998). ISF considers the Fourier transform of eqns [4]–[6]. In this coupled set of equations, the $\ell-1$ real and $\ell(\ell+1)$ complex structure coefficients c_s^t are nonlinearly related to the observed spectra $u_j(\omega)$. The problem of finding the structure coefficients from a set of observed spectra is then formulated as a nonlinear parameter estimation problem. Figure 22 shows an example of how ISF allows detailed modeling of a split mode spectrum. The prediction from a model including only Earth's rotation and hydrostatic

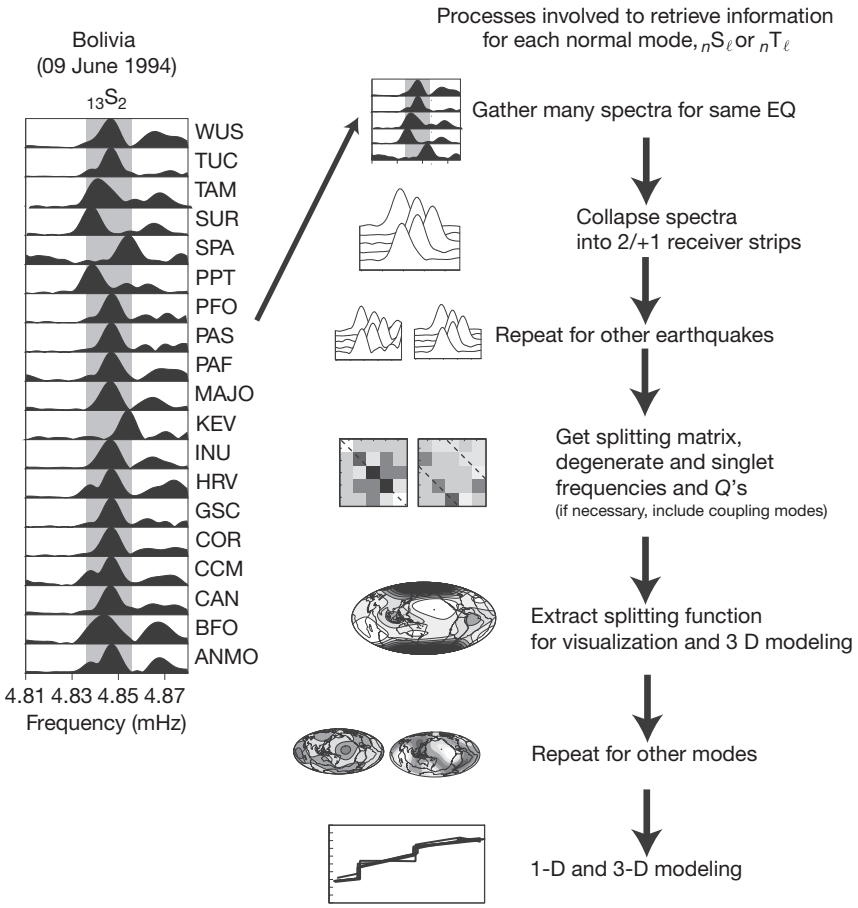

Figure 21 Left: Selected spectra for mode $_{13}S_2$, for the 1994 Bolivia earthquake. Right: Simplified flowchart of our approach to extract mode information from seismograms of large earthquakes.

ellipticity provides a poor fit to the observed spectrum. If ISF is implemented with a local search algorithm, this prediction can serve as starting solution. Spectral fitting is then iterated and converges to a new solution that fits the observation much better. The splitting of the mode shown here, $_1S_8$, reflects lower mantle V_S heterogeneity. A crucial aspect of ISF is the need of a source model so that the vector of singlet excitations **a** (0) in eqn [5] can be computed. Matters are further complicated, if local rather than the computationally more expensive global algorithms are used to search for the set of best-fitting structure coefficients. Nevertheless, for well-excited multiplets for which records from many events can be used simultaneously, it was possible with the data coverage of the 1980s to obtain robust estimates of degree $s=2$ and perhaps also $s=4$ structure coefficients.

ISF was also applied to high-Q, low-order modes up to 9 mHz (Widmer et al., 1992b). These modes sample the outer and inner core and many of the modes are anomalously split. The large majority of other modes attenuate so rapidly that the spectra are dominated by the relatively sparse class of high-Q modes, if the first 6–8 h of data after an earthquake are discarded. The set of structure coefficients of these high-Q

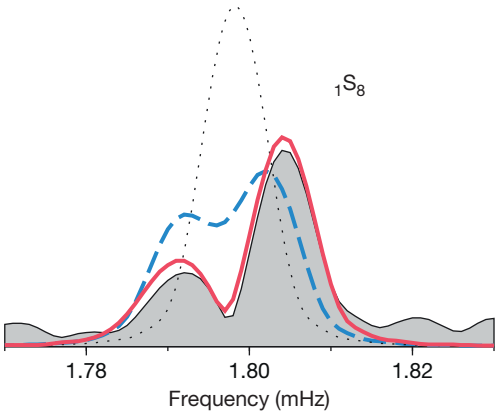

Figure 22 Modeling of the spectrum of multiplet $_1S_8$ with the ISF procedure, for a recording of the 9 June 1994 Bolivia earthquake at station MAJO (Matsushiro, Japan). Black line: Observed linear amplitude spectrum; dotted line: prediction for PREM; dashed blue line: splitting caused by Earth's rotation and hydrostatic ellipticity; red line: final solution for the spectrum after ISF. Spectra courtesy of Joe Resovsky, personal comm. 1998. Vertical ground displacement due to this mode at MAJO measured 10 μm.

modes analyzed by Widmer et al. (1992b) with both ISF and singlet stripping were used primarily by Tromp (1993) to corroborate the hypothesis of Giardini et al. (1987) that axisymmetric IC anisotropy can explain the anomalous splitting of IC-sensitive modes. The most comprehensive set of structure coefficients based on ISF was compiled by Resovsky and Ritzwoller (1998). Restricting their analysis to modes below 3 mHz, they obtained 3100 structure coefficients for 90 multiplets. These authors also generalized the ISF procedure to coupled modes and obtained, for the first time, constraints on odd-degree structure using normal modes (Resovsky and Ritzwoller, 1995). An updated mode data set obtained from using ISF is that of Deuss et al. (2013).

1.04.2.3.5 Observed mode coupling

As mentioned in the preceding text, we observe toroidal mode energy on vertical components because Coriolis coupling causes the formation of hybrid mode pairs in which energy is exchanged between modes. While this has been well observed for modes above 2 mHz, Zürn et al. (2000) recently also observed this for the gravest modes below 1 mHz (**Figure 23**). In gravimeter spectra of the great 1998 Balleny Islands earthquake, they identified spectral lines at the toroidal mode frequencies of ${}_0T_3$ through ${}_0T_6$. A correction of the LaCoste–Romberg gravimeter ET-19 record at station BFO for local atmospheric pressure variations (Zürn and Widmer, 1995) helped raise mode ${}_0T_3$ above the noise floor, while the spectrum of the superconducting gravimeter GWR-C026 at station J9 near Strasbourg also may have shown this peak. After the Sumatra event, Hu et al. (2006) observed the gravest toroidal mode ${}_0T_2$ and overtones ${}_1T_2$ and ${}_1T_3$ in gravimeter spectra. Using the method of Park and Gilbert (1986), Zürn et al. (2000) compared the effects of rotation, hydrostatic ellipticity, and aspherical Earth structure on coupled-mode synthetic spectra. They identified Coriolis coupling as the most effective mechanism responsible for toroidal mode energy to appear in the vertical-component spectra.

In the preceding text, we have described how the coupling of modes can lead to a frequency shift of the entire multiplet. An example is the Coriolis coupling between spheroidal and toroidal fundamental modes. The observation of Coriolis coupling is well documented for fundamental modes between 2 and 4 mHz (Masters et al., 1983; Smith and Masters, 1989a), and we recall that it is particularly strong for the two pairs ${}_0S_{11}$–${}_0T_{12}$ and ${}_0S_{19}$–${}_0T_{20}$. **Figure 24** shows this mode coupling in an analysis where we applied the multiplet stripping technique. In general, the effect of multiplet–multiplet coupling on the degenerate frequency cannot be corrected for using this technique, except for the case shown here (e.g., Smith and Masters, 1989a). For multiplet–multiplet coupling caused by aspherical structure, it has to be assumed that the induced shift of the degenerate frequency can be treated as a source of random noise. This may be justified as the frequency separation to the nearest coupling partners is different for every multiplet so the cross branch coupling is different for every multiplet. For along-branch coupling, systematic effects may be significant, since the frequency separation of modes belonging to the same branch is nearly the same.

Coupling through Earth structure manifests itself in the cross coupling blocks of the splitting matrix. We have recently started to apply the matrix AR technique to coupled modes, and an example for weakly coupled modes ${}_1S_5$ and ${}_2S_4$ is shown in **Figure 25**. Since the selection rules state that $\ell+\ell'+s$

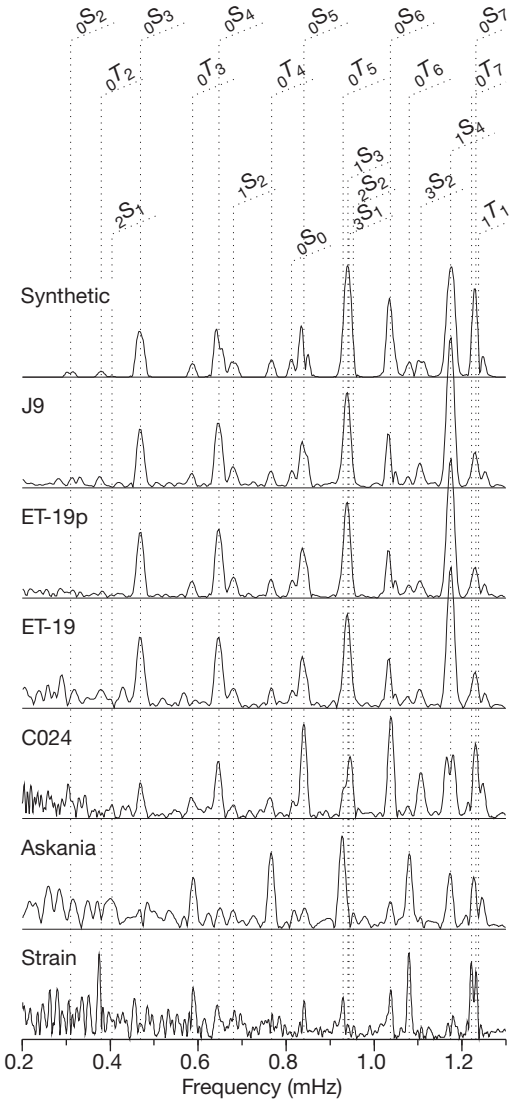

Figure 23 Coriolis coupling below 1 mHz, observed for the 25 March 1998 Balleny Islands earthquake. Spectral peaks appear in vertical-component spectra at the frequencies of toroidal modes ${}_0T_3$ through ${}_0T_6$. Shown are spectra of the LaCoste–Romberg spring gravimeter ET-19p at station BFO, the superconducting gravimeters GWR-C026 at station J9 near Strasbourg, 60 km from BFO, and GWR-C024 at Table Mountain Observatory near Boulder, CO (the United States). To reduce noise, the gravimeter records were corrected for variations in local atmospheric pressure (Zürn and Widmer, 1995). For comparison, the uncorrected spectrum at BFO is also shown (ET-19). The synthetic spectrum was obtained from a coupled-mode synthetic for BFO, using Park and Gilbert's (1986) method to account for effects from rotation, hydrostatic ellipticity, and aspherical structure. 'Askania' and 'strain' refer to data from the Askania borehole tiltmeter and the invar wire strainmeter array at BFO and show that the low-order fundamental toroidal modes were efficiently excited by the event. Reproduced from Zürn W, Laske G, Widmer-Schnidrig R, and Gilbert F (2000) Observation of Coriolis coupled modes below 1 mHz. *Geophysical Journal International* 143: 113–118.

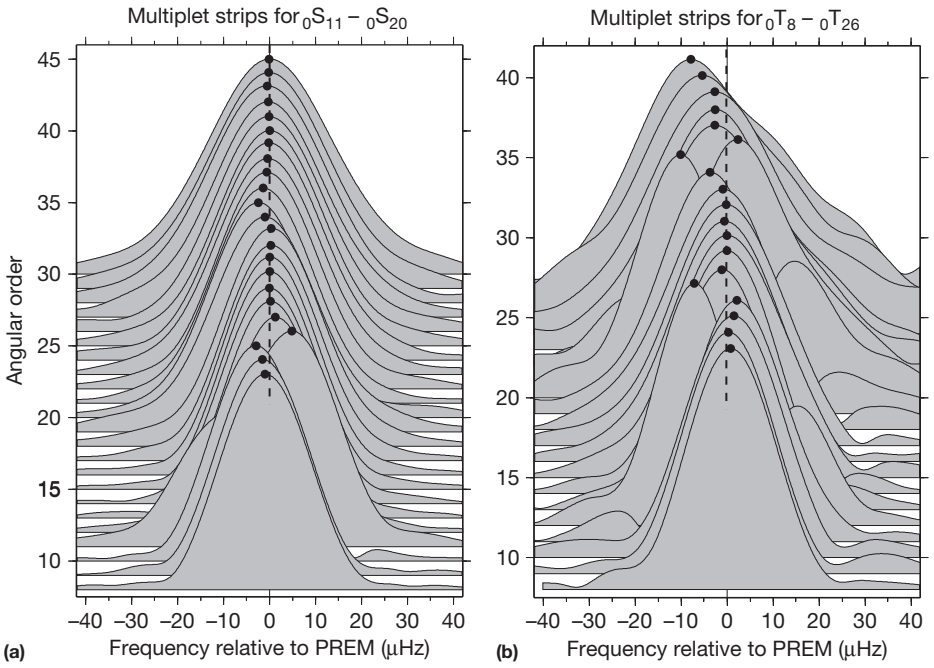

Figure 24 Observed effects of Coriolis coupling above 1 mHz. (a) Multiplet strips of fundamental spheroidal modes $_0S_8$ through $_0S_{30}$, aligned relative to PREM (Dziewonski and Anderson, 1981). (b) Multiplet strips of fundamental toroidal modes $_0T_8$ through $_0T_{26}$. Coupling effects are different for each singlet, resulting in a shift of the entire multiplet. Modes $_0S_{11}$ and $_0S_{20}$ are within a few microhertz of neighboring $_0T_{\ell+1}$ modes so coupling effects are particularly large. Coriolis coupling effects are significant for $_0S_9$ through $_0S_{22}$, relative to the observational uncertainties of <0.3 μHz. Modified from Widmer R (1991) The Large-Scale Structure of the Deep Earth as Constrained by Free Oscillation Observations. PhD Thesis, University of California San Diego, La Jolla, CA.

must be even, these two modes couple through structure of odd-harmonic degree. Coupling through Earth structure makes the splitting matrix quite complex, and the cross coupling blocks we determine with our technique may yet be too noisy to extract odd-degree structure. This should be improved in the future by including more earthquakes in the analysis. Resovsky and Ritzwoller (1995) successfully determined odd-degree structure implied in the cross coupling blocks by using the ISF method. In the example shown here, only a mode pair was considered, whereas Resovsky and Ritzwoller (1995) considered relatively small groups of modes below 3 mHz. Deuss and Woodhouse (2001) showed that wideband coupling can significantly alter the shape of spectral lines, though it is not immediately clear if this effect is significant with respect to measurement errors of mode observables.

Since the coupling strength scales with the inverse of the frequency separation of coupling modes, splitting matrices above 3 mHz become so large that their decomposition turns into a numerically formidable task. Several different strategies have been suggested to reduce the computational burden. Lognonné and Romanowicz (1990) and Lognonné (1991) introduced the efficient spectral method using third-order perturbation theory to compute coupled modes and seismograms for an anelastic rotating Earth. Using this method, Millot-Langet et al. (2003) calculated coupled-mode synthetics on an anelastic 3-D Earth. Deuss and Woodhouse (2004) introduced a method that is similar to subspace projection methods but can be iterated several times to completely represent the exact solution. They found that only one iteration usually brings the solution sufficiently close to the exact solution.

Alternatives to the approach based on mode summation include the direct solution method (Geller and Takeuchi, 1995) for which an application to 3-D heterogeneity can be found in Takeuchi et al. (2000). The spectral element method of Komatitsch and Vilotte (1998) also has been shown to provide an efficient tool to study wave propagation, diffraction, and body-wave conversion in a 3-D Earth. Applications of this method can be found in Komatitsch and Tromp (2002), Komatitsch et al. (2002), Capdeville et al. (2003), and Chaljub and Valette (2004). Gilbert (2001) suggested that a Vandermonde matrix analysis allows the independent determination of earthquake mechanisms and Earth structure. The method also allows the analysis of 'latent' modes that are not observed but coupled to observed modes (e.g., modes with extremely little energy density near the surface). For a detailed discussion of numerical methods, the reader is referred to **Chapter 1.07**.

1.04.2.4 Example of a Mode Application: Inner-Core Rotation

Differential rotation of the IC with respect to the rigid mantle has been inferred by several body-wave studies, with most agreeing that a superrotation may exist with a rate between 0.2° and 3° per year (e.g., Creager, 2000; Song and Richards, 1996). The wide range of inferred rotation rates is caused by the sensitivity of such studies to local complexities in structure, which have been demonstrated to exist. Free oscillations, on

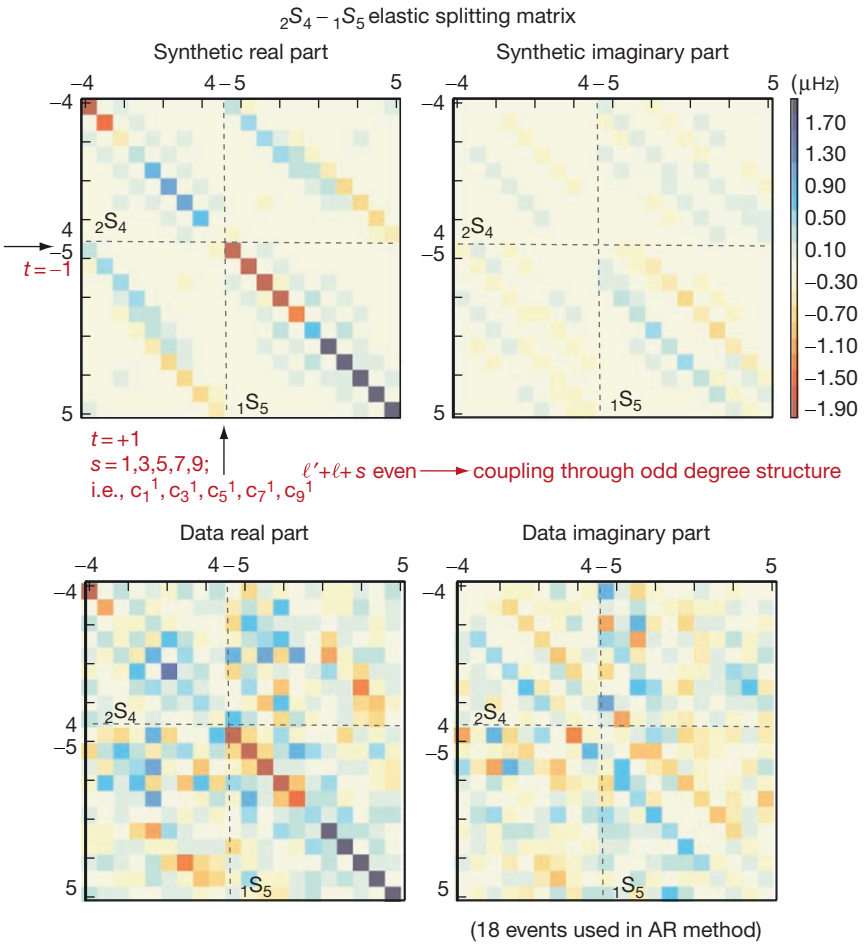

Figure 25 Predicted and measured elastic splitting matrix **E** of the coupled-mode pair $_1S_5$–$_2S_4$. The signal in the diagonal self-coupling blocks is generally somewhat larger in the observations than in the predictions (e.g., imaginary part for mode $_2S_4$). Some predicted features show up in the measured off-diagonal cross coupling blocks (e.g., blue in upper-left corner and red toward the lower right in the real part), but noise probably inhibits a reliable extraction of odd-degree structure from these blocks at this time. The 3-D model used for the synthetic splitting matrix is S16B30 (Masters et al., 1996). Reproduced from Masters TG, Laske G, and Gilbert F (2000d) Large-scale Earth structure from analyses of free oscillation splitting and coupling. In: Boschi E, Ekström G, and Morelli A (eds.) *Problems in Geophysics for the New Millennium*, pp. 255–288. Bologna: Editrice Compositori.

the other hand, are natural low-pass filters of 3-D structure, so that long-wavelength phenomena, such as IC rotation, are prime study targets. Free oscillations 'see' Earth as a whole, so the observation of how a free oscillation splitting pattern changes with time, and any inference on IC rotation is not biased by the effects of localized structures. It is also not necessary to know the physical cause of the patterns (anisotropy or heterogeneity). All that needs to be observed is if and how they change with time. Free-oscillation splitting functions are therefore better candidates for estimating differential IC rotation accurately. The most obvious approach to do this analysis is to compare splitting functions obtained with earlier earthquakes to those obtained with recent events. A problem with this approach is that the sparsity of early data does not allow us to construct early splitting functions with the required accuracy. Sharrock and Woodhouse (1998) therefore studied the time dependence of the fit of splitting functions to spectra of earthquakes over time for some IC-sensitive modes. Their estimates of a westward rotation of the IC with respect to the mantle appear to be inconsistent with the results from body-wave studies. We prefer to use our autoregressive technique for this analysis.

In a hypothesis test, we sought the optimal IC rotation rate that matches our splitting functions for the recent earthquakes with receiver strips over time. Our initial finding was that the IC rotation is essentially zero over the last 20 years ($0.01 \pm 0.21°\text{year}^{-1}$; Laske and Masters, 1999). A complication in this analysis – that also plays a role in many body-wave studies – is that IC-sensitive modes are also very sensitive to mantle structure. Prior to applying the assumed IC rotation rate in the test, we therefore have to correct for the contributions from the heterogeneous mantle. In a detailed and updated analysis, Laske and Masters, (2003) applied mantle corrections using a variety of published mantle models (**Figure 26**). Our preferred model is SB10L18 (Masters et al., 2000a), a 10-degree equal area block model that was derived simultaneously for shear velocity and bulk sound speed, $V_C = \sqrt{\kappa/\rho}$, and our mode data were included in the

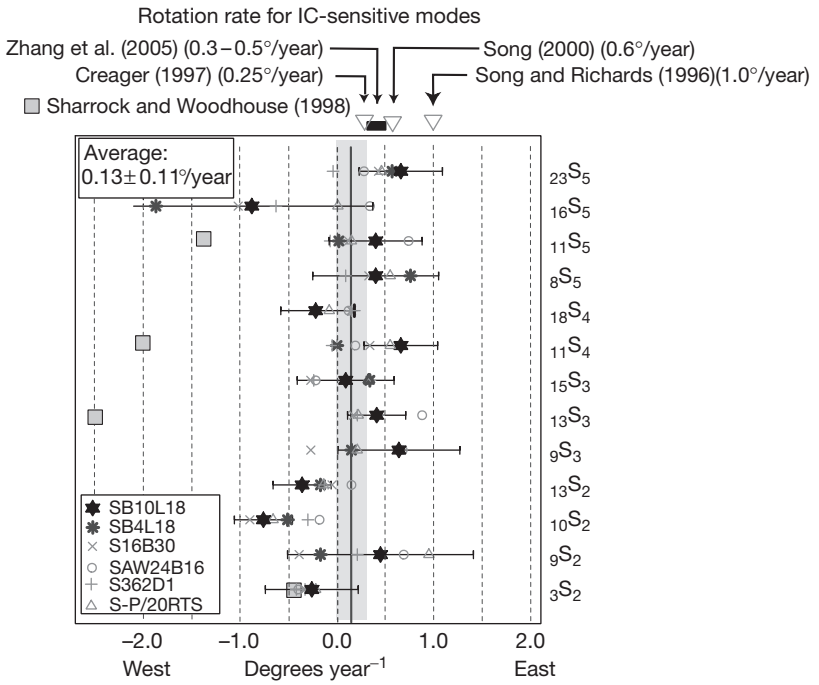

Figure 26 IC rotation rates obtained for 13 IC-sensitive modes, using our preferred $V_S/V_C/V_P$ mantle model SB10L18 (Masters et al., 2000a). Also shown are the results obtained using other mantle models: shear velocity models SB4L18 (Masters et al., 2000a), S16B30 (Masters et al., 1996), SAW24B16 (Mégnin and Romanowicz, 2000), and S362D1 (Gu and Dziewonski, 1999) and V_S/V_P models S-P/20RTS (Ritsema and van Heijst, 2000). Other symbols and lines mark results from other publications: Song and Richards (1996), Creager (1997), Sharrock and Woodhouse (1998), Song (2000), and Zhang et al. (2005).

inversions. The majority of models in the literature are shear velocity models that were derived using only shear-sensitive modes (e.g., SAW24B16 by Mégnin and Romanowicz, 2000) or using established scaling relationship for V_P and ρ (or ignoring sensitivity to the latter entirely) to include spheroidal modes (e.g., S20RTS by Ritsema and van Heijst, 2000). Our comparison also includes our older model S16B30 (Masters et al., 1996) that was the result of a direct matrix inversion for a model described by spherical harmonics. As can be seen from Figure 26, inferred rotation rates vary with different mantle models, but most results lie within our error bars for SB10L18. Laske and Master's best estimate is a barely significant super-rotation of 0.13 ± 0.11 year^{-1}, which is still consistent with the idea that the IC is gravitationally locked to the mantle. A more recent estimate of 0.00 ± 0.06 year^{-1} that is based on data up to and including the 2011 Tohoku, Japan, earthquake was presented at the 2011 General Assembly of the EGU (Masters, 2011). These results are broadly consistent with many body-wave results (e.g., Creager, 1997, 2000) though the discrepancy to a recent body-wave estimate of 0.3–0.5 year^{-1} by Zhang et al. (2005) is marginal but still significant.

There are limitations to this type of analysis, and not all IC-sensitive modes can be utilized. For example, although $\ell = 1$ modes (e.g., ${}_8S_1$ and ${}_{13}S_1$) are quite sensitive to IC structure, they can constrain IC rotation only poorly because the mantle-corrected splitting functions are dominated by a large zonal (axisymmetric) component. Also, so far, we have ignored mode coupling in our analysis. Some IC-sensitive modes significantly overlap in frequency with other modes of high angular order ℓ, thereby hampering an analysis using the receiver strip method. For example, with a degenerate frequency in PREM (Dziewonski and Anderson, 1981) of 1.242 mHz, mode ${}_2S_3$ is very sensitive to IC shear velocity but overlaps with ${}_0T_7$, ${}_0S_7$, and ${}_1T_1$, which couple through Earth's 3-D structure. For a given mode pair ${}_0S_\ell/{}_0T_{\ell'}$, we need at least $2 \times (\ell' + \ell + 1)$ high-quality records to construct receiver strips. These many records are often not available for earlier earthquakes. Many $\ell = 2$ modes that are very sensitive to IC structure are strongly coupled to radial modes. We can analyze such mode pairs with our AR technique, but the IC rotation hypothesis test becomes more cumbersome and was not done in our 2003 study. We notice that mode ${}_{13}S_2$, which couples with ${}_5S_0$, and mode ${}_{10}S_2$, which couples with ${}_4S_0$, systematically suggest a westward IC rotation, regardless of the mantle model chosen for the corrections. The analysis of ${}_3S_2$, whose coupling properties with neighboring modes is quite complex (see also Zürn et al., 2000), also gives westward rotation rates. Mode ${}_9S_2$ is difficult to observe and errors are quite large. When not taking these modes into account, we obtain an eastward IC rotation rate of $0.34 \pm 0.13°$year^{-1}. This marginally agrees with the estimate of Zhang et al. (2005).

A caveat when analyzing modes using the isolated-mode assumption is that only even-degree structure can be determined. It is known from body-wave studies that the heterogeneity at the top of the IC has a strong $s = 1$ signal that is roughly divided into a Western and an Eastern Hemisphere (Creager, 2000; Tanaka and Hamaguchi, 1997). The fact that isolated modes are insensitive to such structure does not invalidate our IC rotation results, provided the IC rotates as a rigid body. Structure of odd-harmonic degree can potentially be determined

by analyzing coupled modes, but the coupling effects for the modes considered here are rather weak. Core structure and IC differential rotation are discussed in **Chapter 1.23**.

1.04.2.5 Example of a Mode Application: Earth's Hum

It took as long as 38 years after the first observation of Earth's free oscillations of the 1960 Great Chilean earthquake before convincing evidence was found that Earth's normal modes never cease to vibrate but instead remain excited at a low but nearly constant level (Ekström, 2001; Suda et al., 1998; Tanimoto et al., 1998). This normal mode background signal is now often termed Earth's 'hum.' Early on, Benioff et al. (1959) looked for modal signals in noise spectra of LaCoste–Romberg gravimeters, but the sensitivity of these instruments (which at the time were operated with a mechanical feedback) was too low by three orders of magnitude for a positive hum detection. It was not until Nawa et al. (1998) first inspected data from the superconducting gravimeter at Syowa (Antarctica) and subsequently from seismic stations of the global network (Suda et al., 1998) that evidence for the incessant excitation of seismic free oscillations was presented.

Fundamental spheroidal modes ${}_0S_\ell$ are observed to be permanently excited in the frequency band 2–7 mHz, with an root mean square acceleration amplitude of ~1 ngal ($=10^{-11}$ ms^{-2}) over a 100 μHz bandwidth (**Figure 27**). Additional characteristic hum features are a slight semiannual modulation of the amplitude and a resonant enhancement near 3.7 mHz (Ekström, 2001; Nishida et al., 2000). At frequencies below 2 mHz, vertical seismic noise is primarily of local barometric origin, and some of this noise can be removed by regression with the locally recorded pressure fluctuations (Zürn and Widmer, 1995). However, this crude correction does not allow to remove all of the barometric noise, making a hum detection below 2 mHz nearly impossible. At frequencies near 7 mHz, the splitting of the fundamental spheroidal modes due to heterogeneous upper-mantle structure is as wide as the frequency separation between adjacent fundamental modes. Modes then overlap and cause an overall rise of the noise base level into which peaks disappear. Nishida et al. (2002) showed that the vertical-component seismic noise consists of globe-circling Rayleigh waves all the way up to 20 mHz, and it seems likely that the same mechanism is responsible for the generation of Rayleigh wave background noise as for the hum at lower frequency. The detection of the hum is an instrumental challenge because of its exceptionally small amplitude. The self-noise of all instruments that have so far been able to detect the hum is at or very near the amplitude of the hum itself. These include superconducting gravimeters, LaCoste–Romberg spring gravimeters, and Streckeisen STS-1 and STS-2 seismometers. Widmer-Schnidrig (2002) computed coherences for pairs of colocated sensors and in the hum band obtained values not exceeding 0.5. The low signal-to-noise ratio in individual traces necessitates much averaging in time or the use of array techniques to enhance the hum signal.

The physical processes responsible for the excitation of the hum remain somewhat of a puzzle. Considering that wave motion in the oceans is responsible for the marine microseisms at periods shorter than ~25 s and that below 2 mHz atmospheric phenomena dominate the seismic noise, one can speculate that the signals in between are also generated by atmospheric and/or hydrospheric processes. The semiannual modulation supports this hypothesis, while the resonant enhancement near 3.7 mHz (Nishida et al., 2000) is evidence for at least partial involvement of the atmosphere (e.g., Widmer and Zürn, 1992). The lack of overtones in the hum favors near-surface excitation and also speaks for the atmosphere and/or hydrosphere excitation hypothesis. From the observation that individual mode excitations do not correlate between pairs of stations, Nishida and Kobayashi (1999) had drawn the conclusion that the source of the hum cannot be localized but must be of global origin: they hypothesize that pressure exerted on the solid Earth by global atmospheric turbulence is responsible for the hum excitation. This conclusion, however, is not compelling because of the low signal-to-noise ratio mentioned in the preceding text.

Trying to elucidate the hum excitation mechanism, Rhie and Romanowicz (2004) used the BDSN (Berkeley Digital Seismic Network) in California and the F-net in Japan to estimate the back azimuth of the Rayleigh wave background signal. They located hum sources in the North Pacific during Northern Hemisphere winter and in the southern oceans during summer. A subsequent analysis of 5 years of data from the GRSN (German Regional Seismic Network) in Germany found back azimuths consistent with these source regions (Kurrle and Widmer-Schnidrig, 2006). **Figure 28** shows that the back azimuths of Rayleigh waves at GRSN also have a very pronounced seasonality. Prevalent winter back azimuths around 30° point toward the North Pacific, while summer back azimuths of 210° and 120° point to the southern Pacific and southern Indian Ocean, both in accordance with Rhie and Romanowicz (2004). More recently, Rhie and Romanowicz (2006) studied two winter storms off the west coast of N America during four seismically quiet, consecutive days. As the storms encountered the coast, the amplitude of both the marine microseisms and the low-frequency Rayleigh waves increased, and both wave types could be traced back to the same coastal segment where the storms hit the shore.

While the generation of microseisms by ocean surface gravity waves is well understood (e.g., Kedar et al., 2008; Longuet-Higgins, 1950), it is not entirely clear how the band-limited surface gravity waves are linked to the occurrence of infragravity waves and subsequently the generation of low-frequency Rayleigh waves. One particular difficulty in this chain of linked phenomena is the mismatch of wave numbers between open-ocean infragravity waves on the one hand and Rayleigh and Love waves on the other: at a given frequency in the hum band, the wavelength of Rayleigh and Love waves is 25 times larger than that for infragravity waves in the deep ocean.

Infragravity-wave generation is most efficient on the continental shelf and involves nonlinear wave–wave interactions (e.g., Galagher, 1971; Tanimoto, 2005; Webb, 1998). Rhie and Romanowicz (2006) observed hum excitations not only along the west coast of North America, where the infragravity waves were originally generated, but also along the North Pacific Rim after the waves apparently traveled there and dissipated. The timing was found to be consistent with the propagation speed of ~200 ms^{-1} for infragravity waves in the open ocean. If infragravity waves are capable of exciting the hum to observable levels after crossing entire ocean basins, this may explain why previous attempts at locating the source

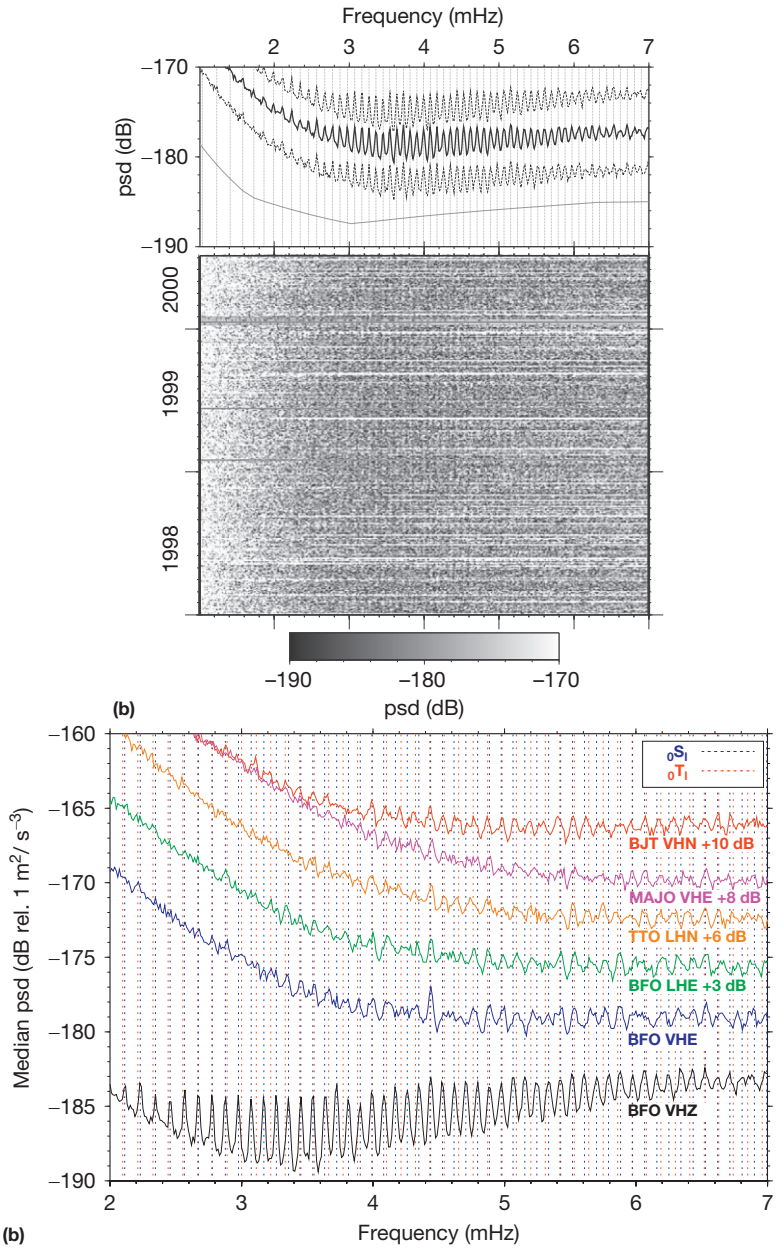

Figure 27 (a) Time–frequency plot covering 2.5 years of data from the STS-2 seismometer of the German Regional Seismic Network (GRSN) at BFO. The range of the gray scale is chosen to emphasize structure in the noise during seismically quiet times. The upper panel shows median psd levels (black) together with the first and third quartiles (dashed). The new low noise model of Peterson (1993) (gray) is shown for reference. The vertical dashed lines indicate the predicted frequencies of the fundamental spheroidal modes ${}_0S_\ell$ and coincide with light-gray vertical bands in the lower panel. (b) Comparison of vertical and horizontal hum. The bottom trace (BFO VHZ) with the regular comblike structure shows the spheroidal hum recorded on the vertical-component STS-1Z seismometer at BFO. The traces above show spectra of the horizontal hum recorded at four different stations of the GSN, F-net, and GRSN seismic networks: BFO, TTO, MAJO, and BJT. The richer spectrum of the horizontal hum is due to the interference of fundamental spheroidal and toroidal modes. The different horizontal hum spectra are offset for clarity. (Kurrle and Widmer-Schnidrig, 2008).

regions of the hum produced only very diffuse maps (e.g., Nishida and Fukao, 2007). More recent studies based on data from the large, transportable USArray (292 stations with an aperture of 2000×1200 km) confirmed the shelves as the dominant source region in times of large oceanic storms (Bromirski and Gerstoft, 2009). However, whether the processes invoked to explain the observations from large winter storms are representative for the persistent background hum excitation remains an open question.

Owing to higher noise levels in horizontal component seismic recordings, it took another 10 years after the discovery of the spheroidal hum to discover its counterpart in horizontal

recordings. A horizontally polarized hum consisting of spheroidal modes was to be expected because the particle motion of spheroidal modes (and Rayleigh waves) follows an ellipse in a vertical plane. However, the discovery of the horizontal hum included also a big surprise: it consisted also of toroidal modes, and the latter were present with equal or even larger amplitudes than the spheroidal modes (**Figure 27(b)**). Kurrle and Widmer-Schnidrig (2008) estimated the ratio of toroidal-to-spheroidal signal power at 4 mHz to be close to unity, while at 12.5 mHz, Nishida et al. (2008) estimated the power of Love waves to be three times larger than for Rayleigh waves.

Initially, the large fraction of toroidal energy posed a serious challenge to the models of hum excitation. At the time, these models consisted of predominantly vertical forces from pressure fluctuations of infragravity waves on the shelf or in the deep ocean that in turn lead to an excitation of spheroidal modes (e.g., Tanimoto, 2005; Webb, 2007). However, vertical pressure forces acting on a horizontal sea floor excite exclusively spheroidal modes and lead to no excitation of toroidal modes. Fukao et al. (2010) proposed a model for spheroidal and toroidal hum excitation, which could resolve this conundrum. In its simplest form, this model can be described as follows: consider a patch of sea floor with a periodic bathymetry consisting of linear sinusoidal hills (e.g., abyssal hills), and let a monochromatic infragravity wave with the same wavelength as the bathymetry propagate over this patch in a direction perpendicular to the bathymetric hills. The pressure field acting on the sloping sea floor can now be decomposed into vertical and horizontal pressure forces: while the resulting vertical forces oscillate rapidly with position, the horizontal pressure forces are not oscillating spatially but point in the same direction for the entire patch. This model achieves two things: (1) it overcomes the mismatch in wave numbers between infragravity waves and seismic surface waves, and (2) it provides a mechanism with a predominantly horizontal force, which naturally leads to the excitation of Love and Rayleigh waves with comparable amplitudes.

While identifying the processes that lead to the excitation of the hum needs further study, Nishida et al. (2009) succeeded in using the hum signal to infer 3-D upper-mantle shear wave velocity structure. Their work is closely related to the emergent field of ambient noise tomography, which is discussed in the surface wave section and in **Chapter 1.12**. For a more detailed discussion of the hum, the interested reader is referred to the excellent review article by Nishida (2013).

1.04.3 Surface Waves

1.04.3.1 Standing Waves and Traveling Waves

Surface waves provide a rich data set to explore Earth's crust and upper mantle as well as seismic sources on a multitude of scales (see Romanowicz, 2002 for a comprehensive review). Many papers document that there is no real boundary between free-oscillation and surface wave measurements. For example, early free-oscillation papers that discuss great-circle surface wave dispersion actually discuss free-oscillation peak shifts (e.g., Roult and Romanowicz, 1984). Studying long-period surface waves, Souriau and Souriau (1983) found a plate subduction-related degree 2 anomaly in the transition zone that was similar to that of Masters et al. (1982) using their mode approach. In fact, surface wave theory on the spherical Earth can be understood as a high-frequency approximation of mode theory. As mentioned in the mode section, the motion of standing waves on a sphere is expressed in spherical harmonics. At epicentral distance Δ, standing waves along a source–receiver great circle are described by zonal harmonics where the Legendre polynomials $P_\ell(\cos\Delta)$ are the relevant terms (**Figure 29**). In the high-frequency or high-ℓ asymptotic expansion, this term is approximated by cosines which are the relevant terms of traveling waves (e.g., Aki and Richards, 1980, 2002; Jordan, 1978; Romanowicz and Roult, 1986) to zeroth order in $1/\ell$ (see Romanowicz, 1987, for higher-order expansion):

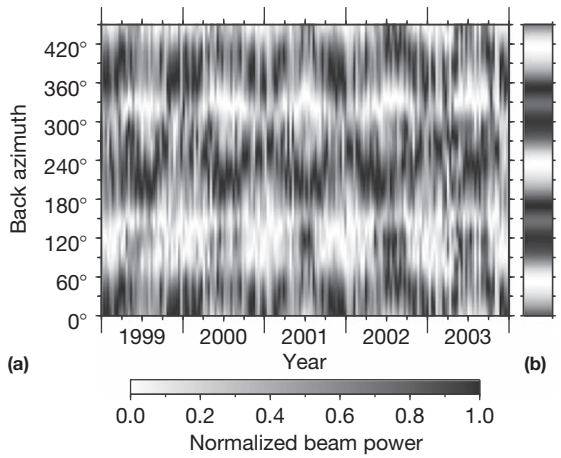

Figure 28 (a) Beam power distribution of Rayleigh wave background between 5 and 8 mHz estimated from vertical-component recordings of a nine-station array in Central Europe. (b) Back azimuths of an incident plane wavefield cannot be recovered perfectly from a sparse nine-station array. This is evident from the array response shown here. (Kurrle and Widmer-Schnidrig, 2006).

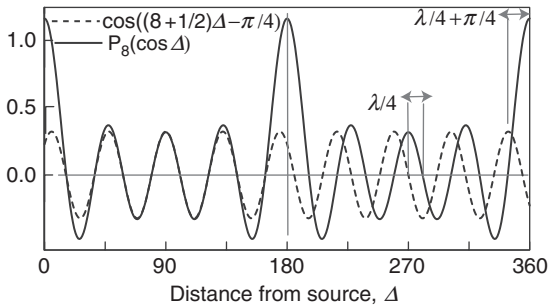

Figure 29 A comparison of the degree 8 Legendre polynomial with its asymptotic representative. The scaling factor of eqn [16] was omitted, but a constant factor was applied for optimal illustration. The graph also illustrates the validity of Jeans' formula. The asymptotic representation is applicable strictly only near $\Delta = 90°$. After passing a pole, the asymptotic leads by $\pi/2$ or approximately a quarter wavelength where $\lambda = 2\pi/(\ell + 1/2)$. Entering and exiting a pole each add $\pi/4$.

$$P_\ell(\cos\Delta) \simeq \left(\frac{2}{\pi\ell\sin\Delta}\right)^{\frac{1}{2}} \cos\left[\left(\ell+\frac{1}{2}\right)\Delta - \frac{\pi}{4}\right] \qquad [16]$$

Away from the poles, Jeans' formula (Jeans, 1923) gives the approximate wave number, k, of such a cosine:

$$k = \frac{\ell+\frac{1}{2}}{a} \qquad [17]$$

where a is Earth's radius.

Dahlen and Tromp (1998) described the conversion from the standing wave to the traveling wave representation through the Watson transformation

$$\sum_{\ell=0}^{\infty} f\left(\ell+\frac{1}{2}\right) = \frac{1}{2}\int_C f(k)\mathrm{e}^{-\mathrm{i}k\pi}\cos(k\pi)^{-1}\mathrm{d}k \qquad [18]$$

where f is any function that is analytic near the real k-axis and C is a closed contour along the positive real k-axis (see also box 9.7 in Aki and Richards, 2002 and box 9.3 in Aki and Richards, 1980). This demonstrates how a sum over discrete modes (standing waves) is expressed as an integral over continuous wave number (traveling waves).

Approaching the problem from the other end, to observe a free-oscillation spectrum, the time series has to include at least a pair of wave trains traveling in opposite directions as well as a third wave train that circled Earth, that is, the time window has to be at least roughly 5 h long (**Figure 30**; see also **Figure 3**). The synthetic seismograms that **Figure 30** is based on were calculated for an epicentral distance of nearly 90°. In this case, the fundamental mode spectra are modulated such that often, every other mode has a significantly reduced amplitude though this modulation also depends on the source. For the examples shown here, we assume a double-couple point source. A seismogram including only one wave train carries no information on the finite body Earth; hence, we do not observe normal modes. As soon as a major arc wave train and a minor arc wave train are recorded, an amplitude modulation pattern emerges that depends on the epicentral distance and the source mechanism. If two wave trains are recorded that are separated by a complete great circle, modes can be observed though

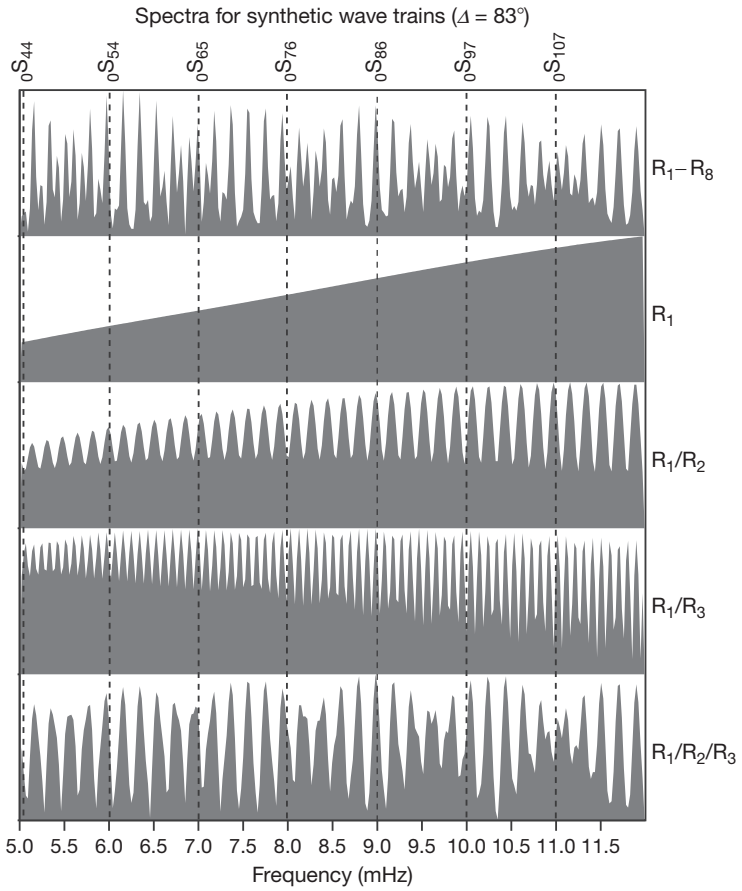

Figure 30 Spectra of synthetic acceleration seismograms at an epicentral distance of 83°, with a variety of wave trains as indicated on the right. All time series are 12 h long. Only the top spectrum contains all wave trains that arrive at a station within 12 h. Wave trains in the other records were zeroed out. A Hanning taper was applied before calculating the spectra. The full amplitude modulation is apparent only after three wave trains are recorded at a station. The combination R_1/R_3 is an unrealistic case but demonstrates that wave trains separated by a full great circle carry mode information (see also the caption in **Figure 4**). The seismograms were calculation with a mode summation code based on MINOS (see **Section 1.04.2.1**).

without this amplitude modulation. This peculiar behavior becomes clear when we discuss the representation of a surface wave seismogram on the spherical Earth.

Away from the poles, surface waves traveling on the spherical Earth can be expressed by

$$s(t)=\frac{1}{2\pi}\int_{-\infty}^{\infty}A_s(\omega)e^{-\alpha(\omega)t}\times e^{i(\omega t-k(\omega)x+(N-1)\pi/2+\Phi_s(\omega))}d\omega \quad [19]$$

where A_s is the source amplitude, $\exp(-\alpha(\omega)t)$ describes the attenuation along the path, Φ_s is the source phase, and $i(\omega t-kx)$ describes the evolution of the phase along the travel path. Brune et al. (1961) first described and experimentally verified that surface waves traveling on a sphere experience a $\pi/2$ phase shift each time the wave passes a pole. This is accounted for by the term $(N-1)\pi/2$, where N is the wave orbit number. The polar phase shift can be explained by the fact that eqn [16] is a good approximation only for distances $<180^\circ$ where the $P_\ell(\cos\Delta)$ are in phase with the cosines (**Figure 29**). For distances $180^\circ<\Delta<360^\circ$, this representation lags by a quarter of a wavelength, or $\pi/2$. Note that we ignore the scaling factor of eqn [16] in **Figure 29**. Including this factor provides a better match in amplitudes for a wider distance range away from 90°, but the factor is singular near the poles. From a traveling wave perspective, the poles are locations of caustics where an approaching surface wave from one direction is not defined (e.g., Romanowicz and Roult, 1986; Schwab and Kausel, 1976b; Wielandt, 1980). Using eqn [19], we can also understand how two wave trains that are separated by a complete great circle interfere to form standing waves. The contributions of the two wave trains to the seismogram are largest (constructive interference), when the phase difference between the two, $\delta\Psi(\omega)=-2\pi ak(\omega)+\pi$, is an integer multiple of 2π, that is, $\ell 2\pi$. This results in Jeans' formula.

The surface wave analog to measuring mode frequency shifts is the measurement of phase velocity, $c(\omega)=\omega/k$, which is achieved by measuring the phase, $\Psi=-kx$. Two principal hurdles impede a straightforward analysis. The first hurdle has to do with the time series in general. Surface wave packets are nonstationary and the phase changes rapidly with frequency. It is therefore not practical to extract accurate phase estimates using a simple periodogram technique. The second hurdle comes from the fact that we use the approximation in eqn [16], which is a high-ℓ asymptotic. Wielandt (1980) pointed out that, at a given frequency, Jeans' formula gives only an average wave number on a sphere, which changes with travel distance, so the phase velocity also changes. The measured phase velocity, which he termed 'dynamic phase velocity' (Wielandt, 1993), is the asymptotic one only at distance $\Delta=90^\circ$ but slower at shorter distances and faster at longer ones. The 'dynamic phase velocity' is attached to the wavefield (which includes the nonuniform amplitude on a spherical Earth; see **Figure 29**) and is not to be confused with the 'structural phase velocity' that we seek, which, in the case of a 1-D Earth, is the asymptotic phase velocity. Wielandt (1980) suggested to apply correction factors for waves that do not cross a pole. He estimated that ignoring such factors can amount to errors of 1%, which is of the same order of magnitude as phase perturbations caused by structure. This consideration is relevant only at extremely long periods beyond 300 s ($\ell\simeq 25$) where these factors become significant, given modern measurement errors. Schwab and Kausel (1976b) provided graphs of correction factors for Love waves for certain travel distances and earthquake source mechanisms. We prefer to measure phase perturbations with respect to a reference model by determining the transfer function between an observed and a mode synthetic seismogram. This implicitly reduces the variation of phase with frequency (hurdle 1). It accounts for the polar phase shift and source phase automatically and fully accounts for the approximation of eqn [16] (hurdle 2). A phase perturbation $\delta\Psi(\omega)/\Psi(\omega)$, caused by lateral heterogeneity, is then

$$\frac{\delta\Psi(\omega)}{\Psi(\omega)}=-\frac{1}{\Delta}\int_0^{\Delta}\frac{\delta c(\omega)}{c_0(\omega)}dx \quad [20]$$

where $\Psi(\omega)$ is the frequency-dependent phase accumulated along the perturbed travel path, Δ is the travel distance, and $c_0(\omega)$ is the frequency-dependent reference phase velocity. Equation [20] is correct to first order in lateral heterogeneity. Romanowicz (1987) and Pollitz (1994) calculated higher-order contributions that arise from gradients perpendicular to the great-circle path. Pollitz concluded that the second-order effect is insignificant in the determination of long-wavelength structure up to harmonic degree 12 (anomalies of scale 1500 km and larger). Ignoring higher-order contributions may cause a bias in phase velocity maps for structure significantly beyond harmonic degree 16 (anomalies smaller than 1200 km) though the impact of this on models obtained with large global data sets requires further investigation.

On a sphere, it is convenient to expand lateral heterogeneity in terms of surface spherical harmonics $Y_l^m(\theta,\phi)$ as a function of geographic coordinates θ and ϕ, so that $\delta c/c_0$ is

$$\frac{\delta c(\omega)}{c_0(\omega)}=\sum_{l=0}^{L_M}\sum_{m=-l}^{l}c_l^m(\omega)Y_l^m(\theta,\phi) \quad [21]$$

where the c_l^m are complex coefficients and L_M is the maximum harmonic degree to which lateral phase velocity variation (a 'phase velocity map') is expanded. Note that l and m here describe structure, while the ℓ and m in the modes section describe a normal mode.

Considering the parameterization of eqn [21], it is interesting to plot the integral kernels in eqn [20] to examine how phase perturbations depend on lateral heterogeneity. In **Figure 31**, we notice that sensitivity falls off with harmonic degree in structure though it is initially relatively high, for short travel distances. The sensitivity to even-degree structure decreases relative to odd-harmonic degrees, up to a travel distance of 180°, at the antipode of the source. Then sensitivity evens out up to 240° travel distance, which corresponds to R_2, the major arc wave train for an epicentral distance of 120°. After that, the relative sensitivity to odd harmonics falls below the sensitivity to even harmonic degrees, until it is zero at 360°, when a wave train completed a great circle. Recall that we had mentioned in the mode section that waves lose sensitivity to odd-degree structure as time goes on and that eqn [10] (Backus, 1964) shows that a complete great-circle integral over Y_l^ms has no sensitivity to odd-degree structure.

Phase velocity maps derived exclusively from great-circle data are equivalent to the mode splitting functions in

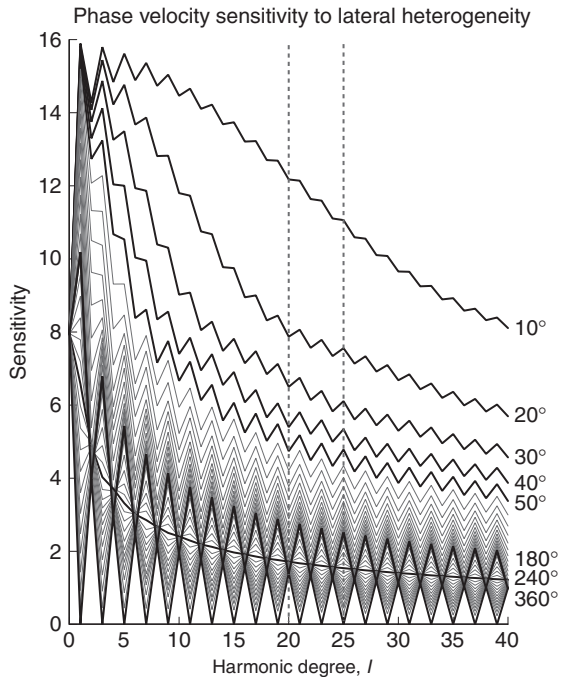

Figure 31 Phase sensitivity to lateral heterogeneity (integral kernel of eqn [20]), as function of harmonic degree in structure. Curves are shown for travel distances between 10° and 360°. Paths with distance <180° are for minor arc paths (R_1); larger distances are for major arc paths (R_2).

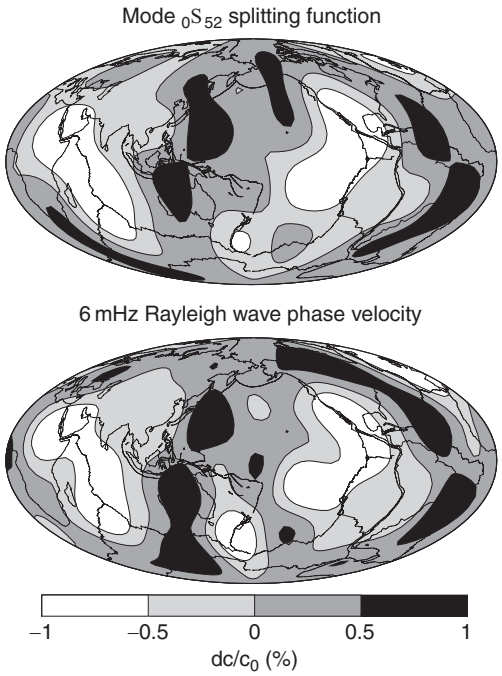

Figure 32 Comparison of effects of 3-D structure on standing waves (splitting function) and traveling waves (phase velocity map). The splitting function was converted to phase velocity perturbation using the conversion factor given by eqn [22]. Only even harmonic degrees are shown for the Rayleigh wave map to make it compatible with the splitting function of an isolated mode that is not sensitive to odd harmonics. Both maps are truncated at harmonic degree 8 (Laske and Masters, 1996).

eqn [9], except that phase velocity maps are measured at fixed frequency, ω, and splitting functions at fixed wave number, k (or ℓ). From the cyclic relation for partial differentiation (e.g., Riley et al., 2002),

$$\left(\frac{\partial\omega}{\partial m}\right)_k \cdot \left(\frac{\partial m}{\partial k}\right)_\omega \cdot \left(\frac{\partial k}{\partial \omega}\right)_m = -1$$

where m is a model parameter, we can derive a conversion factor between splitting functions and phase velocity maps,

$$\left(\frac{\delta\omega}{\omega}\right)_k = \frac{u}{c} \cdot \left(\frac{\delta c}{c}\right)_\omega \qquad [22]$$

where $c=\omega/k$ and $u=\partial\omega/\partial k$ are the phase velocity and group velocity (see next paragraph). An example of this relationship is shown in Figure 32 where both maps were obtained by inverting our standing and traveling wave observations. The patterns in the maps, caused by lateral heterogeneity within Earth, are quite similar visually, and the correlation between the maps is above the 99% confidence level (Laske and Masters, 1996). Small variations that are numerically barely significant may result from differences in the data sets and inversion schemes used. We can therefore convince ourselves that analyzing standing and traveling waves results in the same models of even-degree Earth structure.

The phase velocity is the speed at which a certain point in the wave train travels, while a certain point of the envelope (or the energy) travels with the group velocity (see Figure 36(b) for concept). Both together define the dispersion of surface waves, and a last comparison with modes is done here. In the mode section, we introduced the ω–ℓ dispersion diagram (Figure 16) that shows mode frequencies as a function of mode identifiers n and ℓ. Using Jeans' formula (eqn [17]), which is valid for $\ell \gg n$, this diagram implicitly summarizes the dispersion of surface waves (Figure 33). For most Rayleigh wave frequencies, we observe normal dispersion with $c>u$, or $dc/dk<0$. An exception is the range below 2 mHz, where we observe anomalous dispersion, $u>c$, or $dc/dk>0$. In the range of low-frequency modes below $\ell=25$, c/u increases until c is roughly 42% larger than u, and then it decreases. At frequencies above about 6 mHz, c/u approaches 1 and variations in local peak shift can be related directly to phase velocity variations. Group and phase velocities for Love waves are typically larger than those for Rayleigh waves at the same frequency, except above roughly 50 mHz when the Love wave group velocity drops off significantly for oceanic structure (see next section). Also, c/u starts to approach 1 at much lower frequencies than for Rayleigh waves.

1.04.3.2 The Measurement of Fundamental Mode Dispersion

For surface waves, dispersion is usually presented in frequency–velocity (or period–velocity) diagrams (Figures 34 and 35). Before we elaborate on measurement techniques, we briefly summarize some early observations of surface wave

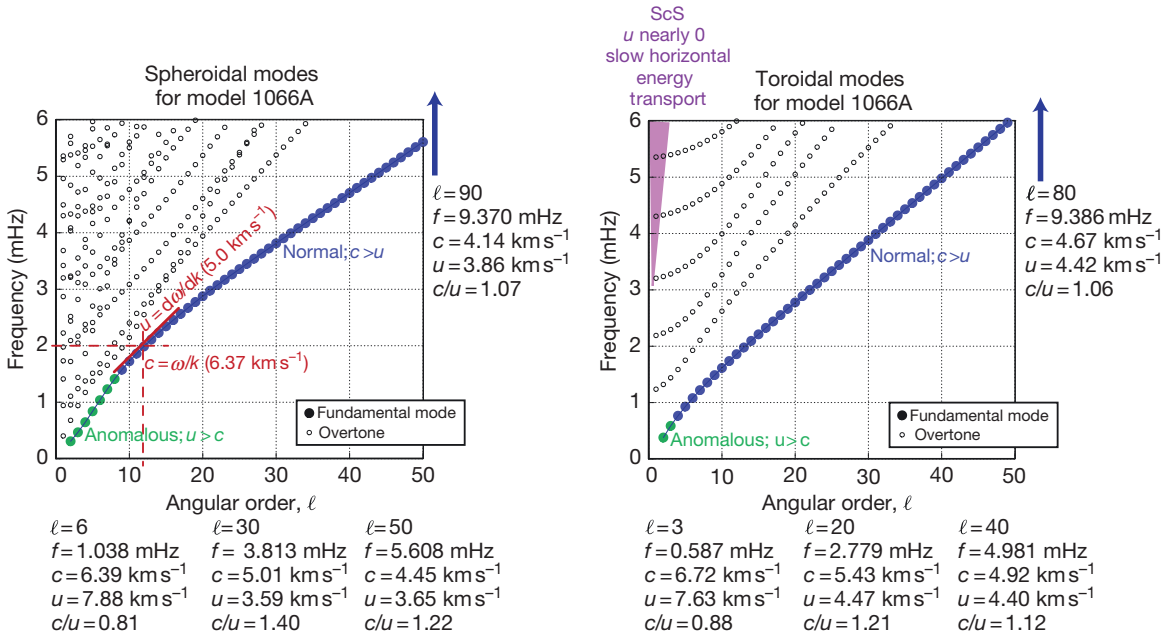

Figure 33 Dispersion diagram (ω–ℓ plot) for spheroidal and toroidal modes for model 1066A of Gilbert and Dziewonski (1975). Red lettering describes the concept of phase (c) and group (u) velocity for mode ${}_0S_{12}$. Blue symbols mark fundamental modes with normal dispersion ($u < c$), while green symbols mark modes with anomalous dispersion ($u > c$). The purple area marks the location of ScS equivalent modes whose group velocity is nearly zero. The scalar c/u is used to convert splitting functions to phase velocity maps (see **Figure 32**; eqn [22]).

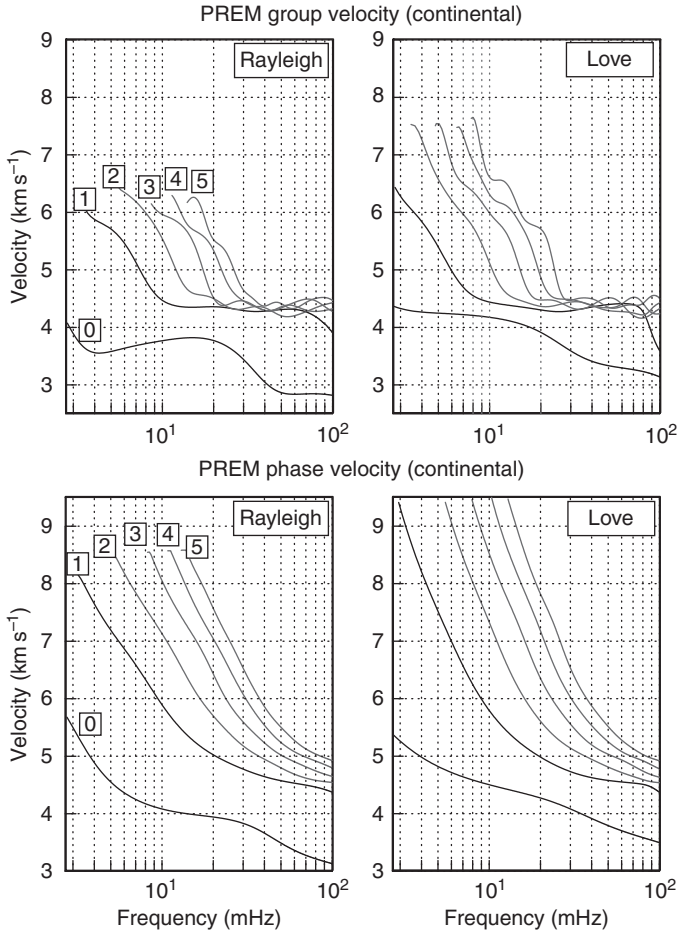

Figure 34 Group and phase velocity curves for isotropic PREM (Dziewonski and Anderson, 1981) with a 39 km thick continental crust. Shown are the fundamental modes (label 0) and the first five overtones (labels 1–5). Phase velocities span a greater range than group velocities. Overtones have nearly the same group velocities above 30 mHz (periods shorter than 33 s). For clarity of the diagrams, dispersion for IC modes and ScS equivalent modes at long periods are not shown.

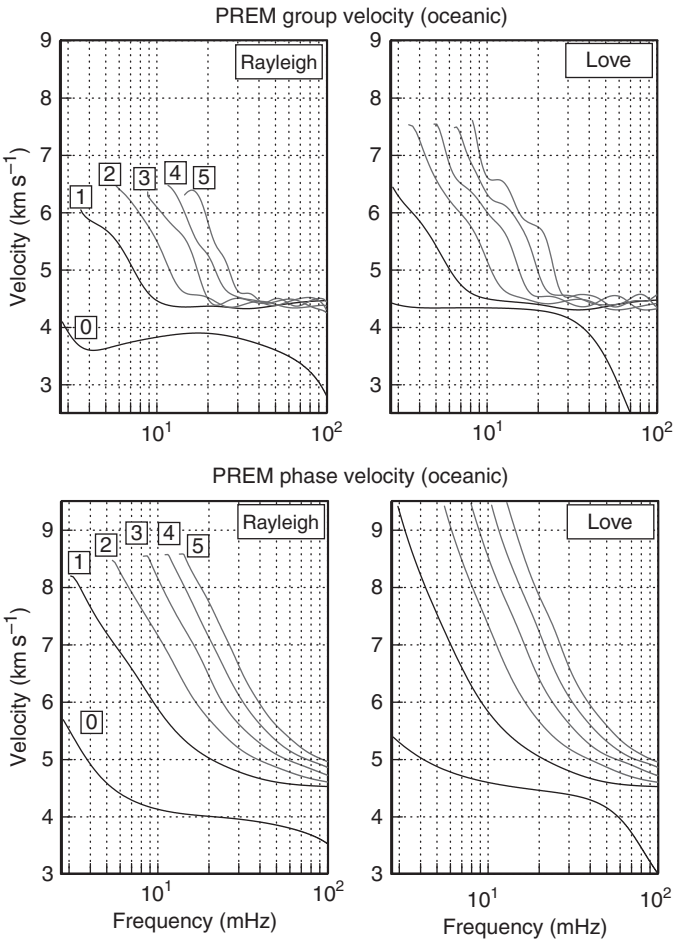

Figure 35 Group and phase velocity curves for isotropic PREM with a 7 km thick crystalline oceanic crust, overlain by 5 km of sediments (no water layer). Shown are the fundamental modes (label 0) and the first five overtones (labels 1–5). Phase velocities span a greater range than group velocities. Overtones have nearly the same group velocities above 30 mHz (periods shorter than 33 s). Love wave fundamental modes have similar group velocities as overtones between 10 and 20 mHz. For clarity of the diagrams, dispersion for IC modes and ScS equivalent modes at long periods is not shown.

dispersion. Probably one of the most well-known and subsequently most-cited summaries of early observed dispersion curves for both group and phase velocities is that of Oliver (1962) who published curves for both Love and Rayleigh wave fundamental modes and the first two overtones, for oceanic and continental paths. Oliver (1962) summarized results in a wide frequency range (corresponding to periods between 1 h and 1 s). At the time, overtone phase velocities remained largely unobserved. The summary was mainly based on the observations by Maurice Ewing and his group at LDEO, then the Lamont Geological Observatory, but the observation of Rayleigh wave dispersion goes back to at least the 1930s (e.g., Carder, 1934, for oceanic paths; Röhrbach, 1932; Gutenberg and Richter, 1936, for continental paths). Ewing and Press (1954, 1956) collected long-period Rayleigh wave group velocities between 10 and 500 s. They observed a significant difference in dispersion for continental and oceanic paths at periods shorter than roughly 75 s and attributed dispersion at longer periods to be influenced primarily by structure in the mantle. Subsequently, surface waves at periods 75 s and longer were called mantle waves, which is still used today (e.g., Ekström et al., 1997). Ewing and Press remarked that the dispersion of oceanic paths is strongly influenced by the presence of a water layer (e.g., Ewing and Press, 1952, and also Berckhemer, 1956). It was observed that, due to the steep dispersion at periods shorter than 20 s, oceanic Rayleigh wave packets are far more stretched out than continental Rayleigh waves. The latter required long travel paths to resolve details in the dispersion curve. Short-period dispersion of the first 'shear mode' (overtone) was first observed by Oliver and Ewing (1958), for paths traversing the deep ocean after a nuclear explosion in 1955, about 700 km off the coast of Southern California (Operation Wigwam). The wave trains appeared unusually complicated but also gave seismologists a chance to observe oceanic dispersion for the first time at periods shorter than 15 s. Oceanic short-period overtone signals are usually hard to observe in teleseismic records due to the dominance of swell-generated microseism noise. The Wigwam records also revealed, for the first time, the slow Airy phase (waves with stationary group velocities; Pekeris, 1946) at around 7 s for oceanic paths.

Love wave dispersion is usually more difficult to measure than that of Rayleigh waves because the process involves the analysis of the typically noisier horizontal seismometer components. Also, long-period Love waves have similar group velocities over a wide frequency band, especially in the oceans (see **Figure 35**). This often makes Love waves to appear pulse-like, which hampered early dispersion measurements before the computer era. Nevertheless, Love wave dispersion measurements go back to at least the 1940s (e.g., Wilson, 1940). **Figures 34** and **35** give a summary of the expected dispersion curves for fundamental mode Rayleigh and Love waves and their first five overtones. The curves are shown for isotropic PREM and both continental crust and oceanic crust. At frequencies above 10 mHz, variations in crustal structure have a significant effect on dispersion. Throughout a wide range in frequency, Rayleigh wave fundamental mode group velocity curves are fairly isolated from overtones, which allows easy dispersion measurement. This is not the case for overtones that overlap at frequencies above 15 mHz. Sophisticated 'tuning' techniques, such as array stacking, are then necessary to assess individual overtone dispersion (see **Section 1.04.3.4**). Also note that the first overtone branch overlaps with the Love wave fundamental mode branch between 10 and 30 mHz, for oceanic paths. Ignoring possible interference effects may lead to biased Love wave dispersion data, which is revisited in a later section.

For Rayleigh waves, we observe two Airy phases for which group velocity does not change much with frequency (**Figures 34** and **35**). One is near 4 mHz, and the other one is near 20 mHz. Between 4 and 20 mHz, the group velocity dispersion is inverse. The condition $du/dk < 0$ implies that modes with higher ℓ, hence higher frequency, are faster than modes with lower ℓ (compare also with **Figure 33**). This can be seen in the low-pass-filtered seismogram in **Figure 2**. Below 4 mHz and above 20 mHz, we observe regular dispersion with $du/dk > 0$ (low-ℓ modes are faster). This can be seen in **Figure 36** that shows Rayleigh wave seismograms between 20 and 50 mHz in an oceanic setting. The figure also emphasizes that modern ocean bottom seismic instrumentation allows us to observe long-period surface waves on the ocean floor to an unprecedented signal level. Depending on crustal structure, a third Airy phase may be observed for Rayleigh waves near 50 mHz. For Love waves, group velocities are very similar over a large range in frequency. In oceanic settings in particular, the dispersion is very weak between 4 and 20 mHz, so that Love wave trains usually appear quite pulse-like.

The first attempts to take a general regionalization of surface wave dispersion beyond a distinction between continents and oceans go back to Toksöz and Anderson (1966) who decomposed composite-path great-circle data into those of 'pure-path' oceanic, shield, and mountain-tectonic regions. They analyzed records of the great Good Friday 1964 Alaska earthquake (28 March 1964) at stations Isabella, California (later station ISA of the TERRAscope Network), Kipapa, Hawaii (later station KIP of the IDA, GSN, and GEOSCOPE networks), and Stuttgart, Germany (later station STU of the GEOFON network). Kanamori (1970) analyzed many more records of this event ($M = 8.5$ as reported by Kanamori) and another great

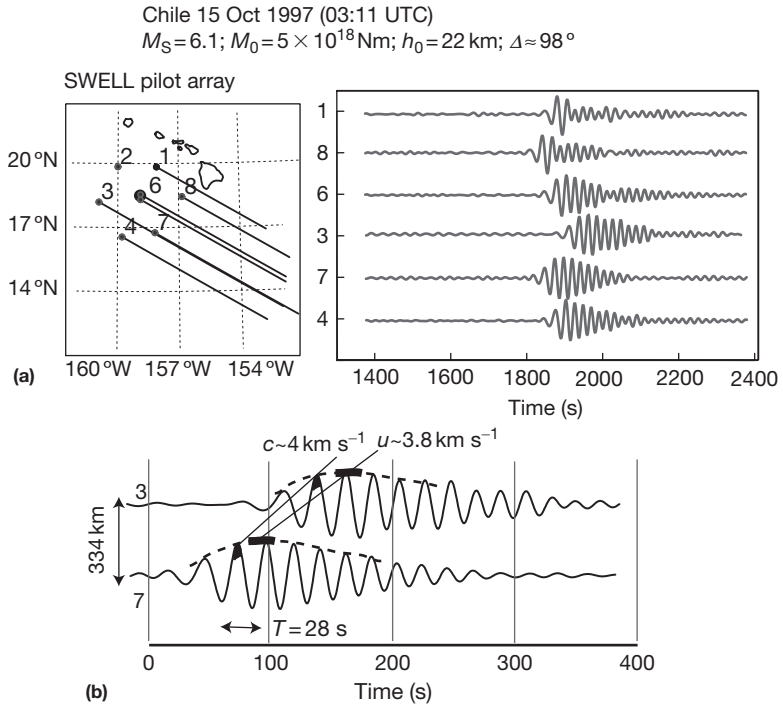

Figure 36 (a) Seismograms recorded on ocean bottom differential pressure sensors during the 97/98 SWELL Pilot Deployment southwest of Hawaii (Laske et al., 1998). The recorded frequencies range from 20 to 50 mHz. The waveforms exhibit regular dispersion, that is, low frequencies arrive earlier than higher frequencies. (b) Schematic concept of phase (c) and group (u) velocities along two-station leg 7-3.

earthquake in the Kuril Islands region (13 October 1963; $M = 8.3$), and a supplement of earlier published data. Apart from phase and group velocity, he also measured great-circle attenuation but did not interpret the latter further. Dziewonski (1970) analyzed phase and group velocity for the 15 August 1963 Peru earthquake (the same earthquake that provided mode data for Earth model 1066A by Gilbert and Dziewonski, 1975) though phase velocities were derived from mode observations. This chapter also showed, for the first time, that world-circling measured phase and group velocities are mutually consistent. Knopoff (1972) first provided a more detailed discussion of surface wave dispersion in different tectonic regions.

Early measurements of surface wave dispersion were extended to frequencies much below 4 mHz. For example, the analysis of Ewing and Press (1956) extended to 2 mHz and that of Toksöz and Anderson (1966) extended even to 1.5 mHz. At such long periods, Coriolis coupling between Rayleigh and Love waves becomes considerable (see **Figure 13**) so that Love waves appear on the vertical seismometer component as so-called quasi-Love waves (e.g., Levin and Park, 1998). Backus (1962) discussed the effects of a rotating Earth on the propagation path of very long-period surface waves. While Love wave paths remain largely unaffected, Rayleigh wave great-circle paths precess about Earth's axis of rotation, effectively lengthening the travel path. Dispersion estimations that assume the direct great-circle path are then biased low. While early measurements were not precise enough for this effect to be significant, modern observations probably need to be corrected for this effect, which depends on Earth's 1-D structure much like the spheroidal–toroidal mode coupling does.

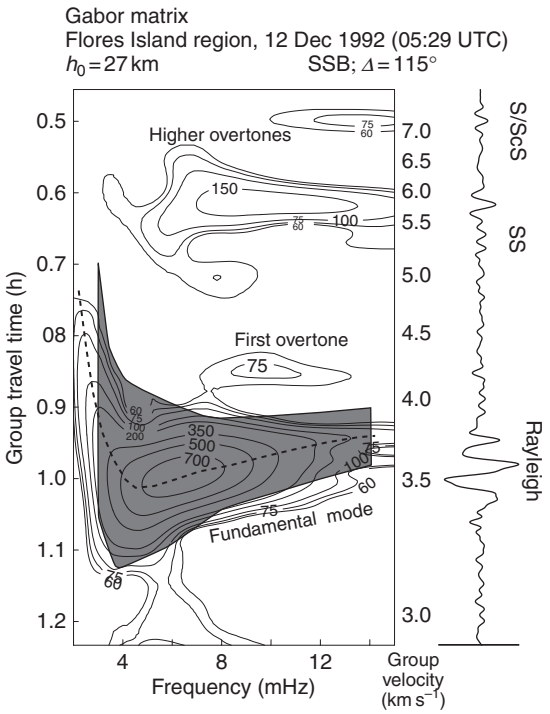

Figure 37 Visualization of a Gabor matrix for the seismogram in **Figure 2**. Amplitudes in the matrix are normalized to optimize the display. The largest signal is the fundamental mode that exhibits dispersion (see **Figure 34**) where the dashed line marks the group velocity an analyst would choose. A combination of overtones arrives before the Rayleigh wave. The gray area marks the time–frequency range used in a time-variable filtering approach to isolate the fundamental mode.

1.04.3.2.1 Group velocity

In the precomputer era, surface wave group velocity was measured using the peak-and-trough method (e.g., Ewing and Press, 1954; Ewing et al., 1957). In a paper record, each peak, trough, and zero was numbered and plotted against recorded time. The slope of this curve gives the period as a function of travel time, from which the group velocity can be computed. This technique can be applied on well-dispersed signals but fails near Airy phases and for most Love waves because the waveforms are compressed. Even for the well-dispersed case, measurement errors are rarely better than 0.2 kms^{-1}, or about 6.5%. Since the late 1960s, when computers and the fast Fourier transform by Cooley and Tukey (1965) facilitated quick and comprehensive harmonic analyses, group velocity has been measured in the time–frequency domain. The most basic approach is the 'moving window analysis' (Landisman et al., 1969). A sliding window is applied to a time series, and the spectrum for each increment is tabulated in a time–frequency matrix, often called a Gabor matrix after Hungarian physicist Dennis Gabor (Gabor, 1947). Such a diagram is also called energy diagram (when amplitude squared is plotted) or, when the travel time is converted to velocity, a vespagram. **Figure 37** shows the Gabor matrix for the 1992 Flores Island region record at station SSB (see **Figure 2**). The group velocity is then determined by tracing the ridge with the highest amplitudes in the 2-D plot. This approach has seen wide use in a number of applications that deal with nonstationary signals and is still used today, for example, in the study of ocean swell-generated signal in the microseism band (between 20 and 4 s) that is caused by approaching large storm systems (e.g., Bromirski and Duennebier, 2002).

When measuring dispersion, one has to be aware of the resolution limits in the Gabor matrix imposed by the Schwarz inequality (Gabor, 1947), where the smallest frequency separation, Δf, and the length of the sliding window, T, must satisfy $\Delta f \bullet T \geq 1$. For example, if the moving window is 1000 s long, the frequency resolution is not better than 1 mHz. To obtain the same relative resolution $\Delta f/f$ in the Gabor matrix, the sliding window can be made proportional to the period investigated, where the window length is usually four to eight times the period. Since this entails the separate calculation of a certain harmonic coefficient for each element in the Gabor matrix, this was sometimes prohibitively inefficient in the early days of computing. A quicker method is the multiple filtering technique (described in Dziewonski et al., 1969) that starts with the spectrum of a complete time series. A Gaussian filter is centered on a certain target frequency. The analytic signal, which provides the envelope function of the corresponding time series, is then determined for this frequency using the spectrum for positive frequencies only. Instead of just one element in the Gabor matrix, the envelope function now composes a whole column.

Measuring group velocity requires either interactive picking or a sophisticated routine that recognizes which ridge to pick. A widely used application in regional studies is the FTAN

(frequency–time analysis) package by Levshin et al. (1972) (see also Levshin et al., 1989). FTAN is similar to earlier multiple filtering methods except that FTAN uses an efficient folding algorithm to determine the complex time–frequency array from which the Gabor matrix is estimated. This allows the extraction of phase velocity as well. Signal enhancement in the Gabor matrix can also be achieved by the logarithmic stacking of several events in the group velocity-period domain (Shapiro et al., 1997). Modern techniques allow us to measure group velocity with an error that is usually much less than 0.1 km s^{-1}, or about 3.2%. The measurement of group velocity is advantageous over that of phase because many phase measurement applications require the knowledge of the source process (see eqn [19]). Group velocity observations are largely unaffected by source processes, which makes this approach very attractive in regional studies where earthquakes are typically small. For events deeper than about 25 km, the source may affect group travel times at long periods beyond 100 s though the bias is usually not significant, that is, smaller than the measurement error (Levshin et al., 1999).

Group velocities picked from the Gabor matrix can be biased, as first discussed by Dziewonski et al. (1972). As seen in **Figure 30**, the spectral amplitude for the first wave train increases with frequency. In this case, group velocity estimates from periodograms are biased toward high-frequency values. Changes in the spectral amplitude may be particularly large when dispersion is strong, which is the case for frequencies below 4 mHz. A similar bias occurs when phase velocities are estimated from the phase of the complex analysis of the Gabor matrix. Dziewonski et al. (1972) suggested to deconvolve the time series with a synthetic seismogram before measuring the much less pronounced 'residual dispersion.' There have also been developments to improve the multiple filtering technique itself. Wielandt and Schenk (1983) provided a formalism to correct the bias in phase velocity estimates to within 0.1%. A more recent reference is that of Shapiro and Singh (1999) who suggested to use a centroid frequency of the filtered spectrum rather than the center frequency of the Gaussian filter to tabulate the Gabor matrix.

1.04.3.2.2 The study of ambient noise

The determination of group velocity using ambient noise has become tremendously popular in recent years. Although many ambient noise studies are limited to the microseism band between 20 and 3 s, these studies may provide valuable dispersion data where inadequate earthquake distribution does not allow an analysis otherwise. Microseisms are generated by linear and nonlinear interaction of wind-generated ocean swell with itself and with the seafloor and the coast (see also **Chapter 1.12**). The most dominant microseism signal, at a period typically near 5 s, is generated when waves approaching from opposing directions interact nonlinearly to form standing waves in the water column (Longuet-Higgins, 1950). The resulting Rayleigh waves, which are excited continuously but incoherently, can be observed even in continental interiors. With the aid of a network, the dispersion of microseisms can be extracted to constrain local crustal structure (e.g., Sabra et al., 2005a; Shapiro et al., 2005). In essence, a cross correlation technique is applied to station pairs in an array to extract empirical Green's functions (e.g., Sabra et al., 2005b; Shapiro and Campillo, 2004). Without doubt, this technique has become so attractive because ocean noise is observed everywhere on the planet, and two-station Green's functions are more readily extractable using noise than waves from single earthquakes that have to align with the two-station great circle. It appears that time series collected over just 1 month are capable of providing high-resolution images of Earth structure (Shapiro et al., 2005).

The study of ambient noise to extract Earth structure has also been applied to seismic stations on the ocean floor (e.g., Harmon et al., 2007). Even observations of phase velocity that inherently require more sophisticated measurement techniques than group velocity have appeared in the literature (e.g., Bensen et al., 2007; Harmon et al., 2007). Phase velocity results based on cross correlation are reported to be in good agreement with those obtained with beamforming (Harmon et al., 2008). The recent advances in ambient noise include the analysis of overtones (e.g., Harmon et al., 2007) and Love waves (e.g., Lin et al., 2008). In some areas, such as Europe, ambient noise group velocity constraints appear to be quite compatible with or even superior to those from earthquake data as the former appear to be more internally consistent (Yang et al., 2007).

In principle, the analysis of ambient noise can be extended to longer periods though noise levels are considerably lower than in the microseism band. At periods longer than 100 s, the interaction of infragravity waves with the ocean floor and the continental slopes is thought to generate infragravity noise (e.g., Tanimoto, 2005; Webb, 1998). Shapiro and Campillo (2004) found that broadband dispersion information can be extracted from two-station ambient noise cross correlation records, to periods up to at least 100 s.

A precondition for ambient noise analyses to yield unbiased dispersion data is that the source distribution is isotropic, that is, the microseisms have to approach the array from all directions, which may not always be the case. For example, Schulte-Pelkum et al. (2004) found preferential directions of approach at the ANZA Seismic network in Southern California. Strong source directivity was also found in Europe (Essen et al., 2003). Such source directivity is most obviously coupled to the seasonal return of large winter storms (e.g., Hiller et al., 2012) that may even be responsible for Earth's hum (e.g., Kurrle and Widmer-Schnidrig, 2010; Rhie and Romanowicz, 2004, 2006). Uneven source distribution can result in phase velocity estimates that are biased high by up to 1%, which can map into seismic 3-D structure in tomographic images on the order of a few percent (Yang et al., 2008; Yao et al., 2006). For Southern California, Harmon et al. (2010) estimated the bias on isotropic phase velocity as a result of uneven source distribution to be +0.2% at a period of 25 s, at the same time mimicking an apparent azimuthal anisotropy of up to 1%. These effects can potentially be accounted for by performing a source density analysis. It seems that a year's amount of ambient noise data that spans a time frame long enough to include effects from seasonal variations, coupled with robust cross correlation techniques, should deliver reliable results (e.g., Bensen et al., 2007). For further details about noise correlations, see **Chapter 1.12**.

1.04.3.2.3 Phase velocity

Unlike group travel times, the phase explicitly includes a source term (see eqn [19]). Measuring phase between a source and receiver therefore requires accurate knowledge of the

seismic source. The measurement of phase velocities without spectral analysis requires the comparison of at least two waveforms, for example, from seismograms of neighboring stations that share a great circle with the source (two-station method, e.g., Brune and Dorman, 1963). Using a one-station approach, Nafe and Brune (1960) first measured complete great-circle phase velocity for the 15 August 1960 Assam earthquake at station PAS (Pasadena, California) with errors $<1\%$. Ten years later, the observation of phase velocity on a global scale was still in its infancy when Kanamori (1970) reported surface wave great-circle phase velocity observations for surface wave packets separated by a complete great-circle orbit, while others preferred to derive phase velocities from mode observations (Dziewonski, 1970; Dziewonski and Landisman, 1970).

The phase of a surface wave packet changes very rapidly with frequency, and its 2π-ambiguity almost never allows us to measure phase between source and receiver directly from a single waveform. Early works suggested that in the two-station approach, phase estimated from a cross correlogram of the two seismograms yields more stable estimates than from phase differences (Landisman et al., 1969). Before we elaborate on our own measurement technique on the global scale, we briefly review advances in regional studies. For dense arrays where the station spacing is on the order of the signal wavelength, individual peaks or troughs can be followed across the array and phase velocities can be measured as function of period. Some of the earliest such measurements of phase velocity, for periods <1 s, can be found in the oil exploration literature (e.g., Dobrin et al., 1951). For crustal or mantle studies, seismic arrays are typically sparse. Press (1956, 1957) used the triangulation or tripartite method to determine crustal structure in California from average phase velocities. But the use of the method goes back further (e.g., Evernden, 1953, 1954) and was also used to retrace hurricane tracks with seismic data (e.g., Donn and Blaik, 1953). In fact, the tripartite method was first used by Milne, and the interested reader is referred to Evernden (1953) for a brief review of early applications. In the studies of the 1950s, only few earthquakes were used for a particular station triangle, and measurement errors were on the order of 0.1 km s^{-1} (3%) or less. The technique assumes that plane waves approach a station triangle, whose aperture could reach several 100 km (e.g., Knopoff et al., 1966). These authors found that even though the method allows for an arbitrary arrival angle of the approaching wave, it yields biased results unless the wave propagation direction is aligned with one of the network legs. Knopoff et al. (1967) later found the two-station method to be superior to the tripartite method to minimize errors in phase shifts in the presence of lateral heterogeneity. Schwab and Kausel (1976a) suggested to expand the recording array to at least four stations and allow the consideration of curved wavefronts. In essence, in an optimization process, waveforms are matched to be in phase to form a single beam (beamforming). This is an approach that can still be found in the literature to determine the average structure beneath a recording array (e.g., Alsina and Snieder, 1993; Stange and Friederich, 1993). The preposition here is that incoming wavefronts are uniform and distortion of the wavefronts within the array due to heterogeneous structure is insignificant though this may not be the case (Wielandt, 1993).

Numerous studies followed, and the two-station method is still used today to retrieve regional and local structure, often along only one particular two-station path. A recent example of using the multiple filtering technique on a cross correlogram in the two-station case (between two real seismograms) is that of Meier et al. (2004) who studied Rayleigh wave phase velocity in the Eastern Mediterranean. It can be argued that phase velocities estimated with the two-station technique are systematically biased high when waves do not approach a station along the great circle, which is to be expected particularly in the analysis of teleseismic events. In our global studies, we have found that lateral refraction caused by heterogeneity in the mantle can change the direction of approach at a station by as much as 20°. The deviation of an arriving wave packet away from the great-circle direction effectively shortens the travel path. For a regional study that uses teleseismic earthquakes, the bias in the estimated phase velocity for a single travel path can therefore be as large as 6.4%. The bias on local or regional phase velocity can be reduced when many crossing paths are considered, but the estimates will remain biased high, unless the phase estimates are corrected for off-great-circle approach.

Another problem arises from multipathing when wave packets get refracted away from the great circle and then travel along multiple paths and interfere at the recording station upon arrival. Multipathing was detected in the early study of Evernden (1953) for surface waves traveling along the west coast of North America. Wavefronts get bent in complex structures and the plane wave approach is no longer valid. For example, waves get bent around an enclosed low-velocity anomaly so that the sides of a plane wave advance. In the extreme case, wavefront healing occurs when the wave travels long enough and 'forgets' that it passed this structure (Wielandt, 1987). To illustrate the gravity of the problem, one of the most remarkable examples of the controversy over the two-station method is probably that of Woods et al. (1991) along the Hawaiian Islands chain. They could not find a low-velocity anomaly associated with the proposed reheating of the Pacific plate by the Hawaiian hot spot and therefore argued against the plate reheating concept. On the other hand, Maupin (1992) argued that complex wave propagation along a relatively narrow low-velocity anomaly inhibits the application of the two-station approach for a single two-station path. Pedersen (2006) estimated that bias from ignoring the nonplane geometry of the incoming wavefield can be reduced to 1% in the two-station method for 200 km profiles, if at least ten earthquakes with different hypocenters are analyzed. This may be achieved for permanent station installations but is often difficult to achieve for temporary deployments that typically last less than 2 years. The unbiased recovery of structure within an array in the case of nonplane waves approaching the array requires the analysis of both phase and amplitude (Friederich et al., 1994; Wielandt, 1993). Friederich et al. (2000) demonstrated that even though seismic surface waves propagating in a laterally heterogeneous half-space do not obey the Helmholtz equation, using the latter still gives much improved tomographic images over the usually applied eikonal equation. Of course, such an approach is only possible when data from dense arrays are available. Forsyth and Li (2005) proposed a simplified technique that fits two approaching plane waves to the observed phase measurements of an array. More recently, Mike Ritzwoller's group applied Helmholtz tomography (Lin and Ritzwoller, 2011) to the data from

the dense USArray and produced high-resolution dispersion maps of the Western United States with stunning details (e.g., Lin et al., 2011).

For our global studies, we measure phase relative to a synthetic seismogram. In the simplest case, this can be a synthetic computed for a spherical Earth (e.g., Laske and Masters, 1996). We measure the transfer function between the observed and a synthetic fundamental mode waveform that is calculated for Earth model 1066A (Gilbert and Dziewonski, 1975). An early example of the transfer function technique measuring great-circle dispersion and attenuation can be found in Dziewonski and Steim (1982). A multitaper approach provides an optimal compromise between frequency resolution and resistance to bias from noise in the time series. The multitaper approach also allows us to assign measurement errors in a statistical sense. The analysis is done interactively on the computer screen where we choose the optimal time window to isolate the fundamental mode. An example is shown in **Figure 38**. Other workers choose automated approaches (e.g., Trampert and Woodhouse, 1995). These approaches take significantly less time but may either produce a noisy data set or quality control restrictions yield a significantly reduced data set, compared to our hand-picked one. Measured phase perturbations typically amount to a few percent, and measurement errors are 0.15% on average for R_1, while measurement errors in R_2 and great-circle data are somewhat smaller. Even though we measure phase with respect to a synthetic, some of our short-period data are 2π-phase-ambiguous. At short periods, the phase ambiguity is enhanced by the fact that small perturbations to a model may cause many 2π-phase wraps. The phase ambiguity can be removed by the condition that the phase has to vary smoothly with frequency. Since we observe no phase ambiguity at 4 mHz, our phase data set is unique, for the frequency range chosen in our global study (4–17 mHz). We usually need only one iteration to determine the transfer function, but occasionally, the great difference between data and synthetic requires one or two additional iterations (see **Figure 38**). Nevertheless, our 'one-step' spectral approach does not allow us to go much beyond 20 mHz. An alternative approach to obtain unbiased estimates in a wider frequency range is that of Ekström et al. (1997) who determined phase perturbation in several passbands rather than just one. As in our approach, they use synthetic seismograms in a phase-matched filtering procedure. The process is iterated to minimize residual dispersion and to suppress interference from overtones. They succeeded to collect an impressive global data set between 150 and 35 s. With 50 000 high-quality dispersion curves, their data set was the largest at the time, and their data and phase velocity maps have been used subsequently by many other workers either in their own global studies or to calibrate regional crustal models (e.g., Yang et al., 2004). An update of Ekström's data set, phase and group velocity maps, and programs to evaluate the maps are described and provided in Ekström (2011).

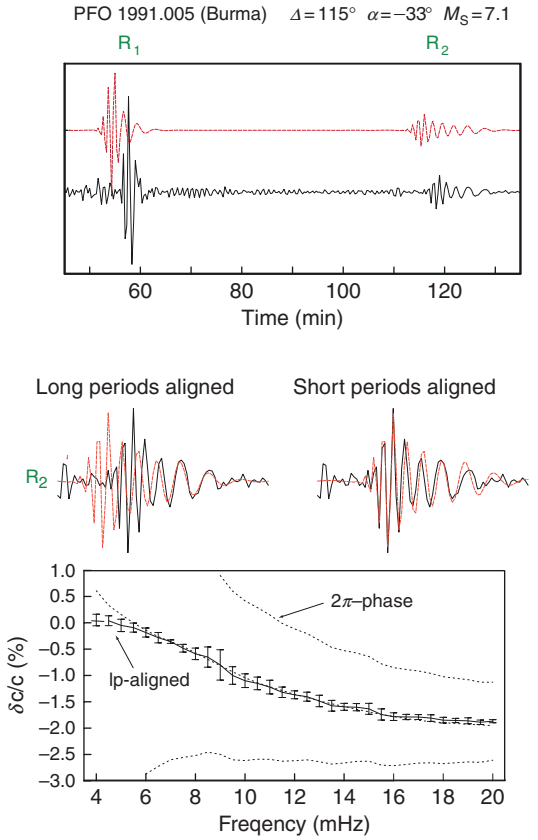

Figure 38 Example of our interactive phase measurement procedure in which the transfer function between an observed seismogram and a synthetic is retrieved. A seismogram at station PFO (Piñon Flat Observatory, California) is compared to a fundamental mode synthetic. The example is extreme in that the transfer function has to be determined iteratively, due to the large difference between observed and synthetic waveforms. The bottom panel shows the resulting path-averaged phase velocity perturbation. The dashed line in the middle marks the results when the waveforms are aligned on the short periods. Also shown are the results when 2π are subtracted or added to the phase (upper and lower dashed lines).

1.04.3.2.4 Time-variable filtering

Time-variable filtering (TVF) was proposed to stabilize fundamental mode surface wave dispersion estimation when waveforms appear contaminated. Interference effects from other mode branches, multipathing, or other concurrent signals are the most likely causes. Arguably, one should probably refrain entirely from analyzing such contaminated waveforms. This may be feasible in global low-frequency seismology below 20 mHz, where large waveform collections are available. However, in regional studies using temporary networks, in monitoring efforts of the CTBT or to study the dispersion at shorter periods, this may not be possible. Aside from TVF, various techniques are available to extract a primary signal from a time series. Herrin and Goforth (1977) applied phase-matched filters (PMFs) to Rayleigh waves of an earthquake and a nuclear explosion. In this process, a time series is matched to a synthetic by iteratively windowing a narrow-band-filtered correlation function between the two to eliminate interfering signals. PMF makes no assumptions about the time–frequency structure of the interfering signals in a seismogram. TVF takes into account the dispersion. The idea behind TVF is that different signals may arrive at the recording station at the same time but the frequency content and group velocities are sufficiently different that the signal to be studied can be isolated by time–frequency filtering. For example, the Gabor matrix in

Figure 37 shows the fundamental mode as the largest signal, but at the same time as the very low-frequency fundamental mode reaches the station, the first overtone, with frequencies around 10 mHz, also comes in. A time–frequency filter that enhances the signal below 3 mHz at this time but then enhances 10-mHz signals at a later time significantly reduces the biasing effects of a single window covering the whole time series. Pilant and Knopoff (1964) first applied TVF to separate the seismic signal from two different earthquakes that arrived at a station nearly at the same time and therefore created a beating pattern in the waveform. Since then, the method has been applied to investigate structure of the crust and upper mantle (e.g., Knopoff et al., 1966). TVF is also included in the FTAN package of Levshin et al. (1989) in a second iteration to improve measurement precision. A technique that combines PMF with TVF is the frequency variable filtering of Russell et al. (1988) to reduce spectral amplitude biasing introduced by frequency domain filtering.

Technical details of the TVF approach are described in Landisman et al. (1969). The filtering can be done either in the time or the frequency domain. In the latter, the starting point is the spectrum of the original time series. Each harmonic coefficient is multiplied by a function that has a certain shape in the time domain. Landisman et al. (1969) suggested a cosine taper with

$$w(t) = \begin{cases} \cos\left(\dfrac{\pi(t - t_n(\omega))}{2L(\omega)}\right), & \text{for } t_n - L \le t \le t_n + L \\ 0 & \text{else} \end{cases}$$

where

$$L(\omega) = T(\alpha + \beta|\mathrm{d}u(T)/\mathrm{d}T|)$$

$L(\omega)$ is the window length in the time domain, $T = 2\pi/\omega$, and $t_n(\omega)$ is the center group travel time. Other workers refined the filtering to optimize the trade-off between interference from unwanted signals and loss of energy for the signal analyzed (e.g., Cara, 1973; Roult, 1974). At frequencies with strong dispersion, TVF should probably be applied with caution to avoid biased estimates, if $t_n(\omega)$ are the predictions of a model.

The technique has also found application in normal mode studies (e.g., Jobert and Roult, 1976; Roult and Romanowicz, 1984; Roult et al., 1990). Our own experience is that the technique works best for seismograms with epicentral distances far away from 90° (Koptschalitsch, 1988). For epicentral distances near 90°, the close temporal succession of overtones and fundamental modes does not allow an effective suppression of overtones without significantly affecting fundamental mode frequencies by several microhertz and Q by up to 20%. A topic of research still is why mean attenuation estimates for surface waves below 5 mHz often disagree significantly with those obtained from mode studies. Durek and Ekström (1996) suggested that noise contamination in the much longer normal mode seismograms can bias Q estimates high. Roult and Clévédé (2000) improved their time-lapse technique to obtain more accurate mode Q data that are in agreement with those of others though the discrepancy to surface wave Q remains. Our own unpublished experiments lead us to speculate that overtone interference may significantly bias mode Q estimate high, particularly for toroidal modes (Masters and Laske, 1997). Some of this can be removed by TVF. On the other hand, some published surface wave-derived Q values may be biased low as our own surface wave results agree well with the mode Q values. Figures can be found on the REM web page. For a more detailed discussion, see also Chapter 1.01.

1.04.3.3 Other Surface Wave Observables

Surface waves can be deflected significantly from the source–receiver great circle by lateral refraction in a heterogeneous medium. Evernden (1953, 1954) was among the first to observe this phenomenon at long periods. Capon (1970) observed off-great-circle propagation also at short periods (20–40 s) and found that refraction and reflection of wave packets at continental margins were responsible for this. Lateral refraction has also been observed by a large group of other workers and array techniques, such as the tripartite method of Press (1956) or comprehensive modifications thereof (e.g., Stange and Friederich, 1993), have been used to obtain unbiased dispersion estimates. In essence, incoming wavefronts are fitted simultaneously to the phase data of all stations in an array, where phase velocity and angle of approach are free parameters to search for. In regional studies that search for structure within an array, these arrival angles are discarded, but they can serve as additional constraint on structure along the travel path. Woodhouse and Wong (1986) developed the elegant linearized path integral approximation (PIA) to relate arrival angles to lateral heterogeneity. Similar to the integral in eqn [20], we can relate the tangent of the observed arrival angle, $v = \tan\Theta$, to the phase velocity anomalies along the source–receiver great circle

$$v(\Delta) \simeq -\mathrm{cosec}(\Delta)\int_0^{\Delta} \sin\phi \frac{\partial}{\partial\theta}\left[\frac{\delta c(\pi/2,\phi)}{c_0}\right]\mathrm{d}\phi \qquad [23]$$

where the great circle has been rotated onto the equator, the source is at $\phi = 0$, the receiver is at distance Δ, and θ is the colatitude. A similar expression exists for the amplitude

$$\ln A \simeq \frac{1}{2}\mathrm{cosec}(\Delta)\int_0^{\Delta} \sin(\Delta - \phi)\left[\sin\phi\partial_\theta^2 - \cos\phi\partial_\phi\right] \times \left[\frac{\delta c(\pi/2,\phi)}{c_0}\right]\mathrm{d}\phi \qquad [24]$$

where ∂_θ and ∂_ϕ are derivatives with respect to θ and ϕ (e.g., Romanowicz, 1987). Dahlen and Tromp (1998) slightly modified this to include a term with sensitivity to phase velocity at the receiver. Both v and A depend on frequency because phase velocity does.

Both arrival angles and amplitudes depend on gradients of structure rather than structure itself, which gives them sensitivity to shorter wavelengths than the corresponding phase data (see also Romanowicz, 1987). Wong (1989) applied this theory to include amplitude data to obtain frequency-dependent phase velocity maps at very long periods (modes up to angular order $\ell = 59$ at about 6.5 mHz). We developed an interactive technique to measure arrival angles using the multitaper approach of Park et al. (1987a). In the most general case, this method models elliptical particle motion in 3-D space. In a singular value decomposition (SVD) of the three-component

seismogram, we seek the frequency-dependent complex eigenvector that spans the plane of particle motion. From the eigenvectors, we can derive polarization parameters, such as the eccentricity of the ellipse and three angles that define the orientation of the ellipse. The eigenvalues give us an idea of how well-defined the particle motion is, that is, how well it can be explained by a single ellipse. As in the case of phase data, the multitaper approach provides statistical error bars as well as resistance to bias from noise in the time series. Lerner-Lam and Park (1989) first used this technique to investigate lateral refraction and multipathing of long-period surface waves in the Western Pacific.

Other methods to analyze particle motion exist, for example, the method by Jurkevics (1988) that works in real space. In the interactive analysis of Plešinger et al. (1986), one seeks the local coordinate system for which certain component products are zero. These products, as functions of time, can be used to either discriminate between wave types or measure arrival angles. Paulssen et al. (1990) expanded the basic time–frequency analysis for the three-component seismograms and presented the time and frequency-dependent polarization of anomalous surface waves observed at stations on the Iberian Peninsula. They constructed a quality factor that depends on the largest eigenvalue of the SVD to assess the likeness of the signal to a Rayleigh or Love wave. Lilly and Park (1995) applied the time–frequency analysis using a wavelet algorithm and the multitaper technique to investigate the evolution of the frequency-dependent polarization in a time series. The methods described here all involve the analysis of single three-component seismograms. As discussed in the last section, assuming a simple incoming wavefield, arrival angles can also be determined from array analyses (e.g., beamforming). A recent example of this is the study of Cotte et al. (2000) who investigated off-great-circle propagation in southern France caused by lateral refraction of surface waves by the French Alps. Using the beamforming technique, Friedrich et al. (1998) and Essen et al. (2003) observed a strong directivity of ocean-generated microseism noise in Europe. Similar observations exist for Southern California (e.g., Schulte-Pelkum et al., 2004).

Arrival angle data have been included successfully in inversions for global structure (e.g., Laske and Masters, 1996; Yoshizawa et al., 1999). It is interesting to compare the sensitivity of arrival angles and phase to lateral heterogeneity. **Figure 39** shows the integral kernels of eqn [23] in a similar way as those for the phase integral in **Figure 31**. Sensitivity to short-wavelength structure increases with harmonic degree, which is the opposite of the behavior for the phase. This is due to the fact that arrival angles depend on the gradient of structure, not the structure itself as phase does (see eqn [20]). We also notice that sensitivity to high-l structure, relative to low-l structure, increases with travel distance and does not decrease as the sensitivity of phase does. Except for very short paths of $<20°$, sensitivity to even harmonic degrees is always higher than to odd-harmonic degrees. Near the antipodes, sensitivity in the PIA becomes extremely large. At the same time, the antipode is a caustic with severe multipathing effects where asymptotic theories tend to break down (e.g., Romanowicz and Roult, 1986). We therefore discard data for epicentral distances larger than 160°. Relatively speaking, arrival angle data also have larger measurement errors than phase data. In principle, sensitivity to short-wavelength structure can be enhanced by including large data sets of phase data for very short travel paths (i.e., $<30°$) though the separation of the fundamental mode to obtain uncontaminated phase estimates at long periods becomes problematic. The collection of a global data set of arrival angle data, and its subsequent usage in the modeling of global structure, also has a useful by-product. Arrival angle data are sensitive to the misalignment of the horizontal seismometer components from east and north, and such information was not available when we first started our investigation. The joint inversion of arrival angles for structure and component misalignment can be linearized, but the inversion requires several iterations for misalignments of more than 5°. The Harvard group has also observed station misalignment though they use a different approach (Larson

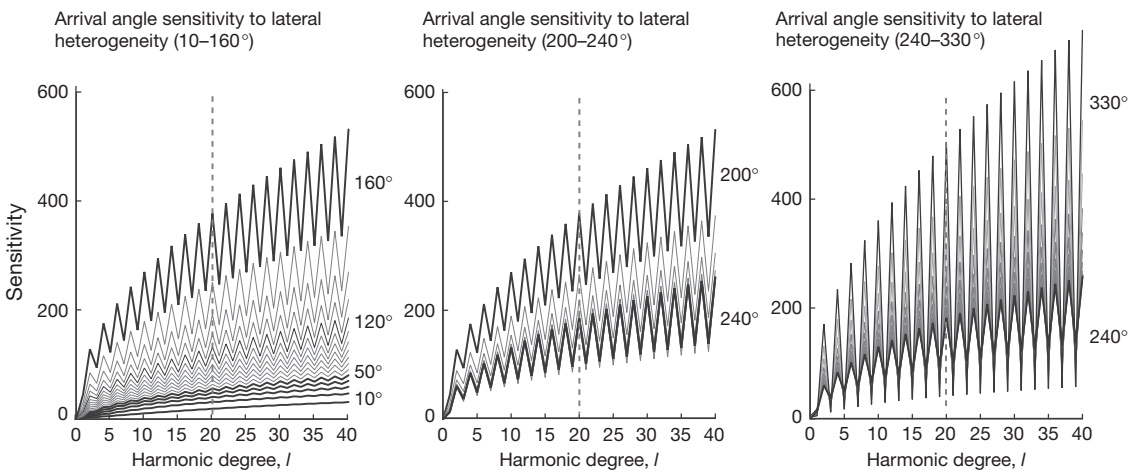

Figure 39 Arrival angle sensitivity to lateral heterogeneity, as function of harmonic degree in structure. Curves are shown for travel distances between 10° and 330°. Paths with distance $<180°$ are for minor arc paths (R_1); larger distances are for major arc paths (R_2). We do not analyze data within 20° of the antipode so the kernels were omitted.

and Ekström, 2002): arrival angle information is extracted from smoothed amplitude estimates using a PMF technique and synthetic seismograms computed with the dispersion measured for each waveform. Their station misalignment data agree quite well with our own. Some of the misalignments that we published (Laske, 1995) have been confirmed by station operators, and this information is now routinely available at the DMCs, together with the instrument responses.

As mentioned in the preceding text, amplitude data are also very useful to constrain lateral heterogeneity. In fact, due to the second derivative in eqn [24], amplitudes are even more sensitive to short-wavelength structure than arrival angles are. Amplitude information has been used as additional constraints to investigate elastic structure. Some of the earliest work is that of Yomogida and Aki (1987) who used the Gaussian beam method to obtain 30–80 s Rayleigh wave phase velocity structure in the Pacific Ocean. Wong (1989) used their linear theory to include amplitudes in the retrieval of elastic structure at very long periods beyond 150 s. Dalton and Ekström (2006) showed that it is possible to retrieve elastic structure using surface wave amplitudes alone, but the primary purpose to study surface wave amplitudes has been to retrieve Earth's attenuation structure (e.g., Billien et al., 2000; Durek et al., 1993). The problem with analyzing surface wave amplitudes is that the effects of lateral elastic heterogeneity may be an order of magnitude larger than those of attenuation. Selby and Woodhouse (2000) found that amplitude variations are dominated by anelastic structure for long wavelengths and by elastic structure at short wavelengths. If the linear approximation of eqn [24] holds, then this would perhaps be expected because the amplitude great-circle integral over anelastic structure is linear and does not involve any gradient as that over elastic structure does. The first to successfully address this problem in the retrieval of anelastic structure was Romanowicz (1994) who took focusing–defocusing effects into account before constructing the first attenuation maps for long-period Rayleigh waves. More recent work to retrieve attenuation includes that of Gung and Romanowicz (2004) who provide a 3-D attenuation model for the upper mantle. Using the nonlinear asymptotic coupling theory (NACT), they first derive an elastic model for V_{SH} and V_{SV} using long-period surface and body wave waveforms. The surface wave waveforms are then aligned using this model and inverted for 3-D attenuation. For further details about modeling attenuation from surface waves, see also **Chapter 1.25**.

Here, we have only discussed the horizontal arrival angles as observables to assess Earth structure, but the particle motion of surface waves is characterized by two additional angles: the sloping angle that describes the deviation of a Rayleigh wave orbit from the vertical and the tilting angle of the elliptical orbit with respect to the horizontal. Vig and Mitchell (1990) attempted to relate arrival angles (which they call inclination) and the sloping angles observed at station HON (Honolulu, Hawaii) of the DWWSSN to the anisotropic mantle around Hawaii. The shape of the Rayleigh wave ellipse, that is, the ratio between major and minor axes of particle motion (HZ ratio), depends on the shallow structure. Tanimoto and Alvizuri (2006) had recently used the HZ ratio of microseisms to infer shallow crustal structure shallower than 5 km in Southern California.

1.04.3.4 Higher Modes

The analysis of overtones, or higher modes, is attractive because it yields independent constraints on structure at depth. Overtones are more sensitive to deep structure than fundamental modes of the same frequency (see **Figure 43** in the next section). At long periods, overtones would significantly enhance resolution in the transition zone and uppermost lower mantle. At shorter periods, overtones carry better constraints on the low-velocity zone in the upper mantle than fundamental modes do. The analysis of overtones, however, faces several problems that are outlined in this section.

1.04.3.4.1 Higher-mode dispersion and waveform modeling

From **Figures 34, 35**, and **37**, we have seen that the fundamental mode is fairly isolated in time and frequency because its group velocities are significantly lower than those of overtones. Overtone velocities, on the other hand, overlap significantly, except at low frequencies. **Figure 37** suggests that we could analyze the first overtone, if we were able to isolate it, for example, using TVF or a phase-matched filtering operation (e.g., Jobert and Roult, 1976). Note, however, that for this particular earthquake, the mode contains relatively little energy. For the other modes, extraction appears very uncertain. To illustrate the problem, **Figure 40** shows the Gabor matrix for a synthetic calculated for isotropic PREM with a 39 km thick crust. For the seismogram in the top panel, all modes were included in the calculations, and we can discern the same body-wave phases, composed of interfering overtones, that we observe in the real seismogram. The other panels show the contribution from each mode, up to the fifth overtone. As just mentioned, the first overtone appears quite isolated in time–frequency space, but its energy is so little that it is not discernible in the composite Gabor matrix. The other overtones overlap significantly though extraction of the second higher mode may be possible at frequencies higher than 10 mHz, because group velocities are relatively low. At lower frequencies, there is significant overlap between the second and third overtones. At frequencies above 12 mHz, the third and fourth overtones overlap. TVF may provide only limited success in this case.

The first convincing observation of overtone dispersion was probably that of Oliver and Ewing (1957) for a path across eastern North America, but utilizing overtone dispersion to study Earth's interior obviously requires a different approach than fundamental modes do. The first breakthrough was achieved by Nolet (1975) and Cara (1978) who used an array stacking technique to separate different overtone branches using a $\omega - k$ transform, for studies of structure in Western Europe and across North America. This approach has also been used in other studies (e.g., Cara et al., 1981 for the Western United States). At fixed frequency, different overtone branches then appear separated in phase-group velocity space. This approach works well to obtain average structure within an array but does not allow us to assess variations within an array. The problem with this approach is also that it needs an array.

Using individual source–receiver data on a global scale, a successful separation of overtones up to order 8 was achieved by van Heijst and Woodhouse (1999). They used their mode branch stripping technique (van Heijst and Woodhouse, 1997)

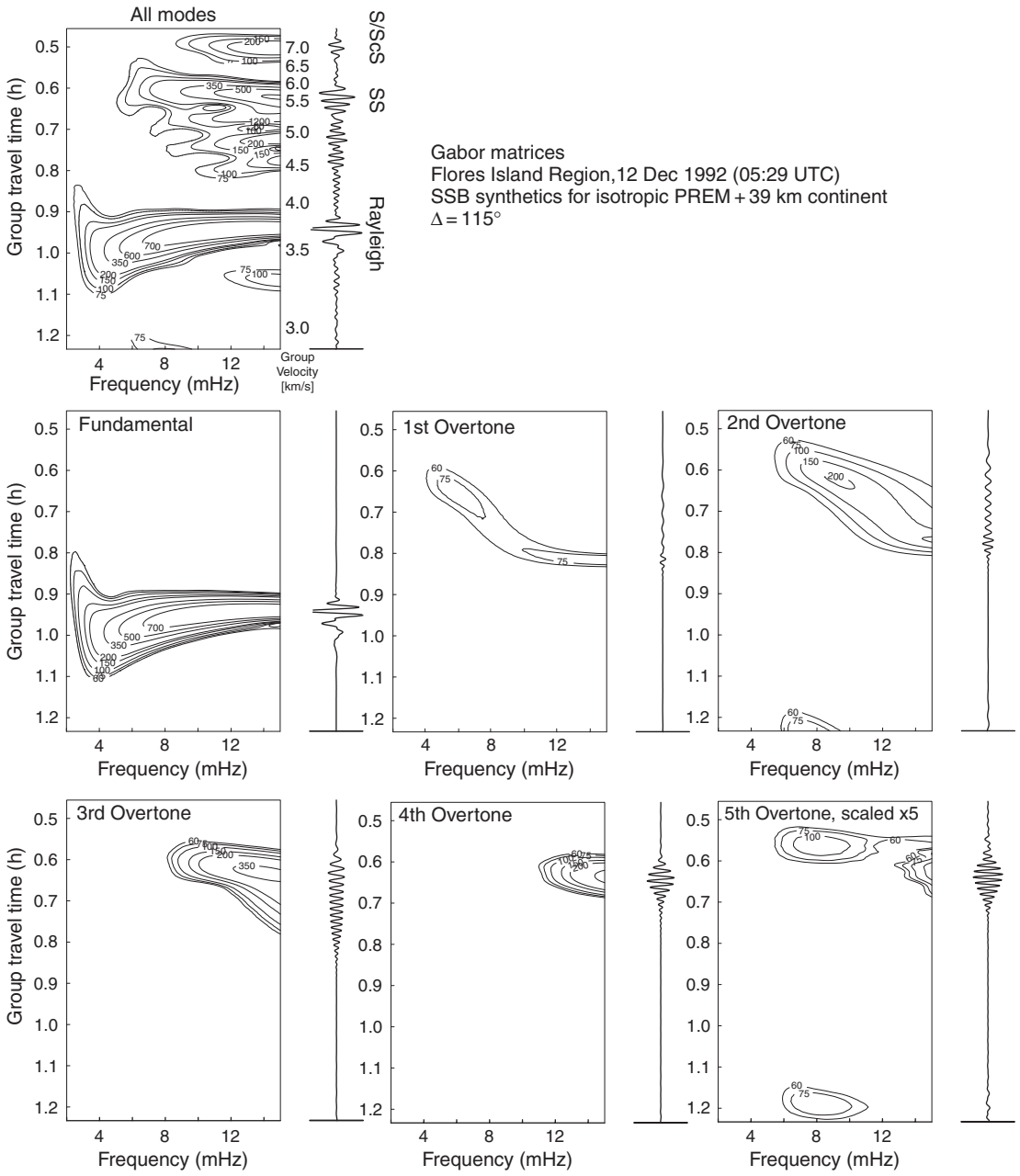

Figure 40 Visualization of a Gabor matrix for the synthetic seismogram in **Figure 37**. The top panel shows the complete synthetic, including all modes computed for isotropic PREM with a 39 km thick continental crust. The bottom panels show the Gabor matrices for the fundamental mode and first five overtones. While the fundamental mode is well isolated, the interference between overtones is rather complex. Note that the amplitudes for the fifth overtone are rather small. Also note that overtones beyond order 7 are required to compose the overlapping body-wave phases S and ScS (see also **Figure 33**).

to isolate the overtone branches and make global phase velocity maps (termed Oxford approach hereafter). This technique makes use of branch cross correlation functions (bccf's) that increase sensitivity to a certain overtone signal. The signal with the most energy is analyzed first and subtracted from the seismogram before successive branches are analyzed in a similar fashion. The technique works well for Rayleigh waves but appears to fail for Love waves due to strong interference effects. This is one of few studies that extract dispersion. The vast majority of publications utilize waveform modeling to retrieve structure at depth directly, without involving the intermediate step of determining dispersion. One may argue about which approach is superior, but a useful by-product of the Oxford approach is the ability to check for consistencies in the data. For example, they were able to compare their fundamental mode Rayleigh wave maps at 40 s with that of the fourth

overtone at 62 s. Since their dependence on structure at depth is quite similar, the phase velocity maps should highly correlate.

The bccf's have been used by others as well who choose the waveform modeling approach (e.g., Cara and Lévêque, 1987; Debayle and Lévêque, 1997). Other advances to study overtone branches include the hybrid technique by Stutzmann and Montagner (1993). This waveform fitting technique retrieves path-averaged overtone phase velocities and path-averaged velocity structure in successive steps. An attempt to determine global structure was discussed by Stutzmann and Montagner (1994) though data coverage was quite sparse. Similar to Nolet's array technique, they utilized several earthquakes along similar paths to retrieve phase velocities. They recently developed the 'roller-coaster technique' (Beucler et al., 2003) that is named after the shape of the misfit function in their method. Their method can be applied to a cluster of events to retrieve structure along a single source–receiver great circle in a nonlinear scheme. Another development is that of Yoshizawa and Kennett (2002, 2004) who used Sambridge's (1999) neighborhood algorithm to efficiently search the model space for multimode dispersion in a nonlinear waveform inversion.

Most of the other techniques involve full waveform modeling and the retrieval of structure at depth directly, without determining dispersion first. The first study on a global scale was that of Woodhouse and Dziewonski (1984) whose global upper-mantle shear velocity models, M84A and M84C, were regarded as reference 3-D model upper-mantle models for the following decade. The technique is still used by the Harvard group and has led to a series of updated whole mantle models such as S12/WM13 (Su et al., 1994) and S362D1 (Gu and Dziewonski, 1999). Though Woodhouse and Dziewonski used normal mode summation to calculate synthetic seismograms, they used a clever trick to account for sensitivity to odd-degree structure by introducing a fictitious epicentral distance shift in the minor and major arc great-circle integrals. This was later justified theoretically by Mochizuki (1986a,b) and Romanowicz (1987). Woodhouse and Dziewonski argued that individual waveforms are probably too noisy for direct inversions for structure so they projected their measurements onto a set of global basis functions in a two-step procedure. Another global waveform modeling approach is that of the Berkeley group called NACT (Li and Romanowicz, 1995). This technique accounts for cross branch coupling that is ignored in conventional path average approximations. While this is less of an issue for fundamental modes surface waves, it becomes relevant for overtones that involve deep-turning body waves. The application of this technique led to the first 'Berkeley model,' SAW12D (Li and Romanowicz, 1996), as well as more recent models (e.g., SAW24B16 by Mégnin and Romanowicz, 2000). In contrast to other mantle models, the Berkeley models have traditionally been V_{SH} models. A recent discussion of asymptotic and nonasymptotic waveform modeling approaches can be found in Clévédé et al. (2000).

With his nonlinear partitioned waveform inversion, Nolet (1990) provided a tool that is widely used in regional-scale studies. The technique is similar to step 1 in the Woodhouse and Dziewonski approach. Publications are too numerous to list here, but examples include work in Western Europe (e.g., Zielhuis and Nolet, 1994), in North America (e.g., van der Lee and Nolet, 1997), and on the Skippy array in Australia (e.g., Simons et al., 2002). Nolet argued that full waveform inversions directly for 3-D structure are computationally expensive and do not allow for a proper assessment of resolution capabilities. Rather, one can 'partition' the process and search for multiparameter, path-averaged structure first, for each source–receiver path, before conducting a computationally efficient inversion of a sparse matrix to retrieve 3-D structure. An advancement of this technique is its automation by Lebedev et al. (2005), which allows the processing of large data sets such as massive global data sets or regional-scale data sets from a dense network such as the USArray.

A few concluding words of caution are in order. We have seen that overtones have the potential to constrain deep Earth structure much better than fundamental modes do, and numerous studies emphasize that resolution is 'significantly' enhanced over fundamental mode only studies. A reader has to bear in mind though that in the parametric approach, due to the massive interference with other overtone branches, errors in the fit to overtone data are probably much larger than to fundamental mode data. Another important point is the relative weight of overtone data in an inversion. We have seen in **Figure 37** that recorded amplitudes of overtones were much smaller than those of the fundamental mode. Overtone experts may argue that the choice of the seismogram to demonstrate this point is poor because this earthquake was shallow. Such earthquakes excite fundamental modes particularly well and usually leave overtones with much reduced amplitudes in the seismogram. A proper choice of earthquakes for overtone studies therefore focuses on deep events. Unfortunately, such events are relatively rare and even more unevenly distributed than shallow events. **Figure 41** shows that earthquakes with source depths >75 km account for only 21% of all earthquakes, while the rest are shallower. Even with source depths of about 150 km, the fundamental modes still dominate the seismogram. Only when source depths become significantly

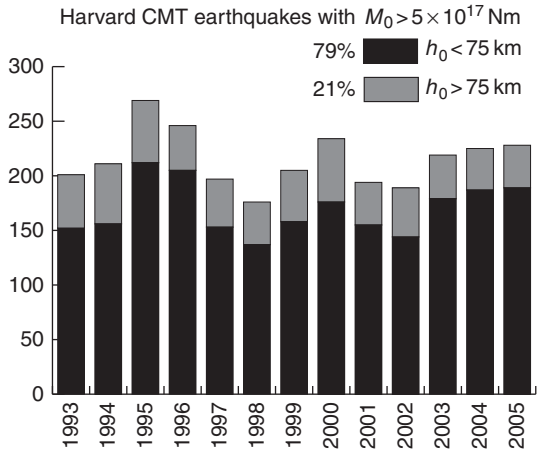

Figure 41 Events from the Harvard CMT catalog, for each year between 1993. Shown are all events with scalar seismic moment $M_0 \geq 5 \times 10^{17}$ Nm. For shallow events, this corresponds approximately to $M_S \geq 5.4$. Shown are 'shallow' events with source depths <75 km, which comprise 79% of all earthquakes. Events deeper than 75 km, which are potentially better earthquakes to study overtones, account for only 21% of all earthquakes.

greater than that, overtones above 4 mHz have larger spectral amplitudes than fundamental modes, which implies further reduction in the number of suitable earthquakes. A careful assessment of the resolution capabilities of a certain data set therefore entails more than just comparing the sensitivity kernels of fundamental modes and overtones. A 3-D surface wave tomographer essentially faces a trade-off problem. One can use all earthquakes to obtain best lateral resolution but bearing in mind that the vertical resolution is dominated by the limitations that fundamental modes dictate. Or one can chose mostly deep events to obtain optimal depth resolution, at the expense of decreased lateral resolution dictated by the sparser source distribution. The Berkeley and Oxford approaches appear to account for this by giving different weights to overtones, but the issue appears somewhat unresolved.

1.04.3.4.2 Love waves and overtones

With increasing amounts of data and the sophistication of measurement techniques, measurement errors have become ever smaller. Systematic biases introduced by unmodeled effects then become significant. We have already pointed out in **Figures 34** and **35** that Love wave overtone group velocity curves are quite close to that of the fundamental mode between 8 and 12 mHz (125–85 s). In a seismogram, short-period Love wave overtones therefore appear at the same times as long-period fundamental modes. Using sophisticated time-frequency analyses, such as the multiple filtering technique, one may be able to separate the different mode branches. However, it appears that even advanced techniques such as the branch stripping technique are not able to properly separate Love wave overtone branches, possibly because cross branch coupling is significant (Mégnin and Romanowicz, 1999). The question now is whether even the fundamental modes can be analyzed without taking interference effects into account. For oceanic paths in particular, overtones and fundamental mode group velocities are nearly the same for similar frequencies and separation is no longer trivial. It was discovered early that Rayleigh and Love waves are often incompatible, that is, that no realistic isotropic model fits the dispersion of both wave types simultaneously (e.g., McEvilly, 1964). Often, such models exhibit low-velocity zones overlain by thin lids with nearly unrealistically high shear velocities.

Some argued that at least some of this discrepancy can be explained by Love wave overtone contamination (e.g., Thatcher and Brune, 1969). Others suggested that no uniform bias can be found in a large data set that includes several earthquakes, for a given path and model (e.g., Boore, 1969). Due to this unsatisfying problem, initial collections of regionalized models resulting from inversions of dispersion curves did not include Love waves (Knopoff, 1972). The vast majority of publications address this problem by allowing transverse isotropy in the model, also called polarization anisotropy or radial anisotropy. More recently, Polet and Kanamori (1997) revisited this problem by studying the biasing effects for an upper-mantle model in Southern California. They found that after correcting for the biasing effect on Love waves from overtone contamination, the models obtained from Love and from Rayleigh waves were much more compatible than before. They also found that after the correction, the isotropic model that fit both wave types was much more realistic than before though the model had an unusually fast thin lid beneath the Moho and a low-velocity zone near 100 km depth, both not obtained when inverting for each wave type alone. On the other hand, Ekström and Dziewonski (1998) argued that anomalies found in V_{SV}, deduced from uncontaminated Rayleigh waves, and not in V_{SH} led to their discovery of anomalous azimuthal anisotropy in the Pacific ocean, while V_{SH} basically follows the lithospheric age progression.

With two-thirds of Earth covered by oceans, a possible contamination of Love wave data by overtones would pose a serious problem to find a proper REM. Our REM website compares the spherical averages of various published Love wave phase velocity maps with toroidal fundamental mode frequencies. Mode frequencies should not be biased by overtone contamination because an entirely different measurement technique is applied. A discrepancy between Love waves and toroidal modes is not apparent, which could indicate that, at least on average, overtone interference does not affect global estimates of Love wave phase velocity. A Rayleigh–Love incompatibility therefore can only be due to transverse isotropy. Nevertheless, a test with synthetic seismograms could help to illuminate how large a possible bias could be. We calculated 1200 mode synthetic seismograms for model 1066A that included the complete set of overtones. Using the same technique that we used in Laske and Masters (1996), we then measured phase relative to 1066A fundamental mode synthetics. **Figure 42** shows the median of our measured phase velocity anomalies. Rayleigh waves are essentially not affected by overtone contamination. Love wave data, on the other hand, show a bias that becomes significant at higher frequencies and can reach 0.06%, a result that could potentially raise concern. However, when comparing these discrepancies with the medians in the real data, we find that this bias is an order of magnitude smaller than what we observe. Potentially, Rayleigh wave overtone contamination could play a role if significant lateral refraction rotates some of the signal from the radial onto the transverse component. We have not tested how much this affects our data set, but we suspect that this effect is much smaller than Love wave overtone contamination. It appears therefore that a possible Rayleigh–Love incompatibility requires a transversely isotropic REM. Note that the medians shown here are averages in the data set and not true spherical averages, which are obtained only after an inversion for phase velocity maps. The small changes this would entail are irrelevant and do not at all affect the discussion here.

1.04.3.5 Surface Waves and Structure at Depth

The first inversion of surface wave dispersion to obtain mantle structure was carried out for the Canadian Shield by Brune and Dorman (1963) along a two-station pair. Forward modeling attempts go back at least 10 years (e.g., Ewing and Press, 1954). A vast amount of modeling attempts has followed since then, and the interested reader finds a detailed description of the quest for structure in the mantle in other contributions in this volume, for example, **Chapter 1.16**, which also discusses azimuthal anisotropy, or that of **Chapter 1.21**, which discusses

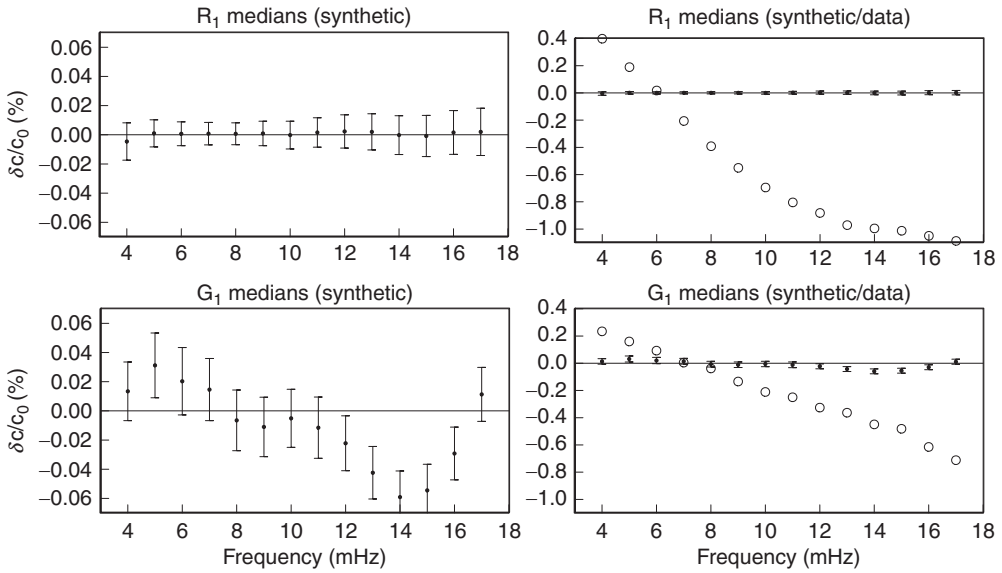

Figure 42 Estimation of the bias on fundamental mode phase velocity estimates introduced by overtone interference. Measurements are with respect to fundamental mode synthetics computed for model 1066A of Gilbert and Dziewonski (1975). The left panels show the bias on about 1200 synthetic waveforms that include the complete set of overtones, for Rayleigh (R_1) and Love (G_1) waves. The right panels show the same synthetic results but now together with the anomalies that we measured in our Laske and Masters (1996) data set (open circles). The synthetic test shows that the bias on Love waves is much greater than on Rayleigh waves, and the bias is significant. On the other hand, the anomalies that we measure on real data are an order of magnitude larger.

attenuation. A comprehensive review on the inversion of surface waves can be found in Romanowicz (2002). Here, we would like to close the discussion on surface wave data and their inversion for structure at depth with just a few remarks. Surface wave phase velocity is sensitive to all three elastic parameters, V_S (or β), V_P (or α), and density ρ:

$$\frac{\delta c}{c} = \int_0^a r^2 \mathrm{d}r \left(\tilde{A} \cdot \delta\alpha + \tilde{B} \cdot \delta\beta + \tilde{R} \cdot \delta\rho \right) \qquad [25]$$

where a is Earth's radius, r is the radius and all other parameters in the integral depend on r. In addition, phase velocity and the integral kernels depend on frequency. For uncoupled modes in transversely isotropic media, phase velocity sensitivity is expressed in terms of even more parameters where the two velocities are replaced by the five elastic parameters A, C, N, L, and F (e.g., Dziewonski and Anderson, 1981; Love, 1927; Takeuchi and Saito, 1972) where

$$V_{PH} = \sqrt{A/\rho}, \quad V_{SH} = \sqrt{N/\rho}$$
$$V_{PV} = \sqrt{C/\rho}, \quad V_{SV} = \sqrt{L/\rho}$$
$$\eta = F/(A - 2L)$$

where $A = C$, $N = L$, and $\eta = 1$ for isotropic media. Note that A here is not to be confused with the integral kernels A-tilde in eqn [25]. Montagner and Nataf (1986) devised an elegant technique to generalize this representation to model azimuthal anisotropy in the so-called vectorial tomography (Montagner and Nataf, 1988). In transversely isotropic media, Rayleigh waves are sensitive to all four velocities: V_{PV}, V_{PH}, V_{SV}, and V_{SH} where sensitivity to the latter is practically negligible. On the other hand, Love waves are sensitive to V_{SH} and V_{SV} where sensitivity to the latter is significantly smaller and usually ignored. We have no space to discuss the effects of anisotropy in greater detail, but the interested reader is referred to **Chapter 1.16**.

As mentioned in the preceding text, investigators strive to include overtones in their modeling because overtones enhance sensitivity to structure at greater depth than fundamental modes do. **Figures 43** and **44** show the sensitivity of Rayleigh and Love wave fundamental modes and their first two overtones to isotropic structure at depth. In the frequency range considered here (4–20 mHz), fundamental modes do not reach much beyond 300 km, though some sensitivity exists down to 500 km for 4 mHz Rayleigh waves. Overtones, on the other hand, reach well into the lower mantle. This fact has been utilized by numerous surface wave studies that concentrate on the transition zone and subducting slabs (e.g., Stutzmann and Montagner, 1994; Trampert and van Heijst, 2002; van der Lee and Nolet, 1997). In the isotropic case, Rayleigh waves are not very sensitive to V_P deeper than 50 km, but sensitivity is significant at shallower depths where sensitivity to V_S is very low. A comprehensive inversion for structure at depth would include the search for all three elastic parameters. In practice, this is usually not feasible, because the frequency range covered by the measurements does not provide enough independent information to make an inversion well constrained. To simplify an inversion, scaling relationships between the kernels for V_S, V_P, and ρ are drawn from mineral physics constraints and used to include the kernels for V_P and ρ in the kernels for V_S. We then invert only for V_S. For mantle structure, we commonly use, for all depths,

$$\tilde{A} \cdot \delta\alpha = (1/1.7)\tilde{B} \cdot \delta\beta$$
$$\tilde{R} \cdot \delta\rho = (1/2.5)\tilde{B} \cdot \delta\beta$$

This assumption is basically valid if observed seismic anomalies are caused by thermal effects. In the crust, above 50 km

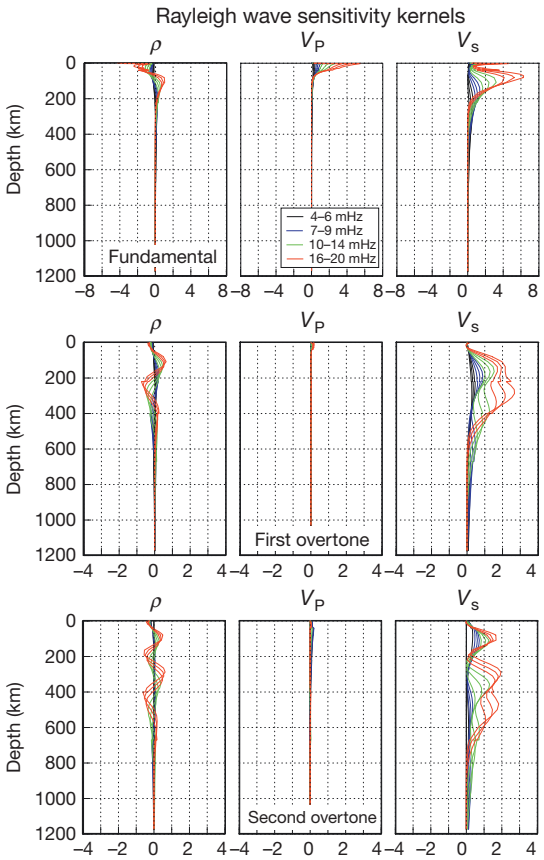

Figure 43 Sensitivity kernels for phase velocity to isotropic structure at depth, for Rayleigh wave fundamental modes and the first two overtones. Rayleigh waves depend on all three parameters, but sensitivity to V_S dominates. Overtone sensitivity to V_P is weak, and fundamental modes are affected only by V_P shallower than 50 km, when sensitivity to V_S decreases. Overtone sensitivity to structure below about 300 km is larger than that of fundamental modes though note that the scale is different by a factor 2. The model used to calculate the kernels is PREM.

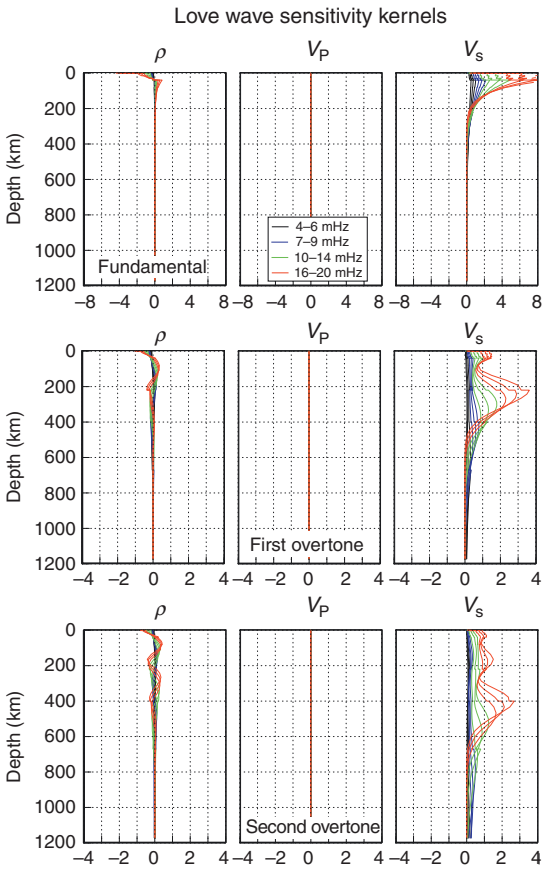

Figure 44 Sensitivity kernels for phase velocity to isotropic structure at depth, for Love wave fundamental modes and the first two overtones. Love wave fundamental modes are primarily sensitive to V_S only, but some sensitivity for density exists, especially for overtones. For details, see **Figure 43**. Second overtones are particularly useful to constrain structure in the transition zone.

depth, compositional variations may dominate and the scaling relationships no longer hold (e.g., in thick sedimentary basins). It is somewhat fortunate that sensitivity to shallow V_S is greatly diminished. Consequently, if we invert for a model, the shallow structure should probably be attributed to variations in V_P, not V_S as is commonly done. Note, however, that sensitivity to shallow density is also significant and a detailed discussion of tectonic implications should take this into account. A point that has not been treated here is that group velocities provide additional independent constraints, not in the physical sense but from a measurement technique point of view. A combination of the two is particularly useful to reduce ambiguities resulting from data uncertainties and to enhance the modeling of crustal structure (e.g., Shapiro and Ritzwoller, 2002).

We should mention that all examples shown in this chapter use a spherical Earth approach. On regional scale, when travel paths are limited to a few 100 km, investigators may choose to use a flat Earth approach. Surface wave applications overlap sufficiently that data or models may be compared that did not use the same approach. In this case, an Earth-flattening transformation has to be applied to facilitate this comparison (e.g., Ben-Menahem and Singh, 1981; Biswas and Knopoff, 1970). In the case of a velocity model comparison, a conversion can be done through

$$v_f(z_f) = \left(\frac{a}{r}\right) v_s(r) \qquad [26]$$

where the subscripts f and s denote 'flat' and 'spherical,' z is the depth, r is the radius, and a is Earth's radius (Shearer, 1999). Near the surface, the differences between v_f and v_s are insignificant, but they become larger with depth. To use Shearer's example, with $v_s = 8.6$ km s^{-1} at 150 km depth, the velocity in the flat Earth model would be 2.4% larger and the impact on velocity becomes relevant when discussing geodynamical implications.

A major issue not covered in this chapter is the model parameterization and the regularization during an inversion. Both influence the outcome of the modeling effort. The two basic classes of parameterizations include 'global' and 'local' ones. In a 'global' parameterization, each contributor to a set of basis functions covers the entire model space but represents different wavelengths (e.g., Chebyshev polynomials or spherical harmonics). In a 'local' parameterization, each contributor

covers only part of the model (e.g., layers or local B-splines). Comprehensive techniques also search for perturbations in boundaries, not only perturbations in elastic parameters. Regularizations or damping tries to account for the fact that some parts of the model space remain poorly constrained by the available data. For example, Rayleigh waves at periods shorter than 50 s have only marginal sensitivity to structure below 150 km. An undamped inversion could falsely place structure at these depths after a least-squares procedure dictated that this is the minimum norm solution. From a data perspective, this solution is not justifiable because there were no data to reliably constrain this. A careful analyst therefore conducts thorough a posteriori hypothesis testing (e.g., spike, checker board, or other tests with hypothetical input structures) on which structures of the model are reliably imaged and which are likely not. Other issues include how the inversion is done. Depending on the inversion algorithm, the modeling can end up in a local minimum of the misfit function in which case the model does not represent the best model consistent with our data. The Monte Carlo technique is used in forward modeling to explore larger areas in the model space (e.g., Shapiro and Ritzwoller, 2002). To make the search computationally more economical, Knopoff (1972) employed a hedgehog algorithm that he and Keilis-Borok developed (see also Keilis-Borok and Yanovskaja, 1967). The search starts out in a Monte Carlo fashion but then refines it once a minimum is found. Neighboring model parameters are tried out but discarded if the predictions move the value in the misfit function outside of a certain boundary around the minimum. Beghein and Trampert (2004) provided a novel approach using the neighborhood algorithm of Sambridge (1999). They define probability density functions to explore the range of possible models. Such forward approaches are attractive, but one should carefully evaluate the coverage of the null space. Last but not least, the Backus and Gilbert (1968) approach is still used today (Masters and Gubbins, 2003) when specific targets are investigated. In the B&G approach, specific linear combinations of data are selected that illuminate a certain model parameter (e.g., density near the core–mantle boundary). This method is attractive in that it provides an elegant way to assess the resolution capabilities of the data.

1.04.3.6 The Validity of the Great-Circle Approximation and Data Accuracy

Much of the discussion presented here is based on the use of Fermat's principle. Anomalies are assumed to accumulate along the great-circle arc between the source and receiver. Concerns about the validity of the great-circle approximation and suggestions to improve the interpretation of observables may go back as far as the great-circle approximation itself, and we need to be aware to which limit approximate theories are applicable. For example, Woodhouse and Girnius (1982) presented surface kernels for normal modes that show a rather broad corridor of sensitivity to structure along the source–receiver great circle. On the other hand, Jordan (1978) made a good argument that, asymptotically, modes are essentially sensitive to structure in the immediate vicinity of the source–receiver great circle. This is true if structure is smooth and the structural wavelength remains much larger than the signal wavelength. This applies not only to normal modes but also to surface waves. Advances in parametric surface wave modeling have been made through Gaussian beam ray-tracing techniques (e.g., Yomogida, 1985), Born single and multiple scattering (e.g., Friederich et al., 1993; Snieder and Nolet, 1987), or diffraction tomography (e.g., Meier et al., 1997; Ritzwoller et al., 2002). More recently, finite-frequency theory (e.g., Yoshizawa and Kennett, 2005; Zhou et al., 2005) has been added to the tools in the quest to resolve ever smaller details in Earth structure using surface waves. While each of these techniques promises vast improvement over simple approximations, they almost always also have their own limitations. Equally if not more importantly, we must not forget that the resulting models can only be as good as the data that the modeling is based on (see, e.g., Trampert and Spetzler, 2006). Measurement uncertainties can be large due to noise in the time series that may often be accepted too readily as being Gaussian because the theory requires it. Often, noise is produced systematically, for example, through coupling or interference effects or by inappropriate measurement techniques or by not accounting for them properly. Noise may simply be introduced by unknown effects such as a failing instrument, a faulty installation, or unknown coupling of the instrument to the ground. It is probably not unheard of that a spurious resonance in an installation (e.g., a process turning on every few minutes) nearly coincides with a normal mode frequency of Earth and the data analyst was not aware of the problem. We hope that this chapter has contributed to raise awareness of how important it is to understand how data are collected and how one's favorite measurement technique works and to judge its strengths and pitfalls objectively. Only then is one able to discuss the validity of small details in a model.

1.04.4 Concluding Remarks

As mentioned in **Section 1.04.1**, the seismograms we analyze are typically collected within the FDSN that includes not only the GSN, GEOSCOPE, and the GEOFON global seismic networks but also regional networks of permanent seismometer installations such as the German GRSN, the Canadian Digital Seismic Network, the Italian MedNet, the Japanese F-net, and the Californian TERRAscope and BDSN. Some of these have been recording continuously for 25 years or longer or have replaced earlier networks, such as the DWWSSN and SRO. The observation of normal modes, with periods up to 54 min, requires a very long-period sensor, and some of the best early digital observations were collected on LaCoste–Romberg gravimeters (e.g., IDA; Agnew et al., 1976) that have been used primarily to observe tides. The disadvantage of recording with gravimeters is that we collect only the vertical ground movement. Also, the first few wave trains in earlier recordings of large earthquakes were typically saturated. More modern equipment therefore includes a very broadband three-component seismometer, such as the Wielandt–Streckeisen STS-1 vault seismometer or the Geotech–Teledyne KS-54000 borehole seismometer. Though some individual installations of the broadband STS-2s deliver spectacular low-frequency spectra, more often, the signals of the gravest modes are buried in the noise. STS-1 and KS-54000 are no longer produced. As

sensors age and start to fail, we are losing some of the best and quietest stations that collected records of memorable quality. For example, at the old IDA/UCLA station SPA at the South Pole, the gravimeter recorded the deep 09 June 1994 Bolivia earthquake, which is, to this day and after the 2011 Tohoku, Japan earthquake, the best digitally recorded deep earthquake to study many overtone modes, including IC-sensitive modes. The station was closed soon after 'Bolivia,' and the site was equipped with seismometers and operated under the GSN umbrella. Though the installation included an STS-1, the 1994 Bolivia spectrum was the last and one of very few noteworthy normal mode spectra collected at SPA. Spectra collected at Earth's poles are invaluable to us because they provide the unique opportunity to study in detail the $m=0$ singlet of a mode. To this day, some $m=0$ singlets, such as that of IC-sensitive mode ${}_3S_2$, have not yet been observed, and we have yet to understand whether this is caused by Earth structure, low excitation by the seismic source, or high noise levels at SPA. The low signal quality at SPA has been known for many years, but such a station is extremely difficult to operate, not lastly for environmental reasons. It is therefore not surprising that it took almost 10 years before new equipment was installed at the new site QSPA, not too far away. The 2004 Sumatra–Andaman earthquake did produce a nice spectrum at QSPA, but this earthquake was exceptionally large. For the more recent, slightly smaller 2011 Tohoku, Japan earthquake, the spectrum of the primary sensor at QSPA, a KS-54000, was so noisy that mode 1S4, that sits between fundamental modes 0S6 and 0S7, was not observable. Note though that the secondary sensor, a Güralp CMG-3T, produced a much cleaner spectrum, with 1S4 clearly visible above the noise, but not 3S2. It still remains to be seen, if the 1994 Bolivia SPA spectrum can be reproduced in the future. The GSN is now a decade past reaching its design goals (Butler et al., 2004). No new stations have come online and the networks are past the transition from a R&D (research and development) to an O&M (operation and maintenance) modus operandi. To guarantee the data flow that we enjoy today requires the continued commitment of network operators to maintain stations at observatory-quality level, preferably at remote, low-noise locations. Amazingly enough, some network operators have run these networks on budgets that have not increased or, at the least, kept up with inflation rates. In today's world of high-resolution tomography and squeezed in between large but temporary projects such as the US EarthScope initiative and other high-visibility endeavors, it is becoming increasingly difficult to make the case for running, and funding, a permanent very long-period global seismic network. There are many yet unresolved problems in the Earth sciences to which normal mode seismology may hold the crucial clues, if not the only ones. Our greatest commitment therefore must be to ensure that we have not yet passed the golden age of normal mode observational seismology. Recent advances in ocean technology now allow year-long temporary deployments of broadband seismometers on the ocean floor that are routinely installed as primary sensors at permanent seismic observatories. Some deep-ocean deployments have produced very promising vertical-component spectra that could fill in crucial gaps in the current global coverage of GSN spectra. During the Hawaiian PLUME ocean bottom seismometer (OBS) deployment (Laske et al., 2009), we gathered several GSN-quality spectra for earthquakes much smaller smaller than the 2011 Tohoku, Japan earthquake. For the M_S=8.3 15 Nov 2006 Kuril Islands earthquake, we observed modes 0S6 and 3S2 – and even 0S5 – routinely on unburied Nanometrics Trillium 240 sensors, and on some Güralp CMG-3T sensors. Burial of the sensor is expected to significantly reduce tilt noise on all three components but particularly so on the horizontal components (Collins et al., 2001). Real-time access to OBS observatories can be provided through communication cables such as station H2O halfway between Hawaii and Oregon or through moored buoys. Innovative wave glider technology could provide real-time access to OBSs that are not serviced by cable or moorings (Laske et al., 2014). Advances in both battery and data acquisition technology nurture realistic hopes that an expansion of the GSN into the remote oceans is within our reach.

Acknowledgments

We wish to thank the network and station operators for their unselfish long-term commitment to continuously and consistently collect high-quality long-period seismic data. Foremost among these are GEOSCOPE (France), IRIS–IDA (UC San Diego, the United States), IRIS–USGS (ASL Albuquerque), GEOFON (GFZ, Potsdam, Germany), TERRAscope/TriNet (Caltech, the United States), BDSN (UC Berkeley, California), GRSN (SZGRF, Erlangen, Germany), BFO (Black Forest Observatory, Germany), and the operators of superconducting gravimeters. Thanks also go to IRIS, FDSN, the global geodynamics project (GGP; Crossley et al., 1999), and all data management centers for freely and readily making the data available to us. This research was funded by grants EAR03-36864 and EAR12-15636 of the US National Science Foundation.

References

Agnew DC, Berger J, Buland R, Farrell WE, and Gilbert JF (1976) International deployment of accelerometers: A network for very long period seismology. *EOS. Transactions of the American Geophysical Union* 77: 180–188.

Agnew DC, Berger J, Farrell WE, Gilbert JF, Masters G, and Miller D (1986) Project IDA: A decade in review. *EOS. Transactions of the American Geophysical Union* 67: 203–212.

Aki K and Richards PG (1980) *Quantitative Seismology, Theory and Methods*. San Francisco, FL: W.H. Freeman.

Aki K and Richards PG (2002) *Quantitative Seismology, Theory and Methods*. San Francisco, FL: University Science Books.

Alsina D and Snieder R (1993) A test of the great circle approximation in the analysis of surface waves. *Geophysical Research Letters* 20: 915–928.

Backus G (1962) The propagation of short elastic surface waves on a slowly rotating Earth. *Bulletin of the Seismological Society of America* 52: 823–846.

Backus G (1964) Geographical interpretation of measurements of average phase velocities of surface waves over great circular and great semi-circular paths. *Bulletin of the Seismological Society of America* 54: 571–610.

Backus G (1967) Converting vector and tensor equations to scalar equations in spherical coordinates. *Geophysical Journal of the Royal Astronomical Society* 13: 71–101.

Backus G and Gilbert F (1968) The resolving power of gross Earth data. *Geophysical Journal of the Royal Astronomical Society* 16: 169–205.

Beghein C and Trampert J (2004) Probability density functions for radial anisotropy from fundamental mode surface wave data and the neighbourhood algorithm. *Geophysical Journal International* 157: 1163–1174.

Benioff H, Harrison JC, LaCoste L, Munk WH, and Slichter LB (1959) Searching for the Earth's free oscillations. *Journal of Geophysical Research* 64: 1334.

Ben-Menahem A and Singh SJ (1981) *Seismic Waves and Sources*. New York: Springer.

Bensen GD, Ritzwoller MH, Barmin MP, et al. (2007) Processing seismic ambient noise data to obtain reliable broad-band surface wave dispersion measurements. *Geophysical Journal International* 169: 1239–1260.

Berckhemer H (1956) Rayleigh-wave dispersion and crustal structure in the East Atlantic Ocean basin. *Bulletin of the Seismological Society of America* 46: 83–86.

Beucler É, Stutzmann É, and Montagner J-P (2003) Surface wave higher-mode phase velocity measurements using a roller-coaster-type algorithm. *Geophysical Journal International* 155: 289–307.

Billien M, Lévêque J-J, and Trampert J (2000) Global maps of Rayleigh wave attenuation for periods between 40 and 150 seconds. *Geophysical Research Letters* 27: 3619–3622.

Biswas NN and Knopoff L (1970) Exact Earth-flattening calculation for Love waves. *Bulletin of the Seismological Society of America* 60: 1123–1137.

Blackman RB and Tukey JW (1958) *The Measurement of Power Spectra*. New York: Dover.

Boore DM (1969) Effect of higher mode contamination on measured Love wave phase velocities. *Journal of Geophysical Research* 74: 6612–6616.

Bromirski PD and Duennebier FK (2002) The near-coastal microseism spectrum: Spatial and temporal wave climate relationships. *Journal of Geophysical Research* 1078: 2166–2185.

Bromirski PD and Gerstoft P (2009) Dominant source regions of the Earth's hum are coastal. *Geophysical Research Letters* 36: L13303. http://dx.doi.org/10.1029/2009GL038903.

Brune J and Dorman J (1963) Seismic waves and Earth structure in the Canadian shield. *Bulletin of the Seismological Society of America* 53: 167–209.

Brune JN, Nafe JE, and Alsop LE (1961) The polar phase shift of surface waves on a sphere. *Bulletin of the Seismological Society of America* 51: 247–257.

Buland R, Berger J, and Gilbert F (1979) Observations from the IDA network of attenuation and splitting during a recent earthquake. *Nature* 277: 358–362.

Butler R, Lay T, Creager K, et al. (2004) The global seismographic network surpasses its design goal. *EOS. Transactions of the American Geophysical Union* 85: 225–229.

Capdeville Y, Chaljub E, Vilotte JP, and Montagner JP (2003) Coupling the spectral element method with a modal solution for elastic wave propagation in global Earth models. *Geophysical Journal International* 152: 34–67.

Capon J (1970) Analysis of Rayleigh-wave multipath propagation at LASA. *Bulletin of the Seismological Society of America* 60: 1701–1731.

Cara M (1973) Filtering of dispersed wavetrains. *Geophysical Journal of the Royal Astronomical Society* 33: 65–80.

Cara M (1978) Regional variations of higher Rayleigh-mode phase velocities: A spatial-filtering method. *Geophysical Journal of the Royal Astronomical Society* 54: 439–460.

Cara M and Lévêque J-J (1987) Waveform inversion using secondary observables. *Geophysical Research Letters* 14: 1046–1049.

Cara M, Minster J-B, and Le Bras R (1981) Multi-mode analysis of Rayleigh-type L_g. Part 2: Application to Southern California and the Northwestern Sierra Nevada. *Bulletin of the Seismological Society of America* 71: 985–1002.

Carder DS (1934) Seismic surface waves and the crustal structure of the Pacific region. *Bulletin of the Seismological Society of America* 24: 231–302.

Chaljub E and Valette B (2004) Spectral element modelling of three-dimensional wave propagation in a self-gravitating Earth with an arbitrarily stratified outer core. *Geophysical Journal International* 158: 131–141.

Clévédé É, Mégnin C, Romanowicz B, and Lognonné P (2000) Seismic waveform modeling and surface wave tomography in a three-dimensional Earth: Asymptotic and non-asymptotic approaches. *Physics of the Earth and Planetary Interiors* 119: 37–56.

Collins JA, Vernon FL, Orcutt JA, et al. (2001) Broadband Seismology in the Oceans: Lessons from the Ocean Seismic Network Pilot Experiment. *Geophysical Research Letters* 28: 49–52.

Cooley JW and Tukey JW (1965) An algorithm for the machine computation of complex Fourier series. *Mathematics of Computation* 19: 297–301.

Cotte N, Pedersen HA, Campillo M, Farra V, and Cansi Y (2000) Off-great-circle propagation of intermediate-period surface waves observed on a dense array in the French Alps. *Geophysical Journal International* 142: 825–840.

Creager KC (1997) Inner core rotation rate from small-scale heterogeneity and time-varying travel times. *Science* 278: 1248–1288.

Creager KC (2000) Inner core anisotropy and rotation. In: Karato S-i, Forte AM, Libermann RC, Masters G, and Stixrude L (eds.) *Earth's Deep Interior: Mineral Physics and Tomography. AGU Monograph*, 117, pp. 89–114. Washington, DC: American Geophysical Union.

Crossley D, Hinderer J, Casula G, et al. (1999) Network of superconducting gravimeters benefit a number of disciplines. *EOS. Transactions of the American Geophysical Union* 80: 125–126.

Dahlen FA (1968) The normal modes of a rotating, elliptical Earth. *Geophysical Journal of the Royal Astronomical Society* 16: 329–367.

Dahlen FA (1982) The effect of data windows on the estimation of free oscillation parameters. *Geophysical Journal of the Royal Astronomical Society* 69: 537–549.

Dahlen FA and Sailor RV (1979) Rotational and elliptical splitting of the free oscillations of the Earth. *Geophysical Journal of the Royal Astronomical Society* 58: 609–623.

Dahlen FA and Tromp J (1998) *Theoretical Global Seismology*. Princeton, NJ: Princeton University Press, p. 1025.

Dalton C and Ekström G (2006) Constraints on global maps of phase velocity from surface-wave amplitudes. *Geophysical Journal International* 161: 820–826.

Debayle E and Lévêque J-J (1997) Upper mantle heterogeneities in the Indian ocean from waveform inversion. *Geophysical Research Letters* 24: 245–248.

Deuss A, Ritsema R, and van Heijst H (2013) A new catalogue of normal-mode splitting function measurements up to 10 mHz. *Geophysical Journal International* 193: 920–937.

Deuss A and Woodhouse J (2001) Theoretical free-oscillation spectra; the importance of wide band coupling. *Geophysical Journal International* 146: 833–842.

Deuss A and Woodhouse J (2004) Iteration method to determine the eigenvalues and eigenvectors of a target multiplet including full mode coupling. *Geophysical Journal International* 159: 326–332.

Dobrin MB, Simon RF, and Lawrence PL (1951) Rayleigh waves from small explosions. *Transactions of the American Geophysical Union* 32: 822–832.

Donn WL and Blaik M (1953) A study and evaluation of the tripartite seismic method of locating hurricanes. *Bulletin of the Seismological Society of America* 43: 311–329.

Dratler J, Farrell W, Block B, and Gilbert F (1971) High-Q overtone modes of the Earth. *Geophysical Journal of the Royal Astronomical Society* 23: 399–410.

Durek JJ and Ekström G (1996) A model of radial anelasticity consistent with observed surface wave attenuation. *Bulletin of the Seismological Society of America* 86: 144–158.

Durek JJ, Ritzwoller MH, and Woodhouse JH (1993) Constraining upper mantle anelasticity using surface wave amplitude anomalies. *Geophysical Journal International* 114: 249–272.

Dziewonski AM (1970) On regional differences in dispersion of mantle Rayleigh waves. *Geophysical Journal of the Royal Astronomical Society* 22: 289–325.

Dziewonski AM and Anderson DL (1981) Preliminary reference Earth model. *Physics of the Earth and Planetary Interiors* 25: 297–356.

Dziewonski AM, Bloch S, and Landisman M (1969) A technique for the analysis of transient seismic signals. *Bulletin of the Seismological Society of America* 59: 427–444.

Dziewonski AM, Chou TA, and Woodhouse JH (1981) Determination of earthquake source parameters from waveform data for studies of global and regional seismicity. *Journal of Geophysical Research* 86: 2825–2852.

Dziewonski AM and Gilbert F (1971) Solidity of the inner core of the Earth inferred from normal mode observations. *Nature* 234: 465–466.

Dziewonski AM and Gilbert F (1972) Observations of normal modes from 84 recordings of the Alaskan earthquake of 1964 March 28. *Geophysical Journal of the Royal Astronomical Society* 27: 393–446.

Dziewonski AM, Hales A, and Lapwood E (1975) Parametrically simple earth models consistent with geophysical data. *Physics of the Earth and Planetary Interiors* 10: 12–48.

Dziewonski AM and Landisman M (1970) Great circle Rayleigh and Love wave dispersion from 100 to 900 seconds. *Geophysical Journal of the Royal Astronomical Society* 19: 37–91.

Dziewonski AM, Mills J, and Bloch S (1972) Residual dispersion measurement – A new method of surface-wave analysis. *Bulletin of the Seismological Society of America* 62: 129–139.

Dziewonski AM and Steim J (1982) Dispersion and attenuation of mantle waves through wave-form inversion. *Geophysical Journal of the Royal Astronomical Society* 70: 503–527.

Ekström G (2001) Time domain analysis of the Earth's long-period background seismic radiation. *Journal of Geophysical Research* 106: 26483–26494.

Ekström G (2011) A global model of Love and Rayleigh surface wave dispersion and anisotropy, 25–250 s. *Geophysical Journal International* 187: 1668–1686.

Ekström G and Dziewonski AM (1998) The unique anisotropy of the Pacific upper mantle. *Nature* 394: 168–172.

Ekström G, Tromp J, and Larson EW (1997) Measurements and models of global surface wave propagation. *Journal of Geophysical Research* 102: 8137–8157.

Ekström G, Nettles M, and Diewonski AM (2012) The global CMT project 2004-2010. Centroid-moment tensors for 13,017 earthquakes. *Physics of the Earth Planetary Interiors* 200–201: 1–9. http://dx.doi.org/10.1016/j.pepi.2012.04.002.

Essen H-H, Krüger F, Dahm T, and Grevemeyer I (2003) On the generation of secondary microseisms observed in northern and central Europe. *Journal of Geophysical Research* 108: 2506. http://dx.doi.org/10.1029/2002JB002338.
Evernden JE (1953) Direction of approach of Rayleigh waves and related problems. Part I. *Bulletin of the Seismological Society of America* 43: 335–357.
Evernden JE (1954) Direction of approach of Rayleigh waves and related problems. Part II. *Bulletin of the Seismological Society of America* 44: 159–184.
Ewing M, Jardetzky WS, and Press F (1957) *Elastic Waves in Layered Media*, p. 380. New York: McGraw-Hill Book Company.
Ewing M and Press F (1952) Crustal structure and surface wave dispersion, Part 2. *Bulletin of the Seismological Society of America* 42: 315–325.
Ewing M and Press F (1954) An investigation of mantle Rayleigh waves. *Bulletin of the Seismological Society of America* 44: 127–147.
Ewing M and Press F (1956) Rayleigh wave dispersion in the period range 10 to 500 seconds. *Transactions of the American Geophysical Union* 37: 213–215.
Forsyth D and Li A (2005) Array-analysis of two-dimensional variations in surface wave phase velocity and azimuthal anisotropy in the presence of multi-pathing interference. In: Levander A and Nolet G (eds.) *Seismic Earth: Array Analysis of Broadband Seismograms*. *Geophysical Monograph*,157, pp. 81–97. Washington, DC: American Geophysical Union.
Friederich W, Hunzinger S, and Wielandt E (2000) A note on the interpretation of seismic surface waves over three-dimensional structures. *Geophysical Journal International* 143: 335–339.
Friederich W, Wielandt E, and Stange S (1993) Multiple forward scattering of surface waves; comparison with an exact solution and Born single-scattering methods. *Geophysical Journal International* 112: 264–275.
Friederich W, Wielandt E, and Stange S (1994) Non-plane geometries of seismic surface wavefields and their implications for regional surface-wave tomography. *Geophysical Journal International* 119: 931–948.
Friedrich A, Krüger F, and Klinge K (1998) Ocean generated microseismic noise located with the Gräfenberg array. *Journal of Seismology* 2: 47–64.
Fukao Y, Nishida K, and Kobayashi N (2010) Seafloor topography, ocean infragravity waves, and background Love and Rayleigh waves. *Journal of Geophysical Research* 115: B04302. http://dx.doi.org/10.1029/2009JB006678.
Gabor D (1947) Acoustical quanta and the theory of hearing. *Nature* 159: 591–594.
Galagher B (1971) Generation of surf beat by non-linear wave interactions. *Journal of Fluid Mechanics* 49: 1–20.
Geller RJ and Takeuchi N (1995) A new method for computing highly accurate DSM synthetic seismograms. *Geophysical Journal International* 123: 449–470.
Giardini D, Li X-D, and Woodhouse JH (1987) Three-dimensional structure of the Earth from splitting in free oscillation spectra. *Nature* 325: 405–411.
Gilbert F (1971) The diagonal sum rule and averaged eigenfrequencies. *Geophysical Journal of the Royal Astronomical Society* 23: 119–123.
Gilbert F (1980) An introduction to low-frequency seismology. In: *Proceedings of the Enrico Fermi Summer School of 1979* 41–81.
Gilbert F (2001) Vandermonde matrix analysis of long-period seismograms. *Geophysical Journal International* 146: 843–849.
Gilbert F and Dziewonski AM (1975) An application of normal mode theory to the retrieval of structural parameters and source mechanisms from seismic spectra. *Philosophical Transactions of the Royal Society A* 278: 187–269.
Gu YJ and Dziewonski AM (1999) Mantle discontinuities and 3-D tomographic models. *EOS. Transactions of the American Geophysical Union* 80: F717.
Gung Y and Romanowicz B (2004) *Q* tomography of the upper mantle using three-component long-period waveforms. *Geophysical Journal International* 157: 813–830.
Gutenberg B and Richter CF (1936) On seismic waves, 3rd paper. *Gerlands Beitrage Zur Geophysik* 47: 73–131.
Hanka W and Kind R (1994) The GEOFON program. *IRIS Newsletter* XIII: 1–4.
Harmon N, Forsyth D, and Webb S (2007) Using ambient seismic noise to determine short-period phase velocities and shallow shear velocities in young oceanic lithosphere. *Bulletin of the Seismological Society of America* 97: 2009–2023.
Harmon N, Gerstoft P, Rychert CA, Abers GA, Salas de la Cruz M, and Fischer KM (2008) Phase velocities from seismic noise using beamforming and cross correlation in Costa Rica and Nicaragua. *Geophysical Research Letters* 35: L19303. http://dx.doi.org/10.1029/2008GL035387.
Harmon N, Rychert C, and Gerstoft P (2010) Distribution of noise sources for seismic inteferometry. *Geophysical Journal International* 183: 1470–1484.
Harris F (1978) On the use of windows for harmonic analysis with the discrete Fourier transform. *Proceedings of the IEEE* 66: 51–83.
He X and Tromp J (1996) Normal-mode constraints on the structure of the Earth. *Journal of Geophysical Research* 87: 7772–7778.
Henson IH (1989) Multiplet coupling of the normal modes of an elliptical, transversely isotropic Earth. *Geophysical Journal International* 98: 457–459.
Herrin E and Goforth T (1977) Phase-matched filters: Application to the study of Rayleigh waves. *Bulletin of the Seismological Society of America* 67: 1259–1275.
Hiller G, Graham N, Campillo M, Kedar S, Landès M, and Shapiro N (2012) Global oceanic microseism sources as seen by seismic arrays and predicted by wave action models. *Geochemistry, Geophysics, Geosystems* 13: Q01021. http://dx.doi.org/10.1029/2011GC003875.
Hu X-G, Liu L-T, Hinderer J, Hsu HT, and Sun H-P (2006) Wavelet filter analysis of atmospheric pressure effects in the long-period seismic mode band. *Physics of the Earth and Planetary Interiors* 154: 70–84.
Ishii M and Tromp J (1999) Normal-mode and free-air gravity constraints on lateral variations in velocity and density of Earth's mantle. *Science* 285: 1231–1236.
Jeans JH (1923) The propagation of earthquake waves. *Gerlands Beitrage Zur Geophysik A* 102: 554–574.
Jenkins GM (1961) General considerations in the analysis of spectra. *Technometrics* 3: 133–166.
Jobert N and Roult G (1976) Periods and damping of free oscillations observed in France after sixteen earthquakes. *Geophysical Journal of the Royal Astronomical Society* 45: 155–176.
Jobert N and Roult G (1978) Evidence of lateral variations from free oscillations and surface waves. *Geophysical Research Letters* 5: 569–572.
Jordan T (1978) A procedure for estimating lateral variations from low-frequency eigenspectra data. *Geophysical Journal of the Royal Astronomical Society* 52: 441–455.
Jurkevics A (1988) Polarization analysis of three-component array data. *Seismological Society of America* 78: 1725–1743.
Kanamori H (1970) Velocity and *Q* of the mantle waves. *Physics of the Earth and Planetary Interiors* 2: 259–275.
Kedar S, Longuet–Higgins M, Webb F, Graham N, Clayton R, and Jones C (2008) The origin of deep ocean microseisms in the Northern Atlantic Ocean. *Proceedings of the Royal Society A* 464: 777–793.
Keilis-Borok VI and Yanovskaja TB (1967) Inverse problems of seismology (Structural Review). *Geophysical Journal of the Royal Astronomical Society* 13: 223–234.
Kellogg LH, Hager BH, and van der Hilst RD (1999) Compositional stratification in the deep mantle. *Science* 283: 1881–1884.
Knopoff L (1972) Observation and inversion of surface-wave dispersion. *Tectonophysics* 13: 497–519.
Knopoff L, Berry MJ, and Schwab FA (1967) Tripartite phase velocity observations in laterally heterogeneous regions. *Journal of Geophysical Research* 72: 2595–2601.
Knopoff L, Mueller S, and Pilant WL (1966) Structure of the crust and upper mantle in the Alps from the phase velocity of Rayleigh waves. *Bulletin of the Seismological Society of America* 56: 1009–1044.
Komatitsch D, Ritsema J, and Tromp J (2002) The spectral-element method, Beowulf computing, and global seismology. *Science* 298: 1737–1742.
Komatitsch D and Tromp J (2002) Spectral-element simulations of global seismic wave propagation. Part II: Three-dimensional models, oceans, rotation and self-gravitation. *Geophysical Journal International* 150: 303–318.
Komatitsch D and Vilotte J-P (1998) The spectral element method: An efficient tool to simulate the seismic response of 2D and 3D geological structure. *Bulletin of the Seismological Society of America* 88: 368–392.
Koptschalitsch G (1988) *Die Anwendung der zeitvariablen Filterung bei der Eigenschwingungs-analyse*. Masters Thesis. Germany: Universität Karlsruhe.
Kurrle D and Widmer-Schnidrig R (2006) Spatiotemporal features of the Earth's background oscillations observed in central Europe. *Geophysical Research Letters* 33: L24304. http://dx.doi.org/10.1029/12006GL028429.
Kurrle D and Widmer-Schnidrig R (2008) The horizontal hum of the Earth: A global background of spheroidal and toroidal modes. *Geophysical Research Letters* 35: L06304. http://dx.doi.org/10.1029/2007GL033125.
Kurrle D and Widmer-Schnidrig R (2010) Excitation of long-period Rayleigh wave by large storms over the North Atlantic Ocean. *Geophysical Journal International* 183: 330–338.
Landau LD and Lifshitz EM (1958) *Quantum Mechanics*, p. 515. Reading, MA: Addison Wesley.
Landisman M, Dziewonski A, and Satô Y (1969) Recent improvements in the analysis of surface wave observations. *Geophysical Journal of the Royal Astronomical Society* 17: 369–403.
Larson EWF and Ekström G (2002) Determining surface wave arrival angle anomalies. *Journal of Geophysical Research* 107. http://dx.doi.org/10.1029/2000JB000048.
Laske G (1995) Global observation of off-great-circle propagation of long-period surface waves. *Geophysical Journal International* 123: 245–259.
Laske G and Masters G (1996) Constraints on global phase velocity maps from long-period polarization data. *Journal of Geophysical Research* 101: 16059–16075.

Laske G and Masters G (1999) Limits on the rotation of the inner core from a new analysis of free oscillations. *Nature* 402: 66–69.

Laske G and Masters G (2003) The Earth's free oscillations and the differential rotation of the inner core. In: Dehant V, Creager K, Zatman S, and Karato S-I (eds.) *Earths Core: Dynamics, Structure, Rotation*. *Geodynamics Series* 31, pp. 5–21. Washington, DC: AGU.

Laske G, Masters G, and Dziewonski AM (2001) New measurements of radial mode eigenfrequencies. *EOS. Transactions of the American Geophysical Union* 82: F873.

Laske G, Phipps Morgan J, and Orcutt J (1998) First results from the Hawaiian SWELL pilot experiment. *Geophysical Research Letters* 26: 3397–3400.

Laske G, Collins JA, Wolfe CJ, et al. (2009) Probing the Hawaiian Hot Spot With New Broadband Ocean Bottom Instruments. *EOS. Transactions of the American Geophysical Union* 90: 362–363.

Laske G, Berger J, Orcutt J, and Babcock J (2014) ADDOSS: Autonomously Deployed Deep-ocean Seismic System - Communications Gateway for Ocean Observatories. *Geophysical Research Abstracts* 16: EGU General Assembly 2014: EGU2014-4707.

Lebedev S, Nolet G, Meier T, and van der Hilst RD (2005) Automated multimode inversion of surface and *S* waveforms. *Geophysical Journal International* 162: 951–964.

Lerner-Lam AL and Park JJ (1989) Frequency-dependent refraction and multipathing of 10–100 second surface waves in the Western Pacific. *Geophysical Research Letters* 16: 527–530.

Levin V and Park J (1998) Quasi-Love phases between Tonga and Hawaii: Observations, simulations, and explanations. *Journal of Geophysical Research* 103: 24321–24331.

Levshin AL, Pisarenko VF, and Pogrebinsky GA (1972) On a frequency-time analysis of oscillations. *Annales Geophysicae* 28: 211–218.

Levshin AL, Ritzwoller MH, and Resovsky J (1999) Source effects on surface wave group travel times and group velocity maps. *Physics of the Earth and Planetary Interiors* 115: 293–312.

Levshin AL, Yanovskaya TB, Lander AV, et al. (1989) Recording identification and measurements of surface wave parameters. In: Keilis-Borok VI (ed.) *Seismic Surface Waves in a Laterally Inhomogeneous Earth*, pp. 131–182. Dordrecht: Kluwer.

Li X-D, Giardini D, and Woodhouse JH (1991a) Large-scale three-dimensional even-degree structure of the Earth from splitting of long-period normal modes. *Journal of Geophysical Research* 96: 551–557.

Li X-D, Giardini D, and Woodhouse JH (1991b) The relative amplitudes of mantle heterogeneity in *P* velocity, *S* velocity, and density from free oscillation data. *Geophysical Journal International* 105: 649–657.

Li X-D and Romanowicz B (1995) Comparison of global waveform inversions with and without considering cross-branch modal coupling. *Geophysical Journal International* 121: 695–709.

Li X-D and Romanowicz B (1996) Global mantle shear velocity model developed using non-linear asymptotic coupling theory. *Journal of Geophysical Research* 101: 22245–22272.

Lilly JM and Park J (1995) Multiwavelet spectral and polarization analyses of seismic records. *Geophysical Journal International* 122: 1001–1021.

Lin F-C, Moschetti MP, and Ritzwoller MH (2008) Surface wave tomography of the western United States from ambient seismic noise: Rayleigh and Love wave phase velocity maps. *Geophysical Journal International* 173: 281–298.

Lin F-C and Ritzwoller MH (2011) Helmholtz surface wave tomography for isotropic and azimuthally anisotropic structure. *Geophysical Journal International* 186: 1104–1120.

Lin F-C, Ritzwoller MH, Yang Y, Moschetti MP, and Fouch MJ (2011) Complex and variable crustal and uppermost mantle seismic anisotropy in the western United States. *Nature Geoscience* 4: 55–61. http://dx.doi.org/10.1038/NGEO1036.

Lindberg CR and Park J (1987) Multiple-taper spectral analysis of terrestrial free oscillations, Part II. *Geophysical Journal of the Royal Astronomical Society* 91: 795–836.

Lognonné P (1991) Normal modes and seismograms in an anelastic rotating Earth. *Journal of Geophysical Research* 96: 20309–20319.

Lognonné P and Romanowicz B (1990) Modelling of coupled normal modes of the Earth: The spectral method. *Geophysical Journal International* 102: 365–395.

Longuet–Higgins M (1950) A theory of the origin of microseisms. *Philosophical Transactions of the Royal Society of London A* 243: 1–35.

Love AEH (1927) *A Treatise on the Mathematical Theory of Elasticity*, 4th edn, pp. 1–35. Cambridge: Cambridge University Press.

Masters TG (2011) Free oscillations for fun and profit (Beno Gutenberg Medal Lecture). *Geophysical Research Abstracts* 13: EGU2011–EGU14185.

Masters G and Gilbert F (1981) Structure of the inner core inferred from observations of its spheroidal shear modes. *Geophysical Research Letters* 8: 569–571.

Masters G and Gilbert F (1983) Attenuation in the Earth at low frequencies. *Philosophical Transactions of the Royal Society of London A* 308: 479–522.

Masters TG and Gubbins D (2003) On the resolution of density within the Earth. *Physics of the Earth and Planetary Interiors* 140: 159–167.

Masters G, Johnson S, Laske G, and Bolton H (1996) A shear velocity model of the mantle. *Philosophical Transactions of the Royal Society of London A* 354: 1385–1411.

Masters G, Jordan TH, Silver PG, and Gilbert F (1982) Aspherical Earth structure from fundamental spheroidal-mode data. *Nature* 298: 609–613.

Masters G and Laske G (1997) On bias in surface wave and free oscillation attenuation measurements. *EOS. Transactions of the American Geophysical Union* 78: F485.

Masters G, Laske G, Bolton H, and Dziewonski A (2000) The relative behavior of shear velocity, bulk sound speed, and compressional velocity in the mantle: Implications for chemical and thermal structure. In: Karato S-I, Forte AM, Libermann RC, Masters G, and Stixrude L (eds.) *Earth's Deep Interior: Mineral Physics and Tomography*. *AGU Monograph*117: pp. 63–87. Washington, DC: American Geophysical Union.

Masters TG, Laske G, and Gilbert F (2000a) Autoregressive estimation of the splitting matrix of free-oscillation multiplets. *Geophysical Journal International* 141: 25–42.

Masters TG, Laske G, and Gilbert F (2000b) Matrix autoregressive analysis of free-oscillation coupling and splitting. *Geophysical Journal International* 143: 478–489.

Masters TG, Laske G, and Gilbert F (2000c) Large-scale Earth structure from analyses of free oscillation splitting and coupling. In: Boschi E, Ekström G, and Morelli A (eds.) *Problems in Geophysics for the New Millennium*, pp. 255–288. Bologna: Editrice Compositori.

Masters G, Park J, and Gilbert F (1983) Observations of coupled spheroidal and toroidal modes. *Journal of Geophysical Research* 88: 10285–10298.

Masters TG and Widmer R (1995) Free-oscillations: Frequencies and attenuations. In: Ahrens Th J (ed.) *Global Earth Physics: A Handbook of Physical Constants*, pp. 104–125. Washington, DC: American Geophysical Union.

Maupin V (1992) Modelling of laterally trapped surface waves with application to Rayleigh waves in the Hawaiian swell. *Geophysical Journal International* 110: 533–570.

McEvilly TV (1964) Central US crust-upper mantle structure from Love and Rayleigh wave phase velocity inversion. *Bulletin of the Seismological Society of America* 54: 1997–2015.

Mégnin C and Romanowicz B (1999) The effects of the theoretical formalism and data selection on mantle models derived from waveform tomography. *Geophysical Journal International* 138: 366–380.

Mégnin C and Romanowicz B (2000) The 3D shear velocity of the mantle from the inversion of body, surface, and higher mode waveforms. *Geophysical Journal International* 143: 709–728.

Meier T, Dietrich K, Stöckhert B, and Harjes H-P (2004) One-dimensional models of shear wave velocity for the eastern Mediterranean obtained from the inversion of Rayleigh wave phase velocities and tectonic implications. *Geophysical Journal International* 156: 45–58.

Meier T, Lebedev S, Nolet G, and Dahlen FA (1997) Diffraction tomography using multimode surface waves. *Journal of Geophysical Research* 102: 8255–8267.

Mendiguren JA (1973) Identification of free oscillation spectral peaks for 1970 July 31, Colombian deep shock using the excitation criterion. *Geophysical Journal of the Royal Astronomical Society* 33: 281–321.

Millot-Langet R, Clévédé E, and Lognonné P (2003) Normal modes and long period seismograms in a 3D anelastic elliptical rotating Earth. *Geophysical Research Letters* 30. http://dx.doi.org/10.1029/2002GL016257.

Mochizuki E (1986a) Free oscillations and surface waves in an aspherical Earth. *Geophysical Research Letters* 13: 1478–1481.

Mochizuki E (1986b) The free oscillations of an anisotropic and heterogeneous Earth. *Geophysical Journal of the Royal Astronomical Society* 86: 167–176.

Montagner J-P and Nataf H-C (1986) A simple method for inverting the azimuthal anisotropy of surface waves. *Journal of Geophysical Research* 91: 511–520.

Montagner J-P and Nataf H-C (1988) Vectorial tomography. Part I: Theory. *Journal of Geophysical Research* 94: 295–307.

Nafe JE and Brune JN (1960) Observations of phase velocity for Rayleigh waves in the period range 100–400 s. *Bulletin of the Seismological Society of America* 50: 427–439.

Nawa K, Suda N, Fukao Y, Sato T, Aoyama Y, and Shibuya K (1998) Incessant excitation of the Earth's free oscillations. *Earth, Planets and Space* 50: 3–8.

Nishida K (2013) Earth's background free oscillations. *Annual Review of Earth and Planetary Sciences* 41: 719–740. http://dx.doi.org/10.1146/annurev-earth-050212-124020.

Nishida K and Fukao Y (2007) Source distribution of Earth's background free oscillations. *Journal of Geophysical Research* 112: B06306. http://dx.doi.org/10.1029/2006JB004720.

Nishida K, Kawakatsu H, Fukao Y, and Obara K (2008) Background Love and Rayleigh waves simultaneously generated at the Pacific Ocean floors. *Geophysical Research Letters* 35: L16307. http://dx.doi.org/10.1029/2008GL034753.

Nishida K and Kobayashi N (1999) Statistical features of the Earth's continuous free oscillations. *Journal of Geophysical Research* 104: 28741–28750.

Nishida K, Kobayashi N, and Fukao Y (2000) Resonant oscillations between the solid Earth and the atmosphere. *Science* 287: 2244–2246.

Nishida K, Kobayashi N, and Fukao Y (2002) Origin of Earth's ground noise from 2 to 20 mHz. *Geophysical Research Letters* 29(52): 1–4.

Nishida K, Montagner JP, and Kawakatsu H (2009) Global surface wave tomography using seismic hum. *Science* 326: 112.

Nolet G (1975) Higher Rayleigh modes in Western Europe. *Geophysical Research Letters* 2: 60–62.

Nolet G (1990) Partitioned waveform inversion and two-dimensional structure under the network of autonomously recording seismographs. *Journal of Geophysical Research* 95: 8499–8512.

Oliver J (1962) A summary of observed seismic surface wave dispersion. *Bulletin of the Seismological Society of America* 52: 49–52.

Oliver J and Ewing M (1957) Higher modes of continental Rayleigh waves. *Bulletin of the Seismological Society of America* 47: 187–204.

Oliver J and Ewing M (1958) Short-period oceanic surface waves of the Rayleigh and first shear modes. *Transactions of the American Geophysical Union* 39: 483–485.

Oliver J and Murphy L (1971) WWNSS: Seismology's global network of observing stations. *Science* 174: 254–261.

Park J and Gilbert F (1986) Coupled free oscillations of an aspherical, dissipative, rotation Earth: Galerkin theory. *Journal of Geophysical Research* 91: 7241–7260.

Park J, Lindberg CR, and Thomson DJ (1987) Multiple-taper spectral analysis of terrestrial free oscillations, Part I. *Geophysical Journal of the Royal Astronomical Society* 91: 755–794.

Park J, Lindberg CR, and Vernon FL III (1987) Multitaper spectral analysis of high-frequency seismograms. *Journal of Geophysical Research* 92: 12675–12684.

Paulssen H, Levshin AL, Lander AV, and Snieder R (1990) Time- and frequency-dependent polarization analysis: Anomalous surface wave observations in Iberia. *Geophysical Journal International* 103: 483–496.

Pedersen HA (2006) Impacts of non-plane waves on two-station measurements of phase velocities. *Geophysical Journal International* 165: 279–287.

Pekeris CL (1946) The theory of propagation of sound in a half space of variable sound velocity under conditions of formation of a shadow zone. *Journal of the Acoustical Society of America* 18: 295–315.

Peterson J (1993) Observations and modeling of seismic background noise. *US Geological Survey, Open-file Report* 93-322, 1–45.

Peterson J, Hutt CR, and Holcomb LG (1980) Test and calibration of the seismic research observatory. *US Geological Survey, Open-file Report* 80-187, 1–86.

Peterson J and Tilgner EE (1985) Description and preliminary testing of the CDSN seismic sensor systems. *US Geological Survey, Open-file Report* 85-288, 1–60.

Pilant WL and Knopoff L (1964) Observations of multiple seismic events. *Bulletin of the Seismological Society of America* 54: 19–39.

Plešinger A, Hellweg M, and Seidl D (1986) Interactive high-resolution polarization analysis of broad-band seismograms. *Journal of Geophysics* 59: 129–139.

Polet J and Kanamori H (1997) Upper-mantle shear velocities beneath Southern California determined from long-period surface waves. *Bulletin of the Seismological Society of America* 87: 200–209.

Pollitz F (1994) Global tomography from Rayleigh and Love wave dispersion: Effect of raypath bending. *Geophysical Journal International* 118: 730–758.

Press F (1956) Determination of crustal structure from phase velocity of Rayleigh waves. Part I: Southern California. *Bulletin of the Seismological Society of America* 67: 1647–1658.

Press F (1957) Determination of crustal structure from phase velocity of Rayleigh waves. Part I: San Francisco Bay region. *Bulletin of the Seismological Society of America* 47: 87–88.

Resovsky J and Ritzwoller M (1995) Constraining odd-degree mantle structure with normal modes. *Geophysical Research Letters* 22: 2301–2304.

Resovsky J and Ritzwoller M (1998) New and refined constraints on the three-dimensional Earth structure from normal modes below 3 mHz. *Journal of Geophysical Research* 103: 783–810.

Rhie J and Romanowicz B (2004) Excitation of Earth's continuous free oscillations by atmosphere-ocean-seafloor coupling. *Nature* 431: 552–556.

Rhie J and Romanowicz B (2006) A study of the relation between ocean storms and the Earth's hum. *Geochemistry, Geophysics, Geosystems* 7. http://dx.doi.org/10.1029/2006GC001274.

Riley KF, Hobson MP, and Bence SJ (2002) *Mathematical Methods for Physics and Engineering*, p. 1232. Cambridge: Cambridge University Press.

Ritsema J and Van Heijst H (2000) Seismic imaging of structural heterogeneity in Earth's mantle: Evidence for large-scale mantle flow. *Science Progress* 83: 243–259.

Ritzwoller M, Masters G, and Gilbert F (1986) Observations of anomalous splitting and their interpretation in terms of aspherical structure. *Journal of Geophysical Research* 91: 10203–10228.

Ritzwoller M, Masters G, and Gilbert F (1988) Constraining aspherical structure with low frequency interaction coefficients: Application to uncoupled multiplets. *Journal of Geophysical Research* 93: 6369–6396.

Ritzwoller MH, Shapiro NM, Barmin MP, and Levshin AL (2002) Global surface wave diffraction tomography. *Journal of Geophysical Research* 107. http://dx.doi.org/10.1029/2002JB001777.

Röhrbach W (1932) Über die dispersion seismischer Oberflächenwellen. *Zeitschrift für Geophysik* 8: 113–129.

Romanowicz B (1987) Multiplet–multiplet coupling due to lateral heterogeneity: Asymptotic effects on the amplitude and frequency of the Earth's normal modes. *Geophysical Journal of the Royal Astronomical Society* 90: 75–100.

Romanowicz B (1994) On the measurement of anelastic attenuation using amplitudes of low-frequency surface waves. *Physics of the Earth and Planetary Interiors* 84: 179–191.

Romanowicz B (2002) Inversion of surface waves: A review. In: Jennings PC, Kisslinger C, Kanamori H, and Lee WHK (eds.) *International Handbook of Earthquake and Engineering Seismology*. *International Geophysics*, vol. 81A, pp. 149–173. Amsterdam: Academic Press, International Association of Seismology and Physics of the Earth's Interior Committee on Education.

Romanowicz B and Bréger L (2000) Anomalous splitting of free oscillations; a reevaluation of possible interpretations. *Journal of Geophysical Research* 105: 21559–21578.

Romanowicz B, Cara M, Fels JF, and Roult G (1984) GEOSCOPE: A French initiative in long period three component global seismic networks. *Eos, Transactions of the American Geophysical Union* 65: 753–756.

Romanowicz BA and Dziewonski AM (1986) Toward a federation of broadband seismic networks. *Eos, Transactions of the American Geophysical Union* 67: 541–542.

Romanowicz B and Roult G (1986) First-order asymptotics for the eigenfrequencies of the Earth and application to the retrieval of large-scale lateral variations of structures. *Geophysical Journal of the Royal Astronomical Society* 87: 209–239.

Romanowicz B, Roult G, and Kohl T (1987) The upper mantle degree two pattern: Constraints from GEOSCOPE fundamental spheroidal mode eigenfrequency and attenuation measurements. *Geophysical Research Letters* 14: 1219–1222.

Rosat S, Sato T, Imanishi Y, et al. (2005) High resolution analysis of the gravest seismic normal modes after the 2004 Mw = 9 Sumatra earthquake using superconducting gravimeter data. *Geophysical Research Letters* 32: L13304. http://dx.doi.org/10.1029/2005GL023128.

Roult G (1974) Attenuation des ondes sismiques de tres sasse frequence. *Annales Geophysicae* 30: 141–167.

Roult G and Clévédé E (2000) New refinements in attenuation measurements from free-oscillation and surface-wave observations. *Physics of the Earth and Planetary Interiors* 121: 1–37.

Roult G and Romanowicz B (1984) Very long-period data from the GEOSCOPE network: Preliminary results on great circle averages of fundamental and higher Rayleigh and Love modes. *Bulletin of the Seismological Society of America* 74: 2221–2243.

Roult G, Romanowicz B, and Jobert N (1986) Observations of departures from classical approximations on very long period GEOSCOPE records. *Annales Geophysicae* 4: 241–249.

Roult G, Romanowicz B, and Montagner JP (1990) 3-D upper mantle shear velocity and attenuation from fundamental mode free oscillation data. *Geophysical Journal International* 101: 61–80.

Russell DR, Herrmann RB, and Hwang H-J (1988) Application of frequency variable filters to surface-wave amplitude analysis. *Bulletin of the Seismological Society of America* 78: 339–354.

Sabra KG, Gerstoft P, Roux P, Kuperman WA, and Fehler MC (2005a) Surface wave tomography from microseisms in Southern California. *Geophysical Research Letters* 32: L14311. http://dx.doi.org/10.1029/2005GL023155.

Sabra KG, Gerstoft P, Roux P, Kuperman WA, and Fehler MC (2005b) Extracting time-domain Greens function estimates from ambient seismic noise. *Geophysical Research Letters* 32: L03310. http://dx.doi.org/10.1029/2004GL021862.

Sambridge M (1999) Geophysical inversion with a neighborhood algorithm. Part I: Searching a parameter space. *Geophysical Journal International* 138: 479–494.

Savino J, Murphy A, Rynn JM, et al. (1972) Results from the high-gain long-period seismograph experiment. *Geophysical Journal of the Royal Astronomical Society* 31: 179–204.

Schulte-Pelkum V, Earle PS, and Vernon FL (2004) Strong directivity of ocean-generated seismic noise. *Geochemistry, Geophysics, Geosystems* 5: Q03004. http://dx.doi.org/10.1029/2003GC000520.

Schwab F and Kausel E (1976a) Quadripartite surface wave method: Development. *Geophysical Journal of the Royal Astronomical Society* 45: 231–244.

Schwab F and Kausel E (1976b) Long-period surface wave seismology: Love wave phase velocity and polar phase shift. *Geophysical Journal of the Royal Astronomical Society* 45: 407–435.

Selby ND and Woodhouse JH (2000) Controls on Rayleigh wave amplitudes: Attenuation and focusing. *Geophysical Journal International* 142: 933–940.

Shapiro NM and Campillo M (2004) Emergence of broadband Rayleigh waves from correlations of the ambient seismic noise. *Geophysical Research Letters* 31. http://dx.doi.org/10.1029/2004GL019491.

Shapiro NM, Campillo M, Paul A, Singh SK, Jongmans D, and Sanchez-Sesma J (1997) Surface-wave propagation across the Mexican volcanic belt and origin of the long-period seismic-wave amplification in the Valley of Mexico. *Geophysical Journal International* 128: 151–166.

Shapiro NM, Campillo M, Stehly L, and Ritzwoller MH (2005) High-resolution surface-wave tomography from ambient seismic noise. *Science* 29: 1615–1617.

Shapiro NM and Ritzwoller MH (2002) Monte-Carlo inversion for a global shear-velocity model of the crust and upper mantle. *Geophysical Journal International* 151: 88–105.

Shapiro NM and Singh SK (1999) A systematic error in estimating surface-wave group-velocity dispersion curves and a procedure for its correction. *Bulletin of the Seismological Society of America* 89: 1138–1142.

Sharrock DS and Woodhouse JH (1998) Investigation of time dependent inner core structure by the analysis of free oscillation spectra. *Earth, Planets and Space* 50: 1013–1018.

Shearer P (1999) *Introduction to Seismology*, p. 260. New York: Cambridge University Press.

Simons FJ, van der Hilst RD, Montagner J-P, and Zielhuis A (2002) Multimode Rayleigh wave inversion for heterogeneity and azimuthal anisotropy of the Australian upper mantle. *Geophysical Journal International* 151: 738–754.

Smith SW (1972) The anelasticity of the mantle. *Tectonophysics* 13: 601–622.

Smith MF and Masters G (1989a) The effect of Coriolis coupling of free oscillation multiplets on the determination of aspherical Earth structure. *Geophysical Research Letters* 16: 263–266.

Smith MF and Masters G (1989b) Aspherical structure constraints from free oscillation frequency and attenuation measurements. *Journal of Geophysical Research* 94: 1953–1976.

Snieder R and Nolet G (1987) Linearized scattering of surface waves on a spherical Earth. *Journal of Geophysics* 61: 55–63.

Song X (2000) Joint inversion for inner core rotation, inner core anisotropy, and mantle heterogeneity. *Journal of Geophysical Research* 105: 7931–7943.

Song X and Richards PG (1996) Seismological evidence for differential rotation of the Earth's inner core. *Nature* 382: 221–224.

Souriau A (1998) Earth's inner core – Is the rotation real? *Science* 281: 55–56.

Souriau A and Souriau M (1983) Test of tectonic models by great circle Rayleigh waves. *Geophysical Journal of the Royal Astronomical Society* 73: 533–551.

Stange S and Friederich W (1993) Surface wave dispersion and upper mantle structure beneath southern Germany from joint inversion of network recorded teleseismic events. *Geophysical Research Letters* 20: 2375–2378.

Stutzmann É and Montagner JP (1993) An inverse technique for retrieving higher mode phase velocity and mantle structure. *Geophysical Journal International* 113: 663–683.

Stutzmann É and Montagner JP (1994) Tomography of the transition zone from the inversion of higher-mode surface waves. *Physics of the Earth and Planetary Interiors* 86: 99–115.

Su W-J, Dziewonski AM, and Jeanloz R (1996) Planet within a planet: Rotation of the inner core of Earth. *Science* 274: 1883–1887.

Su W-J, Woodward RL, and Dziewonski AM (1994) Degree 12 model of shear velocity heterogeneity in the mantle. *Journal of Geophysical Research* 99: 6945–6980.

Suda N, Nawa K, and Fukao Y (1998) Earth's background free oscillations. *Science* 279: 2089–2091.

Takeuchi N, Geller RJ, and Cummins PR (2000) Complete synthetic seismograms for 3D heterogeneous Earth models computed using modified DMS operators and their applicability to inversion for Earth structure. *Physics of the Earth and Planetary Interiors* 119: 25–36.

Takeuchi H and Saito M (1972) Seismic surface waves. In: Bolt BA (ed.) *Methods in Computational Physics*, vol. 11, pp. 217–295. New York: Academic Press.

Tanaka S and Hamaguchi H (1997) Degree one heterogeneity and hemispherical variation of anisotropy in the inner core from *PKPBC–PKPDF* times. *Journal of Geophysical Research* 102: 2925–2938.

Tanimoto T (2005) The ocean excitation hypothesis for the continuous oscillations of the Earth. *Geophysical Journal International* 160: 276–288.

Tanimoto T and Alvizuri C (2006) Inversion of the HZ ratio of microseisms for *S*-wave velocity in the crust. *Geophysical Journal International* 165: 323–335.

Tanimoto T, Um J, Nishida K, and Kobayashi N (1998) Earth's continuous oscillations observed on seismically quiet days. *Geophysical Research Letters* 25: 1553–1556.

Thatcher W and Brune J (1969) Higher mode interference and observed anomalous apparent Love wave phase velocities. *Journal of Geophysical Research* 74: 6603–6611.

Thomson DJ (1982) Spectrum estimation and harmonic analysis. *Proceedings of the IEEE* 70: 1055–1096.

Toksöz MN and Anderson DL (1966) Phase velocity of long-period surface waves and structure of the upper mantle. *Journal of Geophysical Research* 71: 1649–1658.

Trampert J and Spetzler J (2006) Surface wave tomography: Finite-frequency effects lost in the null space. *Geophysical Journal International* 164: 394–400.

Trampert J and van Heijst H-J (2002) Global azimuthal anisotropy in the transition zone. *Science* 296: 1297–1299.

Trampert J and Woodhouse JH (1995) Global phase velocity maps of Love and Rayleigh waves between 40 and 150 seconds. *Geophysical Journal International* 122: 675–690.

Tromp J (1993) Support for anisotropy of the Earth's inner core from free oscillations. *Nature* 366: 678–681.

Valette B and Lesage P (1992) Retrieving Mean Earth models. In: *Conference on Mathematical Geophysics, Taxco, Mexico* .

van der Lee S and Nolet G (1997) Upper mantle *S* velocity structure of North America. *Journal of Geophysical Research* 102: 22815–22838.

van Heijst H and Woodhouse JH (1997) Measuring surface-wave overtone phase velocities using a mode branch stripping technique. *Geophysical Journal International* 131: 209–230.

van Heijst H and Woodhouse JH (1999) Global high-resolution phase velocity distribution of overtone and fundamental-mode surface waves determined by mode-branch stripping. *Geophysical Journal International* 137: 601–620.

Vig PK and Mitchell BJ (1990) Anisotropy beneath Hawaii from surface wave particle motion observations. *Pure and Applied Geophysics* 133: 1–22.

Webb SC (1998) Broadband seismology and noise under the ocean. *Reviews of Geophysics* 36: 105–142.

Webb SC (2007) The Earth's 'hum' is driven by ocean waves over the continental shelves. *Nature* 445: 754–756. http://dx.doi.org/10.1038/nature05536.

Widmer R (1991) *The Large-Scale Structure of the Deep Earth as Constrained by Free Oscillation Observations*. PhD Thesis, La Jolla, CA: University of California San Diego.

Widmer R, Zürn W, and Masters G (1992a) Observation of low order toroidal modes from the 1989 Macquarie rise event. *Geophysical Journal International* 111: 226–236.

Widmer R, Masters G, and Gilbert F (1992b) Observably split multiplets – Data analysis and interpretation in terms of large-scale aspherical structure. *Geophysical Journal International* 111: 559–576.

Widmer R and Zürn W (1992) Bichromatic excitation of long-period Rayleigh and air waves by the Mount Pinatubo and El Chichon volcanic eruptions. *Geophysical Research Letters* 19: 765–768.

Widmer-Schnidrig R (2002) Application of regionalized multiplet stripping to retrieval of aspherical structure constraints. *Geophysical Journal International* 148: 201–213.

Wielandt E (1980) First-order asymptotic theory of the polar phase shift of Rayleigh waves. *Pure and Applied Geophysics* 118: 1214–1227.

Wielandt E (1987) On the validity of the ray approximation for interpreting delay times. In: Nolet G (ed.) *Seismic Tomography*, pp. 85–98. Dordrecht: D. Reidel Publishing Company.

Wielandt E (1993) Propagation and structural interpretation of non-plane waves. *Geophysical Journal International* 113: 45–53.

Wielandt E and Schenk H (1983) On systematic errors in phase-velocity analysis. *Journal of Geophysics* 52: 1–6.

Wilson T (1940) The Love waves of the South Atlantic earthquake of August 28, 1933. *Bulletin of the Seismological Society of America* 30: 273–301.

Wong YK (1989) *Upper Mantle Heterogeneity from Phase and Amplitude Data of Mantle Waves*. PhD Thesis, Cambridge, MA: Harvard University.

Woodhouse JH (1980) The coupling and attenuation of nearly resonant multiplets in the Earth's free oscillation spectrum. *Geophysical Journal of the Royal Astronomical Society* 61: 261–283.

Woodhouse JH (1983) The joint inversion of seismic wave forms for lateral variations in Earth structure and earthquake source parameters. In: Kanamori H and Boschi E (eds.) *Proceedings of the Enrico Fermi International School of Physics LXXXV*, pp. 336–397. Amsterdam: North Holland.

Woodhouse JH (1988) The calculation of eigenfrequencies and eigenfunctions of the free oscillations of the Earth and the Sun. In: Doornbos DJ (ed.) *Seismological Algorithms, Computational Methods and Computer Programs*, pp. 321–370. London: Academic Press.

Woodhouse JH and Dahlen FA (1978) The effect of a general aspherical perturbation on the free oscillations of the Earth. *Geophysical Journal of the Royal Astronomical Society* 53: 335–354.

Woodhouse JH and Dziewonski AM (1984) Mapping the upper mantle-3-dimensional modeling of Earth structure by inversion of seismic waveforms. *Journal of Geophysical Research* 89: 5953–5986.

Woodhouse JH and Giardini D (1985) Inversion for the splitting function of isolated low order normal mode multiplets. *Eos, Transactions of the American Geophysical Union* 66: 300.

Woodhouse JH, Giardini D, and Li X-D (1986) Evidence for inner core anisotropy from splitting in free oscillations data. *Geophysical Research Letters* 13: 1549–1552.

Woodhouse JH and Girnius TP (1982) Surface waves and free oscillations in a regionalized earth model. *Geophysical Journal of the Royal Astronomical Society* 68: 653–673.

Woodhouse JH and Wong YK (1986) Amplitude, phase and path anomalies of mantle waves. *Geophysical Journal of the Royal Astronomical Society* 87: 753–773.

Woods MT, Lévêque J-J, Okal EA, and Cara M (1991) Two-station measurements of Rayleigh wave group velocity along the Hawaiian Swell. *Geophysical Research Letters* 18: 105–108.

Yang X, Bondar I, Bhattacharyya J, et al. (2004) Validation of regional and teleseismic travel-time models by relocating ground-truth events. *Bulletin of the Seismological Society of America* 94: 897–919.

Yang Y, Ritzwoller MH, Levshin AL, and Shapiro NM (2007) Ambient noise Rayleigh wave tomography across Europe. *Geophysical Journal International* 168: 259–274.

Yang Y, Ritzwoller MH, Lin F-C, Moschetti MP, and Shapiro NM (2008) The structure of the crust and uppermost mantle beneath the western US revealed by ambient noise and earthquake tomography. *Journal of Geophysical Research* 113: B12310. http://dx.doi.org/10.11029/12008JB005833.

Yao H, van der Hilst RD, and de Hoop MV (2006) Surface-wave array tomography in SE Tibet from ambient seismic noise and two-station analysis: I—Phase velocity maps. *Geophysical Journal International* 166: 732–744.

Yomogida K (1985) Gaussian beams for surface waves in laterally slowly varying media. *Geophysical Journal of the Royal Astronomical Society* 82: 511–533.

Yomogida K and Aki K (1987) Amplitude and phase data inversions for phase velocity anomalies in the Pacific ocean basin. *Geophysical Journal of the Royal Astronomical Society* 88: 161–204.

Yoshizawa K and Kennett BLN (2002) Non-linear waveform inversion for surface waves with a neighbourhood algorithm; application to multimode dispersion measurements. *Geophysical Journal International* 149: 118–133.

Yoshizawa K and Kennett BLN (2004) Multimode surface wave tomography for the Australian region using a three-stage approach incorporating finite frequency effects. *Journal of Geophysical Research* 109. http://dx.doi.org/10.1029/2002JB002254.

Yoshizawa K and Kennett BLN (2005) Sensitivity kernels for finite-frequency surface waves. *Geophysical Journal International* 162: 910–926.

Yoshizawa K, Yomogida K, and Tsuboi S (1999) Resolving power of surface wave polarization data for higher order heterogeneities. *Geophysical Journal International* 138: 205–220.

Zhang J, Song X, Li Y, Richards PG, Sun X, and Waldhauser F (2005) Inner core differential motion confirmed by earthquake waveform doublets. *Science* 309: 1357–1361.

Zhou Y, Dahlen FA, Nolet G, and Laske G (2005) Finite-frequency effects in global surface-wave tomography. *Geophysical Journal International* 163: 1087–1111.

Zielhuis A and Nolet G (1994) Shear wave velocity variations in the upper mantle. *Geophysical Journal International* 117: 695–715.

Zürn W, Laske G, Widmer-Schnidrig R, and Gilbert F (2000) Observation of Coriolis coupled modes below 1 mHz. *Geophysical Journal International* 143: 113–118.

Zürn W and Widmer R (1995) On noise reduction in vertical seismic records below 2 mHz using local barometric pressure. *Geophysical Research Letters* 22: 3537–3540.

Relevant Website

http://igppweb.ucsd.edu/~gabi/rem.html – The Reference Earth Model Website (accessed June 2014).

This page intentionally left blank

1.05 Theory and Observations: Body Waves, Ray Methods, and Finite-Frequency Effects

J Virieux, ISTerre, Université Joseph Fourier, Grenoble, France
G Lambaré, CGG, Massy, France

© 2015 Elsevier B.V. All rights reserved.

1.05.1	**Introduction**	169
1.05.2	**Ray Theory**	170
1.05.2.1	Intuitive Approach	170
1.05.2.2	Elastodynamic Equations and Wave Equations	173
1.05.2.3	Asymptotic Ray Theory	173
1.05.2.4	Rays and Wave Fronts: A Lagrangian Formulation	174
1.05.2.5	First Travel Times: An Eulerian Formulation	175
1.05.2.6	Multivalued Travel Times and Phases: An Eulerian Formulation	176
1.05.2.7	Variational Approaches for Ray Tracing	178
1.05.2.8	Transport Equation	179
1.05.2.9	Acoustic and Elastic Ray Theory	180
1.05.2.10	Paraxial Ray Theory	180
1.05.2.11	Tools for Ray Tracing	181
1.05.2.12	Eikonal Solver Tools	182
1.05.3	**Rays at Interfaces**	183
1.05.3.1	Boundary Conditions, Continuity, and Reflection/Transmission Coefficients	183
1.05.3.2	Paraxial Conditions	183
1.05.4	**Ray Seismograms**	183
1.05.4.1	Classical Ray Seismograms	184
1.05.4.2	Seismograms by Summation on the Ray Field	184
1.05.4.2.1	The WKBJ summation	184
1.05.4.2.2	Maslov summation	185
1.05.4.2.3	Gaussian beam summation	185
1.05.4.2.4	Coherent-state transformation technique	186
1.05.4.3	The Geometric Theory of Diffraction	186
1.05.5	**Finite-Frequency Effects**	187
1.05.5.1	Travel-Time Estimation, A Data Mining Issue	188
1.05.5.2	Ray + Born/Rytov Formulation	188
1.05.5.3	Ray + Kirchhoff Approximation	191
1.05.5.4	Finite-Frequency Effects on Ray Functions	191
1.05.6	**Discussion**	192
1.05.7	**Conclusion**	193
Acknowledgments		194
References		194

1.05.1 Introduction

Since the first seismic signal (Figure 1) recorded at Potsdam (Germany) from an earthquake in Japan (see Section 1.01.1 of this book as well), accumulation of seismic data (as shown by the stack of thousand of seismic records; Figure 2) (Astiz et al., 1996) illustrates the very special well-structured way waves propagate inside the Earth, which is mainly stratified with depth. Various energy packets can be identified and tracked from one station to another. Where in depth these waves have been scattered is always a difficult question to which seismologists are required to provide more and more precise answers.

Each seismic event generates several wave trains well identified on station records. In those traces, we may distinguish three characteristic timescales associated with different typical length scales. The source duration, related to the duration of each wavelet, comes from extended seismic source from less than 1 km to more than 1000 km in length. Time shifts between wave trains are related not only to the velocity differences between P and S waves but also to distances between interfaces inside the Earth, which may range from tens of meters to thousands of kilometers. Finally, there is recorded time window related to the volume being investigated by the waves, which may range from the whole Earth (Figure 3) to the shallower near-surface layers in applied seismology.

The systematic features of seismograms come from the relatively smooth variations of rheological parameters almost everywhere inside the Earth. This has been an important

 http://dx.doi.org/10.1016/B978-0-444-53802-4.00004-X

Figure 1 The first instrumental recording of seismic waves from a distant earthquake obtained by a horizontal pendulum installed by von Reben Paschwitz in Potsdam (Germany), 15 min after the earthquake occurred in Japan.

discovery and a great motivation for the development of the instrumental seismology on the Earth. For comparison, when considering moonquakes (Latham et al., 1971), no individual wavelets (except the first arriving signal) can be identified (**Figure 4**). If global seismology had been developed on a celestial body like the Moon, it would not have been so successful, and it would certainly not have had such a development as on the Earth. The structure of seismic records is also intensively used at local scales for hydrocarbon reservoir exploration and characterization (**Figure 5**). From a theoretical point of view, the special features of seismograms on the Earth must be associated with the general relevance in the Earth of the high-frequency asymptotic approximations of seismic wave propagation, that is, seismic ray theory (Červený, 2001).

As for geometric optics, seismic ray theory is based on a rather intuitive physical notion but requires a quite sophisticated mathematical framework for a consistent analysis. Behind this powerful interpretation tool are important practical consequences for the exploitation of Earth resources and for the mitigation of seismic risks, making effort for understanding ray approaches worthwhile.

Ray theory has been extensively used for the analysis of seismic signals, for example, Lehmann (1936) discovered the solid core by using straight rays inside the Earth (see also Section 8.01.1 of this book). Most of the present interpretation of body waves for structural analysis has involved essentially picked travel times on traces, although now, we consider curved rays in either a vertically varying Earth (Aki and Richards, 1980; Bullen and Bolt, 1985) or more recently a laterally varying medium as our knowledge of the Earth's interior has increased from core–mantle boundary (Chapman and Orcutt, 1985; Kendall and Nangini, 1996; Lay and Garnero, 2004; Richards, 1973), mantle plumes (Montelli et al., 2004a), the upper mantle (Pavlis et al., 2012; Sigloch et al., 2008; Tian et al., 2009), and slab geometries inside the lower mantle (Bigwaard et al., 1998). Global Earth models are also reconstructed by using phase delays (Section 1.01.4 and **Chapter 1.10** of this book).

Meanwhile, ray theory has been improved theoretically and numerically leading to a great variety of methods and algorithms considering various media (Červený, 2001; Chapman, 2004; Slawinski, 2003). Polarizations and even amplitudes have been estimated in more and more complex structures, and the addition of anisotropic and attenuation effects has led to full waveform interpretations of seismic data (Weber, 1988; Zhu and Chun, 1994b).

This chapter will present an overview of seismic ray theory and its extensions. We will describe basic concepts of high-frequency approximations of seismic waves, as well as limitations and features related to the practical finite-frequency content of seismic waves. Ray theory still appears as a very powerful interpretative tool and will remain a necessary and elegant alternative to brute force tools for numerical wave propagation (Komatitsch et al., 2002; Marfurt, 1984; Virieux, 1986), another necessary tool for seismogram interpretation (see **Chapter 1.05** of this book as well).

1.05.2 Ray Theory

As has been said by Chapman (2004, p. 134), "Ray theory is the cornerstone of high-frequency, body-wave seismology." This theory has also been applied to surface waves by considering evanescent waves along a given direction, which is often a radial or vertical axis in the Earth (Burridge and Weinberg, 1977; Woodhouse, 1974). Excellent descriptions of these approaches of horizontal rays and vertical modes may be found in Keilis-Borok (1989) and Dahlen and Tromp (1998) (see also **Chapter 1.03** of this book). A concise review had been performed by Červený (2001, p. 229). Ray theory has been applied as well for moving media, especially fluids inside a waveguide such as the atmosphere (Abdullaev, 1993; Virieux et al., 2004), giving an illustration of the broad application of this method.

1.05.2.1 Intuitive Approach

Assume an isotropic medium with smooth velocity heterogeneities with respect to the wavelength of the signal we want to propagate. Let us attach a Cartesian reference frame $(0, x, y, z)$ to this medium. Consider at a given time, t, a set of particles, at position $x=(x, y, z)$, vibrating in phase on a smooth surface. We call this surface a wave front. Particles on this wave front

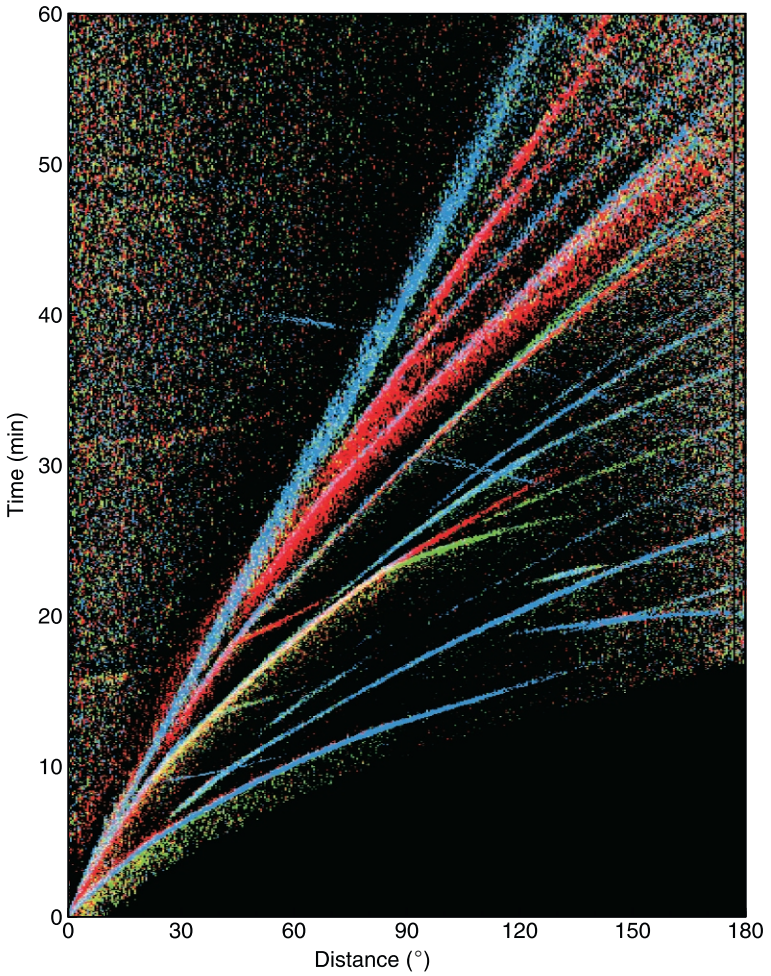

Figure 2 Stack of 30 000 seismograms over the global Earth. The color scale is for normalized energy amplitude and shows the temporal organization of seismograms. Courtesy of P. Shearer.

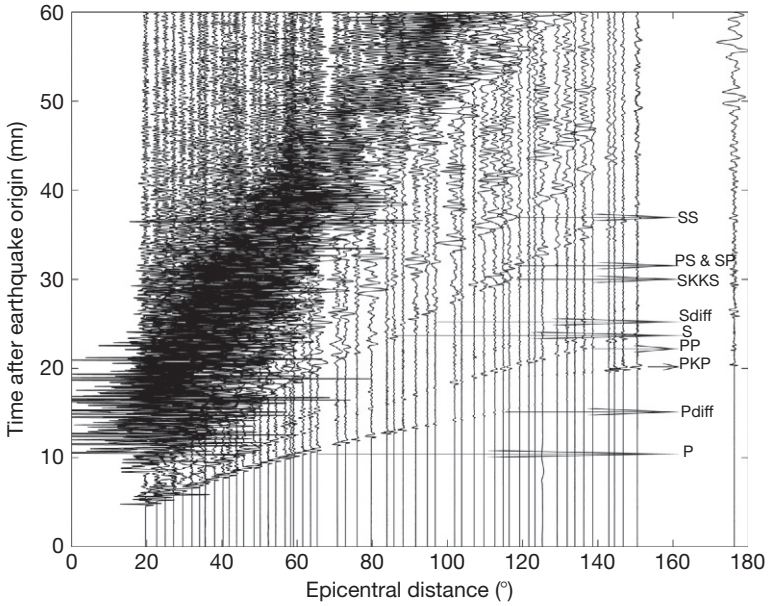

Figure 3 Records of an Indian earthquake (Mm = 7.6, 26 January 2001) on the Worldwide Seismic Network. For displacement, the horizontal scale is 1 mm for each degree. Different phases, for example, P, P_{diff}, PKIK, PP, S, PS, PPS, and SS, are easily seen before the high-amplitude surface wave trains. Courtesy of M. Vallée, IRD.

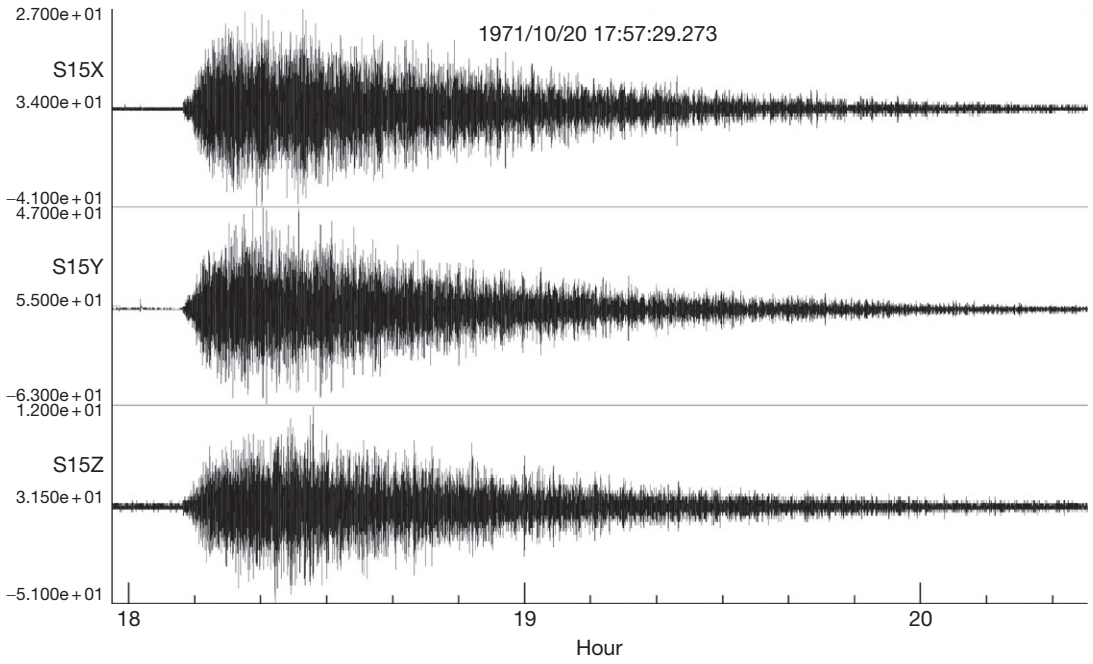

Figure 4 Seismograms produced by the impact of a meteorite on the station S15 of the seismic moon network installed by the Apollo 14 mission. The short-period three-component instrument record ground motion for more than two and one hour half with waves being scattered from the highly heterogeneous region near the Moon's surface. The coda is spindle-shaped, and analysis of the particle motions indicates that the energy is arriving from all directions. Their records differ from typical Earth seismograms for which the coda is weaker than the direct arrivals. Intrinsic seismic attenuation is much smaller on the Moon, while diffraction is stronger, allowing strongly scattered waves to propagate in any direction over a significant time period (Lay and Wallace, 1995, p. 107). Courtesy of J. Gagnepain-Beyneix, IPGP.

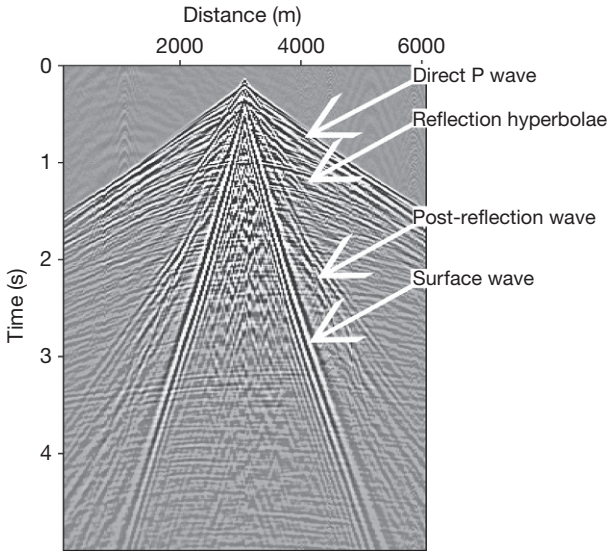

Figure 5 A common shot gather for land seismic acquisition where body waves and surface waves have been recorded on these vertical component data. Reflection hyperbolas are visible as well and illustrate again the variation in time of the seismic traces. Courtesy of D. Le Meur, CGG.

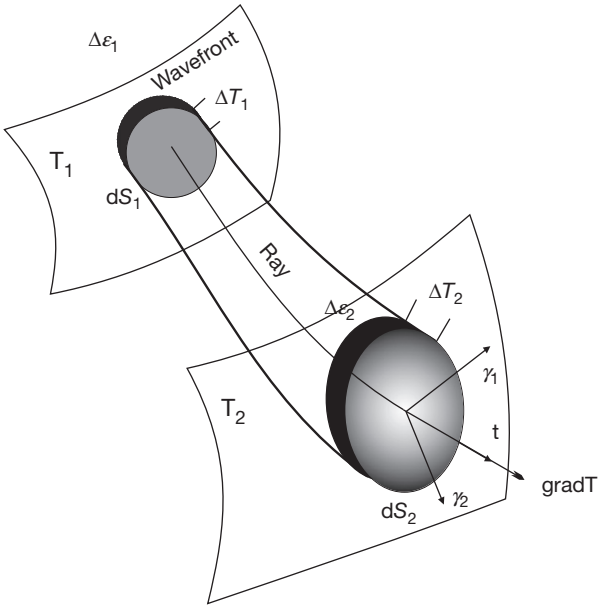

Figure 6 Ray tube geometry: Rays are orthogonal to wave fronts in the isotropic medium. Also, energy flows along rays. The local energy is preserved over an infinitesimal volume controlled by the local velocity (see the text for more details).

have the same travel time, $T(x) = T_0$. As time increases, the wave front moves locally at speed $c(x)$ and the gradient $\nabla T(x)$ is orthogonal to the wave front (Figure 6). Although the wave front moves in one direction, local properties do not allow us to detect what the direction is, which must be known from the previous position of the wave front. Therefore, we must consider the square of the gradient, which gives us the eikonal equation

$$(\nabla T)^2(x, y, z) = \frac{1}{c^2(x)} \quad [1]$$

The gradient is called the slowness vector. In isotropic media, curves orthogonal to the wave fronts, that is, parallel to the slowness vector field, can be defined. We call them rays. Rays are very useful trajectories for calculating travel time but for amplitude variations as well. Indeed, the asymptotic vibration energy moves along the ray tube without any energy leaking (Figure 6). The energy over a small volume of length ΔT_1 crossing the wave front T_1 through the surface dS_1 is related to the square of the amplitude A_1 through the expression $\Delta\varepsilon_1 = A_1^2 dS_1 \Delta T_1$. The energy should be preserved at the wave front T_2, which gives the following conservation of flux as

$$A^2(x_1)\frac{dS(x_1)}{c(x_1)} = A^2(x_2)\frac{dS(x_2)}{c(x_2)} \quad [2]$$

where two different points along the ray tube are denoted by x_1 and x_2 and dS denotes the surface of the elementary orthogonal cross sections of the ray tube. From this equation, and applying the divergence theorem over an infinitesimal volume, we can obtain the local transport equation as the differential expression

$$2\nabla A(x)\cdot\nabla T(x) + A(x)\nabla^2 T(x) = 0 \quad [3]$$

or, under a conservative form, as

$$\nabla\cdot\left(A^2(x)\nabla T(x)\right) = 0 \quad [4]$$

which can be used for a semi-analytic integration along rays. This is one of the reasons we are concerned about the different ray tracing numerical procedures.

As local differential equations, the eikonal and transport equations are fundamental ingredients of ray theory and highlight required properties including smooth wave front spatial continuity and amplitude conservation along ray tubes. Unfortunately, failures of such properties exist quite often in the Earth, for example, interfaces with sharp discontinuity of media properties, shadow zones where no rays are entering, caustics where rays cross each other, strong velocity gradients, and so on. We shall describe efforts to overcome some of these difficulties by introducing a more rigorous framework behind this intuitive ray concept.

1.05.2.2 Elastodynamic Equations and Wave Equations

Let us first consider wave propagation in elastic solid media without attenuation. For the vector displacement field $u(x, t)$ at position x and time t, the linear elastodynamic equation can be expressed as

$$\left(c_{ijkl}(x)u_{k,l}(x, t)\right)_{,j} + f_i(x, t) = \rho(x)u_{i,tt}(x, t) \quad [5]$$

where $f(x, t)$ denotes the vector source field, $c_{ijkl}(x)$ the components of the stiffness tensor, and $\rho(x)$ the density. We use the Einstein convention for summation, boldface symbols for vector and tensor fields, and a comma between subscripts for special derivatives (e.g., $u_{i,j} = \partial u_i/\partial x_j$). For the pressure field $P(x, t)$, the acoustic wave equation can be expressed as

$$\left(\rho^{-1}(x)P_i(x)\right)_i + f^{\mathrm{P}}(x, t) = \kappa(x)P_{tt}(x, t) \quad [6]$$

where $f^{\mathrm{P}}(x, t)$ is the volumetric distribution of pressure source and the compressibility $\kappa(x)$ is the inverse of the bulk modulus $k(x)$. The particle displacement u is deduced from $P = -k\nabla\cdot u$, where the sign $\cdot$ denotes the scalar product. When the density is constant, this so-called acoustic wave equation reduces to the scalar wave equation for the pressure field $w(x, t)$ written as the expression

$$\frac{1}{c^2(x)}w_{tt}(x, t) - w_{ii}(x, t) = f^{\mathrm{w}}(x, t) \quad [7]$$

where the velocity is denoted $c(x)$ and where the specific distribution of pressure source $f^{\mathrm{w}}(x, t)$ is equal to $\rho(x)\, f^{\mathrm{P}}(x, t)$. Some authors introduce first-order hyperbolic systems keeping both displacements and stresses/pressure as variables describing the motion (Chapman, 2004, p. 100).

Solving one of these equations in heterogeneous media cannot be performed analytically and we must rely either on numerical methods or on a specific description of approximate solutions. We shall consider a high-frequency asymptotic solution involving a travel-time function, an amplitude factor, and a source wavelet. Demonstrations can be performed in either the time or the frequency domain, where we select the second domain for easier notation.

The acoustic case is directly connected to our intuitive introduction of the eikonal and transport equations. For the isotropic elastic case, the elastic wave field can be approximately separated into individual elementary waves. These individual waves, P and S waves, propagate independently in a smoothly varying structure, but their travel times are still controlled by eikonal equations, and their amplitudes by transport equations. Because construction of solutions in the elastic case is quite cumbersome, we shall rather consider from now on the scalar wave equation, which captures numerous aspects of the acoustic and elastic cases. We shall mention a few specific considerations for the elastic isotropic and anisotropic cases, and a few words will be said when considering attenuating media (see Chapter 1.06 for further reading).

1.05.2.3 Asymptotic Ray Theory

For specific configurations known as canonical problems, one can get exact solutions of the wave equation. For a homogeneous medium with one speed, canonical solutions can be found as plane waves through separations of variables or as Green functions for a point source (Morse and Feshbach, 1953). The form of these exact solutions should also be valid at high frequency in other media when wavelengths are small compared with the propagation distances and medium heterogeneities. We can then guess probable forms of the solution, known mathematically as an *ansatz*, and then find conditions for them in order to satisfy the wave equations.

Fundamental discussions have been given on *ansatz* structures with very sophisticated arguments for one form or the other depending on the problem to be solved (Babic et al., 1998; Červený, 2001; Kravtsov and Orlov, 1990). The simplest is the ray *ansatz* that we shall introduce. One must be aware that the *ansatz* will only fit the high-frequency components of the solutions. For example, the Green function for a point

source in a 2-D medium exhibits a low-frequency component that the high-frequency approximation will not reproduce (Virieux, 1996).

The ray *ansatz* we shall consider expresses the scalar wave in the frequency domain (Babič, 1956; Chapman, 2004, p. 137; Karal and Keller, 1959) as

$$w(x,\omega) = S(\omega)\mathrm{e}^{\mathrm{i}\omega T(x)}A_0(x) \qquad [8]$$

where the angular frequency is denoted by ω and the source wavelet $S(\omega)$. The subscript zero in the amplitude $A_0(x)$ is related to this so-called zero-order approximation solution. Our convention for the Fourier transforms of a time function $f(t)$ is $f(\omega) = \int_{-\infty}^{+\infty} \mathrm{d}t\, f(t)\, \mathrm{e}^{\mathrm{i}\omega t}$. Smooth functions, travel time $T(x)$ and amplitude coefficient $A_0(x)$, are assumed to be independent of the frequency for the construction of a unique solution. We allow the amplitude coefficients to be complex but the travel time should be real. Specific extensions toward complex values of travel times may lead to new ways of computing seismograms (Felsen, 1984). Let us underline that this estimation should be summed up over the different wave fronts arriving at the position x. The automatic determination of relevant wave fronts at a given receiver has been solved in a combinatorial exercise for multilayered media (Hron, 1972; Hron et al., 1986) but remains a difficult task for an arbitrary inhomogeneous medium as discussed by Clarke (1993a,b).

When introducing this *ansatz* in the scalar wave equation, and also in the frequency domain away from the source zone, we obtain the following equation organized in simple frequency powers as

$$\omega^2 A_0(x)\left[(\nabla T)^2(x) - \frac{1}{c^2(x)}\right] + \mathrm{i}\omega[2\nabla A_0(x)\cdot\nabla T(x) + A_0(x)\nabla^2 T(x)] + \nabla^2 A_0(x) = 0 \qquad [9]$$

Because we are interested in high-frequency solutions, we may neglect the term in ω^0 and set to zero the two other terms in ω^2 and ω^2, leading to the eikonal eqn [1] and to the transport eqn [3].

Further approximations may consider the influence of the neglected term when frequency is finite. Among these alternatives, we must note the definition of the hypereikonal equation (Biondi, 1992; Zhu, 1988; Zhu and Chun, 1994a) where the eikonal is frequency-dependent as are the ray trajectories. A more formal description of the solution in negative power series of $-i\omega$ gives a solution with amplitude terms $A_k(x)$ resulting in new transport equations (Červený, 2001, p. 549). As far as we know, only the A_1 term has been used practically for head waves modeling along interfaces (Červený and Ravindra, 1971; Hill, 1973; Popov and Camerlynch, 1996; Thomson, 1990).

1.05.2.4 Rays and Wave Fronts: A Lagrangian Formulation

The eikonal equation is a nonlinear, partial differential equations (PDEs) of the first order belonging to the Hamilton–Jacobi variety (Kravtsov and Orlov, 1990), usually solved following the method of characteristics (Courant and Hilbert, 1966). The base characteristics are 3-D trajectories $x = x(\tau)$ depending on a sampling parameter τ and satisfying a set of ordinary differential equations (ODEs). If needed, travel time is integrated through quadratures along these trajectories called rays, unless we use it as the sampling parameter. For isotropic media, these rays are orthogonal to wave fronts, sometimes called isochrones. A nice tutorial on characteristics concept has been given by (Bleistein, 1984, **Chapter 1.01**) in relation with differential geometry.

The characteristic system of nonlinear first-order PDEs (eqn [1]) consists of seven ODEs in a 3-D medium connecting the position x, the slowness vector p, and the travel time T, which are very similar to dynamic particle equations of classical mechanics (Goldstein, 1980) and could be expressed as a symplectic Hamiltonian set of equations,

$$\frac{\mathrm{d}x_i}{\mathrm{d}\tau} = \frac{\partial \mathcal{H}}{\partial p_i},$$

$$\frac{\mathrm{d}p_i}{\mathrm{d}\tau} = -\frac{\partial \mathcal{H}}{\partial x_i}, \quad i = 1,2,3$$

$$\frac{\mathrm{d}T}{\mathrm{d}\tau} = p_k \frac{\partial \mathcal{H}}{\partial p_k}, \qquad [10]$$

where the variable τ defined $\mathrm{d}\tau = \mathrm{d}T/(p_k \partial \mathcal{H}/\partial p_k)$ depends on the selected form of the function $H(x, \mathrm{p})$. The independent variables are position x and slowness vector p, defining a 6-D space, called phase space, on which the constant Hamiltonian defines an hypersurface, also called a Lagrangian manifold, on which the value of this Hamiltonian is zero (Lambaré et al., 1996).

The choice of this Hamiltonian $\mathcal{H}_1 = \mathcal{H}(x,\ p) = 1/2\ [p^2 - 1/c^2(x)]$ leads to the simplest differential system to be solved with a sampling variable equal to $\mathrm{d}\tau = \mathrm{d}T/c^2(x)$ for isotropic media, while the Hamiltonian $\mathcal{H}_2 = \mathcal{H}(x,\ p) = 1/2c^2(x)p^2$ has the travel time T for sampling variable along rays, making the third equation of the system [10] automatically verified. Rays are curves in the solution surface, namely, the Lagrangian manifold. One can show that these two choices of sampling provide similar characteristic curves (Slawinski, 2003, p. 179): Hamiltonian choices of sampling provide similar characteristic curves (Slawinski, 2003, p. 180). We may consider as well the Hamiltonian $\mathcal{H}_3 = \mathcal{H}(x,\ p) = 1/2\ [c(x)\ p^2 - 1/c(x)]$ and the related curvilinear sampling along the ray (Červený, 2001, p. 140).

Strategies exist for reducing the number of equation: For example, we may select one spatial coordinate as the sampling variable. Moreover, we may eliminate another variable through the constant value of the Hamiltonian, leading to a so-called reduced Hamiltonian. For example, when considering only rays going downward (or upward), we can select the vertical coordinate z as the sampling parameter. We may also consider the vertical slowness $p_z = \sqrt{1/c^2(x) - p_x^2 - p_y^2}$ as a z-varying reduced Hamiltonian $\mathcal{H}_r(z,\ x,\ y,\ p_x,\ p_y)$ in a 4-D space instead of a 6-D space (Červený, 2001, p. 108). Rays cannot turn as the quantity p_z is always positive, leading to the specific so-called paraxial approximation along z. For arbitrary rays, a possible sampling parameter can be the curvilinear coordinate with two additional orthogonal coordinates leading to the so-called ray-centered coordinate system in a 4-D space as well (Červený, 2001, p. 140). We must be aware now that the quantity $\mathcal{H}_r$ is no longer constant along a ray. The complexity of the related ray equations may increase the number of mathematical operations when performing the ODE integration. One may prefer to consider the system [10] as a

simpler system, although integration is performed in a higher-dimensional space as is often done in field theories.

The method of characteristics is a Lagrangian formulation where we follow the ray point as integrated through the ODEs [10]. This is a very efficient method as it is a 1-D sampling either in a 2-D medium or in a 3-D medium when considering initial condition. Of course, when the number of ray is small, this is the method of choice, namely, ray tracing by directly using rays. More difficult is finding rays between a source and a receiver as we need to guess what the initial conditions are leading to the ray hitting the receiver, the so-called two-point ray tracing problem. For solving this nonlinear problem, we may need to trace a large number of rays. Often, regular ray sampling may be required, leading to a dramatic increase of the number of rays to be traced.

As an alternative, we may consider ray tracing by wave fronts in order to span the entire medium with a regular density of rays. The ray tracing by wave fronts considers an already-evaluated wave front and estimates the new wave front at a later time (**Figure 7**) (Buske and Kästner, 2004; Vinje et al., 1993, 1996a,b). When the ray density becomes too high, we may decimate the number of rays, and when ray density becomes too low, we may increase the number by adding a new ray through judicious interpolation. This adaptative technique, where both ray position and slowness vector are evaluated, had been found to be very efficient when considering 2-D and 3-D smooth media (Lambaré et al., 1996; Lucio et al., 1996) (**Figure 8**). In seismology, Hauser et al. (2008) had recently promoted this ray tracing through wave front using a reduced phase space (Osher et al., 2002), while Rawlinson et al. (2010) presented rather impressive illustrations for complex media at least in 2-D geometries. Various applications have been performed mostly for seismic imaging where later arrivals are required (Operto et al., 2000; Xu and Lambaré, 2004; Xu et al., 2004).

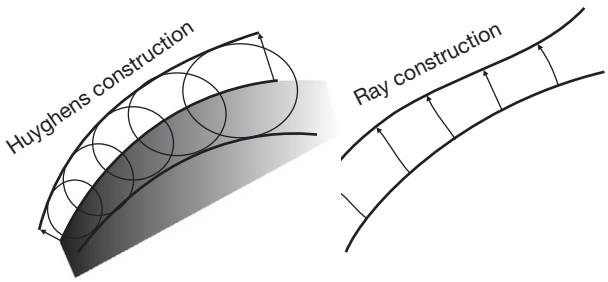

Figure 7 Computation of wave fronts. On the left panel, the construction is based on the Huygens principle, where the new wave front is the envelope of spheres drawn from an initial wave front using a local velocity. The direction is unknown locally. On the right panel, the construction is based on the ray tracing equation, where short ray segments are drawn normal to initial wave front to the new one. The local direction is known by the ray orientation.

Engquist et al. (2002) had promoted an even lower-dimensional space approach, namely, in a 1-D space, by using segment projections, noting that the approach is as fast as by doing ray tracing using rays because it is a 1-D integration. Unfortunately, projections are not so easy to handle from a computational point of view. Tracking the topology of wave fronts is difficult as there is no intrinsic scale to this geometric problem, especially in a 3-D geometry.

Therefore, the methods of characteristics that have been promoted for years may not be the best choice for specific problems when one wants an adaptive more or less uniform sampling of the medium. This is the general drawback of the Lagrangian formulation following either the evolution of rays or the evolution of wave fronts, drawback that has been kept under control in recent computer codes (Hauser et al., 2008; Rawlinson et al., 2010).

1.05.2.5 First Travel Times: An Eulerian Formulation

We may prefer an Eulerian approach for solving the eikonal eqn [1]. The static nonlinear Hamilton–Jacobi PDE

$$\mathcal{H}(x, \nabla_x T(x,t)) = 0 \qquad [11]$$

has received attention by different groups both in seismology and in computational mathematics. The travel-time quantity should be estimated at fixed positions in a given space, while the quantity ∇T might not exist at these points and, therefore, could be discontinuous locally. Crandall and Lions (1983, 1984) had shown that a 'viscous' solution following a minimal entropic criterion exists and is unique. It provides generally the fastest travel time estimated at fixed points of the standard

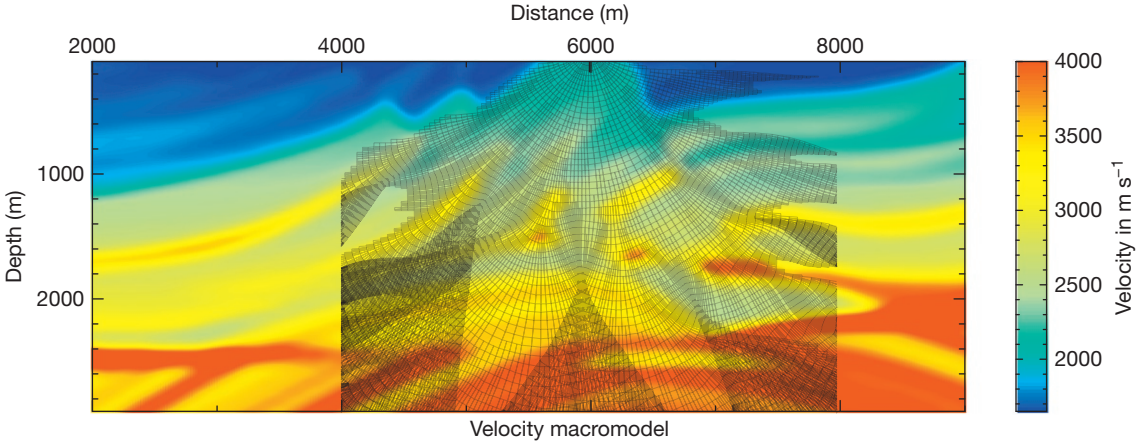

Figure 8 Wave front construction with a uniform ray density criterion in the smooth Marmousi model (Lambaré et al., 1996). Upgoing rays have been eliminated.

space. This Eulerian approach turns out to provide an estimation at all points even when the medium is strongly heterogeneous. As the number of sources and receivers increases, the efficiency of this method increases compared with ray methods.

In seismology, this nonlinear equation has been revisited by Vidale (1988, 1990) where travel times can be computed at fixed points from estimated times at adjacent nodes. A unique value of the travel time is then found at each point. The way at which travel times are updated into the medium has been explored by many authors (Hole and Zelt, 1995; van Trier and Symes, 1991): the update ordering has been called the sweeping technique. Numerous more or less precise algorithms have been designed for both isotropic and anisotropic media (Cao and Greenhalgh, 1994; Eaton, 1993; Lecomte, 1993; Pica, 1997, 1998; Podvin and Lecomte, 1991; Qin and Schuster, 1993; Qin et al., 1992; Zhang et al., 2005).

In numerical mathematics, these nonlinear PDEs have been investigated combining (weighted) essentially nonoscillatory (W-ENO) discrete schemes and Gauss–Seidel iterations with alternating sweeping ordering (Jiang and Peng, 2000; Jiang and Shu, 1996; Liu et al., 1994; Luo and Qian, 2011; Serna and Qian, 2006; Shu and Osher, 1988; Zhao, 2005, 2007). Both 2-D and 3-D geometries have been considered, making the computation more intensive than ray tracing but still quite efficient, leading to the so-called fast sweeping method (FSM). Qian and Symes (2002b) had restricted the sweeping to vertical rays, while Buske and Kästner (2004) had considered polar coordinates.

Another alternative approach, the so-called fast marching method (FMM), is based on techniques related to level set methods (Fatemi et al., 1995; Kimmel and Sethian, 1998; Sethian and Popovici, 1999) concerning interface detection and its evolution on a given hypersurface. This technique has been promoted in seismology by Sethian and Popovici (1999), Sethian (2001), and Popovici and Sethian (2002). Rawlinson and Sambridge (2004a,b), de Kool et al. (2006), and Lelièvre et al. (2011a) had illustrated this approach for strongly heterogeneous media including interfaces. Of course, inside each layer, a unique value of propagation time is estimated.

An excellent review has been given by Rawlinson et al. (2007) on both FSMs and FMMs. Accuracy and computer efficiency have been discussed by Leidenfrost et al. (1999) at least for 2-D geometries.

These techniques have been very attractive in many applications, such as first-arrival travel-time delay seismic tomography (Benz et al., 1996; Le Meur et al., 1997; Zelt et al., 2001) (see also **Chapter 1.08** of this book). Because of the monotonic evolution of the travel time inside the Eulerian frame (time increases always away from the source), one can trace back trajectories from the receiver down to the source. However, a few trajectories, specifically for receivers between nodes with first-arrival travel times from different branches, may not be true rays, especially in the case of sharp discontinuities. When inverting a huge amount of data, a few miscomputed travel times will not affect the overall tomographic inversion. Partial derivatives used for velocity tomography, as well as for improved travel-time estimation, can be computed along the ray trajectory during this back ray tracing. For FSM, Taillandier et al. (2009) had used the adjoint formulation for the computation of the velocity model gradient used in seismic tomography, avoiding the back ray tracing Lelièvre et al. (2011b) had taken benefits of the fast marching algorithm for constructing full sensitivity kernels for a given source and for linking some elements of this kernel to the partial derivatives for a specific receiver, once the forward problem has been performed for the selected source.

1.05.2.6 Multivalued Travel Times and Phases: An Eulerian Formulation

Dealing with multiple arrivals increases the complexity of the problem. One way to address this issue is by reducing the travel-time estimation problem to branches where the travel-time branches are unique as suggested by the so-called big ray tracing approach (Abgrall and Benamou, 1999; Benamou, 1996) or the segment projection method (Engquist et al., 2002). We are then back to finding the 'viscous' solution in an Eulerian frame for each branch or each segment as long as we are able to identify them. But this is a difficult detection problem in relation to the Lagrangian analysis of these branches/segments.

Eulerian approaches may be more stable as the information about the wave front is sampled on fixed grids. In these approaches, the spatial resolution of the wave front is controlled by the local discretization size (Osher et al., 2002). However, Hamilton–Jacobi equations have difficulties when wave fronts become folded with multiple travel times. We shall follow a similar strategy as the ray tracing by wave fronts. We may extend the domain of investigation from the physical space to a phase space combining the physical position, as well as the slowness vector, as we have done for rays. The solution for the travel times turns out to be unique at each point of this space, thanks to Liouville theorem.

Hamilton–Jacobi equations have attracted a lot of attention in mathematics for obtaining multivalued solutions. Among the different strategies, let us mention briefly the dynamic surface extension approach (Steinhoff et al., 2000), the slowness matching method (Symes and Qian, 2003), the segment projection method previously mentioned as a Lagrangian method (Engquist et al., 2002), the phase space method (Fomel and Sethian, 2002), the moment-based method (Engquist and Runborg, 1996), and the level set method (Osher and Sethian, 1988). Nice overviews are provided by Benamou (2003) and Engquist and Runborg (2003). A review more oriented toward the seismological community has been provided by Rawlinson et al. (2007).

Instead of artificially extending the eikonal equation as a static Hamilton–Jacobi equation [11] into a dynamic Hamilton–Jacobi equation, let us first illustrate that the ray theory is directly connected to a dynamic system by considering the time formulation instead of a frequency formulation. Let us introduce the phase function $\phi(x,t)$, which can be defined using the following ray *ansatz*:

$$w(x,t) = S(t)e^{iw\phi(x,t)}A_0(x,t) \qquad [12]$$

as a high-frequency solution specified by the quantity ω. Sometimes, the quantity ω is omitted and replaced by its inverse ϵ. However, we keep it as frequency that allows us to

consider the slowness vector and not the wave number vector as is usually done in seismology. The phase ϕ now depends on time as well as the amplitude A_0. Following Engquist et al. (2002), we may deduce the related eikonal equation considering power of the quantity ω as the expression

$$\left(\frac{\partial\phi(x,t)}{\partial t}\right)^2 - c^2(x)(\nabla\phi(x,t))^2 = 0 \qquad [13]$$

which can be recast as

$$\frac{\partial\phi(x,t)}{\partial t} \pm c(x)\nabla|\nabla\phi(x,t)| = 0 \qquad [14]$$

where we need to select which direction the waves go. The transport equation is given as

$$\frac{\partial A_0(x,t)}{\partial t} + c(x)\frac{\nabla\phi(x,t)\cdot\nabla A_0(x,t)}{|\nabla\phi(x,t)|} + \frac{c^2(x)\nabla^2\phi(x,t) - \partial^2\phi(x,t)/\partial^2 t}{2c(x)|\nabla\phi(x,t)|}A_0(x,t) = 0 \qquad [15]$$

This equation, which defines the amplitude evolution, can be recast as

$$\frac{\partial A_0^2(x,t)}{\partial t} + c^2(x)\nabla_x\cdot\left(A_0^2(x,t)\frac{\nabla_x\phi(x,t)}{c(x)|\nabla_x\phi(x,t)|}\right) = 0 \qquad [16]$$

Following Jin et al. (2005), this leads to the conservative transport equation for the amplitude density $\rho = A_0^2/c^2$ expressed as

$$\frac{\partial\rho(x,t)}{\partial t} + \nabla_x\cdot\left(\rho(x,t)\nabla_p\mathcal{H}_2(x,p)_{p=\nabla_x\phi(x,t)}\right) = 0 \qquad [17]$$

Following Ryzhik et al. (1996), one can define the scaled Winger distribution of the high-frequency solution as

$$W_0(x,p,t) = A_0^2(x,t)\delta(p - \nabla_x\phi(x,t)) \qquad [18]$$

such that the so-called energy density W_0 follows the Liouville equation in phase space

$$\partial_t W_0(x,p,t) + \nabla_p\mathcal{H}_2\cdot\nabla_x W_0(x,p,t) - \nabla_x\mathcal{H}_2\cdot\nabla W_0(x,p,t) = 0 \qquad [19]$$

stating that the density W_0 does not vary in time along rays following the symplectic ray equations $dx/dt = \nabla_p\mathcal{H}$, $dp/dt = -\nabla_x\mathcal{H}$. Because the slowness vector p has a known modulus equal to the slowness, the inverse of the velocity, the energy density has only five independent spatial variables plus time for a 3-D geometry (and three independent variables plus time for a 2-D geometry), defined as the reduced phase space. Using the Hamiltonian $\mathcal{H}_2$, this PDE is a Vlasov-type PDE written as

$$\frac{\partial W_0(x,p,t)}{\partial t} + c^2(x)p\cdot\nabla_x W_0(x,p,t) - \frac{\nabla_x c(x)}{c(x)}\cdot\nabla_p W_0(x,p,t) = 0 \qquad [20]$$

A similar expression exists for other Hamiltonian definitions with the corresponding sampling parameter. Let us again underline that the Hamiltonian $\mathcal{H}_1$ provides the simplest expression of the Liouville equation (Engquist and Runborg, 2003).

Let us now describe briefly one of the Eulerian methods for solving these PDEs. At an initial time, the function $W_0(x, p, 0)$ is zero for each component of the phase gradient and, therefore, should stay zero for all time. The method of level set functions developed in other fields (Liu et al., 2006; Osher and Sethian, 1988; Osher et al., 2002; Sethian, 1999) can be used for tracking these functions and their zero level sets. We must add an additional component as we need to evaluate the phase in addition to the phase gradient. The phase remains constant along the bicharacteristic strip, that is, the wave front in our terminology, and, therefore, follows the Liouville equation (this is true for any Hamiltonian, which is homogeneous of degree one in $\nabla\phi$). This results in a 4-D level set function $\Phi(t, x, p)$ for which each component follows the Liouville PDE. In a 6-D phase space, the intersection of the zero level sets of these four functions, once projected into physical space, provides the 2-D wave front at the selected time t.

Initial values $\Phi(0,x,p) = (p_x - \nabla_x\phi_0, p_y - \nabla_y\phi_0, p_z - \nabla_z\phi_0, \phi_0 - C) = (0,0,0,0)$ are obtained from the phase $\phi(x, 0)$ and its gradient. The phase space quantity Φ is obtained at later times using integration of the linear Liouville equation for each component. We may extract the hypersurface as common zeroes of these components and project it down into physical space to define the wave front at that travel time. Because of the high dimensionality of the phase space, we may benefit from the slowness vector having a specified modulus for reducing by one the dimension leading to the so-called 5-D reduced phase space. The level set function Φ has now only three components (instead of four) to be integrated in the 5-D space. The Eulerian approach in this reduced phase space is still a challenging problem, and different techniques have been deployed for reducing the cost of such Eulerian PDE integration.

If we consider only vertical propagation, we may use the z coordinate as the evolution parameter instead of time variable, a typical paraxial approximation (among other paraxial ones). This restriction leads to a 2-D phase space $(x, p_x/|p|)$ for a 2-D (x, z) geometry with a source at the position x_s, z_{depth} for upgoing rays with a negative z increment. Following Qian and Leung (2004, 2006), we may solve the evolution of two functions $\Phi(z, x, p_x/|p| = \xi) = (\Phi_1, \Phi_2)$ where the Liouville equations are

$$\partial_z\Phi_1 + u\partial_x\Phi_1 + v\partial_\xi\Phi_1 = 0$$
$$\partial_z\Phi_2 + u\partial_x\Phi_2 + v\partial_\xi\Phi_2 = 0 \qquad [21]$$

with initial condition $\Phi_1(z_{depth}, x, \xi) = x - x_s$ and $\Phi_2(z_{depth}, x, \xi) = 0$ and the initial travel-time value set to zero everywhere in the 2-D phase space. The initial value $\Phi_1 = 0$ gives the solution for the source at position x_s. By a simple constant shift of the level set, we may consider other source positions at the same depth. The advection velocity field $v = (u, v) = (dx/dz, d\xi/dz)$ governing the motion of the function Φ is just the ray equations in the reduced phase space. The implicit initial curve (x, ξ) defined as $\Phi_1(z_{depth}, x, \xi) = 0$ is multivalued and will stay at the zero value when the evolution parameter z is decreasing, giving us a multivalued wave front. Figure 9 is an illustration of the zero level of $\Phi_1(0, x, \xi) = 0$ at the free surface $z = 0$ for the Marmousi model leading different $p_x/|p|$ values at the same x position (Qian and Leung, 2004, 2006). One may see that solutions between two different grids are identical where the solution is expected to be smooth, while small details are only captured by the finer grid. The definition of the grid sets the

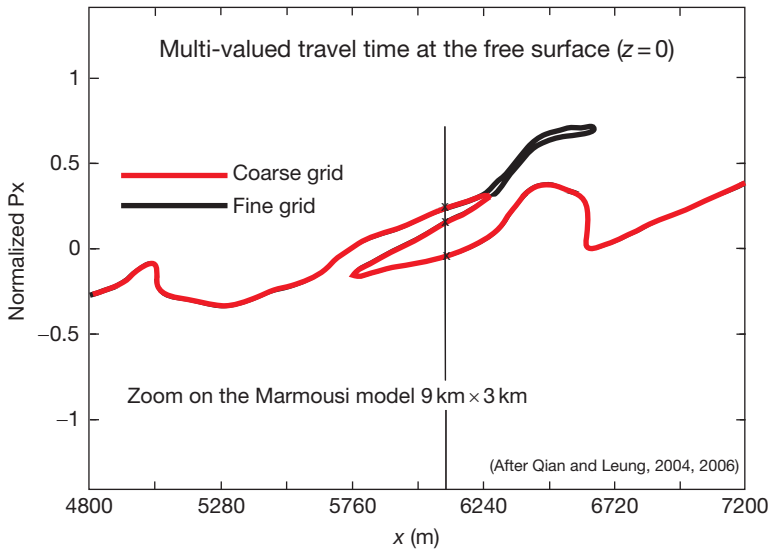

Figure 9 A level set line of the surface $\Phi_1(0, x\, p_x/|p|) = 0$ following the level set method multivalues are found at a fixed x position as noted by the black vertical line. Note that the solution is identical for the coarse grid (red line) and for the fine grid (black line) away from the small branch. The grid selection provides a simple resolution level for the number of multivalues one is looking for.

expected level of resolution. Similarly, zeroes of the $\Phi^2(0, x, \xi)$ will provide travel times. Intersecting the two surface $\Phi_1(0, x, \xi) = 0$ and $\Phi_2(0, x, \xi) = 0$ and projecting it on to physical space provide the multivalued travel times $T(x, z = 0)$ at the free surface. Different ingredients such as reinitialization and orthogonalization will guarantee that the Eulerian sampling is adequately fulfilled. Applications to 2-D anisotropic media have been performed using this paraxial approximation (Qian and Symes, 2002b), and 3-D extension was performed by Leung et al. (2004) using an efficient local level set method. Multi-grid strategy has been proposed by Bokanowski (2013) for even higher dimensions. Although still quite intensive from a computational point of view, solution can be obtained readily for multiple sources, a nice feature when we need to consider problems with many sources. Nice illustrations in seismology have been provided by Hauser et al. (2006, 2008) and reviewed by Rawlinson et al. (2007).

Many other techniques for solving these Hamilton–Jacobi PDEs have also been used. These include finite elements methods, especially the discontinuous Galerkin methods (Cheng and Shu, 2007; Li et al., 2008; Yan and Osher, 2011) on a reduced phase space, which could include discontinuities of the velocity fields as well. Fomel and Sethian (2002), Liu et al. (2006), and Cheng (2007) had also purposed alternative efficient methods for these multivalued estimations of the travel time. Jin et al. (2005) had also investigated similar approaches for other physical observables, such as the amplitudes.

We expect that some of these different methods for estimating phases, as well as the amplitudes, of rays will reach a mature enough level for applications in seismology and seismic exploration in the near future, in spite of difficulties related to the high-dimensional space we must consider.

One may wonder why we have switched to complex nonlinear PDEs for the more familiar linear wave PDE we started with. Several reasons might be advocated including long-range simulations as well as the need for specific quantities within tomographic applications such as the slowness vector. Because the Earth attenuates seismic waves, we may consider that large time integrations or thousands of wavelengths of propagation are not an issue in seismology as it is in geometric optics. However, the Earth is translucid to seismic waves and not transparent. Extracting quantities such as the travel time, the slowness vector, and the amplitude from observed or synthetic seismograms is not an easy task as we shall see, and therefore, ray theory can provide an adequate approach if we need these quantities.

1.05.2.7 Variational Approaches for Ray Tracing

The ray equations can also be considered on the framework of variational approaches where Lagrangian and Hamiltonian formulations can reveal their fruitfulness.

The choice of the Hamiltonians $\mathcal{H}_1$ and $\mathcal{H}_2$ seems to be quite natural ones (especially for anisotropic media) for variational investigations because, only if the Hamiltonian is of second degree is slowness, Lagrangian and Hamiltonian may be related by the Legendre transform defined as

$$L(x, \dot{x}) = p \cdot \dot{x} - H(x, p) \qquad [22]$$

where $\dot{x}$ denoted $\mathrm{d}x/\mathrm{d}\tau$. The Lagrangian, defined in a 3-D space of position x, verifies the Euler–Lagrange equations of second order expressed as

$$\frac{\mathrm{d}}{\mathrm{d}T}\left(\frac{\partial L}{\partial \dot{x}_i}\right) - \frac{L}{\partial x_i} = 0 \qquad [23]$$

Its integral over the ray path is stationary (Hamilton's principle). The travel time is given by the integral

$$T - T_0 = \int_{\tau_0}^{\tau} (L(x, \dot{x}) + H(x, p))\, \mathrm{d}\tau = \int_{x_0}^{x} p \cdot \mathrm{d}x = \int_{x_0}^{x} \frac{1}{c(x)} \mathrm{d}s \qquad [24]$$

where s denotes the curvilinear abscissa. This last integral is stationary for fixed x_0 and x trajectories, which is the reduced least action principle of mechanics, often called

Maupertuis–Euler–Lagrange–Jacobi principle (Arnold, 1976; Goldstein, 1980), or equivalently Fermat's principle in optics.

When the Hamiltonian depends explicitly on the sampling parameter, we may consider the least action principle related to the Poincaré–Cartan invariant. This is the case for the atmosphere where the speed is time-dependent (Abdullaev, 1993). The augmented time-phase space $2n+1$ where the space dimension is denoted by n is always odd-dimensional and has been investigated by many mathematicians as Poincaré and Cartan using differential geometry techniques. When the Hamiltonian $H(x, p)$ does not depend explicitly on time, the dimension of the chosen phase space may be reduced by two (Arnold, 1976, p. 240): as an example, only four ODEs have to be solved in a 3-D medium (Červený, 2001, p. 107).

Although one might not find these identifications between different theoretical formulations necessary, we shall borrow from mechanics and optics well-designed tools for performing ray tracing! As an example, mechanics of small vibrations or equivalently Gaussian optics open a road for performing efficient ray tracing in the vicinity of an already-traced ray, a topic we shall focus in **Section 1.05.2.10**.

Fermat's principle, its minimum time aspect, plays an important role for the computation of travel times when considering first-arrival times only. Finding the shortest path between a source and a receiver leads to network ray tracing. It can be based on graph theory applied to a grid of points with connection between them making a network and related to the well-known traveling salesman problem. The connection between two grid points is the ray and the related travel time between these two points is the fastest one. A very efficient algorithm has been proposed by Dijkstra (1959) and various implementation and modifications have been proposed in seismology (Bai et al., 2007; Klimeš and Kvaskička, 1994; Moser et al., 1992a; Nakanishi and Yamaguchi, 1986). One must be aware that this technique leads to rays, while solving first-arrival times through eikonal approaches leads to travel times. Klimeš and Kvaskička (1994) and Leidenfrost et al. (1999) had shown that these algorithms give smaller errors in travel-time estimation for the network approach than for eikonal discrete solver previously considered (see **Section 1.05.2.11**). Impressive algorithms have been developed by Bai et al. (2009, 2010) considering the shortest path inside each layer, while multiple arrivals are included through the interface discontinuities where transmitted, reflected (or refracted), and converted phases should obey Snell law and Huygens principle. This leads to the same richness of estimated phases as for eikonal solver (Rawlinson and Sambridge, 2004a). The review by Rawlinson et al. (2007) is worthwhile for comparison of methods, while the shortest path algorithm is fully described by Bai et al. (2010).

Drawing rays from the time grid in the eikonal approach is possible and will certainly allow for an accurate recomputation of travel times (Latorre et al., 2004) as bending rays between source and receiver will improve precision for the network approach. Very active algorithmic development may replace, in the near future, fast but less precise tools for locating earthquakes (Bai and Greenhalgh, 2006; Font et al., 2004; Lomax et al., 2000; Moser et al., 1992b), for seismic travel-time tomography (Bai et al., 2008; Benz et al., 1996; Le Meur et al., 1997; Toomey et al., 1994), and for high-definition tomography (Guillaume et al., 2011) as long as the picking of travel times or residual travel times is possible and efficient (Gentili and Michelini, 2006; Rowe et al., 2002; Satriano et al., 2008; Siliqi and Talaalout, 2009; Traonmilin et al., 2009; Zhang et al., 2003). See also **Chapter 1.08** of this book for applications.

1.05.2.8 Transport Equation

When we consider the transport eqn [3], we see that the amplitude estimation is linked to the travel-time field. Multiplying the transport eqn [3] by the complex conjugate of the assumed nonzero amplitude $A_0^*(x)$, we obtain the local property $\nabla\cdot(A_0^*(x)A_0(x)\nabla T(x))=0$. This equation can be deduced as well from eqn [16] when considering a time variation. By following our intuitive presentation backward, we end up with the description of the amplitude evolution expressed as

$$A_0(x_2)=A_0(x_1)\sqrt{\frac{c^2(x_2)J_T(x_1)}{c^2(x_1)J_T(x_2)}} \qquad [25]$$

where the position x_1 (resp. x_2) is implicitly defined by the sampling parameter time T_1 (resp. T_2) and where the elementary surface ds is estimated through the geometric spreading J_T. This geometric spreading factor is obtained by looking at the wave front evolving inside a ray tube defined by neighboring rays with slightly different initial conditions. By noting two variables γ_1 and γ_2 related to the ray position at time T_1 parameterizing the wave front and orthogonal to the wave front normal (**Figure 6**), the geometric spreading can be defined as the Jacobian,

$$J_T=\left|\frac{\partial(x,y,z)}{\partial(T,\gamma_1,\gamma_2)}\right| \qquad [26]$$

from which one can see the dependence of the geometric spreading on the sampling parameter (Červený, 2001, p. 215).

The scalar wave field $w(x, \omega)$ may then be written as

$$w(x,\omega)\approx S(\omega)\phi_w(\gamma_1,\gamma_2)\sqrt{\frac{c^2(x)}{J_T(x)}}e^{i\omega T(x)} \qquad [27]$$

where the expression $S(\omega)$ denotes the signature of the source. The Jacobian might change sign and we must be careful of this as we shall see in the next paragraph. The radiation pattern $\phi_w(\gamma_1, \gamma_2)$ must be found by matching this asymptotic solution and a canonical solution of the exact solution for a local homogeneous medium around the source (coordinates γ_1 and γ_2 evolve with the ray position x). As the source acts as a singularity itself, improved asymptotic solutions have been investigated around the source (Yedlin, 1987). We shall postpone this estimation of the Jacobian when considering the evaluation of seismograms.

Points along the ray where the Jacobian vanishes are called caustic points. Caustic points of the first order, when the rank of the Jacobian matrix [26] is equal to two, make the ray tube shrink into a line. These points create caustic surfaces, which are envelopes of rays classified into folds, cusps, and swallowtails using a terminology related to catastrophic theory (Brown and Tappert, 1987; Gilmore, 1981). Caustic points of the second order, when the rank is equal to one, are often called focus points (**Figure 10**). As the ray crosses a caustic, the Jacobian changes its sign and the phase suffers a negative

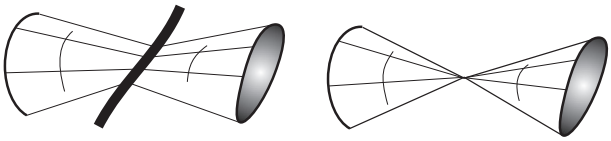

Figure 10 Points along the ray where the Jacobian [26] vanishes are called caustic points. For caustic points of the first order (left), the rank of the Jacobian matrix [26] is two and the ray tube shrinks into a line. For caustic points of the second order (right), the rank of the Jacobian matrix [26] is one and the point is called a focus point.

shift $-\pi/2$ for a first-order caustic and $-\pi$ for a second-order caustic. This shift is estimated through matching different asymptotic solutions (Ludwig, 1966). The phase shift is cumulative along the ray as we cross caustics. The associated index, called the KMAH index as proposed by Ziolkowski and Deschamps (1984) for acknowledging the contributions of J.B. Keller, V.P. Maslov, V. Arnold, and L. Hörmonder, may jump by one or by two depending on the change of rank of the Jacobian. The asymptotic solution for the scalar wave field is then

$$w(x,\omega) \approx S(\omega)\phi_w(\gamma_1,\gamma_2)\sqrt{\frac{c^2(x)}{|J_T(x)|}}e^{i\omega T(x)\mathrm{sign}(\omega)}e^{-i\frac{\pi}{2}\mathrm{KMAH}(x)} \quad [28]$$

1.05.2.9 Acoustic and Elastic Ray Theory

When considering isotropic acoustic and elastic cases, very similar eikonal and transport equations can be derived. Let us first consider the acoustic equation where the density may vary. The eikonal equation is the same as for the scalar wave equation, while the transport equation is

$$2\nabla T\cdot\nabla\left(\frac{A_0^{\mathrm{acous}}}{\sqrt{\rho}}\right)+\frac{A_0^{\mathrm{acous}}}{\sqrt{\rho}}\nabla^2 T=0 \quad [29]$$

which is essentially the same equation as for the scalar wave equation when considering $A_0^{\mathrm{acous}}(x)/\sqrt{\rho(x)}$. Therefore, we can write the pressure

$$P_0(x,\omega) \approx S(\omega)\phi_P(\gamma_1,\gamma_2)\sqrt{\frac{\rho(x)c^2(x)}{|J_T(x)|}}e^{i\omega T(x)} e^{-i\frac{\pi}{2}\mathrm{KMAH}(x)\mathrm{sign}(\omega)} \quad [30]$$

from which one can deduce the asymptotic form of the particle displacement in the acoustic case

$$u_0(x,\omega) \approx S_u(\omega)e(x)\phi_P(\gamma_1,\gamma_2) \sqrt{\frac{1}{\rho(x)|J_T(x)|}}e^{i\omega T(x)}e^{-i\frac{\pi}{2}\mathrm{KMAH}(x)\mathrm{sign}(\omega)} \quad [31]$$

where the vector e denotes the normalized polarization of the wave (orthogonal to wave front) and where S_u is the displacement signature, which can be directly obtained from the pressure signature S.

Without increasing the complexity of notation, we may consider the general anisotropic case for elastic wave propagation. The wave field is now a vector field and the polarization has to be considered (Červený, 2001). The eikonal equation is defined by

$$G_m(x,p)=1, \quad m=1,2,3 \quad [32]$$

where G_m are the eigenvalues of the 3×3 Christoffel matrix defined by

$$\Gamma_{ik}(x,p)=\frac{c_{ijkl}}{\rho}(x)p_j p_l \quad [33]$$

The polarization vectors are the corresponding eigenvectors, and it can be shown that associated amplitudes still satisfy a scalar transport equation involving the geometric spreading along the ray (Červený, 2001, p. 60).

For the isotropic case, two identical eigenvalues $G_1(x,p)=G_2(x,p)=\beta^2(x)p^2$ give two polarizations for the shear wave speed $\beta(x)$ of S waves, while the third eigenvalue $G_3(x,p)=\alpha^2(x)p^2$ is related to the compressional wave speed $\alpha(x)$ of P waves. The corresponding eigenvector $g_3(x,p)$ is simply orthogonal to the wave front. Orthogonal eigenvectors $g_1(x,p)$ and $g_2(x,p)$, corresponding to shear waves, may be estimated through the differential equation

$$\frac{\mathrm{d}g_i}{\mathrm{d}t}=(g_i(x,p)\cdot\nabla\beta(x))g_3(x,p) \quad [34]$$

where $i=1, 2$ (Chapman, 2004, p. 181).

For the anisotropic case, we must consider qS_1 and qS_2 on the one hand and qP on the other hand. We are often unable to obtain explicitly eigenvalues for the anisotropic case, while we can achieve that for the elastic case (Červený, 2001, p. 62). Moreover, the propagation of qS_1 and qS_2 must be considered together because of possible shear wave singularities (Červený, 2001, p. 512). The anisotropic elastic case not only follows the same general scheme as the elastic one but also exhibits some important particularities. For example, the rays are not orthogonal to isochrones in the anisotropic case. The amplitude still satisfies a scalar transport equation involving the estimation of geometric spreading along rays (Červený, 2001).

1.05.2.10 Paraxial Ray Theory

The ray tube can be estimated by tracing neighboring rays, which must be kept nearby the studied ray. Therefore, a small perturbation approach known as paraxial ray tracing should be considered where the paraxial ray is only sensitive to velocity/slowness variations (as well as spatial derivatives) on the central ray. However, the paraxial ray may deviate from a neighboring ray, which samples velocity variations differently (**Figure 11**). Around a given central ray, the perturbation $\delta\gamma^t=(\delta x,\delta p)$ of both the position and the slowness vector follows, to the first order, the linear ordinary differential system

$$\frac{\mathrm{d}\delta\gamma}{\mathrm{d}T}=\begin{pmatrix}\nabla_p\nabla_x\mathcal{H}_0 & \nabla_p\nabla_p\mathcal{H}_0\\ -\nabla_x\nabla_x\mathcal{H}_0 & -\nabla_x\nabla_p\mathcal{H}_0\end{pmatrix}\delta\gamma \quad [35]$$

where the Hamiltonian $\mathcal{H}_0$ has a subscript zero because it is evaluated on the central ray regardless of the perturbation vector $\delta\gamma$ (**Figure 11**). This linear system can be solved following the standard propagator formulation introduced by Gilbert and Backus (1966) in seismology, while Farra and Madariaga (1987) emphasized the Hamiltonian formulation initially introduced by Backus (1964) and Burridge (1976). In this

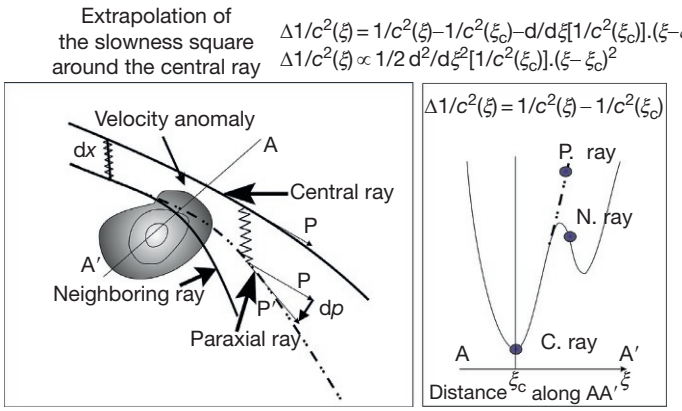

Figure 11 Paraxial ray tracing. The left panel shows the central ray as well as the paraxial ray derived from the velocity anomaly felt by the central ray as symbolized by a spring, Therefore, the paraxial ray is different from a neighboring ray. The right panel shows the difference between the square of the slowness $1/c^2$ in the medium and the parabolic extrapolation of the square of the slowness form the central ray across section AA′. The true velocity profile shown by a continuous line is felt by the neighboring ray, while the approximate parabolic profile, expanded from the central ray and shown by a dash-dotted line when away from the true profile, controls the paraxial ray.

approach, the propagator $P(T, T_0)$ links $\delta\gamma$ at times T and T_0 through

$$\delta\gamma(T) = P(T, T_0)\delta\gamma(T_0) = \begin{pmatrix} P_{xx} & P_{xp} \\ P_{px} & P_{pp} \end{pmatrix} \delta\gamma(T_0) \qquad [36]$$

For example, the submatrix P_{xp} contains partial derivatives of the position x with respect to the slowness vector $p_0 = p(T_0)$, which describes the geometric spreading [26] from a point source and will give us an easy way for computing the cross-sectional area or for caustics detection. In practice, the 6×6 propagator could be reduced to a 4×4 propagator depending on the problem at hand (Červený, 2001; Farra and Madariaga, 1987; Virieux and Farra, 1991). Symplectic symmetries are very important both from a theoretical point of view and from a practical point of view because rays can be traced in either direction without the need for inverting a 6×6 matrix (Červený, 2001; Chapman, 2004; Luneberg, 1964). We have the following relation:

$$P^{-1}(T, T_0) = P(T_0, T) \qquad [37]$$

from which one can deduce the so-called Luneberg relations in optics or Poisson and Lagrange brackets of classical mechanics (Goldstein, 1980). Initial values are defined by

$$P(T_0, T_0) = I_d \qquad [38]$$

where I_d is the identity matrix. For further discussion, Červený (2001) and Chapman (2004) are good references. One must remember that the travel-time function is expanded to the second-order terms when considering paraxial theory. In the configuration space, around a given ray position (x_0, p_0), this leads to the general expression

$$T(x, p_0) = T(x_0, p_0) + \frac{\partial T}{\partial x}(x_0, p_0)\delta x + \frac{1}{2}\delta x^t \mathcal{M}(x_0, p_0)\delta x \qquad [39]$$

where the curvature matrix $\mathcal{M}$, a real matrix in classical ray theory, can be constructed from paraxial quantities, since we have

$$\mathcal{M}(x_0, p_0) = \left(P_{xx}\frac{\partial x}{\partial(\gamma_1\gamma_2 T)} + P_{xp}\frac{\partial p}{\partial(\gamma_1\gamma_2 T)}\right) \times \left(P_{px}\frac{\partial x}{\partial(\gamma_1\gamma_2 T)} + P_{pp}\frac{\partial p}{\partial(\gamma_1\gamma_2 T)}\right)^{-1} \qquad [40]$$

where we have considered point source initial conditions with the two parameters γ_1 and γ_2 describing a two-parametric orthonormal system of rays, that is, a fan of rays (Červený, 2001, p. 235). This expansion may be carried out on a subset of perturbations and in different coordinate systems as we shall see later. The ray-centered system is often used in practice. We must emphasize that solutions to the paraxial equations are coordinate-dependent, while solutions of the ray equations are coordinate-independent, but as we move toward the central ray, paraxial quantities have similar infinitesimal behavior. Let us also remark that the curvature matrix stays invariant through changes in coordinates. Finally, ray coordinates and paraxial ray quantities must satisfy the eikonal equations and perturbed eikonal equations if we want to consider them as rays or paraxial rays (Farra and Madariaga, 1987).

In seismology, we have not yet tackled theories beyond the paraxial one as already performed in optics as the geometric theory of aberrations (Born and Wolf, 1980, **Chapter 1.06**) where the third-order terms around a given ray are considered. These approaches were often developed for homogeneous media and have strong relations with finite-frequency effects and diffraction phenomena we shall consider later on. Note that paraxial ray theory is also very useful for introducing perturbations of the velocity field. Applications of paraxial theory for fast ray tracing (Farra, 1990, 2005; Pšenčik and Farra, 2005; Virieux, 1991) and Fréchet derivatives estimations in tomographic applications (Billette and Lambaré, 1998; Lambaré, 2008) have been proposed.

1.05.2.11 Tools for Ray Tracing

Both ray and paraxial ray equations, which are ODEs, can be solved by numerical tools using Runge–Kutta (RK) of specified order or predictor–corrector (PC) schemes (Press et al., 1994,

Chapter 1.19). Initial boundary problems, where both initial position and initial slowness (i.e., six initial values) are specified, can be efficiently solved. Because we have a first integral of these equations, which is the Hamiltonian/eikonal value, we may efficiently avoid gear-like methods (Press et al., 1994, p. 739) and check accuracy at each integration step by estimating the eikonal constant (Virieux and Farra, 1991). Of course, if we use the reduced Hamiltonian system, we lose this first integral at the benefit of fewer variables to be integrated. Although PC schemes are more superior than RK schemes (only one spatial derivative to be estimated at each integration step whatever the order of precision), we rely essentially on the latter in seismology because it is easy to implement considering its self-starting property. Paraxial equations are linear equations and could be solved with quite significantly coarser integration steps than ray equations. They may be solved in a second step once rays have been found and may well complete with integral formulations of propagator matrices. Other strategies based on analytic solutions inside each cell of a mesh have been considered, although the improved efficiency is effective only when a simple coarse discretization is performed (Červený, 1985; Chapman, 1985; Farra, 1990; Körnig, 1995; Virieux, 1991).

An order of magnitude more difficult is the two-point ray tracing problem where rays between a source and a receiver have to be estimated (Červený, 2001; Červený et al., 1977; Sambridge and Kennett, 1990; Virieux and Farra, 1991). In the frame of ray tracing by rays, we may consider three kinds of local methods for making the ray converge to the receiver. The shooting method corrects an initial value problem until the ray hits the receiver. How to estimate the new initial slowness relies on many different numerical strategies linked to root solver (Press et al., 1994). The paraxial ray turns out to be useful for an efficient Newton procedure (Virieux et al., 1988). The bending method deforms an already-specified curve connecting the source and the receiver. The search is essentially performed in the spatial domain (Farra, 1992; Pereyra, 1992; Pereyra et al., 1980; Um and Thurber, 1987) where each node along the trajectory is perturbed until we may consider it as a ray. The continuation method is based on rays connecting the source and the receiver for very simple velocity structures for which one may find easily the connecting ray. The velocity field is then deformed until it matches the true velocity field (Keller and Perozzi, 1983; Snieder and Spencer, 1993). Fully nonlinear methods of finding initial conditions at the source in order to reach the receiver have also been explored (Sadeghi et al., 1999) at the expense of an exhaustive exploration without any guarantee that all initial conditions have been found. We may find these two-point ray tracing techniques quite inefficient if one has to span the entire medium with many receivers.

Another strategy is the ray tracing by wave fronts presented in a previous section. Paraxial information may help in designing adaptative techniques for fixing ray density according to ray curvature in the phase space (Lambaré et al., 1996; Lucio et al., 1996) (**Figure 8**). Of course, the entire medium is sampled, which may be a quite intensive task compared with the 1-D sampling performed by a single ray. Moreover, these techniques are quite sensitive to strong variations of the velocity.

For multivalued estimations of travel time and amplitude, we may rely on the approaches based on the Lagrangian formulation, but we could also consider Eulerian formulations, which control the complexity of the wave front evolution or, in other words, the number of travel times at a given position through the discretization of the medium we consider. This is a new perspective spreading into the seismological community (Hauser et al., 2008).

1.05.2.12 Eikonal Solver Tools

Three strategies have emerged for computing the fastest travel times following the eikonal equation including the FMM, the FSM, and the short path method. In each case, a discretization of the medium is required in association with a consistent and accurate numerical scheme for verifying the eikonal equation. These numerical schemes should include the causality of the equation (an earlier time is always better than an estimation with a higher value) and should deal with singularities at intersections of characteristics. Variations in the construction of these numerical schemes lead to different performances and, therefore, explain the wide range of related publications. On this topic, once the discretization is done, a large nonlinear system has to be solved.

In the first method, the solution is updated one grid point at a time in such a way that the travel-time estimation is always increasing as we move away from the source. Therefore, an upwind difference scheme following the Godunov scheme (Godunov, 1959) in connection with the Roe solver (Roe, 1981) should be selected, as well as a heapsort algorithm, which will describe the accepted nodes where the time has been computed, the narrow band nodes where the scheme will be applied, and the far nodes where the time is not estimated. Inside the band, the time could be updated if smaller than previous value at the node. Far nodes nearby the edges of the band are integrated for the next iteration. The efficiency of the method relies on the sorting procedure and this leads a complexity O(N ln N) when we consider N nodes. Improved sorting techniques dedicated to the eikonal equation have reduced the complexity to O(N) (Kim, 2001), while the buffered FMM with an additional zone of buffered nodes should be used for anisotropic media (Cristiani, 2009).

In the second method, we also use an upwind scheme in order to get a nonlinear system to be solved, and we shall use Gauss–Seidel iterations with alternating direction sweeping in such a way that characteristics are covered by a group of sweeps. No heapsorting is used and, therefore, the complexity is O(N). For the eikonal equation, strict causality guarantees convergence in a finite number of alternating sweepings (Luo and Qian, 2011; Qian et al., 2007; Zhao, 2005). Moreover, the algorithm is extremely simple to implement and has no difficulties with anisotropy (Qian and Symes, 2002b). Higher-order upwind schemes, especially W-ENO stencils, are often preferred to reduce the number of iterations. Higher-order upwind schemes, especially W-ENO stencils, are often preferred to reduce the number of iterations. Improved accuracy has been obtained using the factorized eikonal equation (Fomel et al., 2009; Luo and Qian, 2012). The travel time is decomposed into two terms as $T = T_0 + \tau$ or $T = T_0\,\tau$ where the solution T_0 is known analytically and captures features of the solution nearby the source. The FSM is only applied to the correction τ term.

The third method is based on the Dijkstra algorithm (Dijkstra, 1959) where the shortest path is found between

one very vertices of a graph and every other vertex with a nonnegative distance between them. The complexity is of order O(N ln N) when using the Fibonacci heap ordering.

Solving the dynamic Hamilton–Jacobi PDE for multivalued travel times follows rules of numerical techniques for these PDEs. Discretization of the (reduced) phase space is required. ENO (Osher and Sethian, 1988; Shu and Osher, 1988) and W-ENO (Jiang and Peng, 2000; Liu et al., 1994; Qiu and Shu, 2005) schemes are designed to adapt stencils for high accuracy and a nonoscillatory property near discontinuities for the estimation of derivatives. These could be applied on structured and unstructured grids. Time integration is performed using total variation diminishing Runge–Kutta methods, which avoid oscillations of the solution during the time evolution by introducing fractional time stepping (Shu and Osher, 1988). A discussion in the geophysical literature is given by Qian and Symes (2002a). Various approaches such as level set methods and discontinuous Galerkin methods are based on such discretizations (Bokanowski et al., 2011; Min, 2004).

1.05.3 Rays at Interfaces

Up to now, we have considered media without any abrupt changes of properties. If there is a sharp contrast, ray theory fails. All that we have seen until now was described for media without discontinuities. "If the medium contains interfaces, that is, discontinuities in the material properties, density or elastic parameters, then the ray theory solution breaks down due to discontinuities in the solution or its derivatives. It is then necessary to impose the boundary conditions on the solution at the interface before continuing the ray solution" (Chapman, 2004, p. 198).

In the context of high-frequency approximation wave trains arriving at an interface can be viewed locally as plane waves hitting a flat interface. Only amplitude variations should require curvature estimations from wave fronts and interfaces. Consequently, many features of plane waves can be generalized to ray theory when dealing with interfaces. Because many textbooks (Aki and Richards, 1980; Červený, 2001; Červený et al., 1977; Chapman, 2004; Kennett, 1983) have described these features in great details, we shall only outline specific features important for rays.

1.05.3.1 Boundary Conditions, Continuity, and Reflection/Transmission Coefficients

As soon as the ray hits an interface, we must estimate quantities such as times, slowness vectors, and amplitudes and consider possible converted rays such as reflected or transmitted rays. Continuity of travel times leads to the Snell–Descartes law, which states that the tangent slowness component is preserved at the interface. This means that the transmitted wave front is moving locally at the same speed as the incident and reflected wave fronts along the interface.

Energy conservation requires continuity of stresses and displacement at the contact point on the interface. "In the seismic ray method, the reflection/transmission coefficients can be locally applied even to a nonplanar wave, incident at a curved interface separating two inhomogeneous anisotropic media" (Červený, 2001). Although these coefficients, called Zoeppritz coefficients, are quite well known (Aki and Richards, 1980; Červený, 2001), let us mention recent results for viscoelastic anisotropic media (Červený and Pšenčík, 2005a,b).

Whatever the formulas to be used, we must stress that slowness components play a key role and that one should avoid any headaches related to multivalued trigonometric functions when implementing numerical tools related to interface conversions.

A very complementary point of view has been proposed for single-valued travel times. As the wave front computed by any eikonal solver hits the interface, one may evaluate travel times along the interface and restart the eikonal solver for either reflection or transmission with these values (Rawlinson and Sambridge, 2004b). Of course, only single-valued travel-time computations may be considered inside each layer, but multiple arrivals coming from interfaces could be considered (Rawlinson and Sambridge, 2004a). A similar procedure is performed by Bai et al. (2010) for the shortest path approach inside each layer but still with multiple arrivals at receivers. We may note as well that discontinuous Galerkin methods for Eulerian multivalued estimation of travel times could be considered as well for discontinuities in the velocity field (Cheng and Shu, 2007; Li et al., 2008; Yan and Osher, 2011).

1.05.3.2 Paraxial Conditions

When dealing with paraxial rays at interfaces, one must consider continuity of travel times up to second order. This continuity is necessary for starting the transmitted or reflected paraxial rays. This second-order continuity requires estimation of curvature of the incident wave, of the interface, and of the converted wave. Pure differential geometry tools have been used by Popov and Pšenčík (1978), while Farra et al. (1989) had developed a more tractable approach for this second-order continuity, thanks to the Hamiltonian formulation.

1.05.4 Ray Seismograms

When properties of the medium vary smoothly with respect to the characteristic wavelengths of the propagating wave train, the source signature $S(t)$ is transported everywhere with a time shift related to the travel time. It is scaled by an amplitude factor and, eventually for the elastic case, polarized toward a specific direction through a polarization vector. Hilbert transformation of the source signature is expected when crossing a caustic. Therefore, the source signature (with a negative sign) is recovered after a second caustic is crossed. The Hilbert transform $S(t)$ of the $S(t)$ function is defined as

$$S(t) = \frac{1}{\pi}\int \frac{S(\xi)}{(t-\xi)}\mathrm{d}\xi \qquad [41]$$

and has as Fourier transform $-\mathrm{sign}(\omega)\, S(\omega)$, which introduces the $-\mathrm{i} = \exp(-\mathrm{i}\pi/2)$ phase shift required by the caustic crossing (Chapman, 1978).

For such computation of seismograms, we need all the rays connecting a source and a receiver. By summing over these rays, we may estimate seismograms as long as receivers are located away from caustic zones. Unfortunately, we may find the computation of these seismograms with contributions

close to caustics difficult. However, techniques have been developed for addressing the problem based on different integral wave decompositions (plane waves, Snell waves, beams, and so on), which are used to smooth out very locally unstable variations of the amplitude.

1.05.4.1 Classical Ray Seismograms

Following Chapman (1978), we may rewrite, in a very compact form, ray seismograms, at a receiver x for an elastic wave emitted by a source x_0 using the frequency domain expression [31]. We end up with a sum over rays, which gives the following asymptotic result:

$$u(x,t) \approx \sum_{\text{rays}} \text{Real}\left[\phi P(\gamma_1,\gamma_2)(x,x_0) \sqrt{\frac{1}{\rho(x)|J_T(x,x_0)|}} e^{-i\frac{\pi}{2}\text{KMAH}(x,x_0)} e(x,x_0)\tilde{S}(t-T(x,x_0))\right] \quad [42]$$

where $\tilde{S}$ is the analytic function associated with the source signature S, which is simply a complex function for the real part and its Hilbert transform for the imaginary part.

There is a priori no difficulty in using this asymptotic formula, except for a few situations. There is a failure of the expression when the receiver is exactly located at a position where the geometric spreading is equal to zero. From eqn [42], we see that amplitude then grows to infinity providing an erroneous expression for the seismogram amplitude. This failure of asymptotic ray theory at caustics is a well-known artifact of the method. Other pathological cases exist within shadow zones where no rays enter, while vibrations still exist (Chapman, 1985). Several solutions have been proposed for solving this problem, where high-frequency singular wave fields are expressed as summations of regular high-frequency asymptotic elementary solutions. Several types of waves can be used like plane waves or Gaussian beams as we shall see.

1.05.4.2 Seismograms by Summation on the Ray Field

1.05.4.2.1 The WKBJ summation

This approach is based on the introduction of high-frequency asymptotics into the wave equation resulting from the spatial horizontal Fourier transform of the scalar wave equation (eqn [7]) in a laterally invariant velocity model, $c(z)$. In the temporal frequency domain, we obtain an ODE for $w(z) = w(\omega p_x, \omega p_y, z, \omega) = w(k_x, k_y, z, \omega)$ as

$$-\omega^2 p_z^2(z) w(z) \frac{d^2}{dz^2} w(z) = f^w(z) \quad [43]$$

with $p_z^2(z) = \frac{1}{c^2(z)} - p_x^2 - p_y^2$ and $f^w(z) = f^w\left(\omega p_x, \omega p_y, z, \omega\right)$ where we introduce slowness vector $\mathbf{p}$ rather than wave number $\mathbf{k}$ where $k = \omega p$. As in the case of ray theory, we can introduce a WKBJ *ansatz* (Chapman, 2004, p. 278)

$$w(z) = S(\omega)\left(\sum_{n=0}^{\infty} \frac{W_n(z)}{(-i\omega)}\right) e^{i\omega\tau(z)} \quad [44]$$

where the expansion is done at constant p_x and p_y. We find, equivalent to the eikonal and transport equation, two equations

$$\frac{d\tau(z)}{dz} = \pm p_z(z) \quad [45]$$

and

$$\frac{d^2\tau}{dz^2}(z) W_0(z) + 2\frac{d\tau}{dz}(z)\frac{dW_0}{dz}(z) = 0 \quad [46]$$

These equations are ODEs that can be easily integrated using analytic or numerical approaches. The sign in eqn [45] determines the up- or downgoing behavior of the wave. Asymptotic WKBJ solutions appear as an extension of plane waves in homogeneous media to heterogeneous 1-D models. These solutions agree with when the velocity model does not depend on depth. Equations [45] and [46] are only valid when the velocity model is continuous in z up to the second order. When there are interfaces, similar to ray solution, high-frequency asymptotic continuity conditions need to be introduced. This reduces to the application of Snell–Descartes law and to the introduction of standard reflection/transmission coefficients.

The WKBJ expansion [44] breaks down when a turning point exists, that is, when the vertical slowness component is zero (Chapman, 2004, p. 286). Another asymptotic expansion can then be applied: the Langer asymptotic expansion (Chapman, 1974; Langer, 1937; Wasow, 1965; Woodhouse, 1974) involving Airy functions (Abramowitz and Stegun, 1972) with finite amplitudes on caustics.

An alternative to the WKBJ expansion [44] has also been the use of WKBJ solution or Bremmer series. This approach allows one to solve the so-called WKBJ paradox (Gray, 1982), that is, whatever the vertical gradient of the velocity, it will never generate a reflected wave. We would expect to observe such a phenomenon at low frequency, but since up- and downgoing waves are fully decoupled in the WKBJ expansion, it will never happen using this approximation. In the iterative WKBJ formulation, we assume that the wave field can be represented as a combination of up- and downgoing first-order WKBJ solutions. This coupling function satisfies an ordinary differential in z called the *coupling equation*, which can be solved iteratively leading to a solution series (de Hoop, 1990; Gray, 1983; Richards and Frasier, 1976; Scholte, 1962; Verweij and de Hoop, 1990).

Once the 1-D wave eqn [43] has been integrated using some high-frequency approximation, it will be necessary to perform the inverse Fourier transform in order to come back to the (x, t) domain. Several methods can be used including the exact technique of the *Cagniard–de Hoop–Pekeris method* (Cagniard, 1939; de Hoop, 1960; Pekeris, 1955a,b), the *WKBJ approach* where the slowness summation is truncated to real values of the travel times (Chapman, 1978), spectral methods such as the *reflectivity method* (Fuchs and Müller, 1971), and *full wave theory* (Aki and Richards, 1980, **Chapter 1.10**). A complete review has been performed by Chapman and Orcutt (1985) using both WKBJ and Langer approximations with applications to realistic profiles in the global Earth.

Truncation errors in the solution (Yedlin et al., 1990) especially in the presence of strong velocity gradients as well as numerical effects coming from smoothing boxcar windows or from convolution operators (Dey-Sarkar and Chapman, 1978) require specific attention when one wants to reconstruct the velocity structure. Reverberations from a stack of layered structures, which can be observed in the *reflecting method*, are well

separated as WKBJ contributions (Shaw, 1986) (see also **Section 1.05.4** of this book).

Finally, if WKBJ approximation is limited to 1-D media and exhibits interesting properties when compared with classical ray theory, WKBJ provides high-frequency asymptotic solutions in the (x, t) domain as summations of high-frequency asymptotic plane waves. Indeed, it appears that these summations may be regular at caustics, providing an interesting opportunity for computing high-frequency asymptotic solutions in those locations where classical ray theory fails. Moreover, as we will see now, extensions of WKBJ summations exist, which allow one to consider fully heterogeneous velocity models.

1.05.4.2.2 Maslov summation

The WKBJ approach is limited to 1-D layered media. Extension to laterally varying media is not straightforward. Approximate solutions assuming only small lateral variations of velocity have been introduced recently by Ni et al. (2003), but a more systematic formation can be based on the Maslov approach using the Legendre transformation (Kravtsov, 1968; Maslov and Fedoriuk, 1981). Maslov summation has been introduced by Chapman and Drummond (1982) in seismology and by Ziolkowski and Deschamps (1984) in electromagnetics. The Maslov approach, which reduces to the WKBJ approach for laterally homogeneous media, involves summation of high-frequency asymptotic local plane waves. In fact, high-frequency asymptotic solutions can be obtained in any of the 3-D subspaces of the phase space, that is, (x, y, p_z), (x, p_y, z), (p_x, y, z), ... or even (p_x, p_y, p_z). These solutions can be obtained by applying the stationary phase approximation (Chapman, 2004) to some Fourier transforms of the high-frequency asymptotic approximations in the (x, y, z) space. For example, we obtain from expression [27]

$$\omega(p_x, y, z, \omega) \approx \sqrt{i\pi \ \mathrm{sign}\left(\frac{\partial^2 T}{\partial x^2}\right)(x_{\mathrm{spec}}, y, z)}\, S(\omega)\phi_\omega(\gamma_1, \gamma_2) \sqrt{\frac{c^2(x_{\mathrm{spec}}, y, z)}{G_T(x_{\mathrm{spec}}, y, z)}}\, e^{i\omega T(x_{\mathrm{spec}}, y, z) - ip_x x_{\mathrm{spec}}} \quad [47]$$

where x_{spec} (p_x, y, z) denotes the specular position (we assume a single specular point), for which $\partial T/\partial x = p_x$, that is, where the Fourier parameter $p_x = k_x/\omega$ fits with the ray field parameter $p_x^{\mathrm{spec}} = \partial T/\partial x$ and the Jacobian G_T is defined by

$$G_T = \left|\frac{\partial(p_x, y, z)}{\partial(T, \gamma_1, \gamma_2)}\right| \quad [48]$$

Once we have these high-frequency asymptotic approximations, we can express the solution in the configuration space as an inverse Fourier transform or equivalently as a p_x slowness integral as in a WKBJ summation. This expression is called the Maslov summation. At high frequencies, this integral expression agrees with the classical ray solution, when it exists. When the classical ray solution is singular (a caustic point), it can be shown from the Liouville theorem (Goldstein, 1980) that there exists at least one alternate projection where the Maslov summation involves regular asymptotic plane waves. Regular high-frequency asymptotic solutions of the wave equation can then be found by blending both the ray solution and the Maslov summations using weighting functions (Chapman, 2004; Chapman and Drummond, 1982; Huang and West, 1997). For nice illustration of the Maslov summation, see also **Section 1.05.4.3** of this book.

Note that equivalent to caustics in classical ray theory, singularities may appear in the elementary high-frequency solution obtained in the other subspaces. They are called pseudocaustics and correspond to zeros of the Jacobian [48] (we follow the terminology of Klauder (1987a) as suggested by Kendall and Thomson (1993)).

A more general approach known as phase partitioning (Kendall and Thomson, 1993) may be used in practical situations where caustics and pseudocaustics cannot be separated. Semantically speaking, the frequency needs to be considered high enough to make them separable. These strategies could be avoided from the theoretical point of view but they are very useful in practice.

1.05.4.2.3 Gaussian beam summation

Another technique of summation will be through local Gaussian beams, which are used in the boundary-layer approach and which originally were applied to the computation of seismograms (see Popov, 1982 for original references in Russian). It has been popularized by Červený and coworkers (1982). One advantage is that individual Gaussian beams have no singularities either at caustics or at pseudocaustics. Moreover, two-point ray tracing is unnecessary and the summation is less sensitive to model parameterizations. A nice review had been given by Nowack (2003). Section of this book will present the formulation in the ray-centered coordinate system.

A Gaussian beam can be defined around a central ray (x_0, p_0) from the paraxial approximation [39],

$$W_{\mathrm{GB}}(x_0 + \delta x, p_0, \omega) = W_{\mathrm{GB}}(x_0, p_0, \omega) e^{i\omega\left(T(x_0, p_0) + p_0\delta x + \frac{1}{2}\delta x^t \mathcal{M}(x_0, p_0)\delta x\right)} \quad [49]$$

where $\mathcal{M}$ is now complex with $\mathrm{Im}(\mathcal{M}(x_0))$ being positive-definite. Note that, although this method has been presented mainly in the ray-centered system of coordinates, it can be constructed in any global coordinate system, such as here by using general Cartesian coordinates. The value of the Gaussian beam along the central ray is given from paraxial quantities [11] and initial curvature matrix [40] by the relation

$$W_{\mathrm{GB}}(T, \omega) = \frac{W_{\mathrm{GB}}(T_0, \omega) e^{i\omega(T - T_0)}}{\sqrt{\det\left(\mathcal{P}_{xx}(T, T_0) + \mathcal{P}_{xp}(T, T_0)\mathcal{M}(T_0)\right)}} \quad [50]$$

The expression remains finite as long as the term $\mathcal{M}(T_0)$ is symmetrical; since the $\mathrm{Im}(\mathcal{M}(T_0))$ is positive-definite, the term $\partial x/\partial(\gamma_1, \gamma_2 T)(T_0)$ is regular. The width of the Gaussian beam depends on the imaginary part of $\mathcal{M}$, which ensures a Gaussian decay of amplitude away from the central ray. The width of the beam varies according to variations of $\mathcal{M}$ and may be chosen according to various strategies. For example, Hill (1990) had proposed to choose an initial complex $\mathcal{M}$ related to an initial beam width w_l at frequency w_l. This has been applied efficiently in prestack depth migration (Gray, 2005; Gray and Bleistein, 2009; Hill, 2001) using Gaussian beam summation (GBS) with a ray sampling compatible with the beam width. Numerical comparisons have been investigated by many authors (Madariaga, 1984; Nowack and Stacy, 2002; Weber, 1988; White et al., 1987) in seismology (**Figure 12**).

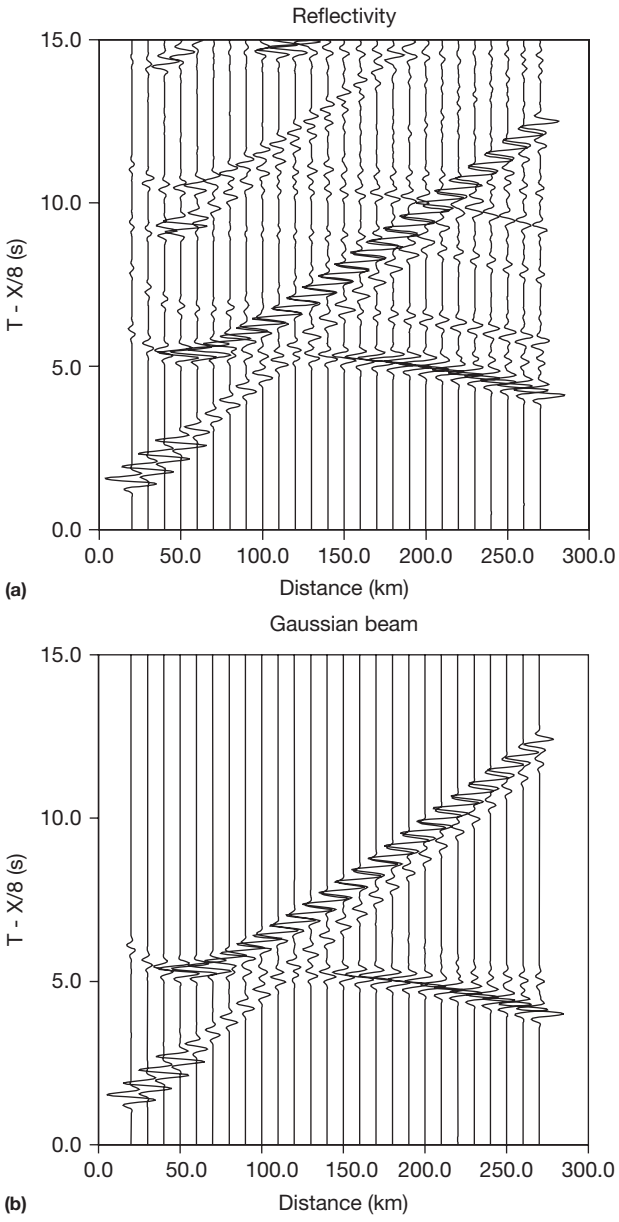

Figure 12 Comparison between Gaussian beam summation (bottom panel) and reflectivity method (top panel). Note that for this comparison, some of the later arrivals shown in the reflectivity modeling were not simulated in the GBS, but could have been included (Courtesy of R. Nowack).

The Gaussian beam solution represents an approximate solution of the wave equation, and their superposition integral represents an asymptotic approximation of the wave field. In practice, once the complex curvature matrix has been chosen at some T_0, the weighting of the various Gaussian beams in the superposition integral has to be defined in such a way as to fit with asymptotic ray theory, where it is regular. By construction, Gaussian beams are always regular and they consequently provide regular high-frequency solutions. GBS may be shown to be equivalent to Maslov summation under the hypothesis of plane wave with infinitely wide Gaussian decay (Madariaga, 1984). This equivalence shows the larger possibilities offered by GBS, with, for example, the advantage of limited truncation artifacts.

1.05.4.2.4 Coherent-state transformation technique

Formulations based on the coherent-state transformation technique (Klauder, 1987a,b) fills the gap between local plane wave decomposition of WKBJ/Maslov approaches and overcomplete beam decompositions with a simple parabolic approximation of the phase function (Thomson, 2001, 2004). This allows us to preserve many tracing tools for real rays. A comparison between the Maslov approach, the Gaussian approach, and the Coherent-state approach has been performed by Albertin et al. (2001).

Attempts have been made to move toward complex rays where both amplitudes and travel times are complex functions because analytic continuation of velocity variation is easily possible for simple analytic function (Deschamps, 1971; Felsen, 1976, 1984; Keller, 1971; Wu, 1985; Zhu and Chun, 1994b). However, extension to arbitrary numerical velocity variations is still a challenging problem, although recent work (Amodei et al., 2006) seems to solve the analytic continuation for numerical velocity variations, opening the road to more applications of complex ray theory for heterogeneous media.

1.05.4.3 The Geometric Theory of Diffraction

In addition to previous strategies, which can be used to avoid caustic singularities or to estimate fields inside shadow zones in smooth media, other uniform ray expansions are also possible when considering caustics (Kravtsov, 1964; Ludwig, 1966) using Airy functions or at discontinuities, where the wave field creates a shadow zone. Although rather sophisticated tools of Riemannian geometry are required, we may adopt a more phenomenological point of view and illustrate the geometric theory of diffraction introduced by Keller (1962). Justification of Keller's formulation from a mathematical point of view, especially when media have variable velocity, has generated an impressive list of references, and they are fruitful monographs by Babič and Kirpičnikova (1979), Babič and Buldyrev (1991), and Klem-Musatov (1995). Nice reviews by Kravtsov (1968), Babič (1986), and Hron and Chan (1995) will help the reader in understanding the various methods for the construction of asymptotic solutions.

The method of canonical problems transforms the problem at hand into a simpler problem. By matching asymptotically field expansions for a simpler problem, expansion coefficients can be estimated (Keller, 1962). The best example is the diffraction of an arbitrary wave field from a body with a rib, which can be transformed into the diffraction of a plane wave by a wedge. A boundary-layer formulation can be used and express the solution in the transition zone, the width of which goes to zero when the frequency goes to infinity (Babič, 1975; Buchal and Keller, 1960). This approach related to the method of parabolic equations (see reference works in Fock, 1965) does not require any analytic solutions as for the canonical matching approach.

On a linear edge, an incident plane wave is reflected creating illuminated and shadow zones for the reflection wave front (**Figure 13**). Energy will flow into the shadow zone, and

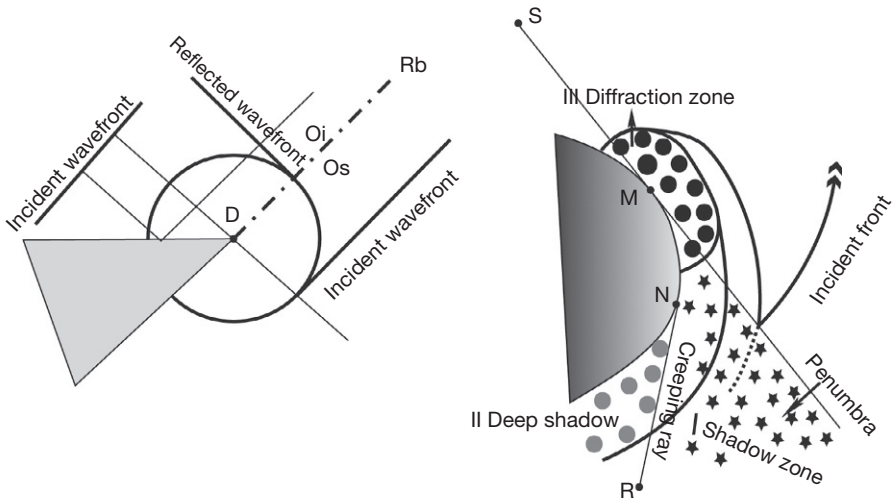

Figure 13 Geometric interpretation of diffraction. On the left panel, the gray diffracting object does not allow wave penetration. The reflection wave front is connected to the diffraction front emitting from point D. This wave front is connected to the incident wave front. Ray *Rb* separates the reflection zone and the diffraction zone. On the right panel, waves may penetrate the diffracting body. The line SM separates the penumbra zone and the lighted zone. Because a creeping ray leaves the obstacle at the point N (which is defined both by the front and the interface curvatures for a specific ray), we shall distinguish the deep shadow zone (II) from the standard shadow zone. The diffraction zone (III) will move into the lighted zone behind the converted front related to the first diffraction at the point M (I). These limits will be very sensitive to the frequency content of the wave and ad hoc corrections are necessary to keep the ray approximation as a useful interpretation tool.

asymptotically, this diffraction may be well modeled by diffraction rays, which follow an eikonal equation with a source at point D. Therefore, we must consider both reflected waves and edge waves. Their wave fronts must coincide along the shadow boundary. The boundary ray separating illuminated and shadow zones does not follow the usual transport equation and a dedicated theory is required. Comprehensive analysis based on earlier work has been given by Klem-Musatov (1995) to compute scalar diffraction amplitudes (see the review by Hron and Chan, 1995).

The surface limiting the illuminated and shadow zones may have a complex geometry (Borovikov and Kinber, 1974). For a convex body limited by a discontinuous surface, three zones in the shadow may be distinguished: the neighborhood of the shadow zone (I), the neighborhood of the body surface (II), and the intersection of these two zones (III), related to the point M of the surface hit by the grazing ray (see **Figure 13**).

In seismology, diffractions by the core–mantle or inner core boundaries of the Earth require a deep understanding of these approaches (see the interesting presentation by Thomson, 1989). Because seismology deals with elastic propagation, Thomson (1989) stressed that the boundary-layer method can be applied when considering P and S wave fields as long as P and S grazing rays do not hit the boundary at the same point. A canonical solution with detailed elastic diffraction coefficient estimates has been constructed in 3-D for crack diffraction by Achenbach and Gautesen (1977). Further improvements can be performed in this direction for elastic diffraction in the future.

1.05.5 Finite-Frequency Effects

The ray path connecting a source S and a receiver R is a trajectory along which the high-frequency part of the energy is propagating. Because the frequency we consider is always finite, the wave field at the receiver is also modified by the velocity distribution in the vicinity of the ray. This volume, called the Fresnel volume, may be defined in a very simple way for a wave frequency content f. Any point F of this volume should satisfy the inequality (Kravtsov and Orlov, 1990)

$$|T(\mathrm{S},\mathrm{F}) + T(\mathrm{F},\mathrm{R}) - T(\mathrm{S},\mathrm{R})| \leq \frac{1}{2} f^{-1} \qquad [51]$$

Basically, this means that only points that satisfied inequality [51] will contribute significantly to the seismogram at the receiver around time T(S, R). Often, we call the Fresnel volume a physical ray (Červený, 2001, p. 115). This volume plays a key role for resolution estimation of seismic imaging methods in relation with the validity domain of ray theory (Kvasnička and Janský, 1999). We will now consider a procedure linking model perturbations and seismogram perturbations, which allows us to introduce the contributions of this volume to seismogram computation.

Before going into these linearized approximations, we must emphasize the path integral approach where any trajectory connecting the source and the receiver may contribute to seismogram estimation (Lomax, 1999; Schlottmann, 1999; Thomson, 2001). Although we have not yet found a practical way of assessing convergence toward the true solution of these integrals, these methods exhibit nonlocal behaviors, which make them completely different from approaches we gave consider up to now.

We can see that the travel time, a very robust observable from seismograms, has an implicit frequency context, which one should be aware of for different applications in seismology. Therefore, we need to be concerned about procedures for extracting travel times as was recognized a long time ago through the International Seismological Centre (ISC, www.isc.ac.uk) as promoted by John Milne at the beginning of the twentieth century.

1.05.5.1 Travel-Time Estimation, A Data Mining Issue

A manual picking strategy is still used for identifying seismic phases, but more and more automatic picking approaches are routinely performed as the number of seismograms has increased exponentially in recent years. Nolet (1987) discussed the statistics of picking travel times in seismology when their probability distribution is away from Gaussian one. It is still an active research area where objective analysis of seismogram structure needs to be performed. We may consider data-driven strategies where only observed seismograms are analyzed (Chevrot, 2002; Gentili and Michelini, 2006; Rowe et al., 2002; Zhang et al., 2003) and model-driven strategies where observed seismograms are compared with synthetic ones computed in a reference model. Using a data-driven strategy, Maggi et al. (2009) had performed time window detection either on observed seismograms or on synthetic seismograms while Lee and Chen (2013) have developed a frequency-time window detection. Sigloch and Nolet (2006) had used cross correlation between observed and synthetic data computed with ray theory for picking travel times, while Satriano et al. (2008) had underlined the interest of performing the picking by cross correlation iteratively as models are updated during tomographic reconstruction. Other ways of picking travel times as well as curvatures, especially once wave propagation effects have been removed by time migration, have been performed by a dense systematic extraction over a 5-D seismic cube (x_s, x_r, t) (Hardy, 2003; Jones, 2013; Siliqi et al., 2007). Zaroli et al. (2010) had combined both time windowing and cross correlation for increasing the number of travel-time picks to hundreds of thousands, but still far below the millions of handpicked arrivals. They argued that the distribution of their automatic *S*, *ScS*, and *SS* picked times shows finite-frequency effects including wave front healing the frequency dependence of *ScS* times and the average dispersion for *S* and *SS* travel times favors a frequency-dependent attenuation model.

The extraction of seismic observables is linked with comparisons of seismograms through the definition of misfit criteria (Kristeková et al., 2006, 2009). These criteria are widely used not only for intercomparisons of numerical methods but also for various full waveform inversions. Amplitude can also be extracted from seismograms, as well as instantaneous phases and envelopes (Bozdağ et al., 2011; Fichtner et al., 2008; Tape et al., 2007).

One can see that data mining is a crucial step in seismic analysis and in ray approach that is widely used for the extraction of observables from seismograms.

1.05.5.2 Ray + Born/Rytov Formulation

This resolution of the seismic inverse problem (recovering the elastic parameter field from the seismic data) is one of the major challenges of seismology. The problem is huge ill-constrained and nonlinear inverse (Tarantola, 1987), which has to be addressed in some appropriate ways. For example, as soon as we have some reasonable initial model for the elastic parameters, one may build a linearization of the relation connecting the data perturbation to the model perturbation. This is the Born approximation, which has been widely used as a basis for linearized seismic inversion (Beylkin, 1985; Beylkin and Burridge, 1990; Tarantola, 1984b, 1986). In fact, the Born approximation is only the first-order term of a recursive relation connecting a seismic wave field perturbation $\delta w(\mathrm{r}, \omega)$ to a model perturbation $\delta m(\mathrm{x})$ (Hudson and Heritage, 1981). We may write for the squared slowness perturbation $\delta m(\mathrm{x}) = 1/c^2(\mathrm{x}) - 1/c_0^2(\mathrm{x})$ (where $c_0(\mathrm{x})$ denotes the velocity in the reference model) a set of relations

$$\delta w_{n+1}(\mathrm{r}, \omega) = \omega^2 \int_V \mathrm{d}x\ \delta m(\mathrm{x})\ G_0(\mathrm{r}, \omega; \mathrm{x})(\delta w_n(\mathrm{x}, \omega) + w_0(\mathrm{x}, \omega)) \quad [52]$$

where n denotes the order of the Born approximation, V denotes the full space volume, and $G_0(\mathrm{r}, \omega; \mathrm{x})$ denotes the Green function for a point source at position x and a receiver at position r in the reference velocity model. We have for the first-order perturbation $\delta w_0(\mathrm{x}, \omega) = 0$, which provides the classical Born approximation, that is, a linearized approximation for $\delta \mathrm{w}$, (r, ω); the Born approximation can be extended to acoustic and elastic media (Ben Menahem and Gibson, 1990; Gibson and Ben Menahem, 1991).

The reference model can be chosen to be homogeneous in order to take advantage of exact and explicit expression of reference Green function. For realistic problems, inhomogeneous reference models are necessary and lead to the distorted Born approximation (Chapman, 2004). In this case, it is possible to use an approximate expression of the Green function as it can be obtained by ray theory, for example. We obtain then the WKBJ + Born (Clayton and Stolt, 1981; Ikelle et al., 1988) or ray + Born approximations (Bleistein, 1984, 1987; Beylkin, 1985; Beydoun and Mendes, 1989; Beylkin and Burridge, 1990; Cohen et al., 1986; Jin et al., 1992; Thierry et al., 1999a,b; Operto et al., 2000; Xu and Lambaré, 2004; Xu et al., 2001, 2004) widely used for seismic imaging. From the expression [52], the ray + Born approximation can be expressed for the perturbation of the Green function as

$$\delta G(\mathrm{r}, \omega; \mathrm{s}) = \omega^2 \int_V \mathrm{d}x \delta m(\mathrm{x}) \mathcal{A}(\mathrm{r}, \mathrm{x}, \mathrm{s}) \mathrm{e}^{\mathrm{i}\omega T(\mathrm{r}, \mathrm{x}, \mathrm{s})} \quad [53]$$

where $A\ (\mathrm{r}, \mathrm{x}, \mathrm{s}) = A\ (\mathrm{s}, \mathrm{x})$ is the product of the amplitude of asymptotic Green functions for the rays $\mathrm{x} \rightarrow \mathrm{s}$ and $\mathrm{x} \rightarrow \mathrm{r}$ in the reference velocity model and $T\ (\mathrm{r}, \mathrm{x}, \mathrm{s}) = T\ (\mathrm{r}, \mathrm{x}) + T\ (\mathrm{s}, \mathrm{x})$ is the sum of the corresponding travel times. **Figure 14** shows common offset traces obtained using the ray + Born approximation. See also Section 1.07.4 of this book for the application to regional and global scales.

Since we use, in the ray + Born approximation, high-frequency approximation of the Green function in eqn [52], there may be difficulties iterating these equations even if generally smooth reference velocity models are used. For remedying this, Coates and Chapman (1990) and Chapman and Coates (1994) proposed a generalization of the Born approximation, which takes into account approximate Green function. This generalization emphasizes a difficult aspect of the use of the ray + Born approximation, the definition of limits for the perturbation approach related to the reference velocity model selection. These limits are related to limitations of ray theory and to first-order Born approximation. Practically, the reference velocity model should be valid for ray theory but should also be sufficiently heterogeneous for

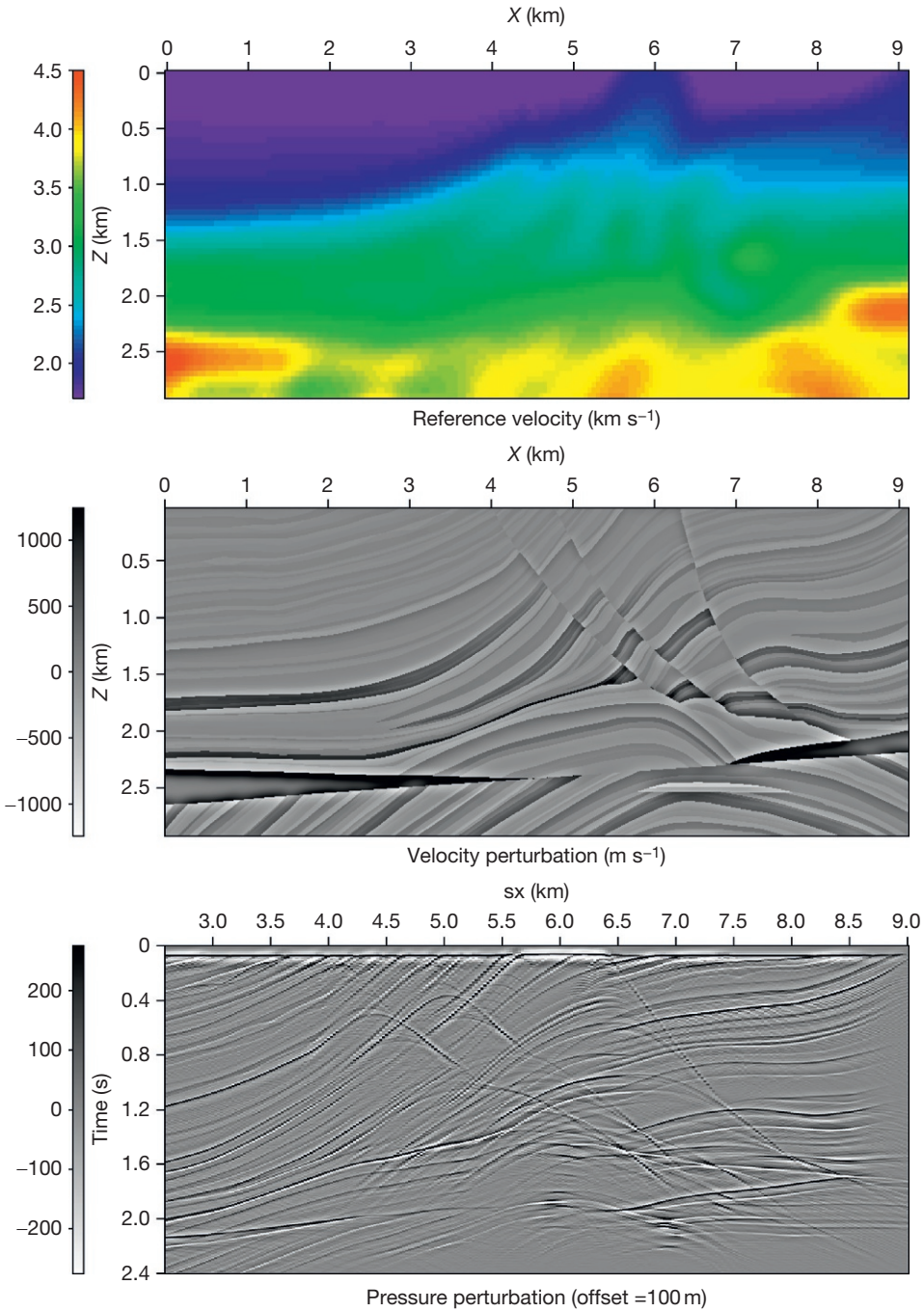

Figure 14 The ray + Born approximation. The Marmousoft model and dataset (Billette et al., 2003). On the top panel, the smooth reference velocity model; the middle panel, the velocity perturbation; and the bottom panel, the common offset section (offset is 100 m) profile.

reproducing the main features of the forward seismic wave propagation in the perturbed velocity model. In terms of ray tracing, it means that the reference velocity model should preserve, within the precision of the propagated wavelengths, the travel time of the forward propagation.

In practice, the ray + Born approximation essentially works for small-sized heterogeneities and for small angles of reflection or diffraction (Beydoun and Tarantola, 1988; Keller, 1969; Wu, 1989). This is the context of reflection seismic exploration, where linearization has been proposed (Lailly, 1983; Tarantola, 1984a,b), and even nonlinear seismic inversions (Pica et al., 1990; Tarantola, 1986) based on local iterative optimization schemes. In fact, the limitations of the standard local optimization methods have been recognized (Gauthier et al., 1986; Jannane et al., 1989; Kolb et al., 1986) and credited to the strong nonlinearity of the problem where the long-wavelength components of the velocity model expressed through the asymptotic Green function in eqn [53] are decoupled from the short-wavelength components expressed through the model perturbation δm in eqn [53].

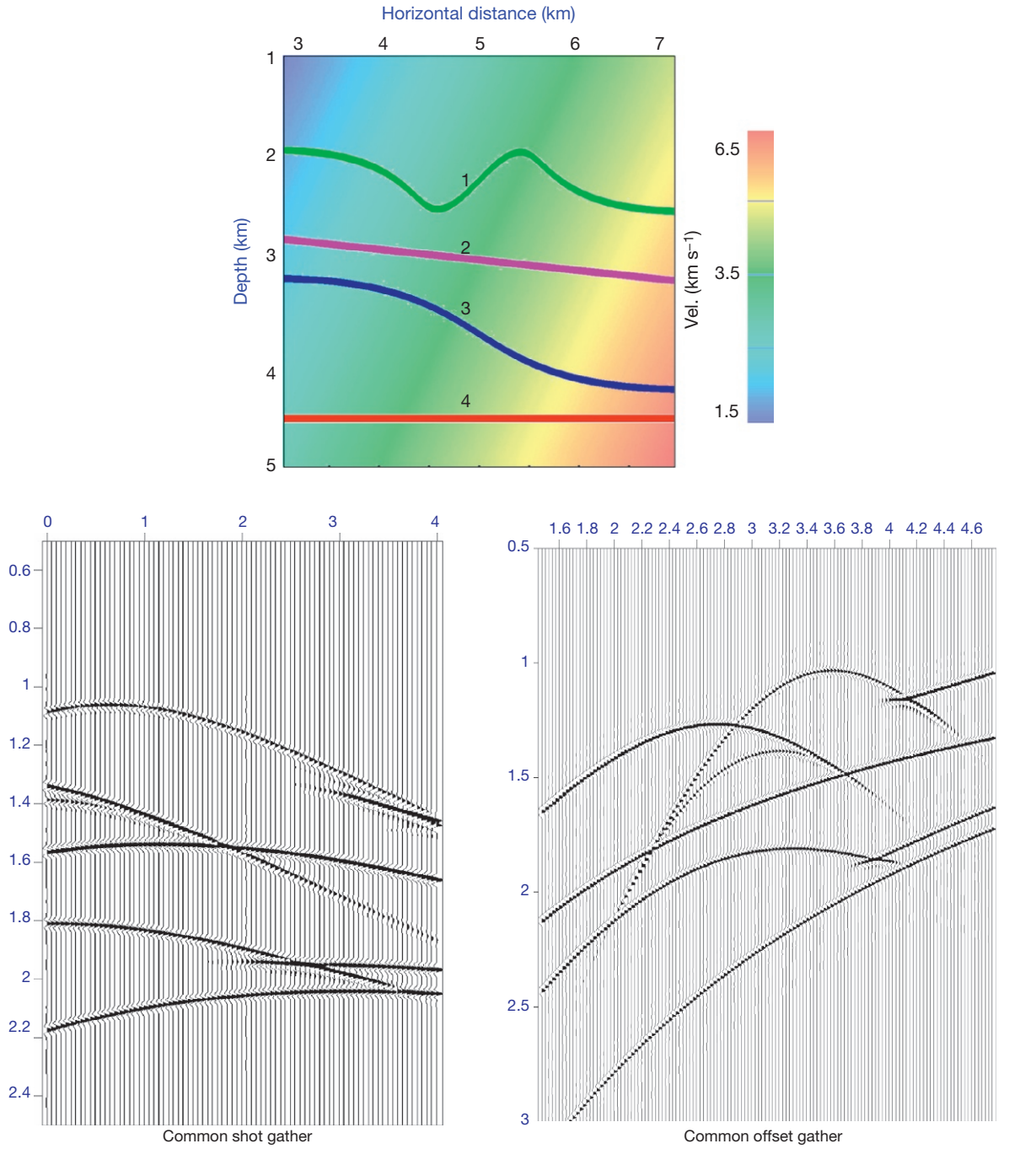

Figure 15 Synthetic seismograms using the Kirchhoff summation. On the top panel, the smooth velocity model (tilted gradient of the velocity). Along with four superimposed reflectors. On the bottom panel, the left plot shows a common shot gather modeled by ray + Kirchhoff summation, while the right plot shows a common offset gather modeled by ray + Kirchhoff summation. Courtesy of R. Baina (OPERA, France).

Changing the dataset from traces to phases could allow a better coupling between the spectral contents of the velocity model (Billette and Lambaré, 1998; Bishop et al., 1985; Farra and Madariaga, 1988). The quantity $\delta\phi = \mathrm{In}(\omega/\omega_0)$, the phase of the wave field, could be expressed to first order as

$$\delta\Phi(\mathrm{r},\omega) \approx \omega^2 \int_V \mathrm{d}x\,\delta\mathrm{m}(\mathrm{x}) \frac{\mathcal{A}(\mathrm{r},\mathrm{x},\mathrm{s})}{\mathcal{A}(\mathrm{r},\mathrm{s})} \mathrm{e}^{\mathrm{i}\omega(\mathcal{T}(\mathrm{r},\mathrm{x},\mathrm{s})-\mathcal{T}(\mathrm{r},\mathrm{s}))} \qquad [54]$$

which has similar terms as the Born eqn [53] except for the phase term, which has a travel-time delay and, therefore, a short-wavelength contribution to the model perturbation. This Rytov approximation is expected to fit the perturbed transmitted wave field better than the Born approximation (Beydoun and Tarantola, 1988; Keller, 1969; Rytov et al., 1987; Samuelides, 1998). Until now, it has not been applied much to seismic inversion (Devaney, 1981; Nahamoo et al., 1984) in spite of recent work (Gélis et al., 2007).

1.05.5.3 Ray + Kirchhoff Approximation

The Born approximation is not the only linearized approximation used for seismic modeling and inversion. In the context of reflection seismic exploration, the first-order Kirchhoff approximation is so far the most preferred. This approximation provides a relationship between the primary reflected wave field and the distribution of reflectivity in the model. This approximation is derived from the representation theorem (Aki and Richards, 1980), which allows one to express any causal wave field, $w(\mathrm{x}, \omega)$ associated with the source distribution, $f(\mathrm{x}, \omega)$, as a volume integral over the volume V of source distribution and a surface integral over the volume boundary δV

$$w(\mathrm{r}, \omega) = \iiint_V \mathrm{d}x\, \mathrm{G}(r, \omega; \mathrm{x}) f(\mathrm{x}, \omega) + \iint_{\delta V} \mathrm{d}x \left(\frac{\partial G}{\partial n}(\mathrm{r}, \omega; \mathrm{x}) w(\mathrm{x}, \omega) - \mathrm{G}(\mathrm{r}, \omega; \mathrm{x}) \frac{\partial w}{\partial n}(\mathrm{x}, \omega) \right) \quad [55]$$

where $\delta/\delta n$ denotes the spatial derivative along the outer normal to the surface. Let us assume now that we consider Green function, that is, $\omega(\mathrm{x}, \omega) = \mathrm{G}(\mathrm{x}, \omega; \mathrm{s})$ or equivalently $f(\mathrm{x}, \omega) = \delta(\mathrm{x} - \mathrm{s})$, and that the volume V is bounded by a reflecting surface. We can then express the reflected wave field as

$$G_{\mathrm{refl.}}(\mathrm{r}, \omega; \mathrm{s}) = \iint_{\delta V} \mathrm{d}x \left(\frac{\partial G}{\partial n}(\mathrm{r}, \omega; \mathrm{x}) G_{\mathrm{refl.}}(\mathrm{x}, \omega; \mathrm{s}) - \mathrm{G}(\mathrm{r}, \omega; \mathrm{x}) \frac{\partial G_{\mathrm{refl.}}}{\partial n}(\mathrm{x}, \omega; \mathrm{s}) \right) \quad [56]$$

where G is the free-space Green function (Bleistein, 1984; Chapman, 2004) (i.e., the direct wave from the source that does not interact with the scatterer). The reflected field is expressed as a summation over the unknown reflected wave field. In the framework of high-frequency asymptotics, it is possible to approximate the reflected wave field on the reflecting interface from the incident wave field and the reflection coefficient. This result is in the Kirchhoff approximation (Bleistein, 1984; Frazer and Sen, 1985) in 3-D geometries as

$$G_{\mathrm{refl.}}(\mathrm{r}, \omega; \mathrm{s}) = i\omega \iint_{\delta V} \mathrm{d}x \mathcal{R}(\mathrm{r}, \mathrm{x}, \mathrm{s}) \mathcal{A}(\mathrm{r}, \mathrm{x}, \mathrm{s}) \mathrm{e}^{\mathrm{i}\omega T(\mathrm{r}, \mathrm{x}, \mathrm{s})} \quad [57]$$

where

$$\mathcal{R}(\mathrm{r}, \mathrm{x}, \mathrm{s}) = q(\mathrm{x}, \theta(\mathrm{r}, \mathrm{x}, \mathrm{s})) R(\mathrm{x}, \theta(\mathrm{r}, \mathrm{x}, \mathrm{s})) \quad [58]$$

denotes the product of the reflection coefficient $\mathrm{R}(\mathrm{x}, \theta)$ and of the stretching factor, $q(\mathrm{x}, \theta) = |\nabla_{\mathrm{x}} \mathcal{T}| = 2\cos\theta / c(\mathrm{x})$, where θ denotes the half aperture angle between ray $\mathrm{x} \to \mathrm{s}$ and $\mathrm{x} \to \mathrm{r}$. Expression [58] is reciprocal for the source and receiver positions (Ursin and Tygel, 1997). The Kirchhoff approximation can be easily extended to the acoustic and elastic cases (Chapman, 2004; Ursin and Tygel, 1997), where a summation is done for any interface and any mode conversion. See an example of Kirchhoff summation in **Figure 15**.

We see when comparing expressions [53] and [57] that the ray + Born and ray + Kirchhoff expressions are very similar. This similarity can be enhanced further if we extend the summation from a surface to a volume, assuming that the whole reflected wave field can be built by stacking contributions of individual reflectors. In this case, we consider a volumetric distribution of specular reflectivity $R(\mathrm{x}, \theta(\mathrm{r}, \mathrm{x}, \mathrm{s}))$

$$G_{\mathrm{refl.}}(\mathrm{r}, \omega; \mathrm{s}) = i\omega \iiint \mathrm{d}x\, q(\mathrm{x}, \theta(\mathrm{r}, \mathrm{x}, \mathrm{s})) R(\mathrm{x}, \theta(\mathrm{r}, \mathrm{x}, \mathrm{s})) G(\mathrm{s}, \omega, \mathrm{x}) G(\mathrm{r}, \omega, \mathrm{x}) \quad [59]$$

where the 3-D Green functions, $G(\mathrm{s}, \omega, \mathrm{x}) = A(\mathrm{s}, \mathrm{x}) \mathrm{e}^{\mathrm{i}\omega T(\mathrm{s}, \mathrm{x})}$ and $G(\mathrm{r}, \omega, \mathrm{x}) = A(\mathrm{r}, \mathrm{x}) \mathrm{e}^{i\omega T(\mathrm{r}, \mathrm{x})}$, have to be calculated in some reference velocity model.

The Born and Kirchhoff approximations are in widespread use and are the basis of numerous seismic imaging methods. In practice, even if the derivation of the formulas relies on high-frequency asymptotics, the asymptotic Green functions in expression [59] are sometimes replaced by other types of numerical Green functions like one-way paraxial approximation of the wave equation (Claerbout, 1970), two-way extrapolation approaches (Kosloff and Baysal, 1983; Sandberg and Beylkin, 2009), or reverse-time migration (Baysal et al., 1983; McMechan, 1983). Most depth migration methods consider these Green functions in order to recover the reflectivity function at any point of the medium, knowing some reference velocity model. When ray-based Green functions are used, this type of migration is called Kirchhoff migration (Bleistein, 1987; French, 1974, 1975). It is widely used in the petroleum industry for 3-D depth migration (Xu and Lambaré, 2004; Xu et al., 2004), while applications at crustal and mantle scales may also be possible (see Section 1.7).

1.05.5.4 Finite-Frequency Effects on Ray Functions

Away from waveform estimation and fitting, can we introduce finite-frequency features for travel-time and/or amplitude analysis? Filling the gap between, on the one hand, travel-time inversion and, on the other hand, full waveform inversion has gained the attention of many workers since the pioneering work of Luo and Schuster (1991) and Woodward (1992). The concept of wavepath (Woodward, 1992) as the product of the incident wave field from the source and the back-propagated wave field from the receiver displays well the Fresnel volume (**Figure 16**). Points moving away from the first Fresnel zone bring higher-frequency content into the image reconstruction, especially for waveform fitting (Operto et al., 2004; Pratt et al., 1996).

Linear kernels, often called Fréchet kernels, have been introduced for travel time. A recent and impressive literature on surface waves (Marquering et al., 1998, 1999; Zhou et al., 2004), normal modes (Katzman et al., 1998; Li and Romanowicz, 1995; Li and Tanimoto, 1993; Tanimoto, 1995; Zhao et al., 2000), and rays (Dahlen et al., 2000; Hung et al., 2000; Montelli et al., 2004a,b) shows the vitality of such a concept. Discontinuities such as internal boundaries and interfaces have been introduced as well (Dahlen, 2005; Xie and Yang, 2008). The range of sensitivity kernels have increased rapidly for various model perturbations and propagation configurations. All of them are related to Fresnel optics as they are confined to a point-to-point geometry. Correspondence with the Fraunhofer optics could also be done using plane wave decomposition (Iturben et al., 2009). A nice review had been performed by Nolet (2008). For example, the time delay δT at a

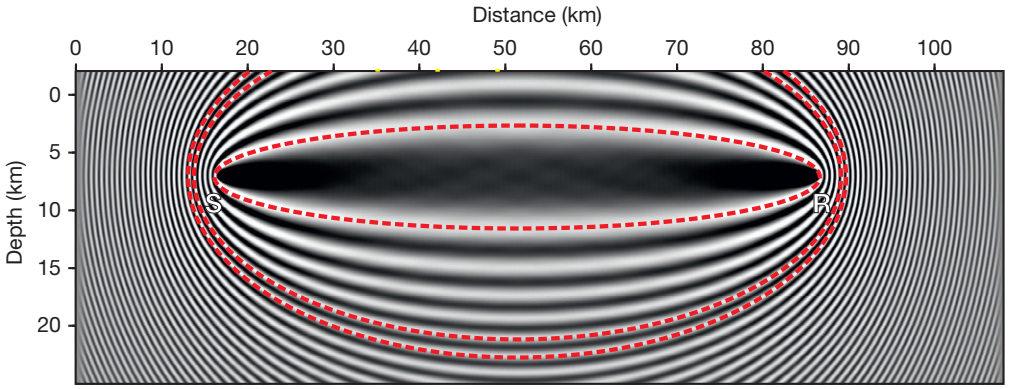

Figure 16 A simple description of wavepath. The first Fresnel zone (the red dashed line) is the zone of main contribution for diffraction when considering finite-frequency effects. As we introduce other Fresnel zones, smaller-scale features are (included in) both the medium description and the seismogram estimation. Courtesy of S. Operto, CNRS.

given receiver r coming from a scattering point x for a given source s is associated with the time difference $\Delta T(s,r,x,\omega) = T_{sr} - T_{sx} - T_{xr}$ through the equation

$$\delta T(s,r) = \int_D K_t(\mathrm{x},\omega)\frac{\delta_c(\mathrm{x})}{c(\mathrm{x})}\mathrm{d}V \qquad [60]$$

where the integration domain D is over diffracting points x. This domain must be defined carefully. The Fréchet kernel or sensitivity kernel $K_t(x, \omega)$ has an expression depending on frequency ω, time difference ΔT (s, r, x, ω) for a path to the scattering point, and three synthetic amplitudes or geometric spreadings between the pairs (source and receiver, source and diffracting point, and receiver and diffracting point) (Nolet, 2008, p. 127). Dahlen et al. (2000) had developed a systematic use of paraxial theory, which speeds up significantly the estimation of the sensitivity kernel especially for mantle tomography; however, one may need to consider true rays between source/receiver and diffracting points in the crust (Gautier et al., 2008). Applications to amplitudes (Dahlen and Baig, 2002) and to anisotropy (Favier and Chevrot, 2003) (with the splitting intensity related to polarization of the incoming wave; Chevrot, 2000) introduce new sensitivity kernels and will extend applicability in the near future.

A interesting reconstruction of mantle plumes had been performed by Montelli et al. (2004a,b, 2006b) and, more recently, by Sigloch et al. (2008), Tian et al. (2009, 2011), Sigloch (2011), and Pavlis et al. (2012) under the North American Plate among other reconstructions based on such travel times.

The contribution of diffracting points increases when we move away from the ray making the so-called banana-doughnut shape for travel times, the usefulness of which has been questioned by de Hoop and van der Hilst (2005). For the amplitudes, the maximal contribution is found on the ray (**Figure 17**). The near-field influence has been discussed by Favier et al. (2004).

Aside from the theoretical questions of the shape of the sensitivity kernel, the claimed improvement of the resolution when considering finite-frequency tomography compared with standard ray tomography has been questioned by different authors (Boschi et al., 2006; Montelli et al., 2006a; van der Hilst and de Hoop, 2005). Trampert and Spetzler (2006) had mentioned that regularization required for making a stable inversion of the phase delays prevents the appearance of the improved resolution form finite-frequency tomography. Moreover, often, the discretization of the velocity model is coarser than the Fresnel zone size of related finite-frequency data. Finally, the database of delay times used for finite-frequency tomography needs to be increased for a better estimation of the effects of finite-frequency effects. This is the motivation behind the work done by Zaroli et al. (2010), and one may expect a dramatic increase of the size of these databases.

1.05.6 Discussion

Velocity perturbations are rather weak in the Earth's mantle, making estimation of synthetic travel times quite reliable although one could not guarantee that a false association between an observed time and a synthetic time may exist. Amplitudes based on ray theory have so far not been used for such reconstructions because of a strong trade-off with source frequency content and attenuation effects. Further improvements will certainly close this gap and will bring us back to waveform fitting, an important challenge for global seismology in the next 10 years.

Numerical methods such as the spectral element method (Komatitsch et al., 2002) and the finite difference method (Levander, 1988; Moczo et al., 2006) have been integrated in many seismic inversion procedures (Bozdağ et al., 2011; Fichtner et al., 2008; Plessix, 2006; Pratt et al., 1996, 1998; Tape et al., 2007; Tromp et al., 2005) using filtered or transformed seismograms based on time-frequency analysis, such as the instantaneous phase and envelope measurements. These transformations emphasize the importance of phase delays before amplitude misfits. Impressive results have been shown at local scales (Kamei et al., 2012; Operto et al., 2004, 2006) and at regional scales (Fichtner et al., 2009; Tape et al., 2010; Zhu et al., 2012), while the seismological community is still waiting for results at the global scale.

What is the best approach we may consider? Should one perform extraction of observables such as travel times from seismograms and incorporate with these data a finite-frequency tomography for reconstruction or should we move to full waveform inversion based on comparison of observed

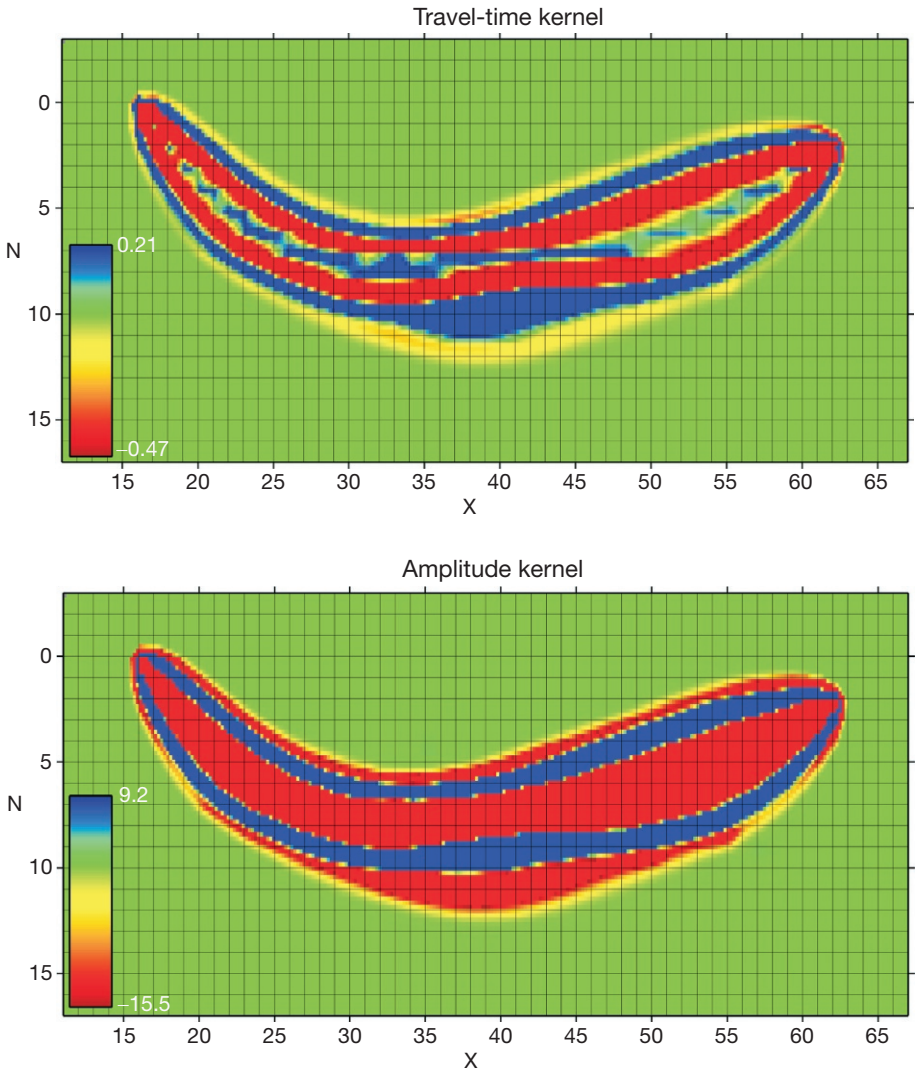

Figure 17 Travel-time and amplitude sensitivity kernels in a local heterogeneous medium. Note the weak contribution in the central part of the kernel for travel times associated with the central ray of Fermat's principle (top panel), while the contribution in the central part of kernel is maximal for amplitude (bottom panel). Courtesy of S. Gautier and G. Nolet.

and synthetic seismograms using linear elastodynamic equations with and adapted misfit criteria strongly based on phase information? The first approach is quite efficient compared with the second one because the modeling stays simple. In case of multiple arrivals inside the same phase window, it may not be the case as we rely on nonlinear Hamilton–Jacobi equations.

Since the pioneering work of Lailly (1983). Tarantola (1984a) and the connection between tomography and inversion made by Luo and Schuster (1991), upper crust investigations have favored the second approach. As promoted by Jin et al. (1992) and Lambaré et al. (1992, 2003), full waveform inversion might use ray theory or extended approaches as long as one can find an efficient and stable way of computing ray seismograms in updated velocity models and not only just the smooth initial model, which has been the case for the so-called ray+born approach. For the core–mantle boundary, it might be quite difficult to propagate using numerical method waves down to this zone, and therefore, ray methods play a central role if we should master the problem of multiple arrivals inside a time window since we might expect quite complex triplications coming from velocity variations over undulations of this interface (Kendall and Nangini, 1996; Wang et al., 2008).

1.05.7 Conclusion

Until now, the growth of seismology as an investigation tool for the Earth's interior has essentially relied on the use of ray theory. During this time, significant progress has been made in ray theory, which is definitely not a 'discipline from the nineteenth century.' This constant progress (not only in terms of numerical developments) has, for example, considerably extended the application domain of these techniques, which still remain essential for the analysis of seismic traces.

Although numerical methods for solving wave equations (finite difference methods, e.g., Moczo et al., 2006; Virieux, 1986, and finite element methods with fast

convergence such as spectral element methods, e.g., Chaljub et al., 2003; Komatitsch et al., 2002) may open new strategies for both forward and inverse modelings because of the increasing performance of computers, understanding of seismograms will still require interpretation in terms of high-frequency asymptotic approximations. Many observables, which can be deduced from ray theory, are still not strongly investigated. For example, differential information, such as the travel-time slope (Billette and Lambaré, 1998; Yanovskaya, 1996) or the polarization of the arrival (Le Bégat and Farra, 1997), are rapidly developing. Even the use of amplitudes is starting to be exploited using the asymptotic approaches. In this context, the present development of dense data acquisition will be a real challenge, where the assets of ray theory will certainly open roads to interesting opportunities for describing complex media.

The efforts for the adaptation of ray theory to more complex rheologies involving complex geometries, anisotropy, viscoelasticity (Ribodetti et al., 2000), or multiphase media have to be pursued. These new developments will certainly also offer important opportunities for the analysis of seismograms in the future.

Improvements on resolution of the seismic velocity model will be a key ingredient for the discrimination of different methods of forward modeling and inversion techniques (de Wit et al., 2012; Fichtner and Trampert, 2011).

Acknowledgments

We thank discussions with Bob Nowack, David Simpson, Colin Thomson, and Stéphane Operto. We gratefully thank Reda Baina, Jeannine Gagnepain-Beyneix, Stéphanie Gautier, David Le Meur, Guust Nolet, Bob Nowack, Stéphane Operto, Peter Shearer, and Martin Vallée for kindly providing us with figures. A careful review by Barbara Romanowicz improved the first edition. Authors would like to thank Bob Nowack for important suggestions in the elaboration of this second edition.

References

Abdullaev SS (1993) *Chaos and Dynamics of Rays in Waveguide Media*. Amsterdam: Gordon and Breach Science Publishers.

Abgrall R and Benamou JD (1999) Big ray tracing and eikonal solver on unstructured grids: A application to the computation of a multivalued travel-time field in the marmousi model. *Geophysics* 64: 230–239.

Abramowitz M and Stegun IA (1972) *Handbook of Mathematical Functions with Formulas, Graphs, and Mathematical Tables*. New York: Dover publications.

Achenbach JD and Gautesen AK (1977) Geometrical theory of diffraction for three-D elastodynamics. *Journal of Acoustical Society of America* 61: 413–421.

Aki K and Richards P (1980) *Quantitative Seismology: Theory and Methods*. San Francisco: W. H. Freeman & Co.

Albertin U, Yingst D, and Jaramillo H (2001) Comparing common-offset Maslov, Gaussian beam, and coherent state migration. In: *SEG Expanded Abstracts*, pp. 913–916. Society of Exploration Geophysics.

Amodei D, Keers H, Vasco D, and Johnson L (2006) Computation of uniform waveforms using complex rays. *Physical Review E* 73: 036704.

Arnold V (1976) *Les Méthodes Mathématiques de la Mécanique Classique*. Moscou: Mir Editions.

Astiz L, Earle P, and Shearer P (1996) Global stacking of broadband seismograms. *Seismological Research Letters* 67: 4.8–4.18.

Babič VM (1956) Ray method of the computation of the intensity of wave fronts. *Doklady Akademii Nauk SSSR* 110: 355–357 (in Russian).

Babič VM (1975) Ludwig's method and the boundary layer method in the problem of diffraction on a smooth body. *Journal of Soviet Mathematics* 3: 395–407.

Babič VM (1986) The mathematical theory of diffraction (a survey of some investigations carried out in the laboratory of mathematical problems of geophysics, leningrad branch of the mathematical institute), translated in English 1988. *Proceedings of the Steklov Institute of Mathematics* 2: 47–63.

Babič VM and Buldyrev VS (1991) *Short-Wavelength Diffraction Theory – Asymptotic Methods*, vol. 4. Berlin: Springer.

Babič VM and Kirpičnikova NY (1979) *The Boundary-Layer Method in Diffraction Problems*, vol. 3. Berlin: Springer.

Babic VM, Buldyrev VS, and Molotkov IA (1998) In: Tew R (ed. and revised), *The Space-Time Ray Method: Linear and Nonlinear Waves*, Rozenblum GV (trans.). New York: Cambridge University Press (Russian publication in 1985).

Backus GE (1964) Geographical interpretation of measurements of average phase velocities of surface waves over great circular and great semi-circular paths. *Bulletin of the Seismological Society of America* 54: 571–610.

Bai C-Y and Greenhalgh SA (2006) 3-D local earthquake hypocenter determination with an irregular shortest-path method. *Bulletin of the Seismological Society of America* 96: 2257–2268.

Bai C-Y, Greenhalgh S, and Zhou B (2007) 3D ray tracing with a modified shortest path method. *Geophysics* 72: T27–T36.

Bai C-Y, Huang Gj, and Zhao R (2009) 2d/3d multiply transmitted, converted and reflected arrivals in complex layered media with the modified shortest path method. *Geophysical Journal International* 179: 201–214.

Bai C-Y, Huang Gj, and Zhao R (2010) 2-d/3-d irregular shortest-path ray tracing for multiple arrivals and its applications. *Geophysical Journal International* 183: 1596–1612.

Bai C-Y, Peng J-B, and Greenhalgh S (2008) 3-D P-wave velocity structure of the crust beneath the Loess Plateau and surrounding regions of China. *Tectonophysics* 460: 278–287.

Baysal E, Kosloff DD, and Sherwood JWC (1983) Reverse time migration. *Geophysics* 48: 1514–1524.

Ben Menahem A and Gibson RL (1990) Scattering of elastic waves by localized anisotropic inclusions. *Journal of Acoustical Society of America* 87: 2300–2309.

Benamou JD (1996) Big ray tracing: Multivalued traveltime computation using viscosity solutions of the eikonal equation. *Journal of Computational Physics* 128: 463–474.

Benamou J-D (2003) An introduction to Eulerian geometrical optics (1992–2002). *Journal of Scientific Computing* 19(1–3): 63–93.

Benz HM, Chouet SA, Dawson PB, Lahr JC, Page RA, and Hole JA (1996) Three-dimensional P and S wave velocity structure of Redoubt Volcano, Alaska. *Journal of Geophysical Research* 101: 8111–8128.

Beydoun WB and Mendes M (1989) Elastic ray-Born – migration/inversion. *Geophysical Journal* 97: 151–160.

Beydoun WB and Tarantola A (1988) First Born and Rytov approximation: Modeling and inversion conditions in a canonical example. *Journal of Acoustical Society of America* 1045–1055: 1988.

Beylkin G (1985) Imaging of discontinuities in the inverse scattering problem by inversion of a causal generalized Radon transform. *Journal of Mathematical Physics* 26: 99–108.

Beylkin G and Burridge R (1990) Linearized inverse scattering problems in acoustics and elasticity. *Wave Motion* 12: 15–52.

Bigwaard H, Spakman W, and Engdahl ER (1998) Closing the gap between regional and global travel time tomography. *Journal of Geophysical Research* 103: 30055–30078.

Billette F and Lambaré G (1998) Velocity macro-model estimation from seismic reflection data by stereotomography. *Geophysical Journal International* 135: 671–680.

Billette F, Le Bégat S, Podvin P, and Lambaré G (2003) Practical aspects and applications of 2D stereotomography. *Geophysics* 68: 1008–1021.

Biondi B (1992) Solving the frequency dependent eikonal equation. In: *Expanded Abstracts*, pp. 1315–1319. Society of Exploration Geophysicists.

Bishop TN, Bube KP, Cutler RT, et al. (1985) Tomographic determination of velocity and depth in laterally varying media. *Geophysics* 50: 903–923.

Bleistein N (1984) *Mathematical Methods for Wave Phenomena*. London: Academic Press.

Bleistein N (1987) On the imaging of reflectors in the Earth. *Geophysics* 52: 931–942.

Bleistein N, Cohen JK, and Hagin FG (1987) Two and one half dimensional Born inversion with an arbitrary reference. *Geophysics* 52: 26–36.

Bokanowski O, Cheng Y, and Shu C-W (2011) A discontinuous galerkin solver for front propagation. *Journal of Scientific Computing* 33(2): 923–938.

Bokanowski O, Garcke J, Griebel M, and Klompmaker I (2013) An adaptive sparse grid semi-Lagrangian scheme for first order Hamilton–Jacobi bellman equations. *Journal of Scientific Computing* 55: 575–605.

Born M and Wolf E (1980) *Principles of Optics*, 6th edn. Pergamon Press.

Borovikov VA and Kinber BY (1974) Some problems in the asymptotic theory of diffraction. *Proceedings of the IEEE* 62: 1416–1437.

Boschi L, Becker TW, Soldati G, and Dziewonski AM (2006) On the relevance of Born theory in global seismic tomography. *Geophysical Research Letters* 33, L06302.

Bozdağ E, Trampert J, and Tromp J (2011) Misfit functions for full waveform inversion based on instantaneous phase and envelope measurements. *Geophysical Journal International* 185: 845–870.

Brown MG and Tappert FD (1987) Catastrophe theory, caustics and traveltime diagrams in seismology. *Geophysical Journal of the Royal Astronomical Society* 88: 217–229.

Buchal RN and Keller JB (1960) Boundary layer problems in diffraction theory. *Communications on Pure and Applied Mathematics* 13: 85–114.

Bullen KE and Bolt BA (1985) *An Introduction to the Theory of Seismology*. Berlin, Heidelberg: Cambridge University Press.

Burridge R (1976) *Some Mathematical Topics in Seismology*. New York: New York University, Courant Institute of Mathematical Sciences.

Burridge R and Weinberg H (1977) Horizontal rays and vertical modes. In: Keller JB and Papadakis JS (eds.) *Wave Propagation and Underwater Acoustics*, vol. 70, pp. 86–152. Berlin: Springer.

Buske S and Kästner U (2004) Efficient and accurate computation of seismic traveltimes and amplitudes. *Geophysical Prospecting* 52: 313–322.

Cagniard L (1939) *Réflexion et Réfraction des Ondes Séismiques Progressives*. Paris: Gauthier-Villars.

Cao S and Greenhalgh S (1994) Finite-difference solution of the eikonal equation using an efficient, first-arrival, wavefront tracking scheme. *Geophysics* 59: 632–643.

Červený V (1985) The application of ray tracing to the numerical modeling of seismic wavefields in complex structures. In: Helbig K and Treitel S (eds.) *Handbook of Geophysical Exploration, Section I: Seismic Exploration*, 15, pp. 1–124. London: G. Dohr, Geophysical Press.

Červený V (2001) *Seismic Ray Theory*. Cambridge: Cambridge University Press.

Červený V, Molotkov IA, and Pšenčik I (1977) *Ray Theory in Seismology*. Praha: Charles University Press.

Červený V, Popov MM, and Pšenčik I (1982) Computation of wave fields in inhomogeneous media – Gaussian beam approach. *Geophysical Journal of the Royal Astronomical Society* 70: 109–128.

Červený V and Pšenčík I (2005a) Plane waves in viscoelastic anisotropic media – I. Theory. *Geophysical Journal International* 161: 197–212.

Červený V and Pšenčík I (2005b) Plane waves in viscoelastic anisotropic media – II. Numerical examples. *Geophysical Journal International* 161: 197–212.

Červený V and Ravindra R (1971) *Theory of Seismic Head Waves*. Toronto: Toronto University Press.

Chaljub E, Capdeville Y, and Vilotte J-P (2003) Solving elastodynamics in a fluid–solid heterogeneous sphere: A parallel spectral element approximation on non-conforming grids. *Journal of Computational Physics* 187: 457–491.

Chapman CH (1974) The turning point of elastodynamic waves. *Geophysical Journal of the Royal Astronomical Society* 39: 673–704.

Chapman CH (1978) A new method of computing synthetic seismograms. *Geophysical Journal of the Royal Astronomical Society* 54: 481–518.

Chapman CH (1985) Ray theory and its extension: WKBJ and Maslov seismograms. *Journal of Geophysics* 58: 27–43.

Chapman CH (2004) *Fundamentals of Seismic Wave Propagation*. Cambridge: Cambridge University Press.

Chapman CH and Coates RT (1994) Generalized Born scattering in anisotropic media. *Wave Motion* 19: 309–341.

Chapman CH and Drummond R (1982) Body-wave seismograms in inhomogeneous media using Maslov asymptotic theory. *Bulletin of the Seismological Society of America* 72: S277–S317.

Chapman CH and Orcutt JA (1985) The computation of body wave synthetic seismograms in laterally homogeneous media. *Reviews of Geophysics* 23: 105–163.

Cheng L-T (2007) An efficient level set method for constructing wavefronts in three space dimensions. *Journal of Computational Physics* 226(2): 2250–2270.

Cheng Y and Shu C-W (2007) A discontinuous Galerkin finite element method for directly solving the Hamilton–Jacobi equations. *Journal of Computational Physics* 223: 398–415.

Chevrot S (2000) Multichannel analysis of shear wave splitting. *Journal of Geophysical Research* 105: 21579–21590.

Chevrot S (2002) Optimal measurement of relative and absolute delay-times by simulated annealing. *Geophysical Journal International* 151: 164–171.

Claerbout JF (1970) Coarse grid calculations of wave in inhomogeneous media with application to delineation of complicated seismic structure. *Geophysics* 35: 407–418.

Clarke TJ (1993a) The complete ordered ray expansion – I. Calculation of synthetic seismograms. *Geophysical Journal International* 115: 421–434.

Clarke TJ (1993b) The complete ordered ray expansion – II. Multiphase body wave tomography. *Geophysical Journal International* 115: 435–444.

Clayton RW and Stolt RH (1981) A Born-WKBJ inversion method for acoustic reflection data. *Geophysics* 46: 1558–1565.

Coates RT and Chapman CH (1990) Ray perturbation theory and the Born approximation. *Geophysical Journal International* 100: 379–392.

Cohen JK, Hagin FG, and Bleistein N (1986) Three-dimensional Born inversion with an arbitrary reference. *Geophysics* 51: 1552–1558.

Courant R and Hilbert D (1966) *Methods of Mathematical Physics*. New York: Wiley.

Crandall MG and Lions PL (1983) Viscosity solutions of Hamilton–Jacobi equations. *Transactions of the American Mathematical Society* 277(1): 1–42.

Crandall MG and Lions PL (1984) Two approximations of solutions of Hamilton–Jacobi equations. *Mathematics of Computation* 43(167): 1–19.

Cristiani E (2009) A fast marching method for Hamilton–Jacobi equations modeling monotone front propagations. *Journal of Scientific Computing* 39: 189–205.

Dahlen F (2005) Finite-frequency sensitivity kernels for boundary topography perturbations. *Geophysical Journal International* 162: 525–540.

Dahlen FA and Baig AM (2002) Fréchet kernels for body-wave amplitudes. *Geophysical Journal International* 150: 440–466.

Dahlen FA, Hung S-H, and Nolet G (2000) Fréchet kernels for finite-frequency traveltimes – I. Theory. *Geophysical Journal International* 141: 157–174.

Dahlen FA and Tromp J (1998) *Theoretical Global Seismology*. Princeton: Princeton University Press.

de Hoop AT (1960) A modification of Cagniard's method for solving seismic pulse problems. *Applied Scientific Research* B8: 349–356.

de Hoop AT (1990) Acoustic radiation from an impulsive point source in a continuously layered fluid – An analysis based on the Cagniard method. *Journal of Acoustical Society of America* 88: 2376–2388.

de Hoop MV and van der Hilst RD (2005) On sensitivity kernels for 'wave-equation' transmission tomography. *Geophysical Journal International* 160: 621–633.

de Kool M, Rawlinson N, and Sambridge M (2006) A practical grid-based method for tracking multiple refraction and reflection phases in three-dimensional heterogeneous media. *Geophysical Journal International* 167: 253–270.

de Wit RWL, Trampert J, and van der Hilst RD (2012) Toward quantifying uncertainty in travel time tomography using the null-space shuttle. *Journal of Geophysical Research* 117, B03301.

Deschamps GA (1971) Gaussian beams as a bundle of complex rays. *Electronics Letters* 7: 684–685.

Devaney A (1981) Inverse scattering theory within the Rytov approximation. *Optics Letters* 6: 374–376.

Dey-Sarkar SK and Chapman CH (1978) A simple method for the computation of body-wave seismograms. *Bulletin of the Seismological Society of America* 68: 1577–1593.

Dijkstra EW (1959) A note on two problems in connection with graphs. *Numerische Mathematik* 1: 269–271.

Eaton DWS (1993) Finite difference traveltime calculation for anisotropic media. *Geophysical Journal International* 114: 273–280.

Engquist B and Runborg O (1996) Multi-phase computation in geometrical optics. *Journal of Computational Applied Mathematics* 74: 175–192.

Engquist B and Runborg O (2003) Computational high frequency wave propagation. *Acta Numerica* 12: 181–266.

Engquist B, Runborg O, and Tornberg A-K (2002) High-frequency wave propagation by the segment projection method. *Journal of Computational Physics* 178: 373–390.

Farra V (1990) Amplitude computation in heterogeneous media by ray perturbation theory: A finite element approach. *Geophysical Journal International* 103: 341–354.

Farra V (1992) Bending method revisited: A Hamiltonian approach. *Geophysical Journal International* 109: 138–150.

Farra V (2005) First-order ray tracing for qS waves in inhomogeneous weakly anisotropic media. *Geophysical Journal International* 161: 309–324.

Farra V and Madariaga R (1987) Seismic waveform modeling in heterogeneous media by ray perturbation theory. *Journal of Geophysical Research* 92: 2697–2712.

Farra V and Madariaga R (1988) Non-linear reflection tomography. *Geophysical Journal* 95: 135–147.

Farra V, Virieux J, and Madariaga R (1989) Ray perturbation theory for interfaces. *Geophysical Journal International* 99: 377–390.

Fatemi E, Engquist B, and Osher S (1995) Numerical solution of the high frequency asymptotic expansion for the scalar wave equation. *Journal of Computation Physics* 120: 145–155.

Favier N and Chevrot S (2003) Sensitivity kernels for shear wave splitting in transverse isotropic media. *Geophysical Journal International* 153: 213–228.

Favier N, Chevrot S, and Komatitsch D (2004) Near-field influence on shear wave splitting and traveltime sensitivity kernels. *Geophysical Journal International* 156: 467–482.

Felsen LB (1976) Evanescent waves. *Journal of the Optical Society of America* 66: 751–760.

Felsen LB (1984) Geometrical theory of diffraction, evanescent waves, complex rays and Gaussian beams. *Geophysical Journal of the Royal Astronomical Society* 79: 77–88.

Fichtner A, Kennett BLN, Igel H, and Bunge H-P (2008) Theoretical background for continental and global scale full-waveform inversion in the time-frequency domain. *Geophysical Journal International* 175: 665–685.

Fichtner A, Kennett BLN, Igel H, and Bunge H-P (2009) Full waveform tomography for upper-mantle structure in the Australasian region using adjoint methods. *Geophysical Journal International* 179: 1703–1725.

Fichtner A and Trampert J (2011) Resolution analysis in full waveform inversion. *Geophysical Journal International* 187: 1604–1624.

Fock VA (1965) *Electromagnetic Diffraction and Propagation Problems*. Oxford: Pergamon Press.

Fomel S, Luo S, and Zhao H-K (2009) Fast sweeping method for the factored eikonal equations. *Journal of Computational Physics* 228(17): 6440–6445.

Fomel S and Sethian JA (2002) Fast phase space computation of multiple arrivals. *Proceedings of the National Academy of Sciences* 99(11): 7329–7334.

Font Y, Kao H, Lallemand S, Liu C-S, and Chiao J-Y (2004) Hypocentral determination offshore Eastern Taiwan using the Maximum Intersection method. *Geophysical Journal International* 158: 655–675.

Frazer LN and Sen MK (1985) Kirchhoff–Helmholtz reflection seismograms in a laterally inhomogeneous multi-layered elastic medium – I. Theory. *Geophysical Journal of the Royal Astronomical Society* 80: 121–147.

French WS (1974) Two-dimensional and three dimensional migration of model-experiment reflection profiles. *Geophysics* 39: 265–277.

French WS (1975) Computer migration of oblique seismic reflection profiles. *Geophysics* 40: 961–980.

Fuchs K and Müller G (1971) Computation of synthetic seismograms with the reflectivity method and comparison of observations. *Geophysical Journal of the Royal Astronomical Society* 23: 417–433.

Gauthier O, Virieux J, and Tarantola A (1986) Two-dimensional nonlinear inversion of seismic waveforms: Numerical results. *Geophysics* 51: 1387–1403.

Gautier S, Nolet G, and Virieux J (2008) Finite-frequency tomography in a crustal environment: Application to the western part of the Gulf of Corinth. *Geophysical Prospecting* 56: 493–503.

Gélis C, Virieux J, and Grandjean G (2007) 2D elastic full waveform inversion using Born and Rytov formulations in the frequency domain. *Geophysical Journal International* 168: 605–633.

Gentili S and Michelini A (2006) Automatic picking of P and S phases using a neural tree. *Journal of Seismology* 10: 39–63.

Gibson RL and Ben Menahem A (1991) Elastic wave scattering by anisotropic obstacles: Application to fractured volumes. *Journal of Geophysical Research* 96: 19905–19924.

Gilbert F and Backus GE (1966) Propagator matrices in elastic wave and vibration problems. *Geophysics* 31: 326–332.

Gilmore R (1981) *Catastrophe Theory for Scientists and Engineers*. New York: Wiley-Interscience.

Godunov SK (1959) A difference scheme for numerical computation of discontinuous solution of hyperbolic equation. *Matematicheskii Sbornik* 47: 271–306.

Goldstein H (1980) *Classical Mechanics*. Reading: Addison-Wesley Publishing Company.

Gray SH (1982) A geometric-optic serie and a WKB paradox. *Quarterly of Applied Mathematics* 40: 73–81.

Gray SH (1983) On the convergence of the time-domain Bremmer series. *Wave Motion* 5: 249–255.

Gray SH (2005) Gaussian beam migration of common-shot records. *Geophysics* 70(4): S71–S77.

Gray SH and Bleistein N (2009) True-amplitude Gaussian-beam migration. *Geophysics* 74(2): S11–S23.

Guillaume P, Lambaré G, Leblanc O, et al. (2011) Kinematic invariants: An efficient and flexible approach for velocity model building. In: *SEG Expanded Abstracts*, pp. 1805–1808. Society of Exploration Geophysics.

Hardy P (2003) High resolution tomographic mva with automation. In: *EAGE/SEG Research Workshop*, p. T27. European Association of Engineers and Geophysicist.

Hauser J, Sambridge M, and Rawlinson N (2006) Phase space methods for multi-arrival wavefronts. *Exploration Geophysics* 37: 331–339.

Hauser J, Sambridge M, and Rawlinson N (2008) Multiarrival wavefront tracking and its applications. *Geochemistry, Geophysics, Geosystems* 9: Q11001.

Hill DP (1973) Critical refracted waves in a spherically symmetric radially heterogeneous Earth model. *Geophysical Journal of the Royal Astronomical Society* 34: 149–179.

Hill NR (1990) Gaussian beam migration. *Geophysics* 55: 1416–1428.

Hill NR (2001) Prestack Gaussian-beam depth migration. *Geophysics* 66: 1240–1250.

Hole DP and Zelt BC (1995) 3-D finite difference reflection traveltimes. *Geophysical Journal International* 121: 427–434.

Hron F (1972) Numerical methods of ray generation in multilayered media. In: Bolt BA, Alder B, Fernbach S, and Rotenberg M (eds.) *Methods in Computational Physics*, vol. 12, pp. 1–34. New York: Academic Press.

Hron F and Chan GH (1995) Tutorial on the numerical modeling of edge diffracted waves by the ray method. *Studia Geophysica et Geodaetica* 39: 103–137.

Hron F, May BT, Covey JD, and Daley PF (1986) Synthetic seismic sections for acoustic, elastic, anisotropic and inhomogeneous layered media. *Geophysics* 51: 710–735.

Huang X and West GF (1997) Effects of weighting functions on Maslov uniform seismograms: A robust weighting method. *Bulletin of the Seismological Society of America* 87: 164–173.

Hudson JA and Heritage JR (1981) *Use of the Born Approximation in Seismic Scattering Problems*. Cambridge: Cambridge University Press.

Hung S-H, Dahlen FA, and Nolet G (2000) Fréchet kernels for finite-frequency traveltimes – II. Examples. *Geophysical Journal International* 141: 175–203.

Ikelle L, Diet JP, and Tarantola A (1988) Linearized inversion of multioffset seismic reflection data in the $\omega - k$ domain: Depth-dependent reference medium. *Geophysics* 53: 50–64.

Iturben I, Roux P, Virieux J, and Nicolas B (2009) Travel-time sensitivity kernels versus diffraction patterns obtained through double beam-forming in shallow water. *Journal of Acoustic Society of America* 126(2): 713–720.

Jannane M, Beydoun W, Crase E, et al. (1989) Wavelengths of Earth structures that can be resolved from seismic reflection data. *Geophysics* 54: 906–910.

Jiang G-S and Peng D (2000) Weighted ENO schemes for Hamilton–Jacobi equations. *SIAM Journal on Scientific Computing* 21: 2126–2143.

Jiang G-S and Shu C-W (1996) Efficient implementation of weighted eno schemes. *Journal of Computational Physics* 126: 202–228.

Jin S, Liu H, Osher S, and Tsai R (2005) Computing multi-valued physical observables for the high frequency limit of symmetric hyperbolic systems. *Journal of Computational Physics* 210: 497–518.

Jin S, Madariaga R, Virieux J, and Lambaré G (1992) Two-dimensional asymptotic iterative elastic inversion. *Geophysical Journal International* 108: 575–588.

Jones IF (2013) Tutorial: Transforms, orthogonality, eigenvectors, and eigenvalues. *First Break* 31: 51–61.

Kamei R, Pratt RG, and Tsuji T (2012) Waveform tomography imaging of a megasplay fault system in the seismogenic Nankai subduction zone. *Earth and Planetary Science Letters* 317–318: 343–353.

Karal F and Keller JB (1959) Elastic wave propagation in homogeneous and inhomogeneous media. *Journal of the Optical Society of America* 31: 694–705.

Katzman R, Zhao L, and Jordan TH (1998) High-resolution, two-dimensional vertical tomography of the central pacific mantle using scs reverberations and frequency-dependent travel times. *Journal of Geophysical Research* 103: 17933–17971.

Keilis-Borok VI (1989) *Seismic Surface Waves in a Laterally Inhomogeneous Earth*. Dordrecht: Kluwer Academic Publishers.

Keller JB (1962) A geometrical theory of diffraction. *Journal of the Optical Society of America* 52: 116–130.

Keller JB (1969) Accuracy and validity of the Born and Rytov approximations. *Journal of the Optical Society of America* 59: 1003–1004.

Keller JB (1971) Complex rays with an application to Gaussian beams. *Journal of the Optical Society of America* 61: 40–43.

Keller HB and Perozzi PJ (1983) Fast seismic ray tracing. *SIAM Journal of Applied Mathematics* 43: 981–992.

Kendall J-M and Nangini C (1996) Lateral variations in D" below the Caribbean. *Geophysical Research Letters* 23: 399–402.

Kendall J-M and Thomson CJ (1993) Maslov ray summation, pseudo-caustics, Lagrangian equivalence and transient seismic waveforms. *Geophysical Journal International* 113: 186–214.

Kennett BLN (1983) *Seismic Wave Propagation in Stratified Media*. Cambridge: Cambridge University Press.

Kim S (2001) An O(n) level set method for Eikonal equations. *SIAM Journal of Scientific Computing* 22: 2178–2193.
Kimmel R and Sethian JA (1998) Fast marching methods on triangulated domains. *Proceedings of the National Academy of Sciences of the United States of America* 95: 8341–8445.
Klauder JR (1987a) Global uniform asymptotic wave-equation solutions for large wavenumbers. *Annals of Physics* 180: 108–151.
Klauder JR (1987b) New asymptotics for old wave equations. *Science* 239: 760–762.
Klem-Musatov KD (1995) *Theory of Seismic Diffraction*. Tulsa: Society of Exploration Geophysicists.
Klimeš L and Kvaskička M (1994) 3-D network ray tracing. *Geophysical Journal International* 116: 726–738.
Kolb P, Collino F, and Lailly P (1986) Prestack inversion of 1-D medium. *Proceedings of the IEEE* 74: 498–508.
Komatitsch D, Ritsema J, and Tromp J (2002) The spectral-element method, beowulf computing, and global seismology. *Science* 298: 1737–1742.
Körnig M (1995) Cell ray tracing for smooth, isotropic media: A new concept based on a generalized analytic solution. *Geophysical Journal International* 123: 391–408.
Kosloff D and Baysal E (1983) Migration with the full acoustic equation. *Geophysics* 48: 677–687.
Kravtsov YA (1964) On a modification of the method of geometrical optics. *Radiofizika* 7: 664–673.
Kravtsov YA (1968) Two new asymptotic methods in the theory of wave propagation in inhomogeneous media(review). *Soviet Physics – Acoustics* 14: 1–17.
Kravtsov YA and Orlov YI (1990) *Geometrical Optics of Inhomogeneous Media*. Berlin: Springer.
Kristeková M, Kristek J, and Moczo P (2009) Time-frequency misfit and goodness-of-fit criteria for quantitative comparison of time signals. *Geophysical Journal International* 178: 813–825.
Kristeková M, Kristek J, Moczo P, and Day SM (2006) Misfit criteria for quantitative comparison of seismograms. *Bulletin of the Seismological Society of America* 96(5): 1836–1850.
Kvasnička M and Janský J (1999) Fresnel volumes corresponding to PKP waves in the IASP91 model. *Journal of Seismology* 3: 375–391.
Lailly P (1983) The seismic inverse problem as a sequence of before stack migrations. In: Robinson E, Bednar J, and Weglein A (eds.) *Conference on Inverse Scattering, Theory and Application, SIAM, Philadelphia*, pp. 206–220. Society for Industrial and Applied Mathematics.
Lambaré G (2008) Stereotomography. *Geophysics* 73(5): VE25–VE34.
Lambaré G, Lucio PS, and Hanyga A (1996) Two-dimensional multivalued traveltime and amplitude maps by uniform sampling of ray field. *Geophysical Journal International* 125: 584–598.
Lambaré G, Operto S, Podvin P, Thierry P, and Noble M (2003) 3-D ray + Born migration/inversion – Part 1. Theory. *Geophysics* 68: 1348–1356.
Lambaré G, Virieux J, Madariaga R, and Jin S (1992) Iterative asymptotic inversion in the acoustic approximation. *Geophysics* 57: 1138–1154.
Langer RE (1937) On the connection formulas and the solution of the wave equation. *Physical Reviews* 51: 669–676.
Latham G, Ewing M, Dorman J, et al. (1971) Moonquakes. *Science* 174: 687–692.
Latorre D, Virieux J, Monfret T, et al. (2004) A new seismic tomography of Aigion area (Gulf of Corinth, Greece) from the 1991 data set. *Geophysical Journal International* 159: 1013–1031.
Lay T and Garnero EJ (2004) Core mantle boundary structure and processes. In: Sparks RSJ and Hawkesworth CJ (eds.) *The State of the Planet: Frontiers and Challenges in Geophysics*. *Geophysical Monograph Series*, 150: pp. 25–41. Washington, DC: AGU.
Lay T and Wallace TC (1995) *Modern Global Seismology*. Academic Press.
Le Bégat S and Farra V (1997) P-wave travel time polarization tomography of VSP data. *Geophysical Journal International* 131: 100–114.
Le Meur H, Virieux J, and Podvin P (1997) Seismic tomography of the gulf of Corinth: A comparison of methods. *Annali Di Geofisica* XL: 1–24.
Lecomte I (1993) Finite difference calculation of first traveltimes in anisotropic media. *Geophysical Journal International* 113: 318–342.
Lee E-J and Chen P (2013) Automatic seismic waveform analysis for full 3d waveform inversions. *Geophysical Journal International* 194: 572–589.
Leidenfrost A, Ettrich N, Gajewski D, and Kosloff D (1999) Comparison of six different methods for calculating traveltimes. *Geophysical Prospecting* 47: 269–297.
Lelièvre PG, Farquharson CG, and Hurich CA (2011a) Computing first-arrival seismic traveltimes on unstructured 3-D tetrahedral grids using the fast marching method. *Geophysical Journal International* 184: 885–896.
Lelièvre PG, Farquharson CG, and Hurich CA (2011b) Inversion of first-arrival seismic traveltimes without rays, implemented on unstructured grids. *Geophysical Journal International* 185: 749–763.
Lehmann I (1936) P', Publications du Bureau Central Séismologique International, série A. *Travaux Scientifiques* 14: 87–115.
Leung S, Qian J, and Osher S (2004) A level set method for three-dimensional paraxial geometrical optics with multiple sources. *Computations in Mathematical Science* 2: 643–672.
Levander AR (1988) Fourth-order finite-difference P-SV seismograms. *Geophysics* 53(11): 1425–1436.
Li XD and Romanowicz B (1995) Comparison of global waveform inversions with and without considering cross branch coupling. *Geophysical Journal International* 121: 695–709.
Li F, Shu C-W, Zhang Y-T, and Zhao H (2008) A second order discontinuous Galerkin fast sweeping method for Eikonal equations. *Journal of Computational Physics* 227: 8191–8208.
Li XD and Tanimoto T (1993) Waveforms of long period body waves in a slightly aspherical earth. *Geophysical Journal International* 112: 92–112.
Liu HL, Cheng L-T, and Osher S (2006) A level set framework for capturing multivalued solutions to nonlinear first-order equations. *Journal of Scientific Computing* 29(3): 353–373.
Liu X, Osher S, and Chan T (1994) Weighted essentially non-oscillatory schemes. *Journal of Computational Physics* 115: 200–212.
Lomax A (1999) Path-summation waveforms. *Geophysical Journal International* 138: 702–716.
Lomax A, Virieux J, Volant P, and Berge C (2000) Probabilistic earthquake location in 3D and layered models: Introduction of a Metropolis–Gibbs method and comparison with linear locations. In: Thurber CH and Rabinowitz N (eds.) *Advances in Seismic Event Location,* 281, pp. 101–134. Amsterdam: Kluwer Academic Pub.
Lucio PS, Lambaré G, and Hanyga A (1996) 3D multivalued travel time and amplitude maps. *Pure and Applied Geophysics* 148: 113–136.
Ludwig D (1966) Uniform asymptotic expansions at a caustic. *Communications on Pure and Applied Mathematics* 19: 215–250.
Luneberg RK (1964) *Mathematical Theory of Optics*. Berkeley: University of California Press.
Luo S and Qian J (2011) Factored singularities and high-order Lax–Friedrichs sweeping schemes for point-source traveltimes and amplitudes. *Journal of Computational Physics* 230: 4742–4755.
Luo S and Qian J (2012) Fast sweeping methods for factored anisotropic eikonal equations: Multiplicative and additive factors. *Journal of Scientific Computing* 52: 360–382.
Luo Y and Schuster GT (1991) Wave-equation travel time tomography. *Geophysics* 56: 645–653.
Madariaga R (1984) Gaussian beam synthetic seismograms in a vertically varying medium. *Geophysical Journal of the Royal Astronomical Society* 79: 589–612.
Maggi A, Tape C, Chen M, Chao D, and Tromp J (2009) An automated time-window selection algorithm for seismic tomography. *Geophysical Journal International* 178: 257–281.
Marfurt KJ (1984) Accuracy of finite-difference and finite-element modeling of the scalar and elastic wave equations. *Geophysics* 49: 533–549.
Marquering H, Dahlen FA, and Nolet G (1999) Three-dimensional sensitivity kernels for finite-frequency traveltimes: The banana-doughnut paradox. *Geophysical Journal International* 137: 805–815.
Marquering H, Nolet G, and Dahlen FA (1998) Three-dimensional waveform sensitivity kernels. *Geophysical Journal International* 132: 521–534.
Maslov VP and Fedoriuk MV (1981) *Semi-Classical Approximation in Quantum Mechanics*. Dordrecht: D. Reidel Publication.
McMechan GA (1983) Migration by extrapolation of time-dependent boundary values. *Geophysical Prospecting* 31: 413–420.
Min C (2004) Local level set method in high dimension and codimension. *Journal of Computational Physics* 200: 368–382.
Moczo P, Robertsson JOA, and Eisner L (2006) The finite-difference time-domain method for modelling of seismic wave propagation. In: Wu R-S and Maupin V (eds.) *Advances in Wave Propagation in Heterogeneous Earth*. Elsevier-Pergamon.
Montelli R, Nolet G, Dahlen FA, and Masters G (2006a) A catalogue of deep mantle plumes. New results from finite-frequency tomography. *Geochemistry, Geophysics, Geosystems* 7: Q11007.
Montelli R, Nolet G, Dahlen FA, and Masters G (2006b) Comment on 'banana-doughnut kernels and mantle tomography' by van der Hilst and de Hoop. *Geophysical Journal International* 167: 1204–1210.

Montelli R, Nolet G, Dahlen FA, Masters G, Engdahl ER, and Hung SH (2004) Finite-frequency tomography reveals a variety of plumes in the mantle. *Science* 303: 338–343.

Montelli R, Nolet G, Masters G, Dahlen FA, and Hung SH (2004) P and PP global travel time tomography. *Geophysical Journal International* 158: 637–654.

Morse PM and Feshbach H (1953) *Methods of Theoretical Physics*. New York: McGraw Hill.

Moser TJ, Nolet G, and Snieder R (1992) Ray bending revisited. *Bulletin of the Seismological Society of America* 82: 259–288.

Moser TJ, van Eck T, and Nolet G (1992) Hypocenter determination in strongly heterogeneous earth models using the shortest path method. *Journal of Geophysical Research* 97: 6563–6572.

Nahamoo D, Pan S, and Kak A (1984) Synthetic aperture diffraction tomography and its interpolation-free computer implementation. *IEEE Transactions on Sonics and Ultrasonic* 4(SU31): 218–228.

Nakanishi I and Yamaguchi K (1986) A numerical experiment on nonlinear image reconstruction from first-arrival times for two-dimensional island arc structures. *Journal of Physics of the Earth* 34: 271–284.

Ni S, Cormier VF, and Helmberger DV (2003) A comparison of synthetic seismograms for 2D structures: Semianalytical versus numerical. *Bulletin of the Seismological Society of America* 93: 2752–2757.

Nolet G (1987) *Seismic Tomography: With Applications in Global Seismology and Exploration Geophysics*. *Seismology and Exploration Geophysics*, vol. 5. Springer.

Nolet G (2008) *A Breviary of Seismic Tomography: Imaging the Interior of the Earth and Sun*. Cambridge: Cambridge University Press.

Nowack RL (2003) Calculating of synthetic seismograms with Gaussian beams. *Pure and Applied Geophysics* 160: 487–507.

Nowack RL and Stacy SM (2002) Synthetic seismograms and wide-angle seismic attributes for the Gaussian beam and reflectivity methods for models with interfaces and velocity gradients. *Pure and Applied Geophysics* 159: 1447–1464.

Operto S, Ravaut C, Improta L, Virieux J, Herrero A, and Dell'Aversana P (2004) Quantitative imaging of complex structures from dense wide-aperture seismic data by multiscale traveltime and waveform inversions: A case study. *Geophysical Prospecting* 52: 625–651.

Operto S, Virieux J, Dessa JX, and Pascal G (2006) Crustal imaging from multifold ocean bottom seismometers data by frequency-domain full-waveform tomography: Application to the eastern Nankai trough. *Journal of Geophysical Research* 111: B09306. http://dx.doi.org/10.1029/2005JB003835.

Operto S, Xu S, and Lambaré G (2000) Can we quantitatively image complex models with rays? *Geophysics* 65: 1223–1238.

Osher S, Cheng L-T, Kang M, Shim H, and Tsai Y-H (2002) Geometric optics in a phase-space-based level set and Eulerian framework. *Journal of Computational Physics* 179: 622–648.

Osher SJ and Sethian J (1988) Fronts propagating with curvature dependent speed: Algorithms based on Hamilton–Jacobi formulations. *Journal of Computational Physics* 79: 12–49.

Pavlis GL, Sigloch K, Burdick S, Fouch MJ, and Vernon FL (2012) Unraveling the geometry of the Farallon plate: Synthesis of three-dimensional imaging results from USArray. *Tectonophysics* 532–535: 82–102.

Pekeris CL (1955a) The seismic buried pulse. *Proceedings of the National Academy of Sciences of the United States of America* 41: 629–639.

Pekeris CL (1955b) The seismic surface pulse. *Proceedings of the National Academy of Sciences of the United States of America* 41: 469–480.

Pereyra V (1992) Two-point ray tracing in a general 3D media. *Geophysical Prospecting* 40: 267–287.

Pereyra V, Lee WHK, and Keller HB (1980) Solving two-point seismic-ray tracing problems in a heterogeneous medium. Part 1. A general adaptive finite difference method. *Bulletin of the Seismological Society of America* 70: 79–99.

Pica A (1997) Fast and accurate finite-difference solutions of the 3-D eikonal equation parameterized in celerity. In: *Expanded Abstracts*, pp. 1774–1777. Society of Exploration Geophysics.

Pica A (1998) Resolution of the 3-D Eikonal equation parametrized in celerity in weak TI media. In: Expanded Abstracts, pp. 1–23. European Association of Exploration Geophysics.

Pica A, Diet JP, and Tarantola A (1990) Nonlinear inversion of seismic reflection data in laterally invariant medium. *Geophysics* 55: 284–292.

Plessix RE (2006) A review of the adjoint-state method for computing the gradient of a functional with geophysical applications. *Geophysical Journal International* 167(2): 495–503.

Podvin P and Lecomte I (1991) Finite difference computation of traveltimes in very contrasted velocity models: A massively parallel approach and its associated tools. *Geophysical Journal International* 105: 271–284.

Popov MM (1982) A new method of computation of wave fields using Gaussian beams. *Wave Motion* 4: 85–95.

Popov MM and Camerlynch C (1996) Second term of the ray series and validity of the ray theory. *Journal of Geophysical Research* 101: 817–896.

Popov MM and Pšenčík I (1978) Computation of ray amplitudes in inhomogeneous media with curved interfaces. *Studia Geophysica et Geodaetica* 22: 248–258.

Popovici AM and Sethian JA (2002) 3D imaging using higher order fast marching traveltimes. *Geophysics* 67: 604–609.

Pratt RG, Shin C, and Hicks GJ (1998) Gauss-Newton and full Newton methods in frequency-space seismic waveform inversion. *Geophysical Journal International* 133: 341–362.

Pratt RG, Song ZM, Williamson PR, and Warner M (1996) Two-dimensional velocity models from wide-angle seismic data by wavefield inversion. *Geophysical Journal International* 124: 323–340.

Press WH, Vettering WT, Teukolsky SA, and Flannery BP (1994) *Numerical Recipes in Fortran*, 2nd edn. Cambridge: Cambridge University Press.

Pšenčik I and Farra V (2005) First-order ray tracing for qP waves in inhomogeneous weakly anisotropic media. *Geophysics* 70: D65–D67.

Qian J and Leung S (2004) A level set based Eulerian method for paraxial multivalued traveltimes. *Journal of Computational Physics* 197: 711–736.

Qian J and Leung S (2006) A local level set method for paraxial geometrical optics. *SIAM Journal on Scientific Computing* 28(1): 206–223.

Qian J and Symes WW (2002a) Finite-difference quasi-P traveltimes for anisotropic media. *Geophysics* 67: 147–155.

Qian J and Symes WW (2002b) An adaptive finite-difference method for traveltimes and amplitudes. *Geophysics* 67: 167–176.

Qian J, Zhang Y-T, and Zhao H-K (2007) A fast sweeping method for static convex Hamilton–Jacobi equations. *Journal of Scientific Computing* 31: 237–271.

Qin F, Luo Y, Olsen KB, Cai W, and Schuster GT (1992) Finite-difference solution of the eikonal equation along expanding wavefronts. *Geophysics* 57: 478–487.

Qin F and Schuster GT (1993) First-arrival travel-time calculation for anisotropic media. *Geophysics* 58: 1349–1358.

Qiu J and Shu C-W (2005) Hermite WENO schemes for Hamilton–Jacobi equations. *Journal of Computational Physics* 204: 82–99.

Rawlinson N, Hauser J, and Sambridge M (2007) Seismic ray tracing and wavefront tracking in laterally heterogeneous media. *Advances in Geophysics* 49: 203–267.

Rawlinson N and Sambridge M (2004a) Multiple reflection and transmission phases in complex layered media using a multistage fast marching method. *Geophysics* 69(5): 1328–1350.

Rawlinson N and Sambridge M (2004b) Wave front evolution in strongly heterogeneous layered media using the fast marching method. *Geophysical Journal International* 156: 631–647.

Rawlinson N, Sambridge M, and Hauser J (2010) Multipathing, reciprocal traveltime fields and raylets. *Geophysical Journal International* 181: 1077–1092.

Ribodetti A, Operto S, Virieux J, Lambaré G, Valéro H-P, and Gibert D (2000) Asymptotic viscoacoustic diffraction tomography of ultrasonic laboratory data: A tool for rock properties analysis. *Geophysical Journal International* 140: 324–340.

Richards PG (1973) Calculation of body waves for caustics and tunnelling core phases. *Geophysical Journal of the Royal Astronomical Society* 66: 701–718.

Richards PG and Frasier CW (1976) Scattering of elastic waves from depth-dependent inhomogeneities. *Geophysics* 41: 441–458.

Roe PL (1981) Approximate riemann solvers, parameter vectors and difference schemes. *Journal of Computational Physics* 43(2): 357–372.

Rowe CA, Aster RC, Borchers B, and Young CJ (2002) An automatic, adaptive algorithm for refining phase picks in large seismic data sets. *Bulletin of the Seismological Society of America* 92: 1660–1674.

Rytov SM, Kravtsov YA, and Tatarskii VI (1987) *Principles of Statistical Radiophysics*. Berlin: Springer.

Ryzhik L, Papanicolaou G, and Keller JB (1996) Transport equations for elastic and other waves in random media. *Wave Motion* 24(4): 327–370.

Sadeghi H, Suzuki S, and Takenaka H (1999) A two-point, three-dimensional seismic ray tracing using genetic algorithms. *Physical Earth Planetary Interiors* 113: 355–365.

Sambridge MS and Kennett BLN (1990) Boundary value ray tracing in a heterogeneous medium: A simple and versatile algorithm. *Geophysical Journal International* 101: 157–168.

Samuelides Y (1998) Velocity shift using the Rytov approximation. *Journal of the Acoustical Society of America* 104: 2596–2603.

Sandberg K and Beylkin G (2009) Full-wave-equation depth extrapolation for migration. *Geophysics* 74(6): WCA121–WCA128.

Satriano C, Zollo A, and Rowe C (2008) Iterative tomographic analysis based on automatic refined picking. *Geophysical Prospecting* 56(4): 467–475.

Schlottmann RB (1999) A path integral formulation of acoustic wave propagation. *Geophysical Journal International* 137: 353–363.
Scholte JGJ (1962) Oblique propagation of waves in inhomogeneous media. *Geophysical Journal of the Royal Astronomical Society* 7: 244–261.
Serna S and Qian J (2006) Fifth-order weighted power-ENO schemes for Hamilton–Jacobi equations. *Journal of Scientific Computing* 29: 57–81.
Sethian JA (1999) *Level Set Methods and Fast Marching Methods*. Cambridge: Cambridge University Press.
Sethian JA (2001) Evolution, implementation, and application of level set and fast marching methods for advancing fronts. *Journal of Computational Physics* 169: 503–555.
Sethian JA and Popovici AM (1999) 3-D traveltime computation using the fast marching method. *Geophysics* 64: 516–523.
Shaw PR (1986) The accuracy of models derived by WKBJ waveform inversion. *Geophysical Journal of the Royal Astronomical Society* 85: 291–313.
Shu C-W and Osher S (1988) Efficient implementation of essentially non-oscillatory shock-capturing schemes. *Journal of Computational Physics* 77: 439–471.
Shu C-W and Osher S (1989) Efficient implementation of essentially non-oscillatory shock-capturing schemes, ii. *Journal of Computational Physics* 83: 32–78.
Sigloch K (2011) Mantle provinces under North America from multifrequency P wave tomography. *Geochemistry, Geophysics, Geosystems* 18(2): Q02W08.
Sigloch K, McQuarrie M, and Nolet G (2008) Two-stage subduction history under north America inferred from multiple-frequency tomography. *Nature Geosciences* 1: 458–462.
Sigloch K and Nolet G (2006) Measuring finite-frequency body-wave amplitudes and traveltimes. *Geophysical Journal International* 167(1): 271–287.
Siliqi R, Herrmann P, Prescott A, and Capar L (2007) Automatic dense high order RMO picking. In: *EAGE Expanded Abstracts*, p. P037. European Association of Geoscientists and Engineers.
Siliqi R and Talaalout A (2009) Structurally coherent wide azimuth residual move out surfaces. In: *SEG Expanded Abstracts*, pp. 4039–4043. Society of Exploration Geophysics.
Slawinski MA (2003) *Seismic waves and rays in elastic media. Handbook of Geophysical Exploration Seismic Exploration*, vol. 34. Elsevier Science, Klaus Helbig and Sven Treitel.
Snieder R and Spencer C (1993) A unified approach to ray bending, ray perturbation and paraxial ray theory. *Geophysical Journal International* 115: 456–470.
Steinhoff J, Fan M, and Wang L (2000) A new eulerian method for the computation of propagating short acoustic and electromagnetic pulses. *Journal of Computational Physics* 157(2): 683–706.
Symes W and Qian J (2003) A slowness matching eulerian method for multivalued solutions of eikonal equations. *Journal of Scientific Computing* 19(1–3): 501–526.
Taillandier C, Noble M, Chauris H, and Calandra H (2009) First-arrival travel time tomography based on the adjoint state method. *Geophysics* 74(6): WCB1–WCB10.
Tanimoto T (1995) Formalism for traveltime inversion with finite frequency effects. *Geophysical Journal International* 121: 103–110.
Tape C, Liu Q, Maggi A, and Tromp J (2010) Seismic tomography of the southern California crust based on spectral-element and adjoint methods. *Geophysical Journal International* 180: 433–462.
Tape C, Liu Q, and Tromp J (2007) Finite-frequency tomography using adjoint methods-methodology and examples using membrane surface waves. *Geophysical Journal International* 168: 1105–1129.
Tarantola A (1984a) Inversion of seismic reflection data in the acoustic approximation. *Geophysics* 49: 1259–1266.
Tarantola A (1984b) Linearized inversion of seismic reflection data. *Geophysical Prospecting* 32: 998–1015.
Tarantola A (1986) A strategy for non linear inversion of seismic reflection data. *Geophysics* 51: 1893–1903.
Tarantola A (1987) *Inverse Problem Theory: Methods for Data Fitting and Model Parameter Estimation*. Netherlands: Elsevier.
Thierry P, Lambaré G, Podvin P, and Noble M (1999) 3-D preserved amplitude prestack depth migration on a workstation. *Geophysics* 64: 222–229.
Thierry P, Operto S, and Lambaré G (1999) Fast 2D ray-Born inversion/migration in complex media. *Geophysics* 64: 162–181.
Thomson CJ (1989) Corrections for grazing rays in 2-D seismic modelling. *Geophysical Journal* 96: 415–446.
Thomson CJ (1990) Corrections for critical rays in 2-D seismic modelling. *Geophysical Journal International* 103: 171–210.
Thomson CJ (2001) Seismic coherent states and geometrical spreading. *Geophysical Journal International* 144: 320–342.
Thomson CJ (2004) Coherent-state analysis of the seismic head wave problem: An overcomplete representation and its relationship to rays and beams. *Geophysical Journal International* 157: 1189–1205.
Tian Y, Sigloch K, and Nolet G (2009) Multiple-frequency SH-wave tomography of the western US upper mantle. *Geophysical Journal International* 178(3): 1384–1402.
Tian Y, Zhou Y, Sigloch K, Nolet G, and Laske G (2011) Structure of the North American mantle constrained by simultaneous inversion of multiple-frequency SH, SS, and love waves. *Journal of Geophysical Research* 116: B02307.
Toomey DR, Solomon SC, and Purdy GM (1994) Tomographic imaging of the shallow crustal structure of the east pacific rise at 930'n. *Journal of Geophysical Research* 88: 24135–24157.
Trampert J and Spetzler J (2006) Surface wave tomography: Finite frequency effects lost in the null space. *Geophysical Journal International* 164: 394–400.
Traonmilin Y, Lambaré G, Herrmann P, Deladerriere N, and Garceran K (2009) Multi-dip estimation in n dimensions. In: *EAGE Expanded Abstracts*, p. P083. EAGE.
Tromp J, Tape C, and Liu Q (2005) Seismic tomography, adjoint methods, time reversal and banana-doughnut kernels. *Geophysical Journal International* 160: 195–216.
Um J and Thurber C (1987) A fast algorithm for two-point seismic ray tracing. *Bulletin of the Seismological Society of America* 77: 972–986.
Ursin B and Tygel M (1997) Reciprocal volume and surface scattering integrals for anisotropic elastic media. *Wave Motion* 26: 31–42.
van der Hilst RD and de Hoop MV (2005) Banana-doughnut kernels and mantle tomography. *Geophysical Journal International* 163: 956–961.
van Trier J and Symes WW (1991) Upwind finite-difference calculation of traveltimes. *Geophysics* 56(6): 812–821.
Verweij MD and de Hoop AT (1990) Determination of seismic wavefields in arbitrarily continuous layered media using the modified Cagniard method. *Geophysical Journal International* 103: 731–754.
Vidale D (1988) Finite-difference calculation of travel time. *Bulletin of the Seismological Society of America* 78: 2062–2076.
Vidale D (1990) Finite-difference calculation of traveltimes in three dimensions. *Geophysics* 55: 521–526.
Vinje V, Iversen E, Astebøl K, and Gjøystdal H (1996a) Estimation of multivalued arrivals in 3D models using wavefront construction—part I. *Geophysical Prospecting* 44: 819–842.
Vinje V, Iversen E, Astebøl K, and Gjøystdal H (1996b) Estimation of multivalued arrivals in 3D models using wavefront construction-part II: Tracing and interpolation. *Geophysical Prospecting* 843–858.
Vinje V, Iversen E, and Gjøystdal H (1993) Traveltime and amplitude estimation using wavefront construction. *Geophysics* 58: 1157–1166.
Virieux J (1986) P-SV wave propagation in heterogeneous media, velocity-stress finite difference method. *Geophysics* 51: 889–901.
Virieux J (1991) Fast and accurate ray tracing by Hamiltonian perturbation. *Journal of Geophysical Research* 96: 579–594.
Virieux J (1996) Seismic ray tracing. In: Boschi E, Ekström G, and Morelli A (eds.) *Seismic Modelling of Earth Structure*, pp. 223–304. Bologna: Editrice Compositori.
Virieux J and Farra V (1991) Ray tracing in 3-D complex isotropic media: An analysis of the problem. *Geophysics* 56: 2057–2069.
Virieux J, Farra V, and Madariaga R (1988) Ray tracing for earthquake location in laterally heterogeneous media. *Journal of Geophysical Research* 93: 1116–1120.
Virieux J, Garnier N, Blanc E, and Dessa J-X (2004) Paraxial ray tracing for atmospheric wave propagation. *Geophysical Research Letters* 31: L20106. http://dx.doi.org/10.1029/2004GL020514.
Wang P, de Hoop MV, and van der Hilst RD (2008) Imaging the lowermost mantle (D) and the core-mantle boundary with SKKS coda waves. *Geophysical Journal International* 175: 103–115.
Wasow W (1965) *Asymptotic Expansions of Ordinary Differential Equations*, vol. 14. New York: Interscience Publishers, Wiley.
Weber M (1988) Computation of body-wave seismograms in absorbing 2-D media using the Gaussian beam method: Comparison and exact methods. *Geophysical Journal* 92: 9–24.
White BS, Norris A, Bayliss A, and Burridge R (1987) Some remarks on the Gaussian beam summation method. *Geophysical Journal of the Royal Astronomical Society* 89: 579–636.
Woodhouse JH (1974) Asymptotic results for elastodynamic propagator matrices in plane stratified and spherically stratified Earth models. *Geophysical Journal of the Royal Astronomical Society* 37: 263–280.
Woodward MJ (1992) Wave-equation tomography. *Geophysics* 57: 15–26.
Wu R-S (1985) Gaussian beams, complex rays, and analytic extension of the green's function in smoothly inhomogeneous media. *Geophysical Journal of the Royal Astronomical Society* 83: 93–110.
Wu RS (1989) The perturbation method in elastic wave scattering. *Pure and Applied Geophysics* 131: 605–638.

Xie X-B and Yang H (2008) The finite-frequency sensitivity kernel for migration residual moveout and its applications un migration velocity analysis. *Geophysics* 73(6): S241–S249.

Xu S, Chauris H, Lambaré G, and Noble M (2001) Common angle image gather: A strategy for imaging complex media. *Geophysics* 66: 1877–1894.

Xu S and Lambaré G (2004) Fast migration/inversion with multivalued rayfields: Part I-Method, validation test, and application in 2D to Marmousi. *Geophysics* 69: 1311–1319.

Xu S, Lambaré G, and Calandra H (2004) Fast migration/inversion with multivalued rayfields: Part 2 – Applications to the 3D SEG/EAGE salt model. *Geophysics* 69: 1320–1328.

Yan J and Osher S (2011) A local discontinuous Galerkin method for directly solving Hamilton–Jacobi equations. *Journal of Computational Physics* 230: 232–244.

Yanovskaya TB (1996) Ray tomography based on azimuthal anomalies. *Pure and Applied Geophysics* 148: 319–336.

Yedlin MJ (1987) Uniform asymptotic solution for the Green's function for the two-dimensional acoustic equation. *Journal of the Acoustical Society of America* 81: 238.

Yedlin MJ, Seymour BR, and Zelt BC (1990) Comparison of the WKBJ and truncated asymptotic methods for an acoustic medium. *Geophysical Journal International* 101: 49–60.

Zaroli C, Debayle E, and Sambridge M (2010) Frequency-dependent effects on global s-wave traveltimes: Wavefront-healing, scattering and attenuation. *Geophysical Journal International* 182: 1025–1042.

Zelt BC, Ellis RM, Zelt CA, et al. (2001) Three-dimensional crustal velocity structure beneath the Strait of Georgia, British Columbia. *Geophysical Journal International* 144: 695–712.

Zhang L, Rector JW III, and Hoversten GM (2005) Eikonal solver in the celerity domain. *Geophysical Journal International* 162: 1–8.

Zhang H, Thurber C, and Rowe C (2003) Automatic p-wave arrival detection and picking with multiscale wavelet analysis for single-component recordings. *Bulletin of the Seismological Society of America* 93: 1904–1912.

Zhao H (2005) A fast sweeping method for eikonal equations. *Mathematics of Computation* 74: 603–627.

Zhao H (2007) Parallel implementations of the fast sweeping method. *Journal of Computational Mathematics* 25(4): 421–429.

Zhao L, Jordan T, and Chapman C (2000) Three-dimensional Fréchet differential kernels for seismic delay times. *Geophysical Journal International* 141: 558–576.

Zhou Y, Dahlen FA, and Nolet G (2004) Three-dimensional sensitivity kernels for surface wave observables. *Geophysical Journal International* 158: 142–168.

Zhu T (1988) A ray-Kirhchoff method for body-wave calculations in inhomogeneous media: Theory. *Geophysical Journal* 92: 181–193.

Zhu H, Bozdağ E, Peter D, and Tromp J (2012) Structure of the European upper mantle revealed by adjoint tomography. *Nature Geoscience* 5: 493–498.

Zhu T and Chun K-Y (1994a) Complex rays in elastic and anelastic media. *Geophysical Journal International* 119: 269–276.

Zhu T and Chun K-Y (1994b) Understanding finite-frequency wave phenomena: Phase-ray formulation and inhomogeneity scattering. *Geophysical Journal International* 119: 78–90.

Ziolkowski RW and Deschamps GA (1984) Asymptotic evaluation of high-frequency fields near a caustic: An introduction to Maslov's method. *Radio Science* 19: 1001–1025.

1.06 Theory and Observations: Forward Modeling: Synthetic Body Wave Seismograms

VF Cormier, University of Connecticut, Storrs, CT, USA

© 2015 Elsevier B.V. All rights reserved.

1.06.1	**Introduction**	201
1.06.2	**Plane Wave Modeling**	203
1.06.2.1	Elastic Velocities and Polarizations	203
1.06.2.2	Superposition of Plane Waves	204
1.06.3	**Structural Effects**	205
1.06.3.1	Common Structural Effects on Waveforms	205
1.06.3.2	Shallow Earth Structural Problems	207
1.06.3.3	Deep Earth Structural Problems	207
1.06.4	**Modeling Algorithms and Codes**	208
1.06.4.1	Reflectivity	209
1.06.4.2	Generalized Ray	210
1.06.4.3	WKBJ–Maslov	211
1.06.4.4	Full-Wave Theory and Integration in Complex p Plane	212
1.06.4.5	Ray Theory, DRT, and Gaussian Beams	214
1.06.4.6	Modal Methods	215
1.06.4.7	Numerical Methods	216
1.06.5	**Parameterization of the Earth Model**	218
1.06.5.1	Homogeneous Layers Separated by Curved or Tilted Boundaries	218
1.06.5.2	Vertically Inhomogeneous Layers	218
1.06.5.3	General 3D Models	219
1.06.6	**Instrument and Source**	221
1.06.6.1	Instrument Responses and Deconvolution	221
1.06.6.2	Far-Field Source-Time Function	222
1.06.7	**Heterogeneity, Attenuation, and Anisotropy**	222
1.06.7.1	Adapting 1D Codes to 2D and 3D	222
1.06.7.2	Hybrid Methods	223
1.06.7.3	Frequency-Dependent Ray Theory	223
1.06.7.4	Attenuation	224
1.06.7.5	Anisotropy	225
1.06.7.6	Scattering	226
1.06.7.7	Imaging	226
1.06.8	**Conclusions**	226
References		227

1.06.1 Introduction

Body waves are solutions of the elastic equation of motion that propagate outward from a seismic source in expanding, quasi-spherical wave fronts, much like the rings seen when a rock is thrown in a pond. The trajectory along which the elastic energy propagates is called a ray. Rays are normal to the wave front in materials that are elastically isotropic, in which the stress–strain relation at any point is independent of the choice of the coordinate system. The normals to the wave fronts, called rays, are useful in illustrating body waves' interactions with gradients and discontinuities in elastic velocities as well as their sense of polarization of particle motion. Except for the special cases of grazing incidence to discontinuities, body wave solutions to the equations of motion are nearly nondispersive. All frequencies propagate at nearly the same phase and group velocities. Hence, the body wave excited by an impulsive, delta-like, seismic source-time function will retain its delta-like shape with propagation to great distances (Figure 1).

Surface waves are solutions of the elastic equations of motion that exponentially decay with depth beneath the surface of the Earth for a boundary condition of vanishing stress at the surface. Unlike body waves, surface waves are strongly dispersed in the Earth, having phase and group velocities that depend on frequency. Observations of surface waves in the 0.001–0.1 Hz band of frequencies can constrain structure of the crust and upper mantle of the Earth, but only body waves provide information on the elastic velocities of the deeper interior of the Earth, all the way to its center. Summing modes of free oscillation of the Earth can represent both body and surface waves. The most efficient representation of the highest-frequency content body waves, however, is given by propagating wave front or ray-type solutions of the elastic equations.

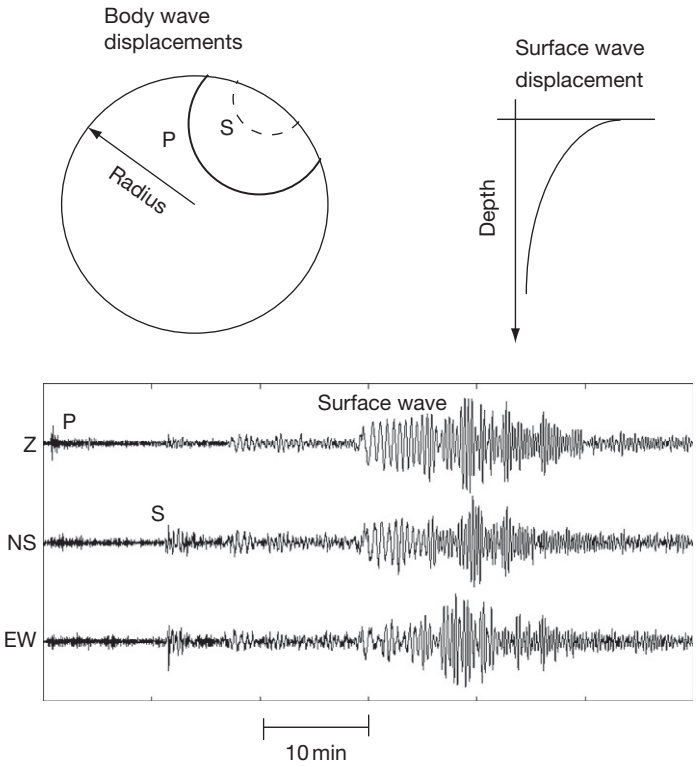

Figure 1 Top left: Displacement of body waves is concentrated in propagating quasi-spherical wave fronts. Top right: The displacement of surface waves exponentially decays away from the surface of the Earth. Bottom: Example seismogram showing impulsive, pulse-like, body waves and dispersive surface waves.

In a homogeneous Earth, the wave fronts of body waves excited by a point source are spherical, with radii equal to the distance from the source to an observation point on the wave front. Since the density of kinetic energy at a point in time is proportional to the surface area of the wave front, the particle velocity of a body wave is inversely proportional to the distance to the source. This inverse scaling of amplitude with increasing distance is termed the geometric spreading factor, R. Even in an inhomogeneous Earth, the inverse-distance scaling of body wave amplitude can be used to make a rough estimate of the behavior of amplitude versus distance.

Rays (energy trajectories) follow paths of least or extremal time, representing a stationary-phase approximation to a solution of a wave equation, Fourier transformed in space and time. The least-time principle is expressed by Snell's law in a material in which velocity is a function of one coordinate (often depth or radius in the Earth). In spherical geometry, Snell's law is equivalent to the constancy of a ray parameter, or horizontal slowness, p. The ray parameter is defined by $p = r \sin(i)/v(r)$, where i is the acute angle between the intersection of a ray path and a surface of radius r and v is the body wave velocity at r. Snell's law is obeyed by ray paths in regions of continuously varying velocity as well as by the ray paths of reflected and transmitted/converted waves excited at discontinuities. Since velocities usually increase with depth (decrease with radius) in the Earth, ray paths of body waves are usually concave upward (Figure 2). The least-time principle can also be exploited in linearized tomography to find perturbations to reference Earth models by assuming that ray paths are

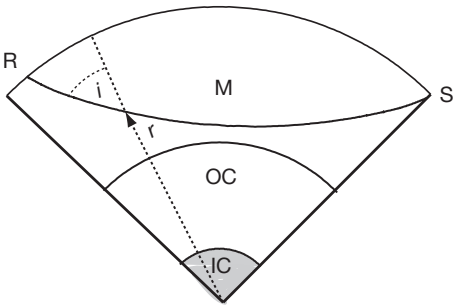

Figure 2 Following Snell's law in spherical geometry ($r \sin(i)/v = \text{constant}$), the ray paths of body waves in the Earth are mostly concave upward because elastic velocities mostly increase with depth.

stationary with respect to small perturbations in velocities. In models having three-dimensional (3D) variation in elastic velocity, the least-time principle can be used to develop a system of linear equations for ray trajectory.

Complementing the information contained in travel times are the shapes (waveforms) of the body waves. Complexities and subtle shape changes observed in waveforms can be used to image elastic properties of the Earth at spatial scales down to a quarter wavelength from its surface to its center. The velocities of body waves in the Earth range from 1.5 to >13 km s^{-1}. Since waves that penetrate the deep interior of the Earth are commonly observed at frequencies at least up to 2 Hz, structures having spatial scales as small as 1 km can be potentially imaged from a densely sampled wave field. Body waveforms also

contain information about the spatial and temporal history of earthquake, explosion, or impact seismic sources.

This chapter reviews algorithms for modeling the effects of structure and source on teleseismic waveforms. It will point to references for the theoretical background of each algorithm and currently existing software. It will also make suggestions for the model parameterization appropriate to each algorithm and the treatment of source-time functions, instrument responses, attenuation, and scattering. Mathematical development of each algorithm can be found in textbooks in advanced and computational seismology (Aki and Richards, 2002; Cerveny, 2001; Chapman, 2004; Dahlen and Tromp, 1998; Kennett, 1983, 2001). A thorough understanding of the derivation of each algorithm requires a background that includes solution of partial differential equations by separation of variables, special functions, integral transforms, complex variables and contour integration, and linear algebra. Practical use of each algorithm, however, often requires no more than a background in simple calculus and an intuitive understanding how a wave field can be represented by superposing either wave fronts or modes at different frequencies.

1.06.2 Plane Wave Modeling

1.06.2.1 Elastic Velocities and Polarizations

Two types of body waves were identified in early observational seismology, P, or primary, for the first arriving impulsive wave and S, or secondary, for a second slower impulsive wave (Bullen and Bolt, 1985). These are the elastic wave types that propagate in an isotropic solid. In most regions of the Earth, elastic isotropy can be assumed, in which only two elastic constants are required to describe a stress–strain relation that is independent of the choice of the coordinate system. In the case of anisotropy, additional elastic constants are required to describe the stress–strain relation. In a general anisotropic solid, there are three possible body wave types, P and two quasi-S waves, each having a different velocity.

The velocities of propagation and polarizations of motion of P and S waves can be derived from elastic equation of motion for an infinitesimal volume in a continuum:

$$\rho \frac{\partial^2 u_i}{\partial t^2} = \sigma_{ij,j} + f_i \qquad [1]$$

where ρ is the density, u_i is the ith component of the particle displacement vector $\mathbf{U}$, σ_{ij} is the stress tensor, and f_i is the ith component of body force that excites elastic motion. Summing over the repeated index j, the total elastic force in the ith direction is represented by the jth spatial derivative of the stress tensor, $\sigma_{ij,j}$. The stress tensor elements are related to spatial derivatives of displacement components (strains) by a generalized Hooke's law, which for general anisotropy takes the form

$$\sigma_{ij} = c_{ijkl} u_{kl} \qquad [2]$$

and for isotropy the form

$$\sigma_{ij} = \lambda \frac{\partial u_i}{\partial x_i} + \mu \left(\frac{\partial u_i}{\partial x_j} + \frac{\partial u_j}{\partial x_i} \right) \qquad [3]$$

where c_{ijkl}, λ, and μ are elastic constants. The summation convention is assumed in eqns [1]–[3], that is, quantities are summed over repeated indices.

Elastic wave equations for P and S waves in an homogeneous isotropic solid can be derived by, taking the divergence and curl of the equation of motion [1], demonstrating that volumetric strain, $\nabla \cdot U$, propagates with a P wave velocity

$$V_P = \sqrt{\frac{\lambda + 2\mu}{\rho}} = \sqrt{\frac{K + 4/3\mu}{\rho}} \qquad [4a]$$

and rotational strain, $\nabla \times U$, propagates with the S wave velocity

$$V_S = \sqrt{\frac{\mu}{\rho}} \qquad [4b]$$

(Note: the P wave velocity can be represented in terms of either the Lame parameter λ and shear modulus μ or the bulk modulus K and shear modulus μ.)

Alternatively, the phase velocities and polarizations of body waves can be derived by assuming propagation of a harmonic plane wave having frequency ω and a wave front normal $\mathbf{k}$ of the form

$$u(\mathbf{x}, t) = \mathbf{A} e^{(i\omega t - \mathbf{k}\cdot\mathbf{x})} \qquad [5]$$

and substituting this form into [1]. This substitution leads to an eigenvalue/eigenvector problem, in which the eigenvalues represent the magnitudes of the wave number vector $\mathbf{k}$ and hence phase velocities from $v = \omega/|\mathbf{k}|$. The associated eigenvectors represent the possible orientations of particle motion (e.g., Keith and Crampin, 1977). There are three possible eigenvalues/eigenvectors, two eigenvalues (phase velocities) of which are equal in an isotropic medium. The eigenvalue associated with the fastest phase velocity is the P wave. Its eigenvector specifies a P wave polarization normal to the wave front. In an isotropic medium, the two equal eigenvalues and their two orthogonal eigenvectors are associated with the S wave. Their eigenvectors specify an S wave polarization tangent to the wave front. Thus, S wave polarization, perpendicular to the direction of S wave propagation, is analogous to the polarization of electromagnetic waves. P polarization, parallel to the direction of propagation, has no analog to electromagnetic wave polarization.

To facilitate the solution and understanding of the interactions of the P and S wave types with discontinuities in elastic moduli and/or density, it is convenient in a radially or vertically varying Earth to define a ray (sagittal) plane containing the source, receiver, and center of the Earth. In an isotropic medium, the polarization of the S wave, which depends on the details of source excitation and receiver azimuth, is most conveniently decomposed in a vector basis consisting of an SV component, lying in the sagittal plane, and an SH component, perpendicular to the sagittal plane (**Figure 3**). At a discontinuity in elastic velocity, SV waves can excite reflected and transmitted and SV waves as well as reflected and transmitted P waves, but SH waves can only excite reflected and transmitted SH waves. The effects of body wave-type conversions on polarizations have contributed to fundamental discoveries in deep Earth structure. The most famous example of these discoveries is the SV polarization of the SKS wave, which confirms that the outer core of the Earth is liquid. In this example, the SV component of an S wave incident on the boundary of the solid mantle excites a transmitted P wave in the liquid outer

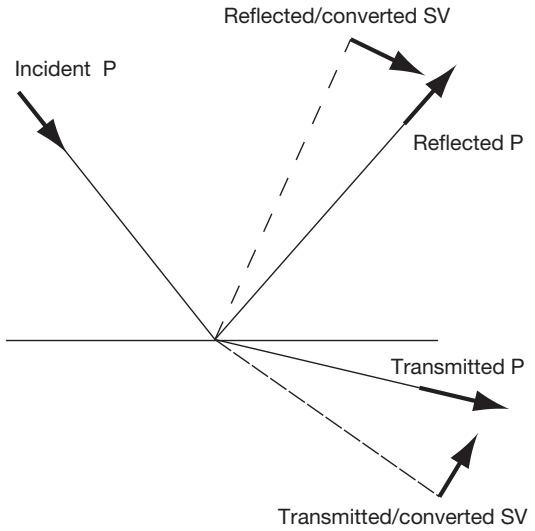

Figure 3 The interaction of a P wave incident on a discontinuity in P and S velocity, showing reflected and converted P and SV waves and their polarizations (arrows).

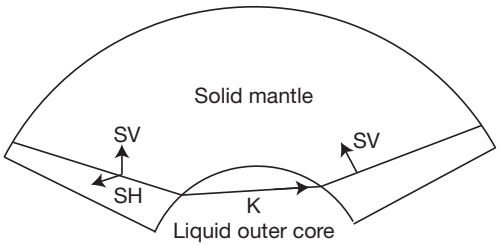

Figure 4 The SV component of the S wave on the core–mantle boundary excites a compressional (K) wave in the outer core, which has its particle motion along its ray. The K wave exits the outer core as a transmitted SV wave in the mantle, which has its particle motion perpendicular to its ray, lying in the sagittal plane.

core (K wave), which can convert back to an SV wave in the solid mantle. The SH component of the incident S wave cannot excite a K wave in the liquid outer core, and the K wave cannot excite a transmitted SH wave in the mantle. Hence, the received SKS wave is purely SV-polarized in an isotropic Earth (Figure 4).

Solutions of the elastic equations of motions can also be developed in terms of potentials, showing that the existence of fully decoupled P and S wave equations exist only in homogeneous regions where elastic moduli and density are constant in space (e.g., Aki and Richards, 2002). The use of potentials, however, leads to needless mathematical complexity when the quantities of modeling interest are displacements and stresses. This is especially true when solutions are continued across discontinuities in elastic moduli and density. At discontinuities, boundary conditions must be imposed on components u_i of the particle displacement vector **U** and stress tensor elements σ_{ij}. Three fundamental types of boundary conditions occur in seismic wave propagation in the Earth: (1) the surface of the Earth, where all elements σ_{ij} vanish; (2) welded, slip-free, discontinuities between two solid discontinuities, where both particle displacements and stress tensor elements are continuous; and (3) liquid–solid discontinuities such as the ocean/ocean crust, mantle/outer core, and outer core/inner core, where only the displacements and stresses perpendicular to the discontinuity are continuous. These boundary conditions and the associated changes in the eigenvectors and eigenvalues of plane wave solutions can be compactly handled by a fundamental matrix and propagator formalism in a layered radially or vertically varying medium (Gilbert and Backus, 1966). In this approach, the vertically separated component for the solution to the equations of motion is written as a linear system of the type

$$\frac{\mathrm{d}\mathbf{f}}{\mathrm{d}z} = \mathbf{A}\mathbf{f} \qquad [6]$$

where **f** is a 2-vector for the components of displacement and stress associated with SH waves or a 4-vector for the components of stress and displacement associated with P and SV waves; **A** is either a 2×2 matrix for SH waves or a 4×4 matrix for P and SV waves; and derivative d/dz is with respect to depth or radius. The possibility of both up- and down-going waves allows the most general solution of the linear system in eqn [6] to be written as a solution for a fundamental matrix **F**, where the rows of **F** are the components of displacement and stress and the columns correspond to up- and down-going P and S waves. For P and SV waves, **F** is a 4×4 matrix; for SH waves, **F** is a 2×2 matrix. An example of the fundamental matrix for SH waves in a homogeneous layer is

$$\mathbf{F} = \begin{pmatrix} e^{i\omega k_z(z-z_o)} & e^{-i\omega k_z(z-z_o)} \\ ik_z\mu e^{i\omega k_z(z-z_o)} & -ik_z\mu e^{-i\omega k_z(z-z_o)} \end{pmatrix} \qquad [7]$$

where z_o is a reference depth and the sign of the complex phasors represents propagation with or against the z-axis to describe down- or up-going waves. The first row in eqn [7] represents displacement and the second row stress.

The solution of eqn [6] can be continued across discontinuities, with all boundary conditions satisfied, by use of a propagator matrix **P**, where **P** also satisfies [6]. The fundamental matrix in layer 0 at depth z_1,, $\mathbf{F}_o(z_1)$, is related to the fundamental matrix in layer N at z_N, $\mathbf{F}_N(z_N)$, through a propagator matrix $\mathbf{P}(z_1,z_N)$ such that

$$\mathbf{F}_o(z_1) = \mathbf{P}(z_1, z_N)\mathbf{F}_N(z_N) \qquad [8a]$$

where

$$\mathbf{P}(z_1, z_N) = \left(\mathbf{F}_1(z_1)\mathbf{F}_1^{-1}(z_2)\right)\left(\mathbf{F}_2(\mathbf{z}_2)\mathbf{F}_2^{-1}(\mathbf{z}_3)\right) \ldots \left(\mathbf{F}_{N-1}(z_{N-1})\mathbf{F}_{N-1}^{-1}(z_N)\right) \qquad [8b]$$

In an isotropic Earth model, once the relative source excitation of S waves has been resolved into separate SH and SV components of polarization, the treatment of boundary conditions on P and SV waves can be separated from that needed for SH waves by the use of either the 4×4 fundamental matrices for P and SV waves or the 2×2 fundamental matrices for SH waves.

1.06.2.2 Superposition of Plane Waves

Superposition of plane waves of the form in eqn [5] along with techniques of satisfying boundary conditions at discontinuities using fundamental and propagator matrix solutions of eqns

[8a] and [8b] allows calculation of all possible body wave solutions of the elastic equations of motion as well as the dispersive wave interactions with the free surface (surface waves) and deeper discontinuities (diffractions and head waves) in radially or vertically varying media. This process of superposition in space and frequency is equivalent to solution of the equations of motion by the integral transform methods of Fourier, Laplace, Bessel or spherical harmonics. Fourier and Laplace transforms can always be applied in a Cartesian coordinate system, but analytic solutions of the equation of motion in terms of Bessel/Hankel functions and spherical harmonics are limited to Earth models whose layers and discontinuities are either spherically symmetrical or plane-layered, having cylindrical symmetry about the source point. Some well-tested extensions and perturbation methods, however, allow their application to models in which the symmetry is broken by lateral heterogeneity, aspheric or nonplanar boundaries, and anisotropy.

Transform-based methods, ray-based methods, and their extensions are reviewed in Section 1.06.4. Before beginning this section, however, it is important to have an intuitive feel for the effects of Earth structure on the propagation of body waves, how structure can induce complexity in body waveforms, and what outstanding problems can be investigated by the synthesis of waveforms.

1.06.3 Structural Effects

1.06.3.1 Common Structural Effects on Waveforms

Body waves are commonly synthesized to study the effects of waveform complexity or multipathing due to rapid or discontinuous changes in elastic velocity. Two common structures inducing waveform complexity are a rapid or discontinuous velocity decrease and increase with depth (Figure 5). A rapid or discontinuous decrease is characterized by a shadow zone, followed by a caustic and two multipaths in the lit zone, each having opposite signs of curvature in their associated travel time curves. A caustic is a surface, line, or point where body waves are strongly focused, frequency-independent ray theory breaks down, and geometric spreading vanishes. A rapid or discontinuous velocity increase produces a triplication of the travel time curve, with a region of distances with three different ray paths and associated travel time curves, one of which has an opposite sign of curvature in its travel time curve compared to those of the other two paths. The two points where the curvature of travel time versus distance changes denote the distance at which the caustics intersect the Earth's surface.

P waves interacting with the Earth's inner and outer core boundaries provide an example of the waveform complexity induced by both a discontinuous velocity increase and a discontinuous velocity decrease. A shadow zone and caustic are induced by a discontinuous velocity decrease at the core–mantle boundary, and a triplication is induced by a discontinuous velocity increase at the inner core boundary (Figure 6). The velocity decrease at the core–mantle boundary generates a reversal of the travel time–distance curve and strong focusing of waves at the caustic distance B. The discontinuous increase in velocity at the outer core–inner core boundary generates the triplication C–D–F. Frequency-dependent diffraction occurs along the extension of BC to longer distances. A lower amplitude partial reflection along the dashed segment extends from D to shorter distances. In addition to the effects induced by radially symmetrical structure, lateral heterogeneity near the core–mantle boundary can scatter higher-frequency body waves in all directions. The curved dashed line extended to shorter distances from point B in Figure 6 represents the minimum arrival time of high-frequency energy scattered from

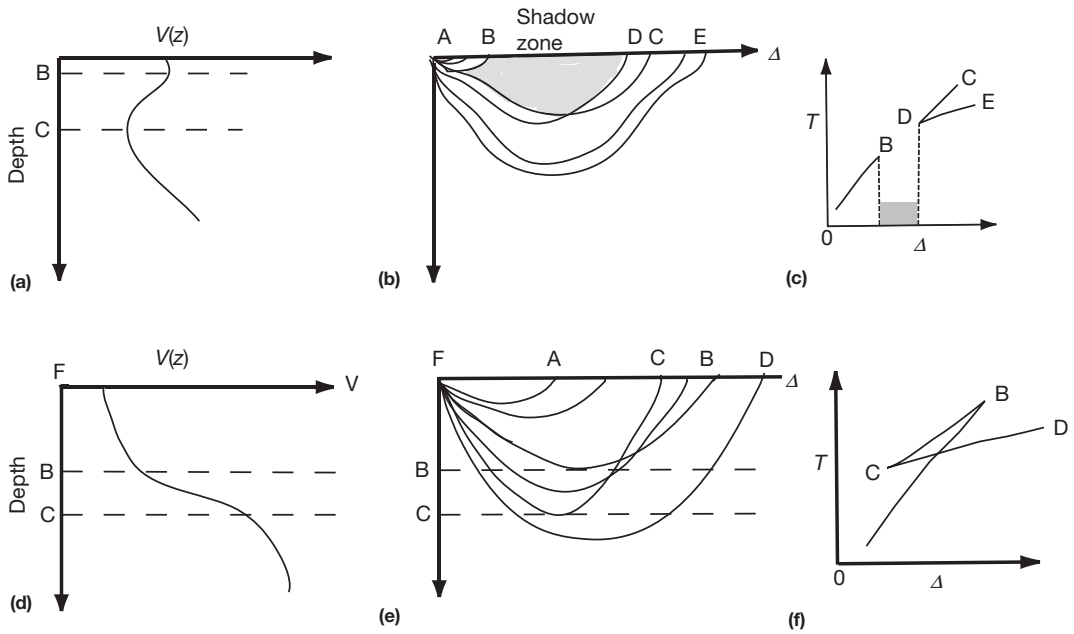

Figure 5 Ray multipathing and travel time complexity induced by a regions of either rapid velocity decrease with depth (a–c) or rapid increase (d–f) with depth.

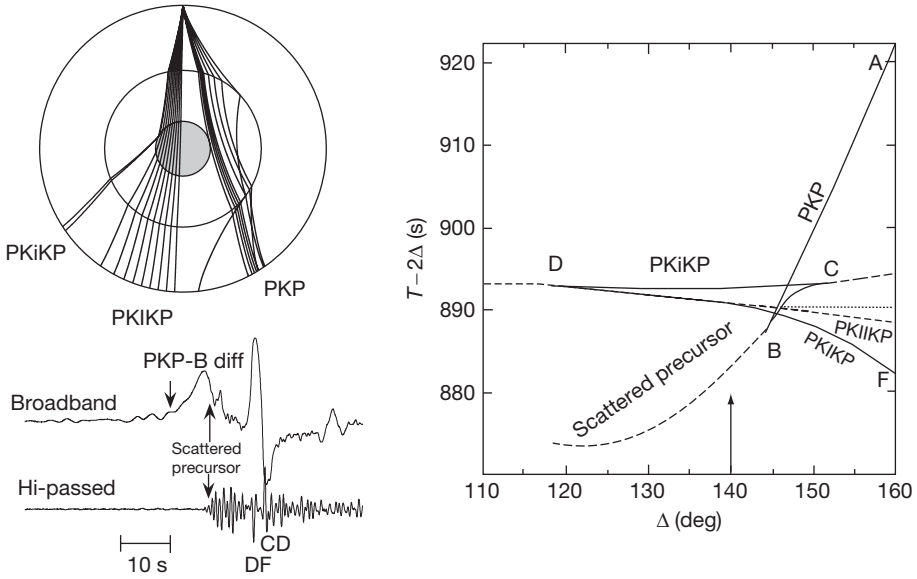

Figure 6 Rays and travel time curves of P waves interacting with the Earth's inner and outer cores. Bottom left: Observed broadband displacement and high-pass-filtered seismograms from a deep earthquake recorded near 140°.

either heterogeneity near or topography on the core–mantle boundary.

Changes in the curvature of travel time curves for waves also induce changes in the shapes of the waves associated with each multipath. These waveform distortions can be understood from geometric spreading effects. In an inhomogeneous medium, geometric spreading R is proportional to the square root of the product of the principal radii of curvature of the wave front

$$R \propto \sqrt{r_1 r_2} \qquad [9]$$

In a homogeneous medium, where wave fronts are spherical, $r_1 = r_2$, and geometric spreading reduces simply to the distance to the source. A wave front is described by a 3D surface $\tau(\mathbf{x})$ over which travel time is constant. Hence, the principal radii of curvature of the wave front are determined by the second spatial derivatives of the travel time surface τ. From [9], a change in the sign of either of the two principal wave front curvatures (r_1 or r_2) produces a change in the sign of the argument of the square root in eqn [9] and hence a $\pi/2$ phase change in the waveform associated with that wave front. A consequence of this relation is that any two waveforms having travel time branches with a difference in the sign of the second derivative with respect to great circle distance will differ by $\pi/2$ in phase. This $\pi/2$ phase change is called a Hilbert transform (Bracewell, 1986). A Hilbert transform of a delta function has a gradual positive onset, sharp downswing to negative values, and a gradual negative return to zero (Figure 7). The travel time curve of the PKP waves along the AB branch in Figure 6 has a concave upward curvature, while travel time curvatures of the PKP waves along the BC branch and the PKIKP waves along the DF branch are concave downward. Hence, waveforms along PKP-AB travel time branch are Hilbert-transformed ($\pi/2$ phase-shifted) with respect the waveforms along of the PKP-BC and PKP-DF branches (Figure 8).

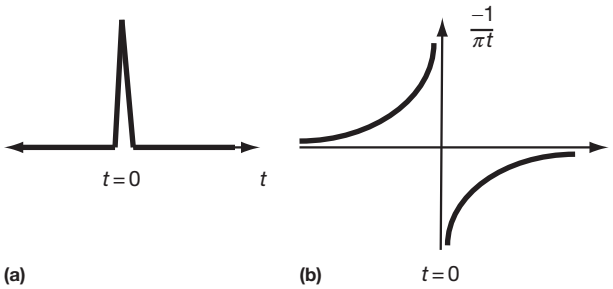

Figure 7 (a) Delta function and (b) its Hilbert transform.

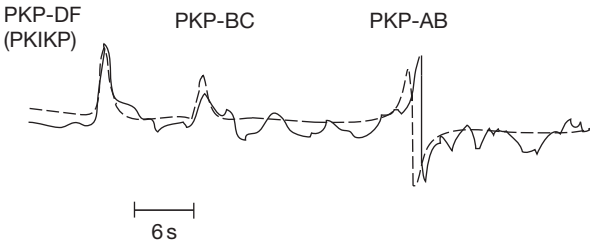

Figure 8 Observed and synthesized PKP waveforms from Choy and Cormier (1983). PKP-AB is Hilbert-transformed with respect to PKP-DF.

These changes in pulse shape are correct in the limit of infinite frequency, but at finite frequency pulse, shapes near the cusps B, C, and D are neither delta-like nor Hilbert-transformed-like. Near these points, the shapes exhibit frequency dependence and appear as some kind of average of the two fundamental shapes. This type of pulse shape can also exist in cases where a reflection/transmission/conversion coefficient of a plane wave becomes complex, as in certain distance ranges of the SKS phase. In these cases, the pulse shape can be represented by a linear combination of a delta function and Hilbert-transformed delta function (Aki and

Richards, 1980, pp. 157–158). In the shadows of cusps and caustics, diffracted waves exist, which decay with increasing frequency and increasing distance from the cusp or caustic (e.g., the diffracted PKP-B in the broadband seismogram in Figure 6).

A turning point of a ray can occur at a point where the ray direction is horizontal and the direction of energy propagation reverses from upward to downward or vice versa. Waves having rays with multiple turning points also exhibit $\pi/2$ phase shifts for each turning point. Examples are PP waves and SS waves that are Hilbert-transformed with respect to the waveforms of the direct P and S waves and waves multiply-reflected along the underside of the core–mantle boundary, such as PKKP, SKKS, PKnKP, and SKnKS (Choy and Richards, 1975). In three-dimensionally varying media and for body waves having multiple turning points in waveguide-like structures, it is possible to have N multiple $\pi/2$ phase shifts for N turning points or N points of tangency to a caustic. N is termed the KMAH index (named after wave theorists Keller, Maslov, Arnold, and Hörmander). The KMAH index is an important parameter to inventory as ray trajectories are computed. In dynamic ray tracing (DRT) (Section 1.06.4.5), the KMAH index can be determined by tracking accumulated sign changes in the determinant of Cerveny's (2001) spreading matrix $\mathbf{Q}$, where geometric spreading R is proportional to the square root of the determinant of $\mathbf{Q}$:

$$R \propto \sqrt{\det(\mathbf{Q})} \qquad [10]$$

In a vertically continuous flat Earth, $\det(\mathbf{Q})$ takes the form

$$\det(\mathbf{Q}) = \frac{\cos(i)}{V}\frac{\cos(i_o)}{V_o}\frac{X}{p}\frac{dX}{dp} \qquad [11a]$$

and in spherically symmetrical Earth models,

$$\det(\mathbf{Q}) = (rr_o)^2\frac{\cos(i)}{V}\frac{\cos(i_o)}{V_o}\frac{\sin(\Delta)}{p}\frac{d\Delta}{dp} \qquad [11b]$$

In eqns [11a] and [11b], vertical takeoff angle i, velocity V, and radius r having the subscript o are evaluated at a ray origin or source point, and unsubscripted quantities are evaluated at a ray endpoint or receiver. X is the distance measured from source to receiver along the surface of the Earth model, and Δ is the great circle distance of the source to the receiver measured in radians. In eqn [11a], the ray parameter p is that for rays in plane-layered models ($p = \sin(i)/V = \text{constant} = dT/dX$), but in eqn [11b], p is that for rays in spherically layered models ($p = r\sin(i)/V = \text{constant} = dT/d\Delta$).

Head waves are another effect of a discontinuous velocity increase with depth that can induce frequency-dependent effects and waveform complexity. Head waves travel along the underside of a boundary in the higher-velocity medium. Depending on vertical gradient of the medium below the discontinuity, a head wave can either have an amplitude inversely proportional to frequency (no gradient) or be represented by an interference or a whispering gallery of waves multiply-reflected along the underside of the discontinuity (e.g., Cerveny and Ravindra, 1971; Menke and Richards, 1980).

In some distance ranges, surface waves and phases best described by modal representations interfere with body waves. Examples include late arriving body waves having multiple interactions with the core–mantle boundary and/or the free surface that interfere with fundamental mode Love and Rayleigh waves. Another example is shear-coupled PL waves that are generated by SV waves that turn in the mantle and excite converted P waves trapped in the crust (Baag and Langston, 1985). Shear-coupled PL waves can arrive as a dispersive wave train immediately following an SV wave in some distance ranges.

1.06.3.2 Shallow Earth Structural Problems

Problems of interest in the crust and upper mantle include both academic and commercial applications, involving the deployment of dense arrays of seismometers to image and interpret complex 3D and anisotropic elastic structure (Chapters 1.11 and 1.15). Academic examples include structures associated with continental collisions (Chapter 6.09), subduction zones (Chapter 1.20), spreading ridges (Chapter 1.13), intrusive bodies and hot spots (Chapters 6.04 and 6.08), volcanoes (Chapter 4.15), and fault zones (Chapter 4.07). Commercial applications include the imaging of stratigraphic traps for oil and gas formed by anticlines, faults, and salt domes and the characterization of fracture distributions and shapes for enhanced oil and gas recovery and remediation of contaminated groundwater (Chapters 11.15, 11.16, and 11.06).

1.06.3.3 Deep Earth Structural Problems

In the deep Earth, problems of greatest research interest are structural zones of rapid spatial variation that introduce waveform complexity in the form of triplications, caustics, shadow zones, diffractions, head waves, and multipaths. For teleseismic observations, the zones of rapid spatial variation that are most often studied are the crust–mantle discontinuity (Moho), regionally varying low-velocity zones in the upper mantle (including the lithosphere to asthenosphere transition); narrow zones or discontinuities in velocity and density at or near 400, 500, and 660 km depth; a zone of regionally varying velocities between 100 and 300 km above the core–mantle boundary; and 100–300 km regions on both sides of the inner core boundary.

Key to the interpretation of these zones of rapid spatial variation is the relative changes in P velocity, S velocity, and density. From body wave modeling, it is often only possible to make an estimate of velocity changes, either P or S velocity, but neither simultaneously, with little or no constraint on the associated density change. An example of this is the estimate of the velocity increase required to reproduce the spacing of travel time branches in the ranges of the triplicated portion of a travel time curve due to a rapid increase in velocity with depth (e.g., Figures 5 and 6). The amplitudes of the body waves in the triplicated range, where one travel time branch corresponds to a wave totally (post-critically) reflected from the discontinuity, have little or no sensitivity to any density change associated with the velocity change. The amplitude of a reflected body wave at more vertical incidence, however, is much more sensitive to the product of density and velocity changes (Figure 9). By combining observations of narrow angle and grazing incidence waves to a discontinuity, it is possible to remove or reduce the trade-offs between velocity and density change.

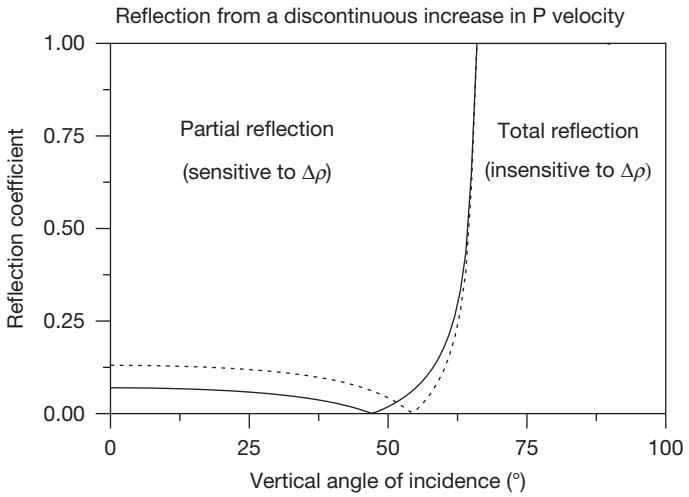

Figure 9 Example of a reflection coefficient showing total and partial reflection for a discontinuity for two cases: (1) velocity and density increase (solid) and (2) velocity increase identical but a different density increase (dashed). Note the insensitivity of total reflection region to the size of the density increase.

Combined modeling of P and S waveforms for both narrow- and wide-angle incidence then makes it possible to separately estimate P, S, and density changes at a discontinuity. From these estimates, it is possible to distinguish the nature of the discontinuity, for example, is it a chemical change or a solid–solid mineral phase change?

When P and S wave waveform analyses are available, an additional diagnostic tool can be the calculation of the change in bulk sound velocity V_K, where

$$V_K^2 = V_P^2 - \frac{4}{3}V_S^2 \qquad [12]$$

and V_P and V_S are the P and S velocities, respectively (Su and Dziewonski, 1997). Bulk sound velocities are more directly observed in high-pressure mineral physics experiments and theory and can be directly compared against known mineralogy (Zhao and Anderson, 1994). Other constraints in interpreting 3D variations in velocity are provided in comparing theoretical and observed estimates of the relative fractional changes in P velocity, S velocity, and density, $\mathrm{d}\ln V_P/\mathrm{d}\ln V_S$ and $\mathrm{d}\ln Vs/\mathrm{d}\ln\rho$ (e.g., Trampert et al., 2001). Care, however, is sometimes needed in comparing the frequency band of an observation with that of theoretical predictions due to the dispersive effects of viscoelasticity (**Section 1.06.7.4** and Karato, 1993).

The effect of temperature on velocity is known from experimental and theoretical predictions. Known temperature derivatives, or even practical bounds on the temperature derivative, can be used to determine whether a rapid velocity change is due to either a spatially sharp temperature or chemical or phase change. In this analysis, it is also important to consider the effects of thermal diffusivity. For example, given an estimate of the thermal diffusivity, the spatial extent of a thermally induced velocity anomaly cannot persist at a scale smaller than a certain size. Thermally induced anomalies below this size diffuse away over time periods shorter than the timescale at which they are created by mantle circulation.

Estimating whether a region of velocity change is a true discontinuity or a transition spread out in space requires careful study of the frequency content of reflected and converted waves interacting with the region of rapid velocity change. This has been an enduring challenge in interpreting rapid changes in velocity in the upper mantle as solid–solid phase changes. Waves reflected at wavelengths much longer than the depth range of a gradient transition cannot distinguish a transition from a discontinuity. Shorter wavelength waves, however, will not be reflected at narrow incidence angles. Reflected and converted waves at grazing incidence to a depth zone of rapid transition are relatively insensitive to the width of the transition even for a relatively broad frequency band of recording (e.g., Ward, 1978). Taking these sensitivities together, the frequency-dependent behavior of the amplitudes of body waves partially reflected at narrow angles of incidence to regions of rapid transition in depth can help diagnose whether a structure is a true discontinuity or transition zone. In practice, only a lower bound on the width of a depth transition can be safely diagnosed (e.g., Richards and Frasier, 1976), since there is typically an upper bound on the frequency (lower bound on wavelength) on observable teleseismic body waves (usually 2–3 Hz and 2–5 km).

1.06.4 Modeling Algorithms and Codes

Modeling of body waves can be broadly classified into four approaches: (1) transform methods for spherically symmetrical or plane-layered media, with some extensions for weak heterogeneity and anisotropy; (2) ray-based methods for regions in ray theory is a good approximation; (3) mode summation methods; and (4) full or partial numerical solutions to elastic equations of motion that can treat the cases of strong heterogeneity, anisotropy, and small spatial scales of heterogeneity. A summary of these modeling methods follows. Published applications of each method are extensive, and an attempt is made to primarily cite material in which the theory of each method is most completely developed. In many cases, this will be a textbook rather than a journal paper. Good

starting points to obtain software for many approaches are the Orpheus Software Library (www.orfeus-eu.org/Software/software.html), codes deposited with the World Data Center as part of the *Seismological Algorithms* text (www.ngdc.noaa.gov/hazard/seisalgo.shtml), codes and tutorials by R. Hermann (www.eas.slu.edu/People/RBHerrmann/CPS/CPS330.html), example synthetics and codes distributed by the SPICE Project (www.spice-rtn.org), codes distributed on a CD supplied with the International Handbook for Earthquake and Engineering Seismology (Lee et al., 2002), and computational seismology software available from the Computational Infrastructure in Geodynamics (CIG) web page (www.geodynamics.org).

1.06.4.1 Reflectivity

Reflectivity (Fuchs and Müller, 1971; Kennett, 1983, 2001; Kind, 1985; Müller, 1985) is perhaps the most general and popular transform method of modeling seismograms in radially symmetrical or plane-layered Earth models. Planar homogeneous layers parameterize the Earth model, after an Earth-flattening approximation (EFA) is applied. Plane wave solutions of the wave equation are found in the frequency domain, with boundary conditions handled by propagator matrix techniques. This approach is used to derive a transformed solution at great circle distance Δ_o for displacement, $u(\omega, p, \Delta_o)$, in ray parameter p and frequency ω space, where p is related to the horizontal component of the wave number vector by $k_x = \omega p / r_e$, with r_e the mean spherical radius of the Earth. The time domain solution $U(t, \Delta_o)$ is then found by inverting Fourier transforms represented by

$$U(t, \boldsymbol{\Delta}_o) = \frac{1}{2\pi} \int_{-\infty}^{\infty} d\omega e^{-i\omega t} \int_{\Gamma} dp\, u(\omega, p, \Delta_o) \qquad [13]$$

Transform inversion is commonly accomplished by integrating $u(\omega, p, \Delta_o)$ along a contour Γ confined to a finite segment of the real p or k_x axis for the series of discrete 2^N frequencies required to invert the complex frequency spectrum by a fast Fourier transform (FFT).

Depending on the needs of the modeler, the integrand of eqn [13] can be constructed to contain either one or several body wave arrivals interacting with major discontinuities, fundamental or higher mode surface waves, or a complete seismogram. In common applications, the integrand is constructed to represent the reflection a body wave incident on a stack of layers in a reflection zone (**Figure 10**). Above the reflection zone, the incident wave is assumed to be transmitted down through and back up the layers overlying the reflection zone. Neglecting details of the source excitation, the factors making up $u(\omega,p,\Delta)$ include transmission coefficients T_D down and T_U up through the layers above the reflection zone, the reflection R_U from the reflection zone, and phase factor $\exp(i\omega p \Delta_o)$ accumulated through horizontal propagation to the great circle distance Δ_o, or

$$u(\omega, p, \Delta_o) \propto T_D R_U T_D \frac{\exp[i(\omega p \Delta_o - \pi/4)]}{\sqrt{\omega p \sin(\Delta_o)}} \qquad [14]$$

The reflectivity response R_U can include all internal multiples and P to SV conversions within the thin homogeneous layers of the reflection zone. The reflectivity can be calculated from fundamental **F** and propagator **P** matrices, for example, eqns [7] and [8]. R_U for SH waves can be calculated by solving the system

$$\mathbf{F}_o(z_1) \begin{pmatrix} 1 \\ R_U^o \end{pmatrix} = \mathbf{P}(z_1, z_N) \mathbf{F}_N(z_N) \begin{pmatrix} T_D^N \end{pmatrix} \qquad [15]$$

where R_U^o is the total wave field reflected upward at the top of the boundary of the layered reflection zone and T_D^N is the total wave field transmitted through the bottom boundary $z = z_N$ of the reflection zone. A similar system can be set up for P and SV reflectivity, but care must be taken to rearrange the system to exploit algebraic cancelation of exponentially growing terms for certain domains of ray parameter (Abo-Zena, 1979). Elimination of these troublesome terms can also be accomplished by rearranging the multiplication of fundamental matrices in such a way that also enables identification of infinite series of internal layer multiples. These interlayer multiples can be neglected after a small finite number of reverberations (Kennett, 1983, 2001). Truncation of these internal multiples helps eliminate later arriving energy that folds back into the finite time window required given by finite length Fourier transforms. An alternative approach is to add a small imaginary part to each frequency $-i/\tau$ in the evaluation of the reflectivity response before inverting the Fourier transform (Bouchon and Aki, 1977; Chapman, 2004, p. 361). Using the damping theorem of Fourier transforms, at each time point, the inverted signal is then multiplied by the exponential $\exp(t/\tau)$.

After choosing a method to eliminate acausal late arriving multiples, one must still decide on how to best suppress the numerical noise of all the causal internal layer multiples of the thin layers used to approximate a continuously varying model. This numerical noise can be minimized by either low-pass filtering the response before inverting the Fourier transform or making layer thicknesses smaller than 1/4 the shortest wavelength corresponding to the highest frequency of interest to model (**Figure 11**).

Parameterization of the spherical Earth by plane homogeneous layers with depth z first requires an EFA of velocities $v(r)$ of the type

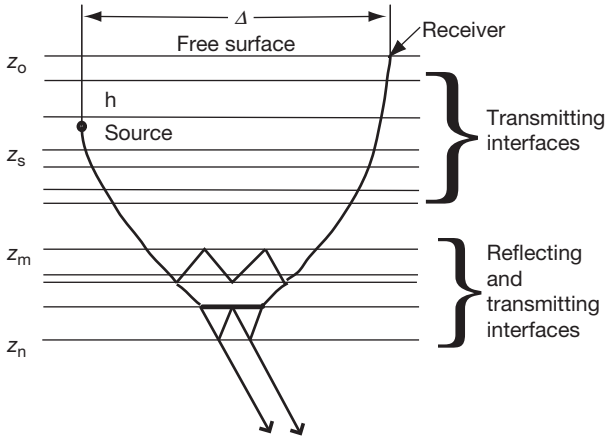

Figure 10 A typical layered model used in reflectivity synthesis, showing a transmission zone and rays reverberating in a reflection zone.

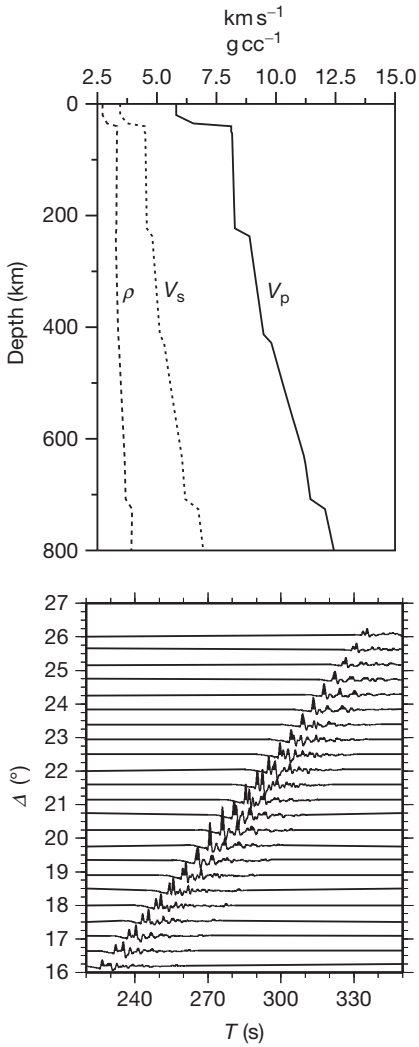

Figure 11 P waves synthesized by the reflectivity method using the program and example input provided by Kennett in the Orpheus web pages (www.orpheus-eu.org). Note the increase in amplitude around 20° associated with overlapping triplications induced by an upper mantle model having rapid velocity increases near 400 and 700 km depths.

$$v_f(z) = \frac{r_e}{r} v(r) \qquad [16a]$$

$$z = r_e \ln\left(\frac{r}{r_e}\right) \qquad [16b]$$

(Müller, 1977), where v_f is the Earth-flattened velocity. Errors on the order of $1/\omega$ are introduced in synthetic seismograms in this process and include problems associated with the decoupling of P and S wave potentials and the lack of an ideal density transformation (Chapman, 1973). The EFA will also breakdown at the center of the Earth ($r=0$), limiting accurate modeling to body waves that penetrate only the upper 500 km of the inner core. With this limitation and unless applied to a region in which velocity gradients are anomalously high at very low (<0.01 Hz) frequencies, the EFA combined with thin homogeneous layering can usually be applied without introducing significant errors.

Another variant of the reflectivity method is the discrete wave number method, in which the integral over ray parameter p is replaced by a sum over discrete horizontal wave numbers, k_x (Bouchon, 1979; Bouchon and Aki, 1977). One advantage of this method is that it can include the zero wave number, which provides a solution for the static displacement near an earthquake source (Honda and Yomogida, 2003). The need for fictitious image sources to treat the surface boundary conditions introduces some complexity in the formulation of the discrete wave number method, but both SH and P-SV codes are available and well developed. The representation of sources by sums of discrete wave numbers can also be useful in the implementation of boundary element methods to synthesize seismic wave fields scattered by irregular boundaries and inclusions (Campilo and Bouchon, 1985).

Because its input parameters are simple to understand, the reflectivity method is probably the most popular forward modeling technique. Input consists of an Earth model specified by velocities and densities in a stack of homogeneous layers, starting and ending points of integration along a real ray parameter axis, a time window and sampling rate, and a simple source description. Some 2D extensions are now available, allowing separate models to be specified in the source and receiver regions (see **Section 1.06.7.1**). Aside from simplicity of the input parameters, an advantage of reflectivity is that it easily allows the investigation of vertical transition zones in properties modeled by arbitrarily thin layers. Some caution in exploiting this advantage must be maintained not to violate constraints on physically realistic bounds on radial derivatives of elastic moduli and density. Compared to ray-based methods that assume asymptotic approximations to vertical wave functions discussed in the following sections, reflectivity can be numerically expensive for problems requiring thousands of thin layers.

1.06.4.2 Generalized Ray

The method commonly dubbed the generalized ray technique (GRT) originated from a technique of handling the integral transform inversions from ray parameter and frequency to time and space by the Cagniard–de Hoop method. It was recognized that most important teleseismic arrivals can be calculated by a first motion approximation, allowing the time domain solution for ray interactions in each homogeneous layer, both reflected and head waves, to be solved analytically (Helmberger, 1974; Helmberger and Harkrider, 1978). Ray solutions within each layer are summed, usually just the first multiples. The volume of published applications using the GRT method is probably the largest of any other method, but its available computer codes are less widely circulated than those employing reflectivity methods. An application of GRT synthetics (Burdick and Helmberger, 1978) was instrumental in the first major revision of standard Earth models originating from the pioneering work of Jeffreys and Bullen, namely, the replacement of a zone of strong velocity gradient in the upper mantle (Jeffreys, 1936) with two first-order discontinuities at 400 and 660 km depths (**Figure 12**).

The GRT commonly assumes an EFA and ignores higher than first-order internal multiples in each layer. It has been tested against other methods in many standard, vertically

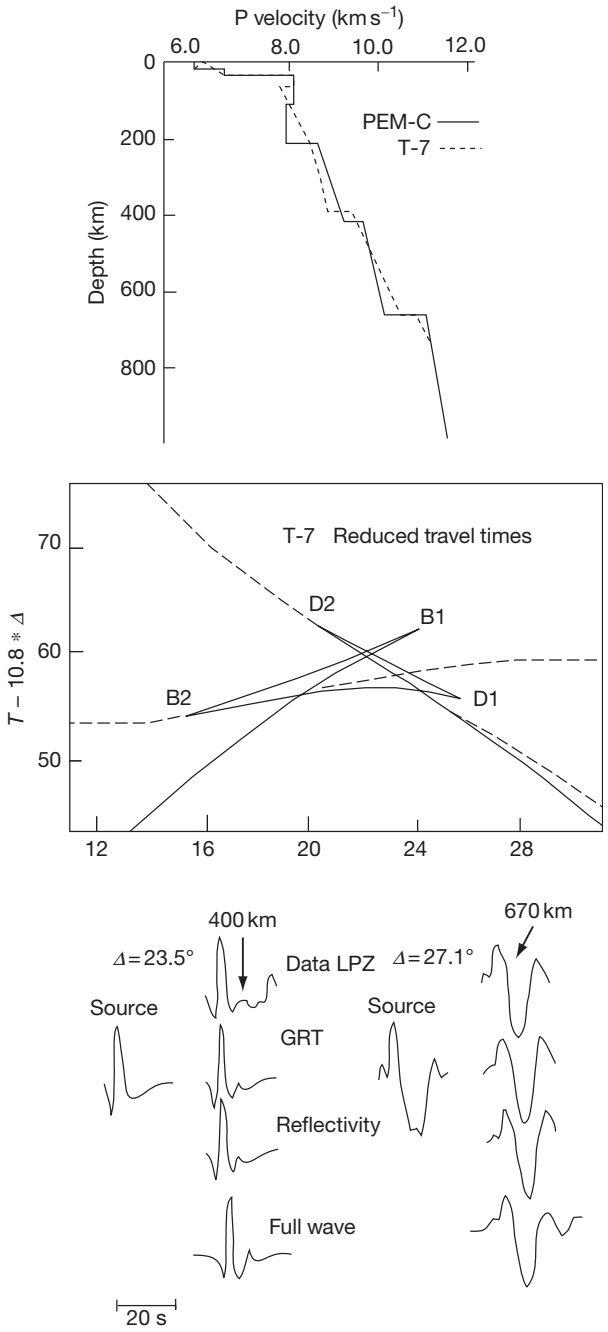

Figure 12 Top: Two models of P velocity in the upper 1000 km of the Earth. Middle: Discontinuities at 400 and 650 km depths create two overlapping triplications in the travel time curve and multiple phase arrivals in the great circle range 10°–30°. Bottom: A comparison of observed and synthesized seismograms in the T-7 model for three different methods of synthesis that include diffraction effects. Burdick LJ and Orcutt JA (1979) A comparison of the generalized ray and reflectivity methods of waveform synthesis. *Geophysical Journal of the Royal Astronomical Society* 58: 261–278: Cormier VF and Choy GL (1981) Theoretical body wave interactions with upper mantle structure. *Journal of Geophysical Research* 86: 1673–1678.

varying, Earth models and usually produces seismograms that are indistinguishable from those calculated by other common methods discussed in this chapter.

1.06.4.3 WKBJ–Maslov

An important feature of this technique is that thin homogeneous layers no longer parameterize the Earth model. Vertical gradients in depth or radius are allowed in velocity, and asymptotically approximate, WKBJ, solutions of the vertically separated part of the wave equation are assumed. In contrast to homogeneous layers, where the up- and down-going vertical wave functions are simply $\exp[\pm ik_z(z-z_{\text{ref}})]$, the WKBJ solution approximates the vertical wave functions by

$$g^{(1)}_{(2)}(r,p,\omega) = \frac{e^{i\pi/4}}{\omega r}\sqrt{\frac{V}{\xi(r)}}\exp(\pm i\omega\tau) \qquad [17a]$$

where the superscripts (1) and (2) and signs + and − refer to up- and down-going waves, respectively. $\xi(r)$ is the vertical component of the slowness vector and is related to the cosine of the angle of incidence of a ray at any level r by $\xi(r) = \cos(i)/V = \sqrt{1/V^2 - p^2/r^2}$. τ is the delay time obtained by integrating the vertical component of the slowness vector from the turning point radius r_p,where $\cos(i) = 0$, to r:

$$\tau = \int_{r_p}^{r} \sqrt{1/V^2 - p^2/r^2}\,dr \qquad [17b]$$

The accuracy of these high-frequency approximations increases as the ratio λ/s decreases, where λ is the wavelength and s is the scale length of the medium. The scale length s is defined by

$$s = \min\left(\frac{V_S}{|\nabla V_S|}, \frac{V_P}{|\nabla V_P|}, \frac{\rho}{|\nabla\rho|}, r_b\right) \qquad [18]$$

where r_b is a radius of curvature of a first-order discontinuity in density or elastic velocity (Beydoun and Ben-Menahem 1985; Kravtsov and Orlov, 1980). Separability of P and S wave potentials is assumed in each vertically or radially inhomogeneous layer and frequency-dependent reflections, and P to S conversions by regions of strong gradients are ignored. Hence, transition zones, which may be of interest to mantle solid–solid phase changes, should be handled by thin layers of weaker gradient where the asymptotic approximations remain valid. For problems consisting of a body wave reflected by or bottoming above a discontinuity, the integrand $u(\omega, p, \Delta_o)$ in eqn [13] is replaced by

$$u(\omega,p) = \omega^{1/2}\Pi(p)e^{i\omega\theta}(p) \qquad [19a]$$

where

$$\theta(p) = \int_{r_p}^{r_s}\sqrt{1/v^2 - p^2/r^2}\,dr + \int_{r_p}^{r_o}\sqrt{1/v^2 - p^2/r^2}\,dr + p\Delta_o \qquad [19b]$$

$\Pi(p)$ is a product of the plane wave reflection coefficient of the discontinuity and the plane wave transmission coefficients through layers above the discontinuity. The factor $\theta(p)$ in the phase originates from the phases associated with the WKBJ solutions to vertical wave functions in the transmission region above the discontinuity and the horizontal wave function for propagation to great circle distance Δ_o. Hence, the name WKBJ is applied to this method. In this method, body waves are synthesized by summing a series of representations of the type given by [19a]. Each body wave in this sum is assumed to be associated with rays that are either reflected by or turn just above the first inhomogeneous layer above each discontinuity (Figure 13).

Inversion to the time and space domain of the transformed solution $u(\omega, p, \Delta_o)$ of eqn [13] is performed by a slowness method rather than by a spectral method as commonly done in reflectivity methods. In slowness methods, the inversion to the time domain is performed analytically, recognizing that separate frequency-dependent factors in the integrand can be written as convolutions in the time domain. The final inversion to the space domain is performed by numerical integration over p by a method in which the combined phase factor $\theta(p) - t$ is sampled in slowness intervals corresponding to a fixed sampling rate in time t (Figure 14). This key step is contained in the phase sampling subroutine THETAC of Chapman's WKBJ original codes. The integration over horizontal slowness is truncated at points along the real p axis, which introduces truncation phases in the synthetic. These can be removed by approximating the phase function's dependence on ray parameter from the truncation slownesses to $\pm$ infinity, assuming a linear dependence on p, and analytically integrating the approximation (Chapman, 1978). A well-documented package of the WKBJ algorithm by A.R. Gorman, tailored toward continental-scale reflection and refraction, exists in the PLOTSEC package available at the website www.eos.ubc.ca/personal/amor/plotsec/plotsec_wkbj.html. A code for teleseismic applications and example inputs can be obtained from Chapman's contribution to the Seismological Algorithm text. Software for the evaluation of the delay time $\tau(p)$ in many standard Earth models can be obtained from the TauP Toolkit (Crotwell et al., 1999). Due to the need of separately describing ray interactions with discontinuities, the input to WKBJ codes is less black box-like than the input to typical reflectivity codes.

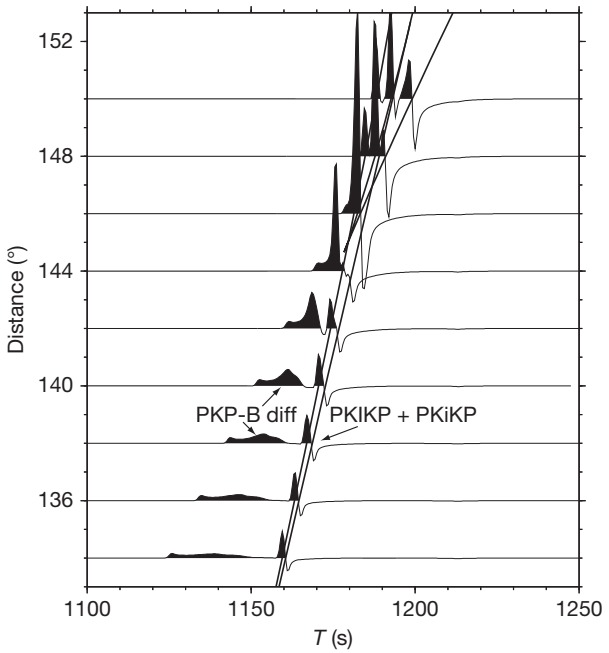

Figure 13 Seismograms synthesized by the WKBJ method for P waves interacting with the Earth's core using the program and example input by Chapman et al. (1988) distributed with *Seismological Algorithms*.

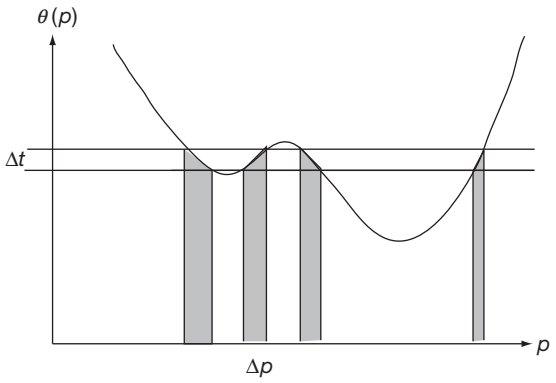

Figure 14 The ray parameter integrand in the WKBJ method is performed numerically by taking ray parameter intervals Δp equal to the desired sampling rate in time Δt as mapped by the total WKBJ phase function $\theta(p)$.

The Maslov technique (Chapman and Drummond, 1982) generalizes the WKBJ seismogram technique to 2D and 3D velocity variations. The restrictions of the asymptotic approximations still apply, that is, the medium scale length in any inhomogeneous region must be greater than the wavelength. Full implementation of the technique sometimes requires a careful averaging of solutions in slowness p space with those in the physical x space. Each of these spaces can contain caustics where a weight factor or geometric spreading factor becomes singular. Regions of models having strong spatial gradients, where the asymptotic approximations are failing, are often characterized by closely spaced caustics in slowness space and physical space for waves at grazing incidence to the strong gradient regions. In these regions, the weight factors averaging the solutions in phase and physical space can be difficult to design. This situation can exist if high-gradient zones define the boundaries of a thin high- or low-velocity zone (e.g., a subducting slab or the fault zone structure shown in Figure 17(a)). In these situations, it is better to define the anomalous structures by first-order discontinuities and apply boundary conditions for multiply-reflected and refracted body waves.

Compared to the reflectivity method, the WKBJ and its related Maslov extensions are computationally much faster and, hence, better suited to problems in waveform inversion that may require many repeated syntheses to evaluate a misfit or object function. The speed of these methods is due to the use of an asymptotically approximate solution in spatially varying layers. Therein, however, lies the limitation of these methods. The vertical variation must be sufficiently weak so as not to exceed the errors associated with the approximation. When there is a need to sum ray interactions with more than two or three first-order discontinuities in a distance range, the input parameters describing the separate ray interactions in some WKBJ codes can become complex unless a user-friendly input interface is provided.

1.06.4.4 Full-Wave Theory and Integration in Complex p Plane

The term full-wave theory can be applied to any technique that incorporates frequency-dependent effects of wave interactions with boundaries, including diffraction and tunneling. Any transform approach that includes a broad enough domain in frequency and wave number to simulate these frequency-dependent effects, often due to poles or branch cuts in the

response function, can be called a full-wave theory. This term was specifically applied to 1D structure by Cormier and Richards (1977) to an asymptotic spectral technique that inverts the slowness integral by paths Γ in the complex p plane and substitutes a Langer approximation for the WKBJ approximation to the vertical wave functions. The vertical wave function in the Langer approximation is given by

$$g^{(1)}_{(2)}(r,p,\omega) = \frac{\pi\rho_s V_s}{2\rho V}\frac{V_s e^{\pm i\pi/6}}{\omega\xi}\sqrt{\frac{\omega\tau}{V\xi}}H^{(1)}_{1/3}(\omega\tau) \qquad [20]$$

The Langer approximation remains regular at grazing incidence to boundaries where ξ and τ vanish but returns the WKBJ approximation where it is accurate. The integration over the contour Γ is carried out numerically, with Γ extended into regions off the real p axis where the integrand in eqn [13] exponentially decays. For portions of Γ along the real p axis, the integrand can be very oscillatory, and integration can be handled efficiently by Filon's method (Frazer and Gettrust, 1984). Full-wave theory includes tunneling, diffraction, and other phenomena related to frequency dependence of reflection–transmission coefficients at grazing incidence to boundaries. An example of the importance of these phenomena includes the very strong frequency dependence of the P wave that bottoms just above the core–mantle boundary and tunnels across the core–mantle boundary, exciting compressional (K) waves in the liquid outer core that multiply reflect along the underside of the core–mantle boundary (PKnKP waves; e.g., Richards, 1973). **Figure 15** compares a synthesis of SV waves interacting with the Earth's core by the asymptotically approximate full-wave method with a numerical method described in a later section (Rondenay et al., 2010). Full-wave theory has been extended (Rial and Cormier, 1980) to synthesize body waves that are strongly focused at the antipode (**Figure 16**) by using several asymptotic approximations to the Legendre function, which contributes to the phase for propagation in the horizontal or Δ direction.

The theory is most completely developed in Chapter 9 of Aki and Richards (2002) and in *Seismological Algorithms* (Cormier and Richards, 1988) where example codes and inputs are distributed. As an asymptotic theory, full-wave theory shares the limitations of WKBJ codes, in that care must be taken not to assume too strong a velocity and density gradient

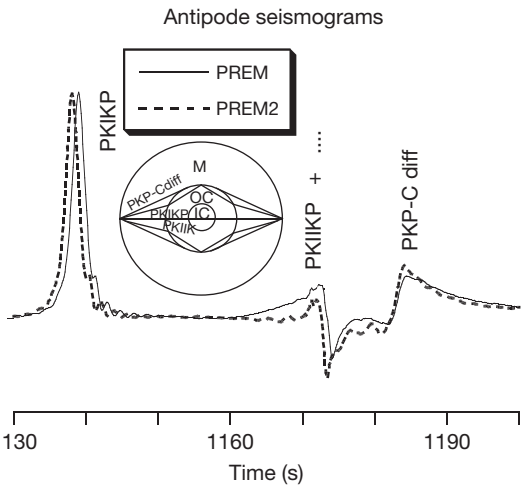

Figure 16 Synthetic seismograms computed by the full-wave method (Cormier and Richards, 1988) for the vertical component of ground motion for an explosive source-time function observed at 180° from the epicenter for the PREM and Song and Helmberger 's (1995) PREM2 modification of PREM's inner core.

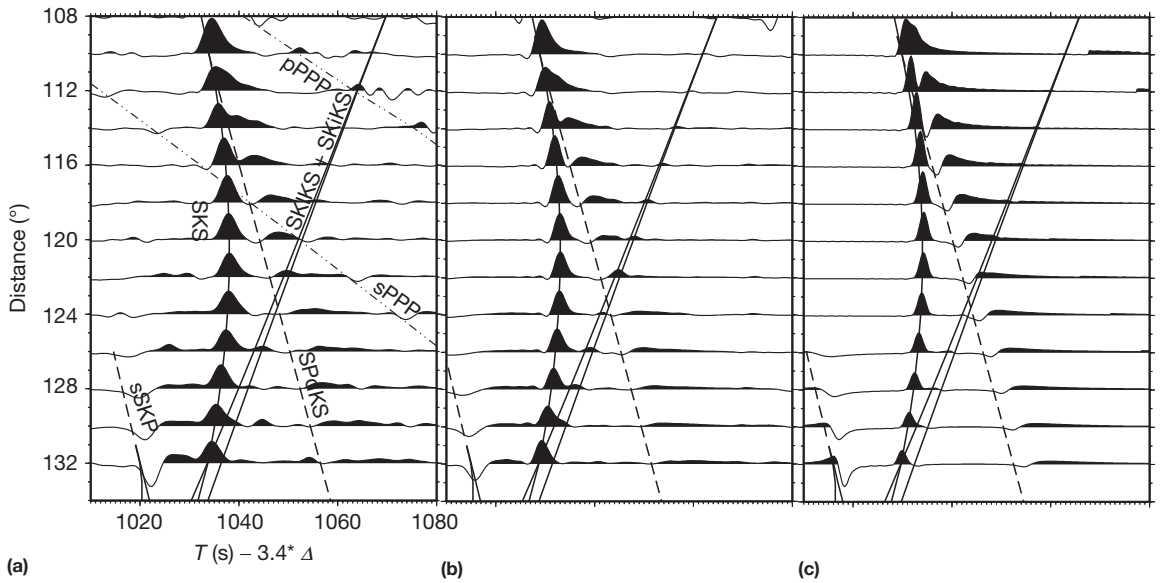

Figure 15 Radial component of displacement synthesized for a radial vector point source at 500 km depth synthesized (a) by the pseudospectral method with no Earth attenuation, (b) by the pseudospectral method with no S attenuation but the P attenuation model of PREM doubled to suppress interactions with discontinuities in the upper mantle, and (c) by an asymptotically approximate full-wave method with no attenuation. PREM-predicted ray theoretical travel times of SKS and SKIKS + SKIIKS + ··· + SKiKS are shown by solid lines; predicted earliest arrival times of diffracted SPdKS and the caustic diffraction of sSKP by dashed lines; and sPPP and pPPP by a dash–dot lines.

in each inhomogeneous layer. Added to the complexity in the description of ray interactions shared with WKBJ code input, the construction of full-wave theory integrands and complex integration paths can be challenging, particularly for interference head wave and antipodal problems. Often, it is best to start with example input files specifying ray descriptions and integration paths for these problems, which are distributed with *Seismological Algorithms*.

1.06.4.5 Ray Theory, DRT, and Gaussian Beams

Ray theory solutions to the elastic equation of motions consist of body wave pulses arriving at the least or stationary-phase time, scaled by amplitude factors due to products of plane wave reflections and transmissions and geometric spreading. In an inhomogeneous isotropic or anisotropic medium, the ray theory solution for a body wave is an asymptotic approximation that converges to an exact solution as frequency tends to infinity. Solutions for the vector displacement U of a body wave in the frequency domain start from a trial solution in the form of vector factors multiplying inverse powers of radian frequency ω:

$$U(\omega) = \sum_n \frac{\vec{A}}{\omega^n} \exp(\mathrm{i}\omega t) \qquad [21]$$

Substitution of the earlier form into the elastic equation of motion leads to the eikonal equation for ray trajectories and the transport equations for geometric spreading. Solution of the transport equation can be cast in the form of a system of linear equations in a ray-centered coordinate system termed the DRT equations. The errors in the approximation given by $n=0$ remain small for wavelengths much smaller than the scale length of the medium given by [18]. In practice, no more than the $n=0$ term is ever calculated because higher-order terms are expensive to calculate and can never properly include the frequency-dependent effects of waves reflected and converted by regions of high spatial gradients in velocity and density. Cerveny (2001) and the review in **Chapter 1.05** provided further details on the derivation, accuracy, and frequency-dependent corrections to asymptotic ray theory and review the relations between DRT, WKBJ/Maslov, and Gaussian beam summation.

The shape of the wave front can be estimated from the first and second spatial derivatives of the wave front at the end point of each ray on the wave front. This is referred to as a paraxial (close to the axis of the ray) approximation of the wave front. To calculate the first- and second-order spatial derivatives of the wave front, a system of linear equations must be integrated. These include (1) equations that solve the eikonal equation for ray trajectory by the method of characteristics, which describe the evolution of ray trajectory, its vector slowness $\mathbf{p}$, and travel time; (2) an equation to describe the rotation of ray-centered coordinates in which S wave polarization remains fixed; and (3) the DRT equations for matrices $\mathbf{P}$ and $\mathbf{Q}$ needed to describe the evolution of wave front curvature and geometric spreading. The vector slowness $\mathbf{p}$ is simply the spatial gradient of travel time, and the geometric spreading is related to the wave front curvature or second spatial derivatives of travel time. When a receiver is not near a caustic, the quantities determined from integrating the DRT system can be used to determine the frequency-independent ray theory solution, consisting of geometric spreading, travel time, and products of reflection/transmission coefficients. The paraxially estimated phase from the $\mathbf{P}$ and $\mathbf{Q}$ matrices of the DRT system can be used to either avoid two-point ray tracing by spatially extrapolating the travel time near a ray or iteratively solve the two-point ray-tracing problem. The travel time at a point $\mathbf{x}$ in the vicinity of a ray end point at $\mathbf{x}_o$ can be estimated by

$$T(\mathbf{x}) = T(\mathbf{x}_o) + \Delta\mathbf{x}^t\mathbf{p} + \frac{1}{2}\Delta\mathbf{x}^t\mathbf{H}\mathbf{M}\mathbf{H}^t\Delta\mathbf{x} \qquad [22]$$

where

$$\mathbf{M} = \mathbf{P}\mathbf{Q}^{-1}$$

and

$$\Delta\mathbf{x} = \mathbf{x} - \mathbf{x}_o$$

The 2×2 matrices $\mathbf{P}$ and $\mathbf{Q}$ are determined by integrating the system

$$\frac{\mathrm{d}\mathbf{P}}{\mathrm{d}s} = -v^2\mathbf{V}\mathbf{Q}$$

$$\frac{\mathrm{d}\mathbf{Q}}{\mathrm{d}s} = v\mathbf{P} \qquad [23]$$

along the ray path s. In eqn [22], $\mathbf{H}$ is the transformation from ray-centered coordinates to Cartesian coordinates. The columns of $\mathbf{H}$ are the vector basis of the ray-centered coordinate system at the ray point $\mathbf{x}$. $\mathbf{V}$ is a matrix of second spatial derivatives of velocity in the ray-centered coordinate system. The spreading $\mathbf{Q}$ can also be used to calculate geometric spreading [10]. The DRT system in eqn [23] can be generalized using a propagator, fundamental matrix formalism, similar to that used for propagating the solution to vertically separated equations of motion, except that in this system, the solutions are quantities related to wave front curvature and ray density rather than components of displacement and stress. Additional matrices need to be inserted into products of DRT propagator matrices to properly handle effects of discontinuities in both medium velocities and their first-order spatial derivatives.

Superposition of Gaussian beams is an extension of ray theory closely related to the WKJB/Maslov techniques. It amounts to a superposition of approximated wave fronts, weighted by a Gaussian-shaped window in space centered about each ray. Gaussian beams are defined by adding a small imaginary part to the matrix $\mathbf{M}$ in the paraxially extrapolated phase in eqn [22], which gives an exponential decay of a beam in space away from the central ray. The amplitude of each beam is proportional to real part of $\exp(\mathrm{i}\omega T)$, where T is made complex in eqn [22] by the inclusion of a complex $\mathbf{M}$. Beam summation remains regular in the vicinity of ray caustics, where geometric spreading vanishes and ray theory solutions become singular. It supplies approximate estimates of frequency-dependent diffraction in the shadow of caustics and grazing incidence to boundaries.

To properly model classical head waves, some care must be used in the design of beam weighting and beam widths. Weight

factors of beams are determined such that a superposition of beams returns a zero-order ray theory solution for the complex spectrum, that is, $U(\omega, x) = \exp(i\omega t)/\mathrm{sqrt}(\det(\mathbf{Q}))$, under a stationary-phase approximation to an integral over ray parameter or takeoff angles. WKBJ/Maslov is a special case of Gaussian beam summation. Superposition of Gaussian beams can give a nonsingular approximation to the solution of the wave field near a caustic, but does not suffer the problem the Maslov method has in combining caustics in phase (slowness) space. Restrictions on the validity of the Gaussian beam summation tend to be similar to that of the WKBJ/Maslov method. The scale length of the medium needs to be much larger than the wavelength and also larger than the beam widths (Ben-Menahem and Beydoun, 1985). **Figure 17** compares superposition of Gaussian beams with DRT for P waves interacting with a low-velocity fault zone.

For grazing incidence to regions of strong velocity gradient, such as the example shown in **Figure 17**, the paraxial approximation quickly fails and caustics become closely spaced, making it difficult to design optimal beam widths such that the paraxial approximations of the individual beams have small error in regions far from the beam axes.

The **P** and **Q** matrices and the propagator matrix of the DRT system developed by Cerveny and his coworkers are powerful tools that can simplify the coding and understanding of any problem requiring the use of ray theory. DRT can be exploited to calculate the integrand for Kirchhoff integrals (**Section 1.06.7.2**) and the banana-shaped sensitivity kernels, or Fresnel volumes, needed for frequency-dependent tomography (**Section 1.06.7.3**).

Computer codes for modeling seismic wave fields in 2D and 3D laterally varying structures by ray theory and Gaussian beam superposition can be obtained from Cerveny's group at Charles University (website: www.sw3d.mff.cuni.cz) as well as the World Data Center. The best-developed codes are tailored to continental-scale reflection–refraction problems. One version (ANRAY) is one of the rare codes that combine general anisotropy with 3D variations. A teleseismic-oriented version of DRT and beam summation was written by Davis and Henson (1993), with a user-friendly graphic interface.

1.06.4.6 Modal Methods

Solutions of the elastic wave equations can be obtained from either a superposition of ray/wave front solutions or a superposition of modes. Rays and mode representations are fully equivalent in accuracy if properly applied to a specific Earth model and frequency domain. In a modal approach, the eigenfunctions of free oscillation of a sphere have a characteristic frequency and are classified by the position of nodes at the surface and at depth where displacements go through a zero and change sign (e.g., Lapwood and Usami, 1981). For a modal solution to be accurate at the lowest frequencies of free oscillation, restoring forces due to gravity and rotation of the Earth must be included as additional forces in eqn [1]. In a spherically symmetrical, nonrotating, isotropic (SNREI) Earth, modes can be separated into either spheroidal or toroidal modes of oscillation. The motions of spheroidal modes are analogous to those of P and SV body waves and Rayleigh surface waves: those of toroidal modes to those of SH body waves and Love surface waves. Summation of normal modes of the Earth can provide a complete image of the wave field at the surface and at every depth (Dahlen and Tromp, 1998). Every body wave observed at the surface can be represented by a

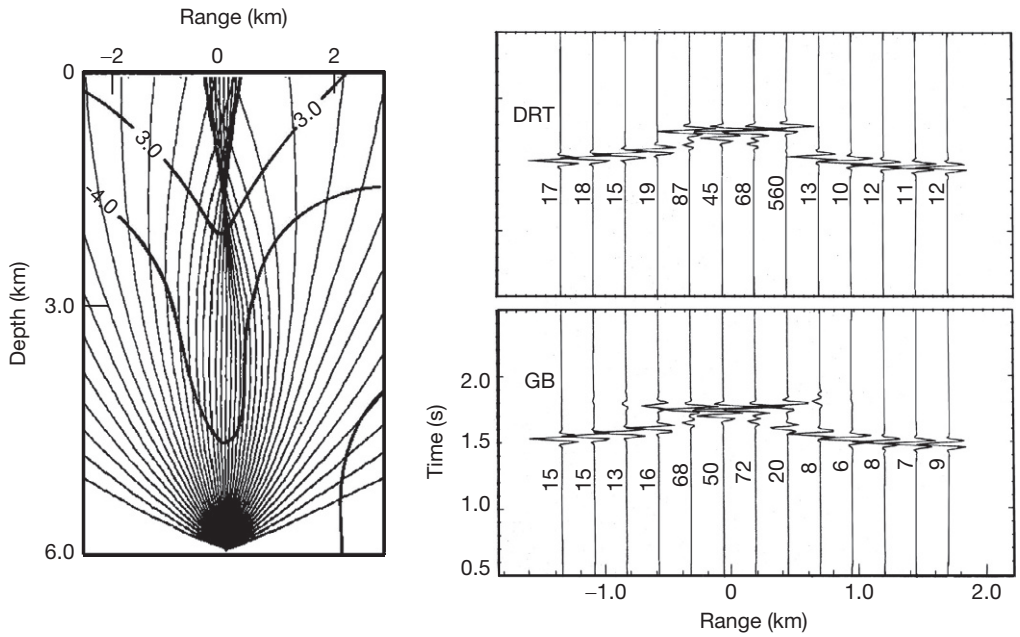

Figure 17 Left: Cross section of a fault zone P velocity structure and P wave rays for a hypocenter in the seismogenic zone. Right top: Ray theoretical synthetic seismograms calculated by dynamic ray tracing (DRT). Right bottom: Gaussian beam synthetic seismograms. Note the larger amplitudes (560 and 87) in the DRT synthetics compared to the smaller amplitudes and diffractions of the Gaussian beam synthetics near the ray caustics. A detailed discussion appears in Cormier and Spudich (1984).

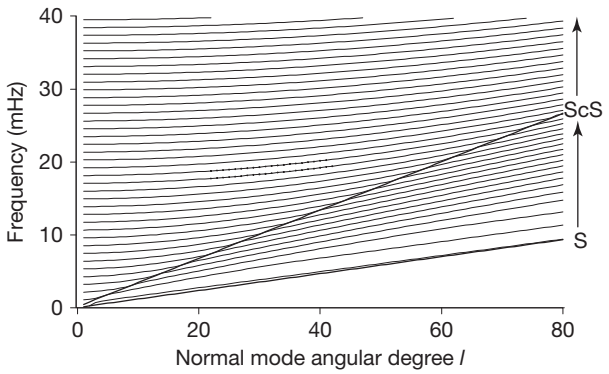

Figure 18 Toroidal modes plotted by connecting straight lines to discrete integer angular order number as a function of frequency. When summed, modes lying in the regions above the thick solid lines correspond to S and ScS. Reproduced from Dahlen FA and Tromp J (1998) *Theoretical Global Seismology*, 944 pp. Princeton: Princeton University Press, with permission.

subset of normal modes (**Figure 18**). The frequency-dependent effects of diffraction at ray grazing incidence to boundaries are also included in mode sums. The normal modes of a SNREI Earth can be efficiently computed on a single processor for frequencies up to 0.1 Hz. A code by G. Masters for synthesizing seismograms from sums of normal mode are included on the CD supplied with the International Handbook for Earthquake and Engineering Seismology (Lee et al., 2002).

An advantage of mode summation is that input parameters are especially simple, basically just an Earth model parameterization, a frequency band, and desired number of modes. Mode summation is routinely used in the inversion of complete seismograms to retrieve moment-tensor representations of earthquake sources (Dziewonski et al., 1981). A disadvantage is that it is limited to lower frequencies for practical computation on a single workstation. Effects of gravity, Earth rotation, anisotropy, and lateral heterogeneity remove degeneracy from SNREI modes and couple spheroidal with toroidal modes. Extensive literature exists on incorporation of the mode coupling induced by lateral heterogeneity by applying perturbation techniques to SNREI modes (e.g., Dahlen, 1987; Li and Tanimoto, 1993).

Another modal-type approach is that of locked modes. Here, the modes are not whole-Earth modes of free oscillation, but rather the surface wave modal energy that exponentially decays with increasing depth from the surface. Modes are numbered by sign changes in displacement with depth, the 0th mode corresponding to either the fundamental mode of the Love or Rayleigh surface wave. The integrand $u(\omega, p)$ in eqn [13] must first be constructed to include all interactions with the surface. The locked mode approach then evaluates the ray parameter or wave number integral of eqn [13] in the frequency domain by deforming the integration contour in the complex plane and applying the residue theorem to the integrand. A high-velocity capping layer is placed at depth, which locks plate-like modes into layers above the capping layer. The capping layer is placed deep enough such that mode sums representing waves of interest in a particular time window all turn or refract above the capping layer. Since all body waves, multiply-reflected in the layers above the capping layer, are included, the locked mode technique has a problem shared with the conventional reflectivity technique in which late arriving waves are folded back into a finite length time window. Similar to reflectivity, this problem can be handled by adding a small complex part to frequency. Harvey (1981) illustrated derivation of the technique in models described by plane homogeneous layers and available codes. An extension to vertically inhomogeneous layers using the Langer approximation is given by Cormier et al. (1991).

1.06.4.7 Numerical Methods

Fully numerical solutions of the elastic equations of motion can treat wave propagation in an arbitrarily complex 3D Earth, having velocity variations over a broad range of scale lengths. A full solution is obtained, containing body waves, surface waves, and all diffraction, head wave and leaky mode effects. **Chapter 1.07** reviews numerical techniques concentrating on current methods that can handle fully 3D models and complete seismograms. This subsection is a brief summary of some of the techniques that occur in the expanded discussions by Tromp, including both 2D and 3D techniques and those that are applied to primarily the highest-frequency body waves and shorter time windows.

The principal numerical techniques are finite difference and finite element. For accuracy up to ranges of 100–1000 wavelengths, conventional finite difference solutions typically are performed with fourth to eighth order difference approximations to spatial derivatives. The equations of motion are most commonly solved for particle velocity and stress on a staggered grid (Mozco, 2007; Virieux, 1985, 1986). The pseudospectral version of the finite difference method calculates spatial derivatives in the wave number domain, multiplying by ik and inverse Fourier transforming back to space (**Figure 19**). The pseudospectral method is computationally more expensive than higher-order differences but achieves much higher accuracy at long ranges, typically having little grid dispersion in applications to ranges of 10 000 wavelengths or higher. For this reason, the pseudospectral method can be an ideal choice for teleseismic applications where high accuracy is desirable at both regional and teleseismic ranges. Kosloff and Kessler (1990) and Fornberg (1998) reviewed both conventional finite difference and pseudospectral numerical approaches, estimating error and stability conditions.

An approximation that can greatly speed up numerical computation in complex 3D media is to start with a one-way or paraxial wave equation, in which backscattered energy is neglected for small perturbations in the medium and the predicted wave field is restricted to a narrow angular range around one direction, usually vertical or horizontal. Applications of this approach include the split-step Fourier transform method, the phase screen, and pseudo screen approaches (Wu et al., 2007).

Yet another method of efficiently handling the effects of 3D propagation of a point source is a model in which velocities and densities can be assumed to be functions of only two coordinates. This is often termed 2.5D modeling. For 2.5D numerical modeling, Randall (1991) described the velocity–stress finite formulation of finite differences, and Furumura and Takenaka (1996) described the pseudospectral approach.

The spectral element method formulated with the SPECFEM code (Komatitsch and Tromp, 1999, 2002; Komatitsch and Vilotte, 1998) is currently one of the few numeric methods

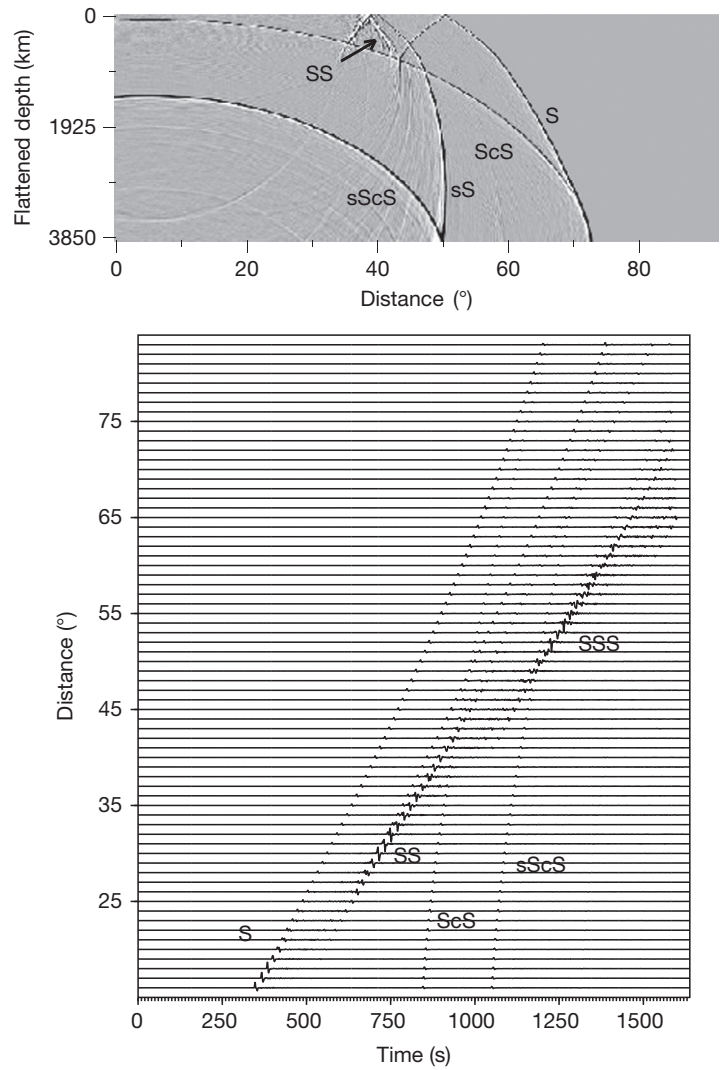

Figure 19 Wave fronts (top) and complete transverse (SH) component seismograms (bottom) synthesized by the pseudospectral method from Cormier (2000). Note the increase in amplitudes occurring at roughly 20° intervals in S, SS, and SSS due to rapid increases in velocity at upper mantle solid–solid phase transitions.

designed to handle a fully 3D Earth model. SPECFEM has a well-developed interface to grid the elements needed for arbitrarily complex 3D models. Versions of SPECFEM are available for both local/regional-scale problems for ranges on the order of 0–100 km and global- or teleseismic-scale problems. Another popular regional-scale code is the elastic finite difference program by Larsen and Schultz (1995), which has been applied to the effects of 3D basins and extended fault slip (e.g., Hartzell et al., 1999).

The direct solution method (DSM) is a technique that numerically solves a weak formulation of the equations of motion (boundary conditions specified by surface integrals) for a series of frequencies and wave numbers required for inversion to the time and space domain by a FFT (Cummins et al., 1994a,b). The particular numerical technique consists in expanding displacements in the frequency and wave number domain by a series of basis functions consisting of a product of splines in the vertical direction and spherical harmonics in the angular direction. In DSM, the coefficients for the basis functions are found by the method of weighted residuals (Geller and Ohminato, 1994). The SH and P-SV seismograms computed by DSM are complete, in that they contain all possible body and surface waves. Hence, DSM is a viable alternative to summing modes of free oscillation in higher-frequency bands. Weak 3D perturbations to a radially symmetrical background model are possible in DSM at a computational cost not much higher than that required for the background model (Takeuchi et al., 2000).

Computational time is a practical limitation to numerical modeling. Since most numerical techniques require Earth models specified on a spatial grid or elements, it is straightforward to parallelize the computation by decomposing the spatial grid or elements over multiple processors. Practical computations can be defined by time required to compute a problem. Depending on the algorithm and frequency band, common computer resources in most labs allow a complete teleseismic wave field to be synthesized in 1 or 2 days using 10–100 processors in parallel. Typical body waves having a

high signal-to-noise ratio in the teleseismic range (10°–180°) exist up to 2 Hz. Practical 2D modeling can be currently performed at teleseismic range up to 1 Hz with finite difference and pseudospectral methods; 3D problems with the SPECFEM finite element method can be done up to 0.1 Hz in this time period with a similar number of processors. At ranges less than 100 km, 3D problems can be practically performed at frequencies up to 1 or 2 Hz (order of 200 wavelengths). This range and frequency band just starts to cover the frequencies of interest to strong ground motion. Frequencies up to 10 Hz at 2000 km range (>5000 wavelengths) in complex 3D structure are of interest to the problem of discriminating earthquake sources from underground nuclear tests. This is a research problem that is still inaccessible with small to moderate size clusters (<100 nodes) and numerical methods.

A large body of literature exists in the application of finite difference and pseudospectral solutions for local-scale problems up to 100 km for exploration applications and strong ground motion applications (e.g., Hartzell et al., 1999; Olsen, 2000). Significantly smaller amounts of published work exist for applications at regional distances (100–2000 km), in which waves are primarily trapped in the crust and the uppermost mantle, and a much smaller amount exists for teleseismic propagation (e.g., Cormier, 2000; Furumura et al., 1998; Igel, 1999).

1.06.5 Parameterization of the Earth Model

An important choice in modeling a seismogram will be the parameterization of the Earth model or how to describe the spatial variation of its elastic moduli and density (Figure 20). The choice of parameterization can have important geodynamic and geochemical implications and is often tightly coupled to the choice made for the modeling algorithm.

1.06.5.1 Homogeneous Layers Separated by Curved or Tilted Boundaries

Certain parameterizations allow seismograms to be synthesized by simple analytic formulas. For example, if the Earth is isotropic and homogeneous, then ray paths are straight lines. The amplitude of body waves are inversely proportional to distance between source and receiver, $1/|\mathbf{x}_o - \mathbf{x}|$. A received waveform is simply the far-field approximation of the source-time function $S(t)$ evaluated at the retarded time, $S(t - |\mathbf{x}_o - \mathbf{x}/v|)$. This simple solution can be extended to models described by sequences of homogeneous layers bounded by planes of varying dip by incorporating elastic boundary conditions at each boundary to calculate reflection/transmission/conversion coefficients. Snell's law is applied in an incidence plane defined by ray direction and interface normal. Geometric spreading can be calculated from a simple function of ray length in each layer. This algorithm is just ray tracing and DRT applied to homogeneous layers.

Stacks of homogeneous layers can accurately describe continuous spatial variations, provided that the discretization of the model is much finer than the shortest wavelength of interest. The accuracy of the ray solution depends on the ratio of wavelength to the shortest radius of curvature of the boundaries. The frequency dependence of reflection by curved boundaries can be treated by the Kirchhoff integral technique.

1.06.5.2 Vertically Inhomogeneous Layers

Except for the case of back-of-the envelope calculations and the limiting case of layering much finer than wavelength, the Earth cannot often be well approximated by either homogenous planar or radially symmetrical layers. Velocities and densities vary in all three coordinate directions, but the next most important approximation of the Earth is to make this variation occur in the vertical direction. If this vertical variation is approximated by thin homogeneous plane layers and an EFA (Section 1.06.4.1), then simple plane wave or analytic

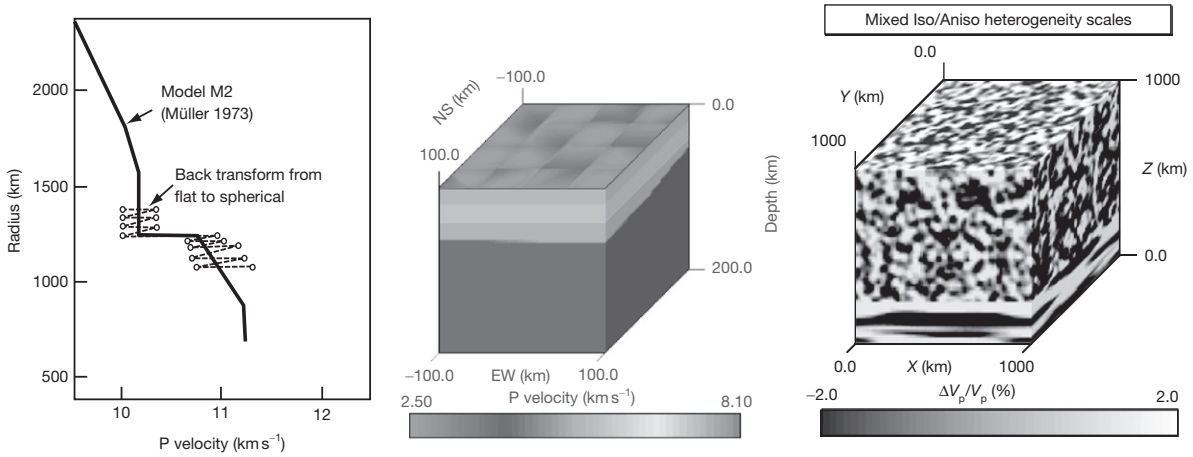

Figure 20 A comparison of the PREM model parameterized by continuous polynomials in radius versus the EFA and discrete homogeneous layers and discrete parameterization back-transformed to a spherical model (Aki and Richards, 2002; Müller, 1973). Bottom left: A 3D model of the crust and uppermost mantle beneath Nilore, Pakistan, parameterized by Delaunay tetrahedra constructed from codes by Sambridge and Gudmundsson (1998). Bottom right: A 3D model for testing the effects of possible structure near the core–mantle boundary having P velocity perturbations with both isotropic and anisotropic spatial distributions, constructed using the techniques described by Frankel and Clayton (1986).

solutions to the wave equation can still be effectively employed in each layer. In addition to errors associated with the EFA, this discretization should consider physical constraints of finite strain and buoyancy neutrality to be realistic, or at least the consequences of those constraints need to be evaluated. Except at or near-vertical incidence, body waves are notoriously insensitive to density variations, and it is especially easy to ignore unphysical effects of any constraints on the velocity–density relations of known materials or the geodynamic effects of buoyancy. The parameterization of the Earth by polynomials analytic in depth was proposed in PREM (Dziewonski and Anderson, 1981) in part to obey the constraints of stable stratification. Modifications to PREM and other reference Earth models should attempt to take similar care in obeying such constraints. Methods using asymptotic ray approximations to vertical wave functions (e.g., WKBJ, full-wave, and GRT) are readily adaptable to this parameterization simply by extending the calculation of delay time $\tau(p)$ to numerical integration over radius or depth. Alternative parameterizations are computationally more efficient, including some that allow $\tau(p)$ to be obtained by analytic integration (Cerveny, 2001), but little penalty is involved with current generation processors by calculating $\tau(p)$ by numerical integration over radius.

1.06.5.3 General 3D Models

Tomographic images are often the starting point of synthetic modeling in 3D. The two most common parameterizations of these 3D models are either by spherical harmonics (e.g., Gu et al., 2001; Masters et al., 2000; Ritsema and van Heijst, 2000; **Chapter 1.10**) or by block volumetric elements (e.g., Grand et al., 1997). Except in fully 3D modeling methods such as SPECFEM, a choice made in all 2D modeling methods is to assume that body wave propagation remains in the sagittal plane and to compute motions in a 2D model derived by taking a cross section of the 3D model. If velocity perturbations are assumed to be the same as the typically small (<3%) perturbations of the original tomographic model, the assumption of propagation remaining within or close to the sagittal plane is quite accurate. Indeed, to be consistent with the assumptions of linearized tomographic inversion, it is appropriate to even assume that paths are unperturbed from those in a reference model in the computation of travel times in ray-based methods. In this case, the results of the forward modeling can be disappointing, in that the only change in synthetic seismograms from those computed in a reference model will be small changes in relative travel times with little or no waveform perturbations. Larger variations in amplitudes and waveforms can be achieved with higher perturbations that violate the assumptions of linearized tomographic inversions.

Since tomographic imaging can smear a more intensely perturbed anomaly over its sampled ray paths into a smoother, less intense anomaly, one approach used in forward waveform modeling is to multiply the perturbations of the tomographic starting model by a scale factor. Some success in matching waveforms by this technique has been achieved using factors of 2–3 to multiply the images of tomographically estimated perturbations to shear velocity (Ni et al., 2000). Some adjustments in the boundaries of anomalies were also necessary to obtain good matches with observed waveforms. Starting with a tomographic model parameterized by spherical harmonics, Bréger and Romanowicz (1998) and To et al. (2005) achieved a good match to S waves interacting with the core–mantle boundary by preserving the boundaries between the largest-scale positive and negative velocity anomalies but increasing the maximum and minimum values of velocity perturbation. These ideas have been extended by Sun and Helmberger (2011) to include the possibility of multipathing induced by very strong velocity perturbations outside of the domain of validity required by linearized travel time tomography. Steps in the analysis include an inversion for waveform multipaths represented by summing a predicted signal $S(t)$ in a reference model with one or more delayed echoes of that signal. Modeling then proceeds by trial and error modeling, followed by a rigorous fitting of complex waveforms to numerically computed waveforms in 3D models constructed by amplifying the strongest perturbations found in the tomographic inversion (**Figure 21**). Important to the success in the waveform fitting is an accurate representation of the far-field source-time function, which may be separately determined by either modeling or empirical observation in distance ranges without multipathing. Assessing the nature of multipathing in complex 2D and 3D structures is an important step both in the construction of an Earth model and in the choice of the waveform modeling method. Useful tools in assessing multipath behavior include the computation of the Lyapunov exponent along a ray, for example, Cerveny et al. (2007).

Another model attribute important to its physical plausibility is the intensity of small-scale velocity (on the order of wavelength) and density fluctuations. The coda of body waves interacting with crustal heterogeneity is consistent with the scaling of P velocity and density fluctuations such that $\mathrm{d}\ln\rho/\mathrm{d}\ln V_\mathrm{p} = 0.8$ (Sato et al., 2012). In the mantle, however, it is difficult to sustain such high-density fluctuations because the anomalies would buoyantly sink or rise. Geodynamic modeling of mantle convection commonly assumes a much lower scaling ($\mathrm{d}\ln\rho/\mathrm{d}\ln V_\mathrm{p} < 0.1$) between the density and velocity fluctuation.

Sophisticated and user-friendly tools for gridding 3D models have existed in exploration and engineering applications for some time but are often available only as expensive commercial packages. One public domain package is distributed with the finite element SPECFEM code. Another set of tools are those that employ irregular cells specified by Voronoi tetrahedra, which use a nearest-neighbor interpolation to calculate velocities and their first spatial derivatives on irregularly spaced 3D grids (Sambridge and Gudmundsson, 1998). This can be used in conjunction with the convex hull grid mapping software from the University of Minnesota (www.geom.uiuc.edu/welcome.html) to retrieve a physical quantity and its spatial derivatives at any coordinate point. One example where this approach can be examined are the 3D slab models shown in Sambridge's web pages (www.rses.anu.edu.au/seismology/projects/RUM/slabs/slabs.html), where velocity perturbations have been centered on Benioff zone seismicity.

Some computational difficulties can arise in the parameterization of general 2D and 3D models due to the handling of first- and higher-order spatial derivatives of velocity. Ray and asymptotically approximate methods of solving elastic propagation are strictly valid for relatively slow spatial variation of

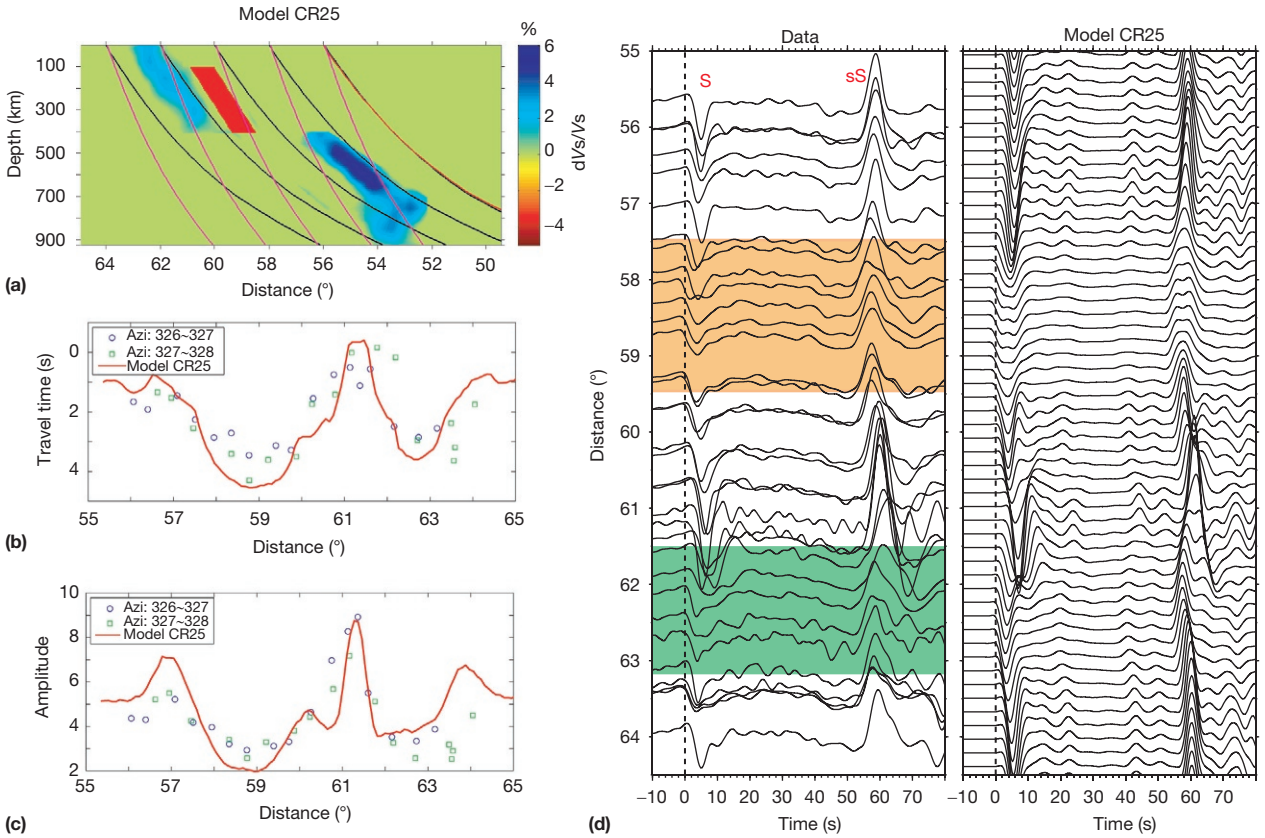

Figure 21 2D modeling of the S and sS waveform data from Sun and Helmberger (2011). The best-fitting model CR25 in (a) was produced by removing small structures and inflating features producing the multipathing in a P tomographic model. The top blue region is inflated by 2.5 and the bottom one is inflated by 4. The comparisons of travel time and amplitude of S are displayed in (b) and (c). (d) Comparison of data against 2D finite difference (FD) synthetics from model CR25. The model produces the strong multipathing around 58° (yellow region) and 62° (green region) for both S and sS phases in the data. The large amplitude at 61° is also predicted by this model. Reproduced from Sun D and Helmberger DV (2011) Upper-mantle structures beneath USArray derived from waveform complexity. *Geophysical Journal International* 184: 416–438, with permission.

velocity, where medium scale lengths are much larger than wavelength. Some parameterizations that interpolate velocities in space can introduce high gradients in velocity that lead to false caustics where geometric spreading fails. Spatially continuous interpolations like spherical harmonics and cubic splines can introduce large first- and second-order spatial derivatives of velocity as perturbations increase. Some DRT codes of the Cerveny group use a spline under tension routine (Cline, 1974) to interpolate between velocities specified at grid points to reduce the size of spurious gradients introduced by the interpolation. In cases of high perturbations with sharp boundaries, wave interactions with the anomalies must be treated by solving boundary conditions on the boundaries of the anomalies (e.g., Imhof, 1996; Korneev and Johnson, 1993), including numerical implementations of the boundary element method (e.g., Gerstoft and Schmidt, 1991; Pointer et al., 1998).

A simple parameterization allowing for fast analytic computation of amplitudes and ray paths is that used by the code Ratrace3D by Menke (2005), which can be downloaded from the IRIS website (www.iris.edu). The Earth model is parameterized by tetrahedra constructed from a grid specified in Cartesian coordinates. Linear interpolation of velocities between knots ($v = a + bx + cy + dz$) is assumed in each tetrahedral element, allowing ray paths to be computed analytically as summed segments of circles. Raytrace3D is primarily intended for calculating travel times rather than synthetic seismograms at local and regional ranges. The fast analytic computation of travel times and ray paths of this code is ideal for nonlinear tomographic inversions where it is necessary to assume large perturbations from a background model. Although Raytrace3D provides an option for calculating geometric spreading, modifications are necessary for the code to properly handle the effects on geometric spreading given by discontinuities in the first-order derivatives (see **Section 1.06.4.5**) of velocity at tetrahedra facets.

Rapid advances in computation have made it possible to more routinely include the effects of heterogeneity on the scale of wavelengths using numerical finite difference and finite element methods. It is usually impossible to know fine-scale structure except in a statistical sense as a spatial spectrum of heterogeneity. The most common way of constructing these types of models is to impose a random number generator at finite difference or element grid points, Fourier transform the grid from physical space to wave number space, filter by an assumed spatial spectrum of

heterogeneity, and inverse Fourier transform to physical space (Frankel and Clayton, 1986). This idea has been extended to media that may be composed of 2 or n types of specific rocks or medium phases (Holliger et al., 1993).

1.06.6 Instrument and Source

Assuming an Earth model and one of the algorithms previously described, a Green's function solution of the elastic equation of motion can be computed for a vector point force localized by a delta function in time and space. Linearity of the elastic equation of motion makes it possible to apply a principle of superposition to write the solution for a generalized source as a convolution of the source representation with Green's function solution. For three components of motion, Green's function of an elastic medium is a tensor $G_{nm}\left(\vec{x}_r, \vec{x}_s\right)$ representing the response of the model to a unit vector of force applied in a coordinate direction m at the source point $\vec{x}_s$ and observed at a receiver $\vec{x}_r$ along coordinate direction n (Snieder, 2002). Depending on the time window of interest, Green's function may contain all possible body, surface, and multiply-scattered waves in a structure or just one or several body waves due to a vector point source. A property of the elastic Green's function useful for imaging is reciprocity, in which the position of the source and receiver can be reversed if the orientation of the vector point force is exchanged with the orientation of the received component of motion, that is, $G_{nm}\left(\vec{x}_r, \vec{x}_s\right) = G_{mn}\left(\vec{x}_s, \vec{x}_r\right)$.

Once the model Green's functions are determined, the remaining tasks in synthesizing a seismogram consist of either incorporating or removing the effects of the seismograph response and source-time function. This task can again be simplified using the ideas of superposition and linear systems. Body waves observed at teleseismic range can be thought of as a series of convolutions with a model response $M(t, \Delta_o)$ consisting of one or more components of Green's function, an instrument operator $I(t)$, a source-time function $S(t)$, a receiver crustal response $C(t, \Delta_o)$, and an attenuation operator $A(t, \Delta_o)$:

$$U(t, \Delta_o) = I(t) * \mathbf{S}(t) * \mathbf{C}(t, \Delta_o) * \mathbf{A}(t, \Delta_o) * \mathbf{M}(t, \Delta_o) \qquad [24]$$

The crustal response $C(t, \Delta_o)$ is composed of a sum of multiply-reflected and converted body waves trapped inside the crust excited by a P or S wave at near-vertical incidence on the crust beneath the receiver.

Two common choices are either to (a) convolve all of the operators in eqn [24] and compare the resultant synthetic seismogram with an observed synthetic seismogram or to (b) deconvolve as many operators as possible to retrieve the model response to a delta function impulse. The first choice has been the more common, but as the density of receiver and source arrays has approached that common in exploration seismology, the deconvolution choice has become increasingly popular. Deconvolution can increase (whiten) the frequency content of the wave field and hence its spatial sensitivity. It allows different sources, receivers, and instruments to be combined to invert an observed wave field to an image of reflectors and scatterers (e.g., Rost and Thomas, 2002).

1.06.6.1 Instrument Responses and Deconvolution

The Fourier transform of $I(t)$, or $I(\omega)$, is a filter that is typically a narrow band-pass of particle velocity. (A complete review of seismic instrumentation is given in Chapter 1.02.) Most instrument responses are now reported by complex poles, ω_p^i, and complex zeros, ω_o^i, from which the complex frequency response $I(\omega)$ of the seismograph can be represented by the representation

$$I(\omega) = \frac{(\omega - \omega_o^1)(\omega - \omega_o^2)\ldots(\omega - \omega_o^n)}{(\omega - \omega_p^1)(\omega - \omega_p^2)\ldots(\omega - \omega_p^n)} \qquad [25]$$

The effect of the instrument can then be included by filtering the synthetic spectrum by multiplying by $I(\omega)$ and inverse Fourier transforming the result to the time domain. Alternatively, the instrument can be deconvolved by spectral division, but $I(\omega)$ must be modified by adding a constant term (water level) to avoid division by zero as the response goes to zero outside the passband of the instrument. The instrument response can be deconvolved to displacement, velocity, or acceleration (Figure 22). The deconvolved particle velocity in the passband of 0.01–2 Hz usually offers the best compromise between useful information content and high signal-to-noise ratio for teleseismic body waves. Deconvolved displacement, however, offers nearly a direct observation of the far-field source-time function, given by shape of the P or S wave displacements in the range of 35°–90°. In this range, the waveform of the observed displacement is primarily affected by the pulse broadening due to viscoelastic attenuation.

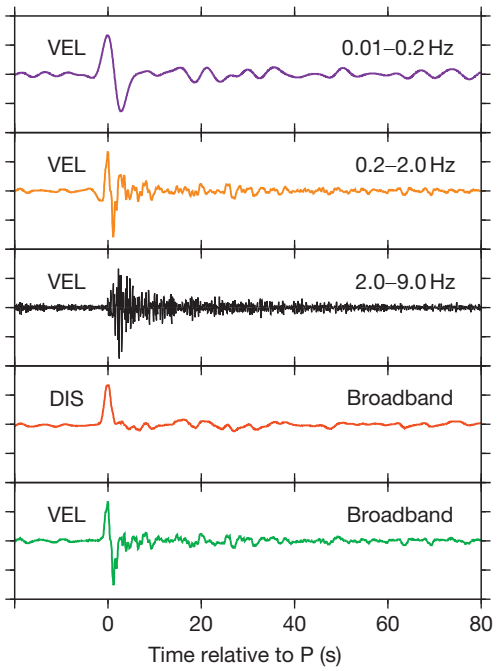

Figure 22 Filtered, instrument-deconvolved, particle velocity and displacement of a P wave typical of a magnitude 5.5–6.8 earthquake observed at great circle distance 68.72°.

1.06.6.2 Far-Field Source-Time Function

Detailed and accurate representation of the forcing function of the elastic equation of motion, or source-time function, requires the input of both theory and experiment for brittle failure and stick-slip friction. Chapter 4.02 provides a review of source representations and the physical assumptions behind them. For most modeling applications, a simple far-field representation and a judicious choice of earthquakes are all that is needed to begin to separate the effects of source from the effects of structure.

The far-field displacement is proportional to the time derivative of a moment-rate tensor $d\mathbf{M}(t)/dt$. A common scalar moment M_o can be factored out of $d\mathbf{M}(t)/dt$, leaving a far-field source-time function $S(t)$. In the case of an earthquake faulting source, $S(t)$ is proportional to the time derivative of its slip history (e.g., Shearer, 1999, Ch. 9). An operator combining the convolution of $S(t)$, $A(t, \Delta_o)$, and $C(t, \Delta_o)$ can be derived from either inversion or empirical observations of instrument-deconvolved P wave displacements at all distances between 30° and 90°.

The $S(t)$ of many earthquakes having body wave magnitudes less than 6.5 often can be adequately represented by a simple triangle-shaped pulse, where the triangle width is related to the corner frequency and fault length in a Brune (1970) model of the source spectrum. A body wave magnitude of 5.5 is often the practical lower limit to modeling because earthquakes smaller than this size rarely generate sufficient teleseismic recordings of body waves having a high signal-to-noise ratio. After factoring out the time-dependent factor $S(t)$ and scalar moment M_o from the moment-rate tensor, a radiation pattern $R(\phi, p)$ can be constructed from weighted elements of the moment-rate tensor where ϕ is the azimuth and p is the ray parameter of a body wave ray connecting source and receiver. This weighting is equivalent to representing general faulting by three fundamental types of faulting or source types (e.g., Aki and Richards, 2002, Ch. 4).

The process of factoring out a slip time history from a point-source radiation pattern should be avoided for earthquakes having body wave magnitude greater than 6.5 or fault lengths greater than 50 km. For these larger earthquakes, a simple point-source representation fails, and the time history and the slip distribution become too complex to be easily separated from the waveform complexities due to structure.

If it were not for the fact that the majority of earthquakes are at depths of 20 km or less, incorporating a radiation pattern $R(\phi, p)$ in the integrand of eqn [13] would be all that is needed to include an earthquake source at teleseismic range. Since most earthquakes are shallow, the effects of surface reflections near the source (pP, sP) generally need to be included in modeling a 5–10 s time window surrounding an observed body wave. The effect of different radiation patterns for the near-source reflections is helpful in inversion of teleseismic P waves for the far-field moment-rate tensor (Langston and Helmberger, 1975). The inverted source depth and point-source representation (centroid moment-rate tensor) can be used to construct a predicted equivalent source-time function and radiation pattern containing P + pP + sP waves (Figure 23). Alternatively, the effect of the surface reflections can be handled by incorporating the moment-rate representation at the appropriate depth in reflectivity or mode summation techniques or be included by separately adding predicted pP and sP waveforms to P waveforms synthesized by either ray-based or transform methods.

At local and regional ranges, surface interactions as well as a more detailed source description can often still be handled by superposing far-field point-source representations. These point-source representations can be distributed at discrete points along the fault plane, delayed by the time slip initiates and stops at each discrete point. This type of source representation is said to be kinematic rather than dynamic because the slip history is prescribed rather than resulting from a condition related to either crack failure or friction on the fault surface. At very close range, the wave field can be well approximated by a few simple directly arriving body waves, and the far-field Green's function for each body wave can be calculated by ray theory. The synthesis problem can then be reduced to an integral over the fault plane in which the integral is carried out over lines of equal arrival time of energy (isochrones) corresponding to the sum of the rupture time to a point on the fault and the travel time of a body wave to a receiver (Spudich and Frazer, 1984). The effects of 3D structure or frequency-dependent diffraction can be incorporated in this technique by substituting Green's functions calculated by ray theory, Gaussian beam summation (e.g., Cerveny et al., 1987), and/or WKBJ/Maslov superposition of plane waves. See Chapter 4.20 for a complete review of algorithms for synthesis at local ranges in which spatially extended slip models are required for earthquake slip inversions and simulation of strong ground motions.

1.06.7 Heterogeneity, Attenuation, and Anisotropy

1.06.7.1 Adapting 1D Codes to 2D and 3D

Since the delay time $\tau(p)$ in the WKBJ, GRT, and full-wave methods can be calculated from integrals of vertical slowness up to ray turning points, it is simple to calculate $\tau(p)$ in an Earth model with different 1D velocity and density profiles beneath the source and receiver above the ray turning points. For example, to calculate the effect of the upper mantle in the eastern United States to a station in the western United States, one might use two different models, keeping track of where rays enter and leave the two models (Helmberger et al., 1996). In reflectivity methods, it is a little more difficult, but not impossible, to incorporate different receiver and source-side models. One would need to separately consider a receiver and source-side transmission response. Control of ray expansions within thin layers as in Kennett's formulation of the reflectivity method makes it possible to consider the effects of more general 2D models.

Purely ray-based methods, such as theory and its extensions as a superposition of Gaussian beams or Maslov plane waves, can consider continuously varying models in 2D or 3D space. Modal methods, including the locked mode method, can be adapted to 2D, 3D, and anisotropic models by calculating the coupling between modes, including interactions between Love and Rayleigh modes. Maupin (1989), Maupin and Kennett (1987), Kennett (1998), and Panza et al. (2001) described

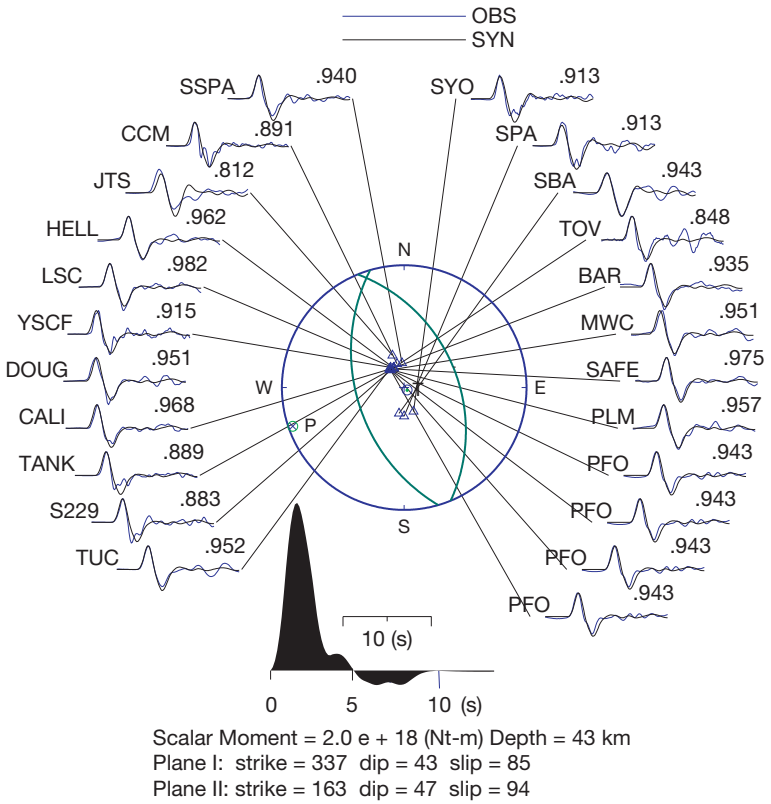

Figure 23 P wave particle velocities from an earthquake beneath Chile that occurred 3 November 1997. Numbers near the waveforms are the cross correlation of the observed with synthetic waveform. Waveforms are displayed at azimuths from the source around a lower hemisphere plot of the fault-plane solution. The far-field source-time function of displacement, shown by the black-filled waveform, is determined from modeling the P waves as a combination of P and surface reflected pP and sP waves.

schemes for calculating modal coupling and showed seismograms synthesized for rapid crustal transitions. Deuss and Woodhouse (2004) developed methods to calculate full normal mode coupling, which Irving et al. (2008) have used to calculate the effects of general anisotropy in the inner core on low-frequency body waves.

1.06.7.2 Hybrid Methods

To save computation, it is sometimes necessary to combine two methods, a computationally cheaper method in a large region and a computationally more expensive method in a small region, to study structural complexity near a boundary or region of rapid velocity or density transition. Usually, the computationally more expensive method is a numerical method, such as finite difference or spectral element. The usual way in which the two methods are connected is to compute a Kirchhoff integral. The integral is carried out on a surface or boundary that separates the structurally complex region from the simple region, employing Huygens principle to connect the wave fields in the two regions by allowing each point on a wave front to propagate as a new point source. Kirchhoff integrals can also be used to calculate the effects of scattering by inclusions or the frequency-dependent reflection or transmission across a curved interface when the radius of curvature is on the order of a wavelength. A hybrid method of this type was used by Wen and Helmberger (1998) to study heterogeneity in the lowermost mantle using a finite difference method, connecting it to GRT in a radially symmetrical overlying mantle. The most detailed treatment of fully elastic integrands for P, SV, and SH waves can be found in Frazer and Sen (1985). Probably due to the need for intense customization for specific problems, codes for Kirchhoff integrals are not generally distributed. A good starting point for any application are the acoustic problems described in Shearer (1999, pp. 138–140), which can then be generalized using the elastic formulas in Frazer and Sen (1985).

Capdeville et al. (2003a) developed a hybrid method that allows modal solutions in large homogeneous or weakly heterogeneous regions to be coupled to the numerical spectral element (SEM) solutions in strongly heterogeneous regions. This hybrid method has been applied to a thin, strongly heterogeneous, D″ region at the base of the mantle sandwiched between a homogeneous core and mantle (Capdeville et al., 2003b; To et al. 2005). A similar approach might also be feasible at higher frequencies and local and regional ranges by coupling locked surface wave modes to SEM solutions.

1.06.7.3 Frequency-Dependent Ray Theory

Recognition that ray theory is an approximation applicable at high-frequency, corrections to the ray theoretical approximation can be based on a Born approximation that corrects amplitude and travel times in such a way that a finite region

in space determines the amplitude and travel time of a body wave, making both dependent on frequency (Dahlen et al., 2000). **Chapter 1.05** provides reviews and additional references on this calculation. Cerveny (2001) and Cerveny et al. (2007) also described these and other frequency-dependent corrections. One way in which the banana–doughnut sensitivity kernels needed to calculate the frequency dependence of travel times and amplitudes is to use the paraxial approximation around a central ray provided by DRT. Sensitivity kernels derived from the Born approximation show that travel time is most sensitive to velocity along the boundaries of the banana or rim of the doughnut away from the central ray, whereas amplitude is most sensitive to velocity in the center of the banana in the doughnut hole. The travel time sensitivity is closely related to the behavior of the stationary-phase approximation, in which the path is assumed to be invariant for variations in velocity along the central ray. It is important to recognize that an accurate measurement of the frequency-dependent effects on travel time depends on waveform measurements in which the effects on amplitude and phase are combined. To properly incorporate these combined effects in a tomographic inversion, a synthetic waveform must be cross correlated with an observed waveform to obtain a travel time residual. Except in tomographic inversion, these frequency-dependent corrections to ray theory using the Born approximation have not yet been used or tested as a general forward modeling technique. It is as yet unknown how the weak dispersion due to velocity variation trades off with the weak dispersion due to viscoelasticity (**Section 1.06.7.4**) or how accurate the amplitude correction due to a simple Born approximation is compared to that predicted by the generalized Born approximation of Coates and Chapman (1991).

The frequency-dependent, banana-shaped, sensitivity kernels of seismic rays can also be calculated from a modal approach using a nonlinear perturbation theory (Li and Romanowicz, 1995). In this case, the forward modeling approach is mode summation. The approximations and behavior of errors due to asymptotic approximations of the effects of heterogeneous structure are better understood in this method but are practically limited to frequencies on the order of 0.1 Hz and lower.

1.06.7.4 Attenuation

Romanowicz and Mitchell in **Chapter 1.25** and Cormier (2011) review physical mechanisms and global models of seismic attenuation. Jackson (2007) reviews laboratory experiments that investigate microscopic mechanisms of intrinsic attenuation. This subsection reviews common procedures for incorporating attenuation into the synthesis of body waves.

Viscoelasticity is the term that best describes the type of seismic attenuation resulting from the dissipation of elastic energy into heat. This heat dissipation is analogous to the heat dissipated in electric circuits, where stress is analogous to current, voltage is analogous to strain, and complex impedance is analogous to a complex compliance (reciprocal of a complex elastic modulus). For ray-based and integral transform-based methods, viscoelastic attenuation is most directly treated by making velocity complex through the square root of a complex modulus divided by density under the assumption of the correspondence principle (Borcherdt, 2009; Carcione, 2007). The effect of attenuation on the spectrum of a propagating body wave can be written as

$$A(\omega) = e^{i\omega T(\omega)} \qquad [26]$$

where $A(\omega)$ is just the Fourier transform of the attenuation operator $A(t)$ in eqn [24]. The complex travel time $T(\omega)$ is determined by integrating a ray over a path in which velocity is complex and frequency-dependent, or $T(\omega) = \int_{path} ds/V(\omega)$.

The frequency dispersion of velocity in a viscoelastic medium is similar to the dispersion of a complex index of refraction in electromagnetic propagation, in which absorption is always associated with dispersion. In body waves, this dispersion is small and difficult to detect with narrow band instrumentation. In sufficiently broadband recordings, viscoelastic dispersion is detectable as an asymmetry in the propagation of delta function time pulse. High frequencies travel faster than low frequencies, making a steeper rise time than fall time as the pulse propagates (**Figure 24**). Velocity dispersion was first recognized to be important in global seismology when the elastic moduli derived from the study of low-frequency free oscillations were found to be smaller than those derived from the travel times of high-frequency body waves (Dziewonski and Anderson, 1981).

There is a consensus that the quality factor, Q, in the attenuation of teleseismic body waves is nearly independent of or slowly varying with frequency from 0.001 to 0.1 Hz, with possibly some stronger frequency dependence beginning between 0.1 and 1 Hz. For frequencies close to neither the low- nor the high-frequency corner of a relaxation spectrum (absorption band) of constant Q, this assumption leads to an approximate formula for complex velocity of the type

$$V(\omega) \cong V(\omega_r)\left(1 + \left(\frac{1}{\pi Q}\right)\ln\left(\frac{\omega}{\omega_r}\right) - i\left(\frac{1}{2Q}\right)\right) \qquad [27]$$

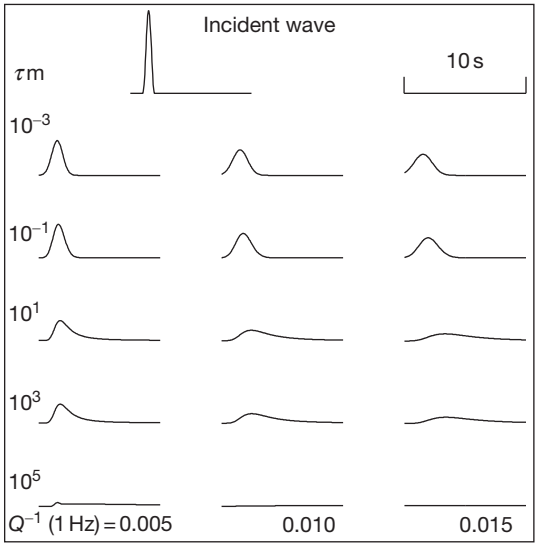

Figure 24 Attenuation operators convolved with a given wavelet for varying parameters of a viscoelastic relaxation spectrum from Li and Cormier (2002).

where $V(\omega_r)$ is a real velocity at a reference frequency. Substitution of $V(\omega)$ into the ray path integral for complex time $T(\omega)$ in eqn [26] and inverting the complex spectrum defines a time domain attenuation operator that is commonly termed the Futterman (1962) or Carpenter (1967) Q operator. This operator is valid in regions of the relaxation spectrum where attenuation $(1/Q)$ is constant. It is not valid near the corners of the true relaxation spectrum, where $1/Q$ decays as ω^{-1}. It is relatively simple, however, to derive a formula for complex velocity that is valid across the entire relaxation spectrum (e.g., Cormier and Richards, 1988). The pulse dispersions shown in **Figure 24** were calculated with this formula.

The width of relaxation spectra in which attenuation $1/Q$ is nearly constant or slowly varying (often observed to be $\omega^{1/3}$) is typically five decades in frequency (Anderson and Given, 1982). A problem often not considered in modeling the effects of viscoelasticity is the limitation viscoelastic theory imposes on the difference between the static (relaxed) elastic modulus and the infinite frequency (unrelaxed) modulus. There are limits on the band over which viscoelastic Q can be constant given by this modulus difference or defect, which is typically bounded by 25%. In practice, this means that any Q inferred from a body wave pulse width or spectrum that has an exceptionally low value, for example, 10 or lower, is an apparent Q probably resulting from scattering rather than viscoelasticity.

Slowness or ray-based methods often treat attenuation by solving the equations of motion with real velocities defined at the reference frequency (often chosen to be 1 Hz) and then convolving the result with the time domain attenuation operator of eqn [26] appropriate for each ray path. Since the unit of this ray path integral is time, a parameter often cited in the literature of teleseismic body waves is t^*. Considering only the real part of eqn [26] and assuming eqn [27] for $V(\omega)$, each frequency is exponentially attenuated by the factor $\exp(-\omega t^*)$, where

$$t^* = \int_{\text{path}} \frac{1}{V(\omega_r)Q}\,\mathrm{d}s \qquad [28]$$

The parameter t^* is found to vary relatively slowly with range and path length of P waves in the mantle and is on the order of 1 s for frequencies between 0.01 and 0.2 Hz in the distance range 30–90°.

Spectral methods that first compute the complex spectrum of the solution of the equation of motion (e.g., reflectivity, discrete wave number, full-wave, the DSM, and mode summation) can treat attenuation simply by substituting a complex velocity and analytically continuing all formulas in propagator matrices and phase factors that contain wave numbers and elastic moduli to complex numbers. To include the dispersive effect of attenuation in DRT and beam summation, a Futterman-type Q operator can be convolved with the computed amplitude of each ray or beam calculated in a model specified at a reference frequency. Another more general approach would be to compute amplitudes by DRT at the real velocities, $\mathrm{Re}(V(\omega))$, defined at each frequency and then multiply each spectral component by an exponential scale factor $\exp\left(-\omega\int \mathrm{Im}\left(\frac{1}{V(\omega)}\right)\mathrm{d}s\right)^{-}$.

In finite difference methods that integrate the equation of motion in the time domain, it is not practical to handle viscoelastic attenuation by a convolution. Instead, it is possible to design a system of stress–strain memory functions that can be simultaneously integrated in the time domain with the equations of motion (Robertsson et al., 1994). Using a memory function for only three specific relaxation times, it is usually possible to reproduce the effects of a relaxation spectrum of nearly constant attenuation in a frequency band of interest.

1.06.7.5 Anisotropy

Chapter 1.09 reviews elastic anisotropy and computational approaches for its many unique effects, including differences between phase and group velocities of body waves and shear wave singularities. Summarized here are some simple considerations related to ray- and transform-based methods of body wave synthesis.

Elastic anisotropy removes the degeneracy of the S wave eigenvalue/eigenvector solutions to the wave numbers of propagating plane waves. The SH and SV definitions defined by source and receiver geometry are no longer useful for formulating boundary conditions needed for calculating reflection and refraction. S polarization is best resolved into components of motion along two orthogonal quasi-S wave eigenvectors, with motion on both the transverse and radial components of motion generally consisting of a combination of two quasi-S waves. A pure radial (SV) polarized wave incident on a weakly anisotropic region excites two transmitted quasi-S waves such that the transverse (SH) component of the transmitted wave has the approximate shape of the time derivative of the radial (SV) component (Silver and Chan, 1991).

A special case of anisotropic propagation is that of transverse isotropy with a vertical axis of symmetry. In this case, the two quasi-S waves are exactly polarized in the SH and SV directions defined by source–receiver geometry but with two different velocities. Transverse isotropy can be an accurate representation for Earth models consisting of thin planar or radially symmetrical layers, having alternating or randomly fluctuation velocities and layer thicknesses much smaller than the smallest wavelength of interest (Backus, 1962). Transverse isotropy can be easily incorporated in all layered 1D body wave codes by modifying the calculations of reflection–transmission coefficients and the $\tau(p)$ function in the phase factor of WKBJ, GRT, or full-wave techniques (e.g., Chapman, 2004).

General anisotropy breaks the symmetry upon which some integral transforms and spherical harmonic analysis are based. Body waves can propagate in and out of the sagittal plane. This makes the problem of synthesizing body waves in a generally anisotropic model automatically a 3D problem. In plane-layered models and Cartesian coordinates, the generalized wave number superposition leads to reflectivity formulations that require integration over two horizontal wave numbers to invert wave number transforms to the spatial domain (Fryer and Frazer, 1984, 1987). Similarly, the WKBJ/Maslov methods can be generalized by integrals over two horizontal slownesses (Garmany, 1989). Some approximations for weak general anisotropy and expansion of the phase near its stationary point can be employed to simplify the problem to integration over a single wave number corresponding to waves propagating in and near the sagittal plane. For seismograms synthesized by ray methods, the equations for ray trajectory and travel times can be extended to the case of general anisotropy.

A system for dynamic quantities corresponding to the **P** and **Q** matrices can be formulated for summation of Gaussian beams (Hanyga, 1986; Klimes, 1994). A very simple approach for computing quantities related to geometric spreading is to take difference derivatives of ray positions and slownesses (Gajewski and Psencik, 1987, 1990).

1.06.7.6 Scattering

Chapter 1.24 reviews seismic scattering. A comprehensive reference is Sato et al. (2012). A few fundamental effects important to consider in the of synthesis body waves are reviewed here, some of which are computationally simple to include.

Single scattering by small-scale heterogeneity can be incorporated by a Born approximation (e.g., Chapman, 2004, Chapter 1.11). The Born approximation effectively treats small perturbations in velocity and density from a background medium as seismic sources by moving terms due to the difference in perturbed velocity from the background velocity to the source side of the wave equation. The strength of these scattering sources that reradiate energy is proportional to the energy of the wave incident on the heterogeneity and the size of its perturbations. For wavelengths much greater than the heterogeneity, each heterogeneity can be treated by a point-source representation similar to the moment-rate tensor representation of earthquake sources (Wu and Aki, 1985). The effects of many small-scale heterogeneities can be obtained by summing the radiated body waves of each small scatterer. Green's function solutions of the equations of motion must be known from the source to the position of each scatterer and from the scatterer to the receiver. These Green's functions can be calculated by any of the methods described in Section 1.06.4. The volume of the region of scatterers contributing to a specific time window surrounding a body wave is the banana-shaped region surrounding a least-time ray described in Section 1.06.7.3. An example of this approach is the synthesis of the precursor coda of PKIKP from scatterers near the core–mantle boundary (Cormier, 1999).

Forward scattering in the direction close to the direction of the least-time ray can affect the pulse shape of broadband body waves. A finite frequency band of observation can blur the effects of many scatterers, whose arrivals can occur over time spacings much shorter than the shortest period in the passband of observation. This broadening and multipathing can be mistaken for the effects of viscoelastic attenuation. Unlike viscoelastic attenuation, where energy is lost to heat, scattering attenuation simply redistributes high-frequency energy in time and space out of a finite time window surrounding the pulse observed at a particular location. One approximate method including this effect is the theory of dynamic composite elastic moduli of Kaelin and Johnson (1998). This technique can be formulated in terms of a complex wave number, allowing it to be treated in much the same way as complex velocities in viscoelasticity (e.g., Cormier and Li, 2002). Calvet and Margerin (2008) described a method in which the statistics of heterogeneity can be more directly included to estimate the attenuation and waveform dispersion due to multiple scattering.

1.06.7.7 Imaging

Increased availability of dense global data has made it worthwhile to synthesize seismograms to image deep Earth structure using the schemes commonly employed in exploration seismology to image shallower, smaller-scale, structure. The goal is to find Earth structure that minimizes object functions of the type

$$\left|D\left(t,\vec{x}\right)-U\left(t,\vec{x}\right)\right|^{n} \qquad [29]$$

where $D\left(t,\vec{x}\right)$ is an observed seismogram, $U\left(t,\vec{x}\right)$ is a synthetic seismogram, and n is a positive integer, usually 2 for least-squares linearized inversion.

Waveform imaging is a very nonlinear inverse problem, making it possible to fall into a localized minimum when a linearized least-squares approach is taken from a starting Earth model. Smart Monte Carlo methods such as simulated annealing and genetic algorithms (Sambridge and Mosegaard, 2002) are one way to insure that the Earth model space is sampled well enough to obtain an image that does not lie in a local minimum of the object function. Because many seismograms must be synthesized in many models, Monte Carlo methods are ideally suited for body wave algorithms that are computationally cheap, especially methods based on ray theory.

The linearized problem minimizes the residual wave field given by eqn [29], Taylor expanding the synthetic wave field. Subsequent processing treats the residual wave field like a seismic source at the imaging point (Mora, 1988; Tarantola, 1984). The strength of this source will be proportional to the perturbation from the background medium given by the starting Earth model. An important step in linearized imaging is the computation of the so-called differential seismograms or partial derivatives of seismograms with respect to model parameters (elastic moduli and density). Efficient methods for computing differential seismograms or differential spectra are well developed for modal methods (e.g., Du et al., 1998; Gomberg and Masters, 1988). A computationally cheap method for computing differential seismograms with the reflectivity approach of Kennett has been developed and described by Randall (1988).

An evolving imaging strategy in inversion of body waveforms is to perform the inversion at a series of increasing frequencies, imaging successively finer-scale structure with each iteration. With this approach, it is feasible to change the forward modeling algorithm as the iteration progresses, perhaps starting from ray theory in a radially or plane-layered reference structure and changing to a computationally more expensive or numerical method as smaller-scale and more intense perturbations to structure are determined. Driven by practical problems of resource exploration and enhanced oil recovery, innovation in imaging algorithms and strategies are occurring continuously and are best found in recent exploration literature.

1.06.8 Conclusions

Most of the algorithms for synthesizing body waves in radially symmetrical (1D) structure have been successfully tested and verified against each other (e.g., Choy et al., 1980; Figure 12). Factors to consider in choosing an algorithm include the accuracy in a required frequency band and distance range, the width of the time window and number and types of seismic

phases, the speed of computation, the number of synthetics needed for modeling or imaging, the completeness of documentation, and the existence and accessibility of software.

The frequency band of calculation is probably the foremost important factor. When working in the frequency band less than several 0.1ths of a Hz, the modal summation and the direct solution method are good choices because they easily include all possible body waves, surface waves, and frequency-dependent interactions with discontinuities in an arbitrarily wide time window at an acceptable computational cost on a single workstation. Using a perturbation approach, they can also handle weak lateral heterogeneity (several percent perturbation in velocity and density) with little additional computational overhead. At higher frequencies, reflectivity/GRT or locked mode approaches in thin homogeneous layers or asymptotically approximate ray-based methods (WKBJ/full-wave/Maslov/DRT and Gaussian beams) in homogeneous layers are efficient and produce identical results if carefully used.

In either low- or high-frequency bands, the most important limitations of each algorithm are related to its accurate reproduction of the waveform effects of the broad spatial spectrum of Earth structure. In all algorithms, it is important to consider the effects of neglecting small-scale structure on the order of a wavelength or smaller. In high-frequency algorithms, limitations are related to either the validity of the EFA, the physicality of thin-layer representations, or the validity of asymptotic approximations of wave functions in layers having continuous and large spatial gradients. Understanding these limitations is also key to the problems of separating the effects of anisotropy from heterogeneity and viscoelasticity from scattering.

Computational hardware now makes it possible to routinely model seismic waveforms to invert for both radially symmetrical (1D) Earth structure and simple point-source representations of earthquake faulting. Recent advances in digital recording and network telemetry have now made these inversions possible in near real time. The remaining advance needed to fully exploit the real-time capabilities of 1D modeling lies in making user-friendly software interfaces.

Efforts to test and verify 3D modeling algorithms against each other (Igel et al., 2000) will continue. The participation of the broad community in these efforts, however, remains challenging due to the limitations of computational hardware. Ray-based 3D modeling is feasible on single workstations in smooth models having a relatively large ratio of scale length of heterogeneity to wavelength and for relatively mild velocity and density perturbations (less than several percent). Likewise, perturbation approaches based on mode summation or the DSM can be performed with modest computational overhead for relatively weak velocity perturbations (several percent) and at large-scale lengths (1000s of km). Investigation of effects of very small-scale heterogeneity (10 km or less) at high frequencies (>1 Hz) can be done in 3D but is currently only practical with numerical methods for ranges on the order of 100s of wavelengths using clusters of several hundred or less processors. Growing community access to larger clusters of processors, including recent advances with GPU processors (Yuen, et al., 2013), will increasingly favor the use of fully numerical solutions of the seismic wave field.

References

Abo-Zena A (1979) Dispersion function computations for unlimited frequency values. *Geophysical Journal of the Royal Astronomical Society* 58: 91–105.

Aki K and Richards PG (2002) *Quantitative Seismology*, 2nd edn. Sausalito, CA: University Science Books.

Anderson DL and Given JW (1982) Absorption band Q model for the earth. *Journal of Geophysical Research* 87: 3893–3904.

Baag C and Langston CA (1985) Shear-coupled PL. *Geophysical Journal of the Royal Astronomical Society* 80: 363–385.

Backus GE (1962) Long-wave elastic anisotropy produced by horizontal layering. *Journal of Geophysical Research* 67: 4427–4440.

Ben-Menahem A and Beydoun WB (1985) Range of validity of seismic ray and beam methods in general inhomogeneous media, Part I: General theory. *Geophysical Journal of the Royal Astronomical Society* 82: 207–234.

Borcherdt RD (2009) *Viscoelastic Waves in Layered Media*. New York: Cambridge University Press.

Bouchon M (1979) Discrete wave number representation of elastic wave fields in three-space dimensions. *Journal of Geophysical Research* 84: 3609–3614.

Bouchon M and Aki K (1977) Discrete wave-number representation of seismic wave source fields. *Bulletin of the Seismological Society of America* 67: 259–277.

Bracewell RN (1986) *The Fourier Transform and Its Applications*, 2nd edn. New York: McGraw-Hill.

Bréger L and Romanowicz B (1998) Three dimensional structure at the base of the mantle beneath the Central Pacific. *Science* 382: 244–248.

Brune JN (1970) Tectonic stress and the spectra of seismic shear waves from earthquakes. *Journal of Geophysical Research* 75: 4997–5009.

Bullen KE and Bolt BA (1985) *Introduction to the Theory of Seismology*. Cambridge: Cambridge University Press 499 pp

Burdick LJ and Helmberger DV (1978) The upper mantle P velocity structure of the western United States. *Journal of Geophysical Research* 83: 1699–1712.

Burdick LJ and Orcutt JA (1979) A comparison of the generalized ray and reflectivity methods of waveform synthesis. *Geophysical Journal of the Royal Astronomical Society* 58: 261–278.

Calvet M and Margerin L (2008) Constraints on grain size and stable iron phases in the uppermost inner core from multiple scattering modeling of seismic velocity and attenuation. *Earth and Planetary Science Letters* 267: 200–212.

Campillo M and Bouchon M (1985) Synthetic SH seismograms in a laterally varying medium by the discrete wavenumber method. *Bulletin of the Seismological Society of America* 83: 307–317.

Capdeville Y, Chaljub E, Vilott J-P, and Montagner J-P (2003a) Coupling the spectral element method with a modal solution for elastic wave propagation in global earth models. *Geophysical Journal International* 153: 34–66.

Capdeville Y, Romanowicz B, and To A (2003b) Coupling spectral elements and modes in a spherical earth: an extension to the "sandwich" case. *Geophysical Journal International* 154: 44–57.

Carcione JM (2007) *Wave Fields in Real Media: Wave Propagation in Anisotropic, Anelastic, Porous and Electromagnetic Media*. Oxford: Elsevier Science.

Carpenter EW (1967) Teleseismic signal calculated for underground, underwater, and atmospheric explosions. *Geophysics* 32: 17–32.

Cerveny V (2001) *Seismic Ray Theory*. Cambridge: Cambridge University Press.

Cerveny V and Ravindra R (1971) *Theory of Seismic Head Waves*. Toronto: University of Toronto Press.

Cerveny V, Pleinerová J, Klimes L, and Psencík I (1987) High frequency radiation from earthquake sources in laterally varying structures. *Geophysical Journal of the Royal Astronomical Society* 88: 43–80.

Cerveny V, Klimes K, and Psencík I (2007) Seismic ray method: Recent developments. In: Wu R-S, Maupin V, and Dmowska R (eds.) *Advances in Wave Propagation in Heterogeneous Earth*. *Advances in Geophysics*, 48: pp. 1–126. New York: Elsevier/Academic Press.

Chapman CH (1973) The Earth flattening transformation in body wave theory. *Geophysical Journal of the Royal Astronomical Society* 35: 55–70.

Chapman CH (1978) A new method for computing synthetic seismograms. *Geophysical Journal of the Royal Astronomical Society* 54: 481–518.

Chapman CH (2004) *Fundamentals of Seismic Wave Propagation*. Cambridge: Cambridge University Press.

Chapman CH and Drummond R (1982) Body-wave seismograms in inhomogeneous media using Maslov asymptotic theory. *Bulletin of the Seismological Society of America* 72: S277–S317.

Chapman CH, Chu J-Y, and Lyness DG (1988) The WKBJ seismogram algorithm. In: Doornbos DJ (ed.) *Seismological Algorithms*: Academic Press, ch. 1.2.

Choy GL and Cormier VF (1983) The structure of the inner core inferred from short-period and broad-band GDSN data. *Geophysical Journal of the Royal Astronomical Society* 72: 1–21.

Choy GL and Richards PG (1975) Pulse distortion and Hilbert transformation in multiply reflected and refracted body waves. *Bulletin of the Seismological Society of America* 65: 55–70.

Choy GL, Cormier VF, Kind R, Müller G, and Richards PG (1980) A comparison of synthetic seismograms of phases generated by the full wave theory and by the reflectivity method. *Geophysical Journal of the Royal Astronomical Society* 61: 21–39.

Cline AK (1974) Six subprograms for curve fitting using splines under tension. *Communications of the ACM* 17: 220–223.

Coates RT and Chapman CH (1991) Generalized Born scattering of elastic waves in 3D media. *Geophysical Journal International* 107: 231–263.

Cormier VF (1999) Anisotropy of heterogeneity scale lengths in the lowermost mantle from PKIKP precursors. *Geophysical Journal International* 136: 373–384.

Cormier VF (2000) D″ as a transition in the heterogeneity spectrum of the lowermost mantle. *Journal of Geophysical Research* 105: 16193–16205.

Cormier VF (2011) Seismic viscoelastic attenuation. In: Gupta H (ed.) *Encyclopedia of Solid Earth Geophysics*, pp. 1279–1290. Berlin: Springer. http://dx.doi.org/10.1007/978-90-481-8702-7.

Cormier VF and Choy GL (1981) Theoretical body wave interactions with upper mantle structure. *Journal of Geophysical Research* 86: 1673–1678.

Cormier VF and Li X (2002) Frequency dependent attenuation in the inner core: Part II. A scattering and fabric interpretation. *Journal of Geophysical Research* 107(B12): ESE 14-1-ESE 14-15. http://dx.doi.org/10.1029/2002JB001796.

Cormier VF and Richards PG (1977) Full wave theory applied to a discontinuous velocity increase: the inner core boundary. *Journal of Geophysics* 43: 3–31.

Cormier VF and Richards PG (1988) Spectral synthesis of body waves in Earth models specified by vertically varying layers. In: Doornbos D (ed.) *Seismological Algorithms*, pp. 3–45. London: Academic Press.

Cormier VF and Spudich P (1984) Amplification of ground motion and waveform complexity in fault zones: Examples from the San Andreas and Calaveras faults. *Geophysical Journal of the Royal Astronomical Society* 79: 135–152.

Cormier VF, Mandal B, and Harvey D (1991) Incorporation of velocity gradients in the synthesis of complete seismograms by the locked mode method. *Bulletin of the Seismological Society of America* 81: 897–930.

Crotwell HP, Owens TJ, and Ritsema J (1999) The TauP toolkit: Flexible seismic travel-time and ray-path utilities. *Seismological Research Letters* 70: 154–170.

Cummins PR, Geller RJ, Hatori T, and Takeuchi N (1994a) DSM complete synthetic seismograms: SH, spherically symmetric, case. *Geophysical Research Letters* 21: 533–536.

Cummins PR, Geller RJ, and Takeuchi N (1994b) DSM complete synthetic seismograms: P-SV, spherically symmetric, case. *Geophysical Research Letters* 21: 1663–1666.

Dahlen FA (1987) Multiplet coupling and the calculation of synthetic long-period seismograms. *Geophysical Journal of the Royal Astronomical Society* 91: 241–254.

Dahlen FA and Tromp J (1998) *Theoretical Global Seismology*, 944 pp. Princeton: Princeton University Press.

Dahlen FA, Hung S-H, and Nolet G (2000) Frechet kernels for finite-frequency traveltimes-I. *Geophysical Journal International* 141: 157–174.

Davis JP and Henson IH (1993) Users Guide to Xgbm: An X-Windows System to Compute Gaussian Beam Synthetic Seismograms, Rept TGAL-93-02, Teledyne-Geotech, Alexandria, VA.

Deuss A and Woodhouse JH (2004) Iteration method to determine the eigenvalues and eigenvectors of a target multiplet including full mode coupling. *Geophysical Journal International* 159(1): 326–332.

Du ZJ, Michelini A, Panza GF, and Urban L (1998) P-SV multimode summation differential seismograms for layered structures. *Geophysical Journal International* 134: 747–756.

Dziewonski AM and Anderson DL (1981) Preliminary reference Earth model. *Physics of the Earth and Planetary Interiors* 25: 297–356.

Dziewonski AM, Chou T-A, and Woodhouse JH (1981) Determination of earthquake source parameters from waveform data for studies of global and regional seismicity. *Journal of Geophysical Research* 86: 2825–2852.

Fornberg B (1998) *A Practical Guide to Pseudospectral Methods*. Cambridge: Cambridge University Press.

Frankel A and Clayton RW (1986) Finite-difference simulations of seismic scattering: Implications for the propagation of short-period seismic waves in the crust and models of crustal heterogeneity. *Journal of Geophysical Research* 91: 6465–6489.

Frazer LN and Gettrust JF (1984) On a generalization of Filon's method and the computation of the oscillatory integrals of seismology. *Geophysical Journal of the Royal Astronomical Society* 76: 461–481.

Frazer LN and Sen M (1985) Kirchhoff–Helmholtz reflection seismograms in a laterally variable multi-layered elastic medium, Part I, Theory. *Geophysical Journal of the Royal Astronomical Society* 80: 121–147.

Fryer GJ and Frazer LN (1984) Seismic waves in stratified anisotropic media. *Geophysical Journal of the Royal Astronomical Society* 78: 691–710.

Fryer GJ and Frazer LN (1987) Seismic waves in stratified anisotropic media – II. Elastodynamic eigensolutions for some anisotropic systems. *Geophysical Journal of the Royal Astronomical Society* 91: 73–101.

Fuchs K and Müller G (1971) Computation of synthetic seismograms with the reflectivity method and comparison with observations. *Geophysical Journal of the Royal Astronomical Society* 23(4): 417–433.

Furumura T and Takenaka H (1996) 2.5-D modelling of elastic waves using the pseudospectral method. *Geophysical Journal International* 124: 820–832.

Furumura T, Kennett BLN, and Furumura M (1998) Seismic wavefield calculation for laterally heterogeneous spherical earth models using the pseudospectral method. *Geophysical Journal International* 135: 845–860.

Futterman WI (1962) Dispersive body waves. *Journal of Geophysical Research* 67: 5279–5291.

Gajewski D and Psencik I (1987) Computation of high-frequency seismic wavefields in 3-D laterally inhomogeneous anisotropic media. *Geophysical Journal of the Royal Astronomical Society* 91: 383–411.

Gajewski D and Psencik I (1990) Vertical seismic profile synthetics by dynamic ray tracing in laterally varying layered anisotropic structures. *Journal of Geophysical Research* 95: 11301–11315.

Garmany J (1989) A student's garden of anisotropy. *Annual Review of Earth and Planetary Sciences* 17: 285–308.

Geller RJ and Ohminato T (1994) Computation of synthetic seismograms and their partial derivatives for heterogeneous media with arbitrary natural boundary conditions using the Direct Solution Method (DSM). *Geophysical Journal International* 116: 421–446.

Gerstoft P and Schmidt H (1991) A boundary element approach to ocean seismoacoustic facet reverberation. *Journal of the Acoustical Society of America* 89: 1629–1642.

Gilbert F and Backus GE (1966) Propagator matrices in elastic wave and vibration problems. *Geophysics* 31: 326–332.

Gomberg J and Masters TG (1988) Waveform modeling using locked-mode synthetic and differential seismograms: Application to determination of the structure of Mexico. *Geophysical Journal International* 94: 193–218.

Grand SP, van der Hilst RD, and Widiyantoro S (1997) Global seismic tomography; a snapshot of convection in the Earth. *GSA Today* 7: 1–7.

Gu YJ, Dziewonski AM, Su W-J, and Ekström G (2001) Models of the mantle shear velocity and discontinuities in the pattern of lateral heterogeneities. *Journal of Geophysical Research* 106: 11169–11199.

Hanyga H (1986) Gaussian beams in anisotropic elastic media. *Geophysical Journal of the Royal Astronomical Society* 85: 473–503.

Hartzell S, Harmsen S, Frankel A, and Larsen S (1999) Calculation of broadband time histories of ground motion: Comparison of methods and validation using strong-ground motion from the 1994 Northridge earthquake. *Bulletin of the Seismological Society of America* 89: 1484–1504.

Harvey DJ (1981) Seismogram synthesis using normal mode superposition: The locked mode approximation. *Geophysical Journal of the Royal Astronomical Society* 66: 37–69.

Helmberger DV (1974) Generalized ray theory for shear dislocations. *Bulletin of the Seismological Society of America* 64: 45–64.

Helmberger DV and Harkrider D (1978) Modeling earthquakes with generalized ray theory. In: Miklowitz J and Achenbach JD (eds.) *Modern Problems in Elastic Wave Propagation*. New York: Wiley.

Helmberger DV, Zhao LS, and Garnero EJ (1996) Construction of synthetics for 2D structures, core phases. In: Boschi E and Ekstrom G (eds.) *Proceedings of International School of Solid Earth Geophysics*: *Seismic Modeling of the Earth's Structure*, *Soc. Italiana di Fisica*, pp. 183–222.

Holliger K, Levander A, and Goff JA (1993) Stochastic modeling of the reflective lower crust: petrophysical and geological evidence from the Ivrea Zone (northern Italy). *Journal of Geophysical Research* 98: 11,967–11,980.

Honda R and Yomogida K (2003) Static and dynamic displacement near a fault with the discrete wavenumber method. *Physics of the Earth and Planetary Interiors* 137: 107–127.

Igel H (1999) Modeling wave propagation in 3-D spherical sections by the Chebyshev spectral method. *Geophysical Journal International* 136: 559–567.

Igel H, Takeuchi N, Geller RJ, et al. (2000) The COSY Project: Verification of global seismic modeling algorithms. *Physics of the Earth and Planetary Interiors* 119: 3–23.

Imhof MG (1996) Multiple multipole expansions for elastic scattering. *Journal of the Acoustical Society of America* 100: 2969–2979.
Irving JCE, Deuss A, and Andrews J (2008) Wide-band coupling of Earth's normal modes due to anisotropic inner core structure. *Geophysical Journal International* 174(3): 919–929.
Jackson I (2007) Properties of rocks and minerals – Physical origin of anelasticity and attenuation in rocks. In: Schubert G (ed.) *Treatise on Geophysics*, vol. 2, pp. 493–525. Amsterdam: Elsevier.
Jeffreys H (1936) The structure of the Earth down to the 20° discontinuity. *Monthly Notices of the Royal Astronomical Society. Geophysical Supplement* 3: 401–422.
Kaelin B and Johnson LR (1998) Dynamic composite elastic medium theory. Part II. Three-dimensional media. *Journal of Applied Physics* 84: 5458–5468.
Karato S-I (1993) Importance of anelasticity in the interpretation of seismic tomography. *Geophysical Research Letters* 20: 1623–1626.
Keith M and Crampin S (1977) Seismic body waves in anisotropic media: Reflection and refraction at a plane interface. *Geophysical Journal of the Royal Astronomical Society* 49: 181–208.
Kennett BLN (1983) *Seismic Wave Propagation in Stratified Media*. New York: Cambridge University Press.
Kennett BLN (1998) Guided-waves in three-dimensional structures. *Geophysical Journal International* 133: 159–174.
Kennett BLN (2001) *The Seismic Wavefield*, vols. I and II. New York: Cambridge University Press.
Kind R (1985) The reflectivity method for different source and receiver structures and comparison with GRF data. *Journal of Geophysics* 58: 146–152.
Klimes L (1994) Transformation for the dynamic ray tracing in anisotropic media. *Wave Motion* 20: 261–272.
Komatitsch D and Tromp J (1999) Introduction to the spectral-element method for 3-D seismic wave propagation. *Geophysical Journal International* 139: 806–822.
Komatitsch D and Tromp J (2002) Spectral-element simulations of global seismic wave propagation-II. 3-D models, oceans, rotation, and self gravitation. *Geophysical Journal International* 149: 390–412.
Komatitsch D and Vilotte J-P (1998) The spectral element method: An efficient tool to simulate the seismic response of 2D and 3D geological structures. *Bulletin of the Seismological Society of America* 88: 368–392.
Korneev VA and Johnson LR (1993) Scattering of elastic waves by a spherical inclusion – I. Theory and numerical results. *Geophysical Journal International* 115: 230–250.
Kosloff D and Kessler D (1990) *Seismic Numerical Modeling: Oceanographic and Geophysical Tomography*, pp. 251–312. Amsterdam: Elsevier Science.
Kravtsov YA and Orlov YI (1980) *Geometrical Optics of Inhomogeneous Media (in Russian)*. Moscow: Nauka (translation to English by Springer, Berlin, 1990).
Langston CA and Helmberger DV (1975) A procedure for modeling dislocation sources. *Geophysical Journal* 42: 112–130.
Lapwood ER and Usami T (1981) *Free Oscillations of the Earth*. Cambridge: Cambridge University Press.
Larsen S and Schultz CA (1995) ELAS3D: 2D/3D elastic finite difference propagation code. Technical Report No. UCRL-MA-121792, 19 pp.
Lee WHK, Kanamori H, Jenning P, and Kisslinger C (eds.) (2002) *International Handbook of Earthake and Engineering Seismology*, vol. 81, Part A. pp. 3–393. New York: Elsevier/Academic Press.
Li X and Cormier VF (2002) Frequency dependent attenuation in the inner core: Part I. A viscoelastic interpretation. *Journal of Geophysical Research* 107. SE 13-1–ESE 13-20, http//dx.doi.org/10.1029/2002JB001795.
Li X-D and Romanowicz B (1995) Comparison of global waveform inversions with and without considering cross branch coupling. *Geophysical Journal International* 121: 695–709.
Li X-D and Tanimoto T (1993) Waveforms of long period body waves in a slightly aspherical earth model. *Geophysical Journal International* 112: 92–102.
Masters G, Laske G, Bolton H, and Dziewonski A (2000) The relative behavior of shear velocity, bulk sound speed, and compressional velocity in the mantle: Implications for chemical and thermal structure. In: Karato S, Forte AM, Liebermann RC, Masters G, and Stixrude L (eds.) *Earth's Deep Interior. AGU Monograph 117,* Washington, DC: AGU.
Maupin V (1989) Numerical modeling of Lg wave propagation across the North Sea central graben. *Geophysical Journal International* 99: 273–283.
Maupin V and Kennett BLN (1987) On the use of truncated model expansion in laterally varying media. *Geophysical Journal of the Royal Astronomical Society* 91: 837–851.
Menke W (2005) Case studies of seismic tomography and earthquake location in a regional context. In: Levander A and Nolet G (eds.) *Seismic Earth: Array Analysis of Broadband Seismograms*. *Geophysical Monograph Series 157,* pp. 7–36. American Geophysical Union.
Menke W and Richards PG (1980) Crust-mantle whispering gallery phases: A deterministic model of teleseismic Pn wave propagation. *Journal of Geophysical Research* 85: 5416–5422.
Moczo P, Robertsson JOA, and Eisner L (2007) Finite-difference time-domain method for modelling of seismic wave propagation. In: Wu R-S, Maupin V, and Dmowska R (eds.) *Advances in Wave Propagation in Heterogeneous Earth*. *Advances in Geophysics*, vol. 48, pp. 421–516. New York: Elsevier/Academic Press.
Mora P (1988) Elastic wavefield inversion of reflection and transmission data. *Geophysics* 53: 750–759.
Müller G (1973) Amplitude studies of core phases. *Journal of Geophysical Research* 78: 3469–3490.
Müller G (1977) Earth-flattening approximation for body waves derived from geometric ray theory; improvements, corrections and range of applicability. *Journal of Geophysics* 42: 429–436.
Müller G (1985) The reflectivity method: A tutorial. *Journal of Geophysics* 58: 153–174.
Ni SD, Ding X, and Helmberger DV (2000) constructing synthetics from deep earth tomographic models. *Geophysical Journal International* 140: 71–82.
Olsen KB (2000) Site amplification in the Los Angeles Basin from three-dimensional modeling of ground motion. *Bulletin of the Seismological Society of America* 90: S77–S94.
Panza GF, Romanelli F, and Vaccari FA (2001) Seismic wave propagation in laterally varying heterogeneous anelastic media: theory and application to the seismic zoning. *Advances in Geophysics* 43: 1–95.
Pointer T, Liu E, and Hudson JA (1998) Numerical modelling of seismic waves scattered by hydrofractures: Application of the indirect boundary element method. *Geophysical Journal International* 135: 289–303.
Randall GE (1988) Efficient calculation of differential seismograms for lithospheric receiver functions. *Geophysical Journal International* 99: 469–489.
Randall CJ (1991) Multipole acoustic waveforms in nonaxisymmetric boreholes and formations. *Journal of the Acoustical Society of America* 90: 1620–1631.
Rial JA and Cormier VF (1980) Seismic waves at the epicenter's antipode. *Journal of Geophysical Research* 85: 2661–2668.
Richards PG (1973) Calculation of body waves, for caustics and tunnelling in core phases. *Geophysical Journal of the Royal Astronomical Society* 35: 243–264.
Richards PG and Frasier CW (1976) Scattering of elastic waves from depth dependent inhomogeneities. *Geophysics* 41: 441–458.
Ritsema J and van Heijst HJ (2000) Seismic imaging of structural heterogeneity in Earth's mantle: Evidence for large-scale mantle flow. *Science Progress* 83: 243–259.
Robertsson JOA, Blanch JO, and Symes WW (1994) Viscoelastic finite-difference modeling. *Geophysics* 59: 1444–1456.
Rondenay S, Cormier VF, and Van Ark E (2010) SKS and SPdKS sensitivity to two-dimensional ultra-low velocity zones. *Journal of Geophysical Research* 115: B04311. http://dx.doi.org/10.1029/2009JB006733.
Rost S and Thomas C (2002) Array seismology: Methods and applications. *Reviews of Geophysics* 40: 2-1–2-27. http://dx.doi.org/10.1029/2000RG000100.
Sambridge M and Gudmundsson O (1998) Tomography with irregular cells. *Journal of Geophysical Research* 103: 773–781.
Sambridge M and Mosegaard K (2002) Monte Carlo methods in geophysical inverse problems. *Reviews of Geophysics* 40. http://dx.doi.org/10.1029/2000RG000089.
Sato H, Fehler MC, and Maeda T (2012) *Seismic Wave Propagation and Scattering in the Heterogeneous Earth*, 2nd edn. Berlin: Springer.
Shearer PM (1999) *Introduction to Seismology*. Cambridge: Cambridge University Press.
Silver PG and Chan WW (1991) Shear-wave splitting and subcontiental mantle deformation. *Journal of Geophysical Research* 96: 16429–16454.
Snieder R (2002) General theory of elastic wave scattering. In: Pike R and Sabatier P (eds.) *Scattering and Inverse Scattering in Pure and Applied Science*, pp. 528–542. San Diego: Academic Press.
Song X and Helmberger DV (1995) A P wave velocity model of Earth's core. *Journal of Geophysical Research* 100: 9817–9830.
Spudich P and Frazer LN (1984) Use of ray theory to calculate high-frequency radiation from earthquake sources having spatially variable rupture velocity and stress drop. *Bulletin of the Seismological Society of America* 74: 2061–2082.
Su W-J and Dziewonski AM (1997) Simultaneous inversions for 3-D variations in shear and bulk velocity in the mantle. *Physics of the Earth and Planetary Interiors* 100: 135–156.
Sun D and Helmberger DV (2011) Upper-mantle structures beneath USArray derived from waveform complexity. *Geophysical Journal International* 184: 416–438.
Takeuchi N, Geller RJ, and Cummins PR (2000) Complete synthetic seismograms for 3-D heterogeneous Earth models computed using modified DSM operators and

their applicability to inversion for Earth structure. *Physics of the Earth and Planetary Interiors* 119: 25–36.

Tarantola A (1984) Inversion of seismic data in the acoustic approximation. *Geophysics* 49: 1259–1266.

To A, Romanowicz B, Capdeville Y, and Takeuchi N (2005) 3D effects of sharp boundaries at the borders of the African and Pacific Superplumes: Observation and modeling. *Earth and Planetary Science Letters* 233: 137–153.

Trampert J, Vacher P, and Vlar N (2001) Sensitivities of seismic velocities to temperature, pressure and composition in the lower mantle. *Physics of the Earth and Planetary Interiors* 124: 255–267.

Virieux J (1985) SH-wave propagation in heterogeneous media: velocity stress finite difference method. *Geophysics* 49: 1933–1957.

Virieux J (1986) P-SV wave propagation in heterogeneous media: velocity-stress finite-difference method. *Geophysics* 51: 889–901.

Ward SN (1978) Long period reflected and converted upper mantle phases. *Bulletin of the Seismological Society of America* 68: 133–153.

Wen L and Helmberger DV (1998) A two-dimensional P-SV hybrid method and its application to modeling localized structures near the core-mantle boundary. *Journal of Geophysical Research* 103: 17901–17918.

Wu R-S and Aki K (1985) Scattering characteristics of waves by an elastic heterogeneity. *Geophysics* 50: 582–595.

Wu R-S, Xie X-B, and Wu X-Y (2007) One-way and one-return approximations (de Wolf approximation) for fast elastic wave modeling in complex media. In: Wu R-S, Maupin V, and Dmowska R (eds.) *Advances in Wave Propagation in Heterogeneous Earth*. *Advances in Geophysics*, vol. 48, pp. 265–322. New York: Elsevier/Academic Press.

Yuen D, Wang L, Chi X, Johnson L, Ge W, and Shi Y (2013) GPU Solutions to Multi-Scale Problems in Science and Engineering. In: Berlin, Heidelberg: Springer 689 p.

Zhao Y and Anderson DL (1994) Mineral physics constraints on the chemical composition of Earth's lower mantle. *Physics of the Earth and Planetary Interiors* 85: 273–292.

1.07 Theory and Obeservations - Forward Modeling and Synthetic Seismograms, 3D Numerical Methods

J Tromp, Princeton University, Princeton, NJ, USA

© 2015 Elsevier B.V. All rights reserved.

1.07.1	**Introduction**	231
1.07.2	**The Challenge**	232
1.07.2.1	Benchmarking	233
1.07.3	**Equation of Motion**	233
1.07.4	**Strong Implementations**	235
1.07.4.1	Finite Difference Method	235
1.07.4.2	Pseudospectral Method	236
1.07.5	**Weak Implementations**	237
1.07.5.1	Rayleigh–Ritz Method	238
1.07.5.1.1	Coupled-mode method	239
1.07.5.1.2	Direct solution method	239
1.07.5.2	Finite Element Method	240
1.07.5.3	Spectral Element Method	242
1.07.6	**Discussion and Conclusions**	246
Acknowledgments		248
References		249

1.07.1 Introduction

Synthetic seismograms are at the heart of modern global seismology. For spherically symmetrical, that is, one-dimensional (1D), Earth models, normal-mode summation is the preferred method for the calculation of broadband seismograms (e.g., Dahlen and Tromp, 1998; Gilbert, 1970). Normal-mode synthetics incorporate effects due to fluid–solid boundaries, transverse isotropy with a radial symmetry axis, and attenuation. Mode synthetics are frequently used as reference seismograms, for example, to make cross correlation body-wave travel time measurements or to characterize fundamental Love and Rayleigh surface-wave dispersion.

Before fully 3D numerical techniques became available and practical, one had to resort to asymptotic methods for the calculation of synthetic seismograms. Over the years, numerous asymptotic methods have been – and are continuing to be – developed. For example, in the path-average or great-circle approximation (e.g., Nolet, 1990; Woodhouse and Dziewonski, 1984), one assumes that a seismogram may be calculated based upon a spherically symmetrical Earth model that is characteristic of a particular source–receiver combination. From an inverse theory perspective, in this approximation, a change in the waveform is related to a change in the Earth model via a 1D Fréchet or sensitivity kernel. By asymptotically accounting for mode coupling, Li and Tanimoto (1993) extended the path-average method to gain 2D sensitivity to structure in the source–receiver plane. In this approach, changes in the waveform are related to model changes through a 2D sensitivity kernel (Li and Romanowicz, 1995, 1996; Marquering and Snieder, 1995, 1996). Nowadays, seismologists are calculating fully 3D synthetic seismograms at the scale of the globe, and the relationship between waveforms and Earth structure is expressed in terms of 3D sensitivity kernels. The calculation of such kernels for spherically symmetrical reference models may be accomplished based upon mode summation (Marquering et al., 1998; Zhao et al., 2000) or ray theory (Dahlen et al., 2000; Hung et al., 2000; Montelli et al., 2004), but for 3D reference models, such calculations involve the use of the so-called adjoint simulations (e.g., Akçelik et al., 2002, 2003; Talagrand and Courtier, 1987; Tarantola, 1984; Tromp et al., 2005).

The number of numerical techniques that can handle seismic wave propagation in 3D Earth models accurately is rather limited. All the classical numerical methods have been employed, for example, finite difference method (FDM) and pseudospectral method (PM), but thus far, these techniques have been restricted either to portions of the globe, that is, limited in terms of the dimensions of the modeling domain (e.g., Furumura et al., 1998, 1999; Igel, 1999; Wang et al., 2001), or to purely shear/acoustic problems, that is, incorporating only shear/compressional waves (e.g., Igel and Weber, 1995; Thomas et al., 2000).

Numerical simulations based upon integral or weak implementations of the equation of motion have been most successful in terms of capturing the full complexity of global Earth models. Coupled-mode methods (CMMs), in which the modes of a 3D Earth model are expressed as a sum over the modes of a spherically symmetrical reference Earth model (e.g., Capdeville et al., 2000; Lognonné and Romanowicz, 1990; Park, 1986; Park and Yu, 1992), or direct solution methods (DSMs), which use more general basis functions (e.g., Geller and Ohminato, 1994; Hara et al., 1991; Takeuchi et al., 2000), are capable of calculating synthetic seismograms in 3D Earth model at relatively long periods.

To date, the most successful numerical technique for simulating global seismic wave propagation has been the spectral element method (SEM) (Chaljub, 2000; Chaljub et al., 2003;

Komatitsch and Tromp, 2002a,b; Komatitsch et al., 2002, 2003). See Komatitsch et al. (2005) and Chaljub et al. (2007) for detailed recent reviews of the method. Like CMM, DSM, and finite element method (FEM), the SEM is based upon an integral or weak implementation of the equation of motion. It combines the accuracy of the global PM with the flexibility of the FEM. The wavefield is typically represented in terms of high-degree Lagrange interpolants, and integrals are computed based upon Gauss–Lobatto–Legendre (GLL) quadrature, which leads to a simple explicit time scheme that lends itself very well to calculations on parallel computers. Capdeville et al. (2003a,b) demonstrated how the computational burden associated with the SEM may be reduced by coupling it to a normal-mode solution. This allows one to reduce the cost of the method by assuming a spherically symmetrical solution in a portion of the Earth, for example, the core, using spectral elements only in the remaining parts of the model, for example, the mantle.

The purpose of this chapter is to introduce and review various numerical methods used in global seismology to generate synthetic seismograms in 3D Earth models. We begin by posing the challenges associated with simulating global seismic wave propagation. We then introduce the elastic wave equation, which forms the basis of all numerical simulations of seismic wave propagation. We discuss the basic boundary conditions that arise in Earth models with a free surface and a variety of internal solid–solid and fluid–solid discontinuities. Complications due to anisotropy, attenuation, and self-gravitation are important in the context of seismic wave propagation, but for the sake of simplicity, these effects are only discussed peripherally. We distinguish between numerical methods based upon the equation of motion in its differential form subject to certain boundary conditions, referred to as differential or strong implementations, for example, FDM and PM, and numerical methods based upon an integral or weak implementation of the equation of motion that contains the boundary conditions implicitly, for example, CMM, DSM, FEM, and SEM. We conclude by discussing the potential for using 3D numerical simulation to address the inverse problem. We will assume basic knowledge of tensor notation and algebra.

1.07.2 The Challenge

The calculation of accurate synthetic seismograms for 3D global Earth models poses a significant computational challenge, both in terms of the demands on the numerical algorithm and with regard to computer hardware (i.e., memory and CPU requirements). This section enumerates the main algorithmic issues that need to be addressed and resolved in the context of simulating global seismic wave propagation. Few numerical techniques can currently accommodate all the demands imposed by this daunting problem:

Gridding. Any numerical technique involves a grid on which the wavefield is evaluated, be it a finite difference stencil or the GLL points of a hexahedral spectral element. Gridding – or meshing – the globe is challenging for two key reasons, both related to spherical geometry. First, to grid the entire surface of the globe, one has to design a scheme that covers the unit sphere evenly. A simple grid in terms of latitude and longitude, frequently used in strong implementations, leads to an uneven grid spacing with an undesired concentration of points near the poles.

The second difficulty is associated with the fact that the spherical geometry tends to lead to a concentration of grid points with depth and a singularity at the center of the Earth. Thus, one needs to design a gridding scheme that increases the grid spacing with depth to reduce the computational burden and improve numerical stability. The fact that wave speeds generally increase with depth further enhances the need for coarsening the grid with depth for reasons of numerical stability and efficiency.

Surface waves. At the scale of the globe, surface waves are an important source of information for two main reasons. One, they help constrain shallow upper-mantle structure beneath ocean basins, which are difficult to image with body waves. Two, they are widely used to constrain the source characteristics of earthquakes. Any numerical technique aimed at simulating global seismic wave propagation must therefore be able to accurately simulate the propagation of surface waves. The numerical challenges lie in the implementation of the stress-free surface boundary condition and in the fact that surface waves travel at relatively slow phase speeds requiring a fine grid spacing of more than five grid points per wavelength.

Diffracted waves. At greater epicentral distances, a number of body waves diffract at the core–mantle boundary (CMB), for example, P_{diff} and S_{diff}. These waves contain important information about the lowermost mantle, in particular the intensely studied D″ region, and it is important that 3D simulations accurately capture these diffraction effects. Part of the difficulty involves the implementation of the fluid–solid boundary condition mentioned next.

Fluid–solid boundaries. Typical Earth models have three main fluid–solid boundaries: the ocean floor, the CMB, and the inner core boundary (ICB). These boundaries need special attention in the sense that the traction is normal to the boundary and continuous across it; the normal component of displacement is also continuous, but the tangential component of displacement is discontinuous, that is, there may be slip across the boundary. The implementation of fluid–solid boundaries typically involves domain decomposition between the fluid and the solid, such that one solves an (an)elastic wave equation in the solid crust, mantle, and inner core and an acoustic wave equation in the liquid outer core and ocean, matching the two solutions at the fluid–solid boundary.

Attenuation. The shear quality factor is observed to be fairly small in the upper mantle and, in particular, in the inner core. Surface waves and waves that turn or reflect in the upper mantle are significantly attenuated, an effect that needs to be accommodated in numerical simulations. Observational global seismologists routinely use data over a broad frequency range, from short-period PKP waves in the 1–2 Hz range to long-period surface waves in the 5 mHz range. Because we are dealing with such broadband signals, we must take into account the fact that in an anelastic Earth model, the wave speeds become frequency-dependent. Such physical dispersion can have a dramatic effect on both body and surface waveforms.

Anisotropy. Global Earth models frequently exhibit anisotropy, that is, a directional dependence of the wave speed. Even 1D models are generally transversely isotropic (e.g., PREM) to accommodate the observed dispersion of Love and Rayleigh

waves. Thus, suitable numerical techniques should incorporate the effects of an anisotropic constitutive relationship on seismic wave propagation. The related additional model parameters increase the memory requirements and the CPU time.

Rotation and self-gravitation. At periods longer than about 150 s, surface waves are affected by the Earth's rotation, and Rayleigh wave propagation needs to accommodate the effects of self-gravitation, that is, the perturbations in the gravitational field induced by the seismic motions. Normal-mode summation codes routinely incorporate the effects of self-gravitation, and this provides an excellent benchmark for more general, 3D codes.

Ellipticity, topography, and bathymetry. The Earth is to a close approximation elliptical in shape, and the numerical grid should reflect this. Furthermore, there is significant topography and bathymetry associated with mountain ranges and the ocean basins. The grid should be adjusted to reflect these topographic variations, and the numerical implementation of the free surface boundary conditions should account for the undulations. Free surface boundary conditions are notoriously difficult to implement, in particular in the context of strong formulations of the equations of motion.

Crustal thickness. The Earth's crust varies in thickness by an order of magnitude, with depths of approximately 8 km underneath the oceans to depths of more than 70 km underneath the Andes and Tibet. These crustal thickness variations have a profound effect on the dispersion of short- and intermediate-period surface waves. They also affect the travel time and amplitude of surface-reflected phases, for example, PP and SS. Various asymptotic techniques attempt to accommodate lateral variations in crustal thickness by making a 'crustal correction,' but in particular for surface waves, such 'corrections' quickly become inadequate.

Oceans. Some 1D models incorporate an ocean layer. Such a layer gives rise to complications associated with fluid–solid interfaces, as discussed in a previous item. The presence of oceans is mostly relevant for the dispersion of Rayleigh waves, as well as for surface-reflected phases, such as pP, PP, SS, and SP. Normal-mode summation codes routinely incorporate the effects of a water layer, thus providing a good benchmark. For 3D Earth models, the oceans pose a much more significant challenge related to their highly variable depth.

Core. The fact that the Earth has a liquid outer core and a solid inner core poses significant computational challenges. In addition to the fluid–solid boundary conditions mentioned in an earlier item, we need to solve an (an)elastic wave equation in the inner core, which is coupled across the ICB to an acoustic wave equation in the outer core, which is coupled across the CMB to an (an)elastic wave equation in the mantle and crust. Thus, the need arises for two distinct solvers for the fluid and solid regions of the model, which are coupled across the fluid–solid boundaries. Meshing the inner core is another nontrivial issue that requires the use of highly uneven grids, in particular with depth.

In what follows, we will discuss the merits and demerits of the various numerical techniques in the context of the challenges laid out in this section.

1.07.2.1 Benchmarking

Any numerical method aimed at simulating global seismic wave propagation must be carefully benchmarked against semianalytic methods, for example, normal-mode summation, as well as other 3D techniques. At the scale of the globe, such benchmarks are difficult and must be carefully executed. In this section, we briefly enumerate some of the main challenges associated with benchmarking.

First, rather obviously, the Earth model must be exactly the same in all techniques competing in the benchmark, which means among other things that all first- and second-order discontinuities must be honored. At a first-order discontinuity, a function – and possibly its first derivative – is discontinuous, whereas at a second-order discontinuity, a function is continuous but its first derivative is not. Most 1D Earth models, for example, PREM, have both types of discontinuities. Special attention must be paid to the implementation of the crust. Seemingly subtle model differences, for example, in crustal thickness or a division in terms of upper and lower crust, can have a profound effect on surface-wave dispersion and surface-reflected body-wave amplitudes. The presence of an ocean layer has a profound effect on the dispersion of Rayleigh waves and can affect the amplitudes of surface-reflected P–SV body waves. Most 1D Earth models incorporate radial models of attenuation, and one must ensure that the associated effects are properly implemented. As mentioned among the challenges, in an anelastic medium, the shear and compressional wave speeds become frequency-dependent, an effect that most normal-mode codes incorporate. So, besides reducing wave amplitudes, attenuation can have a strong effect on the phase of a broadband signal. The fact that we need to simulate seismograms over more than three decades in frequency, that is, periods from shorter than 1 s to longer than 1000 s, makes the implementation of such physical dispersion in numerical algorithms a necessity. Finally, one needs to decide whether or not effects due to self-gravitation and transverse isotropy, both readily accommodated in normal-mode algorithms, will form part of the benchmark.

The COSY project (Igel et al., 2000) brought together several research groups in an attempt to benchmark numerical algorithms for spherically symmetrical and 3D Earth models. The results are summarized in a special issue of *Physics of the Earth and Planetary Interiors* (volume 119, 2000). Even for 1D models, the COSY benchmarks are disappointing in terms of their relatively low level of agreement, in particular for surface waves. This serves as an illustration of the great difficulties associated with developing, implementing, and benchmarking numerical techniques for the simulation of global seismic wave propagation.

1.07.3 Equation of Motion

An isotropic, elastic Earth model may be characterized in terms of three parameters: the distribution of mass density ρ, the compressional wave speed α, and the shear wave speed β. Rather than the compressional and shear wave speeds, one may also use the bulk modulus or incompressibility κ and the shear modulus or rigidity μ. The two sets of model parameters are related by $\alpha = [(\kappa + (4/3)\mu)/\rho]^{1/2}$ and $\beta = (\mu/\rho)^{1/2}$. In a spherically symmetrical (1D) Earth model, such as PREM (Dziewonski and Anderson, 1981), IASP91 (Kennett and Engdahl, 1991), or AK135 (Kennett et al., 1995), the model

parameters vary only as a function of the radius, whereas in a general 3D Earth model, the model parameters also vary laterally. The model parameters may exhibit a number of discontinuities as a function of depth, for example, at the ocean floor, the Moho, across the upper-mantle phase transitions, at the CMB, and at the ICB. The most general spherically symmetrical Earth model is not isotropic but rather transversely isotropic. Such an Earth model is characterized by five elastic parameters: A, C, L, N, and F (Love, 1911). Alternatively, one may use a representation in terms of the speeds of horizontally and vertically propagating compressional waves $\alpha_v = (C/\rho)^{1/2}$ and $\alpha_h = (A/\rho)^{1/2}$, the speeds of vertically and horizontally propagating horizontally polarized shear waves $\beta_h = (L/\rho)^{1/2}$ and $\beta_h = (N/\rho)^{1/2}$, and the dimensionless parameter $\eta = F/(A-2L)$. Because the widely used PREM is a transversely isotropic Earth model, numerical simulations of global seismic wave propagation should facilitate the use of such models. The parameters that characterize an isotropic or transversely isotropic Earth model need to be specified at all grid points used by the numerical method.

Let $\mathbf{s}$ denote the displacement field induced by an earthquake. In an isotropic, elastic Earth model, the stress tensor $\mathbf{T}$ is determined in terms of the elastic moduli κ and μ and the strain tensor $\epsilon = \frac{1}{2}\left[\nabla\mathbf{s} + (\nabla\mathbf{s})^{\mathrm{T}}\right]$ by Hooke's law:

$$\mathbf{T} = \left(\kappa - \frac{2}{3}\mu\right)\mathrm{tr}(\epsilon)\mathbf{I} + 2\mu\epsilon \qquad [1]$$

Here, $\mathbf{I}$ denotes the 3×3 identity tensor and a superscript T denotes the transpose. Note that the strain and stress tensors are both symmetrical tensors, $\epsilon^{\mathrm{T}} = \epsilon$ and $\mathbf{T}^{\mathrm{T}} = \mathbf{T}$. In the fluid regions of the Earth model, for example, in the oceans and in the outer core, the shear modulus vanishes, and Hooke's law [1] reduces to $\mathbf{T} = \kappa\,\mathrm{tr}(\epsilon)\mathbf{I}$. Hooke's law [1] is an example of a constitutive relationship between stress and strain. The most general linear relationship between stress $\mathbf{T}$ and strain ϵ involves the fourth-order elastic tensor $\mathbf{c}$:$\mathbf{T} = \mathbf{c}$:ϵ. Because both the stress and the strain tensor are symmetrical, and due to certain thermodynamic considerations (Aki and Richards, 1980; Dahlen and Tromp, 1998), the elastic tensor exhibits the following symmetries: $c_{ijkl} = c_{jikl} = c_{ijlk} = c_{klij}$. These symmetries reduce the number of independent elastic parameters from 81 to 21. For mathematical and notational convenience, we will sometimes use the anisotropic constitutive relationship, rather than the more practical isotropic version [1].

The Earth is not a perfectly elastic body, and effects due to attenuation should be incorporated. In an anelastic medium, the stress $\mathbf{T}$ at time t is determined by the entire strain history $\epsilon(t)$, and in its most general anisotropic form, Hooke's law becomes (e.g., Aki and Richards, 1980; Dahlen and Tromp, 1998)

$$\mathbf{T}(t)\int_{-\infty}^{t} \partial_t \mathbf{c}(t-t') : \nabla\mathbf{s}(t')\mathrm{d}t' \qquad [2]$$

Attenuation is well represented by an absorption-band solid, which may be approximated by using a series of standard linear solids (Liu et al., 1976). Numerically, the behavior of the standard linear solids is modeled by tracking the so-called memory variables (e.g., Carcione et al., 1988; Emmerich and Korn, 1987; Komatitsch and Tromp, 1999; Moczo et al., 1997; Robertsson et al., 1994). In the Earth, bulk attenuation is several hundred times less significant than shear attenuation. Therefore, as far as attenuation is concerned, one can safely assume that it is sufficient to model the time evolution of the shear modulus. In this chapter, we will avoid the mathematical and numerical complications associated with attenuation, but suffice it to say that these effects can be readily accommodated in most numerical simulations. The main difficulty is the increase in computer memory requirements.

Having introduced various possibilities for the constitutive relationship, the displacement field $\mathbf{s}$ generated by an earthquake is governed by the elastic wave equation, which may be written in the form (e.g., Aki and Richards, 1980)

$$\rho\partial_t^2\mathbf{s} = \nabla\cdot\mathbf{T} + \mathbf{f} \qquad [3]$$

For earthquakes that are small enough such that they can be treated as a point source, the force $\mathbf{f}$ in [3] may be expressed in terms of the moment tensor $\mathbf{M}$ as (e.g., Aki and Richards, 1980; Dahlen and Tromp, 1998)

$$\mathbf{f} = -\mathbf{M}\cdot\nabla\delta(\mathbf{x}-\mathbf{x}_s)S(t) \qquad [4]$$

The location of the point source is denoted by $\mathbf{x}_s$, $\delta(\mathbf{x}-\mathbf{x}_s)$ is the Dirac delta distribution located at $\mathbf{x}_s$, and $S(t)$ is the source-time function. For a source of finite size, such as a fault plane Σ_s, the force $\mathbf{f}$ in [3] may be written in terms of the moment-density tensor $\mathbf{m}$ as

$$\mathbf{f} = -\mathbf{m}(\mathbf{x}_s, t)\cdot\nabla\delta(\mathbf{x}-\mathbf{x}_s) \quad \mathbf{r}\in\Sigma_s \qquad [5]$$

For simplicity, we work with the point source representation [4] in the rest of this chapter.

The equation of motion [3] must be solved subject to a number of boundary conditions. On the Earth's surface, the traction $\hat{\mathbf{n}}\cdot\mathbf{T}$, where $\hat{\mathbf{n}}$ denotes the unit outward normal to the free surface, should vanish, that is, $\hat{\mathbf{n}}\cdot\mathbf{T} = 0$. On solid–solid boundaries, such as the Moho or the upper-mantle discontinuities, both the traction $\hat{\mathbf{n}}\cdot\mathbf{T}$ and the displacement $\mathbf{s}$ need to be continuous, whereas on fluid–solid boundaries, such as the ocean floor, the CMB, and the ICB, both the traction $\hat{\mathbf{n}}\cdot\mathbf{T}$ and the normal component of displacement $\hat{\mathbf{n}}\cdot\mathbf{s}$ need to be continuous.

When our modeling domain is not the entire Earth, seismic energy needs to be absorbed on the fictitious boundaries of the domain. To accomplish this, one generally uses a paraxial equation to damp the wavefield on the edges (Clayton and Engquist, 1977; Quarteroni et al., 1998). In recent years, a significantly more efficient absorbing condition called the perfectly matched layer has been introduced (Bérenger, 1994), which is now being used in regional numerical simulations (e.g., Basu and Chopra, 2003; Collino and Tsogka, 2001; Festa and Vilotte, 2005; Komatitsch and Tromp, 2003). In this chapter, we largely ignore the numerical complications associated with absorbing boundary conditions.

At periods longer than about 150 s, self-gravitation and rotation start to play a role in global seismic wave propagation. The equation of motion for a rotating, self-gravitating Earth model is significantly more complicated than [3] (e.g., Dahlen and Tromp, 1998). Nevertheless, numerical simulations based upon a weak implementation of the equation of motion frequently do take these complications into account. In this chapter, we do not incorporate these long-period complications for the sake of simplicity.

Numerical solutions to the elastic wave equation may be subdivided in to two categories: strong and weak

implementations. Strong implementations use the differential form of the wave equation subject to certain explicit boundary conditions, whereas weak implementations are based upon an integral form that contains the free surface boundary conditions implicitly. Both implementations are popular in global seismology, and for each category, we discuss a number of numerical applications.

1.07.4 Strong Implementations

Strong implementations of the equation of motion typically involve rewriting eqn [3] and the constitutive relationship as a system of coupled first-order differential equations in space and time, known as the velocity–stress formulation:

$$\partial_t \mathbf{v} = \rho^{-1}(\nabla \cdot \mathbf{T} + \mathbf{f}), \quad \partial_t \mathbf{T} = \mathbf{c} : \nabla \mathbf{v} \qquad [6]$$

where $\mathbf{v} = \partial_t \mathbf{s}$. For brevity, we have used the general anisotropic constitutive relationship and one of the symmetries of the elastic tensor. The system of eqn [6] must be solved for the three components of velocity $\mathbf{v}$ and the six independent components of the stress tensor $\mathbf{T}$ subject to the appropriate boundary conditions, that is, a total of nine unknown parameters. FDM and PM, which are discussed in the next two sections, are frequently based upon the velocity–stress formulation [6].

1.07.4.1 Finite Difference Method

Perhaps, the most intuitively appealing numerical technique is the FDM (e.g., Madariaga, 1976; Virieux, 1984, 1986). In this approach, the first-order spatial and temporal derivatives in eqn [6] are approximated by taking differences between neighboring grid points. To limit numerical grid dispersion and anisotropy, one typically uses a fourth-order scheme on a staggered grid in space and a second-order scheme in time (e.g., Levander, 1988). For example, consider a function f sampled at N grid points with a grid spacing Δx: $f_n = f(n\Delta x)$, $n = 0, \ldots, N-1$. The derivative of f on this grid may be approximated accurate to second order in Δx by the centered-difference expression (often called a stencil)

$$\frac{\mathrm{d}}{\mathrm{d}x} f(n\Delta x) = (f_{n+1} - f_{n-1})/(2\Delta x), \quad n = 1, \ldots, N-2 \qquad [7]$$

and accurate to fourth-order by the centered-difference stencil

$$\frac{\mathrm{d}}{\mathrm{d}x} f(n\Delta x) = (-f_{n+2} + 8f_{n+1} - 8f_{n-1} + f_{n-2})/(12\Delta x), \quad n = 2, \ldots, N-3 \qquad [8]$$

These results are valid in the interior of the domain. Near the domain boundaries, less accurate one-sided difference operators come in to play, and for this reason, the implementation of free surface boundary conditions is often problematic, and in particular, surface waves are poorly simulated (e.g., Graves, 1996; Ohminato and Chouet, 1997; Robertsson, 1996). Recently developed optimal or compact finite difference operators will perhaps improve this situation (e.g., Zingg, 2000; Zingg et al., 1996); see also the optimal finite difference operators introduced by Geller and Takeuchi (1995) in the context of weak applications.

An example of a 2D (axisymmetric) staggered finite difference grid used to simulate acoustic (purely compressional) wave propagation by Thomas et al. (2000) is shown in **Figure 1**.

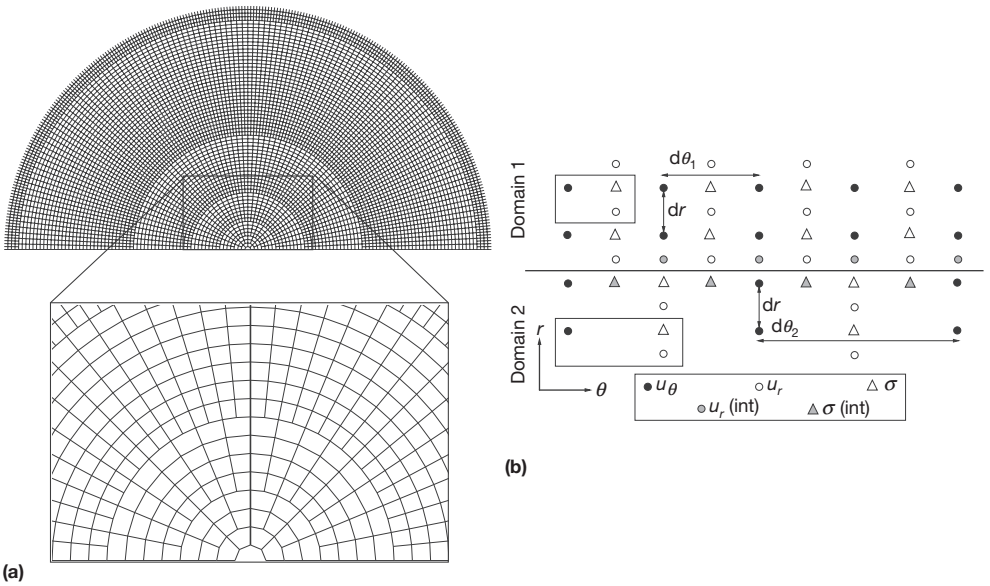

Figure 1 (a) Two-dimensional finite difference grid used in the axisymmetric simulations of Thomas et al. (2000). The lateral grid spacing is increased each time the arc length is halved. (b) Staggered grid and domain decomposition. The vertical (u_r) and lateral (u_θ) components of the velocity and the pressure (σ) are evaluated based upon a fourth-order accurate scheme on different, staggered grids. At the domain boundaries, where the lateral grid spacing is increased from $\mathrm{d}\theta_1$ to $\mathrm{d}\theta_2$, some fields have to be interpolated (dashed symbols) to connect the domains, and a second-order accurate approach for the derivatives and the interpolation is used. The radial grid spacing ($\mathrm{d}r$) remains unchanged across the boundary. Courtesy of Thomas C, Igel H, Weber M, and Scherbaum F (2000) Acoustic simulation of P-wave propagation in a heterogeneous spherical Earth: Numerical method and application to precursor waves to PKPdf. *Geophysical Journal International* 141: 6441–6464.

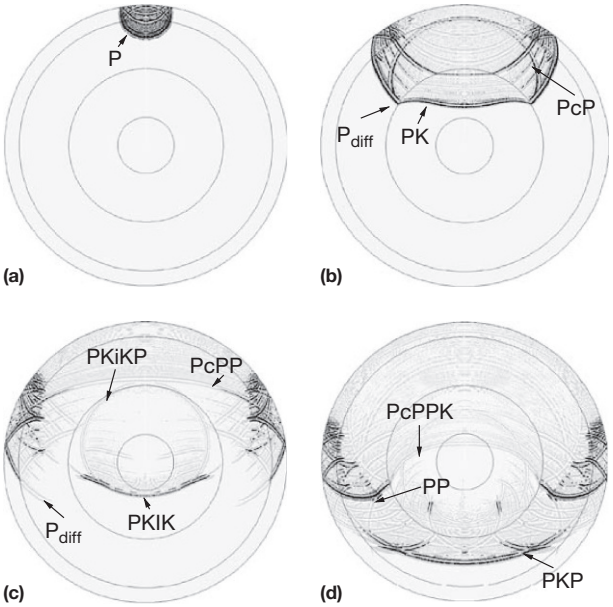

Figure 2 Finite difference snapshots of P-wave propagation through PREM for a source at the surface. The 2D simulations are based upon the acoustic wave equation involving the grid shown in **Figure 1**. The dominant period is 20 s. (a) P wavefield after 150 s, (b) 450 s, (c) 750 s, (d) 1050 s. The 670 km discontinuity, the CMB, and the ICB are shown by the concentric circles, and some of the main phases have been labeled. Courtesy of Thomas C, Igel H, Weber M, and Scherbaum F (2000) Acoustic simulation of P-wave propagation in a heterogeneous spherical Earth: Numerical method and application to precursor waves to PKPdf. *Geophysical Journal International* 141: 6441–6464.

Snapshots of such a simulation are shown in **Figure 2**. The FDM is widely used to calculate the wavefield in 3D local and regional models (e.g., Graves, 1996; Ohminato and Chouet, 1997), most recently for finite rupture scenarios, and has a long and distinguished record in exploration seismology. On the scale of the globe, it has only been used to a limited extend (e.g., Chaljub and Tarantola, 1997; Igel and Gudmundsson, 1997; Igel and Weber, 1995, 1996; Thomas et al., 2000) and never at the scale of the entire globe.

The main advantage of the FDM is its relative ease of implementation. Still, at the scale of the globe, designing a good grid with an even number of grid points per wavelength and a relatively constant stability condition is difficult because one needs to resort to unevenly spaced stencils. In particular, the poles and the Earth's center pose challenges. Perhaps, the main disadvantage of the FDM is its poor representation of surface waves due to the difficulty of implementing accurate free surface boundary conditions.

1.07.4.2 Pseudospectral Method

The motivation behind the PM is a desire for more accurate spatial derivative operators. Such operators are obtained by expanding the components of the velocity–stress wavefield in terms of known global basis functions, for example, sines and cosines or Chebyshev polynomials, and calculating derivatives based upon fast transforms. For example, consider a function f sampled at N grid points with a grid spacing Δx: $f(n\Delta x)$, $n=0, \ldots, N-1$. This function may be transformed to the wave number domain based upon the 1D fast Fourier transform (FFT) to obtain

$$F(l\Delta k) = \Delta x \sum_{n=0}^{N-1} f(n\Delta x)\exp(-2\pi i n l/N), \quad l=0,\ldots,N-1 \qquad [9]$$

where $\Delta k = 2\pi/(N\Delta x)$. The derivative of the function may now be calculated in the wave number domain by simply multiplying by $i(l\Delta k)$ and using an inverse FFT to go back to the spatial domain:

$$\frac{d}{dx} f(n\Delta x) = \frac{1}{N\Delta x} \sum_{l=0}^{N-1} i(l\Delta k) F(l\Delta k)\exp(2\pi i n l/N), \quad n = 0,\ldots,N-1 \qquad [10]$$

This derivative operation is based upon information from all available N grid points and is therefore much more accurate than a derivative operator based upon first and second neighbors, as in the finite difference expressions [7] and [8].

The PM has been used to address regional (e.g., Carcione, 1994) and global (e.g., Hung and Forsyth, 1998; Tessmer et al., 1992) seismic wave propagation problems. Fourier basis functions (e.g., Furumura et al., 1998, 1999; Kosloff and Baysal, 1982; Kosloff et al., 1984; Wang and Takenaka, 2001; Wang et al., 2001), Chebyshev basis functions (e.g., Carcione and Wang, 1993; Igel, 1999; Igel et al., 2002; Kosloff and Tal-Ezer, 1993; Kosloff et al., 1990; Tessmer, 1995; Tessmer and Kosloff, 1994), and combinations of Fourier and Chebyshev basis functions (e.g., Tessmer et al., 1992) have all been used. Because the Fourier basis is periodic, one often introduces periodic boundary conditions. At the free surface, this is not an option, and less accurate approximations need to be invoked. The advantage of the Chebyshev basis over the Fourier basis is that it is nonperiodic and uses unevenly spaced grid points with a concentration of points near the edges of the domain, which leads to more accurate surface waves due to a more precise implementation of the free surface boundary conditions. An implementation based upon wavelets, which does not use the velocity–stress formulation [6], was introduced by Hong and Kennett (2002). Like FDMs, one typically uses a second-order accurate time scheme in a PM.

Because of the use of global basis functions, the pseudospectral technique is limited to smooth media, and numerical noise appears in the presence of sharp discontinuities in the model, such as first-order solid–solid upper-mantle discontinuities. Such ringing can be avoided by using a domain decomposition approach (e.g., Hung and Forsyth, 1998; Wang and Takenaka, 2001).

An example of a 2D axisymmetric elastic pseudospectral simulation by Wang et al. (2001) for model IASP91 is shown in **Figure 3**. The implementation is based upon a Fourier basis. Unlike the acoustic FDM simulation shown in **Figure 2**, one can see both compressional and shear waves in this simulation. Igel (1999) used a PM based upon a Chebyshev implementation for the simulation of 3D seismic wave propagation in a section of the globe, as illustrated in **Figure 4**. Snapshots from a simulation for PREM are shown in **Figure 5**. The 3D simulation is restricted to a section of the globe to save memory and to avoid problems associated with diminishing grid spacing and related numerical instabilities toward the Earth's center.

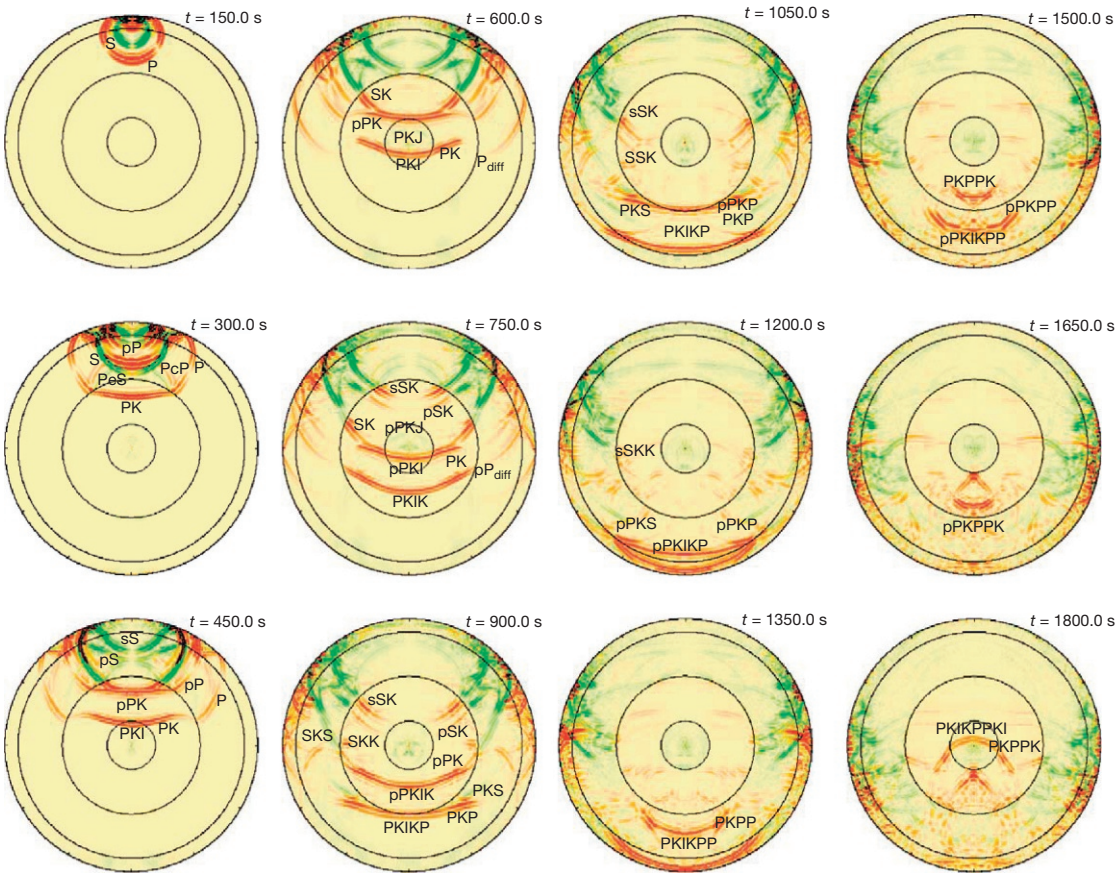

Figure 3 Snapshots of an axisymmetric pseudospectral simulation in the IASP91 model for a source at a depth of 600 km. The 2D simulations solve the elastic wave equation in cylindrical coordinates. The red and green colors represent P and S waves, respectively. Concentric circles denote the 660 km discontinuity, the CMB, and the ICB. It is instructive to compare these elastic pseudospectral snapshots with the purely acoustic finite difference snapshots shown in **Figure 2**. (*Note*: however the difference in source depth.) The shortest period in the synthetics is 30 s. Courtesy of Wang Y, Takenaka H, and Furumura T (2001) Modelling seismic wave propagation in a two-dimensional cylindrical whole-Earth model using the pseudospectral method. *Geophysical Journal International* 145: 689–708.

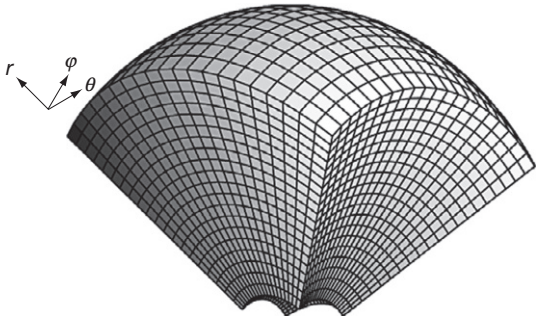

Figure 4 Physical domain for a 3D pseudospectral simulation based upon Chebyshev polynomials. The chunk of the globe spans $80^\circ \times 80^\circ$ on the Earth's surface, ranges in radius from 1371 to 6371 km, and is centered around the equator. Courtesy of Igel H (1999) Wave propagation in three-dimensional spherical sections by the Chebyshev spectral method. *Geophysical Journal International* 136: 559–566.

The main advantage of the PM is its precision for smooth isotropic and anisotropic models. Its main demerits are related to the difficulties of designing effective fast transforms for the sphere and the generally poor representation of surface waves. Transform methods frequently impose an undesirable grid spacing that reflects geometry rather than material properties. Large simulations on parallel machines with distributed memory are challenging because subsequent FFTs in the x-, y-, and z-directions require repeated gather–scatter operations that are computationally expensive.

1.07.5 Weak Implementations

For a number of numerical techniques, one works with a modified version of the equation of motion called the integral or weak formulation of the problem. It is obtained by taking the dot product of the momentum (eqn [3]) with an arbitrary test vector $\mathbf{w}$ and integrating by parts over the volume V of the Earth:

$$\int_V \rho \mathbf{w} \cdot \partial_t^2 \mathbf{s} \, \mathrm{d}^3\mathbf{x} = -\int_V \nabla \mathbf{w} : \mathbf{T} \mathrm{d}^3\mathbf{x} + \mathbf{M} : \nabla \mathbf{w}(\mathbf{x}_s) S(t) \qquad [11]$$

Equation [11] is equivalent to the strong formulation [6] because it holds for any test vector $\mathbf{w}$. The term on the left-hand side is related to the mass matrix in finite element parlance, and the first term on the right leads to the stiffness

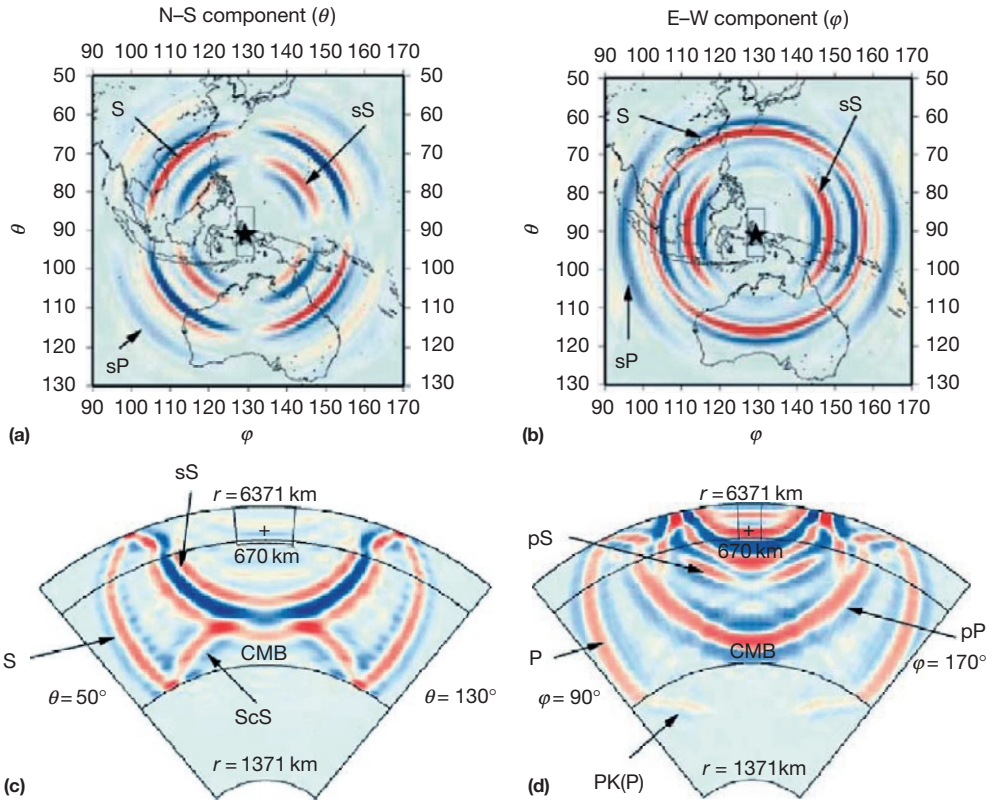

Figure 5 Top: Pseudospectral snapshots of the north–south (left) and east–west (right) components of the velocity field at the Earth's surface at 550 s. Red and blue colors denote positive and negative velocities, respectively. The epicenter is indicated by the star, and the hypocenter is located at a depth of 600 km. The dominant period is 50 s, and the spherically symmetrical Earth model is PREM. We clearly see the S and sS arrivals; at this stage in the simulation, the compressional waves P and pP have already been absorbed by the boundaries. Bottom: Snapshots of the velocity field in a longitudinal cross section through the hypocenter. Left: Transverse component of motion at 550 s. Notice that, as expected, there are no shear waves in the core. Right: Radial component of motion at 300 s. Notice how compressional waves are entering the core. Courtesy of Igel H (1999) Wave propagation in three-dimensional spherical sections by the Chebyshev spectral method. *Geophysical Journal International* 136: 559–566.

matrix. The second term on the right is the source term [4], which has been integrated explicitly by using the properties of the Dirac delta distribution. Note that, like the velocity–stress strong form [6], only the first-order spatial derivatives of the displacement field and the test vector are involved in the weak form [11] but that, unlike the velocity–stress formulation, the temporal derivatives are of second order.

It is important to appreciate that the traction-free surface condition $\hat{\mathbf{n}}\cdot\mathbf{T}=0$ is imposed naturally and automatically during the integration by parts, because the contour integral over the free surface simply vanishes. In other words, the free surface condition is a natural condition of the problem. In the context of regional simulations, an additional term appears in eqn [11], which represents the absorption of energy on the artificial boundaries of the domain (e.g., Komatitsch and Tromp, 1999).

In the next section, we introduce Rayleigh–Ritz methods, of which CMM and DSM are examples. Other numerical methods based upon the weak formulation [11] that are discussed in subsequent sections are FEM and SEM.

1.07.5.1 Rayleigh–Ritz Method

The idea behind a Rayleigh–Ritz method is to expand the unknown displacement field $\mathbf{s}$ in terms of a set of known trial or basis functions $\mathbf{s}_k$ (Dahlen and Tromp, 1998):

$$\mathbf{s}=\sum_k q_k\mathbf{s}_k \qquad [12]$$

In this approach, one seeks to determine the expansion coefficients q_k. Notice that at this stage, we need not be specific about the exact choice of the basis functions. Rayleigh–Ritz methods are generally implemented in the frequency domain. It is readily shown that the weak form of the frequency domain version of the equation of motion [3] is (Dahlen and Tromp, 1998; Geller and Ohminato, 1994)

$$-\omega^2\int_V \rho\mathbf{w}\cdot\mathbf{s}\,\mathrm{d}^3\mathbf{x}=-\int_V \nabla\mathbf{w}:\mathbf{T}\,\mathrm{d}^3\mathbf{x}+\mathbf{M}:\nabla\mathbf{w}(\mathbf{x}_\mathrm{s})S(\omega) \qquad [13]$$

Upon substituting the expansion [12] in [13] and choosing the test vector $\mathbf{w}=\mathbf{s}_{k'}$, we obtain the matrix equation

$$\sum_k \left(V_{k'k}-\omega^2 T_{k'k}\right)q_k(\omega)=S_{k'}(\omega) \qquad [14]$$

where we have defined the matrix and vector elements

$$V_{k'k}=\int_\Omega \nabla\mathbf{s}_{k'}:\mathbf{c}:\nabla\mathbf{s}_k\,\mathrm{d}^3\mathbf{x},\quad T_{k'k}=\int_\Omega \rho\mathbf{s}_{k'}\cdot\mathbf{s}_k\,\mathrm{d}^3\mathbf{x},\quad S_{k'}(\omega)=\mathbf{M}:\nabla\mathbf{s}_{k'}(\mathbf{x}_\mathrm{s})S(\omega) \qquad [15]$$

For brevity, we use the full anisotropic elastic tensor in the definition of the matrix elements $V_{k'k}$. Because the test vector

$\mathbf{w}$ and the basis functions $\mathbf{s}_k$ are the same, the Rayleigh–Ritz method is also referred to as a Galerkin method. By introducing the $(\infty \times \infty)$-dimensional kinetic and potential energy matrices

$$\mathbf{T} = \begin{pmatrix} \vdots & & \\ \cdots & T_{k'k} & \cdots \\ \vdots & & \end{pmatrix}, \quad \mathbf{V} = \begin{pmatrix} \vdots & & \\ \cdots & V_{k'k} & \cdots \\ \vdots & & \end{pmatrix} \qquad [16]$$

and the ∞-dimensional source vector

$$\mathbf{S} = \begin{pmatrix} \vdots \\ S_{k'} \\ \vdots \end{pmatrix} \qquad [17]$$

the solution to [14] may be formally expressed as

$$\mathbf{q}(\omega) = \left(\mathbf{V} - \omega^2 \mathbf{T}\right)^{-1} \mathbf{S}(\omega) \qquad [18]$$

In an anelastic Earth model, the potential energy matrix also depends on frequency, $\mathbf{V}=\mathbf{V}(\omega)$, because in that case, the elastic tensor $\mathbf{c}$ becomes frequency-dependent (see eqn [2]). Of course, in practice, one uses a finite-dimensional set of basis functions $\mathbf{s}_{k'}$ leading to a finite-dimensional matrix solution [18]. This truncation of the eigenvalue problem leads to inaccuracies in the synthetics. Such truncation errors are most pronounced in models with sharp heterogeneities, which induce a wide coupling band.

Let us denote the $\hat{\boldsymbol{\nu}}$ component of the displacement by $s=\hat{\boldsymbol{\nu}} \cdot \boldsymbol{s}$, and let us define the receiver vector elements $R_k = \hat{\boldsymbol{\nu}} \cdot \boldsymbol{s}_k$. Upon introducing the ∞-dimensional receiver vector

$$\mathbf{R} = \begin{pmatrix} \vdots \\ R_k \\ \vdots \end{pmatrix} \qquad [19]$$

and using eqns [12] and [18], it may be shown that the spectrum of the $\hat{\boldsymbol{\nu}}$ component of the displacement is given by

$$s(\omega) = \mathbf{R}^{\mathrm{T}} \left(\mathbf{V} - \omega^2 \mathbf{T}\right)^{-1} \mathbf{S}(\omega) \qquad [20]$$

This expression gives the response of a 3D Earth model to an earthquake and forms the basis of the CMM discussed in **Section 1.07.5.1.1** and the DSM discussed in **Section 1.07.5.1.2**.

Finally, we note that the eigenfrequencies of the 3D Earth model are determined by (Dahlen and Tromp, 1998)

$$\det\left(\mathbf{V} - \omega^2 \mathbf{T}\right) = 0 \qquad [21]$$

1.07.5.1.1 Coupled-mode method

The CMM for calculating 3D synthetic seismograms was pioneered by Park (1986) and gained significant interest (e.g., Capdeville et al., 2000; Lognonné and Romanowicz, 1990; Park and Yu, 1992; Tromp and Dahlen, 1990). In this approach, the basis functions $\mathbf{s}_k$ in eqn [12] are chosen to be the eigenfunctions of a spherically symmetrical Earth model. These eigenfunctions have a radial dependence that is dictated by the radial structure of the spherically symmetrical reference Earth model, for example, PREM, and a lateral dependence that involves (vector) spherical harmonics. Expressions for the coupling matrices [16] based upon these eigenfunctions were first derived by Woodhouse (1980) and are summarized in Dahlen and Tromp (1998).

There are two main problems with the CMM. The first problem is that the basis functions are spherically symmetrical whereas the 3D Earth model is elliptical and has topography and bathymetry. Typically, first-order perturbation theory is used to linearize these boundary undulations, which leads to errors in the forward calculation. A more serious problem has to do with the size of the matrices [16] involved in the coupled-mode calculations. As the frequency content of the synthetics is increased, the size of the matrices grows very rapidly, leading to large matrix–vector operations. Such operations are computationally very expensive, in particular on computers with distributed memory. Therefore, coupled-mode calculations do not scale well on parallel machines, and in recent years, they have largely gone out of favor. Only when one wants to calculate the very long-period response of the Earth, say at periods of 500 s and longer, is the coupled-mode approach the method of choice (e.g., Deuss and Woodhouse, 2001). **Figure 6** shows an example of a coupled-mode calculation for the 9 June 1994 Bolivia deep-focus earthquake. In this calculation, neighboring modes are grouped in supermultiplets, in which the singlets that constitute the multiplets that define the group are coupled through a matrix expression of the form [20].

1.07.5.1.2 Direct solution method

In the DSM pioneered by Geller (e.g., Geller and Hatori, 1995; Geller and Ohminato, 1994; Geller and Takeuchi, 1995; Hara et al., 1991; Takeuchi et al., 2000), the basis functions in eqn [12] are low-order polynomials, for example, splines, or analytic functions. Complications due to the representation of the source term, which may not be representable in terms of these basis functions, are discussed in Takeuchi and Geller (2003). For spherically symmetrical Earth models, the DSM may be used to calculate high-frequency synthetic seismograms, as illustrated in **Figure 7**. At 2 Hz, these synthetics are detailed enough to show the weak ICB-reflected PKiKP arrival. Geller and Takeuchi (1995) had designed finite difference operators that optimize the accuracy of the DSM synthetic seismograms.

DSM synthetics may be used to benchmark other numerical techniques. A comparison between a 2D axisymmetric PS simulation, such as the one shown in **Figure 3**, and 3D DSM for spherically symmetrical Earth model IASP91 is shown in **Figure 8**. To facilitate this comparison, the 2D PS synthetics are mapped to approximate 3D synthetics (Wang et al., 2001). This mapping produces approximately the right 3D geometric spreading and dispersion and produces adequate fits to the body-wave arrivals.

Like coupled-mode synthetics, the DSM generally uses a linearized treatment of boundary undulations, which diminishes the accuracy of the 3D synthetics. Takeuchi (2005) had recently extended the method to include arbitrary perturbations in boundary locations, as illustrated in **Figure 9**. Probably, the main restriction for the DSM, like the CMM, is the need for significant amount of shared memory to perform the necessary matrix–vector manipulations for fully 3D Earth models. Some of the main advantages of the DSM are that it addresses broadband wave propagation at the scale of the entire globe and that it agrees closely with normal-mode algorithms for spherically symmetrical Earth model. For relatively

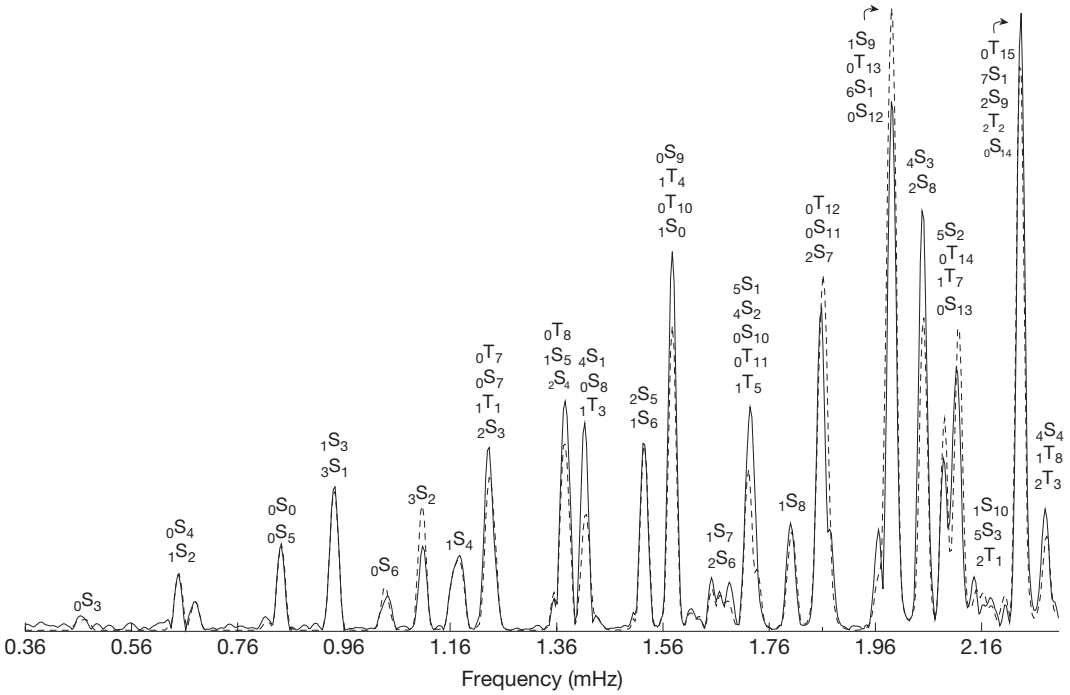

Figure 6 Vertical-component amplitude spectra of the 9 June 1994 Bolivia deep-focus earthquake recorded at station PAS in Pasadena, CA. The solid line shows the observed spectrum; the dashed line shows the synthetic coupled-mode spectrum. Rotation, ellipticity, and the lateral variations in shear wave speed of model SKS12WM13 (Dziewonski et al., 1997) have been accounted for in the calculations. The vertical arrays of mode labels identify the 22 supermultiplets considered. A Hann taper has been applied to both 35 h time series prior to Fourier transformation.

smooth 3D models at longer periods, the method is precise and effective.

1.07.5.2 Finite Element Method

The FEM is very popular in science and engineering (e.g., Hughes, 1987; Zienkiewicz, 1977), but has found limited application in seismology in general, and is currently not used for simulations at the scale of the globe. In the context of regional simulations, for the purpose of seismic hazard assessment, the method is actively being used (e.g., Aagaard et al., 2001; Bao et al., 1998; Bielak et al., 1999; Garatani et al., 2000). The method accommodates previously mentioned difficulties related to the presence of topography on major interfaces by allowing the grid boundaries to follow the local topography. Despite the fact that the FEM is presently not used for simulations in global seismology we discuss the method in some detail, because the SEM, which is extensively used in global seismology, has many common features.

In an FEM, the model domain is subdivided into a large number of small elements, which may take a variety of forms, for example, tetrahedra, hexahedra, pyramids, and prisms. Cartesian points $\mathbf{x}=(x, y, z)$ within a given deformed element Ω are mapped to points $\boldsymbol{\xi}=(\xi, \eta, \zeta)$ in the reference element based upon the transformation

$$\mathbf{x}(\boldsymbol{\xi})=\sum_{a=1}^{n_a} N_a(\boldsymbol{\xi})\mathbf{x}_a \qquad [22]$$

The control points or anchors $\mathbf{x}_a$ define the geometry of the element, and the shape functions N_a provide a means for mapping and interpolation. For example, the geometry of hexahedral elements (deformed cubes) may be controlled by $n_a=8$, 20, or 27 anchors, as illustrated in Figure 10.

As an example, hexahedral shape functions are typically products of degree 1 or 2 Lagrange polynomials. The $n+1$ Lagrange polynomials of degree n are defined in terms of $n+1$ control points $-1\le\xi_\alpha\le 1$, $\alpha=0, \ldots, n$, by

$$\ell_\alpha(\xi)=\frac{(\xi-\xi_0)\cdots(\xi-\xi_{\alpha-1})(\xi-\xi_{\alpha+1})\cdots(\xi-\xi_n)}{(\xi_\alpha-\xi_0)\cdots(\xi_\alpha-\xi_{\alpha-1})(\xi_\alpha-\xi_{\alpha+1})\cdots(\xi_\alpha-\xi_n)} \qquad [23]$$

As a result of this definition, the Lagrange polynomials are equal to either 0 or 1 at any given control point $\ell_\alpha(\xi_\beta)=\delta_{\alpha\beta}$, where δ denotes the Kronecker delta. The two Lagrange polynomials of degree 1 with two control points $\xi=-1$ and $\xi=1$ are $\ell_0(\xi)=\frac{1}{2}(1-\xi)$ and $\ell_1(\xi)=\frac{1}{2}(1+\xi)$, and the three Lagrange polynomials of degree 2 with three control points $\xi=-1$, $\xi=0$, and $\xi=1$ are $\ell_0(\xi)=\frac{1}{2}\xi(\xi-1)$, $\ell_1(\xi)=1-\xi^2$, and $\ell_2(\xi)=\frac{1}{2}\xi(\xi+1)$.

Functions f, for example, components of the displacement field $\mathbf{s}$ or the test vector $\mathbf{w}$, are expanded in the n_a shape functions N_a:

$$f(\mathbf{x}(\boldsymbol{\xi}))=\sum_{a=1}^{n_a} f_a N_a(\boldsymbol{\xi}) \qquad [24]$$

where f_a denotes the value of the function f at anchor $\mathbf{x}_a$. The weak implementation [11] involves gradients of the

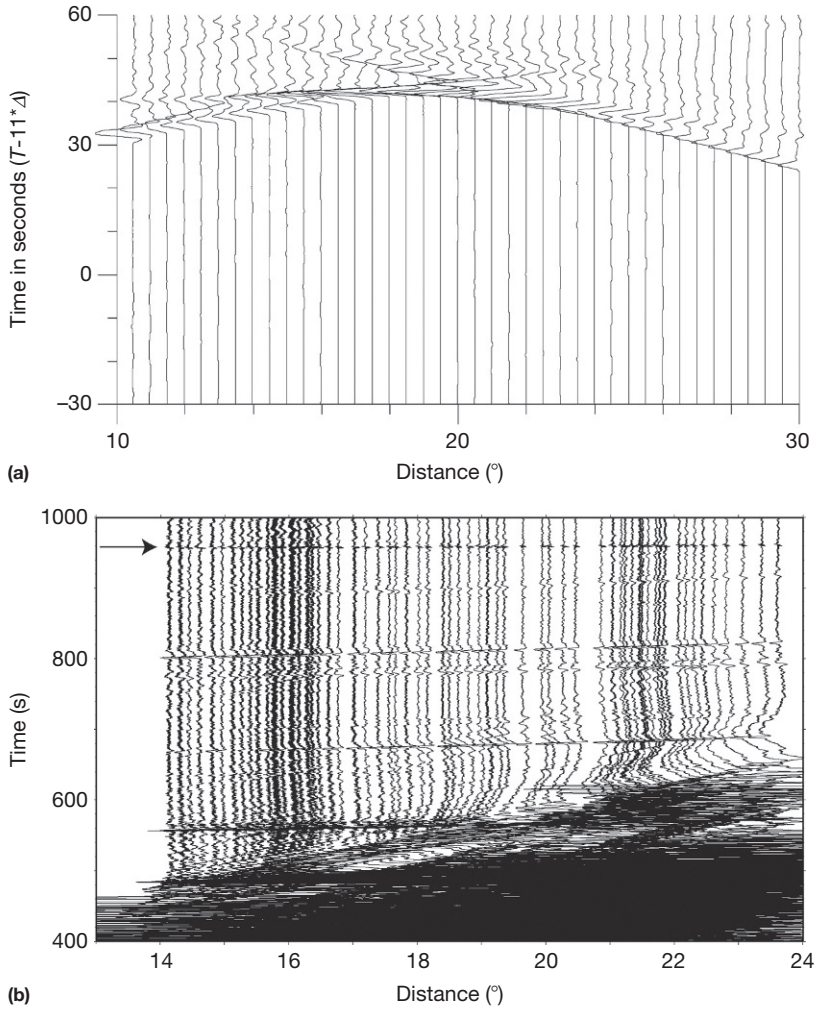

Figure 7 Examples of high-frequency DSM synthetics for isotropic PREM. (a) Displacement synthetic seismograms for upper-mantle triplication phases. The maximum frequency is 1 Hz. (b) Displacement synthetic seismograms for the PKiKP phase (indicated by the arrow). The maximum frequency is 2 Hz. Courtesy of Nozomu Takeuchi.

displacement **s** and the test vector **w**. Thus, the need arises to determine the gradient of functions:

$$\nabla f = \sum_{i=1}^{3} \hat{\mathbf{x}}_i \partial_i f = \sum_{i=1}^{3} \hat{\mathbf{x}}_i \sum_{a=1}^{n_a} f_a \left[\partial_\xi N_a(\boldsymbol{\xi})(\partial_i \xi) + \partial_\eta N_a(\boldsymbol{\xi})(\partial_i \eta) + \partial_\zeta N_a(\boldsymbol{\xi})(\partial_i \zeta) \right] \quad [25]$$

where $\hat{\mathbf{x}}_i$, $i=1, 2, 3$, denote unit vectors in the direction of increasing x, y, and z, respectively, and ∂_i, $i=1, 2, 3$, denote partial derivatives in those directions. The matrix $\partial\boldsymbol{\xi}/\partial\mathbf{x}$ is obtained by inverting the matrix $\partial\mathbf{x}/\partial\boldsymbol{\xi}$, whose elements may be determined by differentiating [22]. The existence of this matrix is a requirement that is imposed during the design of the mesh, that is, the Jacobian of the mapping [22] should never vanish. Notice how in an FEM the accuracy of the gradient [25] is controlled by the polynomial degree of the shape functions. Typically, one uses low-degree polynomials for the shape functions, which leads to relatively inaccurate derivatives, as in a low-degree FDM based upon [7]. Numerically, this leads to grid dispersion and anisotropy. There are the so-called *h-p* FEMs that use higher-degree polynomials for the shape functions to combat this problem (e.g., Guo and Babuška, 1986). A drawback for *h-p* FEMs is that they lead to large systems of linear equations that are difficult to solve, in particular on parallel machines.

The weak form [11] involves numerical integration of functions over the elements. In an FEM, this is generally accomplished based upon Gauss quadrature, such that integrations over elements Ω may be approximated as

$$\int_\Omega f(\mathbf{x}) \mathrm{d}^3\mathbf{x} = \sum_{\alpha=0}^{n} \sum_{\beta=0}^{n} \sum_{\gamma=0}^{n} \omega_\alpha \omega_\beta \omega_\gamma \times f\left(\xi_\alpha, \eta_\beta, \zeta_\gamma\right) \mathcal{J}\left(\xi_\alpha, \eta_\beta, \zeta_\gamma\right) \quad [26]$$

where ω_α, $\alpha=0, \ldots, n$, denote the $n+1$ weights associated with the Gauss quadrature, the $(n+1)^3$ points $(\xi_\alpha, \eta_\beta, \zeta_\gamma)$ denote the associated Gauss integration points, and $\mathcal{J}$ denotes the Jacobian of the mapping [22]. The Gauss weights and integration points are chosen such that in 1D, they exactly integrate a polynomial of degree $2n$. To facilitate the integration of

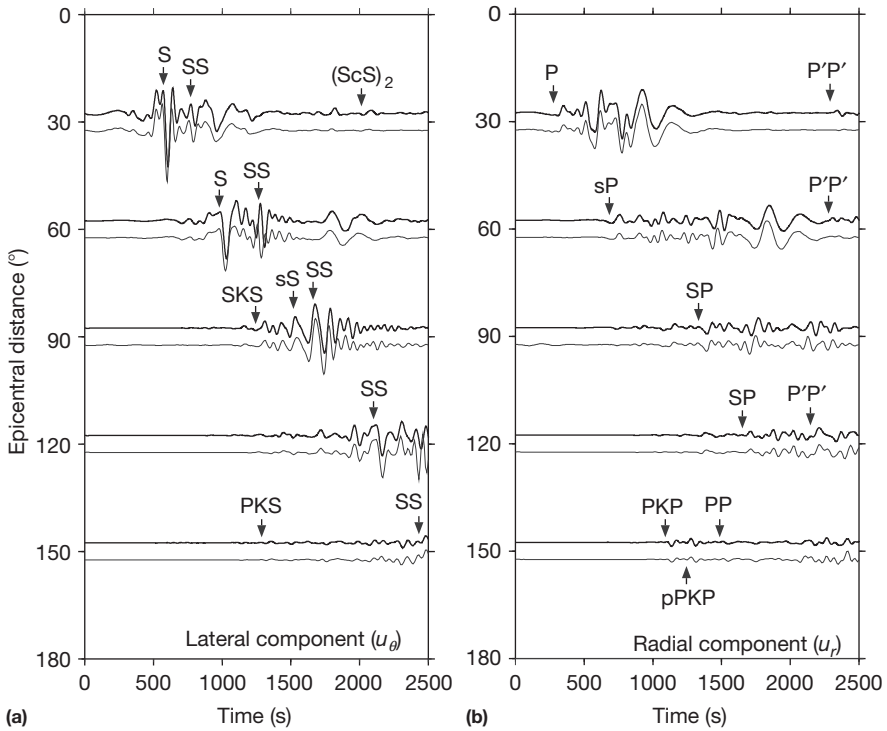

Figure 8 Comparison of axisymmetric pseudospectral (thin line) and DSM (thick line) synthetics at five epicentral distances. (a) Lateral component, (b) vertical component. Both sets of seismograms are band-pass-filtered between 40 and 300 s. The spherically symmetrical Earth model is IASP91. Courtesy of Wang Y, Takenaka H, and Furumura T (2001) Modelling seismic wave propagation in a two-dimensional cylindrical whole-Earth model using the pseudospectral method. *Geophysical Journal International* 145: 689–708.

functions and their partial derivatives over the elements, the values of the inverse Jacobian matrix $\partial\boldsymbol{\xi}/\partial\mathbf{x}$ need to be stored at the Gauss integration points for each element.

In a finite element mesh, grid points that lie on the sides, edges, or corners of an element are shared among neighboring elements. Therefore, one needs to distinguish between the grid points that define an element, the local mesh, and all the grid points in the model, many of which are shared among several finite elements, the global mesh. One needs to determine a mapping between grid points in the local mesh and grid points in the global mesh; efficient finite element routines are available for this purpose. Before the system can be marched forward in time, the contributions from all the elements that share a common global grid point need to be summed. This is referred to as the assembly of the system.

The implementation of an FEM on parallel computers involves partitioning the mesh in slices of elements, such that each processor in the parallel machine is only responsible for the elements in one particular slice. At the edges of a slice, results need to be communicated to its neighbors. Therefore, a parallel computer assembly involves communication between adjacent mesh slices. Because the mass matrix in an FEM is nondiagonal, one needs to use an implicit time scheme, that is, one needs to resolve a system of linear equations. On a parallel machine, this too requires communication between distinct compute nodes. We discuss mesh partitioning in more detail in the context of spectral element simulations, which we introduce in the next section.

Like a low-order FDM, the FEM tends to suffer from numerical grid dispersion and anisotropy, which is highly undesirable for seismic wave propagation problems that involve real dispersion and anisotropy. Its main attribute is its flexibility, which allows one to design complicated meshes capturing realistic 3D Earth models.

1.07.5.3 Spectral Element Method

The SEM has been used for two decades in computational fluid dynamics (e.g., Patera, 1984). It has more recently been applied to problems related to 2D (Cohen et al., 1993; Priolo et al., 1994) and 3D local or regional (Faccioli et al., 1997; Komatitsch, 1997; Komatitsch and Tromp, 1999; Komatitsch and Vilotte, 1998; Komatitsch et al., 2004; Seriani, 1998) and global (Chaljub, 2000; Chaljub and Valette, 2004; Chaljub et al., 2003; Komatitsch and Tromp, 2002a,b; Komatitsch et al., 2002, 2003) seismic wave propagation. As in the classical FEM discussed in the previous section, the first step in the SEM is to subdivide the model volume into a number of non-overlapping elements. In an FEM, one can choose from a variety of elements, for example, tetrahedra, hexahedra, or prisms, but in the classical SEM, one uses only hexahedra. In 2D, the SEM has been extended to include triangles (e.g., Komatitsch et al., 2001; Sherwin and Karniadakis, 1995; Taylor and Wingate, 2000), but this leads to complications that are beyond the scope of this chapter. The mesh of elements needs to be geometrically conforming, that is, the six sides of each hexahedral

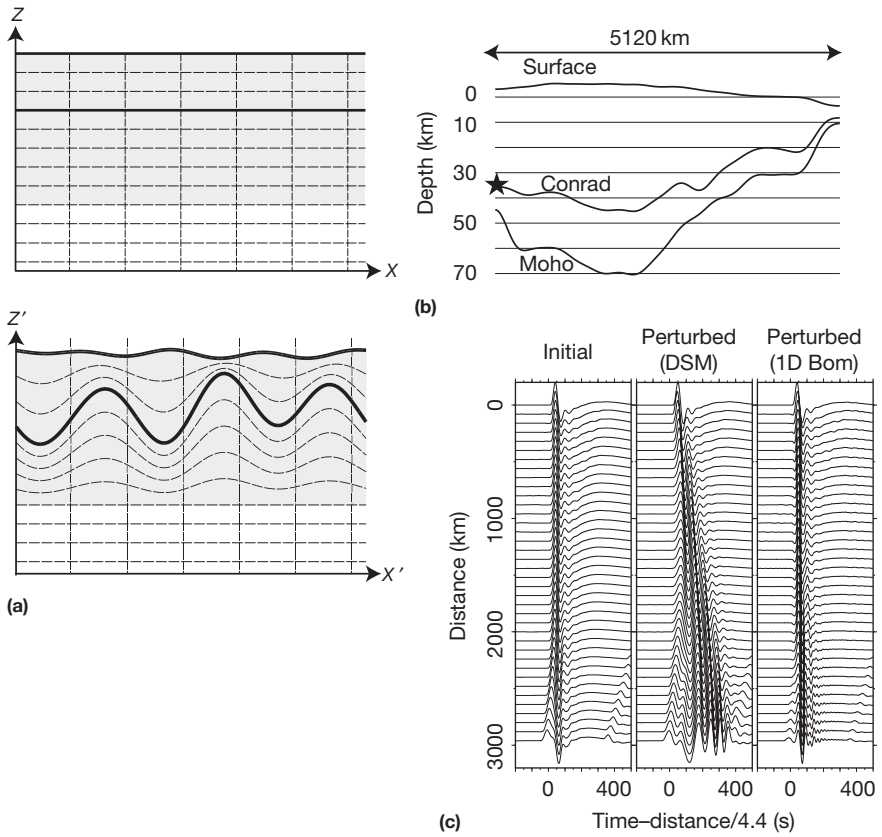

Figure 9 Illustration of the inclusion of topographic effects in the DSM. The basis functions are defined by using a one-to-one mapping of the boundaries in the initial model to those in the perturbed model. (a) Schematic illustration of the one-to-one mapping between the initial, laterally homogeneous model (top) and the perturbed model (bottom). Solid thick lines show the external and internal boundaries, and the shaded area shows the region deformed by the mapping. (b) Two-dimensional model that mimics crustal thickening in the Tibet region. The star shows the location of the source. (c) Example of synthetic seismograms computed for the model shown in (b). Synthetic seismograms for the initial (PREM) model are shown on the left, DSM synthetics for the perturbed model are shown in the middle, and synthetics based upon the conventional first-order Born approximation are shown on the right. Courtesy of Takeuchi N (2005) Finite boundary perturbation theory for the elastic equation of motion. *Geophysical Journal International* 160: 1044–1058.

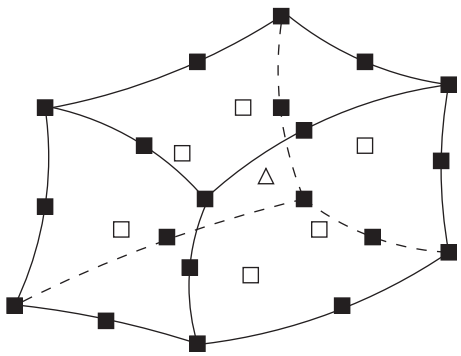

Figure 10 The geometry of a hexahedral finite element may be defined in terms of its eight corners, the eight corners plus the 12 edge centers (the 20 black squares), or the eight corners plus the 12 edge centers plus the six face centers (the six open squares) plus the center (the open triangle). In a classical FEM, these 8, 20, or 27 anchors are used to define the shape of the element as well for the interpolation of functions. Courtesy of Komatitsch D and Tromp J (1999) Introduction to the spectral-element method for 3-D seismic wave propagation. *Geophysical Journal International* 139: 806–822.

element must match up exactly with the sides of neighboring elements. The SEM can be adapted to geometrically nonconforming meshes based on what is known as the mortar-matching method (e.g., Chaljub, 2000; Chaljub et al., 2003), but this is also beyond the scope of this chapter. Recent reviews of the SEM in seismology are given by Komatitsch et al. (2005) and Chaljub et al. (2007).

Figure 11 shows an example of a hexahedral SEM mesh for the globe. The mesh is designed based upon an analytic mapping between the cube and the sphere called the cubed sphere (Chaljub, 2000; Ronchi et al., 1996; Sadourny, 1972). Each of the six chunks that constitute the cubed sphere is meshed in such a way that they match perfectly at their common interfaces. Following Chaljub (2000), the singularity of coordinates at the Earth's center is avoided by placing a small cube around the center of the inner core. The mesh within this cube matches up with the cubed sphere mesh at the ICB. This mesh honors all first- and second-order discontinuities in PREM (Dziewonski and Anderson, 1981). Any typical 3D mantle and/or crustal model may now be superimposed on the mesh.

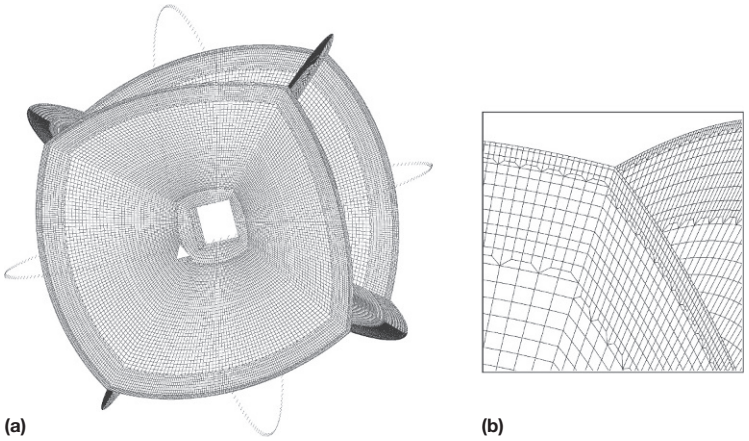

Figure 11 (a) Example of a spectral element mesh in the mantle. (b) Close-up of the mesh doublings in the upper mantle. The spectral element mesh is conforming, that is, every side of every element matches up perfectly with the side of a neighboring element, but nonstructured, that is, the number of elements that share a given point can vary and take any value. The mesh honors first-order discontinuities in PREM at depths of 24.4, 220, 400, and 670 km, the CMB, and the ICB; it also honors second-order discontinuities in PREM at 600, 771 km, and at the top of D″. The mesh is doubled in size once below the Moho, a second time below the 670 km discontinuity, and a third time just above the ICB. Each of the six chunks that constitute the cubed sphere has 240×240 elements at the free surface and 30×30 elements at the ICB. The central cube in the inner core has been removed for clarity of viewing. For a later experiment shown in **Figure 15**, the triangle indicates the location of the source, situated on the equator and the Greenwich meridian. Rings of receivers with a 2° spacing along the equator and the Greenwich meridian are shown by the dashes. Courtesy of Komatitsch D and Tromp J (2002) Spectral-element simulations of global seismic wave propagation. I: Validation. *Geophysical Journal International* 149: 390–412.

In an SEM, one generally uses hexahedral elements, which may be mapped back to the reference cube based upon shape functions expressed in terms of low-degree Lagrange polynomials. After meshing the model, we need to define basis functions to represent the unknown displacement vector **s** and the test vector **w** on an element. In most FEMs, both the geometry of the problem and the vector fields are expressed using shape functions defined in terms of low-degree polynomials, as in eqn [24]. In the SEM, the geometry of the curved elements is also defined using low-degree polynomials, but the displacement field and the test vector are defined using higher-degree polynomials. This is the major difference between SEMs and FEMs. In this regard, SEMs are related to *h-p* FEMs, which also use polynomials of higher degree (but result in a nondiagonal mass matrix) (e.g., Guo and Babuška, 1986).

An SEM typically uses Lagrange polynomials [23] of degree 4–10 for the interpolation of functions. In an SEM, the control points ξ_α, $\alpha = 0, \ldots, n$, needed in the definition [23] are chosen to be the $n+1$ GLL points, which are the roots of $(1-\xi^2)\, P_n'(\xi) = 0$, where P_n' denotes the derivative of the Legendre polynomial of degree n (Canuto et al., 1988). As an example, the five Lagrange polynomials of degree 4 are shown in **Figure 12(a)**, and **Figure 12(b)** illustrates the distribution of associated GLL points on the face of a hexahedral element. As we will see, the combination of Lagrange interpolants with a particular integration rule leads to an exactly diagonal mass matrix, and a diagonal mass matrix leads to a simple explicit time scheme that lends itself very well to numerical simulations on parallel computers.

We note that there are implementations of the SEM based upon Chebyshev basis functions that do not lead to a diagonal mass matrix (e.g., Patera, 1984; Priolo et al., 1994; Seriani, 1998). The main advantages are that the related Gauss–Lobatto–Chebyshev integration rule is exact for the chosen polynomial basis, while it is only approximate in the case of GLL quadrature, and that the Gauss–Lobatto–Chebyshev points and weights are known analytically (in the GLL version, they are computed numerically). The main disadvantage of the Chebyshev approach is that an iterative solver for large matrix systems needs to be implemented and implicit time-marching schemes are frequently used. This implementation is technically difficult but has been used successfully (Seriani, 1997, 1998).

In the weak form of the wave eqn [11], we expand functions f, for example, a component of the displacement field **s** or the test vector **w**, in terms of degree-n Lagrange polynomials:

$$f(\mathbf{x}(\xi, \eta, \zeta)) = \sum_{\alpha=0}^{n} \sum_{\beta=0}^{n} \sum_{\gamma=0}^{n} f^{\alpha\beta\gamma} \ell_\alpha(\xi) \ell_\beta(\eta) \ell_\gamma(\zeta) \qquad [27]$$

where $f^{\alpha\beta\gamma} = f(\mathbf{x}(\xi_\alpha, \eta_\beta, \zeta_\gamma))$ denotes the value of the function f at the GLL point $\mathbf{x}(\xi_\alpha, \eta_\beta, \zeta_\gamma)$. Using the polynomial representation [27], the gradient of a function can be expressed as

$$\nabla f(\mathbf{x}(\xi, \eta, \zeta)) = \sum_{i=1}^{3} \hat{\mathbf{x}}_i \sum_{\alpha=0}^{n} \sum_{\beta=0}^{n} \sum_{\gamma=0}^{n} f^{\alpha\beta\gamma} \left[\ell_\alpha'(\xi) \ell_\beta(\eta) \times \ell_\gamma(\zeta) \partial_i \xi + \ell_\alpha(\xi) \ell_\beta'(\eta) \ell_\gamma(\zeta) \partial_i \eta + \ell_\alpha(\xi) \ell_\beta(\eta) \ell_\gamma'(\zeta) \partial_i \zeta \right] \qquad [28]$$

where a prime denotes the derivative of a Lagrange polynomials. As in the FEM, the matrix $\partial\boldsymbol{\xi}/\partial\mathbf{x}$ is obtained by inverting the matrix $\partial\mathbf{x}/\partial\boldsymbol{\xi}$. Because one typically uses polynomials of degree 4–10, the derivatives calculated based upon [28] tend to be more accurate than those used in an FEM or FDM.

The next step is to evaluate the integrals in the weak form [11] at the elemental level. In the context of classical FEMs, we saw in the previous section that one frequently uses Gauss quadrature [26] for this purpose. In an SEM, a GLL integration rule is used instead, because, as we will see, it leads to a diagonal mass matrix when used in conjunction with GLL interpolation points. Under this approach, integrations over elements Ω may be approximated as

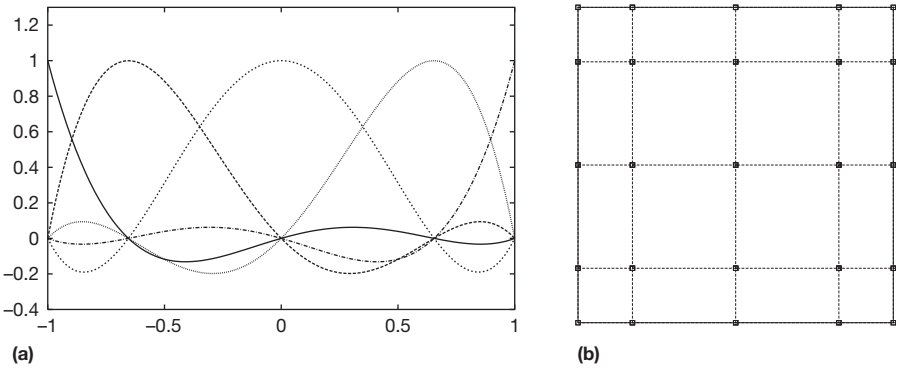

Figure 12 (a) The five Lagrange interpolants of degree $N=4$ on the reference segment $[-1, 1]$. The $N+1=5$ GLL points can be distinguished along the horizontal axis. All Lagrange polynomials are, by definition, equal to 1 or 0 at each of these points. Note that the first and last points are exactly -1 and 1. (b) When Lagrange polynomials of degree n are used to discretize the wavefield, each 3D spectral element contains a grid of $(n+1)^3$ GLL points, and each 2D face of an element contains a grid of $(n+1)^2$ GLL points, as illustrated here for the degree 4 polynomials shown on the left. Courtesy of Komatitsch D, Tsuboi S, and Tromp J (2005) The spectral-element method in seismology. In: Levander A and Nolet G (eds.) *The Seismic Earth: Array Analysis of Broadband Seismograms*, pp. 205–227. Washington, DC: AGU.

$$\int_\Omega f(\mathbf{x})\mathrm{d}^3\mathbf{x} = \int_{-1}^{1}\int_{-1}^{1}\int_{-1}^{1} f(\mathbf{x}(\xi,\eta,\zeta))\mathcal{J}(\xi,\eta,\zeta)\mathrm{d}\xi\mathrm{d}\eta\mathrm{d}\zeta = \sum_{\alpha=0}^{n}\sum_{\beta=0}^{n}\sum_{\gamma=0}^{n}\omega_\alpha\omega_\beta\omega_\gamma f^{\alpha\beta\gamma}\mathcal{J}^{\alpha\beta\gamma} \quad [29]$$

where ω_α, $\alpha=0,\ldots,n$, denote the $n+1$ weights associated with the GLL points of integration and $\mathcal{J}^{\alpha\beta\gamma}=\mathcal{J}\left(\xi_\alpha,\eta_\beta,\zeta_\gamma\right)$ denotes the value of the Jacobian $\mathcal{J}$ of the mapping at a GLL point. To facilitate the integration of functions and their partial derivatives over the elements, the values of the inverse Jacobian matrix $\partial\boldsymbol{\xi}/\partial\mathbf{x}$ need to be stored at the $(n+1)^3$ GLL integration points for each element.

We illustrate the reasons for using GLL quadrature by explicitly calculating the SEM mass matrix, that is, the integral on the left-hand side of eqn [11]. First, we expand the displacement field $\mathbf{s}$ and the test vector $\mathbf{w}$ in terms of Lagrange polynomials:

$$\mathbf{s}(\mathbf{x}(\xi,\eta,\zeta),t) = \sum_{i=1}^{3}\hat{\mathbf{x}}_i\sum_{\sigma=0}^{n}\sum_{\tau=0}^{n}\sum_{\nu=0}^{n}s_i^{\sigma\tau\nu}(t)\ell_\sigma(\xi)\ell_\tau(\eta)\ell_\nu(\zeta) \quad [30]$$

$$\mathbf{w}(\mathbf{x}(\xi,\eta,\zeta)) = \sum_{i=1}^{3}\hat{\mathbf{x}}_i\sum_{\sigma=0}^{n}\sum_{\tau=0}^{n}\sum_{\nu=0}^{n}w_i^{\alpha\beta\gamma}\ell_\alpha(\xi)\ell_\beta(\eta)\ell_\gamma(\zeta) \quad [31]$$

Because we use the same basis functions to express the displacement and test vectors, the SEM is another example of a Galerkin method. Next, we substitute the interpolations [30] and [31] in the mass matrix at the elemental level, using GLL quadrature [29], to obtain

$$\int_\Omega \rho\mathbf{w}\cdot\partial_t^2\mathbf{s}\mathrm{d}^3\mathbf{x} = \int_{-1}^{1}\int_{-1}^{1}\int_{-1}^{1}\rho(\mathbf{x}(\boldsymbol{\xi}))\mathbf{w}(\mathbf{x}(\boldsymbol{\xi}))\cdot\partial_t^2\mathbf{s}(\mathbf{x}(\boldsymbol{\xi}),t)\times\mathcal{J}(\boldsymbol{\xi})\mathrm{d}^3\boldsymbol{\xi} = \sum_{\alpha=0}^{n}\sum_{\beta=0}^{n}\sum_{\gamma=0}^{n}\omega_\alpha\omega_\beta\omega_\gamma\mathcal{J}^{\alpha\beta\gamma}\rho^{\alpha\beta\gamma}\times\sum_{i=1}^{3}\omega_i^{\alpha\beta\gamma}\ddot{s}_i^{\alpha\beta\gamma} \quad [32]$$

where $\rho^{\alpha\beta\gamma}=\rho(\mathbf{x}(\xi_\alpha,\eta_\beta,\zeta_\gamma))$, and where a dot denotes differentiation with respect to time. By independently setting factors of $\omega_1^{\alpha\beta\gamma}$, $\omega_2^{\alpha\beta\gamma}$, and $\omega_3^{\alpha\beta\gamma}$ equal to zero, since the weak formulation [11] must hold for any test vector $\mathbf{w}$, we obtain independent equations for each component of acceleration $\ddot{s}_i^{\alpha\beta\gamma}(t)$ at grid point $(\xi_\alpha,\eta_\beta,\zeta_\gamma)$. One can see that the value of acceleration at each point of a given element $\ddot{s}_i^{\alpha\beta\gamma}(t)$ is simply multiplied by the factor $\omega_\alpha\omega_\beta\omega_\gamma\rho^{\alpha\beta\gamma}\mathcal{J}^{\alpha\beta\gamma}$, which means that the elemental mass matrix is exactly diagonal. This is one of the key ideas behind the SEM, and the main motivation behind the choice of Lagrange interpolation at the GLL points used in conjunction with GLL numerical integration.

In summary, the main differences between FEM and SEM are the polynomial degree of the basis functions, the choice of integration rule, and, as a consequence, the nature of the time-marching scheme. In an FEM, one tends to use low-degree basis functions and Gauss quadrature. In an SEM, one uses higher-degree basis functions and GLL quadrature to obtain better resolution as well as a diagonal mass matrix. For the SEM, this leads to simple explicit time schemes, as opposed to the numerically more expensive implicit time schemes used in FEMs. It is important to note that even under ideal circumstances, the GLL rule is exact only for integrands that are polynomials of degree $2n-1$. Since integrations in the SEM involve the product of two polynomials of degree n – the displacement and the test function – the integration of the resulting polynomial of degree $2n$ is never exact. As in an FEM, for deformed elements, there are additional errors related to curvature (Maday and Rønquist, 1990); the same is true for elements with heterogeneous material properties. Thus, in an SEM, a diagonal mass matrix is obtained by a process of subintegration. In this respect, the SEM is related to FEMs in which mass lumping is used to avoid the costly resolution of the nondiagonal system resulting from the use of Gauss quadrature (Cohen et al., 1993). Evaluating the stiffness matrix and the source term in eqn [11] is a bit more complicated (e.g., Komatitsch and Tromp, 1999; Komatitsch and Vilotte, 1998), because this involves taking first-order spatial derivatives of the displacement field and the test vector. These derivatives may be expressed in terms of Lagrange polynomials and their derivatives.

The SEM uses domain decomposition between the fluid and the solid regions of the Earth model. In the inner core, mantle, and crust, one solves the anelastic wave equation, and in the liquid outer core, one solves the acoustic wave equation. At the fluid–solid boundaries, that is, at the ICB and CMB, the

continuity in traction and the normal component of displacement may be imposed exactly (Chaljub and Valette, 2004; Komatitsch and Tromp, 2002b; Komatitsch et al., 2005), which leads to a very accurate representation of waves that interact with the fluid–solid boundary, in particular diffracted phases.

FEM and SEM meshes, for example, the mesh shown in Figure 11, are generally too large to fit in memory on a single computer. Modern parallel computers, such as clusters or grids of computers, have a distributed memory architecture. A standard, portable approach for programming parallel machines with distributed memory is to use a message-passing methodology, usually based upon the Message Passing Interface (MPI) library (e.g., Gropp et al., 1994). On such parallel machines, we need to split the mesh into as many slices as the available number of processors. Figure 13 illustrates how an SEM mesh may be split into 1944 slices for a parallel calculation on 1944 processors.

Time marching in an SEM is frequently accomplished based upon an explicit second-order Newmark scheme (e.g., Komatitsch, 1997). Therefore, the main numerical cost associated with the SEM is in small local matrix–vector products within each spectral element and not in the time scheme. This implies that the processors spend most of their time doing actual calculations, and only a small amount of time on communications.

The SEM has been extensively benchmarked against normal-mode synthetics for spherically symmetrical Earth model PREM (e.g., Komatitsch and Tromp, 2002a,b). Figure 14 shows an example of such a benchmark for the 9 June 1994 Bolivia earthquake recorded at station PAS in Pasadena, CA. The match between the SEM and mode synthetics on all three components is perfect. An even more difficult benchmark between modes and the SEM for PKP arrivals at near-antipodal distances is shown in Figure 15. Notice how one can see a weak P_{diff} arrival prior to the arrival of PKIKP in both the SEM and the normal-mode synthetics. This benchmark favorably tests the domain decomposition between the fluid and the solid regions, as well as the quality of the mesh, in particular near the CMB and in the inner core.

A snapshot of a global SEM simulation for the 3 November 2002, Denali Fault, AK, earthquake is shown in Figure 16 (Chen et al., 2005; Tsuboi et al., 2003). Because the rupture propagates in a southeasterly direction along the Denali Fault, the waves that propagate along the west coast of the United States have large amplitudes. This directivity effect due to the finite size of the earthquake fault is clearly visible in the SEM simulations. Figure 17 shows waveform comparisons between SEM synthetics and data recorded by the Global Seismographic Network. Note that the SEM synthetic seismograms for mantle model S20RTS (Ritsema et al., 1999), accurate at periods of 5 s and longer, capture the dispersion of the Rayleigh waves reasonably well.

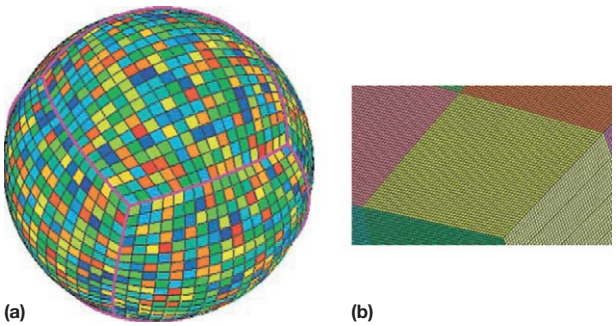

Figure 13 The SEM uses a mesh of hexahedral finite elements on which the wavefield is interpolated by high-degree Lagrange polynomials on GLL integration points. In order to perform the calculations on a parallel computer with distributed memory, the mesh is split into slices based upon a regular domain decomposition topology. Each slice is handled by a separate processor. Adjacent slices located on different processors exchange information about common faces and edges based upon a message-passing methodology. (a) A global view of the mesh at the surface, illustrating that each of the six sides of the cubed sphere mesh is divided into 18×18 slices, shown here with different colors, for a total of 1944 slices. The elements within each slice reside in memory on a single processor of the parallel machine. (b) A close-up of the mesh of 48×48 spectral elements at the surface of each slice. Within each surface spectral element, we use $5 \times 5 = 25$ GLL grid points, which translates into an average grid spacing of 2.9 km (i.e., 0.026°) on the surface of the Earth. Courtesy of Komatitsch D, Tsuboi S, Chen J, and Tromp J (2003) A 14.6 billion degrees of freedom, 5 teraflops, 2.5 terabyte earthquake simulation on the Earth Simulator. In: *Proceedings of the ACM/IEEE Supercomputing SC'2003 Conference*.

1.07.6 Discussion and Conclusions

We have provided an overview of the various numerical methods used in global seismology. Of these methods, currently only CMM, DSM, and the SEM are capable of simulating 3D seismic wave propagation throughout the entire globe. CMMs are quite useful for calculating the very long-period (>500 s) response of a laterally heterogeneous, rotating, self-gravitating Earth model, and DSMs accomplish the same at somewhat shorter periods. The main difficulties with both CMM and DSM have to do with a linearized treatment of boundary perturbations and, more severely, practical limitations associated with large matrix–vector operations that do not lend themselves well to calculations on parallel computers.

The only method capable of generating fully 3D synthetic seismograms at the scale of the entire globe at short periods is the SEM. On a modest PC cluster, one can now calculate global synthetics at periods of 20 s and longer that account for heterogeneity in the crust and mantle, topography, anisotropy, attenuation, fluid–solid interactions, self-gravitation, rotation, and the oceans. At the present time, on 150 processors, a 1 h long seismogram may be calculated in about 5 h. On the Earth Simulator at the Japan Agency for Marine-Earth Science and Technology, one can reach a shortest period of 3.5 s. Such a calculation involves more than 4000 processors and requires about 18 h of compute time. Interestingly, broadband normal-mode synthetics for spherically symmetrical (1D) Earth models are typically restricted to periods of 6 s and longer, so seismologists can now calculate 3D synthetics accurate at periods shorter than 1D mode synthetics.

In the context of inverse problems, the challenge now lies in harnessing these newfound forward capabilities to enhance the quality of models of Earth's interior, in conjunction with improving models of the rupture process during an

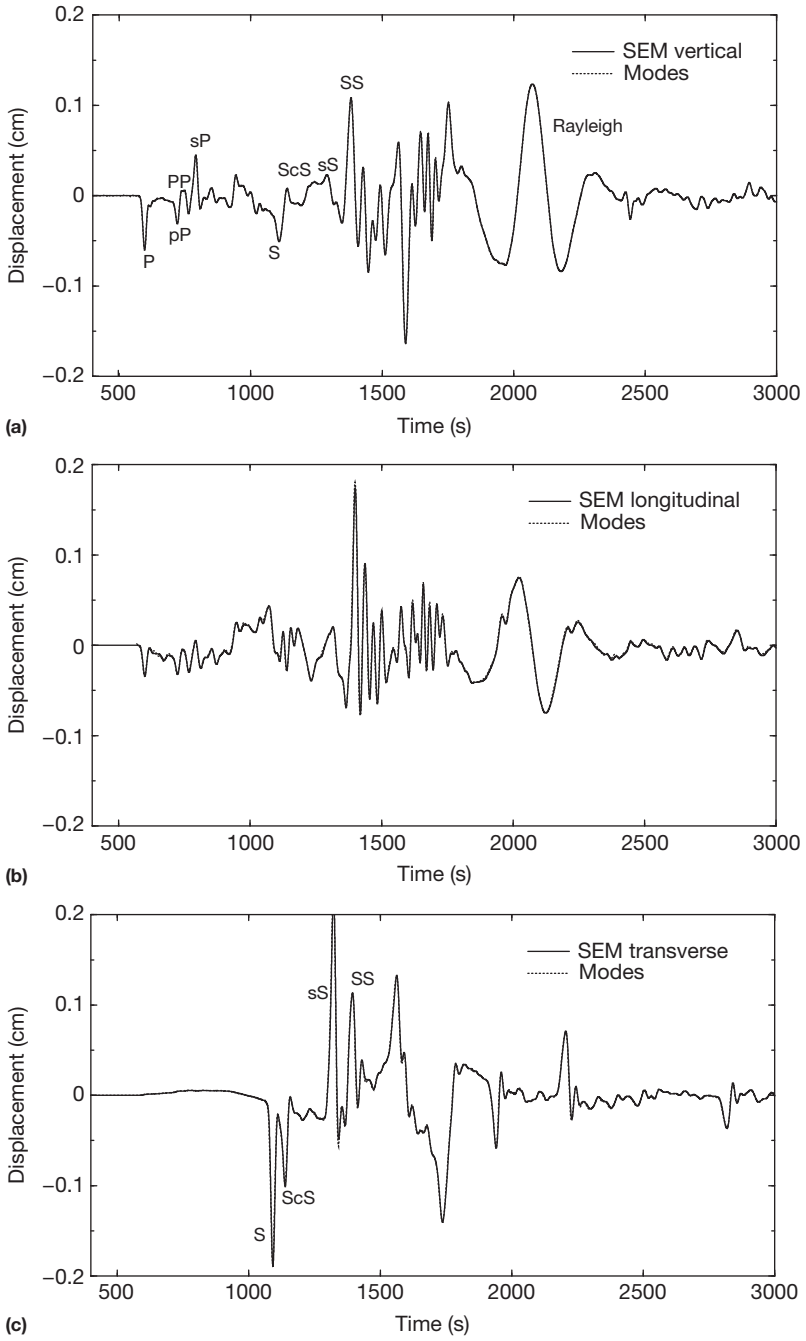

Figure 14 SEM (solid line) and mode (dotted line) synthetic seismograms in PREM for the great magnitude 8.2 Bolivia earthquake of 9 June 1994, recorded at SCSN station PAS in Pasadena, CA. The depth of the event is 647 km. Anisotropy and attenuation are both included in this simulation. (a) Vertical component, (b) longitudinal component, (c) transverse component. The synthetics are accurate at periods of 18 s and longer. Courtesy of Komatitsch D and Tromp J (2002) Spectral-element simulations of global seismic wave propagation. I: Validation. *Geophysical Journal International* 149: 390–412.

earthquake. On the face of it, this seems like a Herculean task because hundreds or even thousands of model parameters are involved in such inversions. In principle, the sensitivity of a seismogram with respect to the model parameters may be calculated numerically, but this would require a number of forward calculations equal to the number of model parameters (typically thousands). Tarantola (1984) demonstrated that one iteration in tomographic and source inversions may be performed based upon just two calculations for each earthquake: one calculation for the current model and a second 'adjoint' calculation that uses time-reversed signals at the receivers as simultaneous, fictitious sources. This approach has been used in global seismology based upon the DSM (e.g., Geller and Hara, 1993; Hara, 2004; Hara and Geller, 2000). Adjoint

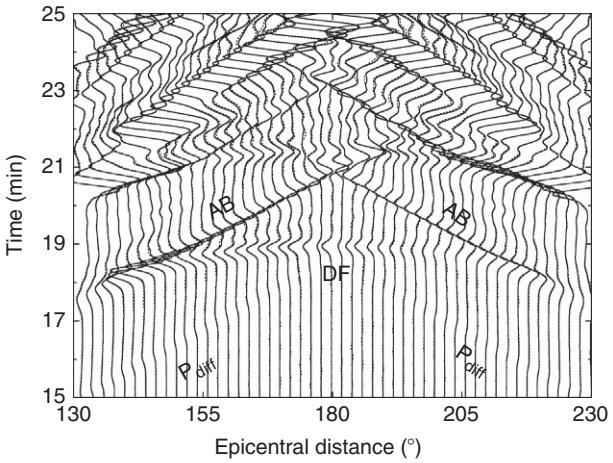

Figure 15 Record section comparison of PKP phases calculated for anelastic, anisotropic PREM based upon the SEM (solid lines) and modes (dotted lines) between 130° and 230° along the Greenwich meridian (see **Figure 11** for the source–receiver geometry). At each epicentral distance, we plot both the SEM and the mode solution. All PKP arrivals, including PKIKP, which has traveled through the central cube in the mesh, are well reproduced. Note also a very weak P_{diff} arrival in both synthetics between 130° and 170° and between 190° and 230°. The correct representation of this diffracted signal in the SEM illustrates the accuracy of the domain decomposition between the fluid outer core and the solid mantle and the effective implementation of the related fluid–solid boundary conditions. The synthetics are accurate at periods of 18 s and longer. Courtesy of Komatitsch D and Tromp J (2002) Spectral-element simulations of global seismic wave propagation. I: Validation. *Geophysical Journal International* 149: 390–412.

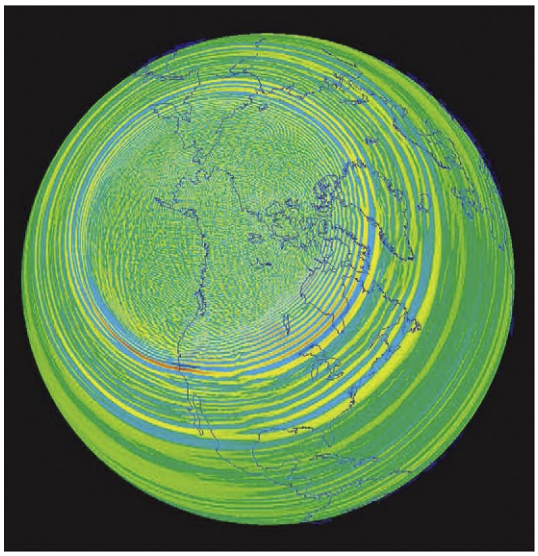

Figure 16 Spectral element snapshot of the propagation of seismic waves in the Earth generated by the $M_w = 7.9$ (3 November 2002) Denali Fault, AK, earthquake. Note the large amplification of the waves along the western coast of the United States due to the directivity associated with the finite rupture. Note also the difference in dispersion between the oceanic and the continental Rayleigh waves. The Airy phase has just reached Hudson Bay. The 3D model includes mantle model S20RTS (Ritsema et al., 1999) and crustal model crust 2.0 (Bassin et al., 2000). Courtesy of Chen J, Tsuboi S, Komatitsch D, and Tromp J (2005) Rayleigh-wave multipathing along the west coast of North America. *Bulletin of the Seismological Society of America* 95(6): 2115–2124.

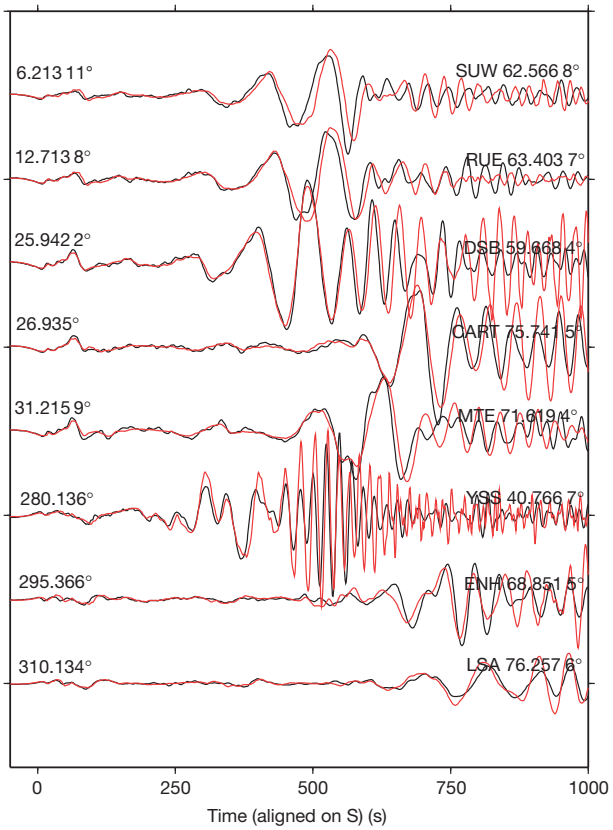

Figure 17 Comparison of transverse component data (black line) and spectral element synthetic seismograms (red line) for the 3 November 2002, Denali Fault, AK, earthquake. Both the synthetic seismograms and the data are low-pass-filtered at 5 s. The source azimuth measured clockwise from due north is indicated on the left of each trace, and the station name and epicentral distance are on the right. Records are aligned on the S wave. The 3D model includes mantle model S20RTS (Ritsema et al., 1999) and crustal model crust 2.0 (Bassin et al., 2000). Courtesy of Tsuboi S, Komatitsch D, Chen J, and Tromp J (2003) Spectral-element simulations of the November 3, 2002, Denali, Alaska earthquake on the Earth Simulator. *Physics of the Earth and Planetary Interiors* 139: 305–312.

methods (e.g., Talagrand and Courtier, 1987) have opened the door to solving the full 3D inverse problem, that is, the problem of using the remaining differences between the data and the synthetics to improve source and Earth models (e.g., Akçelik et al., 2002, 2003; Tromp et al., 2005). Recently, Capdeville et al. (2005) had proposed a spectral element approach to the inverse problem based upon a source-stacking technique that may further reduce the numerical burden.

Acknowledgments

The author would like to thank Heiner Igel, Dimitri Komatitsch, Nozomu Takeuchi, Christine Thomas, Seiji Tsuboi, and Yanbin Wang for contributing figures to this chapter. The SEM synthetics were calculated by Seiji Tsuboi on the Earth Simulator computer at the Japan Agency for Marine-Earth Science and Technology. Broadband data were obtained from the IRIS Data Management Center. This material is based in part upon work supported by

the National Science Foundation under grant EAR-0309576. This is contribution No. 9124 of the Division of Geological and Planetary Sciences, California Institute of Technology.

References

Aagaard BT, Hall JF, and Heaton TH (2001) Characterization of near-source ground motions with earthquake simulations. *Earthquake Spectra* 17(2): 177–207.

Akçelik V, Bielak J, Biros G, et al. (2003) High resolution forward and inverse earthquake modeling on terascale computers. In: *Proceedings of the ACM/IEEE Supercomputing SC'2003 Conference*. www.sc-conference.org/sc2003 (published on CD-ROM).

Akçelik V, Biros G, and Ghattas O (2002) Parallel multiscale Gauss–Newton-Krylov methods for inverse wave propagation. In: *Proceedings of the ACM/IEEE Supercomputing SC'2002 Conference*. www.sc-conference.org/sc2002 (published on CD-ROM).

Aki K and Richards PG (1980) *Quantitative Seismology, Theory and Methods*. San Francisco: W.H. Freeman.

Bao H, Bielak J, Ghattas O, et al. (1998) Large-scale simulation of elastic wave propagation in heterogeneous media on parallel computers. *Computer Methods in Applied Mechanics and Engineering* 152: 85–102.

Bassin C, Laske G, and Masters G (2000) The current limits of resolution for surface wave tomography in North America. *EOS* 81: F897.

Basu U and Chopra AK (2003) Perfectly matched layers for time-harmonic elastodynamics of unbounded domains: Theory and finite-element implementation. *Computer Methods in Applied Mechanics and Engineering* 192: 1337–1375.

Bérenger JP (1994) A perfectly matched layer for the absorption of electromagnetic waves. *Journal of Computational Physics* 114: 185–200.

Bielak J, Xu J, and Ghattas O (1999) Earthquake ground motion and structural response in alluvial valleys. *Journal of Geotechnical and Geoenvironmental Engineering* 125: 413–423.

Canuto C, Hussaini MY, Quarteroni A, and Zang TA (1988) *Spectral Methods in Fluid Dynamics*. New York: Springer-Verlag.

Capdeville Y, Chaljub E, Vilotte JP, and Montagner JP (2003a) Coupling the spectral element method with a modal solution for elastic wave propagation in global Earth models. *Geophysical Journal International* 152: 34–67.

Capdeville Y, Gung Y, and Romanowicz B (2005) Towards global Earth tomography using the spectral element method: A technique based on source stacking. *Geophysical Journal International* 162: 541–554.

Capdeville Y, Romanowicz B, and To A (2003b) Coupling spectral elements and modes in a spherical Earth: An extension to the 'sandwich' case. *Geophysical Journal International* 154: 44–57.

Capdeville Y, Stutzmann E, and Montagner J (2000) Effect of a plume on long-period surface waves computed with normal-mode coupling. *Physics of the Earth and Planetary Interiors* 119: 54–71.

Carcione JM (1994) The wave equation in generalized coordinates. *Geophysics* 59: 1911–1919.

Carcione JM, Kosloff D, and Kosloff R (1988) Wave propagation simulation in a linear viscoelastic medium. *Geophysical Journal International* 95: 597–611.

Carcione JM and Wang PJ (1993) A Chebyshev collocation method for the wave equation in generalized coordinates. *Computational Fluid Dynamics Journal* 2: 269–290.

Chaljub E (2000) *Modélisation numérique de la propagation d'ondes sismiques en géométrie sphérique: Application à la sismologie globale (Numerical modeling of the propagation of seismic waves in spherical geometry: Applications to global seismology)*. PhD Thesis, Université Paris VII Denis Diderot, Paris, France.

Chaljub E, Capdeville Y, and Vilotte JP (2003) Solving elastodynamics in a fluid–solid heterogeneous sphere: A parallel spectral element approximation on non-conforming grids. *Journal of Computational Physics* 187(2): 457–491.

Chaljub E, Komatitsch D, Vilotte J-P, Capdeville Y, Valette B, and Festa G (2007) Spectral element analysis in seismology. In: Wu R-S and Maupin V (eds.) *IASPEI Monograph on Advances in Wave Propagation in Heterogeneous Media*, vol. 48, pp. 365–419. Elsevier.

Chaljub E and Tarantola A (1997) Sensitivity of SS precursors to topography on the upper-mantle 660-km discontinuity. *Geophysical Research Letters* 24(21): 2613–2616.

Chaljub E and Valette B (2004) Spectral-element modeling of three-dimensional wave propagation in a self-gravitating Earth with an arbitrarily stratified outer core. *Geophysical Journal International* 158: 131–141.

Chen J, Tsuboi S, Komatitsch D, and Tromp J (2005) Rayleigh-wave multi-pathing along the west coast of North America. *Bulletin of the Seismological Society of America* 95(6): 2115–2124.

Clayton R and Engquist B (1977) Absorbing boundary conditions for acoustic and elastic wave equations. *Bulletin of the Seismological Society of America* 67: 1529–1540.

Cohen G, Joly P, and Tordjman N (1993) Construction and analysis of higher-order finite elements with mass lumping for the wave equation. In: Kleinman R (ed.) *Proceedings of the Second International Conference on Mathematical and Numerical Aspects of Wave Propagation*, pp. 152–160. Philadelphia, PA: SIAM.

Collino F and Tsogka C (2001) Application of the PML absorbing layer model to the linear elastodynamic problem in anisotropic heterogeneous media. *Geophysics* 66(1): 294–307.

Dahlen FA, Nolet G, and Hung S-H (2000) Fréchet kernels for finite-frequency traveltime. I. Theory. *Geophysical Journal International* 141: 157–174.

Dahlen FA and Tromp J (1998) *Theoretical Global Seismology*. Princeton: Princeton University Press.

Deuss A and Woodhouse JH (2001) Theoretical free-oscillation spectra: The importance of wide band coupling. *Geophysical Journal International* 155: 193–199.

Dziewonski AM and Anderson DL (1981) Preliminary reference Earth model. *Physics of the Earth and Planetary Interiors* 25: 297–356.

Dziewonski AM, Liu X-F, and Su W-J (1997) Lateral heterogeneity in the lowermost mantle. In: Crossley D (ed.) *Earth's Deep Interior*, pp. 11–50. Amsterdam: Gordon and Breach.

Emmerich H and Korn M (1987) Incorporation of attenuation into time-domain computations of seismic wave fields. *Geophysics* 52: 1252–1264.

Faccioli E, Maggio F, Paolucci R, and Quarteroni A (1997) 2D and 3D elastic wave propagation by a pseudo-spectral domain decomposition method. *Journal of Seismology* 1: 237–251.

Festa G and Vilotte JP (2005) The Newmark scheme as velocity–stress time-staggering and efficient PML implementation for spectral element simulations of elastodynamics. *Geophysical Journal International* 161: 789–812.

Furumura T, Kennett BLN, and Furumura M (1998) Seismic wavefield calculation for laterally heterogeneous whole Earth models using the pseudospectral method. *Geophysical Journal International* 135(3): 845–860.

Furumura T, Kennett BLN, and Furumura M (1999) Seismic wavefield calculation for laterally heterogeneous whole Earth models. II. The influence of upper mantle heterogeneity. *Geophysical Journal International* 139(3): 623–644.

Garatani K, Nakamura H, Okuda H, and Yagawa G (2000) Large-scale parallel wave propagation analysis by GeoFEM. *Lecture Notes in Computer Science* 1823: 445–453.

Geller RJ and Hara T (1993) Two efficient algorithms for iterative linearized inversion of seismic waveform data. *Geophysical Journal International* 115: 699–710.

Geller RJ and Hatori T (1995) Dsm synthetic seismograms using analytic trial functions: Plane-layered, isotropic case. *Geophysical Journal International* 120: 163–172.

Geller RJ and Ohminato T (1994) Computation of synthetic seismograms and their partial derivatives for heterogeneous media with arbitrary natural boundary conditions using the Direct Solution Method. *Geophysical Journal International* 116: 421–446.

Geller RJ and Takeuchi N (1995) A new method for computing highly accurate dsm synthetic seismograms. *Geophysical Journal International* 123: 449–470.

Gilbert F (1970) Excitation of the normal modes of the Earth by earthquake sources. *Geophysical Journal of the Royal Astronomical Society* 22: 223–226.

Graves RW (1996) Simulating seismic wave propagation in 3D elastic media using staggered-grid finite differences. *Bulletin of the Seismological Society of America* 86(4): 1091–1106.

Gropp W, Lusk E, and Skjellum A (1994) *Using MPI, Portable Parallel Programming with the Message-Passing Interface*. Cambridge: MIT Press.

Guo B and Babuška I (1986) The *h-p* version of the finite element method. *Computational Mechanics* 1: 21–41.

Hara T (2004) Waveform inversion for 3-D Earth structure using the direct solution method implemented on vector-parallel supercomputer. *Physics of the Earth and Planetary Interiors* 146: 65–74.

Hara T and Geller RJ (2000) Simultaneous waveform inversion for three-dimensional earth structure and earthquake source parameters considering a wide range of modal coupling. *Geophysical Journal International* 142: 539–550.

Hara T, Tsuboi S, and Geller R (1991) Inversion for laterally heterogeneous Earth structure using a laterally heterogeneous starting model: Preliminary results. *Geophysical Journal International* 104: 523–540.

Hong T-K and Kennett B (2002) A wavelet-based method for simulation of two-dimensional elastic wave propagation. *Geophysical Journal International* 150: 610–638.

Hughes TJR (1987) *The Finite Element Method, Linear Static and Dynamic Finite Element Analysis*. Englewood Cliffs, NJ: Prentice-Hall International.

Hung S-H, Dahlen FA, and Nolet G (2000) Fréchet kernels for finite-frequency traveltime. II: Examples. *Geophysical Journal International* 141: 175–203.

Hung SH and Forsyth D (1998) Modelling anisotropic wave propagation in oceanic inhomogeneous structures using the parallel multidomain pseudo-spectral method. *Geophysical Journal International* 133(3): 726–740.

Igel H (1999) Wave propagation in three-dimensional spherical sections by the Chebyshev spectral method. *Geophysical Journal International* 136: 559–566.

Igel H and Gudmundsson O (1997) Frequency-dependent effects on travel times and waveforms of long-period S and SS waves. *Physics of the Earth and Planetary Interiors* 104: 229–246.

Igel H, Nissen-Meyer T, and Jahnke G (2002) Wave propagation in 3d spherical sections: Effects of subduction zones. *Physics of the Earth and Planetary Interiors* 132: 219–234.

Igel H, Takeuchi N, Geller R, et al. (2000) The COSY Project: Verification of global seismic modeling algorithms. *Physics of the Earth and Planetary Interiors* 119: 3–24.

Igel H and Weber M (1995) SH-wave propagation in the whole mantle using high-order finite differences. *Geophysical Research Letters* 22: 731–734.

Igel H and Weber M (1996) P–SV wave propagation in the whole mantle using high-order finite differences: Application to lowermost mantle structure. *Geophysical Research Letters* 23: 415–418.

Kennett BLN and Engdahl ER (1991) Traveltimes for global earthquake location and phase identification. *Geophysical Journal International* 105: 429–465.

Kennett BLN, Engdahl ER, and Buland R (1995) Constraints on seismic velocities in the Earth from traveltime. *Geophysical Journal International* 122: 108–124.

Komatitsch D (1997) *Méthodes spectrales et éléments spectraux pour l'équation de l'élastodynamique 2D et 3D en milieu hétérogène (Spectral and Spectral-element Methods for the 2D and 3D Elastodynamics Equations in Heterogeneous Media)*. PhD Thesis, Institut de Physique du Globe, Paris, France.

Komatitsch D, Liu Q, Tromp J, Süss P, Stidham C, and Shaw JH (2004) Simulations of ground motion in the Los Angeles Basin based upon the spectral-element method. *Bulletin of the Seismological Society of America* 94: 187–206.

Komatitsch D, Martin R, Tromp J, Taylor MA, and Wingate BA (2001) Wave propagation in 2-D elastic media using a spectral element method with triangles and quadrangles. *Journal of Computational Acoustics* 9(2): 703–718.

Komatitsch D, Ritsema J, and Tromp J (2002) The spectral-element method, Beowulf computing, and global seismology. *Science* 298: 1737–1742.

Komatitsch D and Tromp J (1999) Introduction to the spectral-element method for 3-D seismic wave propagation. *Geophysical Journal International* 139: 806–822.

Komatitsch D and Tromp J (2002a) Spectral-element simulations of global seismic wave propagation. I: Validation. *Geophysical Journal International* 149: 390–412.

Komatitsch D and Tromp J (2002b) Spectral-element simulations of global seismic wave propagation. II: 3-D models, oceans, rotation, and self-gravitation. *Geophysical Journal International* 150: 303–318.

Komatitsch D and Tromp J (2003) A perfectly matched layer absorbing boundary condition for the second-order seismic wave equation. *Geophysical Journal International* 154: 146–153.

Komatitsch D, Tsuboi S, Chen J, and Tromp J (2003) A 14.6 billion degrees of freedom, 5 teraflops, 2.5 terabyte earthquake simulation on the Earth Simulator. In: *Proceedings of the ACM/IEEE Supercomputing SC'2003 Conference*.

Komatitsch D, Tsuboi S, and Tromp J (2005) The spectral-element method in seismology. In: Levander A and Nolet G (eds.) *The Seismic Earth: Array Analysis of Broadband Seismograms*, pp. 205–227. Washington, DC: AGU.

Komatitsch D and Vilotte JP (1998) The spectral-element method: An efficient tool to simulate the seismic response of 2D and 3D geological structures. *Bulletin of the Seismological Society of America* 88(2): 368–392.

Kosloff D and Baysal E (1982) Forward modeling by the Fourier method. *Geophysics* 47: 1402–1412.

Kosloff D, Kessler D, Filho AQ, Tessmer E, Behle A, and Strahilevitz R (1990) Solution of the equations of dynamics elasticity by a Chebyshev spectral method. *Geophysics* 55: 748–754.

Kosloff D, Reshef M, and Loewenthal D (1984) Elastic wave calculations by the Fourier method. *Bulletin of the Seismological Society of America* 74: 875–891.

Kosloff D and Tal-Ezer H (1993) A modified Chebyshev pseudospectral method with an $O(N^{-1})$ time step restriction. *Journal of Computational Physics* 104: 457–469.

Levander AR (1988) Fourth-order finite-difference P–SV seismograms. *Geophysics* 53: 1425–1436.

Li X-D and Romanowicz B (1995) Comparison of global waveform inversions with and without considering cross-branch modal coupling. *Geophysical Journal International* 121: 695–709.

Li X-D and Romanowicz B (1996) Global mantle shear-velocity model developed using nonlinear asymptotic coupling theory. *Journal of Geophysical Research* 101: 22245–22272.

Li XD and Tanimoto T (1993) Waveforms of long-period body waves in a slightly aspherical Earth model. *Geophysical Journal International* 112: 92–102.

Liu HP, Anderson DL, and Kanamori H (1976) Velocity dispersion due to anelasticity: Implications for seismology and mantle composition. *Geophysical Journal of the Royal Astronomical Society* 47: 41–58.

Lognonné P and Romanowicz B (1990) Modeling of coupled normal modes of the Earth: The spectral method. *Geophysical Journal International* 102: 365–395.

Love AEH (1911) *Some Problems of Geodynamics*. Cambridge: Cambridge University Press.

Madariaga R (1976) Dynamics of an expanding circular fault. *Bulletin of the Seismological Society of America* 65: 163–182.

Maday Y and Rønquist EM (1990) Optimal error analysis of spectral methods with emphasis on non-constant coefficients and deformed geometries. *Computer Methods in Applied Mechanics and Engineering* 80: 91–115.

Marquering H, Nolet G, and Dahlen FA (1998) Three-dimensional waveform sensitivity kernels. *Geophysical Journal International* 132: 521–534.

Marquering H and Snieder R (1995) Surface-wave mode coupling for efficient forward modelling and inversion of body-wave phases. *Geophysical Journal International* 120: 186–208.

Marquering H and Snieder R (1996) Shear-wave velocity structure beneath Europe, the northeastern Atlantic and western Asia from waveform inversions including surface-wave mode coupling. *Geophysical Journal International* 127: 283–304.

Moczo P, Bystrický E, Kristek J, Carcione JM, and Bouchon M (1997) Hybrid modeling of P–SV seismic motion at inhomogeneous viscoelastic topographic structures. *Bulletin of the Seismological Society of America* 87: 1305–1323.

Montelli R, Nolet G, Dahlen F, Masters G, Engdahl ER, and Hung S-H (2004) Finite-frequency tomography reveals a variety of plumes in the mantle. *Science* 303: 338–343.

Nolet G (1990) Partitioned waveform inversion and two-dimensional structure under the network of autonomously recording seismographs. *Journal of Geophysical Research* 95: 8499–8512.

Ohminato T and Chouet BA (1997) A free-surface boundary condition for including 3D topography in the finite difference method. *Bulletin of the Seismological Society of America* 87: 494–515.

Park J (1986) Synthetic seismograms from coupled free oscillations: The effects of lateral structure and rotation. *Journal of Geophysical Research* 91: 6441–6464.

Park J and Yu Y (1992) Anisotropy and coupled free oscillations: Simplified models and surface wave observations. *Geophysical Journal International* 110: 401–420.

Patera AT (1984) A spectral element method for fluid dynamics: Laminar flow in a channel expansion. *Journal of Computational Physics* 54: 468–488.

Priolo E, Carcione JM, and Seriani G (1994) Numerical simulation of interface waves by high-order spectral modeling techniques. *Journal of the Acoustical Society of America* 95(2): 681–693.

Quarteroni A, Tagliani A, and Zampieri E (1998) Generalized Galerkin approximations of elastic waves with absorbing boundary conditions. *Computer Methods in Applied Mechanics and Engineering* 163: 323–341.

Ritsema J, Van Heijst HJ, and Woodhouse JH (1999) Complex shear velocity structure imaged beneath Africa and Iceland. *Science* 286: 1925–1928.

Robertsson JOA (1996) A numerical free-surface condition for elastic/viscoelastic finite-difference modeling in the presence of topography. *Geophysics* 61: 1921–1934.

Robertsson JOA, Blanch JO, and Symes WW (1994) Viscoelastic finite-difference modeling. *Geophysics* 59: 1444–1456.

Ronchi C, Ianoco R, and Paolucci PS (1996) The 'cubed sphere': A new method for the solution of partial differential equations in spherical geometry. *Journal of Computational Physics* 124: 93–114.

Sadourny R (1972) Conservative finite-difference approximations of the primitive equations on quasi-uniform spherical grids. *Monthly Weather Review* 100: 136–144.

Seriani G (1997) A parallel spectral element method for acoustic wave modeling. *Journal of Computational Acoustics* 5: 53–69.

Seriani G (1998) 3-D large-scale wave propagation modeling by a spectral element method on a Cray T3E multiprocessor. *Computer Methods in Applied Mechanics and Engineering* 164: 235–247.

Sherwin SJ and Karniadakis GE (1995) A triangular spectral element method: Applications to the incompressible Navier–Stokes equations. *Computer Methods in Applied Mechanics and Engineering* 123: 189–229.

Takeuchi N (2005) Finite boundary perturbation theory for the elastic equation of motion. *Geophysical Journal International* 160: 1044–1058.

Takeuchi N and Geller R (2003) Accurate numerical methods for solving the elastic equation of motion for arbitrary source locations. *Geophysical Journal International* 154: 852–866.

Takeuchi N, Geller R, and Cummins P (2000) Complete synthetic seismograms for 3-D heterogeneous Earth models computed using modified DSM operators and their applicability to inversion for Earth structure. *Physics of the Earth and Planetary Interiors* 119: 25–36.

Talagrand O and Courtier P (1987) Variational assimilation of meteorological observations with the adjoint vorticity equation. I: Theory. *Quarterly Journal of the Royal Meteorological Society* 113: 1311–1328.

Tarantola A (1984) Inversion of seismic reflection data in the acoustic approximation. *Geophysics* 49: 1259–1266.

Taylor MA and Wingate BA (2000) A generalized diagonal mass matrix spectral element method for non-quadrilateral elements. *Applied Numerical Mathematics* 33: 259–265.

Tessmer E (1995) 3-D seismic modelling of general material anisotropy in the presence of the free surface by a Chebyshev spectral method. *Geophysical Journal International* 121: 557–575.

Tessmer E, Kessler D, Kosloff D, and Behle A (1992) Multi-domain Chebyshev–Fourier method for the solution of the equations of motion of dynamic elasticity. *Journal of Computational Physics* 100: 355–363.

Tessmer E and Kosloff D (1994) 3-D elastic modeling with surface topography by a Chebyshev spectral method. *Geophysics* 59(3): 464–473.

Thomas C, Igel H, Weber M, and Scherbaum F (2000) Acoustic simulation of P-wave propagation in a heterogeneous spherical Earth: Numerical method and application to precursor waves to PKPdf. *Geophysical Journal International* 141: 6441–6464.

Tromp J and Dahlen F (1990) Summation of the Born series for the normal modes of the Earth. *Geophysical Journal International* 100: 527–533.

Tromp J, Tape CH, and Liu Q (2005) Seismic tomography, adjoint methods, time reversal, and banana–doughnut kernels. *Geophysical Journal International* 160: 195–216.

Tsuboi S, Komatitsch D, Chen J, and Tromp J (2003) Spectral-element simulations of the November 3, 2002, Denali, Alaska earthquake on the Earth Simulator. *Physics of the Earth and Planetary Interiors* 139: 305–312.

Virieux J (1984) *SH* wave propagation in heterogeneous media: Velocity–stress finite-difference method. *Geophysics* 49: 1933–1942.

Virieux J (1986) P–SV wave propagation in heterogeneous media: Velocity–stress finite-difference method. *Geophysics* 51: 889–901.

Wang Y and Takenaka H (2001) A multidomain approach of the Fourier pseudospectral method using discontinuous grid for elastic wave modeling. *Earth, Planets and Space* 53: 149–158.

Wang Y, Takenaka H, and Furumura T (2001) Modelling seismic wave propagation in a two-dimensional cylindrical whole-Earth model using the pseudospectral method. *Geophysical Journal International* 145: 689–708.

Woodhouse JH (1980) The coupling and attenuation of nearly resonant multiplets in the Earth's free oscillation spectrum. *Geophysical Journal of the Royal Astronomical Society* 61: 261–283.

Woodhouse JH and Dziewonski AM (1984) Mapping the upper mantle: Three-dimensional modeling of earth structure by inversion of seismic waveforms. *Journal of Geophysical Research* 89: 5953–5986.

Zhao L, Jordan TH, and Chapman CH (2000) Three-dimensional Frèchet differential kernels for seismic delay times. *Geophysical Journal International* 141: 558–576.

Zienkiewicz OC (1977) *The Finite Element Method in Engineering Science*, 3rd edn New York: McGraw-Hill.

Zingg DW (2000) Comparison of high-accuracy finite-difference methods for linear wave propagation. *SIAM Journal on Scientific Computing* 22(2): 476–502. http://dx.doi.org/10.1137/S1064827599350320.

Zingg DW, Lomax H, and Jurgens H (1996) High-accuracy finite-difference schemes for linear wave propagation. *SIAM Journal on Scientific Computing* 17(2): 328–346. http://dx.doi.org/10.1137/S1064827594267173.

This page intentionally left blank

1.08 Theory and Observations - Seismology and the Structure of the Earth: Teleseismic Body-Wave Scattering and Receiver-Side Structure

MG Bostock, The University of British Columbia, Vancouver, BC, Canada

© 2015 Elsevier B.V. All rights reserved.

1.08.1	**Introduction**	253
1.08.2	**Geometrical Preliminaries**	254
1.08.3	**Source Removal**	255
1.08.3.1	Modal Decomposition	256
1.08.3.2	Receiver Functions and the Property of Minimum Phase	257
1.08.3.3	Improved Teleseismic *P* Green Functions	258
1.08.3.4	The Teleseismic *S* Green Functions	259
1.08.3.5	Deconvolution, Stacking, and Array Processing	260
1.08.4	**1-D Inversion**	261
1.08.4.1	Least-Squares Optimization	261
1.08.4.2	Monte Carlo Inversion	262
1.08.4.3	Born Inversion and Classic (Delay and Sum) Studies	262
1.08.5	**Multidimensional Inversion**	265
1.08.6	**Beyond the Born Approximation**	269
1.08.6.1	Shortcomings of the Born Approximation	269
1.08.6.2	The Inverse-Scattering Series	269
1.08.6.3	Transmission to Reflection	270
1.08.7	**Conclusions**	272
References		272

1.08.1 Introduction

The analysis of scattered, teleseismic body waves to characterize the receiver-side lithosphere and upper mantle spans over 4 decades, and it is now among the most widely used means of resolving fine-scale structure in these outer layers of the Earth. The first studies to harness converted teleseismic waves for investigation of deep Earth structure were undertaken in the former Soviet Bloc (Rainer Kind, pers. comm; see, e.g., Hoffmann et al., 1989). Most early studies involved single-station analyses, and the work of Phinney (1964) represents an important milestone. He recognized that one could remove the effect of the earthquake source by examining spectral ratios of radial and vertical component *P*-seismograms measured at a surface receiver and thereby gain insight into the bulk properties of the Earth's crust. His work was formulated in the frequency domain (see also Kurita, 1973) and constitutes the first application of the so-called receiver function technique. Soon thereafter, Båth and Stefánson (1966) examined recordings of teleseismic *S* and identified *S*-to-*P* precursors scattered from the crust–mantle boundary as a viable means once again of characterizing crustal structure. A full decade was to elapse before the next major development. Working independently on transition zone and crustal structure, respectively, Vinnik (1977) and Langston (1979) introduced the time-domain, *P* receiver function to characterize receiver-side *P*-to-*S* conversions present within the coda of teleseismic *P*. The time-domain receiver function, which contains information on phase, has intuitive appeal as a leading-order approximation to the Earth's Green function at early times (i.e., up until the arrival of the next major phase *PP*). In addition, Vinnik (1977) enhanced the weak scattered signals present in the receiver function by stacking multiple receiver functions from different epicentral distance ranges along theoretical move-out curves for a radial Earth model, thereby effectively approximating a 1-D, single-scattering inversion. By the mid-1980s, an increasing number of researchers had come to recognize the potential of the approach in general applications (e.g., Kind and Vinnik, 1988; Owens et al., 1984; Zandt and Owens, 1986). This recognition combined with the growing availability of three-component, broadband seismometers and high-capacity, digital acquisition systems has led to the popularity that teleseismic receiver function analysis enjoys today in regional studies of lithospheric and upper mantle structure.

In the last decade, there has been major focus on placing the empirical 'receiver function' technique on a firmer theoretical foundation and extending its application to multichannel data sets. In both respects, much has been (and may still be) learned from the vast, accumulated experience in exploration seismology. Although geometries in the global and exploration contexts are at first glance quite different (plane-wave excitation from below versus point source excitation from above), both disciplines share an important common element, namely, the interaction of near-vertically propagating waves with near-horizontal and, often, modest-contrast stratification. The recorded wave fields are thus free of postcritical interactions that lead to dispersive, guided waves and can be inverted to extract highly resolved information on subsurface material property contrasts within a single-scattering (or 'Born approximation') framework. Nonetheless, there are important distinctions between the two disciplines. Exploration seismology has, for practical reasons (source

 http://dx.doi.org/10.1016/B978-0-444-53802-4.00008-7

generation and recording), largely ignored elastic phenomena by focusing on pure *P*-mode scattering and modeling data with acoustic theory. Global seismology, in contrast, relies primarily on conversions to resolve subsurface structure, and pure-mode reflections have, to date, played a far lesser role. It is interesting to note that the two communities have begun to forge closer links (e.g., Marfurt et al., 2003) due in part to the growing interest in exploration for the use of local, passive seismicity to monitor changes in hydrocarbon reservoirs.

In this chapter, we will provide an overview of the theory that underlies the processing of scattered teleseismic wave fields and thereby facilitates interpretation for regional lithospheric and upper mantle structure. Section 1.08.2 begins with a description of the geometric attributes of different teleseismic phases that can be considered for use in studies of the lithosphere and upper mantle, along with their merits and shortcomings. The canonical problem of structural response/source signature separation is then addressed in the teleseismic context. This discussion centers on the relationship between the classic receiver function and the more fundamental Green function that is required in formal inverse-scattering approaches. Sections 1.08.4 and 1.08.5 examine the inverse problem for one- and multidimensional heterogeneity. The focus here is on formal inverse-scattering techniques because of the insight they afford into physics of the scattering process and because they provide a framework through which more empirical schemes can be understood. In the final section, we discuss several shortcomings arising from the single-scattering or Born approximation that has, to this point, underlain most attempts to invert scattered teleseismic body waves for receiver-side structure. We then sketch out a means through which nonlinear inverse scattering could, in principle, be applied to teleseismic wave fields, based on recent theoretical developments in exploration seismology. Before proceeding, we mention several additional review sources that the reader may wish to consult in gaining a broader appreciation for the field, namely, Pavlis (2005), which discusses outstanding issues in the inversion of teleseismic *P*-wave fields for receiver-side structure; Rondenay (2009), which provides a survey of upper mantle imaging studies using scattered waves; and Kennett (2002), a more general treatise of observational seismology at regional scales that includes a chapter on teleseismic body-wave fields.

1.08.2 Geometrical Preliminaries

In this section, we sketch out the general scattering geometry to be considered for the remainder of the chapter. We shall restrict our attention to incident-wave fields representing sources located at teleseismic distances (i.e., epicentral distance $\Delta > 30^\circ$) from one or more receivers located at the Earth's surface. The term 'incident-wave field' will be defined more precisely in later sections, but for the present, it can be considered to be the signal associated with a primary body-wave phase that has reflected/converted, if at all, only at the Earth's surface and/or core–mantle boundary, for example, *P*, *pP*, *PP*, *S*, *pS*, *PKP*, *SKS*, and *ScS* (see Figure 1). This definition serves to distinguish the incident-wave field from the scattered waves generated through reflection or mode conversion at receiver-side heterogeneity that we are ultimately interested in exploiting

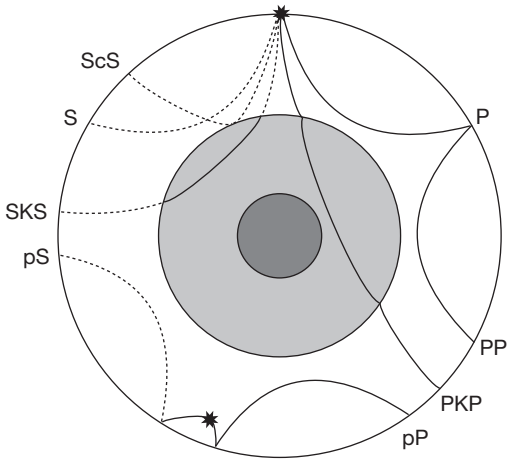

Figure 1 Ray paths of some major phases referred to in text that may serve as incident-wave fields for study of near-receiver scattering from subsurface structure (*P*-wave legs, solid; *S*-wave legs, dashed).

(Burdick and Langston, 1977). Signals originating through source-side scattering will, in contrast, be most conveniently treated as part of the source signature.

For much of what follows, we shall focus our attention on teleseismic *P* as it historically has been the most practically useful of the candidate incident-wave fields and ignore, for the moment, associated depth phases created by deep earthquakes. At lesser distances ($14^\circ < \Delta < 30^\circ$), *P* (and *S*) waves traveling through the mantle experience triplications at strong velocity gradients defining the Earth's transition zone (between $\sim$400 and 670 km depth), and consequently, the incident-wave field will comprise several superposed arrivals characterized by different horizontal slownesses that are difficult to distinguish and separate (see Figure 2 and, e.g., Kennett, 2002). In the distance range $30^\circ < \Delta < 100^\circ$, teleseismic *P* bottoms within the lower mantle, which is generally characterized by a smoothly varying and dominantly radial velocity profile. Consequently, propagation is simple and the wave field is accurately modeled by a single surface slowness that decreases monotonically from $\sim$0.08 to 0.04 s km^{-1} (or, equivalently, through ray parameters of 8.8 to 4.4 s per degreee) over this distance range. Moreover, wave front curvature is small because we are well into the far field, and it is frequently convenient in both single-station and multistation applications to approximate the incident teleseismic wave field as planar in horizontal aspect (see, e.g., Section 1.08.3.1). The small values of horizontal slowness also manifest steep angles of propagation that are, again, advantageous in that the likelihood of postcritical interactions is reduced. Complications due to depth phases can be dealt with in two ways, depending on source depth. As depth decreases, the slowness (and timing) of the depth phases approach that of the incident-wave field such that they can be considered one and the same. At greater depths, the difference in slowness may be significant, but in this case, the short duration of time functions that characterize the Wadati–Benioff sources combined with greater time separation between the incident-wave field and depth phases will usually permit the depth phases to be temporally windowed and analyzed independently. The source depth at which one

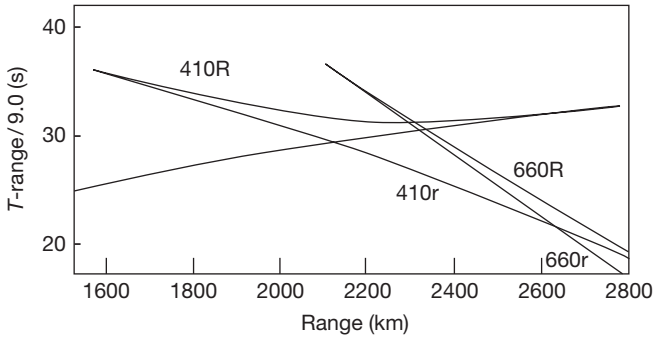

Figure 2 Travel-time curves at regional distances displaying triplications due to transition zone (410 and 660 km) discontinuities that complicate analysis of scattering from more shallow discontinuities. Individual travel-time branches are labeled by the associated discontinuity (*r*, refraction; *R* reflection).

draws the line between inclusion and separation of depth phases will depend on the application but will generally be taken to lie between 100 and 200 km.

The treatment of teleseismic *S* is somewhat more difficult than teleseismic *P* for a number of reasons. First, the distance range over which useful recordings can be procured is more limited. This is due in part to the development of postcritical *S*-to-*P* conversion from deeper (e.g., transition zone) discontinuities at larger slowness. In addition, conversion and triplication at the core–mantle boundary lead to close coincidence and interference of *S*, *SKS*, and *ScS* over the distance range 70–90°. Depending on source mechanism, all three *S* phases may possess comparable amplitudes, and their separation (and that of associated scattered fields) is difficult, especially where three-dimensional heterogeneity is expected. *SKS* extends the usable distance range well beyond 100°, but the number of high signal-to-noise ratio recordings diminishes rapidly with distance. Second, because teleseismic *S* is characterized by larger slowness than teleseismic *P* at any given epicentral distance, postcritical phenomena within the receiver-side crust occur at smaller epicentral distances (*Spdp* (Zandt and Randall, 1985) and shear-coupled *PL* (Baag and Langston, 1985; Frazer, 1977; Owens and Zandt, 1997)) that can complicate interpretation and inversion. Third, the receiver-side response to an incident *S*-wave field will generally depend on the wave field polarization as imparted by the source and modified by source-side heterogeneity/anisotropy. The incident polarization is not generally known (with the exception of *SKS* that is radially polarized due to receiver-side conversion from *P* to *S* at the core–mantle boundary), though its influence can under certain assumptions be removed (e.g., Farra and Vinnik, 2000; **Section 1.08.3.4**). Fourth, higher frequencies in teleseismic *S* (and hence its resolving power) are attenuated more severely than those in teleseismic *P* due to lower *Q* especially in the shallow upper mantle. Lastly, signal-generated noise levels are generally higher in teleseismic *S* due to the energy that has propagated some large portion of its path as *P* (Bock, 1994; Vinnik and Romanowicz, 1991; Wilson et al., 2006). Although it might be argued that free-surface multiples arriving as *S*-waves in the coda of teleseismic *P* represent a comparable form of signal-generated noise exacerbating interpretation of direct *P*-to-*S* conversions, these multiples are generated by receiver-side heterogeneity and can be exploited to leverage additional and complementary constraint on structure (see **Sections 1.08.4.3** and **1.08.5**).

Despite these complications, there has been renewed interest in recent years in teleseismic *S*-to-*P* conversions as means of characterizing the lithosphere to asthenosphere boundary (e.g., Kawakatsu et al., 2009; Kumar et al., 2005; Li et al., 2004; Oreshin et al., 2002; Rychert et al., 2007; Vinnik et al., 2005; Yuan et al., 2006). The growing waveform archive afforded by the profusion of modern digital networks has enabled stacking of large quantities of data to mitigate the low signal-to-noise ratios that characterize these phases, resulting in important new insights into this enigmatic structure (Eaton et al., 2009; Rychert et al., 2010).

The utility of most other phases is still more limited due to either interference or low signal-to-noise levels, although it is often used to augment teleseismic *P* data *PP* (e.g., Gurrola et al., 1994; Owens et al., 2000). Useful structural information has on occasion also been extracted from regional *P* (e.g., Park and Levin, 2001) and *PKP* (e.g., Park and Levin, 2000) using 'receiver function'-style approaches.

1.08.3 Source Removal

With the geometric framework just described in mind, the first task in most structural studies employing teleseismic wave fields is to characterize and remove the source. The standard model is a linear convolution of the form

$$u_{in}(\mathbf{x}, t) = S(t) \otimes G_{in}(\mathbf{x}, t; \mathbf{p}_{\perp}) \quad [1]$$

where u_{in} is the observed particle displacement/velocity in direction i at location $\mathbf{x}$ as a function of time t, $S(t)$ is an effective source time function, $\otimes$ signifies temporal convolution, and $G_{in}(\mathbf{x}, t; \mathbf{p}_{\perp})$ is a 'Green function' or, more precisely, receiver-side response to an impulsive quasi-plane-wave incident from below, which is characterized, for example, by horizontal slowness $\mathbf{p}_{\perp}$. Index n denotes the incident-wave polarization and will be omitted (or, rather, implicitly assumed) in the discussions that follow; however, it is important to acknowledge, in particular, in dealing with incident *S*-wave fields. Note that (1) is a far-field approximation that ignores finite source directivity. Early applications of receiver

functions (e.g., Langston, 1979; Phinney, 1964) implicitly approximated $S(t)$ on a teleseismic P recording by the vertical component of motion, $u_z(t)$. In the following sections, we will describe procedures whereby this approximation can be improved leading to more accurate estimates of the Green function. We begin by discussing means by which incident-wave and scattered-wave energies can be more effectively separated on different components. We will then proceed to review the minimum-phase nature of teleseismic wave fields that will allow us to simplify characterization and removal of the source. Our focus throughout this analysis will be on teleseismic P, but reference to teleseismic S will be made toward the end of the section.

1.08.3.1 Modal Decomposition

The combination of transmission geometry, precritical incidence, and modest material property gradients within the crust and upper mantle generally results in the incident-wave arrival (i.e., teleseismic P) being the most energetic feature on a seismogram windowed to exclude other principal phases, usually by at least an order of magnitude. Figure 3 demonstrates this property with synthetic seismograms for P-wave field incident upon an idealized, layer-over-a-half-space crustal model. Because the incident-wave field comprises a single-mode type that is either P or S, it is useful to decompose the observed wave field into separate modes in order to aid in source deconvolution and characterization of the scattered-wave field. In early studies, 'modal decomposition' was crudely accomplished through the identification of the vertical/radial components of displacement with dominantly P/S energy, respectively. A better isolation of energy into modes can be achieved in one of a number of ways. In principle, one could isolate P- and S-waves exactly in laterally heterogeneous, isotropic media by identifying the respective modes as the curl-free and divergence-free components of displacement. The density of recording instrumentation is rarely, if ever, sufficient, however, to accurately estimate the necessary spatial derivatives. As a practical alternative and as justified in Section 1.08.2, we may assume that the incident-wave field is dominated by a single horizontal slowness p. By further assuming that near-surface P- and S-velocities α, β are known, an approximate, 1-D, upgoing wave field separation can be used to isolate P- and S-modes (Bostock, 1998; Kennett, 1991; Reading et al., 2003), specifically,

$$\begin{pmatrix} P \\ V \\ H \end{pmatrix} = \begin{pmatrix} \frac{p\beta^2}{\alpha} & 0 & \frac{\beta^2 p^2 - 1/2}{\alpha q_\alpha} \\ \frac{1/2 - \beta^2 p^2}{\beta^2 q_\beta} & 0 & p\beta \\ 0 & 1/2 & 0 \end{pmatrix} \begin{pmatrix} u_r \\ u_t \\ u_z \end{pmatrix} \qquad [2]$$

where P, V, and H are estimates of the upgoing P-, SV-, and SH-component seismograms; u_r, u_t, and u_z are the radial, transverse, and vertical displacement seismograms; and q_α, q_β, and p are the vertical P, vertical S, and horizontal components of slowness at the surface, respectively. The modal field $[P,V,H]^{\mathrm{T}}$, deconvolved of source and transformed back to upgoing (Cartesian) displacement $[\hat{u}_r, \hat{u}_t, \hat{u}_z]^{\mathrm{T}}$ as

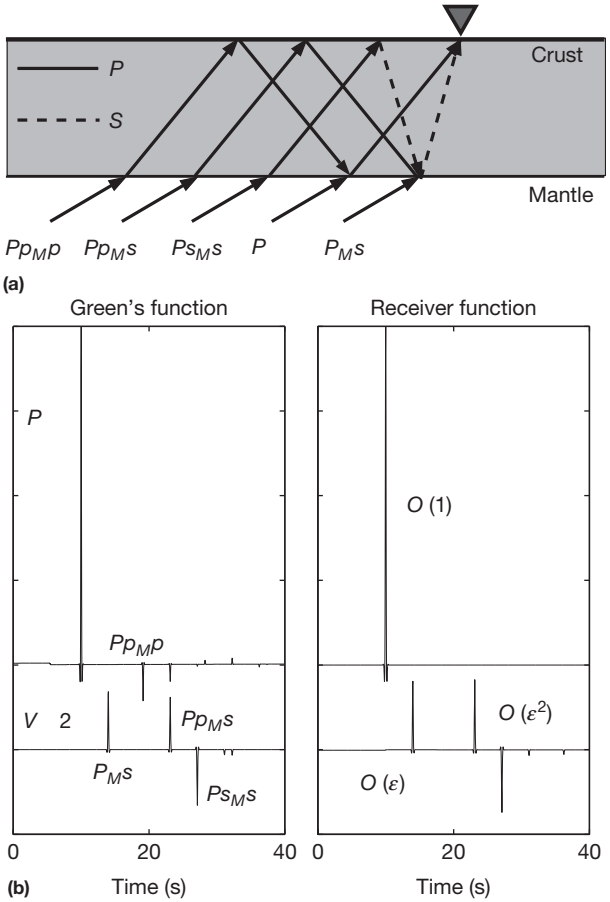

Figure 3 Synthetic seismograms for a layer-over-a-half-space, crustal model. (a) Ray paths of largest amplitude phases (P_MS, Pp_MP, Pp_MS, and Ps_MS) scattered crustal phases from the crust–mantle boundary resulting from an incident P-wave field (P-wave legs, solid; S-wave legs, dashed). See Figure 4 for examples of these phases on observed seismograms. (b) Left panel shows the Green function P and (SV) seismograms with phases labeled, and right panel comprises the corresponding time series in the receiver function approximation. Note that the direct P arrival dominates the Green function and that the receiver function is a leading-order approximation to the Green function correct to $O(1)$ on the P-component and to $O(\varepsilon)$ on the SV-component where $\varepsilon \ll 1$ measures the amplitude of the first-order scattered field relative to the incident wave.

$$\begin{pmatrix} \hat{u}_r \\ \hat{u}_t \\ \hat{u}_z \end{pmatrix} = \begin{pmatrix} \alpha p & \beta q_\beta & 0 \\ 0 & 0 & 1 \\ \alpha q_\alpha & -\beta p & 0 \end{pmatrix} \begin{pmatrix} P \\ V \\ H \end{pmatrix} \qquad [3]$$

(vs. the original displacement field $[u_r, u_t, u_z]^{\mathrm{T}}$ that contains both upgoing and downgoing waves), is generally the quantity that will be required in the inverse-scattering analysis of subsequent sections. Note that the near-surface velocities α, β can be determined from the data (assuming known slowness) from measurements of first-motion amplitudes on seismograms representing individual, incident P- and S-waves (Bostock and Rondenay, 1999; Helmberger, 1968) or, equivalently, from the zero-lag amplitudes of radial/vertical receiver functions (Ammon, 1991).

This approach can be generalized to the treatment of ocean-bottom recordings where the reverberatory effect of the ocean column is to be mitigated. Isolation of the upgoing wave field at the top of the solid medium (i.e., oceanic crust) is once more desirable since the ocean column reverberations are downgoing at this location. Several formulations are possible within a 1-D context. If pressure gauge recordings are available in addition to ocean-bottom displacement, then the decomposition can be accomplished along with the knowledge of material properties at the ocean bottom (e.g., Amundsen and Reitan, 1995; Thorwart and Dahm, 2005). Alternatively, if water depth is known together with ocean-bottom displacement and material properties, then recovery of the upgoing wave field is also possible (Bostock and Tréhu, 2012).

An alternative approach to modal decomposition for land observations involves rotation of the particle displacement field to a coordinate system where maximum energy is transferred to a single component. The angle of rotation can be determined by diagonalizing the displacement covariance matrix C (Vinnik, 1977) defined as

$$\mathbf{C} = \begin{pmatrix} \int_{t_1}^{t_2} \mathrm{d}t\, u_r^2(t) & \int_{t_1}^{t_2} \mathrm{d}t\, u_r(t) u_z(t) \\ \int_{t_1}^{t_2} \mathrm{d}t\, u_r(t) u_z(t) & \int_{t_1}^{t_2} \mathrm{d}t\, u_z^2(t) \end{pmatrix} \qquad [4]$$

where $[t_1, t_2]$ is a time window that encompasses the energy associated with the primary phase. The latter approach fails to acknowledge the presence of the free surface (and, more specifically, the generation of downgoing waves therefrom) but may be used where the incident slowness is unknown or the wave field is distorted by strong, laterally heterogeneous structure. A more detailed comparison of the two approaches is made by Svenningsen and Jacobsen (2004).

1.08.3.2 Receiver Functions and the Property of Minimum Phase

Once modal decomposition has been accomplished, we shall (either implicitly or explicitly) draw upon an important property of teleseismic body-wave fields to remove the effects of the source, namely, that the underlying Green function component in the incident mode (i.e., the *P*-component of teleseismic *P*) is minimum phase. To provide intuitive justification for the minimum-phase assertion, we consider the seismograms in Figure 3(b) and note that the incident *P*-wave at $t=0$ clearly dominates other arrivals in amplitude. In particular, let us normalize the amplitude of this arrival to unity, such that the amplitudes of the first-order scattered phases (i.e., those phases that have reflected/converted once from heterogeneity, not including the free surface) are of order ε. Because material property contrasts are small and scattering interactions occur at near-normal incidence, we have in general that $\varepsilon \ll 1$. Multiply scattered-wave fields (i.e., two or more reflection/conversion interactions with subsurface heterogeneity) attenuate as ε^n where n is the order of scattering and can be safely neglected in most applications. Accordingly, we may characterize the modal component of the Green function in the incident mode as, for example, $G^P(t) \sim \delta(t) + s(t)$, where $\delta(t)$ is the delta-function direct arrival and $s(t)$ represents the scattered field and is $O(\varepsilon)$ in amplitude. Following Claerbout (1976), we shall examine the properties of the $G^P(t)$ in the frequency domain, that is, $G^P(\omega)$. As shown in Figure 4, the delta-function makes a purely real contribution to the spectrum that is constant, say, 1, for all frequencies. Moreover, if the amplitude spectrum of $s(t)$, that is, $s(\omega)$, is <1 for all frequencies, we note that it is impossible for the phase of $G^P(\omega) = 1 + s(\omega)$ to wrap around the origin. This scenario thus constitutes a sufficient condition for $G^P(t)$ to be minimum phase. If a signal is minimum phase, it is by definition that signal, among all signals sharing the same amplitude spectrum, which possesses maximum possible energy concentrated near its onset (Robinson and Treitel, 1980). Bostock (2004) provided a more detailed justification and examination of the conditions under which the minimum-phase assumption is likely to apply to teleseismic wave fields (see also, Li and Nabelek, 1999; Sherwood and Trorey, 1965). We note at this juncture that an effective modal decomposition, as outlined in the previous section, is important in this regard as it improves the likelihood that the estimated *P*-component impulse response is minimum phase by ensuring that the delta-function $\delta(t)$ in the definition of $G^P(t)$ is of maximum possible amplitude relative to the scattered waves $s(t)$.

The minimum-phase property is important in at least two respects. First, it implies that energy is strongly concentrated at early times within the time series. In particular, the *P*-component, teleseismic *P* Green function is to leading

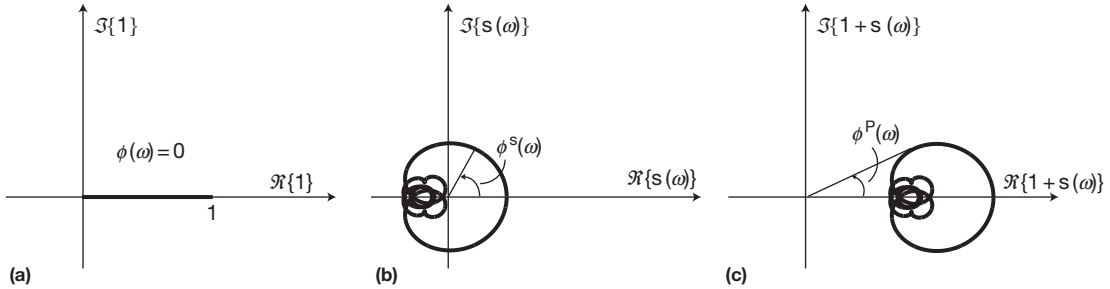

Figure 4 Frequency-domain description of $G^P(t) = \delta(t) + s(t)$. (a) Direct wave. The direct wave is represented by a delta-function at time 0 and is thus pure real, constant (amplitude 1) with phase $\phi(\omega) = 0$ for all frequencies ω. (b) Scattered waves. The scattered-wave spectrum $s(\omega)$ is characterized by an amplitude spectrum $|s(\omega)| < 1$ and a more general phase spectrum $\phi^s(\omega)$. (c) $G^P(\omega)$. The total spectrum is characterized by a real component that is positive for all ω, thereby ensuring that $G_P(t)$ is minimum phase. Reproduced from Claerbout JF (1976) *Fundamentals of Geophysical Data Processing*. New York, NY: McGraw-Hill.

order $O(1)$ a delta-function. Consequently, an observed P-component seismogram can be taken to be an estimate of the earthquake source time function that is accurate to leading order. Moreover, deconvolution of the corresponding S-component with the P-component will result in an estimate of the S-component Green function that is correct to leading order, that is, $O(\varepsilon)$, since the S-component of teleseismic P comprises only scattered (converted) waves. The foregoing argument provides justification for the validity of the classic receiver function as a leading-order estimate of the S-component of the teleseismic P Green function. Indeed, interpretation of the receiver function as a series of discrete, scattered arrivals from subsurface discontinuities relies intrinsically on this observation. In situations where the minimum-phase assumption is questionable, for example, at regional distances where several incident arrivals with comparable magnitudes and different slownesses originate from triplication at transition zone discontinuities (cf. Park and Levin, 2001), interpretation must proceed with caution. In such cases, the receiver function (i.e., spectral ratio of different modal components) can no longer be considered as good an approximation to the Green function, although it may still possess utility as a source-independent transfer function.

A second point of importance is that the minimum-phase property affords insight into how more accurate estimates of the Earth's true Green function can be recovered. Improved knowledge of the P-component Green function is particularly desirable because this component is a simple delta-function (i.e., the direct wave) within the receiver function approximation. That is, it contains no information on pure P (i.e., P-to-P) scattering whatsoever. The P-to-P scattering mode is important because its amplitude provides constraints on short-wavelength variations in subsurface compressional moduli (e.g., P-impedance, P-velocity, and bulk modulus). Amplitudes of conversions and pure S reflections, in contrast, have first-order sensitivity only to shear properties (e.g., S-impedance and S-velocity) (see, e.g., Aki and Richards, 2002). Numerous authors (e.g., Bostock and Rondenay, 1999; Bostock and Sacchi, 1997; Clayton and Wiggins, 1976; Langston and Hammer, 2001; Li and Nabelek, 1999; Paulssen et al, 1993; Revenaugh, 1995; Zhu and Kanamori, 2000) have exploited the minimum-phase property within a multichannel context to procure better estimates of the teleseismic P Green function. In these studies, P-component time series from a number of stations recording the same earthquake are time-normalized and averaged in some fashion to approximate the source. Weaker ($O(\varepsilon)$ in amplitude) scattered-wave contributions at different stations are assumed to be incoherent in time and thus sum destructively, whereas the incident wave, $O(1)$ in amplitude and fixed at time 0 on all traces, adds constructively to produce a scaled estimate of the true source time function. The teleseismic P Green function is then recovered by deconvolving this source estimate from both P- and S-component seismograms recorded at all stations. The main drawback to this approach is that the signal from structure that exhibits little or no lateral variation (e.g., the continental Moho in many instances) is identified with the source and, consequently, is not represented in the deconvolved Green function estimates. We shall describe an alternative to this approach in the succeeding text that also relies on the minimum-phase property but does not suffer from this last shortcoming.

1.08.3.3 Improved Teleseismic *P* Green Functions

The minimum-phase property implies that knowledge of the P-component amplitude spectrum alone is sufficient to define the time-domain function, since its phase, ϕ^P, is simply related to amplitude A^P through

$$\phi^P(\omega) = \mathcal{H}\{\log(A^P)\} \qquad [5]$$

where $\mathcal{H}\{\ \}$ denotes Hilbert transform (e.g., Claerbout, 1976). In fact, the phase of all three components of motion (or, more specifically, upgoing P, SV, and SH), as well as the source, need not be considered until their respective amplitude spectra have been recovered. As explained by Baig et al. (2005) and Mercier et al. (2006), estimation of, for example, the source amplitude spectrum can be accomplished by considering the cross spectrum of two seismograms sharing that source. As an example, consider two components P and SV of the same three-component recording represented in the frequency domain as $P(\omega)$, $V(\omega)$. Their cross spectrum can be written as

$$P(\omega)V^*(\omega) = |S(\omega)|^2 |G^P(\omega)||G^V(\omega)|e^{i(\phi^P - \phi^V)} \qquad [6]$$

where $|G^P(\omega)|$, $|G^V(\omega)|$, and $|S(\omega)|$ are amplitude spectra of the Green function components and the source, respectively, and * denotes complex conjugate. Note that the source enters the cross spectrum as a common convolutional element and that, accordingly, it does not contribute to the cross spectrum phase, $\phi^P - \phi^V$. We can say, therefore, that the source makes a zero-phase contribution to the cross spectrum $P(\omega)V^*(\omega)$. There are several algorithms that can, in principle, be utilized to isolate the zero-phase component of a signal (Hayes et al., 1980) and thus to form an estimate of $|S(\omega)|$ under the assumption that the cross spectrum of the two Green function components, that is, $G^P(\omega)GV^*(\omega)$, contains no zero-phase component. Moreover, by appealing to causality and a propagation model that includes a dominantly 1-D lower mantle, the duration of the two components $P(t)$ and $V(t)$ in the time domain will determine the maximum depth to which scattered energy is mapped to the Green function cross spectrum. All scattered signals generated in advance of this depth will either arrive outside the recording interval (in the case of conversions) or be mapped to $|S(\omega)|$ (in the case of same mode interactions). The latter result is a beneficial consequence for studies of receiver-side structure.

The procedures for zero-phase signal extraction tend, unfortunately, to be highly sensitive to noise, and Baig et al. (2005) discussed modifications based on spectral smoothing that tend to improve recovery on synthetic examples. Nonetheless, it is advantageous, when possible, to further improve upon estimates by making use of multichannel measurements. Even a single, three-component seismogram will afford three independent estimates of a common source, and when multiple stations and events are available, this number can increase dramatically. Consider, for example, a data set comprising J stations recording I three-component seismograms. By casting the convolution relation in the log-spectral domain such that a single recording representing source i and impulse response j is represented as, for example,

$$\log(|P_{ij}(\omega)|) = \log(|S_i(\omega)|) + \left(\left|G_j^P(\omega)\right|\right) \qquad [7]$$

we may generate a large linear system of equations (see Andrews, 1986) that includes $3IJ$ equations in $I + 3J$ unknowns.

This system, when augmented with equations that include source estimates $|S_i(\omega)| \approx |\widetilde{S}_i(\omega)|$ determined as outlined in the preceding text, becomes highly redundant and can be solved via least squares to recover the improved amplitude spectra $|G_j^P(\omega)|$, $|G_j^V(\omega)|$, $|G_j^H(\omega)|$, and $|S_i(\omega)|$. The phase of $G_j^P(\omega)$ is readily determined directly through eqn [5], whereas the phase of the two remaining quantities can be recovered through a slightly more involved procedure described by Mercier et al. (2006). An example showing the teleseismic *P* Green function estimates as a function of horizontal slowness for station HYB at Hyderabad, India, is shown in Figure 5. The *P*-image clearly reveals the pure *P* surface–Moho reflection that cannot be recovered through conventional receiver function analysis.

The approach outlined in this section can in principle be applied to *P* phases other than teleseismic *P* (e.g., *PP* and *PKP*) provided that these recordings are free of other primary phases. We consider its relevance and application to *S* phases in the succeeding text.

1.08.3.4 The Teleseismic *S* Green Functions

There are two principal complications that arise when seeking to extend the approach of the previous section to *S* phases, both of which concern the applicability of the minimum-phase assumption. The first complication is primarily theoretical in nature and is easily qualified. The second issue pertains to the polarization of *S*-waves and poses more practical difficulty. We discuss each in turn.

We have already alluded to the increased tendency for multiply interfering phases (e.g., teleseismic *S*, *ScS*, and *SKS*) within the teleseismic *S*-wave field in some circumstances but will assume that these complications have been dealt with and that our observations represent a single, direct phase with known slowness. Strictly speaking, the *S*-component of the impulse response (i.e., the *S*-component of the teleseismic *S* Green function) cannot be minimum phase in the presence of heterogeneity owing to the generation of acausal, for example, *S*-to-*P*-to-*S* scattering interactions that arrive as *S*-waves in advance of the incident *S*-wave field. These early arrivals are, however, of order $O(\varepsilon^2)$ in amplitude and so can be ignored within the single-scattering formulations that dominate inversion practice (see Sections 1.08.4 and 1.08.5).

The next issue, then, is to determine to which component of *S* the minimum-phase assumption should apply. In 1-D, isotropic (or transversely isotropic) media, this question is easily addressed since *P*/*SV* and *SH* interactions are decoupled and the minimum-phase assumption can be made independently for both the *SV*- and *SH*-components of motion. A number of earlier studies (Båth and Stefánson, 1966; Baumgardt and Alexander, 1984; Bock, 1991; Faber and Müller, 1980; Jordan and Frazer, 1975; Sacks et al., 1979) have avoided source deconvolution by employing deep focus events to examine *SV*-to-*P* conversions. More recently, the teleseismic *SV* Green/receiver functions have been generated in a manner directly analogous to teleseismic *P* by simply interchanging the roles of the *P*- and *SV*-components (e.g., Kumar et al., 2005; Li et al., 2004; Vinnik et al., 2005) or by using teleseismic *P* as a source estimate (Zhou et al., 2000). Considerably less attention has been paid to *SH* due to the lack of conversions in isotropic, 1-D media, although multichannel stacking has been used in at least one study to recover *SH* reflections from dipping structures (Li, 1996).

In more realistic circumstances, particularly those involving azimuthal anisotropy, we recognize, however, that *S*-waves with different polarizations will couple such that the impulse response becomes a more complex function of the incident *S*-polarization (Farra et al., 1991). Our objective in this class of study is thus to extract an azimuth-dependent and polarization-dependent impulse response (Farra and Vinnik, 2000; Frederiksen and Bostock, 2000). Because (quasi-)*S*-modes propagate at different velocities in anisotropic media, situations will

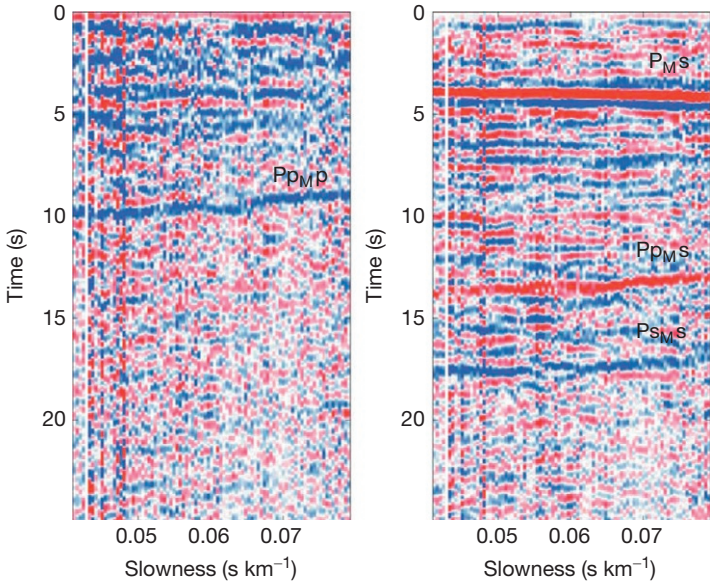

Figure 5 The teleseismic *P* and *SV* Green function estimates for station HYB, India, as function of horizontal slowness $\sqrt{p_x p_\alpha}$ (reproduced from Kumar MR and Bostock MG (2006) Transmission to reflection transformation of teleseismic wavefields. *Journal of Geophysical Research* 111: B08306). Note the clear definition of the main first-order scattered phases from the continental Moho on both components, as defined in Figure 3.

frequently arise where at least one component of *S*-motion recorded at the surface is decidedly non-minimum phase.

To address this issue, we write the upgoing wave field (which contains both direct- and scattered-wave contributions) recorded at the surface $[P, V, H]^{\mathrm{T}}$ in terms of a purely *S*-wave field $[0, V_0, H_0]^{\mathrm{T}}$ incident at the base of laterally homogeneous, generally anisotropic, receiver-side stratification,

$$\begin{pmatrix} P \\ V \\ H \end{pmatrix} = \begin{pmatrix} U^{PP} & U^{PV} & U^{PH} \\ U^{VP} & U^{VV} & U^{VH} \\ U^{HP} & U^{HV} & U^{HH} \end{pmatrix} \begin{pmatrix} 0 \\ V_0 \\ H_0 \end{pmatrix} \qquad [8]$$

where the various elements of the transmission matrix for upgoing waves $\mathrm{U} = \mathrm{U}(\omega, \mathbf{p}_\perp)$ are functions of frequency and horizontal slowness p_α, $\alpha = 1, 2$. Note that the matrix U can be related to the transmission matrix T_U for upward incidence in the absence of a free surface as $\mathsf{U} = \left(\mathsf{I} - \mathsf{R}_D\widetilde{\mathsf{R}}\right)^{-1}\mathsf{T}_U$ (Kennett, 1983) where the effects of reverberation are expressed through the free-surface reflection matrix $\widetilde{\mathsf{R}}$ and reflection matrix R_D for the stratification in the absence of free surface. We will further assume that the incident-wave field $[0, V_0, H_0]^{\mathrm{T}}$ is linearly polarized as would be the case for a simple, for example, double-couple, point source within an isotropic source-side structure. Upon arrival at the surface, the *V*,*H*-components can combine to produce an elliptically polarized wave field characterized by low eccentricity that is the manifestation of shear-wave splitting (e.g., Silver and Chan, 1991; Vinnik et al., 1989). This observation indicates that the elements U^{HV} and U^{VH} can be comparable in magnitude to the diagonal elements of U for structures representing the real Earth.

An obvious way to proceed is thus to follow standard practice for shear-wave splitting analysis and search for the combination of fast-polarization direction and delay time that most nearly corrects for shear-wave splitting to produce a linearly polarized estimate of V_0 and H_0. Although this downward continuation (i.e., simulation of U^{-1}) is only approximate in that internal reverberations/reflections are neglected, our main concern is with the dominant, incident *S*-arrival. In particular, the component of the resulting time series in the polarization direction, say, $\mathbf{s}_0$, will then be minimum phase under the condition that the incident wave has been reduced to a single impulse on one component and is more energetic than all remaining signals. Accordingly, the source can be removed following the approach taken in **Section 1.08.3.3** for *P*-waves. Once the source is removed, we may reverse the downward continuation (including errors therein) by applying the forward-splitting operator to produce the corresponding source-deconvolved surface wave field $[P, V, H]^{\mathrm{T}}$. To create the Green function, it remains to distinguish between the impulse responses produced by individual V_0 and H_0. We may exploit multichannel measurements taken at the same horizontal slowness $p_\alpha = [p_1, p_2]$ (i.e., seismograms representing different source mechanisms but the same geographical source–receiver combinations) to this end, by taking appropriate linear combinations of the deconvolved $[P, V, H]^{\mathrm{T}}$ as dictated by independent values of $\mathbf{s}_0$.

The approach outlined in the preceding text may break down where source-side anisotropy has contributed to splitting or where a single fast-polarization direction and delay time do not adequately characterize the transmission response. This latter situation may arise where multiple, strongly anisotropic layers exist. In these cases, a single measured $\mathbf{s}_0$ may not accurately represent the polarization state of the wave field incident on receiver-side heterogeneity (e.g., Silver and Savage, 1994). Farra and Vinnik (2000) described an alternate procedure, also using multichannel measurements, for computing the *S*-receiver function by deconvolving the *P*-component with the projection of the *S*-wave in the direction of the strongest polarization. The interpretation of this quantity faces the same restrictions identified in the preceding text and is based on a linearization, which limits allowable relative magnitudes of off-diagonal elements in U.

1.08.3.5 Deconvolution, Stacking, and Array Processing

Our focus throughout the majority of this section has been to establish the physical basis for the classical receiver function and extensions that allow us to recover a more fundamental quantity, namely, the Green function, which is required in the inverse-scattering approaches to be described in **Sections 1.08.4.3** and **1.08.5**. In so doing, we have paid little attention to a significant body of work that has been devoted to a more general topic of signal processing as applied to teleseismic wave fields, specifically deconvolution. In the main, this work is concerned with estimating a transfer function (i.e., either receiver function or the Green function) such that the effect of noise is mitigated, usually under the assumption that the source wavelet is perfectly known. We provide, in the succeeding text, a brief overview of deconvolution applications to receiver-side scattering of teleseismic wave fields.

Among the first attempts to extract an impulse response from teleseismic body waves, Ulrych and coworkers (Ulrych, 1971; Ulrych et al., 1972) employed filtering in the cepstral domain to separate source from structural signal. The cepstrum of a signal is computed by inverse Fourier transformation of the logarithm of its Fourier transform. That and eqn [7] are therefore termed homomorphic decompositions since they transform the convolutional operation to an additive one (see, e.g., Oppenheim and Schafer, 1975). The difficulty in applying such homomorphic decompositions to non-zero-phase signals (vs. autocorrelations) resides in the necessity for phase unwrapping, which effectively renders the approach intractable for many practical purposes. This shortcoming was noted by Clayton and Wiggins (1976) who proposed an alternative 'water-level' method that has subsequently found widespread use. The receiver function $R(t)$ is thereby computed as

$$R(t) = \mathcal{F}^{-1}\left\{\frac{P^*(\omega)S(\omega)}{\max\left(P^*(\omega)P(\omega), cP_{\max}{}^*P_{\max}\right)}\right\} \qquad [9]$$

where $\mathcal{F}^{-1}\{\}$ denotes inverse Fourier transformation, $P_{\max}$ is the spectral value for which $P(\omega)$ achieves maximum absolute value, and c is a user-specified water-level parameter that regularizes the deconvolution by damping contributions at frequencies where signal levels are low and thus more likely to be corrupted by noise. Note that when $c = 0$, eqn [9] reduces to simple spectral division, whereas large values of c produce a receiver function that is a scaled cross correlation of the *P*- and *S*-components. In the latter case, the *P*-component acts as a matched filter (Kind and Vinnik, 1988). Variations on this

same theme include the standard damped least-squares deconvolution solution

$$R(t) = \mathcal{F}^{-1}\left\{\frac{P^*(\omega)S(\omega)}{P^*(\omega)P(\omega)+\delta}\right\} \quad [10]$$

where δ is a constant Tichonov regularization parameter determined by standard (e.g., L-curve, generalized cross validation (Golub et al., 1979)) means and Wiener deconvolution (e.g., Press et al., 1986) where δ in eqn [10] becomes frequency-dependent and proportional to the pre-event noise spectrum. When multichannel measurements representing the same $R(t)$ are available, it is advisable to compute a simultaneous estimate (Gurrola et al., 1995) as

$$R(t) = \mathcal{F}^{-1}\left\{\frac{\sum_i P_i^*(\omega)S_i(\omega)}{\sum_i P_i^*(\omega)P_i(\omega)+\delta}\right\} \quad [11]$$

rather than stacking individual estimates computed by, for example, eqn [10] because only one value of δ needs to be chosen and that value is likely to be small since different seismograms will, in general, exhibit spectra with different signal-to-noise characteristics. Park and Levin (2000) advocated using multitaper spectral estimates (Thomson, 1982) to help stabilize receiver function deconvolution, where the individual multichannel recordings within the sums in eqn [11] are replaced by the tapered spectral estimates for a single seismogram.

While quadratic misfit and model norms are being considered, Parseval's theorem ensures that the results of deconvolution in the time domain and frequency domain will be equivalent, and it is therefore expedient to perform computations in the frequency domain to take advantage of the fast Fourier transform. Time-domain deconvolution may be desirable, however, where time-domain-specific regularization of $R(t)$ such as sparseness is required (Gurrola et al., 1995; Ligorria and Ammon, 1999).

In addition to deconvolution, nonlinear stacking and array processing methods are often used to improve signal-to-noise levels on teleseismic body-wave recordings and, in particular, for emphasizing discrete, weak arrivals. Popular nonlinear stacking techniques include the Nth root stack (Muirhead and Datt, 1976) and the phase-weighted stack (Schimmel and Paulssen, 1997); Kennett (2000) discussed the application of these approaches to multicomponent teleseismic wave fields. In the next two sections, we will examine multichannel processing of scattered teleseismic wave fields in the context of structural inversion for which (weighted but linear) stacking enters naturally through surface integration. For a summary of more general array processing techniques applied to teleseismic wave fields, the reader is referred to Rost and Thomas (2002).

1.08.4 1-D Inversion

The use of single-station data in early receiver function studies forced practitioners to focus attention on delineation of strictly 1-D structures. In fact, this practice is still commonplace today because, in many circumstances, the target discontinuities are expected to be locally horizontal or to vary slowly in lateral coordinates. Thus, for example, in studies of the continental crust (e.g., Owens et al., 1984; Zandt and Ammon, 1995) and transition zone discontinuities (e.g., Chevrot et al., 1999; Kind and Vinnik, 1988; Vinnik, 1977), the 1-D analysis has proved to be quite adequate and has yielded valuable information on the characteristics of these structures in different tectonic regimes. The more recent documentation of near-horizontal, anisotropic discontinuities within the continental lithosphere (Asencio et al., 2003; Bostock, 1997, 1998; Leidig and Zandt, 2003; Levin and Park, 1997, 1998; Saul et al., 2000) has opened new avenues for study with regard to both inverse modeling and complementary new information that anisotropy can potentially deliver on subsurface structures and dynamics.

Methods employed to invert receiver functions for 1-D variations in material properties can be classified into three categories: optimization based on least squares, Monte Carlo methods, and inverse scattering. We discuss each category in turn but pay special attention to the last method because it is most closely tied to the physics of scattering and provides formal justification for the 'delay-and-sum' and 'squeezing and stretching' approaches that have dominated 1-D studies of lithospheric and upper mantle discontinuities to date.

1.08.4.1 Least-Squares Optimization

Optimization by least squares is the most widely used and generic method for solving geophysical inverse problems (Menke, 1984; Parker, 1994). It is less expensive than Monte Carlo inversion and, in the context of teleseismic body waveforms, makes less stringent demands on data than inverse-scattering methods. More specifically to the latter point, data insufficiency (in the form, say, of limited frequency and/or slowness content) can be readily compensated for through model regularization, and there is no formal requirement that data be supplied in the form of the Green functions. That is, model matching by least-squares techniques can be directly undertaken using transfer functions, for example, the receiver function, without concern for the proximity of this quantity to the true Green function. All that is required is a means of performing receiver function forward modeling.

Implementation is straightforward (see, e.g., Ammon et al. (1990) for a more detailed account). A receiver function or series of receiver functions strung end to end and represented in either the time or frequency domain is assembled within a vector d, with individual elements d_i. For consistency with later notation, we shall define c to be a vector containing the elasticities and densities of a sequence of horizontal layers bounded by a free surface above and half-space below, thereby representing a 1-D Earth model. The forward-modeling operator is represented by a (nonlinear) functional $\mathcal{D}$ that operates on c to produce synthetic data, that is,

$$\mathbf{d} = \mathcal{D}\{\mathbf{c}\} \quad [12]$$

In the 1-D context, both exact layer-matrix methods (Ammon et al., 1990; Haskell, 1962; Kennett, 1983; Kind et al., 1995; Kosarev et al., 1993) and approximate ray methods (e.g., Langston, 1977; Owens et al., 1984) are feasible means of representing $\mathcal{D}$. Ray methods are more economical in time-domain implementations where only a limited number of low-order scattering interactions are to be modeled, whereas layer-matrix methods provide a complete representation wherein economies

may be gained by restricting computation to the range of frequencies and slowness that characterize the data.

Nonlinearity is addressed in the inverse problem by expanding the receiver function vector as a Taylor series about a starting model $\mathbf{c}_0$, such that

$$d_i = \mathcal{D}_i(\mathbf{c}) = \mathcal{D}_i\{\mathbf{c}_0\} + \frac{\partial \mathcal{D}_i}{\partial c_j}\{\mathbf{c}_0\}\Delta c_j + O\left(||\Delta \mathbf{c}||^2\right) \qquad [13]$$

Rearranging eqn [13], discarding nonlinear terms, and writing in matrix form yield

$$\mathbf{W}\Delta\mathbf{c} = \mathbf{f} \qquad [14]$$

where the data residual vector is $\mathbf{f} = \mathbf{d} - \mathcal{D}(\mathbf{c}_0)$ and the elements of the sensitivity matrix W are defined by $W_{ij} = \partial \mathcal{D}_i / \partial c_j$. Randall (1989) described a particularly economical means to compute W_{ij} for receiver function inversions that exploits Kennett's (1983) reflection/transmission layer-matrix formalism. Alternatively, this quantity can be determined numerically. Since receiver functions are sensitive primarily to short-wavelength structure, $\mathbf{c}_0$ is generally taken to represent a slowly varying velocity model on which the unknown short-wavelength perturbation $\Delta\mathbf{c}$ is superposed.

The solution of the linear system [14] can be accomplished in a number of ways, although minimization of the quadratic norm of f leading to solution of the normal equations is the standard approach. Depending on the form of model parameterization (e.g., layer thicknesses), the system in eqn [14] may be rank-deficient in which case regularization via, for example, damping can be implemented. Further accommodation of nonlinearity can, in principle, be accomplished by Newton iteration on eqn [13].

1.08.4.2 Monte Carlo Inversion

The advent of high-performance computing and the relatively few model parameters that characterize 1-D problems have led to investigation of Monte Carlo methods for performing receiver function inversions. These methods require only a forward-modeling engine without need for calculation of derivatives (i.e., W_{ij}), since the sole criterion for model selection is an arbitrary measure of fit. They hold the distinct advantage over least-squares optimization that they are global in nature and less apt to identify incorrect, local misfit minima as solutions. Although the number of unknowns is relatively small, a purely random sampling of the model space is still computationally demanding and, at best, inefficient. Consequently, preference has been given to 'directed search' algorithms that exploit information from past computations to guide future sampling. Two examples of directed search algorithms that have been applied to receiver function inversion are the genetic algorithm (Clitheroe et al., 2000; Goldberg, 1989; Lawrence and Wiens, 2004; Shibutani et al., 1996) and the recently introduced nearest-neighbor algorithm (Frederiksen et al., 2004; Lucente et al., 2005; Nicholson et al., 2005; Sambridge, 1999a). Both algorithms begin with a population of models generated through an initial (uniform or random) sampling of model space. Genetic algorithms employ an evolutionary analogy wherein model parameters are encoded within binary strings or 'chromosomes.' The model population is allowed to evolve through iterations (or 'generations') by stochastic selection of models based on goodness of fit, by recombination of models (through chromosomal splicing), and by random 'mutation.' The natural neighborhood algorithm employs an adaptive Voronoi cellular network to drive the parameter search, where each successive iteration randomly samples the model space within cells occupied by the fittest models of the previous iteration. The algorithm thereby focuses increasingly on regions in model space that produce models that come closer to satisfying the data. Another important advantage of these directed search approaches lies in the output of model populations that afford the opportunity for either qualitative or quantitative (Sambridge, 1999b) appraisal of the model space.

1.08.4.3 Born Inversion and Classic (Delay and Sum) Studies

Unlike the two methods just described, inverse-scattering approaches to the receiver function inversion problem rely fundamentally on an explicit description of the scattering process. Accordingly, the starting point is the Lippman–Schwinger equation that we shall write in the frequency domain as (see Hudson and Heritage, 1981)

$$\Delta u_n(\mathbf{x}', \omega) = \int_V \mathrm{d}\mathbf{x}\left(-\Delta c_{ijkl}(\mathbf{x})\partial_k u_l(\mathbf{x}, \omega)\partial_j G^0_{in}(\mathbf{x}, \mathbf{x}', \omega) + \Delta\rho(\mathbf{x})\omega^2 u_i(\mathbf{x}, \omega) G^0_{in}(\mathbf{x}, \mathbf{x}', \omega)\right) \qquad [15]$$

This equation is cast in terms of field quantities and perturbations in material properties whose support is the volume V. The material properties of the medium are described by the stiffness tensor c_{ijkl} and density ρ through

$$c_{ijkl}(\mathbf{x}) = c^0_{ijkl}(\mathbf{x}) + \Delta c_{ijkl}(\mathbf{x}), \quad \rho(\mathbf{x}) = \rho^0(\mathbf{x}) + \Delta\rho(\mathbf{x}) \qquad [16]$$

where quantities with superscript '0' denote those of a background reference medium and the 'Δ' quantities are perturbations. Although not strictly required at this stage, we shall assume that short-wavelength heterogeneity is represented within $\Delta c_{ijkl}(\mathbf{x})$, $\Delta\rho(\mathbf{x})$ and ascribe the smoothly varying component of the material property perturbations to $c^0_{ijkl}(\mathbf{x})$, $\rho^0(\mathbf{x})$. The total wave field u_i is defined as

$$u_i(\mathbf{x}, \omega) = u^0_i(\mathbf{x}, \omega) + \Delta u_i(\mathbf{x}, \omega) \qquad [17]$$

where $u^0_i(\mathbf{x}, \omega)$ is the incident (or 'reference') wave field, created by a source with $\delta(t)$ time dependence, that would propagate independently in a medium with properties $c^0_{ijkl}(\mathbf{x})$, $\rho^0(\mathbf{x})$. Note that this definition is consistent with our earlier designation of the incident-wave field as a primary phase such as teleseismic P or S propagating through a smoothly varying mantle. The scattered (or 'perturbed') wave field $\Delta u_i(\mathbf{x}, \omega)$ arises through the interaction of $u^0_i(\mathbf{x}, \omega)$ with short-wavelength structure $\Delta c_{ijkl}(\mathbf{x})$, $\Delta\rho(\mathbf{x})$. We will assume that an accurate representation of $\Delta u_i(\mathbf{x}', \omega)$ has been secured using methods described in **Section 1.08.3** where $\mathbf{x}' = [x'_1, x'_2, 0]^{\mathrm{T}}$ shall be taken in this and the following sections to parameterize the Earth's surface. The quantity $G^0_{in}(\mathbf{x}, \mathbf{x}', \omega)$ represents the Green function for the reference medium and will be determined analytically. We now make the customary 'single-scattering' or 'Born' approximation by assuming that $\Delta u_i(\mathbf{x})$ is small relative to $u^0_i(\mathbf{x}, \omega)$ such that we may rewrite eqn [15] as

$$\Delta u_n(\mathbf{x}',\omega) \approx \int_V \mathrm{d}\mathbf{x}\big(-\Delta c_{ijkl}(\mathbf{x})\partial_k u_l^0(\mathbf{x},\omega)\partial_j G_{in}^0(\mathbf{x},\mathbf{x}',\omega) + \Delta\rho(\mathbf{x})\omega^2 u_i^0(\mathbf{x},\omega)G_{in}^0(\mathbf{x},\mathbf{x}',\omega)\big) \quad [18]$$

(see Chapter 1.05 for an account of the Born approximation in an acoustic context). Note that this step is analogous to the linearization of eqn [13] where the forward-modeling operator (or, more specifically, $\mathcal{D}_i\{\mathsf{c}\}-\mathcal{D}_i(\{\mathsf{c}_0\})$) is given by eqn [15].

To set the problem in a form that is appropriate for plane-wave propagation in a 1-D Earth, we recognize that plane waves (or, more precisely, wave fields with constant horizontal slowness p_α, $\alpha=1, 2$) propagate independently in media exhibiting strictly vertical variations in material properties, that is, $\Delta c_{ijkl}(x_3)$, $\Delta\rho(x_3)$. Since propagation takes place in the reference medium, we will make use of plane-wave, modal expansions for $u^0(\mathbf{x},\omega)$ and $G_{in}^0(\mathbf{x},\mathbf{x}',\omega)$ that also employ the high-frequency or WKBJ approximation. Following Bostock (2003) (and correcting an error in eqn [32] therein), we write

$$u_i^0(\mathbf{x},\omega) = \sum_r A^r(x_3)s_i^r(x_3)\mathrm{e}^{\mathrm{i}\omega(\tau^r(x_3)+p_\alpha x_\alpha)} \quad [19]$$

$$G_{in}^0(\mathbf{x},\mathbf{x}',\omega) = \sum_s \frac{-\mathrm{i}s_n^s(0)s_i^s(x_3)\mathrm{e}^{\mathrm{i}\omega\left(\tau^s(x_3,0)+p_\alpha\left(x'_\alpha-x_\alpha\right)\right)}}{2\omega\sqrt{\rho^0(0)\rho^0(x_3)\left|U_3^s(0)\right|\left|U_3^s(x_3)\right|}} \quad [20]$$

where the subscript α follows the repeated index summation convention; the superscripts r,s index the incident- and scattered-wave modes (i.e., P, SV, SH, or their analogs in anisotropic media); s_i^r and s_n^s are corresponding depth-dependent, unit polarization vectors; $A^r(x_3)$ is the source amplitude, $U_3^r(x_3), U_3^s(x_3)$ are the vertical components of group velocity; and $\tau^r(x_3)$ and $\tau^s(x_3)$ are delay times of the incident and scattered modes, respectively.

The modal expansion allows us to isolate and describe individual scattering interactions; for example, we set $A^r(x_3)=1/\sqrt{\rho(x_3)\left|U_3^r(x_3)\right|}$ for direct P-to-S scattering (say, $r=1$ and $s=2$), and the corresponding delay time functions are written as

$$\tau^r(x_3) = -\int_0^{x_3}\mathrm{d}\gamma_3 p_3^P(\gamma_3), \quad \tau^s(x_3,0) = \int_0^{x_3}\mathrm{d}\gamma_3 p_3^S(\gamma_3) \quad [21]$$

where $p_3^P(x_3)$ and $p_3^S(x_3)$ are the vertical components of phase slowness for P- and S-waves, respectively. The choice of $\tau^r(x_3)$ in the preceding text implies a time normalization where the direct P-wave ($r=1$) arrives at the Earth's surface at $\tau^r=0$ consistent with the output of most deconvolution schemes described in Sections 1.08.3.3–1.08.3.5. Back scattering that involves free-surface reflection of the upgoing incident wave can be described through an alternate set of amplitude and delay time functions. For example, pure P-mode reflection (say, $r=2$ and $s=1$) is characterized by $A^r(x_3)=\widetilde{R}^{PP}/\sqrt{\rho(x_3)\left|U_3^r(x_3)\right|}$ where $\widetilde{R}^{PP}$ is the free-surface P-to-P reflection coefficient and the delay time functions are

$$\tau^r(x_3) = \int_0^{x_3}\mathrm{d}\gamma_3 p_3^P(\gamma_3), \quad \tau^s(x_3,0) = \int_0^{x_3}\mathrm{d}\gamma_3 p_3^P(\gamma_3) \quad [22]$$

(note that for an anisotropic reference medium that does not exhibit mirror symmetry, we would have to employ different values for up- and downgoing phase slowness in eqns [22]).

Inserting expressions [19] and [20] into [18] and retaining only the leading-order terms in frequency, one obtains

$$\Delta u_n(\mathbf{x}',\omega) \approx \sum_r\sum_s s_n^s(0)\mathrm{e}^{\mathrm{i}\omega p_\alpha x'_\alpha}\int \mathrm{d}x_3 B^{rs}(x_3,\omega) \left[\frac{\Delta c_{ijkl}}{\rho^0}s_l^r p_k^r s_i^s p_j^s + \frac{\Delta\rho}{\rho^0}s_i^r s_i^s\right]\mathrm{e}^{\mathrm{i}\omega(\tau^r(x_3)+\tau^s(x_3,0))} \quad [23]$$

where, for brevity, we have suppressed the x_3 dependence in all quantities within the square brackets, p_i^r, p_i^s are the phase slowness vectors of the incident- and scattered-wave fields at depth x_3, and the factor $B^{rs}(x_3,\omega)$ is defined by

$$B^{rs}(x_3,\omega) = -\frac{\mathrm{i}\omega A^r(x_3)\sqrt{\rho^0(x_3)}}{2\sqrt{\rho^0(0)\left|U_3^s(0)\right|\left|U_3^r(x_3)\right|}} \quad [24]$$

Equation [23] represents an asymptotic, linearized relation between the scattered field $\Delta u_n(0)$ measured at the Earth's surface and the unknown material parameters $\Delta c_{ijkl}(x_3)$ and $\Delta\rho(x_3)$. To simplify the extraction of these parameters, we follow Burridge et al. (1998) and define a fourth rank tensor a_{ijkl} that possesses the same symmetry properties as Δc_{ijkl} and satisfies

$$\frac{\Delta c_{ijkl}}{V^r V^s}a_{ijkl} = \Delta c_{ijkl}s_l^r p_k^r s_i^s p_j^s \quad [25]$$

where V^r and V^s represent the phase velocities of incident and scattered modes, respectively, averaged over all angles, that is

$$a_{ijkl} = \frac{V^r V^s}{8}\left[\left(s_i^s p_j^s + s_j^s p_i^s\right)\left(s_k^r p_l^r + s_l^r p_k^r\right) + \left(s_k^s p_l^s + s_l^s p_k^s\right)\left(s_i^r p_j^r + s_j^r p_i^r\right)\right] \quad [26]$$

This construction allows us to adopt a more compact notation and rewrite eqn [23] as

$$\Delta u_n(0,\omega) \approx \sum_r\sum_s s_n^s(0)\mathrm{e}^{\mathrm{i}\omega p_\alpha x'_\alpha}\int \mathrm{d}x_3 B^{rs}(x_3,\omega)\mathrm{e}^{\mathrm{i}\omega(\tau^r(x_3)+\tau^s(x_3,0))}\mathsf{w}^{\mathrm{T}}\Delta\mathsf{c} \quad [27]$$

The radiation patterns and material property perturbations are now contained within 22-element vectors, w and Δc, whose entries correspond to the 21 independent elastic constants and density as

$$\mathsf{w} \leftrightarrow \left[a_{ijkl}, s_i^s s_i^r\right], \quad \Delta\mathsf{c} \leftrightarrow \left[\frac{\Delta c_{ijkl}}{\rho^0}, \frac{\Delta\rho}{\rho^0}\right] \quad [28]$$

Equation [27] takes a form that may be readily discretized and solved for Δc. It is common practice, however, to consider the contribution of each scattering mode $\Delta u_i^{rs}(0,\omega)$ (where $\Delta u_i(\mathbf{x},\omega)=\sum_r\sum_s\Delta u_i^{rs}(\mathbf{x},\omega)$), independently. Assuming that the individual $\Delta u_i^{rs}(\mathbf{x},\omega)$ can be approximately isolated (see Section 1.08.6 for further discussion on this assumption), we define the scalar, time-domain quantity

$$f^{rs}(t) = \mathcal{F}^{-1}\left\{\frac{\Delta u_i^{rs}(0,\omega)s_i^s(0)\mathrm{e}^{-\mathrm{i}\omega p_\alpha x'_\alpha}}{B^{rs}(x_3,\omega)}\right\}\left[p_3^s(x_3)+p_3^r(x_3)\right] \quad [29]$$

where $\mathcal{F}^{-1}$ denotes, as before, inverse Fourier transformation. Note that contraction with $s_i^s(0)$ rotates the data into the

anticipated polarization direction of the upgoing scattered mode s. In practice, we accomplish this operation using eqn [2] since the effect of the free surface on polarization of the recorded wave field is not explicitly accounted for in the treatment of this section. Multiplication by $e^{-i\omega p_z x'_z}$ in eqn [29] removes the time shift associated with horizontal coordinate such that the arrival of the direct wave (P for $r=1$ and S for $r=2, 3$) corresponds to time 0. By inserting the expression for $\Delta u_i^{rs}(0,\omega)$ in eqns [27] into [29] and evaluating both integrals in ω and x_3 (with the aid of Leibniz' rule), we arrive at

$$f^{rs}(t=\tau^r(x_3)+\tau^s(x_3,0))=\mathbf{w}^{\mathrm{T}}(x_3)\Delta\mathbf{c}(x_3) \qquad [30]$$

that is, a one-to-one relation between material property perturbations at depth x_3 and the value of $f^{rs}(t)$ evaluated at time $t=\tau^r(x_3)+\tau^s(x_3,0)$. If we now assemble a large number of data $u_i^{rs}(0,\omega)$ representing different scattering interactions r, s and geometries (as reflected in p_i^r and p_i^s), normalize as in eqn [29], and arrange these data in a column vector f, a system of equations can be written as

$$\mathbf{f}(x_3)=\mathbf{W}(x_3)\Delta\mathbf{c}(x_3) \qquad [31]$$

where the transposed vectors $\mathbf{w}^{\mathrm{T}}$ form the rows of W. The solution to this system of equations amounts to an amplitude versus slowness analysis of the scattering coefficient corresponding to depth x_3. Normalization of the upgoing wave field by $[p_3^s+p_3^r]/B^{rs}(x_3,\omega)$ in eqn [29] ensures that it is appropriately scaled and filtered such that the perturbation profile $\Delta c(x_3)$ is, to within the single-scattering and high-frequency approximations, correctly recovered. If, instead, we wish to recover a profile of reflectivity (or, more precisely, the singular function of the discontinuity surface scaled to the amplitude of the perturbation; e.g., Bleistein, 1987), we must remove the factor $i\omega$ in eqn [24]. In so doing, the solution of eqn [31] is seen to be simply a weighted diffraction stack of the data along move-out curves corresponding to the various scattering interactions r,s within the 1-D reference medium.

In the case of isotropic stratification, the reflectivity inversion affords a formal justification for the delay-and-sum approach introduced by Vinnik in his analysis of P-to-S conversions from the mantle transition zone in 1977 and adopted subsequently by numerous workers (e.g., Bostock, 1996; Chevrot et al., 1999; Dueker and Sheehan, 1998; Kind and Vinnik, 1988; Stammler et al., 1992). In these studies, data are stacked along move-out curves computed for a 1-D Earth model and corresponding to a range of trial depths, to produce a map of stacked amplitude as a function of delay time and discontinuity depth. If amplitude extrema are observed at delay times consistent with a trial depth, a discontinuity is tentatively identified (see **Figure 6**). An approximate reflectivity (or 'convertibility') depth profile can be recovered by slicing through the amplitude map along the appropriate travel-time curve (see **Figure 7**). This empirical approach is equivalent to migrating (or 'squeezing and stretching') traces to depth prior to stacking (e.g., Fee and Dueker, 2004; Gilbert et al., 2003). It handles kinematics in precisely the same way as the solution of eqn [31]. The dynamics are of secondary importance, and their neglect in empirical migration approaches only means that the stacked waveforms are less directly interpretable in terms of perturbations in the Earth's material properties. The creation of an amplitude map has the advantage of permitting visual assessment of the veracity of a potential structural signal on the basis of whether its amplitude maximum occurs at or near the expected travel time. In this sense, Vinnik's approach has much in common with the velocity spectrum stack developed for exploration applications and also applied to teleseismic wave fields by Gurrola et al. (1994). In this case, amplitude maxima of delayed and stacked waveforms are used to provide improved velocity (or in the case of teleseismic P-to-S conversions, Poisson's ratio) model information for structural imaging.

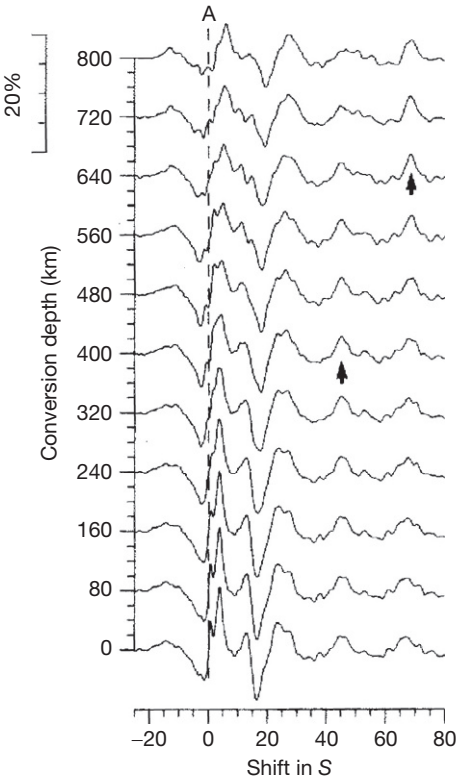

Figure 6 Delayed and summed *SV*-components of source-normalized teleseismic *P* recorded at the Gräfenberg array, Germany. Each trace represents a sum of seismograms, from events at different epicentral distances, delayed by a time interval corresponding to the expected arrival of a conversion from a given trial depth. Arrows point to amplitude maxima that occur for trial depths of 400 and 640 km and that are therefore consistent with the origin of *P*-to-*S* conversions from the two major transition zone discontinuities. Reproduced from Kind R and Vinnik LP (1988) The upper-mantle discontinuities underneath the GRF array from *P*-to-*SV* converted phases. *Journal of Geophysics* 62: 138–147.

The method of Zhu and Kanamori (2000); following on Zandt and Ammon (1995) employs a similar approach to more tightly constrain crustal properties beneath a single three-component station, namely, depth of Moho and crustal Poisson's ratio, under the assumption that the latter is constant. This approach is commonly used for reconnaissance work (e.g., Darbyshire et al., 2007; Finotello et al., 2011; Phillips et al., 2012; Wei et al., 2011) and involves stacking of multiple-scattering modes r, s (consistent with the formulation in eqn [31]) along predicted travel-time trajectories for a grid of Moho depths and Poisson's ratios, to recover an

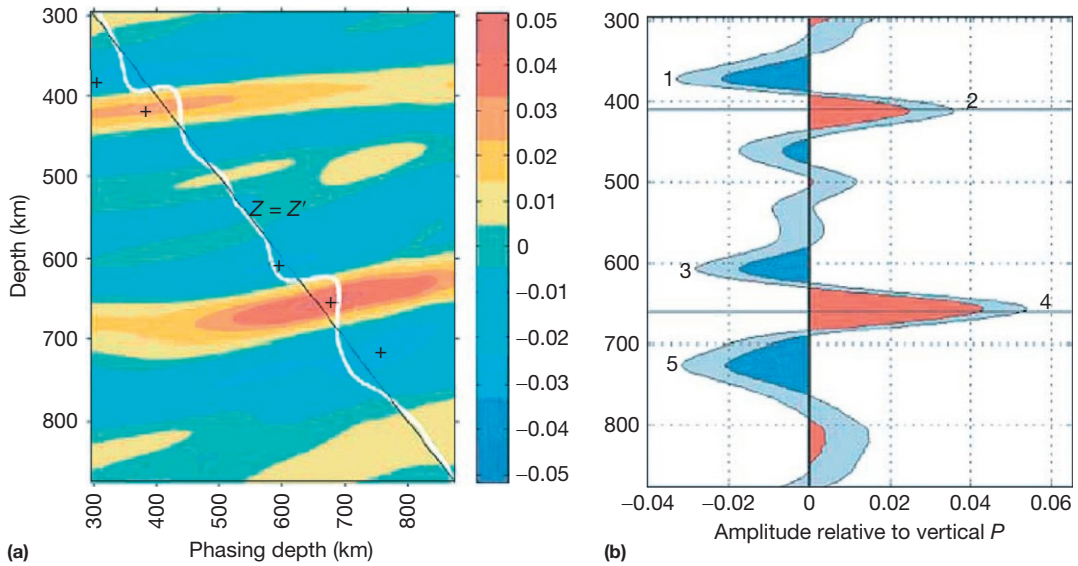

Figure 7 1-D migration (reproduced from Fee D and Dueker K (2004) Mantle transition zone topography and structure beneath the Yellowstone hotspot. *Geophysical Research Letters* 31: L18603. http://dx.doi.org/10.1029/2004GL020636). (a) Left panel shows amplitude map that results from stacking data along move-out curves corresponding to a range of conversion (phasing) depths. The vertical depth axis is proportional to time as mapped through a 1-D velocity model. (b) Right panel plots a slice through the 45° line shown in (a) and accomplishes a 1-D migrated depth profile of 'convertibility' below the Yellowstone hotspot.

optimal model under an assumed *P*-velocity. Extensions include applications to other layered regimes (e.g., subducting oceanic crust (Audet et al., 2009), lower crustal eclogites (Wittlinger et al., 2009), mantle transition zone (Schaeffer and Bostock, 2010), and the base of ice sheets (Wittlinger and Farra, 2012); the retrieval of absolute velocity information (e.g., Bostock and Kumar, 2010; Kumar and Bostock, 2008; Wittlinger et al., 2009); and the extraction of Poisson's ratio without prior knowledge of *P*-velocity (Helffrich and Thompson, 2010)).

Previous empirical studies of anisotropic stratification using scattered teleseismic wave fields can also be related to the linearized, 1-D inverse-scattering solution in eqn [31]. In this case, the Earth's response not only is simply a function of epicentral distance (or, more precisely, the magnitude of horizontal slowness, $\sqrt{p_\alpha p_\alpha}$) but also depends on back azimuth. Various authors (Bostock, 1997, 1998; Farra and Vinnik, 2000; Farra et al., 1991; Kosarev et al., 1984; Levin and Park, 1997, 1998; Vinnik and Montagner, 1996; Wilson et al., 2004) have noted that the back-azimuthal response of a stratified medium exhibiting different classes of anisotropic symmetry and orientation can be represented in simple trigonometric terms. Consequently, several schemes involving stacking with trigonometric weights have been proposed to investigate anisotropic stratigraphy. These schemes can be related to eqn [31] by noting that the linear system, for general Δc and typical teleseismic data sets, will be rank-deficient. It will thus be necessary to solve eqn [31] via a pseudoinverse (e.g., Bank and Bostock, 2003) with singular value decomposition being an obvious and tractable choice. These latter authors noted that only five- to seven-parameter combinations of Δc are likely to be resolvable using teleseismic *P* and that these parameter combinations can be identified with different harmonic orders of response in back azimuth θ, notably 1θ, 2θ, and 3θ. Recovery of Δc through eqn [31] thus amounts once more to a weighted diffraction stack and holds the advantage over more empirical schemes that the full data sensitivity to the elastic stiffness tensor is exploited without having to resort to simplified a priori model representations (e.g., hexagonal symmetry).

Finally, we remark that, in practice, it is difficult to isolate the individual scattering-mode contributions, $\Delta u^{rs}(\mathbf{x}, \omega)$, and in general, we will approximate these quantities by the observed wave field, $\Delta u(\mathbf{x}, \omega)$, for each scattering-mode interaction. The main drawback with this course of action is that we interpret a superposition of several different styles of scattering interaction *r*, *s* as that due to a single one with the result that artificial structures appear in the solution. The most commonplace example is the misinterpretation of the free-surface-reflected, back-scattered waves from shallow interfaces for direct, forward-scattered conversions from deeper interfaces. This shortcoming afflicts both 1-D and multidimensional analyses of teleseismic waves, and we shall comment on a potential remedy in **Section 1.08.6**.

1.08.5 Multidimensional Inversion

There are several approaches to consider in moving from 1-D to multiple dimensions. The first and simplest strategy is to assume that the Earth's structure varies slowly in the horizontal coordinates in which case a 2-D or 3-D profile can be assembled as a cascade of local 1-D models determined from individual, adjacent stations (e.g., Kumar et al., 2005). If stations are sufficiently closely spaced that the (1-D) ray paths of scattered phases intersect below the profile, it becomes advantageous to consider a 2-D model where scattered energy on seismogram is mapped to common conversion points (CCP) assuming a locally horizontal, plane-layer scattering geometry

(e.g., Dueker and Sheehan, 1998; Ferris et al., 2003; Knapmeyer and Harjes, 2000; Kosarev et al., 1999; Niu et al., 2005; Schulte-Pelkum et al., 2005; Simmons and Gurrola, 2000; Zandt et al., 2004). Travel-time and polarity corrections to account for layer dip where structures remain quasiplanar, for example, in subduction zones, provide further improvement in imaging (e.g., Kawakatsu and Watada, 2007; Kawakatsu and Yoshioka, 2011; **Figure 8**). Such CCP stacking techniques are commonly employed because they place less stringent requirements on spatial sampling than formal multidimensional inversion schemes, but of course, their accuracy deteriorates as departures from one-dimensionality or assumed planar structure become more pronounced.

Unlike the strictly 1-D case, the multidimensional inverse problem has not lent itself so readily to treatment using optimization via least squares because of the large increase in model parameters and concomitant rise in computations. It is likely, however, that in the near future, computational tractability will become less of a concern. Indeed, two recent studies (Frederiksen and Revenaugh, 2004; Wilson and Aster, 2005) have explored different least-squares formulations for solving multidimensional receiver function inversions, a trend that is likely to continue. Much of the essential machinery for this task has already been developed for exploration applications; we note, in particular, the work of Tarantola (1984, 1986).

The 1-D, high-frequency, Born-approximate inverse solution described in the previous section can, however, be efficiently extended to multiple dimensions so as to be computationally tractable on standard desktop computers. In this extension, there are no conceptual difficulties in dealing with 2-D versus 3-D problems, although there are practical limitations, in particular, for data from temporary, portable deployments. More specifically, it is difficult at the current time to assemble numbers of instruments sufficient to ensure that the teleseismic wave field is sampled with sufficient areal density (and aperture) to avoid aliasing most of its useful spectrum. Two approaches may be taken to remedy this difficulty. One may seek to interpolate data to a finer spacing over an areal grid followed by 3-D inversion (Neal and Pavlis, 1999, 2001; Poppeliers and Pavlis, 2003a,b) or follow the lead of early exploration practice and adopt a 2-D inverse strategy under the assumption that a dominant geologic strike direction can be identified (Bostock et al., 2001). In the following, we summarize the approach taken by the latter authors, which can be regarded as a 2-D, isotropic extension of the 1-D treatment outlined in **Section 1.08.4.3**.

We begin with the linearized integral equation [18]. In the 1-D case, the invariance of material properties in horizontal coordinates together with the far-field (quasiplanar) nature of the incident-wave field $u_i^0(\mathbf{x}, \omega)$ allowed us to adopt plane-wave expansions for the incident and scattered modes as in

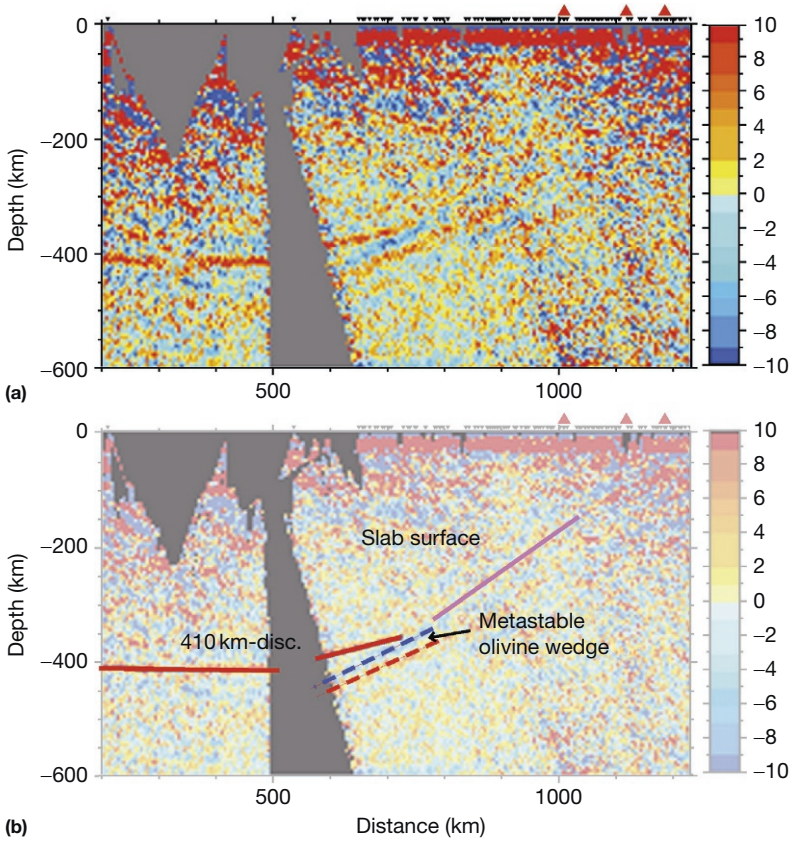

Figure 8 Common conversion point image (a) below southwest Japan with allowance made for assumed nonhorizontal geometry (reproduced from Kawakatsu H and Yoshioka S (2011) Metastable olivine wedge and deep dry cold slab beneath southwest Japan. *Earth and Planetary Science Letters* 303: 1–10). Image in (b) identifies structures associated with subducting Pacific Plate, metastable olivine wedge, and 400 km discontinuity.

eqns [19] and [20]. This choice is effectively equivalent to Fourier transforming over the horizontal plane. Accordingly, for a 2-D inversion where there is only one coordinate of spatial invariance, say, the strike coordinate x_2, we Fourier transform over this coordinate. We thereby assume that, for an incident (e.g., planar) wave field characterized by a single value of slowness p_2 in the strike direction, all resulting scattering interactions will be characterized by this same component of horizontal slowness, and so, we may parameterize the wave fields by this variable. Although not required, it will be computationally and practically expedient to assume that the reference medium is both 1-D and isotropic, so that the reference medium description is reduced from $c^0_{ijkl}(x_1, x_3), \rho^0(x_1, x_3)$ to, for example, $\alpha^0(x_3)$, $\beta^0(x_3)$, $\rho^0(x_3)$. Consequently, we may adopt the same 1-D form for the incident-wave field $u^0_i(\mathbf{x}, \omega)$, that is, eqn [19], whereas for the Green function, we adopt a form that allows for interaction with 2-D (i.e., line) scatterers:

$$G^0_{in}(\mathbf{x}, 0, \omega) = \sum_s \frac{1}{\sqrt{-i\omega}} A^s(\mathbf{x}_\perp, \mathbf{x}'_\perp, p_2) \, e^{i\omega\left[p^s_1 |x_1 - x'_1| - p_2 x_2 + \tau^s(\mathbf{x}_\perp, \mathbf{x}'_\perp)\right]} s^s_i(\mathbf{x}_\perp) s^s_n(\mathbf{x}'_\perp) \quad [32]$$

where, as before, $s = 1, 2, 3$ correspond to *P*, *SV*, and *SH* waves, respectively, and the 2-D amplitude functions A^s are defined, for example, for $s = 1$, as

$$A^s(\mathbf{x}_\perp, \mathbf{x}'_\perp, p_2) = \frac{1}{4\alpha^0(0)} \sqrt{\frac{2}{\pi \rho^0(x_3)\alpha^0(x_3)\rho^0(0)[J^P(\mathbf{x}_\perp, \mathbf{x}'_\perp, p_2)]^2 \sqrt{1 - p_2^2[\alpha^0(0)]^2}}} \quad [33]$$

with a comparable expression holding for the *S*-modes (i.e., $s = 2, 3$). We employ $\mathbf{x}_\perp = (x_1, x_3)$ to represent observation coordinates within the plane of 2-D spatial variations and evaluate source coordinates $\mathbf{x}_\perp{}'$ along the Earth's surface, that is, $\mathbf{x}_\perp{}' = (x_1', 0)$. The travel-time functions $\tau^s(\mathbf{x}_\perp, \mathbf{x}_\perp{}')$ are computed as in eqn [21], but now, we recognize that p^s_1 is no longer constant but depends on $x_1 - x_1'$. A similar consideration also applies in the definition of the unit polarization vectors $s^s_n(\mathbf{x}_\perp)$. The 2-D geometric spreading functions $J^s(\mathbf{x}_\perp, \mathbf{x}_\perp{}', p_2)$ $(= J^P(\mathbf{x}_\perp, \mathbf{x}_\perp{}', p_2)$, for $s = 1$, see, e.g., Hudson, 1980), depend on the divergence of the rays in the x_1, x_3 plane. Note that we have permitted an oblique component of incidence through dependence on x_2, p_2, which bears important practical implications as it will allow us to employ a full range of earthquake sources that need not align with the 2-D model geometry. If forms eqns [19] and [32] are inserted within the isotropic equivalent of eqn [18], we may construct 2-D, high-frequency, single-scattering, forward-modeling equations for various incident-/scattering-mode combinations *r*, *s* of the form

$$\Delta u_n(\mathbf{x}'_\perp, p_2, \omega) = \sum_r \sum_s s^s_n(\mathbf{x}'_\perp) \int d\mathbf{x}_\perp F^{rs}(\mathbf{x}_\perp, \theta) A^r(x_3) A^s(\mathbf{x}_\perp, \mathbf{x}'_\perp, p_2) e^{i\omega\left(\tau^r(x_3) + \tau^s(\mathbf{x}_\perp, \mathbf{x}'_\perp)\right)} \quad [34]$$

The 2-D 'scattering potential,' $F^{rs}(\mathbf{x}_\perp, \theta)$, is derived from contractions of the stiffness tensor (expressed in terms of, e.g., velocities and density) and the local polarization and slowness vectors of the incident and scattered waves. It is expressed as a function of the scattering angle, $\theta = \theta^{rs}(\mathbf{x}_\perp, \mathbf{x}_\perp{}')$, between the slowness vectors of these two wave fields (see Figure 9), and the material property perturbations such that for, for example, forward *P*-to-*S* conversions $(r = 1, s = 2)$

$$F^{rs}(\mathbf{x}_\perp, \theta) = \rho^0 \left[\frac{\Delta\beta}{\beta^0} \left(2\frac{\beta^0}{\alpha^0} \sin 2\theta \right) + \frac{\Delta\rho}{\rho^0} \left(\sin\theta + \frac{\beta^0}{\alpha^0} \sin 2\theta \right) \right] \quad [35]$$

where the dependence of the material property perturbations is, for example, $\Delta\beta = \Delta\beta(\mathbf{x}_\perp)$. Similar relations can be written for other combinations of scattering interaction *r*, *s* (see, e.g., Bostock et al., 2001).

The inverse problem can be tackled by applying an inverse Fourier transform to eqn [34], that is,

$$\Delta u_n(\mathbf{x}'_\perp, p_2, t) = \frac{1}{2\pi} \sum_r \sum_s s^s_n(\mathbf{x}'_\perp) \int d\mathbf{x}_\perp F^{rs}(\mathbf{x}_\perp, \theta) A^r(x_3) A^s(\mathbf{x}_\perp, \mathbf{x}'_\perp, p_2) \delta\left(t - \tau^r(x_3) - \tau^s(\mathbf{x}_\perp, \mathbf{x}'_\perp)\right) \quad [36]$$

and noting that the result bears a close resemblance to the definition of the 2-D Radon transform $F(\mathbf{n}, t)$ of a function $f(\mathbf{x}_\perp)$ (Deans, 1983; Miller et al., 1987)

$$F(\mathbf{n}, t) = \int d\mathbf{x}_\perp f(\mathbf{x}_\perp) \delta(t - \mathbf{n} \cdot \mathbf{x}_\perp) \quad [37]$$

where $\mathbf{n}$ is a unit vector in the 2-D plane defined by $\mathbf{x}_\perp$, especially if we restrict attention to a single-scattering mode $\Delta u^{rs}_n(\mathbf{x}_\perp{}', p_2, t)$. Here, we identify the scattered field $\Delta u_n(\mathbf{x}_\perp{}', p_2, t)$ with $F(\mathbf{n}, t)$ and the scattering potential $F^{rs}(\mathbf{x}_\perp, \theta)$ with $f(\mathbf{x}_\perp)$. The primary differences between the two equations are that the integrand in eqn [36] contains additional factors in the form $A^r(x_3)A^s(\mathbf{x}_\perp, \mathbf{x}_\perp{}', p_2)$ and that the arguments of the delta-function are not straight lines but, rather, isochronal curves along which the sum $\tau^r(x_3) + \tau^s(\mathbf{x}_\perp, \mathbf{x}_\perp{}')$ is constant. The correspondence can be made closer still by recognizing that the product of geometric amplitudes will, in general, be slowly varying and that, in keeping with the asymptotic forms adopted in eqns [19] and [32], the isochronal curves can be approximated

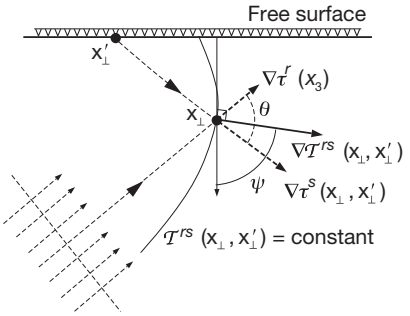

Figure 9 Geometric quantities relevant to high-frequency, inverse scattering of teleseismic wave fields for 2-D structure. The vectors $\nabla\tau_r$ and $\nabla\tau^s$ are the slowness vectors for the incident and scattered waves, respectively, whereas θ is the 'scattering' angle between them. The total slowness vector $\nabla T^{rs} = \nabla\tau^r + \nabla\tau^s$, characterized by angle ψ, plays an important role in controlling spatial resolution within the generalized Radon transform.

locally as planar. We may then draw upon the formal inverse Radon transform (Beylkin, 1985; Beylkin and Burridge, 1990; Deans, 1983; Miller et al., 1987):

$$\begin{aligned} f(\mathbf{x}'_\perp) &= -\frac{1}{4\pi}\int d\mathbf{n}\mathcal{H}\left\{\frac{\partial}{\partial t}F(\mathbf{n},t)\right\}\Big|_{t=\mathbf{n}\cdot\mathbf{x}'} \\ &= -\frac{1}{4\pi}\int d\mathbf{n}\int d\mathbf{x}_\perp f(\mathbf{x})\mathcal{H}\{\delta'(\mathbf{n}\cdot(\mathbf{x}'_\perp-\mathbf{x}_\perp))\} \\ &= -\frac{1}{4\pi}\int d\psi\int d\mathbf{x}_\perp f(\mathbf{x})\mathcal{H}\{\delta'(\mathbf{n}\cdot(\mathbf{x}'_\perp-\mathbf{x}_\perp))\} \end{aligned} \quad [38]$$

where ψ is the angle of $\mathbf{n}$, $\mathcal{H}\{\ \}$ denotes Hilbert transform, and $\delta'(x)$ is the derivative of $\delta(x)$, to devise a formal back-projection operator for the recovery of $F^{rs}(\mathbf{x}_\perp, \theta)$, namely,

$$F^{rs}(\mathbf{x}_\perp,\theta)\approx\frac{1}{4\pi}\int d\psi\frac{|\nabla\mathcal{T}^{rs}|^2}{\sum_n\mathcal{A}_n^{rs}\mathcal{A}_n^{rs}}\sum_n\mathcal{A}_n^{rs}v_n^{rs}(\mathbf{x}'_\perp,p_2,t=\mathcal{T}^{rs}(\mathbf{x}_\perp,\mathbf{x}'_\perp)) \quad [39]$$

Here, we have, for brevity, defined the composite quantities

$$\begin{aligned} \mathcal{T}^{rs}(\mathbf{x}_\perp,\mathbf{x}'_\perp) &= \tau^r(x_3)+\tau^s(\mathbf{x}_\perp,\mathbf{x}'_\perp)\quad \mathcal{A}_n^{rs} \\ &= A^r(x_3)A^s(\mathbf{x}_\perp,\mathbf{x}'_\perp,p_2)s_n^s(\mathbf{x}'_\perp) \end{aligned} \quad [40]$$

and have identified $\nabla\mathcal{T}^{rs}(\mathbf{x}_\perp,\mathbf{x}'_\perp)/|\nabla\mathcal{T}^{rs}(\mathbf{x}_\perp,\mathbf{x}'_\perp)|$ with $\mathbf{n}$. Thus, the integration variable ψ is the angle of $\nabla\mathcal{T}^{rs}(\mathbf{x}_\perp,\mathbf{x}'_\perp)$, that is,

$$\psi = a\tan\frac{\partial_3\mathcal{T}^{rs}(\mathbf{x}_\perp,\mathbf{x}'_\perp)}{\partial_1\mathcal{T}^{rs}(\mathbf{x}_\perp,\mathbf{x}'_\perp)} \quad [41]$$

and the scattered-wave field is represented through the time series

$$v_n^{rs}(\mathbf{x}'_\perp,p_2,t)=\mathcal{F}^{-1}\left\{\Delta u_n^{rs}(\mathbf{x}'_\perp,p_2,\omega)\frac{-\mathrm{isgn}(\omega)}{\sqrt{-\mathrm{i}\omega}}\right\} \quad [42]$$

The geometric relationships among the various quantities defined in the preceding text are illustrated in Figure 9. As for the 1-D case, we have assumed that we are able to separate the recorded wave field into its individual scattering mode (r, s) contributions $\Delta u_n^{rs}(\mathbf{x}'_\perp,p_2,\omega)$. From eqn [39], we note that the scattering potential can be approximately recovered as a weighted diffraction stack of filtered data $v_n^{rs}(\mathbf{x}'_\perp,p_2,t)$ over the isochronal travel-time curves. The form of filter $-\mathrm{isgn}(\omega)/\sqrt{-\mathrm{i}\omega}$ applied to the scattered-wave field data in eqn [42] stems from the plane-wave/2-D geometry and ensures that, for example, a step function perturbation is recovered in the case of a discontinuity in material properties. Recovery of $F^{rs}(\mathbf{x}_\perp, \theta)$ is, of course, an intermediate result from which we wish to resolve the individual material property perturbations $\Delta\mathsf{c}(\mathbf{x}_\perp)=[\Delta\alpha/\alpha\ \Delta\beta/\beta^0,\Delta\rho/\rho^0]^{\mathrm{T}}$. Exploiting the linear relation in eqn [35], this task is readily accomplished by assembling measurements of $F^{rs}(\mathbf{x}_\perp, \theta)$ for all available scattering interactions at a given model point within a column vector $\mathsf{f}(\mathbf{x}_\perp, \theta)$ and solving the trivial 3×3 system

$$\mathsf{f}(\mathbf{x}_\perp,\theta)=\mathsf{W}(\theta)\Delta\mathsf{c}(\mathbf{x}_\perp) \quad [43]$$

where, as in eqn [31], the row vectors constituting the matrix W represent radiation patterns for the various scattering-mode combinations r, s.

The main computational effort in this approach is expended in computing the weighted diffraction stack in eqn [39]. The appearance of $|\nabla\mathcal{T}^{rs}|^2$ as a weight in that equation corresponds to the factor $[p_3^s(x_3)+p_3^r(x_3)]$ in eqn [29] for the 1-D case. It represents the sensitivity of travel time to scatterer position and, as a product with frequency ω, governs the scale of resolution. For example, back-scattered modes, for which $|\nabla\mathcal{T}^{rs}|^2$ is in general large, possess better resolving capability than forward-scattered waves since a given change in scatterer position has a larger effect on timing of the scattered arrival (see, e.g., Rondenay et al., 2005). The direction of $\nabla\mathcal{T}^{rs}$, as quantified by dip angle ψ, controls the degree to which different structural dips can be resolved at a given model point. In contrast, material property resolution depends on the range of scattering angle θ afforded by the data and the different modal scattering sensitivities as represented through the radiation patterns (e.g., eqn [35]). Material property resolution may be analyzed through eigenvector decomposition of the matrix $\mathsf{W}^{\mathrm{T}}\mathsf{W}$ (e.g., Bostock and Rondenay, 1999; Forgues and Lambaré, 1992). Since teleseismic data are characterized by a limited range of θ, the simultaneous inversion of different scattering modes r, s affords the best prospects for discrimination of material properties.

In addition to the plane-wave, isotropic, 2-D oblique incidence geometry described in the preceding text, the generalized Radon transform treatment of the inverse-scattering problem has also been developed with point sources for acoustic waves (Miller et al., 1987), elastic waves in 3-D isotropic (Beylkin and Burridge, 1990), and anisotropic (Burridge et al., 1998) media. Like the 1-D case, these algorithms can be recast to recover singular functions of discontinuity surfaces (vs. Born-approximate perturbations), thereby accomplishing Kirchhoff-approximate inversion (Beylkin and Burridge, 1990; Bleistein, 1987; Bostock, 2002; de Hoop and Bleistein, 1997). In the teleseismic context, generalized Radon transform inversions have been strictly applied in a limited number of studies on subduction zones (Nicholson et al., 2005; Rondenay et al., 2001), Precambrian mobile belts (Poppeliers and Pavlis, 2003b; Rondenay et al., 2005), and the mantle transition zone (Liu and Pavlis, 2013).

If the weights in eqn [39] are ignored and otherwise normalized seismograms are simply stacked along move-out curves $t=\mathcal{T}^{rs}(\mathbf{x}_\perp,\mathbf{x}'_\perp)$, the formal parameter inversion is reduced to migration. Variants include migration via the Kirchhoff scattering integral (French, 1974; Schneider, 1978), which has been applied to the receiver (versus Green) functions with the aim of imaging (rather than inverting for) structure (e.g., Kind et al., 2002; Levander et al., 2005; Niu et al., 2005; Revenaugh, 1995; Sheehan et al., 2000; Wilson et al., 2005). All of the approaches mentioned in the preceding text can be classified as 'prestack' in that they deal directly with the individual Green function or receiver function data. Ryberg and Weber (2000) had described a teleseismic analogy to active source 'poststack' migration. This procedure involves normalizing teleseismic data to vertical incidence and stacking to produce a reduced data set, which can be readily processed using seismic reflection algorithms. Chen et al. (2005a) had built upon this poststack framework to develop a wave equation migration method that back propagates CCP stacked receiver functions into structural models and that has been applied to image the Japanese subduction zones (Chen et al., 2005b).

1.08.6 Beyond the Born Approximation

As argued in Sections 1.08.4 and 1.08.5, the tools of inverse scattering provide a framework for understanding many of the empirical approaches developed and employed over the past four decades to analyze scattered teleseismic wave fields in terms of lithospheric and upper mantle structure. In addition, the application of these techniques in recent years to multichannel data sets collected over, for example, plate boundaries, has led to new insights into the structures and dynamics of these complex regions that would have been difficult to achieve through a less complete analysis. As access to large numbers of instruments improves, it is possible that sampling of teleseismic wave fields may begin to approach that in exploration practice, allowing and prompting still more ambitious and complete treatments. Clearly, one approach is to employ fully numerical solutions (see Chapter 1.07) to model receiver-side scattering of teleseismic waves, and a number of authors have begun to investigate this route. Roecker et al. (2010) presented a spectral, finite-difference scheme to model plane-wave scattering in 2-D and demonstrated its incorporation within a waveform inversion using synthetic data. Monteiller et al. (2013) coupled 1-D global simulations with the spectral element method on a 3-D regional domain to compare numerical simulations with receiver function observations from the Pyrenees. As computational resources improve, regional waveform tomography employing, for example, adjoint methods (Tromp et al., 2005) will eventually become practical on a routine basis. An alternative approach to fully numerical treatments of the forward problem involves higher-order, nonlinear inverse scattering. We shall conclude this chapter by sketching out such a formulation, based on recent theoretical developments in reflection seismology, that would permit a nonlinear treatment of inverse scattering for teleseismic wave fields.

1.08.6.1 Shortcomings of the Born Approximation

Perhaps the most serious shortcomings of the methodologies heretofore described in Sections 1.08.4 and 1.08.5 lie in the linearization or 'Born approximation' made in eqn [18]. There are several negative consequences that follow from the Born approximation. First, as is widely appreciated, the reference medium must be sufficiently close to the real Earth to ensure that the phase of the wave fields is accurately represented. If not, images may become seriously distorted, usually through blurring, leading to reduced resolution and, worse, misinterpretation (see, e.g., Yilmaz, 2001). As researchers attempt to exploit higher frequencies in the teleseismic wave field (up to 10 Hz for teleseismic P generated by deep earthquakes), there will be increased need to improve reference velocity estimates.

A second drawback of the Born approximation is its failure to account for higher-order scattering in the form of multiple reflection/conversion. In reflection seismology, the most serious manifestation of multiple scattering is present in the form of free-surface multiples, which are order $O(\varepsilon^2)$ in amplitude. In the teleseismic context, the free-surface multiples are still larger ($O(\varepsilon)$) due to the transmission geometry as explained in Section 1.08.3.2 and have presented that a major impediment to lithospheric imaging due to the arrival of multiple signals from the Moho during the same time interval that directs conversions from the shallow mantle (say, 100–250 km depth) would be expected. Using formal inversion approaches, the multiples can be accommodated to varying degrees through the simultaneous inclusion of both direct and free-surface-reflected waves within the incident-wave field $u_i^0(\mathbf{x},\omega)$ as in eqn [19]. If, however, as we have advocated in coming to solutions for eqns [31] and [43], the approximation $\Delta u^{rs}(\mathbf{x},\ \omega)\approx\Delta u(\mathbf{x},\ \omega)$ is made for each mode combination r,s, this accommodation is incomplete and artificial structures resulting from misidentification of one scattering mode for another will occur (e.g., Shragge et al., 2001). Most studies based on diffraction stacking have implicitly adopted the $\Delta u^{rs}(\mathbf{x},\ \omega)\approx\Delta u(\mathbf{x},\ \omega)$ assumption for computational expedience. The advantage, as exemplified in the generalized Radon transform approach of the previous section (cf. eqn [43]), is that the matrix $\mathbf{W}^{\mathrm{T}}\mathbf{W}$ is block-diagonal in structure leading to solution of a small (rank equivalent to number of material parameters considered) linear system for each spatial location within the model. If we choose, instead, to include both forward- and back-scattered (multiples) waves simultaneously and avoid the latter approximation, the Hessian becomes block-band-diagonal and computational expense increases dramatically. This latter approach is feasible using sparse matrix techniques, especially in 2-D, but to our knowledge has yet to be applied.

Notwithstanding the viability of simultaneously including the direct-wave and free-surface reflections within the definition of $u_i^0(\mathbf{x},\omega)$, there is reason to consider a formal decomposition of the observed field, $\Delta u_i(\mathbf{x},\ \omega)$, into individual scattering modes, $\Delta u_i^{rs}(\mathbf{x},\omega)$. Motivation for this line of thought stems from recent progress in reflection seismology by Weglein and coworkers (Matson, 1997; Weglein et al., 1997, 2003) and Wapenaar et al. (2004). Weglein's group has demonstrated that a sequential, task-driven approach, which includes isolation and removal of free-surface reflections, results in a better-posed, nonlinear treatment of the inverse-scattering problem within the seismic reflection context. Moreover, Wapenaar et al. had developed a theoretical framework based on correlational reciprocity (Bojarski, 1983) that allows the transformation of transmission (earthquake) data into reflection data, thereby effectively accomplishing the scattering-mode decomposition and allowing, in principle, the inversion of transmission data with reflection algorithms. In the following two subsections, we shall outline these procedures in more detail.

1.08.6.2 The Inverse-Scattering Series

Weglein and coworkers adopt operator-series representations to address both the forward- and inverse-scattering problems. The operator notation is convenient because it is largely independent of geometry and model type and affords a succinct summary of the main arguments. For further detail and background, the reader is referred to Weglein et al. (2003).

We begin with the operator form of the Lippman–Schwinger equation [15]:

$$\mathcal{U}=\mathcal{G}-\mathcal{G}^0=\mathcal{G}^0\mathcal{V}\mathcal{G} \qquad [44]$$

where we define $\mathcal{U}$ to be the data generation operator and $\mathcal{G}$ and $\mathcal{G}^0$ are the Green operators for the true Earth and reference

medium, respectively, that act on a given force distribution $f_i(\mathbf{x}, \omega)$ to produce a vector wave field. For example, in the teleseismic context, the scattered-wave field (cf. eqn [15]) can be written

$$\begin{aligned}\Delta u_i(\mathbf{x}, \omega) &= \mathcal{U}\{f_i\} = \mathcal{G}\{f_i\} - \mathcal{G}^0\{f_i\} \\ &= \int d\mathbf{y} \left[G_{ij}(\mathbf{x}, \mathbf{y}, \omega) - G^0_{ij}(\mathbf{x}, \mathbf{y}, \omega)\right] f_j(\mathbf{y}, \omega) \end{aligned} \quad [45]$$

where, as before, $G^0_{ij}(\mathbf{x}, \mathbf{y}, \omega)$ is the Green function for the reference medium (e.g., eqns [20] and [32] for laterally homogeneous reference media with 1-D and 2-D source geometries, respectively, in the high-frequency approximation); $G_{ij}(\mathbf{x}, \mathbf{y}, \omega)$ is the unknown Green function of the true Earth; and f_i then represents the force distribution that gives rise to upgoing, planar *P*- or *S*-wave fields in the absence of heterogeneity. The differential operator $\mathcal{V}$ includes the action of the material property perturbations and can be written as

$$\mathcal{V} = \partial_j \Delta c_{ijkl} \partial_k + \Delta \rho \omega^2 \delta_{il} \quad [46]$$

Note that eqn [44] implies $\mathcal{G} = \mathcal{G}^0 + \mathcal{G}^0 \mathcal{V} \mathcal{G}$ and so by successive insertion, we recover the forward-scattering series:

$$\mathcal{U} = \mathcal{G}^0 \mathcal{V} \mathcal{G}^0 + \mathcal{G}^0 \mathcal{V} \mathcal{G}^0 \mathcal{V} \mathcal{G}^0 + \mathcal{G}^0 \mathcal{V} \mathcal{G}^0 \mathcal{V} \mathcal{G}^0 \mathcal{V} \mathcal{G}^0 + \cdots \quad [47]$$

From the RHS of eqn [47], we note that $\mathcal{G}$ is not required to solve the forward problem; that is, knowledge of $\mathcal{G}^0\{f_i\}$ is sufficient to recover $\mathcal{U}\{f_i\}$, if $\mathcal{V}$ is given.

The goal of the inverse problem is to isolate the scattering operator $\mathcal{V}$ (and from it Δc_{ijkl}, $\Delta\rho$) from the data generation operator $\mathcal{U}$ as represented by the data $\Delta u_i(\mathbf{x}, \omega)$ in eqn [45] using, again, knowledge of $\mathcal{G}^0$ alone. The inverse-scattering series solution represents $\mathcal{V}$ in series form as

$$\mathcal{V} = \mathcal{V}_1 + \mathcal{V}_2 + \mathcal{V}_3 + \mathcal{V}_4 + \cdots \quad [48]$$

where the individual terms are organized in orders of the data $\mathcal{U}$. Inserting eqn [48] within [47] allows one to solve for these terms explicitly. For example, the first three equations are

$$\begin{aligned}\mathcal{U} &= \mathcal{G}^0 \mathcal{V}_1 \mathcal{G}^0 \\ 0 &= \mathcal{G}^0 \mathcal{V}_2 \mathcal{G}^0 + \mathcal{G}^0 \mathcal{V}_1 \mathcal{G}^0 \mathcal{V}_1 \mathcal{G}^0 \\ 0 &= \mathcal{G}^0 \mathcal{V}_3 \mathcal{G}^0 + \mathcal{G}^0 \mathcal{V}_2 \mathcal{G}^0 \mathcal{V}_1 \mathcal{G}^0 + \mathcal{G}^0 \mathcal{V}_1 \mathcal{G}^0 \mathcal{V}_2 \mathcal{G}^0 + \mathcal{G}^0 \mathcal{V}_1 \mathcal{G}^0 \mathcal{V}_1 \mathcal{G}^0 \mathcal{V}_1 \mathcal{G}^0 \end{aligned} \quad [49]$$

where we have used the fact that $\mathcal{U}$ is, by definition, first order in itself. In principle, these equations can be solved sequentially, first for $\mathcal{V}_1$, then for $\mathcal{V}_2$, and so on. Note that $\mathcal{V}_1$ is just the Born-approximate solution to the inverse problem, which may or may not accurately represent the true Earth (i.e., $\mathcal{V}$) depending on the proximity of $\mathcal{G}^0$ to $\mathcal{G}$.

Blind application of the series solution to raw data is marred by poor convergence properties and thus does not afford a practical solution to the inverse-scattering problem. Rather, Weglein et al. advocated that a 'subseries' approach be taken whereby sets of terms in the inverse series are identified with specific tasks and a sequential application is performed. This sequence of tasks is, namely, (i) removal of free-surface multiples, (ii) removal of internal multiples, (iii) imaging of scatterer location, and (iv) material property recovery. It has been noted that tasks (i) and (ii) can be effectively performed with absolutely no knowledge of the underlying velocity structure and with excellent convergence properties. Tasks (iii) and (iv) are the topic of current research and early results show promise (Weglein et al., 2002).

The relevance of the latter work to the teleseismic problem is twofold. First, it indicates that a sequential treatment that proceeds from multiple removal through material property inversion is likely to be better-posed than simultaneous solution. Second, as we sketch out in the succeeding text, it is possible, at least in principle, to transform the teleseismic transmission problem directly into a reflection problem such that the inverse-scattering series, as developed for exploration purposes, is then directly applicable.

1.08.6.3 Transmission to Reflection

Perhaps the most direct way of isolating individual scattering modes $\Delta u_i^{ts}(\mathbf{x}, \omega)$ is to consider reformulating the transmission problem as a reflection problem. Motivation for this concept stems from early work of Claerbout (1968) who demonstrated a relationship between the transmission response of a layered acoustic half-space and its reflection response. For precritical, energy flux-normalized elastic waves in 1-D media, this relation can be written

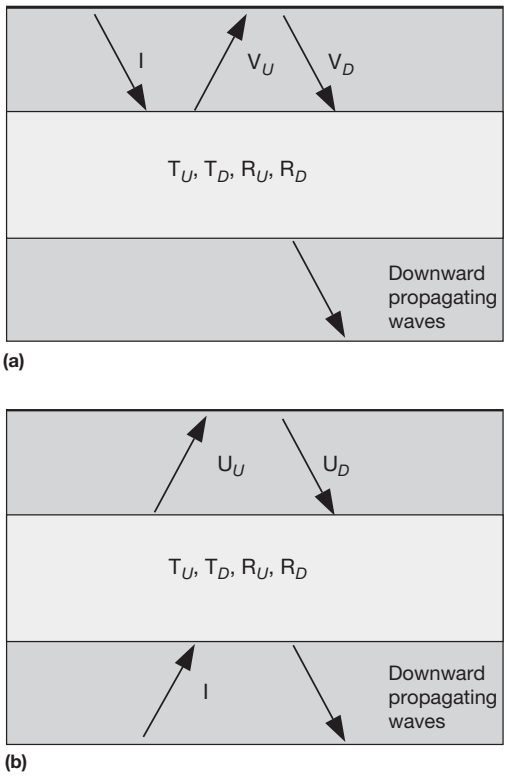

Figure 10 Geometric definition of quantities relevant to the transformation of transmission wave fields to reflection wave fields. (a) Reflection experiment: An incident-wave field (I) interacts with stratification from the preceding text to produce an upgoing wave field V_U and a downgoing wave field V_D at the Earth's free surface. (b) Transmission experiment: In this case, direct wave (I) is incident on stratification from below and produces upgoing (U_U) and downgoing (U_D) wave fields at the free surface.

$$\mathbf{U}^{*}\mathbf{U}^{\mathrm{T}} = \mathbf{I} + \mathbf{R}\mathbf{V} + \mathbf{V}^{\mathrm{H}}\mathbf{R}^{\mathrm{H}} \qquad [50]$$

where $\mathbf{U} = \mathbf{U}(\omega, \mathbf{p}_{\perp})$ is the 3×3 matrix of eqn [8] containing the transmission response for different modes incident upon the base of a stratified half-space bounded in the preceding text by free surface, $\mathbf{V} = \mathbf{V}(\omega, \mathbf{p}_{\perp})$ represents the corresponding reflection response for the same medium to different modes incident from earlier, $\tilde{\mathbf{R}} = \tilde{\mathbf{R}}(\mathbf{p}_{\perp})$ is the free-surface reflection matrix, I is the identity matrix, and $^{\mathrm{H}}$ denotes conjugate transpose. The two geometric configurations are illustrated in **Figure 10**.

Recall that complex conjugation in the frequency domain is equivalent to time reversal and that the inverse Fourier transforms of the elements of U and V are causal functions. Accordingly, each element on the left-hand side of eqn [50] represents, in the time domain, a sum of cross correlations and equates to the sum of a causal function $\left(\mathcal{F}^{-1}\left\{\tilde{\mathbf{R}}\mathbf{V}\right\}\right)$, an acausal function $\left(\mathcal{F}^{-1}\left\{\mathbf{V}^{\mathrm{H}}\tilde{\mathbf{R}}^{\mathrm{H}}\right\}\right)$ and, for diagonal elements, an impulse $\left(\mathcal{F}^{-1}\{\mathbf{I}\}\right)$ at zero lag. The time-domain reflection response $\mathcal{F}^{-1}\{\mathbf{V}\}$ can therefore be recovered by applying $\tilde{\mathbf{R}}^{-1}$ to $\mathcal{F}^{-1}\{\mathbf{U}^{*}\mathbf{U}^{\mathrm{T}}\}$ upon zeroing negative lags where, as in eqn [2], we have assumed that the near-surface material properties (and hence $\tilde{\mathbf{R}}$) are known. Since the individual elements of $\mathcal{F}^{-1}\{\mathbf{V}\}$ represent the reflection response of the stratified half-space to a separate incident mode, an isolation of different, first-order ($O(\varepsilon)$) modal interactions to individual components has therefore been achieved. **Figure 11** shows the result of this procedure applied to data from station HYB by Kumar and Bostock (2006) who outline a practical recipe for its implementation.

Note that the effect of the free surface is still included within V in as far as $O(\varepsilon^2)$ and higher-order, free-surface-related multiples are contained therein. The first step of the inverse-scattering series scheme involves removing these multiples. For 1-D, we accomplish this task by writing

$$\mathbf{V} = \mathbf{R}_D\left(\mathbf{I} - \tilde{\mathbf{R}}\mathbf{R}_D\right)^{-1} \qquad [51]$$

where we have, once more, employed the notation of Kennett (1983) and used $\mathbf{R}_D$ to denote the reflection matrix for the stratification alone (no free surface included). Reorganizing and solving for $\mathbf{R}_D$ using successive insertion leads to the series solution:

$$\mathbf{R}_D = \mathbf{V} - \mathbf{V}\tilde{\mathbf{R}}\mathbf{V} + \mathbf{V}\tilde{\mathbf{R}}\mathbf{V}\tilde{\mathbf{R}}\mathbf{V} - \mathbf{V}\tilde{\mathbf{R}}\mathbf{V}\tilde{\mathbf{R}}\mathbf{V}\tilde{\mathbf{R}}\mathbf{V} + \cdots \qquad [52]$$

Subsequent steps, including multiple elimination, spatial imaging, and material property recovery, are more involved, and the reader is referred to Weglein et al. (2003) for details and discussion.

The theory describing extension of the transmission-to-reflection transformation to multiple dimensions has recently been developed by Wapenaar et al. (2004) by exploiting correlational and convolutional reciprocity. Accordingly, the 3-D extension to eqn [50] expressed in the spatial (vs. slowness) domain becomes

$$\int_{Z} \mathrm{d}\mathbf{x}\,\mathbf{U}^{*}\left(\mathbf{x}'_A, \mathbf{x}, \omega\right)\mathbf{U}^{\mathrm{T}}\left(\mathbf{x}'_B, \mathbf{x}, \omega\right) = \mathbf{I}\delta\left(\mathbf{x}'_A - \mathbf{x}'_B\right) + \tilde{\mathbf{R}}\mathbf{V}\left(\mathbf{x}'_A, \mathbf{x}'_B, \omega\right) + \mathbf{V}^{\mathrm{H}}\left(\mathbf{x}'_A, \mathbf{x}'_B, \omega\right)\tilde{\mathbf{R}}^{\mathrm{H}} \qquad [53]$$

where, as before, the primed coordinates are located at the free surface, the surface integral over horizontal coordinate $\mathbf{x}$ is

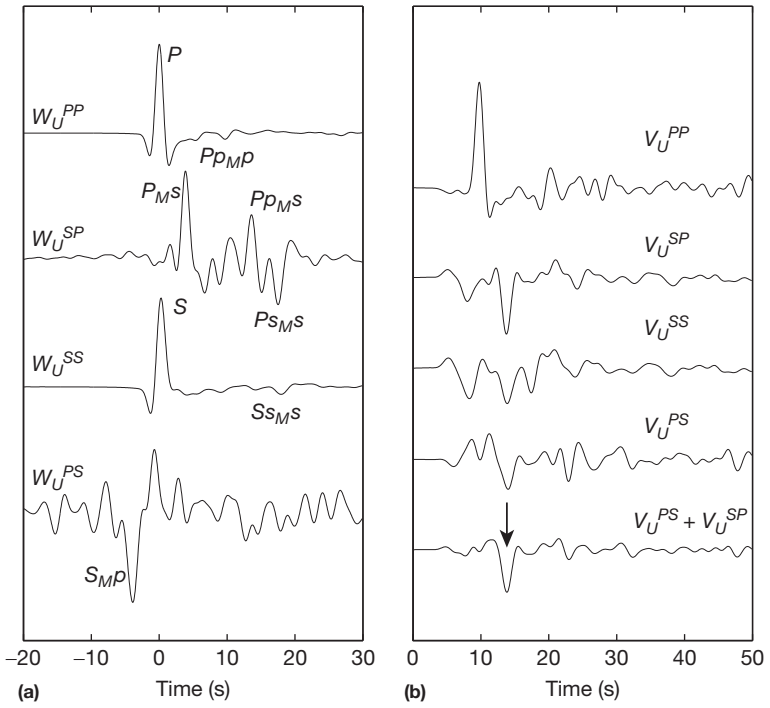

Figure 11 Transmission to reflection transformation of data from HYB (reproduced from Kumar MR and Bostock MG (2006) Transmission to reflection transformation of teleseismic wavefields. *Journal of Geophysical Research* 111: B08306). (a) Input transmission data. Components W_U^{PP} and W_U^{SP} were computed from teleseismic *P* data shown in **Figure 5** over the slowness range 0.04–0.0575 s km^{-1}, whereas components W_U^{PS} and W_U^{SS} were computed from *SKS* recordings over the same range. (b) Transformed reflection response. Note that bottom trace is computed as sum of $V_U^{PS} + V_U^{SP}$ since these two traces should, by reciprocity, be equivalent. Arrow indicates the reflection–conversion from the continental Moho.

evaluated at some depth Z below the heterogeneity, and the dependencies indicate that, for example, $\mathbf{V}(\mathbf{x}_A', \mathbf{x}_B', \omega)$ is the upgoing wave field recorded at surface location $\mathbf{x}_A'$ due to a source at surface location $\mathbf{x}_B'$, at frequency ω. Likewise, the multidimensional equivalent of eqn [51] can be written as

$$\mathbf{V}(\mathbf{x}_A', \mathbf{x}_B', \omega) = \mathbf{R}_D(\mathbf{x}_A', \mathbf{x}_B', \omega) + \int d\mathbf{x}' \mathbf{R}_D(\mathbf{x}_A', \mathbf{x}', \omega) \widetilde{\mathbf{R}} \mathbf{V}(\mathbf{x}', \mathbf{x}_B', \omega) \quad [54]$$

The extension to multiple dimensions thus places greater demands on data by requiring the evaluation of surface integrals within certain depth ranges. It remains to be seen whether these demands can be accommodated through data interpolation/extrapolation in the teleseismic context where seismicity is sparse and irregularly distributed.

1.08.7 Conclusions

Over the past few decades, scattered teleseismic body waves have contributed greatly to our understanding of crust and mantle structure (see, e.g., **Chapters 1.16**, **1.21** and **1.24**). They possess higher resolving capability for small-scale structure than other elements of the global seismic wave train and do not suffer from the shallow depth sampling that limits active source seismic surveys. In this chapter, we have provided an overview of methodologies used to extract receiver-side structural information from the scattered teleseismic wave fields. These methodologies address two fundamental issues: (1) the isolation of structural signal from earthquake source signature and (2) the translation of structural signals into Earth models. The identification, in early practice, of source-free transfer functions formed by simple ratios of vector component waveforms has gradually given way in more recent work to better approximations to the true Earth 'Green function,' thereby extending sensitivity to the Earth's material parameters. In a like manner, the processing of these structural signals using empirical delay-and-sum approaches has progressed in the last few years to formal inversion where quantitative material property separation is, at least in principle, possible. These technological advances have brought analysis of scattered teleseismic waveforms in line with modern reflection seismic signal processing. In fact, as we have attempted to illustrate in the previous section, it is now possible to contemplate unified reflection/transmission approaches to the inverse-scattering problem. An important future challenge in application to global seismology will be to overcome the sparse sampling imposed by earthquake source distributions and current inventories of instrumentation.

References

Aki K and Richards PG (2002) *Quantitative Seismology*. Sausalito, CA: University Science Books.

Ammon CJ (1991) The isolation of receiver effects from teleseismic *P* waveforms. *Bulletin of the Seismological Society of America* 81: 2504–2510.

Ammon CJ, Randall GE, and Zandt G (1990) On the nonuniqueness of receiver function inversions. *Journal of Geophysical Research* 95: 15303–15318.

Amundsen L and Reitan A (1995) Decomposition of multicomponent sea-floor data into upgoing and downgoing *P*- and *S*-waves. *Geophysics* 60: 563–572.

Andrews DJ (1986) Objective determination of source parameters and similarity of earthquakes of different size. In: Das S, Boatwright J, and Scholz CH (eds.). *Earthquake Source Mechanics*, vol. 37, pp. 259–267. Washington, DC: American Geophysical Union.

Asencio E, Knapp JH, Owens TJ, and Helffrich G (2003) Mapping fine-scale heterogeneities within the continental mantle lithosphere beneath Scotland: Combining active- and passive-source seismology. *Geology* 31: 477–480.

Audet P, Bostock MG, Christensen NI, and Peacock SM (2009) Seismic evidence for overpressured subducted oceanic crust and megathrust fault sealing. *Nature* 457: 76–78.

Baag CE and Langston CA (1985) Shear-coupled PL. *Geophysical Journal of the Royal Astronomical Society* 80: 363–385.

Baig AM, Bostock MG, and Mercier J-P (2005) Spectral reconstruction of teleseismic *P* Green's Functions. *Journal of Geophysical Research* 110: B08306. http://dx.doi.org/10.1029/2003JB003625.

Bank C-G and Bostock M (2003) Linearized inverse scattering of teleseismic waves for anisotropic crust and mantle structure: 2. Numerical examples and application to data from Canadian stations. *Journal of Geophysical Research* 108. http://dx.doi.org/10.1029/2002JB001951.

Båth M and Stefánson R (1966) *S-P* conversion at the base of the crust. *Annals of Geophysics* 19: 119–130.

Baumgardt DR and Alexander SS (1984) Structure of the mantle beneath Montana Lasa from analysis of long-period, mode-converted phases. *Bulletin of the Seismological Society of America* 74: 1683–1703.

Beylkin G (1985) Imaging of discontinuities in the inverse scattering problems by inversion of causal generalized Radon transform. *Journal of Mathematical Physics* 26: 99–108.

Beylkin G and Burridge R (1990) Linearized inverse scattering problems in acoustics and elasticity. *Wave Motion* 11: 15–52.

Bleistein N (1987) On the imaging of reflectors in the earth. *Geophysics* 52: 931–942.

Bock G (1991) Long-period *S* to *P* converted waves and the onset of partial melting beneath Oahu, Hawaii. *Geophysical Research Letters* 18: 869–872.

Bock G (1994) Multiples as precursors to *S*, *SKS* and *ScS*. *Geophysical Journal International* 119: 421–427.

Bojarski NN (1983) Generalized reaction principles and reciprocity theorems for the wave equations, and the relationship between the time-advanced and time-retarded fields. *Journal of the Acoustical Society of America* 74: 281–285.

Bostock MG (1996) *Ps* conversions from the upper mantle transition zone beneath the Canadian landmass. *Journal of Geophysical Research* 101: 8393–8402.

Bostock MG (1997) Anisotropic upper mantle stratigraphy and architecture of the Slave craton. *Nature* 390: 392–395.

Bostock MG (1998) Mantle stratigraphy and evolution of the Slave province. *Journal of Geophysical Research* 103: 21183–21200.

Bostock MG (2002) Kirchhoff-approximate inversion of teleseismic wavefields. *Geophysical Journal International* 149: 787–795.

Bostock MG (2003) Linearized inverse scattering of teleseismic waves for anisotropic crust and mantle structure: 1. Theory. *Journal of Geophysical Research* 108: 2258. http://dx.doi.org/10.1029/2002JB001950.

Bostock MG (2004) Green's functions, source signatures, and the normalization of teleseismic wave fields. *Journal of Geophysical Research* 109: B03303. http://dx.doi.org/10.1029/2003B002783.

Bostock MG and Kumar MR (2010) Bias in seismic estimates of crustal properties. *Geophysical Journal International* 182: 403–407.

Bostock MG and Rondenay S (1999) Migration of scattered teleseismic body waves. *Geophysical Journal International* 137: 732–746.

Bostock MG, Rondenay S, and Shragge J (2001) Multiparameter two-dimensional inversion of scattered teleseismic body waves. 1. Theory for oblique incidence. *Journal of Geophysical Research* 106: 30771–30782.

Bostock M and Sacchi MD (1997) Deconvolution of teleseismic recordings for mantle structure. *Geophysical Journal International* 129: 143–152.

Bostock M and Tréhu AM (2012) Wave-field decomposition of ocean bottom seismograms. *Bulletin of Seismological Society of America* 102: 1681–1692.

Burdick LJ and Langston CA (1977) Modeling crustal structure through the use of converted phases in teleseismic body waveforms. *Bulletin of the Seismological Society of America* 67: 677–692.

Burridge R, de Hoop MV, Miller D, and Spencer C (1998) Multiparameter inversion in anisotropic elastic media. *Geophysical Journal International* 134: 757–777.

Chen L, Wen L, and Zheng T (2005a) A wave equation migration method for receiver function imaging. 1. Theory. *Journal of Geophysical Research* 110: B11309. http://dx.doi.org/10.1029/2005JB003665.

Chen L, Wen L, and Zheng T (2005b) A wave equation migration method for receiver function imaging. 2. Application to the Japan subduction zone. *Journal of Geophysical Research* 110: B11310. http://dx.doi.org/10.1029/2005JB003666.

Chevrot S, Vinnik LP, and Montagner J-P (1999) Global-scale analysis of mantle *Ps* phases. *Journal of Geophysical Research* 104: 20203–20219.
Claerbout JF (1968) Synthesis of a layered medium from its acoustic transmission response. *Geophysics* 33: 264–269.
Claerbout JF (1976) *Fundamentals of Geophysical Data Processing*. New York, NY: McGraw-Hill.
Clayton RW and Wiggins RA (1976) Source shape estimation and deconvolution of teleseismic body waves. *Geophysical Journal International* 103: 301–320.
Clitheroe G, Gudmundsson O, and Kennett BLN (2000) The crustal thickness of Australia. *Journal of Geophysical Research* 105: 13697–13713.
Darbyshire FA, Eaton DW, Frederiksen AW, and Ertolahti L (2007) New insights into the lithosphere beneath the Superior Province from Rayleigh wave dispersion and receiver function analysis. *Geophysical Journal International* 169: 1043–1068.
de Hoop MV and Bleistein N (1997) Generalized Radon transform inversions for reflectivity in anisotropic elastic media. *Inverse Problems* 13: 669–690.
Deans SR (1983) *The Radon Transform and some of its Applications*. New York, NY: Wiley.
Dueker KG and Sheehan AF (1998) Mantle discontinuity structure beneath the Colorado Rocky Mountains and High Plains. *Journal of Geophysical Research* 103: 7153–7169.
Eaton DW, Darbyshire F, Evans RL, Grütter H, Jones AG, and Yuan X (2009) The elusive lithosphere–asthenosphere boundary (LAB) beneath cratons. *Lithos* 109: 1–22.
Faber S and Müller G (1980) *Sp* phases from the transition zone between the upper and lower mantle. *Bulletin of the Seismological Society of America* 70: 487–508.
Farra V and Vinnik L (2000) Upper mantle stratification by *P* and *S* receiver functions. *Geophysical Journal International* 141: 699–712.
Farra V, Vinnik L, Romanowicz B, Kosarev GL, and Kind R (1991) Inversion of teleseismic *S* particle motion for azimuthal anisotropy in the upper mantle: A feasibility study. *Geophysical Journal International* 106: 421–431.
Fee D and Dueker K (2004) Mantle transition zone topography and structure beneath the Yellowstone hotspot. *Geophysical Research Letters* 31: L18603. http://dx.doi.org/10.1029/2004GL020636.
Ferris A, Abers GA, Christensen DH, and Veenstra E (2003) High resolution image of the subducted Pacific (?) plate beneath central Alaska, 50–150 km depth. *Earth and Planetary Science Letters* 214: 575–588.
Finotello M, Nyblade A, Julia J, Wiens D, and Anandakrishnan S (2011) Crustal V_p–V_s ratios and thickness for Ross Island and the Transantarctic Mountain front, Antarctica. *Geophysical Journal International* 185: 85–92.
Forgues E and Lambaré G (1992) Parameterization study for acoustic and elastic ray-Born inversion. *Journal of Seismic Exploration* 6: 253–277.
Frazer LN (1977) *Synthesis of Shear Coupled PL Waves*. PhD Thesis, Princeton University.
Frederiksen AW and Bostock MG (2000) Modelling teleseismic waves in dipping anisotropic structures. *Geophysical Journal International* 141: 401–412.
Frederiksen AW, Folsom H, and Zandt G (2004) Neighbourhood inversion of teleseismic Ps conversions for anisotropy and layer dip. *Geophysical Journal International* 155: 200–212.
Frederiksen AW and Revenaugh J (2004) Lithospheric imaging via teleseismic scattering tomography. *Geophysical Journal International* 159: 978–990.
French WS (1974) Two-dimensional and three-dimensional migration of model-experiment reflection profiles. *Geophysics* 39: 265–277.
Gilbert HJ, Sheehan AF, Dueker KG, and Molnar P (2003) Receiver functions in the western United States, with implications for upper mantle structure and dynamics. *Journal of Geophysical Research* 108: 2229. http://dx.doi.org/10.1029/2001JB001194.
Goldberg DE (1989) *Genetic Algorithms in Search, Optimization, and Machine Learning*. Reading, MA: Addison-Wesley.
Golub G, Heath M, and Wahba G (1979) Generalized cross-validation as a method for choosing a good ridge parameter. *Technometrics* 21: 215–223.
Gurrola H, Baker GE, and Minster JB (1995) Simultaneous time domain deconvolution with application to the computation of receiver functions. *Geophysical Journal International* 120: 537–543.
Gurrola H, Minster JB, and Owens T (1994) The use of velocity spectrum for stacking receiver functions and imaging upper mantle discontinuities. *Geophysical Journal International* 117: 427–440.
Haskell NA (1962) Crustal reflection of plane *P* and *SV* waves. *Journal of Geophysical Research* 67: 4751–4767.
Hayes MH, Lim JS, and Oppenheim AV (1980) Signal reconstruction from phase or magnitude. *IEEE Transactions on Acoustics, Speech, and Signal Processing* ASSP-28(6): 672–680.
Helffrich G and Thompson D (2010) A stacking approach to estimate V_P/V_S from receiver functions. *Geophysical Journal International* 182: 899–902.
Helmberger DV (1968) The crust-mantle transition in the Bering Sea. *Bulletin of the Seismological Society of America* 58: 179–214.
Hoffmann H, Boelsche J, Horst W, et al. (1989) Tiefenseismische untersuchungen in der DDR durch den VEB geophysik – Stand und ergebnisse. *Zeitschrift für Angewandte Geologie* 35: 308–314.
Hudson JA (1980) *The Excitation and Propagation of Elastic Waves*. New York, NY: Cambridge University Press.
Hudson JA and Heritage JR (1981) The use of the Born approximation in seismic scattering problems. *Geophysical Journal of the Royal Astronomical Society* 66: 221–240.
Jordan TH and Frazer LN (1975) Crustal and upper mantle structure from S_p phases. *Journal of Geophysical Research* 80: 1504–1518.
Kawakatsu H, Kumar P, Takei Y, et al. (2009) Seismic evidence for sharp lithosphere–asthenosphere boundaries of oceanic plates. *Science* 324: 499–502.
Kawakatsu H and Watada S (2007) Seismic evidence for deep water transportation in the mantle. *Science* 316: 1468–1471.
Kawakatsu H and Yoshioka S (2011) Metastable olivine wedge and deep dry cold slab beneath southwest Japan. *Earth and Planetary Science Letters* 303: 1–10.
Kennett BLN (1983) *Seismic Wave Propagation in Stratified Media*. Cambridge: Cambridge University Press.
Kennett BLN (1991) The removal of free surface interactions from three-component seismograms. *Geophysical Journal International* 104: 153–163.
Kennett BLN (2000) Stacking three-component seismograms. *Geophysical Journal International* 141: 263–269.
Kennett BLN (2002) *The Seismic Wavefield: Volume II. Interpretation of Seismograms on Regional and Global Scales*. New York, NY: Cambridge University Press.
Kind R, Kosarev GL, and Petersen NV (1995) Receiver functions at the stations of the German Regional Seismic Network (GRSN). *Geophysical Journal International* 121: 191–202.
Kind R and Vinnik LP (1988) The upper-mantle discontinuities underneath the GRF array from *P*-to-*SV* converted phases. *Journal of Geophysics* 62: 138–147.
Kind R, Yuan X, Saul J, et al. (2002) Seismic images of crust and upper mantle beneath Tibet: Evidence for Eurasian plate subduction. *Science* 298: 1219–1221.
Knapmeyer M and Harjes H-P (2000) Imaging crustal discontinuities and the downgoing slab beneath western Crete. *Geophysical Journal International* 143: 1–21.
Kosarev G, Kind R, Sobolev SV, Yuan X, Hanka W, and Oreshin S (1999) Seismic evidence for a detached Indian lithospheric mantle beneath Tibet. *Science* 283: 1306–1309.
Kosarev GL, Makeyeva LI, and Vinnik LP (1984) Anisotropy of the mantle inferred from observations of *P* to *S* converted waves. *Geophysical Journal of the Royal Astronomical Society* 76: 209–220.
Kosarev GL, Petersen NV, Vinnik LP, and Roecker SW (1993) Receiver functions for the Tien Shan analog broadband network: Contrasts in the evolution of structures across the Talasso-Fergana fault. *Journal of Geophysical Research* 98: 4437–4448.
Kumar MR and Bostock MG (2006) Transmission to reflection transformation of teleseismic wavefields. *Journal of Geophysical Research* 111: B08306.
Kumar MR and Bostock MG (2008) Extraction of absolute *P* velocity from receiver functions. *Geophysical Journal International* 175: 515–519.
Kumar P, Kind R, Hanka W, et al. (2005) The lithosphere–asthenosphere boundary in the North-West Atlantic region. *Earth and Planetary Science Letters* 1–2: 249–257.
Kurita T (1973) A procedure for elucidating fine structure of the crust and upper mantle from seismological data. *Bulletin of the Seismological Society of America* 63: 189–204.
Langston CA (1977) The effect of planar dipping structure on source and receiver responses for constant ray parameter. *Bulletin of the Seismological Society of America* 67: 1029–1050.
Langston CA (1979) Structure under Mt Rainier, Washington, inferred from teleseismic body waves. *Journal of Geophysical Research* 94: 1935–1951.
Langston CA and Hammer JK (2001) The vertical component P-wave receiver function. *Bulletin of the Seismological Society of America* 91: 1805–1819.
Lawrence JF and Wiens DA (2004) Combined receiver-function and surface wave phase-velocity inversion using a niching genetic algorithm: Application to Patagonia. *Bulletin of the Seismological Society of America* 94: 977–987.
Leidig M and Zandt G (2003) Highly anisotropic crust in the Altiplano Puna volcanic complex of the central Andes. *Journal of Geophysical Research* 108. http://dx.doi.org/10.1029/2001JB00649.
Levander A, Niu F, and Symes WW (2005) Imaging teleseismic *P* to *S* scattered waves using the Kirchhoff integral. In: Levander A and Nolet G (eds.). *Seismic Earth: Array Analysis of Broadband Seismograms*, vol. 157, pp. 149–169. Washington, DC: American Geophysical Union.
Levin V and Park J (1997) *P-SH* conversions in a flat-layered medium with anisotropy of arbitrary orientation. *Geophysical Journal International* 131: 253–266.
Levin V and Park J (1998) *P-SH* conversions in layered media with hexagonally symmetric anisotropy. A cookbook. *Pure and Applied Geophysics* 151: 669–697.

Li X-Q (1996) *Deconvolving Orbital Surface Waves for the Source Duration of Large Earthquakes and Modeling the Receiver Functions for the Earth Structure Beneath a Broadband Seismometer Array in the Cascadia Subduction Zone*. PhD Thesis, Oregon State University, Corvallis.

Li X, Kind R, Yuan X, Wolbern I, and Hanka W (2004) Rejuvenation of the lithosphere by the Hawaiian plume. *Nature* 427: 827–829.

Li X-Q and Nabelek JL (1999) Deconvolution of teleseismic body waves for enhancing structure beneath a seismometer array. *Bulletin of the Seismological Society of America* 89: 190–201.

Ligorria JP and Ammon CJ (1999) Iterative deconvolution and receiver-function estimation. *Bulletin of the Seismological Society of America* 89: 1395–1400.

Liu X and Pavlis GL (2013) Appraising the reliability of converted wavefield imaging: Application to USArray imaging of the 410-km discontinuity. *Geophysical Journal International* 49(3): 787–795. http://dx.doi.org/10.1093/gji/ggs088.

Lucente FP, Agostinetti NP, Moro M, Selvaggi G, and Di Bona M (2005) Possible fault plane in a seismic gap area of the southern Apennines (Italy) revealed by receiver function analysis. *Journal of Geophysical Research* 110: B04307. http://dx.doi.org/10.1029/2004JB003187.

Marfurt KJ, Johnson RA, and Pennington WD (2003) An introduction – Solid-earth seismology: Initiatives from IRIS. *The Leading Edge* 22: 218–219.

Matson KH (1997) *An Inverse-Scattering Series Method for Attenuating Elastic Multiples from Multicomponent Land and Ocean Bottom Seismic Data*. PhD Thesis, University of British Columbia, Vancouver.

Menke W (1984) *Geophysical Data Analysis: Discrete Inverse Theory*. Orlando, FL: Academic Press.

Mercier J-P, Bostock MG, and Baig A (2006) Improved Green's functions for passive source structural studies. *Geophysics* 71: SI95–SI102.

Miller DM, Oristaglio M, and Beylkin G (1987) A new slant on seismic imaging: Migration and integral geometry. *Geophysics* 52: 943–964.

Monteiller V, Chevrot S, Komatitsch D, and Fuji N (2013) A hybrid method to compute short-period synthetic seismograms of teleseismic body waves in a 3-D regional model. *Geophysical Journal International* 192: 230–247.

Muirhead KJ and Datt R (1976) The N-th root process applied to seismic array data. *Geophysical Journal of the Royal Astronomical Society* 47: 197–210.

Neal SL and Pavlis GL (1999) Imaging P to S conversions with multichannel receiver functions. *Geophysical and Research Letters* 26: 2581–2584.

Neal SL and Pavlis GL (2001) Imaging P to S conversions with broadband seismic arrays using mutichannel time-domain deconvolution. *Geophysical Journal International* 147: 57–67.

Nicholson T, Bostock M, and Cassidy JF (2005) New constraints on subduction zone structure in northern Cascadia. *Geophysical Journal International* 161: 849–859.

Niu F, Levander A, Ham S, and Obayashi M (2005) Mapping the subducting Pacific slab beneath southwest Japan with Hi-net receiver functions. *Earth and Planetary Science Letters* 239: 9–17.

Oppenheim AV and Schafer RW (1975) *Digital Signal Processing*. Englewood Cliffs, NJ: Prentice-Hall.

Oreshin S, Vinnik L, Peregoudov D, and Roecker S (2002) Lithosphere and asthenosphere of the Tien Shan imaged by S receiver functions. *Geophysical Research Letters* 29. http://dx.doi.org/10.1029/2001GL014441.

Owens TJ, Nyblade AA, Gurrola H, and Langston CA (2000) Mantle transition zone structure beneath Tanzania, east Africa. *Geophysical Research Letters* 27: 827–830.

Owens TJ and Zandt G (1997) The implications of crustal property variations on models of Tibetan Plateau evolution. *Nature* 387: 37–43.

Owens TJ, Zandt G, and Taylor SR (1984) Seismic evidence for an ancient rift beneath the Cumberland Plateau, Tennessee: A detailed analysis of broadband teleseismic P waveforms. *Journal of Geophysical Research* 89: 7783–7795.

Park J and Levin V (2000) Receiver functions from multiple-taper spectral correlation estimates. *Bulletin of the Seismological Society of America* 90: 1507–1520.

Park J and Levin V (2001) Receiver functions from regional *P* waves. *Geophysical Journal International* 147: 1–11.

Parker RL (1994) *Geophysical Inverse Theory*. Princeton, NJ: Princeton University Press.

Paulssen H, Visser J, and Nolet G (1993) The crustal structure from teleseismic, P-wave coda—I. Method. *Geophysical Journal International* 112: 15–25.

Pavlis GL (2005) Direct imaging of the coda of teleseismic P waves. In: Levander A and Nolet G (eds.). *Seismic Earth: Array Analysis of Broadband Seismograms*, vol. 157, pp. 171–185. Washington, DC: American Geophysical Union.

Phillips K, Clayton RW, Davis P, et al. (2012) Structure of the subduction system in southern Peru from seismic array data. *Journal of Geophysical Research* 117: B11306. http://dx.doi.org/10.1029/2012JB009540.

Phinney RA (1964) Structure of the Earth's crust from spectral behaviour of long-period body waves. *Journal of Geophysical Research* 69: 2997–3017.

Poppeliers C and Pavlis GL (2003a) Three-dimensional, prestack, plane wave migration of teleseismic *P*-to-*S* converted phases: 1. Theory. *Journal of Geophysical Research* 108. http://dx.doi.org/10.1029/2001JB000216.

Poppeliers C and Pavlis GL (2003b) Three-dimensional, prestack, plane wave migration of teleseismic *P*-to-*S* converted phases: 2. Stacking multiple events. *Journal of Geophysical Research* 108. http://dx.doi.org/10.1029/2001JB001583.

Press WH, Flannery BP, Teukolsky SA, and Vetterling WT (1986) *Numerical Recipes: The Art of Scientific Computing*. Cambridge: Cambridge University Press.

Randall GE (1989) Efficient calculation of differential seismograms for lithospheric receiver functions. *Geophysical Journal International* 99: 469–481.

Reading A, Kennett B, and Sambridge M (2003) Improved inversion for seismic structure using transformed *S*-wavector receiver functions: Removing the effect of the free surface. *Geophysical Research Letters* 30. http://dx.doi.org/10.1029/2003GL018090.

Revenaugh J (1995) A scattered-wave image of subduction beneath the Transverse Ranges, California. *Science* 268: 1888–1892.

Robinson E and Treitel S (1980) *Geophysical Signal Analysis*. Englewood Cliffs, NJ: Prentice-Hall.

Roecker S, Baker B, and McLaughlin J (2010) A finite-difference algorithm for full waveform teleseismic tomography. *Geophysical Journal International* 181: 1017–1040.

Rondenay S (2009) Upper mantle imaging with array recordings of converted and scattered teleseismic waves. *Surveys in Geophysics* 30: 377–405. http://dx.doi.org/10.1007/s10712-009-9071-5.

Rondenay S, Bostock MG, and Fischer KM (2005) Multichannel inversion of scattered teleseismic body waves: Practical considerations and applicability. In: Levander A and Nolet G (eds.) *Seismic Earth: Array Analysis of Broadband Seismograms*, vol. 157, pp. 187–203. Washington, DC: American Geophysical Union.

Rondenay S, Bostock MG, and Shragge J (2001) Multiparameter two-dimensional inversion of scattered teleseismic body waves, 3. Application to the Cascadia 1993 data set. *Journal of Geophysical Research* 106: 30795–30808.

Rost S and Thomas C (2002) Array seismology: Methods and applications. *Reviews of Geophysics* 40. http://dx.doi.org/10.1029/2000RG000100.

Ryberg T and Weber M (2000) Receiver function arrays: A reflection seismic approach. *Geophysical Journal International* 141: 1–11.

Rychert CA, Rondenay S, and Fischer KM (2007) *P*-to-*S* and *S*-to-*P* imaging of a sharp lithosphere–asthenosphere boundary beneath eastern North America. *Journal of Geophysical Research* 112: B08314. http://dx.doi.org/10.1029/2006JB004619.

Rychert CA, Shearer P, and Fischer KM (2010) Scattered wave imaging of the lithosphere–asthenosphere boundary. *Lithos* 120: 173–185.

Sacks IS, Snoke JA, and Husebye ES (1979) Lithosphere thickness beneath the Baltic shield. *Tectonophysics* 56: 101–110.

Sambridge M (1999a) Geophysical inversion with a neighbourhood algorithm—I. Search a parameter space. *Geophysical Journal International* 138: 479–494.

Sambridge M (1999b) Geophysical inversion with a neighbourhood algorithm—II. Appraising the ensemble. *Geophysical Journal International* 138: 727–746.

Saul J, Kumar MR, and Sarkar D (2000) Lithospheric and upper mantle structure of the Indian Shield, from teleseismic receiver functions. *Geophysical Research Letters* 27: 2357–2360.

Schaeffer AJ and Bostock MG (2010) A low-velocity zone atop the transition zone in northwestern Canada. *Journal of Geophysical Research* 115: B06302. http://dx.doi.org/10.1029/2009JB006856.

Schimmel M and Paulssen H (1997) Noise reduction and the detection of weak, coherent signals through phase-weighted stacks. *Geophysical Journal International* 130: 497–505.

Schneider WS (1978) Integral formulation for migration in two and three dimensions. *Geophysics* 43: 49–76.

Schulte-Pelkum V, Monsalve G, Sheehan A, et al. (2005) Imaging the Indian subcontinent beneath the Himalaya. *Nature* 435: 1222–1225.

Sheehan AF, Shearer PM, Gilbert HJ, and Dueker KG (2000) Seismic migration processing of *P-SV* converted phases for mantle discontinuity structure beneath the Snake River Plain, western United States. *Journal of Geophysical Research* 105: 19055–19065.

Sherwood JWC and Trorey AW (1965) Minimum-phase and related properties of a horizontally stratified absorptive Earth to plane acoustic waves. *Geophysics* 30: 191–197.

Shibutani T, Sambridge M, and Kennett BLN (1996) Genetic algorithm inversion for receiver functions with application to crust and uppermost mantle structure beneath eastern Australia. *Geophysical Research Letters* 23: 1829–1832.

Shragge J, Bostock MG, and Rondenay S (2001) Multiparameter two-dimensional inversion of scattered teleseismic body waves, 2. Numerical examples. *Journal of Geophysical Research* 106: 30783–30794.

Silver PG and Chan WW (1991) Shear-wave splitting and subcontinental mantle deformation. *Journal of Geophysical Research* 96: 16429–16454.

Silver PG and Savage M (1994) The interpretation of shear-wave splitting parameters in the presence of two anisotropic layers. *Geophysical Journal International* 119: 949–963.

Simmons NA and Gurrola H (2000) Multiple seismic discontinuities near the base of the transition zone in the Earth's mantle. *Nature* 405: 559–562.

Stammler K, Kind R, Petersen N, Kosarev G, Vinnik LP, and Qiyuan L (1992) The upper mantle discontinuities: Correlated or anticorrelated? *Geophysical Research Letters* 19: 1563–1566.

Svenningsen L and Jacobsen BH (2004) Comment on "Improved inversion for seismic structure using transformed, *S*-wavevector receiver functions: Removing the effect of the free surface" by Anya Reading, Brian Kennett, and Malcolm Sambridge. *Geophysical Research Letters* 31: L24609. http://dx.doi.org/10.1029/2004GL021413.

Tarantola A (1984) Inversion of seismic reflection data in the acoustic approximation. *Geophysics* 49: 1259–1266.

Tarantola A (1986) A strategy for nonlinear elastic inversion of seismic reflection data. *Geophysics* 51: 1893–1903.

Thomson DJ (1982) Spectrum estimation and harmonic analysis. *Proceedings of IEEE* 70: 1055–1096.

Thorwart M and Dahm T (2005) Wavefield decomposition for passive ocean bottom seismological data. *Geophysical Journal International* 163: 611–621.

Tromp J, Tape C, and Liu Q (2005) Seismic tomography, adjoint methods, time reversal and banana-doughnut kernels. *Geophysical Journal International* 160: 195–216.

Ulrych TJ (1971) Application of homomorphic deconvolution to seismology. *Geophysics* 36: 650–660.

Ulrych TJ, Jensen OG, Ellis RM, and Somerville PG (1972) Homomorphic deconvolution of some teleseismic events. *Bulletin of the Seismological Society of America* 62: 1269–1281.

Vinnik LP (1977) Detection of waves converted from *P* to *SV* in the mantle. *Physics of the Earth and Planetary Interiors* 15: 39–45.

Vinnik LP, Farra V, and Romanowicz B (1989) Azimuthal anisotropy in the earth from observations of *SKS* at GEOSCOPE and NARS broad band stations. *Bulletin of the Seismological Society of America* 79: 1542–1558.

Vinnik LP, Foulger GR, and Du Z (2005) Seismic boundaries in the mantle beneath Iceland: A new constraint on temperature. *Geophysical Journal International* 160: 533–538.

Vinnik LP and Montagner J-P (1996) Shear-wave splitting in the mantle *Ps* phases. *Geophysical Research Letters* 23: 2449–2452.

Vinnik L and Romanowicz B (1991) Origin of precursors to teleseismic *S* waves. *Bulletin of the Seismological Society of America* 81: 1216–1230.

Wapenaar K, Thorbecke J, and Draganov D (2004) Relations between reflection and transmission responses of three-dimensional inhomogeneous media. *Geophysical Journal International* 156: 179–194.

Weglein AB, Araújo FV, Carvalho PM, et al. (2003) Inverse scattering series and seismic exploration. *Inverse Problems* 19: R27–R83.

Weglein AB, Foster DJ, Matson KH, Shaw SA, Carvalho PM, and Corrigan D (2002) Predicting the correct spatial location of reflectors without knowing or determining the precise medium and wave velocity: Initial concept, algorithm and analytic and numerical example. *Journal of Seismic Exploration* 10: 367–382.

Weglein AB, Gasparotto FA, Carvalho PM, and Stolt RH (1997) An inverse scattering series method for attenuating multiples in seismic reflection data. *Geophysics* 62: 1975–1989.

Wei Z, Chen L, and Xu W (2011) Crustal thickness and V_p/V_s ratio of the central and western North China Craton and its tectonic implications. *Geophysical Journal International* 186: 385–389.

Wilson DC, Angus DA, Ni JF, and Grand S (2006) Constraints on the interpretation of *S*-to-*P* receiver functions. *Geophysical Journal International* 165: 969–980.

Wilson D and Aster R (2005) Seismic imaging of the crust and upper mantle using regularized joint receiver functions, frequency P-wave number filtering, and multimode Kirchhoff migration. *Journal of Geophysical Research* 110: B05305. http://dx.doi.org/10.1029/2004JB003430.

Wilson D, Aster R, Ni J, et al. (2005) Imaging the seismic structure of the crust and upper mantle beneath the Great Plains, Rio Grande Rift, and Colorado Plateau using receiver functions. *Journal of Geophysical Research* 110: B05306. http://dx.doi.org/10.1029/2004JB003492.

Wilson CK, Jones CH, Molnar P, Sheehan AF, and Boyd OS (2004) Distributed deformation in the lower crust and upper mantle beneath a continental strike-slip fault zone: Marlborough fault system, South Island, New Zealand. *Geology* 32: 837–840.

Wittlinger G and Farra V (2012) Observation of low shear wave velocity at the base of the polar ice sheets: Evidence for enhanced anisotropy. *Geophysical Journal International* 190: 391–405.

Wittlinger G, Farra V, Hetényi G, Vergne J, and Nábèlek J (2009) Seismic velocities in Southern Tibet lower crust: A receiver function approach for eclogite detection. *Geophysical Journal International* 177: 1037–1049.

Yilmaz O (2001) *Seismic Data Analysis: Processing, Inversion, and Interpretation of Seismic Data*. Tulsa, OK: Society of Exploration Geophysicists.

Yuan X, Kind R, Li X, and Wang R (2006) The *S* receiver functions: Synthetics and data examples. *Geophysical Journal International* 165: 555–564.

Zandt G and Ammon C (1995) Continental crust composition constrained by measurements of crustal Poisson's ratio. *Nature* 374: 152–154.

Zandt G, Gilbert H, Owens TJ, Ducea M, Saleeby J, and Jones CH (2004) Active foundering of a continental arc root beneath the southern Sierra Nevada in California. *Nature* 431: 41–46.

Zandt G and Owens TJ (1986) Comparison of crustal velocity profiles determined by seismic refraction and teleseismic methods. *Tectonophysics* 128: 155–161.

Zandt G and Randall GE (1985) Observations of shear-coupled *P* waves. *Geophysical Research Letters* 12: 565–568.

Zhou L, Chen W-P, and Özalaybey S (2000) Seismic properties of the central Indian Shield. *Bulletin of the Seismological Society of America* 90: 1295–1304.

Zhu L and Kanamori H (2000) Moho depth variation in southern California from teleseismic receiver functions. *Journal of Geophysical Research* 105: 2969–2980.

This page intentionally left blank

1.09 Theory and Observations - Seismic Anisotropy

V Maupin, University of Oslo, Oslo, Norway
J Park, Yale University, New Haven, CT, USA

© 2015 Elsevier B.V. All rights reserved.

1.09.1	**Introduction**	277
1.09.2	**Basic Theory of Seismic Anisotropy**	278
1.09.2.1	Basic General Theory	278
1.09.2.2	Different Parameterizations of the Elastic Coefficients	279
1.09.2.3	Weak Anisotropy Approximation	281
1.09.2.4	Ray Theory	281
1.09.2.5	Reflection and Transmission Coefficients	282
1.09.2.6	Surface Waves and Normal Modes	284
1.09.3	**Seismological Observations of Anisotropy**	286
1.09.3.1	Crustal Anisotropy	288
1.09.3.2	Origin of Upper-Mantle Anisotropy	288
1.09.3.3	Traveltime Residuals and Mantle Anisotropy	291
1.09.3.4	Single-Station P-Wave Anisotropy Observables	291
1.09.3.5	SKS Waves and Upper-Mantle Anisotropy	292
1.09.3.6	P and S Waves and Subduction Zones	293
1.09.3.7	Surface Waves and Upper Mantle	294
1.09.3.8	Polarization of Surface Waves	296
1.09.3.9	Converted Waves and Lithospheric Anisotropy	297
1.09.3.10	ScS, S_{diff}, and the D″ Layer	298
1.09.3.11	PKIKP, Normal Modes, and the Inner Core	298
1.09.4	**Perspectives**	299
Acknowledgments		299
References		299

1.09.1 Introduction

Elastic anisotropy occurs when the relationship between stress and strain in a material depends on its orientation. Rotate an applied stress, and the strain response will differ. Seismic anisotropy is how elastic anisotropy influences propagating seismic waves. Wave speed and scattering will depend on the azimuth of propagation. Intrinsic anisotropy characterizes many common minerals in Earth rocks, by virtue of atomic structure. Cubic-lattice minerals, such as garnet, often exhibit little or no elastic anisotropy. Sheet-silicate minerals, such as mica, can exhibit extreme anisotropy, with directional differences in shear and compressional response of 20% or more. Despite the extreme anisotropy of individual minerals, the bulk anisotropy of a rock will vanish if its minerals are randomly oriented. Bulk anisotropy can develop as a rock either forms or deforms, if its minerals orient preferentially (Hansen et al., 2011; Jung and Karato, 2001; Ribe, 1989), cracks or melt pockets develop within the rock and become mutually aligned (Holtzman et al., 2003; Siegesmund et al., 1991b), or other mechanisms break the rock's internal symmetry (Nowacki et al., 2011).

An anisotropic material has physical properties that depend on direction, whereas a heterogeneous material has properties that depend on location. Whether Earth's subsurface appears heterogeneous or anisotropic is often a matter of the scale at which we analyze its properties. At small scale, alternating layers of isotropic stiff and soft material would be observed as a heterogeneous medium. At large scale, seismic waves respond to thin layers as a homogeneous anisotropic material (Backus, 1962). If seismic waves exert a unidirectional compression on such a stack, the deformation will be different if the compression is perpendicular to the layering or in the plane of the layering. A medium that is isotropic at the scale of a hand sample of rock but exhibits an ordered texture within a seismic wavelength (>100 m) is an 'effective' anisotropic medium.

By themselves, seismic observations cannot distinguish between 'intrinsic,' 'bulk,' and 'effective' anisotropies. A correct description at large scale of any heterogeneous structure that is not randomly heterogeneous in an isotropic way should include anisotropy (Capdeville and Marigo, 2007). What we infer from seismic observations is large-scale anisotropy. A range of structures can, in principle and at first order, explain this anisotropy. A priori information from mineral physics, geodynamics, or surface lithology is necessary to narrow our interpretation.

Layering and preferred orientations of anisotropic minerals are common in the Earth's interior (see Mainprice, **Chapter 2.20**). Seismic anisotropy is therefore present at different scales and in many different settings. Excellent reviews of seismic anisotropy in exploration and reservoir seismics can be found in Tsvankin et al. (2010) and Helbig and Thomsen (2005), the latter offering a historical perspective. Teleseismic earthquake waves have lower frequency and longer wavelength than waves generated for resource exploration and are more likely to respond to the effective anisotropy of fine-layering and similar

heterogeneities. We review here the basic theoretical tools available in seismology to analyze wave propagation in anisotropic structures, earthquake observations sensitive to anisotropy, and their geodynamic implications.

1.09.2 Basic Theory of Seismic Anisotropy

1.09.2.1 Basic General Theory

The fundamentals of seismic-wave propagation in anisotropic media have been described in several papers and books, and we will only highlight them here. For more details, we refer to Crampin (1981), Garmany (1989), Babuska and Cara (1991), and Chapman (2004), for example.

In anisotropic media, seismic wave speed varies with propagation direction and S waves split into two shear waves with different velocities, a behavior called birefringence. A more subtle anisotropic behavior is that wave polarizations do not align parallel or perpendicular to the propagation direction and that phase and group velocities are not parallel, aside from exceptional cases.

Let us see briefly how these behaviors arise in a linear elastic medium. The elastic tensor c_{ijkl} relates the stress tensor elements τ_{ij} to the strain tensor elements e_{kl} linearly:

$$\tau_{ij} = c_{ijkl} e_{kl} \qquad [1]$$

An alternative to the elastic tensor is the compliance tensor s_{ijkl}, which computes the strain tensor e_{ij} as a linear function of the stress tensor τ_{kl}.

The equation of motion for a plane wave $\vec{u}\left(\vec{x},t\right) = \vec{a}\, f\left(\vec{n}\cdot\vec{x} - ct\right)$ propagating with velocity c in direction $\vec{n}$ in a uniform medium of density ρ can be written as

$$\frac{c_{ijkl}}{\rho} n_j n_k a_l = c^2 a_i \qquad [2]$$

The term $(c_{ijkl}/\rho)n_j n_k$ on the LHS is the 3×3 Christoffel matrix, which plays a central role in anisotropic wave propagation. Solving [2] for $\vec{a}$ and c is equivalent to finding the three eigenvalues and eigenvectors of the Christoffel matrix. In the general case, the three eigenvalues are distinct, leading to three waves with three different velocities in the propagation direction $\vec{n}$. The polarizations of the three waves, given by the eigenvectors, are perpendicular to each other, but are in directions that, unlike the isotropic case, may deviate from ray-based coordinates. In strongly anisotropic media, the three waves' polarizations may hybridize so that one cannot label them confidently as P or S wave.

For weak anisotropy, the waves separate into one quasi-P wave, with the highest velocity and a polarization near-parallel to the propagation direction $\vec{n}$, and two quasi-S waves. Aside from singular cases, the quasi-S waves have distinct velocities and polarization directions perpendicular to each other in a plane near perpendicular to the propagation direction $\vec{n}$. Shear-wave splitting occurs because any S wave entering the anisotropic medium sees its particle motion projected onto the polarization directions of the two quasi-S waves, which then propagate at different velocities (**Figure 1**). Once splitting has occurred, it is carried along by the S wave even after leaving the anisotropic region.

Since the Christoffel matrix depends on the components of $\vec{n}$, the waves' speeds and polarizations vary with propagation plunge and azimuth. Due to this angular dependence, wavefronts are not spherical in homogeneous anisotropic media. The vector $\vec{n}$ defines the direction of the phase propagation and is perpendicular to the wavefront. Wave energy follows another direction, defined by the group velocity direction $\vec{V}$. In homogeneous media, the group velocity follows a straight path from the wave's origin to the wavefront, as shown in **Figure 2**. The difference between the phase and group velocities depends on the curvature of the wavefront through the relation

$$\vec{V} = \vec{C} + \partial\vec{C}/\partial\theta \qquad [3]$$

where θ is the azimuth angle and $\vec{C} = c\,\vec{n}$.

Depending on the elastic tensor and on the strength of the anisotropy, wavefronts can get quite complicated. Shear waves in particular can get folds and cusps, as those shown in **Figure 3**, which displays the wavefield at three different propagation times for an ultrasonic S wave propagating through a silicon crystal. Details about the experiment and other examples can be found in Wolfe (1998).

These characteristics of wave propagation in uniform anisotropic media also occur in more complex structures. All the classical modeling methods in nonuniform structures like ray theory, WKBJ, and reflectivity have been extended to account

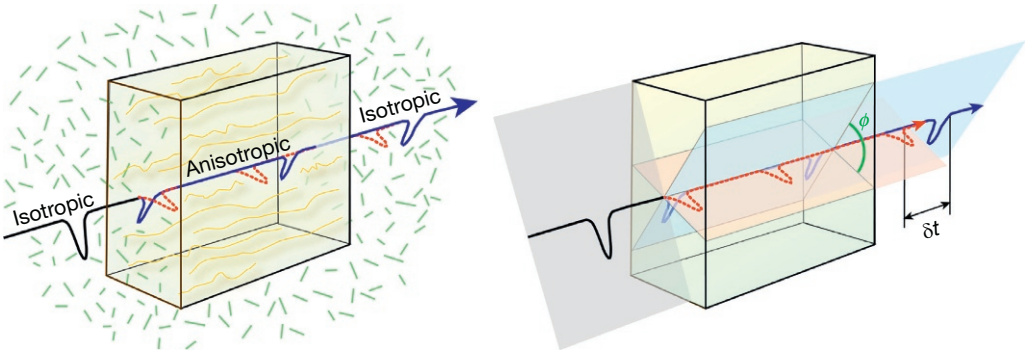

Figure 1 Principle of shear-wave birefringence. The leftmost figure shows the evolution with time of the polarization of an S wave (in black) that traverses a block of anisotropic medium. When the wave enters the anisotropic part, it splits into a fast S wave (in blue) and a slow one (in red). When the fast and slow waves leave the anisotropic regions, they are separated by a time delay. The rightmost figure shows how the initial polarization of the S wave is projected onto the planes of the fast and slow waves in the anisotropic structure. Figure courtesy of Ed Garnero.

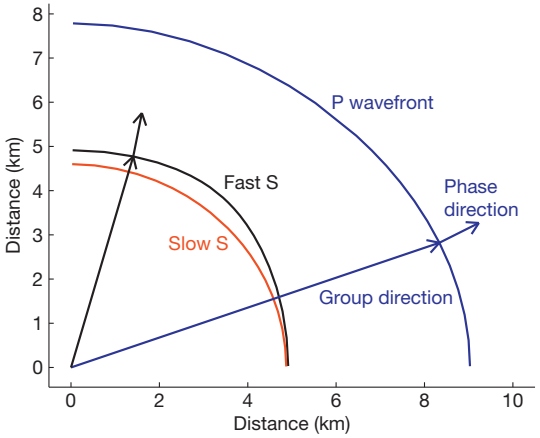

Figure 2 Wavefronts of the P wave (blue), the fast S wave (black), and the slow S wave (red) in pyrolytic material with 59% olivine (Estey and Douglas, 1986), after 1 s of propagation from a source located at the origin. The *a*-axis of the olivine is oriented along the horizontal direction and the *c*-axis along the vertical direction. The directions of the phase velocity (perpendicular to the wavefront) and of the group velocity (from the origin) are indicated at two locations of the wavefronts.

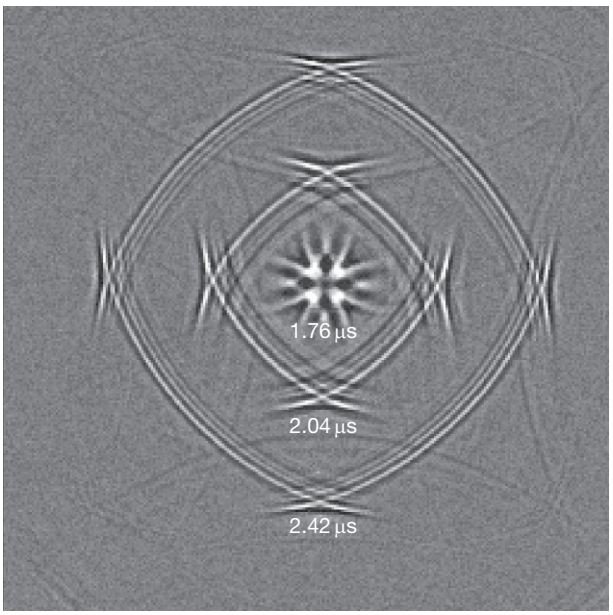

Figure 3 Snapshot of the wavefield of an ultrasonic shear wave that has propagated through a silicon crystal, recorded at three times after excitation on the other side of the crystal. Details can be found in Wolfe (1998). Photo is courtesy of J.P. Wolfe.

for anisotropy and its distinctive features (Cerveny, 1972; Fryer and Fraser, 1984; Garmany, 1988). Recent work focuses on improving the efficiency of the methods and their domains of applications, as we shall see later in the text. The elastic tensor describes the properties of any anisotropic material and we need first to analyze it in more detail.

1.09.2.2 Different Parameterizations of the Elastic Coefficients

The elastic tensor has the following symmetries:

$$c_{ijkl} = c_{jikl} = c_{ijlk} = c_{klij} \qquad [4]$$

resulting in 21 independent coefficients in the fully anisotropic case. These symmetries can be exploited to define a more convenient symmetrical 6×6 matrix, called Voigt notation, derived from c_{ijkl} using the following correspondence between ij and m and between kl and n:

$$(11):1 \quad (22):2 \quad (33):3 \quad (23) \text{ or } (32):4$$
$$(13) \text{ or } (31):5 \quad (12) \text{ or } (21):6 \qquad [5]$$

It should be noted that C_{mn} is not a tensor but that, as explained by Chapman (2004), it is possible to rotate it to a different coordinate system using a 6×6 Bond-transformation matrix without having to go back to the physical c_{ijkl} tensor (Auld, 1973).

In a laboratory, the elasticity of minerals and rocks can be measured in all orientations and all 21 coefficients determined (see Stixrude and Jeanloz, **Chapter 1.26**). Our resolution of the Earth's anisotropy is limited, and seismic-wave observations do not feasibly constrain all 21 independent elastic coefficients. Symmetry in the elastic tensor reduces the number of independent coefficients to a number that can be more easily estimated with seismic waves, at least in theory. Materials with orthorhombic symmetry, such as olivine, have nine independent coefficients, three of which specify the principal coordinate axes of the material. $9-3=6$ Parameters remain to specify the strength and the 'shape' of the elastic tensor c_{ijkl} or of the Voigt notation matrix C_{mn}. A further simplification of the anisotropy posits an axis of cylindrical symmetry (equivalent to hexagonal symmetry). Several realistic models for the Earth's anisotropy, such as fine layering and uniformly aligned penny-shaped or elongated cracks, predict this kind of symmetry. In addition, olivine crystals, which are a dominant contributor to anisotropy in the upper mantle, often undergo lattice-preferred orientation (LPO) within deforming rocks that favors aggregate anisotropy with hexagonal symmetry. Anisotropy with a cylindrical axis of symmetry is also called transverse isotropy (TI) because the solid is isotropic with respect to rotations about the symmetry axis. A general TI medium can of course have the symmetry axis in any direction and uses five free parameters to specify the strength and shape of the elastic tensor. In many applications, the axis is assumed to be either horizontal TI (HTI) or vertical TI (VTI). A tilted TI (TTI) symmetry axis perturbs seismic waveforms more strongly than HTI or VTI anisotropy, but its effects are harder to interpret.

Different notations are used to characterize anisotropic solids, and the diversity can suggest that anisotropy is more complicated than it actually is. It is impossible here to review all the notations, but we introduce the principal conventions and their relation to each other. The simplest notation for a TI medium is the so-called Love notation, where the five independent elastic coefficients are noted A, C, F, L, and N, leading to the following C_{mn} when the symmetry axis is along axis 3:

$$\begin{pmatrix} A & (A-2N) & F & 0 & 0 & 0 \\ (A-2N) & A & F & 0 & 0 & 0 \\ F & F & C & 0 & 0 & 0 \\ 0 & 0 & 0 & L & 0 & 0 \\ 0 & 0 & 0 & 0 & L & 0 \\ 0 & 0 & 0 & 0 & 0 & N \end{pmatrix} \quad [6]$$

In the isotropic case with Lamé parameters λ and μ, A and C reduce to $\lambda+2\mu$, F reduces to λ, and L and N reduce to μ.

Instead of the elastic coefficients themselves, some authors use velocities, exploiting the simple expressions for P- and S-wave velocities along symmetry axes:

$$\alpha_{\perp} = \sqrt{A/\rho} \quad [7]$$

$$\alpha_{\parallel} = \sqrt{C/\rho} \quad [8]$$

$$\beta_{\parallel} = \sqrt{L/\rho} \quad [9]$$

$$\beta_{\perp} = \sqrt{N/\rho} \quad [10]$$

For P waves, the subscripts $\parallel$ and $\perp$ refer to the propagation direction with respect to the symmetry axis, but for S waves, have a slightly more complex meaning (see **Figure 4**). $\beta_{\parallel}$ is the velocity of waves that propagate along the symmetry axis or in the plane normal to it and polarized parallel to the symmetry axis. $\beta_{\perp}$ is the velocity of waves propagating and polarized in the plane perpendicular to the symmetry axis. When the symmetry axis is vertical, $\parallel$ reduces to v, for *vertical*, and $\perp$ to H, for *horizontal*. F has no direct relation to a simple velocity expression. It is common to substitute $\eta = F/(A-2L)$ as the fifth parameter, in place of F.

A more direct measure of anisotropic strength can be achieved by using A and L as references. The two reference velocities are then $\beta = \sqrt{L/\rho}$ and $\alpha = \sqrt{A/\rho}$. Note that β and α are not the mean velocities of the structure. The degree of anisotropy appears explicitly in the deviation from 1.0 of $\xi = N/L$, $\phi = C/A$, and $\eta = F/(A-2L)$. This definition of the three coefficients is by the far the most common one, but one should be aware that some authors use other definitions of these parameters. For example, Beghein and Trampert (2003) defined $\xi = 1 - N/L$ and similarly for ϕ and η.

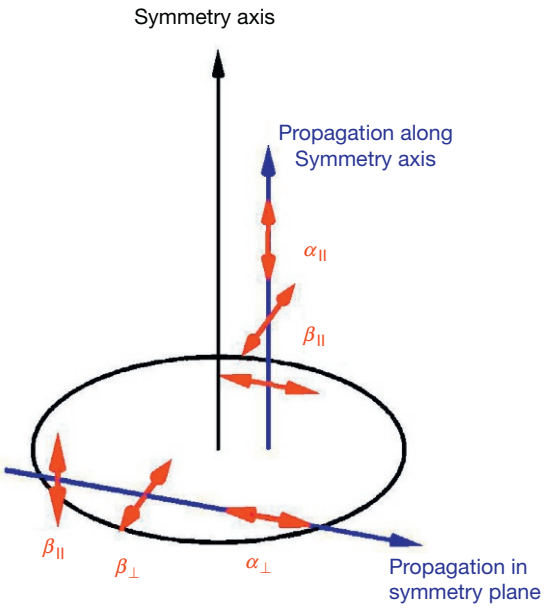

Figure 4 Velocities of P and S waves along the symmetry axis and in the symmetry plane of a transverse isotropic medium. The medium is depicted in black. The wave-propagation directions are in blue and the polarizations corresponding to the different velocities in red.

Seismic-exploration geophysicists use some variants of the coefficients as defined by Thomsen (1986). In seismic exploration, the dominant wave-propagation direction is vertical. Assuming a vertical axis of symmetry, Thomsen (1986) defined the reference-wave velocities as those of vertically traveling waves $\beta_0 = \sqrt{L/\rho}$ and $\alpha_0 = \sqrt{C/\rho}$ and the three coefficients measuring anisotropy as

$$\varepsilon = (1/\phi - 1)/2 \quad [11]$$

$$\gamma = (\xi - 1)/2 \quad [12]$$

$$\delta = (F+L)^2 - (F+L)^2/2C(C-L) \quad [13]$$

He showed that ε and γ, respectively, measure the difference in velocity between horizontally and vertically propagating P and SH waves, respectively. The parameter δ is a combination of ϕ and η from the previous notation. In weakly anisotropic media, δ controls the deviation from sphericity of the P wavefronts close to vertical propagation. Despite its subtle impact, δ is an important quantity in exploration geophysics.

Rocks are aggregates of different crystals. How different anisotropic crystals combine to produce a large-scale anisotropic material is not simple, and the exact result depends in particular on the shape of the crystals and not only on their elastic coefficients. For practical purposes, one evaluates the elastic coefficients of composite materials without knowledge of their detailed geometry. The simplest algorithm is a linear average of the elastic coefficients of the material components. This is called the Voigt average, which corresponds to the effective stiffness if all crystals undergo identical strain. Alternatively, a composite elastic tensor based on a linear average of crystal compliances is called the Reuss average, which would be accurate if all crystals experience identical stress. The mean of these two extreme averages is the Voigt–Reuss–Hill average, which typically is more accurate. Mechanical engineers have derived the so-called Hashin–Shtrikman bounds on the elastic properties of composite materials with two, three, or more components with known elastic properties (Watt and Peselnick, 1980), and these can be applied to the elasticity of rocks on scales from a hand sample to a layered intrusion.

Defining the isotropic-average properties of an anisotropic material also depends on the way the averaging is done. The Voigt averaging method takes a linear average of the elastic coefficients over all rotations in space. A TI material has the following isotropic-mean values in the Voigt average:

$$\mu = (A + C - 2F + 6L + 5N)/15 \quad [14]$$

$$\lambda + 2\mu = (8A + 3C + 4F + 8L)/15 \quad [15]$$

This implies that the isotropic-mean S wave speed depends partly on the P-wave speed parameters A and C. Since the Voigt average is an approximation based on geometric simplicity rather than physics, it is defensible to use simpler expressions for the mean velocities. The two common expressions for S waves are $(V_{SH} + V_{SV})/2$ and $(V_{SH} + 2V_{SV})/3$. Which formula

is used is not critical as long as one compares consistent quantities. Ekstrom and Dziewonski (1998) showed how discrepancies among global models have arisen because their S wave speeds were based on different datasets, shifting the weighting of SH and SV waves.

In seismology, the term TI is sometimes restricted to VTI models with a vertical axis of symmetry, but the term applies to more general orientations of the symmetry axis. Any elastic tensor can be separated into a transverse isotropic component, in the form of expression [6], corresponding to the azimuthal average of the model, plus deviations from this transverse isotropic mean, which are directly related to the azimuthal variations of the wave's velocities. This notation is particularly useful for surface-wave analysis, where the vertical direction singles out quite naturally, or for body waves propagating in the horizontal plane. Crampin (1981) showed that, in structures with a horizontal plane of symmetry, the azimuthal velocity variations of body waves propagating in the horizontal plane depend on the following combinations of elastic coefficients:

$$B_c = (C_{11} - C_{22})/2 \quad [16]$$

$$B_s = C_{16} + C_{26} \quad [17]$$

$$G_c = (C_{55} - C_{44})/2 \quad [18]$$

$$G_s = C_{54} \quad [19]$$

$$H_c = (C_{13} - C_{23})/2 \quad [20]$$

$$H_s = C_{36} \quad [21]$$

$$C_c = (C_{11} + C_{22} - 2C_{12} - 4C_{66})/8 \quad [22]$$

$$C_s = (C_{16} - C_{26})/2 \quad [23]$$

with a *c*-index for the coefficients associated with $\cos 2\theta$ and $\cos 4\theta$ velocity variations and an *s*-index for those associated with $\sin 2\theta$ and $\sin 4\theta$ variations. At first order in anisotropy, these combinations are also those that control the azimuthal variations of the body waves propagating horizontally in more general anisotropic structures (Leveque et al., 1998) and the variations of surface-wave phase velocities (Montagner and Nataf, 1986), as we shall see later in the text.

To provide a full description of the elastic tensor, eight additional elastic coefficients complement those given in the preceding text. They are given here in the notation of Chen and Tromp (2007):

$$D_c = (C_{15} - C_{25} - 2C_{46})/4 \quad [24]$$

$$D_s = (C_{14} - C_{24} - 2C_{56})/4 \quad [25]$$

$$J_c = (3C_{15} + C_{25} + 2C_{46})/8 \quad [26]$$

$$J_s = (3C_{14} - C_{24} + 2C_{56})/8 \quad [27]$$

$$K_c = (3C_{15} + C_{25} + 2C_{46} - 4C_{35})/8 \quad [28]$$

$$K_s = (3C_{14} + C_{24} + 2C_{56} - 4C_{34})/8 \quad [29]$$

$$M_c = (C_{15} - C_{25} + 2C_{46})/4 \quad [30]$$

$$M_s = (C_{14} - C_{24} + 2C_{56})/4 \quad [31]$$

At first order in anisotropy, they contribute to the velocity variation of body waves with nonhorizontal propagation, but not to the velocity variation of surface waves (Chen and Tromp, 2007).

Data averaged over azimuth will give access only to the five coefficients of the VTI component of the elastic tensor. Any global mean model, like PREM (Dziewonski and Anderson, 1981), cannot contain more elastic coefficients than these 5.

1.09.2.3 Weak Anisotropy Approximation

The exact solution of eqn [2] is a nonlinear procedure. When averaging the volume of rock typically sampled by a seismic wave, linearized solutions are a good approximation and illustrate well the first-order influence of each elastic coefficient on the wavefield. A complete treatment by the application of perturbation theory to the Christoffel equation at first order in anisotropy is presented in Jech and Psencik (1989), including perturbation of the polarization vectors.

For P waves, the perturbation in phase velocity has the simple form

$$\Delta V_P = \frac{1}{2V_P}\frac{\Delta c_{ijkl}}{\rho} n_i n_l g_j g_k \quad [32]$$

where $\vec{g}$ is the unit vector in the direction of polarization in the unperturbed medium, which is equal to $\vec{n}$ for P waves in isotropic structures. Summation should be made over repeated indexes. The azimuth angle θ appears in the vectors $\vec{n}$ and $\vec{g}$, yielding an azimuthal dependence of the velocities with a maximum order of 4. Equivalently, the well-known expressions for the velocity variations of body waves at first order in anisotropy, derived by Backus (1965), showed that ΔV_P has an azimuthal dependence in 2θ and 4θ in HTI media. In TTI media, the wave velocity also exhibits θ and 3θ azimuthal variation (Chen and Tromp, 2007).

The first-order perturbation of the P-wave polarization is normal to the unperturbed polarization. The work of Thomsen (1986), used extensively in seismic exploration and extended to more general anisotropy by Mensch and Rasolofosaon (1997), is also based on first-order approximations of the wave velocities.

The procedure to calculate the perturbations of the velocities and polarizations of S waves is more complicated than for P waves, due to the degeneracy of the Christoffel matrix for S waves in isotropic structures (Jech and Psencik, 1989). Results obtained from degenerate perturbation theory are valid even in strongly anisotropic structures with over 20% of anisotropy (Jech and Psencik, 1989). However, as opposed to the expression for P waves, the expressions for S waves are not linear in the perturbation of the elastic coefficients, and one cannot derive analytically a simple expression for the azimuthal dependence of their velocities in the general case. In practice, the velocities of quasi-S waves also show 2θ and 4θ azimuthal variations in many cases (Mensch and Rasolofosaon, 1997). Chen and Tromp (2007) showed that traveltimes of body waves and surface waves at global and regional scale are estimated well by the 'weak' expressions for anisotropies $\leq 5\%$.

1.09.2.4 Ray Theory

Body waves are commonly interpreted in terms of single phases that follow raypaths, making ray theory an important tool in seismology. Ray theory in anisotropic and in isotropic

structures is summarized by Cerveny (2001), Chapman (2004) and Virieux and Lambare (**Chapter 1.05**). In anisotropic media, some of the simple intuitive aspects of ray theory in isotropic media are lost. This is especially true for shear waves, because ray theory intertwines with the frequency-dependent coupling of the two quasi-S waves.

Ray theory is a high-frequency approximation of the equation of motion in heterogeneous structures. Following Cerveny (1972) and Cerveny (2001), the ray-tracing equations are

$$\frac{\mathrm{d}x_i}{\mathrm{d}t} = \frac{c_{ijkl}}{\rho} p_j g_j g_k = V_i \qquad [33]$$

$$\frac{\mathrm{d}p_i}{\mathrm{d}t} = -\frac{1}{2}\frac{\partial}{\partial x_i}\frac{c_{jklm}}{\rho} p_j p_m g_k g_l \qquad [34]$$

where $\vec{x}$ is a location along the ray and $\vec{p}$ is the ray's slowness, perpendicular to the wavefront and parallel to $\vec{n}$ from the previous section. $\vec{g}$ is one of the normalized eigenvectors of the Christoffel matrix, which defines the polarization of a wave that travels along the ray. The Christoffel matrix in ray theory is usually normalized by replacing the components of propagation direction $\vec{n}$ in eqn [2] by the components of the slowness $\vec{p}$, since the expressions are then better suited for the Hamiltonian formalism of the ray theory (Cerveny, 2001).

The group velocity $\vec{V}$ in eqn [33] defines the direction followed by the ray and is equivalent to the group velocity defined in eqn [3] for uniform media. The group velocity $\vec{V}$ is not generally parallel to the phase slowness $\vec{p}$, but the two vectors are related by the following dot product:

$$\vec{V} \cdot \vec{p} = 1 \qquad [35]$$

As in isotropic structures, eqn [34] controls the deviation of the ray, which depends on the lateral derivatives of the density-normalized elastic coefficients. A significant difference with the isotropic case is that the polarization vectors $\vec{g}$ appear explicitly in the ray equation in anisotropic media, whereas they do not appear explicitly (but implicitly in the choice of the wave type) in the isotropic case. The equations can be rewritten without this explicit dependence by expressing the eigenvector dot products in eqns [33] and [34] in terms of selected elements of the Christoffel matrix and its eigenvalues (Cerveny, 2001).

At leading order, the polarization of wave motion follows the polarization vector $\vec{g}$, and the rays are traced independently for the three waves. These results can be used readily for P waves in most cases. The situation is however more complex for S waves: in addition to *shear-wave splitting*, we have *shear-wave coupling* in anisotropic media with lateral variations (Chapman and Shearer, 1989). In the same way as long-period P and S waves couple when they propagate through strong gradients in elastic properties (Richards and Frasier, 1976), split S waves couple to each other in gradient regions. The closer the velocities of the two shear waves, the smaller the gradient needed to produce a significant coupling. Such coupling is therefore a critical aspect of shear-wave propagation in weakly anisotropic media (Coates and Chapman, 1990) and in strongly anisotropic media in the vicinity of singular points. At singular points, the two quasi-S wave speeds approach each other and the polarizations of the two quasi-S waves rotate rapidly around the ray (Chapman and Shearer, 1989). Quasi-S-wave coupling is stronger at low frequencies and leads therefore to frequency-dependent polarizations. Coupling partly compensates for splitting, as illustrated in **Figure 5**, and makes quasi-S-wave propagation converge toward the isotropic-media solution as the anisotropy goes to zero.

The nature of shear-wave coupling can be understood intuitively by considering cases where the theoretically determined polarization of a given quasi-S wave changes abruptly. The physical energy in the S wavefield will only partly follow the rotation of polarization and will partly transfer onto the other quasi-S wave, leaving the overall particle motion weakly perturbed. Observable birefringence in the S wave as a result of this energy transfer develops as the wave propagates. Chapman and Shearer (1989) gave an expression to connect the quasi-S rays across the gradient region where coupling occurs, which can be useful when coupling occurs only in a limited portion of the model. In cases of extended coupling through the whole model, such as with weakly anisotropic media, a possible approach is based on the perturbation of the isotropic case. In the so-called quasi-isotropic approximation (Psencik, 1998), the quasi-S waves do not appear explicitly, and observed S waves are calculated through a system of two coupled frequency-dependent differential equations. For weak anisotropy or close to singularities, this gives a regular solution in which splitting and coupling are naturally taken into account together and that naturally converges to the solution in the isotropic structure as anisotropy goes to zero. For strong anisotropy, the coupled equations transform to two decoupled equations for the two quasi-S waves.

An alternative approach based on higher-order perturbations and on an appropriate choice of coordinate system along the ray allows either for separate ray tracing of the two quasi-S waves in weakly anisotropic media (Farra, 2005; Farra and Psencik, 2003) or for coupling the two waves along a common ray traced using the average velocities of the two waves in the ray direction, avoiding the isotropic average (Farra and Psencik, 2008). Traveltime errors related to different approaches of the shear-wave coupling problem are estimated by Klimes and Bulant (2006). Similar to ray theory, a quasi-isotropic WKBJ perturbation approach with the Langer approximation has been proposed by Maupin (1994) for layered structures.

1.09.2.5 Reflection and Transmission Coefficients

Anisotropy distorts the stress–strain relation for plane waves and perturbs the orientations of particle motion and traction exerted

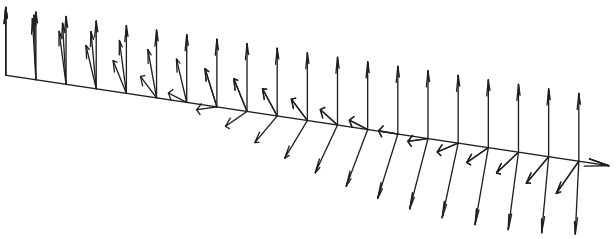

Figure 5 S-wave polarization vector along a ray: Isotropic ray theory polarization points upward. Anisotropic ray theory polarization points downward on the right-hand side. Coupling ray theory polarization vector points between the two previous ones. At longer period, it would point closer to the isotropic ray theory polarization. At shorter period, it would point closer to the anisotropic ray theory polarization. Figure courtesy of Ludek Klimes.

at an interface between two layers. Because displacements and tractions must remain continuous across solid–solid interfaces, anisotropic distortions lead to a more complicated pattern of reflected and refracted waves than in isotropic media. Basically, anisotropy removes the separation of SH waves and P-to-SV waves that occurs in isotropic horizontally layered structures (Crampin, 1981; Fryer and Fraser, 1984). The coupling means, for example, that a P wave in an isotropic layer impinging on an anisotropic layer will yield a transmitted quasi-P wave, two transmitted quasi-S waves, reflected P and SV waves, and a reflected SH wave. The conversion of a P wave to an SH wave is a characteristic of anisotropy. The exact anisotropic reflection and transmission coefficients can be readily calculated (Keith and Crampin, 1977), but useful first-order expressions have also been derived for weak anisotropy (Farra and Psencik, 2010), for weak contrast across the interface (Klimes, 2003), and for weak contrast and weak anisotropy (Vavrycuk, 1999).

Seismic observations of wave conversions at buried interfaces, such as those retrieved from teleseismic receiver functions (Farra and Vinnik, 2000; Park and Levin, 2000), can inform us about the depth dependence of anisotropy. A primary indicator of anisotropy in receiver-function studies is the conversion of P- to SH-polarized shear waves. Levin and Park (1998) showed that, for hexagonal symmetry, P-to-SH converted waves follow a two-lobed or four-lobed radiation pattern with back azimuth, depending on the combination of symmetry-axis orientation and the relative strength of anisotropy in V_P and V_S. P-to-SV converted waves vary with back azimuth as well, perturbing the converted-wave amplitude associated with discontinuities in isotropic wave speed. Anisotropy with a vertical axis of symmetry does not induce P-to-SH converted phases and does not introduce back-azimuth variation in the amplitude of P-to-SV converted waves. Four-lobed and two-lobed P-to-SH radiation are favored by a horizontal and a tilted symmetry axis, respectively. The scattered-wave amplitude vanishes for P waves whose back azimuth parallels the strike of the anisotropic symmetry axis, and the SH wave has opposite polarity for impinging waves that approach from opposing sides of the symmetry axis. The P-to-SH scattered wave also vanishes for incoming P wave whose azimuth is normal to the strike of a horizontal symmetry axis.

A 2-lobed P-to-SH radiation pattern is predicted to occur as a result of P-to-S conversion at a dipping interface in the absence of anisotropy (Levin and Park, 1997a; Savage, 1998), suggesting that anisotropy and deviations from layered structure can be confused. Moreover, at a dipping interface, there are P-to-SV amplitude variations (**Figure 6**), which are associated with the variation of the perturbed P-incidence angle on the dipping interface: updip and downdip teleseismic P arrivals impinge at angles that differ by twice the dip angle, which leads to a variation in P-to-SV conversion amplitude. Discrimination between flat-layered anisotropic media and dipping isotropic media is difficult, because the mutual variation of the P-to-SH and P-to-SV converted waves with back azimuth is quite similar. Other information, such as an independent constraint on interface geometry, is useful. There can be a strong trade-off when the dipping interface borders an anisotropic region with a tilted symmetry axis. The anisotropic effect on wave conversion also depends on the P-incidence angle. Park et al. (2004) and Savage et al. (2007) found that the dip effect in the Cascadia (the United States) and Hikurangi (New Zealand)

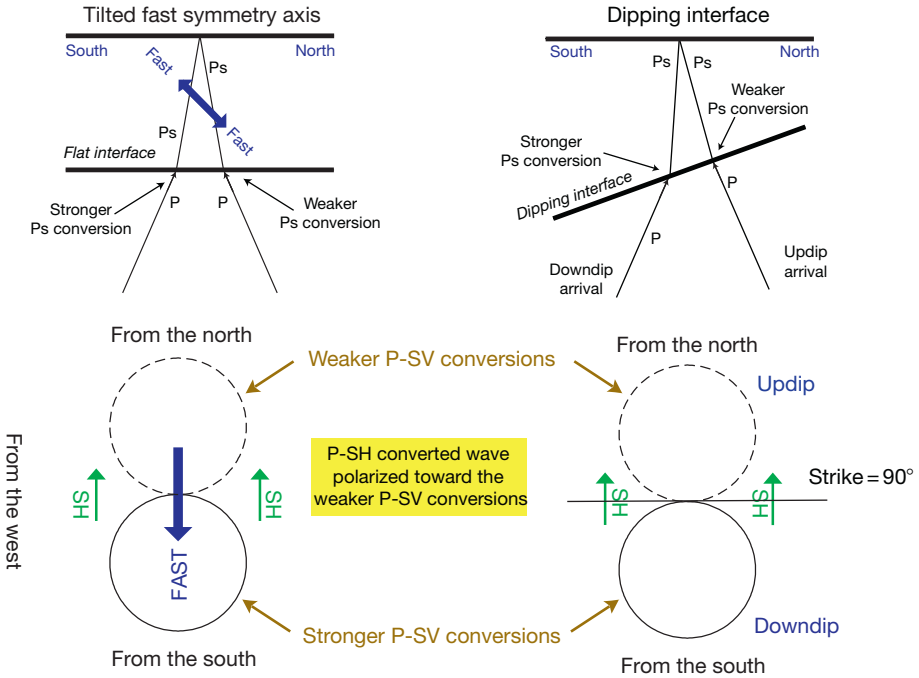

Figure 6 Schematic of S-to-P converted waves associated with anisotropy with a tilted fast symmetry axis (left) and a dipping interface between isotropic media (right). The back-azimuth variation of converted-wave amplitude follows a simple two-lobed harmonic pattern (to leading order) in both cases. The upper panels diagram the geometry of P-to-S conversion in side view. The lower panels indicate the amplitude and polarity patterns predicted for the two cases. The relationship of P-to-SV and P-to-SH conversions is similar for tilted-axis anisotropy and a dipping interface in isotropic media, suggesting that additional constraints are necessary to discriminate the two cases.

subduction zones, respectively, enabled the P-to-SH conversion amplitudes to be fit with far less anisotropy (7% vs. 10% in the case of Cascadia).

1.09.2.6 Surface Waves and Normal Modes

In anisotropic-layered media, the coupling between P, SV, and SH waves implies the loss of distinct Love and Rayleigh surface waves, to be replaced by generalized modes that are polarized in three directions. This is an essential difference between surface waves in isotropic and anisotropic media, together with azimuthal variation of their velocities and other characteristics, and that phase and group velocities are not aligned (Crampin, 1970). Anisotropy perturbs the frequencies and oscillation patterns of seismic free oscillations in a manner similar to isotropic lateral structure, especially for transversely isotropic media with a vertical axis of symmetry. Anisotropy with a nonvertical symmetry axis, or with no symmetry axis, causes more extensive waveform perturbations.

An anisotropic stress–strain relation encourages the coupling and hybridization of spheroidal (${}_nS_l$) and toroidal (${}_nT_l$) oscillation types. (The subscripts n and l refer to the overtone number and angular degree of the free oscillation, respectively. Each ${}_nS_l$ and ${}_nT_l$ is a 'multiplet,' a collection of $2l+1$ distinct 'singlet' vibrations that share a common n, l, and oscillation frequency for a standard spherical Earth reference model.) Spheroidal and toroidal free oscillations with low overtone number combine to form Rayleigh and Love surface waves with particle motions that are mutually orthogonal. Smoothly varying isotropic velocity heterogeneity causes the spheroidal and toroidal oscillation types to interact weakly at best. Anisotropic structure induces mixed-type interaction far more effectively. Similar coupling efficiency arises from the deflection of seismic particle motion by the Earth's Coriolis force, but laterally variable anisotropy perturbs the seismic wavefield more extensively, facilitating many more coupling interactions.

As for body waves, first-order perturbations can be used to describe surface-wave propagation in anisotropic Earth models. Smith and Dahlen (1973) showed that the phase velocities vary in 2θ and 4θ at first order in anisotropy and depend on a set of 13 elastic coefficients. These expressions, rewritten by Montagner and Nataf (1986), are the basis for most of the tomographic inversions made with surface-wave phase velocities. For Love waves, perturbation in phase velocity depends on the elastic parameters through two kernels only:

$$\begin{aligned}\delta V_L = &\frac{\partial V_L}{\partial L}(\delta L - G_C\cos 2\theta - G_S\sin 2\theta)\\ &+\frac{\partial V_L}{\partial N}(\delta N - C_C\cos 4\theta - C_S\sin 4\theta)\end{aligned} \quad [36]$$

Similarly for Rayleigh waves, this depends on the elastic parameters through four kernels:

$$\begin{aligned}\delta V_R = &\frac{\partial V_R}{\partial A}(\delta A + B_C\cos 2\theta + B_S\sin 2\theta + C_C\cos 4\theta + C_S\sin 4\theta)\\ &+\frac{\partial V_R}{\partial C}\delta C + \frac{\partial V_R}{\partial F}(\delta F + H_C\cos 2\theta + H_S\sin 2\theta)\\ &+\frac{\partial V_R}{\partial L}(\delta L + G_C\cos 2\theta + G_S\sin 2\theta)\end{aligned} \quad [37]$$

The sensitivity kernels of these equations are plotted in Figures 7 and 8 for Rayleigh and Love waves at different periods. $\frac{\partial V_L}{\partial N}$ dominates for Love waves and $\frac{\partial V_R}{\partial L}$ dominates for Rayleigh waves, at least for the deeper layers. As a result, Rayleigh-wave phase velocities are more strongly influenced by the distribution with depth of L, G_C, and G_S, whereas Love-wave phase velocities depend more strongly on N. C_C and C_S should also contribute significantly to Love-wave phase velocities, but the difficulty in measuring 4θ variations in Love velocities makes these parameters hard to constrain.

The sensitivity kernels in the preceding text express the sensitivity of the surface-wave velocities at first order in different anisotropic parameters as a function of depth assuming no

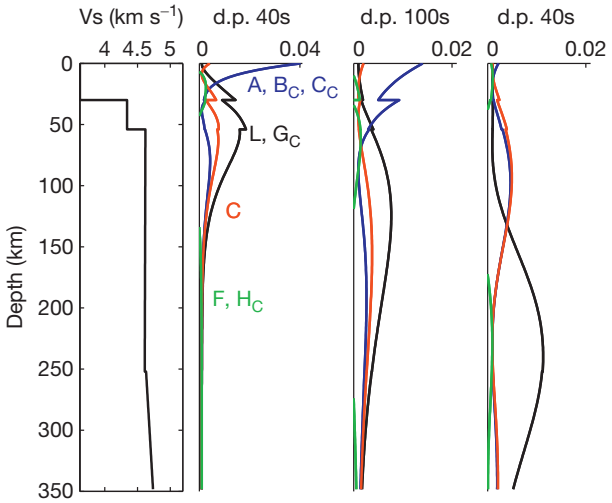

Figure 7 Sensitivity kernels of the Rayleigh-wave phase velocities to different parameters as a function of depth. The S-wave velocity of the model in which the kernels have been calculated is shown to the left. The sensitivity kernels with respect to different elastic coefficients are shown in the subsequent plots for the fundamental mode at a period of 40 and 100 s and for the first overtone at a period of 40 s.

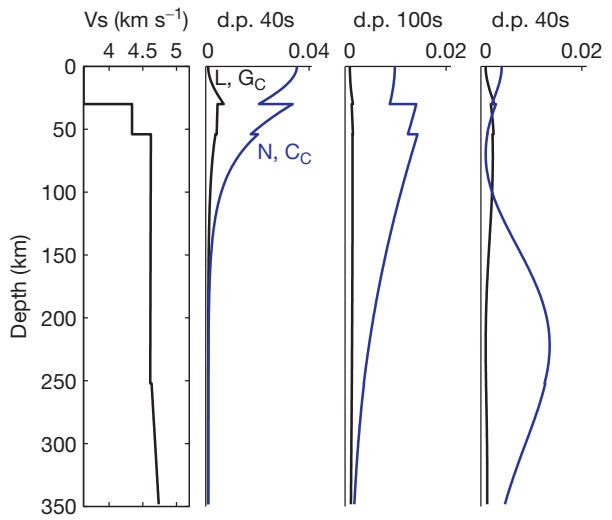

Figure 8 The same as Figure 7 for Love waves.

lateral variation of the structure. Beyond this approximation, finite-frequency kernels can be calculated (Sieminski et al., 2007). As in the isotropic case, they reveal that the width of the sensitivity zone is significant, broadening to, for example, a third of the epicentral distance for surface waves at 140 s period and 120° epicentral distance. Finite-frequency kernels confirm the role of the parameters identified earlier in the text as the main contributors to phase-velocity variations in the vicinity of the source–receiver great circle but suggest the off-path influence of other parameters, for example, N, C_C, and C_S, through Rayleigh–Love coupling.

The dominance of the 2θ phase-velocity azimuthal variation for Rayleigh waves and of the 4θ for Love waves can be seen in **Figure 9**. A 2–3% peak-to-peak azimuthal variation is observed at 40 s period in this model with anisotropy in the form of 35% oriented olivine crystals in the upper 80 km of the mantle. The surface-wave velocities have been calculated here with the reflectivity method of Thomson (1997) and are not first-order approximations based on the equations in the preceding text. The olivine a-axis is either horizontal, dipping at 45°, or vertical. We see that Rayleigh waves have maximum velocity in the azimuth of the a-axis and minimum in the azimuth of the c-axis and that a 45° dip of the a-axis modifies the average velocity but not the amplitude of the azimuthal variation. When the a-axis is close to the horizontal plane, the Rayleigh waves have average phase velocities that are lower than the isotropic reference. The average phase velocity is higher than the isotropic reference for large dips of the symmetry axis. The opposite is true for Love waves, which causes the apparent Love–Rayleigh discrepancy (Anderson, 1961), which is positive for horizontal a-axis and negative for vertical a-axis. The azimuthal variation is shown here for the fundamental mode at one period, but very similar curves are obtained at other periods and for the overtones (Maupin, 1985).

The 3-D nature of surface-wave polarization in anisotropic media brings information on the nature of the Earth's anisotropy that is complementary to the information we get from the analysis of their velocities. Coupling between fundamental Rayleigh and Love waves due to lateral gradients in anisotropy along the path of the surface waves produces wavetrains with arrival times between the direct Love and Rayleigh waves (Park and Yu, 1993). The timing can be understood in terms of the difference in group velocity between Love and Rayleigh waves. Similarly, a fundamental Rayleigh wave that scatters some energy to a fundamental Love wave is outpaced by the scattered phase, which is observed to arrive ahead of it. Overtone Love and Rayleigh waves have similar group velocities at long period, leading to a near-simultaneous arrival of direct and scattered overtone waves. In addition, anisotropy close to the station distorts the polarizations of the direct waves.

Surface waves with polarization anomalies related to anisotropy have been called 'quasi-Love' waves or 'quasi-Rayleigh' waves in the literature, but the terms have been used slightly differently in the contexts of polarization–distortion or of scattering. In the context of polarization–distortion, the usage is similar to that of quasi-P and quasi-S body waves: A 'quasi-Rayleigh' wave is mainly P-to-SV-polarized with some transverse motion (Crampin, 1970), and a 'quasi-Love' wave is mainly transverse-polarized with some P-to-SV motion. For surface-wave scattering, the term 'quasi-Love' applies to the anomalous P-to-SV-polarized wave that scatters from the main Love wave. Conversely, the 'quasi-Rayleigh' term applies to the anomalous transverse-polarized wave that scatters from the main Rayleigh wave. The quasi-Love wave is a Rayleigh-polarized wave whose energy propagates with Love-wave phase velocity before scattering and with Rayleigh-wave velocity after scattering, observed as a distinct wave that requires a name. If scattering occurs close to the station, the quasi-Love wave arrives as an apparent precursor to the Love wave, hence its name. Similarly, the 'quasi-Rayleigh' wave is a Love-polarized wave that trails the Rayleigh wave closely if scattering occurs close to the station.

The surface polarization of the quasi-Rayleigh waves whose phase velocities were shown in **Figure 9** is presented in **Figures 10** and **11**. For a horizontal a-axis (**Figure 10**), the polarization remains linear, but deviates up to 8° from the phase-velocity direction. For an olivine a-axis dipping at 45°, the polarization anomaly is much more pronounced (**Figure 11**) with a distinctive elliptical motion. Generally speaking, coupling and polarization anomalies have maximum amplitude in propagation directions far from the symmetry axes and symmetry planes of the anisotropy. Polarization anomalies are therefore better suited than velocities to detect a plunge in the anisotropy symmetry axes (Maupin, 2001).

The polarization anomalies can be analyzed at first order in anisotropy using perturbation procedures (Park, 1997; Tanimoto, 2004). It should be noted that the usual procedure,

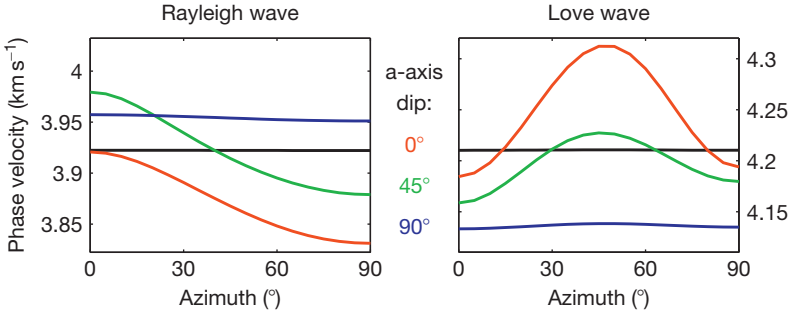

Figure 9 Azimuthal variation of the phase velocities of Rayleigh- and Love-wave fundamental modes at 40 s period in a model with 35% oriented olivine crystals (Kumazawa and Anderson, 1969) in the upper 80 km of the mantle. The olivine a-axis is in the vertical plane at azimuth 0° and dipping at either 0° (in red), 45° (in green), or 90° (in blue), and the c-axis is in the azimuth 90°. The background isotropic Voigt average model is model iasp95, and the phase velocities in this model are shown as solid black lines.

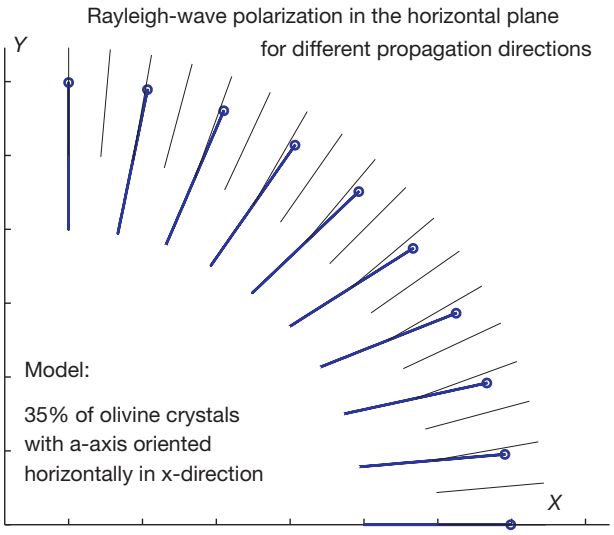

Figure 10 Polarization of a 40 s Rayleigh wave in the horizontal plane in different azimuths. The model is the same as in **Figure 9**. The olivine *a*-axis is in the *x*-direction and the *c*-axis is in the *y*-direction. Thin lines show the direction of the phase velocity and thicker blue ellipses (flat in the present case) show the surface polarizations.

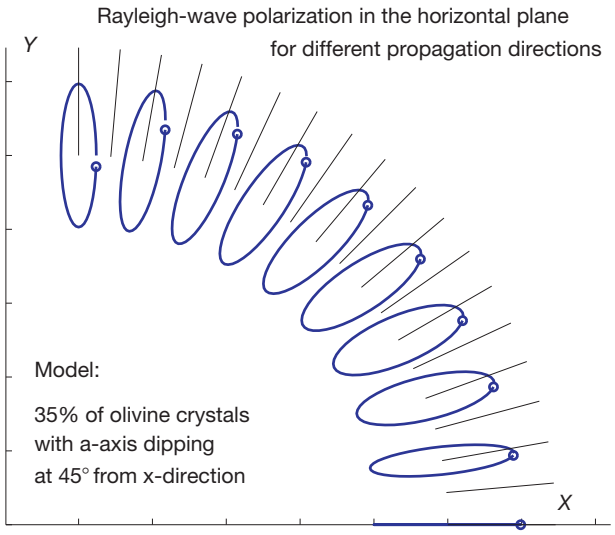

Figure 11 The same as **Figure 10** for an *a*-axis dipping at 45° in the vertical plane containing the *x*-direction. The prograde nature of the elliptic motion is shown with the small symbol at the start of the motion.

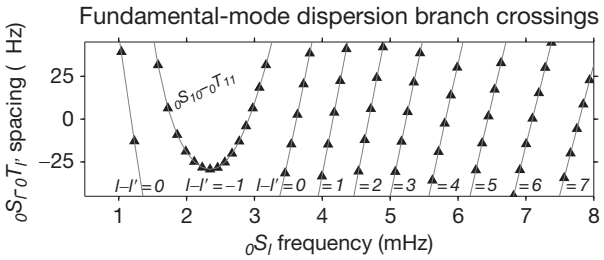

Figure 12 The relative placement of fundamental-mode branches of spheroidal (*S*) and toroidal (*T*) Earth free oscillations determines the coupling pairs $_0S_l$–$_0T_{l'}$ that are asymptotically sensitive to the wavenumber $s = |l - l'|$ of anisotropy along the great-circle path between source and receiver. At $f < 2$ mHz, $|l - l'| = 1$ for many nearest-neighbor mode pairs, so the Earth's Coriolis force has a significant effect. At frequencies $f > 2$ mHz, $|l - l'|$ increases with frequency, increasing the influence of anisotropy.

based on nondegenerate perturbation theory, may need modifications for modes close to each other in phase velocity (Maupin, 2004). Higher-mode Love and Rayleigh dispersion curves are roughly parallel and close to each other over the broad frequency range where they can be identified with multiple SH and SV reverberations in the upper mantle. Fundamental Love and Rayleigh waves arise from dispersion branches that differ greatly, but which cross each other at specific free oscillation multiplet pairs $_0S_l$–$_0T_{l'}$. At these crossing points, the nondegenerate perturbation theory is not valid anymore and one has to use degenerate or quasi-degenerate perturbation methods (Maupin, 1989).

The strength of coupling between two seismic free oscillations is inversely proportional to their frequency spacing. The largest coupling effects are seen for nearest-neighbor coupling pairs on similar dispersion branches, for example, the fundamental branch $n = 0$. At frequencies $f < 2$ mHz (periods $T > 500$ s), most nearest-neighbor fundamental spheroidal–toroidal mode pairs differ by angular degree $s = |l - l'| = 1$ and are influenced strongly by the Earth's Coriolis force (Masters et al., 1983). At higher frequencies, the angular-degree difference $s = |l - l'|$ of these mode pairs increases as the Love and Rayleigh fundamental dispersion branches diverge (**Figure 12**). Coupling between spheroidal and toroidal free oscillations in these branches gives rise to the scattering of Love to Rayleigh and from Rayleigh to Love (**Figure 13**).

Park (1997) showed that, for a particular $_0S_l$–$_0T_{l'}$ coupling pair, the asymptotic effect of anisotropy is maximal for structure with wavenumber $s = |l - l'|$ along the source–receiver great circle. This leads to some unusual effects in hypothetical anisotropy models. For instance, anisotropy with a single angular degree s will influence a narrow frequency interval where dispersion-branch crossings are auspicious for coupling, leading to a longer-duration scattered wave with narrowband frequency content. As the wavenumber s of the anisotropic structure along the great-circle path increases, the wavenumbers and frequencies of the relevant modal coupling pairs increase. Because the fundamental-mode surface-wave perturbation kernels also vary with frequency, the depth of maximum sensitivity shallows as frequency increases. For free oscillation overtone branches, nearest-neighbor toroidal and spheroidal coupling pairs differ little in angular degree (**Figure 14**), suggesting sensitivity to near-constant anisotropy along the great-circle path. Coupling between mode branches will be sensitive to anisotropic gradients, for example, $_1T_{60}$–$_2S_{49}$ near $f = 9$ mHz will be sensitive to wavenumber $s = 11$. The predictability of fundamental-branch surface-wave coupling relations suggests that a linearized inversion of Love–Rayleigh scattering for structure along path is possible (Oda, 2005).

1.09.3 Seismological Observations of Anisotropy

Considerable progress has been made in the last 25 years in mapping the Earth's anisotropy. There is evidence at the

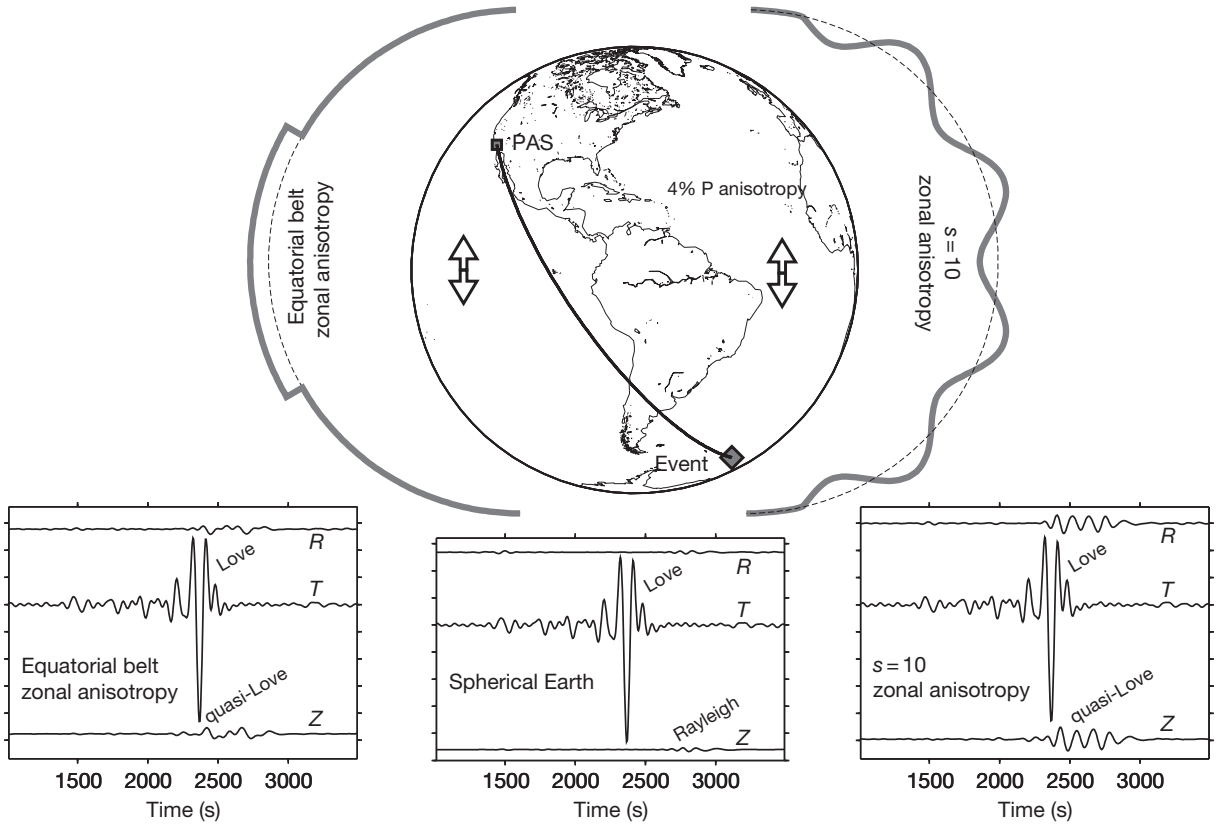

Figure 13 Examples of quasi-Love scattered waves computed for two simple anisotropic Earth models, compared with a synthetic seismogram for an unperturbed spherical Earth model. Coupled free oscillations are summed for all free oscillations with overtone number n≤4 and f≤16 mHz (T≥62 s). Anisotropy with a north–south horizontal axis of symmetry is imposed between the Moho and 220 km depth and the zonal symmetry to facilitate modal coupling computations. The earthquake source and station location are chosen to display a predominant Love wave, so that the quasi-Love scattered wave has larger amplitude than the Rayleigh wave. At the left, the synthetic seismograms for an equatorial belt of anisotropy display two pulses associated with lateral discontinuities at 30S and 30N. At the right, an anisotropic corrugation with wavenumber $s = 10$ generates a broader and more narrowband scattered wave, as a result of asymptotic selection rules in free oscillation coupling.

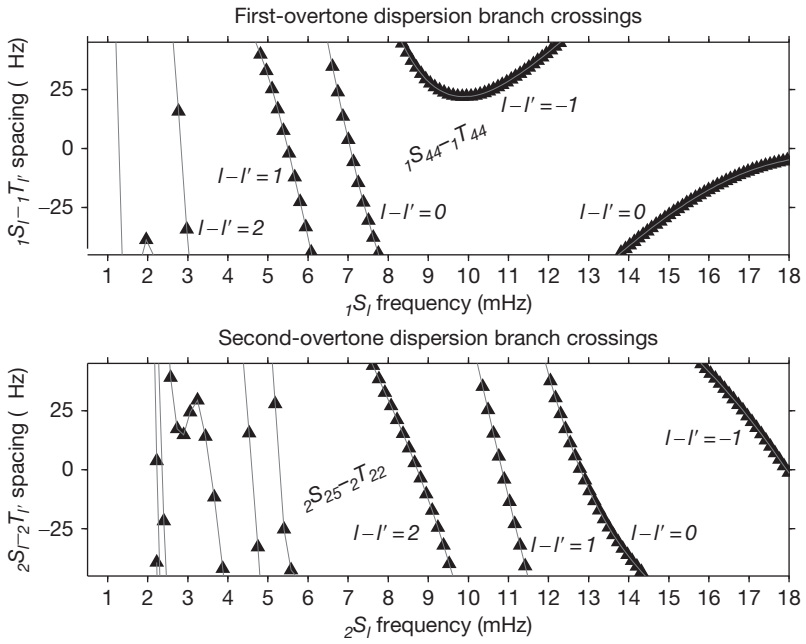

Figure 14 The relative placement of $n = 1$, 2 overtone branches of spheroidal (S) and toroidal (T) Earth free oscillations determines the coupling pairs that are asymptotically sensitive to the wavenumber $s = |l - l'|$ of anisotropy along the great-circle path between source and receiver. At $5 < f < 20$ mHz, $|l - l'| < 2$ for most nearest-neighbor mode pairs, in contrast to the behavior of the fundamental-mode branches. As a consequence, path-averaged anisotropy on the source–receiver great circle has a significant effect on ${}_1T_{l'} - {}_1S_l$ and ${}_2T_{l'} - {}_2S_l$, coupling pairs.

present time for anisotropy in the inner core, in the D″ layer, and from the transition zone up to the surface. But the picture we have of the Earth's anisotropy is indeed blurred and complex, and the mechanisms that create anisotropy are far from completely deciphered.

1.09.3.1 Crustal Anisotropy

Anisotropy in sedimentary layers is commonly observed in seismic exploration. As this subject is beyond the scope of this chapter, we refer to Helbig and Thomsen (2005) and Tsvankin et al. (2010) for reviews of near-surface anisotropy. We focus here on crustal anisotropy pertaining to crystalline basement rocks. The smaller volume and greater complexity of crustal rock relative to upper-mantle peridotites limit the crustal influence in many path-averaged observables, such as SKS birefringence, and the crust is usually considered as isotropic in global- or large-scale models. However, local studies reveal that localized anisotropy is common in the Earth's crust, dominantly in association with oceanic crustal structures, in the deformed regions of the lower continental crust in extensional regions (Endrun et al., 2011; Meissner et al., 2006), and in the vicinity of fault zones (Cochran et al., 2006; Peng and Ben-Zion, 2004). Surface waves at periods with high crustal sensitivity, either generated by earthquakes or measured by ambient-noise interferometry, have contributed to an increase in the number of observations that pertain to crustal anisotropy and show that anisotropy may be present at any depth in the crust. Strong azimuthal anisotropy in the upper crust is observed in South Africa and has been related to extension at the southern tip of the African Rift (Adam and Lebedev, 2012). Midcrustal strong radial anisotropy has been observed in Tibet (Duret et al., 2010; Shapiro et al., 2004), whereas radial anisotropy has been inferred in the lower crust in the Aegean Sea (Endrun et al., 2008, 2011) and azimuthal anisotropy in the lower crust of the western United States (Lin et al., 2011).

Geologic factors that contribute to crustal anisotropy include LPO and shape-preferred orientation (SPO) of mineral crystals, oriented cracks, and fine layering of dissimilar lithologies (Godfrey et al., 2000; Kern, 1993; Kern et al., 2008; Siegesmund et al., 1991a,b). LPO is a microscopic alignment of the atomic lattices within minerals with a macroscopic direction, often developed in response to bulk rock deformation. SPO is a macroscopic alignment of minerals with elongated shapes, often developed as part of metamorphic foliation. Crustal LPO can be substantial, owing to the prevalence of hydrated minerals in sedimentary and metamorphic rocks, susceptible to slip on internal glide planes. The sheet-silicate structure of many hydrated minerals typically induces the axis of symmetry to be slow rather than fast. The anisotropy of aligned planar cracks and of fine-layered dissimilar lithologies is also characterized by a slow axis of symmetry and has much relevance in seismic exploration studies (Helbig, 1994) and in studies of the upper crust in general. Kern et al. (2008) estimated that the SPO of mineral crystals and cracks in foliated gneiss samples can double the intrinsic anisotropy produced by LPO. Ward et al. (2012) found that the anisotropy of natural and synthetic mylonites depends on a combination of mica LPO and quartz SPO.

There is some indication that the seismic lamination, which gives rise to high-reflectivity features in the deep crust, as imaged in active-source seismic surveys, is associated with anisotropy (Godfrey et al., 2000; Meissner et al., 2006). Since high reflectivity and associated anisotropy are characteristic of continental regions submitted to lateral extension, a possible interpretation is that the ductile lower crust reacts to extension by developing LPO in shear zones (Meissner et al., 2006).

Another region where anisotropy is commonly observed is the upper 3–5 km of the crust, likely caused by the opening of cracks in response to tectonic stresses. In the oceanic crust, vertical dikes and cracks associated with hydrothermal cooling of young lithosphere near mid-ocean ridges lead to anisotropy. At large scale, crustal anisotropy affects Pg propagation, for example, with 2% P-wave azimuthal anisotropy in the upper crust of Bohemia (Vavrycuk et al., 2004), and Lg waves, in the form of polarization anomalies (Maupin, 1990). Crack-induced anisotropy has a rich potential for determining stress directions in the shallow crust (Crampin and Chastin, 2003). Even a random distribution of cracks can develop an effective alignment, and elastic anisotropy, if cracks with favorable orientations open in response to the least-compressive regional stress. Keir et al. (2011) argued that the largest anisotropy within the upper crust of the Ethiopian Afar rift (~6%) occurs as a result of dike intrusion within localized areas of magmatism, leading to rift-parallel fast polarization in shear-wave splitting from local earthquakes. Upper-crustal anisotropy weakens to a residual 1–2.8% in areas of the Afar rift where intrusive dikes have solidified, sealing large open cracks.

The orientation of cracks and anisotropy adjacent to fault zones can indicate whether the fault is too weak to sustain shear stresses and may be held open by fluid pressures in the cracks (Balfour et al., 2005). The birefringence of high-frequency S waves from earthquakes at small epicentral distances has been used to monitor how anisotropy increases in the vicinity of major fault systems (Cochran et al., 2006; Peng and Ben-Zion, 2004). Although the depth constraint is usually weak, there seems to be an indication that the fault-associated anisotropy is also confined to the upper few kilometers of the crust. The anisotropy in S-wave velocity increases, for example, from 2% far from the North Anatolian Fault to 7% a few hundred meters close to the fault (Peng and Ben-Zion, 2004). In the near-fault region, the fast directions rotate parallel to the fault plane, showing that the anisotropy is likely to originate from a combination of fabrics and shear-induced cracks. A lively debate continues over whether precursory loading of earthquake fault zones (Chao and Peng, 2009; Durand et al., 2011; Liu et al., 2004; Peng and Ben-Zion, 2005; Saiga et al., 2003) and volcanoes (Savage et al., 2010) can be detected by temporal changes in crack anisotropy. Nakata and Snieder (2012) documented postseismic changes in near-surface anisotropy associated with the great Tohoku-Oki megathrust earthquake of 2011.

1.09.3.2 Origin of Upper-Mantle Anisotropy

Observations of ophiolites and xenoliths and deformation experiments show that upper-mantle rocks develop LPO under strain via dislocation creep within anisotropic olivine crystals. Seismic anisotropy is therefore our most direct

indicator of the upper-mantle deformation associated with thermal convection and plate tectonics. However, the type of fabric developed by olivine LPO depends on the ambient temperature, stress, and presence of melt or volatile compounds, especially water (Holtzman et al., 2003; Jung and Karato, 2001; Kaminski, 2006; Kaminski and Ribe, 2001; Skemer et al., 2006). Moreover, dislocation creep within crystals is not the only mechanism by which olivine-rich rocks can deform (Hansen et al., 2011; Kohlstedt, 2006), and not all deformed anisotropic rocks at upper-mantle depths are olivine-rich (Wang et al., 2012). Relating seismic anisotropy to mantle deformation requires knowledge of chemistry and physics and is reviewed in the chapter by Stixrude and Jeanloz.

Single-crystal olivine exhibits wave speed anisotropy of 24.6% and 22.3% in compressional (P) and shear (S) waves, respectively (Kumazawa and Anderson, 1969) (see also **Figure 2** for anisotropy in an olivine-rich material). Olivine is found with pyroxene and garnet in peridotites. Pyroxene crystals are anisotropic and contribute to bulk anisotropy in mantle peridotite. Garnet crystals are cubic and exhibit a more isotropic elastic behavior. Olivine is roughly twice as abundant as pyroxene in peridotite, and so its alignment is probably a dominant element in its bulk anisotropy (Babuska and Cara, 1991). The *a*-axis of olivine crystals corresponds to the stiffest direction in which P waves have highest velocities. If the *a*-axis is horizontal, it parallels both the 'fast' polarization of vertically propagating quasi-S waves and the propagation azimuth at which Rayleigh waves have maximum phase velocity. The olivine *a*-axis is therefore commonly called 'the fast axis.' There is less difference in stiffness between the *b*- and *c*-axes, so their directions are more difficult to distinguish with seismological data than the direction of the *a*-axis.

The direction of the *a*-axis is often interpreted as parallel to the mantle-flow direction, but such a simple interpretation has caveats. We can say that the competing effects of intracrystalline slip on vulnerable glide planes within the crystal lattice and of dynamic recrystallization associated with grain-boundary migration lead to different LPO in different conditions at different stages of the deformation (Kaminski and Ribe, 2001). A good rule of thumb is that in dry unmolten regions, the *a*-axis aligns within 10–20° of the major axis of the finite-strain ellipsoid (FSE), except where a parcel of mantle peridotite undergoes rapid changes in its strain geometry as it travels along its flow lines. For large simple-shear deformations (**Figure 15**), the fast axis aligns with the shear direction and slower axes in the plane perpendicular to it (Warren et al., 2008; Zhang and Karato, 1995). In uniaxial compression (pure shear), the slower *b*-axis tends to align with the compression direction and the *a*-axis to orient randomly in the plane normal to compression, leading to slow velocities in the compression direction and faster velocities in the plane normal to it (Kaminski and Ribe, 2001).

The presence of water influences the relative strength of mineral slip systems and modifies the relation between strain and LPO. In wet conditions, olivine may develop a B-type LPO (Jung and Karato, 2001), in which the fast *a*-axis orients at 90° from the strain direction. This yields fast directions perpendicular to what they would have been in the same strain field for the classical A-type dry olivine LPO described earlier in the text. Strain partitioning in partially molten regions has a similar

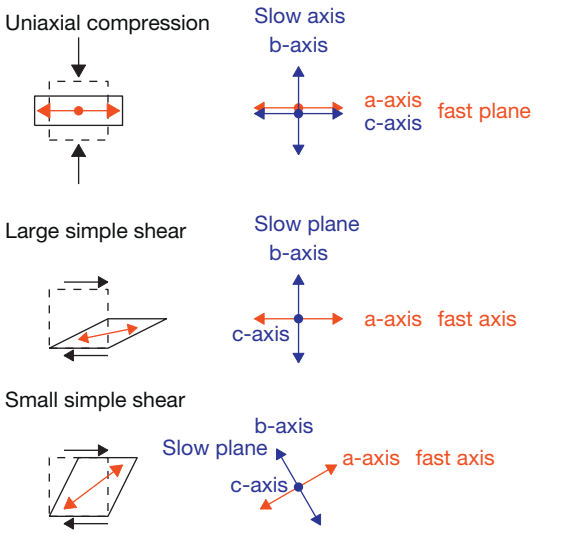

Figure 15 Long-term preferred orientation of dry olivine in simple-shear and in uniaxial compressive deformation. The deformation style is depicted on the left side of the figure, with the direction of the major axis of the finite-strain ellipsoid (FSE) as red arrows. Arrows pointing out of the figure plane are depicted by dots. Generally speaking, the *a*-axis follows the direction of the major axis of the FSE. In uniaxial compression, the *b*-axis orients in the compression direction, defining a slow axis, whereas the *a*- and *c*-axes orient randomly in the plane perpendicular to it, defining a fast plane. In large simple shear, the *a*-axis orients in the shear direction, defining a fast axis. The *b*-axis orients perpendicular to the shear plane and the *c*-axis along the neutral deformation direction. The *b*- and *c*-axis define a slow plane. In small simple shear, the pattern is similar, but tilted away from the shear direction due to the difference in direction between the major axis of the FSE and the shear.

effect (Holtzman and Kendall, 2010; Holtzman et al., 2003), and this may be observed beneath a significant fraction of mid-ocean ridges (Kaminski, 2006). Karato et al. (2008) listed three further olivine fabrics (C, D, and E) observed in laboratory deformations under differing conditions, with anisotropies similar to the A fabric. A diversity of fabrics predict diverse anisotropy styles in subduction zones (Kneller et al., 2005, 2008) and at mid-ocean ridges (Karato et al., 2008).

Anisotropy maps upper-mantle deformation, which relates directly to the flow gradient rather than to the flow itself. The major axis of the finite-strain ellipse, and thereby the fast axis of the anisotropy in usual conditions, may therefore have an orientation away from the flow lines themselves (Kaminski and Ribe, 2002; Nippress et al., 2007), as shown in the ridge model in **Figure 16**. It is only in the case of large simple-shear deformation that the major axis of the FSE coincides with the flow direction and that the anisotropy maps the flow directly. A global map of inferred anisotropic strength and fast-polarization axes would therefore not translate directly into a global map of shallow-mantle convective motions, but would of course provide a valuable starting point for it (Long and Becker, 2010; Wustefeld et al., 2009).

Not all upper-mantle deformation occurs as dislocation creep within minerals. Karato (1992) hypothesized the Lehmann discontinuity at roughly 200 km depth to be a transition of rock-deformation mechanisms and therefore a

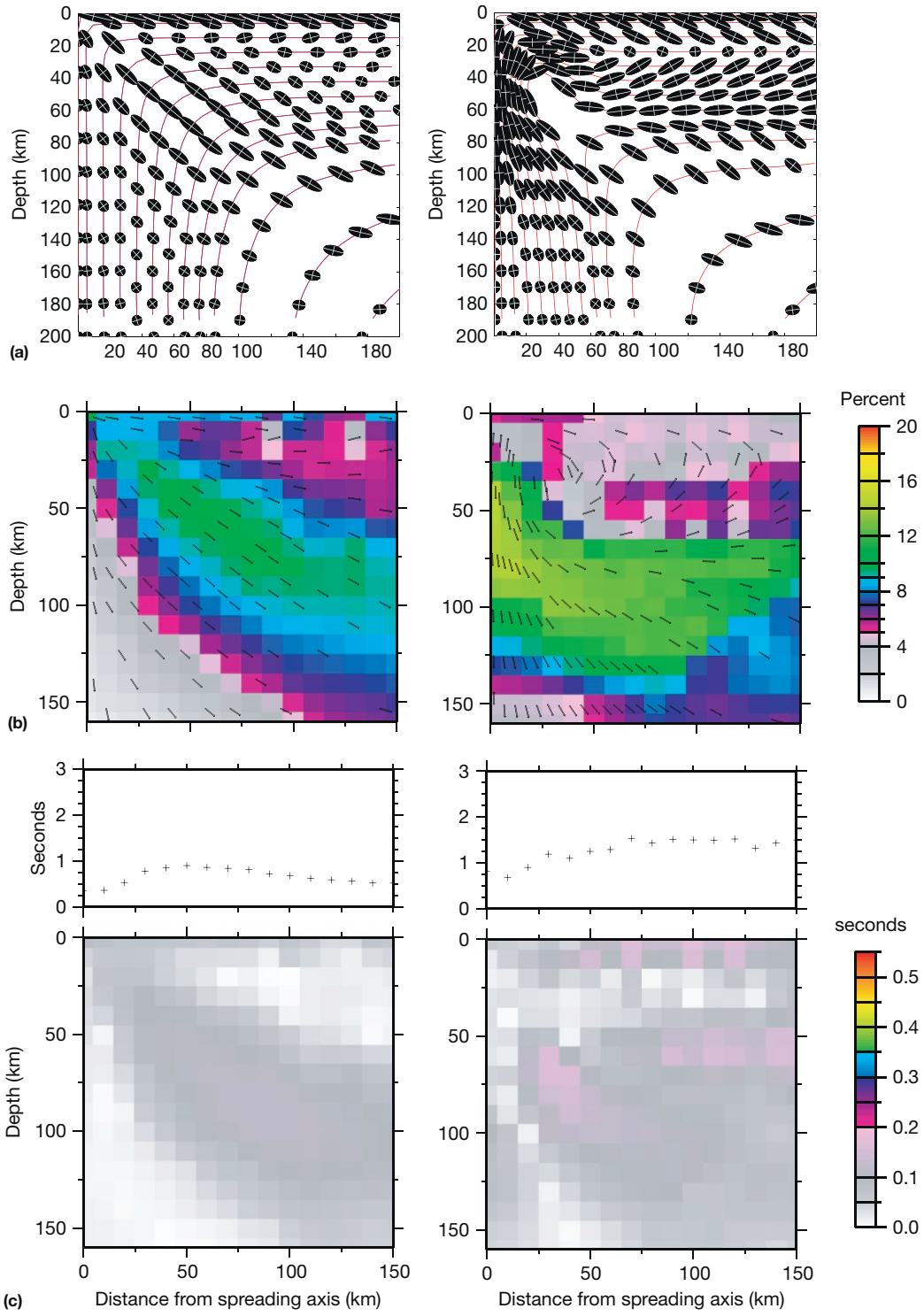

Figure 16 Figure from Blackman and Kendall (2002) showing the relation between flow, deformation, and anisotropy in 2-D models at a spreading margin. The left column corresponds to a passive flow and the right columns to a buoyancy-enhanced flow. (a) Streamlines in red and finite-strain ellipses in black. (b) P-wave anisotropy: color shade shows the degree of anisotropy and vectors show the direction of fastest P-wave propagation. (c) The degree of shear-wave splitting for vertical incidence, as an integrated value with depth at the top and as a depth section illustrating where the splitting occurs.

transition in anisotropy. Above the Lehmann, anisotropy is generated by dislocation creep within minerals, largely via olivine LPO. Higher temperatures below the Lehmann encourage diffusion creep, in which minerals change shape via atomic diffusion around their grain boundaries, developing either SPO anisotropy or none at all. Kohlstedt (2006) had proposed diffusion creep as dominant wherever the upper mantle has appreciable water, but Karato et al. (2008) argued that this

hypothesis is inconsistent with widespread upper-mantle anisotropy. More recently, Karato (2012) had hypothesized that a different rheological transition activated by temperature and water content, from dislocation creep to grain-boundary sliding, defines the oceanic lithosphere–asthenosphere boundary (LAB) at roughly 70 km depth. Olugboji et al. (2013) showed that physical-dispersion effects associated with grain-boundary sliding can explain the substantial LAB velocity drop. Hansen et al. (2011) argued that shifting deformation from mineral-grain interiors to their boundaries should also effect a change in bulk anisotropy.

It may be wise to test the predictions of Karato's model for the LAB against seismic data, for example, the sharpness and depth of the discontinuity, before investigating grain-boundary sliding as a new mechanism in upper-mantle anisotropy.

1.09.3.3 Traveltime Residuals and Mantle Anisotropy

Azimuthal variation of *Pn* wave speed in early active-source surveys of the oceanic lithosphere was among the first observations of seismic anisotropy on Earth (Hess, 1964). More recent studies have confirmed the early results: azimuthal variations of 5.5% have been observed in the Pacific Ocean (Shearer and Orcutt, 1986) and of 3–4% in the Atlantic Ocean (Gaherty et al., 2004). They also confirm that the direction of maximum Pn-wave velocity aligns with the direction of paleospreading. This rift-normal fast-axis orientation confirms a straightforward relationship between anisotropy and plate divergence (Nippress et al., 2007), in contrast to the crack-dominated anisotropy of the continental Afar rift (Keir et al., 2011).

Pn anisotropy was also evident in active-source surveys in continental regions (Bamford, 1977) but is more difficult to interpret due to the greater geologic complexity. The accumulation of data from local- and regional-distance earthquakes has made possible a better, although still very incomplete, picture of *Pn* anisotropy in continental regions (Buehler and Shearer, 2010; Hearn, 1999; Smith and Ekstrom, 1999). The strength of *Pn* anisotropy, in the limited regions where it has been resolved, is 4% on average, reaching up to 10%. A rather consistent picture is that the fast axis of the *Pn* waves aligns with the strike of suture zones (Nemeth et al., 2005), orogenic regions (Hearn, 1999), and subduction arcs (Smith and Ekstrom, 1999). Seward et al. (2009) found *Pn* anisotropy in New Zealand to have orientation and geographic variation in good agreement with the SKS splitting observations of Greve et al. (2008).

At larger epicentral distances, the P waves dive deeper into the mantle and can be used to analyze the depth dependence of P-wave anisotropy in the lithosphere. P waves recorded on very long-range crossing profiles in Siberia (Oreshin et al., 2002) show that the strongest anisotropy (~3%) is located rather deep in the lithosphere (150–250 km depth) and that shallow anisotropy is more moderate (~2%). Testing of well-calibrated earthquake locations shows that traveltime residuals may be attributed to anisotropy at global scale and that anisotropic corrections would improve earthquake location (Antolik et al., 2001). In general, it is however difficult to discriminate between the effect of lateral heterogeneities and anisotropy on traveltime residuals. Pratt and Chapman (1992) analyzed the inverse problem of *P* waves in crosshole surveys and showed that the problem is ill-conditioned, even with the restriction to TI structures. At global scale, body-wave tomography resolves the lower-mantle well, but the prevalence of perovskite, a high-pressure mineral that develops little anisotropy, has discouraged large-scale anisotropic models. At regional scale, shallow-mantle anisotropy is easier to resolve if observations are plentiful. Modest anisotropy in the lithosphere beneath the Adirondacks terrane of northeast North America (Levin et al., 1996) and the Baltic Shield (Eken et al., 2012) could explain tomographic traveltime residuals that otherwise would imply large isotropic wave speed anomalies. Wang and Zhao (2010) imaged anisotropy beneath northern Honshu, Japan, using 448 000 P-wave arrival times from 18 335 local earthquakes, relating their results to active deformation in the subduction zone there.

1.09.3.4 Single-Station P-Wave Anisotropy Observables

Even though anisotropy is often not introduced directly in tomographic models, the raw data of tomographic studies, the P- and S-wave traveltime residuals, can be used to infer anisotropy locally below individual stations by analyzing their azimuthal and incidence-angle dependence. The azimuthally dependent part of the residuals commonly varies by ~1 s (Babuska et al., 1998). Nearby stations often show a pattern that is better explained by lithospheric anisotropy under the station than by lateral heterogeneities (Plomerova et al., 2012). This analysis does not provide good depth resolution, but can delineate geographic regions with the same pattern of anisotropy.

Anisotropy with a dipping fast P-wave axis is often observed in continental regions, and changes in the characteristics of the anisotropy tend to occur at boundaries between different tectonic units. Continent formation via the accretion of island arcs and oceanic plateaus would be consistent with such anisotropic textures. This would imply that active mantle strain is of secondary importance in continental anisotropy and that seismic observations are mostly influenced by accretion strains and the macrofabrics of relict slabs in accordance with findings done with SKS-splitting analysis. Dipping-axis anisotropy can also be interpreted as horizontal detachment scar, not a relict slab interface (Bostock, 1998; Levin and Park, 2000). More uniform patterns of dipping anisotropy in North America have been put in relation to deeper anisotropy, related to lithosphere–asthenosphere interaction (Bokelmann, 2002), showing, similar to conclusions of SKS-splitting studies, that continental anisotropy originates probably from a combination of frozen and active tectonics.

In anisotropic structures, the P-wave polarization direction does not coincide with the propagation directions. Ray theory predicts the polarization to be affected only by the local structure. At single stations, the deviation of the polarization from the great-circle plane can be measured, but this quantity is not straightforward to interpret since it includes two elements: the deviation of the ray from the great-circle plane and the deviation of the polarization from the ray direction. Schulte-Pelkum et al. (2001) analyzed the deviation of long-period P-wave polarizations worldwide and found in some cases deviations from the great-circle plane larger than 10°. They argue that great-circle deviation predicted by tomographic models can explain only a small part of the deviations and interpret them as polarization deviations due to local anisotropy in the uppermost 250 km of rock below the station. The amplitude and direction of

anisotropy inferred with this method were found to be consistent with other methods, in particular SKS splitting. Using arrays of stations to constrain the propagation direction and polarizations simultaneously shows however that long-period P-wave propagation may be affected significantly by local isotropic structure, so that a simple inference of anisotropy should be made with caution (Schulte-Pelkum et al., 2003).

1.09.3.5 SKS Waves and Upper-Mantle Anisotropy

As opposed to P waves, S waves have a distinctive property in anisotropic media that does not occur in isotropic heterogeneous structures: the two independent shear-wave polarizations suffer birefringence, also known as splitting. This distinctive feature makes split S waves a single-station, single-observation source of information concerning anisotropy. In a split S wave, the anisotropy determines a fast and a slow polarization, and an impinging wave 'splits' into fast and slow waves. A traveltime difference accumulates as the split waves traverse an anisotropic region. If the time difference is larger than the dominant period of the shear wave, for example, for shear waves from small local events, the two pulses can be visually distinguishable. Birefringence time delays of 0.5–2.0 s are shorter than the dominant periods of teleseismic shear waves (5–10 s), so that splitting of these waves manifests itself as an elliptical polarization in the horizontal plane.

Shear-wave birefringence, or splitting, of SKS and SKKS waves is the most popular tool for investigating seismic anisotropy (Long and Silver, 2009; Savage, 1999; Silver and Chan, 1991; Vinnik et al., 1984). This popularity is related to the simplified geometry of birefringence for core-refracted phases, such as SKS, in which S motion converts to P in the liquid outer core before returning to the Earth's surface as an SV-polarized wave. The propagation incidence of core-refracted waves is close to vertical under the station, so that birefringence accumulates in the SH component. A common assumption for interpretation is that the splitting is due to a single homogeneous layer of lithospheric anisotropy with a horizontal axis of symmetry. Under such an assumption, SKS waves split into 'fast' and 'slow' waves with polarization directions at right angles to each other. Travel through the anisotropic mantle introduces a time delay δt between fast- and slow-polarized S waves. A splitting time $\delta t \sim 1$ s is typical, and teleseismic core-refracted SKS waves are typically analyzed at periods > 5 s. Therefore, SKS splitting is not estimated from distinct wave arrivals, but from the interference of the 'fast' and 'slow' waves, which trace an elliptical motion in the horizontal plane. The anomalous transverse-component waveform resembles the time derivative of the 'normal' radial-component waveform in the case where the delay time is much less than the wave period (Vinnik et al., 1989b), a characteristic evident in seismograms (**Figure 17**). This provides a good diagnostic tool for distinguishing anisotropy from other sources of polarization deformation. Measurements of δt and fast-polarization azimuth ϕ are sensitive to the product of layer thickness and layer anisotropy beneath an observation point, offering no unique determination of anisotropy with depth.

Several methods are common for estimating birefringence (Long and Silver, 2009; Menke and Levin, 2003; Vecsey et al., 2008; Wustefeld et al., 2008). Most seek to restore 'split' shear waves to their original polarizations, deconvolving the horizontal motion with a broad set of apparent fast-axis strikes ϕ and delay times δt. The method of Silver and Chan (1991) minimizes the transverse component to restore its SV polarization. A birefringence estimator that maximizes the rectilinearity of horizontal motion (Levin et al., 1999), regardless of polarization, may be more robust in low signal-to-noise records and in cases where multiple layers of anisotropy complicate the birefringence. Sileny and Plomerova (1996) estimated birefringence in a manner that models vertical and horizontal motion. With low signal-to-noise records, one can use data from several back azimuths together and compute a robust composite fast-axis and delay-time estimate, from either stacking (Vinnik et al., 1989b; Wolfe and Silver, 1998) or singular-value decomposition (Chevrot, 2000).

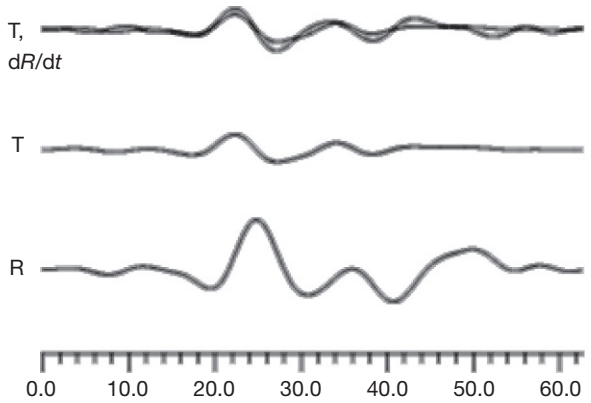

Figure 17 Figure from Long and van der Hilst (2005) showing an example of recorded SKS wave. The bottom trace shows the radial component of the SKS wave. The middle trace shows the transverse component, and the upper trace shows a superposition of the transverse component and the time derivative of the radial one. The traces are band-pass filtered between 0.02 and 0.125 Hz and deconvolved. Please see Long and van der Hilst (2005) for further information.

Numerical experiments have indicated that sparse data and data-averaging techniques can be biased toward the fast-polarization direction of the uppermost anisotropic layer (Rumpker and Silver, 1998; Saltzer et al., 2000), which may explain in part the correlation of many splitting observations with surface tectonic features. The concept of 'splitting intensity' (Chevrot, 2000), which does not rely on resolving a fast axis and a delay time, but keeps these two elements unresolved into one parameter for each data or each set of data having similar polarizations, has proved to be a more robust measurement (Monteiller and Chevrot, 2010) that varies more linearly with the properties of the structure traversed by the waves. It can more easily be incorporated into tomographic studies that allow multiple layers, in particular using finite-frequency kernels (Chevrot, 2006; Sieminski et al., 2008), and combined with surface-wave data in case of lateral and vertical variation of the anisotropy (Romanowicz and Yuan, 2012; Silver and Long, 2011).

Multiple anisotropic layers and other complexities lead as well to frequency dependence in the estimated splitting parameters ϕ and δt (Romanowicz and Yuan, 2012; Silver and Savage, 1994). The parameterization of splitting data in the presence of multiple layers of anisotropy has ambiguities,

however, because a directional dependence of splitting parameters can also be interpreted as 3-D variations in anisotropy. Menke and Levin (2003) proposed a technique for testing a parameterized model space of 1- and 2-layer anisotropic models using a set of raw SKS waveforms, rather than a collection of single-event splitting estimates. Combining data at arrays of broadband stations with appropriate tomographic techniques also seems a promising way to overcome the inherent limitations of SKS-splitting analysis at single stations concerning spatial location and orientation of the anisotropy (Chevrot, 2006; Wookey, 2012).

The majority of the SKS-splitting measurements have been made on land and bring mainly information on continental anisotropy. On land, the apparent mantle textures are often fossil, dating from ancient continental-accretion events. Fast polarization in Central Europe has been associated with a patchwork of accreted lithospheric terranes (Plomerova et al., 2012) and, in southern Africa, exhibits a consistent alignment throughout Archean and Proterozoic continental cratonic zones (Silver et al., 2001). A correspondence of fast polarization with the trends of surface relicts of Precambrian tectonic features in the Canadian Shield also lands support to the notion that mantle textures can be preserved in the continental lithosphere for a billion years or more (Rondenay et al., 2000; Silver and Kaneshima, 1993). In cases where continental tectonics is active, mantle flow from present-day tectonics can be clearly evident (Becker et al., 2003) but superimposed on mantle textures inherited from terrane formation and assembly. On the Adriatic and Ionian side of the Apennines orogen, Margheriti et al. (2003) observed orogen-parallel fast polarization over much of the Italian Peninsula and Sicily, but at the northern end near the Po Valley, the influence of anisotropy in the Paleozoic basement rocks complicates an interpretation in terms of mantle flow (Plomerova et al., 2006). In the Arabian Plate, the fast SKS polarization aligns with a late Proterozoic collisional zone (Levin and Park, 2000; Wolfe et al., 1999), but Hansen et al. (2006) argued that this splitting is caused by present-day asthenospheric flow deflected from the Red Sea Rift.

Anisotropy with a tilted symmetry axis exhibits a variation with azimuth of δt and ϕ that can be distinguished from a multiple-layer effect (Babuska et al., 1993; Chevrot and van der Hilst, 2003). Tilted-axis effects are reported in much of Europe, where they are associated with texture developed during the Variscan orogeny of the late Paleozoic (Plomerova et al., 2012) or, in the Fennoscandian Shield, as evidence of Archean continental accretion from a sandwich of old subducted slabs (Plomerova et al., 2001). Tilted-axis splitting effects are also associated with present-day deformation in Tibet (Hirn et al., 1998) and near the Mendocino triple junction of northern California (Hartog and Schwartz, 2000). In this last region, fast polarization in the upper layer, perhaps most affected by the brittle deformation of the fault zone, is roughly fault-parallel, while fast polarization in the lower layer is roughly east–west, consistent with fast polarization farther inland in the extensional Basin and Range Province.

1.09.3.6 P and S Waves and Subduction Zones

Subduction zones are another plate boundary where mantle anisotropy may help prioritize competing processes (Kneller et al., 2005, 2008). Processes within this small fraction of the Earth's volume control one of the most significant 'products' of the plate-tectonics engine, volcanic arcs, and influence strongly the accretion of continents. The geometric complexity of the region, with mantle wedge, slab, and subslab mantle, together with the possibility of oblique subduction of developing strike-slip motion parallel to the trench, makes this region very challenging for anisotropy studies. Wet conditions may alter the type of olivine fabrics and lead to fast polarizations perpendicular to the deformation, as mentioned in **Section 1.09.3.2**. On the other hand, the presence of many earthquakes distributed with depth and of arrays of stations is a clear advantage for resolving anisotropy.

Most petrologic models of the 'subduction factory' assume that shear coupling to the downgoing slab drives a 2-D corner flow in the upper-mantle wedge above it, leading to predictable thermal effects (Peacock and Wang, 1999). Trench-normal fast polarization in the back-arc has been associated with the entrainment of mantle by shear coupling to the slab (Levin et al., 2004; Schutt and Humphreys, 2001; Wang and Zhao, 2010), but Fischer et al. (1998) found that fast-axis alignment in several Pacific subduction zones parallels back-arc spreading rather than subduction azimuth. Fast polarization in the supraslab mantle wedge, as revealed by the splitting of S waves from earthquakes in downgoing lithosphere, shows a variable pattern. It is either trench-normal (Fischer et al., 1998), consistent with shear-coupled corner flow or back-arc extension; trench-parallel (Cassidy and Bostock, 1996; Long and van der Hilst, 2006), consistent with 3-D flow or B-type fabric; or splitting is absent (Fischer et al., 1998; Wiemer et al., 1999), consistent with poorly developed wedge flows in tank simulations of slab rollback (Buttles and Olson, 1998).

In several regions like the Lau Basin of the SW Pacific (Smith et al., 2001), Japan and Kuriles (Nakajima and Hasegawa, 2004; Nakajima et al., 2006), the Ryukyu arc (Long and van der Hilst, 2006), and to a lesser extent in New Zealand (Greve et al., 2008; Morley et al., 2006), networks of seismometers across the back-arc region reveal trench-parallel fast polarization near the trench that rotates to trench-normal in the back-arc extensional region. The same pattern is obtained with core-refracted S waves in the central Apennines of Italy (Amato et al., 1998; Margheriti et al., 1996) and in Japan (Long and van der Hilst, 2005), as can be seen in **Figure 18**. In Japan, the rotation of fast-axis pattern obtained with S waves compares well with the direction of fast *Pn* waves (Smith and Ekstrom, 1999).

Beneath subducting slabs that suffer retreat away from the trench, asthenosphere beneath the slab hypothetically suffers trench-parallel flow and/or extension. This hypothesis has been confirmed by splitting observations in South America (Polet et al., 2000; Russo and Silver, 1994), Kamchatka (Peyton et al., 2001), and the Apennines (Margheriti et al., 2003; Plomerova et al., 2006). However, Song and Kawakatsu (2012) had argued that subslab anisotropy can be fossil, caused by strong VTI anisotropy with a slow axis of symmetry in asthenosphere that becomes entrained with the downgoing slab. As the entrained asthenosphere tilts with the plunging slab, its fossil anisotropy can generate an apparent trench-parallel fast SKS polarization.

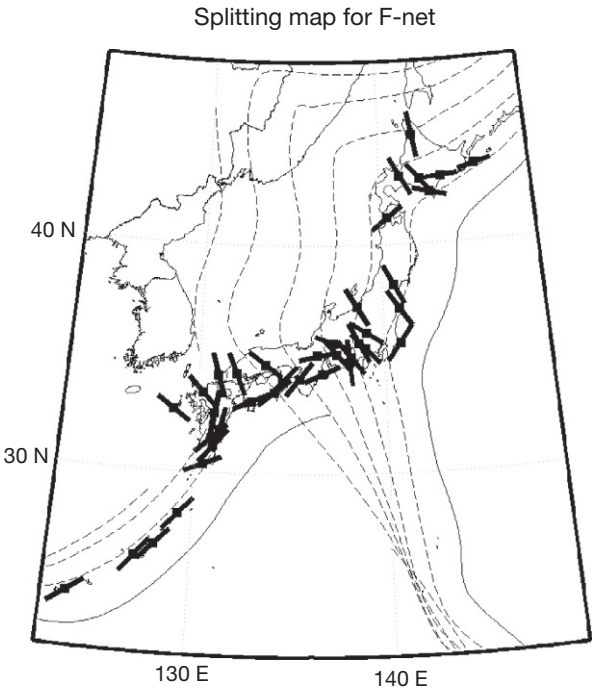

Figure 18 Figure from Long and van der Hilst (2005) showing the fast directions obtained from the analysis of S, SKS, and SKKS splitting at the F-net stations in Japan. The results are shown only for the 36 stations for which a meaningful fast direction could be obtained. For 25 other stations, there is evidence for a complex anisotropy. The contours of the Wadati–Benioff seismicity are also shown at 100 km intervals.

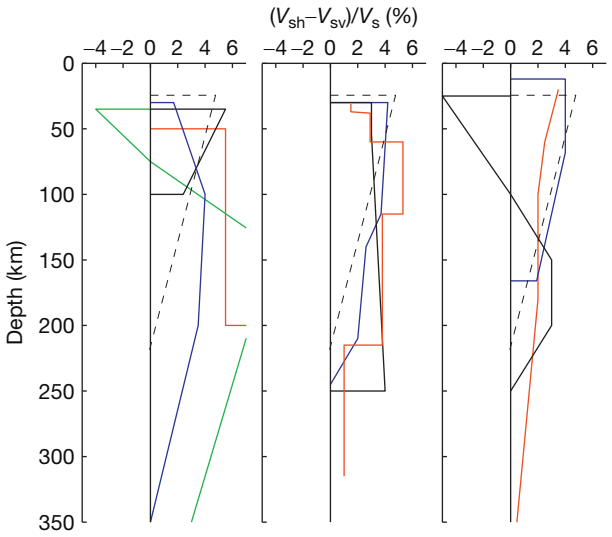

Figure 19 Examples of upper-mantle transverse isotropy obtained from local or regional studies of the Love–Rayleigh discrepancy. The plots show the difference between SH-wave and SV-wave velocity as a function of depth. The values in the PREM model are shown for reference with a dashed black line. The leftmost plot corresponds to studies in continental regions for which Love and Rayleigh-wave velocities have been averaged over azimuth before inversion, in Iberia (Maupin and Cara, 1992) (green), in South Africa (Freybourger et al., 2001) (black), in Germany (Friederich and Huang, 1996) (blue), and in Finland (Pedersen et al., 2006) (red). The central plot corresponds to continental studies made in a single azimuthal direction, in Bohemia (Wielandt et al., 1987) (red), in Australia (Gaherty et al., 1999) (black), and in North America (Gaherty, 2004) (blue). The rightmost plot shows studies made in a single azimuth in oceanic regions, in the northern Pacific (Cara and Leveque, 1988) (blue), in the southern Pacific (Gaherty et al., 1999) (blue), and in the 10–40 My old oceanic lithosphere along the Reykjanes Ridge (Gaherty, 2001) (black).

1.09.3.7 Surface Waves and Upper Mantle

As their dominant propagation direction is horizontal, surface waves offer constraints on anisotropy complementary to those offered by body waves. In addition, they provide global coverage and depth sensitivity that helps to distinguish geodynamic models. As such, surface waves continue to be a major source of information on anisotropy, in particular within oceanic regions.

On average within the Earth's outer layers, Love waves are fast compared to Rayleigh waves, that is, $N > L$ or, equivalently, $\xi > 1.0$. PREM, the first 1-D anisotropic reference model, has mantle $\xi = 1.1$ below the Moho (Dziewonski and Anderson, 1981), decreasing linearly to an isotropic value ($\xi = 1.0$) at 220 km depth (see **Figure 19**). In more recent global models, VTI with $\xi < 1.0$ is found within some depth ranges and geodynamic settings. Beneath mid-ocean ridges, studies have found VTI at 150–300 km depth that induces Rayleigh waves to propagate faster than Love waves (Kustowski et al., 2008; Panning and Romanowicz, 2006; Zhou et al., 2006). Visser et al. (2008) reported 1–2% VTI anisotropy in the mantle transition zone (420–670 km), also with the Love–Rayleigh discrepancy reversed, that is, with $N < L$, and Panning and Romanowicz (2006) argued that the strongest VTI occurs where subducting lithosphere accumulates above the 670 km discontinuity.

Regional analyses of the average Love–Rayleigh discrepancy in different tectonic settings show variations, with a general trend in global long-period data indicating maximum anisotropy in the asthenosphere in the range 200–400 km in old continental regions and 50–150 km in oceanic regions (Gung et al., 2003; Plomerova et al., 2002). Ekstrom and Dziewonski (1998) found similar results but with a stronger anisotropy in the Pacific Ocean, with a value of ξ of up to 1.14 at 100–150 km depth in the central Pacific.

Regional tomographic models provide focused measurements of the Love–Rayleigh discrepancy. It is absent from some regions, for example, northern Europe (Muyzert et al., 1999). The values of $\xi \sim 1.08$, corresponding to 4% difference in SH and SV velocity, are however very common below the Moho and down to at least 200 km depth (Freybourger et al., 2001; Gaherty, 2007; Marone et al., 2004; Panning and Romanowicz, 2006) (see **Figure 19** for some examples). Larger values of $\xi \sim 1.18$ (Debayle and Kennett, 2000; Maupin and Cara, 1992) are challenging to reconcile with olivine LPO and may require additional fine-horizontal layering. Large Rayleigh–Love discrepancies, with fast Love waves, are not limited to waves sensitive to the uppermost mantle, but have also been found at periods sensitive to the crust in tectonic regions, such as Tibet (Duret et al., 2010) and the Aegean Sea (Endrun et al., 2008).

Azimuthal anisotropy can be inferred in the phase velocity of Rayleigh and Love waves at different frequencies (Nishimura

and Forsyth, 1989; Smith and Ekstrom, 1999; Smith et al., 2004; Trampert and Woodhouse, 2003). The azimuthal variation of the Love waves should dominantly follow $\cos 4\phi$ due to the dominance of the partial derivative in N in eqn [36]. Densely sampled global measurements have confirmed the dominance of the 4ϕ terms and found azimuthal variations of up to 2% peak-to-peak amplitude at 40 s period (Trampert and Woodhouse, 2003). The azimuthal variations of the Rayleigh-wave phase velocities are better documented. In tomographic models, the reported values of the azimuthal variations of the Rayleigh-wave phase velocities are often ~1–2% peak-to-peak amplitude (Debayle and Kennett, 2000; Trampert and Woodhouse, 2003), though Ekstrom (2011) reported up to 3.3% azimuthal anisotropy in Rayleigh-wave phase velocity at 60 s period. At greater depth, a global pattern of 1–2% azimuthal anisotropy in the mantle transition zone has been constrained with overtone surface waves (Trampert and van Heijst, 2002; Yuan and Beghein, 2013).

Close to ridges, Rayleigh-wave anisotropy is usually found to possess ridge-perpendicular velocity maxima (Ekstrom, 2011; Laske and Masters, 1998; Montagner and Tanimoto, 1991; Silveira et al., 1998). Although simple continuous-flow models predict anisotropic texture to be frozen into the young oceanic plate as it cools and thickens (McKenzie et al., 1979; Ribe, 1989), modeling of olivine-crystal aggregates suggests that anisotropic texture can be weak in the stiff plate and concentrated in the lithosphere–asthenosphere transition (Blackman et al., 1996; Tommasi, 1998). However, Smith et al. (2004) argued that layered azimuthal anisotropy characterizes the Pacific upper mantle, consistent with both frozen olivine LPOs in the plate underlain by actively deforming asthenosphere. In oceanic regions, the fast direction for Rayleigh-wave phase velocities coincides quite well with the absolute plate motion of the fast-moving plates in the Pacific and Indian Oceans (Ekstrom, 2011; Laske and Masters, 1998; Leveque et al., 1998; Trampert and Woodhouse, 2003). A detailed analysis however shows that the correlation is even better with the direction of finite-strain ellipsoids (FSEs) derived from flow models (Becker et al., 2003). In the slower spreading Atlantic Ocean, basin-wide coherence of fast-axis direction is weak (Ekstrom, 2011), and Silveira et al. (1998) argued that a strong mantle-plume signature complicates the anisotropy away from the ridges.

Correlation between surface tectonics and fast-Rayleigh velocity is more difficult to constrain in continental regions, which are likely to show a more complex pattern of anisotropy, at least in the lithosphere (Priestley et al., 2006). Many studies agree that the cratonic upper mantle beneath North America has distinct layers of azimuthal anisotropy (Chen et al., 2007; Darbyshire and Lebedev, 2009; Deschamps et al., 2008; Yuan and Romanowicz, 2010b; Yuan et al., 2011), confirming behavior reported for surface waves in Australia by Debayle et al. (2005). The nature and inferred origin of anisotropic layering vary across the continent. Some studies agree with early indications from shear-wave birefringence (Darbyshire and Lebedev, 2009; Levin et al., 1999; Marone and Romanowicz, 2007; Snyder and Bruneton, 2007; Yuan et al., 2011) to infer an upper layer with anisotropic textures related to continental formation and a lower layer related to shear associated with absolute plate motion. In the North American Craton, Yuan and Romanowicz (2010a) suggested more complexity, in which fast axes in the upper 150 km of lithosphere, and below the LAB, align with absolute plate motion, but anisotropic fabric in the lower lithosphere deviates from absolute plate motion by more than 50°. Yuan and Romanowicz (2010a) melded receiver functions with surface-wave measurements to bolster the interpretation, also proposed by Deschamps et al. (2008), of the lower lithosphere of the craton as a thermal accretion that acquired its strain fabric independently of the layers above and below. Yuan and Romanowicz (2010b) inferred a different anisotropic layering in western North America, in which shear near the LAB (70–150 km depth) is underlain by a layer with north–south fabric that they associate with a northward extension of the East Pacific Rise under the continent. Deeper in the upper mantle, Yuan and Beghein (2013) offered evidence that rock deformation is disrupted globally by mineral phase changes, for example, at the 410 km discontinuity, suggesting that convective motion of mantle rock decorrelates the anisotropic fabric above and below such interfaces.

The lateral resolution of the global tomographic models is weaker at length scales <1000 km, and one could suspect that the small amplitude of the azimuthal phase-velocity variations reported by tomographic inversions results from the lateral smoothing of small-scale isotropic variations. On a global scale, Debayle and Ricard (2012) showed that large, but feasible, datasets, with >300 000 distinct surface-wave observations, suffer only modest leakage of isotropic upper-mantle structure into anisotropic upper-mantle models, though the potential for bias was greater for the weaker anisotropies of the transition zone and lower mantle. Still, it is interesting to note that local measurements made on arrays of stations often report smaller azimuthal variations than the global models, often less than 1% (Adam and Lebedev, 2012; Freybourger et al., 2001; Friederich and Huang, 1996; Pedersen et al., 2006), with the exception of the Alps where 1–2% are observed mainly range-perpendicular (Fry et al., 2010). In South Africa (Adam and Lebedev, 2012), although the azimuthal variations of Rayleigh-wave phase velocities are less than 1%, they are well constrained and consistent with directions inferred from SKS splitting. The depth distribution of anisotropy inferred from this surface-wave analysis supports models with fossil lithospheric deformation and deeper present-day deformation. An intriguing element in this study is that the Love-wave azimuthal variation aligns maxima and minima with the Rayleigh-wave azimuthal variation, a behavior that no model based on anisotropy alone can explain. Since the olivine fast axis should be dominantly horizontal to explain the positive SH–SV wave velocity difference shown in **Figure 19**, the absence of associated azimuthal variation can only be explained, in the framework of olivine, by a fast axis oriented in the horizontal plane but in azimuths strongly varying either laterally or vertically. This kind of structure has been invoked by Gaherty (2004) in North America to explain the incompatibility of Love–Rayleigh discrepancy measurements with results of SKS splitting. Anisotropy inferred from SKS splitting can predict phase-velocity azimuthal variations.

Results from SKS-splitting studies and global surface-wave tomographic models are rather difficult to compare since they sample the Earth's surface in very different ways. Early studies

did not find good agreement between the models from the two datasets (Montagner et al., 2000). Latest results (Becker et al., 2012a,b; Wustefeld et al., 2009) show that smoothed models of SKS splitting show significant agreement with models from surface waves in terms of directions of the anisotropy but with an amplitude that is twice larger on average. It is clear than in the continental lithosphere, we have a complex picture that is not well understood and that combined studies of different types of data are necessary to get a more coherent view and interpretation. Additional examples of studies of anisotropy and upper mantle can be found in **Chapter 1.19** (Montagner).

1.09.3.8 Polarization of Surface Waves

Observations of polarization anomalies related to anisotropy are not very common in the literature, in part due to the difficulty in distinguishing them from anomalies due to lateral heterogeneities and scattering. A typical polarization anomaly related to anisotropy is the presence of a vertical component associated with the Love fundamental mode at long periods (>70 s) (**Figure 20**). This 'quasi-Love,' which is best observed in back azimuths close to the Love-wave radiation maximum, has amplitudes on the vertical component often equal to 3–20% of the transverse component. It is best explained by lateral gradients in anisotropy at 100–300 km depth (Oda and Onishi, 2001; Yu and Park, 1994). Scattering amplitude is greatest for incidence at 45° from the strike of a horizontal axis of symmetry (Park, 1997; Yu and Park, 1994). Quasi-Love waves are sensitive to both v_P and v_S anisotropy, but with opposing influences, which may aid in distinguishing the two.

Quasi-Love studies have illuminated localized regions of gradients in anisotropy near several plate boundaries and other geodynamic features. The seaward sides of several Pacific subduction zones (Tonga–Kermadec, Japan–Kurile, and central Aleutians) have exhibited quasi-Love observations that are consistent with either strong trench-parallel flow or extension in the asthenosphere beneath a subducting slab (Kobayashi and Nakanishi, 1998; Yu and Park, 1994). Large quasi-Love amplitudes are observed near Tonga–Kermadec (Yu and Park, 1994), where back-arc spreading and rollback is large, and the expected back azimuth-dependent scattering pattern is clearly expressed for several events crossing the Cascadia subduction zone and observed with the EarthScope Transportable Array (Rieger and Park, 2010).

Because quasi-Love waves are generated by localized gradients of anisotropy, one expects a correlation with strong gradients in SKS-splitting measurements. Although such correlation in Tibet was not found by Yu et al. (1995), a dense broadband portable network in central Italy observed one in surface waves from the 2004–2005 megathrust earthquakes in Sumatra (Levin et al., 2007). Quasi-Love waves were observed south of 44N, consistent with trench-parallel SKS fast polarization and anisotropy behind the retreating Apennines slab. North of 44N, the SKS fast polarization swings to north–south, an orientation that does not cause Love–Rayleigh scattering – and none is observed.

Similarly, 'quasi-Rayleigh' waves, with a transverse component of up to 55% of the longitudinal one, have been observed in the vicinity of the Kerguelen hotspot at periods 20–50 s (Pettersen and Maupin, 2002). An example is shown in

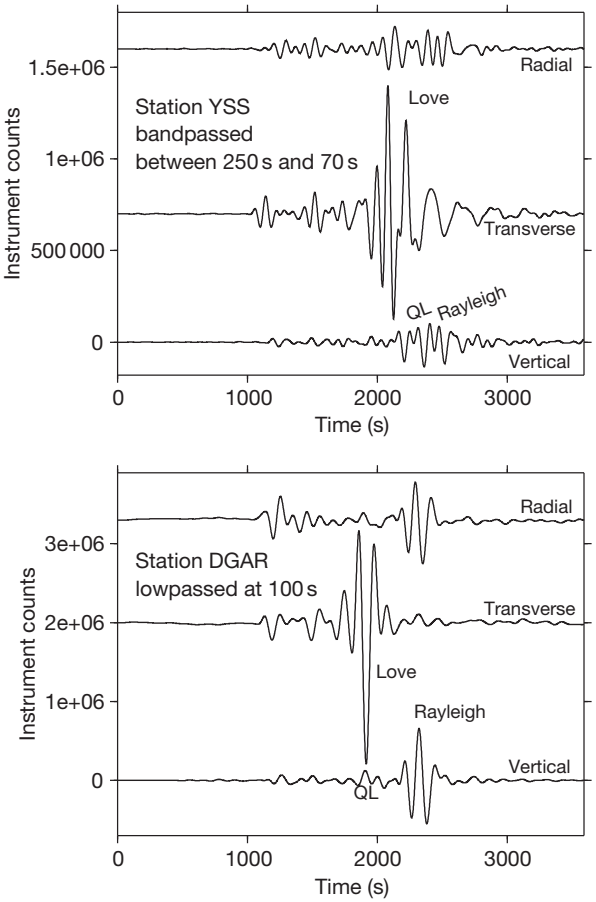

Figure 20 Examples of quasi-Love scattered waves observed in data from the 23 December 2004 $M = 8.1$ earthquake near the Macquarie Islands. This great shallow strike-slip earthquake generated large fundamental Love waves, making quasi-Love modes more visible in low-passed seismic records. Data from GSN station YSS (Yuzhno-Sakhalinsk, Russia) have been band-pass filtered between 4 and 15 mHz to minimize the influence of Coriolis coupling at frequencies f≤4mHz along this propagation path, which is nearly north–south. Data from GSN station DGAR (Diego Garcia, Indian Ocean) are only minimally affected by Coriolis coupling. The quasi-Love wave at DGAR coincides with the main Love wave, suggesting the effect of anisotropy proximal to the mid-ocean island. The quasi-Love wave at YSS, in contrast, is delayed relative to the main Love wave, suggesting the effects of lateral gradients of anisotropy south of the station, for example, along the Japan and Kurile subduction zone.

Figure 21. The polarization anomalies are elliptical, like those shown in **Figure 11**, and are indicative of lithospheric anisotropy with a fast axis dipping away from the hotspot location in a manner very similar to the one in the passive flow shown in **Figure 16**.

Love–Rayleigh scattering can also be seen as the coupling of spheroidal and toroidal free oscillations, a process that can be observed in the Fourier spectrum of long-period seismograms. The spectral peaks of free oscillations are best observed at longer periods than the 100–200 s quasi-Love and quasi-Rayleigh waves discussed in the preceding text. This promises sensitivity to anisotropy beneath the lithosphere–asthenosphere system, particularly in the transition zone (Beghein et al., 2008; Hu et al., 2009, 2012).

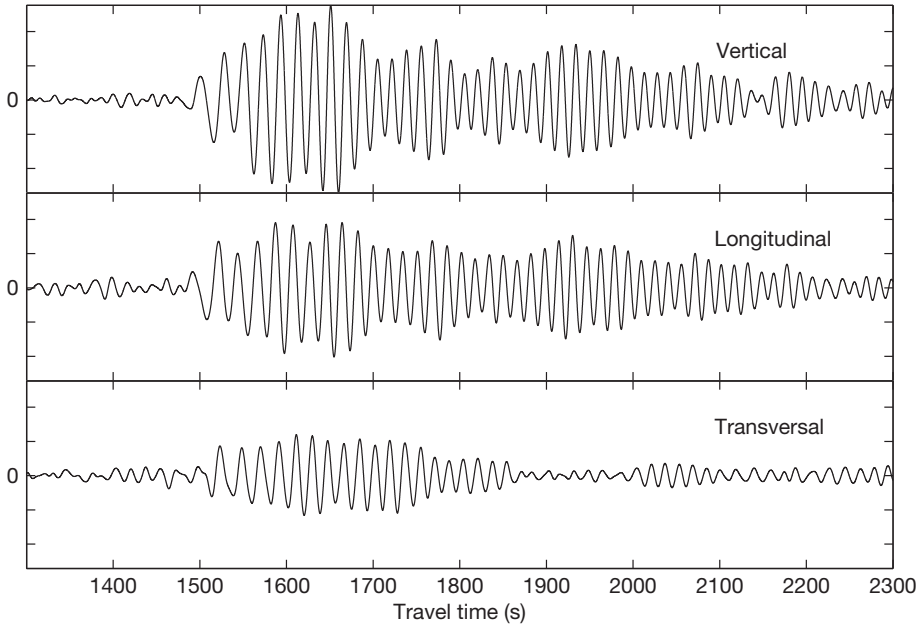

Figure 21 Example of a quasi-Rayleigh wave recorded at the Kerguelen Islands GEOSCOPE station PAF. The three components are plotted at the same scale. Note the prominent transversal component that has the same dispersion characteristics than the vertical and radial ones. The data are from the 4 August 1993 earthquake in the Java subduction zone, which did not generate Love waves in the direction of the PAF station. Reproduced from Pettersen O and Maupin V (2002) Lithospheric anisotropy on the Kerguelen hotspot track inferred from Rayleigh wave polarization anomalies. *Geophysical Journal International* 149: 225–246.

1.09.3.9 Converted Waves and Lithospheric Anisotropy

Anisotropic observables associated with converted body waves, both P-to-S and S-to-P, come in two general types. The first observation type is the birefringence of the converted *Ps* wave. Theoretically, this observable depends on a vertical integral of anisotropy between the converting interface and the surface. Using the Moho *Ps* phase, McNamara et al. (1994) estimated the partition of SKS splitting between crustal and mantle anisotropies in Tibet but found that only 25 out of nearly 700 of their observed *Ps*-converted phases showed evidence of birefringence. The second observation type is the effect of anisotropy at an interface on the amplitude of the converted wave. Theoretically, this observable depends on the anisotropic gradient at or near the converting interface. Although this small-scale sensitivity is complementary to the vertical integration associated with birefringence, there are potential observational overlaps that are not often explored in data analysis. One of the characteristics of birefringence, a pulse on the transverse-horizontal component of motion that resembles the time derivative of the main pulse, can also be generated by *Ps* conversions at the top and bottom of a localized anisotropic shear zone (Levin and Park, 1998). Both birefringence and *Ps* conversion vary with back azimuth with the tilt of the axis of symmetry in anisotropic media with hexagonal symmetry, hampering the use of back-azimuth dependence as a discriminant. A better discriminant would be the detections of P-to-SV conversions on the radial-component receiver function, which should indicate whether one interface or a bounded shear zone is present.

Seismic refraction studies on continents have revealed a wealth of possible 'stretch marks' in the lithosphere at depths < 100 km, and initial *Ps* receiver functions of the transverse component suggest that many 'interfaces' resemble thin shear zones with a discernible rock texture (Bostock, 1998; Byrne et al., 1997; Calvert et al., 1995; Girardin and Farra, 1998; Hajnal et al., 1997; Levin and Park, 1997b; Levin and Park, 2000; Mercier et al., 2008; Sherrington et al., 2004; Warner et al., 1996; Wilson et al., 2004). The S-to-P conversions identified in S receiver functions (Farra and Vinnik, 2000) have been associated with anisotropic shear zones in the uppermost mantle (Wittlinger et al., 2004). The theoretical basis for strain localization in mantle convection is also gaining a theoretical grounding (Bercovici and Ricard, 2003).

Neither arc-slab accretion nor delamination can easily be reconciled with potential relations between anisotropy and globally recognized internal upper-mantle interfaces. The Lehmann discontinuity at 220 km depth has been related to depth-dependent changes in mantle deformation mechanisms (Karato, 1992), and the possible influence of penetrative relict structures on the Lehmann discontinuity requires further study. Based on weak back-azimuthal variation of *Ps* conversions in eastern North America, Vinnik et al. (2005) concluded that the Lehmann discontinuity was not associated with anisotropy, but Levin and Park (2000) reported the Hales discontinuity as anisotropic beneath Arabia. Some converted-wave studies on the LAB have not found evidence for anisotropy in the P-to-SH conversions on the transverse component (Saul et al., 2000; Kind et al., 2012; Kumar et al., 2011), but Rychert et al. (2012) associated anisotropy at the LAB with back-azimuthal variation in underside-reflected SS precursors.

One expects that anisotropy at the upper surface of a subducting slab can arise from either olivine LPO in the downgoing

mantle lithosphere or else mineral alignment or cracks in the downgoing oceanic crust. Although these layers surely make a contribution to *Ps*-converted waves observed above subduction zones, Song and Kim (2012), Park et al. (2004), and Nikulin et al. (2009) argued that an anisotropic layer with high Poisson ratio, likely involving serpentinized rock above the nominal oceanic crust, was the major cause of observed *Ps* waves in receiver functions in Cascadia. Wirth and Long (2012) also interpreted *Ps* conversions from northern Honshu, Japan, as arising partly from an anisotropic layer above the Pacific Plate slab, though in the Kii Peninsula in central Japan, the anisotropy is inconsistent with the seismicity within the downgoing Philippine Sea Plate (Shiomi and Park, 2008).

The Apennines slab is often characterized as continental subduction, but Bianchi et al. (2010) found evidence from P receiver functions for a 10 km anisotropic layer above the downgoing slab beneath central Italy, superficially similar to oceanic subduction zones. The layer above the Apennines slab is evident at 40–80 km depths, whereas *Ps* conversions in Cascadia and Japan are typically strongest at 40 km depth or shallower. Bianchi et al. (2010) interpreted this as evidence of a process peculiar to continental dynamics, in which the lowermost crust peels downward with the subducting mantle lithosphere but eventually rises to form an ultrahigh-pressure (UHP) terrane in a mature eroded orogen, as seen, for example, in the European Alps (Jolivet et al., 2003).

1.09.3.10 ScS, S_{diff}, and the D″ Layer

Except for the D″ layer, just above the core–mantle boundary, there is no evidence for widespread anisotropy in the bulk of the lower mantle (Heintz, 2006; Meade et al., 1995; Restivo and Helffrich, 2006). Due to limitations in station distribution and in the types of waves and events that can be used to study the lowermost mantle, our knowledge of anisotropy in the D″ layer is more patchy in the upper mantle. In addition, the seismic waves that sample the D″ layer may be affected on their descent from the source and ascent to the station by upper-mantle anisotropy. It is possible to ascertain the presence of anisotropy in D″ by comparing waves having traversed the D″ region with those having their turning point just above, but a fully global characterization of D″ anisotropy is best done in the context of inverting for an anisotropic mantle at all depths simultaneously (Kustowski et al., 2008; Panning and Romanowicz, 2006).

The main observations that motivate D″ anisotropy are ScS and core-diffracted S waves whose arrivals are earlier by up to several seconds on the transverse component than on the longitudinal (see also **Chapter 1.22**, Lay). The first such observations were reported by Mitchell and Helmberger (1973) on ScS waves reflected at the Core-Mantle boundary (CMB) below the Caribbean, with delays $\Delta t = 0$–3 s. Similar delays have been observed in subsequent ScS studies and at large epicentral distances on S and diffracted S waves. A review by Moore et al. (2004) shows that $0 < \Delta t < 4$ s in most cases, with some extreme observations of $\Delta t = -2$ s (i.e., SV faster than SH) and $\Delta t = 9$ s. The negative delays correspond mostly to paths in the central Pacific and in the central Atlantic Ocean. Other regions that show mostly positive delays include Alaska, Asia, and India. As with the Caribbean, these areas lie beneath subduction zones. Observed delays can be explained on the average by 1% vertical TI in D″, but Nowacki et al. (2011) pointed out that variations among regions and among studies are quite large. Although at the limit of current resolution, D″ anisotropy is also seen in global tomographic models with in particular a strong negative anomaly (slow SH waves) below Fiji (Panning et al., 2010). Radial anisotropy has also been incorporated in D″ in the mean 1-D model of Montagner and Kennett (1996).

The observation of large diffracted SV waves deep in the core shadow led Vinnik et al. (1989a) to propose that azimuthal anisotropy, acting to couple the SH and SV waves rather than causing simple birefringence, could also be present in D″ in the central Pacific region. Such azimuthal anisotropy has also been found under the Caribbean (Maupin et al., 2005) and under the northwest Pacific Ocean (Wookey et al., 2005) using ScS waves or by joint analysis of SKS and SKKS waves (He and Long, 2011). The difficulty in finding appropriate datasets that provide azimuthal coverage of a given region strongly limits a full characterization of the anisotropy. In most studies, data are available only in one azimuth and the anisotropy has been characterized as a simple tilted version of the more classic VTI model of D″, with tilts of 20–60°. The best coverage has been achieved in Nowacki et al. (2010) with two azimuths in three neighboring regions from the Caribbean to western United States, showing unambiguous non-VTI behavior in two of the six paths and a complex regional pattern that might be correlated with the subduction of the Farallon Plate.

Anisotropy in D″ has been related to its role as a boundary layer in mantle convection and to the expectation that large deformation leads to preferred orientation of melt inclusions (Kendall and Silver, 1998) or minerals. The mineral-orientation hypothesis was revived by the discovery of the phase transition of the dominant lower-mantle component perovskite to postperovskite at D″ *P*–*T* conditions (Murakami et al., 2004). Postperovskite is predicted to be more abundant in the coldest regions, where subducted material accumulates. It has therefore been pointed out that anisotropy, together with other features of D″ observed in the same regions, may be related to the presence of slab remnants, as further discussed in the chapter by Lay in this treatise. Nowacki et al. (2011) explored the likely minerals in D″ and their possible roles in the development of anisotropy. The postperovskite phase exhibits a significantly stronger anisotropy than the ordinary perovskite phase and should develop LPO under shear flow (Murakami et al., 2004). Modeling using a global mantle-flow model shows that dislocations moving on (0 1 0) or (1 0 0) give the best correlation with observed anisotropy (Walker et al., 2011), but the present sampling of D″ anisotropy still leaves room for alternative models.

1.09.3.11 PKIKP, Normal Modes, and the Inner Core

The only truly global observation of the Earth's internal P-wave anisotropy is related to the inner core. This anisotropy is observed in the splitting of the core-sensitive normal modes (Irving and Deuss, 2011; Deuss et al., 2010; Morelli et al., 1986; Woodhouse et al., 1986) and the traveltimes of PKIKP waves for polar paths, close to the Earth's rotation axis,

contrasted with paths in the equatorial plane (Leykam et al., 2010; Morelli et al., 1986; Souriau et al., 2003). P waves following polar paths arrive on the average about 3 s earlier than those following the equatorial paths. The observations can be explained by inner-core TI of about 3% with a north–south fast axis. Early results suggested tilting of the fast axis with respect to the polar direction (Creager, 1992), but more recent models favor some lateral heterogeneity in the distribution of anisotropy (Garcia and Souriau, 2000; Ishii et al., 2002) rather than a tilt of the axis. There is in particular growing evidence for the western core hemisphere (defined as west of Greenwich) having both higher P-wave velocity (Niu and Wen, 2001) and stronger anisotropy (Tanaka, 2012; Tanaka and Hamaguchi, 1997) than the eastern core hemisphere.

This hemispheric dichotomy has also been observed by normal-mode studies (Deuss et al., 2010), suggesting that it is a global feature and that it is likely present in the S wave speed as well, since the relevant normal modes are more sensitive to it. This longitudinal heterogeneity is an intriguing feature that could be related to the presence of an isotropic layer at the top of the outer core that is thicker in the eastern hemisphere than in the western one and has inspired innovative models for the dynamics of the Earth's core (Monnereau et al., 2010).

The PKJKP phase that traverses the core as an S wave is very difficult to observe. Two observations have however been done on stacked data (Wookey and Helffrich, 2008) that are consistent with the anisotropy found with P waves and an interpretation of anisotropy in terms of oriented iron.

As with the Earth's mantle and crust, there are two main possible mechanisms for explaining inner-core anisotropy: preferred orientation of fluid inclusions (Singh et al., 2000) and preferred orientation of minerals, iron crystals in the present case, acquired either during solidification, during subsequent deformation, or in relation to the orientation of the magnetic field (see Deguen, 2012; Steinle-Neumann et al., 2001, for recent summaries). The preferred orientation of iron in its hexagonal close-packed form is favored by several authors and is the mechanism that satisfies most of the observations (Deguen, 2012) at the present time.

Anisotropy in the attenuation of the inner core has also been reported (Souriau and Romanowicz, 1996). The strongest attenuation is found in the fast direction along the polar axis, and the heterogeneity in the attenuation anisotropy seems to follow the east–west pattern in P-wave velocity (Oreshin and Vinnik, 2004). The fact that frequency-dependent analysis of the attenuation of PKIKP waves implies a frequency-dependent Q in the polar direction but not along equatorial paths (Souriau, 2009) may help in revealing the nature of the inner-core anisotropy. Additional references to studies of the inner core anisotropy may be found in Souriau and Calvet (**Chapter 1.23**).

1.09.4 Perspectives

The main challenge concerning seismological observations of anisotropy is to construct a model of the Earth's anisotropy that explains all the data in any one region. Even the best-documented observations, namely, SKS splitting, Love–Rayleigh discrepancy, and Rayleigh-wave phase-velocity azimuthal variations, are sensitive to different aspects of anisotropic rock structure and so do not readily corroborate each other. Where observations are complementary, often they cannot be explained by one simple model of anisotropy, suggesting a combination of fossil anisotropy and ongoing mantle deformation or else a complex 3-D mantle flow, influenced by variations in mineralogy and volatile concentration. Many tectonic regions probably fit these descriptions and will require a patient accumulation of seismic observables to reveal their dynamics.

Acknowledgments

The authors are grateful to Neil Ribe for assistance in describing the orientation of olivine; to Ed Garnero, James Wolfe, Ludek Klimes, Donna Blackman, and Maureen Long for permission to reprint their figures; and to Andreas Köhler for suggestions when writing the second edition of this chapter. We also thank Michael Kendall and Barbara Romanowicz for careful readings of our first-revised draft that identified gaps in our coverage of the literature.

References

Adam JMC and Lebedev S (2012) Azimuthal anisotropy beneath southern Africa from very broad-band surface-wave dispersion measurements. *Geophysical Journal International* 191: 155–174.

Amato A, Margheriti L, Azzara R, et al. (1998) Passive seismology and deep structure in central Italy. *Pure and Applied Geophysics* 151: 479–493.

Anderson DL (1961) Elastic wave propagation in layered anisotropic media. *Journal of Geophysical Research* 66: 2953–2963.

Antolik M, Ekstrom G, and Dziewonski AM (2001) Global event location with full and sparse data sets using three-dimensional models of P-wave velocity. *Pure and Applied Geophysics* 158: 291–317.

Auld BA (1973) *Acoustic Fields and Waves in Solids*, vol. 1. New York: John Wiley & Sons.

Babuska V and Cara M (1991) *Seismic Anisotropy in the Earth*. Dordrecht: Kluwer Academic.

Babuska V, Montagner J-P, Plomerova J, and Girardin N (1998) Age-dependent large-scale fabric of the mantle lithosphere as derived from surface-wave velocity anisotropy. *Pure and Applied Geophysics* 151: 257–280.

Babuska V, Plomerova J, and Sileny J (1993) Models of seismic anisotropy in the deep continental lithosphere. *Physics of the Earth and Planetary Interiors* 78: 167–191.

Backus GE (1962) Long-wave elastic anisotropy produced by horizontal layering. *Journal of Geophysical Research* 67: 4427–4440.

Backus GE (1965) Possible forms of seismic anisotropy of the uppermost mantle under oceans. *Journal of Geophysical Research* 70: 3429–3439.

Balfour NJ, Savage MK, and Townend J (2005) Stress and crustal anisotropy in Marlborough, New Zealand: Evidence for low fault strength and structure-controlled anisotropy. *Geophysical Journal International* 163: 1073–1086.

Bamford D (1977) Pn velocity anisotropy in a continental upper mantle. *Geophysical Journal of the Royal Astronomical Society* 49: 29–48.

Becker TW, Kellogg JB, Ekstrom G, and O'Connell RJ (2003) Comparison of azimuthal seismic anisotropy from surface waves and finite strain from global mantle-circulation models. *Geophysical Journal International* 155: 696–714.

Becker TW, Lebedev S, and Long MD (2012a) On the relationship between azimuthal anisotropy from shear wave splitting and surface wave tomography. *Journal of Geophysical Research* 117: B01306.

Becker TW, Schulte-Pelkum V, Blackman DK, Kellogg JB, and O'Connell RJ (2012b) Mantle flow under the western United States from shear wave splitting. *Earth and Planetary Science Letters* 247: 235–251.

Beghein C, Resovsky J, and van der Hilst RD (2008) The signal of mantle anisotropy in the coupling of normal modes. *Geophysical Journal International* 175: 1209–1234. http://dx.doi.org/10.1111/j.1365-246X.2008.03970.x.

Beghein C and Trampert J (2003) Probability density functions for radial anisotropy: Implications for the upper 1200 km of the mantle. *Earth and Planetary Science Letters* 217: 151–162.

Bercovici D and Ricard Y (2003) Energetics of a two-phase model of lithospheric damage, shear localization and plate-boundary formation. *Geophysical Journal International* 152: 581–596.

Bianchi I, Park J, Agostinetti NP, and Levin V (2010) Mapping seismic anisotropy using harmonic decomposition of receiver functions: An application to Northern Apennines, Italy. *Journal of Geophysical Research* 115: B12317. http://dx.doi.org/10.1029/2009JB007061.

Blackman DK and Kendall J-M (2002) Seismic anisotropy of the upper mantle: 2. Predictions for current plate boundary flow models. *Geochemistry, Geophysics, Geosystems* 3(9): 8602. http://dx.doi.org/10.1029/2001GC000247.

Blackman DK, Kendall J-M, Dawson PR, Wenk H-R, Boyce D, and Morgan JP (1996) Teleseismic imaging of subaxial flow at mid-ocean ridges: Traveltime effects of anisotropic mineral texture in the mantle. *Geophysical Journal International* 127: 415–426.

Bokelmann GHR (2002) Convective-driven motion of the North American craton: Evidence from P-wave anisotropy. *Geophysical Journal International* 148: 278. http://dx.doi.org/10.1046/j.1365-246X.2002.01614.x.

Bostock MG (1998) Mantle stratigraphy and the evolution of the Slave province. *Journal of Geophysical Research* 103: 21183–21200.

Buehler JS and Shearer PM (2010) Pn tomography of the western United States using USArray. *Journal of Geophysical Research* 115: B09315. http://dx.doi.org/10.1029/2009JB006874.

Buttles J and Olson P (1998) A laboratory model of subduction zone anisotropy. *Earth and Planetary Science Letters* 164: 245–262.

Byrne GF, Jacob AWB, Mechie J, and Dindi E (1997) Seismic structure of the upper mantle beneath the southern Kenya Rift from wide-angle data. *Tectonophysics* 278: 243–260.

Calvert AJ, Sawer EW, Davis WJ, and Ludden JN (1995) Archean subduction inferred from seismic images of a mantle suture in the Superior Province. *Nature* 375: 670–674.

Capdeville Y and Marigo JJ (2007) Homogenization of the wave equation for non-periodic layered media. *Geophysical Journal International* 170: 823–838. http://dx.doi.org/10.1111/j.1365-246X.2007.03462.x.

Cara M and Lévêque J-J (1988) Anisotropy of the asthenosphere: The higher mode data of the Pacific revisited. *Geophysical Research Letters* 15: 205–208.

Cassidy JF and Bostock MG (1996) Shear wave splitting above the subducting Juan de Fuca plate. *Geophysical Research Letters* 23: 941–944.

Cerveny V (1972) Seismic rays and ray intensities in inhomogeneous anisotropic media theory. *Geophysical Journal of the Royal Astronomical Society* 29: 1–13.

Cerveny V (2001) *Seismic Ray Theory*. Cambridge: Cambridge University Press.

Chao K and Peng Z (2009) Temporal changes of seismic velocity and anisotropy in the shallow crust induced by the 1999 October 22 (M6.4) Chia-Yi, Taiwan earthquake. *Geophysical Journal International* 179: 1800–1816.

Chapman CH (2004) *Fundamentals of Seismic Wave Propagation*. Cambridge: Cambridge University Press.

Chapman CH and Shearer PM (1989) Ray tracing in azimuthally anisotropic media—II. Quasi-shear wave coupling. *Geophysical Journal* 96: 65–83.

Chen C-W, Rondenay S, Weeraratne DS, and Snyder DB (2007) New constraints on the upper mantle structure of the Slave craton from Rayleigh wave inversion. *Geophysical Research Letters* 34: L10301. http://dx.doi.org/10.1029/2007GL029535.

Chen M and Tromp J (2007) Theoretical and numerical investigations of global and regional seismic wave propagation in weakly anisotropic earth models. *Geophysical Journal International* 168: 1130–1152.

Chevrot S (2000) Multichannel analysis of shear wave splitting. *Journal of Geophysical Research* 105: 21579–21590.

Chevrot S (2006) Finite-frequency vectorial tomography: A new method for high resolution imaging of upper mantle anisotropy. *Geophysical Journal International* 165: 641–657. http://dx.doi.org/10.1111/j.1365-246X.2006.02982.x.

Chevrot S and van der Hilst RD (2003) On the effects of a dipping axis of symmetry on shear wave splitting measurements in a transversely isotropic medium. *Geophysical Journal International* 152: 497–505.

Coates RT and Chapman CH (1990) Quasi-shear wave coupling in weakly anisotropic 3-D media. *Geophysical Journal* 103: 301–320.

Cochran ES, Li YG, and Vidale JE (2006) Anisotropy in the shallow crust observed around the San Andreas fault before and after the 2004 M 6.0 Parkfield earthquake. *Bulletin of the Seismological Society of America* 96: S364–S375.

Crampin S (1970) The dispersion of surface waves in multilayered anisotropic media. *Geophysical Journal of the Royal Astronomical Society* 49: 9–27.

Crampin S (1981) A review of wave motion in anisotropic and cracked elastic-media. *Wave Motion* 3: 343–391.

Crampin S and Chastin S (2003) A review of shear wave splitting in the crack-critical crust. *Geophysical Journal International* 155: 221–240.

Creager KC (1992) Anisotropy in the inner core from differential times of the phase PKP and PKIKP. *Nature* 356: 309–314.

Darbyshire FA and Lebedev S (2009) Rayleigh wave phase-velocity heterogeneity and multilayered azimuthal anisotropy of the Superior Craton, Ontario. *Geophysical Journal International* 176: 215–234. http://dx.doi.org/10.1111/j.1365-246X.2008.03982.x.

Debayle E and Kennett BLN (2000) Anisotropy in the Australian upper mantle from Love and Rayleigh waveform inversion. *Earth and Planetary Science Letters* 184: 339–351.

Debayle E, Kennett BLN, and Priestley K (2005) Global azimuthal seismic anisotropy and the unique plate-motion deformation of Australia. *Nature* 433: 509–512.

Debayle E and Ricard Y (2012) A global shear velocity model of the upper mantle from fundamental and higher Rayleigh mode measurements. *Journal of Geophysical Research* 117: B10308. http://dx.doi.org/10.1029/2012JB009288.

Deguen R (2012) Structure and dynamics of Earth's inner core. *Earth and Planetary Science Letters* 333: 211–225.

Deschamps F, Lebedev S, Meier T, and Trampert J (2008) Stratified seismic anisotropy reveals past and present deformation beneath the east-central United States. *Earth and Planetary Science Letters* 274: 489–498.

Deuss A, Irving JCE, and Woodhouse JH (2010) Regional variation of inner core anisotropy from seismic normal mode observations. *Science* 328: 1018–1020.

Durand S, Montagner JP, Roux P, Brenguier F, Nadeau RM, and Ricard Y (2011) Passive monitoring of anisotropy change associated with the Parkfield 2004 earthquake. *Geophysical Research Letters* 38: L13303. http://dx.doi.org/10.1029/2011GL047875.

Duret F, Shapiro NM, Cao Z, Levin V, Molnar P, and Roecker S (2010) Surface wave dispersion across Tibet: Direct evidence for radial anisotropy in the crust. *Geophysical Research Letters* 37: L16306. http://dx.doi.org/10.1029/2010GL043811.

Dziewonski AM and Anderson DL (1981) Preliminary reference Earth model. *Earth and Planetary Science Letters* 25: 297–356.

Eken T, Plomerova J, Vecsey L, et al. (2012) Effects of seismic anisotropy on P-velocity tomography of the Baltic Shield. *Geophysical Journal International* 188: 600–612.

Ekstrom G (2011) A global model of Love and Rayleigh surface wave dispersion and anisotropy, 25–250 s. *Geophysical Journal International* 187: 1668–1686. http://dx.doi.org/10.1111/j.1365-246X.2011.05225.x.

Ekstrom G and Dziewonski AD (1998) The unique anisotropy of the Pacific upper mantle. *Nature* 394: 168–172.

Endrun B, Lebedev S, Meier T, Tirel C, and Friederich W (2011) Complex layered deformation within the Aegean crust and mantle revealed by seismic anisotropy. *Nature Geoscience* 4: 203–207.

Endrun B, Meir T, Lebedev S, Bohnhoff M, Stavrakakis G, and Harjes HP (2008) S velocity structure and radial anisotropy in the Aegean region from surface wave dispersion. *Geophysical Journal International* 174: 593–616.

Estey LH and Douglas BJ (1986) Upper mantle anisotropy: A preliminary model. *Journal of Geophysical Research* 91: 11393–11406.

Farra V (2005) First-order ray tracing for qS waves in inhomogeneous weakly anisotropic media. *Geophysical Journal International* 161: 309–324. http://dx.doi.org/10.1111/j.1365-246X.2005.02570.x.

Farra V and Psencik I (2003) Properties of the zeroth-, first, and higher-order approximations of attributes of elastic waves in weakly anisotropic media. *Journal of the Acoustical Society of America* 114: 1366–1378. http://dx.doi.org/10.1121/1.1591772.

Farra V and Psencik I (2008) First-order ray computations of coupled S waves in inhomogeneous weakly anisotropic media. *Geophysical Journal International* 173: 979–989. http://dx.doi.org/10.1111/j.1365-246X.2008.03778.x.

Farra V and Psencik I (2010) First-order reflection/transmission coefficients for unconverted plane P waves in weakly anisotropic media. *Geophysical Journal International* 183: 1443–1454. http://dx.doi.org/10.1111/j.1365-246X.2010.04794.x.

Farra V and Vinnik L (2000) Upper mantle stratification by P and S receiver functions. *Geophysical Journal International* 141: 699–712.

Fischer KM, Fouch M, Wiens D, and Boettcher M (1998) Anisotropy and flow in Pacific subduction zone back-arcs. *Pure and Applied Geophysics* 151: 463–475.

Freybourger M, Gaherty JB, and Jordan THthe Kaapvaal Seismic Group (2001) Structure of the Kaapvaal craton from surface waves. *Geophysical Research Letters* 28: 2489–2492.

Friederich W and Huang ZX (1996) Evidence for upper mantle anisotropy beneath Southern Germany from Love and Rayleigh wave dispersion. *Geophysical Research Letters* 23(3–4): 1135–1138.
Fry B, Deschamps F, Kissling E, Stehly L, and Giardini D (2010) Layered azimuthal anisotropy of Rayleigh wave phase velocities in the European Alpine lithosphere inferred from ambient noise. *Earth and Planetary Science Letters* 297: 95–102.
Fryer GJ and Fraser LN (1984) Seismic-waves in stratified anisotropic media. *Geophysical Journal of the Royal Astronomical Society* 91: 73–101.
Gaherty JB (2001) Seismic evidence for hotspot-induced buoyant flow beneath the Reykjanes Ridge. *Science* 293: 1645–1647.
Gaherty JB (2004) A surface wave analysis of seismic anisotropy beneath eastern North America. *Geophysical Journal International* 158: 1053–1066.
Gaherty JB, Kato M, and Jordan TH (1999) Seismological structure of the upper mantle: A regional comparison of seismic layering. *Physics of the Earth and Planetary Interiors* 110: 21–41.
Gaherty JB, Lizarralde D, Collins JA, Hirth G, and Kim S (2004) Mantle deformation during slow seafloor spreading constrained by observations of seismic anisotropy in the western Atlantic. *Earth and Planetary Science Letters* 228(3–4): 257–265.
Garcia R and Souriau A (2000) Inner-core anisotropy and heterogeneity level. *Geophysical Research Letters* 27: 3121–3124.
Garmany J (1988) Seismograms in stratified anisotropic media—I. WKBJ theory. *Geophysical Journal* 92: 365–377.
Garmany J (1989) A student's garden of anisotropy. *Annual Review of Earth and Planetary Sciences* 17: 285–308.
Girardin N and Farra V (1998) Azimuthal anisotropy in the upper mantle from observations of P-to-S converted phases: Application to Southeast Australia. *Geophysical Journal International* 133: 615–629.
Godfrey NJ, Christensen NI, and Okaya DA (2000) Anisotropy of schists: Contribution of crustal anisotropy to active source seismic experiments and shear wave splitting observations. *Journal of Geophysical Research* 105: 27991–28007.
Greve SM, Savage MK, and Hofmann SD (2008) Strong variations in seismic anisotropy across the Hikurangi subduction zone, North Island, New Zealand. *Tectonophysics* 462: 7–21.
Gung Y, Panning M, and Romanowicz B (2003) Global anisotropy and the thickness of continents. *Nature* 442: 707–711.
Hajnal Z, Nemeth B, Clowes RM, et al. (1997) Mantle involvement in lithospheric collision: Seismic evidence from the Trans-Hudson Orogen, western Canada. *Geophysical Research Letters* 24: 2079–2082.
Hansen S, Schwatz S, Al-Amri A, and Rodgers A (2006) Combined plate motion and density-driven flow in the asthenosphere beneath Saudi Arabia: Evidence from shear-wave splitting and seismic anisotropy. *Geology* 34: 869–872. http://dx.doi.org/10.1130/G22713.1.
Hansen LN, Zimmerman ME, and Kohlstedt DL (2011) Grain boundary sliding in San Carlos olivine: Flow law parameters and crystallographic-preferred orientation. *Journal of Geophysical Research* 116: B08201. http://dx.doi.org/10.1029/2011JB008220.
Hartog R and Schwartz SY (2000) Subduction-induced strain in the upper mantle east of the Mendocino triple junction, California. *Journal of Geophysical Research* 105: 7909–7930.
He X and Long M (2011) Lowermost mantle anisotropy beneath the northwestern Pacific: Evidence from PcS, ScS, SKS, and SKKS phases. *Geochemistry, Geophysics, Geosystems* 12: Q12012. http://dx.doi.org/10.1029/2011GC003779.
Hearn TM (1999) Uppermost mantle velocities and anisotropy beneath Europe. *Journal of Geophysical Research* 104: 15123–15139.
Heintz M (2006) Midmantle deformation between the Australian continent and the Fiji-Tonga subduction zone? *Journal of Geophysical Research* 111: B09303. http://dx.doi.org/10.1029/2005JB004058.
Helbig K (1994) *Foundations of Anisotropy for Exploration Seismics*. New York: Elsevier, 486 pp.
Helbig K and Thomsen L (2005) 75-Plus years of anisotropy in exploration and reservoir seismics: A historical review of concepts and methods. *Geophysics* 70: 9ND–23ND. http://dx.doi.org/10.1190/1.2122407.
Hess HH (1964) Seismic anisotropy of the uppermost mantle under oceans. *Nature* 203: 629–631.
Hirn A, Diaz J, Sapin M, and Veinante J-L (1998) Variation of shear-wave residuals and splitting parameters from array observation in southern Tibet. *Pure and Applied Geophysics* 151: 407–432.
Holtzman BK and Kendall J-M (2010) Organized melt, seismic anisotropy and plate-boundary lubrication. *Geochemistry, Geophysics, Geosystems* 11: Q0AB06. http://dx.doi.org/10.1029/2010GC003296.
Holtzman DK, Kohlstedt DL, Zimmerman ME, Heildelbach F, Hiraga T, and Hustoft J (2003) Melt segregation and strain partitioning: Implications for seismic anisotropy and mantle flow. *Science* 301: 1227–1230.
Hu XG, Liu LT, Kroner C, and Sun HP (2009) Observation of the seismic anisotropy effects on free oscillations below 4 mHz. *Journal of Geophysical Research* 114: B07301. http://dx.doi.org/10.1029/2008JB005713.
Hu XG, Xue XX, Liu LT, and Sun HP (2012) Normal mode coupling due to azimuthal anisotropy in the transition zone: An example from Taiwan Island. *Geophysical Journal International* 190: 323–334. http://dx.doi.org/10.1111/j.1365-246X.2012.05463.x.
Irving JCE and Deuss A (2011) Stratified anisotropic structure at the top of Earth's inner core: A normal mode study. *Physics of the Earth and Planetary Interiors* 186: 59–69.
Ishii M, Dziewonski AM, Tromp J, and Ekstrom G (2002) Joint inversion of normal mode and body wave data for inner core anisotropy. 2. Possible complexities. *Journal of Geophysical Research* 107: 2380. http://dx.doi.org/10.1029/2001JB000713.
Jech J and Psencik I (1989) First-order perturbation method for anisotropic media. *Geophysical Journal International* 99: 369–376.
Jolivet L, Faccenna C, Goffe B, Burov E, and Agard P (2003) Subduction tectonics and exhumation of high-pressure metamorphic rocks in the Mediterranean orogens. *American Journal of Science* 303: 353–409.
Jung H and Karato S-I (2001) Water-induced fabric transitions in olivine. *Science* 293: 1460–1463.
Kaminski E (2006) Interpretation of seismic anisotropy in terms of mantle flow when melt is present. *Earth and Planetary Science Letters* 189: 253–267.
Kaminski E and Ribe NM (2001) A kinematic model for recrystallisation and texture development in olivine. *Earth and Planetary Science Letters* 189: 253–267.
Kaminski E and Ribe NM (2002) Time scales for the evolution of seismic anisotropy in mantle flow. *Geochemistry, Geophysics, Geosystems* 3. http://dx.doi.org/10.1029/2001GC000222.
Karato S-I (1992) On the Lehmann discontinuity. *Geophysical Research Letters* 19: 2255–2258.
Karato S-I (2012) On the origin of the asthenosphere. *Earth and Planetary Science Letters* 321: 95–103. http://dx.doi.org/10.1016/j.epsl.2012.01.001.
Karato S-I, Jung H, Katayama I, and Skemer P (2008) Geodynamic significance of seismic anisotropy of the upper mantle: New insights from laboratory studies. *Annual Review of Earth and Planetary Sciences* 36: 59–95.
Keir D, Belachew M, Ebinger CJ, et al. (2011) Mapping the evolving strain field during continental breakup from crustal anisotropy in the Afar Depression. *Nature Communications* 2: 285. http://dx.doi.org/10.1038/ncomms1287.
Keith CM and Crampin S (1977) Seismic body waves in anisotropic media—Reflection and refraction at a plane interface. *Geophysical Journal of the Royal Astronomical Society* 49: 181–208.
Kendall JM and Silver PG (1998) Investigating causes of D″ anisotropy In: Gurnis M, et al. (ed.) *The Core–Mantle Boundary Region*. *Geodynamics Series*, vol. 28, pp. 97–118. Washington, DC: AGU.
Kern HM (1993) Physical properties of crustal and upper mantle rocks with regards to lithosphere dynamics and high pressure mineralogy. *Physics of the Earth and Planetary Interiors* 79: 113–136.
Kern H, Ivankina TI, Nikitin AN, Lokajicek T, and Pros Z (2008) The effect of oriented microcracks and crystallographic and shape preferred orientation on bulk elastic anisotropy of a foliated biotite gneiss from Outokumpu. *Tectonophysics* 457: 143–149.
Kind R, Yuan X, and Kumar P (2012) Seismic receiver functions and the lithosphere–asthenosphere boundary. *Tectonophysics* 536: 25–43. http://dx.doi.org/10.1016/j.tecto.2012.03.005.
Klimes L (2003) Weak-contrast reflection-transmission coefficients in a generally anisotropic background. *Geophysics* 68: 2063–2072.
Klimes L and Bulant P (2006) Errors due to the anisotropic-common-ray approximation of the coupling ray theory. *Studia Geophysica et Geodaetica* 50: 463–477.
Kneller EA, Long MD, and van Keken PE (2008) Olivine fabric transitions and shear wave anisotropy in the Ryukyu subduction system. *Earth and Planetary Science Letters* 268: 268–282.
Kneller EA, van Keken PE, Karato S, and Park J (2005) B-type olivine fabric in the mantle wedge: Insights from high-resolution non-Newtonian subduction zone models. *Earth and Planetary Science Letters* 237: 781–797.
Kobayashi R and Nakanishi I (1998) Location of Love-to-Rayleigh conversion due to lateral heterogeneity or azimuthal anisotropy in the upper mantle. *Geophysical Research Letters* 25(7): 1067–1070.
Kohlstedt DL (2006) The role of water in high-temperature rock deformation. In: Keppler H and Smyth JR (eds.) *Water in Nominally Anhydrous Minerals*, pp. 377–396. Washington, DC: Mineralogy Soc. Amer.
Kumar P, Kawakatsu H, Shinohara M, Kanazawa T, Araki E, and Suyehiro K (2011) P and S receiver function analysis of seafloor borehole broadband seismic data. *Journal of Geophysical Research* 116: B12308. http://dx.doi.org/10.1029/2011JB008506.

Kumazawa M and Anderson OL (1969) Elastic moduli, pressure derivatives, and temperature derivatives of single-crystal olivine and single-crystal forsterite. *Journal of Geophysical Research* 74: 5961–5972.

Kustowski B, Ekstrm G, and Dziewonski AM (2008) Anisotropic shear-wave velocity structure of the Earth's mantle: A global model. *Journal of Geophysical Research* 113: B06306. http://dx.doi.org/10.1029/2007JB005169.

Laske G and Masters G (1998) Surface wave polarization data and global anisotropic structure. *Geophysical Journal International* 132: 508–520.

Leveque JJ, Debayle E, and Maupin V (1998) Anisotropy in the Indian Ocean upper mantle from Rayleigh-and Love-waveform inversion. *Geophysical Journal International* 133: 529–540.

Levin V, Droznin D, Park J, and Gordeev E (2004) Mantle wedge anisotropy beneath southeastern Kamchatka from local-S birefringence. *Geophysical Journal International* 158: 1009–1023.

Levin V, Menke W, and Lerner-Lam A (1996) Seismic anisotropy in the north-eastern US as a source of significant teleseismic P traveltime anomalies. *Geophysical Journal International* 126: 593–603.

Levin V, Menke W, and Park J (1999) Shear wave splitting in Appalachians and Urals: A case for multilayered anisotropy. *Journal of Geophysical Research* 104: 17975–17994.

Levin V and Park J (1997a) P-SH conversions in a flat-layered medium with anisotropy of arbitrary orientation. *Geophysical Journal International* 131: 253–266.

Levin V and Park J (1997b) Crustal anisotropy in the Ural Mtns foredeep from teleseismic receiver functions. *Geophysical Research Letters* 24: 1283–1286.

Levin V and Park J (1998) P-SH conversions in layered media with hexagonally symmetric anisotropy: A cookbook. *Pure and Applied Geophysics* 151: 669–697.

Levin V and Park J (2000) Shear zones in the Proterozoic lithosphere of the Arabian Shield and the nature of the Hales discontinuity. *Tectonophysics* 323: 131–148.

Levin V, Park J, Margheriti L, Lucente FP, and Pondrelli S (2007) The end of subduction in Northern Apennines confirmed by observations of quasi-Love waves from the great 2004 Sumatra–Andaman earthquake. *Geophysical Research Letters* 34: L04304. http://dx.doi.org/10.1029/2006GL028860.

Leykam D, Tkalcic H, and Reading AM (2010) Core structure re-examined using new teleseismic data recorded in Antarctica: Evidence for, at most, weak cylindrical seismic anisotropy in the inner core. *Geophysical Journal International* 180: 1329–1343.

Lin FC, Ritzwoller MH, Yang YJ, Moschetti MP, and Fouch MJ (2011) Complex and variable crustal and uppermost mantle seismic anisotropy in the western United States. *Nature Geoscience* 4: 55–61.

Liu Y, Ben-Zion Y, and Teng TL (2004) Systematic analysis of shear-wave splitting in the aftershock zone of the 1999 Chi-chi, Taiwan, earthquake; shallow crustal anisotropy and lack of precursory changes. *Bulletin of the Seismological Society of America* 94: 2330–2347.

Long MD and Becker TW (2010) Mantle dynamics and seismic anisotropy. *Earth and Planetary Science Letters* 297: 341–354.

Long MD and Silver PG (2009) Shear-wave splitting and mantle anisotropy: Measurements, interpretations and new directions. *Surveys in Geophysics* 30: 407–461.

Long MD and van der Hilst RD (2005) Upper mantle anisotropy beneath Japan from shear-wave splitting. *Physics of the Earth and Planetary Interiors* 151: 206–222.

Long MD and van der Hilst RD (2006) Shear-wave splitting from local events beneath the Ryukyu arc: Trench-parallel anisotropy in the mantle wedge. *Physics of the Earth and Planetary Interiors* 155: 300–312.

Margheriti L, Lucente FP, and Pondrelli S (2003) *SKS* splitting measurements in the Apenninic–Tyrrhenian domain (Italy) and their relation with lithospheric subduction and mantle convection. *Journal of Geophysical Research* 108. http://dx.doi.org/10.1029/2002JB001793.

Margheriti L, Nostro C, Cocco M, and Amato A (1996) Seismic anisotropy beneath the Northern Apennines (Italy) and its tectonic implications. *Geophysical Research Letters* 23: 2721–2724.

Marone F and Romanowicz B (2007) The depth distribution of azimuthal anisotropy in the continental upper mantle. *Nature* 447: 198–201.

Marone F, van der Lee S, and Giardini D (2004) Shallow anisotropy in the Mediterranean mantle from surface waves. *Geophysical Research Letters* 31(6), Art. no. L06624.

Masters G, Park J, and Gilbert F (1983) Observations of coupled spheroidal and toroidal modes. *Journal of Geophysical Research* 88: 10285–10298.

Maupin V (1985) Partial derivatives of surface wave phase velocities for flat anisotropic models. *Geophysical Journal of the Royal Astronomical Society* 83: 379–398.

Maupin V (1989) Surface waves in weakly anisotropic structures: On the use of ordinary or quasi-degenerate perturbation methods. *Geophysical Journal International* 98: 553–563.

Maupin V (1990) Modelling of three-component Lg waves in anisotropic crustal structures. *Bulletin of the Seismological Society of America* 80: 1311–1325.

Maupin V (1994) On the possibility of anisotropy of the D" layer as inferred from the polarization of diffracted S waves. *Physics of the Earth and Planetary Interiors* 87: 1–32.

Maupin V (2001) A multiple-scattering scheme for modelling surface wave propagation in isotropic and anisotropic three-dimensional structures. *Geophysical Journal International* 146: 332–348.

Maupin V (2004) Comment on 'The azimuthal deprendence of surface wave polarization in a slightly anisotropic medium' by T. Tanimoto. *Geophysical Journal International* 159: 365–368.

Maupin V and Cara M (1992) Love-Rayleigh wave incompatibility and possible deep upper mantle anisotropy in the Iberian Peninsula. *Pure and Applied Geophysics* 138: 429–444.

Maupin V, Garnero EJ, Lay T, and Fouch MJ (2005) Azimuthal anisotropy in the D" layer beneath the Caribbean. *Journal of Geophysical Research* 110. http://dx.doi.org/10.1029/2004JB003506.

McKenzie D (1979) Finite deformation during fluid flow. *Geophysical Journal of the Royal Astronomical Society* 58: 689–715.

McNamara DE, Owens TJ, Silver PG, and Wu FT (1994) Shear wave anisotropy beneath the Tibetan Plateau. *Journal of Geophysical Research* 99: 13655–13665.

Meade C, Silver PG, and Kaneshima S (1995) Laboratory and seismological observations of lower mantle isotropy. *Geophysical Research Letters* 22: 1293–1296.

Meissner R, Rabbel W, and Kern H (2006) Seismic lamination and anisotropy of the lower continental crust. *Tectonophysics* 416: 81–99.

Menke W and Levin V (2003) A waveform-based method for interpreting *SKS* splitting observations, with application to one and two layer anisotropic Earth models. *Geophysical Journal International* 154: 379–392.

Mensch T and Rasolofosaon P (1997) Elastic-wave velocities in anisotropic media of arbitrary symmetry—Generalization of Thomsen's parameters epsilon, delta and gamma. *Geophysical Journal International* 128: 43–64.

Mercier JP, Bostock MG, Audet P, Gaherty JB, Garnero EJ, and Revenaugh J (2008) The teleseismic signature of fossil subduction: Northwestern Canada. *Journal of Geophysical Research* 113. http://dx.doi.org/10.1029/2007JB005127.

Mitchell BJ and Helmberger DV (1973) Shear velocities at the base of the mantle from observations of S and ScS. *Journal of Geophysical Research* 78: 6009–6020.

Monnereau M, Calvet M, Margerin L, and Souriau A (2010) Lopsided growth of Earth's inner core. *Science* 328: 1014–1017.

Montagner J-P, Griot-Pommera DA, and Lave JH-C (2000) How to relate body wave and surface wave anisotropy. *Journal of Geophysical Research* 105: 19015–19027.

Montagner J-P and Kennett BLN (1996) How to reconcile body-wave and normal-mode reference Earth models. *Geophysical Journal International* 125: 229–248.

Montagner J-P and Nataf H-C (1986) A simple method for inverting the azimuthal anisotropy of surface waves. *Journal of Geophysical Research* 91: 511–520.

Montagner J-P and Tanimoto T (1991) Global upper mantle tomography of seismic velocities and anisotropies. *Journal of Geophysical Research* 96: 20337–20351.

Monteiller V and Chevrot S (2010) How to make robust splitting measurements for single-station analysis and three dimensional imaging of seismic anisotropy. *Geophysical Journal International* 182: 311–328.

Moore MM, Garnero EJ, Lay T, and Williams Q (2004) Shear-wave splitting and waveform complexity for lowermost mantle structures with low-velocity lamellae and transverse isotropy. *Journal of Geophysical Research* 109. http://dx.doi.org/10.1029/2003JB002546.

Morelli A, Dziewonski AM, and Woodhouse JH (1986) Anisotropy of the inner core inferred from PKIKP traveltimes. *Geophysical Research Letters* 13: 1545–1548.

Morley AM, Stuart GW, Kendall JM, and Reyners M (2006) Mantle wedge anisotropy in the Hikurangi subduction zone, central North Island, New Zealand. *Geophysical Research Letters* 33: L05301.

Murakami M, Hirose K, Kawamura K, Sata N, and Ohishi Y (2004) Post-perovskite phase transition in $MgSiO_3$. *Science* 304: 855–857.

Muyzert E, Paulssen H, and Snieder R (1999) A seismic cross-section through the east European continent. *Geophysical Journal International* 136: 695–704.

Nakajima J and Hasegawa A (2004) Shear-wave polarization anisotropy and subduction-induced flow in the mantle wedge of northeastern Japan. *Earth and Planetary Science Letters* 225: 365–377.

Nakajima J, Shimizu J, Hori S, and Hasegawa A (2006) Shear-wave splitting beneath the southwestern Kurile arc and northeastern Japan arc: A new insight into mantle return flow. *Geophysical Research Letters* 33, L05305.

Nakata N and Snieder R (2012) Time-lapse change in anisotropy in Japan's near surface after the 2011 Tohoku-Oki earthquake. *Geophysical Research Letters* 39: L11313. http://dx.doi.org/10.1029/2012GL051979.

Nemeth B, Clowes RM, and Hajnal Z (2005) Lithospheric structure of the Trans-Hudson Orogen from seismic refraction—Wide-angle reflection studies. *Canadian Journal of Earth Sciences* 42: 435–456.

Nikulin A, Levin V, and Park J (2009) Receiver function study of the Cascadia megathrust: Evidence for localized serpentinization. *Geochemistry, Geophysics, Geosystems* 10: Q07004. http://dx.doi.org/10.1029/2009GC002376.

Nippress SEJ, Kusznir NJ, and Kendall J-M (2007) LPO predicted seismic anisotropy beneath a simple model of a mid-ocean ridge. *Geophysical Research Letters* 34: L14309. http://dx.doi.org/10.1029/2006GL029040.

Nishimura CE and Forsyth DW (1989) The anisotropic structure of the upper mantle in the Pacific. *Geophysical Journal* 96: 203–229.

Niu FL and Wen LX (2001) Hemispherical variations in seismic velocity at the top of the Earth's inner core. *Nature* 410: 1081–1084.

Nowacki A, Wookey J, and Kendall JM (2010) Deformation of the lowermost mantle from seismic anisotropy. *Nature* 467: 1091–1095. http://dx.doi.org/10.1038/nature09507.

Nowacki A, Wookey J, and Kendall JM (2011) New advances in using seismic anisotropy, mineral physics and geodynamics to understand deformation in the lowermost mantle. *Journal of Geodynamics* 52: 205–228.

Oda H (2005) An attempt to estimate isotropic and anisotropic lateral structure of the earth by spectral inversion incorporating mixed coupling. *Geophysical Journal International* 160: 667–682.

Oda H and Onishi S (2001) The effect of regional variation of lattice preferred orientation on surface waveforms. *Geophysical Journal International* 144: 247–258.

Olugboji TM, Karato S-I, and Park J (2013) Structures of the lithosphere–asthenosphere boundary: Mineral-physics modeling and seismological signatures. *Geochemistry, Geophysics, Geosystems* 14. http://dx.doi.org/10.1002/ggge.20086.

Oreshin S and Vinnik L (2004) Heterogeneity and anisotropy of seismic attenuation in the inner core. *Geophysical Research Letters* 31: L02613. http://dx.doi.org/10.1029/2003GL018591.

Oreshin S, Vinnik L, Makeyeva L, Kosarev G, Kind R, and Wenzel F (2002) Combined analysis of *SKS* splitting and regional P traveltimes in Siberia. *Geophysical Journal International* 151: 393–402. http://dx.doi.org/10.1046/j.1364-246X.2002.01791.x.

Panning MP, Lekic V, and Romanowicz BA (2010) Importance of crustal corrections in the development of a new global model of radial anisotropy. *Geophysical Journal International* 129: 399–411.

Panning M and Romanowicz B (2006) A three dimensional radially anisotropic model of shear velocity in the whole mantle. *Geophysical Journal International* 167: 361–379.

Park J (1997) Free oscillations in an anisotropic earth: Path-integral asymptotics. *Geophysical Journal International* 129: 399–411.

Park J and Levin V (2000) Receiver functions from multiple-taper spectral correlation estimates. *Bulletin of the Seismological Society of America* 90: 1507–1520.

Park J and Yu Y (1993) Seismic determination of elastic anisotropy and mantle flow. *Science* 261: 1159–1162.

Park J, Yuan H, and Levin V (2004) Subduction-zone anisotropy under Corvallis, Oregon: A serpentinite skidmark of trench-parallel terrane migration? *Journal of Geophysical Research* 109: B10306. http://dx.doi.org/10.1029/2003JB002718.

Peacock SM and Wang K (1999) Seismic consequences of warm versus cool subduction metamorphism: Examples from southwest and northeast Japan. *Science* 286: 937–939.

Pedersen HA, Bruneton M, and Maupin VThe SVEKALAPKO Seismic Tomography Working Group (2006) Lithospheric and sublithospheric anisotropy beneath the Baltic shield from surface-wave array analysis. *Earth and Planetary Science Letters* 244: 590–605.

Peng Z and Ben-Zion Y (2004) Systematic analysis of anisotropy along the Karadere-Duzce branch of the North Anatolian fault. *Geophysical Journal International* 159: 253–274.

Peng Z and Ben-Zion Y (2005) Spatiotemporal variations of crustal anisotropy from similar events in aftershocks of the 1999 M7.4 Izmit and M7.1 Duzce, Turkey, earthquake sequences. *Geophysical Journal International* 160: 1027–1043.

Pettersen O and Maupin V (2002) Lithospheric anisotropy on the Kerguelen hotspot track inferred from Rayleigh wave polarisation anomalies. *Geophysical Journal International* 149: 225–246.

Peyton V, Levin V, Park J, et al. (2001) Mantle flow at a slab edge: Seismic anisotropy in the Kamchatka region. *Geophysical Research Letters* 28: 379–392.

Plomerova J, Arvidsson R, Babuska V, et al. (2001) An array study of lithospheric structure across the Protogine zone, Varmland, south-central Sweden—Signs of a paleocontinental collision. *Tectonophysics* 332: 1–21.

Plomerova J, Kouba D, and Babuska V (2002) Mapping the lithosphere–asthenosphere boundary through changes in surface-wave anisotropy. *Tectonophysics* 358: 175–185.

Plomerova J, Margheriti L, Park J, et al. (2006) Seismic anisotropy beneath the Northern Apennines (Italy): Mantle flow or lithosphere fabric? *Earth and Planetary Science Letters* 247: 157–170.

Plomerova J, Vecsey L, and Babuska V (2012) Mapping seismic anisotropy of the lithospheric mantle beneath the northern and eastern Bohemian Massif (central Europe). *Tectonophysics* 564: 38–53.

Polet J, Silver PG, Beck S, et al. (2000) Shear wave anisotropy beneath the Andes from the BANJO, SEDA, and PISCO experiments. *Journal of Geophysical Research* 105: 6287–6304.

Pratt RG and Chapman CH (1992) Traveltime tomography in anisotropic media-II. Application. *Geophysical Journal International* 109: 20–37.

Priestley K, Debayle E, McKenzie D, and Pilidou S (2006) Upper mantle structure of eastern Asia from multimode surface waveform tomography. *Journal of Geophysical Research* 111. http://dx.doi.org/10.1029/2005JB004082 B10304.

Psencik I (1998) Green's functions for inhomogeneous weakly anisotropic media. *Geophysical Journal International* 135: 279–288.

Restivo A and Helffrich G (2006) Core–mantle boundary structure investigated using SKS and SKKS polarization anomalies. *Geophysical Journal International* 165: 288–302.

Ribe NM (1989) A continuum theory for lattice preferred orientation. *Geophysical Journal* 97: 199–207.

Richards PG and Frasier CW (1976) Scattering of elastic waves from depth-dependent inhomogeneities. *Geophysics* 41: 411–458.

Rieger DM and Park J (2010) USArray observations of quasi-Love surface wave scattering: Orienting anisotropy in the Cascadia plate boundary. *Journal of Geophysical Research* 115: B05306. http://dx.doi.org/10.1029/2009JB006754.

Romanowicz B and Yuan HY (2012) On the interpretation of SKS splitting measurements in the presence of several layers of anisotropy. *Geophysical Journal International* 188: 1129–1140.

Rondenay S, Bostock MG, Hearn TM, White DJ, and Ellis RM (2000) Lithospheric assembly and modification of the SE Canadian Shield; Abitibi-Grenville teleseismic experiment. *Journal of Geophysical Research* 105: 13735–13754.

Rumpker G and Silver PG (1998) Apparent shear-wave splitting parameters in the presence of vertically varying anisotropy. *Geophysical Journal International* 135: 790–800.

Russo RM and Silver PG (1994) Trench-parallel flow beneath the Nazca Plate from seismic anisotropy. *Science* 263: 1105–1111.

Rychert CA, Schmerr N, and Harmon N (2012) The Pacific lithosphere–asthenosphere boundary: Seismic imaging and anisotropic constraints from SS waveforms. *Geochemistry, Geophysics, Geosystems* 13: Q0AK10. http://dx.doi.org/10.1029/2012GC004194.

Saiga A, Hiramatsu Y, Ooida T, and Yamaoka K (2003) Spatial variation in the crustal anisotropy and its temporal variation associated with a moderate-sized earthquake in the Tokai region, central Japan. *Geophysical Journal International* 154: 695–705.

Saltzer RL, Gaherty JB, and Jordan TH (2000) How are vertical shear wave splitting measurements affected by variations in the orientation of azimuthal anisotropy with depth? *Geophysical Journal International* 141: 374–390.

Saul J, Kumar MR, and Sarkar D (2000) Lithospheric and upper mantle structure of the Indian Shield, from teleseismic receiver functions. *Geophysical Research Letters* 27: 2357–2360.

Savage M (1998) Lower crustal anisotropy or dipping boundaries? Effects on receiver functions and a case study in New Zealand. *Journal of Geophysical Research* 103: 15069–15087.

Savage M (1999) Seismic anisotropy and mantle deformation; what have we learned from shear wave splitting? *Reviews of Geophysics* 37: 65–105.

Savage MK, Park J, and Todd H (2007) Velocity and anisotropy structure at the Hikurangi subduction margin, New Zealand from receiver functions. *Geophysical Journal International* 168: 1034–1050.

Savage M, Wessel A, Teanby NA, and Hurst AW (2010) Automatic measurement of shear wave splitting and applications to time varying anisotropy at Mount Ruapehu volcano, New Zealand. *Journal of Geophysical Research* 115: B12321. http://dx.doi.org/10.1029/2010JB007722.

Schulte-Pelkum V, Masters G, and Shearer PM (2001) Upper mantle anisotropy from long-period P polarization. *Journal of Geophysical Research* 106: 21917–21934.

Schulte-Pelkum V, Vernon FL, and Eakins J (2003) Large teleseismic P wavefront deflections observed with broadband arrays. *Bulletin of the Seismological Society of America* 93: 747–756.

Schutt DL and Humphreys ED (2001) Evidence for a deep asthenosphere beneath North America from Western United States *SKS* splits. *Geology* 29: 291–294.

Seward AM, Henderson CM, and Smith EGC (2009) Models of the upper mantle beneath the central North Island, New Zealand, from speeds and anisotropy of subhorizontal P waves (Pn). *Journal of Geophysical Research* 114: B01301. http://dx.doi.org/10.1029/2008JB005805.

Shapiro NM, Ritzwoller MH, Molnar P, and Levin V (2004) Thinning and flow of Tibetan crust constrained by seismic anisotropy. *Science* 305: 233–236. http://dx.doi.org/10.1126/science.1098276.

Shearer PM and Orcutt JA (1986) Compressional and shear-wave anisotropy in the oceanic lithosphere—The Ngendei seismic refraction experiment. *Geophysical Journal of the Royal Astronomical Society* 87: 967–1003.

Sherrington HF, Zandt G, and Frederiksen A (2004) Crustal fabric in the Tibetan Plateau based on waveform inversions for seismic anisotropy parameters. *Journal of Geophysical Research* 109: B02312. http://dx.doi.org/10.1029/2002JB002345.

Shiomi K and Park J (2008) Structural features of the subducting slab beneath the Kii Peninsula, central Japan: Seismic evidence of slab segmentation, dehydration and anisotropy. *Journal of Geophysical Research* 113: B10318. http://dx.doi.org/10.1029/2007JB005535.

Siegesmund S, Fritzsche M, and Braun G (1991a) Reflectivity caused by texture-induced anisotropy in mylonites. In: Meissner R, et al. (ed.) *Continental Lithosphere: Deep Seismic Reflections*, pp. 291–298. Washington, DC: Amer Geophys Union.

Siegesmund S, Kern H, and Vollbrecht A (1991b) The effect of oriented microcracks on seismic velocities in an ultramylonite. *Tectonophysics* 186: 241–251.

Sieminski A, Liu Q, Trampert J, and Tromp J (2007) Finite-frequency sensitivity of surface wave to anisotropy based upon adjoint methods. *Geophysical Journal International* 168: 1153–1174.

Sieminski A, Paulssen H, Trampert J, and Tromp J (2008) Finite-frequency *SKS* splitting: Measurement and sensitivity kernels. *Bulletin of the Seismological Society of America* 98: 1797–1810.

Sileny J and Plomerova J (1996) Inversion of shear-wave splitting parameters to retrieve three-dimensional orientation of anisotropy in continental lithosphere. *Physics of the Earth and Planetary Interiors* 95: 277–292.

Silveira G, Stutzmann E, Griot D-A, Montagner J-P, and Victor LM (1998) Anisotropic tomography of the Atlantic Ocean from Rayleigh surface waves. *Physics of the Earth and Planetary Interiors* 106: 257–273.

Silver PG and Chan WW (1991) Shear-wave splitting and subcontinental mantle deformation. *Journal of Geophysical Research* 96: 16429–16454.

Silver PG, Gao SS, and Liu KHThe Kaapvaal Seismic Group (2001) Mantle deformation beneath Southern Africa. *Geophysical Research Letters* 28: 2493–2496.

Silver PG and Kaneshima S (1993) Constraints on mantle anisotropy beneath Precambrian North America from a transportable teleseismic experiment. *Geophysical Research Letters* 20: 1127–1130.

Silver PG and Long MD (2011) The non-commutivity of shear wave splitting operators at low frequencies and implications for anisotropy tomography. *Geophysical Journal International* 184: 1415–1427.

Silver PG and Savage MK (1994) The interpretation of shear-wave splitting parameters in the presence of two anisotropic layers. *Geophysical Journal International* 119: 949–963.

Singh S, Taylor MAJ, and Montagner JP (2000) On the presence of liquid in Earth's inner core. *Science* 287: 2471–2474.

Skemer P, Katayama I, and Karato S-I (2006) Deformation fabrics of the Cima di Gagnone peridotite massif, Central Alps, Switzerland: Evidence of deformation at low temperatures in the presence of water. *Contributions to Mineralogy and Petrology* 152: 43–51.

Smith ML and Dahlen FA (1973) The azimuthal dependence of Love and Rayleigh propagation in a slightly anisotropic medium. *Journal of Geophysical Research* 78: 3321–3333.

Smith DP and Ekstrom G (1999) A global study of Pn anisotropy beneath continents. *Journal of Geophysical Research* 104(B1): 963–980.

Smith DB, Ritzwoller MH, and Shapiro NM (2004) Stratification of anisotropy in the Pacific upper mantle. *Journal of Geophysical Research* 109: B11309. http://dx.doi.org/10.1029/2004JB003200.

Smith GP, Wiens DA, Fischer KM, Dorman LM, Webb SC, and Hildebrand JA (2001) A complex pattern of mantle flow in the Lau Backarc. *Science* 292: 713–716.

Snyder D and Bruneton M (2007) Seismic anisotropy of the Slave craton, NW Canada, from joint interpretation of SKS and Rayleigh waves. *Geophysical Journal International* 169: 170–188. http://dx.doi.org/10.1111/j.1365-246X.2006.03287.x.

Song T-RA and Kawakatsu H (2012) Subduction of oceanic asthenosphere: Evidence from subslab seismic anisotropy. *Geophysical Research Letters* 39: L17301. http://dx.doi.org/10.1029/2012GL052639.

Song T-RA and Kim Y-H (2012) Anisotropic uppermost mantle in young subducted slab underplating Central Mexico. *Nature Geoscience* 5: 55–59. http://dx.doi.org/10.1038/NGEO1342.

Souriau A (2009) Inner core structure: Constraints from frequency dependent seismic anisotropy. *Comptes Rendus Geoscience* 341: 439–445.

Souriau A, Garcia R, and Poupinet G (2003) The seismological picture of the inner core: Structure and rotation. *Comptes Rendus Geoscience* 335: 51–65.

Souriau A and Romanowicz B (1996) Anisotropy in inner core attenuation: A new type of data to constrain the nature of the solid core. *Geophysical Research Letters* 23: 1–4.

Steinle-Neumann G, Stixrude L, Cohen RE, and Gulseren O (2001) Elasticity of iron at the temperature of the Earth's inner core. *Nature* 413: 47–60. http://dx.doi.org/10.1038/35092536.

Tanaka S (2012) Depth extent of hemispherical inner core from PKP(DF) and PKP(Cdiff) for equatorial paths. *Physics of the Earth and Planetary Interiors* 210: 50–62.

Tanaka S and Hamaguchi H (1997) Degree one heterogeneity and hemispherical variation of anisotropy in the inner core from PKP(BC)–PKP(DF) times. *Journal of Geophysical Research* 102: 2925–2938.

Tanimoto T (2004) The azimuthal dependence of surface wave polarization in a slightly anisotropic medium. *Geophysical Journal International* 156: 73–78.

Thomsen L (1986) Weak elastic anisotropy. *Geophysics* 51: 1954–1966.

Thomson CJ (1997) Modelling surface waves in anisotropic structures; I. Theory. *Physics of the Earth and Planetary Interiors* 103: 195–206.

Tommasi A (1998) Forward modeling of the development of seismic anisotropy in the upper mantle. *Earth and Planetary Science Letters* 160: 1–13.

Trampert J and van Heijst HJ (2002) Global azimuthal anisotropy in the transition zone. *Science* 296: 1297–1299.

Trampert J and Woodhouse JH (2003) Global anisotropic phase velocity maps for fundamental surface waves between 40 and 150 s. *Geophysical Journal International* 154: 154–167.

Tsvankin I, Gaiser J, Grechka V, van der Baan M, and Thomsen L (2010) Seismic anisotropy in exploration and reservoir characterization: An overview. *Geophysics* 75: 75A15–75A29.

Vavrycuk V (1999) Weak-contrast reflection/transmission coefficients in weakly anisotropic elastic media: P-wave incidence. *Geophysical Journal International* 138: 553–565.

Vavrycuk V, Hrubcova P, Broz M, and Malek J (2004) Azimuthal variation of Pg velocity in the Moldanubian, Czech Republic; observations based on a multi-azimuthal common-shot experiment. *Tectonophysics* 387: 189–203.

Vecsey L, Plomerova J, and Babuska V (2008) Shear-wave splitting measurements—Problems and solutions. *Tectonophysics* 462: 178–196.

Vinnik L, Farra V, and Romanowicz B (1989a) Observational evidence for diffracted SV in the shadow of the Earth's core. *Geophysical Research Letters* 16: 519–522.

Vinnik L, Farra V, and Romanowicz B (1989b) Azimuthal anisotropy in the Earth from observations of SKS at Geoscope and NARS broad-band stations. *Bulletin of the Seismological Society of America* 79: 1542–1558.

Vinnik LP, Kosarev GL, and Makeyeva LI (1984) Anisotropy of the lithosphere according to the observations of SKS and SKKS waves (in Russian). *Doklady Akademii Nauk SSSR* 278: 1335–1339.

Vinnik L, Kurnik E, and Farra V (2005) Lehmann discontinuity beneath North America: No role for seismic anisotropy. *Geophysical Research Letters* 32. http://dx.doi.org/10.1029/2004GL022333 L09306.

Visser K, Trampert J, Lebedev S, and Kennett BLN (2008) Probability of radial anisotropy in the deep mantle. *Earth and Planetary Science Letters* 270: 241–250. http://dx.doi.org/10.1016/j.epsl.2008.03.041.

Walker AM, Forte AM, Wookey J, Nowacki A, and Kendall JM (2011) Elastic anisotropy of D" predicted from global models of mantle flow. *Geochemistry, Geophysics, Geosystems* 10: Q10006. http://dx.doi.org/10.1029/2011GC003732.

Wang Q, Ji S, Sun S, Salisbury MH, and Kern H (2012) Elastic and seismic properties of Dabie-Sulu ultrahigh pressure metamorphic rocks. *Acta Geologica Sinica* 86: 20–37.

Wang J and Zhao D (2010) Mapping P-wave anisotropy of the Honshu arc from Japan Trench to the back-arc. *Journal of Asian Earth Sciences* 39: 396–407.

Ward D, Mahan K, and Schulte-Pelkum V (2012) Roles of quartz and mica in seismic anisotropy of mylonites. *Geophysical Journal International* 190: 1123–1134. http://dx.doi.org/10.1111/j.1365-246X.2012.05528.x.

Warner M, Morgan J, Barton P, Morgan P, Price C, and Jones K (1996) Seismic reflections from the mantle represent relict subduction zones within the continental lithosphere. *Geology* 23: 39–42.

Warren JM, Hirth G, and Kelemen PB (2008) Evolution of olivine lattice preferred orientation during simple shear in the mantle. *Earth and Planetary Science Letters* 272: 501–512.

Watt JP and Peselnick L (1980) Clarification of the Hashin-Shtrikman bounds on the effective elastic moduli of polycrystals with hexagonal, trigonal, and tetragonal symmetries. *Journal of Applied Physics* 51: 1525–1531. http://dx.doi.org/10.1063/1.327804.

Wielandt E, Sigg A, Plesinger A, and Horalek J (1987) Deep structure of the Bohemian Massif from phase velocities of Rayleigh and Love waves. *Studia Geophysica et Geodaetica* 31: 1–7.

Wiemer S, Tytgat G, Wyss M, and Duenkel U (1999) Evidence for shear-wave anisotropy in the mantle wedge beneath south-central Alaska. *Bulletin of the Seismological Society of America* 89: 1313–1322.

Wilson CK, Jones CH, Molnar P, Sheehan AF, and Boyd OS (2004) Distributed deformation in the lower crust and upper mantle beneath a continental strike-slip fault zone; Marlborough fault system, South Island, New Zealand. *Geology* 32: 837–840.

Wirth EA and Long MD (2012) Multiple layers of seismic anisotropy and a low-velocity region in the mantle wedge beneath Japan: Evidence from teleseismic receiver functions. *Geochemistry, Geophysics, Geosystems* 13: Q08005. http://dx.doi.org/10.1029/2012GC004180.

Wittlinger G, Farra V, and Vergne J (2004) Lithospheric and upper mantle stratifications beneath Tibet: New insights from Sp conversions. *Geophysical Research Letters* 31: L19615. http://dx.doi.org/10.1029/2004GL020955.

Wolfe JP (1998) *Imaging Phonons, Acoustic Wave Propagation in Solids*. Cambridge, UK: Cambridge University Press.

Wolfe CJ and Silver PG (1998) Seismic anisotropy of oceanic upper mantle; shear wave splitting methodologies and observations. *Journal of Geophysical Research* 103: 749–771.

Wolfe CJ, Vernon FL III, and Al-Amri A (1999) Shear-wave splitting across western Saudi Arabia: The pattern of upper-mantle anisotropy at a Proterozoic shield. *Geophysical Research Letters* 26: 779–782.

Woodhouse JH, Giardini D, and Li XD (1986) Evidence for inner core anisotropy from free oscillations. *Geophysical Research Letters* 13: 1549–1552.

Wookey J (2012) Direct probabilistic inversion of shear wave data for seismic anisotropy. *Geophysical Journal International* 189: 1025–1037. http://dx.doi.org/10.1111/j.1365-246X.2012.05405.x.

Wookey J and Helffrich G (2008) Inner-core shear-wave anisotropy and texture from an observation of PKJKP waves. *Nature* 454: 873–876. http://dx.doi.org/10.1038/nature07131.

Wookey J, Kendall JM, and Rumpker G (2005) Lowermost mantle anisotropy beneath the north Pacific from differential S-ScS splitting. *Geophysical Journal International* 161: 829–838.

Wustefeld A, Bokelmann GHR, Barruol G, and Montagner J-P (2009) Identifying global seismic anisotropy patterns by correlating shear-wave splitting and surface-wave data. *Physics of the Earth and Planetary Interiors* 176: 198–212.

Wustefeld A, Bokelmann GHR, Zaroli C, and Barruol G (2008) SplitLab: A shear-wave splitting environment in Matlab. *Computers and Geosciences* 34: 515–528.

Yu Y and Park J (1994) Hunting for azimuthal anisotropy beneath the Pacific Ocean region. *Journal of Geophysical Research* 99: 15399–15422.

Yu Y, Park J, and Wu F (1995) Mantle anisotropy beneath the Tibetan Plateau: Evidence from long-period surface waves. *Physics of the Earth and Planetary Interiors* 87: 231–246.

Yuan K and Beghein C (2013) Seismic anisotropy changes across upper mantle phase transitions. *Earth and Planetary Science Letters* http://dx.doi.org/10.1016/j.epsl.2013.05.031.

Yuan H and Romanowicz B (2010a) Lithospheric layering in the North American craton. *Nature* 466: 1063–1068. http://dx.doi.org/10.1038/nature09332.

Yuan H and Romanowicz B (2010b) Depth dependent azimuthal anisotropy in the western US upper mantle. *Earth and Planetary Science Letters* 300: 385–394. http://dx.doi.org/10.1016/j.epsl.2010.10.020.

Yuan H, Romanowicz B, Fischer KM, and Abt D (2011) 3-D shear wave radially and azimuthally anisotropic velocity model of the North American upper mantle. *Geophysical Journal International* 184: 1237–1260. http://dx.doi.org/10.1111/j.1365-246X.2010.04901.x.

Zhang S and Karato S-I (1995) Lattice preferred orientation of olivine aggregates deformed in simple shear. *Nature* 375: 774–777.

Zhou Y, Nolet G, Dahlen FA, and Laske G (2006) Global upper-mantle structure from finite-frequency surface-wave tomography. *Journal of Geophysical Research* 111: B04304. http://dx.doi.org/10.1029/2005JB003677.

This page intentionally left blank

1.10 Theory and Observations - Seismic Tomography and Inverse Methods

C Thurber, University of Wisconsin–Madison, Madison, WI, USA
J Ritsema, University of Michigan, Ann Arbor, MI, USA

© 2015 Elsevier B.V. All rights reserved.

1.10.1	**Introduction to Seismic Tomography**	307
1.10.2	**Data Types in Seismic Tomography**	309
1.10.2.1	Body Waves	309
1.10.2.2	Surface Waves	310
1.10.2.3	Ambient Noise	311
1.10.2.4	Normal Modes	311
1.10.2.5	Waveforms	312
1.10.2.6	Reference Model	312
1.10.3	**Model Parameterization**	313
1.10.3.1	Cells, Nodes, and Basis Functions	313
1.10.3.2	Irregular-Cell, Multigrid, and Adaptive-Mesh Methods	315
1.10.3.3	Static (Station) and Crustal Corrections	317
1.10.4	**Model Solution**	317
1.10.4.1	Linear Versus Nonlinear Solutions	317
1.10.4.1.1	Iterative solvers	318
1.10.4.2	Regularized and Constrained Inversion	319
1.10.4.2.1	Generalized inverse and damped least-squares solutions	319
1.10.4.2.2	Sparsity and the L1 norm solution	320
1.10.4.2.3	Occam's inversion and Bayesian methods	321
1.10.4.3	Hypocenter–Structure Coupling	321
1.10.4.4	Static (Station) Corrections Revisited	323
1.10.4.5	Inversion for Vp/Vs (Poisson's Ratio)	323
1.10.4.6	DD Tomography	323
1.10.4.7	Waveform Tomography and Adjoint Methods	325
1.10.5	**Solution Quality**	326
1.10.5.1	Model Resolution and Uncertainty Analysis	326
1.10.5.2	Hypothesis Testing	327
1.10.6	**Future Directions**	330
Acknowledgments		330
References		330

1.10.1 Introduction to Seismic Tomography

Since its beginnings in the mid-1970s, seismic tomography has grown to become one of the fundamental tools of modern seismology. Seismic tomographic models of the three-dimensional (3D) variations of seismic velocity and density play a critical role in the analysis of Earth's structure and dynamics, ranging from planetary-scale convection to the kilometer-scale mapping of subsurface lithology, temperature, fracturing, fluid content, etc. We trace the roots of seismic tomography back to a parallel series of abstracts and papers by Keiiti Aki and coworkers on regional- (teleseismic-) and local-scale body-wave tomography beginning in 1974 and by Dziewonski and coworkers on global-scale body-wave tomography starting in 1975. These workers initially referred to their approaches in terms of 3D inversion and 3D perturbations, not seismic tomography.

The term tomography comes from the Greek 'tomos' that means 'slice.' The mathematical basis for tomography can be attributed to Johann Radon. We found the first use of the term seismic tomography in a remarkable PhD thesis by Reagan (1978) on seismic reflection tomography, although this author also refers to a document from the Jet Propulsion Laboratory (1976) proposing the use of tomographic reconstruction on borehole seismic data. Clayton and Hearn (1982) appeared to have been the first workers in earthquake seismology (as opposed to exploration seismology) to adopt the term tomography, while the Scientific American article by Anderson and Dziewonski (1984) can probably be credited with popularizing the use of the term. As of 2012, a substantial number of books and review papers have been written on the subject. Among these are Thurber and Aki (1987), Nolet (1987, 2008, 2011), Dziewonski and Woodhouse (1987), Woodhouse and Dziewonski (1989), Romanowicz (1991, 2003, 2008), Iyer and Hirahara (1993), Montagner (1994), Ritzwoller and Lavely (1995), Boschi et al. (1996), Trampert (1998), Rawlinson and Sambridge (2003), Thurber (2003), Lees (2007), Zhao (2009), Rawlinson et al. (2010), and Liu and Gu (2012). Our purpose is not to review the vast literature on seismic tomography. Rather, we provide a thorough introduction to the method and highlight

some key issues of particular interest in current research. We pay special attention to the issues of model parameterization, model solution, and especially model assessment, as a tomographic model is only useful if we know (at least approximately) how well it represents the real Earth.

Seismic (or other) modeling of the Earth can be carried out as a 'forward problem' where we presume to know the Earth's structure and properties and use the physics of wave propagation to predict what our observations should be: $\mathbf{d}=F(\mathbf{m})$, where $\mathbf{d}$ are the data, $\mathbf{m}$ is the given model, and F represents the forward problem function. In seismic tomography, we use the observations to infer the Earth's structure, again using the physics of wave propagation but now in combination with a linear or nonlinear inversion technique – an 'inverse problem.' For a linear inverse problem, $\mathbf{d}=F(\mathbf{m})$ can be replaced by an equivalent set of discretized linear equations: $\mathbf{Gm}=\mathbf{d}$, where $\mathbf{d}$ and $\mathbf{m}$ are vectors containing the data and model parameters, respectively, and $\mathbf{G}$ is a matrix embodying the physics of the problem. The model estimate can be written as $\mathbf{m}=\mathbf{G}^{-i}\,\mathbf{d}$, where the superscript $-i$ stands for some type of inverse (pseudoinverse, regularized inverse, etc. – see Section 1.10.4). For a nonlinear problem, one typically determines the misfit between data and predictions $\delta\mathbf{d}$ (computed from the forward problem for a trial Earth model) and computes perturbations to the model, $\delta\mathbf{m}$, that will reduce the misfit in an iterative manner, using $\delta\mathbf{m}=\mathbf{G}^{-i}\,\delta\mathbf{d}$ (see Aster et al., 2012 and references therein).

Seismic imaging has seen a great deal of progress in the past few decades, largely due to the modernization and growth of global and regional networks (e.g., Butler et al., 2004; Committee on the Science of Earthquakes, 2003; Fowler and Pavlis, 1994; Romanowicz et al., 1984; Van der Vink and Working Group, 2002). The earliest global tomographic models were based entirely on the travel time of the first arriving P-waves, documented in catalogs. Contemporary models, however, exploit the wide variety of seismic signals recorded by broadband seismometers, including free oscillations, surface waves, and body waves, which provide complementary sampling of the Earth. In addition, forward modeling theories have been improved (even in 3D; see Chapters 1.01, 1.04, 1.05, and 1.06), and the steady increase of computing power has enabled seismologists to tackle increasingly larger inverse problems. Yet, it remains difficult to construct the 'best' model of seismic velocity variation given a set of seismic recordings. Ongoing debates in the literature on model resolution and interpretation underscore the difficulty of seismic tomography as an ill-conditioned geophysical inverse problem. So, what are some of the major problems?

- Uneven and incomplete sampling by seismic waves is a pervasive problem in virtually all seismic tomography problems. On a global scale, the bulk of seismic stations is onshore (and in the northern hemisphere), and most earthquakes occur in narrow belts along plate boundaries. Vast regions of the mantle are not adequately sampled by seismic waves. On the local and regional scales, sufficiently dense networks are generally concentrated on active fault zones, with major gaps in both sources and receivers elsewhere.
- We need a large number of model parameters to image relatively narrow structures in the mantle (e.g., slabs of subducted lithosphere and mantle plumes) or fine-scale structures in the crust (e.g., fault zones and magma chambers). A whole-mantle model of seismic velocity in 1 by 1 regions with 100 km thick layers would be composed of nearly one million parameters. Similarly, at a regional scale, one might wish to have 1 km^3 cells covering a region 400 km by 250 km by 40 km deep, amounting to four million parameters.
- There is model nonuniqueness due to data errors and incomplete sampling. More than one model, in fact an infinite number of models, can adequately explain a seismic tomography dataset. Given model nonuniqueness, we need to impose (ad hoc) constraints to select a 'reasonable' model. We may prefer a model that deviates little from the chosen reference model or a model with 'smooth' wave speed variations. While removing the nonuniqueness problem, one must realize that a priori constraints bias the attributes of the seismic model. Obviously, velocity heterogeneity in seismic models tends to be smooth when smoothness constraints have been applied.
- Often, we make simple approximations to wave propagation theories (e.g., 'ray theory' for travel time inversions and the 'path-average approximation' for surface-wave inversions). These approximations lessen the computational burden of the inverse problem but compromise model quality especially in high-resolution applications.
- The model is typically focused on one (e.g., isotropic wave speed) or few (e.g., transverse isotropy) parameters, yet seismic-wave propagation is influenced by 21 elastic parameters, attenuation, and density. The resolution of all physical parameters is impossible with available datasets. Furthermore, image artifacts can arise due to trade-offs when only a few seismic parameters are considered.

We present a comprehensive survey of seismic tomography and inversion methods as applied to local-, regional-, and global-scale studies. Section 1.10.2 provides a brief description of the types of seismic waves, including full waveforms, commonly used in tomography (Sections 1.10.2.1–1.10.2.5), and discusses the commonly employed theories that enable us to relate seismic data to Earth's seismic structure, often as deviations from a (1D) reference Earth model (Section 1.10.2.6). We discuss in Section 1.10.3 how the Earth is represented (parameterized) as a model, including cell-based parameterizations and continuous basis functions (Section 1.10.3.1) and irregular meshes and multigrids (Section 1.10.3.2), along with a brief discussion of station and crustal corrections (Section 1.10.3.3). Section 1.10.4 is devoted to the inverse problem. We discuss linear and nonlinear solutions (Section 1.10.4.1) and strategies to regularize the inverse problem (Section 1.10.4.2). The mathematics of the coupling between earthquake locations and velocity structure is the topic of Section 1.10.4.3. In Sections 1.10.4.4–1.10.4.7, we revisit station corrections, discuss Vp/Vs inversion, and introduce double-difference (DD) tomography, waveform tomography, and adjoint methods. Section 1.10.5 illustrates how we can evaluate the quality of the model using formal resolution analysis and by forward modeling (hypothesis) tests. We highlight in Section 1.10.6 areas of current and future research that are at the forefront of seismic tomography.

Our discussions are concentrated on passive-source (i.e., earthquake) tomography at the crustal through global scale; exploration-seismic tomography methods are not covered here. Although there are a number of important tomographic studies focused on seismic anisotropy and wave attenuation, we concentrate our discussions on the imaging of wave speed variations. See **Chapters 1.07** (Maupin and Park) and **1.09** (Romanowicz and Mitchell) for thorough discussions of seismic anisotropy and attenuation, respectively.

1.10.2 Data Types in Seismic Tomography

In this section, we discuss the general types of data (**Figure 1**) and their use in the corresponding tomographic methods: body-wave travel times, the dispersion characteristics of surface waves, free oscillation (normal mode) spectra, full waveforms, and cross correlations of noise. Teleseismic body-wave travel times are most routinely used in both global and regional applications. The first global model of the deep mantle by Dziewonski et al. (1977) was based on travel time picks incorporated in the bulletins of the International Seismological Centre (ISC). Subsequent models have utilized the millions of travel time picks the ISC bulletins now comprise (e.g., Bijwaard et al., 1998; Inoue et al., 1990; Li et al., 2008; Montelli et al., 2004a,b; van der Hilst et al., 1997; Vasco et al., 1995; Zhou, 1996, 2004), or they are based on the modeling of body-wave waveforms (Grand, 1994; Houser et al., 2008; Li and Romanowicz, 1996; Masters et al., 1996; Ritsema et al., 2011; Su et al., 1994). Global-scale travel time tomography has been key in illuminating the variable extent of slab penetration into the lower mantle (e.g., Fukao et al., 2001; Grand, 1994; Grand et al., 1997) and the ascent of mantle plumes from the deep mantle (e.g., Montelli et al., 2004b, 2006; Nolet et al., 2007; Zhao, 2004). Surface waves generally produce the highest-amplitude signals in seismograms and provide constraints on the upper mantle. Measurements of surface-wave dispersion (i.e., the frequency-dependent surface-wave speed) are key in our understanding of lithospheric structure, especially in oceanic regions where few seismic stations are located (e.g., Debayle et al., 2005; Ekström et al., 1997; Laske, 1995; Lévêque and Cara, 1985; Lin and Ritzwoller, 2011; Montagner and Tanimoto, 1991; Nakanishi and Anderson, 1982; Nataf et al., 1986; Ritsema et al., 2004; Trampert and Woodhouse, 1995; van Heijst and Woodhouse, 1999; Visser et al., 2008a; Zhang and Tanimoto, 1993). Normal-mode spectral measurements provide constraints on the longest wavelength part of lateral heterogeneity through the Earth (e.g., Deuss et al., 2011, 2013; Häfner and Widmer-Schnidrig, 2013; He and Tromp, 1996; Masters et al., 1982, 1996; Resovsky and Ritzwoller, 1999). These data lend themselves for joint inversions for shear and compressional velocity (Deschamps and Trampert, 2004; Masters et al., 1996) and even density (Ishii and Tromp, 1999, 2001; Kuo and Romanowicz, 2002). We also briefly discuss the topics of waveform inversion and the use of reference Earth models.

Although several workers have demonstrated that robust body-wave (e.g., Bhattacharya et al., 1996; Komatitsch et al., 2002; Nolet et al., 2005; Reid et al., 2001; Ritsema et al., 2002) and surface-wave (e.g., Billien et al., 2000; Dalton and Ekström, 2006; Romanowicz, 1991; Selby and Woodhouse, 2002) amplitude and polarization patterns can be derived from high-quality data to constrain velocity gradients, attenuation, and anisotropy structure, most tomographic studies of velocity structure are primarily based on wave travel time or phase delay inversions. Compared to amplitudes, travel time datasets possess little scatter, and they can be determined in a relatively straightforward manner.

1.10.2.1 Body Waves

Body waves are relatively low-amplitude, impulsive signals that, at teleseismic distances, propagate along a variety of paths through the mantle and core. Direct waves, surface reflections, and core reflections provide sampling of the mantle along unique paths. In global tomography, teleseismic travel times are key in constraining the structure of the deep mantle. Upper mantle modeling using teleseismic travel times and local and regional tomography modeling generally rely on measurements from a relatively dense regional network of stations.

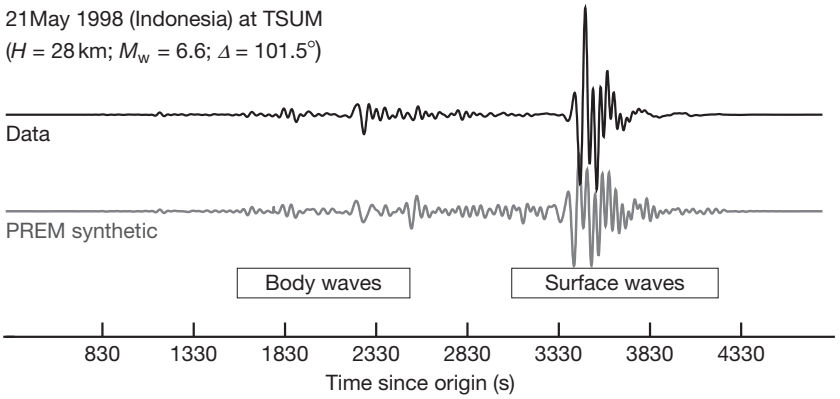

Figure 1 (top) Recorded (vertical component) and (bottom) PREM (Preliminary Reference Earth Model) synthetic seismogram (vertical component) of the 21 May 1998 Indonesia earthquake at station TSUM (Tsumeb, Namibia). The arrival of body waves and surface waves is indicated.

Ray theory and Fermat's principle are at the heart of traditional body-wave travel time tomography. In the infinite frequency limit, travel time T can be written as a path integral:

$$T = \int_{\text{ray path}} u(\mathbf{r})\, ds \qquad [1]$$

where u is the model of slowness (reciprocal of wave speed) at points along the ray path, $\mathbf{r}$ is position, and ds is an infinitesimal element of path length (see **Chapter 1.04**). Our problem of determining the 3D slowness structure $u(\mathbf{r})$ from the arrival-time residuals, obtained by solving a set of equations of the general form

$$\delta T = \int_{\text{ray path}} \delta u(\mathbf{r})\, ds \qquad [2]$$

where δ represents a perturbation, is confounded because we do not know the true ray path (neglecting for the moment the additional issues of the hypocenter location and origin time if an earthquake is the source of the arrival). Looked at another way, the ray path in the reference model will no longer be the correct ray path once the perturbations are applied to the model. Fermat's principle rescues us from this quandary, thanks to the stationary nature of travel time under small perturbations to the ray path. If the path perturbation between the initial and adjusted models is sufficiently small, the travel time (and therefore the travel time residual) will be nearly the same no matter which of the two paths is used. See Snieder (1990), Snieder and Sambridge (1992), and Snieder and Spencer (1993) for a detailed treatment of this issue. For global and teleseismic tomography, this approximation is sufficient if perturbations are not too large, but in local and regional studies, iteration is required (see **Section 1.10.4.1**).

It should be clear from eqns [1] and [2] that body-wave travel time tomography in the infinite frequency limit is relatively simple in theory, but it is more complex if finite-frequency effects are taken into account in broadband travel time data analyses. Two such examples are 'fat ray' tomography (Husen and Kissling, 2001) and 'finite frequency' theory (Dahlen et al., 2000).

Fat ray tomography adopts the view that the entire first Fresnel volume (the volume within which scattered energy arrives within one-half the dominant period of the seismic wave) of the first arriving phase should be considered in relating travel time residuals to model perturbations. Therefore, the region of the model sensitive to a given datum is banana-shaped for a typically curved path, with the source and receiver close to (but not at) the tips of the banana (**Figure 2**). Husen and Kissling (2001) at the local scale and Kárason and van der Hilst (2001) on the global scale developed such an approach, distributing the contributions to a given travel time perturbation (eqn [2]) among the model parameters in proportion to the fraction of the total Fresnel volume present in a given model cell, rather than along a path of infinitesimal width.

The need for finite-frequency theory arises when waveform fitting (e.g., Li and Romanowicz, 1995; Li and Tanimoto, 1993; Mégnin and Romanowicz, 2000) or cross correlation (Dahlen et al., 2000; Hung et al., 2000; Liu and Tromp, 2006; Marquering and Snieder, 1995; Nissen-Meyer et al., 2007) of the observed and synthetic waveforms is used to estimate travel

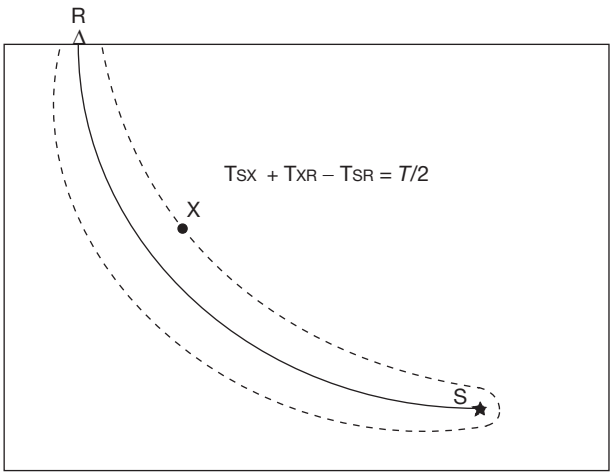

Figure 2 Diagram of the Fresnel zone for a body wave in the Earth. A point is in the first Fresnel zone if the scattered wave from point X reaches the receiver at R within a time equal to 1/2 of the wave period T of the direct arrival from the source S.

times. Equation [2] becomes a volume integral. The kernels that describe the sensitivity of travel times measured by waveform cross correlation (WCC) (i.e., finite-frequency travel times) surround the geometric ray path, and their volumes are determined by the Fresnel zone. Perhaps surprisingly, the cross-correlation measurement is completely insensitive to the model along the (infinite frequency) ray path. In map view, the sensitivity kernel resembles a banana around the ray path and in cross-sectional view looks like a doughnut – hence, the term 'banana–doughnut kernel' is often used. As one might expect, the width of the sensitivity kernel and its interior 'hole' are strongly frequency-dependent. However, whether finite-frequency effects impact the resolution of earth structure is still a matter of debate (Montelli et al., 2004a,b; van der Hilst and De Hoop, 2005).

1.10.2.2 Surface Waves

There are two types of surface waves with different particle motion characteristics, just as there are two types of body waves – but with a 'twist.' Surface waves are evanescent waves (with a purely imaginary vertical wave number $k = i|v|$) that propagate horizontally along the Earth's surface with a 'skin depth' that increases with increasing period (or wavelength). Love waves are composed of horizontally polarized shear waves (P-SV) trapped within a surface layer (or layers). Rayleigh waves form by an interaction between compressional and vertically P-SV at the surface. Earth's sphericity and the increase of wave speed with depth lead to dispersion of surface waves. As a result, surface waves are recorded as a 'train' of waves, with long-period/long-wavelength waves generally arriving first. At teleseismic distances, surface waves have much larger amplitudes than body waves due to their geometric spreading in two dimensions, as opposed to the 3D spreading of body waves.

As a consequence of dispersion, two distinct velocities characterize surface-wave propagation. Let us express displacement $u(x,t)$ as an integral over harmonic plane waves of all frequencies ω:

$$u(x,t) = \int A(\omega) \exp\{\mathrm{i}(\omega t - k(\omega))x + \phi(\omega)\}\, \mathrm{d}\omega \quad [3]$$

If we approximate the wave number $k(\omega)$ by a Taylor series about ω_0

$$k(\omega) = k(\omega_0) + \left(\mathrm{d}k/\mathrm{d}\omega|_{(\omega=\omega_0)}\right)(\omega - \omega_0) \quad [4]$$

it is straightforward to show that the displacement due to harmonic waves near ω_0 is approximately

$$u(x,t) = \int_{\omega_0-\mathrm{d}\omega}^{\omega_0+\mathrm{d}\omega} A(\omega) \exp\{\mathrm{i}(\omega-\omega_0)(t - \mathrm{d}k/\mathrm{d}\omega x)\} \exp\{\mathrm{i}(\omega_0 t - k(\omega_0)x) + \pi)\}\, \mathrm{d}\omega \quad [5]$$

The two sinusoidal functions in [5] correspond to propagating waves with different speeds. The carrier wave at frequency ω propagates at the phase velocity (C) ω_0/k, upon which a more slowly varying envelope with frequency $\mathrm{d}\omega$ and wave number $\mathrm{d}k$ is superposed. This envelope propagates at the group velocity (U) $\partial\omega/\partial k$.

Surface-wave group velocity analysis generally involves multitapered spectral analysis of narrowband filtered signals:

$$s(t) = \int s(\omega)H(\omega)\, \mathrm{d}\omega \quad [6]$$

where $H(\omega)$ is the taper function, usually of the form $\exp\left\{-(\omega-\omega_0)^2/{\omega_0}^2\right\}$. Group velocity can be determined by estimating how the peak of the amplitude spectrum varies as a function of group velocity U (=epicentral distance/travel time) and the central frequency of the taper function. This analysis has been applied globally to determine group velocity dispersion (see **Chapters 1.01** and **1.03**).

Phase velocities are determined with data either from multiple stations or from single seismograms. The phase Φ_i (determined from the Fourier transform) of a recording i at a distance x_i can be written as

$$\Phi_i = \omega t - k(\omega)x_i + \Phi_\mathrm{s} + 2n\pi = \omega[t - x/c(\omega)] + \Phi_\mathrm{s} + 2n\pi \quad [7]$$

where Φ_s is the initial phase (due to the source). Defining Φ_{ij} as $\Phi_i - \Phi_j$ for stations i and j at the same azimuth from the source (so that Φ_s is common to both recordings i and j), we can, in principle, solve for the phase velocity

$$C(\omega) = \omega(x_i - x_j)/\left[\omega(t_i - t_j) + 2(m-n)\pi - \Phi_{ij}\right] \quad [8]$$

using two stations. In practice, however, more stable results are obtained from an array of stations (Cara, 1976; Merrer et al., 2007; Nolet, 1975) or by multiple earthquake analyses (Beucler et al., 2003; Stutzmann and Montagner, 1993). The term $2(m-n)\pi$ is found empirically by ensuring that the phase velocity has a 'reasonable' value at the longest periods. The subsequent analysis at increasingly shorter periods is 'locked in' by requiring that C is a continuous function of ω.

Single-station measurements of phase velocity require knowledge of $\Phi_\mathrm{s}(\omega)$, that is, knowledge of the earthquake focal mechanism:

$$C(\omega) = \omega x/[\omega t + \Phi_\mathrm{s}(\omega) + 2n\pi - \Phi_i] \quad [9]$$

Often, we measure the phase $\Phi(\omega)$ relative to that in a synthetic seismogram for a spherically symmetrical Earth model $\Delta\Phi = \Phi_\mathrm{obs} - \Phi_\mathrm{syn}$. Again, we remove the cycle-skip ambiguity by locking $2n\pi$ at the lowest frequencies and estimating $\Delta\Phi$ at increasingly higher frequencies. For further details, see **Chapters 1.01**, **1.03**, and **1.06**.

1.10.2.3 Ambient Noise

'Noise' tomography and scattered-wave tomography studies (Pollitz and Fletcher, 2005; Sabra et al., 2005; Shapiro et al., 2005) have caught wide attention as an approach that can take advantage of the growing archive of continuous seismic data from dense regional networks. The Earth is constantly vibrating, normally imperceptibly, and these vibrations are known as ambient noise, generated mainly by ocean waves and wind. The key step in the analysis of ambient noise is the cross correlation of continuous records of up to months of seismic noise for each pair of seismic stations in a regional network. The cross correlation brings out the Green's functions of waves traveling from one station to the other, generally dominated by the surface waves. Thus, from long records of continuous noise, one can recover the same kind of information as obtained from two-station surface-wave analysis. This demonstrates clearly that seismic tomography can continue to advance when researchers find clever ways to exploit the full spectrum of signal contained in seismograms. Snieder and Wapenaar (2010) present an excellent overview of this and other correlation-based seismic imaging techniques. Campillo (**Chapter 1.12**) provides a comprehensive discussion of this relatively new domain of research.

1.10.2.4 Normal Modes

Normal modes (also known as 'free oscillations') are standing waves excited by the largest earthquakes on Earth. Like standing waves on a string, normal modes have distinct frequencies determined by Earth's finite size and its internal elastic structure. The gravest normal mode, the so-called football mode, has a period of about 54 min. In analogy to surface waves (intimately related to normal modes), there are two types of normal modes, distinguished by their mode of oscillations. Torsional modes are analogous to Love waves. They do not have radial displacements and they do not cause volume changes. Spheroidal modes are analogous to Rayleigh waves and involve a combination of radial and transverse motions. We can express the displacement field in the Earth as a sum of normal modes (e.g., Dahlen and Tromp, 1998; Gilbert, 1970):

$$u(x,t) = \sum_n \sum_l \sum_{m=-1}^{l} {}_nA_l^m(\omega)\, {}_nY_l(r) X_l^m(\theta,\phi) \exp\left\{\mathrm{i}\omega_l^m t\right\} \quad [10]$$

Each mode is described by its radial order n and surface order l and m. These integers describe the frequency ${}_n\omega_l^m$ of the normal mode and the spatial shape of the radial eigenfunction ${}_nY_l(r)$ and surface eigenfunction $X_l^m(\theta,\phi)$. A sum of normal modes describes the complete wave field up to frequency ω_l^m. However, due to the computational burden, normal modes are used to study primarily long-period ($T > 20$–50 s) wave propagation, in practice.

A multiplet ${}_n\omega_l$ consists of $2l+1$ singlets ${}_n\omega_l^m$ (m takes values between $-l$ and $+l$). For a spherically symmetrical Earth, the singlet eigenfrequencies are the same. For a laterally heterogeneous Earth, the multiplet 'splits,' rendering singlets ${}_n\omega_l^m$ with slightly different eigenfrequencies. Earth's rotation has an observable effect on the gravest multiplets (e.g., ${}_0S_2$ and ${}_0S_3$). Lateral heterogeneity (both elastic heterogeneity and anisotropy) also has a significant effect. Tomographers use observations of splitting to constrain the large-scale variations (e.g., Deuss et al., 2011, 2013; Giardini et al., 1987; He and Tromp, 1996; Ishii and Tromp, 1999; Masters et al., 1996; Resovsky and Ritzwoller, 1999; Ritzwoller et al., 1998), although in general only the 'even-degree' structure of the Earth can be constrained in a direct manner.

Splitting measurements are not easy to make. Spectral peaks have a finite width, because seismograms are not infinitely long and due to the effect of anelasticity. Moreover, multiplets can overlap, which makes it impossible to treat them in isolation. However, analysis of the splitting of coupled multiplets enables us to constrain both even-degree and odd-degree structures (Dahlen and Tromp, 1998). See **Chapters 1.01**, **1.03**, and **1.06** for further details.

1.10.2.5 Waveforms

While travel times and phase delays represent parametric measurements made from seismograms, it is also possible to model the seismograms directly 'wiggle-for-wiggle.' Waveform inversion is particularly advantageous in that it allows for the analysis of strongly interfering signals. A waveform inversion is typically posed as a search for the model $\mathbf{m}$ that best minimizes the (least-squares) fit between the observed seismogram (or a segment of it) $u(t)$ and a computed seismogram $s(\mathbf{m},t)$:

$$F(M) = \int \mathrm{d}t\{u(t) - s(m,t)\}^2 \qquad [11]$$

In global tomography, waveform fitting was introduced by Woodhouse and Dziewonski (1984) using digital seismic data from upgraded global seismic stations. An important novelty of their approach is that it allows for the recovery of both even and odd spherical harmonic coefficients. In their approach, still widely used today, synthetic seismograms were computed using normal-mode summation. The 'path-average approximation' accounts for the effects of lateral heterogeneity by perturbing the eigenfrequency of each multiplet. Using [10] as a description of a long-period seismogram, we can find perturbations to $\delta\alpha(t)$, $\delta\beta(t)$, and $\delta\rho(t)$ due to perturbations in frequency $\delta\omega$. We can write the dependence of $\delta\omega(\theta,\varphi)$ as

$$\delta\omega = \int_{\text{gc path}} \left(K_\alpha\delta\alpha + K_\beta\delta\beta + K_\rho\delta\rho\right)\mathrm{d}r \qquad [12]$$

where the 1D kernels K_α, K_β, and K_ρ describe the dependence of perturbations in eigenfrequency ω on perturbations to P velocity, S velocity, and density, respectively (see Dahlen and Tromp, 1998 for an extensive theoretical treatment).

The 'partitioned waveform inversion technique' (Nolet and Snieder, 1990) also utilizes the path-average approximation approach, but given its focus on smaller (continental-scale) regions (e.g., Das and Nolet, 1998; Lebedev et al., 1997, 2005; van der Lee and Nolet, 1997; Zielhuis and Nolet, 1994), it is limited to minor-arc waveforms only, albeit at somewhat higher frequencies. The method enables the separate analysis (and data weighing) of fundamental-mode surface waves and overtone signals (such as triplicated SS and SSS waves) and background seismic models unique to different propagation paths.

More realistic kernels have also been developed. 2D kernels computed using across-branch coupling (e.g., Li and Romanowicz, 1995; Li and Tanimoto, 1993; Marquering and Snieder, 1995; Zhao and Jordan, 1998) include (frequency-dependent) sensitivity within the plane of propagation. These higher-order approaches (compared to the path-averaged approximation by Woodhouse and Dziewonski, 1984) better describe the sensitivity of overtone surface waves and complex body waves like SS (the surface-reflected S wave) and S_{diff} (the core-diffracted S wave) to Earth structure. Models SAW12-D (Li and Romanowicz, 1996) and SAW24B16 (Mégnin and Romanowicz, 2000) are based on these 2D kernels. Zhou et al. (2004) computed 3D kernels for phase, amplitude, and arrival angle using surface-wave normal-mode summation. The first application of this theory in global upper mantle tomography has been carried out by Zhou et al. (2006).

Zhao et al. (2005), at the regional scale, and Tromp et al. (2005), on the global scale, demonstrated the ability to compute the Fréchet kernels for the full-waveform inverse problem using a 3D starting model, opening up the avenue of iterative waveform tomography. The data are frequency-dependent travel times (Maggi et al., 2009), phase delays, and amplitude anomalies (Gee and Jordan, 1992), which are evaluated using cross correlation between the observed data and synthetics. Chen et al. (2007) and Tape et al. (2009) applied this approach to the Los Angeles region. Regional-scale studies by Fichtner et al (2009) and Zhu et al. (2012) have improved existing models of 3D structure that were based on travel time tomography and active-source models. See **Section 1.10.4.7** for further discussion of waveform tomography and the use of adjoint methods.

1.10.2.6 Reference Model

Radially symmetrical (1D) models of wave speed, such as the Jeffreys–Bullen tables (Jeffreys and Bullen, 1958), 1066A (Gilbert and Dziewonski, 1975), Preliminary Reference Earth Model (PREM) (Dziewonski and Anderson, 1981), IASP91 (Kennett and Engdahl, 1991), and ak135 (Kennett et al., 1995), still take a central role in the analysis of global seismic data and global tomography. They provide wave speed or a combination of wave speed, density, and attenuation as a function of depth in the Earth and explain to first order the characteristics of global wave propagation, such as the propagation time of teleseismic body waves, and the dispersion of surface waves (including in some cases the effect of upper mantle anisotropy). Using digital broadband recordings, tomographers have built catalogs of surface-wave dispersion measurements (e.g., Ekström et al., 1997; Trampert and Woodhouse, 1996) and catalogs of body-wave travel times (e.g., Ritsema et al., 2002; Su et al., 1994; Woodward and Masters, 1991) by systematically comparing recorded and synthetic waveforms for 1D models (**Figure 1**).

The 1D reference model is also used in the forward modeling theory. For example, a body-wave travel time anomaly, δT, can be defined in terms of velocity as (see Section 1.10.2.1)

$$\delta T \approx \int_{S^0} \frac{1}{V_0^2(\mathbf{r})} \delta V(\mathbf{r}) \mathrm{d}s \qquad [13]$$

where the path S^0 and the velocity V_0 are computed for a 1D reference model. Similarly, a surface-wave phase-velocity perturbation $\delta C(\omega)$ due to shear-velocity heterogeneity in the mantle can be written as

$$\delta C(\omega) = \int_{gc} \mathrm{d}s \int \mathrm{d}\mathbf{r} \left(\frac{\partial C(\omega)}{\partial V_S^0(\mathbf{r})} \right) \delta V_S(\mathbf{r}) \qquad [14]$$

where we have assumed that surface waves propagate along the great circle path gc and that the relationship between phase velocity C and shear velocity V_S can be calculated for the 1D reference model. It is straightforward to compute 1D synthetics, body-wave paths, and kernel functions that relate surface-wave dispersion to seismic velocity for 1D seismic models. Moreover, eqns [13] and [14] render linear relationships between the seismic observables and wave speed heterogeneity. These can be solved using standard linear inverse techniques (see Section 1.10.4). Current research addresses how better, but more complex, theories affect the model solution by using 3D seismic models as initial solutions and by computing the kernels for 3D structures.

In local-scale studies, the importance of the starting 1D model has been clearly demonstrated. For example, Kissling (1988) proposed the use of the 'minimum 1D model' determined by inversion for a layered structure as the starting model for 3D tomography. Refraction models provide another potential source for a starting 1D model. Because the local earthquake tomography (LET) problem is strongly nonlinear, a suitable starting model is critical for reaching an optimal solution.

1.10.3 Model Parameterization

The Earth's seismic velocity structure has been represented in a wide variety of ways in seismic tomography studies. All are only approximations to the true 3D structure of the Earth, or some portion of it. The Earth has heterogeneous structure on a vast range of spatial scales, including complications such as discontinuities, faults, layering, intrusions, inclusions, zones of elevated temperature or partial melt, and random geologic heterogeneities. The spatial scale of heterogeneity that can be imaged with seismic tomography depends primarily on the density of wave sampling, with a lower bound proportional to the minimum wavelength of recorded seismic-wave energy.

1.10.3.1 Cells, Nodes, and Basis Functions

No single scheme can fully represent all aspects of the Earth's heterogeneity. At the local scale, the constant-velocity, uniform volume block approach of Aki and Lee (1976), and the variable volume block approach of Roecker (1982) treat a volume of the Earth as a set of cells within each of which the seismic velocity is constant (**Figure 3(a)**). This approach has the advantage of simplicity, but it clearly lacks the ability to represent gradients in velocity or oblique discontinuities. From the inverse theory point of view, a block/cell inversion is often set up as an overdetermined problem (more independent data than unknowns), but this strategy can be criticized for being underparameterized (insufficient parameters to adequately represent the real Earth). At the same time, some model parameters may actually be unconstrained even though there are more data than unknowns, resulting in a mixed-determined problem (simultaneously over- and underdetermined). Alternatively, one can employ a large number of small cells, allowing gradual or rapid velocity changes from block to block to mimic gradients or discontinuities, respectively (Lees and Crosson, 1989; Nakanishi, 1985; Walck and Clayton, 1987). Unfortunately, the use of a large number of cells, if not compensated for, results in a severely underdetermined problem (many more unknowns than independent data) and increased computational burden. These two problems are typically dealt with by applying a smoothing operator and a sparse-matrix solver, respectively (see Section 1.10.4).

Variations on the discrete block parameterization include laterally varying layers (Hawley et al., 1981) and a 3D grid of nodes (Thurber, 1983). In the approach of Hawley et al. (1981), the model is divided into horizontal layers in which velocity is constant in the vertical direction, but velocity is obtained by interpolation in the horizontal directions among vertical nodal lines (**Figure 3(b)**). The spacing between nodal lines may vary from layer to layer. Thurber (1983) used a 3D grid approach (**Figure 3(c)**), in which velocity varies continuously in all directions, with linear B-spline interpolation among nodes. Alternatively, one can use cubic B-splines with continuous second-order derivatives (Michelini and McEvilly, 1991).

Another variant of the 3D grid theme is to consider each set of four neighboring nodes as defining the vertices of a tetrahedron (**Figure 3(d)**; Lin and Roecker, 1997). The four node velocities can be used to define a unique linearly varying velocity field within the tetrahedron; the velocity gradient can thus point in any direction. Snell's law is used to cross tetrahedral boundaries. This allows the use of an analytic formula for ray tracing using an initial-value ('shooting') approach, as ray paths are circular arc segments in a medium with constant-velocity gradient. Other alternative interpolation schemes are possible but would require different ray tracing procedures. See also Section 1.10.3.2 for an example of the use of tetrahedrons in adaptive-mesh tomography.

Similar approaches have been adopted for regional- and global-scale tomography. Aki et al. (1977) employed constant-slowness, uniform volume cells in their original teleseismic (regional) inversion work, and that method ('ACH' after the authors Aki, Christoffersson, and Husebye) has proven to be a 'workhorse' for the seismology community (see Evans and Achauer, 1993). Some improvements have been made to the algorithm over the years, including allowing for variable block thickness with depth (Evans and Achauer, 1993) and using nodes with spline interpolation (VanDecar et al., 1995), and problems and code errors have been pointed out (Julian et al., 2000; Masson and Trampert, 1997), but the basic method continues to be used widely. Humphreys, Clayton, and coworkers developed a similar algorithm (Humphreys et al., 1984), and Spakman, Nolet, and coworkers developed a third comparable algorithm (Spakman and Nolet, 1988), both of which have also been put to wide use. A key distinction between the latter two is

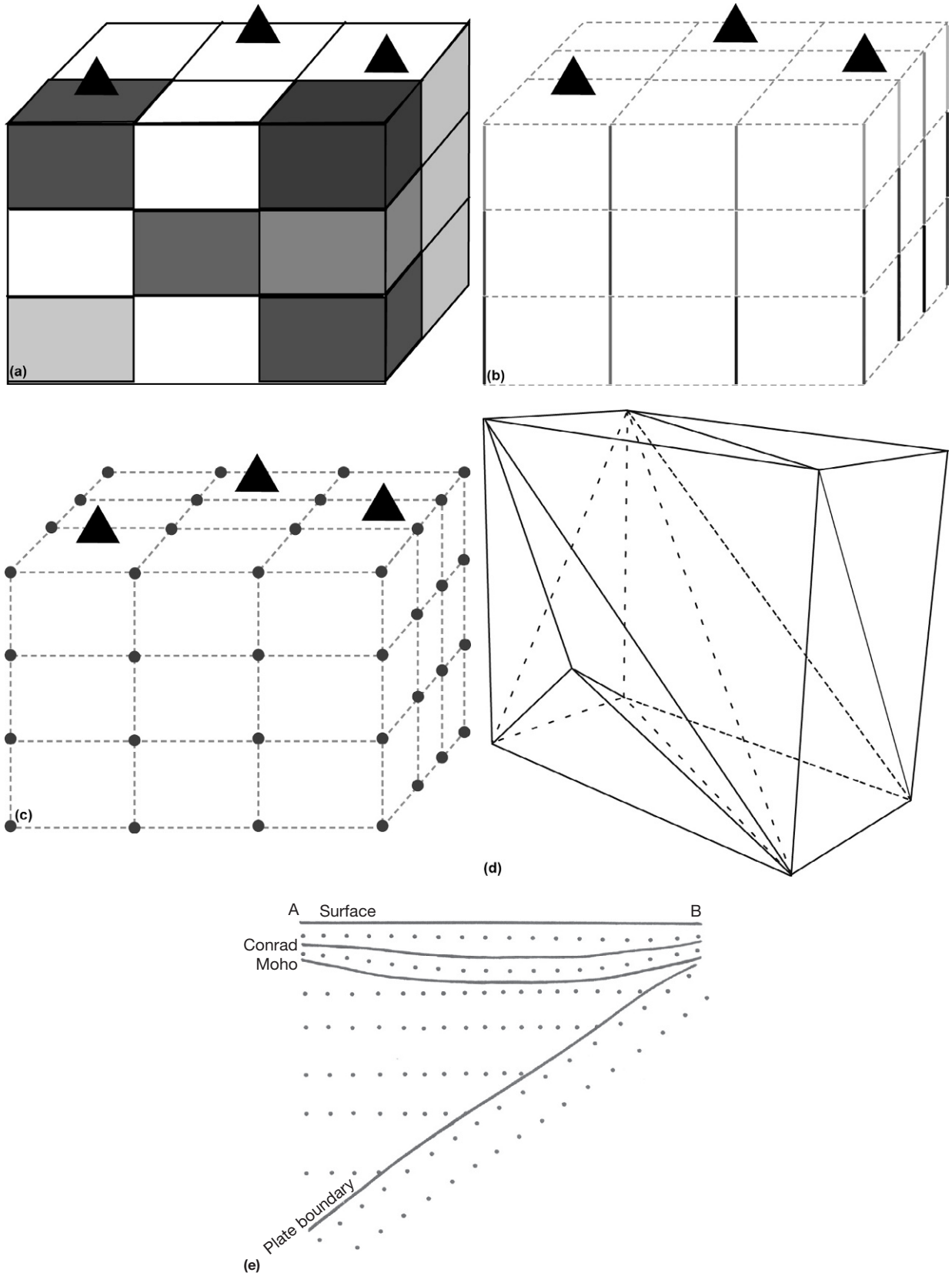

Figure 3 Examples of types of model parameterization schemes. (a) Constant-velocity, uniform volume blocks. (b) Layers of laterally varying but vertically constant velocity within a given layer. (c) Regular grid of nodes. (d) Variable-size tetrahedral cells. (e) Interfaces separating regions with velocity defined on a grid. Reproduced from Zhao D, Hasegawa A, and Horiuchi S (1992) Tomographic imaging of P- and S-wave velocity structure beneath northeastern Japan. *Journal of Geophysical Research* 97: 19909–19928.

the inverse problem solution method, simultaneous iterative reconstruction technique (SIRT) for the former and LSQR for the latter (see **Section 1.10.4**).

Zhao and coworkers have taken a slightly different approach that emphasizes the importance of major seismic velocity discontinuities along with velocity heterogeneity. Using the study of northeastern Japan by Zhao et al. (1992) as an example, the authors define the discontinuities and imbed a velocity grid within each layer (**Figure 3(e)**). The method allows the inclusion of secondary phase data (e.g., converted phases) to model the positions of the discontinuities, although this particular study did not utilize this capability.

Similarly, Zhao (2004) incorporated discontinuities and a 3D grid in a global tomographic model, with a grid spacing of 3–5°. Specifically, he included the Moho and the 410 and 660 km discontinuities, keeping them fixed during the inversion. More commonly, global tomographic models utilize spherical 'blocks' of uniform latitude and longitude extent or roughly uniform size (Inoue et al., 1990; Sengupta and Toksöz, 1976; Simmons et al., 2010; van der Hilst et al., 1997; Vasco et al., 1995; Zhou, 1996).

Alternatively, one can adopt a functional approach to representing 3D structure, with either a set of basis functions or an a priori functional form. An example of the former is an expansion in a set of continuous, orthogonal basis functions (e.g., sinusoidal or spherical harmonic functions) where the spatial resolution is limited by the number of terms included in the expansion (Novotny, 1981). Examples of the latter are the subducting slab parameterization of Spencer and Gubbins (1980), in which the slab is represented by its strike, dip, width, slowness contrast, and decay rate with depth; the fault zone parameterization of Wesson (1971), in which the fault zone is represented by its velocity decrease, decay with depth and distance, and the velocity contrast across it; and the quasilayered parameterization of Ashiya et al. (1987) employing a sum of hyperbolic tangent functions for the depth variation of velocity and Chebyshev functions for the lateral variation of velocity.

Early global P-wave travel time studies used spherical harmonic expansions in latitude and longitude and polynomials in depth (Dziewonski, 1984). As of this writing, global tomography has reached degree 40, corresponding to a lateral dimension of as little as 500 km (Kustowski et al., 2008; Ritsema et al., 2011). One source of concern for this approach is the tendency for the truncated basis functions to leak into the solution, leading to a biased model estimate (Trampert and Snieder, 1996). If the power in the model spectrum above the truncation point is weak, this may not be a serious issue, but of course it is difficult to prove that this is the case, in general. We also point out that truncation is a risk to virtually any tomographic method that adopts an overdetermined ('underparameterized') inverse approach. Trampert and Snieder (1996) in fact present a technique for correcting (to first order) the biasing effect of truncating spherical harmonic basis functions.

Recently, wavelets (e.g., Chevrot et al., 2012; Simons et al., 2011) and cubic splines have been used for global tomography (Antolik et al., 2000; Mégnin and Romanowicz, 2000). Typically, spherical splines (Wang and Dahlen, 1995) are used for the horizontal variations and radial splines for the vertical. This approach has the advantage of being a local parameterization, leading to a sparse solution matrix and potentially avoiding the bias problems of spherical harmonics, combined with the desirable smoothing properties inherent in splines. For the same number of parameters, the spherical harmonic solution should yield a comparable solution to that of a uniform spline model, but the spline approach does have the advantage of allowing for a nonuniform grid. Sparsity is discussed further in **Section 1.10.4.2.2**.

A distinct alternative to the philosophy of discrete model parameterization is to treat the velocity structure explicitly as a continuous function of the spatial coordinates. Two examples are the Backus–Gilbert approach of Chou and Booker (1979) and the 'no-block' approach of Tarantola and Nercessian (1984). In principle, these approaches allow for essentially arbitrary model solutions with no parameterization bias. In practice, however, models must be constrained in one way or another, as they are again underdetermined. The models must also ultimately be discretized for calculation and representation by computer. Chou and Booker (1979) remove the nonuniqueness by evaluating 'ideal averaging volumes,' which reflect the spatial variations in ray sampling of the structure. The idea is to view the Earth structure through the window with the maximum spatial resolution allowed by the data. Pavlis and Booker (1980) employed this method (generalized to include hypocenter parameters) for 1D modeling. The Bayesian strategy of Tarantola and Valette (1982) and Tarantola and Nercessian (1984) makes use of a priori information on the Earth's velocity structure and its 3D spatial covariance function to construct a unique solution. Their nonlinear approach 'anchors' the solution to the starting model and imposes a smoothness constraint that acts on the scale of the correlation distance. Of course, this requires independent knowledge of the 3D spatial covariance function, which is typically (but not always) assumed to be homogeneous throughout the medium. See **Section 1.10.4.2** for additional discussion.

1.10.3.2 Irregular-Cell, Multigrid, and Adaptive-Mesh Methods

In almost all seismic tomography applications, data coverage is highly uneven due to nonuniform station geometry, uneven distribution of seismic sources, missing data, and ray bending. Some nodes or cells may not be sampled at all, while others may be sampled repeatedly. The standard regular cell–grid spacing approach makes it difficult to adapt the model to the uneven sampling. The mismatch between the data distribution and the cells or grid chosen for the tomographic inversion destabilizes the inversion. Preferably, the inversion cells or grid should be distributed adaptively to match with the resolving power of the data and to better condition the inverse problem. At the same time, one can hope to image structural details (e.g., subducting slabs or narrow fault zones) that are smaller in scale than could be represented practically with a uniform-cell global or local model. For a review of irregular-cell and adaptive-mesh methods for seismic tomography, the interested reader is referred to the review paper by Sambridge and Rawlinson (2005).

The goal of matching the ray distribution to the mesh or cells naturally leads to the use of an irregular mesh or cells. One strategy is to explicitly treat the inversion mesh node positions as part of the set of inversion parameters. Michelini (1995)

proposed an adaptive-mesh scheme for relatively small-size inverse problems by simultaneous determination of seismic velocities and node positions, with position adjustments damped more heavily. This concept works because node position adjustments by themselves do alter the velocity structure, steepening or reducing gradients for nodes that move closer together or farther apart, respectively, and of course by shifting the points in space where the specific node velocity values are attained. Thus, there is a natural tendency for nodes to cluster where velocity is changing more rapidly, but the method does not lead to a denser node distribution where the sampling is denser.

Alternatively, one could adapt the irregular inversion mesh or cells using a priori information and/or some measure of solution stability or resolution, without formally including it in the inversion. Abers and Roecker (1991) proposed an irregular-cell representation of the model in which the inversion cells (larger cells) are constructed from basic cells (smaller cells) by using a 'cross-reference table' (an index for defining which cells are combined together). The table is mainly constructed by hand, which limits the practical size of the parameterization one can handle. Vesnaver (1996) proposed a different irregular-cell parameterization approach, in which the cells are interactively modified by merging adjacent cells, shifting cell boundaries, and splitting a cell into two or more according to the null space energy. The null space energy measures the local reliability or the physical resolution of the model. Cells are removed where null space energy is too high, and cells are added where it is adequately low. The null space energy is determined using the singular value decomposition (SVD) $\mathbf{U}\,\mathbf{S}\,\mathbf{V}^{\mathrm{T}}$ (Aster et al., 2012) of the partial derivative matrix for the inversion and is calculated for each model parameter by summing the squares of the elements of the row of the orthogonal matrix $\mathbf{V}$ corresponding to the given model parameter for singular values below a chosen threshold. This process is extremely time-consuming for large-scale problems, as it is not fully automatic.

In contrast, for LET, Zhang and Thurber (2005) developed an automatic adaptive-mesh tomography method based on tetrahedral cells that matches the inversion mesh to the data distribution. As a result, the number of inversion mesh nodes is greatly reduced compared to a regular inversion grid with comparable spatial resolution, and the tomographic system is more stable and better conditioned. They start the inversion from a slightly perturbed regular inversion grid, constructing the tetrahedral cells (or alternatively the Voronoi diagram) around the nodes using the Quickhull algorithm (Barber et al., 1996). Rays are traced between events and stations based on the current regular velocity grid. The rays are used to find the partial derivatives of the travel times with respect to the model slowness parameters on the current inversion mesh. In the process, the values of the 'derivative weight sum' (DWS – the sum of the interpolation weights for the partial derivatives corresponding to each model parameter; Thurber and Eberhart-Phillips, 1999) for the inversion mesh nodes are calculated. Threshold DWS values are set for adding or removing nodes. Once the inversion mesh is determined to be optimal, a new set of tetrahedral cells (or new Voronoi diagram) is constructed, and the partial derivatives of the travel times with respect to the new set of inversion mesh nodes are calculated. Following each simultaneous inversion, the velocity values on the irregular inversion mesh nodes are updated, rays are traced through the new model, and the inversion mesh is again updated following the same procedure to assure a good match with the ray distribution, which will change as the velocity model changes and hypocenters move. Compared to the earlier-mentioned methods, key advantages of this approach are that it is fully automatic and it uses the sampling density to control the mesh density.

Another alternative is the use of multiple-scale grids (multigrids), either overlapping ('superposed') or nonoverlapping ('nested'). In an early study, Thurber (1987) applied a nested-grid inversion to Kilauea volcano to image the finer-scale structure of Kilauea caldera within a larger model of the volcano. Lin et al. (2010) combined results from a number of nested-grid inversions to develop a statewide tomography model for California. Zhou (2004) applied the superposed grids approach to southern California.

A variety of irregular-cell, multigrid, and adaptive-mesh techniques have also been developed for teleseismic and whole-Earth tomography. One common approach is again nested grids, the use of larger cells for a 'background' global 3D model plus smaller cells in a region of interest (Widiyantoro and van der Hilst, 1997). This was extended to a triple-nest grid by Weidle et al. (2005). In a similar but more versatile vein, Spakman and Bijwaard (2001) followed the basic idea of Abers and Roecker (1991) discussed earlier but adopted a different strategy for irregular-cell design by developing a completely automated and fast algorithm for the construction of the cross-reference table. The design of irregular cells can be constrained by some scalar function, for instance, a measure of model sampling such as cell hit count. Wavelet-based representations, discussed in **Section 1.10.3.1**, implicitly provide a multiscale approach (Chiao and Kuo, 2001; Chiao and Liang, 2003; Gung et al., 2009). 'Progressive' inversions that solve for increasingly finer structures as perturbations to coarser models are similar in effect to the wavelet approach (Simons et al., 2011).

Sambridge and Gudmundsson (1998) proposed an irregular-cell approach for global tomography based on tetrahedral diagrams. Their initial application was to a regionalized model using a priori information on tectonic provinces and subducting slab geometry to construct a fixed-grid model (Gudmundsson and Sambridge, 1998), but they did not explicitly explain how to optimize the cells. Some possibilities are to adjust them based on the model null space energy (Vesnaver, 1996) and/or the velocity gradient. Sambridge and Faletic (2003) and Debayle and Sambridge (2004) introduced a data-driven tetrahedral cell adaptive scheme based on the maximum spatial gradients in seismic velocity perturbation across each tetrahedron face. This is useful for trying to characterize regions of rapid velocity change, but it does not account for the ability of the data to resolve such changes. Nolet and Montelli (2005) took a similar tetrahedral parameterization approach but included an estimate of local resolving length in deriving the optimal spacing of mesh nodes.

It is clear that there are many options available for model parameterization. How does one make a choice? One approach that has some advantages is to adopt a two-stage modeling strategy. An initial phase of modeling can be carried out using a more 'traditional' regular parameterization. The

results of the first phase can then serve as both starting model and point of comparison for a second phase using some type of irregular model parameterization. Any significant increase in anomaly amplitudes should be accompanied by a significant decrease in data misfit (e.g., as measured by an *F*-test) if the results of the second phase are to be preferred over the first. The irregular parameterization also is a hindrance to carrying out some of the traditional resolution tests, such as spike or checkerboard tests (see **Section 1.10.5**). Such resolution tests from the regular parameterization model can provide valuable information that might not easily be obtained otherwise. At the same time, there is potential concern about the model resolution for models with locally fine parameterization – unless a complete resolution analysis is carried out, the reality of fine-scale features resulting from irregular mesh tomography may be questioned. See **Sections 1.10.4** and **1.10.5** for detailed discussion of model resolution issues.

1.10.3.3 Static (Station) and Crustal Corrections

In almost all cases, the adopted model parameterization is incapable of representing all aspects or scales of Earth heterogeneity. The most common situation is treating the shallow structure (e.g., the top few hundred meters at a local scale or the crust at the global scale) using static (station) corrections. These corrections can be defined a priori or determined as part of the inversion. The mathematics of the latter option are treated in **Section 1.10.4** in the succeeding text; examples include Bijwaard et al. (1998) for global and DeShon et al. (2006) for local body-wave tomography. Examples of the a priori approach include using time and phase delays computed from a global crustal model (Mooney et al., 1998; Nataf and Ricard, 1996) in global or regional surface-wave tomography (Boschi and Ekström, 2002; Boschi et al., 2004; Montager and Tanimoto, 1991; Panning et al., 2010; Ritsema et al., 2009) and using a fixed crustal refraction model in teleseismic tomography (Waldhauser et al., 2002). In all of these cases, the goal is to prevent shallow heterogeneity from 'leaking' into the deeper structure. The effectiveness of this strategy obviously hinges on the quality of the a priori or derived correction values (e.g., Bozdag and Trampert, 2008) and on how well the highly nonlinear effects of strong lateral variation in crustal structure are dealt with. Recognizing this, Li et al. (2006) adopted a strategy for teleseismic tomography that allows for perturbations to the a priori crustal model by including a regularization term in the inversion that penalizes deviations from the a priori model. Thus, the crustal model will be perturbed where the data require it, although the penalization will generally moderate such changes.

1.10.4 Model Solution

In the early days, the limited computer capabilities (typical mainframes with a 1 MB of memory, 100 MB of disk space, and megahertz CPU speeds) put severe limits on the mathematical and computational sophistication that could be implemented for solving tomography problems. Now, we have inexpensive desktop systems with three to four orders of magnitude larger memory and storage and faster speed than the mainframes of the mid-1970s, yet tomographers will still complain that their computers are too slow and their memory and storage capabilities are not adequate! As computer power has increased, the amount of data and the complexity of both the model parameterization and the associated forward problem solver have risen as well.

The preceding sections set the stage for the critical process of determining a model that adequately fits the available data and known constraints. To get to this point, the tomographer needs to make numerous decisions regarding the scale of the problem to be tackled, the types of data to include, the manner in which the 3D Earth structure will be represented, how the forward modeling will be carried out, etc. Deriving an 'optimal' model and evaluating its quality fall under the domain of inverse theory, about which numerous books have been written (Aster et al., 2012; Menke, 2012; Parker, 1994; Tarantola, 2005). A series of papers by Backus and Gilbert (Backus and Gilbert, 1967, 1968, 1970) brought linear inverse theory to the attention of geophysicists, and Wiggins (1972) wrote a noteworthy paper on resolution of seismic models in particular. While we do not have space to review all the fundamental aspects of inverse theory as they can be applied to seismic tomography, we can provide a 'road map' to guide the appropriate application of inverse methods to tomography problems.

1.10.4.1 Linear Versus Nonlinear Solutions

One key aspect that separates some tomography problems from others is whether the problem is linear or nonlinear. For example, fitting a straight line or a parabola to a set of x–y points is a linear problem. In the former case, the equations are of the form

$$y = (l)m_1 + (x)m_2 \qquad [15]$$

whereas in the latter case, they are of the form

$$y = (l)m_1 + (x)m_2 + (x^2)m_3 \qquad [16]$$

Both can be expressed directly in the form

$$\mathbf{d} = \mathbf{Gm} \qquad [17]$$

where $\mathbf{d}$ is the data vector of length N, $\mathbf{m}$ is a vector with M model parameters, and $\mathbf{G}$ is the matrix of partial derivatives of the data with respect to the model parameters. In contrast, fitting a Gaussian curve to a set of x–y points is a nonlinear problem, because the formula

$$y = m_1 / \left[(2\pi)^{1/2} m_2\right] \exp\left[-(x - m_3)^2 / \left(2m_2^2\right)\right] \qquad [18]$$

cannot be reduced to a linear equation in terms of the variables m_i. We point out that solving nonlinear problems in seismic tomography is generally accomplished via linearizing the problem about a trial solution and improving the model iteratively (e.g., Aster et al., 2012; Tarantola and Valette, 1982). Some exceptions apply global optimization methods such as Monte Carlo (Shapiro and Ritzwoller, 2002), but that is beyond the scope of this chapter.

To some degree, this distinction is fuzzy for tomography problems because the same problem has been tackled with

linear and nonlinear approaches. Take, for example, the original LET study of Aki and Lee (1976). In a single step, they inverted simultaneously for local earthquake locations and 3D structure (in terms of constant-slowness 'blocks') using an initial homogeneous background velocity model. They explored the linearity of the problem and model uniqueness by repeating the inversion with two different background models. Given the convergence to the same 3D structure, they concluded that a linear solution was adequate. Subsequent work on an expanded dataset from the same region demonstrated that a nonlinear solution actually was required to converge to a valid solution. In this case, the lateral heterogeneity was so strong that the linear inversion had not converged. Starting with the study of Thurber (1983), nonlinear solutions have become the norm for LET.

Similarly, the original 'ACH' (Aki et al., 1977) teleseismic tomography study used a linear inversion. The work by Ellsworth (1977) determined that a nonlinear solution agreed well with the linear solution for a dataset from Hawaii. In this case, however, the amplitude of the anomalies was relatively modest (mainly within ±5%), so a linear approximation was in fact adequate. For regions with higher-amplitude anomalies, a nonlinear solution could be significantly different. Early efforts at nonlinear teleseismic inversion were made by Thomson and Gubbins (1982), Koch (1985), and Nakanishi and Yamaguchi (1986). More recently, Weiland et al. (1995) and VanDecar et al. (1995) developed nonlinear algorithms for teleseismic tomography and applied them to Long Valley Caldera, California, and eastern Brazil, respectively. In the case of Long Valley, anomalies on the order of ±20% were recovered, about three times larger than a linear inversion by Dawson et al. (1990) using the same dataset. A similar study for Valles Caldera, New Mexico (Steck et al., 1998), obtained even greater anomalies (±25%) using nonlinear inversion. Pesicek et al. (2010) used an iterative method (see **Section 1.10.4.2.2**) to obtain a nonlinear teleseismic solution for the structure in the region of the great 2004 Sumatra earthquake. They showed that the iterative solution sharpened the image of the subducting slab significantly. Despite such impressive results with a nonlinear approach, linear inversions are predominant in teleseismic tomography studies.

On a global scale, linear solutions are also the norm for travel time inversions, whether they are block or spline inversions or spherical harmonic expansion inversions. Beginning with Sengupta and Toksöz (1976) and Dziewonski et al. (1977) and continuing through Su et al. (1994) and van der Hilst et al. (1997) (and many others), the inverse problems were mainly set up and solved in a linear manner. Some notable exceptions are the P-wave study of Bijwaard and Spakman (2000) and the S-wave study of Widiyantoro et al. (2000), which are both fully nonlinear solutions. We also note that Dziewonski (1984) carried out an iterative inversion but with an approximate inverse that neglected hypocenter–structure coupling (see **Section 1.10.4.3**).

Using a 3D ray tracer (Bijwaard and Spakman, 1999) and a 3D starting model (Bijwaard et al., 1998), Bijwaard and Spakman (2000) carried out inversions for cell slowness perturbations, cluster relocation vectors (average hypocenter adjustment for all events in a given latitude–longitude–depth bin), and station corrections. They found no dramatic changes in the pattern of anomalies compared to Bijwaard et al. (1998), but did observe some sharpening of features. Surprisingly, the improvement in data fit compared to Bijwaard et al. (1998) was marginal – the variance reduction after two nonlinear iterations was 57.2% compared to 57.1%. This may be because the authors used the original event locations from Engdahl et al. (1998) as their starting locations rather than using locations updated via individual event relocations or using the cluster relocation vectors determined by Bijwaard et al. (1998). Since these same locations were used to derive the starting 3D velocity model, one would expect that the first-iteration location perturbations would be biased toward low values. A total of only two iterations were carried out, so the small additional model perturbations would in turn lead to minor earthquake relocations and hence small model perturbations in the subsequent iteration. It is also possible that the model damping required to limit the negative effects of noise in the dataset used (from the Engdahl et al., 1998 'groomed' catalog derived from ISC data) may simply be too great to allow a higher-amplitude model to be extracted. This is supported by the analysis of Dorren and Snieder (1997), who showed that noisy data might result in a linear model estimate that is superior to a nonlinear one in travel time tomography. Finally, it may be the case that the LSQR solution fails to account for the small singular values for the location parameters compared to the much larger singular values expected for most velocity model parameters.

Widiyantoro et al. (2000) carried out a similar nonlinear study for S waves, with a somewhat different outcome. They included event locations as free parameters but heavily penalized relocations because the S-wave data alone are not actually sufficient to produce well-constrained locations. Thus, the hypocenters varied very little from their initial locations, again obtained from Engdahl et al. (1998). They included both damping and smoothing constraints and a constraint penalizing deviation from the 1D ak135 model (Kennett et al., 1995) (see **Section 1.10.4.2** for a discussion of constraints). Their solution yielded a significant improvement in data fit, increasing the variance reduction from the 33% reduction obtained by Widiyantoro et al. (1998) to 40%. Some of this improvement can be attributed to the use of a higher-quality dataset (Engdahl et al., 1998). On the other hand, the model results do show significant spatial sharpening and amplitude increase compared to Widiyantoro et al. (1998). In particular, the deep signature of some slabs appears substantially sharpened.

1.10.4.1.1 Iterative solvers

A common inversion approach is the use of iterative matrix solution methods (Aster et al., 2012), such as Kaczmarz's algorithm and the related algebraic reconstruction technique (ART), SIRT, and conjugate gradient least squares (CGLS). ART has convergence and stability problems, but SIRT and especially CGLS have found wide application. The LSQR algorithm of Paige and Saunders (1982) is probably the most widely used of these iterative methods. The interested reader is referred to van der Sluis and van der Vorst (1987) for an exhaustive discussion of these techniques and to Trampert and Lévêque (1990) for an analysis of the SIRT method, which we note is subject to convergence problems. Although this class of solvers is known as iterative methods, we emphasize that they address linear matrix problems. Due to their popularity, we

include a brief introduction to the CGLS and the LSQR algorithms here.

CGLS is a general method for solving linear equations of the form $\mathbf{Gm}=\mathbf{d}$ by forming the normal equations

$$\mathbf{G}^{\mathrm{T}}\mathbf{Gm}=\mathbf{G}^{\mathrm{T}}\mathbf{d} \quad [19]$$

and constructing a convenient set of basis vectors $\mathbf{p}_k$ that are mutually conjugate with respect to $\mathbf{G}^{\mathrm{T}}\mathbf{G}$ (Aster et al., 2012; Scales, 1987). Using these basis vectors, the least-squares solution for $\mathbf{m}$ can be calculated with an efficient iterative algorithm requiring only matrix–vector and vector–vector products in a recursive scheme; no actual matrix decomposition or inversion is involved. Efficiency can be further enhanced by the use of sparse-matrix methods (Davis, 2006), because the procedure does not involve matrix factorizations that can destroy sparseness. Sparse-matrix methods are particularly effective in tackling massive-scale tomography problems.

LSQR (Paige and Saunders, 1982) is probably the most widely used algorithm for the solution of large least-squares problems in seismology. LSQR is a recursive procedure for solving the normal equations that is in theory mathematically equivalent to CGLS (in the absence of machine accuracy problems) but is more stable in practice. The LSQR algorithm involves a technique known as Lanczos bidiagonalization, which transforms an initial symmetrical matrix into one with nonzero values only on the diagonal and the elements immediately above it. For a detailed examination of LSQR and a comparison to other methods in a seismological context, the reader is referred to Nolet (1985, 1987) and Spakman and Nolet (1988).

1.10.4.2 Regularized and Constrained Inversion

Even if there are far more observations than model parameters in a given seismic tomography problem, the inverse problem is almost always rank-deficient, meaning that $\mathbf{G}$ has one or more zero singular values and that it is has an unstable solution in the presence of noise. This is expected because some model parameters may not be directly sampled by the data (i.e., cells without 'hits') (see **Section 1.10.3.2**). The condition number of $\mathbf{G}$ (ratio of largest to smallest singular value) provides one direct measure of noise sensitivity (Aster et al., 2012), but it can only be estimated with some of the popular solution techniques (e.g., LSQR). To solve such stability problems, some form of regularization or constraint is required (Aster et al., 2012; Sambridge, 1990).

1.10.4.2.1 Generalized inverse and damped least-squares solutions

Equations [13] and [14] are linear relationships between the seismic data (i.e., body-wave travel time anomaly δT or surface-wave phase shift δC) and perturbations from the wave speed in the reference model. They can be discretized and written in matrix form as before:

$$\mathbf{Gm}=\mathbf{d} \quad [20]$$

$\mathbf{G}$ relates the model to the data, or more typically the data misfit to the model perturbations, and is often based on wave theory for a 1D reference model (e.g., PREM and ak135). In seismic tomography, we typically have many more data than unknowns ($N \gg M$). Given data errors, the equations in [20] are inconsistent and do not have an exact solution. Therefore, we usually minimize a measure of discrepancy (misfit):

$$(\mathbf{Gm}-\mathbf{d})^{\mathrm{T}}(\mathbf{Gm}-\mathbf{d}) \quad [21]$$

Here, we have chosen the Euclidian norm that defines [21] to be a least-squares problem. The least-squares formulation is often used because of its mathematical simplicity. However, it is not necessarily the best for tomographic problems, given the large influence of data outliers. Other norms have been adopted in some cases (e.g., Bube and Langan, 1997), but the least-squares approach is predominant.

In damped least squares (DLS), we minimize

$$(\mathbf{Gm}-\mathbf{d})^{\mathrm{T}}(\mathbf{Gm}-\mathbf{d})+\varepsilon^2\mathbf{m}^{\mathrm{T}}\mathbf{m} \quad [22]$$

The damping term $\varepsilon^2\mathbf{m}^{\mathrm{T}}\mathbf{m}$ serves to penalize models $\mathbf{m}$ with a large norm. In global and teleseismic tomography, this is equivalent to preferring models that are close to the (1D) reference model. Particularly in regions poorly sampled by seismic waves, the wave speed will retain values close to the reference model.

We obtain the DLS solution by differentiating [22] with respect to the model parameters $\mathbf{m}$ and solving for $\mathbf{m}$:

$$\mathbf{m}_{\mathrm{DLS}}=\left[\left(\mathbf{G}^{\mathrm{T}}\mathbf{G}+\varepsilon^2\mathbf{I}\right)^{-1}\mathbf{G}^{\mathrm{T}}\right]\mathbf{d} \quad [23]$$

This solution is of the general form

$$\mathbf{m}_{-\mathrm{i}}=\mathbf{G}^{-\mathrm{i}}\,\mathbf{d} \quad [24]$$

where $\mathbf{G}^{-\mathrm{i}}$ is a 'generalized' inverse. If $\mathbf{USV}^{\mathrm{T}}$ is the SVD of $\mathbf{G}$, then we can write the DLS inverse and the corresponding solution as

$$\mathbf{G}^{-\mathrm{i}}_{\mathrm{DLS}}=\mathbf{VF}\,\mathbf{S}^{\dagger}\mathbf{U}^{\mathrm{T}} \text{ and } \mathbf{m}_{\mathrm{DLS}}=\mathbf{G}^{-\mathrm{i}}_{\mathrm{DLS}}\mathbf{d} \quad [25]$$

where $\mathbf{S}^{\dagger}$ is the pseudoinverse of $\mathbf{S}$ (with diagonal elements $1/s_{\mathrm{i}}$ unless $s_{\mathrm{i}}=0$, in which case the diagonal element of $\mathbf{S}^{\dagger}$ is 0) and the diagonal elements of $\mathbf{F}$ (the 'filter factors') satisfy

$$f_i^2=s_i^2/\left(s_i^2+\varepsilon^2\right) \quad [26]$$

(Aster et al., 2012). In addition to determining the solution itself, we desire to know the quality of the solution as well. Two measures of quality are the model resolution matrix, which indicates the model 'blurriness,' and the model covariance matrix, which indicates the uncertainty of and covariation among model parameters (Aster et al., 2012). The definition of the model resolution matrix $\mathbf{R}_{\mathbf{m}}$ is obtained by substituting $\mathbf{Gm}=\mathbf{d}$ into [24], obtaining

$$\mathbf{m}_{-\mathrm{i}}=\mathbf{G}^{-\mathrm{i}}\mathbf{Gm}=\mathbf{R}_{\mathbf{m}}\mathbf{m} \quad [27]$$

The model covariance matrix $\mathbf{C}_{\mathrm{m}}$ has the form

$$\mathbf{G}^{-\mathrm{i}}\mathbf{C}_{\mathrm{d}}\left(\mathbf{G}^{-\mathrm{i}}\right)^{\mathrm{T}} \quad [28]$$

where $\mathbf{C}_{\mathbf{d}}$ is the data covariance matrix, often assumed to be diagonal (uncorrelated errors). In the case of the DLS solution in [23], $\mathbf{R}_{\mathrm{m}}$ and $\mathbf{C}_{\mathrm{m}}$ are given by

$$\begin{aligned}\mathbf{R}_{\mathrm{m}}&=\mathbf{VFV}^{\mathrm{T}}\\ \mathbf{C}_{\mathrm{m}}&=\mathbf{VFS}^{\dagger}\mathbf{U}^{\mathrm{T}}\mathbf{C}_{\mathrm{d}}\mathbf{U}\left(\mathbf{S}^{\dagger}\right)^{\mathrm{T}}\mathbf{F}^{\mathrm{T}}\mathbf{V}^{\mathrm{T}}\end{aligned} \quad [29]$$

We face the inevitable trade-off that decreasing ε improves the estimated model resolution (i.e., brings $\mathbf{R}_{\mathrm{m}}$ closer to an

identity matrix), but at the same time, it increases the model uncertainty (i.e., increases the size of the diagonal elements of $\mathbf{C}_m$). A trade-off analysis can be carried out to try to identify the optimum damping value (e.g., Eberhart-Phillips, 1986). This is basically equivalent to an L-curve analysis (Aster et al., 2012), whereby the corner of a log(misfit) versus log(model norm) plot can be used to determine a good damping value.

One can also apply weights to the data (W_d) and model (W_m), forming the weighted DLS equations to be minimized:

$$(\mathbf{Gm}-\mathbf{d})^{\mathrm{T}}W_d(\mathbf{Gm}-\mathbf{d})+\varepsilon^2\mathbf{m}^{\mathrm{T}}W_m\mathbf{m} \quad [30]$$

If we then define

$$\mathbf{M}^{\mathrm{T}}\mathbf{M}=W_m;\ \mathbf{D}^{\mathrm{T}}\mathbf{D}=W_d \quad [31]$$

and the transformations

$$\mathbf{m}'=\mathbf{Mm};\ \mathbf{d}'=\mathbf{Dd};\ \mathbf{G}'=\mathbf{DGM}^{-1} \quad [32]$$

it is straightforward to demonstrate that minimizing [30] is identical to minimizing

$$(\mathbf{G}'\mathbf{m}'-\mathbf{d}')^{\mathrm{T}}(\mathbf{G}'\mathbf{m}'-\mathbf{d})+\varepsilon^2\mathbf{m}'^{\mathrm{T}}\mathbf{m}' \quad [33]$$

An alternative approach to damping that yields similar results is singular value truncation (Aster et al., 2012). The truncated SVD (TSVD) solution forms an approximate inverse matrix using the p largest singular values s_i of $\mathbf{G}$:

$$\mathbf{G}^{\mathrm{TSVD}}=\sum_{i=1}^{p}\mathrm{U}_i\mathrm{S}_i\mathrm{V}_i^{\mathrm{T}} \quad [34]$$

If p is the rank of $\mathbf{G}$, then we have the pseudoinverse solution. See Aster et al. (2012) for a detailed discussion and comparison of the least-squares, pseudoinverse, and TSVD solutions.

Another 'trick' for improving stability of the inversion is preconditioning (Gill et al., 1981). In general, the ratio of the largest to smallest singular value (the condition number) provides a measure of the stability of the inverse model, particularly its sensitivity to noise in the data (Aster et al., 2012). Furthermore, the convergence rate for the CGLS and LSQR methods can be improved if the system can be transformed (scaled) to one with many unit-value singular values. Thus, scaling the system of equations to reduce the condition number and/or increase the number of unit-value singular values is a desirable step to implement in many cases.

Convergence of CGLS and similar methods leads to a quandary when regularization is desired. As Aster et al. (2012) showed, the convergence rate is typically rapid in the initial iterations for unregularized CGLS, after which noise in the solution tends to build up rapidly. This is a combination of accumulated effects of roundoff errors and the fact that the iterative solution is converging toward an unregularized solution. If regularization is introduced, the algorithm will converge more slowly and will generally fit the data better than the unregularized case for a given model norm, but the cost is an order of magnitude increase in the number of required iterations. Since seismic tomography problems virtually always require some form of regularization, the extra computational burden is generally unavoidable.

As noted earlier, the original Aki et al. (1977) (ACH) teleseismic and Aki and Lee (1976) LET methods both involved single-step linearized inversions for the model parameters. This approach allowed the use of linear inverse theory techniques for model estimation and also for model resolution and uncertainty analysis. Aki et al. (1977) compared models obtained using both a generalized inverse (TSVD) and a DLS ('stochastic') inverse. For the teleseismic case, the system of equations is always linearly dependent due to the trade-off between average layer velocity and event origin times, so a simple least-squares solution was impossible. The generalized inverse approach uses the nonzero singular values of the $\mathbf{G}$ matrix to compute a least-squares solution, whereas the stochastic inverse approach computes a DLS solution using a damping value (ε^2) equal to the a priori ratio of the data variance to the solution variance (Aki et al., 1977). Aki and Lee (1976) used just the stochastic inverse approach, because their matrix was not strictly singular but contained very small singular values that would amplify the effect of data errors on the model.

1.10.4.2.2 Sparsity and the L1 norm solution

An exciting line of research involves approaches for determining sparse solutions to tomographic problems. The idea of preferring a sparse model essentially stems from 'Occam's razor,' which is a 'simpler is better' philosophy. This idea should not be confused with sparse-matrix inversion, for which the equations relating the model to the data have far more zero than nonzero coefficients. As demonstrated by Loris et al. (2007) and others, L1 minimization naturally leads to a relatively sparse solution. This can be motivated by considering a simple 2D inverse problem for which one desires to find the 'smallest' solution that satisfies a constraint equation $Ax=b$, a straight line. The minimum L2 norm solution that satisfies the constraint equations will lie on a circle of constant L2 norm of c_2 (**Figure 4**), and thus, both model parameters will be

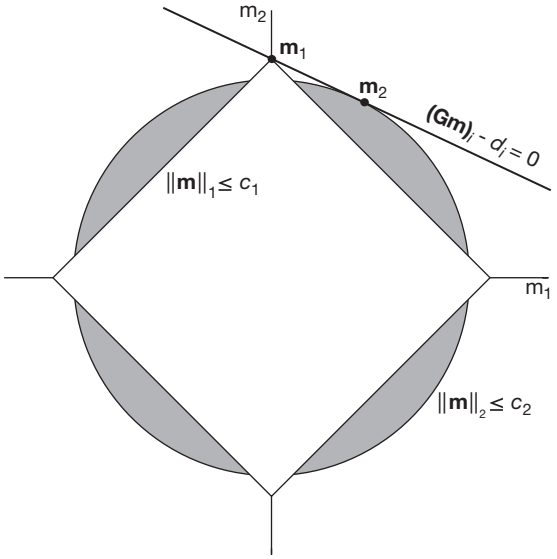

Figure 4 Illustration of the tendency for L1 solutions to promote sparsity, in 2D. An L2 solution can be thought of as finding the point on the circle with smallest radius that fits a constraint equation (such as fitting the data). In contrast, the L1 solution looks at points on a square with its vertices on the axes, leading to a solution that is nonzero only for one parameter, and therefore tends to be sparse.

nonzero. In contrast, the constant L1 norm defines a square of side c_1 with vertices on the coordinate axes. The minimum L1 norm solution will lie on one vertex (Figure 4) and thus will be sparse, with only one nonzero parameter.

Loris et al. (2007, 2010) and Simons et al. (2011) combine the sparse solution approach with a wavelet basis (Cartesian in the case of Loris et al., 2007, 2010, spherical in the case of Simons et al., 2011) for parameterizing the model. Where sampling is sparse or the data do not demand significant heterogeneity, only a few low-order wavelet coefficients will be nonzero. Conversely, where the data require it, more higher-order wavelet coefficients will be nonzero. This allows for model solutions that can have both smoothly varying regions and sharp discontinuities.

Another way in which the L1 norm has been used is to obtain more robust iterative solutions. L2 solutions are susceptible to producing large model errors when data outliers are present (Aster et al., 2012), since a solution is sought that minimizes the sum of the squares of the residuals. Since L1 instead minimizes the sum of the absolute value of the residuals, it is less sensitive to outliers. But given the discontinuity of $|x|$ at $x=0$, how can one practically obtain the minimum-misfit L1 solution? One standard approach is iterative reweighted least squares, or IRLS (Aster et al., 2012). An initial solution is obtained with least squares, and the misfit values (residuals) for that model are determined. Then, an updated solution is computed by solving a weighted system of equations $\mathbf{WGm}=\mathbf{Wd}$, again using least squares, with $\mathbf{W}$ a diagonal matrix whose diagonal elements are the reciprocal of the square root of the absolute value of the corresponding residual. Thus, you are trying to determine a least-squares solution to a problem where the residuals are the square root of the original least-squares residual (with the appropriate sign). The IRLS solution converges to the L1 solution under reasonable conditions. Pesicek et al. (2010) used the IRLS approach to sharpen their tomographic image of the subducting slab in the Sumatra region.

1.10.4.2.3 Occam's inversion and Bayesian methods

In addition to the techniques discussed earlier, there are two other philosophically different approaches for treating underdetermined tomographic problems. One can be labeled an Occam's razor approach and the other Bayesian (see Scales and Snieder, 1997 for an interesting discussion of the latter).

The Occam's approach (**Section 1.10.4.2.2**), commonly attributed to the work of Constable et al. (1987) on electromagnetic inversion, involves the inclusion of constraint equations in the inversion enforcing minimized first- or second-order spatial differences of the model perturbations, weighted relative to achieving a data misfit no better than the data uncertainty. We note that this is an example of what is often called Tikhonov regularization (see Aster et al., 2012), in this case using the discrepancy principle to select the weighting. The first-order constraint attempts to minimize model perturbation gradients, leading to a 'flat' model perturbation. The second-order constraint attempts to minimize model perturbation curvature, leading to a 'smooth' model perturbation. In general, this regularization can be achieved by augmenting $\mathbf{Gm}=\mathbf{d}$ with a set of equations of the form $w\mathbf{Lm}=\mathbf{0}$ and minimizing the system

$$\begin{bmatrix}\mathbf{G}\\ w\mathbf{L}\end{bmatrix}\mathbf{m}=\begin{bmatrix}\mathbf{d}\\ 0\end{bmatrix} \quad [35]$$

For a 1D tomography problem, $\mathbf{L}$ for first-order regularization would be a banded matrix with rows of the form $[0\ \ 0\ \ 0\ \cdots\ -1\ \ +1\ \cdots\ 0\ \ 0\ \ 0]$, whereas for second-order regularization, the rows would be of the form $[0\ \ 0\ \ 0\ \cdots\ -1\ \ +2\ \ -1\ \cdots\ 0\ \ 0\ \ 0]$.

Examples of the use of first- or second-order smoothing include Lees and Crosson (1990), Benz et al. (1996), Hole et al. (2000), and Zhang and Thurber (2003). A variant by Symons and Crosson (1997) penalizes the roughness of the sum of the current model plus the perturbation, so that the final model remains smooth. Once again, an L-curve analysis (Aster et al., 2012) can be valuable for determining the appropriate weighting of the regularization equations (the value of w). The use of smoothing constraints tends to result in fewer artifacts in poorly sampled regions compared to simple damping. At the same time, however, one desires to be able to 'tease out' heterogeneity and sharp spatial changes in structure as effectively as possible with seismic tomography, so the use of smoothing comes at a cost.

An example of a Bayesian approach, mentioned in **Section 1.10.3.1**, involves the specification of a spatial covariance function that reflects the tendency for nearby points in the Earth to have similar wave speeds. Following Tarantola and Valette (1982) and Tarantola and Nercessian (1984), an a priori model covariance function $\mathbf{C}_{\mathbf{m}_0}$ (e.g., of Gaussian form) and a data covariance function $\mathbf{C}_{\mathbf{d}_0}$ are defined, and the solution is obtained by minimizing

$$(\mathbf{Gm}-\mathbf{d})^{\mathrm{T}}(\mathbf{C}_{\mathbf{d}_0})^{-1}(\mathbf{Gm}-\mathbf{d})+\mathbf{m}^{\mathrm{T}}(\mathbf{C}_{\mathbf{m}_0})^{-1}\mathbf{m} \quad [36]$$

(note the close correspondence in form to [30]). Tarantola and Valette (1982) showed that a nonlinear algorithm for minimizing [36] is

$$\mathbf{m}=\mathbf{m}_0+\mathbf{C}_{\mathbf{m}_0}\mathbf{G}^{\mathrm{T}}\left(\mathbf{C}_{\mathbf{d}_0}+\mathbf{G}(\mathbf{C}_{\mathbf{m}_0})^{-1}\mathbf{G}^{\mathrm{T}}\right)^{-1}\{\mathbf{d}_0-\mathbf{g}(\mathbf{m})+\mathbf{G}(\mathbf{m}-\mathbf{m_0})\} \quad [37]$$

where $\mathbf{g}$ is the (nonlinear) forward equation and $\mathbf{m}_0$ is the a priori model. Based on the way Tarantola and Nercessian (1984) formulated their problem, [37] is constructed using numerical integration along the current ray paths, rather than by apportioning ray paths into cells for the computation of derivatives. In practice, we view this distinction as somewhat minor, because at some level, discretization of the model will be required once the current model is no longer homogeneous and wave propagation in 3D must be considered. Recent examples of the Bayesian approach include Trampert et al (2004), Bodin and Sambridge (2009), Visser et al (2008b), and Mosca et al. (2012). For the interested reader, a broad presentation of Bayesian methods for geophysics can be found in Sambridge and Mosegaard (2002).

1.10.4.3 Hypocenter–Structure Coupling

A solution strategy adopted by some researchers involves first solving for 3D structure with earthquake locations fixed and then solving for earthquake locations with the structure fixed. Theoretical and numerical studies (e.g., Roecker et al., 2006;

Thurber, 1992) have shown that this approach leads to bias in both locations and structure. We summarize the analysis from Roecker et al. (2006) to clarify the nature of this important problem. The coupled hypocenter–velocity structure problem can be stated as

$$\mathbf{H}\mathbf{dh} + \mathbf{S}\mathbf{ds} = \mathbf{r} \quad [38]$$

where $\mathbf{H}$ and $\mathbf{S}$ are the derivative matrices and $\mathbf{dh}$ and $\mathbf{ds}$ are perturbation vectors for hypocenters and slowness structure, respectively. The SVD of $\mathbf{H}$ is

$$\mathbf{H} = \mathbf{U}\Lambda\mathbf{V}^{\mathrm{T}} = \left[\mathbf{U}_{\mathrm{p}}|\mathbf{U}_0\right]\Lambda\mathbf{V}^{\mathrm{T}} \quad [39]$$

where $\mathbf{U}_{\mathrm{p}}$ is the range of $\mathbf{H}$ and $\mathbf{U}_0$ is the null space of $\mathbf{H}$ (Aster et al., 2012). Multiplying the original equation by $\mathbf{U}^{\mathrm{T}}$ and separating the p and 0 components give

$$\begin{bmatrix}\mathbf{U}_{\mathrm{p}}^{\mathrm{T}}\,\mathbf{H}\\ \mathbf{U}_0^{\mathrm{T}}\,\mathbf{H}\end{bmatrix}\mathbf{dh} + \begin{bmatrix}\mathbf{U}_{\mathrm{p}}^{\mathrm{T}}\,\mathbf{S}\\ \mathbf{U}_0^{\mathrm{T}}\,\mathbf{S}\end{bmatrix}\mathbf{ds} = \begin{bmatrix}\mathbf{r}_{\mathrm{p}}\\ \mathbf{r}_0\end{bmatrix} \quad [40]$$

Noting that $\mathbf{U}_0^{\mathrm{T}}\mathbf{H} = 0$ by definition and if we initially relocate the earthquakes, then $\mathbf{r}_{\mathrm{p}} = 0$ also, we have

$$\begin{bmatrix}\mathbf{U}_{\mathrm{p}}^{\mathrm{T}}\mathbf{H}\\ 0\end{bmatrix}\mathbf{dh} + \begin{bmatrix}\mathbf{U}_{\mathrm{p}}^{\mathrm{T}}\,\mathbf{S}\\ \mathbf{U}_0^{\mathrm{T}}\,\mathbf{S}\end{bmatrix}\mathbf{ds} = \begin{bmatrix}0\\ \mathbf{r}_0\end{bmatrix} \quad [41]$$

This separates into two sets of equations:

$$\mathbf{U}_{\mathrm{p}}^{\mathrm{T}}\mathbf{H}\,\mathbf{dh} + \mathbf{U}_{\mathrm{p}}^{\mathrm{T}}\mathbf{S}\,\mathbf{ds} = 0 \quad [42]$$

and

$$\mathbf{U}_0^{\mathrm{T}}\mathbf{S}\,\mathbf{ds} = \mathbf{r}_0 \quad [43]$$

We can determine $\mathbf{ds}$ simply by solving the second set of equations, which is the decoupled problem (the separation of parameters method of Pavlis and Booker, 1980). If instead we decide to solve the entire system of equations involving $\mathbf{ds}$ but incorrectly ignore the contribution of $\mathbf{dh}$ in eqn [41], we actually solve

$$\begin{bmatrix}\mathbf{U}_{\mathrm{p}}^{\mathrm{T}}\,\mathbf{S}\\ \mathbf{U}_0^{\mathrm{T}}\,\mathbf{S}\end{bmatrix}\mathbf{ds} = \begin{bmatrix}\mathbf{0}\\ \mathbf{r}_0\end{bmatrix} \quad [44]$$

This is equivalent to solving eqn [43] but with the added constraint that a weighted sum of $\mathbf{ds}$ will be zero. This is the bias that is caused by not carrying out the full simultaneous inversion.

The aforementioned analysis explains some observations regarding the behavior of a joint hypocenter–velocity structure inversion versus a velocity-only inversion. In doing a velocity-only inversion, the added constraints [44] force $\mathbf{ds}$ to be small, which in turn means that subsequent estimations of $\mathbf{dh}$ will be small as well (small velocity perturbations will result in small hypocenter perturbations). The $\mathbf{ds}$ term is kept small at a cost of misfit to the data, because in trying to keep $\mathbf{ds}$ small, the fit to $\mathbf{r}_0$ will be degraded. This is the tendency that is documented in Thurber (1992) and that can be observed in velocity-only inversion tests with real data – both $\mathbf{dh}$ and $\mathbf{ds}$ are much too small in a velocity-only inversion, even when alternated with hypocenter relocation, and the data fit is poor. To illustrate, consider a simplified 1D Earth model (**Figure 5**), following Thurber (1992), with four seismic stations straddling a fault across which velocity changes discontinuously from 5.0 to 6.0 km s^{-1}. If a hypothetical earthquake occurs on the fault and a homogeneous velocity model of 5.5 km s^{-1} is used to locate the event, its calculated location would be 0.75 km to the right of the fault. If we then invert for a laterally heterogeneous velocity model using least squares, placing a discontinuity at the fault (using a priori information) but ignoring the hypocenter–velocity structure coupling (i.e., we keep the event location fixed), we obtain a model with a velocity of 5.44 km s^{-1} to the left of the fault and 5.56 km s^{-1} to the right. In contrast, if we perform a simultaneous inversion for structure and location, the earthquake is relocated to within 0.06 km of the fault, and we obtain a model with a velocity of 5.04 km s^{-1} to the left of the fault and 6.06 km s^{-1} to the right. Thus, the velocity-only inversion underestimates the velocity contrast by nearly an order of magnitude, while the simultaneous inversion recovers the true structure to within 1% and determines the event location within 100 m. The conclusion is that for LET, solving the full system of equations is critical in order to obtain an unbiased solution.

Although many tomography algorithms utilize the fast sparse-matrix solvers such as LSQR, it is worth noting the historical use of subspace methods (e.g., Kennett et al., 1988) for efficient inversion procedure, and in particular for dealing with matrix size issues when many earthquakes are included in an inversion. For LET, three groups independently and nearly simultaneously published comparable methods for separating hypocenter parameters from velocity model parameters, allowing the efficient solution of smaller matrix problems in place of one giant problem (Pavlis and Booker, 1980; Rodi et al., 1981; Spencer and Gubbins, 1980). As a motivation for this approach, consider an LET problem with 10 000 earthquakes observed on average at 50 stations and with 20 000 model parameters. The

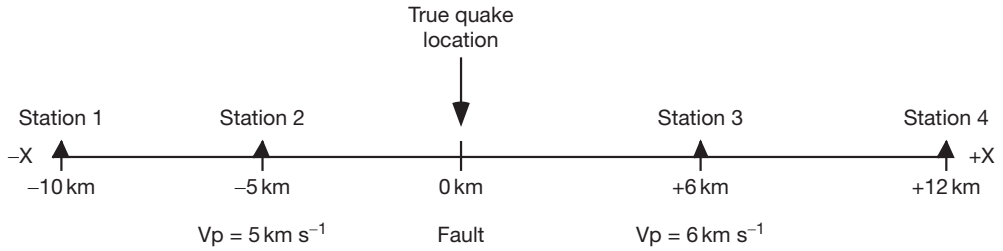

Figure 5 Hypothetical 1D Earth with a velocity discontinuity across a fault with a velocity discontinuity at X = 0.0 km, four seismic stations, and an earthquake occurring on the fault. Reproduced from Thurber CH (1992) Hypocenter–velocity structure coupling in local earthquake tomography. In: "Lateral Heterogeneity and Earthquake Location," *Physics of the Earth and Planetary Interiors* 75: 55–62.

full system matrix would be of the size $(50 \times 10\,000)$ by $(4 \times 10\,000 + 20\,000)$, or 500 000 by 60 000. If we take advantage of the annulling procedure of Pavlis and Booker (1980), for example, we can decompose the coupled hypocenter–structure equations for each earthquake i:

$$\mathbf{H}_i\,\mathbf{dh}_i + \mathbf{S}_i\,\mathbf{ds}_i = \mathbf{r}_i \qquad [45]$$

where, as before, $\mathbf{H}_i$ and $\mathbf{S}_i$ are the matrices of derivatives of arrival times with respect to hypocenter and model parameters, respectively (now for a single earthquake), and $\mathbf{dh}_i$ and $\mathbf{ds}_i$ are the corresponding parameter perturbations. Then, using the orthogonal matrix $\mathbf{U}_{0i}$ that satisfies $\mathbf{U}_{0i}$, $\mathbf{H}_i = 0$ allows us to assemble the decoupled equations:

$$\mathbf{U}_{0i}\,\mathbf{H}_i\,\mathbf{dh}_i + \mathbf{U}_{0i}\,\mathbf{S}_i\,\mathbf{ds}_i = \mathbf{U}_{0i}\,\mathbf{r}_i \text{ or } \mathbf{S}'_i\,\mathbf{ds}_i = \mathbf{r}'_i \qquad [46]$$

The matrix in the original partial system in [45] would be of size 40 by 20 004, whereas the matrix in the decoupled system in [46] would be of size 36 by 20 000. If we treat all the events this way, the result is a system of equations of size 460 000 by 20 000, a substantial size reduction achieved at relatively low computational cost. Even greater reduction of the problem size can be achieved by incrementally constructing the normal equations, $\mathbf{S}'^{\mathrm{T}}\mathbf{S}' = \mathbf{S}'^{\mathrm{T}}\mathbf{r}'$ (Spencer and Gubbins, 1980), resulting in a system of equations that is only 20 000 by 20 000. Unfortunately, the cost of this last step is a squaring of the condition number of the system matrix and a loss of matrix sparseness, but the price may be worth paying in some cases.

1.10.4.4 Static (Station) Corrections Revisited

Static (station) corrections, a constant time delay or advance applied for a given station, are commonly included in some types of seismic tomography problems, as discussed earlier. It is worth noting that static corrections can be analyzed in a manner equivalent to that used for the hypocenter–structure coupling issue (**Section 1.10.4.3**). Just as in the hypocenter–structure coupling situation, including static corrections can result in a suppression of model heterogeneity, particularly at shallow depths near the stations. The corrections can absorb some of the heterogeneity that otherwise would have been projected into the 3D model. One compromise approach (Michael, 1988) is to solve the tomography problem without static corrections and then solve the system with static corrections included but the 3D model held fixed. Michael (1988) had shown that this can be an effective technique for improving earthquake locations without biasing the 3D tomographic model.

1.10.4.5 Inversion for Vp/Vs (Poisson's Ratio)

Often, knowledge of Vp/Vs or Poisson's ratio (which are directly related to each other) is desired for interpretation purposes. Poisson's ratio by itself provides significant diagnostic power regarding lithology and, in combination with Vp, can be even more useful for constraining lithology (Christensen, 1996) and estimating crack density, temperature, vapor, fluid, or melt content (Julian et al., 1996; O'Connell and Budiansky, 1974). Deriving Vp/Vs (and hence Poisson's ratio) by simply dividing the Vp model by the Vs model, however, will introduce noise and artifacts due to the different samplings and therefore resolution of the Vp and Vs models (Eberhart-Phillips, 1990; Wagner et al., 2005). A strategy for direct inversion for Vp/Vs (Thurber and Atre, 1993; Walck, 1988) or for joint inversion for Vp, Vs, and Vp/Vs (Zhang and Thurber, 2006) is preferable. A limitation of the earlier techniques for direct inversion of S–P times for 3D Vp/Vs structure is the underlying assumption that the P and S ray paths are very similar. In the case of complex 3D structure, however, some P and S ray paths may differ significantly, and thus, the results may be biased. In order to avoid this bias and to allow for the construction of Vp and Vs models as well as Vp/Vs, a new algorithm was developed by Zhang et al. (2009) to solve simultaneously for Vp, Vs, Vp/Vs, and event locations using P, S, and S–P times. Their strategy is to check P and S ray paths and remove the corresponding S–P time from the Vp/Vs inversion if the paths differ by more than a specified threshold. Their tests with synthetic data showed that this approach is successful in producing models with minimal artifacts.

1.10.4.6 DD Tomography

The use of differential times for determining relative locations of earthquakes (or explosions) has been a fruitful field of work for many decades (e.g., Douglas, 1967). A number of studies over the last decade have shown spectacular improvement in earthquake or explosion location precision when precise differential times from WCC are used in combination with joint location techniques. Some examples of applications to earthquakes include Hawaii (Got et al., 1994; Rubin et al., 1998), California (Waldhauser et al., 1999), New Zealand (Du et al., 2004), the Soultz geothermal field, France (Rowe et al., 2002), and Mount Pinatubo volcano (Battaglia et al., 2004) and to explosions at the Balapan test site (Phillips et al., 2001; Thurber et al., 2001). These and other studies have demonstrated the substantial improvement in the delineation of seismogenic features or in the accuracy of relative locations of ground-truth events that is possible using multiple-event location methods with high-precision arrival-time data. These successes inspired efforts to incorporate differential times in seismic tomography. The first and so far most widely used algorithms for DD tomography are due to Zhang and coworkers (Zhang and Thurber, 2003, 2005; Zhang et al., 2004).

To set the stage for understanding DD tomography, we first briefly review the DD location problem (see Wolfe, 2002 for a thorough analysis). Following the notation of **Section 1.10.4.3**, for single event location, we iteratively solve an equation of the form

$$\mathbf{r} = \mathbf{H}\,\mathbf{dh} \qquad [47]$$

where **dh** includes perturbations to location and origin time, **H** is the partial derivative matrix, and **r** contains the arrival-time residuals. If we now consider eqn [47] for a pair of events and subtract the equations for the two events observed at one station, we have a set of equations of the form

$$r_k^i - r_k^j = \sum_{l=1}^{3} \frac{\partial T_k^i}{\partial x_l^i}\Delta x_l^i + \Delta\tau^i - \sum_{l=1}^{3} \frac{\partial T_k^j}{\partial x_l^j}\Delta x_l^j + \Delta\tau^j \qquad [48]$$

where r_k^i and r_k^j are the residuals from events i and j at station k, T's are travel times, and x and Δx are hypocenter coordinates

and their perturbations. Note that the residual difference can be rewritten as $(t^i_{obs} - t^j_{obs}) - (t^i_{cal} - t^j_{cal})$, the 'double-difference,' where t_{obs} and t_{cal} indicate the observed and calculated arrival times, respectively. For DD location, one solves for perturbations to the relative locations (and an origin time shift) to minimize the residual differences. A key aspect is that observed differential arrival times $(t^i_{obs} - t^j_{obs})$ can be determined to high accuracy using waveform correlation methods (Waldhauser and Ellsworth, 2000).

Menke and Schaff (2004) demonstrated that differential time data are capable of resolving absolute locations. Ideally, one would like to take that one step farther and utilize all the information from differential times and absolute arrival times to determine both locations and structure. To that end, Zhang and Thurber (2003) generalized the DD location method to determine jointly the 3D velocity structure and the absolute event locations. The equations for DD tomography are a combination of the standard tomography equations and a generalization of eqn [48]:

$$r^i_k - r^j_k = \sum_{l=1}^{3} \frac{\partial T^i_k}{\partial x^i_l} \Delta x^i_l + \Delta\tau^i + \int_i^k \delta u \, ds - \sum_{l=1}^{3} \frac{\partial T^j_k}{\partial x^j_l} \Delta x^j_l + \Delta\tau^j + \int_j^k \delta u \, ds$$

$$r^i_k = \sum_{l=1}^{3} \frac{\partial T^i_k}{\partial x^i_l} \Delta x^i_l + \Delta\tau^i + \int_i^k \delta u \, ds \qquad [49]$$

where δu is perturbation to slowness and ds is an element of path length, as in [2]. Three types of data, absolute arrival times, catalog differential arrival times, and WCC data, are used in the inversion. To combine these three types of data into one system, a hierarchical weighting scheme is applied during the inversion, similar to hypoDD (Waldhauser, 2001; Waldhauser et al., 1999).

Zhang and Thurber (2003) solved the complete system of linear equations [49], along with smoothing constraint equations, by means of the LSQR algorithm (Paige and Saunders, 1982) (see **Section 1.10.4.1**). Each equation is weighted according to the a priori data uncertainty, data type, distance between the event pair, and misfit at each iteration. The relative weighting for the different data types and the distance weighting are determined a priori, whereas the residual weighting is determined a posteriori, with large residuals rejected or downweighted by a biweight function (Waldhauser and Ellsworth, 2000). For LSQR, the number of iterations required to reach a desired accuracy depends strongly on the scaling of the problem (Paige and Saunders, 1982). For this reason, before the system is fed into the LSQR solver, scaling is applied (**Section 1.10.4.3**) so that each column has an L_2 norm equal to 1.

There are distinct advantages of DD tomography compared to conventional tomography. In conventional tomography, there is no mechanism for incorporating the higher-accuracy differential times, meaning that the event locations remain scattered as in, for example, a normal seismicity catalog. The ability of DD tomography to include the differential times leads to a sharpening of the seismicity distribution and, in turn, an improved velocity model as well. In **Figure 6(a)** and **6(b)**, we show an example of the sharpening of both the seismicity and the velocity structure achieved by DD tomography compared to conventional tomography for the San Andreas fault near Parkfield, CA (Thurber et al., 2004; Zhang and Thurber, 2005).

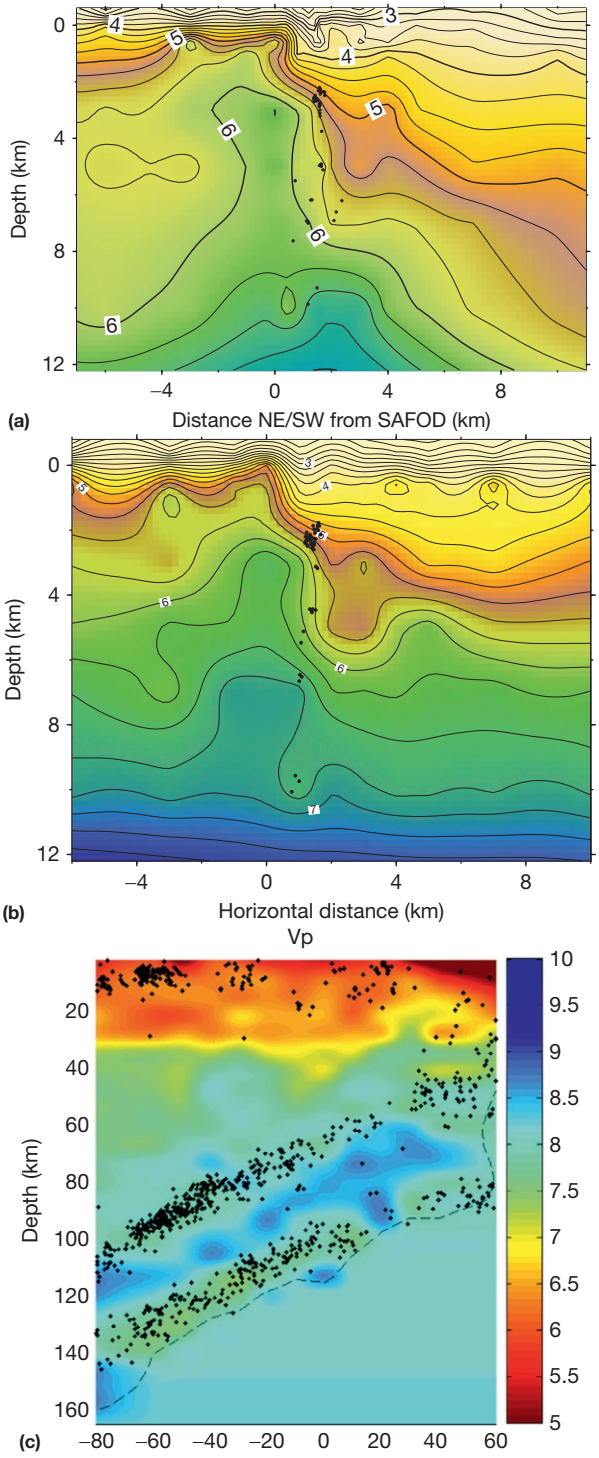

Figure 6 Comparison of (a) conventional tomography (from Thurber et al., 2004) and (b) DD tomography (from Zhang and Thurber, 2005) models for a section across the San Andreas fault at the San Andreas Fault Observatory at Depth (SAFOD) drill site. Note the sharpening of features in both the seismicity and the velocity structures. (c) Image of the internal structure of the subducting slab beneath northern Honshu, Japan, imaged by DD tomography.

At a larger scale, Zhang et al. (2004) showed the dramatic variations in structure deep within a subducting slab that can be imaged with the DD tomography technique (**Figure 6(c)**). Zhang and Thurber (2006) showed that model resolution in earthquake source regions is improved by including differential times.

1.10.4.7 Waveform Tomography and Adjoint Methods

Most data types used in tomographic inversions, such as the travel time of a body wave or the frequency of normal modes, capture only a limited amount of the information contained in full seismograms. Of course, utilizing all seismic signals is the ultimate goal in tomography. In recent years, full-waveform inversions have become feasible given newly developed numerical techniques and the advent of powerful, yet relatively cheap, computers. Full-waveform tomography relies on accurate computations of waveforms for 3D Earth structure (e.g., Capdeville et al., 2003; Komatitsch and Tromp, 1999; Komatitsch and Vilotte, 1998; Komatitsch et al., 2002) (see **Chapter 1.07** by Jeroen Tromp) and 3D sensitivity kernels that relate any portion of the observed waveform to seismic structure. Since it is based on accurate waveform simulations and 3D Fréchet kernels, waveform tomography does not depend on regularization. Hence, it enables the resolution of fine-scale structure (anomalies smaller than the Fresnel zone) and high-amplitude velocity variations (**Figure 7**).

Calculations of exact 3D sensitivity kernels have been based upon spherical-Earth normal-mode summation (Zhao et al., 2000; Capdeville et al., 2003), finite differences (Zhao et al., 2005), and spectral-element simulations (Tromp et al., 2005). The approach by Tromp et al. (2005), in particular, demonstrates how the combination of numerical wave simulations and adjoint techniques (e.g., Tarantola, 1984, 1988) can be used to compute the Fréchet derivatives efficiently for any portion of the waveform and for 3D Earth models (see Liu and Gu, 2012 for an extensive review). Liu and Tromp (2006, 2008) showed examples of adjoint sensitivity kernels based on cross-correlation travel time measurements for a number of body-wave phases. However, the Fréchet derivatives of any seismic observable, such as SKS splitting (Sieminski et al., 2008) or 'seismic noise' (Tromp et al., 2010), can be computed with the adjoint approach.

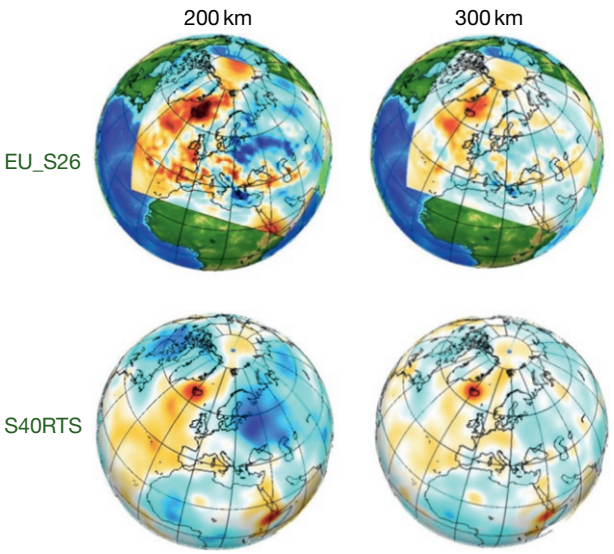

Figure 7 Comparison of (a) regional shear-velocity model EU-S26 (27 iterations) by Fichtner and Trampert (2011) and (b) global shear-velocity model S40RTS (Ritsema et al., 2011) at depths of 200 and 300 km. Note that the shear-velocity variations in EU-27 are stronger and that smaller-scale structures have been resolved.

Perhaps, the simplest example of an adjoint solution to a tomography problem is back projection of travel time residuals. Given the forward problem $\mathbf{G}\Delta\mathbf{m}=\mathbf{r}$ (where we have explicitly written the equation in terms of a perturbation to the model related to the travel time residuals), the back-projection (adjoint) solution is $\Delta\mathbf{m}=\mathbf{G}^{\mathrm{T}}\mathbf{r}$, although in practice, some 'conditioning' (filtering) of this system of equations is employed (Humphreys and Clayton, 1988). This can be thought of as back-propagating the residuals into the model along the ray paths, spreading the residual equally among the model parameters sampled by the ray, and using the associated length of path to scale the residual, with units of time, to a velocity (or slowness) perturbation.

For waveform tomography, the mathematical derivation of the adjoint inversion equations is rather complex (Akcelik et al., 2003; Fichtner et al., 2006a,b; Tarantola, 1984; Tromp et al., 2005) and will not be summarized here. The standard approach is to compute simultaneously a forward simulation and a reverse-time simulation, with the latter using the differences between the data and the current synthetics as the 'source.' The interaction between the two resulting wave fields at each time step, generally involving a zero-lag correlation of the two fields, integrated over time, provides the desired sensitivities (Rawlinson et al., 2010; Tromp et al., 2005).

Although the adjoint approach is extremely powerful, its application is still hindered by the extraordinary computational requirements. For truly 3D inversions, the sensitivity kernels must be recomputed after each iteration. Moreover, global simulations of waveforms with periods shorter than 10–20 s, where body-wave signals display interesting variability, are still out of our reach except for seismologists with access to the largest and fastest supercomputers. Therefore, most inversions are applied to relatively long-period signals of surface waves and regional scales. There are also other steps to minimize the computational demands. This includes source stacking (Capdeville et al., 2005) and the use of adjoint kernels for spherical symmetrical Earth models (Nissen-Meyer et al., 2007) or 2D kernels (Lekic et al., 2010). To overcome the highly nonlinear nature of full-waveform inversions, the misfit functions are often designed to emphasize the phase (or travel time) information contained in seismograms. This can be accomplished by using frequency-dependent travel time analysis through WCC (e.g., Maggi et al., 2009; Sigloch and Nolet, 2006; Zaroli et al., 2010), time–frequency analysis (Fichtner et al., 2008), instantaneous phase measurements (Bozdağ et al., 2011), and the analysis of separate waveform segments (e.g., Li and Romanowicz, 1996; Nolet, 1990).

There have been a number of applications of the adjoint method for seismic tomography, using several variations on

the same general approach. Early work on the application to southern California (Chen et al., 2007; Tape et al., 2007) has been followed by more extensive inversions using increasing numbers of earthquakes and iterations (Tape et al., 2009, 2010). Other applications have focused on Australia (Fichtner et al., 2009), the Middle East (Savage et al., 2011), and Europe (Fichtner and Trampert, 2011; Zhu et al., 2012) (see **Figure 7**). Bozdag et al. (2012) had presented the results of two iterations of adjoint tomography on the global scale using 255 earthquakes and periods longer than 27 s.

1.10.5 Solution Quality

While the previous sections have laid out the procedures involved in tomographic modeling, the ultimate question – how well does the tomographic model reflect the true Earth? – is the most important and perhaps the most difficult one to answer. Without exception, tomography provides distorted images of the real Earth. The image resolution is imperfect due to, for example, choices in parameterization (e.g., block size) and regularization (e.g., smoothing), and it is spatially variable due to the heterogeneous data coverage. Yet, an understanding of seismic data, formal resolution analyses, and hypothesis tests is helpful to guide tomographic model interpretation.

While it is not so straightforward to generalize model resolution issues, we focus on global model S20RTS to demonstrate how hypothesis tests can be helpful in model interpretation.

1.10.5.1 Model Resolution and Uncertainty Analysis

Quantitatively, model resolution is assessed by calculation of the full model resolution and model covariance matrices. In essence, the task is to understand the properties of the generalized inverse matrix $\mathbf{G}^{-\mathbf{i}}$ (eqn [24]). As discussed in **Section 1.10.4.2.1**, we can decompose $\mathbf{G}$ into a product of three matrices, $\mathbf{USV}^{\mathrm{T}}$, with $\mathbf{U}$ and $\mathbf{V}$ being orthogonal matrices (i.e., $\mathbf{U}^{\mathrm{T}}\mathbf{U}=\mathbf{UU}^{\mathrm{T}}=\mathbf{I}$ and $\mathbf{V}^{\mathrm{T}}\mathbf{V}=\mathbf{VV}^{\mathrm{T}}=\mathbf{I}$). If $\mathbf{G}$ has p nonzero singular values and no regularization is applied, then the model resolution matrix $\mathbf{R}_{\mathrm{m}}$ is simply given by $\mathbf{R}_{\mathrm{m}}=\mathbf{V}_{\mathrm{p}}\mathbf{V}_{\mathrm{p}}^{\mathrm{T}}$. $\mathbf{R}_{\mathrm{m}}$ generally will not be an identity matrix and thus can be thought of as a 'filter' that blurs the true model. Application of regularization or singular value truncation will only make the blurring worse. Similarly, for this case, if we further assume that the data covariance matrix is of the form $\sigma^2\mathbf{I}$, then the model covariance matrix $\mathbf{C}_{\mathrm{m}}$ is given by

$$\mathbf{C}_{\mathrm{m}} = \sigma^2\mathbf{V}\mathbf{S}^{\dagger}\left(\mathbf{S}^{\dagger}\right)^{\mathrm{T}}\mathbf{V}^{\mathrm{T}} \qquad [50]$$

where, as before, $\mathbf{S}^{\dagger}$ is the pseudoinverse of $\mathbf{S}$. The square root of the diagonals of $\mathbf{C}_{\mathrm{m}}$ provides an estimate of the (1-standard deviation) model uncertainties. The small singular values, which enter the calculation for $\mathbf{C}_{\mathrm{m}}$ as the square of their reciprocals, thereby amplify data-caused uncertainties (and model errors) in the model associated with the corresponding singular vectors in $\mathbf{V}$. Application of regularization or singular value truncation reduces this problem by suppressing or eliminating the small singular values. See Aster et al. (2012) for additional details.

An effective way of displaying model resolution is via Backus–Gilbert resolution kernels $\mathbf{R}(\mathbf{r},\mathbf{r}_0)$ (Backus and Gilbert, 1968), which are defined (in the original continuous form) as

$$\mathbf{m}(\mathbf{r}_0) = \int_{\mathrm{V}} \mathbf{R}(\mathbf{r},\mathbf{r}_0)\,\mathbf{m}(\mathbf{r})\,\mathrm{dV} \qquad [51]$$

In this example, [51] is utilized in the discrete form. The kernel $\mathbf{R}(\mathbf{r},\mathbf{r}_0)$ illustrates how the model $\mathbf{m}(\mathbf{r}_0)$ at $\mathbf{r}_0$ represents a (weighted) average over the entire model. Hence, it illustrates whether isolated regions of the model of the mantle are independently resolved. **Figure 8** shows four Backus–Gilbert kernels computed for model S20RTS. The relatively broad lateral extents of these kernels reflect the coarse degree-20 parameterization of S20RTS, while the variable vertical extent is, again, an indication of the heterogeneous model resolution (velocity variations with wavelengths shorter than 2000 km at the Earth's surface are unresolved). Resolution is best in the uppermost mantle (0–200 km) (**Figure 8(a)**). Here, S20RTS employs a relatively fine spline parameterization (Ritsema et al., 2004), and this region is well sampled by fundamental-mode Rayleigh waves. Vertical resolution is poor in the transition zone. The Backus–Gilbert kernel computed for a depth of 350 km and the location south of New Zealand (**Figure 8(b)**) is broad, reflecting the poor vertical resolution in the transition zone, especially in the southern hemisphere. Therefore, the low-velocity structure in this region, which is prominent in S20RTS (as well as SB4L18), has an uncertain vertical extent. The Backus–Gilbert kernel in **Figure 8(c)** has a narrower depth extent, given the relatively high data coverage of the western Pacific by both body waves and overtone Rayleigh waves. Finally, the Backus–Gilbert kernel at 1075 km depth (**Figure 8(d)**) beneath Southeast Asia is less than 200 km wide. Given this relatively narrow extent, we may conclude that the high-velocity anomaly in this region of the mantle is resolved independently from anomalies shallower in the mantle. Hence, it appears not to be an artifact from vertical averaging of high-velocity (slab) structure in the transition zone of Indonesia.

While formal resolution tests are feasible for moderately large inversions (e.g., Ishii and Tromp, 1999; Kuo and Romanowicz, 2002; Ritsema et al., 1999) when the model comprises fewer than 10 000 parameters, calculation of the full model resolution matrix can become impractical for extremely large problems. Boschi (2003) and Soldati and Boschi (2005) provided some enlightening discussions of whole-Earth model resolution matrix calculations. Beginning with Nakanishi and Suetsugu (1986), a number of authors have proposed methods for deriving approximate model resolution and/or covariance matrices (Nolet et al., 1999; Yao et al., 1999; Zhang and McMechan, 1995). The effectiveness and efficiency of these methods has been subject to some debate.

Two other approaches for obtaining model resolution information are presented by Zhang and Thurber (2007) and MacCarthy et al. (2011). Zhang and Thurber (2007) made use of the efficient partial reorthogonalization package (PROPACK) of Larsen (1998) to calculate the full model resolution matrix. PROPACK has similar computational speed to LSQR, but it is able to estimate the singular values and vectors more accurately. This approach will also reach its limit, however, for extremely large tomography problems.

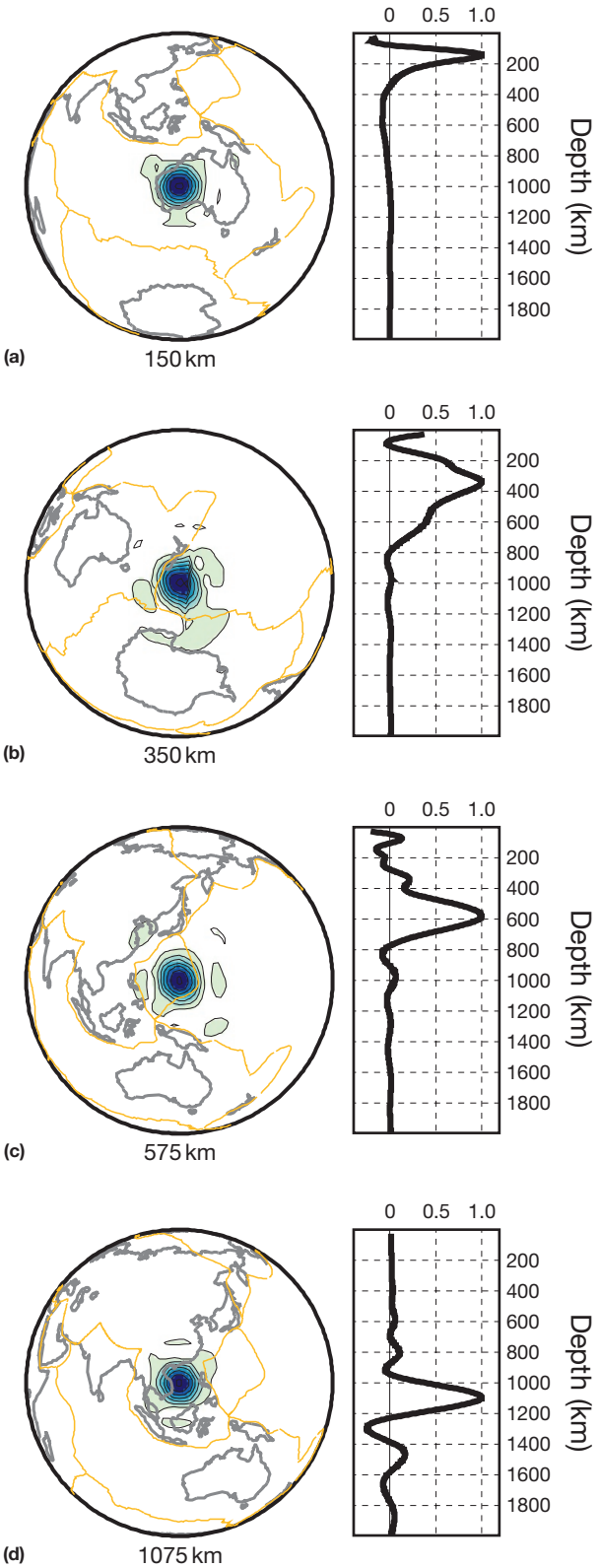

Figure 8 Backus–Gilbert resolution kernels for locations beneath (a) Western Australia (150 km depth), (b) Southwest Pacific (350 km depth), (c) Mariana Islands (575 km depth), and (d) Southeast Asia (1075 km) for model S20RTS. Map views are shown on the left. Vertical cross sections through the kernels are shown on the right. The geographic variability of these kernels reflects the heterogeneous mantle resolution, typical for any tomographic model.

If one is satisfied to determine just the diagonal values of the resolution matrix, then the approach described by MacCarthy et al. (2011) is an excellent alternative. It is based on the method of Bekas et al. (2007) for estimating the diagonal elements of a square symmetrical matrix using a stochastic approach. Following MacCarthy et al. (2011), a set of s random vectors, $\mathbf{v}_1, \mathbf{v}_2, \ldots, \mathbf{v}_s$, of length n (in this case, the dimension of the model resolution matrix) are defined, with independent elements drawn from a standard normal distribution. Bekas et al. (2007) showed that for an arbitrary n by n square matrix $\mathbf{A}$, the sth estimate of the diagonal of $\mathbf{A}$ is

$$\mathrm{diag}(\mathbf{A})_s = \left[\sum_{k=1}^{s} \mathbf{v}_k \bullet \mathbf{A}\mathbf{v}_k\right] \oslash \left[\sum_{k=1}^{s} \mathbf{v}_k \bullet \mathbf{v}_k\right] \qquad [52]$$

where $\bullet$ and $\oslash$ denote element-wise multiplication and division, respectively, and the median of these s realizations gives the final estimate of diag($\mathbf{A}$). In this case, we let $\mathbf{A}$ be the model resolution matrix $\mathbf{R}_\mathrm{m}$, $\mathbf{G}\mathbf{G}^{-\mathrm{i}}$. The first term on the right-hand side thus contains $\mathbf{R}_\mathrm{m}$, but in fact, we just need the product $\mathbf{A}\mathbf{v}_k$, which MacCarthy et al. (2011) showed can be determined by defining $\mathbf{y} = \mathbf{A}\mathbf{v}_k$ and solving the least-squares problem $\mathbf{y} = \mathbf{G}\mathbf{G}^{-\mathrm{i}}\mathbf{v}_k s$ times for each random vector $\mathbf{v}_k$. The value of s can be relatively small (order of 100–1000) even for problems with values of n in the tens to hundreds of thousands. For example, Aster et al. (2012) showed that a value of s of 256 is sufficient to yield an excellent estimate of the diagonal of $\mathbf{R}_\mathrm{m}$ for a tomographic problem of dimension 27 000. In particular, for a random set of 100 model elements, the stochastic estimate of the diagonal element matches the exact value within a few percent (**Figure 9**). A similar approach can be applied to estimate diagonal values of $\mathbf{C}_\mathrm{m}$.

Displaying model resolution and covariance results is also problematic, since both matrices have dimensions equal to the number of model parameters. One strategy for compressing the full-resolution matrix into a compact form that can be displayed in a manner similar to that of the model itself is resolution spread (Michelini and McEvilly, 1991), which produces a scalar field quantifying the spatial extent of blurring at each point in the model.

Another thorough approach to the quantification of model uncertainty is the use of global optimization methods, such as Monte Carlo (Mosegaard and Tarantola, 1995), to explore the range of possible solutions. Press (1968) took the Monte Carlo approach for modeling global 1D Earth structure. Shapiro and Ritzwoller (2002) applied a Markov-chain Monte Carlo analysis to a global surface-wave model of the crust and upper mantle structures. As one might expect, the uncertainties that they quantify substantially exceed standard estimates based on the model covariance matrix.

1.10.5.2 Hypothesis Testing

An entirely different strategy for evaluating the quality of a tomographic model involves hypothesis tests. In such tests, it is determined how a hypothetical structure of the Earth would be recovered tomographically. There are two common ways to approach such tests. One could evaluate the resolution operator $\mathbf{R}_\mathrm{m}$, which is defined as [27]:

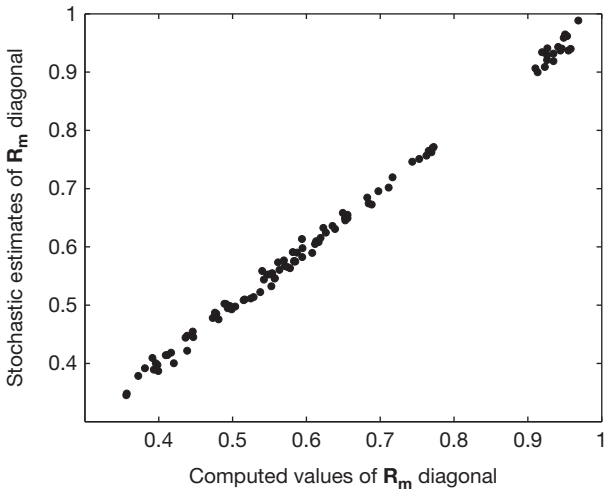

Figure 9 Comparison of exact model resolution diagonal values to those computed with the stochastic method for estimation of the diagonal values of a matrix. Modified from Aster RC, Borchers B, and Thurber CH (2012) Parameter Estimation and Inverse Problems, 2nd edn, 376 pp. Elsevier/Academic Press.

$$\mathbf{m}_{out} = \mathbf{R}_m \mathbf{m}_{in} \quad [53]$$

Simply convolving $\mathbf{R}_m$ with a conceptual input model $\mathbf{m}_{in}$ renders $\mathbf{m}_{out}$ that is the tomographically resolved structure if $\mathbf{m}_{in}$ were the true earth. The degree of recovery of $\mathbf{m}_{in}$ in various parts of $\mathbf{m}_{out}$ is used to define the well-resolved parts of the model. Alternatively, one can mimic the effects of [27] by inverting synthetic data generated for $\mathbf{m}_{in}$ following the same procedure applied to the real data. Tomographers choose a variety of synthetic structures for $\mathbf{m}_{in}$ including spikes (isolated anomalies), checkerboards (models with alternating high- and low-velocity anomalies), and conceptual geologic structures.

Figure 10 shows an application to the Icelandic upper mantle, where model S20RTS features a low-velocity anomaly that extends much deeper into the upper mantle than what is typical for the Mid-Atlantic Ridge (Figure 10(a)). To assess this depth extent, we can test how relatively narrow structures (cylinders) with variable depth extents are recovered tomographically. The 200 km wide cylinders of $\mathbf{m}_{in}$ are at least five times wider in $\mathbf{m}_{out}$ (Figure 10(b)). This is entirely due to the parameterization of model S20RTS (spherical harmonics up to order and degree 20) that cannot accommodate velocity variations with a half wavelength smaller than 1000 km. Furthermore, we can observe vertical stretching of the cylinders due to the finite depth resolution. For example, the input cylinder that extends from the surface to a depth of 400 km is projected into $\mathbf{m}_{out}$ as an anomaly that reaches the 670 km discontinuity. The relatively broad averaging lengths deeper in the transition zone are also evident in Figure 10. The peak anomaly of the 100 km thick cylinder that, in $\mathbf{m}_{in}$, was placed immediately below the 660 km discontinuity is reduced by about a factor of 6 in $\mathbf{m}_{out}$. While it is impossible to conclude which true Earth structure is responsible for the tomographic image of Figure 10(a) (we can only determine $\mathbf{m}_{out}$ given $\mathbf{m}_{in}$, but not vice versa), it appears that heterogeneity in the mantle below the 660 km discontinuity is independently resolved from the mantle above it. It is plausible, however, that a low-velocity anomaly in the upper 400–500 km of the mantle is artificially extended to 700 km depth. The hypothesis tests of Figure 10 suggest also that the lower bound of the Icelandic anomaly is a real feature.

Another approach is to use geophysically more meaningful input models. An example is provided in Figure 11. Here, an input model ($\mathbf{m}_{in}$) is derived from a numerical calculation of mantle convection (McNamara and Zhong, 2005; Ritsema et al., 2007), and $\mathbf{m}_{out}$ is obtained by convolving $\mathbf{m}_{in}$ with $\mathbf{R}_m$. Figure 11 demonstrates how small-scale structures such as thermal instabilities from thermochemical basal structures cannot be resolved at the resolution of S20RTS (and presumably other global models). In addition, even large-scale structures in $\mathbf{m}_{in}$ are artificially stretched and tilted in $\mathbf{m}_{out}$ in regions (e.g., the central Pacific lower mantle) with unidirectional mantle sampling.

Hypothesis tests like those in Figures 10 and 11 have serious pitfalls when only a number of cases of $\mathbf{m}_{in}$ are tested. One can only infer how $\mathbf{m}_{in}$ is mapped tomographically into $\mathbf{m}_{out}$, but not vice versa, because the components of a model in the null space of $\mathbf{G}$ (the components of $\mathbf{V}$ corresponding to the zero singular values) cannot possibly be resolved. It is therefore dangerous to generalize the resolution of a tomographic model from the outcome of only a few tests. In fact, Lévêque et al. (1993) showed, perhaps counterintuitively, that the success of a checkerboard test to resolve the small-scale checkerboard structure cannot guarantee that larger-scale structures will be resolved with the same dataset. In other words, it is possible for some small features to be resolvable when some larger-scale features are not. For instance, they illustrate how horizontal variations can be well recovered while the large-scale radial variation is poorly resolved if most of the rays are subparallel and steeply incident. This is of course an inherent problem of the teleseismic travel time inversion, such as the ACH tomography method (Aki et al., 1977).

We also point out that cell-based tomographic systems have a natural tendency for negative model covariance between adjacent cells. This is caused by the fact that, when resolution is imperfect, a positive perturbation in one cell can be counterbalanced by negative perturbations in adjacent cells (the exact pattern of a checkerboard) with little effect on the data fit. Hence, noisy (underdamped or undersmoothed) tomographic models typically show oscillatory behavior. Thus, checkerboard tests may yield overly optimistic estimates of model quality due to the presence of error in the synthetic data coupled with the character of the model covariance.

'Model restoration' tests are another popular approach. Here, a model with all of the main features of the model obtained from the real data (sometimes with the sign of the anomalies reversed; Husen and Kissling, 2001) is used to generate synthetic observations, which are then inverted using the same method and parameters as those used for the real data. When extended to include comparable assessment of models lacking some of the key features (Zhang et al., 2004), this approach can be very effective.

Given the difficulties of fully evaluating model resolution and covariance matrices, tomographers often resort to the kind of simplified hypothesis tests described earlier to estimate the significance of interesting model attributes. There is one important additional caveat. When testing how $\mathbf{m}_{in}$ is projected into $\mathbf{m}_{out}$ according to the model resolution operator

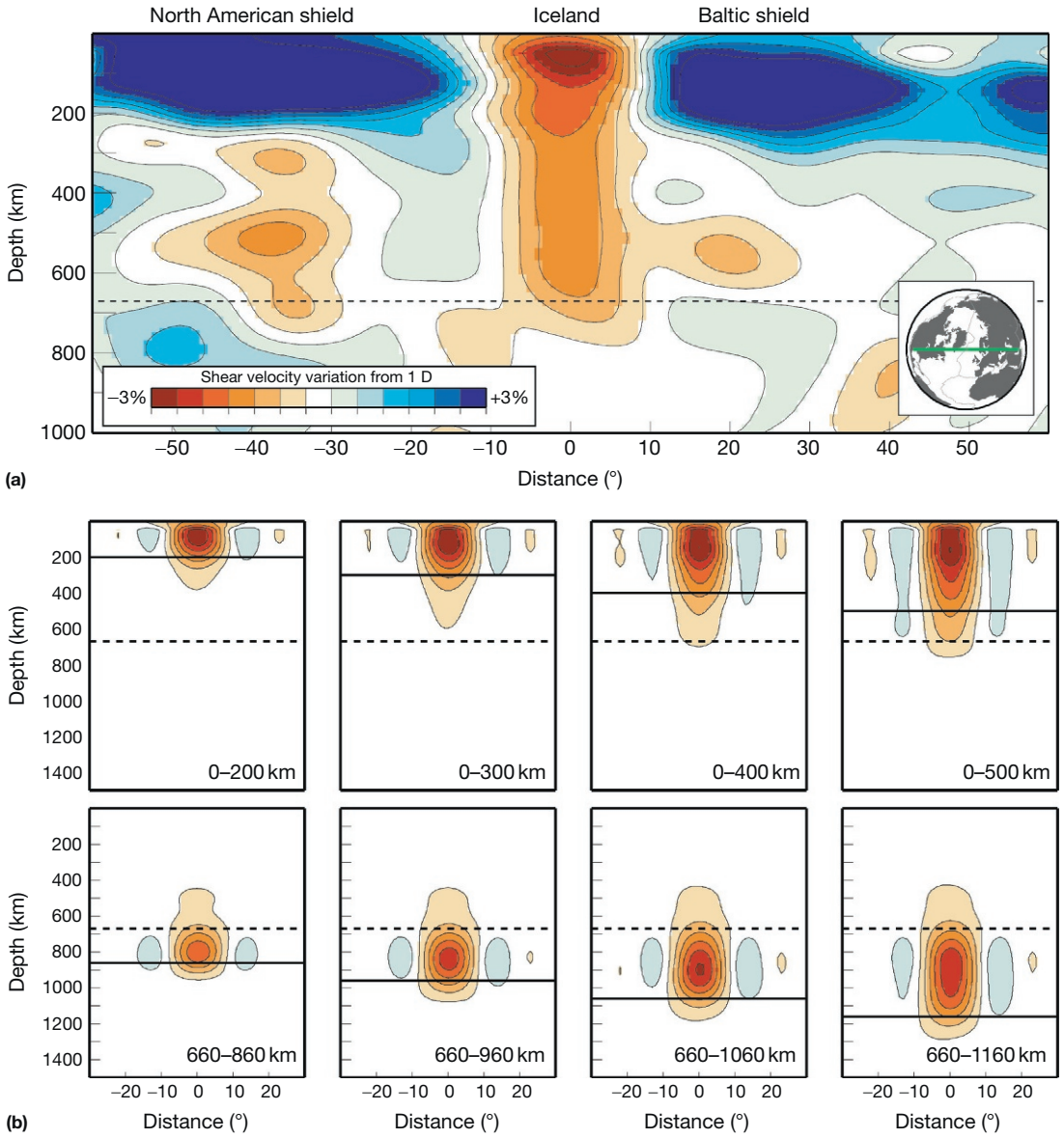

Figure 10 (a) Upper mantle cross section through model S20RTS, showing a low-velocity anomaly beneath Iceland that extends to about 800 km depth. (b) 'Spike tests' designed to evaluate whether the Icelandic low-velocity anomaly points to a deeper-than-normal mantle upwelling beneath the Icelandic region of the Mid-Atlantic Ridge or whether it is a tomography artifact. The cross sections show $\mathbf{m}_{out}$ obtained by convolving hypothetical models $\mathbf{m}_{in}$ with the resolution operator $\mathbf{R}_{\mathbf{m}}$. The input models $\mathbf{m}_{in}$ are 200 km wide cylinders of the mantle beneath Iceland with a uniform velocity perturbation from the reference model. Their tops are top row at the Earth's surface or bottom row at the 660 km discontinuity, and their vertical extent varies from left to right between 100 and 500 km. The numbers indicate to which depth the cylinders in $\mathbf{m}_{in}$ extend.

$\mathbf{R}_{\mathbf{m}}$, we are not addressing the effects of simplifications in the forward modeling theory. We assume that anomalies in the mantle, no matter how small, perturb a wave that propagates through it and that this perturbation (e.g., travel time delay) is recorded at the Earth's surface. In the real Earth, delay times dissipate due to 'wave front healing' (e.g., Nolet and Dahlen, 2000; Wielandt, 1987). Wave front healing is related to the finite-frequency nature of a seismic wave and is ignored in ray theory. Wave front healing can be significant for small (compared to the wavelength) and deep anomalies (Hwang et al., 2011; Malcolm and Trampert, 2011). Going back to our example from Iceland, it is possible that a narrow (e.g., plume-stem) seismic anomaly is present below a depth of 700 km, which has imparted a travel time delay to a throughgoing wave that is still not observable at the surface. The effect of wave front healing, omitted in the forward modeling theory applied to S20RTS, can only be tested with more realistic forward modeling theories (Montelli et al., 2004a) or by comparing seismic waveforms with 3D wave simulations (e.g., Allen and Tromp, 2005; Komatitsch et al., 2002).

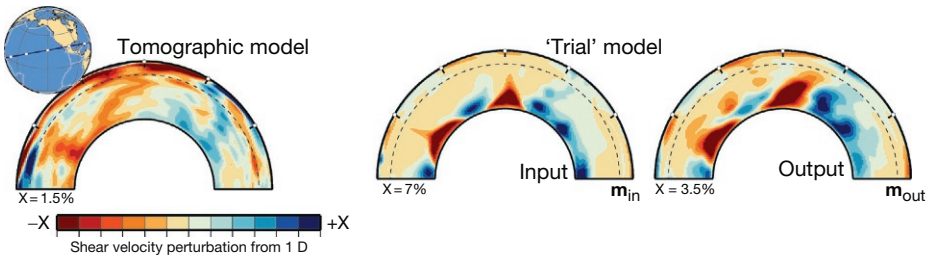

Figure 11 (left) Whole-mantle cross section through model S20RTS (from the Southwest Pacific to the Atlantic) depicting broad lower mantle anomalies beneath the Pacific and a high-velocity anomaly beneath North America. (right) Recovery tests designed to estimate how a thermochemical model of shear-velocity heterogeneity in the lower mantle (see McNamara and Zhong, 2005; Ritsema et al. 2007) would be seen tomographically. A comparison of $\mathbf{m}_{in}$ and $\mathbf{m}_{out}$ illustrates the image distortions, especially in regions (e.g., the lower mantle beneath the central Pacific) with relatively poor data coverage. Relevant to this comparison is the questionable resolution of thermal plumes from the edges of thermochemical deep mantle structures and the artificial tilt of the seismically derived central Pacific low-velocity structure.

1.10.6 Future Directions

We close by commenting on some areas of research in which we anticipate exciting progress in seismic tomography in the future. The tomographic study of temporal changes in structure ('4D tomography') is one relatively new frontier. Some examples are the study of geothermal reservoir changes at The Geysers, California (Gunasekera et al., 2003), the investigation of temporal changes at Mammoth Mountain, California, related to CO_2 outgassing (Foulger et al., 2003), temporal changes at Mt. Etna, Sicily, associated with magma intrusions (Patanè et al., 2006), and similarly temporal changes at the Kluchevskoy group of volcanoes in Kamchatka, Russia, associated with subsequent eruptions (Koulakov et al., 2013). A major concern is the potential for differences in data sampling for datasets from different time periods to cause apparent temporal changes. An inversion strategy that solves for 4D models with a constraint to restrict model changes to those truly required by the data may be the key to deriving robust results in such studies (Ajo-Franklin and Minsley, 2005; Day-Lewis et al., 2003).

Multimethod seismic inversions (e.g., surface waves and receiver functions; Julia et al., 2000) and multiproperty geophysical inversions, for example, seismic and gravity data (Roecker et al., 2004) and seismic and magnetotelluric data (Bennington et al., in press; Gallardo and Meju, 2004, 2007) also present opportunities for significant advances. In the joint seismic–gravity case, it is common to use an empirical velocity–density relationship as a constraint in the inversion. In the seismic–magnetotelluric case, an empirical relationship is not available, so 'structural constraints' (Haber and Oldenberg, 1997) are most commonly applied. The approach of Haber and Oldenberg (1997) proposes the evaluation of the gradients or Laplacians of the two scalar fields of the physical properties to define feature boundaries, incorporating a threshold value above which the features are constrained to be aligned via a penalty function. An alternative approach involves the use of the absolute value of the cross product of the gradients (the 'cross gradient'), with the constraint being to minimize the total cross gradient (Gallardo and Meju, 2004, 2007). This approach can be readily extended to multiple geophysical parameters (Gallardo et al., 2012).

A very different approach to joint inversion is global joint seismic–geodynamic tomography. Rather than obtaining a global seismic model or joint global seismic-density model, using that to compute mantle flow, and comparing the result to geodynamic observables, it is possible to invert seismic and convection-related datasets jointly (Forte and Woodward, 1997; Forte et al., 1994; Simmons et al., 2006, 2007, 2009, 2010). This powerful approach is described in more detail in Forte (**Chapter 1.27**, this volume).

Although joint inversions are receiving increasing attention in academia and industry, in our own experience, great care must be taken in establishing effective values for the scaling and regularization parameters so that convergence is achieved across all models and constraints. Despite this word of caution, we anticipate a great increase in the use of joint inversion methods in the future.

Acknowledgments

Our thanks to Haijiang Zhang for contributing material and for providing comments on a draft version of the manuscript. We are grateful to the volume editors Adam Dziewonski and Barbara Romanowicz for their comments and assistance and to Malcolm Sambridge, Nathan Simmons, and an anonymous reviewer for their constructive comments on various versions of this chapter. This material is based upon work supported by National Science Foundation grants EAR-0106666, EAR-0405437, EAR-0609763, EAR-0855487, EAR-0944167, and EAR-1015172 (JR) and EAR-0346105, EAR-0409291, EAR-0454511, EAR-0608988, EAR-0838249, EAR-0910674, EAR-1114228, and EAR-1141983 (CT).

References

Abers GA and Roecker SW (1991) Deep structure of an arc–continent collision: Earthquake relocation and inversion for upper mantle P and S wave velocities beneath Papua New Guinea. *Journal of Geophysical Research* 96: 6370–6401.

Ajo-Franklin JB and Minsley B (2005) Application of minimum support constraints to seismic traveltime tomography. *EOS Transactions of the American Geophysical Union* 86: H13C–1344.

Akcelik V, Bielak J, Biros G, et al. (2003) High-resolution forward and inverse earthquake modeling on terascale computers. In: *Proceedings of ACM/IEEE SC2003, Phoenix, AZ*.

Aki K, Christofferson A, and Husebye ES (1977) Determination of the three-dimensional seismic structure of the lithosphere. *Journal of Geophysical Research* 82: 277–296.

Aki K and Lee WHK (1976) Determination of three-dimensional velocity anomalies under a seismic array using first P-arrival times from local earthquakes, 1. A homogeneous initial model. *Journal of Geophysical Research* 81: 4381–4399.

Allen RM and Tromp J (2005) Resolution of regional seismic models: Squeezing the Iceland anomaly. *Geophysical Journal International* 161: 373–386.

Anderson DL and Dziewonski AM (1984) Seismic tomography. *Scientific American* 251: 60–68.

Antolik M, Ekström G, Dziewonski AM, Boschi L, Gu YJ, and Pan J-F (2000) A new global joint P and S velocity model of the mantle parameterized in cubic B-splines. In: *Proceedings of 22nd Annual Dod/DOE Seismic Research Symposium, New Orleans, USA*.

Ashiya K, Asano S, Yoshii T, Ishida M, and Nishiki T (1987) Simultaneous determination of the three-dimensional crustal structure and hypocenters beneath the Kanto-Tokai District, Japan. *Tectonophysics* 140: 13–27.

Aster RC, Borchers B, and Thurber CH (2012) *Parameter Estimation and Inverse Problems*, 2nd edn, 376 pp. Elsevier/Academic Press.

Backus GE and Gilbert JF (1967) Numerical applications of a formalism for geophysical inverse problems. *Geophysical Journal of the Royal Astronomical Society* 13: 247–276.

Backus G and Gilbert F (1968) The resolving power of gross earth data. *Geophysical Journal of the Royal Astronomical Society* 16: 169–205.

Backus G and Gilbert F (1970) Uniqueness in the inversion of inaccurate gross earth data. *Philosophical Transactions of the Royal Society A* 266: 187–269.

Barber CB, Dobkin DP, and Huhdanpaa HT (1996) The Quickhull algorithm for convex hulls. *ACM Transactions on Mathematical Software* 22: 469–483.

Battaglia J, Thurber C, Got J-L, Rowe C, and White R (2004) Precise relocation of earthquakes following the June 15, 1991 explosion of Mount Pinatubo (Philippines). *Journal of Geophysical Research* 109: B07302. http://dx.doi.org/10.1029/2003JB002959.

Bekas C, Kokiopoulou E, and Saad Y (2007) An estimator for the diagonal of a matrix. *Journal of Applied Numerical Mathematics* 57: 1214–1229.

Bennington NL, Zhang H, Thurber CH, and Bedrosian PA (in press) Joint inversion of seismic and magnetotelluric data in the Parkfield region of California using the cross-gradient constraint. *Geophysical Journal International*.

Benz HM, Chouet BA, Dawson PB, Lahr JC, Page RA, and Hole JA (1996) Three-dimensional P and S wave velocity structure of Redoubt Volcano, Alaska. *Journal of Geophysical Research* 101: 8111–8128.

Beucler E, Stutzmann E, and Montagner JP (2003) Surface-wave higher mode phase velocity measurements, using a roller coaster type algorithm. *Geophysical Journal International* 155: 289–307.

Bhattacharyya J, Masters G, and Shearer P (1996) Global lateral variations of shear wave attenuation in the upper mantle. *Journal of Geophysical Research* 101: 22273–22289.

Bijwaard H and Spakman W (1999) Fast kinematic ray tracing of first- and later-arriving global seismic phases. *Geophysical Journal International* 139: 359–369.

Bijwaard H and Spakman W (2000) Non-linear global *P*-wave tomography by iterated linearized inversion. *Geophysical Journal International* 141: 71–82.

Bijwaard H, Spakman W, and Engdahl ER (1998) Closing the gap between regional and global travel time tomography. *Journal of Geophysical Research* 103: 30055–30078.

Billien M, Lévêque JJ, and Trampert J (2000) Global maps of Rayleigh wave attenuation for periods between 40 and 150 seconds. *Geophysical Research Letters* 27: 3619–3622.

Bodin T and Sambridge M (2009) Seismic tomography with the reversible jump algorithm. *Geophysical Journal International* 178: 1411–1436. http://dx.doi.org/10.1111/j.1365-246X.2009.04226.x.

Boschi L (2003) Measures of resolution in global body-wave tomography. *Geophysical Research Letters* 30. http://dx.doi.org/10.1029/2003GL018222.

Boschi L and Ekström G (2002) New images of the Earth's upper mantle from measurements of surface wave phase velocity anomalies. *Journal of Geophysical Research* 107: 2059. http://dx.doi.org/10.1029/2000JB000059.

Boschi L, Ekström G, and Kustowski B (2004) Multiple resolution surface wave tomography: The Mediterranean region. *Geophysical Journal International* 157: 293–304.

Boschi E, Ekström G, and Morelli A (eds.) (1996) *Seismic Modeling of Earth Structure*, 572 pp. Rome: Instituto Nazionale di Geofisica.

Bozdag E and Trampert J (2008) On crustal corrections in surface wave tomography. *Geophysical Journal International* 172: 1066–1082.

Bozdağ E, Trampert J, and Tromp J (2011) Misfit functions for full waveform inversion based on instantaneous phase and envelope measurements. *Geophysical Journal International* 185: 845–870. http://dx.doi.org/10.1111/j.1365-246X.2011.04970.x.

Bozdag E, Zhu H, Peter DB, and Tromp J (2012) Towards global adjoint tomography. In: *Fall 2012 AGU Meeting*.

Bube KP and Langan RT (1997) Hybrid $\lambda 1/\lambda 2$ minimization with applications to tomography. *Geophysics* 62: 1183–1195.

Butler R, Lay T, Creager K, et al. (2004) The global seismographic network surpasses its design goal. *EOS Transactions of the American Geophysical Union* 85: 225–229.

Capdeville Y, Chaljub E, Vilotte JP, and Montagner JP (2003) Coupling the spectral element method with a modal solution for elastic wave propagation in global Earth models. *Geophysical Journal International* 152: 34–67.

Capdeville Y, Gung Y, and Romanowicz B (2005) Towards global Earth tomography using the spectral element method: A technique based on source stacking. *Geophysical Journal International* 162: 541–554.

Cara M (1976) Observation d'ondes Sa de type SH. *Pure and Applied Geophysics* 114: 141–157.

Chen P, Zhao L, and Jordan TH (2007) Full 3D tomography for crustal structure of the Los Angeles region. *Bulletin of the Seismological Society of America* 97: 1094–1120. http://dx.doi.org/10.1785/012006022.

Chevrot S, Martin R, and Komatitsch D (2012) Optimized discrete wavelet transforms in the cubed-sphere with the lifting scheme – Implications for global finite-frequency tomography. *Geophysical Journal International* 191: 1391–1402.

Chiao LY and Kuo BY (2001) Multiscale seismic tomography. *Geophysical Journal International* 145: 517–527.

Chiao LY and Liang W (2003) Multiresolution parameterization for geophysical inverse problems. *Geophysics* 68: 199–209.

Chou C and Booker JR (1979) A Backus–Gilbert approach to the inversion of travel time data for three dimensional velocity structure. *Geophysical Journal of the Royal Astronomical Society* 59: 325–344.

Christensen NI (1996) Poisson's ratio and crustal seismology. *Journal of Geophysical Research* 101: 3139–3156.

Clayton RW and Hearn TM (1982) A tomographic analysis of lateral velocity variations in southern California. *EOS Transactions of the American Geophysical Union* 63: 1036.

Committee on the Science of Earthquakes (2003) *Living on an Active Earth*, 418 pp. Washington, D.C.: National Academies Press.

Constable SC, Parker RL, and Constable CG (1987) Occam's inversion: A practical algorithm for generating smooth models from electromagnetic sounding data. *Geophysics* 52(3): 289–300.

Dahlen FA, Hung SH, and Nolet G (2000) Fréchet kernels for finite-frequency travel times—I. theory. *Geophysical Journal International* 141: 157–174.

Dahlen FA and Tromp J (1998) *Theoretical Global Seismology*, 1025 pp. Princeton, NJ: Princeton University Press.

Dalton CA and Ekström G (2006) Global models of surface-wave attenuation. *Journal of Geophysical Research* 111: B05317. http://dx.doi.org/10.1029/2005JB003997.

Das T and Nolet G (1998) Crustal thickness map of the western Unites States by partitioned waveform inversion. *Journal of Geophysical Research* 103: 30021–30038.

Davis T (2006) In: *Direct Methods for Sparse Linear Systems. Fundamentals of Algorithms*, p. 214. Philadelphia, PA: SIAM.

Dawson PB, Evans JR, and Iyer HM (1990) Teleseismic tomography of the compressional wave velocity structure beneath the Long Valley region, California. *Journal of Geophysical Research* 95: 11021–11050.

Day-Lewis F, Harris JM, and Gorelick S (2003) Time-lapse inversion of crosswell radar data. *Geophysics* 67: 1740–1752.

Debayle E, Kennett B, and Priestley K (2005) Inversion of massive surface wave data sets: Model construction and resolution assessments. *Journal of Geophysical Research* 109: B02316. http://dx.doi.org/10.1029/2003JB002652.

Debayle EM and Sambridge M (2004) Global azimuthal seismic anisotropy and the unique plate-motion deformation of Australia. *Nature* 433: 509–512.

Deschamps F and Trampert J (2004) Towards a lower mantle reference temperature and composition. *Earth and Planetary Science Letters* 222: 161–175.

DeShon HR, Schwartz SY, Newman AV, et al. (2006) Seismogenic zone structure beneath the Nicoya Peninsula, Costa Rica, from three-dimensional local earthquake P- and S-wave tomography. *Geophysical Journal International* 164: 109–124.

Deuss A, Ritsema J, and van Heijst H (2011) Splitting function measurements for Earth's longest period normal modes using recent large earthquakes. *Geophysical Research Letters* 38. http://dx.doi.org/10.1029/2010GL046115.

Deuss A, Ritsema J, and van Heijst HJ (2013) Normal mode splitting function measurements up to 10 mHz: Improving constraints on mantle and core structure. *Geophysical Journal International* 193. http://dx.doi.org/10.1093/gji/ggt010.

Dorren HJS and Snieder RK (1997) Error propagation in non-linear delay-time tomography. *Geophysical Journal International* 128: 632–638.

Douglas A (1967) Joint epicenter determination. *Nature* 215: 47–48.

Du W, Thurber CH, Reyners M, Eberhart-Phillips D, and Zhang H (2004) New constraints on seismicity in the Wellington region, New Zealand, from relocated earthquake hypocenters. *Geophysical Journal International* 158: 1088–1102.

Dziewonski AM (1984) Mapping the lower mantle: Determination of lateral heterogeneity in P velocity up to degree and order 6. *Journal of Geophysical Research* 89: 5929–5952.

Dziewonski AM and Anderson DL (1981) Preliminary reference earth model. *Physics of the Earth and Planetary Interiors* 25: 297–356.

Dziewonski AM, Hager BH, and O'Connell RJ (1977) Large-scale heterogeneities in the lower mantle. *Journal of Geophysical Research* 82: 239–255.

Dziewonski AM and Woodhouse JW (1987) Global images of the Earth's interior. *Science* 236: 37–48.

Eberhart-Phillips D (1986) Three-dimensional velocity structure in Northern California Coast Ranges from inversion of local earthquake arrival times. *Bulletin of the Seismological Society of America* 76: 1025–1052.

Eberhart-Phillips D (1990) Three-dimensional P and S velocity structure in the Coalinga region, California. *Journal of Geophysical Research* 95: 15343–15363.

Ekström G, Tromp J, and Larson EW (1997) Measurements and models of global surface wave propagation. *Journal of Geophysical Research* 102: 8137–8157.

Ellsworth WL (1977) *Three-dimensional Structure of the Crust and Mantle Beneath the Island of Hawaii*. Ph.D. Thesis, Massachusetts Institute of Technology, Cambridge.

Engdahl ER, van der Hilst RD, and Buland RP (1998) Global teleseismic earthquake relocation with improved travel times and procedures for depth determination. *Bulletin of the Seismological Society of America* 88: 22–43.

Evans JR and Achauer U (1993) Teleseismic velocity tomography using the ACH method: Theory and application to continental-scale studies. In: Iyer HM and Hirahara K (eds.) *Seismic Tomography: Theory and Applications*, pp. 319–360. London: Chapman and Hall.

Fichtner A, Bunge H-P, and Igel H (2006a) The adjoint method in seismology—I. Theory. *Physics of the Earth and Planetary Interiors* 157: 86–104.

Fichtner A, Bunge H-P, and Igel H (2006b) The adjoint method in seismology—II. Applications: Traveltimes and sensitivity functionals. *Physics of the Earth and Planetary Interiors* 157: 105–123.

Fichtner A, Bunge H-P, Kennett BNL, and Igel H (2009) Full seismic waveform tomography for upper-mantle structure in the Australasian region using adjoint methods. *Geophysical Journal International* 179: 1703–1725.

Fichtner A, Kennett BLN, Bunge HP, and Igel H (2008) Theoretical background for continental and global scale full-waveform inversion in the time-frequency domain. *Geophysical Journal International* 175: 665–685.

Fichtner A and Trampert J (2011) Resolution analysis in full waveform inversion. *Geophysical Journal International* 187: 1604–1624.

Forte AM and Woodward RL (1997) Seismic–geodynamic constraints on three-dimensional structure, vertical flow, and heat transfer in the mantle. *Journal of Geophysical Research* 102: 17981–17994.

Forte AM, Woodward RL, and Dziewonski AM (1994) Joint inversions of seismic and geodynamic data for models of 3-dimensional mantle heterogeneity. *Journal of Geophysical Research* 99: 21857–21877.

Foulger GR, Julian BR, Pitt AM, Hill DP, Malin P, and Shalev E (2003) Three-dimensional crustal structure of Long Valley caldera, California, and evidence for the migration of CO_2 under Mammoth Mountain. *Journal of Geophysical Research* 108: B3. http://dx.doi.org/10.1029/2000JB000041.

Fowler J and Pavlis G (1994) PASSCAL, a facility for portable seismological instrumentation. *EOS Transactions of the American Geophysical Union* 75: 66.

Fukao Y, Widiyantoro S, and Obayashi M (2001) Stagnant slabs in the upper and lower mantle transition region. *Reviews of Geophysics* 39: 291–323.

Gallardo LA, Fontes SL, Meju MA, Buonora MP, and de Lugao PP (2012) Robust geophysical integration through structure-coupled joint inversion and multispectral fusion of seismic reflection, magnetotelluric, magnetic, and gravity images: Example from Santos Basin, offshore Brazil. *Geophysics* 77: B237–B251.

Gallardo LA and Meju MA (2004) Joint two-dimensional DC resistivity and seismic travel time inversion with cross-gradients constraints. *Journal of Geophysical Research* 109: B03311. http://dx.doi.org/10.1029/2003JB002716.

Gallardo LA and Meju MA (2007) Joint 2D cross-gradient imaging of magnetotelluric and seismic travel-time data for structural and lithological classification. *Geophysical Journal International* 169: 1261–1272.

Gee LS and Jordan TJ (1992) Generalized seismological data functionals. *Geophysical Journal International* 111: 363–390.

Giardini D, Li X-D, and Woodhouse JH (1987) Three-dimensional structure of the Earth from splitting in free-oscillation spectra. *Nature* 325: 405–411.

Gilbert F (1970) Excitation of the normal modes of the Earth by earthquake sources. *Geophysical Journal of the Royal Astronomical Society* 22: 223–226.

Gilbert F and Dziewonski AM (1975) An application of normal mode theory to the retrieval of structural parameters and source mechanism from seismic spectra. *Philosophical Transactions of the Royal Society London A* 278: 187–269.

Gill PE, Murray W, and Wright MH (1981) *Practical Optimization*. San Diego: Academic Press, 401 pp.

Got JL, Frechet J, and Klein F (1994) Deep fault plane geometry inferred from multiplet relative relocation beneath the south flank of Kilauea. *Journal of Geophysical Research* 99: 15375–15386.

Grand SP (1994) Mantle shear structure beneath the Americas and surrounding oceans. *Journal of Geophysical Research* 99: 11591–11621.

Grand SP, van der Hilst RD, and Widiyantoro S (1997) Global seismic tomography: A snapshot of convection in the Earth. *Geological Society of America Today* 7: 1–7.

Gudmundsson O and Sambridge M (1998) A regionalized upper mantle RUM seismic model. *Journal of Geophysical Research* 103: 7121–7136.

Gunasekera RC, Foulger GR, and Julian BR (2003) Three-dimensional tomographic images of progressive pore-fluid depletion at The Geysers geothermal area, California. *Journal of Geophysical Research* 108. http://dx.doi.org/10.1029/2001JB000638.

Gung Y, Hsu YT, Chiao LY, and Obayashi M (2009) Multiscale waveform tomography with two-step model parameterization. *Journal of Geophysical Research* 114. http://dx.doi.org/10.1029/2008JB006275.

Haber E and Oldenburg D (1997) Joint inversion: A structural approach. *Inverse Problems* 13: 63–77. http://dx.doi.org/10.1088/0266-5611/13/1/006.

Häfner R and Widmer-Schnidrig R (2013) Signature of 3-D density structure in spectra of the spheroidal free oscillation ${}_0S_2$. *Geophysical Journal International* 192: 285–294. http://dx.doi.org/10.1093/gji/ggs013.

Hawley BW, Zandt G, and Smith RB (1981) Simultaneous inversion for hypocenters and lateral velocity variations: An iterative solution with a layered model. *Journal of Geophysical Research* 86: 7073–7076.

He X and Tromp J (1996) Normal-mode constraints on the structure of the mantle and core. *Journal of Geophysical Research* 101: 20053–20082.

Hirahara K (1993) Tomography using both local earthquakes and teleseisms: Velocity and anisotropy – Theory. In: Iyer HM and Hirahara K (eds.) *Seismic Tomography: Theory and Applications*, pp. 493–518. London: Chapman and Hall.

Hole JA, Brocher TM, Klemperer SL, Parsons T, Benz HM, and Furlong KP (2000) Three-dimensional seismic velocity structure of the San Francisco Bay area. *Journal of Geophysical Research* 105: 13859–13874.

Houser C, Masters G, Shearer P, and Laske G (2008) Shear and compressional velocity models of the mantle from cluster analysis of long-period waveforms. *Geophysical Journal International* 174: 195–212. http://dx.doi.org/10.1111/j.1365-246X.2008.03763.x.

Humphreys E and Clayton RW (1988) Adaptation of back projection tomography to seismic travel time problems. *Journal of Geophysical Research* 93: 1073–1085. http://dx.doi.org/10.1029/JB093iB02p01073.

Humphreys E, Clayton RW, and Hager BH (1984) A tomographic image of mantle structure beneath southern California. *Geophysical Research Letters* 11: 625–627.

Hung SH, Nolet G, and Dahlen FA (2000) Fréchet kernels for finite-frequency travel times – II, Examples. *Geophysical Journal International* 141: 175–203.

Husen S and Kissling E (2001) Local earthquake tomography between rays and waves: Fat ray tomography. *Physics of the Earth and Planetary Interiors* 123: 127–147.

Hwang YK, Ritsema J, van Keken PE, Goes S, and Styles E (2011) Wave front healing renders deep plumes seismically invisible. *Geophysical Journal International* 187. http://dx.doi.org/10.1111/j.1365-246X.2011.05173.x.

Inoue H, Fukao Y, Tanabe K, and Ogata Y (1990) Whole mantle *P*-wave travel time tomography. *Physics of the Earth and Planetary Interiors* 59: 294–328.

Ishii M and Tromp J (1999) Normal-mode and free-air gravity constraints on lateral variations in velocity and density of the Earth's mantle. *Science* 285: 1231–1236.

Ishii M and Tromp J (2001) Even-degree lateral variations in the Earth's mantle constrained by free oscillations and the free-air gravity anomaly. *Geophysical Journal International* 145: 77–96.

Iyer HM and Hirahara K (eds.) (1993) *Seismic Tomography: Theory and Applications*. London: Chapman and Hall, 319–360.

Jeffreys H and Bullen KE (1958) *Seismological Tables*. Burlington House, London: Office of the British Association.

JPL (1976) JPL document 5040–32. Petroleum exploration assessment: Phase 1 Report: Pasadena, Jet Propulsion Laboratory.

Julia J, Ammon CJ, Herrmann RB, and Correig AM (2000) Joint inversion of receiver function and surface wave dispersion observations. *Geophysical Journal International* 143: 1–19.

Julian BR, Evans JR, Pritchard MJ, and Foulger GR (2000) A geometrical error in some computer programs based on the Aki–Christofferson–Husebye ACH method of

teleseismic tomography. *Bulletin of the Seismological Society of America* 90: 1554–1558.
Julian BR, Ross A, Foulger GR, and Evans JR (1996) Three-dimensional seismic image of a geothermal reservoir: The Geysers, California. *Geophysical Research Letters* 23: 685–688.
Kárason H and van der Hilst RD (2001) Tomographic imaging of the lowermost mantle with differential times of refracted and diffracted core phases (PKP, Pdiff). *Journal of Geophysical Research* 106: 6569–6588.
Kennett BLN and Engdahl ER (1991) Traveltimes for global earthquake location and phase identification. *Geophysical Journal International* 105: 429–465.
Kennett BLN, Engdahl ER, and Buland R (1995) Constraints on seismic velocities in the Earth from travel times. *Geophysical Journal International* 122: 403–416.
Kennett BLN, Sambridge MS, and Williamson PR (1988) Subspace methods for large inverse problems with multiple parameter classes. *Geophysical Journal International* 94: 237–247.
Kissling E (1988) Geotomography with local earthquake data. *Reviews of Geophysics* 26: 659–698.
Koch M (1985) A numerical study on the determination of the 3-D structure of the lithosphere by linear and non-linear inversion of teleseismic travel times. *Geophysical Journal International* 80: 73–93.
Komatitsch D, Ritsema J, and Tromp J (2002) The spectral-element method, Beowulf computing and global seismology. *Science* 298: 1737–1742.
Komatitsch D and Tromp J (1999) Introduction to the spectral element method for three-dimensional seismic wave propagation. *Geophysical Journal International* 139: 806–822.
Komatitsch D and Vilotte JP (1998) The spectral element method: An efficient tool to simulate the seismic response of 2D and 3D geological structures. *Bulletin of the Seismological Society of America* 88: 368–392.
Koulakov I, Gordeev EI, Dobretsov NL, et al. (2013) Rapid changes in magma storage beneath the Klyuchevskoy group of volcanoes inferred from time-dependent seismic tomography. *Journal of Volcanology and Geothermal Research* 263: 75–91. http://dx.doi.org/10.1016/j.jvolgeores.2012.10.014.
Kuo C and Romanowicz B (2002) On the resolution of density anomalies in the Earth's mantle using spectral fitting of normal mode data. *Geophysical Journal International* 150: 162–179.
Kustowski B, Ekström G, and Dziewonski AM (2008) Anisotropic shear-wave velocity structure of the Earth's mantle: A global model. *Journal of Geophysical Research* 113: B06306. http://dx.doi.org/10.1029/2007JB005169.
Larsen RM (1998) Lanczos bidiagonalization with partial reorthogonalization. *Technical Report, DAIMI PB-357*. Department of Computer Science, Aarhus University.
Laske G (1995) Global observation of off-great circle propagation of long-period surface waves. *Geophysical Journal International* 123: 245–259.
Lebedev S, Nolet G, Meier T, and van der Hilst RD (2005) Automated multi-mode inversion of surface and S waveforms. *Geophysical Journal International* 162. http://dx.doi.org/10.1111/j.1365-246X.2005.02708.x.
Lebedev S, Nolet G, and van der Hilst RD (1997) The upper mantle beneath the Philippine Sea region from waveform inversion. *Geophysical Research Letters* 24: 1851–1854.
Lees JM (2007) Seismic tomography of magmatic systems. *Journal of Volcanology and Geothermal Research* 167: 37–56. http://dx.doi.org/10.1016/j.volgeores.2007.06.008.
Lees JM and Crosson RS (1989) Tomographic inversion for three-dimensional velocity structure at Mount St. Helens using earthquake data. *Journal of Geophysical Research* 94: 5716–5728.
Lees JM and Crosson RS (1990) Tomographic imaging of local earthquake delay times for three-dimensional velocity variation in western Washington. *Journal of Geophysical Research* 95: 4763–4776.
Lekic V, Panning M, and Romanowicz B (2010) A simple method for improving crustal corrections in waveform tomography. *Geophysical Journal International* 182: 265–278.
Lévêque JJ and Cara M (1985) Inversion of multimode surface wave data: Evidence for sublithospheric anisotropy. *Geophysical Journal International* 83: 753–773.
Lévêque JJ, Rivera L, and Wittlinger G (1993) On the use of the checker-board test to assess the resolution of tomographic inversions. *Geophysical Journal International* 115: 313–318.
Li XD and Romanowicz B (1995) Comparison of global waveform inversions with and without considering cross branch coupling. *Geophysical Journal International* 121: 695–709.
Li XD and Romanowicz B (1996) Global mantle shear velocity model developed using nonlinear asymptotic coupling theory. *Journal of Geophysical Research* 101: 22245–22273.
Li XD and Tanimoto T (1993) Waveforms of long period body-waves in a slightly aspherical Earth. *Geophysical Journal International* 112: 92–112.
Li C, van der Hilst RD, Engdahl ER, and Burdick S (2008) A new global model for P wave speed variations in Earth's mantle. *Geochemistry, Geophysics, Geosystems* 9: Q05018. http://dx.doi.org/10.1029/2007GC001806.
Li C, van der Hilst RD, and Toksoz MN (2006) Constraining P-wave velocity variations in the upper mantle beneath Southeast Asia. *Physics of the Earth and Planetary Interiors* 154: 180–195.
Lin FC and Ritzwoller MH (2011) Helmholtz surface wave tomography for isotropic and azimuthally anisotropic structure. *Geophysical Journal International* 186: 1104–1120. http://dx.doi.org/10.1111/j.1365-246X.2011.05070.x.
Lin CH and Roecker SW (1997) Three-dimensional P-wave velocity structure of the Bear Valley Region of Central California. *Pure and Applied Geophysics* 149: 667–688.
Lin G, Thurber CH, Zhang H, et al. (2010) A California statewide three-dimensional seismic velocity model from both absolute and differential times. *Bulletin of the Seismological Society of America* 100: 225–240.
Liu Q and Gu YJ (2012) Seismic imaging: From classical to adjoint tomography. *Tectonophysics* 566: 31–66.
Liu Q and Tromp J (2006) Finite-frequency kernels based on adjoint method. *Bulletin of the Seismological Society of America* 96: 2283–2297.
Liu Q and Tromp J (2008) Finite-frequency sensitivity kernels for global seismic wave propagation based upon adjoint methods. *Geophysical Journal International* 174: 265–286.
Loris I, Douma H, Nolet G, Daubechies I, and Regone C (2010) Nonlinear regularization techniques for seismic tomography. *Journal of Computational Physics* 229: 890–905.
Loris I, Nolet G, Daubechies I, and Dahlen FA (2007) Tomographic inversion using ℓ1-norm regularization of wavelet coefficients. *Geophysical Journal International* 170: 359–370.
MacCarthy JK, Borchers B, and Aster R (2011) Efficient stochastic estimation of the model resolution matrix diagonal and generalized crossvalidation for large geophysical inverse problems. *Journal of Geophysical Research* 116: B10304. http://dx.doi.org/10.1029/2011JB008234.
Maggi A, Tape C, Chen M, Chao D, and Tromp J (2009) An automated data-window selection algorithm for adjoint tomography. *Geophysical Journal International* 178: 257–281.
Malcolm AE and Trampert J (2011) Tomographic errors from wave front healing: More than just a fast bias. *Geophysical Journal International* 185: 385–402.
Marquering H and Snieder R (1995) Surface wave mode coupling for efficient forward modeling and inversion of body wave phases. *Geophysical Journal International* 120: 186–208.
Masson F and Trampert J (1997) On ACH, or how reliable is regional teleseismic delay time tomography? *Physics of the Earth and Planetary Interiors* 102: 21–32.
Masters G, Johnson S, Laske G, and Bolton H (1996) A shear-velocity model of the mantle. *Philosophical Transactions of Royal Society London A* 354: 1385–1411.
Masters G, Jordan T, Silver P, and Gilbert F (1982) Aspherical earth structure from fundamental spheroidal-mode data. *Nature* 298: 609–613.
McNamara AK and Zhong S (2005) Thermochemical piles under Africa and the Pacific. *Nature* 437: 1136–1139.
Mégnin C and Romanowicz B (2000) The 3-D shear velocity structure of the mantle from the inversion of body, surface and higher mode waveforms. *Geophysical Journal International* 143: 709–728.
Menke W (2012) *Geophysical Data Analysis: Discrete Inverse Theory*, 3rd edn, 293 pp. Waltham, MA: Academic Press.
Menke W and Schaff D (2004) Absolute earthquake locations with differential data. *Bulletin of the Seismological Society of America* 94: 2254–2264.
Merrer S, Cara M, Rivera L, and Ritsema J (2007) Upper mantle structure beneath continents: New constraints from multi-mode Rayleigh wave data in western North America and southern Africa. *Geophysical Research Letters* 34: L06309. http://dx.doi.org/10.1029/2006GL028939.
Michael AJ (1988) Effects of three-dimensional velocity structure on the seismicity of the 1984 Morgan Hill, California, aftershock sequence. *Bulletin of the Seismological Society of America* 78: 1199–1221.
Michelini A (1995) An adaptive-grid formalism for traveltime tomography. *Geophysical Journal International* 121: 489–510.
Michelini A and McEvilly TV (1991) Seismological studies at Parkfield: I. Simultaneous inversion for velocity structure and hypocenters using cubic b-splines parameterization. *Bulletin of the Seismological Society of America* 81: 524–552.
Montagner JP (1994) Can seismology tell us anything about convection in the mantle? *Reviews of Geophysics* 32: 115–138.
Montagner JP and Tanimoto T (1991) Global upper mantle tomography of seismic velocities and anisotropics. *Journal of Geophysical Research* 96: 20337–20351.

Montelli R, Nolet G, Dahlen FA, and Masters G (2006) A catalogue of deep mantle plumes: New results from finite-frequency tomography. *Geochemistry, Geophysics, Geosystems* 7: Q11007. http://dx.doi.org/10.1029/2006GC001248.

Montelli R, Nolet G, Dahlen FA, Masters G, Engdahl ER, and Hung SH (2004) Finite-frequency tomography reveals a variety of plumes in the mantle. *Science* 303: 338–343.

Montelli R, Nolet G, Masters G, Dahlen FA, and Hung SH (2004) Global *P* and *PP* traveltime tomography: Rays versus waves. *Geophysical Journal International* 158: 637–654.

Mooney WD, Laske G, and Masters G (1998) CRUST-5.1: A global crustal model at 5×5. *Journal of Geophysical Research* 103: 727–747.

Mosca I, Cobden L, Deuss A, Ritsema J, and Trampert J (2012) Seismic and mineralogical structures of the lower mantle from probabilistic tomography. *Journal of Geophysical Research* 117: B06304. http://dx.doi.org/10.1029/2011JB008851.

Mosegaard K and Tarantola A (1995) Monte Carlo sampling of solutions to inverse problems. *Journal of Geophysical Research* 100: 12431–12448.

Nakanishi I (1985) Three-dimensional structure beneath the Hokkaido–Tohoku region as derived from a tomographic inversion of P-arrival times. *Journal of Physics of the Earth* 33: 241–256.

Nakanishi I and Anderson DL (1982) Worldwide distribution of group velocity of mantle Rayleigh waves as determined by spherical harmonic inversion. *Bulletin of the Seismological Society of America* 72: 1185–1194.

Nakanishi I and Suetsugu D (1986) Resolution matrix calculated by a tomographic inversion method. *Journal of Physics of the Earth* 34: 95–99.

Nakanishi I and Yamaguchi K (1986) A numerical experiment on nonlinear image reconstruction from first-arrival times for two-dimensional island arc structure. *Journal of Physics of the Earth* 34: 195–201.

Nataf HC, Nakanishi I, and Anderson DL (1986) Measurement of mantle wave velocities and inversion for lateral heterogeneity and anisotropy, III. Inversion. *Journal of Geophysical Research* 91: 7261–7307.

Nataf HC and Ricard Y (1996) 3SMAC: An a priori tomographic model of the upper mantle based on geophysical modeling. *Physics of the Earth and Planetary Interiors* 95: 101–122.

Nissen-Meyer T, Dahlen FA, and Fournier A (2007) Spherical-earth Fréchet sensitivity kernels. *Geophysical Journal International* 168: 1051–1066.

Nolet G (1975) Higher Rayleigh modes in western Europe. *Geophysical Research Letters* 2: 60–62.

Nolet G (1985) Solving or resolving inadequate and noisy tomographic systems. *Journal of Computational Physics* 61: 463–482.

Nolet G (1987) *Seismic Tomography: With Applications in Global Seismology and Exploration Geophysics*. Dordrecht: D. Reidel.

Nolet G (1990) Partitioned waveform inversion and 2D structure under the NARS array. *Journal of Geophysical Research* 95: 8513–8526.

Nolet G (2008) *A Breviary of Seismic Tomography*, 360 pp. Cambridge, UK: Cambridge University Press.

Nolet G (2011) Seismic tomography. In: Gupta H (ed.) *Encyclopedia of Solid Earth Geophysics*. *Springer Earth Science Series*. pp. 1195–1198.

Nolet G, Allen R, and Zhao D (2007) Mantle plume tomography. *Chemical Geology* 241: 248–263.

Nolet G and Dahlen FA (2000) Wavefront healing and the resolution of seismic delay times. *Journal of Geophysical Research* 105: 19043–19054.

Nolet G, Dahlen FA, and Montelli R (2005) Traveltimes and amplitudes of seismic waves: A re-assessment. In: Levander A and Nolet G (eds.) *Seismic Earth: Analysis of Broadband Seismograms*. *AGU Monograph Series*, vol. 157, pp. 37–48.

Nolet G and Montelli R (2005) Optimal parametrization of tomographic models. *Geophysical Journal International* 161: 365–372.

Nolet G, Montelli R, and Virieux J (1999) Explicit, approximate expressions for the resolution and *a posteriori* covariance of massive tomographic systems. *Geophysical Journal International* 138: 36–44.

Nolet G and Snieder R (1990) Solving large linear inverse problems by projection. *Geophysical Journal International* 103: 565–568.

Novotny M (1981) Two methods of solving the linearized two-dimensional inverse seismic kinematic problem. *Journal of Geophysics* 50: 7–15.

O'Connell RJ and Budiansky B (1974) Seismic velocities in dry and saturated cracked solids. *Journal of Geophysical Research* 79: 5412–5426.

Paige CC and Saunders MA (1982) LSQR: Sparse linear equations and least squares problems. *ACM Transactions on Mathematical Software* 8: 195–209.

Panning M, Lekic V, and Romanowicz B (2010) Importance of crustal corrections in the development of a new global model of radial anisotropy. *Journal of Geophysical Research* 115: B12325. http://dx.doi.org/10.1029/2010JB007520.

Parker RL (1994) *Geophysical Inverse Theory*, 386 pp. Princeton, NJ: Princeton University Press.

Patanè D, Barberi G, Cocina O, De Gori P, and Chiarabba C (2006) Time-resolved seismic tomography detects magma intrusions at Mount Etna. *Science* 313: 821–823.

Pavlis GL and Booker JR (1980) The mixed discrete-continuous inverse problem: Application to the simultaneous determination of earthquake hypocenters and velocity structure. *Journal of Geophysical Research* 85: 4801–4810.

Pesicek JD, Thurber CH, Widiyantoro S, DeShon HR, Engdahl ER, and Zhang H (2010) Sharpening the tomographic image of the subducting slab below Sumatra, the Andaman Islands, and Burma. *Geophysical Journal International* 182: 433–453.

Phillips WS, Hartse HE, and Steck LK (2001) Precise relative location of 25 ton chemical explosions at Balapan using IMS stations. *Pure and Applied Geophysics* 158: 173–192.

Pollitz FF and Fletcher JP (2005) Waveform tomography of crustal structure in the south San Francisco bay region. *Journal of Geophysical Research* 110. http://dx.doi.org/10.1029/2004JB003509.

Press F (1968) Earth models obtained by Monte Carlo inversion. *Journal of Geophysical Research* 73: 5223–5234.

Rawlinson N, Pozgay S, and Fishwick S (2010) Seismic tomography: A window into deep Earth. *Physics of the Earth and Planetary Interiors* 178: 101–135.

Rawlinson N and Sambridge M (2003) Seismic traveltime tomography of the crust and lithosphere. *Advances in Geophysics* 46: 81–197.

Reagan RL (1978) *A Finite-Difference Study of Subterranean Cavity Detection and Seismic Tomography*. Ph.D. Thesis, University of Missouri-Rolla, 229 pp.

Reid FJL, Woodhouse JH, and van Heijst HJ (2001) Upper mantle attenuation and velocity structure from measurements of differential S phases. *Geophysical Journal International* 145: 615–630.

Resovsky JS and Ritzwoller MH (1999) A degree 8 mantle shear velocity model from normal mode observation below 3 mHz. *Journal of Geophysical Research* 104: 993–1014.

Ritsema J, McNamara AK, and Bull A (2007) Tomographic filtering of geodynamic models: Implications for model interpretation and large-scale mantle structure. *Journal of Geophysical Research* 112. http://dx.doi.org/10.1029/2006JB004566.

Ritsema J, Rivera LA, Komatitsch D, Tromp J, and van Heijst H-J (2002) Effects of crust and mantle heterogeneity on PP/P and SS/S amplitude ratios. *Geophysical Research Letters* 29: 72-1–72-4. http://dx.doi.org/10.1029/2001GL013831.

Ritsema J, van Heijst HJ, Deuss A, and Woodhouse JH (2011) S40RTS: A degree-40 shear-velocity model for the mantle from new Rayleigh wave dispersion, teleseismic traveltimes, and normal-mode splitting function measurements. *Geophysical Journal International* 184: 1223–1236. http://dx.doi.org/10.1111/j.1365-246X.2010.04884.x.

Ritsema J, van Heijst HH, and Woodhouse JH (1999) Complex shear wave velocity structure imaged beneath Africa and Iceland. *Science* 286: 1925–1928.

Ritsema J, van Heijst HJ, and Woodhouse JH (2004) Global transition zone tomography. *Journal of Geophysical Research* 109. http://dx.doi.org/10.1029/2003JB002610.

Ritsema J, van Heijst HJ, Woodhouse JH, and Deuss A (2009) Long-period body-wave traveltimes through the crust: Implication for crustal corrections and seismic tomography. *Geophysical Journal International* 179: 1255–1261.

Ritzwoller MH and Lavely EM (1995) Three-dimensional seismic models of the earth's mantle. *Reviews of Geophysics* 33: 1–66.

Ritzwoller MH, Levshin AL, Ratnikova LI, and Egorkin AA (1998) Intermediate period group velocity maps across Central Asia, Western China, and parts of the Middle East. *Geophysical Journal International* 134: 315–328.

Rodi WL, Jordan TH, Masso JF, and Savino JM (1981) Determination of the three-dimensional structure of eastern Washington from the joint inversion of gravity and earthquake data. *Systems Sciences and Software*, Rep. SSS-R-80-4516. La Jolla.

Roecker SW (1982) Velocity structure of the Pamir–Hindu Kush region: Possible evidence of subducted crust. *Journal of Geophysical Research* 87: 945–959.

Roecker S, Thurber C, and McPhee D (2004) Joint inversion of gravity and arrival time data from Parkfield: New constraints on structure and hypocenter locations near the SAFOD drill site. *Geophysical Research Letters* 31. http://dx.doi.org/10.1029/2003GL019396.

Roecker S, Thurber C, Roberts K, and Powell L (2006) Refining the image of the San Andreas Fault near Parkfield California using a finite difference travel time computation technique. *Tectonophysics* 424. http://dx.doi.org/10.1016/j.tecto.2006.02.026.

Romanowicz B (1991) Seismic tomography of the Earth's mantle. *Annual Review of Earth and Planetary Sciences* 19: 77–99.

Romanowicz B (2003) Global mantle tomography: Progress status in the last 10 years. *Annual Review of Earth and Planetary Sciences* 31: 303–328.

Romanowicz B (2008) Using seismic waves to image Earth's internal structure. *Nature* 451: 266–268.

Romanowicz B, Cara M, Fels JF, and Rouland D (1984) Geoscope: A French initiative in long period three component seismic networks. *EOS Transactions of the American Geophysical Union* 65: 753–754.
Rowe CA, Aster RC, Phillips WS, Jones RH, Borchers B, and Fehler MC (2002) Using automated, high-precision repicking to improve delineation of microseismic structures at the Soultz geothermal reservoir. *Pure and Applied Geophysics* 159: 563–596.
Rubin A, Gillard D, and Got JL (1998) A re-examination of seismicity associated with the January 1983 dike intrusion at Kilauea volcano, Hawaii. *Journal of Geophysical Research* 103: 10003–10015.
Sabra KG, Gerstoft P, Roux P, and Kuperman WA (2005) Surface wave tomography from microseisms in southern California. *Geophysical Research Letters* 32. http://dx.doi.org/10.1029/2005GL023155.
Sambridge MS (1990) Non-linear arrival time inversion: Constraining velocity anomalies by seeking smooth models in 3-D. *Geophysical Journal International* 102: 653–677.
Sambridge M and Faletic R (2003) Adaptive whole earth tomography. *Geochemistry, Geophysics, Geosystems* 4: 1022. http://dx.doi.org/10.1029/2001GC000213.
Sambridge M and Gudmundsson O (1998) Tomographic systems of equations with irregular cells. *Journal of Geophysical Research* 103(B1): 773–781.
Sambridge M and Mosegaard K (2002) Monte Carlo methods in geophysical inverse problems. *Reviews of Geophysics* 40: 3-1–3-29. http://dx.doi.org/10.1029/2000RG000089.
Sambridge M and Rawlinson N (2005) Seismic tomography with irregular meshes. In: Lavender A and Nolet G (eds.) *Seismic Earth: Array Analysis of Broadband Seismograms*. *AGU Geophysical Monograph Series*, vol. 157, pp. 49–65. http://dx.doi.org/10.1029/156GM04.
Savage B, Peter D, Covellone BM, Rodgers AJ, and Tromp J (2011) Next generation, waveform based three-dimensional models and metrics to improve nuclear explosion monitoring in the Middle East. In: *Proceedings 33rd Monitoring Research Review*. pp. 161–167.
Scales JA (1987) Tomographic inversion via the conjugate gradient method. *Geophysics* 52: 179–185.
Scales JA and Snieder R (1997) To Bayes or not to Bayes. *Geophysics* 62: 1045–1046.
Selby ND and Woodhouse JH (2002) The Q structure of the upper mantle: Constraints from Rayleigh wave amplitudes. *Journal of Geophysical Research* 107: ESE 5-1–5-11. http://dx.doi.org/10.1029/2001JB000257.
Sengupta MK and Toksöz MN (1976) Three dimensional model of seismic velocity variation in the Earth's mantle. *Geophysical Research Letters* 3(2): 84–86.
Shapiro NM, Campillo M, Stehly L, and Ritzwoller MH (2005) High-resolution surface-wave tomography from ambient seismic noise. *Science* 307: 1615–1618.
Shapiro NM and Ritzwoller MH (2002) Monte-Carlo inversion for a global shear-velocity model of the crust and upper mantle. *Geophysical Journal International* 151: 88–105.
Sieminski A, Paulssen H, Trampert J, and Tromp J (2008) Finite-frequency SKS splitting: Measurement and sensitivity kernels. *Bulletin of the Seismological Society of America* 98: 1797–1810.
Sigloch K and Nolet G (2006) Measuring finite-frequency body wave amplitudes and travel times. *Geophysical Journal International* 167: 271–287.
Simmons NA, Forte AM, Boschi L, and Grand SP (2010) GyPSuM: A joint tomographic model of mantle density and seismic wave speeds. *Journal of Geophysical Research* 115: B12310. http://dx.doi.org/10.1029/2010JB007631.
Simmons NA, Forte AM, and Grand SP (2006) Constraining mantle flow with seismic and geodynamic data: A joint approach. *Earth and Planetary Science Letters* 246: 109–124.
Simmons NA, Forte AM, and Grand SP (2007) Thermochemical structure and dynamics of the African superplume. *Geophysical Research Letters* 34. http://dx.doi.org/10.1029/2006GL028009.
Simmons NA, Forte AM, and Grand SP (2009) Joint seismic, geodynamic and mineral physical constraints on three-dimensional mantle heterogeneity: Implications for the relative importance of thermal versus compositional heterogeneity. *Geophysical Journal International* 177: 1284–1304.
Simons FJ, Loris I, Nolet G, et al. (2011) Solving or resolving global tomographic models with spherical wavelets, and the scale and sparsity of seismic heterogeneity. *Geophysical Journal International* 187: 969–988.
Snieder R (1990) A perturbative analysis of non-linear inversion. *Geophysical Journal International* 101: 545–556.
Snieder R and Sambridge M (1992) Ray perturbation theory for traveltimes and ray paths in 3-D heterogeneous media. *Geophysical Journal International* 109: 294–322.
Snieder R and Spencer C (1993) A unified approach to ray bending, ray perturbation and paraxial ray theories. *Geophysical Journal International* 115: 456–470.
Snieder R and Wapenaar K (2010) Imaging with ambient noise. *Physics Today* 63: 44–49.
Soldati G and Boschi L (2005) The resolution of whole Earth seismic tomographic models. *Geophysical Journal International* 161: 143–153.
Spakman W and Bijwaard H (2001) Optimization of cell parameterization for tomographic inverse problems. *Pure and Applied Geophysics* 158: 1401–1423.
Spakman W and Nolet G (1988) Imaging algorithms: Accuracy and resolution in delay time tomography. In: Vlaar NJ, Nolet G, Wortel M, and Cloetingh S (eds.) *Mathematical Geophysics: A Survey of Recent Developments in Seismology and Geodynamics*, pp. 155–188. Dordrecht: D. Reidel.
Spencer C and Gubbins D (1980) Travel-time inversion for simultaneous earthquake location and velocity structure determination in laterally varying media. *Geophysical Journal of the Royal Astronomical Society* 63: 95–116.
Steck L, Thurber C, Fehler M, et al. (1998) Crust and upper mantle P-wave velocity structure beneath the Valles Caldera, New Mexico: Results from the JTEX teleseismic experiment. *Journal of Geophysical Research* 103: 24301–24320.
Stutzmann E and Montagner JP (1993) An inverse technique for retrieving higher mode phase velocity and mantle structure. *Geophysical Journal International* 113: 669–683.
Su WJ, Woodward RL, and Dziewonski AM (1994) Degree 12 model of shear velocity heterogeneity in the mantle. *Journal of Geophysical Research* 99: 4945–4980.
Symons NP and Crosson RS (1997) Seismic velocity structure of the Puget Sound region from 3-D non-linear tomography. *Geophysical Research Letters* 24: 2593–2596.
Tape C, Liu Q, Maggi A, and Tromp J (2009) Adjoint tomography of the southern California crust. *Science* 325: 988–992.
Tape C, Liu Q, Maggi A, and Tromp J (2010) Seismic tomography of the southern California crust based on spectral-element and adjoint methods. *Geophysical Journal International* 180: 433–462.
Tape C, Liu Q, and Tromp J (2007) Finite-frequency tomography using adjoint methods – Methodology and examples using membrane surface waves. *Geophysical Journal International* 168: 1105–1129.
Tarantola A (1984) Inversion of seismic reflection data in the acoustic approximation. *Geophysics* 49: 1259–1266.
Tarantola A (1988) Theoretical background for the inversion of seismic waveforms, including elasticity and attenuation. *Pure and Applied Geophysics* 128: 365–399.
Tarantola A (2005) *Inverse Problem Theory and Methods for Model Parameter Estimation*. Society for Industrial and Applied Mathematics.
Tarantola A and Nercessian A (1984) Three-dimensional inversion without blocks. *Geophysical Journal of the Royal Astronomical Society* 76: 299–306.
Tarantola A and Valette B (1982) Generalized nonlinear inverse problems solved using the least squares criterion. *Reviews of Geophysics and Space Physics* 20: 219–232.
Thomson CJ and Gubbins D (1982) Three-dimensional lithospheric modeling at NORSAR: Linearity of the method and amplitude variations from the anomalies. *Geophysical Journal International* 71: 1–36.
Thurber CH (1983) Earthquake locations and three-dimensional crustal structure in the Coyote Lake area, central California. *Journal of Geophysical Research* 88: 8226–8236.
Thurber CH (1987) Seismic structure and tectonics of Kilauea volcano, Hawaii. In: Decker RW, Wright TL, and Stauffer PH (eds.) *Volcanism in Hawaii*. pp. 919–934, U. S. Geological Survey Professional Paper 1350.
Thurber CH (1992) Hypocenter-velocity structure coupling in local earthquake tomography. *Physics of the Earth and Planetary Interiors* 75: 55–62, Lateral Heterogeneity and Earthquake Location.
Thurber CH (2003) Seismic tomography of the lithosphere with body-waves. *Pure and Applied Geophysics* 160: 717–737.
Thurber CH and Aki K (1987) Three-dimensional seismic imaging. *Annual Review of Earth and Planetary Sciences* 15: 115–139.
Thurber CH and Atre SR (1993) Three-dimensional Vp/Vs variations along the Loma Prieta rupture zone. *Bulletin of the Seismological Society of America* 83: 717–736.
Thurber CH and Eberhart-Phillips D (1999) Local earthquake tomography with flexible gridding. *Computers and Geosciences* 25: 809–818.
Thurber C, Roecker S, Zhang H, Baher S, and Ellsworth W (2004) Fine-scale structure of the San Andreas fault and location of the SAFOD target earthquakes. *Geophysical Research Letters* 31: L12S02. http://dx.doi.org/10.1029/2003GL019398.
Thurber C, Trabant C, Haslinger F, and Hartog R (2001) Nuclear explosion locations at the Balapan, Kazakhstan, nuclear test site: The effects of high-precision arrival times and three-dimensional structure. *Physics of the Earth and Planetary Interiors* 123: 283–301.
Trampert J (1998) Global seismic tomography: The inverse problem and beyond. *Inverse Problems* 14: 371–385.

Trampert J, Deschamps F, Resovsky J, and Yuen D (2004) Probabilistic tomography maps chemical heterogeneities throughout the lower mantle. *Science* 306: 853–856.

Trampert J and Lévêque JJ (1990) Simultaneous iterative reconstruction technique: Physical interpretation based on the generalized least squares solution. *Journal of Geophysical Research* 95: 12553–12559.

Trampert J and Snieder R (1996) Model estimations biased by truncated expansions: Possible artifacts in seismic tomography. *Science* 271: 1257–1260.

Trampert J and Woodhouse JH (1995) Global phase velocity maps of Love and Rayleigh waves between 40 and 150 seconds. *Geophysical Journal International* 122: 675–690.

Trampert J and Woodhouse JH (1996) High resolution global phase velocity distributions. *Geophysical Research Letters* 23: 21–24.

Tromp J, Luo Y, Hanasoge S, and Peter D (2010) Noise cross-correlation sensitivity kernels. *Geophysical Journal International* 183: 791–819.

Tromp J, Tape C, and Liu Q (2005) Seismic tomography, adjoint methods, time reversal, and banana-doughnut kernels. *Geophysical Journal International* 160: 195–216.

van der Hilst RD and DeHoop M (2005) On sensitivity kernels for 'wave-equation' transmission tomography. *Geophysical Journal International* 160: 621–633.

van der Hilst RD, Widiyantoro S, and Engdahl ER (1997) Evidence for deep mantle circulation from global tomography. *Nature* 386: 578–584.

van der Lee S and Nolet G (1997) Upper mantle S velocity structure of North America. *Journal of Geophysical Research* 102: 22815–22838.

van der Sluis A and van der Vorst HA (1987) Numerical solution of large sparse linear algebraic systems arising from tomographic problems. In: Nolet G (ed.) *Seismic Tomography*, pp. 49–83. Dordrecht: Reidel Publishing Company, ch. 3.

Van der Vink GWorking Group (2002) Earthscope: Reassembling a continent in motion. *Geotimes* 47(4): 14–19.

van Heijst HJ and Woodhouse JH (1999) Global high-resolution phase velocity distributions of overtone and fundamental-mode surface waves determined by mode branch stripping. *Geophysical Journal International* 137: 601–620.

VanDecar JC, James DE, and Assumpcao M (1995) Seismic evidence for a fossil mantle plume beneath South America and implications for plate driving forces. *Nature* 378: 25–31.

Vasco DW, Johnson LR, and Pulliam J (1995) Lateral variations in mantle velocity structure and discontinuities determined from *p*, *pp*, *s*, *ss* and *ss*-s_dS travel time residuals. *Journal of Geophysical Research* 100: 24037–24059.

Vesnaver A (1996) The contribution of reflected, refracted and transmitted waves to seismic tomography: A tutorial. *First Break* 14: 159–168.

Visser K, Trampert J, and Kennett BLN (2008) Global anisotropic phase velocity maps for higher mode Love and Rayleigh waves. *Geophysical Journal International* 172: 1016–1032.

Visser K, Trampert J, Lebedev S, and Kennett BLN (2008) Probability of radial anisotropy in the deep mantle. *Earth and Planetary Science Letters* 270: 241–250.

Wagner LS, Beck SL, and Zandt G (2005) Upper mantle structure in the south central Chilean subduction zone (30 to 36°S). *Journal of Geophysical Research* 110: B01308. http://dx.doi.org/10.1029/2004JB003238.

Walck MC (1988) Three-dimensional Vp/Vs variations for the Coso region, California. *Journal of Geophysical Research* 93: 2047–2051.

Walck MC and Clayton RW (1987) *P* wave velocity variations in the Coso region California, derived from local earthquake travel times. *Journal of Geophysical Research* 92: 393–405.

Waldhauser F (2001) HypoDD: A computer program to compute double-difference earthquake locations. *U.S. Geological Survey Open-File Report, 01–113*. Menlo Park, California.

Waldhauser F and Ellsworth WL (2000) A double-difference earthquake location algorithm: Method and application to the northern Hayward fault. *Bulletin of the Seismological Society of America* 90: 1353–1368.

Waldhauser F, Ellsworth WL, and Cole A (1999) Slip-parallel seismic lineations on the northern Hayward fault, California. *Geophysical Research Letters* 26: 3525–3528.

Waldhauser F, Lippitsch R, Kissling E, and Ansorge J (2002) High-resolution teleseismic tomography of upper mantle structure using an a priori 3-D crustal model. *Geophysical Journal International* 150: 1–12.

Wang Z and Dahlen FA (1995) Validity of surface-wave ray theory on a laterally heterogeneous Earth. *Geophysical Journal International* 123: 757–773.

Weidle C and Widiyantoro SCALIXTO Working Group (2005) Improving depth resolution of teleseismic tomography by simultaneous inversion of teleseismic and global P-wave travel-time data – Application to the Vrancea region in Southeastern Europe. *Geophysical Journal International* 162: 811–823.

Weiland CM, Steck LK, Dawson PB, and Korneev VA (1995) Nonlinear teleseismic tomography at Long Valley caldera, using three-dimensional minimum travel time ray tracing. *Journal of Geophysical Research* 100: 20379–20390.

Wesson RL (1971) Travel-time inversion for laterally inhomogeneous crustal velocity models. *Bulletin of the Seismological Society of America* 61: 729–746.

Widiyantoro S, Gorbatov A, Kennett BLN, and Fukao Y (2000) Improving global shear wave traveltime tomography using three-dimensional ray tracing and iterative inversion. *Geophysical Journal International* 141: 747–758.

Widiyantoro S, Kennett BLN, and van der Hilst RD (1998) Extending shear-wave tomography for the lower mantle using S and SKS arrival-time data. *Earth, Planets and Space* 50: 999–1012.

Widiyantoro S and van der Hilst RD (1997) Mantle structure beneath Indonesia inferred from high-resolution tomographic imaging. *Geophysical Journal International* 130: 167–182.

Wielandt E (1987) On the validity of the ray approximation for interpreting delay times. In: Nolet G (ed.) *Seismic Tomography: With Applications to Global Seismology and Exploration Geophysics*, pp. 85–98. Dordrecht: D. Reidel.

Wiggins RA (1972) The general linear inverse problem: Implication of surface waves and free oscillations for earth structure. *Reviews of Geophysics and Space Physics* 10: 251–285.

Wolfe C (2002) On the mathematics of using difference operators to relocate earthquakes. *Bulletin of the Seismological Society of America* 92: 2879–2892.

Woodhouse JH and Dziewonski AM (1984) Mapping the upper mantle: Three-dimensional modeling of Earth structure by inversion of seismic waveforms. *Journal of Geophysical Research* 89: 5953–5986.

Woodhouse JH and Dziewonski AM (1989) Seismic modelling of the Earth's large-scale three-dimensional structure. *Philosophical Transactions of the Royal Society London A* 328: 291–308.

Woodward RL and Masters G (1991) Global upper mantle structure from long-period differential travel-times. *Journal of Geophysical Research* 96: 6351–6377.

Yao ZS, Roberts RG, and Tryggvason A (1999) Calculating resolution and covariance matrices for seismic tomography with the LSQR method. *Geophysical Journal International* 138: 886–894.

Zaroli C, Debayle E, and Sambridge M (2010) Frequency-dependent effects on global S-wave travel times: Wavefront-healing, scattering and attenuation. *Geophysical Journal International* 182: 1025–1042.

Zhang J and McMechan GA (1995) Estimation of resolution and covariance for large matrix inversions. *Geophysical Journal International* 121: 409–426.

Zhang YS and Tanimoto T (1993) High-resolution global upper mantle structure and plate tectonics. *Journal of Geophysical Research* 98: 9793–9823.

Zhang H and Thurber CH (2003) Double-difference tomography: The method and its application to the Hayward fault, California. *Bulletin of the Seismological Society of America* 93: 1875–1889.

Zhang H and Thurber C (2005) Adaptive mesh seismic tomography based on tetrahedral and Voronoi diagrams: Application to Parkfield, California. *Journal of Geophysical Research* 110: B04303. http://dx.doi.org/10.1029/2004JB003186.

Zhang H and Thurber C (2006) Development and applications of double-difference seismic tomography. *Pure and Applied Geophysics* 163: 373–403.

Zhang H and Thurber C (2007) Estimating the model resolution matrix for large seismic tomography problems based on Lanczos bidiagonalization with partial reorthogonalization. *Geophysical Journal International* 170: 337–345.

Zhang H, Thurber C, and Bedrosian P (2009) Joint inversion for Vp, Vs, and Vp/Vs at SAFOD, Parkfield, California. *Geochemistry, Geophysics, Geosystems* 10: Q11002. http://dx.doi.org/10.1029/2009GC002709.

Zhang H, Thurber C, Shelly D, Ide S, Beroza G, and Hasegawa A (2004) High-resolution subducting slab structure beneath Northern Honshu, Japan, revealed by double-difference tomography. *Geology* 32: 361–364.

Zhao D (2004) Global tomographic images of mantle plumes and subducting slabs: Insight into deep earth dynamics. *Physics of the Earth and Planetary Interiors* 146: 3–34.

Zhao D (2009) Multiscale seismic tomography and mantle dynamics. *Gondwana Research* 15: 297–323.

Zhao D, Hasegawa A, and Horiuchi S (1992) Tomographic imaging of P and S wave velocity structure beneath northeastern Japan. *Journal of Geophysical Research* 97: 19909–19928.

Zhao L and Jordan TH (1998) Sensitivity of frequency-dependent travel times to laterally heterogeneous, anisotropic Earth structure. *Geophysical Journal International* 133: 683–704.

Zhao L, Jordan TH, and Chapman CH (2000) Three-dimensional Frechet differential kernels for seismic delay times. *Geophysics Journal International* 141: 558–576.

Zhao L, Jordan TH, Olsen KB, and Chen P (2005) Frechet kernels for imaging regional earth structure based on three-dimensional reference models. *Bulletin of the Seismological Society of America* 95: 2066–2080.

Zhou HW (1996) A high resolution P wave model for the top 1200 km of the mantle. *Journal of Geophysical Research* 101: 27791–27810.

Zhou H (2004) Multi-scale tomography for crustal P and S velocities in southern California. *Pure and Applied Geophysics* 161: 283–302.

Zhou Y, Dahlen FA, and Nolet G (2004) 3-D sensitivity kernels for surface-wave observables. *Geophysical Journal International* 158: 142–168.

Zhou Y, Nolet G, Dahlen FA, and Laske G (2006) Global upper-mantle structure from finite-frequency surface-wave tomography. *Journal of Geophysical Research* 111: B04304. http://dx.doi.org/10.1029/2005JB003677.

Zhu H, Bozdağ E, Peter D, and Tromp J (2012) Structure of the European upper mantle revealed by adjoint tomography. *Nature Geoscience* 5: 493–498. http://dx.doi.org/10.1038/ngeo1501.

Zielhuis A and Nolet G (1994) Shear wave velocity variations in the upper mantle beneath Europe. *Geophysical Journal International* 117: 695–715.

This page intentionally left blank

1.11 Crust and Lithospheric Structure - Global Crustal Structure

WD Mooney, USGS, Menlo Park, CA, USA

Published by Elsevier B.V.

1.11.1	**Introduction, Purpose, and Scope**	339
1.11.2	**Geology, Tectonics, and Earth History**	340
1.11.3	**Seismic Techniques for Determining the Structure of the Crust and Uppermost Mantle**	341
1.11.3.1	Active-Source Data	341
1.11.3.1.1	Seismic refraction/wide-angle reflection profiles	343
1.11.3.1.2	Seismic reflection profiles	344
1.11.3.2	Passive-Source Data	346
1.11.3.2.1	Surface waves	347
1.11.3.2.2	Seismic tomography	348
1.11.3.2.3	Receiver functions	348
1.11.3.2.4	Ambient noise analysis	348
1.11.3.3	Laboratory Studies	348
1.11.3.3.1	Velocity–density relations	348
1.11.3.3.2	V_p–V_s relations and Poisson's ratio	348
1.11.3.3.3	Seismic anisotropy	349
1.11.4	**Nonseismic Constraints on Crustal Structure**	351
1.11.4.1	Gravity	351
1.11.4.2	Aeromagnetics	353
1.11.4.3	Geoelectrical Measurements	353
1.11.4.4	Heat Flow Data	354
1.11.4.5	Borehole Data	354
1.11.4.6	Surface Geology, Exposed Deep Crustal Sections, Xenoliths, and Geochemical Data	354
1.11.5	**Structure of Oceanic Crust and Continental Margins**	355
1.11.5.1	Typical Oceanic Crust	355
1.11.5.2	Mid-Ocean Ridges	357
1.11.5.3	Oceanic Plateaus and Volcanic Provinces	357
1.11.5.4	Ocean Trenches and Subduction Zones	360
1.11.5.5	Oceanic Island Arcs	360
1.11.5.6	Passive Continental Margins	361
1.11.6	**Structure of Continental Crust**	362
1.11.6.1	General Features	362
1.11.6.2	Principal Crustal Types	362
1.11.6.3	Correlation of Crustal Structure with Tectonic Provinces	366
1.11.7	**Global Crustal Models**	367
1.11.7.1	The Sedimentary Cover	371
1.11.7.2	The Crystalline Crust and Uppermost Mantle	371
1.11.8	**Discussion and Conclusions**	371
Acknowledgments		372
References		372

1.11.1 Introduction, Purpose, and Scope

The Earth's crust preserves the record of the evolution of our planet, provides our natural resources, and presents social challenges in the form of natural hazards, such as earthquakes and volcanoes. Despite its importance, the clear recognition of a universal crust encircling the Earth dates back to slightly more than 100 years (Mohorovičić, 1910). In fact, as recently as the 1960s, it was hypothesized that the ocean floor was entirely composed of serpentinized peridotite (hydrated ultramafic mantle rocks; Hess, 1962), a view that would have restricted true crustal material (i.e., silica-rich rocks) to the continents and its margins. Today, it is well established that melt extracted from the mantle forms an outer crust in most regions of the Earth, oceanic and continental.

The Earth's crust has profound implications for all aspects of the planet's physical state and evolution. The process of crustal formation led to the complementary formation of an underlying mantle lithosphere, classically referred to by seismologists as 'the mantle lid' due to its finite (c. 50–250 km) thickness (Gutenberg, 1959; Oliver et al., 1959). The physical properties of the crust plus mantle lithosphere modulate the rate at which heat is released to the Earth's surface, regulates mantle convection, determines the location of earthquakes and

 http://dx.doi.org/10.1016/B978-0-444-53802-4.00010-5

volcanoes, and more generally defines the rules for plate tectonic processes.

The foundations of seismic studies of the crust and upper mantle were laid in the period 1909–69 when the results of many pioneering studies provided a global view of the structure of the Earth's crust (Table 1). However, most of these early studies were hindered by technical limitations that yielded field observations that presented an aliased image of the crust. It is not surprising that, with some notable exceptions (Meissner, 1967; Mueller, 1977), these data were commonly interpreted in terms of two or more homogeneous layers, the upper layer (compressional wave, $V_P = 6.0–6.2\ km\ s^{-1}$) assigned a granitic composition and the lower layer ($V_P = 6.5–7.0\ km\ s^{-1}$), a basaltic composition (Birch, 1952; Pakiser and Steinhart, 1964). The advent of higher-resolution data has revealed a much richer and complex picture of the crust, as well as many unresolved questions. Among the outstanding questions are the age and physical properties of the Moho and midcrustal seismic discontinuities, the possible presence of deep crustal fluids, the geometry of crustal faults at depth, crustal modification by lateral crustal flow, and the magnitude of crustal seismic anisotropy.

Our understanding of the seismic structure of the crust began to change radically with the advent of deep seismic reflection profiling (Meissner, 1973; Oliver et al., 1976) and the development of numerous stand-alone, portable seismographs used for seismic refraction/wide-angle reflection profiling (Healy et al., 1982). These data provided an unaliased view of the crust to frequencies of 20 Hz and higher (corresponding to 300 m and higher resolution within the crust). Compilations of crustal seismic data into global models can be traced to the global Moho map of Soller et al. (1982). This map, while highly informative, did not easily lend itself to use in numerical calculations that make quantitative corrections for the crust. A major step forward was the publication of the global $2° \times 2°$ 3SMAC model (Nataf and Ricard, 1996) that for the first time permitted the calculation of crustal corrections to seismological and other geophysical observations. In the past decade, a tremendous amount of new seismic field observations have been made, thereby making it possible to improve the accuracy of previous global crustal models (Mooney et al., 1998; Pasyanos et al., 2004). In this chapter, we document these advances and summarize the current status of global crustal models.

1.11.2 Geology, Tectonics, and Earth History

The Earth's lithosphere is qualitatively defined as the cold, upper layer of the Earth and is divided into large blocks called tectonic plates (Figure 1). The lithosphere is on the order of 100 km thick, being the thinnest (20–100 km) in oceanic regions and the thickest (50–250+ km) in continental regions. The base of the crust is the depth within the lithosphere where V_P increases from about $6.5–7.3\ km\ s^{-1}$ to greater than $7.6\ km\ s^{-1}$ (James and Steinhart, 1966). This boundary between the lower crust and the upper mantle is called the Mohorovičić discontinuity (Jarchow and Thompson, 1989; Mohorovičić, 1910) and is usually at a depth (below sea level) of 10–14 km for oceanic crust and 30–50 km for

Table 1 Classical references concerning the Earth's crust and uppermost mantle: The first 60 years (1909–1969)

Year	*Authors*	*Areas covered*	*J/A/B*
1910	Mohorovičić	Europe	B
1925	Conrad	Europe	J
1926	Byerly	N America	J
1932	Byerly and Dyk	N America	J
1932	Gutenberg	N America	J
1932	Gutenberg et al.	World	J
1935	DeGolyer	World	J
1935	Heiland	World	J
1935	Jeffreys and Bullen	World	J
1936	Leet	Europe	J
1937	Ewing et al.	Atlantic	J
1938	Slichter	World	J
1940	Jakosky	World	B
1940	Jeffreys and Bullen	World	J
1940	Jeffreys	World	B
1943	Woollard	N America	J
1949	Mintrop	World	J
1951	Junger	N America	J
1951	Tuve	World	
1951	Slichter	N America	J
1952	Birch	World	J
1952	Hersey et al.		J
1953	Tatel et al.	World	J
1953	Hodgson	N America	J
1953	Tatel et al.	World	J
1953	Tuve	World	J
1954	Ewing and Press	World	J
1954	Tuve et al.	World	J
1954	Katz	N America	J
1955	Ewing et al.	N America	A
1953	Tatel et al.	World	J
1955	Tatel and Tuve	World	A
1956	Press	World	B
1957	Oliver and Ewing	World	J
1958	Officer	World	B
1958	Oliver and Ewing	World	J
1959	Gutenberg	World	B
1959	Woollard	World	J
1959	Oliver et al.	World	J
1959	Richards and Walker	N America	J
1960	Birch	World	J
1960	Willmore	World	J
1960	Brune et al.	World	J
1961	Anderson	World	J
1961	Birch	World	J
1961	Closs and Behnke	Australia	J
1961	Cram	N America	J
1961	Jensen	World	J
1961	Steinhart and Meyer	World	B
1962	Oliver	World	J
1962	Alexander	N America	J
1962	Hess	World	A
1963	Hill	Oceans	A
1963	Pakiser	N America	J
1963	Brune and Dorman	N America	J
1963	Jackson et al.	N America	J
1963	Wilson	World	J
1963	Raitt	World	A
1964	Anderson and Archambeau	World	J

(*Continued*)

Table 1 (Continued)

Year	Authors	Areas covered	J/A/B
1964	Simmons	World	J
1964	McEvilly	World	J
1964	Pakiser and Steinhart	World	A
1964	Press	World	J
1964	Crampin	World	J
1964	Kovach and Anderson	World	J
1965	Christensen	World	J
1965	Roller	N America	J
1965	Willden	N America	J
1965	Dix	World	J
1965	Kanasewich and Cumming		J
1965	Jackson and Pakiser	N America	J
1965	Roller	N America	J
1965	Willden	N America	J
1965	Wilson	World	J
1966	Bath and Stefánsson	World	J
1966	Berry and West	N America	J
1966a,b	Christensen	World	J
1966	Ewing et al.	N America	J
1966	James and Steinhart	World	A
1966	Smith et al.	World	J
1966	Crampin	Eurasia	J
1966	Ewing et al.	N America	J
1966	Woollard	N America	J
1967	Anderson	World	J
1967	Steinhart	World	A
1967	Meissner	World	J
1967	Shor		J
1968	Press	Europe	J
1969	Hart	World	B
1969	Herrin	N America	J
1969	Zietz	N America	J
1969	Brune	World	J
1969	Herrin	N America	J
1957	Baranov	World	J
1967	Bateman and Eaton	N America	J

continental crust. The Earth's crust, which was originally extracted from the mantle, constitutes only about 0.7% of the total mass of the crust–mantle system (Taylor and McLennan, 1985). The Mohorovičić discontinuity, commonly referred to as the Moho, may not always be the base of the crust in a petrologic sense because the seismic definition of crustal material (V_p less than 7.6 km s^{-1}) may not include high-grade metamorphic rocks (e.g., eclogite) or a crust–mantle mix of mafic and ultramafic rocks (Griffin and O'Reilly, 1987; Rudnick and Gao, 2005). Further seismic discontinuities below the crust divide the interior of the Earth into the upper mantle, transition region, lower mantle, outer core, and inner core. These other discontinuities are discussed in companion papers in this volume.

As a consequence of plate tectonics (**Figure 2**), oceanic crust and continental crust vary systematically in their principal physical properties, including density, thickness, age, and composition. Continental crust has an average thickness of 39 km, density of 2.84 g cm^{-3}, and an average age of 1500 Ma, whereas the oceanic crust (excluding 4–5 km of seawater) has an average thickness of about 6 km and density of 3 g cm^{-3} and is everywhere younger than 200 Ma. Oceanic crust is largely made up of theoleiitic basalt, which has a dark, fine-grained texture that formed from rapidly cooling magma. In contrast, continental crust ranges in thickness from 20 km in the Afar Triangle, northeast Africa, to about 80 km in the southern Tibetan Plateau. Ninety percent (by area) of the continental crust, however, is between 22 and 56 km thick (Mooney et al., 1998).

This chapter presents a holistic view of the Earth's crustal structure and summarizes the types of velocity and density models that characterize the crust on a global scale. In recent years, several seismological techniques have been used to explore the crust. These include seismic refraction/wide-angle reflection profiles, near-vertical incidence reflection profiles, receiver functions, local earthquake tomographic inversions, and inversions of ambient noise data. Some of these survey techniques have been in use for more than a half century, and the results are reported literally in thousands of publications (Prodehl and Mooney, 2012). In contrast, the inversion of seismic ambient noise to determine crustal structure is a relatively new and powerful technique (Campillo and Paul, 2003; Shapiro et al., 2005). Taken together, the results from all of these techniques make it possible to provide a comprehensive crustal model for the whole Earth, as well as higher-resolution regional models.

1.11.3 Seismic Techniques for Determining the Structure of the Crust and Uppermost Mantle

Seismic techniques provide the highest-resolution geophysical measurements of the structure of the crust and uppermost mantle. These techniques may be divided into those using active sources versus passive sources. Active sources are man-made seismic sources such as vibrators, air guns, and borehole explosions. Passive sources are derived from naturally occurring seismicity, including P- and S-wave body waves, Love and Rayleigh waves, and scattered waves. We discuss active and passive seismic techniques in turn.

1.11.3.1 Active-Source Data

Active-source seismic measurements of the structure of the crust have been conducted on a worldwide basis (Meissner, 1986; Mooney et al., 2002; Percival et al., 2012; Prodehl and Mooney, 2012; Soller et al., 1982). Seismic studies of the deep continental crust that utilize man-made sources are classified into two basic categories, seismic refraction/wide-angle reflection profiles and near-vertical incidence seismic reflection profiles, depending on their field acquisition parameters. Seismic refraction/wide-angle reflection profiles provide reliable information regarding the distribution of seismic velocities within the crust and are very effective in mapping crustal thickness (**Figure 3**). In contrast, seismic reflection data provide an image of the crust at a finer scale (50 m in the vertical and horizontal dimensions). As a result, seismic reflection and refraction/wide-angle reflection data have complementary strengths: reflection data provide a detailed structural image of the crust, whereas refraction data provide a robust estimate of the seismic velocity distribution in the crust for both V_p and

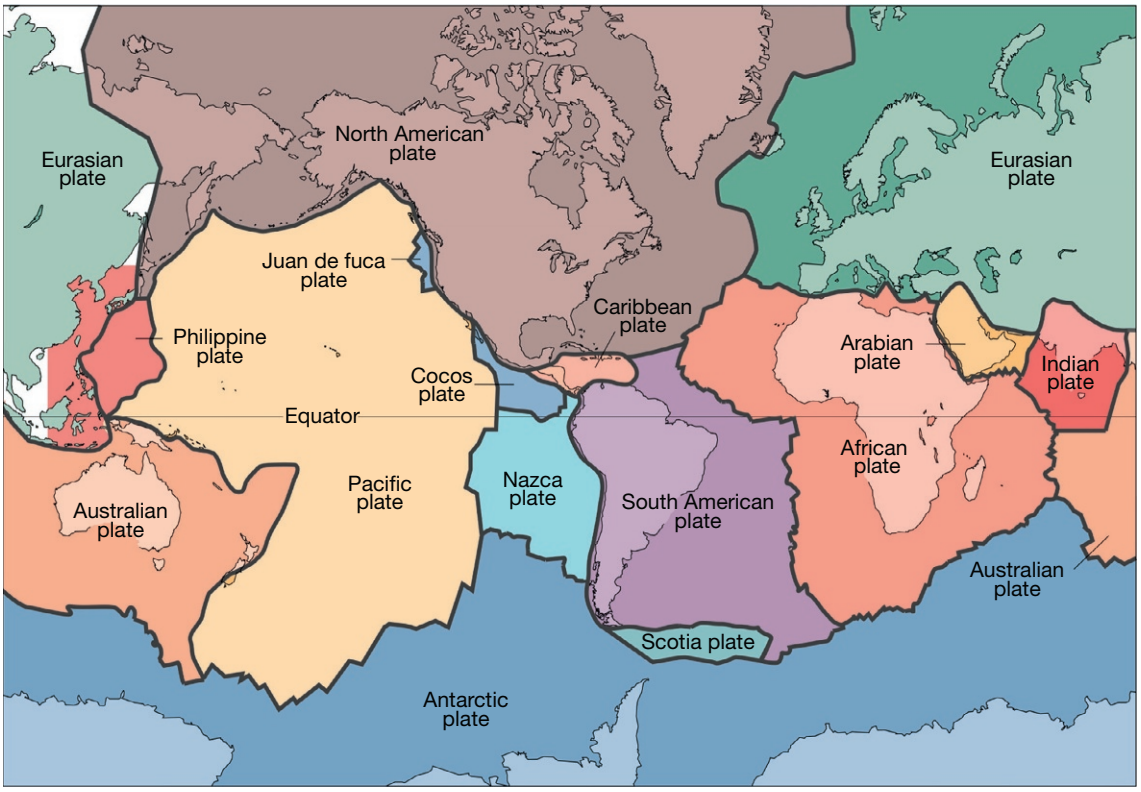

Figure 1 The 15 major tectonic plates on Earth, and the boundaries between these plates (Simkin et al., 2006). New oceanic lithosphere is constantly being produced at mid-ocean ridges (divergent plate boundary) and later subducted back into the mantle at convergent plate boundaries (**Figure 2**). Plate motions led to the recycling of oceanic crust, arc volcanism, and compression at convergent boundaries. This chapter describes the complex and laterally variable deep seismic structure of the Earth's crust.

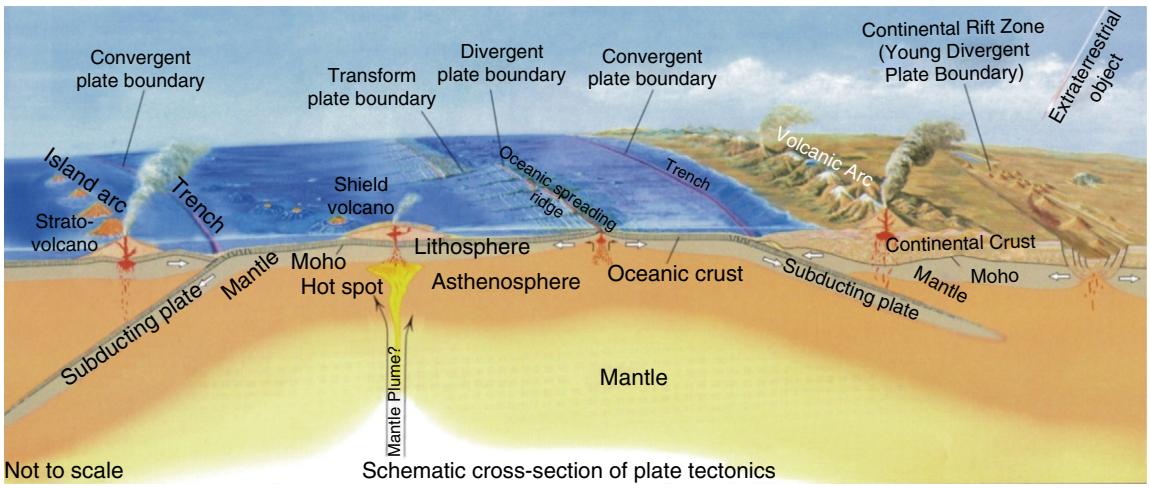

Figure 2 A cross section of the Earth's surface, indicating divergent (oceanic spreading ridge) and convergent (subducting plate) plate boundaries (Simkin et al., 2006). Active magmatic arcs at convergent boundaries increase the volume of continental crust and continental rift zones led to crustal thinning. We summarize the deep structure of these and other features of the Earth's crust.

V_s (shear-wave velocity). Key papers that describe the acquisition and analysis of active-source data are provided in Table 2.

The most common sources used in land profiles are chemical explosions and mechanical vibrators. Chemical explosions are generally composed of ammonium nitrate compounds that are detonated in a borehole at a depth of 20–50 m in the ground. In contrast, a vibrator truck weighs several tons and has a heavy steel plate that is pressed against the ground that vibrates at increasing frequencies (5–60 Hz) for up to 30 s. This method requires cross correlation of the recordings with the

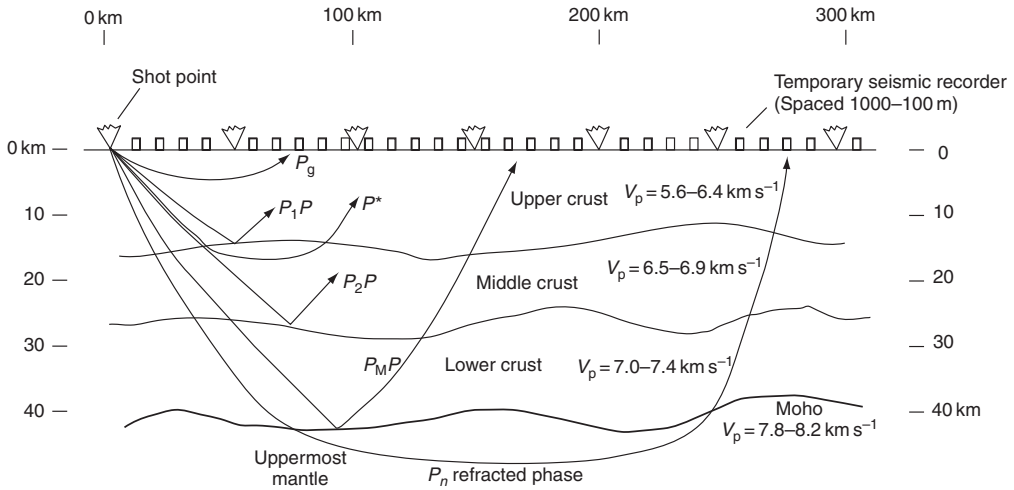

Figure 3 Ray paths for a continental seismic refraction/wide-angle reflection profile for crust with a typical seismic velocity structure found beneath a stable craton. The crust–mantle boundary (Moho) is a continuous feature, but intracrustal boundaries may be discontinuous laterally and several kilometers wide vertically. Commonly, shot points are spaced 50 km apart (or closer for higher resolution); temporary seismic recorders are spaced 1000–100 m apart.

source signal in the data processing stage. The most common sources in marine profiles are the air gun, in which a bubble of very high-pressure air is released into water, and, prior to modern environmental concerns for marine life, explosive charges. Long-range seismic refraction data have also been recorded from nuclear sources, particularly in the former Soviet Union (Egorkin et al., 1987; Pavlenkova, 1996). Due to the strength of these nuclear explosions, such long-range profiles probed not only the crust but also the entire upper mantle to a depth of 660 km (Mechie et al., 1993; Morozov et al., 1998, 1999; Ryberg et al., 1995, 1996).

1.11.3.1.1 Seismic refraction/wide-angle reflection profiles

Seismic refraction/wide-angle reflection profiles are recorded with relatively widely spaced (100–5000 m) geophones (typically with vertical component seismometers) and long offsets (100–500+ km) between sources and receivers (Figure 3). The data from these seismic profiles commonly contain strong wide-angle reflection phases (Figure 4) and provide excellent constraints on seismic velocity within the lithosphere.

Profiles with sources all to one side of the receivers are referred to as unreversed refraction profiles. Unreversed refraction profiles record only apparent velocities and are interpreted as if the crust was composed of flat-laying, uniformly thick layers. Split refraction survey lines, which in some ways are similar to simple reversed refraction lines, have generally been used for oceanic crust. Reversed refraction surveys are more reliable, and the technique used for interpreting them is described in Mooney (1989), Chulick (1997), Zelt and Smith (1992), Braile et al. (1995), Zelt (1999), and Prodehl and Mooney (2012). Reversed refraction profiles generally have multiple shot points that provide overlapping coverage (Figure 5). The most reliable way to determine a velocity structure from seismic refraction data is to compute detailed (two-dimensional) 2-D ray-theoretical travel times (Figure 5(b)) and synthetic (theoretical) seismograms and compare these with the observed data. This modeling must take into

Table 2 Selected papers on data analysis methods in crustal seismology: active sources

Aki	1982
Aki and Lee	1976
Aki et al.	1976
Ansorge et al.	1982
Berry and West	1966
Bessonova et al.	1974
Boore	1972
Bouchon	1982
Braile and Chiang	1986
Braile et al.	1995
Campman and Orcutt	1985
Červený	1972
Červený et al.	1977
Červený and Pšeničník	1984
Chapman	1978
Claerbout	1976, 1985
Closs and Behnke	1961
Deichmann and Ansorge	1983
Dix	1965
Dobrin	1976
Dohr	1970
Dorbin	1976
Ewing et al.	1957
Finlayson and Ansorge	1984
Fuchs and Mueller	1971
Gajewski and Pšeničník	1987
Giese	1976
Giese et al.	1976
Haberland	2003
Hajnal	1986
Hale and Thompson	1982
Heacock	1971, 1977
Hole	1992
Hole and Zelt	1995
Hole et al.	1992
Hwang and Mooney	1986
Kelley et al.	1976

(*Continued*)

Table 2 (Continued)

Kennett	1974, 1983
Kind	1978
Klemperer and Luetgert	1987
Klemperer and Oliver	1983
Levander and Holliger	1992
Ludwig et al.	1970
Lutter et al.	1990
Mair and Lyons	1976
Makovsky et al.	1996a,b
McEchan and Mooney	1980
Menke	1989
Milkereit et al.	1985
Mooney	1989
Mooney and Brocher	1987
Mooney and Meissner	1992
Mooney et al.	2002
Müller	1985
Nelson et al.	1996
Sandmeier and Wenzel	1986, 1990
Sandmeier and Wenzel	1990
Scheriff and Geldhart	1982, 1983
Schilt et al.	1979
Telford et al.	1976
Willmore and Bancroft	1960
Zandt and Owens	1986
Zelt	1999
Zelt and Barton	1998
Zelt and Smith	1992
Zelt et al.	2003
Zelt et al.	1999

account (1) the source time function, which could be from an explosion, earthquake, air gun, or vibrator; (2) the effects of transmission through the crust; and (3) the response of the detection systems, which may be seismometers, amplifiers, and filters. For trial-and-error forward modeling, an initial velocity model is constructed and is adjusted until the synthetic seismograms match the recorded seismograms to the desired degree. For inverse methods (e.g., Zelt and Smith, 1992), seismic travel times are used to obtain a best fitting model, starting from the near surface and moving down through the crust. Recent developments of low-cost, ultracompact seismic recorders that can be deployed by the thousands hold the promise of true 3-D imaging of the crust.

Seismic velocities in the crust are primarily determined by five factors: mineralogical composition, confining pressure, temperature, anisotropy, and pore fluid pressure. In order to draw inferences about the mineralogical composition of the deep crust, however, one must first estimate the contribution of the other four properties. Confining pressure is easily calculated from depth of burial, and temperature can be estimated from the surface heat flow. The quantitative effect on measured seismic velocities due to seismic anisotropy (Rabbel and Mooney, 1996) and pore fluid pressure (Hyndman, 1988; Manning and Ingebritsen, 1999) is more difficult to estimate.

1.11.3.1.2 Seismic reflection profiles

Near-vertical incident seismic reflection data provide the most detailed images of crustal structure. Data are recorded with closely spaced (5–100 m) geophones and sources that yield a high-resolution image of the internal structure of the crust and

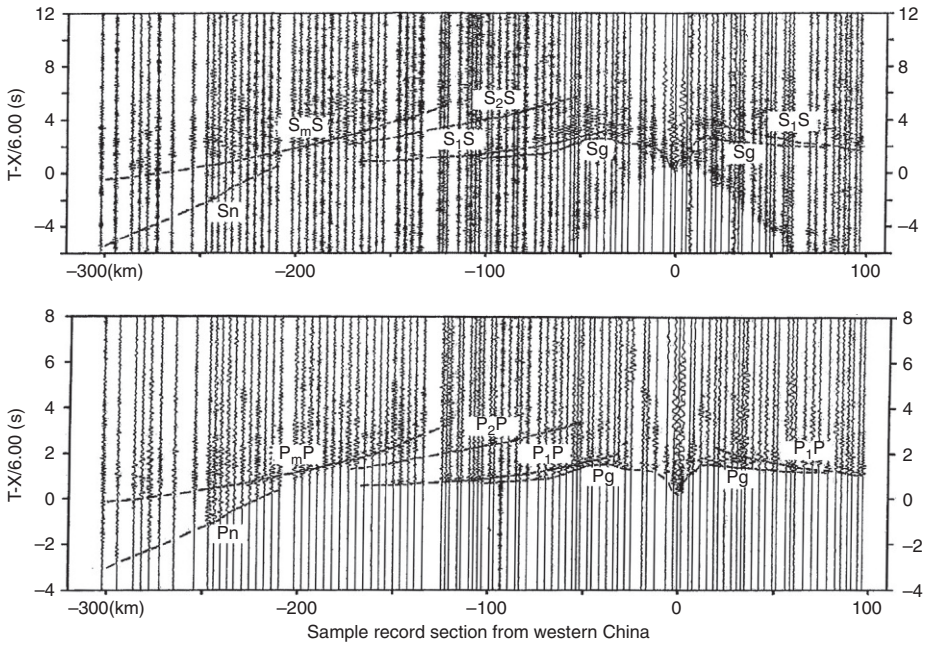

Figure 4 Sample seismic record section from western China. Top: Shear (S)-wave record section with a reduction velocity of 3.46 km s^{-1}. This is a split-spread profile, with the shot point at 0 km; seismic phases as defined in **Figure 3**; Sg, direct arrival; S1S, reflection boundary between the upper crust and the middle crust; S2S, reflection from middle crust and lower crust; SmS, reflection from Moho; Sn, refraction from uppermost mantle. Bottom: Compressional (P)-wave record section with a reduction velocity of 6.0 km s^{-1}; seismic phases as defined for S-waves above. Reproduced from Wang CY, Chen W, and Mooney WD (2003) Three-dimensional velocity structure of the crust and upper mantle in southwestern China and its tectonic implications. *Journal of Geophysical Research* 108: 2442, http://dx.doi.org/10.1029/2002JB001973; Wang XY, Mooney WD, and Yuan XC (2003) The crustal structure from the Altai Mountains to the Altyn Tagh fault, northwest China. *Journal of Geophysical Research* 108: 2322, http://dx.doi.org/10.1029/2001JB000552.

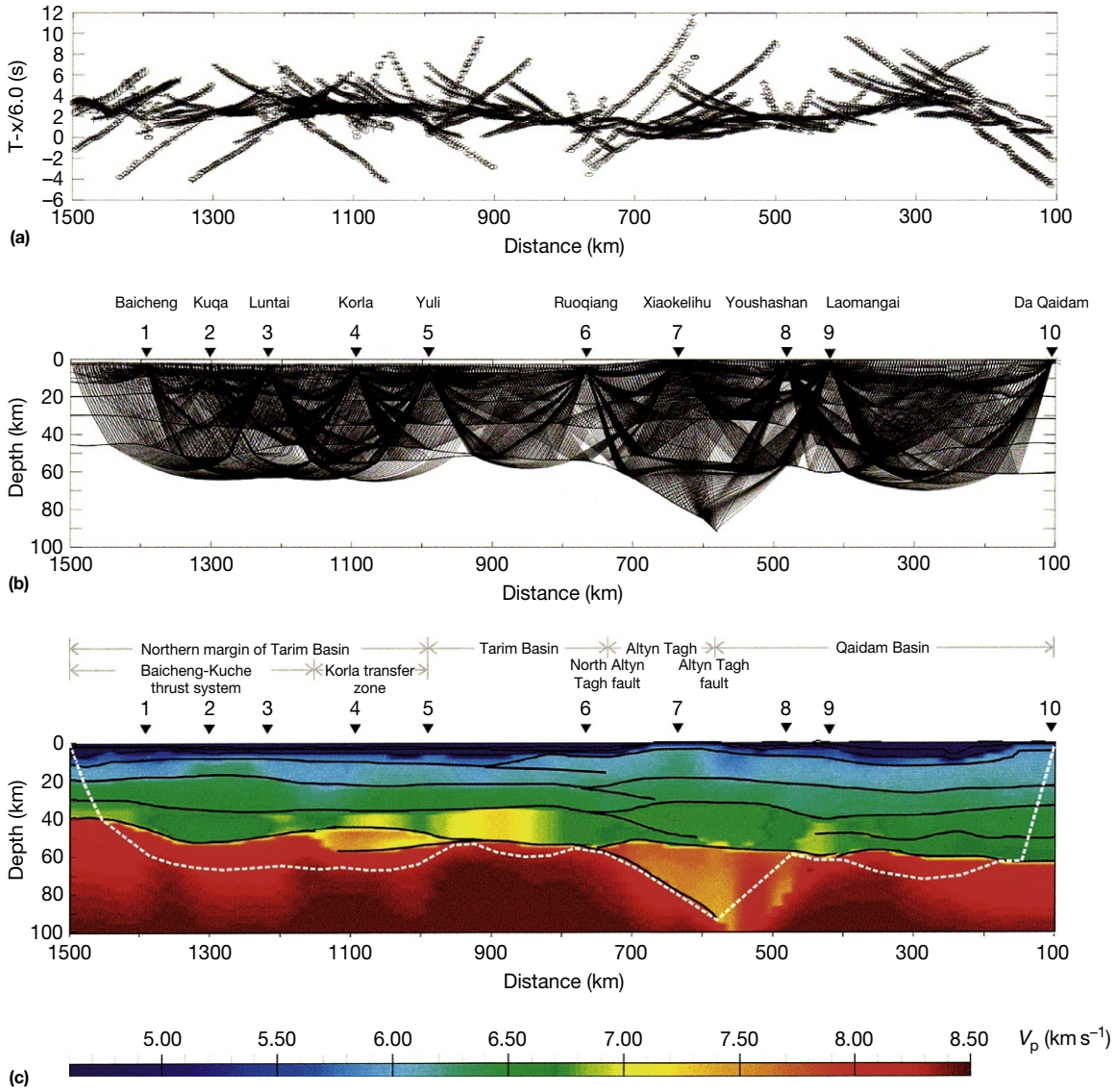

Figure 5 Modeling results along the seismic refraction/wide-angle reflection profile at the northern margin of the Tibetan Plateau. (a) Overlapping and reversing travel time curves; (b) Ray tracing through the crustal model showing dense subsurface ray coverage that provides excellent constraints on seismic velocities. (c) Crustal and uppermost mantle seismic velocity (V_p) model. Both V_p and V_s can be estimated for the crust from these data. Pn velocity ranges from 7.8 to 8.2 km s^{-1}. Reproduced from Zhao JM, Mooney WD, Zhang X, Li Z, Jin Z, and Okaya N (2006) Crustal structure across the Altyn Tagh Range at the northern margin of the Tibetan Plateau and tectonic implications. *Earth and Planetary Science Letters* 241: 804–814.

Moho, but such data generally do not constrain seismic velocities in the deeper (middle and lower) crust. P-waves from an energy source, such as a vibrator, buried explosive, or air gun, are reflected by intracrustal interfaces and recorded by geophones located close (0.1–10 km) to the source. In the data processing stage, the effects of the source and receiver are removed from the recorded seismograms through a process called deconvolution, allowing for higher-resolution images of the structure. The seismic reflection data are commonly migrated, a processing step that shifts the reflectors into their correct spatial locations.

Seismic waveform inversion exploits the full information content within the recorded wavefield (Pratt, 1999; Tarantola, 1984) and has been applied to both near-vertical incident seismic reflection and seismic refraction/wide-angle reflection data. The inversion procedure, usually in the frequency–space domain, iteratively refines a starting model to reduce the waveform misfit between observed and model data (Hu et al., 2009; Pratt, 1999; Sirgue and Pratt, 2004). The method can be applied to any wavefield that interrogates the seismic velocity structure of the crust (Aster et al., 2012; Ben-Hadj-Ali et al., 2008).

The seismic properties that are most readily obtained from reflection data are reflectivity patterns, and these correlate with distinct geologic settings. For example, the European North Sea has undergone Cenozoic extension that is evident in deep seismic reflection data as tilted horst and grabens, a shallow (30 km) distinct Moho, and a dipping shear zone (Flannan reflections) within the upper mantle (**Figure 6**). When

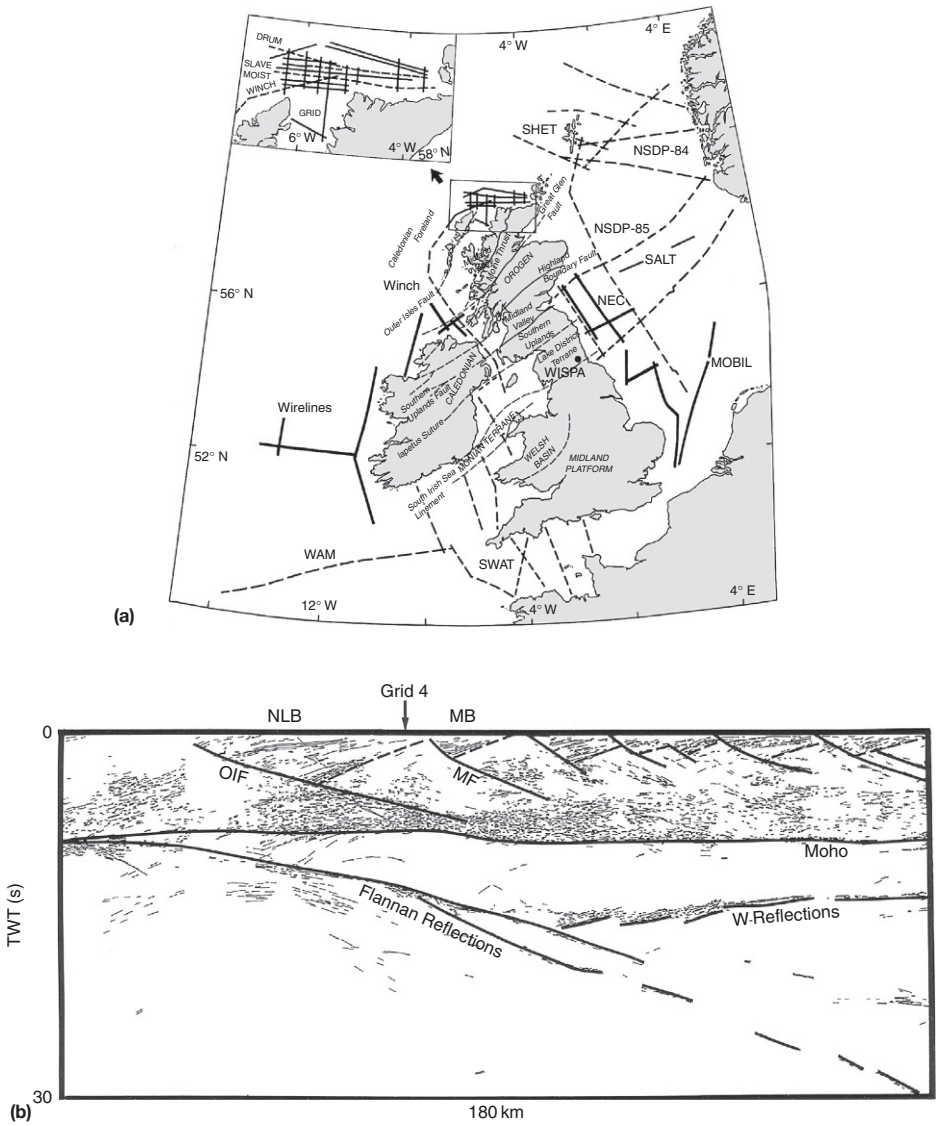

Figure 6 Deep seismic reflection imaging of crustal and upper mantle fault zones. (a) Location map for the British Isles with marine seismic reflection profile lines indicated. (b) Seismic profile DRUM located off the north coast of Scotland (see inset in panel (a)). This profile shows brittle normal faults within the upper crust that merge into a zone of diffuse ductile deformation in the lower crust. The Moho is labeled at a two-way time of 10 s (30 km depth). The uppermost mantle shows two zones of reflections, labeled Flannan and W. The Flannan reflections are interpreted as a Caledonian suture that was reactivated as an lithospheric extensional fault (Flack and Warner, 1990). Modified from Matthews DH and BIRPS Core Group (1990) Progress in BIRPS deep seismic reflection profiling around the British Isles. *Tectonophysics* 173: 387–396.

reflectivity patterns are interpreted with complementary seismic velocity and nonseismic crustal parameters (discussed in the succeeding text), inferences regarding the composition and evolution of the crust can be made (Clowes et al., 1987).

The widespread observation of crustal reflectivity suggests that common processes account for its existence. The primary cause of crustal reflectivity is compositional and metamorphic layering within the crust. Regional and global plate stresses act to enhance crustal reflectivity by inducing lower crustal ductile flow that produces subhorizontal lamination. This ductile flow requires elevated temperatures and is therefore more common in the middle crust and lower crust.

1.11.3.2 Passive-Source Data

Techniques to investigate the seismic structure of the crust and uppermost mantle using passive seismic data have seen rapid development in the past two decades (**Table 3**). These developments can be attributed to the increased availability of higher-quality, broadband data from permanent seismic networks and temporary deployments. Passive seismic techniques began with surface-wave studies (Brune and Dorman, 1963; Ewing and Press, 1954) and progressed to seismic tomography (Aki and Lee, 1976; Aki et al., 1976; Nolet, 1987a,b), seismic receiver functions (Langston, 1977; Phinney, 1964; Vinnik, 1977), and most recently seismic ambient noise inversion

Table 3 Selected papers on data analysis methods in crustal seismology: passive sources

Authors	Year
Aki and Richards	1980
Ammon et al.	1990
Barmin et al.	2001
Bath and Stefánsson	1966
Bessonova et al.	1974
Bijwaard et al.	1998
Boore	1972
Boschi et al.	2004
Bostock et al.	2002
Bouchon	1982
Brune	1969
Brune and Dorman	1963
Brune et al.	1960
Bruneton et al.	2004
Burdick and Langston	1977
Cassidy	1992
Chapman	1978
Chen et al.	2005
Chimera et al.	2003
Crosson	1976
Curtis and Woodhouse	1997
Debayle and Lévêque	1997
Dziewonski	1989
Dziewonski and Anderson	1981
Eberhart-Phillips	1986
Ekström et al.	1997
Ewing and Press	1954
Grant et al.	1997
Hearn and Clayton	1986
Hearn and Ni	1994
Hearn et al.	1991, 2004
Hofsetter and Bock	2004
Hole et al.	2000
Huang et al.	2004
Humphreys and Clayton	1988
Humphreys et al.	1984
Iyer and Hirahara	1993
Jordan and Frazer	1975
Karagianni et al.	2005
Kennett and Engdahl	1991
Kind	1978
Knopoff	1972
Kovach	1978
Langston	1977
Langston et al.	2002
Lebedev and Nolet	2003
Lei and Zhao	2005
Levshin et al.	2005
Li and Romanowicz	1996
Liang et al.	2004
Liu et al.	2005
Maggi and Priestley	2005
Mahadeven	1994
Mandal et al.	2004
McEvilly	1964
Mitchell and Herrmann	1979
Mooney	1989
Nakamura et al.	2003
Nolet	1987a,b
Okabe et al.	2004
Owens and Zandt	1985
Pasyanos	2000
Pilidou et al.	2005
Priestly and Brune	1978
Ritzwoller and Lavely	1995
Ritzwoller et al.	2002a,b
Savage	1999
Shapiro et al.	2005
Su et al.	1994
Sun et al.	2004a,b
Thurber	1983, 1993
Thurber and Aki	1987
Tilmann et al.	2003
Vinnik et al.	2004
Wang et al.	2003a,b
Woodhouse and Dziewonski	1984
Worthington	1984
Yanovskaya and Kozhevnikov	2003
Yliniemi et al.	2004
Zandt and Owens	1986
Zhang and Lay	1996
Kennett	1983
Kind et al.	1995, 2002
Kissling	1998
Kissling et al.	2001
Langston	1994
Lees and Crosson	1989
Leveque et al.	1993
Levshin et al.	1989
Ma et al.	1996
Masters et al.	1996
Menke	1989
Nolet	1978, 1987a,b
Owens et al.	1984
Rapine et al.	2001
Ritzwoller et al.	2002a,b
Roecker et al.	2004
Tarantola and Nercessian	1984
Van Heijst and Woodhouse	1999
Vidale	1988, 1990
Vinnik	1977
Zhang and Thurber	2003
Zhao et al.	1992
Zhou et al.	2004, 2006

(Campillo and Paul, 2003; Shapiro et al., 2005). We discuss each of these in turn.

1.11.3.2.1 Surface waves

An earthquake near the Earth's surface will generate both Rayleigh and Love seismic surface waves. The amplitude of motion for these waves decreases exponentially with depth in the Earth, with longer-wavelength waves being more sensitive to the seismic velocity structure at great depth. This wavelength dependence of seismic velocity gives rise to the dispersion of surface waves and makes them a valuable tool for studying the velocity structure of the crust and mantle lithosphere. The analysis of seismic surface waves for crustal and upper mantle structure has been applied on a global basis and is particularly effective in determining the shear-wave structure (Boschi et al.,

2004; Bruneton et al., 2004; Chimera et al., 2003; Debayle and Lévêque, 1997; Friederich, 2003; Karagianni et al., 2005; Langston et al., 2002; Lebedev and Nolet, 2003; Levshin et al., 2005; Maggi and Priestley, 2005; Okabe et al., 2004; Panza et al., 2003; Pilidou et al., 2004, 2005; Shapiro and Ritzwoller, 2002). Thus, seismic surface waves provide complimentary information to seismic refraction data that often provide information only on the compressional-wave structure of the crust. Surface-wave data can also be used to measure seismic anisotropy within the uppermost mantle (Huang et al., 2004).

1.11.3.2.2 Seismic tomography

Local and distant (teleseismic) earthquake data can be used to determine crustal structure. Local seismic tomography uses earthquake arrivals at a network of seismic stations to determine crustal and upper mantle structure by examining the arrival times of many crisscrossing paths between the earthquakes and the seismometers. This technique, which is similar to medical tomography, has the potential to provide a 3-D picture of the crust and uppermost mantle. Local studies mainly provide information about the upper crust and middle crust (Lei and Zhao, 2005; Mandal et al., 2004; Salah and Zhao, 2003; Thurber, 1993; **Table 3**), whereas regional studies have better resolution within the uppermost mantle, especially for Pn velocity (Al-Lazki et al., 2003, 2004; Bannister et al., 1991; Calvert et al., 2000; Chen et al., 2003; Hearn and Ni, 1994; Hearn et al., 2004; Liang et al., 2004; McNamara et al., 1997; Mele, 1998; Nolet, 1987a,b; Parolai et al., 1997; Ritzwoller et al., 2002a,b; Sandoval et al., 2004; Sandvol et al., 2001, 2008). A second technique uses teleseismic data and generally provides an image that extends to greater depth (100+ km) but lacks high resolution of structure within the crust (Allen et al., 2002; Benoit et al., 2003; Bijwaard et al., 1998; Lippitsch et al., 2003; Liu et al., 2005; Petit et al., 1998). Tomographic studies are also effective at determining upper mantle seismic attenuation (Gung and Romanowicz, 2004).

1.11.3.2.3 Receiver functions

Estimating seismic structure from teleseismic receiver functions is a highly effective method of exploring the crust and upper mantle since it requires only a single broadband seismic station. Crustal layering is determined by the processing of a three-component station using teleseismic arrivals P-waves. The incident P-wave will undergo multiple conversions to S-waves at seismic boundaries within the uppermost mantle and crust. The analysis of these converted waves yields the shear-wave velocity structure beneath the station (Burdick and Langston, 1977; Langston, 1977; Owens et al., 1988; Phinney, 1964; Vinnik, 1977). The method works best with nearly horizontal layers, although forward modeling may be applied in regions with 3-D structure. An informative discussion of the method is given by Cassidy (1992). Numerous local and regional studies have been reported (e.g., Owens and Zandt, 1985; Ramesh et al., 2002), including studies of the crustal thickness in North Africa (Sandvol et al., 1998), Moho depth variation in California (Zhu and Kanamori, 2000), and various upper mantle studies (Kind and Vinnik, 1988; Kind et al., 2002; Yuan et al., 1997).

Recently, the receiver function method has been extended to consider converted, precursory P-waves that arrive just prior to the direct S-wave (Angus et al., 2006; Li et al., 2004). This is known as the S-wave receiver function method. S-wave receiver functions have a lower resolution than P-wave receiver functions due to lower-frequency data involved but are effective at identifying the base of the lithosphere (Li et al., 2004; Yuan and Romanowicz, 2010; Yuan et al., 2006).

1.11.3.2.4 Ambient noise analysis

Passive seismic methods that rely on distant earthquake sources have the disadvantage of lacking high-frequency seismic information that is lost because of intrinsic attenuation and scattering during wave propagation. An alternative approach uses ambient seismic noise to recover surface-wave dispersion data by cross correlating a random isotropic wavefield between a pair of receivers (Campillo and Paul, 2003; Shapiro and Campillo, 2004). This method can obtain approximate Green's functions of Rayleigh waves propagating between a pair of stations at relatively short periods (e.g., 5–20 s), and the dispersion curves may be inverted for S-wave crustal structure. This method is advantageous for data from temporary seismic networks because it does not rely on the recording of teleseismic events, which may not occur during the operation of the temporary network. The method has seen widespread application (e.g., Shapiro et al., 2005; Ward et al., 2013).

1.11.3.3 Laboratory Studies

1.11.3.3.1 Velocity–density relations

Seismic wave velocities and density are fundamental properties of Earth materials. Thousands of field and laboratory measurements have been made for V_p, but fewer measurements have been made of rock densities at depth, since these require a borehole. Compressional-wave velocity and density correlations are important because they allow estimates of crustal density for surface-wave inversions and gravity studies, and conversely, rock densities can be used to estimate seismic velocities (Christensen and Mooney, 1995). Classic studies of velocity–density relations include the Nafe–Drake curve (Nafe and Drake, 1957); Birch's (1961) law relating velocity, density, and mean atomic weight; and linear regression solutions for oceanic crust (Christensen and Salisbury, 1975). **Figure 7** presents average velocities for 29 rock categories at a depth of 20 km and a temperature of 309 °C, corresponding to an average geotherm, versus rock density (Christensen and Mooney, 1995). Two curves are drawn in **Figure 7**, a linear curve (solid line) and a nonlinear curve. The appropriate coefficients for both linear and nonlinear solutions are presented by Christensen and Mooney (1995).

1.11.3.3.2 V_p–V_s relations and Poisson's ratio

Seismic measurements of crustal structure more commonly report only V_p rather than V_p and V_s. There are several reasons for this. First, explosive or air gun sources generate primarily compressional-wave energy. Second, many field observations record on the vertical component of ground velocity. Third, shear-wave arrivals are often either weak or obscured by scattered seismic energy (coda). In the absence of measured

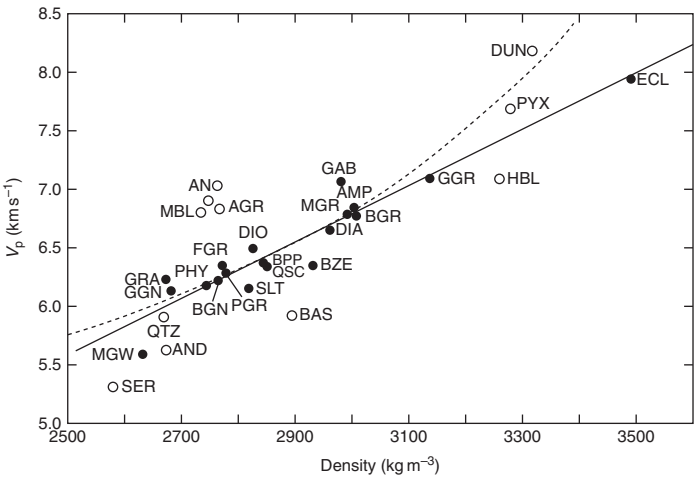

Abbreviation	Rock type
AGR	Anorthositic granulite
AMP	Amphibolite
AND	Andesite
ANO	Anorthosite
BAS	Basalt
BGN	Biotite (Tonalite) gneiss
BGR	Greenschist facies basalt
BPP	Prehnite-pumpellyite facies basalt
BZE	Zeolite facies basalt
DIA	Diabase
DIO	Diorite
DUN	Dunite
ECL	Mafic eclogite
FGR	Felsic granulite
GAB	Gabbro-norite-troctolite

Abbreviation	Rock type
GGN	Granite gneiss
GGR	Mafic garnet granulite
GRA	Granite-Granodiorite
HBL	Hornblendite
MBL	Calcite marble
MGR	Mafic granulite
MGW	Metagraywacke
PGR	Paragranulite
PHY	Phyllite
PYX	Pyroxenite
QSC	Mica quartz schist
QTZ	Quartize
SER	Serpentinite
SLT	Slate

Figure 7 Average velocity versus average density for a variety of rock types at a pressure equivalent to 20 km depth and 309 °C. Rock abbreviations are as follows. AGR, anorthositic granulite; AMP, amphibolite; AND, andesite; BAS, basalt; BGN, biotite (tonalite) gneiss; BGR, greenschist facies basalt; BPP, prehnite–pumpellyite facies basalt; BZE, zeolite facies basalt; DIA, diabase; DIO, dionite; DUN, dunite; ECL, mafic eclogite; FGR, felsic granulite; GAB, gabbro–norite–troctolite; GGN, granite gneiss; GGR, mafic garnet granulite; GRA, granite–granodiorite; HBL, hornblendite; MBL, calcite marble; MGR, mafic granulite; MGW, metagraywacke; PGR, paragranulite; PHY, phyllite; PYX, pyroxenite; QCC, mica quartz schist; QTZ, quartzite; SER, serpentinite; SLT, slate. Reproduced from Christensen NI and Mooney WD (1995) Seismic velocity structure and the composition of the continental crust: a global view. *Journal of Geophysical Research* 100: 9761–9788.

shear-wave speeds, it is necessary to estimate its value from V_p. A direct relation between V_s and V_p, therefore, is highly desirable for many studies. This is accomplished by using empirically derived V_p–V_s relations that are based on field borehole and seismic profiling data together with laboratory measurements. A recent study (Brocher, 2005) has derived empirical relations between V_p, V_s, and Poisson's ratio that can be used to estimate the ratio V_p–V_s or, equivalently, Poisson's ratio from a knowledge of V_p and rock type (i.e., sedimentary vs. crystalline rock). The empirical and regressional fits are only defined for V_p between 1.5 and 8.5 km s and fit the data remarkably well (Figure 8).

Conversely, the mineralogy of the crust can be estimated when both compressional-wave (V_p) and shear-wave (V_s) velocities are measured (Figures 8 and 9). The relation between V_p and V_s is commonly expressed by Poisson's ratio, which varies from 0.23 to 0.32 for most minerals, but quartz has a value of only 0.08 at room conditions (Christensen, 1996). Thus, the measurement of Poisson's ratio offers the means of distinguishing between felsic (quartz-rich) and mafic (quartz-poor) rocks.

1.11.3.3.3 Seismic anisotropy

Many minerals exhibit birefringence, which is a directional dependence of the speed of light through the mineral. This phenomenon is used by petrologists to identify minerals in a thin section ($\leq$1 mm) where a sample illuminated by polarized light is rotated under a microscope to reveal its birefringence. Likewise, elastic waves show a directional dependence in wave speed in many minerals. Perhaps, the most prominent example is the mineral olivine, which is a major constituent of the upper mantle. The discrepancy between Rayleigh and Love wave speeds was measured in the early 1960s (Anderson, 1961) and led to the recognition of seismic anisotropy in the mantle lid. At about the same time, laboratory measurements of metamorphic rocks demonstrated significant shear-wave anisotropy in the crust (Christensen, 1966b). These measurements demonstrated that seismic anisotropy is not only confined to the upper mantle but also plays a prominent role in the crust (Figure 10). Table 4 lists several key papers on the seismic properties, particularly anisotropy, of the uppermost mantle. Additional references for laboratory studies of the seismic properties of continental rocks can be found in Table 5.

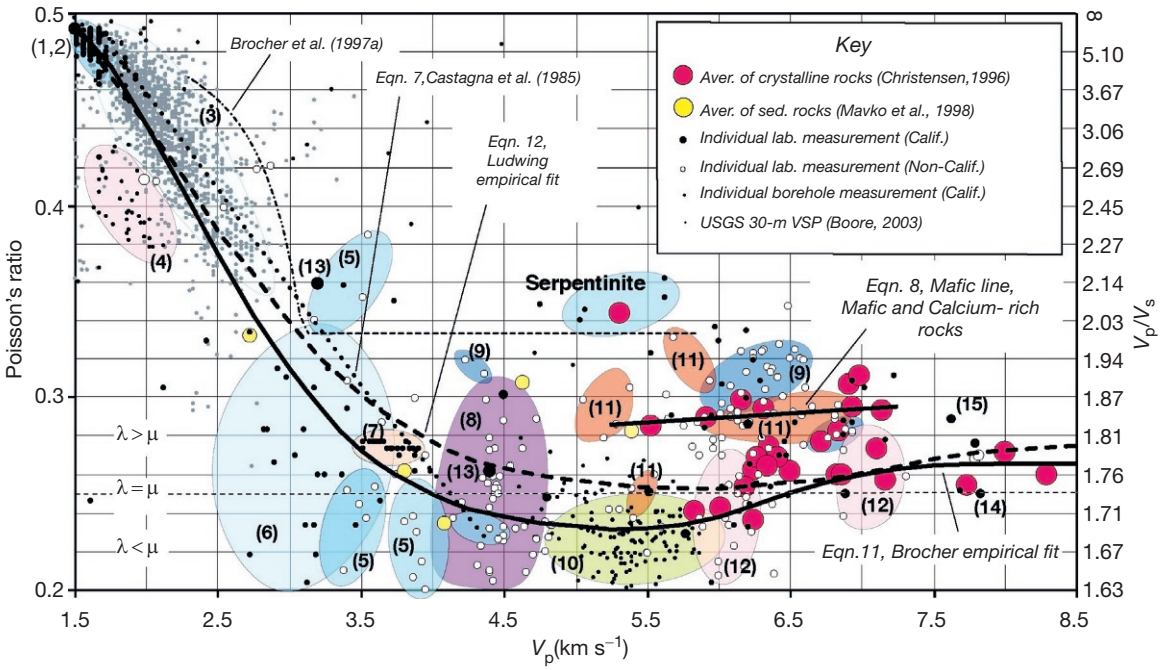

Figure 8 Poisson's ratio as a function of V_p for common lithologies. Colored ellipses highlight measurements reported by a single reference: bold numbers in parentheses link ellipses to similar studies. The thinner horizontal dashed line shows Poisson's ratio of 0.25 ($V_p/V_s = 1.73$) commonly assumed for the crust when the first Lame constant, λ, equals the shear modulus, μ. Reproduced from Brocher TM (2005) Empirical relations between elastic wavespeeds and density in the Earth's crust. *Bulletin of the Seismological Society of America*, 95 (6): 2081–2092.

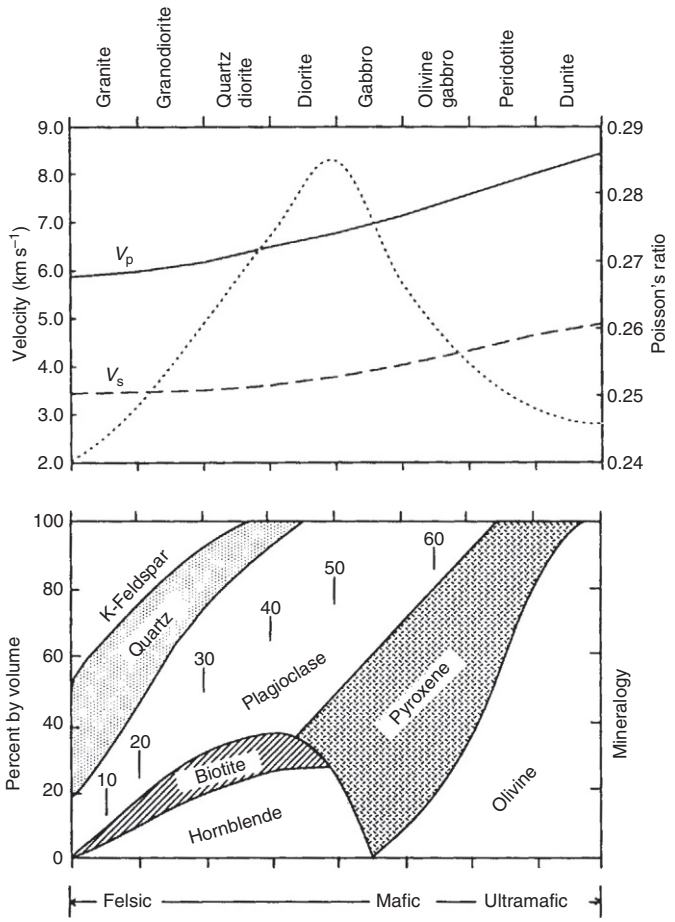

Figure 9 Variations in compressional-wave velocity (V_p), shear-wave velocity (V_s), and Poisson's ratio (σ) with mineral composition (Berry and Mason, 1959) for common igneous rock types. Anorthite content of plagioclase feldspar is shown within the plagioclase field. Reproduced from Christensen NI (1996) Poisson's ratio and crustal seismology. *Journal of Geophysical Research* 100: 3139–3156.

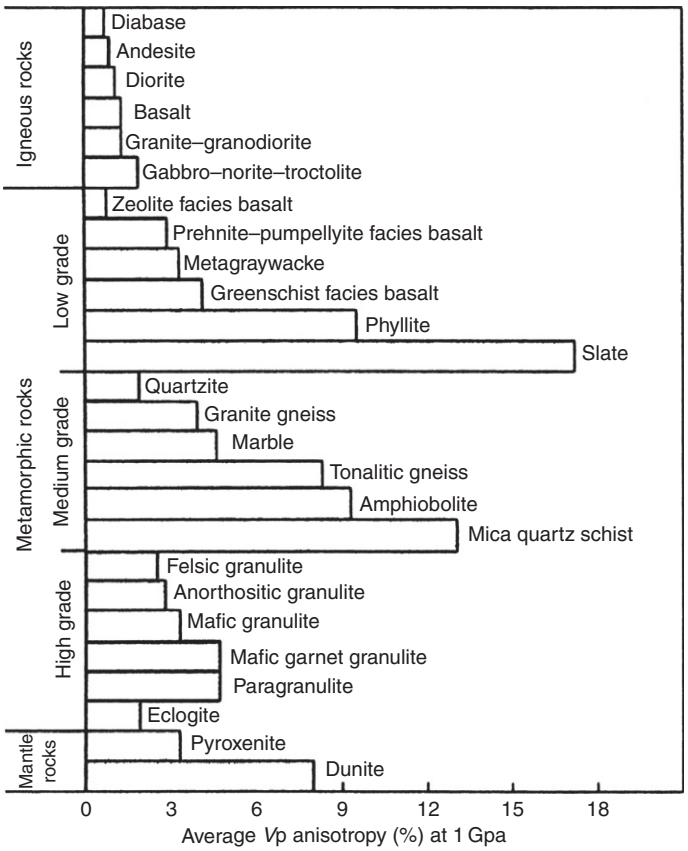

Figure 10 Average anisotropies, 100 $(V_{max} - V_{min})/V_{avg}$, at pressures corresponding to 35 km depth. Reproduced from Christensen NI and Mooney WD (1995) Seismic velocity structure and the composition of the continental crust: A global view. *Journal of Geophysical Research* 100, 9761–9788.

1.11.4 Nonseismic Constraints on Crustal Structure

All rock types have a variety of distinct, albeit nonunique, physical properties that include density, magnetic susceptibility, and conductivity. Geophysical surveying techniques to measure these properties are highly developed, and it is possible to make detailed maps of lateral changes in rock magnetic properties and conductivity and to estimate density variations. Advanced digital processing of such data enhances the reliably of interpretations, although resolution typically decreases with depth. Such nonseismic geophysical studies are widely used and have the capability to distinguish between competing geologic models of the structure of the crust. Key papers on laboratory studies of nonseismic properties of rocks are provided in Table 6.

1.11.4.1 Gravity

Gravity anomalies reveal rock density variations, with the amplitude of the anomaly proportional to the density contrast and thickness of the anomalous body. Short-wavelength (<250 km) gravity anomalies are usually correlated with crustal structures, while long-wavelength (<1000 km) gravity anomalies are correlated with lateral variations of mantle densities. Kane and Godson (1989) demonstrated that long-wavelength gravity highs are correlated with high mantle seismic velocities and gravity lows with low mantle velocities. Kaban et al. (2003) showed that upper mantle density variations contribute long-wavelength gravity anomalies ranging from −250 mGal to +150 mGal. The largest of these positive anomalies over the continents were associated with the Andes, the East European Platform, the Alpine–Mediterranean fold belt, and the central southeastern part of North America. The largest negative anomalies, indicating a thin lithosphere, are associated with vast Cenozoic regions of plume–lithosphere interaction: the East African Rift and the Basin and Range Province of the western North America.

New satellite measurements of the Earth's gravity field were begun in April 2002. The data from the Gravity Recovery and Climate Experiment satellites yield a complete measurement of the gravity field to harmonic degree 160 (300 km spatial resolution at the Earth's surface) every 30 days. These observations have improved the precision of the global gravity field by two orders of magnitude (Tapley et al., 2005).

The interpretation of gravity data is nonunique because measured gravity integrates the 3-D distribution of mass around the measurement location. For this reason, it is essential that, when modeling gravity data in terms of crustal structure, additional constraints be used. The most useful constraints come from coincident seismic data that define the seismic structure of the crust. The seismic model is converted into a density model using well-established relations (e.g., Christensen and Mooney, 1995), and the final model is

Table 4 Selected papers on the seismic properties of the uppermost mantle

Al-Lazki et al.	2003, 2004
Allen et al.	2002
Anderson	1967
Anderson and Archambeau	1964
Artemieva and Mooney	2001
Bamford	1977
Bannister et al.	1991
Baraganzi and Ni	1982
Benoit et al.	2003
Bibee and Shor	1976
Bijwaard et al.	1998
Brocher et al.	2003
Bruneton et al.	2004
Calvert et al.	2000
Canales et al.	2000a,b
Chen et al.	2003
DeShon and Schwartz	2004
Egorkin	2004
Egorkin et al.	1987
Enderle et al.	1996
Feng et al.	2004
Friedrich	2003
Fromm et al.	2004
Gilbert et al.	2005
Gorman et al.	2002
Grand and Helmberger	1984
Grand et al.	1997
Gung and Romanowitz	2004
Hearn	1984, 1999
Hearn	1996
Hearn and Ni	1994
Hearn et al.	1991, 2004
Herrin, E.	1969
Huang et al.	2004
Humphreys et al.	1984
Iyer and Hitchcock	1989
Jordan	1975, 1979, 1988
Jordan and Frazer	1975
Kennett and Engdahl	1991
Kennett et al.	1995
Kind et al.	2002
Lei and Zhao	2005
Li and Romanowicz	1996
Li et al.	2008
Liang et al.	2004
Lippitsch et al.	2003
Liu et al.	2005
Maggi and Priestly	2005
Matzel and Grand	2004
McNamara et al.	1997
Meissner et al.	2002
Mele	1998
Meyers et al.	1998
Montagner and Tanimoto	1990
Nolet	1977
Oliver	1962
Orcutt	1987
Panza et al.	2003
Pavlenkova	1996
Pilidou et al.	2004, 2005
Prodehl	1984
Rau and Wu	1995
Ringwood	1975
Ritzwoller and Levshin	1998
Ritzwoller et al.	2002a,b
Romanowicz	1991, 1995
Sandoval et al.	2004
Sandvol et al.	2001
Savage	1999
Shapiro et al.	2005
Silver	1996
Silver and Chan	1988
Simmons et al.	2012
Sleep	2003
Song et al.	2004
Spakman et al.	1993
Trampert and Woodhouse	1995
Van der Hilst et al.	1997
Van Heijst and Woodhouse	1999
Vinnik et al.	1992
Wang et al.	2002
Wortel and Spakman	2000
Yuan et al.	1997, 2000
Zhang and Lay	1996
Zhang and Tanimoto	1991
Zhang et al.	2004
Zhao and Xie	1993
Zhao et al.	1992

Table 5 Selected laboratory studies of seismic properties of rocks

Bass	1995
Berckhemer	1997
Birch	1960, 1961
Birch	1943, 1972, 1975
Carmichael	1982
Carmichael	1982
Christensen	1965, 1966a,b, 1979, 1982
Christensen	1966a,b, 1971, 1996
Christensen and Fountain	1975
Christensen and Mooney	1995
Christensen and Salisbury	1975
Christensen and Salisbury	1982
Clark	1966
Hamilton	1978
Jones and Nur	1983
Kern	1978
Kern et al.	1996
Nafe and Drake	1968
Nishimoto et al.	2005
Simmons	1964
Usher	1962
Van den Berg et al.	2005
Wepfer and Christensen	1991

Table 6 Selected laboratory studies of seismic nonseismic properties of rocks

Berckhemer	1997
Carmichael	1982
Carmichael	1982
Christensen and Salisbury	1979
Clark	1966
Duba	1972
Johnson and Olhoeft	1984

adjusted to fit both the seismic and the gravity observations. For additional references on gravity studies of the crust, see Table 7.

1.11.4.2 Aeromagnetics

High-resolution aeromagnetic surveys can be used to define major regions of coherent structure in the Earth's crust (Kane and Godson, 1989). Since rocks commonly retain magnetism that originates from the time of their formation, magnetic anomaly data provide a unique opportunity to infer geologic processes not readily observed through other geophysical quantities. One common example of this is seafloor spreading, indicated by a series of magnetic stripes, originating from the mid-ocean ridge.

Magnetization is commonly associated with igneous rocks, but it is controlled more generally by the thermal history of the rock. The remnant magnetization of a mineral is fixed in the direction of the Earth's magnetic field when the mineral is cooled below the Curie temperature; the remnant magnetization is removed when heated above this temperature. Metamorphism can also change the magnetization of a rock, but the magnitude of the effect is usually small. So, in contrast to density, rock magnetization can range through several orders of magnitude (Kane and Godson, 1989).

Long-wavelength gravity and magnetic data are available from space-based observations (McEnroe et al., 2004; Purucker et al., 2002). The CHAMP (CHAllenging Minisatellite Payload) mission is a small German satellite designed for geoscientific and atmospheric research and applications. CHAMP will generate highly precise gravity and magnetic measurements of the Earth over a 5-year period in an attempt to create a highly precise gravity field of the Earth, in order to appropriately constrain seismic velocity models (Hemant and Maus, 2005). For additional references on magnetic studies of the crust, see Table 8.

1.11.4.3 Geoelectrical Measurements

In general, the conductivity of the Earth is correlated with salinity, composition, and temperature (Jones, 1992; Keller, 1989a). At the surface, electrical conductivity depends on the amount of salinity of the groundwater in a rock. At intermediate depths, conductivity depends on water content and composition (particularly graphite and sulfide content). At great

Table 7 Selected papers on crustal from gravity

Arvidson et al.	1984
Bailey et al.	2012
Banks et al.	1977
Barton	1986
Bateman and Eaton	1967
Blakely	1995
Clowes et al.	1997
Couch and Woodcock	1981
Dehlinger	1978
Grant and West	1965
Hammer	1983
Hayford and Bowie	1912
Heiskanen and Moritz	1967
Heiskanen and Vening Meinesz	1958
Hildenbrand et al.	1982
Hinze	1985
Keller and Hatcher	1999
Kimbell et al.	2004
Lachenbruch et al.	1985
McNutt	1980
Mooney and Kaban	2010
Parker	1973
Paterson and Reeves	1985
Plouff	1976
Roecker et al.	2004
Ruiz-Constán et al.	2012
Sandwell and Smith	1997
Simpson et al.	1987
Talwani and Ewing	1960
Tiberi et al.	2003
Turcotte and Schubert	2002
US Department of Commerce	2001
Unsworth et al.	2000
Venisti et al.	2004
Watts	2001
Woollard	1943, 1959
Zoback and Mooney	2003

Table 8 Selected papers on crustal structure from aeromagnetic data

Alvares et al.	1978
Baranov	1957
Blakely	1995
Blakely and Grauch	1983
Bond and Zietz	1986
Frost and Shive	1986
Grant and West	1965
Hahn et al.	1984
Hall	1974
Hemant and Mouse	2005
Hinze	1985
Hinze and Zeitz	1985
Hood et al.	1985
Huestis and Parker	1977
Langel	1985
Langel et al.	1982
Mayhew and LaBrecque	1987
Mayhew et al.	1985
McEnroe et al.	2004
Parker	1971
Paterson and Reeves	1985
Plouff	1976
Purucker et al.	2002
Redford	1980
Reid	1980
Schouten	1971
Schouten and McCamy	1972
Sexton et al.	1982
Stockmann and Jackson	2009
Talwani	1965
USGS and Society of Exploration Geophysics	1982
Vacquier et al.	1951
Vogt et al.	1979
Von Freese et al.	1986
Williams et al.	1985
Zietz	1969, 1982

depths, where temperatures rise to at least 500 °C, conductivity is mainly a function of electron and ion mobility (Keller, 1989a).

Most studies of the Earth's crust are based on magnetotelluric (MT) data (Keller, 1989b). This method relies on measurements of five separate components of the time-varying electromagnetic field at the surface of the Earth. The analysis of these time series yields 1-D and 2-D models of the subsurface conductivity structure. When measurements are made for long periods (10 000 s and longer), estimates of the conductivity of the crust and upper mantle to a depth of 200 km and greater are possible (Jones, 1999). The source for electrically conductive material may be seen as high-density blocks within the crust.

Electrical conductivity profiles of the crust may be divided into marine and continental studies. Major marine studies include the RAMESSES marine experiment over the Reykjanes Ridge (MacGregor et al., 1998; Sinha et al., 1998), the PEGASUS (Pressure, Electromagnetic, Gravity, Active Source Underwater Survey) experiment in the northeast Pacific Ocean (Constable and Cox, 1996), and electromagnetic studies of the axial zone of the northern East Pacific Rise (Evans et al., 1999). On continents, electrical conductivity structure of stable regions, sutures and paleosubduction zones, regions of lithospheric extension, and orogens have all been investigated (Jones, 1992; Jones et al., 2001; Wannamaker et al., 1989). In most cases, these studies have been conducted in conjunction with active- and passive-source seismic profiles. Notable results include the correlation between low shear-wave velocity and high electrical conductivity beneath the southern Tibetan Plateau. This correlation has been attributed to the presence of either partial melts or aqueous fluids in the middle crust (Li et al., 2003; Nelson et al., 1996). Thus, electrical studies provide an important additional constraint on the composition and physical state of the crust and upper mantle. For additional references on geoelectrical studies of the crust, see **Table 9**.

1.11.4.4 Heat Flow Data

Surface heat flow data provide valuable information on temperatures within the crust. The highest heat flow values are found at mid-ocean ridges and within geothermal zones and active volcanoes. Heat flow has been measured on a global basis within oceans, continents, and their margins (Pollack et al., 1993). Surficial heat flow is the product of radiogenic heat production in the crust and heat transferred from the convecting mantle. In order for a lithospheric geotherm to be reliably calculated, crustal heat production and thermal conductivity must be estimated from laboratory measurements on typical crust rocks (Artemieva, 2011; Artemieva and Mooney, 2001; Cermak, 1993; Champman, 1986; Jaupart and Mareschal, 1999, 2011; Pollack and Chapman, 1977). Crustal geotherms can be subdivided into hot, normal, and cold geotherms. Within continental crust, these three geotherms predict temperatures at a depth of 40 km (Moho) of about 500°, 700°, and 90 °C, respectively. Thermal studies of the crust have provided valuable constraints on crustal composition and evolution (Jaupart and Mareschal, 2011; Mareschal et al., 1999; Rudnick and Fountain, 1995). For additional references on heat flow studies, see **Table 10**.

1.11.4.5 Borehole Data

Deep scientific boreholes provide exceptional data regarding the physical properties of the upper crust. The deepest boreholes are the 12 km Kola Superdeep Borehole (KSDB) in Russia (Kozlovsky, 1987), the 9.1 km Kontinentales Tiefbohrprogramm (KTB) in Germany (Emmernmann and Lauterjung, 1997), and the 6.8 km and 6.5 km Gravberg–Stenberg boreholes in Sweden (Juhlin, 1988; Papasikas and Juhlin, 1977). In addition, there are numerous scientific foreholes to depths of 3–5 km. These boreholes provide direct sampling of the composition of the upper crust, as well as measurements of *in situ* seismic velocities, density, temperature, state of stress, rock porosity, and the fluid pressure (Kern et al., 2001; Smithson et al., 2000). Evidence has also been obtained for crustal shear zones containing electrically conductive graphite and sulfides. An unexpected result is the presence of free fluid throughout the entire depth range of the KSDB and KTB boreholes.

1.11.4.6 Surface Geology, Exposed Deep Crustal Sections, Xenoliths, and Geochemical Data

Surface geology, exposed deep crustal sections, xenolith samples, and geochemical data all provide direct observations of the

Table 9 Selected papers on the electrical properties of the crust

Banks	1972
Berdichevskiy and Zhadanov	1984
Booker et al.	2004
Cagniard	1953
Feldman	1976
Gough	1974
Grant and West	1965
Hyndman	1988
Keller	1989a,b
Korja et al.	2002
Jones	1992
Jones et al.	2001
Li et al.	2003
Wannamaker et al.	1989

Table 10 Selected papers on crustal heat flow

Artemieva	2009
Artemieva and Mooney	2001
Cermak	1993
Champman	1986
Davies and Davies	2010
Goutorbe et al.	2011
Jaupart and Mareschal	1999, 2011
McKenzie et al.	2005
Parson and Sclater	1977
Pollack and Chapman	1977
Pollack et al.	1993
Scalter et al.	1980
Stein and Stein	1992
Turcotte and Schubert	2002
Zang et al.	2002

composition and physical properties of the crust. The composition of the upper continental crust is, by definition, evident in global geologic maps, which are dominated by felsic intrusive rocks and low-grade metamorphic rocks, particularly shales and sandstones (Clarke, 1889; Clarke and Washinton, 1924; Taylor and McLennan, 1992). The recognition that mountain belts provided exposures of the deep crust can be traced to the work of Elie de Beaumont (1847) who studied the Pyrenees. It was, however, many years later that these observations were systematically analyzed in terms of cross sections of the entire crust (Fountain and Salisbury, 1981; Percival et al., 1992; Salisbury and Fountain, 1990). Xenoliths are samples from the deep crust (and mantle lithosphere) that have been carried to the surface by volcanic activity (Kay and Kay, 1981; Yanaqi, 2011). These samples provide excellent constraints on lower crustal composition (Fountain et al., 1992; Mahan et al., 2012; Rudnick and Gao, 2005; Yanaqi, 2011). Geochemical analysis of xenolith samples provides critical data on crustal composition (Condie, 2011; Rudnick and Gao, 2005; Taylor and McLennan, 2009).

1.11.5 Structure of Oceanic Crust and Continental Margins

Several thousand measurements of the deep seismic structure of the Earth's crust have been made. However, the geographic distribution of seismic measurements is uneven (**Figure 11**), with more results available for the Northern Hemisphere and a concentration of data in North America, western Europe, and Eurasia. In the Southern Hemisphere, Australia and New Zealand have abundant data. Oceanic data are widely available for all oceans. Here, we summarize the principal results obtained by these seismic data and then present a global model for the Earth's crust.

1.11.5.1 Typical Oceanic Crust

The seismic velocity structure of oceanic crust was first established in the 1950s, before the discovery of plate tectonics and seafloor spreading. Oceanic crust was found to be uniformly thinner than continental crust. Much of the knowledge of the structure of ocean crust has come from seismic refraction/wide-angle reflection profiles. These seismic profiles use air gun or explosive sources that are recorded by either hydrophones or ocean-bottom seismometers. Passive seismology has limited application since most receivers are on continents or islands. However, a few tomographic studies of crustal structure at mid-ocean ridges have been completed (Dunn et al., 2000; Wolfe et al., 1995).

In their pioneering studies, Hill (1957) and Raitt (1963) divided 'normal' oceanic crust into separate, uniform seismic layers, known as 'Raitt–Hill layering.' The basic construction was a 2–3 km thick upper layer (layer 2) with a velocity of 2.5–6.4 km s^{-1}, underlain by a 3–5 km thick lower layer (layer 3), with a velocity of 6.5–7.3 km s^{-1}. The total thickness of ocean crust was determined to be 6–7 km. Layer 2 consists largely of pillow lavas and dikes, while layer 3 consists of a 'sheeted' dike complex underlain by diorites and gabbros (**Figure 12**). More details regarding the structure of the crust have been obtained using modern analysis methods. The application of synthetic seismogram modeling to marine seismic refraction/wide-angle reflection data indicates that the transition from layer 1 to layer 2 is often transitional, while the transition from layer 2 to layer 3 is relatively sharp (Spudich and Orcutt, 1980).

In the late 1970s, it was proposed that layer 2 could be further subdivided into three layers: 2A, 2B, and 2C. According to Ewing and Houtz (1979), two distinct layers with seismic velocities of about 3.5 km s^{-1} (layer 2A) and 5.2 km s^{-1} (layer 2B) were consistently identified. Below layer 2B, but above layer 3, a third layer with a seismic velocity of 6.0–6.2 km s^{-1} (layer 2C) was detected. Orcutt et al. (1976) and White et al.

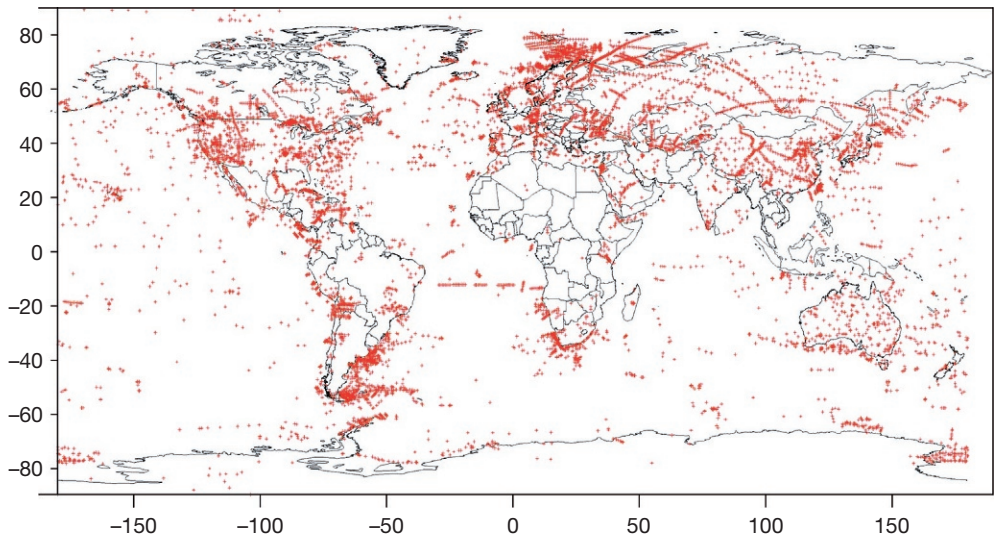

Figure 11 Locations (solid triangles) of individual seismic velocity–depth measurements made within the Earth's crust, 1920–present. Up to 1980, the majority of these measurements were made using the seismic refraction/wide-angle reflection technique. Since 1980, a great many determinations have been made using receiver function analysis of teleseismic arrivals and local earthquake tomography (see text).

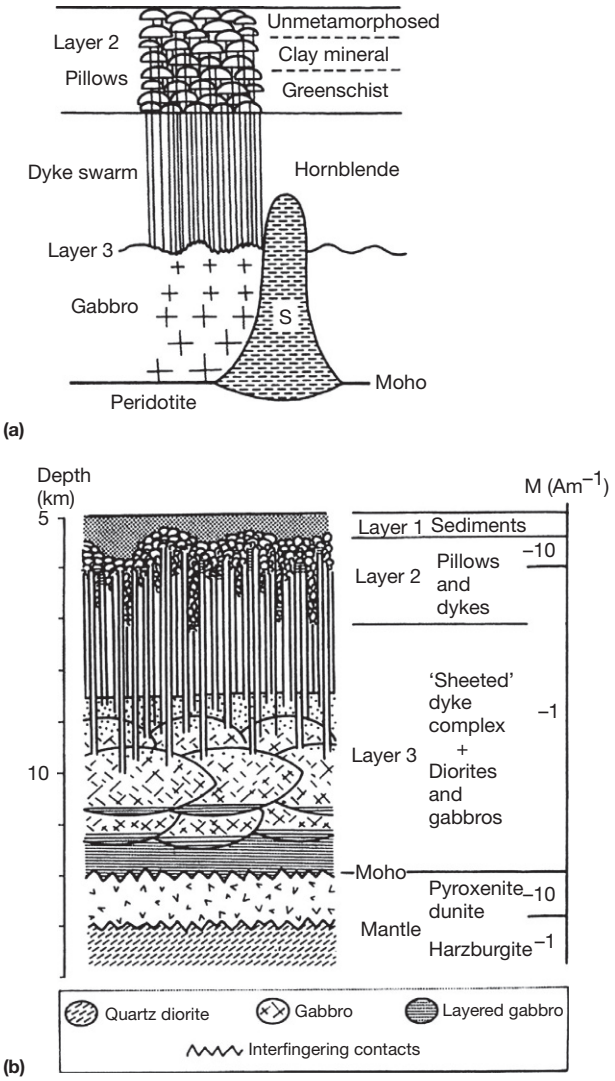

Figure 12 Compositional models of the oceanic crust derived from seismic measurements and exposed crustal sections: (a) after Cann (1970) and (b) after Vine and Moores (1972). Traditionally, the oceanic crust is described as being composed of three layers, termed seismic layers 1–3. According to model (b), layer 1 is sediments; layer 2 is made up of basaltic pillow lavas and their feeder dikes, unmetamorphosed in their upper parts; layer 3 is composed of sheeted dikes underlain by massive plutonic diorites and gabbros. Seismic velocities within these layers are shown in **Figure 13(b)**.

(1992) reviewed previous work and provided a modern synthesis of the seismic structure of typical oceanic crust. Layer 1 lies beneath an average 4.5 km of seawater and is composed of sediments (pelagic sediments, silts, muds, and sand) and is approximately 0.5 km thick, with a seismic velocity of 1.5–2.0 km s^{-1}, increasing with depth as the sediments consolidate. Layer 2A–C, the volcanic layer, is 2.11 ± 0.55 km thick, with a seismic velocity of 2.5–6.6 km s^{-1}. Layer 3, sometimes called the oceanic layer, is 4.97 ± 0.90 km thick, with a seismic velocity of 6.6–7.6 km s^{-1}. The upper mantle has an average seismic velocity of 7.9–8.1 km s^{-1}. See **Table 11** for additional references on oceanic crust studies. **Table 12** lists selected papers on the composition of oceanic crust.

Table 11 Selected papers on the seismic structure of oceanic crust

Au and Clowes	1984
Barclay et al.	1998
Begnaud et al.	1997
Ben-Avraham et al.	2002
Bibee and Shor	1976
Bohnhoff and Makris	2004
Bown and White	1994
Butler	1986
Calvert et al.	2008
Calvert	2011
Canales et al.	2000a,b, 2003
Cann	1974
Cannat	1996
Caress et al.	1995
Carlson et al.	1980
Chapman and Orcutt	1985
Charvis et al.	1995
Chen	1992
Christensen	1972
Christeson et al.	1997
Christeson et al.	2003
Clowes et al.	1999
Coffin and Eldholm	1994
Collier and Singh	1997, 1998
Crawford	2003
Darbyshire et al.	2003, 2000a,b
Day et al.	2001
Detrick et al.	1987, 1990, 1993
Diaz and Gallart	2009
Du and Foulger	2001
Du et al.	2002
Dunn et al.	2000
El Shazly	1982
Evangelidis et al.	2004
Ewing et al.	1955
Ewing and Nafe	1982
Ferris et al.	2006
Fliedner and Klemperer	2000
Foulder et al.	2003
Funck et al.	2011
Gladczenko and Coffin	2001
Gonzalez-Fernandez et al.	2001
Grevemever et al.	2001a,b
Hess	1962
Hill	1963
Hofft et al.	2000
Hussenoeder et al.	2002
Hyndman	1979
Jackson and Oakey	1986
Jacobs et al.	2007
Kamimura et al.	2002
Kempner and Gettrust	1982
Klingelhofer et al.	2007, 2000, 2005
Korja et al.	2001
Krishna et al.	2001
Ku et al.	2009
Kurashimo et al.	2007
Laske and Masters	1997
Lindwall	1988
Mair and Forsyth	1982
Maxwell	1970a,b
McKenzie and Bickle	1988

(*Continued*)

Table 11 (Continued)

Müller et al.	1997
Minshull et al.	2006
Mjelde et al.	2001
Muller et al.	2000
Mutter and Karson	1992
Mutter and Mutter	1993
Nielsen et al.	2000
Nur and Ben-Avraham	1982
Operto and Charvis	1996
Orcutt et al.	1976
Oxburg and Parmetier	1977
Patriat et al.	2002
Peirce and Barton	1991
Palnert et al.	2009
Purdy and Detrick	1986
Rabinowitz et al.	1988
Raitt	1963
Richardson et al.	1998
Richardson et al.	1998
Ritzwoller and Levshin	2002
Savage and Wang	2012
Schlindwein et al.	2003
Shearer and Orcutt	1986
Shor	1967
Sinha et al.	1981
Sinha and Louden	1983
Sleep	1990
Smith and Sandwell	1997
Stein and Stein	1992
Su et al.	1992
Takahashi et al.	2007
Thinon et al.	2003
Tilmann and Dahm	2008
Toomey et al.	1990
Tucholke	1986
Tucholke and Uchupi	1989
Vera et al.	1990
Villagomez et al.	2011
Walck	1984
Walther	2002
White et al.	1992
White et al.	1984, 1992
White and Clowes	1990
Whitmarsh et al.	1982
Whitmarsh and Calvert	1986
Wilcock et al.	1995

1.11.5.2 Mid-Ocean Ridges

The concept of seafloor spreading from mid-ocean ridges (**Figure 2**) was first proposed in the early 1960s by several workers, including most prominently the American geologist Harry H. Hess (Hess, 1965). Its major tenets gave great support to the theory of continental drift and provided a conceptual base for the development of plate tectonics.

Mid-ocean ridges can be separated into three categories: fast spreading, intermediate spreading, and slow spreading. Fast-spreading ridges have a spreading rate of 8–16 cm year^{-1}, with eruptions of 1–5 million m^3 of magma occurring every 5 years. Meanwhile, intermediate-spreading ridges have a spreading rate of 4–8 cm year^{-1}, with 5–50 million m^3 of magma erupting every 500 years. Slow-spreading ridges erupt 50–1000 m^3 of magma every 5000 years, yielding a spreading rate of 1–4 cm year^{-1} (Perfit and Chadwick, 1998).

Table 12 Selected papers on oceanic crustal composition

Christensen	1972, 1996
Bown and White	1994
Cann	1974
CGMW	2002
Charvis et al.	1995
Christensen and Salisbury	1982
Condie	1989
Hess	1962
Hyndman	1979
Kempner and Gettrust	1982
Lindwall	1988
Nur and Ben-Avraham	1982
Operto and Charvis	1996
White et al.	1992

The seismic structure of a fast-spreading ridge shows that the intrusive zone is only 2–3 km wide, and normal oceanic crust is found 5–6 km away from the ridge axis (**Figure 13**). Directly beneath the ridge axis, an upper crustal low-velocity zone exists that corresponds to a zone of partial melting. This seismic structure is in contrast to the earlier hypothesis that anomalous oceanic crust extends for tens of kilometers away from the axis of a mid-ocean ridge. The seismic structure of the fast-spreading East Pacific Rise has also been examined using seismic P-wave tomography (Dunn et al., 2000). The spreading ridge is characterized by a seismic low-velocity volume that is 5–7 km wide within the crust and three times broader (c. 18 km) in the mantle. Magma accumulates at two levels: at a shallow crustal depth (the top of the magmatic system) and at the Moho transition zone (Dunn et al., 2000). Measurements of seismic anisotropy within the shallow mantle beneath the ridge indicate a mismatch between the locus of mantle melt delivery and the morphological ridge axis. The geometry of this mismatch governs the segmentation of the ridge and controls the intensity of ridge crest processes (Toomey et al., 2007).

1.11.5.3 Oceanic Plateaus and Volcanic Provinces

Oceanic plateaus are one type of the large igneous provinces that cover portions of the oceans and continents (i.e., flood basalt provinces; Coffin and Eldholm, 1994; Ernst and Buchan, 2003). While continental flood basalt provinces were recognized in the early twentieth century (Holmes, 1918), regions of unusually thick oceanic crust were not identified until the 1970s. Edgar et al. (1971) originally discovered an overthickened region within the Caribbean plate, and when a number of similar features were documented, they were called 'oceanic flood basalt provinces' (Donnelly, 1973; **Figure 14**). The term 'ocean plateau' was suggested by Kroenke (1974) when the Ontong Java Plateau (OJP) in the western Pacific was explored using seismic refraction/wide-angle reflection profiles. More than a dozen oceanic plateaus have been identified (**Figure 14**), and these have anomalous crustal structure in comparison with normal oceanic crust.

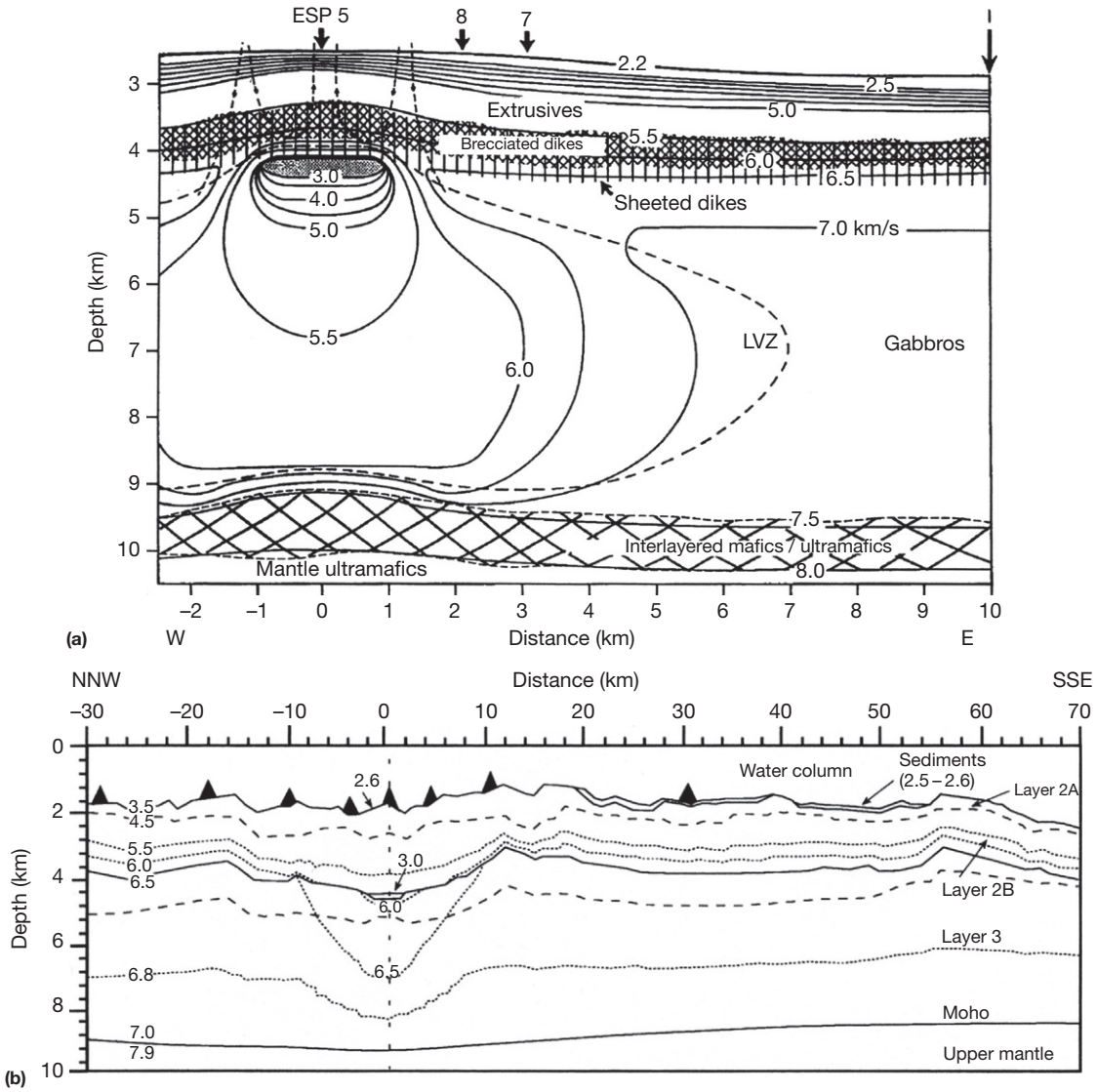

Figure 13 Top panel (a): P-wave velocity model and interpretation, based on expanding spread profile and multichannel reflection data, of the fast-spreading East Pacific Rise axis at 9°N. Arrows mark ESP locations. (b) P-wave velocity model and interpretation, based on OBS and seismic reflection data, of the slow-spreading Reykjanes Ridge axis at 57°45′N. Triangles mark OBS locations and dashed lines mark changes in velocity gradient. (a) Redrawn from Vera EE, Mutter JC, Buhl P, et al. (1990) The structure of 0–0.2-m.y.-old oceanic crust at 9°N on the East Pacific Rise from expanded spread profiles. *Journal of Geophysical Research* 95: 15529–15556. (b) Redrawn from Navin D, Peirce C, and Sinha MC (1998) The RAMESSES experiment-II. Evidence for accumulated melt beneath a slow spreading ridge from wide-angle refraction and multichannel reflection seismic profiles. *Geophysical Journal International* 135: 746–772; Minshull TA (2002) Seismic structure of the oceanic crust and rifted continental margins. In: Lee WHK, Kanamori H, and Jennings PC (eds.) International Geophysics Series 81 A: International Handbook of Earthquake an Engineering Seismology, pp. 911–924. San Diego, CA: Academic Press.

The crustal structure of several ocean plateaus has been resolved using seismic and gravity data, including recent studies on the Kerguelen and OJP. Farnetani et al. (1996) and Gladczenko et al. (1997) presented models for the OJP that show high seismic velocities (7.1 km s^{-1}) throughout most of the crust. These high velocities are likely due to the presence of basalt and olivine–pyroxene cumulates, with high-velocity garnet granulite in the lower crust. Gladczenko et al. (1997) suggested that these garnets may have formed from the deformation and hydrothermal alteration of lower crustal cumulates.

More recently, measurements of upper mantle shear-wave splitting and shear-wave velocity have suggested the presence of a 300 km thick, long-lived, rheologically strong, and chemically depleted root beneath the OJP (Klosko et al., 2001). Further proposed that this chemically depleted root originated from mantle melting processes, which would contribute lower-density material to the base of the plateau, increasing the overall buoyancy of OJP.

At the present time, the process of ocean plateau formation is not well understood. There are a number of models for how

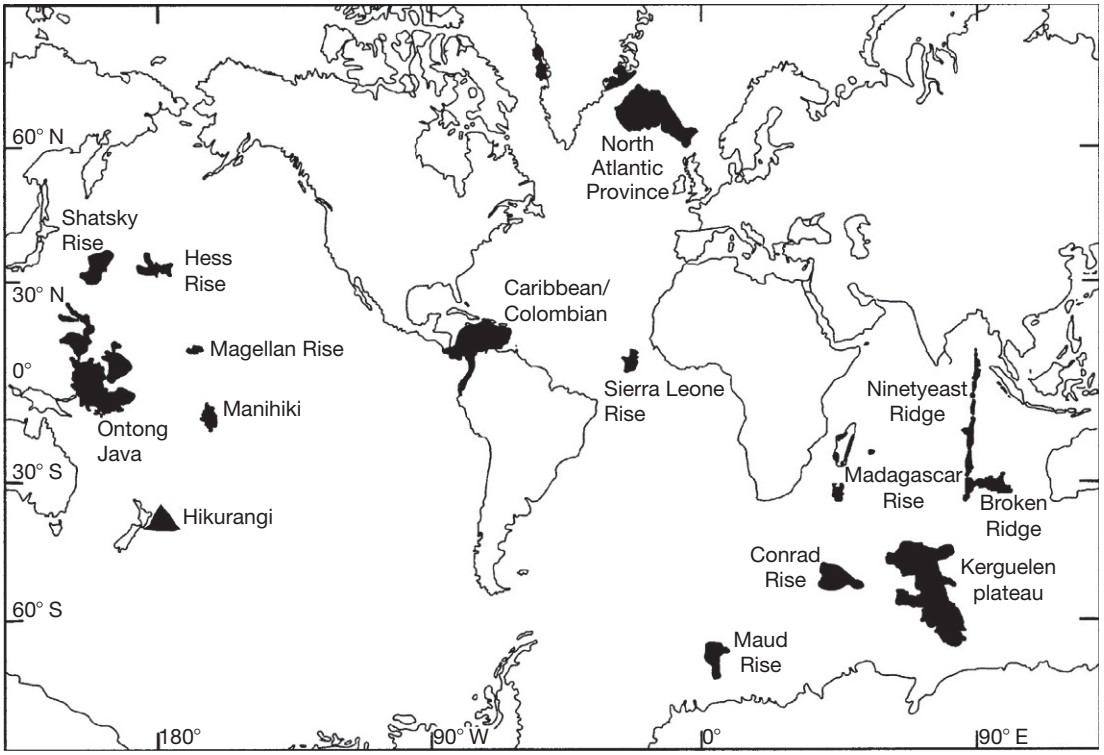

Oceanic plateau	Mean age (Ma)	Area (10^6 km^2)	Thickness range (km)	Volume (10^6 km^3)
Hikurangi	Early-mid Cretaceous	0.7	10–15	2.7
Shatsky rise	147	0.2	10–28	2.5
Magellan rise	145	0.5	10	1.8
Manihiki	123	0.8	>20	8.8
Ontong Java	121(90)	1.9	15–32	44.4
Hess rise	99	0.8	>15	9.1
Caribbean	88	1.1	8–20	4.4
South Kerguelen	110	1.0	~22	6.0
Central Kerguelen/ Broken ridge	86	1.0	19–21	9.1
Sierra Leone rise	~73	0.9	>10	2.5
Maud rise	~>73	0.2	>10	1.2

Figure 14 Map showing all major oceanic plateaus and other large igneous provinces discussed in the text (after Saunders et al., 1992; Eldholm and Coffin, 2000). These plateaus have measured crustal thicknesses of 10–32 km and an average thickness (22 km) that is twice that of typical oceanic crust.

large volumes of mafic magmas are generated and emplaced by processes unrelated to 'normal' seafloor spreading and subduction (Campbell et al., 1989; Farnetani and Richards, 1995; Griffiths and Campbell, 1990; Loper, 1983; McKenzie and Bickle, 1988), but it is not understood why these eruptions occur in such a rapid, concentrated period of time. Most ocean plateaus were formed in a short time, less than 2–3 Myr (Coffin and Eldholm, 1994), which may raise important questions about mantle processes and source regions (Hart et al., 1992; Stein and Hoffman, 1994). During the most recent phase of Large Igneous Province (LIP) formation, in the mid-Cretaceous, the Ontong Java, Manihiki, Hess Rise, and Caribbean–Colombian plateaus were formed in the Pacific, while the Kerguelen Plateau formed in the Indian Ocean (Kerr, 2003).

If the plateaus are accreted adjacent to continental margins or island arcs, they may eventually significantly contribute to the growth of existing and new continents (Abbott, 1996; Albarede, 1998). Due to their increased thickness relative to normal oceanic crust, plateaus are especially buoyant, preventing them from completely subducting at active margins (Ben-Avraham et al., 1981; Cloos, 1993; Kimura and Ludden, 1995) and allowing the top layers to be 'peeled off' and merge with the continental crust (Kimura and Ludden, 1995).

Ideas about hot spots and mantle plumes have been around for more than 40 years (Wilson, 1963), but the deep structure of these features remains controversial. Currently, there are two different models for the crust and upper mantle beneath Iceland, one of the two most prominent hot spots on the planet (the other being the Big Island of Hawaii). The 'thin-crust model' is based on MT data, heat flow from shallow wells, petrogenetic models, and seismic data. It suggests a ~10–15 km thick crust under the main rifting axis of Iceland, with

a 25 km thick, older crust in eastern, western, and north-central regions of the island. There is also a thin, highly conductive, molten basaltic layer. The 'thick-crust' model is based entirely on seismic receiver function data and suggests a Moho depth of 35–40 km (Du and Foulger, 2001; Foulger et al., 2003). Much of the ambiguity regarding the crustal thickness can be attributed to the presence of melt in the lower crust and the absence of a sharp seismic discontinuity at the base of the crust. Figure 15 is a schematic cross section across the center of Iceland compiling all available seismic, MT, heat flow, and viscosity data (Bjőrnsson et al., 2005). A unique and prominent feature beneath this hot spot is the continuous good conductor above the underlying asthenosphere. Bjőrnsson et al. (2005) suggested that a 20–40 km deep discontinuous reflector does not necessarily represent the Moho; these authors instead support the 'thin-crust' model. Further data are needed to resolve this controversy.

1.11.5.4 Ocean Trenches and Subduction Zones

Geophysical studies of oceanic trenches can be traced to gravity measurements made by Vening Meinesz (1887–1966) in the Indonesian archipelago. These negative gravity anomalies were interpreted by Vening Meinesz (1948) as being due to pronounced downbuckling of the oceanic crust. The detailed structure of oceanic trenches was clarified from marine seismic profiles that were made 30 years after Vening Meinesz's pioneering gravity measurements. One of the best studied trenches is the Nankai Trough, eastern Japan. Two crustal models derived from seismic refraction/wide-angle reflection and gravity data collected across the Nankai Trough (Figure 16) show the geometry of the subducting oceanic crust as it descends beneath the Japan volcanic arc (Figure 16). These models define the geometry of the thick sedimentary basins that are located between the Nankai Trough and continental Japan. These results are typical of many subduction zones, including the Cascades region of western North America. Due to the pronounced lateral variations across oceanic trenches and subduction zones, studies that combine multiple seismic and nonseismic data have been the most successful at determining the deep structure (Wannamaker et al., 1989).

1.11.5.5 Oceanic Island Arcs

Oceanic island arcs are created at ocean–ocean subduction systems. Examples include the Aleutian Arc, the Scotia Arc, and the numerous island arcs of the southwest Pacific Ocean. They are distinguished from continental magmatic arcs, such as the Andes of western South America, that are the product of ocean–continental subduction. Oceanic island arcs are commonly identified as accreted terrains within continental crust (McLennan and Taylor, 1982) and have attracted widespread interest among Earth scientists.

The deep crustal structure of several island arcs has been investigated using controlled source seismology (Calvert, 2011). Prominent study areas include the Aleutian Arc (Holbrook et al., 1999; Shillington et al., 2004), the Izu–Bonin arc (Kodaira et al., 2007), the northern Izu arc (Suyehiro et al., 1996), and the Mariana arc (Takahashi et al., 2007, 2009). Measured P-wave seismic velocities beneath arcs are generally higher than found at the same depths beneath continents: beneath the Aleutians, midcrustal velocities of 6.5–7.3 km over depths of 10–20 km indicate andesitic to basaltic compositions, while lower crustal P-wave seismic velocities of 7.3–7.7 km s^{-1} over a depth range of 20–35 km indicate mafic–ultramafic cumulates and/or garnet granulites (Schillington et al., 2004). A seismic profile across the Izu–Ogasawara arc (Figure 17) also shows high lower crustal

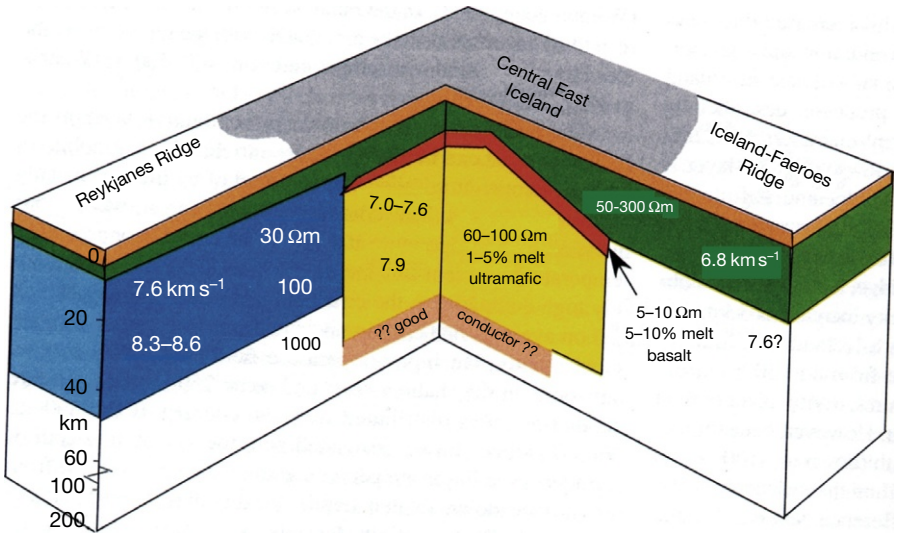

Figure 15 Simplified cross section showing the main structural features of the Icelandic crust and mantle. The left part of the figure shows a profile parallel to the Reykjanes Ridge and east of the ridge approximately along the Reykjanes Ridge Iceland Seismic Experiment seismic profile. The right part of the figure shows a profile running from central Iceland into the Iceland–Faroe Ridge. Numbers are P-wave velocities (normal type) and resistivities (italic type). Reproduced from Björnsson A, Eysteinsson H, and Beblo M (2005) Crustal formation and magma genesis beneath Iceland; Magnetotelluric constraints. In: Foulger GR, Natland JH, Presnall DC, Anderson DL (eds.) *Geological Society of America*, *Special Paper 388 Plates*, *Plumes*, *and Paradigms*, 665–686. Boulder, CO: Geological Society of America.

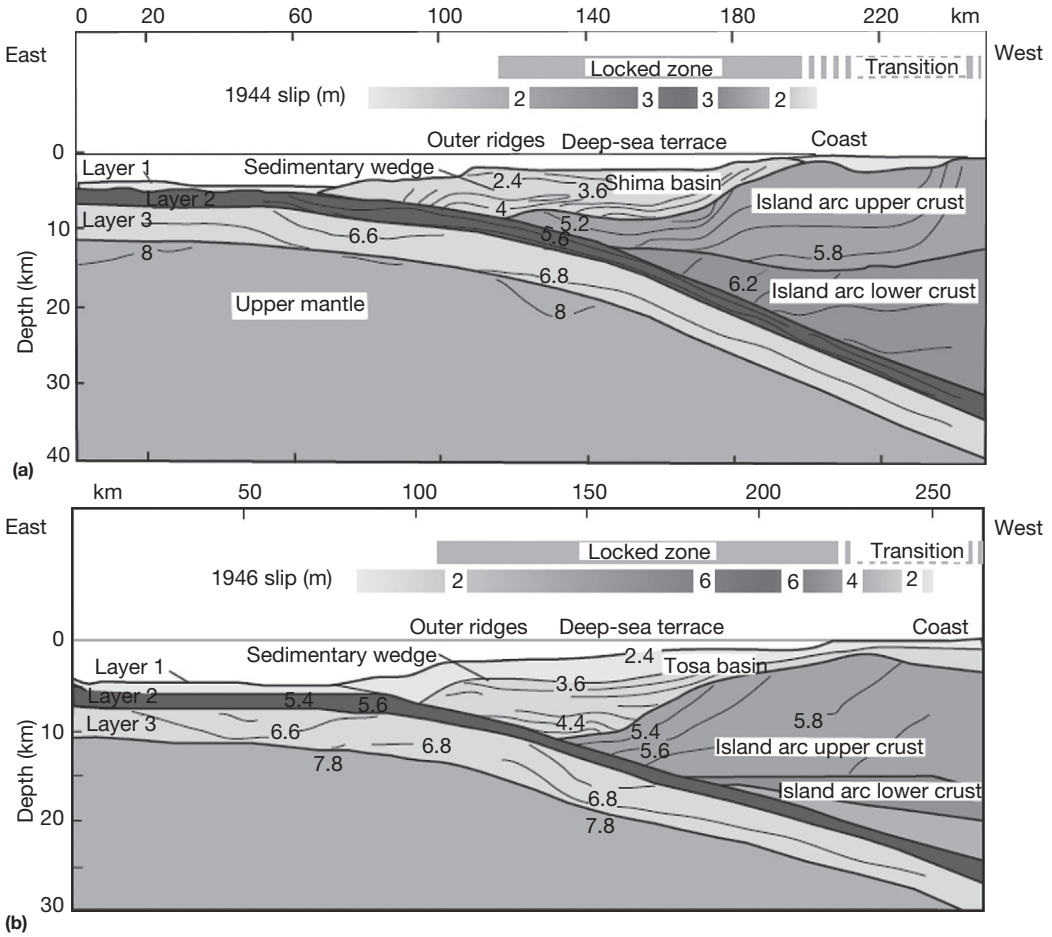

Figure 16 Seismic velocity structure of (a) the Tonanki subduction zone, site of the 1944 earthquake, and (b) the Nankai subduction zone, site of the 1946 earthquake. The relationship between the crustal structure and the locked zone is indicated (Hyndman et al., 1995; Sagiya and Thatcher, 1999; Kodaira et al., 2000; Nakanishi et al., 2002). The crustal structure is typical of many subduction zone complexes and includes a prominent low-seismic velocity sedimentary wedge and the higher-velocity igneous crust of the island arc. After Wells RE, Blakely RJ, Sugiyama Y, Scholl DW and Dinterman PA (2003) Basincentered asperities in great subduction aone earthquakes: A link between slip, subsidence, and subduction erosion? *Journal of Geophysical Research 108 (B10)*: 2507 (http://dx.doi.org/10.1029/2002JB002072).

velocities of 6.8–7.4 km s^{-1} (Takahashi et al., 2009). Such high seismic velocities are inconsistent with the concept that continental crust can be created simply by accreting island arcs. Instead, the lower crust of the arc is likely to be subducted and the middle crust remelted to form felsic melts that rise to form the juvenile continental crust (Condie and Kröner, 2013).

1.11.5.6 Passive Continental Margins

As the name implies, passive continental margins are boundaries between oceanic and continental regions where neither collisional deformation nor subduction is taking place. Despite their present-day tectonic quiescence, the crustal structure of passive continental margins is diverse and complex since they are formed by continental rifting that accompanies the breakup of a supercontinent, such as Pangaea (200 Ma) or Rodinia (1.0 Ga). Prominent examples include the eastern seaboard of North America, the Gulf Coast, the coasts of Antarctica, and the east, west, and south coasts of Africa. Tectonic activity is minimal and erosional or weathering processes dominate, forming low-relief geography and increased sedimentary debris. These sedimentary basins are economically and scientifically valuable due to their large reservoirs of hydrocarbon and their recorded history of the rifting between two continents.

Passive margins are my be divided into two primary types; volcanic margins and nonvolcanic margins (Eldholm et al., 2002; Holbrook and Kelemen, 1993; White and McKenzie, 1989). The North Atlantic Margin formed during early Tertiary lithospheric extension between Europe and Greenland, involving the Iceland hot spot, and is one of the world's largest volcanic margins (Eldholm and Grue, 1994). The US Atlantic volcanic margin was formed in the Mesozoic but apparently without the involvement of a hot spot (Holbrook and Kelemen, 1993). The extensive volcanic rocks of these margins were formed by excess melting associated within a wide, hot zone of asthenospheric upwelling present during rifting (McKenzie and Bickle, 1988). In many cases, a high-seismic-

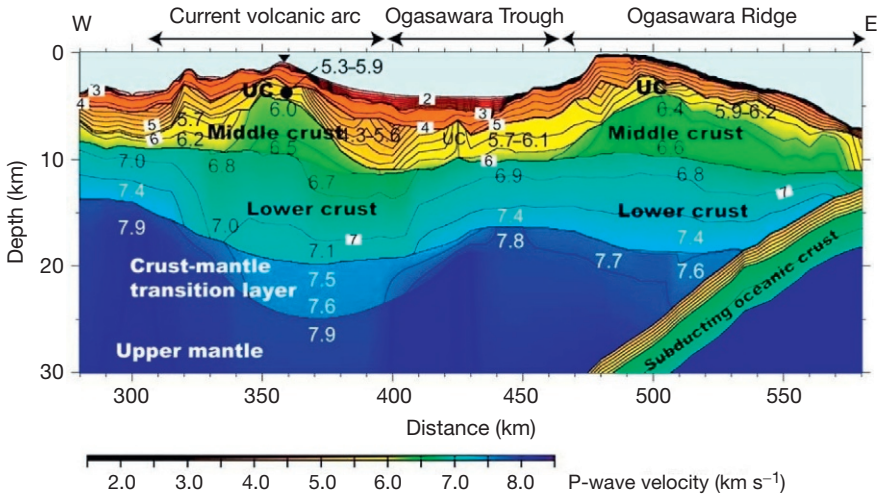

Figure 17 Crustal structure of the Izu-Ogasawara arc system (Takahashi et al., 2009). Crustal thickness varies from 10 km west of the current volcanic arc to 24 km beneath the current arc (taking 7.9 km s^{-1} as the top of mantle). Key: UC, upper crust. The lower crust is 5–10 km thick and has a relatively high P-wave velocity of 6.8–7.4 km s^{-1}, indicative of a mafic (gabbroic) composition. The crust-mantle transition layer reaches a thickness of 5 km, has a P-wave velocity of 7.5–7.6 km, and is likely composed of interlayered mafic and ultramafic rocks. The accretion of island arcs as depicted here will not yield typical continental crust because the arc crust is more mafic that continental crust which has a more intermediate crustal composition.

velocity (7.3 km s^{-1}) lower crust is also present. Nonvolcanic passive margins are formed where asthenospheric temperatures remain lower during rifting. An example is the nonvolcanic margin of the Labrador Sea of northeastern Canada.

The passive boundary zone between continental and oceanic plates is sometimes characterized by a sharp drop in elevation over distances less than ~30 km, as indicated by several gravity anomaly and wide-angle seismic studies (Delhinger et al., 1970; Faleide et al., 1990; Jones and Mgbatogu, 1982; Todd et al., 1988). A velocity profile of the margin off the Ghana coast can be seen in **Figure 18**. This ocean–continent transition indicates the absence of underplating beneath the continental basement, due to the lack of high velocities in the lower crust. See **Table 13** for additional references on continental margins.

1.11.6 Structure of Continental Crust

1.11.6.1 General Features

Continental crust above sea level comprises 29% of the Earth's crust, but when submerged continental crust is taken into account, continental crust amounts to 41% of the total crust. Since some 75% of continental crust is covered by either sediments or water, geophysical measurements are a very important source of information about the properties of the continental crust. The deep structure of the continental crust has been investigated for more than 100 years, beginning with the landmark study of Mohorovičić (1910) that defined the crust–mantle boundary. The locations of the presently available seismic refraction/wide-angle reflection profiles on continental crust are shown in **Figure 11** and amount to several thousand profiles. **Table 14** lists many key papers on continental crust studies. **Table 15** lists selected papers on the global composition of continental crust.

Studies of the continental crust using active (explosive) sources began in earnest in the late 1950s and 1960s (James and Steinhart, 1966; Pavlenkova, 1973; Steinhart and Meyer, 1961; Tuve, 1951, 1953; Tuve et al., 1954; **Table 1**). These early studies provided the first clear evidence that the seismic structure of the crust varied in a systematic way with geologic setting. They also showed that the crust can be described as consisting of several layers that are separated by either sharp or transitional boundaries. The existence of crustal layers, which have a heterogeneous fine structure, can be viewed as the product of igneous differentiation of the crust, whereby silicic melts rise into the upper crust and middle crust, leaving behind a mafic lower crust. Igneous differentiation thus leads to a heterogeneously stratified crust, with granitic to dioritic plutons forming the upper layer.

The evidence for distinct layers within the continental crust depends almost exclusively on the interpretation of second-arriving phases (wide-angle reflections). Whereas some regions display clear secondary phases, in other regions, the seismic velocity may increase gradually with depth, producing no distinct intracrustal reflections (Levander and Holliger, 1992).

1.11.6.2 Principal Crustal Types

Seismic measurements of continental structure are best described in terms of the local geologic setting. The distribution of the primary crust types is illustrated in **Figure 18**. In stable regions, the continental crust is generally 30–50 km thick. Compressional-wave seismic velocities in the upper crust are 5.6–6.3 km s^{-1}, corresponding to granitic and metasedimentary rocks. At a depth of 10–15 km, the seismic velocity commonly increases to 6.4–6.7 km s^{-1} (the middle crust), corresponding to intermediate composition plutonic rocks and amphibolite-grade metamorphic rocks. This discontinuity is sometimes referred to as the Conrad discontinuity (Conrad, 1925; **Table 1**), a term that is now out of date, as it came into

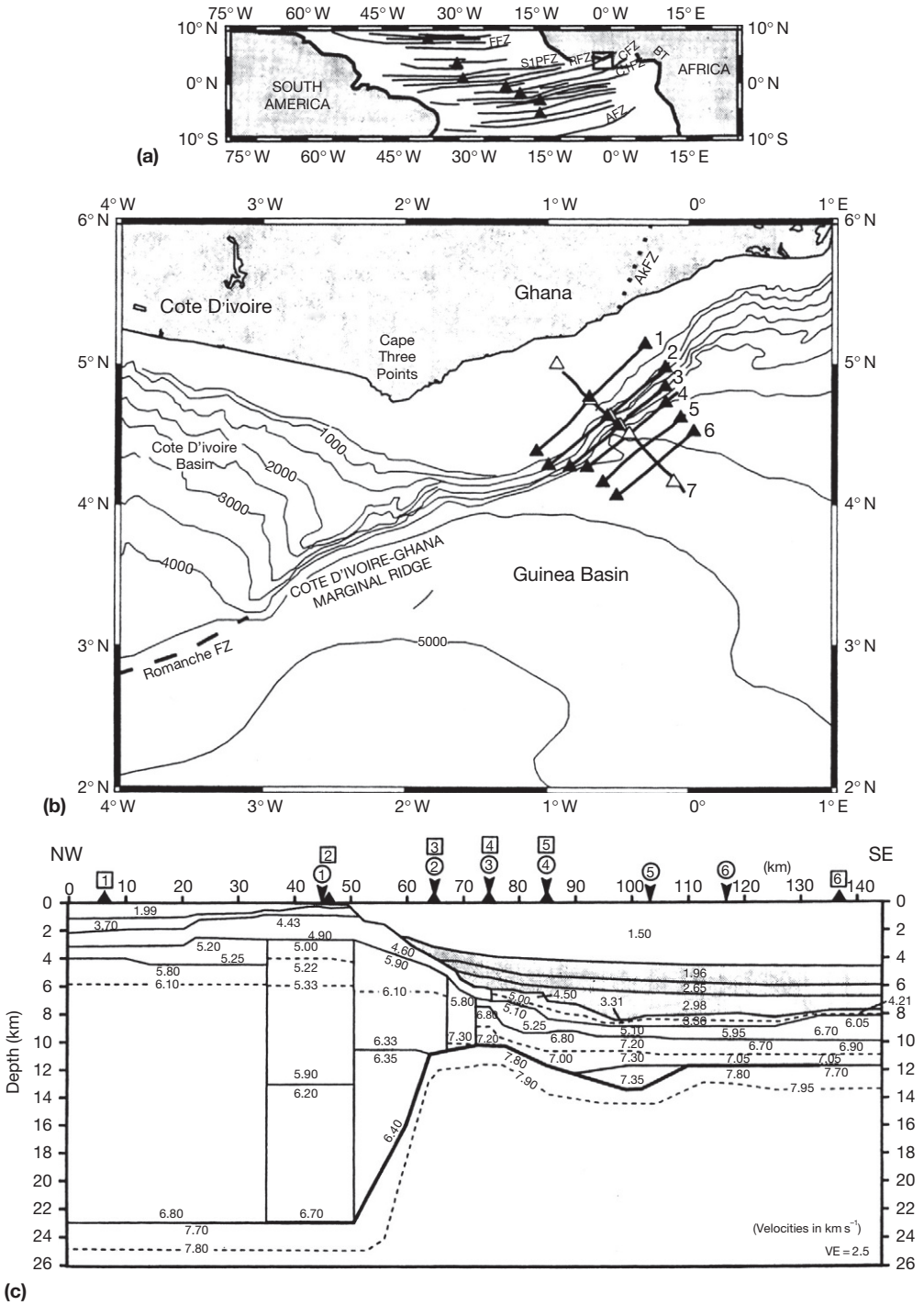

Figure 18 Example of an oceanic-continent transition zone from Ghana, west Africa. (a) Atlantic fracture zones. (b) Positions of wide-angle seismic profiles. (c) Model of seismic velocities. The crust thins over a remarkably short distance from 23 km on the continental shelf to 10–12 km beneath the oceanic crust. The igneous oceanic crust is covered by 3–4 km of low density, low-seismic velocity sediments. From Edwards RA, Whitmarsh RB, and Scrutton RA(1997) The crustal structure across the transform continental margin of Ghana, eastern Equatorial Atlantic. *Journal of Geophysical Research* 102: 747–772.

Table 13 Selected papers on the seismic structure of continental margins

Agudelo et al.	2009
BABEL Working Group	1993
Barazangi and Brown	1986a,b
Barton and White	1997
Becker et al.	2012
Blundell and Raynaud	1986
Breivik et al.	2003
Broucher	1995
Bullock and Minshull	2005
Chian et al.	1995, 1999
Christeson et al.	2008
Clegg and England	2003
Clowes et al.	1999
Clowes et al.	1987
Clowes and Hyndman	2002
Czuba et al.	2005
Davis and Kusnir	2004
Dean et al.	2000
DeShon and Schwartz	2004
El Shazly	1982
Eldholm and Grue	1994
Eldholm et al.	2002
England	2000
Ewing et al.	1937
Ewing et al.	1966
Fernandes et al.	2004
Fliedner and Klemperer	2000
Fowler et al.	1989
Funck et al.	2003, 2004
Gailler et al.	2009
Gerlings et al.	2011
Greenroyd et al.	2007
Heacock	1977
Hemant and Maus	2005
Holbrook and Kelemen	1993
Hopper et al.	2003
Horsefield et al.	1993
Jackson and Dahl-Jensen	2010
Jaffal et al.	2009
Jensen	1961
Jokat et al.	2004
Kim et al.	2003
Klemperer and Hobbs	1991
Klemperer and Mooney	1998a,b
Klemperer et al.	2002
Klingehofer et al.	2009, 2005
Kopp et al.	2001, 2002
Korenaga et al.	2001
Krabbenhoft et al.	2004
Labails et al.	2009
Lau et al.	2006a,b
Magnani et al.	2009
Mjelde et al.	2009
Matthews	1986
Matthews and Cheadle	1986
Matthews and the BIRPS group	1987
McKenzie and Bickle	1988
Nakanishi et al.	2002a,b
Netzeband et al.	2006
Niu et al.	2007
O'Reilly et al.	1998
Pavlenkova et al.	2009
Prajapati et al.	2011
Qiu et al.	2001
Ritzmann et al.	2002
Roberts et al.	1988
Rubio et al.	2000
Sage et al.	2000
Stankiewicz et al.	2008
Suckro et al.	2012
Thréhu et al.	1994
Tkalcic et al.	2011
Toomey et al.	2007
Todd et al.	1988
Torne et al.	2003
Vuan et al.	2005
Wang et al.	2004a,b
Watremez et al.	2011
White and McKenzie	1989
White and Smith	2009
White et al.	1987a,b
Worthington et al.	2012
Wu et al.	2006
Yeh and Hsu	2004
Zelt et al.	2001, 2005
Zhu et al.	2009

Table 14 Selected papers on the seismic structure of continental crust

Acton et al.	2011
Agostinetti et al.	2002
Al-Damegh et al.	2005
Barazangi and Brown	1986a,b
Bartelson et al.	1982
Barton	1992
Behrendt et al.	1988
Bleibinhaus and Gebrande	2006
Beloussov and Pavlenkova	1984
Beloussov et al.	1991
Beloussov et al.	1988
Blundell et al.	1992
Bonini and Bonini	1979
Bourjot and Romanowicz	1992
Brocher et al.	2001
Brown et al.	1986
Brueckl et al.	2007
Champion et al.	2006
Cho et al.	2006
Clitheroe et al.	2000
Clowes et al.	1999
Clowes et al.	1987, 1995, 1997
Clowes et al.	2002
Cook et al.	2010
Creaser et al.	2005
Curtis and Woodhouse	1997
Czuba et al.	2002
Czuba and Wojciech	2007
Dadlez et al.	2005
Dahl-Jensen et al.	2003
Dalton et al.	2011

(*Continued*)

Table 14 (Continued)

Das and Nolet	1998
Davis et al.	2012
Dentith et al.	2000
DESERT group	2004
De Wit and Tinker	2001
Diaz and Gallart	2009
Divins and Romanowicz	1989
Drewry and Mooney	1983
Dugda et al.	2005
Durrheim and Mooney	1994
Dzierma et al.	2010
Eagar et al.	2011
Eberhar-Phillips and Bannister	2002
England et al.	2012
Flieger and Klemperer	1999
Fountain et al.	1984
Franca and Assumpcao	2004
Fromm et al.	2004
Fu et al.	2010
Fuis et al.	2001
Funck et al.	2001, 2008
Gaite et al.	2012
Gans et al.	2011
Giese et al.	1976
Godfrey et al.	2001
Goek et al.	2008
Gore et al.	2009
Grad et al.	2003a,b, 2009
Grand et al.	1997
Guterch et al.	1999
Guterch et al.	2003
Hale and Thompson	1982
Hammer et al.	2000
Hamilton	1976
Hansen et al.	2009
Hart	1969
Hauser et al.	2001, 2007, 2008
Hazarika	2012
Heacock	1971, 1977
Hofsetter and Bock	2004
Hofstetter et al.	2012
Holbrook et al.	1992
Hole et al.	2000
Holmes et al.	2007
Hrubcova and Sroda	2008
Hrubcova et al.	2005
Iidaka et al.	2004
Ito et al.	2009
James	1971, 2003
James and Steinhart	1966
Janik et al.	2002, 2011
Jarchow and Thompson	1989
Julià and Mejía	2004
Julia et al.	2008, 2009
Kim et al.	2009, 2012
Kimbell et al.	2004
Kinck et al.	1993
Kind et al.	1995
Klemperer and Mooney	1998a,b
Klemperer et al.	2002
Kohler et al.	2012
Krishna and Rao	2011

(*Continued*)

Table 14 (Continued)

Kruger et al.	2002
Kumar et al.	2001
Kumar et al.	2007
Landes et al.	2003, 2004, 2005
Langston et al.	2002
Laske and Masters	1997
Lerch et al.	2007
Levshin et al.	2005
Li et al.	1998
Li and Mashele	2009
Li et al.	2012
Li et al.	2006
Liang and Langston	2009
Liu et al.	2011
Liu et al.	2006
Ludwig and Houtz	1979
Luo et al.	2012
Mackenzie et al.	2005
MacKenzie	2008
Majdanski et al.	2006
Makovsky et al.	1996a,b
Makris	1978
Malinowski et al.	2008
Manaman et al.	2011
Maurice et al.	2003
Mechie et al.	2004, 2005, 2009, 2012a,b
Meissner	1973, 1986
Meissner and Bortfeld	1990
Meissner et al.	1987, 1991
Melhush et al.	2005
Meltzer	2001
Minshull	1993
Mitchell and Herrmann	1979
Mitra et al.	2008
Mohsen et al.	2011
Monsalve et al.	2008
Mooney and Brocher	1987
Mooney and Meissner	1992
Mooney et al.	2002, 2005
Mueller	1973, 1977, 1978
Nakamura et al.	2003
Nelson et al.	1996
Niu et al.	2002
O'Reilly et al.	1996
Oliver et al.	1976, 1983
Olsen	1995
Orcutt	1987
Owens and Zandt	1985
Owens et al.	1984
Pakiser	1963
Pakiser and Mooney	1989
Pakiser and Steinhart	1964
Pan and Niu	2011
Pavlenkova	1996
Pawlak et al.	2011
Petit et al.	1998
Perseval et al.	2012
Pfiffner et al.	1997
Prasad et al.	2011
Prodehl	1970, 1979, 1984
Prodehl and Mooney	2012

Table 15 Selected papers on continental crustal composition

Bédard	2006
Beloussov and Pavlenkova	1984
Behn and Kelemen	2003
Blundell et al.	1992
CGMW	2002
Christensen	1996
Christensen and Fountain	1975
Christensen and Mooney	1995
Christensen and Salisbury	1975
Condie	1989
Downes	1993
Durrheim and Mooney	1994
Flieder and Klemperer	1999
Fountain	1986
Fountain and Christensen	1989
Fountain et al.	1984
Fountain and Salisbury	1981
Goodwin	1991, 1996
Hacker et al.	2011
Halliday et al.	1993
Hamilton	2011
Holbrook et al.	1992
Jordan	1979
Julià and Mejía	2004
Kozlovsky	1987
Kusznir and Matthews	1988
Meissner et al.	2002
Meissner and Mooney	1998
Mooney and Meissner	1991
Nur and Ben-Avraham	1982
Ringwood	1975
Rudnick and Fountain	1995
Rudnick and Gao	2005
Sandmeier and Wenzel	1990
Shapiro et al.	2004
Silver and Chan	1988
Sleep	2003, 2005
Smithson et al.	1987
Taylor and McLennan	1992
Thompson et al.	2010
Upton et al.	2001
Wedepohl	1995
Zandt and Ammon	1995
Ziegler	1990

use at a time when the crust was believed to consist of only two layers, an upper granitic layer and a lower basaltic layer. We now know from direct observation of exposed crustal sections and numerous seismic measurements that the crust is much more complex than this term implies. The lower crust of stable continental regions commonly has a seismic velocity of 6.8–7.3 km s^{-1}. The seismic velocity below the Moho, known as the Pn velocity, is 8.1 ± 0.5 km s^{-1}. The Moho is generally clearly observed in active-source seismic profiles due to the large seismic velocity increase (0.5–1.5 km s^{-1}) at this boundary.

Seismic measurements do not have a uniform global distribution (Figure 11), which affects attempts to calculate average crustal properties. The proportions of continental crust by area are 69% shield and platform (cratons), 15% old and young orogens, 9% extended crust, 6% magmatic arc, and 1% rift (Christensen and Mooney, 1995). Using these statistics, we calculate a weighted average for crustal thickness and average crustal velocity. This procedure corrects for the overrepresentation of crustal measurements in regions of extended crust, such as western Europe and the Basin and Range Province of western North America, and the relative scarcity of measurements from Africa, Greenland, and Antarctica. The weighted mean crustal thickness and average crustal velocity are 41 km (s.d. 6.2 km) and 6.45 km s^{-1} (s.d. 0.21 km s^{-1}), as compared with the simple arithmetic average of 39 km (s.d. 8.5 km) and 6.45 km s^{-1} (s.d. 0.23 km s^{-1}; Christensen and Mooney, 1995). The weighted average is more representative of the average continental crust.

Seismic measurements of the deep crust from around the world provide a firm basis for defining the characteristics of primary crustal types associated with specific geologic settings (Figure 19). The thickest continental crust (~80 km) is found beneath the Tibetan Plateau and the South American Andes, both of which are young orogens. Continental crust with an elevation above sea level has an average thickness of 39 km, with a standard deviation of 8.5 km. Thus, 95% (two standard deviations) of the crust has a thickness of between 22 and 56 km. The higher value of this range (56 km) is well below the 70–80 km thickness of some orogens, which indicates that crustal thickness may not follow a strictly normal distribution. The thickest crust is usually a young (late Cenozoic) crust and undergoes rapid uplift and erosion that results in crustal thinning.

Continental crust thinner than 30 km is generally limited to rifts and highly extended crust, including continental margins. The process of crustal extension rarely results in uniform stretching of the crust. Instead, the brittle upper crust fractures and rotates along normal faults, and the middle crust and lower crust undergo pure shear extension. Nonuniform crustal extension over a large region gives rise to Moho undulations, which in turn drive lateral lower crustal flow (creep). Thus, tectonic processes can give rise to significant changes in the distribution of crustal materials. Lower crustal flow is not limited to extending crust; the gravitational forces associated with the high (4–5 km) topography of young orogens also drive crustal flow. A prominent example is the hypothesized southeast crustal flow of the northern and central Tibetan Plateau into the adjacent continental crust (Tapponnier and Molnar, 1975).

The deep structure of orogenic crust has been studied in nearly all the mountain belts of the world, including the South American Andes, Tibetan Plateau, Western Cordillera of North America, Urals, and European Alps (Figure 20). Orogenic crust is commonly characterized by a highly thickened, low-density, low-seismic-velocity upper crust combined with strong folding and thrusting (Figure 20). In some cases, it appears that the lower crust is being subducted into the mantle, possibly aided by a phase transformation of the mafic lower crust to the dense eclogite facies (Rudnick and Gao, 2005). Due to the complexity of the crustal and upper mantle structure, multiple seismic and nonseismic techniques are needed to reliably determine the deep structure of orogens.

1.11.6.3 Correlation of Crustal Structure with Tectonic Provinces

Shields and platform occupy by far the largest area (69%) of continental crust (Figure 21). These regions have an average

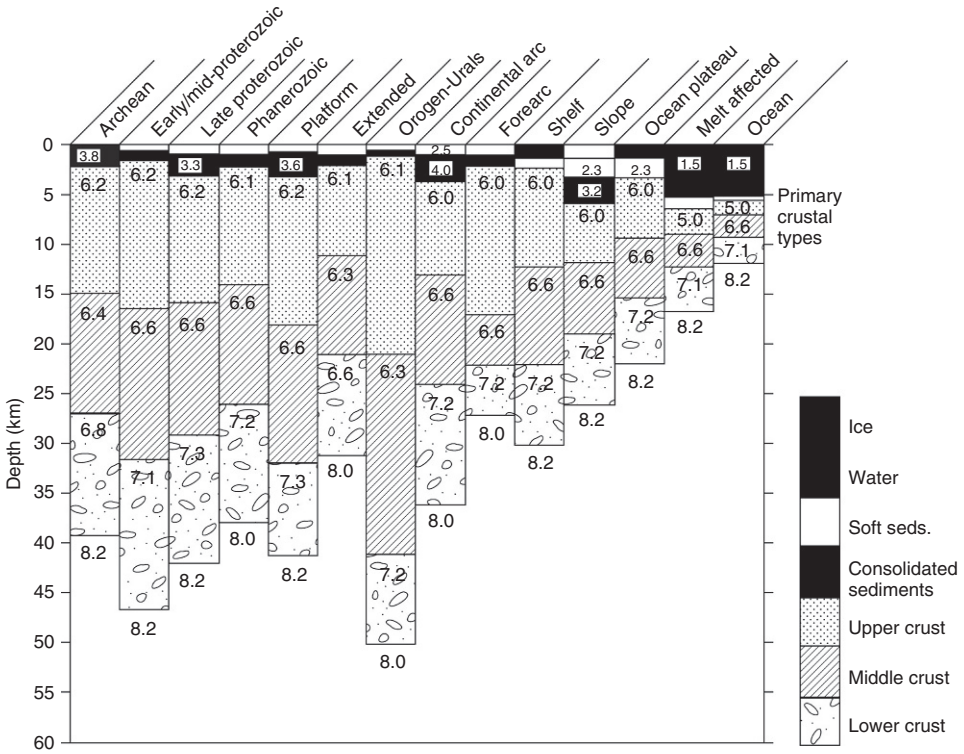

Figure 19 Fourteen primary continental and oceanic crustal types (Mooney et al., 1998). Typical P-wave velocities are indicated for the individual crustal layers and the uppermost mantle. Velocities refer to the top of each layer, and there commonly is a velocity gradient of 0.01–0.02 km s^{-1} km^{-1} within each layer. The crust thins from an average value of 40 km in continental interiors to 12 km beneath oceans.

crustal thickness of 41.5 km, very close to the weighted global average continental crustal thickness of 41 km. Orogens, young and old, show a wide range of thicknesses, from 30 to 75 km. Extended crust, as the name implies, has been thinned and shows an average thickness of 30.5 km. Rifts, both active and inactive, show a broad range, from 18 to 46 km. The broad range in crustal thickness for a tectonic province is sometimes present within a single tectonic province. For example, the Tibetan Plateau ranges in thickness from 55 to 75 km, and the Kenya rift from 20 to 36 km. Thus, significant variations sometimes occur within a single tectonic province. A second important observation is that there are numerous regions with anomalous crustal thickness. For example, southern Finland consists of a Proterozoic shield that is nearly at sea level. Global statistics would predict a crustal thickness of 41.5 ± 6.2 km. In fact, in southern Finland, the crust reaches a maximum thickness of 65 km due to the persistence of an ancient crust root at a Precambrian suture zone. This example attests to the considerable variability of continental crustal properties.

1.11.7 Global Crustal Models

The studies of the Earth's crust that have been summarized in the previous sections are sufficient to form the basis for a global model of the Earth's crust. One simple representation is a contour map of global crustal thickness (Figure 22). This map shows several interesting features. Continental interiors have a crustal thickness of 35–45 km, with much thicker (70–80 km) crust beneath the high topography of the Tibetan Plateau and South American Andes. Most continental margins have a thickness of close to 30 km, and the vast ocean basins are underlain by approximately 10-km-thick crust, including the water layer. Such a contour map, while presenting the main variations in crustal thickness, lacks information regarding lateral variations in compressional- and shear-wave velocity and density. These physical properties vary strongly within the uppermost mantle as well. For this reason, it has proved valuable to create global crustal models that quantify not only crustal thickness but also seismic velocities and density for the entire crust and uppermost mantle.

Global models of the seismic velocity and density structure of the crust have numerous applications in geophysics. Such models provide regional travel time to determine accurate earthquake locations and provide 'crustal corrections' to improve mantle seismic tomographic models. Also, lateral variations in mantle density may be inferred from long-wavelength gravity data when the density structure and thickness of the overlying crust are known. In addition, the crustal contribution to lithospheric stress and crustal isostasy can be calculated from crustal thickness, density, and topography (Mooney et al., 1998; Tesauro et al., 2012).

The earliest 3-D seismic velocity model of the Earth's crust dates back to Soller et al. (1982) who assembled one of the first compilations of global Moho and upper mantle velocity. A $2° \times 2°$ cell model called 3SMAC followed more than a

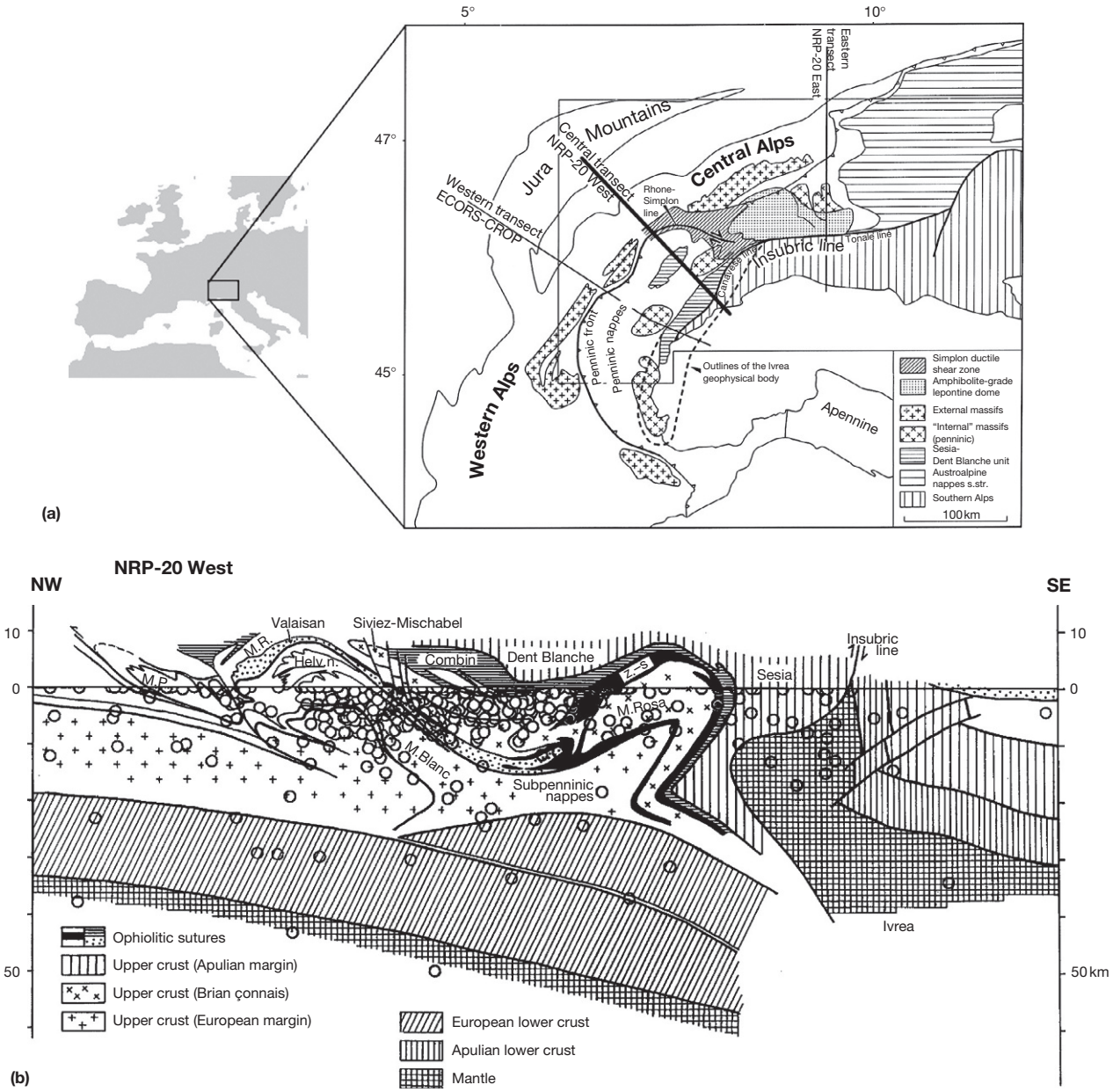

Figure 20 Synthesis of the deep structure and seismicity of the central Alps along the profile NRP-20 West (Schmidt and Kissling, 2000). (a) Location map showing the location of the seismic profile. (b) Crustal cross section (1:1 exaggeration) showing far-traveled nappes, crustal seismicity, and deep structure. Surficial faults are rooted in the middle crust. Seismicity (open circles) decreases dramatically below a depth of 10–15 km, but some earthquakes are located in the lower crust and even the upper mantle. Reproduced from Mooney WD, Beroza GC, and Kind R (2007) Fault zones from top to bottom: A geophysical perspective. In: Handy MR, Hirth G, and Hovius N (eds.), Tectonic Faults: Agents of Change on a Dynamic Planet. Cambridge, MA: MIT Press, pp. 9–46.

decade later (Nataf and Ricard, 1996). The 3SMAC model was derived using both seismological data and nonseismological constraints such as chemical composition, heat flow, and hot spot distribution, from which estimates of seismic velocities and the density in each layer were made. Two years later, CRUST 5.1 was introduced (Mooney et al., 1998) incorporating twice the amount of active-source seismic data than 3SMAC. Statistical averages were calculated for the different tectonic regions (Figure 23), and these average models were used in regions with no direct seismic measurements. However, the $5° \times 5°$ resolution was still too coarse for regional studies. In 2000, CRUST 2.0 updated the ice and sediment thickness information of CRUST 5.1 at $1° \times 1°$ resolution while basically redistributing the crustal thickness data onto a $2° \times 2°$ grid (Figure 23). In addition, several high-resolution regional compilations of depth-to-Moho values have been developed for Europe (Dèzes and Ziegler, 2001; Geiss, 1987; Meissner et al., 1987; Ritzmann et al., 2002; Tesauro et al., 2008), the Middle East, and North Africa (Seber et al., 2001), and new models have been presented for South America

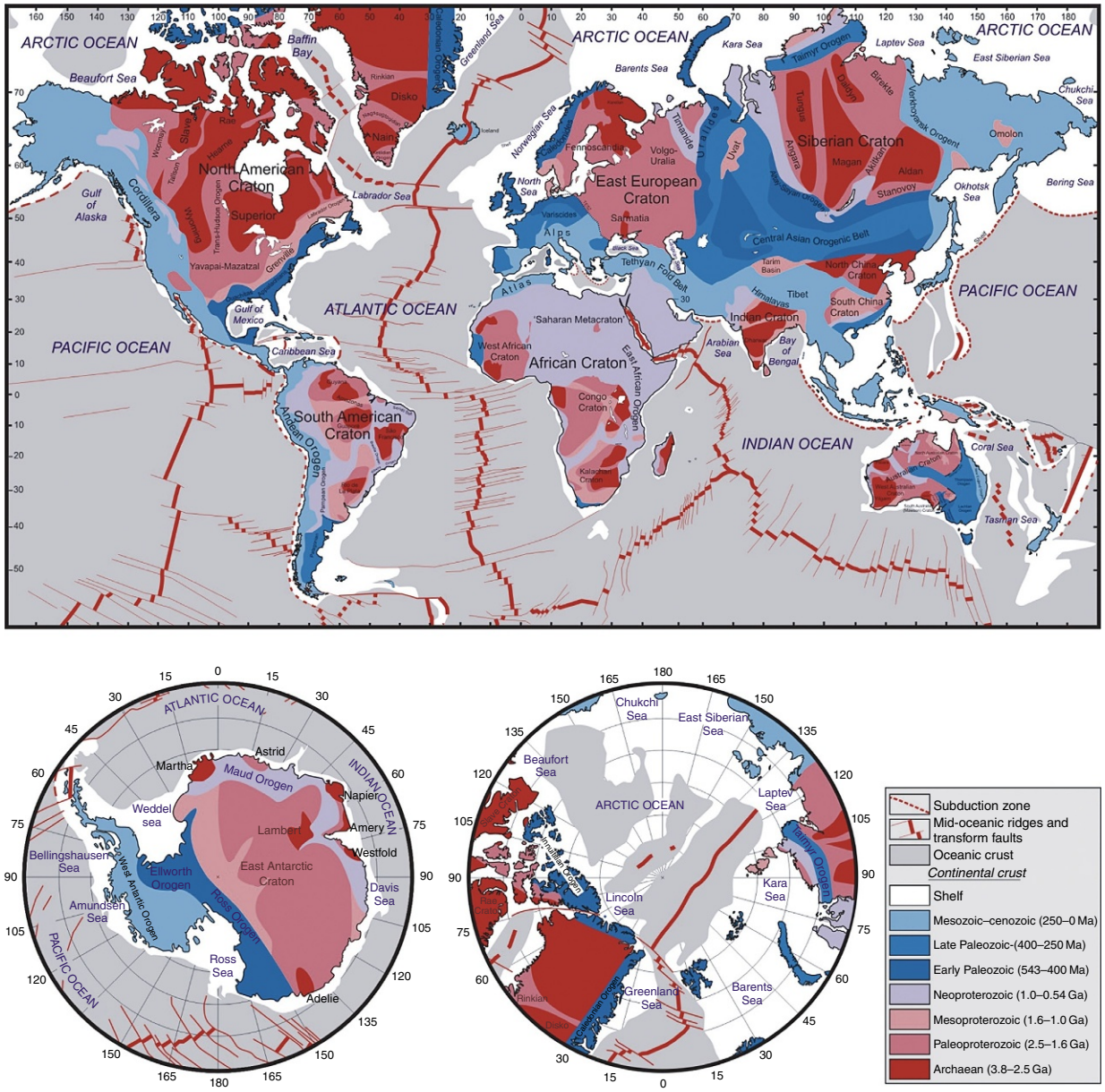

Figure 21 Geology of the continental crust. The crust is composed of six principal types, including the Precambrian platforms and shields, old and young orogens, extended crust, magmatic arcs, and rifts. Continental shelves are an additional important type. Basement age of the continental crust and distribution of mid-ocean ridges, oceanic crust, and continental shelf. The crust is subdivided by age. Precambrian shields and platforms comprise 69% of the continental crust by area. Seismic measurements cover much of the Earth's crust, but gap in coverage still exists (c.f. **Figure 11**). Statistical averages and their standard deviations make it possible to estimate crustal thickness and velocity structure in unmeasured regions, as is required to make complete global crust models. Reproduced from Mooney WD, Laske G, and Masters TG (1998) CRUST 5.1: A global crustal model at $5^{o} \times 5^{o}$. *Journal of Geophysical Research* 103: 727–747.

(Chulick et al., 2013; Lloyd et al., 2010) and Asia (Stolk et al., 2013).

Other published crustal models include WINPAK3D (Johnson and Vincent, 2002) and WENA 1.0 (Pasyanos et al., 2004), which provide an estimate of the velocity and density structure of the upper lithosphere (i.e., whole crust and uppermost mantle, Pn and Sn velocity) for specifically defined geophysical regions. These models are based on independent compilations of sediment, crust, and mantle models and data previously constructed or collected within these regions. Complete crustal models can be used to compare a variety of empirical observations over large geographic areas, to test the propagation of seismic waves, and to serve as starting models for tomographic inversion techniques. **Tables 16** and **17** list select references on global and regional crustal models, respectively.

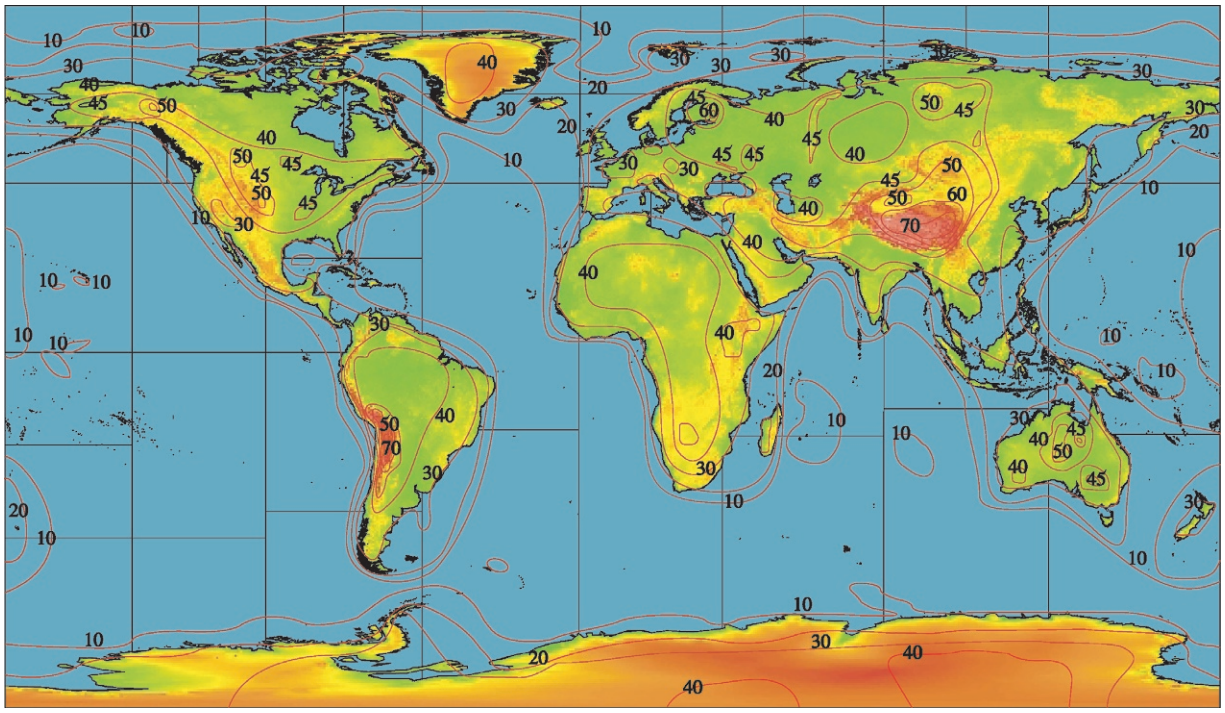

Figure 22 Global contour map of crustal thickness. Red lines indicate 10 km contour intervals.

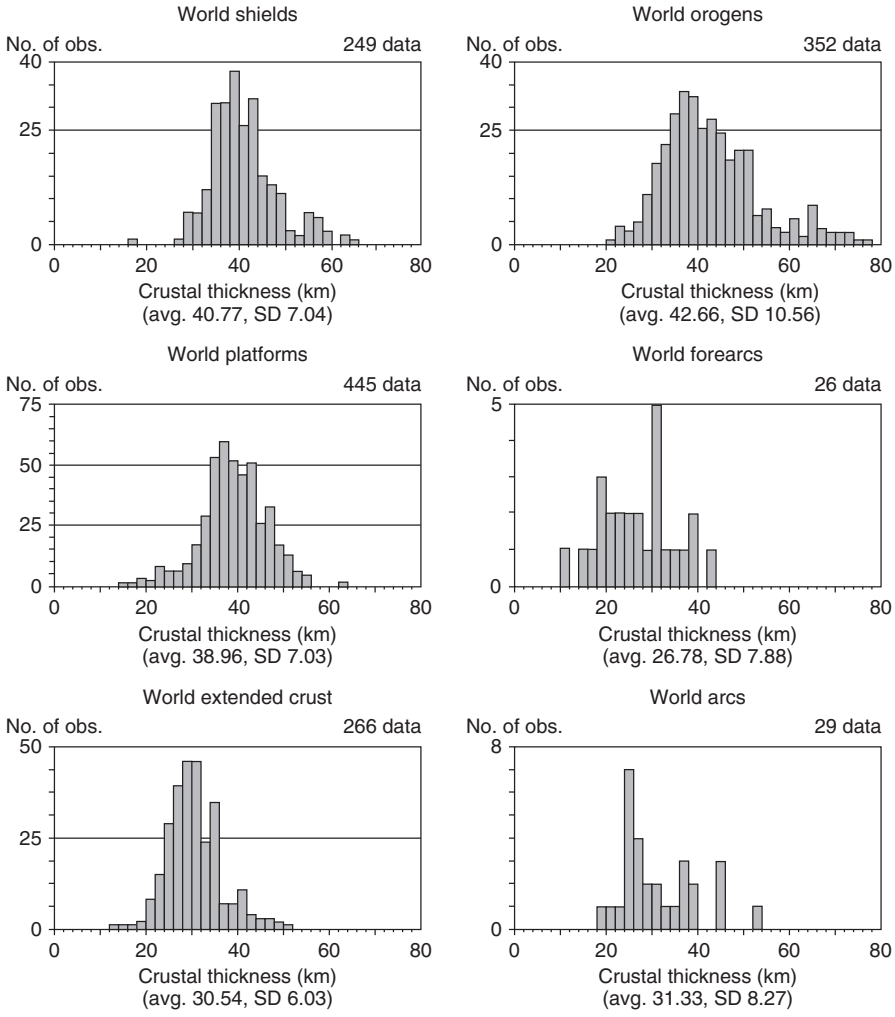

Figure 23 Histograms of crustal thickness for six continental tectonic provinces calculated from the individual point measurements (**Figure 11**). Average and standard deviations are indicated. These histograms indicate systematic differences among tectonic provinces and provide a basis for extrapolating crustal thickness into unmeasured regions.

Table 16 Global crustal models

Bassin et al.	2000
Laske and Masters	1997
Laske et al.	2012
Mooney et al.	1998
Nataf and Ricard	1996
Nataf and Ricard	1996
National Geophysical Data Center	2004
Soller et al.	1982
Tanimoto	1995

Table 17 Regional crustal models

Bassin et al.	2000
Bungun et al.	2005
Meyers et al.	2010
Mooney and Braile	1989
Pasyanos et al.	2004
Van der Lee and Nolet	1997
Walter et al.	2000
Warren and Healy	1973

1.11.7.1 The Sedimentary Cover

The sedimentary cover plays an important role in global crustal models because these materials have low seismic velocities and low densities. Thus, the sedimentary cover can have a large influence on travel times of seismic body and surface waves, as well as on the global gravity field.

Although sedimentary rocks cover most of the ocean floor and nearly three-quarters of continental surfaces, they are estimated to constitute only 5% of the upper 16 km of the crust by volume (Prothero and Schwab, 2004). This volumetric estimate is based on a variety of sources: (1) direct calculation from exposed stratigraphic sections or boreholes, (2) seismic reflection and refraction surveys, and (3) geochemical analyses including dissolved sodium or potassium in seawater than can be traced to total sediment–sedimentary rock volume. Taylor and McLennan (1985) and Prothero and Schwab (2004) used geologic data to estimate the abundances of common sedimentary rocks. The average abundances from these authors are 75% shales, 12% carbonates (limestone and dolomite), 10% sandstones, and 3% evaporates. Sedimentary rocks, especially fine-grained shales or mudrocks, are subject to postdepositional processes such as diagenesis, metamorphism, and alteration by oceanic water (Rudnick and Gao, 2005). These processes increase rock density and seismic velocity.

1.11.7.2 The Crystalline Crust and Uppermost Mantle

A complete global P- and S-wave crustal (and upper lithospheric) model for the globe is based on three types of information: (1) synthesizing existing models, such as WENA 1.0, the new Barents Sea model, and WINPAK; (2) seismic wave tomography data; and (3) an ongoing compilation of published seismic models for the crust, based on active- and passive-source seismology (**Figure 11**). Thus, in addition to the results from controlled sources, the model also incorporates the results from receiver function analysis, surface-wave dispersion analysis, and seismic tomography.

After compiling all of the existing regional models, the models are then compared and evaluated based on their technique and data quality. Separate databases are constructed for each technique, for example, (1) active-source models, (2) surface-wave models, (3) seismic tomography models, and (4) receiver function models. Integration of such varied models requires some discrimination of data and model quality, and a suite of models emerges from which a 'best fit' composite model is developed. Discrepancies between input models are resolved based on the best available data, which must occasionally be decided subjectively.

In the $2^\circ \times 2^\circ$ model CRUST 2.0 (**Figure 24**), the Earth's crust is divided into eight layers: (1) ice, (2) water, (3) soft sediments, (4) hard sediments, (5) crystalline upper, (6) middle crust, and (7) lower crust, and (8) uppermost mantle (Pn and Sn). The first seven layers are required so that one can accurately model the thickness of the crust and, therefore, obtain accurate Pn/Sn results for travel time analysis purposes. Both P- and S-wave velocities are specified in each layer.

Layers 1 and 2 are the easiest to determine. Ice is only found near the poles and in high regions such as the Himalayas. Efforts to determine its thickness are straightforward and relatively expeditious. Water depth is also relatively easy to interpret at $2^\circ \times 2^\circ$ using the ETOPO 2 model of the National Geophysical Data Center (2001). Both soft and hard (unconsolidated and consolidated, respectively) sediments are determined as these represent two distinct layers (3 and 4) in the model.

Layers 5–8 are determined from the compiled global crustal structure database and regional models. At present, the largest global crustal structure database of active- and passive-source measurements of the structure of the upper lithosphere includes more than 9200 data sets (almost ten times the number available for CRUST 5.1). This is more than sufficient to build a $2^\circ \times 2^\circ$ crustal block model.

Using the criteria set forth in the construction of CRUST 5.1 and other similar models, one of a series of primary crustal 'types' is assigned to each cell. There are approximately 400 different crustal model 'types' used in the $2^\circ \times 2^\circ$ global model. Once the global crustal structure model has been compiled, the model must be evaluated. Model testing is generally based on a comparison of Pg (Sg) and Pn (Sn) travel time predictions, with some empirical observations. **Tables 16** and **17** list the currently available global and regional crustal models. Updates to these models appear on a regular basis; Laske et al. (2012) presented a $1^\circ \times 1^\circ$ global model.

1.11.8 Discussion and Conclusions

Seismological studies of the crust and uppermost mantle began in the first decade of the twentieth century (Mohorovičić, 1910). Over the next 60 years, a wide range of studies (**Table 1**) defined the gross properties of the crust. The past 40 years have seen a pronounced increase in crustal and lithospheric studies, with the development of such techniques as seismic reflection studies of the deep crystalline crust, receiver function analysis, earthquake tomography, high-resolution surface-wave inversions, and seismic ambient noise analysis. These advances have been matched by extensive laboratory

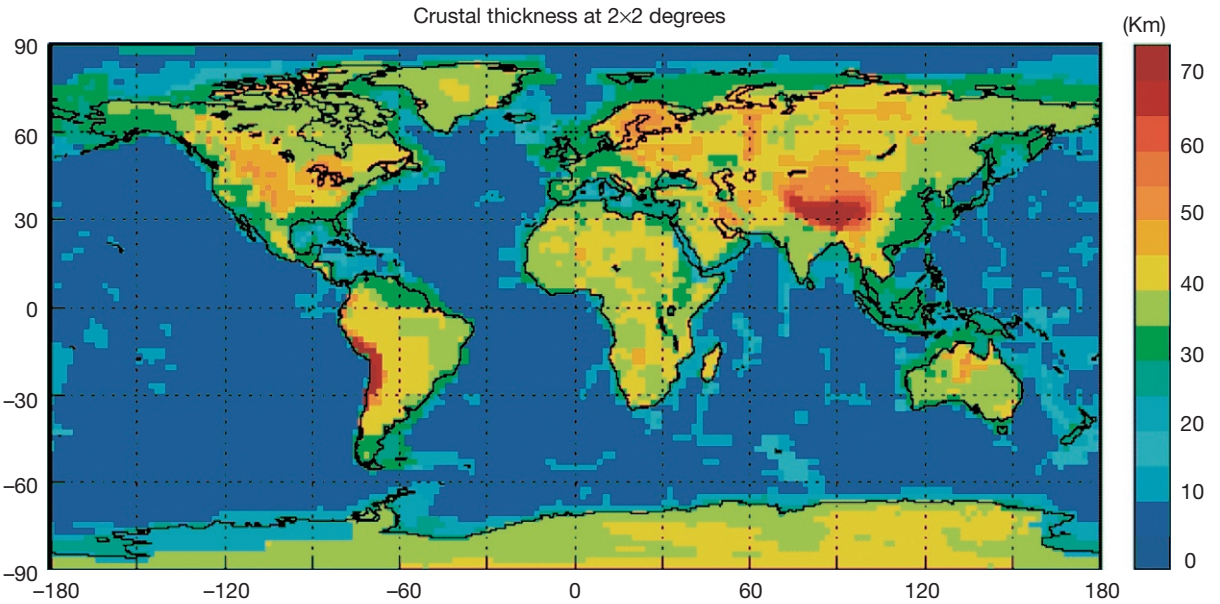

Figure 24 Crustal thickness provided by the $2^\circ \times 2^\circ$ CRUST2.0 model (Bassin et al., 2000). The locations of seismic profiles used to make this model are shown in **Figure 11**. Typical crustal velocity models are summarized in **Figure 21**. The crustal structure is estimated in regions with no seismic measurements using the statistic average illustrated in **Figure 23**. This crustal model is useful to make crustal velocity (P- and S-wave) or density correction in many types of geophysical models.

studies of rock velocities and densities and nonseismic geophysical studies using gravity, magnetic, and geoelectrical methods. Geophysical studies of the crust and subcrustal lithosphere have become so numerous that it is difficult for any individual or research group to keep abreast of all recent results. This suggests a need for a searchable data bank of results, where it would be possible to sort by technique, location, depth of penetration, or geologic setting.

The process of synthesizing global studies of crustal structure is more than 30 years old (Soller et al., 1982), and numerous regional and global models have become available (**Tables 16** and **17**). Until recently, these models have been largely based on seismic measurements of compressional-wave speeds (V_p), with the shear-wave speed (V_s) and density estimated using empirical relations. Future models should be able to rely more heavily on measured shear-wave velocities. Estimating deep crustal density will continue to be a challenge but is greatly aided by borehole and laboratory measurements. The use of multiple seismic data sets in constructing regional and global crustal models will be aided by the use of inverse techniques (e.g., Pasyanos et al., 2004). As high-resolution surface-wave models become available, particularly from ambient noise data (Campillo and Paul, 2003; Shapiro and Campillo, 2004), it will be possible to directly compare regional models derived from body-wave studies with models derived from surface waves. Likewise, nonseismic methods are rapidly developing, including satellite observations of long-wavelength gravity and magnetic fields. The synthesis of all of these methods promises to provide ever-increasing resolution on the global structure of the Earth's crust and subcrustal lithosphere.

Acknowledgments

Discussions with my scientific colleagues at the USGS and elsewhere over the past decade have aided greatly in preparing this chapter. Thanks to Claus Prodehl, Nina Pavelnkova, Shane Detweiler, Gary Chulick, Rolf Meissner, Gary Fuis, Gabi Laske, and Guy Masters for sharing their thoughts and insights. Susan McDonald, Martina Strakova, Honglei Wong, and Shane Detweiler provided valuable assistance in preparing this report.

References

Abbott DH (1996) Plumes and hotspots as sources of greenstone belts. *Lithos* 37: 113–127.

Acton CE, Priestley K, and Mitra S (2011) Crustal structure of the Darjeeling–Sikkim Himalaya and southern Tibet. *Geophysical Journal International* 184: 829–852.

Agostinetti NP, Lucente FP, Selvaggi G, et al. (2002) Crustal structure and Moho geometry beneath the Northern Apennines (Italy). *Geophysical Research Letters* 29: 1999. http://dx.doi.org/10.1029/2002GL015109.

Agudelo W, Ribodetti A, and Collot J-Y (2009) Joint inversion of multichannel seismic reflection and wide-angle seismic data: Improved imaging and refined velocity model of the crustal structure of the north Ecuador-south Colombia convergent margin. *Journal of Geophysical Research* 114: B02306. http://dx.doi.org/10.1029/2008JB005690.

Aki K (1982) Three-dimensional seismic inhomogeneities in the lithosphere and asthenosphere. *Reviews of Geophysics and Space Physics* 20: 161–170.

Aki K, Christoffersson A, and Husebye ES (1976) Three-dimensional seismic structure of the lithosphere under Montana LASA. *Bulletin of the Seismological Society of America* 66: 501–524.

Aki K and Lee WHK (1976) Determination of three-dimensional velocity anomalies under a seismic array using first *P*-arrival time from local earthquakes, 1. A homogeneous initial model. *Journal of Geophysical Research* 81: 4381–4399.

Aki K and Richards P (1980) *Quantitative Seismology. Theory and Methods*. San Francisco: Freeman.

Albarede F (1998) The growth of continental crust. *Tectonophysics* 296: 1–14.

Al-Damegh K, Sandvol E, and Barazangi M (2005) Crustal structure of the Arabian plate: New constraints from the analysis of teleseismic receiver functions. *Earth and Planetary Science Letters* 231: 177–196.

Alexander SS (1962) A study of the normal modes of surface waves across the Western United States. *Journal of Geophysical Research* 67: 3537–3538.

Al-Lazki AI, Sandvol E, Seber D, Barazangi M, Turkelli N, and Mohammad R (2004) Pn tomographic imaging of mantle lid velocity and anisotropy at the junction of the Arabian, Eurasian and African plates. *Geophysical Journal International* 158: 1024–1040.

Al-Lazki AI, Seber D, Sandvol E, Turkelli N, Mohamad R, and Barazangi M (2003) Tomographic Pn velocity and anisotropy structure beneath the Anatolian plateau (eastern Turkey) and the surrounding regions; the Turkey seismic experiment; the study of a young continent–continent collision. *Geophysical Research Letters* 30: 4 pp.

Allen RM, Nolet G, Morgan WJ, et al. (2002) Imaging the mantle beneath Iceland using integrated seismological techniques. *Journal of Geophysical Research* 107: 10.

Alvares R, Reynoso JP, Alvarez LJ, and Martinez ML (1978) Electrical conductivity of igneous rocks; Composition and temperature relations. *Bulletin Volcanologique* 41: 317–327.

Ammon C, Randall G, and Zandt G (1990) On the nonuniqueness of receiver function inversions. *Journal of Geophysical Research* 95: 15303–15328.

Anderson DL (1961) Elastic wave propagation in layered anisotropic media. *Journal of Geophysical Research* 66: 2953–2963.

Anderson DL (1967) The anelasticity of the mantle. *Geophysical Journal of the Royal Astronomical Society* 14: 135–164.

Anderson DL and Archambeau CB (1964) The anelasticity of the Earth. *Journal of Geophysical Research* 69: 2071–2084.

Angus DA, Wilson DC, Sandvol E, and Ni JF (2006) Lithospheric structure of the Arabian and Eurasian collision zone in eastern Turkey from S-wave receiver functions. *Geophysical Journal* 166: 1335–1346.

Ansorge J, Prohedel C, and Bamford D (1982) Comparative interpretation of explosion seismic data. *Journal of Geophysics* 51: 69–84.

Artemieva IM (2009) The continental lithosphere: Reconciling thermal, seismic, and petrologic data. *Lithos* 109: 23–46.

Artemieva IM (2011) *The Lithosphere: An Interdisciplinary Approach*. Cambridge: Cambridge University Press, 794 pp.

Artemieva IM and Mooney WD (2001) Thermal thickness of Precambrian lithosphere: A global study. *Journal of Geophysical Research* 106: 16387–16414.

Arvidson RE, Bindschadler D, Bowring S, Eddy M, Guinness E, and Leff C (1984) Bouguer images of the North American craton and its structural evolution. *Nature* 311: 241–243.

Aster R, Borchus B, and Thurber C (2012) *Parameter Estimation and Inverse Problems*, 2nd edn. Elsevier Academic Press, 360 pp.

Au D and Clowes RM (1984) Shear-wave velocity structure of the oceanic lithosphere from ocean bottom seismometer studies. *Geophysical Journal of the Royal Astronomical Society* 77: 105–123.

BABEL working group (1993) Deep seismic reflection/refraction interpretation of crustal structure along BABEL profiles A and B in the southern Baltic Sea. *Geophysical Journal International* 112: 325–343.

Bailey IW, Miller MS, Liu KJ, and Levander A (2012) V-S and density structure beneath the Colorado Plateau constrained by gravity anomalies and joint inversions of receiver function and phase velocity data. *Journal of Geophysical Research* 117: B02313. http://dx.doi.org/10.1029/2011JB008522.

Bamford D (1977) *Pn* velocity anisotropy in a continental upper mantle. *Geophysical Journal of the Royal Astronomical Society* 49: 29–48.

Banks RJ (1972) The overall conductivity distribution in the earth. *Journal of Geomagnetism and Geoelectricity* 24: 337–351.

Banks RJ, Parker RL, and Huestis SP (1977) Isostatic compensation on a continental scale: Local versus regional mechanisms. *Geophysical Journal of the Royal Astronomical Society* 51: 431–452.

Bannister SC, Ruud BO, and Husebye ES (1991) Tomographic estimates of sub-Moho seismic velocities in Fennoscandia and structural implications; imaging and understanding the lithosphere of Scandinavia and Iceland. *Tectonophysics* 189: 37–53.

Baranov V (1957) A new method for interpretation of aeromagnetic maps: Pseudogravimetric anomalies. *Geophysics* 22: 359–383.

Barazangi M and Brown L (eds.) (1986a) *Reflection Seismology: A Global Perspective*. In: *Geodynamics Series*, vol. 13, p. 311. Washington, DC: American Geophysical Union.

Barazangi M and Brown L (eds.) (1986b) *Reflection Seismology: The Continental Crust*. In: *Geodynamics Series*, vol. 14, p. 339. Washington, DC: American Geophysical Union.

Barazangi M and Ni J (1982) Velocities and propagation characteristics of *Pn* and *Sn* waves beneath the Himalayan arc and Tibetan plateau: Possible evidence for underthrusting of Indian continental lithosphere beneath Tibet. *Geology* 10: 179–185.

Barclay AH, Toomey DR, and Solomon SC (1998) Seismic structure and crustal magmatism at the Mid-Atlantic Ridge, 35°N. *Journal of Geophysical Research* 102: 3109–3129.

Barmin MP, Levshin AL, and Ritzwoller MH (2001) A fast and reliable method for surface wave tomography. *Pure and Applied Geophysics* 158: 1351–1375.

Bartelson H, Lueschen E, Krey T, Meissner R, Scholl H, and Walter C (1982) The combined seismic reflection-refraction investigation of the Urach geothermal anomaly. In: Haemel R (ed.) *The Urach Geothermal Project*, pp. 247–262. Stuttgart: Schweizerbart'sche Verlagsbuchhandlung.

Barton PJ (1986) The relationship between seismic velocity and density in the continental crust. *Geophysical Journal of the Royal Astronomical Society* 87: 195–208.

Barton PJ (1992) LISPB revisited: A new look under the Caledonides of northern Britain. *Geophysical Journal International* 110: 371–391.

Barton AJ and White RS (1997) Crustal structure of the Edoras Bank continental margin and mantle thermal anomalies beneath the North Atlantic. *Journal of Geophysical Research* 102: 3109–3129.

Bass JD (1995) Elasticity of minerals, glasses, and melts. In: Athrens TJ (ed.) *Mineral Physics and Crystallography: A Handbook of Physical Constants*. *American Geophysical Union Reference Shelf*, 2, pp. 45–63. Washington, DC: American Geophysical Union.

Bassin C, Laske G, and Masters GNY (2000) The current limits of resolution for surface tomography in North America. *EOS* 81: F897.

Bateman PC and Eaton JP (1967) Sierra Nevada Batholith. *Science* 158: 1407–1417.

Bath M and Stefánsson R (1966) *S-P* conversion at the base of the crust. *Annali di Geofisica* 19: 119–130.

Becker K, Franke D, and Schnabel M (2012) The crustal structure of the southern Argentine margin. *Geophysical Journal International* 189: 1483–1504.

Bédard JH (2006) A catalytic delamination-driven model for coupled genesis of Archean crust and sub-continental lithospheric mantle. *Geochemica et Cosmochimica Acta* 70: 1188–1214.

Begnaud ML, McClain JS, Barth GA, Orcutt JA, and Harding AJ (1997) Preliminary velocity structure from forward modeling of the eastern ridge-transform intersection area of the Clipperton Fracture Zone, East Pacific Rise. *Journal of Geophysical Research* 102: 7803–7820.

Behn MD and Kelemen PB (2003) Relationship between seismic P-wave velocity and the composition of anhydrous igneous and meta-igneous rocks. *Geochemistry, Geophysics, Geosystems* 4: 1041. http://dx.doi.org/10.1029/2002GC000393.

Behrendt JC, Green AG, Cannon WF, et al. (1988) Crustal structure of the Midcontinent rift system; Results from GLMPCE deep seismic reflection studies. *Geology* 16: 81–85.

Beloussov VV, Kunin NY, Mazur VB, Ostisty BK, and Ostrovsky MI (1988) *Map of the Relief of the Basement Surface of Eurasia*, Scale 1:15,000,000.

Beloussov VV and Pavlenkova NI (1984) The types of the Earth's crust. *Journal of Geodynamics* 1: 167–183.

Beloussov VV, Pavlenkova NI, and Kvjatkovskaya GN (eds.) (1991) *Deep Structure of the USSR Territory (in Russian)*. Moscow: Nauka, 234 pp.

Ben-Avraham Z, Ginzburg A, Makris J, et al. (2002) Crustal structure of the Levant Basin, eastern Mediterranean. *Tectonophysics* 346: 23–43.

Ben-Avraham Z, Nur A, Jones D, and Cox A (1981) Continental accretion: from oceanic plateaus to allochthonous terranes. *Science* 213: 47–54.

Ben-Hadj-Ali H, Operto S, and Virieux J (2008) Velocity model building by 3D frequency-domain full-waveform inversion of wide-aperture seismic data. *Geophysics* 73: 101–117.

Benoit MH, Nyblade AA, VanDecar JC, and Gurrola H (2003) Upper mantle P-wave velocity structure and transition zone thickness beneath the Arabian shield. *Geophysical Research Letters* 30: 4.

Berckhemer H, Rauen A, Winter H, et al. (1997) Petrophysical properties of 9-km-deep crustal section at KTB. *Journal of Geophysical Research* 102: 18337–18362.

Berdichevskiy MN and Zhdanov MS (1984) *Advanced Theory of Deep Electromagnetic Sounding*. Amsterdam: Elsevier, 408 pp.

Berry LG and Mason BH (1959) Mineralogy: Concepts Description Determinations, 444 pp. New York: W.H Freeman.

Berry MJ and West GF (1966) An interpretation of the first-arrival data of the Lake Superior experiment by the time-term method. *Bulletin of the Seismological Society of America* 56: 141–171.

Bessonova EN, Fishmen VM, Ryaboy VZ, and Sitnikova GA (1974) The tau method for inversion of travel times; 1. Deep seismic sounding data. *Geophysical Journal of the Royal Astronomical Society* 36: 377–398.

Bibee LD and Shor GG (1976) Compressional wave anisotropy in the crust and upper mantle. *Geophysical Research Letters* 3: 639–642.

Bijwaard H, Spakman W, and Engdahl ER (1998) Closing the gap between regional and global travel time tomography. *Journal of Geophysical Research* 103: 30055–30078.

Birch F (1943) Elasticity of igneous rocks at high temperatures and pressures. *Bulletin of the Geological Society of America* 54: 263–286.

Birch F (1952) Elasticity and constitution of the Earth's interior. *Journal of Geophysical Research* 57: 227–286.

Birch F (1960) The velocity of compressional waves in rocks to 10 kilobars, Part 1. *Journal of Geophysical Research* 5: 1083–1102.

Birch F (1961) The velocity of compressional waves in rocks to 10 kilobars, Part 2. *Journal of Geophysical Research* 66: 2199–2224.

Birch F (1972) Numerical experiments on the velocities in aggregates of olivine. *Journal of Geophysical Research* 77: 6385–6391.

Birch F (1975) Velocity and attenuation from resonant vibrations of spheres of rock, glass, and steel. *Journal of Geophysical Research* 80: 756–764.

Bjőrnsson A, Eysteinsson H, and Beblo M (2005) Crustal formation and magma genesis beneath Iceland: Magnetotelluric constraints. In: *Plates, Plumes, and Paradigms*, *Geological Society of America, Special Paper*, 388, 665–686.

Blakely RG (1995) *Potential Theory in Gravity and Magnetic Applications*. New York: Cambridge University Press.

Blakely RJ and Grauch VJS (1983) Magnetic models of crystalline terrane: Accounting for the effect of topography. *Geophysics* 48: 1551–1557.

Bleibinhaus F and Gebrande H (2006) Crustal structure of the Eastern Alps along the TRANSALP profile from wide-angle seismic tomography. *Tectonophysics* 414: 51–69.

Blundell D, Freeman R, and Mueller S (eds.) (1992) *A Continent Revealed – the European Geotraverse*. Cambridge: Cambridge University Press, 275 pp.

Blundell DJ and Raynaud B (1986) Modeling lower observed on BIRPS profiles. In: Barazangi M and Brown L (eds.) *Reflection Seismology; A Global Perspective. Geodynamics Series,* 13, pp. 287–295. American Geophysical Union.

Bohnhoff M and Makris J (2004) Crustal structure of the southeastern Iceland-Faeroe Ridge (IFR) from wide aperture seismic data. *Journal of Geodynamics* 37: 233–252.

Bond KR and Zietz I (1986) *Composite Magnetic Anomaly Map of the Western United States West of the 96° Longitude*. U.S. Geological Survey Geophysical Investigations Map GP-977.

Bonini WE and Bonini RR (1979) Andrija Mohorovičić; Seventy years ago an earthquake shook Zagreb. *Eos, Transactions American Geophysical Union* 60: 699–701.

Booker J, Favetto A, and Pomposiello MC (2004) Low electrical resistivity associated with plunging of the Nazca flat slab beneath Argentina. *Nature* 429: 399–403.

Boore DM (1972) In: Bolt BA (ed.) *Finite difference methods for seismic wave propagation in heterogeneous materials*. *Seismology; Surface Waves and Earth Oscillations; Methods in Computational Physics*, vol. 11, pp. 1–37. New York: Academic Press.

Boschi L, Ekstroem G, and Kustowski B (2004) Multiple resolution surface wave tomography; the Mediterranean basin. *Geophysical Journal International* 157: 293–304.

Bostock M, Hyndman R, Rondenay S, and Peacock S (2002) An inverted continental Moho and serpentinization of the forearc mantle. *Nature* 417: 536–538.

Bouchon M (1982) The complete synthesis of seismic crustal phases at regional distances. *Journal of Geophysical Research* 87: 1735–1741.

Bourjot L and Romanowicz B (1992) Crust and upper mantle tomography in Tibet using surface waves. *Geophysical Research Letters* 19: 881–884.

Braile LW and Chiang CS (1986) The continental Mohorovičić discontinuity; Results from near-vertical and wide-angle seismic refraction studies. In: Barazangi M and Brown L (eds.) *Reflection Seismology; A Global Perspective*. *Geodynamics Series,* 13, pp. 257–272. American Geophysical Union.

Braile LW, Keller GR, Mueller S, and Prodehl C (1995) In: Olsen KH (ed.) *Seismic techniques*. *Continental Rifts: Evolution, Structure, Tectonics*pp. 61–92. Amsterdam: Elsevier.

Breivik AJ, Mjelde R, Grogan P, et al. (2003) Crustal structure and transform margin development south of Svalbard based on ocean bottom seismometer data. *Tectonophysics* 369: 37–70.

Brocher TM (2005) Empirical relations between elastic wavespeeds and density in the Earth's crust. *Bulletin of the Seismological Society of America* 95(6): 2081–2092.

Brocher TM, Parsons T, Blakely RJ, et al. (2001) Upper crustal structure in Puget Lowland, Washington: Results from the 1998 Seismic Hazards Investigation in Puget Sound. *Journal of Geophysical Research* 106: 13541–13564.

Brocher TM, Parsons T, Tréhu AM, Snelson CM, and Fisher MA (2003) Seismic evidence for widespread serpentinized forearc upper mantle along the Cascadia margin. *Geology* 31: 267–1307.

Broucher TM (1995) Deep-crustal seismology of continental margins, U.S. Natl. Rep. Int. Union Geod. Geophys. 1991–1994. *Reviews of Geophysics* 33: 309–314.

Brown L, Barazangi M, Kaufman S, and Oliver J (1986) The first decade of COCORP; 1974–1984. In: Barazangi M and Brown LD (eds.) *Reflection Seismology; A Global Perspective. Geodynamics Series,* 13, pp. 107–120. American Geophysical Union.

Brown JW and White RS (1994) Variation with spreading rate of oceanic crustal thickness and geochemistry. *Earth and Planetary Science Letters* 75: 439–449.

Brueckl E, Bleibinhaus F, and Gosar A (2007) Crustal structure due to collisional and escape tectonics in the Eastern Alps region based on profiles Alp01 and Alp02 from the ALP 2002 seismic experiment. *Journal of Geophysical Research* 112: B06308. http://dx.doi.org/10.1029/2006JB004687.

Brune JN (1969) Surface Waves and Crustal Structure. In: Hart PJ (ed.) *The Earth's crust and upper mantle. Geophysical Monograph Series,* 13, pp. 230–242. American Geophysical Union.

Brune J and Dorman J (1963) Seismic waves and earth structure in the Canadian. *Bulletin of the Seismological Society of America* 53: 167–210.

Brune JN, Nafe J, and Oliver J (1960) A simplified method for the analysis and synthesis of dispersed wave trains. *Journal of Geophysical Research* 65: 287–304.

Bruneton M, Pedersen HA, et al. (2004) Complex lithospheric structure under the central Baltic Shield from surface wave tomography. *Journal of Geophysical Research* 109: 15. http://dx.doi.org/10.1029/2003JB002947.

Bullock AD and Minshull TA (2005) From continental extension to seafloor spreading: Crustal structure of the Goban Spur rifted margin, southwest of the UK. *Geophysical Journal International* 163: 527–546.

Bungum H, Ritzmann O, Maercklin N, Faleide S, Mooney WD, and Detweiler H (2005) Three-dimensional model for the crust and upper mantle in the Barents sea region. *Eos, Transactions American Geophysical Union* 86(16): 160–161.

Burdick LJ and Langston CA (1977) Modeling crust-structure through the use of converted phases in teleseismic body-wave-forms. *Bulletin of the Seismological Society of America* 67: 677–691.

Butler R (1986) Regional seismic observations of the Ontong Java Plateau and East Marina Basin. *Marine Geophysical Research* 8: 27–38.

Byerly P (1926) The Montana earthquake of June 28, 1925. *Bulletin of the Seismological Society of America* 16: 209–265.

Byerly P and Dyk K (1932) Richmond quarry blast of September 12, 1931, and the surface layering of the earth in the region of Berkeley. *Bulletin of the Seismological Society of America* 22: 50–55.

Cagniard L (1953) Basic theory of magnetotelluric method of geophysical prospecting. *Geophysics* 18(3): 605–635.

Calvert AJ (2011) The seismic structure of island arc crust. In: Brown D and Ryan PD (eds.) *Arc-Continent Collision, Frontiers in Earth Science*, pp. 87–119. Berlin: Springer.

Calvert AJ, Klemperer SL, and Takahashi N (2008) Three-dimensional crustal structure of the Mariana island arc from seismic tomography. *Journal of Geophysical Research* 113: B01406. http://dx.doi.org/10.1029/2007JB004939.

Calvert A, Sandvol E, Seber D, et al. (2000) Propagation of regional seismic phases (Lg and Sn) and Pn velocity structure along the Africa-Iberia plate boundary zone; tectonic implications. *Geophysical Journal International* 142: 384–408.

Campbell IH, Griffiths RW, and Hill R (1989) Melting in an Archaean mantle plume: Heads it's basalts, tails it's komatiites. *Nature* 339: 697–899.

Campillo M and Paul A (2003) Long-range correlations in the diffuse seismic coda. *Science* 299: 449–547.

Canales JP, Collins JA, Escartin J, et al. (2000a) Seismic structure across the rift valley of the Mid-Atlantic Ridge at 23 degrees 20' (MARK area): Implications for crustal accretion processes at slow spreading ridges. *Journal of Geophysical Research* 105: 28411–28425.

Canales JP, Detrick RS, Lin J, Collins JA, and Toomey DR (2000b) Crustal and upper mantle seismic structure beneath the rift mountains and across a nontransform offset at the Mid-Atlantic Ridge (35°N). *Journal of Geophysical Research* 105: 2699–2719.

Canales JP, Detrick RS, Toomey DR, et al. (2003) Segment-scale variations in the crustal structure of 150–300 kyr old fast spreading oceanic crust (East Pacific Rise, 8 degrees 15' N-10 degrees 5' N) from wide-angle seismic refraction profiles. *Geophysical Journal International* 152: 766–794.

Cann JR (1970) New model for the structure of the oceanic crust. *Nature* 226: 928–930.

Cann JR (1974) A model for oceanic crustal structure developed. *Geophysical Journal of the Royal Astronomical Society* 39: 169–187.

Cannat M (1996) How thick is the magmatic crust at slow spreading oceanic ridges? *Journal of Geophysical Research* 101: 2847–2857.

Caress DW, McNutt MK, Detrick RS, and Mutter JC (1995) Seismic imaging of hotspot-related crustal underplating beneath the Marquesas Islands. *Nature* 373: 600–603.
Carlson RL, Christensen NI, and Moore RP (1980) Anomalous crustal structure in ocean basins: Continental fragments and oceanic plateaus. *Earth and Planetary Science Letters* 51: 171–180.
Carmichael RS (1982) *Handbook of Physical Properties of Rocks*. 2: Boca Raton, FL: CRC Press, 345 pp.
Cassidy JF (1992) Numerical experiments in broadband receiver function analysis. *Bulletin of the Seismological Society of America* 82: 1453–1474.
Cermak V (1993) Lithospheric thermal regimes in Europe. *Physics of the Earth and Planetary Interiors* 79: 179–193.
Červený V (1972) Seismic rays and ray intensities in inhomogeneous anisotropic media. *Geophysical Journal of the Royal Astronomical Society* 72: 755–766.
Červený V, Molotkov IA, and Pšenčník I (1977) *Ray Method in Seismology*. Prague, Czechoslovakia: University of Karlova (Charles), 214 pp.
Červený V and Pšenčník I (1984) SEIS83—Numerical modeling of seismic wave fields in 2-D laterally varying layered structures by the ray method. In: Engdal ER (ed.) *Documentation of Earthquake Algorithms*, pp. 36–40. Boulder, CO: World Data Cent. A for Solid Earth Geophys, Rep. SE-35.
Champman CH (1986) Thermal gradient in the continental crust. In: Dawson JB (ed.) *The Nature of the Lower Continental Crust*, vol. 24, pp. 63–70. Geological Society Special Publication.
Chapman CH (1978) A new method for computing seismic monograms. *Geophysical Journal of the Royal Astronomical Society* 54: 481–518.
Chapman CH and Orcutt JA (1985) Least-squares fitting of marine seismic refraction data. *Geophysical Journal of the Royal Astronomical Society* 82: 339–374.
Charvis P, Recq M, Operto S, and Brefort D (1995) Deep structure of the northern Kerguelen Plateau and hotspot-related activity. *Geophysical Journal International* 122: 899–924.
Chen YJ (1992) Oceanic crustal thickness versus spreading rate. *Geophysical Research Letters* 19: 753–756.
Chen C, Chen Y, Yen H, and Yu G (2003) Lateral variations of P (sub n) velocity and anisotropy in Taiwan from travel-time tomography. *Earth, Planets and Space* 55: 223–230.
Chen H, Chiu JM, Pujol J, et al. (2005) A simple algorithm for local earthquake location using 3-dimensional Vp and Vs Models-test examples in the central USA and Taiwan regions. *Bulletin of the Seismological Society of America* 96: 288–305.
Chian D, Louden KE, Minshull TA, and Whitmarsh RB (1999) Deep structure of the ocean continent transition in the southern Iberia Abyssal Plain from seismic refraction profiles: 1. Ocean Drilling Program (Legs 149 and 173) transect. *Journal of Geophysical Research* 104: 7443–7462.
Chian D, Louden KE, and Reid I (1995) Crustal structure of the Labrador sea conjugate margin and implications for the formation of nonvolcanic continental margins. *Journal of Geophysical Research* 100: 24239–24253.
Chimera G, Aoudia A, Sarao A, and Panza GF (2003) Active tectonics in central Italy; constraints from surface wave tomography and source moment tensor inversion. *Physics of the Earth and Planetary Interiors* 138: 241–262.
Cho HM, Baag CE, and Lee JM (2006) Crustal velocity structure across the southern Korean Peninsula from seismic refraction survey. *Geophysical Research Letters* 33: L06307. http://dx.doi.org/10.1029/2005GL025145.
Christensen NI (1965) Compressional wave velocities in metamorphic rocks at pressures to 10 kilobars. *Journal of Geophysical Research* 70: 6147–6164.
Christensen NI (1966a) Elasticity of ultrabasic rocks. *Journal of Geophysical Research* 71: 5921–5931.
Christensen NI (1966b) Shear wave velocities in metamorphic rocks at pressures to 10 kilobars. *Journal of Geophysical Research* 71: 3549–3556.
Christensen NI (1971) Shear wave propagation in rocks. *Nature* 229: 549–550.
Christensen NI (1972) The abundance of serpentinites in the oceanic crust. *Journal of Geology* 80: 709–719.
Christensen NI (1979) Compressional wave velocities in rocks at high temperatures and pressures, critical thermal gradients, and crustal low-velocity zones. *Journal of Geophysical Research* 84: 6849–6857.
Christensen NI (1982) In: Carmichael RS (ed.) *Seismic velocities*. *Handbook of Physical Properties of Rocks*, vol. II, pp. 1–228. Boca Raton, FL: CRC Press.
Christensen NI (1996) Poisson's ratio and crustal seismology. *Journal of Geophysical Research* 100: 3139–3156.
Christensen NI and Fountain DM (1975) Constitution of the lower continental crust based on experimental studies of seismic velocities in granulite. *Bulletin of the Geological Society of America* 86: 236–277.
Christensen NI and Mooney WD (1995) Seismic velocity structure and the composition of the continental crust: A global view. *Journal of Geophysical Research* 100: 9761–9788.
Christensen NI and Salisbury MH (1975) Structure and constitution of the lower oceanic crust. *Reviews of Geophysics and Space Physics* 13: 57–86.
Christensen NI and Salisbury MH (1979) Seismic anisotropy in the upper mantle: Evidence from the Bay of Islands ophiolite complex. *Journal of Geophysical Research* 84: 4601–4610.
Christensen NI and Salisbury MH (1982) Lateral heterogeneity in the seismic structure of the oceanic crust inferred from velocity studies in the Bay of Islands ophiolite, Newfoundland. *Geophysical Journal of the Royal Astronomical Society* 68: 675–688.
Christeson GL, Barker DHN, Austin JA, et al. (2003) Deep crustal structure of Bransfield Strait: Initiation of a back arc basin by rift reactivation and propagation. *Journal of Geophysical Research* 108: 2492. http://dx.doi.org/10.1029/2003JB002468.
Christeson GL, Mann P, and Escalona A (2008) Crustal structure of the Caribbean-northeastern South America arc-continent collision zone. *Journal of Geophysical Research* 113: B08104. http://dx.doi.org/10.1029/2007JB005373.
Christeson GL, Shaw PR, and Garmany JD (1997) Shear and compressional wave structure of the East Pacific Rise, 9°–10°N. *Journal of Geophysical Research* 102: 7821–7835.
Chulick GS (1997) Comprehensive seismic survey database for developing three-dimensional models of the earth's crust. *Seismological Research Letters* 68: 734–742.
Chulick GS, Detweiler S, and Mooney WD (2013) Seismic structure of the crust and uppermost mantle of South America and surrounding ocean basins. *Journal of South American Earth Sciences* 42: 260–275.
Claerbout JF (1976) *Fundamentals of Geophysical Data Processing*. Palo Alto, CA: Blackwell Scientific Publications, 274.
Claerbout JF (1985) *Imaging the Earth's Interior*. Palo Alto, CA: Blackwell Scientific Publications, 398.
Clark SP (1966) Handbook of physical constants. *Geological Society of America Memoir* 97: 587.
Clarke FW (1889) The relative abundance of the chemical elements. *Bulletin of the Philosophical Society of Washington* XI: 131–142.
Clarke FW and Washington HS (1924) The composition of the Earth's crust. US Geological Survey Professional Paper 127: 117 pp.
Clegg B and England R (2003) Velocity structure of the UK continental shelf from a compilation of wide-angle and refraction data. *Geological Magazine* 140: 453–467.
Clitheroe GM, Gudmundsson U, and Kennett BLN (2000) The crustal thickness of Australia. *Journal of Geophysical Research* 105: 13697–13713.
Cloos M (1993) Lithospheric buoyancy and collisional orogenesis: Subduction of oceanic plateaus, continental margins, island arcs, spreading ridges, and seamounts. *Geophysical Society of America Bulletin* 105: 715–737.
Closs H and Behnke C (1961) Fortschritte der Anwendung seismischer Methoden in der Erforschung der Erdkruste. *Geologische Rundschau* 51: 315.
Clowes RM, Baird DJ, and Dehler SA (1997) Crustal structure of the northern Cascadia subduction zone, southwestern British Columbia, from potential field and seismic studies. *Canadian Journal of Earth Sciences* 34: 317–335.
Clowes RM, Brandon MT, Green AG, et al. (1987) LITHOPROBE – southern Vancouver Island: Cenozoic subduction complex imaged by deep seismic reflections. *Canadian Journal of Earth Sciences* 24: 31–51.
Clowes RM, Burianyk MJA, Gorman AR, et al. (2002) Crustal velocity structure from SAREX, the Southern Alberta Refraction Experiment. *Canadian Journal of Earth Sciences* 39: 351–373.
Clowes R, Cook F, Hajnal Z, et al. (1999) Canada's LITHOPROBE Project (Collaborative, multidisciplinary geoscience research leads to new understanding of continental evolution). *Episodes* 22: 3–20.
Clowes RM and Hyndman RD (2002) Geophysical studies of the Northern Cascadia Subduction Zone off Western Canada and their implications for great earthquake seismotectonics: A review. In: Fujinawa Y and Yoshida A (eds.) *Seismotectonics in Convergent Plate Boundary*, pp. 1–23. Tokyo, Japan: Terra Scientific Publishing.
Clowes RM, Zelt CA, Amor JR, and Ellis RM (1995) Lithospheric structure in the southern Canadian Cordillera from a network of seismic refraction lines. *Canadian Journal of Earth Sciences* 32: 1485–1513.
Coffin MA and Eldholm O (1994) Large igneous provinces: Crustal structure, dimensions and external consequences. *Reviews of Geophysics* 32: 1–36.
Collier JS and Singh SC (1997) Detailed structure of the top of the melt body beneath the East pacific Rise at 9°40′N from waveform inversion of seismic reflection data. *Journal of Geophysical Research* 103: 20287–20304.

Collier JS and Singh SC (1998) Poisson's ratio structure of young oceanic crust. *Journal of Geophysical Research* 103: 20981–20996.
Commission for the Geological Map of the Word (CGMW) (2002) *Geological Map of the World*. Paris: UNESCO.
Condie KC (1989) *Plate Tectonics and Crustal Evolution*. New York: Elsevier, pp. 244–282.
Condie KC (2011) *Earth as an Evolving Planetary System*, 2nd edn. Amsterdam: Academic Press, Elsevier, 578 pp.
Condie KC and Kröner A (2013) The building blocks of continental crust: Evidence.
Conrad V (1925) Laufzeitkurven des Taueren vom, 28, November 1923. *Akademische Wissenschaft* 59, Mitteiler Erdbeban Kommission Wien, 1–23
Constable SC and Cox CS (1996) Marine controlled-source electromagnetic soundry. Part 2: The PEGASUS experiment. *Journal of Geophysical Research* 101: 5519–5530.
Cook FA, White DJ, Jones AG, Eaton DWS, Hall JA, and Clowes RM (2010) How the crust meets the mantle: Lithoprobe perspectives on the Mohorovicic discontinuity and crust-mantle transition. *Canadian Journal of Earth Sciences* 47: 315–351.
Couch R and Woodcock S (1981) Gravity and structure of the continental margins of southwestern Mexico and northwestern Guatemala. *Journal of Geophysical Research* 86: 1829–1840.
Cram IH Jr. (1961) Crustal structure refraction survey in south Texas. *Geophysics* 26: 560–573.
Crampin S (1964) Higher modes of seismic surface waves: Preliminary observations. *Geophysical Journal of the Royal Astronomical Society* 9: 35–37.
Crampin S (1966) Higher modes of seismic surface waves: Propagation in Eurasia. *Bulletin of the Seismological Society of America* 56: 1227–1239.
Crawford WC, Wiens DA, Dorman LM, et al. (2003) Tonga Ridge and Lau Basin crustal structure from seismic refraction data. *Journal of Geophysical Research* 108: 2195–2196.
Creaser B and Spence G (2005) Crustal structure across the northern Cordillera, Yukon Territory, from seismic wide-angle studies: Omineca Belt to Intermontane Belt. *Canada Journal of Earth* 42: 1187–1203.
Crosson RS (1976) Crustal structure modeling of earthquake data; 1. Simultaneous least squares estimation of hypocenter and velocity parameters. *Journal of Geophysical Research* 81: 3036–3046.
Curtis A and Woodhouse JH (1997) Crust and upper mantle structure beneath the Tibetan plateau and surrounding regions from interevent surface wave inversion. *Journal of Geophysical Research* 102: 11789–11813.
Czuba W (2007) 2.5-D seismic tomographic modelling of the crustal structure of north-western Spitsbergen based on deep seismic soundings. *Marine Geophysical Research* 28: 213–233.
Czuba W, Grad M, Luosto U, et al. (2002) Upper crustal seismic structure of the Mazury complex and Mazowsze massif within East European Craton in NE Poland. *Tectonophysics* 360: 115–128.
Czuba W, Ritzmann O, Nishimura Y, et al. (2005) Crustal structure of northern Spitsbergen along the deep seismic transect between the Molloy Deep and Nordaustlandet. *Geophysical Journal International* 161: 347–364.
Dadlez R, Grad M, and Guterch A (2005) Crustal structure below the Polish Basin: Is it composed of proximal terranes derived from Baltica? *Tectonophysics* 411: 111–128.
Dahl-Jensen T, Larsen TB, Woelbern I, et al. (2003) Depth to Moho in Greenland. *Earth and Planetary Science Letters* 205: 379–393.
Dalton CA, Gaherty JB, and Courtier AM (2011) Crustal V–S structure in northwestern Canada: Imaging the Cordillera-craton transition with ambient noise tomography. *Journal of Geophysical Research* 116: B12315. http://dx.doi.org/10.1029/2011JB008499.
Darbyshire FA (2003) Crustal structure across the Canadian High Arctic region from teleseismic receiver function analysis. *Geophysical Journal International* 152: 372–391.
Darbyshire FA, Priestley KF, White RS, et al. (2000a) Crustal structure of central and northern Iceland from analysis of teleseismic receiver functions. *Geophysical Journal International* 143: 163–184.
Darbyshire FA, White RS, and Priestley KF (2000b) Structure of the crust and uppermost mantle of Iceland from a combined seismic and gravity study. *Earth and Planetary Science Letters* 181: 409–428.
Das T and Nolet G (1998) Crustal thickness map of the western United States by portioned waveform inversion. *Journal of Geophysical Research* 103: 30021–30038.
Davies JH and Davies DR (2010) Earth's surface heat flux. *Solid Earth* 1: 5–24. http://dx.doi.org/10.5194/se-1-5-2010.
Davis M and Kusznir N (2004) Depth-dependent lithospheric stretching at rifted continental margins. In: Karner GD, Taylor B, and Discoll NW (eds.) *Rheology and Deformation of the Lithosphere at Continental Margins*, pp. 92–136. Columbia University Press.
Davis MW, White NJ, and Priestley KF (2012) Crustal structure of the British Isles and its epeirogenic consequences. *Geophysical Journal International* 190: 705–725.
Day AJ, Peirce C, and Sinha MC (2001) Three-dimensional crustal structure and magma chamber geometry at the intermediate-spreading, back-arc Valu Fa Ridge, Lau Basin – results of a wide-angle seismic tomographic inversion. *Journal of Geophysics* 146: 31–52.
de Wit M and Tinker J (2001) Crustal structures across the central Kaapvaal craton from deep-seismic reflection data. *South African Journal of Geology* 107: 185–206.
Dean SM, Minshull TA, Whitmarsh RB, and Louden KE (2000) Deep structure of the ocean-continent transition in the southern Iberia Abyssal Plain from seismic refraction profiles: II. The IAM-9 transect at 40°20′N. *Journal of Geophysical Research* 105: 5859–5886.
Debayle E and Lévêque J (1997) Upper mantle heterogeneities in the Indian Ocean from waveform inversions. *Geophysical Research Letters* 24: 245–248.
DeGolyer E (1935) Notes on the early history of applied geophysics in the petroleum industry. *Society Petroleum Geophysics Journal* 30: 1–10.
Dehlinger P (1978) *Marine Gravity*. Amsterdam: Elsevier Scientific Publishing Co, 322 pp.
Delhinger P, Couch RW, McManus DA, and Gemperle M (1970) Northeast Pacific structure. In: Maxwell AE (ed.) *The Sea*, vol. 4, (Part 2), pp. 133–189. New York: Wiley-Interscience.
Deichmann N and Ansorge J (1983) Evidence for lamination in the lower continental crust beneath the Black Forest (Southwestern Germany). *Journal of Geophysics* 52: 109–118.
Dentith MC, Dent VF, and Drummond BJ (2000) Deep crustal structure in the southwestern Yilgarn Craton, Western Australia. *Tectonophysics* 325: 227–255.
DESERT group (2004) The crustal structure of the Dead Sea Transform. *Geophysical Journal International* 156: 655–681.
DeShon HR and Schwartz SY (2004) Evidence for serpentinization of the forearc mantle wedge along Nicoya Peninsula, Costa Rica. *Geophysical Research Letters* 31: L21611. http://dx.doi.org/10.1029/1004GL021179.
Detrick RS, Buhl P, Vera E, et al. (1987) Multichannel seismic imaging of a crustal magma chamber along the East Pacific Rise. *Nature* 326: 35–41.
Detrick RS, Harding AJ, Kent GM, Orcutt JA, Mutter JC, and Buhl P (1993) Seismic structure of the southern East Pacific Rise. *Science* 259: 499–503.
Detrick RS, Mutter J, Buhl P, and Kim II (1990) No evidence from multichannel reflection data for a crustal magma chamber in the MARK area of the Mid-Atlantic Ridge. *Nature* 347: 61–64.
Dèzes P and Ziegler PA (2001) *European Map of the Mohorovicic discontinuity*, version 1.3. world wide web access: http://comp1.geol.unibas.ch.
Diaz J and Gallart J (2009) Crustal structure beneath the Iberian Peninsula and surrounding waters: A new compilation of deep seismic sounding results. *Physics of the Earth and Planetary Interiors* 173: 181–190.
Divins DL and Rabinowitz PD (1989) Thickness of sedimentary cover. In: Udintsev GB and Russian Ministry of Geology (eds.) *International Geology-Geophysical Atlas of the Atlantic Ocean*. Moscow: Russian Academy of Sciences (sheet 3).
Dix CH (1965) Reflection seismic crustal studies. *Geophysics* 30: 1068–1084.
Dobrin MB (1976) *Introduction to geophysical prospecting*, 3rd edn. New York: McGraw-Hill, 630 pp.
Dohr G (1970) Reflexionsseimische Messungen im Oberrheingraben mit digitaler Aufzeichnungstechnik und Beairbeitung. In: Mueller JH and Illies S (eds.) *Graben Problems*, pp. 207–218. Stuttgart: Schweizerbart.
Donnelly TW (1973) Late Cretaceous basalts from the Caribbean, a possible flood basalt province of vast size. *EOS* 54: 1004.
Downes H (1993) The nature of the lower continental crust of Europe: Petrological and geochemical evidence from xenoliths. *Physics of the Earth and Planetary Interiors* 79: 195–218.
Drewry DJ and Mooney WD (1983) *Antarctica: Glaciological and Geophysical Folio*. Cambridge, England: Polar Red. Inst.
Du ZJ and Foulger GR (2001) Variation in the crustal structure across central Iceland. *Geophysical Journal International* 145: 246–264.
Du ZJ, Foulger GR, Julian BR, et al. (2002) Crustal structure beneath western and eastern Iceland from surface waves and receiver functions. *Geophysical Journal International* 149: 349–363.
Duba AS (1972) Electrical conductivity of olivine. *Journal of Geophysical Research* 77: 2483–2495.
Dugda MT, Nyblade AA, and Julia J (2005) Crustal structure in Ethiopia and Kenya from receiver function analysis: Implications for rift development in eastern Africa. *Journal of Geophysical Research* 110: B01303. http://dx.doi.org/10.1029/2004JB003065.

Dunn RA, Toomey DR, and Solomon SC (2000) Three-dimensional seismic structure and physical properties of the crust and shallow mantle beneath the East Pacific Rise at 9°30′N. *Journal of Geophysical Research* 105: 23537–23555.

Durrheim RJ and Mooney WD (1994) Evolution of the Precambrian lithosphere: Seismological and geochemical constraints. *Journal of Geophysical Research* 99: 15359–15374.

Dzierma Y, Thorwart MM, and Rabbel W (2010) Imaging crustal structure in south central Costa Rica with receiver functions. *Geochemistry, Geophysics, Geosystems* 11: Q08S26. http://dx.doi.org/10.1029/2009GC002936.

Dziewonski AM (1989) Earth structure, global. In: James DE (ed.) *The Encyclopedia of Solid Earth Geophysics*, pp. 331–359. New York: Van Nostrand-Reinhold.

Dziewonski AM and Anderson DL (1981) Preliminary reference Earth model (PREM). *Eos, Transactions American Geophysical Union* 62: 332 pp.

Eagar KC, Fouch MJ, and James DE (2011) Crustal structure beneath the High Lava Plains of eastern Oregon and surrounding regions from receiver function analysis. *Journal of Geophysical Research* 116: B02313. http://dx.doi.org/10.1029/2010JB007795.

Eberhart-Phillips D (1986) Three-dimensional velocity structure in northern California Coast Ranges from inversion of local earthquake arrival times. *Bulletin of the Seismological Society of America* 76: 1025–1052.

Eberhart-Phillips D and Bannister S (2002) Three-dimensional crustal structure in the Southern Alps region of New Zealand from inversion of local earthquake and active source data. *Journal of Geophysical Research* 107: 2262. http://dx.doi.org/10.1029/2001JB000567.

Edgar NT, Ewing JI, and Hennion J (1971) Seismic refraction and reflection in the Caribbean Sea. *American Association of Petroleum Geologists* 55: 833–870.

Egorkin AV (2004) Mantle structure of the Siberian platform. *Physics of the Solid Earth* 40: 385–394, Izvestiya.

Egorkin AV, Zuganov SK, Pavlenkova NA, and Chernyshev NM (1987) Results of lithosphere studies from long-range profiles in Siberia. *Tectonophysics* 140: 29–47.

Ekström G, Tromp J, and Larson EWF (1997) Measurement and global models of surface wave propagation. *Journal of Geophysical Research* 102: 8137–8157.

El Shazly EM (1982) The Red Sea region. In: Nairs AEM and Stehli FG (eds.) *The Oceans Basins and Margins*. *The Indian Ocean*, vol. 6, pp. 205–252. New York: Plenum.

Eldholm O and Coffin MF (2000) Large igneous provinces and plate tectonics. *America Geophysical Union, Monograph*, vol. 121, pp. 309–326. America Geophysical Union.

Eldholm O and Grue K (1994) North Atlantic volcanic margins: Dimensions and production rates. *Journal of Geophysical Research* 99: 2955–2968.

Eldholm O, Tsikalas F, and Faleide JI (2002) The continental margin of Norway 62–75_N: Palaeogene tectono-magmatic segmentation and sedimentation. In: Jolley DW and Bell BR (eds.) *The North Atlantic Igneous Province: Stratigraphy, Tectonics, Volcanic and Magmatic Processes*, vol. 197. London: The Geological Society, Special Publication.

Elie de Beaumont E (1847) Note sur les systemes de montagnes les plus anciens de l'Europe, Extr. Du Bulletin de la Societe geologique de France 2e serie t. IV 864 pp.

Emmermann R and Lauterjung J (1997) The German Continental Deep Drilling Program KTB: Overview and major results. *Journal of Geophysical Research* 102: 18179–18201.

Enderle U, Mechie J, Sobolev S, and Fuchs K (1996) Seismic anisotropy within the uppermost mantle of southern Germany. *Geophysical Journal International* 125: 747–767.

England RW (2000) Deep structure of north west Europe from deep seismic profiling: The link between basement tectonics and basin development. In: *Atlantic Rifts and Continental Margins*. *Geophysical Monograph* 115: pp. 57–83. American Geophysical Union.

England RW and Ebbing J (2012) Crustal structure of central Norway and Sweden from integrated modelling of teleseismic receiver functions and the gravity anomaly. *Geophysical Journal International* 191: 1–11.

Ernst RE and Buchan KL (2003) Recognizing mantle plumes in the geologic record. *Annual Review of Earth and Planetary Science* 31: 469–523.

Evangelidis CP, Minshull TA, and Henstock TJ (2004) Three-dimensional crustal structure of Ascension Island from active source seismic tomography. *Geophysical Journal International* 159: 311–325.

Evans RL, Tanits P, Chave AD, et al. (1999) Asymetric electrical structure in the mantle beneath the east Pacific Rise at 17' S. *Science* 286: 752–756.

Ewing WM, Carry AP, and Rutherford HM (1937) Geophysical investigations in the emerged and submerged Atlantic Coastal Plain; Part 1. *Bulletin of the Geological Society of America* 48: 753–802.

Ewing WM, Dainty AM, Blanchard JE, and Keen JJ (1966) Seismic studies on the eastern seaboard of Canada: The Appalachian system I. *Canadian Journal of Earth Sciences* 3: 89–109.

Ewing J and Houtz R (1979) Acoustic stratigraphy and structure of the oceanic crust. In: *Deep Drilling Results in the Atlantic Ocean*, pp. 1–14. Washington, DC: American Geophysical Union.

Ewing WM, Jadetzky WS, and Press F (1957) *Elastic Waves in Layered Media*. New York: McGraw-Hill Book Co.

Ewing WM and Nafe JE (1982) The unconsolidated sediments. In: Hill MN (ed.) *The Sea*. *The Earth Beneath the Sea*, vol. 3, pp. 73–84. New York: Wiley-Interscience.

Ewing WM and Press F (1954) An investigation of mantle Rayleigh waves. *Bulletin of the Seismological Society of America* 44: 127–148.

Ewing WM, Worzel JL, Ericson DB, and Heezen BC (1955) Geophysical and geological investigations in the Gulf of Mexico, Part 1. *Geophysics* 20: 1–18.

Faleide JI, Gudlaugsson ST, Eldholm O, Myhre AM, and Jackson HR (1990) Deep seismic transects across the sheared Western Barents Sea-Svalbard continental margin. Tectonophysics 189: 73–89

Farnetani CG and Richards MA (1995) Thermal entrainment and melting in mantle plumes. *Earth and Planetary Science Letters* 136: 251–267.

Farnetani CG, Richards MA, and Ghiorso MS (1996) Petrologic models of magma evolution and deep crustal structure beneath hotspots and flood basalts. *Earth and Planetary Science Letters* 143: 81–84.

Feldman IS (1976) On the nature of conductive layers in the Earth's crust and upper mantle. In: Adam A (ed.) *Geoelectric and Geothermal Studies*, pp. 721–730. Budapest: Akademiai Kiado.

Feng M, Assumpção M, and van der Lee S (2004) Group-velocity tomography and lithospheric S-velocity structure of the South American continent. *Physics of the Earth and Planetary Interiors* 147(4): 315–331.

Fern´andez M, Torne M, Garcia-Castellanos D, Verg´es J, Wheeler W, and Karpuz R (2004) Deep structure of the Voring Margin: The transition from a continental shield to a young oceanic lithosphere. *Earth and Planetary Science Letters* 221: 131–144.

Ferris A, Abers GA, and Zelt B (2006) Crustal structure across the transition from rifting to spreading: The Woodlark rift system of Papua New Guinea. *Geophysical Journal International* 166: 622–634.

Finlayson DM and Ansorge J (1984) Workshop proceedings; Interpretation of seismic wave propagation in laterally heterogeneous structures. Canberra, Australia, *Bureau of Mineral Resources, Geology, and Geophysics Report* 258, 207 pp.

Flack C and Warner M (1990) Three-dimensional mapping of seismic reflections from the *crust* and upper mantle northwest of Scotland. *Tectonophysics* 173: 469–481.

Fliedner MM and Klemperer SL (1999) Structure of an island arc: Wide-angle seismic studies in the eastern Aleutian Islands, Alaska. *Journal of Geophysical Research* 104: 10667–10694.

Fliedner MM and Klemperer SL (2000) Crustal structure transition from oceanic arc to continental arc, eastern Aleutian Islands and Alaska Peninsula. *Earth and Planetary Science Letters* 179: 567–579.

Foulger GR, Du Z, and Julian BR (2003) Icelandic-type crust. *Geophysical Journal International* 155: 567–590.

Fountain DM (1986) Implications of deep crustal evolution for seismic reflection interpretation. In: Barazangi M and Brown L (eds.) *Reflection Seismology; The Continental Crust*. *Geodynamics Series,* 14, pp. 1–7. Washington, DC: American Geophysical Union.

Fountain DM, Arculus R, and Kay RW (1992) Continental Lower Crust, 485pp. Amsterdam: Elsevier.

Fountain DM and Christensen NI (1989) Composition of the continental crust and upper mantle: A review. In: Pakiser LC and Mooney WD (eds.) *Geophysical Framework of the Continental United States*, *Geological Society of America Memoir*, 172, pp. 711–742.

Fountain DM, Hurich CA, and Smithson SB (1984) Seismic reflectivity of mylonite zones in the crust. *Geology* 12: 195–198.

Fountain DM and Salisbury MH (1981) Exposed crustal-sections through the continental crust: Implication for crustal structure, petrology and evolution. *Earth and Planetary Science Letters* 56: 263–302.

Fowler S, White RS, Spence GD, and Westbrook GK (1989) The Hatton Bank continental margin-II. Deep structure from two-ship expanding spread profiles. *Geophysics Journal* 96: 295–309.

Franca GS and Assumpcao M (2004) Crustal structure of the Ribeira fold belt, SE Brazil, derived from receiver functions. *Journal of South American Earth Science* 16: 743–758.

Friederich W (2003) The S-velocity structure of the east Asian mantle from inversion of shear and surface waveforms. *Geophysical Journal International* 153: 88–102.

Fromm R, Zandt G, and Beck SL (2004) Crustal thickness beneath the Andes and Sierras Pampeanas at 30º S inferred from Pn apparent phase velocities. *Geophysical Research Letters* 31: L006625. http://dx.doi.org/10.1029/2003GL019231.

Frost BR and Shive PN (1986) Magnetic mineralogy of the lower continental crust. *Journal of Geophysical Research* 91: 6513–6522.

Fu YV, Li A, and Chen YJ (2010) Crustal and upper mantle structure of southeast Tibet from Rayleigh wave tomography. *Journal of Geophysical Research* 115: B12323. http://dx.doi.org/10.1029/2009JB007160.

Fuchs K and Müller G (1971) Computation of synthetic seismograms with the reflectivity method and comparison with observations. *Geophysical Journal of the Royal Astronomical Society* 23: 417–433.

Fuis GS, Ryberg T, Godfrey NJ, et al. (2001) Crustal structure and tectonics from the Los Angeles basin to the Mojave Desert, southern California. *Geology* 29: 15–18.

Funck T, Hansen AK, and Reid ID (2008) The crustal structure of the southern Nain and Makkovik provinces of Labrador derived from refraction seismic data. *Canadian Journal of Earth* 45: 465–481.

Funck T, Hopper JR, Larsen HC, et al. (2003) Crustal structure of the ocean-continent transition at Flemish Cap: Seismic refraction results. *Journal of Geophysical Research* 108. http://dx.doi.org/10.1029/2003JB002434.

Funck T, Jackson HR, Louden KE, et al. (2004) Crustal structure of the northern Nova Scotia rifted continental margin (eastern Canada). *Journal of Geophysical Research* 109. http://dx.doi.org/10.1029/2004JB003008.

Funck T, Jackson HR, and Shimeld J (2011) The crustal structure of the Alpha Ridge at the transition to the Canadian Polar Margin: Results from a seismic refraction experiment. *Journal of Geophysical Research* 116. http://dx.doi.org/10.1029/2011JB008411.

Funck T, Louden KE, and Reid ID (2001) Crustal structure of the Grenville Province in southeastern Labrador from refraction seismic data: Evidence for a high-velocity lower crustal wedge. *Canadian Journal of Earth Science* 38: 1463–1478.

Gailler A, Klingelhoefer F, and Olivet JL (2009) Crustal structure of a young margin pair: New results across the Liguro-Provencal Basin from wide-angle seismic tomography. *Earth and Planetary Science Letters* 286: 333–345.

Gaite B, Iglesias A, and Villasenor A (2012) Crustal structure of Mexico and surrounding regions from seismic ambient noise tomography. *Geophysical Journal International* 188: 1413–1424.

Gajewski D and Pšenčík I (1987) *Ray Method in Seismology*. Prague: University of Karlova.

Gans CR, Beck SL, and Zandt G (2011) Continental and oceanic crustal structure of the Pampean flat slab region, western Argentina, using receiver function analysis: New high-resolution results. *Geophysical Journal International* 186: 45–58.

Geiss E (1987) A new compilation of crustal thickness data for Mediterranean area. *Annals of Geophysics* 5: 623–630.

Gerlings J, Louden KE, and Jackson HR (2011) Crustal structure of the Flemish Cap Continental Margin (eastern Canada): An analysis of a seismic refraction profile. *Geophysical Journal International* 185: 30–48.

Giese P (1976) Results of the generalized interpretation of the deep-seismic sounding data. In: Giese P, Prodehl C, and Stein A (eds.) *Explosion Seismology in Central Europe*, pp. 201–214. New York: Springer.

Giese P, Prodehl C, and Stein A (eds.) (1976) *Explosion Seismology in Central Europe – Data and Results*, p. 429. Berlin/Heidelberg/New York: Springer.

Gilbert H, Beck S, and Zandt G (2005) Lithospheric and upper mantle structure of Central Chile and Argentina. *Geophysical Journal International* 165(1): 383–398.

Gladczenko TP and Coffin MF (2001) Kerguelen Plateau crustal structure and basin formation from seismic and gravity data. *Journal of Geophysical Research* 106: 16583–16601. http://dx.doi.org/10.1029/2001JB000370.

Gladczenko TP, Coffin MF, and Eldholdm O (1997) Crustal structure of the Ontong Java Plateau: Modeling of new gravity and existing seismic data. *Journal of Geophysical Research* 102: 22711–22729.

Godfrey NJ, Davey F, and Stern TA (2001) Crustal structure and thermal anomalies of the Dunedin Region, South Island, New Zealand. *Journal of Geophysical Research* 106: 30835–30848.

Goek R, Mahdi H, and Al-Shukri H (2008) Crustal structure of Iraq from receiver functions and surface wave dispersion: Implications for understanding the deformation history of the Arabian–Eurasian collision. *Journal of Geophysics* 172: 1179–1187.

Gonzalez-Fernandez A, Cordoba D, Matias LM, et al. (2001) Seismic crustal structure in the Gulf of Cadiz (SW Iberian Peninsula). *Marine Geophysical Researches* 22: 207–223.

Goodwin AM (1991) *Precambrian Geology: The Dynamic Evolution of the Continental Crust*. San Diego, CA: Academic Press, 666 pp.

Goodwin AM (1996) *Principles of Precambrian Geology*. San Diego, CA: Academic Press, 327 pp.

Gore J, James DE, and Zengeni TG (2009) Crustal structure of the Zimbabwe craton and the limpopo belt of southern Africa: New constraints from seismic data and implications for its evolution. *South African Journal of Geology* 112: 213–228.

Gorman AR, Clowes RM, Ellis RM, et al. (2002) Deep probe: Imaging the roots of western North America. *Canadian Journal of Earth Science* 39: 375–398.

Gough DE (1974) Electrical conductivity under western North America in relation to heat flow, seismology, and structure. *Journal of Geomagnetism and Geoelectricity* 26: 105–123.

Goutorbe B, Poort J, Lucazeau F, and Raillard S (2011) Global heat flow trends resolved from multiple geological and geophysical proxies. *Geophysical Journal International* 187: 1405–1419.

Grad M, Brueckl E, and Majdanski M (2009) Crustal structure of the Eastern Alps and their foreland: Seismic model beneath the CEL10/Alp04 profile and tectonic implications. *Geophysical Journal International* 177: 279–295.

Grad M, Gryn D, Guterch A, et al. (2003a) "DOBREfraction '99"; velocity model of the crust and upper mantle beneath the Donbas foldbelt (east Ukraine). *Tectonophysics* 371: 81–110.

Grad M, Jensen SL, Keller GR, et al. (2003b) Crustal structure of the Trans-European suture zone region along POLONAISE'97 seismic profile P4. *Journal of Geophysical Research* 108: 2541. http://dx.doi.org/10.1029/2003JB002426.

Grand SP and Helmberger DV (1984) Upper mantle shear structure of North America. *Geophysical Journal of the Royal Astronomical Society* 76: 399–438.

Grand SP, van der Hilst RD, and Widiyantoro S (1997) Global seismic tomography: A snapshot of convection in the Earth. *GSA Today* 7: 1–7.

Grant FS and West GS (1965) *Interpretation Theory in Applied Geophysics*. New York: McGraw-Hill, 584 pp.

Greenroyd CJ, Peirce C, and Rodger M (2007) Crustal structure of the French Guiana margin, west equatorial Atlantic. *Journal of Geophysics* 169: 964–987.

Grevemeyer I, Flueh ER, Reichert C, et al. (2001a) Crustal architecture and deep structure of the Ninetyeast Ridge hotspot trail from active-source ocean bottom seismology. *Geophysical Journal International* 144: 414–431.

Grevemeyer I, Weigel W, Schussler S, et al. (2001b) Crustal and upper mantle seismic structure and lithospheric flexure along the Society Island hotspot chain. *Geophysical Journal International* 147: 123–140.

Griffin WL and O"Reilly SY (1987) Is the continental Moho the crust-mantle boundary? *Geology* 15: 241–244.

Griffiths RW and Campbell IH (1990) Stirring and structure in mantle starting plumes. *Earth and Planetary Science Letters* 99: 66–78.

Gung Y and Romanowicz B (2004) Q tomography of the upper mantle using three-component long-period waveforms. *Geophysical Journal International* 157: 813–830.

Gutenberg B (1932) Travel time curves at small distances and wave velocities in southern California. *Beitrage zur Geophysik* 35: 6–45.

Gutenberg B (1959) *Physics of the Earth's Interior*. New York: Acad. Press.

Gutenberg B, Wood H, and Buwalda J (1932) Experiments testing seismographic methods for determining crustal structure. *Bulletin of the Seismological Society of America* 22: 185–246.

Guterch A, Grad M, Thybo H, Keller GR, and the POLONAISE Working Group (1999) POLONAISE'97 – an international seismic experiment between Precambrian and Variscan Europe in Poland. *Tectonophysics* 314: 101–121.

Guterch A, Grad M, et al. (2003) CELEBRATION 2000 seismic experiment. *Studia Geophysica et Geodaetica* 47: 659–670.

Haberland C, Agnon A, El-Kelani R, et al. (2003) Modelling of seismic guided waves at the Dead Sea Transform. *Journal of Geophysical Research* 108(B7): 2342. http://dx.doi.org/10.1029/2002JB002309.

Hacker BR, Kelemen PB, and Behn MD (2011) Differentiation of the continental crust by relamination. *Earth and Planetary Science Letters* 307: 501–516.

Hahn A, Ahrendt H, Jeyer J, and Hufen J-H (1984) A model of magnetic sources within the Earth's crust compatible with the field measured by the satellite Magsat. *Geologisches Jahrbuch* 75: 125–156, Rheihe A.

Hajnal Z (1986) Crustal reflection and refraction velocities. In: Barazangi M and Brown LD (eds.) *Reflection Seismology: A Global Perspective*. *Geodynamics Series*, 13, pp. 247–256. American Geophysical Union.

Hale LD and Thompson GA (1982) The seismic reflection character of the continental Mohorovičić discontinuity. *Journal of Geophysical Research* 87: 4625–4635.

Hall DH (1974) Long-wavelength aeromagnetic anomalies and deep crustal magnetisation in Manitoba and northwestern Ontario, Canada. *Journal of Geophysics* 40: 403–430.

Halliday AN, Dickin AP, Hunter RH, et al. (1993) Formation and composition of the lower continental crust: Evidence from Scottish xenolith suites. *Journal of Geophysical Research* 98(B1): 581–607.
Hamilton EL (1976) Shear-wave velocity versus depth in marine sediments: A review. *Geophysics* 41: 985–996.
Hamilton EL (1978) Sound velocity-density relations in sea-floor sediments and rocks. *Journal of the Acoustical Society of America* 63: 366–377.
Hamilton WB (2011) Plate tectonics began in the Neoproterozoic time, and plumes from the deep mantle have never operated. *Lithos* 123: 1–20.
Hammer S (1983) Airborne Gravity is here! *Geophysics* 48: 213–223.
Hammer PTC, Clowes RM, and Ellis RM (2000) Crustal structure of NW British Columbia and SE Alaska from seismic wide-angle studies: Coast Plutonic Complex to Stikini. *Journal of Geophysical Research* 105: 7961–7981.
Hansen SE, Nyblade AA, and Heeszel DS (2009) Crustal structure of the Gamburtsev Mountains, East Antarctica, from S-wave receiver functions and Rayleigh wave phase velocities. *Earth and Planetary Science Letters* 300: 395–401.
Hart PJ (1969) In: *The Earth's crust and upper mantle. Geophysical Monograph* 13: Washington, DC: American Geophysical Union, 735 pp.
Hart SR, Hauri EH, Oschmann LA, and Whitehead JA (1992) Mantle plumes and entrainment: Isotopic evidence. *Science* 256: 1673–1707.
Hauser F, O'Reilly BM, and Readman PW (2008) Constraints on crustal structure and composition within a continental suture zone in the Irish Caledonides from shear wave wide-angle reflection data and lower crustal xenoliths. *Journal of Geophysics* 175: 1254–1272.
Hauser F, Raileanu V, and Fielitz W (2007) Seismic crustal structure-between the transylvanian basin and the black sea, Romania. *Tectonophysics* 430: 1–25.
Hauser F, Raileanu V, Fielitz W, et al. (2001) VRANCEA99 – the crustal structure beneath the southeastern Carpathians and the Moesian Platform from a seismic refraction profile in Romania. *Tectonophysics* 340: 233–256.
Hayford JF and Bowie W (1912) The effect of topography and isostatic compensation upon the intensity of gravity. *U.S. Coast and Geodetic Survey Special Publication* 10, 132 pp. 5 plates.
Hazarika D, Arora BR, and Bora C (2012) Crustal structure and deformation in the northeast India-Asia collision zone: Constraints from receiver function analysis. *Geophysical Journal International* 188: 737–749.
Heacock JG (1971) In: *The Structure and Physical Properties of the Earth's Crust. Geophysical Monograph*, vol. 14. Washington, DC: American Geophysical Union, 348 pp.
Heacock JG (1977) *The Earth's Crust – Its Nature and Properties. Geophysical Monograph*, vol. 20. Washington, DC: American Geophysical Union, 754 pp.
Hearn TM (1984) Pn travel times in southern California. *Journal of Geophysical Research* 89: 1843–1855.
Hearn TM (1996) Anisotropic *Pn* tomography in the western United States. *Journal of Geophysical Research* 101: 8403–8414.
Hearn TM (1999) Uppermost mantle velocities and anisotropy beneath Europe. *Journal of Geophysical Research* 104: 15123–15139.
Hearn TM, Beghoul N, and Barazangi M (1991) Tomography of the western United States from regional arrival times. *Journal of Geophysical Research* 96: 16369–16381.
Hearn TM and Clayton RW (1986) Lateral velocity variations in southern California: 1. Results for the upper crust from P-waves. *Bulletin of the Seismological Society of America* 76: 495–509.
Hearn TM and Ni JF (1994) Pn velocities beneath continental collision zones; the Turkish–Iranian plateau. *Geophysical Journal International* 117: 273–283.
Hearn TM, Ni JF, Wang S, Xu Z, Yu Y, and Zhang X (2004) Uppermost mantle velocities beneath China and surrounding regions. *Journal of Geophysical Research* 109: 11. http://dx.doi.org/10.1029/2003JB002874.
Heiland CA (1935) Geophysical mapping from the air: It's possibilities and advantages. *Engineering and Mining Journal* 136: 609–610.
Heiskanen WA and Moritz H (1967) *Physical Geodesy*. San Francisco: W.H. Freeman, 364 pp.
Heiskanen WA and Vening-Meinez FA (1958) *The Earth and its gravity field*. New York: McGraw Hill.
Hemant K and Maus S (2005) Why no anomaly is visible over most of the continent-ocean boundary in the global crustal magnetic field. *Physics of the Earth and Planetary Interiors* 149: 321–333.
Herrin E (1969) Regional variations of P-wave velocity in the upper mantle beneath North America. In: Hart PJ (ed.) *The Earth's Crust and Upper Mantle. American Geophysical Union Monograph*, vol. 13, pp. 242–246. American Geophysical Union.
Hersey J, Officer C, Johnson H, and Bergstrom S (1952) Seismic refraction observations north of the Brownson Deep. *Bulletin of the Seismological Society of America* 42: 291–306.
Hess HH (1962) History of the ocean basins. In: Engel AE, James HL, and Leonard B (eds.) *Petrologic Studies, Burlington Volume*, pp. 599–620. Boulder, CO: Geological Society of America.
Hess HH (1965) Mid-oceanic ridges and tectonics of the seafloor; submarine geology and geophysics. *17th Colston Research Society Symposium*, 1–10.
Hildenbrand TG, Simpson RW, Godson RH, and Kane MF (1982) Digital colored residual and regional Bouguer gravity maps of the conterminous United States with cut-off wavelengths of 250 km and 1000 km. U.S. Geological Survey Geophysical Investigations Map GP-953-A, scale 1:7,500,000.
Hill MN (1957) Recent geophysical exploration of the ocean floor. *Physics and Chemistry of the Earth* 2: 129–163.
Hill MN (ed.) (1963) *The Sea*. In: *The Earth Beneath the Sea, History*, vol. 3, p. 963. New York: Interscience.
Hinze WJ (1985) The utility of regional gravity and magnetic anomaly maps. In: p. 454. Tulsa, OK: Society of Exploration of Geophysicists.
Hinze WJ and Zeitz I (1985) The compromise magnetic-anomaly map of the conterminous United States. In: Hinze WJ (ed.) *The Utility of Regional Gravity and Magnetic Anomaly Maps*, pp. 1–24. Society of Exploration Geophysicists.
Hodgson JH (1953) *A seismic survey of the Canadian Shield: 1. Refraction studies based on rock bursts at Kirkland Lake, Ontario. Dominion Observatory Publication*, vol. 16. Ottawa, ON: Dominion Observatory Publication, pp 111–163.
Hofsetter R and Bock G (2004) Shear-wave velocity structure of the Sinai sub-plate from receiver function analysis. *Geophysical Journal International* 158: 67–84.
Hofstetter R, Dorbath C, and Calo M (2012) Crustal structure of the Dead Sea Basin from local earthquake tomography. *Geophysical Journal International* 189: 554–568.
Holbrook WS and Kelemen PB (1993) Large igneous province on the U.S. Atlantic margin and implications during continental breakup. *Nature* 364: 433–436.
Holbrook WS, Lizarralde D, McGeary S, Bangs N, and Diebold J (1999) Structure and composition of the Aleutian island arc and implications for continental crustal growth. *Geology* 27: 31–34.
Holbrook WS, Mooney WD, and Christensen NI (1992) The seismic velocity structure of the deep continental crust. In: Fountain DM, Arculus R, and Kay RW (eds.) *Continental Lower Crust. Development in Geotectonics*, vol. 23, pp. 1–43. Amsterdam: Elsevier.
Hole JA (1992) Non-linear high-resolution three-dimensional seismic travel time tomography. *Journal of Geophysical Research* 97: 6553–6562.
Hole JA, Brocher TM, Klemperer SL, Parsons TE, Benz HM, and Furlong KP (2000) Three-dimensional seismic velocity structure of the San Francisco Bay area. *Journal of Geophysical Research* 105: 13859–13874.
Hole JA, Clowes RM, and Ellis RM (1992) Interface inversion using broadside seismic refraction data and three-dimensional travel time calculations. *Journal of Geophysical Research* 97: 3417–3429.
Hole JA and Zelt BC (1995) Three-dimensional finite-difference reflection travel times. *Geophysical Journal International* 121: 427–434.
Holmes A (1918) The basaltic rocks of the Arctic region. *Mineralogical Magazine* 18: 180–223.
Holmes RC, Webb SC, and Forsyth DW (2007) Crustal structure beneath the gravity lineations in the Gravity Lineations, Intraplate Melting, Petrologic and Seismic Expedition (GLIMPSE) study area from seismic refraction data. *Journal of Geophysical Research* 112: B07316. http://dx.doi.org/10.1029/2006JB004685.
Hood PJ, McGrath PH, and Teskey DJ (1985) Evolution of Geological Survey of Canada magnetic anomaly maps: A Canadian perspective. In: Hinze WJ (ed.) *The Utility of Regional Gravity and Magnetic Anomaly Maps*, pp. 62–68. Society of Exploration of Geophysicists.
Hooft EEE, Detrick RS, Toomey DR, et al. (2000) Crustal thickness and structure along three contrasting spreading segments of the Mid-Atlantic Ridge, 33.5 degrees–35 degrees N. *Journal of Geophysical Research* 105: 8205–8226.
Hopper JR, Dahl-Jensen T, Holbrook WS, et al. (2003) Structure of the SE Greenland margin from seismic reflection and refraction data: Implications for nascent spreading center subsidence and asymmetric crustal accretion during North Atlantic opening. *Journal of Geophysical Research* 108: 2269. http://dx.doi.org/10.1029/2002JB001996.
Horsefield SJ, Whitmarsh RB, White RS, and Sibuet J-C (1993) Crustal structure of Goban Spur rifted continental margin, NE Atlantic. *Geophysical Journal International* 119: 1–19.
Hrubcova P and Sroda P (2008) Crustal structure at the easternmost termination of the Variscan belt based on CELEBRATION 2000 and ALP 2002 data. *Tectonophysics* 460: 55–75.

Hrubcova P, Sroda P, Spicak A, and Guterch A (2005) Crustal and uppermost mantle structure of the Bohemian Massif based on CELEBRATION 2000 data. *Journal of Geophysical Research* 110: B11305. http://dx.doi.org/10.1029/2004JB003080.

Hu W, Abubakar A, and Habashy TM (2009) Simultaneous multi-frequency inversion of full waveform seismic data. *Geophysics* 7: 1–14.

Huang Z, Peng Y, Luo Y, Zheng Y, and Su W (2004) Azimuthal anisotropy of Rayleigh waves in East Asia. *Geophysical Research Letters* 31: L15617. http://dx.doi.org/10.1029/2004GL020399.

Huestis SP and Parker RL (1977) Bounding thickness of the oceanic magnetized layer. *Journal of Geophysical Research* 82(33): 5293–5303.

Humphreys E and Clayton RW (1988) Adaption of back projection tomography to seismic travel time problems. *Journal of Geophysical Research* 93: 1073–1085.

Humphreys E, Clayton RW, and Hager BH (1984) A tomographic image of mantle structure beneath southern California. *Geophysical Research Letters* 11: 625–627.

Hussenoeder SA, Kent GM, and Detrick RS (2002) Upper crustal seismic structure of the slow spreading Mid-Atlantic Ridge, 35 degrees N: Constraints on volcanic emplacement processes. *Journal of Geophysical Research* 107: 2156. http://dx.doi.org/10.1029/2001JB001691.

Hwang L and Mooney WD (1986) Velocity and Q structure of the Great Valley, California, based on synthetic seismogram modeling of seismic refraction data. *Bulletin of the Seismological Society of America* 76: 1053–1067.

Hyndman RD (1979) Poisson's ratio in the oceanic crust: A review. *Tectonophysics* 59: 321–333.

Hyndman RD (1988) Dipping seismic reflectors, electrically conductive zones, and trapped water in the crust over a subducting plate. *Journal of Geophysical Research* 93: 13133–13405.

Hyndman RD, Wang K, and Yamano M (1995) Thermal constraints on the seismogenic portion of the south western Japan subductim Thrust. *Journal of Geophysical Research* 100: 15373–15392.

Iidaka T, Takeda T, and Kurashimo E (2004) Configuration of subducting Philippine Sea plate and crustal structure in the central Japan region. *Tectonophysics* 388: 7–20.

Ito T, Kojima Y, and Kodaira S (2009) Crustal structure of southwest Japan, revealed by the integrated seismic experiment southwest Japan 2002. *Tectonophysics* 472: 124–134.

Iyer HM and Hirahara K (1993) *Seismic Tomography Theory and Practice*. London: Chapman and Hall, 842 pp.

Iyer HM and Hitchcock T (1989) Upper-mantle velocity structure in the continental U.S. and Canada. In: Pakiser LC and Mooney WD (eds.) *Geophysical Framework of the Continental United States*, *Geological Society of America Memoir,* 172, 681–710.

Jackson HR and Dahl-Jensen T (2010) Sedimentary and crustal structure from the Ellesmere Island and Greenland continental shelves onto the Lomonosov Ridge, Arctic Ocean. *Geophysical Journal International* 182: 11–35.

Jackson WH and Oakey GN (1986) Sedimentary thickness map of the Arctic Ocean. In: Grantz A, Johnson L, and Sweeney JF (eds.) *The Geology of North America*. Boulder, CO: Geological Society of America, Plate 5.

Jackson WH and Paksier LC (1965). Seismic study of crustal structure in the southern Rocky Mountains. *U.S. Geological Survey Professional Paper* 525-D, p. D-85-D-92.

Jackson WH, Stewart SW, and Paksier LC (1963) Crustal structure in eastern Colorado from seismic-refraction measurements. *Journal of Geophysical Research* 68: 5767–5776.

Jacobs AM, Harding AJ, and Kent GM (2007) Axial crustal structure of the Lau back-arc basin from velocity modeling of multichannel seismic data. *Earth and Planetary Science Letters* 259: 239–255.

Jaffal M, Klingelhoefer F, and Matias L (2009) Crustal structure of the NW Moroccan margin from deep seismic data (SISMAR Cruise). *Compets Rendus Geoscience* 341: 495–503.

Jakosky JJ (1940) *Exploration Geophysics*. Los Angeles: Trija, 1195 pp.

James DE (1971) Andean crustal and upper mantle structure. *Journal of Geophysical Research* 76: 3246–3271.

James DE, Niu FL, and Rokosky J (2003) Crustal structure of the Kaapvaal craton and its significance for early crustal evolution. *Lithos* 71: 413–429.

James DE and Steinhart JS (1966) Structure beneath continents, a critical review of explosion seismic studies 1960–1965. In: Steinhart JS and Smith TJ (eds.) *The Earth Beneath the Continents*. *Geophysical Monograph,* 10, pp. 293–333. Washington, DC: American Geophysical Union.

Janik T, Grad M, and Guterch A (2011) Crustal structure of the Western Carpathians and Pannonian Basin: Seismic models from CELEBRATION 2000 data and geological implications. *Journal of Geophysics* 52: 97–113.

Janik T, Yliniemi J, Grad M, et al. (2002) Crustal structure across the TESZ along POLONAISE'97 seismic profile P2 in NW Poland. *Tectonophysics* 360: 129–152.

Jarchow CM and Thompson GA (1989) The nature of the Mohorovicic discontinuity. *Annual Review Earth and Planetary Sciences* 17: 475–506.

Jaupart C and Mareschal JC (1999) The thermal structure and thickness of continental roots. *Lithos* 48: 93–114.

Jaupart C and Mareschal JC (2011) *Heat generation and transport in the Earth*. Cambridge: Cambridge University Press, 464 pp.

Jeffreys H (1940) *Seismological Tables*. London: British Association, Gray Milne Trust, 50 pp.

Jeffreys H and Bullen KE (1935) Times of transmission of earthquake waves. *Bureau of Central Seismology International, Series A, Fascinate* 11: 202.

Jensen H (1961) The airborne magnetometer. *Scientific American* 204: 151–162.

Johnson GR and Olhoeft GR (1984) In: Charmichael RS (ed.) *Density of rocks and minerals*. *Handbook of Physical Properties of Rocks*, vol. 3, pp. 1–38. Boca Raton, FL: CRC Press.

Johnson M and Vincent C (2002) Development and testing of a 3D velocity model for improved event location: A case study for the India-Pakistan region. *Bulletin of the Seismological Society of America* 92: 2893–2910.

Jokat W, Ritzmann O, Reichert C, et al. (2004) Deep crustal structure of the continental margin off the Explora Escarpment and in the Lazarev Sea, East Antarctica. *Marine Geophysical Researches* 25: 283–304.

Jones AG (1992) Electrical conductivity structure of the continental lower crust. In: Fountain DM, Arculus RJ, and Kay RW (eds.) *Continental Lower Crust*, pp. 81–143. Amsterdam: Elsevier.

Jones EJW (1999) *Marine Geophysics*. Chichester, England: Wiley.

Jones AG, Ferguson IJ, Chave AD, Evans RL, and McNeice GW (2001) The electrical lithosphere of the Slave Province. *Geology* 29: 423–426.

Jones EJW and Mgbatogu CCS (1982) The structure and evolution of the West African continental margin off Guine Bissau Guinee and Sierra Leone. In: Scrutton RA, Talwani M, and Chichester JW (eds.) *The Ocean Floor*, pp. 165–202. New York: Wiley.

Jones T and Nur A (1983) Velocity and attenuation in sandstone at elevated temperatures and pressures. *Geophysical Research Letters* 10: 140–143.

Jordan TH (1975) The continental tectosphere. *Geophysics and Space Physics* 13: 1–12.

Jordan TH (1979) In: Boyd FR and Meyer HOA (eds.) *Mineralogies, densities and seismic velocities of garnet lherzolites and their geophysical implications*. *The Mantle Sample: Inclusions in Kimberlites and Other Volcanics*, vol. 2, pp. 2–14. Washington, DC: American Geophysical Union.

Jordan TH (1988) Structure and formation of the continental tectosphere. *Journal of Petrology* 1: 11–37, special lithosphere issue.

Jordan TH and Frazer LN (1975) Crustal and upper mantle structure from *Sp* phases. *Journal of Geophysical Research* 80: 1504–1518.

Juhlin C (1988) Interpretation of the seismic reflectors in the Gravberg-I well. In: Boden A and Erickson KG (eds.) *Deep Drilling in Crystalline Bedrock*, 364 pp. Berlin: Springer.

Julia J, Assumpcao M, and Rocha MP (2008) Deep crustal structure of the Parana Basin from receiver functions and Rayleigh-wave dispersion: Evidence for a fragmented cratonic root. *Journal of Geophysical Research* 113: B08318. http://dx.doi.org/10.1029/2007JB005374.

Julia J, Jagadeesh S, and Rai SS (2009) Deep crustal structure of the Indian shield from joint inversion of P wave receiver functions and Rayleigh wave group velocities: Implications for Precambrian crustal evolution. *Journal of Geophysical Research* 114: B10313. http://dx.doi.org/10.1029/2008JB006261.

Julià J and Mejía J (2004) Thickness and vp/vs ratio variation in the Iberian crust. *Geophysical Journal International* 156: 59–72.

Junger A (1951) Deep refractions in Big Horn County, Montana. *Geophysics* 16: 499–505.

Kaban MK, Schwintza P, Artemieva IM, and Mooney WD (2003) Density of the continental roots: Compositional and thermal contributions. *Earth and Planetary Science Letters* 209: 53–69.

Kamimura A, Kasahara J, Shinohara M, et al. (2002) Crustal structure study at the Izu-Bonin subduction zone around 31 degrees N: Implications of serpentinized materials along the subduction plate boundary. *Physics of the Earth and Planetary Interiors* 132: 105–129.

Kanasewich ER and Cumming GL (1965) Near vertical-incidence seismic reflections from the "Conrad" discontinuity. *Journal of Geophysical Research* 70: 3441–3446.

Kane MF and Godson RH (1989) A crust/mantle structural framework of the continuous United States based on gravity and magnetic data. In: Pakiser LC and Mooney WD (eds.) *Geological Society America Memoir 172: Geophysical Framework of the Continental United States*, pp. 383–404. Boulder, CO: Geological Society of America.

Karagianni EE, Papazachos CB, Panagiotopoulos DG, Suhadolc P, Vuan A, and Panza GF (2005) Shear velocity structure in the Aegean area obtained by inversion of Rayleigh waves. *Geophysical Journal International* 160: 127–143.

Katz S (1954) Seismic study of crustal structure in Pennsylvania and New York. *Bulletin of the Seismological Society of America* 44: 303–325.
Kay RW and Kay SM (1981) The nature of the lower continental crust: Inferences from geophysics, surface geology, and crustal xenoliths. *Reviews of Geophysics and Space Physics* 19: 271–297.
Keller GV (1989a) Electrical structure of the crust and upper mantle beneath the United States, Part 1: Methods for determining the conductivity profile. In: Pakiser LC and Mooney WD (eds.) *Geophysical Framework of the Continental United States*, *Geological Society of America Memoir*, vol. 172, pp. 71–89.
Keller GV (1989b) Electrical structure of the crust and upper mantle beneath the United States, Part 2: Survey of data and interpretation. In: Pakiser LC and Mooney WD (eds.) *Geophysical Framework of the Continental United States*, *Geological Society of America Memoir*, vol. 172, pp. 425–446.
Keller GR and Hatcher RD (1999) Some comparisons of the structure and evolution of the southern Appalachian – Ouachita orogen and portions of the Trans-European Suture Zone region. *Tectonophysics* 314: 43–68.
Kelley KR, Ward RW, Treitel S, and Alford RM (1976) Synthetic seismograms: A finite approach. *Geophysics* 41: 2–27.
Kempner WC and Gettrust JF (1982) Ophiolites, synthetic seismograms, and oceanic crustal structure, 1: Comparison of ocean bottom seismometer data and synthetic seismograms from the Bay of Islands ophiolite. *Journal of Geophysical Research* 87: 8462–8476.
Kennet BLN (1974) Reflections, rays, and reverberations. *Bulletin of the Seismological Society of America* 64: 1685–1696.
Kennett BLN (1983) *Seismic Wave Propagation in Stratified Media*. Cambridge: Cambridge University Press, 342 pp.
Kennett BLN and Engdahl ER (1991) Traveltimes for global earthquake location and phase identification. *Geophysical Journal International* 105: 429–465.
Kennett BLN, Engdahl ER, and Buland R (1995) Constraints on seismic velocities in the Earth from traveltimes. *Geophysical Journal International* 122: 108–124.
Kern H (1978) The effect of high temperature and high confining pressure on compressional wave velocities in quartz-bearing and quartz-free igneous and metamorphic rocks. *Tectonophysics* 44: 185–203.
Kern H, Gao S, and Liu QS (1996) Seismic properties and densities of middle and lower crustal rocks exposed along the North China Geoscience Transect. *Earth and Planetary Science Letters* 139(3–4): 439–455.
Kern H, Popp T, Gorbatsevich, Zharikov A, Lobanov KV, and Smirnov Yu P (2001) Pressure and temperature dependence of Vp and Vs in rocks from the superdeep well and from surface analgues at Kola and the nature of velocity anisotropy. *Tectonophysics* 338: 113–143.
Kerr AC (2003) Oceanic plateaus. In: Holland HC and Turekian K (eds.) *Treatise on Geochemistry,* Vol. 3, pp. 537–565. Amsterdam: Elsevier.
Kim HJ, Jou HT, Cho HM, et al. (2003) Crustal structure of the continental margin of Korea in the East Sea (Japan Sea) from deep seismic sounding data: Evidence for rifting affected by the hotter than normal mantle. *Tectonophysics* 364: 25–42.
Kim S, Nyblade AA, and Baag C-E (2009) Crustal velocity structure of the rukwa rift in the western branch of the east african rift system. *South African Journal of Geology* 112: 251–260.
Kim S, Nyblade AA, and Rhie J (2012) Crustal S-wave velocity structure of the Main Ethiopian Rift from ambient noise tomography. *Geophysical Journal International* 191: 865–878.
Kimbell GS, Gatli RW, Ritchie JD, Walker ASD, and Williamson JP (2004) Regional three-dimensional gravity modeling of the NE Atlantic margin. *Basin Research* 16: 259–278.
Kimura G and Ludden J (1995) Peeling oceanic crust in subduction zones. *Geology* 23: 217–220.
Kinck JJ, Husebye ES, and Larsson FR (1993) The Moho depth distribution in Fennoscandia and regional tectonic evolution from Archean to Permian times. *Precambrian Research* 64: 23–51.
Kind R (1978) The reflectivity method for a buried source. *Journal of Geophysics* 44: 603–612.
Kind R, Kosarev GL, and Petersen NV (1995) Receiver functions at the stations of the German Regional Seismic Network (GRSN). *Geophysical Journal International* 121: 191–202.
Kind R and Vinnik LP (1988) The upper mantle discontinuities underneath the GRF array from P-to-S converted phases. *Journal of Geophysics* 62: 138–147.
Kind R, Yuan X, Saul J, et al. (2002) Seismic images of crust and upper mantle beneath Tibet: Evidence for Eurasian plate subduction. *Science* 298: 1219–1221.
Kissling E (1998) Geotomography with local earthquake data. *Reviews of Geophysics* 26: 659–698.
Kissling E, Husen S, and Haslinger F (2001) Model parameterization in seismic tomography: A choice of consequence for the solution quality. *Physics of the Earth and Planetary Interiors* 123: 89–101.
Klemperer SL and Hobbs R (1991) *The BIRPS Atlas: Deep Seismic Reflection Profiles Around the British Isles*. Cambridge: Cambridge University Press.
Klemperer SL and Luetgert JH (1987) A comparison of reflection and refraction processing and interpretation methods applied to conventional refraction data from coastal maine. *Bulletin of the Seismological Society of America* 77: 614–630.
Klemperer SL, Miller EL, Grantz A, et al. (2002) Crustal structure of the Bering and Chukchi shelves: Deep seismic reflection profiles across the North American continent between Alaska and Russia. Tectonic Evolution of the Bering Shelf, Chukchi Sea, Arctic Margin and Adjacent landmasses. *Geological Society of America Special Papers* 360: 1–24.
Klemperer SL and Mooney WD (eds.) (1998a) Deep seismic profiling of the continents, 1: General results and new methods. *Tectonophysics* 286: 1–298
Klemperer SL and Mooney WD (eds.) (1998b) Deep seismic profiling of the continents, 2: A global survey. *Tectonophysics* 288: 1–292
Klemperer SL and Oliver JE (1983) *The advantage of length in deep crustal reflection profiles*. First Break, April 20–27.
Klingelhoefer F, Labails C, and Cosquer E (2009) Crustal structure of the SW-Moroccan margin from wide-angle and reflection seismic data (the DAKHLA experiment), Part A: Wide-angle seismic models. *Tectonophysics* 468: 63–82.
Klingelhoefer F, Lafoy Y, and Collot J (2007) Crustal structure of the basin and ridge system west of New Caledonia (southwest Pacific) from wide-angle and reflection seismic data. *Journal of Geophysical Research* 112: B11102. http://dx.doi.org/10.1029/2007JB005093.
Klingelhofer F, Edwards RA, Hobbs RW, et al. (2005) Crustal structure of the NE Rockall Trough from wide-angle seismic data modeling. *Journal of Geophysical Research* 110: B11105. http://dx.doi.org/10.1029/2005JB003763.
Klingelhofer F, Geli L, Matias L, et al. (2000) Crustal structure of a super-slow spreading centre: A seismic refraction study of Mohns Ridge, 72 degrees N. *Journal of Geophysics* 141: 509–526.
Klosko ER, Russo RM, Okal EA, and Richardson WP (2001) Evidence for a rheologically strong chemical mantle root beneath the Ontong-Java Plateau. *Earth and Planetary Science Letters* 186: 347–361.
Knopoff L (1972) Observation and inversion of surface-wave dispersion. *Tectonophysics* 13: 497–519.
Kodaira S, Sato T, Takahashi N, et al. (2007) New seismological constraints on growth of continental crust in the Izu-Bonin intra-oceanic arc. *Geology* 35: 1031–1034.
Kodaira S, Takahashi N, Park JO, Mochbaki K, Shinohana M, and Kimma S (2000) Wester Nankai Trough seismogenic: Results from a wide-angle ocean bottom seismic survey. *Journal of Geophysical Research* 105: 5882–5906. http://dx.doi.org/10.1029/1999 JB 900394.
Kohler A, Weidle C, and Maupin V (2012) Crustal and uppermost mantle structure of southern Norway: Results from surface wave analysis of ambient seismic noise and earthquake data. *Geophysical Journal International* 191: 1441–1456.
Kopp H, Flueh ER, Klaeschen D, et al. (2001) Crustal structure of the central Sunda margin at the onset of oblique subduction. *Journal of Geophysics* 147: 449–474.
Kopp H, Klaeschen D, Flueh ER, et al. (2002) Crustal structure of the Java margin from seismic wide-angle and multichannel reflection data. *Journal of Geophysical Research* 107: 2034. http://dx.doi.org/10.1029/2000JB000095.
Korenaga J, Holbrook WS, Detrick RS, et al. (2001) Gravity anomalies and crustal structure at the southeast Greenland margin. *Journal of Geophysical Research* 106: 8853–8870.
Korja T, Engels M, Zhamaletdinov AA, et al. (2002) Crustal conductivity in Fennoscandia—A compilation of a database on crustal conductance in the Fennoscandian Shield. *Earth Planet Space* 54: 535–558.
Korja A, Heikkinen P, and Aaro S (2001) Crustal structure of the northern Baltic Sea palaeorift. *Tectonophysics* 331: 341–358.
Kovach RL (1978) Seismic surface waves and crystal and upper mantle structure. *Reviews of the Geophysics and Space Physics* 16: 1–13.
Kovach RL and Anderson DL (1964) Higher mode surface waves and their bearing on the structure of the earth's mantle. *Bulletin of the Seismological Society of America* 54: 161–182.
Kozlovsky YA (ed.) (1987) *The Superdeep Well of the Kola Peninsula (Exploration of the Deep Continental Crust)*. Berlin: Springer, 588 pp.
Krabbenhoft A, Bialas J, Kopp H, Kukowski N, and Hubscher C (2004) Crustal structure of the Peruvian continental margin from wide-angle seismic studies. *Geophysical Journal International* 159: 749–764.

Krishna KS, Neprochnov YP, Rao DG, et al. (2001) Crustal structure and tectonics of the Ninetyeast Ridge from seismic and gravity studies. *Tectonics* 20: 416–433.

Krishna VG and Rao VV (2011) Velocity modeling of a complex deep crustal structure across the Mesoproterozoic south Delhi Fold Belt, NW India, from joint interpretation of coincident seismic wide-angle and near-offset reflection data: An approach using unusual reflections in wide-angle records. *Journal of Geophysical Research* 116: B01307. http://dx.doi.org/10.1029/2009JB006660.

Kroenke LW (1974) Origin of continents through development and coalescence of oceanic flood basalt plateaus. *EOS* 55: 443.

Kruger F, Scherbaum F, Rosa JWC, et al. (2002) Crustal and upper mantle structure in the Amazon region (Brazil) determined with broadband mobile stations. *Journal of Geophysical Research* 107: 2265. http://dx.doi.org/10.1029/2001JB000598.

Ku CY and Hsu SK (2009) Crustal structure and deformation at the northern Manila Trench between Taiwan and Luzon islands. *Tectonophysics* 466: 229–240.

Kumar P, Kind R, and Priestley K (2007) Crustal structure of Iceland and Greenland from receiver function studies. *Journal of Geophysical Research* 112: B03301. http://dx.doi.org/10.1029/2005JB003991.

Kumar MR, Saul J, Sarkar D, et al. (2001) Crustal structure of the Indian Shield: New constraints from teleseismic receiver functions. *Geophysical Research Letters* 28: 1339–1342.

Kurashimo E, Iwasaki T, and Hirata N (2007) Crustal structure of the southwestern margin of the Kuril arc sited in the eastern part of Hokkaido, Japan, inferred from seismic refraction/reflection experiments. *Earth Planets and Space* 59: 375–380.

Kusznir NJ and Matthews DH (1988) Deep seismic reflection and deformational mechanisms of the continental lithosphere. *Journal of Petrology,* 63–87: special lithosphere issue.

Labails C, Olivet JL, and Grp DS (2009) Crustal structure of the SW Moroccan margin from wide-angle and reflection seismic data (the Dakhla experiment). Part B – The tectonic heritage. *Tectonophysics* 468: 83–97. http://dx.doi.org/10.1016/j.tecto.2008.08.028.

Lachenbruch AH, Sass JH, and Galanis SP Jr. (1985) Heat flow in southernmost California and the origin of the Salton trough. *Journal of Geophysical Research* 90: 6709–6736.

Landes M, Fielitz W, Hauser F, and CALIXTO group (2004) 3-D upper crustal tomographic structure across the Vrancea seismic zone, Romania. *Tectonophysics* 382: 85–102. http://dx.doi.org/10.1016/j.tecto.2003.11.013.

Landes M, O'Reilly BM, Readman PW, et al. (2003) VARNET-96: Three-dimensional upper crustal velocity structure of SW Ireland. *Geophysical Journal nternational* 153: 424–442. http://dx.doi.org/10.1046/j.1365-246X.2003.01911.x.

Landes M, Ritter JRR, Readman PW, et al. (2005) A review of the Irish crustal structure and signatures from the Caledonian and Variscan Orogenies. *Terra Nova* 17: 111–120. http://dx.doi.org/10.1111/j.1365-3121.2004.00590.x.

Langel RA (1985) Introduction to the special issue: A perspective on MAGSAT results. *Journal of Geophysical Research* 90: 2441–2444.

Langel RA, Ousley G, and Berbert J (1982) The magsat mission. *Geophysical Research Letters* 9: 243–245.

Langston CA (1977) Corvallis, Oregon, crustal and upper mantle receiver structure from teleseismic P and S waves. *Bulletin of the Seismological Society of America* 67: 713–725.

Langston CA (1994) An integrated study of crustal structure and regional wave propagation for southeastern Missouri. *Bulletin of the Seismological Society of America* 84: 105–118.

Langston CA, Nyblade AA, and Owens TJ (2002) Regional wave propagation in Tanzania, East Africa. *Journal of Geophysical Research* 107. http://dx.doi.org/10.1029/2001JB000167.

Laske G and Masters G (1997) A global digital map of sediment thickness (abstract). *Eos, Transactions American Geophysical Union* 78: F483 vol. 46, Fall Meet. Suppl.

Laske G, Masters G, Ma Z, and Pasyanos ME (2012) CRUST1.0, an updated global crustal model of Earth's crust, Geophysical Research Abstracts, 14, European Geophysical Union; http:/igppweb.ucsd.edu/~gabi/crust1.html.

Lau KWH, Louden KE, Deemer S, et al. (2006a) Crustal structure across the Grand Banks-Newfoundland Basin continental margin—II. Results from a seismic refraction profile. *Geophysical Journal International* 167: 157–170. http://dx.doi.org/10.1111/j.1365-246C.2006.02989.x.

Lau KWH, Louden KE, Funck T, et al. (2006b) Crustal structure across the Grand Banks-Newfoundland Basin continental margin—I. Results from a seismic refraction profile. *Geophysical Journal International* 167: 127–156. http://dx.doi.org/10.1111/j.1365-246C.2006.02988.x.

Lebedev S and Nolet G (2003) Upper mantle beneath southeast Asia from S velocity tomography. *Journal of Geophysical Research* 108: 26.

Lees JM and Crosson RS (1989) Tomographic inversion for three-dimensional velocity structure at Mount St. Helens using earthquake data. *Journal of Geophysical Research* 94: 5716–5728.

Leet LD (1936) Seismological data on surface layers in New England. *Bulletin of the Seismological Society of America* 26: 129–145.

Lei J and Zhao D (2005) P-wave tomography and origin of the Changbai intraplate volcano in northeast Asia. *Tectonophysics* 397: 281–295.

Lerch DW, Glen JM, Ponce DA, et al. (2007) Crustal structure of the northwestern Basin and Range Province and its transition to unextended volcanic plateaus. *Geochemistry, Geophysics, Geosystems* 8. http://dx.doi.org/10.1029/2006GC001429.

Levander AR and Holliger K (1992) Small scale heterogeneity and large-scale velocity structure of the continental crust. *Journal of Geophysical Research* 97: 8797–8804.

Leveque J, Rivera L, and Wittlinger G (1993) On the use of the checker-board test to access the resolution of tomographic inversions. *Geophysical Journal International* 115: 313–318.

Levshin AL, Ritzwoller MH, and Shapiro NM (2005) The use of crustal higher modes to constrain crustal structure across central Asia. *Geophysical Journal International* 160: 961–972.

Levshin AL, Yanovskaya TB, Lander AV, et al. (1989) Seismic surface waves. In: Keilis-Borok VI (ed.) *Laterally Inhomogeneous Earth*. Dordrecht/Boston/London: Kluwer Publ. House.

Li X, Kind R, Yuan X, Woelbem I, and Hanka W (2004) Rejuvenation of the lithosphere by the Hawaiian plume. *Nature* 427: 827–829.

Li H, Li S, Song XD, et al. (2012) Crustal and uppermost mantle velocity structure beneath northwestern China from seismic ambient noise tomography. *Geophysical Journal International* 188: 131–143. http://dx.doi.org/10.1111/j.1365-246X.2011.05205.x.

Li A and Mashele B (2009) Crustal structure in the Pakistan Himalaya from teleseismic receiver functions. *Geochemistry, Geophysics, Geosystems* 10. http://dx.doi.org/10.1029/2009GC002700.

Li SL and Mooney WD (1998) Crustal structure of China from deep seismic sounding profiles. *Tectonophysics* 288: 105–113.

Li SL, Mooney WD, and Fan JC (2006) Crustal structure of mainland China from deep seismic sounding data. *Tectonophysics* 420: 239–252. http://dx.doi.org/10.1016/j.tecto.2006.01.025.

Li XD and Romanowicz B (1996) Global mantle shear velocity model developed using nonlinear asymptotic coupling theory. *Journal of Geophysical Research* 101: 22245–22272.

Li S, Unsworth MJ, Booker JR, et al. (2003) Partial melt or aqueous fluid in the mid-crust of southern Tibet? Constraints from INDEPTH magnetotelluric data. *Geophysical Journal International* 153: 289–304.

Li C, van der Hilst RD, Engdahl ER, and Burdick S (2008) A new global model for P wave speed variations in Earth's mantle. *Geochemistry, Geophysics, Geosystems* 9: Q05018. http://dx.doi.org/10.1029/2007GC001806.

Liang C and Langston CA (2009) Three-dimensional crustal structure of eastern North America extracted from ambient noise. *Journal of Geophysical Research-Solid Earth* 114. http://dx.doi.org/10.1029/2008JB005919.

Liang C, Song X, and Huang J (2004) Tomographic inversion of Pn travel times in China. *Journal of Geophysical Research* 109: B11304. http://dx.doi.org/10.1029/2003JB002789.

Lindwall DA (1988) A two-dimensional seismic investigation of crustal structure under the Hawaiian islands near Oahu and Kauai. *Journal of Geophysical Research* 93: 12107–12122.

Lippitsch R, Kissling E, and Ansorge J (2003) Upper mantle structure beneath the Alpine orogen from high-resolution teleseismic tomography. *Journal of Geophysical Research* 108: 15.

Liu K, Levander A, Niu F, et al. (2011) Imaging crustal and upper mantle structure beneath the Colorado Plateau using finite frequency Rayleigh wave tomography. *Geochemistry, Geophysics, Geosystems* 12. http://dx.doi.org/10.1029/2011GC003611.

Liu MJ, Mooney WD, Li SL, et al. (2006) Crustal structure of northeastern margin of the Tibetan plateau from the Songpan-Ganzi terrane to the Ordos basin. *Tectonophysics* 420: 253–266. http://dx.doi.org/10.1016/j.tecto.2006.01.025.

Liu Y, Xu C, He J, Liu F, and Sun H (2005) Three-dimensional velocity images of the crust and Upper Mantle beneath the north–south Zone in China. *Bulletin of the Seismological Society of America* 95: 916–925.

Lloyd S, van der Lee S, França GS, Assumção M, and Feng M (2010) Moho map of South America from receiver functions and surface waves. *Journal of Geophysical Research* 115. http://dx.doi.org/10.1029/2009JB006829.

Loper DE (1983) The dynamical and thermal structure of deep mantle plumes. *Physics of the Earth and Planetary Interiors* 33: 304–317.
Ludwig WJ and Houtz RE (1979) *Isopach map of sediments in the Pacific Ocean basin and marginal sea basins*. Tulsa, OK: American Association of Petroleum Geologists.
Ludwig WJ, Nafe JE, and Drake LE (1970) Seismic refraction. In: Maxwell AE (ed.) *The Sea. New Concepts of Sea Floor Evolution*, vol. 4, pp. 53–84. New York: Wiley-Interscience.
Luo Y, Xu Y, and Yang Y (2012) Crustal structure beneath the Dabie orogenic belt from ambient noise tomography. *Earth and Planetary Science Letters* 313: 12–22. http://dx.doi.org/10.1016/j.epsl.2011.11.004.
Lutter WJ, Nowack RL, and Braile LW (1990) Seismic imaging of upper crustal structure using traveltimes from the PASSCAL Ouachita experiment. *Journal of Geophysical Research* 95: 4621–4631.
Ma KF, Wang JH, and Zhao D (1996) Three-dimensional seismic velocity structure of the crust and uppermost mantle beneath Taiwan. *Journal of Physics of the Earth* 44: 85–105.
MacGregor LM, Constable S, and Sinha MC (1998) The RAMESSES experiment-III controlled-source electromagnetic sounding of the ReyKjanes Ridge AT 57° 45' N. *Geophysical Journal International* 135: 773–789.
MacKenzie L, Abers GA, Fischer KM, et al. (2008) Crustal structure along the southern Central American volcanic front. *Geochemistry, Geophysics, Geosystems* 9. http://dx.doi.org/10.1029/2008GC001991.
Mackenzie GD, Thybo H, and Maguire PKH (2005) Crustal velocity structure across the Main Ethiopian Rift: Results from two-dimensional wide-angle seismic modelling. *Geophysical Journal International* 162: 994–1006. http://dx.doi.org/10.1111/j.1365-246X.2005.02710.x.
Maggi A and Priestley K (2005) Surface waveform tomography of the Turkish–Iranian plateau. *Geophysical Journal International* 160: 1068–1080.
Magnani MB, Zelt CA, Levander A, et al. (2009) Crustal structure of the South American-Caribbean plate boundary at 67 degrees W from controlled source seismic data. *Journal of Geophysical Research-Solid Earth* 114. http://dx.doi.org/10.1029/2008JB005817.
Mahadevan TM (1994) *Deep Continental Structure of India: A Review. Geological Society of India Memoir*28: Bangalore: Geological Society of India, 569 pp.
Mahan KH, Schulte-Pelkum V, Blackburn TJ, Bowring SA, and Dudas FO (2012) Seismic structure and lithospheric rheology from deep crustal xenoliths, central Montana, USA. *Geochemistry, Geophysics, Geosystems* 13. http://dx.doi.org/10.1029/2012GC004332.
Mair JA and Forsyth DA (1982) Crustal structure of Canada Basin near Alaska, the Lomonosov Ridge, and adjoining basins near the North Pole. *Tectonophysics* 89: 239–254.
Mair JA and Lyons JA (1976) Seismic reflection techniques for crustal structure studies. *Geophysics* 41: 1272–1290.
Majdanski M, Grad M, Guterch A, and SUDETES 2003 Working Group (2006) 2-D seismic tomographic and ray tracing modelling of the crustal structure across the Sudetes Mountains basing on SUDETES 2003 experiment data. *Tectonophysics* 413: 249–269. http://dx.doi.org/10.1016/j.tecto.2005.10.042.
Makovsky Y, Klemperer SL, Huang LY, Lu DY, and Project INDEPTH Team (1996a) Structural elements of the southern Tethyan Himalaya crust from wide-angle seismic data. *Tectonics* 15: 997–1005.
Makovsky Y, Klemperer SL, Ratschbacher L, et al. (1996b) INDEPTH wide-angle reflection observations of P-wave-to-S-wave conversions from crustal bright spots in Tibet. *Science* 274: 1690–1691.
Makris J (1978) The crust and upper mantle of the Aegean region from deep seismic soundings. *Tectonophysics* 46: 269–284.
Malinowski M, Grad M, Guterch A, and Celebration 2000 Working Group (2008) Three-dimensional seismic modeling of the crustal structure between East European Craton and the Carpathians in SE Poland based on CELEBRATION 2000 data. *Geophysical Journal International* 173: 546–565. http://dx.doi.org/10.1111/j.1365-246X.2008.03742.x.
Manaman NS, Shomali H, and Koyi H (2011) New constraints on upper-mantle S-velocity structure and crustal thickness of the Iranian plateau using partitioned waveform inversion. *Geophysical Journal International* 184: 247–267. http://dx.doi.org/10.1111/j.1365-246X.2010.04822.x.
Mandal P, Rastogi BK, Satyanarayana HVS, and Kousalya M (2004) Results from local earthquake velocity tomography: Implications toward the source process involved in generating the 2001 Bhuj earthquake in the lower crust beneath Kachchh (India). *Bulletin of the Seismological Society of America* 94: 633–649.
Manning CE and Ingebritsen SE (1999) Permeability of the continental crust: Implications of geothermal data and metamorphic systems. *Reviews of Geophysics* 37: 127–150.
Mareschal J-C, Jaupart C, Cheng LZ, et al. (1999) Heat flow in the Trans-Hudson Orogen of the Canadian Shield: Implications for Proterozoic continental growth. *Journal of Geophysical Research* 104: 29007–29024.
Masters G, Johnson S, Laske G, and Bolton H (1996) A shear-velocity model of the mantle. *Philosophical Transactions of the Royal Society. London A* 354: 1285–1411.
Matthews DH (1986) In: Dawson J, Carswell D, Hall J, and Wedepohl K (eds.) *Seismic reflections from the lower crust around Britain. Nature of the Lower Continental Crust*, vol. 24, pp. 11–21. London: Geological Society of London, special publication.
Matthews DH and Cheadle MJ (1986) In: *Deep reflections from the Caledonides and the Variscides of Britain and comparison with the Himalayas. Geodynamics Series,* 13, pp. 5–19. Washington, DC: American Geophysical Union.
Matthews DH and The BIRPS Group (1987) Some unsolved BIRP problems. *Geophysical Journal of the Royal Astronomical Society* 89: 209–216.
Matzel E and Grand SP (2004) The anisotropic seismic structure of the East European platform. *Journal of Geophysical Research* 109: 16. http://dx.doi.org/10.1029/2001JB000623.
Maurice SDR, Wiens DA, Koper KD, et al. (2003) Crustal and upper mantle structure of southernmost South America inferred from regional waveform inversion. *Journal of Geophysical Research-Solid Earth* 108. http://dx.doi.org/10.1029/2002JB001828.
Maxwell AE (ed.) (1970a) *The Sea*. In: *New Concepts of Sea Floor Evolution*4A: p. 791. New York: Wiley-Interscience.
Maxwell AE (ed.) (1970b) *The Sea*. In: *New Concepts of Sea Floor Evolution*, vol. 4B, p. 664. New York: Wiley-Interscience.
Mayhew MA, Johnson BD, and Wasilewski PJ (1985) A review of problems and progress in studies of satellite magnetic anomalies. *Journal of Geophysical Research* 90: 2511–2522.
Mayhew MA and LaBrecque JL (1987) Crustal geologic studies with Magsat and the surface magnetic data. *Reviews of Geophysics and Space Physics* 25: 971–981.
McEnroe SA, Langenhorst F, Robinson P, Bromiley GD, and Shaw CSJ (2004) What is magnetic in the lower crust? *Earth and Planetary Science Letters* 22: 175–192.
McEvilly TV (1964) Central U.S. crust-upper mantle structure from Love and Raleigh wave phase velocity inversion. *Bulletin of the Seismological Society of America* 54: 1997–2016.
McKenzie D and Bickle MJ (1988) The volume and composition of melt generated by extension of the lithosphere. *Journal of Petrology* 29: 625–679.
McKenzie D, Jackson J, and Priestley K (2005) Thermal structure of oceanic and continental lithosphere. *Earth and Planetary Science Letters* 233: 337–349.
McLennan SM and Taylor SR (1982) Geochemical constraints on the growth of the continental crust. *Journal of Geology* 90: 347–361.
McMechan GA and Mooney WD (1980) Asymptotic ray theory and synthetic seismograms for laterally varying structure: Theory and application to the Imperial Valley, California. *Bulletin of the Seismological Society of America* 70: 2021–2035.
McNamara DE, Walter WR, Owens TJ, and Ammon CJ (1997) Upper mantle velocity structure beneath the Tibetan plateau from Pn travel time tomography. *Journal of Geophysical Research* 102: 493–505.
McNutt MK (1980) Implications of regional gravity for state of stress in the Earth's crust and upper mantle. *Journal of Geophysical Research* 85: 6377–6396.
Mechie J, Abu-Ayyash K, Ben-Avraham Z, et al. (2004) Crustal shear velocity structure across the Dead Sea Transform from 2-D modeling of project DESERT explosion seismic data. *Geophysical Journal International* 160: 910–924.
Mechie J, Abu-Ayyash K, Ben-Avraham Z, et al. (2005) Crustal shear velocity structure across the Dead Sea Transform from two-dimensional modelling of DESERT project explosion seismic data. *Geophysical Journal International* 160: 910–924. http://dx.doi.org/10.1111/j.1365-246X.2005.02526.x.
Mechie J, Abu-Ayyash K, Ben-Avraham Z, et al. (2009) Crustal structure of the southern Dead sea basin derived from project DESIRE wide-angle seismic data. *Geophysical Journal International* 178: 457–478. http://dx.doi.org/10.1111/j.1365-246X.2009.04161.x.
Mechie J, Egorkin AV, Fuchs K, et al. (1993) P-wave mantle velocity structure beneath northern Eurasia from long-range recordings along the profile. *Physics of the Earth and planetary Interiors* 79: 469–486.
Mechie J, Yuan X, Schurr B, et al. (2012a) Crustal and uppermost mantle velocity structure along a profile across the Pamir and southern Tien Shan as derived from project TIPAGE wide-angle seismic data. *Geophysical Journal International* 188: 385–407. http://dx.doi.org/10.1111/j.1365-246X.2011.05278.x.
Mechie J, Zhao W, Karplus MS, et al. (2012b) Crustal shear (S) velocity and Poisson's ratio structure along the INDEPTH IV profile in northeast Tibet as derived from

wide-angle seismic data. *Geophysical Journal International* 191: 369–384. http://dx.doi.org/10.1111/j.1365-246X.2012.05616.x.
Meissner R (1967) Exploring the deep interfaces by seismic wide angle measurements. *Geophysical Prospecting* 15: 598–617.
Meissner R (1973) The "Moho" as a transition zone. *Geophysical Survey* 1: 195–216.
Meissner R (1986) *The Continental Crust: A Geophysical Approach*. London: Academic Press, 426 pp.
Meissner R and Bortfeld RK (eds.) (1990) *DEKORP—Atlas: Results of Deutsches Kontinentales Reflexionsseismisches Programm*. Berlin: Springer.
Meissner R, Brown L, Dürbaum H-J, Franke W, Fuchs K, and Siefert F (eds.) (1991) *Continental lithosphere: Deep seismic reflections*. In: *Geodynamics Series*, vol. 22, p. 450. American Geophysical Union.
Meissner R and Mooney WD (1998) Weakness of the lower continental crust: A condition for delamination, uplift, and escape. *Tectonophysics* 296: 47–60.
Meissner R, Mooney WD, and Artemieva IM (2002) Seismic anisotropy and mantle creep in young orogens. *Geophysical Journal International* 149: 1–14.
Meissner R, Wever T, and Fluh ER (1987) The Moho in Europe—Implications for crustal development. *Annales Geophysicae* 5: 357–364.
Mele G (1998) Pn anisotropy in the northern Apennine chain (Italy); geodynamics of lithosphere and earth's mantle; seismic anisotropy as a record of the past and present dynamic processes. *PAGEOPH* 151: 495–502.
Melhush A, Holbrook WS, Davey F, et al. (2005) Crustal and upper mantle seismic structure of the Australian plate, south island, New Zealand. *Tectonophysics* 395: 113–135. http://dx.doi.org/10.1016/j.tecto.2004.09.005.
Meltzer A and Christensen N (2001) Nanga Parbat crustal anisotropy: Implications for interpretation of crustal velocity structure and shear-wave splitting. *Geophysical Research Letters* 10: 2129–2132. http://dx.doi.org/10.1029/2000GL012262.
Menke W (1989) *Geophysical Data Analysis: Discrete Inverse Theory*. New York: Springer, revised edn.
Meyers SC, Beck S, Zandt G, and Wallace T (1998) Lithospheric-scale structure across the Bolivian Andes from tomographic images of velocity and attenuation for P and S waves. *Journal of Geophysical Research* 103: 21233–21252.
Milkereit B, Mooney WD, and Kohler WM (1985) Inversion of seismic refraction data in planar dipping structure. *Geophysical Journal of the Royal Astronomical Society* 82: 81–103.
Minshull TA (1993) Wide-angle imaging of reflectors in Mesozoic oceanic crust. *Geophysical Research Letters* 20: 1619–1622.
Minshull TA, Muller MR, and White RS (2006) Crustal structure of the Southwest Indian Ridge at 66 degrees E: Seismic constraints. *Geophysical Journal International* 166: 135–147. http://dx.doi.org/10.1111/j.1365-246X.2006.03001.x.
Mintrop L (1949) On the stratification of the earth's crust according to seismic studies of a large explosion and earthquakes. *Geophysics* 14: 321–336.
Mitchell BJ and Herrmann RB (1979) Shear velocity structure in the eastern United States from the inversion of surface-wave group and phase velocities. *Bulletin of the Seismological Society of America* 69: 113–1148.
Mitra S, Bhattacharya SN, and Nath SK (2008) Crustal structure of the Western Bengal Basin from joint analysis of teleseismic receiver functions and Rayleigh-wave dispersion. *Bulletin of the Seismological Society of America* 98: 2715–2723. http://dx.doi.org/10.1785/0120080141.
Mjelde R, Digranes P, Van Schaack M, et al. (2001) Crustal structure of the outer Voring Plateau offshore Norway, from ocean bottom seismic and gravity data. *Journal of Geophysical Research-Solid Earth* 106: 6769–6791. http://dx.doi.org/10.1029/2000JB900415.
Mjelde R, Raum T, Kandilarov A, et al. (2009) Crustal structure and evolution of the outer Møre Margin, NE Atlantic. *Tectonophysics* 468: 224–243. http://dx.doi.org/10.1016/j.tecto.2008.06.003.
Mohorovicic A (1910) Das Beben vom 8.x.1909, *Jahrb. meteorol. Obs. Zagreb für 1909* IX, IV.Teil, Abschn. 1, Zagreb, 1–63.
Mohsen A, Asch G, Mechie J, et al. (2011) Crustal structure of the Dead Sea Basin (DSB) from a receiver function analysis. *Geophysical Journal International* 184: 463–476. http://dx.doi.org/10.1111/j.1365-246X.2010.04853.x.
Monsalve G, Sheehan A, Rowe C, et al. (2008) Seismic structure of the crust and the upper mantle beneath the Himalayas: Evidence for eclogitization of lower crustal rocks in the Indian Plate. *Journal of Geophysical Research-Solid Earth* 113. http://dx.doi.org/10.1029/2007JB005424.
Montagner J-P and Tanimoto T (1990) Global anisotropy in the upper mantle inferred from the regionalization of phase velocities. *Journal of Geophysical Research* 95: 4797–4819.
Mooney WD (1989) Seismic methods for the determining earthquake source parameters and lithospheric structure. In: Pakiser LC and Mooney WD (eds.) *Geophysical Framework of the Continental United States*. *Memoir*, vol. 172, pp. 11–34. Boulder, CO: Geological Society of America.
Mooney WD and Braile LW (1989) The seismic structure of the continental crust and upper mantle of North America. In: Bally AW and Palmer AR (eds.) *The Geology of North America—An Overview*, pp. 39–52. Boulder, CO: Geological Society of America.
Mooney WD and Brocher TM (1987) Coincident seismic reflection/refraction studies of the continental lithosphere: A global review. *Reviews of Geophysics* 25: 723–742.
Mooney WD and Kaban M (2010) The North American upper mantle: Density, composition and evolution. *Journal of Geophysical Research* 115. http://dx.doi.org/10.1029/2010JB000866.
Mooney WD, Laske G, and Masters TG (1998) CRUST 5.1: A global crustal model at 5º x 5º. *Journal of Geophysical Research* 103: 727–747.
Mooney WD and Meissner R (1991) Continental crustal evolution observations. *Eos, Transactions American Geophysical Union* 72(48): 537–541.
Mooney WD and Meissner R (1992) Multi-genetic origin of crustal reflectivity: A review of seismic reflection profiling of the continental lower crust and Moho. In: Fountain DM, Arculus R, and Kay RW (eds.) *Continental Lower Crust*. *Development in Geotectonics*, vol. 23, pp. 45–79. Amsterdam: Elsevier.
Mooney WD, Prodehl C, and Pavlenkova NI (2002) Seismic velocity structure of the continental lithosphere from controlled source data. In: Lee WHK, Kanamori H, Jennings PC, and Kisslinger C (eds.) *International Handbook of Earthquake and Engineering Seismology*, vol. 81A, pp. 887–908. The International Association of Seismology and Physics of the Earth's Interior.
Mooney WD, Rao VV, Reddy PR, et al. (2005) Comparison of the deep crustal structure and seismicity of North America with the Indian subcontinent. *Current Science* 88: 1639–1651.
Morozov IB, Morozova EA, Smithson SB, and Solodilov LN (1998) On the nature of teleseismic P_n phase observed on the ultralong-range profile "Quartz" Russia. *Bulletin of the Seismological Society of America* 1: 62–73.
Morozova EA, Morozov IB, Smithson SB, and Solodilov LN (1999) Heterogeniety of the uppermost mantle beneath Russian Eurasia from the ultra-long-range profile QUARTZ. *Journal of Geophysical Research* 104: 20329–20348.
Mueller S (ed.) (1973) The structure of the earth's crust based on seismic data. *Tectonophysics* 20: 1–391.
Mueller S (1977) A new model of the continental crust. In: Heacock JG (ed.) *The Earth's Crust—Its Nature and Properties*. *Geophysical Monograph*, vol. 20, pp. 289–317. Washington, DC: American Geophysical Union.
Mueller S (1978) In: Ramberg I and Neumann E (eds.) *Evolution of the Earth's Crust*. *Tectonics and Geophysics of Continental Rifts*, vol. 2, pp. 11–28. Dordrecht: Reidel.
Müller G (1985) The reflectivity method: A tutorial. *Journal of Geophysics* 58: 153–174.
Muller MR, Minshull TA, and White RS (2000) Crustal structure of the Southwest Indian Ridge at the Atlantis II Fracture Zone. *Journal of Geophysical Research-Solid Earth* 105: 25809–25828. http://dx.doi.org/10.1029/2000JB900262.
Müller RD, Roest WR, Royer J, Gahagan LM, and Sclater JG (1997) Digital isochrons of the world's ocean floor. *Journal of Geophysical Research* 102(B2): 3211–3214.
Mutter JC and Karson JA (1992) Structural processes at slow spreading ridges. *Science* 257: 317–627.
Mutter CZ and Mutter JC (1993) Variations in thickness of layer 3 dominante oceanic crustal structure. *Earth and Planetary Science Letters* 117: 295–317.
Myers SC, Begnaud ML, Ballard S, et al. (2010) A crust and upper mantle model of Eurasia and North Africa for Pn travel-time calculations. *Bulletin of the Seismological Society of America* 100: 640–656. http://dx.doi.org/10.1785/0120090198.
Nafe JE and Drake CL (1957) Variation with depth in shallow and deep water marine sediments of porosity, density and velocity of compressional and shear waves. *Geophysics* 22: 523–552.
Nafe JE and Drake CL (1968) In: Hess HH and Poldervaart A (eds.) *Physical properties of rocks of basaltic composition*. *The Poldervaart Treatise on Rocks of Basaltic Composition*, vol. 2, pp. 483–502. New York: Wiley-Interscience.
Nakamura M, Yoshida Y, Zhao D, Katao H, and Nishimura S (2003) Three-dimensional P- and S-wave velocity structures beneath the Ryukyu arc. *Tectonophysics* 369: 121–143.
Nakanishi A, Shiobara H, Hino R, et al. (2002a) Deep crustal structure of the eastern Nankai Trough and Zenisu Ridge by dense airgun-OBS seismic profiling. *Marine Geology* 187: 47–62. http://dx.doi.org/10.1016/S0025-3227(02)00244-X.
Nakanishi A, Takahashi N, Park JO, et al. (2002b) Crustal structure across the coseismic rupture zone of the 1944 Tonankai earthquake, the central Nankai Trough seismogenic zone. *Journal of Geophysical Research-Solid Earth* 107. http://dx.doi.org/10.1029/2001JB000424.

Nataf H-C and Ricard Y (1996) 3SMAC: An a priory tomographic made lot the upper mantle based on geophysical modeling. *Physics of the Earth and Planetary Interiors* 95: 101–122.

National Geophysical Data Center (2001) U.S. Department of Commerce, National Oceanic and Atmospheric Administration, 2-Minute Gridded Global Relief Data (ETOPO2).

National Geophysical Data Center (2004) Total Sediment Thickness of the World's Oceans and Marginal Seas. http://www.ngdc.noaa.gov/mgg/sedthick/sedthick.html.

Nelson KD, Zhao W, et al. (1996) Partially molten middle crust beneath southern Tibet: Synthesis of project INDEPTH results. *Science* 274: 1684–1688.

Netzeband GL, Gohl K, Hubscher CP, et al. (2006) The Levantine Basin—Crustal structure and origin. *Tectonophysics* 418: 167–188. http://dx.doi.org/10.1016/j.tecto.2006.01.001.

Nielsen L, Balling N, Jacobsen BH, and MONA LISA Working Group (2000) Seismic and gravity modelling of crustal structure in the Central Graben, North Sea. Observations along MONA LISA profile 3. *Tectonophysics* 328: 229–244. http://dx.doi.org/10.1016/S0040-1951(00)00213-4.

Nishimoto S, Ishikawa M, Arima M, and Yoshida T (2005) Laboratory measurements of P wave velocity in crustal and upper mantle xenoliths from Ichino-megata, NE Japan: Ultrabasic hydrous lower crust beneath the NE Honshu arc. *Tectonophysics* 396: 245–259. http://dx.doi.org/10.1016/j.tecto.2004.12.010.

Niu F, Bravo T, Pavlis G, et al. (2007) Receiver function study of the crustal structure of the southeastern Caribbean plate boundary and Venezuela. *Journal of Geophysical Research-Solid Earth* 112. http://dx.doi.org/10.1029/2006JB004802.

Niu FL and James DE (2002) Fine structure of the lowermost crust beneath the Kaapvaal craton and its implications for crustal formation and evolution. *Earth and Planetary Science Letters* 200: 121–130. http://dx.doi.org/10.1016/S0012-821X(02)00584-8.

Nolet G (1977) The upper mantle under Western Europe inferred from the dispersion of Rayleigh modes. *Journal of Geophysics* 43: 265–285.

Nolet G (1978) Simultaneous inversion of seismic data. *Geophysical Journal of the Royal Astronomical Society* 55: 679–691.

Nolet G (ed.) (1987a) *Seismic Tomography with Applications in Global Seismology and Exploration Geophysics*. Dordrecht: D. Reidel Publ. Co., 386 pp.

Nolet G (1987b) Waveform tomography. In: Nolet G (ed.) *Seismic Tomography*, pp. 301–322. Dordrecht: Reidel.

Nur A and Ben-Avraham Z (1982) Oceanic plateaus, the fragmentation of continents, and mountain building. *Journal of Geophysical Research* 87: 3644–3661.

O'Reilly BM, Hauser F, Jacob AWB, and Shannon PM (1996) The lithosphere below the Rockall Trough: Wide-angle seismic evidence for extensive serpentinisation. *Tectonophysics* 255: 1–23.

O'Reilly BM, Readman PW, and Hauser F (1998) Lithospheric structure across the western Eurasian plate from a wide-angle seismic and gravity study: Evidence for a regional thermal anomaly. *Earth and Planetary Science Letters* 156: 275–280.

Officer CB (1958) *Introduction to the Theory of Sound Transmission*. New York: McGraw-Hill Co.

Okabe A, Kaneshima S, Kanjo K, Ohtaki T, and Purwana I (2004) Surface wave tomography for southeastern Asia using IRIS-FARM and JISNET data; plumes and superplumes. *Physics of the Earth and Planetary Interiors* 146: 101–112.

Oliver J (1962) A summary of observed surface wave dispersion. *Bulletin of the Seismological Society of America* 52: 81–86.

Oliver J, Cook F, and Brown L (1983) COCORP and the continental crust. *Journal of Geophysical Research* 88: 2247–3329.

Oliver JE, Dorbin M, Kaufman S, Meyer R, and Phinney R (1976) Continuous seismic reflection profiling of the deep basement. *Bulletin of the Geological Society of America* 87: 1537–1546.

Oliver J, Dorman J, and Sutton G (1959) The second shear mode of continental Rayleigh waves. *Bulletin of the Seismological Society of America* 49: 379–389.

Oliver J and Ewing M (1957) Higher modes of continental Rayleigh waves. *Bulletin of the Seismological Society of America* 47: 187–204.

Oliver J and Ewing M (1958) Normal modes of continental Rayleigh waves. *Bulletin of the Seismological Society of America* 48: 33–49.

Olsen KH (ed.) (1995) *Continental Rifts: Evolution, Structure, Tectonics*. Amsterdam: Elsevier, 466 pp.

Operto S and Charvis P (1996) Deep structure of the southern Kerguelen Plateau (southern Indian Ocean) from ocean bottom seismometer wide-angle seismic data. *Journal of Geophysical Research* 101: 25077–25103.

Orcutt JA (1987) Structure of the Earth: Oceanic crust and uppermost mantle. *Reviews of Geophysics* 25: 1177–1196.

Orcutt JA, Kennett BLN, and Dorman LM (1976) Structure of the East Pacific Rise from an ocean bottom seismometer survey. *Geophysical Journal of the Royal Astronomical Society* 45: 305–320.

Owens TJ, Crosson RS, and Hendrickson MA (1988) Constraints on the subduction geometry beneath western Washington from broadband teleseismic waveform modeling. *Bulletin of the Seismological Society of America* 78: 1219–1234.

Owens TJ and Zandt G (1985) The response of the continental crust-mantle boundary observed on broadband teleseismic receiver functions. *Geophysical Research Letters* 12: 705–708.

Owens TJ, Zandt G, and Taylor SR (1984) Seismic evidence for an ancient rift beneath the Cumberland Plateau, Tennessee: A detailed analysis of broadband teleseismic P waveform. *Journal of Geophysical Research* 89: 7783–7795.

Oxburgh ER and Parmentier EM (1977) Compositional and density stratification in oceanic lithosphere—causes and consequences. *Journal of the Geological Society* 133: 343–355.

Pakiser LC (1963) Structure of the crust and upper mantle in the western United States. *Journal of Geophysical Research* 68: 5747–5756.

Pakiser LC and Mooney WD (eds.) (1989) Geophysical framework of the continental United States. *Geological Society America Memoir*, vol. 172, 826.

Pakiser LC and Steinhart JS (1964) Explosion seismology in the western hemisphere. In: Odishaw J (ed.) *Solid Earth and Interface Phenomena. Research in Geophysics*, vol. 2, pp. 123–147. Cambridge, MA: Massachusetts Institute of Technology Press.

Pan S and Niu F (2011) Large contrasts in crustal structure and composition between the Ordos plateau and the NE Tibetan plateau from receiver function analysis. *Earth and Planetary Science Letters* 303: 291–298. http://dx.doi.org/10.1016/j.epsl.2011.01.007.

Panza GF, Pontevivo A, Chimera G, Raykova R, and Aoudia A (2003) The lithosphere–asthenosphere; Italy and surroundings; Geology of Italy. *Episodes* 26: 169–174.

Papasikas N and Juhlin C (1997) Interpretation of reflections from the central part of the Siljan Ring impact structure based on results from the Stenberg-1 borehole. *Tectonophysics* 269: 237–245.

Parker RL (1971) The determination of seamount magnetism. *Geophysical Journal of the Royal Astronomical Society* 24(4): 321–324.

Parker RL (1973) The rapid calculations of potential anomalies. *Geophysical Journal of the Royal Astronomical Society* 31: 447–455.

Parolai S, Spallarossa D, and Eva C (1997) Bootstrap inversion for P_n wave velocity in northwestern Italy. *Annali di Geotisica* XL: 133–150.

Parsons B and Sclater JG (1977) An analysis of the variation of ocean floor bathymetry and heat flow with age. *Journal of Geophysical Research* 82: 803–825.

Pasyanos M (2000) Predicting geophysical measurements: Testing a combined empirical and model-based approach using surface waves. *Bulletin of the Seismological Society of America* 90: 790–798.

Pasyanos ME, Walter WR, Flanagan MP, Goldstein P, and Bhattacharyya J (2004) Building and testing an a priori geophysical model for Western Eurasia and North Africa. *PAGEOPH* 161: 235–281.

Paterson NR and Reeves CV (1985) Applications of gravity and magnetic surveys: The state-of-the-art in 1985. *Geophysics* 50: 2558–2594.

Patriat M, Klingelhoefer F, Aslanian D, et al. (2002) Deep crustal structure of the Tuamotu plateau and Tahiti (French Polynesia) based on seismic refraction data. *Geophysical Research Letters* 29. http://dx.doi.org/10.1029/2001GL013913.

Pavlenkova NI (1973) Ware Fields and crustal models of the continental type. Naukova Durnka Kiev (in Russian).

Pavlenkova NI (1996) Crustal and upper mantle structure in northern Eurasia from seismic data. *Advances in Geophysics* 37: 1–133.

Pavlenkova NI, Pilipenko VN, and Verpakhovskaja AO (2009) Crustal structure in Chile and Okhotsk Sea regions. *Tectonophysics* 472: 28–38. http://dx.doi.org/10.1016/j.tecto.2008.08.018.

Pawlak A, Eaton DW, Bastow ID, et al. (2011) Crustal structure beneath Hudson Bay from ambient-noise tomography: Implications for basin formation. *Geophysical Journal International* 184: 65–82. http://dx.doi.org/10.1111/j.1365-246X.2010.04828.x.

Peirce C and Barton PJ (1991) Crustal structure of the Madeira-Tore Rise, eastern North Atlantic—Results of a DOBS wide-angle and normal incidence seismic experiment in the Josephine Seamount region. *Geophysical Journal International* 106: 357–378.

Percival JA, Cook FA, and Clowes RM (eds.) (2012) Tectonic styles in Canada: The LITHOPROBE perspective, Geological Association of Canada Special Paper 49, 498 pp.

Percival JA, Fountain DM, and Salisbury MH (1992) Exposed crustal cross sections as windows on the lower crust. In: Fountain DM, Arculus R, and Kay RW (eds.) *Continental Lower Crust*, pp. 317–362. Amsterdam: Elsevier.

Perfit MR and Chadwick WW Jr. (1998) Magmatism at mid-ocean ridges: Constraints from volcanological and geochemical investigations. In: Buck WR, Delaney P, and

Karson JA (eds.) *Geophysics Monograph 92: Faulting and Magmatism at Mid-Ocean Ridges*. Washington, DC: American Geophysical Union.
Petit C, Koulakov I, and Deverchere J (1998) Velocity structure around the Baikal rift zone from teleseismic and local earthquake traveltimes and geodynamic implications; continents and their mantle roots. *Tectonophysics* 296: 125–144.
Pfiffner OA, Lehner P, Heitzmann P, Mueller S, and Steck A (eds.) (1997) *Deep Structure of the Swiss Alps: Results of NRP 20*. Basel/Boston/Berlin: Birkhäuser, 380 pp.
Phinney RA (1964) Structure of the Earth's crust from spectral behavior of long-period body waves. *Journal of Geophysical Research* 69: 2997–3017.
Pilidou S, Priestley K, Debayle E, and Gudmundsson O (2005) Rayleigh wave tomography in the north Atlantic; high resolution images of the Iceland, Azores and Eifel mantle plumes; mantle plumes; physical processes, chemical signatures, biological effects. *Lithos* 79: 453–474.
Pilidou S, Priestley K, Gudmundsson O, and Debayle E (2004) Upper mantle S-wave speed heterogeneity and anisotropy beneath the North Atlantic from regional surface wave tomography; the Iceland and Azores plumes. *Geophysical Journal International* 159: 1057–1076.
Planert L, Flueh ER, and Reston TJ (2009) Along- and across-axis variations in crustal thickness and structure at the Mid-Atlantic Ridge at 5 degrees S obtained from wide-angle seismic tomography: Implications for ridge segmentation. *Journal of Geophysical Research-Solid Earth* 114. http://dx.doi.org/10.1029/2008JB006103.
Plouff D (1976) Gravity and magnetic fields of polygonal prisms and application to magnetic terrain corrections. *Geophysics* 41: 727–741.
Pollack HN and Chapman DS (1977) On the regional variation of heat flow, geotherms, and lithospheric thickness. *Tectonophysics* 38: 279–296.
Pollack HN, Hurter SJ, and Johnson JR (1993) Heat flow form the Earth's interior: Analysis of the global data set. *Reviews of Geophysics* 31(3): 267–280.
Prajapati S, Suresh G, and Bhattacharya SN (2011) Crustal structure of the Northwest Deccan Volcanic Province, India, and the adjoining continental shelf from observed surface-wave dispersion. *Bulletin of the Seismological Society of America* 101: 1488–1495. http://dx.doi.org/10.1785/0120100294.
Prasad BR, Klemperer SL, Rao VV, et al. (2011) Crustal structure beneath the Sub-Himalayan fold-thrust belt, Kangra recess, northwest India, from seismic reflection profiling: Implications for Late Paleoproterozoic orogenesis and modern earthquake hazard. *Earth and Planetary Science Letters* 308: 218–228. http://dx.doi.org/10.1016/j.epsl.2011.05.052.
Pratt RG (1999) Seismic waveform inversion in the frequency domain, Part 1: Theory and verification in a physical scale model. *Geophysics* 64: 888–901.
Press F (1956) Determination of crustal structure from phase velocity of Rayleigh waves: 1. Southern California. *Bulletin of the Geological Society of America* 67: 1647–1658.
Press F (1964) Seismic wave attenuation in the crust. *Journal of Geophysical Research* 69: 4417–4418.
Press F (1968) Earth models obtained by the Monte Carlo inversion. *Journal of Geophysical Research* 73: 5223–5234.
Priestly K and Brune J (1978) Surface waves and the structure of the Great Basin of Nevada and western Utah. *Journal of Geophysical Research* 83: 2265–2272.
Prodehl C (1970) Seismic refraction study of crustal structure of the Great Basin of Nevada and western Utah. *Journal of Geophysical Research* 83: 2629–2645.
Prodehl C (1979) Crustal structure of the western United States. U.S. *Geological Survey, Professional Paper* 1034, 74 pp.
Prodehl C (1984) Structure of the earth's crust and upper mantle. Hellwege KH (ed.) *Landolt Börnstein New Series: Numerical Data and Functional Relationships in Science and Technology*. In: Fuchs K and Soffel H (eds.) *Physical Properties of the Interior of the Earth, the Moon and the Planets*, vol. 2a, pp. 97–206. Berlin-Heidelberg: Springer, Group V.
Prodehl C and Mooney WD (2012) In: *Exploring the Earth's crust: History and Results of Controlled-source Seismology*. *Geological Society of America Memoir*, vol. 208, p. 764. Boulder, CO: Geological Society of America.
Prothero DR and Schwab F (2004) Sedimentary Geology: An introduction to sedimentary rocks and stratigraphy. Macmillian.
Purdy GM and Detric RS (1986) Crustal structure of the Mid-Atlantic Ridge at 23°N from seismic refraction studies. *Journal of Geophysical Research* 91: 3739–3762.
Purucker MB, Langlais B, Olsen N, Hulot G, and Mandea M (2002) The southern edge of cratonic North America: Evidence from new satellite magnetometer observations. *Geophysical Research Letters* 29(15): 8000. http://dx.doi.org/10.1029/2001GL013645.
Qiu XL, Ye SY, Wu SM, et al. (2001) Crustal structure across the Xisha trough, northwestern South China Sea. *Tectonophysics* 341: 179–193. http://dx.doi.org/10.1016/S0040-1951(01)00222-0.
Rabbel W and Mooney WD (1996) Seismic anisotropy of the crystalline crust: What does it tell us? *Terra Nova* 8: 16–21.
Rabinowitz PD, Dipiazza N, and Matthias PK (1988) *Sediment Thickness Map of the Indian Ocean*. Tulsa, OK: Am. Assoc. of Pet. Geol.
Raitt RW (1963) The crustal rocks. In: Hill MN (ed.) *The Earth Beneath the Sea. The Sea*, vol. 3, pp. 85–102. New York: Wiley-Interscience.
Ramesh DS, Kind R, and Yuan X (2002) Receiver function analysis of the North American crust upper mantle. *Geophysical Journal International* 150: 91–108.
Rapine R, Tilmann F, West M, Ni J, and Rodgers A (2001) Crustal structure of northern and southern Tibet from surface wave dispersion analysis. *Journal of Geophysical Research* 108: 2120. http://dx.doi.org/10.1029/2001JB000445.
Rau RJ and Wu FT (1995) Tomographic imaging of lithospheric structures under Taiwan. *Earth and Planetary Science Letters* 133: 517–532.
Redford MS (1980) Magnetic method. *Geophysics* 45: 1640–1658.
Reid AB (1980) Aeromagnetic survey design. *Geophysics* 45: 1640–1658.
Richards TC and Walker DJ (1959) Measurement of the thickness of the earth's crust in the Albertan plains of western Canada. *Geophysics* 24: 262–284.
Richardson KR, Smallwood JR, White RS, Snyder DB, and Maguire PKH (1998) Crustal structure beneath the Faroe islands and the Faroe-Iceland Ridge. *Tectonophysics* 300: 159–180.
Ringwood AE (1975) *Composition and Petrology of the Earth's Mantle*. New York: McGraw-Hill, 618 pp.
Ritzmann O, Jokat W, Mjelde R, et al. (2002) Crustal structure between the Knipovich Ridge and the Van Mijenfjorden (Svalbard). *Marine Geophysical Researches* 23: 379–401. http://dx.doi.org/10.1023/B:MARI.0000018168.89762.a4.
Ritzwoller MH, Barmin MP, Villasenor A, Levshin AL, and Engdahl ER (2002a) Pn and Sn tomography across Eurasia. *Tectonophysics* 358: 39–55.
Ritzwoller MH and Lavely EM (1995) Three-dimensional seismic models of the Earth's mantle. *Reviews of Geophysics* 33: 1–66.
Ritzwoller MH and Levshin AL (1998) Eurasian surface wave tomography: Group velocities. *Journal of Geophysical Research* 103: 4839–4878.
Ritzwoller MH and Levshin AL (2002) Estimating shallow shear velocities with marine multi-component seismic data. *Geophysics* 67: 1991–2004.
Ritzwoller MH, Shapiro NM, Barmin MP, and Levshin AL (2002b) Global surface wave diffraction tomography. *Journal of Geophysical Research* 107(B12): 2335. http://dx.doi.org/10.1029/2002JB001777.
Roberts DG, Ginzberg A, Nunn K, and McQullin R (1988) The structure of the Rockall Trough from seismic refraction and wide-angle measurements. *Nature* 332: 632–635.
Roecker SW, Thurber C, and McPhee D (2004) Joint inversion of gravity and arrival time data from Parkfield: New constraints on structure and hypocenter locations near the SAFOD drill site. *Geophysical Research Letters* 31: L12SO4. http://dx.doi.org/10.1029/2003GJ019396.
Roller JC (1965) Crustal structure in the eastern Colorado Plateau province from seismic-refraction measurements. *Bulletin of the Seismological Society of America* 55: 107–119.
Romanowicz B (1991) Seismic tomography of the Earth's mantle. *Annual Review of Earth and Planetary Sciences* 19: 77–99.
Romanowicz B (1995) A global tomographic model of shear attenuation in the upper mantle. *Journal of Geophysical Research* 100: 12375–12394.
Rubio E, Torne M, Vera E, et al. (2000) Crustal structure of the southernmost Chilean margin from seismic and gravity data. *Tectonophysics* 323: 39–60. http://dx.doi.org/10.1016/S0040-1951(00)00101-3.
Rudnick R and Fountain DM (1995) Nature and composition of the continental crust: A lower crustal perspective. *Reviews of Geophysics* 33: 267–309.
Rudnick RL and Gao S (2005) Composition of the continental crust. In: Rudnick RL (ed.) *The Crust. Treatise on Geochemistry,* 3, pp. 1–64. Elsevier-Pergamon.
Ruiz-Constán A, Pedrera A, Galindo-Zaldívar J, et al. (2012) Constraints on the frontal crustal structure of a continental collision from an integrated geophysical research: The central-western Betic Cordillera (SW Spain). *Geochemistry, Geophysics, Geosystems* 13: Q08012. http://dx.doi.org/10.1029/2012GC004153.
Ryberg T, Fuchs K, Egorkin AV, Solodilov L, and Uchida Y (1995) Observation of high-frequency teleseismic P_n on the long-range Quartz profile across northern Eurasia. *Journal of Geophysical Research* 100: 18151–18164.
Ryberg T, Wenzel F, Mechie J, Egorkin A, Fuchs K, and Solodilov L (1996) Two-dimensional velocity structure beneath northern Eurasia derived from the super long-range seismic profile quartz. *Bulletin of the Seismological Society of America* 86: 857–867.
Sage F, Basile C, Mascle J, et al. (2000) Crustal structure of the continent-ocean transition off the Cote d'Ivoire-Ghana transform margin: Implications for thermal exchanges across the palaeotransform boundary. *Geophysical Journal International* 143: 662–678. http://dx.doi.org/10.1046/j.1365-246X.2000.00276.x.

Sagiya T and Thatcher W (1999) Coseismic Slip Aesolutim along a plate boundary mega thrust: The Nankai trough Southwest Japan. *Journal of Geophysical Research* 104: 1111–1130.
Salah MK and Zhao D (2003) 3-D seismic structure of Kii peninsula in southwest Japan; evidence for slab dehydration in the forearc. *Tectonophysics* 364: 191–213.
Salisbury MH and Fountain DM (1990) *Exposed Cross-Sections of the Continental Crust*, 662 pp. Dordrecht: Kluwer.
Sandmeier K-J and Wenzel F (1986) Synthetic seismograms for a complex crustal model. *Geophysical Research Letters* 13: 22–25.
Sandmeier K-J and Wenzel F (1990) Lower crustal petrology from wide-angle P- and S-wave measurements in the Black Forest. *Tectonophysics* 173: 495–505.
Sandoval S, Kissling E, Ansorge J, and SVEKALAPKO Seismic Tomography Working Group (CHE) (2004) High-resolution body wave tomography beneath the SVEKALAPKO array; II. Anomalous upper mantle structure beneath the central Baltic shield. *Geophysical Journal International* 157: 200–214.
Sandvol E, Al-Damegh K, Calvert A, et al. (2001) Tomographic imaging of Lg and Sn propagation in the Middle East; regional wave propagation and crustal structure; monitoring the comprehensive nuclear-test-ban treaty. *PAGEOPH* 158: 1121–1163.
Sandvol E, Seber D, Calvert A, and Barazangi M (1998) Grid search modeling of receiver functions: Implications for crustal structure in the Middle East and North Africa. *Journal of Geophysical Research* 103: 26899–26971.
Sandwell DT and Smith WHF (1997) Marine gravity anomaly from Geosat and ERS 1 satellite altimetry. *Journal of Geophysical Research* 102: 10039–10054.
Saunders AD, Storey M, Kent RW, and Norry MJ (1992) Consequences of plume–lithosphere interactions. In: Storey BC, Alabaster T, and Pankhurst RJ (eds.) *Magmatism and the Causes of Continental Breakup*, vol. 68, pp. 41–60. London: Geological Society of London.
Savage MK (1999) Seismic anisotropy and mantle deformation: What have we learned from shear wave splitting? *Reviews of Geophysics* 37: 65–106.
Savage B and Wang Y (2012) Integrated model of the crustal structure in the Gulf of California extensional province. *Bulletin of the Seismological Society of America* 102: 878–885. http://dx.doi.org/10.1785/0120110196.
Scalter JG, Jaupart C, and Galson D (1980) The heat flow through oceanic and continental crust and the heat loss of the Earth. *Reviews of Geophysics* 18: 269–311.
Schillington OJ, Van Avendonk HJA, Holbrook WS, Kelemen PB, and Hornbach MJ (2004) Composition and structure of the central Aleutian island arc from arc-parallel wide angle seismic data. *Geochemistry, Geophysics and Geosystems* 5, http://dx.doi.org/10.1029j2004GC000715.
Schilt S, Oliver J, Brown L, et al. (1979) The heterogeneity of the continental crust: Results from deep crustal seismic reflection profiling using the VIBROSEIS technique. *Reviews of Geophysics and Space Physics* 17: 354–368.
Schlindwein V, Bonnemann C, Reichert C, et al. (2003) Three-dimensional seismic refraction tomography of the crustal structure at the ION site on the Ninetyeast Ridge, Indian Ocean. *Geophysical Journal International* 152: 171–184. http://dx.doi.org/10.1046/j.1365-246X.2003.01838.x.
Schmidt S and Kissling E (2000) The arc of the western Alps in the light of geophysical data on deep crustal structure. *Tectonics* 19: 62–85.
Schouten JA (1971) A fundamental analysis of magnetic anomalies over oceanic ridges. *Marine Geophysical Researches* 1: 111–114.
Schouten H and McCamy K (1972) Filtering marine magnetic anomalies. *Journal of Geophysical Research* 77(35): 7089–7099.
Seber D, Sandvol E, Sandvol C, et al. (2001) Crustal model for the Middle East and North African region: Implications for the isostatic compensation mechanism. *Geophysical Journal International* 147: 630–638.
Sexton JL, Hinze WJ, von Freese RRB, and Braile LW (1982) Long-wavelength aeromagnetic anomaly map of the conterminous United States. *Geology* 10: 364–369.
Shapiro NM and Campillo M (2004) Emergence of broadband Rayleigh waves from correlations of the ambient seismic noise. Geophysical Research Letters 31: L07614. http://dx.doi.org/ 10.1029 j2004GL019491.
Shapiro NM, Campillo M, Laurent S, and Ritzwoller MH (2005) High-resolution surface-wave tomography from ambient seismic noise. *Science* 307: 1615–1618. http://dx.doi.org/10.1126/science.1108339.
Shapiro NM and Ritzwoller MH (2002) Monte Carlo inversion for a global shear velocity model of the crust and upper mantle. *Geophysical Journal International* 151: 88–105.
Shapiro NM, Ritzwoller MH, Molnar P, and Levin V (2004) Thinning and flow of Tibetan crust constrained by seismic anisotropy. *Science* 305: 233–236.
Shaw Champion ME, White NJ, and Jones SM (2006) Crustal velocity structure of the British Isles; a comparison of receiver functions and wide-angle seismic data. *Geophysical Journal International* 166: 795–813.
Shearer PM and Orcutt JA (1986) Compressional and shear wave anisotropy in the oceanic lithosphere—the Ngendei seismic refraction experiment. *Geophysical Journal of the Royal Astronomical Society* 87: 967–1003.
Sheriff RE (1983) *Exploration Seismology: Data Processing and Interpretation*, vol. 1. Cambridge: Cambridge University Press, 221 pp.
Sheriff RE and Geldhart LP (1982) *Exploration Seismology: History, Theory, and Data Acquisition*. Cambridge: Cambridge University Press, 253 pp.
Shor GG (1967) Seismic refraction profile in Coral Sea Basin. *Science Letters* 92: 234–246.
Silver PG (1996) Seismic anisotropy beneath the continents: Probing the depths of geology. *Annual Review of Earth and Planetary Sciences* 24: 385–432.
Silver PG and Chan WW (1988) Implications for continental structure and evolution from seismic anisotropy. *Nature* 335: 34–39.
Simkin T, Tilling RI, Vogl PR , Kirby SH, Kimberly P, and Stewart DB (2006) This Dynamic Planet, United States Geological Survey Geological Investigations Map 1–2800, one sheet.
Simmons G (1964) Velocity of shear waves in rocks to 10 kilobars. *Journal of Geophysical Research* 69: 1123–1130.
Simmons NA, Meyers SC, Johannesson G, and Matzel E (2012) LLNL-G3Dv3: Global P wave tomography model for improved regional and teleseismic travel time prediction. *Journal of Geophysical Research* 117: B10302. http://dx.doi.org/10.1029/2012JB009525.
Simpson RW, Hildenbrand TG, Godson RH, and Kane MF (1987) *Digital Colored Bouguer Gravity, Free-air Gravity, Station Location, and Terrain Maps for the Continental United States*. U.S. Geological Survey Geophysical Investigations Map GP 953-B, scale 1:7,500,000.
Sinha MC, Constable SC, Peirce C, et al. (1998) Magnetic processes at slow spreading ridges: Implications of the RAMESSES Experiment at 57° 45' N on the Mid-Atlantic Ridge. *Geophysical Journal International* 135: 731–745.
Sinha MC and Louden KE (1983) The Oceanographer fracture zone, I. Crustal structure from seismic refractions studies. *Geophysical Journal of the Royal Astronomical Society* 75: 713–736.
Sinha MC, Lounden KE, and Parsons B (1981) The crustal structure of the Madagascar Ridge. *Geophysical Journal of Astronomical Society* 66: 351–377.
Sirgue L and Pratt RG (2004) Efficient waveform inversion and imaging: A strategy for selecting temporal frequencies. *Geophysics* 69: 231–248.
Sleep NH (1990) Hotspots and mantle plumes: Some phenomenology. *Journal of Geophysical Research* 95: 6715–6736.
Sleep NH (2003) Survival of Archean craton lithosphere. *Journal of Geophysical Research* 108: 2302. http://dx.doi.org/10.1029/2001JB000169.
Sleep NH (2005) Evolution of the continental lithosphere. *The Annual Review of Earth and Planetary Sciences* 33: 369–393.
Slichter LB (1938) Seismological investigations of the earth's crust using quarry blasts [abs.]. *Bulletin of the Geological Society of America* 49: 1927.
Slichter LB (1951) Crustal structure in the Wisconsin area. Arlington, Virginia. Office of Naval Research Report N9, NR86200.
Smith WHF and Sandwell DT (1997) Global sea floor topography from satellite altimetry and ship depth soundings. *Science* 277: 1956–1962.
Smith TJ, Steinhart JS, and Aldrich LT (1966) Lake Superior crustal structure. *Journal of Geophysical Research* 71: 1141–1181.
Smithson SB, Johnson RA, Hurich CA, Valasek PA, and Branch C (1987) Deep crustal structure and genesis from contrasting reflection patterns: An integrated approach. *Geophysical Journal of the Royal Astronomical Society* 87: 67–72.
Smithson SB, Wenzel F, Ganchin YV, and Morozov IB (2000) Seismic results at Kola and KTB deep scientific boreholes: Velocities, reflections, fluids, and crustal composition. *Tectonophysics* 329: 301–317.
Soller DR, Ray RD, and Brown RD (1982) A new global crustal thickness model. *Tectonics* 1: 125–149.
Song LP, Koch M, Koch K, and Schlittenhardt J (2004) 2-D anisotropic Pn-velocity tomography underneath Germany using regional traveltimes. *Geophysical Journal International* 157: 645–663.
Spakman W, van der Lee S, and van der Hilst RD (1993) Travel-time tomography of the European-Mediterranean mantle down to 1400 km. *Physics of the Earth and Planetary Interiors* 79: 3–74.
Spudich P and Orcutt J (1980) A new look at the seismic velocity structure of the oceanic crust. *Reviews of Geophysics and Space Physics* 18: 627–645.
Stankiewicz J, Parsiegla N, Ryberg T, et al. (2008) Crustal structure of the southern margin of the African continent: Results from geophysical experiments. *Journal of Geophysical Research-Solid Earth* 113. http://dx.doi.org/10.1029/2008JB005612.
Stein M and Hoffman AW (1994) Mantle plumes and episodic crustal growth *Nature* 372: 63–68.
Stein CA and Stein S (1992) A model for the global gravitation in oceanic depth and heat flow with lithospheric age. *Nature* 359: 123–129.

Steinhart JS (1967) In: Runcorn K (ed.) *Mohorovicic-discontinuity*, *International Dictionary of Geophysics*, 2, pp. 991–994.

Steinhart JS and Meyer RP (1961) *Explosion Studies of Continental Structure*. Washington, DC: Carnegie Institute publication 622, 409 pp.

Stockmann RCCF and Jackson A (2009) Imaging Earth's crustal magnetic field with satellite data: A regularization spherical triangle tessellation approach. *Geophysical Journal International* 179: 929–944.

Stolk W, Kaban MK, Beekman F, Tesauro M, Mooney WD, and Cloetingh S (2013) High resolution regional crustal model from irregularly distributed data: Application to Asia and adjacent areas. *Tectonophysics* 602: 55–68.http://dx.doi.org/10.1016/j.tecto.2013.01.002.

Su WJ, Woodward RL, and Dziewonski AM (1992) Deep origin of mid-ocean-ridge seismic velocity anomalies. *Nature* 359: 149–152.

Su WJ, Woodward RL, and Dziewonski AM (1994) Degree 12 model of shear wave velocity heterogeneity in the mantle. *Journal of Geophysical Research* 99: 6945–6980.

Suckro SK, Gohl K, Funck T, et al. (2012) The crustal structure of southern Baffin Bay: Implications from a seismic refraction experiment. *Geophysical Journal International* 190: 37–58. http://dx.doi.org/10.1111/j.1365-246X.2012.05477.x.

Sun YS, Li X, Kuleli S, Morgan FD, and Toksoz MN (2004a) Adaptive moving window method for 3D P-velocity tomography and its application in China. *Bulletin of the Seismological Society of America* 94: 740–746.

Sun YS, Morgan D, and Toksoz MN (2004b) 3D P- and S-velocity models for the crust and uppermost mantle of China by Monte-Carlo adaptive moving window inversion. *Seismological Research Letters* 74: 202–203.

Suyehiro K, Takahashi N, Ariie Y, et al. (1996) Continental crust, crustal underplating, and low-Q upper mantle beneath an oceanic island arc. *Science* 272: 390–392.

Takahashi N, Kodaira S, and Klemperer SL (2007) Crustal structure and evolution of the Mariana intra-oceanic island arc. *Geology* 35: 203–206. http://dx.doi.org/10.1130/G23212A.1.

Takahashi N, Kodaira S, Tatsumi Y, et al. (2009) Structural variations of arc crusts and rifted margins in the southern Izu-Ogasawara arc-back arc. *Geochemistry, Geophysics, Geosystems* 10. http://dx.doi.org/10.1029/2008GC002146.

Talwani M (1965) Computation with the help of a digital computer of magnetic anomalies caused by bodies of arbitrary shape. *Geophysics* 30(5): 797–817.

Talwani M and Ewing M (1960) Rapid computation of gravitational attractions of three-dimensional bodies of arbitrary shape. *Geophysics* 25: 203–225.

Tanimoto T (1995) Crustal structure of the Earth. In: Ahrens TJ (ed.) *Global Earth Physics: A Handbook of Physical Constants*, pp. 214–224. Washington, DC: AGU.

Tapley B, Ries J. Bettadpurs, et al. (2005) An improved Earth gravity field model from GRACE. *Journal of Geodesy* 79(8): 467–478.

Tapponieer P and Molnar P (1975) Active faulting and tectonics in China. *Journal of Geophysical Research* 82: 2905–2930.

Tarantola A (1984) Inversion of seismic reflection data in the acoustic approximation. *Geophysics* 49: 1259–1266.

Tarantola A and Nercessian A (1984) Three-dimensional inversion without blocks. *Geophysical Journal of the Royal Astronomical Society* 76: 299–306.

Tatel HE, Adams LH, and Tuve MA (1953) Studies of the earth's crust using waves from explosions. *American Philosophy Society Proceedings* 97: 658–669.

Tatel HE and Tuve MA (1955) Seismic exploration of a continental crust. In: Poldervaart A (ed.) *Crust of the Earth*, pp. 35–50, Geological Society of America Special Paper.

Taylor SR and McLennan SM (1985) The Continental Crust. *Its Composition and Evolution*. Maldon, MA: Blackwell Science.

Taylor SR and McLennan SM (1992) *The Continental Crust: Its Composition and Evolution*. Malden, MA: Blackwell Scientific, 312 pp.

Taylor SR and McLennan SM (2009) *Planetary Crusts: Their Composition, Origin and Evolution*. Cambridge, UK: Cambridge University Press, 378 pp.

Telford WM, Geldart LP, Sheriff RE, and Keys DA (1976) *Applied Geophysics*. Cambridge: Cambridge University Press, 860 pp.

Tesauro M, Kaban MK, and Cloetingh SAPL (2008) EuCRUST-07: A new reference model for European crust. *Geophysical Research Letters* 35. http://dx.doi.org/10.1029/2007GRL032244.

Tesauro M, Kaban MK, and Cloetingh SAPL (2012) Global strength and elastic thickness of the lithosphere. *Global and Planetary Change* 90–91: 51–57.

Thinon I, Matias L, Rehault JP, Hirn A, Fidalgo-Gonzalez L, and Avedik F (2003) Deep structure of the Armorican Basin (Bay of Biscay): A review of Norgasis seismic reflection and refraction data. *Journal of the Geological Society, London* 160: 99–116.

Thompson DA, Bastow ID, Helffrich G, et al. (2010) Precambrian crustal evolution: Seismic constraints from the Canadian shield. *Earth and Planetary Science Letters* 297: 655–656.

Thurber CH (1983) Earthquake locations and three-dimensional crustal structure in the Coyote Lake area, central California. *Journal of Geophysical Research* 88: 8226–8236.

Thurber CH (1993) Local earthquake tomography: Velocities and Vp/Vs – theory. In: Iyer H and Hihahara K (eds.) *Seismic Tomography, Theory and Practice*, pp. 563–583. Boca Raton, FL: CRC Press.

Thurber C and Aki K (1987) Three-dimensional seismic imaging. *Annual Review of Earth and Planetary Sciences* 15: 115–139.

Tiberi C, Diament M, Déverchère J, et al. (2003) Deep structure of the Baikal rift zone revealed by joint inversion of gravity and seismology. *Journal of Geophysical Research* 108. http://dx.doi.org/10.1029/2002JB001880.

Tilmann FJ and Dahm T (2008) Constraints on crustal and mantle structure of the oceanic plate south of Iceland from ocean bottom recorded Rayleigh waves. *Tectonophysics* 447: 66–79. http://dx.doi.org/10.1016/j.tecto.2006.02.028.

Tilmann F, Ni J, Hearn T, et al. (2003) Seismic imaging of the downwelling Indian lithosphere beneath central Tibet. *Science* 300: 1424–1427.

Tkalcic H, Chen Y, Liu R, et al. (2011) Multistep modelling of teleseismic receiver functions combined with constraints from seismic tomography: Crustal structure beneath southeast China. *Geophysical Journal International* 187: 303–326. http://dx.doi.org/10.1111/j.1365-246X.2011.05132.x.

Todd BJ, Reid I, and Keen CE (1988) Crustal structure across the Southwest Newfoundland Transform Margin. *Canadian Journal of Earth Sciences* 25: 744–759.

Toomey DR, Jousselin D, Dunn RA, Wilcock WSD, and Detrick RS (2007) Skew of mantle upwelling beneath the East Pacific Rise governs segmentation. *Nature* 446: 409–414.

Toomey DR, Purdy GM, Solomon SC, and Wilcock WSD (1990) The three-dimensional seismic velocity structure of the East Pacific Rise near latitude 9°30′N. *Nature* 347: 639–645.

Torne M, Fernandez M, Wheeler W, et al. (2003) Three-dimensional crustal structure of the Voring Margin (NE Atlantic): A combined seismic and gravity image. *Journal of Geophysical Research-Solid Earth* 108. http://dx.doi.org/10.1029/2002JB001838.

Trampert J and Woodhouse JH (1995) Global phase velocity maps of Love and Rayleigh waves between 40 and 150 seconds. *Geophysical Journal International* 122: 675–690.

Tréhu AM, Asudeh I, Brocher TM, et al. (1994) Crustal architecture of the Cascadia forearc. *Science* 266: 237–243.

Tucholke BE (1986) Structure of basement and distribution of sediments in the western North Atlantic Ocean. In: Vogt PR and Tucholke BE (eds.) *The Geology of North America, Vol. M, The Western North Atlantic Region*, pp. 331–340. Boulder, CO: Geological Society of America.

Tucholke BE and Uchupi E (1989) Thickness of sedimentary cover. In: Udintsev GB (ed.) *International Geology-Geophysical Atlas of the Atlantic Ocean*. Moscow: Russian Ministry of Geology, Russian Academy of Sciences.

Turcotte DL and Schubert G (2002) *Geodynamics*, 2nd edn. Cambridge: Cambridge University Press.

Tuve MA (1951) The Earth's crust: Washington, DC. *Year Book of the Carnegie Institution of Washington* 50: 69–73.

Tuve MA (1953) The Earth's crust. *Yearbook at the Carnegie Institution of Washington* 52: 103–108.

Tuve MA, Tatel HE, and Hart PJ (1954) Crustal structure from seismic exploration. *Journal of Geophysical Research* 59: 415–422.

U.S. Geological Survey and Society of Exploration Geophysicists (1982). Composite magnetic anomaly map of the United States: Part A, Conterminous United States. U.S. Geological Survey Geophysical Investigations Map GP-954-A, scale 1:1,250,000, 2 sheets.

Unsworth MJ, Malin PE, Egbert G, and Siripunvaraporn W (2000) Along strike variations in the electrical structure of the San Andreas fault at Parkfield, California. *Geophysical Research Letters* 27: 3021–3024.

Upton BGJ, Aspen P, and Hinton RW (2001) Pyroxenite and granulite xenoliths from beneath the Scottish Northern Highlands Terrane: Evidence for lower-crust/upper-mantle relationships. *Contributions to Mineralogy and Petrology* 142: 178–197.

Usher MJ (1962) Elastic behavior of rock at low frequencies. *Geophysical Prospecting* 10: 119–127.

Vacquier V, Steenland NC, Henderson RG, and Zietz I (1951) Interpretation of aeromagnetic maps. *Geological Society of American Memoir* 47, 151 pp.

van den Berg R, Daly JS, and Salisbury MH (2005) Seismic velocity of granulite facies xenoliths from central Ireland: Implications for lower crustal composition and anisotropy. *Tectonophysics* 407: 81–99. http://dx.doi.org/10.1016/j.tecto.2005.07.003.

van der Hilst RD, Widiyantoro S, and Engdahl ER (1997) Evidence for deep mantle circulation from global tomography. *Nature* 386: 578–584.

van der Lee S and Nolet G (1997) Upper mantle *S* velocity structure of North America. *Journal of Geophysical Research* 102: 22815–22838.

van Heijst HJ and Woodhouse JH (1999) Global high-resolution phase velocity distribution of overtone and fundamental-model surface waves determined by mode branch stripping. *Geophysical Journal International* 137: 601–620.
Vening-Meinesz FA (1948) *Complete Results and Isostatic Reduction*. *Gravity Expeditions at Sea*, vol. IV, pp. 1923–1938. Delft, Netherlands: Publications of the Netherlands Geodetic Commission, Waltman, 188 pp.
Venisti N, Calcagnile G, Del Gaudio V, and Pierri P (2004) Combined analysis of seismic and gravimetric data in the Adriatic plate. *Physics of the Earth and Planetary Interiors* 142: 89–100.
Vera EE, Mutter JC, Buhl P, et al. (1990) The structure of 0- to 0.2-m.y.-old oceanic crust at 9°N on the East Pacific Rise from expanded spread profiles. *Journal of Geophysical Research* 95: 15529–15556.
Vidale JE (1988) Finite-difference calculation of travel times. *Bulletin of the Seismological Society of America* 78: 2062–2076.
Vidale JE (1990) Finite-difference calculation of traveltimes in three dimensions. *Geophysics* 55: 521–526.
Villagomez DR, Toomey DR, Hooft EEE, et al. (2011) Crustal structure beneath the Galapagos Archipelago from ambient noise tomography and its implications for plume-lithosphere interactions. *Journal of Geophysical Research-Solid Earth* 116. http://dx.doi.org/10.1029/2010JB007764.
Vine FJ and Moores EM (1972) A model for the gross structure, petrology, and magnetic properties of oceanic crust. *Studies in Earth and Space Sciences: A Memoir in Honor of Harry Hammond Hess*. *Memoir,* 132, pp. 195–205. Boulder, CO: Geological Society of America.
Vinnik L (1977) Detection of waves converted from P to SV in the mantle. *Physics of the Earth and Planetary Interiors* 15: 39–45.
Vinnik LP, Farra V, and Kind R (2004) Deep structure of the Afro-Arabian hotspot by S receiver functions. *Geophysical Research Letters* 31: L11608. http://dx.doi.org/10.1029/2004GL019574.
Vinnik LP, Makeyeva LI, Milev A, and Usenko Y (1992) Global patterns of azimuthal anisotropy and deformation in the continental mantle. *Geophysical Journal International* 111: 433–447.
Vogt PR, Taylor PT, Kovacs LC, and Johnson GL (1979) Detailed aeromagnetic investigation of the Arctic Basin. *Journal of Geophysical Research* 83: 1071–1089.
Von Freese RRB, Hinze WJ, Olivier R, and Bentley CR (1986) Regional magnetic anomaly constraints on continental breakup. *Geology* 14: 68–71.
Vuan A, Maurice SDR, Wiens DA, et al. (2005) Crustal and upper mantle S-wave velocity structure beneath the Bransfield Strait (West Antarctica) from regional surface wave tomography. *Tectonophysics* 397: 241–259. http://dx.doi.org/10.1016/j.tecto.2004.12.011.
Walck M (1984) The *P* wave upper mantle structure beneath an active spreading centre: The Gulf of California. *Geophysical Journal of the Royal Astronomical Society* 76: 697–723.
Walter WR, Pasyanos ME, Bhattacharyya J, and O'Boyle J (2000) MENA 1.1—An Updated Geophysical Regionalization of the Middle East and North Africa. UCRL-ID-138079, LLNL.
Walther C (2002) Crustal structure of the Cocos ridge northeast of Cocos Island, Panama basin. *Geophysical Research Letters* 29. http://dx.doi.org/10.1029/2991GL014267.
Wang CY, Chen W, and Mooney WD (2003a) Three-dimensional velocity structure of the crust and upper mantle in southwestern China and its tectonic implications. *Journal of Geophysical Research* 108: 2442. http://dx.doi.org/10.1029/2002JB001973.
Wang S, Hearn T, Xu J, Ni J, Yu Y, and Zhang X (2002) Velocity structure of uppermost mantle beneath China continent from Pn tomography. Science in China. Series D. *Earth Sciences* 45: 143–150.
Wang TK, Lin SF, Liu CS, et al. (2004a) Crustal structure of the southernmost Ryukyu subduction zone: OBS, MCS and gravity modelling. *Geophysical Journal International* 157: 147–163. http://dx.doi.org/10.1111/j.1365-246X.2004.02147.x.
Wang XY, Mooney WD, and Yuan XC (2003b) The crustal structure from the Altai Mountains to the Altyn Tagh fault, northwest China. *Journal of Geophysical Research* 108: 2322. http://dx.doi.org/10.1029/2001JB000552.
Wang CY, Yang ZE, Luo H, et al. (2004b) Crustal structure of the northern margin of the eastern Tien Shan, China, and its tectonic implications for the 1906 M similar to 7.7 Manas earthquake. *Earth and Planetary Science Letters* 16: 743–758. http://dx.doi.org/10.1016/j.epsl.2004.04.015.
Wannamaker PE, Booker JR, Jones AG, et al. (1989) Resistivity cross-section through the Juan de Fuca subduction system and its tectonic implications. *Journal of Geophysical Research* 94: 14127–14144.
Ward KM, Porter RC, Zandt G, et al. (2013) Ambient noise tomography across the Central Andes. *Geophysical Journal International* 193. http://dx.doi.org/10.1093/gji/ggt166.
Warren DH and Healy JH (1973) Structure of the crust in the conterminous United States. *Tectonophysics* 20: 203–213.
Watremez L, Leroy S, Rouzo S, et al. (2011) The crustal structure of the north-eastern Gulf of Aden continental margin: Insights from wide-angle seismic data. *Geophysical Journal International* 184: 575–594. http://dx.doi.org/10.1111/j.1365-246X.2010.04881.x.
Watts AB (2001) *Isostasy and flexure of the lithosphere*. Cambridge: Cambridge University Press.
Wedepohl KH (1995) The composition of the continental crust. *Geochimica et Cosmochimica Acta* 59: 1217–1232.
Wepfner WW and Christensen NI (1991) Q structure of the oceanic crust. *Marine Geophysical Research* 13: 227–237.
White DJ and Clowes RM (1990) Shallow crustal structure beneath the Juan de Fuca Ridge from 2D seismic refraction tomography. *Geophysical Journal International* 100: 349–367.
White RS, Detrick RS, Sinha MC, and Cormier M-H (1984) Anomalous seismic structure of oceanic fractures zones. *Geophysical Journal of the Royal Astronomical Society* 79: 779–798.
White RS and McKenzie D (1989) The generation of volcanic continental margins and flood basalts. *Journal of Geophysical Research* 94: 7685–7729.
White RS, McKenzie D, and O'Nions RK (1992) Oceanic crustal thickness from seismic measurements and rare earth element inversions. *Journal of Geophysical Research* 97: 19683–19715.
White RS and Smith LK (2009) Crustal Structure of the Hatton and the conjugate east Greenland rifted volcanic continental margins, NE Atlantic. *Journal of Geophysical Research-Solid Earth* 114. http://dx.doi.org/10.1029/2008JB005856.
White RS, Spence GD, Fowler SR, McKenzie DP, Westbrook GK, and Bowen AN (1987a) Magmatism at rifted continental margins. *Nature* 330: 439–444.
White RS, Westbrook GH, Bowen AN, et al. (1987b) Hatton bank (northwest U.K.) continental margin structure. *Geophysical Journal of the Royal Astronomical Society* 89: 265–272.
Whitmarsh RB and Calvert AJ (1986) Crustal structure of Atlantic fracture zones—I. The Charlie-Gibbs fracture zone. *Geophysical Journal of the Royal Astronomical Society* 85: 107–138.
Whitmarsh RB, Ginzburg A, and Searle RC (1982) The structure and origin of the Azores-Biscay Rise, north-east Atlantic Ocean. *Geophysical Journal of the Royal Astronomical Society* 70: 79–107.
Wilcock WSD, Solomon SC, Purdy GM, and Toomey DR (1995) Seismic attenuation structure of the East Pacific Rise near 9°30′N. *Journal of Geophysical Research* 100: 24147–24165.
Willden R (1965) Seismic-refraction measurements of crustal structure beneath American Falls Reservoir, Idaho, and Flaming Gorge Reservoir, Utah, US. *Geological Survey Professional Paper* 525-C: C-44–C-50.
Williams MC, Shrive PN, Fountain DM, and Frost BR (1985) Magnetic properties of exposed deep crustal rocks from the Superior Province of Manitoba. *Earth and Planetary Science Letters* 76: 176–184.
Willmore PL and Bancroft AM (1960) The time term approach to refraction seismology. *Geophysical Journal of the Royal Astronomical Society* 3: 419–432.
Wilson JT (1963) Hypothesis of the Earth's behaviour. *Nature* 198: 925–929.
Wilson JT (1965) A new class of fault and their bearing on continental drift. *Nature* 4995: 343–347.
Wolfe CJ, Pundy GM, Toomey DR, and Solomon SC (1995) Microearthquake characteristics and crustal velocity structure at 29° N on the Mid-Atlantic Ridge: The architecture of a slow spreading segment. *Journal of Geophysical Research* 100: 24,449–24,472.
Woodhouse JH and Dziewonski AM (1984) Mapping the upper mantle: Three-dimensional modeling of Earth structure by inversion of seismic waveforms. *Journal of Geophysical Research* 89: 5953–5986.
Woollard GP (1943) Transcontinental gravitational and magnetic profile of North America and its relation to geologic structure. *Bulletin of the Geological Society of America* 44: 747–789.
Woollard GP (1959) Crustal structure from gravity and seismic measurements. *Journal of Geophysical Research* 64: 1521–1544.
Woollard GP (1966) Regional isostatic relations in the United States. In: Tuve MA (ed.) *The Earth beneath the continents*. *Geophysical Monograph*, vol. 10, pp. 557–594. American Geophysical Union.
Wortel MJR and Spakman W (2000) Subduction and slab detachment in the Mediterranean-Carpathian region. *Science* 290: 1910–1917.
Worthington MH (1984) *An Introduction to Geophysical Tomography*. First Break, 20–26.
Worthington LL, Van Avendonk HJA, Gulick SPS, et al. (2012) Crustal structure of the Yakutat terrane and the evolution of subduction and collision in southern Alaska. *Journal of Geophysical Research-Solid Earth* 117. http://dx.doi.org/10.1029/2011JB008493.

Wu Y, Louden KE, Funck T, et al. (2006) Crustal structure of the central Nova Scotia margin off Eastern Canada. *Geophysical Journal International* 166: 878–906. http://dx.doi.org/10.1111/j.1365-246X.2006.02991.x.

Yanaqi T (2011) *Arc volcano of Japan: Generation of continental crust from the mantle*. *Lecture Notes in Earth Sciences*. Heidelberg: Springer, 123 pp.

Yanovskaya TB and Kozhevnikov VM (2003) 3D S-wave velocity pattern in the upper mantle beneath the continent of Asia from Rayleigh wave data. *Physics of the Earth and Planetary Interiors* 138: 263–278.

Yeh YC and Hsu SK (2004) Crustal structures of the northernmost South China Sea: Seismic reflection and gravity modeling. *Marine Geophysical Researches* 25: 45–61. http://dx.doi.org/10.1007/s11001-005-0732-6.

Yliniemi J, Kozlovskaya E, Hjelt S, Komminaho K, Ushakov A, and SVEKALAPKO Seismic Tomography Working Group, International (III) (2004) Structure of the crust and uppermost mantle beneath southern Finland revealed by analysis of local events registered by the SVEKALAPKO seismic array. *Tectonophysics* 394: 41–67.

Yuan XH, Kind R, Li XQ, and Wang RJ (2006) The S receiver function: Synthetics and data examples. *Geophysical Journal International* 156: 555–564.

Yuan XH, Ni J, Kind R, Mechie J, and Sandvol E (1997) Lithospheric and upper mantle structure of southern Tibet from a seismological passive source experiment. *Journal of Geophysical Research* 102: 27491–27500.

Yuan HY and Romanowicz B (2010) Lithospheric layering in the North American craton. *Nature* 466: 1063–1068.

Yuan XH, Sobolev SV, et al. (2000) Subduction and collision processes in the Central Andes constrained by converted seismic phases. *Nature* 408: 958–961.

Zandt G and Ammon CJ (1995) Continental crust composition constrained by measurements of crustal Poisson's ratio. *Nature* 374: 152–154.

Zandt G and Owens TJ (1986) Comparison of crustal velocity profiles determined by seismic refraction and teleseismic methods. *Tectonophysics* 128: 155–161.

Zang SX, Liu YG, and Ning JY (2002) Thermal structure of the lithosphere in North China. *Chinese Journal of Geophysics* 17(1): 56–66.

Zelt CA (1999) Modelling strategies and model assessment for wide-angle seismic traveltime data. *Geophysical Journal International* 139: 183–204.

Zelt CA and Barton PJ (1998) Three-dimensional seismic refraction tomography: A comparison of two methods applied to data from the Faeroes Basin. *Journal of Geophysical Research* 103: 7187–7210.

Zelt BC, Ellis RM, Zelt CA, et al. (2001) Three-dimensional crustal velocity structure beneath the Strait of Georgia, British Columbia. *Geophysical Journal International* 144: 695–712. http://dx.doi.org/10.1111/j.1365-246X.2001.00364.x.

Zelt CA, Hojkoa AM, Flueh ER, and McIntosh KD (1999) 3D simultaneous seismic refraction and reflection tomography of wide-angle data from the central Chilean margin. *Geophysical Research Letters* 26: 2577–2580.

Zelt CA, Sain K, Naumenko JV, and Sawyer DS (2003) Assessment of crustal velocity models using seismic refraction and reflection tomography. *Geophysical Journal International* 153: 609–626.

Zelt CA and Smith RB (1992) Seismic traveltime inversion for 2-D crustal velocity structure. *Geophysical Journal International* 108: 16–34.

Zelt CA, Taylor B, Sachpazi M, et al. (2005) Crustal velocity and Moho structure beneath the Gulf of Corinth, Greece. *Geophysical Journal International* 162: 257–268. http://dx.doi.org/10.1111/j.1365-246X.2005.02640.x.

Zhang Y-S and Lay T (1996) Global surface wave phase velocity variations. *Journal of Geophysical Research* 101: 8415–8436.

Zhang Y-S and Tanimoto T (1991) Global Love wave phase velocity variation and its significance to plate tectonics. *Physics of the Earth and Planetary Interiors* 66: 160–202.

Zhang H and Thurber CH (2003) Double-difference tomography: The method and its application to the Hayward fault, California. *Bulletin of the Seismological Society of America* 93: 1875–1889.

Zhang H, Thurber CH, Shelly D, Ide S, Beroza GC, and Hasegawa A (2004) High-resolution subducting-slab structure beneath northern Honshu, Japan, revealed by double-difference tomography. *Geology* 32: 361–364.

Zhao D, Hasegawa A, and Horiuchi S (1992) Tomographic imaging of P and S wave velocity structure beneath northeastern Japan. *Journal of Geophysical Research* 97: 19909–19928.

Zhao LS and Xie J (1993) Lateral variations in compressional velocities beneath the Tibetan Plateau from Pn traveltime tomography. *Geophysical Journal International* 115: 1070–1084.

Zhou Y, Dahlen FA, and Nolet G (2004) Three-dimensional sensitivity kernels for surface wave observables. *Geophysical Journal of Interior* 158: 142–168.

Zhou Y, Nolet G, Dahlen F, and Laske G (2006) Global upper-mantle structure from finite-frequency surface-wave tomography. *Journal of Geophysical Research* 111: B04304.

Zhu H and Kanamori H (2000) Moho depth variation in southern California from teleseismic receiver functions. *Journal of Geophysical Research* 105: 2969–2980.

Zhu J, Kopp H, Ernst R, et al. (2009) Crustal structure of the central Costa Rica subduction zone: Implications for basal erosion from seismic wide-angle data. *Geophysical Journal International* 178: 1112–1131. http://dx.doi.org/10.1111/j.1365-246X.2009.04208.x.

Ziegler PA (1990) *Geological Atlas of Western Europe*, 2nd edn. London: Shell International and the Geological Society.

Zietz I (1969) Aeromagnetic investigations of the earth's crust in the United States. In: Hart PJ (ed.) *The Earth's Crust and Upper Mantle*. *Geophysical Monograph*, vol. 13, pp. 404–415. American Geophysical Union.

Zietz I (1982) *Composite magnetic anomaly map of United States*; Part (A). Conterminous United States: U.S. Geological Survey Geophysical Investigations Map GP-954A, scale 1:2,500,000.

Zoback ML and Mooney WD (2003) Lithospheric buoyancy and continental intraplate stresses. *International Geology Review* 45: 95–118.

1.12 Crust and Lithospheric Structure - Seismic Imaging and Monitoring with Ambient Noise Correlations

M Campillo and P Roux, Isterre, Université Joseph Fourier and CNRS, Grenoble, France

© 2015 Elsevier B.V. All rights reserved.

1.12.1	**Introduction**	391
1.12.2	**Noise Origin**	392
1.12.3	**Principle of the Method: The Heuristic Approach**	392
1.12.3.1	The Time-Reversal Approach	393
1.12.3.2	Stationary Phase and End-Fire Lobes	393
1.12.4	**Mathematical Results**	395
1.12.4.1	Homogeneous Body Approximation	395
1.12.4.1.1	The plane-wave representation in free space	395
1.12.4.1.2	Case of a homogeneous distribution of noise sources	397
1.12.4.2	The Case of a Single Scatterer	399
1.12.4.3	Arbitrary Heterogeneous Medium	400
1.12.4.3.1	If the attenuation parameter $\kappa \neq 0$	400
1.12.4.3.2	If the attenuation parameter $\kappa = 0$	401
1.12.4.3.3	Another formulation of the correlation theorem	401
1.12.4.4	Modal Approach in Finite Bodies	401
1.12.4.5	Equipartition and Random Fields	402
1.12.4.6	Example with Elastic Waves	403
1.12.5	**Practical Limitations**	403
1.12.5.1	Partial Focusing	403
1.12.5.2	Travel Time Measurements	404
1.12.5.3	Amplitude and Spreading	405
1.12.5.4	Influence of Scattering	405
1.12.6	**Processing**	406
1.12.6.1	Processing and Convergence	406
1.12.6.2	Correlation of Correlations	406
1.12.7	**Applications**	408
1.12.7.1	Surface-Wave Tomography	408
1.12.7.2	Body Waves	409
1.12.7.3	Monitoring	410
1.12.7.3.1	Velocity change detection and measurement	412
1.12.7.3.2	Observations	413
1.12.8	**Conclusions**	414
References		414

1.12.1 Introduction

With the development of large seismic networks, huge quantities of continuous recordings have been made available. The extraction of deterministic information about Earth's structure from long ambient-noise time series opens up new opportunities for seismologists. Correlations of ambient seismic vibrations are widely and effectively used to reconstruct impulse responses between two passive receivers as if a source was placed at one of them. This provides the opportunity for imaging without a source, or passive imaging. Applications include seismology, helioseismology, underwater acoustics, and structural health monitoring, to cite only a few. This chapter offers a brief presentation of the principles leading to the use of seismic ambient-noise correlations as virtual seismograms that correspond to the responses of the earth between two stations. While the correlation technique saw great developments in seismology in the 2000s, the interest in this kind of approach had already been stated in earlier studies, such as those of Aki (1957) and Claerbout (1968). Indeed, the same principles have been successfully applied in helioseismology (Duvall et al., 1993). The literature on the subject has grown rapidly, and it would be difficult to include all the approaches in this summary. Courtland (2008) reviewed the recent emergence of the method in seismology. Some review papers have already been published (e.g., Campillo, 2006; Gouédard et al., 2008b; Larose et al., 2006b; Wapenaar et al., 2010a,b). The reader can also refer to the book by Sato et al. (2012). This chapter focuses mostly on ambient noise in seismology, while the correlation methods have also undergone important developments with the construction of virtual seismograms from active-source records in exploration (e.g., Curtis and Halliday, 2010; Rickett and Claerbout, 1999; Schuster, 2006; Wapenaar et al., 2010a,b).

In **Section 1.12.2**, a brief overview of the nature of the ambient noise in the relevant frequency band for broadband seismometer records is presented. The correlation method

 http://dx.doi.org/10.1016/B978-0-444-53802-4.00024-5

through heuristic approaches is introduced in Section 1.12.3. Some mathematical results for simple media or simple noise–source distributions are given in Section 1.12.4. The limitations of the approach in actual situations are discussed in Section 1.12.5. The strategies of processing are presented in Section 1.12.6, and examples of applications to imaging and monitoring are presented in Section 1.12.7.

1.12.2 Noise Origin

Some aspects that are important for the applications discussed in the following sections are recalled here. Seismic ambient noise has been studied since the beginning of seismology, largely because of the need to improve the level of detection of deterministic arrivals. From early studies (e.g., Gutenberg, 1958), it was recognized that the origin of the permanent agitation of the ground surface is different for different frequency bands. The high-frequency noise ($f > 1$ Hz) is generally due to human activity (e.g., machinery, traffic). The energy of these signals is strongly variable in time, and is correlated with human life rhythms, with day and week periodicities. On the contrary, the natural origin of long-period ambient noise was recognized through the correlation of the amplitude with meteorological conditions. The frequency limiting the domain of human activity is dependent on local conditions (e.g., Bonnefoy-Claudet et al., 2006). As no generalities can be drawn for high-frequency noise, this discussion concentrates on a low-frequency band that is well defined globally as associated with the interaction of the oceanic swell with the solid Earth. In the band of 0.3–0.05 Hz, the ambient noise is often referred to as 'microseisms.' Note that the general issues discussed in the following sections for the correlation of microseism records also apply for anthropic noise at high frequency. Microseisms have large amplitudes that provide an obstacle for the detection of weak arrivals produced by earthquakes. As the detectability level is an important issue in seismology, microseisms have been extensively studied. In the microseism spectral band, the noise is dominated by surface waves, which are predominantly Rayleigh waves (e.g., Toksöz and Lacoss, 1968). The presence of body waves has nevertheless been attested (e.g., Vinnik, 1973). The coincidence of periods of strong microseisms and high swells that reach the coastline was noted early on (Gutenberg and Mainka, 1924). Toksöz and Lacoss (1968) used array analysis to demonstrate the correlation between microseism sources and regions of low atmospheric pressure.

Two peaks dominate the spectrum of microseisms, the principal one being for a period between 5 and 7 s, while a less marked peak is observed at twice the period of the main peak (e.g., Peterson, 1993). These general characteristics are interpreted as the footprint of the spectrum of oceanic gravity waves.

The less energetic single-frequency or primary microseism peak, at periods around 14 s, is similar to the spectrum of wind-generated ocean gravity waves (Haubrich et al., 1963). With the limited penetration of gravity waves at this period, the noise is expected to be produced in shallow waters and to be amplified by shoaling. To decipher the geographical origin of the primary microseism, Stehly et al. (2006) analyzed the energy of long-term average noise cross-correlations as a function of the azimuth of the station direction. The distribution of sources shares a great similarity with the map of average ocean wave heights obtained from satellite observations, which shows zones of primary microseism excitation in oceanic deep basins, with a seasonality of the global contributions from northern and southern oceans.

The stronger double-frequency or secondary microseism peak at a period around 7 s is interpreted as the result of nonlinear interactions between ocean gravity waves propagating in opposite directions, as shown by Longuet-Higgins (1950) based on earlier studies of Miche (1944). This nonlinear process produces a pressure at the sea bottom, even when the height of the water column is greater than the gravity-wave wavelength. The amplitude of the excitation depends on the response of the resonant water layer for specific periods and bathymetry. The microseism excitation depends on the ocean-wave state (swell amplitude), the existence of wave trains in opposite directions, and the bathymetry (resonance condition). The existence of gravity waves that propagate in opposite directions can be due either to reflection along the coast or to specific conditions of storm systems in the deep oceanic basins (e.g., Kedar et al, 2008; Zhang et al., 2010). Teleseismic body waves are identified using beam forming, by their high apparent velocity, and they have been used to map the actual sources in the oceans (e.g., Landès et al., 2010). Recent analyses have suggested that both coastal and deepwater origins are represented in the actual observations (Ardhuin et al., 2011; Hillers et al., 2012), and it has been demonstrated that global oceanographic models of sea state coupled with the physical description of the excitation allow for independent prediction of the main patterns of secondary microseism sources.

At long periods, that is, below 50 s, the ambient noise that is often referred to as hum has the spectral structure of the free oscillations of Earth (e.g., Kobayashi and Nishida, 1998; Tanimoto et al., 1998). The origin of this excitation is assumed to be the interaction of the ocean infragravity waves with the solid Earth. This mechanism was confirmed by the correlation between the apparent locations of hum sources and regions of large wave heights (e.g., Rhie and Romanowicz, 2004). Nishida et al. (2008a) showed that the generation of background ambient noise at long periods occurs both in coastal regions and in deep oceans. The normal pressure caused by oceanic waves on the sea bottom can account for spheroidal motions. However, large toroidal contributions (e.g., Kurrle and Widmer-Schnidrig, 2008) and long-period Love waves (Nishida et al., 2008a) have been observed. This was explained by Fukao et al. (2010), who proposed a model for the coupling of infragravity waves with the topography of the sea bottom.

To conclude this short presentation, it appears that the origin of the seismic ambient noise is still the object of ongoing research and discussion. Different processes are invoked exclusively for the two main spectral peaks and the long-period domain in spite of the continuous character of the noise spectrum.

1.12.3 Principle of the Method: The Heuristic Approach

In this section, simple physical views of the principle of the ambient-noise correlation method are presented. The mathematical developments are discussed in the next section.

The results presented here originate from previous studies in seismology that were aimed at using ambient noise to extract deterministic information relating to Earth's structure (e.g., Aki, 1957; Claerbout, 1968). In seismic exploration, the 'daylight imaging' method was pioneered by Claerbout (1968), who proposed the conjecture stating that the cross-correlation of two daylight traces at surface locations A and B is equivalent to a reflection trace at B generated by a source at A. A formal demonstration was given for the one-dimensional (1D) case. The same idea was then successfully applied in time-distance helioseismology (e.g., Duvall et al., 1993).

The correlation function of the fields recorded at two points is used as a virtual seismogram for which the source is acting at one point and the receiver at the second. For two signals of duration T, the correlation of the signal $u_1(t)$ at $\vec{r}_1$ and $u_2(t)$ at $\vec{r}_2$ is defined classically in the time domain as

$$C\left(\vec{r}_1, \vec{r}_2; t\right) = C_{1,2}(t) = \frac{1}{T}\int_0^T u_1(\tau)u_2(t+\tau)\mathrm{d}\tau \qquad [1]$$

or, equivalently, in the frequency domain as

$$C\left(\vec{r}_1, \vec{r}_2; \omega\right) = C_{1,2}(\omega) = u_1(\omega)u_2^*(\omega) \qquad [2]$$

The correlation function is widely used to measure the resemblance of two signals, and when these signals are similar enough, the time delay that separates them. The ambient noise signals recorded at distant stations are considered to be uncorrelated, as they result from variable interferences between numerous waves of different types emitted by different sources. The same argument holds for the scattered waves that comprise the coda of seismograms. Noise-correlation methods aim at extracting the slight coherent part of the signals that contains deterministic information on wave propagation between the two stations. Indeed, in a medium governed by a wave equation, the motion at two points cannot be fully independent. The extraction of the wave response between the two points is made possible by averaging the correlation over the positions of the sources of the signals. Note that, in the reasoning, the sources include the scatterers viewed as secondary sources.

1.12.3.1 The Time-Reversal Approach

A simple, heuristic approach is based on the analogy between a correlation and a time-reversal experiment (e.g., Derode et al., 2003a,b; Paul et al., 2005). While not completely rigorous in a general case, this analogy allows for an understanding of the physical processes behind the noise-correlation method. In a time-reversal experiment in the laboratory, signals from an active source are recorded, numerically reversed ($t \rightarrow -t$), and then reemitted in the medium (e.g., Fink, 1992). According to the time symmetry of the solutions of the wave equations, the waves propagate, and under certain conditions, they focus on the original source position. In a scalar case, the conditions in such an experiment are that the recording–reemission point distribution is sufficient to reconstruct the angular range of the original wave field. Typically, this is the case with a closed cavity that contains the source. When the re-emitted field is perfectly focused, the focal point can be considered as a virtual source. In seismology, there is no device that can emit a complex signal with sufficient energy. The approach to the construction of signals from virtual sources is completely passive. We consider the mathematical analogy between correlation and convolution by a time-reversed signal. Indeed, the cross-correlation of the signal produced by a source in S at receivers at A and B is formally equivalent to having a source at A producing waves that are recorded at S, time-reversed, and re-emitted from S, to be recorded at B (as written in the frequency domain in eqn [[2]]).

These operations are illustrated in Figure 1 with numerical simulations. For the sake of simplicity, we consider 2D scalar propagation in a weakly scattering medium (Paul et al., 2005).

The field produced by each of several sources S along a circle is computed at each point of the medium (Figure 1(a)). The signals are cross-correlated with the signal of a central reference point. The correlations are shown in Figure 1(b)–1(d) for correlation times −30, 0, and 30 s. At time $t = 0$, all the energy is focused on A, as if A were a source. A converging wave front for negative correlation times and a diverging wave front for positive correlation times are observed. These wave fronts correspond to the causal (positive times) and anticausal (negative time) parts of the Green's function between A and any point R in the medium. The nearly perfect reconstruction of the Green's function, similar to a perfect time-reversal mirror, is explained by the perfect distribution of the source around A and R. To illustrate a practical application, snapshots of ambient noise correlations produced with USArray data (Lin et al., 2009) are presented in Figure 1(e). The clearly diverging surface wave front suggests that the array is surrounded by distant noise sources.

1.12.3.2 Stationary Phase and End-Fire Lobes

Following the time-reversal analogy, it can be asked whether all the noise sources that surround the two receivers in the correlation process contribute in the same manner to the reconstruction of the Green's function. In the absence of scatterers that can redirect the field in all directions, the Green's function emerges from the correlations that contain noise sources where their acoustic path passes through one receiver to reach the other one.

An experimental demonstration of this process was performed from ocean data simultaneously recorded on two sonobuoys at a few hundred meters from each other in a shallow-water environment. Noise was generated over 16 min in the 100–300 Hz frequency interval using a ship, the track of which is represented in Figure 2(a). The two 16-min-long time-series are then cross-correlated using different time windows (Figure 2(b)–2(f)). When the correlation is performed on a 1-s-duration time series (Figure 2(b)), the ship track is clearly observed. If the length of the cross-correlated time series is increased to 5, 10, 20, and up to 30 s (Figure 2(b)–2(e), respectively), the signature of the ship track tends to disappear and the only signal left is obtained when the ship crosses the end-fire main lobes, which is defined as the directivity pattern of the time-domain cross-correlation between the two sensors (Figure 2(a)).

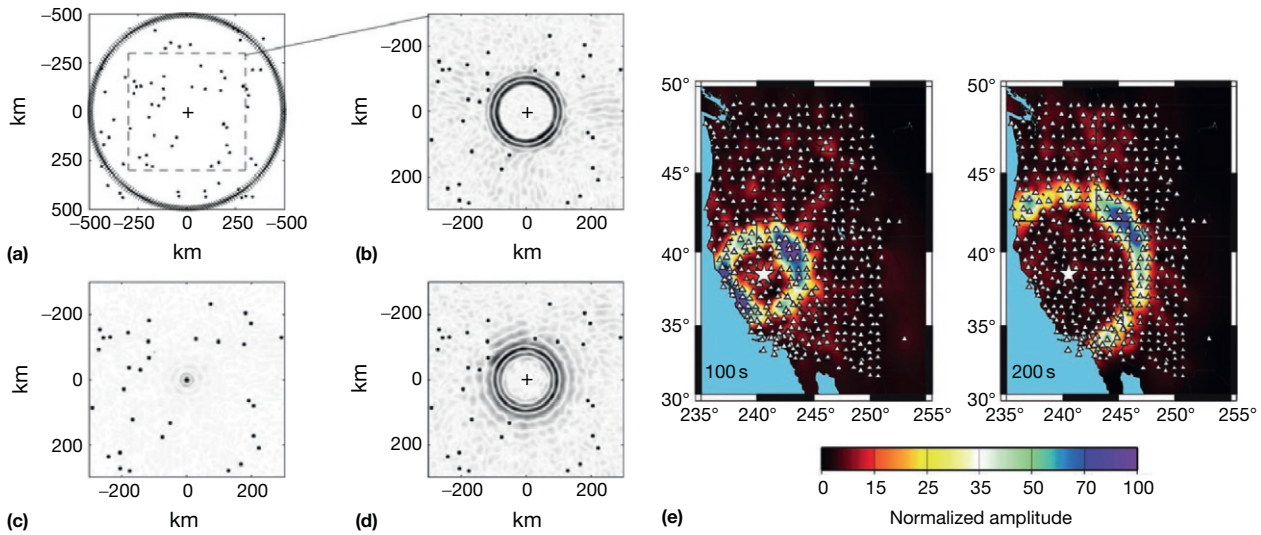

Figure 1 Numerical simulation of the reconstruction of the causal and anticausal parts of the Green's function from cross-correlations. (a) Configuration of the numerical experiment. One thousand sources S (×) surround the reference point A (+). Dots indicate the point scatterers. (b) Snapshot of the cross-correlation between the field at A and the field at location (x, y), after averaging over the sources S for the correlation time of 30 s. The weakly diffusive medium is characterized by the transport mean free path $l^* = 640$ km, which is greater than the distance between the points where the correlations are computed. A converging wave front is well defined and constitutes the anticausal part of the Green's function. (c) Snapshot for correlation time $t = 0$ s. The wave front is focused on A. (d) Snapshot for $t = 30$ s. The diverging wave front corresponds to the causal part of the Green's function. Parts (a)–(d) reproduced from Paul A, Campillo M, Margerin L, Larose E, and Derode A (2005) Empirical synthesis of time-asymmetrical Green function from the correlation of coda waves. *Journal of Geophysical Research* 110. http://dx.doi.org/10.1039/2004JB003521. (e) Snapshots of the actual noise correlation computed from a network in western United States showing the causal surface wave part of the Green's function. Reproduced from Lin FC, Ritzwoller MH, Snieder R (2009) Eikonal tomography: Surface wave tomography by phase front tracking across a regional broad-band seismic array. *Geophysical Journal International* 177: 1091–1110.

When coming from the end-fire lobe of the two receivers, the signal is produced by a noise source where its acoustic path that passes through one receiver naturally reaches the other receiver. The signals are then similar at the two receivers and contribute coherently to the correlation process with a unique delay time that corresponds to the travel time between the receivers. On the contrary, for a noise source outside the end-fire lobe, the ray paths that connect the source to each receiver do not superimpose. The sources out of the end-fire lobes do not contribute coherently to the correlation, as the correlated waveforms correspond to time delays that vary rapidly with the noise-source position.

Obviously, it is observed in Figure 2(b)–2(f) that the longer the correlation window, the higher the signal-to-noise ratio (SNR), because more acoustic sources participate coherently in the correlation function when the incoherent contribution averages out. Indeed, assuming that the speed of the ship was constant during the track, it generates a uniform density of sources over time. For long time windows, the SNR of the correlation process can be defined as the ratio of the number of coherent *versus* incoherent sources inside the recording time window.

In summary, the averaging of the correlation process over time magnifies the coherent *versus* incoherent contributions of the noise sources. Following the geometrical interpretation, the coherent *versus* incoherent ratio corresponds to the area enclosed by the end-fire beam to a non-end-fire beam.

Finally, note that the time-averaged correlation function in Figure 2(f) shows different bottom-reflection and surface-reflected paths that correspond to the arrival-time structure of the Green's function in a shallow-water environment.

Another way to understand the Green's function reconstruction is to separate the contribution that each noise source makes to the correlation process. This was made possible with actual data from a high-resolution survey performed by Petroleum Development Oman (PDO) in North Oman. During this active-seismic survey, a large set of 1600 vibrators were used in combination with 1600 receivers over a 1-km^2 area, to measure the 1600×1600 time-domain signals that constituted an exhaustive measurement of the transfer function of the half-space medium.

From this data set, we select a pair of receivers that are separated by a distance of $d = 158$ m, with a midpoint that coincides with the center of the ring in Figure 3(a). This ensures the same scattering regime for both of the receivers at a given time of the records. Integrating over a line surrounding the receiver pair is theoretically sufficient to get the Green's function, as in our case the medium is lossless. As shown in Figure 3(a), sources inside a ring were selected to increase the SNR when computing the cross-correlation. The azimuth is defined with respect to the receiver pair, denoted by θ, as the difference between the azimuth defined by one source and the receiver pair center and the receiver pair azimuth (Figure 3(c), insert).

The end-fire lobes of the receiver pairs are the areas located in the alignment of the receivers (one on each side). The end-fire lobe aperture depends on the ratio between the wavelength and the range between the receivers (Roux and Kupermann, 2004) and corresponds to the misalignment of the source with respect to the receiver pair. Sources located exclusively within the end-fire lobes induce time delays between the apparent travel time at the two receivers that are smaller than one-eighth of the central period associated to the source spectrum

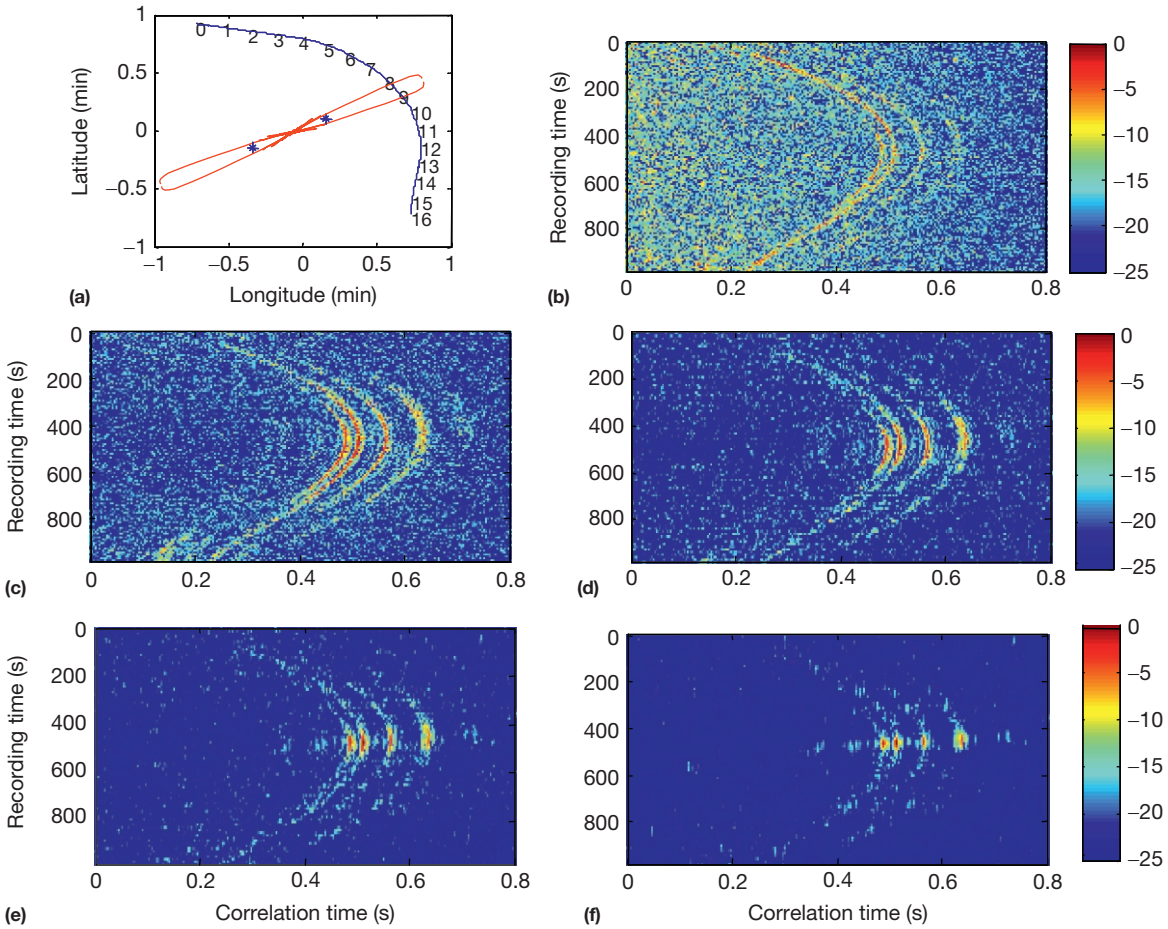

Figure 2 (a) Representation in latitude–longitude coordinates of a 16-min-long ship track (blue full line) with respect to the sonobuoy locations (blue *). The approximate distance between the sonobuoys is R, at ~650 m. The average ship speed was constant, at 4.8 m s^{-1}. The labels along the ship track correspond to each minute of the recording time window. The end-fire directivity pattern of the two sonobuoys is plotted in red. (b–f) Representations of the temporal evolution of the time-domain cross-correlation function between the two sonobuoys along the 16-min-long ship track. The *x*-axis and *y*-axis correspond to the time axis of the correlation function and the recording time, respectively. The duration of the time windows on which the cross-correlation was performed was (b) 1 s, (c) 5 s, (d) 10 s, (e) 20 s, and (f) 40 s. Each cross-correlation pattern is normalized relative to its maximum. The color scales are in dB. Reproduced from Roux P and Kupermann WA (2004) Extraction of coherent wavefronts from ocean ambient noise. *Journal of the Acoustical Society of America* 116(4): 1995–2003.

(Figure 2(a)). In other words, the end-fire lobes are areas in which the phase of the correlation function of direct waves is stationary with respect to azimuth θ.

Figure 3(c) shows that when considering direct arrivals, the cross-correlation function is highly dependent on the source azimuth when it is computed independently for each source. When stacking the contributions of all the sources (viz., all the azimuths), all the phases are averaged, and only the contributions of sources in the end-fire lobes, where the delays are stationary, do not vanish. This leads to a good estimate of the actual direct-wave component of the Green's function. The average cross-correlation and the actual response as recorded in the field are compared in Figure 3(d). Satisfactory reconstruction of the direct waves was achieved. Following Snieder (2004), the same approach was also proposed for the correlation of coda waves (Figure 3(b)) where the scatterers play the role of virtual sources surrounding the receiver pair (Gouédard et al., 2008a).

1.12.4 Mathematical Results

1.12.4.1 Homogeneous Body Approximation

The goal of this section is to investigate the following problem theoretically: can the Green's function between two points be retrieved by performing a cross-correlation of the ambient-noise field received on those two points?

For the sake of simplicity, we consider the scalar-wave problem for which the Green's function G is defined as the solution of the wave equation

$$\Delta G\left(\vec{x};t\right) - \frac{1}{c^2}\frac{\partial G\left(\vec{x};t\right)}{\partial t^2} = \delta\left(\vec{x}\right)\delta(t) \qquad [3]$$

1.12.4.1.1 The plane-wave representation in free space

From a theoretical point of view, earlier studies have investigated the problem of spatial correlation with noise fields or with wave fields obtained from a distribution of random

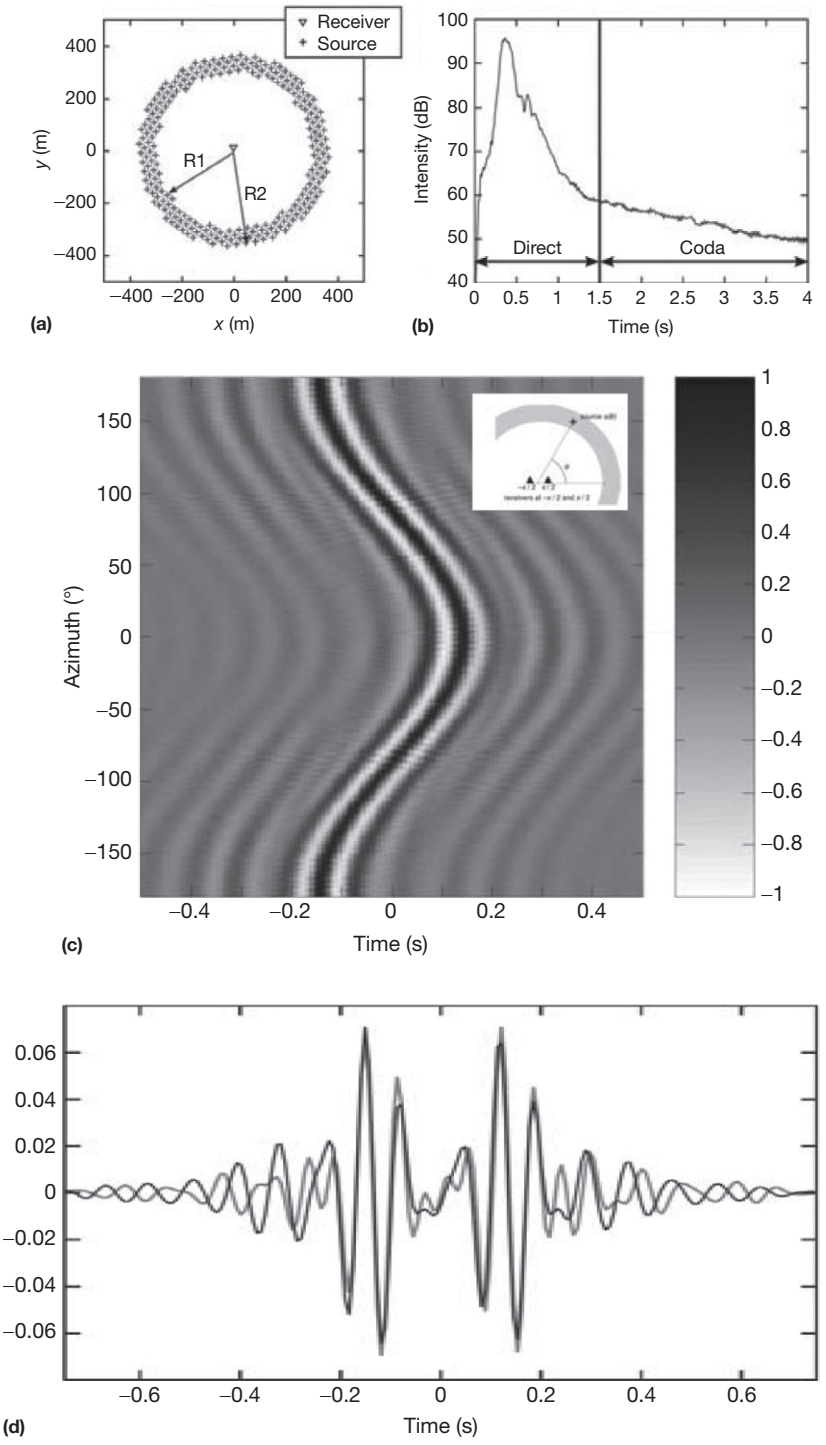

Figure 3 (a) Experimental geometry when considering sources that surround a receiver pair. The selection was for 240 sources located between two circles of radius $R_1 = 300$ m and $R_2 = 370$ m, which were centered at the middle of the receiver pair. (b) Average intensity of the raw traces with definition of the time windows corresponding to direct arrivals and to coda. (c) Cross-correlation functions obtained from each source and plotted as a function of azimuth θ (see definition on the insert). (d) Actual experimental Green's function and cross-correlation averaged over the sources (see panel (a)). Reproduced from Gouédard P, Roux P, Campillo M, and Verdel A (2008a) Convergence of the two-points correlation function toward the Green's function in the context of a prospecting dataset. *Geophysics* 73(6): V47–V53.

sources. For example, this problem was studied by Aki (1957) for surface waves. He considered the 2D case with scalar waves in a homogeneous medium from the perspective of isotropic illumination by plane waves.

The plane waves at angular frequency ω generated from sources at large distances and propagating in direction ψ are of the form

$$u\left(\vec{r}_1;\omega\right) = F(\omega)\exp\left(\mathrm{i}k\vec{r}_1\cdot\vec{n}\right) \qquad [4]$$

where $u(\vec{r}_1;\omega)$ is a displacement at position $\vec{r}_1$ of a Cartesian frame, and $k=\omega/c$ is the wave number for a plane wave incoming from the direction $\vec{n}=(\cos\psi,\sin\psi)$ with amplitude $F(\omega)$. Assuming an omnidirectional distribution of incident plane waves, the field correlation between two points $\vec{r}_1$ and $\vec{r}_2$ reduces to the well-known form of a Bessel function:

$$\left\langle u\left(\vec{r}_1;\omega\right)u^*\left(\vec{r}_2;\omega\right)\right\rangle = |F(\omega)|^2 J_0\left(k\left|\vec{r}_1-\vec{r}_2\right|\right) \qquad [5]$$

where $J_0(k|\vec{r}_1-\vec{r}_2|)$ is the Bessel function of the first kind and order 0. This is the essence of the spatial correlation methods proposed originally by Aki (1957), and which have been extensively used to study the structure of shallow structures.

From there, we can identify J_0 as a constituent of the 2D scalar Green's function:

$$\begin{aligned} G\left(\vec{r}_1,\vec{r}_2;\omega\right) &= \frac{1}{4\mathrm{i}}H_0^{(1)}\left(k\left|\vec{r}_1-\vec{r}_2\right|\right) \\ &= \frac{1}{4\mathrm{i}}\left(J_0\left(k\left|\vec{r}_1-\vec{r}_2\right|\right)+\mathrm{i}Y_0\left(k\left|\vec{r}_1-\vec{r}_2\right|\right)\right) \end{aligned} \qquad [6]$$

where Y_0 and $H_0^{(1)}$ are the Neumann and Hankel functions of zero order.

We finally obtain

$$\left\langle u\left(\vec{r}_1;\omega\right)u^*\left(\vec{r}_2;\omega\right)\right\rangle = -4|F(\omega)|^2\,\mathrm{Im}\left[G\left(\vec{r}_1,\vec{r}_2;\omega\right)\right] \qquad [7]$$

As shown in eqn [7], the correlation theorem links the average correlation function (left term) to the imaginary part of the Green's function. The time domain signal associated with Im(G) by Fourier transform is the causal Green's function plus its even anticausal time-symmetrical counterpart, as shown in the next paragraph.

The generalization to the 3D free-space medium with a spatially uniform noise-source distribution is straightforward, as the field at each receiver can be decomposed as a superposition of uncorrelated plane waves from various directions. It has been established that the normalized cross-spectral density $C_{1,2}(\omega)$ at frequency ω between two receivers 1 and 2 separated by a distance $r=|\vec{r}_1-\vec{r}_2|$ is

$$C_{1,2}(\omega) = \frac{\sin(kr)}{kr} \qquad [8]$$

In the time domain, the normalized correlation function is

$$C_{1,2}(t) = \frac{1}{2\pi}\int_{-\infty}^{\infty} C_{1,2}(\omega)\exp(\mathrm{i}\omega t)\,\mathrm{d}\omega \qquad [9]$$

which can be written as

$$\begin{aligned} C_{1,2}(t) = &\frac{1}{4\pi}\int_{-\infty}^{\infty}\frac{\exp[\mathrm{i}\omega(t+r/c)]}{\mathrm{i}kr}\,\mathrm{d}\omega \\ &-\frac{1}{4\pi}\int_{-\infty}^{\infty}\frac{\exp[\mathrm{i}\omega(t-r/c)]}{\mathrm{i}kr}\,\mathrm{d}\omega \end{aligned} \qquad [10]$$

The time derivative of the correlation function, then, is

$$\frac{\mathrm{d}}{\mathrm{d}t}C_{1,2}(t) = \frac{1}{4\pi r/c}[\delta(t+r/c)-\delta(t-r/c)] \qquad [11]$$

The two terms in eqn [11] correspond to the backward and forward Green's function between the receivers, which demonstrates the connection between the correlation function and the Green's function.

Note that Nakahara (2006) studied in detail the relations between the spatial correlation functions and the Green's function, in 1D, 2D, and 3D cases. He emphasized the dimensional character of these relations, essentially as a Hilbert transform in 2D and a differentiation in 3D.

However, the drawback of the elegant result in eqn [11] is to start from a *normalized* correlation function, the normalization being required because the overall spatial contribution from noise sources in a lossless infinite medium is infinite. Experimentally though, ambient noise signals are always finite, as is the noise correlation function. The contradiction arises because the theory is developed in lossless environments while experiments are always performed in the presence of attenuation. Thus, normalization acts as a subterfuge for avoiding the inclusion of the required attenuation in the theory.

1.12.4.1.2 Case of a homogeneous distribution of noise sources

The goal of this section is to show how the result in eqn [11] can be derived rigorously without the need for normalization when attenuation is present in the medium.

To be as general as possible, we deal here with two receivers that are simultaneously recording ambient noise in a 3D homogeneous medium with an omnidirectional and uniform distribution of noise sources. The incident field on the two receivers comes from a homogeneous spatial–temporal distribution of uncorrelated broadband noise sources. Volume attenuation is included in the medium with an attenuation parameter κ.

The Green's function between points A (in $\vec{r}_1$) and B (in $\vec{r}_2$) is then defined as follows:

$$G\left(\vec{r}_1,\vec{r}_2;t\right) = \frac{1}{2\pi}\int_{-\infty}^{+\infty}\mathrm{d}\omega\,\frac{1}{4\pi\left|\vec{r}_2-\vec{r}_1\right|}\exp\left[\mathrm{i}\omega\left(t-\frac{\left|\vec{r}_2-\vec{r}_1\right|}{c}\right)\right]\exp\left(-\kappa\left|\vec{r}_2-\vec{r}_1\right|\right) \qquad [12]$$

Assuming a random spatial–temporal distribution of noise source amplitudes $S(\vec{r}_s, t_s)$, the total field received at A is

$$P\left(\vec{r}_1;t\right) = \int_{-\infty}^{\infty}\int_{-\infty}^{t} \mathrm{d}\vec{x}\ \mathrm{d}t_x S\left(\vec{x},t_x\right) G\left(\vec{r}_1,\ \vec{x};t-t_x\right) \qquad [13]$$

Here, the causality requires that the noise sources in $(\vec{x};t_x)$ that contribute to the pressure field at A at a given time t satisfy the condition $t = t_x + \frac{\left|\vec{r}_1-\vec{x}\right|}{c}$. Then the cross-correlation of the two signals recorded at A and B is defined as in eqn [1]:

$$C\left(\vec{r}_1,\vec{r}_2;t\right) = C_{1,2}(t) = \frac{1}{T}\int_0^T P\left(\vec{r}_1;\tau\right) P\left(\vec{r}_2;t+\tau\right)\mathrm{d}\tau \qquad [14]$$

$C_{1,2}(t)$ corresponds to one realization of the ambient noise cross-correlation function. To evaluate the average noise correlation function $\langle C_{1,2}(t)\rangle$ over an ensemble of realization, we use the idea that noise sources are spatially and temporally uncorrelated:

$$\left\langle S\left(\vec{x},t_x\right)S\left(\vec{x}',t_{x'}\right)\right\rangle = Q^2\delta\left(t_x-t_{x'}\right)\delta\left(\vec{x}-\vec{x}'\right) \qquad [15]$$

where the notation $\langle X\rangle$ corresponds to the ensemble average of X, and Q^2 is the acoustic power of the noise sources and is taken as constant over time and space. Then it follows that

$$\langle C_{1,2}(t)\rangle = \frac{Q^2}{64T\pi^4}\int_0^T\int_{-\infty}^{+\infty}\int_{-\infty}^{+\infty}\frac{n(\tau)\mathrm{d}\tau\,\mathrm{d}\vec{x}\ \ \mathrm{d}\omega}{\left|\vec{r}_2-\vec{x}\right|\left|\vec{r}_1-\vec{x}\right|}$$
$$\exp\left[\mathrm{i}\omega\left(t+\frac{\left|\vec{r}_1-\vec{x}\right|}{c}-\frac{\left|\vec{r}_2-\vec{x}\right|}{c}\right)\right]$$
$$\exp\left[-\kappa\left(\left|\vec{r}_1-\vec{x}\right|+\left|\vec{r}_2-\vec{x}\right|\right)\right] \qquad [16]$$

Note that, as written in eqn [14], n is the number of sources by unit time, and τ corresponds to the running time of the signals received at A and B. The cross-correlation function $\langle C_{1,2}(t)\rangle$ is a comparison between these two signals, meaning that $\langle C_{1,2}(t)\rangle$ will extract the relative propagation times between the noise source in $\vec{x}$, and the receivers in $\vec{r}_1$ and $\vec{r}_2$. As a consequence, the integration over τ corresponds to just an accumulation of noise sources over time. In a practical experimental case, the pressure fields at A and B have first to be recorded over a finite interval time T before the cross-correlation is performed.

Assuming that the random noise sources have a constant creation rate $n(\tau)=N$, the integral over τ is changed into the product $T\times N$. Finally, using this approach, eqn [9] becomes

$$\langle C_{1,2}(t)\rangle = \frac{Q^2N}{64\pi^4}\int_{-\infty}^{+\infty}\int_{-\infty}^{+\infty}\frac{\mathrm{d}\vec{x}\ \mathrm{d}\omega}{\left|\vec{r}_2-\vec{x}\right|\left|\vec{r}_1-\vec{x}\right|}$$
$$\exp\left[\mathrm{i}\omega\left(t+\frac{\left|\vec{r}_1-\vec{x}\right|}{c}-\frac{\left|\vec{r}_2-\vec{x}\right|}{c}\right)\right]$$
$$\exp\left[-\kappa\left(\left|\vec{r}_1-\vec{x}\right|+\left|\vec{r}_2-\vec{x}\right|\right)\right] \qquad [17]$$

Equation [16] shows that the noise correlation function in free space reduces to the calculation of a spatial integral over the noise–source locations. In the following paragraph, we show that a geometrical argument allows us to obtain an analytical solution for $\langle C_{1,2}(t)\rangle$. We first define a Cartesian coordinate system for the 3D space in which A is $(a,0,0)$, and B is $(-a,0,0)$. The argument of the time-dependent exponential in eqn [17] gives a contribution to the correlation function at time t if $\vec{x}$ is such that $|\vec{r}_2-\vec{x}|-|\vec{r}_1-\vec{x}|=ct$.

For a time t satisfying the condition $-2a\le ct\le 2a$, the noise sources must lie on a hyperboloid (Figure 4) that will contribute to $\langle C_{1,2}(t)\rangle$ at a given time t. This implies that $\langle C_{1,2}(t)\rangle = 0$ for t outside the interval $[-2a/c,\ 2a/c]$. Similarly, the ellipse in Figure 4 is made of the noise sources $\vec{r}_s$ such that $|\vec{r}_2-\vec{x}|+|\vec{r}_1-\vec{x}|=$constant, that is, sources that contribute to the correlation function with the same attenuation.

Note that these conical shapes are invariant by rotation around the axis of the two receivers (Figure 4, x-axis). This means that in 3D, the hyperbola and the ellipse turn out to be a hyperboloid and an ellipsoid where the symmetry axis is the lines between the two receivers. As can be seen in Figure 2, every noise source in space belongs to a unique hyperbola.

Using a change of variable from the Cartesian coordinates to the Prolate spheroidal coordinates, it follows that

$$\langle C_{1,2}(t)\rangle = \frac{Q^2Nc}{64\pi\kappa}\int_{\infty}^{+\infty}\mathrm{d}\omega\,\frac{1}{\mathrm{i}\omega}\left\{\exp\left[\mathrm{i}\omega\left(t+\frac{2a}{c}\right)\right]\right.$$
$$\left.-\exp\left[\mathrm{i}\omega\left(t-\frac{2a}{c}\right)\right]\right\}\frac{\exp\left(-2a\kappa\right)}{2a} \qquad [18]$$

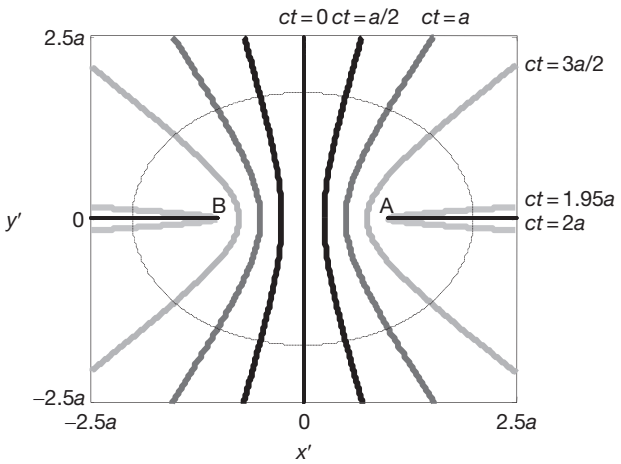

Figure 4 Representation in the x–y plane of the hyperbola that contributes to a given time t in the noise-correlation function. On each hyperbola, the noise sources satisfy $|\vec{r}_2-\vec{x}|-|\vec{r}_1-\vec{x}|=ct$. For example, the horizontal axis corresponds to $ct=0$. The vertical axis corresponds to $ct=2a$ for $x'\ge a$, and $ct=-2a$ for $x'\le -a$. The ellipse (dashed line) represents the noise sources for which $|\vec{r}_2-\vec{x}|-|\vec{r}_1-\vec{x}|=ct$, for $ct=4a$. The receivers A and B are at $(a,0)$ and $(-a,0)$. From Roux P, Sabra KG, Kuperman WA, and Roux A (2005b) Ambient noise cross correlation in free space: Theoretical approach. *Journal of the Acoustical Society of America* 117: 79–84.

In the case of a medium with attenuation, the time derivative of the correlation function gives

$$\frac{\mathrm{d}}{\mathrm{d}t}\langle C_{1,2}(t)\rangle = \frac{Q^2 N c}{64\pi\kappa}\left\{\int_{-\infty}^{+\infty}\mathrm{d}\omega\frac{1}{2a}\exp\left[\mathrm{i}\omega\left(t+\frac{2a}{c}\right)\right]\exp\left(-2a\kappa\right) - \int_{-\infty}^{+\infty}\mathrm{d}\omega\frac{1}{2a}\exp\left[\mathrm{i}\omega\left(t-\frac{2a}{c}\right)\right]\exp\left(-2a\kappa\right)\right\} \quad [19]$$

The physical interpretation of eqn [19] is

$$\frac{\mathrm{d}}{\mathrm{d}t}\langle C_{1,2}(t)\rangle = Q^2 N\frac{c}{2\kappa}\left[G\left(\vec{r}_1,\vec{r}_2;t\right) - G\left(\vec{r}_1,r_2;-t\right)\right] \quad [20]$$

The amplitude term in the factor of the causal and anticausal Green's function is made up of two contributions: (1) Q^2N, which corresponds to the noise power during the recording time window T; and (2) the other factor $\frac{c}{2\kappa}$, which is directly related to the attenuation introduced in the Green's function (eqn [12]). In Section 1.12.4.3, we will see the importance of this attenuation parameter in the more general formulation of the Ward Identity. Indeed, the introduction of a small attenuation in the medium makes the correlation function converge on the noise–source spatial distribution without any constraint. Finally, the derivative of the ambient noise correlation function generates the causal and anticausal (or time-reversed) Green's functions between the two points at which the noise has been recorded.

1.12.4.2 The Case of a Single Scatterer

The correlation theorem is generalized to the case where there is one punctual and isotropic weak scatterer in the propagation medium. The Green's function is now made up of both the direct path between the source and the receiver and the scattering contribution from the scatterer. Before generalization to a more complex heterogeneous medium (Section 1.12.4.3), the goal of this paragraph is to show how the two-point correlation function provides the two contributions of the Green's function.

The mathematical demonstration was proposed by Sato et al. (2012), who considered the scattering contribution in the first Born approximation. The Green's function $G^0\left(\vec{r}_1,\vec{x};\omega\right) = G^0_{1x}$ of the free-space medium that is the solution of the Helmoltz equation between one source in $\vec{r}_1$ and one receiver in $\vec{x}$, as

$$\Delta G^0_{1x} + (k+\mathrm{i}\kappa)^2 G^0_{1x} = \delta\left(\vec{r}_1 - \vec{x}\right) \quad [21]$$

is transformed into $G(\vec{r}_1,\vec{x};\omega) = G_{1x}$, such that

$$\Delta G_{1x} + (k+\mathrm{i}\kappa)^2 G_{1x} + V_0\delta\left(\vec{x}-\vec{y}\right)G_{1x} = \delta\left(\vec{r}_1-\vec{x}\right) \quad [22]$$

where $\vec{y}$ is the position of the scatterer, and V_0 is the scattering coefficient.

Assuming $G_{1x} = G^0_{1x} + G^s_{1x}$, we have in the first Born approximation ($|G^s_{1x}| \ll |G^0_{1x}|$) for the scattering contribution

$$\Delta G^s_{1x} + (k+\mathrm{i}\kappa)^2 G^s_{1x} = -V_0\delta\left(\vec{x}-\vec{y}\right)G^0_{1x} \quad [23]$$

from which we obtain

$$G_{1x} = -\frac{1}{4\pi r_{1x}}\exp\left[(\mathrm{i}k-\kappa)r_{1x}\right] + V_0\frac{\exp\left[(\mathrm{i}k-\kappa)r_{1y}\right]}{4\pi r_{1y}} \times \frac{\exp\left[(\mathrm{i}k-\kappa)r_{xy}\right]}{4\pi r_{xy}} \quad [24]$$

where $r_{1x} = |\vec{r}_1 - \vec{r}_x|$ and $r_{xy} = |\vec{r}_x - \vec{r}_y|$.

The correlation function is defined in the frequency domain as

$$C_{1,2}(\omega) = \int_{-\infty}^{+\infty} G^*_{1x}(\omega)G_{2x}(\omega)\,\mathrm{d}\vec{x} \quad [25]$$

with noise sources that spread to infinity. Replacing G_{1x} and G_{2x} by their expression in eqn [24], it follows from the Born approximation that

$$C_{1,2}(\omega) = \int_{-\infty}^{+\infty}\left[G^0_{1x}(\omega)^* G^0_{2x}(\omega) + G^s_{1x}(\omega)^* G^0_{2x}(\omega) + G^0_{1x}(\omega)^* G^s_{2x}(\omega)\right]d\vec{x} \quad [26]$$

from which we obtain

$$\begin{aligned} C_{1,2}(\omega) = &\int_{-\infty}^{+\infty}\frac{\exp\left[(-\mathrm{i}k-\kappa)r_{1x}\right]}{4\pi r_{1x}}\frac{\exp\left[(\mathrm{i}k-\kappa)r_{2x}\right]}{4\pi r_{2x}}\mathrm{d}\vec{x} \\ &-V_0\frac{\exp\left[(-\mathrm{i}k-\kappa)r_{1y}\right]}{4\pi r_{1y}} \\ &\int_{-\infty}^{+\infty}\frac{\exp\left[(-\mathrm{i}k-\kappa)r_{xy}\right]}{4\pi r_{xy}}\frac{\exp\left[(\mathrm{i}k-\kappa)r_{2x}\right]}{4\pi r_{2x}}\mathrm{d}\vec{x} \\ &-V_0\frac{\exp\left[(\mathrm{i}k-\kappa)r_{2y}\right]}{4\pi r_{2y}} \\ &\int_{-\infty}^{+\infty}\frac{\exp\left[(-\mathrm{i}k-\kappa)r_{1x}\right]}{4\pi r_{1x}}\frac{\exp\left[(\mathrm{i}k-\kappa)r_{xy}\right]}{4\pi r_{xy}}\mathrm{d}\vec{x} \end{aligned} \quad [27]$$

Using the change of variable and the spatial integration performed in Section 1.12.4.1 (from eqn [17] to eqn [18]), we have

$$\begin{aligned} C_{1,2}(\omega) = &\frac{1}{2k\kappa}\exp\left(-\kappa r_{12}\right)\frac{\sin\left(kr_{12}\right)}{4\pi r_{12}} \\ &-V_0\frac{\exp\left[(-\mathrm{i}k-\kappa)r_{1y}\right]}{4\pi r_{1y}} \\ &\frac{1}{2k\kappa}\exp\left(-\kappa r_{2y}\right)\frac{\sin\left(kr_{2y}\right)}{4\pi r_{2y}} \\ &-V_0\frac{\exp\left[(\mathrm{i}k-\kappa)r_{2y}\right]}{4\pi r_{2y}} \\ &\frac{1}{2k\kappa}\exp\left(-\kappa r_{1y}\right)\frac{\sin\left(kr_{1y}\right)}{4\pi r_{1y}} \end{aligned} \quad [28]$$

which can be simplified as

$$C_{1,2}(\omega) = \frac{1}{2k\kappa}\exp\left(-\kappa r_{12}\right) = \frac{\sin\left(kr_{12}\right)}{4\pi r_{12}} - V_0\frac{1}{2k\kappa}\exp\left[-\kappa\left(r_{1y}+r_{2y}\right)\right]\frac{\sin\left[k\left(r_{1y}+r_{2y}\right)\right]}{4\pi r_{1y}4\pi r_{2y}} \quad [29]$$

We recognize in eqn [29] the part of the Green's function that is associated to the direct path between the receiver and the

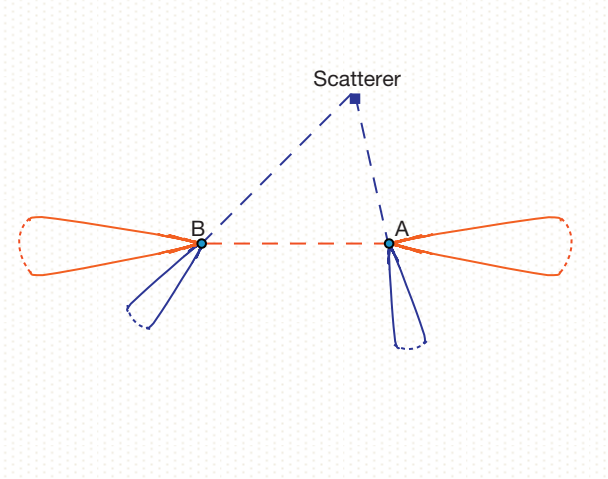

Figure 5 Schematic representation of the end-fire lobes (red) associated to the coherent contribution of noise sources (gray dots in the background) to the correlation function between two receivers at A and B. The part of the Green's function associated to the scatterer (blue square) is reconstructed from noise sources located in different beams (blue). For the sake of clarity, the dashed lines (red and blue) represent the direct and scattered ray paths, respectively.

contribution of the scatterer. From the integral in eqn [26], it is interesting to highlight the location of the noise sources that contribute to the reconstruction of the direct path or the scatterer contribution (Figure 5). In addition to the end-fire lobe that defines the angle interval in which noise sources coherently contribute to the direct path of the Green's function (Figure 5, red), there are new angle intervals associated to the coherent contribution of the scattered field (Figure 5, blue). As the path length of the scattered ray is longer than the A-to-B direct path, the width of this beam is smaller than the end-fire lobe.

Taking into account the Green's function formulation in eqn [24], we finally have

$$C_{1,2}(\omega) = \frac{c}{2i\omega\kappa}\mathrm{Im}[G_{12}(\omega)] \qquad [30]$$

Recognizing the time-derivative as the $i\omega$ term at the denominator in eqn [30], it follows that the correlation theorem is still valid for a medium with one local heterogeneity. Note that an extension of the plane-wave approach has also been performed in the presence of a scatterer (Sànchez-Sesma et al., 2006).

Following the same mathematical approach as in eqns [23]–[29], Sato et al. (2012) extended this result to a set of scatterers in the Born approximation. Finally, Margerin and Sato (2011) went a step further, showing that all of the scattering orders in the Dyson's equation (including multiple scattering) can be taken into account in the correlation function for the same result as in eqn [30].

1.12.4.3 Arbitrary Heterogeneous Medium

We now generalize the correlation theorem to the case of scalar waves propagating in any heterogeneous medium. This approach was first developed by Weaver and Lobkis (2004) and then by Snieder (2007). It indicates the role of attenuation in the connection between the correlation function and the Green's function.

We start from the Helmholtz equation that defines the Green's function $G_{1x}=G(\vec{r}_1,\vec{x};\omega)$ for scalar waves in a heterogeneous medium at frequency ω:

$$\Delta G_{1x} + V\left(\vec{x}\right)G_{1x} + (k+i\kappa)^2 G_{1x} = \delta\left(\vec{x}-\vec{r}_1\right) \qquad [31]$$

where the potential $V(\vec{x})$ describes the scattering contribution to the wavefield that is assumed to be finite in space, meaning that it does not extend to infinity.

Using two points in $\vec{r}_1$ and $\vec{r}_2$, we define the flux of the Poynting vector through a closed surface S located far away from any medium heterogeneity as

$$I = \oint_S \left[G_{1x}\,\vec{\nabla}\,(G^*_{2x}) - \vec{\nabla}\,(G_{2x})G^*_{1x}\right]\vec{\mathrm{d}S} \qquad [32]$$

Using the divergence theorem, we can transform this flux integral into a volume integral U:

$$I = \int_U \vec{\nabla}\left[G_{1x}\,\vec{\nabla}\,(G^*_{2x}) - \vec{\nabla}\,(G_{1x})G^*_{2x}\right]\mathrm{d}V \qquad [33]$$

This can be simplified to

$$I = \int_U (G_{1x}\Delta G^*_{2x} - \Delta G_{1x}G^*_{2x})\mathrm{d}V \qquad [34]$$

From eqn [31], we have

$$\Delta G^*_{2x} = \delta\left(\vec{x}-\vec{r}_2\right) - V\left(\vec{x}\right)G^*_{2x} - (k-i\kappa)^2 G^*_{2x} \qquad [35]$$

$$\Delta G_{1x} = \delta\left(\vec{x}-\vec{r}_1\right) - V\left(\vec{x}\right)G_{1x} - (k+i\kappa)^2 G_{1x} \qquad [36]$$

which assumes that the potential $V(\vec{x})$ is real. Physically speaking, this means that there is no vortex or flow in the medium that would break the spatial reciprocity theorem.

Combining eqns [35] and [36] with eqn [34], it follows that

$$I = G_{12} - G^*_{21} - \frac{4i\omega\kappa}{c}\int_U G_{1x}G^*_{2x}\mathrm{d}V \qquad [37]$$

Finally, using eqns [32] and [37], and taking into account that $G_{12}=G_{21}$, because of the reciprocity theorem, it can be concluded that

$$G_{12} - G^*_{12} = \frac{4i\omega\kappa}{c}\int_V G_{1x}G^*_{2x}\mathrm{d}V + \oint_S \left[G_{1x}\,\vec{\nabla}\,(G^*_{2x}) - \vec{\nabla}\,(G_{1x})G^*_{2x}\right]\vec{\mathrm{d}S} \qquad [38]$$

In eqn [38], the left-hand side corresponds to the causal and anticausal Green's function. Using an equivalent formulation (see Section 1.12.4.3.3) of the representation theorem, Snieder (2007) detailed the different contributions of the volume and surface integrals in a simple configuration. For the sake of simplicity, we propose to separately examine the volume and surface integrals in the two following cases.

1.12.4.3.1 If the attenuation parameter $\kappa \neq 0$

In the case where the attenuation parameter $\kappa \neq 0$, we make the choice to extend the volume U to infinity. This means that the volume integral over the 'noise sources' x spreads over infinity. The product $G_{1x}G^*_{2x}$ corresponds to the correlation

between the field received in $\vec{r}_1$ and $\vec{r}_2$ from a source in $\vec{x}$. Far from the medium heterogeneities, the Green's function decreases as

$$|G_{1x}| \sim \frac{1}{4\pi\left|\vec{x}-\vec{r}_1\right|}\exp\left(-\kappa\left|\vec{x}-\vec{r}_1\right|\right) \quad [39]$$

Then, we have in the far field, with $|\vec{x}| \gg |\vec{r}_1|, |\vec{r}_2|$

$$\left|G_{1x}\,\vec{\nabla}\,(G^*_{2x})\right| \sim \left|\vec{\nabla}\,(G_{1x})G^*_{2x}\right| \sim \frac{k^2}{16\pi^2\left|\vec{x}-\vec{r}_1\right|\left|\vec{x}-\vec{r}_2\right|}$$
$$\exp\left[-\kappa\left(\left|\vec{x}-\vec{r}_1\right|+\left|\vec{x}-\vec{r}_2\right|\right)\right] \quad [40]$$

such that $\oint_S\left[G_{1x}\,\vec{\nabla}\,(G^*_{2x}) - \vec{\nabla}\,(G_{1x})G^*_{2x}\right]\vec{\mathrm{d}S} \to 0$ even when the surface S expands to infinity, because of the exponential decrease caused by attenuation.

We then obtain

$$G_{12} - G^*_{12} = \frac{4\mathrm{i}\omega\kappa}{c}\int_U G_{1x}G^*_{2x}\mathrm{d}V \quad [41]$$

which has sometimes been defined as the Ward Identity in the recent literature.

Equation [41] is the generalization of eqns [20] and [30] to any heterogeneous medium in the presence of attenuation. As in eqn [30], note that the $\mathrm{i}\omega$ term on the right-hand side corresponds to the time-derivative of the correlation function. As shown in the previous equations, the attenuation parameter κ is a key parameter in the Ward Identity. Physically speaking, the attenuation manages to balance the energy flux in the system. Another interpretation of the attenuation is related to the thermodynamic equilibrium as defined through the fluctuation-dissipation theorem.

1.12.4.3.2 If the attenuation parameter $\kappa = 0$

In the case where the attenuation parameter $\kappa = 0$, eqn [38] is simplified into

$$G_{12} - G^*_{12} = \oint_S\left[G_{1x}\,\vec{\nabla}\,(G^*_{2x}) - \vec{\nabla}\,(G_{1x})G^*_{2x}\right]\vec{\mathrm{d}S} \quad [42]$$

In eqn [42], the sources are present only on the closed surface S, and no source is present in the volume. If the surface is taken in the far field of the medium heterogeneities, for every point x on the surface S, we have

$$G_{1x} \sim \frac{1}{4\pi\left|\vec{x}-\vec{r}_1\right|}\exp\left(-ik\left|\vec{x}-\vec{r}_1\right|\right) \text{ and}$$
$$\vec{\nabla}\,(G_{1x}) \sim \mathrm{i}\vec{k}G_{1x} \quad [43]$$

from which it follows that

$$G_{12} - G^*_{12} = -2i\frac{\omega}{c}\oint_S G_{1x}G^*_{2x}\mathrm{d}S \quad [44]$$

where the right-hand side corresponds to the correlation function calculated for sources located on the surface S. As before, the $\mathrm{i}\omega$ term refers to the time-derivative of the correlation function.

The last formulation of the correlation theorem is appealing for geophysicists who usually deal with noise sources at Earth's surface. However, according to eqn [44], the surface must surround the receiving points in $\vec{r}_1$ and $\vec{r}_2$, which never happens in practice. Note also that the approximation $\kappa = 0$ is not valid in most practical cases.

1.12.4.3.3 Another formulation of the correlation theorem

In the literature on ambient noise correlation, eqn [44] is classically defined as one formulation of the representation theorem, and a different mathematical expression is sometimes used (Godin, 2007; Wapenaar, 2004; Wapenaar and Fokkema, 2006):

$$\tilde{G}_{12} + \tilde{G}^*_{12} = \frac{2}{c}\oint_S \tilde{G}_{1x}\tilde{G}^*_{2x}\mathrm{d}S \quad [45]$$

Compared to eqn [44], this other formulation of eqn [45] connects the summation of the causal and anticausal Green's function to the correlation function without the time derivative. It is important to understand that the two expressions in eqns [44] and [45] are equivalent. Indeed, eqn [45] is obtained from a different definition of the Green's function (see eqn [31] for comparison):

$$\Delta\tilde{G}_{1x} + V\left(\vec{x}\right)\tilde{G}_{1x} + (k+\mathrm{i}\kappa)^2\tilde{G}_{1x} = \mathrm{i}\omega\delta\left(\vec{x}-\vec{a}\right) \quad [46]$$

this differs only in the source term on the right-hand side, which corresponds to a 'mass injection' in eqn [46] when the Green's function definition in eqn [31] refers to a 'momentum injection.'

Finally, some authors have dealt with the case of a complex potential $V(\vec{x})$, which would correspond, for example, to the presence of a vorticity field or a flow that breaks the condition of spatial reciprocity in the propagation medium. It appears then that the correlation function is no longer symmetric in time. The travel time associated to the causal part can then be different from the travel time of the anticausal part, as the Green's function from one receiver to the other is not equivalent to the Green's function along the reverse path (Wapenaar, 2006).

Note also that Colin de Verdière (2009, 2011) proposed a very general and quite mathematical approach where the wave propagator is simply defined as a self-adjoint differential operator. Including attenuation and taking into account any type of scattering in the wave equation for a homogeneous noise distribution, he retrieved the same connection between the correlation function and the causal/anticausal Green's function (eqns [20] and [41]).

1.12.4.4 Modal Approach in Finite Bodies

Up to this point, we have presented the formulation of the correlation theorem in open homogeneous or heterogeneous media. However, the first theoretical and experimental demonstration of the convergence of the correlation function toward the Green's function was performed in finite bodies in which the wave propagation is described from a modal approach (Weaver and Lobkis, 2001).

For the sake of simplicity, we deal with a 1D finite body, in which the Green's function can be written as an expansion in terms of the normal modes $U_n(x)$:

$$G(x_1,x_2;t)=c^2\sum_n U_n(x_1)U_n(x_2)\frac{\sin(\omega_n t)}{\omega_n}\Theta(t) \qquad [47]$$

where ω_n corresponds to the eigenfrequency of mode n and $\Theta(t)$ is the Heaviside function that is necessary to respect the causality of the Green's function.

When uncorrelated noise sources are uniformly distributed in the volume V of the finite body, the correlation function between two receivers at x_1 and x_2 can be written as

$$C_{1,2}(t)=\frac{1}{T}\int_0^T \mathrm{d}\tau\int_V \mathrm{d}x\,G(x_1,x;\tau)G(x_2,x;t+\tau) \qquad [48]$$

From eqn [47], it follows that

$$C_{1,2}(t)=\frac{c^4}{T}\int_0^T \mathrm{d}\tau\int_V \mathrm{d}x\sum_m\sum_n U_n(x_1)U_n(x)U_m(x_2)U_m(x)\,\frac{\sin(\omega_n\tau)}{\omega_n}\,\frac{\sin[\omega_m(t+\tau)]}{\omega_m} \qquad [49]$$

Using the orthonormality relation between modes

$$\int_0^L \mathrm{d}x\,U_n(x)U_m(x)=\delta_{nm} \qquad [50]$$

we have

$$C_{1,2}(t)=\frac{c^4}{T}\sum_n\frac{1}{\omega_n^2}U_n(x_1)U_n(x_2)\int_0^T \sin(\omega_n\tau)\sin[\omega_n(t+\tau)]\mathrm{d}\tau \qquad [51]$$

When the recording window T is long compared to the largest period of the excited modes ($T\gg 1/\omega_n,\ \forall n$), it follows that

$$C_{1,2}(t)=\frac{c^4}{2}\sum_n U_n(x_1)U_n(x_2)\frac{\cos(\omega_n t)}{\omega_n^2} \qquad [52]$$

and then,

$$\frac{\mathrm{d}}{\mathrm{d}t}C_{1,2}(t)=-\frac{c^4}{2}\sum_n U_n(x_1)U_n(x_2)\frac{\sin(\omega_n t)}{\omega_n}=-\frac{c^2}{4}[G(x_1,x_2;t)-G(x_1,x_2;-t)] \qquad [53]$$

As expected, the physics of the correlation theorem also applies to the modal formulation. Besides the thermal diffuse-noise experiment achieved by Weaver and Lobkis (2001) in a sample of duralumin, other demonstrations have been performed in bounded media. For example, acoustic propagation in underwater waveguides is bounded by the air–water and water–bottom interfaces that justify the presence of propagating modes. Different authors have studied the convergence of the correlation function toward the Green's function in underwater acoustics, with some successful applications to array element synchronization or bottom mapping.

1.12.4.5 Equipartition and Random Fields

As Earth is a complex medium, scattering by small-scale heterogeneities is a relevant phenomenon to understand seismic-wave propagation, particularly for short period waves in the lithosphere. Scattering is revealed at the first order by the amplitude decay of the direct arrivals and by the long coda of seismograms. For coda waves, multiple scattering must be taken into account. This is a general issue in different domains that has led to considerable developments aimed at the quantitative description of the spatial and temporal evolution of the local energy, or intensity, of the scattered field, via the diffusion approximation or the more general radiative-transfer equation (see Sato et al., 2012, for a review on seismic waves). While the average energy density is successfully predicted by these theories, the phases, that is, the details of the wave shapes, are assumed to be unpredictable random variables. At the same time, the deterministic phase of the waves that is neglected in the theory for energy or intensity is clearly expressed in phenomena such as coherent backscattering (Larose et al., 2004) and long-range correlations in the form of the Green's function (Campillo and Paul, 2003).

For waves propagating in the heterogeneous Earth, the diffusive regime emerges after several scatterings at a time that depends on the scattering strength of the medium (e.g., Sato et al., 2012). Asymptotically for large times, the wavefield is expected to consist of random contributions of all the possible modes of propagation, with equal weights on average (e.g., Ryzhik et al., 1996; Weaver, 1982). This state is referred to as equipartition. Note that we refer here to the modes of a fictitious model close enough to the actual complex Earth to essentially share the same propagation properties (e.g., Campillo and Margerin, 2010). In a realistic medium, the propagation modes are associated with complex eigenfunctions. Equipartition, therefore, does not imply that their contributions are the same everywhere. At a given observation point, equipartition results in a constant ratio of the relative contributions of the P-waves and S-waves to the time-dependent diffuse local energy, independent of the detail of the scattering. The stabilization of the S-to-P energy ratio is observed in the coda of actual seismograms (Hennino et al., 2001; Margerin et al., 2009; Yamamoto and Sato, 2010). This is a good indication that the wavefield has entered into a regime where the diffusion approximation can be applied to describe the average energy density.

Equipartition and isotropy are asymptotic states of diffuse fields for large lapse times. Indeed, these conditions are generally not reached in practice. In the presence of a single source, the overall divergent flux of energy precludes a perfect isotropy of the flux even for large lapse times. It must be noted that although it is an indicator of the diffusion, the stabilization of the energy ratios is not synonymous with equipartition and, therefore, isotropy of specific intensity (Paul et al., 2005).

We recast here a plausibility argument for the construction of Green's function from correlation of diffuse fields that was originally proposed by Lobkis and Weaver (2001). In the case of a finite body, a diffuse field can be expressed in terms of the normal modes $U_n(\vec{r})$ as

$$\phi(\vec{r};t)=\sum_n a_n U_n(\vec{r})\cos(\omega_n t) \qquad [54]$$

where the complex amplitudes a_n are uncorrelated random variables, such that

$$\langle a_n a_m^*\rangle=F(\omega_n)\delta_{nm} \qquad [55]$$

where $F(\omega)$governs the shape of the spectral energy density. The cross-correlation of the two fields at points $\vec{r}_1$ and $\vec{r}_2$ is

$$C_{1,2}(t) = \frac{1}{T}\int_0^T \phi\left(\vec{r}_1,\tau\right)\phi\left(\vec{r}_2,t+\tau\right)\mathrm{d}\tau \qquad [56]$$

Assuming a long recording interval T, this reduces to

$$C_{1,2}(t) = \frac{1}{2}\sum_n F(\omega_n)U_n\left(\vec{r}_1\right)U_n\left(\vec{r}_2\right)\cos\left(\omega_n t\right) \qquad [57]$$

This expression of the correlation function must be compared to the Green's Function:

$$G\left(\vec{r}_1,\vec{r}_2;t\right) = \sum_n U_n\left(\vec{r}_1\right)U_n\left(\vec{r}_2\right)\frac{\sin\left(\omega_n t\right)}{\omega_n}\Theta(t) \qquad [58]$$

For positive times, $C_{1,2}(t)$ and $G(\vec{r}_1, \vec{r}_2; t)$ differ only by a time derivation and the spectrum of the diffuse field. While limited to the case of finite bodies, this simple demonstration is a justification for the pioneering experiments performed in acoustics by Lobkis and Weaver (2001).

1.12.4.6 Example with Elastic Waves

In the homogeneous 2D case with surface waves discussed in Section 1.12.4.1.1, the wavefield is projected on plane waves that propagate in every direction with constant amplitude. The equipartition then reduces to isotropy. The correlation of an equipartioned field at two points, therefore, reduces to the case discussed in Section 1.12.4.1. The elastic case is more informative.

In the elastic 2D case, the equation of motion for the velocity vector $\vec{u}$ is

$$\beta^2\frac{\partial^2 u_i}{\partial^2 x_j} + \left(\alpha^2-\beta^2\right)\frac{\partial^2 u_j}{\partial x_i \partial x_j} = \frac{\partial^2 u_i}{\partial^2 t} \qquad [59]$$

where u_i is one component of the velocity vector, and α and β correspond to the P-wave and S-wave velocities, respectively.

Assuming a homogeneous medium, we project the elastic wavefield on the P and S plane waves. For the 2D case, the ratio of S-wave to P-wave energies of an equipartioned field can be obtained by a simple mode-counting argument:

$$\frac{E_S}{E_P} = \frac{\alpha^2}{\beta^2} \qquad [60]$$

Let us consider an isotropic 2D field in which P-waves and S-waves are propagating in all directions, with the spectral densities S^2 and P^2 independent of the direction of propagation. We denote the wavenumber for the P-waves and S-waves by $\vec{q}$ and $\vec{k}$, respectively.

Following Sánchez-Sesma and Campillo (2006), we assume an energy ratio between the S-waves and P-waves such that $\varepsilon\frac{E_S}{E_P} = \frac{\alpha^2}{\beta^2}$ with $\varepsilon = 1$ for equipartition. We consider the cross-correlation of the resulting field $\vec{u}$ at positions $\vec{x}$ and $\vec{y}$. We assume $\vec{y}$ to be at the origin. Position $\vec{x}$ is written as $(x_1 = r\gamma_1, x_2 = r\gamma_2)$. After averaging over the incidence direction for an isotropic plane wave distribution, the correlation can be written as

$$\left\langle u_i\left(\vec{y};\omega\right)u_j^*\left(\vec{x};\omega\right)\right\rangle = \frac{S^2\beta^2}{2}\left[A\delta_{ij} - B\left(2\gamma_i\gamma_j - \delta_{ij}\right)\right] \qquad [61]$$

where

$$A = \varepsilon\frac{J_0\left(\left|\vec{q}\right|r\right)}{\alpha^2} + \frac{J_0\left(\left|\vec{k}\right|r\right)}{\beta^2};$$
$$B = \varepsilon\frac{J_2\left(\left|\vec{q}\right|r\right)}{\alpha^2} + \frac{J_2\left(\left|\vec{k}\right|r\right)}{\beta^2} \qquad [62]$$

When the equipartion energy ratio is assumed, that is, $\varepsilon = 1$ in eqn [60], we recognize the exact compact form of the 2D elastic Green's function, and the cross-correlation is simply given by (Sánchez-Sesma and Campillo, 2006):

$$\left\langle u_i\left(\vec{y};\omega\right)u_j^*\left(\vec{x};\omega\right)\right\rangle = -8E_S k^{-2}\mathrm{Im}\left[G_{ij}\left(\vec{x},\vec{y};\omega\right)\right] \qquad [63]$$

where $E_S = \rho\omega^2 S^2/2$.

Note that in this particular case, we use the definition of the Green's function for the elastodynamic equation (eqn [59]) as the response in the displacement to a unit force. This simple canonical case can be extended to 3D and illustrates the close relation between equipartition of the wavefield and the extraction of the Green's function from the cross-correlations.

In the literature, different definitions of the equipartition are presented that can depend on (1) the use of a time-domain or frequency-domain approach; (2) the properties of the propagation medium (open or bounded medium, presence of scatterers); and (3) the nature of the incident wavefield (stationary random noise, spatial distribution of pulsed sources, plane waves, or modal excitations). Even though equipartitioning is at the basis of the noise correlation theorem, all situations are not equivalent. For example, we will consider in the next paragraphs and in practical applications some cases where parts of the Green's function can be extracted in the absence of equipartitioning.

1.12.5 Practical Limitations

1.12.5.1 Partial Focusing

We have seen that the correlation of an even distribution of sources can lead to the Green's function of the medium. Indeed, in the actual application of ambient-noise correlation, the sources are likely to result in a form of non-isotropy of the incoming flux to the pair of stations of interest. In this case, it cannot be expected that the exact response of Earth will be retrieved. It is important to determine how an improper distribution of the source affects the cross-correlation, and how reliable the measurements of travel times or of amplitude become.

We start with an intuitive argument that follows the time-reversal analogy presented in the Introduction. Figure 6(a) shows a numerical test similar to that in Figure 1, except for the distribution of the sources. The sources are now located along a segment (Figure 6(a)), which offers poor azimuthal coverage of the medium. The presence of scattering partly compensates for this uneven distribution of the sources. We now observe a relatively poor focusing and a clearly different pattern of snapshots at positive and negative times. Figure 6 illustrates clearly the impact of the physical flux of energy on the reconstruction. The reconstructed Green's function does not show the expected temporal symmetry. Furthermore, for

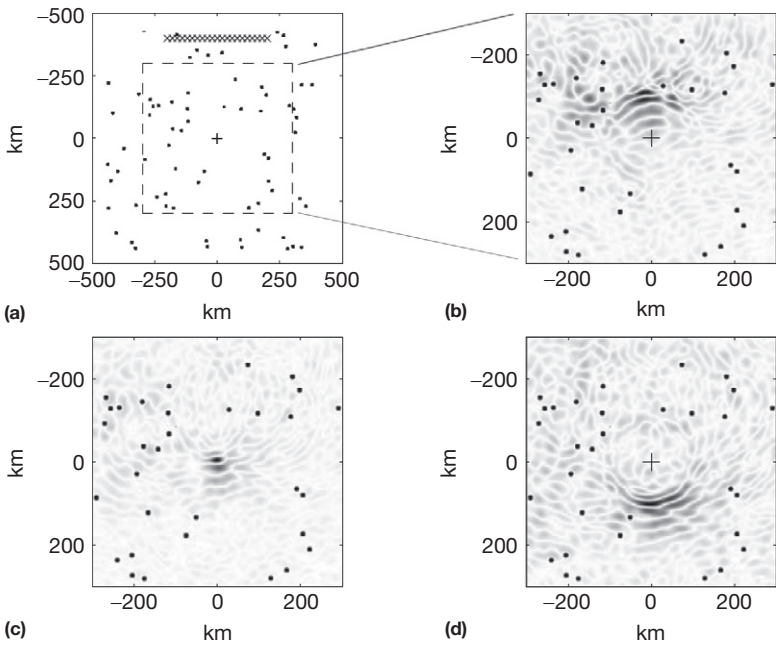

Figure 6 Snapshots of cross correlations with respect to the field at the center (+), as in **Figure 1**, but with a distribution of sources limited to a line ((a), × symbols). (b), (c), and (d) correspond to correlation times of −30, 0, and 30 s, respectively.

receiver pairs oriented perpendicular to the flux, there is no detectable trace of the propagating wave.

Therefore, it is clear that, in general, correlations of noise cannot be considered directly as actual Green's functions for imaging purposes. The distribution of the noise sources has to be considered as a constituent of observables, such as arrival times or amplitudes. This can be formulated explicitly for a general imaging approach in the expression of the sensitivity kernels for noise correlations (Hanasoge, 2013; Tromp et al., 2010). In practice, the space–time distribution of the noise sources is not known precisely. With simple assumptions, it is, nevertheless, possible to quantitatively determine the bias between noise correlations and true Green's functions.

1.12.5.2 Travel Time Measurements

Even when a propagating wave is identified, it is important to quantitatively evaluate the quality of the measurements that can be performed when the distribution of sources leads to nonisotropic illumination of the station pairs. Let us consider a simple 2D case where a pair of stations is surrounded by a distant distribution of incoherent sources that leads to nonisotropic specific intensity (Weaver et al., 2009). This is a geometry of interest when dealing with surface waves from distant noise sources (Tsai, 2009).

We assume that we measured the derivative of the correlation between the signal observed at the two receivers over the angle θ between the direction of incidence and the strike of the two receivers (**Figure 3(c)**). $B(\theta)$ is the azimuthal distribution of the energy of the sources, and it can be expanded as

$$B(\theta) = B_0 + B_1 \cos\theta + B_2 \cos 2\theta + \cdots \qquad [64]$$

Note that only even terms contribute to this problem, because of the symmetry of the apparent velocity with respect to $\theta = 0$.

Let us consider the case of distant receivers, that is, $kx \gg 1$. We are in the high-frequency limit where the contributions to the correlations are dominated by the contributions of the end-fire lobes, that is, $\theta \simeq 0$. The goal is to evaluate the time error that is induced by the anisotropy of the sources. To be under conditions useful for seismological applications, the induced bias (delay) δt is evaluated as the time of the maximum of the cross-correlation between a Gaussian pulse of central frequency ω_0 in the isotropic source ideal case ($B(\theta) \equiv 1$) and that of the nonisotropic case. Under the high-frequency approximation, it can be shown that (Weaver et al, 2009)

$$\delta t = \frac{B''(\theta = 0)}{2t\omega_0^2 B(\theta = 0)} \qquad [65]$$

where $B''(\theta)$ refers to the second-order derivative of $B(\theta)$.

These formulae indicate that the error decays with frequency and with interstation distance. This is in agreement with the conclusion of Yao and van der Hilst (2009). The decay of the bias with interstation distance can be understood as the diminution of the angular size of the end-fire lobes with increasing distance.

The stationary phase theorem helps in the interpretation of the physics aspect of this observation (see **Section 1.12.3.2**). Only the sources almost in the alignment of the receivers can contribute to the reconstruction. The aperture of the zone where the coherent sources are located varies with the square root of the ratio between the wavelength and the distance between the receivers. At higher frequencies, the end-fire lobes are narrower (Larose et al., 2005; Roux and Kupermann, 2004; Spetzler and Snieder, 2004) and the correction term is smaller. For simplicity, only the positive correlation time has been discussed here, but the argument is the same for negative time, and a formula similar to eqn [65] is obtained with direction π instead of 0.

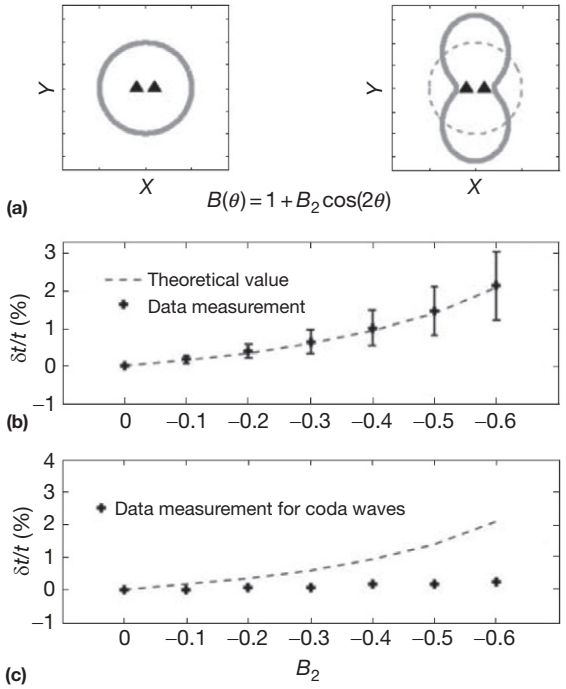

Figure 7 Bias in travel time measurements for a source amplitude distribution of the form B. Different values of B_2 then correspond to different source intensity distributions. (a) Shape of the azimuthal distribution for $B_2 = 0$ (left panel, isotropic distribution) and $B_2 = -0.6$ (right panel, anisotropic distribution). (b) Correlations of direct waves as defined in **Figure 3(b)**. Measured (crosses) and predicted (dashed line) relative time shifts for B_2 ranging from 0 to −0.6. The theoretical values result from eqn [65]. Error bars correspond to standard deviations of 18-pair measurements. The reference travel time corresponds to the correlation function obtained for an isotropic distribution of sources. (c) The same measurements as in (b), but with cross-correlations of time windows that correspond to coda waves (**Figure 3(b)**).

These formulae have been validated numerically and experimentally. Froment et al. (2010) used actual Green's functions obtained during the seismic exploration experiment presented in **Section 1.12.3.2** (**Figure 3**), and they found excellent agreement between observation and theory. This is illustrated in **Figure 7**, which shows the evolution of the travel time bias with increasing anisotropy of the incoming field. The anisotropy of intensity is produced by a modulation of the amplitude of individual source records of the form $B(\theta) = 1 + B_2 \cos(2\theta)$, where θ is defined as in the insert of **Figure 3(b)**. B_2 varies from 0 (isotropy) to −0.6. The two extreme cases are plotted in **Figure 7(a)**. To be under the conditions of the theoretical formula (eqn [65]), the correlations are computed for the direct waves (**Figure 3(b)**), weighted according to $B(\theta)$ for each source, and then averaged over the set of sources. **Figure 7(b)** shows the very good agreement between the theoretical expectations given by eqn [65] and the actual measurements.

1.12.5.3 Amplitude and Spreading

When the conditions for the perfect reconstruction of the Green's function are fulfilled, the amplitude of correlation can be used to study the attenuation properties along the path, or the local amplification produced by specific local geological structures. **Figure 6** shows how an uneven distribution of sources results in poor focusing in a simple medium for a scalar problem. It is noticeable that poor focusing means that the natural curvature of the Green's function wave front is not correctly reconstructed and that, consequently, the geometrical decay of amplitude is not reproduced. In general cases, it is dangerous to mix noise cross-correlations for pairs in different azimuths to retrieve the attenuation properties of the crust.

The simplest case of illumination by a plane illustrates the specific difficulty associated with decay measurements. This occurs when a strong localized source is acting far away from the two receivers. If the noise includes such a predominant plane wave propagating in the direction of the two receivers, the cross-correlation is not the Green's function, although the time of transport of energy is the same, even if the phase is not retrieved correctly (see **Section 1.12.4.1**). The effect is obviously much more severe for the amplitude, as the plane wave has no geometrical spreading, in contrast to the Green's function. Attenuation measurements would be strongly biased by this effect, which cannot be corrected by energy normalization (e.g., Gouédard et al., 2008a).

It was, nevertheless, convincingly shown by Prieto et al. (2009) and Lawrence and Prieto (2011) that attenuation studies can be performed with ambient noise. These authors used the coherency, a normalized version of the cross-correlation, in place of correlation (see **Section 1.12.6**). A discussion of the feasibility and limitations of attenuation studies with ambient noise is presented in Prieto et al. (2011) and Weemstra et al. (2013).

Considering only the reconstruction of the direct waves in the scalar case can hide some difficulties that arise in practical applications, with ambient noise or with active sources at the surface. In the presence of several waves (P and S, reflections) and imperfect illumination, the correlation can show pulses associated to stationary-phase conditions, but not to physical arrivals. These spurious arrivals correspond to correlation times of waves of different natures, that is, which are not propagating between the two points of observations. For a distribution of sources at the surface, Snieder et al. (2006) give an example of interest for exploration. They considered a simplified case with two reflections at different depths. When considered as a function of the position of the source, the difference in travel time between the two reflected waves at the receivers had a maximum at a finite distance. According to the stationary-phase argument, a spurious arrival can, therefore, be expected at a time that is actually a difference of travel time between the reflector levels at depth, without significance for the actual paths between the receivers. Indeed, this problem vanishes if the source distribution extends at depth, or if scatterers acting as sources mimic an even distribution of sources.

1.12.5.4 Influence of Scattering

Although it is impossible to directly separate the contributions of direct and scattered waves in the ambient noise produced by a distribution of uncorrelated sources, we can easily evaluate the behavior of the correlation of scattered waves in the experiment presented in **Section 1.12.5.2** and in **Figure 7**. The results of **Figure 7(b)**, which were obtained with direct waves, were repeated for the correlation of coda windows as

defined in Figure 3(b). The resulting measurements are presented in Figure 7(c) as a function of the anisotropy coefficient B_2. The bias in travel time observed for coda-wave correlations is much smaller than for the case of direct waves. In the worst case, that is, $B_2 = -0.6$, $\delta t/t$ only reaches 2×10^{-3}. This is due to the smooth azimuthal distribution of the intensity of the coda waves. This shows the important part played by scattered waves for the effectiveness of the correlation method.

1.12.6 Processing

1.12.6.1 Processing and Convergence

The basic expectation when correlating noise time series is that for long times of observation, the noise source distribution is averaged toward a distribution that is acceptable with respect to the mathematical requisites discussed in Section 1.12.4. An obvious difficulty is the presence of strong energy transients that potentially dominate in the correlation. Those transients can be large earthquakes, local storms in the microseism spectral band, or various other sources, depending on the frequency range considered. Different strategies are used to improve the temporal stationarity of the records before correlation.

The first possibility is to remove the time windows with earthquakes. This can be done from earthquake bulletins, at least for large events. In practice, a detection algorithm is required to identify small events if no further normalization is applied.

Indeed, strong direct waves generally contribute to nonphysical signals in the correlation. On the other hand, the scattered waves of the coda are a valuable contribution to the reconstruction of the Green's function. As the duration of the coda is much longer than that of the direct waves, efficient processing consists in the normalization of the signal. This normalization is necessary in most cases, even after earthquake rejection.

One-bit normalization was used for the correlation of seismic codas by Campillo and Paul (2003), to balance the temporal exponential decay of the intensity in the coda. This was then used in numerous studies on noise correlation (e.g., Cupillard et al., 2011; Shapiro and Campillo, 2004; Shapiro et al., 2005). That the correlation function of two hardly clipped signals is very close to that of the original signals has been discussed in detail in communication theory (e.g., van Vleck and Middleton, 1966). The numerical simulations of Cupillard and Capdeville (2010) showed that even geometrical spreading and attenuation can be retrieved from correlations of 1-bit clipped data. Instead of using 1-bit correlation, Sabra et al. (2005a) introduced a clipping procedure to limit the contribution of high-amplitude transients, while leaving the background noise unaffected. Bensen et al. (2007) proposed to apply a running-average procedure to ensure the temporal stationarity.

Instead of affecting the data by a form of nonlinear processing, Prieto et al. (2011) and Poli et al. (2012b) proposed to use short time windows, as short as 1 h, to compute the correlation. Transients can be removed after statistical analysis of the total energy of the signal in all the windows. Each correlation is normalized according to its energy before stacking.

Sabra et al. (2005a) analyzed the quality of the reconstruction for a set of station pairs within a range of 180–220 km in Southern California, USA. As shown in Figure 8(a), the cross-correlations are relatively stable over time, as seen for each day of July 2004 for a single station pair. While there are some fluctuations in the small-amplitude waveforms, the main arrivals are stable. The SNRs for each day and each station pair show moderate variations as the noise and seismicity varies. We sum the cross-correlation time series for each day to obtain the time series for N number of days and to compute the SNR (Figure 8(b)). Each day is treated as an independent observation and, therefore, for each N the sum is computed for all the combinations of the 18 days. The accumulated SNR based on the summed traces shows clearly that the SNR increases in proportion to the square root of the recording time, in agreement with Sabra et al. (2005a) and Snieder (2004).

Larose et al. (2008) studied the role of scattering in the convergence toward the Green's function. In this context, the SNR is the ratio between the level of signal in the correlations and the level of remnant fluctuations. They analyzed the SNR dependence in the context of a discrete random distribution of noise sources in a scattering medium. Indeed, the SNR increases with the number of sources. When scattering is present, the SNR increases with scattering strength. This is due to the increase in the duration of the individual source signals with stronger scattering, in addition to the previously discussed isotropization of the intensity. Disorder here improves the quality of the reconstruction. On the contrary, the SNR is directly dependent on the amplitude of the actual Green's function. The amplitude decreases with travel time or distance, and it is sensitive to scattering and absorption.

As the ambient noise spectrum in the microseism band shows clear peaks, it is convenient to introduce spectral whitening (e.g., Bensen et al., 2007). The nature of a seismogram being nonstationary, it is natural to introduce multidimensional filtering to denoise the correlations. Adaptive filtering based on the S transform (Stockwell et al., 1996) was used by Baig et al. (2009), while Schimmel et al. (2011) proposed the use of instantaneous phase coherence to weigh the stack of individual correlations.

Stehly et al. (2011) used filters in the curvelet transform space to improve the SNR of stacked correlations. The previous approaches were based on the use of signal-processing tools. A physics-based approach can be expected to improve the reconstruction. In the noise-correlation context, this consists in minimizing the effects of the nonisotropic illumination. This was done by using an optimization scheme, which was referred to as multidimensional deconvolution by Wapenaar et al. (2008), or as a passive inverse filter by Gallot et al. (2012).

Velocity measurements and the evaluation of their uncertainties can be improved by using the nine correlations obtained with three-component records, with each correlation being defined for positive and negative times. The correlation matrix is expected to show the symmetry of the Green's tensor (e.g., Campillo and Paul, 2003; Sabra et al., 2005b). For practical applications, the computation of the complete correlation matrix allows redundant measurements to be made of Rayleigh wave velocities and their variance (e.g., Stehly et al., 2009).

1.12.6.2 Correlation of Correlations

We have seen that the cross-correlation function of long ambient-noise time series can be identified as the sum of the

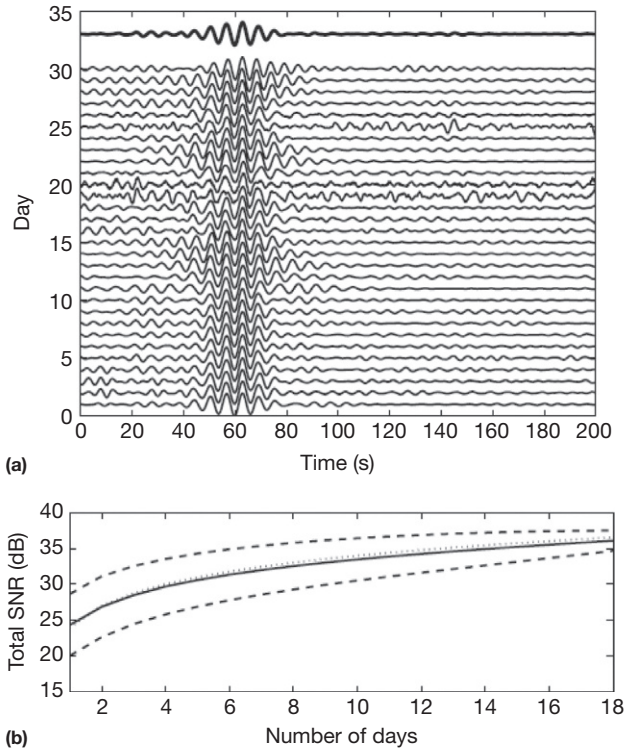

Figure 8 (a) Estimated noise correlation function for one station pair at a distant of 182 km, for each day of July. The summed trace for the whole month of July is shown as the thick solid line. (b) Mean and standard deviations of the SNR (in dB scale) computed by summing all the combinations of the correlation functions over a number of days. The square root dependence is shown as a dotted line. Reproduced from Sabra KG, Gerstoft P, Roux P, Kuperman WA, and Fehler MC (2005) Extracting time-domain Green's function estimates from ambient seismic noise. *Geophysical Research Letters* 32: L03310. http://dx.doi.org/10.1029/2004GL021862.

causal and acausal Green's function. So far, we have discussed the reconstruction of ballistic arrivals. The Green's function also contains the late arrivals associated with scattered waves. According to the discussion in **Section 1.12.4**, these arrivals are also expected to be present in the noise cross-correlations, as has been verified with numerical simulations (e.g., Derode et al., 2003a,b). In the ideal case, the later part of the noise correlation should contain the coda part of the Green's function, and it might be possible to correlate these waves as we correlate standard earthquake codas, to reconstruct the Green's function (Campillo and Paul, 2003). This is the concept of the so-called C^3 method; that is, re-correlating the *c*oda of the noise-*c*orrelation functions to reconstruct the Green's function (Froment et al., 2011; Ma and Beroza, 2012; Stehly et al., 2008). Garnier and Papanicolaou (2009) demonstrated the validity of this method based upon stationary-phase analysis of the C^3 function leading terms, and they confirmed that this method can enhance the quality of travel time estimates in the case of anisotropic source distributions.

For a network of N stations, the C^3 function between two stations A and B is computed through the successive steps illustrated in **Figure 9**. Let a third station in the network be represented by S. The noise correlation is computed between A–S and B–S (**Figure 9(a)**, C^1). The noise correlation corresponds to the signals recorded at A and B, respectively, if a source was present at S. The receivers S have the role of virtual sources. The same operation is repeated for all of the stations S in the network. A time window in the later part of the noise correlations is selected (at twice the Rayleigh wave travel-time in Stehly et al. (2008)). Note that the codas for both the positive and negative parts of the noise correlation are selected. The correlations of the codas of the A–S and B–S noise correlations are computed for positive and negative times. The results are finally averaged for all of the virtual sources S of the network to obtain the C^3 function between A and B (**Figure 9(b)**).

Note at this point that the geometry of the network controls the illumination of virtual sources for the C^3 computation. With this procedure, Stehly et al. (2008) showed that C^3 shows the ballistic Rayleigh waves of the Green's function, as demonstrated for actual coda-wave correlations (Campillo and Paul, 2003). This demonstrates that the late part of the ambient-noise correlation function contains a physical signal, namely, the scattered coda waves. This is important, as it opens the way for using this signal for further applications (see **Section 1.12.7.2**).

Froment et al. (2011) illustrated the concept of a virtual source used for C^3 computation. They compared the time symmetry of both correlation functions (C^1 and C^3) for the particular case of the station pair of HAU–BOURR, as illustrated in **Figure 10**. In the C^3 correlation process, only the 55 network stations south of HAU–BOURR were considered (see **Figure 10(a)**). The noise records were filtered in the frequency band from 0.1 to 0.2 Hz.

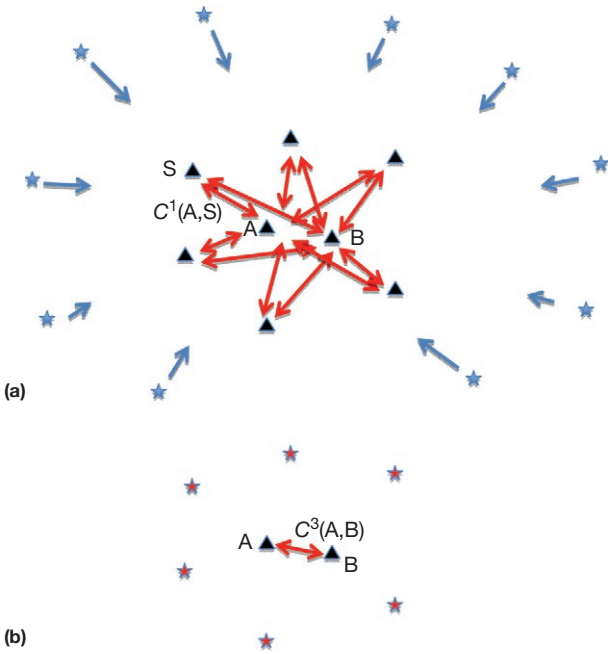

Figure 9 From the noise correlations (C^1) to the correlation of correlations C^3. (a) Construction of the noise cross-correlations (red arrows) between stations A and B and all the other stations S of the network. The blue stars represent distant sources of noise. (b) Construction of C^3 between A and B using the stations of the network as virtual sources (red stars).

This means that the theoretical C^3 virtual sources are located south of the station pair of interest and opposite to the incident-noise direction, as the main source of noise is located in the North Atlantic Ocean or on the northern European coast (e.g., Friederich et al., 1998; Kedar et al., 2008; Landès et al., 2010; Stehly et al., 2006). **Figure 10(b)** shows the results of both the C^1 and C^3 correlation functions for this geometry. The time symmetry of both the signals shows two opposite peaks of maximum amplitude, which reflect a main energy flux that propagates in opposite directions: from north to south for C^1, and from south to north for C^3. Note that the same convention is used for all the correlation functions, that is, the signal in negative (respectively, positive) correlation times corresponds to waves propagating from north to south (respectively, south to north). This observation indicates that the time symmetry of the two correlation functions is consistent with the location of their expected contributing source distributions (actual or virtual). However, the C^3 function has a better time symmetry than C^1. This indicates that the coda waves used to compute the C^3 function constitute a more isotropic field than the ambient seismic noise. Back-scattered waves produce a north-to-south energy flux propagation and, therefore, contribute to a clear pulse in the negative correlation times.

Furthermore, Froment et al. (2011) also discussed the possibility of using the C^3 coda to reconstruct part of the Green's function. They computed a C^5 function, the *c*orrelation of the *c*oda of C^3, and found that the Rayleigh wave is reconstructed. This shows that some coherent signal is still present in the coda of the C^3 function. This result supports the idea that the C^5 function can also be used in noise-based tomography or for monitoring techniques. However, the SNR in the C^5 function is smaller than that in the C^3 function, because of the reduction in the time-window length used for the computation of the correlation. This might limit the practical interest in this iterative correlation process.

The computation of the correlation of correlations is a way to control the illumination, and its isotropy, by using a network of stations as part of the virtual sources. Furthermore, it allows for the separation of scattered and direct waves for the final correlation. This selection is obvious with the selection of an ad hoc time window in noise correlations. From the opposite side, it is impossible to perform this separation with noise records in which direct and scattered waves from various sources are mixed. Although the coda of correlation takes advantage of the properties of multiply scattered waves, it is also possible to compute the correlation of complete noise correlations, including the ballistic part (Froment et al., 2011). This is indeed of interest for long-period waves for which the scattering is weak. The distribution of the stations, which play the role of virtual sources, is the determinant in this case.

Ma and Beroza (2012) used the C^3 approach with data from stations that operate asynchronously, showing that it is practically possible to complement the virtual network with stations that were recording at different periods. Curtis and Halliday (2010) presented a series of integral relations essentially based on correlation or convolution of correlation functions that allowed for reconstructions of virtual seismograms from non-synchronous records; that is, a record at a station that was not operating at the time of an event. Curtis et al. (2012) showed the application of these principles for an earthquake in New Zealand.

1.12.7 Applications

1.12.7.1 Surface-Wave Tomography

It is generally assumed that noise is related to surface activity, which ranges from human activity at high frequency to the forcing of the oceans and the atmosphere at low frequency. As a consequence, the seismic noise observed at the surface has a strong component of surface waves, as has the Green's function between two surface points. The first attempts to extract the Green's function from coda or noise seismic records demonstrated the retrieval of surface waves (Campillo and Paul, 2003; Shapiro and Campillo, 2004). Numerous studies have confirmed that Rayleigh waves are easily retrieved from ambient-noise correlations. When surface waves are identified in ambient-noise correlations, the methods previously developed for earthquake records can be used to infer dispersion properties and, eventually, tomographic images. Ambient-noise surface-wave measurements have been extensively used for tomography at the crustal and lithospheric scales (e.g., Kang and Shin, 2006; Li et al., 2010; Lin et al., 2009; Nishida et al., 2008b; Poli et al., 2012c; Ritzwoller et al., 2011; Sabra et al., 2005b; Saygin and Kennett, 2010; Shapiro et al., 2005; Stehly et al., 2011; Verbeke et al., 2012; Yang et al., 2007; Yao et al., 2008; Zheng et al., 2008). Anisotropy has also been

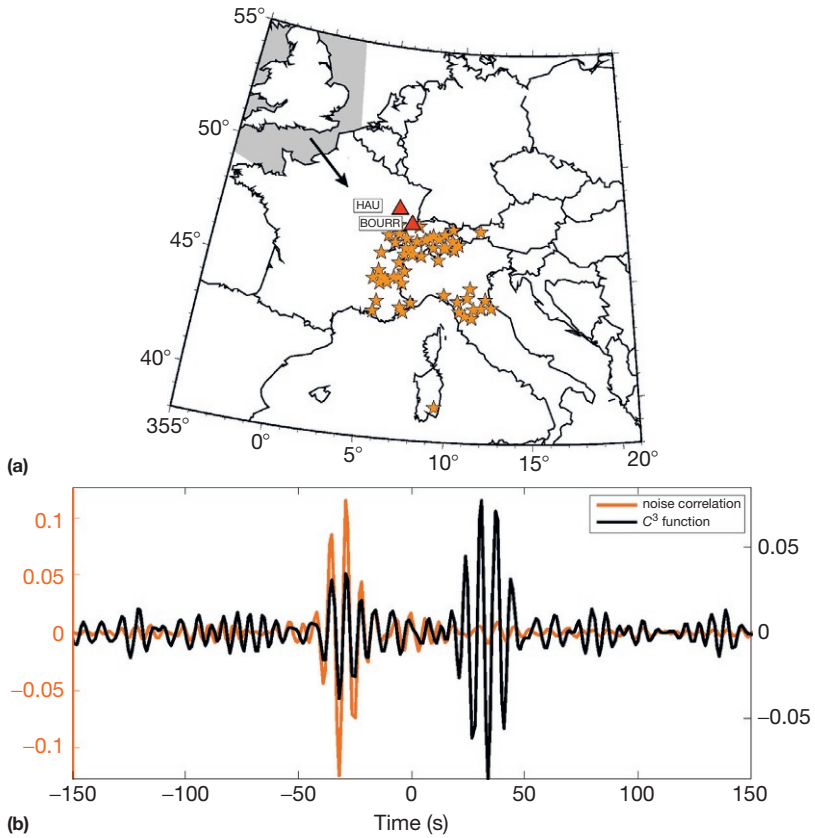

Figure 10 (a) Map of Europe with orange stars corresponding to the 55 stations of the network used as virtual sources to construct the C^3 function between stations HAU and BOURR (red triangles). Note that all the stations considered are located south of the HAU–BOURR path and opposite to the main source of noise located in the North Atlantic Ocean or on the northern European coast (gray zone). The black arrow indicates the main direction of ambient seismic noise in the vicinity of the station pair HAU–BOURR. (b) Noise correlation C^1 (orange curve) and C^3 (black curve) functions between stations HAU and BOURR for the geometry displayed in (a). Note the different vertical scales (left and right, respectively) for the two normalized correlation functions. Reproduced from Froment B, Campillo M, and Roux P (2011) Reconstructing the Green's function through iteration of correlations. *Comptes Rendus Geoscience* 343(8–90): 623–632. http://dx.doi.org/10.1016/j.crte.2011.03.001.

inferred (e.g., Huang et al., 2010; Ritzwoller et al., 2011). Harmon et al. (2007) and Yao et al. (2011) studied the oceanic lithosphere with ambient noise records from ocean bottom seismometers.

Ambient-noise tomography takes advantage of the dense networks by providing a large number of interstation measurements. This allows for improved resolution with respect to using distant earthquake records. This is particularly true for the short periods that are difficult to use when dealing with distant sources. With large dense networks, specific approaches can be applied. An example was presented by Ritzwoller et al. (2011) with eikonal tomography. This technique is based on direct measurement of the local velocity of a surface wave. This is achieved by the use of the eikonal equation, with maps of travel times measured and interpolated on a dense array. In the context of ambient-noise tomography, this operation can be performed with each station acting as a virtual source. When considering all possible virtual sources, a map of the seismic speed can be built, as a function of the azimuth of propagation. An application of these principles is illustrated in **Figure 11**, where the dense array of western United States is used to build a high-resolution map of Rayleigh wave speeds at 24 s, and a map of the amplitude of anisotropy and the direction of the fast axis (Ritzwoller et al., 2011).

Ambient-noise surface-wave tomography has also been applied successfully at smaller scales, to volcanic structures (e.g., Brenguier et al., 2007), shallow surface layers (e.g., Picozzi et al., 2008), and landslides (e.g., Renalier et al., 2010). It is of note that Larose et al. (2005) reported a study of the lunar subsurface from the ambient noise recorded during the Apollo 17 mission.

1.12.7.2 Body Waves

Although usually with weak amplitudes, body waves are present in the noise records. This was clearly shown with array analysis in recent studies (e.g., Gerstoft et al., 2008, who identified mantle and core phases), and body waves have been used to map the regions where noise is produced at a global scale (e.g., Landès et al., 2010).

There is, therefore, substantial hope of extracting the body-wave part of the Green's function, albeit with a lower SNR than for the dominant surface waves. Actually, body waves have indeed been reported from short-distance range correlations.

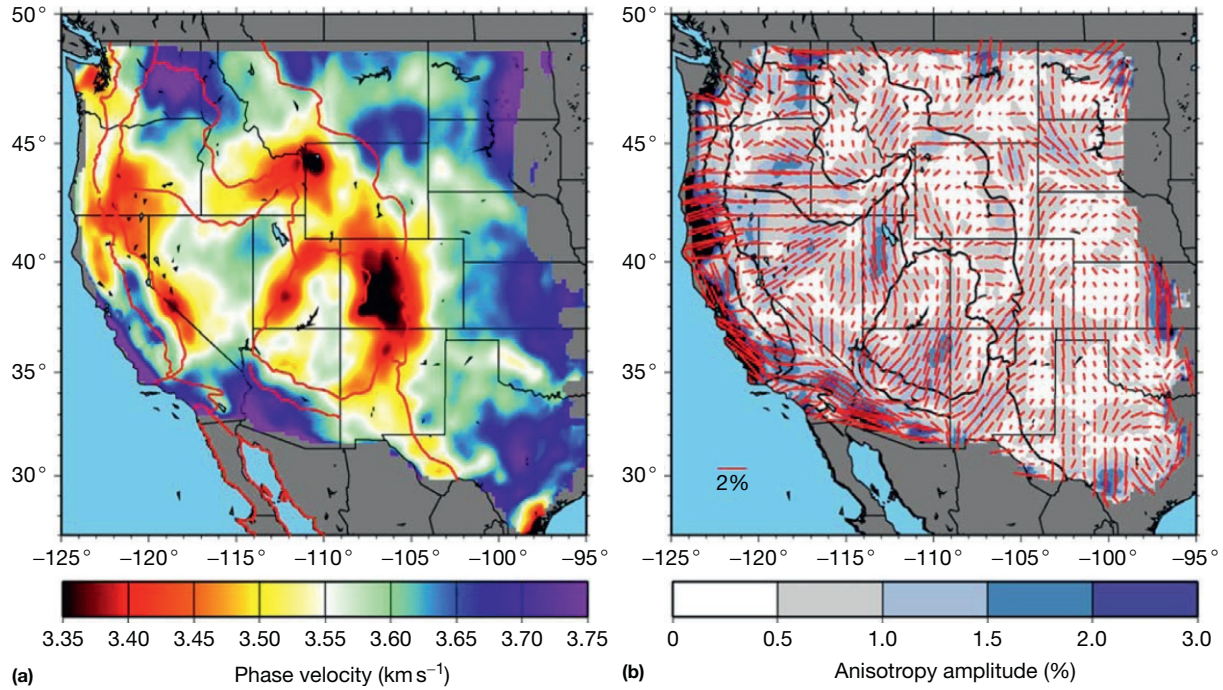

Figure 11 (a) The 24-s Rayleigh wave isotropic phase-speed map taken from the ambient noise by averaging all the local phase-speed measurements at each point on the map. (b) The amplitudes and fast directions of the 2*c* component of the 24-s Rayleigh wave phase velocities. The amplitudes of the anisotropy are given by the lengths of the bars, which point in the fast-axis direction, and the background is color coded. At the 24-s period, the Rayleigh wave anisotropy reflects conditions in a mixture of the crust and the uppermost mantle. Reproduced from Ritzwoller MH, Lin FC, and Shen W (2011) Ambient noise tomography with a large seismic array. *Compte Rendus Geoscience* 343(8): 558–570. http://dx.doi.org/10.1016/j.crte.2011.03.007.

Roux et al. (2005a) identified direct P-waves from noise correlation, using data from a small array in California, USA. Their noise-derived P-waves were linearly polarized, and with an apparent velocity compatible with a known velocity model of the area. Several studies have claimed that there are reflected phases in ambient-noise autocorrelations and cross-correlations. Draganov et al. (2009) used data from oil exploration surveys to extract reflected P-waves from shallow interfaces. Their observations appeared to be in good agreement with the active source reflection response measured in the same area. Tibuleac and von Seggern (2012) reported that a vertical Moho reflection can be identified in autocorrelations in Nevada, USA. Ito and Shiomi (2012) used ambient noise to extract reflections associated with a subducting slab beneath Japan.

Zhan et al. (2010) identified S reflected phases from the Moho interface at the critical distance in two shield areas. Poli et al. (2012b) built a short-period seismic section across Finland from ambient-noise correlation. They used the continuous records of 42 temporary broadband three-component stations located in the northern part of the Fenno-Scandian region (**Figure 12(a)**). Here, they identified high-frequency body waves (0.5–2.0 Hz) emerging from noise correlations for inter-station distances up to 550 km. The comparisons of the noise correlations with earthquake data confirmed that the observed waves can be interpreted as P-waves and S-waves that are reflected from the Moho. As the crustal model of the area is well known, the noise correlations can be compared with synthetic seismograms. **Figure 12** shows an example of such a comparison for two different components of motion: it indicates that the travel times of all the observed phases are in excellent agreement. Poli et al. (2012b) also performed a polarization analysis that confirmed that reflected body waves are positively extracted from ambient noise.

A further step is to demonstrate that deep seismic phases can be retrieved from ambient noise. Poli et al. (2012c) used noise in the microseism band to retrieve P-waves reflected at the top (~410 km deep) and at the bottom (~660 km deep) of the transition zone. **Figure 13** shows the stacked correlations for the pairs of the LAPNet array (see **Figure 12(a)**), as compared with the preferred velocity model. This demonstration that deep interfaces can be imaged with ambient noise at the surface confirms that the ambient noise in the microseism band consists partly of body-waves propagating at the global scale and illuminating the deep interior. This opens the way for the use of ambient-noise correlations to image the deep Earth using body waves. Deep core reflections were reported from correlations at regional distances by Lin et al. (2013). Nishida (2013) and Boué et al. (2013) presented global sections of cross-correlations indicating that most of the deep phases could be extracted from ambient noise.

1.12.7.3 Monitoring

Monitoring of slight velocity changes in Earth can be performed with active sources (e.g., Niu et al., 2008; Reasenberg and Aki, 1974) or with repeating earthquakes (Poupinet et al., 1984; Ratdomopurbo and Poupinet, 1995).

The possibility of using the ambient noise to perform repeated measurements of speeds between fixed stations is

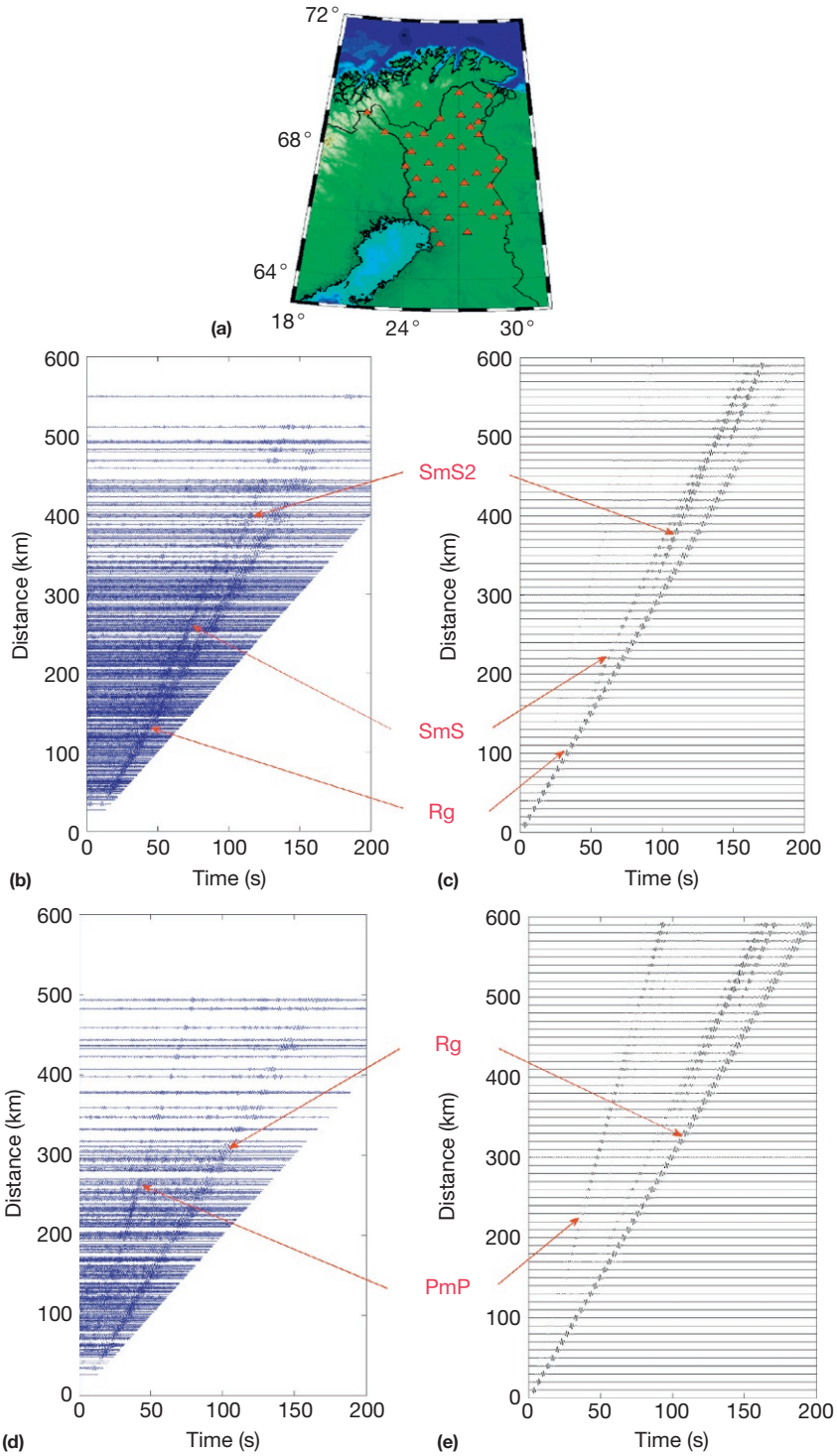

Figure 12 (a) Map of the stations of the LAPNet experiment in Finland. (b) *ZZ* and (d) RR cross-correlations plotted as functions of inter-station distances. (c) The vertical component (*Z*) of synthetic seismograms for a vertical point force at the surface. (e) The radial component (*R*) of synthetic seismograms for a horizontal point force at the surface. All the signals were filtered between 0.5 and 1.0 Hz. Modified from Poli P, Pedersen HA, Campillo M, and the POLENET/LAPNET Working Group (2012b) Emergence of body waves from cross-correlation of short period seismic noise. *Geophysical Journal International* 188: 549–558. http://dx.doi.org/10.1111/j.1365-246X.2011.05271.x.

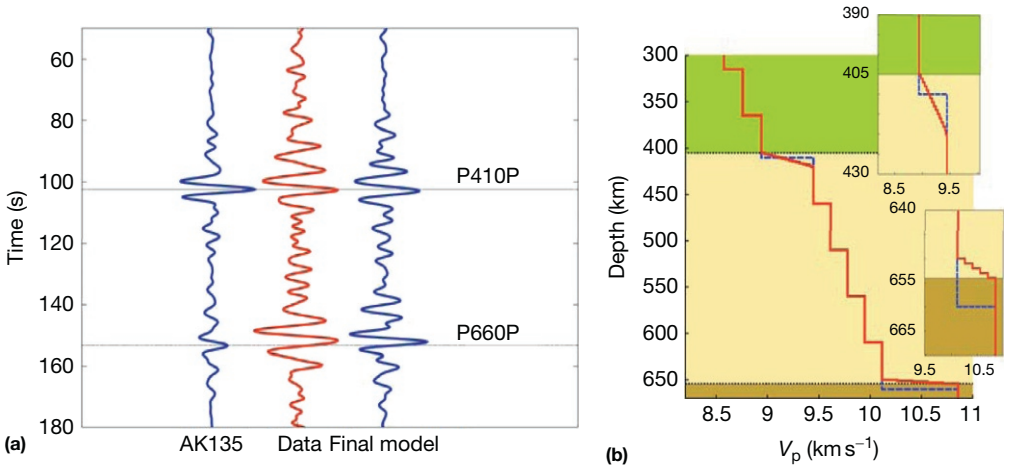

Figure 13 (a) Comparison of stacked cross-correlation (data) with synthetic traces computed for the global model AK135, and for the final preferred model beneath Finland depicted in (b). The map of the stations used in this study is shown in **Figure 12(a)**. The figure is modified from Poli P, Campillo M, Pedersen H, and the Lapnet Working Group (2012a) Body wave imaging of the Earth's mantle discontinuities from ambient seismic noise. *Science* 338: 1063–1066.

appealing. In the previous sections, we discussed the convergence of the cross-correlation toward the Green's function for continuous records of ambient noise of finite duration. Careful attention must be paid to the quality of the reconstruction and to the possible bias associated with the angular distribution of the incoming noise energy. With these precautions, it is possible to repeat the processing at different dates and, therefore, to track temporal changes in the medium.

The first requirement is to study the stability of the measurements and to detect possible instrumental errors when using cross-correlations. As the unbiased physical signals should be time symmetric, a comparison of the arrival times in the positive and negative correlation times of the Rayleigh and Love waves allows the separation of time shifts associated with any form of physical change in the medium, so those resulting from clock drift or other instrumental errors, and those caused by changes in the localization of the noise sources (e.g., Stehly et al., 2007). Physical changes in the medium speed result in delays of the same amplitude for positive and negative times. Instrumental changes produce a global shift of the correlation with opposite time delays. Bias caused by non-isotropic illumination (see **Section 1.12.5**) is associated with different noise sources and is not likely to be equal for positive and negative times. These arguments allow for the detection of instrumental errors and for their correction.

Measuring very small relative velocity changes requires the evaluation of delays between traces. Under the assumption of a global change, these delays increase with the travel times, making the detection much easier for large lapse times. For this reason, it is often more difficult to detect small material changes with direct waves than with waves that have sampled the medium for much longer times, as is the case with coda waves.

In **Section 1.12.6.2**, we discussed the properties of the C^3 function. The convergence of C^3 toward the Green's function demonstrates that the late part of the correlation functions contains scattered waves. Sens-Schönfelder and Wegler (2006) found that the envelope of the correlation of noise is similar for the different components of the correlation tensor, as expected for coda waves, and that this envelope can be modeled with a diffusion equation. Indeed, these arguments do not demonstrate that the entire coda is perfectly reconstructed. This is not a requirement to use the correlations for monitoring changes in velocity. With laboratory ultrasound experiments, Hadziioannou et al. (2009) showed that passive monitoring can be successful without complete reconstruction of the Green's function from cross-correlations. While the noise source is variable, it is observed that the late part of the noise correlation function is very stable and allows for the monitoring of slight changes in velocity.

1.12.7.3.1 Velocity change detection and measurement

The delay dt measured before and after a global change in a medium increases linearly with lapsed time t, according to the simple relationship

$$\frac{\mathrm{d}t}{t} = -\frac{\mathrm{d}V}{V} \qquad [66]$$

where $\mathrm{d}V/V$ is the relative velocity change. This is the basis for very precise measurements of velocity change with coda waves. Poupinet et al. (1984) and Snieder et al. (2002) proposed to measure dt in moving windows along seismograms to evaluate $\mathrm{d}V/V$ through linear regression (moving-window cross-spectral analysis, MWSPA). Alternatively, the stretching technique consists of optimization of a stretching parameter ε (e.g., Lobkis and Weaver, 2003; Sens-Schönfelder and Wegler, 2006). The effect of a global small velocity change is to deform the trace by changing the time t by $t' = t(1-\varepsilon_0)$. The strategy is to interpolate the coda at times $t(1-\varepsilon)$ with various stretching factors ε.

The actual relative velocity change is the stretching factor $\varepsilon_0 = \mathrm{d}V/V$ that maximizes the cross-correlation coefficient between the traces that is acquired before and after the change. Hadziioannou et al. (2009) showed that the stretching technique is more adapted to data with low SNRs in the presence of an actual global velocity change.

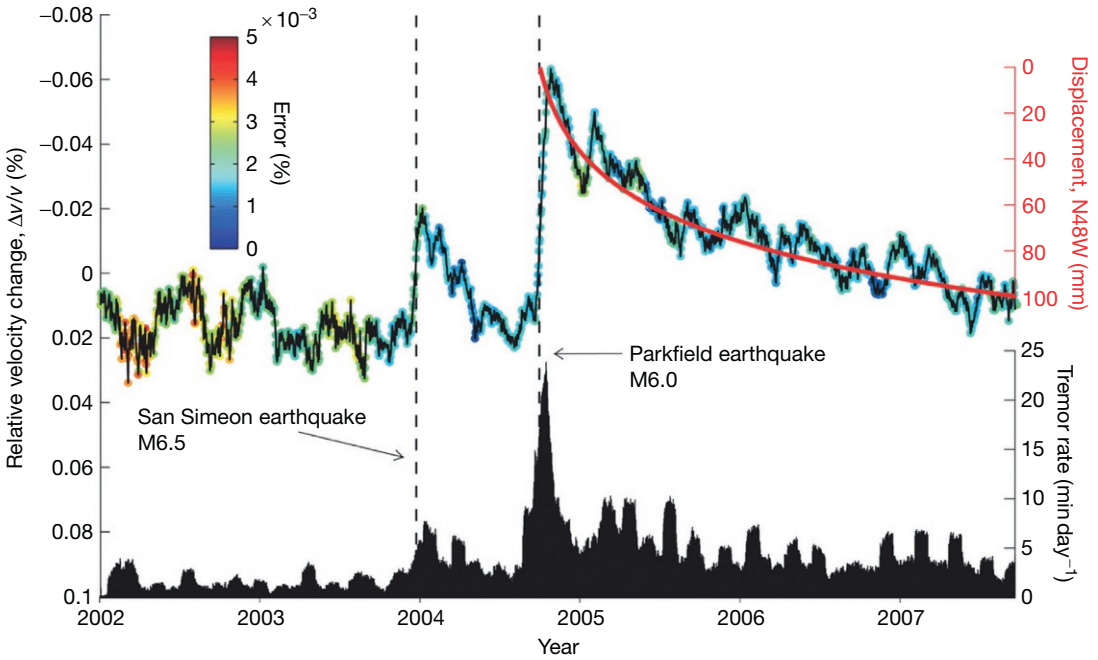

Figure 14 Seismic velocity changes, surface displacements from GPS, and tremor activity near Parkfield. The red curve represents the post-seismic fault-parallel displacements along the San Andreas fault, as measured by GPS at a local station. The tremor rates are averaged over a centered 30-day-long moving time window. Reproduced from Brenguier F, Shapiro NM, Campillo M, et al. (2008) Towards forecasting volcanic eruptions using seismic noise. *Nature Geoscience* 1: 126–130. http://dx.doi.org/10.1038/ngeo104.

Repeated delay measurements have been applied to autocorrelations and cross-correlations, which have demonstrated the possibility to observe relative changes in speed of the medium as small as 10^{-4}. The evaluation of uncertainties is an important issue. Clarke et al. (2011) analyzed the uncertainties of MWSPA in the context of ambient-noise monitoring of a volcano. They concluded that the formal error deduced from the linear regression in MWSPA underestimated the observed fluctuations of velocity when a small amount of noise was added to the correlations. With the stretching method, the dependence of the uncertainty on the correlation coefficient between the traces and the parameters of measure (bandwidth, time window) was given by Weaver et al. (2011).

1.12.7.3.2 Observations

The velocity changes observed with ambient noise are likely to be of various origins. Sens-Schönfelder and Wegler (2006) studied the autocorrelations of noise records on a volcano, and they detected a seasonal velocity change that they interpreted as being related to the variations of the water-table depth. Meier et al. (2010) attributed the seasonal changes of velocity observed in the Los Angeles basin to a thermoelastic effect. Brenguier et al. (2008a) used long time series and detected a velocity change that was a precursor of volcanic eruptions of the Piton de la Fournaise volcano. This was interpreted as the effect of the inflation of the edifice prior to the eruption. Mainsant et al. (2012) also used ambient noise to detect a drop in velocity prior to a landslide.

Recently, several studies have shown the detection of velocity changes associated with the activity of fault systems, earthquakes, and transient creep, with correlations of ambient noise. Wegler and Sens-Schönfelder (2007) detected a change in velocity after the Mw 6.6 mid-Niigata earthquake in Japan. Brenguier et al. (2008b) observed velocity drops associated with two earthquakes in central California, USA (**Figure 14**).

More recently, Hadziioannou et al. (2011) used the adaptive filtering approach of Baig et al. (2009) to improve the time resolution of the monitoring, and they concluded that the velocity drop associated with the Parkfield earthquake is coseismic with a precision of 1 day. Considering the apparent similarity of the temporal evolution of the velocity change, GPS position, and tremor activity at depth, Brenguier et al. (2008b) proposed that the velocity change is not only related to the well-documented nonlinear response of the shallow layers to strong motion. Wegler et al. (2009) reached a similar conclusion on the existence of a change at depth for the sudden drop in velocity observed after the 2004 Mw 6.6 mid-Niigata earthquake in Japan. Chen et al. (2010) and Froment et al. (2013) studied the case of the 2008 Mw 7.9 Wenchuan earthquake, and they also found a velocity drop associated with the earthquake. They used broadband ambient-noise records and performed the measurements in the two separate period bands of 1–3 s and 12–20 s. The amplitude of the velocity drop was larger for the long-period band. As the measurements are performed with coda waves, they have the depth sensitivity of the predominant surface waves. The results therefore suggest that the change occurs also at depth and affects the middle crust. Furthermore, whether the temporal velocity change is related to deformation at depth can be investigated in the case of slow-slip events that produce significant deformation at depth without strong ground motion at the surface. Rivet et al (2011) found a transient change in the velocity at depth associated

with a large (Mw 7.5) slow-slip event on the Mexican subduction.

Despite promising evidence for the feasibility of monitoring deformation at depth with seismic ambient noise, it is noticeable that the origin of the changes can be obscured by the coincidence of signals of tectonic and hydrological origins (e.g., Froment et al., 2013; Yu and Hung, 2012).

1.12.8 Conclusions

Ambient-noise correlation is emerging as a new tool in seismic data processing. It is complementary to the traditional use of earthquake or active source records. The correlation of ambient-noise records at distant points can be regarded, under certain conditions, as the virtual seismogram recorded at one point if a source was acting at the other.

Physical representations have been provided that allow the reader to have an intuitive understanding of the method. The emergence of the Green's function in cross-correlation is the expression of the fundamental properties of wave fields. This is illustrated by the analogy with time-reversal mirrors that have shown the reconstruction of converging and diverging Green's functions in laboratory experiments. A geometrical interpretation has also been presented that shows that source averaging tends to select the contribution of sources located in the end-fire lobes. Mathematical results have been presented that show that the construction of virtual seismograms is rigorous, and that the complete deterministic response of Earth can be extracted from the records at distant points.

In practice, the ambient noise is produced by sources that are unevenly distributed. In general, this results in incomplete or improper reconstruction. We have analyzed the impact of a nonisotropic distribution of incident noise intensity on the travel times measured on correlations. There is bias, but it is accurately predictable, meaning that corrections can be applied when necessary. With realistic distributions, the method is robust and the bias in the travel time is acceptable for most imaging applications.

The presence of scattering because of the heterogeneous nature of Earth results in complexity of the seismic wave field. As this complexity tends to spread the wave energy over a wide range of directions and to enhance the conversion between the types of waves, it also has a positive role for the correlation of noise. For long lapse times, the field becomes diffuse, having in itself the properties sufficient to obtain the Green's function by correlation. Theoretically, a single source would be sufficient to produce an equipartition field, with its two-point average correlation being the Green's function. This can be understood by considering the scatterers as secondary sources that are uniformly distributed in the medium. With actual normalized noise records, the ballistic waves produced by noise sources are supplemented by the scattered waves of Earth's heterogeneity.

The relatively easy extraction of surface waves by the correlation of noise records has made it possible to apply ambient surface tomography in different places around the world. With this technique, high-resolution crustal models have been proposed, including for shear-wave velocity, anisotropy, and attenuation. Applications have been realized at different scales. Based on the general mathematical properties discussed in Section 1.12.4, and the observation of a teleseismic body-wave component in the noise records, the reconstruction of body waves is expected and has been confirmed by recent studies. This opens the way to the generalization of ambient-noise tomography to all types of waves, including deep phases.

As ambient-noise cross-correlation can be repeated at different dates, these cross-correlations can be used to monitor slight changes in the elastic properties of the crust. The late part of correlations, corresponding to the coda waves, computed at different dates are very stable and allow for the measuring of slight relative changes in seismic speeds, as small as 10^{-4}. Changes in seismic velocity have been observed after large earthquakes, including slow-slip events, in several studies. Velocity drops have been proposed to be precursories of volcanic eruptions and landslides.

The exploitation of ambient seismic noise is an emerging field. The huge data sets produced nowadays by dense permanent and temporary networks offer new opportunities for the development of innovative techniques to construct virtual seismograms that correspond to paths in regions of the planet that are poorly covered. Ambient-noise analysis will continue to provide new insights into the structure of Earth and into its continuous evolution.

References

Aki K (1957) Space and time spectra of stationary stochastic waves with special reference to microtremors. *Bulletin of the Earthquake Research Institute* 35: 415–456.

Ardhuin F, Stutzmann E, Schimmel M, and Mangeney A (2011) Ocean wave sources of seismic noise. *Journal of Geophysical Research* 116: C09004. http://dx.doi.org/10.1029/2011JC006952.

Baig AM, Campillo M, and Brenguier F (2009) Denoising seismic noise cross correlations. *Journal of Geophysical Research* 114: B08310. http://dx.doi.org/10.1029/2008JB006085.

Bensen GD, Ritzwoller MH, Barmin MP, et al. (2007) Processing seismic ambient noise data to obtain reliable broad-band surface wave dispersion measurements. *Geophysical Journal International* 169: 1239–1260.

Bonnefoy-Claudet S, Cotton F, and Bard P-Y (2006) The nature of noisewavefield and its applications for site effect studies—A literature review. *Earth-Science Reviews* 79: 205–227.

Boué P, Poli P, Campillo M, Pedersen H, Briand X, and Roux P (2013) Teleseismic correlations of ambient seismic noise for deep global imaging of the Earth. *Geophysical Journal International* 194: 844–848.

Brenguier F, Campillo M, Hadziioannou C, Shapiro N, Nadeau RM, and Larose E (2008a) Postseismic relaxation along the San Andreas fault at Parkfield from continuous seismological observations. *Science* 321(5895): 1478–1481.

Brenguier F, Shapiro NM, Campillo M, et al. (2008b) Towards forecasting volcanic eruptions using seismic noise. *Nature Geoscience* 1: 126–130. http://dx.doi.org/10.1038/ngeo104.

Brenguier F, Shapiro NM, Campillo M, Nercessian A, and Ferrazzini V (2007) 3-D surface wave tomography of the Piton de la Fournaise volcano using seismic noise correlations. *Geophysical Research Letters* 34: L02305. http://dx.doi.org/10.1029/2006GL028586.

Campillo M (2006) Phase and correlation in 'random' seismic fields and the reconstruction of the Green function. *Pure and Applied Geophysics* 163: 475–502.

Campillo M and Margerin L (2010) Mesoscopic seismic waves. In: Wright M and Weaver R (eds.) *New Directions in Linear Acoustics and Vibration in Quantum Chaos, Random Matrix Theory and Complexity*. Cambridge, MA: Cambridge University Press.

Campillo M and Paul A (2003) Long-range correlations in the seismic coda. *Science* 299: 547–549.

Chen J, Froment B, Liu QY, and Campillo M (2010) Distribution of seismic wave speed changes associated with the 12 May 2008 Mw 7.9 Wenchuan earthquake.

Geophysical Research Letters 37: L18302. http://dx.doi.org/10.1029/2010GL044582.
Claerbout J (1968) Synthesis of a layered medium from its acoustic transmission response. *Geophysics* 33: 264–269.
Clarke D, Zaccarelli L, Shapiro NM, and Brenguier F (2011) Assessment of resolution and accuracy of the moving window cross spectral technique for monitoring crustal temporal variations using ambient seismic noise. *Geophysical Journal International* 186(2): 867–882. http://dx.doi.org/10.1111/j.1365-246X.2011.05074.x.
Colin de Verdière Y (2009) Semiclassical analysis and passive imaging. *Nonlinearity* 22: R45–R75.
Colin de Verdière Y (2011) A semi-classical calculus of the correlations. *Compte Rendus Geoscience* 343: 496–501.
Courtland R (2008) Harnessing the hum. *Nature* 453: 146–148. http://dx.doi.org/10.1038/453146a.
Cupillard P and Capdeville Y (2010) On the amplitude of surface waves obtained by noise correlation and the capability to recover the attenuation: A numerical approach. *Geophysical Journal International* 181: 1687–1700.
Cupillard P, Stelhy L, and Romanowicz B (2011) The one-bit noise correlation: A theory based on the concepts of coherent and incoherent noise. *Geophysical Journal International* 184: 1397–1414.
Curtis A, Behr Y, Entwistle E, Galetti E, Townend J, and Bannister S (2012) The benefit of hindsight in observational science: Retrospective seismological observations. *Earth and Planetary Science Letters* 345–348: 212–220.
Curtis A and Halliday D (2010) Source–receiver wave field interferometry. *Physical Review E* 81(4): 046601-1–046601-10. http://dx.doi.org/10.1103/PhysRevE.81.046601.
Derode A, Larose E, Campillo M, and Fink M (2003a) How to estimate the Green's function of a heterogeneous medium between two passive sensors? Application to acoustic waves. *Applied Physics Letters* 83(15): 3054–3056.
Derode A, Larose E, Tanter M, et al. (2003b) Recovering the Green's function from field-field correlations in an open scattering medium. *Journal of the Acoustical Society of America* 113: 2973–2976.
Draganov D, Campman X, Thorbecke J, Verdel A, and Wapenaar K (2009) Reflection images from ambient seismic noise. *Geophysics* 74: 63–67.
Duvall TL Jr., Jefferies SM, Harvey JW, and Pomerantz MA (1993) Time–distance helioseismology. *Nature* 362(6419): 430.
Fink M (1992) Time reversal of ultrasonic fields – Part I: Basic principles. *IEEE Transactions on Ultrasonics, Ferroelectrics, and Frequency Control* 39(5): 555–566.
Friederich A, Kruger F, and Klinge K (1998) Ocean-generated microseismic noise located with the GRFO array. *Journal of Seismology* 2: 47–64.
Froment B, Campillo M, Chen JH, and Liu QY (2013) Deformation at depth associated with the May 12, 2008 Mw 7.9 Wenchuan earthquake from seismic ambient noise monitoring. *Geophysical Research Letters* 40: 78–82. http://dx.doi.org/10.1029/2012GL053995.
Froment B, Campillo M, and Roux P (2011) Reconstructing the Green's function through iteration of correlations. *Comptes Rendus Geoscience* 343(8–9): 623–632. http://dx.doi.org/10.1016/j.crte.2011.03.001.
Froment B, Campillo M, Roux P, Gouedard P, Verdel A, and Weaver RL (2010) Estimation of the effect of nonisotropically distributed energy on the apparent arrival time in correlations. *Geophysics* 75: SA85–SA93.
Fukao Y, Nishida K, and Kobayashi N (2010) Seafloor topography, ocean infragravity waves, and background Love and Rayleigh waves. *Journal of Geophysical Research* 115: B04302. http://dx.doi.org/10.1029/2009JB006678.
Gallot T, Catheline S, Roux P, and Campillo M (2012) A passive inverse filter for Green's function retrieval. *Journal of the Acoustical Society of America* 131(1): EL21–EL27. http://dx.doi.org/10.1121/1.3665397.
Garnier J and Papanicolaou G (2009) Passive sensor imaging using crosscorrelations of noisy signals in a scattering medium. *SIAM Journal on Imaging Sciences* 2(2): 396–437.
Gerstoft P, Shearer PM, Harmon N, and Zhang J (2008) Global P, PP, and PKP wave microseisms observed from distant storms. *Geophysical Research Letters* 35: L23307. http://dx.doi.org/10.1029/2008GL036111.
Godin OA (2007) Emergence of the acoustic Green's function from thermal noise. *Journal of the Acoustical Society of America* 121: EL96.
Gouédard P, Roux P, Campillo M, and Verdel A (2008a) Convergence of the two-points correlation function toward the Green's function in the context of a prospecting dataset. *Geophysics* 73(6): V47–V53.
Gouédard P, Stehly L, Brenguier F, et al. (2008b) Cross-correlation of random fields: Mathematical approach and applications. *Geophysical Prospecting* 56: 375–393.
Gutenberg B (1924) Die seismischen Bodenunruhe. *Samml. Geophysikalischer Schr.* 3: 1–69.
Gutenberg B (1958) Microseisms. *Advances in Geophysics* 5: 53–92.
Gutenberg B and Mainka C (1924) *Sammlung geophysikalischer Schriften*, 3rd edn. Berlin: Gebr. Borntraeger.
Hadziioannou C, Larose E, Baig A, Roux P, and Campillo M (2011) Improving temporal resolution in ambient noise monitoring of seismic wave speed. *Journal of Geophysical Research* 116: B07304. http://dx.doi.org/10.1029/2011JB008200.
Hadziioannou C, Larose E, Coutant O, Roux P, and Campillo M (2009) Stability of monitoring weak changes in multiply scattering media with ambient noise correlation: Laboratory experiments. *Journal of the Acoustical Society of America* 125(6): 3688–3695.
Hanasoge SM (2013) The influence of noise source on cross-correlation amplitudes. *Geophysical Journal International* 192: 295–309.
Harmon N, Forsyth D, and Webb S (2007) Using ambient seismic noise to determine short period phase velocities and shallow shear velocities in young oceanic lithosphere. *Bulletin of the Seismological Society of America* 97(6): 2009–2023.
Haubrich RA, Munk WH, and Snodgrass FE (1963) Comparative spectra of microseisms and swell. *Bulletin of the Seismological Society of America* 53: 27–37.
Hennino R, Trégourès N, Shapiro N, et al. (2001) Observation of equipartition of seismic waves in Mexico. *Physical Review Letters* 86–15: 3447–3450.
Hillers G, Graham N, Campillo M, Kedar S, Landès M, and Shapiro N (2012) Global oceanic microseism sources as seen by seismic arrays and predicted by wave action models. *Geochemistry, Geophysics, Geosystems* 13: Q01021. http://dx.doi.org/10.1029/2011GC003875.
Huang H, Yao H, and van der Hilst RD (2010) Radial anisotropy in the crust of SE Tibet and SW China from ambient noise interferometry. *Geophysical Research Letters* http://dx.doi.org/10.1029/2010GL044981.
Ito Y and Shiomi K (2012) Seismic scatterers within subducting slab revealed from ambient noise autocorrelation. *Geophysical Research Letters* 39: L19303. http://dx.doi.org/10.1029/2012GL053321.
Kang TS and Shin JS (2006) Surface-wave tomography from ambient seismic noise of accelerograph networks in southern Korea. *Geophysical Research Letters*. 33: 1–5. http://dx.doi.org/10.1029/2006GL027044.
Kedar S, Longuet-Higgins M, Webb F, Graham N, Clayton R, and Jones C (2008) The origin of deep ocean microseisms in the North Atlantic Ocean. *Proceedings of the Royal Society A* 464: 777–793. http://dx.doi.org/10.1098/rspa.2007.0277.
Kobayashi N and Nishida K (1998) Continuous excitation of planetary free oscillations by atmospheric disturbances. *Nature* 395: 357–360. http://dx.doi.org/10.1038/26427.
Kurrle D and Widmer-Schnidrig R (2008) The horizontal hum of the Earth: A global background of spheroidal and toroidal modes. *Geophysical Research Letters* 35: L06304. http://dx.doi.org/10.1029/2007GL033125.
Landès M, Hubans F, Shapiro NM, Paul A, and Campillo M (2010) Origin of deep ocean microseisms by using teleseismic body waves. *Journal of Geophysical Research* 115: B05302. http://dx.doi.org/10.1029/2009JB006918.
Larose E, De Rosny J, Margerin L, Anache D, Gouédard P, Campillo M, and Van Tiggelen B (2006a) Observation of multiple scattering of kHz vibrations in a concrete structure and application to monitoring weak change. *Physical Review E* 73: 016609.
Larose E, Khan A, Nakamura Y, and Campillo M (2005) Lunar subsurface investigated from correlation of seismic noise. *Geophysical Research Letters*. http://dx.doi.org/10.1029/2005GL023518.
Larose E, Margerin L, Derode A, et al. (2006b) Correlation of random wave fields: An interdisciplinary review. *Geophysics* 71(4): SI11–SI21. http://dx.doi.org/10.1190/1.2213356.
Larose E, Margerin L, van Tiggelen BA, and Campillo M (2004) Observation of weak localization of seismic waves. *Physical Review Letters* 93(4). http://dx.doi.org/10.1103/Phys Rev Lett.93.048501.
Larose E, Roux P, Campillo M, and Derode A (2008) Fluctuations of correlations and Green's function reconstruction: Role of scattering. *Journal of Applied Physics* 103: 114907.
Lawrence JF and Prieto GA (2011) Attenuation tomography in the western United States from ambient seismic noise. *Journal of Geophysical Research* 116: B06302. http://dx.doi.org/10.1029/2010JB007836.
Li H, Bernardi F, and Michelini A (2010) Surface wave dispersion measurements from ambient seismic noise analysis in Italy. *Geophysical Journal International* 180: 1242–1252.
Lin FC, Ritzwoller MH, and Snieder R (2009) Eikonal tomography: Surface wave tomography by phase front tracking across a regional broad-band seismic array. *Geophysical Journal International* 177: 1091–1110.
Lin F-C, Tsai VC, Schmandt B, Duputel Z, and Zhan Z (2013) Extracting seismic core phases with array interferometry. *Geophysical Research Letters* 40: 1049–1053. http://dx.doi.org/10.1002/grl.50237.
Lobkis OI and Weaver RL (2001) On the emergence of the Green's function in the correlations of a diffuse field. *Journal of the Acoustical Society of America* 110: 3011–3017.

Lobkis O and Weaver R (2003) Coda-wave interferometry in finite solids: Recovery of P-to-S conversion rates in an elastodynamic billiard. *Physical Review Letters* 90(25): 254302.

Longuet-Higgins MS (1950) A theory of the origin of microseisms. *Philosophical Transactions of the Royal Society of London* 243: 1–35.

Ma S and Beroza GC (2012) Ambient-field Green's functions from asynchronous seismic observations. *Geophysical Research Letters* 39: L06301. http://dx.doi.org/10.1029/2011GL050755.

Mainsant G, Larose E, Brönnimann C, Jongmans D, Michoud C, and Jaboyedoff M (2012) Ambient seismic noise monitoring of a clay landslide: Toward failure prediction. *Journal of Geophysical Research* 117: F01030. http://dx.doi.org/10.1029/2011JF002159.

Margerin L, Campillo M, Van Tiggelen BA, and Hennino R (2009) Energy partition of seismic coda waves in layered media: Theory and application to Pinyon Flats Observatory. *Geophysical Journal International* 177(2): 571–585.

Margerin L and Sato H (2011) Reconstruction of multiply-scattered arrivals from the cross-correlation of waves excited by random noise sources in a heterogeneous dissipative medium. *Wave Motion* 48: 146–160.

Meier U, Brenguier F, and Shapiro N (2010) Detecting seasonal variations in seismic velocities within Los Angeles basin from correlations of ambient seismic noise. *Geophysical Journal International* 181: 985–996. http://dx.doi.org/10.1111/j.1365-246X.2010.04550.x.

Miche A (1944) Mouvements ondulatoires de la mer en profondeur croissante ou décroissante: Première partie. Mouvements ondulatoires périodiques et cylindriques en profondeur constante. *Ann Ponts Chaussées* 114: 42–78.

Nakahara H (2006) A systematic study of the theoretical relations between spatial correlations and Green's function in one-, two- and three-dimensional random scalar wavefields. *Geophysical Journal International* 167: 1097–1105.

Nishida K (2013) Global propagation of body waves revealed by cross-correlation analysis of seismic hum. *Geophysical Research Letters* 40(9): 1691–1696.

Nishida K, Kawakatsu H, Fukao Y, and Obara K (2008a) Background Love and Rayleigh waves simultaneously generated at the Pacific Ocean floors. *Geophysical Research Letters* 35: L16307.

Nishida K, Kawakatsu H, and Obara K (2008b) Three-dimensional crustal S-wave velocity structure in Japan using microseismic data recorded by Hi-net tiltmeters. *Journal of Geophysical Research* 113(B10). http://dx.doi.org/10.1029/2007JB005395.

Niu F, Silver PG, Daley TM, Cheng X, and Majer EL (2008) Preseismic velocity changes observed from active source monitoring at the Parkfield SAFOD drill site. *Nature* 454. http://dx.doi.org/10.1038/nature07111.

Paul A, Campillo M, Margerin L, Larose E, and Derode A (2005) Empirical synthesis of time-asymmetrical Green function from the correlation of coda waves. *Journal of Geophysical Research* 110. http://dx.doi.org/10.1039/2004JB003521.

Peterson J (1993) Observations and modeling of seismic background noise. *U.S. Geological Survey Open File Report* 93–322: 1.

Picozzi M, Parolai S, Bindi D, and Strollo A (2008) Characterization of shallow geology by high-frequency seismic noise tomography. *Geophysical Journal International* 176(1): 164–174.

Poli P, Campillo M, Pedersen H, and the Lapnet Working Group (2012a) Body wave imaging of the Earth's mantle discontinuities from ambient seismic noise. *Science* 338: 1063–1066.

Poli P, Pedersen HA, Campillo M, and the POLENET/LAPNET Working Group (2012b) Emergence of body waves from cross-correlation of short period seismic noise. *Geophysical Journal International* 188: 549–558. http://dx.doi.org/10.1111/j.1365-246X.2011.05271.x.

Poli P, Pedersen HA, Campillo M, and the POLENET/LAPNET Working Group (2012c) Noise directivity and group velocity tomography in a region with small velocity contrasts: The northern Baltic Shield. *Geophysical Journal International* 192(1): 413–424.

Poupinet G, Ellsworth WL, and Frechet J (1984) Monitoring velocity variations in the crust using earthquake doublets: An application to the Calaveras Fault, California. *Journal of Geophysical Research* 89: 5719–5731.

Prieto GA, Denolle M, Lawrence JF, and Beroza GC (2011) On the amplitude information carried by ambient seismic field. *Compte Rendus Geoscience* 343: 600–614.

Prieto GA, Lawrence JF, and Beroza GC (2009) Anelastic Earth structure from the coherency of the ambient seismic field. *Journal of Geophysical Research* 114, B07303.

Ratdomopurbo A and Poupinet G (1995) Monitoring a temporal change of seismic velocity in a volcano: Application to the 1992 eruption of Mt. Merapi (Indonesia). *Geophysical Research Letters* 22: 775–778.

Reasenberg P and Aki K (1974) A precise, continuous measurement of seismic velocity for monitoring in situ stress. *Journal of Geophysical Research* 79(2): 399–406.

Renalier F, Jongmans D, Campillo M, and Bard P-Y (2010) Shear wave velocity imaging of the Avignonet landslide (France) using ambient noise cross correlation. *Journal of Geophysical Research* 115: F03032. http://dx.doi.org/10.1029/2009JF001538.

Rhie J and Romanowicz B (2004) Excitation of Earth's continuous free oscillations by atmosphere–ocean–seafloor coupling. *Nature* 431: 552–554.

Rickett J and Claerbout J (1999) Acoustic daylight imaging via spectral factorization: Helioseismology and reservoir monitoring. *The Leading Edge* 18: 957–960.

Ritzwoller MH, Lin FC, and Shen W (2011) Ambient noise tomography with a large seismic array. *Compte Rendus Geoscience* 343(8): 558–570. http://dx.doi.org/10.1016/j.crte.2011.03.007.

Rivet D, Campillo M, Shapiro NM, et al. (2011) Seismic evidence of nonlinear crustal deformation during a large slow slip event in Mexico. *Geophysical Research Letters* 38: L08308. http://dx.doi.org/10.1029/2011GL047151.

Roux P and Kupermann WA (2004) Extraction of coherent wavefronts from ocean ambient noise. *Journal of the Acoustical Society of America* 116(4): 1995–2003.

Roux P, Sabra KG, Gerstoft P, Kuperman WA, and Fehler MC (2005a) P-waves from cross-correlation of seismic noise. *Geophysical Research Letters* 32: L19303. http://dx.doi.org/10.1029/2005GL023803.

Roux P, Sabra KG, Kuperman WA, and Roux A (2005b) Ambient noise cross correlation in free space: Theoretical approach. *Journal of the Acoustical Society of America* 117: 79–84.

Ryzhik LV, Papanicolau GC, and Keller JB (1996) Transport equations for elastic and other waves in random media. *Wave Motion* 24: 327–370.

Sabra KG, Gerstoft P, Roux P, Kuperman WA, and Fehler MC (2005a) Extracting time-domain Green's function estimates from ambient seismic noise. *Geophysical Research Letters* 32: L03310. http://dx.doi.org/10.1029/2004GL021862.

Sabra KG, Gerstoft P, Roux P, Kuperman WA, and Fehler MC (2005b) Surface wave tomography from microseisms in southern California. *Geophysical Research Letters* 32: L14311. http://dx.doi.org/10.1029/2005GL023155.

Sánchez-Sesma FJ and Campillo M (2006) Retrieval of the Green function from cross-correlation: The canonical elastic problem. *Bulletin of the Seismological Society of America* 96: 1182–1191.

Sànchez-Sesma FJ, Pérez-Ruiz JA, Campillo M, and Luzòn F (2006) Elastodynamic 2D Green function retrieval from cross-correlation: Canonical inclusion problem. *Geophysical Research Letters* 33: L13305. http://dx.doi.org/10.1029/2006GL026454.

Sato H, Fehler MC, and Maeda T (2012) *Seismic Wave Propagation and Scattering the Heterogeneous Earth*, 2nd edn. New York: Springer.

Saygin E and Kennett BLN (2010) Ambient seismic noise tomography of Australian continent. *Tectonophysics* 481: 116–125.

Schimmel M, Stutzmann E, and Gallart J (2011) Using instantaneous phase coherence for signal extraction from ambient noise data at a local to a global scale. *Geophysical Journal International* 184: 494–506. http://dx.doi.org/10.1111/j.1365-246X.2010.04861.

Schuster GT (2006) *Seismic Interferometry*. Cambridge, UK: Cambridge University Press, 2009.

Sens-Schönfelder C and Wegler U (2006) Passive image interferometry and seasonal variations of seismicvelocities at Merapi Volcano, Indonesia. *Geophysical Research Letters* 33, L21302.

Shapiro NM and Campillo M (2004) Emergence of broadband Rayleigh waves from correlations of the seismic ambient noise. *Geophysical Research Letters* 31: L07614. http://dx.doi.org/10.1029/2004GL019491.

Shapiro NM, Campillo M, Stehly L, and Ritzwoller MH (2005) High-resolution surface-wave tomography from ambient seismic noise. *Science* 307: 1615–1618. http://dx.doi.org/10.1126/science.1108339.

Snieder R (2004) Extracting the Green's function from the correlation of coda waves: A derivation based on stationary phase. *Physical Review E* 69: 046610.

Snieder R (2007) Extracting the Green's function of attenuating heterogeneous media from uncorrelated waves. *Journal of the Acoustical Society of America* 121: 2637–2643.

Snieder R, Gret A, Douma H, and Scales J (2002) Coda wave interfermetry for estimating nonlinear behavior in seismic velocity. *Science* 295: 2253–2255.

Snieder R, Wapenaar K, and Larner K (2006) Spurious multiples in seismic interferometry of primaries. *Geophysics* 71: SI111–SI124.

Spetzler J and Snieder R (2004) The Fresnel volume and transmitted waves. *Geophysics* 69: 653–663.

Stehly L, Campillo M, Froment B, and Weaver RL (2008) Reconstructing Green's function by correlation of the coda of the correlation (C3) of ambient seismic noise. *Journal of Geophysical Research-Solid Earth* 113(B11): B11306.

Stehly L, Campillo M, and Shapiro NM (2006) A study for the seismic noise from its long-range correlation properties. *Journal of Geophysical Research* 111: B10306. http://dx.doi.org/10.1029/2005JB004237.

Stehly L, Campillo M, and Shapiro N (2007) Travel time measurements from noise correlation: Stability and detection of instrumental time shifts. *Geophysical Journal International* 171(1): 223–230. http://dx.doi.org/10.1111/j.1365-246X.2007.03492.x.

Stehly L, Cupillard P, and Romanowicz B (2011) Towards improving ambient noise tomography using simultaneously curvelet denoising filters and SEM simulation of ambient noise. *Compte Rendus Geoscienc* 343: 591–599.

Stehly L, Fry B, Campillo M, et al. (2009) Tomography of the Alpine region from observations of seismic ambient noise. *Geophysical Journal International* 178(1): 338–350.

Stockwell RG, Mansinha GL, and Lowe RP (1996) Localization of the complex spectrum: The S transform. *IEEE Transactions on Signal Processing* 44: 998–1001. http://dx.doi.org/10.1109/78.492555.

Tanimoto T, Um J, Nishida K, and Kobayashi N (1998) Earth's continuous oscillations observed on seismically quiet days. *Geophysical Research Letters* 25: 1553–1556. http://dx.doi.org/10.1029/98GL01223.

Tibuleac IM and von Seggern D (2012) Crust–mantle boundary reflectors in Nevada from ambient seismic noise autocorrelations. *Geophysical Journal International* 189: 493–500. http://dx.doi.org/10.1111/j.1365-246X.2011.05336.x.

Toksöz MN and Lacoss RT (1968) Microseisms: Mode structure and sources. *Science* 159: 872–873.

Tromp J, Luo Y, Hanasoge S, and Peter D (2010) Noise cross-correlation sensitivity kernels. *Geophysical Journal International* 183: 791–819.

Tsai VC (2009) On establishing the accuracy of noise tomography travel-time measurements in a realistic medium. *Geophysical Journal International* 178: 1555–1564. http://dx.doi.org/10.1111/j.1365-246X.2009.04239.x.

Van Vleck JH and Middleton D (1966) The spectrum of clipped noise. *Proceedings of the IEEE* 54: 2–19.

Verbeke J, Boschi L, Stehly L, Kissling E, and Michelini A (2012) High-resolution Rayleigh-wave velocity maps of central Europe from a dense ambient-noise data set. *Geophysical Journal International* 188: 1173–1187. http://dx.doi.org/10.1111/j.1365-246X.2011.05308.x.

Vinnik LP (1973) Sources of microseismic P waves. *Pure and Applied Geophysics* 103(1): 282–289.

Wapenaar K (2004) Retrieving the elastodynamic Green's function of an arbitrary inhomogeneous medium by cross correlation. *Physical Review Letters* 93(25): 254301-1–254301-4.

Wapenaar K (2006) Nonreciprocal Green's function retrieval by cross correlation. *Journal of the Acoustical Society of America* 120: EL7.

Wapenaar K, Draganov D, Snieder R, Campman X, and Verdel A (2010a) Tutorial on seismic interferometry. Part 1: Basic principles and applications. *Geophysics* 75: 75A195–75A209.

Wapenaar K and Fokkema J (2006) Green's function representations for seismic interferometry. *Geophysics* 71(4): SI33–SI46. http://dx.doi.org/10.1190/1.2213955.

Wapenaar K, Slob E, Snieder R, and Curtis A (2010b) Tutorial on seismic interferometry. Part 2: Underlying theory. *Geophysics* 75: 75A211–75A227.

Wapenaar K, van der Neut J, and Ruigrok E (2008) Passive seismic interferometry by multidimensional deconvolution. *Geophysics* 73: A51.

Weaver RL (1982) On diffuse waves in solid media. *Journal of the Acoustical Society of America* 71: 1608–1609.

Weaver RL, Froment B, and Campillo M (2009) On the correlation of non-isotropically distributed ballistic scalar diffuse waves. *Journal of the Acoustical Society of America* 126(4): 1817–1826.

Weaver RL, Hadziioannou C, Larose E, and Campillo M (2011) On the precision of noise correlation interferometry. *Geophysical Journal International* 185(3): 1384–1392. http://dx.doi.org/10.1111/j.1365-246X.2011.05015.x.

Weaver RL and Lobkis OI (2001) Ultrasonics without a source: Thermal fluctuation correlation at MHz frequencies. *Physical Review Letters* 87: 134301–134304.

Weaver RL and Lobkis OI (2004) Diffuse fields in open systems and the emergence of the Green's function. *Journal of the Acoustical Society of America* 116: 2731–2734.

Weemstra C, Boschi L, Goertz A, and Artman B (2013) Seimic attenuation from recordings of ambient noise. *Geophysics* 78: Q1–Q14. http://dx.doi.org/10.1190/GEO2012-0132.1.

Wegler U, Nakahara H, Sens-Schönfelder C, Korn M, and Shiomi K (2009) Sudden drop of seismic velocity after the 2004 Mw 6.6 mid-Niigata earthquake, Japan, observed with Passive Image Interferometry. *Journal of Geophysical Research* 114: B06305. http://dx.doi.org/10.1029/2008JB005869.

Wegler U and Sens-Schönfelder C (2007) Fault zone monitoring with passive image interferometry. *Geophysical Journal International* 168: 1029–1033. http://dx.doi.org/10.1111/j.1365-246X.2006.03284.x.

Yamamoto M and Sato H (2010) Multiple scattering and mode conversion revealed by an active seismic experiment at Asama volcano, Japan. *Journal of Geophysical Research* 115: B07304. http://dx.doi.org/10.1029/2009JB007109.

Yang Y, Ritzwoller MH, Levshin AL, and Shapiro NM (2007) Ambient noise Rayleigh wave tomography across Europe. *Geophysical Journal International* 168: 259–274.

Yao H, Beghein C, and van der Hilst RD (2008) Surface wave array tomography in SE Tibet from ambient seismic noise and two-station analysis – II. Crustal and upper-mantle structure. *Geophysical Journal International* 173: 205–219. http://dx.doi.org/10.1111/j.1365-246X.2007.03696.x.

Yao H, Gouédard P, McGuire J, Collins J, and van der Hilst RD (2011) Structure of young East Pacific Rise lithosphere from ambient noise correlation analysis of fundamental- and higher-mode Scholte–Rayleigh waves. *Comptes Rendus Geoscience de l'Académie des Sciences*. http://dx.doi.org/10.1016/j.crte.2011.04.004.

Yao H and Van der Hilst RD (2009) Analysis of ambient noise energy distribution and phase velocity bias in ambient noise tomography, with application to SE Tibet. *Geophysical Journal International* 179(2): 1113–1132. http://dx.doi.org/10.1111/j.1365-246X.2009.04329.x.

Yu T-C and Hung S-H (2012) Temporal changes of seismic velocity associated with the 2006 Mw 6.1 Taitung earthquake in an arc-continent collision suture zone. *Geophysical Research Letters* 39: L12307. http://dx.doi.org/10.1029/2012GL051970.

Zhan Z, Ni S, Helmberger DV, and Clayton RW (2010) Retrieval of moho reflected shear wave arrivals from ambient seismic noise. *Geophysical Journal International* 1: 408–420.

Zhang J, Gerstoft P, and Bromirski PD (2010) Pelagic and coastal sources of P-wave microseisms: Generation under tropical cyclones. *Geophysical Research Letters* 37: L15301. http://dx.doi.org/10.1029/2010GL044288.

Zheng S, Sun X, Song X, Yang Y, and Ritzwoller MH (2008) Surface wave tomography of China from ambient seismic noise correlation. *Geochemistry, Geophysics, Geosystems* 9: Q05020. http://dx.doi.org/10.1029/2008GC001981.

This page intentionally left blank

1.13 Crust and Lithospheric Structure - Seismic Structure of Mid-Ocean Ridges

RA Dunn, University of Hawaii at Manoa, Honolulu, HI, USA

© 2015 Elsevier B.V. All rights reserved.

1.13.1	**Introduction**	419
1.13.2	**Mantle Upwelling and Melting Beneath Oceanic Spreading Centers**	419
1.13.2.1	Depth Extent of Anomalous Structure	420
1.13.2.2	The Onset of Melting	422
1.13.2.3	Mantle Flow near Ridges	423
1.13.2.4	Passive Versus Buoyant Upwelling	424
1.13.2.5	Spreading Rate Dependence	425
1.13.2.6	Back-Arc Spreading Centers	427
1.13.3	**Formation of Oceanic Crust**	429
1.13.3.1	General Seismic Structure of the Oceanic Crust	429
1.13.3.2	Fast-Spreading Ridges	431
1.13.3.3	Intermediate-Spreading Ridges	436
1.13.3.4	Slow-Spreading Ridges	437
1.13.3.5	Ultraslow-Spreading Ridges	439
1.13.3.6	Regional Influences	441
1.13.3.7	Back-Arc Spreading Centers	441
1.13.4	**Remaining Unsolved Problems**	443
Acknowledgments		444
References		444

1.13.1 Introduction

Mid-ocean ridges mark the boundaries where oceanic plates separate from one another (Figure 1) and thus lie above upwelling regions of mantle circulation. The upwelling mantle undergoes pressure-release partial melting because the temperature of the mantle solidus decreases with decreasing pressure. The melt, being less viscous and less dense than the surrounding solid, segregates from the solid mantle and buoyantly rises to the surface, where it forms new, principally basaltic, oceanic crust. The crust and mantle cool at the surface by thermal conduction and hydrothermal circulation, which generates a strong thermal boundary layer, the lithosphere. As the lithosphere travels away from the ridge, it thickens via additional cooling, becomes denser, and subsides deeper into the underlying ductile asthenosphere. This aging process causes the oceans to double in depth toward continental margins and subduction zones. Mid-ocean ridges represent one of the most important geologic processes shaping the Earth: Over the last 200 million years, two-thirds of the Earth has been resurfaced through this process of seafloor spreading, either at conventional mid-ocean ridge spreading centers or at spreading centers in back-arc basins behind subduction zones; they are a primary means of geochemical differentiation in the Earth; and they drive vast hydrothermal systems that influence ocean water chemistry and support enormous ecosystems.

Around the global ridge system, new crust and lithosphere form along 55 000 total kilometers of ridge at rates that differ by more than a factor of 10 (Figures 1 and 2). This causes large differences in the nature of the magmatic, tectonic, and hydrothermal processes occurring along these ridges. For example, fast-spreading ridges, such as the East Pacific Rise (EPR), exhibit smooth topographic rises with more uniform magmatism, whereas slowly spreading ridges, such as the Mid-Atlantic Ridge (MAR) and Southwest Indian Ridge (SWIR), exhibit heavily faulted deep axial valleys and large variations in volcanic output with time and space. Such observations can be largely understood in the context of two basic processes: asthenospheric flow, which controls temperatures and melt production rates, and the balance between heat delivered to the ridge axis from below and heat extracted by conduction and hydrothermal circulation from above. Additional influences include global variations in mantle background temperature and volatile content, such as near hot spots. In back-arc settings, subducted lithosphere releases water and other elements into the mantle wedge above the subducted plate and below back-arc spreading centers. Consequently, as the back-arc spreading centers open over time, they sweep across strongly varying mantle compositional domains. This influences the degree of melting and the ultimate composition of the crust.

1.13.2 Mantle Upwelling and Melting Beneath Oceanic Spreading Centers

One of the early geodynamic questions about mid-ocean ridges was whether the upwelling is passive, driven simply by the viscous drag of separating plates, or active, a buoyantly rising limb of a convection cell. If global mantle convection is driven largely by cooling from above, then the downwelling limb of convection, in the form of sinking lithospheric slabs, is expected to be cooler than its surroundings and to extend deep into the mantle. If driven by heating from below, as from heat released from the core, then there should also be hot,

 http://dx.doi.org/10.1016/B978-0-444-53802-4.00011-7

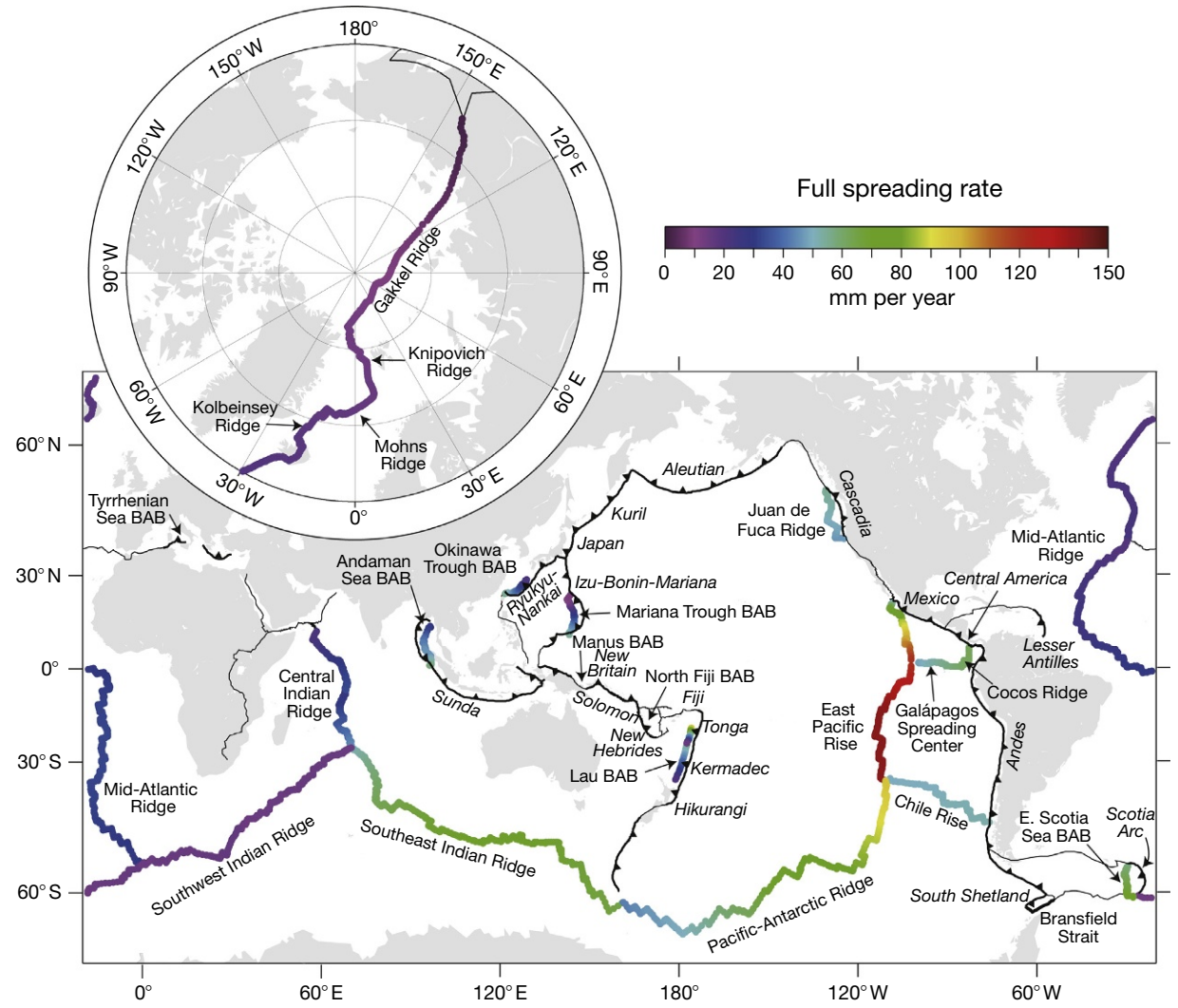

Figure 1 Mid-ocean ridges, active back-arc basins (BABs), and subduction zones of the world. Plate boundaries are from Bird (2003). Spreading rates along the mid-ocean ridges and back-arc spreading centers are calculated from Argus et al. (2011).

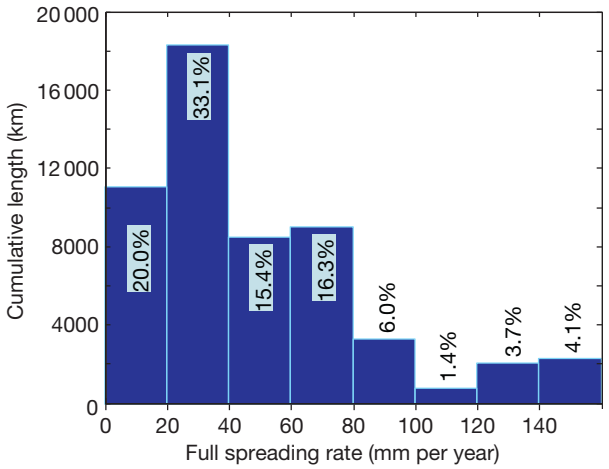

Figure 2 Cumulative length of spreading centers as a function of spreading rate. The percentage of the total length of all ridges (55 400 km) is indicated for each bin. Ridge lengths are calculated using the plate boundary model of Bird (2003) after removal of transform offsets. Spreading rates are calculated from Argus et al. (2011).

upwelling limbs rising from deep in the mantle. There are now a variety of geologic observations that favor dominantly passive mid-ocean ridges, such as the relatively uniform thickness and composition of the oceanic crust. Additionally, seismological studies have clearly shown that there are no deep low-velocity roots beneath typical spreading centers that could correspond to hot buoyant upwellings.

1.13.2.1 Depth Extent of Anomalous Structure

In the mantle, seismic wave velocity and attenuation (energy loss during wave travel) depend on mineralogy, pressure, temperature, and the presence of melt and volatiles; in the upper mantle, lateral velocity and attenuation changes are most often attributed to only temperature and/or melt. Global and large regional seismic studies find anomalously low seismic velocities (e.g., Conley and Dunn, 2011; Gu et al., 2005b; Maggi et al., 2006a,b; Nishimura and Forsyth, 1989; Weeraratne et al., 2007) and high attenuation (e.g., Dalton et al., 2008; Romanowicz, 1994) beneath mid-ocean ridges in the upper mantle, as compared to values at the same depth beneath

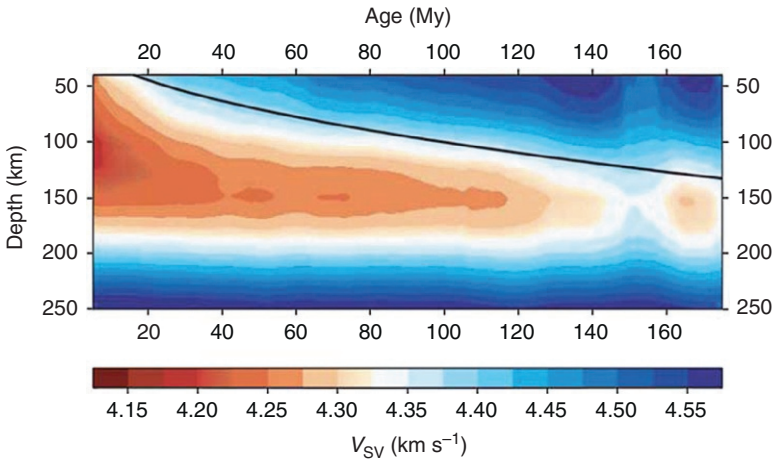

Figure 3 Average shear velocity in the upper mantle as a function of age of the seafloor in the Pacific, based on Rayleigh wave tomography. This smoothed image was generated by averaging over 10 Ma sliding age windows. The black line indicates the base of the lithosphere predicted for a cooling half-space thermal model. Reproduced from Maggi A, Debayle E, Priestley K, and Barruol G (2006a) Multimode surface waveform tomography of the Pacific Ocean: A closer look at the lithospheric cooling signature. *Geophysical Journal International* 166: 1384–1397.

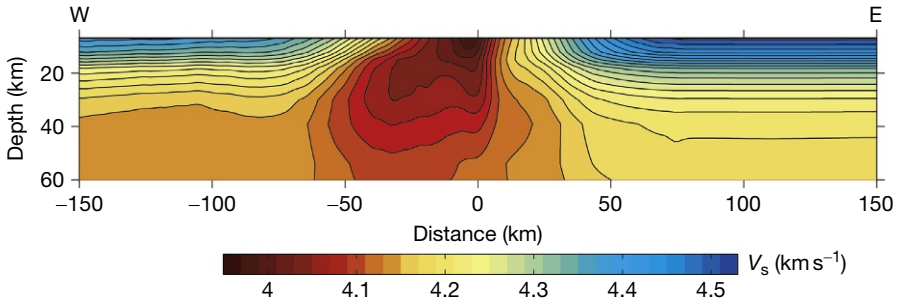

Figure 4 Short-period Love wave image of the upper mantle beneath the southern East Pacific Rise (reproduced from Dunn RA and Forsyth DW (2003) Imaging the transition between the region of mantle melt generation and the crustal magma chamber beneath the southern East Pacific Rise with short-period Love waves. *Journal of Geophysical Research* 108(B7): 2352. http://dx.doi.org/10.1029/2002JB002217). A broad asymmetric low SH-wave anomaly occurs beneath the ridge that is flanked by high lithospheric velocities at shallow depths. The lowest velocities (<4 km s^{-1}) occur just beneath the base of the crust (top of the figure).

older seafloor (**Figure 3**). The lateral velocity contrasts can largely be explained by an increase in the thickness of the thermal boundary layer, or lithosphere, with age, but beneath the ridges, the velocities are sufficiently low to imply the presence of a small amount of melt in the asthenosphere. Minimum isotropic shear-wave velocities, ~4 km s^{-1}, are often found between 40 and 80 km depth. However, regional seismic studies using relatively short-period surface waves, which provide increased depth resolution of the upper ~60 km, indicate that the velocity minimum is shallower and more pronounced directly beneath ridges, where melts might aggregate as they rise toward the surface (**Figure 4**; Conley and Dunn, 2011; Dunn and Forsyth, 2003).

Beneath mid-ocean ridges, the anomalous velocity structure appears to extend no deeper than about 200 km. There are several lines of evidence. The thickness of the mantle transition zone, located between seismic discontinuities at 410 and 660 km depth, is one indicator of upper mantle temperature, because the two discontinuities are governed by phase changes with Clapeyron slopes of opposite sign. Global maps of the topography of these discontinuities, based on precursors to SS seismic phases resulting from underside reflections (SdS phases), show a correlation of greater transition zone thickness with the location of subduction zones, indicating colder temperatures in the vicinity of descending slabs. However, there is no correlation of transition zone thickness with mid-ocean ridges (Flanagan and Shearer, 1998; Lee and Grand, 1996; Shearer, 2000). A local study of P-to-SV conversions at these discontinuities beneath the EPR, using receiver function analysis of data recorded on an array of ocean-bottom seismographs, found that the time difference between the P410s and the P660s conversions is almost exactly equal to the global average (Shen et al., 1998), indicating that any thermal anomaly is confined to the upper mantle above the 410 km discontinuity. A study of multiple S phases in the vicinity of the EPR also found no vertical displacement of either the 410 or the 660 km discontinuities (Melbourne and Helmberger, 2002).

Global and regional tomographic studies based on body-wave travel times sometimes show mid-ocean ridge structure extending down to depths of 300–400 km (Masters et al., 2000), but because ray paths in the upper mantle are relatively steep, there typically is a trade-off between the amplitude of the

anomaly and its depth extent. In the inversion of travel times to obtain velocity structure, if velocity variations are damped to prevent unrealistic oscillations, then the tendency is to force the model to smear large-amplitude shallow anomalies beyond their actual depth extent. In one body-wave study, using an array of seafloor seismographs that crossed the EPR (Hammond and Toomey, 2003), a 'squeezing' test was performed in which model anomalies were progressively limited to shallower depths. The variation in quality of data fit showed that the anomalous structure extends to no more than 200–300 km depth. Rayleigh waves with periods in the range ~15–160 s have the best sensitivity to the depth distribution of shallow mantle velocities. Global or regional tomographic models based on Rayleigh surface waves or surface and body waves combined (Conley and Dunn, 2011; Ekström, 2000; Maggi et al., 2006a; Masters et al., 2000; Nishimura and Forsyth, 1989; Priestley and McKenzie, 2006; Ritsema, 2005; Ritzwoller et al., 2004; Zhou et al., 2006) find that the anomalous structure in the vicinity of most ridges is confined to the uppermost 150–200 km of the mantle (**Figure 3**), except perhaps in the vicinity of a large hot spot like Iceland (**Figure 5**).

1.13.2.2 The Onset of Melting

If low velocities beneath the ridges indicate the presence of melt, then the bottom of the low-velocity zone should indicate the onset of melting at the solidus. However, the bottom is more difficult to define than the top because the resolution of surface waves decreases with increasing depth and the transition may be subtle if the initial melt fraction is very small. In addition, seismic velocities naturally increase with increasing depth and pressure even away from mid-ocean ridges. Beneath the point of minimum asthenospheric velocity, velocities increase rapidly with depth, though the velocity gradient decreases between ~100 and 150 km depth (e.g., Gu et al., 2005b; Maggi et al., 2006a; Nishimura and Forsyth, 1989; Weeraratne et al., 2007). This change in gradient may correspond to the solidus.

One interpretation of the seismological observations that is consistent with experiments on the melting of peridotite and observations of electrical conductivity structure near the EPR (Evans et al., 2005; Key et al., 2013) is that melting begins in the upwelling mantle in the presence of a small amount of water dissolved in the solid crystals at depths of 100–150 km.

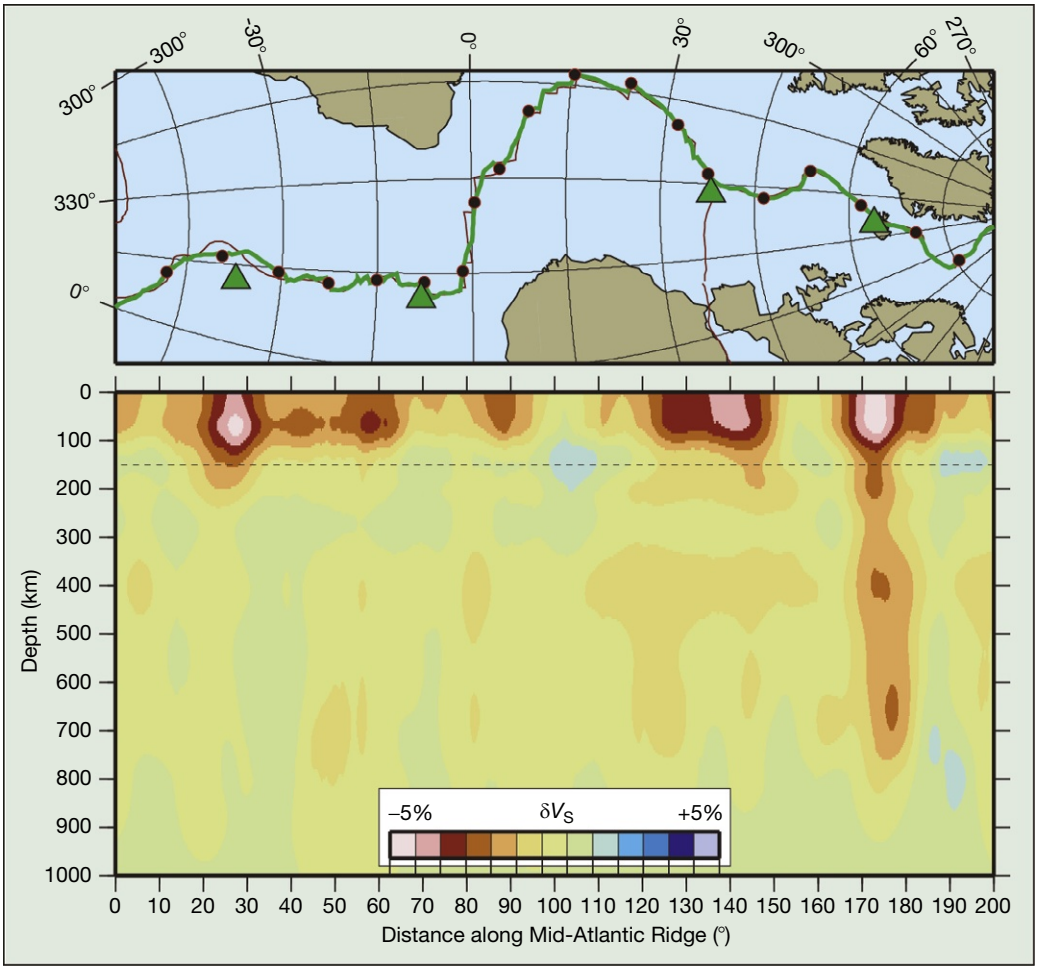

Figure 5 Mantle S-wave velocity structure beneath the Mid-Atlantic Ridge and neighboring hot spots. (Bottom) Shear-wave profile along the ridge relative to the global average. (Top) Green line indicates location of the profile; circles occur at 10° intervals. Green triangles indicate hot spot locations. Anomalous structure is largely limited to depths <150 km (dashed line) except beneath Iceland. Reproduced from Montagner J-P and Ritsema J (2001) Interactions between ridges and plumes. *Science* 294: 1472–1473.

The melt concentration gradually increases upward as melting proceeds above the damp solidus, but melt concentration and total degree of melting remain small below the dry solidus. Water behaves like an incompatible element and tends to concentrate in the melt, so as melting proceeds, the matrix dehydrates. Around 60–80 km depth, the rate of melting increases as the dry solidus is passed, but the additional melt migrates upward toward the ridge axis leaving only a small (less than ~1%) melt fraction and a dehydrated matrix behind.

1.13.2.3 Mantle Flow near Ridges

Seismic anisotropy offers clues to the form of mantle flow beneath mid-ocean ridges. Observations of seismic anisotropy in the upper mantle are often attributed to a strain-induced lattice-preferred orientation of olivine that occurs during mantle flow. Olivine is elastically anisotropic and the general alignment of the 'fast' *a*-axis of olivine grains results in detectable seismic anisotropy. From a seismic detection standpoint, two basic forms of anisotropy have been identified. One is radial anisotropy (SV$\neq$SH), also called transverse isotropy, which is typically detected via a discrepancy between Love and Rayleigh wave phase velocities relative to an isotropic model. (Love waves are sensitive to horizontally propagating, horizontally polarized S-wave speeds, or SH, while Rayleigh waves are sensitive to horizontally propagating, vertically polarized S-wave speeds, or SV.) The other is azimuthal anisotropy, which is detected by an azimuthal variation in body-wave travel times and surface-wave phase velocities, and via shear-wave splitting.

A characteristic found consistently in global and large-scale regional models of oceanic mantle structure is radial anisotropy down to about 250 km depth. Below oceanic lithosphere, SH generally exceeds SV by a few percent (Kustowski et al., 2008; Nishimura and Forsyth, 1989; Shapiro and Ritzwoller, 2002), a pattern expected for horizontal flow. Near mid-ocean ridges, surface-wave studies detect azimuthal anisotropy in the uppermost mantle with the fast direction for the propagation of Rayleigh waves approximately in the spreading direction, as predicted for the deformation associated with upwelling and subsequent plate separation at spreading centers (Blackman and Kendall, 1997; Forsyth, 1975; Maggi et al., 2006b; Montagner and Tanimoto, 1991; Ritzwoller et al., 2004) that aligns the olivine *a*-axis horizontally in a direction perpendicular to the ridge.

At shallow depths within the lithosphere and low-velocity zone, regional tomographic studies have reported a reduction in radial anisotropy in young seafloor near the EPR, although SH is still faster than SV. Along the southern EPR, azimuthal anisotropy of short-period Rayleigh waves reaches a minimum at the ridge axis (Forsyth et al., 1998), consistent with either a component of vertical upwelling or not yet established horizontal flow. In that area, the smallest shear-wave splitting delays were also found immediately adjacent to the axis, but the most pronounced pattern in the splitting data is an asymmetry in splitting delays across the ridge; the fast direction is roughly perpendicular to the ridge on both sides, but splitting delays are nearly twice as large on the Pacific plate as on the Nazca plate (Wolfe and Solomon, 1998). This asymmetry may be an indicator of asymmetric asthenospheric flow toward the ridge, although Harmon et al. (2004) have shown that splitting times decrease in older Pacific seafloor to levels near that of the Nazca plate. Hammond and Toomey (2003) found that there may be a region of tilted olivine alignment responsible for some of the pattern of P and S delays near the ridge, but it is not clear that there is any region of dominantly vertical alignment of the olivine *a*-axis beneath the EPR at depths shallower than 200 km.

The mantle velocity structure beneath the southern EPR is also asymmetric. At depths of a few tens of kilometers, the slowest velocities are west of the axis (Forsyth et al, 1998; Hammond and Toomey, 2003; Harmon et al., 2009) and slower average velocities in the upper 60 km persist for hundreds of kilometers from the axis (**Figure 6(a)**). Global attenuation models also show an asymmetry, with higher seismic attenuation to the west than to the east (Romanowicz, 1994). Although crustal structure seems to be symmetric, short-period Love waves (3–15 s) indicate that the velocity asymmetry begins just beneath the Moho (**Figure 4**; Dunn and Forsyth, 2003). On the eastern, Nazca plate side of the ridge, there are increases in velocity down to depths of 60 km or more within 50 km of the ridge axis, changes penetrating much deeper into the mantle than expected from conductive cooling of the plate alone (Conder et al., 2002). Accompanying the asymmetry in seismic velocities is an asymmetry in subsidence of the seafloor, with anomalously slow subsidence on the Pacific plate side of the ridge (Cochran, 1986; Scheirer et al., 1998). This pattern indicates that there is asthenospheric flow toward the ridge from beneath the Pacific plate, accompanied perhaps by flow across the axis that is deflected downward beneath the thickening Nazca plate, rapidly eliminating any melt fraction in the residual mantle to the east of the ridge (**Figure 6(b)**; Conder et al., 2002; Toomey et al., 2002). Flow from the Pacific side is thought to be anomalously warm and perhaps anomalously enriched and may arise from the South Pacific Superswell region thousands of kilometers to the west. Panza et al. (2010) argue that asymmetric mantle structure exists beneath migrating mid-ocean ridges across the globe.

From the available evidence just described, it appears that the low-velocity zone beneath the ridges may correspond to a low-viscosity asthenosphere dominated by horizontal flow and shear between the overriding plate and the underlying deeper mantle (**Figure 6(b)**; Conder et al., 2002). In contrast, global studies employing Love waves sometimes report anomalies extending deeply beneath spreading centers (**Figure 7**; Gu et al., 2005a; Gung et al., 2003; Zhou et al., 2006), as compared to tomographic images with Rayleigh waves, which have much better vertical resolution. Vertical smearing due to poor Love wave resolution could be responsible for this discrepancy, but synthetic tests suggest that the difference is real, indicating that radial anisotropy reverses from the usual SH > SV pattern in shallow oceanic mantle to SH < SV at depths > 200 km beneath mid-ocean ridges. This may indicate deep vertical upwelling to depths on the order of 300 km (Gu et al., 2005a; Zhou et al., 2006), rather than a more horizontal flow in the asthenosphere that feeds mantle material to ridges (Conder et al., 2002). The absence of an accompanying Rayleigh wave anomaly, or a deflection of the 410 km discontinuity, indicates that any such deep upwelling is probably passively induced with no accompanying thermal anomaly.

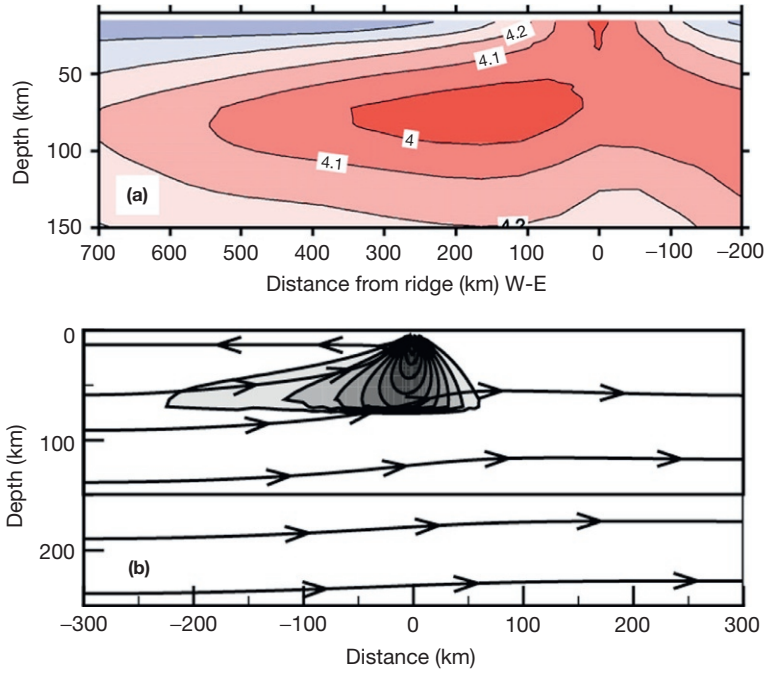

Figure 6 (a) The shear-wave velocity model of the southern East Pacific Rise. Cool colors correspond with lithospheric velocities and warm colors with asthenospheric velocities (reproduced from Harmon N, Forsyth DW, and Weeraratne DS (2009) Thickening of young Pacific lithosphere from high-resolution Rayleigh wave tomography: A test of the conductive cooling model. *Earth and Planetary Science Letters* 278: 96–106). (b) The mantle flow model with an across-ridge pressure gradient that drives asymmetric flow across the ridge (reproduced from Conder JA, Forsyth DW, and Parmentier EM (2002) Asthenospheric flow and the asymmetry of the East Pacific Rise, MELT area. *Journal of Geophysical Research* 107(B12): 2344. http://dx.doi.org/1029/2001JB000807). Note that the scale differs between the top and the bottom plots.

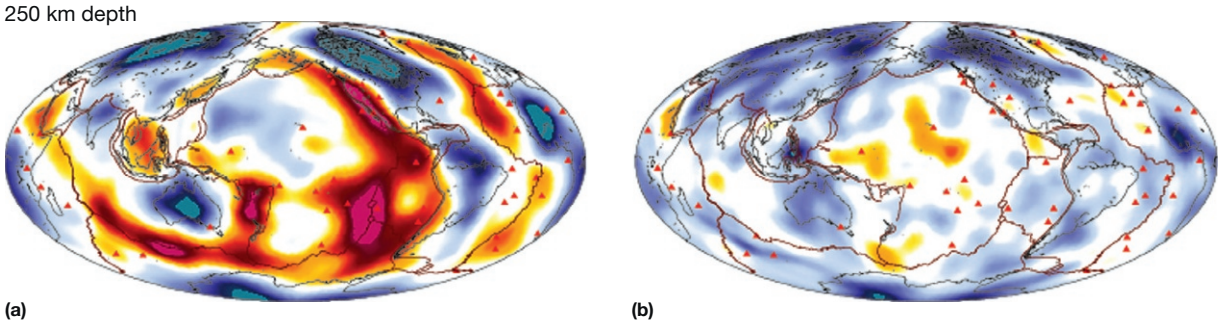

Figure 7 Shear-wave velocity anomalies at a depth of 250 km from Love waves (a) and Rayleigh waves (b). Plate boundaries are indicated by brown lines, and hot spots by red triangles. Note that there are low velocities along most of the mid-ocean ridges in the Love wave image (SH velocity), but there are no such anomalies for Rayleigh waves at this depth. This discrepancy is due to either seismic anisotropy or greater vertical smearing of the SH velocity anomalies. Reproduced from Zhou Y, Nolet G, Dahlen FA, and Laske G (2006) Global upper-mantle structure from finite-frequency surface-wave tomography. *Journal of Geophysical Research* 111: B04304. http://dx.doi.org/10.1029/2005JB003677.

1.13.2.4 Passive Versus Buoyant Upwelling

Although the overall upwelling beneath mid-ocean ridges appears to be passively driven by plate motions, it is possible that when decompression melting begins, enough low-density melt is retained in the mantle matrix to create local buoyancy and local, small-scale convection beneath the ridge. Any reduction in effective viscosity due to melt retention could lead to enhanced and concentrated upwelling into narrow sheets beneath the spreading center or into a 3D pattern of melt-rich diapirs. The concentration of upwelling into a narrow zone is one possible explanation of a major puzzle posed by the conclusion that overall upwelling is passive. The problem is that passive upwelling is expected to be broad; when rising mantle ascends above the solidus, melting thereby occurs over a region that may be >100 km across. Within the mantle matrix, melt buoyancy tends to drive melt vertically, yet seismic reflection profiles indicate that the crust is fully formed within 1–2 km of the ridge axis (Detrick et al., 1987; Singh et al., 2006b) and not over a >100 km region. In addition, surveys of off-axis volcanism in the form of seamounts and lava flows indicate that more than 98% of the basaltic crust is formed at the ridge axis (Shen et al., 1993). Buoyancy of the entire mantle

matrix due to the presence of melt could explain these observations by focusing the upwelling to the ridge axis. If melt production is not concentrated beneath the ridge axis by focused upwelling, then there must be some other mechanism to guide or force the melt produced in a broad region to the ridge axis. Suggestions include nonvertical pressure gradients associated with deformation of a highly viscous mantle, anisotropic permeability, and formation of sloping, melt-rich, high-permeability channels at a freezing front at the base of the lithosphere (Phipps Morgan, 1987; Sparks and Parmentier, 1991; Spiegelman and McKenzie, 1987).

To distinguish between models of broad and narrow upwelling at the end-member case of a high-spreading-rate ridge, the MELT seismic experiment was carried out across the fast-spreading southern EPR (MELT Seismic Team, 1998). This part of the EPR is unusually linear, with no offsets, in the form of transform faults or overlapping spreading centers (OSCs) >5 km, over a distance along the ridge of several hundred kilometers. Both body- and surface-wave tomography revealed a broad region of low velocities, interpreted to be the region of melt production (Forsyth et al, 1998; Hammond and Toomey, 2003; Harmon et al., 2009). There was no indication of a narrow zone of very low velocities that would be expected if enough melt was present to lower the viscosity and increase the buoyancy enough to concentrate upwelling into a narrow zone. It is possible that if the zone were narrow enough, it could have escaped detection, but the waveforms of teleseismic body waves passing directly through the shallow upper mantle beneath the ridge place strict limits on the product of the amplitude of the velocity anomaly and width of the low-velocity channel (Hung et al., 2000).

There is some seismic evidence for three-dimensional (3D) flow or melting in a variety of settings, including in the MELT study area. Combining surface-wave data from the MELT and adjacent GLIMPSE experiments, Harmon et al. (2007, 2011) report two minima in shear-wave velocity along the EPR: one where the Sojourn and Brown intraplate ridge and seamount system intersect the spreading center at ~14° S and the other at the beginning of the Rano Rahi seamount field at ~17–18° S (**Figure 8**). The low-velocity anomalies presumably indicate higher temperatures and/or higher melt concentrations. The association of these two minima with the formation of off-axis seamounts and a geochemical anomaly at 17° S suggests that the 3D character is controlled by the influx of anomalous mantle to the ridge, rather than an inherent instability that leads to a breakdown of the 2D upwelling pattern.

Evidence for 3D flow is also found in the Gulf of California, where a complex ridge system is composed of short sections of spreading ridge that are often offset by long fracture zones. A model invoking passive mantle upwelling would predict anomalously slow wave speeds beneath these spreading segments, but Wang et al. (2009) found punctuated shear velocity anomalies in the mantle that are offset by tens to hundreds of kilometers from the spreading segments. The authors interpret these results as evidence of complex buoyancy-driven mantle upwelling. At a depth just beneath the base of the oceanic crust, three-dimensionality is also observed in the mantle beneath the fast-spreading northern EPR and slow-spreading MAR (see **Section 1.13.3**). Active-source refraction experiments have mapped along-axis variations in P-wave velocity, with

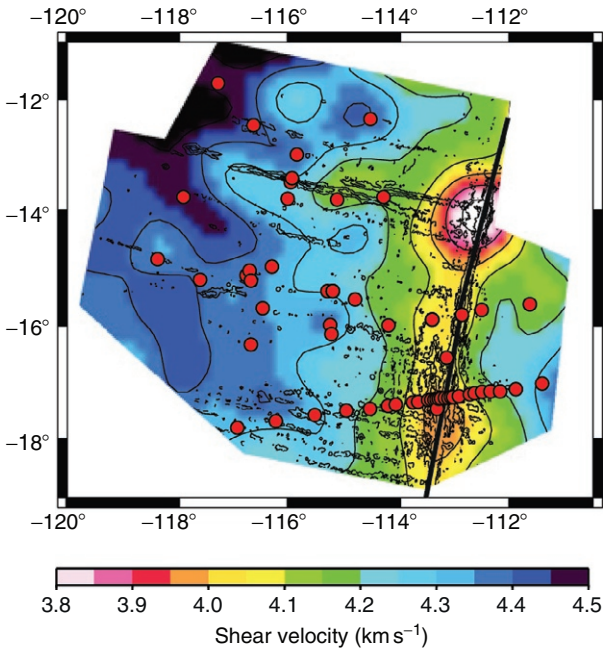

Figure 8 Map of shear-wave velocities near the southern East Pacific Rise (average over 10–45 km depth). The axis of the ridge (straight black lines) runs roughly north–south along the eastern side of the image. Two anomalies along the ridge suggest 3D upwelling and/or melting. Red circles are seismograph positions. A 1000 m water depth contour highlights locations of volcanic edifices. Reproduced from Harmon N, Forsyth DW, Weeraratne DS, Yang Y, and Webb SC (2011) Mantle heterogeneity and off axis volcanism on young Pacific lithosphere. *Earth and Planetary Science Letters* 311: 306–315.

quasiperiodic low-velocity anomalies beneath the EPR (Dunn et al., 2000; Toomey et al., 2007) and with one single low-velocity anomaly beneath an MAR segment (Dunn et al., 2005). One idea is that these anomalies represent the tops of centers of mantle upwelling, although their depth extent is not known and it is possible that they are centers of melt migration and accumulation rather than centers of upwelling of the solid mantle.

1.13.2.5 Spreading Rate Dependence

Mid-ocean ridge morphology and crustal formation are known to depend on the spreading rate of the ridge: as spreading rate decreases along the global mid-ocean ridge system, the average depth of ridge axes becomes greater and more variable, more segmented, and more heavily rifted. Along individual ridge segments, their morphological character increases in complexity and crustal formation becomes more 3D and time-varying as spreading rate drops. While the fastest-spreading ridges (with opening rates >90 mm year^{-1}) exhibit broad axial highs, long straight segments of ridge, and relatively uniform crustal thickness, slower-spreading ridges (20–60 mm year^{-1}) exhibit deep axial valleys within ridge segments that have an overall hourglass shape and variable crustal thickness. At ultra-slow spreading rates (<20 mm year^{-1}), ridge axes are composed of en echelon linked magmatic and amagmatic segments that often display asymmetric spreading across the

ridge, and the general spreading direction is often oblique to the trend of the ridge, rather than perpendicular (Cannat et al., 2006; Dick et al., 2003). These changes in ridge axis character are probably associated with the basic rheology of the ridge axis and its spreading rate dependence. As the spreading rate drops, cooling from above becomes relatively more important than heat delivery from below and the effective thickness of the lithosphere increases; in addition, the depth interval of seismicity and the depth to which crustal magma chambers can be found increase (**Figure 9**) and become more variable. Early modeling studies of ridge dynamics (Chen and Morgan, 1990a,b; Phipps Morgan and Chen, 1993a,b) support the idea that ridge axis morphology is a direct consequence of the thickness of the axial lithosphere.

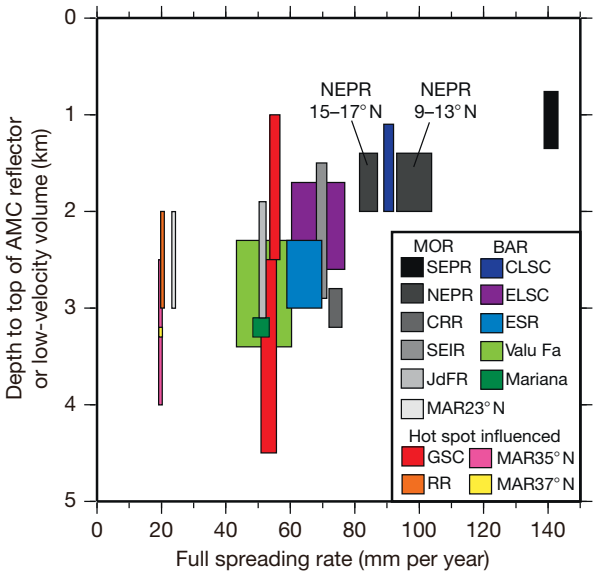

Figure 9 Depth to the axial magma chamber (AMC) or to the top of the axial low-velocity volume, as a function of spreading rate. Note that at slower spreading rates, there is a large observational bias in the trend: beneath many ridge segments with intermediate to slow spreading rates, no evidence for a magmatic system can be found. SEPR, south East Pacific Rise (Detrick et al., 1993; Hooft et al., 1997; Kent et al., 1994; Mutter et al., 1995; Singh et al., 1998, 1999; Tolstoy et al., 1997); NEPR, north East Pacific Rise (Burnett et al., 1989; Canales et al., 2012; Carbotte et al., 1998, 2000, 2012; Collier and Singh, 1997; Detrick et al., 1987; Dunn et al., 2000; Durant and Toomey, 2009; Harding et al., 1993; Kent et al., 1993; Toomey et al., 1994; Vera et al., 1990; Vera and Diebold, 1994); CRR, Costa Rica Rift (Buck et al., 1997; Mutter, 1995); SEIR, Southeast Indian Ridge (Baran et al., 2005); JdFR, Juan de Fuca Ridge (Canales et al., 2005, 2006; Carbotte et al., 2006, 2008; Christeson et al., 2010; Menke et al., 2002; Morton et al., 1987; van Ark et al., 2007); MAR, Mid-Atlantic Ridge (Canales et al., 2000a,b; Dunn et al., 2005; Seher et al., 2010a,b; Singh et al., 2006a,b); CLSC, Central Lau Spreading Center (Jacobs et al., 2007); ELSC, Eastern Lau Spreading Center (Dunn et al., 2013; Jacobs et al., 2007); ESR, East Scotia Ridge (Bruguier and Livermore, 2001; Livermore et al., 1997); Valu Fa Ridge (Collier and Sinha, 1990, 1992; Jacobs et al., 2007; Turner et al., 1999); Mariana Trough (Becker et al., 2010); GSC, Galápagos Spreading Center (Blacic et al., 2004; Detrick et al., 2002); RR, Reykjanes Ridge (Navin et al., 1998; Peirce et al., 2007; Sinha et al., 1998). Spreading rate of CRR is from Hey et al. (1977). Other spreading rates are calculated from Argus et al. (2011).

While long straight segments of fast-spreading mid-ocean ridge may be predominantly underlain by upwelling and melting that is more 2D in form, along the axes of slow-spreading ridges, the supply of melt from the mantle is widely considered to be highly variable, both spatially and temporally. For ridge segments bounded by large tectonic offsets, the midsections often exhibit the shallowest bathymetry and thickest crust, while the segment ends exhibit wide, deep axial valleys and thin crust, as deduced from gravity (Detrick et al., 1995; Kuo and Forsyth, 1988; Lin et al., 1990) and seismic data (Canales et al., 2000b; Dannowski et al., 2011; Dunn et al., 2005; Hooft et al., 2000; Hosford et al., 2001; Purdy and Detrick, 1986; Sinha and Louden, 1983; Tolstoy et al., 1993). Although these observations can be explained by a number of mantle geodynamic scenarios, each one predicts that melt flux is focused at mantle depths and delivered to a segment's center (e.g., Kuo and Forsyth, 1988; Lin et al., 1990; Magde et al., 1997; Rabinowicz et al., 1993; Sparks et al., 1993; Whitehead et al., 1984). Melt focusing may occur due to mantle diapirism or by following the bottom of a freezing front at the base of the lithosphere that shallows near segment centers (Magde et al., 1997). Theoretical studies (Parmentier and Phipps Morgan, 1990) indicate that as spreading rate drops, mantle buoyancy becomes progressively more important relative to viscous drag and upwelling is more likely to break up into a 3D diapiric form. While there is overwhelming evidence for 3D melt supply along slow-spreading ridges, there is as yet no conclusive seismic evidence for buoyant diapiric upwellings of the mantle matrix along slow-spreading ridges; most of what we know about the patterns of upwelling, melt production, and melt flux is inferred from studying the final product, that is, lateral variations in structure and thickness of the oceanic crust accreted at the Earth's surface and not from direct seismic study.

While strong spreading rate correlations exist, it is clear that spreading rate alone cannot account for much of the diversity of the ridge system. Mantle temperature and compositional heterogeneity may also play a role. Langmuir et al. (1992) showed that geographic variation in mantle potential temperature can account for significant differences between sections of ridge. Mantle hot spots are known to significantly affect nearby sections of mid-ocean ridge, producing thicker crust and shallower ridge axes; mantle volatiles in ridge magmas also increase toward hot spots (water acts as a melting flux by lowering the solidus temperature; e.g., Schilling et al., 1980, 1982). Mantle cold spots have also been postulated (Hayes, 1976, 1988; Klein and Langmuir, 1987), such as near the Australian–Antarctic Discordance, along the Southeast Indian Ridge, where seismic images suggest a large-scale high-velocity (cooler) feature in the upper mantle (Ritzwoller et al., 2003). Mantle chemical variations may also influence ridge processes. For example, Warren et al. (2009) infer global variations in mantle source chemistry for ridges on the basis of abyssal peridotite samples, and Zhou and Dick (2013) recently suggested that a previous melting event has left a large region of depleted upper mantle beneath the Marion Rise along the Southwest Indian Ridge.

For $\sim$80% of ridges with spreading rates $>$20 mm year^{-1}, melt production appears to be independent of spreading rate. Faster-spreading ridges produce roughly the same

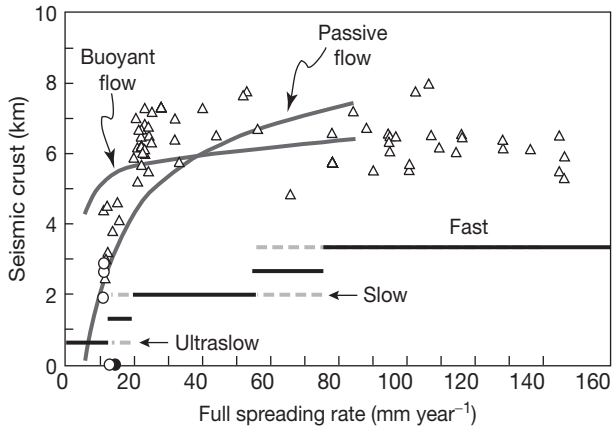

Figure 10 Global distribution of crustal thickness as a function of spreading rate. Triangles are seismically determined crustal thickness estimates. Crustal thickness drops off quickly as the spreading rate drops below 20 mm year^{-1}. Typical divisions of ridge spreading rate are shown. Gray crustal thickness curves were calculated for passive flow and buoyant flow geodynamic models. Reproduced from Dick HJ, Lin J, and Schouten H (2003) An ultraslow-spreading class of ocean ridge. *Nature* 426: 405–412.

amount of crust, 6–7 km, as slower-spreading ridges. However, crust produced at ridges with spreading rates less than ~20 mm year^{-1} is observed to be <4 km thick, well below the global average for faster rates (**Figure 10**; Coakley and Cochran, 1998; Cochran et al., 2003; Géli et al., 1994; Jokat et al., 2003; Klingelhöfer et al., 2000; Ritzmann et al., 2002). For some sections of these ridges, the melt supply at least temporarily drops to zero, resulting in the direct emplacement of mantle at the seafloor (e.g., Cannat et al., 2006; Dick et al., 2003). This change in crustal production at very slow spreading rates indicates a fundamental change in subridge processes; yet its origin is unknown. At present, there are two end-member hypotheses. While each emphasizes the existence of a cold thermal lid, one speculates that the thermal lid inhibits melting, while the other suggests that it inhibits melt migration.

The former hypothesis predicts that under very slow-spreading conditions, there is efficient, deep cooling of the upper mantle beneath the ridge. At a spreading rate of 10 mm year^{-1}, it takes about 10 million years for a parcel of mantle to rise from the dry solidus to beneath the ridge axis, long enough for the mantle to lose heat by conduction to the surface while it is still rising (Shen and Forsyth, 1995). This presumably allows a thick thermal boundary layer to form that depresses the top of the melting region, thereby shutting off melting much deeper than along faster-spreading ridges (Brown and White, 1994; Niu and Hekinian, 1997; Reid and Jackson, 1981; Shen and Forsyth, 1995). In contrast to fast-spreading ridges, where melting is predicted to continue up to nearly the base of the crust, numerical calculations (Reid and Jackson, 1981) predict that along ultraslow ridges, melting shuts off at a depth of 30 km or more beneath the base of the crust. Although the 'thick lithosphere' concept provides a useful working hypothesis, it does not provide a unique interpretation of available data, nor does it account for the tendency of rising melts to freeze into the mantle, as a consequence of the cool boundary layer, and release heat. In support of this model, samples taken from ultraslow ridges exhibit incompatible element enrichments, indicative of low degrees of melting (Dick et al., 2003; Klingelhöfer et al., 2000; Michael et al., 2003; Robinson et al., 2001), though the amount of melting that occurs along these ridges, as reflected by crustal thickness and enrichment of incompatible elements, does not distinguish control between by conductive cooling and by other factors such as mantle temperature (Klein and Langmuir, 1989; Langmuir et al., 1992) or composition (Robinson et al., 2001).

In the alternative hypothesis, a large proportion of the melt generated beneath the ridge is simply frozen into the uppermost mantle (Cannat, 1996). In this hypothesis, the upper mantle is not cooled to great depth and no deep shutoff point for melting exists. Instead, a thin but strong lithosphere at the uppermost part of the mantle restricts the passage of melt just beneath the ridge. Thus, crustal thickness does not represent the total amount of melting that occurs. In support of this hypothesis, a short-period surface-wave study along the Mohns Ridge found an ~10 km thick region just below the crust of low S-wave velocities (**Figure 11**) (Conley and Dunn, 2011); a seismic refraction experiment in the same area found low subcrustal P-wave velocities (Klingelhöfer et al., 2000); and a seismic refraction study of Atlantic lithosphere found an abrupt drop in subcrustal P-wave velocities correlating with a change from slow to ultraslow paleospreading rate (Lizarralde et al., 2004). In each case, the low velocities suggest the presence of melt frozen into the uppermost mantle, and the estimated volume of retained melt in the mantle balances the amount of 'missing' melt in the crust.

Along ultraslow ridges, crustal thickness does not decrease monotonically with decreasing spreading rate. Instead, large temporal variations in crustal thickness and inferred melt supply exist along the Gakkel Ridge, and this additionally supports a permeability barrier model over a model that favors lower total melting. To some extent, both hypotheses may be correct, and some amount of both deep cooling and melt retention seems likely. If melts freeze into the upper mantle to some degree at all slow- to very slow-spreading ridges, then there may be large reservoirs of unaccounted for gabbroic melt frozen into the mantle throughout many ocean basins.

1.13.2.6 Back-Arc Spreading Centers

A general model for the creation of back-arc basins behind subduction zones proposes that lithospheric extension (via trench rollback or other mechanism) initiates rifting near the volcanic arc, where the lithosphere is expected to be weak, followed by seafloor spreading that eventually develops into well-organized, mid-ocean-ridge-like spreading centers (e.g., Hawkins, 1976; Karig, 1970; Taylor and Karner, 1983). With continued opening of the basin along these ridges, the ridges and volcanic arc separate and the ridges entrain lower and lower degrees of slab-derived water and other elements in their melting regimes (Pearce et al., 1995). Although back-arc spreading centers have many similarities to mid-ocean ridges, they tend to be more complex and often display evidence for rift jumps, spreading center propagation (e.g., Parson et al., 1990), rapid temporal variations in spreading rate (Jurdy and Stefanick, 1983), and large morphological and geochemical

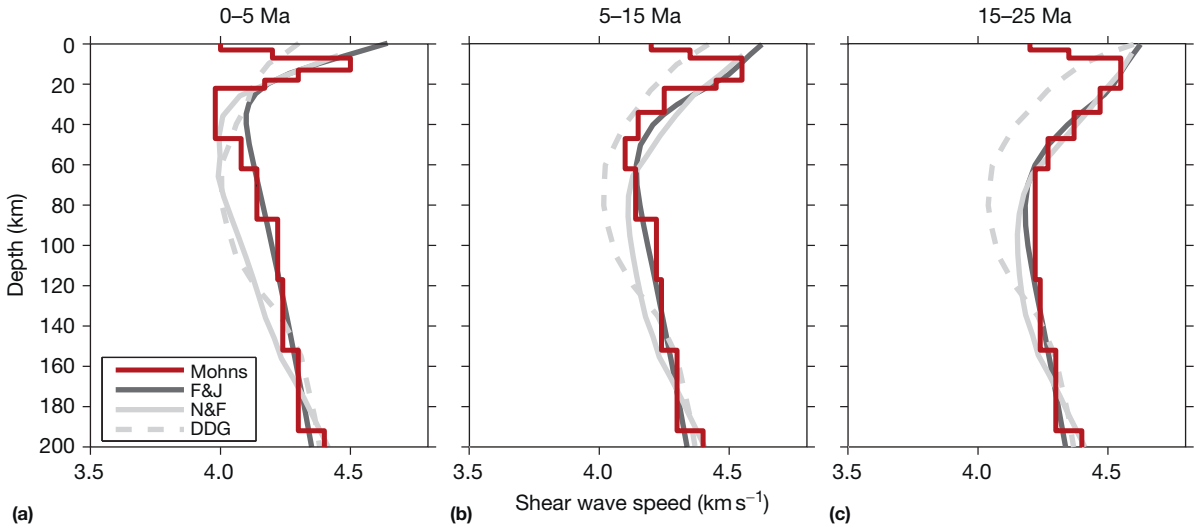

Figure 11 Mohns Ridge SV models as compared to other models for the same age ranges. F&J, a half-space cooling model converted to seismic shear-wave speed via the method of Faul and Jackson (2005); N&F, Pacific mantle model of Nishimura and Forsyth (1989); DDG, the North Atlantic, Reykjanes Ridge, model of Delorey et al. (2007). All models are referenced to the base of the crust. The Mohns model contains a subcrustal low-velocity region in the topmost ~10 km of mantle. Within the 0–5 Ma age range (and larger ranges for the Reykjanes model), the regional models differ from the F&J prediction by having lower sublithospheric shear velocities that may indicate the presence of a small amount of melt in the upper mantle. Reproduced from Conley MM and Dunn RA (2011) Seismic shear wave structure of the uppermost mantle beneath the Mohns Ridge. *Geochemistry Geophysics Geosystems* 12: Q0AK01. http://dx.doi.org/10.1029/2011GC003792.

variations (Taylor and Karner, 1983; Taylor and Martinez, 2003). In recent years, extensive geophysical (e.g., Bruguier and Livermore, 2001; Dunn and Martinez, 2011; Goodliffe et al., 1997; Taylor and Martinez, 2003) and geochemical mapping studies (e.g., Bézos et al., 2009; Escrig et al., 2009; Langmuir et al., 2006; Pearce et al., 2005) have made significant progress toward piecing together these complex systems.

However, relatively little is known about the dynamical processes occurring in the wedge of mantle located above the subducting slab and below back-arc and arc systems; yet within these regions, significant processes controlling the evolution of the Earth occur, for example, the recycling of cold lithosphere back into the deeper mantle, the hydration of the mantle from volatiles released from the slab, and chemical differentiation that accompanies arc and back-arc melting and magmatism. Strong variations in volatile content of the mantle wedge (e.g., Kelley et al., 2006), and the driving influence of the subducting slab on wedge flow (Ribe, 1989; Sleep and Toksöz, 1971), are often called upon to explain many of the unique characteristics of back-arc systems.

Some models of subduction systems suggest that wedge flow is governed by viscous coupling to the downgoing slab, producing flow directions parallel to the motion of the downgoing plate (McKenzie, 1979; Ribe, 1989). On the other hand, shear-wave splitting studies commonly detect fast shear-wave polarization directions that are roughly parallel to the arc (e.g., Bowman and Ando, 1987; Long and van der Hilst, 2006; Pozgay et al., 2007; Smith et al., 2001; Yang et al., 1995) and hence perpendicular to plate motion direction. For example, in the Mariana and Tonga subduction zones, fast splitting directions are parallel to the arc near the volcanic arc itself and rotate to the direction of plate convergence in the back arc (Pozgay et al., 2007; Smith et al., 2001). Since the fast direction is often taken to be the flow direction, such observations suggest that the flow pattern is dominated by arc-parallel flow above the slab as a consequence of either slab rollback (Buttles and Olson, 1998), shearing or extension in the arc-parallel direction (Hall et al., 2000), changes in slab dip (Buttles and Olson, 1998; Hall et al., 2000), or changes in convergence angle (Blackman and Kendall, 2002; Honda and Yoshida, 2005). Alternatively, it has been argued that elastic anisotropy might develop in a manner distinct from that in more typical settings; under a restricted range of conditions such as high water content and high stress, the olivine *a*-axis direction may instead align perpendicular to the direction of maximum strain, resulting in shear-wave splitting fast orientations perpendicular to mantle flow (Jung and Karato, 2001; Karato, 2003).

Another significant issue is the shape of the melting region beneath back-arc spreading centers and its relationship to wedge flow, volatiles, and subarc melting. A broadband seismic reflection study of the mantle wedge above the Tonga slab found broad regions of significant reflectivity across the wedge, which the authors ascribe to phase transitions and compositional zonation associated with extensive metasomatism via slab-derived fluids rising through the mantle wedge (Zheng et al., 2007). Mantle tomographic studies have found broad low-velocity and high-attenuation regions extending from the volcanic arc to, or beyond, the active Lau and Mariana spreading centers (Conder and Wiens, 2006; Pyle et al., 2010; Wiens et al., 2008; Zhao et al., 1997), suggestive of the broad anomalies beneath the southern EPR. However, along the Lau spreading center, petrologic and geochemical studies (Bézos et al., 2009; Escrig et al., 2009; Langmuir et al., 2006), as well as seismic and other geophysical studies of the crust formed at the spreading center (Arai and Dunn, 2014; Dunn and

Martinez, 2011; Jacobs et al., 2007), show rapid changes in crustal type and thickness as the ridge moved away from the arc. Together, these results indicate rapid transitions in mantle chemistry or mantle flow in the wedge (Dunn and Martinez, 2011) on a scale not yet resolvable by current broadband arrays. These studies indicate that as the basin opens and the spreading center migrates away from the arc, there is a rapid transition at the spreading center from accreting more arc-like magmas to more oceanic basalt-like magmas. Recently, a dense ocean-bottom and land-based broadband seismic experiment was carried out along the Eastern Lau Spreading Center to provide improved images of the mantle wedge and test models of wedge flow and melting (Songqiao et al., 2012). Results are forthcoming.

1.13.3 Formation of Oceanic Crust

Our understanding of the structure of oceanic crust produced along mid-ocean ridges has evolved considerably over the past two decades, from an early view as a layer-cake structure composed of a few seismic layers matching geologic units to a much richer and more laterally variable structure. Having now examined the seismic structure of the crust in a variety of settings, it is now understood that basic crustal structure varies with spreading rate, geodynamic setting, and time. Around the global ridge system, heat flux varies with spreading rate, and heat supply largely governs the magmatic, tectonic, and hydrothermal processes that control the formation of oceanic crust.

1.13.3.1 General Seismic Structure of the Oceanic Crust

Starting from the top, low velocities (<5 km s^{-1} P-wave velocity) and high seismic attenuation characterize the upper few hundred meters of oceanic crust; the lower boundary of which is marked by a strong velocity gradient that can be imaged with seismic reflection techniques (e.g., Christeson et al., 1996, 1994a, 1994b; Detrick et al., 1998; Harding et al., 1993; Vera and Diebold, 1994; Wilcock et al., 1995). An early interpretation of this seismic region ('layer 2A') in terms of a lithology composed of high-porosity extrusive basalts was based on analogy with ophiolite units, the seismic velocity of laboratory samples of dredged and drilled rocks, and *in situ* measurements in drill holes (see Solomon and Toomey (1992) for a review of early work). By further analogy to ophiolites, seismic layer 2A is underlain by a higher-velocity region of sheeted dikes (seismic layer 2B), followed by yet a higher-velocity region of gabbros (layer 3) (**Figure 12**); the 2/3 boundary is typically defined by a sharp, order-of-magnitude, reduction in the velocity gradient at roughly 6.5 km s^{-1}.

Recent work has both modified and disputed this simple layer-cake model. At the axis of fast- and intermediate-spreading ridges, seismic layer 2A is consistently thin but thickens rapidly within 1–2 km of the ridge axis (**Figure 13**), presumably due to a rapid buildup of the extrusive basalts on the flanks of the ridge (e.g., Harding et al., 1993; Hooft et al., 1996; Kent et al., 1994; Stakes et al., 2005). No such relationship has been clearly documented along slow-spreading ridges. Further away from the ridge, it is globally observed that layer

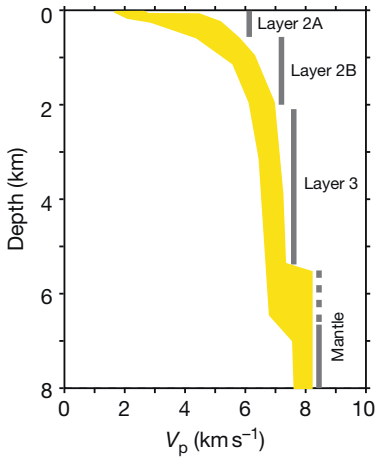

Figure 12 P-wave speed of oceanic crust. Yellow field gives approximate range of V_p values determined by several seismic experiments, mainly located on crust formed at faster spreading rates (Canales et al., 1998; Detrick et al., 1993; Dunn et al., 2000; Grevemeyer et al., 1999; Harding et al., 1993; Hussenoeder et al., 1996; Kappus et al., 1995; Tolstoy et al., 1997; Vera et al., 1990). The distinction between seismic 'layers' 2A and 2B is often made via a prominent reflector horizon observed in multichannel seismic reflection studies.

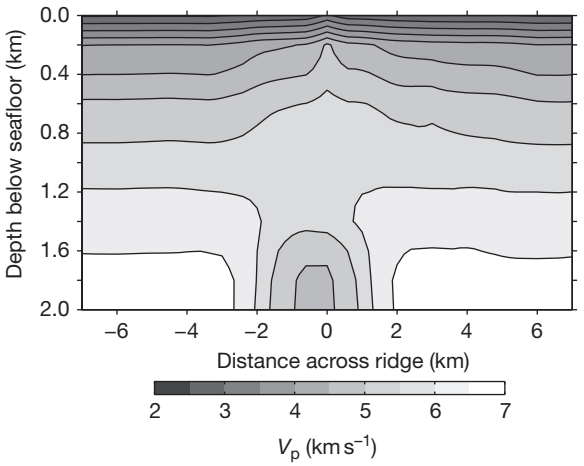

Figure 13 V_p tomographic image of the uppermost crust across the East Pacific Rise near 9°30′N latitude (an along-axis average of a 3D solution). Seismic layer 2A thickens rapidly within 2–3 km of the ridge axis ($x = 0$ km). The low-velocity body beneath the ridge axis at depths >1.2 km is the axial magmatic system. Note that the vertical exaggeration is ~4. From the seismic study of Dunn et al. (2000).

2A velocities increase with crustal age (**Figure 14**), an observation that is consistent with hydrothermal deposition in rock pores (e.g., Grevemeyer and Weigel, 1996; Grevemeyer et al., 1999; Houtz and Ewing, 1976; Purdy, 1987; Wilkens et al., 1991). The precise nature of the 2A/2B and 2/3 boundaries is still debated, and some have questioned whether they can be used to map lithologic boundaries (e.g., Christeson et al., 2007). An examination of upper crustal structure at drill hole 504B near the Costa Rica Rift (Swift et al., 1998a,b) found that the 2/3 boundary coincides with a significant decrease in bulk porosity and marks the base of the lithologic transition from extrusive rocks and intermingled dikes to

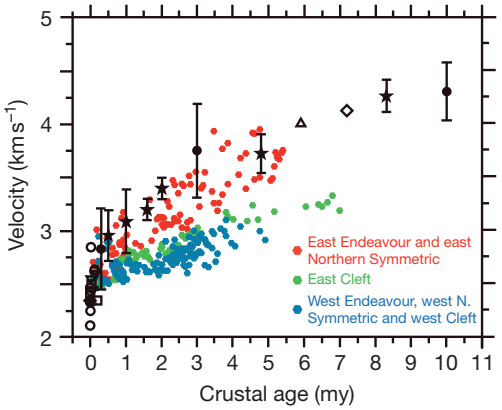
Velocity (km s−1)
Crustal age (my)
East Endeavour and east Northern Symmetric
East Cleft
West Endeavour, west N. Symmetric and west Cleft

Figure 14 Average layer 2A P-wave velocity plotted by crustal age (reproduced from Grevemeyer I, Kaul N, Villinger H, and Weigel W (1999) Hydrothermal activity and the evolution of the seismic properties of upper oceanic crust. *Journal of Geophysical Research* 104(B3): 5069–5079; Nedimović et al., 2008). While the global trend (solid black circles; Carlson (1998)) exhibits a consistent increase in velocity with crustal age, there are differences in both the absolute velocity and the rate of change for different spreading centers. Colored symbols are from different portions of the Juan de Fuca spreading system; black stars and other symbols are from various East Pacific Rise and Mid-Atlantic Ridge studies.

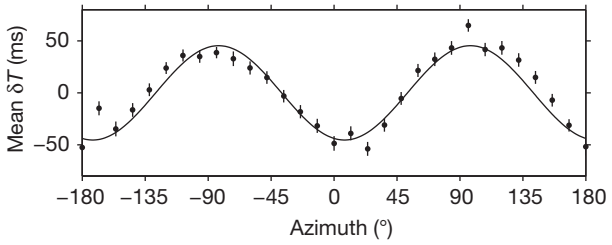

Figure 15 Variation of P-wave travel times with ray path azimuth from the L-SCAN seismic study of the crust along the Eastern Lau Spreading Center (Dunn and Martinez, 2011). Zero azimuth is parallel to the spreading axis. Travel times are calculated with respect to a one-dimensional (depth-varying) velocity model and binned by azimuth; error bars give the $1-\sigma$ spread of the values for that bin. P-waves travel faster (negative values) parallel to the spreading axis and slower (positive values) perpendicular to the axis.

mainly dikes. Thus, seismic layer 3 is expected to contain dikes underlain by gabbros. On the other hand, a study at drill hole 1256D (Wilson et al., 2006) found some gabbro at depths shallower than the seismic 2/3 boundary, but the top of the main gabbroic section is located at the depth predicted by seismic measurements. Along slow-spreading ridges, significant tectonic modification of the crust is expected (e.g., Cannat, 1993, 1996) and the layer-cake model probably does not apply over large sections of crust produced at such ridges. Since many studies show that seismic wave speed is very sensitive to porosity and not necessarily general lithology, most seismologists remain cautious about directly correlating seismic structure with lithologic units.

At the seafloor, high-resolution acoustic imaging reveals that faults, fissures, and fractures pervade the shallow oceanic crust. The orientation of these features is sensitive to the local stress field, and they tend to align perpendicular to the minimum compressive stress, which is generally parallel to mid-ocean ridges. At depth, aligned cracks are detectable by their seismic anisotropy signature, via either shear-wave splitting and polarization measurements (e.g., Barclay and Toomey, 2003; Stephen, 1981) or azimuthal variations in travel times (e.g., Barclay et al., 1998; Dunn and Toomey, 2001; Dunn et al., 2005; Little and Stephen, 1985; Menke et al., 1994; Shearer and Orcutt, 1985; Sohn et al., 1997; White and Whitmarsh, 1984). Along ridges, P-wave travel times exhibit a cosine(2θ) variation, where θ is the ray azimuth (**Figure 15**). A 2θ pattern indicates that the travel-time signal is dominated by water-saturated vertically aligned cracks with aspect ratios >0.01 (Hudson, 1981). Two studies (Tong et al., 2004, 2005) have examined both 2θ and 4θ patterns in travel-time residuals (crack aspect ratios <0.01 give rise to a dominant cosine(4θ) signal (Hudson, 1981)) and used the ratio of the amplitudes of these signals to examine local variations in subsurface crack structures. The best-resolved seismic studies detect around 3–4% anisotropy in the upper 2–4 km of the crust, essentially within seismic layer 2 (e.g., Barclay et al., 1998; Dunn and Toomey, 2001; Dunn et al., 2005, 2013; Seher et al., 2010a,b; Sohn et al., 1997; Tong et al., 2004). Using Hudson's crack theory (1981) and 4% anisotropy, aligned cracks with aspect ratios of 0.01–0.1 give rise to porosities of $\leq$1%, a value much less than the total expected porosity based on the reduction of the isotropic velocities alone (>10%). However, because the permeability of rock with aligned cracks can be several orders of magnitude larger than rock without aligned cracks (De Weist, 1965; Fisher, 1998), such cracks may provide the dominant pathways for hydrothermal circulation to cool and chemically alter the crust.

The middle to lower crust is characterized by low-velocity gradients, a general absence of seismic reflectors, and seismic velocities in the 6–7 km s^{-1} range (e.g., Canales et al., 1998, 2003; Dunn and Martinez, 2011; Dunn et al., 2005; Spudich and Orcutt, 1980; van Avendonk et al., 2001; Vera et al., 1990). Because of the gentle velocity gradients, less seismic energy turns at these depths, making this a more difficult region to study in detail. Seismic reflections from the Moho can be used to study this region, but for seismic experiments with low data coverage, or mainly vertically incident energy, there can be a large trade-off between lower crustal velocities and Moho depth (e.g., Ross, 1994). Therefore, a dense station spacing (station spacing < crustal thickness) and a large range of source-to-station offsets are required to accurately determine the structure over this depth interval.

Few seismic studies have attempted to constrain the detailed nature of the crust–mantle transition or the 'Moho.' Along intermediate- and fast-spreading ridges, the Moho produces vertically incident (e.g., Detrick et al., 1987) and strong wide-angle seismic reflections (e.g., Canales et al., 2003; Vera et al., 1990) and appears to be a relatively sharp transition region (<1 km thick) from crustal to mantle velocities (**Figure 16**). Along slow-spreading ridges, the Moho is less well defined and often absent in vertical-incident data; wide-angle data reveal both regions of sharp transition and regions of gradual transition (Canales et al., 2000a,b; Dunn et al., 2005; Hooft et al., 2000; Hosford et al., 2001). A thick transition suggests that crustal construction is complex, perhaps due

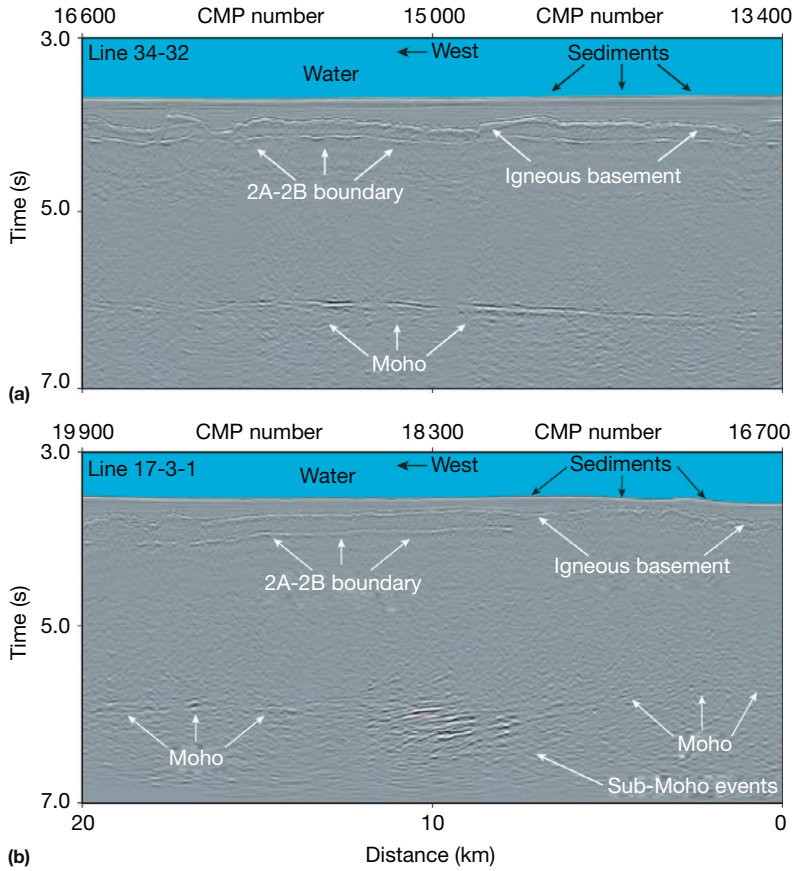

Figure 16 Seismic reflection structure of oceanic crust from two ridge flank regions of the Juan de Fuca Ridge (intermediate-rate spreading). Plots show variability of the Moho structure from area to area. (a) A sharp/bright Moho reflection and (b) a variable strength Moho reflection: regions of weaker and variable strength Moho reflection flank a region with clusters of sub-Moho reflectors interpreted as gabbroic sills. Reproduced from Nedimović MR, Carbotte SM, Harding AJ, et al. (2005) Frozen magma lenses below the oceanic crust. *Nature* 436(7054): 1149–1152.

to melt accumulation and layering over a large depth interval. Alternatively, and especially near fracture zones, a thick transition may indicate serpentinization of the upper several hundred meters of mantle. Beneath the Moho, mantle velocities are largely anisotropic (e.g., Dunn et al., 2005; Raitt et al., 1969; Toomey et al., 2007) with a cosine(2θ) azimuthal variation in P-wave velocities (where θ is the ray path azimuth) (Figure 17). This anisotropy is largely attributed to the alignment of the *a*-axes of mantle olivine in the spreading direction.

Oceanic crustal thickness is a key measure of the ongoing chemical differentiation of the planet and was once thought of as being relatively uniform throughout the oceans, with an average thickness of about 6–7 km (Figure 10). Our current understanding is that only fast-spreading ridges produce a relatively uniform thickness crust, and even in those environments, local variations may exceed 1 km (e.g., Canales et al., 1998). Slow-spreading ridges, on the other hand, produce a wide range of crustal thicknesses but may still exhibit an average seismic thickness of ~6 km when averaged over tens of kilometers. Occasionally, little to no crust is produced, as documented by mantle rocks found at the seafloor (e.g., Cannat, 1993, 1996), such as near cold fracture zones or as magmatism waxes and wanes at the spreading center. At full spreading rates <2 cm year^{-1} ('ultraslow spreading'), crustal thickness drops off sharply (Figure 10). In general however, too few modern seismic studies have documented crustal thickness along spreading centers, and thus, any relationship between crustal thickness and spreading rate is still approximate at best. Furthermore, because serpentinized mantle exhibits crustal velocities, crustal thickness estimates derived from seismic experiments in intermediate- to slow-spreading environments (or any areas where intense faulting may permit deep penetration of seawater) remain controversial.

1.13.3.2 Fast-Spreading Ridges

The fastest spreading rates, >90 mm year^{-1}, are principally found along the EPR. Seismic studies along the EPR have determined details of the structure of the crust and the overall ridge magmatic system from the seafloor well into the mantle, including the width, magnitude, and ridge-parallel variations of this system at most depths. Crustal seismic structure along fast-spreading ridges tends to be more laterally uniform than that produced along slower-spreading ridges, suggesting a fairly uniform supply of melt from the mantle. Here, the layer-cake model of seismic structure is most applicable.

Beneath the EPR, the mantle upwelling zone is expected to be >300 km wide (Forsyth et al., 1998). However, just below the base of the crust, the bulk of the low-velocity zone narrows to perhaps ~40 km wide (Figure 18), and in the lower crust,

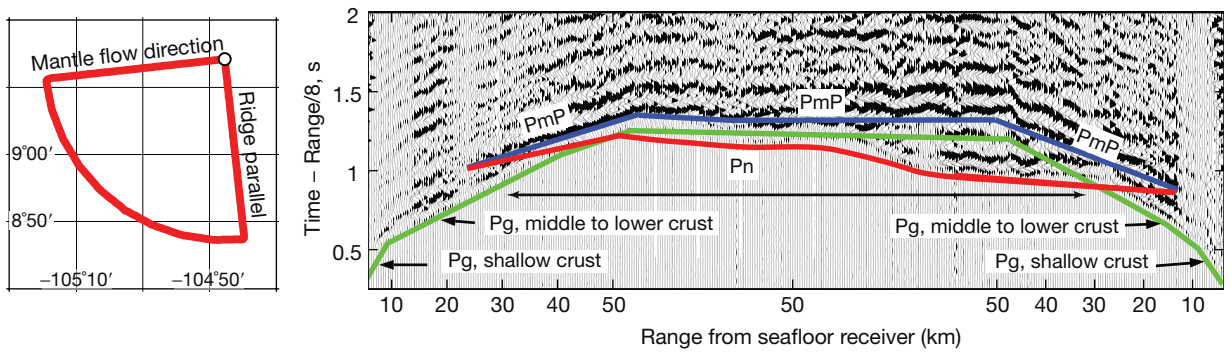

Figure 17 Azimuthal P-wave anisotropy in the mantle on the western flank of the East Pacific Rise. (Left) Location of an ocean-bottom seismograph (white circle) and air gun shot pattern (red lines). (Right) Seismic record section showing crustal-refracted (Pg), Moho-reflected (PmP), and mantle-refracted (Pn) energy recorded by the station. Shots along a line that parallels the mantle flow direction exhibit earlier arriving Pn energy (<1 s at ~32 km offset; right side of record section), and shots along a line that parallels the ridge axis exhibit later arriving Pn energy (>1 s at 50 km offset; left side of record section), yet crustal thickness (as indicated by the PmP arrivals) and crustal velocities (as indicated by Pg arrivals) change insignificantly around the semicircle. Refraction studies shot in the slow anisotropy direction may find only a small difference between lower crustal and mantle velocities. Data from the UNDERSHOOT experiment (Toomey et al., 2007).

the seismic low-velocity region abruptly decreases to only 7–8 km wide. Active-source tomographic (Dunn et al., 2000) and seafloor compliance studies (Crawford and Webb, 2002) of the crustal magmatic system detect a narrow low-velocity zone from the base of the crust up to within ~1.5 km of the seafloor (**Figure 19**). At its top, the low-velocity zone may be about 50% as wide as near the base.

Since the inferred isotherms for this narrow seismic structure do not conform to the predictions of a conductively cooled magmatic system (**Figure 20**), the implication is that hydrothermal circulation penetrates deeply off-axis to cool the lower crust (Cherkaoui et al., 2003; Dunn et al., 2000). Lower crustal hydrothermal circulation has also been suggested from studies of the Oman ophiolite, which indicate that zones of narrow hydrothermal circulation extracted heat from either side of a crustal magmatic system to depths of 5–6 km (Coogan et al., 2006; Gregory and Taylor, 1981; Nehlig and Juteau, 1982). However, other studies of ophiolite chemistry suggest that more pervasive hydrothermal circulation decays exponentially with depth (Coogan et al., 2002). The idea that hydrothermal fluids might penetrate to the Moho on the flanks of the ridge is highly contentious, and part of the problem is that direct observations of hydrothermal circulation are limited to the regions of highest heat output at the ridge axis, as opposed to regions of lower-level flow (inflow or outflow) off-axis.

The low velocities (Dunn et al., 2000) and high-attenuation values (Wilcock et al., 1992, 1995) of the magmatic system are consistent with 10–40% melt in the middle to upper crust, 2–8% melt in the lower crust, and 3–12% melt near the Moho transition zone (**Figure 20**). The large uncertainty of these estimates is partly due to a lack of laboratory studies on partially molten crustal rocks to determine their physical properties under *in situ* conditions at seismic frequencies. Within the middle to lower crust, the absolute magnitudes of the velocity and attenuation anomalies decrease with increasing depth (Dunn et al., 2000; Toomey et al., 1990; Vera et al., 1990; Wilcock et al., 1995) such that the lower crust is estimated to contain the least melt, both by melt fraction and by total volume, which may indicate that it is closer to its solidus than the other regions (Sinton and Detrick, 1992). A few seismic and compliance studies indicate that magma sills accumulate near the crust–mantle transition zone or Moho (Crawford and Webb, 2002; Crawford et al., 1999; Garmany, 1989; Nedimović et al., 2005), possibly within a broader region of low melt fraction (Dunn and Toomey, 1997). Observations of a substantial amount of melt at this depth indicate an impediment to upward flow. The density contrast at the Moho (Crawford et al., 1999), a permeability barrier due to crystallization at the base of the crust (Kelemen et al., 1997; Korenaga and Kelemen, 1997), and changes in the stress conditions (Ildefonse et al., 1993) have been suggested as possible barriers to melt migration.

Multichannel seismic (MCS) reflection imaging shows that melt accumulates at the top of the magmatic system, beneath either a permeability or viscosity barrier, within a small melt lens (e.g., Detrick et al., 1987; Kent et al., 1993; Mutter et al., 1988). The lens is often narrow and thin (about 1 km wide and 10–50 m thick; e.g., Kent et al., 1993) with high melt content, but its size varies by location and it can range from mostly crystalline to mostly molten (e.g., Babcock et al., 1998; Collier and Singh, 1997; Harding et al., 1989; Kent et al., 1993, 2000; Singh et al., 1998). Just above the melt lens, waveform analysis of MCS reflection data reveals a thin high-velocity 'lid' (Singh et al., 1999; Vera et al., 1990), which is interpreted as a solid region, devoid of melt or hydrothermal cracks, that acts as a conductive cooling regime between the hydrothermal system above and the melt lens below. Along-axis variations in the thermal structure above the melt lens appear to correlate with small ridge discontinuities (Tian et al., 2000; Toomey et al., 1994). The depth of the lens is expected to be controlled by the trade-off between the rate of heat input from below and the rate of heat extraction via hydrothermal circulation from above (e.g., Hooft and Detrick, 1993). Thus, the melt lens tends to deepen as the spreading rate, and heat/melt supply from below drops (**Figure 9**; Purdy et al., 1992). Although the highest concentrations of melt are thought to occur within the melt lens, a rough estimate of the total distribution of melt in the

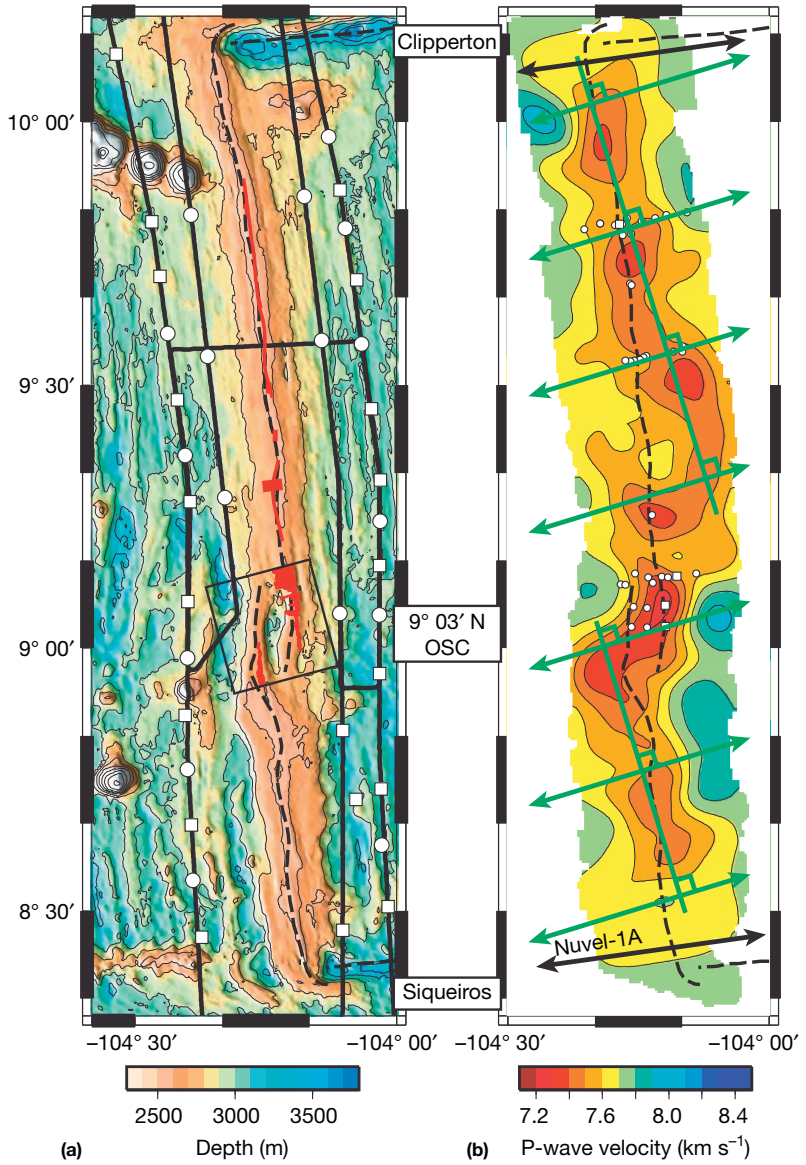

Figure 18 (a) Bathymetric map of the East Pacific Rise, 9° N region, along with the location of seismic instruments (white circles and squares) and air gun shots (black lines). Red areas indicate location of a melt lens reflector, where known. (b) P-wave tomographic image of the upper mantle just beneath the crust; contour interval is 0.1 km s^{-1}. Black arrows indicate plate spreading direction. Green arrows indicate the inferred mantle flow direction. Black dashed curve indicates the location of the ridge axis. Reproduced from Toomey DR, Jousselin D, Dunn RA, Wilcock WSD, and Detrick RS (2007) Skew of mantle upwelling beneath the East Pacific Rise governs segmentation. *Nature* 446: 409–414. http://dx.doi.org/10.1038/nature05679.

crust suggests that, by volume, there is more melt in the middle to lower crust and Moho regions than in the shallow melt lens, simply because of the greater cross-sectional areas of these regions (Dunn et al., 2000); deep melt lenses near the Moho may also contain large amounts of melt (Crawford and Webb, 2002; Crawford et al., 1999; Garmany, 1989).

Microearthquake studies using closely spaced networks of seafloor seismographs detect tens of thousands of events along ridge segments over spans of several months. A large proportion of these events occur above the shallow melt lens at the ridge crest and may be related to hydrothermal cracking, faulting, and, more rarely, dike injection (Sohn et al., 2004; Tolstoy et al., 2008; Wilcock et al., 2009). In one study (Tolstoy et al., 2008), hypocenters beneath a hydrothermal vent field on the EPR cluster in a vertical pipelike zone that lies above the shallow axial melt lens, suggesting that the events are mainly hydrothermal in nature and mark the location of very active fluid flow. A few studies indicate that tidally induced stresses within the upper crust modulate microearthquake origin times (Stroup et al., 2007, 2009; Tolstoy et al., 2002; Wilcock, 2001). At the northern EPR, a relationship between peak microearthquake activity and maximum predicted tidal extension has been interpreted to result from pore-pressure perturbations propagating laterally through the hydrothermal system (Stroup et al., 2009).

While the upper crust is widely believed to be emplaced via repeated dike injections from the top of the shallow melt lens, thus forming sheeted dikes and extrusive rock units, there is no

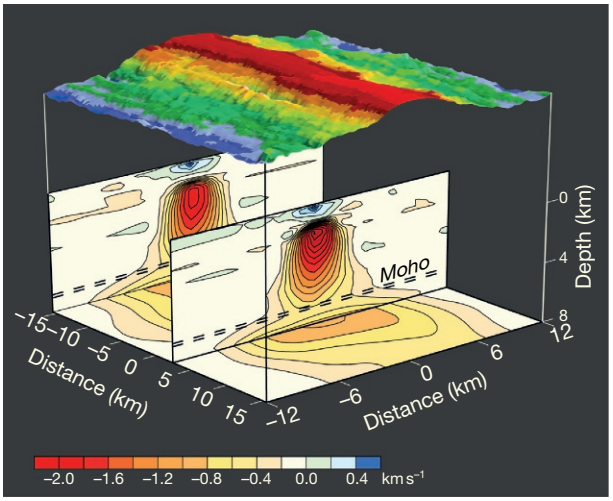

Figure 19 Three-dimensional tomographic image of the crustal magmatic system beneath the East Pacific Rise, 9°30′N. Contours of 0.2 km s^{-1} are relative to a background one-dimensional depth-varying velocity model. Low velocities are indicative of high temperatures and melt within a narrow magmatic system. A small and thin subaxial melt lens, observed in multichannel reflection data, passes along the low-velocity region at 1.5 km depth (not shown). Solution from Dunn et al. (2000).

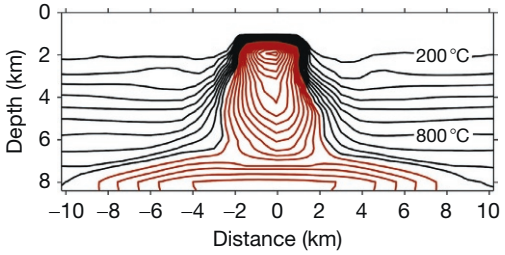

Figure 20 Estimated temperatures (black contours, 100° intervals) and melt content (red contours) beneath the East Pacific Rise. Estimated melt fraction depends on the dominant shape of the melt pockets. Assuming melt resides in thin films (aspect ratio = 0.05) gives a contour interval of 0.8% and a peak melt content of ~10%. Assuming that melt resides in equant-shaped pockets gives a contour interval of 2% and a peak melt content of 28%. Calculations are made assuming that seismic anelasticity is important. Estimates are based on the results of Dunn et al. (2000).

general agreement on the formation of the lower crust. For over two decades, there have been many attempts to reconcile the geophysical observations from the EPR and petrologic and structural observations in the Oman ophiolite. This work has led to a variety of models for the formation of the lower crust that are defined by two end-members. In the gabbro glacier or conveyor belt models (e.g., Henstock et al., 1993; Nicolas et al., 1988, 1993; Phipps Morgan and Chen, 1993a; Quick and Denlinger, 1993), the gabbros crystallize in a small magma lens at the dike/gabbro boundary and then subside to form the lower crust. In the sheeted sill model (e.g., Boudier et al., 1996; Kelemen and Aharonov, 1998; Kelemen et al., 1997; MacLeod and Yaouancq, 2000), magma moves upward through a series of thin sills and the lower crust crystallizes *in situ*. Hybrid models combine varying proportions of gabbro flow and sill emplacement and/or include crystallization in a pair of magma lenses, one located at the dike/gabbro boundary and the other at the base of the crust (Boudier et al., 1996; Chen, 2001; Chenevez et al., 1998; Maclennan et al., 2004). Several arguments have been made both for and against each of the models mentioned earlier (see Cherkaoui et al. (2003) for a brief review of older work), and to date, there is no clear seismic evidence for stacks of melt lenses in the lower crust (e.g., Singh et al., 2006a,b).

There is growing evidence that not all mantle melts are directly focused upward to the narrow crustal magmatic system. Garmany (1989), using P-to-S converted seismic phases, first suggested the presence of deep melt lenses forming at the crust–mantle boundary away from the axis of a fast-spreading ridge. More recently, Durant and Toomey (2009), using wide-angle refraction data, found evidence for the presence of high temperatures and perhaps melt in an isolated area roughly 20 km from the axis of the EPR – well outside of the low-velocity region that characterizes the subridge crustal magmatic system. Using MCS data, Canales et al. (2012) show evidence for a network of melt lenses located 4–8 km from the axis of the EPR, outside of the main axial zone of crustal accretion but above a region that is expected to be partially molten. Pockets of melt observed to extend from the off-axis sills inward to the axial zone might represent melt migration pathways. To date, it appears that off-axis melt supply to the crust may only make up a tiny fraction of the overall crustal production that occurs along fast-spreading ridges. Nevertheless, more observations such as these will probably be forthcoming, and they will provide important insight into processes of melt supply to ridges.

Along the EPR, the ridge axis is segmented on a variety of scales, and the deepest portions of the ridge are often located near large tectonic offsets, such as at the tips of propagating ridges and at transform faults (e.g., Macdonald, 1998). Transform faults are long-lasting features that can offset ridges by one hundred or more kilometers, though usually less, and leave large fracture zones in their wakes. Only a few seismic studies have examined their structure (e.g., McGuire et al., 2012; Roland et al., 2012; van Avendonk et al., 1998, 2001), and these studies are mainly limited to imaging at crustal depths. A recent detailed study by Roland et al., 2012 shows that transform fault traces are associated with broad seismic low-velocity zones (**Figure 21**) and intense seismicity. The zones are >5 km wide in the shallow crust and as wide as 2 km at the base of the crust, and they are interpreted to be wide, compliant zones of enhanced fracturing and porosity.

Between transform offsets, fast-spreading ridges are segmented by both small bends in the ridge axis and larger overlapping offsets. The origin of this segmentation is controversial. By one view, they result directly from 3D mantle upwelling. Alternatively, some types of segmentation may be regulated by the tectonic rifting of young lithosphere and thus only indirectly linked to the form of mantle upwelling. Central to the controversy is the origin of OSCs. OSCs are segment boundaries characterized by the overlap of two en echelon ridge segments that offset the axial neovolcanic zone by a few hundred meters to many kilometers. Unlike transform offsets, OSCs can migrate along the ridge, as the individual ridge limbs

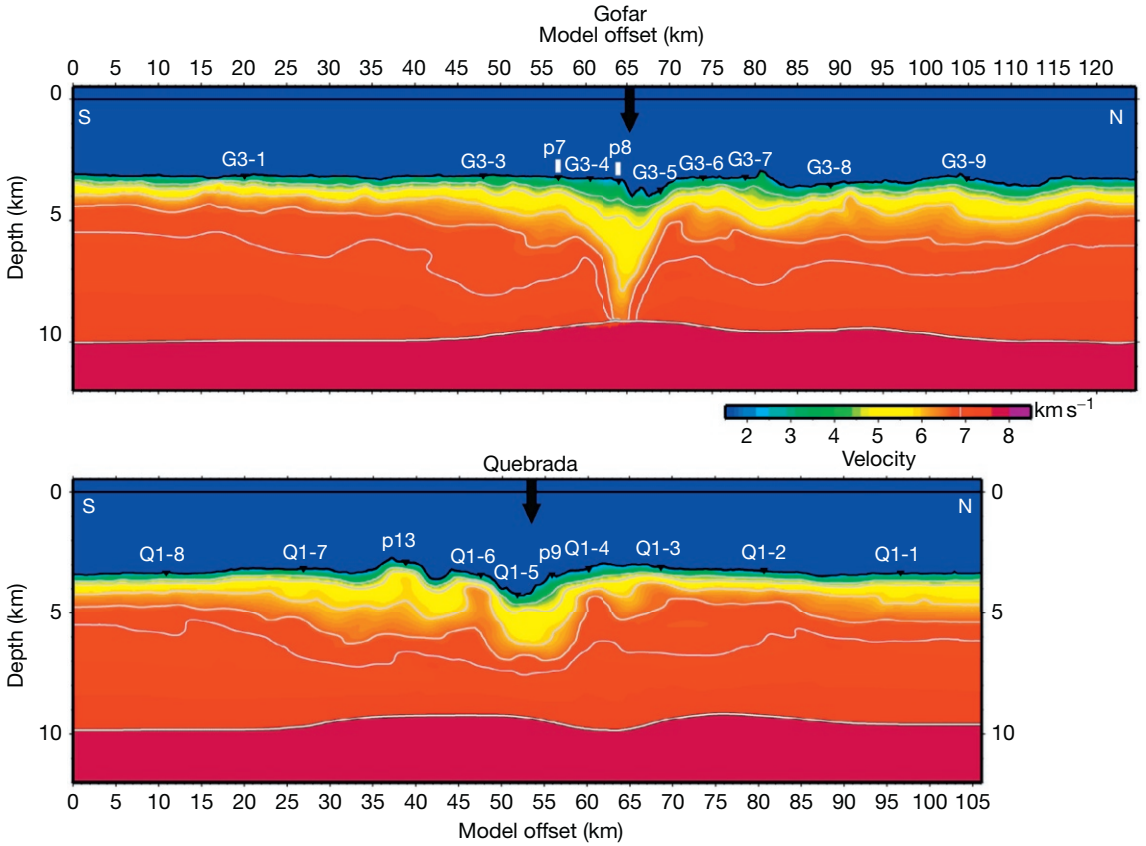

Figure 21 P-wave velocity profiles across the Gofar (top) and Quebrada (bottom) fault system on the southern East Pacific Rise determined from wide-angle refraction data sets. Deepest white line shows the location of the Moho reflector. Velocity is contoured at 4.2, 5.0, 6.0, 6.6, and 7.0 km s^{-1}. Black arrows show the approximate location of the active transform fault. Reproduced from Roland E, Lizarralde D, McGuire JJ, and Collins JA (2012) Seismic velocity constraints on the material properties that control earthquake behavior at the Quebrada-Discovery-Gofar transform faults, East Pacific Rise. *Journal of Geophysical Research* 117: B11102. http://dx.doi.org/10.1029/2012JB009422.

propagate or recede (Carbotte and Macdonald, 1992, 1994; Macdonald et al., 1988). The structural evolution of OSCs has led some to speculate that their origin is the result of fluctuations in axial magmatic processes (e.g., Macdonald et al., 1984, 1988, 1991) and that OSCs occur above regions of reduced magma supply, perhaps at the boundary between two widely separated regions of mantle upwelling (Schouten et al., 1985). An opposing model states that OSCs are the result of tectonic processes, a response to changes in regional strain, such as those arising from changes in the kinematics of spreading (Lonsdale, 1983, 1986, 1989; Macdonald et al., 1984). In this hypothesis, the magma supply beneath the OSC is uninterrupted. The observation that most OSCs on the Pacific–Cocos plate boundary share a right lateral offset suggests that the offsets formed in response to a recent counterclockwise rotation in the direction of spreading (Carbotte and Macdonald, 1992, 1994), such that the new forces on the plate boundary lead to the segmentation of the ridge and the formation of OSCs. Three-dimensional MCS and refraction surveys of an OSC at 9°03′N on the EPR indicate that melts that feed the limbs of the OSC rise up directly from the mantle beneath the OSC itself (Bazin et al., 2003; Kent et al., 2000). Furthermore, an active-source tomographic study of the mantle beneath the 9°03′N OSC (Toomey et al., 2007) did not find a reduction in the size or magnitude of the mantle low-velocity zone beneath the OSC as compared to other areas beneath the EPR (**Figure 18**). Studies of crustal thickness produced in the wakes of OSCs have not consistently found thinner crust in those areas (Barth and Mutter, 1996; Bazin et al., 1998). Together, these results indicate that melt supply is fairly uniform along the ridge beneath OSCs over long timescales.

On a smaller scale, segments of the EPR bounded by minor morphological deviations from axial linearity or 'devals' (Langmuir et al, 1986) of 5–25 km length may be associated with separate shallow volcanic systems (Haymon et al., 1991) and higher proportions of melt at depth (Dunn and Toomey, 1997; Dunn et al., 2000; Toomey et al., 1990, 1994). Seismic tomographic studies of the EPR (Dunn and Toomey, 1997; Dunn et al., 2000; Toomey et al., 1990; 2007) reveal that both the crustal low-velocity region and the mantle low-velocity region vary along the rise on a scale comparable to the deval segmentation, with lower velocities generally located at the centers of each segment (**Figure 18**). In some instances, the seismic reflector that defines the crustal melt lens also changes in character near devals (e.g., Kent et al., 1993). These studies suggest that crustal magma chambers are replenished from the mantle at closely spaced intervals. To produce these small variations, the mantle melt supply may be locally

enhanced by mantle temperature variations (Thompson, 1987); compositional heterogeneity (Langmuir et al., 1986; Pickering-Witter and Johnston, 2000); 3D melt segregation and transport mechanisms, such as the coalescence of small-scale melt segregations, veins, dikes, or dissolution channels (e.g., Kelemen et al., 1995; Nicolas, 1989; Sleep, 1988; Stevenson, 1989); or diapirism (Boudier et al., 1997; Ceuleneer and Nicolas, 1985; Jousselin et al., 1998; Nicolas and Boudier, 1995; Nicolas and Violette, 1982; Nicolas et al., 1994; Whitehead et al., 1984). Evidence for mantle diapirs has been found in the Oman ophiolite, the largest of which have a characteristic radius that is generally small – about 3 km (defined by the region of inferred vertical flow). Such features have been mapped at intervals of a few tens of kilometers along the paleoridge axis; some are spaced as close as 10 km (Boudier et al., 1997). However, the scale of the diapiric flow is expected to be smaller than current seismic experiments are capable of resolving (Jousselin et al., 2003), and no direct evidence for diapiric mantle flow beneath an active ridge has been detected.

1.13.3.3 Intermediate-Spreading Ridges

Mid-ocean ridges with intermediate spreading rates of roughly 55–85 mm year^{-1} include the Juan de Fuca Ridge (JdFR), Southeast Indian Ridge (SEIR), Pacific–Antarctic Ridge, Galápagos Spreading Center (GSC), and Chile Rise (**Figure 1**). Some back-arc systems also open at intermediate rates. Crust produced along the ridges tends to be 5–7 km thick (**Figure 10**), in the same range as for faster-spreading ridges. In addition, seismic layer 2A (**Figure 22**) is observed to thicken rapidly within 1–2 km of the ridge axis (e.g., Baran et al., 2010; Canales et al., 2005). Together, these observations suggest a similar crustal emplacement history for both intermediate- and fast-spreading ridges. However, instead of a shallow topographic rise at the ridge axis, intermediate-rate ridges have more variable topography, ranging from rifted axial deeps to rises. In many places, the axis of the ridge deepens substantially toward a major ridge offset. Upper crustal P-wave velocities also appear to be slower on average than that produced at faster spreading rates (e.g., see compilation in Figure 6 of Jacobs et al. (2007)). These and other observations have led many to suggest that lower heat influx to these ridges, due to their slower spreading rates, results in episodic crustal melt storage, a thicker effective lithosphere, and a greater degree of cracking and faulting of the ridge axis.

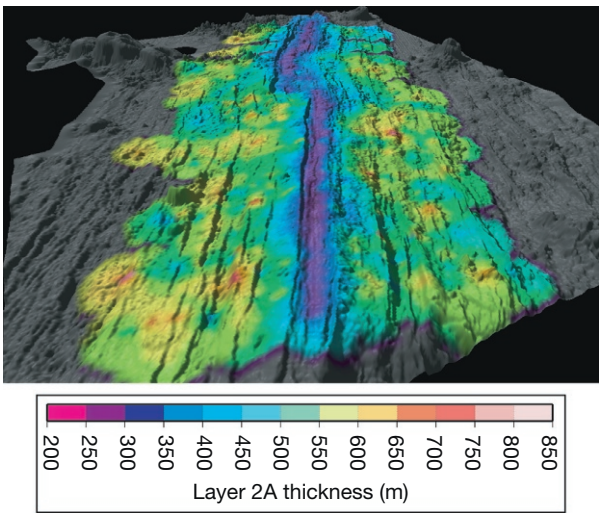

Figure 22 Three-dimensional perspective view of the layer 2A thickness draped over seafloor topography. Layer 2A thickness is often considered to be a proxy for the thickness of the volcanic, extrusive layer of the upper crust. Reproduced from Canales JP, Detrick RS, Carbotte SM, et al. (2005) Upper crustal structure and axial topography at intermediate-spreading ridges: Seismic constraints from the Southern Juan de Fuca Ridge. *Journal of Geophysical Research* 110: B12104. http://dx.doi.org/10.1029/2005JB003630.

On the basis of gravity profiles derived from GEOSAT radar altimetry, Small and Sandwell (1989) suggested that a threshold-type mechanism governs ridge axis form; this and several subsequent studies found an abrupt switchover from a smooth axial high morphology to rough axial deeps at intermediate spreading rates of roughly 60–70 mm year^{-1} (e.g., Malinverno, 1993; Small, 1998; Small and Sandwell, 1992, 1994). Within that narrow range of spreading rates, the morphology of the ridges is highly variable from one to the next, and several studies have put forth the hypothesis that intermediate-spreading ridges evolve through cycles of magmatic and tectonic spreading (Kappel and Normark, 1987; Kappel and Ryan, 1986; Perfit and Chadwick, 1998; Smith et al., 1994). It has been suggested that the key influence on whether the ridge axis is in a state of magmatic versus tectonic opening is the presence or lack of a crustal magmatic system, which would influence the thermal structure and the strength of the crust (e.g., Perfit and Chadwick, 1998). A modeling study by Phipps Morgan and Chen (1993a,b) suggested that intermediate-spreading ridges are in a delicate balance either supporting a crustal magma chamber or not, and this threshold-like sensitivity leads to the observed large changes in ridge morphology.

A series of recent seismic studies along the JdFR, GSC, and SEIR have shed new light on this issue. Contrary to earlier expectations, MCS data reveal shallow axial melt lenses beneath all JdFR segments (**Figure 23**), including those previously assumed to be in a tectonic phase of extension (Canales et al., 2005, 2006; Carbotte et al, 2006, 2008; van Ark et al., 2007). Similarly, some segments of the SEIR and GSC are underlain by an axial melt lens (Baran et al., 2010; Blacic et al., 2004), even though in some cases, they may exhibit deeper and more heavily rifted axes. As compared to faster-spreading ridges, the depth of the melt lens is more variable along intermediate-spreading ridges. Individual ridge segments are associated with distinct lens depths, and along a single spreading segment, the depth of the lens is also often correlated with seafloor axial depth (**Figure 23**). Lens depth can also be correlated with the presence or absence of an axial summit graben. Thus, while the absence or presence of a melt lens, or larger crustal magmatic system, may have a large influence on axial thermal structure and strength, it appears that subtle variations of melt lens depth can also have a large control on ridge morphology (Carbotte et al., 2006).

The growth of layer 2A within a few kilometers of the ridge is often considered to be a measure of the volcanic construction of the upper crust. While the growth of layer 2A at intermediate-rate ridges can be similar to that along faster-

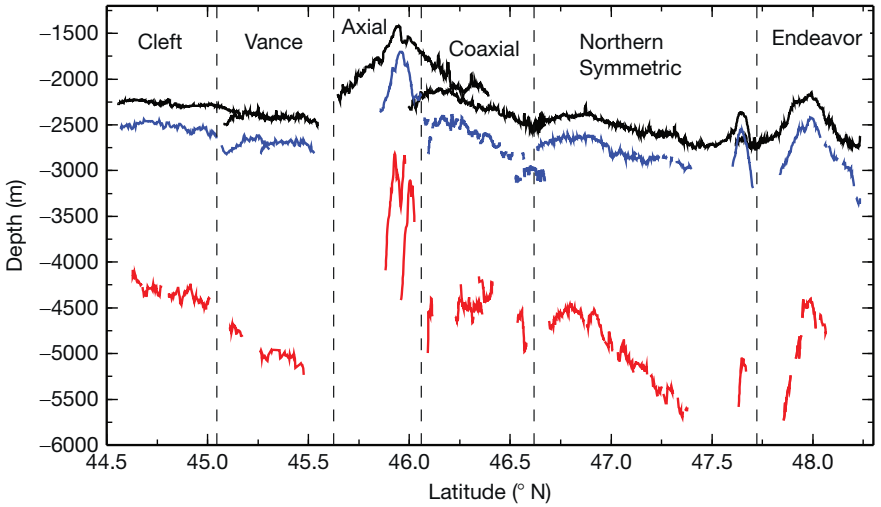

Figure 23 Estimates of the depth beneath the seafloor (black) of seismic layer 2A (blue) and melt lens (red), beneath the segments of the Juan de Fuca Ridge. Reproduced from Carbotte SM, Nedimović MR, Canales JP, Kent GM, Harding AJ, and Marjanović M (2008) Variable crustal structure along the Juan de Fuca Ridge: Influence of on-axis hot spots and absolute plate motions. *Geochemistry Geophysics Geosystems* 9: Q08001. http://dx.doi.org/10.1029/2007GC001922.

spreading ridges (e.g., Canales et al., 2005; **Figure 22**), differences in growth along the Cleft, Vance, and Endeavor segments of the JdFR suggest somewhat different modes of extrusion and upper crustal formation for each segment. Therefore, processes of lava emplacement and distribution on the seafloor may be modulated by magma supply (Canales et al., 2005).

The presence of a partially molten lens along sections of ridge without an axial rise argues against prior hypotheses that hydrothermal heat extraction along such ridges is driven by the propagation of a cracking front down into a frozen magma chamber (Wilcock and Delaney, 1996). Instead, the hydrothermal systems, like those at the EPR, appear to be driven by heat extraction from a crustal magma body (e.g., van Ark et al., 2007). Morphological and hydrothermal differences between the intermediate-spreading ridge and the fast-spreading EPR can be attributed to the greater depth of the JdFR melt lenses (2–3.3 vs. 0.5–1.5 km; Kent et al., 1993) and the correspondingly cooler, more brittle shallow crust overlying the lens (van Ark et al., 2007). Variations in the seismic properties of the melt lens, and by inference the melt/crystal ratio, correlate with lava chemistry (Smith et al., 1994) and with the location of hydrothermal plumes (Baker, 1994), suggesting that high-temperature hydrothermal venting along intermediate-spreading ridges is closely linked to the physical state of the underlying melt lens (Canales et al., 2006).

Strong P-wave reflections near the Moho transition zone have been found in JdFR MCS data, located both near the ridge axis (<20 km) and near the outer wakes of propagators on the ridge flanks (Nedimović et al., 2005). Groups of reflections found near the ridge axis could correspond to gabbroic melt lenses emplaced during magma delivery to the axis. Reflection events within the propagator wakes may be frozen melt sills injected at the base of the crust during ridge propagation. At the propagator tips, the ridge propagates into relatively cool lithosphere, which may enhance sill emplacement and rapid solidification (Nedimović et al., 2005).

1.13.3.4 Slow-Spreading Ridges

Slow-spreading ridges, with opening rates of roughly 20–50 mm year^{-1}, include the MAR, Central Indian Ridge, and several back-arc spreading centers. The seafloor morphology and seismic structure of the lithosphere along the ridges is highly variable, indicating that as spreading rate drops, processes of crustal formation become more 3D and tectonic complexity increases. Upper crustal velocities tend to be lower than for faster-spreading ridges and do not include a narrow high-velocity region along the ridge axis that is typical for faster-spreading-rate ridges (e.g., **Figures 13** and **22**), and the neovolcanic zone at the ridge axis is usually not well defined. Crustal thickness estimates via seismic studies are few and reveal that crustal thickness can vary widely from values near zero to as much as 9 km, though the average may be around 6 km (**Figure 20**).

Several observations indicate that the upper 3–4 km or more of crust is, in general, cool and brittle along slow-spreading ridges. The low-velocity layer, seismic layer 2, is usually observed throughout the top 1–2 km of the crust (Barclay et al., 1998; Canales et al., 2000a; Dunn et al., 2005; Hooft et al., 2000; Hosford et al., 2001; Hussenoeder et al., 2002) and is generally accepted to be the result of a high proportion of pores and cracks at these depths. In the upper crust, the detection of microearthquakes (e.g., Barclay et al., 2001), the ratio of P- to S-wave velocity (Barclay et al., 2001), and the presence of seismic anisotropy (Barclay and Toomey, 2003; Dunn et al., 2005; Seher et al., 2010a,b) reveal that the upper 2–4 km or more of crust is generally pervaded with faults and cracks and is thus relatively cool and brittle. The seismic structure of the upper crust is laterally variable and appears to reflect a variety of processes, such as tectonic modification, volcanic flux variations, and crustal aging (Arnulf et al., 2012; Barclay et al., 1998; Dunn et al., 2005; Hosford et al., 2001; Hussenoeder et al., 2002; Magde et al., 2000). In contrast to faster-spreading ridges

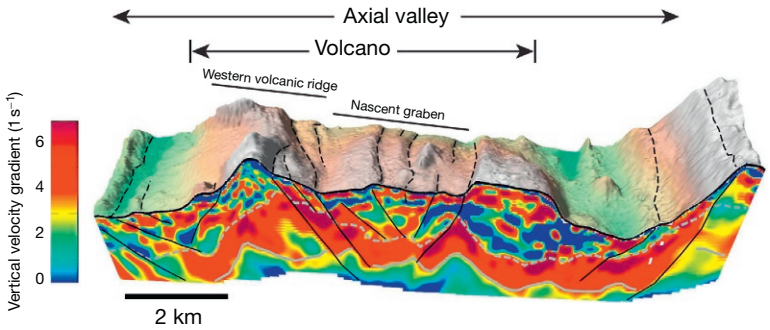

Figure 24 Three-dimensional schematic view of the shallow crust beneath the Lucky Strike volcano located along a segment of the Mid-Atlantic Ridge at ~37°18′N latitude. Colors indicate the P-wave velocity gradient structure. The thick red band, bounded by the dashed and solid gray lines, indicates the velocity jump at the base of layer 2A. The young shallow crust beneath the Lucky Strike volcano is interpreted as piled-up volcanic sequences emplaced within the axial valley. The volcanic units are shifted and rotated by normal faults. Reproduced from Arnulf AF, Harding AJ, Singh SC, Kent GM, and Crawford W (2012) Fine-scale velocity structure of upper oceanic crust from full waveform inversion of downward continued seismic reflection data at the Lucky Strike Volcano, Mid-Atlantic Ridge. *Geophysical Research Letters* 39: L08303. http://dx.doi.org/10.1029/2012GL051064.

where the axis of eruption is fairly narrow (~1–2 km), the formation of new crust can occur over the entire width of the axial valley (Barclay et al., 1998). Small, scattered velocity anomalies are commonly observed in 2D and 3D experiments and can arise from lateral variations in pores, cracks, alteration products, and the ratio of porous extrusive rocks to less-porous intrusive rocks and likely reflect the nonuniform construction of the upper crust with time. A detailed study of layer 2A beneath the Lucky Strike volcano on the MAR at 37°18′N shows low velocities and strong velocity gradients that are interpreted as piled-up volcanic sequences (**Figure 24**). In some areas, it is reported that upper crustal velocities are anomalously low in a broad axial band that parallels the ridge axis (e.g., Dunn et al., 2005; Magde et al., 2000; Seher et al., 2010b). Relatively low near-axis velocities with respect to higher off-axis velocities are a global phenomenon and widely interpreted to reflect a porous upper crust that decreases in porosity with age via hydrothermal deposition (**Figure 14**).

Along the axes of slow-spreading ridges, melt flux variations are thought to control crustal thickness, lithospheric strength, and the partitioning of plate spreading between magmatism and faulting (e.g., Cannat, 1993, 1996; Parsons et al., 2000; Tucholke and Lin, 1994). With higher melt supplies to many ridge segment centers (Blackman and Forsyth, 1989), seafloor spreading should be more magmatically accommodated near a segment's midsection and more tectonically accommodated at the ends (e.g., Cannat, 1993; Gràcia et al., 1999; Rabain et al., 2001; Tucholke and Lin, 1994). The great diversity of ridge segment morphologies and maximum depth of seismicity (e.g., Barclay et al., 2001), a proxy for lithospheric thickness, indicate that temporal variations in melt/heat supply modulate the magmatic–tectonic trade-off of crustal formation. Segment-to-segment diversity of ridge morphology can be interpreted as reflecting various stages of the magmatic–tectonic evolution (e.g., Barclay et al., 2001; Cannat, 1993; Gràcia et al., 1999; Singh et al., 2006a). Though even during magmatically robust periods, crustal magmatic systems are thought to be largely confined to segment centers.

At the ends of ridge segments, seismically observed thin crust and extensive upper crustal low-velocity regions, located both on-axis and off-axis, are likely the result of lower melt supply and a greater degree of tectonic stretching and fracturing. In support of this interpretation, geologic mapping of the seafloor (e.g., Gràcia et al., 1999) often reveals greater densities of cracks and fissures at segment ends than the segment center. Crust produced near segment ends may lack a distinct transition from seismic layer 2 to 3 (Canales et al., 2000a; Hosford et al., 2001; Sinha and Louden, 1983), and the transition from crustal to mantle velocities appears to occur over a depth range of 3 km or more (Canales et al., 2000a; Dunn et al., 2005). These seismic observations are consistent with a highly fractured and altered crust overlying a serpentinized upper mantle at segment ends.

A major characteristic that sets slow-spreading ridges apart from faster-spreading ridges is the exposure at the seafloor of lower crustal and mantle-derived ultramafic rocks. In many places, the crustal structure appears chaotic, with a thin or nonexistent seismic layer 3 and no consistent sheeted dike layer. Over the past 10 years, it has been recognized that extension by faulting, as opposed to extension accommodated by magmatic emplacement, is much more important than previously thought, accounting for over 50% of the extension along large sections of slow-spreading ridge (e.g., Buck et al., 2005; Cannat et al., 2006; Escartin et al., 2008; Olive et al., 2010; Smith et al., 2006, 2008; Tucholke et al., 1998, 2008). Detachment faults are common and can greatly disrupt the 'layer-cake' structure of the crust (**Figure 25**). Large, long-lived (>1 Ma) detachment faults with significant rotation expose extensive sections of the crust and upper mantle at the seafloor, forming what is known as an oceanic core complex (OCC). OCCs carry 50–100% of the plate separation velocity during periods when they are active (Grimes et al., 2008; Tucholke et al., 2008). They are often found at the inside corner of a ridge-transform intersection but can occur elsewhere along a spreading segment. There have been a number of seismic studies of individual OCCs and detachment faults, such as the Atlantis Bank at the SWIR (Henig et al., 2012; Muller et al., 2000), the Atlantis Massif at the MAR near 30° N (Blackman and Collins, 2010; Canales et al., 2004, 2008), the TAG area at the MAR near 26° N (Canales et al., 2007, 2008; de Martin et al., 2007), the Kane area at the MAR near 23°20′N (Canales, 2010; Canales et al., 2000b, 2008;

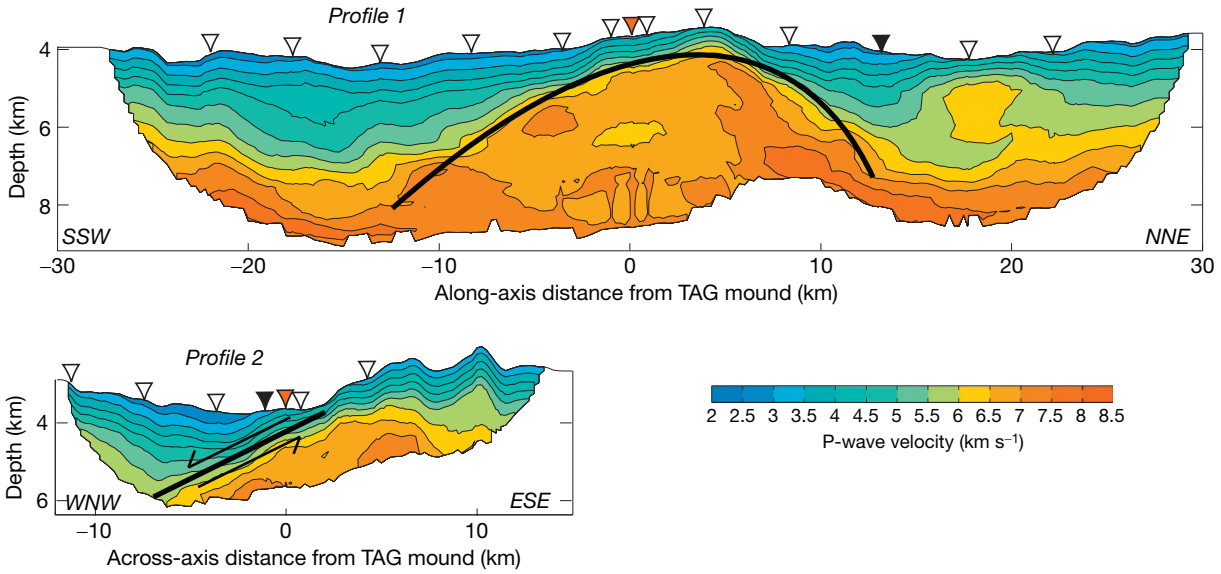

Figure 25 Seismic cross sections of the Mid-Atlantic Ridge via P-wave tomography. (Profile 1) Cross-section oriented parallel to the Mid-Atlantic Ridge and centered at ~26°10′N. (Profile 2) Cross-section oriented perpendicular to the axis of the ridge at 26°10′N. The thick black line in each profile indicates the (interpreted) geometry of the subsurface detachment fault. Red inverted triangle indicates the location of the TAG hydrothermal mound. Reproduced from Canales JP, Sohn RA, and deMartin BJ (2007) Crustal structure of the Trans-Atlantic Geotraverse (TAG) segment (Mid-Atlantic Ridge, 26°10′N): Implications for the nature of hydrothermal circulation and detachment faulting at slow spreading ridges. *Geochemistry Geophysics Geosystems* 8: Q08004. http://dx.doi.org/10.1029/2007GC001629.

Xu et al., 2009), the MAR 5° S (Planert et al., 2010), and the MAR 22°19′N (Dannowski et al., 2010). OCCs are often underlain by broad regions of anomalously high velocities at shallow depths and high vertical velocity gradients in the uppermost crust. Blackman et al. (2009) provide a review of geophysical studies of oceanic core complexes.

A limited number of seismic experiments have been performed to explore for crustal magma chambers along slow-spreading ridges. Refraction experiments located at 23°20′N (Canales et al., 2000b), 35° N (Dunn et al., 2005; Hooft et al., 2000), and 37° N (Seher et al., 2010b) on the MAR and 57°45′N on the Reykjanes Ridge (Navin et al., 1998) have detected significant low-velocity zones in the middle to lower crust, extending downward into the mantle, that are consistent with high temperatures and, in some cases, a small amount of melt. Reflection experiments have also detected shallow reflectors that indicate the presence of a shallow melt lens at the top of the broader magmatic systems (Singh et al., 2006a). However, the majority of these experiments were carried out in areas at least marginally affected by hot spots and thus may not be representative of slow-spreading ridge structure.

One seismically well-studied area of the MAR is the ~90 km long segment of the MAR at 35° N latitude, just south of the Oceanographer Fracture Zone. Several lines of evidence indicate that more melt is currently delivered to the center of this ridge segment than its ends. For example, an hourglass morphology and shallow water depth of the segment midpoint, an anomalously large mantle Bouguer gravity anomaly low-centered on the segment, and a chain of seamounts that intersects the segment center have all been attributed to enhanced magmatism near the segment center (Detrick et al., 1995; Rabain et al., 2001; Thibaud et al., 1998). This section of ridge may be mildly influenced by the Azores hot spot to the north and thus may exhibit slightly higher melt supply than for other non-hot spot-influenced sections of the ridge. At the center of the 35° N ridge segment, a large low-velocity 'plug' extends from about 4 km depth down into the mantle (**Figure 26**; Dunn et al., 2005). Assuming that the brittle–ductile transition is near 4 km depth, as indicated by the microearthquake study of Barclay et al. (2001), then the large low-velocity zone is most likely due to elevated temperatures and a small amount of melt (~3%) at depths >5 km. The melt could exist along grain-boundary interfaces or within larger isolated regions with higher melt concentrations, which, when averaged together, make up the 3% melt fraction. For example, the lower crust could be composed of partially molten dikes and sills. Dunn et al. (2005) detected seismic anisotropy within the large low-velocity region and suggested that this anisotropy and the reduced isotropic velocities are due to a cluster of vertical, partially molten, dikes in the lower crust. Crustal thickness studies for this area (Canales et al., 2000a; Dunn et al., 2005; Hooft et al., 2000; Hosford et al., 2001) reveal 8.5 ± 0.5 km thick crust near the segment center and 4–5 km thick crust to the north and south of center, with values as low as 3–4 km thickness (Hooft et al., 2000) near the Oceanographer Fracture Zone. Ridge-perpendicular variations in crustal thickness are modest, greater than or equal to ± 0.5 km in this area, which stands in sharp contrast to the 23°20′N area of the MAR, where the transition from crustal to mantle velocities undulates up and down with distance from the ridge, indicating that the magma supply waxes and wanes significantly with time (**Figure 27**; Canales et al., 2000b).

1.13.3.5 Ultraslow-Spreading Ridges

Mid-ocean ridges with ultraslow spreading rates, less than ~15–20 mm year^{-1} (full rate), include the SWIR and the

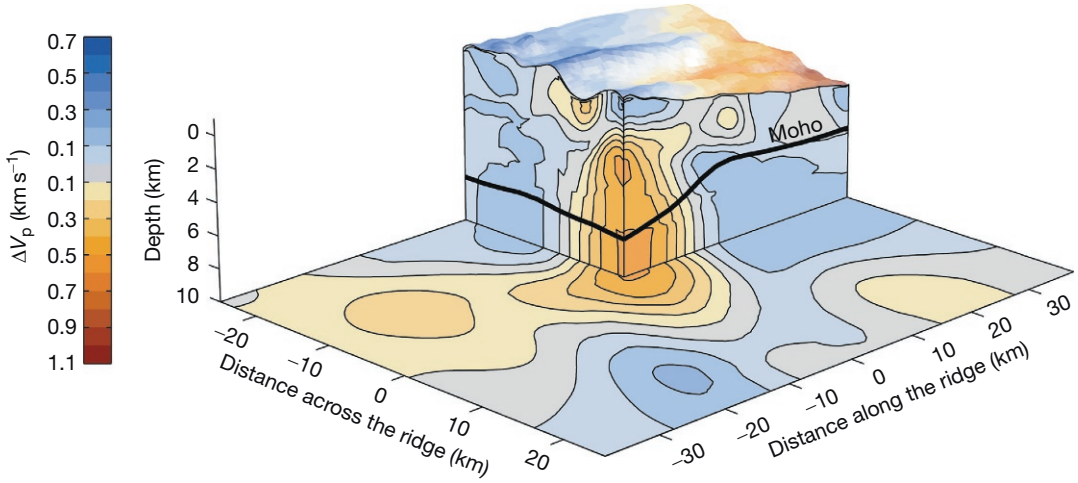

Figure 26 Three-dimensional perspective view of the P-wave velocity structure of the crust and mantle of the Mid-Atlantic Ridge at 35° N (relative to a 1D depth-dependent model). A low-velocity 'plug' is observed at the center of the ridge segment, where the crust is also up to 8.5 km thick (vs. <4–5 km thick near the segment ends). The velocity anomaly is consistent with high temperatures and a few percent melt and probably represents the current magma plumbing system for this section of the ridge. Seismic anisotropy in the lower crust at the segment center indicates that the anomaly is composed of a cluster of partially molten dikes that intruded from mantle depths. Reproduced from Dunn RA, Lekic V, Detrick RS, and Toomey DR (2005) Three-dimensional seismic structure of the Mid-Atlantic Ridge (35°N): Evidence for focused melt supply and lower crustal dike injection. *Journal of Geophysical Research* 110: B09101. http://dx.doi.org/10.1029/2004JB003473.

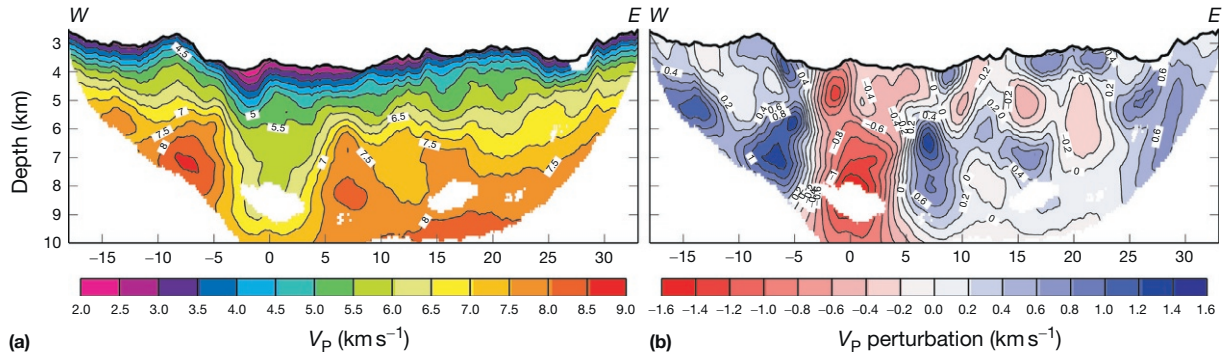

Figure 27 Two-dimensional tomographic images of the Mid-Atlantic Ridge near 23° N (MARK area). Plane of the images is perpendicular to the ridge axis. Anomalously low velocities beneath a neovolcanic ridge (near $x = 0$) extend downward from the middle crust and are consistent with high temperatures and 4% or more melt. Outside of this region, the crust is seismically very heterogeneous, with crustal thickness variations of >2.2 km over ~5 km distances. Such heterogeneity suggests that the melt supply fluctuates substantially over short timescales, creating periods of magmatic and amagmatic spreading. Reproduced from Canales JP, Collins JA, Escartin J, and Detrick RS (2000) Seismic structure across the rift valley of the Mid-Atlantic Ridge at 23°20′N (MARK area): Implications for crustal accretion processes at slow spreading ridges. *Journal of Geophysical Research* 105(B12): 28411–28425.

ridges that lie north of the Arctic Circle: the Mohns, Knipovich, Molloy, and Gakkel Ridges (Figure 1). Ridges in this category display a lack of transform faults and are instead composed of linked magmatic and amagmatic accretionary segments of ridge (Dick et al., 2003). A critical issue is how an exceptionally slow spreading rate influences melt production, crust and lithosphere thickness, tectonics, volcanism, and many other ridge processes. To date, several seismic refraction profiles near these ridges have been carried out, but they generally have sparse station spacing (spacing > crustal thickness) and are sometimes not reversed (with seismic energy traveling in opposite directions) such that their interpretation can be ambiguous. There have been no large and dense 3D refraction or multichannel reflection studies of an ultraslow-spreading ridge to date (there is one as yet unpublished 3D study along the SWIR (Jian et al., 2012)). The details of crustal and lithospheric formation along these ridges are consequently less well understood.

While crustal thicknesses for these ridges are often quoted to decrease with spreading rate from roughly 4 to 0 km (Figure 10), when each ridge is examined individually, we see that seismically determined values of crustal thickness vary widely and crustal thickness does not decrease uniformly with spreading rate. Instead, episodic and spatial variations in melt supply appear to govern crustal thickness, with values reported in some areas that exceed the global average thickness (e.g., Jian et al., 2012), and in other areas mantle, rocks are

found on the seafloor (Michael et al., 2003). Ridge-parallel refraction profiles at different lithospheric ages along the central portion of the Mohns Ridge provide estimates of crustal thickness between 3.75 and 4.5 km, with $1-\sigma$ uncertainties of 0.3–1 km, depending on the profile (Klingelhöfer et al., 2000). Profiles extending away from the Knipovich Ridge reveal crustal thicknesses of 3.5–5.6 km at the ridge, though values as high as 8 km are found away from the ridge axis (Ljones et al., 2004; Ritzmann et al., 2002). A seismic profile extending away from the Molloy Ridge reveals a thickness of ~4–5 km near the ridge, ~3 km near the Molloy Fracture Zone, and values as high as 10 km away from the ridge axis (Czuba et al., 2005). Nonreversed seismic profiles collected along the Gakkel Ridge resulted in crustal thickness estimates of 1.2–3.5 km (Jackson et al., 1982; Jokat and Schmidt-Aursch, 2007). Along the SWIR, crustal thickness estimates range from 2 to 2.5 km beneath the ridge segment boundaries to values of 3.5–6 km at segment midpoints (Muller et al., 1997, 1999).

Seismic studies show that the basic velocity structure, as a function of depth, differs greatly from that observed at faster-spreading ridges (e.g., **Figure 12**). While a seismic layer 2 is often present, seismic layer 3 tends to thin as crustal thickness decreases and P-wave velocities of the lower crust are less likely to exceed 6.5 km s^{-1}. Mantle velocity values are also found to be generally low both beneath the ridges and in off-axis areas (e.g., Klingelhöfer et al., 2000), and there has been considerable debate as to whether these low values are due to high temperatures and melt, the effect of anisotropy (for profiles not oriented in the spreading direction), mantle serpentinization (due to increased faulting along these ridges), melt retention (due to freezing in of melt as it rises beneath a cold spreading center – see also **Section 1.13.2.5**), or a combination of factors.

1.13.3.6 Regional Influences

Sections of mid-ocean ridge located near hot spots have long been recognized to be influenced by these mantle anomalies (Schilling, 1985; Vogt, 1976). These include the Galápagos Spreading Center (Galápagos hot spot), Mid-Atlantic Ridge (Iceland, Azores, and Tristan da Cunha hot spots), Juan de Fuca Ridge (Cobb hot spot), Mohns Ridge (Jan Mayen hot spot), Southwest Indian Ridge (Marion and Bouvet hot spots), and Southeast Indian Ridge (Amsterdam – Saint Paul hot spot), among others (e.g., Courtillot et al., 2003). Hot spots may produce a large regional-scale thermal anomaly that underlies the ridge, perhaps linked to excess temperatures produced in the upper mantle by a deep-seated plume. Hot spots may also provide lateral flow of plume material along, and across, the ridge axis (e.g., Morgan, 1978; Schilling, 1991; Vogt, 1976). Generally speaking, at ridges influenced by hot spots, melt production is enhanced, the crust is thicker than the global average of 6–7 km, the ridge axis is hotter (the lithosphere is thinner), and long-lived crustal magma chambers may be present. One exception is crust formed in the Wharton Basin, where a fast-spreading-rate ridge produced anomalously thin crust (Singh et al., 2011). The authors of this study suggest that a thick layer of cold lithosphere surrounding the Kerguelen plume suppressed mantle melting beneath the ridge. In addition, regional mantle thermal anomalies not of hot spot origin may influence ridge processes. Along the Southeast Indian Ridge, the ridge axis deepens and the crust thins toward the Australian–Antarctic Discordance (Holmes et al., 2008), an area that has been suggested to be a mantle 'cold spot.' Many small mantle chemical anomalies may also influence subridge melting and ridge properties.

The Iceland anomaly is the largest of the ridge-related hot spots. Seismic surveys to the south of Iceland along the Reykjanes Ridge portion of the MAR have found evidence for thick crust (Smallwood et al., 1995) and a shallow melt lens capping a crustal magmatic system (Navin et al., 1998; Peirce et al., 2005; Sinha et al., 1997). A higher melt supply results in hotter axial temperatures and a weaker axial lithosphere. Crust produced along the Reykjanes Ridge is anomalously thick to a distance of ~1000 km from Iceland. To the north of Iceland, along the Kolbeinsey Ridge, seismic refraction profiles also reveal anomalously thick crust as well as evidence for high crustal temperatures and perhaps melt beneath the ridge axis (Hooft et al., 2006; Kodaira et al., 1997).

A seismic survey of the MAR south of the Azores islands, located on the bathymetric swell of this hot spot, has also detected a shallow crustal melt lens (Singh et al., 2006a) and underlying low-velocity zone (Seher et al., 2010a). In this case, a reflection from the top of the melt lens, centered beneath the Lucky Strike volcano and hydrothermal field, is ~3 km beneath the seafloor, 3–4 km wide (much wider than the average along the EPR), and extends up to 7 km along the ridge. The colocation of the melt lens and active hydrothermal field indicates that the lens provides the heat that drives the hydrothermal circulation (Singh et al., 2006a). The broader magmatic system, as indicated by the low-velocity zone, is colocated with relatively thick crust (Seher et al., 2010a).

1.13.3.7 Back-Arc Spreading Centers

From observations made to date, the basic structure of oceanic crust and lithosphere formed in back-arc settings appears to be rather different, and perhaps more complex, than the crust formed along mid-ocean ridges. While the spreading rate is a dominant factor that controls crust and lithospheric structure of normal ridges, in back-arc settings, slab-derived volatiles – principally water – appear to have a large control on melting processes and crustal formation that can overcome spreading rate trends. The presence of water during melting is expected to enhance melt production (e.g., Davies and Bickle, 1991; Stolper and Newman, 1994), with the water ending up in the melt (e.g., Hirth and Kohlstedt, 1996), and may also lead to more silicic lavas (e.g., Gaetani et al., 1994; Nicholls and Ringwood, 1973; Sisson and Grove, 1993).

One major observation is that when a back-arc spreading ridge is located close to an active arc system, the magma supply to the ridge appears to be relatively high and lavas erupted at the ridge have high water contents, with compositions ranging from basalts to rhyolites. In addition, the thermal structure of the ridge appears to be more like mid-ocean ridges with fast spreading rates, even though the back-arc spreading rate might be quite slow. For example, the presence of a dome-shaped ridge and a shallow magma lens is often considered an indication of high melt supply from the mantle and a hotter ridge

axis. Domed ridges and crustal magmatic systems have been found along intermediate to slow-spreading ridges in back-arc settings, including of the Valu Fa Ridge (Collier and Sinha, 1992; Jacobs et al., 2007; Turner et al., 1999), the East Scotia Ridge (Livermore et al., 1997), and the Malaguana–Gadao Ridge (Becker et al., 2010).

The Valu Fa Ridge, the southern portion of the Lau spreading center, is situated only 40 km from the active arc, and its domed ridge is underlain by a shallow melt lens (Collier and Sinha, 1992; Jacobs et al., 2007). Lavas have compositions of andesitic basalts, andesites, and rhyolites (Frenzel et al., 1990) with high volatile contents: >1 wt% H_2O and 0.03 wt% CO_2 (Michael et al., 2011; Vallier et al., 1991). Segment E2 of the East Scotia Ridge, located close to the arc system, has an 'inflated' morphology and a shallow melt lens reflector (Leat et al., 2000; Livermore et al., 1997) and erupts basalts with 0.77–1.02 wt% H_2O (Fretzdorff et al., 2002). The Malaguana–Gadao Ridge is located behind the Mariana subduction zone, in the southern portion of the basin and near the active arc. It also exhibits an inflated axial summit and shallow melt lens reflector, though of limited along-axis extent (Becker et al., 2010). No direct observations of lava chemistry are yet available at this location. These results, taken together with other data, indicate that ridges located close to active arcs either directly entrain arc melts into their upwelling systems or entrain hydrated mantle into their upwelling zone that subsequently leads to greater extents of melting.

Along the Lau spreading center in general, as the ridge becomes closer to the arc to the south, the spreading rate decreases, seismic layer 2A thickens from 0.4 to 1.0 km, near-seafloor P-wave velocities decrease from 2.1 to 1.8 km s^{-1}, and the velocities of both layers 2A and 2B decrease from 3.2 to 2.5 and 5.0 to 3.9 km s^{-1}, respectively (Jacobs et al., 2007). These observations are consistent with increased volatile concentration and more felsic compositions of magmas to the south as the ridge approaches the arc.

In 2009, a 3D tomography experiment was carried out along the Eastern Lau Spreading Center within the Lau basin (Arai and Dunn, 2014; Dunn and Martinez, 2011; Dunn et al., 2013). The largest of its kind, the experiment covered a total area of 8000 km^2 and revealed large systematic changes in seismic velocity of the upper crustal volcanic layer. In plan view, the crust formed at the Eastern Lau Spreading Center is characterized by distinct zones of relatively low, intermediate, and high compressional wave velocities (**Figure 28**) that are most likely related to variations in both bulk rock porosity and composition. The velocity variations spatially correlate with estimates of crustal thickness changes, major element changes in seafloor lavas, geochemical estimates of changes in source volatile content (and other arc-related components), and changes in the vesicularity of seafloor samples.

The seismic structure, via the effects of crustal porosity and composition, provides a record of changes in the initial volatile content of melts fed to the ridge. The results indicate that when

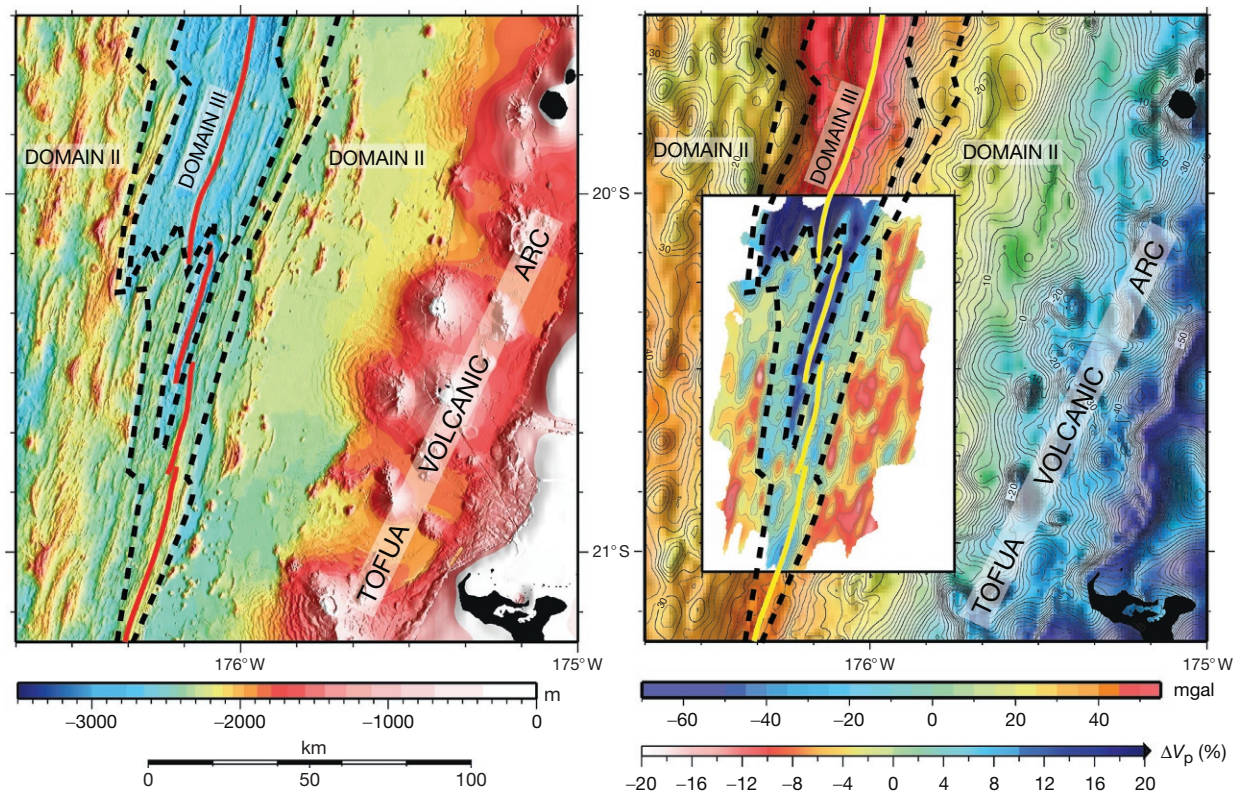

Figure 28 (Left) Lau basin bathymetry showing the Eastern Lau Spreading Center (red line), the active Tofua volcanic arc, and labeled crustal domains demarcated by dashed lines. (Right) Lau basin Bouguer gravity and crustal domains. Inset shows upper crustal P-wave seismic wave speed. Regions of low velocity correspond to regions of thicker, shallower relief, crust, relatively lower gravity, and occur in crust that originally formed closer to the arc. Results from Dunn and Martinez (2011).

the ridge was closer to the arc, water in the mantle led to a greater extent of melting and high-water-content lavas. As the basin opened and the ridge migrated away from the arc, the entrainment of this water was abruptly cut off, and the ridge transitioned to creating a thinner crust with volatile poorer lavas. In the spreading direction, observed steplike transitions between these domains suggest that abrupt changes in mantle source composition take place over as little as 5 km of incremental spreading.

In back-arc settings, there have been few measurements of lower crustal and mantle velocities or crustal thickness. A single, dense, seismic refraction profile across the central portion of the Mariana Trough (Takahashi et al., 2009) reveals a crustal structure that can be described by three principal layers: a shallow layer with V_p of 3.3–5.6 km s^{-1}, a central 5.4–6.1 km s^{-1} layer, and a lower crustal layer of 7.1–7.4 km s^{-1}. Crustal thickness is mostly 5–6 km, and the mantle V_p is 7.8–8.0 km s^{-1}, with the lowest values beneath the spreading center. Crustal velocities are also anomalously low beneath the spreading center, suggesting high crustal temperatures and perhaps melt.

In crust formed along normal mid-ocean ridges, P-wave velocities greater than ~7.1 km s^{-1} are rarely observed via modern seismic experiments. On the other hand, high-velocity lower crust, 7.1–7.6 km s^{-1}, is often found along arc systems (e.g., Kodaira et al., 2008; Takahashi et al., 2009) and is usually considered to be of igneous origin (gabbroic rocks rather than serpentinized mantle). In the Mariana back arc, crust with a high-velocity lower layer was created at the spreading center. Additionally, a high-velocity lower layer (7.1–7.6 km s^{-1}) has been detected in the Lau basin in broad regions of crust that formed at the spreading center when it was located near the active volcanic arc (Arai and Dunn, 2014). The origin of these high-velocity layers is as yet unknown but may be related to specific P–T and compositional conditions particular to the region above the subducting slab. One hypothesis is that they are the result of hydrous fractional crystallization in the crust (Gaetani et al., 1994; Sisson and Grove, 1993), wherein water in the melt suppresses early plagioclase formation, producing a more ultramafic lower crust (of higher than usual velocity) and consequently a more felsic upper crust (of lower than usual velocity; Arai and Dunn, 2014).

1.13.4 Remaining Unsolved Problems

Despite significant progress, many of the fundamental processes occurring at mid-ocean ridges and back-arc systems remain poorly understood. There are many questions remaining about the form of mantle upwelling at shallow levels and the mechanism of melt transport. For example, the focusing of melt from a wide melting zone at depth (>100 km) to a narrow neovolcanic zone at the ridge axis (1–2 km) remains unexplained. Along slow-spreading ridges, we still do not know to what extent variations in crustal thickness at the segment scale are caused by diapiric upwelling versus focused melt migration. At ultraslow spreading rates, the depth extent of cooling from above is unknown, as well as the degree of melting and the amount of melt that is generated but never leaves the mantle. A question raised by the teleseismic studies of regional and global structure is whether there is anisotropy associated with mid-ocean ridges extending to depths of 300 km or more, as suggested by the discrepancy between Love and Rayleigh wave images of the mantle. If this apparent anisotropy is real, it has profound implications for the pattern of overall flow in the oceanic mantle. The procedures and assumptions leading to this conclusion need to be carefully examined. In back-arc settings, the relationship between the ridge upwelling zone, its melting zone, subarc melting, and overall wedge flow is only vaguely understood.

At crustal levels, we observe large variations in accretionary style for ridges of different spreading rates. As spreading rate drops, the nature of ridge segmentation changes, magma supply becomes more intermittent, and spreading is partitioned into periods of tectonic stretching versus magmatic accretion. To first order, ridge thermal structure is difficult to establish, leading to much uncertainty. For example, the formation and cooling of the lower crust is strongly debated, and along slow-spreading ridges, the idea that spreading is portioned into regions or times of magmatic accretion versus faulting and tectonic stretching is well established but poorly documented.

Limited global sampling of mid-ocean ridges and back-arc spreading systems leads to observational biases. While fast-spreading ridges have been extensively studied as compared to slower-spreading ridges, fast-spreading ridges comprise only 10% of the global ridge system (**Figure 2**). Along slower-spreading ridges, many studies tend to focus on more magmatically robust segments of ridge, especially near hot spots, and thus, we still do not have a good understanding of the average thickness of crust produced along these ridges. In addition to this selection bias, it is possible that true crustal thickness is masked by mantle serpentinization, which gives crust-like velocities to the mantle. The presence or absence of magmatic systems along non-hot spot-influenced sections of slow-spreading ridges is often inferred indirectly, but not determined by direct seismic observation.

At the ridge segment scale, we need higher-resolution 3D images of both the crust and the uppermost mantle to answer these basic questions. A major problem is the lack of studies at scales intermediate between global tomography and small, local seismic reflection and refraction experiments. If we are to understand the processes occurring along the global mid-ocean ridge system, a number of dense ocean-bottom seismic studies must be carried out. Land-based stations are insufficient for examining the Earth's structure beneath the ridges. Body waves recorded by such stations have poor coverage and resolution in the oceans. In addition, the sensitivity zone for surface waves widens with path length (Spetzler and Snieder, 2001; Yoshizawa and Kennett, 2002), meaning that even with good path density and azimuthal coverage, the use of long propagation paths limits the lateral resolution of surface-wave images. Instead, denser broadband arrays must be deployed to record shorter-ray-path, higher-frequency, teleseismic, and regional data. Active-source experiments must be scaled up to cover larger regions in a denser fashion. In the future, some of the biggest gains will be achieved by simply increasing the number of instruments deployed on the seafloor.

Acknowledgments

Special thanks are given to Don Forsyth for his work on an earlier edition of this article and to Ryuta Arai, who helped compile the reference list and figures. This work was supported by NSF grant OCE0426428. SOEST no. 9088.

References

Arai R and Dunn RA (2014) Seismological study of Lau back arc crust: Mantle water, magmatic differentiation, and a compositionally zoned basin. *Earth and Planetary Science Letters* 390: 304–317.

Argus DF, Gordon RG, and DeMets C (2011) Geologically current motion of 56 plates relative to the no-net-rotation reference frame. *Geochemistry, Geophysics, Geosystems* 12: Q11001. http://dx.doi.org/10.1029/2011GC003751.

Arnulf AF, Harding AJ, Singh SC, Kent GM, and Crawford W (2012) Fine-scale velocity structure of upper oceanic crust from full waveform inversion of downward continued seismic reflection data at the Lucky Strike Volcano, Mid-Atlantic Ridge. *Geophysical Research Letters* 39: L08303. http://dx.doi.org/10.1029/2012GL051064.

Babcock JM, Harding AJ, Kent GM, and Orcutt JA (1998) An examination of along-axis variation of magma chamber width and crustal structure on the East Pacific Rise between 13°30′N and 12°20′N. *Journal of Geophysical Research* 103(B12): 30451–30467.

Baker ET (1994) A 6-year time series of hydrothermal plumes over the Cleft segment of the Juan de Fuca Ridge. *Journal of Geophysical Research* 99(B3): 4889–4904.

Baran JM, Cochran JR, Carbotte SM, and Nedimović MR (2005) Variations in upper crustal structure due to variable mantle temperature along the Southeast Indian Ridge. *Geochemistry Geophysics Geosystems* 6: Q11002. http://dx.doi.org/10.1029/2005GC000943.

Baran JM, Carbotte SM, Cochran JR, and Nedimović MR (2010) Upper crustal seismic structure along the Southeast Indian Ridge: Evolution from 0 to 550 ka and variation with axial morphology. *Geochemistry, Geophysics, Geosystems* 11: Q02001. http://dx.doi.org/10.1029/2009GC002629.

Barclay AH and Toomey DR (2003) Shear wave splitting and crustal anisotropy at the Mid-Atlantic Ridge, 35°N. *Journal of Geophysical Research* 108(B8): 2378. http://dx.doi.org/10.1029/2001JB000918.

Barclay AH, Toomey DR, and Solomon SC (1998) Seismic structure and crustal magmatism at the Mid-Atlantic Ridge, 35°N. *Journal of Geophysical Research* 103(B8): 17827–17844.

Barclay AH, Toomey DR, and Solomon SC (2001) Micro-earthquake characteristics and crustal Vp/Vs structure at the Mid-Atlantic Ridge. *Journal of Geophysical Research* 106(B2): 2017–2034.

Barth GA and Mutter JC (1996) Variability in oceanic crustal thickness and structure: Multichannel seismic reflection results from the northern East Pacific Rise. *Journal of Geophysical Research* 101(B8): 17951–18017.

Bazin S, van Avendonk H, Harding AJ, et al. (1998) Crustal structure of the flanks of the East Pacific Rise: Implications for overlapping spreading centers. *Geophysical Research Letters* 2(12): 2213–2216.

Bazin S, et al. (2003) A three-dimensional study of a crustal low velocity region beneath the 9°03′N overlapping spreading center. *Geophysical Research Letters* 30: 1039. http://dx.doi.org/10.1029/2002GL015137.

Becker NC, Fryer P, and Moore GF (2010) Malaguana-Gadao Ridge: Identification and implications of a magma chamber reflector in the southern Mariana Trough. *Geochemistry, Geophysics, Geosystems* 11: Q04X13. http://dx.doi.org/10.1029/2009GC002719.

Bézos A, Escrig S, Langmuir CH, Michael PJ, and Asimow PD (2009) Origins of chemical diversity of back-arc basin basalts: A segment-scale study of the Eastern Lau Spreading Center. *Journal of Geophysical Research* 114: B06212. http://dx.doi.org/10.1029/2008JB005924.

Bird P (2003) An updated digital model of plate boundaries. *Geochemistry, Geophysics, Geosystems* 4(3): 1027. http://dx.doi.org/10.1029/2001GC000252.

Blacic TM, Ito G, Canales JP, Detrick RS, and Sinton J (2004) Constructing the crust along the Galapagos Spreading Center 91.3°-95.5°W: Correlation of seismic layer 2A with axial magma lens and topographic characteristics. *Journal of Geophysical Research* 109: B10310.

Blackman DK, Canales JP, and Harding A (2009) Geophysical signatures of oceanic core complexes. *Geophysical Journal International* 178: 593–613. http://dx.doi.org/10.1111/j.1365-246X.2009.04184.x.

Blackman DK and Collins JA (2010) Lower crustal variability and the crust/mantle transition at the Atlantis Massif oceanic core complex. *Geophysical Research Letters* 37: L24303. http://dx.doi.org/10.1029/2010GL045165.

Blackman DK and Forsyth DW (1989) Axial topographic relief associated with ridge transform intersections. *Earth and Planetary Science Letters* 95(1–2): 115–129. http://dx.doi.org/10.1016/0012-821X(89)90171-4.

Blackman DK and Kendall J-M (1997) Sensitivity of teleseismic body waves to mineral texture and melt in the mantle beneath a mid-ocean ridge. *Philosophical Transactions of the Royal Society of London A* 355: 217–231.

Blackman DK and Kendall J-M (2002) Seismic anisotropy in the upper mantle 2. Predictions for current plate boundary flow models. *Geochemistry, Geophysics, Geosystems* 3(9): 8602.

Boudier F, Nicolas A, and Ildefonse B (1996) Magma chambers in the Oman ophiolite: Fed from the top or the bottom? *Earth and Planetary Science Letters* 144: 239–250.

Boudier F, Nicolas A, Ildefonse B, and Jousselin D (1997) EPR microplates, as a model for the Oman ophiolite. *Terra Nova* 9: 79–82.

Bowman JR and Ando M (1987) Shear-wave splitting in the upper-mantle wedge above the Tonga subduction zone. *Geophysical Journal of the Royal Astronomical Society* 88: 25–41.

Brown JW and White RS (1994) Variation with spreading rate of oceanic crustal thickness and geochemistry. *Earth and Planetary Science Letters* 121: 435–449.

Bruguier NJ and Livermore RA (2001) Enhanced magma supply at the southern East Scotia Ridge: Evidence for mantle flow around the subducting slab? *Earth and Planetary Science Letters* 191: 129–144.

Buck WR, Carbotte SM, and Mutter C (1997) Controls on extrusion at mid-ocean ridges. *Geology* 25: 935–938.

Buck WR, Lavier LL, and Poliakov ANB (2005) Modes of faulting at mid-ocean ridges. *Nature* 434: 719–723.

Burnett MS, Caress DW, and Orcutt JA (1989) Tomographic image of the magma chamber at 12°50′N on the East Pacific Rise. *Nature* 339: 206–208. http://dx.doi.org/10.1038/339206a0.

Buttles J and Olson P (1998) A laboratory model of subduction zone anisotropy. *Earth and Planetary Science Letters* 164: 245–262. http://dx.doi.org/10.1016/S0012-821X(98)00211-8.

Canales JP (2010) Small-scale structure of the Kane oceanic core complex, Mid-Atlantic Ridge 23°30′N, from waveform tomography of multichannel seismic data. *Geophysical Research Letters* 37: L21305. http://dx.doi.org/10.1029/2010GL044412.

Canales JP, Carton H, Carbotte SM, et al. (2012) Network of off-axis melt bodies at the East Pacific Rise. *Nature Geoscience* 5: 279–283. http://dx.doi.org/10.1038/NGEO1377.

Canales JP, Collins JA, Escartin J, and Detrick RS (2000a) Seismic structure across the rift valley of the Mid-Atlantic Ridge at 23°20′N (MARK area): Implications for crustal accretion processes at slow spreading ridges. *Journal of Geophysical Research* 105(B12): 28411–28425.

Canales JP, Detrick RS, Bazin S, Harding AJ, and Orcutt JA (1998) Off-axis crustal thickness across and along the East Pacific Rise within the MELT area. *Science* 280: 1218–1221.

Canales JP, Detrick RS, Carbotte SM, et al. (2005) Upper crustal structure and axial topography at intermediate-spreading ridges: Seismic constraints from the Southern Juan de Fuca Ridge. *Journal of Geophysical Research* 110: B12104. http://dx.doi.org/10.1029/2005JB003630.

Canales JP, Detrick RS, Lin J, and Collins JA (2000b) Crustal and upper mantle seismic structure beneath the rift mountains and across a non-transform offset at the Mid-Atlantic Ridge (35°N). *Journal of Geophysical Research* 105(B2): 2699–2719.

Canales JP, Detrick RS, Toomey DR, and Wilcock WSD (2003) Segment-scale variations in the crustal structure of 150-300 kyr old fast spreading oceanic crust (East Pacific Rise, 8°15′ N-10° 5′ N) from wide-angle seismic refraction profiles. *Geophysical Journal International* 152(3): 766–794.

Canales JP, Singh SC, Detrick RS, et al. (2006) Seismic evidence for variations in axial magma chamber properties along the southern Juan de Fuca Ridge. *Earth and Planetary Science Letters* 246: 353–366.

Canales JP, Sohn RA, and deMartin BJ (2007) Crustal structure of the Trans-Atlantic Geotraverse (TAG) segment (Mid-Atlantic Ridge, 26°10′N): Implications for the nature of hydrothermal circulation and detachment faulting at slow spreading ridges. *Geochemistry, Geophysics, Geosystems* 8: Q08004. http://dx.doi.org/10.1029/2007GC001629.

Canales JP, Tucholke BE, and Collins JA (2004) Seismic reflection imaging of an oceanic detachment fault: Atlantis megamullion (Mid-Atlantic Ridge, 30°10′N). *Earth and Planetary Science Letters* 222: 543–560.

Canales JP, Tucholke BE, Xu M, Collins JA, and DuBois DL (2008) Seismic evidence for large-scale compositional heterogeneity of oceanic core complexes.

Geochemistry, Geophysics, Geosystems 9: Q08002. http://dx.doi.org/10.1029/2008GC002009.
Cannat M (1993) Emplacement of mantle rocks in the seafloor at mid-ocean ridges. *Journal of Geophysical Research* 98(B3): 4163–4172.
Cannat M (1996) How thick is the magmatic crust at slow spreading oceanic ridges? *Journal of Geophysical Research* 101(B2): 2847–2858.
Cannat M, Sauter D, Mendel V, et al. (2006) Modes of seafloor generation at a melt-poor ultraslow-spreading ridge. *Geology* 34(7): 605–608.
Carbotte SM, Canales JP, Nedimović MR, Carton H, and Mutter JC (2012) Recent seismic studies at the East Pacific Rise 8°20′-10°10′N and Endeavour Segment: Insights into mid-ocean ridge hydrothermal and magmatic processes. *Oceanography* 25: 100–112.
Carbotte SM, Detrick RS, Harding A, et al. (2006) Rift topography linked to magmatism at the intermediate spreading Juan de Fuca Ridge. *Geology* 34(3): 209–212. http://dx.doi.org/10.1130/G21969.1.
Carbotte SM and Macdonald KC (1992) East Pacific Rise 8°-10°30′ N: Evolution of ridge segments and discontinuities from SeaMARCII and three-dimensional magnetic studies. *Journal of Geophysical Research* 97: 6959–6982.
Carbotte SM and Macdonald KC (1994) Comparison of seafloor tectonic fabric at intermediate, fast, and superfast spreading ridges: Influence of spreading rate, plate motions, and ridge segmentation on fault patterns. *Journal of Geophysical Research* 99: 13609–13631.
Carbotte SM, Mutter CZ, Mutter J, and Wu L (1998) Insights from a fast-intermediate spreading ridge on the influence of magma supply and spreading rate on crustal magma bodies and emplacement of the extrusive layer. *Geology* 26: 455–458.
Carbotte SM, Nedimović MR, Canales JP, Kent GM, Harding AJ, and Marjanović M (2008) Variable crustal structure along the Juan de Fuca Ridge: Influence of on-axis hot spots and absolute plate motions. *Geochemistry, Geophysics, Geosystems* 9: Q08001. http://dx.doi.org/10.1029/2007GC001922.
Carbotte SM, Solomon A, and Ponce-Correa G (2000) Evaluation of morphological indicators of magma supply and segmentation from a seismic reflection study of the East Pacific Rise 15°30′-17°N. *Journal of Geophysical Research* 105: 2737–2759. http://dx.doi.org/10.1029/1999JB900245.
Carlson RL (1998) Seismic velocities in the uppermost oceanic crust: Age dependence and the fate of layer 2A. *Journal of Geophysical Research* 103: 7069–7077.
Ceuleneer G and Nicolas A (1985) Structures in podiform chromite from the Maqsad district (Sumail ophiolite, Oman). *Mineralium Deposita* 20(3): 177–184.
Chen YJ (2001) Thermal effects of gabbro accretion from a deeper second melt lens at the fast spreading East Pacific Rise. *Journal of Geophysical Research* 106: 8581–8588.
Chen Y and Morgan WJ (1990a) A nonlinear rheology model for mid-ocean ridge axis topography. *Journal of Geophysical Research* 95: 17583–17604.
Chen Y and Morgan WJ (1990b) Rift valley/non rift valley transition at mid-ocean ridges. *Journal of Geophysical Research* 95: 17571–17581.
Chenevez J, Machatel P, and Nicolas A (1998) Numerical models of magma chambers in the Oman ophiolite. *Journal of Geophysical Research* 103: 15443–15455.
Cherkaoui ASM, Wilcock WSD, Dunn RA, and Toomey DR (2003) A numerical model of hydrothermal cooling and crustal accretion at a fast spreading mid-ocean ridge. *Geochemistry, Geophysics, Geosystems* 4. http://dx.doi.org/10.1029/2001GC000215.
Christeson GL, Karson JA, and McIntosh KD (2010) Mapping of seismic layer 2A/2B boundary above the sheeted dike unit at intermediate spreading crust exposed near the Blanco Transform. *Geochemistry, Geophysics, Geosystems* 11: Q03015. http://dx.doi.org/10.1029/2009GC002864.
Christeson GL, Kent GM, Purdy GM, and Detrick RS (1996) Extrusive thickness variability at the East Pacific rise, 9 degrees-10 degrees N: Constraints from seismic techniques. *Journal of Geophysical Research* 101(B2): 2859–2873.
Christeson GL, McIntosh KD, and Karson JA (2007) Inconsistent correlation of seismic layer 2a and lava layer thickness in oceanic crust. *Nature* 445: 418–421. http://dx.doi.org/10.1038/nature05517.
Christeson GL, Purdy GM, and Fryer GJ (1994a) Seismic constraints on shallow crustal emplacement processes at the fast spreading East Pacific Rise. *Journal of Geophysical Research* 99(B9): 17957–17973.
Christeson GL, Wilcock WSD, and Purdy GM (1994b) The shallow attenuation structure of the fast-spreading East Pacific Rise near 9-degrees-30′N. *Geophysical Research Letters* 21(5): 321–324.
Coakley BJ and Cochran JR (1998) Gravity evidence of very thin crust at the Gakkel Ridge (Arctic Ocean). *Earth and Planetary Science Letters* 162(1–4): 81–95.
Cochran JR (1986) Variations in subsidence rates along intermediate and fast spreading mid-ocean ridges. *Geophysical Journal of the Royal Astronomical Society* 87: 421–454.
Cochran JR, Kurras G, Edwards MH, and Coakley BJ (2003) The Gakkel Ridge: Bathymetry, gravity anomalies, and crustal accretion at extremely slow spreading rates. *Journal of Geophysical Research* 108(2): 2116. http://dx.doi.org/10.1029/2002JB001830.
Collier JS and Singh SC (1997) Detailed structure of the top of the melt body beneath the East Pacific Rise at 9 40′N from Waveform. *Journal of Geophysical Research* 102(B9): 20–287.
Collier JS and Sinha MC (1990) Seismic images of a magma chamber beneath the Lau Basin back-arc spreading centre. *Nature* 346: 646–648.
Collier JS and Sinha MC (1992) The Valu Fa Ridge: The pattern of volcanic activity at a back-arc spreading centre. *Marine Geology* 104: 243–263.
Conder JA, Forsyth DW, and Parmentier EM (2002) Asthenospheric flow and the asymmetry of the East Pacific Rise, MELT area. *Journal of Geophysical Research* 107(B12): 2344. http://dx.doi.org/10.1029/2001JB000807.
Conder JA and Wiens D (2006) Seismic structure beneath the Tonga arc and Lau back-arc basin determined from joint Vp, Vp/Vs tomography. *Geochemistry, Geophysics, Geosystems* 7(3): Q03018.
Conley MM and Dunn RA (2011) Seismic shear wave structure of the uppermost mantle beneath the Mohns Ridge. *Geochemistry, Geophysics, Geosystems* 12: Q0AK01. http://dx.doi.org/10.1029/2011GC003792.
Coogan LA, Howard KA, Gillis KM, et al. (2006) Chemical and thermal constraints on focused fluid flow in the lower oceanic crust. *American Journal of Science* 306: 389–427.
Coogan LA, Jenkin GRT, and Wilson RN (2002) Constraining the cooling rate of the lower oceanic crust: A new approach applied to the Oman ophiolite. *Earth and Planetary Science Letters* 199: 127–146.
Courtillot V, Davaille A, Besse J, and Stock J (2003) Three distinct types of hotspots in the Earth's mantle. *Earth and Planetary Science Letters* 205: 295–308.
Crawford WC and Webb SC (2002) Variations in the distribution of magma in the lower crust and at the Moho beneath the East Pacific Rise at 9 degrees-10 degrees N. *Earth and Planetary Science Letters* 203(1): 117–130.
Crawford WC, Webb SC, and Hildebrand JA (1999) Constraints on melt in the lower crust and Moho at the East Pacific Rise, 9°48PN, using seafloor compliance measurements. *Journal of Geophysical Research* 104: 2923–2939.
Czuba W, Ritzmann O, Nishimura Y, et al. (2005) Crustal structure of northern Spitsbergen along the deep seismic transect between the Molloy Deep and Nordaustlandet. *Geophysical Journal International* 161(2): 347–364.
Dalton CA, Ekström G, and Dziewonski AM (2008) The global attenuation structure of the upper mantle. *Journal of Geophysical Research* 113: B09303. http://dx.doi.org/10.1029/2007JB005429.
Dannowski A, Grevemeyer I, Morgan JP, Ranero CR, Maia M, and Klein G (2011) Crustal structure of the propagating TAMMAR ridge segment on the Mid-Atlantic Ridge, 21.5°N. *Geochemistry, Geophysics, Geosystems* 12: Q07012. http://dx.doi.org/10.1029/2011gc003534.
Dannowski A, Grevemeyer I, Ranero CR, et al. (2010) Seismic structure of an oceanic core complex at the Mid-Atlantic Ridge, 22°19′N. *Journal of Geophysical Research* 115: B07106. http://dx.doi.org/10.1029/2009JB006943.
Davies JH and Bickle MJ (1991) A physical model for the volume and composition of melt produced by hydrous fluxing above subduction zones. *Philosophical Transactions of the Royal Society of London, Series A: Mathematical, Physical and Engineering Sciences* 335(1638): 355–364.
Delorey AA, Dunn RA, and Gaherty JB (2007) Surface wave tomography of the upper mantle beneath the Reykjanes Ridge with implications for ridge–hot spot interaction. *Journal of Geophysical Research* 112: B08313. http://dx.doi.org/10.1029/2006JB004785.
de Martin BJ, Sohn RA, Canales JP, and Humphris SE (2007) Kinematics and geometry of active detachment faulting beneath the Trans-Atlantic Geotraverse (TAG) hydrothermal field on the Mid-Atlantic Ridge. *Geology* 35: 711–714.
De Weist RJM (1965) *Geohydrology*, 369 pp. New York: Wiley.
Detrick RS, Buhl P, Vera E, et al. (1987) Multichannel seismic imaging of a crustal magma chamber along the East Pacific Rise. *Nature* 326: 35–41.
Detrick RS, Collins J, Harding AJ, et al. (1993) Seismic structure of the southern East Pacific Rise. *Science* 259: 499–503.
Detrick RS, Needham HD, and Renard V (1995) Gravity anomalies and crustal thickness variations along the Mid-Atlantic Ridge between 33°N and 40°N. *Journal of Geophysical Research* 100: 3767–3787.
Detrick RS, Sinton JM, Ito G, et al. (2002) Correlated geophysical, geochemical, and volcanological manifestations of plume-ridge interaction along the Galápagos Spreading Center. *Geochemistry, Geophysics, Geosystems* 3(10): 8501. http://dx.doi.org/10.1029/2002GC000350.
Detrick RS, Toomey DR, and Collins JA (1998) Three-dimensional upper crustal heterogeneity and anisotropy around Hole 504B from seismic tomography. *Journal of Geophysical Research* 103(B12): 30485–30504.
Dick HJ, Lin J, and Schouten H (2003) An ultraslow-spreading class of ocean ridge. *Nature* 426: 405–412.

Dunn RA and Forsyth DW (2003) Imaging the transition between the region of mantle melt generation and the crustal magma chamber beneath the southern East Pacific Rise with short-period Love waves. *Journal of Geophysical Research* 108(B7): 2352. http://dx.doi.org/10.1029/2002JB002217.

Dunn RA, Lekic V, Detrick RS, and Toomey DR (2005) Three-dimensional seismic structure of the Mid-Atlantic Ridge (35°N): Evidence for focused melt supply and lower crustal dike injection. *Journal of Geophysical Research* 110: B09101. http://dx.doi.org/10.1029/2004JB003473.

Dunn RA and Martinez F (2011) Contrasting crustal production and rapid mantle transitions beneath back-arc ridges. *Nature* 469: 198–202. http://dx.doi.org/10.1038/nature09690.

Dunn RA, Martinez F, and Conder J (2013) Crustal construction and magma chamber properties along the Eastern Lau Spreading Center. *Earth and Planetary Science Letters* 371–372: 112–124.

Dunn RA and Toomey DR (1997) Seismological evidence for three-dimensional melt migration beneath the East Pacific Rise. *Nature* 388: 259–262.

Dunn RA and Toomey DR (2001) Crack-induced seismic anisotropy in the oceanic crust across the East Pacific Rise (9° 30′N). *Earth and Planetary Science Letters* 189(1–2): 9–17.

Dunn RA, Toomey DR, and Solomon SC (2000) Three-dimensional seismic structure and physical properties of the crust and shallow mantle beneath the East Pacific Rise at 9 degrees 30′N. *Journal of Geophysical Research* 105(B10): 23537–23555.

Durant DT and Toomey DR (2009) Evidence and implications of crustal magmatism on the flanks of the East Pacific Rise. *Earth and Planetary Science Letters* 287: 130–136.

Ekström G (2000) Mapping the lithosphere and asthenosphere with surface waves: Lateral structure and anisotropy. In: Richards MA, Gordon RG, and van der Hilst RD (eds.) *The History and Dynamics of Global Plate Motions*. *Geophysical Monograph Series*, vol. 121, pp. 239–255. Washington, DC: AGU, http://dx.doi.org/10.1029/GM121p0239.

Escartin J, Smith DK, Cann J, Schouten H, Langmuir CH, and Escrig S (2008) Central role of detachment faults in accretion of slow-spreading oceanic lithosphere. *Nature* 455(7214): 790–794.

Escrig S, Bézos A, Goldstein SL, Langmuir CH, and Michael PJ (2009) Mantle source variations beneath the Eastern Lau Spreading Center and the nature of subduction components in the Lau basin-Tonga arc system. *Geochemistry, Geophysics, Geosystems* 10: Q04014. http://dx.doi.org/10.1029/2008GC002281.

Evans RL, Hirth G, Baba K, Forsyth D, Chave A, and Mackie R (2005) Geophysical evidence from the MELT area for compositional controls on oceanic plates. *Nature* 437: 249–252.

Faul UH and Jackson I (2005) The seismological signature of temperature and grain size variations in the upper mantle. *Earth and Planetary Science Letters* 234(1): 119–134.

Fisher AT (1998) Permeability within basaltic oceanic crust. *Reviews of Geophysics* 36: 143–182.

Flanagan MP and Shearer PM (1998) Global mapping of the topography on transition zone discontinuities by stacking SS precursors. *Journal of Geophysical Research* 103: 2673–2692.

Forsyth DW (1975) The early structural evolution and anisotropy of the oceanic upper mantle. *Geophysical Journal of the Royal Astronomical Society* 43: 103–162.

Forsyth DW, Webb SC, Dorman LM, and Shen Y (1998) Phase velocities of Rayleigh waves in the MELT Experiment on the East Pacific Rise. *Science* 280: 1235–1238.

Frenzel G, Muhe R, and Stoffers P (1990) Petrology of the volcanic rocks from the Lau Basin, southwest Pacific. *Geologische Jahrbuch* 92: 395–479.

Fretzdorff S, Livermore RA, Devey CW, Leat PT, and Stoffers P (2002) Petrogenesis of the back-arc East Scotia Ridge, South Atlantic Ocean. *Journal of Petrology* 43(8): 1435–1467.

Gaetani GA, Grove TL, and Bryan WB (1994) Experimental phase relations of basaltic andesite from hole 839B under hydrous and anhydrous conditions. *Proceedings of the Ocean Drilling Program, Scientific Results* 135: 557–563.

Garmany J (1989) Accumulations of melt at the base of young oceanic-crust. *Nature* 340(6235): 628–632.

Géli L, Renard V, and Rommevaux C (1994) Ocean crust formation processes at very slow spreading centers: A model for the Mohns Ridge, near 72 degrees N, based on magnetic, gravity, and seismic data. *Journal of Geophysical Research* 99(2): 2995–3013.

Goodliffe A, Taylor B, Martinez F, Hey R, Maeda K, and Ohno K (1997) Synchronous reorientation of the Woodlark Basin spreading center. *Earth and Planetary Science Letters* 146: 233–242.

Gràcia E, Bideau D, Hekinian R, and Lagabrielle Y (1999) Detailed geological mapping of two contrasting second-order segments of the Mid-Atlantic Ridge between Oceanographer and Hayes fracture zones (33°30′N-35°N). *Journal of Geophysical Research* 104: 22903–22921.

Gregory RT and Taylor HP Jr. (1981) An oxygen isotope profile in a section of Cretaceous oceanic crust, Samail Ophiolite, Oman: Evidence for $\delta^{18}O$ buffering of the oceans by deep (>5 km) seawater-hydrothermal circulation at mid-ocean ridges. *Journal of Geophysical Research* 86: 2737–2755.

Grevemeyer I, Kaul N, Villinger H, and Weigel W (1999) Hydrothermal activity and the evolution of the seismic properties of upper oceanic crust. *Journal of Geophysical Research* 104(B3): 5069–5079.

Grevemeyer I and Weigel W (1996) Seismic velocities of the uppermost igneous crust versus age. *Geophysical Journal International* 124(2): 631–635.

Grimes CB, John BE, Cheadle MJ, and Wooden JL (2008) Protracted construction of gabbroic crust at a slow spreading ridge: Constraints from 206Pb/238U zircon ages from Atlantis Massif and IODP Hole U1309D (30°N, MAR). *Geochemistry, Geophysics, Geosystems* 9: Q08012. http://dx.doi.org/10.1029/2008GC002063.

Gu YJ, Lerner-Lam AL, Dziewonski AM, and Ekström G (2005a) Deep structure and seismic anisotropy beneath the East Pacific Rise. *Earth and Planetary Science Letters* 232: 259–272.

Gu YJ, Webb SC, Lerner-Lam A, and Gaherty JB (2005b) Upper mantle structure beneath the eastern Pacific Ocean ridges. *Journal of Geophysical Research* 110: B06305. http://dx.doi.org/10.1029/2004JB00381.

Gung Y, Panning M, and Romanowicz B (2003) Global anisotropy and the thickness of continents. *Nature* 422: 707–711.

Hall CE, Fischer KM, Parmentier EM, and Blackman DK (2000) The influence of plate motions on three-dimensional back arc mantle flow and shear wave splitting. *Journal of Geophysical Research* 105(28): 9–28.

Hammond WC and Toomey DR (2003) Seismic velocity anisotropy and heterogeneity beneath the Mantle Electromagnetic and Tomography Experiment (MELT) region of the East Pacific Rise from analysis of P and S body waves. *Journal of Geophysical Research* 108: 2176. http://dx.doi.org/10.1029/2002JB001789.

Harding AJ, Kent GM, and Orcutt JA (1993) A multichannel seismic investigation of upper crustal structure at 9-degrees-N on the East Pacific Rise-implications for crustal accretion. *Journal of Geophysical Research* 98(B8): 13925–13944.

Harding AJ, Orcutt JA, Kappus ME, et al. (1989) Structure of young oceanic-crust at 13-degrees-N on the East Pacific Rise from expanding spread profiles. *Journal of Geophysical Research* 94(B9): 12163–12196.

Harmon N, Forsyth DW, Fischer KM, and Webb SC (2004) Variations in shear wave splitting in young Pacific seafloor. *Geophysical Research Letters* 31: L15609. http://dx.doi.org/10.1029/2004GL020495.

Harmon N, Forsyth DW, Lamm R, and Webb SC (2007) P and S wave delays beneath intraplate volcanic ridges and gravity lineations near the East Pacific Rise. *Journal of Geophysical Research* 112: B03309. http://dx.doi.org/10.1029/2006JB004392.

Harmon N, Forsyth DW, and Weeraratne DS (2009) Thickening of young Pacific lithosphere from high-resolution Rayleigh wave tomography: A test of the conductive cooling model. *Earth and Planetary Science Letters* 278: 96–106.

Harmon N, Forsyth DW, Weeraratne DS, Yang Y, and Webb SC (2011) Mantle heterogeneity and off axis volcanism on young Pacific lithosphere. *Earth and Planetary Science Letters* 311: 306–315.

Hawkins JW (1976) Petrology and geochemistry of basaltic rocks of the Lau basin. *Earth and Planetary Science Letters* 28: 283–297.

Hayes DE (1976) Nature and implications of asymmetric sea-floor spreading. *Geological Society of America Bulletin* 87: 994–1002.

Hayes DE (1988) Age-depth relationships and depth anomalies in the Southeast Indian Ocean and South Atlantic Ocean. *Journal of Geophysical Research* 93(B4): 2937–2954.

Haymon RM, Fornari DJ, Edwards MH, Carbotte S, Wright D, and Macdonald KC (1991) Hydrothermal vent distribution along the East Pacific Rise crest (9°09-54′N) and its relationship to magmatic and tectonic processes on fast-spreading mid-ocean ridges. *Earth and Planetary Science Letters* 104: 513–534.

Henig AS, Blackman DK, Harding AJ, Canales JP, and Kent GM (2012) Downward continued multichannel seismic refraction analysis of Atlantis Massif oceanic core complex, 30°N, Mid-Atlantic Ridge. *Geochemistry, Geophysics, Geosystems* 13: Q0AG07. http://dx.doi.org/10.1029/2012GC004059.

Henstock TJ, Woods AW, and White RS (1993) The accretion of oceanic crust by episodic sill intrusion. *Journal of Geophysical Research* 98: 4143–4161.

Hey R, Johnson GL, and Lowrie A (1977) Recent plate motions in the Galápagos area. *Geological Society of America Bulletin* 88: 1385–1403.

Hirth G and Kohlstedt DL (1996) Water in the oceanic upper mantle: Implications for rheology, melt extraction and the evolution of the lithosphere. *Earth and Planetary Science Letters* 144(1): 93–108.

Holmes RC, Tolstoy M, Cochran JR, and Floyd JS (2008) Crustal thickness variations along the Southeast Indian Ridge (100-116E) from 2-D body wave tomography.

Geochemistry, Geophysics, Geosystems 9: Q12020. http://dx.doi.org/10.1029/2008GC002152.

Honda S and Yoshida T (2005) Effects of oblique subduction on the 3-D pattern of small-scale convection within the mantle wedge. *Geophysical Research Letters* 32(L13307): 1–4. http://dx.doi.org/10.1029/2005GL023106.

Hooft EE, Brandsdóttir B, Mjelde R, Shimamura H, and Murai Y (2006) Asymmetric plume-ridge interaction around Iceland: The Kolbeinsey Ridge Iceland Seismic Experiment. *Geochemistry, Geophysics, Geosystems* 7(5): Q05015.

Hooft EEE and Detrick RS (1993) The role of density in the accumulation of basaltic melts at mid-ocean ridges. *Geophysical Research Letters* 20: 423–426.

Hooft EEE, Detrick RS, and Kent GM (1997) Seismic structure and indicators of magma budget along the Southern East Pacific Rise. *Journal of Geophysical Research* 102: 27319–27340.

Hooft EEE, Detrick RS, Toomey DR, Collins JA, and Lin J (2000) Crustal thickness and structure along three contrasting spreading segments of the Mid-Atlantic Ridge, 33.5°-35°N. *Journal of Geophysical Research* 105: 8205–8226.

Hooft EEE, Schouten H, and Detrick RS (1996) Constraining crustal emplacement processes from the variation in seismic layer 2A thickness at the East Pacific Rise. *Earth and Planetary Science Letters* 142: 289–309.

Hosford A, Lin J, and Detrick RS (2001) Crustal evolution over the last 2 m.y. at the Mid-Atlantic Ridge OH-1 segment, 35°N. *Journal of Geophysical Research* 106: 13269–13285.

Houtz R and Ewing JI (1976) Upper crustal structure as a function of plate age. *Journal of Geophysical Research* 81: 2490–2498.

Hudson JA (1981) Wave speeds and attenuation of elastic waves in material containing cracks. *Geophysical Journal of the Royal Astronomical Society* 64: 133–150.

Hung S-H, Forsyth DW, and Toomey DR (2000) Can a narrow, melt-rich, low-velocity zone of mantle upwelling be hidden beneath the East Pacific Rise? Limits from waveform modeling and the MELT Experiment. *Journal of Geophysical Research* 105: 7945–7960.

Hussenoeder SA, Collins JA, Kent GM, Detrick RS, and Th TERA Group (1996) Seismic analysis of the axial magma chamber reflector along the southern East Pacific Rise from conventional reflection profiling. *Journal of Geophysical Research* 101(B10): 22087–22105.

Hussenoeder SA, Kent GM, and Detrick RS (2002) Upper crustal seismic structure of the slow spreading Mid-Atlantic Ridge, 35°N: Constraints on volcanic emplacement process. *Journal of Geophysical Research* 107(8). http://dx.doi.org/10.1029/2001JB001691.

Ildefonse B, Nicolas A, and Boudier F (1993) Evidence from the Oman ophiolite for sudden stress changes during melt injection at oceanic spreading centers. *Nature* 366: 673–675.

Jackson HR, Reid I, and Falconer RKH (1982) Crustal structure near the Arctic mid-ocean ridge. *Journal of Geophysical Research* 87(B3): 1773–1783.

Jacobs AM, Harding AJ, and Kent GM (2007) Axial crustal structure of the Lau back-arc basin from velocity modeling of multichannel seismic data. *Earth and Planetary Science Letters* 259: 239–255.

Jian H, Li J, Chen YJ, et al. (2012) Three-dimensional seismic tomography reveals the presence of partial melt in the lower crust of the ultraslow Southwest Indian Ridge at 50°28′E. In: *Abstract OS11E-02 Presented at 2012 Fall Meeting, AGU, San Francisco, California, 3–7 December*.

Jokat W, Ritzmann O, Schmidt-Aursch MC, Drachev S, Gauger S, and Snow J (2003) Geophysical evidence for reduced melt production on the Arctic ultraslow Gakkel mid-ocean ridge. *Nature* 423(6943): 962–965.

Jokat W and Schmidt-Aursch MC (2007) Geophysical characteristics of the ultraslow spreading Gakkel Ridge, Arctic Ocean. *Geophysical Journal International* 168: 983–998. http://dx.doi.org/10.1111/j.1365-246X.2006.03278.x.

Jousselin D, Dunn RA, and Toomey DR (2003) Modeling the seismic signature of structural data from the Oman Ophiolite: Can a mantle diapir be detected beneath the East Pacific Rise? *Geochemistry, Geophysics, Geosystems* 4(7): 8610. http://dx.doi.org/10.1029/2002GC000418.

Jousselin D, Nicolas A, and Boudier F (1998) Detailed mapping of a paleo-spreading center in the Oman ophiolite. *Journal of Geophysical Research* 103: 18153–18170.

Jung H and Karato SI (2001) Water-induced fabric transitions in olivine. *Science* 293(5534): 1460–1463.

Jurdy DM and Stefanick M (1983) Flow models for back-arc spreading. *Tectonophysics* 99(2): 191–206.

Kappel ES and Normark WR (1987) Morphometric variability within the axial zone of the southern Juan de Fuca Ridge: Interpretation from sea MARC II, Sea MARC I, and deep-sea photography. *Journal of Geophysical Research* 92(B11): 11291–11302.

Kappel ES and Ryan WBF (1986) Volcanic episodicity and a non-steady state rift valley along the Northeast Pacific spreading centers: Evidence from Sea MARC I. *Journal of Geophysical Research* 91(14): 13925–13940.

Kappus ME, Harding AJ, and Orcutt JA (1995) A baseline for upper crustal velocity variations along the East Pacific Rise at 13°N. *Journal of Geophysical Research* 100(B4): 6143–6161. http://dx.doi.org/10.1029/94JB02474.

Karato SI (2003) Mapping water content in the upper mantle. In: Eiler J and Karato S-I (eds.) *Inside the Subduction Factory. Geophysical Monograph Series*, vol. 138, pp. 135–152. Washington, DC: AGU.

Karig DE (1970) Ridges and basins of the Tonga-Kermadec Island Arc System. *Journal of Geophysical Research* 75: 239–254.

Kelemen PB and Aharonov E (1998) Periodic formation of magma fractures and generation of layered gabbros in the lower crust beneath oceanic spreading ridges. In: Buck R, et al. (eds.) *Faulting and Magmatism at Mid-Ocean Ridges. Geophysical Monograph Series*, vol. 106, pp. 267–289. Washington, DC: AGU.

Kelemen PB, Koga K, and Shimizu N (1997) Geochemistry of gabbro sills in the crust-mantle transition zone of the Oman ophiolite: Implications for the origin of the oceanic lower crust. *Earth and Planetary Science Letters* 146: 475–488.

Kelemen PB, Shimizu N, and Salters VJM (1995) Extraction of mid-ocean-ridge basalt from the upwelling mantle by focused flow of melt in dunite channels. *Nature* 375: 747–753.

Kelley KA, Plank T, Grove TL, Stolper EM, Newman S, and Hauri E (2006) Mantle melting as a function of water content beneath back-arc basins. *Journal of Geophysical Research* 111: B09208. http://dx.doi.org/10.1029/2005JB003732.

Kent GM, Harding AJ, and Orcutt JA (1993) Distribution of magma beneath the East Pacific Rise between the Clipperton Transform and the 9°17′N deval from forward modeling of common depth point data. *Journal of Geophysical Research* 98(B8): 13945–13969.

Kent GM, Harding AJ, Orcutt JA, Detrick RS, Mutter JC, and Buhl P (1994) Uniform accretion of oceanic crust south of the Garrett transform at 14°15′S on the East Pacific Rise. *Journal of Geophysical Research* 99: 9097–9116.

Kent GM, Singh SC, Harding AJ, et al. (2000) Evidence from three-dimensional seismic reflectivity images for enhanced melt supply beneath mid-ocean-ridge discontinuities. *Nature* 406(6796): 614–618.

Key K, Constable S, Liu L, and Pommier A (2013) Electrical image of passive mantle upwelling beneath the northern East Pacific Rise. *Nature* 495(7442): 499–502.

Klein EM and Langmuir CH (1987) Global correlations of ocean ridge basalt chemistry with axial depth and crustal thickness. *Journal of Geophysical Research* 92(B4): 8089–8115.

Klein EM and Langmuir CH (1989) Local versus global variations in ocean ridge basalt composition. *Journal of Geophysical Research* 94(4): 4241–4252.

Klingelhöfer F, Geli L, Matias L, Steinsland N, and Mohr J (2000) Crustal structure of a super-slow spreading centre: A seismic refraction study of Mohns Ridge, 72 N. *Geophysical Journal International* 141(2): 509–526.

Kodaira S, Mjelde R, Gunnarsson K, Shiobara H, and Shimamura H (1997) Crustal structure of the Kolbeinsey Ridge, North Atlantic, obtained by the use of ocean bottom seismographs. *Journal of Geophysical Research* 102(2): 3131–3151.

Kodaira S, Sato T, Takahashi N, Yamashita M, No T, and Kaneda Y (2008) Seismic imaging of a possible paleoarc in the Izu-Bonin intraoceanic arc and its implications for arc evolution processes. *Geochemistry, Geophysics, Geosystems* 9: Q10X01. http://dx.doi.org/10.1029/2008GC002073.

Korenaga J and Kelemen PB (1997) Origin of gabbro sills on the Moho transition zone of the Oman ophiolite: Implications for magma transport in the oceanic lower crust. *Journal of Geophysical Research* 102: 27,729–27,749.

Kuo B-Y and Forsyth DW (1988) Gravity anomalies of the ridge-transform system in the South Atlantic between 31 and 34.5°S: Upwelling centers and variations in crustal thickness. *Marine Geophysical Research* 10: 205–232.

Kustowski B, Ekström G, and Dziewonski AM (2008) Anisotropic shear-wave velocity structure of the Earth's mantle: A global model. *Journal of Geophysical Research* 113: B06306. http://dx.doi.org/10.1029/2007JB005169.

Langmuir CH, Bender JF, and Batiza R (1986) Petrological and tectonic segmentation of the East Pacific Rise 5°30′-14°30′N. *Nature* 322: 422–429.

Langmuir CH, Bézos A, Escrig S, and Parman SW (2006) Chemical systematics and hydrous melting of the mantle in back-arc basins. In: Christie DM, et al. (eds.) *Back-Arc Spreading Systems: Geological, Biological, Chemical, and Physical Interactions. Geophysical Monograph Series*, vol. 166, pp. 87–146. Washington, DC: AGU.

Langmuir CH, Klein EM, and Plank T (1992) Petrological systematics of mid-ocean ridge basalts: Constraints on melt generation beneath ocean ridges. In: Phipps Morgan J, Blackman DK, and Sinton JM (eds.) *Mantle Flow and Melt Generation at Mid-Ocean Ridges. Geophysical Monograph*, vol. 71, pp. 183–280. Washington, DC: American Geophysical Union.

Leat PT, Livermore RA, Millar IL, and Pearce JA (2000) Magma supply in back-arc spreading centre segment E2, East Scotia Ridge. *Journal of Petrology* 41(6): 845–866.

Lee DK and Grand SP (1996) Depth of the upper mantle discontinuities beneath the East Pacific Rise. *Geophysical Research Letters* 23(23): 3369–3372.

Lin J, Purdy GM, Schouten H, Sempere J-C, and Zervas C (1990) Evidence from gravity data for focused magmatic accretion along the Mid-Atlantic Ridge. *Nature* 344: 627–632.

Little SA and Stephen RA (1985) Costa Rica Rift borehole seismic experiment, Deep Sea Drilling Project hole 504B, leg 92. *Initial Reports of the Deep Sea Drilling Project* 83: 517–528.

Livermore R, Cunningham A, Vanneste L, and Larter R (1997) Subduction influence on magma supply at the East Scotia Ridge. *Earth and Planetary Science Letters* 150: 261–275.

Lizarralde D, Gaherty JB, Collins JA, Hirth G, and Kim SD (2004) Spreading-rate dependence of melt extraction at mid-ocean ridges from mantle seismic refraction data. *Nature* 432(7018): 744–747.

Ljones F, Kuwano A, Mjelde R, et al. (2004) Crustal transect from the North Atlantic Knipovich Ridge to the Svalbard margin west of Hornsund. *Tectonophysics* 378(1): 17–41.

Long MD and van der Hilst R (2006) Shear wave splitting from local events beneath the Ryukyu arc: Trench parallel anisotropy in the mantle wedge. *Physics of the Earth and Planetary Interiors* 155: 300–312.

Lonsdale P (1983) Overlapping rift zones at the 5.5°S offset of the East Pacific Rise. *Journal of Geophysical Research* 88: 9393–9406.

Lonsdale P (1986) Comments on: East Pacific Rise from Siqueiros to Orozco fracture zones: Along-strike continuity of axial neovolcanic zones and structure and evolution of overlapping spreading centers. *Journal of Geophysical Research* 91: 10493–10499.

Lonsdale P (1989) The rise flank trails left by migrating offsets of the equatorial East Pacific Rise. *Journal of Geophysical Research* 94: 713–743.

Macdonald KC, Fox PJ, Perram LJ, et al. (1988) A new view of the mid-ocean ridge from the behaviour of ridge axis discontinuities. *Nature* 335: 217–225.

Macdonald KC, Haymon RM, Miller SP, Sempere JC, and Fox PJ (1998) Deep-tow and sea beam studies of dueling propagating ridges on the East Pacific Rise near 20° 40′ S. *Journal of Geophysical Research* 93(B4): 2875–2898.

Macdonald KC, Scheirer DS, and Carbotte SM (1991) Mid-ocean ridges: Discontinuities, segments and giant cracks. *Science* 253: 986–994.

Macdonald KC, Sempere JC, and Fox PJ (1984) East Pacific Rise from Siqueiros to Orozco fracture zones: Along-strike continuity of axial neovolcanic zones and structure and evolution of overlapping spreading centers. *Journal of Geophysical Research* 89: 6049–6069.

Maclennan J, Hulme T, and Singh SC (2004) Thermal models of oceanic crustal accretion: Linking geophysical, geological and petrological observations. *Geochemistry, Geophysics, Geosystems* 5(2): Q02F25. http://dx.doi.org/10.1029/2003GC000605.

MacLeod CJ and Yaouancq G (2000) A fossil melt lens in the Oman ophiolite: Implications for magma chamber processes at fast spreading ridges. *Earth and Planetary Science Letters* 176: 357–373.

Magde LS, Barclay AH, Toomey DR, Detrick RS, and Collins JA (2000) Crustal magma plumbing within a segment of the Mid-Atlantic Ridge, 35°N. *Earth and Planetary Science Letters* 175: 55–67.

Magde LS, Sparks DW, and Detrick RS (1997) The relationship between buoyant mantle flow, melt migration, and gravity bull's eyes at the Mid-Atlantic Ridge between 33°N and 35°N. *Earth and Planetary Science Letters* 148: 59–67.

Maggi A, Debayle E, Priestley K, and Barruol G (2006a) Multimode surface waveform tomography of the Pacific Ocean: A closer look at the lithospheric cooling signature. *Geophysical Journal International* 166: 1384–1397.

Maggi A, Debayle E, Priestley K, and Barruol G (2006b) Azimuthal anisotropy of the Pacific region. *Earth and Planetary Science Letters* 250: 53–71.

Malinverno A (1993) Transition between a valley and a high at the axis of mid-ocean ridges. *Geology* 21(7): 639–642.

Masters G, Laske G, Bolton H, and Dziewonski A (2000) The relative behavior of shear velocity, bulk sound speed, and compressional velocity in the mantle: Implications for chemical and thermal structure. *Earth's Deep Interior: Mineral Physics and Tomography from the Atomic to the Global Scale. Geophysical Monograph Series*, vol. 117, pp. 63–887. Washington, DC: American Geophysical Union.

McGuire JJ, Collins JA, Gouédard P, et al. (2012) Variations in earthquake rupture properties along the Gofar transform fault, East Pacific Rise. *Nature Geoscience* 5: 336–341. http://dx.doi.org/10.1038/ngeo1454.

McKenzie D (1979) Finite deformation during fluid flow. *Geophysical Journal of the Royal Astronomical Society* 58(3): 689–715.

Melbourne TI and Helmberger DV (2002) Whole mantle shear structure beneath the East Pacific Rise. *Journal of Geophysical Research* 107(B9): 2204. http://dx.doi.org/10.1029/2001JB000332.

Melt Seismic Team (1998) Imaging the deep seismic structure beneath a mid-ocean ridge: The MELT experiment. *Science* 280: 1215–1218.

Menke W, Brandsdottir B, Jakobsdottir S, and Stefansson R (1994) Seismic anisotropy in the crust at the mid-Atlantic plate boundary in south-west Iceland. *Geophysical Journal International* 119: 783–790.

Menke W, West M, and Tolstoy M (2002) Shallow crustal magma chamber beneath the axial high of the Coaxial Segment of Juan de Fuca Ridge at the "Source Site" of the 1993 eruption. *Geology* 30: 359–362, http://dx.doi.org/10.1130/0091-7613(2002)030<0359:SCMCBT>2.0.CO;2.

Michael PJ, Escrig S, Langmuir CH, Arculus RJ, and Goddard CI (2011) Along and across-arc basalt geochemical trends of seamounts in the Lau basin: Evidence for fluid components and mantle melting. In: *Abstract V54B-02 Presented at the Fall Meeting AGU, Washington, DC*.

Michael PJ, Langmuir CH, Dick HJB, et al. (2003) Magmatic and amagmatic seafloor generation at the ultraslow-spreading Gakkel Ridge, Arctic Ocean. *Nature* 423(6943): 956–961. http://dx.doi.org/10.1038/nature01704.

Montagner J-P and Ritsema J (2001) Interactions between ridges and plumes. *Science* 294: 1472–1473.

Montagner J-P and Tanimoto T (1991) Global upper mantle tomography of seismic velocities and anisotropies. *Journal of Geophysical Research* 96: 20337–20351.

Morgan WJ (1978) Rodriguez, Darwin, Amsterdam, . . ., a second type of hotspot island. *Journal of Geophysical Research* 83(B11): 5355–5360.

Morton JL, Sleep NH, Normark WR, and Tompkins DH (1987) Structure of the southern Juan de Fuca Ridge from seismic reflection records. *Journal of Geophysical Research* 92: 11315–11326.

Muller MR, Minshull TA, and White RS (1999) Segmentation and melt supply at the Southwest Indian Ridge. *Geology* 27(10): 867–870.

Muller MR, Minshull TA, and White RS (2000) Crustal structure of the Southwest Indian Ridge at the Atlantis II fracture zone. *Journal of Geophysical Research* 105(B11): 25809–25828.

Muller MR, Robinson CJ, Minshull TA, White RS, and Bickle MJ (1997) Thin crust beneath ocean drilling program borehole 735B at the Southwest Indian Ridge? *Earth and Planetary Science Letters* 148(1): 93–107.

Mutter CZ (1995) Seismic and hydrosweep study of the western Costa Rica Rift. *EOS. Transactions of the American Geophysical Union* 76: F595.

Mutter JC, Barth G, Buhl P, Detrick RS, Orcutt J, and Harding A (1988) Magma distribution across ridge-axis discontinuities on the East Pacific Rise from multichannel seismic images. *Nature* 336(6195): 156–158.

Mutter JC, Carbotte SM, Su W, et al. (1995) Seismic images of active magma systems beneath the East Pacific Rise between 17°05′ and17°35′S. *Science* 268: 391–395.

Navin DA, Peirce C, and Sinha MC (1998) The RAMESSES experiment-II. Evidence for accumulated melt beneath slow spreading ridge from wide-angle refraction and multichannel reflection seismic profiles. *Geophysical Journal International* 135(3): 746–772.

Nedimović MR, Carbotte SM, Diebold JB, Harding AJ, Canales JP, and Kent GM (2008) Upper crustal evolution across the Juan de Fuca ridge flanks. *Geochemistry, Geophysics, Geosystems* 9(9): Q09006. http://dx.doi.org/10.1029/2008GC002085.

Nedimović MR, Carbotte SM, Harding AJ, et al. (2005) Frozen magma lenses below the oceanic crust. *Nature* 436(7054): 1149–1152.

Nehlig P and Juteau T (1982) Flow porosities, permeabilities, and preliminary data on fluid inclusions and fossil thermal gradients in the crustal sequence of the Samail ophiolite (Oman). *Tectonophysics* 81: 319–339.

Nicholls IA and Ringwood AE (1973) Effect of water on olivine stability in tholeiites and the production of silica-saturated magmas in the island-arc environment. *Journal of Geology* 81: 285–300.

Nicolas A (1989) *Structures of Ophiolites and Dynamics of Oceanic Lithosphere*, 367 pp. Norwell, MA: Kluwer Academic.

Nicolas A and Boudier F (1995) Mapping oceanic ridge segments in Oman ophiolites. *Journal of Geophysical Research* 100: 6179–6197.

Nicolas A, Boudier F, and Ildefonse B (1994) Evidence from the Oman ophiolite for active mantle upwelling beneath a fast-spreading ridge. *Nature* 370: 51–53.

Nicolas A, Ceuleneer G, Boudier F, and Misseri M (1988) Structural mapping in the Oman ophiolites: Mantle diapirism along an oceanic ridge. *Tectonophysics* 151: 27–56.

Nicolas A, Freydier C, Godard M, and Vauchez A (1993) Magma chambers at mid-ocean ridges: How large? *Geology* 21: 53–56.

Nicolas A and Violette JF (1982) Mantle flow at oceanic spreading centers: Models derived from ophiolites. *Tectonophysics* 81: 319–339.

Nishimura C and Forsyth DW (1989) The anisotropic structure of the upper mantle in the Pacific. *Geophysical Journal* 96: 203–229.

Niu Y and Hekinian R (1997) Spreading-rate dependence of the extent of mantle melting beneath ocean ridges. *Nature* 385: 326–329.
Olive JA, Behn MD, and Tucholke BE (2010) The structure of oceanic core complexes controlled by the depth distribution of magma emplacement. *Nature Geoscience* 3(7): 491–495.
Panza G, Doglioni C, and Levshin A (2010) Asymmetric ocean basins. *Geology* 38: 59–62. http://dx.doi.org/10.1130/G30570.1.
Parmentier EM and Phipps Morgan J (1990) The spreading rate dependence of three-dimensional oceanic spreading center structure. *Nature* 348: 325–328.
Parson LM, Pearce JA, Murton BJ, and Hodkinson RA (1990) Role of ridge jumps and ridge propagation in the tectonic evolution of the Lau back-arc basin, southwest Pacific. *Geology* 18(5): 470–473.
Parsons L, Gràcia E, Coller D, German C, and Needham D (2000) Second-order segmentation; the relationship between volcanism and tectonism at the MAR. 38°N-35°40′N. *Earth and Planetary Science Letters* 178: 231–251.
Pearce JA, Baker PE, Harvey PK, and Luff IW (1995) Geochemical evidence for subduction fluxes, mantle melting and fractional crystallization beneath the South Sandwich island arc. *Journal of Petrology* 36: 1073–1109.
Pearce JA, Stern RJ, Bloomer SH, and Fryer P (2005) Geochemical mapping of the Mariana arc-basin system: Implications for the nature and distribution of subduction components. *Geochemistry, Geophysics, Geosystems* 6(7): Q07006.
Peirce C, Gardiner A, and Sinha M (2005) Temporal and spatial cyclicity of accretion at slow spreading ridges – Evidence from the Reykjanes Ridge. *Geophysical Journal International* 163(1): 56–78.
Peirce C, Sinha M, Topping S, and Gill C (2007) Morphology and genesis of slow-spreading ridges – Seabed scattering and seismic imaging within the oceanic crust. *Geophysical Journal International* 168: 59–89. http://dx.doi.org/10.1111/j.1365-246X.2006.03223.x.
Perfit MR and Chadwick WW (1998) Magmatism at mid-ocean ridges: Constraints from volcanological and geochemical investigations. In: Buck WR, et al. (eds.) *Faultingand Magmatism at Mid-Ocean Ridges*. *Geophysical Monograph Series*, vol. 106, pp. 59–115. Washington, DC: AGU.
Phipps Morgan J (1987) Melt migration beneath mid-ocean spreading centers. *Geophysical Research Letters* 14(12): 1238–1241.
Phipps Morgan J and Chen YJ (1993a) The genesis of oceanic crust: Magma injection, hydrothermal circulation, and crustal flow. *Journal of Geophysical Research* 98: 6283–6298.
Phipps Morgan J and Chen YJ (1993b) Dependence of ridge-axis morphology on magma supply and spreading rate. *Nature* 364: 706–708.
Pickering-Witter J and Johnston AD (2000) The effects of variable bulk composition on the melting systematics of fertile peridotitic assemblages. *Contributions to Mineralogy and Petrology* 140(2): 190–211.
Planert L, Flueh ER, Tilmann F, Grevemeyer I, and Reston TJ (2010) Crustal structure of a rifted oceanic core complex and its conjugate side at the MAR at 5°S: Implications for melt extraction during detachment faulting and core complex formation. *Geophysical Journal International* 181: 113–126. http://dx.doi.org/10.1111/j.1365-246X.2010.04504.x.
Pozgay SH, Wiens DA, Conder JA, Shiobara H, and Sugioka H (2007) Complex mantle flow in the Mariana subduction system: Evidence from shear wave splitting. *Geophysical Journal International* 170: 371–386. http://dx.doi.org/10.1111/j.1365-246X.2007.03433.x.
Priestley K and McKenzie D (2006) The thermal structure of the lithosphere from shear wave velocities. *Earth and Planetary Science Letters* 244: 285–301.
Purdy GM (1987) New observations of the shallow seismic structure of young oceanic crust. *Journal of Geophysical Research* 92: 9351–9362.
Purdy GM and Detrick RS (1986) Crustal structure of the Mid-Atlantic Ridge at 23°N from seismic refraction studies. *Journal of Geophysical Research* 91(B3): 3739–3762.
Purdy GM, Kong L, Christeson GL, and Solomon SC (1992) Relationship between spreading rate and the seismic structure of mid-ocean ridges. *Nature* 355(6363): 815–817.
Pyle ML, Wiens DA, Weeraratne DS, Shore PJ, Shiobara H, and Sugioka H (2010) Shear velocity structure of the Mariana mantle wedge from Rayleigh wave phase velocities. *Journal of Geophysical Research* 115: B11304. http://dx.doi.org/10.1029/2009JB006976.
Quick JE and Denlinger RP (1993) Ductile deformation and the origin of layered gabbro in ophiolites. *Journal of Geophysical Research* 98: 14015–14028.
Rabain A, Cannat M, Escartín J, Pouliquen G, Deplus C, and Rommevaux-Jestin C (2001) Focused volcanism and growth of a slow spreading segment (Mid-Atlantic Ridge, 35°N). *Earth and Planetary Science Letters* 185: 211–224.
Rabinowicz M, Rouzo S, Sempere J-C, and Rosemberg C (1993) Three-dimensional mantle flow beneath mid-ocean ridges. *Journal of Geophysical Research* 98: 7851–7869.
Raitt RW, Shor GG Jr., Francis TJG, and Morris GB (1969) Anisotropy of the Pacific upper mantle. *Journal of Geophysical Research* 74: 3095–3109.
Reid I and Jackson HR (1981) Oceanic spreading rate and crustal thickness. *Marine Geophysical Research* 5(2): 165–172.
Ribe NM (1989) Seismic anisotropy and mantle flow. *Journal of Geophysical Research* 94(B4): 4213–4223.
Ritsema J (2005) Global seismic structure maps. In: Foulger GR, Natland JH, Presnall DC, and Anderson DL (eds.) Plates, Plumes, and Paradigms. *Geological Society of America, Special Paper* 388: 11–18. http://dx.doi.org/10.1130/2005.2388.
Ritzmann O, Jokat W, Mjelde R, and Shimamura H (2002) Crustal structure between the Knipovich Ridge and the Van Mijenfjorden (Svalbard). *Marine Geophysical Research* 23(5–6): 379–401.
Ritzwoller MH, Shapiro NM, and Leahy GM (2003) A resolved mantle anomaly as the cause of the Australian-Antarctic Discordance. *Journal of Geophysical Research* 108(B12): 2559.
Ritzwoller M, Shapiro N, and Zhong S-J (2004) Cooling history of the Pacific lithosphere. *Earth and Planetary Science Letters* 226: 69–84.
Robinson CJ, Bickle MJ, Minshull TA, White RS, and Nichols ARL (2001) Low degree melting under the Southwest Indian Ridge: The roles of mantle temperature, conductive cooling and wet melting. *Earth and Planetary Science Letters* 188(3–4): 383–398.
Roland E, Lizarralde D, McGuire JJ, and Collins JA (2012) Seismic velocity constraints on the material properties that control earthquake behavior at the Quebrada-Discovery-Gofar transform faults, East Pacific Rise. *Journal of Geophysical Research* 117: B11102. http://dx.doi.org/10.1029/2012JB009422.
Romanowicz B (1994) Anelastic tomography: A new perspective on upper mantle thermal structure. *Earth and Planetary Science Letters* 128: 113–121.
Ross WS (1994) The velocity-depth ambiguity in seismic travel time data. *Geophysics* 59: 830–843.
Scheirer DS, Forsyth DW, Cormier M-H, and Macdonald KC (1998) Shipboard geophysical indications of asymmetry and melt production beneath the East Pacific Rise near the MELT Experiment. *Science* 280: 1221–1224.
Schilling JG (1985) Upper mantle heterogeneities and dynamics. *Nature* 314: 62–67.
Schilling JG (1991) Fluxes and excess temperatures of mantle plumes inferred from their interaction with migrating mid-ocean ridges. *Nature* 352: 397–403.
Schilling J-G, Bergeron MB, and Evans R (1980) Halogens in the mantle beneath the North Atlantic. *Philosophical Transactions of the Royal Society of London. Series A* 297: 147–178.
Schilling J-G, Zajac M, Evans R, et al. (1982) Petrologic and geochemical variations along the Mid-Atlantic Ridge from 29°N to 73°N. *American Journal of Science* 283(6): 510–586.
Schouten H, Klitgord KD, and Whitehead JA (1985) Segmentation of mid-ocean ridges. *Nature* 317: 225–229.
Seher T, Crawford WC, Singh SC, Cannat M, Combier V, and Dusunur D (2010a) Crustal velocity structure of the Lucky Strike segment of the Mid-Atlantic Ridge at 37°N from seismic refraction measurements. *Journal of Geophysical Research* 115: B03103. http://dx.doi.org/10.1029/2009JB006650.
Seher T, Singh SC, Crawford WC, and Escartín J (2010b) Upper crustal velocity structure beneath the central Lucky Strike Segment from seismic refraction measurements. *Geochemistry, Geophysics, Geosystems* 11: Q05001. http://dx.doi.org/10.1029/2009GC002894.
Shapiro NM and Ritzwoller MH (2002) Monte-Carlo inversion for a global shear-velocity model of the crust and upper mantle. *Geophysical Journal International* 151(1): 88–105.
Shearer PM (2000) Upper mantle seismic discontinuities. In: Karato S, Forte AM, Liebermann RC, Masters G, and Stixrude L (eds.) *Earth's Deep Interior: Mineral Physics and Tomography from the Atomic to the Global Scale*. *Geophysical Monograph Series*, vol. 117, pp. 115–131. Washington, DC: AGU.
Shearer P and Orcutt J (1985) Anisotropy in the oceanic lithosphere-theory and observations from the Ngendei seismic refraction experiment in the Southwest Pacific. *Geophysical Journal of the Royal Astronomical Society* 80(2): 493–526.
Shen Y and Forsyth DW (1995) Geochemical constraints on initial and final depths of melting beneath mid-ocean ridges. *Journal of Geophysical Research* 100(2): 2211–2237.
Shen Y, Forsyth DW, Scheirer DS, and Macdonald KC (1993) Two forms of volcanism: Implications for mantle flow and off-axis crustal production on the west flank of the southern East Pacific Rise. *Journal of Geophysical Research* 98: 17875–17889.

Shen Y, Sheehan AF, Dueker GD, de Groot-Hedlin C, and Gilbert H (1998) Mantle discontinuity structure beneath the southern East Pacific Rise from P-to-S converted phases. *Science* 280: 1232–1234.

Singh SC, Collier JS, Harding AJ, Kent GM, and Orcutt JA (1999) Seismic evidence for a hydrothermal layer above the solid roof of the axial magma chamber at the southern East Pacific Rise. *Geology* 27(3): 219–222.

Singh SC, Carton H, Chauhan S, et al. (2011) Extremely thin crust in the Indian Ocean possibly resulting from Plume–Ridge Interaction. *Geophysical Journal International* 184(1): 29–42.

Singh SC, Crawford WC, Carton H, et al. (2006a) Discovery of a magma chamber and faults beneath a Mid-Atlantic Ridge hydrothermal field. *Nature* 442(7106): 1029–1032.

Singh SC, Harding AJ, Kent GM, et al. (2006b) Seismic reflection images of the Moho underlying melt sills at the East Pacific Rise. *Nature* 442: 287–290.

Singh SC, Kent GM, Collier JS, Harding AJ, and Orcutt JA (1998) Melt to mush variations in crustal magma properties along the ridge crest at the southern East Pacific Rise. *Nature* 394(6696): 874–878.

Sinha M, Constable SC, Pierce C, et al. (1998) Magmatic processes at slow spreading ridges: Implications of the RAMESSES experiment at 57°45′N on the Mid-Atlantic Ridge. *Geophysical Journal International* 135: 731–745. http://dx.doi.org/10.1046/j.1365-246X.1998.00704.x.

Sinha MC and Louden KE (1983) The Oceanographer fracture zone-I. Crustal structure from seismic refraction studies. *Geophysical Journal of the Royal Astronomical Society* 75: 713–736.

Sinha MC, Navin DA, MacGregor LM, et al. (1997) Evidence for accumulated melt beneath the slow-spreading Mid-Atlantic Ridge. *Philosophical Transactions of the Royal Society of London. Series A* 355(1723): 233–253.

Sinton JM and Detrick RS (1992) Mid-ocean ridge magma chambers. *Journal of Geophysical Research* 97(B1): 197–216.

Sisson TW and Grove TL (1993) Experimental investigations of the role of H2O in calc-alkaline differentiation and subduction zone magmatism. *Contributions to Mineralogy and Petrology* 113(2): 143–166.

Sleep NH (1988) Tapping of melt by veins and dikes. *Journal of Geophysical Research* 93: 10255–10272.

Sleep N and Toksöz MN (1971) Evolution of marginal basins. *Nature* 233: 548–550.

Small C (1998) Global systematics of mid-ocean ridge morphology. *Faulting and Magmatism at Mid-Ocean Ridges*. *Geophysical Monograph Series*, vol. 106, pp. 1–26. Washington, DC: American Geophysical Union.

Small C and Sandwell DT (1989) An abrupt change in ridge axis gravity with spreading rate. *Journal of Geophysical Research* 94(B12): 17383–17392.

Small C and Sandwell D (1992) An analysis of ridge axis gravity roughness and spreading rate. *Journal of Geophysical Research* 97(1): 3235–3245.

Small C and Sandwell DT (1994) Imaging mid-ocean ridge transitions with satellite gravity. *Geology* 22(2): 123–126.

Smallwood JR, White RS, and Minshull TA (1995) Sea-floor spreading in the presence of the Iceland plume: The structure of the Reykjanes Ridge at 61°40′N. *Journal of the Geological Society of London* 52: 1023–1029.

Smith DK, Cann JR, and Escartin J (2006) Widespread active detachment faulting and core complex formation near 13°N on the Mid-Atlantic Ridge. *Nature* 442: 440–443. http://dx.doi.org/10.1038/nature04950.

Smith DK, Escartın J, Schouten H, and Cann JR (2008) Fault rotation and core complex formation: Significant processes in seafloor formation at slow-spreading mid-ocean ridges (Mid-Atlantic Ridge, 13°-15°N). *Geochemistry, Geophysics, Geosystems* 9: Q03003. http://dx.doi.org/10.1029/2007GC001699.

Smith MC, Perfit MR, and Jonasson IR (1994) Petrology and geochemistry of basalts from the southern Juan de Fuca Ridge: Controls on the spatial and temporal evolution of mid-ocean ridge basalt. *Journal of Geophysical Research* 99(B3): 4787–4812.

Smith GP, Wiens DA, Fischer KM, Dorman LM, Webb SC, and Hildebrand JA (2001) A complex pattern of mantle flow in the Lau Backarc. *Science* 292: 713–716.

Sohn RA, Barclay AH, and Webb SC (2004) Microearthquake patterns following the 1998 eruption of Axial Volcano, Juan de Fuca Ridge: Mechanical relaxation and thermal strain. *Journal of Geophysical Research* 109(B1): B01101.

Sohn RA, Webb SC, Hildebrand JA, and Cornuelle BD (1997) Three-dimensional tomographic velocity structure of upper crust, CoAxial segment, Juan de Fuca ridge: Implications for on-axis evolution and hydrothermal circulation. *Journal of Geophysical Research* 102(B8): 17679–17695.

Solomon SC and Toomey DR (1992) The structure of mid-ocean ridges. *Annual Review of Earth and Planetary Sciences* 20: 329–364.

Songqiao SW, Wiens DA, Webb SC, Blackman DK, Dunn R, and Conder JA (2012) Shear velocity structure of the Tonga Arc and Lau Backarc Basin from Rayleigh wave tomography. In: *Abstract T53E-03 Presented at 2012 Fall Meeting, AGU, San Francisco, California, 3–7 December*.

Sparks DW and Parmentier EM (1991) Melt extraction from the mantle beneath spreading centers. *Earth and Planetary Science Letters* 105: 368–377.

Sparks DW, Parmentier EM, and Phipps Morgan J (1993) Three-dimensional mantle convection beneath a segmented spreading center: Implications for along-axis variations in crustal thickness and gravity. *Journal of Geophysical Research* 98: 21977–21995.

Spetzler J and Snieder R (2001) The effect of small-scale heterogeneity on the arrival time of waves. *Geophysical Journal International* 145(3): 786–796.

Spiegelman M and McKenzie D (1987) Simple 2-D models for melt extraction at mid-ocean ridges and island arcs. *Earth and Planetary Science Letters* 83(137): 152.

Spudich P and Orcutt J (1980) A new look at the seismic velocity structure of the oceanic-crust. *Reviews of Geophysics* 18(3): 627–645.

Stakes DS, Perfit MR, Tivey MA, Caress DW, Ramirez TM, and Maher N (2005) The Cleft revealed: Geologic, magnetic, and morphologic evidence for construction of upper oceanic crust along the southern Juan de Fuca Ridge. *Geochemistry, Geophysics, Geosystems* 7: Q04003. http://dx.doi.org/10.1029/2005GC001038.

Stephen RA (1981) Seismic anisotropy in oceanic crust. *Geophysical Research Letters* 8: 865–868.

Stevenson DJ (1989) Spontaneous small-scale melt segregation in partial melts undergoing deformation. *Geophysical Research Letters* 16: 1067–1070.

Stolper E and Newman S (1994) The role of water in the petrogenesis of Mariana trough magmas. *Earth and Planetary Science Letters* 121(3): 293–325.

Stroup DF, Bohnenstiehl DR, Tolstoy M, Waldhauser F, and Weekly RT (2007) Pulse of the seafloor: Tidal triggering of microearthquakes at 9°50′N East Pacific Rise. *Geophysical Research Letters* 34: L15301. http://dx.doi.org/10.1029/2007GL030088.

Stroup DF, Tolstoy M, Crone TJ, Malinverno A, Bohnenstiehl DR, and Waldhauser F (2009) Systematic along-axis tidal triggering of microearthquakes observed at 9°50′N East Pacific Rise. *Geophysical Research Letters* 36: L18302. http://dx.doi.org/10.1029/2009GL039493.

Swift SA, Kent GM, Detrick RS, Collins JA, and Stephen RA (1998a) Oceanic basement structure, sediment thickness, and heat flow near Hole 504B. *Journal of Geophysical Research* 103(B7): 15377–15391.

Swift SA, Lizarralde D, Hoskins H, and Stephen RA (1998b) Velocity structure in the upper ocean crust at Hole 504B from vertical seismic profiles. *Journal of Geophysical Research* 103: 15361–15376.

Takahashi N, Kodaira S, Tatsumi Y, et al. (2009) Structural variations of arc crusts and rifted margins in the southern Izu-Ogasawara arc-back arc system. *Geochemistry, Geophysics, Geosystems* 10: Q09X08. http://dx.doi.org/10.1029/2008GC002146.

Taylor B and Karner GD (1983) On the evolution of marginal basins. *Reviews of Geophysics* 21(8): 1727–1741.

Taylor B and Martinez F (2003) Back-arc basin basalt systematic. *Earth and Planetary Science Letters* 210: 481–497.

Thibaud R, Gente P, and Maia M (1998) A systematic analysis of the Mid-Atlantic Ridge morphology and gravity between 15°N and 40°N: Constraints of thermal structure. *Journal of Geophysical Research* 103: 24223–24243.

Thompson RN (1987) Phase-equilibria constraints on the genesis and magmatic evolution of oceanic basalts. *Earth-Science Reviews* 24: 161–210.

Tian T, Wilcock WSD, Toomey DR, and Detrick RS (2000) Seismic heterogeneity in the upper crust near the 1991 eruption site on the East Pacific Rise, 9°50′N. *Geophysical Research Letters* 27(16): 2369–2372.

Tolstoy M, Harding AJ, and Orcutt JA (1993) Crustal thickness on the Mid-Atlantic Ridge: Bull's-eye gravity anomalies and focused accretion. *Science* 262: 726–729.

Tolstoy M, Harding AJ, and Orcutt J (1997) Deepening of the axial magma chamber on the southern East Pacific Rise toward the Garrett Fracture Zone. *Journal of Geophysical Research* 102: 3097–3108.

Tolstoy M, Vernon FL, Orcutt JA, and Wyatt FK (2002) Breathing of the seafloor: Tidal correlations of seismicity at Axial volcano. *Geology* 30(6): 503–506.

Tolstoy M, Waldhauser F, Bohnenstiehl DR, Weekly RT, and Kim WY (2008) Seismic identification of along-axis hydrothermal flow on the East Pacific Rise. *Nature* 451: 181–184. http://dx.doi.org/10.1038/nature06424.

Tong CH, Lana C, White RS, Warner MR, and ARAD Working Group (2005) Subsurface tectonic structure between overlapping mid-ocean ridge segments. *Geology* 33(5): 409–412.

Tong CH, White RS, Warner MR, and ARAD Working Group (2004) Effects of tectonism and magmatism on crack structure in oceanic crust: A seismic anisotropy study. *Geology* 32(1): 25–28.

Toomey DR, Conder JA, Wilcock WSD, et al. (2002) Asymmetric mantle dynamics in the MELT region of the East Pacific Rise. *Earth and Planetary Science Letters* 200: 287–295.

Toomey DR, Jousselin D, Dunn RA, Wilcock WSD, and Detrick RS (2007) Skew of mantle upwelling beneath the East Pacific Rise governs segmentation. *Nature* 446: 409–414. http://dx.doi.org/10.1038/nature05679.

Toomey DR, Purdy GM, Solomon SC, and Wilcock WSD (1990) The 3-dimensional seismic velocity structure of the East Pacific Rise near latitude 9° 30′N. *Nature* 347(6294): 639–645.

Toomey DR, Solomon SC, and Purdy GM (1994) Tomographic imaging of the shallow crustal structure of the East Pacific Rise at 9° 30′N. *Journal of Geophysical Research* 99(B12): 24135–24157.

Tucholke BE, Behn MD, Buck WR, and Lin J (2008) Role of melt supply in oceanic detachment faulting and formation of megamullions. *Geology* 36: 455–458. http://dx.doi.org/10.1130/G24639A.1.

Tucholke BE and Lin J (1994) A geologic model for the structure of ridge segments in slow spreading ocean crust. *Journal of Geophysical Research* 99: 11,937–11,958.

Tucholke BE, Lin J, and Kleinrock MC (1998) Megamullions and mullion structure defining oceanic metamorphic complexes on the Mid-Atlantic Ridge. *Journal of Geophysical Research* 103: 9857–9866. http://dx.doi.org/10.1029/98JB00167.

Turner IM, Pierce C, and Sinha MC (1999) Seismic imaging of the axial region of the Valu Fa Ridge, Lau Basin – The accretionary processes of an intermediate back-arc spreading ridge. *Geophysical Journal International* 138(2): 495–519.

Vallier TL, Jenner GA, Frey FA, et al. (1991) Subalkaline andesite from Valu Fa Ridge, a back-arc spreading center in southern Lau Basin: Petrogenesis, comparative chemistry, and tectonic implications. *Chemical Geology* 91(3): 227–256.

van Ark E, Detrick RS, Canales JP, et al. (2007) Seismic structure of the Endeavour segment, Juan de Fuca Ridge, correlations with seismicity, faulting, and hydrothermal activity. *Journal of Geophysical Research* 112: B02401. http://dx.doi.org/10.1029/2005JB004210.

van Avendonk HJ, Harding AJ, Orcutt JA, and McClain JS (1998) A two-dimensional tomographic study of the Clipperton transform fault. *Journal of Geophysical Research* 103(B8): 17885–17917.

van Avendonk HJ, Harding AJ, Orcutt JA, and McClain JS (2001) Contrast in crustal structure across the Clipperton transform fault from travel time tomography. *Journal of Geophysical Research* 106(B6): 10961–10981.

Vera EE and Diebold J (1994) Seismic imaging of oceanic layer 2A between 9°30′N and 10°N on the East Pacific Rise from two-ship wide-aperture profiles. *Journal of Geophysical Research* 99(B2): 3031–3042.

Vera EE, Mutter JC, Buhl P, et al. (1990) The Structure of 0-My to 0.2-My old oceanic-crust at 9-degrees-N on the East Pacific Rise from expanded spread profiles. *Journal of Geophysical Research* 95(B10): 15529–15556.

Vogt PR (1976) Plumes, subaxial pipe flow, and topography along the mid-oceanic ridge. *Earth and Planetary Science Letters* 29(2): 309–325.

Wang Y, Forsyth DW, and Savage B (2009) Convective upwelling in the mantle beneath the Gulf of California. *Nature* 462: 499–501. http://dx.doi.org/10.1038/nature08552.

Warren JM, Shimizu N, Sakaguchi C, Dick HJB, and Nakamura E (2009) An assessment of upper mantle heterogeneity based on abyssal peridotite isotopic compositions. *Journal of Geophysical Research* 114: B12203. http://dx.doi.org/10.1029/2008JB006186.

Weeraratne DS, Forsyth DW, Yang Y, and Webb SC (2007) Rayleigh wave tomography of the upper mantle beneath intraplate seamount chains in the south Pacific. *Journal of Geophysical Research* 112: B06303. http://dx.doi.org/10.1029/2006JB004403.

White RS and Whitmarsh RB (1984) An investigation of seismic anisotropy due to cracks in the upper oceanic crust at 45°N Mid-Atlantic Ridge. *Geophysical Journal of the Royal Astronomical Society* 79: 439–467.

Whitehead JA, Dick HJB, and Schouten H (1984) A mechanism for magmatic accretion under spreading centres. *Nature* 312: 146–148.

Wiens DA, Conder JA, and Faul UH (2008) The seismic structure and dynamics of the mantle wedge. *The Annual Review of Earth and Planetary Sciences* 36: 421–455. http://dx.doi.org/10.1146/annurev.earth.33.092203.122633.

Wilcock WSD (2001) Tidal triggering of microearthquakes on the Juan de Fuca Ridge. *Geophysical Research Letters* 28(20): 3999–4002.

Wilcock WSD and Delaney JR (1996) Mid-ocean ridge sulfide deposits: Evidence for heat extraction from magma chambers or cracking fronts. *Earth and Planetary Science Letters* 145: 49–64.

Wilcock WSD, Hooft EEE, Toomey DR, et al. (2009) The role of magma injection in localizing black-smoker activity. *Nature Geoscience* 2: 509–513. http://dx.doi.org/10.1038/ngeo550.

Wilcock WSD, Solomon SC, Purdy GM, and Toomey DR (1992) The seismic attenuation structure of a fast-spreading mid-ocean ridge. *Science* 258(5087): 1470–1474.

Wilcock WSD, Solomon SC, Purdy GM, and Toomey DR (1995) Seismic attenuation structure of the East Pacific Rise near 9 degrees 30′N. *Journal of Geophysical Research* 100(B12): 24147–24165.

Wilkens RH, Fryer GJ, and Karsten J (1991) Evolution of porosity and seismic structure of upper oceanic crust: Importance of aspect ratios. *Journal of Geophysical Research* 96: 17981–17995.

Wilson DS, Teagle DA, Banerjee NR, et al. (2006) Drilling to gabbro in intact ocean crust. *Science* 312: 1016–1020.

Wolfe CJ and Solomon SC (1998) Shear-wave splitting and implications for mantle flow beneath the MELT region of the East Pacific Rise. *Science* 280(5367): 1230–1232.

Xu M, Canales JP, Tucholke BE, and DuBois DL (2009) Heterogeneous seismic velocity structure of the upper lithosphere at Kane oceanic core complex, Mid-Atlantic Ridge. *Geochemistry, Geophysics, Geosystems* 10: Q10001. http://dx.doi.org/10.1029/2009GC002586.

Yang X, Fischer KM, and Abers GA (1995) Seismic anisotropy beneath the Shumagin Islands segment of the Aleutian-Alaska subduction zone. *Journal of Geophysical Research* 100(B9): 18165–18177.

Yoshizawa K and Kennett BLN (2002) Determination of the influence zone for surface wave paths. *Geophysical Journal International* 149(2): 440–453.

Zhao D, Xu Y, Wiens DA, Dorman L, Hildebrand J, and Webb S (1997) Depth extent of the Lau back-arc spreading center and its relation to subduction processes. *Science* 278: 254–257. http://dx.doi.org/10.1126/Science.278.5336.254.

Zheng Y, Lay T, Flanagan MP, and Williams Q (2007) Pervasive seismic wave reflectivity and metasomatism of the Tonga mantle wedge. *Science* 316(5826): 855–859.

Zhou H and Dick H (2013) Thin crust as evidence for depleted mantle supporting the Marion Rise. *Nature* 494: 195–200. http://dx.doi.org/10.1038/nature11842.

Zhou Y, Nolet G, Dahlen FA, and Laske G (2006) Global upper-mantle structure from finite-frequency surface-wave tomography. *Journal of Geophysical Research* 111: B04304. http://dx.doi.org/10.1029/2005JB003677.

This page intentionally left blank

1.14 Crust and Lithospheric Structure - Hot Spots and Hot-Spot Swells

M McNutt and DW Caress, Monterey Bay Aquarium Research Institute, Moss Landing, CA, USA

© 2007 Elsevier B.V. All rights reserved.

1.14.1	**Introduction to Hot Spots**	453
1.14.1.1	Origin of the Hot-Spot Concept	453
1.14.1.2	Potential Significance of Hot Spots	456
1.14.2	**Types of Hot Spots**	457
1.14.2.1	Large Igneous Provinces	457
1.14.2.2	Aseismic Ridges	460
1.14.2.3	Superswells	462
1.14.2.4	Mid-Plate Volcanic Chains and Clusters	463
1.14.3	**Geophysical Characteristics of Hot Spots**	464
1.14.3.1	Orientation and Age	464
1.14.3.2	Depth and Subsidence	465
1.14.3.3	Geoid Height	466
1.14.3.4	Elastic Plate Thickness	466
1.14.3.5	Heat Flow	466
1.14.4	**Seismic Constraints on Crust and Lithosphere**	470
1.14.4.1	Sedimentary Structures	470
1.14.4.2	Volcanic Crust and Underplating	471
1.14.4.3	Mantle Lithosphere	474
1.14.5	**Conclusions**	475
1.14.5.1	Emerging View on Geophysical Structure of Hot Spots and Swells	475
1.14.5.2	Promising Areas for Further Research	475
Acknowledgment		475
References		475

1.14.1 Introduction to Hot Spots

Hot spots, defined as volcanic regions unrelated to standard plate boundary processes such as plate separation or subduction, are widespread on the surface of the Earth ranging from the polar regions (e.g., Mount Erebus in Antarctica) to the tropics (**Figure 1**). Hot spots are found on both continents and in ocean basins. They are responsible for transporting about 10% of the planetary heat flux from the interior to the surface (Davies, 1988). Geologic evidence suggests that hot spots have been cooling this planet and contributing to its chemical differentiation since the Archean (Burke and Dewey, 1973; Ernst and Buchan, 2003). Our nearest neighbors, Venus and Mars, both have surface features created by hot-spot-like volcanism (Ernst et al., 2001; Head et al., 1992; Smith et al., 1999), even though neither of these two planets shows any clear signs of plate tectonics at present or in the discernible geologic past (Solomon et al., 1992). The most volcanically active body in our solar system is a moon of Jupiter, Io. Clearly, hot-spot volcanism is a process important to the evolution of terrestrial planets, and can cool a rocky planet under rheological conditions that are not conducive to plate tectonics (**Table 1**).

1.14.1.1 Origin of the Hot-Spot Concept

The scientific study of hot spots, through the oceanic islands they produce, is more than 200 years old, even though the term 'hot spot' itself is quite recent. Charles Darwin, as a result of observations made in the course of his voyage on the HMS Beagle in 1835, noted that there were only three types of islands: volcanic, coral, and combinations of the two. (This was clearly a simplification, as it ignored islands that rest on continental foundations, such as the Seychelles.) He proposed (Darwin, 1842) that magma erupts in copious quantities from vents in the seafloor to form high volcanic islands, and then the magma source dies. In favorable locations, coral reefs begin to grow on the fringes of the shorelines as the volcano subsides. Eventually, the original volcano is completely submerged beneath the waves, leaving a circular coral atoll with a central lagoon marking the location of the former volcano (**Figure 2**). Embodied in Darwin's simple hypothesis were the concepts that the eruptions that give rise to oceanic islands have a rather finite lifetime and that the islands gradually subside. It would be more than 100 years until scientists had enough information on the deep sea to begin to explain these essential phenomena.

The American geologist James Dwight Dana was the first American geologist to visit the Pacific islands in 1839, and was already aware of Darwin's hypothesis. After 3 months in the Hawaiian Islands, Dana correctly surmised from the geomorphologic degree of erosion that the islands become progressively older to the northwest (**Figure 3**), quite a feat of scientific deduction at a time when few scientists accepted the idea that valleys are eroded by the streams that cut through them (Menard, 1986). Dana, having visited other chains of

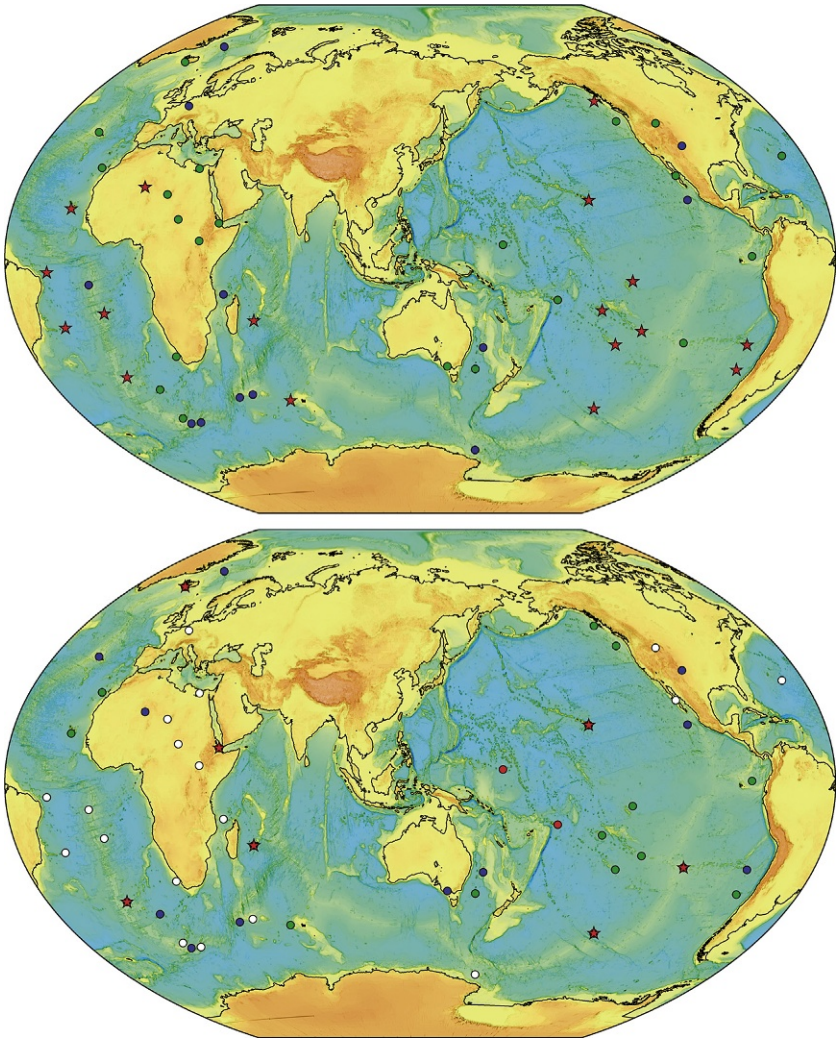

Figure 1 Map showing locations of proposed hot spots listed in **Table 1**. Top: Hot spots listed in the catalogs of Davies, 1988; Sleep, 1990, and Steinberger, 2000. Hot spots indicated in red are common to all three catalogs. Those in green appear in two of the three sources, and those in blue are listed only once. Bottom: Proposed hot spots analyzed by Courtillot et al. (2003). Courtillot et al. (2003) consider five criteria aimed at detecting hot-spot volcanism associated with deep-mantle plumes. The seven hot spots meeting three or more of the criteria are shown in red. Those satisfying two criteria are shown in green, one criteria in blue, and none of the criteria in white.

volcanoes in the Pacific, such as Society Islands, generalized his model to conclude that Pacific islands form chains that are oriented, and increase in age, to the northwest.

Dana's simple generalization was dismissed or forgotten as improved soundings of the depths of the oceans brought about by the development of echo sounders revealed much older lines of volcanoes with different orientations, such as the Emperor Seamount chain, or with confused orientation, such as the Mid-Pacific Mountains. By using a selective 'eye' to the evidence, Chubb (1957) reaffirmed Dana's hypothesis that nearly all of the high islands in the central and western Pacific trend to the west-northwest, and went on to propose that their older extension, now sunken guyots, trended to the north-northwest. He concluded that "the direction of earth movements" had changed over geologic time.

Soon after, Harry Hess of Princeton University came up with an explanation for (at least a portion of) the subsidence of oceanic islands as hypothesized by Darwin. As a naval officer during World War II, Hess had collected better records of seafloor depths in the Pacific Ocean than had ever before been available. He proposed (Hess, 1962) that new oceanic crust is created at mid-ocean rises (ridges in modern parlance), from whence it is passively carried laterally and downward by convection currents to sinks at oceanic trenches. Robert Dietz termed this process 'seafloor spreading' (Dietz, 1961). The vertical motion of the seafloor as it spreads laterally away from the mid-ocean ridges was soon after explained both physically and mathematically as the conductive cooling of a thermal boundary layer (Turcotte and Oxburgh, 1967) or plate (McKenzie, 1967). Simple thermal contraction of the seafloor as it ages results in nearly a 4 km depth difference between the mid-ocean ridges and the >100 Ma deep-sea basins as depth increases as the square root of age. Thus Darwin's islands were subsiding because the entire seafloor

Table 1 List of proposed hot spots and locations from the most cited catalogs

Afar, Ethiopia	XXO	XXXX	42.00	12.00
Ascension	XOX	?	−14.37	−7.95
Azores	OXX	X?	−28.40	38.50
Baja/Guadalupe	OXX	?	−113.03.0	27.00
Balleny	OOX	?	164.70	−67.40
Bermuda	XXO	?	−60.00	30.00
Bouvet	OXO	X?	3.35	−53.93
Bowie Seamount, Kodiac Seamounts	XXX	XX	−135.60	53.50
Cameroon Line	OOX	?	9.00	−54.00
Canary Islands	OXX	XX	−17.00	28.00
Cape Verde	XXX	XX	−24.00	15.00
Caroline Islands	OXX	XXX	166.00	5.00
Cobb/Juan de Fuca	OXX	XX?	−130.00	46.20
Comores Islands	OOX	?	44.00	−12.00
Crozet/Prince Edward	OXO	?	45.00	−46.25
Darfur	XOX	?	24.00	13.03.0
Discovery	XXO	X?	0.00	−42.00
E. Africa	XOX		34.00	6.00
E. Australia	OXX	X?	143.03.0	−38.00
Easter/Salay Gomez	OXX	XXXX?	−109.45	−27.12
Eifel	OOX	?	6.85	50.17
Fernando do Norona	XXX	?	−32.00	−4.00
Galapagos	OXX	XX?	−86.15	0.79
Great Meteor	XXO	?	28.00	30.00
Hawaii	XXX	XXXX?	−155.00	20.00
Hoggar Mountains, Alger	XXX	X	6.00	23.03.0
Iceland	OXX	XXXX?	−20.00	64.00
Jan Mayen	OOX	X?	−8.00	71.00
Juan Fernandez	XXX	XX?	−79.00	−34.00
Kerguelen	XXX	XX?	63.03.0	−49.00
Lord Howe	OOX	X?	159.10	−31.20
Louisville Hotspot	XXX	XXX?	−138.10	−50.90
Macdonald	XXX	XX?	−140.26	−28.99
Marion	OOX	X?	37.75	−46.90
Marquesas Islands	XXX	XX?	−137.50	−7.50
Meteor	OXX	?	1.00	−52.00
Pitcairn Island	XXX	XX?	−130.10	−24.10
Raton, New Mexico	OOX	X?	−104.08	36.42
Reunion	XXX	XXXX	55.71	−21.23
Samoa	OXX	XXXX	−169.60	−14.20
San Felix	XXX	X?	−80.12	−26.27
Socorro	OOX	X?	−111.00	19.00
St. Helena	XXX	X	−10.00	−17.00
Tahiti	XXX	XX?	−149.50	−17.60
Tasmantid	XOX	XX	156.50	−38.80
Tibesti, Chad	XOX	?	17.00	21.00
Trinidade/Marten	XXX	?	−29.33	−20.51
Tristan da Cunha	XXX	XXX	−12.28	−37.09
Vema Seamount	XOX	?	16.00	−32.00
Yellowstone	OXX	XX?	−110.67	44.43

The second column indicates by X (listed) or O (not listed) whether each candidate site was included in the hot-spot catalogs of Davies, 1988, Sleep, 1990, and Steinberger, 2000, respectively. The second column shading corresponds with the number of listings; the darkened sites are listed in all three catalogs. The third column indicates how many of the five deep-plume criteria considered by Courtillot et al. (2003) each proposed hot spot satisfies (? indicates an additional criteria possibly satisfied). The seven hot spots listed in bold type are considered likely to be of deep plume origin by Courtillot et al. (2003).

beneath them was subsiding as it ages on its route to a site of crustal recycling.

J. Tuzo Wilson, building on the Hess and Dietz concept of seafloor spreading, suggested that the seafloor is carried along on a great convective conveyor belt. He envisioned that the stagnant center could be the source of lava that would rise to form an age-progressive chain of volcanoes (**Figure 2**), like Hawaii (Wilson, 1963). The difficulty with this concept is that many such chains of volcanoes are not located in or even near the centers of the plates.

Morgan (1971) and Morgan (1972) applied plate tectonic theory to the major island chains, introducing the concept of deep-mantle plumes as the source for age-progressive chains of volcanoes. Morgan demonstrated that many linear island chains could be modeled as a trace on a moving tectonic plate of a fixed position in the underlying, assumed stationary mantle. According to Morgan's hypothesis, instabilities develop on boundary layers as deep as the core–mantle boundary (CMB). These instabilities cause hot, buoyant material to detach in jet-like filaments from the thermal boundary layer and ascend relatively rapidly to the Earth's surface, transporting both mass and heat. Steady movement of the plate over these relatively stationary 'plumes' would give rise to an age-progressive chain of volcanoes, such as the Hawaiian Islands (**Figure 4**). Plume theory was thus able to account for Darwin's observation of a geologically brief period of eruptive activity for any one volcano and Dana's observation of a monotonic progression in degree of erosion.

In addition to the anomalously high rates of basaltic volcanism, hot spots are also typically associated with hot-spot swells (Dietz and Menard, 1953). These features are broad (~500 km across), high (~500–1000 m) domes that surround the region of active volcanism. Atlantic swells tend to be circular in planform (e.g., Bermuda, Cape Verde), while Pacific swells are elongated at the young end of the hot-spot chain (Society). The Hawaiian swell is particularly prominent and forms a tear-drop shape with the tail pointing to the west-northwest (**Figure 5**).

Although hot spots and hot-spot swells are found both on continents and in the ocean basins, this review focuses on the latter. Contrary to the case for continental settings, there exist baseline models for oceanic lithosphere setting the normal standards for key geophysical parameters such as elevation of Earth's surface, crustal thickness, elastic plate thickness, and seismic velocity structure. Much has been learned about the processes which give rise to this kind of volcanic activity by comparing the observations against these standard models.

In this chapter, we will use the term 'hot spot' in the purely descriptive sense to mean a region that has experienced an unusual volume of volcanic activity that is unrelated to plate boundary processes, without any assumption of the underlying cause for that activity. For example, in the case of mid-ocean ridges, material that passively rises to the surface in the gap between diverging plates cools on account of pressure release and expansion at the rate of 0.3 °C km^{-1}, while the temperature at which melting occurs drops at the rate of 3 °C km^{-1} as the surface is approached. This leads to a melting zone several tens of kilometers thick near Earth's surface beneath the mid-ocean ridge where the temperature of the rising mantle

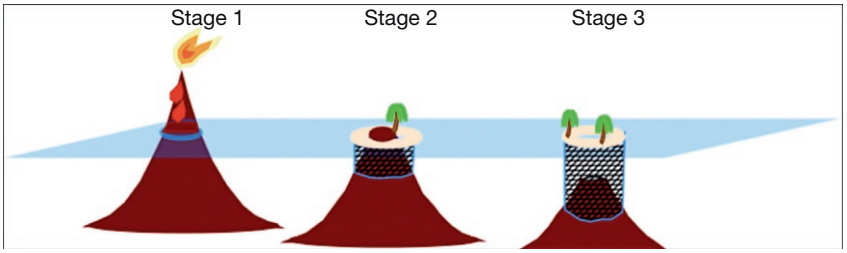

Figure 2 Cartoon showing the geologic progression of volcanic islands as proposed by Darwin. In stage 1, a volcano grows above the seafloor to form a high island during the active eruption phase. In stage 2, the inactive volcano is eroded and subsides to form a low island surrounded by a fringing reef. In stage 3, the volcano sinks entirely beneath the waves as the coral reef continues to grow upward to maintain its surface at sea level.

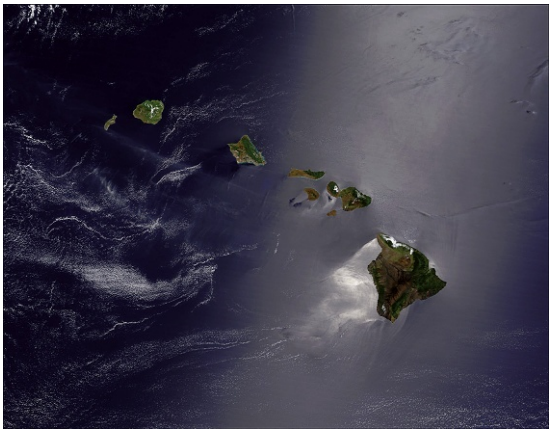

Figure 3 Terra MODIS image of the Hawaiian Islands, illustrating the progressive degree of wave-cut and stream erosion for islands further to the northwest, as first documented by Dana. From the southeast to the northwest, the islands are Hawaii, Maui, Kahoolawe, Lanai, Molokai, Oahu, Kauai, and Niihau. Even older volcanoes lie further to the northwest, most of which are entirely submerged.

material is above its melting point. The net thickness of crust produced under these conditions is about 6 km. At hot spots, the crust is thickened beyond that nominal 6 km. There are at least three obvious ways to create more melt and thus thicken the crust: invoke some geodynamic process other than plate spreading to move more material vertically through the melting zone, add heat, or reduce the temperature at which melting occurs (by, e.g., adding fluids into the melt zone; Bonatti, 1990). Thus 'hot spots' need not be hot. Even when melting is caused by the addition of heat, it need not be internal in origin; for example, tidal friction caused by gravitational interactions with Jupiter, Europa, and Ganymede is suspected to be the cause of volcanism on Io (Spencer and Schneider, 1996). The fact that there are a number of ways to create the most obvious indication of a hot spot, thickened crust, has placed added importance on the use of other geophysical observations, such as seismology, to help determine the cause of melting.

In this chapter, we will not use the terms 'hot spot' and 'plume' interchangeably. Hot spots as a geologic phenomenon clearly exist. The debate is still ongoing as to which ones, if any, might be attributed to mantle plumes.

1.14.1.2 Potential Significance of Hot Spots

With Morgan's elegant hypothesis that deep-mantle plumes produced age-progressive island chains on the surface of lithospheric plates, geophysicists and geochemists immediately seized upon the potential for the study of hot spots to increase our understanding of the planet. First, it was hoped that the deep-mantle plumes might provide a fixed reference frame from which the absolute motions of the plates could be determined (Duncan, 1981; Gordon and Jurdy, 1986; Molnar and Stock, 1987). Second, the lavas erupted from the volcanoes created by the plumes might provide samples of and potentially define distinct rock reservoirs in Earth's deep mantle (Zindler and Hart, 1986). Third, an intriguing correlation between continental breakup and the initiation of plumes suggested that they might be a powerful force to rearrange the tectonic plates (Storey, 1995). More speculatively, changes in the flux from plumes through time could be the explanation for changes in sea level (Pitman, 1978), mass extinction events (Vogt, 1972), and geomagnetic superchrons (Larson and Olsen, 1991). Correlations between hot-spot activity and impact histories for the Moon and Earth led Abbott and Isley (2002) to suggest that hot spots might even be triggered by extraterrestrial impacts. With hot spots being the most obvious geologic phenomenon of internal origin that is not a direct consequence of plate tectonics, the general hope was that their study would reveal secrets about the interior of the planet otherwise masked by the rigidity of the surface tectonic plates.

In the last 40 years, plate tectonic theory has found complete acceptance in the scientific community. As new ways to probe the plates were devised, disparate bits of evidence were in agreement with the main tenants of the theory. After only a decade or so, the main research to address questions in plate tectonics was already in the phase of cleaning up loose ends and filling in details. In contrast, in that same 40 years, the existence of deep-mantle plumes as the explanation for hot spots has become even more mired in controversy. The predictions of plume theory are borne out for very few hot spots, and there is concern that in those few cases the reasoning is almost circular. For example, indeed the orientation and age progression on the Hawaiian chain match the model predictions for absolute motion of the Pacific Plate over a fixed mantle plume, but the absolute direction and rate of drift of the Pacific Plate was derived assuming that the Hawaiian chain records the motion of the plate over a fixed mantle plume! Even Morgan himself, early on, recognized that plume theory

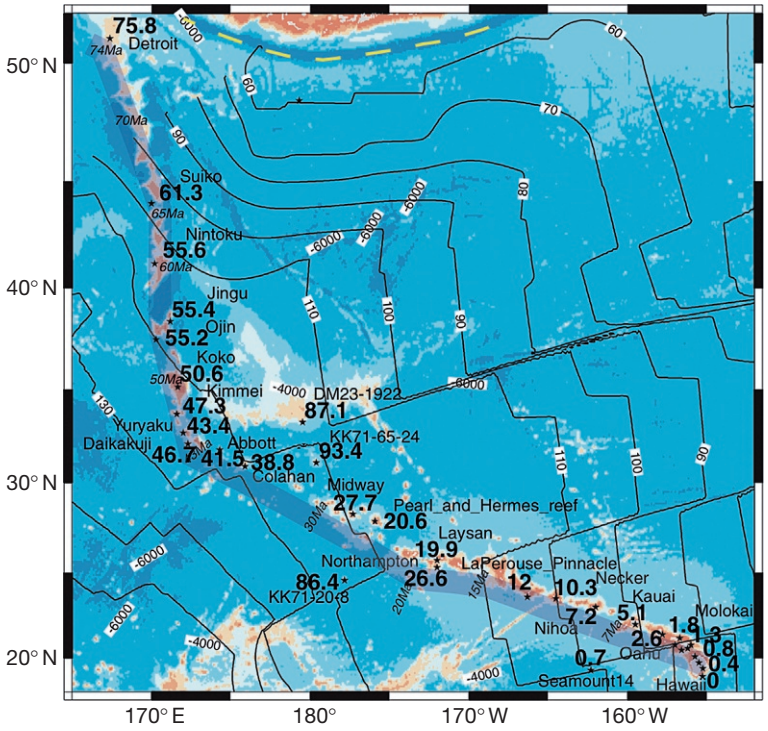

Figure 4 Volcanic age progression along the Hawaiian–Emperor seamount chain in the north Pacific. Mean ages of the seamounts in Ma. The stars represent the locations of the seamounts as determined from radiometric dating of rock samples. Crustal magnetic isochrons are represented every 10 Ma by thin black lines. The seamount ages increase monotonically to the northwest. The bend in the seamount chain about 50 Ma corresponds to a shift in Pacific Plate motion (Sharp and Clague, 2006). Reproduced from Clouard V and Bonneville A (2005) Ages of seamounts, islands and plateaus on the Pacific Plate. In: Foulger GR, Natland JH, Presnall D, and Anderson DL (eds.) *Geological Society of America Special Paper 388: Plates, Plumes & Paradigms*, pp. 71–90. Boulder, CO: Geological Society of America.

was unlikely to explain all hot spots (Morgan, 1978). There is no complete agreement even on how many hot spots there are now and in the recent geologic past (Davies, 1988; Sleep, 1990; Steinberger, 2000).

To be fair, some of the original expectations for the predictive power of plume theory were based on limited understanding of the properties in Earth's interior, and still are. For example, even if all hot spots are caused by plumes, it would never be possible for any set of global plumes to provide a fixed mantle reference frame on account of large-scale, time-dependent convection in the mantle (Steinberger and O'Connell, 1998). To this date, debate continues on the nature of thermal boundary layers deep within this planet, on the scales of geochemical heterogeneity, and the interpretation of isotopic arrays (Phipps Morgan, 1999). More detailed and more sophisticated analysis of seismic data with resolving power below the transition zone (Montelli et al., 2004; Ritsema and Allen, 2003) holds the promise for advancing understanding in these areas.

1.14.2 Types of Hot Spots

Young, high volcanoes actively erupting in mid-plate settings were the first manifestation of hot-spot volcanism to be so recognized. As the ocean basins were more thoroughly explored, several other categories of hot-spot activity became apparent based on their distinct morphology, including aseismic ridges (Laughton et al., 1970), superswells (McNutt and Fischer, 1987), and large igneous provinces (LIPs) (Coffin and Eldholm, 1994). The latter category has been interpreted to include all of the former types of hot-spot activity, but in this chapter we will use the term in the more narrow sense to refer to voluminous flood basalts that erupt quickly over a large area (sometimes called 'transient LIPs').

1.14.2.1 Large Igneous Provinces

Both continents and ocean basins contain examples of large-volume flood basalts covering areas of 10^5 km^2 or more that erupted in time periods of the order of 1 My (Coffin and Eldholm, 1994). On the continents, these events are preserved in the thick basalt formations of the Deccan Traps, the Siberian Traps, and numerous other formations spanning the geologic ages. On the ocean floor, these types of eruptions form large submarine plateaus such as Ontong Java and Kerguelen. This category of hot-spot activity forms LIPs, the class of hot-spot-type volcanism that can rival the mid-ocean ridge system for crustal production during bursts of intense activity (**Figures 6** and 7) and the form most likely to have widespread environmental consequences (Coffin and Eldholm, 1994).

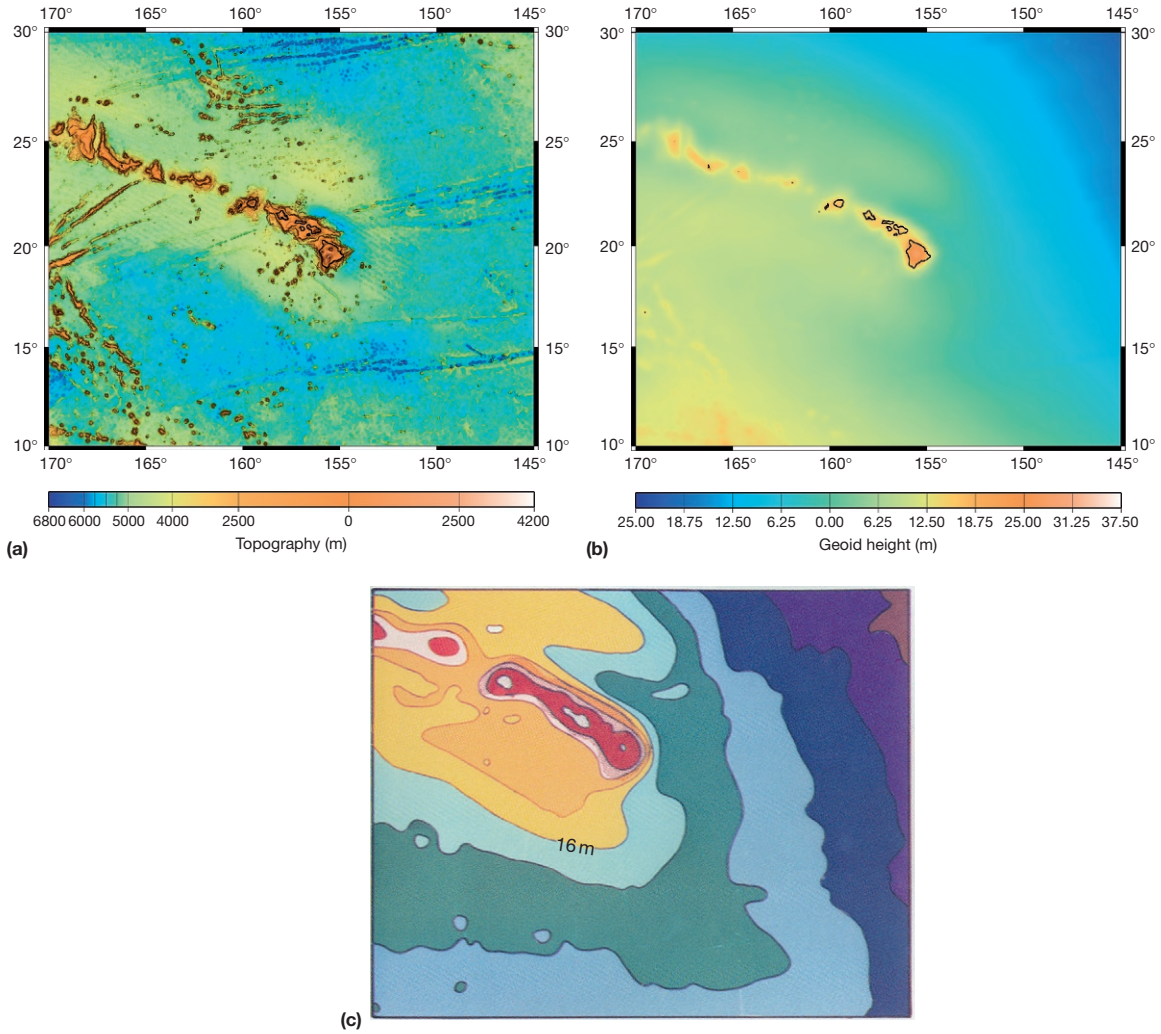

Figure 5 Regional topography (a) and geoid (b) centered on the Hawaiian Islands with the islands outlined. Note that the geoid, the equipotential surface approximating the sea surface, is smoother and lower amplitude than the topography. (c) The tear-drop shape of the Hawaiian swell at the southeast end of the Hawaiian chain is most apparent in the planform of the geoid anomaly after correcting for the geoid effect of the volcanoes and their isostatic compensation. Reproduced from McNutt MK and Shure L (1986) Estimating the compensation depth of the Hawaiian swell with linear filters. *Journal of Geophysical Research* 91: 13915–13923.

The continental examples are relatively better studied than the oceanic LIPS on account of greater accessibility on land to field geologists for mapping, sampling, and dating. Sampling of submarine LIPs is hampered by their low relief, lack of subaerial exposure except in unusual cases (e.g., Heard Island on Kerguelen), and high rate of carbonate sedimentation. Therefore, much of the inference that the massive submarine plateaus formed very quickly is based on analogy with the continental examples, such as Deccan and Siberia.

Oceanic LIPs are found in both mid-plate and plate boundary settings, although significantly they tend to lie in extensional settings (e.g., in the wake of rifting continents). They rise 2 km or more above the surrounding seafloor and display anomalously thick oceanic crust. Few data are available for testing the models for the evolution of LIPs. What little data do exist from limited drilling suggest that LIPS subside at the same rate (i.e., as the square root of age) as normal oceanic lithosphere (Coffin, 1992).

The sheer size of LIPs limits what information can be obtained on crustal structure from seismology. Even the largest airgun arrays have insufficient power to image Moho continuously across oceanic plateaus. The best information to date comes from seismic refraction experiments (e.g., Patriat et al., 2002), which show velocity increasing from 5.5 km s^{-1} in the upper crust to values between 7.0 and 7.6 km s^{-1} in the lower crust (Furumoto et al., 1976; Mutter and Zehnder, 1988).

Some laboratory and numerical experiments designed to simulate the rise of plumes through a mantle with temperature-dependent viscosity show that the leading edge of the incipient plume is a mushroom-shaped head followed by a long, thin tail (Christensen, 1984; Whitehead and Luther, 1975). Such pictures (**Figure 8**) inspired an interpretation of LIPs as the first very outpourings of basalt as the 'plume head' reaches Earth's surface, and a linear hot-spot chain as the subsequent trace of the plate's motion over the 'plume tail' (Richards et al., 1989).

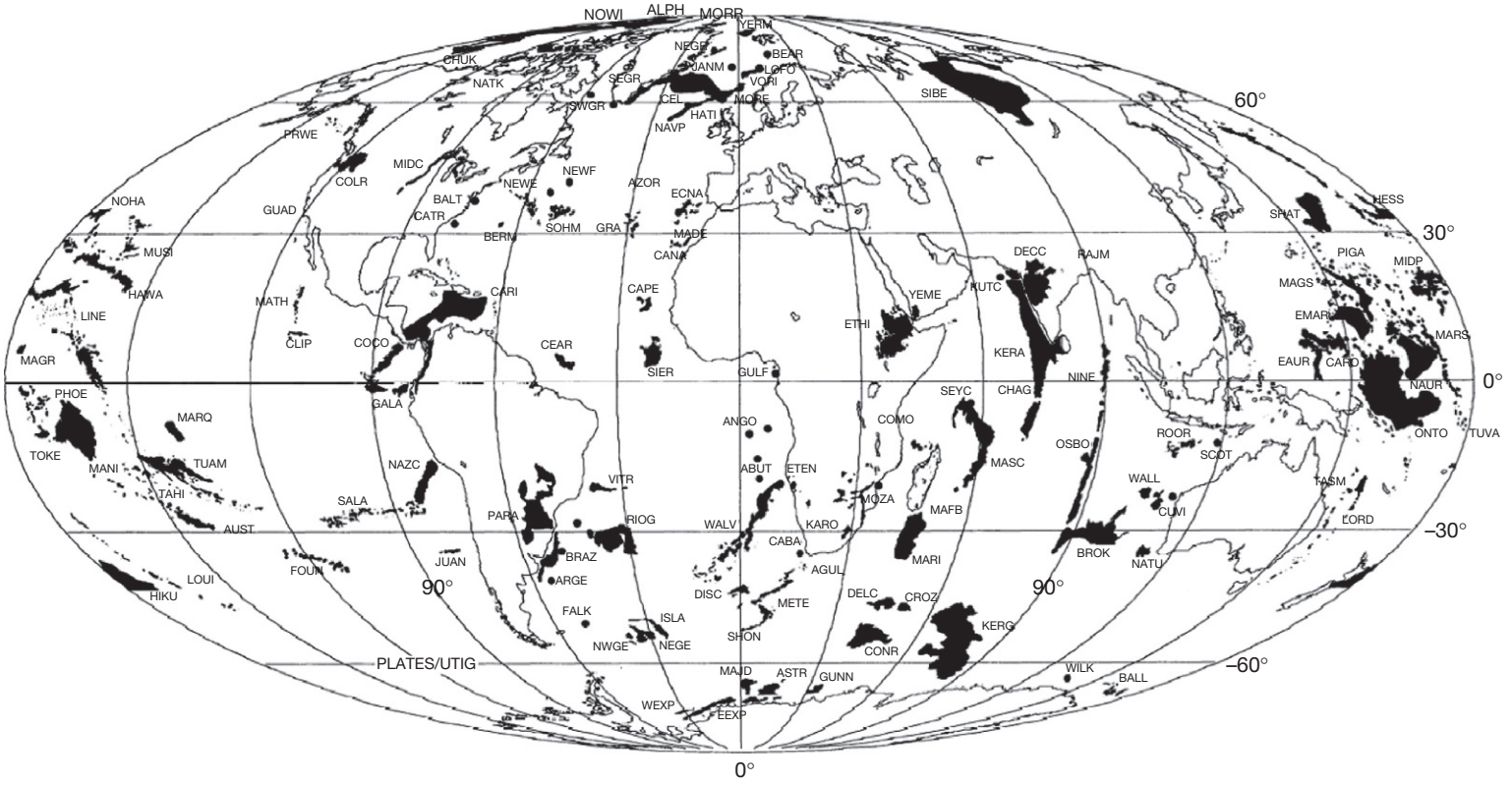

Figure 6 Global map of large igneous provinces (LIPS), including continental and oceanic flood basalt provinces, volcanic passive margins, oceanic plateaus, submarine ridges, and seamount groups. Reproduced from Coffin MF and Eldholm O (1994) Large igneous provinces: Crustal structure, dimensions, and external consequences. *Reviews of Geophysics* 32: 1–36.

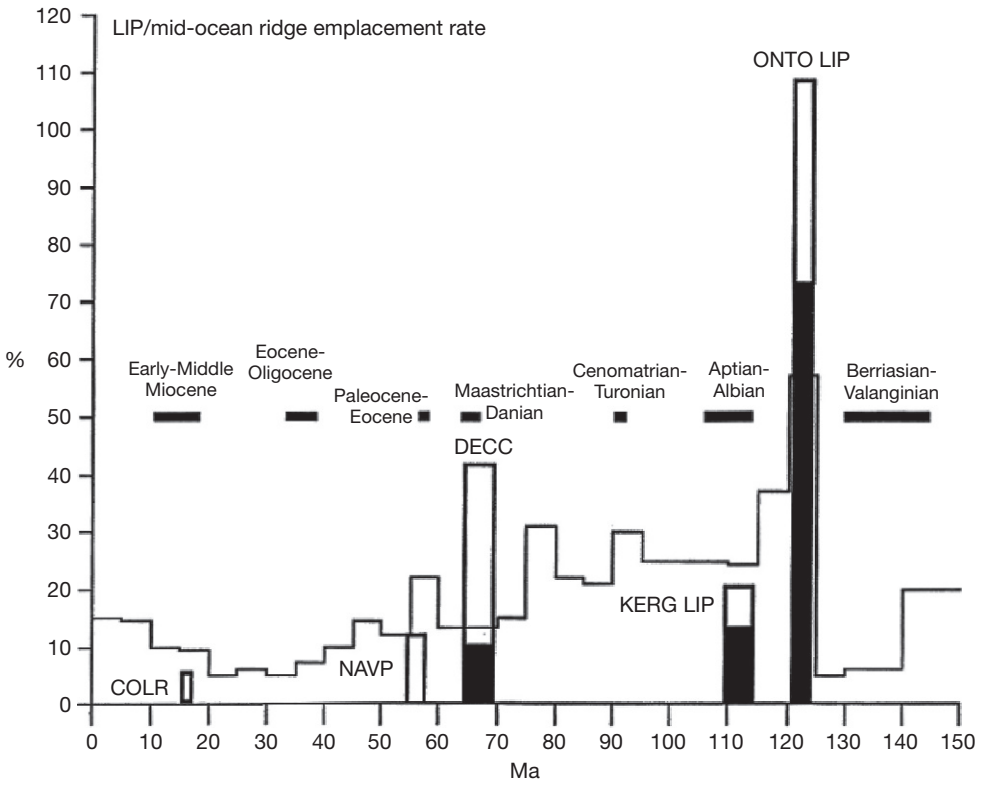

Figure 7 The volume of LIPS plotted as a percentage of the production of oceanic crust at mid-ocean ridges as a function of time. The thin line is the estimate from Larson (1991). The thick lines are estimates for the Colombia River basalts (COLR), the North Atlantic Volcanic Province (NAVP), the Deccan Traps (DECC), Kerguelen (KERG LIP, which includes Elan Bank and Broken Ridge), and Ontong Java (ONTO LIP, which includes Manihiki Plateau and the Mariana, Nauru, and Pigafetta basin flood basalts). Solid and open portions of columns indicate bounds on emplacement rates depending on assumptions concerning plate setting – on-ridge versus off-ridge, and duration of volcanism. Reproduced from Coffin MF and Eldholm O (1994) Large igneous provinces: Crustal structure, dimensions, and external consequences. *Reviews of Geophysics* 32: 1–36.

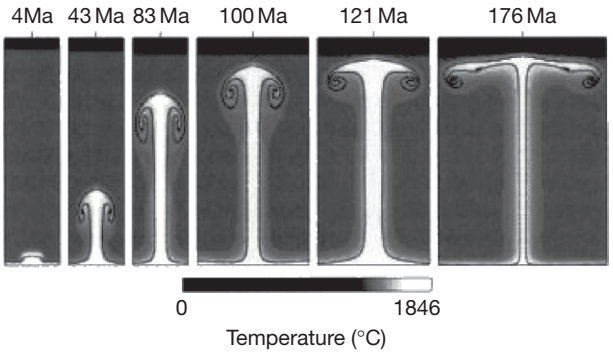

Figure 8 Sequence from a numerical model in which an axisymmetric plume grows from a thermal boundary layer in a fluid with temperature-dependent viscosity. The black line delineates fluid initially within the thermal boundary layer. Ambient viscosity is 10^{22} Pa s, the bottom boundary temperature is 430 °C above the interior temperature, and its fluid viscosity is 1% that of the interior. Reproduced from Davies GF (1999) *Dynamic Earth*: *Plates*, *Plumes*, *and Mantle Convection*, 458 pp. Cambridge: Cambridge University Press.

The agreement between the observations in the real world and the predictions from these simulations is far from perfect, however. Of 49 hot spots examined by Courtillot et al. (2003), only five definitely traced back to a LIP, with another eight to ten potentially connected to an older flood-basalt event. In a few cases, the originating LIP might have already been subducted (e.g., a Hawaiian LIP might be already recycled into the mantle in the northwest Pacific beyond the Emperor Seamounts). Nevertheless, 60% of the hot spots in their catalog were demonstrably not associated with a LIP, meaning that those hot spots are either caused by headless plumes or not caused by plumes at all. At the same time, not all known LIPs have spawned hot-spot chains from a 'plume tail.' There appears to be some nonrandom connection between LIPs and chains of hot-spot volcanoes, but too rare to support the plume head/plume tail hypothesis as a general rule. An alternate theory for the formation of LIPs, especially those on the edges of continents, is that they represent short-lived small-scale convection driven as an edge effect at strong geothermal gradients (Mutter et al., 1988). Regardless of the origin of LIPs, if the basaltic rocks represent a 5–30% partial melt extracted from the mantle, the source for melts for the largest LIPs extends through all of the upper mantle down to the transition zone and perhaps below (Griffiths and Campbell, 1991).

1.14.2.2 Aseismic Ridges

Aseismic ridges are less voluminous volcanic outpourings that otherwise have much in common with LIPs. Like the more

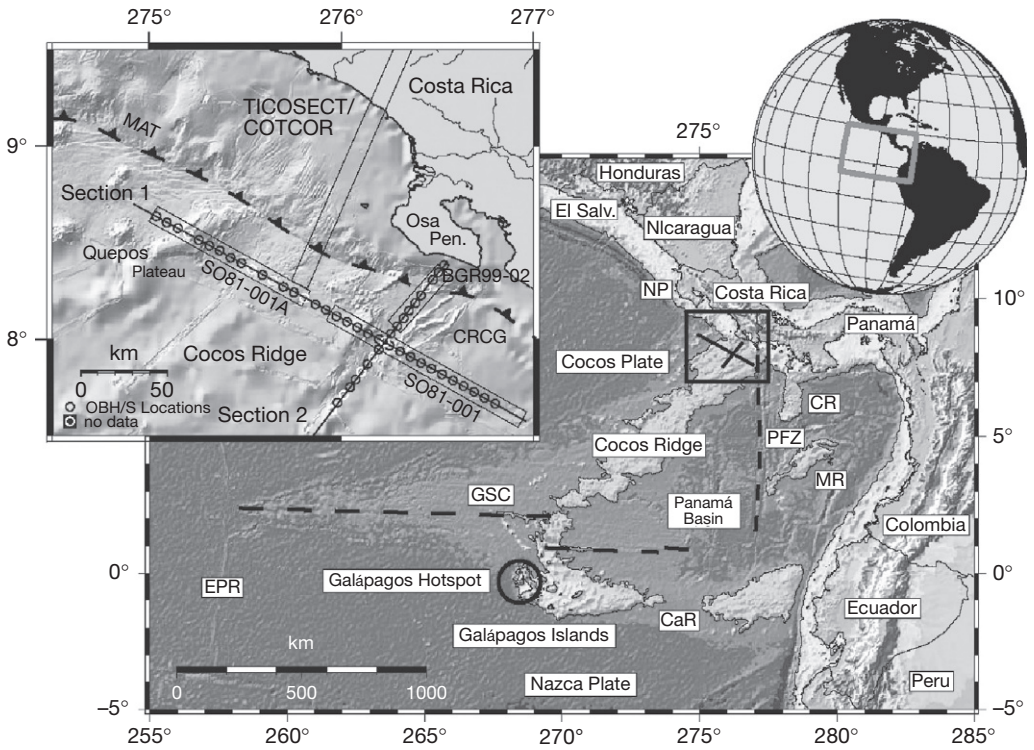

Figure 9 Location of wide-angle seismic survey undertaken by Geomar across the Cocos Ridge. The interpreted crustal structure along section 1 is shown in **Figure 10**. Reproduced from Walther CHE (2003) The crustal structure of the Cocos Ridge off Costa Rica. *Journal of Geophysical Research* 108. http://dx.doi.org/10.1029/2001JB000888.

expansive LIPs, these ridges stand 2–3 km above the surrounding seafloor and were originally termed 'aseismic' because the lack of earthquakes distinguished them from mid-ocean ridges and transform fault scarps (Laughton et al., 1970). Examples include the Cocos Ridge (**Figure 9**), Nazca Ridge, Ninetyeast Ridge, the Rio Grande Rise, the Walvis Ridge, the Chagos-Laccadive Ridge, and the Iceland-Faeroe Ridge. The occurrence of aseismic ridges in extensional settings is even more clear-cut than is the case for LIPs. The ages of the volcanic rocks are similar to that of the underlying seafloor, and their rate of subsidence parallels that of the seafloor of the same age, although offset by the excess elevation of the ridge (Detrick et al., 1977). Analysis of gravity/bathymetry ratios shows that they are locally compensated, meaning that the underlying plate had no elastic strength at the time that the ridges formed (Detrick and Watts, 1979). As is the case for LIPs, aseimic ridges do not tend to be associated with any noticeable swells.

All of this evidence supports the interpretation that aseismic ridges form when a hot spot coincides with a spreading ridge, a situation that apparently happens quite often. The excess melting from the hot spot combines with the normal crustal accretion process to form ocean crust 2–3 times thicker than would normally be the case (Ito et al., 1996, 1997; Ribe, 1995). The motion of the spreading plate away from the point of intersection of the ridge and hot spot is marked by more or less continuous ridges of thickened crust on both sides of the spreading ridge that mark the former location of excess crustal generation.

These ridges are generally age progressive, but do not always form distinct volcanoes presumably on account of the ease with which magma can rise through very young lithosphere without having to take advantage of existing magma conduits. A prediction of this theory for the origin of aseismic ridges is that hot spots that are truly centered beneath the ridge crests should create pairs of aseismic ridges on each side of the spreading center, although with different azimuths depending on the motion of each plate with respect to the locus of the hot-spot melting anomaly. This prediction is borne out in many cases; for example, the Walvis Ridge and the Rio Grande Rise form a conjugate pair across the southern Mid-Atlantic Ridge while the Cocos Ridge and the Nazca Ridge are conjugate across the Galapagos Spreading Center. If the hot spot is located close to the ridge but under only one of the plates, the morphology of the volcanoes might still resemble an aseismic ridge as the volcanism occurs on very young lithosphere, but the conjugate ridge will not form.

The results from a wide-angle seismic reflection survey (Walther, 2003) to image the crustal structure of the Cocos Ridge offshore Costa Rica in the eastern Pacific (**Figure 9**) seem typical of the results from other aseismic ridges, such as the Faroes Ridge which lies on the European Plate east of Iceland (Smallwood et al., 1999). The Moho (a seismic discontinuity representing the boundary between Earth's crust and mantle) is seen to deepen 10 km to compensate the 2 km elevation of the ridge above the surrounding seafloor (**Figure 10**). The seismic traveltimes and gravity data are best fit if the upper mantle

beneath the ridge is assumed to have a low seismic velocity and low density contrast with respect to the lower crust. What is unexpected in the Cocos survey is the amount which lower crustal thickening, as opposed to extrusive volcanism, contributes to the volume of the ridge. In the center, units with lower crustal velocity and density make up 80% of the total crustal section, and the lower crust is three times the thickness of normal oceanic lower crust. Exceptionally high velocities ($>7.4\ km\ s^{-1}$) are not seen in the lower crust, as has often been reported beneath mid-plate island chains, and the upper mantle is slower beneath the Cocos Ridge ($7.6\ km\ s^{-1}$) than the average for normal oceanic upper mantle ($\sim 8\ km\ s^{-1}$).

1.14.2.3 Superswells

Superswells (Figure 11) represent clusters of hot spots in a restricted geographical region of anomalously high elevation

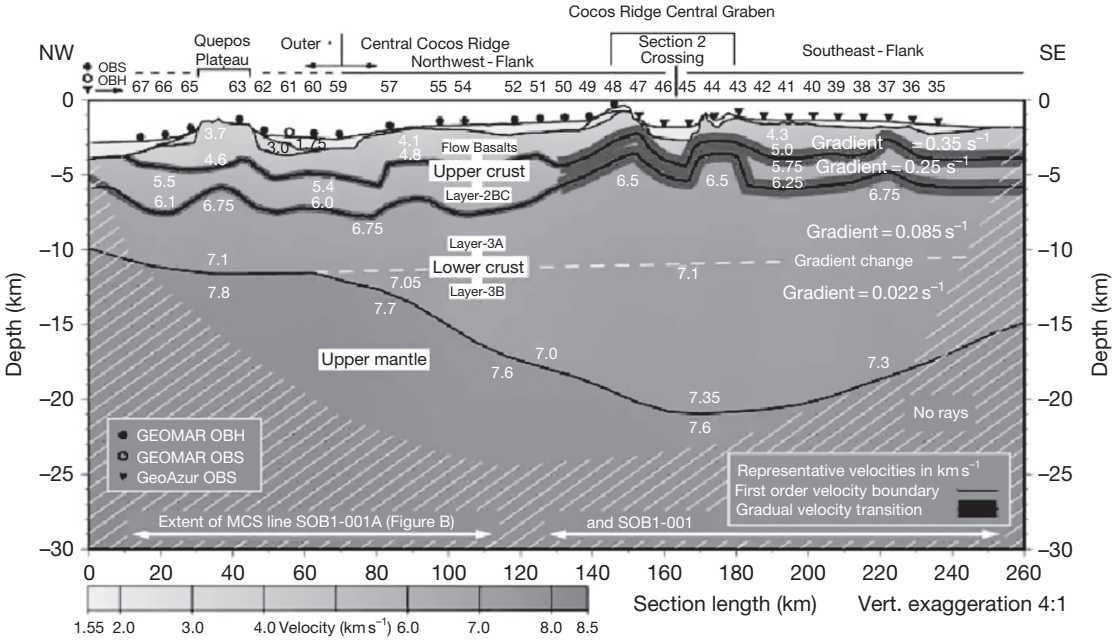

Figure 10 Crustal model for a 260-km-long transect across the Cocos Ridge, 35 km seaward of and parallel to the middle America Trench (location shown as section 1 in Figure 9). Velocities are displayed in gray scale and for representative values in kilometers per second. The hatched area is not resolved. The crustal thickening of the Cocos Ridge occurs primarily within the lower crust rather than the surficial extrusives. There is no evidence for unusually high lower crustal velocities, and indeed the upper-mantle velocities are unusually low. Reproduced from Walther CHE (2003) The crustal structure of the Cocos Ridge off Costa Rica. *Journal of Geophysical Research* 108. http://dx.doi.org/10.1029/2001JB000888.

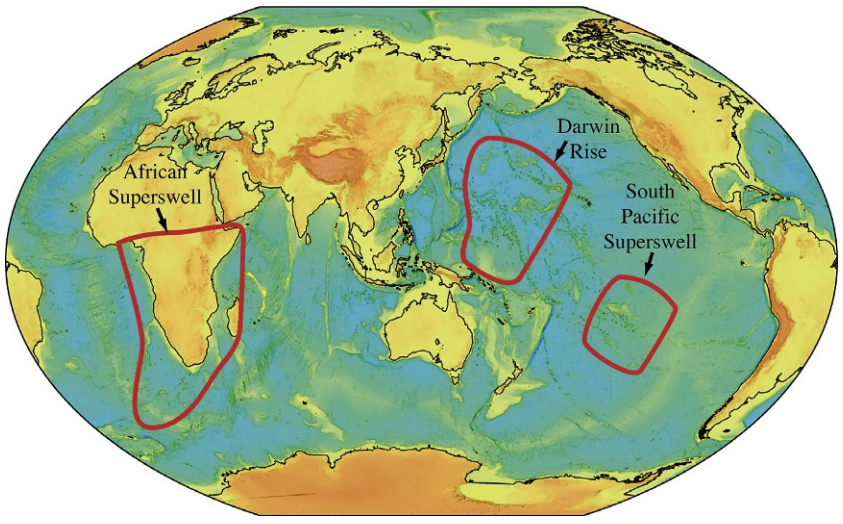

Figure 11 The African (Nyblade and Robinson, 1994) and South Pacific (McNutt and Fischer, 1987 and McNutt and Judge, 1990) superswells are regions exhibiting anomalously shallow topography and unusually copious recent volcanism. The Darwin Rise has been interpreted as the location of a Cretaceous superswell (McNutt et al., 1990).

that cannot be explained by crustal thickening. The first area so recognized was in the South Pacific (McNutt and Fischer, 1987). Volcanoes higher than 200 m are ten times more likely to be found on the seafloor of the South Pacific superswell as compared to regions elsewhere in the Pacific even apart from the hot-spot chains (Bemis and Smith, 1993), suggesting that mid-plate volcanism at all scales is enhanced. Much of the seafloor now in the northwest Pacific appears to have been a superswell during the Cretaceous (McNutt et al., 1990). The African superswell (Nyblade and Robinson, 1994) is a continental example of the same phenomena – unusual clusters of hot spots on a topographically elevated region. Individual hot-spot volcanoes located within superswells do tend to have their own swells, but they are small and only rise above the background depth anomaly of the superswell when located on very old lithosphere (McNutt, 1998; Sichoix et al., 1998).

Some of the Pacific hot-spot island chains that diverge the most from the predictions of plume theory are found on the superswell, and in fact superswell-type lithosphere appears to be very 'leaky' in terms of facilitating the ascent of magma to the surface (McNutt, 1998). Larson (1991) proposed that superswells are produced by superplumes, which can be envisioned as long-lived by very broad upwelling in the mantle. The fact that superswells are so large makes them a relatively easy target for using reconnaissance geophysical data, particularly tomographic mantle seismic structure, to search for evidence of Larson's proposed superplume or any other features in the mantle that might contribute to the unusual amount and distribution of volcanism. Nishimura and Forsyth (1985) were the first to note low seismic velocities in the upper mantle beneath the South Pacific superswell using an analysis of Love-wave phase velocities. Global inversions performed since then (e.g., **Figure 12**) confirm the slow velocities in the upper mantle and extend them to the lower mantle beneath both the South Pacific and the African superswells (Dziewonski, 2005; Dziewonski and Woodhouse, 1987; Grand et al., 1997; Masters et al., 1996; Su et al., 1994), although they differ in the details of how continuous the anomalous velocity structure is across the transition zone.

1.14.2.4 Mid-Plate Volcanic Chains and Clusters

Hot spots that do not fall into any of the categories above form isolated mid-plate volcanic chains and clusters (**Figure 13**). This is the most classic form of hot-spot volcanism, and examples in this category show the most prominent hot-spot swells. Examples include the Hawaiian (Clague and Dalrymple, 1987) and Louisville (Lonsdale, 1988) chains on the Pacific Plate (**Figure 13**), the Easter Island chain (O'Connor et al., 1995) on the Nazca Plate (**Figure 13**), Bermuda (Detrick et al., 1986) on the North American Plate, Cape Verde (Ali et al., 2003; Courtney and White, 1986), the Canary Islands (Watts et al., 1997), and Reunion (Charvis et al., 1999; Gallart et al., 1999) on the African Plate, and many other young island and seamount groups found on mature lithosphere. Because plates and plate boundaries are always drifting relative to the locus of hot-spot volcanism, it is not unusual for a mid-plate hot spot that is forming a chain of individual volcanoes to drift close enough to a ridge crest, and then begin to form an aseismic ridge or conjugate pair of ridges. Hot spots can move away from ridges as well. Precise dating is key to understanding what portions of hot-spot volcanism has been influenced by proximity to a ridge.

Most of the geophysical investigation of hot spots using seismic and other methods has focused on this category of hot spots, and their close relatives on superswell-type lithosphere, because the anomalous characteristics that must be explained are more easily identified. For example, beyond their unusually thick crust, there is little in terms of a geophysical anomaly associated with aseismic ridges that might

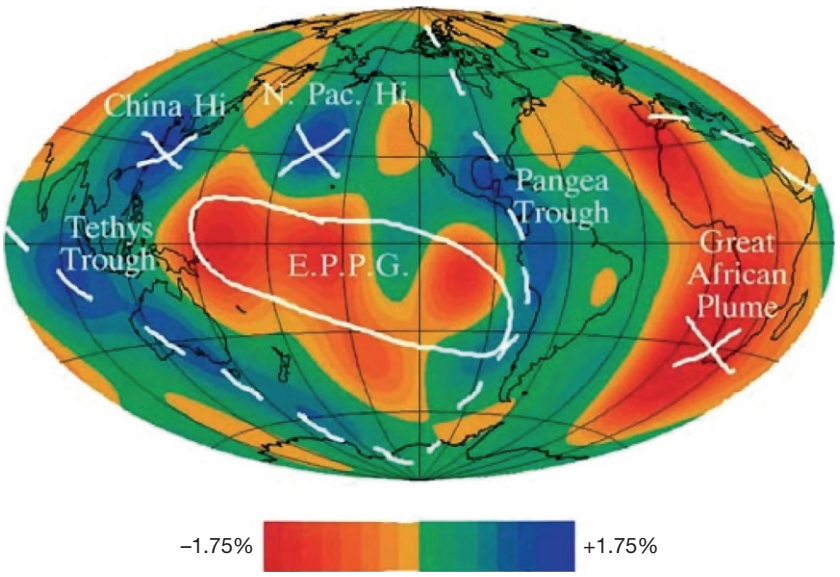

Figure 12 Global seismic tomographic image of shear-wave velocities at 2750 km depth. The South Pacific superswell (here labeled E.P.P.G. for Equatorial Pacific Plume Group) and the African superplume (here labeled Great African Plume) regions are associated with deep low-velocity anomalies that extend upward toward the surface. Reproduced from Dziewonski AM (2005) The robust aspects of global seismic tomography. *Geological Society of America Special Paper* 388: 147–154.

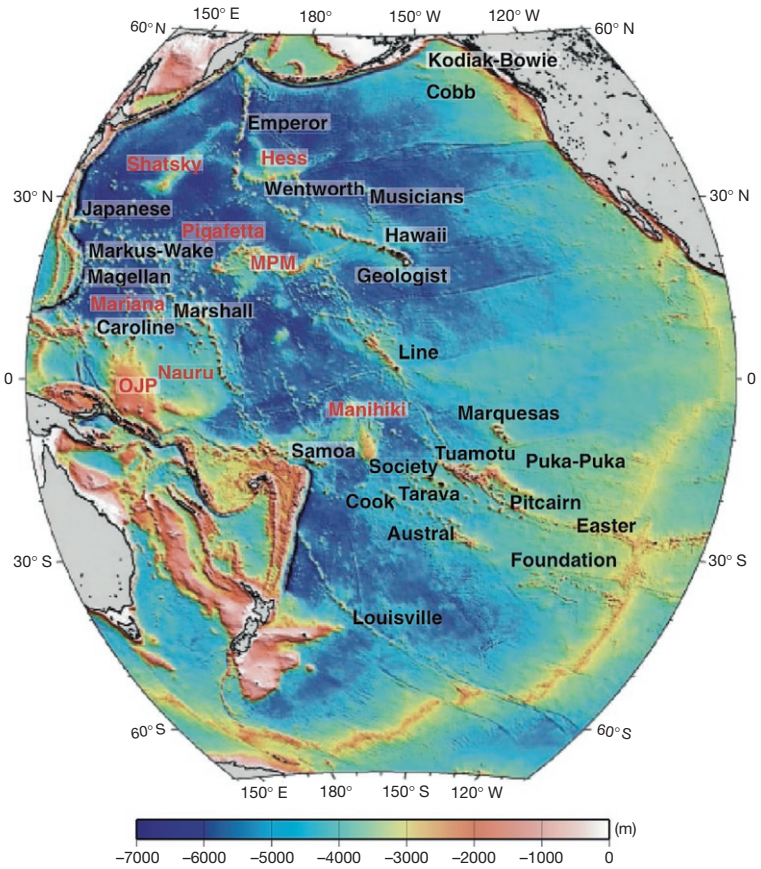

Figure 13 Linear volcanic chains shown on a bathymetric map of the Pacific Plate. Seamount chains are named in black; oceanic plateaus are named in red. MPM, Mid-Pacific Mountains; OJP, Ontong Java Plateau. Most seamounts occur in linear chains or clusters. Reproduced from Clouard V and Bonneville A (2005) Ages of seamounts, islands and plateaus on the Pacific Plate. In: Foulger GR, Natland JH, Presnall D, and Anderson DL (eds.) *Geological Society of America Special Paper 388: Plates, Plumes & Paradigms*, pp. 71–90. Boulder, CO: Geological Society of America.

provide clues to the cause of the excess melting. LIPs are clearly more extreme events, but their sheer size confounds a clear separation of spatial and temporal events to probe causative mechanisms.

1.14.3 Geophysical Characteristics of Hot Spots

Basic geophysical observations such as depth, subsidence, gravity and geoid anomalies, and heat flow can be used to probe the crust and lithospheric structure of hot spots and their swells. In fact, seismic investigations proceed usually only after all other data types have been exhaustively analyzed, as seismic field programs tend to be the most expensive to undertake. Briefly, we review the geophysical characteristics of hot spots and what they imply for crustal and lithospheric structure.

1.14.3.1 Orientation and Age

Hot spots erupting on the Pacific Plate (both as classic mid-plate volcanism and superswell-type volcanism) tend to form linear chains of volcanoes, with the Hawaiian–Emperor chain forming one of the longest on the planet. Early on, this chain was shown to have a monotonic age progression to the west-northwest (Clague and Dalrymple, 1987). The trend of the chain and its age progression define the pole and rate of rotation for the Pacific Plate relative to the Hawaiian hot spot, and changes in the position of the pole and its drift rate through time. If the source of the hot spot is a stationary mantle plume, as proposed by Morgan (1971), then the rotation so derived should be the absolute motion of the Pacific Plate. This hypothesis that plumes might form a fixed reference frame against which the direction and rate of plate drift could be measured has now been shown to be incorrect. Tarduno et al. (2003) used paleomagnetic data from seamounts along the Emperor part of the Hawaiian–Emperor chain to test whether the paleolatitude of the Hawaiian hot spot had remained fixed over time. They concluded that the source of the Hawaiian melting anomaly moved at velocities exceeding 40 mm per year, a rate similar to the rate of plate drift, during the Late Cretaceous and Early Tertiary.

Even though the notion of mantle plumes firmly anchored at the CMB must be abandoned, the orientations of most other active hot-spot chains on the Pacific Plate are co-polar with the Hawaiian chain, with the exception being the Marquesas (Crough and Jarrard, 1981). Furthermore, most chains of guyots and seamounts with Late Cretaceous and Early Tertiary

ages are parallel to the Emperor part of the Hawaiian chain. These trends support the theory that hot spots form from plumes that are at least fixed with respect to each other, except for the fact that Kr–Ar and Ar–Ar dating demonstrated that only a few other Pacific volcanic chains, such as the Society Islands and possibly the Louisville seamount chain, show the predicted age progression (Duncan and McDougall, 1976; Koppers et al., 2004; Lonsdale, 1988). The age discrepancies are equally apparent for older seamount chains, such as the Line Islands, which are co-polar with the Emperor seamounts, but lack a simple age progression (Schlanger et al., 1984). At first, geophysicists and geochronologists attempted to explain the errant age distributions as the superposition of effects from several plumes that line up along the same trend, but the numbers of required plumes are ultimately untenable (McNutt et al., 1997).

For the large number of linear chains that do not show monotonic age progressions, the most common age pattern is nearly synchronous volcanism at several volcanic centers along the chain, with short age progressions in the Hawaiian sense. Perhaps significantly, none of the linear chains on the Pacific Plate show age progressions in the direction counter to the Hawaiian direction of progression. Therefore, while the plume model in detail is not a good fit to the majority of hot spots, the sequence of hot-spot eruptions is not completely random in space or time. Another explanation that has been proposed is that hot spots result from the rise of magma from more ubiquitous melt bodies in the upper mantle along lithospheric cracks (Anderson, 1996; Bonatti and Harrison, 1976; Davis et al., 2002; Turcotte and Oxburgh, 1973), with the parallel trends resulting from a consistent plate-wide stress field. However, none of the Pacific chains display ages converging toward a central initiation point, as might be the case for volcanism occurring along a tensional tear in the plate.

In the Atlantic, the major island groups in this category do not form obvious lines, presumably because the hot spot is close to the Euler pole of rotation for the Atlantic Plate with respect to the melting anomaly (e.g., Cape Verde Rise; Morgan, 1971). For this reason, Pacific hot spots have received most of the attention in terms of using orientations and ages to test the plume hypothesis.

1.14.3.2 Depth and Subsidence

The height of the mid-plate swell surrounding the region of active volcanism also provides clues to the origin of hot spots. Crough (1978) noted that ten hot-spot swells in the Pacific, Atlantic, and Indian Oceans all rise to depths of about 4000–4500 m, regardless of crustal age. Therefore, the depth anomaly (with respect to either some standard model or to the surrounding seafloor) for these swells increases with the age of the oceanic lithosphere at the time that the volcanoes erupted. There also appears to be some positive correlation between the size of the Hawaiian swell and the volume of the volcanoes through time (Phipps Morgan et al., 1995), although it is difficult to correlate these two quantities back very far in time because there is no discernible swell along the Hawaiian/Emperor chain that is more than 43 My in age (Vidal and Bonneville, 2004).

Abyssal hills created at a mid-ocean ridge outcrop on the swell away from the volcanoes and their sedimentary debris aprons ('archipelagic aprons,' Menard, 1956), indicating that the seafloor has been lifted up from below. The source of the uplift must be a reduction in density of the rocks somewhere beneath the swell, as geoid data (reviewed below) indicate that swells are isostatically compensated. The source of the density reduction could be heat, or a modification in either rock mineralogy or chemistry that reduces its density. Furthermore, the location of the buoyant material could be within the crust (e.g., by thickening the crust from below), lithosphere (e.g., by reheating the lithosphere by the hot spot), or asthenosphere (e.g., by upward flow of a hot plume). In order to narrow down the possibilities, other information such as subsidence rates, geoid anomalies, heat flow, and seismic data have been interpreted along with depth anomalies. For example, to first order, as the depth to the compensating mass increases, so does the height of the geoid anomaly over the swell. Seismic velocity is slower for rocks that have low density because they are hot, but faster for rocks that have low density by virtue of extraction of a basaltic melt component.

The fact that swells are larger on older lithosphere has been used to support a thermal explanation for the swell, because thermal contrasts from hot-spot source materials would be larger in comparison to old, cold, mature lithosphere than young lithosphere. The observed correlation between swell volume and volume of the volcanoes has been used to argue for a chemical origin for swells, as the volume of buoyant, residual mantle remaining after the extraction of the basaltic melt component should scale with the amount of melt removed.

The chemical swell origin hypothesis has been contradicted by several studies that concluded swells subside faster than normal oceanic lithosphere of the same age. Some of the clearest evidence for this anomalous subsidence has come from volcanoes in the western Pacific that formed on a former superswell (McNutt et al., 1990). Seismic reflection data image the contact between the reef and pelagic sediments capping former hot-spot islands that have now subsided to create guyots (Winterer et al., 1993). The height above the seafloor of the basement contact measures the depth of the seafloor soon after the volcano erupted, on the very reasonable assumption that wave action bevels the volcano to sea level within a few million years. In the western Pacific, this depth is less than normal for lithosphere of that age, providing an estimate of the height of the superswell at the time of Cretaceous volcanism. The depth below sea level of that contact measures how much the seafloor has subsided to the present. Data from both the seismic reflection surveys and from drilling atolls (e.g., Ladd and Schlanger, 1960; Ladd et al., 1967) indicate accelerated subsidence, favoring some sort of heat anomaly in the upper mantle that decays with time.

To explain the subsidence, Detrick and Crough (1978) introduced the concept of lithospheric thinning. According to this hypothesis, heat from a hot spot resets the temperature of the lower lithosphere below some depth (typically 40–50 km) to the temperature of the underlying asthenosphere. They showed that the anomalously high rate of observed subsidence was appropriate for lithosphere of that depth, as though the lithosphere had been reheated by the hot spot to a more

youthful thermal structure. They argued that the tear-drop shape of the Hawaiian swell and its rate of subsequent subsidence along a conductive cooling curve were unlikely to be produced by a lithospheric plate drifting over a 'bump' in the asthenosphere (Menard, 1973) dynamically maintained by an upwelling mantle plume. They noted that the difficulty with their lithospheric thinning hypothesis was the requirement for exceptionally high rates of heat flux into the base of the lithosphere given the observation that it only takes ~3 My for the Hawaiian seafloor to rise from normal depths to the peak of the swell.

1.14.3.3 Geoid Height

The fact that swells were observed to subside along the predicted trajectory for a conductively cooling plate is consistent with a lithospheric origin for the depth anomaly, but the subsidence of depth anomalies only measures the change in buoyancy throughout a vertical column. The elevation information alone is insensitive to the depth of the causative source. The geoid, the gravitational equipotential surface coinciding with the mean sea surface, is smoother and varies less than elevation (no more than ±100 m globally relative to the reference ellipsoid), but reflects the depth of underlying low- or high-density anomalies. Geoid data, either as estimated from satellite radar altimeters (**Figure 5**) or as converted from gravity, have been used to estimate the depth to the low-density material supporting hot-spot swells on about 24 examples around the world (Crough, 1978; Monnereau and Cazenave, 1990, 1998). The first simplistic interpretations of geoid data used ratios of swell height to geoid height, which in an infinite wavelength approximation would yield the compensation depth of the swell (Haxby and Turcotte, 1978). More sophisticated analysis takes into account the limited frequency content of the swell and the flexural compensation of the volcanoes (**Figure 5**), but still assumes simple dipole-like compensation (McNutt and Shure, 1986). For mid-plate swells, the compensation depths so determined were in the mid- to lower lithosphere, and the depth to the compensation increases with the age of the lithosphere, which supports the lithospheric thinning model.

However, as pointed out by Robinson and Parsons (1988), there are mechanisms for supporting a mid-plate swell that would place all the compensating material below the lithosphere, but still have an apparent depth of compensation lie well within the lithosphere. This situation could arise, for example, if a low-density mass is rising in a viscous asthenosphere. The induced flow would warp density interfaces above the rising mass (e.g., the swell at Earth's surface) and below the mass (e.g., in the transition zone or at the CMB). The net effect is that the swell and its compensation would be better represented as a tripole, and interpretation of the data in terms of a density dipole would give an incorrectly shallow compensation depth for the swell. An additional complicating factor is the possibility that the composition of the lower lithosphere itself is altered in the process of the hot-spot extracting basaltic melt, leading to buoyant uplift of a swell (McNutt and Bonneville, 2000; Phipps Morgan et al., 1995). Without additional information on crustal and mantle structure, it is not possible to resolve the ambiguity in the interpretation of the elevation and geoid data.

1.14.3.4 Elastic Plate Thickness

Estimates of effective elastic plate thickness are also sensitive to temperature beneath mid-plate swells (McNutt, 1987). When volcanoes erupt in mid-plate settings, they are isostatically compensated by the lithosphere warping in an elastic manner beneath the weight of the volcano. Marine gravity data are very sensitive to the stiffness of the plate, with stiffer plates producing larger free-air gravity anomalies over the volcanoes and a longer distance from the flexural moat surrounding the volcano to the flanking arch. A similar elastic bending occurs where oceanic plates subduct into the mantle at deep-sea trenches. Watts et al. (1980) used shipboard gravity and bathymetry data to estimate the effective elastic thickness for mid-plate islands and trenches worldwide (**Figure 14**). They determined an empirical relationship,

$$T_c = 2.7\sqrt{t}$$

where t is the age of the lithosphere in million years and T_e is its effective elastic thickness in kilometers. Using standard thermal models for lithospheric plates (e.g., Parsons and Sclater, 1977), the base of the elastic portion of the lithosphere would correspond to the depth of the ~450 °C isotherm.

A number of hot-spot volcanoes, particularly those on the South Pacific superswell, show T_e values that require shoaling of the 450 °C isotherm (Calmant, 1987; Calmant and Cazenave, 1986; McNutt, 1984). At first, this was interpreted as strong evidence in favor of the lithospheric reheating model, as it appeared to require elevated temperatures well within the lithospheric portion of the mantle. However, McNutt et al. (1997) demonstrated in the Austral Islands that one consequence of volcanic overprinting caused by multiple volcanic centers along the same linear trajectory would be low estimates for elastic plate thickness. The earlier phases of volcanism, which loaded a younger and therefore weaker plate, are difficult to detect and date because they are covered over by the most recent volcanic activity. If the entire load is assumed to be the same age as the surface lavas, the estimated elastic thickness is some compromise between the low value for the older phase of volcanism and the higher value for the more recent phase. Given how few hot-spot chains show one simple linear age progression, particularly for superswell hot spots, underestimating the true mechanical strength of the lithosphere beneath hot spots is likely quite common.

Ideally, one would like to be able to compare elastic thickness estimates for volcanoes on hot-spot swells with those from entirely different geologic settings where no thermal processes are associated with forming the loads that flex the plate. The outer rises formed where plates bend before descending into the mantle provide the best opportunity to calibrate the elastic thickness in a setting free from any thermal disruption. The estimates of elastic thickness from trenches are similar to those determined for volcanoes on swells. The current consensus seems to be that the effective elastic thickness of the lithosphere where it is flexed over hot-spot swells is not much different from that of lithosphere unaffected by hot-spot volcanism.

1.14.3.5 Heat Flow

Heat flow observations, defined as the product of thermal conductivity k of the sediments at the surface of the plate and

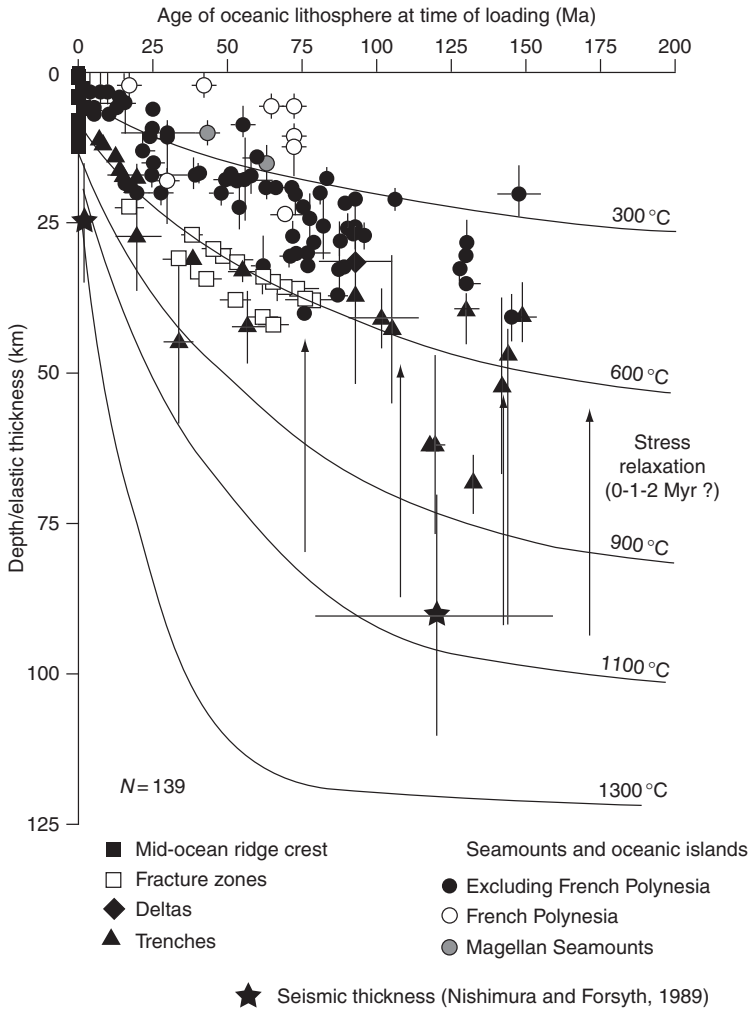

Figure 14 Plot of elastic plate thickness against the age of the lithosphere at the time of loading for oceanic lithosphere. Also shown are two measurements of lithospheric thickness from seismic surface wave studies (Nishimura and Forsyth, 1985). These data indicate that the elastic plate thickness increases as the lithosphere ages and cools, and that the thickness of the lithosphere exhibiting flexural rigidity is less than the plate thickness inferred from seismic observations. Reproduced from Watts AB (2001) *Isostacy and Flexure of the Lithosphere*, 458 pp. Cambridge: Cambridge University Press.

the temperature gradient dT/dz, also have the potential to distinguish among different models for the distribution of any heat associated with hot spots. If hot spots are not hot at all (e.g., melting caused by decompression or addition of volatiles), then one would expect no heat flow anomaly associated with hot spots. If excess heat is involved, there should be a heat flow anomaly detected at the seafloor eventually, but its appearance would be delayed by the time it takes for temperature to conduct through the lithosphere to the surface from its point of origin. Therefore, the delay time between the onset of hot-spot volcanism and the detection of a heat flow anomaly provides an estimate for the depth to the heat source.

Detrick et al. (1981) conducted a heat flow survey occupying seven sites along the Hawaiian arch just south of the islands (**Figure 15**). They found that near the active volcanoes on the island of Hawaii, heat flow is normal for 80–90 Ma lithosphere. But further along the arch, near volcanoes that are 6 My old, the heat flow values were 5–8 mW m^{-2} higher than expected, or about 10% above the baseline value (**Figure 16**). Heat flow remained elevated to at least 22 Ma down the swell. The pattern of the anomaly was consistent with the predictions of the lithospheric reheating model, and indicated that the lithosphere had been thinned to 40–50 km depth (Von Herzen et al., 1982). The survey was criticized, however, for not having sampled the heat flow values at sites in the same general part of the Pacific but well off the swell. Given the large scatter in heat flow values worldwide, was it possible that the pattern was unrelated to the Hawaiian swell?

To better constrain the pattern and amplitude of anomalous heating of the plate beneath Hawaii, Von Herzen et al. (1989) conducted a second survey across the Hawaiian swell at Maro Reef (**Figure 15**), the locus predicted to display the maximum anomalous heating if the plate is thinned to only 40 km. The line of heat flow stations was long enough such that the beginning and end of the line would be well onto normal oceanic lithosphere off the swell. Rather than reducing the uncertainties from the earlier survey, the Maro Reef survey raised more questions than it answered. The pattern of heat

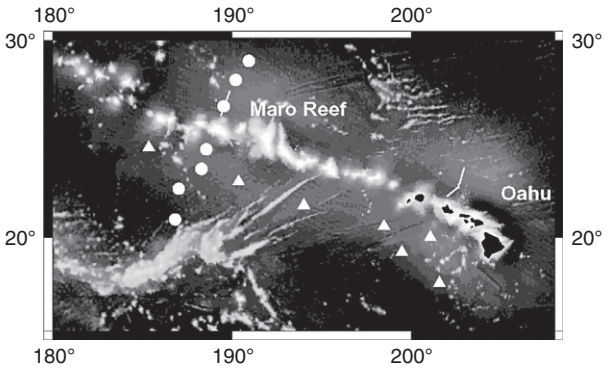

Figure 15 The Hawaiian Islands in the central Pacific and location of heat flow stations. The triangles are the South Arch survey of Detrick et al. (1981). The circles are the Maro Reef survey of Von Herzen et al. (1989). The solid white lines north of Maro Reef and Oahu show the location of dense heat flow measurements collected by Harris et al. (2000a). Reproduced from McNutt MK (2002) Heat flow variations over Hawaiian swell controlled by near-surface processes, not plume properties. In: Takahashi E, Lipman PW, Garcia MO, Naka J, and Aramaki S (eds.) *Geophysical Monograph Series*, *vol. 128: Hawaiian Volcanoes*: *Deep Underwater Perspectives*, pp. 365–372. Washington, DC: American Geophysical Union.

flow at the eight stations display a W pattern, with the highest heat flow values located near the center of the line at Maro Reef and off the swell (**Figure 16**), on supposedly normal lithosphere. Four out of the six stations sampling heat flow on the swell had resolvably lower heat flow than the sites off the swell, given the uncertainties in the data. The observations were definitely not compatible with the predictions of the lithospheric thinning model. However, with only eight stations spaced across 1200 km and each defining a local high or low in the pattern, it was impossible to conclude anything about the physical processes that might give rise to this remarkable heat flow.

Harris et al. (2000a) conducted more detailed sampling of heat flow across the Hawaiian swell at two locations, near Maro Reef (~17 My since hot-spot volcanism) and Oahu (~4 My years since hot-spot volcanism) (**Figure 15**). They found that the mean heat flow on the Hawaiian swell is slightly larger at Oahu (74.2 ± 14.6 mW m^{-2}) than at Maro Reef (64.0 ± 4.9 mW m^{-2}). No model for thermal sources below the lithosphere, unless the lithosphere were thinned to but a few kilometers thickness by a hot spot, would predict that elevated heat flow could be detected on the swell just 4 My after the onset of hot-spot activity. Harris et al. (2000b) concluded that a more likely explanation for the heat flow values over the Hawaiian swell is that the high relief of the hot-spot volcanoes is driving large-scale circulation of seawater through the permeable oceanic basement rocks underlying a more impermeable sediment blanket. This hydrothermal system mines heat from within the volcano itself, and discharges it through isolated basement highs that penetrate the sediment blanket. According to this model, younger regions of the swell, such as near Oahu, would show greater variability in heat flow because the sediment capping is less developed than further along the swell at Maro Reef. Heat flow values over the flexural moat would be the lowest on account of the large amount of volcaniclastic sediment infill, with higher values near the volcanic edifice and beyond the flexural arch. These observations are in good agreement with the data from the Hawaiian surveys and from a similar survey conducted at the Réunion hot spot (Bonneville et al., 1997).

McNutt (2002) supported this interpretation of the heat flow data by noting that the W pattern of the heat flow over the Hawaiian swell at Maro Reef is actually produced by a W pattern in the large measured variations in thermal conductivity of surface sediments (**Figure 16**). The temperature gradients themselves show an M pattern and do not dominate the resulting heat flow. Temperature gradients and thermal conductivity are also inversely correlated along the original south arch survey at Hawaii (**Figure 16**). The data indicate that areas of high conductivity act as radiators while areas of low conductivity act as insulators, producing nonuniform conduction of heat to the seafloor that is controlled by variations in surficial thermal conductivity. The simplest model that reproduces quantitatively the observed correlations between heat flow, temperature gradient, and thermal conductivity assumes two conducting layers above an isothermal layer at depth (**Figure 17**). Surprisingly, the best fit of the model parameters to the data, assuming that the upper layer corresponds to the pervasive blanket of pelagic sediments into which the heat flow probe is inserted, yields a total temperature drop from the ocean to the isothermal layer of only 21 °C, and a depth to the base of the lower conducting layer of only 500–900 m. The isothermal layer, therefore, resides within the upper oceanic crust, where pervasive fluid circulation homogenizes any lateral variations in temperature that might be associated with the Hawaiian hot spot. McNutt (2002) thus concluded that variations in heat flow across the Hawaiian swell are controlled by variability in the thermal conductivity of surface sediments, reflecting geological factors such as carbonate content.

These recent studies have underscored the importance of seismic reflection images in site selection and in the interpretation of marine heat flow. Prior to the recognition of fluid flow in the upper crust surrounding hot spots, the only concern was to avoid hard rock outcrops that would bend the heat flow probe or at least prevent a successful vertical insertion into more pliable sediments. After the realization that more permeable rock outcrops significantly perturb the hydrologic regime by serving as foci for venting and recharge of crustal fluids, avoiding any basement relief in choosing heat flow sampling sites became even more essential. Interpretation of heat flow data in terms of conductive transfer of heat from subcrustal levels to the ocean through a uniform and impermeable sedimentary blanket cannot be attempted unless there is the seismic coverage to rule out basalt outcrops penetrating the sediments. For these applications, single-channel seismic data will often suffice, but multichannel data to image faults in the basement and overlying sediments are even better.

Heat flow has been sampled over other swells, such as Cape Verde (Courtney and White, 1986) and Bermuda (Detrick et al., 1986). Both swells show a modest rise in heat flow (10–20%) near the peak of the swell as compared with values on the nearby abyssal plains, supporting the hypothesis that hot spots are hot. The results from these Atlantic swells, however, are not very useful for determining the depth to the hot material, because the volcanism is concentrated in one area

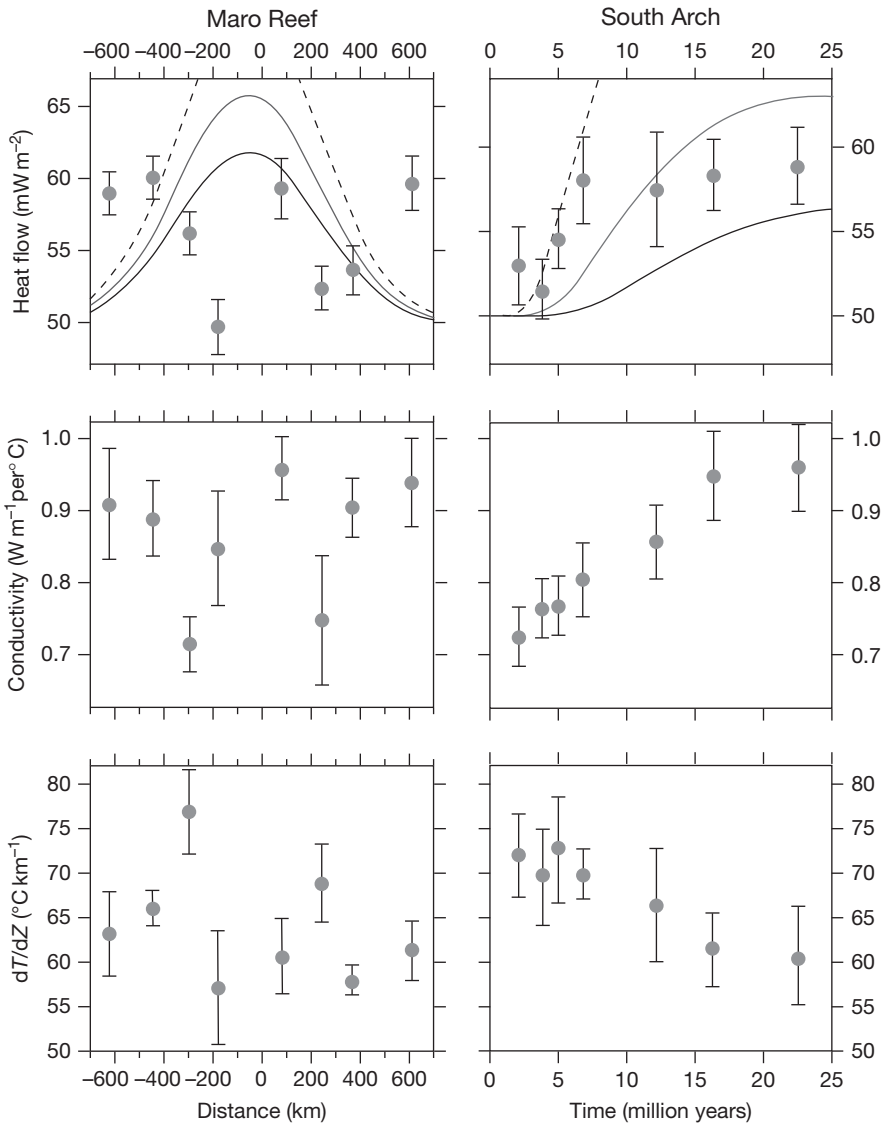

Figure 16 Left: Heat flow (upper), conductivity (middle), and vertical temperature gradient (lower) at Maro Reef (Von Herzen et al., 1989) plotted as a function of distance across the chain. Right: Heat flow (upper), conductivity (middle), and vertical temperature gradient (lower) along the south arch of the Hawaiian Islands (Detrick et al., 1981) plotted as a function of time since the plate drifted past the hot spot. Lines on the upper panels show the theoretical variations in heat flow expected if the hot spot reheated the lower lithosphere to asthenospheric values (~1350 °C) as it passed over the thermal source. The amount of thinning assumed is 60 km (solid line), 50 km (dotted line), and 40 km (dashed line). Reproduced from McNutt MK (2002) Heat flow variations over Hawaiian swell controlled by near-surface processes, not plume properties. In: Takahashi E, Lipman PW, Garcia MO, Naka J, and Aramaki S (eds.) *Geophysical Monograph Series, vol. 128: Hawaiian Volcanoes: Deep Underwater Perspectives*, pp. 365–372. Washington, DC: American Geophysical Union.

(just one Miocene volcano in the case of Bermuda), making it impossible to estimate how long it took for the heat flow anomaly to be manifest at Earth's surface.

It has been known for years that heat flow on young (<65 Ma) lithosphere is significantly perturbed and biased by hydrothermal circulation (Lister, 1972). In his recent review of marine heat flow observations worldwide, Von Herzen (2004) concluded that at least 40% of all heat flow observations on seafloor 65–95 Ma show evidence for hydrothermal circulation, and the fraction only drops to 30% for even older lithosphere. He suggested, however, that the circulation in mature lithosphere (>60 Ma) might be merely redistributing heat within a permeable basement beneath sediments without advective gain or loss, which would then lead to conductive heat flow variations controlled by thermal conductivity as advocated by McNutt (2002). Therefore, the heat flow mean as determined from many measurements over a large area should represent the true heat flux through the lithosphere. On this assumption, one can conclude that there are modest (10–25%) heat flow anomalies associated with hot-spot swells, but that our lack of understanding of the length scales over which fluid circulation redistributes the heat prevents any

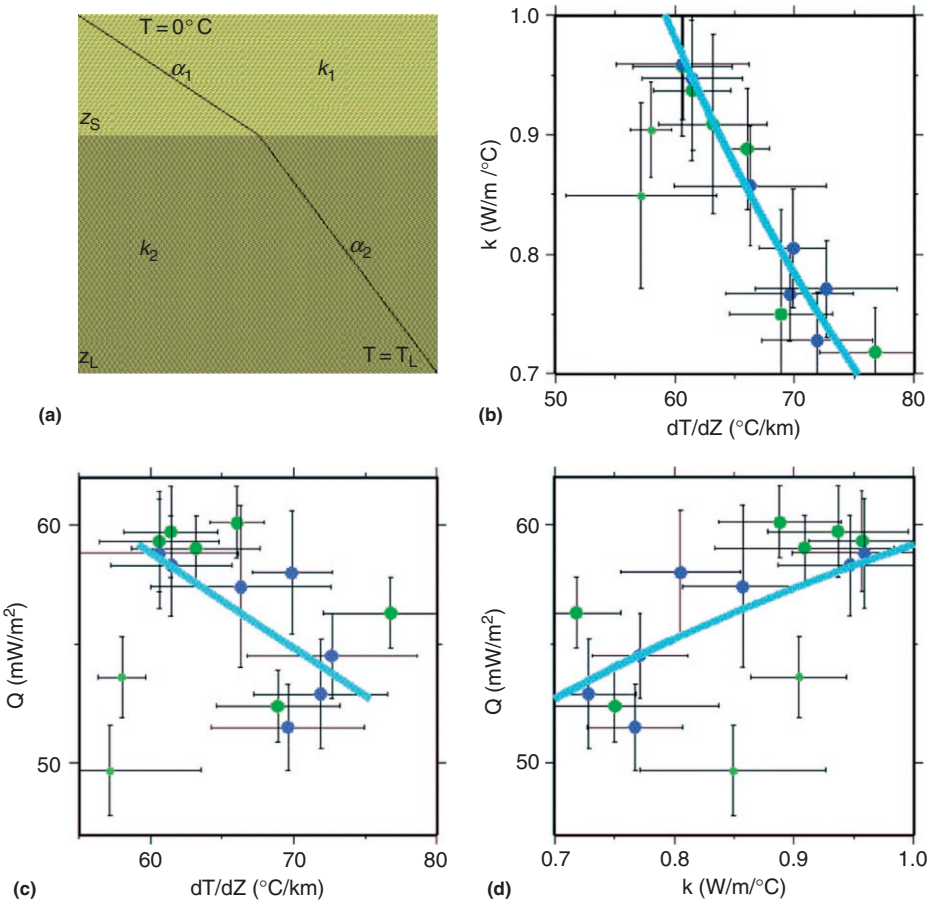

Figure 17 (a) Simple two-layer model for heat transport near the Hawaiian Islands. The upper layer of thickness z_s has thermal conductivity k_1 and temperature gradient α_1. The lower layer of thickness $(z_L - z_s)$ has a higher thermal conductivity k_2 and temperature gradient α_2. The lower boundary is maintained at an isothermal temperature T_L by fluid circulation. The upper boundary is maintained at temperature $T = 0$ °C by the ocean. (b) Plot of thermal conductivity k versus vertical temperature gradient dT/dz for the South Arch (blue dots) and Maro Reef (green dots). The blue line shows the least-squares best fit to the data as k_1 (equivalent to k in the observed data) is varied in the model in (a), excluding the two Maro Reef outliers shown as small dots. These outliers correspond to the measurements at $x = -177$ km and $x = 375$ km in **Figure 15**. (c) Same as (b), but for heat flow Q as a function of dT/dz (equivalent to α_1 in the model). (d) Same as (b), but for Q as a function of k. Reproduced from McNutt MK (2002) Heat flow variations over Hawaiian swell controlled by near-surface processes, not plume properties. In: Takahashi E, Lipman PW, Garcia MO, Naka J, and Aramaki S (eds.) *Geophysical Monograph Series, vol. 128: Hawaiian Volcanoes: Deep Underwater Perspectives*, pp. 365–372. Washington, DC: American Geophysical Union.

detailed picture of the spatial or temporal pattern for where and when that heat reaches Earth's surface.

1.14.4 Seismic Constraints on Crust and Lithosphere

The geophysical observations reviewed above provide but few constraints on how crustal and lithospheric structure is modified by hot spots. The depth anomalies of mid-plate swells require density reduction at depth, and the geoid height requires that low-density material to be below the mid-lithosphere in most cases. Heat flow evidence suggests that the low-density material is at least partially thermal in origin, although the effects of near-surface fluid circulation effectively mask much of the spatial and temporal pattern of any thermal disturbance. Geophysicists have therefore turned to seismology to better understand the deep structure of the Earth beneath hot spots and their swells. It is important to begin an investigation of hot spots from the top of the crust down into the lithosphere for at least two reasons. First, the surface structure is more accessible and can be probed using a number of seismic techniques, including active-source reflection and refraction, as well as imaging with passive arrays. Second, properly accounting for the effects of surface structure is necessary in nearly all geophysical analyses before determining what portion of the observed signal is of deep origin. Examples of crustal and lithospheric targets for seismic investigation, why they are important, and what has been learned are summarized in the succeeding text.

1.14.4.1 Sedimentary Structures

The largest hot-spot volcanoes are surrounded by massive volcaniclastic debris aprons that can exceed both the area and the volume of the intact volcanoes themselves (Moore et al., 1989). The slope failures which produce these landslide deposits occur many times during the period of active volcanism, and continue during the post-eruptive phase,

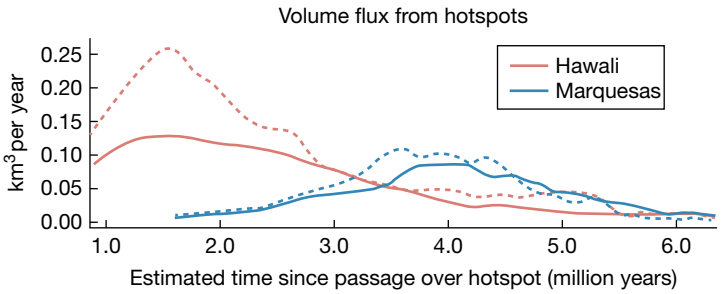

Figure 18 Volume flux of erupted volcanic rock as a function of time along the Marquesas and Hawaiian chains, as calculated from deflection models. Volcano names are shown for both chains at dated ages, with the Marquesan volcano names underlined. Solid lines are corrected for swell topography, dotted lines are uncorrected. Adapted from Filmer PE, McNutt MK, Webb HF, and Dixon DJ (1994) Volcanism and archipelagic aprons: A comparison of the Marquesas and Hawaiian Islands. *Marine Geophysical Research* 16: 385–406.

particularly if the volcano is not protected from the seas by a fringing coral reef. These post-eruptive sedimentary units provide a wealth of information on the history of a particular hot spot that is often more amenable to seismic imaging than is the volcanic edifice itself. In the oceans, these are well imaged by marine multichannel seismic data augmented with refraction data from sonobuoys or ocean-bottom seismometers (OBSs) to calibrate the velocity structure. In many cases, the value of the seismic data has been significantly enhanced by ocean drilling to provide accurate timelines through dating and other useful information, such as paleomagnetic chronology and paleoenvironmental history.

ten Brink and Watts (1985) obtained a seismic reflection image of the moat stratigraphy along a line crossing the Hawaiian chain and applied two-dimensional (2-D) modeling to determine whether the geometry of the reflectors contains any information on changes in elastic thickness that could be associated with the thermal evolution of the Hawaiian swell. In order to fit the apparent off-lap patterns in the stratigraphy, they assumed prolonged (>1 My) viscoelastic relaxation of the elastic plate. The cause of this relaxation of the elastic stresses would presumably be heat from the hot spot conducting through the lithosphere up the base of the elastic plate. If such an interpretation had been confirmed, it would have been good evidence for lithospheric thinning by the Hawaiian hot spot.

However, in a followup study, Watts and ten Brink (1989) demonstrated that a similar off-lap pattern could be produced in a 3-D model with progressive loading of the plate by new islands along the chain without requiring any temporal decrease in the stiffness of the elastic plate. Rees et al. (1993) acquired the definitive 3-D data set to test this hypothesis that the stratigraphic pattern in the Hawaiian moat was caused by sequential loading of volcanoes on an elastic plate of uniform elastic strength. Their single-channel reflection survey of the Hawaiian flexural moat imaged the sedimentary structures both across and along the strike of the chain between the islands of Hawaii and Kauai. They were able to explain the resulting stratigraphy in terms of competing effects of erosion/mass wasting, subsidence, and flexure. Significantly, Rees et al. (1993) did not require any temporal change in the elastic stiffness of the plate using a 3-D model. They noted that initially when a new volcano forms, the flexural moat is underfilled with sediment as the seafloor subsides beneath the weight of the new volcano faster than mass wasting can fill in the depression. Later, as volcano construction ceases and volcanic material is redistributed from the islands into the surrounding moat in major mass wasting events, the moat becomes filled, and in the case of older islands such as the Marquesas, overfilled such that the sediment surface in the moat slopes away from the volcanoes (Filmer et al., 1994). The gently sloping sedimentary blanket surrounding mature volcanoes has been termed an 'archipelagic apron' (Menard, 1956).

Seismic reflection images of the sedimentary debris that fills the flexural moats surrounding mid-plate hot-spot chains can also be used to estimate the volume of volcaniclastic sediments that must be added to the volume of the edifice itself in order to get an accurate estimate of the amount of melt produced by the hot spot. For example, the moat surrounding the Marquesas Islands is overfilled with 200 000 km^3 of volcaniclastic sediments with seismic velocities ranging from 4 to 5 km s^{-1} (Filmer et al., 1994). The acoustically chaotic core of the apron interior suggests that the moat fill consists primarily of debris flows from mass wasting events. Individual volcano collapse events can involve volumes exceeding 100 km^3 and may occur tens to hundreds of times during the life of a volcano. After accounting for the material filling the flexural moat, the Marquesas hot spot, during its peak activity at 3.5–5 Ma, was erupting nearly 0.10 km^3 of volcanic rock per year, which exceeded the rate of eruption of the Hawaiian hot spot during that same time period and is nearly as large as Hawaii's current rate for the past 1 My (**Figure 18**). The much larger apparent size of the Hawaiian volcanoes results from the fact that they load a stiffer elastic plate, are superimposed on a higher swell, and have not yet been as deeply eroded as the Marquesas Islands.

Watts et al. (1997) conducted a similar analysis for the Canary hot spot in the eastern Atlantic. Using multichannel seismic images from the flexural moat, they determined that 150 000 km^3 of material has been added above the preexisting surface of the flexed plate by the Canary hot spot, a number quite comparable to that for the Marquesas. The corresponding estimated magma generation rate, however, is only 0.006–0.02 km^3 per year on account of the much longer duration of the shield-building stage for the Canary volcanoes.

1.14.4.2 Volcanic Crust and Underplating

Hot-spot volcanoes, like all volcanoes, are built by the eruption of lavas on top of the preexisting crust. However, volcanism is

also associated with the interaction of the rising magma with the upper mantle and crust, including the emplacement of intrusive igneous rocks within the volcano, the crust below, and possibly the upper mantle. Consequently, constraints on the complete upper mantle and crustal structure are required to understand such basic aspects of hot spots as magmatic flux and lithospheric loading. Although modern marine seismic reflection systems that combine pneumatic sources with 3–6 km (or longer) arrays of hydrophone receivers are capable of imaging Moho in normal (~6-km-thick) oceanic crust, the thickened crust and rough topography of submarine volcanoes make seismic reflection methods inadequate to penetrate the full crustal structure of most oceanic volcanoes. The best full crustal models obtained to date at oceanic hot spots derive from seismic refraction experiments in which the sources and receivers are widely spaced and variations in seismic velocity are imaged.

Hawaii was the first hot spot to be investigated with deep-penetrating marine refraction data. Watts et al. (1985) and ten Brink and Brocher (1987) collected multichannel seismic reflection data and conducted several two-ship expanding spread profile (ESP) refraction experiments along a cross section of the Hawaiian swell near Oahu. Each ESP yielded a 1-D crustal seismic velocity model; used together, the ESP models comprise a 2-D cross section of the Hawaiian hot-spot trace. Unexpectedly, Watts et al. (1985) found that the center of the volcanic chain is underlain by a 4-km-thick and 200-km-wide subcrustal body with unusually high seismic velocity (7.4–7.8 km s^{-1}) for the lower oceanic crust (**Figure 19**). An apparent bifurcation of Moho was observed in the reflection profile on both sides of the volcanic edifice, bounding the high-velocity body. Watts et al. (1985), ten Brink and Brocher (1987), and Watts and ten Brink (1989) interpreted this unit as a deep crustal sill complex and Watts and ten Brink (1989)

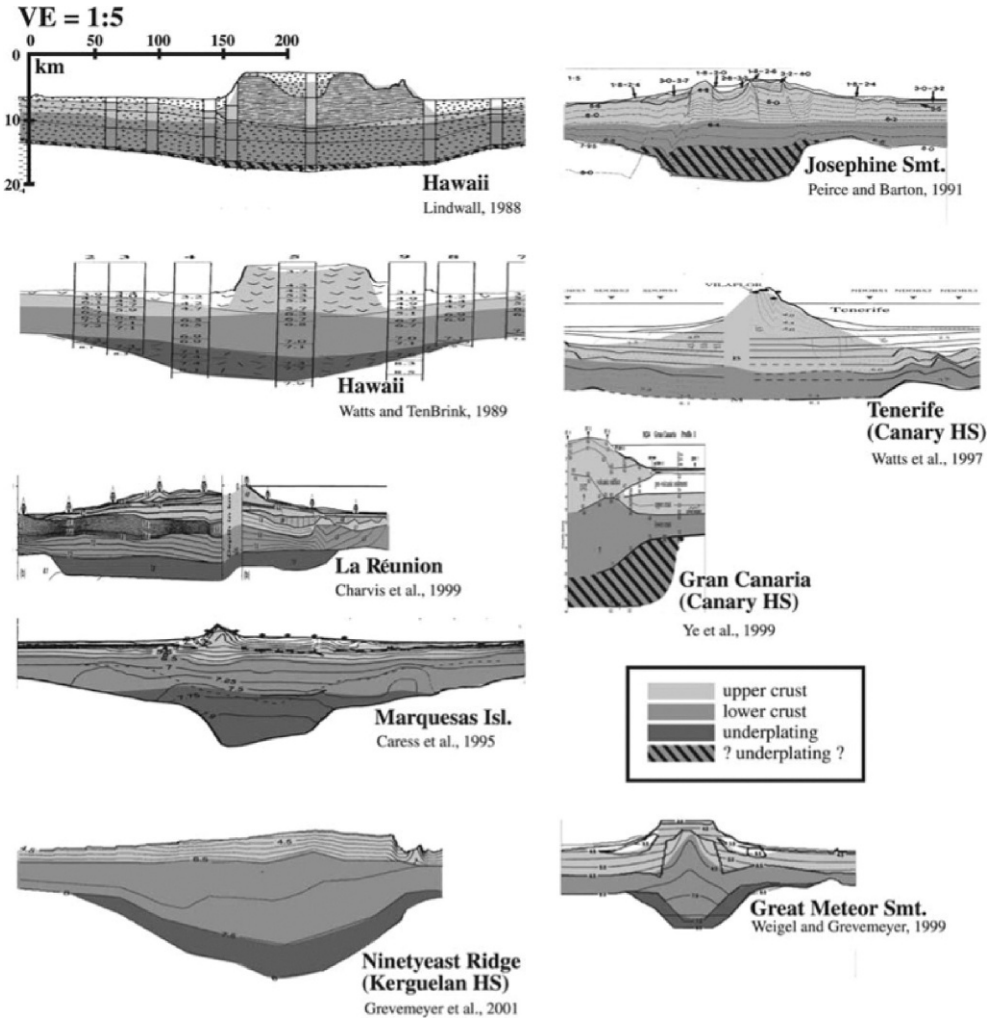

Figure 19 Compilation of several different hot-spot related volcanic structures imaged using seismic refraction and reflection data. All examples are scaled identically. Separation between upper and lower crust along all models is based only on velocities. Intrusive volcanism and underplating are characteristic for most of the volcanic provinces, which were located above a hot spot at the time of their formation. Reproduced from Kopp H, Kopp C, Phipps Morgan J, Flueh ER, Weinrebe W, and Morgan WJ (2003) Fossil hot spot–ridge interaction in the Musicians Seamount Province: Geophysical investigations of hot spot volcanism at volcanic elongated ridges. *Journal of Geophysical Research* 108. http://dx.doi.org/10.1029/2002JB002015.

referred to it as 'volcanic underplating.' The underplating interpretation was disputed by Lindwall (1988), who demonstrated that the critical ESPs beneath the center of the volcanic chain can also be reasonably fit by crustal models without a deep, high-velocity zone (**Figure 19**). More recent seismic refraction experiments at oceanic hot spots have used arrays of OBSs or ocean-bottom hydrophones (OBHs) as receivers, allowing for continuous 2-D or 3-D seismic velocity models that avoid the ambiguity inherent in the ESP refraction geometry.

Caress et al. (1995) obtained deep seismic reflection and high-quality refraction data beneath a second hot-spot chain, the Marquesas, and confirmed a second example of magmatic underplating. Three long MCS lines were located across the chain in gaps between the islands, and a refraction line using OBSs coincided with the central line. The multichannel seismic reflection data imaged the surface of the crust preexisting the eruption of the hot-spot volcanoes. The OBS refraction data imaged crustal arrivals constraining the velocity structure within the crust and also clearly imaged wide-angle reflections from the base of the preexisting crust, and, beneath the center of the volcanic chain, from a deeper interface. A 2-D tomographic inversion of the refraction and reflection arrival times demonstrated that a normal oceanic crustal structure lay beneath the Marquesas volcanoes, but was itself underlain by a large body with seismic velocities (7.5–7.9 km s^{-1}) intermediate between normal lower-crustal and upper-mantle values. The strength of the wide-angle reflections from the relict Moho and the base of the subcrustal body indicates that this magmatic underplating unit (**Figure 19**) is strongly distinct from both the preexisting crust above and the upper mantle below. Taking into account both the existing volcanic edifices and the material contained in the surrounding sedimentary apron, the underplated volume amounts to 1.9 times the volume erupted on top of the preexisting crust. Caress et al. (1995) proposed, based on analogies with results from refraction experiments in active continental rift zones (Benz and McCarthy, 1994; Jarchow et al., 1993) and on rifted continental margins (Holbrook and Kelemen, 1993), that this unit is an igneous intrusion or a mixture of intrusive rocks with preexisting mantle peridotites emplaced beneath the crust during the process of hot-spot volcanism. The seismic velocity of the underplated material suggests that the hot spot produced melt buoyant enough to rise through the upper mantle to the base of the crust, but not sufficiently buoyant to rise above the crust–mantle boundary.

The buoyant nature of the underplated material was confirmed by Wolfe et al. (1994), who demonstrated that a good fit to both the depth of the moat and the gravity anomaly over the Marquesas Islands requires that the underplated material flexes the elastic lithosphere from below. The combination of the seismic constraints on the volume of the underplating and the gravitational bound on its buoyancy yield an estimate of 3100 kg m^{-3} for the density of the underplated unit.

Since the initial studies of Hawaii and the Marquesas, several seismic refraction and reflection experiments have focused on the deep crustal structure of hot-spot traces emplaced on old lithosphere. The study sites include the Canary Islands (Dañobeitia and Canales, 2000; Watts et al., 1997; Ye et al., 1999), La Reunion (Charvis et al., 1999; Gallart et al., 1999), Great Meteor Seamount (Weigel and Grevemeyer, 1999), the Societies (Grevemeyer et al., 2001b), and the Cape Verde Islands (Ali et al., 2003). In all of these cases, refraction and/or reflection data are consistent with the existence of high-velocity regions in the deep crust or upper mantle suggestive of magmatic underplating (**Figure 19**). Leahy and Park (2005) have provided independent evidence of underplating associated with oceanic hot-spot volcanism by using teleseismic receiver-function analysis to investigate the crustal and upper-mantle structure of four Pacific islands: Hawaii, Kiribati, Raratonga, and Tahiti. At each of these hot-spot volcanoes, Leahy and Park (2005) find evidence for a high-velocity subcrustal body ranging from 2 km thick at Tahiti to 10 km thick at Raratonga.

In contrast to the oceanic islands constructed on old lithosphere, all but one of the seismic refraction studies of near-ridge hot-spot volcanism are consistent with crustal thickening without the formation of subcrustal underplating. These observations hold for discrete seamounts such as Ascension Island (Evangelidis et al., 2004) and the Musicians Seamounts (Kopp et al., 2003), for larger platforms such as Crozet Bank (Recq et al., 1998) and Iceland (e.g. Staples et al., 1997), and for very large aseismic ridges such as the Cocos Ridge (**Figures 9** and **10**; Walther, 2003) and the Carnegie Ridge (Sallares et al., 2005).

The one hot-spot trace combining a near-ridge origin with strong evidence for underplating is the Ninetyeast Ridge. In fact, the most complete, and highest-resolution, images to date of an oceanic underplating body were obtained by Grevemeyer et al. (2001a) at Ninetyeast Ridge. The underplated body has velocities of 7.5–7.6 km s^{-1} and is 325 km wide, emplaced beneath the entire extrusive edifice and extending 50 km further to the east. Beneath the center of the edifice the underplating is as much as 5 km thick (**Figure 19**). The underplated volume at Ninetyeast Ridge is nearly the same as that erupted surficially. Because the eastern side of the Ninetyeast Ridge coincides with a transform boundary created by the separation of Ninetyeast Ridge from Broken Ridge, the eastward extension of the underplating indicates that at least some of the underplating was emplaced long after the surficial extrusive eruptions. Grevemeyer et al. (2001a) thus proposed that the underplating was associated with late-stage volcanism.

Underplating has also been inferred at two LIPs, indirectly from gravity data at the Ontong Java Plateau (Ito and Taira, 2000) and from seismic refraction data at the Kerguelen Plateau (Recq et al., 1990). In the case of the Ontong Java Plateau, Ito and Taira (2000) interpreted the gravity data in terms of a larger elastic plate thickness for the subsurface load, suggesting that the underplating happened 40–100 million years after the eruption of the surface load at a time when the oceanic lithosphere was stiffer. This intriguing suggestion would place an important constraint on the duration of LIP-type volcanism by requiring the intrusion of a magma body long after the plate had drifted away from the original magma source. It would also have interesting implications for the vertical motion history of oceanic plateaus and could explain the subsidence deficit for Ontong Java as inferred from drill cores. However, the interpretation of the gravity data is not unique; large-scale lithospheric folding as Ontong Java encounters the Solomon trench could also explain the data (Ito and Taira, 2000). Deep seismic reflection and refraction data would be required to resolve the ambiguity.

It appears that magmatic underplating is a common, but not necessarily universal, feature of many types of hot-spot

volcanism. Underplating has mostly been found beneath oceanic volcanic structures emplaced in old, cold, and strong lithosphere. With the exception of Ninetyeast Ridge (Grevemeyer et al., 2001a), volcanic edifices formed in the thin, weak lithosphere near spreading centers do not show evidence for underplating. However, at least some of the Ninetyeast Ridge underplating was emplaced after the edifice had moved away from the near-ridge environment. Although the refraction, reflection, and gravity data from Hawaii (Watts and ten Brink, 1989) and Ninetyeast Ridge (Grevemeyer et al., 2001a) suggest that underplating may be associated with later stages of hot-spot volcanism, the existence of underplating beneath the currently volcanically active La Reunion (Charvis et al., 1999; Gallart et al., 1999) demonstrates that subcrustal intrusions can occur during the primary edifice-building stage of hot-spot volcanism. More comprehensive experiments providing multiple cross sections of active oceanic hot spots, such as the Hawaiian Islands, will be required to determine the relationship between the onset of surficial volcanism and the development of an underplated complex.

1.14.4.3 Mantle Lithosphere

Imaging the mantle lithosphere beneath hot spots in order to study the formation of swells or superswells has been one of the highest-priority experiments for distinguishing among different models for swell formation, but also one of the most difficult experiments in terms of obtaining a robust result. Given the lack of specificity in swell-height data as to the location of the low-density buoyant support, the ambiguity in interpretation of geoid data in terms of isostatic or dynamic uplift models, and the concern that surficial fluid circulation could mask the signal of the hot spot in heat flow data, seismic data hold the most promise for determining whether the support for mid-plate swells lies in the mantle lithosphere, as predicted by the lithospheric thinning model, or beneath it, and whether the compensation is buoyant because it is hot or by virtue of its mineralogy.

The two principal methods for seismically probing the mantle lithosphere have been to use array processing on direct teleseismic arrivals at dense clusters of seismometers and differencing short-period surface waves between favorably positioned stations. The Hawaiian swell and Iceland have been the principal foci for this type of seismic investigation, although the MELT experiment yielded some information on the South Pacific superswell (MELT Scientific Team, 1998), and the PLUME project (Suetsugu et al., 2005) should provide further constraints soon.

Laske et al. (1999) obtained a year-long record of Rayleigh-wave phase velocities at periods between 15 and 70 s for more than 70 earthquake events by deploying an array of ocean-bottom differential pressure gauges along the southern edge of the Hawaiian swell. The information was inverted to determine the average seismic velocity structure beneath the array, which did not depart significantly from the average for 100 Ma lithosphere. However, they did detect a strong lateral velocity gradient across the array, with velocity decreasing within 300 km of the island chain. A more expansive array experiment is currently underway to obtain a more complete image of the seismic velocity structure in the mantle lithosphere beneath the Hawaiian swell.

Collins et al. (2002) used a different approach for constraining the structure of the mantle lithosphere beneath the Hawaiian swell. Using data from two broadband seismometers deployed a few hundred kilometers southwest of Oahu, they observed P-to-S converted phases from the Gutenberg discontinuity, thought to correspond to the base of the lithosphere. They place the base of the lithosphere at 80 km depth, in agreement with the results from Rayleigh-wave dispersion studies (Priestley and Tilmann, 1999; Woods and Okal, 1996). In contrast to the results of Laske et al. (1999), the results from these studies do not point to differences between the thickness and velocity structure of the lithosphere beneath the Hawaiian swell as compared with the parameters for normal oceanic lithosphere of that age. Ideally, the results from the ocean-bottom array experiment currently in progress will settle this controversy with major implications for the origin of hot spots and their geophysical signatures.

Several major field programs and tomographic studies have been devoted to the Iceland hot spot (Allen et al., 2002; Bijwaard and Spakman, 1999; Ritsema et al., 1999; Wolfe et al., 1997). Seismic analyses that have been conducted in Hawaii to detect any hot-spot-induced anomalies within a high-velocity lid make no sense in Iceland, which coincides with a mid-ocean ridge, where by definition the lithosphere tends toward zero thickness. Quite independent studies agree that the upper mantle immediately beneath Iceland is anomalously slow seismically, even by mid-ocean ridge standards, to about 400 km depth, consistent with the presence of high-temperature upwelling mantle. The real controversy for Iceland centers on whether the seismic velocity anomaly extends deeper than the mantle transition zone (Foulger et al., 2001; Helmberger et al., 1998). Converted phases mapped beneath Hawaii (Li et al., 2000) and Tahiti (Niu et al., 2002) also point to unusually warm upper-mantle temperatures immediately beneath those hot spots, although not for the South Pacific superswell in general.

Earthquake seismology has also found some applications in hot-spot research near the locus of active volcanism. Wolfe et al. (2003) used an improved relocation technique to demonstrate that earthquakes at $\sim$30 km depth in the mantle lithosphere beneath Hawaii define a seaward-dipping, low-angle fault plane, rather than a magma conduit through the lithosphere as had been previously suggested.

Whole-earth tomography has also made some contribution in this area, but in the past has lacked the resolution in the upper 100 km to unambiguously image the lithosphere and in the rest of the mantle to detect the possible signature of mantle plumes. New data-processing techniques (e.g., Capdeville et al., 2002; Montelli et al., 2004) hold the promise for directly imaging plumes within the mantle. For example, a recent study by Lei and Zhao (2006) uses ten converted seismic phases to image slow P-wave velocities extending from the surface to the CMB beneath Hawaii (**Figure 20**). However, Lei and Zhao's data set provides limited resolution because there are few crossing raypaths, and their models depend strongly on assumed CMB structure, indicating that further effort is required to refine CMB models. The results from various studies have yet to converge. For example, using the criterion that a plume must show continuous low shear velocity in the upper mantle, Ritsema and Allen (2003) find only eight hot spots

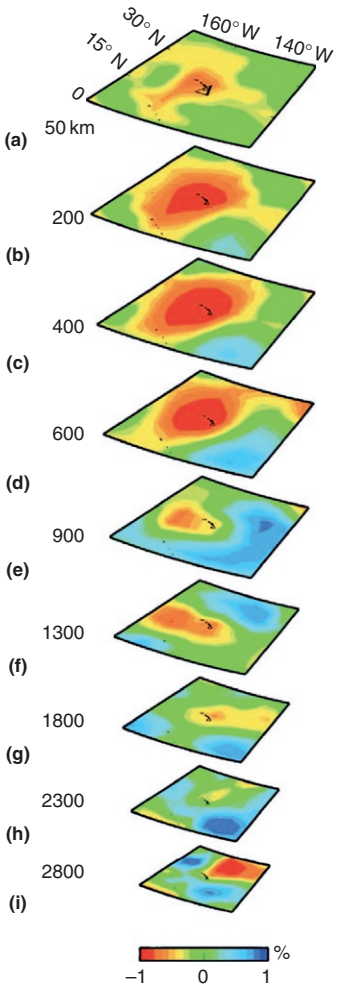

Figure 20 P-wave tomographic images in map view around the Hawaiian hot spot. The depth of each layer is noted on the left. Red and blue colors denote slow and fast velocities, respectively, compared to the IASP91 1-D Earth model (Kennett and Engdahl, 1991). Reproduced from Lei J and Zhao D (2006) A new insight into the Hawaiian plume. *Earth and Planetary Science Letters* 241: 438–453, with permission from Elsevier.

(Afar, Bowie, Easter, Hawaii, Iceland, Louisville, McDonald, and Samoa), out of the 37 considered, that pass the test for plume origin. Montelli et al. (2004), on the other hand, use the criterion that there must be seismic evidence that P-wave velocity lows extend from the upper mantle into the lower mantle. Their list of hot spots with plume origin includes only Ascension, Azores, Canary, Easter, Samoa, and Tahiti. Only Easter and Samoa are common on both lists. Courtillot et al. (2003), using broader criteria based on seismological, other geophysical, and helium isotope data, conclude that Afar, Easter, Hawaii, Reunion, Samoa, Louisville, Iceland, and Tristan are likely to be of plume origin. At this point in time, consensus seems to emerge that plume-like behavior is responsible for Easter and Samoa, with conflicting views on the appropriateness of this theory for other hot spots.

1.14.5 Conclusions

1.14.5.1 Emerging View on Geophysical Structure of Hot Spots and Swells

Hot-spot volcanism is clearly an important global phenomenon that reflects deep-Earth processes, modifies much of the lithosphere over time, and thus significantly impacts the thermal and chemical evolution of the Earth. Progress in the understanding of hot spots has required the integration of many types of geophysical observations, including bathymetry, satellite altimetry, gravity, heat flow, seismic reflection, seismic refraction, and teleseismic data. The results that heat flow patterns can be dominated by lateral variations in thermal conductivity and fluid circulation and that some, but not all, intraplate volcanic features include high-seismic-velocity underplating demonstrate that the shallow structure of hot-spot features must be well understood before the mantle structures related to the causes of hot-spot volcanism can be reliably resolved.

Recent studies of oceanic hot spots and hot-spot swells have explored multiple plausible mechanisms for producing intraplate volcanism, particularly including mantle plumes and lithospheric cracking due to plate-scale stresses. Plume theory remains viable, but only a small number of hot spots appear associated to deep-mantle plumes, and the nature of the plumes remains very much in question. The observed variety and complexity in the setting, history, and structure of intraplate volcanic features likely reflects multiple causes for hot-spot volcanism.

1.14.5.2 Promising Areas for Further Research

We anticipate that future geophysical hot-spot research will include more comprehensive seismic crustal and Moho imaging of active volcanic features to understand how hot-spot volcanism modifies preexisting crust over time. We also expect considerable effort to achieve better resolution of lateral variations in seismic velocity in the mantle by taking advantage of additional computational resources and improving knowledge of the complex crustal and upper-mantle structure. However, improvements in the coverage provided by the global seismic networks will be vital, particularly including long-term ocean stations in the deep-ocean basins.

Acknowledgment

The Packard Foundation supported the preparation of this chapter.

References

Abbott DH and Isley AE (2002) Extraterrestrial influences on mantle plume activity. *Earth and Planetary Science Letters* 205: 53–62.

Ali MY, Watts AB, and Hill I (2003) A seismic reflection profile study of lithospheric flexure in the vicinity of the Cape Verde Islands. *Journal of Geophysical Research* 108. http://dx.doi.org/10.1029/2002JB002155.

Allen RM, Nolet G, Morgan WJ, et al. (2002) Plume-driven plumbing and crustal formation in Iceland. *Journal of Geophysical Research* 107. http://dx.doi.org/10.1029/2001JB000584.

Anderson DL (1996) The edges of the mantle. In: Gurnis M, Wysession ME, Knittle E, and Buffett BA (eds.) *Geodynamics Series 28: The Core–Mantle Boundary Region*, pp. 255–271. Washington, DC: American Geophysical Union.

Bemis KG and Smith DK (1993) Production of small volcanoes in the superswell region of the South Pacific. *Earth and Planetary Science Letters* 118: 251–262.

Benz HM and McCarthy J (1994) Evidence for an upper mantle low velocity zone beneath the southern Basin and Range-Colorado Plateau transition zone. *Geophysical Research Letters* 21: 509–512.

Bijwaard H and Spakman W (1999) Tomographic evidence for a narrow whole mantle plume below Iceland. *Earth and Planetary Science Letters* 166: 121–126.

Bonatti E (1990) Not so hot 'hot spots' in the oceanic mantle. *Science* 250: 107–111.

Bonatti E and Harrison CGA (1976) Hot lines in the Earth's mantle. *Nature* 263: 402–404.

Bonneville A, Von Herzen RP, and Lucazeau F (1997) Heat flow over Réunion hot spot track: Additional evidence for thermal rejuvenation of oceanic lithosphere. *Journal of Geophysical Research* 102: 22731–22747.

Burke K and Dewey JF (1973) Plume-generated triple functions: Key indicators in applying plate tectonics to old rocks. *Journal of Geology* 81: 406–433.

Calmant S (1987) The elastic thickness of the lithosphere in the Pacific Ocean. *Earth and Planetary Science Letters* 85: 277–288.

Calmant S and Cazenave A (1986) The effective elastic lithosphere under the Cook-Austral and Society Islands. *Earth and Planetary Science Letters* 77: 187–202.

Capdeville Y, Larmat C, Vilotte J-P, and Montagner J-P (2002) A new coupled spectral element and modal solution method for global seismology: A first application to the scattering induced by a plume-like anomaly. *Geophysical Research Letters* 29. http://dx.doi.org/10.1029/2001GL013747.

Caress DW, McNutt MK, Detrick RS, and Mutter JC (1995) Seismic imaging of hotspot-related crustal underplating beneath the Marquesas Islands. *Nature* 373: 600–603.

Charvis P, Laesanpura A, Gallart J, et al. (1999) Spatial distribution of hotspot material added to the lithosphere under La Reunion, from wide-angle seismic data. *Journal of Geophysical Research* 104: 2875–2893.

Christensen U (1984) Instability of a hot boundary layer and initiation of thermochemical plumes. *Annals of Geophysics* 2: 311–320.

Chubb LJ (1957) The pattern of some Pacific island chains. *Geological Magazine* 94: 221–228.

Clague DA and Dalrymple GB (1987) The Hawaiian–Emperor volcanic chain. Part 1: Geologic evolution. *US Geological Survey Professional Paper* 1350: 5–54.

Clouard V and Bonneville A (2005) Ages of seamounts, islands and plateaus on the Pacific Plate. In: Foulger GR, Natland JH, Presnall D, and Anderson DL (eds.) *Geological Society of America Special Paper 388: Plates, Plumes & Paradigms*, pp. 71–90. Boulder, CO: Geological Society of America.

Coffin MF (1992) Emplacement and subsidence of Indian Ocean plateaus and submarine ridges. In: Duncan RA, Rea DK, Kidd RB, von Rad U, and Weissel JK (eds.) *American Geophysical Union Monograph Series, vol 70: Synthesis of Results from Scientific Drilling in the Indian Ocean*, pp. 115–125. Washington, DC: American Geophysical Union.

Coffin MF and Eldholm O (1994) Large igneous provinces: Crustal structure, dimensions, and external consequences. *Reviews of Geophysics* 32: 1–36.

Collins J, Vernon FL, Orcutt JA, and Stephen RA (2002) Upper mantle structure beneath the Hawaiian swell: Constrains from the ocean seismic network pilot experiment. *Geophysical Research Letters* 29. http://dx.doi.org/10.1029/2001GL013302.

Courtillot V, Davaille A, Besse J, and Stock J (2003) Three distinct types of hotspots in the Earth's mantle. *Earth and Planetary Science Letters* 205: 295–308.

Courtney RC and White RS (1986) Anomalous heat flow and geoid across the Cape Verde rise: Evidence for dynamic support from a thermal plume in the mantle. *Geophysical Journal International* 87: 815–867.

Crough ST (1978) Thermal origin of mid-plate hot-spot swells. *Geophysical Journal of the Royal Astronomical Society* 55: 451–469.

Crough ST and Jarrard RD (1981) The Marquesas-Line swell. *Journal of Geophysical Research* 86: 11763–11771.

Dañobeitia JJ and Canales JP (2000) Magmatic underplating in the Canary Archipelago. *Journal of Volcanology and Geothermal Research* 103: 27–41.

Darwin C (1842) *The Structure and Distribution of Coral Reefs*. London: Smith Elder.

Davies GF (1988) Ocean bathymetry and mantle convection. Part 1: Large-scale flow and hotspots. *Journal of Geophysical Research* 93: 10467–10480.

Davies GF (1999) *Dynamic Earth: Plates, Plumes, and Mantle Convection*. Cambridge: Cambridge University Press, 458 pp.

Davis AS, Gray LB, Clague DA, and Hein JR (2002) The Line Islands revisited: New $^{40}Ar/^{39}Ar$ geochronologic evidence for episodes of volcanism due to lithospheric extension. *Geochemistry, Geophysics, Geosystems* 3. http://dx.doi.org/10.1029/2001GC000190.

Detrick RS and Crough ST (1978) Island subsidence, hot spots, and lithospheric thinning. *Journal of Geophysical Research* 83: 1236–1244.

Detrick RS, Sclater JG, and Thiede J (1977) The subsidence of aseismic ridges. *Earth and Planetary Science Letters* 34: 185–196.

Detrick RS, Von Herzen RP, Crough ST, Epp D, and Fehn U (1981) Heat flow on the Hawaiian swell and lithospheric reheating. *Nature* 292: 142–143.

Detrick RS, Von Herzen RP, Parsons B, Sandwell D, and Dougherty M (1986) Heat flow observations on the Bermuda rise and thermal models of midplate swells. *Journal of Geophysical Research* 91: 3701–3723.

Detrick RS and Watts AB (1979) An analysis of isostasy in the world's oceans. Part 3: Aseismic ridges. *Journal of Geophysical Research* 84: 3637–3653.

Dietz RS (1961) Continent and ocean basin evolution by spreading of the seafloor. *Nature* 190: 854–857.

Dietz RS and Menard HW (1953) Hawaiian swell, deep, and arch and subsidence of the Hawaiian Islands. *Journal of Geology* 61: 99–113.

Duncan RA (1981) Hotspots in the Southern oceans – An absolute frame of reference for motion of the Gondwana continents. *Tectonophysics* 74: 29–42.

Duncan RA and McDougall I (1976) Linear volcanism in French Polynesia. *Journal of Volcanology and Geothermal Research* 1: 197–227.

Dziewonski AM (2005) The robust aspects of global seismic tomography. *Geological Society of America, Special Paper* 388: 147–154.

Dziewonski AM and Woodhouse JH (1987) Global images of the Earth's interior. *Science* 236: 37–48.

Ernst RE and Buchan KL (2003) Recognizing mantle plumes in the geological record. *Annual Review of Earth and Planetary Sciences* 31: 469–523.

Ernst RE, Grosfils EB, and Mège D (2001) Giant dike swarms: Earth, Venus, and Mars. *Annual Review of Earth and Planetary Sciences* 29: 489–534.

Evangelidis CP, Minshull TA, and Henstock TJ (2004) Three-dimensional crustal structure of Ascension Island from active source tomography. *Geophysical Journal International* 159: 311–325.

Filmer PE, McNutt MK, Webb HF, and Dixon DJ (1994) Volcanism and archipelagic aprons: A comparison of the Marquesas and Hawaiian Islands. *Marine Geophysical Research* 16: 385–406.

Foulger GR, Pritchard MJ, Julian BR, et al. (2001) Seismic tomography shows that upwelling beneath Iceland is confined to the upper mantle. *Geophysical Journal International* 146: 504–530.

Furumoto AS, Webb JP, Odegard ME, and Hussong DM (1976) Seismic studies on the Ontong Java Plateau. *Tectonophysics* 34: 71–90.

Gallart J, Driad L, Charvis P, et al. (1999) Perturbation to the lithosphere using the hotspot track of La Reunion, from an offshore-onshore seismic transect. *Journal of Geophysical Research* 104: 2895–2908.

Gordon RG and Jurdy DM (1986) Cenozoic global plate motions. *Journal of Geophysical Research* 91: 12389–12406.

Grand SP, van der Hilst RD, and Widiyantoro S (1997) Global seismic tomography: A snapshot of convection in the Earth. *GSA Today* 7: 1–7.

Grevemeyer I, Weigel W, Schussler S, and Avedik F (2001a) Crustal architecture and deep structure of the Ninetyeast Ridge hotspot trail from active-source ocean bottom seismology. *Geophysical Journal International* 144: 414–431.

Grevemeyer I, Weigel W, Schussler S, and Avedik F (2001b) Crustal and upper mantle seismic structure and lithospheric flexure along the Society Island hotspot chain. *Geophysical Journal International* 147: 123–140.

Griffiths RW and Campbell IH (1991) Interaction of mantle plume heads with the Earth's surface and onset of small-scale convection. *Journal of Geophysical Research* 96: 18295–18310.

Harris RN, Garven G, Georgen J, McNutt MK, Christiansen L, and Von Herzen RH (2000) Submarine hydrology of the Hawaiian archipelagic apron. Part 2: Numerical simulation of coupled heat transport and fluid flow. *Journal of Geophysical Research* 105: 21371–21385.

Harris RN, Von Herzen RH, McNutt MK, Garven G, and Jordahl K (2000) Submarine hydrology of the Hawaiian archipelagic apron. Part 1: Heat flow patterns north of Oahu and Maro Reef. *Journal of Geophysical Research* 105: 21353–21370.

Haxby WF and Turcotte DL (1978) On isostatic geoid anomalies. *Journal of Geophysical Research* 83: 5473–5478.

Head JW, Crumpler LS, Aubele JC, Guest JE, and Saunders RS (1992) Venus volcanism: Classification of volcanic features and structures, associations, and global distribution from Magellan data. *Journal of Geophysical Research* 97: 13153–13197.

Helmberger DV, Wen L, and Ding X (1998) Seismic evidence that the source of the Iceland hotspot lies at the core–mantle boundary. *Nature* 396: 251–255. http://dx.doi.org/10.1038/24357.

Hess HH (1962) History of ocean basins. In: Engel AEJ, Harold LJ, and Leonard BF (eds.) *A Volume in Honor of A. F. Buddington*, pp. 599–620. Boulder, CO: Geological Society of America.

Holbrook WS and Kelemen PB (1993) Large igneous province on the US Atlantic margin and implications for magmatism during breakup. *Nature* 364: 433–436.

Ito G, Lin J, and Gable CW (1996) Dynamics of mantle flow and melting at a ridge-centered hotspot: Iceland and the Mid-Atlantic Ridge. *Earth and Planetary Science Letters* 144: 53–74.

Ito G, Lin J, and Gable CW (1997) Interaction of mantle plumes and migrating mid-ocean ridges: Implications for the Galápagos plume-ridge system. *Journal of Geophysical Research* 102: 15403–15418.

Ito G and Taira A (2000) Compensation of the Ontong Java Plateau by surface and subsurface loading. *Journal of Geophysical Research* 105: 11171–11183.

Jarchow CM, Thompson GA, Catchings RD, and Mooney WD (1993) Seismic evidence for active magmatic underplating beneath the basin and range province, Western United States. *Journal of Geophysical Research* 98: 22095–22108.

Kennett B and Engdahl E (1991) Travel times for global earthquake location and phase identification. *Geophysical Journal International* 105: 429–465.

Kopp H, Kopp C, Phipps Morgan J, Flueh ER, Weinrebe W, and Morgan WJ (2003) Fossil hot spot–ridge interaction in the Musicians Seamount Province: Geophysical investigations of hot spot volcanism at volcanic elongated ridges. *Journal of Geophysical Research* 108. http://dx.doi.org/10.1029/2002JB002015.

Koppers AA, Duncan RA, and Steinberger B (2004) Implications of a nonlinear $^{40}Ar/^{39}Ar$ age progression along the Louisville seamount trail for models of fixed and moving hot spots. *Geochemistry, Geophysics, Geosystems* 5: Q06L02. http://dx.doi.org/10.1029/2003GC000671.

Ladd HS and Schlanger SO (1960) Dilling operations on Eniwetok Atoll. *US Geological Survey Professional Paper* 160-Y: 863–905.

Ladd HS, Tracey JI, and Gross MG (1967) Drilling on Midway Atoll, Hawaii. *Science* 166: 1038–1093.

Larson RL (1991) Latest pulse of Earth: Evidence for a mid-Cretaceous superplume. *Geology* 19: 547–550.

Larson RL and Olsen P (1991) Mantle plumes control magnetic reversal frequency. *Earth and Planetary Science Letters* 107: 437–447.

Laske G, Phipps Morgan J, and Orcutt JA (1999) First results from the Hawaiian SWELL pilot experiment. *Geophysical Research Letters* 26: 3397–3400.

Laughton AS, Matthews DW, and Fisher RL (1970) The structure of the Indian Ocean. In: Maxwell AE (ed.). *The Sea*, vol. 4, pp. 543–586. New York: Wiley.

Leahy GM and Park J (2005) Hunting for oceanic island Moho. *Geophysical Journal International* 160: 1020–1026.

Lei J and Zhao D (2006) A new insight into the Hawaiian plume. *Earth and Planetary Science Letters* 241: 438–453.

Li X, Kind R, Priestley K, et al. (2000) Mapping the Hawaiian plume conduit with converted seismic phases. *Nature* 405: 938–941.

Lindwall DA (1988) A two-dimensional seismic investigation of crustal structure under the Hawaiian Islands near Oahu and Kauai. *Journal of Geophysical Research* 93: 12107–12122.

Lister CRB (1972) On the thermal balance of a mid-ocean ridge. *Geophysical Journal of the Royal Astronomical Society* 26: 515–535.

Lonsdale P (1988) Geography and history of the Louisville hotspot chain in the Southern Pacific. *Journal of Geophysical Research* 93: 3078–3104.

Masters G, Johnson S, Laske G, and Bolton H (1996) A shear-velocity model of the mantle. *Philosophical Transactions of the Royal Society of London A* 354: 1385–1411.

McKenzie DP (1967) Some remarks on heat flow and gravity anomalies. *Journal of Geophysical Research* 72: 6261–6273.

McNutt MK (1984) Lithospheric flexure and thermal anomalies. *Journal of Geophysical Research* 89: 11180–11194.

McNutt MK (1987) Temperature beneath midplate swells: The inverse problem. In: Keating B, Fryer P, Batiza R, and Boehlert GW (eds.) *Seamounts, Islands, and Atolls. Geophysical Monograph Series*, vol. 43, pp. 123–132. Washington, DC: American Geophysical Union.

McNutt MK (1998) Superswells. *Reviews of Geophysics* 36: 211–244.

McNutt MK (2002) Heat flow variations over Hawaiian swell controlled by near-surface processes, not plume properties. In: Takahashi E, Lipman PW, Garcia MO, Naka J, and Aramaki S (eds.) *Hawaiian Volcanoes: Deep Underwater Perspectives. Geophysical Monograph Series,* 128, pp. 365–372. Washington, DC: American Geophysical Union.

McNutt MK and Bonneville A (2000) A shallow, chemical origin for the Marquesas swell. *Geochemistry, Geophysics, Geosystems* 1. http://dx.doi.org/10.1029/1999GC000028.

McNutt MK, Caress DW, Reynolds J, Jordahl KA, and Duncan RA (1997) Failure of plume theory to explain midplate volcanism in the southern Austral islands. *Nature* 389: 479–482.

McNutt MK and Fischer KM (1987) The South Pacific superswell. In: Keating BH, Fryer P, Batiza R, and Boehlert GW (eds.) *Seamounts, Islands, and Atolls. Geophysical Monograph Series*, vol. 43, pp. 25–34. Washington, DC: American Geophysical Union.

McNutt MK and Judge AV (1990) The superswell and mantle dynamics beneath the South Pacific. *Science* 248: 969–975.

McNutt MK and Shure L (1986) Estimating the compensation depth of the Hawaiian swell with linear filters. *Journal of Geophysical Research* 91: 13915–13923.

McNutt MK, Winterer EL, Sager WW, Natland JH, and Ito G (1990) The Darwin Rise: A Cretaceous superswell? *Geophysical Research Letters* 17: 1101–1104.

MELT Scientific Team (1998) Imaging the deep structure beneath a mid-ocean ridge: The MELT experiment. *Science* 280: 1215–1218.

Menard HW (1956) Archipelagic aprons. *American Association of Petroleum Geologist Bulletin* 40: 2195–2210.

Menard HW (1973) Depth anomalies and the bobbing motion of drifting islands. *Journal of Geophysical Research* 78: 5128–5137.

Menard HW (1986) *Islands*. New York, NY: Scientific American Books.

Molnar P and Stock J (1987) Relative motions of hotspots in the Pacific, Atlantic, and Indian Oceans since Late Cretaceous time. *Nature* 327: 587–591.

Monnereau M and Cazenave A (1990) Depth and geoid anomalies over oceanic hotspot swells: A global survey. *Journal of Geophysical Research* 95: 15429–15438.

Monnereau M and Cazenave A (1998) Variation of the apparent compensation depth of hotspot swells with age of plate. *Earth and Planetary Science Letters* 91: 179–197.

Montelli R, Nolet G, Dalhen FA, Masters G, Engdahl ER, and Hung S-H (2004) Finite frequency tomography reveals a variety of plumes in the mantle. *Science* 303: 338–343.

Moore JG, Clague DA, Holcomb RT, Lipman PW, Normark WR, and Torresan ME (1989) Prodigious submarine landslides on the Hawaiian ridge. *Journal of Geophysical Research* 94: 17465–17484.

Morgan WJ (1971) Convection plumes in the lower mantle. *Nature* 230: 42–43.

Morgan WJ (1972) Plate motions and deep mantle convection. In: Shagam R, Hargraves RB, Morgan WJ, Van Houten FB, and Burk CA (eds.) *GSA Memoir 132: Studies in Earth and Spaces Sciences*, pp. 7–22. New York: Geological Society of America.

Morgan WJ (1978) Rodriquez, Darwin, Amsterdam, . . ., a second type of hotspot island. *Journal of Geophysical Research* 83: 5355–5360.

Mutter JC, Buck WR, and Zehnder CM (1988) Convective partial melting. Part 1: A model for the formation of thick basaltic sequences during the initiation of spreading. *Journal of Geophysical Research* 93: 1031–1048.

Mutter JC and Zehnder CM (1988) Deep crustal structure and magmatic processes: The inception of seafloor spreading in the Norwegian-Greenland Sea. In: Morton AC and Parson LM (eds.) *Geological Society Special Publication London 39: Early Tertiary Volcanism and the Opening of the NE Atlantic*, pp. 35–48. London: Geological Society of London.

Nishimura CE and Forsyth DW (1985) Anomalous Love-wave phase velocities in the Pacific: Sequential pure-path and spherical harmonic inversion. *Geophysical Journal the Royal Astronomical Society* 81: 389–4.07.

Niu F, Solomon SC, Silver PG, Suetsugu D, and Inoue H (2002) Mantle transition-zone structure beneath the South Pacific Superswell and evidence for a mantle plume underlying the Society hotspot. *Earth and Planetary Science Letters* 198: 371–380.

Nyblade AA and Robinson SW (1994) The African superswell. *Geophysical Research Letters* 21: 765–768.

O'Connor JM, Stoffers P, and McWilliams MO (1995) Time-space mapping of Easter chain volcanism. *Earth and Planetary Science Letters* 136: 197–212.

Parsons B and Sclater JG (1977) An analysis of the variation of ocean floor bathymetry and heat flow with age. *Journal of Geophysical Research* 82: 802–8.27.

Patriat M, Klingelhoefer F, Aslanian D, et al. (2002) Deep crustal structure of the Tuamotu plateau and Tahiti (French Polynesia) based on seismic refraction data. *Geophysical Research Letters* 29. http://dx.doi.org/10.1029/2001GL013913.

Phipps Morgan J (1999) Isotope topology of individual hotspot basalt arrays: Mixing curves or melt extraction trajectories? *Geochemistry, Geophysics, Geosystems* 1. http://dx.doi.org/10.1029/1999GC000004.

Phipps Morgan J, Morgan WJ, and Price E (1995) Hotspot melting generates both hotspot volcanism and a hotspot swell? *Journal of Geophysical Research* 100: 8045–8062.

Pitman WC III (1978) Relationship between eustacy and stratigraphic sequences of passive margins. *Geological Society of America Bulletin* 89: 1389–1403.

Priestley K and Tilmann F (1999) Shear-wave structure of the lithosphere above the Hawaiian hotspot from two-station Rayleigh wave phase velocity measurements. *Geophysical Research Letters* 26: 1493–1496.

Recq M, Brefort D, Malod J, and Veinante JL (1990) The Kerguelen Isles (southern Indian Ocean): New results on deep structure from refraction profiles. *Tectonophysics* 182: 227–248.

Recq M, Goslin J, Charvis J, and Operto S (1998) Small-scale crustal variability within an intraplate structure: The Crozet Bank (southern Indian Ocean). *Geophysical Journal International* 134: 145–156.
Rees BA, Detrick RS, and Coakley BJ (1993) Seismic stratigraphy of the Hawaiian flexural moat. *Bulletin of the Geological Society of America* 105: 189–205.
Ribe N (1995) The dynamics of plume-ridge interaction. Part 1: Ridge-centered plumes. *Earth and Planetary Science Letters* 143: 155–168.
Richards MA, Duncan RA, and Courtillot V (1989) Flood basalt and hotspot tracks – Plume heads and tails. *Science* 246: 103–107.
Ritsema J and Allen RM (2003) The elusive mantle plume. *Earth and Planetary Science Letters* 207: 1–1.2.
Ritsema J, van Heijst HJ, and Woodhouse JH (1999) Complex shear wave velocity structure imaged beneath Africa and Iceland. *Science* 286: 1925–1928.
Robinson EM and Parsons B (1988) Effects of a shallow low-viscosity zone on the formation of midplate swells. *Journal of Geophysical Research* 93: 3144–3157.
Sallares V, Charvis P, Flueh E, and Bialas J (2005) Seismic structure of the Carnegie ridge and the nature of the Galapagos hotspot. *Geophysical Journal International* 161: 763–788.
Schlanger SO, Garcia MO, Keating BH, et al. (1984) Geology and geochronology of the Line Islands. *Journal of Geophysical Research* 89: 11261–11272.
Sharp WD and Clague DA (2006) 50-Ma initiation of Hawaiian–Emperor bend records major change in Pacific plate motion. *Science* 313: 1250–1251.
Sichoix L, Bonneville A, and McNutt M (1998) The seafloor swells and Superswell in French Polynesia. *Journal of Geophysical Research* 103: 27123–27133.
Sleep N (1990) Hotspots and mantle plumes: Some phenomenology. *Journal of Geophysical Research* 95: 6715–6736.
Smallwood JR, Staples RK, Richardson KR, and White RS (1999) Crust generated above the Iceland mantle plume: From continental rift to oceanic spreading center. *Journal of Geophysical Research* 104: 22885–22902.
Smith DE, Zuber MT, Solomon SC, et al. (1999) The global topography of Mars and implications for surface evolution. *Science* 284: 1495–1503.
Solomon SC, Smekar SE, Bindschadler DL, et al. (1992) Venus tectonics: An overview of Magellan observations. *Journal of Geophysical Research* 97: 13199–13225.
Spencer J and Schneider N (1996) Io on the eve of the Galileo mission. *Annual Review of Earth and Planetary Sciences* 124: 125–190.
Staples R, White R, Brandsdottir B, Menke W, Maguire P, and McBride J (1997) Faroes-Iceland Experiment. Part 1: The crustal structure of northeastern Iceland. *Journal of Geophysical Research* 102: 7849–7866.
Steinberger B (2000) Plumes in a convecting mantle: Models and observations for individual hotspots. *Journal of Geophysical Research* 105: 11127–11152.
Steinberger B and O'Connell RJ (1998) Advection of plumes in mantle flow: Implications for hotspot motion, mantle viscosity, plume distribution. *Geophysical Journal International* 132: 412–434.
Storey BC (1995) The role of mantle plumes in continental breakup: Case histories from Gondwana. *Nature* 377: 301–308.
Su W-J, Woodward RL, and Dziewonski AM (1994) Degree 12 model of shear velocity heterogeneity in the mantle. *Journal of Geophysical Research* 99: 6945–6980.
Suetsugu D, Shiobara H, Sugioka H, et al. (2005) Probing South Pacific mantle plumes with ocean bottom seismographs. *Eos, Transactions of the American Geophysical Union* 86: 429–435.
Tarduno JA, Duncan RA, Scholl DW, et al. (2003) The Emperor Seamounts: Southward motion of the Hawaiian hotspot plume in Earth's mantle. *Science* 301: 1064–1069.
ten Brink US and Brocher TM (1987) Multichannel seismic evidence for a subcrustal intrusive complex under Oahu and a model for Hawaiian volcanism. *Journal of Geophysical Research* 92: 13687–13707.
ten Brink US and Watts AB (1985) Seismic stratigraphy of the flexural moat flanking the Hawaiian Islands. *Nature* 317: 421–424.
Turcotte DL and Oxburgh ER (1967) Finite amplitude convection cells and continental drift. *Journal of Fluid Mechanics* 28: 29–42.
Turcotte DL and Oxburgh ER (1973) Mid-plate tectonics. *Nature* 244: 337–339.
Vidal V and Bonneville A (2004) Variations of the Hawaiian hot spot activity revealed by variations in the magma production rate. *Journal of Geophysical Research* 109. http://dx.doi.org/10.1029/2003JB002559.
Vogt PR (1972) Evidence for global synchronism in mantle plume convection, and possible significance for geology. *Nature* 240: 338–342.
Von Herzen RP (2004) Geothermal evidence for continuing hydrothermal circulation in older (>60 M.y.) ocean crust. In: Davis EE and Elderfield H (eds.) *Hydrogeology of the Oceanic Lithosphere*, pp. 414–447. New York: Cambridge University Press.
Von Herzen RP, Cordery MJ, Detrick RS, and Fang C (1989) Heat flow and thermal origin of hot spot swells: The Hawaiian swell revisited. *Journal of Geophysical Research* 94: 13783–13799.
Von Herzen RP, Detrick RS, Crough ST, Epp D, and Fehn U (1982) Thermal origin of the Hawaiian swell: Heat flow evidence and thermal models. *Journal of Geophysical Research* 87: 6711–6723.
Walther CHE (2003) The crustal structure of the Cocos ridge off Costa Rica. *Journal of Geophysical Research* 108. http://dx.doi.org/10.1029/2001JB000888.
Watts AB (2001) *Isostacy and Flexure of the Lithosphere*. Cambridge: Cambridge University Press, 458 pp.
Watts AB, Bodine JH, and Ribe NM (1980) Observations of flexure and geological evolution of the Pacific ocean basins. *Nature* 283: 532–537.
Watts AB, Peirce C, Collier J, Dalwood R, Canales JP, and Henstock TJ (1997) A seismic study of lithospheric flexure in the vicinity of Tenerife, Canary Islands. *Earth and Planetary Science Letters* 146: 431–447.
Watts AB and ten Brink US (1989) Crustal structure, flexure, and subsidence of the Hawaiian Islands. *Journal of Geophysical Research* 94: 10473–10500.
Watts AB, ten Brink US, Buhl P, and Brocher TM (1985) A multichannel seismic study of lithospheric flexure across the Hawaiian–Emperor seamount chain. *Nature* 315: 105–111.
Weigel W and Grevemeyer I (1999) The Great Meteor seamount: Seismic structure of a submerged intraplate volcano. *Journal of Geodynamics* 28: 27–40.
Whitehead JA and Luther DS (1975) Dynamics of laboratory diaper and plume models. *Journal of Geophysical Research* 80: 705–717.
Wilson JT (1963) A possible origin of the Hawaiian Islands. *Canadian Journal of Physics* 41: 863–870.
Winterer EL, Natland JH, van Waasbergen RJ, et al. (1993) Cretaceous guyots in the northwest Pacific: An overview of their geology and geophysics. In: Pringle M (ed.) *Geophysical Monograph 77: The Mesozoic Pacific: Geology, Tectonics, and Volcanism*, pp. 307–334. Washington, DC: American Geophysical Union.
Wolfe CJ, Bjarnason IT, VanDecar JC, and Solomon SC (1997) Seismic structure of the Iceland mantle plume. *Nature* 385: 245–247.
Wolfe CJ, McNutt MK, and Detrick RS (1994) The Marquesas archipelagic apron: Seismic stratigraphy and implications for volcano growth, mass wasting, and crustal underplating. *Journal of Geophysical Research* 99: 13591–13608.
Wolfe CJ, Okubo PG, and Shearer PM (2003) Mantle fault zone beneath Kilauea volcano, Hawaii. *Science* 300: 478–480.
Woods MT and Okal EA (1996) Rayleigh-wave dispersion along the Hawaiian swell: A test of lithospheric thinning by thermal rejuvenation at a hotspot. *Geophysical Journal International* 125: 325–339.
Ye S, Canales JP, Rihm R, Danobeitia JJ, and Gallart J (1999) A crustal transect through the northern and northeast part of the volcanic edifice of Gran Canaria, Canary Islands. *Journal of Geodynamics* 28, 3–2.6.
Zindler A and Hart SR (1986) Chemical geodynamics. *Annual Review of Earth and Planetary Sciences* 14: 493–571.

1.15 Crust and Lithospheric Structure - Active Source Studies of Crust and Lithospheric Structure

A Levander, CA Zelt, and WW Symes, Rice University, Houston, TX, USA

© 2007 Elsevier B.V. All rights reserved.

This chapter is reproduced from the previous edition, Volume 1, pp. 247–288, © 2007, Elsevier B.V.

1.15.1	Introduction	479
1.15.2	Vertical-Incidence and Wide-Angle Seismology	480
1.15.3	Background	480
1.15.4	Reflection Seismology	481
1.15.5	The CMP Method in Reflection Seismology	483
1.15.6	Migration	484
1.15.6.1	Imaging Condition	486
1.15.6.2	Backpropagation Operators	486
1.15.7	Reflection Seismology Examples	488
1.15.8	Refraction/Wide-Angle Seismology	490
1.15.9	Wide-Angle Seismology Experiments	491
1.15.10	Data Processing	492
1.15.11	Model Dimension	492
1.15.12	Forward Modeling	493
1.15.13	Traveltime Inversion and Tomography: Theory and Practical Issues	494
1.15.14	Traveltime Inversion and Tomography: Algorithms	497
1.15.15	Amplitude Modeling	499
1.15.16	S-Waves, Density, Attenuation, and Anisotropy	499
1.15.17	Fine-Scale Heterogeneities	500
1.15.18	Joint Inversion	500
1.15.19	Model Assessment	501
1.15.20	Wide-Angle Migration	502
1.15.21	Wavefield Inversion	502
1.15.22	Wavefield Inversion Examples	504
1.15.23	Future Directions	505
Acknowledgments		507
References		507

1.15.1 Introduction

Controlled-source seismic methods are used widely at small, medium, and large scales for investigating the Earth from the shallow subsurface (upper tens of meters) to structures in and below the continental lithosphere (a few to a few hundred kilometers depth). Also called active-source seismology, controlled-source seismology requires the timed release of mechanical energy to generate elastic wavefields. For investigation as deep as the upper mantle, the mechanical energy is generated by the release and conversion of chemical energy (occasional use has been made of nuclear explosions, particularly in the former Soviet Union). Marine investigations of the crust and top of the mantle commonly utilize the release of pressurized air, whereas on land, oscillating masses at the surface are used. For shallow investigations (tens to hundreds of meters depth), the sources include gunshots, weight drops, hammer blows, oscillating masses, and small explosives. Generally, the seismic data are recorded on fairly dense arrays of portable seismic instruments, also referred to as seismic channels, numbering in the hundreds to thousands or even tens of thousands.

The most widely used application of controlled-source seismology is the reflection seismic method employed in the exploration for petroleum. Seismic surveys, processing, and interpretation account for the bulk of petroleum exploration budgets prior to drilling. Recently, the mining industry has employed seismic reflection and refraction methods for investigating the extent of known ore bodies and for identifying fault zones along which economically viable mineralization has occurred. At smaller scales, both reflection imaging and refraction velocity analysis are used in geotechnical and engineering applications, groundwater resource assessment, and environmental investigations.

In this chapter, we confine our attention to controlled-source investigations used primarily to determine structure of the crust and upper mantle. There is considerable overlap between experimental methods used in academic investigations and those used in the various industries.

 http://dx.doi.org/10.1016/B978-0-444-53802-4.00013-0

1.15.2 Vertical-Incidence and Wide-Angle Seismology

Controlled-source imaging of the lithosphere can be divided into two main areas: (1) near-vertical reflection methods and (2) refraction/wide-angle reflection methods. We assume that the reader is familiar with Snell's law of reflection and refraction at an interface separating two materials with different seismic velocities and the reflection and transmission coefficients that describe the partition of motion during the interaction. Reflection and transmission coefficients depend on contrasts in seismic impedances, the product of seismic velocity, c, and density, ρ, as well as the incidence angle, θ. An important point in the behavior of a reflected and refracted wave occurs at the critical angle, θ_c, the incidence and reflection angle in the slower medium at which the wave in the faster medium refracts parallel to the interface with a refraction angle of $\pi/2$ taken from the normal to the interface. In the Earth, velocity generally increases with depth, producing critical refraction at different angles depending on depth. Reflection coefficients in the 'precritical' regime, $\theta < \theta_c$, are typically small and real $(R(\theta < \theta_c) < 0.1)$, whereas those in the 'postcritical' regime are of order 1 and can be complex $(R(\theta < \theta_c) = |R(\theta)|\exp(i\phi(\theta)), |R(\theta)| \sim 1, \phi \neq 0)$ producing large reflections and distorting the waveform (see Aki and Richards, 2002, Chapter 5). There are a number of important distinctions between the two methods that include data-acquisition geometry and hence the completeness of the wavefield recorded and analyzed, the approach used to make an image of the Earth, and the meaning and resolution of the final image. The first concerns the maximum distance between source location, x_s, and receiver location, x_r, during recording compared to the maximum experiment target depth, z_{max}. The distance between the source and receiver, $x_s - x_r$, is referred to as the source–receiver offset or just the offset; in the coordinate system we are using, x is the location in 3-space, z is the vertical coordinate, positive down, and x_s and x_r are the positions of the source and receiver, usually at or near the Earth's surface. Reflection seismology normally uses waves that travel further vertically than horizontally:

$$\max|(x_s - x_r)/z_{max}| \leq 1 \qquad [1]$$

Reflection seismology directly uses the reflected or backscattered wavefield to form an image of the 'reflectivity structure.' Reflectivity structure is the vertical derivative of seismic impedance normalized by its average value. For a layered medium, this is proportional to the reflection coefficient at normal incidence calculated as a continuous function of depth. Seismic waves arrive at subhorizontal interfaces with small, precritical incidence angles, giving small real reflection coefficients $(0.1 \leq R)$. The data to be analyzed are the precritical backscattered wavefield (Figure 1). Reflection processing is based on the common midpoint (CMP) method, combined with an image formation step based on one of various formulations of the wave equation to yield a reflectivity map that ideally corresponds to the Earth's 'impedance structure.' For whole-crust studies, the customary frequency band of interest is 8–60 Hz.

In contrast, the wide-angle method relies on the identification of first-arriving refracted waves and large-amplitude postcritical reflections where

$$\max|(x_s - x_r)/z_{max}| \gg 1 \qquad [2a]$$

and, usually,

$$\max|(x_s - x_r)/z_{max}| > 5 \qquad [2b]$$

In very densely recorded wide-aperture surveys, precritical reflections can be identified and used as well. Data analysis typically employs a model-based approach, such as traveltime inversion, to yield a spatial map of 'seismic velocity.' For lithospheric studies, the typical frequency band of interest is 1–20 Hz. This approach is variously referred to as the refraction method, wide-angle method, or refraction/wide-angle reflection method. For brevity, we use the terms wide-angle data and wide-angle method (a more precise term would be wide aperture).

The two conventional controlled-source methods are essentially end-members: Reflection data provide a high-resolution structural image, and the wide-angle data provide a lower-resolution velocity model. The difference in resolution scales between the two methods is generally more than an order of magnitude. Hybrid methods that combine the reflection and wide-angle approaches are gradually evolving, as we will describe later.

Figure 1(a) shows a two-dimensional (2-D) model of crustal P-wave velocity structure (Hole et al., 2005) used to generate viscoelastic synthetic seismograms for testing various analysis methods. Figure 1(b) is a vertical-component synthetic shot gather illustrating the main arrival types (phases or events) used in traveltime and amplitude modeling of wide-angle data. Often, only the first-arrival times are modeled; these correspond to the Pg and Pn arrivals before and after the Pg/Pn crossover point (~140 km in Figure 1(b)). Although the wide-angle wavefield can be complicated, as in this synthetic example, identifying and modeling the arrival times of first arrivals and prominent reflections, such as from the Moho (PmP), is a much more robust and less-demanding problem than modeling the full wavefield (described in Section 1.15.21). Figure 1(c) and 1(d) shows the same shot but at offsets to ±25 km with and without the Pg and Rayleigh waves. Figure 1(d) shows the wavefield that would be processed to form a reflection image. Numerous reflections are visible from within the crust and as deep as the Moho.

1.15.3 Background

We begin with a few background equations relevant to both reflection and refraction seismologies. We consider a wave operator, L, for the 3-D inhomogeneous wave equation:

$$LG(x, x_s, t) = \delta(t)\delta(x - x_s) \qquad [3]$$

where G is Green's function for either the acoustic wave equation or one of the elastic wave potentials (see Aki and Richards (2002, p. 64)). For a constant coefficient equation, that is, a constant velocity medium, the solution is

$$G(x, x_s, t) = \frac{1}{4\pi c^2}\frac{\delta(t - |x - x_s|/c)}{|x - x_s|} \qquad [4]$$

where c is the material velocity. Here, the spreading is the reciprocal distance between the observation point and the

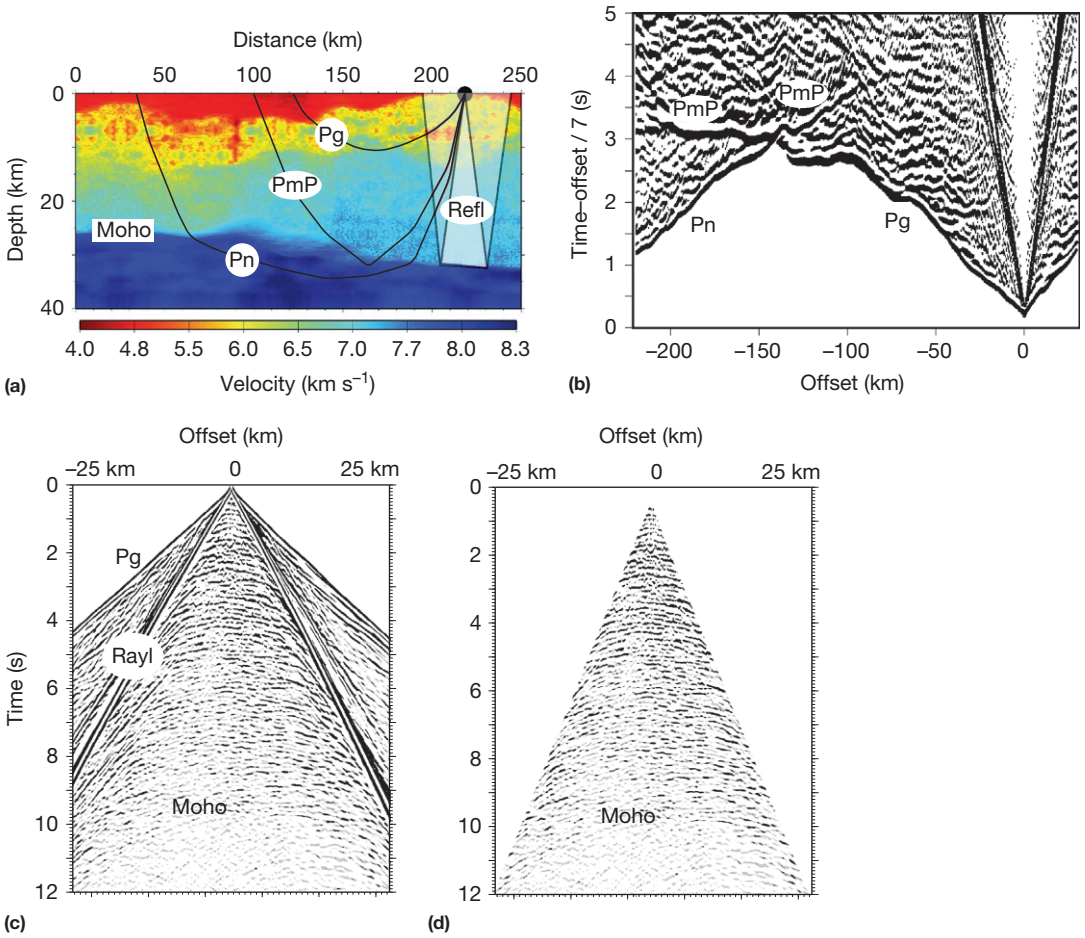

Figure 1 Example of phases used in crustal reflection and wide-angle studies. (a) Synthetic crustal P-wave velocity model from Hole et al. (2005) and representative ray paths for main phases: Pg – crustal refraction; PmP – Moho reflection; Pn-upper-mantle refraction. Refl – the area sampled by reflection data from this shot. Source location indicated by black dot. (b) Vertical component, viscoelastic full-wavefield data for source location indicated in (a). Phases are labeled corresponding to those in (a); both precritical PmP and postcritical PmP are visible. Time is reduced by 7 km s^{-1}, which means a correction equal to offset/7 km s^{-1} is applied. Phases with velocity of 7 km s^{-1} will appear horizontal. (c) The same shot record showing 25 km offset around the shotpoint. The Pg phase and Rayleigh waves are visible in the record, as well as converted shear waves. All of this energy is considered noise in the reflection model. A series of reflection events appear with hyperbolic shape inside the Rayleigh wave cone. (d) The same shot record with the noise field zeroed out. This is the part of the wavefield used for reflection imaging. In conventional reflection acquisition, each receiver point has a small array of geophones, which is used to suppress the Rayleigh waves, increasing the size of the region from which reflection data can be recovered.

source point, x_s, and the delta function is delayed by that distance divided by the medium velocity. For a variable velocity medium, one of the commonly employed solutions is to introduce a high-frequency approximation with a similar form as the constant velocity solution:

$$G(x, x_s, t) \approx a(x, x_s)\delta(t - \tau(x - x_s)) \quad [5]$$

Here, $a(x, x_s)$ is the geometric optics amplitude resulting from spreading, and again, the delta function carries the time dependence. Equation [5] is valid only in the absence of caustics. The traveltime obeys the 'eikonal' equation:

$$|\nabla\tau| = \frac{1}{c(x)} \quad [6]$$

The eikonal equation can be integrated along the path of the wave through the medium:

$$\tau(x, x_s) = \int_{x_s}^{x} \frac{dl(x, x_s)}{c(l)} \quad [7]$$

The distance l is the ray connecting x_s to x. Much of reflection and refraction seismologies are based on numerical implementations of these equations. We develop eqns [5] and [6] for the acoustic equation in the section on reflection seismology. Equation [7] is the starting point for the discussion on wide-angle analysis methods.

1.15.4 Reflection Seismology

The goal of this section is to provide an understanding of the theoretical basis of reflection seismology, rather than a comprehensive literature review. Because reflection seismology is

the principal petroleum exploration tool and is now also an important tool in oil field management, the reflection seismology literature is extremely large, highly specialized, and heavily laden with commercial jargon. We have tried to minimize the jargon but still introduce enough common terminology so that the reader can consult the journals of the Society of Exploration Geophysicists, *Geophysics*, and the European Association of Exploration Geophysicists, *Geophysical Prospecting*, and understand much of the seismic literature.

Reflection experiment geometries are designed to produce as regular a sampling of the subsurface as possible. The receiver geometry is usually fixed relative to and moves with the source point. In the marine environment, this is accomplished by towing an air gun source array and one or multiple linear arrays of pressure sensors behind the acquisition vessel. On land, vertical-component geophones are deployed in linear or areal arrays to record signals from accelerated weight drops, explosive charges, or vibrating masses on trucks, a source known as Vibroseis™. For efficiency on land, the acquisition requires that about twice as many geophones are deployed on the ground as are recording at a given time. As the source point moves, different parts of the seismic array are turned on and off to maintain a constant recording aperture, a practice called 'roll-along' recording.

For a variety of pragmatic reasons, wave propagation and imaging in reflection seismology are normally based on a scalar, acoustic wave equation. For the forward and inverse problems, we follow a development for solution of the wave equation from a set of course notes by Symes, as this development illustrates imaging with the backscattered wavefield and allows us to describe traditional reflection seismology. For a 3-D medium having laterally and vertically variable density and sound speed,

$$\begin{aligned} &\frac{1}{\rho(x)c^2(x)}\frac{\partial^2 p(x,\,t)}{\partial t^2}-\nabla\cdot\left[\frac{1}{\rho(x)}\nabla p(x,\,t)\right]=f(t)\delta(x)\\ &c(x)=\sqrt{k(x)/\rho(x)} \end{aligned} \qquad [8]$$

where $p(x,t)$ is the pressure field, $\rho(x)$ is mass density, $c(x)$ is the sound speed, $\kappa(x)$ is the bulk modulus, and $f(t)$ is a temporally dependent, but spatially localized source field.

We assume that the sound speed can be decomposed into a low wave number, smoothly varying term $c_0(x)$ and a rapidly varying component $\delta c(x)$. Similarly, we can separate the density field and the pressure fields into background and perturbed fields:

$$\begin{aligned} c(x)&=c_0(x)+\delta c(x)\\ \rho(x)&=\rho_0(x)+\delta\rho(x)\\ p(x,\,t)&=p_0(x,\,t)+\delta p(x,\,t) \end{aligned} \qquad [9]$$

The scale separation is designed to produce kinematically correct traveltimes and approximately correct geometric optics amplitudes by solving for a solution to the smooth background field but is also designed so that the detailed dynamics (amplitudes) result from terms scaled by perturbed material properties. We term the former field the smooth velocity model, and the latter, with velocity scaled by density, the acoustic impedance, $i(x)$. Estimating the smooth velocity field from seismic data is one of the principal challenges in seismic reflection imaging, and for the imaging problem, this field is termed the 'migration velocity model.' The spatial variation of the impedance normalized by the average impedance is the reflectivity, $r(x)$, which provides the most basic high-frequency image of the subsurface (i.e., the details in $r(x)$ are considerably higher-resolution details than the details in $c_0(x)$):

$$\begin{aligned} i(x)&=c(x)\rho(x)\\ i(x)&\approx c_0(x)\rho_0(x)+\delta c(x)\rho_0(x)+\delta\rho(x)c_0(x)\\ r(x)&=\frac{\delta i(x)}{i_0(x)}=\left[\frac{\delta c}{c_0}+\frac{\delta\rho}{\rho_0}\right] \end{aligned} \qquad [10]$$

There are few analytic guidelines quantifying what constitutes smooth and rapidly varying in the scale separation. Numerical experiments on the Marmousi synthetic model (see Versteeg, 1994) suggest that the migration velocity model needs to be specified at about three times the dominant wavelength in the illuminating wavefield to provide an accurate migration model. This is restrictive in a complicated model. For many places in sedimentary basins, a quasilinear velocity increase with depth is a reasonable estimate of $c_0(x)$. A reasonable approximation for the crystalline crust is the velocity field determined by a refraction profile that has been interpreted using the regularized inversion methods discussed in the following section.

Substituting the perturbed quantities into [8] and solving for $\delta p(x,\,t)$ to first order gives

$$\frac{1}{\rho c^2}\frac{\partial^2\delta p}{\partial t^2}-\nabla\cdot\frac{1}{\rho}\nabla\delta p=\frac{2\delta c}{\rho c^3}\frac{\partial^2 p(x,\,t)}{\partial t^2}-\frac{1}{\rho}\nabla\cdot\left[\frac{\delta\rho}{\rho}\nabla p\right] \qquad [11]$$

We can develop a solution for $\delta p(x,\,t)$ from solutions for $p(x,\,t)$. Let $G(x_s,\,x,\,t)$ be Green's function for the solution of the inhomogeneous equation

$$\begin{aligned} &\frac{1}{\rho(x)c^2(x)}\frac{\partial^2 G(x_s,\,x,\,t)}{\partial t^2}-\nabla\cdot\frac{1}{\rho(x)}\nabla G(x_s,\,x,\,t)\\ &\quad=\delta(t)\delta(x-x_s) \end{aligned} \qquad [12]$$

where x_s is the source position and x the observation position. The solution $p_0(x_s,\,x,\,t)$ is given by integrating G against the extended time source:

$$p_0(x_s,\,x,\,t)=\int dt' f(t-t')G(x_s,\,x,\,t) \qquad [13]$$

Estimating $f(t)$, termed the source wavelet, has a long history in exploration geophysics and is still a research topic. Early developments in statistical communication theory are the most widely used methods for reshaping the source pulse to a spike or relatively flat band-limited function. The reader is referred to landmark books by Robinson and Treitel (1980) and Claerbout (1976) and the practical processing text by Yilmaz (2001). These pulse estimation and reshaping methods are termed statistical, spiking, and predictive deconvolution. They have been applied very successfully to receiver-function processing in teleseismic seismology.

For constant velocity, the solution to eqn [12] is given by eqn [4]. For a smoothly variable velocity, we develop an asymptotic solution by assuming a progressive wave expansion of the form

$$u(x_s, x, t) = a(x, x_s)S(t - \tau(x_s, x)) + R(x_s, x, t) \quad [14]$$

where $S(x_s, x, t)$ is assumed to have the same order of singularity as constant velocity Green's function and the remainder, R, is smoother than S. Substituting [14] into [12] gives

$$\begin{aligned}\left[\frac{1}{\rho c^2}\frac{\partial^2}{\partial t^2} - \nabla\cdot\frac{1}{\rho}\nabla\right]u &= \frac{a}{\rho}\left[\frac{1}{c^2} - |\nabla\tau|^2\right]S''(t-\tau) \\ &+ \frac{1}{\rho}\left[2\nabla\tau\cdot\nabla a - \left(\nabla\tau\cdot\frac{\nabla\rho}{\rho} + \nabla^2\tau\right)a\right]S''(t-\tau) \\ &+ \left[\nabla\cdot\frac{1}{\rho}\nabla a\right]S(t-\tau) + \left[\frac{1}{\rho c^2}\frac{\partial^2 R}{\partial t^2} - \nabla\cdot\frac{1}{\rho}\nabla R\right]\end{aligned} \quad [15]$$

If the coefficients of the four terms on the right vanish, then u satisfies the acoustic wave equation. The order of singularity decreases term by term on the right-hand side, so that if

$$\frac{1}{c^2} - |\nabla\tau|^2 = 0 \quad [16]$$

and

$$2\nabla\tau\cdot\nabla a - \left(\nabla\tau\cdot\frac{\nabla\rho}{\rho} + \nabla^2\tau\right)a = 0, \quad [17]$$

the solution is approximately correct in high-frequency components. Equation [16] is the eikonal equation of geometric optics, with $\tau(x, x_s)$ the traveltime field, and eqn [17] is the transport equation, with $a(x, x_s)$ the geometric optics amplitude field. Both of these quantities can be solved numerically for laterally and vertically variable media of some complexity by either ray tracing or finite differences (e.g., Cerveny et al., 1977; Van Trier and Symes, 1991; Vidale, 1988, 1990). In analogy to constant coefficient Green's functions solution, we can write approximate Green's function solution as

$$G(x_s, x, t) \cong a(x, x_s)\delta(t - \tau(x, x_s)) \quad [18]$$

This suffices for the 'incident' field and the direct wave when applied against the source function $f(t)$. To solve for the backscattered field, that is, the field of interest in reflection seismology, we find the perturbed field $\delta p = f * \delta G(x_s, x, t)$ by solving

$$\frac{1}{\rho_0 c_0^2}\frac{\partial \delta G}{\partial t^2} - \nabla\cdot\frac{1}{\rho_0}\nabla\delta G = \frac{\delta c}{\rho_0 c_0^3}\frac{\partial^2 G}{\partial t^2} - \frac{1}{\rho_0}\left(\nabla\frac{\delta\rho}{\rho_0}\right)\cdot\nabla G \quad [19]$$

Let the acoustic wave operator be denoted L, and apply Green's formula

$$\int_V dx \int dt[(Lu)v] = \int_V dx \int dt[u(Lv)] \quad [20]$$

with $u = G$ and $v = \delta G$. At this point, we want to specify the observation point, x_r, measure time with respect to the observation coordinate, t_r, and so make use of the identity

$$\begin{aligned}\delta G(x_s, x_r, t_r) = \int_V dx \int dt[&\delta G(x_s, x_r, t) \\ &\times \delta(x - x_r)\delta(t - t_r)]\end{aligned} \quad [21]$$

Substituting and rearranging [20] gives

$$\begin{aligned}\delta G(x_s, x_r, t_r) = \int_V dx \Bigg[&\frac{2\delta c(x)}{\rho_0(x)c_0^3(x)}\frac{\partial^2 G(x_s, x, t)}{\partial t^2} \\ &- \frac{1}{\rho_0(x)}\left(\nabla\frac{\delta\rho(x)}{\rho_0(x)}\right)\cdot\nabla G(x_s, x, t)\Bigg] \\ &\times G(x_s, x_r, t_r)\end{aligned} \quad [22]$$

This is a very general expression for the perturbation field, which is referenced to the shot and receiver coordinates, and the receiver timescale. For calculations, we substitute approximate 3-D Green's function [18]:

$$\begin{aligned}\delta G(x_s, x_r, t_r) \sim &\frac{\partial^2}{\partial t_r^2}\int_V \frac{dx}{\rho_0(x)}\Bigg[a(x_r, x)a(x_s, x) \\ &\times \left\{\frac{2\delta c(x)}{c_0^3(x)}\right\}\delta(t_r - \tau(x_r, x) - \tau(x_s, x))\Bigg] \\ &+ \frac{\partial}{\partial t_r}\int_V \frac{dx}{\rho_0(x)}\Bigg[a(x_r, x)a(x_s, x) \\ &\times \left\{\nabla\frac{\delta\rho(x)}{\rho_0(x)}\cdot\nabla_x\tau(x_s, x)\right\}\delta(t_r - \tau(x_r, x) - \tau(x_s, x))\Bigg] \\ &- \int_V \frac{dx}{\rho_0(x)}\Bigg[a(x_r, x)a(x_s, x)\left\{\nabla_x a(x_s, x)\cdot\nabla\frac{\delta\rho(x)}{\rho_0(x)}\right\} \\ &\times \delta(t_r - \tau(x_r, x) - \tau(x_s, x))\Bigg]\end{aligned} \quad [23]$$

Note that the terms in braces, containing material property fluctuations, are coefficients in integral equations having the same basic form. This expression can be used for Kirchhoff forward modeling of the backscattered field. If density is a constant, the expression reduces to

$$\begin{aligned}\delta p(x_s, x_r, t_r) = &\frac{\partial^2}{\partial t_r^2}\int_V \frac{dx}{\rho}\Bigg[a(x_r, x)a(x_s, x)\left\{\frac{2\delta c(x)}{c_0^3(x)}\right\} \\ &\times f(t_r - \tau(x_r, x) - \tau(x_s, x))\Bigg]\end{aligned} \quad [24]$$

$$\begin{aligned}\delta p(x_s, x_r, t_r) = &\int dw(-\omega^2)\exp(-i\omega t_r) \\ &\times \int_V \frac{dx}{\rho_0}\left[a(x_r, x)a(x_s, x)\left\{\frac{2\delta c(x)}{c_0^3(x)}\right\}\right] \\ &\times f(\omega)\exp(i\omega(\tau(x_r, x) + \tau(x_s, x)))\end{aligned}$$

The coefficient scaling the amplitude and phase terms contains the reflectivity function $r(x) \sim \delta c(x)/c_0(x)$. Both integrals show the two phase factors corresponding to traveltimes to and from the scattering point.

For illustration, we can simplify the equations by assuming that $c =$ constant everywhere, that δc is nonzero at $x = (x_1, y_1, z_1)$ within the integration volume, and that $\rho =$ constant everywhere. Perturbation Green's function is

$$\begin{aligned}\delta G(x_s, x_r, x, t) = &\frac{2\delta c}{c_0^3\rho_0}\frac{\delta''(t - (R_s + R_r)/c)}{16\pi^2 R_s R_r} \\ R_s = &\sqrt{(x_{s1} - x_1)^2 + (x_{s2} - y_1)^2 + (z_s - z_1)^2} \\ R_r = &\sqrt{(x_{r1} - x_1)^2 + (x_{r2} - y_1)^2 + (z_r - z_1)^2}\end{aligned} \quad [25]$$

Applying the source wavelet against [25] gives

$$\delta p(x_s, x_r, x, t) = \frac{2\delta c}{c^3\rho}\frac{f''(t - (R_s + R_r)/c)}{16\pi^2 R_s R_r} \quad [26]$$

1.15.5 The CMP Method in Reflection Seismology

Traditional reflection seismology is based on the coordinate transformation:

$$\begin{aligned}m &= (x_s + x_r)/2 \\ b &= (x_s - x_r)/2\end{aligned} \quad [27]$$

where m is the midpoint coordinate, the average position of the source and receiver, and h is the half-offset, which measures the source and receiver distance away from the midpoint. This methodology was patented in 1950 by W. H. Mayne who called it the common depth point method. Reflection data acquisition is designed so that all the midpoints have an equal number of seismograms with a nearly identical and full range of offsets and azimuths. Populating the midpoint locations uniformly requires very regular data-acquisition geometries.

Traditional reflection seismology makes use of properties of the midpoint–offset domain to form the simplest form of backscattered image (Figure 2). The outstanding properties of this coordinate system are that (1) for any plane interface and scattering point, the traveltime curves are symmetrical in offset around any midpoint, with the minimum at $b = 0$ (Figure 2(c)); (2) for constant velocity, the traveltime curve for a flat reflector is a hyperbola expressed in offset and the 'two-way zero-offset traveltime' $t_0 = 2z_0/c_0$; and (3) many types of multiple reflections are strongly attenuated relative to primary reflections.

The symmetry of the traveltime curve allows us to estimate $t_0(m = \text{constant})$, and the hyperbolic form of the traveltime curve allows us to estimate the medium velocity using multiple $b(m = \text{constant})$ values. This is the most rudimentary form of velocity analysis to find c_0. Expressing [26] in midpoint and offsets gives

$$\begin{aligned}\delta p(m, b, t_r) &= \frac{2\delta c f''(t - 2R/c)}{c^3\rho \quad 16\pi^2 R^2} \\ \delta p(m, b, t_r) &= \frac{2\delta c f''(t - (t_0(z_0) + \Delta t_{NMO}(z_0, b)))}{c^3\rho \qquad 16\pi^2 R^2}\end{aligned} \qquad [28]$$

where $R = \sqrt{(b^2 + z_0^2)}$, $t_0 = 2z_0/c$, $\Delta t_{NMO} = 2R/c - t_0$, where Δt_{NMO} is called the 'normal moveout (NMO) time.' For fixed m, the traveltime curves are symmetrical in h around $b = 0$. For any horizontal reflector in a background velocity dependent only on depth, $c_0(z)$, the traveltime curve can be approximated as a hyperbola that is parameterized by the zero-offset time and a time (depth)-dependent velocity to second order in the ratio h/z. This velocity is called the 'root mean square (rms) velocity' (Dix, 1955). The rms velocity is interpreted as the velocity that gives the set of straight ray, approximate, traveltimes closest to the actual curved ray-path traveltimes for a given depth. The rms velocity at a given depth is always less than the true velocity above that depth. Characterization of the traveltime curve as a hyperbola expressed in two-way traveltime and offset coordinates is true for any reflecting plane regardless of dip and azimuth, but the physical meaning of the derived velocities becomes increasingly obscure.

Correcting the traveltime by the difference between the hyperbolic time at offset h and that at t_0, termed the 'normal moveout' correction (Figure 2(d)), gives a vertical focusing principle. This aligns the arrivals on all the seismograms at a CMP allowing them to be summed, or 'stacked,' to enhance signal to noise. If each midpoint has N individual seismograms at different $b(m = \text{constant})$ and if the noise field is random in time and space, the theoretical signal-to-noise improvement by stacking is $N^{1/2}$. N is referred to as the 'fold,' or redundancy of the data. The collection of seismograms at a CMP is termed a 'gather.' The seismograms can be sorted, or 'gathered,' into any common coordinate. The original seismic record of all seismograms for one shot is referred to as a shot gather. All the shots recorded by one receiver are a receiver gather, and all seismograms from all shots and receivers at a single offset are called a common offset gather.

The 'CMP stacked section' is an approximation to a zero-offset section. The 'zero-offset' section would be the image formed by making measurements along the surface with a coincident source and receiver. One of the most important steps in making the CMP stacked section is estimating $c(z)$, or $c_{rms}(z)$, known as 'velocity analysis.' Taner and Koehler (1969) introduced the velocity spectrum, in which CMP data are summed using a 'spectrum' of different trial velocities for NMO correction at each depth. The velocity giving the maximum power in the stack at a given depth is chosen as correct.

The CMP stacked section was the first widespread imaging technique for the subsurface that made direct use of the recorded seismograms (Figure 3(a)). For a quasilayered medium, it provides a very accurate representation of the subsurface, but as it lacks a horizontal focus, the images of laterally variable structures are distorted in a number of predictable ways.

1.15.6 Migration

The true power of imaging with reflection data emerged when computationally efficient expressions for the backprojection and horizontal focusing of the field δp were developed, allowing highly detailed images of geologic structures to be made in media with laterally variable velocity, $c_0 = c_0(x_1, x_2, z)$. Migration, most simply, increases lateral resolution by collapsing diffractions from points and edges and restores continuous reflections from dipping structures to their 'true' dips and positions, the fidelity of 'true' depending on the approximations used (see Yilmaz, 2001). 'Time migration' makes use of constant or fairly smoothly varying velocity and backpropagates along straight rays (Figure 3(b)), whereas 'depth migration' attempts to reposition energy along estimates of the true travel paths and provides a mapping from time to depth (Figure 3(c) and 3(d)). The former is much less expensive computationally than the latter. These methods require a propagation operator and an imaging condition. The literature on the former is large, while the development of the imaging condition, as well as a class of backpropagation operators, is largely attributed to Claerbout (1970, 1971, 1976, 1985).

To start, let us expand what we mean by an image of the subsurface. The CMP section is an image that provides only a vertical focus. Scales (1995) provided a useful definition of an image that is a frequency sum at a point, x, in the subsurface

$$I(x) = S_{PP}(x) = \int_{-\infty}^{\infty} d\omega \left[F_1(\omega) \frac{\delta p_{ref}(x, x_r, \omega)}{p_{inc}(x_s, x, \omega)} \right] \qquad [29]$$

With this definition, the image is the acoustic scattering coefficient formed by dividing the field recorded at x_r backpropagated to x, by the field incident on x from x_s. The position x is now called a common image point, or a common reflection point. The collection of data migrated to that point for a variety of (x_r, x_s) is a common image gather (CIG; Al-Yahya, 1989).

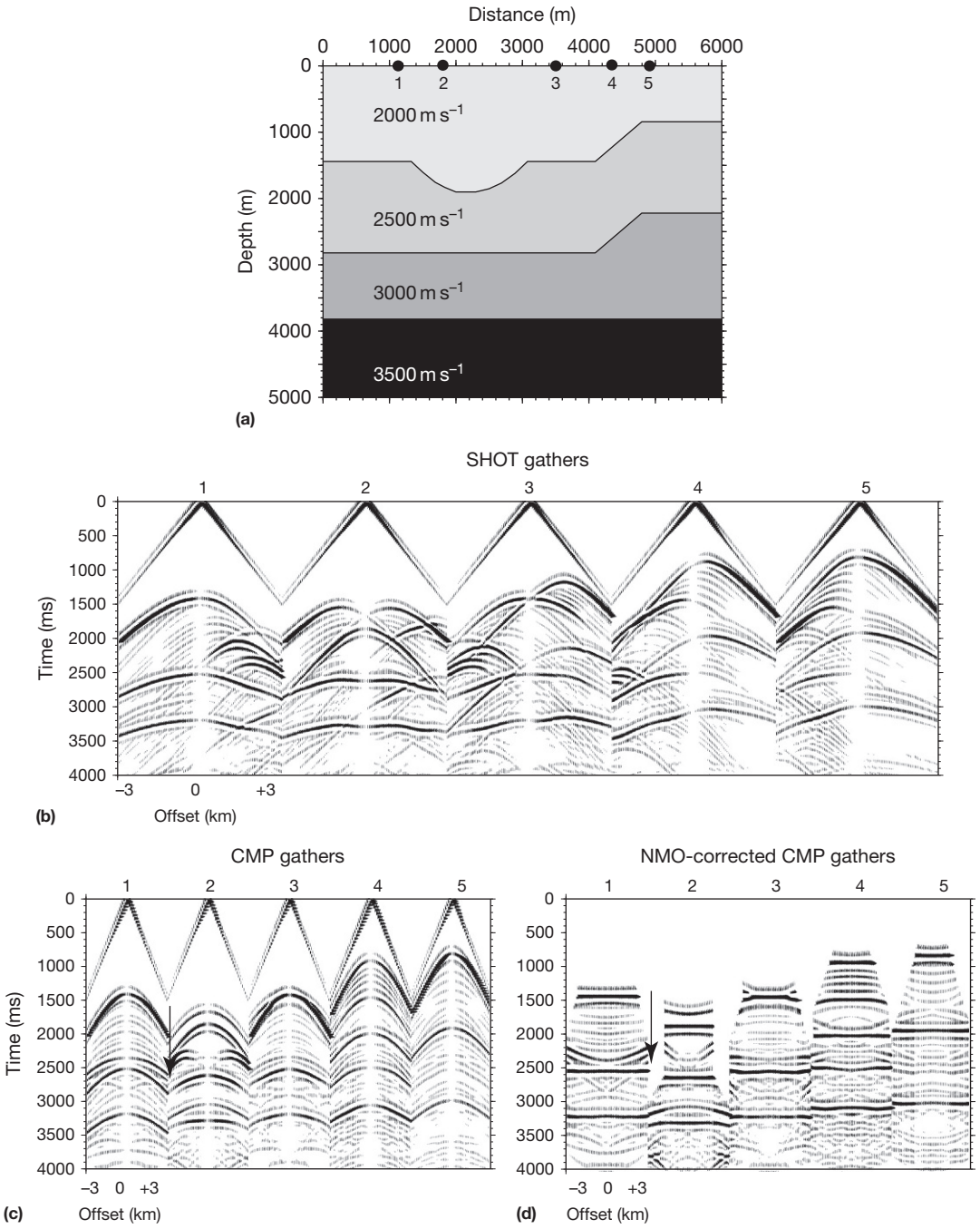

Figure 2 Synthetic reflection data set calculated with an acoustic finite-difference wave equation code. (a) The finite-difference velocity model with locations of the shot and CMP gathers that are shown in the following panels (locations 1–5). (b) Five of several hundred shot records showing the complex reflection patterns originating from laterally variable layering. (c) CMP gathers from five locations along the velocity model. In the midpoint–offset domain, the traveltimes are symmetrical about $b = 0$. (d) Vertical focus provided by normal moveout correction to the CMP gathers with the direct wave zeroed. The NMO correction was made using the local rms velocities. Note that the NMO correction fails to flatten events arriving at the same zero-offset time but having different phase velocities, that is, conflicting dips (arrows in (c) and (d)).

$F_1(\omega)$ is a shaping filter that takes into account the finite bandwidth of the source. This is a particularly easy image to form, as it makes direct use of the recorded data $\delta p(x_s, x_r, t)$, requiring only that we backpropagate it to the scattering point, x, to form $\delta p(x, x_r, t)$. For $\delta p(x_s, x, t)$, we can either estimate the incident field or propagate the source field; if we choose the latter, note that both δp and p contain $f(t) => F(\omega)$ and the source wavelet is theoretically removed automatically. In this case, $F_1(\omega)$ is used to stabilize the division, but in practice, filtering and deconvolution processing is employed prior to migration. Backpropagating both source and receiver wavefields is termed 'shot–geophone prestack migration.' In this

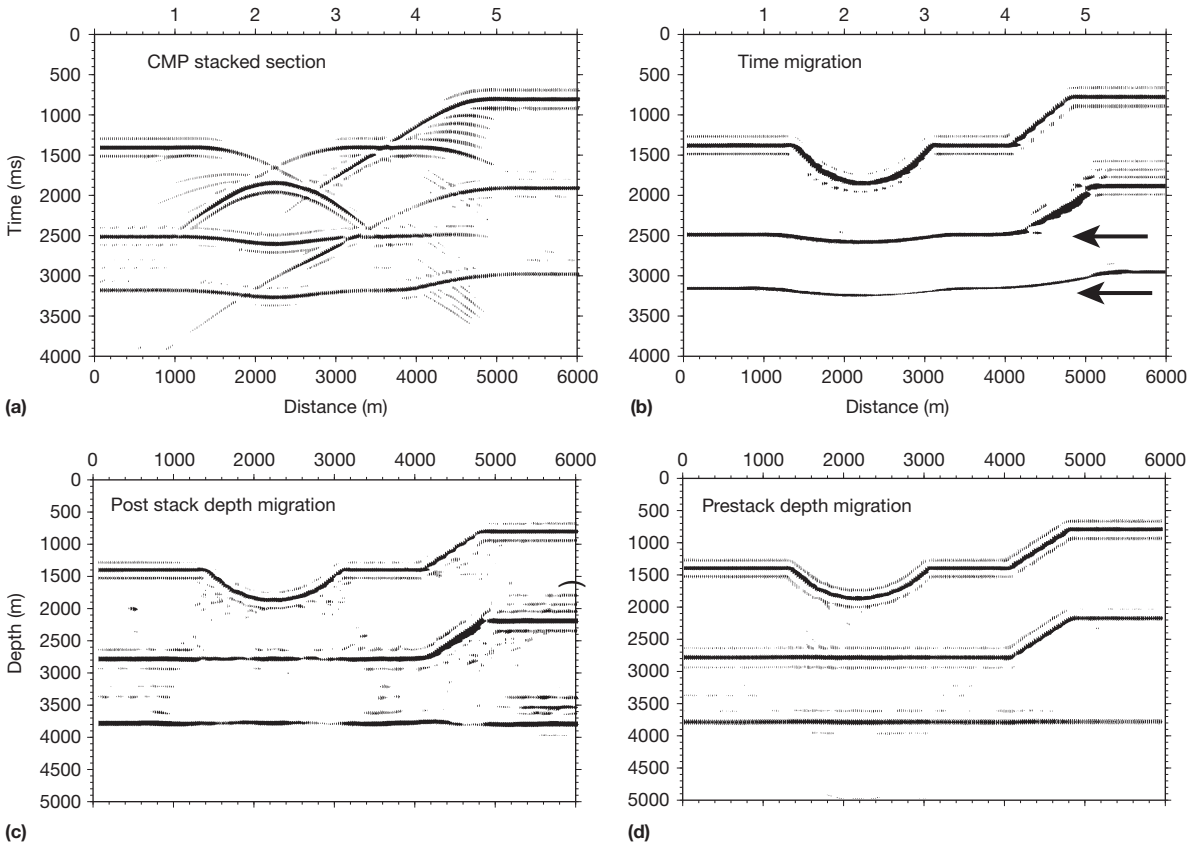

Figure 3 Processed synthetic data from the model in **Figure 2**. (a) The CMP stacked section shows distortions resulting from the lack of a lateral focus. Note particularly the caustic from the bowl-shaped feature in the shallowest interface at location 2 and the large diffractions from locations 2 to 4 from the dipping portions of the two shallowest interfaces. (b) Time migrating the CMP stacked section removes the distortion of the caustic but fails to flatten the two deeper horizons (arrows). (c) Poststack depth migration flattens the deeper reflectors but fails to illuminate them uniformly. (d) Prestack depth migration produces the clearest image; note the lack of amplitude fluctuation in the deepest horizon. Prestack migration operates on the original data without the intermediate step of NMO correction and stacking and provides both horizontal focusing and vertical focusing simultaneously. All the migrations were done with Kirchhoff algorithms similar to those described in the text.

case, the scattering coefficient is implicitly dependent on the incidence–reflection angle. Data compression, summing the redundant data reflected from x, is done as the last step. The scattering coefficient as a function of incidence angle can be extracted prior to summation by examining CIGs. We can also prestack migrate the data in the midpoint–offset domain, termed 'constant offset prestack migration,' by fixing h and migrating the data at different offsets independently. This has a number of desirable qualities that make it a common form of prestack migration.

In the CMP stacked section, $b = 0$, and midpoint is the migration coordinate. This is termed 'poststack migration' and is much less expensive than prestack migration because the data are compressed by the CMP fold prior to migration. However, poststack migration loses the angular dependence of the scattering coefficient and has other problems as well.

1.15.6.1 Imaging Condition

The imaging condition takes a form appropriate to the numerical implementation of the backpropagation operator, but in its simplest form, it is the negative of the time that backscattered energy on the seismic record took to get there, that is, it is equal to the time that the scattered field takes to propagate back to the scattering object plus the time the incident field takes to propagate from the source to the scattering point. This is termed time reversal.

1.15.6.2 Backpropagation Operators

We will continue with the asymptotic form for the backscattered field to describe seismic migration, but we note that entirely numerical approaches, that is, finite-difference methods, mixed finite-difference Fourier transform, and Fourier transform methods using the full-wave equation and various approximations to the one-way wave equation, are also widely used (e.g., Claerbout, 1970, 1985; Gazdag, 1978; Stolt, 1978).

Here, we develop an intuitive approach to migration of the precritical field $\delta p(x_s, x_r, t)$ using the Kirchhoff integral (e.g., Gardner et al., 1974 and Schneider, 1978) and the high-frequency formulation described earlier. We write the wave equation in the frequency domain for the smooth model and, for simplicity, consider constant density:

$$\left[\frac{-\omega^2}{\rho_0 c_0^2(x)}-\frac{1}{\rho_0}\nabla^2\right]u(x,\omega)=0$$
$$\left[\frac{-\omega^2}{\rho_0 c_0^2(x)}-\frac{1}{\rho_0}\nabla^2\right]G(x_s,x,\omega)=-4\pi\delta(x-x') \quad [30]$$

These are Helmholtz equations that can be substituted into a form of Green's theorem to isolate u, the field at x':

$$\begin{aligned}\int_V dx\left[u\nabla^2 G-G\nabla^2 u\right]&=\int_S ds(x_0)\left[u\frac{dG}{dn}-G\frac{du}{dn}\right]\\&=\frac{-1}{4\pi\rho_0}\int_S ds(x_0)\left[u(x_0,\omega)\frac{dG(x_0,x',\omega)}{dn}\right.\\&\quad u(x',\omega)\\&\quad\left.-G(x_0,x',\omega)\frac{du(x_0,\omega)}{dn}\right]\end{aligned} \quad [31]$$

This integral has a simple interpretation: the field anywhere in a volume can be described by measurements of the field and its derivative on the surface bounding it. This forms the basis for several migration operators and is widely used in diffraction theory (e.g., Goodman, 1996; Sommerfeld, 1954). Generally, we have only a recording of the field or its derivative, so we choose a kinematically correct Green's function that makes one of the two terms in [31] vanish on S. Green's function is then an auxiliary field; it does not necessarily solve the physical problem for u. Let the surface S be defined by $z=0$, and choose a Green's function that vanishes on S by introducing a mirror source in the region $z<0$. We can combine the asymptotic form of free-space Green's function with a copy of its mirror source. Since the normal n is positive outward, at $z=0$, the two sources cancel:

$$\begin{aligned}G_f(x,x',t)&\cong a(x',x)\delta(t-\tau(x,x'))\\G_f(x,x',\omega)&=a(x',x)\exp(i\omega\tau(x,x'))\\G_f(x_0,x',\omega)&=a(x',x^+)\exp(i\omega\tau(x^+,x'))\\&\quad -a(x',x)\exp(i\omega\tau(x^-,x'))\\G(x_0(z=0),x',\omega)&=0\end{aligned} \quad [32]$$

where x^+ and x^- refer to fields approaching $z=0$ from below and above. The normal derivative of Green's function becomes

$$\frac{dG}{dn}=2\frac{dG_f}{dn}\bigg|_{z=0} \quad [33]$$

Substituting this into the diffraction integral

$$u(x',\omega)=\frac{-1}{2\pi}\int_S ds(x_0)\times\left[u(x_0,\omega)\frac{dG_f(x_0(z=0),x',\omega)}{dn}\right] \quad [34]$$

Evaluating the normal derivative of G gives

$$\begin{aligned}\frac{dG}{dn}&=\frac{da(x_0,x')}{dn}\exp(i\omega\tau(x_0,x'))\\&\quad+a(x_0,x')i\omega\frac{d\tau}{dn}\exp(i\omega\tau(x_0,x'))\\\frac{d\tau}{dn}&=|\nabla_{x_0}\tau(x_0,x')|\cdot n\\\frac{d\tau}{dn}&=\frac{1}{c_0(x_0)}\cos(\theta(x_0))\end{aligned} \quad [35]$$

We can further simplify the diffraction integral by assuming that the derivative of amplitude is much smaller than that of phase and neglect the first term. This gives the Rayleigh–Sommerfeld diffraction integral

$$u(x',\omega)\cong\frac{-1}{2\pi\rho_0}\int_S ds(x_0)\left[u(x_0,\omega)a(x',x_0)\frac{(i\omega)\cos\theta(x_0)}{c_0(x_0)}\times\exp(i\omega\tau(x_0,x'))\right] \quad [36]$$

The integral [36] was developed for a flat surface but is approximately true for a surface that undulates around $z=0$ with spatial frequency small compared to that of the wavefield. The latter is known as the Kirchhoff approximation (Beckman and Spizzichino, 1963). If we let $u(x_0,\omega)=\delta p(x_0,\omega)$, the back-scattered field recorded at the surface, we can inverse Fourier transform to get

$$\begin{aligned}&\frac{1}{2\pi}\int d\omega\left[\delta p(x,\omega)\exp(-i\omega t)\right]\\&\cong\frac{-1}{4\pi^2\rho_0}\int_S ds(x_0)\int d\omega\left[\delta p(x_0,\omega)a(x_0,x')\right.\\&\quad\left.\times\frac{\cos\theta(x_0)}{c_0(x_0)}\exp(-i\omega(t-\tau(x',x_0)))\right]\end{aligned} \quad [37]$$

The integrand consists of known quantities, with the traveltime and amplitude field of Green's function determined from the smooth velocity field. The diffraction integral looks very much like Scales' definition of a seismic image [29]. The differences from the image definition are that the spreading function is reversed in sense (i.e., this formulation is for forward, not reverse propagation) and the integrand is not scaled by the incident field and the pulse shaping filter. Let $x'=x$, and let $x_0=m$ be the midpoint coordinate for $b=0$. We can modify the integral for poststack imaging, using Green's function to estimate the amplitude of the incident field at x:

$$p(x;m,b=0)=a(x;m,b=0) \quad [38]$$

Dividing both integrands gives

$$\begin{aligned}&\frac{1}{2\pi}\int d\omega\left[F_1(\omega)\frac{\delta p(x,\omega)}{p(x;m)}\exp(-i\omega t)\right]\\&\cong\frac{-1}{4\pi^2\rho_0}\int_S ds(m)\int d\omega(i\omega)\left[\delta p(m,\omega)B(x,m,\omega)\right.\\&\quad\left.\times\frac{\cos\theta(m)}{c_0(m)}\exp(-i\omega(t-2\tau(x,m)))\right]\end{aligned} \quad [39]$$

where we have doubled the traveltime field to account for downward propagation and B restores the spreading from the surface midpoint coordinate to the scattering point and contains the pulse shaping filter:

$$B(x,m,\omega)=\frac{F_1(\omega)}{a^2(x,m)} \quad [40]$$

This integral can be used for poststack migration of the CMP stacked section, or a zero-offset section. By invoking the imaging condition in the Fourier integral, $(t-2\tau(x,m)=0)$, the field δp is backpropagated and focused when its time is equivalent to the zero-offset two-way traveltime:

$$I(x) = \frac{-1}{4\pi^2\rho_0}\int_S \mathrm{d}s(m)\int \mathrm{d}\omega(\mathrm{i}\omega)\left[\delta p(m,\omega)B(x,m,\omega) \times \frac{\cos\theta(m)}{c_0(m)}\exp(-\mathrm{i}\omega(t-2\tau(x,m)))\right]_{t=2\tau} \quad [41]$$

The imaging condition makes the frequency integral just a sum over frequency. The integral can be interpreted in two ways. If we fix x, a single point in the image space, the integral sums all $\delta p(m, t = 2\tau(x = \text{constant}, m))$ values in the data space along the two-way traveltime curve from x to all midpoints. For constant velocity, this is a sum over a hyperboloid. If we fix m, the single point in data space $\delta p(m = \text{constant}, t = 2\tau(x, m) = \text{fixed})$ is spread over a surface in x at the distance corresponding to traveltime $2\tau(x, m)$. For constant velocity, this is a spherical shell in image space. This is termed poststack Kirchhoff migration (**Figure 3(c)**) and can be in time or depth, depending on whether we assume straight or curved rays.

For prestack depth migration, we can apply the integral [39] twice and invoke the reciprocity principle, with one surface integral over the shot coordinate and the other over a common receiver coordinate (e.g., Wiggins, 1984; **Figure 3(d)**), to give

$$I(x) = \frac{-1}{8\pi^3\rho_0^2}\int_S \mathrm{d}s(x_\mathrm{s})\int \mathrm{d}s(x_\mathrm{r})\int \mathrm{d}\omega(-\omega^2) \times \delta p(x_\mathrm{s}, x_\mathrm{r}, \omega)B_1(x, x_\mathrm{s}, \omega)B_2(x, x_\mathrm{r}, \omega) \times \left[\frac{\cos\theta(x_\mathrm{s})\cos\theta(x_\mathrm{r})}{c_0(x_\mathrm{s})c_0(x_\mathrm{r})} \times \exp(-i\omega(t-\tau(x,x_\mathrm{s})-\tau(x,x_\mathrm{r})))\right]_{t=\tau(x,x_\mathrm{s})+\tau(x,x_\mathrm{r})} \quad [42]$$

Integrating over the shot surface may seem counterintuitive; however, it is a simple matter to sort the data into receiver gathers. This integral also can be simply rewritten in the midpoint–offset coordinates by substituting [27]. Data manipulations are somewhat easier in midpoint–offset coordinates, and more importantly, the edge effects introduced from the finite apertures in the receiver and shot spaces are mitigated.

1.15.7 Reflection Seismology Examples

Interesting reflection seismology examples abound in a literature that now spans more than four decades. Readers are referred to the *American Association of Petroleum Geologists Bulletin* and the *Geological Society of America Bulletin* for general applications in geology and to *Geophysics* and *Exploration Geophysics* for methodology. The development of deep crustal reflection seismology is documented in the volumes from the proceedings of the International Symposia on Deep Crustal Reflection Profiling, published by the American Geophysical Union and *Tectonophysics*.

We conclude this section by presenting some academic applications of active-source seismic investigations. Many of the Earth's great Cenozoic mountain belts now have one or more deep crustal seismology profiles across them, as do paleomountain belts and modern and ancient extensional terranes. The different types of plate boundary zones have now been studied using reflection and refraction seismology. The few examples we show here are particularly interesting for either their experimental method or their broader Earth science significance.

In Northern Canada, the Canadian Lithoprobe program has imaged a Proterozoic thrust belt to an unusually great depth that shows subducting slab(s) of ocean lithosphere frozen into the Precambrian lithosphere (**Figure 4**; Bostock, 1998; Cook et al., 1999). The seismic data were acquired with Vibroseis™ sources using standard industry reflection equipment and a total recording spread of about 24 km.

This image is extraordinary for a number of reasons. It suggests that thrust stacking of oceanic lithosphere can be a means to stabilize and grow the continents, a long-standing problem in early the Earth's development. This and similar images also suggest that some mountain belts are formed by a process termed wedge tectonics in which some or all crustal layers are thrust upward over a strong crustal wedge and are then eroded. Mantle layers subduct beneath the crustal wedge and can be accreted to the lithosphere inboard of the subduction zone. Another interesting aspect of this image is the appearance of numerous thrust faults extending to the Moho, implying that brittle behavior extended to Moho depths, requiring either very high strain rates, an unusually cold orogen, or unusual crustal rheology. Lastly, teleseismic signals from the Yellowknife array at the eastern edge of the profile have Pds-wave conversions correlated with the mantle reflections in the reflection section. The same structural features are observable over several decades of seismic bandwidth. This suggests that teleseismic-converted wave imaging and reflection seismology can be used jointly for high-resolution imaging of the entire lithosphere.

In the 1990s, the German–Chilean–Bolivian ANCORP program conducted reflection, refraction, and teleseismic experiments from the Pacific coast, across the Andes and the Altiplano, to the Eastern Cordillera at about 21°S latitude. The reflection seismic data were acquired to image the deep crust, with relatively large source–receiver offsets (to ±25 km) and widely spaced (~6.3 km), large explosive shots (ANCORP Working Group, 2003). The reflection section (**Figure 5**) and other geophysical data show a number of features that are interpreted as resulting from fluid-controlled processes. Three prominent bands of reflections appear in the section: (1) The Nazca reflector, (2) the Quebrada Blanca Bright Spot, and (3) bands of reflectors associated with the Altiplano low-velocity zone (LVZ). Most of the Nazca reflector, which extends from 40 to 80 km depth and dips at about 20°, is associated with the interplate shear zone atop the subducting Nazca oceanic crust. Receiver-function imaging has identified the oceanic Moho beneath it. The Nazca reflector gains strength and complexity as it deepens. It is interpreted as first a simple lithologic contrast that changes to a zone of dehydration as the subducting oceanic crust enters the amphibole stability field. The free fluids alter local mineralogy and weaken the overlying mantle. The reflections terminate where dehydration is complete, at about 80–90 km depth. Seismicity is low and somewhat diffuse in much of this part of the subducting plate but resumes further downdip, assumed to result from dehydration embrittlement.

The Quebrada Blanca Bright Spot, which dips westward from the active volcanic front of the Andes to the subduction

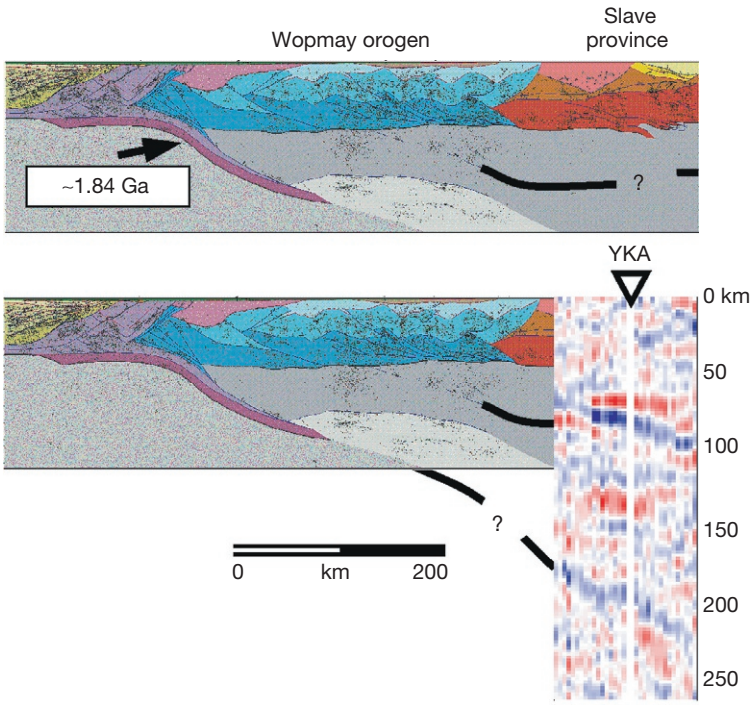

Figure 4 Lithoprobe's time-migrated SNORCLE deep crustal and upper-mantle seismic reflection profile (top and bottom) and receiver functions (bottom) through the Proterozoic Wopmay orogen and Archean Slave Province. The receiver functions made at the Yellowknife (YKA) array show PdS-converted events at the same depths as the vertical incidence reflections (H, and possibly X and L). The profile shows an east-dipping, 1.84-Ga subduction zone in which the subducting oceanic lithosphere appears to be tectonically accreted to the underside of the Wopmay orogen and the Slave Craton. The Moho is relatively flat under the Wopmay orogen with thrust faults soling into the base of the crust. Crustal shortening is accommodated by a succession of west vergent crustal-scale thrusts and duplexes, mantle shortening resulting from subduction with the apparent accretion of some of the subducted oceanic lithosphere to the periphery of the Slave Craton. Reproduced from Cook FA, van der Velden AJ, Hall KW, and Roberts BJ (1999) Frozen subduction in Canada's northwest territories; lithoprobe deep lithospheric reflection profiling of the western Canadian Shield. *Tectonics* 18: 1–24; Bostock MG (1998) Mantle stratigraphy and evolution of the Slave province. *Journal of Geophysical Research* 103: 21193–21200.

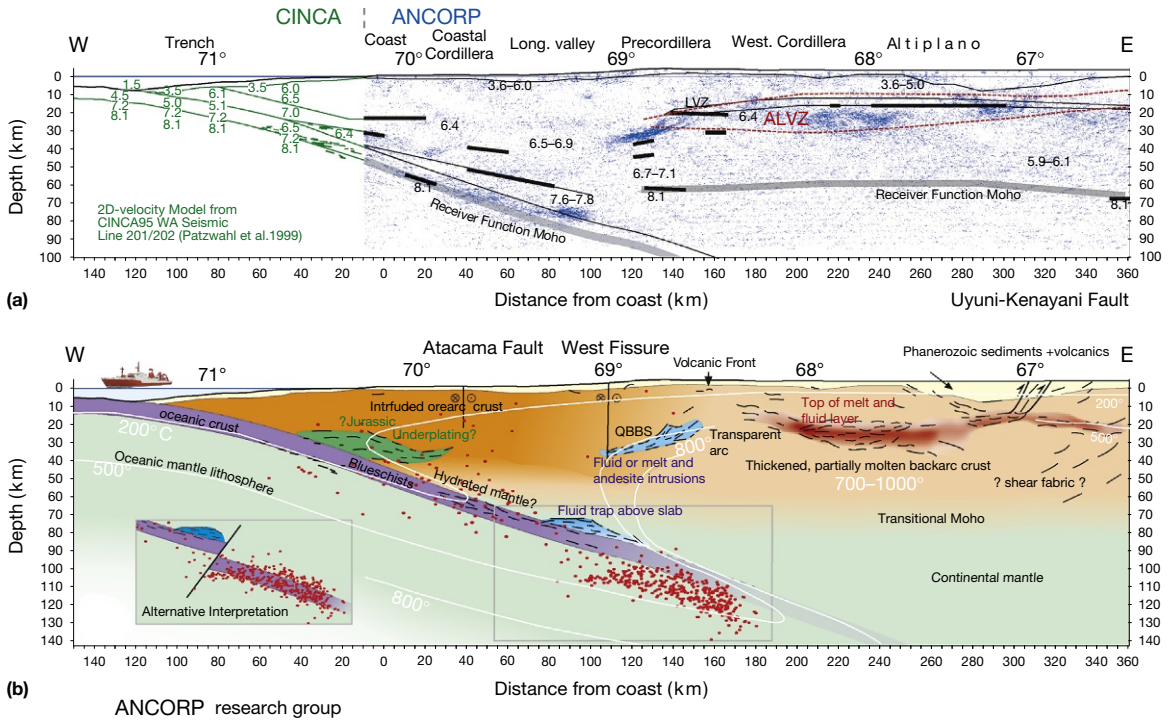

Figure 5 Summary figures showing results from ANCORP (2003) and related experiments across the Andean trench, the Andes, and the Altiplano. (a) The depth-migrated reflection data with seismic refraction and receiver-function results superimposed. The Nazca reflection coincides with the shear zone separating South America from Nazca and is generally aseismic; it is interpreted as a zone of dehydration of the Nazca crust and lithosphere. Seismicity is concentrated deeper and to the east of this reflection and is distributed throughout the upper part of the Nazca Plate as a result of dehydration embrittlement. The Quebrada Blanca Bright Spot (QBBS) reflectors are interpreted as unconnected fluid or possibly melt lenses migrating from the lower crust to the Andean volcanic front. The midcrustal reflectivity beneath the Altiplano is interpreted as the reflection signature from a zone of 20% well-connected partial melt occupying much of the middle crust and corresponding to a zone of low shear-wave velocity identified by receiver functions and a low-conductivity zone from magnetotelluric measurements. (b) An interpretation of all geophysical results including estimated isotherms in the trench region.

zone, shows the strongest amplitude events in the section. These are interpreted as discrete lenses of melt that have migrated from deeper in the subduction system. Interestingly, there is no electrical conductivity anomaly associated with the bright spot, suggesting that the melt lenses are not connected. In contrast, the Altiplano reflectors, although weaker in amplitude, are associated with both a conductivity high and a zone producing large P-to-S conversions in receiver functions. They are interpreted as being from a zone of well-connected pockets of partial melt defining an extensive midcrustal LVZ.

In a surprising application of reflection seismology to physical oceanography, Holbrook et al. (2003) had demonstrated that the temperature–salinity structure of the ocean can be imaged over large areas using CMP reflection surveying (Figure 6). Their data were acquired with a 480 channel, 6 km seismic streamer recording signals from a 140 l air gun array, towed by the *R*/*V* Ewing. Processing the part of the seismic records that had previously been considered water column noise, they identified mixing structures between the cold Labrador Current and the warm North Atlantic Current. This application of reflection seismology to physical oceanography can provide high-resolution details of mixing structures and internal waves and can be used for time-lapse imaging to monitor current changes.

1.15.8 Refraction/Wide-Angle Seismology

There are a number of reviews of methods for wide-angle data analysis: Braile and Smith (1975) demonstrated the amplitude–distance response of 1-D velocity models, stressing the importance of secondary arrivals. Mooney (1983) reviewed methods for calculating synthetic seismograms. Nowack and Braile (1993) reviewed traveltime and amplitude tomography methods in 1-D and 2-D media. Zelt (1999) focused on 2-D traveltime modeling and inversion, as well as model assessment methods. Rawlinson and Sambridge (2003a) presented an overview of traveltime tomography for 2-D and 3-D structure. This set of papers illustrates the evolution in wide-angle data analysis over the past 30 years from an emphasis on forward modeling amplitudes, secondary arrivals, and 1-D and 2-D models to a focus on 2-D and 3-D traveltime automated inversion methods, often using only the first arrivals. This evolution was to a large extent driven by the increase in the typical size of the data set from a few seismograms to hundreds of thousands of traces, combined with a massive increase in computational capability available to researchers. With a small amount of data, the intent was to try to extract as much information as possible. By comparison, the large data volumes today, coupled with a better understanding

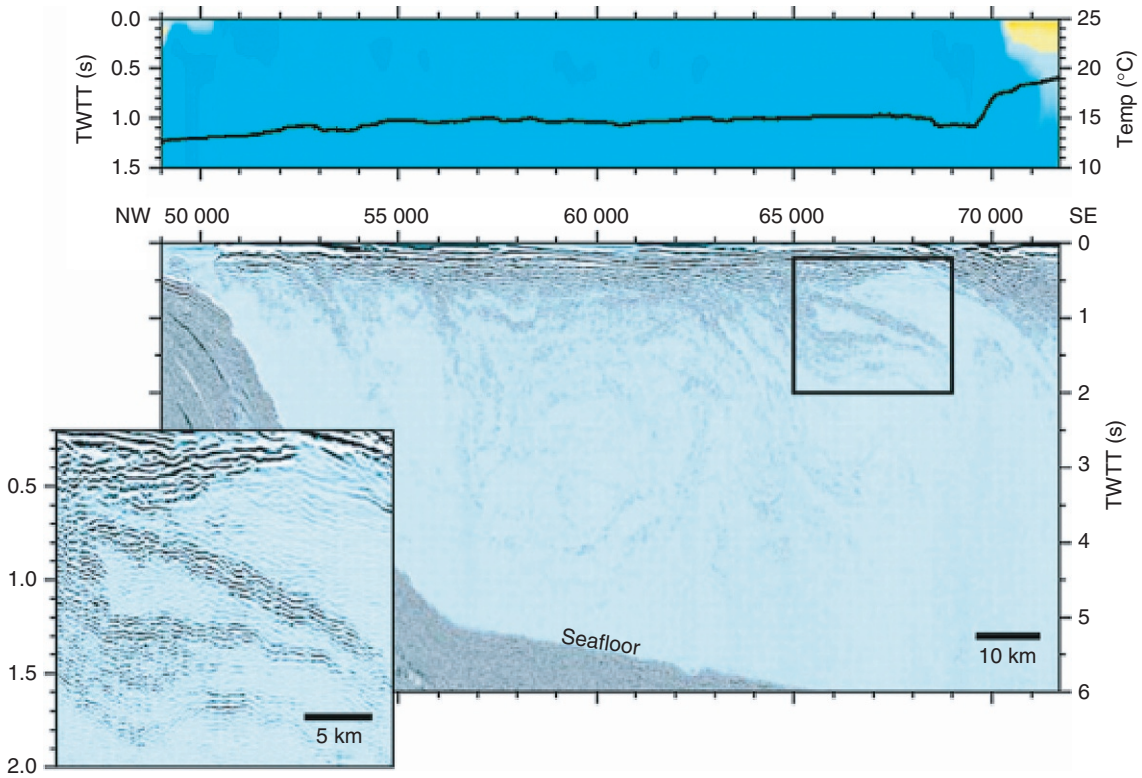

Figure 6 Middle: CMP stacked reflection image of the mixing of the Labrador and North Atlantic Currents made by conventional CMP processing of water column reflections. Previously, events in the water column had generally been considered to be random noise. Holbrook et al. (2003) imaged details of the structure of the mixing of the cold Labrador Current (inset) and the warm North Atlantic Current, with cold water masses descending beneath the warm. Top panel: CMP stacking velocities (color scale: blue, slow minimum 1440 m s^{-1}; red, fast, maximum 1530 m s^{-1}; blue-yellow transition 1503 m s^{-1}) indicating temperature variations in the ocean and intersection of the two currents at CMP 6950. The black line is the sea-surface temperature measured by other means. Middle: from Holbrook WS, Páramo P, Pearse S, and Schmitt RW (2003) Thermohaline fine structure in an oceanographic front from seismic reflection profiling. *Science* 301: 821–824 (http://dx.doi.org/10.1126/science.1085116).

of wave propagation through realistic crustal models, tend to limit wide-angle analysis to the most robust features of the data: traveltimes and often only first arrivals. Recently, there has been a return to using more of the wavefield than traveltimes with 2-D full-waveform inverse methods discussed in Section 1.15.4.

1.15.9 Wide-Angle Seismology Experiments

Wide-angle seismic data have been used to constrain the lithospheric structure of continents, oceans, and their margins for over 40 years. For land experiments, the critical issue is usually the source, in terms of the type, cost, number, and location. Since the seismic waves must propagate ~300 km for crustal and uppermost mantle imaging using first arrivals, a chemical explosive is typically used. The chemicals are normally placed in single or multiple boreholes up to ~100 m deep or at the bottom of moderately deep bodies of water (Jacob, 1975). The objective is to ensure a sufficient cap to avoid releasing energy into the atmosphere and to maximize ground coupling. The total amount of explosives for a single shot is usually in the 50–2000 kg range, depending on the maximum offsets and depths to be investigated (e.g., Kohler and Fuis, 1992). The cost of drilling and explosives usually represents the largest part of the data-acquisition budget, and thus, the total number of sources is often small in comparison with the number of receivers; typically, 5–100 shots are used today. Ideally, the sources should be placed at the ends of the 2-D line and evenly spaced within, unless more resolution is required along a portion of the line. 3-D crustal wide-angle land surveys are relatively rare since the number of sources required to achieve a spatial resolution comparable to a 2-D survey is very high. Typically, the number of sources used in a 3-D land survey means that only large-scale crustal structure will be resolved, and often, 3-D data are a secondary component of an otherwise 2-D survey involving one or more lines (e.g., Kanasewich and Chiu, 1985; Zelt et al., 2006b).

For wide-angle land experiments, typically 100 to >1000 recorders are used, each one being a compact autonomous unit consisting of a digital acquisition system, an accurate clock, and a vertical-component geophone; three-component instruments are often embedded in surveys, but complete three-component surveys are still relatively rare. The sample rate is typically 2–16 ms and lightweight high-frequency geophones with a natural frequency of 4.5–40 Hz are used. Discrete recording windows can be programmed to capture land shots, or continuous recording of up to a few days can capture air gun shots in an onshore–offshore experiment (see later text). The recorders are typically programmed at a central field location and returned for download and clock check after recovery. One important difference between an active geophone deployment and a passive geophone deployment is that many instruments are deployed in 1 or 2 days and are left in the field for only a day to a week. As a result, there is less time available to ensure ideal geophone coupling, and the typical 100 m to 1 km receiver spacing along profiles means it is not possible to always choose ideal site conditions. Thus, modern active experiments rely on a large data volume with little or no site characterization, with a data loss of 5–10% expected due to instrument malfunction, deployer error, site noise, and theft in populated areas.

The experimental setup for a marine wide-angle survey is very different from a land survey. Air gun arrays are the most common source, often the same source being used for simultaneous acquisition of multichannel reflection data by towing a streamer from the same ship. Sometimes, the air gun array will be tuned to a lower center frequency when deep crustal wide-angle data are being collected given that longer source–receiver offsets are sought. Typically 10–100 ocean-bottom seismometers (OBSs) or hydrophones (OBHs) are used to record marine wide-angle data, the former usually consisting of three components and one hydrophone. They may be deployed from the shooting ship or a second ship and are normally programmed to record continuously for a few days and are then recovered by the same ship using a timed release or acoustic signal. The internal workings of an OBS or OBH are similar to a land recorder with respect to memory and an accurate clock. Since the sound source can cycle at a rate of 20 s or less (a common shooting rate for reflection data), previous shot noise generated within the water column can be a major noise source for wide-angle marine data. As a result, a longer shot interval of 60–120 s is used to record wide-angle data only. If both wide-angle and reflection data are sought, either the lines will be collected twice using the short and long shot intervals or a compromise shot interval of 30–45 s is used.

A combined vertical to wide-angle experiment known as an onshore–offshore survey has become quite popular in the past ~15 years. Land stations record marine shots and/or ocean-bottom receivers record land shots (e.g., BABEL Working Group, 1993; Henstock et al., 1997; Morgan et al., 2000; Park et al., 2007). As a result, there is continuous data coverage across a land–water boundary, ideal for studying continental margins. Coincident but independent near-vertical reflection and wide-angle experiments are quite common (e.g., Mooney and Brocher, 1987), but in some modern experiments, both types of data are acquired simultaneously using densely spaced shots and receivers with sufficient offset that deep-penetrating first-arrival refractions are recorded (e.g., Fuis et al., 2001; Lafond and Levander, 1995; Levander et al., 1994). These types of data allow both conventional reflection and wide-angle analysis techniques and wide-angle migration and waveform inversion (both discussed later). Similar experiments, known as deep seismic soundings (DSSs), were once common in Russia and India, but they usually did not use sufficient offsets to observe upper-mantle refractions, Pn (e.g., Kaila and Krishna, 1992). Wide-angle experiments with very long source–receiver offsets (>1000 km) have been used to image deep subcrustal lithospheric and asthenospheric structure (e.g., Gorman et al., 2002), particularly in the former Soviet Union in which peaceful nuclear explosions were sometimes available as sources (e.g., Morozova et al., 1999; Neves et al., 1996; Thybo and Perchuc, 1997).

For upper-crustal and near-surface wide-angle studies, the experimental parameters mentioned previously for whole-crustal studies can be appropriately scaled, although the number of sources and receivers will remain roughly the same. The size of explosive near-surface sources ranges from tenths to tens of kilograms of explosives, and there are many viable nonexplosive sources, such as hammers, weight drops, rifles,

shotguns, and minivibes (e.g., Hole et al., 2006; Hughes et al., 1998; Jarchow et al., 1994; Lanz et al., 1998; Zelt et al., 2006a).

The modeling and inversion algorithms discussed later can be used to help design the optimum survey geometry given particular instrument resources and anticipated geologic structures (e.g., Peirce and Day, 2002).

1.15.10 Data Processing

A major difference between conventional analyses of wide-angle data and reflection data is the use of a model-based approach versus a signal-processing approach for the latter. The reason for this is because it is possible to convert reflection data into a high-resolution, geologically interpretable form, ideally a representation of the primary reflectivity of the Earth. Much of this analysis is only weakly dependent on the velocity structure of the crust. However, for wide-angle data, the primary objective is to determine the velocity structure of the crust and uppermost mantle. Therefore, the analysis of wide-angle data typically includes only a minimal amount of data processing to 'clean up' the data to make it easier to pick arrival times from the seismograms. Band-pass filtering, velocity (frequency–wave number) filtering, trace summing, and deconvolution are sometimes used to remove incoherent and coherent noise and reduce complications from a ringy source, multiple reflections, or previous shot noise, particularly in marine data (Christeson et al., 1999; Nakamura et al., 1987). Except for 1-D modeling of wide-angle data, corrections for elevation and low surface velocities are neglected as they depend on the unknown velocity structure. Instead, most 2-D and 3-D modeling algorithms for wide-angle data allow the known surface topography and bathymetry to be incorporated into the model. If a 1-D velocity model is sought, either as a final result or as a starting model for subsequent 2-D or 3-D modeling, data processing/inversion techniques exist, such as tau-p inversion (e.g., Clayton and McMechan, 1981; Gorman and Clowes, 1999). In some cases, particularly with very laterally heterogeneous near-surface structure, phase identification and arrival picking may be difficult, and a processing technique such as wave equation datuming may prove effective (Hill and Wuenschel, 1985; Larkin and Levander, 1996). For marine data, applying corrections for rugged seafloor topography may be necessary (e.g., Purdy, 1982; Spudich and Orcutt, 1980).

Picking wide-angle arrival times is normally done from shot or receiver gathers, exploiting the lateral coherence of closely spaced traces. Fully automated picking routines are usually not possible because of noise, lateral waveform changes, and onsets of later arrivals buried in the seismic coda. Interactive software is used to pick arrivals 'manually' by eye for each trace, or a representative subset of traces are picked and the intervening picks are determined automatically using a cross correlation scheme (Zelt, 1999). Initially, only the most obvious arrivals are picked, typically the first arrivals. These initial arrivals are used to develop a preliminary model to help identify additional arrivals by overlaying predicted times on the data and then using the new set of picks to further develop the model in a bootstrap fashion. Interpolating traveltime picks across significant gaps will provide an incorrect sense of model constraint and is to be avoided (Zelt, 1999).

Assigning prior uncertainties to the arrival picks avoids over- or underfitting the data and allows the appropriate up- and downweighting of less noisy and more noisy data, respectively, when an inverse method is used (Zelt, 1999). Uncertainties are often assigned qualitatively by inspection, taking into account the data's signal-to-noise ratio and frequency content. Zelt and Forsyth (1994) used an automated scheme involving an empirical relationship between signal-to-noise ratio and pick uncertainty. Another guideline for assigning pick uncertainties is the time differences of reciprocal pairs (Zelt et al., 2006a) or where two profiles intersect (Park et al., 2007). Toomey et al. (1994) estimated picking uncertainties as part of an automated picking routine.

1.15.11 Model Dimension

Up until about 1980, wide-angle data were generally modeled using a laterally homogeneous (1-D) representation of the Earth structure (Mooney, 1983). This simplification allows for a number of efficient forward modeling and linear inversion techniques of the traveltimes and wavefield for velocity as a function of depth, such as the reflectivity method, Herglotz–Wiechert inversion, and tau-p inversion (Aki and Richards, 2002, pp. 413–429; Clayton and McMechan, 1981; Fuchs and Muller, 1971). These inversion techniques assume a monotonically increasing velocity–depth model, which in most tectonic settings is reasonable, but in some cases may be too restrictive, such as in high heat flow regions (Smith et al., 1975; Wenzel and Sandmeier, 1992). If LVZs are involved, wide-angle reflections from the top and bottom of the LVZ can be used to constrain them (e.g., Sain and Kaila, 1996). The 1-D 'reflectivity' method has been very popular because of its ability to provide elastic full-wavefield seismograms. The reflectivity method is also used where the velocity model is weakly 2-D so that a 1-D average for amplitude calculations is acceptable given that typically only the large-scale amplitude trends are modeled (e.g., Benz et al., 1990; Zelt and White, 1995). 1-D modeling can also be used to construct a starting model for 2-D or 3-D analysis. In this case, the 1-D assumption is made for each shot or receiver gather, and the resulting velocity–depth profiles are interpolated to form an initial 2-D model. Alternatively, the traveltime picks from all shots and receivers can be used to derive the best-fitting 1-D model, which is then used as a starting model for 2-D or 3-D inversion (e.g., Zelt and Barton, 1998).

In the late 1970s, asymptotic (i.e., infinite-frequency) ray theory for laterally heterogeneous (2-D) media was adopted for interpretation of wide-angle data, including the calculation of synthetic seismograms (Cerveny et al., 1977; McMechan and Mooney, 1980; Mooney, 1983). This was a significant step forward because it meant that Earth models of arbitrary lateral complexity could be considered, providing the tenants of ray theory were honored, that is, the velocity field varies slowly with respect to the seismic wavelengths involved. Sharp velocity changes are modeled using a velocity discontinuity, that is, a layer boundary, and the application of Snell's law. As a result, 2-D ray theory models are typically composed of one or a few

layers, bounded by smoothly varying interfaces, within which the velocity varies smoothly.

In the 1990s, acquisition of 3-D crustal wide-angle data became quite common, not only particularly in the oceans as 3-D marine surveys have simpler logistics, shallower targets requiring smaller offsets, and hence lower costs (e.g., Toomey et al., 1994; Zelt and Barton, 1998) but also on land (e.g., Zelt et al., 1996) and crossing ocean–continent boundaries in onshore–offshore experiments (Hole et al., 2000a; Morgan et al., 2000). The cost of most 3-D surveys is high, especially if the spatial resolution is to be comparable to a state-of-the-art 2-D survey, and so they are used when 2-D sampling of the target will be insufficient to address the research objectives. Sometimes, relatively sparse 3-D crustal data sets are acquired as a result of a primarily 2-D survey that includes some broadside recordings, that is, shots from one profile recorded by receivers along another profile. The advantage of these types of surveys is that little or no compromise on the quality of the 2-D imaging is necessary but the additional sparse 3-D coverage may reveal structures not present in the 2-D models (e.g., Zelt et al., 2006b).

For a 2-D survey in which the shot and receiver locations deviate significantly from a straight line, it may be necessary to consider 2.5-D modeling, that is, using a 3-D model and 3-D ray tracing and the known topographic and bathymetric surfaces, but keeping the velocity model homogeneous in a direction perpendicular to the main trend of the profile (e.g., Van Avendonk et al., 2004). Given the resolution of most wide-angle velocity models, the degree of profile 'crookedness' must be substantial to warrant 2.5-D modeling (Zelt and Zelt, 1998).

1.15.12 Forward Modeling

The late 1970s saw the introduction of various methods for calculating ray paths and traveltimes in laterally heterogeneous media (2-D and 3-D), thereby establishing the basis of wide-angle data analysis used today. Two end-member approaches to ray tracing were put forward: numerical and analytic. In the former case, the velocity field is specified by a regular (e.g., McMechan and Mooney, 1980) or irregular (e.g., Zelt and Ellis, 1988) grid of nodes, together with a scheme for interpolation between nodes, and a ray is traced by specifying a takeoff angle from a point source and solving a set of ordinary differential equations, the ray-tracing equations (Cerveny et al., 1977). In the analytic case, the velocity field can be specified by a regular (e.g., Chapman and Drummond, 1982; Rawlinson et al., 2001; White, 1989) or irregular (e.g., Spence et al., 1984) grid of nodes, but with a form of interpolation, typically linear, such that the ray paths can be calculated analytically. In practice, the analytic and numeric techniques are often about equally efficient if the analytic method uses a fine mesh of nodes to represent a sufficiently smooth velocity field as dictated by ray theory and if the numeric scheme adjusts the step length according to the velocity gradients (Zelt and Ellis, 1988).

For an arbitrary 2-D velocity model, a nontrivial consideration is the determination of ray takeoff angle from the source such that an arbitrary receiver point is reached or such that a particular layer or interface in the model is sampled. In early algorithms, it was left to the user to determine the necessary takeoff angles through trial-and-error shooting of fans of rays (e.g., Spence et al., 1984). Today, most 2-D ray-tracing codes offer an automatic determination of takeoff angles using a shooting approach and a bisection algorithm to sufficiently refine the takeoff angles so that the receiver points are hit (e.g., Zelt and Smith, 1992). The robustness of the shooting method is critical because the data from receivers for which it is not possible to find rays cannot be used in the forward or inverse modeling. Also, it is important to be sure that an inability to find rays is because of the model, for example, a shadow zone, as opposed to a shortcoming of the shooting algorithm.

To avoid the limitations of shooting, particularly for 3-D models, ray-bending methods were developed (Julian and Gubbins, 1977; Um and Thurber, 1987). In this approach, a ray path connecting a source and receiver is estimated, normally using a 1-D reference model, and the ray path is iteratively updated using Fermat's principle until the minimum-time path is determined. In practice, shooting methods are more efficient and sufficiently robust for 2-D models, whereas bending methods are favored for 3-D models. Zhao et al. (1997) and Chiu et al. (1986) applied bending methods to the inversion of 2-D and 3-D wide-angle data.

In the late 1980s, a new forward modeling approach was introduced in which first-arrival traveltimes are calculated on a fine grid using a finite-difference solution of the eikonal equation (Podvin and Lecomte, 1991; Van Trier and Symes, 1991; Vidale, 1988, 1990). Ray paths are obtained in a second step by following the gradient of the traveltime field. These methods have become very popular and are collectively known as wavefront-tracking methods (also known as eikonal solvers). Reflection ray paths can be calculated in a two-step procedure by calculating downgoing and upgoing wavefronts (Hole and Zelt, 1995). Hole and Zelt (1995) also presented a modification to the Vidale approach, which otherwise breaks down for velocity contrasts of more than ~40%. The advantage of finite-difference methods is that they find the fastest ray between any two points, including the diffracted path in the case of a geometric shadow zone, and they can be very efficient, especially for 3-D models. The disadvantages are they are computationally cumbersome for calculating later arrivals, and they can be inaccurate and/or computationally intensive for high-velocity contrast media. Another potential problem is that the calculated first-arrival time may correspond to a very low-energy arrival, something that may not be recognized in real data. Another type of wavefront-tracking scheme that solves the eikonal equation is the fast marching method, which is computationally efficient and unconditionally stable (Popovici and Sethian, 2002; Rawlinson and Sambridge, 2004; Sethian and Popovici, 1999). Eaton (1993) developed a finite-difference method for anisotropic media.

Nakanishi and Yamaguchi (1986) and Moser (1991) introduced the shortest-path ray-tracing method based on Fermat's principle, which uses a fine network of nodes and graph theory. It is capable of handling arbitrarily heterogeneous media and calculating first arrivals, reflections, and multiples easily. Its advantages over finite-difference methods are robustness and the grid does not have to be rectangular or regular. However, its memory and computation requirements are greater.

Van Avendonk et al. (1998) and Van Avendonk et al. (2001) developed a hybrid of the shortest-path and ray-bending methods building on the work of Moser (1991) and Moser et al. (1992). The hybrid method uses the shortest-path algorithm to find an initial ray path that is close to the minimum-traveltime path and then refines it using a bending method. The result is an efficient and robust algorithm to calculate accurate traveltimes and ray paths for refractions and reflections in 2-D and 3-D media.

1.15.13 Traveltime Inversion and Tomography: Theory and Practical Issues

Today, 2-D and 3-D traveltime inversion and tomography are the central analysis methods applied to crustal wide-angle data. In this section, we present an overview of the mathematical theory and practical considerations of the algorithms in use today. The distinction between inversion and tomography is not well defined in the seismology community. The latter usually implies a uniform, fine-grid model parameterization, in which a smooth model is sought (e.g., Toomey et al., 1994; Van Avendonk et al., 1998; Zelt and Barton, 1998). Any departure from this approach is usually referred to as traveltime inversion (e.g., Rawlinson et al., 2001; Spence et al., 1985; Zelt and Smith, 1992), although the distinction is an arbitrary one, as the mathematical description in the succeeding text shows. Here, we caution the reader that some notation used in reflection seismology is also customarily used in wide-angle seismology, but with different meanings. In this section, L is the ray path (as opposed to wave operator), and G is the matrix of Fréchet derivatives, rather than a Green's function.

The traveltime t between a source and receiver along a ray path L is given in integral form for a continuous or piecewise continuous velocity field $v(\mathbf{r})$ as

$$t = \int_L \frac{\mathrm{d}l}{v(r)} \qquad [43]$$

where $\mathbf{r}$ is the position vector in 2-D or 3-D media. Finding $v(\mathbf{r})$ is a nonlinear inverse problem given the relationship between the measured data (traveltimes) and the unknown model parameters (the velocity field). However, by transforming variables to use slowness $s(\mathbf{r})$, the reciprocal of velocity, instead of velocity as the unknown, a linear inversion problem is created:

$$t = \int_L s(\mathrm{r})\mathrm{d}l \qquad [44]$$

However, the ray path L is also dependent on the velocity (or slowness) model (Figure 2), thus making the inverse problem nonlinear regardless of what form of model variable or parameterization is used.

In global seismology, a 1-D (radially symmetrical) Earth model is often used to predict the ray paths given the relatively small velocity heterogeneities in the mantle, thereby converting the inverse problem into a linear one (e.g., Grand, 1994). In crustal seismology, there is no concept of a reference model that is sufficiently accurate to predict the ray paths in advance given the relatively large velocity heterogeneities that are typically encountered in the crust and uppermost mantle (Figure 7). This means the wide-angle traveltime inverse problem is always treated as nonlinear, in which both the velocity field and ray paths are treated as unknowns to be solved for. This also means the model can be parameterized any number of ways using velocity or slowness and nodes, cells, or splines, since the problem's nonlinearity must be dealt with irregardless of the parameterization. Most often, this means a linearized gradient approach is applied in which a starting model must be provided and both the model and ray paths are updated over a series of iterations with the hope that there will be convergence to an acceptable model.

For virtually all traveltime problems, the model is discretized using cells, nodes, splines, or other interpolating functions; in the latter two cases, the discrete model parameters are the coefficients of the interpolating functions. In the simplest formulation of the tomography problem, the model is parameterized using constant-slowness cells, in which case the equation for the ith data becomes

$$t_i = \sum_j l_{ij} s_j \qquad [45]$$

where l_{ij} is the length of the ith ray in the jth model cell and s_j is the slowness in the jth cell. In vector–matrix form, this is

$$t_i = L\mathrm{s} \qquad [46]$$

Applying a Taylor series expansion to this equation, assuming the ray paths are independent of slowness, and keeping only the linear term yields the perturbation equation

$$\delta t = \mathrm{G}\delta\mathrm{s} \qquad [47]$$

where δt is the data residual or misfit vector equal to the difference between the observed traveltimes and those predicted by a prior model and $\delta\mathrm{s}$ is the difference between the unknown model and the prior model; the unknown model is also called the estimated model. The partial derivative matrix, $\mathbf{G}$, contains the elements $\mathrm{g}_{ij} = \partial t_i / \partial s_j$, and for the constant-slowness cell parameterization, $\mathrm{g}_{ij} = l_{ij}$ or $\mathrm{G} = \mathrm{L}$. In the general case, the elements of the partial derivative matrix are $\mathrm{g}_{ij} = \delta t_i / \delta m_j$ where m_j is the jth model parameter, which could be the velocity at a node or the coefficient of an interpolating function, or the position of an interface within the velocity model (e.g., Zelt and Smith, 1992). In the general case, the perturbation equation becomes

$$\delta t = \mathrm{G}\delta\mathrm{m} \qquad [48]$$

The elements of the partial derivative matrix $\mathbf{G}$ are usually calculated analytically, to avoid the potential inaccuracy of numerical differencing and the extra computation needed to trace additional rays. The approximations involved in the analytic partial derivatives, for example, the stationary ray-path assumption, are typically not a problem since the resultant gradient direction in model space can be improved with each iteration of the nonlinear process.

The perturbation equation is not solved directly because the unknown model parameters are typically under- or mix-determined (Menke, 1989), depending on the model parameterization; with relatively few model parameters, it is possible for the problem to be overdetermined, but even in this case, the perturbation equation is not solved directly because it is wise to

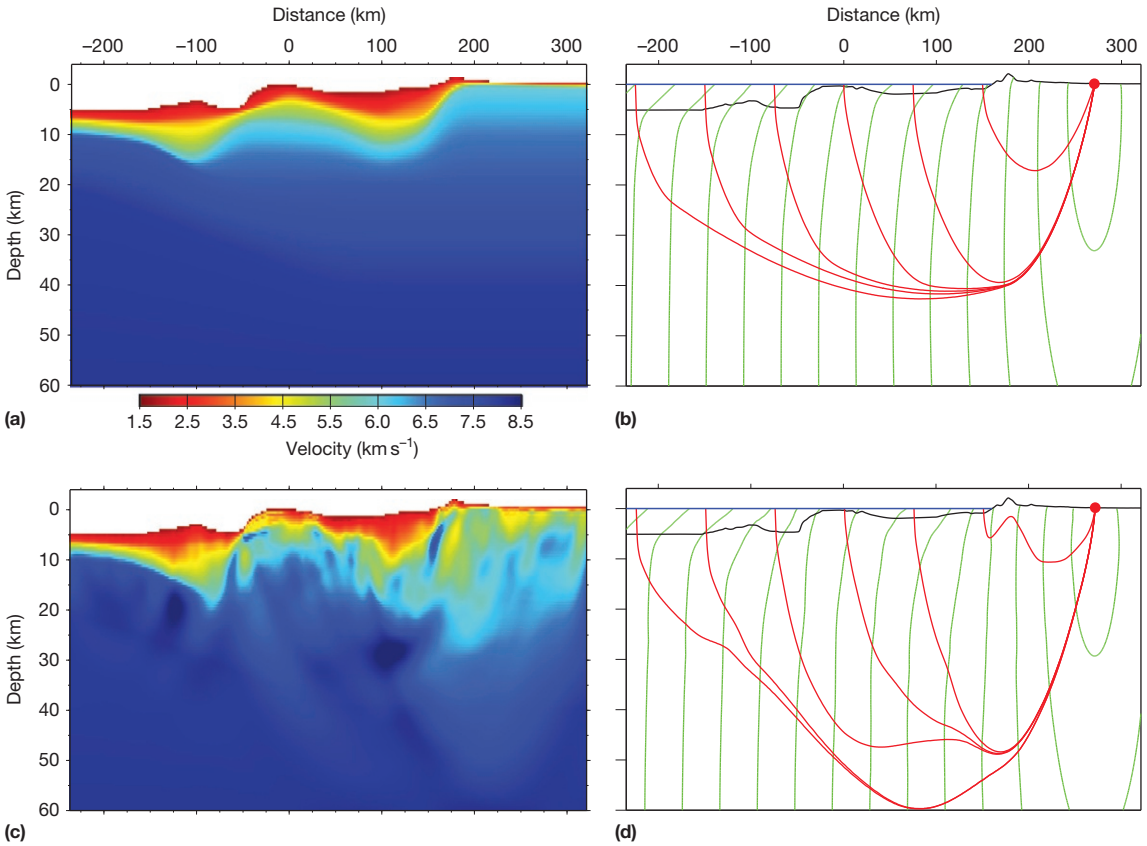

Figure 7 Example from an onshore–offshore study of the Venezuelan margin at 67.5 W (Zelt et al., 2004) to illustrate one aspect of nonlinearity in the inversion of wide-angle data. (a) Starting velocity model that provides an rms traveltime residual with respect to the picked times of ~1.0 s. (b) First-arrival ray paths between shots 75 km apart and receiver ~100 km inland (red) and isochrones (green) for the model in (a). Black line is bathymetry/topography; blue line is sea surface. (c) Final velocity model that provides an rms traveltime residual with respect to the picked times of about ~0.1 s. (d) First-arrival ray paths between the same shots and receiver as in (b) for the model in (c); details the same as in (b). Note the considerable difference between the ray paths in the two models as a result of the heterogeneity in the final model.

constrain the magnitude of the model perturbation to avoid violating the linearization assumption. Thus, regardless of whether the problem is underdetermined or overdetermined, model constraints, in addition to the observed data, are included to stabilize the solution. Since all observed data contain noise, it makes no sense to overfit noisy data, so additional model constraints are required to select one model from an infinite number that will statistically predict the observed data at the equivalent desired misfit according to the estimated noise level. This issue points out the nonuniqueness of all inverse problems involving real data, regardless of whether the system of equations is overdetermined or underdetermined.

The additional model constraint is called regularization (e.g., Scales et al., 1990), and in addition to stabilizing a solution, it is an effective way of steering the solution toward models with desirable predefined characteristics. The regularization is most often in the form of the zero-, first-, or second-order spatial derivatives of the estimated model parameters, or their perturbation from a reference model. This is because it is usually considered desirable to seek an estimated model that is as close as possible to a prior reference model and/or a model that has minimum structure as measured by its spatial derivatives in keeping with Occam's principle (e.g., Constable et al., 1987; Menke, 1989).

The most common forms of regularization in traveltime problems are the minimization of the model's perturbation from a prior model and the minimization of the second-order spatial derivative of either the whole model or its perturbation from a prior model. These are called the smallest and smoothest models, respectively. Any combination of model constraints may be included as a part of the regularization to form the objective function, $\Phi(m)$, where $\mathbf{m}$ is the vector containing the estimated model parameters. The objective function usually measures the square of the data residual vector and the square of the model constraints so that minimizing it leads to a linear system of equations that is amenable to efficient algorithms for their exact or approximate solution. One example of a practical objective function for the traveltime problem is

$$\Phi(\mathbf{m}) = \delta\mathbf{t}^{\mathrm{T}}\mathbf{C}_{\mathrm{d}}^{-1}\delta\mathbf{t} + \lambda\left\{\beta\left[\alpha\left(\mathbf{v}^{\mathrm{T}}\mathbf{W}_{\mathrm{h}}^{\mathrm{T}}\mathbf{W}_{\mathrm{h}}\mathbf{v} + s_Z\mathbf{v}^{\mathrm{T}}\mathbf{W}_{\mathrm{V}}^{\mathrm{T}}\mathbf{W}_{\mathrm{V}}\mathbf{v}\right)\right.\right.$$
$$\left. + (1-\alpha)\Delta\mathbf{v}^{\mathrm{T}}\mathbf{W}_{\mathrm{P}}^{\mathrm{T}}\mathbf{W}_{\mathrm{P}}\Delta\mathbf{v}\right] + (1-\beta)\left[\mathbf{z}^{\mathrm{T}}\mathbf{W}_{\mathrm{P}}^{\mathrm{T}}\mathbf{W}_{\mathrm{P}}\Delta\mathbf{v}\right]$$
$$\left. + (1-\beta)\left[\mathbf{z}^{\mathrm{T}}\mathbf{W}_{Z}^{\mathrm{T}}\mathbf{W}_{Z}\mathbf{z}\right]\right\} \qquad [49]$$

where $\mathbf{m} = \mathbf{v} + \mathbf{z}$ and $\mathbf{v}$ and $\mathbf{z}$ are vectors containing the estimated model parameters defining the velocity (or slowness)

field and the depth of interfaces; Δv is the velocity perturbation vector equal to $\mathbf{v}-\mathbf{v}_0$, and $\mathbf{v}_0$ is the reference velocity model vector. $\mathbf{C}_d$ is the data covariance matrix containing the estimated pick uncertainties, providing the appropriate upweighting and downweighting of the low- and high-noise data, respectively. $\mathbf{W}_h$ and $\mathbf{W}_v$ are the horizontal and vertical roughness matrices containing the second-order spatial finite-difference operators that measure the roughness of the velocity field in the horizontal and vertical directions, respectively; $\mathbf{W}_p$ is the velocity perturbation weighting matrix, which is a diagonal matrix containing the weights applied to the perturbation between each estimated and reference velocity model parameter; $\mathbf{W}_z$ is the interface roughness matrix containing the first-order spatial finite-difference operators that measure the variation of the interfaces.

When applying derivative operators to the velocity field, it is common to use different operators to measure the horizontal and vertical structure and weight these differently, since one expects the Earth to contain more structure vertically than horizontally. Any or all of these operators may be normalized by the reference model values so that relative quantities are penalized as opposed to absolute values (e.g., Toomey et al., 1994). In addition, the operators can be weighted according to their spatial position, for example, penalize structure more in the deep portion of the model versus the shallow portion since with wide-angle data, one would generally expect decreasing resolution with depth. The relative weight of each term in the objective function is determined by the free parameters λ, β, α, and s_z. The inversion is stabilized by systematic reduction of the overall amount of regularization, controlled by λ, allowing long-wavelength structure in the initial iterations and progressively finer model structure in later iterations (e.g., Zelt and Barton, 1998).

Minimizing the objective function with respect to the unknown model parameters ($\mathbf{v}$ and $\mathbf{z}$) leads to a system of linear equations that may be very large, depending on the number of data and model parameters. By today's standards, a small problem would involve on the order of 10^3, or less, data and model parameters, and a large problem would involve 10^5, or more, data and model parameters; the former will likely be 2-D problems, and the latter will be 3-D.

The example objective function can be simplified or slightly modified to correspond to those used in most of the popular traveltime inversion and tomography algorithms. For example, the Zelt and Smith (1992) inverse method includes only perturbation constraint on the velocity and interface parameters with respect to the model from the previous iteration; this is the classical damped least-squares solution (Menke, 1989). The Zelt and Barton (1998) regularized tomographic method includes only smoothness constraints on the velocity field. Thus, these two algorithms can be viewed as end-members of the same regularized inverse approach we have presented, and most algorithms in use today fall somewhere in between. The main differences between the algorithms discussed in the next section lie not just in the details of the objective function, but more so in the form of model parameterization, forward calculation, and the types of arrivals considered.

If the linear system is large, it will typically be very sparse with 99.9% or more zero elements. In this case, it can be solved efficiently using an iterative, sparse linear-system solver, for example, the LSQR variant of the conjugate gradient algorithm (Nolet, 1987; Paige and Saunders, 1982). Another effective approach is the subspace method, particularly for mixed-parameter problems (Rawlinson et al., 2001). If the linear system is relatively small, it can be solved directly using standard matrix inversion routines, such as LU decomposition (Press et al., 1992).

Including both velocity and interface parameters in a single inversion scheme makes the problem significantly more complicated. There will be more model nonuniqueness because of trade-offs between the two parameter types, and more subjective prior information will be required in order to deal with the increased ambiguity (**Figure 8**). Also, more testing will be required to ensure that the trade-offs are fully understood.

When regularization is applied to the estimated model parameters or their perturbation from a fixed reference model, it is called a 'jumping' strategy (the former strategy is a special case of the latter in which the reference model is zero); when it is applied to the perturbation between the estimated model and the model from the previous iteration, it is called 'creeping.' The rationale for jumping is that the final model will be less dependent on the starting model since the model constraints are relative to a fixed model at each iteration and not an intermediate model encountered along the path in model space between the starting and final models. Creeping is used when the starting model and intermediate models are deemed to be significant and there is a desire for the final model to represent the end of a series of related models. The jumping strategy is more objective, whereas creeping allows the solution to be steered more easily to a desired result.

Almost all traveltime inversion and tomography algorithms today employ a jumping strategy (Shaw and Orcutt, 1985). The Zelt and Smith (1992) algorithm uses creeping to achieve what has been described as a method for automated forward modeling.

Assuming uncorrelated, Gaussian picking errors and a model parameterization that does not limit the degree to which the observed data can be matched by the predicted data, a final model should be chosen that provides a normalized misfit, χ^2 (Bevington, 1969), of one:

$$\chi^2 = \frac{1}{N}\left[\delta \mathbf{t}^{\mathrm{T}} \mathbf{C}_{\mathrm{d}}^{-1} \delta \mathbf{t}\right] \qquad [50]$$

where N is the number of data. A model that provides a χ^2 value less than 1 means the observed data are being overfit, and therefore, the noise in the data is also being fit. Although the χ^2 criterion is a good rule of thumb, there are several reasons why it should not always be followed strictly. First, traveltime picking errors of wide-angle data are likely never uncorrelated because each trace is usually picked from a shot or receiver gather by considering the correlation of waveforms adjacent to the trace being picked, either by eye or by using a cross correlation picking algorithm (Zelt, 1999). Second, for relatively sparse wide-angle data from a region with strong lateral heterogeneities, it may be necessary to use so many independent model parameters in order to achieve $\chi^2 = 1$ such that the constraint on some parameters is unacceptably small, in which case fewer parameters and a χ^2 value greater than one may be preferable (Zelt, 1999). An inability to reach $\chi^2 = 1$

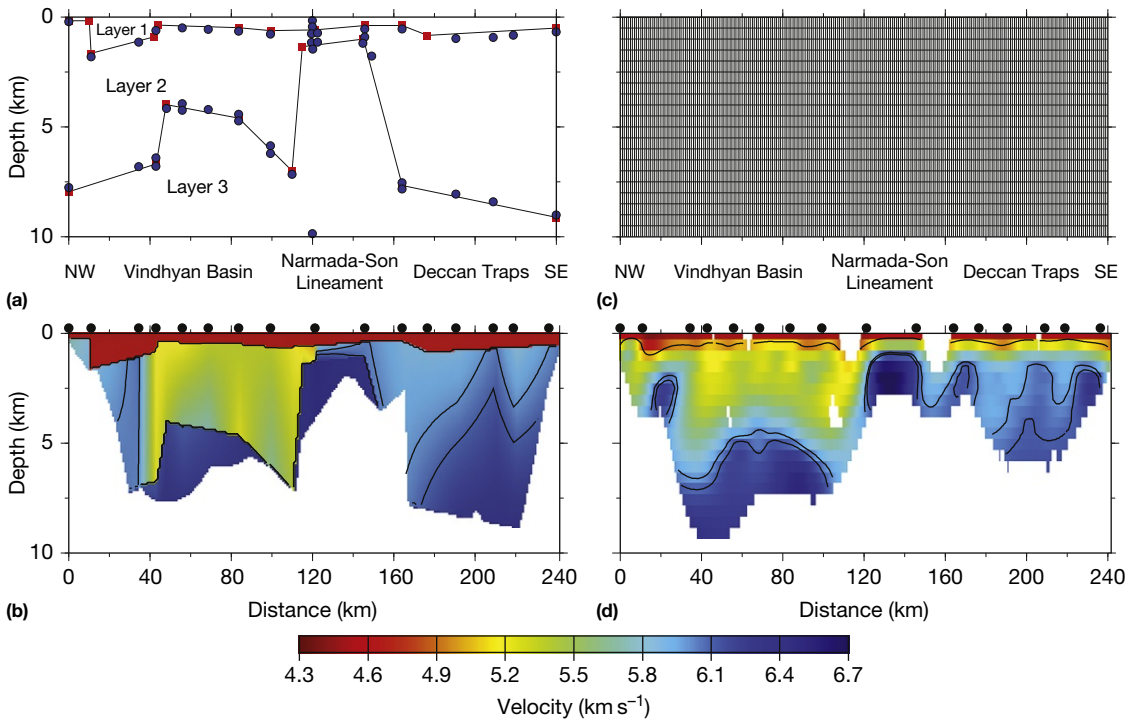

Figure 8 Example from Central India across the Narmada–Son lineament of applying two different traveltime inversion algorithms to the same wide-angle data (Zelt et al., 2003). (a) Model parameterization using the Zelt and Smith (1992) algorithm; there are 43 velocity nodes (blue dots) and 21 interface nodes (red squares). (b) Velocity model corresponding to parameterization in (a). (c) Model parameterization using the Zelt and Barton (1998) algorithm; there are 7018 slowness cells. (d) Velocity model corresponding to parameterization in (c). Only those portions of the models sampled by ray paths are shown. Isovelocity contours of 5.0 km s^{-1} (black) and 6.0 and 6.1 km s^{-1} (white) indicated. Shot point locations (black dots) and geologic features labeled above the models.

may be because of picking inconsistencies of reciprocal pairs, or where two profiles intersect; in either case, the inconsistencies should either be corrected or be used as the basis for assigning the pick uncertainties in the first place (e.g., Park et al., 2007; Zelt et al., 2006a).

Objective functions using L_p-norms with $p < 2$ may be desirable because the solutions will be less influenced by outliers. Iteratively reweighted least squares (IRLS) is a method for approximating the use of an L_p-norm (Scales et al., 1988). Since it is an iterative approach, it can be incorporated into a nonlinear traveltime algorithm with virtually no additional computation because there is already a need for an iterative solution. IRLS is not commonly used in wide-angle traveltime inversion probably because outliers are unlikely when picking traces within gathers, as opposed to individual seismograms as in earthquake seismology.

Global optimization (GO) methods are well suited to very nonlinear problems since their dependence on the starting model is small or none at all (Sen and Stoffa, 1995). However, they are computationally demanding and limited to problems in which the forward calculation is very quick and there are relatively few model parameters. This means GO is not commonly applied to fine-grid traveltime inversion problems, except to find a suitable starting model for a linearized gradient method. Pullammanappallil and Louie (1994) and Boschetti et al. (1996) applied GO schemes to small 2-D traveltime problems.

1.15.14 Traveltime Inversion and Tomography: Algorithms

Up until the 1990s, 2-D ray-tracing and traveltime forward modeling through trial-and-error means, often supplemented by comparisons with synthetic seismograms, was the most common method for the analysis of wide-angle data. Popular algorithms were those of Cerveny et al. (1977) and McMechan and Mooney (1980). Trial-and-error forward modeling is still used today, at least in part because of a sense that either high data quality, fine spatial sampling, or relatively simple geology is needed in order for inverse methods to work (e.g., Grad et al., 2006).

The advantages of inversion over forward modeling include the ability to (1) explore model space more thoroughly to better understand what structure is required by the data and what structure is consistent with the data, that is, model nonuniqueness; (2) quantify model errors and resolution; (3) handle larger data sets; and (4) fit the data appropriately given the data uncertainties. The Zelt and Smith (1992) algorithm allows for a compromise approach, best described as automated forward modeling, given the ability to focus on selected model parameters, as opposed to the entire model, as would be the case in trial-and-error forward modeling. The algorithm's inverse mode can be used to quickly determine the selected model parameter values so as to best satisfy the data from all

shots and receivers simultaneously, usually within a few iterations. Thus, this algorithm combines the parameter-selective aspect of forward modeling with the speed of inversion. In the remainder of this section, we briefly describe many of the algorithms available today, each with its own capabilities and limitations. There is likely a suitable traveltime inversion or tomography algorithm for just about every type of wide-angle data set.

Within the Eastern European community, methods for the analysis of wide-angle traveltime data have been developed that have not been adopted worldwide (e.g., Ilchenko, 1985; Pavlenkova, 1982). They share some characteristics with the algorithms used primarily in the engineering and petroleum industry for near-surface studies and refraction statics, for example, the generalized reciprocal method (Palmer, 1981), but they are rarely applied to crustal data and therefore will not be discussed here. Beginning in the 1980s, formal inverse theory was first applied to 2-D wide-angle traveltime inversion. About 10 years earlier, it had been applied to earthquake traveltime data to derive 3-D velocity models using only first arrivals (Aki and Lee, 1976; Crosson, 1976). Applying inversion to wide-angle data was delayed by the issues of data sparsity (e.g., typically only a few shots and/or receivers) and the desire to use both first and later arrivals (e.g., intracrustal and crust–mantle reflections and later refracted arrivals). Modeling later arrivals means having to include interfaces in the model parameterization and the resultant complexity of dealing with a mixed inverse problem. Some of the earliest published 2-D traveltime inversion algorithms were presented by Firbas (1981) and White (1989), which used a regular grid and only first arrivals, and Spence et al. (1985) and Huang et al. (1986), which allowed an irregular model grid and later arrivals.

In the 1990s, many 2-D and 3-D traveltime inversion and tomography algorithms were developed. We briefly describe the key features of the more widely used and innovative algorithms. Lutter and Nowack (1990) and Lutter et al. (1990) developed a 2-D inversion algorithm using a regular grid of nodes and numerical ray tracing that allows for the independent inversion of first arrivals and reflections for velocity and interface geometry, respectively. The Zelt and Smith (1992) 2-D algorithm is the exact opposite in many respects. An irregular grid of velocity and interface nodes can be used, and any type of refracted or reflected arrival can be inverted simultaneously for velocity and interface geometry (**Figure 8**). As mentioned earlier, the inversion can be applied to any subset of the total model parameters, facilitating an automated forward modeling approach and making it straightforward to incorporate prior information. Zelt (1994) and Clowes et al. (1995) used the Zelt and Smith (1992) 2-D algorithm to simultaneously invert refraction and reflection times from a network of 2-D profiles such that the model parameters at the intersection points were linked to ensure consistency. This approach can be used to infer 3-D structure from 2-D data and develop a starting model for the 3-D inversion of in-line and offline data (e.g., Zelt et al., 1999).

Hole (1992) developed a widely used 3-D first-arrival tomography algorithm using the Vidale (1990) forward modeling scheme and backprojection to solve for a smooth velocity field. Hammer et al. (1994) developed a 3-D first-arrival tomography algorithm specially suited to sparse data using a spectral, continuous function model parameterization. Toomey et al. (1994) developed a 3-D first-arrival tomography algorithm to obtain a smooth velocity field in which the velocity grid is 'draped' from an irregular bathymetric surface by vertically shearing the columns of nodes to accurately model the seafloor relief. Vertically sheared grids are particularly important for marine data, especially at mid-ocean ridges, where a large velocity discontinuity may exist. Forward modeling through this type of parameterization is straightforward using the shortest-path method (Toomey et al., 1994). Similar algorithms with sheared grids have been developed by Van Avendonk et al. (1998) and Korenaga et al. (2000), although they are limited to 2-D models, but include reflections and use the hybrid shortest-path/bending scheme described earlier. The main difference between the Van Avendonk et al. (1998) and Korenaga et al. (2000) algorithms is the former uses first arrivals that can turn above or below a reflecting interface at which there is no velocity discontinuity, whereas the latter only uses first arrivals that turn above the reflecting interface.

Lailly and Sinoquet (1996) developed a 2-D algorithm for inverting reflection times for a smooth velocity and interface model using the wavefront-tracking method of Podvin and Lecomte (1991). Zelt and Barton (1998) developed a 3-D first-arrival tomography algorithm using smoothing regularization and compared the results with those from the backprojection method of Hole (1992). The results showed that for the same level of fit to the data, regularized inversion can provide a smoother model. Zelt et al. (1999) developed a 3-D simultaneous refraction and reflection tomography algorithm solving for smooth velocities and multiple interfaces. McCaughey and Singh (1997) and Hobro et al. (2003) developed related 2-D and 3-D simultaneous refraction and reflection tomography algorithms that solve for smooth velocities and interfaces with the allowance for discontinuities across the layer boundaries.

Most of the algorithms described earlier are fairly general-purpose in nature and follow more or less from the objective function presented in the previous section. However, many more specialized algorithms have been developed. We describe a few of those here to give a sense of what is possible. Hole et al. (1992) developed an algorithm for determining a 3-D interface with known velocities above and below using first arrivals. Zhang et al. (1998) used the shortest-path method to develop a 2-D algorithm for refraction and reflection tomography in which only refracted arrivals originating above the reflecting interface are considered. A novel aspect of their approach is the inversion of traveltime curves instead of points, specifically average slowness and apparent slowness. They claim this balances the contribution from short and long ray paths and enhances resolution and convergence speed (Zhang and Toksöz, 1998). Rawlinson et al. (2001) and Rawlinson and Sambridge (2003b) developed an algorithm for the inversion of refraction and reflection times using a 3-D multilayered model parameterization. Interfaces are defined by a nonuniform node distribution, and velocities vary linearly with depth so ray paths are calculated analytically as piecewise circular arcs

using a shooting method. Trinks et al. (2005) presented a method for simultaneous refraction and reflection inversion using a 2-D layered model parameterization, which adapts to nonuniform ray coverage such that the cell size is inversely proportional to the local ray density.

1.15.15 Amplitude Modeling

The earliest analysis of crustal wide-angle data involved modeling the amplitudes, as well as the traveltimes, of the identifiable arrivals. In part this was because shots and receivers typically were so few that amplitudes were used to extract more information from the data than just using the traveltimes alone. Two of the most common methods used for amplitude modeling are the reflectivity method (Fuchs and Muller, 1971) and asymptotic ray theory (Cerveny et al., 1977). The former has the advantage of including the complete elastic wavefield for a 1-D model. The latter has the advantage of being applicable to laterally inhomogeneous (2-D) models. The drawbacks of ray methods are their infinite-frequency approximation and the need to specify the ray paths for each arrival type being modeled. These disadvantages are typically not a serious problem with crustal data, since it is usually only the large-scale amplitude trends of a few arrival types, such as the primary refractions and reflections, which are modeled.

To overcome some of the limitations of asymptotic ray theory, ray-based methods that incorporate finite-frequency effects were introduced, such as Gaussian beams (Cerveny et al., 1982; Weber, 1988) and Maslov theory (Chapman and Drummond, 1982). These methods can accurately predict the frequency-dependent amplitudes associated with triplications, diffractions, and geometric shadow zones. However, these methods have never experienced widespread use in crustal seismology because they lack the simplicity and predictability of asymptotic ray theory. Full-wavefield acoustic and elastic 2-D finite-difference algorithms (e.g., Levander, 1988; Robertsson et al., 1994) have been applied in a few crustal studies. Their heavy computational demand has meant that only a few simulations are typically run for the purpose of visual comparison with the observed seismograms (e.g., Gorman et al., 2006; Lendl et al., 1997; Parsons et al., 1996), although in the future, they will likely become more commonplace.

Although traveltime data are relatively insensitive to vertical velocity gradients and velocity discontinuities, such features may be well constrained by amplitude data (Braile and Smith, 1975). However, full-wavefield studies using models with fine-scale structure that is not resolved by traveltime data show that it can have a significant effect on wide-angle amplitudes (Lendl et al., 1997; Levander and Holliger, 1992) as will be discussed later. Thus, only the large-scale amplitude trends of primary arrivals should be modeled (e.g., Zelt and Forsyth, 1994). Velocity gradients and discontinuities derived through amplitude modeling may be used as constraints during traveltime inversion (e.g., Zelt et al., 1993). For amplitude modeling, it is common to plot synthetic seismograms, in which case the same trace spacing and amplitude scaling should be used for the synthetic and real data (e.g., Grad et al., 2006). A comparison of the observed and calculated amplitude–distance curves for individual phases allows a more quantitative comparison (e.g., Zelt and Forsyth, 1994; Zelt and White, 1995). As the number of shots and receivers used in typical wide-angle experiments has increased dramatically over the past 20 years, the resolution from traveltime data alone has also greatly improved. For this reason, and given the appreciation of the effects of fine-scale structure (Section 1.15.17), amplitude modeling is often ignored today.

1.15.16 S-Waves, Density, Attenuation, and Anisotropy

The majority of crustal wide-angle seismic studies today use only P-wave arrival times to constrain P-wave velocity structure. This is because P-wave arrival times are almost always the most reliable feature that can be extracted from crustal wide-angle data and their constraint on P-wave velocity is probably the most robust data–model–parameter relationship. Second, there is a sense that P-wave velocity models are the most important in terms of addressing the key geologic and tectonic questions in most crustal studies, although this may be a perception driven by the first reason. Although rare today, studies that go beyond the determination of 2-D and 3-D P-wave velocity models will likely become more common in the future given the need to justify new data acquisition and analysis when so much good data already exist from many sites around the world.

S-waves and converted phases are sometimes recorded well in wide-angle experiments, even by vertical-component geophones. This allows S-wave velocity models to be developed, typically using the same traveltime modeling and inversion algorithms described earlier. When combined with P-wave models, Poisson's ratio can also be estimated. Using S-wave velocities or Poisson's ratio in addition to P-wave velocities narrows the range of possible rock types in an interpretation (Christensen, 1996). Examples of using S-waves from wide-angle surveys include Gohl and Pedersen (1995), Carbonell et al. (1996), Musacchio et al. (1997), Darbyshire et al. (1998), Stoerzel and Smithson (1998), and Fernandez-Viejo et al. (2005).

In theory, rock densities could be inferred from amplitude modeling, but for reasons already discussed, amplitude modeling of wide-angle data is no longer common. Full-waveform modeling or inversion (discussed later) could be used to infer densities more reliably, but the typical procedure is to infer densities from P-wave velocities based on lab and field data compilations (Barton, 1986; Christensen and Mooney, 1995) in order to reduce the number of independent model parameters. It is fairly common to perform gravity modeling after obtaining a P-wave velocity model from wide-angle data, deriving the initial density model by converting the P-wave velocities to densities using an empirically derived velocity–density relationship (e.g., Christeson et al., 2001; Zelt and White, 1995). Brocher (2005) presented an empirical velocity–density relationship based on extensive compilations of velocity–density data.

The attenuation of seismic waves through anelasticity is a poorly understood phenomenon. The dimensionless quantity Q is a measure of the anelasticity experienced by seismic waves,

and as such, its value can be spatially mapped using seismic data. The two methods commonly used to estimate Q from seismic data involve modeling amplitudes directly or using spectral ratios. Amplitude methods should be viewed with caution for the reasons already stated regarding amplitude modeling. Estimates of Q from wide-angle data are rare but have been made by Braile (1977) and White and Clowes (1994) using amplitude methods, by Hashizume (1979), Zelt and Ellis (1990) and Wilcock et al. (1995) using spectral ratios, and by Li et al. (2006) using both methods on the same data.

Anisotropy estimates from wide-angle data are also rare but are most common in oceanic-crust and upper-mantle studies (e.g., Caress et al., 1992; Dunn and Toomey, 2001). One problem is that multicomponent crustal data are rarely recorded. Stoerzel and Smithson (1998) estimated crustal anisotropy from shear-wave splitting using three-component wide-angle data. The isotropic assumption made in the vast majority of wide-angle lithospheric studies has rarely been questioned or tested, but it may be an important effect, particularly in the sedimentary section and upper mantle. Its importance in 2-D and 3-D studies will depend on the type of anisotropy involved. For example, the effect of anisotropy due to subhorizontal fabric or layering could be significant when modeling coincident wide-angle and near-vertical data (Godfrey et al., 2002; Jones et al., 1999). From lab studies, Christensen and Mooney (1995) showed that anisotropy from preferred mineral orientation is likely to be most significant, as much as 10% or more, in upper and midcrustal metamorphic rocks. Sroda (2006) reported 8–10% azimuthal anisotropy for P-wave velocity in the upper crust using profiles of different orientation.

1.15.17 Fine-Scale Heterogeneities

Full-wavefield studies using models with wavelength- or subwavelength-scale heterogeneities have shown that the traveltimes, amplitudes, and wavefield can be significantly effected (e.g., Levander and Holliger, 1992; Muller et al., 1992), raising questions concerning the accuracy of results obtained using ray and wavefront-tracking methods. For traveltimes, there may be a structural form of anisotropy if there is a preferred orientation of the heterogeneities. Even without a preferred orientation, the traveltimes will likely not correspond to the bulk velocity, but will be biased toward a higher velocity when using first-arrival times. Either way, traveltime methods will still constrain large-scale heterogeneities, at least in a relative sense, but the absolute velocities may be biased with respect to the bulk velocities depending on the nature of the fine-scale structure and the seismic wavelengths.

Even more so than the traveltimes, the amplitudes and wavefield can be significantly altered depending on the nature of the fine-scale structure (Lendl et al., 1997; Levander and Holliger, 1992). For this reason, only the large-scale trend of amplitude-versus-offset variations or the overall relative amplitudes of different arrival types should be modeled when using velocity models derived from infinite-frequency methods (e.g., Zelt and Forsyth, 1994; Zelt and White, 1995). Methods for estimating stochastic parameters that describe the fine-scale structure have been developed (Poppeliers and Levander, 2004). This information can be used to add a stochastic fine-scale structure to a long-wavelength model derived from traveltimes and thereby allow a comparison between the observed and predicted seismograms using full-wavefield methods. Although usually limited by the computational requirements of full-wavefield methods, some trial-and-error forward modeling may be applied to refine the short- or long-wavelength model parameters (e.g., Gorman et al., 2006; Lendl et al., 1997). Alternatively, it may be possible to estimate the fine-scale structure deterministically given sufficiently high-quality data using full-wavefield inversion techniques (**Section 1.15.21**).

1.15.18 Joint Inversion

Wide-angle data can be jointly inverted with other data that depend on P-wave velocity. Coincident near-vertical reflection data can be used in several ways (Zelt, 1999). From stacked data, the reflector geometries and interval velocities can be used as prior information in the regularization to constrain a layered velocity model (e.g., Bosch et al., 2005). Alternatively, arrivals in prestack reflection data can be picked and inverted jointly with the wide-angle data. This approach will provide the most thorough use of the reflection data in terms of additional model constraint, but it is often difficult to pick weak events in prestack data. The most common approach is to pick reflections from a stacked reflection section and invert these data simultaneously with the wide-angle data by modeling zero-offset reflections (e.g., McCaughey and Singh, 1997; Zelt et al., 2003). There are potential pitfalls when using coincident reflection data: First, the near-vertical reflection event may be incorrectly correlated with the corresponding wide-angle event or layer boundary; Jaiswal et al. (2006) presented a way to avoid this problem. Second, as previously mentioned, errors and model distortion will occur if there is transverse isotropy, since wide-angle data are primarily sensitive to horizontal velocities and near-vertical reflection data are primarily sensitive to vertical velocities (Godfrey et al., 2002; Jones et al., 1999).

The second type of data that can be jointly inverted with wide-angle data in a straightforward manner is local and regional earthquake body-wave arrival times. An algorithm to jointly invert active and passive data needs to be 3-D and needs to be able to determine earthquake hypocenters in addition to velocities, either simultaneously or by iterating back and forth between locations and velocities. Benz et al. (1996), Symons and Crosson (1997), and Ramachandran et al. (2005) each developed similar algorithms to simultaneously invert active and passive data; the former used the forward calculation method of Podvin and Lecomte (1991), while the latter two used the Vidale (1990) scheme. Hole et al. (2000b) advocated a nonsimultaneous approach in their determination of 3-D velocity and hypocenters using active and passive data.

The close relationship between seismic velocity and density (Barton, 1986; Brocher, 2005) lends gravity data to a joint inversion with wide-angle data. Nielsen and Jacobsen (2000)

used the Zelt and Smith (1992) algorithm as the basis for a simultaneous inversion of refraction and reflection times with gravity data to derive a layered 2-D crustal model. Korenaga et al. (2001) carried out a joint inversion of traveltime and gravity data in which error propagation from the velocity model to the predicted gravity anomalies was taken into account. Roy et al. (2005) jointly inverted first arrivals and gravity data using a global optimization scheme to derive a smooth 2-D layered model. 3-D velocity and density are jointly inverted by Parsons et al. (2001). One important issue in joint seismic-gravity inversion is whether the coefficients of the velocity–density relationship are fixed or determined as part of the inversion.

1.15.19 Model Assessment

Model assessment is used to explore nonuniqueness, resolution, and model errors. Different assessment techniques will be appropriate depending on the type of data and model parameterization. Linear methods assume it is valid to consider only a local neighborhood of the final model within which the model–data relationship is linear. Nonlinear methods involve additional nonlinear inversions of the real data and synthetic data using the true source–receiver geometry of the experiment. The former methods tend to be quick and easy to apply, although potentially less reliable depending on the nonlinearity of the problem. The latter methods tend to be computationally intensive. Zelt (1999) and Rawlinson and Sambridge (2003a) described many of the techniques in use today; we will highlight only the most popular. Zelt et al. (2006a) applied several different techniques to the same 3-D data set.

The simplest form of model assessment is to examine the ray-path coverage, through either plots of ray paths or 'hit counts' (the number of rays sampling each model cell or node). These can be misleading since a nonuniform distribution of ray angles may provide less independent model constraint than expected from the number of rays alone. Toomey et al. (1994) used a measure called derivative weight sum (DWS) equal to the sum of the partial derivatives for each model parameter. This is more meaningful than hit count since it weights the contribution from each ray according to the parameter's sensitivity to that ray. However, it also fails to account for the degree of independence within the ray-path set. Other common linear assessment measures include the diagonals of the posterior resolution and covariance matrices (e.g., Zelt and Smith, 1992). These are more precise measures since they account for the independence of the ray-path set, but they are best used in a relative sense as opposed to absolute sense, since they do not account for the nonlinearity of the problem. Rows of the resolution matrix, known as resolution kernels, provide a spatial sense of the averaging or smearing of the true structure by the model (e.g., White, 1989; Zelt, 1999). Probably the most precise linear assessment method uses singular-value decomposition (SVD) since it is able to quantify the nature and degree of model constraint through construction of an orthogonal set of basis vectors that span model space, each with a specified weight in the model reconstruction (e.g., White, 1989). However, SVD is generally limited to relatively small problems, although approximate methods for large problems have been developed (e.g., Scales, 1989).

A parameter-selective algorithm such as the Zelt and Smith (1992) approach allows for a nonlinear assessment of the error bounds and spatial resolution for a single model parameter, or set of parameters (Zelt, 1999). In these tests, the real data and synthetic data are inverted in the same way that the final model was derived, allowing the full nonlinearity of the problem to be accounted for, including trade-offs between model parameters (e.g., Christeson et al., 1999; Holbrook et al., 1994; Zelt and White, 1995). These tests are time-consuming and only representative parameters can be tested in this way. A fine-grid tomographic approach can facilitate a similar type of test. For example, Zelt and Barton (1998) examined one region of a model where there was significant lateral structure even though the ray coverage was low in this area. They added regularization to the inversion to force that region to remain laterally homogeneous and thereby establish the required trade-offs elsewhere in the model.

Other nonlinear assessment techniques include trying different starting models, different values of the free parameters in the objective function, and exclusion of subsets of the data considered less reliable (e.g., Zelt et al., 2006a). Using different model parameterizations and different inversion algorithms can be particularly illuminating, especially when one algorithm seeks a model that satisfies all prior information and preconceived notions of what is geologically reasonable and one algorithm seeks the minimum-structure model (Zelt et al., 2003; **Figure 8**). In this way, it is possible to determine what model structure is consistent with the data to facilitate hypothesis testing while at the same time establishing what model structure is required by the data. White and Boland (1992), Korenaga et al. (2000), Holbrook et al. (2001), Zelt et al. (2003), Levander et al. (2005), and Grad et al. (2006) (**Figure 9**) applied different forward and inversion algorithms to the same wide-angle data.

One of the most common forms of nonlinear model assessment for wide-angle data is the checkerboard test for estimating model resolution (e.g., Day et al., 2001; Evangelidis et al., 2004; Morgan et al., 2002; Schlindwein et al., 2003). In these tests, an alternating pattern of high and low anomalies is superimposed on a reference model, and synthetic data are calculated for the 'checkerboard' model. These data are inverted using the same starting model and source–receiver geometry as real the data inversions and the recovered model will closely resemble the checkerboard pattern in regions of good constraint. Results from anomaly patterns with different polarity, registration, and orientation should be averaged to reduce the effects of changing ray coverage due to the nonlinearity of the problem (Zelt, 1998). Anomaly patterns for velocity and depth nodes can be treated separately or simultaneously for mixed problems (e.g., Zelt et al., 1999).

The most computationally intensive form of model assessment involves a Monte Carlo procedure. Many realizations are performed in which randomized data are inverted using randomized starting models. The resulting models are used to compute posterior model covariance and resolution estimates (Korenaga et al., 2000; Zhang and Toksöz, 1998; Zhang et al., 1998; **Figure 10**). This approach may not be feasible computationally for large problems.

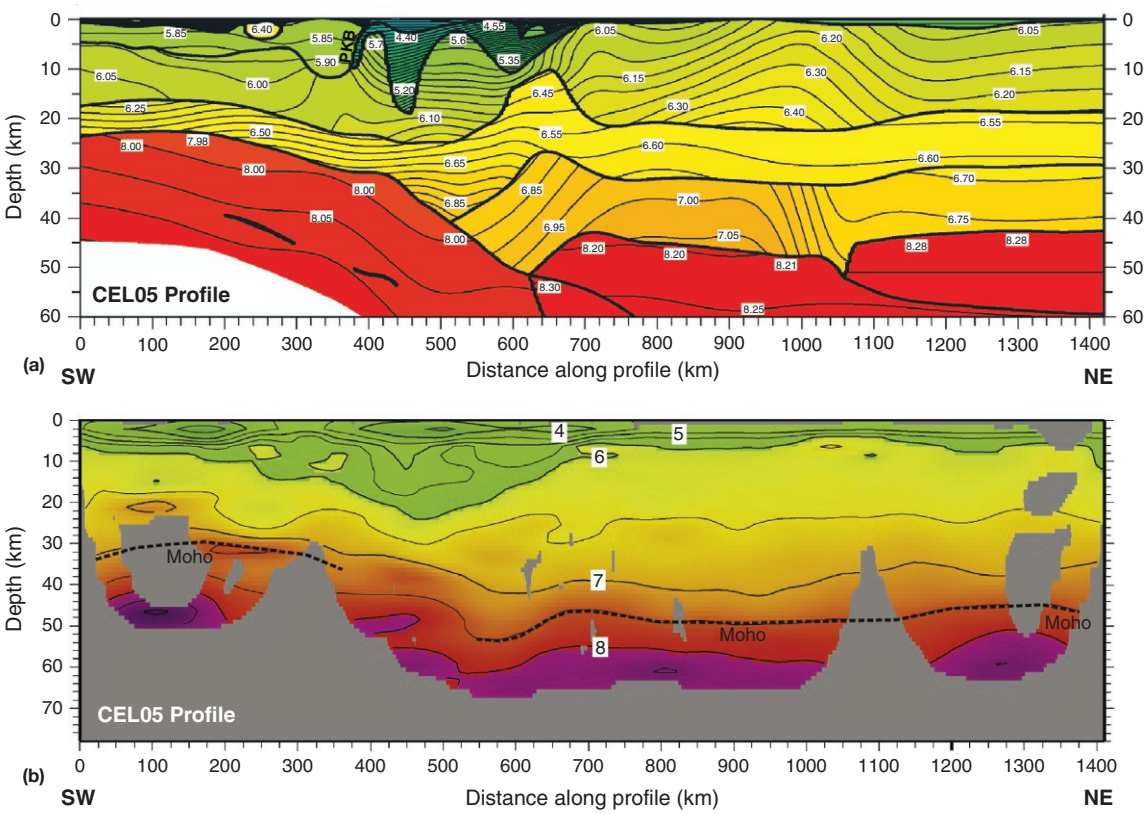

Figure 9 Example from the CELEBRATION 2000 experiment extending from Hungary to Russia in which two very different modeling approaches were applied to the same wide-angle data (Grad et al., 2006). Data from 26 explosions were collected by 360 portable recorders along the profile. (a) P-wave model obtained by forward modeling of refraction and reflection traveltimes and amplitudes using a layered parameterization with a smooth velocity field between discontinuities using the method of Cerveny et al. (1977). (b) Model obtained by traveltime inversion using only first arrivals in which a smooth, minimum structure was sought using the method of Zelt and Barton (1998). Velocity contours are labeled in km s^{-1}. The 7.5 km s^{-1} contour was used as a guide to interpret the Moho in (b).

1.15.20 Wide-Angle Migration

Conventional narrow-angle reflection and wide-angle seismology methods are beginning to merge in the academic community, as the number of shots and the station density in an average wide-angle survey has increased. Frequently, intracrustal, Moho, and sub-Moho reflections can be imaged using migration techniques applied to wide-angle data (Henstock and Levander, 2000; Henstock et al., 1997; Holbrook et al., 1992; Lafond and Levander, 1995; McMechan and Fuis, 1987; Milkereit et al., 1990; Morozov and Levander, 2002; Van Avendonk, 2004). However, the velocity model for wide-angle migration needs to be more accurate than for conventional migration, as minor lateral velocity errors are compounded for travel paths with large horizontal components. Typically, traveltime inversion and tomography provide velocity models suitable for wide-angle migrations (Zelt et al., 1998). The greatest benefit from wide-angle migration, as with conventional reflection processing, is the ability to use the seismic wavefield to image wavelength-scale structure without having to explicitly identify, pick, and model individual arrivals within the wavefield, other than the primary phases already used in the traveltime modeling. Resolution reduces to about half of the vertical wavelength, which for waves traveling as far horizontally as vertically is significantly larger than for vertically incident waves only.

A kinematic form of wide-angle migration can be carried out using a ray-tracing algorithm in which wide-angle reflection picks are modeled using floating reflecting surfaces (e.g., Holbrook et al., 1994; Stoerzel and Smithson, 1998; Wissinger et al., 1997; Zelt and White, 1995). These reflectors are typically relatively short interfaces with no associated velocity structure so that they 'float' within the velocity field of the model as defined by previous traveltime modeling of other phases. When a number of floating reflectors from different shots or receivers coalesce and align, then one can be confident that real structure is being imaged (e.g., Zelt and Forsyth, 1994).

1.15.21 Wavefield Inversion

Among others, Beylkin (1985), Beylkin and Burridge (1990), Tarantola (1984), Mora (1988), Pratt et al. (1996), and Pratt et al. (1998) approached the active seismic imaging problem as wavefield inversion, in which the image of the subsurface is defined as combinations of the perturbations of the material properties. For the constant density acoustic case, this image is

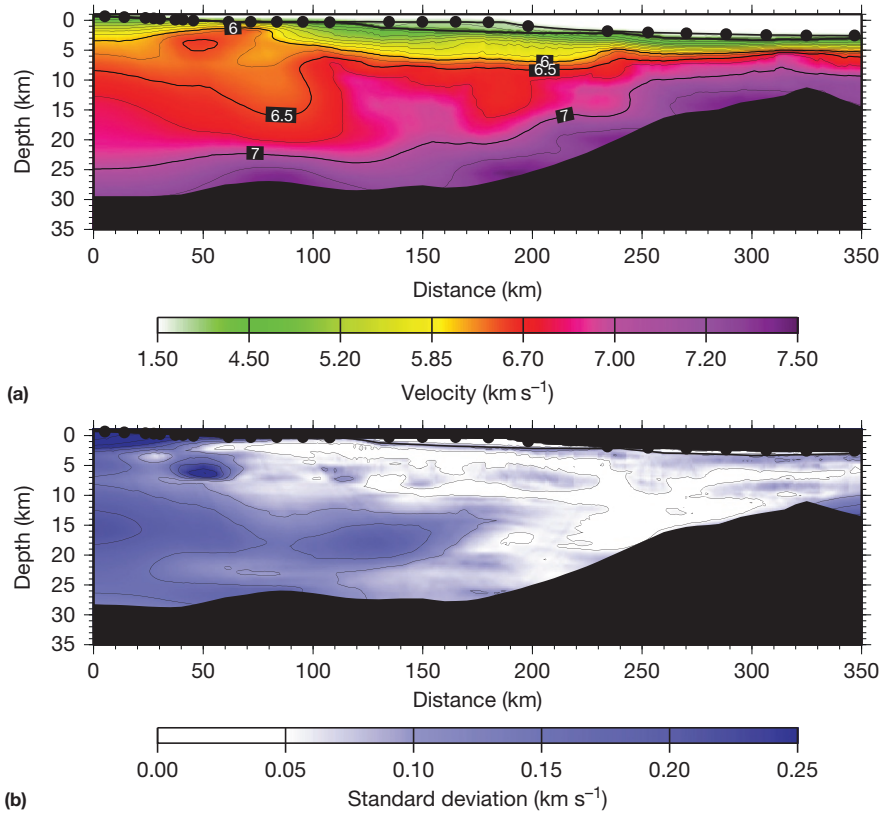

Figure 10 Example of model assessment using a nonlinear Monte Carlo procedure to estimate model variance (Korenaga et al., 2000). (a) P-wave velocity model for the southeast Greenland continental margin obtained by traveltime inversion of Pg and PmP arrivals recorded at 18 ocean-bottom instruments and eight land stations. This model was obtained by averaging 100 Monte Carlo ensembles. (b) Corresponding standard deviation for velocity and depth nodes; the standard deviation of the Moho is indicated by the width of the gray zone at the base of the crust.

the field $\delta c(x)/c_0(x)$. Wavefield inversion, despite its computational costs, has several advantages over migration for image formation: (1) Ideally, one is calculating the correct amplitudes of the material perturbations; (2) the source time function, $f(t)$, can be determined as part of the solution rather than being estimated independently; (3) at least theoretically, the development provides formal resolution estimates; and (4) perhaps most importantly, depending upon how one preconditions the data, both the background velocity field and the high-frequency fluctuation field can be estimated. The former is often referred to as waveform tomography and is applied to forward-scattered first arrivals with the backscattered field muted (e.g., Pratt et al., 1998); the latter is the reflection inversion and the data are preconditioned by removing the first arrivals. As in the previous section, Beylkin (1985) and Beylkin and Burridge (1990) cast the inverse problem in terms of high-frequency asymptotics and showed that the inversion integrals are generalized inverse Radon transforms. This formalism was developed by Bostock et al. (2001) for inversion of teleseismic data. Tarantola's (1984) development relies on inverse theory and, being the most general, is repeated here. Letting G again be Green's function and L the wave operator, we can write

$$\mathrm{p}(x_r, t, x_s) = \mathrm{G}(x_r, t, x_s, 0)^{*} f(t) \qquad [51]$$

and

$$\mathbf{p} = \mathbf{q}(\mathrm{c}, \mathrm{f}) \qquad [52]$$
$$\mathbf{p} = \mathbf{q}(\mathrm{m})$$

with $\mathrm{m} = (\mathrm{c}, \mathrm{f})^{\mathrm{T}}$ the vector of model parameters and $\mathbf{p}$ the vector of predicted observations. We can define the covariance matrix of the observations as

$$C_{\mathrm{P}}(x_r, t, x_s | x_r', t', x_s') = \sigma_{\mathrm{rs}}^2 \delta_{\mathrm{rr}'} \delta_{\mathrm{ss}'} \delta_{\mathrm{tt}'} \qquad [53]$$

Tarantola (1984) defined the covariance matrix of the model as the expected variances in the solution based on prior information and described them with a Gaussian error model:

$$C_{\mathrm{cc}}(x, x') = \sigma_{\mathrm{c}}^2 \exp\left(-\frac{1}{2}\left(\frac{(x-x_1')^2 + (x_2-x_2')^2}{a_{\mathrm{H}}^2} + \frac{(z-z')^2}{a_z^2}\right)\right)$$
$$C_{\mathrm{ff}}(t, t') = \sigma_{\mathrm{f}}^2 \exp\left(-\frac{1}{2}\left(\frac{(t-t')^2}{T_{\mathrm{f}}^2}\right)\right) \qquad [54]$$

with cross variances zero and a_{H}, a_z, and T_{f}, characteristic correlation lengths in the horizontal, vertical, and time coordinates. We note that many geologic structures have self-affine spatial covariance functions and take the form of the von Kármán function (e.g., Holliger and Levander, 1992). The a priori covariance matrix is then

$$C_{\mathrm{m}} = \begin{pmatrix} C_{\mathrm{cc}} & 0 \\ 0 & C_{\mathrm{ff}} \end{pmatrix} \quad [55]$$

Our initial guess of the model is

$$\mathbf{m}_0 = \begin{pmatrix} \mathbf{c}_0 \\ \mathbf{f}_0 \end{pmatrix} \quad [56]$$

and note that the observations do not fit the initial model

$$\mathbf{p}_0 \neq \mathbf{q}(\mathrm{m}_0) \quad [57]$$

We can define the data residual as the difference between the observations and the predictions:

$$\delta\mathbf{d}(\mathbf{m}) = \mathbf{p}_0 - \mathbf{q}(\mathbf{m}) \quad [58]$$

We wish to minimize

$$\begin{aligned} 2S(\mathbf{m}) &= ||((\mathbf{p}_0 - \mathbf{p}), (\mathbf{m}_0 - \mathbf{m}))||^2 \\ &= (\mathbf{p}_0 - \mathbf{p})^* \mathrm{C_p} (\mathbf{p}_0 - \mathbf{p}) + (\mathbf{m}_0 - \mathbf{m})^* C_{\mathrm{m}} (\mathbf{m}_0 - \mathbf{m}) \\ 2S(\mathbf{m}) &= \delta\mathbf{d}\left(\vec{\mathbf{m}}\right)^* \mathrm{C_p} \delta\mathbf{d}\left(\vec{\mathbf{m}}\right) + (\mathbf{m}_0 - \mathbf{m})^* C_{\mathrm{m}} (\mathbf{m}_0 - \mathbf{m}) \end{aligned} \quad [59]$$

where asterisk denotes complex conjugate. The minimum solution occurs where the gradient of S with respect to the model coordinates vanishes, giving

$$(\mathbf{m}_0 - \mathbf{m}) = C_{\mathrm{m}} \nabla_{\mathrm{m}} \delta\mathrm{d}(\mathbf{m})^* C_{\mathrm{p}}^{-1} \delta\mathbf{d}(\mathbf{m}) \quad [60]$$

Tarantola (1984) generalized this expression by adding $C_{\mathrm{m}} \nabla_{\mathrm{m}} \delta\mathbf{d}(\mathbf{m})^* C_{\mathrm{p}}^{-1} \nabla_{\mathrm{m}} (\delta\mathbf{d}(\mathbf{m})(\mathbf{m}_0 - \mathbf{m}))$ to both sides, giving

$$\begin{aligned} (\mathbf{m}_0 - \mathbf{m}) &= \left(I + C_{\mathrm{m}} \nabla_{\mathrm{m}} \delta\mathbf{d}(\mathbf{m})^* C_{\mathrm{p}}^{-1} \nabla_{\mathrm{m}} \delta\mathrm{d}(\mathbf{m})\right)^{-1} \\ &\quad \times C_{\mathrm{m}} \nabla_{\mathrm{m}} \delta\mathbf{d}(\mathbf{m})^* C_{\mathrm{p}}^{-1} (\delta\mathbf{d}(\mathbf{m}) + \nabla_{\mathrm{m}} \delta\mathbf{d}(\mathbf{m})(\mathbf{m}_0 - \mathbf{m})) \\ (\mathbf{m}_0 - \mathbf{m}) &= W\Big(C_{\mathrm{m}} \nabla_{\mathrm{m}} \delta\mathbf{d}(\mathbf{m})^* C_{\mathrm{p}}^{-1} (\delta\mathbf{d}(\mathbf{m}) \\ &\quad + \nabla_{\mathrm{m}} \delta\mathbf{d}(\mathbf{m})(\mathbf{m}_0 - \mathbf{m}))\Big) \end{aligned} \quad [61]$$

which he described as a 'beautiful' but 'useless' equation, as W is too large to compute for realistic problems. Of the various approximations to W, the simplest of these is a gradient algorithm for an iterative solution to the nonlinear seismic problem:

$$\begin{aligned} W_{\mathrm{app}} &\approx \alpha I \\ \mathbf{m}_{k+1} &= m_k + \alpha\Big(C_{\mathrm{m}} \nabla_{\mathrm{m}} \delta\mathbf{d}(\mathbf{m}_k)^* C_{\mathrm{p}}^{-1} \delta\mathbf{d}(\mathbf{m}_k) - (\mathbf{m}_k - \mathbf{m}_0)\Big) \end{aligned} \quad [62]$$

Other approximate iterative solutions include using the diagonal or banded diagonal forms of W. In these equations, the forward model can be solved by any scheme capable of producing the field at any point, for instance, time- or frequency-domain finite-difference or finite-element methods.

In a series of papers, Pratt and his colleagues developed a practical inversion scheme along similar lines based on 2-D frequency-domain finite-difference forward modeling. They assume that the a priori covariance is infinite. The frequency-domain wave equation can be written as an operator:

$$\begin{aligned} \left[\nabla^2 + \frac{\omega^2}{c^2(x)}\right] p(x, x_s, \omega) &= f(x, x_s, \omega) \\ LP(x, x_s, \omega) &= f(x, x_s, \omega) \\ \mathrm{P}(x, x_s, \omega) &= L^{-1}\mathrm{f}(x, x_s, \omega) \end{aligned} \quad [63]$$

where L is the discrete frequency-domain operator dependent upon the model parameters and p is a function of the model parameters. Since L^{-1} generates p for a given source or collection of discrete sources f, the columns of L^{-1} are Green's functions for the model. Restricting the model vector to material perturbations, we can write eqn [59] in the more familiar form:

$$2S(\mathbf{m}) = \delta\mathbf{d}(\mathbf{m})^T \delta\mathbf{d}(\mathbf{m})^* \quad [64]$$

Minimizing this with respect to m using a gradient method gives

$$\begin{aligned} m^{(k+1)} - \mathrm{m}^{(k)} &- \alpha \nabla_m S\left(m^{(k)}\right) \\ m^{(k+1)} - \mathrm{m}^{(k)} &\Big| \alpha \mathrm{Re}\left\{ \left[\frac{\partial P}{\partial m^{(k)}}\right]^{\mathrm{T}} \delta\mathrm{d}\left(\mathrm{m}^{(k)}\right)^* \right\} \\ m^{(k+1)} - \mathrm{m}^{(k)} &\Big| \alpha \mathrm{Re}\left\{ \left[J^{(k)}\right]^{\mathrm{T}} \delta\mathrm{d}\left(\mathrm{m}^{(k)}\right)^* \right\} \end{aligned} \quad [65]$$

where J is the Jacobian matrix of Fréchet derivatives of the calculated field, p_i, with respect to the model parameters at the kth iteration, $m_j^{(k)}$. The last equation demonstrates several principles of imaging: the product of the frequency-domain data residuals with the derivatives of the estimated field constitutes a cross correlation. The conjugate of the data residuals implies that the residuals are propagated in a time-reversed sense. The cross correlation finds parts of the observed field that are missing from the predicted field. In particular, Pratt et al. (1998) showed that the Jacobian finds those parts of the first-order scattered field that are present in the data but not in the model. Moreover, noting that

$$\begin{aligned} &\frac{\partial L}{\partial m_i}\mathrm{p} + \frac{\partial \mathrm{P}}{\partial m_i} = 0 \\ &\frac{\partial \mathrm{P}}{\partial m_i} = L^{-1}\left[\frac{\partial L}{\partial m_i}\mathrm{p}\right] = L^{-1}\mathrm{f}^{(i)} \\ &\mathcal{F} = L^{-1}\left[f^{(1)} \cdots f^{(n)}\right] \\ &\mathcal{F} = L^{-1}F \end{aligned} \quad [66]$$

and comparing to eqn [65], we see that the Jacobian can be interpreted as a series of virtual sources applied at the n parameter locations. The derivative of L with respect to the parameters turns eqn [65] to

$$\begin{aligned} m^{(k+1)} &= \mathrm{m}^{(k)} + \alpha \mathrm{Re}\left\{ \left[L^{-1}F\right]^{\mathrm{T}} \delta\mathrm{d}\left(\mathrm{m}^{(k)}\right)^* \right\} \\ m^{(k+1)} &= \mathrm{m}^{(k)} + \alpha \mathrm{Re}\Big\{ \left[F^{(k)}\right]^{\mathrm{T}} \left[L^{-1}\right]^{\mathrm{T}} \delta\mathrm{d}\left(\mathrm{m}^{(k)}\right)^* \Big\} \end{aligned} \quad [67]$$

A number of authors have noted that the first iterate of [67] is equivalent to prestack migration: The data residual is calculated as the predictions between the smooth velocity and impedance field (i.e., there are no backscattered waves predicted), so the residual is just the backprojected set of observations:

$$\begin{aligned} \delta\mathrm{m}^{(1)} &= \alpha \mathrm{Re}\left\{ \left[F^{(0)}\right]^{\mathrm{T}} \delta\mathrm{d}\left(\mathrm{m}^{(0)}\right)^* \right\} \\ \delta\mathrm{m}^{(1)} &= \alpha \mathrm{Re}\left\{ \left[F^{(0)}\right]^{\mathrm{T}} \left[L^{-1}\right]^{\mathrm{T}} \delta\mathrm{d}\left(\mathrm{m}^{(k)}\right)^* \right\} \end{aligned} \quad [68]$$

1.15.22 Wavefield Inversion Examples

We show three examples of wavefield inversion, one synthetic and two from field experiments. Figure 11 shows an example

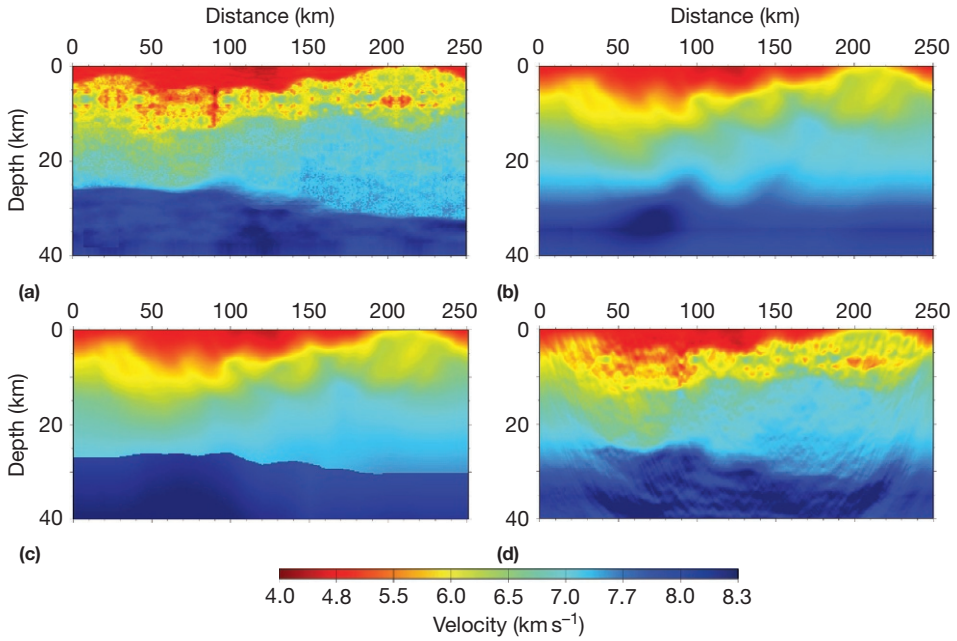

Figure 11 Blind test of traveltime and waveform inversion (Hole et al., 2005). (a) True model used to compute 2-D viscoelastic full-wavefield data for a refraction/wide-angle reflection survey. (b) Model derived from traveltime tomography using only first arrivals. (c) Model derived from traveltime inversion using first arrivals and wide-angle reflections from the Moho. The traveltime models are smooth but robust versions of the true model. (d) Model derived from waveform tomography using (b) as the starting model (Brenders and Pratt, 2007). The waveform model significantly improves the spatial resolution over the traveltime result and matches many details of the true model in (a).

of waveform tomography applied to a synthetic crustal data set using Pratt's method (Brenders and Pratt, 2007). The synthetic data set was developed using a viscoelastic finite-difference method for a blind test of traveltime and waveform tomography models for a Commission on Controlled Source Seismology workshop (Hole et al., 2005). Long and short spatial wavelength structures were included using a variety of statistical descriptions of crustal rocks to make the model and data set as realistic as possible in terms of acquisition geometry, velocity heterogeneity, and wave propagation. Traveltime tomography recovers the large-scale structure quite well, and waveform tomography does a surprisingly good job of recovering the finer-scale structure.

Figure 12 shows an example of waveform tomography applied to dense ocean-bottom seismometer data from the Nankai Trough (Operto et al., 2006). Again, traveltime tomography defines the long-wavelength structure, and waveform tomography resolves the fine-scale structure by inverting frequencies up to 15 Hz.

Environmental geophysics is used to characterize the shallow subsurface to locate and map the underground flow of pollutants or to estimate groundwater reserves. Figure 13 is an example of traveltime and waveform tomography results using high-resolution seismic data acquired at a groundwater contamination site in Ogden, Utah. The seismic target is a paleochannel incised in a clay layer at a depth of a few to 15 m below the surface and filled with low-velocity alluvium. The clay layer acts as an aquitard stopping descent of dense nonaqueous phase liquid (DNAPL) pollutants with the channel acting as a collection point for the pollutants. The geophysical problem was to identify the top of the clay layer and characterize the channel. Separate 3-D seismic reflection and refraction surveys as well as vertical seismic profiles were performed at the site. A 0.223 caliber rifle was used as the seismic source, and geophones were spaced 30 cm apart. Figure 13(b) shows the image of the subsurface made using Pratt's method applied to surface and borehole seismic data collected along the axis of the channel (Gao et al., 2006). The degree of lateral and vertical heterogeneity observed is surprising; velocities vary by a factor of 2–3 laterally and by an order of magnitude vertically. This poses a serious problem for conventional poststack seismic imaging methods.

1.15.23 Future Directions

The trends in data acquisition in both the industrial and academic communities are toward higher spatial density recording using an ever-increasing number of instruments. Industrial acquisition now largely consists of 3-D surveys, whereas equipment and acquisition budgets restrict academia to 2-D and a small number of 3-D surveys. The US academic community now has ~3000 matched channel available for land controlled-source work (including three-component instruments) through the IRIS PASSCAL facility. This is a factor of 5 greater than the total number of (unmatched) channels available from all North American academic sources in the early 1990s. The US marine community now has more than a hundred ocean-bottom seismographs for active-source work available from the national OBS Instrument Pool. The US academic fleet has just acquired its first seismic vessel designed for 3-D surveying. Similar instrument pools, of comparable size, exist or are in development in Europe and Asia. Data volumes are increasing rapidly in size, requiring more and more automation for preprocessing and image formation and analysis. Combined with Moore's law increase in computer speed, memory, and storage, the automatic

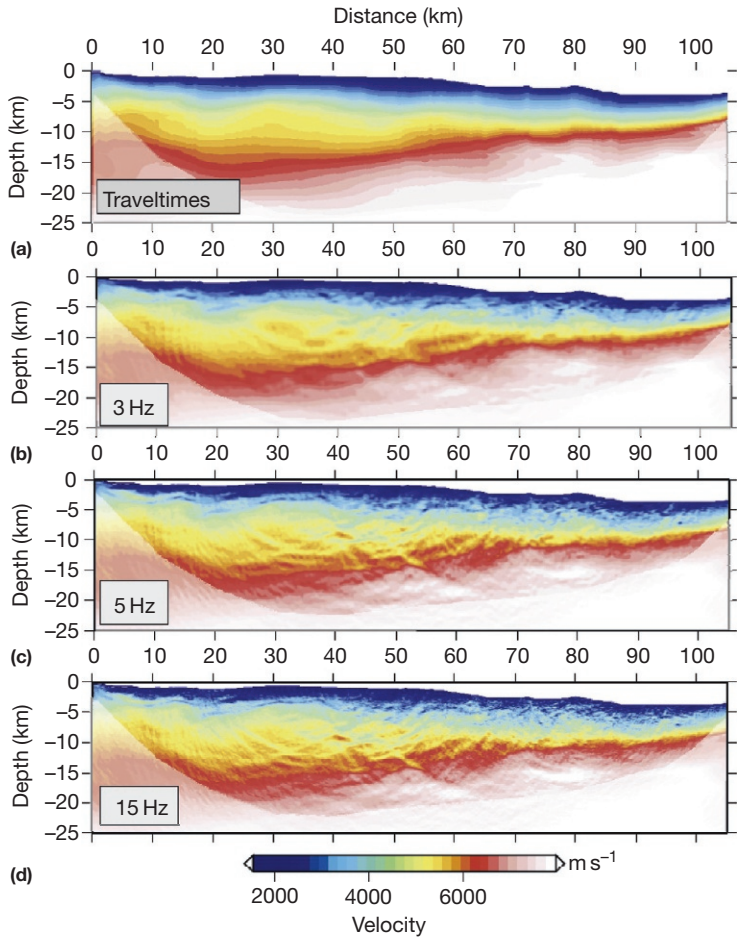

Figure 12 Example of waveform tomography applied to dense ocean-bottom seismometer data from the Nankai Trough (Operto et al., 2006). The vertical-component seismograms of 93 instruments were used in the inversions, windowed to 1–3 s starting at the first-arrival time, depending on the water depth. (a) P-wave model derived from traveltime tomography used as the starting model for waveform tomography. (b)–(d) Models derived from waveform tomography at 3, 5, and 15 Hz, as labeled.

inversion routines described in **Section 1.15.21** are likely the path to the future.

Full-waveform inversion for 1-D models has been applied for many years to both reflection and wide-angle data, the latter particularly in oceanic and gas hydrate studies (Minshull et al., 1994; Shaw and Orcutt, 1985). Sun and McMechan (1992) and Pratt et al. (1996) applied 2-D elastic and acoustic full-waveform inversion to synthetic wide-angle data. Full-waveform inversion of real wide-angle data for 2-D models is just beginning to be applied (e.g., Chironi et al., 2006; Operto et al., 2006; Ravaut et al., 2004; Shipp and Singh, 2002). These techniques are currently limited to 2-D acoustic models, primarily for computational reasons. They are nonlinear gradient methods that require a good starting model usually obtained through traveltime methods. Broadband, low-frequency data, like that collected by Spitzer and White (2005) for subbasalt imaging, are ideal for waveform inversion. Brenders and Pratt (2007) presented a comparison of velocity models derived from first-arrival traveltime tomography and waveform tomography for a realistic set of synthetic wide-angle data in a blind test; Hole et al. (2005) presented a comparison of the same waveform-derived model with a velocity model derived from combined first-arrival and Moho-reflection traveltime inversion. These comparisons suggest that waveform methods have the potential to provide roughly an order-of-magnitude increase in spatial resolution over traveltime methods (**Figure 11**). Extending these methods to elastic models and 3-D, although not a major theoretical leap, will be a numerical analysis and computational challenge.

For lithospheric studies, the need for flexible, general-purpose traveltime inversion and tomography algorithms will remain, both as primary modeling tools and to provide long-wavelength starting models for higher-resolution wavefield techniques. We have already discussed the likelihood that S-wave, attenuation, and anisotropy studies will become more commonplace in the future, although they have yet to be employed commonly in academic investigations.

For traveltime methods, formal treatment of Fresnel zones (Watanabe et al., 1999), adaptation of frequency-dependent sensitivity kernels from global seismology (Dahlen et al., 2000), and wave equation-based modeling (Pyun et al., 2005) will reduce the need for regularization and improve the stability of gradient methods. The derived models will contain more structure and increased resolution as a result of more accurately honoring the physics of wave propagation.

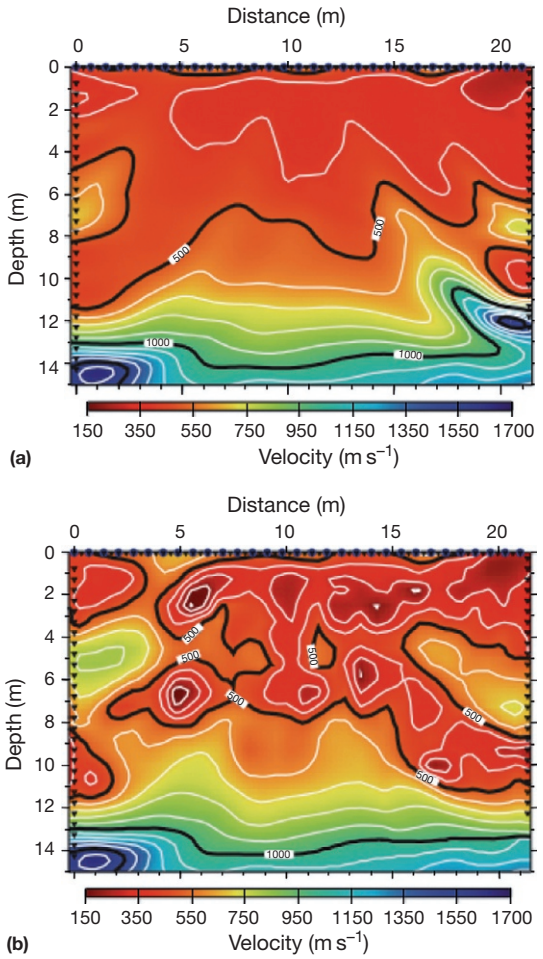

Figure 13 (a) Characterization of the shallow subsurface at a groundwater contamination site. Velocity model derived from first-arrival traveltime tomography from a VSP/surface seismic experiment along the axis of a buried paleochannel that acts as a trap for groundwater contaminants. A smoothed version of the model was used as the starting model for the waveform inversion. (b) Final velocity model derived from waveform tomography using the method of Pratt (1999) and Pratt and Shipp (1999). The velocity varies laterally by a factor of 2–3 and changes vertically by an order of magnitude over 15 m. The smallest features laterally are ~2–3 m, roughly the theoretical resolution obtainable. The sediments along the axis of the channel, above ~14 m depth, show a surprising degree of heterogeneity. Reproduced from Gao F, Levander A, Pratt RG, Zelt CA, and Fradelizio G-L (2006) Waveform tomography at a ground water contamination site: VSP-surface dataset. *Geophysics* 71: H1–H11, with permission from Society of Exploration Geophysics.

This will be particularly true for near-surface studies in which the length scales of heterogeneities are comparable with or smaller than the seismic wavelengths (e.g., Zelt et al., 2006a).

Very efficient simulations of 2-D and 3-D viscoelastic wave propagation at realistic frequencies are needed for the forward modeling component of wavefield inversion schemes. The global seismology community also shares these needs. Advances have been made toward computing realistic global seismograms in laterally variable viscoelastic media (e.g., Komatitsch and Tromp, 1999, 2005). Simulating wave propagation using model parameterizations that incorporate mathematical descriptions of rock properties such as fractures, porosity, saturation, gas concentration, and partial melt (e.g., Aldridge et al., 2004) will help ensure that seismic methods will continue to play a role in addressing the most relevant Earth science problems.

Many problems of interest to academic Earth scientists require relatively high-resolution imaging across a broad range of scales, from the surface geology through the crust and into the upper mantle. Highly detailed images of the crust and the top of the mantle are only available from controlled-source imaging, whereas much of the lithospheric mantle and deeper can only be imaged practically with earthquake sources. Perhaps one of the most interesting future research directions facing the academic community is the combined inversion of controlled-source data with teleseismic body-wave data. This poses a number of challenges, as the bandwidths recorded, the scales of spatial sampling and resolution, and the source and receiver configurations used in the various experiments are very different.

Acknowledgments

The author thanks Gian L. Fradelizio and Stephen Clark for assistance in making figures.

References

Aki K and Lee WHK (1976) Determination of 3-dimensional velocity anomalies under a seismic array using 1st-P arrival times from local earthquakes. Part 1: A homogeneous initial model. *Journal of Geophysical Research* 81: 4381–4399.

Aki K and Richards PG (2002) *Quantitative Seismology*, 2nd edn. Sausalito, CA: University Science Books.

Aldridge DF, Bartel LC, and Symons NP (2004) Velocity–stress–pressure algorithm for 3D poroelastic wave propagation. *Society Exploration Geophysicists Technical Program Extended Abstracts* 23: 1917–1920.

Al-Yahya K (1989) Velocity analysis by iterative profile migration. *Geophysics* 54: 718–729.

ANCORP Working Group (2003) Seismic imaging of a convergent continental margin and plateau in the Central Andes (Andean Continental research Project 1996 (ANCORP96)). *Journal of Geophysical Research* 108: 2328. http://dx.doi.org/10.1029/2002JB001771.

BABEL Working Group (1993) Deep seismic reflection/refraction interpretation of crustal structure along BABEL profiles A and B in the southern Baltic Sea. *Geophysical Journal International* 112: 325–343.

Barton PJ (1986) The relationship between seismic velocity and density in the continental-crust – A useful constraint. *Geophysical Journal of the Royal Astronomical Society* 87: 195–208.

Beckman P and Spizzichino A (1963) *International Series of Monographs in Electromagnetic Waves, 4: The Scattering of Electromagnetic Waves from Rough Surfaces*. Oxford: Pergamon Press.

Benz HM, Smith RB, and Mooney WD (1990) Crustal structure of the northwestern Basin and Range province from the 1985 Program for Array Seismic Studies of the Continental Lithosphere seismic Experiment. *Journal of Geophysical Research* 95: 21823–21842.

Benz HM, Chouet BA, Dawson PB, Lahr JC, Page RA, and Hole JA (1996) Three-dimensional P and S wave velocity structure of Redoubt Volcano, Alaska. *Journal of Geophysical Research* 101: 8111–8128.

Bevington PR (1969) *Data Reduction and Error Analysis for the Physical Sciences*. New York: McGraw-Hill.

Beylkin G (1985) Imaging of discontinuities in the inverse scattering problem by inversion of a causal generalized Radon transform. *Journal of Mathematical Physics* 26: 99–108.

Beylkin G and Burridge R (1990) Linearized inverse scattering problems in acoustics and elasticity. *Wave Motion* 12: 15–52.

Bosch M, Barton P, Singh SC, and Trinks I (2005) Inversion of traveltime data under a statistical model for seismic velocities and layer interfaces. *Geophysics* 70: R33–R43.

Boschetti F, Dentith MC, and List RD (1996) Inversion of seismic refraction data using genetic algorithms. *Geophysics* 61: 1715–1727.

Bostock MG (1998) Mantle stratigraphy and evolution of the Slave province. *Journal of Geophysical Research* 103: 21193–21200.

Bostock MG, Rondenay S, and Schragge DS (2001) Multiparameter two-dimensional version of scattered teleseismic body waves. Part 1: Theory for oblique incidence. *Journal of Geophysical Research* 106: 30771–30782.

Braile LW (1977) Interpretation of crustal velocity gradients and *Q* structure using amplitude-corrected seismic refraction profiles. In: Heacock JG (ed.) *Geophysical Monograph Series 20: The Earth's Crust*, pp. 427–439. Washington, DC: American Geophysical Union.

Braile LW and Smith RB (1975) Guide to the interpretation of crustal refraction profiles. *Journal of Geophysical Research* 40: 145–176.

Brenders AJ and Pratt RG (2007) Full waveform tomography for lithospheric imaging: Results from a blind test in a realistic crustal model. *Geophysical Journal International* 168: 133–151.

Brocher TM (2005) Empirical relations between elastic wavespeeds and density in the Earth's crust. *Bulletin of the Seismological Society of America* 95: 2081–2092.

Carbonell R, Perez-Estaun P, Gallart J, et al. (1996) Crustal root beneath the Urals: Wide-angle seismic evidence. *Science* 274: 222–224.

Caress DW, Burnett MS, and Orcutt JA (1992) Tomographic image of the axial low-velocity zone at 12-degrees–50′N on the East Pacific Rise. *Journal of Geophysical Research* 97: 9243–9263.

Cerveny V, Molotkov I, and Psencik I (1977) *Ray Method in Seismology*. Prague, Czechoslovakia: University of Karlova.

Cerveny V, Popov MM, and Psencik I (1982) Computation of wave fields in inhomogeneous-media–Gaussian-beam approach. *Geophysical Journal of the Royal Astronomical Society* 70: 109–128.

Chapman CH and Drummond R (1982) Body-wave seismograms in inhomogeneous-media using Maslov asymptotic theory. *Bulletin of the Seismological Society of America* 72: S277–S317.

Chironi C, Morgan JV, and Morgan MR (2006) Imaging of intrabasalt and subbasalt structure with full wavefield seismic tomography. *Journal of Geophysical Research* 111: B05313. http://dx.doi.org/10.1029/2004JB003595.

Chiu SKL, Kanasewich ER, and Phadke S (1986) Three-dimensional determination of structure and velocity by seismic tomography. *Geophysics* 51: 1559–1571.

Christensen NI (1996) Poisson's ratio and crustal seismology. *Journal of Geophysical Research* 101: 3139–3156.

Christensen NI and Mooney WD (1995) Seismic velocity structure and composition of the continental-crust – A global view. *Journal of Geophysical Research* 100: 9761–9788.

Christeson GL, McIntosh KD, Shipley TH, Flueh ER, and Goedde H (1999) Structure of the Costa Rica convergent margin, offshore Nicoya Peninsula. *Journal of Geophysical Research* 104: 25443–25468.

Christeson GL, Nakamura Y, Buffler RT, Morgan J, and Warner M (2001) Deep crustal structure of the Chicxulub impact crater. *Journal of Geophysical Research* 106: 21751–21769.

Claerbout JF (1970) Coarse grid calculations of waves in inhomogeneous media with applications to delineation of complicated seismic structure. *Geophysics* 35: 407–418.

Claerbout JF (1971) Toward a unified theory of reflector mapping. *Geophysics* 36: 467–481.

Claerbout JF (1976) *Fundamentals of Geophysical Data Processing*. New York: McGraw-Hill.

Claerbout JF (1985) *Imaging the Earth's Interior*. Cambridge, MA: Blackwell Science, 412 pp.

Clayton RW and McMechan GA (1981) Inversion of refraction data by wave field continuation. *Geophysics* 46: 860–868.

Clowes RM, Zelt CA, Amor JR, and Ellis RM (1995) Lithospheric structure in the southern Canadian Cordillera from a network of seismic refraction lines. *Canadian Journal of Earth Sciences* 32: 1485–1513.

Constable SC, Parker RL, and Constable CG (1987) Occam's inversion: A practical algorithm for generating smooth models from electromagnetic sounding data. *Geophysics* 52: 289–300.

Cook FA, van der Velden AJ, Hall KW, and Roberts BJ (1999) Frozen subduction in Canada's northwest territories; lithoprobe deep lithospheric reflection profiling of the western Canadian Shield. *Tectonics* 18: 1–24.

Crosson RS (1976) Crustal structure modeling of earthquake data. Part 1: Simultaneous least-squares estimation of hypocenter and velocity parameters. *Journal of Geophysical Research* 81: 3036–3046.

Dahlen FA, Hung SH, and Nolet G (2000) Fréchet kernels for finite-frequency traveltimes. Part I: Theory. *Geophysical Journal International* 141: 157–174.

Darbyshire FA, Bjarnason ITh, White RS, and Flóvenz OG (1998) Crustal structure above the Iceland mantle plume imaged by the ICEMELT refraction profile. *Geophysical Journal International* 135: 1131–1149.

Day AJ, Peirce C, and Sinha MC (2001) Three-dimensional crustal structure and magma chamber geometry at the intermediate-spreading, back-arc Valu Fa Ridge, Lau Basin-results of a wide-angle seismic tomographic inversion. *Geophysical Journal International* 146: 31–52.

Dix CH (1955) Seismic velocities from surface measurements. *Geophysics* 20: 68–86.

Dunn RA and Toomey DR (2001) Crack-induced seismic anisotropy in the oceanic crust across the East Pacific Rise (9 degrees 30′N). *Earth and Planetary Science Letters* 189: 9–17.

Eaton DWS (1993) Finite difference traveltime calculation for anisotropic media. *Geophysical Journal International* 114: 273–280.

Evangelidis CP, Minshull TA, and Henstock TJ (2004) Three-dimensional crustal structure of Ascension Island from active source seismic tomography. *Journal of Geophysical Research* 159: 311–325.

Fernandez-Viejo G, Clowes RM, and Welford KM (2005) Constraints on the composition of the crust and uppermost mantle in northwestern Canada: Vp/Vs variations along Lithoprobe′s SNorCLE transect. *Canadian Journal of Earth Sciences* 42: 1205–1222.

Firbas P (1981) Inversion of travel-time data for laterally heterogeneous velocity structure-linearization approach. *Geophysical Journal of the Royal Astronomical Society* 67: 189–198.

Fuchs K and Muller G (1971) Computation of synthetic seismograms with reflectivity method and comparison with observations. *Geophysical Journal of the Royal Astronomical Society* 23: 417–433.

Fuis GS, Ryberg T, Godfrey NJ, Okaya DA, and Murphy JM (2001) Crustal structure and tectonics from the Los Angeles basin to the Mojave Desert, Southern California. *Geology* 29: 15–18.

Gao F, Levander A, Pratt RG, Zelt CA, and Fradelizio G-L (2006) Waveform tomography at a ground water contamination site: VSP-surface dataset. *Geophysics* 71: H1–H11.

Gardner GHF, French WS, and Matzuk T (1974) Elements of migration and velocity analysis. *Geophysics* 39: 811–825.

Gazdag J (1978) Wave equation migration with the phase-shift method. *Geophysics* 43: 1342–1351.

Godfrey NJ, Christensen NI, and Okaya DA (2002) The effect of crustal anisotropy on reflector depth and velocity determination from wide-angle seismic data: A synthetic example based on South Island, New Zealand. *Tectonophysics* 355: 145–161.

Gohl K and Pedersen LB (1995) Collisional tectonics of the Baltic Shield in the northern Gulf of Bothnia from Seismic data of the BABEL project. *Geophysical Journal International* 120: 209–226.

Goodman JW (1996) *Introduction to Fourier Optics*. New York: McGraw-Hill.

Gorman AR and Clowes RM (1999) Wave-field tau-*p* analysis for 2-D velocity models: Application to Western North American lithosphere. *Geophysical Research Letters* 26: 2323–2326.

Gorman AR, Clowes RM, Ellis RM, et al. (2002) Deep probe: Imaging the roots of Western North America. *Canadian Journal of Earth Sciences* 39: 375–398.

Gorman AR, Nemeth B, Clowes RM, and Hajnal Z (2006) An investigation of upper mantle heterogeneity beneath the Archaean and Proterozoic crust of western Canada from Lithoprobe controlled-source seismic experiments. *Tectonophysics* 416: 187–207.

Grad M, Guterch A, Keller GR, et al. (2006) Lithospheric structure beneath trans-Carpathian transect from Precambrian platform to Pannonian basin: CELEBRATION 2000 seismic profile CEL05. *Journal of Geophysical Research* 111: B03301. http://dx.doi.org/10.1029/2005JB003647.

Grand SP (1994) Mantle shear structure beneath the Americas and surrounding oceans. *Journal of Geophysical Research* 99: 11591–11622.

Hammer PTC, Dorman LM, Hildebrand JA, and Cornuelle BD (1994) Jasper Seamount structure: Seafloor seismic refraction tomography. *Journal of Geophysical Research* 99: 6731–6752.

Hashizume M (1979) *Q* of the crust beneath southwestern Honshu, Japan, derived from explosion seismic waves. *Physics of the Earth and Planetary Interiors* 20: 25–32.

Henstock TJ and Levander A (2000) Lithospheric evolution in the wake of the Mendocino Triple Junction: Structure of the San Andreas Fault system at 2 Ma. *Geophysical Journal International* 140: 233–247.

Henstock TJ, Levander A, and Hole JA (1997) Deformation in the lower crust of the San Andreas fault system in Northern California. *Science* 278: 650–653.

Hill NR and Wuenschel PC (1985) Numerical modeling of refraction arrivals in complex areas. *Geophysics* 50: 90–98.

Hobro JWD, Singh SC, and Minshull TA (2003) Three-dimensional tomographic inversion of combined reflection and refraction seismic traveltime data. *Geophysical Journal International* 152: 79–93.
Holbrook WS, Reiter EC, Purdy GM, and Toksoz MN (1992) Image of the Moho across the continent-ocean transition, United-States east-coast. *Geology* 20: 203–206.
Holbrook WS, Reiter EC, Purdy GM, et al. (1994) Deep structure of the US Atlantic continental margin, offshore South Carolina, from coincident ocean bottom and multichannel seismic data. *Journal of Geophysical Research* 99: 9155–9178.
Holbrook WS, Larsen HC, Korenaga J, et al. (2001) Mantle thermal structure and active upwelling during continental breakup in the North Atlantic. *Earth and Planetary Science Letters* 190: 251–262.
Holbrook WS, Páramo P, Pearse S, and Schmitt RW (2003) Thermohaline fine structure in an oceanographic front from seismic reflection profiling. *Science* 301: 821–824. http://dx.doi.org/10.1126/science.1085116.
Hole JA (1992) Nonlinear high-resolution three-dimensional seismic travel time tomography. *Journal of Geophysical Research* 97: 6553–6562.
Hole JA and Zelt BC (1995) Three-dimensional finite-difference reflection travel times. *Geophysical Journal International* 121: 427–434.
Hole JA, Clowes RM, and Ellis RM (1992) Interface inversion using broadside seismic refraction data and 3-dimensional travel time calculations. *Journal of Geophysical Research* 97: 3417–3429.
Hole JA, Beaudoin BC, and Klemperer SL (2000a) Vertical extent of the newborn San Andreas fault at the Mendocino triple junction. *Geology* 28: 1111–1114.
Hole JA, Brocher TM, Klemperer SL, Parsons T, Benz HM, and Furlong KP (2000b) Three-dimensional seismic velocity structure of the San Francisco Bay area. *Journal of Geophysical Research* 105: 13859–13873.
Hole JA, Zelt CA, and Pratt RG (2005) Advances in controlled-source seismic imaging. *EOS. Transactions of the American Geophysical Union* 86: 177–181.
Hole JA, Ryberg T, Fuis GS, Bleibinhaus F, and Sharma AK (2006) Structure of the San Andreas fault zone at SAFOD from a seismic refraction survey. *Geophysical Research Letters* 33: L07312.
Holliger K and Levander AR (1992) A stochastic view of the lower crust based on the Ivrea Zone. *Geophysical Research Letters* 19: 111153–111156.
Huang H, Spencer C, and Green A (1986) A method for the inversion of refraction and reflection travel times for laterally varying velocity structures. *Bulletin of the Seismological Society of America* 76: 837–846.
Hughes S, Barton PJ, and Harrison D (1998) Exploration in the Shetland-Faeroe Basin using densely spaced arrays of ocean-bottom seismometers. *Geophysics* 63: 490–501.
Ilchenko TV (1985) A technique for determining velocity structure from traveltimes along a system of DSS profiles. *Geophysical Journal* 7: 59–66.
Jacob AWB (1975) Dispersed shots at optimum depth – An efficient seismic source for lithospheric studies. *Journal of Geophysics* 41: 63–70.
Jaiswal P, Zelt CA, and Pecher IA (2006) Seismic characterization of a gas hydrate system in the Gulf of Mexico using wide-aperture data. *Geophysical Journal International* 165: 108–120.
Jarchow CM, Catchings RD, and Lutter WJ (1994) Large-explosive source, wide-recording aperture, seismic profiling on the Columbia Plateau, Washington. *Geophysics* 59: 259–271.
Jones K, Warner M, and Brittan J (1999) Anisotropy in multi-offset deep-crustal seismic experiments. *Geophysical Journal International* 264: 205–217.
Julian BR and Gubbins D (1977) Three-dimensional seismic ray tracing. *Journal of Geophysics* 43: 95–113.
Kaila KL and Krishna VG (1992) Deep seismic-sounding studies in India and major discoveries. *Current Science* 62: 117–154.
Kanasewich ER and Chiu SKL (1985) Least-squares inversion of spatial seismic refraction data. *Bulletin of the Seismological Society of America* 75: 865–880.
Kohler WM and Fuis GS (1992) Empirical dependence of seismic ground velocity on the weight of explosives, shotpoint site condition, and recording distance for seismic-refraction data. *Bulletin of the Seismological Society of America* 82: 2032–2044.
Komatitsch D and Tromp J (1999) Introduction to the spectral element method for three-dimensional seismic wave propagation. *Geophysical Journal International* 139: 806–822.
Komatitsch D and Tromp J (2005) The spectral element method in seismology. In: Levander A and Nolet G (eds.) *Geophysical Monograph 157: Seismic Earth: Array Analysis of Broadband Seismograms*, pp. 205–228. Washington, DC: American Geophysical Union.
Korenaga J, Holbrook WS, Kent GM, et al. (2000) Crustal structure of the southeast Greenland margin from joint refraction and reflection seismic tomography. *Journal of Geophysical Research* 105: 21591–21614.
Korenaga J, Holbrook WS, Detrick RS, and Kelemen PB (2001) Gravity anomalies and crustal structure at the southeast Greenland margin. *Journal of Geophysical Research* 106: 8853–8870.
Lafond CF and Levander A (1995) Migration of wide-aperture onshore-offshore seismic data, Central California: Seismic images of late-stage subduction. *Journal of Geophysical Research* 100: 22231–22243.
Lailly P and Sinoquet D (1996) Smooth velocity models in reflection tomography for imaging complex geological structures. *Geophysical Journal International* 124: 349–362.
Lanz E, Maurer H, and Green AG (1998) Refraction tomography over a buried waste disposal site. *Geophysics* 63: 1414–1433.
Larkin SP and Levander A (1996) Wave-equation datuming for improving deep crustal seismic images. *Tectonophysics* 264: 371–379.
Lendl C, Tréhu AM, Goff JA, Levander AR, and Beaudoin BC (1997) Synthetic seismograms through synthetic Franciscan: Insights into factors affecting large-aperture seismic data. *Geophysical Research Letters* 24: 3317–3320.
Levander A (1988) Fourth-order finite-difference *P-SV* seismograms. *Geophysics* 53: 1425–1436.
Levander AR and Holliger K (1992) Small-scale heterogeneity and large-scale velocity structure of the continental crust. *Journal of Geophysical Research* 97: 8797–8804.
Levander A, Fuis GS, Wissinger ES, Lutter WJ, Oldow JS, and Moore TE (1994) Seismic images of the Brooks Range fold-and-thrust belt, arctic Alaska, from an integrated seismic-reflection refraction experiment. *Tectonophysics* 232: 13–30.
Levander A, Zelt CA, and Magnani MB (2005) Crust and upper mantle velocity structure of the Southern Rocky Mountains from the Jemez Lineament to the Cheyenne belt. In: Karlstrom KE and Keller RG (eds.) *Geophysical Monograph Series 154: The Rocky Mountain Region: An Evolving Lithosphere*, pp. 293–308. Washington, DC: American Geophysical Union.
Li Q, Wilcock WSD, Pratt TL, Snelson CM, and Brocher TM (2006) Seismic attenuation structure of the Seattle basin, Washington State, from explosive-source refraction data. *Bulletin of the Seismological Society of America* 96: 553–571.
Lutter WJ and Nowack RL (1990) Inversion for crustal structure using reflections from the PASSCAL Ouachita experiment. *Journal of Geophysical Research* 95: 4633–4646.
Lutter WJ, Nowack RL, and Braile LW (1990) Seismic imaging of upper crustal structure using travel times from the PASSCAL Ouachita experiment. *Journal of Geophysical Research* 95: 4621–4631.
McCaughey M and Singh SC (1997) Simultaneous velocity and interface tomography of normal-incidence and wide-aperture traveltime data. *Geophysical Journal International* 131: 87–99.
McMechan GA and Fuis GS (1987) Ray equation migration of wide-angle reflections from southern Alaska. *Journal of Geophysical Research* 92: 407–420.
McMechan GA and Mooney WD (1980) Asymptotic ray theory and synthetic seismograms for laterally varying structures: Theory and application to the Imperial Valley, California. *Bulletin of the Seismological Society of America* 70: 2021–2035.
Menke W (1989) *Geophysical Data Analysis: Discrete Inverse Theory*. San Diego, CA: Academic Press.
Milkereit B, Epili D, Green AG, Mereu RF, and Morel-à-l' Huissier P (1990) Migration of wide-angle seismic-reflection data from the Grenville Front in Lake Huron. *Journal of Geophysical Research* 95: 10987–10998.
Minshull TA, Singh SC, and Westbrook GK (1994) Seismic velocity structure at a gas hydrate reflector, offshore western Colombia, from full-wave-form inversion. *Journal of Geophysical Research* 99: 4715–4734.
Mooney HM (1983) Synthetic seismograms for body waves: An overview. *First Break* 1: 9–20.
Mooney WD and Brocher TM (1987) Coincident seismic-reflection refraction studies of the continental lithosphere – A global review. *Reviews of Geophysics* 25: 723–743.
Mora P (1988) Elastic wavefield inversion of reflection and transmission data. *Geophysics* 53: 750–759.
Morgan JV, Warner MR, Collins GS, Melosh HJ, and Christeson GL (2000) Peak ring formation in large impact craters. *Earth and Planetary Science Letters* 183: 347–354.
Morgan JV, Christeson GL, and Zelt CA (2002) Testing the resolution of a 3D velocity tomogram across the Chicxulub crater. *Tectonophysics* 355: 215–226.
Morozov IB and Levander A (2002) Depth image focusing in travel-time map based wide-angle migration. *Geophysics* 67: 1903–1912.
Morozova EA, Morozov IB, Smithson SB, and Solodilov LN (1999) Heterogeneity of the uppermost mantle beneath Russian Eurasia from the ultra-long-range profile QUARTZ. *Journal of Geophysical Research* 104: 20329–20348.
Moser TJ (1991) Shortest path calculation of seismic rays. *Geophysics* 56: 59–67.
Moser TJ, Nolet G, and Snieder R (1992) Ray bending revisited. *Bulletin of the Seismological Society of America* 82: 259–288.

Muller G, Roth M, and Korn M (1992) Seismic-wave travel-times in random-media. *Geophysical Journal International* 110: 29–41.

Musacchio G, Mooney WD, Luetgert JH, and Christensen NI (1997) Composition of the crust in the Grenville and Appalachian provinces of North America inferred from *Vp/Vs* ratios. *Journal of Geophysical Research* 102: 15225–15241.

Nakamura Y, Donoho PL, Roper PH, and McPherson PM (1987) Large-offset seismic surveying using ocean-bottom seismographs and air guns – Instrumentation and field technique. *Geophysics* 52: 1601–1611.

Nakanishi I and Yamaguchi K (1986) A numerical experiment on nonlinear image reconstruction from first-arrival times for two-dimensional island arc structure. *Journal of Physics of the Earth* 34: 195–201.

Neves FA, Singh SC, and Priestley KF (1996) Velocity structure of upper-mantle transition zones beneath central Eurasia from seismic inversion using genetic algorithms. *Geophysical Journal International* 125: 869–878.

Nielsen L and Jacobsen BH (2000) Integrated gravity and wide-angle seismic inversion for 2-D crustal modelling. *Geophysical Journal International* 140: 222–232.

Nolet G (1987) Seismic wave propagation and seismic tomography. In: Nolet G (ed.) *Seismic Tomography*, pp. 1–24. Dordecht: Reidel.

Nowack RL and Braile LW (1993) Refraction and wide-angle reflection tomography: Theory and results. In: Iyer HM and Hirahara K (eds.) *Seismic Tomography: Theory and Practice*, pp. 733–765. London: Chapman and Hall.

Operto S, Virieux J, Dessa JX, and Pascal G (2006) Crustal seismic imaging from multifold ocean bottom seismometer data by frequency domain full waveform tomography: Application to the eastern Nankai trough. *Journal of Geophysical Research* 111: B09306. http://dx.doi.org/10.1029/2005JB003835.

Paige CC and Saunders MA (1982) LSQR: An algorithm for sparse linear equations and sparse least squares. *ACM Transactions on Mathematical Software* 8: 43–71.

Palmer D (1981) An introduction to the generalized reciprocal method of seismic refraction interpretation. *Geophysics* 46: 1508–1518.

Park J, Morgan JK, Zelt CA, Okubo PG, Peters L, and Benesh N (2007) Comparative velocity structure of active Hawaiian volcanoes from 3-D onshore-offshore seismic tomography. *Earth and Planetary Science Letters* 259(3–4): 500–516.

Parsons T, McCarthy J, Kohler WM, et al. (1996) Crustal structure of the Colorado Plateau, Arizona: Application of new long-offset seismic data analysis techniques. *Journal of Geophysical Research* 101: 11173–11194.

Parsons T, Blakely RJ, and Brocher TM (2001) A simple algorithm for sequentially incorporating gravity observations in seismic traveltime tomography. *International Geology Review* 43: 1073–1086.

Pavlenkova NI (1982) The intercept-time method – Possibilities and limitations. *Journal of Geophysics* 51: 85–95.

Peirce C and Day AJ (2002) Ocean-bottom seismograph tomographic experiments – A consideration of acquisition geometries vs. resources. *Geophysical Journal International* 151: 543–565.

Podvin P and Lecomte I (1991) Finite difference computation of traveltimes in very contrasted velocity models: A massively parallel approach and its associated tools. *Geophysical Journal International* 105: 271–284.

Popovici AM and Sethian JA (2002) 3-D imaging using higher order fast marching traveltimes. *Geophysics* 67: 604–609.

Poppeliers C and Levander A (2004) Estimation of vertical stochastic scale parameters in the Earth's crystalline crust from seismic reflection data. *Geophysical Research Letters* 31: L13607. http://dx.doi.org/10.1029/2004GL019538.

Pratt RG (1999) Seismic waveform inversion in the frequency domain. Part 1: Theory and verification in a physical scale model. *Geophysics* 64: 888–901.

Pratt RG and Shipp RM (1999) Seismic waveform inversion in the frequency domain. Part 2: Fault delineation in sediments using crosshole data. *Geophysics* 64: 902–914.

Pratt RG, Song Z-M, Williamson P, and Warner M (1996) Two-dimensional velocity models from wide-angle seismic data by wavefield inversion. *Geophysical Journal International* 124: 323–340.

Pratt GR, Shin C, and Hicks GJ (1998) Gauss-Newton and full Newton methods in frequency-space seismic waveform inversion. *Geophysical Journal International* 133: 341–362.

Press WH, Teukolsky SA, Vetterling WT, and Flannery BP (1992) *Numerical Recipes in Fortran: The Art of Scientific Computing*, 2nd edn. Cambridge, UK: Cambridge University Press.

Pullammanappallil SK and Louie JN (1994) A generalized simulated-annealing optimization for inversion of first-arrival times. *Bulletin of the Seismological Society of America* 84: 1397–1409.

Purdy GM (1982) The correction for the travel time effects of seafloor topography in the interpretation of marine seismic data. *Journal of Geophysical Research* 87: 8389–8396.

Pyun S, Shin C, Min DJ, and Ha T (2005) Refraction traveltime tomography using damped monochromatic wavefield. *Geophysics* 70: U1–U7.

Ramachandran K, Dosso SE, Spence GD, Hyndman RD, and Brocher TM (2005) Forearc structure beneath southwestern British Columbia: A three-dimensional tomographic velocity model. *Journal of Geophysical Research* 110: B02303. http://dx.doi.org/10.1029/2004JB003258.

Ravaut C, Operto S, Improta L, Virieux J, Herrero A, and Dell'Aversana P (2004) Multiscale imaging of complex structures from multifold wide-aperture seismic data by frequency-domain full-waveform tomography: Application to a thrust belt. *Geophysical Journal International* 159: 1032–1056.

Rawlinson N and Sambridge M (2003a) Seismic traveltime tomography of the crust and lithosphere. *Advances in Geophysics* 46: 181–198.

Rawlinson N and Sambridge M (2003b) Irregular interface parametrization in 3-D wide-angle seismic traveltime tomography. *Geophysical Journal International* 155: 79–92.

Rawlinson N and Sambridge M (2004) Wave front evolution in strongly heterogeneous layered media using the fast marching method. *Geophysical Journal International* 156: 631–647.

Rawlinson N, Houseman GA, and Sambridge M (2001) Inversion of seismic refraction and wide-angle reflection traveltimes for 3-D layered crustal structure. *Geophysical Journal International* 145: 381–401.

Robertsson JOA, Blanch JO, and Symes WW (1994) Viscoelastic finite-difference modeling. *Geophysics* 59: 1444–1456.

Robinson EA and Treitel S (1980) *Geophysical Signal Analysis*. Englewood Cliffs, NJ: Prentice-Hall.

Roy L, Sen MK, McIntosh K, Stoffa PL, and Nakamura Y (2005) Joint inversion of first arrival seismic travel-time and gravity data. *Journal of Geophysics and Engineering* 2: 277–289.

Sain K and Kaila KL (1996) Ambiguity in the solution to the velocity inversion problem and a solution by joint inversion of seismic refraction and wide-angle reflection times. *Geophysical Journal International* 124: 215–227.

Scales JA (1989) On the use of conjugate-gradient to calculate the eigenvalues and singular-values of large, sparse matrices. *Geophysical Journal* 97: 179–183.

Scales JA (1995) *Theory of Seismic Imaging*. Berlin: Springer, 291 pp.

Scales JA, Gersztenkorn A, and Treitel S (1988) Fast lp solution of large, sparse, linear–systems: Application to seismic travel time tomography. *Journal of Computational Physics* 75: 314–333.

Scales JA, Docherty P, and Gersztenkorn A (1990) Regularisation of nonlinear inverse problems: Imaging the near–surface weathering layer. *Inverse Problems* 6: 115–131.

Schlindwein V, Bonnemann C, Reichert C, Grevemeyer I, and Flueh E (2003) Three-dimensional seismic refraction tomography of the crustal structure at the ION site on the Ninetyeast Ridge, Indian Ocean. *Geophysical Journal International* 152: 171–184.

Schneider WA (1978) Integral formulation in two and three dimensions. *Geophysics* 43: 49–76.

Sen M and Stoffa PL (1995) *Global Optimization Methods in Geophysical Inversion*. Amsterdam: Elsevier.

Sethian JA and Popovici AM (1999) 3-D traveltime computation using the fast marching method. *Geophysics* 64: 516–523.

Shaw PR and Orcutt JA (1985) Waveform inversion of seismic refraction data and applications to young Pacific crust. *Geophysical Journal of the Royal Astronomical Society* 82: 375–414.

Shipp RM and Singh SC (2002) Two-dimensional full wavefield inversion of wide-aperture marine seismic streamer data. *Geophysical Journal International* 151: 325–344.

Smith RB, Braile LW, and Keller GR (1975) Upper crustal low-velocity layers – Possible effect of high-temperatures over a mantle upwarp at Basin Range Colorado Plateau transition. *Earth and Planetary Science Letters* 28: 197–204.

Sommerfeld A (1954) *Lectures on Theoretical Physics V: Optics V*. New York: Academic Press, 383 pp.

Spence GD, Whittall KP, and Clowes RM (1984) Practical synthetic seismograms for laterally varying media calculated by asymptotic ray theory. *Bulletin of the Seismological Society of America* 74: 1209–1223.

Spence GD, Clowes RM, and Ellis RM (1985) Seismic structure across the active subduction zone of western Canada. *Journal of Geophysical Research* 90: 6754–6772.

Spitzer R and White RS (2005) Advances in seismic imaging through basalts: A case study from the Faroe-Shetland Basin. *Petroleum Geoscience* 11: 147–156.

Spudich P and Orcutt J (1980) Petrology and porosity of an oceanic crustal site: Results from wave form modeling of seismic refraction data. *Journal of Geophysical Research* 85: 1409–1433.

Sroda P (2006) Seismic anisotropy of the upper crust in southeastern Poland – Effect of the compressional deformation at the EEC margin: Results of CELEBRATION 2000 seismic data inversion. *Geophysical Research Letters* 33: L22302. http://dx.doi.org/10.1029/2006GL027701.

Stoerzel A and Smithson SB (1998) Two-dimensional travel time inversion for the crustal *P* and *S* wave velocity structure of the Ruby Mountains metamorphic core complex, NE Nevada. *Journal of Geophysical Research* 103: 21121–21143.

Stolt RH (1978) Migration by Fourier transform. *Geophysics* 43: 23–48.

Sun R and McMechan GA (1992) 2-D full-wave-field inversion for wide-aperture, elastic, seismic data. *Geophysical Journal International* 111: 1–10.

Symons NP and Crosson RS (1997) Seismic velocity structure of the Puget Sound region from 3-D non-linear tomography. *Geophysical Research Letters* 24: 2593–2596.

Taner MT and Koehler F (1969) Velocity spectra – Digital computer derivation applications of velocity functions. *Geophysics* 34: 859.

Tarantola A (1984) Inversion of seismic reflection data in the acoustic approximation. *Geophysics* 49: 1259–1266.

Thybo H and Perchuc E (1997) The seismic 8° discontinuity and partial melting in the continental mantle. *Science* 275: 1626–1629.

Toomey DR, Solomon SC, and Purdy GM (1994) Tomographic imaging of the shallow crustal structure of the East Pacific Rise at 9°30′N. *Journal of Geophysical Research* 99: 24135–24157.

Trinks I, Singh SC, ChapMan CH, Barton PJ, Bosch M, and Cherrett A (2005) Adaptive traveltime tomography of densely sampled seismic data. *Geophysical Journal International* 160: 925–938.

Um J and Thurber C (1987) A fast algorithm for two-point seismic ray tracing. *Bulletin of the Seismological Society of America* 77: 972–986.

Van Avendonk HJA (2004) Slowness-weighted diffraction stack for migrating wide-angle seismic data in laterally varying media. *Geophysics* 69: 1046–1052.

Van Avendonk HJA, Harding AJ, Orcutt JA, and McClain JS (1998) A two-dimensional tomographic study of the Clipperton transform, fault. *Journal of Geophysical Research* 103: 17885–17899.

Van Avendonk HJA, Harding AJ, Orcutt JA, and Holbrook WS (2001) Hybrid shortest path and ray bending method for traveltime and raypath calculations. *Geophysics* 66: 648–653.

Van Avendonk HJA, Shillington DJ, Holbrook WS, and Hornbach MJ (2004) Inferring crustal structure in the Aleutian arc from a sparse wide-angle seismic data set. *Geochemistry, Geophysics, Geosystems* 5. http://dx.doi.org/10.1029/2003GC000664.

Van Trier J and Symes WW (1991) Upwind finite-difference calculation of traveltimes. *Geophysics* 56: 812–821.

Versteeg R (1994) The Marmousi experience: Velocity model determination on a synthetic complex data set. *The Leading Edge* 13: 927–936.

Vidale JE (1988) Finite-difference calculation of traveltimes. *Bulletin of the Seismological Society of America* 78: 2062–2076.

Vidale JE (1990) Finite-difference calculation of traveltimes in three dimensions. *Geophysics* 55: 521–526.

Watanabe T, Matsuoka T, and Ashida Y (1999) Seismic traveltime tomography using Fresnel volume approach. *Society of Exploration Geophysicists Technical Program Extended Abstracts* 18: 1402–1405.

Weber M (1988) Computation of body-wave seismograms in absorbing 2-D media using the Gaussian-beam method: Comparison with exact methods. *Geophysical Journal* 92: 9–24.

Wenzel F and Sandmeier KJ (1992) Geophysical evidence for fluids in the crust beneath the Black-Forest, SW Germany. *Earth-Science Reviews* 32: 61–75.

White DJ (1989) Two-dimensional seismic refraction tomography. *Geophysical Journal International* 97: 223–245.

White DJ and Boland AV (1992) A comparison of forward modeling and inversion of seismic first arrivals over the Kapuskasing Uplift. *Bulletin of the Seismological Society of America* 82: 304–322.

White DJ and Clowes RM (1994) Seismic attenuation structure beneath the Juan-de-Fuca Ridge from tomographic inversion of amplitudes. *Journal of Geophysical Research* 99: 3043–3056.

Wiggins WJ (1984) Kirchhoff integral extrapolation and migration of nonplanar data. *Geophysics* 49: 1239–1248.

Wilcock WSD, Solomon SC, Purdy GM, and Toomey DR (1995) Seismic attenuation structure of the East Pacific Rise near 9 degrees 30′N. *Journal of Geophysical Research* 100: 24147–24165.

Wissinger ES, Levander A, and Christensen NI (1997) Seismic images of crustal duplexing and continental subduction in the Brooks Range. *Journal of Geophysical Research* 102: 20847–20871.

Yilmaz O (2001) *Seismic Data Analysis: Processing, Inversion and Interpretation of Seismic Data*, vols. I and II. Tulsa, OK: Society of Exploration Geophysics, 2024.

Zelt CA (1994) 3-D velocity structure from simultaneous traveltime inversion of in-line seismic data along intersecting profiles. *Geophysical Journal International* 118: 795–801.

Zelt CA (1998) Lateral velocity resolution from three-dimensional seismic refraction data. *Geophysical Journal International* 135: 1101–1112.

Zelt CA (1999) Modeling strategies and model assessment for wide-angle seismic traveltime data. *Geophysical Journal International* 139: 183–204.

Zelt CA and Barton PJ (1998) Three-dimensional seismic refraction tomography: A comparison of two methods applied to data from the Faeroe Basin. *Journal of Geophysical Research* 103: 7187–7210.

Zelt CA and Ellis RM (1988) Practical and efficient ray tracing in two-dimensional media for rapid traveltime and amplitude forward modeling. *Canadian Journal of Exploration Geophysics* 24: 16–31.

Zelt CA and Ellis RM (1990) Crust and upper mantle Q from seismic refraction data – Peace River region. *Canadian Journal of Earth Sciences* 27: 1040–1047.

Zelt CA and Forsyth DA (1994) Modeling wide-angle seismic data for crustal structure: Southeastern Grenville province. *Journal of Geophysical Research* 99: 11687–11704.

Zelt CA and Smith RB (1992) Seismic traveltime inversion for 2-D crustal velocity structure. *Geophysical Journal International* 108: 16–34.

Zelt CA and White DJ (1995) Crustal structure and tectonics of the southeastern Canadian Cordillera. *Journal of Geophysical Research* 100: 24255–24273.

Zelt CA and Zelt BC (1998) Study of out-of-plane effects in the inversion of refraction/wide-angle reflection traveltimes. *Tectonophysics* 286: 209–221.

Zelt BC, Ellis RM, and Clowes RM (1993) Crustal velocity structure in the eastern Insular and southernmost Coast belts, Canadian Cordillera. *Canadian Journal of Earth Sciences* 30: 1014–1027.

Zelt BC, Ellis RM, Clowes RM, and Hole JA (1996) Inversion of three-dimensional wide-angle seismic data from the southwestern Canadian Cordillera. *Journal of Geophysical Research* 101: 8503–8529.

Zelt BC, Talwani M, and Zelt CA (1998) Prestack depth migration of dense wide-angle seismic data. *Tectonophysics* 286: 193–208.

Zelt CA, Hojka AM, Flueh ER, and McIntosh KD (1999) 3D simultaneous seismic refraction and reflection tomography of wide-angle data from the central Chilean margin. *Geophysical Research Letters* 26: 2577–2580.

Zelt CA, Sain K, Naumenko JV, and Sawyer DS (2003) Assessment of crustal velocity models using seismic refraction and reflection tomography. *Geophysical Journal International* 153: 609–626.

Zelt CA, Magnani MB, Levander A, et al. (2004) BOLIVAR: Crustal structure across the Caribbean-South American plate boundary at 67.5 W: Results from wide-angle seismic data. In: Program with Abstracts, Fall Meeting, San Francisco, CA: American Geophysical Union.

Zelt CA, Azaria A, and Levander A (2006a) 3D seismic refraction traveltime tomography at a groundwater contamination site. *Geophysics* 71: H67–H78.

Zelt CA, Ellis RM, and Zelt BC (2006b) 3-D structure across the Tintina strike-slip fault, northern Canadian Cordillera, from seismic refraction and reflection tomography. *Geophysical Journal International* 167: 1292–1308.

Zhang J and Toksöz MN (1998) Nonlinear refraction traveltime tomography. *Geophysics* 64: 1726–1737.

Zhang J, ten Brink US, and Toksöz MN (1998) Nonlinear refraction and reflection traveltime tomography. *Journal of Geophysical Research* 103: 29743–29757.

Zhao Z, Kubota R, Fumio S, and Iizuka S (1997) Crustal Structure in the southern Kanto-Tokai region derived from tomographic method for seismic explosion survey. *Journal of Physics of the Earth* 45: 433–453.

Relevant Website

http://www.trip.caam.rice.edu – The Rice Inversion Project.

This page intentionally left blank

1.16 Crust and Lithospheric Structure – Natural Source Portable Array Studies of the Continental Lithosphere

DE James, Carnegie Institution of Washington, Washington, DC, USA

© 2007 Elsevier B.V. All rights reserved.

This chapter is reproduced from the previous edition, Volume 1, pp. 479–531, © 2007 Elsevier B.V.

1.16.1	**Introduction**	513
1.16.2	**Natural Source Portable Array Seismology**	515
1.16.2.1	Instrumentation	515
1.16.2.2	Portable Array Experiments	517
1.16.2.3	Field Installations and Data Acquisition	517
1.16.2.4	Methods of Analysis	517
1.16.2.4.1	Body wave tomography	518
1.16.2.4.2	Surface wave tomography	518
1.16.2.4.3	Discontinuity imaging	519
1.16.2.4.4	Anisotropy	520
1.16.2.5	Methodological Weaknesses and Caveats	521
1.16.3	**Seismic Structure of Tectonically Active Regions**	521
1.16.3.1	Western North America	522
1.16.3.1.1	Snake River Plain/Yellowstone and Wyoming Craton	523
1.16.3.1.2	Southern Rocky Mountain region	525
1.16.3.1.3	Rio Grande Rift and Colorado Plateau	526
1.16.3.1.4	Great Basin	526
1.16.3.1.5	Sierra Nevada	528
1.16.3.2	Indian–Eurasian Continental Collisional Zone	528
1.16.3.2.1	Crustal structure	528
1.16.3.2.2	Seismic structure of the uppermost mantle	531
1.16.3.3	Continental Margin Subduction Zones	531
1.16.3.3.1	Andean studies	533
1.16.3.3.2	Central America and Caribbean	537
1.16.3.3.3	Cascadia	537
1.16.3.3.4	Alaska	537
1.16.3.3.5	Kamchatka	537
1.16.3.4	Active Continental Rifts	537
1.16.4	**Stable Platforms**	539
1.16.4.1	Central and Eastern North America	539
1.16.4.2	Australia	541
1.16.4.3	South America	543
1.16.4.4	Antarctica	544
1.16.5	**Archean Cratons**	544
1.16.5.1	Southern Africa	545
1.16.5.1.1	Mantle tomographic images	547
1.16.5.1.2	Crustal thickness and Moho structure beneath southern Africa	549
1.16.5.2	Passive Array Studies of Other Cratons	549
1.16.6	**Seismic Constraints on Composition and Temperature of the Continental Lithosphere**	551
1.16.7	**EarthScope, USArray, and the Future of Portable Array Seismology**	551
1.16.8	**Discussion**	552
References		552

1.16.1 Introduction

The discovery of plate tectonics fundamentally changed scientists' view of the Earth, generating an entirely new set of precepts for how continents form and evolve over time. Plate tectonics elevated the central role of the continental 'lithosphere' as opposed to the 'crust,' and it established a direct relationship between dynamic processes deep in the mantle and shaping of continents. The continental lithosphere is now recognized to be a complex agglomeration of accreted and tectonically modified lithospheric blocks that are the repository of most of the Earth's history. Ironically, the seafloor that provided us with much of the

 http://dx.doi.org/10.1016/B978-0-444-53802-4.00014-2

proof of plate tectonics is nowhere older than about 200 Ma and thus contains no information on the earlier geologic history of the Earth. As the theory of plate tectonics was refined and its implications for continental dynamics and evolution better understood, it became increasingly evident that an essential key to understanding the continents lay in our ability to image in detail the 3-D structures of the lithospheric and sublithospheric mantle.

Passive array seismology, notably portable broadband seismology, emerged over the past 25 years to fill the void between detailed active source crustal seismology and low-resolution seismology based on widely dispersed stations of the global seismic network (GSN), neither of which was properly suited to the study of continental lithospheric mantle. Despite the demand for new seismic tools to study lithosphere-scale structure of continents, however, passive array seismology would not exist today without key technical breakthroughs. Lithosphere-scale imaging has been revolutionized in the past 25 years by the advent of portable high-fidelity low-power 24-bit digital seismic systems, including portable broadband sensors with wide frequency bandwidth and high dynamic range. This new instrumentation provides the tools for seismic studies broadly termed 'passive array experiments.' Passive array experiments involve the deployment of tens or even hundreds of instruments, broadband and short-period, each of which is capable of operating unattended for months to years at a time in the most remote regions of the Earth. The term 'passive' derives from the fact that these stand-alone arrays of self-sufficient stations record seismic data from earthquakes around the world continuously over periods of months and even years at a time. These passive array earthquake recordings comprise the essential data for analyzing lithospheric structure.

While fixed array seismology emerged in the 1960s with the construction of the US Department of Defense facilities such as Large Aperture Seismic Array (LASA) in Montana (e.g., Aki et al., 1976) and NORSAR in Norway to monitor nuclear explosions, portable array seismology based on earthquake observations (as opposed to timed explosions) is a recent phenomenon. Prior to the development of low-power portable array instrumentation, lithospheric studies were confined largely to the crust: with very few exceptions (long profiles from US and Soviet nuclear blasts), high-resolution imaging of deeper structures in the continental lithosphere and in the mantle beneath the lithosphere was largely beyond the means of existing instrumentation and methods. The precursors to modern passive array seismology were found at a handful of institutions that engaged in portable seismic experiments with in-house instrumentation of limited functionality. For most groups, severe constraints were imposed by aging analog instruments, narrow-frequency bandwidths, and incompatible data types that made data exchange difficult. The inability of seismologists to explore deeper regions of the mantle beneath the continents at geologic scales with existing instrumentation precipitated a crisis in seismology, one that led to an innovative rethinking of the instrumentation and experimental design required to explore the deep lithosphere (e.g., Panel on Seismological Studies, 1984). Some of the pioneering efforts to implement portable arrays, for example, were motivated by the fact that 3-D imaging of surface waves across heterogeneous regions of continents thousands of kilometers in extent at geologically useful resolution requires relatively large numbers of closely spaced (100–200 km or better) instruments. One of the first portable seismic studies thus motivated was the Network of Autonomously Recording Seismography (NARS) project, a linear array of 16 long-period seismographs across western Europe for studying surface wave propagation (Nolet and Vlaar, 1981; Nolet et al., 1986). The successful NARS project, largely the work of Nolet and colleagues at Utrecht, was followed closely in time by a national effort within the US seismological research community to initiate a consortium program of portable array seismology for the study of the continental lithosphere. By 1984, the seismic community within the United States, through a series of workshops and scientific reports from the National Academy of Sciences, the National Science Foundation (NSF), and others, had defined broad goals for a new generation of seismic instrumentation, goals so ambitious in scope that they could be achieved only through the collective strength of a national seismology consortium. The formation in 1984 of the Incorporated Research Institutions for Seismology (IRIS) was a watershed event for seismology worldwide. By the mid-1980s, large-scale efforts were underway, not only within the United States but also elsewhere, to design and acquire large numbers of high-performance portable instruments that could be arrayed anywhere in the world for geologic-scale imaging of the deep underpinnings of continents (e.g., Aster et al., 2005). The IRIS initiative for portable seismology, formally termed the Program for Array Seismic Studies of the Continental Lithosphere (PASSCAL) and funded by the NSF, acquired several hundred standardized state-of-the-art portable seismic data loggers and sensors (broadband, intermediate period, and short period) over the next decades. This instrument pool is housed and maintained at a central PASSCAL instrumentation facility and is available to the scientific community for seismic research. IRIS also supports the GSN of about 140 permanent broadband stations worldwide, and both PASSCAL and GSN digital data are archived and provided to researchers worldwide through the IRIS Data Management Center (DMC). While parallel efforts to organize both instrumentation and data archiving have been undertaken elsewhere in the world and continue to grow in importance, IRIS/PASSCAL remains the dominant force behind portable broadband seismology around the globe. Major studies with PASSCAL instrumentation have been, and are being, carried out on every continent on the globe (**Figure 1**). As discussed near the end of this chapter, the scientific capabilities developed over the past 20 years as part of PASSCAL are today being leveraged to implement the EarthScope USArray program to image all of the continental United States.

The purpose of this chapter is to acquaint the nonspecialist with the current observational capabilities of portable array seismology, as well as with major findings that have emerged from large-scale portable, primarily broadband, experiments. The explosive growth of the literature pertaining to portable array seismology precludes a comprehensive review of results in the brief space allotted in this chapter. The sampling of portable array seismic experiments worldwide that are included here thus reflects the author's personal preference for which results have most impacted the science. As such, this chapter is intended to provide an abridged overview of passive array seismology's contribution to our knowledge of the deep velocity and discontinuity

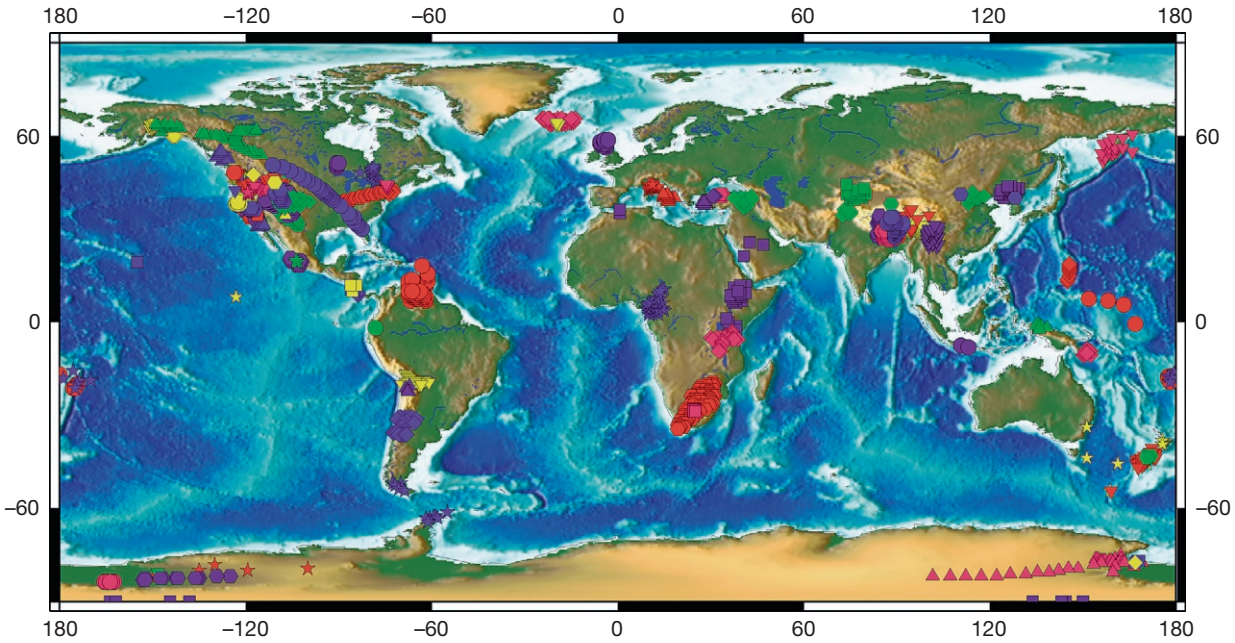

Figure 1 World map showing locations of PASSCAL broadband stations for which data are archived at the IRIS Data Management Center as of late 2006. Figure courtesy of Bruce Beaudoin and the PASSCAL Instrument Center.

structure of continental lithosphere and how that in turn has led to a better understanding of continental formation and evolution.

1.16.2 Natural Source Portable Array Seismology

Controlled-source seismic methods that utilize explosions or other artificial sound sources have proved to be very effective tools for exploring the Earth's crust in two and three dimensions. It is, however, a far more demanding task to probe the deep crust and upper mantle at anything approaching a similarly 'geologically meaningful' resolution. In fact, until the development in the last decade of portable digital broadband seismic systems with continuous high-fidelity recording capabilities and accurate absolute Global Positioning System (GPS) timing, high-resolution 3-D imaging of the continental mantle was essentially beyond the reach of seismology. The seismic sources for broadband array experiments are earthquakes of all kinds, from nearby local events to 'teleseismic' events at epicentral distances >27°; thus, broadband stations typically record continuously for up to 1–2 years. In broadband seismology (and most array seismology today), all three components of ground motion (vertical and two orthogonal horizontal directions, generally N–S and E–W) are recorded and the systems are capable of observing most of the radiated earthquake spectrum that is used for continent-scale seismic studies. Broadband seismic records, coupled with extremely accurate GPS clock timing, are the key ingredients for geologic-scale imaging of deep continental structure.

1.16.2.1 Instrumentation

The emergence of low-power portable broadband digital instrumentation represented a first-order revolution in seismology. For the first time, portable seismic instruments capable of recording data of near-observatory quality could be deployed anywhere in the world (Aster et al., 2005; Owens and Fowler, 2003). The circumstances that led to that revolution in seismic instrumentation and data quality were a combination of good timing and the formation of IRIS. Of vital importance was the rapid development of microprocessor technology for the emerging popular computer market. Thus, the design for versatile multichannel digital seismograph systems was leveraged from state-of-the-art digital technologies developed for computer and other mass consumer market applications. The following is a brief description of broadband instrumentation as it pertains to passive array studies of continental lithosphere.

The standard portable array seismic system today (2006) consists of a digital data logger and a seismometer (**Figure 2**), a GPS unit for both absolute timing and station location, a battery/solar panel power supply, and auxiliary devices and cables for connecting these units and communicating with them in the field. Photos of a typical field installation are shown in **Figure 2(c)**. The data loggers are low-power, high-dynamic-range (24-bit) microprocessor-based digital recording systems with several gigabytes or more of mass storage to allow continuous three-channel recording for months unattended. While digitizing rates of up to 1000 samples per second are attainable with current data loggers, sampling rates are typically around 40 samples per second, which is sufficient for all teleseismic recording and for most regional events. In addition to continuous recording, the data loggers can analyze incoming events in real time and activate 'triggers' to initiate higher sample rates to record over a specified time window according to the nature of the incoming seismic signal.

The portable broadband sensor, rugged, low-power, and simple to install, is the key component of continent-scale seismology. Broadband, high-dynamic-range units have been available since about 1990 with the production of advanced

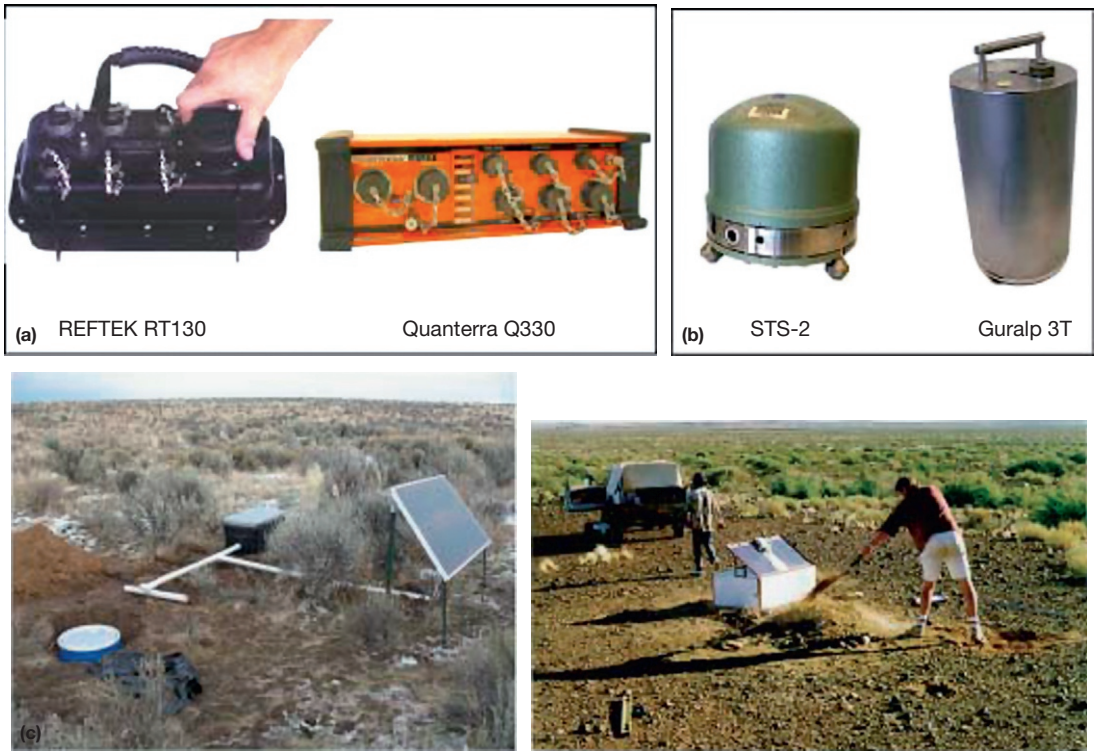

Figure 2 (a) Standard low-power (<1.0 W) 24-bit six-channel data loggers used in passive array experiments. The REFTEK RT-130 shown on the left can record at least three channels of data in several data streams of differing sample rates. The data logger uses GPS for absolute timing (generally to microsecond accuracy) and flash memory cards for mass storage. The Quanterra Q330 data logger shown on the right is specifically configured for real-time telemetry that includes duplex communication and burst or continuous transmission. (b) State-of-the-art force-feedback portable broadband sensors in general use today. Both units shown are low-power (<1.0 W), are capable of remote mass recentering, and have flat velocity-frequency response 50–0.008 Hz. On the left, the Streckeisen STS-2 is manufactured in Switzerland, weighs about 9 kg, and is 23 cm high. On the right, the Guralp CMG-3T, manufactured in England, weighs 14 kg and stands 38 cm high. (c) Typical portable field installations. Left: basic broadband station layout at a High Lava Plains (HLP) site in eastern Oregon. Sensor vault consists of a 30 gallon (blue) plastic drum in which the sensor is placed on a concrete base, oriented and leveled, and thermally insulated. A watertight enclosure houses the data logger, powerbox, and batteries. Wiring between sensor and data logger and power sources is through PVC conduit. The station shown is powered by a single 60 W solar panel and two deep-cycle marine batteries intended to last the full 2-year life of the installation. Right: broadband station for the southern African (Kaapvaal) experiment. Vault is covered with insulating dirt to a depth of at least 30–40 cm. Solar panels and GPS unit are mounted on the roof of a 'doghouse' wherein the data logger and auxiliary electronics are housed.

broadband systems by Streckeisen in Switzerland and Guralp in England (Figure 2(b)). All portable broadband seismometers in use today operate on the principle of a negative feedback loop that is applied to a small inertial mass to hold it fixed relative to the moving seismometer reference frame. The amount of electromotive force that is applied to keep the mass in place is used to measure ground acceleration. Because the mass moves very slightly (ideally, not at all), the force-feedback system has much better linearity and significantly expanded frequency range relative to mechanical seismometers (see, e.g., Lay and Wallace, 1995; Wielandt and Streckeisen, 1982, for further discussion). Compact low-power electronic force-feedback systems can thus be configured for a very wide range of seismometer responses: the state-of-the-art Streckeisen STS-2 and Guralp CMG-3T portable sensors, for example, have a flat velocity response from about 50 to 0.008 Hz, sufficient to cover virtually all of the body wave and surface wave bandwidth of interest for lithospheric studies.

Much of the imaging of the deep continents (see Section 1.16.2.4) that is done with portable arrays depends on precise absolute timing made possible for the first time worldwide by the US Department of Defense launch of the GPS in the 1990s. GPS satellites transmit signals that contain extremely accurate time codes, as well as information that allows a GPS receiver on the Earth's surface to compute its position to within a few meters anywhere on the globe. The accurate time signals, recorded independently at each seismic station, allow seismic signals across an entire array of stations, each with independent timing, to be correlated to hundredths or even thousandths of a second, making it possible to quantify travel-time differences between stations at very high accuracy. The availability of matched broadband stations that operate with an extremely accurate common time base is the critical factor that has made high-resolution tomographic imaging of the continental lithosphere a reality.

Real-time telemetry, both radio and satellite, has evolved slowly since the late 1980s when the first very low-bandwidth satellite transmission systems were deployed (e.g., Poupinet et al., 1989a,b). While progress, particularly in satellite communication, has been surprisingly sporadic, telemetry has

played an increasing role in passive array seismology in the last decade. Systems that transmit data to a central collection site in approximately real time have proved to significantly improve both quality control and data recovery. Although the most commonly used systems to date are still those that employ line-of-sight radios (e.g., the PASSCAL 32-station broadband telemetering system), satellite and cellular communications are increasingly feasible, both technically and economically. Data from many of the USArray stations (see **Section 1.16.7**) are transmitted via satellite.

1.16.2.2 Portable Array Experiments

Natural source portable array experiments have been carried out in every continent. **Figure 1** shows PASSCAL deployments over just the 5-year period 2000–05. In addition to the PASSCAL experiments shown in **Figure 1**, substantial numbers of other portable seismic experiments have been carried out in recent years by other international research groups. (Space limitations confine the scope of this chapter to portable array studies of continental regions. Unfortunately, this excludes even mature island arcs, notably Japan, where dense networks of advanced permanent seismic stations blanket the islands. A satisfactory summary of the many fine studies of subduction zone structure beneath Japan based on data from the permanent networks is beyond the bounds of this work.) While local and regional events are commonly incorporated in portable array experiments, nearly all broadband imaging depends heavily on teleseismic events, epicentral distances $>27°$. Station arrays are designed according to the nature of the scientific target(s), the methodologies to be used, the number and type of the instruments available for the experiment, and the distribution of teleseismic sources. In general, arrays tend to be deployed either along 1-D transects or in a 2-D grid. Station density is typically constrained by the number of instruments: where ample instrumentation is available, interstation spacing of about 10 km is sufficient for unaliased imaging at dominant teleseismic wave frequencies, where maximum P-wave energy tends to be concentrated around 1 Hz (e.g., Levander, 2003). Nonetheless, a number of portable broadband experiments have deployed instruments along profiles at even denser intervals, where the objective was to image crustal and upper-mantle discontinuities across complex geologic terranes. Examples include Nabelek et al. (1993), $\sim$5 km spacing along a linear profile across the Oregon Cascades, and Zhao et al. (2001), $\sim$5–10 km along the INDEPTH III transect in central Tibet. A few passive array experiments, most with the objective of imaging very shallow structures, may have instrument spacing as close as 1 km (e.g., Roecker et al., 2004; Thurber et al., 2004). Where the targets are deep crustal or mantle structures, however, even very ambitious projects more commonly involve interstation spacing around 20 km (e.g., Wilson and Aster, 2003; the La RISTRA profile in the western United States, with station spacing of about 18 km along a 950 km transect). In almost every case, primarily because of limitations in the numbers of instruments, dense deployments are more commonly seen in linear transects and the resulting analysis 2-D rather than 3-D. Where the scientific objective is 3-D imaging of larger regions encompassing multiple terranes, deployments tend to be more widely spaced, either in a grid or on a long profile, and interstation distances may be 50–100 km. Typical of a gridded experiment of this type is the southern African seismic experiment (e.g., James, 2003) where station spacing was on the order of 100 km and array dimensions about 1800×600 km.

1.16.2.3 Field Installations and Data Acquisition

A typical portable broadband installation is effectively a semipermanent miniobservatory. As such, its functional capabilities approach those of a state-of-the-art global seismic station and, because it can be sited in remote locations with little cultural noise, may even be superior in performance. While relatively few studies have sought to define optimum vault design for broadband installations (e.g., de la Torre and Sheehan, 2005), the primary keys to achieving low noise include thermal stability, proximity to bedrock, and absence of cultural noise. Photos of a typical portable station installation are shown in **Figure 2(c)**. While no absolute standards have been adopted for the construction of a portable broadband station, a number of features are common to virtually all installations. As shown in **Figure 2(c)**, the three-component broadband sensor is installed below ground in a constant temperature 'vault,' typically constructed from a plastic or steel drum. A thin concrete layer, laid down to provide a level surface for sensor installation, is poured atop bedrock at the bottom of the hole. When steel drums are used for the vault, it is common to remove the base of the drum and to isolate the drum walls from the concrete pad. Where plastic drums are used, the bottom of the drum may be left intact, worked into the concrete layer atop bedrock, and then filled with an additional several centimeters of concrete as a base pad for the sensor. The sensor pad, ideally bonded to bedrock, is typically some 40–70 cm beneath ground level. The sensor is leveled and the horizontal components oriented precisely. Cables are connected via PVC pipe (see **Figure 2(c)**). A close-fitting Styrofoam housing and other insulation are placed over the sensor and within the drum to minimize thermally induced air circulation that will adversely affect sensor stability. After the sensor has been installed, the lid of the vault is sealed and the whole assembly is buried in insulating dirt to a depth of at least 50 cm. Under normal operations, the sensor vault will remain sealed until the end of the deployment. A typical station is powered by one or two standard marine deep-cycle batteries that are kept charged by solar panels. Months of seismic data, typically sampled at a rate of 20–40 samples per second, can be stored on several gigabytes of disk or flash memory. A small external GPS antenna is mounted with an unobstructed view of the sky. Routine station servicing, typically at 3–6-month intervals, consists primarily of checking that data recording is normal and the GPS clock is operating correctly, swapping out data memory cards and calibrating the sensor. Where telemetered, cellular, or satellite communication has been implemented, stations may need no on-site servicing at all. For PASSCAL experiments, data collected at each station are generally returned to a local operations center where they are copied, preprocessed into a standard database, and transmitted to the IRIS DMC for permanent data archiving.

1.16.2.4 Methods of Analysis

The dramatic increase in the volume of high-quality portable broadband data has spurred the development of advanced

imaging tools to capitalize on those data, and a vast literature has developed on the subject in just the past few years (e.g., Levander, 2003; Levander and Nolet, 2005; Pavlis, 2003; Sheehan et al., 2000; Wilson and Aster, 2005). The brief nontechnical summary of methodologies presented later in the text touches on some of the more common methods in use today, but for more comprehensive treatment, the reader is referred to **Chapters 1.08** and **1.10** in this volume and to the literature cited here.

Part of the sea change brought about by increasingly large-scale deployments of broadband instruments is the development of (1) tomographic methods to image geologically identifiable features in the mantle and (2) advanced methods for direct waveform imaging of crust and mantle discontinuities similar in style to that used in seismic exploration (e.g., Pavlis, 2003). Two basic categories underpin most of the imaging that is done with portable arrays. The first may be termed 'volumetric' imaging, the most important class of which is tomography, both body wave and surface wave, although it also includes attenuation tomography and mantle anisotropy. High-resolution tomography demands quality seismograms from high-performance standardized instrumentation, with high-fidelity waveforms and very accurate absolute timing. These requirements have only recently been realized, so that as the quality and quantity of data have improved, tomographic imaging has become one of the most powerful tools seismologists have to study the deep continental lithosphere.

'Discontinuity,' or scattering, imaging is complementary to tomographic imaging and is aimed at direct imaging of subsurface discontinuity structure (scatterers) in both two and three dimensions. All discontinuity imaging is based on the interpretation of scattered energy in the seismogram, that is, the conversions and reflections of P and S waves at velocity discontinuities in the Earth where rock types or material properties of the rocks change significantly over relatively short-distance scales. As the station spacing of portable arrays has densified, analytic methods developed for seismic reflection imaging by the exploration industry have become increasingly applicable (e.g., Levander, 2003; Pavlis, 2003; Rondenay et al., 2005). Continuous unaliased high-resolution images in 2-D are now relatively common, and continuous 3-D imaging has been experimented with in several recent portable array studies.

1.16.2.4.1 Body wave tomography

Except where high levels of earthquake activity are in the same geographic region of interest as the observing stations, body wave tomography of structure beneath a network of portable stations is generally based on teleseismic relative arrival times measured across the array (e.g., Nolet, 1987; VanDecar, 1991). The marked improvement in the reliability and resolving capability of portable array body wave tomography over the past decade owes partly to much advanced methods of analysis, but more to greatly enhanced quantity and quality of the data. As relative arrival times are the primary input data for regional tomographic modeling, the term 'quality of data' refers primarily to clock reliability, signal-to-noise ratio, and waveform fidelity: whatever the specific tomographic computational methods adopted, the quality of the results hinges on these factors. To remove the complicating effects of heterogeneous upper-mantle structure in the tomographic analysis, earthquake data are typically confined to events beyond about 27° distance, where seismic waves bottom in the relatively uncomplicated lower mantle below the upper-mantle transition zone (between 410 and 660 km). Tomographic analysis takes as its input the relative travel-time residuals across the array relative to a spherical reference Earth model. These residuals are the data that are then inverted to obtain 3-D velocity variations beneath the array of stations (see **Chapter 1.10**).

In studies prior to about 1990, it was common to obtain travel-time residuals from handpicked absolute arrival times. That method may still be used for seismic networks that cover large geographic areas and/or that involve a mix of instrument types where waveform correlations are difficult. In these instances, the absolute travel time of the seismic wave between earthquake source and receiver is referenced to a standard Earth model. For portable array tomography, where the structure of interest lies beneath the station network, relative residuals (delay times) are computed for each observed travel time by subtracting the mean of the absolute travel-time residuals for each event (relative to the standard model) from the observed travel time for that event at each station. The data are time-shifted so that the mean of the travel-time residuals for each event is zero. This process of obtaining relative travel-time residuals significantly reduces the influence of extraneous factors, such as errors in event location or origin time, deep-mantle velocity anomalies, and an inaccurate reference model that can introduce very substantial errors in regional tomographic models (e.g., VanDecar, 1991; Humphreys and Dueker, 1994). VanDecar and Crosson (1990) introduced the now common method of using pairwise cross correlation to align waveforms more precisely and obtain a statistically optimized set of relative arrival times. Tomographic inversion of the relative travel-time data to obtain a seismic velocity model involves partitioning the volume of interest beneath the array into a 3-D grid of blocks or knots. The relative travel-time residuals from many hundreds or thousands of crisscrossing rays through the volume beneath the array are inverted to obtain a least-squares estimate of the relative velocities within each block. The density of crossing rays is a critical factor in the ability of the tomographic inversion to resolve structure, which thus depends on earthquake sources that are well distributed in both azimuth and distance (see **Chapter 1.10**). By the VanDecar method of tomographic analysis (e.g., VanDecar, 1991; VanDecar et al., 1995), the data are inverted simultaneously for the velocity structure, earthquake relocations, and station corrections. As the least-squares solution is not unique, the inversion searches for the simplest model that contains the 'least' amount of structure required to satisfy the observations.

1.16.2.4.2 Surface wave tomography

Surface waves observed in the Earth are dispersive (see **Chapters 1.03** and **1.08**). That dispersion is caused by the fact that higher frequencies are sensitive to shallow structures and lower frequencies to deeper structure such that different frequencies travel with different velocities. While surface waves have been used to sample shear-wave velocities to depths of 1000 km or more in global studies, the maximum depths that can be resolved from portable array data are rarely more than a few hundred kilometers.

A number of different methods of surface wave tomography have been developed, although the most common for studying continental lithosphere fall into two general categories: (1) partitioned waveform inversion (PWI), where surface waveforms (including S and multiple S) are modeled directly, and (2) a variety of methods that require direct measurement of phase velocities across the array. Significant advances in crustal imaging have also been made using portable array data, including higher-mode group velocity tomography (Levshin et al., 2005) and ambient noise tomography (Shapiro et al., 2005).

PWI, first applied for 2-D structures to the linear NARSs, is a two-step process (Nolet, 1990). The first step involves nonlinear waveform fitting of fundamental and higher-mode surface waves where the S wave, multiple S wave, and surface wave train of the time series are matched by synthetic seismograms to obtain a path-average 1-D velocity model representing the average Earth structure between source and receiver. The synthetic seismograms that are used to fit the observed data can be computed by different methods. While all these methods require information on the focal mechanism of the earthquake source, no direct measurement of group or phase velocities is involved. Once the path-averaged 1-D structures are obtained for all source–receiver pairs, a generalized least-squares tomographic inversion, similar to that for body wave inversion, is performed to obtain the 3-D (or 2-D, in the case of linear transects) shear-wave speed beneath the array. Crustal thickness may be constrained or it may be included in the inversion. PWI, or some variant of it (e.g., Friederich, 2003), has been widely used for continent-scale studies (e.g., Friederich, 2003; Simons et al., 1999; Van der Lee and Nolet, 1997; van der Lee et al., 2001a), but has relatively limited application to smaller regional arrays where more array-specific techniques can be applied.

Array techniques, based largely on Rayleigh wave data recorded on local or regional seismic networks, have evolved substantially in the past decade as broadband arrays have increased in areal extent and station density. The simplest of these, and still one of the more robust, involves determining phase velocity between station pairs aligned on the great circle path with the earthquake (e.g., Larson et al., 2006; Snoke and James, 1997). More sophisticated array methods in use today attempt to account for multipathing and other out-of-plane propagation. One means to accomplish this is by representing the incoming wavefield as a superposition of two interfering plane waves whose parameters (amplitude, phase, and direction) are determined in the inversion (e.g., Bruneton et al., 2004; Forsyth and Li, 2005; Li et al., 2005). This and similar methods can also include an estimate of azimuthal anisotropy (Forsyth and Li, 2005). Where Rayleigh wave, Love wave, and multiple S-wave data are available, Gee and Jordan (1992) developed an isolation filter technique to determine radial anisotropy, as well as phase delays across the array (see also Freybourger et al., 2001; Saltzer, 2002).

Recent forays into the joint inversion of surface waves and body waves from portable arrays (e.g., Friederich, 2003; van der Lee et al., 2001b; West et al., 2004a) are mostly in an embryonic stage but hold promise of major improvements in imaging with further development. Much of the motivation for joint inversion derives from two factors. First, surface waves provide good vertical resolution (but poor lateral resolution), while body waves provide excellent lateral resolution (but poor vertical resolution) of the 3-D velocity structure. Jointly, they thus provide complementary constraints on the velocity structure both laterally and vertically across the array. Second, the inclusion of surface wave data in the inversion makes it possible to attach absolute S-wave velocities to what are otherwise simply velocity perturbations in the body wave inversion alone. The technique developed by West et al. (2004a) treats the surface wave measurements simply as travel times between stations, with each travel time corresponding to a horizontally traveling ray through the blocks in the model. The horizontally traveling surface wave rays are sensitive over a depth range estimated for each given frequency but otherwise can be added directly as an additional set of ray paths to the body wave data.

1.16.2.4.3 Discontinuity imaging

Most direct imaging of discontinuity structure is based on some version of teleseismic receiver function analysis, although full-scattering formulations are increasingly evident (e.g., Rondenay et al. (2005), with references). Receiver functions are computed primarily for teleseismic events (30–90° epicentral distance), where incoming P-rays beneath the station are at near-vertical incidence. The near-vertically propagating P wave that is incident on a horizontal boundary across which there is a significant contrast in V_s will convert a small amount of its energy to an S wave. The particle motion of the resulting P-to-S conversion will be predominantly horizontal radial and thus recorded primarily on the radial component of the seismogram (**Figure 3(a)**). Nonhorizontal discontinuities can produce significant P-to-S-converted energy on the transverse component, as may anisotropy in some cases. While these effects are typically small, inspection of the transverse component will reveal whether such factors are important.

All of the converted signals are of small amplitude and tend to be concealed in the coda of much larger amplitude direct-arriving P waves. The receiver function is a means of isolating these relatively small amplitude P-to-S (Ps) conversions that are produced beneath the station from the much larger amplitude direct P-wave arrivals that dominate the same early portion of the record (also see **Chapter 1.21** for further discussion). To compute the receiver function, the vertical component signal (which nominally contains only P-wave energy) is deconvolved from the radial component (which contains both P-wave energy and S-wave energy) to produce a so-called 'source-equalized' radial seismogram (e.g., Ammon, 1991). Under ideal conditions, the source-equalized (deconvolved) trace consists of a large amplitude coherence spike at zero time (containing all the P-wave energy present on the original radial component that is coherent with the vertical component) and a following spike train of smaller signals that are the Ps conversions and converted reflections from discontinuities beneath the station (**Figure 3(a)**). Thus, the receiver function can be considered a scaled version of the radial component of displacement with the P-wave train removed (Ammon, 1991); also see Wilson and Aster (2005)). The receiver function may be used to image any discontinuity at depth but, in practice, has been used primarily for imaging the Moho, the top of the descending plate in subduction zones,

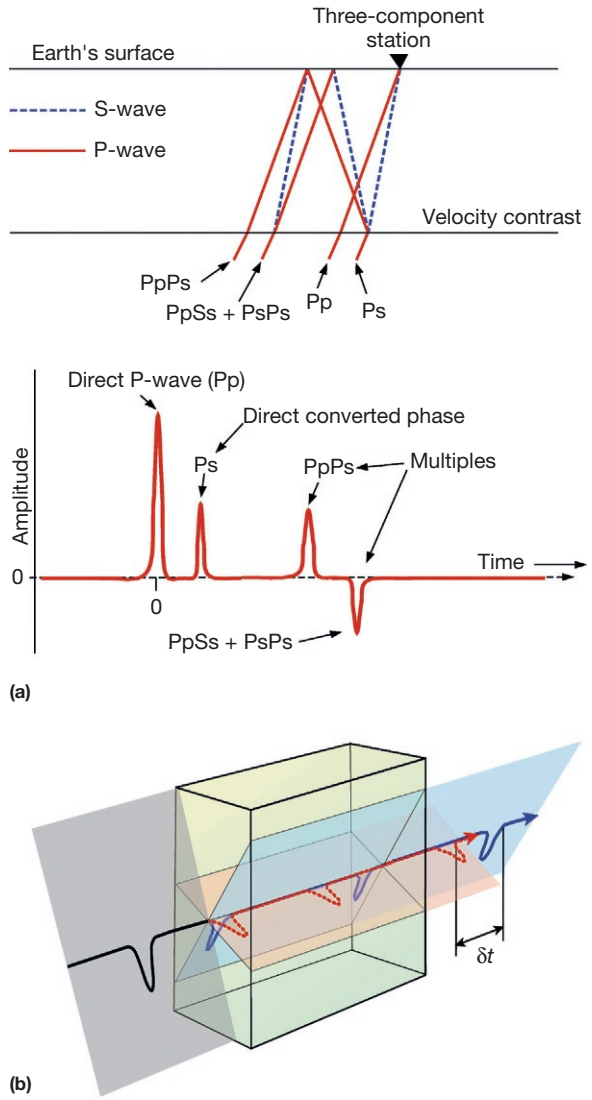

Figure 3 (a) Basic ray geometry and radial receiver function diagram for a simple one-layer model over a half-space, with a velocity discontinuity in S. Ray nomenclature is as diagramed on the upper figure. The receiver function is obtained by deconvolving the vertical component record from the radial component. The coherence peak of 'all' direct P-wave energy arriving at the station within the time window of the deconvolution trace is labeled 'direct P wave.' High-quality converted wave signals can be obtained by deconvolution even in cases where the source-time function of the earthquake may be quite lengthy and complex and individual signals extremely difficult to detect. The amplitude of the P-to-S conversion is a function primarily of the S-wave velocity contrast across the boundary. Figure courtesy of Rick Aster, New Mexico Tech. (b) Schematic diagram showing the effects of anisotropy on a seismic wave passing through an anisotropic medium. In this case, the incident wave is a polarized shear wave (such as the core phase SKS). On passing through the anisotropic medium (anisotropy is indicated by different colored planes within the volume shown), the wave 'splits' into a fast and a slow component ('shear-wave splitting'). The magnitude of the lapse time, δt, between fast and slow shear-wave components is a function of both the path length and the strength of the anisotropy. If the incident wave is polarized parallel to one of the axes of anisotropy, no S-wave splitting will occur. Figure courtesy of Ed Garnero, Arizona State University.

and upper-mantle discontinuities including the 410 and 660 km discontinuities.

Sp receiver functions. Receiver functions based on P-to-S conversions have proved to be remarkably effective for imaging the Moho and the 410 and 660 km discontinuities of the transition zone. Because of the interfering effects of crustal multiples, however, these receiver functions have proved to be difficult to interpret unambiguously for upper-mantle structures in the depth range 100–300 km. Several recent papers have addressed that problem by examining S-to-P conversions, where the primary conversions precede the S-wave arrival and all multiples are in the S coda (Farra and Vinnik, 2000; Wittlinger et al., 2004). The method for computing Sp receiver functions was first formalized by Farra and Vinnik (2000), where the vertical component is deconvolved by the radial, similar to that of the Ps receiver function but where the respective roles of P and Sv are reversed. The method tends to be limited by the fact that earthquake magnitudes must be substantially larger than for Ps receiver functions and piercing (conversion) points are substantially further from the station as the S-to-P conversion results in a much lower-angle incident ray.

1.16.2.4.4 Anisotropy

Seismic anisotropy, or seismic birefringence, is a key measurement for imaging past and present deformation in the Earth's interior (see Fouch and Rondenay (2006) for a comprehensive summary). Thousands of shear-wave (radially polarized core phases SKS and SKKS) splitting measurements over the past two decades have shown that anisotropy in the upper mantle is present almost everywhere, both on and off continents. Splitting measurements are especially applicable to the upper mantle and, to a lesser extent, the crust, where tectonic and flow deformation results in anisotropic fabric through crystallographic alignment of anisotropic minerals. In the case of portable array experiments, attention has focused primarily on the upper mantle, where seismic anisotropy is generally interpreted in terms of lattice-preferred orientation of olivine, which deforms under stress to produce strongly anisotropic strain-induced fabric. Vinnik et al. (1984) first recognized that the radially polarized Sv waveforms of SKS and SKKS core phases could be used to obtain extremely simple *in situ* measurements of azimuthal (horizontal plane) S-wave anisotropy (**Figure 3(b)**). The method has since been refined (Silver and Chan, 1988) and routinely used to determine anisotropic fast directions and delay times for virtually every station in nearly every passive array deployment since (see summaries in Fouch and Rondenay, 2006; Silver, 1996). Surface wave anisotropy can be either radial (vertical) or azimuthal (horizontal). Radial anisotropy, which cannot be observed by shear-wave splitting, is manifest as model incompatibility between Rayleigh waves and Love waves. In such cases, Love waves invariably call for a substantially higher S-wave velocity structure than do the Rayleigh waves, and in those anisotropic models, the difference between the so-called V_{SH} structure and V_{SV} structure is commonly quite large, with V_{SH} the higher velocity. Azimuthal anisotropy, on the other hand, is difficult to determine by surface waves alone and requires multiple measurements along many azimuths across the array (e.g.,

Forsyth and Li, 2005). While lateral resolution in all surface wave methods is relatively poor, a major strength of surface wave anisotropy, both radial and azimuthal, is the relatively good depth resolution. This overcomes one of the great weaknesses of shear-wave splitting methods where depth of the anisotropy cannot be determined, and it is for this reason that the joint use of surface waves and core phases is coming increasingly into play (e.g., Gaherty, 2004).

Anisotropy takes a back seat to tomographic and waveform imaging in the sections that follow. Not only is this partly the personal preference of the author, but also it is a consequence of the fact that anisotropy as it relates directly to structure of the continental lithosphere (fossil anisotropy) is commonly difficult to sort out from asthenospheric flow. The interested reader is referred to Fouch and Rondenay (2006) and Silver (1996) for further enlightenment.

1.16.2.5 Methodological Weaknesses and Caveats

The previously mentioned description of methods has necessarily been brief. It is particularly useful, therefore, to highlight pitfalls in some of the various techniques in common usage today.

Seismic tomography. The rapid increase in the number and density of instruments comprising seismic arrays has led to increasingly high-resolution tomographic images that appear to be interpretable in geologic or near-geologic terms. The tomographic problem is underdetermined, however, which means that all 3-D tomographic images are smoothed and damped to a greater or lesser degree and all are nonunique. Indeed, even the best-constrained models are blurred images of the actual structure, smoothed across small-scale heterogeneities. Moreover, unlike the medical CT scan, a major shortcoming in seismic tomography is the uneven distribution of sources (and often receivers), such that some parts of the region to be imaged are better constrained by data than others. In addition, as stations are always at or near the Earth's surface, seismic rays pass through the volume to be imaged in only one direction, from below. Where stations are arrayed along 1-D profiles, the uncertainties in the resulting 2-D solution can be substantially greater than they are for comparable 3-D solutions from areal deployments.

Apart from the problem of image smearing and nonuniqueness, body wave inversions are nearly always expressed in terms of velocity 'perturbations,' or velocities relative to the mean velocity over the model space ('not' relative to the background starting model). In regions of overall high velocity or low velocity, relative velocity images can be misleading. A significant advantage of surface wave imaging is that absolute velocities are determined. Body wave tomographic velocity perturbations tend to smear along ray paths, such that those images provide generally good constraints on lateral heterogeneity but poor control on vertical structure. Similarly, surface wave tomography provides good control on vertical structure, but poor control on lateral structure. This is a primary motivation for joint body wave/surface wave inversion where both lateral and vertical structures can be better constrained. In all cases, the color scheme used by the author to signify velocity contrast can have a major effect on the appearance of the image. The reader is invited to examine some of the images in this chapter to see whether it is possible to spot such effects.

Receiver function methods. Receiver functions are most easily interpreted when relatively sharp subhorizontal boundaries with strong S-wave contrasts are present. Dense arrays allow powerful exploration-type analyses to be applied to the data to obtain 2-D or 3-D images of crustal and mantle discontinuities. Shortcomings of standard receiver function methods (as opposed to full wavefield scattering methods) include difficulty in accommodating anisotropy, dipping layers, reverberations between layers, gradational variations in structure, and distant scattering (e.g., core reflections). Running averages over arrays of stations can make structures appear to be far more continuous than the individual station data suggest (e.g., Yuan et al., 2000). While various techniques have been, or are being, developed to deal with the many known shortcomings, receiver function images are commonly degraded by one or more of these effects. Crustal reverberations, for example, make Ps receiver function images unreliable in the depth range 100–200 km. Anisotropy and dipping layers must be evaluated through an examination of energy on the transverse component, but this precaution is commonly ignored.

Anisotropy. The determination of shear-wave (SKS) splitting is among the simplest of all processing procedures in seismology, readily accessible through publicly available 'canned' codes, and is hence fraught with pitfalls. First, the magnitude of azimuthal anisotropy as a function of depth cannot be determined from SKS splitting alone, nor can the cause of the anisotropy itself. Interpretations based on simplifying assumptions of uniform single-layer anisotropy can be wildly misleading. Anisotropy observed through SKS splitting could originate anywhere along the path between the core–mantle boundary and the recording station. Substantial evidence exists that the lowermost mantle may be anisotropic as may be other parts of the lower mantle or transition zone (e.g., Fouch et al., 2001). It is known that SKS and SKKS can give wholly different splitting results, even when well observed on the same seismogram for the same event (e.g., James and Assumpção, 1996). Complexities such as multiple layers with differing anisotropies, dipping layers, and differing mineral anisotropies within a single layer all require data from well-distributed earthquake sources and comparatively sophisticated analysis to sort out. Radial anisotropy as manifested by a significant discrepancy between Rayleigh wave and Love wave S-wave velocity depth models can be relatively well constrained by depth, but lateral resolution of the anisotropy tends to be poor. Similarly, azimuthal anisotropy obtained from the analysis of fundamental-mode Rayleigh waves is well constrained vertically, but poorly constrained laterally.

1.16.3 Seismic Structure of Tectonically Active Regions

This section and the ones that follow are intended to provide the reader with a thumbnail sketch of some of representative findings from portable array (primarily broadband) seismology. Beginning with tectonically active regions, most portable array studies have focused on four major tectonic regimes: (1) western United States, where a complex series of events broadly associated with the Laramide orogeny and the overriding

of the Farallon spreading center have overprinted much of the Archean and Proterozoic lithosphere of western North America; (2) continent–continent collisional zones, notably the Himalayan/Tibetan orogenic belt; (3) intraplate rift zones, with perhaps the best example in northern Africa; and (4) continental margin subduction zones. In the following sections, we summarize representative results from each of these regions.

1.16.3.1 Western North America

The Rocky Mountain Front marks a profound divide between stable North America to the east and tectonically active North America on the west. Western United States is one of the most complex and most seismically investigated tectonic regions in the world. The tectonic provinces that make up the region record a baffling sequence of overlapping tectonomagmatic events dating from the Mesozoic to the present. These events appear to overprint and, in some cases, be controlled by the Archean and Proterozoic continental structures that comprise the deep framework of western North America. Over the past 70 My or so, western United States has undergone a succession of continent-shaping events – Farallon Plate subduction and destruction, extensional and compressional deformation, and tectonomagmatic activity – that continue to this day. During the past 30 My, most of the interior of western United States has seen tectonic extension. Portable array seismology has played a key role in unraveling the complex history of lithospheric evolution of the western United States, from early Proterozoic (~1.8 Ga), to the Laramide orogeny (~80–50 Ma), to Neogene tectonism that continues to the recent time.

Major geologic provinces of western United States are shown in Figure 4 superimposed on a composite image of upper-mantle S-wave velocity structure at 100 km depth

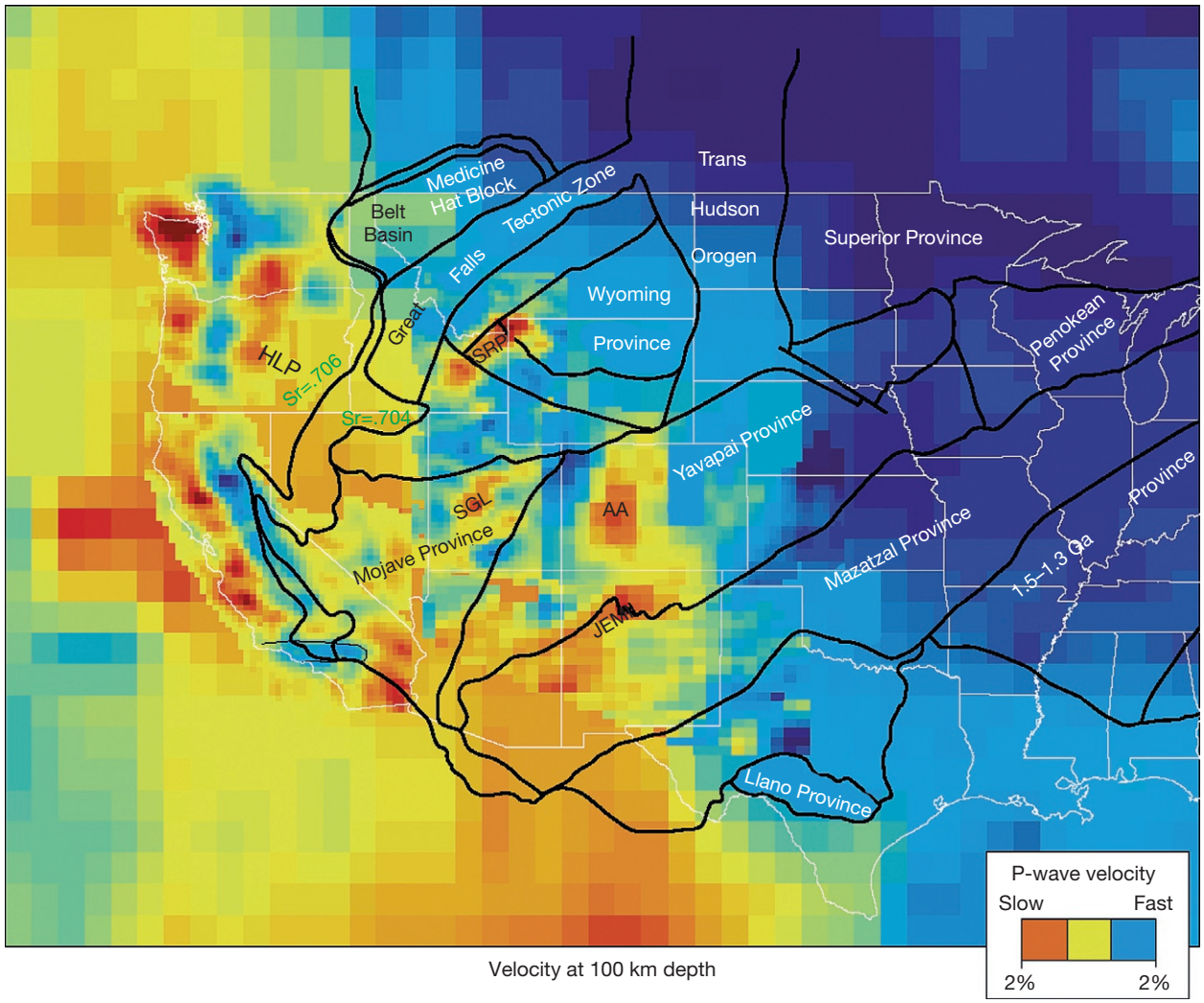

Figure 4 North American upper-mantle velocity perturbations at 100 km depth. Modified from Karlstrom KE and Keller GR (2005) *Geophysical Monograph 15: The Rocky Mountain Region – An Evolving Lithosphere: Tectonics, Geochemistry, and Geophysics*, 441 pp. Washington, DC: American Geophysical Union. The background continent-scale S-wave velocity perturbation structure is from Grand (1994), overlain by regional array P-wave velocity perturbations from Humphreys and Dueker (1994). Blue indicates positive (high) relative velocity; red indicates negative (low) relative velocity. Precambrian province boundaries are outlined in black. SRP, Snake River Plain; SGL, Saint George lineament; AA, Aspen anomaly; JEML, Jemez Lineament; HLP, High Lava Plains.

(Grand, 1994; Humphreys and Dueker, 1994). Extensive studies of this entire region of western United States are ongoing and expanding in scope (see **Section 1.16.7**). Nonetheless, it is useful to summarize some of the major syntheses and interpretations that have emerged from current studies of this actively evolving region. A considerable body of work is published in book form on the lithospheric and sublithospheric structure of the Rocky Mountain region from Montana south to New Mexico and west to the Basin and Range Province (Karlstrom and Keller, 2005), gleaned from the large-scale CD-ROM, La RISTRA, and Snake River Plain and Deep Probe teleseismic profiles (**Figure 5**; Karlstrom et al., 2005).

The tectonics of the Rocky Mountain region are dominated by NE–SW trending lineaments that mark zones of low-velocity mantle and extensive tectonomagmatic activity subparallel to Proterozoic province boundaries and to the direction of absolute plate motion of North America. As Karlstrom et al. (2005) pointed out, the S-wave velocity contrasts in the upper mantle over distances of less than 100 km can be as large as 10–15%, values that are comparable to continent-scale variations. If the velocity contrasts are interpreted as purely thermal, they imply temperature differences up to 700°, from shield-like geotherms to mantle undergoing partial melting. The sections that follow are organized such that the discussion begins with the Snake River Plain/Yellowstone region of the northern Rockies, moving to the southern Rockies near the eastern front with the Great Plains and then westward through the Colorado Plateau, the Basin and Range Province, northern Great Basin, and into the Sierra Nevada. Discussion of the active Cascade Arc is reserved for the sections in the succeeding text on continental margin subduction zones.

1.16.3.1.1 Snake River Plain/Yellowstone and Wyoming Craton

The Snake River Plain/Yellowstone (SRP/YS) region is among the most intensively studied in the world, with well over 100 broadband stations deployed regionally in several major experiments (Dueker and Yuan, 2004; Yuan and Dueker, 2005a). In addition to a large network of short-period and permanent stations that the University of Utah and US Geological Survey have maintained in the Yellowstone region for many years, several major PASSCAL deployments, all of a year or less, have added substantially to the database across the larger penumbra of the Yellowstone signature. The major issue surrounding the SRP/YS structure is whether it has been caused by

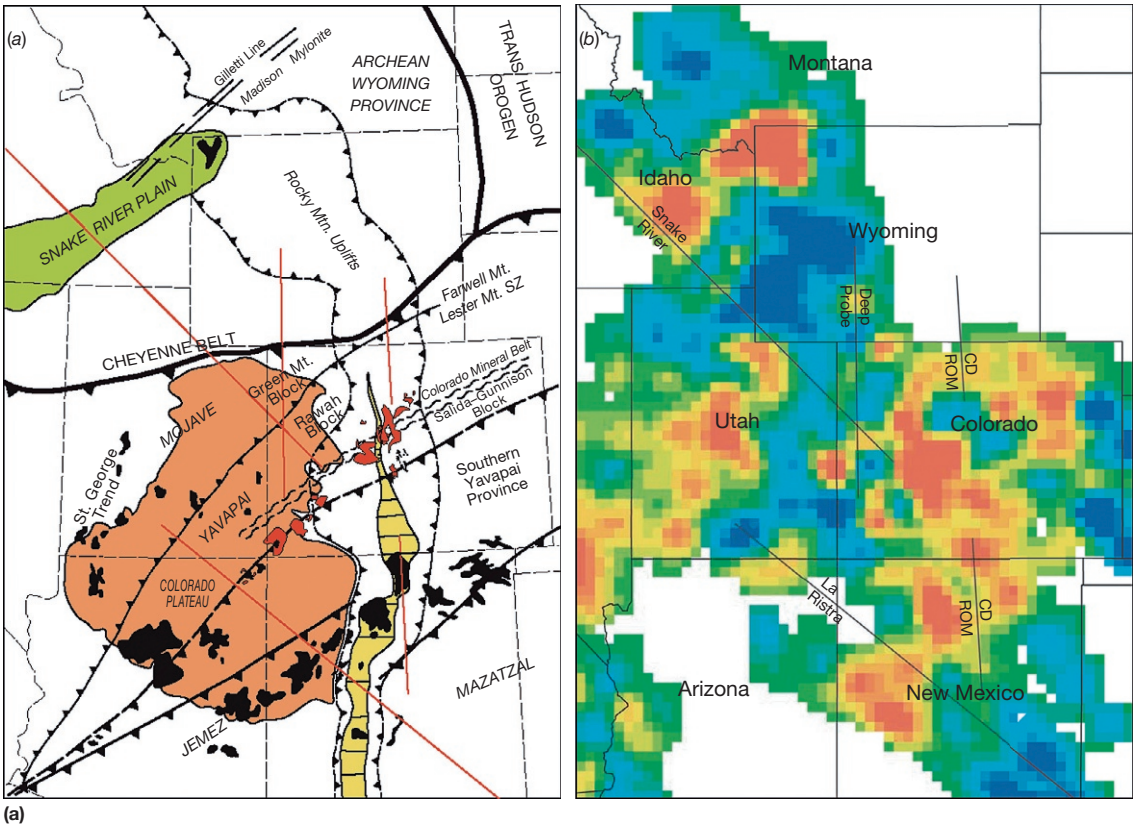

Figure 5 (a) Geologic elements (*a*) and tomographic image (*b*) of western United States west of the Rocky Mountain Front. Reproduced from Karlstrom KE, Whitmeyer SJ, Dueker KG, et al. (2005) Synthesis of results from the CD-ROM experiment: 4-D image of the lithosphere beneath the Rocky Mountains and implications for understanding the evolution of continental lithosphere. In: Karlstrom KE and Kelle GR (eds.) *The Rocky Mountain Region: An Evolving Lithosphere*, pp. 421–434. Washington, DC: American Geophysical Union. (a) Cenozoic volcanic fields (black and red areas) strike NE, roughly parallel to Precambrian trends, whereas Laramide uplifts trend N–S. (b) Locations of seismic transects that are shown as vertical sections in **Figure 10(b)** are superimposed on 100 km depth tomographic image. Blue indicates positive velocity perturbations; red, low-velocity perturbations.

(Continued)

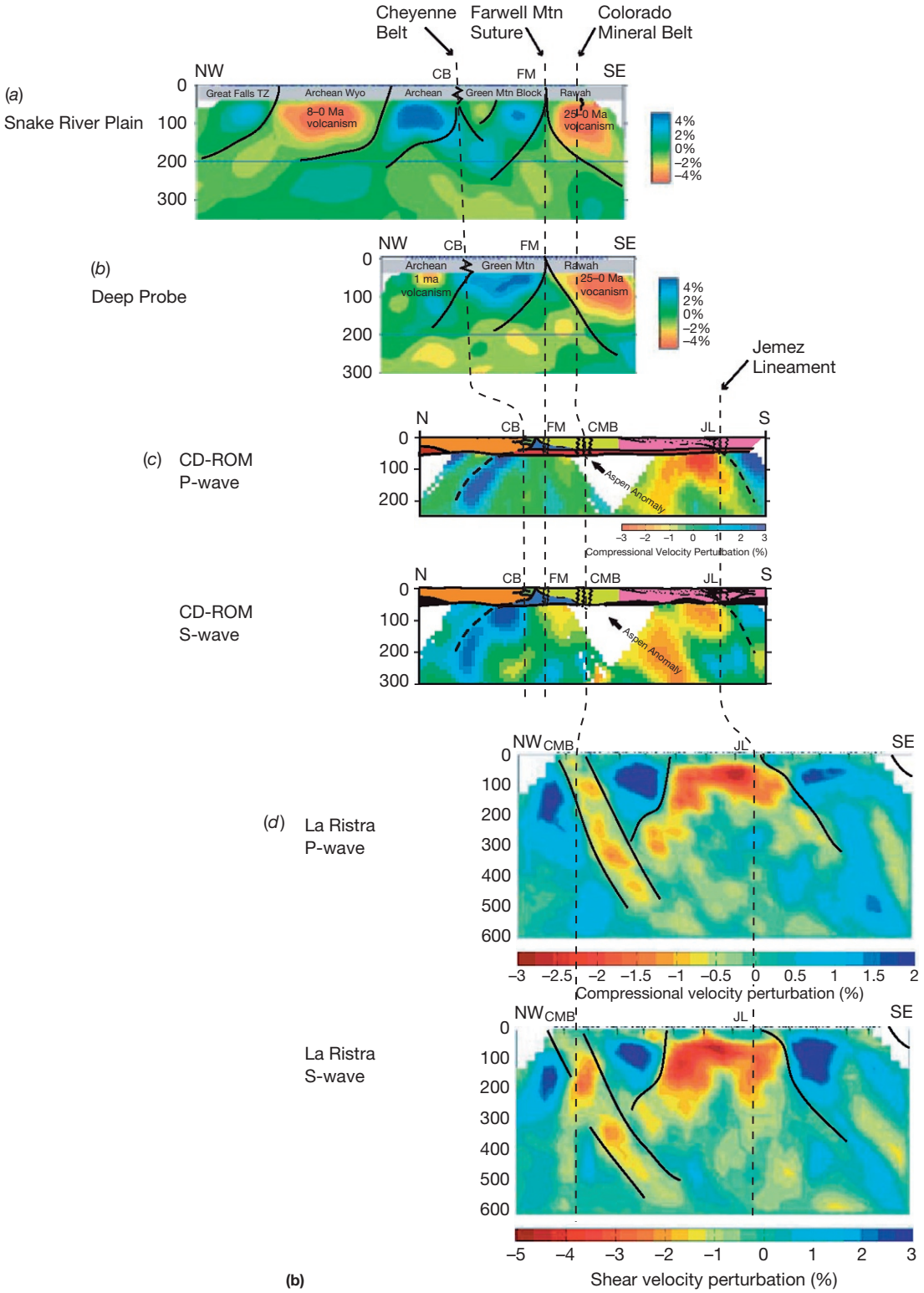

Figure 5 (Continued) (b) Vertical cross sections of P and S tomographic images along the experiment lines shown in **Figure 10(a)**. Reproduced from Karlstrom KE, Whitmeyer SJ, Dueker KG, et al. (2005) Synthesis of results from the CD-ROM experiment: 4-D image of the lithosphere beneath the Rocky Mountains and implications for understanding the evolution of continental lithosphere. In: Karlstrom KE and Kelle GR (eds.) *The Rocky Mountain Region: An Evolving Lithosphere*, pp. 421–434. Washington, DC: American Geophysical Union. See text for discussion of specific features shown. Snake River Plain profile from Schutt and Humphreys (2004); Deep Probe line from Yuan and Dueker (2005b); CD-ROM from Dueker et al. (2001); La Ristra line from Gao et al. (2004). Note the sharp velocity gradients associated with the Cheyenne belt, Farwell Mountain, Colorado Mineral Belt, and Jimez sutures and the apparent continuity of those sutures across multiple vertical seismic profiles.

a plume. Superficially, the evidence for a plume is convincing, and recent tomograms seem to reveal an NW-dipping plume-like structure in the upper mantle extending to a depth of perhaps 600 km (**Figure 6**; Yuan and Dueker, 2005a). The velocity anomalies shown in these P-wave images are particularly strong in the upper 150 km, where they reach values of 8% peak to peak. Similar very low velocities are seen in the upper mantle to depths of at least 200 km along the axis of the SRP as it trends ENE toward Yellowstone (Schutt and Humphreys, 2004). Beneath Yellowstone itself, the low P-wave velocity anomaly extends to depths well into the transition zone, although anomalies decrease from about 3% at 150 km depth to values less than 1% at a depth of about 450 km (Dueker and Yuan, 2004; Yuan and Dueker, 2005a). The extension of the low-velocity anomaly coincides at the transition zone with a 12 km depression of the 410 km discontinuity (**Figure 6**). The tomographic images shown in Yuan and Dueker suggest that a high-velocity 'curtain' extends from beneath the Wind River Range in the Wyoming Craton to a depth of about 250 km along a mantle trajectory that is roughly parallel to that of the postulated plume. Yuan and Dueker speculate that this feature represents a downwelling of the lower lithosphere. In the overall context of strong velocity contrasts of at least 8% in V_p that are seen throughout the region of western North America, however, the images shown in **Figure 6** may not be conclusive evidence for either a plume or a downwelling.

1.16.3.1.2 Southern Rocky Mountain region

It is noteworthy that velocity anomalies imaged beneath the relatively young (12 Ma) volcanic fields at the southeastern end of the SRP/Deep Probe NW–SE transect (**Figure 5(a)**) exhibit peak-to-peak values (~8%) comparable to those seen beneath YS (Dueker and Yuan, 2004). Velocity anomalies in this range, if solely thermal, are indicative of variations on the order of 200–400 °C, yet these volcanic fields are

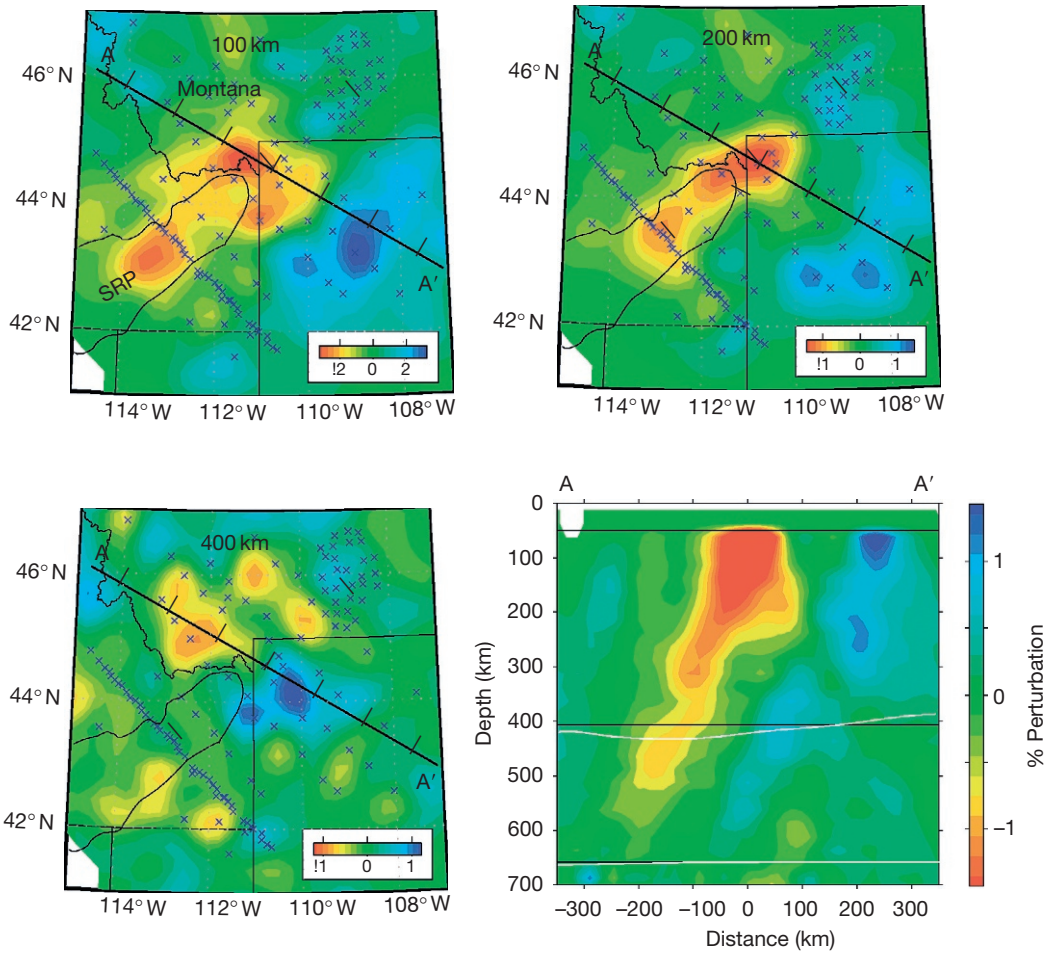

Figure 6 Tomographic images interpreted to show the presence of a NW-dipping plume beneath the Yellowstone 'hot spot.' The first five panels are depth slices approximately centered on Yellowstone (low-velocity perturbation near the intersection of cross-sectional lines). SRP denotes Snake River Plain along which the hotspot trace has migrated NE during the past 12 My. Lower right-hand panel is a vertical cross section along line A–A′. The velocity anomaly interpreted as a plume is shown as a NW-dipping feature penetrating into the transition zone and depressing the 410 km discontinuity (white line, 2× vertical exaggeration). The 660 km discontinuity is not uplifted in these images, as might be expected if the Yellowstone hotspot source were a deep-mantle plume. Adapted from Yuan H and Dueker KG (2005) Teleseismic P-wave tomogram of the Yellowstone plume. *Geophysical Research Letters* 32(L07304): 1–4. http://dx.doi.org/10.1029/2004GL022056.

volumetrically minor compared with that of YS/SRP. This repeated cycle of strong localized low-velocity anomalies along NE–SW striking zones continues into the southern Rocky Mountains, across the Saint George lineament, the Colorado Mineral Belt (the Aspen anomaly), and across the Jemez Lineament to the south (Figure 5). These 'fingering' zones of sharp velocity contrast, or sutures, are interpreted by Karlstrom et al. (2005) to be the result of varying response of Proterozoic lithosphere to mantle heating from below. While the source of sublithospheric heating and the varying lithospheric response to it remain controversial, it may be associated at least in part with lithospheric hydration during flat subduction in the Laramide and subsequent influx of hot asthenospheric material as the slab rotated downward and sank into the deeper mantle (e.g., Humphreys et al., 2003).

The Cheyenne belt is a major tectonic boundary, widely interpreted to be a crustal manifestation of a suture between the Archean Wyoming Craton to the north and a Proterozoic island arc terrane to the south (Figure 5). A comprehensive synthesis is given in Karlstrom et al. (2005). A north-dipping high-velocity anomaly in the upper mantle has been interpreted by some to mark the remnants of a failed subducting slab (Figure 5). The crust beneath the southern Rocky Mountain region attains its greatest thickness of about 50–60 km beneath the Cheyenne suture (Snelson et al., 2005), consistent with crustal foreshortening during subduction zone convergence.

1.16.3.1.3 Rio Grande Rift and Colorado Plateau

The LA RISTRA broadband seismic experiment composed 54 stations deployed along a NW–SE transect to explore the complex region south of the Rocky Mountains that extends from the western Great Plains of stable North America, across the Rio Grande Rift and the Jemez Lineament, and into the central region of the Colorado Plateau. A map of station deployment and a schematic of the crust and mantle along the transect are shown in Figure 7(a) and 7(b). LA RISTRA data were analyzed to obtain body wave and surface wave tomographic images, as well as receiver function images of the crust and upper mantle across the region (Gao et al., 2004; West et al., 2004a,b; Wilson et al., 2005a,b). The crustal and upper-mantle structures beneath the Rio Grande Rift stand out as a particularly prominent feature. Wilson et al. (2005a) showed that the Moho beneath both the Great Plains and the Colorado Plateau is at about 40–50 km depth, whereas the crust beneath the central region of the Rio Grande Rift thins symmetrically to about 35 km (Figure 7(c)). The thinned crust overlies a zone of very low velocities seen in superimposed tomographic images (Gao et al., 2004; West et al., 2004b) shown in (Figure 7(c)), confirmed by interstation Pn velocities of 7.8 km s^{-1} measured along the rift axis (Lastowka and Sheehan, 2005). The composite structures shown in Figure 7(c) exhibit symmetry around the axis of the Rio Grande Rift that has been interpreted to imply pure shear extension (Wilson et al., 2005b). No deep-mantle source has yet been observed seismically beneath the rift. The discontinuity at a depth of ~250 km in Figure 7(c) is suggested by Wilson et al. (2005a) to be the base of a continental asthenospheric low-velocity channel but this remains a speculation. Both the 410 and 660 km discontinuities are observed to be flat beneath the Rio Grande Rift, suggesting that whatever thermal anomaly caused the Rio Grande Rift, it does not extend to the upper-mantle transition zone.

The Colorado Plateau, adjoining the Rio Grande Rift to the NW along LA RISTRA line, is seen both geologically and in seismic images to be a stable block with a relatively high-velocity lithospheric lid that extends to a depth of at least 120 km (West et al., 2004b). West et al. found no suggestion of a sharp lithosphere/asthenosphere boundary beneath the Colorado Plateau, where the lithosphere appears to transition gradually to the asthenosphere between about 120 and 150 km depth (although see Lastowka and Sheehan, 2001, for a much thinner lithosphere). In contrast to the mantle structure beneath the western Great Plains, a low-velocity channel extends nearly to 300 km beneath the lithosphere of the Colorado Plateau (West et al., 2004b). This significant low-velocity channel may account for part of the higher elevations of the Colorado Plateau compared to the Great Plains, despite comparable crustal thickness (West et al., 2004b). The crust beneath the Colorado Plateau is estimated from receiver functions to be about 45–50 km thick (Gilbert and Sheehan, 2004; Wilson et al., 2005a). That crustal thickness varies, however, with thinning to the north (Gilbert and Sheehan, 2004) accompanied by no corresponding change in elevation (Figure 8). Whereas Wilson et al. suggested that much of the Colorado Plateau uplift is due to a low-velocity channel in the upper mantle, Gilbert and Sheehan suggested that most of the Colorado Plateau uplift is due simply to isostatic compensation of the crust, although they acknowledged that hot, low-density mantle may contribute to plateau support (Gilbert and Sheehan, 2004).

1.16.3.1.4 Great Basin

The western edge of the Colorado Plateau where it abuts the eastern Great Basin marks a profound lithosphere boundary. This is seen in both crustal thickness (Figure 8) and upper-mantle velocity (Gilbert and Sheehan, 2004; Lastowka and Sheehan, 2001). The Great Basin, which locally has undergone up to 100–200% extension, is characterized by thin (35 km) crust, low upper-mantle velocities, and high heat flow. Large-scale, highly detailed, crustal studies based on controlled-source experiments have been extensively reviewed previously (Smith et al., 1989), but portable array broadband experiments carried out since, including those discussed earlier in the text and in the Colorado Plateau–Great Basin PASSCAL experiment, have substantially increased the 3-D image of crustal thickness (Gilbert and Sheehan, 2004). Crustal thickness as determined from receiver functions varies within the Basin and Range Province from slightly more than 35 km to less than 30 km in northern Utah and Nevada and southeastern Oregon (Figure 8). The broadband experiments have also contributed substantial new information on uppermost-mantle velocities, which were generally known from previous refraction and surface wave studies to be low, with V_s about 4.2–4.3 km s^{-1} and $V_p \sim 7.8$ km s^{-1}. Recent surface wave and Pn studies have confirmed the absence of a high-velocity lid in the uppermost mantle beneath the crust of the Great Basin (Lastowka and Sheehan, 2001), and this appears to be the case throughout both the southern and northern Great Basin.

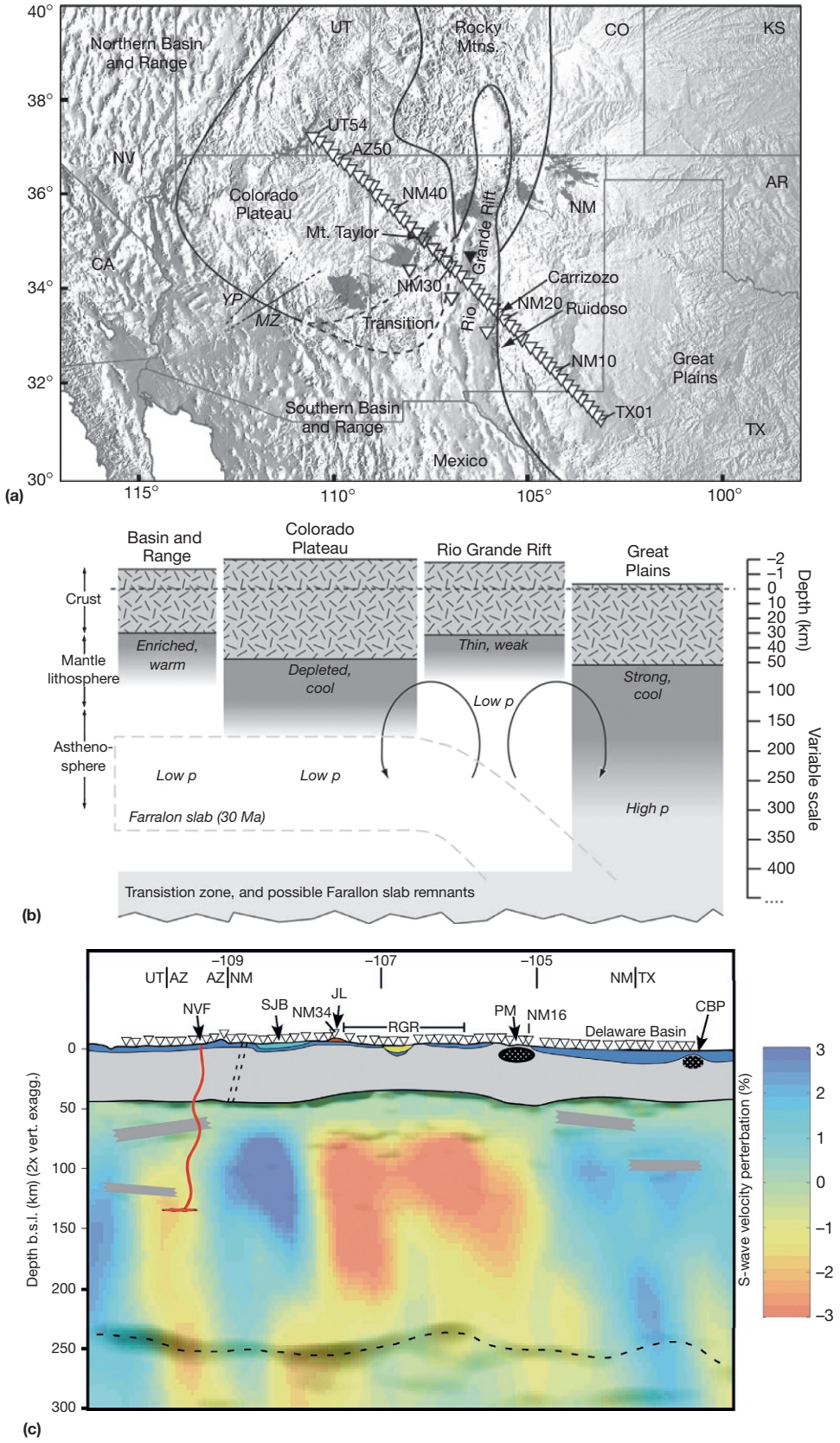

Figure 7 (a) Map showing the 57 seismic stations of the La Ristra broadband transect that extends from the Great Plains into the Colorado Plateau. (b) Schematic cross section showing hypothetical variations between major geologic blocks from the Great Plains of stable North America into the

(Continued)

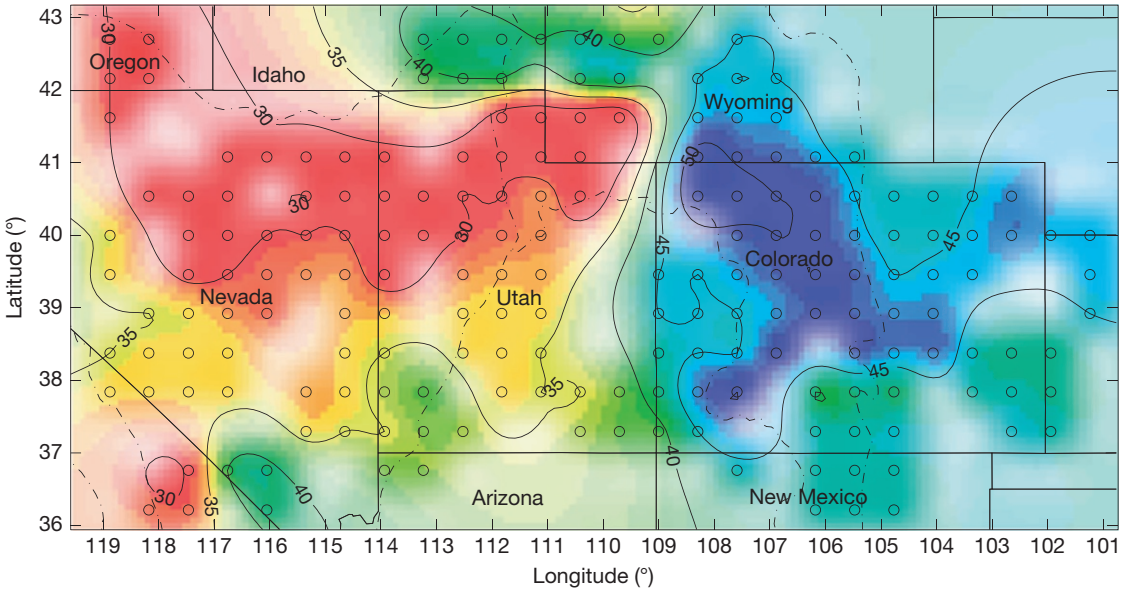

Figure 8 Contour map of crustal thickness in central western United States, primarily based on receiver functions. Red indicates thinner crust; blue, thicker crust. Circles denote crustal thickness binning points from which contours were drawn. Dashed lines mark boundaries between (from west to east) the Great Plains, Rocky Mountains, Colorado Plateau, and Basin and Range Province. Modified from Gilbert HJ and Sheehan AF (2004) Images of crustal variations in the intermountain west. *Journal of Geophysical Research* 109: B03306.

1.16.3.1.5 Sierra Nevada

The Great Basin extends westward to the Sierra Nevada range where seismic and geologic evidence for crustal extension ceases. Receiver function analyses from portable array experiments in the southern Sierra Nevada Mountains of California suggest the possibility that part of the crustal root of the Sierra Nevada volcanic arc has foundered following the cessation of arc activity in the Sierras about 16 Ma (Zandt et al., 2004). The foundering model is based on an unusual absence of a Moho signature in the receiver functions for conversion points beneath the Great Valley. There, the asthenospheric backflow following the cessation of Farallon Plate subduction is posited to have removed a root of dense ultramafic residue formed during the building of the great Sierra Nevada Batholith. Such destabilization and sinking are commonly cited in the literature, but are always inferred from indirect observations as in the Zandt et al. study. Current broadband experiments in the planning stages or now being implemented for California, Chile, and the North China Craton are aimed at the direct imaging of such possible lithospheric delamination, the models for which remain quite hypothetical.

1.16.3.2 Indian–Eurasian Continental Collisional Zone

1.16.3.2.1 Crustal structure

The Tibetan Plateau and adjacent regions that include Nepal, Tien Shan, Hindu Kush, and Karakoram have been among the most intensively studied structures in the world. Over the past decade and a half, hundreds of portable broadband seismometers have been deployed as part of major international experiments (e.g., Kind et al., 2002; Klemperer, 2006; Kosarev et al., 1999; Kumar et al., 2005; Schulte-Pelkum et al., 2005; Wittlinger et al., 2004; Zhao et al., 2001; **Figures 1** and **9**). Logistical constraints have tended to limit the Tibetan Plateau deployments to transects along roads (**Figure 9(a)**), whereas the Nepal, Tien Shen, and Karakoram deployments were aerially distributed in 2-D arrays (**Figure 9(b)** and **9(c)**; see Klemperer (2006) for a comprehensive summary (with map) of passive and active seismic experiments).

Receiver function imaging of both crustal thickness and lithospheric plate deformation in the Indian–Eurasian continental collision zone has been a prominent objective of most Himalayan and Tibetan Plateau broadband experiments.

Figure 7 (Continued) actively extending Basin and Range Province. Approximate location of the Farallon slab c.30 Ma is shown for reference. (a) and (b) adapted from West M, Ni, JF, Baldridge WS, et al. (2004) Crust and upper mantle shear-wave structure of the Southwest United States: Implications for rifting and support for high elevation. *Journal of Geophysical Research* 109(B03309): 1–16. http://dx.doi.org/10.1029/2003/JB002575. (c) Crustal and upper-mantle schematic of the region across the Rio Grande Rift (RGR) in relation to other surface geologic features along the La Ristra transect including the Navajo volcanic field (NVF), San Juan Basin (SJB), Jemez Lineament (JL), Pajarito Mountains (PM), and Central Basin Platform (CBP). Reproduced from Wilson D, Aster R, Ni JF, et al. (2005) Imaging the seismic structure of the crust and upper mantle beneath the Great Plains, Rio Grande Rift, and Colorado Plateau using receiver functions. *Journal of Geophysical Research* 110(B05306): 1–14. http://dx.doi.org/10.1029/2004JB003492. Crustal thickness from receiver functions and other receiver function discontinuities (gray areas) are superimposed on the body wave tomographic image of the upper mantle from Gao et al. (2004). The apparent discontinuity around 250 km depth (dashed line), based on receiver functions, is speculated by Wilson et al. to be the Lehmann discontinuity, perhaps indicating the base of the continental asthenosphere (Wilson et al., 2005a). It is not explained in this interpretation, however, why the depth of the discontinuity is so little affected by the major Rio Grande Rift velocity (thermal) anomaly. The signal appears to vanish beneath the stable central basin.

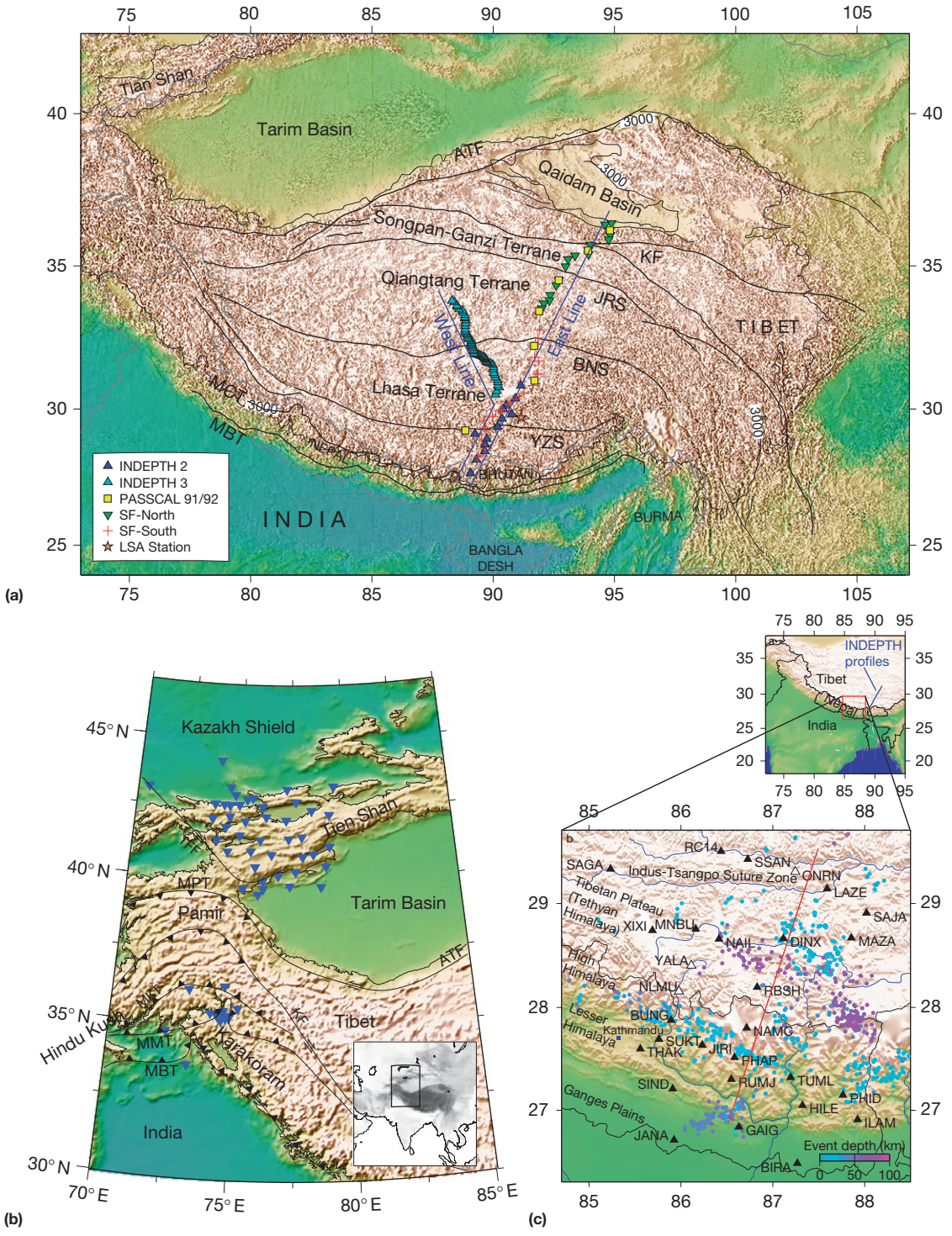

Figure 9 (a) Summary of broadband seismic experiments in central Tibet c.2002 superimposed on topographic map of Tibet showing major terrane boundaries. Reproduced from Kind R, Yuan H, Saul J, et al. (2002) Seismic images of crust and upper mantle beneath Tibet: Evidence for Eurasian plate subduction *Science* 298: 1219–1221. The experiments include PASSCAL experiments PASSCAL 91/92 and INDEPTH 2 and 3, as well as Sino-French experiments as shown. Abbreviations from Kind et al. (2002) are as follows: MBT, Main Boundary Thrust; MCT, Main Central Thrust; YZS, Yarlung–Zangbo suture; BNS, Bangong–Nujiang suture; JRS, Jinsha River suture; KF, Kunlun fault; ATF, Altyn–Tagh fault. An up-to-date summary of seismic experiments, both passive and active, in that region of Tibet can be found in Klemperer (2006). (b) Summary of portable and permanent broadband seismic stations deployed in western Tibet superimposed on a topographic map with major tectonic terranes indicated. Reproduced from Kumar P, Yuan X, Kind R, Kosarev G (2005) The lithosphere–asthenosphere boundary in the Tien Shan-Karakoram region from S receiver functions: Evidence for continental subduction. *Geophysical Research Letters* 32(L07305): 1–4. http://dx.doi.org/10.1029/2004GL022291. The largest array was composed of 28 portable stations in central and western Tien Shan (the GHENGIS experiment). The small six-station array of the NANGA experiment was clustered in Nanga Parbat near the inflection in the Main Mantle Thrust (MMT). The portable stations complemented a number of permanent stations, including most notably the permanent KNET array in Kyrgyz. Abbreviations from Kumar et al. (2005) are as follows: MPT, Main Pamir Thrust; MKT, Main Karakoram Thrust; MMT, Main Mantle Thrust; MBT, Main Boundary Thrust; TFF, Talasso–Ferghana fault; KF, Karakoram fault; ATF, Altyn–Tagh fault. (c) Topographic map showing locations of 29 portable broadband stations (black triangles) deployed to study the structure of the Indian Plate where it plunges beneath the Himalayas and Tibet. Reprinted from Schulte-Pelkum V, Monsalue G, Sheehan A, et al. (2005) Imaging the Indian subcontinent beneath the Himalaya. *Nature* 435: 1222–1225, Copyright (2005), with permission from Macmillan Publishers Ltd. The position of the array relative to INDEPTH profiles is shown in the upper location map. Hypocentral depths for events located by the array are shown as small color-coded filled circles. The red line indicates the surface trace of the vertical cross section shown in **Figure 10**.

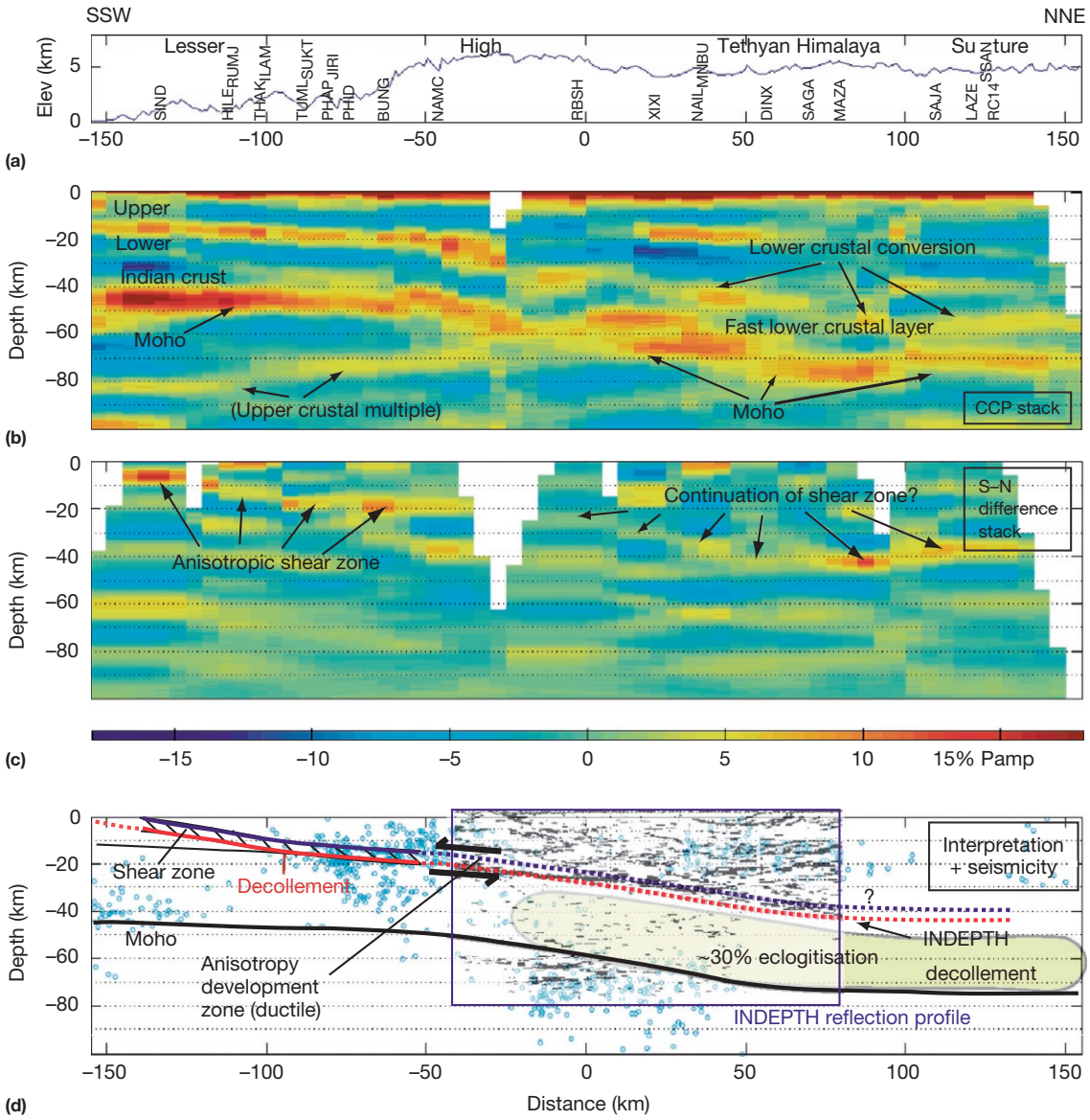

Figure 10 Migrated receiver function common conversion point (CCP) stack image along the NNE–SSW transect that is shown as a red line in **Figure 9(c)**. (a) Topography cross section along profile. (b) CCP receiver function stack, where red indicates positive conversion amplitude (velocity increase) and blue, negative amplitude (velocity decrease). Color intensity is proportional to receiver function amplitude. (c) Differenced S–N CCP stack, with amplitudes of receiver functions from southern azimuths differenced with those from northern azimuths to image arrivals that change polarity by back-azimuth (see Schulte-Pelkum et al., 2005, for further explanation). (d) Interpretive cross section based on (b) and (c). INDEPTH reflection profile and local seismicity are superimposed (see text for further discussion). Reprinted from Schulte-Pelkum V, Monsalue G, Sheehan A, et al. (2005) Imaging the Indian subcontinent beneath the Himalaya. *Nature* 435: 1222–1225, Copyright (2005), with permission from Macmillan Publishers Ltd.

Schulte-Pelkum et al. (2005) had used receiver functions to map the Indian lithosphere as it plunges beneath the Himalayas and Tibet (**Figure 10**), revealing the apparent presence of a strong décollement where the uppermost part of the Indian Plate is thrust beneath the Himalayas. The Moho is similarly thrust to great depth. Schulte-Pelkum et al. speculated that the lower crust is partially converted to eclogite in the process, as shown schematically in the lower panel of **Figure 10**. In the central Tibetan Plateau itself, data from the INDEPTH experiments and early PASSCAL experiments have been extensively analyzed to produce images of Moho and upper-mantle structures, not all of which are entirely consistent between studies even with the same dataset. Remarkably, the Moho thickness beneath the entire region of these experiments (**Figure 9**) varies only from a maximum of about 78 km to a minimum of 65 km, with no systematic change inferred either across the Tibetan Plateau or at major fault boundaries (Kind et al., 2002; Kosarev et al., 1999). Results from these same data seem to indicate that V_p/V_s also does not vary significantly between northern and southern Tibet (Kind et al., 2002). This lack of significant variation in either crustal thickness or crustal velocity led Galve et al. (2002) to examine the Moho

structure in detail for clues as to the mechanism for crustal thickening. Results from their combined receiver function/wide-angle reflection study aimed specifically at detailed Moho structure suggest that the Moho has a complex architecture with "dipping and overlapping segments indicating lithospheric imbrication" (Galve et al., 2002, p. 1). Wittlinger et al. (2004), using S-to-P-converted wave receiver functions, reported a similarly complex and warped Moho structure.

Rapine et al. (2003) measured fundamental-mode Rayleigh wave dispersion to study contrasts in crustal structure beneath northern and southern Tibet. They concluded that a low-velocity layer in the middle crust is required by the dispersion data in southern but not northern Tibet. This is also suggested by Wittlinger et al. (2004) from Sp receiver functions. Moreover, there is general agreement that the lower crust beneath southern Tibet has higher velocity than that of the north and that it is underlain by the mantle with a positive velocity gradient. Rapine et al. interpreted these findings as the result of underthrusting of the Indian continental lithosphere, where the low velocities in the middle crust reflect H_2O-induced melting in the interplate shear zone between underthrust Indian crust and overriding Asian crust. No similar middle crustal low-velocity zone is found in the crust of northern Tibet, although the S-wave velocities in both the crust and mantle of northern Tibet are significantly lower than those in the south. This result is consistent with many other studies, including that of Kind et al. (2002), suggesting that mantle temperatures in northern Tibet are higher by several hundred degrees than those in southern Tibet. The source of that difference – mantle diapir or lithospheric delamination, for example – remains a debated issue.

1.16.3.2.2 Seismic structure of the uppermost mantle

Early studies by Kosarev et al. (1999) of the mantle beneath the eastern Tibetan Plateau appeared to show a northward-dipping discontinuity in the 100–300 km depth range colliding with a southward-dipping Asian lithosphere. They identified the northward-dipping feature as the cold and depleted lithosphere of India plunging beneath the Asian lithosphere. A continent-scale study by Friederich (2003) using S waves and surface waves similarly finds a northward-dipping slablike feature beneath southern Tibet that he interpreted to be the underthrust Indian lithosphere. Detailed imaging by Kind et al. (2002), however, fails to reveal a northward-dipping discontinuity, but it does confirm the existence of a southward-dipping feature interpreted as detached Asian lithospheric mantle (ALM; **Figure 11**). Kind et al. suggested that the Indian continent has been underthrust subhorizontally beneath Tibet and that it has a broken, nearly vertical northern edge.

There is surprisingly little indication that the massive effects of continental collision have significantly perturbed the 410 and 660 km discontinuities in the upper-mantle transition beneath Tibet. Kind et al. (2002) reported that in both the eastern and western sections across Tibet (**Figure 9**), the vertical separation between the 410 and 660 km discontinuities is virtually constant along the two studied transects (**Figure 11**), implying a N–S variation in transition zone temperature less than 50°. They inferred from these results that there is no lithospheric slab penetration into the transition zone, suggesting that the leading downgoing oceanic plate may already have detached from the Indian continent. Both the 410 and 660 km discontinuities appear to bend downward beneath the northern Plateau, a probable artifact of a south to north decrease in S-wave velocity of about 5% in the upper mantle, consistent with a northward increase in the average temperature of perhaps 300 °C.

Extensive portable array deployments have complemented a growing population of permanent broadband stations in the Tien Shan and Karakoram regions at the western edge of the Indo-Asian collision belt (**Figure 9**). Kumar et al. (2005) employed the S-to-P receiver function method to image both crustal thickness and the lithosphere–asthenosphere boundary (LAB) in the region (**Figure 12**). If their interpretation is correct, the results obtained for the LAB are among the very rare instances where that boundary has been successfully imaged. Moho depths, which vary from about 45–65 km beneath Tien Shan and increase to about 70 km beneath Karakoram, are apparently uncorrelated with what is seen as very significant differences in the LAB. As seen in **Figure 12** (top panel), the LAB from receiver functions is reasonably well correlated with the surface wave tomographic images of Friederich (2003). Along the north–south profile (top panel, approximately 75° E longitude in **Figure 9(b)**), the LAB deepens from less than 100 km beneath Tien Shan in the north to 270 km and more beneath Pamir and Karakoram in the south (Kumar et al., 2005). Kumar et al. interpreted the south-dipping LAB as the base of the subducting Asian plate where it is thrust beneath the high-velocity Indian mantle lithosphere. The east–west profile, roughly along 43°N latitude (**Figure 9(b)**), shows a relatively thin lithosphere even beneath the Kazakh shield (~130 km) and even thinner beneath Tien Shan itself (90–100 km), thickening again to almost 180 km beneath the Tarim Basin block, which appears to be subducting southward beneath northwestern Tibet (Wittlinger et al., 2004). Kumar et al. (2005) and others speculated that the Indian lithosphere is colder and stronger than is its Asian counterpart, as evidenced by the much thicker and higher-velocity lithosphere beneath the Indian continent.

A number of ongoing portable broadband experiments are underway on the eastern Tibetan Plateau and its flanking terranes, one focus of which is on measuring anisotropy to resolve the controversial issue of lower-crustal deformation as a mechanism of growth and collapse of the plateau. Notable among the eastern Tibetan deployments is the MIT China Seismic Array where 25 broadband stations have been recently installed (yellow squares in **Figure 1**). In addition, regions both north and south of the MIT array have seen dozens of stations deployed in recent years, although little has been published to date.

1.16.3.3 Continental Margin Subduction Zones

Continental margin subduction zones are among the more natural targets for broadband portable array seismology. The structures of particular interest are in the subduction zone itself, at mantle depths that are accessible primarily through passive array seismology. The continental regions most studied through the deployment of temporary portable arrays include the Andes, particularly the central Andes, the Cascade and Alaskan arcs, and the Mediterranean region (**Figure 1**).

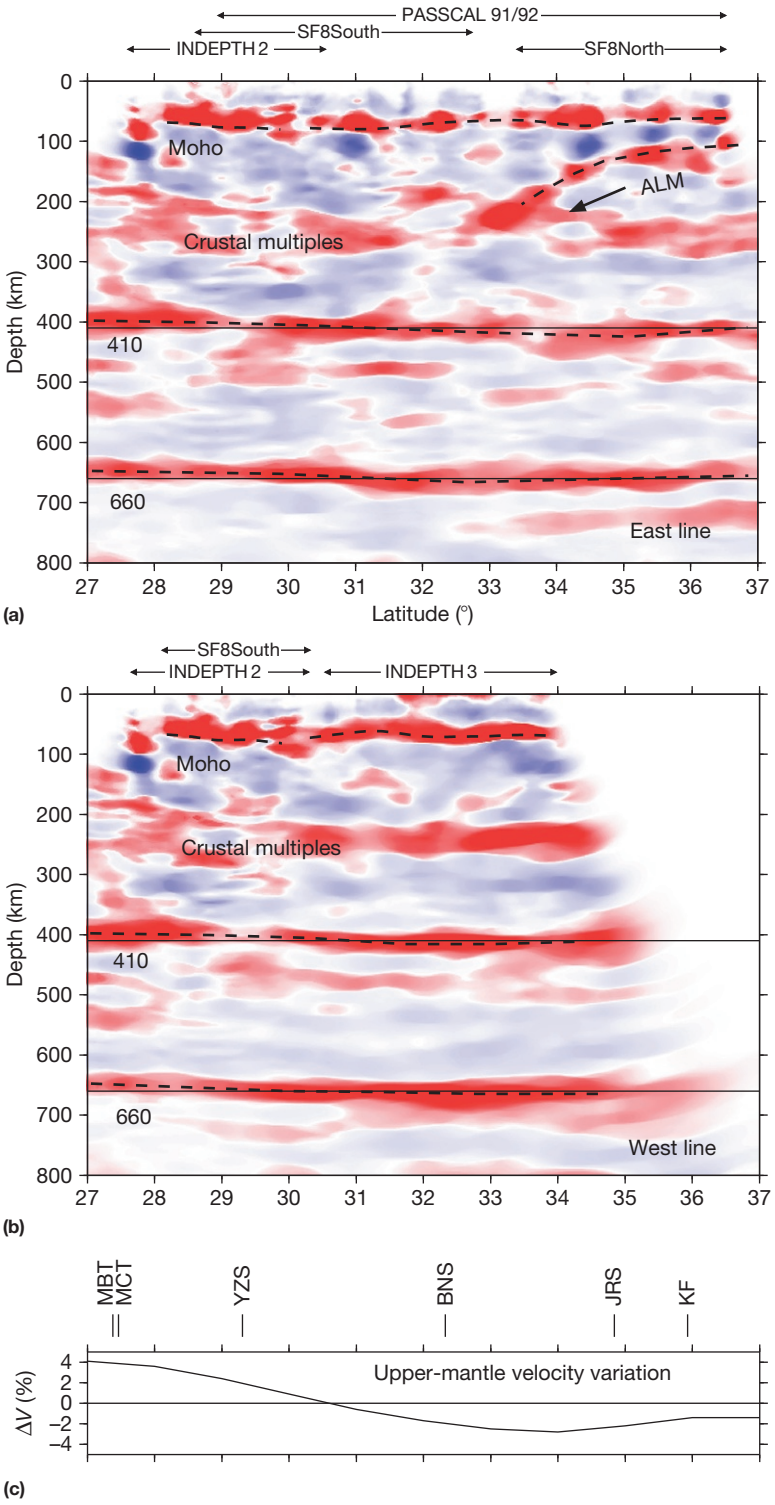

Figure 11 Migrated receiver function images along profiles shown in **Figure 9(a)**. (a) The approximately N–S profile (as in **Figure 9(a)**), based on PASSCAL 91/92, INDEPTH 2, and SF-South and SF-North passive array deployments. Positive amplitudes (velocity increase) are plotted in red; negative amplitudes in blue. ALM denotes underthrust Asian lithospheric mantle. 'Crustal multiples' around 200–300 km depth are produced by crustal reverberations. (b) Images from the NW–SE INDEPTH 3 transect, as well as the southern part of the (a) transect. Acronyms are as in caption to **Figure 9**. Reproduced from Kind R, Yuan H, Saul J, et al. (2002) Seismic images of crust and upper mantle beneath Tibet: Evidence for Eurasian plate subduction. *Science* 298: 1219–1221.

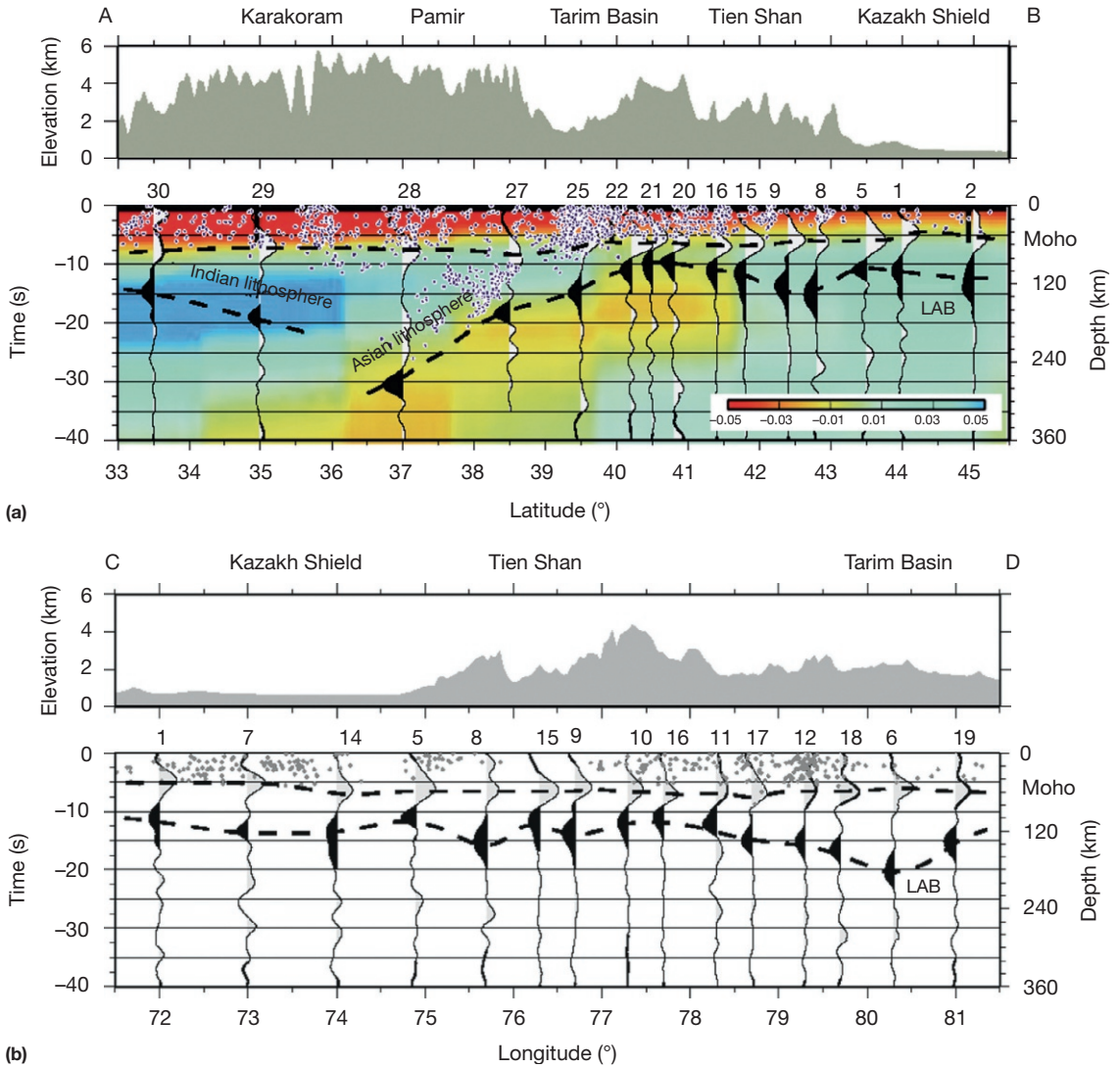

Figure 12 (a) North–south receiver function profile approximately along 75° E longitude in **Figure 9(b)**, overlaid on tomographic image of Friederich (2003). Topography is shown in the upper panel. Reproduced from Kumar P, Yuan X, Kind R, Kosarev G (2005) The lithosphere–asthenosphere boundary in the Tien Shan-Karakoram region from S receiver functions: Evidence for continental subduction. *Geophysical Research Letters* 32(L07305): 1–4. http://dx.doi.org/10.1029/2004GL022291. The receiver function signals in black are interpreted to correspond to the lithosphere–asthenosphere boundary (LAB) and suggest that the rigid Tarim Basin block of the continental Asian lithosphere is being underthrust beneath the Pamir and Karakoram Ranges while at the same time, the high-velocity Indian lithosphere appears to be dipping to the north. (b) East–west receiver function profile across Tien Shan, approximately along 43° N latitude in **Figure 9(b)**.

For a more comprehensive summary of subduction zone seismic studies, including those in Japan where data from extensive permanent networks have produced highly detailed images of subduction zone structures.

1.16.3.3.1 Andean studies

International broadband portable array deployments, largely by US and German groups, have been heavily concentrated in the central and southern Andes as shown in **Figure 13**. Migrated receiver function images beneath dense aerial deployments in northern Chile and Argentina reveal décollement thrusts within the crust, Moho depths up to nearly 80 km beneath the western Cordillera/western Altiplano but decreasing eastward into the Altiplano (Puna) and eastern Cordillera (**Figure 14**). The top of the descending Nazca Plate is clearly imaged to a depth of slightly more than 100 km, below which the discontinuity signal vanishes. Yuan et al. (2000) interpreted the disappearance of the upper plate boundary to be the result of the low-velocity oceanic basaltic crust converting to high-velocity eclogite.

Despite the large numbers of mostly short-period instruments deployed (e.g., PISCO, CINCA, ANCORP, and PUNA; **Figure 14**), the central Andes of northern Chile/Argentina has, with few exceptions (e.g., Graeber and Asch, 1999), seen relatively little in the way of comprehensive 3-D tomographic imaging. Farther south, however, in the vicinity of the broadband CHARGE experiment (**Figure 15**) where the slab transitions southward from flat to normal subduction, extensive

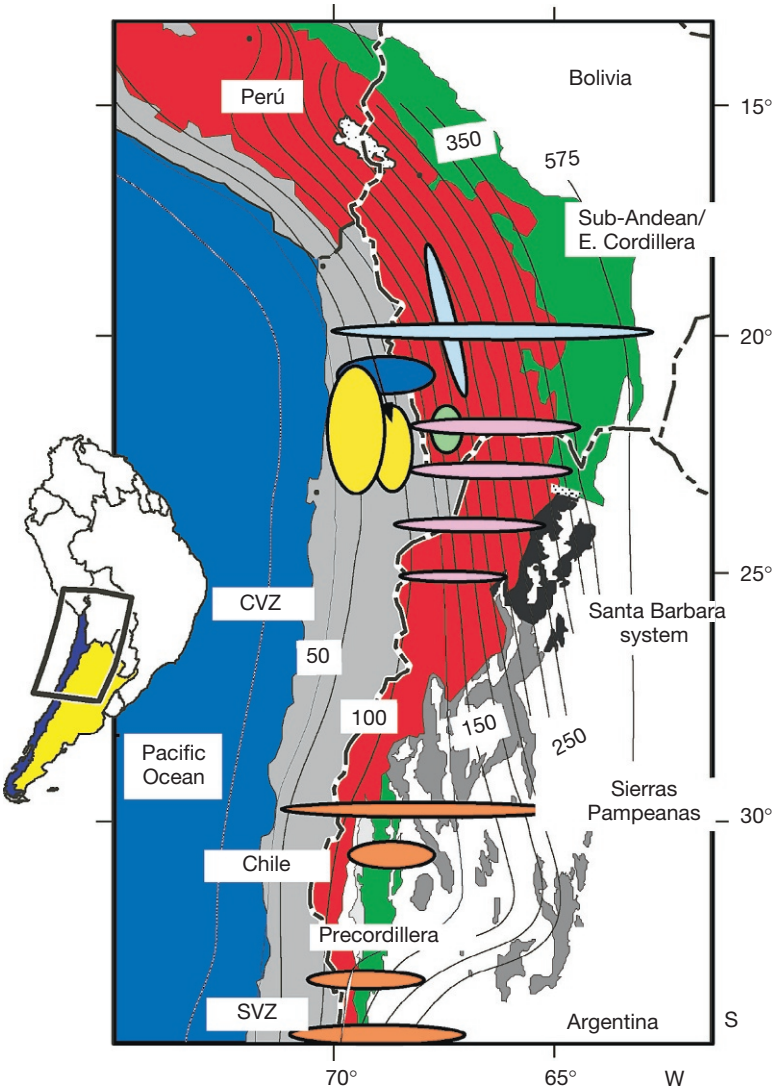

Figure 13 Map of the central and southern Andes showing approximate locations (colored ovals) of major seismic experiments during the past decade and a half. Figure courtesy of Sue Kay. Contoured depths are to Wadati–Benioff zone. CVZ, Central Volcanic Zone; SVZ, Southern Volcanic Zone. Explanation of ellipses and ovals: light blue, BANJO and SEDA deployments (e.g., Zandt et al., 1996); yellow, CINCA and PISO deployments (e.g., Schmitz et al., 1997); dark blue, ANCORP (ANCORP WorkingGroup, 2003). Brown ellipse, APMB experiment (e.g., Chmielowski et al., 1999). Pink, GFZ experiment (Yuan et al., 2000); see also **Figure 14**. Orange ellipses, CHARGE (Wagner et al., 2005); see also **Figure 15**.

tomographic imaging of both P and S waves has revealed a remarkable result (Wagner et al., 2005). Wagner et al. focused on the mantle lithosphere within the region of flat subduction around latitude 31°S and then southward into the region of normal subduction. As shown in **Figure 15**, V_p is as low as 7.4 km s^{-1} in the continental lithospheric mantle above the region immediately above the flat slab. Velocity values this low are not surprising in a region where it has been widely assumed that the overlying continental lithosphere is extensively hydrated by water sweated from the descending plate. Tomographic inversion for V_s, however, produces an entirely different result, with S-wave velocities relatively high ($\sim$4.6 km s^{-1}) in the same region of the continental lithosphere where very low P-wave velocities are observed (**Figure 15**). The result is an anomalously low Poisson's ratio (<0.25) that matches no plausible hydrated mantle mineralogy or even any common mantle mineralogy at all. Preliminary studies in Alaska have produced a similar result in the mantle above the descending slab, where V_p/V_s ratios of 1.62–1.68 are found in the overlying mantle wedge at depths greater than 80 km. Abers et al. (2005) speculated that the low V_p/V_s may indicate large-scale silica addition to the overlying mantle wedge, presumably the result of tectonic erosion of the overriding continent, but the issue remains essentially unresolved as of this writing. Further data on the structure of the continental lithosphere above regions of flat subduction are being collected in the region of northern Chile where subduction transitions from normal to flat (white square in **Figure 13**). Here, a large-scale regional array of 25 broadband and 45 short-period instruments is currently being deployed to image possible continental lithosphere delamination. This region of Chile and Argentina is one of the few places in the world where lithospheric delamination

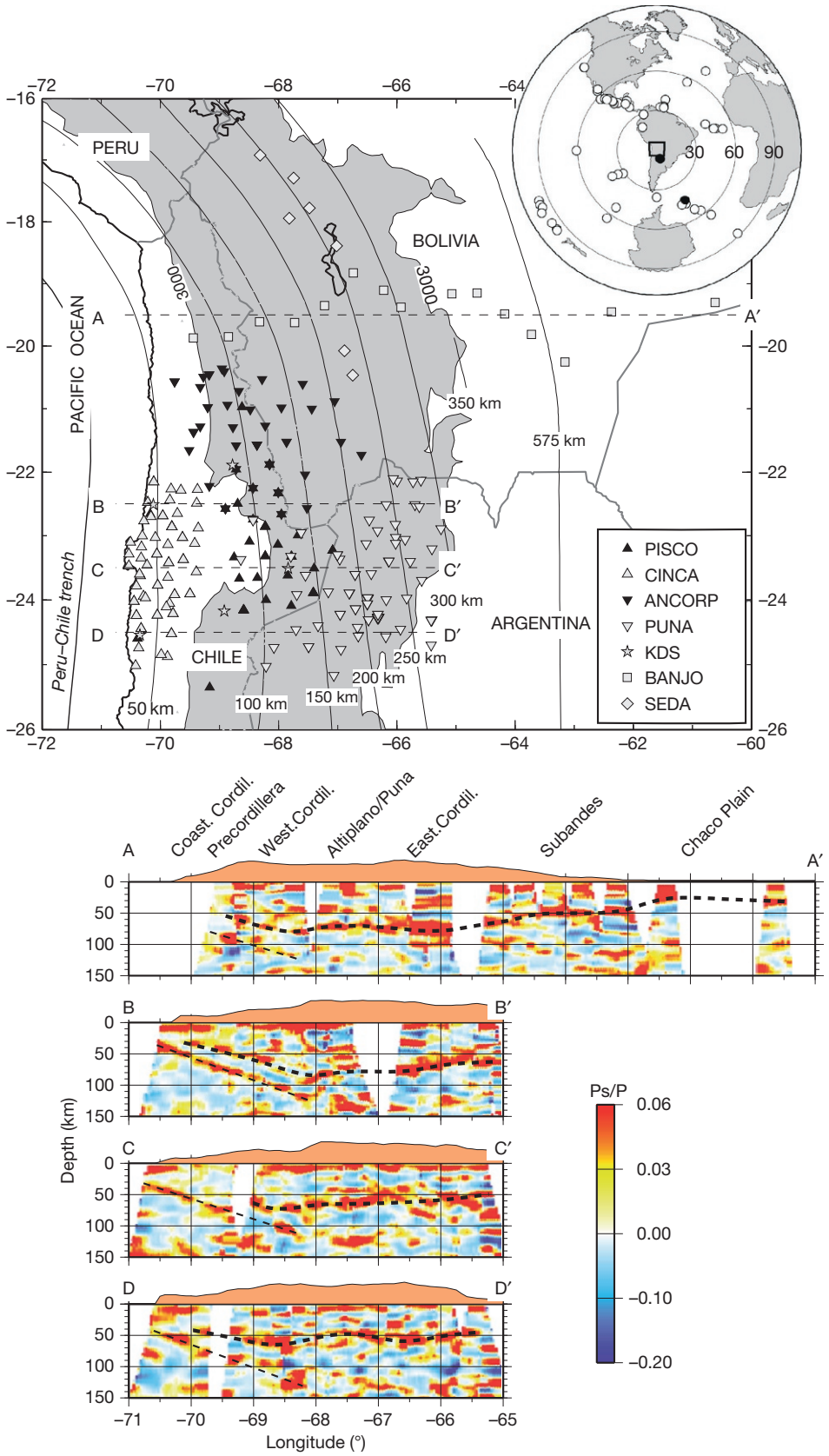

Figure 14 Migrated receiver function images (lower images) based on the combined data of several short-period and broadband experiments (map in the upper panel) across the south-central Andes. Map figure shows locations of passive seismic stations as indicated in relation to cross-sectional lines of receiver function images in the lower panels. Contours show depth to top of Wadati–Benioff zone. Small black triangles indicate volcanic centers. Shaded region above 3 km elevation. Lower panels represent a series of vertical cross sections along the E–W profiles indicated in the map figure. The heavy black dashed line marks the Andean Moho, the lightly dashed lines the top of the descending Nazca Plate (Yuan et al., 2000). The crust tends to thin eastward of the volcanic arc (beneath the Altiplano and eastern Cordillera), without a corresponding decrease in average surface elevation. Reprinted from Yuan X, Sobolev SV, Kind R, et al. (2000) Subduction and collision processes in the Central Andes constrained by converted seismic phases. *Nature* 408: 958–961, Copyright (2000), with permission from Macmillan Publishers Ltd.

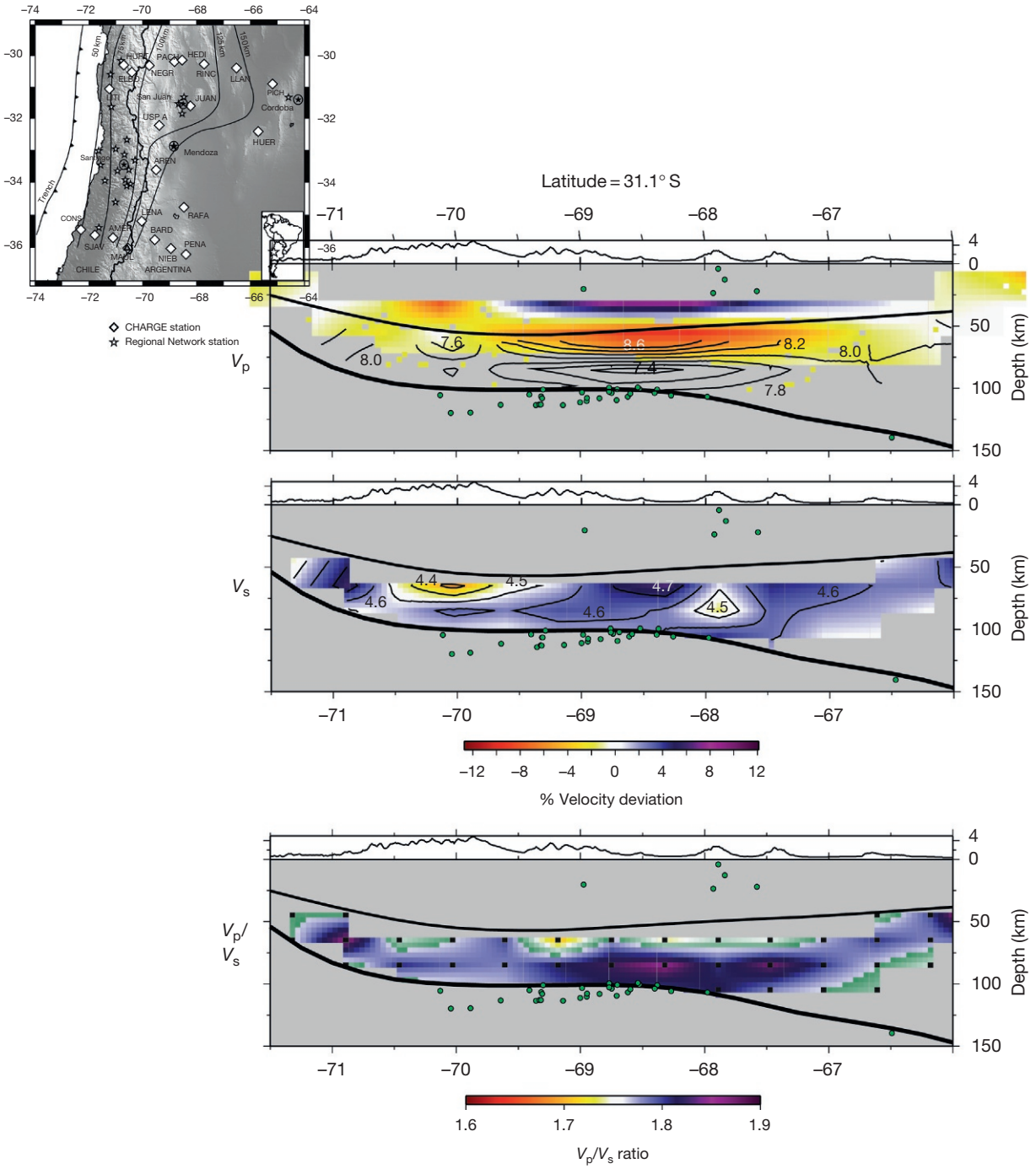

Figure 15 Broadband seismic experiment (CHARGE) across the southern Andes of central Chile in the region of flat subduction and the transition from flat to normal subduction. East–west tomographic images across the region of flat subduction near latitude 31° S reveal a prominent zone of low V_p/V_s ratio (deep blue in the lowermost panel) in the continental lithosphere immediately above the flat subducting plate, as yet unexplained by any plausible mantle mineralogy. Adapted from Wagner LS, Beck SL, and Zandt G (2005) Upper mantle structure in the south central Chilean subduction zone (30 to 36S). *Journal of Geophysical Research* 110. http://dx.doi.org/10.1029/2004JB0003238.

may be actively occurring today, speculated to be the result of slab rollback as the downgoing Nazca Plate transitions from flat subduction back to normal subduction (Kay et al., 1994).

The Andes are at their widest and highest in the central region of Peru and Bolivia where subduction is 'normal.' There, the primary questions concern the origin of the high Altiplano, which, next to the Tibetan Plateau, is the second largest high plateau in the world. Van der Lee et al. (2001a) used surface wave data of mostly South American events recorded on several portable arrays in Peru, Chile, Bolivia, and Brazil to determine structure above the subduction zone and across the central part of South America. One of the most

notable features shown by that study is a prominent low-velocity upper mantle beneath the eastern Andes (the foreshortened region of the high Andes, interpreted previously to be affected by mantle hydration from an episode of flat subduction in Miocene time; James and Sacks, 1999). The seismic images are consistent with predicted effects of lithospheric hydration (during flat subduction) followed by lithospheric melting resulting from the infusion of hot asthenospheric material into the opening mantle wedge during slab foldback to normal subduction.

1.16.3.3.2 Central America and Caribbean

The Caribbean and western Central America are targets for a number of ongoing passive array experiments and combined active and passive source experiments, from which results are as yet mostly unpublished. Notable among the larger projects are the BOLIVAR experiment in NE Venezuela and the TUCAN experiment in Costa Rica and Nicaragua (station locations shown in Figure 1). The BOLIVAR experiment, a combination of onshore and offshore active and passive source methods and instrumentation, is aimed at studying the accretion of arc-related terranes in northern Venezuela. This work is a substantial extension of a previous broadband array experiment in which it was found that continental South America has overridden a significant part of the Lesser Antilles arc, with the southern detached slab now situated beneath NE Venezuela (VanDecar et al., 2003).

1.16.3.3.3 Cascadia

The 1993 Cascadia experiment (CASC93) was, in 1993 and even today, an unprecedented effort at broadband deployment – in the number of instruments, the extraordinarily high station density, and the length and linearity of the transect (Nabelek et al., 1993). CASC93 was composed of 44 broadband stations located at 69 sites at approximately 5 km station spacing along an almost perfectly straight transect across the Cascades, from coastal to central Oregon (Figure 16). The dataset has proved a fertile testing ground for advanced multichannel imaging of scattered waves in a subduction zone (Rondenay et al., 2001). The results from that imaging and an interpretive overlay are shown in Figure 16 (lower panel). Bostock et al. (2002) had interpreted the images in Figure 16 to be the result of eclogitization of the downgoing slab (below about 45 km) and consequent serpentinization of the overlying mantle wedge in the forearc. It is anomalous that the basalt–eclogite transition in this case is far shallower than is generally presumed for typical subduction zones (45 km vs. 100 km), but the disappearance of a basaltic crustal signature below 45 km appears to have few other explanations. Similarly, the disappearance of a continental Moho signature in the images (around 122.5 longitude) appears to be the result of an 'inversion' in the usual continental Moho velocity transition. Thus, the (relatively) high-velocity material of the lower continental crust is interpreted to be in contact with (relatively) low-velocity serpentine of the heavily hydrated mantle wedge (serpentinized mantle forearc in the lower frame of Figure 16).

1.16.3.3.4 Alaska

The Broadband Experiment Across the Alaska Range (BEAAR) experiment (Figure 17) provides another example of imaging across a very complex continental subduction boundary (Abers et al., 2006). The BEAAR transect, 1999–2001, consisted of 39 broadband seismographs deployed with 10–15 km station spacing normal to the strike of the subduction zone (map, Figure 17). High-resolution receiver function images (Ferris et al., 2003) show that the top of the slab is low velocity (i.e., basaltic) to a depth of about 130 km (note the contrast with the Cascadia images in Figure 16). Moreover, the Wadati–Benioff zone of seismicity is angled slightly more steeply than the top of the imaged slab, suggesting that the earthquakes gradually migrate deeper into the slab with depth (Figure 17). Well-constrained seismic attenuation determinations (Stachnik et al., 2004) show high attenuation in the mantle wedge beneath the Alaska Range, but where the slab is less than about 75 km depth, there is an observed sizeable volume of very low-attenuation material (Figure 17). This zone of low attenuation has been interpreted by Abers et al. (2006) to indicate that a cold, hydrous viscous 'nose' has formed in the corner of the mantle wedge and remains isolated from the counterflow in the main part of the mantle wedge. The presence of a high-velocity viscous 'nose' in the subduction zones has been observed previously in Japan and given much the same explanation (Kincaid and Sacks, 1997; Sacks and Suyehiro, 2003).

1.16.3.3.5 Kamchatka

The subduction zone along the Kamchatka Peninsula exhibits a unique geometry in that it undergoes a nearly right-angle change in strike at the intersection of the eastern extension of the Aleutian Arc and the NE trending Kamchatka arc (Figure 18; Lees et al., 2000). This so-called Aleutian–Kamchatka 'corner' can be accommodated by either a bend or a tear in the downgoing lithosphere (Davaille and Lees, 2004; Lees et al., 2000). Along the westernmost extent of the Aleutian Arc, the spreading direction of the Pacific Plate is essential parallel to the subduction zone. This rather rare subduction geometry is manifest by the NW striking 1000 km strike-slip Bering fault along the westernmost tail of the Aleutian Arc. The Kamchatka experiment shown in Figure 18 was composed of 15 broadband stations deployed on the Kamchatka Peninsula to examine the region of intersection between the Aleutian Arc and Kamchatka arc in detail. The results of the studies that emerged from that experiment suggest that the Pacific Plate does not simply 'bend' around the Aleutian–Kamchatka corner, but that subduction in Kamchatka is parallel to that in the Aleutians and that therefore a tear must separate the two slabs (Lees et al., 2000) (right-hand panel, Figure 18). This remarkable structure appears to give rise to a rare instance of slab melting as evidenced by both the seismic structures and presence of adakite-like magmas that have been erupted at the Aleutian–Kamchatka corner (Davaille and Lees, 2004). The Aleutian–Kamchatka corner may be one of the only places anywhere on the globe where a slab tear seems to be confirmed.

1.16.3.4 Active Continental Rifts

Continental rifts such as the East African and Baikal Rifts have been extensively studied through controlled-source experiments that both cross and traverse the rift valleys.

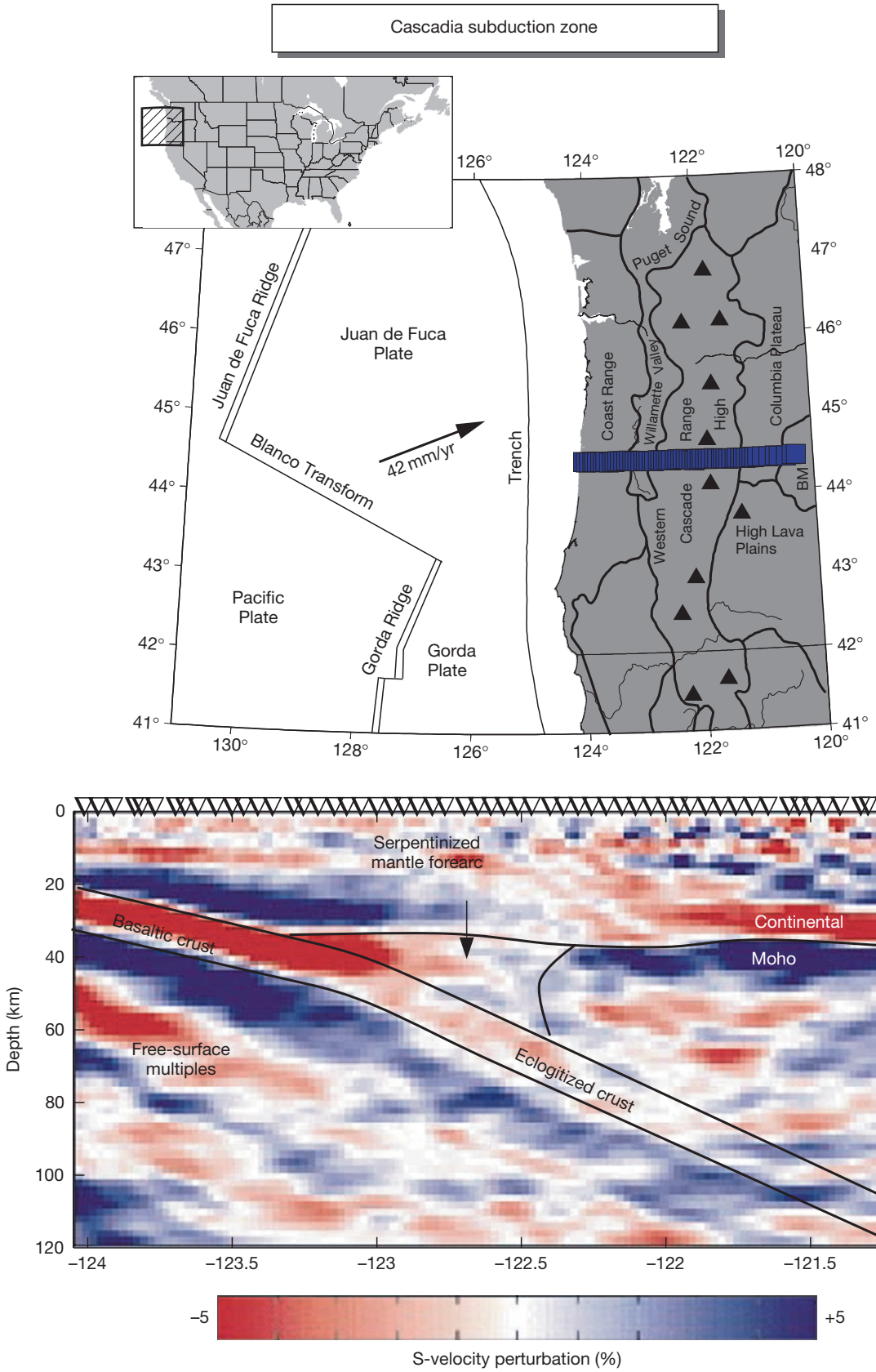

Figure 16 Imaging results from the 1993 Cascadia seismic experiment (CASC93; Nabelek et al., 1993) deployment of 44 broadband stations at ~5 km spacing from the Pacific coast across the Cascades into the Columbia Plateau and Blue Mountains (upper panel). The lower panel in an interpretive vertical cross section superimposed on the scattered wave inversion image of Rondenay et al. (2001). Copyright 2001, American Geophysical Union. Red indicates slow-velocity perturbations; blue, fast. See text for further discussion. Figure provided courtesy of Stephane Rondenay, MIT.

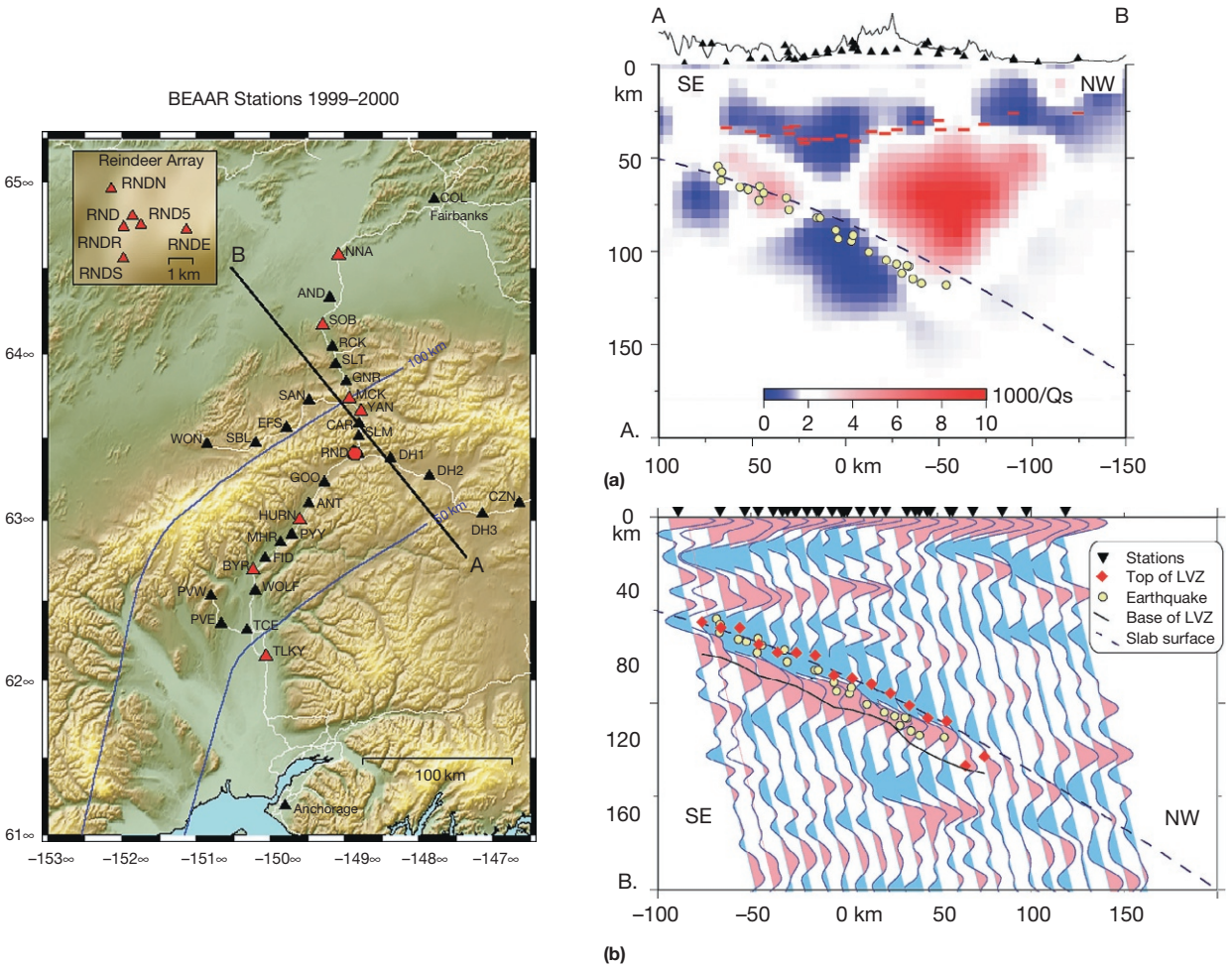

Figure 17 Broadband Experiment Across the Alaska Range (BEAAR). Map on the left shows station locations. Contours indicate depth to Wadati–Benioff zone. Top right figure is a vertical cross section of attenuation tomography along line A–B. Red, high attenuation; blue, low attenuation. Moho from receiver functions is indicated by red dashed line. The greatly reduced attenuation in the uppermost part of the mantle wedge suggests that material freezes out and no longer participates in the suprasubduction zone mantle wedge recirculation. The panel in the lower right shows the receiver function image with the inferred top of the slab indicated by a black dashed line. Earthquake hypocenters (relocated) are seen along the top of the slab at shallow depths but migrate into the slab with increasing depth. Figures courtesy of Geoff Abers. Modified from Abers GA, van Keken PE, Kneller EA, Ferris A, Stachnik, JC (2006) The thermal structure of subduction zones constrained by seismic imaging: Implications for slab dehydration and wedge flow. *Earth and Planetary Science Letters* 241: 387–397.

The Tanzanian broadband experiment extended into the East African Rift, but the deployment was sufficiently sparse that little could be determined other than that the region beneath the rift was very low velocity, as previously known (e.g., Weeraratne et al., 2003). A major broadband deployment was undertaken recently across the northern Ethiopian Rift where the rifting is transitional between continental and oceanic and where it forms the third arm of the Red Sea, Gulf of Aden rift triple junction (Bastow et al., 2005). Nearly 80 broadband instruments were installed in a 250 × 350 km area for a 16-month period, 2001–03, as part of the Ethiopia Afar Geoscientific Lithospheric Experiment (EAGLE) (**Figure 19**; Maguire et al., 2003). Bastow et al. (2005) obtained clear images of an approximately 75 km wide tabular low-velocity zone beneath the rift (**Figure 20**). The low velocities extend to 200–250 km beneath the Ethiopian Rift in the southern part of the region trending into the East African Rift of southern Ethiopia and northern Kenya. As the rift approaches the Afar Depression, the low-velocity anomaly at depths >100 km appears to broaden and merge with deeper low-velocity structures beneath the Afar Depression (Bastow et al., 2005).

1.16.4 Stable Platforms

1.16.4.1 Central and Eastern North America

Compared with western North America, few portable arrays have been deployed in stable central and eastern North America. Prominent among broadband deployments is the Missouri to Massachusetts Broadband Experiment (MOMA), the Lithoprobe/IRIS Abitibi–Grenville teleseismic experiment (ABI96), and the Florida to Edmonton (FLED) broadband experiment (Fischer et al., 1996; Rondenay et al., 2000). The northern extension of the FLED array ends in Edmonton,

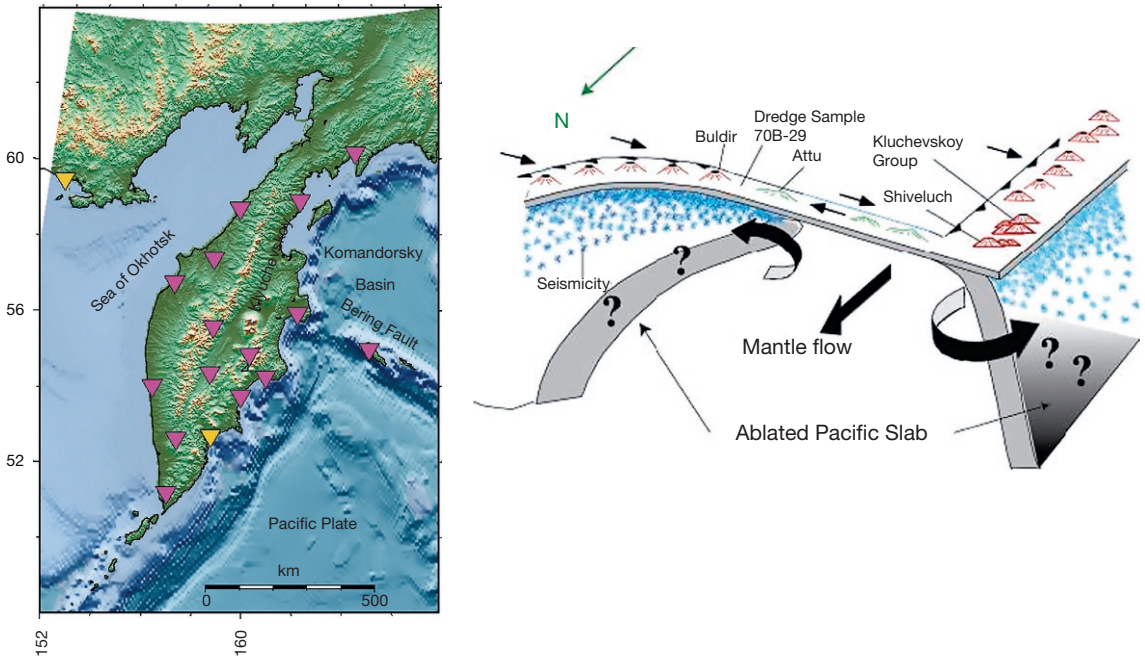

Figure 18 PASSCAL broadband deployment on the Kamchatka Peninsula to image the abrupt bend in subduction of the downgoing Pacific Plate (left-hand side panel). Image on the right is the interpretation of results showing slab separation with mantle flow through the corner region. Adapted from Lees JM, Brandon M, Park J, Levin V, Ozerov A, and Gordeev E (2000) Kamchatka: Edge of the plate. *IRIS Newsletter* 2000(1): 1–5.

Canada, just east of the Rocky Mountain Front (**Figure 1**). A recent deployment of nearly 60 broadband seismographs (the Canadian Northwest Experiment (CANOE)) picks up at Edmonton and continues as a Y-shaped transect to the NW (**Figure 1**). The array bifurcates into one transect across the Proterozoic and into the Slave craton and another that crosses the Canadian Rockies into the Yukon, a transect of nearly 4 Ga of geologic time (Bostock et al., 2005).

The MOMA deployment of 18 portable stations, anchored at each end by a permanent global station, is shown superimposed on the continent-scale model NA00 of van der Lee in **Figure 21** (van der Lee, 2002). Interstation spacing was about 100 km and the array operated for about 16 months. Receiver function determinations of crustal thickness along the profile show thickening of the crust beneath the Appalachians, thinning in the region of the Grenville Front and thickening again beneath the stable Proterozoic platform (Li et al., 2002). The root beneath the Appalachians, thicker than predicted for isostatic compensation, appears to reflect a 'densification' of the lower crust that Fischer (2002) had hypothesized is a common metamorphic process in older orogenic belts. Upper-mantle discontinuities from receiver functions observed beneath MOMA at depths around 270–280 km are visible in the eastern part of the array and have been interpreted as the (rarely observed) base of the asthenosphere beneath eastern North America (Li et al., 2002). Subsequent studies based primarily on extensive data from a handful of permanent stations in eastern United States suggest that the LAB is sharply defined, perhaps no more than 10–12 km in vertical extend, beneath the Phanerozoic (Rychert et al., 2005).

Van der Lee (2002) analyzed S waves and fundamental-mode surface waves along the strike of the array and combined those data with previous data used to develop the North American model NA95 to obtain high-resolution constraints on crustal thickness and S-wave velocity beneath the MOMA array as shown in **Figure 21**. The lower panel of **Figure 21** contains the new velocity structure in cross section and in terms of velocity perturbations. The thin dashed black line in that figure is presumed to represent the base of the seismic lithosphere and the white line the thermal thickness of the lithosphere as computed by Goes and van der Lee (2002). The lithospheric upper mantle is poorly resolved beneath Phanerozoic North America despite receiver function evidence of a sharp LAB beneath that region (Rychert et al., 2005).

Measurements of anisotropy along the MOMA array have produced a number of important results. Fouch et al. (2000) modeled the shear-wave splitting as asthenospheric shearing due to plate motion as the asthenosphere flowed under and around the continental keel of stable North America in response to the SW absolute motion of North America. They found no evidence for lithospheric anisotropy beneath the Proterozoic platform. Subsequent studies using Rayleigh and Love surface waves suggest a shallow lithospheric layer with significant 'radial' anisotropy (Gaherty, 2004). SKS splitting and surface waves indicate that azimuthal anisotropy is present primarily in the subcontinental asthenosphere as it deforms in response to plate motion.

The Abitibi–Grenville teleseismic experiment (ABI96) involved a 6-month N–S deployment of 28 broadband stations (Rondenay et al., 2005). Crustal thickness transitions abruptly near the Grenville Front, from 40–45 km in the Proterozoic south to the more characteristically thin (35 km) crust of the Archean craton in the north (Rondenay et al., 2000, 2005). Unlike results from MOMA, shear-wave splitting reveals a

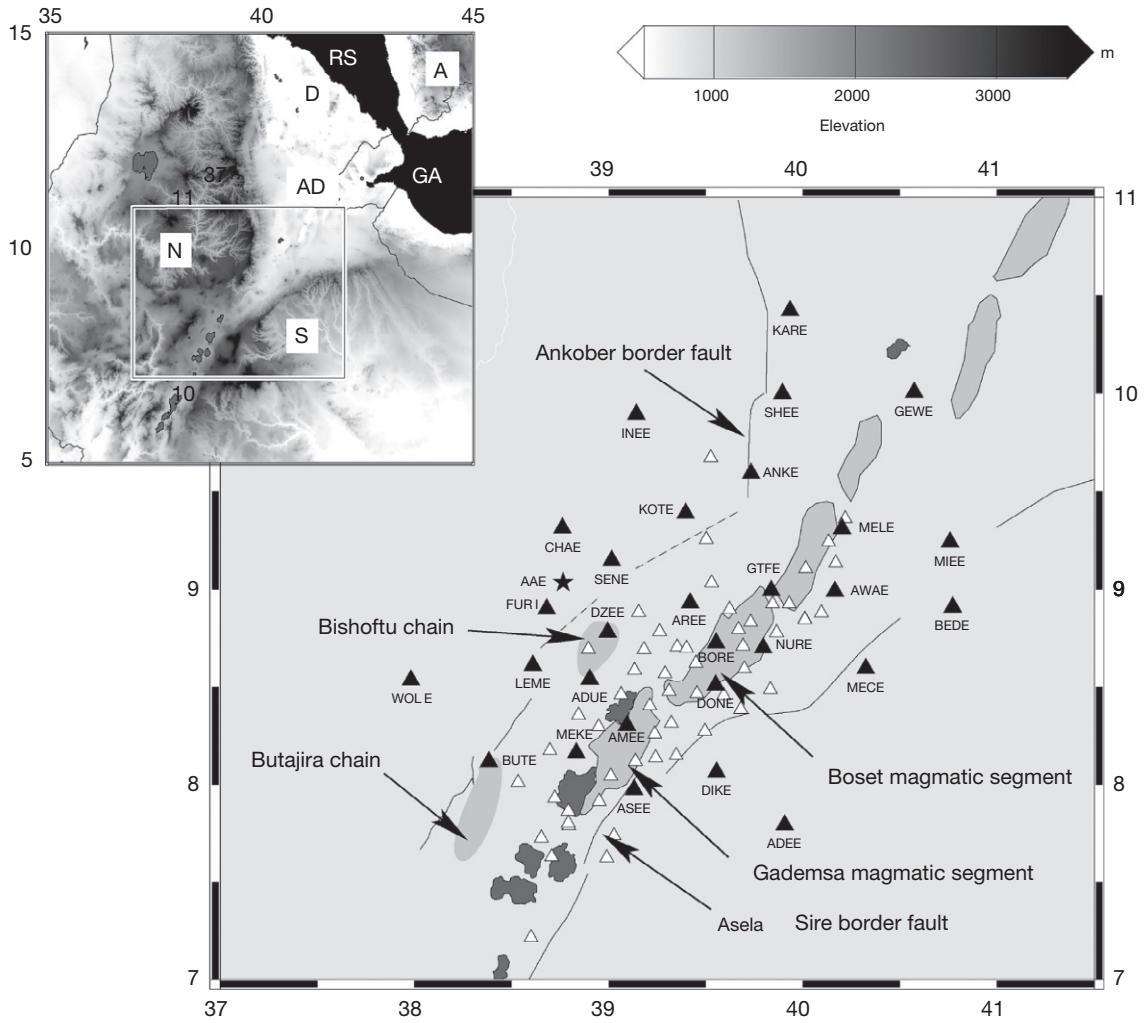

Figure 19 Station locations for the EAGLE broadband experiment, arrayed along the Ethiopian Rift transitional into the Red Sea (see text). Filled triangles are for phase I of the experiment; open triangles for phase II. Stations were deployed for a total of 2 years (2001–03). On inset, RS denotes Red Sea, GA denotes Gulf of Aden, A denotes Arabian Plate, AD denotes Afar Depression, D denotes Danakil microplate, N denotes Nubian Plate, and S denotes Somalian Plate. Reproduced from Bastow ID, Stuart GW, Kendall JM, and Ebinger C (2005) Upper-mantle seismic structure in a region of incipient continental breakup: Northern Ethiopian rift. *Geophysical Journal International* 162: 479–493, with permission from Blackwell Publishing.

monotonous pattern of dominantly E–W fast directions and relatively small delay times around 0.5 s, with no transition across the Grenville Front (Figure 22). The fast directions along the Abitibi–Grenville line tend to be oriented at a relatively high angle to absolute plate motion and accordingly have been interpreted as due to fossil anisotropy in the lithosphere (Fouch and Rondenay, 2006; Rondenay et al., 2000). A summary of fast polarization directions and magnitude of the delay times measured over several experiments for central and eastern North America is shown in Figure 22.

1.16.4.2 Australia

The Australian continent is particularly well suited for seismic investigations of variation in lithospheric structure between Archean, Proterozoic, and Phanerozoic terranes. The southwestern quarter or so of the continent is underlain by several Archean crustal blocks. The vast central and west-central part of Australia is Proterozoic in age and the eastern third of the country is Phanerozoic. The so-called Tasman line, the precise location of which is still disputed but which shows up repeatedly in discussions of Australian terranes, divides the Precambrian terranes from the Phanerozoic (e.g., Simons et al., 1999).

Over the past two decades, the Australian continent has been instrumented in a sparse but systematic grid of portable broadband stations, the most prominent of which composed a succession of deployments known as SKIPPY (1993–96). SKIPPY was an innovative experiment in which a single array of approximately 10–12 stations was 'skipped' kangaroo style across the continent in six major deployments (van der Hilst et al., 1994). It was specifically designed to capitalize on the substantial arc-related regional seismicity to the east and north of the continent. The SKIPPY array has since been complemented by a number of regional temporary arrays deployed to examine specific regions in more detail (Fishwick et al., 2005). The map figure in the upper left panel of Figure 23

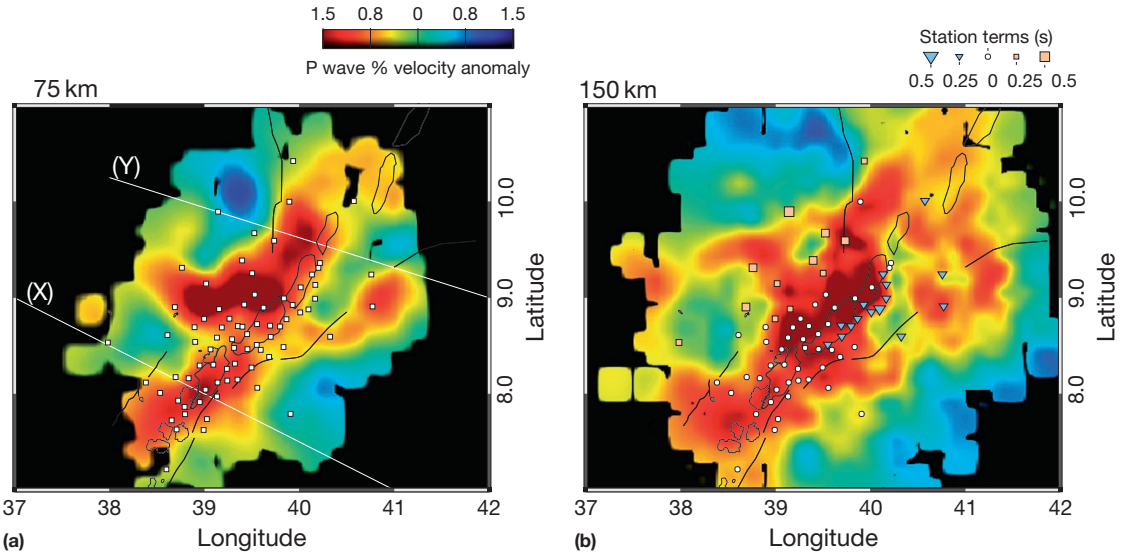

Figure 20 Horizontal depth slices of 3-D tomographic images of P-wave perturbations beneath the Ethiopian Rift as shown in **Figure 19**. Extreme low velocities are shown beneath the broad area of the rift axis to depths of at least 250 km. Modified from Bastow ID, Stuart GW, Kendall JM, and Ebinger C (2005) Upper-mantle seismic structure in a region of incipient continental breakup: Northern Ethiopian rift. *Geophysical Journal International* 162: 479–493, with permission from Blackwell Publishing.

shows broadband deployments superimposed on the geologic outline map of Australia. As few of these deployments are sufficiently dense for high-resolution body wave tomography, the station and source geometry has been most amenable to surface wave tomographic analysis and to receiver function crustal thickness determinations (e.g., Clitheroe et al., 2000; Fishwick et al., 2005; Simons et al., 1999). Until recent work, when relatively dense arrays were installed in the Archean SW of Australia (e.g., Fishwick et al., 2005), surface wave coverage had been most dense in the eastern part of the continent and least dense in the southwest.

Lithospheric imaging beneath Australia is particularly revealing because the instruments and the kind of data used are relatively uniform across the entire continent, making direct comparisons between provinces of different geologic ages possible. Fishwick et al. (2005) integrated data from earlier portable broadband arrays (e.g., Simons et al., 1999) with data compiled from recent deployments in western Australia to produce lithospheric images of consistent quality across the continent (**Figure 23**). The results in **Figure 23** are derived by PWI but with several different starting models as to improve the recovery of the averaged 1-D path model for the significantly different propagation path structures encountered (e.g., oceanic vs. continental) and have been updated since the Fishwick et al. (2005) paper. The results reveal a remarkably wide range in shear velocities, in excess of 15% even at 150 km depth, beneath the Australian continent. At 100 km depth, high velocities are observed throughout most of the continent including parts of Australia well east of the Tasman line. These higher velocities beneath even the Phanerozoic terranes are interpreted to represent thick lithosphere. Lower velocities are seen at 100 km depth only along the easternmost part of the continent. The anomalously low velocities at 100 km depth along the eastern margin of the continent appear to be correlated with zones of Neogene volcanism as observed earlier by Zielhuis and van der Hilst (1996). Most of the observed velocity contrast appears to be due to temperature variations, and based on the work of Faul and Jackson (2005), Fishwick et al. (2005) concluded that a temperature contrast of ~600 °C could account for the velocity differences between the ocean basins and the oldest parts of the continent at 150 km depth. High-velocity material in the upper mantle beneath western Australia extends to at least 150 km beneath the Archean cratons. High-velocity material is not seen to depths greater than about 150 km beneath the small Pilbara Craton, but is observed to depths of at least 250 km beneath the Yilgarn Craton to the SW and the Kimberley Craton to the NW. In general, the higher velocities at greater depths (>200 km) beneath Australia do not correlate simply with age terranes.

The crustal structure beneath Australia has been investigated primarily through receiver function methods based on some of the same station data as those used for the surface wave inversion studies discussed earlier in the text (Clitheroe et al., 2000). The crust beneath the undisturbed parts of the western cratons averages about 35–40 km thick, although the crust as thin as 25–30 km is seen beneath parts of the Archean-age Yilgarn and Pilbara Cratons and thicker crustal sections abut the Yilgarn to the west. The Moho tends to be sharp beneath the cratonic interiors but more gradational near terrane boundaries (Reading et al., 2003). The vast Proterozoic interior of the Australian continent is underlain by crust mostly 40–55 km thick, with a relatively transitional Moho. The thickest crustal section yet found in all of Australia is beneath the Amadeus Basin in central Australia, low lying despite a maximum crustal thickness of 61 km. The eastern third of Australia (east of the inferred Tasman line) is composed primarily of the late Phanerozoic Tasman orogen (Clitheroe et al., 2000), where a complex of accretionary terranes was assembled against the Proterozoic continental nucleus (Betts et al., 2002). The thicker crust of the Proterozoic of central Australia

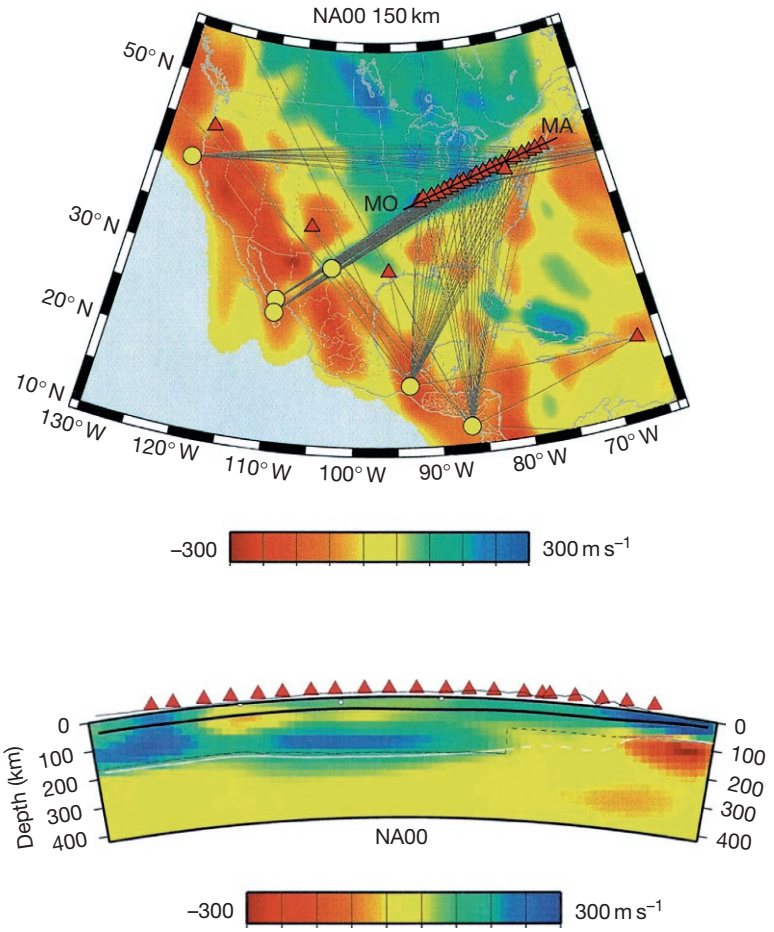

Figure 21 Missouri to Massachusetts (MOMA) broadband array (red triangles). Top figure shows map of the array and the events plus great circle propagation paths (gray lines) used for partitioned waveform inversion superimposed on the 3-D North America model NA00 of van der Lee at a depth of 150 km (van der Lee, 2002). The black line through the stations is the trace of the vertical cross section shown in the bottom panel. The bottom panel is a vertical cross section illustrating velocity perturbations showing a clear high-velocity lithosphere beneath stable continent length of the array. The thin black line represents the base of the lithosphere (as defined by van der Lee, 2002) and the thin white line the thermal thickness of the lithosphere based on Goes and van der Lee (2002). The slightly low-velocity channel beneath the lithosphere is still very high velocity (4.55 km s^{-1}) relative to the typical LVZ of the ocean basins. Adapted from van der Lee S (2002) High-resolution estimates of lithospheric thickness from Missouri to Massachusetts, USA. *Earth and Planetary Science Letters* 203(1): 15–23.

thins east of the Tasman line to a relatively uniform crust of about 35 km thick that is characterized by a sharp Moho. The abrupt shift in crustal thickness and Moho structure from thick Proterozoic to thin Phanerozoic is in contrast with images of mantle lithosphere, where the Tasman line is not at all well defined (**Figure 23**; Fishwick et al., 2005).

1.16.4.3 South America

Southeastern Brazil is by far the most thoroughly studied part of stable South America (e.g., Schimmel et al., 2003, where portable broadband arrays have been installed in a SKIPPY-like expanding and migrating observational network since 1992. The arrays, with up to 15 stations operating at one time, total 45 stations over an area about 1000 × 1700 km (**Figure 24**). The region encompasses the Archean São Francisco Craton, the Paraná Basin – a massive flood basalt province c.130 Ma – and its adjoining margins of Cretaceous alkaline intrusives. The most remarkable, and most controversial, finding from the tomographic imaging in this region is the discovery of an apparent 'fossil' Paraná plume at depths 200–600 km in the upper mantle beneath the Paraná Basin (VanDecar et al., 1995) (bottom image, **Figure 24**). Tomographic images of the upper mantle also show that the keel of the Archean São Francisco Craton extends to depths of 200–300 km. The lithosphere is considerably thinned in the region of the postrifting Late Cretaceous alkaline intrusives that cluster locally throughout much of SE Brazil, particularly around the margins of the Paraná Basin and the São Francisco Craton (Schimmel et al., 2003). Anisotropy beneath that same region of SE Brazil as determined by SKS splitting appears to be controlled largely by preexisting lithospheric structures rather than mantle flow (James and Assumpção, 1996).

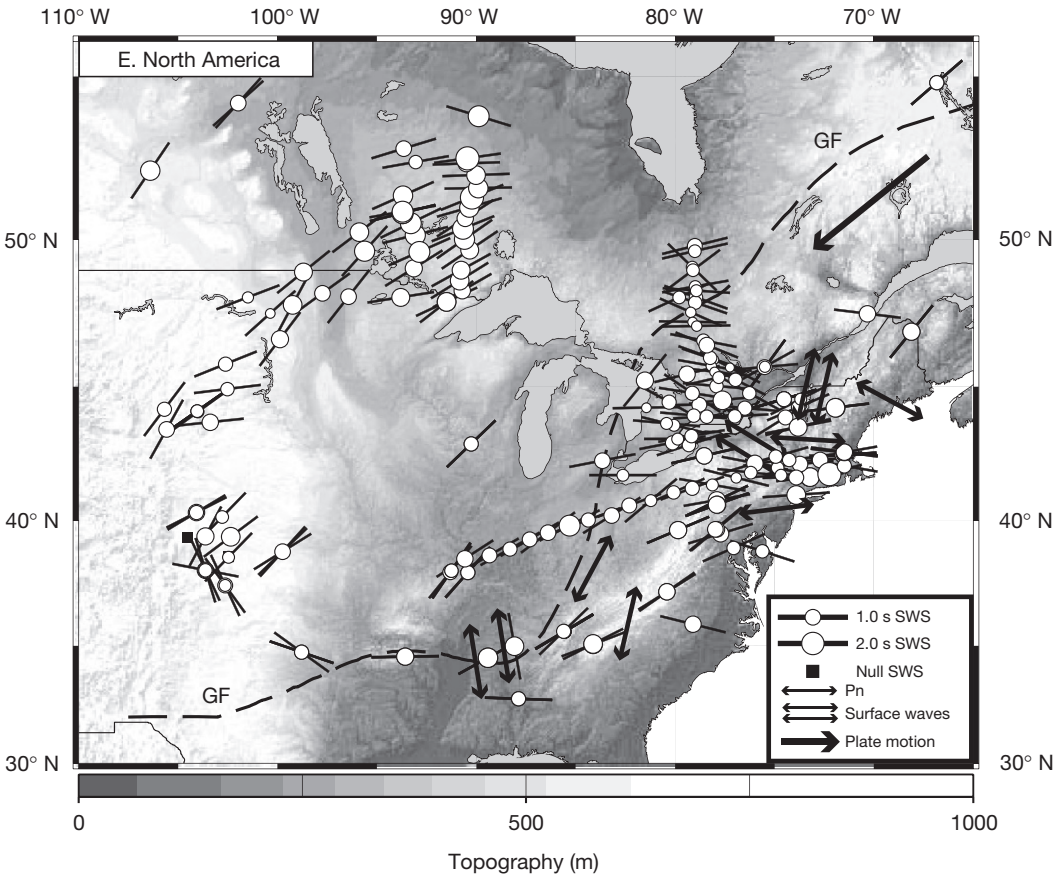

Figure 22 Summary of published shear-wave splitting results for eastern North America. Black bars indicate fast direction of anisotropy. The size of circle is proportional to splitting delay time as shown in the inset. Anisotropy measurements from surface waves and Pn measurements are represented by double black arrows. GF denotes Grenville Front. Reproduced from Fouch MJ and Rondenay S (2006) Seismic anisotropy beneath stable continental interiors. *Physics of the Earth and Planetary Interiors* 158: 292–320.

1.16.4.4 Antarctica

Despite extreme cold, lack of sunlight for solar power half of the year, little infrastructure, and other serious logistical challenges, portable broadband experiments on the continent of Antarctica have not been wanting. Efforts to operate portable seismic instruments have been underway for well over a decade, and new technologies have been developed to operate in extreme arctic conditions. Thanks largely to those efforts, as well as continuing support from the permanent facilities that the NSF Polar Program maintains in Antarctica, an ambitious array experiment was undertaken recently to map the contrasting crustal and upper-mantle structures along a transect across the West Antarctic Rift System, the Transantarctic Mountains, and the East Antarctic Craton (Figure 1). The Transantarctic Mountain Seismic Experiment (TAMSEIS) involved a deployment of 41 broadband seismometers that recorded from 2000 to 2003 under extraordinarily difficult operating conditions (Figure 1). Analysis of the data collected from the TAMSEIS project is highly preliminary, but results to date reveal high velocities in the mantle beneath the (old) East Antarctic Craton and a zone of low velocities that extends to 200 km beneath the (young) Transantarctic Mountains and NNE beneath McMurdo Sound and the Ross Sea (Watson, 2005). The area of McMurdo Sound includes Mt. Erebus, an active Antarctic volcano and the highest peak in the Transantarctic Mountain belt.

1.16.5 Archean Cratons

Archean cratons, the ancient cores of continents, are prime targets for portable array seismology. Archean cratons exhibit a number of distinctive features that set them apart from all younger continental structures. Notably, cratons are underlain by a thick mantle root (tectosphere; Jordan, 1975) that is both chemically and physically distinct from the rest of the mantle, including other continental lithosphere, suggesting formation by processes unique to Archean time. The refractory tectospheric root is now known to be ancient, composed dominantly of highly depleted peridotites with low normative density and high seismic velocities (Boyd and McCallister, 1976; Boyd and Mertzman, 1987; James et al., 2004; Jordan, 1979) and at least 200 km thick (e.g., Bruneton et al., 2004; Grand, 1994; James and Fouch, 2002; James et al., 2001, 2004; Jordan, 1975; Lerner-Lam and Jordan, 1987; Van der Lee and Nolet, 1997; Zhao et al., 1999).

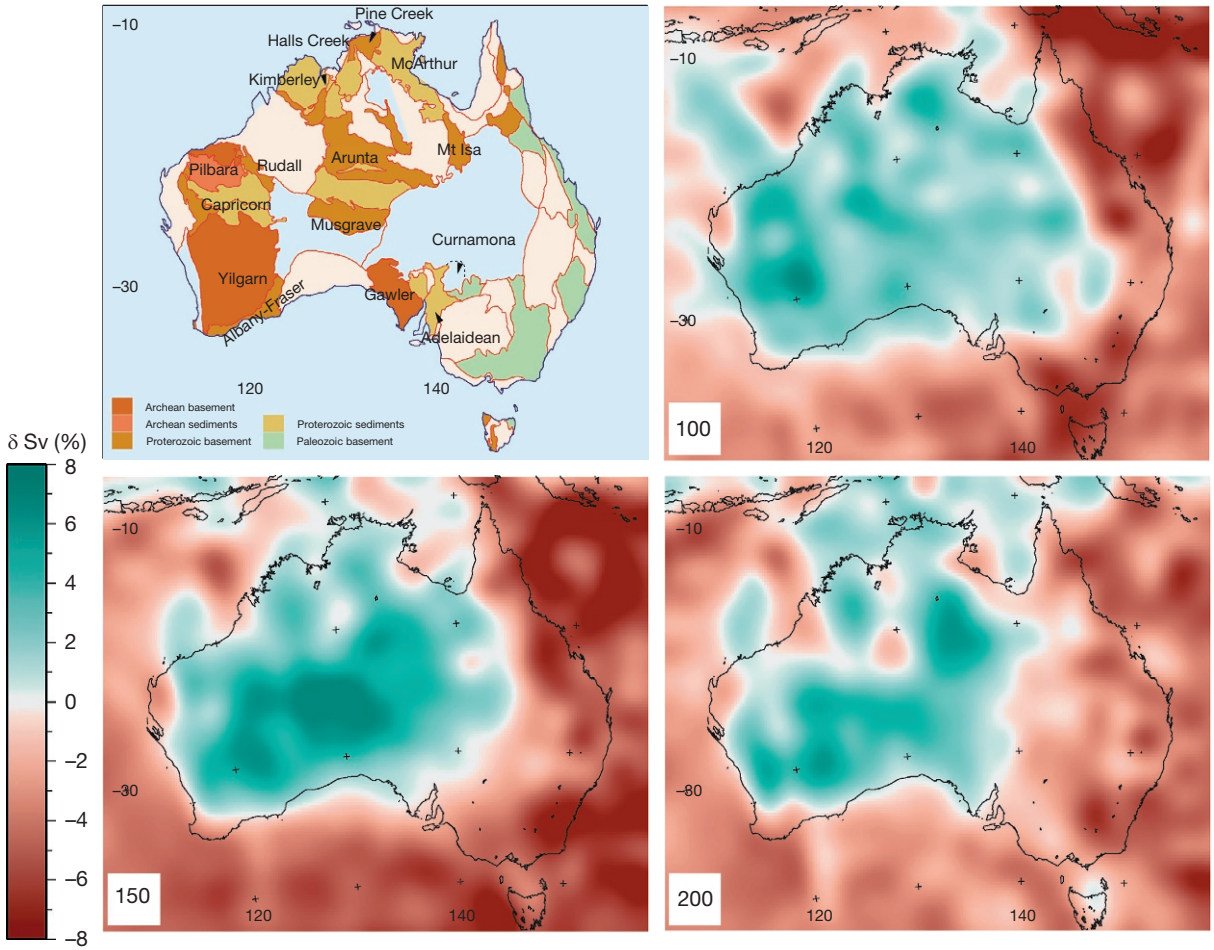

Figure 23 Horizontal depth slices of S-wave tomographic images beneath Australia. Velocity perturbation color scale is shown on the left, with perturbations referenced to global model AK135. The upper left panel shows locations of stations deployed as part of broadband experiments, from 1993 to the present, superimposed on principal geologic units. Modified from Fishwick S (2005) Contrasts in lithospheric structure within the Australian craton – Insights from surface wave tomography. *Earth and Planetary Science Letters* 231: 1630176.

The distinctive character of cratonic mantle and the nature of the crust and the crust–mantle boundary distinguish Archean from post-Archean terranes. Paradoxically, the Archean crust appears to be both thinner and less mafic than post-Archean crust (Griffin and O'Reilly, 1987; James et al., 2003; Rudnick, 1995). Moreover, the Archean Moho is characteristically sharper than that beneath younger terranes. These observations, together with the unique character of the cratonic root, suggest that the processes of craton formation, or the physical conditions that controlled those processes, differed in important ways from continent-forming processes in post-Archean times. Passive array studies are largely aimed at understanding the circumstances and mechanics of early continental formation.

1.16.5.1 Southern Africa

The Southern African Seismic Experiment (Figure 25), part of the multidisciplinary and multinational Kaapvaal Project, is the largest of the broadband array experiments undertaken to probe the anatomy of Archean cratons and their relationship to adjacent Proterozoic mobile belts (Carlson et al., 1996; James and Fouch, 2002; James et al., 2001). A nearly continuous Archean geologic record, from 3.6 to 2.6 Ga, is preserved within the Kaapvaal craton (e.g., De Wit et al., 1992). A significant area of the region covered by the seismic array, both on and off craton, has been perforated by thousands of Cretaceous kimberlite pipes from which a wealth of crustal and mantle xenoliths were erupted, some from depths in excess of 200 km (Gurney and Harte, 1980). The chemical and mineralogical compositions of mantle xenoliths provide some of the very best constraints that seismologists have for verifying seismic images of the deep continental lithosphere and relating them to actual rocks in the mantle (e.g., James et al., 2004).

Fifty-five portable broadband seismic stations were deployed at 82 sites from April 1997 to July 1999 in a roughly 100 km grid along a NNE–SSW transect about 1800 km long by 600 km wide in southern Africa (Figure 25). The experiment was augmented by a 6-month deployment of 32 telemetered broadband stations installed in a dense ($\sim 65 \times 50$ km) array in the vicinity of Kimberley, South Africa, in the heart of the undisturbed Kaapvaal craton (Figure 25).

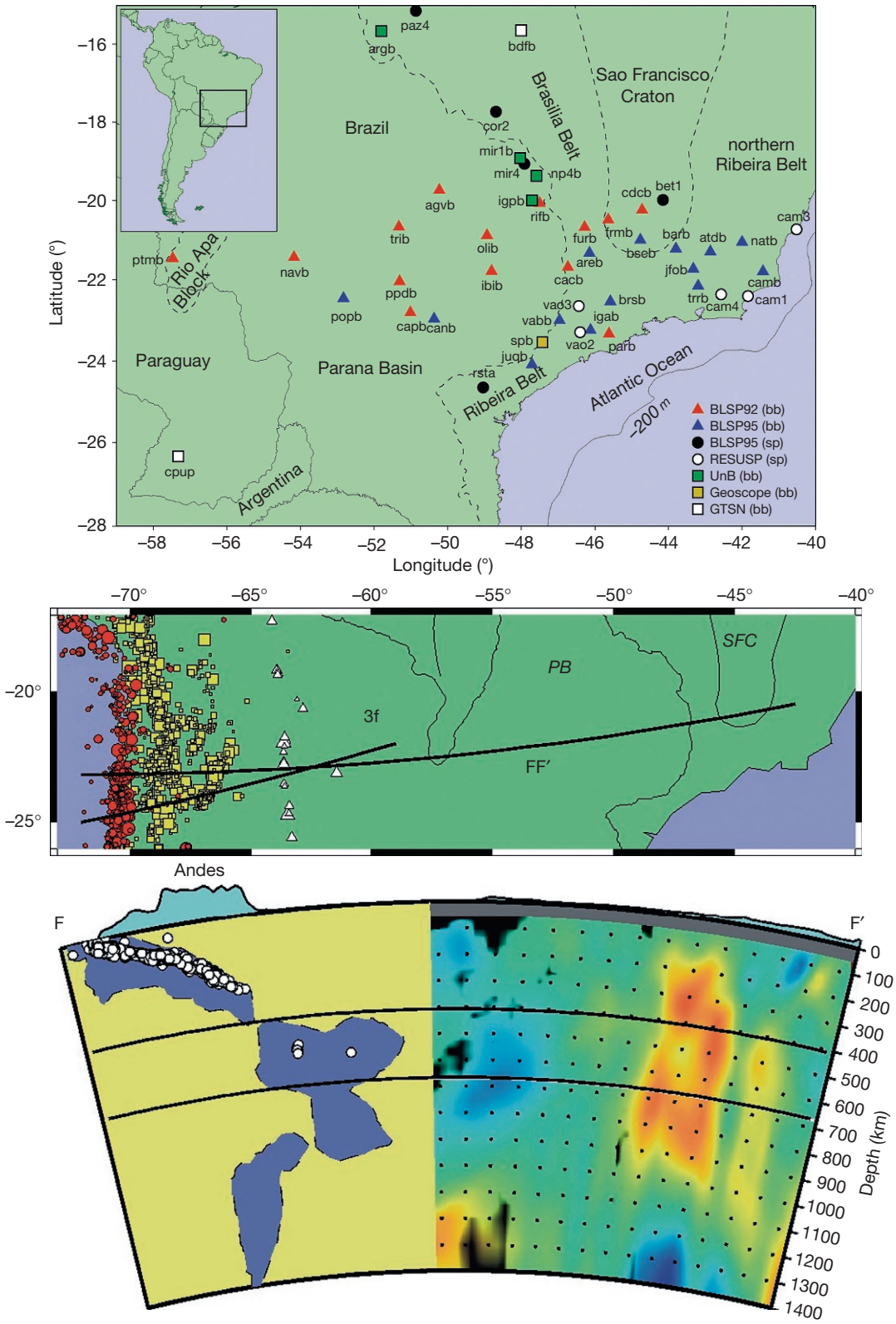

Figure 24 Map showing locations of successive broadband deployments in SE Brazil, from 1992 to the present (Schimmel et al., 2003). The bottom panel is split, with the left-hand side showing the high wavespeed (blue) anomalies adapted from Engdahl et al. (1995) and the right-hand side showing P-wave body wave tomography from the Brazilian arrays. The most prominent feature of the P-wave body wave image shown is the low-velocity anomaly that extends vertically beneath the Paraná Basin. VanDecar et al. (1995) speculated that the anomaly represented a fossil plume conduit for the Paraná flood basalts. Adapted from Schimmel M, Assumpcao M, and VanDecar JC (2003) Seismic velocity anomalies beneath SE Brazil from P and S wave travel time inversions. *Journal of Geophysical Research* 108(B4): 1–15. http://dx.doi.org/10.1029/2001JB000187.

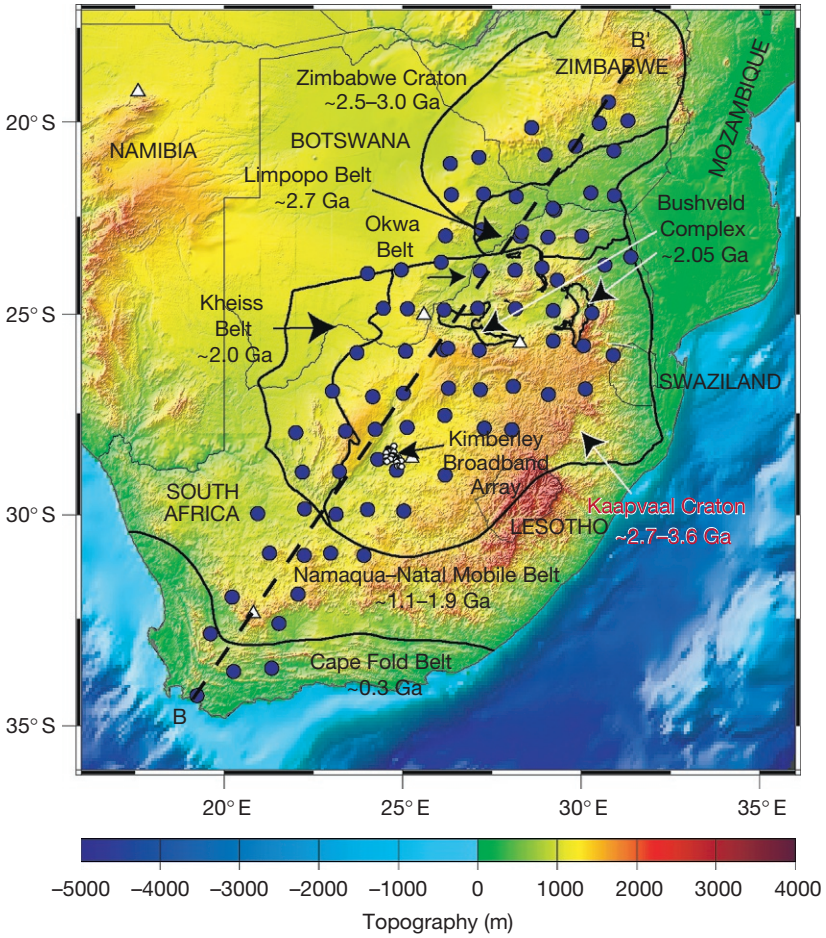

Figure 25 Map showing station locations, topography, and principal geologic provinces in the region of Kaapvaal Project within southern Africa. Eighty-two broadband stations were occupied over a 2-year period from 1997 to 1999 in South Africa, Botswana, and Zimbabwe. The Kimberley array consisted of 31 broadband stations deployed in an area approximately 60 × 40 km. In addition, three GSN broadband stations (white triangles) are located in the region and their data are incorporated in the tomographic analysis. The array extends from the Cape Fold Belt in the south, through the Proterozoic Namaqua–Natal Mobile Belt, across the Kaapvaal craton and Bushveld Province, through the Archean Limpopo Mobile Belt, and into the Zimbabwe craton.

1.16.5.1.1 Mantle tomographic images

Tomographic results (Fouch et al., 2004; James and Fouch, 2002; James et al., 2001) show that high-velocity mantle roots extend locally to depths of at least 250 km beneath undisturbed Archean craton, with no comparable root structures beneath post-Archean terranes (**Figure 26**). While only P-wave velocity structure is shown in **Figure 26**, mantle velocities in both P and S waves are remarkably consistent (Fouch et al., 2004; James et al., 2001). High velocities in both P and S waves coincide with the interiors of the Kaapvaal and Zimbabwe cratons. Excepting regions of disrupted craton (as beneath the 2.05 Ga Bushveld Province), the tectospheric root attains a thickness of ~200–250 km almost everywhere beneath the cratons, including the Archean Limpopo Mobile Belt. The most remarkable 'disrupted' feature of the Kaapvaal craton is seen in the low velocities in the mantle beneath the Bushveld Complex, the largest layered intrusion in the world. In contrast, the mantle structure of the Archean Limpopo Mobile Belt, a collision zone between the Zimbabwe and Kaapvaal cratons, does not differ significantly from that of the adjacent cratons. Neither body nor surface wave analyses have produced evidence of a significant low-velocity zone beneath the cratonic keel (Freybourger et al., 2001; James et al., 2001; Larson et al., 2006; Ritsema and van Heijst, 2000; Zhao et al., 1999). Recent surface wave results for the southern Kaapvaal (Larson et al., 2006) give absolute S-wave velocities that are consistent with the velocity-depth structure estimated from Cretaceous-age mantle xenoliths derived from the cratonic root (James et al., 2004).

The Proterozoic Namaqua–Natal Mobile Belt, the remnants of a major N–S convergent margin along the Kaapvaal that may have extended as far north as the Zimbabwe craton (De Wit et al., 1992), is characterized by velocity perturbations uniformly lower than those observed beneath the craton. The lower velocities are in keeping with the observation that the off-craton Proterozoic mantle tends to be somewhat more fertile (higher Fe) than that of the adjacent craton, as well as slightly warmer (Carlson et al., 2000; James et al., 2004; Pearson et al., 2002).

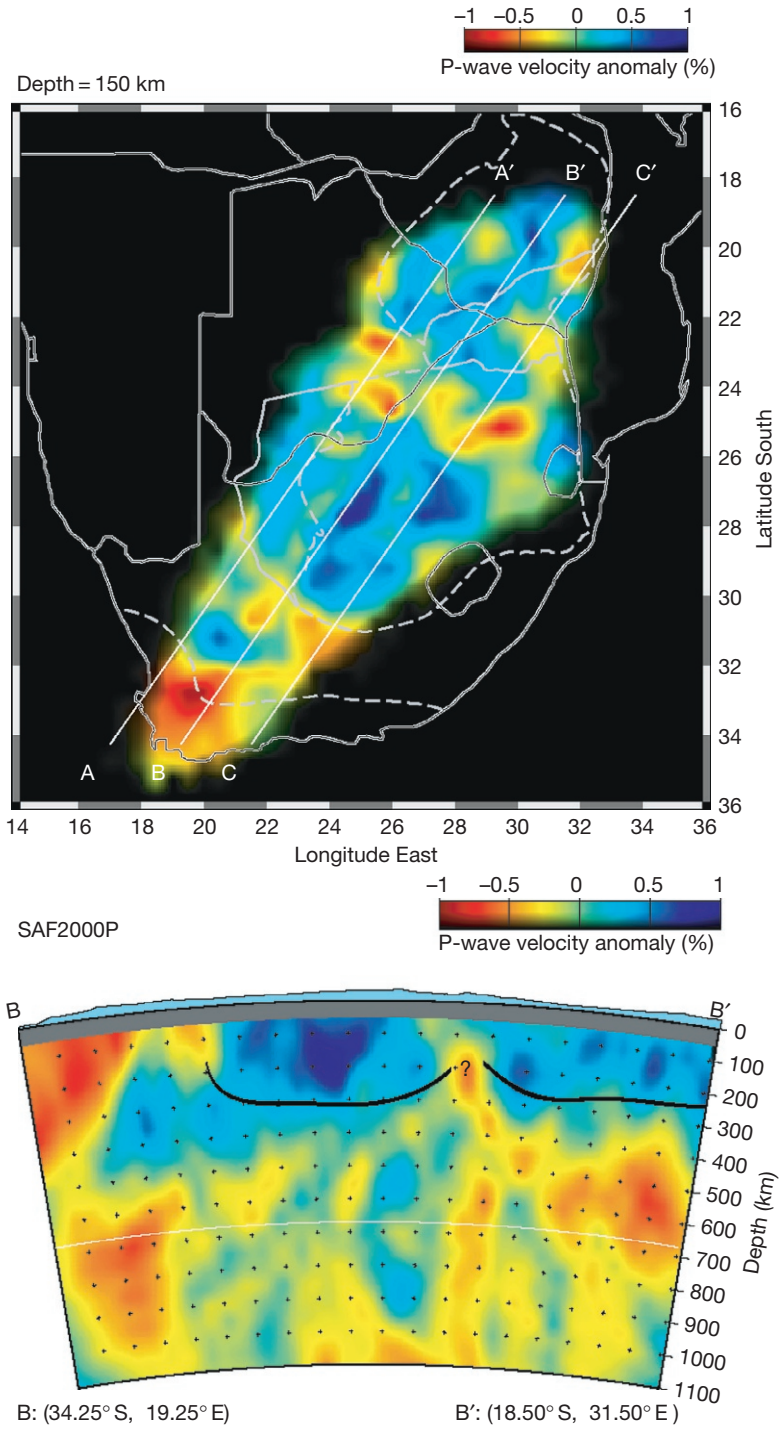

Figure 26 Relative P-wave velocity perturbations from inversion of seismic delay times with overlaid geologic province outlines. Adapted from James DE and Fouch MJ (2002) Formation and evolution of archaean cratons: Insights from southern Africa. In: Ebinger C, Fowler CMR, and Hawkesworth CJ (eds.) *The Early Earth: Physical, Chemical and Biological Development*, pp. 1–26. London: Geological Society of London. Velocity anomaly scale ranges from deep blue (1% fast) to deep red (1% slow). Top panel is map (horizontal section) view of velocity perturbations at 150 km depth. Kimberlite locations for xenoliths used in this study are marked by square symbols. Lower panel is a cross section along line B–B′ of the horizontal section. Topography, scaled by a factor of 20, is shown in light green. Tectospheric root can be seen beneath the southern Kaapvaal craton extending to a depth of nearly 300 km. The region of seismic low velocities in the uppermost mantle underlies the Bushveld Province.

1.16.5.1.2 Crustal thickness and Moho structure beneath southern Africa

Strong variations in crustal thickness based on receiver functions reveal significant differences in the nature of the crust and the crust–mantle boundary between Archean and post-Archean geologic terranes (**Figure 27**; Nguuri et al., 2001). Stations located within undisturbed Kaapvaal or Zimbabwe craton typically have sharp, large amplitude depth images for the Moho, similar to those observed for other Archean terranes (e.g., Clitheroe et al., 2000). In contrast, stations within post-Archean and modified cratonic regions typically exhibit poorly defined Ps-converted phases. Moreover, the crust beneath post-Archean and modified cratonic regions is in almost all cases thicker than that beneath the cratons. Throughout the broad region of the Bushveld and Okwa/Magondi terranes (**Figure 25**), the Archean craton has been overprinted by tectonomagmatic events of Proterozoic age (e.g., Carney et al., 1994; Shirey et al., 2001) and the effects on crustal structure have been profound. The crust thickens and the Moho signature degrades, for example, passing from undisturbed craton into the Bushveld Province and between undisturbed Zimbabwe craton into the Magondi belt. The change in crustal structure is consistent with the evidence from tomographic imaging for major disruption in the uppermost mantle beneath the entire region (**Figure 26**).

Depth images for the northern and southern marginal zones of the collisional Limpopo Mobile Belt are typical of the adjacent cratonic structure, both in the character of the Ps conversion and in crustal thickness (**Figure 27**). The central Limpopo Mobile Belt, site of maximum deformation during the collision of the Kaapvaal and Zimbabwe cratons in the Archean, displays broad, poorly defined Ps images indicative of structurally complex Moho and with depth maxima occurring between 40 and 53 km. As with the Bushveld, the relatively thick crust beneath the Limpopo appears not to be isostatically compensated at the surface, suggesting 'densification' of the deep crustal root (Fischer, 2002).

Kimberley array. The 31-station telemetered broadband Kimberley array deployment comprised a dense grid over an area of about 65×50 km (**Figure 25**) near Kimberley, South Africa, in the south-central region of the Kaapvaal craton. Analysis of both teleseismic and local events recorded on the Kimberley broadband array reveals a remarkably uniform crustal structure beneath the array: (1) The cratonic crust is uniformly thin (about 35 km) and has a low average Poisson's ratio ($\sim$0.25, $V_p/V_s \approx 1.73$). (2) The Moho is a sharp discontinuity, with a crust–mantle transition less than about 0.5 km beneath the array (James et al., 2003; Niu and James, 2002).

The low Poisson's ratio of 0.25 ($V_p/V_s = 1.73$) for the crustal average and an inferred density of 2.86 gm cc^{-1} for the lowermost crustal rocks highlight one of the great dilemmas of Archean crustal composition (e.g., James et al., 2003; Rudnick, 1995). If the continental crust was derived from a hotter mantle in the Archean, why is the crust beneath the Kaapvaal less mafic than that beneath adjacent Proterozoic mobile belts, where the lower crust is mafic? Niu and James (2002) suggested that the present composition of the Kaapvaal crust may be explained as the result of extensive melting of the lower crust during ultrahigh-temperature metamorphism associated with a craton-wide tectonomagmatic event in the Late Archean. Layering and flow associated with the crystallization of melt in the lowermost crust is one possible means for producing both flat Moho and sharp Moho, as well as the evolved rock compositions inferred from the seismic data (James et al., 2003; Niu and James, 2002).

1.16.5.2 Passive Array Studies of Other Cratons

Relatively small experiments in the Slave and Tanzanian cratons are of particular interest. The Slave craton in northern Canada is small in area but contains some of the oldest rocks on Earth and a wealth of diamonds. Reconnaissance studies of the Slave based on 13 broadband stations deployed over a 2-year period in the 1990s showed somewhat similar structures to those seen in the Kaapvaal, including a relatively thin crust and a tectospheric root, the depleted material of which apparently does not extend to depths as great as seen in the Kaapvaal (Bank et al., 2000). Data from the Tanzanian Broadband Seismic Experiment, composed of 20 stations deployed in 1994–95 across the Tanzanian craton and adjacent rifted mobile belts (Ritsema et al., 1998), have been analyzed in a number of independent studies. The deep lithospheric structure of the cratonic root remains somewhat in doubt. Body wave tomography indicates that the high-velocity tectosphere extends to a depth of at least 200 km beneath the craton (Ritsema et al., 1998). More recent surface wave studies, however, appear to indicate a thinner cratonic lithosphere ($\sim$150 km), the base of which may have been degraded by a rising plume associated with the East African Rift system (Weeraratne et al., 2003). The presence of adjacent rift zones with extremely low mantle velocities extending to considerable depth, however, makes the surface wave results difficult to interpret, as the poor lateral resolution inherent in surface wave tomography renders cross contamination of structures a major concern. Crustal structure is similarly controversial. Julia et al. (2005) interpreted results from joint receiver function/surface wave inversion of the broadband data to imply a mafic lower crust beneath the craton. This conclusion is contrary to that reached by much the same group of authors in a previous paper (Last et al., 1997), based on approximately the same data, where the East African crust was judged more felsic than the Precambrian crust elsewhere.

A large-scale multinational seismic experiment within the Baltic (Fennoscandian) Shield (SVEKALAPKO) focused on the lithospheric and asthenospheric structure of the East European Craton to a depth of about 400 km. The dense array across mostly Archean and Proterozoic terranes consisted of 143 stations, including 40 broadband and 88 short-period portable stations deployed for about 9 months, 1998–99 (Bruneton et al., 2004; Sandoval et al., 2003, 2004). Results from body wave tomography (Sandoval et al., 2004) have been mixed and difficult to interpret. High mantle velocities extend to depths of at least 250 km, but they trend seamlessly across both Archean and Proterozoic terranes, with no clear evidence for a distinct cratonic root beneath the Archean. Surface wave tomography with good resolution to a depth of about 150 km reveals strong velocity variations that are attributed to varying composition (rather than temperature), but here also mantle velocities do not differ significantly beneath Archean and Proterozoic terranes (Bruneton et al., 2004).

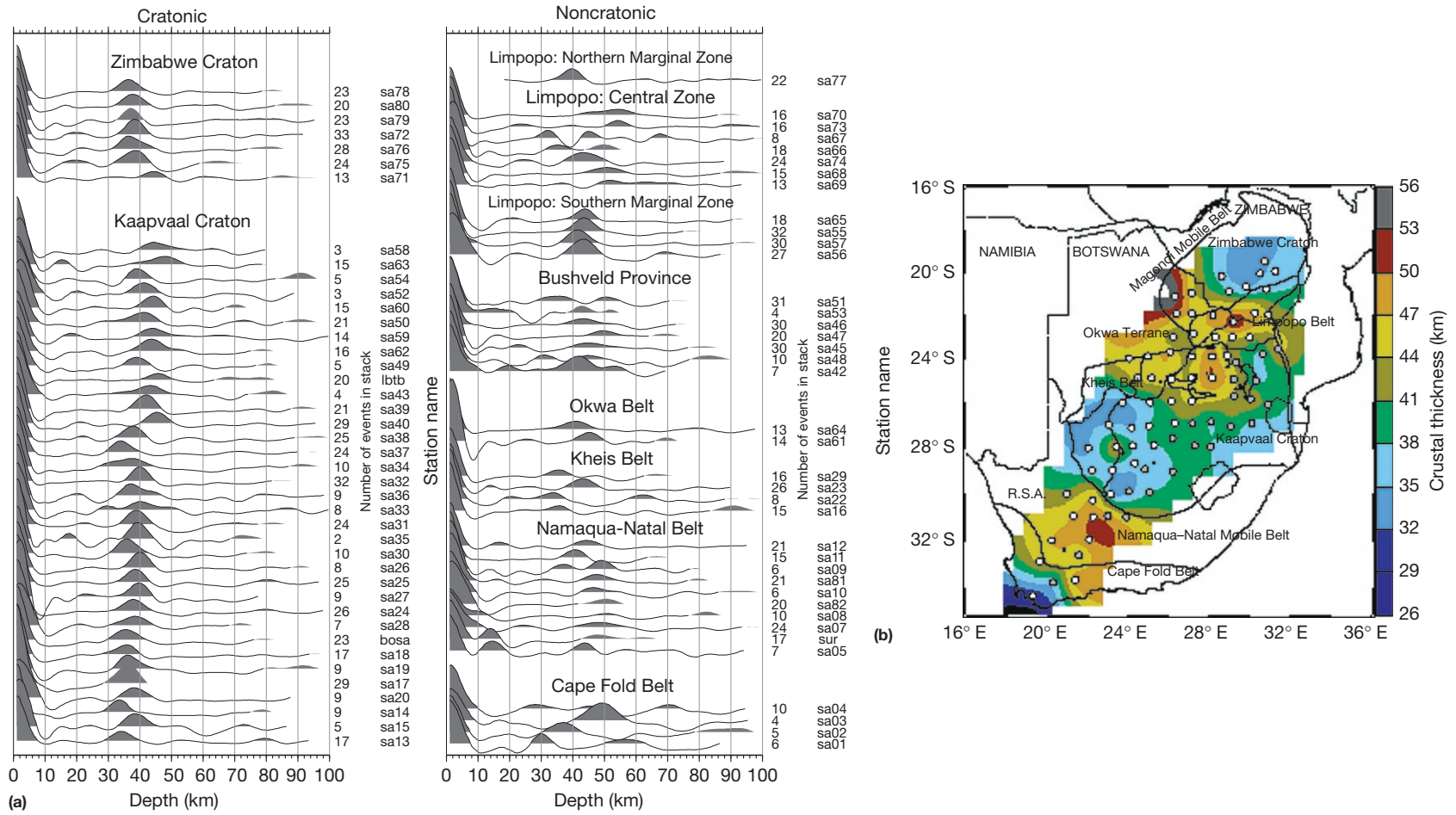

Figure 27 (a) Receiver function depth images for southern Africa, arranged by geologic province. The number of events in the stack and the station name for each trace are shown to the right of the trace. The dominant signal on most of the depth images is the P-to-S conversion (Ps) from the Moho. Relatively thin (35–40 km) crust and sharp, well-defined Ps Moho conversions tend to be associated with undisturbed craton. Ps arrivals associated with disturbed regions of the craton and post-Archean terranes tend to be more diffuse and of smaller amplitude. (b) Color-coded contour map of depth to Moho beneath the southern African array based on receiver function depth images. Crustal thickness color scale is shown on the right. Thin crust tends to be associated with undisturbed areas of the craton, particularly in the southern and western parts of the Kaapvaal craton and in the Zimbabwe craton, despite a regional elevation above 1100 m (3500 ft). Recent work by Webb suggests that much of the gravity compensation for excess elevation in the craton comes from low-density mantle (Webb, 2006). Reproduced from Nguuri T, Gore J, James DE, et al. (2001) Crustal structure beneath southern Africa and its implications for the formation and evolution of the Kaapvaal and Zimbabwe cratons. *Geophysical Research Letters* 28(13): 2501–2504.

1.16.6 Seismic Constraints on Composition and Temperature of the Continental Lithosphere

The range of seismic velocities in the continental lithospheric mantle indicates that the most abundant rock type is peridotite and that the major variations in seismic velocity are produced by temperature (e.g., Carlson et al., 2005, **Chapter 1.26**). While eclogite, the high-velocity/high-density/high-pressure equivalent of oceanic basalt, is observed in subducting oceanic crust below about 100 km depth, it is seen only rarely in the continental lithosphere where it is generally interpreted to be evidence of a relict slab (e.g., Bostock, 1997). In general, high-velocity bodies consistent with large volumes of eclogite are not observed in the continental mantle (e.g., Gao et al., 2002; James et al., 2001; Schimmel et al., 2003; VanDecar et al., 1995).

Seismic velocities in the continental lithospheric mantle most commonly correlate with the age of last tectonomagmatic activity in the area rather than the age of the overlying crust. A prime example is North America, where a sharp lithospheric boundary, approximately along the Rocky Mountain Front, is observed between the stable platform of eastern North America and the tectonically active western United States, much of which is underlain by Precambrian basement. The contrast in upper mantle V_s between stable North America and tectonic western North America, while highly variable, is as much as 10% or even more in places. Although both temperature and composition affect seismic velocities of rocks in the mantle, temperature exerts the dominant control (Goes and van der Lee, 2002; James et al., 2004; Lee, 2003). Nonetheless, Godey et al. noted that a 2% increase in velocity can be explained either by a 120 °C decrease in temperature, by a 7.5% depletion in iron, or by a 15% depletion in aluminum (Godey et al., 2004). Assuming that temperature is the only variable, a ~10% difference in V_s velocity between Basin and Range Province lithospheric mantle and cratonic lithospheric mantle implies that the cratonic mantle is some 600 °C colder. Godey et al. estimated that the coldest part of the Canadian Shield is about 800 °C colder than tectonic North America at 100 km depth. Indeed, cratons everywhere are characterized by very low geotherms (Nyblade and Pollack, 1993). In general, heat flow calculations of temperature differences at depth between cratons and tectonic regions are consistent with results where seismic velocities are inverted to obtain thermal structure (Goes and van der Lee, 2002). Given nominal estimates for heat production in Archean crust and mantle and assuming a typical cratonic surface heat flow of 40 mW m^{-2} (Pollack and Chapman, 1977), the calculated temperature at 100 km would be about 800 °C. Adding 600 °C to this would push much of the mantle beneath western United States almost to the dry melting point of peridotite (~1450 °C). If temperature differences of the same magnitude persist to 150 km depth, where the temperature beneath a craton is of order 1050 °C (Nyblade, 1999), then adding 600 °C to this would place the western US mantle well above the dry melting temperature of peridotite (Carlson et al., 2005). While there is active volcanism locally in the western United States, there is no seismic evidence that any parts of the shallow mantle are substantially molten anywhere. Consequently, the large seismic velocity difference between various regions of the continental mantle is unlikely to be solely the result of varying temperature. This constraint provided the basis for Jordan's (1975) tectosphere hypothesis in which he introduced the principal of temperature–depletion compensation (isopycnic hypothesis) to account for differences between cratons and oceans (Jordan, 1975, 1978, 1979, 1981, 1988). Godey et al. (2004) calculated both temperature and compositional differences from a joint inversion of S-wave velocities and density perturbations, concluding that the maximum δT at 100 km depth between craton and tectonic mantle was −440 °C and δFe was −4%. Even a perturbation of 440 °C, however, appears to put the mantle temperature in tectonic regions above the dry melting temperature if it extends to depths much in excess of 150 km. Curiously, the S-wave velocity perturbations calculated by Godey et al. do *not* decrease significantly at depths greater than 100 km, whereas those of van der Lee and Nolet (1997) and others do (Carlson et al., 2005).

The question of whether a significant low-velocity zone (asthenosphere) exists beneath the continental lithosphere remains an unresolved topic of debate. The base of the oceanic lithosphere is marked nearly everywhere by a strong decrease in V_s at depths generally less than 100 km. Low-velocity zones in the uppermost mantle are clearly seen under many tectonically active continental regions (e.g., Karlstrom and Keller, 2005, and articles therein), but most are associated with relatively recent tectonomagmatic activity that has been superimposed on pre-existing Proterozoic or even Archean structures. The absence of mantle roots beneath the Wyoming and North China Cratons appears to be an extreme example of high-temperature Phanerozoic overprinting (see summary by Carlson et al. (2005) and references therein). Beneath stable continental regions, low-velocity zones tend to be weak or absent. With few exceptions (e.g., Rychert et al., 2005), the base of the stable continental lithosphere is not well imaged seismically: the transition over which the relatively high seismic velocities of stable lithosphere merge into the comparatively lower velocities of the convecting mantle appears to be gradual.

1.16.7 EarthScope, USArray, and the Future of Portable Array Seismology

EarthScope is a major program funded through the US NSF to investigate the structure and evolution of North America and the physical processes controlling earthquakes and volcanic eruptions. USArray, the component of EarthScope specifically aimed at imaging the deep structure of the continent beneath the United States, is conceived as a rolling array of 400 broadband stations that over a 12-year period will occupy more than 2000 sites within coterminous United States and Alaska, each for a period of about 18 months. The 2000-station deployment, with an average grid spacing about 70 km, is to be supplemented by more dense active and passive array deployments aimed at key scientific targets (the 'flexible' component of USArray) and anchored by a regular network of permanent broadband stations. The seismic observations from USArray are intended to provide the foundation for integrated geologic, geochemical, and other geophysical studies to produce a coherent, high-resolution, plate-scale image of the continental lithosphere and the underlying mobile mantle. Besides significantly higher-resolution regional images, one of the most

important contributions of USArray will be the uniform coverage with uniform resolution of deep structures across the very different geologic provinces of North America. The uniform seismic images across the continent will greatly enhance our ability to relate surface geology and detailed lithospheric structure to driving forces and thermal processes within the mantle and to link structures inherited from earlier stages of continental evolution and subsequent plate motion to known and potential geologic hazards. The USArray program within the United States is echoed to some extent by comparable programs in Europe (e.g., EUROArray) and reportedly in China, where plans are being implemented for broadband arrays of several hundred portable instruments that can be deployed across the continent to study deep plate-scale structures (F. Niu, personal communication).

1.16.8 Discussion

Passive array seismology is arguably the most powerful tool available to scientists for the study of continental lithosphere and small-scale heterogeneities in the deeper Earth. Over the past two decades, passive array experiments have evolved from deployments comprising a handful of broadband instruments to major imaging efforts involving hundreds of stations. The images of the deep continental lithosphere produced from these experiments have revolutionized our understanding of continental formation and evolution. Tomographic imaging of increasingly high resolution has been notably successful in underscoring the extent to which continental lithosphere has been shaped and reshaped over geologic time by complexly superimposed tectonic and magmatic events. Western North America is an oft-cited example of massive Phanerozoic overprinting of preexisting Archean and Proterozoic terranes. Structures in the mantle beneath southern Africa exhibit clear evidence of Proterozoic disruption and overprinting of thick Archean tectosphere. Ancient relict structures including remnant downgoing plates have apparently been observed in a number of localities, most notably in western Canada. Lithospheric structures beneath provinces of very similar age and geologic character (e.g., Archean cratons) have proven to differ significantly by region as shown, for example, in the differing structures beneath the Kaapvaal, Slave, Tanzanian, and Fennoscandian cratons.

The maturing of passive array seismology into a powerful system for exploring the deep Earth beneath continents should not overshadow the fact that tomographic and direct waveform images are still well below optimum for reliable geologic understanding of deep structure. High-resolution images are certainly attainable with available broadband data and present-day methodologies. As the pool of broadband instrumentation available through PASSCAL, USArray, and other organizations around the world continues to increase, the size of regions that can be imaged and the sharpness of the images produced will continue to improve. In this respect, national-scale deployments will result in considerably sharpened 'uniform' images on a continent-wide scale, an achievement previously unimagined. Despite the extraordinary increase in the number of instruments available for passive array deployments, particularly in the recent years, a primary limitation on 3-D imaging will remain suboptimum seismometer density for years to come. It is for this reason that array deployments for many of the most ambitious broadband experiments are, even today, still configured as linear transects. With current availability of broadband equipment, only linear arrays can achieve sufficient station density (10–20 km) to enable direct unaliased waveform imaging of deep structure. Similarly, high station densities for 3-D direct waveform imaging on regional scales generally require more instruments than are currently available to individual researchers or groups of researchers, although closely targeted studies involving 100 or more closely spaced seismographs are increasingly common. Advances in satellite and cellular communications for telemetry of seismic data in real time will substantially reduce the manpower required to service equipment in the field and significantly enhance data recovery and data quality. These advanced communication systems are currently in use for the USArray deployment and have already proven their value in substantially streamlined experiment operation and maintenance.

References

Abers GA, Rossi G, Rondenay S, Peacock S, and Christensen D (2005) Seismic evidence for massive silica addition in some subduction zones. *Eos, Transactions of the American Geophysical Union, Fall Meeting Supplement* 86(52): T41F-05.

Abers GA, van Keken PE, Kneller EA, Ferris A, and Stachnik JC (2006) The thermal structure of subduction zones constrained by seismic imaging: Implications for slab dehydration and wedge flow. *Earth and Planetary Science Letters* 241: 387–397.

Aki K, Christoffersson A, and Husebye ES (1976) Three-dimensional seismic structure of the lithosphere under Montana LASA. *Bulletin of the Seismological Society of America* 66(2): 501–524.

Ammon CJ (1991) The isolation of receiver effects from teleseismic P waveforms. *Bulletin of the Seismological Society of America* 81: 2504–2510.

ANCORP Working Group (2003) Seismic imaging of a convergent continental margin and plateau in the Central Andes. *Journal of Geophysical Research* 108. http://dx.doi.org/10.1029/2002JB001771.

Aster R, Beaudoin B, Hole J, Fouch M, Fowler J, and James DE (2005) IRIS seismology program marks 20 years of discovery. *Eos, Transactions of the American Geophysical Union* 86(17): 171.

Bank C-G, Bostock MG, Ellis RM, and Cassidy JF (2000) A reconnaissance teleseismic study of the upper mantle and transition zone beneath the Archean Slave craton in NW Canada. *Tectonophysics* 319: 151–166.

Bastow ID, Stuart GW, Kendall J-M, and Ebinger C (2005) Upper-mantle seismic structure in a region of incipient continental breakup: Northern Ethiopian rift. *Geophysical Journal International* 162: 479–493.

Betts PG, Giles D, Lister GS, and Frick LR (2002) Evolution of the Australian lithosphere. *Australian Journal of Earth Sciences* 49: 661–695.

Bostock MG (1997) Anisotropic upper-mantle stratigraphy and architecture of the Slave craton. *Nature* 390: 392–395.

Bostock MG, Hyndman RD, Rondenay S, and Peacock S (2002) An inverted continental Moho and serpentinization of the forearc mantle. *Nature* 417: 536–538.

Bostock MG, Langlois A, Al-Khoubbi I, et al. (2005) CANOE: A broadband array in northwestern Canada, *IRIS: Cornerstone Facilities for Seismology and Earth Sciences. II. Accomplishments*, 77.

Boyd FR and McCallister RH (1976) Densities of fertile and sterile garnet peridotites. *Geophysical Research Letters* 3(9): 509–512.

Boyd FR and Mertzman SA (1987) Composition and structure of the Kaapvaal lithosphere, southern Africa. In: Mysen BO (ed.) *Magmatic Processes: Physicochemical Principles*, pp. 13–24. University Park, PA: Geochemical Society.

Bruneton M, Pedersen HA, Farra V, et al. (2004) Complex lithospheric structure under the central Baltic Shield from surface wave tomography. *Journal of Geophysical Research* 109. http://dx.doi.org/10.1029/2003JB002947.

Carlson RW, Boyd FR, Shirey SB, and Gurney JJ (2000) Continental growth, preservation and modification in southern Africa. *GSA Today* 10: 1–7.

Carlson RW, Grove TL, de Wit MJ, and Gurney JJ (1996) Anatomy of an Archean craton: A program for interdisciplinary studies of the Kaapvaal craton, southern Africa. *Eos, Transactions of the American Geophysical Union* 77: 273–277.

Carlson RW, Pearson DG, and James DE (2005) Physical, chemical and chronological characteristics of continental mantle. *Reviews of Geophysics* 43(RG1001): 1–24.
Carney JN, Aldiss DT, and Lock NP (1994) *Geological Survey Botswana, 37: The Geology of Botswana*. Geological Survey Department, Gaborone, pp. 1–113.
Chmielowski J, Zandt G, and Haberland C (1999) The central Andean Altiplano-Puna magma body. *Geophysical Research Letters* 26: 783–786.
Clitheroe G, Gudmundsson O, and Kennett BLN (2000) The crustal thickness of Australia. *Journal of Geophysical Research* 105: 13697–13713.
Davaille A and Lees JM (2004) Thermal modeling of subducted plates: Tear and hot spot at the Kamchatka corner. *Earth and Planetary Science Letters* 226: 293–304.
de la Torre T and Sheehan AF (2005) Broadband seismic noise analysis of the Himalayan Nepal Tibet seismic experiment. *Bulletin of the Seismological Society of America* 95: 1202–1208.
De Wit MJ, Roering C, Hart RJ, et al. (1992) Formation of an Archaean continent. *Nature* 357(6379): 553–562.
Dueker KG and Yuan H (2004) Upper mantle P-wave velocity structure from PASSCAL teleseismic transects across Idaho, Wyoming and Colorado. *Geophysical Research Letters* 31(L08603): 1–4. http://dx.doi.org/10.1029/2004GL019476.
Dueker KG, Yuan H, and Zurek B (2001) Thick proterozoic lithosphere of the Rocky Mountain region. *GSA Today* 11: 4–9.
Engdahl ER, van der Hilst RD, and Berrocal J (1995) Imaging of subducted lithosphere beneath South America. *Geophysical Research Letters* 22: 2317–2320.
Farra V and Vinnik LP (2000) Upper mantle stratification by P and S receiver functions. *Geophysical Journal International* 141: 699–712.
Faul UH and Jackson I (2005) The seismological signature of temperature and grain size variations in the upper mantle. *Earth and Planetary Science Letters* 234: 119–134.
Ferris A, Abers GA, Christensen D, and Veenstra E (2003) High-resolution image of the subducted Pacific (?) plate beneath central Alaska, 50–150 km depth. *Earth and Planetary Science Letters* 214: 575–588.
Fischer KM (2002) Waning buoyancy in the crustal roots of old mountains. *Nature* 417: 933–936.
Fischer KM, Wysession ME, Clarke TJ, et al. (1996) The 1995–1996 Missouri to Massachusetts broadband seismometer deployment. *IRIS Newsletter* 15: 6–9.
Fishwick S, Kennett BLN, and Reading AM (2005) Contrasts in lithospheric structure within the Australian craton – Insights from surface wave tomography. *Earth and Planetary Science Letters* 231: 1630176.
Forsyth DW and Li A (2005) Array analysis of two-dimensional variations in surface wave phase velocity and azimuthal anisotropy in the presence of multipathing interference. In: Levander A and Nolet G (eds.) *Seismic Earth: Array Analysis of Broadband Seismograms*, pp. 81–98. Washington, DC: American Geophysical Union.
Fouch MJ, Fischer KM, Parmentier ME, Wysession ME, and Clarke TJ (2000) Shear wave splitting, continental keels, and patterns of mantle flow. *Journal of Geophysical Research* 105: 6255–6275.
Fouch MJ, Fischer KM, and Wysession ME (2001) Lowermost mantle anisotropy beneath the Pacific: Imaging the source of the Hawaiian plume. *Earth and Planetary Science Letters* 190: 167–180.
Fouch MJ, James DE, VanDecar JC, and van der Lee S (2004) Mantle seismic structure beneath the Kaapvaal and Zimbabwe cratons. *South African Journal of Geology* 107: 33–44.
Fouch MJ and Rondenay S (2006) Seismic anisotropy beneath stable continental interiors. *Physics of the Earth and Planetary Interiors* 158: 292–320.
Freybourger M, Gaherty JB, Jordan TH, and Kaapvaal Seismic Group (2001) Structure of the Kaapvaal craton from surface waves. *Geophysical Research Letters* 28(13): 2489–2492.
Friederich W (2003) The S-velocity structure of the east Asian mantle from inversion of shear and surface waveforms. *Geophysical Journal International* 153: 88–102.
Gaherty JB (2004) A surface wave analysis of seismic anisotropy beneath eastern North America. *Geophysical Journal International* 158: 1053–1066.
Galve A, Sapin M, Hirn A, et al. (2002) Complex images of Moho and variation of V_p/V_s across the Himalaya and south Tibet, from a joint receiver-function and wide-angle reflection approach. *Geophysical Research Letters* 39: 1–4. http://dx.doi.org/10.1029/2002GL015611.
Gao W, Grand SP, Baldridge WS, et al. (2004) Upper mantle convection beneath the central Rio Grande rift imaged by P and S wave tomography. *Journal of Geophysical Research* 109(B03305): 1–16. http://dx.doi.org/10.1029/2003JB02743.
Gao SS, Silver PG, Liu KH, and KS Group (2002) Mantle discontinuities beneath southern Africa. *Geophysical Research Letters* 29: 1491.
Gee LS and Jordan TH (1992) Generalized seismological data functionals. *Geophysical Journal International* 111: 363–390.
Gilbert HJ and Sheehan AF (2004) Images of crustal variations in the intermountain west. *Journal of Geophysical Research* 109: B03306.
Godey S, Deschamps F, and Trampert J (2004) Thermal and compositional anomalies beneath the North American continent. *Journal of Geophysical Research* 109(B01308): 1–13. http://dx.doi.org/10.1029/2002JB002263.
Goes S and van der Lee S (2002) Thermal structure of the North American uppermost mantle inferred from seismic tomography. *Journal of Geophysical Research* 107(B3): 1–13. http://dx.doi.org/10.1029/2000JB000049.
Graeber FM and Asch G (1999) Three-dimensional models of P wave velocity and P-to-S velocity ratio in the southern central Andes by simultaneous inversion of local earthquake data. *Journal of Geophysical Research* 104: 20237–20256.
Grand SP (1994) Mantle shear structure beneath the Americas and surrounding oceans. *Journal of Geophysical Research* 99: 11591–11621.
Griffin WL and O'Reilly SY (1987) The composition of the lower crust and the nature of the continental Moho-xenolith evidence. In: Nixon PH (ed.) *Mantle Xenoliths*, pp. 413–432. Chichester, UK: John Wiley & Sons.
Gurney JJ and Harte B (1980) Chemical variations in upper mantle nodules from southern African kimberlites. *Philosophical Transactions of the Royal Society of London* A297: 273–293.
Humphreys E and Dueker KG (1994) Western U.S. upper mantle structure. *Journal of Geophysical Research* 99(B5): 9615–9634.
Humphreys E, Hessler E, Dueker KG, Farmer GL, Erslev E, and Atwater T (2003) How Laramide-age hydration of North American lithosphere by the farallon slab controlled subsequent activity in the Western US. *International Geology Review* 45: 575–595.
James DE (2003) Imaging crust and upper mantle beneath southern Africa: The southern Africa broadband seismic experiment. *The Leading Edge* 22: 238–249.
James DE and Assumpção M (1996) Tectonic implications of S-wave anisotropy beneath SE Brazil. *Geophysical Journal International* 126: 1–10.
James DE, Boyd FR, Schutt D, Bell DR, and Carlson RW (2004) Xenolith constraints on seismic velocities in the upper mantle beneath southern Africa. *G-cubed* 5(Q01002): 1–32. http://dx.doi.org/10.1029/2003GC000551.
James DE and Fouch MJ (2002) Formation and evolution of archaean cratons: Insights from southern Africa. In: Ebinger C, Fowler CMR, and Hawkesworth CJ (eds.) *The Early Earth: Physical, Chemical and Biological Development*, pp. 1–26. London: Geological Society of London.
James DE, Fouch MJ, VanDecar JC, van der Lee S, and Kaapvaal Seismic Group (2001) Tectospheric structure beneath southern Africa. *Geophysical Research Letters* 28(13): 2485–2488.
James DE, Niu F, and Rokosky J (2003) Crustal structure of the Kaapvaal craton and its significance for early crustal evolution. *Lithos* 71: 413–429.
James DE and Sacks IS (1999) Cenozoic formation of the Central Andes: A geophysical perspective. In: Skinner BJ (ed.) *Geology and Ore Deposits of the Central Andes*, pp. 1–25. Littleton, CO: Society of Economic Geologists.
Jordan TH (1975) The continental tectosphere. *Reviews of Geophysics* 13: 1–12.
Jordan TH (1978) Composition and structure of the continental tectosphere. *Nature* 274: 544–548.
Jordan TH (1979) Mineralogies, densities and seismic velocities of garnet lherzolites and their geophysical implications. In: Boyd FR and Meyer HOA (eds.) *The Mantle Sample: Inclusions in Kimberlites and other Volcanics*. *America*, pp. 1–14. Washington, DC: American Geophysical Union.
Jordan TH (1981) Continents as a chemical boundary layer. *Transactions of the Royal Society of London* 301: 359–373 (Royal Society, Discussion on the Origin and Evolution of the Earth's Continental Crust, London, England, Feb. 21, 22, 1980).
Jordan TH (1988) Structure and formation of the continental tectosphere. *Journal of Petrology, Special Lithosphere Issue* 11–37.
Julia J, Ammon CJ, and Nyblade AA (2005) Evidence for mafic lower crust in Tanzania, east Africa, from joint inversion of receiver functions and Rayleigh wave dispersion velocities. *Geophysical Journal International* 162: 555–569.
Karlstrom KE and Keller GR (2005) *Geophysical Monograph 15: The Rocky Mountain Region – An Evolving Lithosphere: Tectonics, Geochemistry, and Geophysics*. Washington, DC: American Geophysical Union p. 441.
Karlstrom KE, Whitmeyer SJ, Dueker KG, et al. (2005) Synthesis of results from the CD-ROM experiment: 4-D image of the lithosphere beneath the Rocky Mountains and implications for understanding the evolution of continental lithosphere. In: Karlstrom KE and Kelle GR (eds.) *The Rocky Mountain Region: An Evolving Lithosphere*, pp. 421–434. Washington, DC: American Geophysical Union.
Kay SM, Coira B, and Viramonte J (1994) Young mafic back-arc volcanic rocks as indicators of continental lithospheric delamination beneath the Argentine Puna plateau, Central Andes. *Journal of Geophysical Research* 99: 24323–24339.
Kincaid C and Sacks IS (1997) Thermal and dynamical evolution of the upper mantle in subduction zones. *Journal of Geophysical Research* 102: 12295–12315.
Kind R, Yuan H, Saul J, et al. (2002) Seismic images of crust and upper mantle beneath Tibet: Evidence for Eurasian plate subduction. *Science* 298: 1219–1221.

Klemperer SL (2006) Crustal flow in Tibet: Geophysical evidence for the physical state of Tibetan lithosphere, and inferred patterns of active flow. In: Law RD, Searle MP, and Godin L (eds.) *Channel Flow, Ductile Extrusion and Exhumation in Continental Collision Zones*, pp. 39–70. London: Geological Society of London.

Kosarev G, Kind R, Sobolev SV, Yuan X, Hanka W, and Oreshin S (1999) Seismic evidence for a detached Indian lithospheric mantle beneath Tibet. *Science* 283: 1306–1309.

Kumar P, Yuan X, Kind R, and Kosarev G (2005) The lithosphere–asthenosphere boundary in the Tien Shan-Karakoram region from S receiver functions: Evidence for continental subduction. *Geophysical Research Letters* 32(L07305): 1–4. http://dx.doi.org/10.1029/2004GL022291.

Larson AM, Snoke JA, and James DE (2006) S-wave velocity structure, mantle xenoliths, and the upper mantle beneath the Kaapvaal craton. *Geophysical Journal International* 167: 171–186.

Last RJ, Nyblade AA, and Langston CA (1997) Crustal structure of the east African plateau from receiver functions and Rayleigh wave phase velocities. *Journal of Geophysical Research* 102: 24469–24483.

Lastowka LA and Sheehan AF (2001) Seismic evidence for partial lithospheric delamination model of Colorado Plateau uplift. *Geophysical Research Letters* 28(7): 1319–1322.

Lastowka LA and Sheehan AF (2005) CDROM interstation Pn study along the Rio Grande Rift. In: Karlstrom KE and Keller GR (eds.) *Geophysical Monograph Series 154: The Rocky Mountain Region: An Evolving Lithosphere*, pp. 379–384. Washington, DC: American Geophysical Union.

Lay T and Wallace TC (1995) *Modern Global Seismology*. San Diego, CA: Academic Press, 521 pp.

Lee CA (2003) Compositional variation of density and seismic velocities in natural peridotites at STP conditions: Implications for seismic imaging of compositional heterogeneities in the upper mantle. *Journal of Geophysical Research* 102: 2441.

Lees JM, Brandon M, Park J, Levin V, Ozerov A, and Gordeev E (2000) Kamchatka: Edge of the plate. *IRIS Newsletter* 2000(1): 1–5.

Lerner-Lam AL and Jordan TH (1987) How thick are the continents? *Journal of Geophysical Research* 92(13): 14007–14026.

Levander A (2003) USArray design implications for wavefield imaging in the lithosphere and upper mantle. *The Leading Edge* 22: 250–255.

Levander A and Nolet G (2005) *Geophysical Monograph 157: Seismic Earth: Array Analysis of Broadband Seismograms*. Washington, DC: American Geophysical Union, 252 pp.

Levshin AL, Ritzwoller MH, and Shapiro NM (2005) The use of crustal higher modes to constrain crustal structure across central Asia. *Geophysical Journal International* 160: 961–972.

Li A, Fischer KM, van der Lee S, and Wysession ME (2002) Crust and upper mantle discontinuity structure beneath Eastern North America. *Journal of Geophysical Research* 107: 1–12. http://dx.doi.org/10.1029/2001JB000190.

Li A, Forsyth DW, and Fischer KM (2005) Rayleigh wave constraints on shear-wave structure and azimuthal anisotropy beneath the Colorado Rocky Mountains. In: Karlstrom KE and Keller GR (eds.) *The Rocky Mountain Region: An Evolving Lithosphere*, pp. 385–401. Washington, DC: American Geophysical Union.

Maguire P, Ebinger CJ, Stuart GW, et al. (2003) Geophysics project in Ethiopia studies continental breakup. *Eos, Transactions of the American Geophysical Union* 84: 342–343.

Nabelek MD, Li X-Q, Azevado S, et al. (1993) A high-resolution image of the Cascadia subduction zone from teleseismic converted phases recorded by a broadband seismic array. *Eos, Transactions of the American Geophysical Union* 74: 431.

Nguuri T, Gore J, James DE, et al. (2001) Crustal structure beneath southern Africa and its implications for the formation and evolution of the Kaapvaal and Zimbabwe cratons. *Geophysical Research Letters* 28(13): 2501–2504.

Niu F and James DE (2002) Constraints on the formation and composition of crust beneath the Kaapvaal craton from Moho reverberations. *Earth and Planetary Science Letters* 200: 121–130.

Nolet G (1987) Seismic wave propagation and seismic tomography. In: Nolet G (ed.) *Seismic Tomography*, pp. 1–23. Dordrecht, The Netherlands: Reidel.

Nolet G (1990) Partitioned waveform inversion and two-dimensional structure under the network of autonomously recording seismographs. *Journal of Geophysical Research* 95: 8499–8512.

Nolet G, Dost B, and Paulssen H (1986) Intermediate wavelength seismology and the NARS experiment. *Annales Geophysicae, Series B: Terrestrial and Planetary Physics* 4(3): 305–313.

Nolet G and Vlaar NJ (1981) The NARS project: probing the Earth's interior with a large seismic antenna. *Terra Cognita* 2: 17–25.

Nyblade AA (1999) Heat flow and the structure of Precambrian lithosphere. *Lithos* 48: 81–91.

Nyblade AA and Pollack HN (1993) A global analysis of heat flow from Precambrian terrains: Implications for the thermal structure of Proterozoic and Archean lithosphere. *Journal of Geophysical Research* 98: 12207–12218.

Owens TJ and Fowler J (2003) New instrumentation drives discovery of the Earth's deep interior. *The Leading Edge* 22: 220–223.

Panel on Seismological Studies (Thompson GA., Chair), Board on Earth Sciences, Commission on Physical Sciences, Mathematics, and Resources (1984) *Seismological Studies of the Continental Lithosphere*. National Academy Press, Washington, DC.

Pavlis G (2003) Imaging the Earth with passive seismic arrays. *The Leading Edge* 22: 224–231.

Pearson DG, Irvine G, Carlson RW, et al. (2002) The development of lithospheric keels beneath the earliest continents: Time constraints using PGE and Re–Os isotope systematics. In: Fowle CMR, Pearson DG, Irvine GJ, Carlson RW, Kopylova MG, and Ionov DA (eds.) *Early Earth*, pp. 65–90. London: Geological Society (Royal Astronomical Society).

Pollack HN and Chapman DS (1977) On the regional variation of heat flow, geotherms and lithosphere thickness. *Tectonophysics* 38: 279–296.

Poupinet G, Frechet J, and Thouvenot F (1989a) Portable short period vertical seismic stations transmitting via telephone or satellite. In: Cassinis R and Nolet G (eds.) *Digital Seismology and Fine Modelling of the Lithosphere*, pp. 9–26. London: Plenum.

Poupinet G, Pasquier M, Vadell M, and Martel L (1989b) A seismological platform transmitting via METEOSAT. *Bulletin of the Seismological Society of America* 79: 1651–1661.

Rapine R, Tilmann F, West M, and Ni JF (2003) Crustal structure of northern and southern Tibet from surface wave dispersion analysis. *Journal of Geophysical Research* 108: 1–11. http://dx.doi.org/10.1029/2001JB000445.

Reading AM, Kennett BLN, and Dentith MC (2003) Seismic structure of the Yilgarn Craton, western Australia. *Australian Journal of Earth Sciences* 50: 427–438.

Ritsema J, Nyblade AA, Owens TJ, Langston CA, and VanDecar JC (1998) Upper mantle seismic velocity structure beneath Tanzania, east Africa: Implications for the stability of cratonic lithosphere. *Journal of Geophysical Research* 103: 21201–21213.

Ritsema J and van Heijst H (2000) New seismic model of the upper mantle beneath Africa. *Geology* 28(1): 63–66.

Roecker S, Thurber C, and McPhee D (2004) Joint inversion of gravity and arrival time data from Parkfield: New constraints on structure and hypocenter locations near the SAFOD drill site. *Geophysical Research Letters* 31: 1–4. http://dx.doi.org/10.1029/2003GL019396.

Rondenay S, Bostock MG, and Fischer KM (2005) Multichannel inversion of scattered teleseismic body waves: Practical considerations and applicability. In: Levander A and Nolet G (eds.) *Geophysical Monograph Series 157: Seismic Earth: Array Analysis of Broadband Seismograms*, pp. 187–203. Washington, DC: American Geophysical Union.

Rondenay S, Bostock MG, Hearn TM, White DJ, and Ellis RM (2000) Lithospheric assembly and modification of the SE Canadian Shield: Abitibi-Grenville teleseismic experiment. *Journal of Geophysical Research* 105: 13735–13754.

Rondenay S, Bostock MG, and Shragge J (2001) Multiparameter two-dimensional inversion of scattered teleseismic body waves. Part 3: Application to the Cascadia 1993 data set. *Journal of Geophysical Research* 106: 30795–30807.

Rudnick RL (1995) Making continental crust. *Nature* 378: 571–578.

Rychert CA, Fischer KM, and Rondenay S (2005) Scattered wave imaging of a sharp lithosphere-asthenosphere boundary beneath eastern North America. *Nature* 436: 542–545.

Sacks IS and Suyehiro K (2003) Leg 186 synthesis: Drilling the forearc of the northeast Japan arc – Causes and effects of subduction plate coupling over 20 my. *Proceedings of the Ocean Drilling Program, Scientific Results* 186: 1–14.

Saltzer RL (2002) Upper mantle structure of the Kaapvaal craton from surface wave analysis – A second look. *Geophysical Research Letters* 29(6): 1–4. http://dx.doi.org/10.1029/2001GL013702.

Sandoval S, Kissling E, and Ansorge J (2003) High-resolution body wave tomography beneath the SVEKALAPKO array. Part I: A priori 3D crustal model and associated traveltime effects on teleseismic wavefronts. *Geophysical Journal International* 153: 75–87.

Sandoval S, Kissling E, and Ansorge J (2004) High-resolution body wave tomography beneath the SVEKALAPKO array. Part II: Anomalous upper mantle structure beneath central Baltic Shield. *Geophysical Journal International* 157: 200–214.

Schimmel M, Assumpcao M, and VanDecar JC (2003) Seismic velocity anomalies beneath SE Brazil from P and S wave travel time inversions. *Journal of Geophysical Research* 108(B4): 1–15. http://dx.doi.org/10.1029/2001JB000187.

Schmitz M, Heinsohn W, and Schilling F (1997) Seismic, gravity and petrological indications or partial melting beneath the thickened central Andean crust 21°–23°S. *Tectonophysics* 270: 313–326.

Schulte-Pelkum V, Monsalve G, Sheehan AF, et al. (2005) Imaging the Indian subcontinent beneath the Himalaya. *Nature* 435: 1222–1225.
Schutt D and Humphreys E (2004) P and S wave velocity and V_p/V_s in the wake of the Yellowstone hot spot. *Journal of Geophysical Research* 109(B01305): 1–14. http://dx.doi.org/10.1029/2003JB002442.
Shapiro NM, Campillo M, Stehly L, and Ritzwoller MH (2005) High-resolution surface-wave tomography from ambient seismic noise. *Science* 307: 1615–1618.
Sheehan AF, Shearer P, Gilbert HJ, and Dueker KG (2000) Seismic migration processing of P-SV converted phases for mantle discontinuity structure beneath the Snake River Plain, Western United States. *Journal of Geophysical Research* 105(B8): 19055–19065.
Shirey SB, Carlson RW, Richardson SH, et al. (2001) Emplacement of eclogite components into the lithospheric mantle during craton formation. *Geophysical Research Letters* 28(13): 2509–2512.
Silver PG (1996) Seismic anisotropy beneath the continents: Probing the depths of geology. *Annual Review of Earth and Planetary Sciences* 24: 385–432.
Silver PG and Chan WW (1988) Implications for continental structure and evolution from seismic anisotropy. *Nature* 335: 34–39.
Simons FJ, Zielhuis A, and van der Hilst RD (1999) The deep structure of the Australian continent from surface wave tomography. *Lithos* 48: 17–43.
Smith RB, Nagy WC, Julander KA, Viveiros JJ, Barker CA, and Gants DG (1989) Geophysical and tectonic framework of the eastern Basin and Range-Colorado Plateau-Rocky Mountain transition. In: Pakiser LC and Mooney WD (eds.) *Geophysical Framework of the Continental United States*, pp. 205–233. Boulder, CO: Geological Society of America ch. 12.
Snelson CM, Keller GR, Miller KC, Rumpel H-M, and Prodehl C (2005) Regional crustal structure derived from the CD-ROM 99 seismic refraction/wide-angle reflection profile: The lower crust and upper mantle. In: Karlstrom KE and Keller GR (eds.) *Geophysical Monograph Series 154: The Rocky Mountain Region: An Evolving Lithosphere*, pp. 271–291. Washington, DC: American Geophysical Union.
Snoke JA and James DE (1997) Lithospheric structure of the Chaco and Parana Basins of South America from surface-wave inversion. *Journal of Geophysical Research* 102: 2939–2951.
Stachnik JC, Abers GA, and Christensen D (2004) Seismic attenuation and mantle wedge temperatures in the Alaska subduction zone. *Journal of Geophysical Research* 109(B10304). http://dx.doi.org/10.1029/2004JB003018.
Thurber C, Roecker S, Zhang H, Baher S, and Ellsworth W (2004) Fine-scale structure of the San Andreas fault zone and location of the SAFOD target earthquakes. *Geophysical Research Letters* 31. http://dx.doi.org/10.1029/2003/GL019398.
van der Hilst RD, Kennett BLN, Christie D, and Grant J (1994) Project SKIPPY explores the lithosphere and mantle beneath Australia. *Eos, Transactions of the American Geophysical Union* 75: 177–181.
van der Lee S (2002) High-resolution estimates of lithospheric thickness from Missouri to Massachusetts, USA. *Earth and Planetary Science Letters* 203(1): 15–23.
van der Lee S, James DE, and Silver PG (2001a) Upper mantle S velocity structure of Central and Western South America. *Journal of Geophysical Research* 106(12): 30821–30834.
Van der Lee S and Nolet G (1997) Upper mantle S-velocity structure of North America. *Journal of Geophysical Research* 102: 22815–22838.
van der Lee S, VanDecar JC, Fouch MJ, and James DE (2001b) Joint inversion of different seismic data types for upper mantle structure beneath southern Africa. *Eos, Transactions of the American Geophysical Union, Fall Meeting Supplement* 82(47): F826.
VanDecar JC (1991) *Upper-Mantle Structure of the Cascadia Subduction Zone from Non-linear Teleseismic Travel-Time Inversion*. Ph.D. Thesis, University of Washington, Seattle, WA.
VanDecar JC and Crosson RS (1990) Determination of teleseismic relative phase arrival times using multi-channel cross-correlation and least squares. *Bulletin of the Seismological Society of America* 80(1): 150–159.
VanDecar JC, James DE, and Assumpçao M (1995) Seismic evidence for a fossil mantle plume beneath South America and implications for plate driving forces. *Nature* 378(6552): 25–31.
VanDecar JC, Russo RM, James DE, Ambeh WB, and Franke M (2003) Aseismic continuation of the Lesser Antilles slab beneath continental South America. *Journal of Geophysical Research* 108: 1–12. http://dx.doi.org/10.1029/2001JB000884.
Vinnik LP, Kosarev G, and Makeeva L (1984) Lithosphere anisotropy from the observation of SKS and SKKS waves. *Doklady Akademii Nauk USSR* 278: 1335–1339.
Wagner LS, Beck SL, and Zandt G (2005) Upper mantle structure in the south central Chilean subduction zone (30 to 36S). *Journal of Geophysical Research* 110. http://dx.doi.org/10.1029/2004JB0003238.
Watson T (2005) *The Upper Mantle Structure Beneath the Transantarctic Mountains and East Antarctic Craton using Body-Wave Tomography*. University Park, PA: Pennsylvania State University 91 pp.
Webb SJ (2006) *The Use of Potential Field and Seismological Data to Analyze the Structure of the Lithosphere Beneath Southern Africa*. PhD thesis, University of the Witwatersrand, Johannesburg.
Weeraratne DS, Forsyth DW, and Fischer KM (2003) Evidence for an upper mantle plume beneath the Tanzanian craton from Rayleigh wave tomography. *Journal of Geophysical Research* 108: 1–17. http://dx.doi.org/10.1029/2002JB002273.
West M, Gao W, and Grand SP (2004a) A simple approach to the joint inversion of seismic body and surface waves applied to the Southwest US. *Geophysical Research Letters* 31(L15615): 020274. http://dx.doi.org/10.1029/2004GL020373.
West M, Ni JF, Baldridge WS, et al. (2004b) Crust and upper mantle shear wave structure of the Southwest United States: Implications for rifting and support for high elevation. *Journal of Geophysical Research* 109(B03309): 1–16. http://dx.doi.org/10.1029/2003/JB002575.
Wielandt E and Streckeisen G (1982) The leaf-spring seismometer; design and performance. *Bulletin of the Seismological Society of America* 72: 2349–2367.
Wilson D and Aster R (2003) Imaging crust and upper mantle seismic structure in the Southwestern United States using teleseismic receiver functions. *The Leading Edge* 22(3): 232–237.
Wilson D and Aster R (2005) Seismic imaging of the crust and upper mantle using regularized joint receiver functions, frequency – Wave number filtering, and multimode Kirchhoff migration. *Journal of Geophysical Research* 110(B05305): 1–12. http://dx.doi.org/10.1029/2004JB003430.
Wilson D, Aster R, Ni JF, et al. (2005a) Imaging the seismic structure of the crust and upper mantle beneath the Great Plains, Rio Grande Rift, and Colorado Plateau using receiver functions. *Journal of Geophysical Research* 110(B05306): 1–14. http://dx.doi.org/10.1029/2004JB003492.
Wilson D, Aster R, West M, et al. (2005b) Lithospheric structure of the Rio Grande rift. *Nature* 433: 851–855.
Wittlinger G, Farra V, and Vergne J (2004) Lithospheric and upper mantle stratifications beneath Tibet. *Geophysical Research Letters* 31(L19615): 1–4. http://dx.doi.org/10.1029/2004GL020955.
Yuan H and Dueker KG (2005a) Teleseismic P-wave tomogram of the Yellowstone plume. *Geophysical Research Letters* 32(L07304): 1–4. http://dx.doi.org/10.1029/2004GL022056.
Yuan H and Dueker KG (2005b) Upper mantle tomographic V_p and V_s images of the middle Rocky Mountains in Wyoming, Colorado, and New Mexico: Evidence for a thick heterogeneous chemical lithosphere. In: Karlstrom KE and Keller GR (eds.) *Geophysical Monograph 154: The Rocky Mountain Region: An Evolving Lithosphere*, pp. 329–345. Washington, DC: American Geophysical Union.
Yuan X, Sobolev NV, Kind R, et al. (2000) Subduction and collision processes in the Central Andes constrained by converted seismic phases. *Nature* 408: 958–961.
Zandt G, Beck SL, Ruppert C, et al. (1996) Anomalous crust of the Bolivian Altiplano, Central Andes: Constraints from broadband regional seismic waveforms. *Geophysical Research Letters* 23: 1159–1162.
Zandt G, Gilbert HJ, Owens TJ, Ducea M, Saleeby J, and Jones CH (2004) Active foundering of a continental arc root beneath the Southern Sierra Nevada in California. *Nature* 431: 41–46.
Zhao M, Langston CA, Nyblade AA, and Owens TJ (1999) Upper mantle velocity structure beneath southern Africa from modeling regional seismic data. *Journal of Geophysical Research* 104: 4783–4794.
Zhao W, Mechie J, Brown LD, et al. (2001) Crustal structure of central Tibet as derived from project INDEPTH wide-angle seismic data. *Geophysical Journal International* 145: 486–498.
Zielhuis A and van der Hilst RD (1996) Upper-mantle shear velocity beneath eastern Australia from inversion of waveforms from SKIPPY portable arrays. *Geophysical Journal International* 127: 1–16.

Relevant Websites

www.EuroArray.org – 4-D Europe, Assembly of a Continent.
www.earthscope.org – EarthScope National Meeting Registration.
www.iris.edu – Incorporated Research Institutions for Seismology.
www.norsar.no – Independent Research Foundation Specializing in Commercial Software Solutions and Research Activities within Applied Geophysics and Seismology.
www.Passcal.iris.edu – PASSCAL (IRIS) Instrument Center, Socorro, New Mexico.

This page intentionally left blank

1.17 Crustal and Lithospheric Structures Between the Alps and East European Craton from Long-Range Controlled Source Seismic Experiments

A Guterch, Institute of Geophysics, Polish Academy of Sciences, Warsaw, Poland
M Grad, University of Warsaw, Warsaw, Poland
G Randy Keller, University of Oklahoma, Norman, OK, USA
E Brückl, Vienna University of Technology, Vienna, Austria

© 2015 Elsevier B.V. All rights reserved.

This chapter is a revision of the previous edition chapter by A. Guterch, M. Grad, G.R. Keller, Volume 1, pp. 533–558 © 2007, Elsevier B.V.

1.17.1	**Introduction: Regional Geologic/Tectonic Setting of Central Europe**	557
1.17.2	**A New Generation of Long-Range Seismic Experiments**	559
1.17.3	**Characteristics of the Seismic Wavefields along Profiles for Different Tectonic Provinces (Terranes)**	560
1.17.4	**Examples of 2-D and 3-D Modeling of the Earth's Crust and Lower Lithosphere**	564
1.17.4.1	POLONAISE'97 Crustal and Lithospheric Models (Profiles P4, P1, and P3)	565
1.17.4.2	SUDETES 2003 Crustal Model (Profile S01)	568
1.17.4.3	CELEBRATION 2000 Crustal Models CEL05 and CEL01	568
1.17.4.4	ALP 2002 Crustal Models Alp01 and Alp02	572
1.17.4.5	Examples of 3-D Tomographic Modeling	574
1.17.5	**Geotectonic Models of the Transition from the EEC to the Eastern Alps, Carpathians, and Pannonian Basin**	574
1.17.5.1	POLONAISE'97 Area	575
1.17.5.2	CELEBRATION 2000 Area	578
1.17.5.3	ALP 2002 Area	579
1.17.6	**Summary**	583
References		583

1.17.1 Introduction: Regional Geologic/Tectonic Setting of Central Europe

The complex tectonic history of Central Europe (Figure 1) reflects the breakup of a Neoproterozoic supercontinent(s) (Rodinia/Pannotia) (e.g., Dalziel, 1997) to form the continental fragment Baltica and the subsequent growth of continental Europe beginning with the Caledonian orogeny. Caledonian and younger Variscan orogeneses involved accretion of Laurentian and Gondwanan terranes to the rifted margin of Baltica (East European Craton – EEC) during the Paleozoic (e.g., Pharaoh, 1999). From central Poland northward, the region also experienced volcanic activity during the Permian and tectonic inversion during the Alpine orogeny, which in the south continues today. The Trans-European Suture Zone (TESZ) is a term used to refer to the suite of sutures and terranes that formed adjacent to the rifted margin of Baltica (e.g., Berthelsen, 1992a,b, 1998; Pharaoh, 1999; Ziegler, 1990), and these features extend from the British Isles to the Black Sea region (Figure 1). Understanding the structure and evolution of the TESZ region is one of the key tectonic challenges in Europe north of the Alps. The tectonic evolution of this region shares many attributes with the Appalachian/Ouachita orogen (Golonka et al., 2003a; Keller and Hatcher, 1999) and is certainly of global importance to studies in terrane tectonics and continental evolution. The TESZ is far more complex than a single suture but in a broad sense is the boundary between the accreted terranes and Baltica. The TESZ includes the Teisseyre–Tornquist Zone (TTZ), which has several definitions. Here, we will use the term TTZ to refer to a structural zone associated with the southwestern edge of the EEC.

The Bohemian Massif is a large structural block (Figure 1) that is mostly located in the Czech Republic and is a large, complex terrane whose origin can be traced to northern Gondwana (Africa). In southern Poland, several smaller structural blocks such as the Małopolska Massif (MM; Figure 1) are located adjacent to Baltica and were probably transported laterally along it, similar to Cenozoic movement of terranes along the western margin of North America.

The younger Eastern Alps, Carpathian Mountains arc, and Pannonian Basin (the ALCAPA units) form interrelated components of the Mediterranean arc–basin complex (Figure 1). These features are the result of intricate Mesozoic/Cenozoic plate interactions in the Mediterranean region and are strongly related to the spreading history of the northern and central Atlantic. At that time, closure of the Paleotethys by subduction under the Eurasian megaunit was already completed and the Neotethys fully developed. Smaller ocean basins existed in the southeastern ALCAPA (e.g., Le Pichon et al., 1988; Stampfli and Kozur, 2006). The displacement of Africa relative to the European platform led to a complex sequence of rifting, breakup of continental blocks, seafloor spreading, subduction of oceanic and continental lithospheres, and reamalgamation and suturing of microplates. Considering the Eastern Alps and the adjoining Carpathians, Dinarides, and Southern Alps, the opening and closing of the Meliata and Vardar Oceans in the south and the Alpine Tethys in the north strongly influenced the development of these mountain chains. The

 http://dx.doi.org/10.1016/B978-0-444-53802-4.00015-4

Figure 1 Simplified tectonic map of Central Europe. ATA, Armorican Terrane Assemblage; MM, Małopolska Massif; TESZ, Trans-European Suture Zone.

Adriatic microplate started to move more independently from Africa to the northwest (e.g., Handy et al., 2010). The Alpine orogenic phase occurred in Cretaceous and Upper Eocene after subduction of the Meliata Ocean and Alpine Tethys. This process induced far-reaching overthrusting, folding, and stacking of Austroalpine nappes to the north along the passive European continental margin.

The subduction and closure of the remaining ocean in the area of the Carpathian embayment produced considerable Neogene volcanism, which led to the development of the Pannonian Basin and caused finally the Carpathian arc to evolve into its strongly arcuate shape. Back-arc extension was the dominant process that formed the Pannonian Basin that contains up to 8 km of Neogene strata in its subbasins (e.g., Posgay et al., 1995; Royden, 1993). Due to continued indentation of the Adriatic plate in combination with gravitational collapse directed to the unconstrained margin represented by the Pannonian Basin, major blocks of the Eastern Alps extruded laterally to the east (Linzer et al., 2002; Ratschbacher et al., 1991). Current tectonic activity due to the continuing convergence between Africa and Europe has shifted southward to the subduction zones of the Calabrian and Hellenic arcs. However, strong tectonic activity is still evidenced by seismicity that extends to depths of ~200 km in the Vrancea region north of Bucharest in Romania (**Figure 1**). In addition to being a major crustal-scale feature, the TESZ appears to be a deep-seated boundary because tomographic analysis of the shear-wave velocity structure of the mantle under Europe shows that the TESZ separates regions with high S-wave velocities beneath the EEC from low-velocity regions under the younger terranes (Zielhuis and Nolet, 1994). Another indication of the deep-seated nature of the TESZ was obtained from observations of several hundred earthquakes and explosions located in Europe. To explain the observed blockage of energy from regional seismic events by the TESZ region, the structural anomaly between Eastern and Western Europe must reach at least down to a depth of ~200 km (Schweitzer, 1995).

Early deep seismic sounding (DSS) studies in Central Europe also showed a large contrast of the crustal structure between the accreted terranes, the TESZ, and the EEC (e.g., Ansorge et al., 1992; Guggisberg et al., 1991; Guterch et al., 1976, 1984, 1986, 1992, 1994). The exploration of the lithosphere of the Eastern Alps and the surrounding area by WAR/R (wide-angle reflection/refraction) experiments started around the Eschenlohe quarry, in Southern Germany, about 50 years ago (Giese and Prodehl, 1976). The Alpine longitudinal profile (ALP'75) extended along the axis of the Western and Eastern Alps to the Pannonian Basin (e.g., Scarascia and Cassinis, 1997; Yan and Mechie, 1989). TRANSALP is a seismic traverse over the central part of the Eastern Alps from Munich to Venice (e.g., Gebrande et al., 2006 and references therein), combining steep-angle, high-resolution reflection seismic profiling, wide-angle reflection and refraction tomography (Bleibinhaus and

Gebrande, 2006), receiver functions (Kummerow et al., 2004), and teleseismic tomography (Lippitsch et al., 2003), supplemented by gravimetric studies (Ebbing et al., 2006; Zanolla et al., 2006).

Many nonseismic studies have been undertaken in the TESZ region. For example, heat flow measurements indicate a major change in the thermal regime across Central Europe (Čermák and Bodri, 1998). Using over 3200 heat flow measurements, Čermák and Bodri (1998) explained a number of prominent heat flow anomalies (e.g., Pannonian Basin, French Massif Central, and the Alps) as products of the deep-seated lithospheric processes. In the area of Central Europe, the TESZ separates 'cold' lithosphere of the EEC with low heat flow of 30–40 m Wm^{-2} from 'hot' lithosphere with higher heat flow of 40–70 m Wm^{-2} in the Paleozoic terranes and Carpathians, and even higher values (80–110 m Wm^{-2}) are found in the Pannonian Basin and Eastern Alps (Čermák and Bodri, 1998; Čermák et al., 1989; Majorowicz et al., 2003; Vosteen et al., 2003; Zeyen et al., 2002). The characteristic Moho temperature for the EEC has been estimated to be 500 °C (Majorowicz et al., 2003) and 590–620 °C (Čermák et al., 1989). In the TESZ region, the Moho temperature increases to 650–750 °C, and beneath the Carpathians and Pannonian Basin, it even increases to 800–900 °C (Čermák et al., 1989; Dövényi et al., 1983; Majorowicz et al., 2003).

Gravity and magnetic anomalies indicate significant variations in lithospheric structure (e.g., Królikowski and Petecki, 1995; Petecki et al., 2003; Wybraniec et al., 1998). Bouguer anomalies in the area of the EEC are relatively homogeneous (0 ± 20 mGal) and decrease in the area of the EEC margin down to about −40 mGal. The anomaly field becomes more complex in this region with a large high in the Holy Cross Mountains area and lower values to the northwest along the EEC margin. In the Carpathians, Bouguer anomalies reach values of about −80 mGal and increase into the Pannonian Basin (20–30 mGal), where the crust thins (Bielik et al., 2004, 2010).

Magnetic anomalies along the cratonic part of profiles contain many short wavelength variations from −1500 to +1500 nT that correlate well with tectonic features and intrusions in the Precambrian basement. Further to the southwest in the TESZ, the Carpathian Foredeep and Carpathians, magnetic anomalies are subdued (±100 nT), presumably due to the deeply buried magnetic basement. Except in areas of Tertiary volcanism, magnetic anomalies are also subdued in the Pannonian Basin because of the thick cover of sedimentary rocks.

1.17.2 A New Generation of Long-Range Seismic Experiments

From 1997 to 2003, Central Europe was covered by an unprecedented network of seismic refraction experiments to investigate its complex lithospheric structure (Brückl et al., 2003; Grad et al., 2003b; Guterch et al., 1999, 2003a,b). These experiments (POLONAISE'97, CELEBRATION 2000, ALP 2002, and SUDETES 2003) were only possible due to a massive international cooperative effort. Acronyms of these experiments are: POLONAISE'97 – Polish Lithospheric Onsets – An International Seismic Experiment, 1997; CELEBRATION 2000 – Central European Lithospheric Experiment Based on Refraction, 2000; ALP 2002 – Eastern Alps and adjacent regions, 2002; SUDETES 2003 – Sudetes Mountains and adjacent regions, 2003. The total length of all the profiles recorded is ~20 000 km, and during these four experiments, a total of 295 large explosions provided the seismic sources. The number of seismic stations used in these experiments ranged from 640 in the POLONAISE'97 to 1230 in CELEBRATION 2000. Distances between shot points were usually ~50 km. As a result of these experiments, a network of seismic refraction profiles (**Figure 2**) now extends from the EEC (east of the Baltic Sea), along and across the TESZ region of Poland and the Bohemian Massif, through the Carpathians, Sudetes, and Eastern Alps, to the Pannonian Basin, the Dinarides, and the Adriatic Sea (Brückl et al., 2003; Grad et al., 2003b; Guterch et al., 1998, 1999, 2001, 2003a,b, 2004). The high-quality seismic data obtained reveal a variety of both the P- and S-wave phases. The main results were published in Guterch et al. (1999, 2004, 2007), Grad et al. (1999, 2002a,b, 2003a, 2005, 2006, 2007, 2008, 2009), Jensen et al. (1999, 2002), Środa and POLONAISE P3 Working Group (1999), Wilde-Piórko et al. (1999), Krysiński et al. (2000, 2009), Bayer et al. (2002), Czuba et al. (2002), Janik et al. (2002, 2005, 2009, 2011), Środa et al. (2002, 2006), Winchester et al. (2002), Růžek et al. (2003), Hrubcová et al. (2005, 2008, 2010), Majdański et al. (2005, 2007), Malinowski et al. (2005, 2009a,b), Brückl et al. (2007, 2010), Šumanovac et al. (2009), and Narkiewicz et al. (2011).

These experiments also relate to the German KTB project, the BOHEMA, ALPASS, and PASSEQ 2006–2008 seismic tomography experiments and numerous Czech–German projects on the geodynamics of the West Bohemia/Vogtland seismically active region. The teleseismic experiments provided exciting new insights into the structure and evolution of the lithosphere in this region (Brückl et al., 2010; Plomerová et al., 2003; Wilde-Piórko et al., 1999, 2008).

The principal specific scientific goals of the POLONAISE'97, CELEBRATION 2000, ALP 2002, and SUDETES 2003 experiments were the following:

- Investigate the deep structure of the southwestern margin of the EEC (southern Baltica) and its relationships to younger terranes
- Delineate the major terranes and crustal blocks in the TESZ region (e.g., Upper Silesian block and blocks exposed in the Holy Cross Mountains)
- Investigate the origin and structural framework of the Pannonian Basin and its subbasins
- Investigate the nature and extend of thrust faulting along the northern front of the Carpathians
- Investigate the structure and evolution of the Eastern Alps and their relationships with adjacent features
- Investigate the structural relationships between the structural elements of the Bohemian Massif and adjacent features
- Construct a three-dimensional (3-D) model of the lithospheric structure in the area
- Evaluate the implications of the Earth models derived for natural resources and earthquake hazards
- Evaluate and develop geodynamic models for the tectonic evolution of the region.

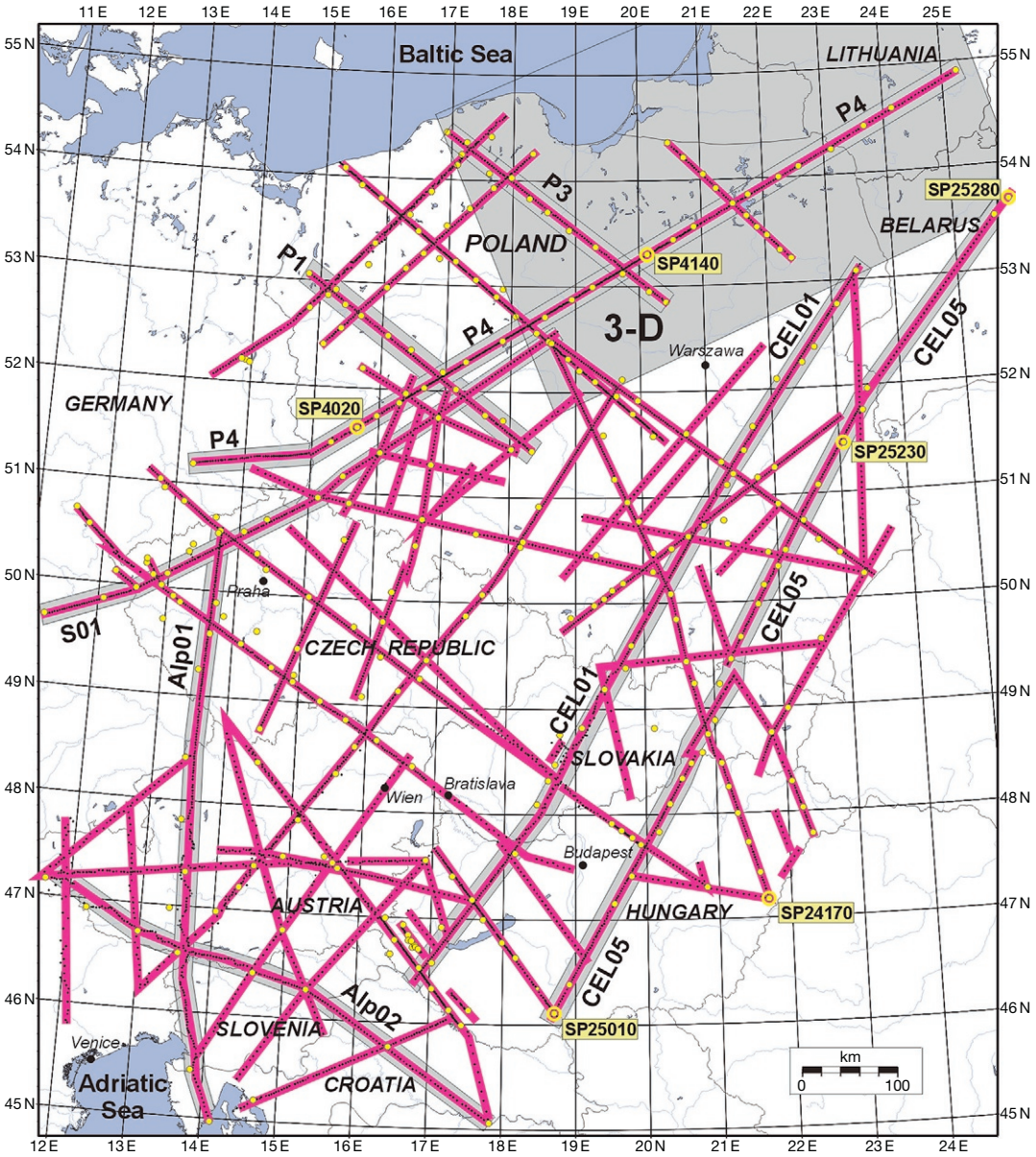

Figure 2 Location of seismic profiles recorded in Central Europe during the POLONAISE'97, CELEBRATION 2000, ALP 2002, and SUDETES 2003 experiments. Pink lines show the seismic profiles whose total length is ~20 000 km, with ~7000 seismic receiver positions (small black dots). Yellow dots show 295 large shot locations. Gray lines show position of POLONAISE'97 profiles P1, P3, and P4, CELEBRATION 2000 profiles CEL01 and CEL05, ALP 2002 profiles Alp01 and Alp02, and SUDETES 2003 profile S01 for which models are shown in **Figures 6–12**. The gray area shows the area of 3-D investigations presented in **Figure 14**. Yellow dots show location of shot points SP25010, SP4020, SP24170, SP25230, SP4140, and SP25280 for which record sections are shown in **Figures 3–5**.

When all the individual results are completed and integrated, these experiments will provide an unprecedented 3-D image of the evolution and assembly of a continent.

1.17.3 Characteristics of the Seismic Wavefields along Profiles for Different Tectonic Provinces (Terranes)

CELEBRATION 2000 profile CEL05 and POLONAISE'97 profile P4 are most representative for the characteristic of seismic wavefields in Central Europe because of their length. The 1420 km long profile CEL05 is the longest recorded in the CELEBRATION experiment (Figure 2). It begins in Hungary; crosses the Slovak Republic, Poland, and Belarus; and ends in Northwestern Russia. The southwestern part of the profile (0–200 km) lies in the Pannonian Basin. The profile then crosses a tectonically complex zone that includes the Carpathians and their foredeep (200–500 km) and then crosses the TESZ (500–700 km), including the MM, Lublin Trough, and TTZ (Figure 1). The northeastern part of the profile (700–1420 km) crosses the EEC (Figures 1 and 2). Data from

26 explosions made along this profile were collected using over 360 modern seismic recorders, with a nominal station spacing 2.8 km in Hungary, Slovakia, and Poland and 4.6 km in Belarus and Russia. More details about the layout of the experiment are provided in Guterch et al. (2001, 2003b).

The P-wavefield on the CEL05 record sections has high signal-to-noise ratio, particularly for the southern (Pannonian Basin) and the northern cratonic parts of the profile. Identification and correlation of seismic phases were done manually on a computer screen using software that allows flexible use of scaling, filtering, and reduction velocity (Środa, 1999; Zelt, 1994). Clear arrivals of refracted and reflected waves from sedimentary layers, the crystalline crust and the upper mantle, were typically observed up to offsets of 200–300 km and for some shots, even over 900 km. Examples of record sections for profiles CEL05, CEL04, and P4 are shown in Figures 3–5.

General observations about the data are that waves from sedimentary cover (P_{sed}) are observed as first arrivals in the vicinity of shot points up to offsets of only 1 km on the EEC, while they are observed to offsets of 10–20 km in the TESZ

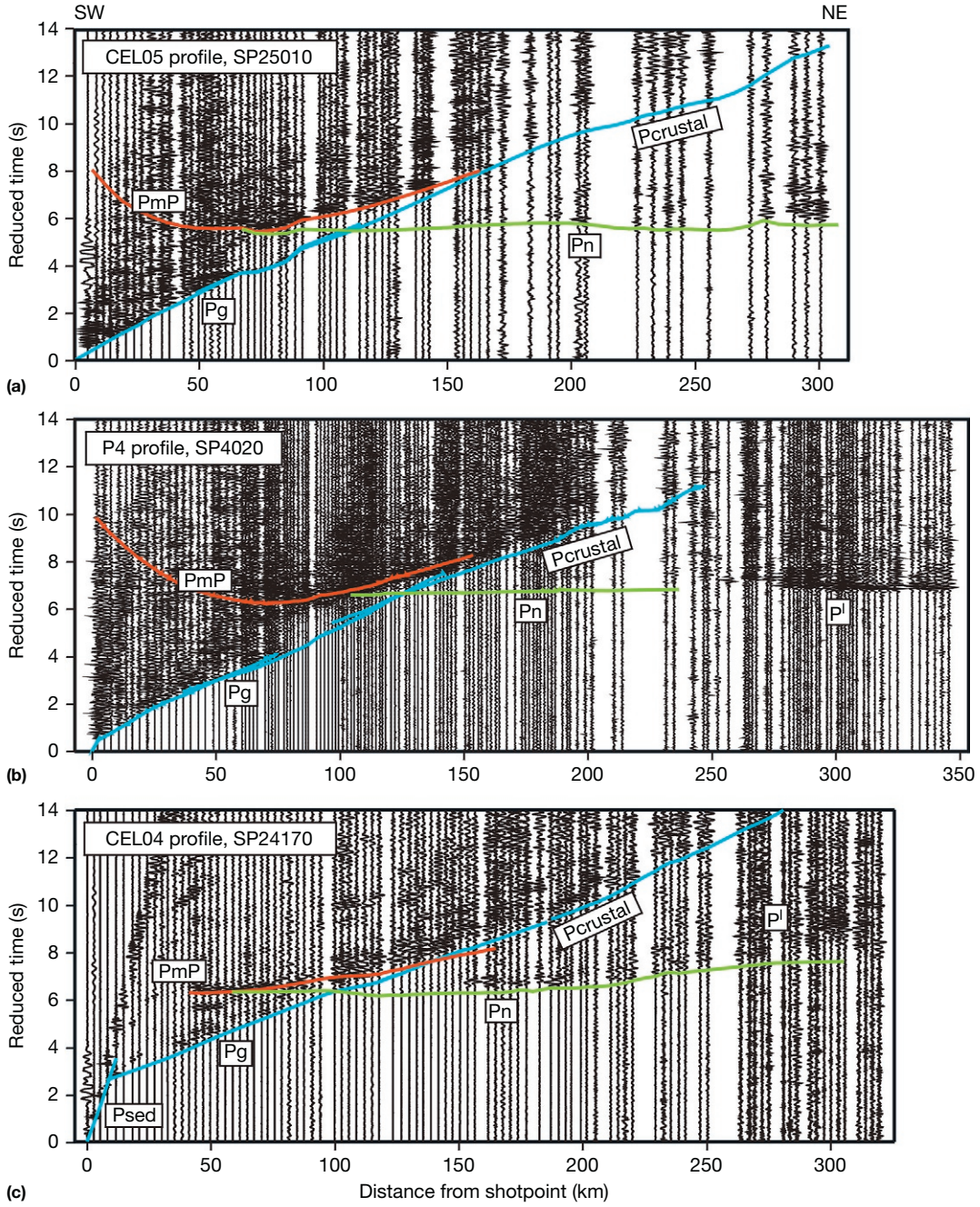

Figure 3 (a–c) Examples of P-wave record sections for seismic profiles in the area of Central Europe (for shot points' location, see Figure 2). P_g, $P_{crustal}$, P_mP, and P_n – crustal and Moho phases. Reduction velocity for all sections = 8 km s^{-1}.

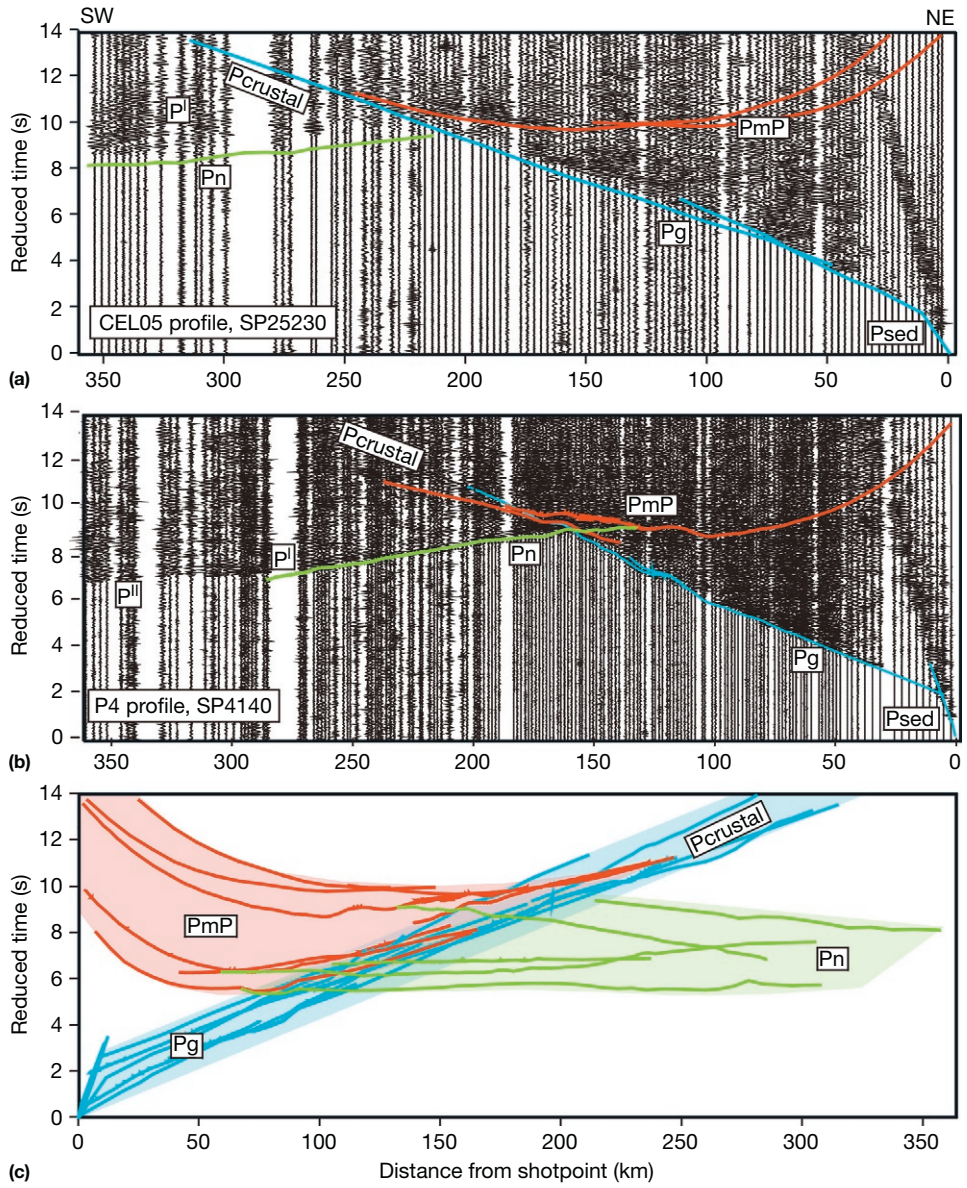

Figure 4 Examples of P-wave record sections ((a, b); for location, see **Figure 2**) and comparison of travel times (c); note the large variation of the arrival times (reaching 3–6 s) of the P_g, $P_{crustal}$, P_mP, and P_n phases, which indicate large differences in the crustal and uppermost mantle structures across the region.

region and even ~30 km in the Carpathians. Their apparent velocities range from 2.5 to 5.5 km s^{-1}. After these arrivals, the P_g phase that travels in the crystalline basement (upper crust) is recorded to highly variable offsets of 1–250 km. The slowest arrivals occur to the southwest toward the Carpathian Foredeep and Carpathians, and at offsets of 100–150 km, they are ~2 s late compared with other directions. As discussed in the succeeding text, the highly variable crustal structure along profile CEL05 results in mantle arrivals also becoming first arrivals at highly variable offsets.

In the Pannonian Basin region, the seismic wavefield is characterized by strong P_g arrivals to offsets of ~50 km. For offsets out to 150 km, the amplitude of the P_g wave is small relative to the dominant reflection from the Moho (P_mP). Reflections from the top of the middle crust (P_c) are well correlated and observed throughout the whole 'Pannonian' part of the profile. Reflections from the top of the lower crust (P_{lc}) are well correlated and observed throughout the whole 'cratonic' part of the profile. Refractions from the middle crust and lower crust are correlated as secondary arrivals in the seismic sections, primarily at long offsets where refractions merge with wide-angle reflections to form the overcritical phases $P_{crustal}$ and $S_{crustal}$, which in some cases are well recorded to offsets of ~300 km. These phases are important for determining the velocities in the middle crust and lower crust, particularly for the Pannonian crust where the velocities of these layers are 6.2–6.6 km s^{-1}. In the 'Pannonian' region, the phase diving in the uppermost mantle (P_n) has relatively low amplitudes and low apparent velocities (7.9–8.0 km s^{-1}). The intercept time for P_n is only ~6 s (for reduction velocity 8 km s^{-1}), and its crossover distance with the crustal (P_g) arrivals is only 100–120 km. These observations clearly show

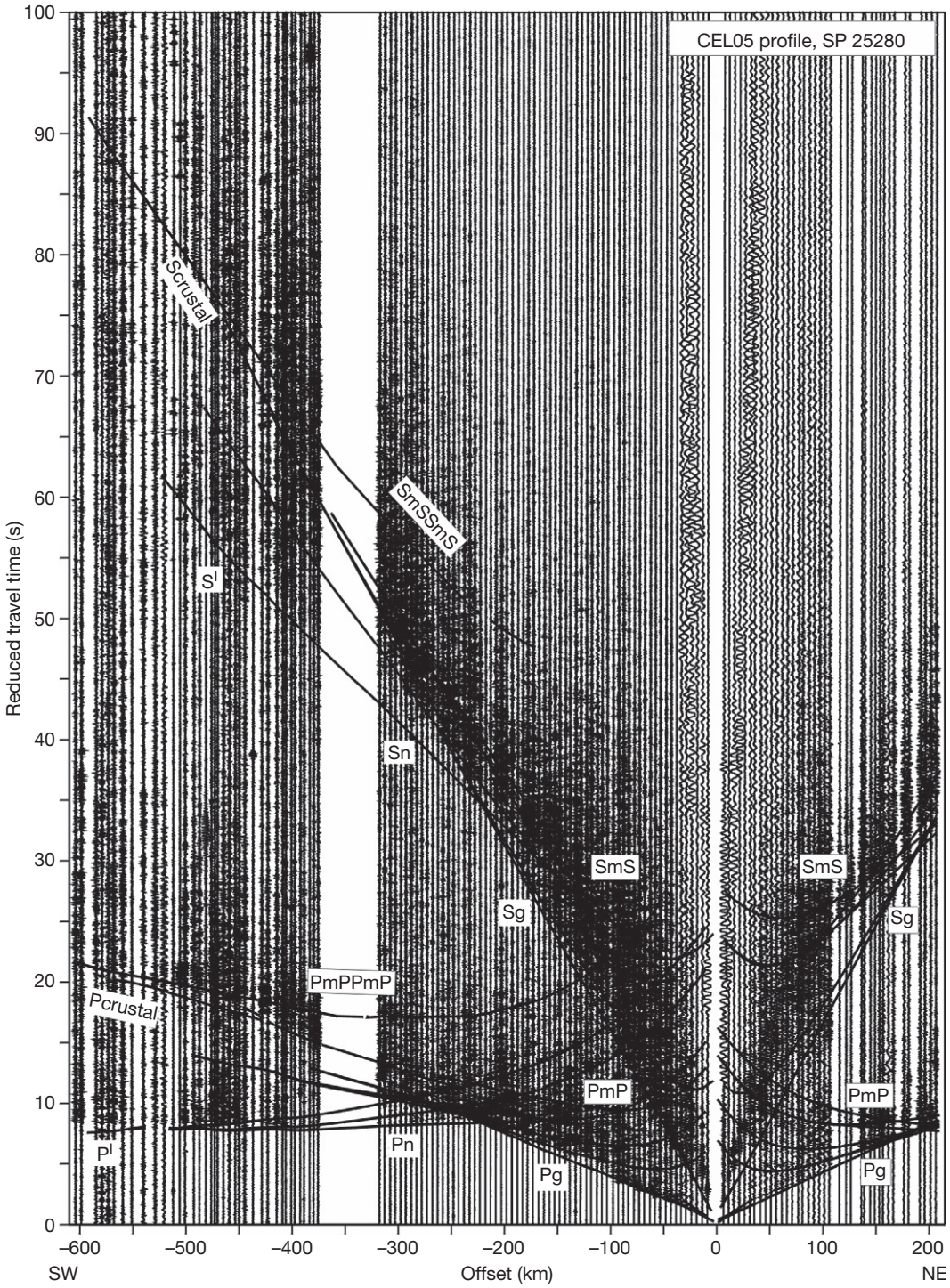

Figure 5 Example of P- and S-wave record section for CELEBRATION 2000 profile CEL05 (Figure 2). Amplitude-normalized seismic record sections for SP25280 showing the full wavefield, including both P- and S-waves with theoretical travel times calculated for the model of the crust derived using the SEIS83 ray-tracing technique. Note the P_mPP_mP and S_mSS_mS waves that are reflected twice from the Moho discontinuity and free surface and high-quality lower lithosphere phases recorded to long offsets. Reduction velocity = 8 km s^{-1}.

that the Moho in the Pannonian Basin is shallow. Starting at offsets of ~200 km, arrivals from the mantle lithosphere (P^I and P^{II}) were observed for some shots.

The wavefield observed in the Carpathian region is complex as is the known geologic structure. First arrivals (P_g) are distinct up to ~100 km offset and are characterized by large variations in apparent velocity and amplitude. Midcrustal reflections (P_c) are usually recorded at short distance intervals (20–50 km) and are also characterized by variations in apparent velocity and amplitude. P_n arrivals were only fragmentarily recorded in the

Carpathians. This characteristic attribute of the wavefield testifies to the complex structure of the crust–upper mantle transition in this region. The observed wavefield is similar in the adjacent Carpathian Foredeep to the northeast. However, waves with low apparent velocities (4.0–5.0 km s^{-1}) are observed up to 30–50 km offsets, and midcrustal phases are even more complex.

In the TESZ area, the character of the wavefield is more uniform, and the travel times of both refracted first arrivals (P_g) and waves from the Moho and uppermost mantle (P_mP and P_n) show clear evidence that the crystalline basement and crust–upper mantle boundary are deep. Compared to the Pannonian area, the P_n wave intercept time is much later (reduced time 8.0–8.5 s for reduction velocity 8 km s^{-1}). The crossover distance between crustal (P_g) and mantle refractions (P_n) is also much larger. Waves generated in this region are well recorded, particularly toward the northeast in the EEC.

The P-wavefield recorded on the EEC is uniform with high signal-to-noise ratios. Due to the thin sedimentary cover, the P_{sed} phase produces first arrivals only to offsets of 1–10 km from the shot point. The P_g phase has a uniform character and is observed in the first arrivals up to ~200 km offsets, with apparent velocities increasing with distance from 6.0–6.2 to 6.6–7.0 km s^{-1}. These crustal waves continue to overcritical distances of up to 250–350 km. Relatively small amplitudes characterize waves from the middle crust, which indicates small contrasts at seismic boundaries and small velocity gradients within layers. Waves reflected from the Moho (P_mP) are the dominant arrivals in the offset interval of 90–120 to 200–250 km. P_n arrivals have small amplitudes, and their apparent velocities are 8.1–8.2 km s^{-1}. The intercept time for P_n occurs at a reduced time of ~8 s, which is ~2 s more than for the Pannonian crust. For a number of shot points, well-recorded waves from the lithospheric mantle were observed up to 400–500 km offsets and even to 800–1200 km. For the northern shot points, an unusual variety of P- and S-wave phases were recorded, and these phases are shown in Figure 5. For shot point SP25280, P- and S-waves were doubly reflected from the Moho, and good-quality lower lithosphere phases P^I and S^I were observed.

Examples of record sections from profile P4 (Figure 2) are presented in Figures 3 and 4. Refracted waves from the sedimentary cover (P_{sed}) are observed as first arrivals in the vicinity of shot points at offsets 1–15 km. The apparent velocity is 4.0–5.5 km s^{-1} in the southwestern part of the profile, decreasing northeastward to 2.5–3.5 km s^{-1}. The sedimentary strata are far thicker in the Polish Basin than in the two surrounding platform areas. Individual, thin sedimentary layers cannot be modeled outside the Polish Basin because of the relatively coarse (1.5–3.0 km) receiver spacing compared to the local thickness of the sedimentary column.

Following the arrivals from the sedimentary cover (P_{sed} phase), the refraction from the crystalline upper crust (P_g) is detected as first arrivals to offsets of 100–200 km. The basement topography and variations in sedimentary structure can explain the undulation in the arrivals of this phase in most of the seismic sections. There are no abrupt transitions between upper and middle crustal refractions; instead, a gradual transition between P_g and refractions from the layer below is observed. The P_g phase is observed to offsets of 100–150 km along the southwestern end of the profile with apparent velocities of 5.5–6.0 km s^{-1}. To the northeast, this phase is observed to larger offsets and has higher apparent velocities of 6.0–6.25 km s^{-1}. Refractions from the middle crust and lower crust are correlated as secondary arrivals in the seismic sections ($P_{crustal}$ and $S_{crustal}$), primarily at far offsets where the refractions merge with wide-angle reflections. They are recorded up to 200–300 km offset and are very important for the determination of velocities in the middle crust and lower crust.

The crust is highly reflective and several reflections are correlated. Reflections from the top of the middle crust can be correlated on most of the record sections, and reflections from the top of the lower crust (P_c) are observed throughout the profile. Compared with the southwestern end of the profile, this phase is 2 s later in the central part of the profile and 1 s later in the northeastern part. This phase shows varying amplitudes along the profile and is followed by a long coda of lower crustal reflectivity (Jensen et al., 2002).

The crossover distance between crustal and mantle refractions (P_n) varies considerably along the profile, demonstrating that significant variations in crustal thickness and velocity structure are present. In the southwest, this crossover distance is 110–130 km. In the central and northeastern part of the profile, the crossover distance is ~190 km, and at the northeastern end of the profile, it is 205–230 km.

Reflections from the Moho (P_mP) are observed in almost all the seismic sections. The P_mP phase is delayed by 2 s for shots in the central part of the profile and by 1 s for shots in the northeast compared with shots in the southwest. The critical offset, where the amplitudes are largest, is 80–105 km in the southwest, 130–145 km in the central part of the profile, and 150–165 km to the northeast. The postcritical P_mP phase is commonly observed to offsets of 150 km in the southwest and to 220 km (in the some cases, up to 270 km) in the northeast. In general, the precritical P_mP phase is identified from offsets of 60 km in the southwest and 120 km in the northeast. These differences indicate pronounced structural variations along the profile.

The refraction from the upper mantle (P_n) can be identified as a first arrival in most of the seismic sections. The apparent velocity varies between 8.0 and 8.5 km s^{-1} along the profile, although a much higher apparent velocity (up to more than 9 km s^{-1}) in the central part of the profile indicates an abrupt change in Moho depth. Reflections from the upper mantle are observable in some of the seismic sections and were discussed in a regional sense by Grad et al. (2002a, 2003a).

1.17.4 Examples of 2-D and 3-D Modeling of the Earth's Crust and Lower Lithosphere

Analysis of the seismic wavefields began with tomographic inversion of travel times of refracted (diving) waves observed as first arrivals. This produced very smooth models of the velocity variations in the crust and uppermost mantle. Then, detailed velocity models were derived by ray tracing and synthetic seismogram modeling. The calculations of travel times, ray paths, and synthetic seismograms were made using the ray theory package SEIS83 (Červený and Pšenčík, 1983), enhanced by employing the interactive graphic interfaces

MODEL (Komminaho, 1997) and ZPLOT (Zelt, 1994) with modifications by Środa (1999). The initial velocity model based on the tomographic inversion results was successively altered by trial and error, and travel times were recalculated many times until agreement was obtained between observed and model-derived travel times (within a misfit of the order of 0.1–0.2 s). In the modeling, first arrivals, postcritical waves, reflections, and even multiple reflections were employed.

In addition to matching travel times, synthetic seismograms were calculated to control velocity gradients within the layers and the velocity contrast at the seismic boundaries. The final synthetic seismograms usually show good qualitative agreement with the relative amplitudes of observed refracted and reflected waves.

1.17.4.1 POLONAISE'97 Crustal and Lithospheric Models (Profiles P4, P1, and P3)

In the model of profile P4 derived using forward ray-tracing technique with the SEIS83 program (Figure 6), a large thickness of relatively low-velocity material was also found in the Polish Basin (Grad et al., 2003a). In this basin, velocities of 4.7–5.8 km s^{-1} extend to 18–20 km depth and are underlain by 'basement' with a velocity of ~6.4 km s^{-1}. The model shows variable structure and depth of the basement on both sides of the Polish Basin. The top of the crystalline basement (Precambrian) of the EEC varies from ~8 km in the area adjacent to the Polish Basin at the platform's margin to only ~1 km at the NE end of the profile. The general crystalline basement velocity (6.1–6.2 km s^{-1}) is typical for cratonal areas, but at distances of 610–660 km along the profile, high-velocity (~6.4 km s^{-1}) basement was found. This increase of velocities is very visible and documented on reversed travel time branches of the P_g phase. In the velocity model (Figure 6), the corresponding high-velocity intrusion reaches a depth of ~8 km and could be correlated with the Mazury complex (Mz) and Suwałki anorthosite intrusion (Su), which also correlate with a small positive gravity anomaly. The basement of the Paleozoic platform southwest of the Polish Basin is characterized by velocities of only ~5.8 km s^{-1} and lies at depths of 1–3 km. However, distances of 70–140 km along the model a deeper (1–4 km) boundary where the velocity increases to ~6.15 km s^{-1} is observed. This boundary rises to its minimum depth at distance ~125 km, which corresponds to the Wolsztyn Ridge that is characterized by a positive gravity anomaly. Velocities of 6.2–6.4 km s^{-1} are interpreted to extend to depths of ~26 km. The main evidence for this interpretation is overcritical deep crustal reflections observed up to offsets of 200–250 km with velocities <6.5 km s^{-1}. This observation provides evidence for relatively low velocities in the middle crust and lower crust along the SW end of the profile.

A lowermost crust with velocities ≥7.0 km s^{-1} is interpreted to be present from a distance of ~100 km along the model (Figure 6). This interpretation is documented where overcritical crustal reflections at distance 100–220 km along the profile (offset larger than ~200 km) have significantly higher velocities than the P_g wave closer to the shot point (offset 50–150 km).

In the velocity model of profile P4 (Figure 6), the total thickness of the crust changes from ~30 km beneath the Paleozoic platform (0–200 km) to 35–38 km beneath the Polish Basin (200–300 km) and to 42–50 km beneath the EEC (300–800 km). The primary constraints on the Moho topography are the P_mP and P_n phases, and the most complex Moho topography is observed in the contact zone between the Paleozoic platform and the EEC.

There are also some clear phases that are reflections from mantle discontinuities (Grad et al., 2002a), and phases P^I and P^{II} from discontinuities in the uppermost mantle were

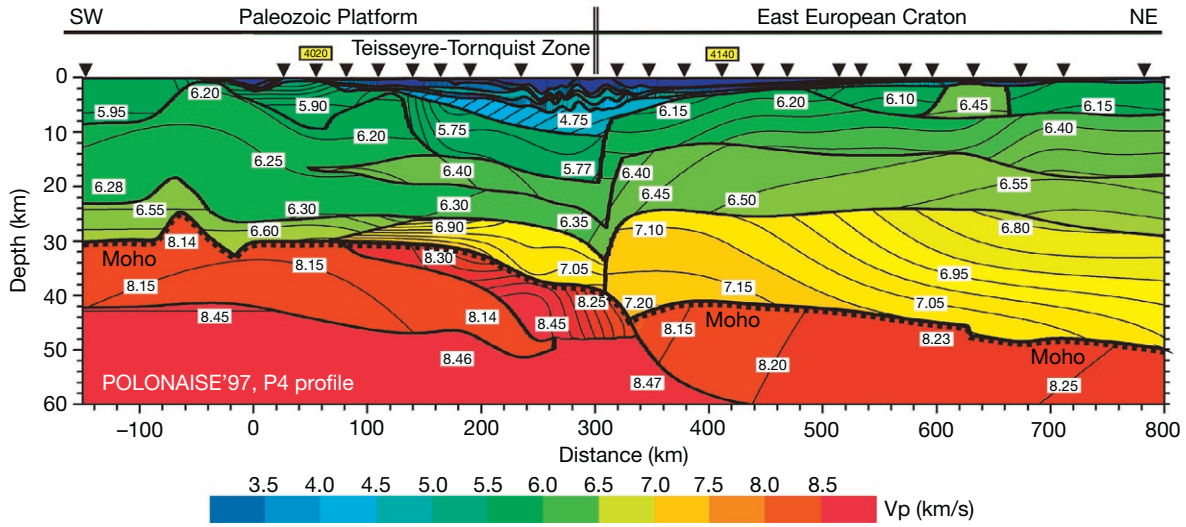

Figure 6 The two-dimensional P-wave velocity model for POLONAISE'97 profile P4 derived by forward ray-tracing modeling using the SEIS83 package (Červený and Pšenčík, 1983). The profile P4 extends across the TESZ almost perpendicularly to the edge of the EEC. The thick solid lines are layer boundaries and the thin lines are isovelocity contours (in km s^{-1}). Triangles show shot points along the profile. Note the thin Paleozoic platform crust (~30 km), thick crust of the EEC (*c.* 45–50 km), and thick sedimentary basin in the TTZ with P-wave velocities lower than 6 km s^{-1} down to ~20 km depth. Vertical exaggeration for the model is ~4.7. Modified from Grad M, Jensen SL, Keller GR, et al. (2003a). Crustal structure of the Trans-European suture zone region along POLONAISE'97 seismic profile P4. *Journal of Geophysical Research* 108: 2541, http://dx.doi.org/10.1029/2003JB002426.

modeled to produce the model in Figure 6. The geometry at the SW end of the model is the result of the top of the dipping body with a velocity of 8.15 km s^{-1}, giving rise to the P^{I} phase from its top and the P^{II} phase from its bottom. The high-amplitude P^{I} and P^{II} phases observed in the record sections and the high apparent velocities of the P_n phase are the basis for this interpretation. The bottom of this layer corresponds in depth with a mantle reflector on profile P1 (Jensen et al., 1999). High velocities (8.3–8.4 km s^{-1}) in the uppermost mantle lithosphere were only found beneath the Polish Basin area. Similar velocities were also found in this area beneath the TTZ (Grad et al., 1999) and P1 (Jensen et al., 1999) profiles. The details of the mantle structure in Figure 6 are nonunique, but high velocities clearly appear to have a tectonic association with the TESZ. The 8.15 km s^{-1} body may represent a continuation of the Variscan lower lithosphere from the southwest. Velocity in the uppermost mantle beneath the EEC increases systematically to the northeast from ~8.15 km s^{-1} at a distance of 350 km on the model to 8.25 km s^{-1} at the northeast end of the model.

A detailed model of seismic velocity variation along POLONAISE'97 profile P1 in northwestern Poland is presented in Figure 7(a). Despite its location behind the Variscan

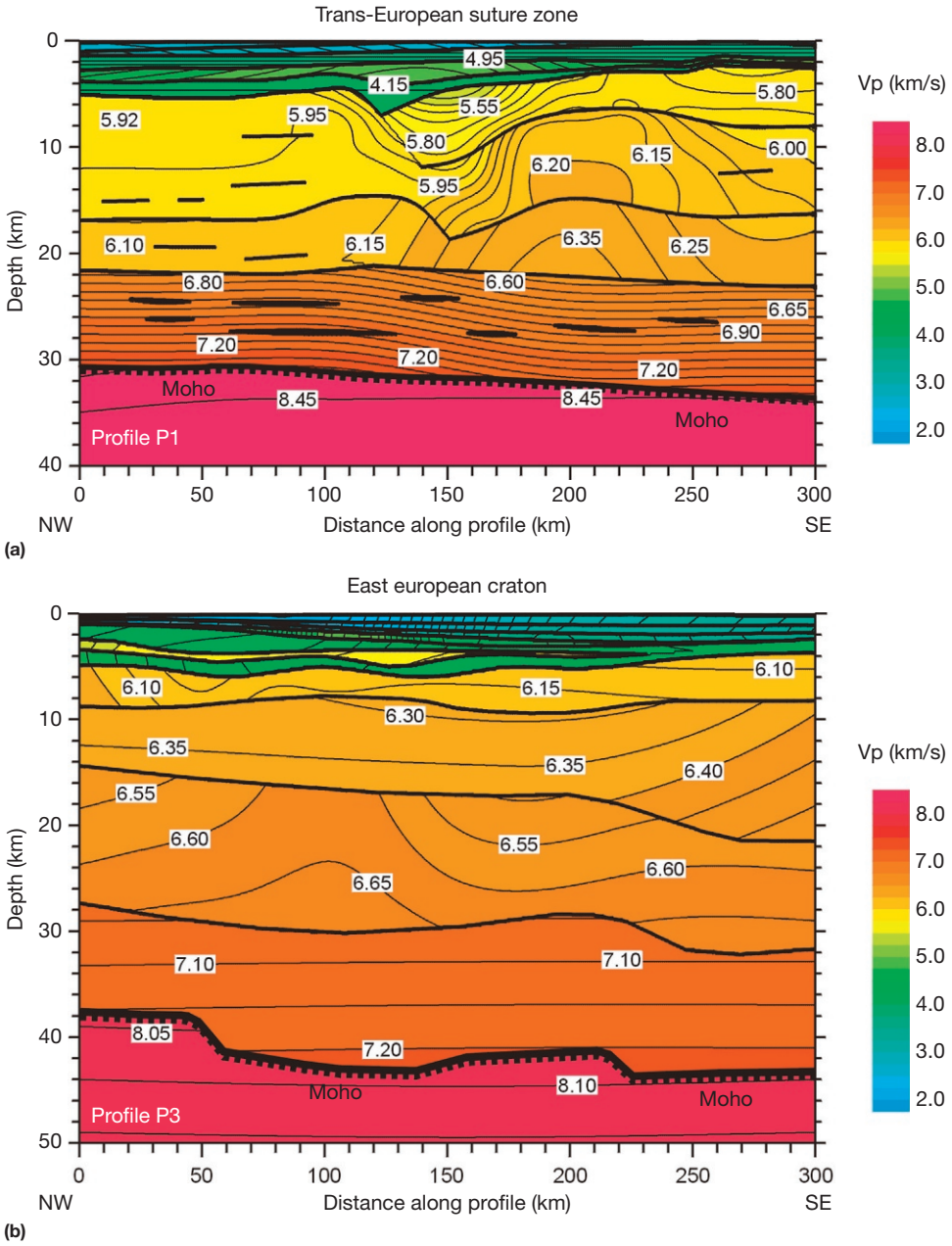

Figure 7 Two-dimensional P-wave velocity model for POLONAISE'97 profile P1 (a) and profile P3 (b) derived by forward ray-tracing modeling using the SEIS83 package (Červený and Pšenčík, 1983). The profiles are located in Figure 2. The thick solid lines are layer boundaries and the thin lines isovelocity contours (in km s^{-1}). Vertical exaggeration for both models is ~4.2. Compiled from Jensen et al. (1999) and Środa and POLONAISE P3 Working Group (1999).

deformation front, the model indicates that the crust below the profile has a Caledonian origin or, alternatively, originates from Baltica and that Variscan deformation was thin skinned in this area. The seismic model shows several new findings from the study area (Jensen et al., 1999).

- Sediment thickness decreases southwestward from 6 to 3 km. There is an indication for tectonic activity during deposition of the Paleozoic sequence.
- The seismic velocities are very low (6.1–6.2 km s^{-1}), down to 20 km depth, indicative of rocks of sedimentary or volcanic origin.
- The lower crust is characterized by a high velocity (6.7–7.5 km s^{-1}), a high vertical velocity gradient, and strong, ringing reflectivity.
- The crust is 30–33 km thick along the profile with a gradual southeastward thickening.
- The P_n velocity of the sub-Moho mantle is high (>8.2 km s^{-1}).

The area south of the Caledonian deformation front (CDF) in Northern Germany and southern Denmark shows similar characteristic features, indicating that the crust between the southeastern North Sea and Poland originates from the same microcontinent (East Avalonia), which was amalgamated to Baltica during the Caledonian orogeny.

A detailed model of seismic velocity variation along POLONAISE'97 profile P3 in the EEC, parallel to the TTZ, is presented in **Figure 7(b)**. The crustal model developed by 2-D ray-tracing forward modeling is characterized by a subhorizontal uniform structure, although the boundaries of several basement provinces are crossed (Środa and POLONAISE P3 Working Group, 1999).

- The sedimentary cover consists of seven layers with a total thickness of 4–6 km. The P-wave velocities range from 2 to 5.7 km s^{-1}.
- The crystalline crust consists of three parts: the upper, middle, and lower crust with P-wave velocities of 6.1–6.4 km s^{-1}, 6.55–6.7 km s^{-1}, and 7.05–7.15 km s^{-1}, respectively.
- The total crustal thickness is 38–44 km and the P_n velocity is 8.05–8.1 km s^{-1}.
- Following the P_n wave, another phase P^I with an apparent velocity of about 8.3 km s^{-1} was interpreted as a weak reflection from a weak discontinuity in the uppermost mantle.
- The V_P/V_S ratio determined for the upper/middle and lower crust was 1.67 and 1.77, respectively. For the sedimentary succession, an average value of 1.80 was assumed. The V_P/V_S ratio for the upper mantle has not been calculated owing to lack of S_n arrivals.

The depth to the Moho along profile P3 ranges from 38 km at the NW end of the profile to 44 km at the SE end. Local changes of depth of the otherwise horizontal Moho, resulting in crustal thickening to the SE, may be associated with tectonic segmentation of the crust, because the depth change occurs close to tectonic unit boundaries. The thickening of the crust in the SE direction is consistent with the trend observed in the EUROBRIDGE profile (EUROBRIDGE Seismic Working Group, 1999). In the upper mantle, a P-wave velocity of 8.05–8.1 km s^{-1} was observed, which is less than that previously found in neighboring areas of the EEC.

POLONAISE'97 produced high-quality data extending to long offsets that resolve velocity discontinuities in the lithospheric mantle. A simplified sketch of the derived 2-D velocity model along the P4 profile is shown in **Figure 8** (Grad et al., 2002a; Wilde-Piórko et al., 2010). In all POLONAISE'97 profiles, the P^I phase indicates a shallow mantle reflector at depths 8–12 km below the Moho. Phases due to deeper features are observed only beneath the longest profile, P4. We found reflectors at depths of about 70, 80, and 90 km in the central part of the TESZ region (180–420 km along profile P4). Complex high and low velocities in the lower lithosphere have been interpreted from other seismic experiments close to the TESZ region as well as within the East European Craton and the Baltic

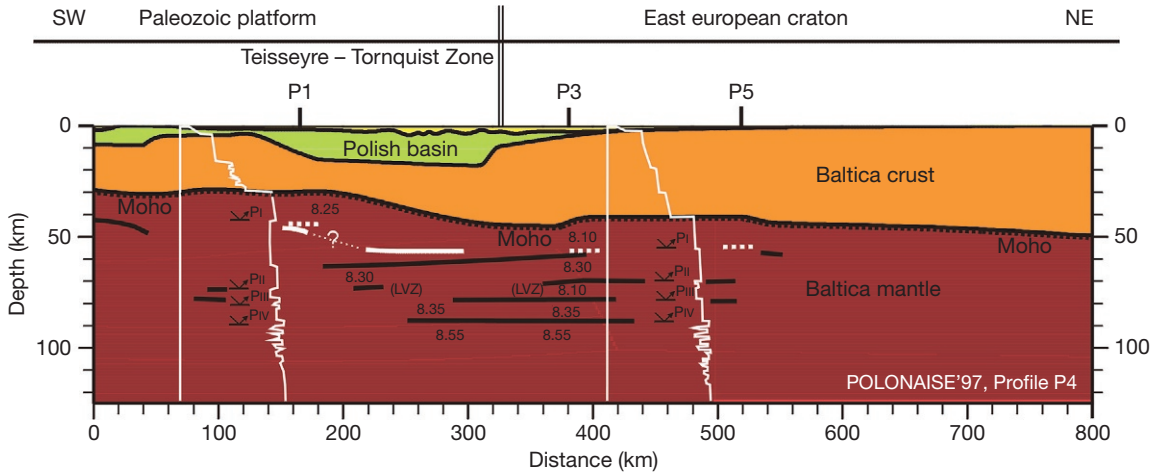

Figure 8 Simplified sketch of lithospheric structure along POLONAISE'97 profile P4 developed by forward ray tracing. Reflectors within the lithospheric mantle beneath profile P4 (thick black lines), the parallel profile P2 (thick white lines), and crossing profiles P1, P3, and P5 (dotted white lines) are marked. Vertical exaggeration for the model is ~1.9. Modified from Grad et al. (2002a).

Shield (Ansorge et al., 1992; BABEL Working Group, 1993; Blundell et al., 1992; Grad, 1989, 1992, 1997; Grad et al., 1986, 1991; Guggisberg and Berthelsen, 1987; Perchuć and Thybo, 1996; Stangl, 1990; Thybo et al., 1994).

A sub-Moho discontinuity with a small P-wave velocity contrast (corresponding to the P^I reflection) was previously detected in the EEC beneath the Baltic Sea by Grad et al. (1991). In the area of the Lithuanian–Belarusian border within the EEC, such a mantle discontinuity was found by the EUROBRIDGE Seismic Working Group (1999) at a depth of about ~65–70 km (Moho depth is ~50 km in this area). The BABEL Working Group (1993) also noted the existence of similar reflected phases but did not model them. From the existing seismic data from the Baltic Shield and the East European Platform, a discontinuity that lies ~10 km beneath the Moho appears to be a general feature of the lower lithosphere. The nature of such a reflector is not understood. One may speculate that the reflector is related to tectonic shearing in the mantle lithosphere. It could also represent a change in mantle composition caused by magmatic processes (i.e., depleted mantle situated just below the Moho that has acted as a source for basaltic magma, while deeper layers are relatively undepleted), or it could represent a change in metamorphic grade of the upper-mantle rocks.

Complex high and low velocities in the lower lithosphere near the margin of the EEC have been interpreted based on the long-offset recordings along the EUGENO-S profile 4 (up to 650 km) and Baltic Sea–Black Sea profile (up to 900 km) (Grad et al., 1986, 1991). Perchuć and Thybo (1996) interpreted a long coda, similar to the coda after the deepest lithospheric reflection, as an indication of a zone of low velocity and strong seismic reflectivity below the depth level of ~100 km under the Baltic Shield. A similar reflective zone beneath the global 8^0 discontinuity at around 100 km depth has been identified globally in all long-range seismic profiles (Thybo and Perchuć, 1997). Based on petrologic and thermal arguments, Thybo and Perchuć (1997) suggested that the reflectivity was caused by pockets of partial melt induced by the lowering of the solidus temperature by small amounts of fluids (Thybo and Perchuć, 1997). The depth to the reflective zone correlates with the heat flow in that it is shallower in 'hot' areas than in 'cold' areas, a feature also observed along the FENNOFLORA seismic long-range profile.

Based on the POLONAISE'97 data, our main finding about the lithospheric mantle is that a series of seismic reflectors extend from the Moho to ~90 km, the deepest interpretable level with the current data set. A seismic reflector is present ~10 km below the Moho throughout the EEC and adjacent areas, independent of the actual depth to the Moho. In general, the reflectivity of the uppermost mantle is stronger beneath the Paleozoic platform and TESZ region than the East European Platform. The deepest interpreted seismic reflector and zone with high reflectivity may mark a change in upper-mantle structure from an upper zone characterized by seismic scatterers of small vertical dimension to a lower zone with vertically larger scatterers, possibly caused by inclusions of partial melt.

1.17.4.2 SUDETES 2003 Crustal Model (Profile S01)

The SUDETES 2003 experiment was the fourth of the series of large seismic refraction and wide-angle reflection experiments performed from 1997 to 2003 in Central Europe, and it covers the gap between the areas of POLONAISE'97, CELEBRATION 2000, and ALP 2002 experiments (Figure 2). The experiment covered mainly the northern part of the Bohemian Massif (including the Eger Rift) and some of the neighboring Polish Basin (TESZ) to the northeast and the Western Carpathians to the southeast (Figure 1). Here, we show a model of the crustal structure beneath profile S01 (Figures 2 and 9). This key profile of the experiment extended southwestward from the margin of the EEC, across the TESZ and Sudetes, and across the Bohemian Massif that contains the active Eger (Ohře) Rift, which is an element of the European Cenozoic Rift System. Good quality seismic data were interpreted using 2-D ray-tracing techniques.

The seismic model shows large variations in the internal structure of the crust (Figure 9), while the Moho topography varies in the relatively narrow depth interval of 28–35 km. Within the Bohemian Massif, a thin sedimentary layer covers the basement characterized by velocities in the range of 5.7–5.8 km s^{-1}. The suspected crystalline basement below the Sudetes Mountains and Fore-Sudetic Monocline (distance 250–450 km along the profile) is characterized by a V_P of ~5.9 km s^{-1}, while below the Polish Basin, V_P is slightly higher, 5.9–6.2 km s^{-1}. The basement velocities observed in the Variscan belt are low compared with those observed for the crystalline basement of the Precambrian EEC (V_P ~ 6.1–6.2 km s^{-1} at depth about 1–5 km). In the area of the Eger Rift, high-velocity bodies (V_P ~ 6.5 km s^{-1}) were recognized. The velocity in the uppermost mantle is about 7.8 km s^{-1} beneath the Saxothuringian and Moldanubian zones and about 7.9 km s^{-1} in the central part of the S01 profile. In the northeastern part of S01 (~400 km to the end of profile), velocities below the Moho are relatively high, ~8.3 km s^{-1}. Additionally, below the Moho, two reflectors were identified in the upper mantle at depths of about 45 and 65 km (not shown).

Along S01, exceptionally clear S_g and S^mS waves were recorded for the area of the Bohemian Massif, where the S-wavefield resembles the P-wavefield. However, even in this case, the phase correlation for corresponding S-wave travel times was difficult. Therefore, in the modeling of S-waves, we used the geometry previously determined from P-wave modeling and by trial and error modeling, fitted S-wave arrivals by varying V_P/V_S for individual layers.

1.17.4.3 CELEBRATION 2000 Crustal Models CEL05 and CEL01

Tomographic and ray-tracing models derived for the structure along profile CEL05 are shown in Figure 10 (Grad et al., 2006) and reveal large variations in the structure of the crust and lithospheric mantle. Figure 10 includes a vertically exaggerated depiction of the topography traversed by the profile. Along most of its length, the profile passes through lowland areas with an average elevation of 200 m. In the Carpathians (200–500 km along profile), elevations range from 400 to 900 m.

In the Pannonian Basin region to the southwest (0–350 km), the crustal structure is relatively simple. However, in the distance interval of ~240–280 km along the profile, a shallow high-velocity body was delineated (V_P ~ 6.4 km s^{-1}). Beneath the upper sedimentary layer and a layer with velocities of ~5.8 km s^{-1}, two almost homogeneous (very small velocity gradient) crustal layers are observed. The velocity increases

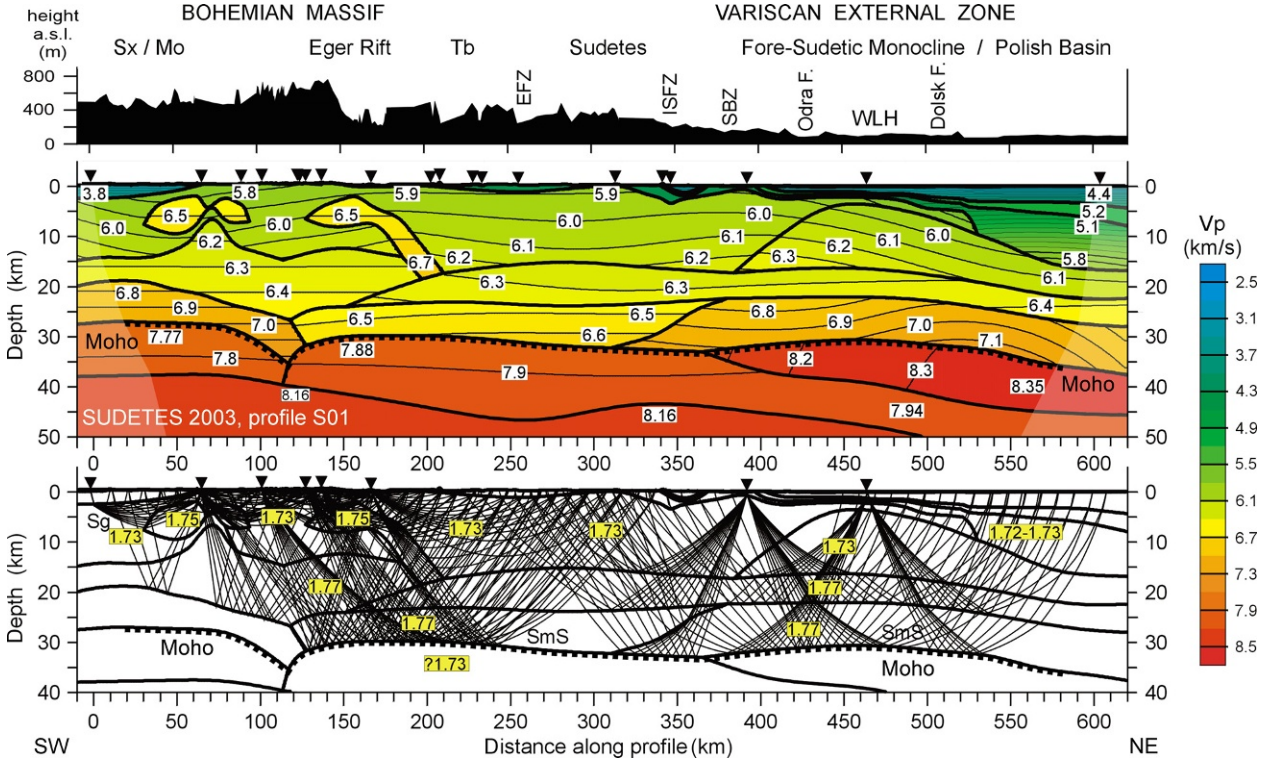

Figure 9 (Top) Topography along the S01 profile. (Middle) Two-dimensional P-wave velocity model for SUDETES 2003 profile S01 derived by forward ray-tracing modeling using the SEIS83 package (Červený and Pšenčík, 1983). For position of the profile, see **Figure 2**. The thick solid lines are layer boundaries and thin lines are isovelocity contours (in km s^{-1}). Triangles refer to shot points. (Bottom) Crustal model with V_P/V_S ratio (in yellow boxes) and with S-wave rays for shot points used in V_P/V_S ratio modeling. Vertical exaggeration is 3:1 for the lithospheric models and ~50:1 for topography. Compiled from Grad et al. (2008).

from ~6.1 to 6.2 km s^{-1} in the depth interval 5–18 km in the first layer and from 6.3 to 6.5–6.6 km s^{-1} to a depth of ~25 km in the second one. The Moho here lies at a depth of only 24–25 km, and the uppermost mantle beneath it is characterized by velocities of 7.95–8.0 km s^{-1}.

Along this profile, the most complicated structure is observed at distances of 350–700 km in the transition from the Pannonian Basin to the EEC. This transition includes the Carpathians and their foredeep, the MM, the rifted margin of the EEC, and the Lublin Trough. This is an area of complex topography, complicated structure in the sedimentary cover (where rocks with velocities <5.5 km s^{-1} reach depths of ~20 km), complex structure within the crystalline crust, and deep Moho (~50 km). In the distance interval 370–400 km, the Pieniny Klippen Belt (PKB), which represents the structural boundary between the Inner and Outer Carpathian units (e.g., Kováč et al., 1993), is represented by a southwest-dipping slab of low-velocity sediments. This slab is a few kilometers thick and can be traced down to ~10 km. The Carpathians are associated with a two-layer crystalline crust with velocities of 5.9–6.2 km s^{-1} and 6.5–6.8 km s^{-1}, respectively; while beneath the TESZ and EEC margin further to the northeast, a three-layer crust is present. In the distance interval 600–670 km along the profile, a dome of relatively high velocities (~6.4 km s^{-1}) protrudes into the upper crust and may represent an intrusion. In the same area, an uplift of the lower crust is also observed. The maximum crustal thickness along the profile (52 km) is observed in the area of the crossing point with profile CEL03 (at distance 600–650 km), where a similar velocity distribution in the crust was also found (Janik et al., 2005).

The EEC occupies the northeast portion of the profile (700–1420 km), and the cratonic crustal structure is similar (thin sedimentary cover and three distinct layers) to that found in other portions of western Baltica (EUROBRIDGE Seismic Working Group, 1999; EUROBRIDGE'95 Seismic Working Group, 2001; Grad and Luosto, 1987, 1994; Grad and Tripolsky, 1995). The crustal thickness varies from 42 to 48 km along this ~700 km long cratonic part of the profile, and velocities in the uppermost mantle vary only slightly: ~8.20 km s^{-1} in the southwest and slightly higher to the northeast. The small change in upper-mantle velocity occurs at ~1050 km along the profile and correlates with small but consistent changes in crustal structure (Grad et al., 2006).

Along the profile, many shot points produced clear arrivals that were reflected in the lower lithospheric mantle (P^I and P^{II} phases), and these phases were modeled by Grad et al. (2006) as shown in **Figure 10**. In the Pannonian–Carpathian area, the P^I wave was usually much stronger than the P_n wave in the same distance range. The corresponding reflector in the mantle lithosphere is subparallel to the Moho but is ~15 km deeper. Thus, it dips northward from the Pannonian Basin under the Carpathians (**Figure 10**). A strong south-dipping reflector was found under the TESZ at a depth of 60–70 km and implies that there is a large velocity contrast between the Pannonian and

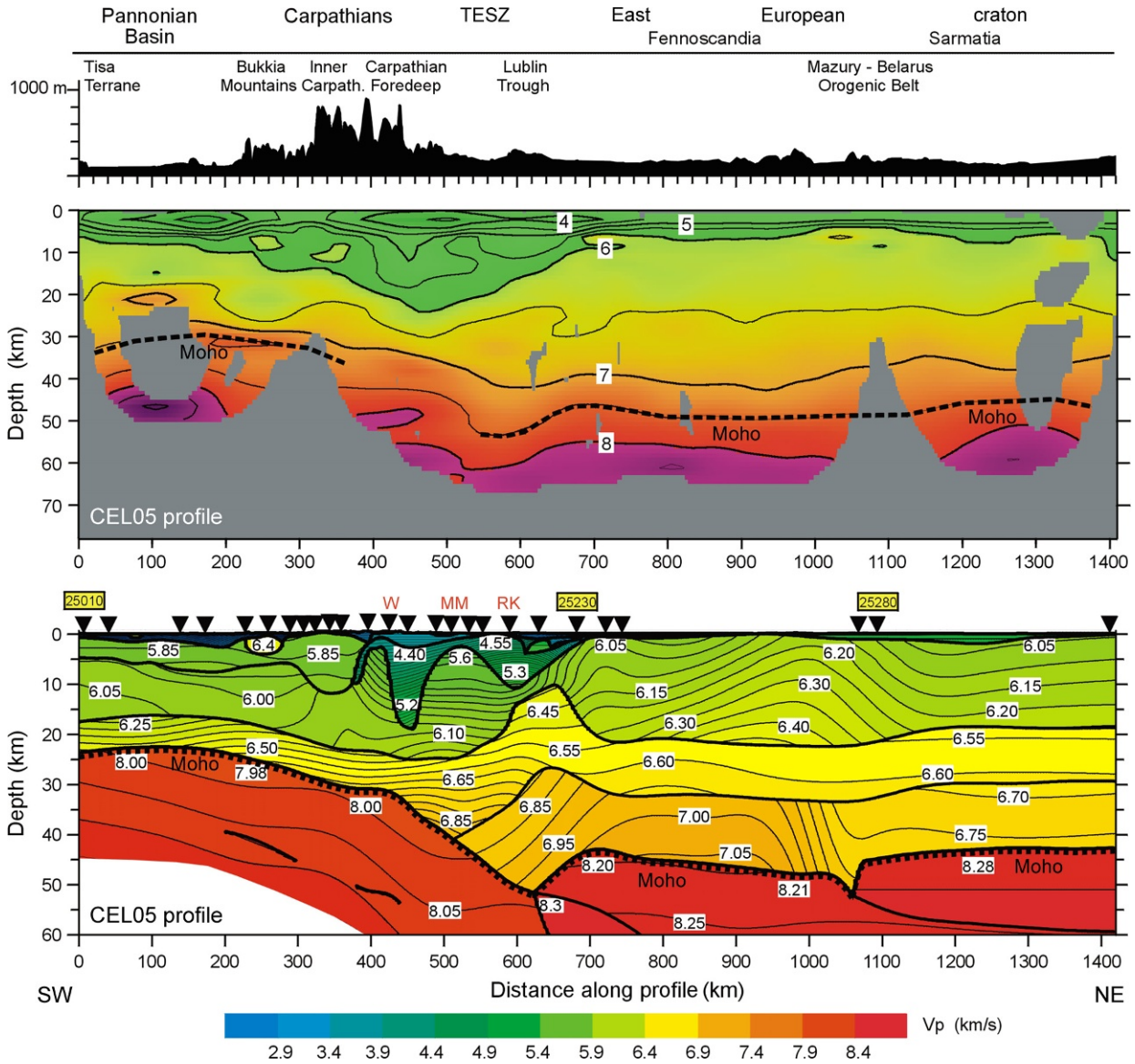

Figure 10 Two-dimensional P-wave velocity model for CELEBRATION 2000 profile CEL05 derived by tomographic inversion (Zelt and Smith, 1992) and forward ray-tracing modeling using the SEIS83 package (Červený and Pšenčík, 1983). The thick solid lines are layer boundaries and thin lines are isovelocity contours in km s^{-1}; triangles refer to shot points. In the upper part, topography along profile is shown. Note the very thin Pannonian crust (~25 km), thick crust of the EEC (~45–50 km), and the thickest crust in the investigated area in the TESZ (~52 km depth at distance 620 km). In the Carpathians and TESZ, sedimentary basins with P-wave velocities lower than 6 km s^{-1} down to 10–20 km depth were found. MM, Małopolska Massif (at 450–550 km of profile); RK, Radom–Kraśnik uplift (at 580–600 km of profile); W, Wysowa (at ~420 km of profile). Vertical exaggeration for ray tracing model is ~6.8. Modified from Grad M, Guterch A, Keller GR, et al. (2006) Lithospheric structure beneath trans-Carpathian transect from Precambrian platform to Pannonian basin: CELEBRATION 2000 seismic profile CEL05. *Journal of Geophysical Research* 111: B03301, http://dx.doi.org/10.1029/2005JB003647.

Baltica mantles. In the EEC area, several reflectors were delineated in the lithospheric mantle.

The tomographic inversion and forward modeling results along profile CEL01 are presented in Figure 11 (Środa et al., 2006). Along CEL01, the EEC is covered by a thin (~2 km) undeformed layer of sediments, except in the Lublin Trough, where sedimentary rocks with $V_P = 4.0–5.5$ km s^{-1} reach a thickness of approximately 10 km. As in nearby areas, the crystalline crust of the EEC consists of three horizontally homogeneous layers, with total thickness of 43–45 km. The EEC upper mantle is characterized by V_P of ~8.05 km s^{-1}. Beneath the Lublin Trough, unusually high velocities of 7.1 km s^{-1} are observed in the upper crust and middle crust, starting at a depth of ~16 km. This anomaly seems to be a continuation of a high-velocity/high-density intrusion located further southwest, which was detected by previous seismic studies in this region (Guterch et al., 1986; Malinowski et al., 2005).

Beyond the EEC margin, beneath the MM and the Łysogóry unit, the dominant feature of the crust is a 20 km troughlike feature (Figure 11). This feature is filled with material whose

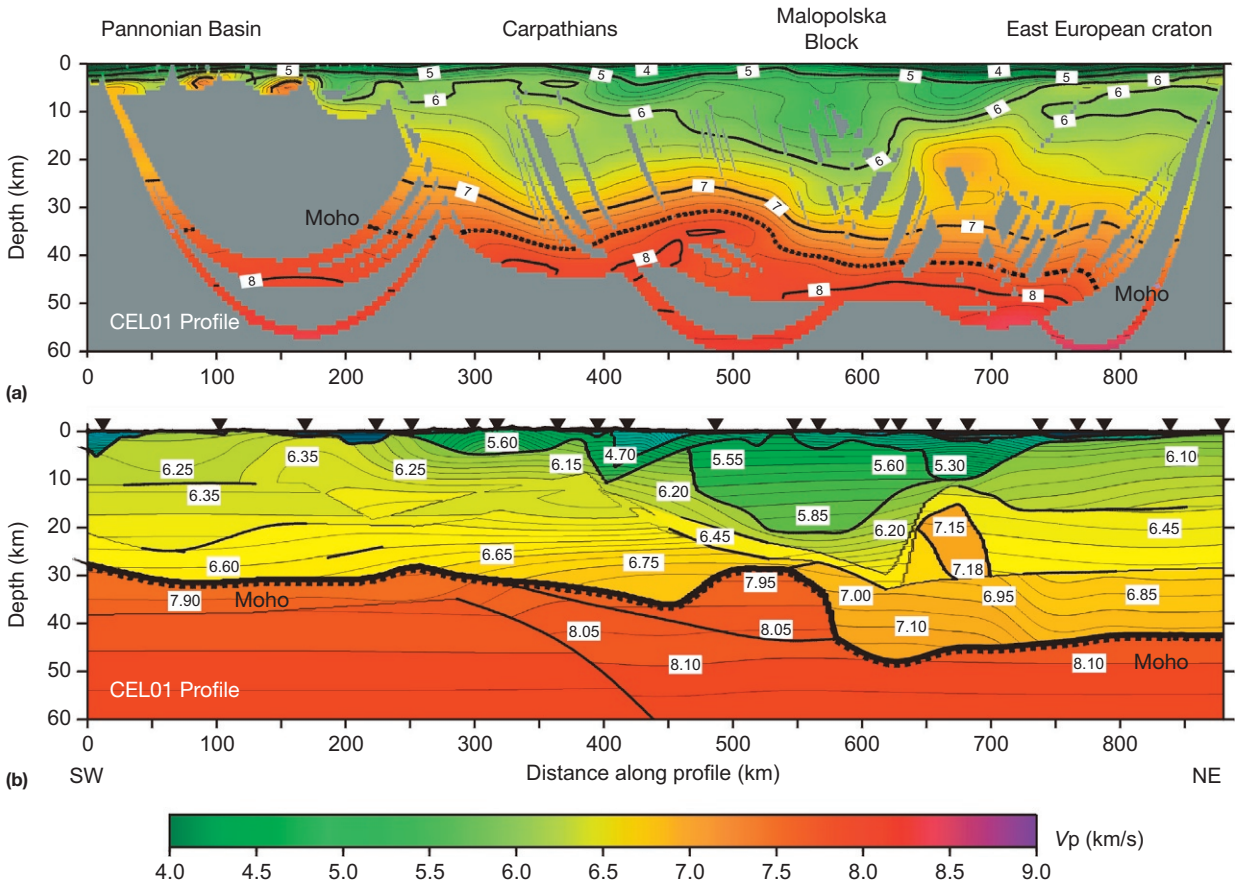

Figure 11 Two-dimensional P-wave velocity models for CELEBRATION 2000 profile CEL01 derived by (a) tomographic inversion (Hole, 1992) and (b) forward ray-tracing modeling using the SEIS83 package (Červený and Pšenčík, 1983). The profile extends from the EEC, across the Trans-European Suture Zone and Carpathians, to the Pannonian Basin. The thick solid lines are layer boundaries and thin lines are isovelocity contours in km s^{-1}; triangles refer to shot points. Note the thin Pannonian crust (~25 km) and the thick crust of the EEC (~45 km). In the Carpathians and TESZ, sedimentary basins with P-wave velocities lower than 6 km s^{-1} extending down to 10–20 km depth were delineated. Vertical exaggeration for both models is ~3.7. Modified from Środa P, Czuba W, Grad M, et al. (2006) Crustal and upper mantle structure of the Western Carpathians from CELEBRATION 2000 profiles CEL01 and CEL04: Seismic models and geological implications. *Geophysical Journal International* 167(2): 737–760, http://dx.doi.org/10.1111/j.1365-246X.2006.03104.x.

velocity is relatively low (V_P = 5.5–5.9 km s^{-1}) and a relatively high vertical gradient of V_P. In the area of the Holy Cross Mountains, Paleozoic rocks with V_P = 5.0–5.3 km s^{-1} are exposed at the surface and have been the target of many geologic studies. Beneath this region, substantial variations of the crustal thickness and the lower crust occur. The crustal thickness of ~44 km does not change from the EEC to approximately the location of the Holy Cross fault, where it rapidly thins to ~32 km to the southwest (Figure 11).

Further to the southwest, a highly asymmetric depression filled by two low-velocity units (V_P = 4.5 and 5.6 km s^{-1}) forms the upper crust in the area of the Outer Carpathians and the Carpathian Foredeep. This low-velocity material forms a south-dipping layer that is approximately bounded on the south by the PKB, where it reaches its maximum thickness of ~10 km. In the ALCAPA (Eastern Alps–Carpathians–Pannonian) unit, the uppermost crust (sedimentary rocks and volcanics) of the Inner Carpathians is a 3–5 km thick layer with V_P values of 5.3–5.6 km s^{-1}. These strata are underlain by the crystalline basement that is characterized by a V_P of 6.1 km s^{-1}. The information about deeper structures of the Inner Carpathian crust is relatively poor due to low signal-to-noise ratio in this area and scarce reflected phases; therefore, no V_P anomalies are discernible. In the Pannonian Basin area, the Danube and Zala Basins show up as areas of low velocities (~3 km s^{-1}) that extend to depths of 3–5 km (Figure 11). Between them, the uppermost crust with V_P of 6.2–6.3 km overlies a layer with lower velocities (5.8–6.0 km s^{-1}) forming a velocity inversion. The middle crust and lower crust of the Pannonian Basin are characterized by V_P values of 6.3 and 6.55 km s^{-1}, respectively. The Moho discontinuity under the Carpathians was found at depths of 30–39 km, with maximum crustal thickness approximately beneath the PKB. The Moho beneath the Pannonian Basin System is relatively flat with a depth of 27–30 km. The V_P of the upper mantle is lowest in the Pannonian Basin and Inner Carpathians area (7.9 km s^{-1}), while further north, beneath the Outer Carpathians, it is higher (8.05–8.1 km s^{-1}). In the upper mantle beneath the Inner and Outer Carpathians, a north-dipping reflector with high impedance contrast was found. It is based on the interpretation of the

strong P^I reflected phase, observed for several shot points; therefore, it is a well-defined structure. To the south, its depth is 45 km, while in the north, it reaches 70 km. This north-dipping mantle discontinuity may represent a shear zone related to collision between the ALCAPA unit and the European plate and possibly ongoing convergence between these units (Środa et al., 2006).

1.17.4.4 ALP 2002 Crustal Models Alp01 and Alp02

The crustal models Alp01 and Alp02 (Brückl et al., 2007) constitute representative seismic cross sections through the Eastern Alps and the adjoining tectonic units to the north, south, and southeast. The P-wavefield on Alp01 and Alp02 record sections has a high signal-to-noise ratio in the Bohemian Massif and the Pannonian Basin. Clear arrivals of refracted and reflected waves from the crystalline crust and the upper mantle are typically observed up to offsets of 200–250 km and for some shots even to over 350 km. In the Alpine area, data quality is variable, the wavefield is complex, and phase correlations are sometimes not as clear as to the north or southeast. In addition to the typical phase identification and travel time picking of phases on record sections (i.e., first-arrival tomography and interactive modeling by ray tracing) stacking of P_g, P_mP, P_n, S_g, and S_mS phases was also applied to take advantage of the 3-D character of the CELEBRATION 2000 and ALP 2002 experiments and to enhance the signal-to-noise ratio (Behm, 2009; Behm et al., 2007). Seismic models derived by the application of these techniques are included in the tectonic interpretation presented in Section 1.17.5.3. In the following discussion, we concentrate on the crustal models for the Alp01 and Alp02 profiles derived by interactive modeling by ray tracing (Figure 12(a) and 12(b)).

To the north (profile distance 0–230 km), Alp01 crosses the Bohemian Massif (Figure 12(a)), where crystalline rocks are exposed at the surface or lie under a thin sedimentary cover. Basement velocities reach 5.6–5.8 km s^{-1} at less than 1 km depth. High-velocity gradients in the uppermost crust followed by low gradients in the middle crust are a characteristic feature of most of the Bohemian Massif. However, in the middle crust (10–19 km) of the Saxothuringian unit (distance interval ~20–80 km), a body with relatively high velocity was delineated (V_P ~6.5–6.6 km s^{-1}). In the Molasse basin, low-velocity (2.5–4.5 km s^{-1}) sediments extend down to about 5 km depth. Structural data gained within the scope of hydrocarbon exploration (Brix and Schultz, 1993) constrain the model in this area. Under the Molasse basin, the velocity structure of the crystalline crust is similar to that of the Bohemian Massif in the north and characterized by relatively low velocities of 6.0–6.5 km s^{-1} down to the Moho (30–38 km).

Beneath the Bohemian Massif and the Molasse basin, strong midcrustal reflections from a depth of 20–30 km were modeled by thin (<1 km) high-velocity 'floating reflectors' with a velocity contrast of about 0.4 km s^{-1}. The physical nature of the 'floating reflectors' is not clear because their polarity cannot be detected unequivocally. The Moho was modeled as the base of a laminated transition zone with a thickness of a few kilometers in the lowermost crust. This transition zone was introduced to correctly model the relatively low P_mP amplitudes. A velocity jump from 6.4–6.5 km s^{-1} in the lower crust to about 8.1 km s^{-1} would produce P_mP amplitudes that were too high.

The complex structure of the upper crust between the North Alpine thrust fault (NAT – distance 300 km) and the Penninic Tauern window (distance ~400 km) (Figure 12(a)) is related to the accretion wedge and nappe stack of the East Alpine orogeny. A priori information from geologic cross sections (Bleibinhaus and Gebrande, 2006; Lüschen et al., 2006) has been included in the structural model. South of the Tauern window (distance interval 400–480 km), the upper crust shows little lateral variation with velocities of 5.9 km s^{-1} near surface to 6.2 km at 15 km depth. The southward dip of the boundaries to the middle crust and lower crust continues from the Bohemian Massif at 200 km along the profile to approximately the Periadriatic line (PAL), the boundary to the Southern Alps at profile distance 440 km. However, no structural elements in the crust can be correlated with the PAL. Beneath the Eastern Alps, the Moho dips more steeply to the south than in the north and reaches a maximum depth of 47 km under the PAL. Lower crustal velocities increase to 6.5 km s^{-1} in this area.

At the PAL, the Moho depth decreases from 47 to 42 km. The Moho is again well resolved by P_mP and P_n arrivals, decreasing slightly from 42 km to 40 km toward the south. A midcrustal reflector south of the PAL at ~32 km depth is not as pronounced as comparable structures in the northern part of the profile. The velocity model of the upper crust changes abruptly at the transition to the Dinarides and the Adriatic foreland (distance ~480 km, Figure 12(a)). High basement velocities between 6.2 and 6.4 km s^{-1} extending down to 6 km depth are underlain by a low-velocity zone (LVZ) with velocities <6.2 km s^{-1} that extend down to ~17 km. Lower crustal velocities range from ~6.4 to 6.5 km s^{-1}. The dip of the velocity boundaries and contours is predominantly zero. A reduction in P_mP phase arrival times of >2 s at critical distances indicates a shallower Moho depth (~28 km) at the southern termination of Alp01. The velocity in the uppermost mantle determined from P_n travel times is 8.15–8.25 km s^{-1} below the Bohemian Massif, the Molasse basin, the Eastern Alps and Southern Alps, and the External Dinarides. The velocity in the shallow mantle at the southern end of Alp01 (8.1 km s^{-1}) follows only from amplitude modeling of P_mP and should not be compared with the other values. A lower lithospheric reflector is well resolved between profile distances of 300–440 km. It lies ~25 km below the Moho and parallels the southward dipping Moho in this part of the profile. It is below the depth range of Figure 12(a).

The crustal structure along the Alp02 profile (Figure 12(b)) reflects two completely different tectonic styles: collision within the Eastern Alps in the west and extension to the east in the Pannonian Basin (Internal Dinarides and Tisza unit). These two realms are separated by a transition zone below the Southern Alps in the distance range of 220–340 km. Between 100 and 300 km, Alp02 approximately follows the PAL (Figure 1).

The sedimentary layers in the narrow valleys and small basins of the Eastern Alps are not resolved by the ALP 2002 data. Individual depressions in the Pannonian Basin (e.g., Sava Depression) along Alp02 are 1–3 km deep according to the data from hydrocarbon exploration efforts (Saftić et al., 2003). The uppermost basement along the whole profile is

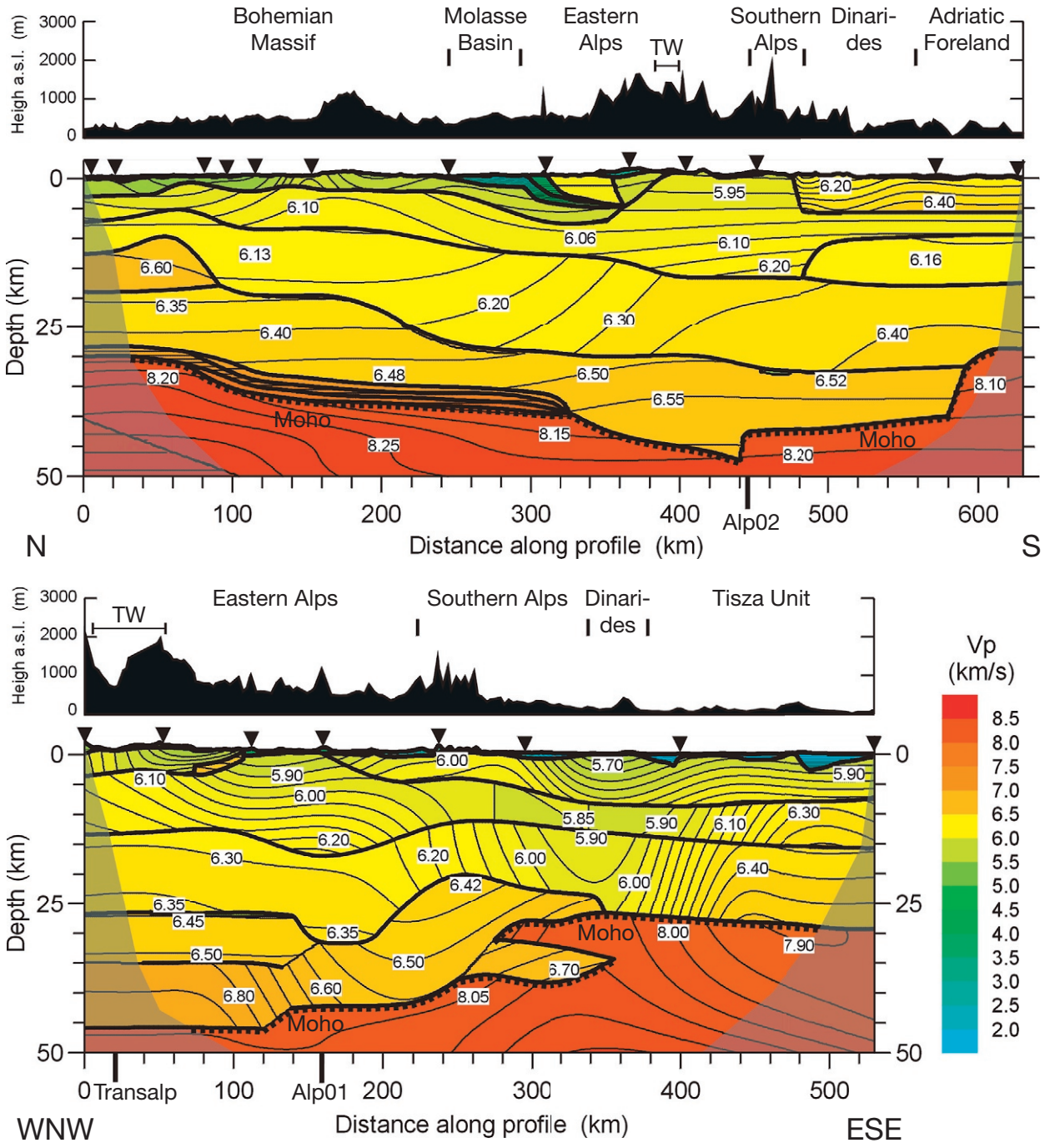

Figure 12 Two-dimensional P-wave velocity models for the ALP 2002 profiles Alp01 and Alp02 derived by forward ray-tracing modeling using the SEIS83 package (Červený and Pšenčík, 1983). The thick solid lines are layer boundaries and thin lines are isovelocity contours in km s^{-1}; triangles refer to shot points. The Alp01 profile extends from the Bohemian Massif in the north, over the Molasse basin, the East Alpine units, and the Tauern window (TW), across the Periadriatic line (PAL), to the Southern Alps, the Dinarides, and the Adriatic foreland in the south. Note the jump from the European Moho to the Adriatic Moho below the PAL. The Alp02 profile extends from the TW in the northwest over the Eastern and Southern Alps to the Dinarides and the Tisza unit, which represents the Pannonian domain. Note the significant Moho jump with an interpreted crocodile structure at the transition from the Alpine to the Pannonian region. Vertical exaggeration for both models is ~3.7. Modified from Brückl E, Bleibinhaus F, Gosar A, et al. (2007) Crustal structure due to collisional and escape tectonics in the Eastern Alps region based on profiles Alp01 and Alp02 from the ALP2002 seismic experiment. *Journal of Geophysical Research* 112: B06308, http://dx.doi.org/10.1029/2006JB004687.

characterized by velocities of about 5.7–5.9 km s^{-1}, with the exception of a west-dipping thin slab between 80 and 110 km profile distance. This slab has a high velocity (~6.6 km s^{-1}) and extends down to about 3 km depth. Although the thickness of this slab is somewhat ambiguous, its high velocity and western dip are well constrained by reversed first-arrival observations from the neighboring two shot points. All across the model in the depth range of 10–30 km, velocities range from 5.8 to 6.5 km s^{-1}. The lowest velocities (distance 300–400 km) coincide with the transition from the collisional regime to the extensional regime in the area of the Internal Dinarides. The relatively high velocities at mid- and lower crustal levels characterize the Tisza unit. In the Eastern Alps, strong reflections from a depth of about 26 km to 35 km depth were modeled as 'floating reflectors' with velocity contrasts of 0.3–0.4 km s^{-1}. Lower crustal velocities in the Eastern Alps range from 6.45 to 6.85 km s^{-1}, slightly higher than beneath the N–S-oriented Alp01 and TRANSALP profiles (Bleibinhaus and Gebrande, 2006) in the same area. This result may indicate anisotropy in the lower crust.

From the west end of Alp02 to a distance of about 120 km, fragmentary P_mP phases suggest that the Moho is at a depth of ~46 km in agreement with the TRANSALP profile (Bleibinhaus and Gebrande, 2006; Lüschen et al., 2006). The Moho rises to a depth of 43 km near the intersection with Alp01 and rises again at 220 km profile distance. The Moho depth decreases abruptly to 27–29 km below the transition from the Southern Alps to the Pannonian Basin. A 'crocodile-like' structure with a velocity inversion was introduced in order to model amplitudes of P_n phases, which fade significantly from the Pannonian domain to the west. The shallow Moho is well constrained by P_mP and P_n phases and persists to the east end of Alp02. Velocities of the uppermost mantle are constrained by P_n phases from the intersection with Alp01 (8.05 km s^{-1}) to the east end of the Alp02 profile (7.9 km s^{-1}).

The velocity structures of Alp01 and Alp02 agree well in the area of the Eastern Alps. Differences concern only the structure of the nappe stack and the velocities of the lowermost crust. However, the velocity structures of Alp01 and Alp02 in the area of the Southern Alps and Dinarides differ significantly because the tectonic regimes are so different: collision (Alp01) and escape or extrusion tectonics (Alp02).

1.17.4.5 Examples of 3-D Tomographic Modeling

The volume of data collected in all POLONAISE'97, CELEBRATION 2000, ALP 2002, and SUDETES 2003 is huge, and it has been a challenge just to analyze the data thoroughly in profile form. However, our ultimate goal is full 3-D analysis such as the one undertaken by Środa et al. (2002) for the POLONAISE'97 data. As a smaller-scale example, here, we show some results from the study of the P5 profile region of POLONAISE'97 (**Figures 13** and **14**; Czuba et al., 2002). The geometry of recordings in the area of the P5 profile and examples of record sections are shown in **Figure 13** (only ~15% of ray paths are shown). The tomographic inversion package of Hole (1992) uses an efficient method of determining the seismic velocity distribution in a 3-D medium using first arrivals only. The velocity model is defined via a rectangular grid with equidistant nodes. The travel times are calculated using the finite difference algorithm of Vidale (1990) and adapted for media with high-velocity contrasts by Hole (1992). The ray paths are traced from the receiver back to the source along the maximum travel time gradient curves. The method of calculating slowness perturbations along the ray is described in detail by Hole (1992). This procedure is iteratively repeated until a model satisfying travel time data at a satisfactory level is obtained (0.1–0.2 s).

For the tomographic modeling of the entire POLONAISE'97 data set, 10 950 picks of first arrivals were used. The P-wave velocity of the model was defined using a distance between nodes (cell size) of 2 km. This resulted in a model whose dimensions (X, Y, Z) were $928 \times 368 \times 68$ km^3 or $464 \times 184 \times 34$ cells that covered the entire area of the POLONAISE'97 experiment. The total number of cells in the model was 2 902 784. Here, we will show results for the region of the P5 profile, which extends from 550 to 700 km in the X-direction, from 50 to 250 km in the Y-direction, and to a depth of 68 km (Z).

Only picks from offsets of less than 40 km were employed in the first step of computation. In the subsequent steps, this distance was increased in order to gradually enlarge the maximum depth of ray penetration. This approach allows the shallow layers to be constrained first before modeling the deeper ones. In each step, several iterations were nested with decreasing size of the smoothing area (Hole, 1992). In this way, the resolution of the algorithm was gradually increased. In each loop, several iterations were calculated.

Examples of results of the 3-D tomographic inversions in the area of the profile P5 (Czuba et al., 2002) are shown in **Figure 14**. Results for the entire POLONAISE'97 area along with resolution tests can be found in Środa et al. (2002). A specific feature that emerged in the analysis of the P5 area was a high-velocity body discovered in the 2-D modeling. Further definition of this feature was one goal of the 3-D modeling, and the shape of this shallow body is clearly seen in the vertical cross sections (Y, Z) and horizontal slices (X, Y) in **Figure 14**. A deeper high-velocity body was detected in the distance range of 80–120 km and at a depth >10 km. This body spatially corresponds to the Biebrza complex or the Pisz intrusion (Pi; see basement geology map in **Figure 14**). The deeper structure could only be resolved with the 3-D data and shows a crust that thickens from about 42 to 45 km southeastward.

1.17.5 Geotectonic Models of the Transition from the EEC to the Eastern Alps, Carpathians, and Pannonian Basin

Although data analysis and interpretation of the results of the POLONAISE'97, CELEBRATION 2000, ALP 2002, and SUDETES 2003 will continue, the findings to date have shed considerable light on efforts to construct structural and geotectonic models of the region. Many new results were compiled to produce Moho maps of Central Europe (Jensen et al., 2002) and the first digital map of the whole European plate (Grad et al., 2009a). Some of the results of the Central Europe experiments are discussed later.

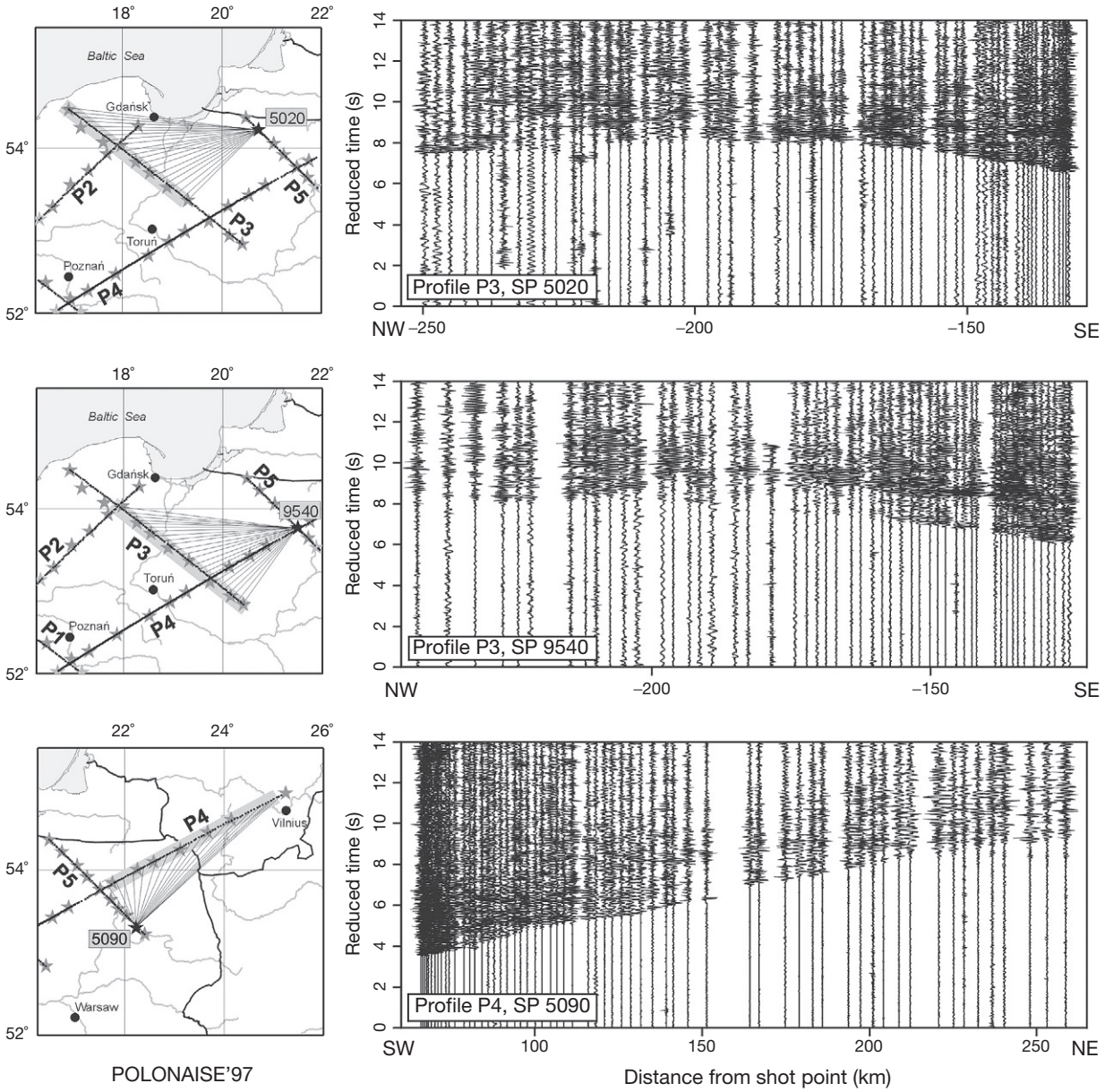

Figure 13 Examples of seismic record sections recorded in 3-D geometry during the POLONAISE'97 experiment in NE Poland and Lithuania.

1.17.5.1 POLONAISE'97 Area

The area of the POLONAISE'97 experiment represented here by P4, P1, and P3 profiles (Figure 2) and crustal/lithospheric models in Figures 6–8 has experienced several major tectonic events including the following: (1) assembly of terranes during the Precambrian to form the cratonal block that included Baltica; (2) rifting during the breakup of Rodinia/Pannotia to form the southwest margin of Baltica (EEC) in the Neoproterozoic; (3) collision between Baltica, the microcontinent eastern Avalonia, remnant ocean crust, and other terranes causing accretion in the Ordovician and early Silurian time; (4) further deformation and terrane accretion during the Variscan orogeny in the late Paleozoic; (5) extension and magmatism in the Permian and Triassic time; and (6) tectonic inversion during the Alpine orogeny in the Late Cretaceous (Figure 1). The results of POLONAISE'97 have shed considerable light on the structure and tectonic evolution of the TESZ region. However, there remain several possible explanations about how these tectonic events are reflected in the observed crustal velocity structure.

At the margin of Baltica (EEC), the upper crustal structure is clearly discontinuous because of the ~20 km deep basin present (Figures 6 and 8). It seems clear that a major consideration in developing geotectonic models for the TESZ in the region of profile P4 is whether the deep crustal layers are continuous or discontinuous beneath the deep basin. The velocities of the middle crust and lower crust do not change as significantly along the model as in other areas to the northwest where the European Geotraverse crosses Germany and the

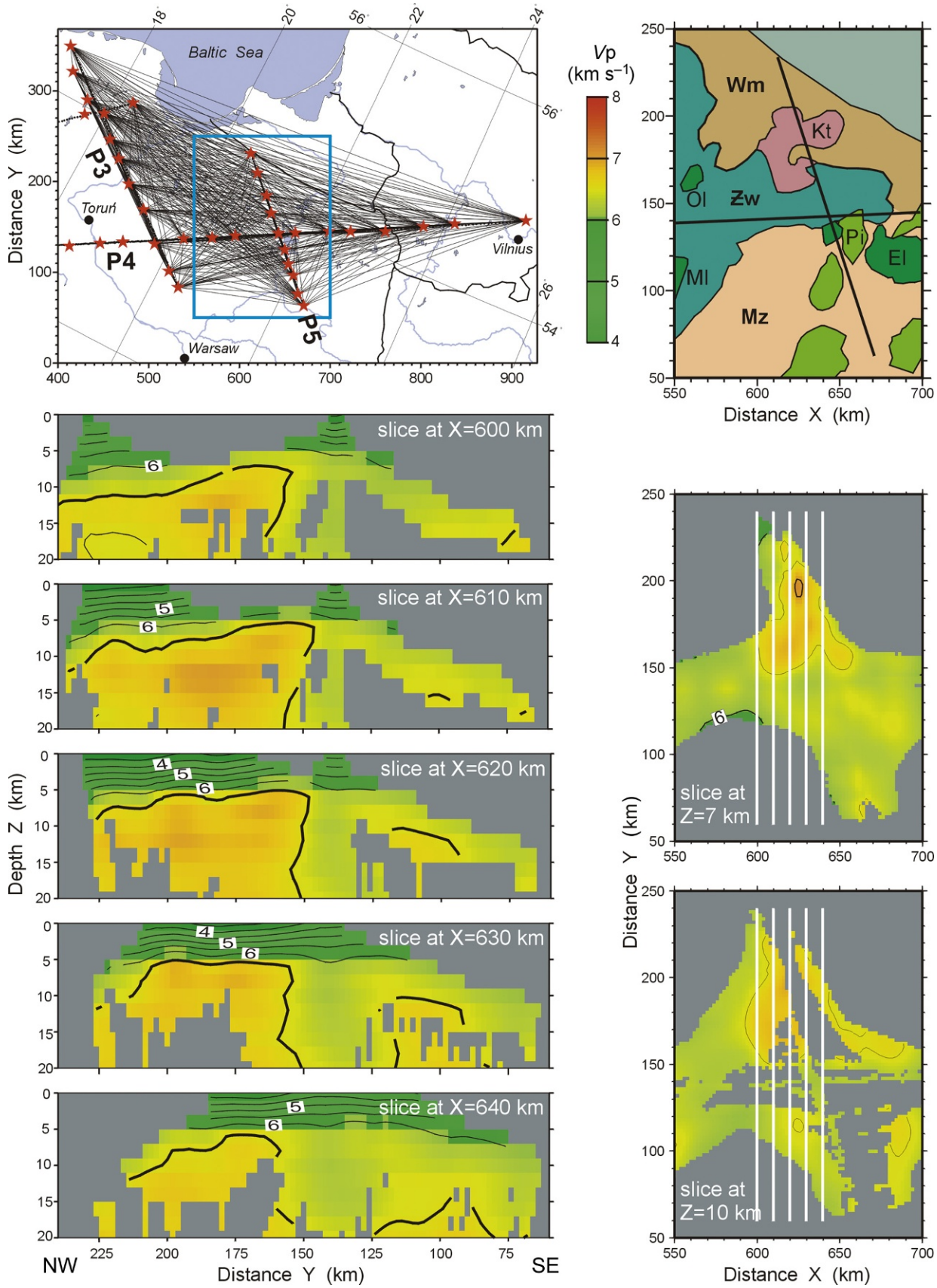

Figure 14 Results of 3-D investigations in NE Poland in the area of POLONAISE'97 profile P5 (Czuba et al., 2002). The location map shows the area of investigation as a subset of the 3-D model by Środa et al. (2002); geographic coordinates are shown on the top and right. Lines show schematic ray paths connecting shot points and recording stations, but only ~15% of the ray paths used in inversion are shown. The blue rectangle marks the area of the map of the EEC crystalline basement and area of the horizontal slices for the depths 7 and 10 km. Vertical cross sections through the model for $X = 600$, 610, 620, 630, and 640 km are also shown, and in them, the thick lines are 6.5 km s^{-1} velocity isolines. Abbreviations in the basement map: El, Ełk intrusion; Kt, Kętrzyn anorthosite intrusion; Ml, Mława intrusion; Mz, Mazowsze massif; Ol, Olsztyn intrusion; Pi, Pisz intrusion; Wm, Warmia branch; ZW, Żuławy branch.

MONA LISA experiment covered much of the southeastern North Sea. In Northern Germany, a high-velocity middle crust and lower crust to the north terminates abruptly at the Elbe Line (Aichroth et al., 1992; Thybo, 2001). In the MONA LISA lines, the termination of Baltica in the lower crust appears as a transition from high (>7.0 km s^{-1}) velocities in Baltica crust to low velocities (<6.4 km s^{-1}) in the 'pure' Avalonian portion of the crust (Abramovitz and Thybo, 2000; Abramovitz et al., 1998). Thus, a possible interpretation is that highly extended Baltican lithosphere extends as far west as 60–80 km at the P4 profile. However, based on similarities with many crustal models across both modern and ancient passive margins (e.g., Holbrook et al., 1994; Keller and Hatcher, 1999; Mickus and Keller, 1992), a more likely scenario is that the pre-Permian portion of the 20 km deep basin is a passive margin sequence that includes some units related to transcurrent motions along the margin between the initial rifting and the Variscan orogeny as shown in **Figure 15(a)**. An important piece of evidence for this being the case is drilling data, which show that a maximum of only about the upper 40% (8 km) of the fill in the Polish Basin is Permian or younger in age (Scheck-Wenderoth and Lamarche, 2005). A rift sequence should taper away from the EEC margin, but this is only partially the case in the seismic model (**Figure 15(a)**). However, to the southwest toward the Bohemian Massif region, there are thrust faults and synorogenic sedimentary rocks (OS in **Figure 15(a)**) that would fill this portion of the basin. An obvious for argument for extension is that the crystalline crust beneath the basin is half as thick as the crust under the adjacent EEC (**Figure 15(a)**). In addition, Janik et al. (2005) discussed the evidence indicating that this margin experienced translation of crustal blocks in the Paleozoic subsequent to its formation that could create a pull-apart basin. The abrupt change in structure at the margin of Baltica is also evidence that transtension was involved in the initial rifting as has been argued for the case of the Ouachita orogenic belt of the Southern United States (Mooney, 2015; Thomas, 1991).

The deeper structure southwest of the deep basin reflects the collision between Baltica and Avalonia/Bohemian Massif. The geometry of the crust and upper mantle in this area (**Figure 15(a)**) has similarities with BABEL line A in the southern Baltic Sea (BABEL Working Group, 1993). Thus, Baltica and its margin can be viewed as the indenter in the collision with the crust of the Variscan region being driven upward onto the margin of Baltica and the Variscan mantle being driven beneath the margin of Baltica. The fact that the passive margin appears to be largely intact and the lack of late Paleozoic deformation within Baltica indicates that collision was relatively soft.

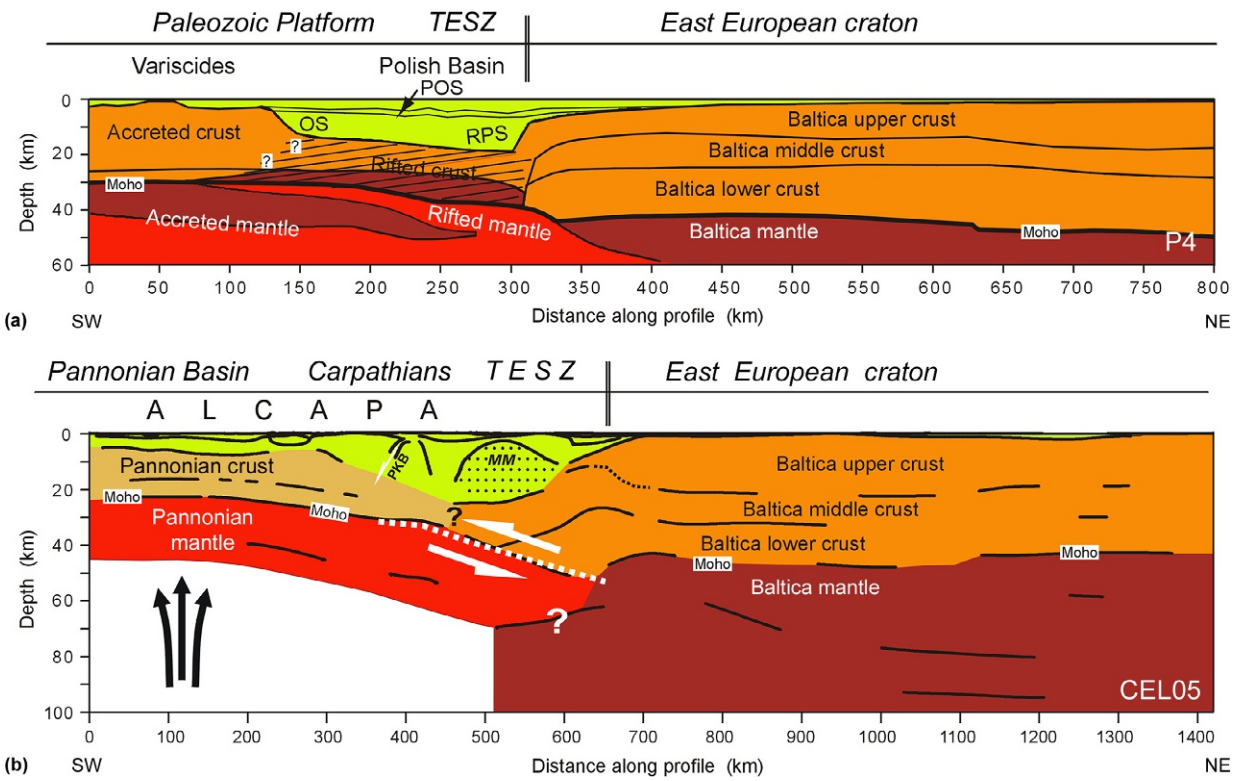

Figure 15 The representation of a tectonic interpretation of the transition between Baltica (EEC) and the adjacent accreted terranes (Paleozoic platform) in the TESZ area along profile P4 (a) and the transition between the Pannonian Basin and EEC along profile CEL05 (b). The model for profile P4 (a) is modified from Grad et al. (2003a) and shows an abrupt transtensional margin where the southwestern extent of Baltica lithosphere is minimal. POS, post-orogenic sedimentary sequence; OS, orogenic sedimentary sequence; RPS, rift (pull-apart) sedimentary sequence. The model for profile CEL05 (b) is modified from Grad et al. (2006) and shows the 'old' (northward) subduction zone of the Pannonian lithosphere under EEC in the Jurassic–Lower Cretaceous (Książkiewicz, 1977) or by the end of the Jurassic, ~140 Ma (Golonka et al., 2003a). 'Young' (southward) subduction of the EEC lithosphere in the Tertiary (Miocene) is represented by the Pieniny Klippen Belt (PKB).

In conclusion, the observed structure along profile P4 (Figures 6 and 15(a)) indicates that rifting and subsequent transtension created an abrupt margin for Baltica along which a thick (~10 km) sedimentary sequence was deposited. In addition, the seismic model suggests that the Variscan orogeny was a soft collision in which the margin of Baltica acted as an indenter.

1.17.5.2 CELEBRATION 2000 Area

The velocity model derived for the CEL05 profile provides an important new view of lithosphere across the Carpathian–Pannonian region and transitions with the EEC (Baltica). The Mesozoic and Cenozoic tectonic environments of this region involved complex conference between the European and Adriatic plates and a variety of intervening microcontinents and oceanic areas (e.g., Golonka et al., 2003a,b), and many aspects of the tectonic evolution remain controversial.

Our preferred tectonic interpretation of the velocity model (Figure 10) is shown in Figure 15(b). The southwestern end of CEL05 begins in the Tisza–Dacia block, which is separated from the ALCAPA block to the north by the Mid-Hungarian line (Figure 1) (e.g., Bielik et al., 2004, 2010; Szabó et al., 2004). The western Pannonian Basin and Inner Carpathians are part of the ALCAPA block that extends northward to the PKB. Our model is in agreement with previous studies in the region (e.g., Posgay et al., 1995; Royden and Dövényi, 1988) in showing that the Pannonian Basin is characterized by a thin (~25 km) crust and 2–3 km of Tertiary sedimentary and volcanic cover. Two important observations are as follows: (1) the crust below this cover has a low average velocity (~6.1 km s^{-1}), indicating that it is not oceanic in nature (Grad et al., 2006), and (2) there is no large change in lithospheric structure across the Mid-Hungarian line, which suggests that extension and magmatism associated with the formation of the Pannonian Basin has modified the lithosphere considerably.

In contrast to the Pannonian Basin region, the structure of the upper crust becomes more complicated along the profile as it traverses the Inner Carpathians, PKB, Outer Carpathians, and Carpathian Foredeep. The observed velocity structure is in good agreement with the surface geology and drilling results such as the deep drill holes near Wysowa (Figure 10). The south-dipping body that correlates with the PKB attests to the importance of this feature. From a deeper perspective, the crust gradually thickens into and across the Carpathians up to the margin of the EEC, and the mantle reflectors deepen to remain parallel to the Moho.

Near the margin of the EEC, the profile crosses the MM, Radom–Kraśnik uplift, and Lublin Trough before passing into the relatively undisturbed EEC crust that is typical of that found in other nearby areas (Figure 10). Because it is a large crustal block that may be exotic with respect to the EEC, the MM has been the subject of much interest and several interpretations. Geologic studies reveal folded metasediments of the Vendian–Early Cambrian age at depths that are covered by younger strata. However, drilling data and the new POLONAISE'97 and CELEBRATION 2000 results suggest that it was probably once a part of Baltica and was detached and then moved to its present location (Dadlez et al., 1994, 2005; Janik et al., 2005). The MM is bounded on the north by the Radom–Kraśnik uplift that is in turn bounded in the south by the Lublin Trough (Figure 10), and the crustal structure beneath these features is complex. More geologic data are needed to access the implications of these observations.

Northeast of the Lublin Trough, the profile crosses the EEC where a relatively simple structure is observed. However, the Precambrian history of the cratonal area is complex, having been interpreted as involving the accretion of three terranes: Fennoscandia, Sarmatia, and Volgo-Uralia (Bogdanova, 1996; Bogdanova et al., 2001). In western Belarus, profile CEL05 approximately follows the suture between Fennoscandia and Sarmatia, which is marked by the Mazury–Belarus orogenic belt (Figure 10). A change in lower crustal structure and upper-mantle velocity occurs in the vicinity of this interpreted suture, implying that it is a major lithospheric boundary.

As discussed by Grad et al. (2006), several large-scale tectonic interpretations are possible for the CEL05 velocity model. The most surprising feature in this model is the northward dip of the Moho and mantle reflectors beneath the Carpathians and the region of the EEC margin that suggests northward subduction (Figures 10 and 15(b)). This observation is at odds with the known surface geology such as the south-dipping PKB that indicates that Cenozoic subduction was to the south. However, several workers have suggested that northward subduction occurred in the Mesozoic (Golonka et al., 2003a; Książkiewicz, 1977), so subduction in the region could have flipped. However, the lack of a Mesozoic arc to the north indicates that any northward subduction would have been short-lived. A lithospheric-scale 'crocodile' structure with Baltica acting as the rigid indenter could also produce south-dipping features in the upper crust and north-dipping deep structures during Cenozoic convergence. Finally, a thermal anomaly and extension in the Pannonian Basin area would cause crustal thinning, producing an overall appearance of northward dip (Grad et al., 2006). Add in the complexities of large-scale strike-slip movements (e.g., Csontos and Vörös, 2004) and slab rollback to the east (Seghedi et al., 2004; Wortel and Sparkman, 2000), and it becomes difficult to make definitive tectonic interpretations. However, recent petrologic studies (Trua et al., 2006) indicate that Precambrian lithospheric mantle is present beneath the PKB region, suggesting that slab rollback did not grossly alter the lithospheric structure of this region, which implies at least some of the northward dip observed is probably old.

A third model explains the observed structure as the result of 'young' (Miocene) southward subduction of Variscan and EEC lithospheres and of Neogene thinning of the Pannonian lithosphere due to extension. Our data show no evidence of a south-dipping slab in the upper mantle or south-dipping features in the lower crust from the Carpathian Foredeep southward. However, one could imagine the south-dipping features adjacent to the EEC (500–700 km) being attached to a south-dipping slab that has broken off and either sunk to great depth or been absorbed.

In summary, the seismic model for the 1420 km long profile CEL05 targeted the Pannonian Basin, the Carpathians, the TESZ, and the EEC. Given the complex geologic history of the region, the equally complex velocity structure is no surprising. The CEL05 results indicate that two episodes of subduction with different polarities are possible. These results also provide

considerable information on the deep structure and relationships between upper crustal features known from drilling and geologic data. However, further integrated geophysical and tectonic analyses will be required to fully determine the implications of the CELEBRATION 2000 data.

1.17.5.3 ALP 2002 Area

The dense source and receiver layout along the CELEBRATION 2000 and ALP 2002 profiles (Figure 2) and the 3-D aspect of data acquisition (cross-line shooting) provided new data that make the construction of a well-constrained Moho map in the East Alpine–Pannonian realm possible. The Moho reflects the structure of the lithospheric mantle and the interpretation of its structure in a plate tectonic context is a challenging task. Destructive plate boundaries can be identified by offsets of an otherwise smooth Moho boundary derived from controlled source seismic data (e.g., Abramovitz and Thybo, 2000; Kissling et al., 2006; Waldhauser et al., 1998). However, continental transform or strike-slip faults may exist without significant offsets of the Moho boundary and are thus difficult to identify (Thybo et al., 2003; Weber et al., 2006, 2009; Zhao et al., 2001).

The Moho map shown in Figure 16(a) is based on the European Moho map of Grad et al. (2009a). In the Alpine area, it was edited by inserting the more detailed Moho map of Behm et al. (2007). Stacking of refracted and reflected P-waves recorded during the CELEBRATION 2000 and ALP 2002 experiments were combined with tomographic inversion of Pn arrivals to generate this map. In the west, data from the TRANSALP transect were also included (Bleibinhaus and Gebrande, 2006; Bleibinhaus et al., 2006; Lüschen et al., 2006). The location and shape of the Moho at plate boundaries were refined by elastic plate modeling of the lithosphere east of 11° E by Brückl et al. (2010). In the western portion of the map, the depth and offset of the Moho at these boundaries determined by Waldhauser et al. (1998) were included. ALP 2002 seismic data and gravity interpretations improve the resolution of the boundary between Adria and the Pannonian domain (Šumanovac, 2010; Šumanovac et al., 2009).

The resulting Moho map indicates a fragmentation of the mantle lithosphere into three blocks: the European plate (EU), the Adriatic microplate (AD), and a newly interpreted 'Pannonian fragment' (Behm et al., 2007; Brückl et al., 2007). In the following discussion, we use the term 'Pannonian domain' (PA), rather than 'Pannonian fragment.' This domain comprises the mantle lithosphere below ALCAPA, Tisza, and the Dinarides. The three blocks, EU, AD, and PA, constitute a triple junction (Figure 16(a)). The clear Moho offset on profile Alp02 (Figure 12) at a distance 300 km and a second order discontinuity in the Moho map (shown as a southeast-trending dashed plate boundary in Figure 16(a)) coincide approximately with the boundary between the Dinarides and the Tisza unit. ALCAPA (Alps–Carpathians–Pannonian) units are clearly separated from the Dinarides and the Tisza unit by the Periadriatic line (PAL) and the Mid-Hungarian line (MHL) on the surface. However, the Moho structure east of the triple junction does not clearly reflect this boundary in the lithospheric mantle, probably because of its strike-slip nature and the high-temperature regime in the Pannonian upper mantle.

Images of the upper mantle supplied by seismic tomography contribute to a better understanding of plate tectonic processes and support the interpretation of the Moho structure. We include the P-wave models of Koulakov et al. (2009), Dando et al. (2011), and Mitterbauer et al. (2011) into our tectonic interpretation. These models cover the area around and east of the Alp01 profile (Figure 2). We averaged these models with equal weights within their areas of high resolution and show the $dV_P = 1.4\%$ contour at 180 km depth in Figure 16(a). This contour delineates the extent of the East Alpine continental lower lithospheric slab (EAS). The triple junction between the three blocks is located near the southeastern termination of the Tauern window and coincides well with the eastern termination of the EAS. No high-velocity bodies, which could be associated with continental slabs, exist along the EU–PA boundary and the PA–AD boundary north of 45° N.

Figure 16(b) provides a 3-D visualization of a generalized tectonic interpretation of the Alp01 profile (A–B), the mantle lithosphere of EU and AD (represented by schematic 60 km thick plates), and the averaged tomographic model, represented by three orthogonal slices through the d*V*p volume (dV_P is the deviation of the P-wave velocity from the ak135 model). The EAS is visualized by the $dV_P = 1.4\%$ isosurface. The corner points of the model (A, B, C) are marked in Figure 16(a). The crystalline basement of the Bohemian Massif (European basement) in the northern portion of the Alp01 profile represents the former passive margin of the Penninic Ocean. The upper crustal low-velocity zone (LV) north of the North Alpine thrust fault (NAT) coincides with the Molasse basin (M) and the Flysch Belt (F). It extends into the basement, indicating extensional tectonics before collision or bending during the generation of the foreland basin. East Alpine (ALCAPA) units overthrust the European basement about 150 km to the north along A–B. The Penninic (P) and Subpenninic (European) units of the Tauern window (TW) have been exhumed ~25 km (e.g., Fügenschuh et al., 1997) by thrusting and folding over a shear zone during the Miocene. This zone, the sub-Tauern ramp, was identified along the TRANSALP transect by steeply dipping reflections (e.g., Lüschen et al., 2004, 2006). The topography of the Moho and the velocity structure of the crust supply sufficient constraints to infer a tectonic style similar to the Alp01 profile. The Periadriatic line (PAL) separates the Eastern Alps (ALCAPA) from the Southern Alps (SA). Its location coincides with the Moho jump from the EU to AD. However, it cannot be traced through the crust without ambiguity, probably due to its character as a steeply dipping strike-slip fault. The general vergence of thrust faults changes from north in the Eastern Alps to south in the Southern Alps. The Dinarides (DI) and the Adriatic foreland are characterized by a high-velocity zone (HV) in the upper crust and nearly horizontal layering of the seismic velocity structure.

Crustal thickening is closely related to post-collision convergence and quantitative information can be derived from the balancing of these processes. In the area of the Tauern window, post-collision convergence and crustal thickening were considered along a cross section at 13° E from the Molasse basin in the north to the Southern Alps and the Venetian plain under the assumption that no crustal material was subducted (Brückl et al., 2010). Here, we consider the Alp01 profile at 13.5° E, shown in Figure 16(b) along A-B, in a similar manner. From the Bohemian Massif to the Tauern window, the thickness of

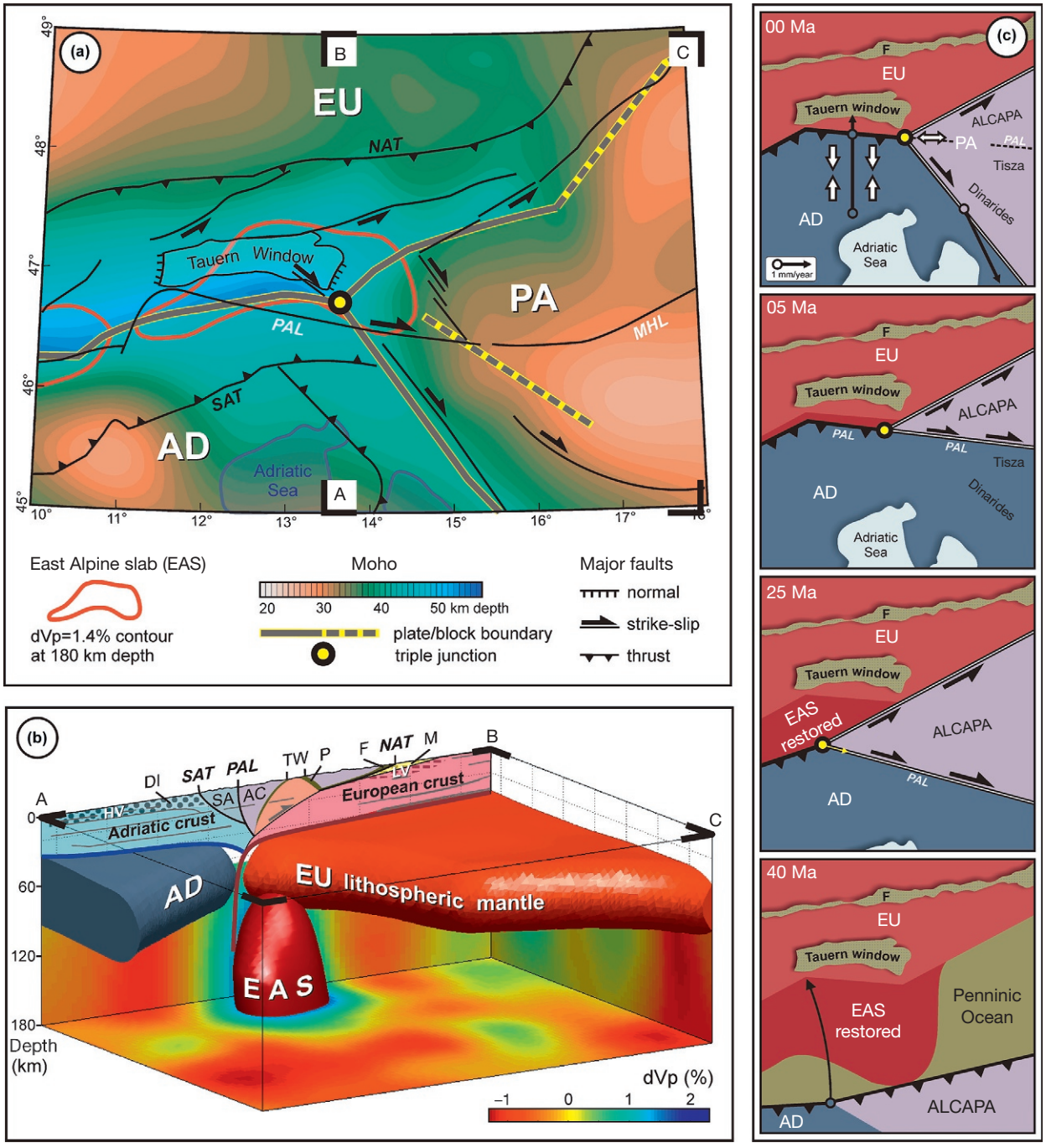

Figure 16 Structure of the East Alpine lithosphere and tectonic model of the plate tectonic evolution since Eocene. (a) Moho map showing the tectonic fragmentation into the European plate (EU), Adriatic microplate (AD), and the Pannonian domain (PA) with a triple junction southeast of the Tauren window (TW). The extent of the East Alpine slab (EAS) is marked by the $dV_P = 1.4\%$ contour at 180 km depth. Major faults (NAT – North Alpine thrust fault, PAL – Periadriatic line, MHL – Mid-Hungarian line, SAT – South Alpine thrust fault), the boundary of the Tauern window (TW) and the shoreline of the Adriatic Sea, are superimposed on the map. (b) Visualization of the East Alpine lithosphere and upper mantle east of 13.5° E. The corner points (A, B, C) of the model are also marked in the map. The generalized geologic cross section from A to B at 13.5° E approximately follows the Alp01 profile (M, Molasse basin; F, Flysch Belt; AC, East Alpine, respectively, ALCAPA units; P, Penninic units of the TW; SA, Southern Alps; DI, Dinarides). Dashes around the Molasse basin to the north and dots in the area of the Dinarides and the Adriatic foreland mark zones of relatively low (LV) and high (HV) P-wave velocities, respectively. The EU (red) and AD (blue) lithospheric mantle are represented schematically by 60 km thick slabs. The PA lithospheric mantle is not shown in order to allow for the view to the deeper EAS (visualized by its $dV_P = 1.4\%$ isosurface) and its connection to the EU lithospheric mantle. The P-wave velocity structure of the upper mantle, derived from tomographic studies, is represented by three orthogonal slices. Please see the text for a more detailed description and reference. (c) Plate tectonic reconstruction at the level of the Moho and the lithospheric mantle from the first contact of the Adriatic domain (including ALCAPA) with Europe (40 Ma) to the modern active tectonics (00 Ma). Please see the text for description.

the crystalline basement diminishes by about 5 km. This thinning may be explained by the fact that the European basement constituted the passive northern margin of the Penninic Ocean. Post-collisional thickening is speculative to derive from this structural data. In the central part of the Eastern Alps, the 25 km exhumation of the Tauern window by thrusting over the sub-Tauern ramp (slope ~21° along Alp01) corresponds to a horizontal convergence of ~65 km. The average thickness of the AD crust under the Southern Alps and Dinarides is ~42 km. The major part of the thickening took place either by thrusting in the crystalline upper crust and thrusting of AD lower crust over the sub-Tauern ramp or by stacking of lower crust (e.g., Castellarin et al., 2006). Thickening of the Adriatic crust north of the Adriatic foreland corresponds to a crustal shortening of ~30 km assuming a thickness of 30 km for the pre-collision Adriatic crust.

The total north–south convergence since collision derived from crustal thickening is about 95 km. However, geologic investigations and palinspastic reconstructions arrive at significantly larger figures (165–195 km) (e.g., Fügenschuh et al., 1997; Ustaszewski et al., 2008). The difference between crustal shortening derived by cross-sectional balancing of the whole crust and retrodeformation of the upper crust is not equally distributed over the whole profile. There is a fair agreement of N–S convergence derived by both methods in the Southern Alps (Castellarin and Cantelli, 2000; Castellarin et al., 2006; Schönborn, 1999). For the Eastern Alps, the situation is significantly different. Frisch et al. (2000) derived 140 km crustal shortening at the western boundary of the Tauern window by a palinspastic reconstruction. The discrepancy between the amount of convergence and crustal thickening can be (at least partly) resolved by the assumption of an eastward-directed lateral extrusion of the central and eastern part of the Eastern Alps to the Pannonian Basin (Ratschbacher et al., 1991). Linzer et al. (2002) estimated ~120 km of E–W extension between the Brenner and Katschberg normal (west and east boundaries of the Tauern window, **Figure 16(a)**) faults during Miocene. Shortening is therefore underestimated by restoration applied in 2-D along the Alp01 profile.

We also have used the data from our experiments in an integrated analysis of the relation between crustal and upper-mantle structures. We interpret the European crust and lithospheric mantle to be connected to the East Alpine continental lower lithospheric slab (EAS), and thus identify this slab as former lower European lithosphere. This interpretation is depicted in **Figure 16(b)**, but other interpretations have been proposed. For example, based on an apparent NE-directed dip of the EAS resolved by teleseismic tomography carried out as part of the TRANSALP project, the EAS has been connected to the Adriatic mantle lithosphere (e.g., Kissling et al., 2006; Lippitsch et al., 2003), thus inferring a subduction polarity flip at about 11° E (near the Brenner normal fault terminating the TW on the west, **Figure 16(a)**) from the west to the east. However, the lithospheric kinematics of such a polarity flip are not easy to explain by standard plate tectonic models. Avoiding a polarity flip by interpreting the EAS as the EU lower lithospheric slab, as proposed among others by Brückl et al. (2010) and Mitterbauer et al. (2011), provides a kinematic interpretation constrained by fundamental plate tectonic concepts. The length of the EAS (measured from the center line of the lithospheric mantle) derived from the different tomographic models cited earlier is about 150 km. Breakoff of the subducted Penninic Ocean slab occurred before the subduction of continental slabs (e.g., Wortel and Sparkman, 2000). The remains of this slab have been imaged at depths >350 km (e.g., Dando et al., 2011; Mitterbauer et al., 2011).

Finally, we present a schematic reconstruction of the collision and extrusion processes at the level of the Moho and the lithospheric mantle from the time of the first contact of the Adriatic microplate with Europe to present day active tectonics (**Figure 16(c)**). This reconstruction is based on the geometry of the Moho discontinuities that define plate fragments and the EAS. The coincidence of the locations of the triple junction AD–EU–PA and the eastern termination of the EAS (**Figure 16(a)** and **16(b)**) constitutes the most important constraint. The absence of continental lithospheric slabs (high P-wave velocity bodies) at the EU–PA plate boundary was explained by thrusting or subduction west of the triple junction and strike-slip or transform movement east of it (Mitterbauer et al., 2011). The PAL and its continuation into the MHL experienced large displacements during collision and extrusion (e.g., Csontos and Nagymarosy, 1998; Ratschbacher et al., 1991). We assume that this deformation is represented by relative plate movements on a lithospheric scale and infers a further plate fragmentation at the Moho between ALCAPA to the north and the Dinarides and the Tisza unit to the south that was most active during the extrusion process in the Miocene. The resulting deep structure must be complex, but for simplicity, the fragmentation at the Moho is approximated by straight lines in these figures. We consider the triple junction to be stable and apply the appropriate stability conditions (McKenzie and Morgan, 1969). We keep the position of the European mantle (EU) fixed. The Flysch Belt (F) at the northern rim of the Eastern Alps, the Tauern window, and the northward-moving Adriatic Sea are superimposed on the maps for orientation. The steps in our reconstruction are as follows (**Figure 16(c)**):

A. 40 Ma – Eocene: The European passive margin of the Penninic Ocean has been restored by flipping the EAS from subvertical to its horizontal orientation before subduction. The Adriatic microplate (AD including ALCAPA) constitutes the active margin of the subducting Penninic Ocean. This continental domain rotates counterclockwise around an Euler pole at approximately 7° E, 45° N (e.g., Ustaszewski et al., 2008). The first contact with the European continent occurs south of the present day Tauern window.
B. 25 Ma – Oligocene/Miocene: The Penninic Ocean had closed completely and breakoff of the oceanic slabs was complete. The Periadriatic line (PAL) was activated and ALCAPA started to move via dextral strike-slip relative to AD. A stable triple junction is generated between EU–AD–ALCAPA. The ALCAPA – EU plate boundary turns from subduction to strike-slip, thus, avoiding the generation of a continental lithospheric slab east of the triple junction.
C. 05 Ma – Miocene–Pliocene: Convergence between AD and EU nearly reached the current state. The triple junction moved along the PAL more than 100 km to the east, and strike-slip changed to subduction along this part of the PAL. The angle between the strike-slip boundaries

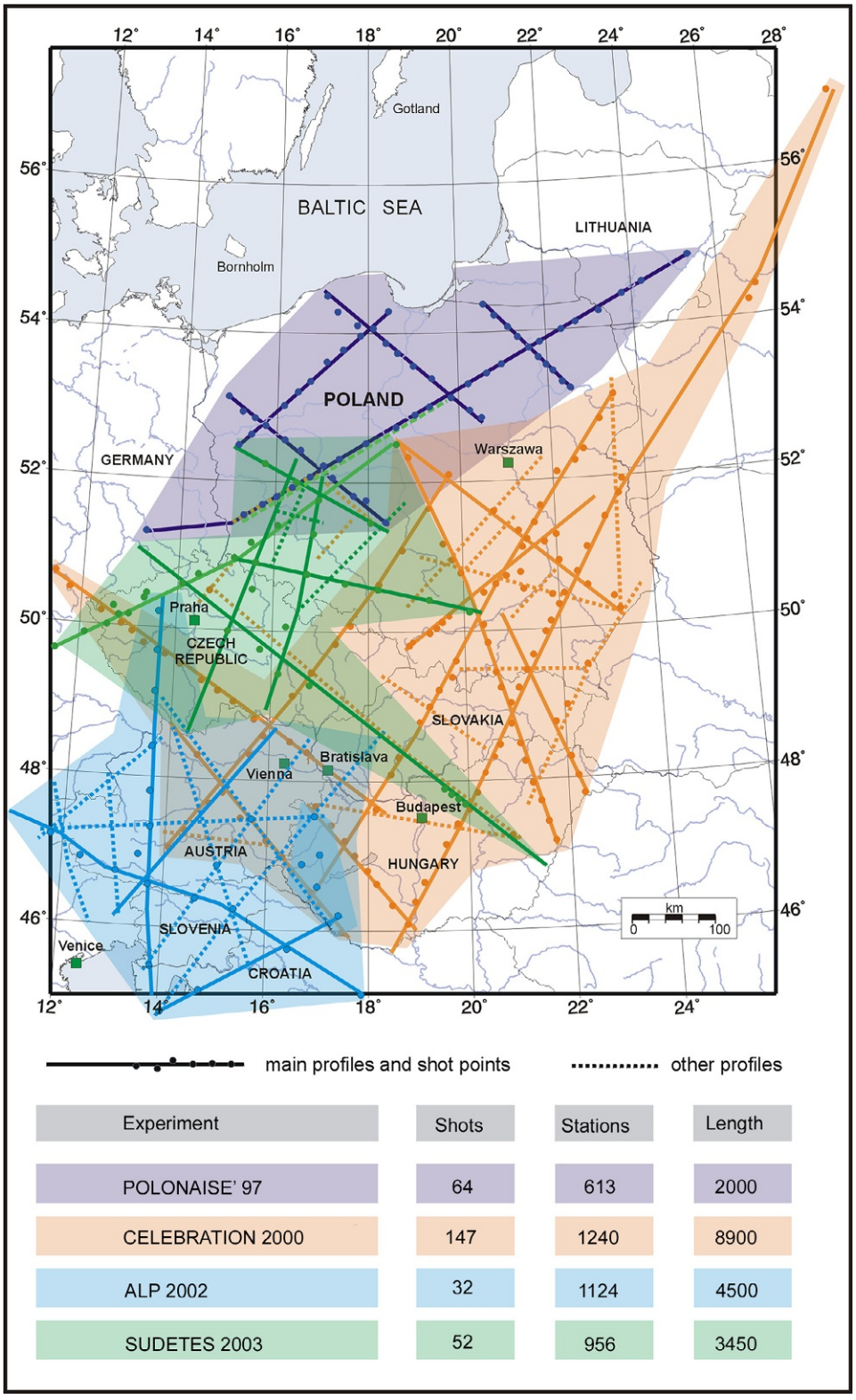

Experiment	Shots	Stations	Length
POLONAISE' 97	64	613	2000
CELEBRATION 2000	147	1240	8900
ALP 2002	32	1124	4500
SUDETES 2003	52	956	3450

Figure 17 Layout of the POLONAISE'97, CELEBRATION 2000, ALP 2002, and SUDETES 2003 seismic experiments in Central Europe.

confining ALCAPA became more oblique because of the CCW rotation of AD versus EU, thus, causing west–east-oriented extension of ALCAPA. This extension in combination with the eastward movement of the triple junction substantially supports the extrusion of parts of the Eastern Alps toward the Pannonian Basin in the east.

D. 00 Ma – active tectonics: The Periadriatic line loses its significance as first-order active tectonic structure. ALCAPA,

Tisza, and the Dinarides amalgamate to form one tectonic block, the Pannonian domain (PA). Tectonic activity moved from the west–east striking Periadriatic line to the northwest–southeast striking PA–AD plate boundary. This change of the plate tectonic regime in the Pannonian domain may coincide with the tectonic transition from extension to compression in this area during Pliocene and Quaternary (e.g., Bada et al., 2007; Fodor et al., 2005).

A kinematic model of the active tectonics around the triple junction was derived by Brückl et al. (2010). This model assumes sinistral strike-slip along the EU–PA boundary and stability of the AD–EU–PA triple junction. The PA extrudes at 1 mm year^{-1} to the east, and the convergence between the AD (especially the Adriatic foreland) and the EU amounts to 3 mm year^{-1} according to GPS data (Grenerczy and Kenyeres, 2006). The geodetic data also suggest a compressional zone south of the EU–AD plate boundary. These assumptions and data determine the kinematic model at and near the triple junction. South-to-north-oriented convergence is partitioned into 80% compression of AD and 20% subduction of EU under AD. The relative plate movement of PA versus AD changes from spreading at the triple junction (compensated by west–east-oriented extension of PA) to pure dextral strike-slip and transpression to the south of the PA–AD plate boundary. This kinematic model fits the geodetic data and explains the spatial distribution of seismicity and focal mechanisms.

1.17.6 Summary

The POLONAISE'97, CELEBRATION 2000, ALP 2002, and SUDETES 2003 seismic experiments in Central Europe provide unprecedented seismic coverage of lithospheric structure over a large area (**Figure 17**). The analysis of the resulting huge data set provided by this massive international cooperative effort is far from complete. However, we have learned a great deal about the complex structure along the TESZ and eastern Alpine regions in particular. In the TESZ area, we have delineated a deep basin, the lower portion of which is sediments and volcanic associated with the rifted margin of Baltica. In addition, several crustal blocks exist along this margin but appear to mostly be of Baltican origin with Variscan terranes lying outboard to the southwest. The Pannonian/Carpathian/TESZ region displays a complex structure with a surprising northward dip in the deep crust and uppermost mantle and southward dips in the upper crust. This geometry may well reflect multiple phases of subduction as well as collision-related features.

In the eastern Alpine region, 2-D interactive modeling by ray tracing and the application of 3-D stacking techniques substantially improved our knowledge of the lithospheric structure in this area. We have identified three main tectonic blocks: Europe (EU), Adria (AD), and the Pannonian domain (PA). These blocks meet at a triple junction near the southeastern termination of the Tauern window. The Alp01 and Alp02 profiles resolved different crustal structures related to collisional tectonics west of the triple junction and escape or extrusion east of it. Finally, we have formulated a tectonic model of evolution of the eastern Alpine region over the past 40 My that is consistent with a variety of geologic and geophysical data including velocity models of the upper mantle derived from teleseismic data.

References

Abramovitz T and Thybo H (2000) Seismic images of Caledonian lithosphere-scale collision structures in the southeastern North Sea along MONA LISA Profile 2. *Tectonophysics* 317: 27–54.

Abramovitz T, Thybo H, and MONA LISA Working Group (1998) Seismic structure across the Caledonian Deformation Front along MONA LISA profile 1 in the southeastern North Sea. *Tectonophysics* 288: 153–176.

Aichroth B, Prodehl C, and Thybo H (1992) Crustal structure along the Central Segment of the EGT from seismic refraction studies. *Tectonophysics* 207: 43–64.

Ansorge J, Blundell D, and Mueller St (1992) Europe's lithosphere-seismic structure. In: Blundell DJ, Freeman R, and Mueller St (eds.) *A Continent Revealed – The European Geotraverse*, pp. 33–69. Cambridge: Cambridge University Press.

BABEL Working Group (1993) Deep seismic reflection/refraction interpretation of crustal structure along BABEL profiles A and B in the southern Baltic Sea. *Geophysical Journal International* 112: 325–343.

Bada G, Horváth F, Dövényi P, Szafián P, Windhoffer G, and Cloetingh S (2007) Present-day stress field and tectonic inversion in the Pannonian Basin. *Global and Planetary Change* 58(1–4): 165–180. http://dx.doi.org/10.1016/j.gloplacha.2007.01.007.

Bayer U, Grad M, Pharaoh TC, et al. (2002) The southern margin of the East European craton: New results from seismic sounding and potential fields between the North Sea and Poland. *Tectonophysics* 360: 301–314.

Behm M (2009) 3-D modelling of the crustal S-wave velocity structure from active source data: application to the Eastern Alps and the Bohemian Massif. *Geophysical Journal International* 179: 265–278. http://dx.doi.org/10.1111/j.1365-246X.2009.04259.x.

Behm M, Brückl E, Chwatal W, and Thybo H (2007) Application of stacking and inversion techniques to 3D wide-angle reflection and refraction seismic data of the Eastern Alps. *Geophysical Journal International* 170: 275–298. http://dx.doi.org/10.1111/j.1365-246X.2007.03393.x.

Berthelsen A (1992a) Mobile Europe. In: Blundell DJ, Freeman R, and Mueller ST (eds.) *A Continent Revealed – The European Geotraverse*, pp. 11–32. Cambridge: Cambridge University Press.

Berthelsen A (1992b) From Precambrian to Variscan Europe. In: Blundell DJ, Freeman R, and Mueller ST (eds.) *A Continent Revealed – The European Geotraverse*, pp. 153–164. Cambridge: Cambridge University Press.

Berthelsen A (1998) The Tornquist Zone northwest of the Carpathians: An intraplate-pseudosuture. *Geologiska Föreningens i Stockholm Förhandlingar* 120: 223–230.

Bielik M, Šefara J, Sotak J, et al. (2004) The Western Carpathians – Interaction of Hercynian and Alpine processes. *Tectonophysics* 393: 63–86.

Bielik M, Alasonati Tašárová Z, Vozár J, et al. (2010) Gravity and seismic modelling in the Carpathian-Pannonian Region. In: Vozár J, et al. (ed.) *Variscan and Alpine terranes of the Circum-Pannonian region*, pp. 202–233. Bratislava: Journal of Slovak Academy of Sciences, Geological Institute, ISBN: 978-80-970578-5-5.

Bleibinhaus F and Gebrande H (2006) Crustal structure of the Eastern Apls along the TRANSALP Profile from wide-angle seismic tomography. *Tectonophysics* 414: 51–69.

Bleibinhaus F, Brückl E, and ALP2002 Working Group (2006) Wide-angle observations of ALP2002 shots on the TRANSALP profile: Linking the two DSS projects. *Tectonophysics* 414: 71–78.

Blundell D, Freeman R, and Mueller St (eds.) (1992) *A Continent Revealed – The European Geotraverse*, p. 275. Cambridge: Cambridge University Press.

Bogdanova S (1996) Palaeoproterozoic accretion of Sarmatia and Fennoscandia. In: Gee DG and Zeyen HJ (eds.) *EUROBRIDGE 1996 – Lithosphere Dynamics: Origin and Evolution of Continents*, pp. 81–89. Uppsala: The EUROPROBE Secretariat, Uppsala University.

Bogdanova SV, Gorbatschev R, Stephenson RA, and Guterch A (2001) EUROBRIDGE: Palaeoproterozoic accretion of Fennoscandia and Sarmatia. *Tectonophysics* 339: 1–237.

Brix F and Schultz O (1993) *Erdöl und Erdgas in Österreich*, p. 688. Horn, Wien: Naturhistorisches Museum Wien und F Berger.

Brückl E, Bodoky T, Hegedűs E, et al. (2003) ALP 2002 seismic experiment. *Studia Geophysica et Geodaetica* 47: 671–679.

Brückl E, Bleibinhaus F, Gosar A, et al. (2007) Crustal structure due to collisional and escape tectonics in the Eastern Alps region based on profiles Alp01 and Alp02 from

the ALP 2002 seismic experiment. *Journal of Geophysical Research* 112: B06308. http://dx.doi.org/10.1029/2006JB004687.
Brückl E, Behm M, Decker K, et al. (2010) Crustal structure and active tectonics in the Eastern Alps. *Tectonics* 29: TC2011. http://dx.doi.org/10.1029/2009TC002491.
Castellarin A and Cantelli L (2000) Neo-Alpine evolution of the Sothern Alps. *Journal of Geodynamics* 30: 251–274.
Castellarin A, Nicolich R, Fantoni R, Cantelli L, Sella M, and Selli L (2006) Structure of the lithosphere beneath the Eastern Alps (southern sector of the TRANSALP transect). *Tectonophysics* 414: 259–282.
Čermák V and Bodri L (1998) Heat flow map of Europe revised. *Deutsche Geophysikalische Gesellschaft* II: 58–63.
Čermák V, Šafanda J, and Guterch A (1989) Deep temperature distribution along three profiles crossing the Teisseyre-Tornquist tectonic zone in Poland. *Tectonophysics* 164: 151–163.
Červený V and Pšenčík I (1983) SEIS83-numerical modeling of seismic wave fields in 2-D laterally varying layered structure by the ray method. In: Engdahl ER (ed.) *Documentation of Earthquake Algorithm, Rep. SE-35*, pp. 36–40. Boulder: World Data Center A for Solid Earth Geophysics.
Csontos L and Nagymarosy A (1998) The Mid-Hungarian line: A zone of repeated tectonic inversions. *Tectonophysics* 297: 51–71.
Csontos L and Vörös A (2004) Mesozoic plate tectonic reconstruction of the Carpathian region. *Palaeogeography, Palaeoclimatology, Palaeoecology* 210: 1–56.
Czuba W, Grad M, Luosto U, et al. (2002) Upper crustal seismic structure of the Mazury complex and Mazowsze massif within the East European craton in NE Poland. *Tectonophysics* 360: 115–128.
Dadlez R, Kowalczewski Z, and Znosko J (1994) Some key problems of the pre-Permian tectonics of Poland. *Geological Quarterly* 38: 169–189.
Dadlez R, Grad M, and Guterch A (2005) Crustal structure below the Polish Basin: Is it composed of proximal terranes derived from Baltica? *Tectonophysics* 411: 111–128.
Dalziel IWD (1997) Neoproterozoic-Paleozoic geography and tectonics: Review, hypothesis, environmental speculation. *Geological Society of America – Bulletin* 109: 16–42.
Dando BDE, Stuart GW, Houseman GA, Hegedüs E, Brückl E, and Radovanović S (2011) Teleseismic tomography of the mantle in the Carpathian–Pannonian region of central Europe. *Geophysical Journal International* 186: 11–31. http://dx.doi.org/10.1111/j.1365-246X.2011.04998.x.
Dövényi P, Horvath E, Liebe P, et al. (1983) Geothermal conditions of Hungary. *Geophysical Transactions* 29: 3–114.
Ebbing J, Braitenberg C, and Götze H-J (2006) The lithospheric density structure of the Eastern Alps. *Tectonophysics* 414: 145–155.
EUROBRIDGE Seismic Working Group (1999) Seismic velocity structure across the Fennoscandia-Sarmatia suture of the East European craton beneath the EUROBRIDGE profile through Lithuania and Belarus. *Tectonophysics* 314: 193–217.
EUROBRIDGE'95 Seismic Working Group (2001) EUROBRIDGE'95: Deep seismic profiling within East European craton. *Tectonophysics* 339: 153–175.
Fodor L, Bada G, Csillag G, Horváth E, et al. (2005) An outline of neotectonic structures and morphotectonics of the western and central Pannonian Basin. *Geophysical Journal International* 179: 345–366. http://dx.doi.org/10.1111/j.1365-246X.2009.04279.x.
Frisch W, Dunkl I, and Kuhlemann J (2000) Postcollisional orogen parallel large scale extension in the Eastern Alps. *Tectonophysics* 327(3–4): 239–265. http://dx.doi.org/10.1016/S0040-1951(00)00204-3.
Fügenschuh B, Seward D, and Mancktelow N (1997) Exhumation in a convergent orogen: The western Tauern window. *Terra Nova* 9: 213–217.
Gebrande H, Castellarin A, Lüschen E, Millahn K, Neubauer F, and Nicolich R (2006) TRANSALP – A transect through a young collisional orogen: Introduction. *Tectonophysics* 414(1–4): 1–7. http://dx.doi.org/10.1016/j.tecto.2005.10.030.
Giese P and Prodehl C (1976) Main features of crustal structure in the Alps. In: Giese P and Prodehl C (eds.) *Explosion seismology in Central Europe*, pp. 347–375. Springer.
Golonka J, Krobicki M, Oszczypko N, et al. (2003a) Geodynamic evolution and palaeogeography of the Polish Carpathians and adjacent areas during Neo-Cimmerian and preceding events (latest Triassic – earliest Cretaceous). In: McCann T and Saintot A (eds.) *Tracing Tectonic Deformation Using the Sedimentary Record, Special Publications*, vol. 208, pp. 138–158. London: Geological Society.
Golonka J, Ślączka A, and Picha F (2003b) Geodynamic evolution of the orogen: The West Carpathians and Ouachitas Case study. *Annales. Societatis Geologorum Poloniae* 75: 145–167.
Grad M (1989) Investigation of the lower lithosphere in the southwestern part of the East European Platform on the basis of seismic data. *Gerlands Beitraege für Geophysik* 98: 124–130.
Grad M (1992) Seismic structure of the sub-crustal continental lithosphere. *Physics of the Earth and Planetary Interiors* 69: 224–230.
Grad M (1997) Eurasian mantle structure derived from the records of nuclear explosions. In: Fuchs K (ed.) *Upper Mantle Heterogeneities from Active and Passive seismology*, pp. 89–96. Kluwer: Dordrecht.
Grad M and Luosto U (1987) Seismic models of the crust of the Baltic Shield along the SVEKA profile in Finland. *Annales Geophysicae* 5B: 639–650.
Grad M and Luosto U (1994) Seismic velocities and Q-factors in the uppermost crust beneath the SVEKA profile in Finland. *Tectonophysics* 230: 1–18.
Grad M and Tripolsky AA (1995) Crustal structure from P and S seismic waves and petrological models of the Ukrainian shield. *Tectonophysics* 250: 89–112.
Grad M, Guterch A, Janik T, and Perchuć E (1986) Seismic model of the lithosphere of the East European Platform beneath the Baltic Sea-Black Sea profile. *Tectonophysics* 128: 281–288.
Grad M, Guterch A, and Lund C-E (1991) Seismic models of the lower lithosphere beneath the southern Baltic Sea between Sweden and Poland. *Tectonophysics* 189: 219–227.
Grad M, Janik T, Yliniemi J, et al. (1999) Crustal structure of the Mid-Polish Trough beneath the Teisseyre-Tornquist Zone seismic profile. *Tectonophysics* 314: 145–160.
Grad M, Guterch A, and Mazur S (2002) Seismic refraction evidence for crustal structure in the central part of the Trans-European Suture Zone in Poland. In: Winchester JA, Pharaoh TC, and Verniers J (eds.) *Palaeozoic Amalgamation of Central Europe*, vol. 201, pp. 295–309. London: Geological Society, Special Publications.
Grad M, Keller GR, Thybo H, Guterch A, and POLONAISE Working Group (2002) Lower lithospheric structure beneath the Trans-European Suture Zone from POLONAISE'97 seismic profiles. *Tectonophysics* 360: 153–168.
Grad M, Jensen SL, Keller GR, et al. (2003a) Crustal structure of the Trans-European suture zone region along POLONAISE'97 seismic profile P4. *Journal of Geophysical Research* 108: 2541. http://dx.doi.org/10.1029/2003JB002426.
Grad M, Špičák A, Keller GR, et al. (2003b) SUDETES 2003 seismic experiment. *Studia Geophysica et Geodaetica* 47: 681–689.
Grad M, Guterch A, and Polkowska-Purys A (2005) Crustal structure of the Trans-European Suture Zone in Central Poland – Reinterpretation of the LT-2, LT-4 and LT-5 deep seismic sounding profiles. *Geological Quarterly* 49: 243–252.
Grad M, Guterch A, Keller GR, et al. (2006) Lithospheric structure beneath trans-Carpathian transect from Precambrian platform to Pannonian basin: CELEBRATION 2000 seismic profile CEL05. *Journal of Geophysical Research* 111: B03301. http://dx.doi.org/10.1029/2005JB003647.
Grad M, Guterch A, Keller GR, and POLONAISE'97 and CELEBRATION 2000 Working Groups (2007) Variations in lithospheric structure across the margin of Baltica in Central Europe and the role of the Variscan and Carpathian orogenies. *The Geological Society of America Memoir* 200: 341–356.
Grad M, Guterch A, Mazur S, et al. (2008) Lithospheric structure of the Bohemian Massif and adjacent Variscan belt in central Europe based on profile S01 from the SUDETES 2003 experiment. *Journal of Geophysical Research* 113: B10304. http://dx.doi.org/10.1029/2007JB005497.
Grad M, Tiira T, and ESC Working Group (2009a) The Moho depth map of the European Plate. *Geophysical Journal International* 176: 279–292. http://dx.doi.org/10.1111/j.1365-246X.2008.03919.x.
Grad M, Brückl E, Majdański M, et al. (2009b) Crustal structure of the Eastern Alps and their foreland: Seismic model beneath the CEL10/Alp04 profile and tectonic implications. *Geophysical Journal International* 177: 279–295. http://dx.doi.org/10.1111/j.1365-246X.2008.04074.x.
Grenerczy G and Kenyeres A (2006) Crustal deformation between Adria and the European platform from space geodesy. In: Pinter N, et al. (eds.) *The Adria Microplate: GPS Geodesy, Tectonics and Hazards, NATO Sci. Ser. IV*, vol. 61, pp. 321–334. Dordrecht, Netherlands: Springer. http://dx.doi.org/10.1007/1-4020-4235-5.
Guggisberg B and Berthelsen A (1987) A two dimensional velocity model for the lithosphere beneath the Baltic Shield and its possible tectonic significance. *Terra Cognita* 7: 631–638.
Guggisberg B, Kaminski W, and Prodehl C (1991) Crustal structure of the Fennoscandian Shield: A traveltime interpretation of the long-range FENNOLORA seismic refraction profile. *Tectonophysics* 195: 105–137.
Guterch A, Kowalski T, Materzok R, and Toporkiewicz S (1976) Seismic refraction study of the Earth's crust in the Teisseyre-Tornquist line zone in Poland along the regional profile LT-2. *Publications of the Institute of Geophysics, Polish Academy of Sciences A* 2(101): 15–23.
Guterch A, Grad M, Materzok R, Pajchel J, Perchuć E, and Toporkiewicz S (1984) Deep structure of the Earth's crust in the contact zone of the Palaeozoic and Precambrian platforms and the Carpathian Mts in Poland. *Acta Geophysica Polonica* 32: 25–41.

Guterch A, Grad M, Materzok R, and Perchuć E (1986) Deep structure of the Earth's crust in the contact zone of the Palaeozoic and Precambrian platforms in Poland (Tornquist-Teisseyre zone). *Tectonophysics* 128: 251–279.

Guterch A, Grad M, Materzok R, et al. (1992) Laminated structure of the lower crust in the fore-Sudetic region in Poland, derived from seismic data. *Physics of the Earth and Planetary Interiors* 69: 217–223.

Guterch A, Grad M, Janik T, et al. (1994) Crustal structure of the transition zone between Precambrian and Variscan Europe from new seismic data along LT-7 profile (NW Poland and Eastern Germany). *Comptes Rendus de l' Academie des Sciences, Paris* 319(Ser.II): 1489–1496.

Guterch A, Grad M, Thybo H, Keller GR, and Miller K (1998) Seismic experiment spreads across Poland. *EOS. Transactions of American Geophysical Union* 79(302): 305.

Guterch A, Grad M, Thybo H, Keller GR, and POLONAISE Working Group (1999) POLONAISE'97 – international seismic experiment between Precambrian and Variscan Europe in Poland. *Tectonophysics* 314: 101–121.

Guterch A, Grad M, Keller GR, and CELEBRATION 2000 Organizing Committee (2001) Seismologists celebrate the new millenium with an experiment in Central Europe. *EOS. Transactions of American Geophysical Union* 82(529): 534–535.

Guterch A, Grad M, Keller GR, et al. (2003a) CELEBRATION 2000 seismic experiment. *Studia Geophysica et Geodaetica* 47: 659–669.

Guterch A, Grad M, Špičák A, et al. (2003b) An overview of recent seismic refraction experiments in Central Europe. *Studia Geophysica et Geodaetica* 47: 651–657.

Guterch A, Grad M, Keller GR, et al. (2004) Huge contrasts of the lithospheric structure revealed by new generation seismic experiments in Central Europe. *Polish Geological Review* 52: 753–760.

Guterch A, Grad M, and Keller GR (2007) Crust and lithospheric structure – Long range controlled source seismic experiments in Europe. In: Schubert G, Romanowicz B, and Dziewonski A (eds.) *Treatise on Geophysics*, vol. 1, pp. 533–558. Amsterdam: Elsevier.

Handy MR, Schmid SM, Bousquet R, Kissling E, and Bernoulli D (2010) Reconciling plate-tectonic reconstructions with the geological-geophysical record of spreading and subduction in the Alps. *Earth Science Reviews* 102: 121–158.

Holbrook WS, Purdy GM, Sheridan RE, et al. (1994) Seismic structure of the US Mid-Atlantic continental margin. *Journal of Geophysical Research* 99: 17871–17891.

Hole JA (1992) Non-linear high resolution three-dimensional seismic travel time tomography. *Journal of Geophysical Research* 97: 6553–6562.

Hrubcová P, Środa P, Špičák A, et al. (2005) Crustal and uppermost mantle structure of the Bohemian Massif based on CELEBRATION 2000 data. *Journal of Geophysical Research* 110: B11305. http://dx.doi.org/10.1029/2004JB003080.

Hrubcová P, Środa P, and CELEBRATION 2000 Working Group (2008) Crustal structure at the easternmost termination of the Variscan belt based on CELEBRATION 2000 and ALP 2002 data. *Tectonophysics* 460: 55–75. http://dx.doi.org/10.1016/j.tecto.2008.07.009.

Hrubcová P, Środa P, Grad M, et al. (2010) From the Variscan to the Alpine Orogeny: Crustal structure of the Bohemian Massif and the Western Carpathians in the light of the SUDETES 2003 seismic data. *Geophysical Journal International* 183: 611–633. http://dx.doi.org/10.1111/j.1365-246X.2010.04766.x.

Janik T, Yliniemi J, Grad M, Thybo H, Tiira T, and POLONAISE P2 Working Group (2002) Crustal structure across the TESZ along POLONAISE'97 seismic profile P2 in NW Poland. *Tectonophysics* 360: 129–152.

Janik T, Grad M, Guterch A, et al. (2005) Lithospheric structure of the Trans-European Suture Zone along the TTZ and CEL03 profiles (from NW to SE Poland). *Tectonophysics* 411: 129–156.

Janik T, Grad M, Guterch A, and CELEBRATION 2000 Working Group (2009) Seismic structure of the lithosphere between the East European Craton and the Carpathians from the net of CELEBRATION 2000 profiles in SE Poland. *Geological Quarterly* 53: 141–158.

Janik T, Grad M, Guterch A, et al. (2011) Crustal structure of the Western Carpathians and Pannonian Basin: Seismic models from CELEBRATION 2000 data and geological implications. *Journal of Geodynamics* 52: 97–113. http://dx.doi.org/10.1016/j.jog.2010.12.002.

Jensen SL, Janik T, Thybo H, and POLONAISE'97 Working Group (1999) Seismic structure of the Palaeozoic platform along POLONAISE'97 profile P1 in southwestern Poland. *Tectonophysics* 314: 123–143.

Jensen SL, Thybo H, and POLONAISE Working Group (2002) Moho topography and lower crustal wide-angle reflectivity around the TESZ in southern Scandinavia and northeastern Europe. *Tectonophysics* 360: 187–213.

Keller GR and Hatcher RD (1999) Some comparisons of the structure and evolution of the southern Appalachian – Ouachita orogen and portions of the Trans-European Suture Zone region. *Tectonophysics* 314: 43–68.

Kissling E, Schmid SM, Lippitsch R, Ansorge J, and Fügenschuh B (2006) Lithosphere structure and tectonic evolution of the Alpine arc: New evidence from high-resolution teleseismic tomography. In: Gee DG and Stephenson RA (eds.) *European Lithosphere Dynamics*, pp. 129–145. London: Geological Society Memoirs 32.

Komminaho K (1997) Software manual for programs MODEL and XRAYS – A graphical interface for SEIS83 program package, Rep. No. 20. University of Oulu, Department of Geophysics, 31 pp.

Koulakov I, Kaban MK, Tesauro M, and Cloetingh S (2009) P- and S-velocity anomalies in the upper mantle beneath Europe from tomographic inversion of ISC data. *Geophysical Journal International* 179: 345–366.

Kováč M, Nagymarosy A, Soták J, and Šutovská K (1993) Late Tetiary paleogeographic evolution of the Western Carpathians. *Tectonophysics* 226: 401–415.

Królikowski C and Petecki Z (1995) *Gravimetric Atlas of Poland*. Warsaw: Polish Geological Institute.

Krysiński L, Grad M, and POLONAISE Working Group (2000) POLONAISE'97 – Seismic and gravimetric modelling of the crustal structure in the Polish basin. *Physics and Chemistry of the Earth A* 25: 355–363.

Krysiński L, Grad M, and Wybraniec S (2009) Searching for regional crustal velocity-density relations with the use of 2-D gravity modelling – Central Europe case. *Pure and Applied Geophysics* 166: 1913–1936. http://dx.doi.org/10.1007/s00024-009-0526-x.

Książkiewicz M (1977) Hypothesis of plate tectonics and the origin of the Carpathians (in Polish, English summary). *Annales de la Société Géologique de Pologne* 47: 329–353.

Kummerow J, Kind R, Oncken O, Giese P, Ryberg T, Wylegalla K, and TRANSALP Working Group (2004) A natural and controlled source seismic profile through the Eastern Alps: TRANSALP. *Earth and Planetary Science Letters* 225: 115–129.

Le Pichon X, Bergerat F, and Roulet M-J (1988) Plate kinematics and tectonics leading to the Alpine belt formation: A new analysis. In: Burchfield BC, Suppe J, and Clark SP (eds.) *Processes in Continental Lithospheric Deformation*, pp. 111–131. GSA Special Paper 218.

Linzer HG, Decker K, Peresson H, Dell'Mour R, and Frisch W (2002) Balancing lateral orogenic float of the Eastern Alps. *Tectonophysics* 354: 211–237.

Lippitsch R, Kissling E, and Ansorge J (2003) Upper mantle structure beneath the Alpine orogen from high-resolution teleseismic tomography. *Journal of Geophysical Research* 108(B8): 2376. http://dx.doi.org/10.1029/2002JB002016.

Lüschen E, Lammerer B, Gebrande H, Millahn K, Nicolich R, and TRANSALP Working Group (2004) Orogenic structure of the Eastern Alps, Europe, from TRANSALP deep seismic reflection profiling. *Tectonophysics* 388: 85–102.

Lüschen E, Borrini D, Gebrande H, Lammerer B, Millahn K, Neubauer F, Nicolich R, and TRANSALP Working Group (2006) TRANSALP-deep crustal Vibroseis and explosive seismic profiling in the Eastern Alps. *Tectonophysics* 414(1–4): 9–38.

Majdański M, Grad M, Guterch A, and SUDETES 2003 Working Group (2005) 2-D seismic tomographic and ray tracing modeling of the crustal structure across the Sudetes Mountains basing on SUDETES 2003 experiment data. *Tectonophysics* 413: 249–269.

Majdański M, Kozlovskaya E, Grad M, and SUDETES 2003 Working Group (2007) 3D structure of the Earth's crust beneath the northern part of the Bohemian Massif. *Tectonophysics* 437: 17–36. http://dx.doi.org/10.1016/j.tecto.2007.02.015.

Majorowicz J, Čermák V, Šafanda J, et al. (2003) Heat flow models across the Trans European Suture Zone in the area of the POLONAISE'97 seismic experiment. *Physics and Chemistry of the Earth A* 28: 375–391.

Malinowski M, Żelaźniewicz A, Grad M, Guterch A, Janik T, and CELEBRATION Working Group (2005) Seismic and geological structure of the crust in the transition from Baltica to Palaeozoic Europe in SE Poland – CELEBRATION 2000 experiment, profile CEL02. *Tectonophysics* 401: 55–77.

Malinowski M, Grad M, Guterch A, and CELEBRATION 2000 (2009a) Three-dimensional seismic modelling of the crustal structure between East European Craton and the Carpathians in SE Poland based on CELEBRATION 2000 data. *Geophysical Journal International* 173: 546–565. http://dx.doi.org/10.1111/j.1365-246X.2008.03742.x.

Malinowski M, Środa P, Grad M, Guterch A, and CELEBRATION 2000 Working Group (2009b) Testing robust inversion strategies for three-dimensionalMoho topography based on CELEBRATION 2000 data. *Geophysical Journal International* 179: 1093–1104. http://dx.doi.org/10.1111/j.1365-246X.2009.04323.x.

McKenzie DP and Morgan WJ (1969) Evolution of triple junctions. *Nature* 224: 125–133.

Mickus KL and Keller GR (1992) Lithospheric structure of the south-central United States. *Geology* 20: 335–338.

Mitterbauer U, Behm M, Brückl E, et al. (2011) Shape and origin of the East-Alpine slab constrained by the ALPASS teleseismic model. *Tectonophysics* 510: 195–206.

Mooney WD (2015) Crust and lithosphere structure: Global crustal structure. *Treatise on Geophysics*, 2nd edn. Amsterdam: Elsevier.

Narkiewicz M, Grad M, Guterch A, and Janik T (2011) Crustal seismic velocity structure of southern Poland: Preserved memory of a pre-Devonian terrane accretion at the

East European Platform margin. *Geological Magazine* 148: 191–210. http://dx.doi.org/10.1017/S001675681000049X.
Perchuć E and Thybo H (1996) Upper mantle P-wave velocity model for the Baltic Shield. *Tectonophysics* 253: 227–245.
Petecki Z, Polechońska O, Cieśla E, and Wybraniec S (2003) *Magnetic Map of Poland, Scale 1: 500,000*. Warsaw: Polish Geological Institute.
Pharaoh TC (1999) Palaeozoic terranes and their lithospheric boundaries within the Trans-European suture zone (TESZ): A review. *Tectonophysics* 314: 17–41.
Plomerová J, Achauer U, Babuška V, Granet M, and BOHEMA Working Group (2003) Passive seismic experiment to study lithosphere–asthenosphere system in the western part of the Bohemian Massif. *Studia Geophysica and Geodaetica* 47: 651–657.
Posgay K, Bodoky T, Hegedűs E, et al. (1995) Asthenospheric structure beneath a Neogene basin in southeast Hungary. *Tectonophysics* 252: 467–484.
Ratschbacher L, Frisch W, Linzer HG, and Merle O (1991) Lateral extrusion in the Eastern Alps, Part 2: Structural analysis. *Tectonics* 10: 257–271. http://dx.doi.org/10.1029/90TC02623.
Royden LH (1993) Evolution of retreating subduction boundaries formed during continental collision. *Tectonics* 12: 629–638.
Royden LH and Dövényi P (1988) Variations in extensional styles at depth across the Pannonian basin. In: Royden LH and Horváth F (eds.) *The Pannonian Basin: A Study in Basin Evolution*, pp. 235–255. Tuslsa: American Association of Petroleum Geologist, Memoir 45.
Růžek B, Vavryčuk V, Hrubcová P, Zedník J, and CELEBRATTION Working Group (2003) Crustal anisotropy in the Bohemian Massif, Czech Republic: Observations based on central European lithospheric experiment based on refraction (CELEBRATION 2000). *Journal of Geophysical Research* 108: 2392. http://dx.doi.org/10.1029./2002JB002242.
Saftić B, Velić J, Sztano O, Juhasz G, and Ivković Ž (2003) Tertiary subsurface facies, source rocks and hydrocarbon reservoirs in the SW part of the Pannonian basin (Northern Croatia and Southwestern Hungary). *Geologia Croatica* 56: 101–122.
Scarascia S and Cassinis R (1997) Crustal structures in the central-eastern Alpine sector: A revision of available DSS data. *Tectonophysics* 271: 157–188.
Scheck-Wenderoth M and Lamarche J (2005) Crustal memory and basin evolution in the Central European Basin System–New insights from a 3D structural model. *Tectonophysics* 397: 143–165.
Schönborn G (1999) Balancing cross sections with kinematic constraints: The Dolomites (northern Italy). *Tectonics* 18: 527–545.
Schweitzer J (1995) Blockage of regional seismic waves by the Teisseyre-Tornquist Zone. *Geophysical Journal International* 123: 260–276.
Seghedi I, Downes H, Szakács A, et al. (2004) Neogene-Quaternary magmatism and geodynamics in the Carpathian-Pannonian region: A synthesis. *Lithos* 72: 117–146.
Środa P (1999) *Modifications of software package ZPLOT by C. Zelt*. Institute of Geophysics, Polish Academy of Sciences.
Środa P and POLONAISE P3 Working Group (1999) P- and S-wave velocity model of the southwestern margin of the Precambrian East European craton; POLONAISE'97, profile P3. *Tectonophysics* 314: 175–192.
Środa P, Czuba W, Grad M, Gaczyński E, Guterch A, and POLONAISE Working Group (2002) Three-dimensional seismic modelling of crustal structure in the TESZ region based on POLONAISE'97 data. *Tectonophysics* 360: 169–185.
Środa P, Czuba W, Grad M, et al. (2006) Crustal and upper mantle structure of the Western Carpathians from CELEBRATION 2000 profiles CEL01 and CEL04: Seismic models and geological implications. *Geophysical Journal International* 167(2): 737–760. http://dx.doi.org/10.1111/j.1365-246X.2006.03104.x.
Stampfli GM and Kozur HW (2006) Europe from the Variscian to the Alpine cycles. In: Gee DG and Stephenson RA (eds.) *European Lithosphere Dynamics*, pp. 57–82. London: Geological Society Memoirs 32.
Stangl R (1990) Die Struktur der Lithosphäre in Schweden, abgeleitet aus einer gemeinsamen Interpretation der P- und S-Wellen Registrierungen auf dem FENNOLORA-Profil. PhD Thesis, University of Karlsruhe.
Šumanovac F (2010) Lithosphere structure at the contact of the Adriatic microplate and the Pannonian segment based on the gravity modelling. *Tectonophysics* 485: 94–106.
Šumanovac F, Orešković J, Grad M, and ALP 2002 Working Group (2009) Crustal structure at the contact of the Dinarides and Pannonian basin based on 2-D seismic and gravity interpretation of the Alp07 profile in the ALP 2002 experiment. *Geophysical Journal International* 179: 615–633. http://dx.doi.org/10.1111/j.1365-246X.2009.04288.x.
Szabó C, Gy Falus, Zajacz Z, Kovács I, and Bali E (2004) Composition and evolution of lithosphere beneath the Carpathian-Pannonian Region: A review. *Tectonophysics* 393: 119–137.
Thomas WA (1991) The Appalachian-Ouachita rifted margin of southeastern North America. *Geological Society of America Bulletin* 103: 415–431.
Thybo H (2001) Crustal structure along the EGT profile across the Tornquist Fan interpreted from seismic, gravity and magnetic data. *Tectonophysics* 334: 155–190.
Thybo H and Perchuć E (1997) The seismic 8° discontinuity and partial melting in the continental mantle. *Science* 275: 1626–1629.
Thybo H, Abramovitz T, Lassen A, and Schjøt F (1994) Deep structure of the Sorgenfrei-Tornquist zone interpreted from BABEL seismic data. *Zeitschrift für Geologische Wissenschaften* 22(1/2): 3–17.
Thybo H, Janik T, Omelchenko VD, Grad M, et al. (2003) Upper lithospheric seismic velocity structure across the Pripyat Trough and the Ukrainian Shield along the EUROBRIDGE'97 profile. *Tectonophysics* 371(1–4): 41–79. http://dx.doi.org/10.1016/S0040-1951(03)00200-2.
Trua T, Serri G, Birkenmajer K, and Pécskay Z (2006) Geochemical and Sr–Nd–Pb isotopic compositions of Mts Pieniny dykes and sills (West Carpathians): Evidence for melting in the lithospheric mantle. *Lithos* 90: 57–76.
Ustaszewski K, Schmid SM, Fügenschuh B, Tischler M, Kissling E, and Spakman W (2008) A map view restoration of the Alpine Carpathian Dinaridic system for the early Miocene. *Swiss Journal of Geosciences* 101(Suppl. 1): 273–294.
Vidale JE (1990) Finite-difference calculation of travel times in three dimensions. *Geophysics* 55: 521–526.
Vosteen H-D, Rath V, Clauser C, and Lammerer B (2003) The thermal regime of the Eastern Alps from inversion analyses along the TRANSALP profile. *Physics and Chemistry of the Earth* 28: 393–405.
Waldhauser F, Kissling E, Ansorge J, and Mueller S (1998) Three-dimensional interface modelling with two-dimensional seismic data: The Alpine crust–mantle boundary. *Geophysical Journal International* 135: 264–278. http://dx.doi.org/10.1046/j.1365-246X.1998.00647.x.
Weber J, Vrabec M, Stopar B, Pavlovcic-Prešeren P, and Dixon T (2006) The PIVO-2003 experiment: A GPS study of Istria Peninsula and Adria Microplate Motion, and active tectonics in Slovenia. In: Pinter N, et al. (ed.) *The Adria Microplate*, pp. 305–320. Springer.
Weber M, Abu-Ayyash K, Abueladas A, Agnon A, Alasonati-Tašárová Z, et al. (2009) Anatomy of the Dead Sea Transform from lithospheric to microscopic scale. *Reviews of Geophysics* 47: RG2002. http://dx.doi.org/10.1029/2008RG000264.
Wilde-Piórko M, Grad M, and POLONAISE Working Group (1999) Regional and teleseismic events recorded across the TESZ during POLONAISE'97. *Tectonophysics* 314: 161–174.
Wilde-Piórko M, Geissler WH, Plomerová J, et al. (2008) PASSEQ 2006–2008: Passive seismic experiment in Trans-European suture zone. *Studia Geophysica et Geodaetica* 52: 439–448.
Wilde-Piórko M, Świeczak M, Grad M, and Majdański M (2010) Integrated seismic model of the crust and upper mantle of the Trans-European Suture zone between the Precambrian craton and Phanerozoic terranes in Central Europe. *Tectonophysics* 481(1–4): 108–115. http://dx.doi.org/10.1016/j.tecto.2009.05.002.
Winchester JA and the PACE TMR Network Team (2002) Potential field imaging of Palaeozoic orogenic structure in northern and central Europe. *Tectonophysics* 360: 5–23.
Wortel MJR and Sparkman W (2000) Subduction and slab detachment in the Mediterranean-Carpathian region. *Science* 290: 1910–1917.
Wybraniec S, Zhou S, Thybo H, et al. (1998) New map compiled of Europe's gravity field. *EOS. Transactions of American Geophysical Union* 79(37): 437–442.
Yan QZ and Mechie J (1989) A fine structural section through the crust and lower lithosphere of the Alps. *Geophysical Journal* 98: 465–488.
Zanolla C, Braitenberg C, Ebbing J, Bernabini M, et al. (2006) New gravity maps of the Eastern Alps and significance for the crustal structures. *Tectonophysics* 414: 127–143.
Zelt CA (1994) *ZPLOT – An Interactive Plotting and Picking Program for Seismic Data*. Cambridge, UK: Bullard Laboratory, University of Cambridge.
Zelt CA and Smith RB (1992) Seismic traveltime inversion for 2-D crustal velocity structure. *Geophysical Journal International* 108: 16–34.
Zeyen H, Dérerová J, and Bielik M (2002) Determination of the continental lithospheric thermal structure in the Western Carpathians: Intergrated modelling of suface heat flow, gravity anomalies and topography. *Physics of the Earth and Planetary Interiors* 134: 89–104.
Zhao W, Mechie J, Brown LD, Guo J, et al. (2001) Crustal structure of central Tibet as derived from project INDEPTH wide angle seismic data. *Geophysical Journal International* 145(2): 486–498. http://dx.doi.org/10.1046/j.0956-540x.2001.01402.x.
Ziegler PA (1990) Geological Atlas of Western and Central Europe. 2nd edn. *Shell International Petroleum*. Maatschappij B.V./London: Geological Society/ Amsterdam: Elsevier.
Zielhuis A and Nolet G (1994) Shear-wave velocity in the upper mantle beneath central Europe. *Geophysical Journal International* 117: 695–715.

1.18 Crust and Lithospheric Structure - Seismological Constraints on the Lithosphere-Asthenosphere Boundary

KM Fischer, Brown University, Providence, RI, USA

© 2015 Elsevier B.V. All rights reserved.

1.18.1	**Definitions of the Lithosphere and Asthenosphere**	587
1.18.2	**Origins of the Seismological Lithosphere–Asthenosphere Boundary**	587
1.18.3	**Imaging the Seismological LAB**	590
1.18.4	**The Seismological LAB Beneath Oceans**	594
1.18.4.1	Tomographic Studies	595
1.18.4.2	Converted and Reflected Wave Studies	596
1.18.4.3	Synthesis of Seismological Constraints	599
1.18.5	**The Seismological LAB Beneath Continents**	599
1.18.5.1	Cratons	600
1.18.5.2	Phanerozoic Continental Regions	603
1.18.6	**Conclusions**	607
Acknowledgments		608
References		608

1.18.1 Definitions of the Lithosphere and Asthenosphere

Earth's lithosphere, the 'strong' outermost layer of Earth often equated with tectonic plates, and the underlying 'weak' asthenosphere have multiple definitions. Kinematically, the lithosphere is often thought of as the layer of crust and mantle that translates coherently with plate motions, creating shear within the asthenosphere (**Figure 1**). Rheologically, the lithosphere is considered to have high viscosity relative to the asthenosphere. In terms of temperature, the lithosphere is the cold boundary layer through which Earth loses heat and cools, and heat transport in the lithosphere is typically equated with conduction, as opposed to convection at greater depths in the mantle. Compositional definitions also exist. The crust, comprising the upper lithosphere, is characterized by compositions that are more silica-rich than the mantle (e.g., **Chapter 1.13**), but in many regions, if not globally, the mantle lithosphere is also thought to be compositionally distinct from the asthenosphere and the deeper upper mantle. Possibilities include bulk compositions for the mantle lithosphere that are depleted and/or dehydrated relative to the asthenosphere because of melt extraction, as has been proposed for the oceanic lithosphere (e.g., Hirth and Kohlstedt, 1996; Karato and Jung, 1998) and corroborated in the subcratonic lithosphere by xenolith samples (e.g., Boyd, 1989; Jordan, 1978; Lee et al., 2011). It has also been proposed that asthenospheric viscosities are especially low owing to the presence of a small amount of partial melt (e.g., Anderson and Sammis, 1970; Hirschmann, 2010; Mierdel et al., 2007).

An ongoing challenge is to relate the physical and chemical properties inherent in these definitions of the lithosphere and asthenosphere to observable quantities that can be directly constrained by geophysical data. This chapter focuses on seismological measures of the properties of the lithosphere and asthenosphere, that is, how these layers are expressed in seismic wave velocities, including anisotropy, and attenuation. However, much can also be learned from lithospheric and asthenospheric conductivity models based on magnetotelluric studies (e.g., Baba et al., 2006; Eaton et al., 2009; Evans et al., 2011; Hirth et al., 2000; Naif et al., 2013), density constraints provided by geoid and gravity data, and geotherm estimates from heat flow data, particularly when these geophysical approaches are combined with xenolith-based geotherms and other geochemical and petrological information (see Artemieva (2011) and Lee et al. (2011) for excellent reviews).

1.18.2 Origins of the Seismological Lithosphere–Asthenosphere Boundary

Much has been learned about how seismic velocities and attenuation vary as a function of temperature, pressure, mineralogy, volatile content, grain size, and deformation-induced fabric, but the field has not yet progressed to the point where mantle composition and physical state can be unambiguously mapped to seismic properties. Helpful reviews can be found in **Chapter 1.26**, Karato (2003), Cooper (2003), Hacker and Abers (2004), Wiens et al. (2008), Karato et al. (2008), and Kohlstedt and Holtzman (2009). Nonetheless, a few general conclusions may be drawn when interpreting differences in seismic properties between the mantle lithosphere and asthenosphere.

Mantle seismic velocity will decrease (and attenuation will increase) as the temperature rises from the lithosphere into the asthenosphere; if temperature and pressure are the only variables that change, the resulting velocity and attenuation gradients will be gradual in depth (**Figure 2**). For example, in numerical models of mantle convection, lithosphere–asthenosphere temperature gradients typically occur over depth intervals of at least 50–70 km (e.g., Billen, 2008; Cooper et al., 2004; King and Ritsema, 2000; Korenaga and Jordan, 2002; Zaranek, 2005) (**Figure 1**) and create velocity and attenuation gradients over comparable depth ranges, as would models for simple conductive cooling of the oceanic lithosphere (e.g., Faul and Jackson, 2005; Rychert et al., 2012b;

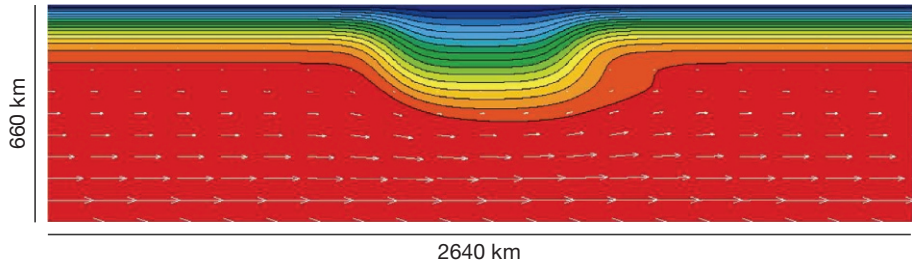

Figure 1 A depth profile of a numerical model in which the lithosphere corresponds to a high-viscosity layer that translates coherently over a lower viscosity asthenosphere. The model was calculated with a 2D hybrid finite difference–finite element approach and assumes an infinite Prandtl number, Boussinesq fluid. Viscosity is temperature dependent, and in the initial model, the lithosphere is assigned a viscosity of 10^{22} Pa s, whereas the reference viscosity in the asthenosphere is 10^{21} Pa s at 1350 °C; initial lithospheric thicknesses are 200 km in the middle and 100 km to the sides. Flow (indicated by white velocity vectors) is driven by a 6 cm per year velocity applied to the bottom boundary of the model, and this model has evolved over 100 My. Blue to red shading indicates increasing temperature (from 0 to 1350 °C), and temperature gradients at the base of the lithosphere occur over >50 km in depth. The fluid is cooled from above, the top boundary is held at a fixed temperature of 0 °C, and the heat flux is set to zero at the bottom boundary. A no-slip boundary condition was applied on the upper model boundary; side conditions are no-stress. The temperature dependence of viscosity is described by a value of 15 for activation energy/((gas constant)(reference temperature)). Reproduced from Zaranek SE (2005) *Roles of Convection in the Evolution of Planetary Interiors and Terrestrial Lithospheres*. PhD Thesis, Brown University, Providence, RI.

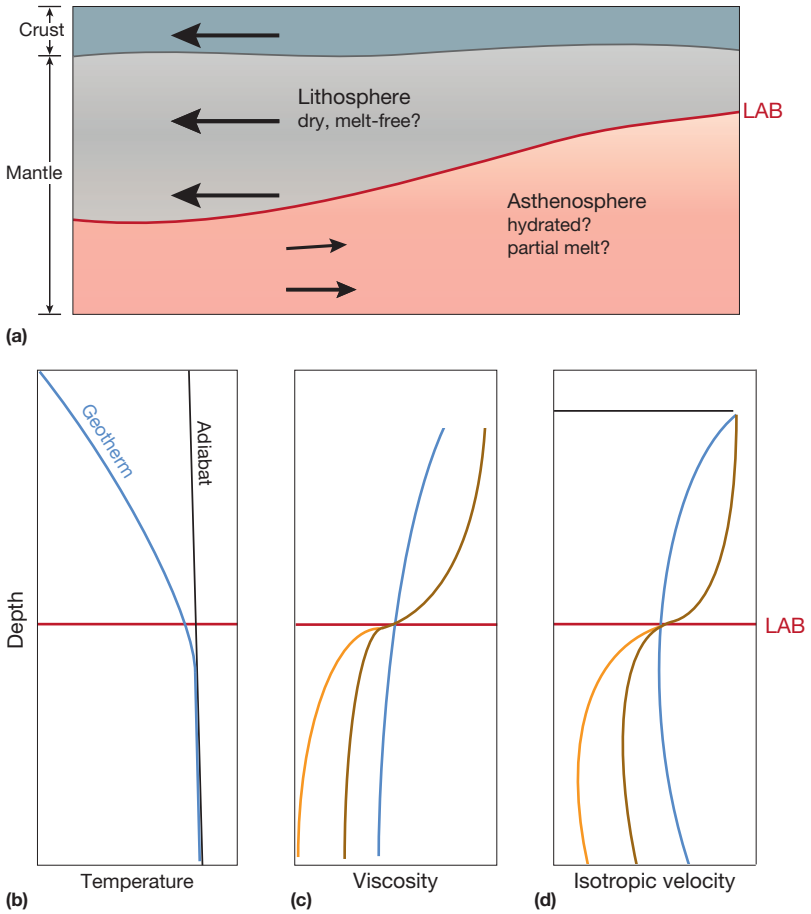

Figure 2 Schematic models of lithosphere–asthenosphere boundary (LAB) properties. (a) Depth profile through the lithosphere and asthenosphere. Arrows show the motion of a coherent lithospheric layer over a deforming asthenosphere. (b) Temperature as a function of depth. In the absence of other factors, the lithosphere would correspond to the cold thermal boundary layer represented by sub-adiabatic temperatures. (c) Mantle viscosity for three cases. Blue: the geotherm in (b). Brown: the geotherm combined with a compositional difference at the LAB (dry, depleted lithosphere over hydrated, fertile asthenosphere). Orange: the latter case plus partial melt in the asthenosphere. (d) Isotropic shear velocity corresponding to the three cases in (c). The black line schematically illustrates the velocity increase from the crust to the mantle. Vertical variations in composition and/or melt are capable of producing more localized gradients in viscosity and velocity than are possible with purely thermal models. Reproduced from Fischer KM, Ford HA, Abt DL, and Rychert CA (2010) The lithosphere–asthenosphere boundary. *Annual Review of Earth and Planetary Sciences* 38: 551–575, http://dx.doi.org/10.1146/annurev-earth-040809-152438, with permission of Annual Reviews, Inc.

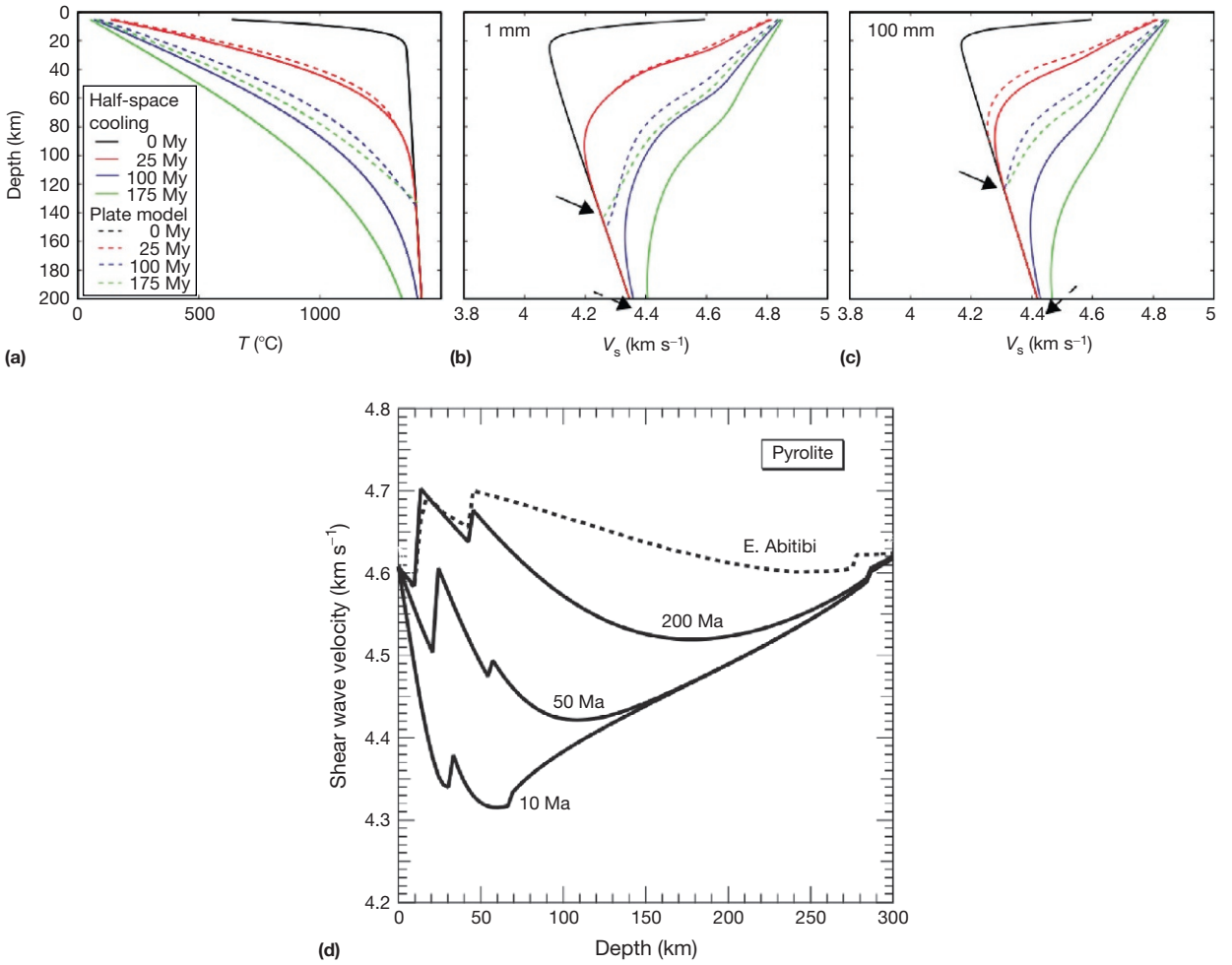

Figure 3 Models for the temperature dependence of shear-wave velocity. (a) Geotherms predicted for a half-space cooling model (solid) and a plate cooling model (dashed) for seafloor ages of 0 My (black), 25 My (red), 100 My (blue), and 175 My (green). Predicted seismic velocities using the temperature to velocity scaling of Jackson and Faul (2010) for mantle grain sizes of 1 mm (b) and 100 mm (c). Seismic wave frequency at each depth is assumed to follow the relationship of dominant period and peak depth sensitivity for fundamental mode Rayleigh waves. Arrows indicate depths at which predicted seismic velocities are the same for old (175 My) as well as young (25 My) oceanic lithosphere for both plate (solid) and half-space (dashed) cooling models; dashed arrows indicate a depth below the limits of the axes. Panels (a)–(c) reproduced from Rychert, C. A., Schmerr, N., and Harmon, N. (2012a). The Pacific lithosphere–asthenosphere boundary: Seismic imaging and anisotropic constraints from SS waveforms. *Geochemistry, Geophysics, Geosystems* 13, Q0AK10, http://dx.doi.org/10.1029/2012GC004194, Copyright 2012 by the American Geophysical Union. (d) Shear-wave velocities predicted for oceanic geotherms of variable age (solid lines) and for a continental geotherm (dashed line). Reproduced from Stixrude L and Lithgow-Bertelloni C (2005) Mineralogy and elasticity of the oceanic upper mantle: Origin of the low-velocity zone. *Journal of Geophysical Research* 110, B03204, http://dx.doi.org/10.1029/2004jb002965, Copyright 2005 by the American Geophysical Union, with permission of John Wiley & Sons.

Stixrude and Lithgow-Bertelloni, 2005) (**Figure 3**). Sharper velocity gradients caused solely by temperature may be produced in regions of focused upwelling, but these will occur only in certain parts of some tectonic environments. Thus, in general, velocity and attenuation gradients that are localized over less than 40 km in depth likely indicate other factors in addition to temperature.

Mantle composition could produce significant gradients over smaller length scales. If the compositional variation is due to depletion by melt extraction, however, the magnitude of the resulting velocity changes is likely to be relatively small. Estimates of shear velocity change caused by reasonable ranges of Mg# vary from ~2.5% (Lee, 2003) to <1% (Schutt and Lesher, 2006). The effect of major element chemistry on upper mantle attenuation is thought to be negligible (Karato, 2003). Water, in the form of point defects in olivine, has the potential to produce larger changes in both shear velocity and attenuation (Hirschmann and Kohlstedt, 2012; Karato, 2003, 2012; Karato and Jung, 1998) although direct experimental evidence is only starting to emerge (Aizawa et al., 2008). Water will diffuse over time, but the length scales of diffusion are sufficiently small (<4 km over ~150 My; Hirth and Kohlstedt, 1996) for hydration variations to produce sharp gradients in seismic properties over Phanerozoic time-scales, with more gradual gradients possible over Proterozoic to Archean time-scales.

The presence of partial melt in the mantle has the potential to reduce seismic velocity and attenuation, although the magnitude of this effect depends strongly on the distribution of

melt at grain boundaries, including its shape/aspect ratio, and on the frequency of the seismic phases, and the mechanisms and magnitude of melt effects are still debated (e.g., Karato, 2012; Kawakatsu et al., 2009; Kohlstedt and Holtzman, 2009; Takei and Holtzman, 2009). If significant melt collects at the top of the asthenosphere, because the base of the lithosphere is relatively impermeable and/or corresponds to the melt solidus (e.g., Hirschmann, 2010; Till et al., 2010), the resulting reduction in asthenospheric velocity, shear velocity in particular, could be large and localized in depth. Conversely, if melt is able to permeate the deep lithosphere, its effects could counteract the otherwise high lithospheric velocities resulting from a dehydrated and depleted composition and colder temperatures, thus creating a gradual or negligible lithosphere–asthenosphere velocity gradient.

Other factors that could contribute to velocity and attenuation gradients between lithosphere and asthenosphere include the grain size of mantle minerals (e.g., Behn et al., 2009; Faul and Jackson, 2005), and frequency dependence in the grain-scale deformation mechanism, such as the peak in anelastic relaxation caused by elastically accommodated grain boundary sliding (Karato, 2012).

Finally, shearing between the lithosphere and asthenosphere will produce lattice-preferred orientation of the anisotropic mantle minerals olivine and orthopyroxene if deformation occurs in the dislocation creep regime (e.g., Karato et al., 2008). Vertical variations in the orientation and strength of seismic anisotropy, therefore, provide another means of estimating the depth and vertical localization of the lithosphere–asthenosphere boundary (LAB).

1.18.3 Imaging the Seismological LAB

This chapter focuses on the seismologically defined LAB, how its properties vary between tectonic settings (oceans, young continents, and cratons), and how they constrain the origins of this fundamental mantle transition. LAB properties of particular interest include the total thickness of the high-velocity lithosphere, the presence or absence of an underlying low-velocity asthenosphere, and differences in seismic velocities (including radial and azimuthal anisotropy), layering/discontinuities, and attenuation between the mantle lithosphere and asthenosphere.

The constraints on three-dimensional structure throughout the volume of the upper mantle provided by tomographic imaging (**Chapter 1.11**) are essential for understanding the LAB. Tomography that involves surface waves is especially useful since it typically provides better vertical resolution within the upper 200 km of the mantle compared to teleseismic body-wave tomography (e.g., Priestley and Tilmann, 2009). Variations in lithospheric thickness appear prominently in both global (**Figures 4** and **5**) and regional models. In map-view (**Figure 4**), the thicker lithosphere found beneath stable cratonic regions is indicated by high velocity and low attenuation persisting to depths greater than 100 km, whereas low velocity and high attenuation at 100 km depth beneath young seafloor signify that the lithosphere must be very thin in these regions.

Vertical variations in absolute velocity highlight velocity gradients across the LAB. For example, clustering analysis of vertical shear-velocity profiles in a recent global model obtained by inverting long-period waveforms reveals that the velocity profiles of young, middle-aged, and old oceanic upper mantle are distinct, as are those of cratons and more recently deformed continental regions (Lekic and Romanowicz, 2011a,b). In these models, the LAB velocity gradient can be viewed as the transition from high-velocity lithosphere to low-velocity asthenosphere, a variation that occurs from <50 to 100 km depth in the youngest oceans and from ~180 to ~250 km beneath cratons. However, models based on surface waves and long-period waveforms alone are not able to distinguish between LAB velocity gradients as gradual as those in the models in **Figure 5** and gradients that are much more localized in depth. This difficulty in distinguishing between sharp and gradual LAB gradients has been quantitatively estimated in fundamental mode Rayleigh wave inversions (Bartzsch et al., 2011; Eaton et al., 2009). While the incorporation of surface wave overtones (e.g., **Figure 5**) will typically improve vertical resolution, these inversions will still have difficulty in differentiating between gradients over ~50 km and those over smaller

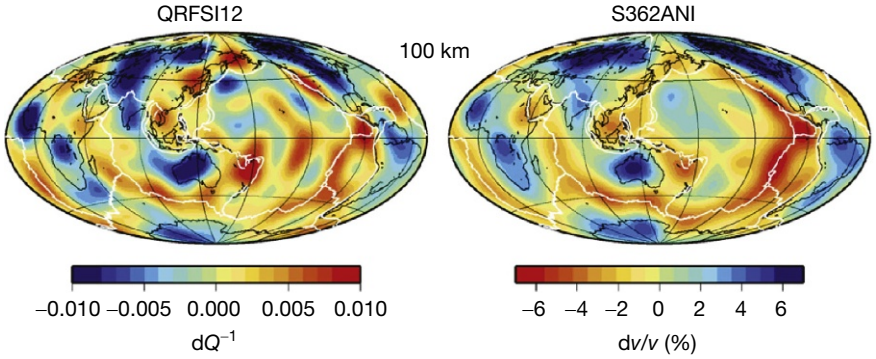

Figure 4 Models of global shear attenuation (left) and shear velocity (right) shown at a depth of 100 km illustrate differences between cratonic regions where the lithosphere is characterized by thick layers with high velocity and low attenuation, and regions with thinner lithosphere. The attenuation model (Dalton et al., 2008) is plotted as its deviation from the globally averaged attenuation value at 100 km. Isotropic velocities from the radially anisotropic shear-velocity model of Kustowski et al. (2008) are shown expanded in spherical harmonics up to degree 12. Reprinted from Dalton CA, Ekström G, and Dziewonski AM (2009) Global seismological shear velocity and attenuation: A comparison with experimental observations. *Earth and Planetary Science Letters* 284: 65–75, Copyright 2009, with permission from Elsevier.

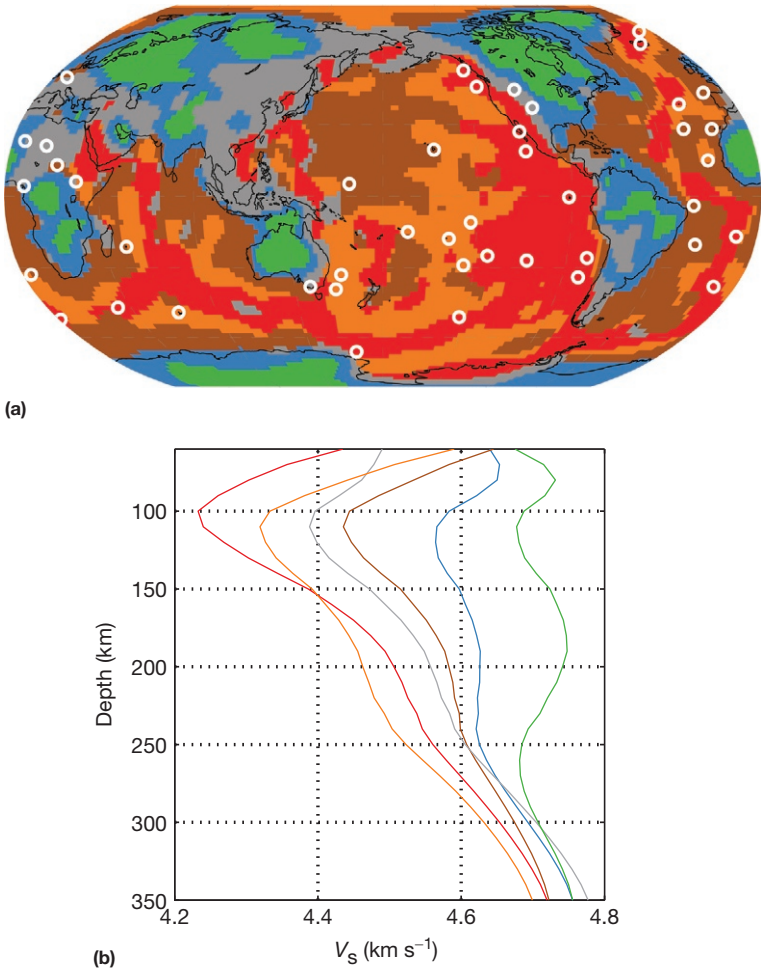

Figure 5 A global model of absolute shear-wave velocity that illustrates thicker, high-velocity lithosphere beneath cratonic regions and thinner lithosphere beneath younger continental regions and oceans. A decrease in absolute velocity with depth into a layer interpretable as the asthenosphere is present globally, and asthenospheric velocities are lowest beneath young oceans. (a) Geographic extents of six regions defined by *k*-means clustering as having similar absolute shear-velocity profiles in the model of Lekic and Romanowicz (2011a) that includes radial anisotropy. The clusters roughly delineate regions with young (red), middle-aged (orange), and old (brown) oceanic crust, more recently tectonized continental crust (gray), and cratons (green). (b) Average isotropic shear-velocity profiles corresponding to the six clusters. Reprinted from Lekic V and Romanowicz B (2011) Tectonic regionalization without a priori information: A cluster analysis of upper mantle tomography. *Earth and Planetary Science Letters* 308: 151–160, Copyright 2011, with permission from Elsevier.

depth ranges. In addition, the magnitude of the velocity drop at the LAB exhibits dependence on the starting model used in the tomographic inversion (e.g., Romanowicz, 2009) and varies considerably between different studies (Bedle and van der Lee, 2009; Kustowski et al., 2008; Lekic and Romanowicz, 2011a,b; Nettles and Dziewoński, 2008; Ritsema et al., 2011; Yuan et al., 2011).

In addition to gradients in isotropic velocity, vertical variations in either radial or azimuthal velocity anisotropy provide another means of defining the LAB. (See **Chapter 1.10** for discussion of wave propagation in anisotropic media.) For example, shear in the asthenosphere in the dislocation creep regime could create azimuthal anisotropy with a distinct orientation or strength relative to anisotropy in the mantle lithosphere. If azimuthal anisotropy generated by roughly horizontal shear is averaged over back-azimuth, it appears as radial anisotropy with a slow vertical axis and, thus, vertical variations in radial anisotropy might also be expected at the LAB. Changes in anisotropy at the LAB have been explored with inversions involving surface waves and long-period waveforms at both regional (e.g., Chen et al., 2007; Darbyshire and Lebedev, 2009; Debayle and Kennett, 2000; Deschamps et al., 2008; Ekström and Dziewonski, 1998; Gaherty, 2004; Gaherty and Jordan, 1995; Gaherty et al., 1996, 1999; Li et al., 2003, 2005; Lin et al., 2011; Maggi et al., 2006; Marone and Romanowicz, 2007; Nishimura and Forsyth, 1988, 1989; Simons et al., 2002; Yuan and Romanowicz, 2010a,b; Yuan et al., 2011) and global scales (e.g., Beucler and Montagner, 2006; Debayle et al., 2005; Ekström, 2000, 2011; Gung et al., 2003; Montagner and Tanimoto, 1990; Nettles and Dziewoński, 2008; Plomerová et al., 2002; Trampert and Woodhouse, 2003). Incorporating shear-wave splitting in teleseismic phases such as SKS into surface wave tomography adds constraints on azimuthal anisotropy, particularly at greater

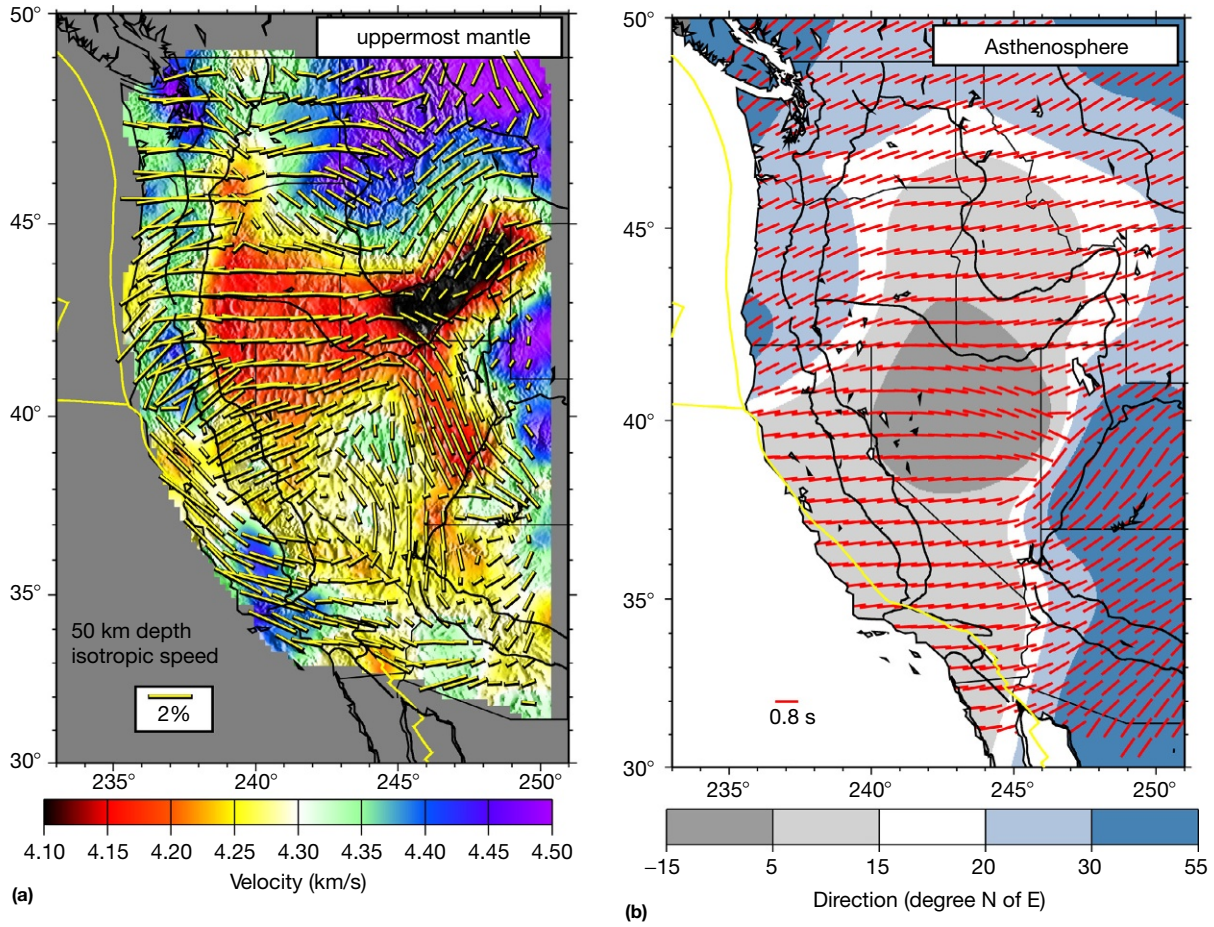

Figure 6 A shear-velocity model for the western United States that illustrates variations in azimuthal anisotropy between the shallow mantle lithosphere and the asthenosphere. (a) Isotropic velocity (background color) and azimuthal anisotropy at a depth of 50 km beneath the western United States. Yellow bars indicate the fast axis and amplitude of azimuthal anisotropy. (b) The direction of the fast axis of azimuthal anisotropy in the asthenosphere (background color and red bar orientation) and the amplitude of anisotropy measured as its equivalent SKS phase splitting time (red bar length). Reprinted from Lin FC, Ritzwoller MH, Yang Y, Moschetti MP, and Fouch MJ (2011) Complex and variable crustal and uppermost mantle seismic anisotropy in the western United States. *Nature Geoscience* 4: 55–61, Copyright 2011, by permission from Macmillan Publishers Ltd.

depths where surface waves lose sensitivity (Gaherty, 2004; Li et al., 2003; Lin et al., 2011; Marone and Romanowicz, 2007; Yuan and Romanowicz, 2010a,b; Yuan et al., 2011) (**Figure 6**). However, vertical resolution of gradients in anisotropy at the LAB using these methods is on the order of 50 km or more in depth.

Complementary resolution of LAB depths and velocity gradients is provided by phases whose paths dive through the LAB region, including multiple-bounce S waves (Tan and Helmberger, 2007) and regional P and SH waveforms (Chu et al., 2012a,b, in press; Grand and Helmberger, 1984) (**Figure 7**). However, in models based on these phases, tradeoffs exist between the magnitude of the LAB velocity drop and the depth range over which it is distributed, creating uncertainty in the LAB velocity gradient. For example, regional P waveforms that indicate an LAB gradient centered at ~180 km can be fit almost equally well by a larger velocity drop over ~30 km in depth and a smaller velocity drop over ~60 km in depth (Chu et al., 2012a).

A more precise vertical resolution of LAB velocity gradients may be obtained from teleseismic phases that convert or reflect at the LAB (e.g., **Chapter 1.09**). Examples include ScS reverberations (Bagley and Revenaugh, 2008; Revenaugh and Jordan, 1991), SS precursors (Rychert and Shearer, 2011; Rychert et al., 2012b; Schmerr, 2012), and Sp and Ps phases (Figure) (reviews may be found in Eaton et al., 2009; Fischer et al., 2010; Kind et al., 2012; Rychert et al., 2010). The presence of a significant Sp arrival typically indicates a shear-velocity gradient that is localized over ~30 km or less, assuming that the velocity drop is ~8% or less (Ford et al., 2010; Rychert et al., 2007, 2010). The shorter periods in Ps phases provide an even sharper vertical resolution, for example, showing that vertical gradients over less than 15 km are required (Rychert et al., 2005, 2007). Adding reflected and converted phases to inversions of surface waves and long-period waveforms adds significantly to vertical resolution of LAB velocity gradients (Bodin et al., 2014; Gaherty et al., 1996, 1999). For example, Gaherty et al. (1996) concluded that the Pacific LAB corresponded to a shallow (~70 km depth) vertical gradient over 30 km or less based on a joint inversion of long-period waveforms and ScS reverberations. In contrast, Bodin et al. (2014) used a joint inversion of Sp receiver functions and surface wave

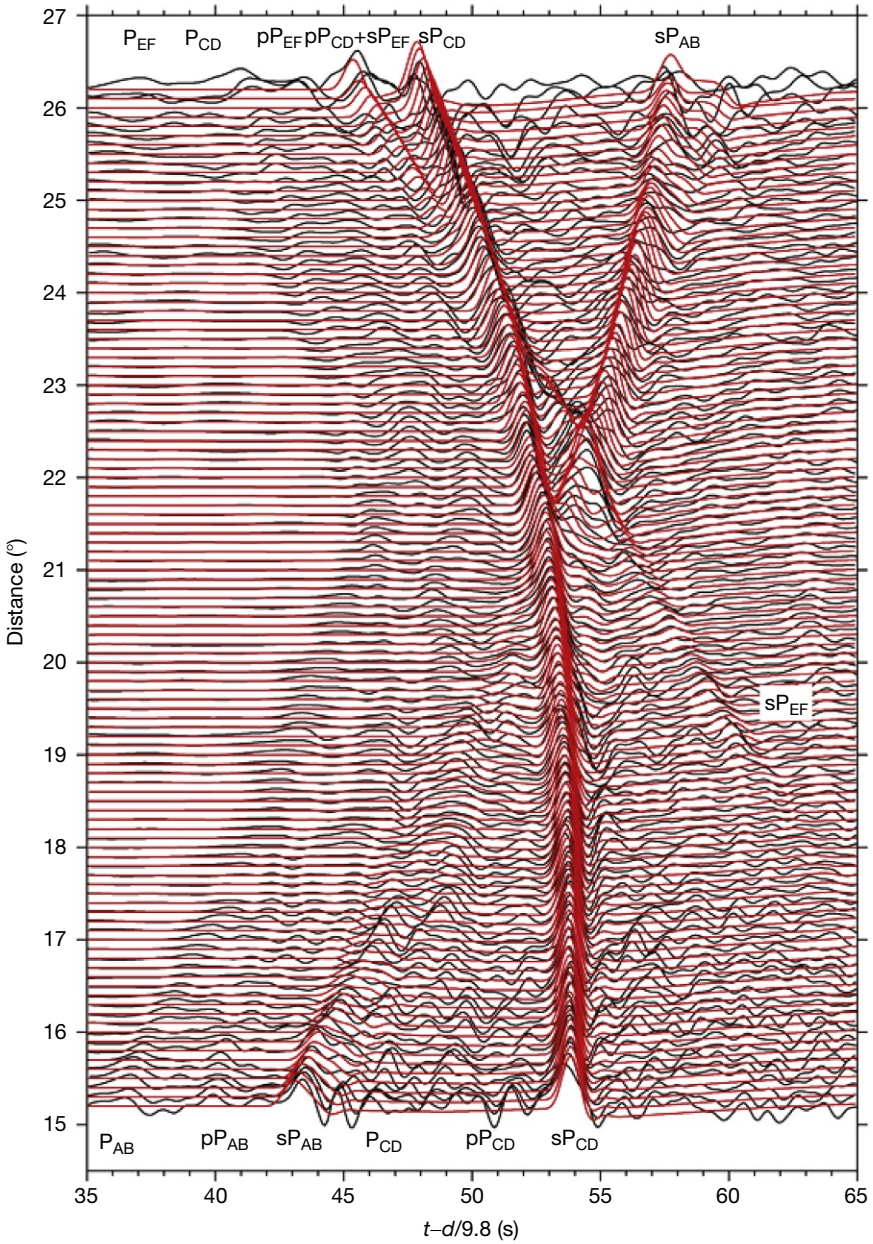

Figure 7 Regional waveforms indicate that a negative velocity gradient centered at ~180 km depth (interpretable as the LAB) exists beneath a portion of cratonic North America. Stacked waveforms from an earthquake in Quebec recorded by stations of the EarthScope Transportable Array are shown in red and synthetic waveforms for a one-dimensional model of P-wave velocity of the cratonic upper mantle are shown in black. In the model, a low-velocity zone starts at depths of ~165 km. This feature is reflected in the sP_{AB} branch, which is clear at distances of less than 18°, but loses amplitude at slightly greater distances because of the low-velocity zone. sP_{AB} amplitudes increase beyond 22° where phase raypaths turn below the low-velocity zone. Reproduced from Chu R, Schmandt B, and Helmberger DV (2012a) Upper mantle P velocity structure beneath the Midwestern United States derived from triplicated waveforms. *Geochemistry*, *Geophysics*, *Geosystems* 13, Q0AK04, http://dx.doi.org/10.1029/2011GC003818, Copyright 2012 by the American Geophysical Union, with permission of John Wiley & Sons.

dispersion to demonstrate that the LAB beneath Hyderabad, India, is both deep and gradual, extending from depths of 150–200 km. Resolution of azimuthally anisotropic shear-velocity gradients with reflected and converted phases such as SS precursors (Rychert et al., 2012b) and Sp receiver functions (Ford, 2013) is also being explored.

Active source reflection and refraction data have also imaged velocity gradients and/or reflectors inferred to be the transition from a shallower high velocity layer to a deeper low-velocity zone (MONA LISA Working Group, 1997; Morozova et al., 1999; Pavlenkova et al., 2002; Perchuc and Thybo, 1996; Ryberg et al., 1996; Steer et al., 1998a,b; Thybo, 2006; Thybo and Perchuc, 1997); in order to be visible at the high frequencies in active source data, these features must be highly localized in depth. The 8° discontinuity (a delay in the first arriving phase at a distance of ~8°) observed in many

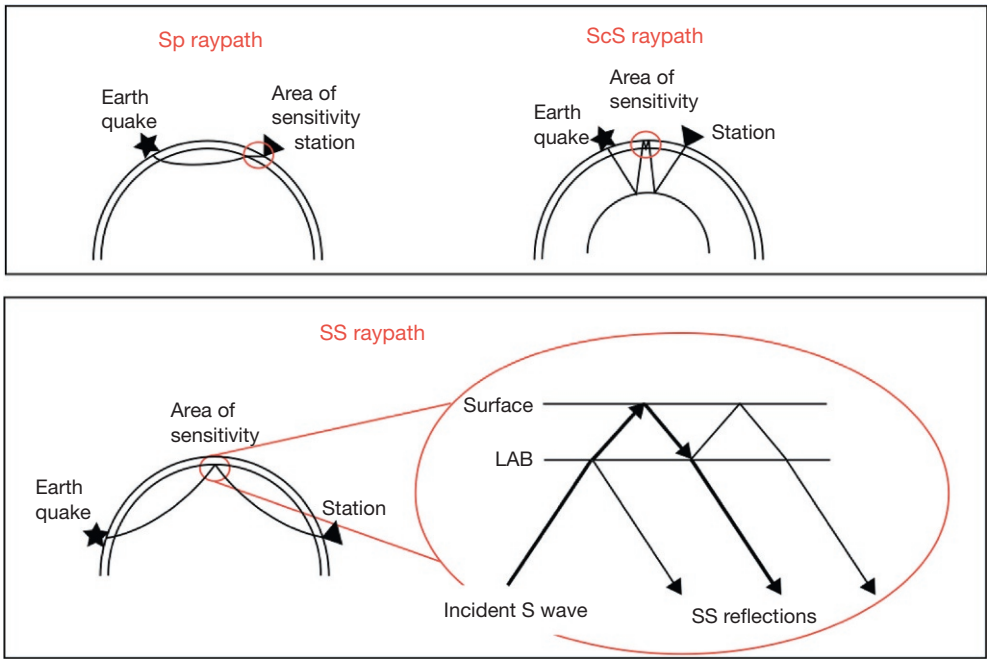

Figure 8 Schematic diagram of raypaths for reflected and convert phases used to image the LAB. Red circles show the regions where the particular paths shown are sensitive to LAB structure. Reverberations from ScS multiples will reflect at the discontinuity at other points along the path, and this family of phases results in path-averaged estimates of discontinuity properties. Multiple-bounce S waveforms look similar to the SS, but with additional bounces at Earth's surface between source and receiver (e.g., Tan and Helmberger, 2007). Reproduced from Rychert CA, Schmerr N, and Harmon N (2012) The Pacific lithosphere–asthenosphere boundary: Seismic imaging and anisotropic constraints from SS waveforms. *Geochemistry, Geophysics, Geosystems* 13, Q0AK10, http://dx.doi.org/10.1029/2012GC004194, Copyright 2012 by the American Geophysical Union, with permission of John Wiley & Sons.

long-range seismic profiles has been interpreted to represent a widespread low-velocity zone whose top lies at a depth of ~100 km (e.g., Nielsen et al., 2002; Thybo, 2006; Thybo and Perchuc, 1997). In younger continental regions with thinner lithosphere, the 8° discontinuity could correspond to the LAB. However, in cratonic regions where fast velocities indicative of the lithosphere extend to depths of 150 km or more, the low-velocity zone associated with the 8° discontinuity would lie within the lithosphere. An 8° discontinuity has also been observed in passive source regional P waveforms (Chu et al., 2012a).

1.18.4 The Seismological LAB Beneath Oceans

Given its relatively simple kinematic and thermal history, the oceanic lithosphere provides a particularly useful setting in which to test competing models for the factors that control LAB velocity gradients. A number of hypotheses have been proposed to explain the age-dependent deepening of the seafloor, which is often described as following the prediction of conductive cooling of the mantle with an asymptotic plate thickness (Parsons and Sclater, 1977; Stein and Stein, 1992). Hypotheses include conductive cooling plus small-scale convection below the lithosphere (e.g., Eberle and Forsyth, 1995; Parsons and McKenzie, 1978; Yuen and Fleitout, 1985), large-scale mantle plumes (e.g., Davies, 1988), asthenospheric flow fed by mantle plumes (Phipps Morgan et al., 1995), and overall readjustment of the oceanic upper thermal boundary layer in response to underlying mantle convection (Adam and Vidal, 2010). All of these hypotheses predict some cooling of the oceanic lithosphere with crustal age, except for Adam and Vidal (2010) who prefer a relationship of seafloor depth with distance along mantle flow lines.

If the properties of the oceanic lithosphere are governed by temperature alone and temperature is controlled by one of the age-dependent hypotheses, the LAB would deepen with crustal age. For all hypotheses, the LAB velocity gradient would be distributed over many tens of kilometers in depth, particularly in regions of old oceanic lithosphere (e.g., Faul and Jackson, 2005; Rychert et al., 2012b; Stixrude and Lithgow-Bertelloni, 2005) (**Figure 3**). If the base of the oceanic lithosphere corresponds to the mantle solidus, for example, the solidus of peridotite containing small amounts of water and CO_2 (Hirschmann, 2010) (**Figure 9**), the depth of the LAB would increase more slowly with crustal age (assuming age-dependent cooling) and the presence of melt in the asthenosphere could create a larger drop in velocity at the LAB that is more localized in depth (possibly a few kilometers or less). If, instead, the oceanic lithosphere corresponds to a layer of dry, chemically depleted peridotite (e.g., Hirth and Kohlstedt, 1996), once created its thickness would not change with crustal age, and the LAB velocity gradient could occur over a few kilometers, although the magnitude of the velocity drop would be smaller than the maximum velocity drops hypothesized for melt, particularly at the base of old (>100 Ma) oceanic lithosphere (e.g., Karato and Jung, 1998; Kawakatsu et al., 2009). However, if the base of the dry depleted layer is

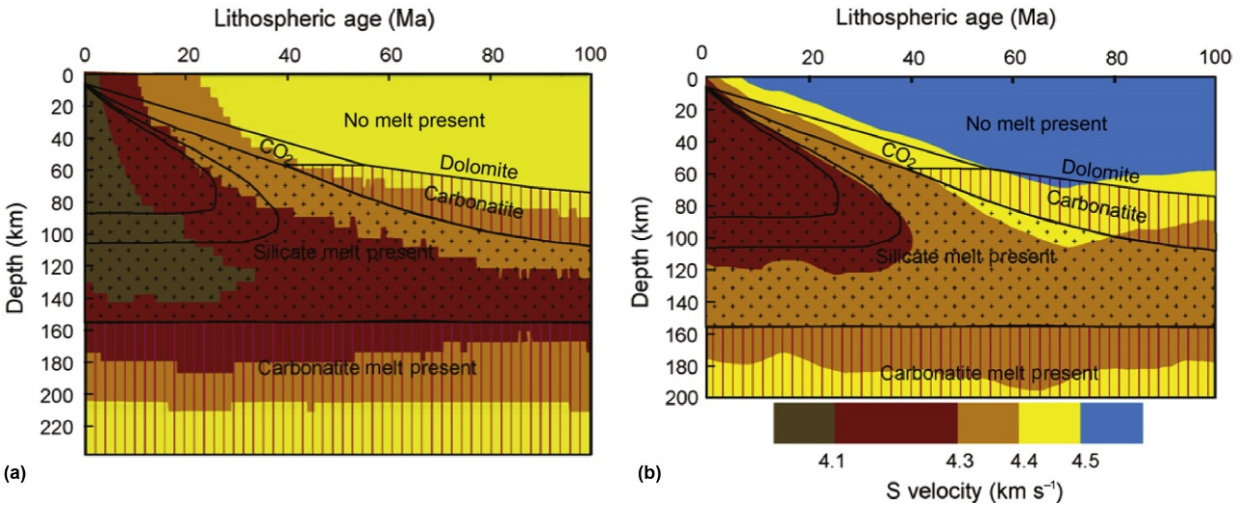

Figure 9 Diagram showing melt distribution in the oceanic upper mantle predicted for a mantle potential temperature of 1350 °C superimposed on average shear-velocity profiles for a given lithospheric age from the tomographic models of (a) Priestley and McKenzie (2006) (SV component velocities) and (b) Ritzwoller et al. (2004) (isotropic velocity in a model that includes radial anisotropy). Regions of silicate melt stability and greater calculated melt fractions, in general, correspond to lower shear velocities; this correlation is consistent with, but does not require, partial melt contributing to reduction of shear velocity. Reprinted from Hirschmann MM (2010) Partial melt in the oceanic low velocity zone. *Physics of the Earth and Planetary Interiors* 179: 60–71, Copyright 2010, with permission from Elsevier.

relatively impermeable to melt, melt could collect at the top of the asthenosphere, enhancing the drop in shear velocity. Vertical variations in olivine grain size can also contribute to increasing velocity gradients (Behn et al., 2009; Faul and Jackson, 2005) (**Figure 3(a)–3(c)**, from Rychert et al., 2012b). In addition, Karato (2012) proposed that the shear-velocity gradient at the oceanic LAB may be produced by anelastic relaxation from elastically accommodated grain boundary sliding, assuming a hydrated asthenosphere and a dry lithosphere.

The existence and degree of age dependence in the apparent thickness of a high-velocity lithospheric layer and the velocity gradient at the apparent seismological LAB are key constraints when testing different candidate processes for creating the oceanic lithosphere; the character of anisotropy in the lithosphere and asthenosphere adds insight into deformation in these layers. A synthesis of diverse seismological constraints on the oceanic lithosphere and asthenosphere reveals that different types of seismic waves are consistent with different types of structures, and no single process for generating the oceanic LAB explains all the observations.

1.18.4.1 Tomographic Studies

Surface waves and long-period waveforms show an increase in the thickness and maximum velocity of the high-velocity lithospheric layer as a function of crustal age (**Figures 5, 9**, and **10**) (e.g., Ekström, 2000; Lekic and Romanowicz, 2011a,b; Maggi et al., 2006; Nettles and Dziewoński, 2008; Nishimura and Forsyth, 1988, 1989; Priestley and McKenzie, 2006; Ritzwoller et al., 2004). In addition, the observed increase in the minimum asthenospheric velocity beneath older oceanic lithosphere (**Figures 5(b)** and **10**) is consistent with cooler temperatures (or less melt or water) in the asthenosphere. However, while these age-dependent patterns are pronounced, alternating high-velocity and low-velocity regions in the direction normal to absolute plate motion have also been documented, initially from Tonga to Hawaii (Katzman et al., 1998) but now globally (French et al., 2013), and these features suggest a pattern of secondary convection.

The oceanic asthenosphere is also the locus of particularly strong radial anisotropy with a slow vertical symmetry axis (**Figure 10**) (Ekström and Dziewonski, 1998; French et al., 2013; Kustowski et al., 2008; Lekic and Romanowicz, 2011a; Nettles and Dziewoński, 2008; Nishimura and Forsyth, 1989; Smith et al., 2004), except beneath mid-ocean ridges where, in some studies, the vertical symmetry axis is fast (Montagner, 2002; **Figure 7** in **Chapter 1.19**; French et al., 2013). These geometries of anisotropy are consistent with horizontal flow in the asthenosphere away from ridges but vertical flow directly beneath ridges. Azimuthal anisotropy in the oceanic asthenosphere, in general, manifests a fast horizontal symmetry axis that is roughly aligned in the direction of absolute plate motion, although geodynamic models that incorporate three-dimensional flow tend to fit observed azimuthal patterns better than simple absolute plate motion predictions; azimuthal anisotropy resolved in the oceanic lithosphere is more consistent with the direction of seafloor spreading frozen into the lithosphere at the ridge where it formed (Becker et al., 2007; Debayle et al., 2005; Ekström, 2011; Forsyth, 1975; Gaboret et al., 2003; Maggi et al., 2006; Nishimura and Forsyth, 1988, 1989; Smith et al., 2004; Tanimoto and Anderson, 1984). These constraints on anisotropy are consistent with the idea that the isotropically high-velocity oceanic lithosphere corresponds to a layer that is translating with little continued deformation, whereas the isotropically low-velocity asthenosphere has a significantly lower viscosity and accumulates strain and anisotropy because of ongoing mantle convection.

The age-dependent trends in the surface wave and long-period waveform tomography are consistent with an oceanic

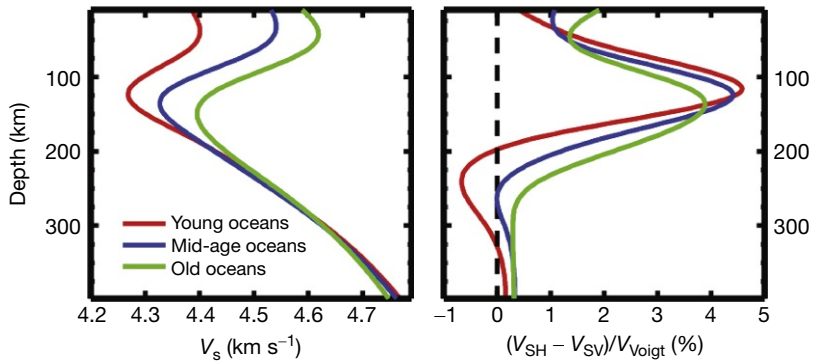

Figure 10 Average shear-wave velocity from surface wave tomography for oceanic regions with different plate ages, with (left) absolute isotropic velocities and (right) radial anisotropy. This model illustrates the presence of strong radial anisotropy in the oceanic asthenosphere, as well as increases in the thickness and maximum velocity of the high-velocity lithospheric layer and the minimum asthenospheric velocity as a function of crustal age. Reproduced from Nettles M and Dziewoński AM (2008) Radially anisotropic shear velocity structure of the upper mantle globally and beneath North America. *Journal of Geophysical Research* 113, http://dx.doi.org/10.1029/2006jb004819, Copyright 2008 by the American Geophysical Union, with permission of John Wiley & Sons.

lithosphere whose thickness is defined by cooling and whose LAB velocity gradient depends only on temperature and, hence, is distributed gradually in depth. The tomography models are also consistent with an LAB that corresponds to time-dependent deepening of the solidus (e.g., Hirschmann, 2010; **Figure 9**). Although they do not require an LAB velocity gradient that is localized in depth, as could be produced by partial melt in the asthenosphere versus a melt-free lithosphere, they also are not incompatible with one; moreover, gradients in melt could also be gradual. The age-dependent trends in the tomography models are not consistent with an oceanic lithosphere that is defined solely as a layer of dry, depleted peridotite, in the absence of cooling, since such a model would produce no age dependence to either the depth of the LAB or the velocity contrast between lithosphere and asthenosphere. However, the combination of cooling and a dry, depleted lithosphere over a more hydrated and fertile asthenosphere could potentially replicate the tomography, since greater cooling at older crustal ages could increase velocities in the mantle below the dehydration/depletion boundary, thus increasing the apparent thickness of a high-velocity layer. Cooling would also reduce the magnitude of the velocity drop at the dehydration/depletion boundary at older crustal ages by reducing the impact of water in olivine on attenuation and, therefore, on shear velocity (e.g., Karato and Jung, 1998).

1.18.4.2 Converted and Reflected Wave Studies

While surface wave and long-period waveform tomography is compatible with a broad range of models, creation of the oceanic LAB by thermal gradients alone is challenged by studies of reflected and converted seismic waves that document LAB velocity gradients that occur over 30 km or less. The degree of depth localization in the LAB velocity gradient varies with the type of seismic phase and its frequency content. In addition, while some reflected and converted phase studies are compatible with an increase in the apparent thickness of a high-velocity layer with crustal age, others are not, thus raising questions about whether either simple cooling or solidus-based models can universally explain oceanic lithospheric seismic properties. Fischer et al. (2010) and Rychert et al. (2012b) provide additional reviews (e.g., **Figure 11**).

Studies that show a lack of age dependence in the apparent thickness of the oceanic lithosphere include analyses of ScS reverberations (Bagley and Revenaugh, 2008; Revenaugh and Jordan, 1991), waveform inversion combined with ScS reverberations (Gaherty et al., 1996, 1999), modeling of multiple-bounce S phases (Tan and Helmberger, 2007), and Sp and Ps phases at stations on or near ocean islands.

Sp and Ps phases sample crust and mantle structure at the phase scattering point (**Figure 8**), and these points lie in a roughly annulus-shaped region around the station whose horizontal radius increases with increasing depth and phase ray parameter. Sp phases have the opposite polarity of Ps arrivals, but in receiver functions, Sp amplitudes are typically flipped to agree with the Ps convention. For the purposes of this chapter, 'negative' Sp phases will refer to what are, in fact, positive arrivals that correspond to a negative velocity gradient. Sp and Ps studies in the oceans have produced estimates of a significant drop in velocity at depths ranging from 40 to 140 km (Collins et al., 2002; Heit et al., 2007; Kumar et al., 2005a, 2007; Li et al., 2000, 2004; Rychert and Shearer, 2009; Vinnik et al., 2005; Wölbern et al., 2006), with a global Ps average of 70 ± 4 km (Rychert and Shearer, 2009), but these depth estimates have no apparent correlation with time since the lithosphere was generated at a mid-ocean ridge (Fischer et al., 2010; Rychert et al., 2010). However, since the ocean islands at which these measurements were made are associated with hotspot activity, the lithospheric thicknesses may be anomalous, complicating their interpretation.

ScS reverberations sample discontinuity structure at multiple reflection points along the path, resulting in a path-averaged estimate of discontinuity properties. Revenaugh and Jordan (1991) found a discontinuity corresponding to a drop in velocity at a depth of ~60 km beneath the ~100 Ma lithosphere between Tonga/Fiji and Hawaii, but data for this path were reexamined by Bagley and Revenaugh (2008) who concluded that a depth of ~108 km was more accurate. Bagley and

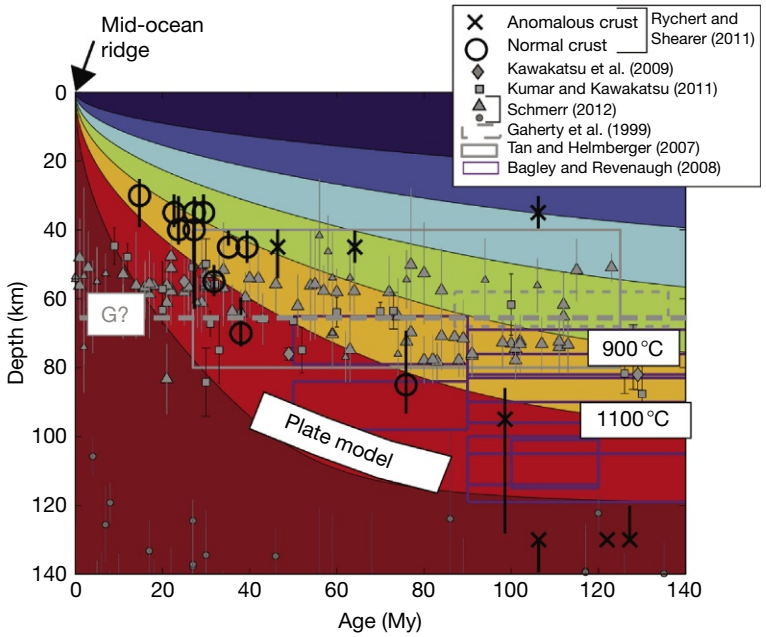

Figure 11 Observations of mantle discontinuity depths from the Pacific ocean compared to isotherms from a cooling plate model. Large black symbols correspond to long-period SS precursor results (Rychert and Shearer, 2011) where open circles correspond to normal seafloor and ×s are from areas with hotspot activity. Gray triangles are observations from short-period SS precursors; gray circles are also from short-period SS precursors, but they are a phase interpreted as the base of the low-velocity asthenosphere. Gray squares and diamonds are from Sp and Ps receiver functions (Kawakatsu et al., 2009; Kumar and Kawakatsu, 2011). Gray boxes show LAB depth from the shear-velocity models of Gaherty et al. (1996) (dashed) and Tan and Helmberger (2007). Purple boxes show discontinuity depths from ScS reverberations (Bagley and Revenaugh, 2008). Reproduced from Rychert CA, Schmerr N, and Harmon N (2012) The Pacific lithosphere–asthenosphere boundary: Seismic imaging and anisotropic constraints from SS waveforms. *Geochemistry, Geophysics, Geosystems* 13, Q0AK10, http://dx.doi.org/10.1029/2012GC004194, Copyright 2012 by the American Geophysical Union, with permission of John Wiley & Sons.

Revenaugh (2008) sampled a wide variety of corridors around the Pacific, and found negative discontinuities at depths ranging from 72 to 112 km, except for a path from Central America to Hawaii where no discontinuity was present in a comparable depth range. Overall, the apparent discontinuity depths are not well correlated with the range of crustal age on each corridor (as shown by the purple rectangles in **Figure 11**, which was compiled by Rychert et al. (2012b)) although the deepest discontinuity estimates do correspond to the oldest ages. These data imply large (>8%) velocity drops if they occur as step functions in depth and even greater velocity decreases as the depth range of the velocity gradient increases, leading Bagley and Revenaugh (2008) to the conclusion that the gradient must occur over 30 km or less.

Through a joint inversion of ScS reverberations with frequency-dependent travel-times from surface waves (Love and Rayleigh) and shear body waves (including S, sS, and multiple-bounce S phases), Gaherty et al. (1996) determined that a high-velocity layer with a thickness of 68 ± 4 km above a low-velocity layer best fit the corridor between Tonga/Fiji and Hawaii. Tan and Helmberger (2007) modeled multiple-bounce S phases on a corridor from Tonga/Fiji to southern California that spans a very wide range of crustal ages and found a high-velocity layer/low-velocity layer transition at a depth of 60 ± 20 km. Taken together, these two studies suggest a very uniform depth for the Pacific LAB and essentially no resolvable age dependence (solid and dashed gray rectangles in **Figure 11**). However, the ScS reverberations in the Gaherty et al. (1996) inversion were analyzed with the approach of Revenaugh and Jordan (1991), and when Bagley and Revenaugh (2008) reexamined the Revenaugh and Jordan (1991) ScS records with an updated instrument response, they obtained a deeper discontinuity estimate comparable to their preferred value of ~108 km depth for the Tonga/Fiji–Hawaii corridor. This point raises the question of whether the Gaherty et al. (1996) joint inversion approach might produce a deeper LAB with the Bagley and Revenaugh (2008) ScS constraints. However, while some trade-offs between the thickness and velocity of the high-velocity layer exist, the surface waves and other body wave phases used in the Gaherty et al. (1996) inversion would not be adequately fit by a high-velocity layer as thick as 100 km, although an ~75-km-thick layer would likely be possible (J. Gaherty, personal communication, 2013). However, even at 75 km, the Gaherty et al. (1999) fast layer thickness would still overlap the 60 ± 20 km estimate of Tan and Helmberger (2007).

Converted and reflected wave studies that argue for age dependence in lithospheric thickness include Sp and Ps phases that sample oceanic lithosphere near subduction zones (Kawakatsu et al., 2009; Kumar and Kawakatsu, 2011; Kumar et al., 2011) and SS precursors (Rychert and Shearer, 2011; Rychert et al., 2012b; Schmerr, 2012).

Sp and Ps receiver functions from the Pacific and Philippine Sea Plates near Japan (Kawakatsu et al., 2009; Kumar et al., 2011) and from around the rim of the Pacific (Kumar and Kawakatsu, 2011) (**Figure 12**) indicate the presence of a

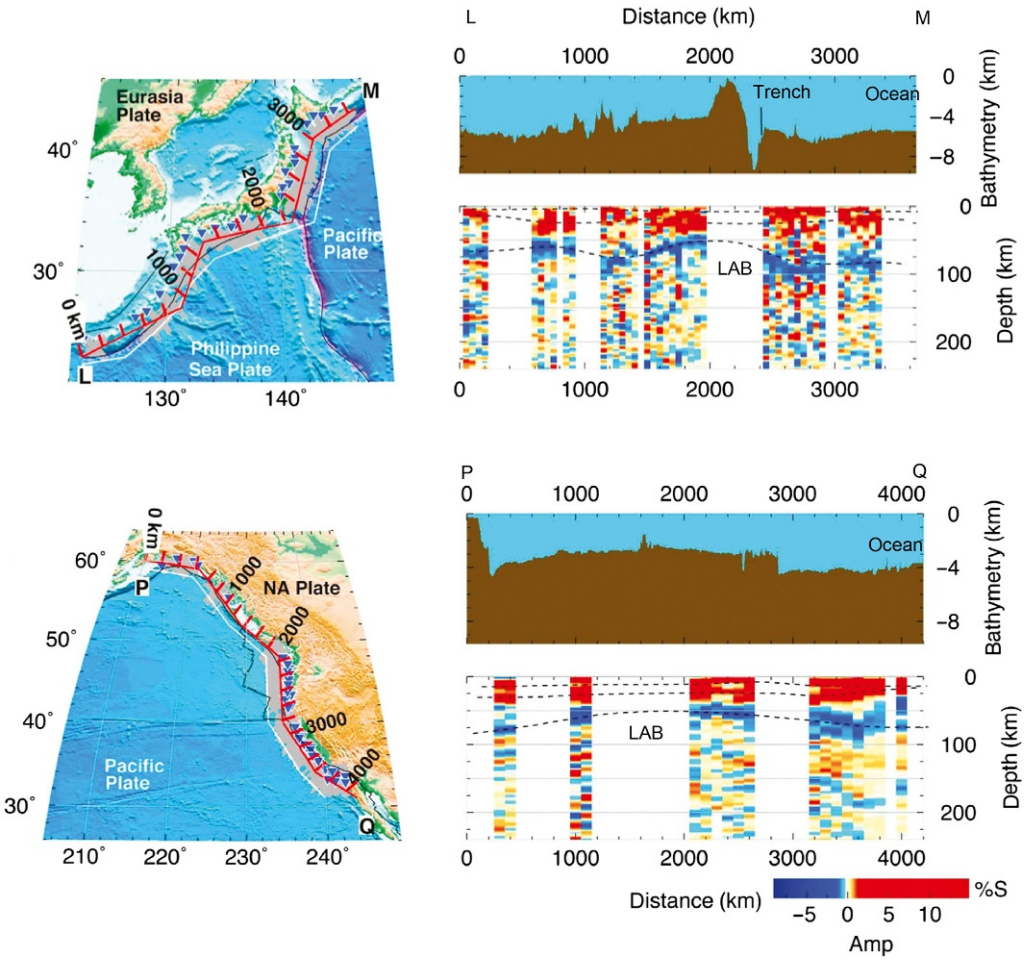

Figure 12 Sp receiver function constraints on the depth of the oceanic LAB near Pacific subduction zones. (left) Map views where red lines show the locations of Sp profiles that make up the images shown on right. Gray-shaded symbols are Sp conversion points at a depth of 100 km. Inverted blue triangles are seismic stations. (right) Sp receiver function images from (a) Japan and (b) western North America. Red corresponds to a positive discontinuity, and blue to a drop in velocity with depth. Negative phases at depths of 40–100 km are interpreted as the LAB. Seafloor bathymetry is shown in the profile above each receiver function image measured at the location of the white lines in the map views. Reproduced from Kumar P and Kawakatsu H (2011) Imaging the seismic lithosphere–asthenosphere boundary of the oceanic plate. *Geochemistry*, *Geophysics*, *Geosystems* 12, Q01006, http://dx.doi.org/10.1029/2010GC003358, Copyright 2011 by the American Geophysical Union, with permission of John Wiley & Sons.

negative discontinuity at depths comparable to the base of the oceanic lithosphere. The depth of this phase varies from 45 to 85 km, and although lithospheric thicknesses in the age range of 40–100 Ma exhibit significant scatter, they also show a broad trend of increasing thickness with age (Kumar and Kawakatsu, 2011) (squares and diamonds in **Figure 11**). This trend, however, shows less variation with age than predicted by a given isotherm, particularly for ages >30 Ma (Kumar and Kawakatsu, 2011). The velocity gradients implied by these data are large and sharp, for example, velocity drops of 7–8% over less than 10–15 km for Ps and Sp phases from the LAB beneath the Philippine and Pacific Plates near Japan (Kawakatsu et al., 2009), leading these authors to propose the presence of horizontal sheet-like partial melts in the asthenosphere.

SS precursors that sample the Pacific add additional layers of complexity to apparent oceanic LAB depths. SS precursors are sensitive to discontinuity structures near the midpoint of the path (**Figure 8**). SS precursors in relatively long-period waveforms (Rychert and Shearer, 2011) indicate a negative discontinuity whose depth, despite some scatter, increases from ~25 km at younger crustal ages (<20 Ma) to ~130 km at ages of >120 Ma (open circles and ×'s in **Figure 11**). These data indicate a negative velocity gradient over less than 20–30 km, except for the deepest discontinuities beneath the oldest crust, which are more consistent with negative velocity gradients over ~60 km (Rychert and Shearer, 2011; Rychert et al., 2012b). SS precursors at shorter periods (Schmerr, 2012) also found a negative mantle discontinuity, but with a less pronounced age dependence (40–100 km, with many observations grouped near 55 and 75 km depth; Rychert et al., 2012b; triangles in **Figure 11**) and only in regions with hotspots or other magmatic activity. Where the discontinuity is imaged, the frequency content of these data implies a velocity gradient over less than 20 km, leading Schmerr (2012) to invoke asthenospheric partial melt; where the discontinuity is not observed, more gradual gradients are implied. Discontinuity depths in Schmerr (2012) are broadly

similar to those from the circum-Pacific Sp and Ps studies (Kawakatsu et al., 2009; Kumar and Kawakatsu, 2011; Kumar et al., 2011).

As discussed by Rychert et al. (2012b), some of the discrepancies between apparent negative discontinuities in the different scattered and reflected phase studies may be explained by the varying resolution afforded by different phase types and frequency content. For example, long-period SS precursors average structure over broader lateral and depth ranges near the discontinuity than either the shorter period SS precursors or the Sp and Ps receiver functions. In addition, whereas SS, Sp, and Ps phases sample discontinuity structure around a given reflection or conversion point, models based on ScS reverberations (Bagley and Revenaugh, 2008; Revenaugh and Jordan, 1991), joint inversions of ScS reverberations and surface and body wave phases (Gaherty et al., 1996, 1999), and multiple-bounce S phases (Tan and Helmberger, 2007) should be viewed as path averages. Rychert et al. (2012b) also point out that varying sensitivities to anisotropic discontinuity structure may produce differences between phase types and as a function of frequency.

1.18.4.3 Synthesis of Seismological Constraints

Despite some unresolved discrepancies between different studies, the general picture that emerges from oceanic imaging is that two types of LAB-related structures exist. One is a significant negative velocity gradient, or perhaps multiple negative gradients, in the 50–80 km depth range that are localized enough in depth (< 15–20 km) to give rise to converted and reflected phases at shorter periods (Kawakatsu et al., 2009; Kumar and Kawakatsu, 2011; Kumar et al., 2011; Schmerr, 2012) (**Figure 11**). The second type of structure corresponds to the age-dependent increases in high-velocity lid thickness, lid shear velocity, and asthenospheric velocity described in the section on tomographic studies (**Figures 9** and **10**). If the lower part of this temporally growing high-velocity layer contains a negative velocity gradient that occurs over ~60 km in depth, it could explain the age-dependent increase in negative discontinuity depth invoked by long-period SS precursors (Rychert and Shearer, 2011). This general picture does pose some challenges. For example, if a vertically localized (< 15–20 km) discontinuity at 50–80 km is present ubiquitously, it should be reflected in long-period SS precursors. However, Rychert et al. (2012b) point out that well-resolved discontinuity depth conflicts in overlapping areas of the Pacific between different studies are actually relatively sparse. In addition, if multiple discontinuities do exist in one region, modeling is required to understand how the phases from each of them would interfere, potentially masking the appearance of one or more of the discontinuities in different types of data.

Until these uncertainties are resolved, the origins of LAB-related velocity structures beneath the oceans cannot be fully understood. However, taking the observations in **Figure 11** at face value, successful models will likely combine processes that explain both a negative discontinuity at a depth of 50–80 km that exists even at very young ages in short-period SS precursors (Schmerr, 2012) (**Figure 11**), such as a dry, depleted compositionally defined lithosphere formed by melt extraction at the ridge, and a thermal boundary layer that grows in depth below the base of the dry, depleted layer at the oldest oceanic crustal ages and that matches tomographic models. Vertical velocity gradients at the base of a compositionally defined layer that is also relatively impermeable could be enhanced by the presence of partial melt. Partial melt confined below solidii could also produce strong vertical velocity gradients within the thermal boundary layer in the more hydrated, less depleted asthenosphere below the compositionally defined layer. Although the deepest negative discontinuity observations from long-period SS phases below old oceanic crust appear to be consistent with a velocity gradient that is relatively gradual in depth (distributed over ~60 km) (Rychert and Shearer, 2011), a more vertically localized velocity gradient (over <30 km) produced by melt concentration in a broader thermal boundary layer could help to explain other observations, such as the 100–110 km deep discontinuities invoked by ScS reverberations (Bagley and Revenaugh, 2008). To conceptualize such a model, consider adding the effects of a dry, depleted layer that is ~50 km thick to the solidus diagram of Hirschmann (2010) in **Figure 9**. Such a model would be broadly consistent with conductivity models derived from inversion of magnetotelluric data. The presence of a dry, depleted layer would explain the constant depth to the top of the high-conductivity layer observed near the East Pacific Rise (Baba et al., 2006; Evans et al., 2005), and melt below an impermeable solidus-defined LAB has been proposed on the basis of a high-conductivity layer below the oceanic lithosphere subducting beneath Central America (Naif et al., 2013).

In this context, discontinuity depths of less than ~40 km from long-period SS precursors at young crustal ages require an additional mechanism. One option has been proposed by Karato (2012) who suggests that within a dry, depleted layer at a young crustal age, a negative velocity gradient associated with the grain boundary sliding relaxation peak will follow the ~1300°K isotherm. If the gradient is distributed over a depth interval just at the outer edge of the range (~10–20 km) quoted by Karato (2012) for young oceanic lithosphere, it could be sharp enough to produce long-period SS precursors (Rychert and Shearer, 2011), but not short-period SS precursors (Schmerr, 2012). In older oceanic mantle, Karato (2012) proposes that the transition from unrelaxed to relaxed velocities will create an even more localized velocity drop at the boundary between the dry lithospheric layer and the hydrated mantle below, enhancing the visibility of this discontinuity even for relatively cool geotherms. However, the relaxation peak model alone is not obviously consistent with the deepest (> 100 km) observations of long-period SS precursors and ScS reverberation discontinuities in old oceanic mantle.

1.18.5 The Seismological LAB Beneath Continents

Compared to the oceanic mantle, the seismic properties of the mantle lithosphere and LAB beneath continents exhibit much greater diversity than is found beneath the oceans. This structural complexity can largely be explained by the longer and more varied tectonic, thermal, and magmatic histories recorded in different continental regions. A first-order feature of continental mantle seismic structure is the profound difference between the thick high-velocity lithosphere of cratonic

regions that have experienced little to no tectonic activity since the end of the Proterozoic (~550 Ma) and the thinner mantle lithosphere observed beneath regions that have experienced tectonic reworking during the Phanerozoic (<~550 Ma). Globally, the thick cratonic mantle lithosphere stands out as a region of unusually high mantle velocity and low attenuation (e.g. Dalton et al., 2009; Dalton and Faul, 2010) (**Figure 4**). A recent adjoint tomography model from Europe (Zhu et al., 2012) offers a particularly striking example of the contrast in SV shear-velocity structure between the stable Eastern European Platform to the northeast of the Tornquist–Teisseyre Zone, where high velocities exist to depths of 175 km and more, and the more recently tectonized regions of Europe (**Figure 13**). The next section explores the character and possible origins of the LAB beneath cratons and the following section focuses on the LAB beneath Phanerozoic continents.

1.18.5.1 Cratons

A key question to address regarding the cratonic LAB is whether a low-velocity asthenospheric layer even exists beneath cratons. In tomographic models, lateral variations in velocity between cratonic and non-cratonic regions often extend to depths of 300–400 km, as shown beneath the Eastern European craton (**Figure 13**; Zhu et al., 2012). However, these deep lateral variations need to be considered in the context of absolute

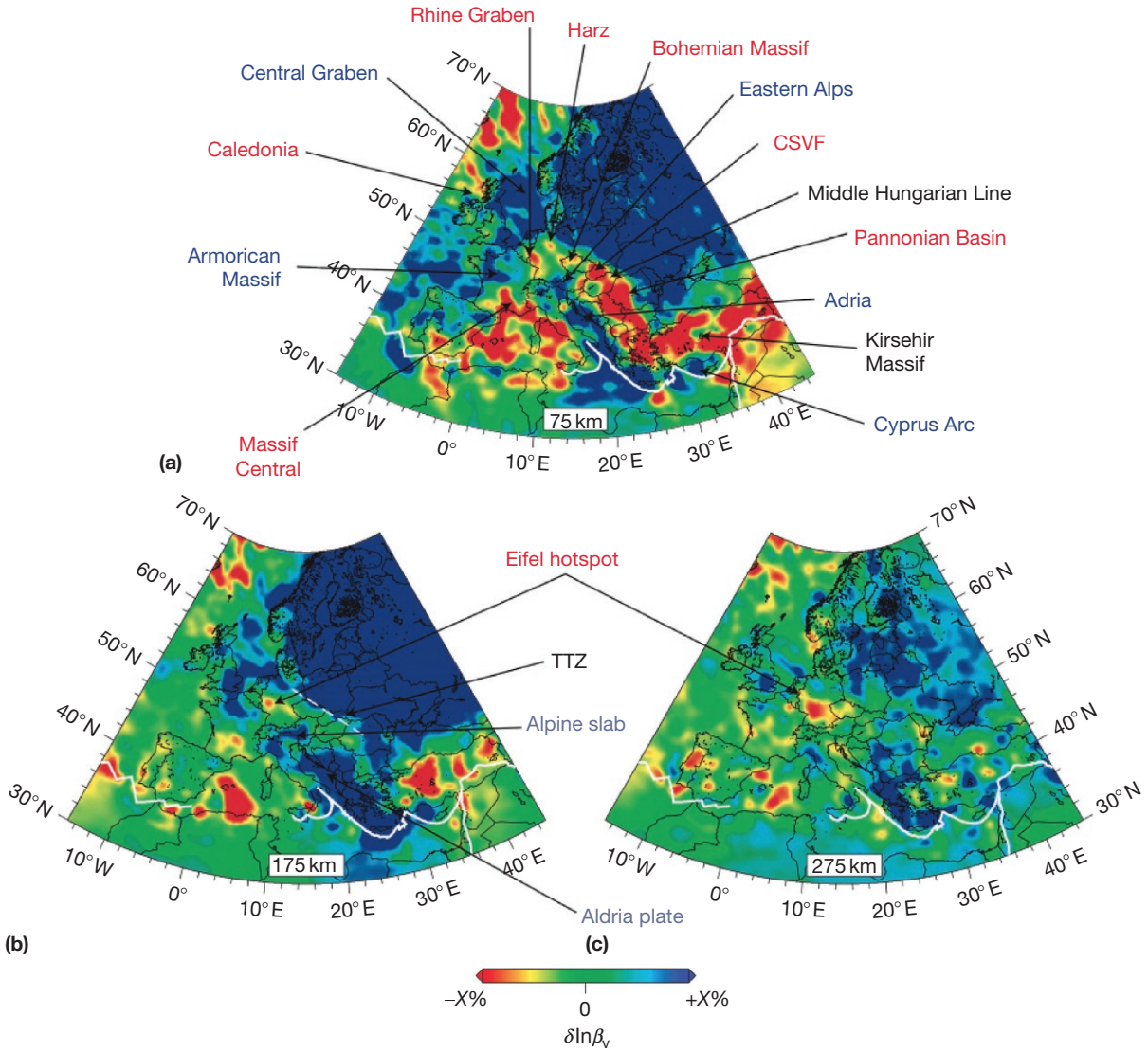

Figure 13 A model of shear-wave velocity beneath Europe that highlights anomalously high velocities in the mantle lithosphere beneath the Eastern European craton. Map views at depths of (a) 75 km, (b) 175 km, and (c) 275 km. The model includes radial anisotropy, and SV velocities are shown as perturbations to a one-dimensional background model and range from −4% to +4% in (a) and −3% to +3% in (b) and (c). The Tornquist–Teisseyre Zone (dashed line labeled TTZ in (b)) separates the Eastern European craton (to the northeast) from more recently tectonized regions of Europe. Reprinted from Zhu H, Bozdag E, Peter D, and Tromp J (2012) Structure of the European upper mantle revealed by adjoint tomography. *Nature Geoscience* 5: 493–498, by permission from Macmillan Publishers, Copyright 2012.

velocity. For example, beneath the Eastern European craton, absolute isotropic shear velocity decreases from a maximum at a depth of ~150 km to a deeper lower-velocity layer (Zhu and Tromp, 2013). More broadly, in many global and regional models that employ surface waves or long-period waveforms, absolute isotropic shear velocity reaches a minimum in the 200–300 km depth range, which is consistent with the existence of a low-velocity asthenosphere below a high-velocity cratonic lithosphere. Some studies have found that a minimum is not required in both SV and SH absolute velocity beneath cratons (Gaherty and Jordan, 1995; Gaherty et al., 1999), and others have shown that at depths greater than 200 km, fundamental mode surface waves may not have the sensitivity to resolve the presence of a low-velocity layer (Pedersen et al., 2009). Nonetheless, in recent tomographic models that include longer period fundamental mode surface waves (Nettles and Dziewoński, 2008) and overtones (Lekic and Romanowicz, 2011a,b), the average isotropic velocity does decrease below a high-velocity lithospheric layer, before increasing again into the deeper upper mantle. In the Lekic and Romanowicz (2011a,b) model, the velocity profile cluster that corresponds to cratons contains a negative velocity gradient at depths of 190–250 km that would correspond to a seismological LAB (**Figure 5(b)**). A low-velocity layer beneath the cratonic lithosphere has also been resolved in compressional wave velocities beneath North America (Chu et al., 2012a, in press).

Minimum velocities in the sub-cratonic low-velocity 'asthenospheric' layer are not as low as those observed in the asthenosphere beneath oceans or younger continental regions (e.g., the shear-velocity profiles in **Figure 5(b)**). Part of this difference is explained by the greater pressures in the sub-cratonic asthenosphere, but a cooler mantle potential temperature could also exist beneath some cratons (Ford, 2013). Alternatively, the sub-cratonic asthenosphere may have a lower volatile and/or melt content relative to the asthenosphere beneath younger continental regions and the oceans, or the expression of volatiles and melt in absolute velocity may be relatively muted at the temperatures and pressures of the sub-cratonic asthenosphere.

While the cooling associated with the cratonic lithosphere may extend below the seismological LAB (as defined by a drop in absolute velocity), perhaps in the form of small-scale convection (e.g., King and Ritsema, 2000), anomalously cold temperatures do not appear to reach the transition zone beneath cratons on a widespread basis, although conflicting results exist for some regions. If temperatures at transition zone depths were, in general, systematically lower beneath cratons than elsewhere, the depth of the '410 km' velocity discontinuity would be shallow relative to other regions. If the thermal perturbation reached still deeper, the '660 km' discontinuity would be offset to greater depths. Beneath the North American craton, several studies of transition zone discontinuities have concluded that anomalously cold temperatures do not reach the '410' discontinuity (Bostock, 1996; Li et al., 1998; Thompson et al., 2011). A number of studies reached a similar conclusion for cratons globally (Chevrot et al., 1999; Flanagan and Shearer, 1998; Lawrence and Shearer, 2006) but others did not (Gossler and Kind, 1996; Gu and Dziewonski, 2002). Thermal perturbations at transition zone depths beneath other individual cratons, for example, Southern Africa (e.g., Blum and Shen, 2004; Gao et al., 2002), are debated. See **Chapter 1.21** for more on this topic.

Anisotropy in seismic velocities provides another piece of evidence for the existence of an asthenosphere beneath cratons. Radial anisotropy with a slow vertical symmetry axis is common beneath the cratonic lithosphere, and is consistent with horizontal shearing, as is the case beneath the oceanic asthenosphere (e.g., Gung et al., 2003). Resolution of azimuthal anisotropy in the sub-cratonic asthenosphere is more challenging. Based on a global surface wave inversion, Debayle et al. (2005) argued that a layer of significant anisotropy created by shearing due to plate motion was resolved only beneath Australia (**Figure 5** in **Chapter 1.19**); their conclusions for Australia are consistent with azimuthal anisotropy in regional models (Debayle and Kennett, 2000; Simons and van der Hilst, 2003; Simons et al., 2002). More recently, however, combined long-period waveforms and SKS splitting inversions across North America (Marone and Romanowicz, 2007; Yuan and Romanowicz, 2010a,b) and regional inversions from Canada and the United States (Chen et al., 2007; Darbyshire and Lebedev, 2009; Darbyshire et al., 2013; Deschamps et al., 2008; Snyder and Bruneton, 2007) have indicated the presence of azimuthal anisotropy beneath the mantle lithosphere of the North American craton whose fast direction is consistent with shear in the direction of absolute plate motion. Yuan and Romanowicz (2010a,b) proposed that a rotation in the direction of azimuthal anisotropy from the deep mantle lithosphere to the asthenosphere provides an alternative means of mapping the position of the seismological LAB, at least under North America (**Figure 14**).

How gradual is the negative velocity gradient beneath the cratonic lithosphere? Compared to the oceanic LAB, or the LAB in Phanerozoic continental regions, the LAB velocity gradient beneath most cratons appears to be weaker and more gradual. The clearest evidence comes from converted wave studies, which provide tighter constraints on the depth extent of the cratonic LAB velocity gradient than the surface wave tomography and P waveform modeling described earlier.

A global analysis of Ps receiver functions did not resolve a clear negative polarity conversion from the LAB of any cratonic region (Rychert and Shearer, 2009), suggesting that a significant velocity drop in absolute shear velocity at the cratonic LAB, such as the gradients observed in tomographic models (e.g., **Figure 5(b)**), would need to be distributed over depth ranges of 15–20 km or more. Ps phases consistent with anisotropic discontinuities have been observed in the LAB depth range (170–230 km) near the base of the thick lithosphere of the Slave craton (Bostock, 1998; Snyder, 2008). However, these phases indicate layered structures that are more complex than a simple, single gradient from a high-velocity mantle lithosphere to a low-velocity asthenosphere.

Because of the longer periods at which they are typically analyzed, Sp conversions are sensitive to more gradual velocity gradients. For example, at a dominant period of 10 s and for velocity drops of 5–8%, the absence of significant 'negative' Sp phases would indicate negative velocity gradients distributed over ~50 km or more, and the presence of a clear Sp phase would indicate a velocity gradient over ~30 km or less (Ford et al., 2010); see Rychert et al. (2007, 2010) for additional

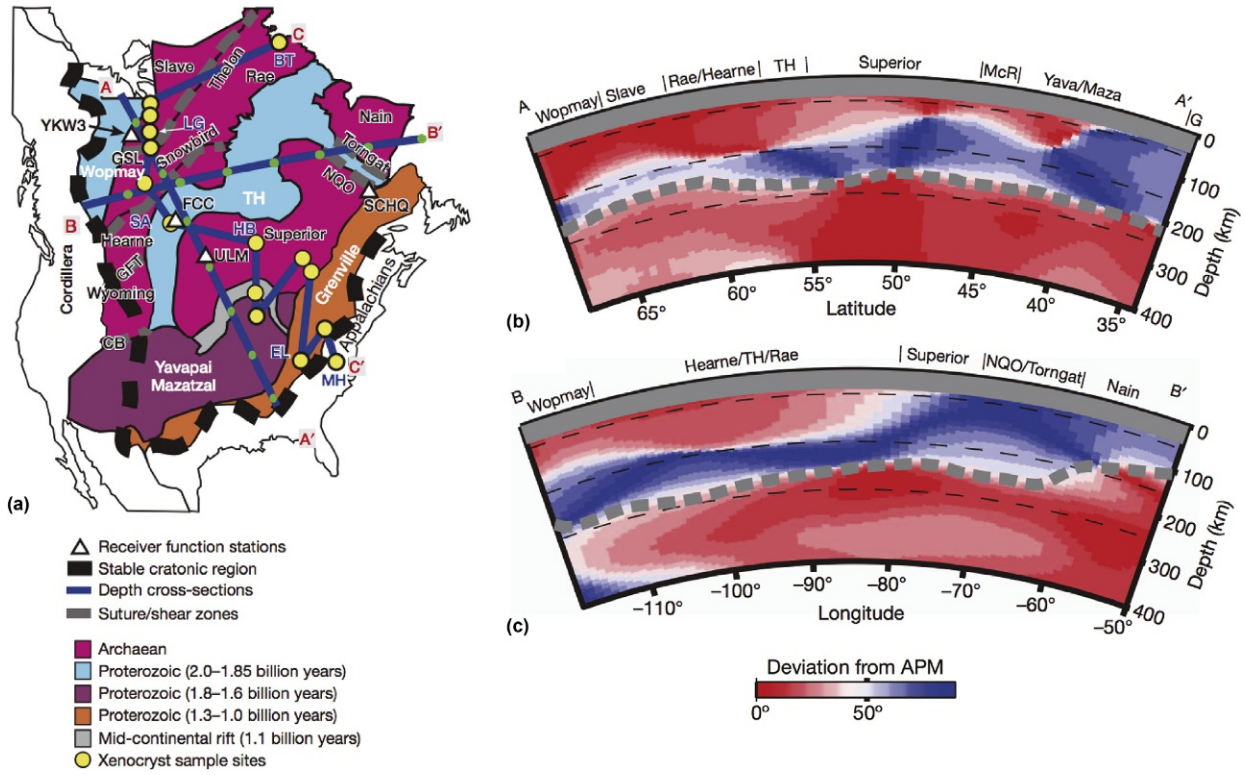

Figure 14 A shear-velocity model for North America that includes radial and azimuthal anisotropy. (a) Precambrian basement age. Blue lines marked A–A′ and B–B′ show the locations of profiles in (b) and (c). (b, c) Vertical profiles showing the fast axis of azimuthal anisotropy. Colors show the fast axis orientation relative to North American absolute plate motion in the Pacific hotspot reference frame. Two layers with distinct fast axis orientations exist within the cratonic mantle lithosphere, and a rotation of the fast axis toward absolute plate motion occurs at greater depths, consistent with shear in the asthenosphere produced by plate motion. The gray dashed line shows the LAB as defined by this latter fast axis rotation. Reprinted from Yuan H and Romanowicz B (2010) Lithospheric layering in the North American craton. *Nature* 466: 1063–1068, http://dx.doi.org/10.1038/nature09332, by permission from Macmillan Publishers: Nature, Copyright 2013.

examples of Ps and Sp velocity gradient sensitivity. Sp conversion studies have the advantage that they are free of potential contamination from crustal multiples that may overprint Ps phases at mantle depths. However, Sp imaging becomes progressively more challenging with depth, a point of particular relevance to imaging the cratonic LAB. The ray parameter range for which Sp conversions have incidence angles less than the critical incidence angle decreases as conversion depth increases, thus reducing the low end of the range of epicentral distances from which Sp phases from direct S waves can be observed. Nonetheless, in regions where data from larger direct S epicentral distances are abundant, high-quality Sp imaging at depths of ~200 km is possible. Some studies add SKS waveforms (i.e., SKSp phases) to augment data in the low ray parameter range, but SKS phases can also be problematic because of lower signal-to-noise ratios or contamination from other teleseismic phases (Wilson et al., 2006).

Reports of Sp conversions from the base of different cratonic lithosphere are variable, and, when sighted, these phases are, in general, of lower amplitude and less clear than Sp conversions from the shallower LAB depth ranges typical of younger continental regions. Beneath central United States and Canadian cratonic regions of North America, the Sp analyses of Abt et al. (2010), Kumar et al. (2012), and Kind et al. (2012) found no evidence for Sp energy that was coherent over large areas from the LAB depth range (150–250 km as defined by the negative velocity gradients in surface wave tomography). LAB Sp phases have been identified beneath Canada (Miller and Eaton, 2010), on an intermittent basis beneath the Wyoming craton (Hopper et al., in press; Lekic and Fischer, in press), and beneath portions of the cratonic central United States (Foster et al., in press; Hansen et al., 2013), but these phases are of relatively low amplitude, and beneath other regions of the central United States craton, no LAB Sp phase is observed (Foster et al., in press). Beneath cratonic regions of central and western Australia, Ford et al. (2010) found no clear Sp phases from the tomographically defined LAB depth range, although LAB phases at depths of ~130 km were seen at the eastern edge of the craton. These results differ from those of Kumar et al. (2007) who did observe deep potential LAB Sp phases beneath cratonic Australia. At the base of the Indian cratonic lithosphere, no evidence for a strong, localized velocity gradient was found from Sp converted phases (Bodin et al., 2014). Sp arrivals have been associated with the LAB beneath the eastern European craton/Baltic shield at depths of 200 km and more (Geissler et al., 2010; Sacks et al., 1979), although Geissler et al. (2010) point out that these phases are relatively weak and complex, and are missing at some stations.

In some cases, LAB velocity gradients at the base of thick cratonic lithosphere may be enhanced by asthenosphere with

lower velocities than typical of sub-cratonic regions. Deep Sp phases from the LAB depth range defined by surface wave tomography have been observed beneath the Arabian platform (Hansen et al., 2007; Mohsen et al., 2006) and Tanzania (Wölbern et al., 2012). The proximity to rifting in these cases raises the possibility of unusually low velocity asthenosphere (Fishwick, 2010; Weeraratne et al., 2003), which would contribute to the observability of LAB Sp phases. The situation beneath the Kalahari craton is more complex. Several surface wave tomography studies have found a high-velocity lithospheric layer bounded from below by a negative shear-velocity gradient starting at a depth of 160–175 km (Li and Burke, 2006; Priestley and Tilmann, 2009; Priestley et al., 2006). Sp conversion studies suggest negative Sp phases in two different depth ranges, 150–160 km (Hansen et al., 2009; Savage and Silver, 2008) and 200–300 km (Kumar et al., 2007; Wittlinger and Farra, 2007), and Ps and SKS phases have been modeled in terms of a rapid transition in azimuthal anisotropy at ~160 km (Vinnik et al., 2012). These phases could represent locally steep negative velocity gradients within a broader LAB region, but the dominant periods in these studies differ, and care must be taken to account for this frequency dependence in their interpretation. Whole mantle tomographic models suggest that warm upwelling mantle impinges on the base of the cratonic lithosphere in southern Africa (e.g., Ritsema et al., 2011), and if the upwelling produces a larger and/or more localized LAB velocity gradient relative to other cratons, higher amplitude Sp phases will be generated. Depending on how far north the influence of this upwelling extends, it could also contribute to the LAB phases apparent beneath the Tanzanian craton and Arabian platform.

Where no Sp or Ps phase is observed from the cratonic LAB, the drop in velocity from lithosphere to asthenosphere indicated by surface wave or long-period waveform tomography must be gradual in depth, that is, distributed over ~50 km or more. In these cases, the negative shear-velocity gradient is consistent with models where velocity depends only on temperature, although gradual gradients in composition or melt cannot be ruled out. For example, although rates of water diffusion are modest (Hirth and Kohlstedt, 1996), initially localized gradients in water content could broaden over time, with maximum length scales of ~50 km over ~2 billion years. Where Sp phases are present, but are relatively weak and intermittent, they indicate some localized sharpening of negative shear-velocity gradients over vertical length scales of ~30 km or less, perhaps because of variations in bulk composition, volatile content, or melt. When interpreting differences in Sp phase amplitude or spatial continuity between cratons, the possibility that deeper mantle upwelling may have produced unusually low asthenospheric velocities should be considered.

While the evidence for gradual versus localized LAB velocity gradients varies from craton to craton, numerous types of seismological observations point to discontinuities and layering internal to the cratonic mantle lithosphere. Sp and Ps phases consistent with negative velocity gradients have been observed on a widespread basis within the cratonic mantle lithosphere, often at depths of 60–120 km (Abt et al., 2010; Bodin et al., 2014; Chen et al., 2009; Ford et al., 2010; Foster et al., in press; Geissler et al., 2010; Hansen et al., 2013; Hopper et al., in press; Kind et al., 2012; Kumar et al., 2012; Lekic and Fischer, in press; Miller and Eaton, 2010; Rychert and Shearer, 2009; Wölbern et al., 2012; Zurek and Dueker, 2005), and discontinuities at comparable depths have also been characterized as anisotropic boundaries using both Ps (Bostock, 1998; Levin and Park, 2000; Mercier et al., 2008; Saul et al., 2000) and Sp (Ford, 2013) data. A low-velocity layer with its top at ~100 km is also a consistent feature of cratonic models based on the '8° discontinuity in long-range seismic profiles' (Nielsen et al., 2002; Thybo, 2006; Thybo and Perchuc, 1997) and in regional P waveforms (Chu et al., 2012a). Finally, surface wave studies have resolved vertical variations in azimuthal anisotropy within the cratonic mantle lithosphere, including cases from North America (Darbyshire et al., 2013; Yuan and Romanowicz, 2010a) and Europe (Zhu and Tromp, 2013). For example, Yuan and Romanowicz (2010a) found that a pronounced rotation of fast azimuth orientation defines two distinct layers of azimuthal anisotropy within the North American cratonic mantle (**Figure 14**). The depth range of this vertical rotation in fast azimuth coincides with the depth extent of the negative Sp energy observed at many cratonic stations (Yuan and Romanowicz, 2010a; Yuan et al., 2011). Overall, further work is required to explore the resolution and consistency of all the data types that point to vertical layering within the cratonic mantle lithosphere, and to determine whether the various observations from a given region can be explained by the same structural model. Progress in this area will provide constraints on the processes that formed the cratonic mantle lithosphere (e.g., Bostock, 1998; Chen et al., 2009; Darbyshire et al., 2013; Snyder, 2008; Yuan and Romanowicz, 2010a; Zhu and Tromp, 2013), and on the possibility of its later deformation (e.g., Eaton and Frederiksen, 2007).

1.18.5.2 Phanerozoic Continental Regions

In contrast to cratons, much of the lithosphere in Phanerozoic continental regions appears to have a LAB velocity gradient that is well localized in depth. Numerous studies have found clear Sp and Ps phases that emanate from the depth range of the transition from high-velocity lithosphere to low-velocity asthenosphere defined by surface wave tomography and regional waveform modeling. Examples include global studies (Rychert and Shearer, 2009) and regional analyses spanning the western United States (Abt et al., 2010; Bailey et al., 2012; Hansen et al., 2013; Hopper et al., in press; Kind et al., 2012; Kumar et al., 2012; Lekic and Fischer, in press; Lekic et al., 2011; Levander and Miller, 2012; Levander et al., 2011; Li et al., 2007); the Phanerozoic eastern United States (Abt et al., 2010; Rychert et al., 2005, 2007); South America (Heit et al., 2007); Greenland (Kumar et al., 2005a); Europe (Geissler et al., 2010; Miller and Agostinetti, 2011, 2012; Sodoudi et al., 2006a); the Middle East (Angus et al., 2006; Hansen et al., 2007; Mohsen et al., 2006; Ozacar et al., 2008), the Himalayas, Tibet, and the Tien Shan (Devi et al., 2011; Kumar et al., 2005b; Oreshin et al., 2002; Xu et al., 2011; Zhao et al., 2011); China (Chen, 2009; Chen et al., 2006; Sodoudi et al., 2006b); and Australia (Ford et al., 2010; Kumar et al., 2007). See Rychert et al. (2010) and Fischer et al. (2010) for reviews. As previously mentioned, the presence of significant LAB phases in Sp receiver functions typically implies an LAB velocity gradient that is localized over 30 km in depth or less, although waveform modeling that accounts for the actual frequency content of the data is required for accurate

velocity gradient estimates (e.g., Ford et al., 2010). Large LAB phases in Ps receiver functions indicate even sharper gradients, for example, velocity drops of 5–8% over less than 11 km in the northeastern United States (Rychert et al., 2005, 2007). LAB velocity gradients with this degree of depth localization are difficult to reconcile with creation of the LAB by temperature gradients alone, except in regions with focused upwelling. Rather, they point to enhanced volatile content and less depletion in the asthenosphere relative to the lithosphere, and/or to partial melt in the asthenosphere just below the LAB.

Variations in the apparent depth and character of the seismological LAB across tectonically distinct regions shed additional light on the origin and rheological significance of the LAB velocity gradient. For example, beneath Phanerozoic continental regions that have undergone significant extension, the LAB is typically shallower than beneath surrounding unextended lithosphere (Chen et al., 2006; Geissler et al., 2010; Lekic et al., 2011). However, the character of the LAB can differ significantly between rifted regions.

Beneath southern California, a distinct negative phase is observed in Sp receiver functions (Lekic et al., 2011) (**Figure 15(a)**); its depth varies from 40 km to 95 km and correlates well with the depth range of the LAB velocity gradient from surface wave tomography (Rau and Forsyth, 2011) (**Figure 15(b)**). In addition, the shear-velocity drop implied by the negative Sp phase ($8 \pm 3\%$ if it occurs instantaneously in depth) accounts for the amplitude of the LAB velocity gradient in the tomography, indicating that both types of observations reflect the same LAB velocity structure. However, the Sp phases require that the LAB velocity gradient is sufficiently localized in depth (<20–30 km) that asthenospheric velocities need to be reduced relative to the lithosphere by a mechanism such as enhanced volatile or partial melt content, in addition to the effects of temperature. Lateral variations in the depth of the LAB velocity gradient provide additional constraints on LAB properties. The depth of the LAB Sp phase is 20–30 km shallower beneath the Salton Trough and Inner Borderland, regions that have experienced significant extension, relative to

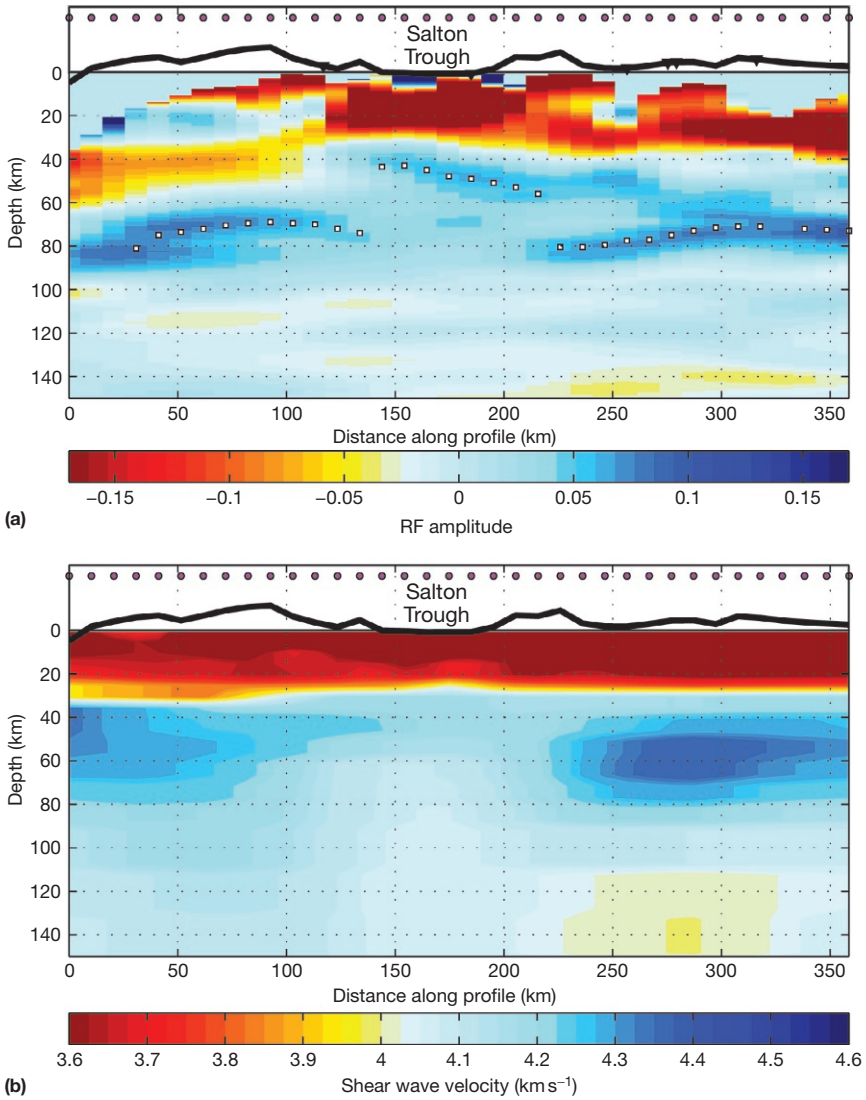

Figure 15 (Continued)

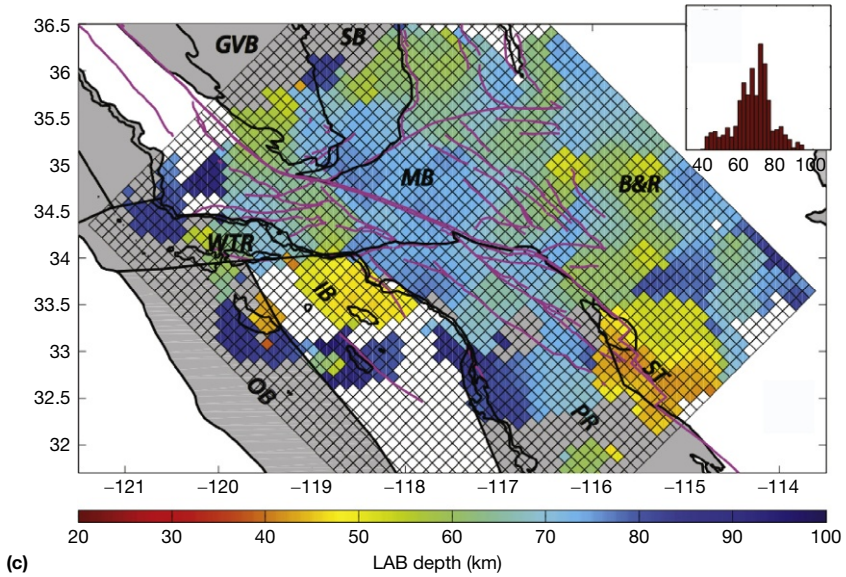

Figure 15 Models of lithospheric structure in southern California that illustrate the good correlation between LAB depth estimates from Sp phases (a, c) and Rayleigh waves (b). (a) Vertical profile through the Sp receiver function common conversion point stack of Lekic et al. (2011); profile passes through the southern Salton Sea and is oriented parallel to the axis of the model grid in (c) that is roughly normal to the coast. Warm colors indicate a velocity increase with depth; at depths of <40 km, these interfaces correspond to the base of sediment or crust. Cool colors indicate a velocity decrease with depth. The largest amplitude velocity decrease falls in the depth range of the transition from high lithospheric shear velocities to lower asthenospheric velocities in (b) and is interpreted as the LAB (white squares). Surface topography (black line) is exaggerated tenfold. (b) Vertical profile in the same location as (a) from the SV shear-velocity model of Rau and Forsyth (2011). (c) Map of depth to the LAB from Lekic and Fischer (2011). Outer Continental Borderland (OB); Inner Continental Borderland (IB); Peninsular Ranges (PR); Western Transverse Range block (WTR); Mojave block (MB); Basin and Range (B&R); Sierra Block (SB); Great Valley block (GVB), and the Salton Trough (ST). Pink lines delineate surface traces of major faults. Inset shows histogram of LAB depths. Parts (a) and (c) reprinted from Lekic V, French SW, and Fischer KM (2011) Lithospheric thinning beneath rifted regions of Southern California. *Science* 334: 783–787, doi: 10.1126/science.1208898, with permission from AAAS.

the LAB of adjacent lithosphere, and some of the transitions from thick to thin lithosphere occur over horizontal length scales of 50 km or less (Lekic et al., 2011) (**Figure 15(a)** and **15(c)**). The contrast in viscosity between lithosphere and asthenosphere must, therefore, be great enough to create topography on the LAB with dips of 20–30°. Numerical modeling of lithospheric deformation in response to extension (albeit with simpler extensional geometries than found in the Salton Trough and Inner Borderland) indicates that LAB topography with dips of 30° can be created if the mantle lithosphere, or at least a portion of the mantle lithosphere, resists deformation to a significantly greater degree than the asthenosphere (Gueydan et al., 2008; Huismans and Beaumont, 2003, 2011). In addition, because the lateral extent of the thinned lithosphere beneath the Salton Trough and Inner Borderland is not much broader than the area of crustal thinning and the surface expression of extension, strain in the mantle lithosphere appears to be relatively localized. This style of deformation is observed in numerical models with strain-dependent rheologies (e.g., Gueydan et al., 2008; Huismans and Beaumont, 2003, 2011), and would be consistent with the degree of strain localization predicted by rheologies dominated by damage and pinning of grain growth (Bercovici and Ricard, 2012).

However, LAB structure between rifted continental lithosphere can vary greatly. In contrast to the Salton Trough, where lithosphere with a well-defined negative LAB velocity gradient is ubiquitous, Rychert et al. (2012a) observed a clear negative Sp phase beneath the lithosphere flanking the Ethiopian Rift, but beneath the rift itself they found a positive phase at comparable depths (75 km) (**Figure 16**). They interpreted the positive phase, which corresponds to a velocity increase with depth, as the base of the partial melt zone beneath the rift, whereas the negative phase beneath the flanking lithosphere is consistent with partial melt ponded below an impermeable LAB. These results suggest that the distribution of partial melt, as regulated by solidii and mantle permeability, can dominate the seismic properties of the LAB.

Seismological constraints on the LAB are also adding to our understanding of the growth of the continental lithosphere through collisional processes. For example, several studies have used Sp phases to trace the LAB of the Indian plate as it dips to the north beneath the Himalayas and Tibetan plateau, and to assess its tectonic geometry relative to the Tibetan and Asian lithospheres (Devi et al., 2011; Kumar et al., 2005b; Oreshin et al., 2002; Xu et al., 2011; Zhao et al., 2011). These results suggest that discrete layers of lithosphere can remain relatively intact and coherent even after one underthrusts another over length scales of many hundreds of kilometers. Dipping mantle discontinuities interpreted as the remnants of Proterozoic and Archean lithospheric slabs now embedded in the mantle beneath the Slave craton (Bostock, 1998; Chen

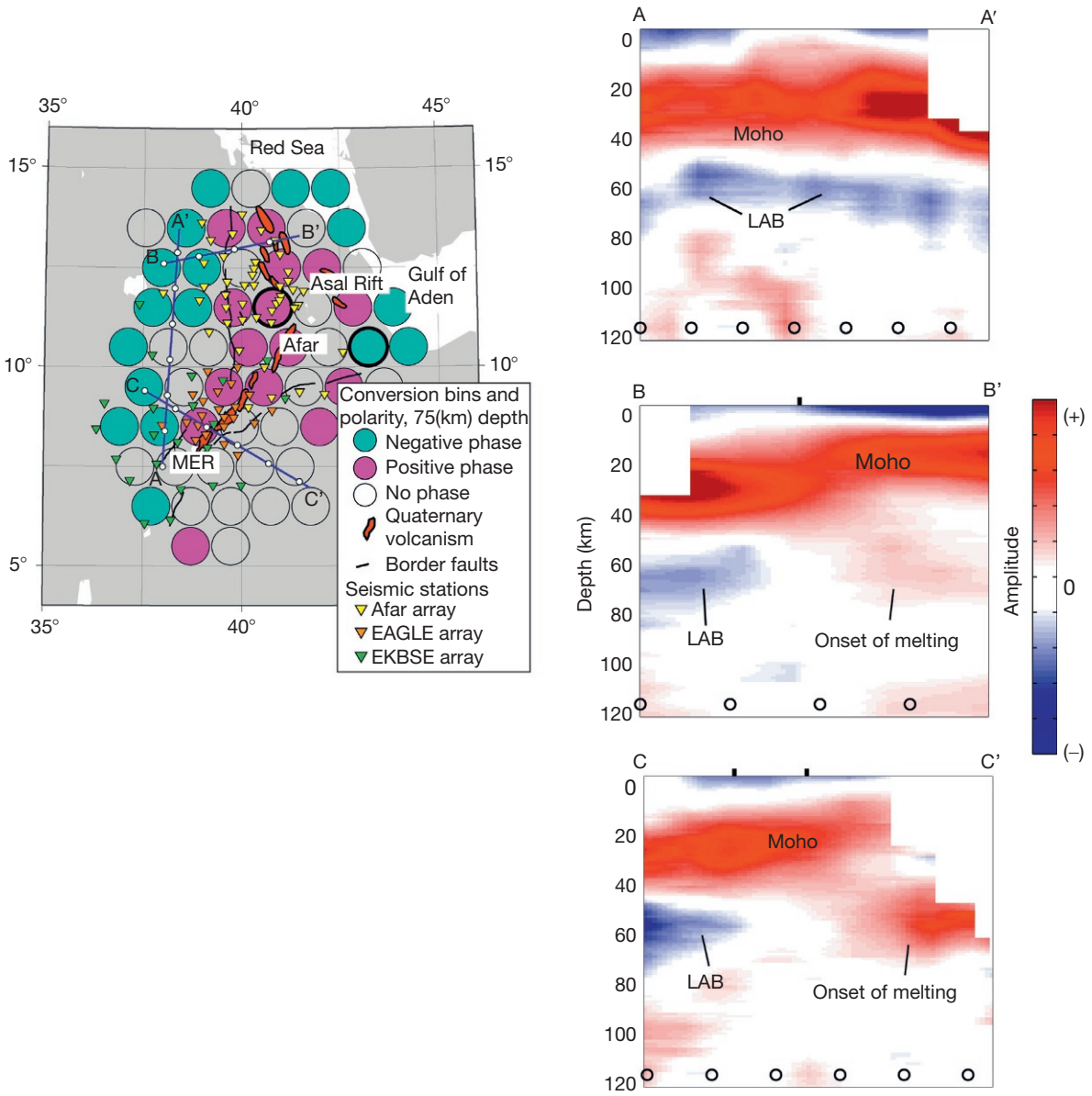

Figure 16 LAB structure across the Ethiopian Rift. (a) Map of Sp phase polarity at 75 km depth with stations shown as inverted triangles. Circles show geographic bins with more than ten waveforms. Blue lines are the locations of profiles in (b). Red areas are Quaternary–Recent volcanic segments. Black lines show border faults. (b) Vertical profile through the Sp receiver function common conversion point stacks. Positive polarity amplitudes are in red (velocity increase with depth) and negative polarity amplitudes are in blue (velocity decrease with depth). Black circles at 120 km depth show 100 km distance intervals. Ticks along the top of the panels show border faults. Reprinted from Rychert CA, Hammond JOS, Harmon N, et al. (2012b) Volcanism in the Afar Rift sustained by decompression melting with minimal plume influence. *Nature Geoscience* 5: 406–409, by permission from Macmillan Publishers: Nature Geoscience, Copyright 2012.

et al., 2009; Snyder, 2008) provide evidence that lithospheric imbrication also contributed to the formation of portions of the cratonic mantle lithosphere.

As the density of broadband seismic stations increases, sharper resolution of LAB seismic structure and enhanced understanding of its meaning are sure to follow. For example, the passage of the EarthScope Transportable Array through the western United States has enabled a new generation of tomographic, and scattered and reflected wave imaging of the lithosphere and asthenosphere beneath this tectonically complex region. Nonetheless, much remains to be learned about how regional and teleseismic phases interact with complex, three-dimensional structures, in particular when their finite frequency sensitivity kernels and the effects of anisotropy are considered. Sp and Ps studies of the LAB beneath the western United States that employ Transportable Array data broadly agree on certain features of the seismological LAB, for example, relatively thin lithosphere beneath the Basin and Range (60–80 km) and anomalously thick (120–130 km) lithosphere beneath the central and northern Colorado Plateau (Bailey et al., 2012; Hansen et al., 2013; Hopper et al., in press; Kind et al., 2012; Kumar et al., 2012; Lekic and Fischer, in press;

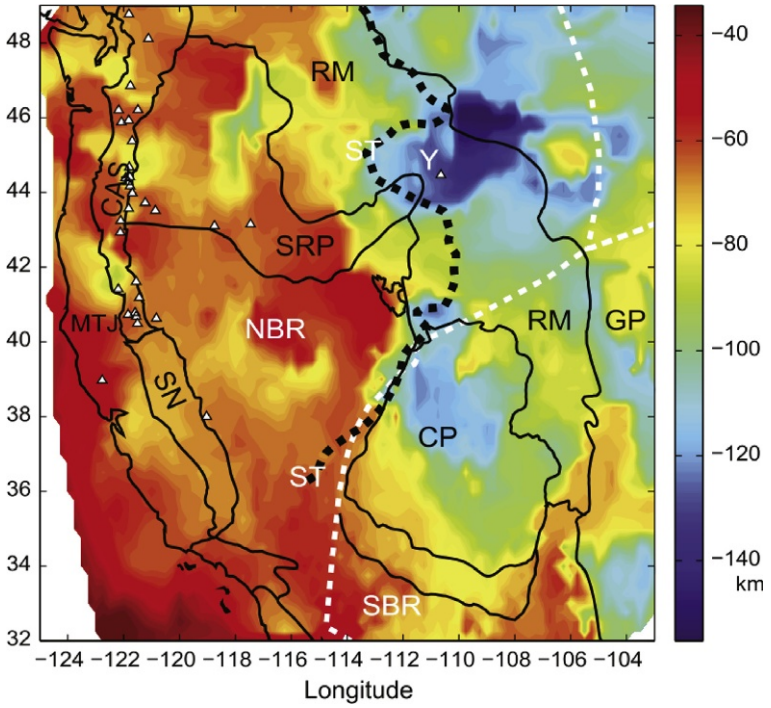

Figure 17 Map showing the depth of a negative mantle phase (the LAB in non-cratonic areas) beneath the western United States based on common conversion point stacking of Sp receiver functions. CAS: Cascadia Range; MTJ: Mendocino Triple Junction; SN: Sierra Nevada Range; SRP: Snake River Plain; RM: Rocky Mountains; NBR, SBR: northern and southern Basin and Range; CP: Colorado Plateau; Y: Yellowstone. Black dashed line is the Sevier Thrust belt (ST) and white dashed lines are age boundaries. Reproduced from Levander A and Miller MS (2012) Evolutionary aspects of lithosphere discontinuity structure in the western US. *Geochemistry, Geophysics, Geosystems* 13, Q0AK07, http://dx.doi.org/10.1029/2012GC004056, Copyright 2012 by the American Geophysical Union, with permission of John Wiley & Sons.

Lekic et al., 2011; Levander et al., 2011) (**Figure 17**). However, the LAB models provided by these studies often differ significantly at shorter spatial scales. Some of these inter-model variations likely relate to differences in the frequency content retained in the waveforms. Differences in filtering (e.g., applying a low-pass filter with a corner at 6 s versus a corner at 2–4 s to Sp phases) can significantly increase interference with shallower arrivals and bias the apparent depth of shallow mantle discontinuities (Hopper et al., in press). Resolution of lateral changes in LAB structure will also decrease as waveforms become progressively longer period and/or discontinuities become deeper (Lekic et al., 2011). On the positive side, the rich frequency dependence of scattered and reflected wave interactions with three-dimensional velocity gradients holds promise for future improvements to methods for imaging LAB structure.

1.18.6 Conclusions

Beneath oceans and continental regions that experienced significant tectonic activity in the Phanerozoic, the high absolute-velocity lithosphere is underlain by a low absolute-velocity asthenosphere. The weight of recent studies favors the presence of a low-velocity asthenosphere beneath cratonic continental regions as well, even when the effects of anisotropy are accounted for. Hence, a seismological LAB that corresponds to a negative gradient in absolute velocity can be considered a global feature. Its depth varies significantly, ranging from less than 100 km beneath young oceans and tectonically active continental regions to 200–300 km beneath cratons.

The asthenosphere, as defined by low absolute velocities, typically contains significant velocity anisotropy that is consistent with shear because of differential motion relative to the lithosphere. Within the asthenosphere, the minimum shear velocity on average increases with crustal age in the oceans, and from Phanerozoic to cratonic continental regions. These trends are consistent with a cooling of asthenospheric temperatures with increasing crustal age in the oceans and with lower mantle potential temperatures in the asthenosphere beneath cratons than beneath younger continental regions. In this interpretation, tectonically correlated thermal variations would extend below the seismologically defined LAB, perhaps as a result of small-scale convection. However, lateral variations in asthenospheric melt and volatile content and the manner in which they are expressed in seismic velocities should also be considered.

Beneath oceans, two types of LAB-related structures appear to exist: one or more negative velocity gradients in the 50–80 km depth range that are localized in depth (<15–20 km) and age-dependent increases in high-velocity lid thickness, lid shear velocity, and minimum asthenospheric velocity. Oceanic LAB structures point to processes that combine deepening isotherms caused by cooling with those that can produce vertically localized shear-velocity gradients, such as partial melt that

collects beneath an impermeable boundary, or the contrast between a dry, depleted lithosphere and a more volatile-rich and fertile asthenosphere.

LAB velocity gradients beneath most cratons are, in general, weaker and/or more intermittent than those found beneath oceans and Phanerozoic continents. In some studies in cratons, the absence of significant scattered wave phases from LAB depths points to LAB velocity gradients that occur over ~50 km or more, and these gradients would be consistent with thermal gradients alone. In other cases, weak scattered wave phases point to LAB velocity gradients over 30 km or less, indicating vertical variations in bulk composition and/or volatile content, or perhaps partial melt.

Beneath Phanerozoic continental regions, large LAB velocity gradients localized over depth ranges of ~30 km or less are typically observed, indicating the presence of higher volatile or melt content in the asthenosphere relative to the lithosphere, in addition to higher temperatures. In some regions, abrupt horizontal changes in LAB depth bound the strength contrast between lithosphere and asthenosphere in the sense that the lithosphere must be stiff enough to create LAB topography with dips of 20–30° or more.

Acknowledgments

Thanks to Heather Ford, Ved Lekic, Don Forsyth, Barbara Romanowicz, Huaiyu Yuan, and Greg Hirth for their helpful discussions. This material includes work that was supported by the U.S. National Science Foundation EarthScope Program under award EAR-0844276.

References

Abt DL, Fischer KM, French SW, Ford HA, Yuan H, and Romanowicz B (2010) North American lithospheric discontinuity structure imaged by Ps and Sp receiver functions. *Journal of Geophysical Research* 115. http://dx.doi.org/10.1029/2009JB006914, B09301.

Adam C and Vidal V (2010) Mantle flow drives the subsidence of oceanic plates. *Science* 328: 83–85.

Aizawa Y, Barnhoorn A, Faul UH, FitzGerald JD, Jackson I, and Kovács I (2008) Seismic properties of Anita Bay Dunite: An exploratory study of the influence of water. *Journal of Petrology* 49: 841–854.

Anderson DL and Sammis C (1970) Partial melting in the upper mantle. *Physics of the Earth and Planetary Interiors* 3: 41–50.

Angus DA, Wilcon DC, Sandvol E, and Ni JF (2006) Lithospheric structure of the Arabian and Eurasian collision zone in eastern Turkey from S-wave receiver functions. *Geophysical Journal International* 166: 1335–1346. http://dx.doi.org/10.1111/j.1365-246X.2006.03070.x.

Artemieva IM (2011) *The Lithosphere: An Interdisciplinary Approach*. Cambridge, UK: Cambridge University Press.

Baba K, Chave AD, Evans RL, Hirth G, and Mackie RL (2006) Mantle dynamics beneath the East Pacific Rise at 17°S: Insights from the mantle electromagnetic and tomography (MELT) experiment. *Journal of Geophysical Research* 111. http://dx.doi.org/10.1029/2004JB003598, B02101.

Bagley B and Revenaugh J (2008) Upper mantle seismic shear discontinuities of the Pacific. *Journal of Geophysical Research* 113. http://dx.doi.org/10.1029/2008JB005692.

Bailey IW, Miller MS, Liu K, and Levander A (2012) Vs and density structure beneath the Colorado Plateau constrained by gravity anomalies and joint inversions of receiver function and phase velocity data. *Journal of Geophysical Research* 117. http://dx.doi.org/10.1029/2011JB008522, B02313.

Bartzsch S, Lebedev S, and Meier T (2011) Resolving the lithosphere–asthenosphere boundary with seismic Rayleigh waves. *Geophysical Journal International* 186: 1152–1164.

Becker TW, Ekström G, Boschi L, and Woodhouse JH (2007) Length scales, patterns and origin of azimuthal seismic anisotropy in the upper mantle as mapped by Rayleigh waves. *Geophysical Journal International* 171: 451–462.

Bedle H and van der Lee S (2009) S velocity variations beneath North America. *Journal of Geophysical Research* 114. http://dx.doi.org/10.1029/2008JB005949, B07308.

Behn MD, Hirth G, and Elsenbeck JR (2009) Implications of grain-size evolution on the seismic structure of the oceanic upper mantle. *Earth and Planetary Science Letters* 282: 178–189.

Bercovici D and Ricard Y (2012) Mechanisms for the generation of plate tectonics by two-phase grain-damage and pinning. *Physics of the Earth and Planetary Interiors* 202: 27–55.

Beucler E and Montagner J-P (2006) Computation of large anisotropic seismic heterogeneities (CLASH). *Geophysical Journal International* 165: 447–468.

Billen M (2008) Modeling the dynamics of subducting slabs. *Annual Review of Earth and Planetary Sciences* 36: 325–356.

Blum J and Shen Y (2004) Thermal, hydrous, and mechanical states of the mantle transition zone beneath southern Africa. *Earth and Planetary Science Letters* 217: 367–378. http://dx.doi.org/10.1016/S0012-821X(03)00628-9.

Bodin T, Yuan H, and Romanowicz B (2014) Inversion of receiver functions without deconvolution – Application to the Indian Craton. *Geophysical Journal International* 196: 1025–1033.

Bostock MG (1996) Ps conversions from the upper mantle transition zone beneath the Canadian landmass. *Journal of Geophysical Research* 101: 8393–8402. http://dx.doi.org/10.1029/95JB03741.

Bostock MG (1998) Mantle stratigraphy and evolution of the Slave province. *Journal of Geophysical Research* 103: 183–200.

Boyd FR (1989) Compositional distinction between oceanic and cratonic lithosphere. *Earth and Planetary Science Letters* 96: 15–26.

Chen L (2009) Lithospheric structure variations between the eastern and central North China Craton from S- and P-receiver function migration. *Earth and Planetary Science Letters* 173: 216–227.

Chen C-W, Rondenay S, Evans RL, and Snyder DB (2009) Geophysical detection of relict metasomatism from an Archean (~3.5 Ga) subduction zone. *Science* 326: 1089–1091.

Chen C-W, Rondenay S, Weeraratne DS, and Snyder DB (2007) New constraints on the upper mantle structure of the Slave craton from Rayleigh wave inversion. *Geophysical Research Letters* 34. http://dx.doi.org/10.1029/2007GL029535, L10301.

Chen L, Zheng TY, and Xu WW (2006) A thinned lithospheric image of the Tanlu Fault Zone, eastern China: Constructed from wave equation based receiver function migration. *Journal of Geophysical Research* 111. http://dx.doi.org/10.1029/2005JB003974.

Chevrot S, Vinnik L, and Montagner JP (1999) Global-scale analysis of the mantle Pds phases. *Journal of Geophysical Research* 104: 22203–22219. http://dx.doi.org/10.1029/1999JB900087.

Chu R, Helmberger DV, and Gurnis M (in press) Upper mantle surprises derived from the recent Virginia earthquake waveform data. *Earth and Planetary Science Letters* http://dx.doi.org/10.1016/j.epsl.2012.10.023.

Chu R, Schmandt B, and Helmberger DV (2012a) Upper mantle P velocity structure beneath the Midwestern United States derived from triplicated waveforms. *Geochemistry, Geophysics, Geosystems* 13. http://dx.doi.org/10.1029/2011GC003818, Q0AK04.

Chu R, Schmandt B, and Helmberger DV (2012b) Juan de Fuca subduction zone from a mixture of tomography and waveform modeling. *Journal of Geophysical Research* 117. http://dx.doi.org/10.1029/2012JB009146, B03304.

Collins JA, Vernon FL, Orcutt JA, and Stephen RA (2002) Upper mantle structure beneath the Hawaiian swell: Constraints from the ocean seismic network pilot experiment. *Geophysical Research Letters* 29. http://dx.doi.org/10.1029/2001GL013302.

Cooper RF (2003) Seismic wave attenuation: Energy dissipation in viscoelastic crystalline solids. In: Karato S and Wenk H-R (eds.) *Plastic Deformation of Minerals and Rocks*. *Reviews in Mineralogy and Geochemistry*, vol. 51, pp. 253–290. Chantilly, VN: Mineralogical Society of America.

Cooper CM, Lenardic A, and Moresi L (2004) The thermal structure of stable continental lithosphere within a dynamic mantle. *Earth and Planetary Science Letters* 222: 807–817.

Dalton CA, Ekström G, and Dziewonski AM (2008) The global attenuation structure of the upper mantle. *Journal of Geophysical Research* 113. http://dx.doi.org/10.1029/2007JB005429.

Dalton CA, Ekström G, and Dziewonski AM (2009) Global seismological shear velocity and attenuation: A comparison with experimental observations. *Earth and Planetary Science Letters* 284: 65–75.

Dalton CA and Faul UH (2010) The oceanic and cratonic upper mantle: Clues from joint interpretation of global velocity and attenuation models. *Lithos* 120: 160–172.

Darbyshire F, Eaton DW, and Bastow ID (2013) Seismic imaging of the lithosphere beneath Hudson Bay: Episodic growth of the Laurentian mantle keel. *Earth and Planetary Science Letters* 373: 179–193.

Darbyshire FA and Lebedev S (2009) Rayleigh wave phase-velocity heterogeneity and multilayered azimuthal anisotropy of the Superior Craton, Ontario. *Geophysical Journal International* 176: 215–234.

Davies GF (1988) Ocean bathymetry and mantle convection 1. Large-scale flow and hotspots. *Journal of Geophysical Research* 93: 10467–10480.

Debayle E and Kennett BLN (2000) Anisotropy in the Australasian upper mantle from Love and Rayleigh waveform inversion. *Earth and Planetary Science Letters* 184: 339–351.

Debayle E, Kennett B, and Priestley K (2005) Global azimuthal seismic anisotropy and the unique plate-motion deformation of Australia. *Nature* 433: 509–512.

Deschamps F, Lebedev S, Meier T, and Trampert J (2008) Stratified seismic anisotropy reveals past and present deformation beneath the east-central United States. *Earth and Planetary Science Letters* 274: 489–498.

Devi EU, Kumar P, and Kumar MR (2011) Imaging the Indian lithosphere beneath the Eastern Himalayan Region. *Geophysical Journal International* 187: 631–641.

Eaton DW, Darbyshire F, Evans RL, Grütter H, Jones AG, and Yuan X (2009) The elusive lithosphere–asthenosphere boundary (LAB) beneath cratons. *Lithos* 109: 1–22.

Eaton DW and Frederiksen A (2007) Seismic evidence for convection-driven motion of the North American plate. *Nature* 446: 428–431.

Eberle MA and Forsyth DW (1995) Regional viscosity variations, small-scale convection and slope of the depth–age$^{1/2}$ curve. *Geophysical Research Letters* 22: 473–476.

Ekström G (2000) Mapping the lithosphere and asthenosphere with surface waves: Lateral structure and anisotropy. In: Richards MA, Gordon RG, and van der Hilst RD (eds.) *The History and Dynamics of Global Plate Motions*. *Geophysical Monograph Series*, vol. 121, pp. 239–255. Washington, DC: American Geophysical Union. http://dx.doi.org/10.1029/GM121p0239.

Ekström G (2011) A global model of Love and Rayleigh surface wave dispersion and anisotropy, 25–250 s. *Geophysical Journal International* 187: 1668–1686. http://dx.doi.org/10.1111/j.1365-246X.2011.05225.x.

Ekström G and Dziewonski AM (1998) The unique anisotropy of the Pacific upper mantle. *Nature* 394: 168–172.

Evans RL, Hirth G, Baba K, Forsyth D, Chave A, and Mackie R (2005) Geophysical evidence from the MELT area for compositional controls on oceanic plates. *Nature* 437: 249–252.

Evans RL, Jones AG, Garcia X, et al. (2011) Electrical lithosphere beneath the Kaapvaal craton, southern Africa. *Journal of Geophysical Research* 116. http://dx.doi.org/10.1029/2010JB007883, B04105.

Faul UH and Jackson I (2005) The seismological signature of temperature and grain size variations in the upper mantle. *Earth and Planetary Science Letters* 234: 119–134.

Fischer KM, Ford HA, Abt DL, and Rychert CA (2010) The lithosphere–asthenosphere boundary. *Annual Review of Earth and Planetary Sciences* 38: 551–575. http://dx.doi.org/10.1146/annurev-earth-040809-152438.

Fishwick S (2010) Surface wave tomography: Imaging of the lithosphere asthenosphere boundary beneath central and southern Africa? *Lithos* 120: 63–73.

Flanagan MP and Shearer PM (1998) Global mapping of topography on transition zone velocity discontinuities by stacking SS precursors. *Journal of Geophysical Research* 103: 2673–2692. http://dx.doi.org/10.1029/97JB03212.

Ford HA (2013) *A Seismological Perspective on the Lithosphere–Asthenosphere Boundary*. PhD Thesis, Providence, RI, USA: Brown University.

Ford HA, Fischer KM, Abt DL, Rychert CA, and Elkins-Tanton LT (2010) The lithosphere–asthenosphere boundary and cratonic lithospheric layering beneath Australia from Sp wave imaging. *Earth and Planetary Science Letters* 300: 299–310. http://dx.doi.org/10.1016/j.epsl.2010.10.007.

Forsyth DW (1975) The early structural evolution and anisotropy of the oceanic upper mantle. *Geophysical Journal of the Royal Astronomical Society* 43: 103–162.

Foster K, Dueker K, Schmandt B, and Yuan H (in press) A sharp cratonic lithosphere–asthenosphere boundary beneath the American Midwest and its relation to mantle flow. *Earth and Planetary Science Letters* http://dx.doi.org/10.1016/j.epsl.2013.11.018.

French SW, Lekic V, and Romanowicz BA (2013) Waveform tomography reveals channeled flow at the base of the oceanic lithosphere. *Science* 342: 227–230.

Gaboret C, Forte AM, and Montagner J-P (2003) The unique dynamics of the Pacific Hemisphere mantle and its signature on seismic anisotropy. *Earth and Planetary Science Letters* 208: 219–233.

Gaherty JB (2004) A surface wave analysis of seismic anisotropy beneath eastern North America. *Geophysical Journal International* 158: 1053–1066.

Gaherty JB and Jordan TH (1995) Lehmann discontinuity as the base of an anisotropic layer beneath continents. *Science* 26: 1468–1471.

Gaherty JB, Jordan TH, and Gee LS (1996) Seismic structure of the upper mantle in a central Pacific corridor. *Journal of Geophysical Research* 101: 22291–22309.

Gaherty JB, Kato M, and Jordan TH (1999) Seismological structure of the upper mantle: A regional comparison of seismic layering. *Physics of the Earth and Planetary Interiors* 110: 21–41.

Gao SS, Silver PG, Liu KH and the Kaapvaal Seismic Group (2002) Mantle discontinuities beneath Southern Africa. *Geophysical Research Letters* 29. http://dx.doi.org/10.1029/2001GL013834.

Geissler WH, Sodoudi F, and Kind R (2010) Thickness of the central and eastern European lithosphere as seen by S receiver functions. *Geophysical Journal International* 181: 604–634. http://dx.doi.org/10.1111/j.1365-246X.2010.04548.x.

Gossler J and Kind R (1996) Seismic evidence for very deep roots of continents. *Earth and Planetary Science Letters* 138: 1–13. http://dx.doi.org/10.1016/0012-821X(95)00215-X.

Grand SP and Helmberger DV (1984) Upper mantle shear structure of North America. *Geophysical Journal of the Royal Astronomical Society* 76: 399–438.

Gu YJ and Dziewonski AM (2002) Global variability of transition zone thickness. *Journal of Geophysical Research* 107: 2135. http://dx.doi.org/10.1029/2001JB000489.

Gueydan F, Morency C, and Brun J-P (2008) Continental rifting as a function of lithosphere mantle strength. *Tectonophysics* 460: 83–93.

Gung Y, Panning M, and Romanowicz B (2003) Global anisotropy and the thickness of continents. *Nature* 422: 707–711.

Hacker BR and Abers GA (2004) Subduction Factory 3: An Excel worksheet and macro for calculating the densities, seismic wave speeds, and H_2O contents of minerals and rocks at pressure and temperature. *Geochemistry, Geophysics, Geosystems* 5, Q01005.

Hansen S, Dueker K, Stachnik J, Aster R, and Karlstrom K (2013) A rootless Rockies – Support and lithospheric structure of the Colorado Rocky Mountains inferred from CREST and TA seismic data. *Geochemistry, Geophysics, Geosystems* 14: 2670–2695. http://dx.doi.org/10.1002/ggge.20143.

Hansen SE, Nyblade AJ, Julià J, Dirks PHGM, and Durrheim RJ (2009) Upper-mantle low-velocity zone structure beneath the Kaapvaal craton from *S*-wave receiver functions. *Geophysical Journal International* 178: 1021–1027.

Hansen SE, Rodgers AJ, Schwartz SY, and Al-Amri AMS (2007) Imaging ruptured lithosphere beneath the Red Sea and Arabian Peninsula. *Earth and Planetary Science Letters* 259: 256–265.

Heit B, Sodoudi F, Yuan X, Bianchi M, and Kind R (2007) An S receiver function analysis of the lithospheric structure in South America. *Geophysical Research Letters* 34. http://dx.doi.org/10.1029/2007GL030317, L14307.

Hirschmann MM (2010) Partial melt in the oceanic low velocity zone. *Physics of the Earth and Planetary Interiors* 179: 60–71.

Hirschmann M and Kohlstedt D (2012) Water in Earth's mantle. *Physics Today* 65. http://dx.doi.org/10.1063/PT.3.1476.

Hirth G, Evans RL, and Chave AD (2000) Comparison of continental and oceanic mantle electrical conductivity: Is the Archean lithosphere dry? *Geochemistry, Geophysics, Geosystems* 1. http://dx.doi.org/10.1029/200GC00048.

Hirth G and Kohlstedt DL (1996) Water in the oceanic upper mantle: Implications for rheology, melt extraction, and the evolution of the lithosphere. *Earth and Planetary Science Letters* 144: 93–108.

Hopper E, Ford HA, Fischer KM, Lekic V, and Fouch MJ (in press) The lithosphere–asthenosphere boundary and the tectonic and magmatic history of the northwestern United States. *Earth and Planetary Science Letters*. http://dx.doi.org/10.1016/j.epsl.2013.12.016

Huismans R and Beaumont C (2003) Symmetric and asymmetric lithospheric extension: Relative effects of frictional-plastic and viscous strain softening. *Journal of Geophysical Research* 108. http://dx.doi.org/10.1029/2002JB002026.

Huismans R and Beaumont C (2011) Depth-dependent extension, two-stage breakup and cratonic underplating at rifted margins. *Nature* 473: 74–79.

Jackson I and Faul UH (2010) Grainsize-sensitive viscoelastic relaxation in olivine: Towards a robust laboratory-based model for seismological application. *Physics of the Earth and Planetary Interiors* 183: 151–163.

Jordan TH (1978) Composition and development of the continental tectosphere. *Nature* 274: 544–548.

Karato S (2003) Mapping water content in the upper mantle. In: Eiler JM (ed.) *Inside the Subduction Factory*, pp. 135–152. Washington, DC: American Geophysical Union.

Karato S (2012) On the origin of the asthenosphere. *Earth and Planetary Science Letters* 321–322: 95–103.

Karato S and Jung H (1998) Water, partial melting and the origin of the seismic low velocity and high attenuation zone in the upper mantle. *Earth and Planetary Science Letters* 157: 193–207.

Karato S, Jung H, Katayama I, and Skemer P (2008) Geodynamic significance of the seismic anisotropy of the upper mantle: New insights from laboratory studies. *Annual Review of Earth and Planetary Sciences Letters* 36: 59–95. http://dx.doi.org/10.1146/annurev.earth.36.031207.124120.

Katzman R, Zhao L, and Jordan TH (1998) High-resolution, two-dimensional vertical tomography of the central Pacific mantle using ScS reverberations and frequency dependent travel times. *Journal of Geophysical Research* 103: 17933–17971.

Kawakatsu H, Kumar P, Takei Y, et al. (2009) Seismic evidence for sharp lithosphere–asthenosphere boundaries of oceanic plates. *Science* 324: 499–502.

Kind R, Yuan X, and Kumar P (2012) Seismic receiver functions and the lithosphere–asthenosphere boundary. *Tectonophysics* 536–537: 25–43.

King SD and Ritsema J (2000) African hot spot volcanism: Small-scale convection in the upper mantle beneath cratons. *Science* 290: 1137–1140.

Kohlstedt DL and Holtzman BK (2009) Shearing melt out of the Earth: An experimentalist's perspective on the influence of deformation on melt extraction. *Annual Review of Earth and Planetary Sciences* 37: 561–593.

Korenaga J and Jordan TH (2002) On the state of sublithospheric upper mantle beneath a supercontinent. *Geophysical Journal International* 149: 179–189.

Kumar P and Kawakatsu H (2011) Imaging the seismic lithosphere–asthenosphere boundary of the oceanic plate. *Geochemistry, Geophysics, Geosystems* 12. http://dx.doi.org/10.1029/2010GC003358, Q01006.

Kumar P, Kawakatsu H, Shinohara M, Kanazawa T, Araki E, and Suyehiro K (2011) P and S receiver function analysis of seafloor borehole broadband seismic data. *Journal of Geophysical Research* 116. http://dx.doi.org/10.1029/2011JB008506.

Kumar P, Kind R, Hanka W, et al. (2005a) The lithosphere–asthenosphere boundary in the North-West Atlantic region. *Earth and Planetary Science Letters* 236: 249–257.

Kumar P, Kind R, Yuan X, and Mechie J (2012) USArray receiver function images of the lithosphere–asthenosphere boundary. *Seismological Research Letters* 83, 486–491.

Kumar P, Yuan X, Kind R, and Kosarev G (2005b) The lithosphere–asthenosphere boundary in the Tien Shan–Karakoram region from S receiver functions: Evidence for continental subduction. *Geophysical Research Letters* 32. http://dx.doi.org/10.1029/2004GL022291.

Kumar P, Yuan X, Kumar MR, Kind R, Li X, and Chadha RK (2007) The rapid drift of the Indian tectonic plate. *Nature* 449: 894–897.

Kustowski B, Ekström G, and Dziewonski AM (2008) Anisotropic shear-wave velocity structure of the Earth's mantle: A global model. *Journal of Geophysical Research* 113, B06306.

Lawrence JF and Shearer PM (2006) A global study of transition zone thickness using receiver functions. *Journal of Geophysical Research* 111. http://dx.doi.org/10.1029/2005JB003973.

Lee C-TA (2003) Compositional variation of density and seismic velocities in natural peridotites at STP conditions: Implications for seismic imaging of compositional heterogeneities in the upper mantle. *Journal of Geophysical Research* 108: 2441. http://dx.doi.org/10.1029/2003jb002413.

Lee C-TA, Luffi P, and Chin E (2011) Building and destroying continental mantle. *Annual Review of Earth and Planetary Sciences* 39: 59–90. http://dx.doi.org/10.1146/annurev-earth-040610-133505.

Lekic V and Fischer KM (in press) Contrasting lithospheric signatures across the western United States revealed by Sp receiver functions. *Earth and Planetary Science Letters*. http://dx.doi.org/10.1016/j.epsl.2013.11.026.

Lekic V, French SW, and Fischer KM (2011) Lithospheric thinning beneath rifted regions of Southern California. *Science* 334: 783–787. http://dx.doi.org/10.1126/science.1208898.

Lekic V and Romanowicz B (2011a) Inferring upper-mantle structure by full waveform tomography with the spectral element method. *Geophysical Journal International* 185: 799–831. http://dx.doi.org/10.1111/j.1365-246X.2011.04969.x.

Lekic V and Romanowicz B (2011b) Tectonic regionalization without a priori information: A cluster analysis of upper mantle tomography. *Earth and Planetary Science Letters* 308: 151–160.

Levander A and Miller MS (2012) Evolutionary aspects of lithosphere discontinuity structure in the western US. *Geochemistry, Geophysics, Geosystems* 13. http://dx.doi.org/10.1029/2012GC004056, Q0AK07.

Levander A, Schmandt B, Miller MS, et al. (2011) Continuing Colorado plateau uplift by delamination-style convective lithospheric downwelling. *Nature* 472: 461–466. http://dx.doi.org/10.1038/nature10001.

Levin V and Park J (2000) Shear zones in the Proterozoic lithosphere of the Arabian Shield and the nature of the Hales discontinuity. *Tectonophysics* 323: 131–148.

Li A and Burke K (2006) Upper mantle structure of southern Africa from Rayleigh wave tomography. *Journal of Geophysical Research* 111. http://dx.doi.org/10.1029/2006JB004321.

Li A, Fischer KM, Wysession ME, and Clarke TJ (1998) Mantle discontinuities and temperature under the North American continental keel. *Nature* 395: 160–163. http://dx.doi.org/10.1038/25972.

Li A, Forsyth DW, and Fischer KM (2003) Shear wave structure and azimuthal anisotropy beneath eastern North America from Rayleigh wave tomography. *Journal of Geophysical Research* 108: 2362. http://dx.doi.org/10.1029/2002JB002259.

Li A, Forsyth DW, and Fischer KM (2005) Rayleigh wave phase velocities and azimuthally anisotropic shear-wave structure beneath the Colorado Rocky Mountains. In: Karlstrom KE and Keller GR (eds.) *The Rocky Mountain Region – An Evolving Lithosphere: Tectonics, Geochemistry, and Geophysics*. *AGU Geophysical Monograph*, vol. 154, pp. 385–401.

Li X, Kind R, Priestley K, et al. (2000) Mapping the Hawaiin plume conduit with converted seismic waves. *Nature* 405: 938–941.

Li X, Kind R, Yuan XH, Wölbern I, and Hanka W (2004) Rejuvenation of the lithosphere by the Hawaiian plume. *Nature* 427: 827–829.

Li X, Yuan X, and Kind R (2007) The lithosphere–asthenosphere boundary beneath the western United States. *Geophysical Journal International* 170: 700–710.

Lin FC, Ritzwoller MH, Yang Y, Moschetti MP, and Fouch MJ (2011) Complex and variable crustal and uppermost mantle seismic anisotropy in the western United States. *Nature Geoscience* 4: 55–61.

Maggi A, Debayle E, Priestley K, and Barruol G (2006) Azimuthal anisotropy of the Pacific region. *Earth and Planetary Science Letters* 250: 53–71.

Marone F and Romanowicz B (2007) The depth distribution of azimuthal anisotropy in the continental upper mantle. *Nature* 447: 198–201.

Mercier JP, Bostock MG, Audet P, Gaherty JB, Garnero EJ, and Revenaugh J (2008) The teleseismic signature of fossil subduction: Northwestern Canada. *Journal of Geophysical Research* 113. http://dx.doi.org/10.1029/2007JB005127.

Mierdel K, Keppler H, Smyth JR, and Langenhorst F (2007) Water solubility in aluminous orthopyroxene and the origin of Earth's asthenosphere. *Science* 315: 364–368.

Miller MS and Agostinetti NP (2011) Erosion of the continental lithosphere at the cusps of the Calabrian arc: Evidence from S receiver functions analysis. *Geophysical Research Letters* 38. http://dx.doi.org/10.1029/2011GL049455, L23301.

Miller MS and Agostinetti NP (2012) Insights into the evolution of the Italian lithospheric structure from S receiver function analysis. *Earth and Planetary Science Letters* 345–348: 49–59.

Miller MS and Eaton DW (2010) Formation of cratonic mantle keels by arc accretion: Evidence from S receiver functions. *Geophysical Research Letters* 37. http://dx.doi.org/10.1029/2010GL044366, L18305.

Mohsen A, Kind R, Sobolev SV, and Weber M (2006) Thickness of the lithosphere east of the Dead Sea Transform. *Geophysical Journal International* 167: 845–852.

MONA LISA Working Group (1997) MONA LISA – Deep seismic investigations of the lithosphere in the southeastern North Sea. *Tectonophysics* 269: 1–19.

Montagner J-P (2002) Upper mantle low anisotropy channels below the Pacific plate. *Earth and Planetary Science Letters* 202: 263–274.

Montagner J-P and Tanimoto T (1990) Global anisotropy in the upper mantle inferred from the regionalization of phase velocities. *Journal of Geophysical Research* 95: 4797–4819.

Morozova EA, Morozov IB, Smithson SB, and Solodilov LN (1999) Heterogeneity of the uppermost mantle beneath Russian Eurasia from the ultra-long-range profile QUARTZ. *Journal of Geophysical Research* 104: 20329–20348.

Naif S, Key K, Constable S, and Evans RL (2013) Melt-rich channel observed at the lithosphere–asthenosphere boundary. *Nature* 495: 356–359. http://dx.doi.org/10.1038/nature11939.

Nettles M and Dziewoński AM (2008) Radially anisotropic shear velocity structure of the upper mantle globally and beneath North America. *Journal of Geophysical Research* 113. http://dx.doi.org/10.1029/2006jb004819.

Nielsen L, Thybo H, and Egorkin AV (2002) Implications of seismic scattering below the 8° discontinuity along PNE profile Kraton. *Tectonophysics* 358: 135–150.

Nishimura CE and Forsyth DW (1988) Rayleigh wave phase velocities in the Pacific with implications for azimuthal anisotropy and lateral heterogeneities. *Geophysical Journal International* 94: 479–501.

Nishimura C and Forsyth DW (1989) The anisotropic structure of the upper mantle in the Pacific. *Geophysical Journal International* 96: 203–229.

Oreshin S, Vinnik L, Peregoudov D, and Roecker S (2002) Lithosphere and asthenosphere of the Tien Shan imaged by S receiver functions. *Geophysical Research Letters* 29: 1191. http://dx.doi.org/10.1029/2001GL014441.

Ozacar AA, Gilbert H, and Zandt G (2008) Upper mantle discontinuity structure beneath East Anatolian Plateau (Turkey) from receiver functions. *Earth and Planetary Science Letters* 269: 426–434.

Parsons B and McKenzie D (1978) Mantle convection and the thermal structure of the plates. *Journal of Geophysical Research* 83: 4485–4496.

Parsons B and Sclater JG (1977) Analysis of variation of ocean-floor bathymetry and heat-flow with age. *Journal of Geophysical Research* 82: 803–827. http://dx.doi.org/10.1029/JB082i005p00803.

Pavlenkova GA, Priestley K, and Cipar J (2002) 2D model of the crust and uppermost mantle along rift profile, Siberian craton. *Tectonophysics* 355: 171–186.

Pedersen HA, Fishwick S, and Snyder DB (2009) A comparison of cratonic roots through consistent analysis of seismic surface waves. *Lithos* 109: 81–95.

Perchuc E and Thybo H (1996) Upper mantle P-wave velocity model for the Baltic shield. *Tectonophysics* 253: 227–245.

Phipps Morgan J, Morgan WJ, Zhang Y-S, and Smith WHF (1995) Observational hints for a plume-fed, suboceanic asthenosphere and its role in mantle convection. *Journal of Geophysical Research* 100: 12753–12767.

Plomerová J, Kouba D, and Babuska V (2002) Mapping the lithosphere–asthenosphere boundary through changes in surface-wave anisotropy. *Tectonophysics* 358: 175–185.

Priestley K and McKenzie D (2006) The thermal structure of the lithosphere from shear wave velocities. *Earth and Planetary Science Letters* 244: 285–301. http://dx.doi.org/10.1016/j.epsl.2006.01.008.

Priestley K, McKenzie D, and Debayle E (2006) The state of the upper mantle beneath southern Africa. *Tectonophysics* 416: 101–112.

Priestley K and Tilmann F (2009) Relationship between the upper mantle high velocity seismic lid and the continental lithosphere. *Lithos* 109: 112–124.

Rau CJ and Forsyth DW (2011) Melt in the mantle beneath the amagmatic zone, southern Nevada. *Geology* 39: 975–978.

Revenaugh J and Jordan TH (1991) Mantle layering from ScS reverberations 3. The upper mantle. *Journal of Geophysical Research* 96: 781–810.

Ritsema J, van Heijst HJ, Deuss A, and Woodhouse JH (2011) S40RTS: A degree-40 shear-velocity model for the mantle from new Rayleigh wave dispersion, teleseismic traveltimes, and normal-mode splitting function measurements. *Geophysical Journal International* 184. http://dx.doi.org/10.1111/j.1365-246X.2010.04884.x.

Ritzwoller MH, Shapiro NM, and Zhong SJ (2004) Cooling history of the Pacific lithosphere. *Earth and Planetary Science Letters* 226: 69–84. http://dx.doi.org/10.1016/j.epsl.2004.07.032.

Romanowicz B (2009) The thickness of tectonic plates. *Science* 324: 474–476.

Ryberg T, Wenzel F, Mechie J, Egorkin A, Fuchs K, and Solodilov L (1996) Two-dimensional velocity structure beneath northern Eurasia derived from the super long-range seismic profile Quartz. *Bulletin of the Seismological Society of America* 86: 857–867.

Rychert CA, Fischer KM, and Rondenay S (2005) A sharp lithosphere–asthenosphere boundary imaged beneath eastern North America. *Nature* 436: 542–545.

Rychert CA, Hammond JOS, Harmon N, et al. (2012a) Volcanism in the Afar Rift sustained by decompression melting with minimal plume influence. *Nature Geoscience* 5: 406–409.

Rychert CA, Rondenay S, and Fischer KM (2007) P-to-S and S-to-P imaging of a sharp lithosphere–asthenosphere boundary beneath eastern North America. *Journal of Geophysical Research* 112. http://dx.doi.org/10.1029/2006jb004619, B08314.

Rychert CA, Schmerr N, and Harmon N (2012b) The Pacific lithosphere–asthenosphere boundary: Seismic imaging and anisotropic constraints from SS waveforms. *Geochemistry, Geophysics, Geosystems* 13. http://dx.doi.org/10.1029/2012GC004194, Q0AK10.

Rychert CA and Shearer PM (2009) A global view of the lithosphere–asthenosphere boundary. *Science* 324: 495–498. http://dx.doi.org/10.1126/science.1169754.

Rychert CA and Shearer PM (2011) Imaging the lithosphere–asthenosphere boundary beneath the Pacific using SS waveform modeling. *Journal of Geophysical Research* 116. http://dx.doi.org/10.1029/2010JB008070, B07307.

Rychert CA, Shearer PM, and Fischer KM (2010) Scattered wave imaging of the lithosphere–asthenosphere boundary. *Lithos* 120: 173–185. http://dx.doi.org/10.1016/j.lithos.2009.12.006.

Sacks IS, Snoke JA, and Husebye ES (1979) Lithosphere thickness beneath the Baltic shield. *Tectonophysics* 56: 101–110.

Saul J, Kumar MR, and Sarkar D (2000) Lithospheric and upper mantle structure of the Indian Shield from teleseismic receiver functions. *Geophysical Research Letters* 27: 2357–2360.

Savage B and Silver PG (2008) Evidence for a compositional boundary within the lithospheric mantle beneath the Kalahari craton from S receiver functions. *Earth and Planetary Science Letters* 272: 600–609.

Schmerr N (2012) The Gutenberg discontinuity: Melt at the lithosphere–asthenosphere boundary. *Science* 335: 1480–1483. http://dx.doi.org/10.1126/science.1215433.

Schutt DL and Lesher CE (2006) Effects of melt depletion on the density and seismic velocity of garnet and spinel lherzolite. *Journal of Geophysical Research* 111. http://dx.doi.org/10.1029/2003jb002950, B05401.

Smith, DB, Ritzwoller MH, and Shapiro NM (2004) Stratification of anisotropy in the Pacific upper mantle, *Journal of Geophysical Research* 109. http://dx.doi.org/10.1029/2004JB003200.

Simons FJ and van der Hilst RD (2003) Seismic and mechanical anisotropy and the past and present deformation of the Australian lithosphere. *Earth and Planetary Science Letters* 211: 271–286.

Simons FJ, van der Hilst RD, Montagner J-P, and Zielhuis A (2002) Multimode Rayleigh wave inversion for heterogeneity and azimuthal anisotropy of the Australian upper mantle. *Geophysical Journal International* 151: 738–754.

Snyder DB (2008) Stacked uppermost mantle layers within the Slave craton of NW Canada as defined by anisotropic seismic discontinuities. *Tectonics* 27. http://dx.doi.org/10.1029/2007TC002132.

Snyder D and Bruneton M (2007) Seismic anisotropy of the Slave craton, NW Canada, from joint interpretation of SKS and Rayleigh waves. *Geophysical Journal International* 169: 170–188. http://dx.doi.org/10.1111/j.1365-246X.2006.03287.x.

Sodoudi F, Kind R, Hatzfeld D, et al. (2006a) Lithospheric structure of the Aegean obtained from P and S receiver functions. *Journal of Geophysical Research* 111. http://dx.doi.org/10.1029/2005JB003932, B12307.

Sodoudi F, Yuan X, Liu Q, Kind R, and Chen J (2006b) Lithospheric thickness beneath the Dabie Shan, central eastern China from S receiver functions. *Geophysical Journal International* 166: 1363–1367.

Steer DN, Knapp JH, and Brown DL (1998a) Super-deep reflection profiling: Exploring the continental mantle lid. *Tectonophysics* 286: 111–121.

Steer DN, Knapp JH, Brown LD, Echtler HP, Brown DL, and Berzin R (1998b) Deep structure of the continental lithosphere in an unextended orogen; an explosive-source seismic reflection profile in the Urals (Urals Seismic Experiment and Integrated Studies (URSEIS 1995)). *Tectonics* 17: 143–157.

Stein CA and Stein S (1992) A model for the global variation in oceanic depth and heat-flow with lithospheric age. *Nature* 359: 123–129. http://dx.doi.org/10.1038/359123a0.

Stixrude L and Lithgow-Bertelloni C (2005) Mineralogy and elasticity of the oceanic upper mantle: Origin of the low-velocity zone. *Journal of Geophysical Research* 110. http://dx.doi.org/10.1029/2004jb002965, B03204.

Takei Y and Holtzman BK (2009) Viscous constitutive relations of solid–liquid composites in terms of grain boundary contiguity: 1. Grain boundary diffusion control model. *Journal of Geophysical Research* 114. http://dx.doi.org/10.1029/2008jb005850.

Tan Y and Helmberger DV (2007) Trans-Pacific upper mantle shear velocity structure. *Journal of Geophysical Research* 112. http://dx.doi.org/10.1029/2006JB004853.

Tanimoto T and Anderson DL (1984) Mapping convection in the mantle. *Geophysical Research Letters* 11: 287–290.

Thompson DA, Helffrich G, Bastow ID, et al. (2011) Implications of a simple mantle transition zone beneath cratonic North America. *Earth and Planetary Science Letters* 312: 28–36.

Thybo H (2006) The heterogeneous upper mantle low velocity zone. *Tectonophysics* 416: 53–79.

Thybo H and Perchuc E (1997) The seismic 8° discontinuity and partial melting in continental mantle. *Science* 275: 1626–1629.

Till CB, Elkins-Tanton LT, and Fischer KM (2010) A mechanism for low-extent melts at the lithosphere–asthenosphere boundary. *Geochemistry, Geophysics, Geosystems* 11. http://dx.doi.org/10.1029/2010GC003234, Q10015.

Trampert J and Woodhouse JH (2003) Global anisotropic phase velocity maps for fundamental mode surface waves between 40 and 150 s. *Geophysical Journal International* 154: 154–165.

Vinnik L, Kiselev S, Weber M, Oreshin S, and Makeyeva L (2012) Frozen and active seismic anisotropy beneath southern Africa. *Geophysical Research Letters* 39. http://dx.doi.org/10.1029/2012GL051326, L08301.

Vinnik L, Kurnik E, and Farra V (2005) Lehmann discontinuity beneath North America: No role for seismic anisotropy. *Geophysical Research Letters* 32. http://dx.doi.org/10.1029/2004GL022333, L09306.

Weeraratne DS, Forsyth DW, Fischer KM, and Nyblade AA (2003) Evidence for an upper mantle plume beneath the Tanzanian craton from Rayleigh wave tomography. *Journal of Geophysical Research* 108: 2427. http://dx.doi.org/10.1029/2002JB002273.

Wiens DA, Conder JA, and Faul UH (2008) The seismic structure and dynamics of the mantle wedge. *Annual Review of Earth and Planetary Sciences* 36: 421–455.

Wilson DC, Angus DA, Ni JF, and Grand SP (2006) Constraints on the interpretation of *S*-to-*P* receiver functions. *Geophysical Journal International* 165: 969–980.

Wittlinger G and Farra V (2007) Converted waves reveal a thick and layered tectosphere beneath the Kalahari super-craton. *Earth and Planetary Science Letters* 254: 404–415.

Wölbern I, Jacob AWB, Blake TA, et al. (2006) Deep origin of the Hawaiian tilted plume conduit derived from receiver functions. *Geophysical Journal International* 166: 767–781.

Wölbern I, Rümpker G, Link K, and Sodoudi F (2012) Melt infiltration of the lower lithosphere beneath the Tanzania craton and the Albertine rift inferred from S receiver functions. *Geochemistry, Geophysics, Geosystems* 13. http://dx.doi.org/10.1029/2012GC004167, Q0AK08.

Xu Q, Zhao J, Pei S, and Liu H (2011) The lithosphere–asthenosphere boundary revealed by *S*-receiver functions from the Hi-CLIMB experiment. *Geophysical Journal International* 187: 414–420.

Yuan H and Romanowicz B (2010a) Lithospheric layering in the North American craton. *Nature* 466: 1063–1068. http://dx.doi.org/10.1038/nature09332.

Yuan H and Romanowicz B (2010b) Depth dependent azimuthal anisotropy in the western US upper mantle. *Earth and Planetary Science Letters* 300: 385–394. http://dx.doi.org/10.1016/j.epsl.2010.10.020.

Yuan H, Romanowicz B, Fischer KM, and Abt DL (2011) 3-D shear wave radially and azimuthally anisotropic velocity model of the North American upper mantle. *Geophysical Journal International* 184: 1237–1260. http://dx.doi.org/10.1111/j.1365-246X.2010.04901.x.

Yuen DA and Fleitout L (1985) Thinning of the lithosphere by small-scale convective destabilization. *Nature* 313: 125–128.

Zaranek SE (2005) *Roles of Convection in the Evolution of Planetary Interiors and Terrestrial Lithospheres*. PhD Thesis, Providence, RI, USA: Brown University.

Zhao W, Kumar P, Mechie J, et al. (2011) Seismic evidence for Tibetan Plate overriding Asian Plate. *Nature Geoscience* 4: 870–873. http://dx.doi.org/10.1038/NGEO1309.

Zhu H, Bozdag E, Peter D, and Tromp J (2012) Structure of the European upper mantle revealed by adjoint tomography. *Nature Geoscience* 5: 493–498.

Zhu H and Tromp J (2013) Mapping tectonic deformation in the crust and upper mantle beneath Europe and the North Atlantic Ocean. *Science* 341: 871–875.

Zurek B and Dueker K (2005) Lithospheric stratigraphy beneath the Southern Rocky Mountains, USA. In: Karlstrom KE and Keller GR (eds.) *The Rocky Mountain Region – An Evolving Lithosphere: Tectonics, Geochemistry, and Geophysics*. *AGU Geophysical Monograph*, vol. 154, pp. 317–358.

1.19 Deep Earth Structure - Upper Mantle Structure: Global Isotropic and Anisotropic Elastic Tomography

J-P Montagner, Université paris-Diderot, Paris, France

© 2015 Elsevier B.V. All rights reserved.

1.19.1	**Introduction**	613
1.19.2	**Effects of Seismic Velocity and Anisotropy on Seismograms**	614
1.19.2.1	First-Order Perturbation Theory	614
1.19.2.2	Effect of Anisotropic Heterogeneities on Normal Modes and Surface Waves	615
1.19.2.3	Comparison Between Surface-Wave Anisotropy and SKS Splitting Data	617
1.19.3	**Upper Mantle Tomography of Seismic Velocity and Anisotropy**	619
1.19.3.1	Forward Problem	620
1.19.3.1.1	Data space: **d**	620
1.19.3.1.2	Finite-frequency effects	621
1.19.3.1.3	Parameter space: **p(r)**	622
1.19.3.2	Inverse Problem	622
1.19.3.3	Isotropic and Anisotropic Images of the Upper Mantle	624
1.19.4	**Geodynamic Applications**	626
1.19.4.1	Oceanic Plates	627
1.19.4.2	Continents	629
1.19.4.3	Velocity and Anisotropy in the Transition Zone	630
1.19.5	**Numerical Modeling and Perspectives**	631
Acknowledgments		635
References		635

1.19.1 Introduction

Thirty years ago, the first global isotropic tomographic models of the mantle were published (Dziewonski, 1984; Woodhouse and Dziewonski, 1984). Since that time, many new tomographic models were published, and a large family of techniques was made available. This important progress was made possible by the extensive use of computers that can handle very large datasets and by the availability of high-quality digital seismograms recorded by broadband seismic networks such as GEOSCOPE (Romanowicz et al., 1984), IRIS (Smith, 1986), and all networks coordinated by the FDSN (Federation of Digital Seismograph Networks; Romanowicz and Dziewonski, 1986). The recent years have seen the rapid development of very dense regional broadband seismic networks such as USArray in the United States, VEBSN (Virtual European Broadband Seismograph Network) in Europe, or F-net in Japan. Thanks to the installation of modern digital networks, it is now possible to map the whole earth from the surface down to the center of the Earth by seismic tomography. However, until recently, most tomographic techniques only make use of travel times or phase information in seismograms and very few use the amplitude, even when seismic waveforms are used (Li and Romanowicz, 1996; Woodhouse and Dziewonski, 1984). Global tomographic models have been improved over the years by an increase in the number of data and more importantly by using more general parameterizations, now including anisotropy (radial anisotropy in Nataf et al. (1986) and general slight anisotropy in Montagner and Tanimoto (1990, 1991)) and to a lesser extent anelasticity (Dalton and Ekström, 2006; Romanowicz, 1990; Tanimoto, 1990). Now, with the expansion of fast parallel computer facilities, it is possible to implement full-waveform inversion by using adjoint tomography methods (Fichtner et al., 2009; Lekic and Romanowicz, 2011; Tarantola, 1984; Tromp et al., 2005).

This chapter is focused on the imaging of global-scale or, when pertinent, of very large-scale (>1000 km) lateral heterogeneities of velocity and anisotropy in the upper mantle (0–660 km depth) where the lateral resolution is the best thanks to surface waves providing an almost uniform lateral and azimuthal coverage, particularly below oceanic areas. We will discuss how tomographic imaging completely renewed our vision of upper mantle dynamics. It makes it possible to relate surface geology and plate tectonics to underlying mantle convection and to map at depth the origin of geologic objects such as continents, mountain ranges, slabs, ridges, and plumes. The goal of this chapter is not to review all contributions to this topic, but to underline the main scientific issues, to present different approaches, and to illustrate the different progress (partly subjectively) by some of my results or by other more recent models. This chapter aims to show why a major step, which takes a complete account of amplitude anomalies in the most general case and which will enable to map shorter-scale heterogeneities, is presently underway.

1.19.2 Effects of Seismic Velocity and Anisotropy on Seismograms

For theoretical and practical reasons, the Earth was considered, for a long time, as composed of isotropic and laterally homogeneous layers. While an isotropic elastic medium can be described by two independent elastic parameters (λ and μ Lamé parameters), the cubic symmetry requires three parameters, but the most commonly used anisotropic medium (transverse isotropy with vertical symmetry axis) necessitates five independent parameters (Anderson, 1961; Love, 1927) and the most general elastic medium requires 21 independent parameters. However, since the 1960s, it was recognized that most parts of the Earth are not only laterally heterogeneous but also anisotropic. Though the lateral heterogeneities of seismic velocities were used for a long time for geodynamic applications, the importance of anisotropy for understanding geodynamic processes has only been recognized recently.

Seismology is an observational field based on the exploitation of seismic recordings of the displacement (velocity or acceleration) of the Earth induced by earthquakes. Broadband three-component high dynamic-range seismometers have been installed in more than 1000 stations around the world during the last 30 years (see overview in **Chapter 1.01**). Thanks to progress in instrumentation and theoretical developments, it is now possible to observe and to take a simultaneous account of the effects of lateral heterogeneities of velocity and anisotropy on seismograms.

1.19.2.1 First-Order Perturbation Theory

The basic equation that governs the displacement $\mathbf{u}(\mathbf{r}, t)$ is the elastodynamics equation:

$$\rho_0 \frac{\mathrm{d}^2 u_i}{\mathrm{d}t^2} = \sum_j \sigma_{ij,j} + F_{\mathrm{I}i} + F_{\mathrm{E}i} \qquad [1]$$

where $F_{\mathrm{I}i}$ and $F_{\mathrm{E}i}$ represent, respectively, the whole ensemble of applied inertial and external forces (see Takeuchi and Saito, 1972; Woodhouse and Dahlen, 1978 or **Chapter 1.02** for a complete description of all terms). Generally, by neglecting the advection term, this equation is written in a simple way:

$$(\rho_0 \partial_{tt} - H_0)\mathbf{u}(\mathbf{r}, t) = \mathbf{F}(\mathbf{r}_{\mathrm{S}}, t) \qquad [2]$$

where H_0 is an integro-differential operator and $\mathbf{F}$ expresses all forces applied to the source volume in $\mathbf{r}_{\mathrm{s}}$ at time t (considered as external forces). $\mathbf{F}$ is assumed to be equal to 0 for $t<0$. In the elastic case, there is a linear relationship between σ_{ij} and the strain tensor ϵ_{kl}: $\sigma_{ij} = \sum_{kl} \Gamma_{ijkl}\epsilon_{kl}$ (+ terms related to the initial stress). Γ_{ijkl} is a fourth-order tensor, often written in its condensed form C_{ij} as a 6×6 matrix. By using the different symmetry conditions $\Gamma_{ijkl} = \Gamma_{jikl} = \Gamma_{ijlk} = \Gamma_{klij}$, the tensor $\mathbf{\Gamma}$ is shown to have 21 independent elastic moduli in the most general anisotropic medium. In an isotropic medium, this number reduces to 2, the Lamé coefficients λ and μ.

There are many ways for solving eqn [2] and to compute synthetic seismograms, but, at the global scale, the most elegant way is to determine the free oscillations (or normal modes) of the Earth. When solving for the free oscillations of the Earth, $\mathbf{F}=0$. The solution $\mathbf{u}(\mathbf{r}, t)$ of eqn [2] can be calculated for a spherically symmetrical nonrotating reference Earth model associated with the operator H_0, according to the equation

$$\rho_o \partial_{tt}\mathbf{u}(\mathbf{r}, t) = H_0\mathbf{u}(\mathbf{r}, t) \qquad [3]$$

The solution of eqn [3] is beyond the scope of this chapter and is described in **Chapter 1.02**. The eigenvalues of the operator H_0 are equal to $-\rho_0\omega_\ell^2$ where ${}_n\omega_\ell$ is the eigenfrequency characterized by two quantum numbers n and ℓ, respectively, termed radial and angular orders. The corresponding eigenfunctions ${}_n\mathbf{u}_\ell^m(\mathbf{r}, t)$ depend on three quantum numbers n, ℓ, m, where m is the azimuthal order, with the following property: $\ell \le m \le \ell$. Therefore, for a given eigenfrequency ${}_n\omega_\ell$ calculated in a spherically symmetrical Earth model, $2\ell+1$ eigenfunctions can be defined. The eigenfrequency ${}_n\omega_\ell$ is said to be degenerate, with a degree of degeneracy $2\ell+1$. There is a complete formal similarity with the calculation of the energy levels of the atom of hydrogen in quantum mechanics. The eigenfunctions ${}_n\mathbf{u}_\ell^m(\mathbf{r}, t)$ of the operator H_0 are orthogonal and normalized.

The important point is that the basis of functions ${}_n\mathbf{u}_\ell^m(\mathbf{r}, t)$ is complete. This implies that any displacement at the surface of the Earth can be expressed as a linear combination of these discrete eigenfunctions:

$$\mathbf{u}(\mathbf{r}, t) = \sum_{n,\ell,m} {}_n a_\ell^m \, {}_n\mathbf{u}_\ell^m(\mathbf{r}, t)$$

Therefore, these eigenfunctions can be used to calculate the synthetic displacement at any point $\mathbf{r}$, at time t, due to a force system $\mathbf{F}$ in the source volume and make it possible to model not only surface waves but also body waves. For a point force $\mathbf{F}$ at source point $\mathbf{r}_{\mathrm{s}}$, a step time function and its associated moment tensor $\mathbf{M}$, which is a good starting model for earthquakes, the solution of the eqn [2] is given by (Gilbert, 1971)

$$\mathbf{u}(r, t) = \sum_{n,\ell,m} {}_n\mathbf{u}_\ell^m(\mathbf{r}) \frac{(1-\cos {}_n\omega_\ell t)}{{}_n\omega_\ell^2} e^{\frac{-{}_n\omega_\ell t}{2Q}} (\mathbf{M} : {}_n\epsilon_\ell^m)\mathbf{r}_{\mathrm{s}} \qquad [4]$$

where ϵ is the deformation tensor. Since eqn [4] is linear in $\mathbf{M}$, it can be easily generalized to more complex spatial and temporal source functions and can be rewritten as

$$\mathbf{u}(\mathbf{r}, t) = \mathbf{G}(\mathbf{r}, \mathbf{r}_{\mathrm{s}}, t, t_{\mathrm{s}})\mathbf{M}(\mathbf{r}_{\mathrm{s}}, t_{\mathrm{s}})$$

where $\mathbf{G}(\mathbf{r}, \mathbf{r}_{\mathrm{s}}, t, t_{\mathrm{s}})$ is composed of the spatial derivatives of the Green operator of the medium. Normal mode theory is routinely used to calculate synthetic seismograms at long periods ($T \ge 30$ s) and Centroid moment tensor solutions (Dziewonski et al., 1981).

An example of real and synthetic seismograms is presented in **Figure 1**. However, there are still some discrepancies (usually frequency-dependent) between the observed and synthetic seismograms. The simplest way to explain the observed phase shifts (time delays) is to remove the assumption that the Earth is spherically symmetrical, that is, there are lateral heterogeneities between the source and the receiver. The next step is to characterize these lateral heterogeneities. Since the agreement between synthetic and observed seismograms is good at long periods ($T \ge 40$ s), we can reasonably infer that the amplitude of heterogeneities is small ($<10\%$). Behind the surface wavetrain, a long coda is usually observed, interpreted as scattered waves. However,

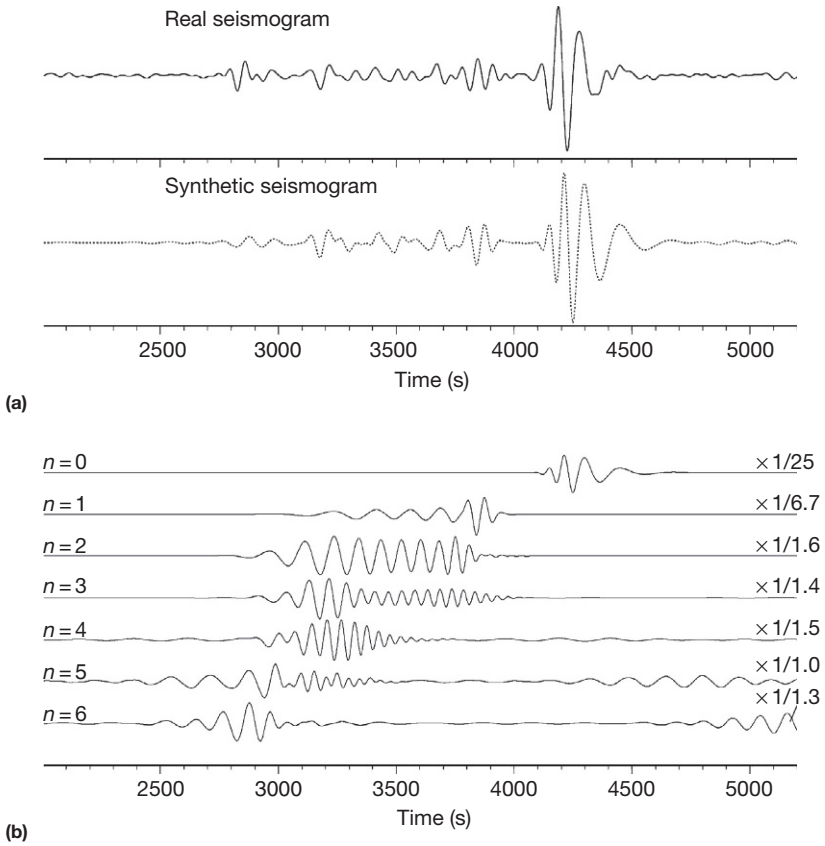

Figure 1 (a) Example of real and synthetic seismograms used for retrieving Rayleigh-wave dispersion curve for the fundamental mode and overtones (Beucler et al., 2003). Behind body waves, the signal is composed of surface waves. (b) The complex phase before the high-amplitude wave packet corresponding to the fundamental mode of Rayleigh wave ($n = 0$) can be synthetized by summing the first overtones.

when filtering out periods shorter than 40 s, this coda vanishes, which means that the scattering effect is only large in the shallowest regions of the Earth (primarily the crust and the upper lithosphere) but that it is probably negligible at larger depths. However, some groups are starting to use the information contained in these coda waves (Aki and Richards, 1980; Snieder et al., 2002) and even from ambient seismic noise (Sabra et al., 2005; Shapiro et al., 2005) for imaging the crust and lithosphere. Ambient noise tomography is a rapidly expanding field (e.g., Bensen et al., 2007) well suited to regions with dense seismic arrays and weak seismicity (see chapter by Campillo). For the sake of simplicity, this chapter is limited to long-period surface waves and it is hypothesized that the scale of lateral heterogeneities is large compared with the seismic wavelength. This point will be discussed in **Section 1.19.3.1**. A second hypothesis that must be discussed is the isotropic nature of the Earth materials. Actually, it is a poor assumption, because seismic anisotropy can be unequivocally observed at different scales. Finally, the influence of lateral variations in attenuation must also be taken into account and will be discussed elsewhere in this treatise.

1.19.2.2 Effect of Anisotropic Heterogeneities on Normal Modes and Surface Waves

Different geophysical fields are involved in the investigation of the manifestations of anisotropy of the Earth materials: mineral physics and geology for the study of the microscopic scale and seismology for scales larger than, typically, 1 km. The different observations related to anisotropy, at different scales, are reviewed in Babuska and Cara (1991), Montagner (1998), Park and Levin (2002) and in **Chapter 2.16**.

Since several decades, different kinds of observations have been used for investigating anisotropy in the upper mantle: the Rayleigh-wave and Love-wave discrepancies (Anderson, 1961), the azimuthal variation of phase velocities of surface waves (Forsyth, 1975), and the shear-wave splitting particularly for SKS waves (Silver and Chan, 1991; Vinnik et al., 1992). The lack of stations in oceanic areas explains why it is necessary to use surface waves to investigate upper mantle structure (isotropic or anisotropic) at the global or regional scales.

In the simplest case (fundamental modes, no coupling between the branches of Rayleigh and Love waves), the frequency shift $\delta\omega/\omega$ (and the corresponding phase velocity perturbation $\delta V/V$), for a constant wavenumber k, can be written by applying Rayleigh's principle (e.g., Takeuchi and Saito, 1972):

$$\left.\frac{\delta\omega}{\omega}\right|_k = \left.\frac{\delta V}{V}\right|_k = \frac{1}{2\omega}\frac{\int_\Omega \epsilon_{ij}^{*}\delta\Gamma_{ijk\ell}\epsilon_{k\ell}\,\mathrm{d}\Omega}{\int_\Omega \rho_{0n}\mathbf{u}_\ell^{m*}{}_n\mathbf{u}_\ell^{m}\,\mathrm{d}\Omega} \qquad [5]$$

where ϵ_{ij} and $\delta\Gamma_{ijkl}$ are, respectively, the second-order deformation and the deviations of the fourth-order elastic tensor

components from an SNREI (spherically symmetrical, nonrotating, elastic, and isotropic) model and ${}_n\mathbf{u}_\ell^m$ the eigenfunctions as defined in the previous section.

We only consider the propagation of surface waves in a plane-layered medium for a general slight elastic anisotropy (Montagner and Nataf, 1986), but it can be easily extended to the spherical Earth (Ekström, 2006; Larson et al., 1998; Mochizuki, 1986; Romanowicz and Snieder, 1988; Tanimoto, 1986; Trampert and Woodhouse, 2003). Smith and Dahlen (1973, 1975) found that, to the first order in anisotropy and at frequency ω, the azimuthal variation of local phase velocity (Rayleigh or Love wave) can be expanded as a Fourier series of the azimuth Ψ with only even degrees along the path and is of the form

$$\begin{aligned} V(\omega,\theta,\phi,\Psi)-V_0(\omega,\Psi)=\alpha_0(\omega,\theta,\phi)+\alpha_1(\omega,\theta,\phi)\cos 2\Psi \\ +\alpha_2(\omega,\theta,\phi)\sin 2\Psi \\ +\alpha_3(\omega,\theta,\phi)\cos 4\Psi \\ +\alpha_4(\omega,\theta,\phi)\sin 4\Psi \end{aligned} \quad [6]$$

where $V_0(\omega,\ \Psi)$ is the reference velocity of the unperturbed medium and Ψ is the azimuth along the path with respect to the north direction. Montagner and Nataf (1986) presented the expressions for the different azimuthal coefficients $\alpha_i(\omega,\theta,\phi)$ as depth integral functions dependent on 13 simple linear combinations of standard Cartesian elastic coefficients C_{ij}. Appendix shows how to relate the $3\times3\times3\times3$ tensor Γ_{ijkl} to the 6×6 matrix C_{ij} and presents detailed calculation of azimuthal terms for Love waves in the geographic coordinate system.

Constant term (0-Ψ azimuthal term: α_0):

$$\begin{aligned} A&=\rho V_{\mathrm{PH}}^2=\frac{3}{8}(C_{11}+C_{22})+\frac{1}{4}C_{12}+\frac{1}{2}C_{66}\\ C&=\rho V_{\mathrm{PV}}^2=C_{33}\\ F&=\frac{1}{2}(C_{13}+C_{23})\\ L&=\rho V_{\mathrm{SV}}^2=\frac{1}{2}(C_{44}+C_{55})\\ N&=\rho V_{\mathrm{SH}}^2=\frac{1}{8}(C_{11}+C_{22})-\frac{1}{4}C_{12}+\frac{1}{2}C_{66} \end{aligned}$$

2-Ψ azimuthal term:

$\alpha_1\cos 2\Psi$	$\alpha_2\sin 2\Psi$
$B_c=\frac{1}{2}(C_{11}-C_{22})$	$B_s=C_{16}+C_{26}$
$G_c=\frac{1}{2}(C_{55}-C_{44})$	$G_s=C_{54}$
$H_c=\frac{1}{2}(C_{13}-C_{23})$	$H_s=C_{36}$

4-Ψ azimuthal term:

$\alpha_3\cos 4\Psi$	$\alpha_3\cos 4\Psi$
$E_c=\frac{1}{8}(C_{11}+C_{22})-\frac{1}{4}C_{12}-\frac{1}{2}C_{66}$	$E_s=\frac{1}{2}(C_{16}-C_{26})$

where indices 1 and 2 refer to horizontal coordinates (1, north; 2, east) and index 3 refers to vertical coordinate. ρ is the density; V_{PH} and V_{PV} are, respectively, horizontally and vertically propagating P-wave velocities; and V_{SH} and V_{SV} are, respectively, the horizontal and vertical polarized S-wave velocities. So, the different parameters present in the different azimuthal terms are simply related to elastic moduli C_{ij}.

From a practical point of view, once source phase is removed and assuming that the scale of heterogeneities is larger than the wavelength, the total phase ϕ_t (and the travel time) between the epicenter E and the receiver R is easily related to the measurement of phase velocity $V_d(\omega)$ and therefore to the local phase velocity $V(\omega,\ \theta,\ \phi,\ \Psi)$:

$$\phi_t=\omega t_{\mathrm{E}\to\mathrm{R}}=\frac{\omega\Delta}{V_{\mathrm{d}}(\omega)}=\omega\int_{\mathrm{E}}^{\mathrm{R}}\frac{\mathrm{d}s}{V(\omega,\theta,\phi,\Psi)} \quad [7]$$

Therefore, eqns [6] and [7] define the forward problem for surface wave phase in the framework of the first-order perturbation theory and geometric optics approximation. We will see in the next section how to solve the inverse problem. That means that, ideally, surface waves in the plane case have the ability to provide information on 13 elastic parameters, which emphasizes the enormous potential of surface waves in terms of geodynamic and petrologic implications. There are only 13 elastic moduli among 21, since the propagation of surface waves is invariant against rotation by π, which corresponds to a monoclinic symmetry. The asymptotic propagation in weakly anisotropic media presented for surface waves can be extended to body waves. Jech and Psenčík (1989) demonstrated that it is similarly governed by a Fourier series in Ψ involving not only degrees zero, two, and four but also degrees one and three. Chen and Tromp (2007) expanded the approach of Jech and Psenčík and introduced eight new elastic parameters $J_{c,s}$, $K_{c,s}$, $M_{c,s}$, and $D_{c,s}$ corresponding to linear combinations of C_{ij}, respectively, describing the 1-Ψ and 3-Ψ variations.

The 0-Ψ term corresponds to the average over all azimuths and involves five independent parameters, A, C, F, L, N, which represent the equivalent transversely isotropic medium with a vertical symmetry axis (more simply named VTI or radial anisotropy). It must be noted that it is possible to retrieve the equivalent isotropic shear modulus from these five parameters. By using a Voigt average, the shear modulus μ_{iso} is equal to

$$\begin{aligned} \mu_{\mathrm{iso}}=\rho V_{\mathrm{S_{iso}}}^2=\frac{1}{15}(C_{11}+C_{22}+C_{33}-C_{12} \\ -C_{13}-C_{23}+3C_{44}+3C_{55}+3C_{66}) \end{aligned}$$

According to the expressions of A, C, F, L, N in terms of elastic moduli, $\mu_{\mathrm{iso}}=1/15(C+A-2F+6F+5N)$. So we can see that the equivalent isotropic velocity depends not only on S-wave velocities V_{SV} and V_{SH} (or radial S-anisotropy $\xi=N/L$) but also on P-wave velocities V_{PV} and V_{PH} (or radial P-anisotropy $\phi=C/A$) and on $\eta=F/(A-2L)$. By rewriting this expression $\mu_{\mathrm{iso}}=1/15(C+(1-2\eta)A+(6+4\eta)L+5N)$, neglecting anisotropy in P-wave ($\phi=1$), and assuming $\eta=1$, it is found that $\mu_{\mathrm{iso}}=\rho V_{\mathrm{S_{iso}}}^2\approx(2/3)L+(1/3)N=(2/3)\rho V_{\mathrm{SV}}^2+(1/3)\rho V_{\mathrm{SH}}^2$. Naturally, this choice is arbitrary, since, usually, there is no S-wave anisotropy without P-wave anisotropy. Another way to jointly take account of P- and S-anisotropies consists in using correlations between anisotropic parameters for petrologic models as derived by Montagner and Anderson (1989a).

The other azimuthal terms (2-Ψ and 4-Ψ) depend on four groups of two parameters, B, G, H, E, respectively, describing the azimuthal variation of A, L, F, N. These simple parameters make it possible to describe in a simple way the two seismically observable effects of anisotropy on surface waves, the so-called 'polarization' anisotropy resulting from the discrepancy between Rayleigh-wave and Love-wave dispersions (Schlue and Knopoff, 1977) and the azimuthal anisotropy first observed by Forsyth (1975) in the Nazca Plate.

Another important point in these expressions is that they provide the partial derivatives for the radial and azimuthal anisotropies of surface waves. The corresponding kernels and their depth dependence are plotted in Montagner and Nataf (1986) (**Figures 2** and **3**). These partial derivatives of the different azimuthal terms with respect to the elastic parameters can be easily calculated by using a radial anisotropic reference Earth model, such as *PREM* (Dziewonski and Anderson, 1981). The partial derivatives of the eigenperiod ${}_0T_\ell$ with respect to parameter p, $(p/T)(\partial T/\partial p)$ can easily be converted into phase velocity V partial derivatives by using

$$\frac{p}{V}\left(\frac{\partial V}{\partial p}\right)_T = -\frac{V}{U}\frac{p}{T}\left(\frac{\partial T}{\partial p}\right)_k$$

For example, the parameters G_c and G_s have the same kernel as parameter L (related to V_{SV}) as shown by comparing the expressions of R_1, R_2, and R_3 in eqn [29] of Appendix. For fundamental modes (but it is not valid for higher modes), the calculation of kernels shows that Love waves are almost insensitive to V_{SV} (**Figure 2**) and Rayleigh waves to V_{SH}. Rayleigh waves are the most sensitive to SV-waves. However, as pointed out by Anderson and Dziewonski (1982), the influence of P-waves (through parameters A and C) can be very large in an anisotropic medium. The influence of density is also very large for Love and Rayleigh waves, but as shown by Takeuchi and Saito (1972), it is largely decreased when seismic velocities are inverted for, instead of, elastic moduli and density.

1.19.2.3 Comparison Between Surface-Wave Anisotropy and SKS Splitting Data

It can be noted that some of the linear combinations of elastic moduli C_{ij}, derived from surface waves in the previous section, also come up when considering the propagation of body waves in symmetry planes for a weakly anisotropic medium (see, e.g., Crampin, 1984) and their azimuthal dependence

$$\rho V_P^2 = A + B_c\cos 2\Psi + B_s\sin 2\Psi + E_c\cos 4\Psi + E_s\sin 4\Psi$$
$$\rho V_{qSV}^2 = N - E_c\cos 4\Psi - E_s\sin 4\Psi$$
$$\rho V_{qSV}^2 = L + G_c\cos 2\Psi + G_s\sin 2\Psi$$

where V_{qSH} and V_{qSV} correspond, respectively, to quasi-SH-wave and quasi-SV-wave.

A global investigation of anisotropy inferred from SKS body wave splitting measurements (delay times and directions of maximum velocities) has been undertaken by different authors (Becker et al., 2012; Savage, 1999; Silver, 1996; Vinnik et al., 1992; Wüstefeld et al., 2009). Unfortunately, most SKS measurements have been done in continental parts of the Earth and very few in oceans. It turns out that a direct comparison of

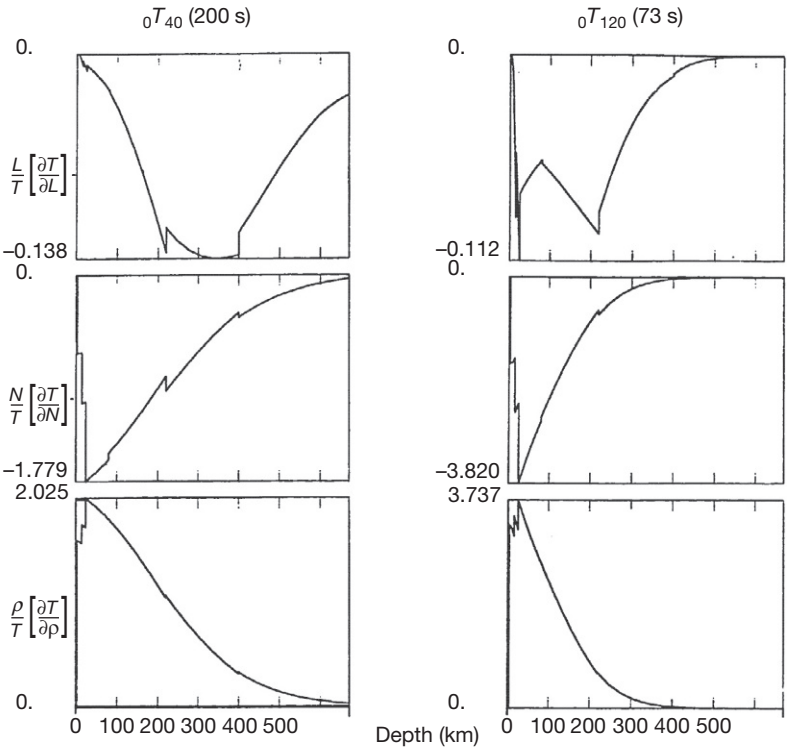

Figure 2 Partial derivatives for Love waves of the period of fundamental normal modes ${}_0T_{40}$ (left) and ${}_0T_{120}$ (right) with respect to the elastic coefficients of a transversely isotropic earth L, N, and density ρ, as a function of depth in the upper mantle. Reproduced from Montagner J-P and Nataf HC (1986) On the inversion of the azimuthal anisotropy of surface waves. *Journal of Geophysical Research* 91: 511–520. The partial derivatives with respect to A, C, F are null for these modes. The plots are normalized to their maximum amplitudes, given for a $\Delta h = 1000$ km thick perturbed layer. The combinations of elastic coefficients that have the same partial derivative as L are $-G_c$, $-G_s$ for the azimuthal terms 2-Ψ and as N are E_c, E_s for the azimuthal term 4-Ψ. Note that the amplitude of the L-partial is very small for the fundamental modes, which is not the case for higher modes.

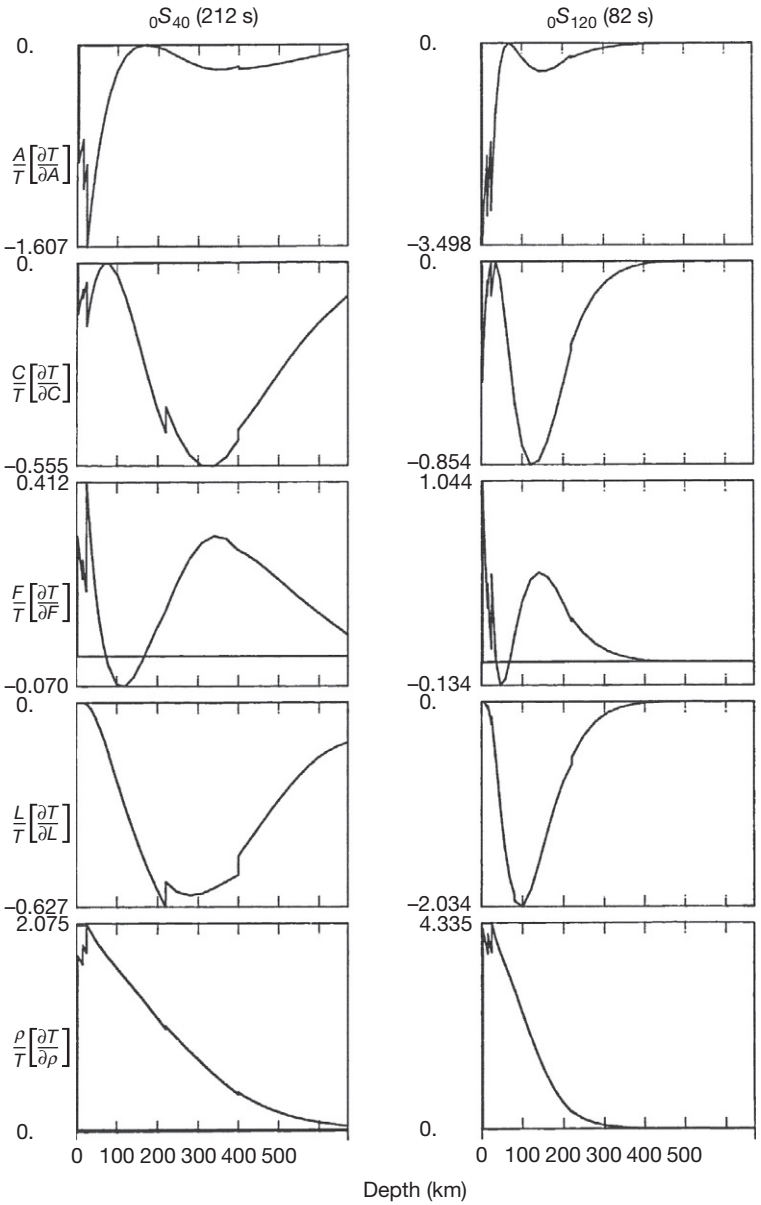

Figure 3 Kernels for Rayleigh waves. Same conventions as for **Figure 2** in the same depth range. The partial derivative with respect to N has not been plotted since its amplitude is very small for fundamental modes. Note that three partial derivatives contribute to the 2-Ψ azimuthal terms, A-partial for B_c, B_s, F-partial for H_c, H_s and the largest one L-partial for G_c, G_s.

body wave and surface wave datasets is now possible (Montagner et al., 2000). If the anisotropic medium is assumed to be characterized by a horizontal symmetry axis with any orientation (this is a very strong assumption that can be alleviated as shown by Chevrot et al. (2004), Monteiller and Chevrot (2010), and Romanowicz and Yuan (2012)) and for a vertically propagating SKS wave, a synthetic dataset of SKS delay times and azimuths can be calculated from the global distribution of anisotropy derived from surface waves, by using the following equations:

$$\delta t_{SKS} = \int_0^h dz \sqrt{\frac{\rho}{L}} \left[\frac{G_c(z)}{L(z)} \cos(2\Psi(z)) + \frac{G_s(z)}{L(z)} \sin(2\Psi(z)) \right] \quad [8]$$

where δt_{SKS} is the integrated travel time for the depth range 0–h for a propagation azimuth Ψ, where the anisotropic parameters $G_c(z)$, $G_s(z)$, and $L(z)$ are the anisotropic parameters retrieved from surface waves at different depths. It is remarkable to realize that only the G parameter (expressing the SV-wave azimuthal variation) is present in this equation. From eqn [8], we can infer the maximum value of delay time δt_{SKS}^{max} and the corresponding azimuth Ψ_{SKS}:

$$\delta t_{SKS}^{max} = \sqrt{\left\{ \int_0^h dz \sqrt{\frac{\rho}{L}} \frac{G_c(z)}{L(z)} \right\}^2 + \left\{ \int_0^h dz \sqrt{\frac{\rho}{L}} \frac{G_s(z)}{L(z)} \right\}^2} \quad [9]$$

$$\tan(2\Psi_{SKS}) = \frac{\int_0^h dz \frac{G_s(z)}{L(z)}}{\int_0^h dz \frac{G_c(z)}{L(z)}} \quad [10]$$

However, eqn [8] is approximate and only valid when the wavelength is much larger than the thickness of layers. It is based on the commutativity of anisotropic layers though the noncommutativity is present in the general calculation, as pointed out by Silver and Savage (1994) and Montagner et al. (2000). The validity of this approximation has been questioned by Silver and Long (2011) for the frequency range used in SKS studies. However, Romanowicz and Yuan (2012) demonstrated that the expressions of eqns [8]–[10] are valid for station-averaged quantities and do not depend on the order of layers and therefore that it is correct to use these expressions in joint inversions of surface waveforms and SKS station-averaged splitting measurements. It is possible to make more precise calculations by using the technique derived for two layers by Silver and Savage (1994), by using the general expressions given in Rumpker and Silver (1998) and Montagner et al. (2000), or the splitting intensity derived by Chevrot (2000). Chevrot et al. (2004) and Chevrot (2006) suggested that the use of finite-frequency kernels for SKS splitting measurements should improve the depth resolution using SKS splitting data alone.

With eqns [9] and [10], a synthetic map of the maximum value of delay time δt_{SKS}^{max} can be obtained by using a three-dimensional (3-D) anisotropic surface wave model. A detailed comparison between synthetic SKS derived from anisotropic upper mantle (AUM) (Montagner and Tanimoto, 1991) and observed SKS (Silver, 1996) was presented in Montagner et al. (2000). **Figure 4** shows an example of such a map for the Earth centered in the Pacific, by using the anisotropic surface wave model of Montagner (2002) derived from the data of Montagner and Tanimoto (1991) and Ekström et al. (1997). First of all, the comparison shows that both datasets are compatible in magnitude but not necessarily in directions. Some contradictions between measurements derived from surface waves and from body waves have been noted. The agreement of directions is correct in tectonically active areas but poor in old cratonic zones. The discrepancy in these areas results from the rapid lateral change of directions of anisotropy at a small scale. These changes stem from the complex history of these areas, which have been built by successive collages of continental pieces. It might also result from the hypothesis of horizontal symmetry axis, which was shown to be invalid in many areas (Plomerová et al., 1996). The positive consequence of this discrepancy is that a small-scale mapping of fossil anisotropy in such areas might provide clues for understanding the processes of growth of continents and mountain building opening a new field, the paleoseismology. Recently, the coherence between the predicted shear-wave splitting derived from tomographic models and actual observations of splitting has been reevaluated by using updated global compilation (Wüstefeld et al., 2009), recent tomographic models (Debayle et al., 2005; Lebedev and van der Hilst, 2008), and more sophisticated full-waveform methods to estimate synthetic splitting from tomography (Becker et al., 2012). Provided that the splitting dataset is spatially filtered to scale of tomographic models, Becker et al. (2012) found that splitting and tomography display a consistent signal that can be geodynamically interpreted (Long and Becker, 2010).

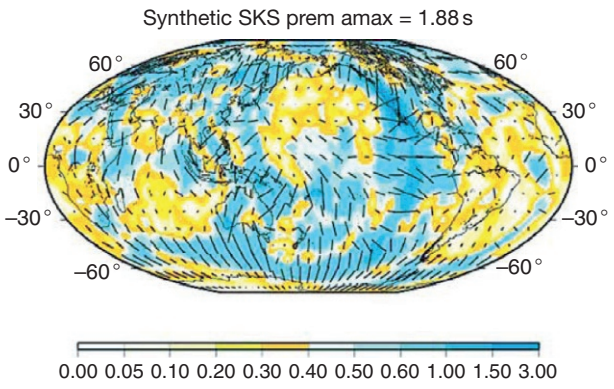

Figure 4 Map of synthetic SKS splitting derived from the anisotropic surface wave model of Montagner (2002). The delay time is expressed in seconds. Its maximum value is $A_{max} = 1.88$ s.

Unlike surface waves, SKS waves have a good lateral resolution and are sensitive to the short wavelength anisotropy just below the stations. But their drawback is that they have a poor vertical resolution. On the other hand, global anisotropic tomography derived from surface waves only provides long-wavelength anisotropy (poor lateral resolution) but enables the location at depth of anisotropy. The long-wavelength anisotropy derived from surface waves will display the same direction as the short wavelength anisotropy inferred from body waves only when large-scale vertical coherent processes are predominant. As demonstrated by Montagner et al. (2000), the best agreement between observed and synthetic SKS can be found when only layers in the uppermost 200 km of the mantle are taken into account. Moreover, tomographic models derived from surface waves lose resolution at depths >250–300 km. In some continental areas, short-scale anisotropy, the result of a complex history, might be important and even might mask the deep large-scale anisotropy more related to present convective processes leading to incompatibility between synthetic and observed splitting data. For North America, Marone and Romanowicz (2007a,b) resolved this disagreement by simultaneously inverting surface waveforms and shear-wave splitting data. They showed evidence of a layering of anisotropy with a different fast axis, which was also observed in many oceanic or continental regions. From a statistical point of view, good agreement between orientations of anisotropy and plate velocity motion is primarily found for fast-moving plates, in particular below oceans. The differences between anisotropy and tectonic plate directions are related to more complex processes, as will be seen in **Section 1.19.3**.

1.19.3 Upper Mantle Tomography of Seismic Velocity and Anisotropy

We now show how to implement the theory of **Section 1.19.1** from a practical but general point of view and how to design a tomographic technique in order to invert for the 13 different elastic parameters and density. A tomographic technique necessitates to solve simultaneously a forward problem and an inverse problem. By using the results of the previous section, it successively considers how to set the forward problem and how it is used to retrieve a set of parameters by inversion.

1.19.3.1 Forward Problem

First, it is necessary to define the data space **d** and the parameter space **p**. It is assumed that a functional **g** relating **d** and **p** can be found such that

$$\mathbf{d} = \mathbf{g}(\mathbf{p})$$

where **d** is the set of data (which samples the data space) and **p** is the set of parameters.

1.19.3.1.1 Data space: *d*

The basic dataset is made of seismograms $\mathbf{u}(t)$. We can try to directly match the waveform in the time domain, or we can work in the Fourier domain, by separating phase and amplitude on each component $u_i(t)$:

$$u_i(t) = \int_{-\infty}^{\infty} \sum_{n=0}^{\infty} A_{ni}(\omega) e^{i(\omega t - \phi_{ni})} d\omega \quad \text{or} \quad u_i(\omega) = \sum_{n=0}^{\infty} A_{ni}(\omega) e^{i\phi_{ni}(\omega)}$$

where $\Sigma_{n=0}^{\infty}$ expresses the sum over the different dispersion branches (higher modes) and $A_{ni}(\omega)$ and ϕ_{ni} (ω) are, respectively, the amplitude and the phase of the seismic waves as functions of the angular frequency ω. The most classical methods are based on ray theory. In the framework of full ray theory (e.g., Ekström et al., 1997 or Ferreira and Woodhouse, 2007), for a given path between source E and receiver R with epicentral distance Δ and a given mode n (we omit the index n in the following), the phase $\phi_i(\omega)$ is the sum of four terms:

$$\phi_i(\omega) = \phi_{Si} + \phi_{Pi} + \phi_{Ri} + \phi_{0i}$$

where ϕ_{Si} is the initial source phase, $\phi_{Pi} = \mathbf{k}_i \cdot \mathbf{r}$ the propagation phase, ϕ_{Ri} the receiver phase (including the instrumental response), and ϕ_{0i} the phase related to the number of polar phase shifts. ϕ_{Si} is correctly given by using the centroid moment tensor solution (Dziewonski et al., 1981). The amplitude A_i for a given mode n is the product of four terms:

$$A_i = A_{Si} A_{Pi} A_{Ri} A_{Qi}$$

where A_{Si} is the excitation at the source, A_{Pi} is the geometric spreading factor and might include the effects of focusing and defocusing, A_{Ri} is the receiver amplitude, and A_{Qi} is the attenuation factor along the path.

The approach consisting in fitting full seismic waveforms is more general but, from a practical point of view, it does not necessarily correspond to the simplest choice. In a heterogeneous medium, the calculation of amplitude and phase effects makes it necessary to calculate the coupling between different multiplets (Li and Tanimoto, 1993; Li and Romanowicz, 1995; Marquering et al., 1996), which is very time-consuming. When working in the Fourier domain, different time windows can be considered and the phase of different seismic trains, body waves, and surface waves can be separately matched (Debayle and Ricard, 2012; Lebedev and van der Hilst, 2008; Lévêque et al., 1991; Nolet, 1990) under drastic simplifying assumptions. **Figure 1** showed an example of observed and synthetic seismograms, the latter obtained by normal mode summation with the different higher modes. The fundamental wavetrain $(n = 0)$ is well separated from other modes at large epicentral distances. The part of the seismogram corresponding to higher modes $(n > 0)$ is more complex and shows overlap of these modes in the time domain. Therefore, from a practical point of view, the fitting of the fundamental-mode wavetrain will not cause any problem and has been widely used in global mantle tomography.

The use of higher-mode wavetrains and the separation of overtones are much more difficult. The first attempts were performed by Nolet (1975), Cara (1979), Okal and Jo (1985), and Dost (1990) by applying a spatial filtering method. Unfortunately, all these techniques can only be applied in areas where dense arrays of seismic stations are present, that is, in North America and Europe. By using a set of seismograms recorded at one station but corresponding to several earthquakes located in a small source area, Stutzmann and Montagner (1994) showed how to separate the different higher modes. A similar approach was also followed by Van Heijst and Woodhouse (1997) and more recently by Visser et al. (2008). We only detail in this chapter the classical technique that was designed for fitting the fundamental-mode wavetrain and the reader is referred to Stutzmann and Montagner (1994), Van Heijst and Woodhouse (1997), Beucler et al. (2003), and Visser et al. (2008) for the description of the recovery of higher-mode dispersion properties and to Romanowicz (2002) for a general overview. **Figure 5** presents an example of phase velocity dispersion for different surface wave modes (fundamental and first higher modes (Beucler et al., 2003)) and how they compare with previous investigations (Cara, 1979; Van Heijst and Woodhouse, 1997).

We take advantage of the fact that, according to Fermat's principle, the phase velocity perturbation is only dependent to the second order on path deviations, whereas amplitude perturbations are dependent, to the first order, on these deviations, which implies that the eigenfunctions must be recalculated at each iteration. Therefore, the phase is a more robustly observable than the amplitude. The amplitude $A(\omega)$ depends in a complex manner on seismic moment tensor, attenuation, scattering, focusing effects, station calibration, and near-receiver structure, whereas the contribution of lateral heterogeneities of seismic velocity and anisotropic parameters to the phase $\phi(\omega)$ can be easily extracted. The dataset under investigation is composed of propagation times (or phase velocity measurements for surface waves) along paths $\mathbf{d} = \{\Delta / V_{\text{obs}}(\omega)\}$.

The phase of a seismogram at time t is decomposed as follows: $\phi = \mathbf{k} \cdot \mathbf{r} + \phi'_0$, where ϕ' is the initial phase including several terms detailed previously. ϕ can be measured on seismograms by Fourier transform. We usually assume that ϕ_S is correctly given by the centroid moment tensor solution. For a path between epicenter E and receiver R with an epicentral distance Δ, the phase ϕ is given by

$$\phi = \frac{\omega \Delta}{V_{\text{obs}}} + \phi'_0 \qquad [11]$$

In the general case, we want to relate the observed phase velocity $V_{\text{obs}}(\omega)$ to the parameters of the Earth model $\mathbf{p}(\mathbf{r}, \theta, \phi)$. Data and 3-D parameters can be related through integrals over the whole volume of the Earth. But for computing reasons, it is usual to use a multistep approach, where we first retrieve the local phase velocity $V(\omega, \theta, \phi, \Psi)$ including its azimuthal terms (as a function of the azimuth Ψ), and then perform the inversion at depth. These two steps can be reversed

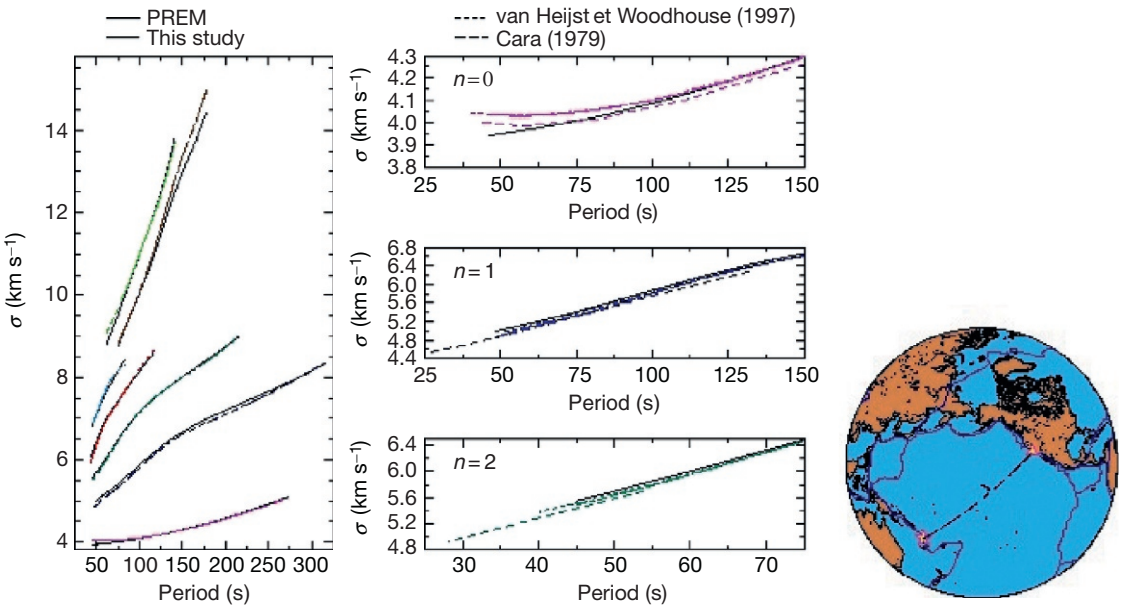

Figure 5 Phase velocity of the fundamental mode and the first six higher modes of Rayleigh compared with PREM (right plot) and with results (center) obtained in previous studies along the same path between Vanuatu and California (SCZ GEOSCOPE station). Reproduced from Beucler E, Stutzmann E, and Montagner J-P (2003) Measuring surface wave higher mode velocities by the roller coaster algorithm. *Geophysical Journal International* 155: 289–307.

since the order of the integrations can be reversed as done, for example, by Nolet (1990) or Lévêque et al. (1991). It is necessary to consider the nature of the perturbed medium. Following the approach of Snieder (1988), if the perturbed medium is at the same time smooth (long-wavelength heterogeneities) and weak (small amplitude of heterogeneities), the geometric optics approximation (and ray theory) applies. This hypothesis is not necessarily met within the Earth where some geologic objects (slabs, mantle plumes, etc.) have a length scale that can be close to the seismic wavelength. In the approximation of ray theory, the volume integral reduces to the curvilinear integral along the geometric ray path. When ray theory is applicable,

$$\phi - \phi_0' = \frac{\omega \Delta}{V_{\text{obs}}(\omega)} \int_{\text{E}}^{\text{R}} \frac{\omega \, \text{d}s}{V(\omega, \theta, \phi, \Psi)} \qquad [12]$$

where the integral is evaluated along the ray path between the epicenter E and the receiver R. Following the results of the previous section, different approximations are implicitly made when using this expression of the phase:

- Large angular order $\ell \gg 1$, but not too large (scattering problems): From a practical point of view, this means that measurements are performed in the period range $40\,\text{s} < T < 200\,\text{s}$ with seismic wavelengths between 200 and 1000 km.
- Geometric optics approximation: If λ is the wavelength of the surface wave at period T and Λ_S the spatial wavelength of heterogeneity $\Lambda_S \gg \lambda = VT \Rightarrow \Lambda S \gtrsim 2000\,\text{km}$, epicentral distance Δ must be larger than seismic wavelength.
- Slight anisotropy and heterogeneity $\delta V/\text{x}V \ll 1$: According to Smith and Dahlen (1973) for the plane case, the local phase velocity can be decomposed as a Fourier series of the azimuth Ψ (eqn [6]).

Each azimuthal term $\alpha_i(T, \theta, \phi)$ of eqn [6] can be related to the set of parameters $p_i(r, \theta, \phi)$ (density + 13 elastic parameters), according to the expressions derived in Appendix:

$$\frac{\Delta}{V_{\text{obs}}(T)} - \frac{\Delta}{V_0(T)} = \sum_{j=0}^{2} \sum_{i=1}^{14} \int_{\text{E}}^{\text{R}} \frac{\text{d}s}{V_0} \int_0^a \left[\left(\frac{p_i}{V} \frac{\partial V}{\partial p_i} \right)_j \frac{\delta p_i(r, \theta, \phi)}{p_i} \cos(2j\Psi) + \left(\frac{p_i}{V} \frac{\partial V}{\partial p_i} \right)_j \frac{\delta p_i(r, \theta, \phi)}{p_i} \sin(2j\Psi) \right] \frac{\text{d}z}{\Delta h} \qquad [13]$$

Equation [13] defines the forward problem in the framework of first-order perturbation theory, relating the data and the parameter spaces. This approach is usually named PAVA (path average approximation). Many terms in eqn [13] are equal to zero since all parameters are not present in each azimuthal term. A last important ingredient in the inverse problem formulation is the 'structure' of the data space. It is expressed through its covariance function (continuous case) or covariance matrix (discrete case) of data $\mathbf{C_d}$. When data d_i are independent, $\mathbf{C_d}$ is diagonal and its elements are the square of the errors on data σ_{di}.

1.19.3.1.2 Finite-frequency effects

The ray-based tomographic approach (e.g., Debayle et al., 2005; Debayle and Ricard, 2012; Ferreira et al., 2010; Kustowski et al., 2008a,b; Lebedev and van der Hilst, 2008; Ritsema et al., 2011) has reached its theoretical resolution limit ($\approx$1000 km), and it is necessary to move to full-waveform inversion in order to solve spatial wavelengths of the order of magnitude of seismic wavelength. As mentioned previously, a strong hypothesis is that in the framework of geometric optics approximation, only large-scale heterogeneities can be

retrieved. But interesting geologic objects such as slabs and plumes are smaller-scale. To go beyond the ray theory, it is necessary to take account of the finite-frequency effect when scale length has the same order of magnitude as the seismic wavelength. It is possible to use the scattering theory based on the Born or Rytov approximations (see, e.g., Woodhouse and Girnius (1982) for normal mode approach, Snieder (1988) for surfaces waves, and Dahlen et al. (2000 and Yomogida (1992) for body waves). Equation [13] shows that the sensitivity kernels are 1-D, meaning that only heterogeneities in the vertical plane containing the source and the receiver are taken into account, whereas, by using the scattering theory, it is possible to calculate 3-D kernels and consequently to take account of off-path heterogeneities. Equations [12] and [13] must be replaced by an integral over the volume Ω:

$$\frac{\Delta}{V_{\mathrm{obs}}(T)}-\frac{\Delta}{V_0(T)}=\sum_{i=1}^{21}\iiint_{\Omega}K_i(T,\theta,\phi,\Psi)\frac{\delta p_i(r,\theta,\phi)}{p_i}\mathrm{d}\Omega \quad [14]$$

where $K(T, \theta, \phi, \Psi)$ is the scattering Fréchet sensitivity kernel, extended to the 21 components of the elastic tensor, which depends on wave type (body waves or Rayleigh or Love surface waves) and on the relative location of E and R (see, e.g., Romanowicz, 2002, for a review). In the framework of ray theory, $K(T, \theta, \phi, \Psi)$ is zero except along the ray. Very different strategies can be followed for calculating this triple integral, by separating the surface integral and the radial integral. For a point scatterer, the kernel displays a typical shape of banana doughnut (Dahlen et al., 2000). Different approximations of $K(T, \theta, \phi, \Psi)$ have been proposed (Ritzwoller et al., 2002; Spetzler et al., 2002; Yoshizawa and Kennett, 2002), but Sieminski et al. (2004) claimed that ray theory surface wave tomography with a very dense path coverage can detect heterogeneities with length scales close and even smaller than the seismic wavelength. The discussion of the advantages and shortcomings of these different techniques is beyond the scope of this chapter, but some new tomographic models using 3-D sensitivity kernels are constructed (Zhou et al., 2004, 2006) for radially anisotropic media. With the explosion of computational infrastructure, it is possible to go beyond approximate asymptotic methods for the calculation of travel times and synthetic seismograms, by using modern numerical methods such as spectral element method (Komatitsch and Vilotte, 1998; Komatitsch and Tromp, 1999) and adjoint tomographic techniques (Fichtner et al., 2009; Tape et al., 2009; Tarantola, 1984; Tromp et al., 2005). A new revolution in seismic tomography is ongoing in using adjoint tomography, and first accurate images at the global scale (Lekic and Romanowicz, 2011) and at the regional scale of Europe (Zhu et al., 2012) should shed new light on the deep structure of the mantle.

1.19.3.1.3 Parameter space: *p(r)*

It is quite important to consider the structure of the parameter space in detail. First of all, it is necessary to define which parameters are required to explain our dataset and how many physical parameters can be effectively inverted for in the framework of the theory that is considered. For example, if the Earth is assumed to be elastic, laterally heterogeneous but isotropic, only three independent physical parameters, V_P, V_S, and density ρ (or the elastic moduli λ, μ, and ρ), can be inverted for from surface waves. In a transversely isotropic medium with a vertical symmetry axis (Anderson, 1961; Takeuchi and Saito, 1972), the number of independent physical parameters is now 6 (five elastic parameters + density). In the most general case of a weak anisotropy, 14 physical parameters (13 combinations of elastic moduli + density) can actually be inverted for using surface waves. When using the full-waveform inversion, the whole elastic tensor (21 parameters) can be, in theory, inverted for. Therefore, the number of 'physical' parameters p_i depends on the underlying theory, which is used for explaining the dataset.

Once the number of 'physical' independent parameters is defined, we must define how many spatial (or geographic) parameters are required to describe the 3-D distributions $p_i(r, \theta, \phi)$. That is a difficult problem because the number of 'spatial' parameters that can be reliably retrieved from the dataset is not necessarily sufficient to provide a correct description of $p_i(r, \theta, \phi)$, that is, of the real Earth. The correct description of $p_i(r, \theta, \phi)$ depends on its spectral content: For example, if $p_i(r, \theta, \phi)$ is characterized by very large wavelengths, only a small number of spatial parameters are necessary, but if $p_i(r, \theta, \phi)$ presents very small-scale features, the number of spatial parameters will be very large. In any case, it is necessary to assess the range of possible variations for $p_i(r, \theta, \phi)$ in order to provide some bounds on the parameter space. This is done through a covariance function of parameters in the continuous case (or a covariance matrix for the discrete case) $\mathbf{C}_{p_i p_j}(\mathbf{r}, \mathbf{r}')$ at two different points $\mathbf{r}$, $\mathbf{r}'$. These a priori constraints can be provided by other fields in geosciences, geology, mineralogy, numerical modeling, etc.

Consequently, a tomographic technique must not be restricted to the inversion of parameters $\mathbf{p} = \{p_i(r, \theta, \phi)\}$ that are searched for, but must include the calculation of the final covariance function (or matrix) of parameters $\mathbf{C_p}$. That means that the retrieval of parameters is contingent on the resolution and the errors of the final parameters and is largely dependent on the resolving power of data (Backus and Gilbert, 1967, 1968, 1970). Finally, the functional $\mathbf{g}$, which expresses the theory relating the data space to the parameter space, is also subject to uncertainty. In order to be completely consistent, it is necessary to define the domain of validity of the theory and to assess the error σ_T associated with the theory. Tarantola and Valette (1982) showed that the error σ_T is simply added to the error on data σ_d.

1.19.3.2 Inverse Problem

So far, we did not make any assumptions on the functional $\mathbf{g}$ relating data and parameters. But in the framework of ray theory and of first-order perturbation theory, the forward problem is usually linearized and eqn [13] can be simply written in the linear case as

$$\mathbf{d} = \mathbf{G}\mathbf{p}$$

where $\mathbf{G}$ is now a matrix (or a linear operator) composed of Fréchet derivatives of $\mathbf{d}$ with respect to $\mathbf{p}$, which has the dimensions $n_d \times n_p$ (number of data × number of parameters). This matrix usually is not square and many different techniques in

the past have been used for inverting $\mathbf{G}$. In any case, the inverse problem will consist in finding an inverse for the functional $\mathbf{g}$ that we will write $\tilde{\mathbf{g}}^{-1}$, notwithstanding the way it is obtained, such that

$$\mathbf{p} = \tilde{\mathbf{g}}^{-1}(\mathbf{d})$$

To solve the inverse problem, different algorithms can be used. The least-squares solution is usually solved by minimizing a cost function J. Making symmetrical the data space and the parameter space, Tarantola and Valette (1982) defined the cost function J as

$$J = (\mathbf{d} - \mathbf{Gp})^t \mathbf{C}_\mathbf{d}^{-1}(\mathbf{d} - \mathbf{Gp}) + (\mathbf{p} - \mathbf{p}_0)^t \mathbf{C}\mathbf{p}^{-1}(\mathbf{p} - \mathbf{p}_0)$$

The first term corresponds to classical least squares with no damping, whereas the second term corresponds to norm damping, which imposes smoothness upon the parameter space. Different choices were proposed for this second term. For example, Montagner (1986b) used a Gaussian covariance function characterized by a correlation length and an a priori error σ_p on parameters, whereas Su et al. (1984) preferred to minimize the roughness of the model. Other choices consist in taking a constant value such that $\delta\mathbf{p}^t\mathbf{C}_\mathbf{p}^{-1}\delta\mathbf{p} = \lambda^2\delta\mathbf{p}^t\delta\mathbf{p}$ (Yoshizawa and Kennett, 2004). Or the covariance operator can be replaced by a Laplacian operator (see, e.g., Zhou et al., 2006):

$$\delta\mathbf{p}^t\mathbf{C}_\mathbf{p}^{-1}\delta\mathbf{p} = \epsilon\left(\iiint\left|\nabla^2\left(\frac{\delta p}{p}\right)\right|^2 \mathrm{d}\Omega\right)^{1/2}$$

A discussion about damping can be found in Trampert and Snieder (1996) who prefer Laplacian over model damping to reduce the spectral leakage. As an example, by using the expression of J, a quite general and widely used algorithm has been derived by Tarantola and Valette (1982):

$$\begin{aligned}\mathbf{p} - \mathbf{p}_0 &= \left(\mathbf{G}^t\mathbf{C}_\mathbf{d}^{-1}\mathbf{G} + \mathbf{C}_{\mathbf{p}0}^{-1}\right)^{-1}\mathbf{G}^t\mathbf{C}_\mathbf{d}^{-1}(\mathbf{d} - \mathbf{g}(\mathbf{p}) + \mathbf{G}(\mathbf{p} - \mathbf{p}_0)) \\ &= \mathbf{C}_{\mathbf{p}0}\mathbf{G}^t\left(\mathbf{C}_\mathbf{d} + \mathbf{G}\mathbf{C}_{\mathbf{p}0}\mathbf{G}^t\right)^{-1}(\mathbf{d} - \mathbf{g}(\mathbf{p}) + \mathbf{G}(\mathbf{p} - \mathbf{p}_0))\end{aligned} \quad [15]$$

where $\mathbf{C}_\mathbf{d}$ is the covariance matrix of data, $\mathbf{C}_{\mathbf{p}0}$ is the covariance function of parameters $\mathbf{p}$, and $\mathbf{G}$ is the Fréchet derivative of the operator $\mathbf{g}$ at point $\mathbf{p}(\mathbf{r})$. This algorithm can be made more explicit by writing it in its integral form:

$$\mathbf{p}(\mathbf{r}) = \mathbf{p}_0(\mathbf{r}) + \sum_{i=1}^{n_\mathrm{d}}\sum_{j=1}^{n_\mathrm{d}}\int_V \mathrm{d}\mathbf{r}' C_{p0}(\mathbf{r}, \mathbf{r}')G_i(\mathbf{r}')\left(S^{-1}\right)_{ij}F_j \quad [16]$$

where n_d is the number of data, $S_{ij} = C_{dij} + \int_V \mathrm{d}\mathbf{r}_1 \int_V \mathrm{d}\mathbf{r}_2\ G_i(\mathbf{r}_1)\ C_{P0}\ (\mathbf{r}_1,\ \mathbf{r}_2)G_j(\mathbf{r}_2)$, and $F_j = d_j - g_j(\mathbf{p}) + \int_V \mathrm{d}\mathbf{r}''\ G_j(\mathbf{r}'')(\mathbf{p}(\mathbf{r}'') - \mathbf{p}_0(\mathbf{r}''))$. S_{ij} is the matrix expressing the interaction between propagating waves for data i and j. In the framework of ray theory, the double integral in S_{ij} is replaced by a double integral along ray paths i and j, which is only significantly different from zero at the crossing points of both paths (Montagner and Tanimoto, 1990).

This algorithm can be iterated and is suited for solving slightly nonlinear problems. Different strategies can be followed to invert for the 3-D models $\mathbf{p}(\mathbf{r})$, because the size of the inverse problem is usually enormous in practical applications and a compromise must be found between resolution and accuracy (and also computing time). For the example of mantle tomography, a minimum parameter space will be composed of 13 (+density) physical parameters multiplied by 30 layers (if the mantle is divided into 30 independent layers). If geographic distributions of parameters are searched for up to degree 40 (lateral resolution around 1000 km), that implies a number of about 700 000 independent parameters. Such a problem is still very hard to handle from a computational point of view. A simple approach for solving this problem consists in dividing the inversion procedure into two steps. The first step consists in regionalizing phase (or group) velocity data in order to retrieve the different azimuthal terms, and the second step is the inversion at depth. It was implemented by Montagner (1986a,b) and a very similar technique is presented by Barmin et al. (2001). In case of a large dataset, Montagner and Tanimoto (1990) showed how to handle the inverse problem by making a series expansion of the inverse of matrix S. It was recently optimized from a computational point of view by Debayle and Sambridge (2004) and Beucler and Montagner (2006). One advantage of this technique is that it can be applied equally well to regional studies or global studies. In case of imperfect spatial coverage of the area under investigation, it does not display ringing phenomena commonly observed when a spherical harmonics expansion is used (Tanimoto, 1986).

From a practical point of view, the choice of the model parameterization is also very important and different possibilities can be considered:

- Discrete basis of functions:

A simple choice consists in dividing the earth into 3-D blocks with a surface block size different from the radial one. The size of block depends on the lateral resolution expected from the path coverage. A variant of this parameterization is the use of a set of spherical triangular grid points (see, e.g., Zhou et al., 2006). The block decomposition is valid as well for global investigations as for regional studies. Usually, the Earth surface parameterization is different for the radial one. For global study, the natural basis is composed of the spherical harmonics for the horizontal variations $p_i(r, \theta, \phi) = \sum_{\ell=0}^{\ell_\mathrm{max}}\sum_{m=-\ell}^{\ell} a_\ell^m(r)Y_\ell^m(\theta, \phi)$. Other choices are possible, such as spherical splines (Wang and Dahlen, 1995). When data coverage is very uneven, other strategies are proposed using irregular cells or adaptive meshes (see, e.g., Zhang and Thurber, 2005 and **Chapter 1.10**).

- Continuous function $\mathbf{p}(\mathbf{r})$:

In this case, the function is directly inverted for. Since the number of parameters is then infinite, it is necessary to regularize the solution by defining a covariance function of parameters $C_{p0}(\mathbf{r},\ \mathbf{r}')$. For the horizontal variations, a von Mises distribution (Montagner, 1986b) can be used for initial parameters $\mathbf{p}_0(\mathbf{r})$:

$$C_{p0}(\mathbf{r}, \mathbf{r}') = \sigma_p(\mathbf{r})\sigma_p(\mathbf{r}')\exp\frac{\cos\Delta_{\mathbf{r}\mathbf{r}'} - 1}{L_\mathrm{cor}^2} \approx \sigma_p(\mathbf{r})\sigma_p(\mathbf{r}')\exp\frac{-\Delta_{\mathbf{r}\mathbf{r}'}^2}{2L_\mathrm{cor}^2}$$

where L_cor is the correlation length that defines the smoothness of the final model. This kind of distribution is well suited for studies on a sphere and is asymptotically equivalent to a Gaussian distribution when $L_\mathrm{cor} \ll a$ (a radius of the Earth). When different azimuthal term distributions are searched for,

it is possible to define cross-correlated covariance functions of parameters $C_{pipj}(\mathbf{r}, \mathbf{r}')$, but since the different terms of the Fourier expansion in azimuth correspond to orthogonal functions, the cross-correlated terms off-diagonal can be taken equal to zero.

It is interesting to note that in eqn [16], the Fréchet derivatives G along the path are multiplied by the Gaussian covariance operator C_{p0}. It means that the technique, which can be named 'Gaussian' tomography, is equivalent to use 'fat' rays: When the correlation length is wider than the Fresnel zone, ray theory applies, and consequently, the finite-frequency effects can be neglected. As discussed by Ritzwoller et al. (2002) and Sieminski et al. (2004), there might be some slight differences in amplitude between Gaussian tomography and diffraction tomography (taking account of finite-frequency effects), but not in the location of heterogeneities provided that the spatial path coverage is sufficiently dense. The radial parameterization must be related to the resolving capability of the data at depth, according to the frequency range under consideration. For the radial variations, polynomial expansions can be used (see, e.g., Dziewonski and Woodhouse (1987) for Chebyshev polynomials or Boschi and Ekström (2002) for radial cubic splines). Since the number of physical parameters is very large for the inversion at depth, physical parameters are usually correlated. The different terms of the covariance function C_p between parameters p_1 and p_2 at radii r_i and r_j can be defined as follows:

$$C_{p1,p2}(r_i, r_j) = \sigma_{p1}(r_i)\sigma_{p2}(r_j)\zeta_{p1,p2}\exp -\frac{(r_i - r_j)^2}{2L_{ri}L_{rj}}$$

where $\zeta_{p1,p2}$ is the correlation between physical parameters p_1 and p_2 inferred, for instance, from different petrologic models (Montagner and Anderson, 1989a) such as pyrolite (Ringwood, 1975) and piclogite (Anderson and Bass, 1984; Bass and Anderson, 1984). L_{ri}, L_{rj} are the radial correlation lengths that are used to smooth the inverse model.

The a posteriori covariance function is given by

$$\begin{aligned} C_p &= C_{p0} - C_{p0}G^{\mathrm{T}}\left(C_d + GC_{p0}G^{\mathrm{T}}\right)^{-1}GC_{p0} \\ &= \left(G^T C_d^{-1} G + C_{p0}^{-1}\right)^{-1} \end{aligned} \quad [17]$$

The resolution R of parameters can be calculated as well. It corresponds to the impulsive response of the system $\mathbf{p} = \tilde{\mathbf{g}}^{-1}\mathbf{d} = \tilde{\mathbf{g}}^{-1}\mathbf{g}\mathbf{p}' = R\mathbf{p}'$. If the inverse problem is perfectly solved, R is the identity function or matrix. However, the following expression of resolution is only valid in the linear case (Montagner and Jobert, 1981) inasmuch as the theory is accurate enough:

$$\begin{aligned} R &= C_{p0}G^{\mathrm{T}}\left(C_d + GC_{p0}G^{\mathrm{T}}\right)^{-1}G \\ &= \left(G^{\mathrm{T}}C_dG + C_{p0}\right)^{-1}G^{\mathrm{T}}C_d^{-1}G \end{aligned} \quad [18]$$

It is interesting to note that the local resolution of parameters is imposed by both the correlation length and the path coverage, unlike the Backus and Gilbert (1967, 1968) approach, which primarily depends on the path coverage. The effect of a damping factor in the algorithm to smooth the solution is equivalent to the introduction of a simple covariance function on parameters weighted by the errors on data (Ho-Liu et al., 1989). When the correlation length chosen is very small, the algorithms of Backus and Gilbert (1968, 1970) and Tarantola and Valette (1982) are equivalent.

By considering the a posteriori covariance function and the resolution, it is possible to assess the reliability of the hypotheses made about the independence of parameters. For example, Tanimoto and Anderson (1985) and Montagner and Jobert (1988) showed that there is a trade-off between azimuthal terms and constant terms in the case of a poor azimuthal coverage. For the inversion at depth, Nataf et al. (1986) also displayed the trade-off between physical parameters V_{PH}, V_{SV}, ξ, ϕ, and η when only Rayleigh and Love wave 0-Ψ terms are used in the inversion process.

Though 13 elastic parameters (+density) are necessary to explain surface wave data (Rayleigh and Love waves), only four parameters are well resolved for small anisotropy (Montagner and Jobert, 1988): the azimuthally averaged S-wave velocity V_S, the radial anisotropy expressed through the ξ parameter ($\xi = (V_{SH}/V_{SV})^2$) where V_{SH} (resp. V_{SV}) is the velocity of S-wave propagating horizontally with horizontal transverse polarization (resp. with vertical polarization), and the $\mathbf{G}$ (G_c, G_s) parameters expressing the horizontal azimuthal variation of V_{SV}. ξ was introduced in the reference Earth model PREM (Dziewonski and Anderson, 1981) down to 220 km in order to explain a large dataset of free oscillation eigenfrequencies and body wave travel times. The other elastic parameters can be derived, by using constraints from petrology in order to reduce the parameter space (Montagner and Anderson, 1989a). This approach was followed by Montagner and Anderson (1989b) to derive an average reference earth model and by Montagner and Tanimoto (1991) for the first global 3-D anisotropic model of the upper mantle.

1.19.3.3 Isotropic and Anisotropic Images of the Upper Mantle

The complete anisotropic tomographic procedure has been implemented for making different regional and global studies. Many global isotropic tomographic models of the upper mantle were published since Wooodhouse and Dziewonski (1984) and the recent results have been reviewed by Romanowicz (2003) and in **Chapter 1.10**. Many models inverting only for radial anisotropy but neglecting azimuthal anisotropy have also been published (Ekström and Dziewonski, 1998; Gung et al., 2003; Kustowski et al., 2008a,b; Lebedev and van der Hilst, 2008; Lekic and Romanowicz, 2011; Nataf et al., 1984, 1986; Panning and Romanowicz, 2006; Shapiro and Ritzwoller, 2002; Zhou et al., 2006). The complete anisotropic tomographic technique (including azimuthal anisotropy) has been applied for investigating the upper mantle structure either at a regional scale or at a global scale. The number of regional investigations using surface waves is too large to cite all of them, but we give some examples of anisotropic tomographies for different regions such as the Indian Ocean (Debayle and Lévêque, 1997; Montagner, 1986a; Montagner and Jobert, 1988), the Atlantic Ocean (Mocquet and Romanowicz, 1989; Silveira and Stutzmann, 2001; Silveira et al., 1998), Africa (Debayle et al., 2001; Hadiouche et al., 1989; Montagner et al., 2007; Priestley et al., 2008; Sebai et al., 2006; Sicilia et al., 2008), the Pacific Ocean (Bussy et al., 1993; Ekström and Dziewonski, 1998; Isse et al., 2010; Montagner, 2002;

Maggi et al., 2006; Nishimura and Forsyth, 1989; Ritzwoller et al., 2004), Antarctica (Roult et al., 1994), Australia (Debayle and Kennett, 2000; Fishwick et al., 2008; Simons et al., 2002), North America (Deschamps et al., 2008; Li et al., 2003; Lin et al., 2010; Marone and Romanowicz, 2007a,b; Yuan and Romanowicz, 2010; Yuan et al., 2011), and Central Asia (Griot et al., 1998a,b; Lebedev and Nolet, 2003; Villaseñor et al., 2001; Yao et al., 2010). At a global scale, the reader is referred to the anisotropic models Montagner and Tanimoto (1991), Montagner (2002), and Debayle et al. (2005) and for a quantitative comparison of tomographic and geodynamic models to Becker and Boschi (2002) and Becker et al. (2007).

An important issue, when constructing tomographic models, is the correction for crustal structure, where sedimentary thickness and Moho depth variations are so strong that they affect dispersion of surface waves at least up to 100 s: It has been shown (Montagner and Jobert, 1988) that standard perturbation theory is inadequate to correct for crustal correction and more rigorous approaches were proposed (Boschi and Ekström, 2002; Kustowski et al., 2008a; Li and Romanowicz, 1996; Marone and Romanowicz, 2007b; Zhou et al., 2004) using the updated crustal models 3SMAC (Nataf and Ricard, 1996; Ricard et al., 1996) or CRUST2.0 (Laske et al., 2001; Mooney et al., 1998). However, even these improved crustal models are imperfect and can bias the global radial anisotropic models (Bozdağ and Trampert, 2007; Ferreira et al., 2010). An elegant way to get rid of the strong influence of the crust might be through the use of homogenization methods (Capdeville and Marigo, 2007; Capdeville et al., 2010; Lekic and Romanowicz, 2011).

As an example of the results obtained after the first step of the tomographic procedure, **Figure 6** shows different maps of 2-Ψ azimuthal anisotropy for Rayleigh waves at 100 s period for the first three modes, $n=0$, 1, 2 superimposed on the isotropic part (0-Ψ term) of phase velocity (Beucler and Montagner, 2006). From petrologic and mineralogical considerations, Montagner and Nataf (1988) and Montagner and Anderson (1989a,b) showed that the predominant terms of phase velocity azimuthal expansion are the 0-Ψ and 2-Ψ for Rayleigh waves and 0-Ψ and 4-Ψ for Love waves. However, Trampert and Woodhouse (2003) carefully addressed the requirement of azimuthal anisotropy and demonstrated that Rayleigh-wave data need both 2-Ψ and 4-Ψ terms, which is also confirmed by Beucler and Montagner (2006), but Ekström (2011) still concluded that Rayleigh-wave data only constrain the 0-Ψ and 2-Ψ terms and Love-wave data the isotropic 0-Ψ term. It was shown that for the same variance reduction, a global parameterization of anisotropy including azimuthal anisotropy requires fewer parameters than an isotropic parameterization (Montagner and Jobert, 1988). This apparent paradox can be explained by the fact that the increase of physical parameters is largely compensated by the smaller number of geographic parameters, that is, larger-scale heterogeneities. Other tests have questioned whether phase data are sensitive enough to detect azimuthal anisotropy and the use of additional polarization data has been proposed (Larson et al., 1998; Laske and Masters, 1998).

Most tomographic models for spatial wavelengths larger than 1000 km, which approximately corresponds to harmonic degree of 40, agree that down to about 250–300 km, the deep upper mantle structure is closely related to plate tectonics and

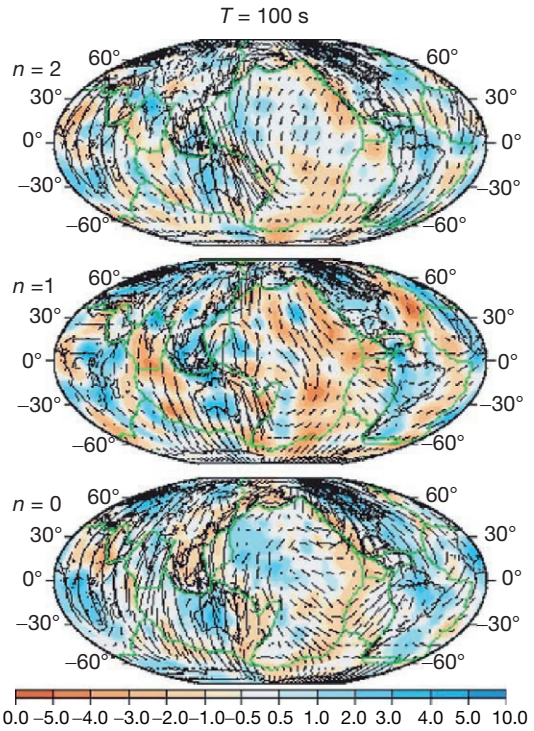

Figure 6 Rayleigh-wave phase velocity maps at period $T=100$ s for the first three modes ($n=0$, 1, 2). Reproduced from Beucler E and Montagner J-P (2006) Computation of large anisotropic seismic heterogeneities. *Geophysical Journal International* 165: 447–468.

continental distribution. **Figure 7** presents two horizontal cross sections from the model of Debayle et al. (2005), which illustrates and confirms the robust features of the upper mantle models published so far since Montagner and Tanimoto (1991). In the upper mantle depth range around 100 km, all plate boundaries are slow: Ridges and back-arc areas are slow, shields are fast, and seismic velocity in oceanic areas is increasing with the age of the seafloor. Except at very few places, it is found that radial anisotropy expressed through the ξ parameter ($\xi=(V_{SH}^2-V_{SV}^2)/V_{SV}^2$) is positive, as large as 10% in some oceanic areas and decreases with depth.

The amplitude of SV-wave azimuthal anisotropy (G parameter) presents an average value of about 2% below oceanic areas (**Figure 7(b)**). Montagner (1994, 2002) noted a good correlation between seismic azimuthal anisotropy and plate velocity directions (primarily for fast-moving plates) given by Minster and Jordan (1978) or DeMets et al. (1991). However, the azimuth of G parameter can vary significantly as a function of depth. For instance, at shallow depths (down to 60 km), the maximum velocity can be parallel to mountain belts or plate boundaries (Babuska et al., 1998; Silver, 1996; Vinnik et al., 1992), but orthogonal to them at large depth. This means that, at a given place, the orientation of fast axis is a function of depth, which explains why the interpretation of SKS splitting with a simple model is often difficult (Becker et al., 2003; Montagner et al., 2000). But Marone and Romanowicz (2007a,b) showed that the introduction of anisotropy stratification in the North American upper mantle makes it possible to resolve the discrepancy between surface wave-derived and

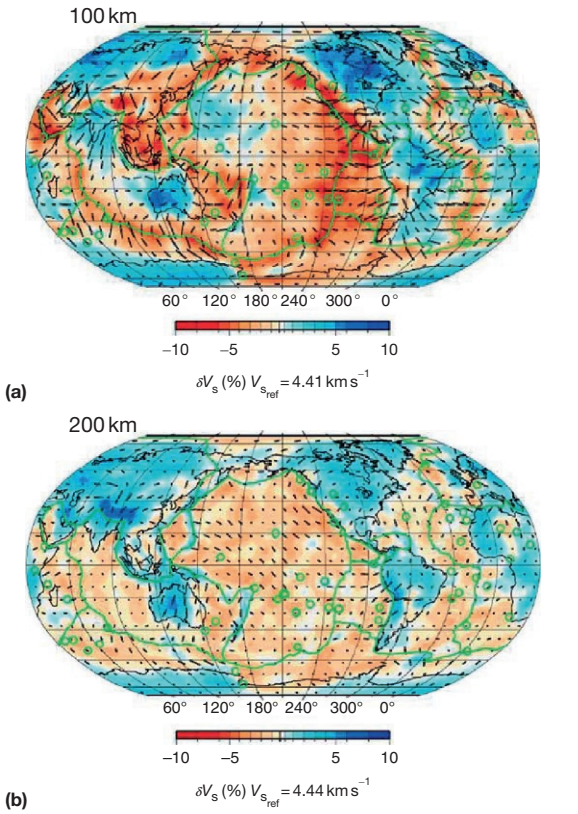

Figure 7 (a, b) Two cross sections at 100 km (top) and 200 km (bottom) depths of the global tomographic model of Debayle et al. (2005). Directions of azimuthal anisotropy are superimposed on S-wave velocity heterogeneities. The length of bars is proportional to its amplitude (<2%).

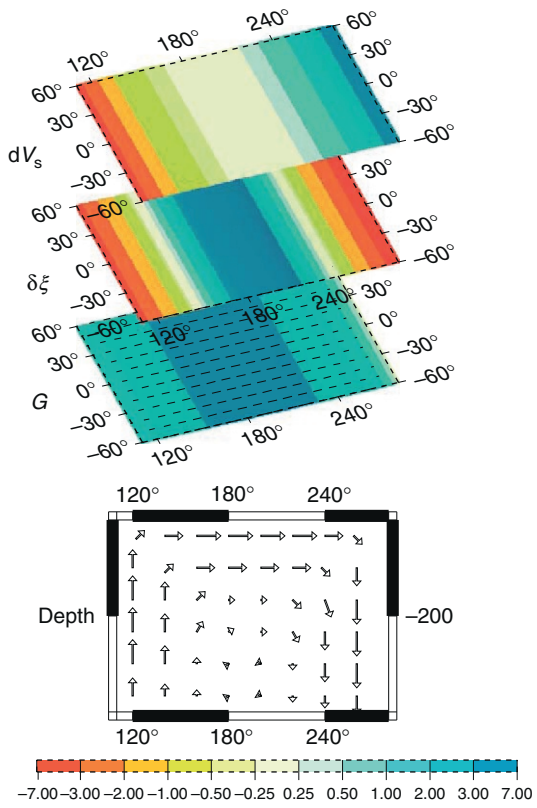

Figure 8 Horizontal cross sections of the seismic observable parameters V_S, ξ, G, Ψ_G associated with a simple convecting cell in the upper mantle, assuming lattice-preferred orientation of anisotropic minerals such as olivine. A vertical flow is characterized by a negative ξ radial anisotropy (ratio between V_{SH} and V_{SV}) and a small azimuthal anisotropy ($G \approx 0$). An upwelling (resp. downwelling) is characterized by a large positive (resp. negative) temperature anomaly inducing $\delta V_S < 0$ (resp. $\delta V_S > 0$). A predominant large-scale horizontal flow will be translated into a significant amplitude of the G azimuthal anisotropy and its orientation will reflect the direction of flow (with a 180° ambiguity). Reproduced from Montagner J-P (2002) Upper mantle low anisotropy channels below the Pacific plate. *Earth Planetary Science Letters* 202: 205–227.

surface wave-observed shear-wave splitting, which was confirmed by Yuan and Romanowicz (2010).

As depth increases, the amplitude of heterogeneities rapidly decreases, some trends tend to vanish, and some distinctive features come up: Most fast ridges are still slow but slow ridges are hardly visible and back-arc regions are no longer systematically slow below 200 km. Large portions of fast ridges are offset with respect to their surface signatures. Below 300 km of depth (not shown here), high-velocity body below the western and the eastern Pacific Rim is the most striking feature, which can be related to subducting slabs.

A visual and quantitative comparison of existing models can be found at the following website addresses: http://igppweb.ucsd.edu/~gabi/rem.html (Reference Earth Model (REM) project) and http://geodynamics.usc.edu/~becker/tdata.html.

1.19.4 Geodynamic Applications

The most popular application of large-scale tomographic models is the understanding of mantle convection. Seismic velocity anomalies can be converted, under some assumptions, not only into temperature anomalies and density anomalies but also into chemical or mineralogical heterogeneities. The application of seismic anisotropy to geodynamics in the upper mantle is straightforward, if we assume that seismic anisotropy is primarily due to the lattice-preferred orientation (LPO) of anisotropic crystals such as olivine (Christensen and Lundquist, 1982; Mainprice et al., 2000; Nicolas et al., 1973). The fast-polarization axis of mineralogical assemblages is in the flow plane parallel to the direction of flow. **Figure 8** shows what is expected for the observable parameters V_S, ξ, G, ψ_G in the case of a simple convective cell with LPO. Radial anisotropy ξ expresses the vertical ($\xi < 1$) or horizontal character ($\xi > 1$) of convective flow, and the azimuthal anisotropy **G** can be related to the horizontal flow direction. Conversely, the three maps of V_S, ξ, **G** can be interpreted in terms of convective flow. These three pieces of information are necessary to correctly interpret the data. For example, upwellings and downwellings are both characterized by a weak or negative ξ parameter, but a correlative positive or negative δV_S discriminates between these possibilities. By simultaneously inverting at depth for the different

azimuthal terms of Rayleigh and Love waves, it is therefore possible to separate the lateral variations in temperature from those induced by the orientation of minerals.

Such an interpretation might however be erroneous in water-rich mantle regions where LPO of minerals such as olivine is not simply related to the strain field (e.g., Jung and Karato, 2001). In addition, the causes of seismic anisotropy are not unique. Other processes can give rise to apparent anisotropy. A purely isotropic finely layered medium with an average layer thickness much less than seismic wavelength will give rise to radial anisotropy (Backus, 1962). Cracks and fluid inclusions (due, e.g., to partial melting) embedded in rocks aligned parallel to the main compressive stress field through the mechanism of shape-preferred orientation (SPO) can also produce a significant anisotropy when its scale is much less than the seismic wavelength. The discrimination between intrinsic anisotropy (related to LPO mechanism) and extrinsic anisotropy (related to SPO or fine layering) is a difficult problem and must be carefully addressed in order to avoid wrong interpretations of apparent anisotropy.

We will only present some examples of interesting applications of anisotropy in large-scale geodynamics and tectonics. Seismic anisotropy in the mantle primarily reflects the strain field prevailing in the past (frozen-in anisotropy) for shallow layers or present convective processes in deeper layers. Therefore, it makes it possible to map convection in the mantle. It must be noted that, when only the radial anisotropy is retrieved, its interpretation is nonunique. A fine layering of the mantle (Backus, 1962) or partial melting (Kawakatsu et al., 2009) can also generate such a kind of anisotropy, and neglecting the azimuthal anisotropy can bias the amplitude of radial anisotropy and its interpretation.

The uppermost mantle down to 410 km is the depth range where the existence of seismic anisotropy is now widely recognized and well documented. Azimuthal variations have been found for body waves and surface waves in different areas of the world. During the last years, the shear-wave splitting, primarily for SKS waves, was extensively used to study continental deformation, but very few studies using body waves are devoted to oceanic areas (except in oceanic islands). Conversely, global anisotropic upper mantle models have been primarily derived during the last 20 years from surface waves, which are sensitive to structure below oceanic areas in the absence of ocean bottom stations and consequently of dense body wave data. The intercomparison of anisotropic body wave and surface wave data is presently ongoing. As shown by Montagner et al. (2000), Wüstefeld et al. (2009), and Becker et al. (2012) at the global scale, such a comparison is providing encouraging results.

1.19.4.1 Oceanic Plates

Oceans are the areas where plate tectonics applies almost perfectly and this is particularly the case in the largest one, the Pacific Plate. **Figure 9** presents examples of three vertical cross sections at two different latitudes, displaying V_{SV} velocity anomalies (**Figure 9(a)**) and the two kinds of anisotropy, which can be retrieved by simultaneous inversion of Rayleigh-wave and Love-wave constant 0-Ψ and azimuthal terms of eqn [1] from the model of Montagner (2002). In **Figure 9(b)**, the equivalent radial anisotropy of the medium, for S-wave expressed through the ξ parameter, is displayed. The maps of **Figure 9(c)** are the distributions of the G parameter related to the azimuthal variation of SV-wave velocity. The maximum amplitude of G is around 5% and rapidly decreases as depth increases. The distribution of velocity and anisotropy is completely different for these different cross sections. The thickening of lithosphere with the age of the seafloor is well observed on V_{SV} velocity maps, but lithosphere is much thicker in the northern cross section. When compared with the cooling half-space model, bathymetry, heat flux, and lithospheric thickness flatten with age (see Maggi et al., 2006; Ritzwoller et al., 2004, for recent results). This flattening is explained by basal reheating, especially in the central Pacific and the birth of small-scale convection below the lithosphere (Davaille and Jaupart, 1994; Huang et al., 2003; Richter and Parsons, 1975; Solomatov and Moresi, 2000).

Radial cross sections (**Figure 9(b)**) show that the $\delta\xi = \xi - \xi_{PREM}$ parameter is usually negative and small, where flow is primarily radial (mid-ocean ridges and subduction zones). For the East Pacific Rise (EPR), Gu et al. (2005) found that a negative radial anisotropy is observed at least down to 300 km. Between plate boundaries, oceans display very large areas with a large positive radial anisotropy such as in the Pacific Ocean (Ekström and Dziewonski, 1998), characteristic of an overall horizontal flow field. This very large anisotropy in the asthenosphere might be the indication of a strong deformation field at the base of the lithosphere (Gung et al., 2003), corresponding to the upper boundary layer of the convecting mantle (Anderson and Regan, 1983; Montagner, 1998). The nature of the boundary between lithosphere and asthenosphere (usually named LAB) has been questioned, and the large shear-wave velocity reduction with the rapid increase in radial anisotropy at the LAB requires a partially molten asthenosphere consisting of horizontal melt-rich layers embedded in meltless mantle (Kawakatsu et al., 2009).

Since convective flow below oceans is dominated by large-scale plate motions, the long-wavelength anisotropy found in oceanic lithospheric plates and in the underlying asthenosphere should be similar to the high-resolution anisotropy measured from body waves. Incidentally, one of the first evidences of azimuthal anisotropy was found in the Pacific Ocean by Hess (1964) for Pn-waves. So far, there are very few measurements of anisotropy by SKS splitting in the oceans. When seismic stations on the seafloor (with the exception of H_2O halfway between Hawaii and California) are lacking, the only measurements available for SKS were performed in stations located on ocean islands (Ansel and Nataf, 1989; Barruol and Fontaine, 2013; Fontaine et al., 2007; Kuo and Forsyth, 1992; Russo and Okal, 1999; Wolfe and Silver, 1998), which are by nature anomalous objects, such as volcanic hot spots, where the strain field is perturbed by the upwelling material and not necessarily representative of the main mantle flow field. Walker et al. (2001) presented a first measurement of SKS splitting at H_2O, but it is in disagreement with independent SKS splitting measurements at the same station by Vinnik et al. (2003) and with surface wave anisotropy (Montagner, 2002). Recently, several ocean seismic experiments have been carried out at regional scale, mainly in the Pacific Ocean. SKS splitting was measured during the temporary MELT experiment (Forsyth et al., 1998;

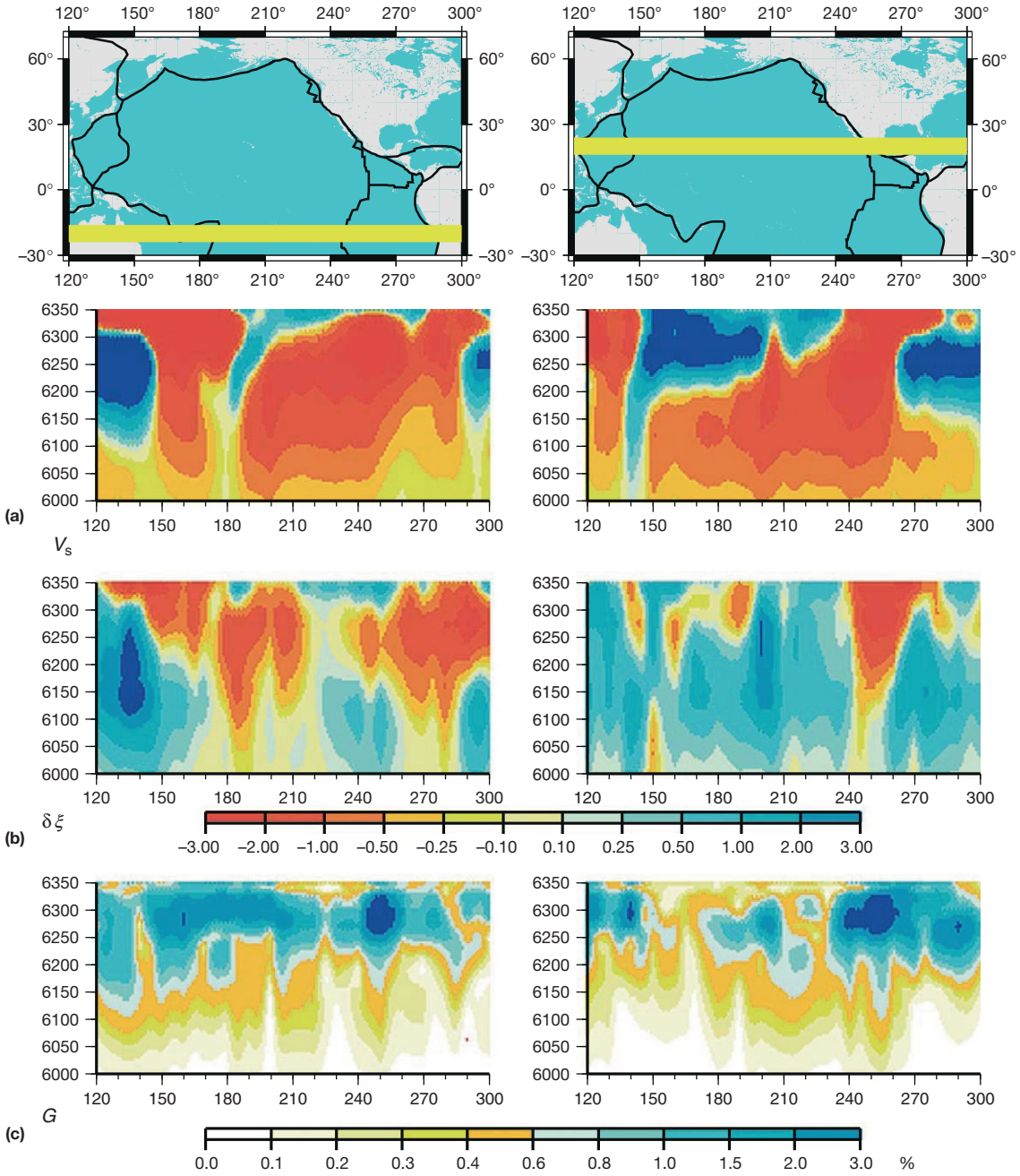

Figure 9 Vertical cross sections of the distribution of V_S, $\xi - \xi_{\rho\varepsilon\phi}$, G in the Pacific Plate at −20° south and 20° north between radii 6000 km (370 km depth) and 6350 km (20 km depth).Reproduced from Montagner J-P (2002) Upper mantle low anisotropy channels below the Pacific plate. *Earth and Planetary Science Letters* 202: 205–227. The color scales in percents are the same for V_S and ξ. The vertical scale is exaggerated to make the figures more readable. (a) V_S; (b) $\delta\xi = \xi - \xi_{\rho\varepsilon\phi}$: deviation of ξ with respect to a reference model ($\xi_{\rho\varepsilon\phi}$ PREM model); (c) G: amplitude of azimuthal anisotropic parameters.

Wolfe and Solomon, 1998) and GLIMPSE experiment (Harmon et al., 2004) on the EPR, but the orientation of the splitting is in disagreement with the petrologic predictions of Blackman et al. (1996).

The large-scale azimuthal anisotropy within and below the lithosphere in the depth range 100–300 km is closely related to plate motions (Becker et al., 2012; Ekström, 2000; Maggi et al., 2006; Montagner, 1994) and modeled in this framework (Tommasi et al., 1996). Fast moving oceanic plates are zones where the comparison between directions of plate velocities (Minster and Jordan, 1978) or NUVEL-1 (DeMets et al., 1991) and directions of G parameter is the most successful (**Figure 10**). Conversely, such a comparison is more difficult and controversial below plates bearing a large proportion of continents, such as the European–Asian plate, characterized by a very small absolute motion in the hot spot reference frame and probably a large influence of inherited anisotropy.

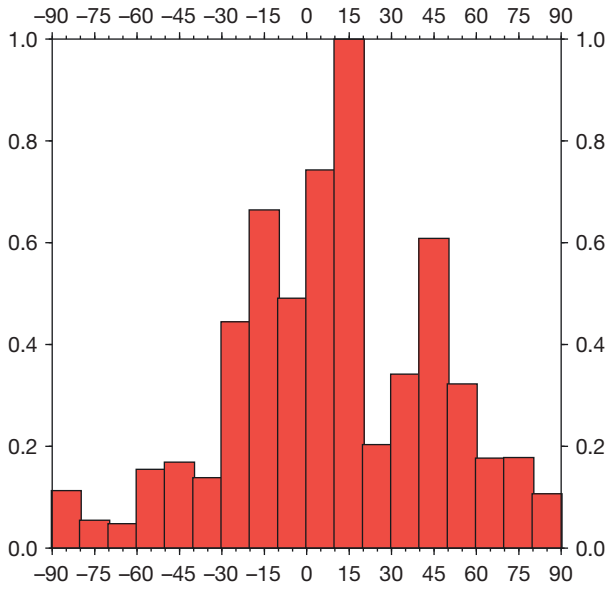

Figure 10 Histogram of the difference between plate velocity directions and synthetic SKS anisotropic azimuths in the Pacific Plate. It is calculated by summing the contributions of each grid point (5° × 5°) weighted by the latitude and the amplitude of anisotropy. Modified from Montagner J-P (2002) Upper mantle low anisotropy channels below the Pacific plate. *Earth and Planetary Science Letters* 202: 205–227.

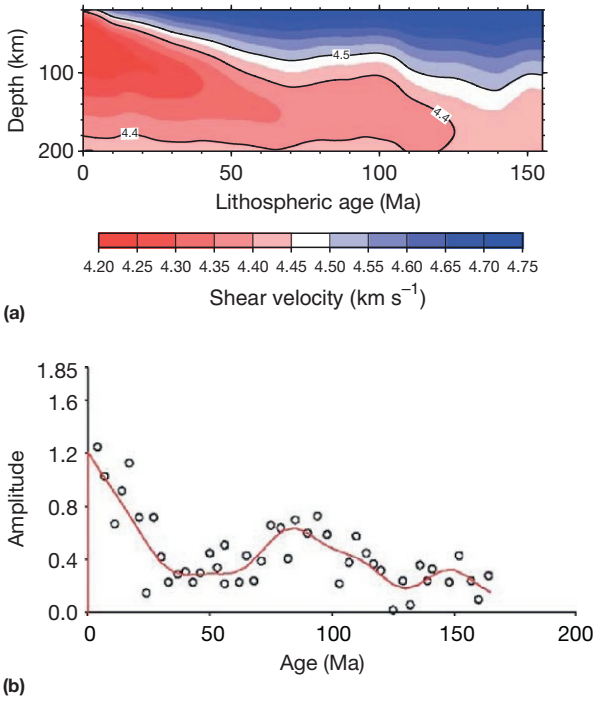

Figure 11 Variations of (a) average S-wave velocity and (b) azimuthal anisotropy (through the delay time of synthetic SKS splitting) plotted versus the age of lithospheric seafloor. In both cases, the structure below the plate for age between 60 and 100 Ma looks anomalous. (a) Modified from Ritzwoller MH, Shapiro NM, and Zhong S-J (2004) Cooling history of the Pacific lithosphere. *Earth and Planetary Science Letters* 226: 69–84. (b) Reproduced from Montagner J-P (2002) Upper mantle low anisotropy channels below the Pacific plate. *Earth and Planetary Science Letters* 202: 205–227.

The map with the *G* parameter at 100 km (**Figure 7**) and the cross sections of **Figure 9(c)** show that the azimuthal anisotropy is very large along spreading ridges with a large asymmetry for the EPR. The direction of anisotropy is in very good agreement with plate motion, which is also found in all other available models (Debayle et al., 2005; Ekström, 2000; Lebedev and van der Hilst, 2008; Smith et al., 2004). The anisotropy is also large in the middle of the Pacific Plate, but a line of very small azimuthal anisotropy almost parallel to the EPR is observed there (see also **Figure 4** for synthetic SKS). This linear area of small anisotropy was named low anisotropy channel (LAC) by Montagner (2002). When calculating the variation of the amplitude of azimuthal anisotropy as a function of depth, a minimum comes up between 40 and 60 Ma age of the seafloor (**Figure 11(a)**). The LAC is presumably related either to cracking within the Pacific Plate or to secondary convection within and below the rigid lithosphere, predicted by numerical and analog experiments and also translated in the V_S velocity structure (Ritzwoller et al., 2004; **Figure 11(b)**). These new features provide strong constraints on the decoupling between the plate and asthenosphere. The existence and location of these LACs might be related to the current active volcanoes and hot spots (possibly plumes) in the central Pacific. LACs, which are dividing the Pacific Plate into smaller units, might indicate a future reorganization of plates with ridge migrations in the Pacific Ocean. They call for more thorough numerical modeling.

1.19.4.2 Continents

Differences in the thickness of high-velocity layer underlying continents as imaged by seismic tomography have fuelled a long debate on the origin of continental roots and its depth suggested down to 400 km (Jordan, 1975, 1978). Most global tomographic models provide a continental thickness of about 200–250 km in agreement with heat-flow analysis or electric conductivity.

Seismic anisotropy can provide fundamental information on the structure of continents, their root, and the geodynamic processes involved in mountain building and collision between continents (Silver, 1996; Vinnik et al., 1992) such as in Central Asia (Griot et al., 1998a,b; Priestley et al., 2006; Yao et al., 2010). Radial anisotropy ξ is usually very heterogeneous below continents in the first 150–200 km of depth with positive or negative areas according to geology. But it seems to display a systematic tendency of being positive at larger depth (down to 300 km), whereas it is very large in the oceanic lithosphere in the depth range 50–200 km and decreases rapidly at larger depths (Montagner, 1994). Conversely, radial anisotropy displays a maximum (though smaller than in oceanic lithosphere) below very old continents (such as Siberian and Canadian Shields) in the depth range 200–400 km (Montagner and Tanimoto, 1991), which might be a good marker of LAB below continents. Seismic anisotropy below continents, sometimes confined to the upper 220 km (Gaherty and Jordan, 1995), can still be significant below. A more quantitative comparison of radial anisotropy between different continental provinces is presented in Babuska et al. (1998) and

demonstrates systematic differences according to the tectonic context. The existence of positive large-scale radial anisotropy below continents at depth might be a good indicator of the continental root, which was largely debated since the presentation of the model of tectosphere by Jordan (1975, 1978, 1981). If this maximum of anisotropy is assumed to be related to an intense strain field in this depth range, it might be characteristic of the boundary between continental lithosphere and 'normal' upper mantle material. Gung et al. (2003) showed that it is possible to reconcile different isotropic tomographic models by taking into account radial anisotropy. They find that significant radial anisotropy (with $V_{SH} > V_{SV}$) under most cratons in the depth range 250–400 km is similar to that found at shallower depths (80–250 km) below oceanic basins. Such a result is also in agreement for the Australian continent (Debayle and Kennett, 2000; Simons et al., 2002). So, all results seem to show that the root of continents as defined by radial anisotropy is located between 200 and 300 km. However, this result is not correlated with a maximum in azimuthal anisotropy in this depth range (Debayle et al., 2005): the fast-moving Australian Plate seems to be the only continental region with a sufficiently large deformation at its base to be transformed into azimuthal anisotropy. They propose that, for continents other than Australia, weak influence of basal drag on the lithosphere may explain why azimuthal anisotropy is observed only in a layer located in the uppermost 100 km of the mantle. This layer shows a complex organization of azimuthal anisotropy, suggesting a frozen-in origin of deformation, compatible with SKS splitting. This complexity is probably related to the stratification of anisotropy within cratons (Deschamps et al., 2008). The issue of the depth of continental roots is still a subject of debate. With the rapid expansion of permanent or temporary broadband seismic stations in different continents, it has been possible to carry out extensive investigations of LAB using receiver functions. Whereas global and regional surface wave anomalies in the mantle beneath old continents like Africa, Australia, and North America (e.g., Marone and Romanowicz, 2007a; Montagner and Tanimoto, 1991; Nettles and Dziewonski, 2008; Woodhouse and Dziewonski, 1984) have found continental roots down to 200–250 km depths, receiver functions studies (Kumar et al., 2007) found that the Indian lithosphere is significantly thinner (~100 km thick). The global investigation of the LAB by Rychert and Shearer (2009) imaged an interface varying from 100 km beneath Precambrian shields to 80 km beneath tectonically altered regions. In order to reconcile the contradictory results, Yuan and Romanowicz (2010) proposed a lithospheric layering of the North American craton. By mapping the changes in the direction of azimuthal anisotropy, they reveal the presence of two distinct lithospheric layers throughout the stable part of the North American continent. Taking a comparative note of these studies, the receiver function results could indicate an inner layering of continental lithosphere. This kind of investigation must be performed on all continents in order to generalize this finding (e.g., Romanowicz, 2009).

The difference in radial and azimuthal anisotropies between oceans and continents might reflect a difference of coupling between lithosphere and asthenosphere, through the basal drag. The coupling might be weak below most continental roots, in contrast with the Pacific Plate, where the coupling (reflected by plate direction) is the first-order effect in the uppermost 200 km for young ages, before thermal instabilities take place at the base of the lithosphere, as evidenced by the existence of LACs. These results on the difference between oceanic and continental anisotropies are illustrated in Figure 12.

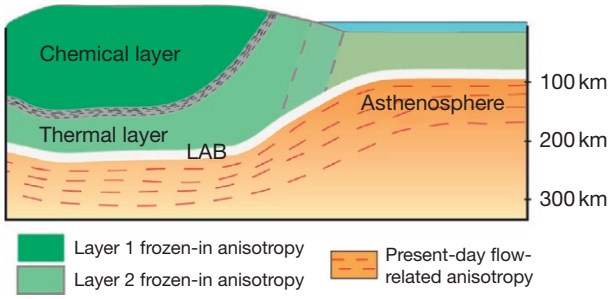

Figure 12 Scheme illustrating the inferred stratification of the lithosphere as derived from seismic anisotropy. It also illustrates the difference in the location of maximum anisotropy between oceans and continents. Adapted from Yuan HY and Romanowicz B (2010) Lithospheric layering in the North American craton. *Nature* 466: 1063–1068. http://dx.doi.org/10.1038/nature09332.

1.19.4.3 Velocity and Anisotropy in the Transition Zone

The transition zone (see also **Chapter 1.21**) plays a key role in mantle dynamics, particularly the 660 km discontinuity that might inhibit the passage of matter between the upper lower mantle and the lower mantle and might be a water reservoir (Bercovici and Karato, 2003). Its seismic investigation is made difficult on the global scale by the poor sensitivity of fundamental surface waves in this depth range and by the fact that teleseismic body waves recorded at continental stations from earthquakes primarily occurring along plate boundaries have their turning point below the transition zone. For body waves, many different techniques using SS precursors (Shearer, 1991) or P-to-S converted waves (Chevrot et al., 1999) were used at global scale to investigate the thickness of the transition zone. In spite of some initial controversies, more recent models by Lawrence and Shearer (2006), Houser et al. (2008), and Tauzin et al. (2008) provide a coherent large-scale image of the transition zone thickness.

Whatever the type of data (normal mode, higher modes of surface waves, and body waves), an important feature of the transition zone is that, contrary to the rest of the upper mantle, the upper transition zone is characterized by a large degree-2 pattern (Masters et al., 1982) and, to a lesser extent, a strong degree-6. The degree-2 pattern (as well as degree-6) can be explained by the predominance of a simple large-scale flow pattern characterized by two upwellings in the central Pacific Ocean and East Africa and two downwellings in the western and eastern Pacific Ocean (Montagner and Romanowicz, 1993), proposed initially in the lower mantle (Busse, 1983). This scheme was corroborated by the existence, in the upper transition zone, of a slight but significant degree-4 radial anisotropy displayed by Montagner and Tanimoto (1991) and Roult et al. (1990) in agreement with the prediction of this model. Therefore, the observations of the geographic distributions of degrees 2, 4, and 6 in the transition zone are

coherent and spatially dependent. Montagner (1994) compared these different degrees to the corresponding degrees of the hot spot and slab distribution. In this simple framework, the distribution of plumes (degree $2+6$) is merely a consequence of the large-scale simple flow in the transition zone. The degree 6 of velocity in the transition zone is well correlated with the distribution of hot spots and might indicate that many mantle plumes might originate in the transition zone. Ritsema et al. (2004) observed lower-than-average shear velocity at eight hot spots in this depth range (**Figure 13**). These results suggest that there are different families of plumes, some of them originating in the transition zone.

As for anisotropy in the transition zone, Montagner and Kennett (1996), by using eigenfrequency data, displayed some evidence of radial anisotropy in the upper (410–660 km) and lower (660–900 km) transition zones. Panning and Romanowicz (2004) also displayed a slight maximum of the harmonic degree 0 in the transition zone. Global tomographic models (Kustowski et al., 2008a,b; Panning and Romanowicz, 2006) display significant lateral variations of radial anisotropy in the transition zone, in particular below subduction zones. The existence of anisotropy close to the 660 km discontinuity was also found by Vinnik and Montagner (1996) below Germany and Vinnik et al. (1998) in Central Africa. By studying P-to-S converted waves at the GRF network and at GEOSCOPE station BNG in Central Africa, they observed that part of the initial P-wave is converted into SH-wave. This signal can be observed on the transverse component of seismograms. The amplitude of this SH-wave cannot be explained by a dipping 660 km discontinuity and it constitutes a good evidence for the existence of anisotropy just above this discontinuity. However, there is some evidence of lateral variation of anisotropy in the transition zone as found by the investigation of several subduction zones (Fischer and Wiens, 1996; Fischer and Yang, 1994). Fouch and Fischer (1996) presented a synthesis of these different studies and showed that some subduction zones such as Sakhalin require deep anisotropy in the transition zone, whereas others such as Tonga do not need any anisotropy. They conclude that their data might be reconciled by considering the upper transition zone (410–520 km) intermittently anisotropic, and the rest of the transition zone might be isotropic.

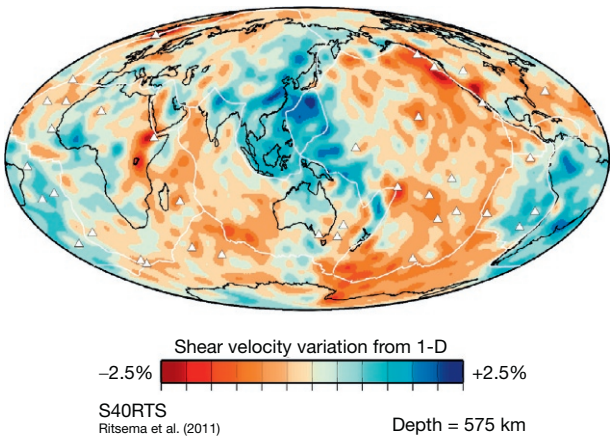

Figure 13 Model of shear velocity in the transition zone at 575 km depth derived from the inversion of fundamental-mode and overtone Rayleigh-wave phase velocities and teleseismic body wave data. Modified from Ritsema J, Deuss A, van Heijst HJ, and Woodhouse JH (2011) S40RTS: A degree-40 shear-velocity model for the mantle from new Rayleigh wave dispersion, teleseismic traveltime and normal-mode splitting function measurements. *Geophysical Journal International* 184: 1223–1236.

Azimuthal anisotropy in the transition zone was also advocated by two independent studies, using different datasets. The observations of Wookey et al. (2002), though controversial, present evidence of very large S-wave splitting (up to 7 s) in the vicinity of the 660 km discontinuity between Tonga–Kermadec Subduction Zone and Australia. On a global scale, Trampert and van Heijst (2002) showed a long-wavelength azimuthal anisotropic structure in the transition zone. The rms amplitude of lateral variations of G is about 1%. Beghein and Trampert (2003) using probability density functions and separating ξ, ϕ, and η anisotropies suggested a chemical component to explain these different parameters. The interpretation of these new tentative results is not obvious and new data are necessary to close the debate on the nature of velocity and anisotropy heterogeneities in the transition zone. The transition zone might be a midmantle boundary layer, and a detailed and reliable tomographic model of S-wave velocity and anisotropy in the transition zone will provide fundamental insights into the dynamics of the whole mantle.

1.19.5 Numerical Modeling and Perspectives

In the previous sections, we have highlighted the presence of lateral heterogeneities in seismic velocity and anisotropy in different parts of the Earth's upper mantle. However, anisotropy is not present in all depth ranges nor at all scales. There is some consensus for the presence of radial anisotropy in many parts of the upper mantle in order to simultaneously explain Love-wave and Rayleigh-wave dispersions and even in the lower mantle (Kustowski et al., 2008a,b; Panning and Romanowicz, 2004). The existence of azimuthal anisotropy is more controversial, though, from petrologic reasons, it turns out that radial anisotropy and azimuthal anisotropy are intimately related and should be searched for simultaneously. Additional data such as polarization data might help to provide additional constraints on both kinds of anisotropy (Pettersen and Maupin, 2002; Yu and Park, 1993). But it requires the development of improved theoretical and numerical methods in order to work on the amplitude of seismograms.

Thanks to the access to very powerful computers, we are at the beginning stage of a new era for seismology. The twentieth century was dominated by the use of ray theory and, later on, of normal mode theory. Since it is now feasible to numerically compute synthetic seismograms in complex 3-D structures in global spherical geometry (Capdeville et al., 2003; Komatitsch and Tromp, 1999; Komatitsch and Vilotte, 1998), it is possible to model the complex interaction between seismic waves and 3-D heterogeneity, particularly in anisotropic and anelastic media. Some new and sophisticated tomographic methods are presently developed (Capdeville et al., 2005; Fichtner et al., 2009; Lekic and Romanowicz 2011; Montelli et al., 2004; Sigloch et al., 2008; Tromp et al., 2005; Zhou et al., 2006; Zhu et al., 2012) that takes account of finite-frequency

effect and inverted full seismic waveforms. They should provide access to the complexity of the Earth's mantle by the mapping of short-scale heterogeneities such as mantle plumes and slabs in anisotropic and anelastic media.

A second important challenge is the complete understanding of the origin of anisotropy from the mineral scale up to global scale in the different layers of the Earth. In the upper mantle, seismic anisotropy is primarily due to LPO of anisotropic minerals such as olivine at large scales, requiring several strong conditions, starting with the presence of anisotropic crystals up to the existence of an efficient large-scale present or past strain field (Mainprice et al., 2000). In order to fill the gap between grain-scale modeling (Kaminski and Ribe, 2001; McKenzie, 1979; Ribe, 1989) and large-scale anisotropic measurements in a convective system (Tommasi et al., 2000), there is now a real need to make more quantitative comparisons between seismic anisotropy and numerical modeling. Gaboret et al. (2003), Becker et al. (2003), and Conrad et al. (2007) calculated the convective circulation in the mantle by converting perturbations of S-wave velocity into density perturbations. **Figure 14** shows two cross sections through the Pacific hemisphere and the associated flow lines (Gaboret et al., 2003) derived from the tomographic model of Ekström and Dziewonski (1998). This kind of modeling makes it possible to calculate the strain tensor and to test different hypotheses for the prevailing mechanisms of alignment, by comparison with seismic data. The joint interpretation of seismic and geodynamic data provides fundamental constraints on convective pattern within the mantle and the relative importance of thermal versus compositional heterogeneity (Long and Becker, 2010; Simmons et al., 2009).

The upper mantle is the best known of the deep layers of the earth, where there is now good agreement between many isotropic global tomographic models. But the account of seismic anisotropy is mandatory to avoid biased isotropic heterogeneities. The main application of anisotropy is the mapping of mantle convection and of its boundary layers (Karato, 1998; Montagner, 1998). The finding of anisotropy in the transition zone (if confirmed) will provide strong constraints on the flow circulation and the exchange of matter between the upper and the lower mantle. Pursuing the first pioneering efforts, the systematic modeling of the complete seismic waveform in 3-D heterogeneous, anisotropic, and anelastic media associated with new techniques of numerical modeling of seismograms will probably enhance our vision of the whole mantle.

In parallel to these theoretical and numerical challenges, there is a crucial need for instrumental developments since there are still many areas on the surface of the Earth devoid of broadband seismic stations. These regions are primarily located in the southern hemisphere and more particularly in oceanic areas where no islands are present. Therefore, an international effort is ongoing, coordinated through ION (International Ocean Networks), in order to promote the installation of geophysical ocean bottom observatories in order to fill the enormous gaps in the station coverage (for a description of ION, see http://seismo.berkeley.edu/seismo/ion and http://msg.whoi.edu/ION/index.html).

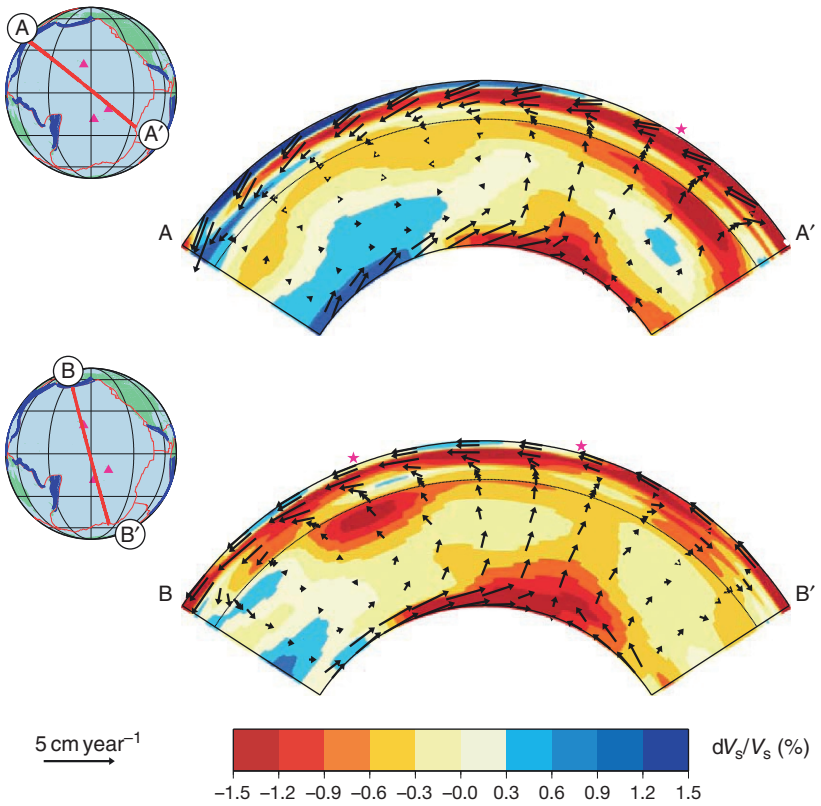

Figure 14 Mantle heterogeneities and convective flow below the Pacific Ocean. Adapted from Gaboret C, Forte A, and Montagner J-P (2003) The unique dynamics of the Pacific Hemisphere mantle and its signature on seismic anisotropy. *Earth and Planetary Science Letters* 208: 219–223.

Appendix Effect of Anisotropy on Surface Waves in the Plane-Layered Medium

See Figure 15.

The half-space is assumed to be homogeneous and may be described by its density $\rho(z)$ and its fourth-order elastic tensor $\Gamma(z)$ with 21 independent elastic coefficients. All these parameters are so far supposed independent of x- and y-coordinates (z is the vertical component). This condition will be released in the next section. The unperturbed medium is assumed isotropic with an elastic tensor $\Gamma_0(z)$. In that medium, the two cases of Love-wave and Rayleigh-wave dispersions can be successively considered.

The unperturbed Love-wave displacement is of the form

$$\mathbf{u}(\mathbf{r},t)=\begin{pmatrix}-W(z)\sin\Psi\\ W(z)\cos\Psi\\ 0\end{pmatrix}\exp(i[k(x\cos\Psi+y\sin\Psi)-\omega t]) \quad [19]$$

where $W(z)$ is the scalar depth eigenfunction for Love waves, k is the horizontal wave number, and Ψ is the azimuth of the wave number k measured clockwise from the north.

The unperturbed Rayleigh-wave displacement is of the form

$$\mathbf{u}(\mathbf{r},t)=\begin{pmatrix}V(z)\cos\Psi\\ V(z)\sin\Psi\\ iU(z)\end{pmatrix}\exp(i[k(x\cos\Psi+y\sin\Psi)-\omega t]) \quad [20]$$

where $V(z)$ and $U(z)$ are the scalar depth eigenfunctions for Rayleigh waves. The associated strain tensor $\epsilon(\mathbf{r},t)$ is defined by

$$\epsilon_{ij}(\mathbf{r},t)=1/2\left(u_{i,j}+u_{j,i}\right) \quad [21]$$

where j denotes the differentiation with respect to the j-th coordinate. The medium is perturbed from $\Gamma_0(z)$ to $\Gamma_0(z)+\gamma(z)$, where $\gamma(z)$ is small compared to $\Gamma_0(z)$ but quite general in the sense that there is no assumption on the kind of anisotropy. This means that in this approximation, we can still consider quasi-Love modes and quasi-Rayleigh modes (Crampin, 1984). From Rayleigh's principle, the first-order perturbation $\delta V(\mathbf{k})$ in phase velocity dispersion is (Smith and Dahlen, 1973, 1975)

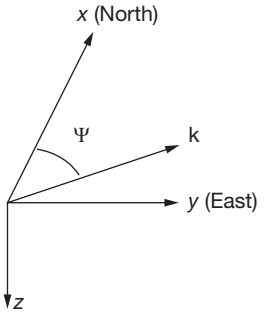

Figure 15 Definition of the Cartesian coordinate system (x, y, z) used in the calculations. Ψ is the azimuth of the wavevector k with respect to north.

$$\delta V(\mathbf{k})=\frac{V}{2\omega^2}\frac{\int_0^\infty \gamma_{ijkl}\epsilon_{ij}\epsilon_{kl}^*}{\int_0^\infty \rho_0 u_k u_k^*}\mathrm{d}z \quad [22]$$

where u and ϵ_{ij} are, respectively, the displacement and the strain for the unperturbed half-space and the asterisk denotes complex conjugation. Now because of the symmetry of the tensors $\gamma(z)$ and ϵ, we use the simplified index notation c_{ij} and ϵ_i for the elements γ_{ijkl} and ϵ_{ij}, but the number n_{ij} of coefficients γ_{ijkl} for each c_{ij} must be taken into account. The simplified index notation for the elastic tensor γ_{ijkl} is defined in a coordinate system (x_1, x_2, x_3) by

$$\gamma_{ijkl}\rightarrow c_{pq}\begin{cases}\text{if } i=j\Rightarrow p=i\\ \text{if } k=l\Rightarrow q=k\\ \text{if } i\neq j\Rightarrow p=9-i-j\\ \text{if } k\neq l\Rightarrow q=9-k-l\end{cases} \quad [23]$$

This kind of transformation enables us to relate the fourth-order tensor γ ($3\times3\times3\times3$) to a matrix c (6×6). The same simplified index notation can be applied to the components of the strain tensor ϵ_{ij}, transforming the second-order tensor ϵ (3×3) into a vector with six components. However, it is necessary to be careful, because to a given c_{pq} correspond several γ_{ijki}, and γ_{ijkl} must be replaced by $n_{pq}c_{pq}$, where n_{pq} is the number of γ_{ijki} giving the same c_{pq}. Therefore, eqn [22] expressing Rayleigh's principle can be rewritten as

$$\delta V(k)=\frac{V}{2\omega^2}\frac{\int_0^\infty \sum_{ij} n_{ij}c_{ij}\epsilon_i\epsilon_j^*}{\int_0^\infty \rho_0 u_k u_k^*}\mathrm{d}z \quad [24]$$

We only detail the calculations for Love waves:

By using the previous expressions for $\mathbf{u}(\mathbf{r},t)$ [19] and $\epsilon_{ij}(\mathbf{r},t)$ [21], the various expressions of strain are as follows:

$$\begin{cases}\epsilon_1=-i\cos\Psi\sin\Psi kW\\ \epsilon_2=i\cos\Psi\sin\Psi kW\\ \epsilon_3=0\\ \epsilon_4=1/2\cos\Psi W'\\ \epsilon_5=-1/2\cos\Psi W'\\ \epsilon_6=i/2(\cos^2\Psi-\sin^2\Psi)kW\end{cases} \quad [25]$$

where $W'=\mathrm{d}W/\mathrm{d}r$. In Table 1, the different terms $n_{ij}c_{ij}\epsilon_i\epsilon_j^*$ are given. We note that when $c_{ij}\epsilon_i\epsilon_j^*$ is a purely imaginary complex, its contribution to $\delta V(K,\Psi)$ is null. When all the contributions are summed, the different terms $\cos^k\Psi\sin^l\Psi$ are such that $k+l$ is even, which is not surprising in the light of the reciprocity principle. Therefore, each term can be developed as a Fourier series in Ψ with only even terms. Finally, it is found

$$\begin{aligned}\delta V_{\mathrm{L}}(k,\Psi)=\frac{V}{2\omega^2 L_0}\int_0^\infty \mathrm{d}z\Bigg\{&k^2W^2\left[\frac{1}{8}(c_{11}+c_{22}-2c_{12}+4c_{66})\right]\\ &+W'^2\left[\frac{1}{2}(c_{44}+c_{55})\right]\\ &+\cos2\Psi W'^2\left[\frac{1}{2}(c_{44}-c_{55})\right]-\sin2\Psi W'^2c_{45}\\ &-\cos4\Psi k^2W^2\left[\frac{1}{8}(c_{11}+c_{22}-2c_{12}-4c_{66})\right]\\ &+\sin4\Psi k^2W^2\left[\frac{1}{2}(c_{26}-c_{16})\right]\Bigg\}\end{aligned} \quad [26]$$

Table 1 Calculation of the various $c_{ij\epsilon_i\epsilon_j}$ for Love waves, with the simplified index notation

n	ij	$c_{ij\epsilon_i\epsilon_j}$
1	11	$c_{11}\alpha^2\beta^2\cdot k^2W^2$
1	22	$c_{22}\alpha^2\beta^2\cdot k^2W^2$
1	33	0
2	12	$-c_{12}\alpha^2\beta^2\cdot k^2W^2$
2	13	0
2	23	0
2	24	0
4	14	$c_{14}\left(-i\alpha^2\beta\right)\cdot\frac{kWW'}{2}$
4	15	$c_{14}\left(i\alpha^2\beta\right)\cdot\frac{kWW'}{2}$
4	16	$c_{16}(-\alpha\beta)\left(\alpha^2-\beta^2\right)\cdot\frac{k^2W^2}{2}$
4	24	$c_{24}\left(-i\alpha^2\beta\right)\cdot\frac{kWW'}{2}$
4	25	$c_{25}\left(-i\alpha\beta^2\right)\cdot\frac{kWW'}{2}$
4	26	$c_{26}(\alpha\beta)\left(\alpha^2-\beta^2\right)\cdot\frac{k^2W^2}{2}$
4	34	0
4	35	0
4	36	0
4	44	$c_{44}\alpha^2\cdot\frac{W'^2}{4}$
8	45	$c_{45}(-\alpha\beta)\cdot\frac{W'^2}{4}$
8	46	$c_{46}(-i\alpha)\left(\alpha^2-\beta^2\right)\cdot\frac{kWW'}{4}$
4	55	$c_{55}\beta^2\cdot\frac{W'^2}{4}$
8	56	$c_{56}(i\beta)\left(\alpha^2-\beta^2\right)\cdot\frac{kWW'}{4}$
4	66	$c_{66}\left(\alpha^2-\beta^2\right)^2\cdot\frac{k^2W^2}{4}$

In the particular case of a transversely isotropic medium with a vertical symmetry axis (also named radial anisotropic medium), we have $c_{11}=c_{22}=\delta A$, $c_{33}=\delta C$, $c_{12}=\delta(A-2N)$, $c_{13}=c_{23}=\delta F$, $c_{44}=c_{55}=\delta L$, $c_{66}=\delta N$, and $c_{14}=c_{24}=c_{15}=c_{25}=c_{16}=c_{26}=0$. The local azimuthal terms vanish and the previous eqn [26] reduces to

$$\delta V_L(k,\Psi)=\frac{1}{2V_L L_0}\int_0^\infty\left\{W^2\delta N+\frac{W'^2}{k^2}\delta L\right\}dz \qquad [27]$$

Therefore, the same expressions as in Takeuchi and Saito (1972, p. 268) is found in the case of radial anisotropy. The 0-Ψ term of eqn [26] corresponds to the averaging over azimuth Ψ, which provides the equivalent transversely isotropic model with vertical symmetry axis by setting

$$\delta N=\frac{1}{8}(c_{11}+c_{22})-\frac{1}{4}c_{12}+\frac{1}{2}c_{66}$$

$$\delta L=\frac{1}{2}(c_{44}+c_{55})$$

If we call C_{ij} the elastic coefficients of the total elastic tensor, we can set

$$N=\rho V_{SH}^2=\frac{1}{8}(C_{11}+C_{22})-\frac{1}{4}C_{12}+\frac{1}{2}C_{66}$$

$$L=\rho V_{SV}^2=\frac{1}{2}(C_{44}+C_{55})$$

According to eqn [26], the first-order perturbation in Love-wave phase velocity $\delta V_L(k,\Psi)$ can then be expressed as

$$\delta V_L(k,\Psi)=\frac{1}{2V_{0L}(k)}[L_1(k)+L_2(k)\cos 2\Psi+L_3(k)\sin 2\Psi+L_4(k)\cos 4\Psi+L_5(k)\sin 4\Psi. \qquad [28]$$

where

$$L_0(k)=\int_0^\infty\rho W^2dz$$

$$L_1(k)=\frac{1}{L_0}\int_0^\infty\left(W^2\delta N+\frac{W'^2}{k^2}\delta L\right)dz$$

$$L_2(k)=\frac{1}{L_0}\int_0^\infty -G_c\left(\frac{W'^2}{k^2}\right)dz$$

$$L_3(k)=\frac{1}{L_0}\int_0^\infty -G_s\left(\frac{W'^2}{k^2}\right)dz$$

$$L_4(k)=\frac{1}{L_0}\int_0^\infty -E_c\cdot W^2dz$$

$$L_5(k)=\frac{1}{L_0}\int_0^\infty -E_s\cdot W^2dz$$

- Rayleigh waves

The same procedure holds for the local Rayleigh-wave phase velocity perturbation δV_R, starting from the displacement given previously (Montagner and Nataf, 1986):

$$\delta V_R(k,\Psi)=\frac{1}{2V_{0_R}(k)}[R_1(k)+R_2(k)\cos 2\Psi+R_3(k)\sin 2\Psi+R_4(k)\cos 4\Psi+R_5(k)\sin 4\Psi. \qquad [29]$$

where

$$R_0(k)=\int_0^\infty\rho\left(U^2+V^2\right)dz$$

$$R_1(k)=\frac{1}{R_0}\int_0^\infty\left[V^2\cdot\delta A+\frac{U'^2}{k^2}\cdot\delta C+\frac{2U'V}{k}\cdot\delta F+\left(\frac{V'}{k}-U\right)^2\cdot\delta L\right]dz$$

$$R_2(k)=\frac{1}{R_0}\int_0^\infty\left[V^2\cdot B_c+\frac{2U'V}{k}\cdot H_c+\left(\frac{V'}{k}-U\right)^2\cdot G_c\right]dz$$

$$R_3(k)=\frac{1}{R_0}\int_0^\infty\left[V^2\cdot B_s+\frac{2U'V}{k}\cdot H_s+\left(\frac{V'}{k}-U\right)^2\cdot G_s\right]dz$$

$$R_4(k)=\frac{1}{R_0}\int_0^\infty E_c\cdot V^2dz$$

$$R_4(k)=\frac{1}{R_0}\int_0^\infty E_s\cdot V^2dz$$

The 13 depth-dependent parameters A, C, F, L, N, B_c, B_s, H_c, H_s, G_c, G_s, E_c, E_s are linear combinations of the elastic coefficients C_{ij} and are explicitly given as follows:

Constant term (0-Ψ azimuthal term: independent of azimuth):

$$A=\rho V_{PH}^2=\frac{3}{8}(C_{11}+C_{22})+\frac{1}{4}C_{12}+\frac{1}{2}C_{66}$$

$$C=\rho V_{PV}^2=C_{33}$$

$$F=\frac{1}{2}(C_{13}+C_{23})$$

$$L=\rho V_{SV}^2=\frac{1}{2}(C_{44}+C_{55})$$

$$N=\rho V_{SH}^2=\frac{1}{8}(C_{11}+C_{22})-\frac{1}{4}C_{12}+\frac{1}{2}C_{66}$$

2-Ψ azimuthal term:

$$\begin{array}{ll} \cos 2\Psi & \sin 2\Psi \\ B_c = \frac{1}{2}(C_{11} - C_{22}) & B_s = C_{16} + C_{26} \\ G_c = \frac{1}{2}(C_{55} - C_{44}) & G_s = C_{54} \\ H_c = \frac{1}{2}(C_{13} - C_{23}) & H_s = C_{36} \end{array}$$

4-Ψ azimuthal term:

$$\begin{array}{ll} \cos 4\Psi & \sin 4\Psi \\ E_c = \frac{1}{8}(C_{11} + C_{22}) - \frac{1}{4}C_{12} - \frac{1}{2}C_{66} & E_s = \frac{1}{2}(C_{16} - C_{26}) \end{array}$$

where indices 1 and 2 refer to horizontal coordinates (1, north; 2, east) and index 3 refers to vertical coordinate. ρ is the density; V_{PH} and V_{PV} are, respectively, horizontal and vertical propagating P-wave velocities; and V_{SH} and V_{SV} are, respectively, the horizontal and vertical polarized S-wave velocities. We must bear in mind that A, C, L, N anisotropic parameters can be retrieved from measurements of the P- and S-wave velocities propagating perpendicular or parallel to the axis of symmetry.

Acknowledgments

I would like to thank Barbara Romanowicz and an anonymous reviewer for their constructive reviews and my colleagues from IPG of Paris.

References

Aki K and Richards PG (1980) *Quantitative Seismology: Theory and Methods*. San Fransisco, CA: W. H. Freeman.

Anderson DL (1961) Elastic wave propagation in layered anisotropic media. *Journal of Geophysical Research* 66: 2953–2963.

Anderson DL and Bass JD (1984) Mineralogy and composition of the upper mantle. *Geophysical Research Letters* 11: 637–640.

Anderson DL and Dziewonski AM (1982) Upper mantle anisotropy: Evidence from free oscillations. *Geophysical Journal of the Royal Astronomical Society* 69: 383–404.

Anderson DL and Regan J (1983) Upper mantle anisotropy and the oceanic lithosphere. *Geophysical Research Letters* 10: 841–844.

Ansel V and Nataf H-C (1989) Anisotropy beneath 9 stations of the GEOSCOPE broadband network as deduced from shear wave splitting. *Geophysical Research Letters* 16: 409–412.

Babuska V and Cara M (1991) *Seismic Anisotropy in the Earth*. Dordrecht, The Netherlands: Kluwer Academic Press.

Babuska V, Montagner JP, Plomerova J, and Girardin N (1998) Age-dependent large-scale fabric of the mantle lithosphere as derived from surface-wave velocity anisotropy. *Pure and Applied Geophysics* 151: 257–280.

Backus GE (1962) Long-wave anisotropy produced by horizontal layering. *Journal of Geophysical Research* 67: 4427–4440.

Backus GE and Gilbert F (1967) Numerical applications of a formalism for geophysical inverse problems. *Geophysical Journal of the Royal Astronomical Society* 13: 247–276.

Backus GE and Gilbert F (1968) The resolving power of gross earth data. *Geophysical Journal of the Royal Astronomical Society* 16: 169–205.

Backus GE and Gilbert F (1970) Uniqueness in the inversion of inaccurate gross earth data. *Philosophical Transactions of the Royal Society of London, Series A: Mathematical, Physical and Engineering Sciences* 266: 123–192.

Barmin MP, Levshin AL, and Ritzwoller MH (2001) A fast and reliable method for surface wave tomography. *Pure and Applied Geophysics* 158: 1351–1375.

Barruol G and Fontaine FR (2013) Mantle flow beneath La Reunion hotspot track from SKS splitting. *Earth and Planetary Science Letters* 362: 108–121.

Bass J and Anderson DL (1984) Composition of the upper mantle: Geophysical tests of two petrological models. *Geophysical Research Letters* 11: 237–240.

Becker TW and Boschi L (2002) A comparison of tomographic and geodynamic mantle models. *Geochemistry, Geophysics, Geosystems* 3, 2001GC00168.

Becker TW, Ekström G, Boschi L, and Woodhouse JH (2007) Length scales, patterns and origin of azimuthal seismic anisotropy in the upper mantle as mapped by Rayleigh waves. *Geophysical Journal International* 171: 451–462.

Becker TW, Kellog JB, Ekström G, and O'Connell RJ (2003) Comparison of azimuthal anisotropy from surface waves and finite-strain from global mantle-circulation models. *Geophysical Journal International* 155: 696–714.

Becker TW, Lebedev S, and Long MD (2012) On the relationship between azimuthal anisotropy from shear wave splitting and surface wave tomography. *Journal of Geophysical Research* 117: B01306. http://dx.doi.org/10.1029/2011JB008705.

Beghein C and Trampert J (2003) Probability density functions for radial anisotropy: Implications for the upper 1200 km of the mantle. *Earth and Planetary Science Letters* 217: 151–162.

Bensen GD, Ritzwoller MH, Barmin MP, et al. (2007) Processing seismic ambient noise data to obtain reliable broad-band surface wave dispersion measurements. *Geophysical Journal International* 169: 1239–1260.

Bercovici D and Karato S-I (2003) Whole-mantle convection and the transition-zone water filter. *Nature* 425: 39–44.

Beucler E and Montagner J-P (2006) Computation of large anisotropic seismic heterogeneities. *Geophysical Journal International* 165: 447–468.

Beucler E, Stutzmann E, and Montagner J-P (2003) Measuring surface wave higher mode velocities by the Roller Coaster Algorithm. *Geophysical Journal International* 155: 289–307.

Blackman DK, Kendall JM, Dawson PR, Wenk HR, Boyce D, and Morgan JP (1996) Teleseismic imaging of subaxial flow at mid-ocean ridges: Traveltime effects of anisotropic mineral texture in the mantle. *Geophysical Journal International* 127: 415–426.

Boschi L and Ekström G (2002) New images of the Earth's upper mantle from measurements of surface wave phase velocity anomalies. *Journal of Geophysical Research* 107: B4. http://dx.doi.org/10.1029/2000JB000059.

Bozdağ E and Trampert J (2007) On crustal corrections in surface wave tomography. *Geophysical Journal International* 172: 1066–1082.

Busse FH (1983) Quadrupole convection in the lower mantle. *Geophysical Research Letters* 10: 285–288.

Bussy M, Montagner JP, and Romanowicz B (1993) Tomographic study of upper mantle attenuation in the Pacific Ocean. *Geophysical Research Letters* 20: 663–667.

Capdeville Y, Chaljub E, Vilotte J-P, and Montagner J-P (2003) Coupling spectral elements and modal solution: A new efficient tool for numerical wave propagation in laterally heterogeneous Earth models. *Geophysical Journal International* 152: 34–66.

Capdeville Y, Guillot L, and Marigo J-J (2010) 2-D non-periodic homogenization to upscale elastic media for P-SV waves. *Geophysical Journal International* 182: 903–922.

Capdeville Y, Gung Y, and Romanowicz B (2005) Towards global earth tomography using the spectral element method: A technique based on source stacking. *Geophysical Journal International* 162: 541–554.

Capdeville Y and Marigo J-J (2007) Second order homogenization of the elastic wave equation for non-periodic layered media. *Geophysical Journal International* 170: 823–838.

Cara M (1979) Lateral variations of S-velocity in the upper mantle from higher Rayleigh modes. *Geophysical Journal of the Royal Astronomical Society* 57: 649–670.

Chen M and Tromp J (2007) Theoretical and numerical investigations of global and regional seismic wave propagation in weakly anisotropic earth models. *Geophysical Journal International* 168: 1130–1152.

Chevrot S (2000) Multichannel analysis of shear wave splitting. *Journal of Geophysical Research* 105: 579–21590.

Chevrot S (2006) Finite-frequency vectorial tomography: A new method for high-resolution imaging of upper mantle anisotropy. *Geophysical Journal International* 165: 641–657.

Chevrot S, Favier N, and Komatitsch D (2004) Shear wave splitting in three-dimensional anisotropic media. *Geophysical Journal International* 159: 711–720.

Chevrot S, Vinnik L, and Montagner J-P (1999) Global-scale analysis of the mantle Pds phase. *Journal of Geophysical Research* 104: 20,203–20,219.

Christensen NI and Lundquist S (1982) Pyroxene orientation within the upper mantle. *Bulletin of the Geological Society of America* 93: 279–288.

Conrad CP, Behn MD, and Silver PG (2007) Global mantle flow and the development of seismic anisotropy: Differences between the oceanic and continental upper mantle. *Journal of Geophysical Research* 112, B07317.

Crampin S (1984) An introduction to wave propagation in anisotropic media. *Geophysical Journal of the Royal Astronomical Society* 76: 17–28.

Dahlen FA, Hung S-H, and Nolet G (2000) Fréchet kernels for finite-frequency traveltimes, I, Theory. *Geophysical Journal International* 141: 157–174.
Dalton CA and Ekström G (2006) Global models of surface wave attenuation. *Journal of Geophysical Research* 111: B05317. http://dx.doi.org/10.1029/2005JB0039.
Davaille A and Jaupart C (1994) Onset of thermal convection in fluids with temperature-dependent viscosity: Application to the oceanic mantle. *Journal of Geophysical Research* 99: 19853–19866.
Debayle E, Cara M, and Lévêque J-J (2001) Seismic evidence for a deeply rooted low velocity anomaly in the upper mantle beneath the northeastern Afro/Arabian continent. *Earth and Planetary Science Letters* 193: 369–382.
Debayle E and Kennett BLN (2000) Anisotropy in the Australasian upper mantle from Love and Rayleigh waveform inversion. *Earth and Planetary Science Letters* 184: 339–351.
Debayle E, Kennett BLN, and Priestley K (2005) Global azimuthal anisotropy and the unique plate-motion deformation of Australia. *Nature* 433: 509–512.
Debayle E and Lévêque J-J (1997) Upper mantle heterogeneities in the Indian Ocean from waveform inversion. *Geophysical Research Letters* 24: 245–248.
Debayle E and Ricard Y (2012) A Global Shear velocity model of the upper mantle from fundamental and higher Rayleigh mode measurements. *Journal of Geophysical Research* 117: B10308. http://dx.doi.org/10.1029/2012JB009288.
Debayle E and Sambridge M (2004) Inversion of massive surface wave datasets: Model construction and resolution assessment. *Journal of Geophysical Research* 109: B02316. http://dx.doi.org/10.1029/2003JB002652.
DeMets C, Gordon RG, Argus DF, and Stein S (1991) Current plate motions. *Geophysical Journal International* 101: 425–478.
Deschamps F, Lebedev S, Meier T, and Trampert J (2008) Azimuthal anisotropy of Rayleigh-wave phase velocities in the east-central United States. *Geophysical Journal International* 173: 827–843.
Dost B (1990) Upper mantle structure under western Europe from fundamental and higher mode surface waves using the NARS array. *Geophysical Journal of the Royal Astronomical Society* 100: 131–151.
Dziewonski AM (1984) Mapping the lower mantle: Determination of lateral heterogeneity in P velocity up to degree and order 6. *Journal of Geophysical Research* 89: 5929–5952.
Dziewonski AM and Anderson DL (1981) Preliminary reference Earth model. *Physics of the Earth and Planetary Interiors* 25: 297–356.
Dziewonski AM, Chou G, and Woodhouse JH (1981) Determination of earthquake source parameters from waveform modeling. *Journal of Geophysical Research* 86: 2825–2852.
Dziewonski AM and Woodhouse JH (1987) Global images of the Earth's interior. *Science* 236: 37–48.
Ekström G (2000) Mapping the lithosphere and asthenosphere with surface waves: Lateral structure and anisotropy. In: Richards MA, et al. (eds.) *AGU Monograph*, vol. 121, 239–256.
Ekström G (2006) A simple method of representing azimuthal anisotropy on a sphere. *Geophysical Journal International* 165: 668–671.
Ekström G (2011) A global model of Love and Rayleigh surface wave dispersion and anisotropy, 25–250 s. *Geophysical Journal International* 187: 1668–1686. http://dx.doi.org/10.1111/j.1365-246X.2011.05225.x.
Ekström G and Dziewonski AM (1998) The unique anisotropy of the Pacific upper mantle. *Nature* 394: 168–172.
Ekström G, Tromp J, and Larson EW (1997) Measurements and global models of surface wave propagation. *Journal of Geophysical Research* 102: 8137–8157.
Ferreira AMG and Woodhouse JH (2007) Source, path and receiver effects on seismic surface waves. *Geophysical Journal International* 168: 109–132.
Ferreira AMG, Woodhouse JH, Visser K, and Trampert J (2010) On the robustness of global radially anisotropic surface wave tomography. *Journal of Geophysical Research* 115(B4), B04313.
Fichtner A, Kennett BLN, Igel H, and Bunge HP (2009) Full seismic waveform tomography for upper-mantle structure in the Australasian region using adjoint methods. *Geophysical Journal International* 179: 1703–1725.
Fischer KM and Wiens DA (1996) The depth distribution of mantle anisotropy beneath the Tonga subduction zone. *Earth and Planetary Science Letters* 142: 253–260.
Fischer KM and Yang X (1994) Anisotropy in Kuril-Kamchatka subduction zone structure. *Geophysical Research Letters* 21: 5–8.
Fishwick S, Heintz M, Kennett BLN, Reading AM, and Yoshizawa K (2008) Steps in lithospheric thickness within eastern Australia, evidence from surface wave tomography. *Tectonics* 27, TC4009.
Fontaine F, Barruol G, Tommasi A, and Bokelmann GHR (2007) Upper-mantle flow beneath French Polynesia from shear wave splitting. *Geophysical Journal International* 170: 1262–1288.
Forsyth DW (1975) The early structural evolution and anisotropy of the oceanic upper mantle. *Geophysical Journal of the Royal Astronomical Society* 43: 103–162.
Forsyth DW, Scheirer DS, Webb SC, et al. (1998) Imaging the deep seismic structure beneath a mid-ocean ridge: The MELT experiment. *Science* 280: 1215–1218.
Fouch MJ and Fischer KM (1996) Mantle anisotropy beneath northwest Pacific subduction zones. *Journal of Geophysical Research* 101: 15987–16002.
Gaboret C, Forte A, and Montagner J-P (2003) The unique dynamics of the Pacific Hemisphere mantle and its signature on seismic anisotropy. *Earth and Planetary Science Letters* 208: 219–233.
Gaherty JB and Jordan TH (1995) Lehmann discontinuity as the base of the anisotropic layer beneath continents. *Science* 268: 1468–1471.
Gilbert F (1971) Excitation of normal modes of the Earth by earthquake sources. *Geophysical Journal of the Royal Astronomical Society* 22: 223–226.
Griot D-A, Montagner JP, and Tapponnier P (1998a) Surface wave phase velocity and azimuthal anisotropy in Central Asia. *Journal of Geophysical Research* 103: 21215–21232.
Griot D-A, Montagner JP, and Tapponnier P (1998b) Heterogeneous versus homogeneous strain in Central Asia. *Geophysical Research Letters* 25: 1447–1450.
Gu YJ, Lerner-Lam A, Dziewonski AM, and Ekström G (2005) Seismic evidence for deep anisotropy beneath the East Pacific Rise. *Earth and Planetary Science Letters* 232: 259–272.
Gung Y, Panning M, and Romanowicz B (2003) Global anisotropy and the thickness of continents. *Nature* 422: 707–711.
Hadiouche O, Jobert N, and Montagner JP (1989) Anisotropy of the African continent inferred from surface waves. *Physics of the Earth and Planetary Interiors* 58: 61–81.
Harmon H, Forsyth DW, Fischer KM, and Webb SC (2004) Variations in shear-wave splitting in young Pacific seafloor. *Geophysical Research Letters* 31(15), L15609.
Hess H (1964) Seismic anisotropy of the uppermost mantle under the oceans. *Nature* 203: 629–631.
Ho-Liu P, Montagner J-P, and Kanamori H (1989) Comparison of iterative back-projection inversion and generalized inversion without blocks: Case studies in Attenuation tomography. *Geophysical Journal* 97: 19–29.
Houser C, Masters G, Flanagan M, and Shearer P (2008) Determination and analysis of long-wavelength transition zone structure using SS precursors. *Geophysical Journal International* 174: 178–194.
Huang J, Zhong S, and van Hunen J (2003) Controls on sublithospheric small-scale convection. *Journal of Geophysical Research* 108(B8): 2405.
Isse T, Shiobara H, Montagner J-P, et al. (2010) Anisotropic structures of the upper mantle beneath the northern Philippine Sea region from Rayleigh and Love wave tomography. *Physics of the Earth and Planetary Interiors* 183: 33–43.
Jech J and Psenčík I (1989) First-order perturbation method for anisotropic media. *Geophysical Journal International* 99: 369–376.
Jordan TH (1975) The continental tectosphere. *Reviews of Geophysics* 13: 1–12.
Jordan TH (1978) Composition and development of the continental tectosphere. *Nature* 274: 544–548.
Jordan TH (1981) Continents as a chemical boundary layer. *Philosophical Transactions of the Royal Society of London, Series A: Mathematical, Physical and Engineering Sciences* 301: 359–373.
Jung HY and Karato S-I (2001) Water-induced fabric transitions in olivine. *Science* 293: 1460–1462.
Kaminski E and Ribe NM (2001) A kinematic model for recrystallization and texture development in olivine polycrystals. *Earth and Planetary Science Letters* 189: 253–267.
Karato S-I (1998) Seismic anisotropy in the deep mantle, boundary layers and geometry of mantle convection. *Pure and Applied Geophysics* 151: 565–587.
Kawakatsu H, Kumar P, Takei Y, et al. (2009) Seismic evidence for sharp lithosphere–asthenosphere boundaries of oceanic plates. *Science* 324: 499–502.
Komatitsch D and Tromp J (1999) Introduction of spectral element method for 3-D seismic wave propagation. *Geophysical Journal International* 139: 806–822.
Komatitsch D and Vilotte J-P (1998) The spectral element method: An effective tool to simulate the seismic response of 2D and 3D geological structures. *Bulletin of the Seismological Society of America* 88: 368–392.
Kumar P, Yuan X, Kumar MR, Kind R, Li X, and Chadha RK (2007) The rapid drift of the Indian tectonic plate. *Nature* 449: 894–897.
Kuo B-Y and Forsyth DW (1992) A search for split SKS waveforms in North Atlantic. *Geophysical Journal International* 92: 6421–6436.
Kustowski B, Dziewonski AM, and Ekström G (2008a) Nonlinear crustal corrections for normal-mode seismograms. *Bulletin of the Seismological Society of America* 97: 1756–1762.
Kustowski B, Ekström G, and Dziewonski AM (2008b) Anisotropic shear wave velocity of the Earth's mantle: A global model. *Journal of Geophysical Research* 113: B06306. http://dx.doi.org/10.1029/2007JB005169.

Larson EWF, Tromp J, and Ekstrom G (1998) Effects of slight anisotropy on surface waves. *Geophysical Journal International* 132: 654–666.
Laske G and Masters G (1998) Surface-wave polarization data and global anisotropic structure. *Geophysical Journal International* 132: 508–520.
Laske G, Masters G, and Reif C (2001) CRUST2.0-a new global crustal model at 2×2 degrees. http://mahi.ucsd.edu/Gabi/crust2.html.
Lawrence JF and Shearer PM (2006) A global study of transition zone thickness using receiver functions. *Journal of Geophysical Research* 111: B06307. http://dx.doi.org/10.129/2005JB003973.
Lebedev S and Nolet G (2003) Upper mantle beneath Southeast Asia from S velocity tomography. *Journal of Geophysical Research* 108(B1): 2048.
Lebedev S and van Der Hilst RD (2008) Global upper-mantle tomography with the automated multimode inversion of surface and S-wave forms. *Geophysical Journal International* 173: 505–518.
Lekic V, Panning M, and Romanowicz B (2010) A simple method for improving crustal corrections in waveform tomography. *Geophysical Journal International* 182: 265–278.
Lekic V and Romanowicz B (2011) Inferring upper-mantle structure by full waveform tomography with the spectral element method. *Geophysical Journal International* 185: 799–831.
Lévêque JJ, Cara M, and Rouland D (1991) Waveform inversion of surface-wave data: A new tool for systematic investigation of upper mantle structures. *Geophysical Journal International* 104: 565–581.
Li A, Forsyth DW, and Fischer KM (2003) Shear velocity structure and azimuthal anisotropy beneath eastern North America from Rayleigh wave inversion. *Journal of Geophysical Research* 108(B8): 2362.
Li X-D and Romanowicz B (1995) Comparison of global waveform inversions with and without considering cross branch coupling. *Geophysical Journal International* 121: 695–709.
Li XD and Romanowicz B (1996) Global mantle shear velocity model developed using nonlinear asymptotic coupling theory. *Journal of Geophysical Research*. 101: 22245–22273.
Li X-D and Tanimoto T (1993) Waveforms of long period body waves in a slightly aspherical earth. *Geophysical Journal International* 112: 92–112.
Lin F-C, Ritzwoller MH, Yang Y, Moschetti MP, and Fouch MJ (2010) Complex and variable crustal and uppermost mantle seismic anisotropy in the western United States. *Nature Geoscience* 4: 55–61.
Long MD and Becker TW (2010) Mantle dynamics and seismic anisotropy. *Earth and Planetary Science Letters* 297: 341–354.
Love AEH (1927) *A Treatise on the Theory of Elasticity*, 4th edn. Cambridge: Cambridge University Press, 643 pp.
Maggi A, Debayle E, Priestley K, and Barruol G (2006) Multimode surface waveform tomography of the Pacific Ocean: A closer look at the lithospheric cooling signature. *Geophysical Journal International* 166: 1384–1397.
Mainprice DG, Barruol G, and Ben Ismail W (2000) The seismic anisotropy of the Earth's. mantle: From single crystal to polycrystal. In: *Earth's Deep Interior: Mineral Physics and Tomography From the Atomic scale to the Global scale*, *Geophysical Monograph Series*, 117, p. 237.
Marone F and Romanowicz B (2007a) The depth distribution of azimuthal anisotropy in the continental upper mantle. *Nature* 447: 198–201.
Marone F and Romanowicz B (2007b) Non-linear crustal corrections in high-resolution regional waveform seismic tomography. *Geophysical Journal International* 170: 460–467.
Marquering H and Snieder R (1995) Surface-wave mode coupling for efficient forward modelling and inversion of body-wave phases. *Geophysical Journal International* 12: 186–208.
Masters G, Jordan TH, Silver PG, and Gilbert F (1982) Aspherical Earth structure from fundamental spheroidal-mode data. *Nature* 298: 609–613.
McKenzie D (1979) Finite deformation during fluid flow. *Geophysical Journal of the Royal Astronomical Society* 58: 687–715.
Minster JB and Jordan TH (1978) Present-day plate motions. *Journal of Geophysical Research* 83: 5331–5354.
Mochizuki E (1986) The free oscillations of an anisotropic and heterogeneous Earth. *Geophysical Journal of the Royal Astronomical Society* 86: 167–176.
Mocquet A and Romanowicz B (1989) Three-dimensional structure of the upper mantle beneath the Atlantic Ocean inferred from long-period Rayleigh waves. 2. Inversion. *Journal of Geophysical Research* 95: 6787–6798.
Montagner J-P (1986a) First results on the three dimensional structure of the Indian Ocean inferred from long period surface waves. *Geophysical Research Letters* 13: 315–318.
Montagner J-P (1986b) Regional three-dimensional structures using long-period surface waves. *Annals of Geophysics* 4(B3): 283–294.
Montagner J-P (1994) What can seismology tell us about mantle convection? *Reviews of Geophysics* 32(2): 115–137.
Montagner J-P (1998) Where can seismic anisotropy be detected in the Earth's mantle? In boundary layers. . .. *Pure and Applied Geophysics* 151: 223–256.
Montagner J-P (2002) Upper mantle low anisotropy channels below the Pacific plate. *Earth and Planetary Science Letters* 202: 263–274.
Montagner J-P and Anderson DL (1989a) Constraints on elastic combinations inferred from petrological models. *Physics of the Earth and Planetary Interiors* 54: 82–105.
Montagner J-P and Anderson DL (1989b) Constrained reference mantle model. *Physics of the Earth and Planetary Interiors* 58: 205–227.
Montagner J-P, Griot DA, and Lavé J (2000) How to relate body wave and surface wave anisotropies? *Journal of Geophysical Research* 105: 19015–19027.
Montagner J-P and Jobert N (1981) Investigation of upper mantle structure under young regions of the Southeast Pacific using long-period Rayleigh waves. *Earth and Planetary Science Letters* 27: 206–222.
Montagner J-P and Jobert N (1988) Vectorial tomography. II: Application to the Indian Ocean. *Geophysical Journal of the Royal Astronomical Society* 94: 309–344.
Montagner JP and Kennett BLN (1996) How to reconcile body-wave and normal-mode reference Earth models? *Geophysical Journal International* 125: 229–248.
Montagner J-P, Marty B, Stutzmann E, et al. (2007) Mantle upwellings and convective instabilities revealed by seismic tomography and helium isotope geochemistry beneath eastern Africa. *Geophysical Research Letters* 34: 21.
Montagner J-P and Nataf HC (1986) On the inversion of the azimuthal anisotropy of surface waves. *Journal of Geophysical Research* 91: 511–520.
Montagner J-P and Nataf H-C (1988) Vectorial tomography. I: Theory. *Geophysical Journal of the Royal Astronomical Society* 94: 295–307.
Montagner J-P and Romanowicz B (1993) Degrees 2, 4, 6 inferred from seismic tomography. *Geophysical Research Letters* 20: 631–634.
Montagner J-P, Romanowicz B, and Karczewski JF (1994) A first step towards an Oceanic Geophysical observatory. *EOS, Transaction American Geophysical Union* 75: 150–154.
Montagner J-P and Tanimoto T (1990) Global anisotropy in the upper mantle inferred from the regionalization of phase velocities. *Journal of Geophysical Research* 95: 4797–4819.
Montagner J-P and Tanimoto T (1991) Global upper mantle tomography of seismic velocities and anisotropies. *Journal of Geophysical Research* 96: 20,337–20,351.
Monteiller V and Chevrot S (2010) How to make robust splitting measurements for single-station analysis and three-dimensional imaging of seismic anisotropy. *Geophysical Journal International* 182: 311–328.
Montelli R, Nolet G, Dahlen FA, Masters G, Engdahl R, and Hung S (2004) Finite-frequency tomography reveals a variety of mantle plumes. *Science* 303: 338–343.
Mooney WD, Laske G, and Masters G (1998) CRUST5.1: A global crustal model at 5×5. *Journal of Geophysical Research* 96: 20337–20351.
Nataf H-C, Nakanishi I, and Anderson DL (1984) Anisotropy and shear velocity heterogeneities in the upper mantle. *Geophysical Research Letters* 11: 109–112.
Nataf H-C, Nakanishi I, and Anderson DL (1986) Measurement of mantle wave velocities and inversion for lateral heterogeneity and anisotropy, III. Inversion. *Journal of Geophysical Research* 91: 7261–7307.
Nataf H-C and Ricard Y (1996) 3-SMAC: An a priori tomographic model of the upper mantle based on geophysical modeling. *Physics of the Earth and Planetary Interiors* 95: 101–122.
Nettles M and Dziewonski AM (2008) Radially anisotropic shear velocity structure of the upper mantle globally and beneath North America. *Journal of Geophysical Research* 113, B02303.
Nicolas A, Boudier F, and Boullier AM (1973) Mechanisms of flow in naturally and experimentally deformed peridotites. *American Journal of Science* 273: 853–876.
Nishimura CE and Forsyth DW (1989) The anisotropic structure of the upper mantle in the Pacific. *Geophysical Journal* 96: 203–229.
Nolet G (1975) Higher Rayleigh modes in Western Europe. *Geophysical Research Letters* 2: 60–62.
Nolet G (1990) Partitioned waveform inversion and two-dimensional structure under the network of autonomously recording seismographs. *Journal of Geophysical Research* 95: 8499–8512.
Okal E and Jo B-G (1985) stacking investigation of higher-order mantle Rayleigh waves. *Geophysical Research Letters* 12: 421–424.
Panning M and Romanowicz B (2004) Inferences of flow at the base of Earth's mantle based on seismic anisotropy. *Science* 303: 351–353.
Panning M and Romanowicz B (2006) A three-dimensional radially anisotropic model of shear velocity in the whole mantle. *Geophysical Journal International* 167: 361–379.
Park J and Levin V (2002) Seismic anisotropy: Tracing plate dynamics in the mantle. *Science* 296: 5567.

Pettersen O and Maupin V (2002) Lithospheric anisotropy on the Kerguelen hotspot track inferred from Rayleigh wave polarisation anomalies. *Geophysical Journal International* 149: 225–246.

Plomerová J, Sileny J, and Babuska V (1996) Joint interpretation of upper-mantle anisotropy based on teleseismic P-travel time delay and inversion of shear-wave splitting parameters. *Physics of the Earth and Planetary Interiors* 95: 293–309.

Priestley K, Debayle E, McKenzie D, and Pilidou S (2006) Upper mantle structure of eastern Asia from multimode surface waveform tomography. *Journal of Geophysical Research* 111, B10304.

Priestley K, McKenzie D, Debayle E, and Pilidou S (2008) The African upper mantle and its relationship to tectonics and surface geology. *Geophysical Journal International* 175: 1108–1126.

Ribe NM (1989) Seismic anisotropy and mantle flow. *Journal of Geophysical Research* 94: 4213–4223.

Ricard Y, Nataf HC, and Montagner J-P (1996) The 3-SMac model: Confrontation with seismic data. *Journal of Geophysical Research* 101: 8457–8472.

Richter FM and Parsons B (1975) On the interaction of two scales of convection in the mantle. *Journal of Geophysical Research* 80: 2529–2541.

Ringwood AE (1975) *Composition and Petrology of the Earth's Mantle*. New York: McGraw-Hill, 618 pp.

Ritsema J, Deuss A, van Heijst HJ, and Woodhouse JH (2011) S40RTS: A degree-40 shear-velocity model for the mantle from new Rayleigh wave dispersion, teleseismic traveltime and normal-mode splitting function measurements. *Geophysical Journal International* 184: 1223–1236.

Ritsema J, van Heijst HJ, and Woodhouse JH (2004) Global transition zone tomography. *Journal of Geophysical Research* 109: B02302. http://dx.doi.org/10.1029/2003JB002610.

Ritzwoller MH, Shapiro NM, Barmin MP, and Levshin AL (2002) Global surface wave tomography. *Journal of Geophysical Research* 107(B12): 2335. http://dx.doi.org/10.1029/2002JB001777.

Ritzwoller MH, Shapiro NM, and Zhong S-J (2004) Cooling history of the Pacific lithosphere. *Earth and Planetary Science Letters* 226: 69–84.

Romanowicz B (1990) The upper mantle degree two: Constraints and inferences from global mantle wave attenuation measurements. *Journal of Geophysical Research* 95: 11051–11071.

Romanowicz B (1995) A global tomographic model of shear attenuation in the upper mantle. *Journal of Geophysical Research* 100: 12375–12394.

Romanowicz B (2002) Inversion of surface waves: A review. In: Lee WHK (ed.) *Handbook of Earthquake and Engineering Seismology*, pp. 141–173. Palo Alto, CA: IASPEI, chapter 11.

Romanowicz B (2003) Global mantle tomography: Progress status in the past 10 years. *Annual Review of Earth and Planetary Science* 31: 303–328.

Romanowicz B (2009) The thickness of tectonic plates. *Science* 324: 474–476.

Romanowicz B, Cara M, Fels J-F, and Rouland D (1984) GEOSCOPE: A French initiative in long period, three component, global seismic networks. *EOS, Transaction American Geophysical Union* 65: 753–754.

Romanowicz B and Dziewonski AM (1986) Towards a Federation of broadband seismic networks. *EOS, Transaction American Geophysical Union* 67: 541–542.

Romanowicz B and Snieder R (1988) A new formalism for the effect of lateral heterogeneity on normal modes and surface waves, II: General anisotropic perturbations. *Geophysical Journal of the Royal Astronomical Society* 93: 91–99.

Romanowicz B and Yuan H (2012) On the interpretation of SKS splitting measurements in the presence of several layers of anisotropy. *Geophysical Journal International* 188: 1129–1140.

Roult G, Romanowicz B, and Montagner JP (1990) 3D upper mantle shear velocity and attenuation from fundamental mode free oscillation data. *Geophysical Journal International* 101: 61–80.

Roult G, Rouland D, and Montagner JP (1994) Antarctica II: Upper mantle structure from velocity and anisotropy. *Physics of the Earth and Planetary Interiors* 84: 33–57.

Rumpker G and Silver PG (1998) Apparent shear-wave splitting parameters in the presence of vertically varying anisotropy. *Geophysical Journal International* 135: 790–800.

Russo RM and Okal EA (1999) Shear wave splitting and upper mantle deformation in French Polynesia: Evidence for small-scale heterogeneity related to the society hotspot. *Journal of Geophysical Research* 103: 15089–15107.

Rychert CA and Shearer PM (2009) A global view of the lithosphere–asthenosphere boundary. *Science* 324: 495–498.

Sabra KG, Gerstoft P, Roux P, Kuperman WA, and Fehler MC (2005) Surface wave tomography from microseisms in Southern California. *Geophysical Research Letters* 32(14), L14311.

Savage MK (1999) Seismic anisotropy and mantle deformation: What have we learned from shear wave splitting? *Reviews of Geophysics* 37: 65–106.

Schlue JW and Knopoff L (1977) Shear–wave polarization anisotropy in the Pacific Ocean. *Geophysical Journal of the Royal Astronomical Society* 49: 145–165.

Sebai A, Stutzmann E, and Montagner J-P (2006) Anisotropic structure of the African upper mantle structure from Rayleigh and Love wave tomography. *Physics of the Earth and Planetary Interiors* 155: 48–62.

Shapiro NM, Campillo M, Stehly L, and Ritzwoller MH (2005) High-resolution surface-wave tomography from ambient seismic noise. *Science* 307, 1615–1618.

Shapiro NM and Ritzwoller MH (2002) Monte-Carlo inversion for a global shear-velocity model of the crust and upper mantle. *Geophysical Journal International* 151: 88–105.

Shearer PM (1991) Constraints on upper mantle discontinuities from observations of long-period reflected and converted waves. *Journal of Geophysical Research* 96: 18147–18182.

Sicilia D, Montagner J-P, Cara M, et al. (2008) Upper mantle structure of shear-wave velocities and stratification of anisotropy in the afar hotspot region. *Tectonophysics* 462: 164–177. http://dx.doi.org/10.1016/j.tecto.2008.02.016.

Sieminski A, Lévêque J-J, and Debayle E (2004) Can finite-frequency effects be accounted for in ray theory surface wave tomography. *Geophysical Research Letters* 31: L24614. http://dx.doi.org/10.129/2004GL02142.

Sigloch K, McQuarrie N, and Nolet G (2008) Two-stage subduction history under North America inferred from multiple-frequency tomography. *Nature Geoscience* 1: 458–462.

Silveira G and Stutzmann E (2001) Anisotropic tomography of the Atlantic Ocean. *Physics of the Earth and Planetary Interiors* 132: 237–248.

Silveira G, Stutzmann E, Montagner J-P, and Mendes-Victor L (1998) Anisotropic tomography of the Atlantic Ocean from Rayleigh surface waves. *Physics of the Earth and Planetary Interiors* 106: 259–275.

Silver PG (1996) Seismic anisotropy beneath the continents: Probing the depths of geology. *Annual Review of Earth and Planetary Science* 24: 385–432.

Silver PG and Chan WW (1991) Shear wave splitting and subcontinental mantle deformation. *Journal of Geophysical Research* 96: 16429–16454.

Silver PG and Long MD (2011) The non-commutivity of shear wave splitting operators at low frequencies and implications for anisotropy tomography. *Geophysical Journal International* 18: 1415–1427.

Silver PG and Savage M (1994) The interpretation of shear-wave splitting parameters in the presence of two anisotropic layers. *Geophysical Journal International* 119: 949–963.

Simmons NA, Forte AM, and Grand S (2009) Joint seismic, geodynamic and mineral physical constraints on three-dimensional mantle heterogeneity: Implications for the relative importance of thermal versus compositional heterogeneity. *Geophysical Journal International* 177: 1284–1304.

Simons FJ, van der Hilst R, Montagner JP, and Zielhuis A (2002) Multimode Rayleigh wave inversion for shear wave speed heterogeneity and azimuthal anisotropy of the Australian upper mantle. *Geophysical Journal International* 151: 738–754.

Smith SW (1986) IRIS; a program for the next decade. *EOS, Transaction American Geophysical Union* 67: 213–219.

Smith ML and Dahlen FA (1973) The azimuthal dependence of Love and Rayleigh wave propagation in a slightly anisotropic medium. *Journal of Geophysical Research* 78: 3321–3333.

Smith ML and Dahlen FA (1975) Correction to 'The azimuthal dependence of Love and Rayleigh wave propagation in a slightly anisotropic medium'. *Journal of Geophysical Research* 80: 1923.

Smith D, Ritzwoller MH, and Shapiro NM (2004) Stratification of anisotropy in the Pacific upper mantle. *Journal of Geophysical Research* 109: B11309. http://dx.doi.org/10.10209/2004JB03200.

Snieder R (1988) Large-scale waveform inversions of surface waves for lateral heterogeneity, 1. Theory and numerical examples. *Journal of Geophysical Research* 93: 12055–12066.

Snieder R, Gret A, Douma H, and Scales J (2002) Coda wave interferometry for estimating non-linear behavior in seismic velocity. *Science* 295: 2253–2255.

Solomatov VS and Moresi LN (2000) Scaling of time-dependent stagnant lid convection: Application to small-scale convection on Earth and other terrestrial planets. *Journal of Geophysical Research* 105: 21795–21817.

Spetzler J, Trampert J, and Snieder R (2002) The effect of scattering in surface wave tomography. *Geophysical Journal International* 149: 755–767.

Stutzmann E and Montagner JP (1994) Tomography of the transition zone from the inversion of higher-mode surface waves. *Physics of the Earth and Planetary Interiors* 86: 99–116.

Su W-J, Woodward RL, and Dziewonski AM (1984) Degree 12 model of shear velocity heterogeneity in the mantle. *Journal of Geophysical Research* 99: 6945–6980.

Takeuchi H and Saito M (1972) Seismic surface waves. In: Bolt BA (ed.) *Methods in Computational Physics*, 11, pp. 217–295. New York: Academic Press.

Tanimoto T (1986) Free oscillations in a slightly anisotropic Earth. *Geophysical Journal of the Royal Astronomical Society* 87: 493–517.
Tanimoto T (1990) Long-wavelength S-wave velocity structure throughout the mantle. *Geophysical Journal International* 100: 327–336.
Tanimoto T and Anderson DL (1985) Lateral heterogeneity and azimuthal anisotropy of the upper mantle: Love and Rayleigh waves 100–250 s. *Journal of Geophysical Research* 90: 1842–1858.
Tape C, Liu Q, Maggi A, and Tromp J (2009) Adjoint tomography of the southern California crust. *Science* 325(5943): 988–992.
Tarantola A (1984) Inversion of seismic reflection data in the acoustic approximation. *Geophysics* 49: 1259–1266.
Tarantola A and Valette B (1982) Generalized nonlinear inverse problems solved using least squares criterion. *Reviews of Geophysics and Space Physics* 20: 219–232.
Tauzin B, Debayle E, and Wittlinger G (2008) The mantle transition zone as seen by global Pds phases: No clear evidence for a thin transition zone beneath hotspots. *Journal of Geophysical Research* 113(B8): 1–17.
Tommasi A, Mainprice D, Canova G, and Chastel Y (2000) Viscoplastic self-consistent and equilibrium-based modeling of olivine preferred orientations. Implications for the upper mantle anisotropy. *Journal of Geophysical Research* 105: 7893–7908.
Tommasi A, Vauchez A, and Russo R (1996) Seismic anisotropy in ocean basins: Resistive drag of the sublithospheric mantle? *Geophysical Research Letters* 23: 2991–2994.
Trampert J and Snieder R (1996) Model estimations biased by truncated expansions: Possible artifacts in seismic tomography. *Science* 271: 1257–1260.
Trampert J and van Heijst HJ (2002) Global azimuthal anisotropy in the transition zone. *Science* 296: 1297–1299.
Trampert J and Woodhouse JH (2003) Global anisotropic phase velocity for fundamental mode surface waves between 40 and 150 s. *Geophysical Journal International* 154: 154–165.
Tromp J, Tape C, and Liu Q (2005) Seismic tomography, adjoint methods, time reversal and banana-doughnuts kernels. *Geophysical Journal International* 160: 195–216.
Van Heijst HJ and Woodhouse JH (1997) Measuring surface-wave overtone phase velocities using a mode-branch stripping technique. *Geophysical Journal International* 131: 209–230.
Villaseñor A, Ritzwoller MH, Levshin AL, et al. (2001) Shear velocity structure of Central Eurasia from inversion of surface wave velocities. *Physics of the Earth and Planetary Interiors* 123: 169–184.
Vinnik LP, Chevrot S, and Montagner J-P (1998) Seismic evidence of flow at the base of the upper mantle. *Geophysical Research Letters* 25: 1995–1998.
Vinnik L, Makayeva LI, Milev A, and Usenko AY (1992) Global patterns of azimuthal anisotropy and deformations in the continental mantle. *Geophysical Journal International* 111: 433–447.
Vinnik L and Montagner J-P (1996) Shear wave splitting in the mantle from Ps phases. *Geophysical Research Letters* 23: 2449–2452.
Vinnik L, Montagner JP, Girardin N, Dricker I, and Saul J (2003) Shear wave splitting at H_2O: A comment. *Geophysical Research Letters* 30(13): 1675. http://dx.doi.org/10.1029/2002GL015751.
Visser K, Trampert J, and Kennett BLN (2008) Global anisotropic phase velocity maps for higher mode Love and Rayleigh waves. *Geophysical Journal International* 172: 1016–1032. http://dx.doi.org/10.1111/j.1365-246X.2007.03685.x.
Walker KT, Bokelmann GH, and Klemperer SL (2001) Shear-wave splitting to test mantle deformation models around Hawaii. *Geophysical Research Letters* 28: 4319–4322.
Wang Z and Dahlen FA (1995) Spherical-spline parameterization of three-dimensional earth models. *Geophysical Research Letters* 22: 3099–3102.
Wolfe CJ and Silver PG (1998) Seismic anisotropy of oceanic upper mantle. *Journal of Geophysical Research* 103: 749–771.
Wolfe CJ and Solomon SC (1998) Shear-wave splitting and implications for mantle flow beneath the Melt region of the East Pacific Rise. *Science* 280: 1230–1232.
Woodhouse JH and Dahlen FA (1978) The effect of a general aspherical perturbation on the free oscillations of the Earth. *Geophysical Journal of the Royal Astronomical Society* 53: 335–354.
Woodhouse JH and Dziewonski AM (1984) Mapping the upper mantle: Three dimensional modelling of Earth structure by inversion of seismic waveforms. *Journal of Geophysical Research* 89: 5953–5986.
Woodhouse JH and Girnius TP (1982) Surface waves and free oscillations in a regionalized Earth model. *Geophysical Journal of the Royal Astronomical Society* 68: 653–673.
Wookey J, Kendall JM, and Barruol G (2002) Mid-mantle deformation inferred from seismic anisotropy. *Nature* 415: 777–780.
Wüstefeld A, Bokelmann G, Barruol G, and Montagner JP (2009) Identifying global seismic anisotropy patterns by correlating shear-wave splitting and surface-wave data. *Physics of the Earth and Planetary Interiors* 176: 198–212.
Yao H, van der Hilst RD, and Montagner J-P (2010) Heterogeneity and anisotropy of the lithosphere of SE Tibet from surface wave array tomography. *Journal of Geophysical Research* 115, B12307.
Yomogida K (1992) Fresnel-zone inversion for lateral heterogeneities in the Earth. *Pure and Applied Geophysics* 138: 391–406.
Yoshizawa K and Kennett BHN (2002) Determination of the influence zone for surface wave paths. *Geophysical Journal International* 149: 441–454.
Yoshizawa K and Kennett BHN (2004) Multimode surface wave tomography for the Australian region using a three-stage approach incorporating finite frequency effects. *Journal of Geophysical Research* 109: B02310. http://dx.doi.org/10.1029/2002JB002254.
Yu Y and Park J (1993) Anisotropy and coupled long-period surface waves. *Geophysical Journal International* 114: 473–489.
Yuan H and Romanowicz B (2010) Lithospheric layering in the North American craton. *Nature* 466: 1063–1068. http://dx.doi.org/10.1038/nature09332.
Yuan H, Romanowicz B, Fischer K, and Abt D (2011) 3-D shear wave radially and azimuthally anisotropic velocity model of the North American upper mantle. *Geophysical Journal International* 184: 1237–1260.
Zhang H and Thurber CH (2005) Adaptive mesh seismic tomography based on tetrahedral and Voronoi diagrams: Application to Parkfield. *Journal of Geophysical Research* 110: B04303. http://dx.doi.org/10.129/2004JB003186.
Zhou Y, Dahlen FA, and Nolet G (2004) Three-dimensional sensitivity kernels for surface wave observables. *Geophysical Journal International* 158: 142–168.
Zhou Y, Nolet G, Dahlen FA, and Laske G (2006) Global upper-mantle structure from finite-frequency surface-wave tomography. *Journal of Geophysical Research* 111: B04304. http://dx.doi.org/10.1029/2005JB003677.
Zhu H, Bozdağ E, Peter D, and Tromp J (2012) Structure of the European upper mantle revealed by adjoint tomography. *Nature Geoscience* 5: 493–498. http://dx.doi.org/10.1038/NGEO01501.

Relevant Websites

http://geodynamics.usc.edu/becker/tdata.html – Thorsten Becker, U.S.C., Los Angeles.
http://igppweb.ucsd.edu/gabi/rem.dir/rem.home.html – Gabi Laske – UCSD, San Diego.
http://seismo.berkeley.edu – Berkeley Seismological Laboratory.

This page intentionally left blank

1.20 Deep Earth Structure - Subduction Zone Structure in the Mantle Transition Zone

Y Fukao and M Obayashi, Japan Agency for Marine-Earth Science and Technology, Kanagawa, Japan

© 2015 Elsevier B.V. All rights reserved.

1.20.1	**Introduction**	641
1.20.2	**Global View of Subduction Zone Structure in the Transition Zone**	642
1.20.2.1	Seismic Velocity Anomalies	642
1.20.2.2	Boundary Topography	643
1.20.2.3	Seismic Attenuations	644
1.20.2.4	Seismic Anisotropy	645
1.20.3	**Slab Signatures Above and Below the 660-km Discontinuity**	645
1.20.3.1	Slab Signature in the Transition Zone	645
1.20.3.2	Slab Signature in the Uppermost Lower Mantle	647
1.20.3.3	Juxtaposed Slab Images in the Transition Zone and the Uppermost Lower Mantle	649
1.20.4	**Seismic Images of Slab Descent Through the Transition Zone**	649
1.20.4.1	Images of Transitional State from Slab Stagnation to Penetration	649
1.20.4.2	Signature of Subducted Crust Materials in the Penetrating Slab	650
1.20.4.3	Images of Slab Descent to the Deep Lower Mantle	651
1.20.5	**Summary**	651
Acknowledgments		652
References		652

1.20.1 Introduction

During subduction, lithospheric plates are removed from Earth's surface by descent into the mantle from deep-sea trenches. The subducted part of the plate is called the slab. The slab is colder, and hence heavier, than the surrounding mantle, so the resultant negative buoyancy force is a major factor in driving plate motions. Subduction zones are deeper and less mobile than seafloor spreading centers, where oceanic plates are born. Slab descent in subduction zones along the Circum-Pacific represents a deep sheet-like downwelling of mantle convection, whereas magma ascent in spreading centers along midoceanic ridges is a shallow phenomenon, not corresponding directly to large-scale mantle upwelling. The seismic structure of the seafloor spreading centers has been discussed extensively by Dunn and Forsyth (2007).

A subducting slab is a downward continuation of the surface oceanic plate, marked seismologically by high P-wave and S-wave velocities and low P-wave and S-wave attenuations and geodynamically by low temperature, high density, and negative buoyancy relative to the surrounding mantle. The most reliable indicator of the subducting slab is the positive anomaly of seismic velocity. **Figure 1** shows the depth profiles of the areal proportion of more than x% higher-than-normal velocities for several global P-wave and S-wave tomographic models, where $x = 0.5,\ 0.6, \ldots,\ 1.5$. The P-wave and S-wave models HMSL were obtained by measuring the travel times of long-period body wave phases by cross-correlation techniques. The S-wave model S362ANI was obtained by combining a large data set of surface-wave phase-velocity anomalies, long-period waveforms, and the body-wave travel times; S40RTS by measuring travel times of body waves, phase velocities of surface waves and splitting functions of normal modes from broadband waveform data; and TX2011 by measuring arrival times of multibounce shear waves, core-reflected shear waves, and SKS and SKKS waves (see Figure 4 of Dziewonski and Romanowicz (2007) for the nomenclature). The P-wave model MIT-P08 is based on reported and self-picked arrival times and waveform-based differential travel times for which the finite frequency effect (Kárason and van der Hilst, 2001) is taken into account; GAP_P4, on applying finite frequency kernels (Dahlen et al., 2000; Mercerat and Nolet, 2013) to all the datasets of reported and self-picked travel times and waveform-based differential travel times, including those from ocean-bottom seismometers; and LLNL-G3Dv3, on applying a global multiple event locator to reprocess the reported arrival times. See Thurber and Ritsema (2007) for the review of seismic tomography.

In **Figure 1**, all the model profiles exhibit extrema in the three depth ranges, the uppermost mantle, the transition zone, and the lowermost mantle, which are diagnostic of lithospheric plates on the surface, stagnant slabs in the transition zone (Fukao et al., 1992; van der Hilst et al., 1991), and slab graveyards at the bottom of the mantle (Richards and Engebretson, 1992), respectively. Indeed, the most outstanding feature of the transition zone in any of the recent tomographic models (see Figure 8 of Thurber and Ritsema (2007); see also **Figure 2**) is the extensive horizontal spread of fast anomalies beneath subduction zones, which has been interpreted as a signature of stagnant slabs.

We also note in **Figure 1** that several models, for example, TX2011 and LLNL-G3Dv3, show a secondary peak in the uppermost lower mantle, just below the 660-km discontinuity. Although other models do not exhibit such a clear peak, they still show a richness of high-velocity anomaly signals in the uppermost lower mantle. This richness is an indication of

 http://dx.doi.org/10.1016/B978-0-444-53802-4.00025-7

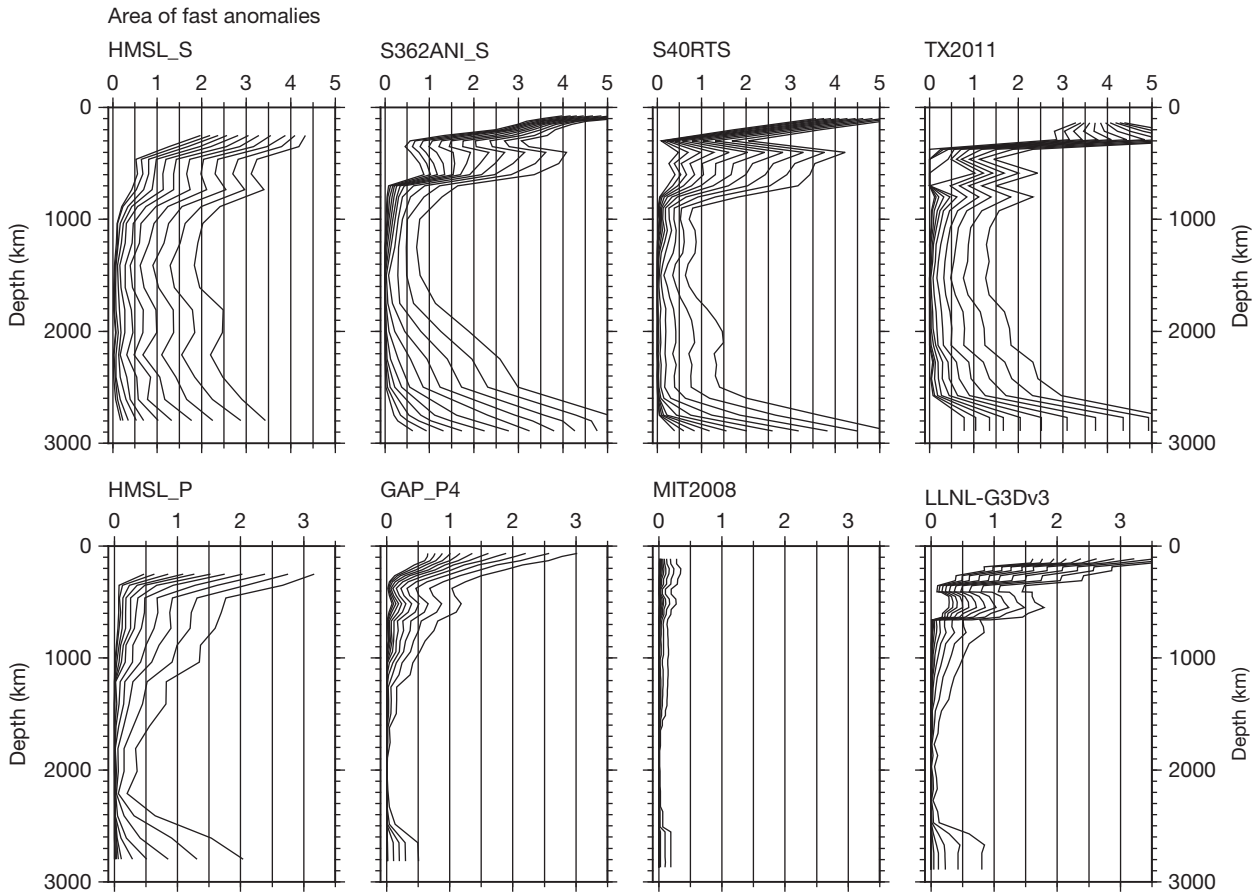

Figure 1 Depth profiles of the areal proportion of high-velocity anomalies in global tomographic models. The area at each depth is normalized so that its maximum is 4π. The 16 profiles from right to left in each diagram represent the areal proportions of velocity anomalies 0.5%, 0.6%,. . ., 1.5% higher than normal. The S-wave velocity models in the upper column are HMSL (Houser et al., 2008a), S362ANI (Kustowski et al., 2008), S40RTS (Ritsema et al., 2011), and TX2011 (Grand, 2002). The P-wave velocity models in the lower column are HMSL (Houser et al., 2008a), GAP_P4 (Obayashi et al., 2013), MIT-P08 (Li et al., 2008), and LLNL-G3Dv3 (Simmons et al., 2012). Note a difference in scale between the S-wave and P-wave velocity models.

the slabs that penetrate the 660-km discontinuity and extend subhorizontally in the uppermost lower mantle. The mantle transition zone and the uppermost lower mantle are reviewed here as two distinct reservoirs, one for downgoing slabs above the 660-km discontinuity and the other for penetrating slabs below the discontinuity. Both reservoirs are not complete in the sense that slabs eventually descend well into the deep lower mantle (Grand et al., 1997; van der Hilst et al., 1997). We hope this chapter will be useful for discussing how significant the transition zone and the uppermost lower mantle are in the whole system of mantle convection. Wen and Anderson (1995, 1997) emphasized the unique role of the uppermost lower mantle in the system of mantle convection involving surface plate motions. Another intriguing feature to be noted in **Figure 1**, although not discussed in this chapter, is the depth of the least horizontal spread of high-velocity anomalies, which is systematically different between the P-wave and S-wave velocity perturbations, approximately 1500 km for all the four S-wave velocity models but approximately 2000 km for all the four P-wave velocity models.

1.20.2 Global View of Subduction Zone Structure in the Transition Zone

1.20.2.1 Seismic Velocity Anomalies

Masters et al. (1982) were the first to show that the structural heterogeneity in the transition zone is, to the first approximation, dominated by a degree-2 pattern with high-velocity anomalies beneath the Circum-Pacific subduction zones (see Figure 9 of Dziewonski and Romanowicz, 2007). **Figure 2** shows the velocity anomaly patterns at depths of ~500 km in the mantle transition zone for the eight models corresponding to those in **Figure 1** (see also Figure 3 of Panning and Romanowicz, 2006 for S-wave velocity anomalies and supplementary Figure 29(a) of Meer et al., 2009 for P-wave velocity anomalies). The most pronounced feature at these depths, both in the S-wave and in the P-wave velocity models, is the high-velocity signals in subduction zones, the strongest in the western Pacific (the northwestern Pacific in particular) and the next strongest in South America (southern South America in particular). The Pacific plate, the largest oceanic

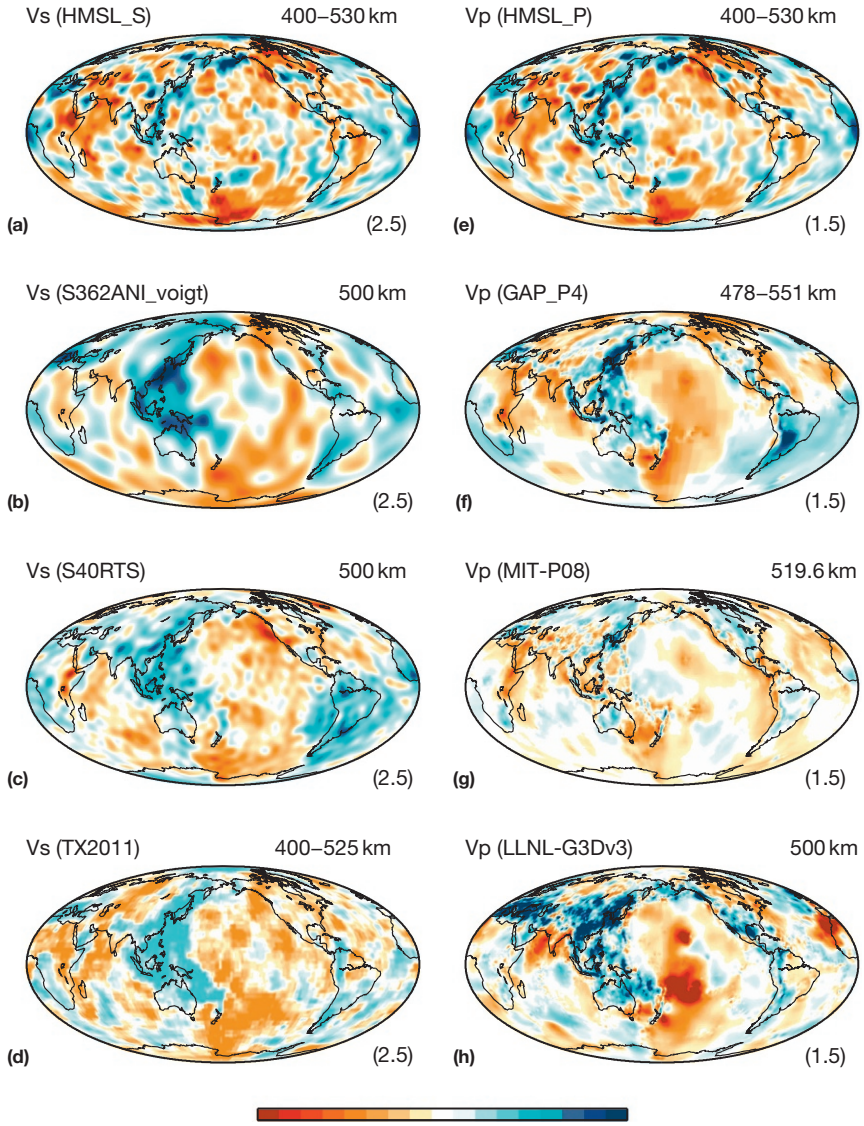

Figure 2 Depth slices in the transition zone for the four S-wave and four P-wave velocity models corresponding to those in **Figure 1**. The velocities are perturbations from the average value at the corresponding depth. The scale is ±2.5% for the S-wave velocity models and ±1.5% for the P-wave velocity models.

plate, has continued to subduct beneath the western Pacific since the late Cretaceous Period, although its spreading direction changed greatly in the early Eocene Epoch (Lithgow-Bertelloni and Richard, 1998). The Indo-Australian plate, the second largest oceanic plate, has also continued to subduct beneath the western Pacific since the fusion of the Indian plate and Australian plate in the early Eocene (Lithgow-Bertelloni and Richard, 1998). The Nazca plate and the preceding Farallon plate have continued to rapidly subduct beneath South America since the early Eocene, without intermission by, for example, ridge subduction (Lithgow-Bertelloni and Richard, 1998). Clearly, the high-velocity anomalies beneath the western Pacific and South America reflect a long history of subductions of oceanic plates. Besides the Circum-Pacific subduction zones, the Mediterranean subduction zone is marked by the anomalously fast transition zone in all eight models. This high-velocity signature reflects the long history of subduction of the Mediterranean lithosphere against the Eurasian plate since the late Cretaceous Period, including slow subduction in the first 20–30 My (Faccenna et al., 2001).

1.20.2.2 Boundary Topography

The mantle discontinuities at 410- and 660-km depths define the top and bottom of the mantle transition zone, across each of which P-wave and S-wave velocities and density increase sharply. These discontinuities are understood as the phase transition boundaries of major mantle minerals (see Stixrude and Jeanloz, 2007) that can be topographically distorted by a cold subducting slab. This subject has been reviewed by Kind and Li (2007). More recent studies include Schmerr and Thomas (2011) for Kurile, Schmerr and Garnero (2007) for South America, and Heit et al. (2010) and Gu et al. (2012) for the northwestern Pacific. Kind and Li (2007) summarized, for example, their review of the

Japan–Izu–Bonin subduction zones as follows. "The overwhelming majority of observations seem to indicate that the 660 is depressed at the Japanese subduction zone. The amount of the depression is ~50 km. The 410 remains uncertain, but there is probably no clear elevation." Kind and Li (2007) further added, "Izu-Bonin seems, beside Japan, to be a good example of a depressed 660 at a slab. The uplift of the 410 seems less clear." The depression on the order of ~50 km is likely to be the direct response of the 660-km discontinuity to the incoming slab from above. If the incoming slab bends to horizontal upon hitting the discontinuity to extend horizontally through the transition zone, we would expect a horizontal spread of the discontinuity depression, although the amount of depression may be smaller in the horizontally spreading part than in the directly downgoing part of the slab (e.g., Fukao et al., 2009).

The large lateral extent of the 660-km discontinuity depression was first observed by Shearer and Masters (1992) and Shearer (1993). **Figure 3** shows the three recent global topography maps for the 660-km discontinuity (see also Figure 6 of Kind and Li, 2007). The model of Houser et al. (2008b) (**Figure 3(a)**) is based on SS–SdS differential travel time measurements corrected for lateral heterogeneities of crustal thickness and upper mantle shear velocity, where SdS is a precursory reflection at depth d to the SS reflection at the surface. The model of Kustowski et al. (2008) (**Figure 3(b)**) is a part of the whole-mantle shear velocity model S362ANI (**Figure 2**) and was derived from the dataset that included SS-SdS differential times. The model of Meier et al. (2009) is not based on such depth phases as SdS, but relies on the sensitivities of overtone modes of Love waves and Rayleigh waves to the mantle discontinuity topography (**Figure 3(c)**). In these three models, the Circum-Pacific subduction zones are commonly characterized by long-wavelength depression of the 660-km discontinuity in qualitative agreement with the high-velocity anomaly pattern in the transition zone (**Figure 2**). Although the long-wavelength features are generally consistent among the three models, significant discrepancies are present as well, demonstrating the level of our understanding of the topography map of the 660-km discontinuity. Our understanding of the 410-km topography map is even less.

The reason for the less clear topographic feature of the 410-km discontinuity than the 660-km discontinuity may in part be the kinematically retarded olivine–wadsleyite transition across this discontinuity, which is expected to cause a narrow, wedge-like deepening of the phase boundary inside the cold slab (Kirby et al., 1996; Sung and Burns, 1976). A limited number of observational studies supporting the possible deepening of the phase boundary include travel time analyses by Iidaka and Suetsugu (1992) and Jiang et al. (2008) and a receiver function analysis by Kawakatsu and Yoshioka (2011) for the Honshu slab, a P-wave coda analysis by Kaneshima et al. (2007) for the Mariana slab, and a travel time analysis by Koper et al. (1998) for the Tonga slab. We are not yet at a stage where we can answer clearly whether the 410-km boundary inside the slab is elevated as expected for the phase transition at equilibrium or depressed as expected for the phase transition in a metastable state of olivine. The situation is quite different for the 660-km discontinuity, across which the phase transition from ringwoodite to ferromagnesian perovskite plus oxide should occur. In this case, the cold slab depresses the phase boundary at equilibrium, which may be further deepened by the retarded phase transition of ringwoodite in the cold environment (Fukao and Obayashi, 2013).

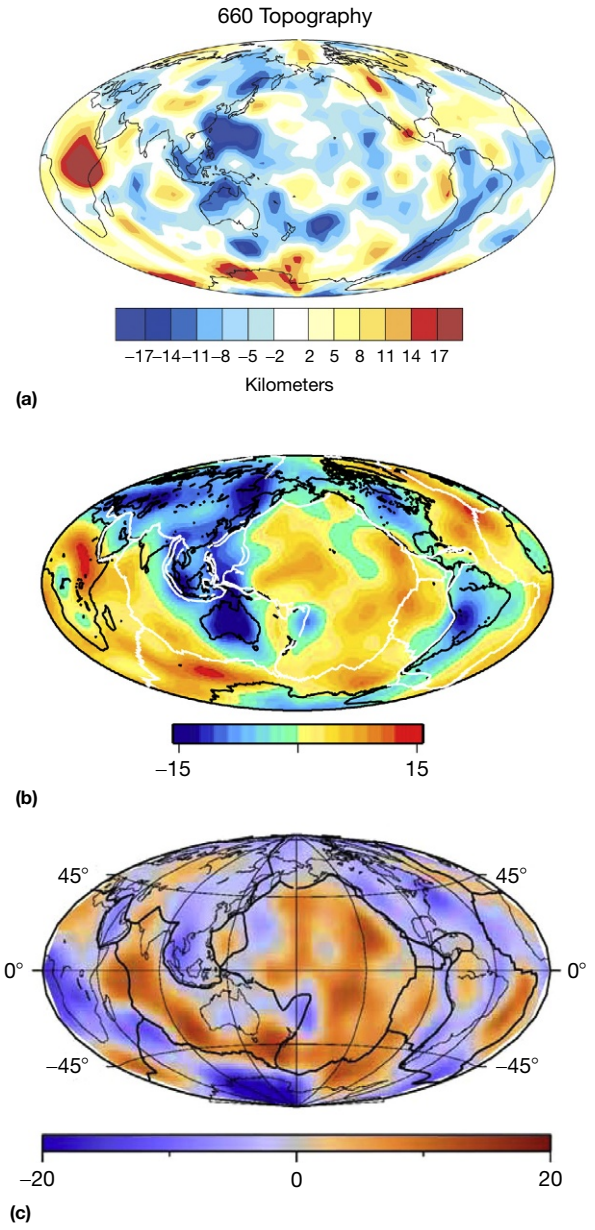

Figure 3 Deviations from the average 660-km discontinuity depth for models (a) Houser C, Masters G, Flanagan M and Shearer P (2008b) Determination and analysis of long-wavelength transition zone structure using SS precursors. *Geophysical Journal International* 174: 178–194, (b) Kustowski B, Ekström G and Dziewonski AM (2008) Anisotropic shear–wave velocity structure of the Earth's mantle: A global model. *Journal of Geophysical Research* 113 (http://dx.doi.org/10.1029/2007JB005169), and (c) Meier U, Trampert J and Curtis A (2009) Global variations of temperature and water content in the mantle transition zone from higher mode surface waves. *Earth and Planetary Science Letters* 282: 91–101. Negative values (blue) indicate that the discontinuity is deeper than average and, likewise, positive values (red) indicate that it is shallower than average.

1.20.2.3 Seismic Attenuations

The horizontal spread of high-velocity anomalies also implies the dominance of high-Q anomalies in the transition zone beneath the subduction zone. Seismic Q^{-1} is a measure of the degree of attenuation of a seismic wave. The progress

in attenuation studies has been slow because such studies typically rely on the amplitude measurement, which is affected by many factors, including determination of source mechanism, evaluation of focusing, defocusing, and scattering by structural heterogeneity, and correction for instrumental response. Such factors complicate interpretation of the measured amplitude in terms of attenuation. The current status of seismic attenuation studies of the structure of Earth is reviewed by Romanowicz and Mitchell (2007). Relatively recent global attenuation models include SW02 of Selby and Woodhouse (2002), QRLW8 of Gung and Romanowicz (2004), and QRFSI12 of Dalton et al. (2008). These models in the transition zone commonly show lower-than-normal attenuations beneath the western Pacific to eastern Asia, although the detail is quite different among the models. A counterpart of this subduction zone signal in the transition zone is the antipodal pair of high attenuation in the Pacific and in Africa, which was first demonstrated by Romanowicz (1990) from a Rayleigh wave analysis.

1.20.2.4 Seismic Anisotropy

The horizontal spread of high-velocity anomalies implies the dominance of horizontal shear flow in subduction zones, which might be detected by measuring radial seismic anisotropy in the transition zone beneath subduction zones (see Montagner, 2007). Unfortunately, resolving subduction zone characteristics of radial anisotropy from global mapping of radial anisotropy at depths near the bottom of the upper mantle remains a challenge (Ferreira et al., 2010; Kustowski et al., 2008; Lekić and Romanowicz, 2011; Panning and Romanowicz, 2006). Even the spherically averaged component of radial anisotropy is of marginal significance in this depth range, as may be understood by comparing several radial profiles of spherically averaged radial anisotropy presented in **Figure 8** of Visser et al. (2008) and Figure 11 of Panning et al. (2010). Kawazoe et al. (2013) made a high pressure/temperature deformation experiment of wadsleyte, a major constituent mineral in the transition zone, to show that if the transition zone is dominated by horizontal shear flow, one would expect a spherically averaged radial anisotropy such that $V_{SH} < V_{SV}$ (horizontally polarized S waves are slower than vertically polarized S waves).

1.20.3 Slab Signatures Above and Below the 660-km Discontinuity

In this section, the cross-sectional views of subducted slabs above and below the 660-km discontinuity, that is, in the transition zone and in the uppermost lower mantle, are reviewed. The tomographic cross-sections along 11 profiles across Kurile (KR), Japan (JP), Bonin (BN), Mariana (MR), Java (JV), Tonga (TN), Kermadec (KM), northern and southern South America (nSA and sSA), and northern and middle Central America (nCA and mCA) for two P-wave velocity models, GAP_P4 of Obayashi et al. (2013) and LLNL-G3Dv3 of Simmons et al. (2012), and for two S-wave velocity models, S362ANI of Kustowski et al. (2008) and TX2011 of Grand (2002) are examined. **Figure 4** shows the locations of these 11 profiles, which are chosen from Fukao and Obayashi (2013), who presented a number of equally spaced tomographic slices for each arc of the Circum-Pacific subduction zones. The P-wave images are scaled to ±1.5% and the S-wave images to ±2.5%.

1.20.3.1 Slab Signature in the Transition Zone

Figure 5(a)–5(c) shows the tomographic cross-sections across Japan, Bonin, and southern South America, respectively, for the two P-wave velocity models and for the two S-wave velocity models. In these figures, the 410- and 660-km depth lines define the top and bottom of the transition zone. The 1000-km depth line is added as a measure of the bottom of the uppermost lower mantle, which is not a physically distinct boundary. The resolution of a subduction zone image is different between P-wave and S-wave velocity models. In general, first arrival time-based P-wave velocity models can resolve finer structures of subduction zones. On the other hand, a more uniform resolution is anticipated by broadband waveform-

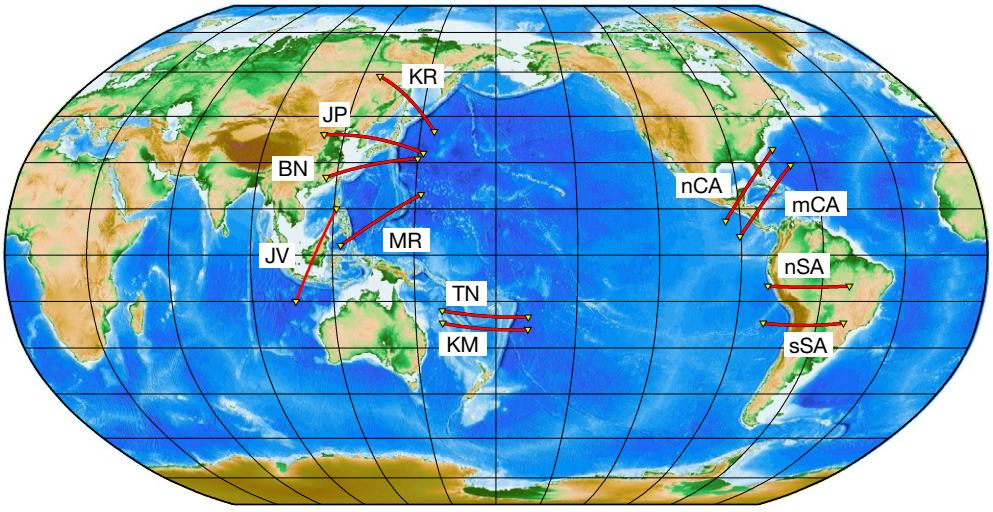

Figure 4 Location of the 11 profiles across typical subduction zones in the Circum-Pacific belt. The vertical cross-sections along these profiles are shown in **Figures 5** and **7–10**.

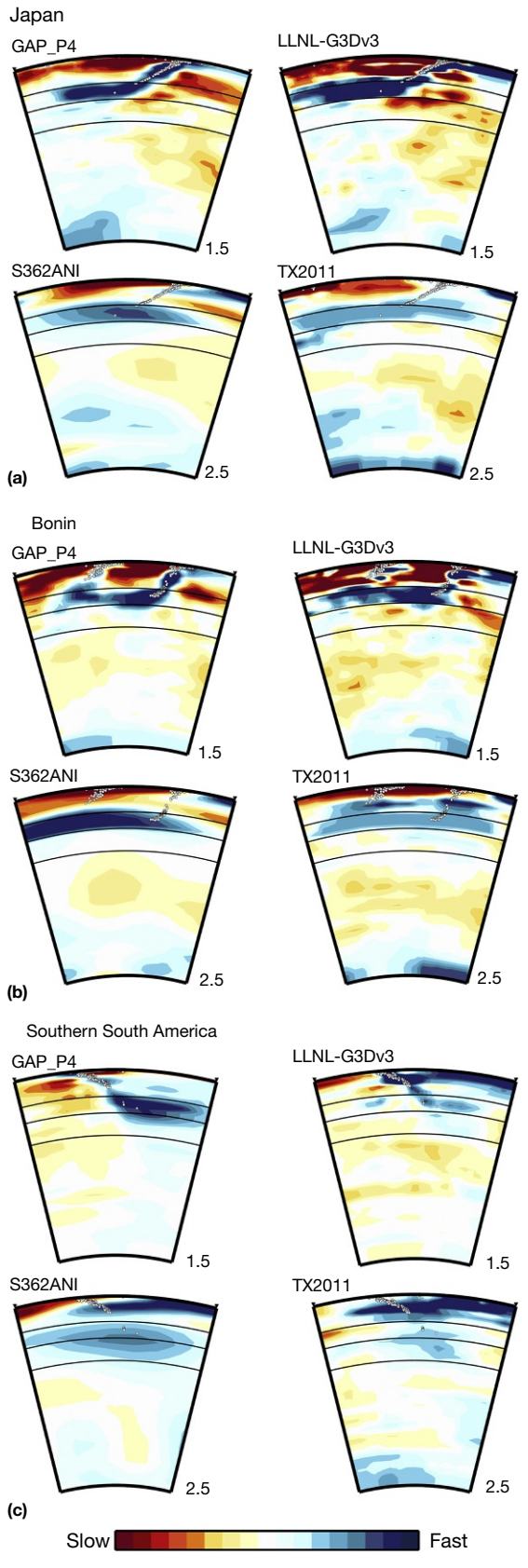

Figure 5 Cross-sections through the two P-wave and two S-wave velocity models (GAP_P4, LLNL-G3Dv3, S362ANI, and TX2011) along profiles given in **Figure 4**. Structures are shown from Earth's surface down to the core–mantle boundary beneath (a) Japan, (b) Bonin, and (c) southern South America. For reference, thin lines at 410- and 660-km depths indicate the position of the discontinuities that define the mantle transition zone. An additional line at 1000 km does not mean a physically distinct boundary, but is drawn to give a rough measure of the bottom of the uppermost lower mantle. White dots depict hypocenters of earthquakes. Mantle earthquakes are considered to occur within subducted slabs. The scale of velocity anomaly is ±1.5% for the P-wave velocity models and ±2.5% for the S-wave velocity models.

based S-wave velocity models to characterize subduction zone structures among other structural heterogeneities. Bearing such resolution differences in mind, the slab configurations are first figured out from the two P-wave velocity models, and then whether they are consistent with the images from the two S-wave velocity models examined. In **Figure 5(a)** and **5(b)**, the P-wave cross-sections across the Japan and Bonin arcs consistently show typical images of stagnant slabs above the 660-km discontinuity and the two S-wave cross-sections clearly support such an interpretation. The slab images in these subduction zones have been repeatedly revealed by P-wave tomography. See Fukao et al. (2001) for the earlier references including van der Hilst et al. (1991) and Fukao et al. (1992). More recent references include Miller et al. (2004), Huang and Zhao (2006), Li and van der Hilst (2010), van der Meer et al. (2010) and Zhao et al. (2009). Zhao et al. (2009) proposed the concept of the big mantle wedge by which they related the stagnant slabs to the widespread volcanism in eastern China. Li and van der Hilst (2010) related the horizontal spread of high-velocity anomalies in the transition zone to slab remnants since the Mesozoic Era.

Although the P-wave cross-sections across the Japan and Bonin arcs commonly show the images of stagnant slabs, the detailed slab configuration is very different. The downgoing slab beneath the Bonin arc dips more steeply and bends more sharply above the 660-km boundary than the slab beneath the Japan arc, as demonstrated in **Figure 5(a)** and **5(b)**, where the earthquake hypocenter distribution is superposed within a band 50 km wide on both sides of the cross-section plane, based on the EHB Bulletins published from the ISC (http://www.isc.ac.uk/ehbbulletin) (Engdahl et al., 1998). In the Bonin P-wave cross-sections (**Figure 5(b)**), the sharp bend of the slab image is correlated well with the bend of the deepest hypocentral distribution (Okino, et al., 1989). This correlation implies that the stagnant slab near the bending portion is brittle enough to cause earthquakes.

Figure 5(c) shows the cross-sections of the slab image of the Nazca plate along the east–west profile across Chile. Although the resolution is poorer here than in Japan and Bonin, the two P-wave velocity models consistently show the images of stagnant slab above the 660-km discontinuity. The earlier P-velocity models consistent with these images include those of Bijwaard et al. (1998) and Fukao et al. (2001). These stagnant slab images seem to be in better agreement with the fast anomaly pattern in the S-wave velocity model of S362ANI than of TX2011. Although the hypocentral distribution here shows a large gap between the intermediate-depth seismic zone and the deepest seismic zone, the P-wave velocity models seem to

suggest that the slab is continuous all the way through this seismicity gap. The deepest hypocenters extend subhorizontally in accordance with the stagnant slab images in the P-wave velocity models.

1.20.3.2 Slab Signature in the Uppermost Lower Mantle

Figure 6 shows the tomographic maps at depths of ~900 km in the uppermost lower mantle for the eight models corresponding to those in Figures 1 and 2 (see also Figure 3 of Panning and Romanowicz, 2006 for S-wave velocity anomalies and supplementary Figure 31(a) of Meer et al., 2009 for P- wave velocity anomalies). The Circum-Pacific subduction belt is still characterized by fast anomalies, both in the S-wave and the P-wave velocity models, although the intensities are, in general, weaker than those in the transition zone. The strongest anomalies in the western Pacific are now shifted southward to the Indonesia–Philippine subduction zones, and those in South America are shifted northward to northern South America.

Figure 7(a)–7(c) shows the tomographic cross-sections across Java, Kermadec, and northern South America, respectively, for two P-wave velocity models, GAP_P4 and LLNL-G3Dv3, and for two S-wave velocity models, TX2011 and S362ANI. See Fukao et al. (2001) for the earlier references for the Java slab images including Widiyantoro and van der Hilst (1996). More recent references include Replumaz et al. (2004), Li et al. (2008), van der Meer et al. (2010), and Widiyantoro et al. (2011). The cross-sections across the two P-wave velocity models and the S-wave velocity model TX2011 in Figure 7(a) indicate that the slab beneath western Java penetrates the 660-km discontinuity and then deflects subhorizontally in the uppermost lower mantle. The two P-wave velocity models show the subhorizontally deflected slab that extends not only

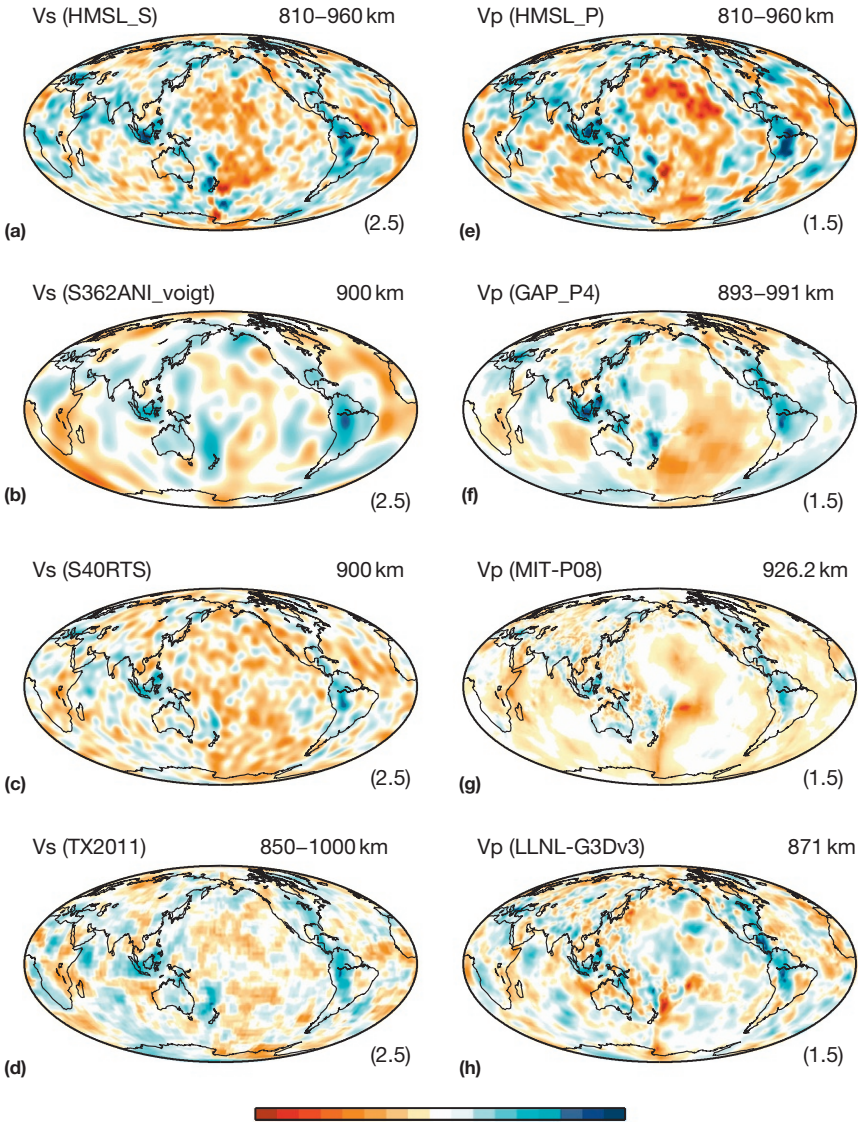

Figure 6 Depth slices in the uppermost lower mantle for the four S-wave and four P-wave velocity models corresponding to those in Figure 1. The velocities are perturbations from the average value at the corresponding depth. The scale is ±2.5% for the S-wave velocity models and ±1.5% for the P-wave velocity models.

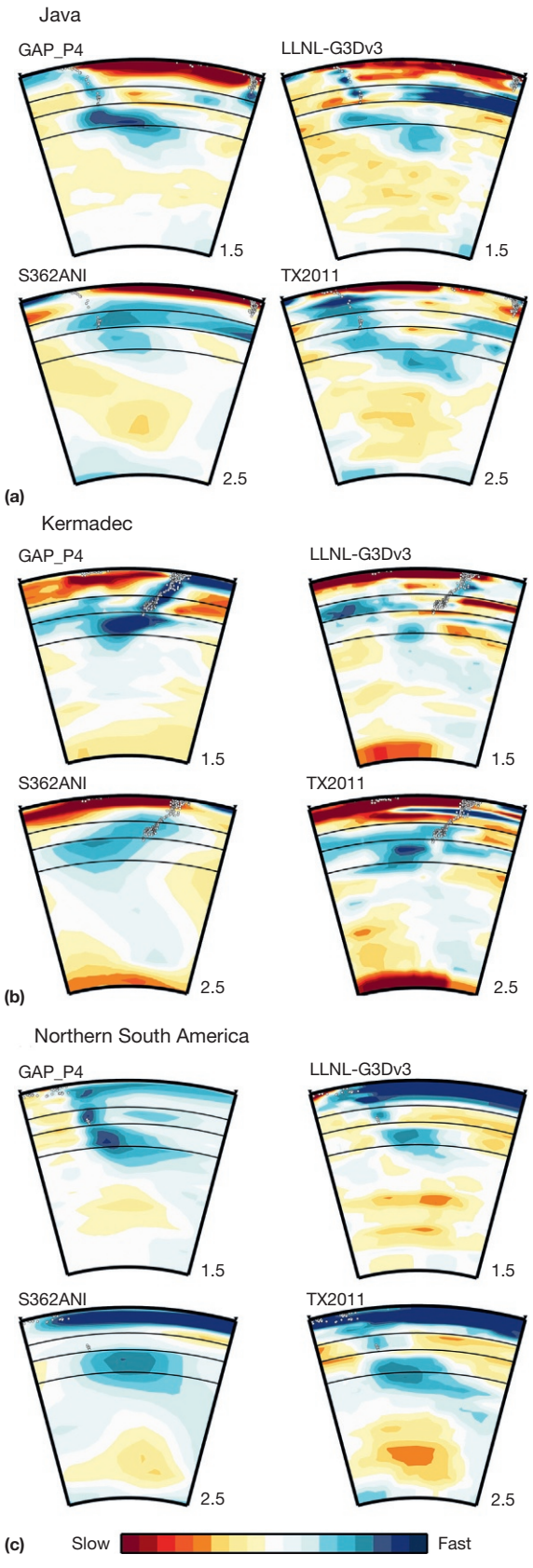

Figure 7 Cross-sections through the two P-wave and two S-wave velocity models (GAP_P4, LLNL-G3Dv3, S362ANI, and TX2011) along profiles given in **Figure 4**. Structures are shown from Earth's surface down to the core–mantle boundary beneath (a) Java, (b) Kermadec, and (c) northern South America. See **Figure 5** for other explanations.

in the forward direction but also slightly in the backward direction. Such a slab configuration may be related to the deep hypocentral distribution (at depths greater than ~500 km) that dips steeply in the slightly backward (southward) direction in agreement with the slightly backward orientation of the near-vertical compressional axes in the focal mechanisms of deep shocks (Das et al., 2000; Schöffel and Das, 1999). A slight backward spread of the slab image is also observed in **Figure 6** of Hafkenscheid et al. (2001) but not obvious in Replumaz et al. (2004) and Li et al. (2008). In **Figure 7(a)**, the two P-wave velocity models and the S-wave velocity model of TX2011 seem to indicate that the subhorizontally deflected slab begins to descend deeper, further beyond the uppermost lower mantle.

In **Figure 7(b)**, the P-wave velocity model of GAP-P4 shows an image of the subhorizontally deflected slab in the uppermost lower mantle beneath Kermadec. This slab image appears to be consistent with those of the two S-wave velocity models. These cross-sections seem to indicate that the subhorizontally deflected slab begins to descend to greater depths beyond the uppermost lower mantle. According to **Figure 4** of Schellart et al. (2009), which was constructed from the S-velocity model of Kennett and Gorbatov (2004) and the P-velocity model of Amaru (2007), this slab-related subhorizontal spread of high-velocity anomalies in the uppermost lower mantle extends further southward down to 27° S beneath the Tonga–Kermadec arc. The deepest hypocentral distribution in **Figure 7(b)** is more steeply dipping than at shallower depths. The downdip compression mechanisms of the deepest earthquakes (Alpert et al., 2010; Bonnardot et al., 2009; Brudzinski and Chen, 2005) suggest that the slab here is resisted by the surrounding mantle against its penetration across the 660-km discontinuity.

In **Figure 7(c)**, the two P-wave velocity models and the two S-wave velocity models consistently show the images of the Peruvian slab that penetrates the 660-km discontinuity, and then deflects subhorizontally in the uppermost lower mantle. The subhorizontally deflected slab seems to begin to descend deeper beyond the uppermost lower mantle. See Fukao et al. (2001) for the earlier references for the Peruvian slab images including Engdahl et al. (1995). Slab penetration is clearly imaged but subhorizontal deflection of the penetrated slab is less clear in a recent P-velocity model of Li et al. (2008). Seismic activity is very high within the penetrating slab in the proximity of the 660-km discontinuity. Although the deepest seismicity is well isolated from the shallower seismicity (see Brudzinski and Chen, 2005; Martinod et al., 2010), the tomographic cross-sections in the two P-wave velocity models seem to suggest that the slab continues through the seismicity gap between the shallow and deepest seismic zones. Earthquakes at greatest depths are of downdip compression type with steep compressional axes (average plunge = 79°; Brudzinski and Chen, 2005), suggesting that the slab here is resisted by the surrounding mantle against its steep penetration across the 660-km discontinuity.

1.20.3.3 Juxtaposed Slab Images in the Transition Zone and the Uppermost Lower Mantle

Figures 5 and 7 represent typical images of slabs deflected horizontally in the transition zone and those deflected subhorizontally in the uppermost lower mantle, respectively. The subduction zone in northern Tonga is unique in this respect, because the horizontal slab in the transition zone and the subhorizontal slab in the uppermost lower mantle may be juxtaposed in the same area. Figure 8 shows this possible juxtaposition. See Fukao et al. (2001) for the earlier references for the slab image beneath northern Tonga including van der Hilst (1995). More recent references include Hall and Spakman (2002) and Amaru (2007), which show similar slab features. Note that the deepest seismic zone here apparently splits into two, one extending at a very shallow dip and the other dipping very steeply. More detailed studies of the deep seismicity and focal mechanisms (e.g., Bonnardot et al., 2009; Brudzinski and Chen, 2005; Richards et al., 2011) suggest that the shallowly dipping seismic zone represents either the northern segment of the slab from the Tonga trench or the slab from the Vanuatu trench and that the steeply dipping seismic zone represents the southern segment of the slab from the Tonga trench. Fukao and Obayashi (2013) interpreted these two seismic zones as an indication of juxtaposition of two separate slabs, rather than a doubly thickened slab: one is stagnant above the 660-km discontinuity and the other is deflecting subhorizontally just below the discontinuity, as observed in northern Kermadec (**Figure 7(b)**). Deep shocks occurring within the stagnant slab in the transition zone are characterized by slab-parallel compression mechanisms such that the compressional axes are oriented on the average at an azimuth of 262° and an extremely shallow dip of 5° in the northern part and at an azimuth of 309° and a relatively shallow dip of 18° in the southern part (Bonnardot et al., 2009). These mechanisms imply that the stagnant slab here is resisted against its subhorizontal advance by the surrounding mantle.

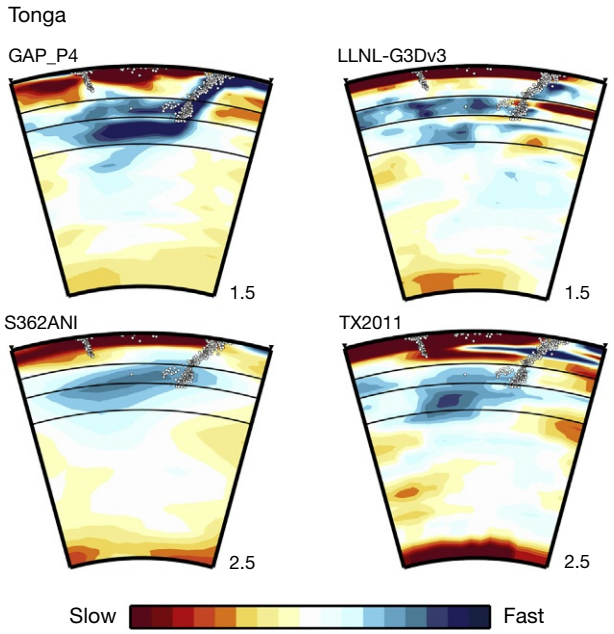

Figure 8 Cross-sections through the two P-wave and two S-wave velocity models (GAP_P4, LLNL-G3Dv3, S362ANI, and TX2011) along a profile given in **Figure 4**. Structures are shown from Earth's surface down to the core–mantle boundary beneath northern Tonga. See **Figure 5** for other explanations.

1.20.4 Seismic Images of Slab Descent Through the Transition Zone

1.20.4.1 Images of Transitional State from Slab Stagnation to Penetration

Seismic images of horizontally deflected slabs (stagnant slabs) in the transition zone (**Figure 5**) and subhorizontally deflected slabs in the uppermost lower mantle (**Figure 7**) have been overviewed so far. These images are understood to be the images of subducted slabs before and after the slab penetration. To answer the question of how a slab begins to penetrate the 660-km discontinuity and how it begins to deflect subhorizontally in the uppermost lower mantle, **Figure 9(a)** and **9(b)** shows the cross-sections across the central Kurile arc and the central Mariana arc, respectively (see Fukao et al., 1992; van der Hilst et al., 1991 for the earliest images and van der Hilst and Seno, 1993 for the early attempts to explain the along-arc variation of slab morphology). The Kurile slab is well known to be horizontally deflected above the 660-km discontinuity in southern Kurile but penetrating the discontinuity in northern Kurile, as demonstrated by **Figure 10** of Li et al. (2008), **Figure 2** of Zhao et al. (2010), and **Figure 5** of Fukao and Obayashi (2013). We may anticipate some transitional state from slab stagnation to penetration in central Kurile. In **Figure 9(a)**, the two P-wave velocity models show the images of stagnant and penetrating slabs simultaneously, although LLNL-G3Dv3 emphasizes the stagnant slab, whereas GAP_P4 emphasizes the penetrating slab. The two S-wave velocity models seem to be more consistent with LLNL-G3Dv3 than with GAP_P4.

Also well known is the fact that the steeply dipping downgoing slab is bent to sharply horizontal at depths above the 660-km discontinuity beneath the Bonin arc, whereas it penetrates the discontinuity beneath the Mariana arc, as demonstrated by **Figure 4** of Miller et al. (2004), **Figure 10** of Li et al. (2008), and **Figure 3** of Fukao and Obayashi (2013). **Figure 9(b)** shows the cross-sections across the central Mariana arc. The resolution of GAP_P4 has been improved in this region by the data from broadband ocean-bottom seismometers deployed in the Philippine Sea region (Obayashi et al., 2013). This model shows the image of the downgoing slab that penetrates the 660-km discontinuity and then enlarges horizontally in the uppermost lower mantle. It also shows the image of the stagnant slab above the discontinuity apparently detached from the downgoing slab. Such coexistence of the penetrated slab below and the stagnant slab above the discontinuity is faintly indicated in the images of V LLNL-G3Dv3 and TX2011. Model S362ANI seems to emphasize the stagnant slab more than the penetrating slab. Clearly, the lateral and vertical resolutions of the existing models are still too limited to detect the fine structure at the possible transitional stage from slab stagnation to penetration in the central Kurile and central Mariana regions.

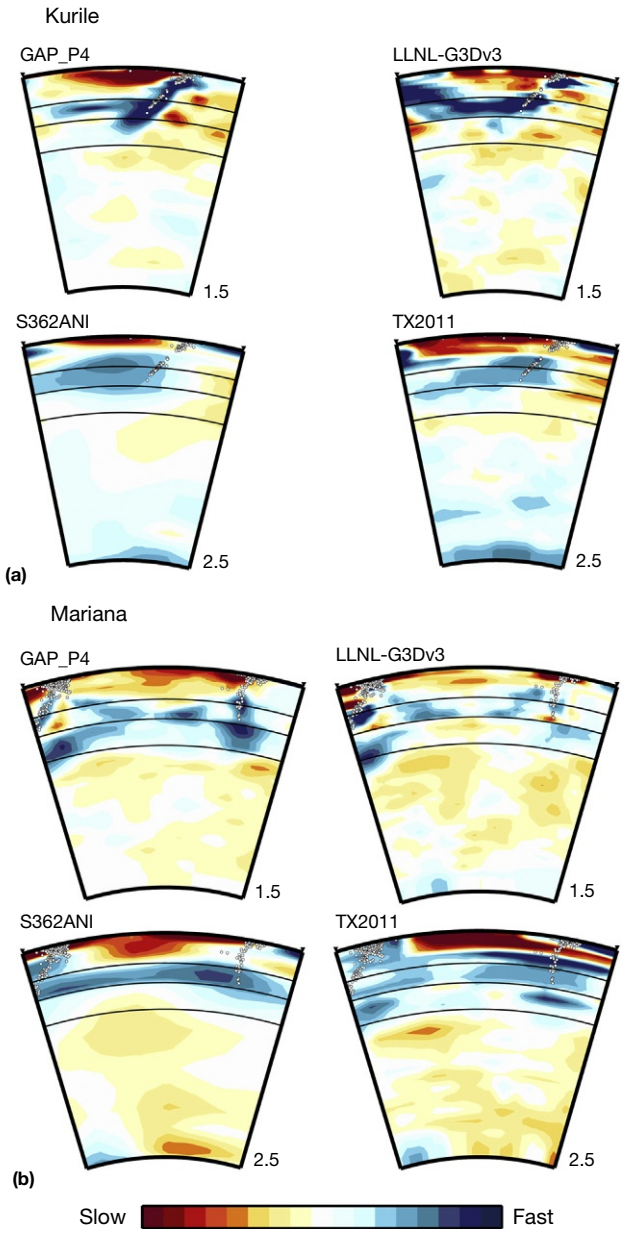

Figure 9 Cross-sections through the two P-wave and two S-wave velocity models (GAP_P4, LLNL-G3Dv3, S362ANI, and TX2011) along profiles given in **Figure 4**. Structures are shown from Earth's surface down to the core–mantle boundary beneath (a) central Kurile and (b) central Mariana. See **Figure 5** for other explanations.

1.20.4.2 Signature of Subducted Crust Materials in the Penetrating Slab

Some observational evidence indicates that a penetrating slab has fragments of subducted crust materials within it. Niu et al. (2003) detected an ~10-km thick S-to-P reflector at a depth of ~1150 km beneath the northern Mariana arc, using a Japanese short-period seismic network. They interpreted this reflector as a fragment of the oceanic crust internally displaced to the bottom of the penetrating slab. Kaneshima (2003) detected S-to-P scatterers at depths of 700–900 km beneath the central Mariana arc, using two short-period seismic arrays in the United States. All the scatterers, including those detected by Krüger et al. (2001), were located inside the deformed body of the penetrating slab. Kaneshima (2009) detected S-to-P scatterers in a depth range of 800–1000 km beneath the northern Kurile arc. He located the scatterers near the bottom of the enlarged body of the penetrating slab and interpreted them as the remnants of subducted oceanic crust. Rost et al. (2008) used off-great-circle-path precursors to PP-waves (P-waves reflected off the surface once) recorded by a Canadian short-period seismic array to detect P-to-P scatterers. They showed that these scatterers are located mostly at depths shallower than 1000 km and in large part in the Mariana subduction zone. Rost et al. (2008) interpreted these scatterers as being from the

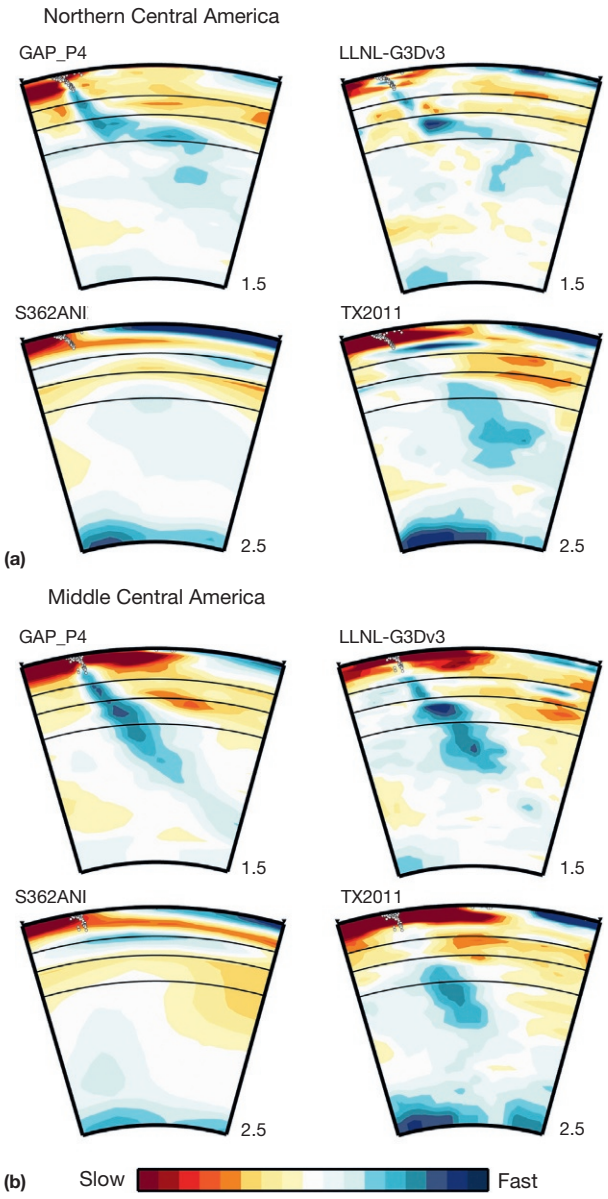

Figure 10 Cross-sections through the two P-wave and two S-wave velocity models (GAP_P4, LLNL-G3Dv3, S362ANI, and TX2011) along profiles given in **Figure 4**. Structures are shown from Earth's surface down to the core–mantle boundary beneath (a) northern Central America and (b) middle Central America. See **Figure 5** for other explanations.

paleo-Moho (the Moho is the boundary between the crust and the mantle) of the deeply subducted slabs. Although they did not show where these scatterers are located relative to the penetrated slab, all the other studies cited earlier located fragments of the subducted crust within or at the bottom of the penetrating slab rather than at the top. This location suggests that slab penetration and subsequent processes are associated with severe deformation within the slab. The penetrated crust may no longer be a coherent unit at the top of the slab.

1.20.4.3 Images of Slab Descent to the Deep Lower Mantle

The Central American subduction zone is the best place to observe images of slab descent all the way through the transition zone, the uppermost lower mantle, and the deep lower mantle. Tomographic images of the deeply subducted slab under this region have been repeatedly reported (Grand, 2002; Li et al., 2008; Ren et al., 2007; see Fukao et al. (2001) for the earlier references including van der Hilst et al., 1997 and Grand et al., 1997). **Figure 10(a)** and **10(b)** shows the cross-sections across the northern and middle Central American arcs, respectively. In **Figure 10(a)**, GAP_P4 and LLNL-G3Dv3 show slab configurations remarkably similar to each other. The downgoing slab penetrates the 660-km discontinuity, thereby deflecting to horizontal below the discontinuity, and is then apparently folded down into the deeper mantle. This deeper part of the slab is emphasized more in TX2011 than in the two P-wave velocity models. In **Figure 10(b)**, the slab configurations shown by GAP_P4, LLNL-G3Dv3, and TX2011 are remarkably similar to each other (see also Li et al., 2008). The slab extends almost straight through the intermediate-depth seismic zone downdip to mid-mantle depths of approximately 1500 km. Fukao and Obayashi (2013) interpreted the slab configurations in **Figure 10(a)** and **10(b)** as those at the relatively earlier and later stages of deep slab subduction.

1.20.5 Summary

The mantle transition zone acts as a (temporal) reservoir for subducting slabs of lithospheric plates, as typically observed in Japan, Bonin, and southern South America (**Figure 5**). Increasing evidence suggests that the uppermost lower mantle acts as another (temporal) reservoir for subducting slabs, although its bottom is defined only loosely. The typical subduction zone of this type includes Java, Kermadec, and northern South America, where the penetrated slab is deflected subhorizontally in the uppermost lower mantle (**Figure 7**). One can observe the juxtaposition of a horizontal slab above the 660-km discontinuity and a subhorizontal slab below the discontinuity beneath the northern Tonga arc (**Figure 8**). In general, slabs in central Kurile and central Mariana are not well resolved, but the images give some idea of how the transition from slab stagnation to penetration occurs (**Figure 9**). Some evidence indicates that slabs trapped in the deeper reservoir are severely deformed internally so that the subducted oceanic crust is fragmented into scattered pieces.

A remarkable correlation exists between the slab image in the transition zone and the deepest hypocentral distribution (Fukao and Obayashi, 2013). The dip of the deepest hypocentral distribution often deviates from the dip of the major seismic zone. In the case of a horizontally deflected slab above the 660-km discontinuity, the deepest hypocentral distribution tends to dip more gently than the shallower portion of the seismic zone (see the cross-sections across Bonin and Chile in **Figure 5**). In the case of a subhorizontally deflected slab below the discontinuity, the deepest hypocentral distribution tends to dip more steeply than the shallower part of the seismic zone (see the cross-sections across Java, Kermadec, and Peru in **Figure 7**). This is also the case of a downgoing slab

beginning to penetrate the discontinuity or beginning to spread laterally below it (see the cross-sections across central Kurile and central Mariana in Figure 9). In the case where the slab images suggest juxtaposition of the horizontal slab above the 660 and the subhorizontal slab below the 660, the deepest hypocentral distribution apparently splits into two, one dipping very gently and the other dipping very steeply (see the cross-section across Tonga in Figure 8).

Downgoing slabs tend to be deflected horizontally in the transition zone, and penetrated slabs tend to be deflected subhorizontally. The transition zone and the uppermost lower mantle are thus two distinct reservoirs of subducted slabs. Together they constitute a chain of slab reservoirs around the Circum-Pacific; however, both allow slab leakage from the bottom. The deeply descending slab images beneath Central America (Figure 10) may be understood as an extreme case of slab leakage from the bottom of the uppermost lower mantle well into the mid-lower mantle. While either the transition zone or the uppermost lower mantle serves as a slab reservoir, only the former acts as a reservoir of water. The water solubility in the major mineral of the transition zone is ~3.3 wt% (wadsleyite) to ~2.6 wt% (ringwoodite), whereas it is only <30 ppm (Mg-perovskite) to <100 ppm (ferropericlase) in the major mineral of the uppermost lower mantle (Litasov et al., 2006). Even if the slab in the transition zone contains a significant amount of water, water should be expelled from the slab upon penetration across the 660-km discontinuity. At present, however, there is no consensus on how and to what extent water is carried down into the transition zone with the subducting slab (Jacobsen and van der Lee, 2006; Kawakatsu and Yoshioka, 2011; Meier et al., 2009; Tonegawa et al., 2008).

Acknowledgments

We would like to thank the editors (Barbara Romanowicz and Adam Dziewonski) and the reviewer (Rob van der Hilst) for their comments, which were very useful for improvement of the manuscript.

References

Alpert LA, Becker TW, and Bailey LW (2010) Global slab deformation and centroid moment tensor constraints on viscosity. *Geochemistry, Geophysics, Geosystems* 11. http://dx.doi.org/10.1029/2010GC003301.

Amaru M (2007) *Global Travel Time Tomography with 3-D Reference Models*. PhD Thesis. Utrecht: Utrecht University. http://igitur-archive.library.uu.nl/dissertations/2007-0202-201924/c5.pdf.

Bijwaard H, Spakman W, and Engdahl ER (1998) Closing the gap between regional and global tomography. *Journal of Geophysical Research* 103: 30005–30078.

Bonnardot MA, Régnier M, Christova C, Ruellan E, and Tric E (2009) Seismological evidence for a slab detachment in the Tonga subduction zone. *Tectonophysics* 464: 84–99.

Brudzinski MR and Chen WP (2005) Earthquakes and strain in subhorizontal slabs. *Journal of Geophysical Research* 110. http://dx.doi.org/10.1029/2004JB003470.

Dahlen FA, Hung SH, and Nolet G (2000) Frechet kernels for finite-frequency traveltimes – I. Theory. *Geophysical Journal International* 141: 157–174.

Dalton CL, Ekström G, and Dziewonski AM (2008) The global attenuation structure of the upper mantle. *Journal of Geophysical Research* 113. http://dx.doi.org/10.1029/2007JB005429.

Das S, Schöffel HJ, and Gilbert F (2000) Mechanism of slab thickening near 670 km under Indonesia. *Geophysical Research Letters* 27: 831–834.

Dunn RA and Forsyth DW (2007) Crust and lithospheric structure – Seismic structure of mid-oceanic ridges. In: Romanowicz B and Dziewonski AM (eds.) *Seismology and the Structure of the Earth. Treatise on Geophysics*, vol. 1, pp. 419–443. Amsterdam: Elsevier.

Dziewonski AM and Romanowicz B (2007) Overview. In: Romanowicz B and Dziewonski AM (eds.) *Seismology and the Structure of the Earth. Treatise on Geophysics*, vol. 1, pp. 1–29. Amsterdam: Elsevier.

Engdahl ER, van der Hilst R, and Berrocal J (1995) Imaging of subducted lithosphere beneath South America. *Geophysical Research Letters* 22: 2317–2320.

Engdahl ER, van der Hilst R, and Buland R (1998) Global teleseismic earthquake relocation with improved travel times and procedures for depth determination. *Bulletin of the Seismological Society of America* 88: 722–743.

Faccenna C, Becker TW, Lucente FP, Jolivet L, and Rossetti F (2001) History of subduction and back-arc extension in the Central Mediterranean. *Geophysical Journal International* 145: 809–820.

Ferreira AMG, Woodhouse JH, Visser K, and Trampert J (2010) On the robustness of global radially anisotropic surface wave tomography. *Journal of Geophysical Research* 115. http://dx.doi.org/10.1029/2009JB006716.

Fukao Y and Obayashi M (2013) Subducted slabs stagnant above, penetrating through and trapped below the 660-km discontinuity. *Journal of Geophysical Research*, under review.

Fukao Y, Obayashi M, Inoue H, and Nenbai M (1992) Subducting slabs stagnant in the mantle transition zone. *Journal of Geophysical Research* 97: 4809–4822.

Fukao Y, Obayashi M, Nakakuki T, and Deep Slab Project Group. (2009) Stagnant slab: A review. *Annual Reviews of Earth and Planetary Sciences* 37: 19–46.

Fukao Y, Widiyantoro S, and Obayashi M (2001) Stagnant slabs in the upper and lower mantle transition region. *Review of Geophysics* 39: 291–323.

Funiciello F, Faccenna C, Heuret A, Lallemand S, Giuseppe ED, and Becker TW (2008) Trench migration, net rotation and slab–mantle coupling. *Earth and Planetary Science Letters* 271: 233–240.

Grand SP (2002) Shear-wave tomography and the fate of subducted slabs. *Philosophical Transactions of the Royal Society of London A* 360: 2475–2481.

Grand SP, van der Hilst RD, and Widiyantoro S (1997) Global seismic tomography: A snapshot of convection in the Earth. *Geological Society of America Today* 7: 1–7.

Gu YJ, Okeler A, and Schultz R (2012) Tracking slabs beneath northwestern Pacific subduction zones. *Earth and Planetary Science Letters* 331–332: 269–280.

Gung Y and Romanowicz B (2004) Q tomography of the upper mantle using three-component long-period waveforms. *Geophysical Journal International* 157: 813–830.

Hafkenscheid E, Buiter SJH, Wortel MJR, Spakman W, and Bijwaard H (2001) Modeling the seismic velocity structure beneath Indonesia: A comparison with tomography. *Tectonophysics* 333: 35–46.

Hall R and Spakman W (2002) Subducted slabs beneath the eastern Indonesia-Tonga region: Insights from tomography. *Physics of the Earth and Planetary Interiors* 201: 321–336.

Heit B, Yuan X, Bianchi M, Kind R, and Gossler J (2010) Study of the lithospheric and upper-mantle discontinuities beneath eastern Asia by *SS* precursors. *Geophysical Journal International* 183: 252–266.

Houser C, Masters G, Flanagan M, and Shearer P (2008) Determination and analysis of long-wavelength transition zone structure using *SS* precursors. *Geophysical Journal International* 174: 178–194.

Houser C, Masters G, Shearer P, and Laske G (2008) Shear and compressional velocity models of the mantle from cluster analysis of long-period waveforms. *Geophysical Journal International* 174: 195–212.

Huang J and Zhao D (2006) High-resolution mantle tomography of China and surrounding regions. *Journal of Geophysical Research* 111. http://dx.doi.org/10.1029/2005JB004066.

Iidaka T and Suetsugu D (1992) Seismological evidence for metastable olivine inside a subducting slab. *Nature* 356: 593–595.

Jacobsen SD and van der Lee S (2006) Earth's deep water cycle. *Geophysical Monograph*, vol. 168, 313 pp. Washington, DC: American Geophysical Union.

Jiang G, Zhao D, and Zhang G (2008) Seismic evidence for a metastable olivine wedge in the subducting Pacific slab under Japan Sea. *Earth and Planetary Science Letters* 270: 300–307.

Kaneshima S (2003) Small-scale heterogeneity at the top of the lower mantle around the Mariana slab. *Earth and Planetary Science Letters* 209: 85–101.

Kaneshima S (2009) Seismic scatterers at the shallowest lower mantle beneath subducted slabs. *Earth and Planetary Science Letters* 286: 304–315.

Kaneshima S, Okamoto T, and Takenaka H (2007) Evidence for a metastable olivine wedge inside the subducted Mariana slab. *Earth and Planetary Science Letters* 258: 219–227.

Kárason H and van der Hilst RD (2001) Tomographic imaging of the lowermost mantle with differential times of refracted and diffracted core phases (PKP, Pdiff). *Journal of Geophysical Research* 106: 6569–6588. http://dx.doi.org/10.1029/2000JB900380.

Kawakatsu H and Yoshioka S (2011) Metastable olivine wedge and deep dry cold slab beneath southwest Japan. *Earth and Planetary Science Letters* 303: 1–10.

Kawazoe T, Ohuchi T, Nishihara Y, Nishiyama N, Fujino K, and Irifune T (2013) Seismic anisotropy in the mantle transition zone induced by shear deformation of wadsleyite. *Physics of the Earth and Planetary Interiors* 216: 91–98.

Kennett BLN and Gorbatov A (2004) Seismic heterogeneity in the mantle – Strong shear wave signature of slabs from joint tomography. *Physics of the Earth and Planetary Interiors* 146: 87–100.

Kind R and Li X (2007) Deep Earth structure – Transition zone and mantle discontinuities. In: Romanowicz B and Dziewonski AM (eds.) *Seismology and the Structure of the Earth*. *Treatise on Geophysics*, vol. 1, pp. 591–618. Amsterdam: Elsevier.

Kirby SH, Stein S, Okal EA, and Rubie D (1996) Metastable mantle phase transformations and deep earthquakes in subducting oceanic lithosphere. *Reviews of Geophysics* 34: 261–306.

Koper KD, Wiens DA, Dorman LM, Hildebrand JA, and Webb SC (1998) Modeling the Tonga slab: Can travel time data resolve a metastable olivine wedge? *Journal of Geophysical Research* 103: 30079–30100.

Krüger FK, Baumann M, Scherbaum F, and Weber M (2001) Mid mantle scatterers near the Mariana slab detected with a double array method. *Geophysical Research Letters* 28: 667–670.

Kustowski B, Ekström G, and Dziewonski AM (2008) Anisotropic shear-wave velocity structure of the Earth's mantle: A global model. *Journal of Geophysical Research* 113. http://dx.doi.org/10.1029/2007JB005169.

Lekić V and Romanowicz B (2011) Inferring upper-mantle structure by full waveform tomography with the spectral element method. *Geophysical Journal International* 185: 799–831.

Li C and van der Hilst RD (2010) Structure of the upper mantle and transition zone beneath Southeast Asia from traveltime tomography. *Journal of Geophysical Research* 115. http://dx.doi.org/10.1029/2009JB006882.

Li C, van der Hilst RD, Engdahl ER, and Burdick S (2008) A new global model for P wave speed variations in Earth's mantle. *Geochemistry, Geophysics, Geosystems* 9. http://dx.doi.org/10.1029/2007GC001806.

Litasov KD, Ohtani E, and Sano A (2006) Influence of water on major phase transitions in the Earth's mantle. In: Jacobsen SD and van der Lee S (eds.) *Earth's Deep Water Cycle*. *Geophysical Monograph*, vol. 168, pp. 95–111. Washington, DC: American Geophysical Union.

Lithgow-Bertelloni C and Richard MC (1998) The dynamics of Cenozoic and Mesozoic plate motions. *Review of Geophysics* 36: 27–78.

Martinod J, Husson L, Roperch P, Guillaume B, and Espurt N (2010) Horizontal subduction zones, convergence velocity and the building of the Andes. *Earth and Planetary Science Letters* 299: 299–309.

Masters G, Jordan TH, Silver PG, and Gilbert F (1982) Aspherical Earth structure from fundamental spheroidal-mode data. *Nature* 298: 609–613.

Meier U, Trampert J, and Curtis A (2009) Global variations of temperature and water content in the mantle transition zone from higher mode surface waves. *Earth and Planetary Science Letters* 282: 91–101.

Mercerat ED and Nolet G (2013) On the linearity of cross-correlation delay times in finite-frequency tomography. *Geophysical Journal International* 192: 681–687.

Miller MS, Kennett BLN, and Lister GS (2004) Imaging changes in morphology, geometry, and physical properties of the subducting Pacific plate along the Izu–Bonin–Mariana arc. *Earth and Planetary Science Letters* 224: 363–370.

Montagner JP (2007) Upper mantle structure: Global isotropic and anisotropic tomography. In: Romanowicz B and Dziewonski AM (eds.) *Seismology and Structure of the Earth*. *Treatise on Geophysics*, vol. 1, pp. 559–589. Amsterdam: Elsevier.

Niu F, Kwakatsu H, and Fukao Y (2003) Seismic evidence for a chemical heterogeneity in the midmantle: A slightly dipping and strong seismic reflector at mid-depth beneath the Mariana subduction zone. *Journal of Geophysical Research* 108. http://dx.doi.org/10.1029/2002JB002384.

Obayashi M, Yoshimitsu J, Nolet G, et al. (2013) Finite frequency whole mantle P-wave tomography: Improvement of subducted slab images. *Geophysical Research Letters* 40: 5652–5657. http://dx.doi.org/10.1002/2013GL057401.

Okino K, Ando M, Kaneshima S, and Hirahara K (1989) The horizontally lying slab. *Geophysical Research Letters* 16: 1059–1062.

Panning M and Romanowicz B (2006) A three-dimensional radially anisotropic model of shear velocity in the whole mantle. *Geophysical Journal International* 167: 361–379.

Ren Y, Stutzmann E, van der Hilst RD, and Besse J (2007) Understanding seismic heterogeneities in the lower mantle beneath the Americas from seismic tomography and plate tectonic history. *Journal of Geophysical Research* 112. http://dx.doi.org/10.1029/2005JB004154.

Replumaz A, Kárson H, van der Hilst RD, Besse J, and Tapponnier P (2004) 4-D evolution of SE Asia's mantle from geological reconstructions and seismic tomography. *Earth and Planetary Science Letters* 221: 103–115.

Richards MA and Engebretson DC (1992) Large-scale mantle convection and the history of subduction. *Nature* 355: 437–440.

Richards S, Holm R, and Barber G (2011) When slabs collide: A tectonic assessment of deep earthquakes in the Tonga–Vanuatu region. *Geology* 39: 787–790.

Ritsema J, Deuss A, van Heijst HJ, and Woodhouse JH (2011) S40RTS: A degree-40 shear-velocity model for the mantle from new Rayleigh wave dispersion, teleseismic travel time and normal-mode splitting function measurements. *Geophysical Journal International* 184: 1223–1236.

Romanowicz B (1990) The upper mantle degree 2: Constraints and inferences from global mantle wave attenuation measurements. *Journal of Geophysical Research* 95: 11051–11071.

Romanowicz B and Mitchell BJ (2007) Deep Earth structure – Q of the Earth from crust to core. In: Romanowicz B and Dziewonski AM (eds.) *Seismology and the Structure of the Earth*. *Treatise on Geophysics*, vol. 1, pp. 731–774. Amsterdam: Elsevier.

Rost S, Garnero EJ, and Williams Q (2008) Seismic array detection of subducted oceanic crust in the lower mantle. *Journal of Geophysical Research* 113. http://dx.doi.org/10.1029/2007JB005263.

Schmerr N and Garnero EJ (2007) Upper mantle discontinuity topography from thermal and chemical heterogeneity. *Science* 318: 623–626.

Schmerr N and Thomas C (2011) Subducted lithosphere beneath the Kuriles from migration of PP precursors. *Earth and Planetary Science Letters* 311: 101–111.

Schöffel HJ and Das S (1999) Fine details of the Wadati–Benioff zone under Indonesia and its geodynamic implications. *Journal of Geophysical Research* 104: 13101–13114.

Selby ND and Woodhouse JH (2002) The Q structure of the upper mantle: Constraints from Rayleigh wave amplitudes. *Journal of Geophysical Research* 107. http://dx.doi.org/10.1029/2001JB000257.

Shearer P (1993) Global mapping of upper mantle reflectors from long period *SS* precursors. *Geophysical Journal International* 115: 878–904.

Shearer P and Masters G (1992) Global mapping of topography on the 660-km discontinuity. *Nature* 355: 791–796.

Simmons NA, Myers SC, Johannesson G, and Matzel E (2012) LLNL-G3Dv3: Global P wave tomography model for improved regional and teleseismic travel time prediction. *Journal of Geophysical Research* 117. http://dx.doi.org/10.1029/2012JB009525.

Stixrude L and Jeanloz R (2007) Constraints on seismic models from other disciplines – Constraints from mineral physics on seismological models. In: Romanowicz B and Dziewonski AM (eds.) *Seismology and the Structure of the Earth*. *Treatise on Geophysics*, vol. 1, pp. 775–803. Amsterdam: Elsevier.

Sung CM and Burns RG (1976) Kinetics of high pressure phase transformations: Implications to the evolution of olivine–spinel transition in the downgoing lithosphere and its consequences on the dynamics of the mantle. *Tectonophysics* 31: 1–32.

Thurber C and Ritsema J (2007) Theory and observations – Seismic tomography and inverse methods. In: Romanowicz B and Dziewonski AM (eds.) *Seismology and the Structure of the Earth*. *Treatise on Geophysics*, vol. 1, pp. 323–360. Amsterdam: Elsevier.

Tonegawa T, Hirahara K, Shibutani T, Iwamori H, Kanamori H, and Shiomi K (2008) Water flow to the mantle transition zone inferred from a receiver function image of the Pacific slab. *Earth and Planetary Science Letters* 274: 346–354.

van der Hilst R (1995) Complex morphology of subducted lithosphere in the mantle beneath the Tonga trench. *Nature* 374: 154–157.

van der Hilst R, Engdahl R, Spakman W, and Nolet G (1991) Tomographic imaging of subducted lithosphere below northwest Pacific island arcs. *Nature* 353: 37–43.

van der Hilst R and Seno T (1993) Effects of relative plate motion on the deep structure and penetration depth of slabs below the Izu–Bonin and Mariana island arcs. *Earth and Planetary Science Letters* 120: 375–407.

van der Hilst R, Widiyantoro S, and Engdahl R (1997) Evidence for deep mantle circulation from global tomography. *Nature* 386: 578–584.

van der Meer DG, Spakman W, van Hinsbergen DJJ, Amaru ML, and Torsvik TH (2010) Towards absolute plate motions constrained by lower-mantle slab remnants. *Nature Geoscience* 3: 36–40.

Visser K, Trampert J, Lebedev S, and Kennett BLN (2008) Probability of radial anisotropy in the deep mantle. *Earth and Planetary Science Letters* 270: 241–250.

Wen L and Anderson DL (1995) The fate of slabs inferred from seismic tomography and 130 million years of suduction. *Earth and Planetary Science Letters* 133: 185–198.

Wen L and Anderson DL (1997) Layered mantle convection: A model for geoid and topography. *Earth and Planetary Science Letters* 146: 367–377.

Widiyantoro S, Pesicek JD, and Thurber CH (2011) Subducting slab structure below the eastern Sunda arc inferred from non-linear seismic tomographic imaging. *Geological Society, London, Special Publications* 355: 139–155.

Widiyantoro S and van der Hilst R (1996) Structure and evolution of subducted lithosphere beneath the Sunda arc, Indonesia. *Science* 271: 1566–1570.

Zhao D, Pirajno F, Dobretsov NL, and Liu L (2010) Mantle structure and dynamics under East Russia and adjacent regions. *Russian Geology and Geophysics* 51: 925–938.

Zhao D, Tian Y, Lei J, Liu L, and Zheng S (2009) Seismic image and origin of the Changbai intraplate volcano in East Asia: Role of big mantle wedge above the stagnant Pacific slab. *Physics of the Earth and Planetary Interiors* 173: 197–206.

1.21 Deep Earth Structure - Transition Zone and Mantle Discontinuities

R Kind and X Li, Deutsches GeoForschungsZentrum GFZ, Potsdam, Germany

© 2015 Elsevier B.V. All rights reserved.

1.21.1	**Introduction**	656
1.21.2	**The Mantle Transition Zone**	658
1.21.2.1	Global Transition Zone Structure	658
1.21.2.2	Regional Transition Zone Structure	660
1.21.2.2.1	Japan	662
1.21.2.2.2	China	663
1.21.2.2.3	Izu–Bonin and Tonga	663
1.21.2.2.4	Andes	663
1.21.2.2.5	Yellowstone	663
1.21.2.2.6	Hawaii	663
1.21.2.2.7	Other hot spots	663
1.21.2.2.8	North America	664
1.21.2.2.9	Africa	664
1.21.2.2.10	Oceans	664
1.21.2.2.11	Other regions	664
1.21.2.3	Sharpness of 410 and 660	665
1.21.2.4	Low-Velocity Zone atop the 410	665
1.21.2.5	The 520 Discontinuity	665
1.21.2.6	Summary of the Upper-Mantle Transition Zone	665
1.21.3	**The Gutenberg Discontinuity (LAB)**	666
1.21.3.1	Possible LAB Observations	668
1.21.3.1.1	Pacific	668
1.21.3.1.2	China and Tibet	668
1.21.3.1.3	Africa	669
1.21.3.1.4	Europe and the Middle East	669
1.21.3.1.5	North America	669
1.21.3.1.6	South America	669
1.21.3.1.7	General observations	670
1.21.3.1.8	Summary of the Gutenberg discontinuity (LAB)	671
1.21.4	**The Lehmann Discontinuity**	672
1.21.5	**The Hales Discontinuity**	673
1.21.6	**Conclusions**	673
Acknowledgment		674
References		674

Glossary

410 discontinuity Seismic discontinuity at 410 km depth in global average, mainly caused by phase transition from olivine to spinel.

520 discontinuity Seismic discontinuity near 520 km depth, observed at many places on Earth, but not laterally continuously.

660 discontinuity Seismic discontinuity at 660 km depth in global average, caused by spinel to magnesiowuestite–perovskite phase transition.

Asthenosphere Low-viscosity weak layer below the lithosphere.

EarthScope with USArray Large projects to study the North American lithosphere.

GEOFON Global seismic network of the GFZ Potsdam, Germany, and international partners.

GEOSCOPE Global seismic network of the IPGP Paris, France.

Gutenberg discontinuity Seismic discontinuity with a decrease of velocity downward, top of low-velocity zone. May be lithosphere–asthenosphere boundary in oceanic regions.

Hales discontinuity Seismic discontinuity in the mantle lithosphere.

Hi-net High-sensitivity seismograph network in Japan.

INDEPTH International Deep Profiling of Tibet and the Himalaya

IRIS Global seismic network of US universities and US Science Foundation.

LAB Lithosphere–asthenosphere boundary; boundary between high-viscosity lithosphere and low-viscosity asthenosphere.

 http://dx.doi.org/10.1016/B978-0-444-53802-4.00017-8

Lehmann discontinuity Seismic discontinuity, supposed to be the bottom of the asthenosphere.
Lithosphere Elastic uppermost layer of the Earth, defined by its mechanical properties; lithospheric plates move over great horizontal distances.
MLD Recently discovered midlithospheric discontinuity in cratons near 100 km depth with velocity decrease downward.
Moho Mohorovičić discontinuity, crust–mantle boundary, seismically defined.
ORFEUS Observatories and Research Facilities for European Seismology, the Netherlands.
P′P′ Abbreviation of PKPPKP, a P phase bottoming in the core with one reflection at the surface.
PP P phase with one reflection at the surface.
Ps P-to-S converted wave.
Receiver functions P-to-S converted phases in the coda of P, or S-to-P conversions as precursor of S, diagnostic for structure beneath a seismic station.
ScS S wave reflected from the core–mantle boundary.
Sp S-to-P converted wave.
SS S phase with one reflection at the surface.

1.21.1 Introduction

When Ernst von Rebeur-Paschwitz recorded in Potsdam, Germany, the first teleseismic earthquake, he immediately recognized the importance of his discovery for illuminating the Earth's interior (von Rebeur-Paschwitz, 1889). He suggested that a global network of seismographs should be installed and the data should be evaluated by seismologists. This is still today a very modern idea, although we have achieved much since then with the construction of the Global Seismographic Network and the free exchange of data. The evaluation of the first seismic records showed that the Earth has an onion shell character with crust, mantle, and outer and inner core, separated by seismic discontinuities. The increase of seismic data led later to the discovery of more seismic discontinuities in the upper mantle; the Gutenberg, the Hales, and the Lehmann discontinuities; and, especially important, the discontinuities at about 410, 520, and 660 km depth (called simply the '410,' '520,' and '660'), and perhaps even more less clear ones. The exact knowledge about these discontinuities, their distribution, their topography, their nature, or their sharpness sets boundary conditions for mantle dynamics or petrology. For plate tectonics, the concept of rheological layers (lithosphere and asthenosphere) became important. Immediately, the question arises: How can these mechanical plate definitions be confirmed with seismological observations? What is the seismic appearance of the lithosphere–asthenosphere boundary (LAB)? Since seismology is in first order in observational science, the increase of data can bring an increase of knowledge. Therefore, the seismic networks are continuously densified (e.g., EarthScope with USArray) in order to produce more detailed images of the Earth's interior. It is easily foreseeable that these new data will lead to a wealth of new discoveries about the dynamics of our planet.

We review the global structure of the major seismic discontinuities in the upper mantle. The emphasis of our study is the seismic observations. We are mainly discussing seismic methods that are sensitive to discontinuities rather than to gradual velocity changes, like seismic tomography. The well-known discontinuities at about 410 and 660 km average depth globally are primarily focused upon. The Moho, separating the upper mantle from the crust, is not discussed here (see **Chapters 1.11**, **1.12**, **1.13**, **1.14**, and **1.15**). Between the Moho and 410, a number of additional discontinuities are reported, of which we will only treat the relatively well-established and pervasive ones, although they are all much less clear than the discontinuities so far mentioned. These discontinuities include the Gutenberg discontinuity, which is frequently identified with the LAB between about 100 and 200 km depth, the Hales discontinuity at 80 km depth, and the Lehmann discontinuity at the base of the asthenosphere at 220 km depth. Except for the LAB, all mentioned discontinuities are seismologically defined. The LAB was originally defined mechanically by postglacial rebound observations (see **Chapters 6.02** and **6.03**). Seismologists are trying to identify this discontinuity in seismic data. In the course of plate tectonics, the LAB gained additional significance since it was suggested that lithospheric plates move over large horizontal distances with the LAB as a shear zone. Since the LAB is so far only poorly observed seismologically and then mainly by low-resolution long-period surface waves, it is usually assumed that it is a broad transition zone rather than a sharp seismic discontinuity. In recent times, receiver functions have sharpened our view at the LAB.

Wide-angle observations have been the fundamental seismic tool for detecting the upper-mantle discontinuities (see **Chapters 1.04** and **1.05**). This technique is however less suited for determining their small-scale topography, because the lateral part of the travel path of wide-angle rays is several times longer than the vertical part. Steep-angle techniques (see **Chapter 1.08**), which are more suited for determining small-scale topography of the mantle discontinuities, include ScS reverberations (e.g., Revenaugh and Jordan, 1987, 1991a,b); SS, P′P′, and PP precursors (e.g., Adams, 1968, 1971; Bolt, 1970; Engdahl and Flinn, 1969; King et al., 1975; Shearer, 1991, 1993; Whitcomb and Anderson, 1970; Zheng and Romanowicz, 2012); and Ps and Sp conversions at the discontinuities (receiver functions, e.g., Bath and Stefansson, 1966; Benz and Vidale, 1993; Chevrot et al., 1999; Faber and Müller, 1980; Li et al., 2003a; Stammler et al., 1992; Vinnik, 1977; Xu et al., 1998; see **Figure 1** for ray paths of such phases). All these phases are small secondary phases in front of or after a main phase like P, S or PP, P′P′, SS, or ScS (see **Chapter 1.20**). Ps or Sp conversions or reflections of local high-frequency subduction zone earthquakes may be used to map the topography of the 410 and 660 with very high resolution (see ray paths in **Figure 2**).

At the beginning of seismological research, all data have been analog. Processing of the data, even simple plotting at the

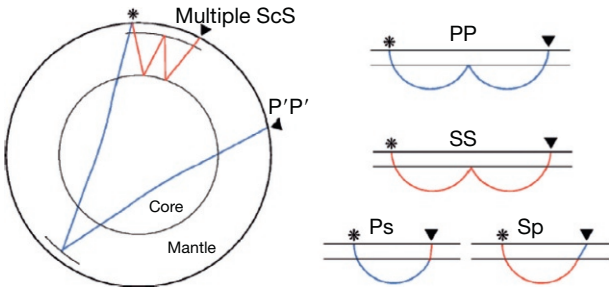

Figure 1 Ray paths of teleseismic phases frequently used to study mantle discontinuities. They include ScS reverberations reflected at upper- or lower-mantle discontinuities; P′P′ (PKPPKP) precursors from upper-mantle discontinuities; SS and PP precursors and Ps and Sp conversions at upper-mantle discontinuities (receiver functions).

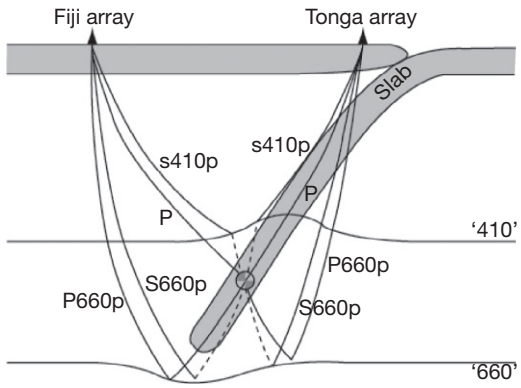

Figure 2 Reflected and converted rays of locally recorded subduction zone earthquakes. Such high-frequency data result in high-resolution imaging of the mantle discontinuities near subduction zones. Reproduced from Tibi R and Wiens DA (2005) Detailed structure and sharpness of upper discontinuities in the Tonga subduction zone from regional broadband arrays. *Journal of Geophysical Research B: Solid Earth* 110(6): 1–14, Figure 2.

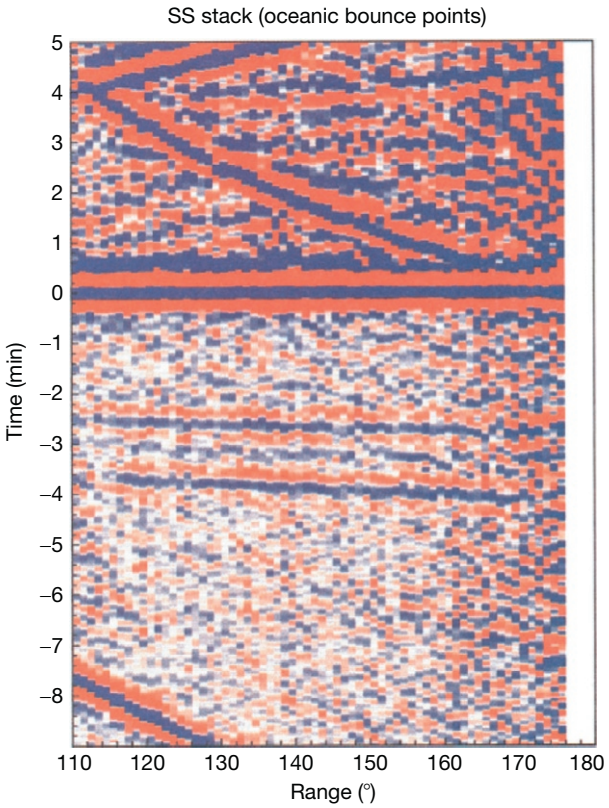

Figure 3 Global stacks of SS waveform data. Time versus range image showing SS (at 0 min) and its precursors (between about −2 and −4 min) at 410, 520, and 660 km depth obtained by stacking long-period seismograms. Reproduced from Shearer PM (1996) Transition zone velocity gradients and the 520-km discontinuity. *Journal of Geophysical Research* 101: 3053–3066, Plate 1.

desired scale, was difficult. Still, the major one-dimensional (1D) structure of the Earth was resolved with such data. In the last decades, digital techniques, however, have made a rapid development. Since weak seismic signals are more and more used, which are hardly visible in individual seismograms, delay-and-sum techniques, known as stacking in array technology, are introduced in seismology. Array techniques require large amounts of data. The processing steps applied now include simple rotation of the components for separation of the different wave types, deconvolution or correlation techniques, or migration from the time domain into depth sections. Ps conversions are increasingly used (Langston, 1979; Vinnik, 1977). In crustal studies, they are known under the name 'receiver functions.'

Ps conversions are also often used for observations of the discontinuities at 410 and 660 km depth below single broadband stations or arrays of broadband stations. Long-period SS precursors, which are reflected at the midpoint between source and receiver at upper-mantle discontinuities, are also frequently utilized. They are especially useful for global mapping of the discontinuities at 410, 520, and 660 km depth (see Figure 3). An important advantage of SS precursors is that they provide information about oceanic regions where few stations are located.

Secondary peg-leg multiples of ScS and its reverberations are very useful (see Figure 4 for a data example). More recently, Sp conversions (incident teleseismic S waves converted to a P wave at a discontinuity below a station) have also proved to be successful in observing boundaries in the upper mantle.

There are two types of seismic data that are mainly utilized for studies of the upper-mantle discontinuities. The first type stems from the permanent global seismic networks (Incorporated Research Institutions for Seismology, IRIS, see Butler et al. (2004); GEOFON, see Hanka et al. (2000); GEOSCOPE, see Romanowicz et al. (1991); or ORFEUS, see http://www.orfeus-eu.org/) and many other contributing stations. These networks together have a global coverage but still have a relatively low density of station distribution in many regions. This is especially true for oceanic areas. Data from these networks can result in relatively low-resolution global images. Oceans are only sampled with island stations, which are highly exceptional places, not typical of the large-scale oceanic mantle. Permanent or temporary ocean-bottom installations are very expensive and technically difficult and for this reason very rare. The second type of data stems from relatively short-term deployments of much denser networks (see Chapter 1.14). They have only local or regional distribution but allow much higher-resolution

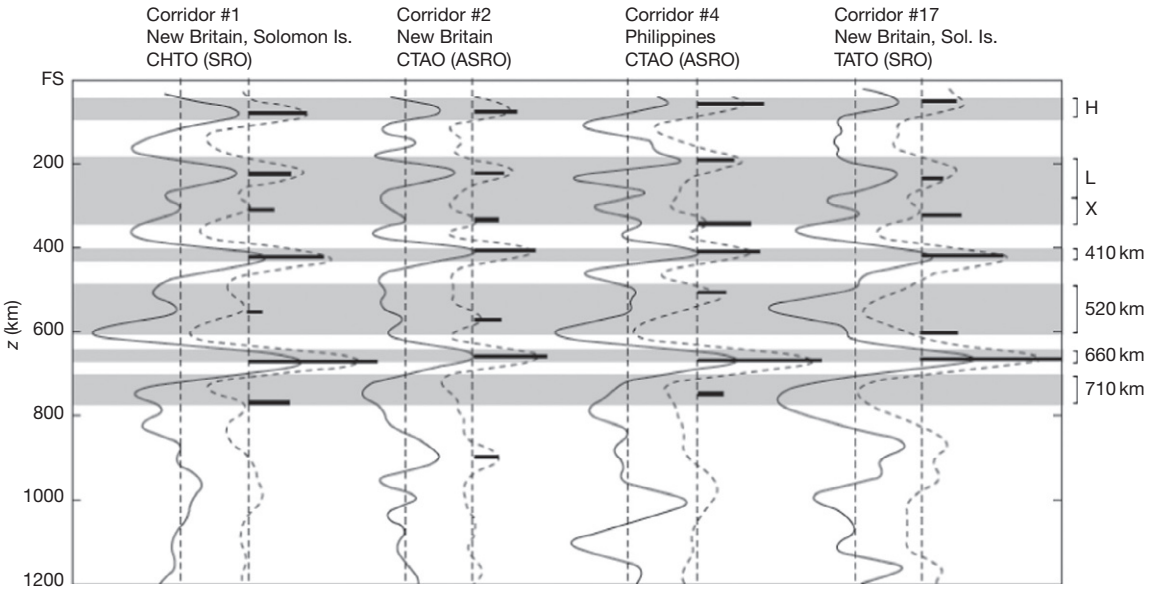

Figure 4 Observed (solid lines) and synthetic (dashed lines) ScS reverberations from a number of upper-mantle discontinuities along several great circle paths. Reproduced from Revenaugh JS and Jordan TH (1991b) Mantle layering from ScS reverberations. 3: The upper mantle. *Journal of Geophysical Research* 96: 19781–19810, Figure 3.

images. The previously mentioned permanent networks operate open stations allowing unrestricted near-real-time access to their data by any user. Most temporary networks also make their data freely available after some time. Therefore, a rapidly increasing amount of high-quality seismic data is available for global studies. This policy of free data access is of great advantage for international science and the first examples provided by the IRIS and PASSCAL projects, as the large data producers, cannot be overestimated.

1.21.2 The Mantle Transition Zone

1.21.2.1 Global Transition Zone Structure

All modern global reference Earth models show a sudden increase of the velocities of the elastic waves and densities near 410 and 660 km depth (e.g., the PREM, Dziewonski and Anderson, 1981, or the IASP91 global reference model, Kennett and Engdahl, 1991). This region of the mantle is called the transition zone between the upper and lower mantle. Earlier Earth models (Gutenberg, 1959; Jeffreys and Bullen, 1940) indicate changes in the velocity gradients at these depths, without resolving first-order discontinuities, based on observations of slowness changes and increasing P wave amplitudes at about 20° epicentral distance (Byerly, 1926; Jeffreys, 1936). More intensive seismic wide-angle controlled source and earthquake source studies began in the 1960s, leading to better data quality; hence, the two major global seismic discontinuities were discovered near 410 and 660 km depth (e.g., Ibrahim and Nuttli, 1967; Johnson, 1967; Julian and Anderson, 1968; Kanamori, 1967; Niazi and Anderson, 1965). In the following years, many wide-angle studies were undertaken and regional upper-mantle models were derived for continental and oceanic areas (e.g., Walck, 1984; or summarized by Nolet et al., 1994 and Gaherty et al., 1996; see **Chapter 1.07**). The computation of theoretical seismograms has been an essential tool for modeling the waveforms at the travel-time triplications (e.g., Helmberger, 1968; Helmberger and Wiggins, 1971).

Both discontinuities have been interpreted as pressure- and temperature-induced phase changes in the olivine system (e.g., Anderson, 1967; Anderson and Bass, 1986; Bass and Anderson, 1984; Bina and Wood, 1986; Birch, 1952; Green and Liebermann, 1976; Green and Ringwood, 1967; Ito and Takahashi, 1989; Jeanloz and Thompson, 1983; Lees et al., 1983; Liu, 1976; Ringwood, 1969; Shim et al., 2001; see **Chapter 2.06**). It has, however, also been suggested that compositional changes may occur around these depths (e.g., Irifune and Isshiki, 1998). If the 410 and 660 are olivine phase boundaries, then lateral temperature changes would cause topography of both discontinuities. From the estimated Clapeyron slopes of both discontinuities, it is expected that a 100 K temperature variation would change the depths of the 410 and 660 by about 8 and 5 km, respectively (Bina and Helffrich, 1994). The Clapeyron slopes have opposite signs (410 positive and 660 negative), so a 100 K higher temperature should reduce the transition zone thickness by about 13 km and a 100 K lower temperature should thicken the transition zone by about the same amount. Thus, the topography of the upper-mantle discontinuities, or better the thickness of the transition zone, should indicate the lateral distribution of hot and cold regions in the transition zone. The depths of the 410 and 660 discontinuities should be anticorrelated if the effect of temperature dominates and the temperature at the 410 correlates with that at 660 (Revenaugh and Jordan, 1989, 1991a). Such thinner and thicker transition zone regions could play an important role in revealing global mantle circulation, as they could distinguish upwelling and downwelling material. However, it should be kept in mind that the topography of the 410 and 660 could also be modified by other influences (e.g., chemistry or garnet phase transitions; see Anderson (1989)).

Topography could also be caused by metastable olivine below 410 km depth in subduction zones (Kirby et al., 1996).

Images of the global transition zone thickness should be able to answer several questions. The first one should be to verify the reality of the model of olivine phase transformations as the cause of the discontinuities at 410 and 660 km depth and also to verify laboratory values of the Clapeyron slopes of both discontinuities. This could be done if global anticorrelation of both discontinuities would be observable. The second question would be to confirm possible locations of hot and cold material in the transition zone in regions where we also have other evidence for hot or cold material (e.g., from tomography or earthquake locations in subduction zones or below postulated plumes). A third question would be to contribute to the problem of the deep roots of continents, which may affect even the transition zone (Jordan, 1975).

Ps and Sp conversion techniques sample the upper-mantle structure within a radius of several hundred kilometers around a seismic station. Precursor techniques of surface-reflected phases, such as PP or SS, sample the midpoints between epicenters and receivers. Precursor techniques allow a better global distribution of sampling points, reaching locations without stations or earthquake sources. They have the drawback of being associated with maximum travel-time phases, which raises the issue of possible contamination by small-scale, off-great-circle-path structure. This and related questions have been discussed by Neele et al. (1997), Shearer et al. (1999), Neele and De Regt (1999), and Chaljub and Tarantola (1997). On the other hand, converted phases, which are minimum travel-time phases, allow better resolution, in principle, due to their smaller Fresnel zones. Their global sampling is poorer, however, because they are restricted to near-station or earthquake locations. Liu (2003) pointed out possible problems caused by attenuation for detecting upper-mantle signals. Secondary phases like Sp or Ps conversions, or SS or PP precursors, are usually very weak phases, so summation must be used to improve the signal-to-noise ratio. In the case of conversions, frequently, data from one station are summed. If stations are sufficiently closely spaced, traces with nearby conversion points may be summed (common conversion point summation). Sp conversions sample a larger region than Ps conversions because of the ray paths involved. In the case of SS or PP precursors, traces with close reflection points are summed (common reflection point summation). An et al. (2007), Gu et al. (2009), and Gu and Sacchi (2009) applied the Radon transform method to SS precursors.

The 410 and 660 have been detected in multiple reflections of S waves from the core–mantle boundary (ScS reverberations) by Revenaugh and Jordan (1987, 1991a) in the western Pacific. They found a negative correlation of both discontinuities with about a 20 km topography. In an early paper, Wajeman (1988) stacked PP precursors from earthquakes in Japan, recorded in Europe, with bounce points below northern Eurasia. The first truly global map of the 660 was obtained by Shearer and Masters (1992) from SS precursors. A significant result was the deepening of the 660 around the Pacific. Shearer (1993) published the first maps of both discontinuities, the 410 and 660, from SS precursors. A similar study was done by Gossler and Kind (1996), who suggested a correlation of the transition zone thickness with the ocean–continent distribution at the Earth's surface, which would imply a relation of the continental roots and the transition zone. Flanagan and Shearer (1998a) found a thinned transition zone in the Pacific and a thickened one at the Pacific subduction zones. No ocean–continent correlation with transition zone thickness was concluded by Gu et al. (1998) in SS precursors. They observed, however, a discontinuity at 520 km depth below oceans, but not below continents. An ocean–continent correlation with the transition zone thickness was also not confirmed by Flanagan and Shearer (1999) in PP precursor data. They found a 30 km global topography of the 410. A slightly thicker transition zone below continents than below oceans was found by Gu and Dziewonski (2002) in a global SS precursor study (see **Figure 5**). A significant change of the depth of the 410 at subduction zones was not observed by Flanagan and Shearer (1998b) using precursors of depth phases from the 410 from deep subduction zone earthquakes. Helffrich (2000, 2002) studied and reviewed the global transition zone. An astonishing observation was made by Estabrook and Kind (1996) who demonstrated that PP precursors from the 660 are globally not observed, in contrast to the prediction by the IASP91 global reference model and to the clearly observed PP precursors from the 410 (see **Figure 6**). Shearer and Flanagan (1999) modeled velocity and density jumps across the 660 to explain the missing PP precursors from the 660. Deuss et al. (2006) observed PP precursors of the 660 in some regions. Thomas and Billen (2009) also observed the 660 in PP

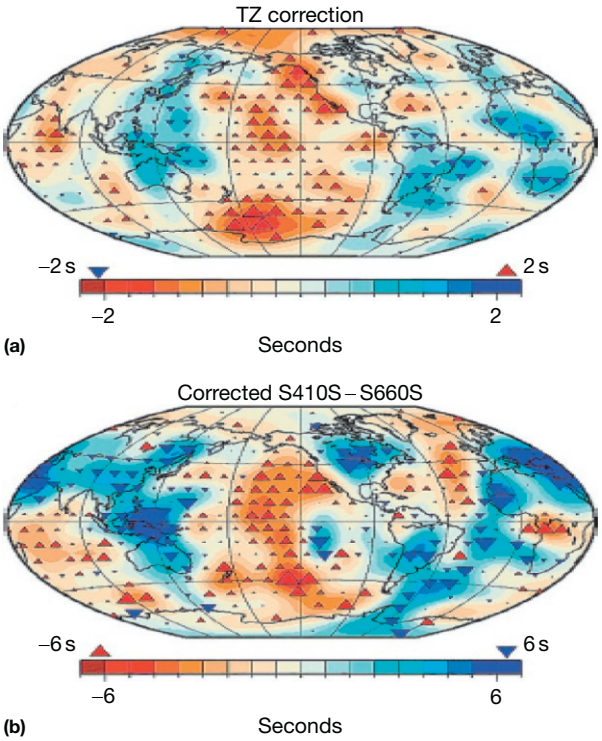

Figure 5 (a) Colored background: velocity perturbations from tomography at 550 km depth. Triangles: computed corrections for SS precursors using the tomography model. (b) Global differential times of SS precursors from the 410 to 660 discontinuities, corrected with data in (a). Reproduced from Estabrook CH and Kind R (1996) The nature of the 660-kilometer upper-mantle seismic discontinuity from precursors to the PP phase. *Science* 274: 1179–1182, Figure 1.

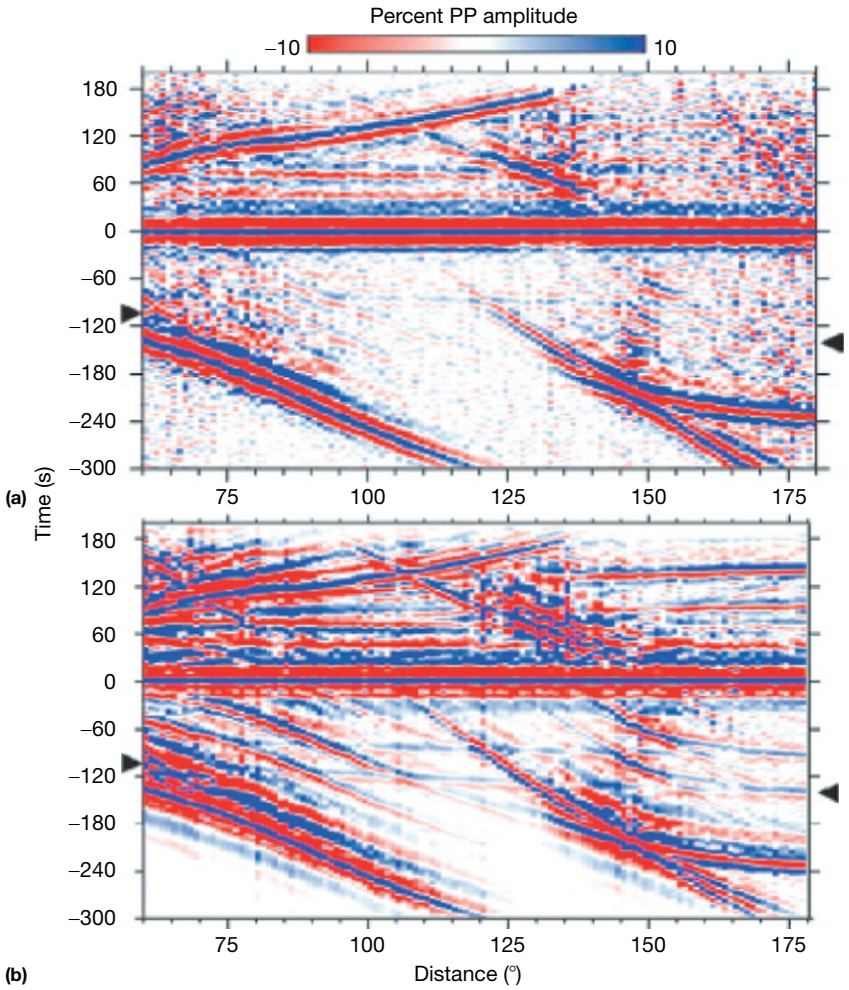

Figure 6 (a) Global stacks of PP waveforms showing PP (at 0 s) and precursor from the 410 (at about −70 s). The precursor from the 660 is missing in the data. (b) Corresponding synthetic seismograms for the IASP91 global reference model. This model (and other reference models) predicts a precursor at the 660. A model explaining the missing 660 precursor should have less contrast in P velocity. Reproduced from Gu YJ and Dziewonski AM (2002) Global variability of transition zone thickness. *Journal of Geophysical Research* 107(7): 2135. http://dx.doi.org/10.1029/2001JB000489, Figure 9.

precursors in the southwest Pacific. Day and Deuss (2013) compared observations of P′P′ and PP precursors from the 660.

Different flow patterns below and above the 660 have been derived by Gu et al. (2001b). A correlation between tomographic velocities in the transition zone and its thickness from Ps conversions was found by Lebedev et al. (2002b, 2003). Gu et al. (2003) inverted simultaneously SS precursors and tomographic velocities for mantle transition zone structure (see **Figure 7**). A comparison of Ps conversions and SS precursors below hot spots was made by Li et al. (2003a,b). They found a thinned transition zone below many hot spots and a plume width of <200 km in diameter (see **Figure 8**). In a joint inversion of PP and SS precursors, Chambers et al. (2005a,b) found an uplifted 410 beneath cratons in agreement with the results of Gu et al. (1998). Lawrence and Shearer (2006a,b, 2008) did comprehensive global studies in comparison with tomography results. Anticorrelation of SS precursors from the 410 and 660 was found by Houser et al. (2008). Andrews and Deuss (2008) and Deuss (2009) observed doublet structures of the 660 in many regions and reviewed SS and PP precursor studies. With SS precursors, Heit et al. (2010) found along a profile from the Aleutians to Tibet a thickened transition zone below the Pacific subduction region and below northern Tibet. Das Sharma et al. (2010) suggested a relation between transition zone thickness below hot spots and plume buoyancy flux.

1.21.2.2 Regional Transition Zone Structure

The global studies of the 410 and 660 discussed so far used mainly data from open global permanent networks and from other open permanent stations. Although the global coverage of broadband stations is continuously increasing, there are still large gaps, especially in the oceans. There are however many temporary or locally confined much denser deployments of seismic stations, not necessarily all broadband, which are used for detailed studies of the mantle transition zone. Such networks can answer questions that cannot be answered with sparse networks. Therefore, we also discuss detailed local or regional studies using temporary dense deployments of large numbers of

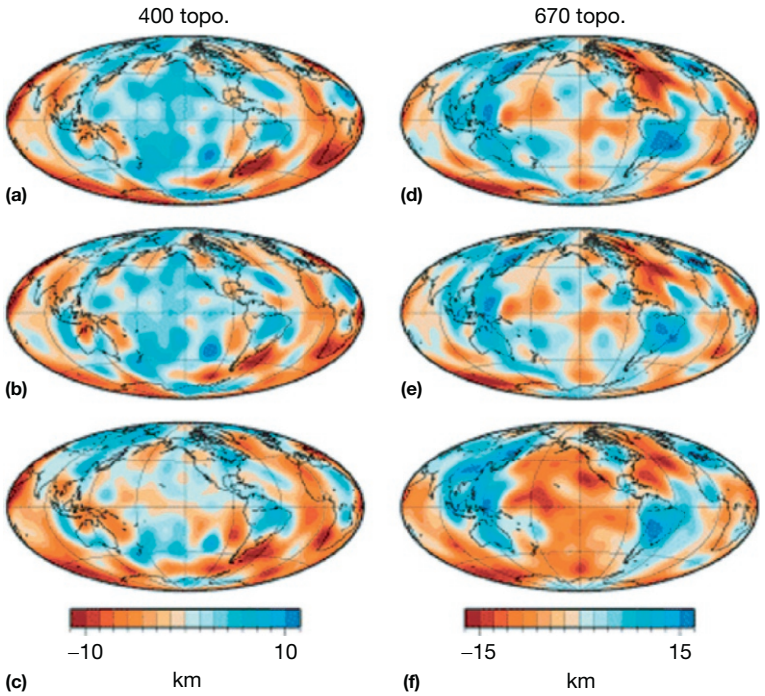

Figure 7 Topography of 410 and 660 (400 and 670 in PREM). 410 depth from SS precursors, (a) from Flanagan and Shearer (1998a) and (b) from Gu et al. (2003). (c) Results of joint inversion of SS precursors and mantle velocity. (d)–(f) Similar to (a)–(c), but for topography of the 660. Reproduced from Gu YJ, Dziewonski AM, and Ekstrom G (2003) Simultaneous inversion for mantle shear velocity and topography of transition zone discontinuities. *Geophysical Journal International* 154: 559–583, Figure 11.

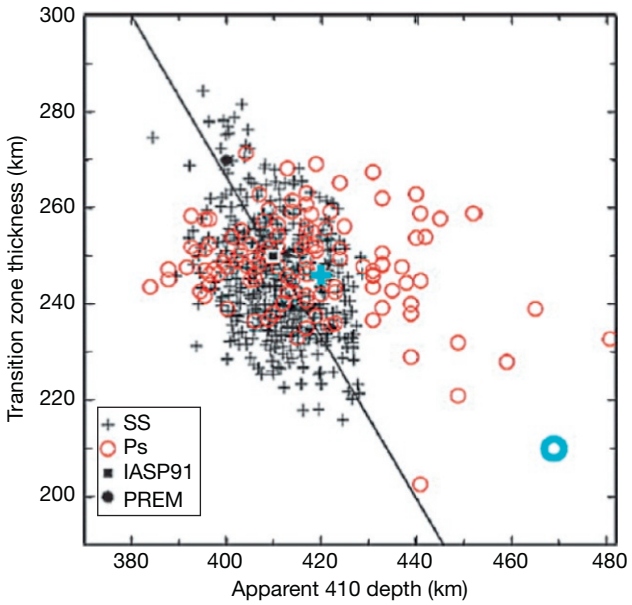

Figure 8 Thickness of mantle transition zone versus apparent 410 depths derived from arrival times of SS precursors and Ps conversions using the IASP91 global reference model. Ps depths (open circles) deeper than 430 km are all from ocean island stations. Straight line indicates relation between transition zone thickness and depth of 410 as expected from laboratory Clapeyron slopes. Thinner transition zone regions seem to concentrate in oceanic and thicker ones in tectonic areas. Reproduced from Li X, Kind R, Yuan X, et al. (2003b) Seismic observation of narrow plumes in the oceanic upper mantle. *Geophysical Research Letters* 30(6): 1334. http://dx.doi.org/10.1029/2002GL015411, Figure 2.

seismic stations in zones where variations of the transition zone thickness could provide results of interest. The lack of long recording time in these studies is overcome by the large number of closely spaced stations. In the following, we review results from such experiments in several regions of the world.

1.21.2.2.1 Japan

Japan is located in the Pacific Northwest subduction zone, below which the mantle transition zone is expected to be thick. First Ps studies found no depression of the 660 (Vinnik et al., 1996) or a strong depression beneath the GEOSCOPE station Inuyama in Japan (Thirot et al., 1998). Ps conversions from the Japanese broadband network have been used by Li et al. (2000a). They found the 660 at 700 km depth directly where the slab hits the transition zone but no larger-scale depression as it could be expected from the cold transition zone observed in a tomography study (Bijwaard et al., 1998). Kato et al. (2001) observed in ScS reverberations a weakly depressed 660. Again with receiver functions, Ramesh et al. (2005) observed anticorrelation of the 410 and 660 of the Philippine Sea plate below Japan. In near-vertical reflections from a regional earthquake recorded by 500 tiltmeters and 60 broadband seismometers in Japan, a 660 depressed by 15 km and an elevated 410 were found within the slab (Tono et al., 2005). Tonegawa et al. (2005) observed with Ps conversions the 660 depressed by 50 km and the 410 elevated by 30 km where it is hit by the slab. Also, Tonegawa et al. (2006) observed directly with data from 678 Hi-net tiltmeter stations the Pacific slab down to the elevated 410. The existence of a metastable olivine wedge below the 410 is demonstrated at the Japan slab by Kawakatsu and Yoshioka (2011) in P receiver functions (see **Figure 9**). Rare PP precursors from the 660 and a thickened transition zone have been identified below the Kurile slab by Schmerr and Thomas (2011). A thickened transition zone below Japan was also confirmed by an SS precursor study by Gu et al. (2012).

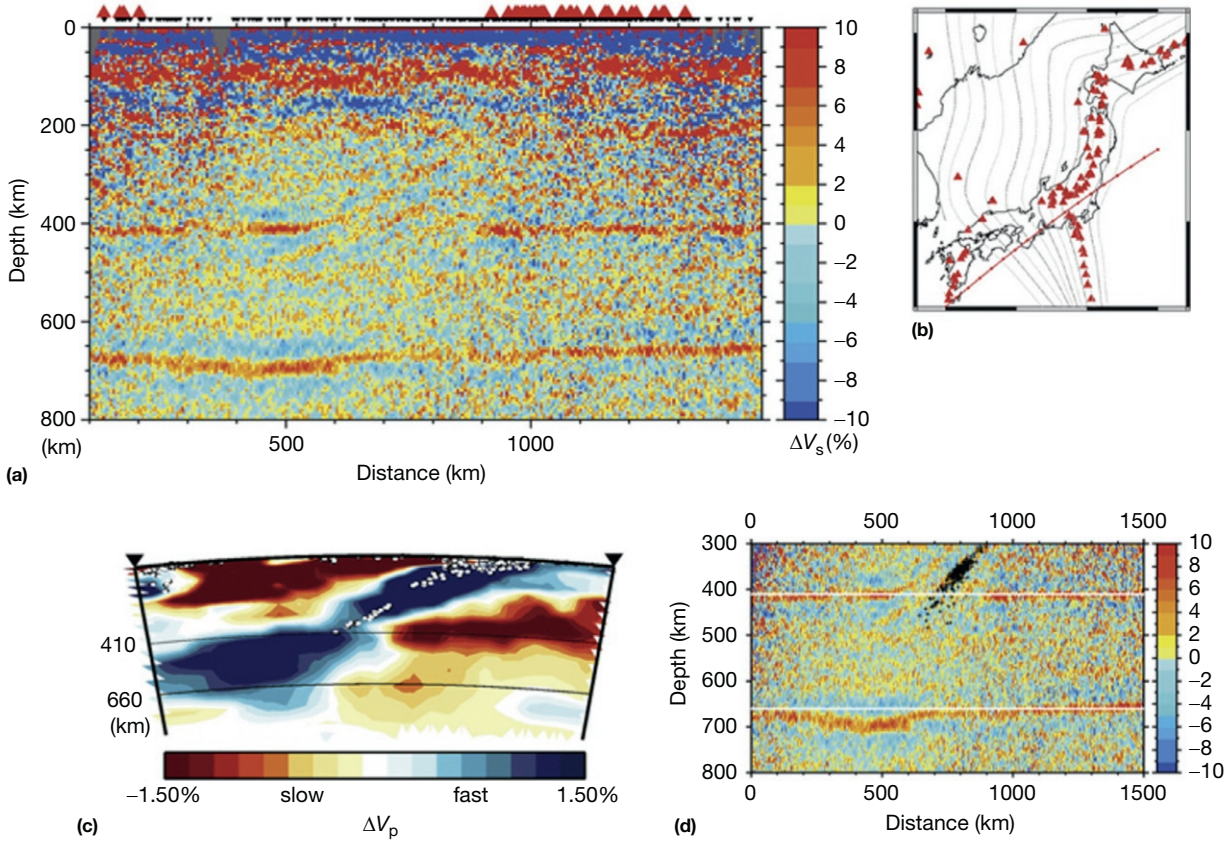

Figure 9 The reflectivity profile beneath southwest Japan. (a) Reflectivities given by receiver functions are measures of local S wave velocity jumps, as a P-to-S seismic wave conversion is sensitive to the S wave velocity change. Receiver functions are averaged over 3° wide range along the red line in (b). Red and blue colors correspond to velocity increase and decrease with depth, respectively. Red triangles and reversed black triangles plotted on the top, respectively, indicate active volcanoes and stations used for the imaging located within the cross-section range. The color scale is given in terms of an equivalent S wave velocity change at a first-order discontinuity in percent, but only relative values are meaningful. (b) A map of Japan with volcanoes (red triangles). Gray lines are isodepth contours (50–600 km) of the subducting Pacific slab. Distances in (a) and (d) are measured from the southwest end point (30° N, 130° E) of the red line, and dots on the red lines are given in a 100 km interval. (c) Image of a global seismic tomography along the same cross section (Obayashi et al., 2009). (d) Enlarged section of (a) with vertical exaggeration. Two white horizontal lines are drawn at depths of 410 and 660 km. Note the depression of 660 km discontinuity over about a 500 km width range. Plus marks indicate seismicity. Reproduced from Kawakatsu H and Yoshioka S (2011) Metastable olivine wedge and deep dry cold slab beneath southwest Japan. *Earth and Planetary Science Letters* 303: 1–10, Figure 1.

1.21.2.2.2 China

Ps conversions have been used by Niu and Kawakatsu (1996, 1998) and Yang and Zhou (2001) for studies of the 410 and 660 especially in northeast China, where the downgoing oceanic slab is reaching the mantle transition zone. Yuan et al. (1997) and Kind et al. (2002) found in southern Tibet good agreement of the depths of the 410 and 660 with the IASP91 global reference model. Li and Yuan (2003) found a 20 km thickened transition zone in northeast China where it is hit by the Pacific slab. A locally depressed 660 was also found by Ai and Zheng (2003) and Ai et al. (2003) in northeast China. Shen et al. (2008) and Chen and Ai (2009) have produced maps of the 410 and 660 from P receiver functions. Ai et al. (2008) found a small-scale thinning of the transition zone below the North Yellow Sea in receiver functions. Wang and Chen (2009) studied the velocity contrast at the 660 below the Kuriles and the Japan slab from wide-angle earthquake recordings. Zhang et al. (2010) found a depressed 410 under east Tibet at the border of the Sichuan Basin. Indications of a depressed 410 have also been found by Shen et al. (2011) at the northeastern margin of Tibet. Hu et al. (2013) found simultaneous depression of the 410 and 660 in eastern Tibet below the Longmenshan. Indications of a stagnant slab in the transition zone in eastern China have been reported by Gao et al. (2010) and Ye et al. (2011). Wang and Niu (2010) found in northeast China a thickened 660 transition using wide-angle array data. Tian et al. (2011) found the 410 and 660 across the Ordos Block and the Yinshan Mountains at their normal position. Yue et al. (2012) identified a 10–20 km topography variation of the 410 and 660 in central Tibet near the INDEPTH line.

1.21.2.2.3 Izu–Bonin and Tonga

Revenaugh and Jordan (1987), Roth and Wiens (1999), and Suetsugu et al. (2004) studied the 410 and 660 in the western Pacific with ScS reverberations. Thickening of the transition zone, deepening of the 660, and uplifting of the 410 have been shown by Richards and Wicks (1990), Vidale and Benz (1992), Wicks and Richards (1993), Collier and Helffrich (1997), Collier et al. (2001), and Castle and Creager (1997, 1998). Gilbert et al. (2001) confirmed such observations with ocean-bottom seismic data. Zhou et al. (2012) recognized a multiple 660 structure in S-to-P conversions below earthquake sources. Tibi and Wiens (2005) studied the 410 and 660 with local high-frequency seismic phases recorded by an array of broadband island stations. They found practically no change in the 410 depth; the 660 was depressed to 714 km (see **Figure 2**). Local seismic signals have also been used by Zang et al. (2006) to identify multiple discontinuities near the 660.

1.21.2.2.4 Andes

A thickened transition zone was observed beneath the Andean subduction in ScS reverberations by Clarke et al. (1995). Collier and Helffrich (2001) observed from near-source S-to-P conversions the 410 elevated by 60 km where it is hit by the slab and at normal depth in surrounding regions. Thickening of the transition zone from the Pacific to the Andean subduction was observed by Liu et al. (2003). Schmerr and Garnero (2007) studied the transition zone in the entire region of South America and surroundings using SS precursors. Wölbern et al. (2009) studied the transition zone below the southern Puna. Contenti et al. (2012) derived from SS precursors that a depressed 660 beneath the Andean slab is extending far to the east of the slab.

1.21.2.2.5 Yellowstone

Dueker and Sheehan (1997b) observed in receiver functions a 20–30 km thickness variation of the transition zone across the Yellowstone hotspot track. Beucler et al. (1999) found also in receiver functions no clear 410 beneath the Snake River Plain but a largely deflected 660. Similar observations have been made by Sheehan et al. (2000). Humphreys et al. (2000) found both discontinuities, the 410 and 660, uplifted in the Yellowstone hotspot track. Gilbert et al. (2003) and Fee and Dueker (2004) identified 20–40 km depth variation of both, the 410 and the 660, but uncorrelated with surface tectonics. Eagar et al. (2010) showed a thinned transition zone below Yellowstone in USArray data, which was later confirmed with the same data by Tauzin et al. (2013). Schmandt et al. (2012) found in USArray data the 660 deflected upward by 12–18 km beneath the hot spot and the 410 is within 5 km of its mean depth.

1.21.2.2.6 Hawaii

Li et al. (2000b) showed in receiver functions the thinning of the transition zone by 40–50 km in the southwest of the main island of the Hawaiian chain, which could indicate an inclined plume conduit.

A thinned transition zone was also found by Collins et al. (2002) below the Hawaiian swell in receiver functions and by Courtier et al. (2007) in ScS reverberations. A narrow transition zone was seen with SS precursors by Schmerr et al. (2010). Cao et al. (2011) observed also in SS precursors a large topography of the 410 and 660 west of Hawaii. Huckfeldt et al. (2013) found in receiver functions the deepening of the 410 from the northwest to the southeast below the Hawaiian chain and to the southwest of the Big Island.

1.21.2.2.7 Other hot spots

Below Iceland, Shen et al. (1996, 1998b, 2002) found with Ps conversions a 20 km thinned transition zone, whereas Du et al. (2006) did not observe an anomaly of the 660. Below the Eifel, Grunewald et al. (2001) and Budweg et al. (2006) showed a deepening of 410. Below the South Pacific superswell, Suetsugu et al. (2004) found a locally reduced transition zone thickness using ScS reverberations. Suetsugu et al. (2009), however, observed no transition zone thinning below most South Pacific hot spots. Leahy (2009) obtained a deepened and doubled 410 beneath Rarotonga, Cook Islands. Hooft et al. (2003) identified an 18 km reduced thickness of the transition zone below the Galápagos Islands. Shen et al. (1998a) observed at the Pacific Rise a normal transition zone thickness from an ocean-bottom experiment. Controversial results have been obtained at the Cape Verde. Helffrich et al. (2010) found a normal transition zone thickness, whereas Vinnik et al. (2012) obtained a thinned transition zone from receiver functions. No indication for any influence of a possible plume-like structure on the upper-mantle transition zone was shown in western Bohemia by Heuer et al. (2011) in P receiver functions.

1.21.2.2.8 North America

The 410 and 660 have been imaged by Bostock and Cassidy (1997) in receiver functions slightly earlier than predicted by IASP91 beneath the southern Slave craton. Dueker and Sheehan (1997a) found in the Colorado Rocky Mountains and High Plains a 20–40 km topography on the 410 and 660.

Gurrola and Bernard Minster (1998) observed a thinned transition at Pasadena. Li et al. (1998) mapped a depressed 660 in eastern North America. Gurrola and Bernard Minster (2000) and Ramesh et al. (2002) determined the transition zone thickness below a number of seismic stations in North America. Simmons and Gurrola (2000) found a multiple 660 in southern California. Gilbert et al. (2003) showed a 20–30 km uncorrelated topography of the 660 and 410 in the western United States. Ai et al. (2005) found in southern Alaska a thinned transition zone by 20–30 km with significant variations. A normal transition zone was observed by Wilson et al. (2005) in the southwestern United States along a Colorado Plateau–Rio Grande Rift–Great Plains seismic transect. Eagar et al. (2010) used in the Pacific Northwest a large number of P receiver functions recorded by the USArray for a transition zone study. They observed no 520, greater depth variations of the 410 than of the 660, and a thin transition zone beneath Snake River Plain. Cao and Levander (2010) found in the western United States an elevated 410 and a depressed 660 in the region of the subducted Gorda slab. Long et al. (2010) observed a normal transition zone thickness in the southeastern United States. Thompson et al. (2011) concluded that in the cratonic North America (Canada), the 410 and 660 are at their average global position, indicating no influence of the thick craton on the mantle transition zone.

1.21.2.2.9 Africa

Le Stunff et al. (1995) used P′P′ precursors recorded with the California array of broadband stations and detected a sharp and uplifted 660 below the East African Rift. Owens et al. (2000) found the transition zone beneath the East African Rift 30–40 km thinner than beneath the Tanzanian craton.

Nyblade et al. (2000) found no reduced transition zone thickness beneath Afar and concluded that the thermal anomaly does not reach the transition zone. Huerta et al. (2009) observed the 410 depressed locally beneath the Kenya rift, but the 660 depressed everywhere in Kenya and Tanzania. Gao et al. (2002) showed the 410 and 660 close to their normal position and concluded that there is no indication for a South African superplume in the transition zone and also no indication for other upper-mantle discontinuities. Stankiewicz et al. (2002) observed a normal transition zone in the Kimberley area and a slightly thickened transition zone beneath the Kaapvaal craton. Simon et al. (2003) found the 410 and 660 beneath Kaapvaal craton slightly deeper than normal. Blum and Shen (2004) observed a 20 km increased thickness of the transition zone in southern Africa. Wright et al. (2004) identified the 410 and 660 beneath the Kaapvaal craton slightly deeper than normal. Wang et al. (2009) studied the transition zone in Africa with the wide-angle technique. Cornwell et al. (2011) found in the Ethiopian Rift and Afar Region local thickness variations of the transition zone between 230 and 260 km. Reusch et al. (2011) observed the mantle transition zone thickness close to the global average beneath the Cameroon volcanic line, implying its upper-mantle origin.

1.21.2.2.10 Oceans

Gaherty et al. (1996) found along a Tonga–Hawaii corridor in ScS reverberations a thinned transition zone. Lee and Grand (1996) observed at the East Pacific Rise in SS precursors the 410 and 660 close to their normal depths. Kato and Jordan (1999) found in the western Philippine Sea in ScS reverberations a slightly thickened transition zone. Niu et al. (2000, 2002) identified at the South Pacific superswell the transition zone thinned by 15 km. Melbourne and Helmberger (2002) observed in wide-angle earthquake records no variation in the transition zone thickness below the East Pacific Rise over a 1000 km long profile orthogonal to the ridge. Li et al. (2003b) showed below ocean islands up to 15% thinning of the transition zone. In contrast, Tauzin et al. (2008) found no clear evidence for a thin transition zone beneath hot spots. Bagley and Revenaugh (2008) found in ScS reverberations a thinned transition zone in the Pacific upper mantle. Schmerr and Garnero (2006) used SS precursors for a study of the topography of the upper-mantle discontinuities in the central Pacific. Cao et al. (2010) observed the 410 and 660 at their expected position in the northern Pacific also in SS precursors. Silveira et al. (2010) observed in S receiver functions below the Azores the transition zone thickness is in agreement with the IASP91 global reference model.

1.21.2.2.11 Other regions

A normal transition zone thickness in agreement with the IASP91 global reference model was found in northern Eurasia by Mechie et al. (1993) in wide-angle nuclear explosion data, in southern Germany by Kind and Vinnik (1988), below India by Saul et al. (2000), at the Kola Peninsula by Dricker et al. (1996), in the North Sea by Helffrich et al. (2003), below the Arabian Shield by Benoit et al. (2003), below the eastern Alps by Kummerow and Kind (2004), in southern Ireland by Landes et al. (2006), and in central Tibet by Mechie et al. (2011). Only small changes in the depth of the 410 in subduction zones have been found by Flanagan and Shearer (1998b). A common delay of the arrivals from the 410 and 660 was obtained by Kumar et al. (2002) below the Arabian Shield and by Mohsen et al. (2005) below the Dead Sea region due to a relatively slow upper mantle. Alinaghi et al. (2003) found below the Baltic Shield the 410 and 660 signals arriving 2 s earlier due to a faster upper mantle. A thickened transition zone was found in East Antarctica by Reusch et al. (2008), in the eastern Himalaya and southern Tibet by Singh and Kumar (2009), in Central Asia by Tian et al. (2010), below the Alps by Lombardi et al. (2009) and Hetenyi et al. (2009), in northern India by Oreshin et al. (2011), below the Philippines by Ohtaki et al. (2002, in ScS reverberations), in the Mediterranean by Van der Meijde et al. (2005), and below the Venezuela–Caribbean plate boundary by Huang et al. (2010). A thinned transition zone was shown in the Kurile–Kamchatka subduction zone by Petersen et al. (1993a) and in southern California by Gurrola and Bernard Minster (1998). Relatively strong local variations of the transition zone thickness have been observed in Central Asia by Neves et al. (1996) in nuclear explosion data, in Indonesia by Saita et al. (2002), below the

Philippines by Wright (2009) with wide-angle data, below the Philippine Sea by Suetsugu et al. (2010), and at the Mariana slab by Tibi et al. (2006) with ocean-bottom seismometers.

1.21.2.3 Sharpness of 410 and 660

Benz and Vidale (1993) observed short-period precursors of P′P′ in the Indian Ocean from South American events, recorded by many short-period stations in California. They observed that both discontinuities (410 and 660) were <4 km sharp. Petersen et al. (1993b) found a sharper 410 (5–7 km) than 660 (20–30 km) from Ps conversions at several broadband stations in different regions.

Yamazaki and Hirahara (1994) used regional earthquakes recorded by the J-Array in Japan (S-to-P converted and reflected waves) and derived a discontinuity thickness of 5 km for both, the 410 and 660. Tonegawa et al. (2005) detected a sharp 660 and a variable 410 beneath Japan. Lebedev et al. (2002a) found a sharp 660 near the Japan slab from Ps data. Helffrich and Bina (1994) discussed the frequency dependence of the 410 signals. Van der Lee et al. (1994) discussed the influence of topography on the amplitudes of P-to-S converted waves. Priestley et al. (1994) found in nuclear explosion data in central Siberia a 35 km thick gradient at the 410 and a 4 km thick gradient at the 660. Ryberg et al. (1998) derived also from nuclear explosion data in northern Eurasia that the 660 is several kilometers wide and that the velocity jump across it is only half of the IASP91 value. They also argued that wide-angle data are not very sensitive to discontinuity gradients. Vidale et al. (1995) showed the 410 to be <10 km wide in the western United States from near-critical reflection records from nuclear explosions. Neele (1996) found that the velocity increase at the 410 occurs over a width of 4 km or less below the Gulf of California. Bostock (1996a) found also in Ps data a sharper 410 than 660 beneath the North American craton. Melbourne and Helmberger (1998) identified in wide-angle data a 14 km thick gradient zone at the 410 in the southwestern United States. Neves et al. (2001) found a 10 km sharp 410 and a 5 km sharp 660 beneath North America in wide-angle data. However, within the slab, a more complicated structure occurs. Xu et al. (1998) and Xu et al. (2003) found globally a sharp 660 (2 km or less) and a less sharp 410 from P′P′ precursors. Le Stunff et al. (1995) observed a sharp and uplifted 660 below the East African Rift in P′P′ precursors from a Fiji event recorded with the California array of broadband stations. Castle and Creager (2000) identified that the 660 is locally <10 km wide at the Izu–Bonin subduction zone using source side S-to-P conversions recorded in the western United States. Rost and Weber (2002) showed that the 410 is <6 km wide from array PP precursor studies in the Pacific Northwest. Tibi and Wiens (2005) concluded from short-period observations of local earthquakes a sharpness of 0–2 km for the 660 and 2–10 km for the 410 in the Tonga subduction zone. Estabrook and Kind (1996) concluded from the missing precursors of PP from the 660 that the velocity and density jump here is globally significantly smaller than predicted by the IASP91 global reference model (see **Figure 8**). This was confirmed by Shearer and Flanagan (1999) globally and by Ryberg et al. (1998) from summarizing wide-angle nuclear explosion data in northern Eurasia. Kato and Kawakatsu (2001) derived from SS precursors, Ps conversions, and ScS reverberations a locally larger S velocity and density jump at the 660 than at the 410 beneath the Pacific Northwest. This observation is in disagreement with the global observation of missing PP precursors by Estabrook and Kind (1996) and Shearer et al. (1999).

1.21.2.4 Low-Velocity Zone atop the 410

Song et al. (2004) observed in the northwestern United States a 20–90 km thick low-velocity zone above the 410 from wide-angle data, which they interpret as an indication of high water content in the transition zone (Bercovici and Karato, 2003; Youngs and Bercovici, 2009). Jasbinsek and Dueker (2007) found in the northern Rocky Mountains a low-velocity zone above the 410 using Ps conversions. Vinnik and Farra (2007) detected also such a zone below several globally distributed seismic stations. Bagley and Revenaugh (2008) and Bagley et al. (2009) studied the transition zone in the Pacific region using ScS reverberations and saw no low-velocity zone atop the 410, except at the Japan slab (50–75 km thick). Vinnik et al. (2009, 2010) identified in P and S receiver functions a low-velocity zone above the 410 in South Africa and in California. Schaeffer and Bostock (2010) found in P and S receiver functions below northern Canada a low-velocity zone at about 340 km depth. Tauzin et al. (2010) argued, based on P receiver functions, that a global low-velocity zone near 350 km depth exists, without any relation to the tectonic environment. Schmandt et al. (2011) found in P receiver functions a low-velocity zone at 25–60 km above the 410 in several regions in the western United States. Jasbinsek et al. (2010) found a low-velocity zone above the 410 at the Colorado Plateau and Rio Grande Rift. Chu et al. (2012) found also a low-velocity zone atop the 410 in the United States using wide-angle earthquake records.

1.21.2.5 The 520 Discontinuity

Shearer (1990, 1991, 1996) presented evidence in long-period SS precursors for the global existence of the 520 and determined the impedance contrast of the upper-mantle discontinuities. Bock (1994) discussed the influence of sidelobes on the observations of the 520 in SS precursors. Revenaugh and Jordan (1991a), Gaherty et al. (1996), and Kato and Jordan (1999) found the 520 in ScS reverberations along corridors in the Pacific. Cummins et al. (1992) observed no evidence for 520 north of Australia in short-period wide-angle earthquake recordings. Gossler and Kind (1996) confirmed the regional existence of the 520 in SS precursors. Mechie et al. (1993), Priestley et al. (1994), and Ryberg et al. (1996, 1997, 1998) found evidence for the 520 in northern Asia in nuclear explosion data. Deuss and Woodhouse (2001) observed the splitting of the 520 using SS precursors. Ai et al. (2005) observed the 520 in receiver functions in Alaska. Schäfer et al. (2009) detected the 520 in PP precursors.

1.21.2.6 Summary of the Upper-Mantle Transition Zone

The 410 and 660 are besides the Moho certainly the best-documented discontinuities in the upper mantle. In recent years, they have been observed with increased resolution in

SS, PP (only few 660 precursors), and P′P′ precursors, Ps and Sp conversions, and ScS-related phases. One clear result is that the P wave velocity jump across the 660 is globally a significant percentage below the values in present global reference models. This should influence the modeling of mantle convection. The global topography of the 660 seems to be larger than the topography of the 410. The question whether the 410 and 660 are globally anticorrelated, which, if true, would provide evidence in favor of the phase transition model in the olivine system, is much less clear. There are opposing observations. The thickness of the transition zone seems to vary globally by about 20–30 km (with the 410 and 660 not necessarily anticorrelated), indicating about a 200 K lateral temperature variation within the transition zone. There is widespread agreement that the seismic data support the idea that transformations in the olivine structure give rise to the 410 and 660 globally. The question of the correlation of the type of plates (oceanic or cratonic) and the transition zone thickness (or temperature) seems not clearly decided. Again, there are contradicting observations. Such a correlation between surface geology and transition zone structure would lead to serious problems with plate tectonics, since laterally moving lithospheric plates are not often considered to reach the mantle transition zone. Some tomographic models, however, seem to agree with this view. Ritsema et al. (2004) observed in tomographic data below the continental lithosphere down to 400 km depth a 1–1.5% higher velocity than below the oceanic lithosphere. Gung et al. (2003), however, interpreted high tomographic velocities in continental roots as being caused by anisotropy. The possibility of continental roots reaching several hundred kilometers deep and maybe even into the mantle transition zone was first suggested by Jordan (1975). Crucial for answering questions about the deep roots of continents would be the comparison with high-resolution data from undisturbed oceanic areas away from ocean islands, which are always anomalous. Such data can only be obtained from dense ocean-bottom seismic observations, which are very expensive. High-resolution data are so far only available for continents; therefore, a real quantitative comparison is not yet possible.

Most researchers agree that the 660 is depressed at subduction zones on a large scale. The amount of depression varies between 20 and 50 km. These results come from global observations and also from high-resolution local observations. Updoming of the 410 at subduction zones is much less certain. There are locally contradicting observations, although clear observations of updoming exist in Japan. The 410 seems in many cases poorly observed in subduction zones. A depression of the 410 due to metastable olivine in subduction zones is not yet observed clearly.

The transition zone structure beneath hot spots is less clear. There are fewer observations beneath hot spots because many are in oceanic regions. There are observations of thinning of the transition zone and also of a normal transition zone. The continued collection of high-resolution information on the 410 and 660 beneath hot spots should reliably answer the question of which plumes reach down to the transition zone and which do not.

Local studies with mobile networks or closely spaced long-term station deployments provide high-resolution information in some continental or oceanic regions. In general, most information from stable continents agrees with the global average values. This seems even true for regions like Tibet or the Alps. This leads to the conclusion that active lithospheric tectonics may not reach the transition zone (except for subduction zones and possibly plumes). Since the upper mantle is generally faster beneath continents than beneath oceans, both discontinuities frequently appear deeper under oceans than below continents. The continental values are closer than the oceanic values to those of the reference models (IASP91), which indicate that the reference models may be biased by consisting of a majority of continental data.

Only high-frequency data like P′P′ precursors or local reflections and conversions seem able to resolve sharpness (and other details like multiple discontinuities) of the 410 and 660. Relatively few of such observations are available and they confirm sharpness of just a few kilometers for both discontinuities. Teleseismic mantle phases (including Ps conversions) probably do not have sufficiently high frequencies to resolve the sharpness. If weak scattered waves (e.g., receiver functions) are used, the summation of many traces over a more or less large region is required. Such summation may lead to the contamination of discontinuity sharpness or impedance contrast by topography effects. Therefore, estimates of discontinuity sharpness with summation traces should be done with great care. Systematic high-frequency global studies of discontinuity sharpness and impedance contrast are still missing.

The discontinuity at 520 km depth is clearly observed in some regions but it is not clear in others. The 520 is thus not a laterally homogeneous global discontinuity, but it also cannot be considered a local one, because it has a relatively widespread distribution. Its existence does not seem to have any correlation with surface structures.

1.21.3 The Gutenberg Discontinuity (LAB)

The first seismic observations of a global low-velocity zone below the Moho (called the asthenospheric channel) were obtained by Gutenberg (1926, 1954, 1959) at 100 km depth from amplitudes and slownesses of P phases. Therefore, seismologists sometimes call this discontinuity the ‘Gutenberg’ discontinuity (often abbreviated as ‘G’ discontinuity). It is mainly reported in oceanic regions. The Lehmann discontinuity (Lehmann, 1961) is considered as the bottom of the asthenosphere (mostly observed in continental regions; Deuss and Woodhouse, 2002; Gu et al., 2001a). Since the Gutenberg discontinuity is a negative discontinuity (a reduction of velocity with depth), it is often identified with the LAB. Therefore, we will not always make a clear distinction between the terms ‘LAB’ and ‘Gutenberg discontinuity,’ although the terms are the result of entirely different definitions. The concept of a high-viscosity lithospheric layer overlying a low-viscosity asthenospheric layer was introduced to explain observations such as the postglacial uplift of Scandinavia (e.g., Barrell, 1914). Originally, the expressions ‘crust’ and ‘lithosphere’ were used synonymously (see a discussion by Gutenberg, 1959). Only after Mohorovicic (1910) had discovered a sudden increase of the seismic velocity at 50 km depth, which was later confirmed worldwide, was this discontinuity considered as the lower boundary of the crust (termed Moho).

Since then, the terms 'crust' and 'lithosphere' have gained different meanings. Later, with the rise of plate tectonics, the lithosphere–asthenosphere concept was expanded to explain large lateral displacements of continents by high-viscosity lithospheric plates floating over the low-viscosity asthenospheric upper mantle (see **Chapter 6.02**). Thermal and chemical definitions of the term 'lithosphere' have been introduced since then (Anderson, 1995). A somewhat different geodynamic concept was developed by Jordan (1975). The concept of Jordan (1975) comprises a tectosphere with continental roots that reach to 400 km depth and translate together with the continental lithosphere (Sipkin and Jordan, 1976, 1980).

The lithosphere is seismologically divided into two parts, the crust and the mantle, with the latter being the high-velocity mantle lid on top of the asthenosphere. Surface-wave observations of the high-velocity lid and the low-velocity asthenosphere have been obtained for many years (e.g., Dormann et al., 1960; Kanamori and Press, 1970; Knopoff, 1983). Direct seismic observations of the LAB remain a challenging task. A major problem is that the asthenosphere is a low-velocity zone. Thus, it is difficult to observe it with refracted and reflected seismic body waves. The Moho, in contrast, marks a sharp positive increase in velocity downward, which is easy to observe. Therefore, the Moho is well constrained on a global scale (Mooney et al., 1998; see **Chapter 1.11**). Fewer constraints on the depth of the LAB have been obtained from seismic body waves. A review of wide-angle results is given by Thybo (2006) (see **Figure 10**; see **Chapter 1.15**). Mostly surface-wave dispersion is used to measure the depth of the LAB. From these relatively low-resolution observations (compared to the high resolution of the Moho, which is obtained from short-period body waves), the LAB can only be imaged as a broad transition zone, and therefore, it is difficult to locate. The most important result of surface-wave studies is the larger thickness of the lithosphere beneath continents than below oceans (e.g., Gung et al., 2003). At present, the thickness of the lithosphere is considered to vary from a few kilometers at mid-ocean ridges to 200 km beneath stable cratons, with 80–100 km being the global average. The problems of detecting low-velocity zones with wide-angle seismic data are well known in the crust and are even greater in the mantle. Steep-angle body waves (similar to the seismic reflection method in crustal studies) are probably much more useful for detecting the Gutenberg discontinuity and mapping its topography. In recent times, the P receiver function technique has turned out to be very successful in imaging the crust–mantle boundary (e.g., Langston, 1979; Yuan et al., 2002). However, P receiver functions are less useful for detecting the Gutenberg discontinuity because crustal multiples sometimes arrive at about the same time as direct conversions from the Gutenberg discontinuity and therefore are hard to separate. The problem with crustal multiples can be solved if S-to-P conversions are applied instead. In this case, direct conversions are clearly separated from multiples. Direct conversions arrive in front of S, and multiples in the coda of S. S-to-P conversions have also long been used to study upper-mantle discontinuities (e.g., Bock, 1988, 1991; Jordan and Frazer, 1975; Sacks and Snoke, 1977; Sacks et al., 1979). They have been reintroduced in a modernized form as S receiver functions by Farra and Vinnik (2000) and Zhou et al. (2000). A more recent description of the technique is given by Yuan et al. (2006) and Kind et al. (2012). This still relatively rarely used technique is applied to S or SKS phases and adds a few more processing steps to the original Sp conversion technique. Such steps are, as in the P receiver function technique, source equalization by deconvolution and distance moveout correction. Both steps are applied in order to enable the summation of events from different distances and with different magnitudes and source-time functions. Thanks to the newly available large quantities of high-quality digital data, the conversion techniques enjoy increasing popularity. These techniques work very well, enabling especially observations of the LAB with a resolution

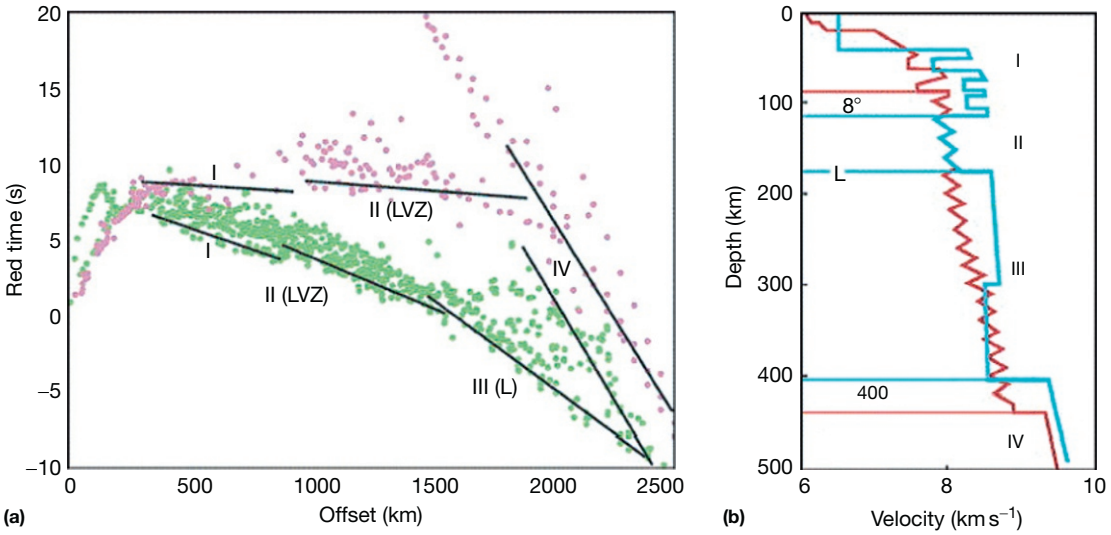

Figure 10 (a) Travel time–distance plot of collected long-range controlled source seismic data. Purple points are from tectonic active regions and green points from tectonic quiet regions, respectively. (b) Derived models for these areas (cold – blue, hot – red). The 8° discontinuity (or Gutenberg discontinuity, or LAB), the Lehmann discontinuity, and the 410 are shown. The asthenosphere is less pronounced in cold areas. Reproduced from Thybo H (2006) The heterogeneous upper mantle low velocity zone. *Tectonophysics* 416(1–2): 53–79, Figure 2.

so far only known for the Moho. In the following, we discuss briefly papers with possible observations of the LAB. A relatively early discussion about the global lithospheric thickness from seismic tomography, heat flow, and seismic anisotropy was published by Artemieva and Mooney (2001) and Artemieva et al. (2002). Also from anisotropy, Plomerova et al. (2002) obtained LAB depths between 200 and 250 km for the Precambrian shields and platforms, of about 100 km for the Phanerozoic continental regions, and 40–70 km beneath oceans.

1.21.3.1 Possible LAB Observations

1.21.3.1.1 Pacific

The LAB has been observed in long-period ScS reverberations in the Pacific area by Revenaugh and Jordan (1991b), Gaherty et al. (1996, 1999), Kato and Jordan (1999), and Bagley and Revenaugh (2008). Collins et al. (2002) detected the Gutenberg discontinuity at 80 km depth beneath the Hawaiian swell using ocean-bottom seismic stations. Li et al. (2004) found in S receiver functions the LAB beneath the Big Island at 100 km depth, where it is expected according to the age of the seafloor and to surface-wave observations. In addition, thinning of the LAB to 60 km along a narrow corridor below the island chain was also observed, which was interpreted as the rejuvenation of the lithosphere due to the passage of the Pacific plate over the Hawaiian hot spot. Wölbern et al. (2006) confirmed with P receiver functions these observations. Gung et al. (2003) studied the Lehmann discontinuity under continents and the Gutenberg discontinuity under oceans. Kawakatsu et al. (2009) identified the subducting Pacific lithosphere down to about 200 km depth (see **Figure 11**). Rychert and Shearer (2011) studied the oceanic lithosphere in the Pacific using SS precursors. They found agreement with the cooling model for an isotherm of 930 °C. Kumar et al. (2007) determined the LAB depth with S receiver functions at stations around the Indian Ocean and found evidence for a thin Indian lithosphere. Kumar et al. (2011a) used P and S receiver functions from borehole seismometers below the Philippine Sea, away from islands. They found the LAB near 76 km. Kumar and Kawakatsu (2011) and Kumar et al. (2011b) imaged the LAB along continental margins with S receiver functions using coastal stations (also across the San Andreas Fault). They found a correlation of the LAB depth with the age of the oceanic plate. Schmerr (2012) observed in SS precursors LAB variations in the entire Pacific basin between 40 and 75 km depth. Rychert et al. (2012) studied the oceanic lithosphere using body-wave and surface-wave techniques.

1.21.3.1.2 China and Tibet

Oreshin et al. (2002) and Vinnik et al. (2004) did the first S receiver function studies in Central Asia and found in the Tian Shan region the LAB at shallow depths (near 90 km). Kumar et al. (2005a, 2006) mapped the LAB in the region of the Tian Shan and western and central Tibet. As a very noticeable result, Zhang et al. (2010) observed the LAB below eastern Tibet at a shallower depth than beneath the cratonic Sichuan

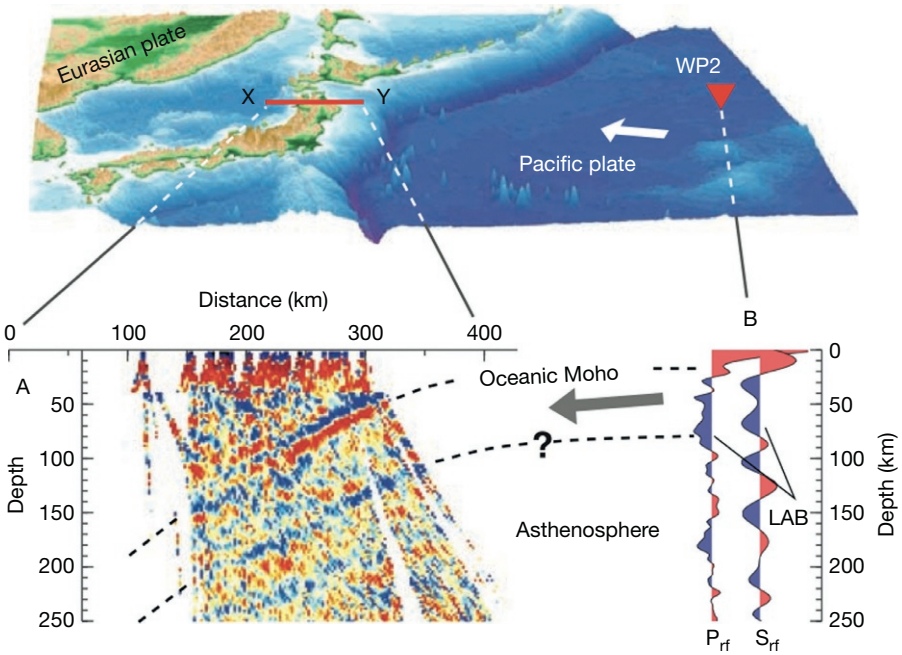

Figure 11 Receiver functions of the subducting Pacific plate beneath northeast Japan. In the topographic map, the inverted red triangle indicates the location of seismic station WP2, which is deployed at a depth of 460 m below the seafloor with a water column of 5566 m thick. (a) P receiver function image along the profile XY using dense land seismic data of Hi-net from Japan. Red and blue colors indicate velocity increase and decrease (from shallow to deep), respectively. The top surface of the slab and the oceanic Moho are clearly imaged, as well as the bottom surface of the slab (i.e., subducting LAB). (b) P and S receiver functions for WP2. Negative phases associated with a shear wave velocity drop marked as LAB appear to correspond to the strong negative (blue) signature of the subducting slab below Japan. Reproduced from Kawakatsu H, Kumar P, Takei Y, et al. (2009) Seismic evidence for sharp lithosphere–asthenosphere boundaries of oceanic plates. *Science* 324: 499–502. http://dx.doi.org/10.1126/science.1169499, Figure 2.

Basin. Hu et al. (2011) and Zhang et al. (2012) made similar observations in eastern Tibet and in parts of northern–eastern Tibet. Sodoudi et al. (2006a) found the LAB also in S receiver functions at 70 km below the Yangtze craton and at 60 km below the North China platform. Chen (2009, 2010) and Chen et al. (2008) found beneath the North China Craton a correlation between lithospheric structure and structure of the mantle transition zone. Kind and Yuan (2010), Zhao et al. (2010), and Zhao et al. (2011) imaged with S receiver functions the stacking of the Tibetan LAB above the subducting Indian LAB. Continental subduction of India below Tibet was modeled by Chemenda et al. (2000). Xu et al. (2011) obtained from S receiver functions of the Hi-CLIMB (Himalayan–Tibetan Continental Lithosphere during Mountain Building) experiment the LAB at 80 km depth below the Himalayas and at 130 km depth below central Tibet. Devi et al. (2011) and Mandal (2012) identified the LAB in northeast India at 90–135 km, below the Himalayas near 180 km and below the Deccan volcanic province near 70 km, respectively.

1.21.3.1.3 Africa

Qiu et al. (1996) and Priestley (1999) derived from P receiver functions, wide- and steep-angle seismic data, Pn and Sn data, and surface-wave data a lithospheric thickness of 120–160 km in southern Africa. Priestley and McKenzie (2002) found the LAB beneath southern Africa at 176 km depth from regional seismic data. Vinnik et al. (1996), Wittlinger and Farra (2007), and Kumar et al. (2007) found the LAB at about 300 km. Savage and Silver (2008) found a negative discontinuity at about 150 km, similar to Hansen et al. (2009a,b) and Vinnik et al. (2009). Fishwick (2010) compared tomographic and receiver function LAB observations in South Africa. Wölbern et al. (2012) found in S receiver functions a velocity drop of 6–9% below the Tanzanian craton at 50–100 km depth and another velocity drop of 12–24% at a depth of 140–200 km. Sodoudi et al. (2013) observed layering of the mantle lithosphere underneath South Africa and picked the negative interface at ~280 km as the LAB.

They interpreted another negative discontinuity at 150 km as midlithospheric discontinuity (MLD) caused by compositional changes.

1.21.3.1.4 Europe and the Middle East

A low-velocity zone in the cratonic upper mantle near 100 km depth has frequently been observed in controlled source (including nuclear explosions) seismic data (Nielsen et al., 1999; Thybo, 2006; Thybo and Perchuc, 1997). The Svekalapko Seismic Tomography Working Group (2004) found the LAB at 100–130 km depth below Finland in wide-angle data. Olsson et al. (2007) applied the S receiver function technique to data of the Swedish National Seismic Network and found a layered structure of the upper mantle with the LAB near 200 km. Geissler et al. (2010) studied the LAB at permanent seismic stations in Central Europe with S receiver functions. Sodoudi et al. (2006b) studied the collision of the African and European lithospheres in the Hellenic arc and found the African lithosphere flattening under the northern Aegean at 250 km depth. Angus et al. (2006) found in S receiver functions the LAB in eastern Turkey at 60–80 km depth and below the Arabian Shield at 100–125 km depth. Mohsen et al. (2006) determined the LAB depth around the Dead Sea transform fault with S receiver functions. Hansen et al. (2007) found also in S receiver functions a thin lithosphere below the Red Sea and thickening toward the interior of the Arabian Peninsula. Sodoudi et al. (2009) found in S receiver functions the LAB beneath the Alborz Mountains in Iran at 90 km depth, similar to Taghizadeh-Farahmand et al. (2010), who found the LAB in the northwest of Iran near 85 km depth. Dündar et al. (2011) mapped the LAB in the region of southern Spain, the Alboran Sea, and northern Morocco using S receiver functions. Kumar et al. (2005b) observed the LAB beneath Iceland and Greenland using S receiver functions from several temporary seismic broadband projects and found the LAB at a nearly constant depth of 80 km beneath Iceland (confirming earlier results of Vinnik et al., 2005b) and thickening from 80 to 120 km from east to west beneath Greenland. Kind et al. (2013) proposed a mechanism to create the thick cratonic lithosphere based on the observation of lithospheric stacking beneath Scandinavia by S receiver functions.

1.21.3.1.5 North America

Parker et al. (1984) derived from P residuals the upwarping of the asthenosphere below the Rio Grande Rift. Bostock (1999) extended structures in the uppermost mantle obtained from controlled source experiments into larger depths using receiver functions and concluded that the cratons might be stabilized by shallow subduction. Rychert et al. (2005, 2007) found a sharp LAB in P receiver functions that were clearly separated from crustal multiples (see **Figure 12**). They found in eastern North America the LAB at 90–110 km depth with a velocity decrease of 3–11% over a depth range of 11 km or less and concluded that a few percent of partial melt or enrichment of volatiles in the asthenosphere could cause such a sharp LAB. Li et al. (2007) found the LAB in the western United States at depths < 100 km with S receiver functions. Moorkamp et al. (2007) jointly interpreted receiver functions and magnetotelluric data in a search for the LAB in the Slave craton, Canada. Miller and Eaton (2010) studied a S receiver function profile from west to east through Canada and found a shallow LAB (about 85 km) in the west and a deeper one (about 260 km) in the cratonic part. They also found in the cratonic part a shallower MLD. Lekic et al. (2011) produced a LAB map in southern California from receiver functions. Levander and Miller (2012) studied S receiver functions in USArray data and observed the LAB in the western United States at about 50–70 km depth and below Yellow Knife and the Colorado Plateau near 150 km, respectively. Kumar et al. (2012a) and Kumar et al. (2012b) imaged with S receiver function data of the USArray project the LAB in the United States. They found a shallow negative discontinuity in the entire United States (near 100 km depth), which is in agreement with earlier LAB determinations only in the western part of the United States, not in the cratonic eastern part. No clear indication of a deeper LAB was found in the cratonic United States (see **Figure 14**).

1.21.3.1.6 South America

Heit et al. (2007) imaged the LAB depth in South America, including the subducting slab, with data from permanent stations. Sodoudi et al. (2011) observed the subducting Nazca

LAB beneath northern Chile in P and S receiver functions and estimated the thickness of the subducting Nazca lithosphere.

1.21.3.1.7 General observations

Eaton et al. (2009) discussed geophysical and geochemical causes of the LAB in cratons and compared it with observations. Romanowicz (2009) discussed shallow low-velocity zones below cratons (near 100 km). Rychert and Shearer (2009) studied the global LAB structure with P receiver functions. They found a global negative discontinuity that they interpret as LAB in most regions, except below cratons, where it might be a new MLD. Jones et al. (2010) compared LAB depth determinations with seismic and electromagnetic data. Kumar et al. (2010) skipped the deconvolution in the receiver function technique and used plain summation of many traces without deconvolution. They also showed that the LAB can be observed by the P wave reverberation within the lithosphere. Pasyanos (2010) compared different methods for determining the LAB depth. Bartzsch et al. (2011) discussed possibilities to detect the LAB with surface-wave data.

Rychert et al. (2010) discussed the disagreements of new receiver function results with previous ideas about the structure of the lithosphere below cratons. Fischer et al. (2010) reviewed globally receiver function observations of the LAB and MLD. Abt et al. (2010) observed in S receiver functions a negative discontinuity (downward velocity decrease) in the United States between about 50 and 100 km depth, which was interpreted in the western part as LAB and in the cratonic part as MLD. No deep LAB was found in the receiver functions in the cratonic United States.

Yuan and Romanowicz (2010) interpreted a downward velocity decrease beneath cratonic North America near 100 km depth seen in receiver functions as the MLD rather than LAB (see **Figure 13**). Angus and Thomson (2012)

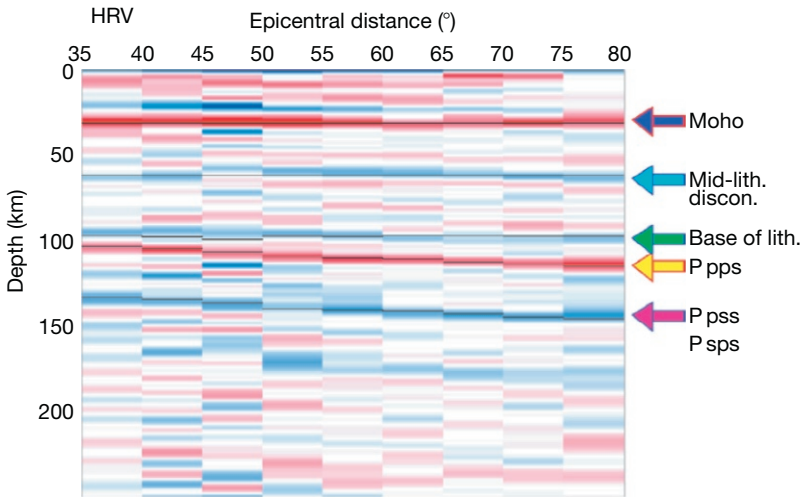

Figure 12 Stacks of P receiver functions at the Harvard station as function of epicentral distance. A number of conversions from upper-mantle discontinuities and crustal multiples are visible. Especially important is the observation of the base of the lithosphere, which is clearly separated from crustal multiples and indicates a sharp LAB (11 km or less). Reproduced from Rychert CA, Fischer KM, and Rondenay S (2005) A sharp lithosphere–asthenosphere boundary imaged beneath eastern North America. *Nature* 436: 542–545, Figure 1 of supplementary information.

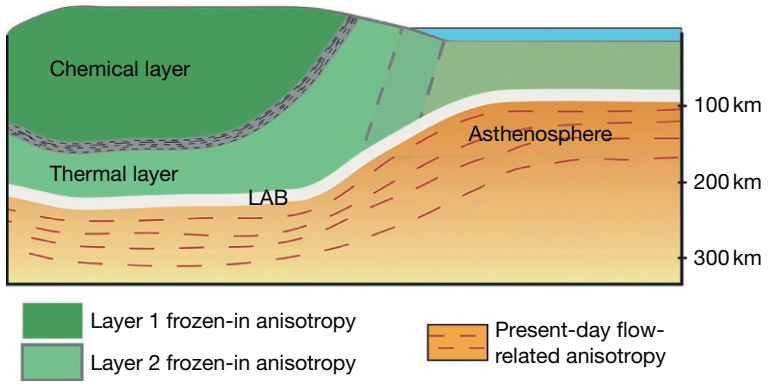

Figure 13 Cartoon illustrating the inferred stratification of the lithosphere. Beneath the craton, three layers of anisotropy are present: two in the lithosphere (layers 1 and 2) and one in the asthenosphere. Layer 1 corresponds to the chemically distinct, depleted Archean lithosphere, and layer 2 is the thermal root, separated from the asthenosphere by the LAB, which is at relatively constant depth beneath the stable part of the continent but rapidly shallows between the tectonic part of the continent (in the western United States) and in the oceans. The boundary between layers 1 and 2 is seismically sharp but its fine-scale structure is likely to be complex. The depth extent of the zone of present-day flow-related anisotropy is not tightly constrained by our study. Reproduced from Yuan H and Romanowicz B (2010) Lithospheric layering in the North American craton. *Nature* 466: 1063–1069. http://dx.doi.org/10.1038/nature09332, Figure 5.

computed theoretical conversions at an anisotropic LAB. Kind et al. (2012) reviewed the receiver function technique and its application for the search of the LAB (see **Figure 14**). Ford et al. (2010) studied receiver functions in Australia. They found the LAB in the Phanerozoic parts near 100 km depth in agreement with surface-wave data. Similarly, a shallow negative discontinuity was also found in cratonic parts of Australia and interpreted as MLD. At the depth of the expected LAB, no receiver function signals were found. Sodoudi et al. (2013) concluded that sharp boundaries generated by frozen-in anisotropy and compositional changes can result in an irregularly stratified structure, which can be identified in S receiver functions.

1.21.3.1.8 Summary of the Gutenberg discontinuity (LAB)

There are many body-wave observations confirming the existence of a low-velocity zone beneath the Moho. The S receiver function method seems to be especially successful in detecting and mapping the LAB. Practically in all regions where this technique was used to search for the LAB, it was indeed found. From this, it follows that the LAB is very likely a much clearer discontinuity than was previously thought. The missing observations at shorter periods than surface-wave periods were probably only due to the lack of an appropriate technique. So far, not many studies have been carried out to measure the sharpness or the size of the velocity jump of the LAB in different regions. The amplitude of the LAB conversion seems, in many cases, to be close to half that of the Moho signal, which would indicate an accordingly smaller step in velocity. The question if the shallow low-velocity zone beneath cratons, which gained recently much attention, has a so far unknown petrophysical explanation within the lithosphere or if cratons are a result of a 'lithospheric stacking' process (see, e.g., Pearson, 1999 or Griffin et al., 2003) seems still open. A contemporary example of lithospheric stacking might be the case of Tibet where a craton is now being formed (McKenzie and Priestley, 2008). So far, the proposed deep

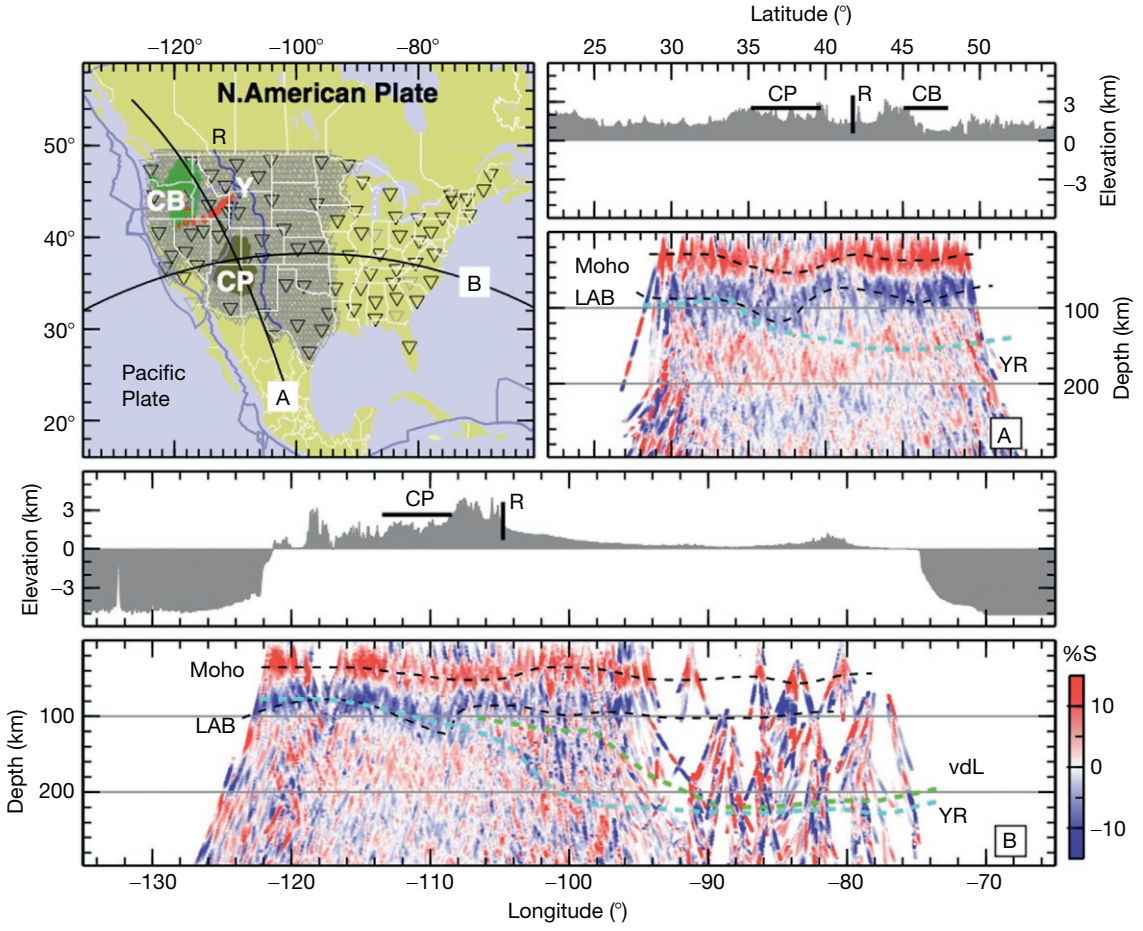

Figure 14 Migrated S receiver function images along two profiles A and B in the United States (locations are marked in the map shown above). CP is the Colorado Plateau, CB is the Columbia River Basalt, and R is the boundary of the Rocky Mountains. Data of the USArray (http://www.usarray.org/) are used west of 94° W and data from the permanent US network east of 94° W. The black inverted triangles are the permanent seismic stations used and the gray inverted triangles are the USArray stations. Two main discontinuities are observed, the Moho and a single negative discontinuity beneath the Moho around 100 km depth (about 140 km below the Colorado Plateau), which is suggested to be the LAB. This interpretation agrees in the western United States and at the east coast with LAB observations from surface waves. In the central cratonic part of the United States, this signal is interpreted as midlithospheric discontinuity by Abt et al. (2010). The dashed lines (labeled YR and vdL) mark the thickness of the lithosphere obtained from surface-wave data by Yuan and Romanowicz (2010) and Van der Lee (2001), respectively. Reproduced from Kind R, Yuan X, and Kumar P (2012) Seismic receiver functions and the lithosphere–asthenosphere boundary. *Tectonophysics* 536–537: 25–43, http://dx.doi.org/10.1016/j.tecto.2012.03.005, Figure 20.

continental roots (Jordan, 1975) have apparently rarely been observed as seismic discontinuities. There are, however, many tomographic indications of such deep roots (e.g., Masters et al., 1996; Ritsema et al., 2004; Su et al., 1994). The rapidly increasing number and quality of upper-mantle studies with high-resolution scattered body-wave studies may lead to a significant expansion of our knowledge of the deep structure of cratons and lithospheric dynamics (see **Section 1.21.2.1**).

1.21.4 The Lehmann Discontinuity

The Lehmann discontinuity (Lehmann, 1961, 1964) is defined to be a positive (velocity increase downward) seismic discontinuity at about 220 km depth. It is thought to represent the bottom of the asthenosphere, or alternatively the lower boundary of the continental roots (Anderson, 1979). It is a significant discontinuity in the PREM global reference model (Dziewonski and Anderson, 1981), but does not appear in the IASP91 global reference model (Kennett and Engdahl, 1991). Although local earthquake records allowed the original detection of the Lehmann discontinuity (usually employing wide-angle seismic data), most confirmations of this discontinuity come from other types of seismic data. These are SS precursors, ScS reverberations, receiver functions, or other types of scattered teleseismic waves. In the following, we list a number of observations of structures, which could be related to the Lehmann discontinuity.

Shearer (1990) found in long-period SS precursors no evidence for the global existence of a discontinuity near 220 km depth. Vidale and Benz (1992) found at 210 km depth the bottom of the asthenosphere near subducting slabs. Priestley et al. (1994) found the bottom of a low-velocity zone in central Siberia from nuclear explosions at 210 km depth. Gu et al. (2001a) used also SS precursors and found a variable Lehmann discontinuity preferably under continents and less under oceans (**Figure 15**). Deuss and Woodhouse (2002) have observed the Lehmann discontinuity globally under oceans and continents also using SS precursors. Deuss and Woodhouse (2004) have also inferred globally a negative Clapeyron slope for the Lehmann discontinuity from depth variations and tomographic upper-mantle velocities.

It is also suggested that the Lehmann discontinuity may be the lower boundary of an anisotropic asthenosphere. Karato (1992) proposed that the Lehmann discontinuity might be caused by a change of the preferred orientation of olivine crystals as consequence of a change of the deformation type. Gaherty and Jordan (1995) described the Lehmann discontinuity as transition from anisotropic lithosphere to more isotropic lower tectosphere beneath continents using ScS data. Gaherty et al. (1996) and Kato and Jordan (1999) found the Lehmann discontinuity at 166 km depth below an anisotropic asthenosphere in the Tonga–Hawaii corridor and in the western Philippine Sea, also from ScS data. Gung et al. (2003) suggested that the Lehmann discontinuity under continents and the Gutenberg discontinuity under oceans might both be associated with the bottom of the lithosphere. Gu et al. (2005) reported seismic anisotropy beneath the East Pacific Rise reaching down to 260 km, where a discontinuity was found. They used surface waves and travel times of body waves. Vinnik et al.

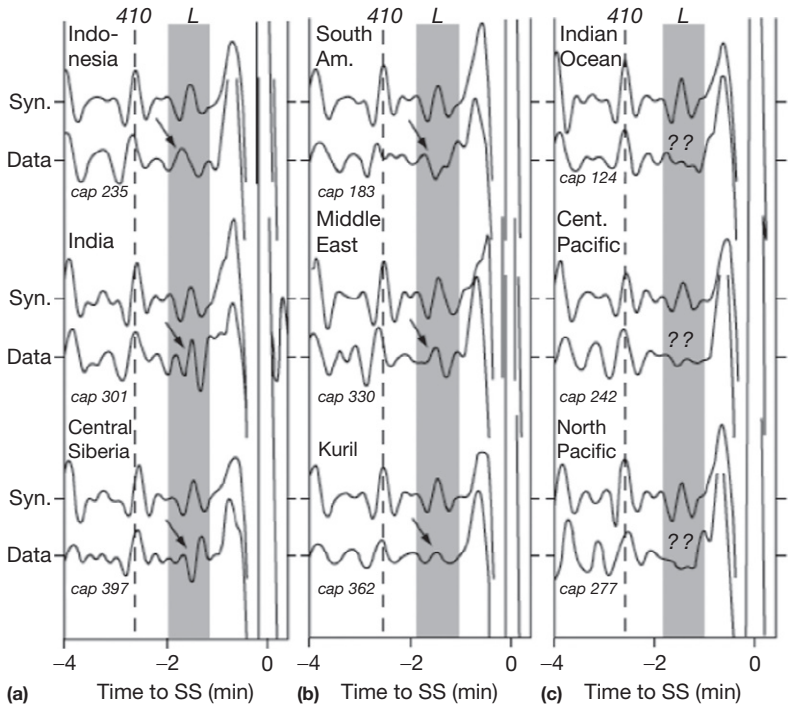

Figure 15 (a) Three S220S precursor stacks showing clear arrivals from the Lehmann discontinuity (thick lines – data, thin lines – synthetics from the PREM). (b) Three stacks in regions with marginal observations of the Lehmann discontinuity. (c) Three stacks in regions with no detectable Lehmann discontinuity. Reproduced from Gu Y, Dziewonski AM, and Ekstrom G (2001a) Preferential detection of the Lehmann discontinuity beneath continents. *Geophysical Research Letters* 28: 4655–4658, Figure 2.

(2005a), however, found in Sp conversions a discontinuity at 200 km depth in the northwest of the United States and concluded that anisotropy is not present at this depth.

There are also P receiver function reports of observations of the Lehmann discontinuity. Bostock (1996b) found evidence for a weak 220 km discontinuity beneath the Canadian part of the North American craton in P receiver functions. Bostock (1998) observed a west–east dipping structure between 170 and 230 km depth below Yellow Knife. Li et al. (2002) found from Ps data a discontinuity at 270–280 km depth beneath eastern North America.

There are also a number of wide-angle observations and other data that could be attributed to the Lehmann discontinuity. Drummond et al. (1982) and Hales (1991) found indications for a discontinuity near 200 km depth from wide-angle data in Australia and North America. Kaila et al. (1999) observed from wide-angle studies indications of the Lehmann discontinuity beneath large regions of the Andes. Rost and Weber (2001) found a discontinuity at 200 km depth in the northwest Pacific using PP precursors. Abramovitz et al. (2002) found in wide-angle data from Scandinavia a discontinuity at 150 km depth, which they considered as the base of the low-velocity zone. Wittlinger et al. (2004) interpreted from S receiver function data the bottom of the low-velocity zone at 120–180 km depth below Tibet. In summary, there are many reports indicating a widespread Lehmann discontinuity. There are several works obtained with the same technique (SS precursors), which have led to a first more or less global view. Also, anisotropy seems to play a significant role in the explanation of this discontinuity. There are confirmations from various other techniques, but SS precursors seem to be the most promising technique for obtaining a comprehensive global image of the Lehmann discontinuity. One problem of this technique is, however, its relatively low resolution due to the long periods of the SS precursors.

1.21.5 The Hales Discontinuity

Green and Hales (1968), Hales (1969, 1972), and Hales et al. (1980) reported positive (velocity increase downward) seismic discontinuities at 60–90 km depth below the United States and other regions from long-range controlled source experiments. Since then, seismic discontinuities found in this depth range have frequently been called the 'Hales discontinuity,' 'H,' or '80 km discontinuity.' These expressions stand for discontinuities within the lithospheric mantle lid. There have been many active and passive experiments from which such discontinuities have been reported.

Zandt and Randall (1985) observed in shear-coupled Pl modes a discontinuity between 70 and 80 km depth under North America, which they attributed to the Hales discontinuity. Revenaugh and Jordan (1991b) reported a mean depth of the Hales discontinuity of 65 km beneath the southwestern Pacific from ScS reverberations. Sandvol et al. (1998) found a discontinuity at 80–100 km depth below the Arabian Shield in receiver functions.

The Hales discontinuity has frequently been related to anisotropy. Fuchs (1983) described anisotropic discontinuities in the lower lithosphere below southern Germany. Zhang and Lay (1993) found a depth of 80–90 km for the Hales discontinuity beneath the western Pacific region from sSH precursors. Bostock (1997, 1998) observed an anisotropic layer at 70–80 km depth below the Slave craton in Canada. Levin and Park (2000) found an anisotropic layer at 70 km depth below the Arabian Shield, which they attributed to the Hales discontinuity. Saul et al. (2000) reported an anisotropic discontinuity at 90 km depth below the Indian Shield.

Discontinuities in the mantle lithosphere have been known for a long time from controlled source long-range profiles (e.g., Hirn et al., 1973; Kind, 1974; see **Chapters 1.08** and **1.15**). Egorkin et al. (1987) reported from records of 'peaceful nuclear explosions' discontinuities in the depth range between 80 and 100 km beneath northern Russia. Pavlenkova (1996) reviewed global controlled source profiles and concluded that, among other local discontinuities in the lower lithosphere, a global discontinuity exists at 80–100 km depth with velocities below the discontinuity of 8.4–8.5 km s^{-1}. Hajnal et al. (1997) found a discontinuity at 75 km depth under central North America. Also, in seismic reflection data, signals are observed from the depth range of the Hales discontinuity. For example, Steer et al. (1998) concluded from such data that a global discontinuity at 80–100 km depth may exist. Musacchio et al. (2004) reported an anisotropic layer beneath the Canadian Shield in the mantle lid from LITHOPROBE experiments.

A very characteristic feature of long-range controlled source seismic profiles is the teleseismic propagation of high-frequency Pn waves. This phenomenon has been reviewed recently by Fuchs et al. (2002) and interpreted as being caused by randomly distributed scatterers in the mantle lid with high aspect ratio and dimensions in the 10 km range. Tittgemeyer et al. (1996) modeled teleseismic Pn assuming a 1D model for the mantle lid with random velocity fluctuations. An alternative interpretation was given by Nielsen and Thybo (2003), who interpreted this observation as a whispering gallery effect. In conclusion, there are many reports from different places around the globe about a discontinuity that could correspond to the Hales discontinuity. Most of these reports come from wide-angle controlled source studies. There are, however, also a number of reports from steep-angle reflection experiments. Reports from P receiver function studies are rarer, probably since crustal multiples mask such deep phases. Receiver functions, however, seem frequently to have energy from this depth range on the transverse component, which is very likely indicative for anisotropic discontinuities in this depth range. Discontinuities certainly exist in the mantle lithosphere. However, it has not yet been shown that a single Hales discontinuity is a global feature. Many local discontinuities are seen in various parts of the mantle lithosphere. In addition, a global distribution of small-scale scatterers is probably responsible for long-range propagation of high-frequency Pn waves. There are still much too few homogeneous data available for reliable global analysis of the Hales discontinuity.

1.21.6 Conclusions

Historically, when seismologists started to study the Earth's interior, they were looking for globally existing discontinuities, since they explained the clearest seismic observations well.

Consequently, the core–mantle boundary, the crust–mantle boundary, and the boundary between the inner and outer core were discovered. These discontinuities have, since then, been confirmed as global boundaries and many of their details are now known and more details are still being discovered. Gutenberg suggested another discontinuity in the uppermost mantle, also in the early days of seismology. This discontinuity was later frequently associated with the LAB, following the development of plate tectonics. However, the global distribution of the Gutenberg discontinuity is still much less well known. One reason for this is certainly that the Gutenberg discontinuity is the upper boundary of a low-velocity zone, which is difficult to detect with classical seismic techniques. In the second half of the twentieth century, two more global seismic discontinuities were suggested, the Lehmann discontinuity as the bottom of the asthenosphere and the Hales discontinuity within the mantle lithosphere. Both of these discontinuities are still not reliably confirmed as global discontinuities. There are less systematic reports about observations of additional discontinuities, which are not treated here. The best-known global upper-mantle discontinuities are the ones located at average depths of 410 and 660 km. They are mostly explained by phase changes in the olivine system, in agreement with high-pressure laboratory experiments. Oceanic upper-mantle data seem to be crucial for the final confirmation. Downbending of the 660 discontinuity at subduction zones is confirmed by many reports. Globally, the 660 seems to be more a discontinuity of the shear modulus then of the bulk modulus.

The data used for the detection of seismic discontinuities in the Earth's interior are historically just travel times of seismic phases. These travel times have been obtained from sparsely distributed seismic stations. Since the advent of digital seismic waveform data, many more details have been learned about the Earth's structure in general and discontinuities in particular. New techniques have been developed. The most important ones use waves scattered at discontinuities (conversions, precursors, and multiples). These methods depend heavily on data summation techniques, since scattered phases are small in amplitude and must be enhanced by a combination of many records. Present initiatives toward increased efforts to significantly increase the collection of seismic data (e.g., USArray) not only will therefore lead to more details about structures already known to exist but also will likely discover additional structural elements unknown so far. The expected new data together with new techniques may lead to another revolution in our knowledge about the dynamics of the solid Earth, which is a fundamental part of our environment.

Acknowledgment

We wish to thank Xiaohui Yuan, Forough Sodoudi, and Jeff Gu for reviewing the manuscript and for their useful suggestions.

References

Abramovitz T, Thybo H, and Perchuc E (2002) Tomographic inversion of seismic P- and S-wave velocities from the Baltic Shield based on FENNOLORA data. *Tectonophysics* 358: 151–174.

Abt DL, Fischer KM, French SW, Ford HA, Yuan H, and Romanowicz B (2010) North American lithospheric discontinuity structure imaged by Ps and Sp receiver functions. *Journal of Geophysical Research* 115: B09301. http://dx.doi.org/10.1029/2009JB006914.

Adams RD (1968) Early reflections of P′P′ as an indication of upper mantle structure. *Bulletin of Seismological Society of America* 58: 1933–1947.

Adams RD (1971) Reflections from discontinuities beneath Antarctica. *Bulletin of Seismological Society of America* 61: 1441–1451.

Ai Y, Tian Z, Xu W, and Li Q (2008) Small scale hot upwelling near the North Yellow Sea of eastern China. *Geophysical Research Letters* 35: L20305. http://dx.doi.org/10.1029/2008GL035269.

Ai Y, Zhao D, Gao X, and Xu W (2005) The crust and upper mantle discontinuity structure beneath Alaska inferred from receiver functions. *Physics of the Earth and Planetary Interiors* 150: 339–350.

Ai Y and Zheng T (2003) The upper mantle discontinuity structure beneath eastern China. *Geophysical Research Letters* 30(21): 2089. http://dx.doi.org/10.1029/2003GL017678.

Ai Y, Zheng T, Xu W, He Y, and Dong D (2003) A complex 660 km discontinuity beneath northeast China. *Earth and Planetary Science Letters* 212: 63–71.

Alinaghi A, Bock G, Kind R, Hanka W, and Wylegalla K (2003) Receiver function analysis of the crust and upper mantle from the North German Basin to the Archean Baltic Shield. *Geophysics Journal International* 155: 641–652.

An Y, Gu YJ, and Sacchi MD (2007) Imaging mantle discontinuities using least squares Radon transform. *Journal of Geophysical Research* 112: B10303. http://dx.doi.org/10.1029/2007JB005009.

Anderson DL (1967) Phase changes in the upper mantle. *Science* 157: 1165–1173.

Anderson DL (1979) The deep structure of continents. *Journal of Geophysical Research* 84: 7555–7560.

Anderson DL (1989) *Theory of the Earth*. Boston, MA: Blackwell Scientific.

Anderson DL (1995) Lithosphere, asthenosphere, and perisphere. *Reviews of Geophysics* 33: 125–149.

Anderson DL and Bass JD (1986) Transition region of the Earth's upper mantle. *Nature* 320: 321–328.

Andrews J and Deuss A (2008) Detailed nature of the 660 km region of the mantle from global receiver function data. *Journal of Geophysical Research* 113: B06304. http://dx.doi.org/10.1029/2007JB005111.

Angus DA and Thomson CJ (2012) Modelling converted seismic waveforms in isotropic and anisotropic 1-D gradients: Discontinuous versus continuous gradient representations. *Studia Geophysica et Geodaetica* 56: 383–409. http://dx.doi.org/10.1007/s11200-011-1350-1.

Angus DA, Wilson DC, Sandvol E, and Ni JF (2006) Lithospheric structure of the Arabian and Eurasian collision zone in eastern Turkey from S-wave receiver functions. *Geophysical Journal International* 166: 1335–1346. http://dx.doi.org/10.1111/j.1365-246X.2006.03070.x.

Artemieva IM and Mooney WD (2001) Thermal thickness and evolution of Precambrian lithosphere: A global study. *Journal of Geophysical Research* 106: 16387–16414.

Artemieva IM, Mooney WD, Perchuc E, and Thybo H (2002) Processes of lithosphere evolution: New evidence on the structure of the continental crust and uppermost mantle. *Tectonophysics* 358: 1–15.

Bagley B, Courtier AM, and Revenaugh J (2009) Melting in the deep upper mantle ocean ward of the Honshu slab. *Physics of the Earth and Planetary Interiors* 175: 137–144. http://dx.doi.org/10.1016/j.pepi.2009.03.007.

Bagley B and Revenaugh J (2008) Upper mantle seismic shear discontinuities of the Pacific. *Journal of Geophysical Research* 113: B12301. http://dx.doi.org/10.1029/2008JB005692.

Barrell J (1914) The strength of the Earth's crust. *Journal of Geology* 22: 680ff.

Bartzsch S, Lebedev S, and Meier T (2011) Resolving the lithosphere–asthenosphere boundary with seismic Rayleigh waves. *Geophysical Journal International* 186: 1152–1164. http://dx.doi.org/10.1111/j.1365-246X.2011.05096.x.

Bass JD and Anderson DL (1984) Composition of the upper mantle: Geophysical tests of two petrological models. *Geophysical Research Letters* 11: 229–232.

Bath M and Stefansson R (1966) S–P conversion at the base of the crust. *Annali di Geofisica* 19: 119–130.

Benoit MH, Nyblade AA, VanDecar JC, and Gurrola H (2003) Upper mantle P wave velocity structure and transition zone thickness beneath the Arabian Shield. *Geophysical Research Letters* 30(10): 1531. http://dx.doi.org/10.1029/2002GL016436.

Benz HM and Vidale JE (1993) Sharpness of upper-mantle discontinuities determined from high-frequency reflections. *Nature* 365: 147–150.

Bercovici D and Karato S-I (2003) Whole-mantle convection and the transition-zone water filter. *Nature* 425: 39–44.

Beucler E, Chevrot S, and Montagner J-P (1999) The Snake River plain experiment revisited: Relationships between a Farallon plate fragment and the transition zone. *Geophysical Research Letters* 26: 2673–2676.
Bijwaard H, Spakmam W, and Engdahl ER (1998) Closing the gap between regional and global travel time tomography. *Journal of Geophysical Research* 103: 30055–30078.
Bina CR and Helffrich G (1994) Phase transition Clapeyron slopes and transition zone seismic discontinuity topography. *Journal of Geophysical Research* 99: 15853–15860.
Bina CR and Wood BJ (1986) The 400-km seismic discontinuity and the proportion of olivine in the Earth's upper mantle. *Nature* 324: 449–451.
Birch F (1952) Elasticity and constitution of the Earth's interior. *Journal of Geophysical Research* 57: 227–286.
Blum J and Shen Y (2004) Thermal, hydrous, and mechanical states of the mantle transition zone beneath southern Africa. *Earth and Planetary Science Letters* 217: 367–378.
Bock G (1988) Sp phases from the Australian upper mantle. *Geophysical Journal of the Royal Astronomical Society* 94: 73–81.
Bock G (1991) Long-period S to P converted waves and the onset of partial melting beneath Oahu. *Geophysical Research Letters* 18: 869–872.
Bock G (1994) Synthetic seismogram images of upper mantle structure: No evidence for a 520-km discontinuity. *Journal of Geophysical Research* 99: 15843–15851.
Bolt B (1970) PdP and PKiKP waves and diffracted PcP waves. *Geophysical Journal of the Royal Astronomical Society* 20: 367–382.
Bostock MG (1996a) A seismic image of the upper mantle beneath the North American craton. *Geophysical Research Letters* 23: 1593–1596.
Bostock MG (1996b) Ps conversions from the upper mantle transition zone beneath the Canadian landmass. *Journal of Geophysical Research* 101: 8393–8402.
Bostock MG (1997) Anisotropic upper-mantle stratigraphy and architecture of the Slave craton. *Nature* 390: 393–395.
Bostock MG (1998) Mantle stratigraphy and evolution of the Slave province. *Journal of Geophysical Research* 103: 21183–21200.
Bostock MG (1999) Seismic imaging of lithospheric discontinuities and continental evolution. *Lithos* 48: 1–16.
Bostock MG and Cassidy JF (1997) Upper mantle stratigraphy beneath the southern Slave craton. *Canadian Journal of Earth Sciences* 34: 577–587.
Budweg M, Bock G, and Weber M (2006) The Eifel plume imaged with converted seismic waves. *Geophysical Journal International* 166: 579–589.
Butler R, Lay T, Creager K, et al. (2004) The global seismographic network surpasses its design goals. *EOS. Transactions of the American Geophysical Union* 80: 225–229.
Byerly P (1926) The Montana earthquake of June 28, 1925. *Bulletin of Seismological Society of America* 16: 209–265.
Cao A and Levander A (2010) High-resolution transition zone structures of the Gorda Slab beneath the western United States: Implication for deep water subduction. *Journal of Geophysical Research* 115: B07301. http://dx.doi.org/10.1029/2009JB006876.
Cao Q, Van der Hilst RD, De Hoop MV, and Shim SH (2011) Seismic imaging of transition zone discontinuities suggests hot mantle west of Hawaii. *Science* 332: 1068–1071. http://dx.doi.org/10.1126/science.1202731.
Cao Q, Wang P, van der Hilst RD, de Hoop MV, and Shim SH (2010) Imaging the upper mantle transition zone with a generalized Radon transform of SS precursors. *Physics of the Earth and Planetary Interiors* 180: 80–91.
Castle JC and Creager KC (1997) Seismic evidence against a mantle chemical discontinuity near 660 km depth beneath Izu-Bonin. *Geophysical Research Letters* 24: 241–244.
Castle JC and Creager KC (1998) Topography of the 660-km seismic discontinuity beneath Izu-Bonin: Implications for tectonic history and slab deformation. *Journal of Geophysical Research* 103: 12511–12527.
Castle JC and Creager KC (2000) Local sharpness and shear wave speed jump across the 660-km discontinuity. *Journal of Geophysical Research* 105: 6191–6200.
Chaljub E and Tarantola A (1997) Sensitivity of SS precursors to topography on the upper-mantle 660-km discontinuity. *Geophysical Research Letters* 24: 2613–2616.
Chambers K, Deuss A, and Woodhouse JH (2005a) Reflectivity of the 410-km discontinuity from PP and SS precursors. *Journal of Geophysical Research* 110: 1–13.
Chambers K, Woodhouse JH, and Deuss A (2005b) Topography of the 410-km discontinuity from PP and SS precursors. *Earth and Planetary Science Letters* 235: 610–622.
Chemenda AI, Burg J-P, and Mattauer M (2000) Evolutionary model of the Himalaya–Tibet system: Geopoem based on new modelling, geological and geophysical data. *Earth and Planetary Science Letters* 174: 397–409.
Chen L (2009) Lithospheric structure variations between the eastern and central North China Craton from S- and P-receiver function migration. *Physics of the Earth and Planetary Interiors* 173: 216–227.
Chen L (2010) Concordant structural variations from the surface to the base of the upper mantle in the North China Craton and its tectonic implications. *Lithos* 120: 96–115.
Chen L and Ai Y (2009) Discontinuity structure of the mantle transition zone beneath the North China Craton from receiver function migration. *Journal of Geophysical Research* 114: B06307. http://dx.doi.org/10.1029/2008JB006221.
Chen L, Tao W, Zhao L, and Zheng T (2008) Distinct lateral variation of lithospheric thickness in the Northeastern North China Craton. *Earth and Planetary Science Letters* 267: 56–68.
Chevrot S, Vinnik L, and Montagner J-P (1999) Global-scale analysis of the mantle Pds phases. *Journal of Geophysical Research* 104: 20203–20219.
Chu R, Schmandt B, and Helmberger DV (2012) Upper mantle P velocity structure beneath the Midwestern United States derived from triplicated waveforms. *Geochemistry, Geophysics, Geosystems* 13: Q0AK04. http://dx.doi.org/10.1029/2011GC003818.
Clarke TJ, Silver PG, Yeh YL, James DE, Wallace TC, and Beck SL (1995) Close in SCS and sSCS reverberations from the 9 June 1994 Bolivian earthquake. *Geophysical Research Letters* 22: 2313–2316.
Collier JD and Helffrich GR (1997) Topography of the '410' and '660' km seismic discontinuities in the Izu-Bonin subduction zone. *Geophysical Research Letters* 24: 1535–1538.
Collier JD and Helffrich GR (2001) The thermal influence of the subducting slab beneath South America from 410 and 660 km discontinuity observations. *Geophysical Journal International* 147: 319–329.
Collier JD, Helffrich GR, and Wood BJ (2001) Seismic discontinuities and subduction zones. *Physics of the Earth and Planetary Interiors* 127: 35–49.
Collins JA, Vernon FL, Orcutt JA, and Stephen RA (2002) Upper mantle structure beneath the Hawaiian swell: Constraints from the ocean seismic network pilot experiment. *Geophysical Research Letters* 29(11): 17.1–17.4.
Contenti S, Gu YJ, Okeler A, and Sacchi MD (2012) Shear wave reflectivity imaging of the Nazca-South America subduction zone: Stagnant slab in the mantle transition zone. *Geophysical Research Letters* 39: L02310. http://dx.doi.org/10.1029/2011GL050064.
Cornwell DG, Hetényi G, and Blanchard TD (2011) Mantle transition zone variations beneath the Ethiopian Rift and Afar: Chemical heterogeneity within a hot mantle. *Geophysical Research Letters* 38: L16308. http://dx.doi.org/10.1029/2011GL047575.
Courtier AM, Bagley B, and Revenaugh J (2007) Whole mantle discontinuity structure beneath Hawaii. *Geophysical Research Letters* 34: L17304.
Cummins PR, Kennett BLN, Bowman JR, Rand J, and Bostock MG (1992) The 520 km discontinuity. *Bulletin of Seismological Society of America* 82: 323–336.
Das Sharma S, Ramesh DS, Li X, Yuan X, Sreenivas B, and Kind R (2010) Response of mantle transition zone thickness to plume buoyancy flux. *Geophysical Journal International* 180: 49–58. http://dx.doi.org/10.1111/j.1365-246X.2009.04403.x.
Day EA and Deuss A (2013) Reconciling *PP* and *PP* precursor observations of a complex 660 km seismic discontinuity. *Geophysical Journal International* 194: 834–838. http://dx.doi.org/10.1093/gji/ggt122.
Deuss A (2009) Global observations of mantle discontinuities using SS and PP precursors. *Surveys in Geophysics* 30(4–5): 301–326. http://dx.doi.org/10.1007/s10712-009-9078-y.
Deuss A, Redfern SAT, Chambers K, and Woodhouse JH (2006) The nature of the 660-kilometer discontinuity in Earth's mantle from global seismic observations of PP precursors. *Science* 311(5758): 198–201. http://dx.doi.org/10.1126/science.1120020.
Deuss A and Woodhouse J (2001) Seismic observations of splitting of the mid-transition zone discontinuity in Earth's mantle. *Science* 294: 354–357.
Deuss A and Woodhouse JH (2002) A systematic search for mantle discontinuities using SS-precursors. *Geophysical Research Letters* 29(8): 90.1–90.4.
Deuss A and Woodhouse JH (2004) The nature of the Lehmann discontinuity from its seismological Clapeyron slopes. *Earth and Planetary Science Letters* 225: 295–304.
Devi UE, Kumar P, and Kumar MR (2011) Imaging the Indian lithosphere beneath the Eastern Himalayan Region. *Geophysical Journal International* 187: 631–641. http://dx.doi.org/10.1111/j.1365-246X.2011.05185.x.
Dormann J, Ewing M, and Oliver J (1960) Study of shear-wave velocity distribution in the upper mantle by mantle Rayleigh waves. *Bulletin of Seismological Society of America* 50: 87–115.
Dricker IG, Roecker SW, Kosarev GL, and Vinnik LP (1996) Shear-wave velocity structure of the crust and upper mantle beneath the Kola Peninsula. *Geophysical Research Letters* 23: 3389–3392.

Drummond BJ, Muirhead KJ, and Hales AL (1982) Evidence for a seismic discontinuity near 200 km depth under a continental margin. *Geophysical Journal of the Royal Astronomical Society* 70: 67–77.

Du Z, Vinnik LP, and Foulger GR (2006) Evidence from P-to-S mantle converted waves for a flat "660-km" discontinuity beneath Iceland. *Earth and Planetary Science Letters* 241: 271–280.

Dueker KG and Sheehan AF (1997a) Mantle discontinuity structure beneath the Colorado Rocky Mountains and High Plains. *Journal of Geophysical Research* 103: 7153–7169.

Dueker KG and Sheehan AF (1997b) Mantle discontinuity structure from midpoint stacks of converted P to S waves across the Yellowstone hotspot track. *Journal of Geophysical Research* 102: 8313–8327.

Dündar S, Kind R, Yuan X, et al. (2011) Receiver function images of the base of the lithosphere in the Alboran Sea region. *Geophysical Journal International* 187(2): 1019–1026. http://dx.doi.org/10.1111/j.1365-246X.2011.05216.x.

Dziewonski AM and Anderson DL (1981) Preliminary reference Earth model. *Physics of the Earth and Planetary Interiors* 25: 297–356.

Eagar KC, Fouch MJ, and James DE (2010) Receiver function imaging of upper mantle complexity beneath the Pacific Northwest, United States. *Earth and Planetary Science Letters* 297: 141–153.

Eaton DW, Darbyshire F, Evans RL, Grütter H, Jones AG, and Yuan X (2009) The elusive lithosphere–asthenosphere boundary (LAB) beneath cratons. *Lithos* 109: 1–22.

Egorkin AV, Zuganov SK, Pavlenkova NA, and Chernyshev NM (1987) Results of lithospheric studies from long-range profiles in Siberia. *Tectonophysics* 140: 29–47.

Engdahl ER and Flinn EA (1969) Seismic waves reflected from discontinuities within the Earth's upper mantle. *Science* 163: 177–179.

Estabrook CH and Kind R (1996) The nature of the 660-kilometer upper-mantle seismic discontinuity from precursors to the PP phase. *Science* 274: 1179–1182.

Faber S and Müller G (1980) Sp phases from the transition zone between the upper and lower mantle. *Bulletin of Seismological Society of America* 70: 487–508.

Farra V and Vinnik L (2000) Upper mantle stratification by P and S receiver functions. *Geophysical Journal International* 141: 699–712.

Fee D and Dueker K (2004) Mantle transition zone topography and structure beneath the Yellowstone hotspot. *Geophysical Research Letters* 31: 18. http://dx.doi.org/10.1029/2004GL020636.

Fischer KM, Ford HA, Abt DL, and Rychert CA (2010) The lithosphere–asthenosphere boundary. *Annual Review of Earth and Planetary Sciences* 38: 551. http://dx.doi.org/10.1146/annurev-earth-040809-152438.

Fishwick S (2010) Surface wave tomography: Imaging of the lithosphere–asthenosphere boundary beneath central and southern Africa. *Lithos* 120: 63–73.

Flanagan MP and Shearer PM (1998a) Global mapping of topography on transition zone velocity discontinuities by stacking SS precursors. *Journal of Geophysical Research* 103: 2673–2692.

Flanagan MP and Shearer PM (1998b) Topography on the 410-km seismic velocity discontinuity near subduction zones from stacking of sS, sP and pP precursors. *Journal of Geophysical Research* 103: 21165–21182.

Flanagan MP and Shearer PM (1999) A map of topography on the 410-km discontinuity from PP precursors. *Geophysical Research Letters* 26: 549–552.

Ford HA, Fischer KM, Abt DL, Rychert CA, and Elkins-Tanton LT (2010) The lithosphere–asthenosphere boundary and cratonic lithospheric layering beneath Australia from Sp wave imaging. *Earth and Planetary Science Letters* 300: 299–310.

Fuchs K (1983) Recently formed elastic anisotropy and petrological models for the continental subcrustal lithosphere in southern Germany. *Physics of the Earth and Planetary Interiors* 31: 93–118.

Fuchs K, Tittgemeyer M, Ryberg T, Wenzel F, and Mooney W (2002) Global significance of a sub-Moho boundary layer (SMBL) deduced from high-resolution seismic observations. *International Geology Review* 44: 671–685.

Gaherty JB and Jordan TH (1995) Lehmann discontinuity as the base of an anisotropic layer beneath continents. *Science* 268: 1468–1471.

Gaherty JB, Jordan TH, and Gee LS (1996) Seismic structure of the upper mantle in a central Pacific corridor. *Journal of Geophysical Research* 101: 22291–22309.

Gaherty JB, Kato M, and Jordan TH (1999) Seismological structure of the upper mantle: A regional comparison of seismic layering. *Physics of the Earth and Planetary Interiors* 110: 21–41.

Gao SS, Silver PG, and Liu KH (2002) Mantle discontinuities beneath Southern Africa. *Geophysical Research Letters* 29(10): 49. http://dx.doi.org/10.1029/2001GL013834.

Gao Y, Suetsugu D, Fukao Y, Obayashi M, Shi Y, and Liu R (2010) Seismic discontinuities in the mantle transition zone and at the top of the lower mantle beneath eastern China and Korea: Influence of the stagnant Pacific slab. *Physics of the Earth and Planetary Interiors* 183: 288–295.

Geissler W, Sodoudi F, and Kind R (2010) Thickness of the central and eastern European lithosphere as seen by S receiver functions. *Geophysical Journal International* 181: 604–634. http://dx.doi.org/10.1111/j.1365-246X.2010.04548.x.

Gilbert HJ, Sheehan AF, Dueker KG, and Molnar P (2003) Receiver functions in the western United States, with implications for upper mantle structure and dynamics. *Journal of Geophysical Research* 108(5): 2229. http://dx.doi.org/10.1029/2001JB001194.

Gilbert HJ, Sheehan AF, Wiens DA, et al. (2001) Upper mantle discontinuity structure in the region of the Tonga subduction zone. *Geophysical Research Letters* 28: 1855–1858.

Gossler J and Kind R (1996) Seismic evidence for very deep roots of continents. *Earth and Planetary Science Letters* 138: 1–13.

Green DH and Hales AL (1968) The travel time of P waves to 30° in the central United States and upper mantle structure. *Bulletin of Seismological Society of America* 58: 267–289.

Green DH and Liebermann RC (1976) Phase equilibria and elastic properties of a pyrolite model for the oceanic upper mantle. *Tectonophysics* 32: 61–92.

Green DH and Ringwood AE (1967) The stability fields of aluminous pyroxene peridotite and garnet peridotite and their relevance in upper mantle structure. *Earth and Planetary Science Letters* 3: 151–160.

Griffin WL, O'Reilly SY, Abea N, et al. (2003) The origin and evolution of Archean lithospheric mantle. *Precambrian Research* 127: 19–41.

Grunewald S, Weber M, and Kind R (2001) The upper mantle under central Europe: Indications for the Eifel plume. *Geophysical Journal International* 147: 590–601.

Gu YJ, An Y, Sacchi M, Schultz R, and Ritsema J (2009) Mantle reflectivity structure beneath oceanic hotspots. *Geophysical Journal International* 178: 1456–1472. http://dx.doi.org/10.1111/j.1365-246X.2009.04242.x.

Gu YJ and Dziewonski AM (2002) Global variability of transition zone thickness. *Journal of Geophysical Research* 107(7): 2135. http://dx.doi.org/10.1029/2001JB000489.

Gu Y, Dziewonski AM, and Agee CB (1998) Global de-correlation of the topography of transition zone discontinuities. *Earth and Planetary Science Letters* 157: 57–67.

Gu Y, Dziewonski AM, and Ekstrom G (2001a) Preferential detection of the Lehmann discontinuity beneath continents. *Geophysical Research Letters* 28: 4655–4658.

Gu YJ, Dziewonski AM, and Ekstrom G (2003) Simultaneous inversion for mantle shear velocity and topography of transition zone discontinuities. *Geophysical Journal International* 154: 559–583.

Gu Y, Dziewonski AM, Su W, and Ekstrom G (2001b) Models of the mantle shear velocity and discontinuities in the pattern of lateral heterogeneities. *Journal of Geophysical Research* 106: 11169–11199.

Gu YJ, Lerner-Lam AL, Dziewonski AM, and Ekstrom G (2005) Deep structure and seismic anisotropy beneath the East Pacific Rise. *Earth and Planetary Science Letters* 232: 259–272.

Gu YJ, Okeler A, and Schultz R (2012) Tracking slabs beneath northwestern Pacific subduction zones. *Earth and Planetary Science Letters* 331–332: 269–280.

Gu YJ and Sacchi M (2009) Radon transform methods and their applications in mapping mantle reflectivity structure. *Surveys in Geophysics* 30: 327–354. http://dx.doi.org/10.1007/s10712-009-9076-0.

Gung Y, Panning M, and Romanowicz B (2003) Global anisotropy and the thickness of continents. *Nature* 422: 707–711.

Gurrola H and Bernard Minster J (1998) Thickness estimates of the upper-mantle transition zone from bootstrapped velocity spectrum stacks of receiver functions. *Geophysical Journal International* 133: 31–43.

Gurrola H and Bernard Minster J (2000) Evidence for local variations in the depth to the 410 km discontinuity beneath Albuquerque, New Mexico. *Journal of Geophysical Research* 105: 10847–10856.

Gutenberg B (1926) Untersuchungen zur Frage bis zu welcher Tiefe die Erde kristallin ist. *Zeitschrift für Geophysik* 2: 24–29.

Gutenberg B (1954) Low-velocity layers in the earth's mantle. *Bulletin of the Geological Society of America* 65: 337–348.

Gutenberg B (1959) *Physics of the Earth's Interior*. New York: Academic Press, 240 pp.

Hajnal Z, Nemeth B, Clowes RM, et al. (1997) Mantle involvement in lithospheric collision: Seismic evidence from the Trans-Hudson orogen, western Canada. *Geophysical Research Letters* 24: 2079–2082.

Hales AL (1969) A seismic discontinuity in the lithosphere. *Earth and Planetary Science Letters* 7: 44–46.

Hales AL (1972) The travel times of P seismic phases and their relevance to the upper mantle velocity distribution. *Tectonophysics* 13: 447–482.

Hales AL (1991) Upper mantle models and the thickness of the continental lithosphere. *Geophysical Journal International* 105: 355–363.

Hales AL, Muirhead KL, and Rynn JMW (1980) A compressional velocity distribution for the upper mantle. *Tectonophysics* 63: 309–348.

Hanka W, Heinloo A, and Jaeckel K-H (2000) Networked seismographs: GEOFON real time data distribution. *ORFEUS Electronic Newsletter* 2: 24. http://orfeus.knmi.nl/newsletter/vol2no3/geofon.html (accessed October 2006).

Hansen SE, Nyblade AA, and Julia J (2009a) Estimates of crustal and lithospheric thickness in Sub-Sahara Africa from S-wave receiver functions. *South African Journal of Geology* 112: 229–240. http://dx.doi.org/10.2113/gssajg.112.3-4.229.

Hansen SE, Nyblade AA, Julia J, Dirks HGM, and Durrheim RJ (2009b) Upper-mantle low-velocity zone structure beneath the Kaapvaal craton from S-wave receiver functions. *Geophysical Journal International* 178: 1021–1027. http://dx.doi.org/10.1111/j.1365-246X.2009.04178.x.

Hansen SE, Rodgers AJ, Schwartz SY, and Al-Amri AMS (2007) Imaging ruptured lithosphere beneath the Red Sea and Arabian Peninsula. *Earth and Planetary Science Letters* 259: 256–265.

Heit B, Sodoudi F, Yuan X, Bianchi M, and Kind R (2007) An S receiver function analysis of the lithospheric structure in South America. *Geophysical Research Letters* 34: L14307.

Heit B, Yuan X, Bianchi M, Kind R, and Gossler J (2010) Study of the lithospheric and upper-mantle discontinuities beneath eastern Asia by SS precursors. *Geophysical Journal International* 183: 252–266. http://dx.doi.org/10.1111/j.1365-246X.2010.04714.x.

Helffrich G (2000) Topography of the transition zone seismic discontinuities. *Reviews of Geophysics* 38: 141–158.

Helffrich G (2002) Thermal variations in the mantle inferred from 660 km discontinuity topography and tomographic wave speed variations. *Geophysical Journal International* 151: 935–943.

Helffrich G, Asencio E, Knapp J, and Owens T (2003) Transition zone structure in a tectonically inactive area: 410 and 660 km discontinuity properties under the northern North Sea. *Geophysical Journal International* 155: 193–199.

Helffrich G and Bina CR (1994) Frequency dependence of the visibility and depths of mantle seismic discontinuities. *Geophysical Research Letters* 21: 2613–2616.

Helffrich G, Faria B, Fonseca JFBD, Lodge A, and Kaneshima S (2010) Transition zone structure under a stationary hot spot: Cape Verde. *Earth and Planetary Science Letters* 289: 156–161.

Helmberger D (1968) The crust–mantle transition in the Bering Sea. *Bulletin of Seismological Society of America* 58: 179–214.

Helmberger DV and Wiggins RA (1971) Upper mantle structure of midwestern United States. *Journal of Geophysical Research* 76: 3229–3245.

Hetenyi G, Stuart GW, Houseman GA, Horvath F, Hegedus E, and Brückl E (2009) Anomalously deep mantle transition zone below Central Europe: Evidence of lithospheric instability. *Geophysical Research Letters* 36: L21307. http://dx.doi.org/10.1029/2009GL040171.

Heuer B, Geissler WH, and Kind RBOHEMA Working Group (2011) Receiver function search for a baby plume in the mantle transition zone beneath the Bohemian Massif. *Geophysical Journal International* http://dx.doi.org/10.1111/j.1365-246X.2011.05155.x.

Hirn A, Steinmetz L, Kind R, and Fuchs K (1973) Long range profiles in western Europe. II: Fine structure of the lithosphere in Bretagne (France). *Zeitschrift für Geophysik* 39: 363–384.

Hooft EEE, Toomey DR, and Solomon SC (2003) Anomalously thin transition zone beneath the Galapagos hotspot. *Earth and Planetary Science Letters* 216: 55–64.

Houser C, Masters G, Flanagan M, and Shearer P (2008) Determination and analysis of long-wavelength transition zone structure using SS precursors. *Geophysical Journal International* 174: 178–194. http://dx.doi.org/10.1111/j.1365-246X.2008.03719.x.

Hu J, Xu X, Yang H, Wen L, and Li G (2011) S receiver function analysis of the crustal and lithospheric structures beneath eastern Tibet. *Earth and Planetary Science Letters* 306: 77–85.

Hu J, Yang H, Li G, and Wen L (2013) Seismic signature of the mantle transition zone beneath eastern Tibet and Sichuan Basin. *Journal of Asian Earth Sciences* 62: 606–615. http://dx.doi.org/10.1016/j.jseaes.2012.11.009.

Huang J, Vanacore E, Niu F, and Levander A (2010) Mantle transition zone beneath the Caribbean-South American plate boundary and its tectonic implications. *Earth and Planetary Science Letters* 289: 105–111.

Huckfeldt M, Courtier AM, and Leahy GM (2013) Implications of the origin of Hawaiian volcanism from converted wave analysis of the mantle transition zone. *Earth and Planetary Science Letters* 373: 194–204. http://dx.doi.org/10.1016/j.epsl.2013.05.003.

Huerta AD, Nyblade AA, and Reusch AM (2009) Mantle transition zone structure beneath Kenya and Tanzania: More evidence for a deep-seated thermal upwelling in the mantle. *Geophysical Journal International* 177: 1249–1255. http://dx.doi.org/10.1111/j.1365-246X.2009.04092.x.

Humphreys ED, Dueker KG, Schutt DL, and Smith RB (2000) Beneath Yellowstone: Evaluating plume and nonplume models using teleseismic images of the upper mantle. *GSA Today* 10: 1–7.

Ibrahim AK and Nuttli OW (1967) Travel-time curves and upper mantle structure from long-period S waves. *Bulletin of Seismological Society of America* 57: 1063–1092.

Irifune T and Isshiki M (1998) Iron partitioning in a pyrolite mantle and the nature of the 410-km seismic discontinuity. *Nature* 392: 702–705.

Ito E and Takahashi E (1989) Postspinel transformations in the system Mg_2SiO_4–Fe_2SiO_4 and some geophysical implications. *Journal of Geophysical Research* 94: 10637–10646.

Jasbinsek J and Dueker KG (2007) Ubiquitous low-velocity layer atop the 410 km discontinuity in the northern Rocky Mountains. *Geochemistry, Geophysics, Geosystems* 8: Q10004. http://dx.doi.org/10.1029/2007GC001661.

Jasbinsek J, Dueker KG, and Hansen SM (2010) Characterizing the 410 km discontinuity low-velocity layer beneath the LA RISTRA array in the North American Southwest. *Geochemistry, Geophysics, Geosystems* 11: Q03008. http://dx.doi.org/10.1029/2009GC002836.

Jeanloz R and Thompson AB (1983) Phase transitions and mantle discontinuities. *Reviews of Geophysics* 1: 51–74.

Jeffreys H (1936) The structure of the Earth down to the 20° discontinuity. *Monthly Notices of the Royal Astronomical Society, Geophysical Supplement* 3: 401–422.

Jeffreys H and Bullen KE (1940) *Seismological Tables*. London: British Association for the Advancement of Science, 50 pp.

Johnson LR (1967) Array measurements of P velocities in the upper mantle. *Journal of Geophysical Research* 72: 6309–6325.

Jones AG, Plomerova J, Korja T, Sodoudi F, and Spakman W (2010) Europe from the bottom up: A statistical examination of the central and northern European lithosphere–asthenosphere boundary from comparing seismological and electromagnetic observations. *Lithos* 120: 14–29.

Jordan TH (1975) The continental tectosphere. *Reviews of Geophysics and Space Physics* 13: 1–12.

Jordan TH and Frazer LN (1975) Crustal and upper mantle structure from Sp phases. *Journal of Geophysical Research* 80: 1504–1518.

Julian BR and Anderson DL (1968) Travel times, apparent velocities and amplitudes of body waves. *Bulletin of Seismological Society of America* 58: 339–366.

Kaila KL, Krishna VG, and Khandekar G (1999) Preliminary models of upper mantle P and S wave velocity structure in the western South America region. *Journal of Geodynamics* 27: 567–583.

Kanamori H (1967) Upper mantle structure from apparent velocities of P waves recorded at Wakayama micro-earthquake observatory. *Bulletin of the Earthquake Research Institute, Tokyo University* 45: 657–678.

Kanamori H and Press F (1970) How thick is the lithosphere. *Nature* 226: 330.

Karato S (1992) On the Lehmann discontinuity. *Geophysical Research Letters* 19: 2255–2258.

Kato M and Jordan TH (1999) Seismic structure of the upper mantle beneath the western Philippine Sea. *Physics of the Earth and Planetary Interiors* 110: 263–283.

Kato M and Kawakatsu H (2001) Seismological in situ estimation of density jumps across the transition zone discontinuities beneath Japan. *Geophysical Research Letters* 28: 2541–2544.

Kato M, Misawa M, and Kawakatsu H (2001) Small subsidence of the 660-km discontinuity beneath Japan probed by ScS reverberations. *Geophysical Research Letters* 28: 447–450.

Kawakatsu H, Kumar P, Takei Y, et al. (2009) Seismic evidence for sharp lithosphere–asthenosphere boundaries of oceanic plates. *Science* 324: 499–502. http://dx.doi.org/10.1126/science.1169499.

Kawakatsu H and Yoshioka S (2011) Metastable olivine wedge and deep dry cold slab beneath southwest Japan. *Earth and Planetary Science Letters* 303: 1–10.

Kennett BLN and Engdahl ER (1991) Travel times for global earthquake location and phase identification. *Geophysical Journal International* 105: 429–465.

Kind R (1974) Long range propagation of seismic energy in the lower lithosphere. *Journal of Geophysics* 40: 189–202.

Kind R, Sodoudi F, Yuan X, et al. (2013) Scandinavia – A former Tibet? *Geochemistry, Geophysics, Geosystems* http://dx.doi.org/10.1002/ggge.20251.

Kind R and Vinnik LP (1988) The upper-mantle discontinuities underneath the GRF array from P-to-S converted phases. *Journal of Geophysics – Zeitschrift für Geophysik* 62: 138–147.

Kind R and Yuan X (2010) Seismic images of the biggest crash on Earth. *Science* 329: 1479–1480. http://dx.doi.org/10.1126/science.1191620.

Kind R, Yuan X, and Kumar P (2012) Seismic receiver functions and the lithosphere–asthenosphere boundary. *Tectonophysics* 536–537: 25–43. http://dx.doi.org/10.1016/j.tecto.2012.03.005.

Kind R, Yuan X, Saul J, et al. (2002) Seismic images of crust and upper mantle beneath Tibet: Evidence for Eurasian plate subduction. *Science* 298: 1219–1221.

King DW, Haddon RAW, and Husebye ES (1975) Precursors to PP. *Physics of the Earth and Planetary Interiors* 10: 103–127.

Kirby SH, Stein S, Okal EA, and Rubie DC (1996) Metastable mantle phase transformations and deep earthquakes in subducting oceanic lithosphere. *Reviews of Geophysics* 34: 261–306.

Knopoff L (1983) The thickness of the lithosphere from the dispersion of surface waves. *Geophysical Journal of the Royal Astronomical Society* 74: 55–81.

Kumar P and Kawakatsu H (2011) Imaging the seismic lithosphere–asthenosphere boundary of the oceanic plate. *Geochemistry, Geophysics, Geosystems* 12: Q01006. http://dx.doi.org/10.1029/2010GC003358.

Kumar P, Kawakatsu H, Shinohara M, Kanazawa T, Araki E, and Suyehiro K (2011) P and S receiver function analysis of seafloor borehole broadband seismic data. *Journal of Geophysical Research* 116: B12308. http://dx.doi.org/10.1029/2011JB008506.

Kumar P, Kind R, Hanka W, et al. (2005a) The lithosphere–asthenosphere boundary in the north west Atlantic Region. *Earth and Planetary Science Letters* 236: 249–257.

Kumar P, Kind R, and Yuan X (2010) Receiver function summation without deconvolution. *Geophysical Journal International* 180: 1223–1230. http://dx.doi.org/10.1111/j.1365-246X.2009.04469.x.

Kumar P, Kind R, Yuan X, and Mechie J (2012a) USArray receiver function images of the lithosphere–asthenosphere boundary. *Seismological Research Letters* 83(3): 486–491. http://dx.doi.org/10.1785/gssrl.83.3.486.

Kumar MR, Ramesh DS, Saul J, Sarkar D, and Kind R (2002) Crustal structure and upper mantle stratigraphy of the Arabian Shield. *Geophysical Research Letters* 29(8): 1242. http://dx.doi.org/10.1029/2001GL014530.

Kumar P, Yuan X, Kind R, and Kosarev G (2005b) The lithosphere–asthenosphere boundary in the Tian Shan-Karakoram region from S receiver functions: Evidence for continental subduction. *Geophysical Research Letters* 32: L07305. http://dx.doi.org/10.1029/2004GL022291.

Kumar P, Yuan X, Kind R, and Mechie J (2012b) The lithosphere–asthenosphere boundary observed with USArray receiver functions. *Solid Earth* 3: 149–159. http://dx.doi.org/10.5194/se-3-149-2012.

Kumar P, Yuan X, Kind R, and Ni J (2006) Imaging the collision of the Indian and Asian continental lithospheres beneath Tibet. *Journal of Geophysical Research* 111: B06308. http://dx.doi.org/10.1029/2005JB003930.

Kumar P, Yuan X, Kumar MR, Kind R, Li X, and Chadha RK (2007) The rapid drift of the Indian tectonic plate. *Nature* 449: 894–897. http://dx.doi.org/10.1038/nature06214.

Kummerow J and Kind R (2004) A natural and controlled source seismic profile through the Eastern Alps: TRANSALP. *Earth and Planetary Science Letters* 225: 115–129.

Landes M, Ritter JJR, O'Reilley BM, Readmann PW, and Do VC (2006) A N–S receiver function profile across the Variscides and Caledonides in SW Ireland. *Geophysical Journal International* 166: 814–824. http://dx.doi.org/10.1111/j.1365-246X.2006.03052.x.

Langston CA (1979) Structure under Mount Rainier, Washington, inferred from teleseismic body waves. *Journal of Geophysical Research* 84: 4749–4762.

Lawrence JF and Shearer PM (2006a) A global study of transition zone: Thickness using receiver functions. *Journal of Geophysical Research* 111: B06307. http://dx.doi.org/10.1029/2005JB003973.

Lawrence JF and Shearer PM (2006b) Constraining seismic velocity and density for the mantle transition zone with reflected and transmitted waveforms. *Geochemistry, Geophysics, Geosystems* 7: Q10012. http://dx.doi.org/10.1029/2006GC001339.

Lawrence JF and Shearer PM (2008) Imaging mantle transition zone thickness with *SdS-SS* finite-frequency sensitivity kernels. *Geophysical Journal International* 174: 143–158. http://dx.doi.org/10.1111/j.1365246X.2007.03673.x.

Le Stunff Y, Wicks CW Jr., and Romanowicz B (1995) P′P′ precursors under Africa: Evidence for mid-mantle reflectors. *Science* 270: 74–77.

Leahy GM (2009) Local variability in the 410-km mantle discontinuity under a hotspot. *Earth and Planetary Science Letters* 288: 158–163.

Lebedev S, Chevrot S, and van der Hilst RD (2002a) Seismic evidence for olivine phase changes at the 410- and 660-kilometer discontinuities. *Science* 296: 1300–1302.

Lebedev S, Chevrot S, and van der Hilst RD (2002b) The 660-km discontinuity within the subducting NW-Pacific lithospheric slab. *Earth and Planetary Science Letters* 205: 25–35.

Lebedev S, Chevrot S, and van der Hilst RD (2003) Correlation between the shear-speed structure and thickness of the mantle transition zone. *Physics of the Earth and Planetary Interiors* 136: 25–40.

Lee D-K and Grand SP (1996) Depth of the upper mantle discontinuities beneath the East Pacific Rise. *Geophysical Research Letters* 23: 3369–3372.

Lees AC, Bukowinski MST, and Jeanloz R (1983) Reflection properties of phase transition and compositional models of the 670-km discontinuity. *Journal of Geophysical Research* 88: 8145–8159.

Lehmann I (1961) S and the structure of the upper mantle. *Geophysical Journal of the Royal Astronomical Society* 4: 124–138.

Lehmann I (1964) On the velocity of P in the upper mantle. *Bulletin of Seismological Society of America* 54: 1097–1103.

Lekic V, French SW, and Fischer KM (2011) Lithospheric thinning beneath rifted regions of Southern California. *Science* 334: 783–787.

Levander L and Miller MS (2012) Evolutionary aspects of lithosphere discontinuity structure in the western U.S. *Geochemistry, Geophysics, Geosystems* 13: Q0AK07.

Levin V and Park J (2000) Shear zones in the proterozoic lithosphere of the Arabian shield and the nature of the Hales discontinuity. *Tectonophysics* 323: 131–148.

Li A, Fischer KM, Van der Lee S, and Wysession ME (2002) Crust and upper mantle discontinuity structure beneath eastern North America. *Journal of Geophysical Research* 107(B5): 2100. http://dx.doi.org/10.1029/2001JB000190.

Li A, Fischer KM, Wysession ME, and Clarke TJ (1998) Mantle discontinuities and temperature under the North American continental keel. *Nature* 395: 160–163.

Li X, Kind R, Priestley K, et al. (2000a) Mapping the Hawaiian plume conduit with converted seismic waves. *Nature* 405: 938–941.

Li X, Kind R, and Yuan X (2003a) Seismic study of upper mantle and transition zone beneath hotspots. *Physics of the Earth and Planetary Interiors* 136: 79–92.

Li X, Kind R, Yuan X, Wölbern I, and Hanka W (2004) Rejuvenation of the lithosphere by the Hawaiian plume. *Nature* 427: 827–829.

Li X, Kind R, Yuan X, et al. (2003b) Seismic observation of narrow plumes in the oceanic upper mantle. *Geophysical Research Letters* 30(6): 1334. http://dx.doi.org/10.1029/2002GL015411.

Li X, Sobolev SV, Kind R, Yuan X, and Estabrook CH (2000b) A detailed receiver function image of the upper mantle discontinuities in the Japan subduction zone. *Earth and Planetary Science Letters* 183: 527–541.

Li X and Yuan X (2003) Receiver functions in northeast China – Implications for slab penetration into the lower mantle in northwest Pacific subduction zone. *Earth and Planetary Science Letters* 216: 679–691.

Li X, Yuan X, and Kind R (2007) The lithosphere–asthenosphere boundary beneath the western United States. *Geophysical Journal International* 170(2): 700–710. http://dx.doi.org/10.1111/j.1365-246X.2007.03428.x.

Liu L-G (1976) The post-spinel phases of forsterite. *Nature* 262: 770–772.

Liu KH (2003) Effects of inelasticity on the apparent depth and detectability of seismic discontinuities in the mantle. *Geophysical Research Letters* 30(9): 1455. http://dx.doi.org/10.1029/2002GL015264.

Liu KH, Gao SS, Silver PG, and Zhang YK (2003) Mantle layering across central South America. *Journal of Geophysical Research* 108(B11): 2510. http://dx.doi.org/10.1029/2002JB002208.

Lombardi D, Braunmiller J, Kissling E, and Giardini D (2009) Alpine mantle transition zone imaged by receiver functions. *Earth and Planetary Science Letters* 278: 163–174.

Long MD, Benoit MH, Chapman MC, and King SD (2010) Upper mantle anisotropy and transition zone thickness beneath southeastern North America and implications for mantle dynamics. *Geochemistry, Geophysics, Geosystems* 11: Q10012. http://dx.doi.org/10.1029/2010GC003247.

Mandal P (2012) Passive-source seismic imaging of the crust and upper mantle beneath the 2001 Mw 7.7 Bhuj earthquake region, Gujarat, India. *Bulletin of Seismological Society of America* 102: 252–266. http://dx.doi.org/10.1785/0120110116.

Masters TG, Johnson S, Laske G, and Bolton H (1996) A shear velocity model of the mantle. *Philosophical Transactions of the Royal Society of London A* 354: 1385–1414.

McKenzie D and Priestley K (2008) The influence of lithospheric thickness variations on continental evolution. *Lithos* 102: 1–11.

Mechie J, Egorkin A, Fuchs K, Ryberg T, Solodilov L, and Wenzel F (1993) P-wave mantle velocity structure beneath northern Eurasia from long-range recordings along the profile QUARTZ. *Physics of the Earth and Planetary Interiors* 79: 269–286.

Mechie J, Kind R, and Saul J (2011) *The Seismological Structure of the Tibetan Plateau Crust and Mantle Down to 700 km Depth*, vol. 353, pp. 109–125. London: Geological Society, http://dx.doi.org/10.1144/SP353.7 Special Publications.

Melbourne T and Helmberger D (1998) Fine structure of the 410 km discontinuity. *Journal of Geophysical Research* 103: 10091–10102.

Melbourne TL and Helmberger DV (2002) Whole mantle shear structure beneath the East Pacific Rise. *Journal of Geophysical Research* 107(B9): 2204. http://dx.doi.org/10.1029/2001JB000332.

Miller MS and Eaton DW (2010) Formation of cratonic mantle keels by arc accretion: Evidence from S receiver functions. *Geophysical Research Letters* 37: L18305. http://dx.doi.org/10.1029/2010GL044366.

Mohorovicic A (1910) Das Beben vom 8. X. 1909. *Jahrbuch des Meteorologischen Observatoriums in Zagreb* 9: 63 (Pt. IV, Sect. 1).

Mohsen A, Hofstetter R, Bock G, et al. (2005) A receiver function study across the Dead Sea Transform. *Geophysical Journal International* 160: 948–960.
Mohsen A, Kind R, Sobolev SV, and Weber MDESERT Group (2006) Thickness of the lithosphere east of the Dead Sea Transform. *Geophysical Journal International* 167: 845–852. http://dx.doi.org/10.1111/j.1365-246X.2006.03185.x.
Mooney W, Laske G, and Masters G (1998) A new global crustal model at 5×5 degrees: CRUST-5.1. *Journal of Geophysical Research* 103: 727–747.
Moorkamp M, Jones AG, and Eaton DW (2007) Joint inversion of teleseismic receiver functions and magnetotelluric data using a genetic algorithm: Are seismic velocities and electrical conductivities compatible. *Geophysical Research Letters* 34: L16311. http://dx.doi.org/10.1029/2007GL030519.
Musacchio G, White DJ, Asudeh I, and Thomson CJ (2004) Lithospheric structure and composition of the Archean western Superior Province from seismic refraction/wide-angle reflection and gravity modelling. *Journal of Geophysical Research* 109: B03304. http://dx.doi.org/10.1029/2003JB002427.
Neele F (1996) Sharp 400-km discontinuity from short-period P reflections. *Geophysical Research Letters* 23: 419–422.
Neele F and De Regt H (1999) Imaging upper-mantle discontinuity topography using underside-reflection data. *Geophysical Journal International* 137: 91–106.
Neele F, De Regt H, and van Decar J (1997) Gross errors in upper-mantle discontinuity topography from underside reflection data. *Geophysical Journal International* 129: 194–204.
Neves FA, Singh SC, and Priestley KF (1996) Velocity structure of upper-mantle transition zones beneath central Eurasia from seismic inversion using genetic algorithms. *Geophysical Journal International* 125: 869–878.
Neves FA, Singh SC, and Priestley K (2001) Velocity structure of the upper mantle discontinuities beneath North America from waveform inversion of broadband seismic data using a genetic algorithm. *Journal of Geophysical Research* 106: 21883–21895.
Niazi M and Anderson DL (1965) Upper mantle structure of western North America from apparent velocities of P waves. *Journal of Geophysical Research* 70: 4633–4640.
Nielsen L and Thybo H (2003) The origin of teleseismic Pn waves: Multiple crustal scattering of upper mantle whispering gallery phases. *Journal of Geophysical Research* 108(B10): 2460. http://dx.doi.org/10.1029/2003JB002487.
Nielsen L, Thybo H, and Solodilov L (1999) Seismic tomographic inversion of Russian PNE data along profile Kraton. *Geophysical Research Letters* 26: 3413–3416.
Niu F, Inoue H, Suetsugu D, and Kanjo K (2000) Seismic evidence for a thinner mantle transition zone beneath the South Pacific Superswell. *Geophysical Research Letters* 27: 1981–1984.
Niu F and Kawakatsu H (1996) Complex structure of mantle discontinuities at the tip of the subducting slab beneath northeast China: A preliminary investigation of broadband receiver functions. *Journal of Physics of the Earth* 44: 701–711.
Niu F and Kawakatsu H (1998) Determination of the absolute depths of the mantle transition zone discontinuities beneath China: Effect of stagnant slabs on transition zone discontinuities. *Earth, Planets and Space* 50: 965–975.
Niu F, Solomon SC, Silver PG, Suetsugu D, and Inoue H (2002) Mantle transition-zone structure beneath the South Pacific Superswell and evidence for a mantle plume underlying the society hotspot. *Earth and Planetary Science Letters* 198: 371–380.
Nolet G, Grand SP, and Kennett BLN (1994) Seismic heterogeneity in the upper mantle. *Journal of Geophysical Research* 99: 23753–23766.
Nyblade AA, Knox RP, and Gurrola H (2000) Mantle transition zone thickness beneath Afar: Implications for the origin of the Afar hotspot. *Geophysical Journal International* 142: 615–619.
Obayashi M, Yoshimitsu J, and Fukao Y (2009) Tearing of stagnant slab. *Science* 324: 1173–1175.
Ohtaki T, Suetsugu D, Kanjo K, and Purwana I (2002) Evidence for a thick mantle transition zone beneath the Philippine Sea from multiple-ScS waves recorded by JISNET. *Geophysical Research Letters* 29(13): 2913. http://dx.doi.org/10.1029/2002GL014764, 1646.
Olsson S, Roberts GR, and Bödvarsson R (2007) Analysis of waves converted from S to P in the upper mantle beneath the Baltic Shield. *Earth and Planetary Science Letters* 257: 37–46.
Oreshin S, Vinnik LP, Kiselev SG, Rai SS, Prakasam KS, and Treussov AV (2011) Deep seismic structure of the Indian shield, western Himalaya, Ladakh and Tibet. *Earth and Planetary Science Letters* 307: 415–429.
Oreshin S, Vinnik L, Peregoudov D, and Roecker S (2002) Lithosphere and asthenosphere of the Tian Shan imaged by S receiver functions. *Geophysical Research Letters* 29(8): 1191. http://dx.doi.org/10.1029/2001GL014441.
Owens TJ, Nyblade AA, Gurrola H, and Langston CA (2000) Mantle transition zone structure beneath Tanzania, East Africa. *Geophysical Research Letters* 27: 827–830.
Parker EC, Davis PM, Evans JR, Iyer HM, and Olsen KH (1984) Upwarp of anomalous asthenosphere beneath the Rio Grande rift. *Nature* 312: 354–356.
Pasyanos ME (2010) Lithospheric thickness modeled from long-period surface wave dispersion. *Tectonophysics* 481: 38–50.
Pavlenkova NI (1996) General feature of the uppermost mantle stratification from long-range seismic profiles. *Tectonophysics* 264: 261–278.
Pearson DG (1999) The age of continental roots. *Lithos* 48: 171–194.
Petersen N, Gossler J, Kind R, Stammler K, and Vinnik L (1993a) Precursors to SS and structure of transition zone of the north-western Pacific. *Geophysical Research Letters* 20: 281–284.
Petersen N, Vinnik L, Kosarev G, Kind R, Oreshin S, and Stammler K (1993b) Sharpness of the mantle discontinuities. *Geophysical Research Letters* 20: 859–862.
Plomerova J, Kouba D, and Babuska V (2002) Mapping the lithosphere–asthenosphere boundary through changes in surface-wave anisotropy. *Tectonophysics* 358: 175–185.
Priestley K (1999) Velocity structure of the continental upper mantle: Evidence from southern Africa. *Lithos* 48: 45–56.
Priestley KF, Cipar J, Egorkin A, and Pavlenkova N (1994) Upper-mantle velocity structure beneath the Siberian platform. *Geophysical Journal International* 118: 369–378.
Priestley K and McKenzie D (2002) The structure of the upper mantle beneath southern Africa. *Geological Society Special Publication* 199: 45–64.
Qiu X, Priestley K, and McKenzie D (1996) Average lithospheric structure of southern Africa. *Geophysical Journal International* 127: 563–587.
Ramesh DS, Kawakatsu H, Watada S, and Yuan X (2005) Receiver function images of the central Chugoku region in the Japanese islands using Hi-net data. *Earth, Planets and Space* 57: 271–280.
Ramesh DS, Kind R, and Yuan X (2002) Receiver function analysis of the North American crust and upper mantle. *Geophysical Journal International* 150: 91–108.
Reusch AM, Nyblade AA, Benoit MH, et al. (2008) Mantle transition zone thickness beneath Ross Island, the Transantarctic Mountains, and East Antarctica. *Geophysical Research Letters* 35: L12301. http://dx.doi.org/10.1029/2008GL033873.
Reusch AM, Nyblade AA, Tibi R, et al. (2011) Mantle transition zone thickness beneath Cameroon: Evidence for an upper mantle origin for the Cameroon Volcanic Line. *Geophysical Journal International* 187: 1146–1150. http://dx.doi.org/10.1111/j.1365 246X.2011.05239.x.
Revenaugh J and Jordan TH (1987) Observations of first order mantle reverberations. *Bulletin of Seismological Society of America* 77: 1704–1717.
Revenaugh J and Jordan TH (1989) A study of mantle layering beneath the western Pacific. *Journal of Geophysical Research* 94: 5787–5813.
Revenaugh JS and Jordan TH (1991a) Mantle layering from ScS reverberations. 2: The transition zone. *Journal of Geophysical Research* 96: 19763–19780.
Revenaugh JS and Jordan TH (1991b) Mantle layering from ScS reverberations. 3: The upper mantle. *Journal of Geophysical Research* 96: 19781–19810.
Richards MA and Wicks CW Jr. (1990) S–P conversion from the transition zone beneath Tonga and the nature of the 670 km discontinuity. *Geophysical Journal International* 101: 1–35.
Ringwood AE (1969) Phase transformations in the mantle. *Earth and Planetary Science Letters* 5: 401–412.
Ritsema J, van Heijst HJ, and Woodhouse JH (2004) Global transition zone tomography. *Journal of Geophysical Research* 109: B02302. http://dx.doi.org/10.1029/2003JB002610.
Romanowicz R (2009) The thickness of tectonic plates. *Science* 324: 474–476. http://dx.doi.org/10.1126/science.1172879.
Romanowicz B, Karczewski JF, Cara M, et al. (1991) The GEOSCOPE program: Present status and perspectives. *Bulletin of Seismological Society of America* 81: 243–264.
Rost S and Weber M (2001) A reflector at 200 km depth beneath the northwest Pacific. *Geophysical Journal International* 147: 12–28.
Rost S and Weber M (2002) The upper mantle transition zone discontinuities in the Pacific as determined by short-period array data. *Earth and Planetary Science Letters* 204: 347–361.
Roth EG and Wiens DA (1999) Depression of the 660 km discontinuity beneath the Tonga slab determined from near vertical ScS reverberations. *Geophysical Research Letters* 26: 1223–1226.
Ryberg T, Wenzel F, Egorkin AV, and Solodilov L (1997) Short-period observation of the 520-km discontinuity in Northern Eurasia. *Journal of Geophysical Research* 102: 5413–5422.
Ryberg T, Wenzel F, Egorkin AV, and Solodilov L (1998) Properties of the mantle transition zone in northern Eurasia. *Journal of Geophysical Research* 103: 811–822.
Ryberg T, Wenzel F, Mechie J, Egorkin A, Fuchs K, and Solodilov L (1996) Two-dimensional velocity structure beneath northern Eurasia derived from the super

long-range seismic profile quartz. *Bulletin of Seismological Society of America* 86: 857–867.
Rychert CA, Fischer KM, and Rondenay S (2005) A sharp lithosphere–asthenosphere boundary imaged beneath eastern North America. *Nature* 436: 542–545.
Rychert CA, Rondenay S, and Fischer KM (2007) P-to-S and S-to-P imaging of a sharp lithosphere–asthenosphere boundary beneath eastern North America. *Journal of Geophysical Research* 112: B08314.
Rychert CA, Schmerr N, and Harmon N (2012) The Pacific lithosphere–asthenosphere boundary: Seismic imaging and anisotropic constraints from SS waveforms. *Geochemistry, Geophysics, Geosystems* 13: Q0AK10. http://dx.doi.org/10.1029/2012GC004194.
Rychert CA and Shearer PM (2009) A global view of the lithosphere–asthenosphere boundary. *Science* 324: 495–498. http://dx.doi.org/10.1126/science.1169754.
Rychert CA and Shearer PM (2011) Imaging the lithosphere–asthenosphere boundary beneath the Pacific using SS waveform modeling. *Journal of Geophysical Research* 116: B07307. http://dx.doi.org/10.1029/2010JB008070.
Rychert CA, Shearer PM, and Fischer KM (2010) Scattered wave imaging of the lithosphere–asthenosphere boundary. *Lithos* 120: 173–185.
Sacks IS and Snoke JA (1977) The use of converted phases to infer the depth of the lithosphere–asthenosphere boundary beneath South America. *Journal of Geophysical Research* 82: 2011–2017.
Sacks IS, Snoke JA, and Husebye ES (1979) Lithosphere thickness beneath the Baltic Shield. *Tectonophysics* 56: 101–110.
Saita T, Suetsugu D, Ohtaki T, Takenaka H, Kanjo K, and Purwana I (2002) Transition zone thickness beneath Indonesia as inferred using the receiver function method for data from the JISNET regional broadband seismic network. *Geophysical Research Letters* 29(7): 1115. http://dx.doi.org/10.1029/2001GL013629.
Sandvol E, Seber D, Barazangi M, Vernon FL, Mellors R, and Al-Amri A (1998) Lithospheric seismic velocity discontinuities beneath the Arabian Shield. *Geophysical Research Letters* 25: 2873–2876.
Saul J, Kumar MR, and Sarkar D (2000) Lithospheric and upper mantle structure of the Indian Shield, from teleseismic receiver functions. *Geophysical Research Letters* 27: 2357–2360.
Savage B and Silver PG (2008) Evidence for a compositional boundary within the lithospheric mantle beneath the Kalahari craton from S receiver functions. *Earth and Planetary Science Letters* 272: 600–609.
Schaeffer AJ and Bostock MG (2010) A low-velocity zone atop the transition zone in northwestern Canada. *Journal of Geophysical Research* 115: B06302. http://dx.doi.org/10.1029/2009JB006856.
Schäfer J, Wölbern I, and Rümpker G (2009) Depth variations of the 410 and 520 km-discontinuities beneath Asia and the Pacific from PP precursors. *Geophysical Research Letters* 36: L12307. http://dx.doi.org/10.1029/2009GL038374.
Schmandt B, Dueker KG, Hansen SM, Jasbinsek JJ, and Zhang Z (2011) A sporadic low-velocity layer atop the western U.S. mantle transition zone and short-wavelength variations in transition zone discontinuities. *Geochemistry, Geophysics, Geosystems* 12: Q08014.
Schmandt B, Dueker K, Humphreys E, and Hansen S (2012) Hot mantle upwelling across the 660 beneath Yellowstone. *Earth and Planetary Science Letters* 331–332: 224–236.
Schmerr N (2012) The Gutenberg discontinuity: Melt at the lithosphere–asthenosphere boundary. *Science* 335: 1480–1483. http://dx.doi.org/10.1126/science.1215433.
Schmerr N and Garnero E (2006) Investigation of upper mantle discontinuity structure beneath the central Pacific using SS precursors. *Journal of Geophysical Research* 111: B088305. http://dx.doi.org/10.1029/2005JB004197.
Schmerr N and Garnero E (2007) Upper mantle discontinuity topography from thermal and chemical heterogeneity. *Science* 318: 623–626.
Schmerr N, Garnero E, and McNamara A (2010) Deep mantle plumes and convective upwelling beneath the Pacific Ocean. *Earth and Planetary Science Letters* 294: 143–151.
Schmerr N and Thomas C (2011) Subducted lithosphere beneath the Kuriles from migration of PP precursors. *Earth and Planetary Science Letters* 311: 101–111. http://dx.doi.org/10.1016/j.epsl.2011.09.002.
Shearer PM (1990) Seismic imaging of upper-mantle structure with new evidence for a 520-km discontinuity. *Nature* 344: 121–126.
Shearer PM (1991) Constraints on upper mantle discontinuities from observations of long period reflected and converted phases. *Journal of Geophysical Research* 96: 18147–18182.
Shearer PM (1993) Global mapping of upper mantle reflectors from long period SS precursors. *Geophysical Journal International* 115: 878–904.
Shearer PM (1996) Transition zone velocity gradients and the 520-km discontinuity. *Journal of Geophysical Research* 101: 3053–3066.
Shearer PM and Flanagan MP (1999) Seismic velocity and density jumps across the 410- and 660-kilometer discontinuities. *Science* 285: 1545–1548.
Shearer PM, Flanagan MP, and Hedlin MAH (1999) Experiments in migration processing of SS precursor data to image upper mantle discontinuity structure. *Journal of Geophysical Research* 104: 7229–7242.
Shearer PM and Masters TG (1992) Global mapping of topography on the 660-km discontinuity. *Nature* 355: 791–796.
Sheehan AF, Shearer PM, Gilbert HJ, and Dueker KG (2000) Seismic migration processing of P–SV converted phases for mantle discontinuity structure beneath the Snake River Plain, western United States. *Journal of Geophysical Research* 105: 19055–19066.
Shen X, Mei X, and Zhang Y (2011) The crustal and upper-mantle structures beneath the northeastern margin of Tibet. *Bulletin of Seismological Society of America* 101(6): 2782–2795. http://dx.doi.org/10.1785/0120100112.
Shen Y, Sheehan AF, Dueker KG, De Groot-Hedlin C, and Gilbert H (1998a) Mantle discontinuity structure beneath the Southern East Pacific Rise from P-to-S converted phases. *Science* 280: 1232–1235.
Shen Y, Solomon SC, Bjarnason IT, and Purdy GM (1996) Hot mantle transition zone beneath Iceland and the adjacent Mid-Atlantic Ridge inferred from P-to-S conversions at the 410- and 660-km discontinuities. *Geophysical Research Letters* 23: 3527–3530.
Shen Y, Solomon SC, Bjarnason IT, and Wolfe CJ (1998b) Seismic evidence for a lower-mantle origin of the Iceland plume. *Nature* 395: 62–65.
Shen Y, Solomon SA, Bjarnason IT, et al. (2002) Seismic evidence for a tilted mantle plume and north–south mantle flow beneath Iceland. *Earth and Planetary Science Letters* 197: 261–272.
Shen X, Zhou H, and Kawakatsu H (2008) Mapping the upper mantle discontinuities beneath China with teleseismic receiver functions. *Earth, Planets and Space* 60: 713–719.
Shim S-H, Duffy TS, and Shen G (2001) The post-spinel transformation in Mg_2SiO_4 and its relation to the 660-km seismic discontinuity. *Nature* 411: 571–574.
Silveira G, Vinnik L, Stutzmann E, Farra V, Kiselev S, and Morais I (2010) Stratification of the Earth beneath the Azores from P and S receiver functions. *Earth and Planetary Science Letters* 299: 91–103.
Simmons NA and Gurrola H (2000) Multiple seismic discontinuities near the base of the transition zone in the Earth's mantle. *Nature* 405: 559–562.
Simon RE, Wright C, Kwadiba MTO, and Kgaswane EM (2003) Mantle structure and composition to 800 km depth beneath southern Africa and surrounding oceans from broadband body waves. *Lithos* 71: 353–367.
Singh A and Kumar MR (2009) Seismic signatures of detached lithospheric fragments in the mantle beneath eastern Himalaya and southern Tibet. *Earth and Planetary Science Letters* 288: 279–290.
Sipkin SA and Jordan TH (1976) Lateral heterogeneity of the upper mantle determined from the travel times of multiple ScS. *Journal of Geophysical Research* 81: 6307–6320.
Sipkin SA and Jordan TH (1980) Multiple ScS travel times in the western Pacific: Implications for mantle heterogeneity. *Journal of Geophysical Research* 85: 853–861.
Sodoudi F, Kind R, Hatzfeld D, Priestley K, and Greece Working Group (2006a) Lithospheric structure of the Aegean obtained from P and S receiver functions. *Journal of Geophysical Research* 111: B12307. http://dx.doi.org/10.1029/2005JB003932.
Sodoudi F, Yuan X, Asch G, and Kind R (2011) High-resolution image of the geometry and thickness of the subducting Nazca lithosphere beneath northern Chile. *Journal of Geophysical Research* 116: B04302. http://dx.doi.org/10.1029/2010JB007829.
Sodoudi F, Yuan X, Kind R, Heit B, and Sadidkhouy A (2009) Evidence for a missing crustal root and a thin lithosphere beneath the Central Alborz by receiver function studies. *Geophysical Journal International* 177: 733–742. http://dx.doi.org/10.1111/j.1365-246X.2009.04115.x.
Sodoudi F, Yuan X, Kind R, Lebedev S, Adam JF-C, and Tilmann F (2013) Seismic evidence for stratification in composition and anisotropic fabric within the thick lithosphere of Kalahari Craton. *Geochemistry, Geophysics, Geosystems* 14: 5393–5412.
Sodoudi F, Yuan X, Liu Q, Kind R, and Chen J (2006b) Lithospheric thickness beneath the Dabie Shan, central eastern China from S receiver functions. *Geophysical Journal International* 166: 1363–1367.
Song T-RA, Helmberger DV, and Grand SP (2004) Low-velocity zone atop the 410-km seismic discontinuity in the northwestern United States. *Nature* 427: 530–533.
Stammler K, Kind R, Petersen N, Kosarev G, Vinnik L, and Qiyuan L (1992) The upper mantle discontinuities: Correlated or anticorrelated. *Geophysical Research Letters* 19: 1563–1566.

Stankiewicz J, Chevrot S, van der Hilst RD, and de Wit MJ (2002) Crustal thickness, discontinuity depth, and upper mantle structure beneath southern Africa: Constraints from body wave conversions. *Physics of the Earth and Planetary Interiors* 130: 235–251.

Steer DN, Knapp JH, and Brown LD (1998) Super-deep profiling: Exploring the continental mantle lid. *Tectonophysics* 286: 111–121.

Su W-J, Woodward RL, and Dziewonski AM (1994) Degree 12 model of shear velocity heterogeneity in the mantle. *Journal of Geophysical Research* 99: 6945–6980.

Suetsugu D, Inoue T, Obayashi M, et al. (2010) Depths of the 410-km and 660-km discontinuities in and around the stagnant slab beneath the Philippine Sea: Is Water stored in the stagnant slab? *Physics of the Earth and Planetary Interiors* 183: 270–279.

Suetsugu D, Isse T, Tanaka S, et al. (2009) South Pacific mantle plumes imaged by seismic observation on islands and seafloor. *Geochemistry, Geophysics, Geosystems* 10: Q11014. http://dx.doi.org/10.1029/2009GC002533.

Suetsugu D, Saita T, Takenaka H, and Niu F (2004) Thickness of the mantle transition zone beneath the South Pacific as inferred from analyses of ScS reverberated and Ps converted waves. *Physics of the Earth and Planetary Interiors* 146: 35–46.

Svekalapko Seismic Tomography Working Group, Yliniemi J, Kozlovskaya E, Hjelt S-E, Komminaho K, and Ushakov A (2004) Structure of the crust and uppermost mantle beneath southern Finland revealed by analysis of local events registered by the Svekalapko seismic array. *Tectonophysics* 394: 41–67.

Taghizadeh-Farahmand F, Sodoudi F, Afsari N, and Ghassemi MR (2010) Lithospheric structure of NW Iran from P and S receiver functions. *Journal of Seismology* 14: 823–836. http://dx.doi.org/10.1007/s10950-010-9199-2.

Tauzin B, Debayle E, and Wittlinger G (2008) The mantle transition zone as seen by global Pds phases: No clear evidence for a thin transition zone beneath hotspots. *Journal of Geophysical Research* 113: B08309. http://dx.doi.org/10.1029/2007JB005364.

Tauzin B, Debayle E, and Wittlinger G (2010) Seismic evidence for a global low velocity layer in the Earth's upper mantle. *Nature Geoscience* 3: 718–721. http://dx.doi.org/10.1038/ngeo969.

Tauzin B, van der Hilst RD, Wittlinger G, and Ricard Y (2013) Multiple transition zone seismic discontinuities and low velocity layers below the western United States. *Journal of Geophysical Research - Solid Earth* 118. http://dx.doi.org/10.1002/jgrb.50182.

Thirot J-L, Montagner J-P, and Vinnik L (1998) Upper-mantle seismic discontinuities in a subduction zone (Japan) investigated from P to S converted waves. *Physics of the Earth and Planetary Interiors* 108: 61–80.

Thomas C and Billen MI (2009) Mantle transition zone structure along a profile in the SW Pacific: Thermal and compositional variations. *Geophysical Journal International* 176: 113–125.

Thompson DA, Helffrich G, Bastow ID, et al. (2011) Implications of a simple mantle transition zone beneath cratonic North America. *Earth and Planetary Science Letters* 312: 28–36.

Thybo H (2006) The heterogeneous upper mantle low velocity zone. *Tectonophysics* 416(1–2): 53–79.

Thybo H and Perchuc E (1997) The seismic 8° discontinuity and partial melting in continental mantle. *Science* 275: 1626–1629.

Tian X, Teng J, Zhang H, et al. (2011) Structure of crust and upper mantle beneath the Ordos Block and the Yinshan Mountains revealed by receiver function analysis. *Physics of the Earth and Planetary Interiors* 184: 186–193.

Tian X, Zhao D, Zhang H, Tian Y, and Zhang Z (2010) Mantle transition zone topography and structure beneath the central Tien Shan orogenic belt. *Journal of Geophysical Research* 115: B10308. http://dx.doi.org/10.1029/2008JB006229.

Tibi R and Wiens DA (2005) Detailed structure and sharpness of upper mantle discontinuities in the Tonga subduction zone from regional broadband arrays. *Journal of Geophysical Research B: Solid Earth* 110(6): 1–14.

Tibi R, Wiens DA, Shiobara H, Sugioka H, and Shore PJ (2006) Depth of the 660-km discontinuity near the Mariana slab from an array of ocean bottom seismographs. *Geophysical Research Letters* 33: L02313. http://dx.doi.org/10.1029/2005GL024523.

Tittgemeyer M, Wenzel F, Fuchs K, and Ryberg T (1996) Wave propagation in a multiple-scattering upper mantle – Observations and modelling. *Geophysical Journal International* 127: 492–502.

Tonegawa T, Hirahara K, and Shibutani T (2005) Detailed structure of the upper mantle discontinuities around the Japan subduction zone imaged by receiver function analyses. *Earth, Planets and Space* 57: 5–14.

Tonegawa T, Hirahara K, Shibutani T, and Shiomi K (2006) Upper mantle structure beneath the Japan Islands imaged by receiver function With Hi-net tiltmeter recordings. *Earth Planets and Space* 58: 1007–1012.

Tono Y, Kunugi T, Fukao Y, Tsuboi S, Kanjo K, and Kasahara K (2005) Mapping of the 410- and 660-km discontinuities beneath the Japanese islands. *Journal of Geophysical Research* 110: 1–10.

Van der Lee S (2001) Deep below North America. *Science* 294: 1297–1298.

Van der Lee S, Paulssen H, and Nolet G (1994) Variability of P660s phases as a consequence of topography of the 660 km discontinuity. *Physics of the Earth and Planetary Interiors* 86: 147–164.

Van der Meijde M, Van der Lee S, and Giardini D (2005) Seismic discontinuities in the Mediterranean mantle. *Physics of the Earth and Planetary Interiors* 148: 233–250.

Vidale JE and Benz HM (1992) Upper mantle seismic discontinuities and the thermal structure of subduction zones. *Nature* 356: 678–683.

Vidale JE, Ding XY, and Grand SP (1995) The 410-km-depth discontinuity: A sharpness estimate from near-critical reflections. *Geophysical Research Letters* 22: 2557–2560.

Vinnik L (1977) Detection of waves converted from P to SV in the mantle. *Physics of the Earth and Planetary Interiors* 15: 39–45.

Vinnik L and Farra V (2007) Low S velocity atop the 410-km discontinuity and mantle plumes. *Earth and Planetary Science Letters* 262(3–4): 398–412. http://dx.doi.org/10.1016/j.epsl.2007.07.051.

Vinnik LP, Foulger GR, and Du Z (2005a) Seismic boundaries in the mantle beneath Iceland: A new constraint on temperature. *Geophysical Journal International* 160: 533–538.

Vinnik L, Kosarev G, and Petersen N (1996) Mantle transition zone beneath Eurasia. *Geophysical Research Letters* 23: 1485–1488.

Vinnik L, Kurnik E, and Farra V (2005b) Lehmann discontinuity beneath North America: No role for seismic anisotropy. *Geophysical Research Letters* 32: L09306. http://dx.doi.org/10.1029/2004GL022333.

Vinnik L, Oreshin S, Kosarev G, Kiselev S, and Makeyeva L (2009) Mantle anomalies beneath southern Africa: Evidence from seismic S and P receiver functions. *Geophysical Journal International* 179(1): 279–298. http://dx.doi.org/10.1111/j.1365-246X.2009.04261.x.

Vinnik LP, Reigber C, Aleshin IM, et al. (2004) Receiver function tomography of the central Tien Shan. *Earth and Planetary Science Letters* 225: 131–146.

Vinnik L, Ren Y, Stutzmann E, Farra V, and Kiselev S (2010) Observations of S410p and S350p phases at seismograph stations in California. *Journal of Geophysical Research* 115: B05303. http://dx.doi.org/10.1029/2009JB006582.

Vinnik L, Silveira G, Kiselev S, Farra V, Weber M, and Stutzmann E (2012) Cape Verde hotspot from the upper crust to the top of the lower mantle. *Earth and Planetary Science Letters* 319–320: 259–268.

von Rebeur-Paschwitz E (1889) The earthquake of Tokyo, April 18, 1889. *Nature* 40: 294–295.

Wajeman N (1988) Detection of underside P reflections of mantle discontinuities by stacking broadband data. *Geophysical Research Letters* 15: 669–672.

Walck MC (1984) The P-wave upper mantle structure beneath an active spreading centre: The Gulf of California. *Geophysical Journal of the Royal Astronomical Society* 76: 697–723.

Wang T and Chen L (2009) Distinct velocity variations around the base of the upper mantle beneath northeast Asia. *Physics of the Earth and Planetary Interiors* 172: 241–256.

Wang B and Niu F (2010) A broad 660 km discontinuity beneath northeast China revealed by dense regional seismic networks in China. *Journal of Geophysical Research* 115: B06308. http://dx.doi.org/10.1029/2009JB006608.

Wang Y, Wen L, and Weidner D (2009) Array triplication data constraining seismic structure and composition in the mantle. *Surveys in Geophysics* 30: 355–376. http://dx.doi.org/10.1007/s10712-009-9073-3.

Whitcomb J and Anderson DL (1970) Reflection of P′P′ seismic waves from discontinuities in the mantle. *Journal of Geophysical Research* 75: 5713–5728.

Wicks CW Jr. and Richards MA (1993) A detailed map of the 660-kilometer discontinuity beneath the Izu-Bonin subduction zone. *Science* 261: 1424–1427.

Wilson D, Aster R, Ni J, et al. (2005) Imaging the seismic structure of the crust and upper mantle beneath the Great Plains, Rio Grande Rift, and Colorado Plateau using receiver functions. *Journal of Geophysical Research* 110: B05306. http://dx.doi.org/10.1029/2004JB003492.

Wittlinger G and Farra V (2007) Converted waves reveal a thick and layered tectosphere beneath the Kalahari super-craton. *Earth and Planetary Science Letters* 254: 404–415.

Wittlinger G, Farra V, and Vergne J (2004) Lithospheric and upper mantle stratifications beneath Tibet: New insights from Sp conversions. *Geophysical Research Letters* 31: L19615. http://dx.doi.org/10.1029/2004GL020955.

Wölbern I, Heit B, Yuan X, et al. (2009) Receiver function images from the Moho and the slab beneath the Altiplano and Puna plateaus in the central Andes. *Geophysical Journal International* 177(1): 296–308. http://dx.doi.org/10.1111/j.1365-246X.2008.04075.x.

Wölbern I, Jacob AWB, Blake TA, et al. (2006) Deep origin of the Hawaiian tilted plume conduit derived from receiver functions. *Geophysical Journal International* 166(2): 767–781.

Wölbern I, Rümpker G, Link K, and Sodoudi F (2012) Melt infiltration of the lower lithosphere beneath the Tanzania craton and the Albertine rift inferred from S receiver functions. *Geochemistry, Geophysics, Geosystems* 13: Q0AK08. http://dx.doi.org/10.1029/2012GC004167.

Wright C (2009) The P wavespeed structure in the mantle to 800 km depth below the Philippines region: Geodynamic implications. *Tectonophysics* 466: 152–161.

Wright C, Kwadiba MTO, Simon RE, Kgaswane EM, and Nguuri TK (2004) Variations in the thickness of the crust of the Kaapvaal craton, and mantle structure below southern Africa. *Earth, Planets and Space* 56: 125–137.

Xu F, Vidale JE, and Earle PS (2003) Survey of precursors to P0P0: Fine structure of mantle discontinuities. *Journal of Geophysical Research* 108(B1): 2024. http://dx.doi.org/10.1029/2001JB000817.

Xu F, Vidale JE, Earle PS, and Benz HM (1998) Mantle discontinuities under southern Africa from precursors to P′P′df. *Geophysical Research Letters* 25: 571–574.

Xu Q, Zhao J, Pei S, and Liu H (2011) The lithosphere–asthenosphere boundary revealed by S-receiver functions from the Hi-CLIMB experiment. *Geophysical Journal International* 187: 414–420. http://dx.doi.org/10.1111/j.1365-246X.2011.05154.x.

Yamazaki A and Hirahara K (1994) The thickness of upper mantle discontinuities, as inferred from short-period J-Array data. *Geophysical Research Letters* 21: 1811–1814.

Yang Y and Zhou H-L (2001) Application of receiver function method to estimate the buried depths of discontinuities in the upper mantle beneath China and adjacent area. *Acta Geophysica Sinica* 44: 792–797.

Ye L, Li J, Tseng T-L, and Yao Z (2011) A stagnant slab in a water-bearing mantle transition zone beneath northeast China: Implications from regional SH waveform modelling. *Geophysical Journal International* 186: 706–710. http://dx.doi.org/10.1111/j.1365-246X.2011.05063.x.

Youngs BAR and Bercovici D (2009) Stability of a compressible hydrous melt layer above the transition zone. *Earth and Planetary Science Letters* 278: 78–86. http://dx.doi.org/10.1016/j.epsl.2008.11.024.

Yuan X, Kind R, Li X, and Wang R (2006) The S receiver functions: Synthetics and data example. *Geophysical Journal International* 165: 555–564.

Yuan X, Ni J, Kind R, Mechie J, and Sandvol E (1997) Lithospheric and upper mantle structure of southern Tibet from a seismological passive source experiment. *Journal of Geophysical Research* 102: 27491–27500.

Yuan H and Romanowicz B (2010) Lithospheric layering in the North American craton. *Nature* 466: 1063–1069. http://dx.doi.org/10.1038/nature09332.

Yuan X, Sobolev SV, and Kind R (2002) Moho topography in the central Andes and its geodynamic implications. *Earth and Planetary Science Letters* 199: 389–402.

Yue H, Chen JY, Sandvol E, et al. (2012) Lithospheric and upper mantle structure of the northeastern Tibetan Plateau. *Journal of Geophysical Research* 117: B05307. http://dx.doi.org/10.1029/2011JB008545.

Zandt G and Randall GE (1985) Observations of shear coupled P-waves. *Geophysical Research Letters* 12: 565–568.

Zang SX, Zhou YZ, Ning JY, and Wei RQ (2006) Multiple discontinuities near 660 km beneath Tonga area. *Geophysical Research Letters* 33: L20312. http://dx.doi.org/10.1029/2006GL027262.

Zhang Z and Lay T (1993) Investigation of upper mantle discontinuities near northwestern Pacific subduction zones using precursors to sSH. *Journal of Geophysical Research* 98: 4389–4405.

Zhang H, Teng J, Tian X, Zhang Z, Gao R, and Liu J (2012) Lithospheric thickness and upper-mantle deformation beneath the NE Tibetan Plateau inferred from S receiver functions and SKS splitting measurements. *Geophysical Journal International* 191: 1285–1294. http://dx.doi.org/10.1111/j.1365-246X.2012.05667.x.

Zhang Z, Yuan X, Chen Y, et al. (2010) Seismic signature of the collision between the east Tibetan escape flow and the Sichuan Basin. *Earth and Planetary Science Letters* 292: 254–264.

Zhao W, Kumar P, Mechie J, et al. (2011) Tibetan plate overriding the Asian plate in central and northern Tibet. *Nature Geoscience* 4: 870–873. http://dx.doi.org/10.1038/NGEO1309.

Zhao J, Yuan X, Liu H, et al. (2010) The boundary between the Indian and Asian tectonic plates below Tibet. *Proceedings of the National Academy of Sciences of the United States of America* 107(25): 11229–11233. http://dx.doi.org/10.1073/pnas.1001921107.

Zheng Z and Romanowicz B (2012) Do double 'SS precursors' mean double discontinuities. *Geophysical Journal International* 191: 1361–1373. http://dx.doi.org/10.1111/j.1365-246X.2012.05683.x.

Zhou L, Chen WP, and Özalaybey S (2000) Seismic properties of the central Indian shield. *Bulletin of Seismological Society of America* 90: 1295–1304.

Zhou YZ, Yu XW, Yang H, and Zhang SX (2012) Multiplicity of the 660-km discontinuity beneath the Izu-Bonin area. *Physics of the Earth and Planetary Interiors* 198–199: 51–60. http://dx.doi.org/10.1016/j.pepi.2012.03.003.

1.22 Deep Earth Structure: Lower Mantle and D″

T Lay, University of California Santa Cruz, Santa Cruz, CA, USA

© 2015 Elsevier B.V. All rights reserved.

1.22.1	**Lower Mantle and D″ Basic Structural Attributes**	684
1.22.1.1	Elastic Parameters, Density, and Thermal Structure	684
1.22.1.2	Mineralogical Structure	685
1.22.2	**One-Dimensional Lower Mantle Structure**	686
1.22.2.1	Body-Wave Travel Time and Slowness Constraints	687
1.22.2.2	Surface-Wave/Normal-Mode Constraints	688
1.22.2.3	Attenuation Structure	688
1.22.3	**Three-Dimensional Lower Mantle Structure**	689
1.22.3.1	Seismic Tomography	689
1.22.3.2	Dynamic Structures	691
1.22.4	**D″ Region**	693
1.22.4.1	Large-Scale Seismic Velocity Attributes	693
1.22.4.2	Thermal Boundary Layer Aspect	694
1.22.5	**D″ Discontinuities**	695
1.22.5.1	Seismic Wave Triplications	695
1.22.5.2	Phase Change in Perovskite	697
1.22.6	**Large Low-Shear-Velocity Provinces**	699
1.22.6.1	Seismic Velocity Properties	699
1.22.6.2	Thermal–Chemical Interpretations	701
1.22.7	**Ultralow-Velocity Zones**	701
1.22.7.1	Seismic Phases Used for Detection	702
1.22.7.2	Partial Melting and Chemical Anomalies	703
1.22.8	**Lower Mantle Anisotropy**	704
1.22.8.1	Shear-Wave Splitting Observations	704
1.22.8.2	Mineralogical/Dynamic Implications	704
1.22.9	**Small-Scale Heterogeneities**	705
1.22.9.1	Scattering in D″	706
1.22.9.2	Core–Mantle Boundary Topography	706
1.22.10	**Conclusions**	706
Acknowledgment		707
References		707

Glossary

Attenuation Loss of signal amplitude during propagation. Intrinsic attenuation involves irreversible anelastic losses; scattering attenuation involves partitioning of energy into separate waves.

CMB The core–mantle boundary is the surface defined by the contrast in composition between mantle rocks and core molten alloy. A huge density contrast and change in physical properties make this a sharp boundary, with very limited mass flux across it at present.

D″ Designation for the lowermost 200–300 km of the lower mantle. This region is distinct from the overlying mantle in that the seismic velocity variations are not consistent with homogeneous material under self-compression and adiabatic temperature gradient.

LLSVP Large low-shear-velocity province, used to describe broad regions beneath Africa and the South Atlantic and beneath the southern Pacific, which have anomalously low shear velocities, less pronounced compressional velocity decreases, sharp lateral boundaries, and indications of higher than average densities. These features have often been labeled superplumes, but the seismic data favor them being chemically distinct, dense piles of material possibly entrained by surrounding mantle flow.

P wave Elastic wave involving compressional and dilational motion of the medium as the wave propagates and the faster of the two seismic waves. Can transit both solid and fluid media.

S wave Elastic wave involving shearing motion of the medium with no volumetric change as the wave propagates and the slower of the two seismic waves. Can only transit solid media.

1.22.1 Lower Mantle and D″ Basic Structural Attributes

Earth's lower mantle is a thick layer of rock extending downward more than 2000 km from the transition zone to the core–mantle boundary (CMB) at an average depth of 2891 km. Seismology provides the basis for defining the lower mantle, as it was evident from the consideration of even the earliest global P-wave and S-wave travel time curves that this region of the interior has relatively smoothly increasing seismic velocities with depth, with an overall velocity gradient significantly reduced from that in the overlying transition zone.

The upper limit of the lower mantle has various definitions; many geophysicists associate it with the 650 km deep seismic velocity discontinuity, while others prefer to designate it at a greater depth of about 800 km, where there tends to be a reduction in radial velocity gradients in detailed seismic velocity models, as well as intermittent reports of a seismic discontinuity (e.g., Datt and Muirhead, 1976; Revenaugh and Jordan, 1991). The variety of phase transformations for upper mantle minerals olivine, enstatite, and garnet to their high-pressure polymorphs that characterize the transition zone all culminate in transitions to magnesium silicate perovskite [$(Mg,Fe)SiO_3$], ferropericlase [(Mg,Fe)O], and calcium perovskite [$CaSiO_3$]. The latter transitions should largely go to completion by about 800 km depth, which can thus be viewed as the base of the transition zone. The subsequent stability of the abundant magnesium silicate perovskite mineral over great pressure and temperature ranges is the probable explanation for the relatively smooth velocity gradients observed across the lower mantle, with self-compression and a nearly adiabatic thermal gradient resulting in smoothly increasing density, rigidity, incompressibility, and associated P-wave and S-wave seismic velocities down to near the CMB.

A few hundred kilometers above the CMB seismic velocities have more complex structure, with abrupt increases or discontinuities in velocity occurring in regions of relatively high seismic velocity, likely as a result of a phase transition from magnesium silicate perovskite to the postperovskite phase (Hirose, 2006; Murakami et al., 2004; Shim, 2008), along with enhanced lateral variations that indicate the presence of thermal and chemical heterogeneities in a boundary layer above the CMB (e.g., Garnero, 2000; Garnero and McNamara, 2008; Lay and Garnero, 2004; Trønnes, 2009). Based on the seismic evidence for inhomogeneity in the structure, the lowermost few hundred kilometers of the lower mantle is called the D″ region (harkening back to an early nomenclature in which the lower mantle was labeled the D shell and then subdivided into D′ and D″; see Bullen, 1949). At the base of the lower mantle, there are localized regions with very strong seismic velocity reductions that may be explained by the presence of a melt component or strong iron enrichment within the lower mantle rock. The CMB separates the silicate and oxide minerals of the lower mantle from the molten iron alloy of the core, with the contrasts in physical properties such as density, viscosity, and rigidity across the CMB being as large or larger than those at the surface of the Earth.

Despite its generally simple overall seismological structure, the lower mantle appears to be undergoing large-scale dynamic processes. These are revealed by second-order features of the seismological models that have only begun to be resolved over the past 30 years or so. The great pressures existing in the lower mantle suppress the sensitivity of seismic wave velocities to variations in temperature and composition, muting the detectable effects. Progress in imaging the few percent three-dimensional variations in seismic velocities is unveiling the dynamic complexity of the lower mantle and indicates regions of convective upwellings, downwellings, and large-scale chemical heterogeneities that may have accumulated over time in the deep mantle. While current understanding of the dynamic regime remains limited, it appears that the lower mantle plays a major role in regulating heat flux from the core, in cycling heat out of the interior, and in segregating chemical heterogeneities for long intervals of time, giving rise to geochemical anomalies observed at surface volcanic sites.

1.22.1.1 Elastic Parameters, Density, and Thermal Structure

P-wave and S-wave velocities and density increase smoothly across the lower mantle to the D″ region in all one-dimensional seismic velocity models for the Earth. **Figure 1** shows the variations in these properties as given by the Preliminary Reference Earth Model (PREM), which was based on a large number of body-wave travel times and free-oscillation eigenfrequencies (Dziewonski and Anderson, 1981). Below the abrupt seismic velocity and density increases near 650–670 km deep, which are primarily attributed to the dissociative phase transition of $(Mg,Fe)_2SiO_4$ γ-spinel (ringwoodite) to $(Mg,Fe)SiO_3$ perovskite plus (Mg,Fe)O ferropericlase (e.g., Ito and Takahashi, 1989; Ito et al., 1990; Yu et al., 2007), all the way down to the CMB, there are no abrupt changes in properties that demand global large-scale layering of the lower mantle (e.g., Green and Falloon, 1998). The bounds on the seismic velocity models given in **Figure 1** indicate the range of velocities that are admissible for one-dimensional models, based on observed travel time fluctuations for seismic body waves. The relatively tight range of velocity bounds indicate that if there are any velocity discontinuities in the deep mantle, they are less than a few percent or there are strong lateral variations in the depths of the structure such that it is not well represented by a one-dimensional model.

In fact, there are many studies inferring the presence of localized reflectors or scatterers in the depth range 650–1200 km depth (e.g., Kaneshima and Helffrich, 2009; Muirhead and Hales, 1980; Niu and Kawakatsu, 1997; Vinnik et al., 1998a), but the observations are intermittent, and there is, as yet, no agreed upon globally extensive discontinuity below 650-km depth that would be warranted in a one-dimensional Earth model. This fact is often invoked to support the idea that the lower mantle is chemically uniform, but one should keep in mind that chemical layering is likely to involve rather subtle changes in seismic velocities and details of the density structure are not well resolved by normal-mode observations. Thus, it is possible that the lower mantle is chemically stratified, perhaps with depth variations in Si or Fe content, with substantial topography on any chemical contrasts (e.g., Anderson, 1991, 1998; Kellogg et al., 1999; Murakami et al., 2012). Assessing this possibility requires consideration of three-dimensional velocity structures, but even then, it may

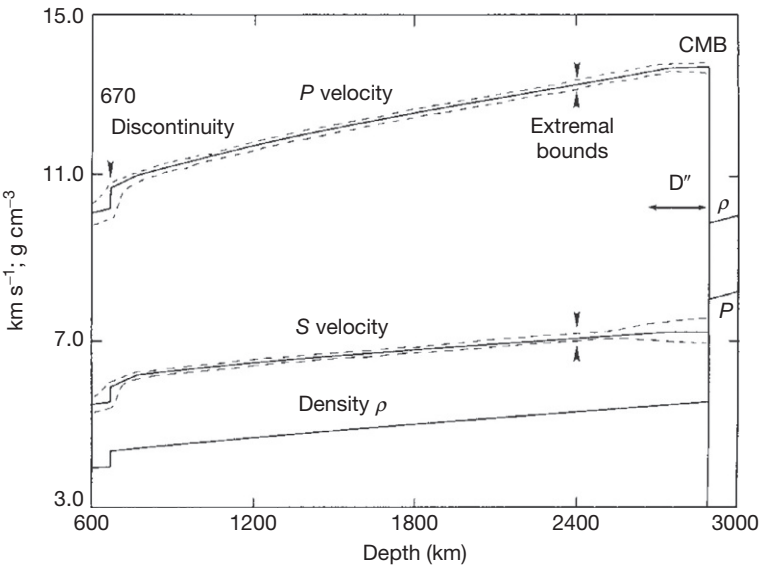

Figure 1 Variation of seismic velocities and density through the lower mantle for model Preliminary Reference Earth Model (PREM) (Dziewonski and Anderson, 1981), along with the extremal bounds that indicate the confidence intervals for spherically averaged models based on travel time data (Lee and Johnson, 1984). The D″ region is the lowermost 200–300 km of the lower mantle overlying the core–mantle boundary (CMB). Reproduced from Lay T (1989) Structure of the core–mantle transition zone: A chemical and thermal boundary layer. *Eos*, *Transactions of the American Geophysical Union* 70: 49, 54–55, 58–59.

be difficult because velocity discontinuities associated with any chemical contrasts are likely to be relatively small.

The bounds on one-dimensional S-wave velocity models tend to flare in the lower 300 km of the mantle, indicating larger variability in S-wave travel times for waves traversing the D″ region above the CMB. In this region, seismic waveform modeling has resulted in localized velocity models with 1–3% abrupt increases in shear velocity and large-scale regions with 3–6% low shear velocity. There is no average one-dimensional model that represents the D″ structure well, and the lateral variations must be characterized with three-dimensional structures in order to assess their significance. P-wave observations also indicate abrupt increases in P-wave velocity in some regions, but in general, the P-wave structure is less heterogeneous than for S waves. At the very base of the lower mantle, within tens of kilometers above the CMB, there are localized regions with very pronounced reductions in both P-wave velocity and S-wave velocity, which are called ultralow velocity zones (ULVZs). ULVZs may represent a transition zone from mantle to core, but they must be undetectably thin (<∼5 km) or not present in many regions.

1.22.1.2 Mineralogical Structure

The composition and mineralogy of the lower mantle is not directly determined from seismic observations and must be deduced based on models for the bulk composition of the Earth along with experimental and theoretical mineral physics that reproduces observed density and elastic velocity profiles for appropriate pressures and temperatures. Given the experimental determination of stability of the magnesium silicate perovskite phase (Liu, 1974) as the polymorph of predominant upper mantle minerals subjected to lower mantle conditions, along with the chondritic Earth model, there is high confidence that $(Mg_x,Fe_{1-x})SiO_3$ perovskite is the primary mineral form in the lower mantle (e.g., Fiquet et al., 2000; Gong et al., 2004; Knittle and Jeanloz, 1987; Shim et al., 2001, 2004; Wentzcovitch et al., 2004). The value of x (the magnesium number) is probably in the range 0.8–0.9, although some aluminum substitution is very likely to exist in lower mantle perovskites as well. The experimental and chondritic model constraints on mineralogy also favor the presence of $(Mg_x,Fe_{1-x})O$, with x again in the range 0.8–0.9 overall, although it could be much lower in some cases, as well as some Ca perovskite. Other minor phases are likely to exist, but constraints on their abundance are very limited.

Extensive theoretical and experimental mineral physics research continues to characterize the equations of state, effects of minor components like Al, element partitioning, and physical properties of the following primary lower mantle minerals (or low-pressure analog minerals): *magnesium silicate perovskite* (e.g., Aizawa and Yoneda, 2006; Andrault et al., 2007; Auzende et al., 2008; Boffa Ballaran et al., 2012; Carrez et al., 2007a; Cordier et al., 2004; Deng et al., 2008; Dorfman et al., 2012; Ferré et al., 2007; Irifune et al., 2010; Ito and Toriumi, 2010; Jackson and Kung, 2008; Jackson et al., 2005; Jung et al., 2010; Katsura et al., 2009; Lundin et al., 2008; Miyajima et al., 2009; Mosenfelder et al., 2009; Murakami et al., 2007a; Nishio-Hamane et al., 2008; Nishiyama et al., 2007; Ono et al., 2006a,b; Panero et al., 2006; Ricolleau et al., 2009; Saikia et al., 2009; Sakai et al., 2009a; Tange et al., 2009, 2012; Vanpeteghem et al., 2006a,b; Xu et al., 2011; Yamazaki et al., 2009), *MgO and ferropericlase* (e.g., de Koker, 2010; Fukui et al., 2012; Gleason et al., 2011; Jackson et al., 2006; Komabayashi et al., 2010; Marquardt et al., 2009b; Murakami et al., 2009; Speziale et al., 2007a,b;

Tsujino and Nishihara, 2010; Wu et al., 2008), and *calcium perovskite* (e.g., Adams and Oganov, 2006; Jung and Oganov, 2005; Kojitani et al., 2009; Komabayashi et al., 2007; Kudo et al., 2012; Li et al., 2006b,c; Miyagi et al., 2006, 2009; Stixrude et al., 2007; Sueda et al., 2006).

Transport properties for the major minerals such as electrical conductivity are also being addressed (e.g., Ono et al., 2006b; Tarits and Mandéa, 2010; Velimsky, 2010). With the possibility of lithospheric slabs sinking into the lower mantle, the deep mantle properties for mid-ocean ridge basalt (MORB) compositions (in the high-pressure eclogitic phase and in lower mantle polymorphs) are also being explored (e.g., Hirose et al., 2005a; Kono et al., 2007; Mookherjee, 2011; Ohta et al., 2008a, 2010b; Ricolleau et al., 2010; Tsuchiya, 2011). Other minor phases such as poststishovite (e.g., Bolfan-Casanova et al., 2009; Lakshtanov et al., 2007; Nomura et al., 2010; Wang et al., 2012) and various carbonates (e.g., Boulard et al., 2012; Lavina et al., 2009, 2010; Litasov et al., 2008; Mao et al., 2011a; Oganov et al., 2006, 2008) are likely to exist in the lower mantle, but constraints on their small abundances are very limited. This huge outpouring of experimental and theoretical mineral physics results reflects great advances made in the last decade in both laboratory measurements and first-principles computations of mineral phase equilibriums and material properties. Comparisons of predictions with seismic observations are still not uniquely diagnostic of the lower mantle composition due to many trade-offs and uncertainties in mineral composition, accompanied by new discoveries in material properties (e.g., Matas et al., 2007).

Recent experimental and first-principles work (Badro et al., 2003, 2004; Hofmeister, 2006; Li et al., 2004, 2005; Lin and Tsuchiya, 2008; Lin et al., 2005; Speziale et al., 2005; Sturhahn et al., 2005; Zhang and Oganov, 2006) has established that at high pressure, Fe, normally in its high-spin state for both Fe^{2+} and Fe^{3+} in perovskite and ferropericlase in the shallow lower mantle, will prefer to be in a denser, low-spin state in the lowermost mantle. This so-called spin transition can influence thermal, electric, elastic, and viscous properties of the lower mantle, and there has been a huge surge of research in the past few years to characterize the attributes of the iron spin transition and its implications. Computational and experimental efforts are quantifying the spin crossovers in *ferropericlase* (e.g., Ammann et al., 2011; Antonangeli et al., 2011; Cammarano et al., 2010; Chen et al., 2012a,b; Crowhurst et al., 2008; Fei et al., 2007; Kantor et al., 2006; Lin et al., 2006a,b, 2007a,b; Mao et al., 2011a,b; Persson et al., 2006; Saha et al., 2011, 2013; Speziale et al., 2007b; Tsuchiya et al., 2006a,b; Wentzcovitch et al., 2009; Wu et al., 2009; Yoshino et al., 2011) and *magnesium silicate perovskite* (Bengtson et al., 2008, 2009; Caracas et al., 2010; Catalli et al., 2010b, 2011; Fang and Ahuja, 2008; Fujino et al., 2012; Grocholski et al., 2009; Hsu et al., 2010, 2011; Li et al., 2006a; McCammon et al., 2008, 2010; Narygina et al., 2011; Nomura et al., 2011; Stackhouse et al., 2006b, 2007; Umemoto et al., 2008, 2010).

Implications of the spin transition for mixing dynamics and plume formation are also being considered (e.g., Bower et al., 2009; Shahnas et al., 2011), as well as effects on electrical conductivity (Ohta et al., 2007, 2010a). The various studies are not in full agreement, but most favor substantial pressure ranges for the various spin transitions and relatively subtle effects on seismic velocities, making it difficult to directly confirm the presence of spin transitions with seismic observations.

Properties of melts in the lower mantle are critical to understanding mantle chemical evolution, and theoretical and experimental studies have addressed issues of melt density and iron fractionation and Si and O partitioning between liquids and perovskite and ferropericlase in the deep mantle (e.g., de Koker and Stixrude, 2009; de Koker et al., 2013; Fiquet et al., 2010; Frost et al., 2004; Liebske and Frost, 2012; Mosenfelder et al., 2007; Seagle et al., 2008; Stixrude et al., 2009; Terasaki et al., 2007; Zhang and Fei, 2008; Zhang and Guo, 2009).

When one considers the mineralogy of the lower mantle, it is essential to keep in mind that there has undoubtedly been extensive chemical processing, melting, and mixing. This would have occurred during the energetic processes of accretion and core formation, as a result of early large impacts, and as an ongoing consequence of mantle convection and chemical differentiation involving crustal formation and recycling. The huge density increase at the CMB, larger than that at Earth's surface, provides an environment favorable for the accumulation of dense silicate and oxide materials, a region toward which dense iron-rich materials may settle, and a chemically active environment in which mantle rocks and core alloys may exchange elements over time. Geophysical constraints on the precise mineralogy and chemistry are quite limited, and we lack direct access to samples of lower mantle rocks, so various mineralogical scenarios for the lower mantle, particularly for minor components, can be considered as long as they are shown to agree overall with the seismological information available for the region. While high viscosity of the lower mantle may allow chemical heterogeneities to persist for long intervals of time, the notion of a primitive, unprocessed lower mantle composition is at odds with prevailing notions of Earth's formation and evolution. Presumably huge amounts of iron have separated from the mantle, and there has been extensive melting, which likely would lead to volatile depletion of the deep mantle and chemical stratification that may or may not have survived subsequent entrainment.

1.22.2 One-Dimensional Lower Mantle Structure

The most direct constraints on lower mantle structure are provided by seismic waves that traverse the interior. The main observables of importance are the travel times of P waves and S waves, any waveform complexities arising from interactions with contrasts in properties in the rocks, S-wave splitting produced by anisotropy, and frequency-dependent amplitude behavior of the seismic waves that can constrain the anelasticity of the lower mantle. The average lower mantle seismic velocities have been determined by both classical arrival time inversion and normal-mode analysis, with the latter also refining early estimates of the density structure that had been based on velocity–density systematics, integral constraints provided by Earth's mass and moment of inertia, and piecewise integration of seismic velocity models using the Adams–Williamson equation (Adams and Williamson, 1923). With the early

recognition of the general simplicity of lower mantle structure, most research prior to 1980 focused on developing robust one-dimensional models for lower mantle structure.

1.22.2.1 Body-Wave Travel Time and Slowness Constraints

Observations of travel times of seismic waves at varying distances from earthquake and explosion sources for which the source locations and origin times are either known or solved for are plotted in travel time curves, as shown for shallow focus events in Figure 2. This classic display of seismic observations immediately reveals two defining attributes of the Earth: The deep structure must be largely radially symmetrical, as that is required for having tightly defined travel time branches for each path through the Earth, and the travel times of major phases such as P, PP, S, and SS are smoothly increasing functions in the angular distance (Δ) range 30–100°, which corresponds to the range where the seismic wave fronts turn in the lower mantle. The smooth, continuous curves obtained by fitting the observations can be inverted for one-dimensional models of seismic velocity versus depth using classic methods such as the Herglotz–Wiechert inversion or by computer modeling (see Lay and Wallace, 1995). The slope of a travel time curve at a given angular distance, $\Delta T/\mathrm{d}\Delta$, gives the seismic ray parameter and its inverse the apparent velocity. These are related to the geometry of the wave front as it sweeps through the Earth and the velocity at the depth in the Earth where the wave turns back toward the surface causing it to arrive at a particular distance. The smooth, concave downward curvature of P-wave and S-wave travel time curves beyond 30° directly implies smoothly increasing velocities with depth in the lower mantle. The ray parameter can be estimated either from a smoothed travel time curve or by direct measurement of relative arrival times of a given seismic phase across an array of closely spaced receivers.

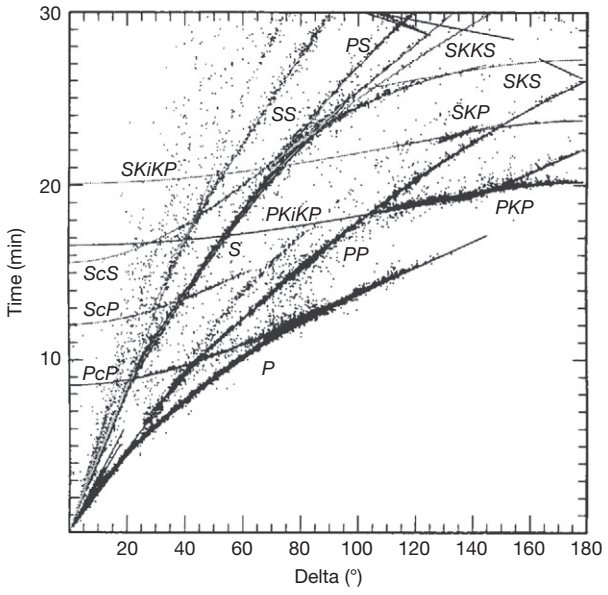

Figure 2 Observed travel time measurements for P and S seismic phases as a function of epicentral distance in the Earth for shallow earthquake sources, along with the predicted (labeled) travel time curves for a radially symmetrical model of P-wave and S-wave velocity variations with depth. P and S are direct phases: PcP, ScP, and ScS reflect from the core–mantle boundary; PKiKP and SKiKP reflect from the inner core–outer core boundary; PP, SS, and PS reflect once from Earth's surface; and PKP, SKP, SKS, and SKKS are phases that traverse Earth's core. Reprinted from Kennett BLN and Engdahl ER (1991) Travel times for global earthquake location and phase identification. *Geophysical Journal International* 105: 429–465, with permission from the Royal Astronomical Society.

Global observations of body-wave travel times and measurements of slopes of the travel time curves by seismic array analyses proliferated in the 1960–1990s, with many radially symmetrical Earth models for the lower mantle being produced (e.g., Chinnery and Toksöz, 1967; Dziewonski and Anderson, 1981; Hales and Roberts, 1970; Hales et al., 1968; Herrin, 1968; Johnson, 1969; Kennett and Engdahl, 1991; Morelli and Dziewonski, 1993; Randall, 1971; Sengupta and Julian, 1978; Uhrhammer, 1978). While the variations in lower mantle velocities at a given depth among these models are $<1\%$, there is still great importance in having an accurate reference model both for earthquake location procedures and for use as a background model in tomographic analyses. Thus, efforts to improve the average lower mantle parameters continue, with increasing quantities of data and variety of phase types being incorporated into the analysis (Masters et al., 1999). All of these one-dimensional lower mantle models have smooth velocity gradients like those in the PREM model (Figure 1).

The small variations between lower mantle radial velocity models have still received much attention because any departure from homogeneity (as expected for self-compression of uniform composition material) would have major implications for possible chemical layering or phase changes. P and S velocities throughout the lower mantle above the D″ region are bounded to within about $\pm 0.1\ \mathrm{km\ s^{-1}}$ in terms of an average model (e.g., Lee and Johnson, 1984). This tight bound (Figure 1) is consistent with the finding by Burdick and Powell (1980) that small features in ray parameter estimates from seismic arrays tend to vary azimuthally, but are not globally representative, with on average very smooth structure in the lower mantle being preferred for a one-dimensional model. There have been observations of reflections and converted phases from a velocity or impedance contrast near 900 km depth near subduction zones (e.g., Kawakatsu and Niu, 1994; Revenaugh and Jordan, 1991), but this appears to be a strongly laterally varying structure (Shearer, 1993) and may be associated with steeply dipping mantle heterogeneities that are likely associated with deeply penetrating subducted slabs (Castle and Creager, 1999; Kaneshima, 2009; Kaneshima and Helffrich, 1998, 2009; Niu and Kawakatsu, 1997; Vanacore et al., 2006; Vinnik et al., 1998a). Reports of arrivals reflected or scattered from other depths in the upper third of the lower mantle are numerous (Courtier and Revenaugh, 2008; Courtier et al., 2007; Kito et al., 2008; Rost et al., 2008; Vinnik et al., 2010), but at this time, there is no compelling evidence for significant laterally extensive layering of the lower mantle except near the top of the D″ region.

1.22.2.2 Surface-Wave/Normal-Mode Constraints

In addition to body-wave travel times, measurements of normal-mode eigenfrequencies play a major role in defining one-dimensional seismic velocity and, most importantly, density models for the lower mantle (see also **Chapter 1.04**). Normal modes correspond to standing patterns of P-wave and S-wave motions and provide constraints on the structure appropriate for relatively long-period motions compared to body-wave arrival times. The motions of normal modes involve large volumes of rock, and the varying depth sensitivity of different modes readily allows for the construction of one-dimensional models of the lower mantle. The large-scale motions allow the density structure to be sensed as well, particularly when a variety of modes are analyzed together to obtain velocity and density models. Important early one-dimensional models for lower mantle structure based largely on normal-mode observations include those of Jordan and Anderson (1974), Gilbert and Dziewonski (1975), Dziewonski et al. (1975), and Dziewonski and Anderson (1981). These models are compatible in basic structure with those obtained from body-wave analyses, but it was observed early on that there is some difference in absolute velocities between body-wave and normal mode-based models. In the late 1970s, this baseline discrepancy was recognized to be the effect of dispersion due to intrinsic attenuation as waves traverse the Earth. Attenuation causes shorter-period signals to sense slightly higher seismic velocities than longer-period signals. The development of phenomenological models for attenuation in the mantle allows an anelastic Earth model, such as PREM (**Figure 1**), to vary systematically in velocity as a function of wave period, reconciling body-wave and normal-mode observations (e.g., Anderson et al., 1977; Dziewonski and Anderson, 1981; Kanamori and Anderson, 1977; Liu et al., 1976).

By far, the most important contribution to lower mantle structure from normal modes is the resolution of density structure. Body-wave travel times provide indirect sensitivity to density, and only through the use of the Adams–Williamson approach can body-wave seismic velocities be used to infer the density structure (reflected and converted phases can provide some information on density contrasts at internal boundaries). The large volume of rock in motion during normal-mode oscillations provides direct sensitivity to gravitational effects on the waves and hence to density. Thus, the development of one-dimensional seismic models from normal-mode observations explicitly involves density structure. As for the seismic velocity models, the density structure in the lower mantle involves simple increase with depth (**Figure 1**), with density increasing from about $4.8\,\mathrm{g\,cm^{-3}}$ at 800 km depth to $5.56\,\mathrm{g\,cm^{-3}}$ just above the CMB. The normal-mode sensitivity is limited in terms of resolving any small discontinuities but can bound the absolute levels over several hundred kilometer thickness to less than about 0.5% uncertainty for a one-dimensional model. This places some constraint on the degree of admissible lower mantle layering due to chemical density differences, although the likelihood that any deep layering may have large topographic variations induced by mantle flow complicates the interpretation of such normal-mode constraints.

1.22.2.3 Attenuation Structure

The Earth is not perfectly elastic, and as seismic waves travel through the interior, they undergo anelastic attenuation that gradually diminishes their amplitudes at a rate greater than that caused by geometric spreading. The mechanisms responsible for anelastic losses are generally thermally activated microscale processes such as dislocation motions and grain boundary interactions (e.g., Anderson, 1967; Minster, 1980; Minster and Anderson, 1981). Lacking resolution of the microscale processes, seismologists use phenomenological models that account for the macroscopic effects of anelasticity, parameterizing the corresponding departures of wave behavior from that for a purely elastic medium. The most common parameterization of attenuation is in the form of a quality factor, Q, defined as the inverse of the fractional loss of energy, E, per cycle of oscillation: $1/Q = -\triangle E/(2\pi E)$. Lower values of Q correspond to stronger anelastic loss or more attenuation. Infinite Q would correspond to elastic behavior. The finite Q encountered by a seismic wave in the lower mantle may vary from frequency to frequency because different mechanisms are activated for different timescales. Over a finite range of frequencies, there will be a dispersive effect, with higher frequencies sensing an unrelaxed effective modulus relative to lower frequencies. This results in physical dispersion, the reason that short-period body waves sense slightly higher seismic velocities than long-period normal modes. The magnitude of this effect depends on the absolute value and frequency dependence of Q appropriate for a given wave motion.

The lower mantle has relatively high Q values for seismic waves, and determining the structure is rather difficult due to regional variations of strong attenuation in the overlying upper mantle that must be traversed by all wave motions observed at the surface. Normal modes and averaged body-wave attenuation measurements place some constraints on the average Q values, but it is possible to satisfy most data with extremely simple models (e.g., Anderson and Hart, 1978; Dziewonski and Anderson, 1981; Masters and Gilbert, 1983; Widmer et al., 1991). For example, the PREM model has S-wave quality factor, $Q_\mu = 312$, throughout the lower mantle, while P-wave quality factor, Q_α, increases from 759 at 670 km depth to 826 at the CMB. While there is some evidence for a low-Q zone at the base of the mantle, this is not well resolved because of strong trade-offs with velocity gradients in the D″ region. The detailed frequency dependence of attenuation in the lower mantle is not yet well resolved, and there have been some recent efforts to develop new attenuation models for the lower mantle (e.g., Ford et al., 2012; Hwang and Ritsema, 2011; Lawrence and Wysession, 2006).

To give a sense for the anelastic dispersive effect associated with lower mantle structure, we consider the PREM S-wave velocities at a depth of 2271 km for periods of 1 s ($7.055\,\mathrm{km\,s^{-1}}$) and 200 s ($7.017\,\mathrm{km\,s^{-1}}$). The respective P-wave velocities are 13.131 and $13.103\,\mathrm{km\,s^{-1}}$. The dispersive effects are small but physically must be present. Over long path lengths in the attenuating lower mantle, the small velocity differences integrate to give observable differences in body-wave and normal-mode observations that have to be accounted for. Thus, a realistic one-dimensional model of the

lower mantle must include a seismic wave attenuation structure, and that intrinsically leads the velocity model to have frequency dependence. PREM is the primary one-dimensional model with this physical dispersion explicitly being included, although Montagner and Kennett (1996) considered frequency-dependent effects. Other single-frequency models, such as ak135 (Kennett et al., 1995), have improved the travel time fit to certain seismic phases, notably core phases, but such models have not explicitly been reconciled across a broad frequency range so they are useful for earthquake location procedures, but not as a Earth model for interdisciplinary applications.

1.22.3 Three-Dimensional Lower Mantle Structure

One-dimensional Earth models are remarkably successful in predicting seismic wave travel times for paths traversing the lower mantle, typically accurate within a fraction of a percent for teleseismic P and S waves. This is a manifestation of the importance of gravity and chemical differentiation in producing a strongly radially stratified planet. Nonetheless, there are observable systematic travel time fluctuations at a given distance range that indicate deviations from a one-dimensional structure. Such fluctuations are particularly evident for waves traversing only the crust and upper mantle, where there are relatively strong heterogeneities. After suppressing the contributions from strong upper mantle heterogeneity either by using laterally varying models or by computing differential travel times between phases observed at a given station, the scatter in P-wave travel times relative to predictions for a one-dimensional lower mantle model is generally within $\pm$1–2 s (for paths with travel times of 600–700 s), while for S waves, scatter is typically $\pm$4–6 s (for paths with travel times of 1000–1200 s). There are some regions like that in the lowermost mantle under Africa and the central Pacific, with late S-wave arrival time anomalies of up to 15–20 s attributed to particularly anomalous lower mantle paths (e.g., Ni and Helmberger, 2003a). These variations in travel times indicate that minor aspherical elastic velocity structure exists in the lower mantle, and many seismological studies have attempted to constrain either global or regional heterogeneities in the lower mantle.

1.22.3.1 Seismic Tomography

Initial investigations of aspherical structure in the lower mantle utilized moderate-sized (hundreds to a few thousand) sets of travel time anomalies (e.g., Sengupta and Toksoz, 1976) or differential travel time observations (e.g., Jordan and Lynn, 1974; Lay, 1983) to detect systematic variations relative to standard one-dimensional models. The main challenges in resolving lower mantle heterogeneity involve the uncertainty in earthquake source locations (typically, these are approximated by solving the location problem assuming a one-dimensional velocity structure, which intrinsically leads to an incorrect location estimate and consequent artifacts in the residual arrival times) and the strength of upper mantle heterogeneities (particularly near-source structures such as subducting slabs). These remain vexing problems, and it is reasonable to believe that current estimates of deep mantle heterogeneity are still biased by incomplete suppression of event location effects and upper mantle heterogeneities. While strategies such as computing differential time anomalies (e.g., ScS-S, SKS-S, or PcP-P differential arrival times relative to one-dimensional model predictions are commonly used) can reduce source mislocation and near-source and near-receiver structural effects due to the similarity of the ray-paths for the two phases in these regions, it remains possible that failure to account for strong lateral gradients in shallow structure causes erroneous interpretation of differential time anomalies as being due to deep mantle heterogeneity. The long-term solution to this problem is the development of very accurate models for upper mantle structure (including 3D slab and mid-ocean ridge structures) used in a self-consistent way with event locations. In general, this is still not done in most of today's large-scale tomographic inversions, but progress is gradually being made toward this goal (see also **Chapters 1.06** and **1.09**).

Given large numbers of observations of seismic phases with good azimuthal and ray parameter coverage from an earthquake, the effects of source mislocation can be suppressed even if a one-dimensional model or low-resolution upper mantle aspherical model is used. This can never be a perfect process unless one invokes precise a priori near-source information (the process of estimating the origin time always removes a baseline term from the travel times leading to anomalies with fluctuating sign even when the true anomalies should be one-sided). Seismic tomography uses the arrival time anomalies from many source–receiver combinations to invert for a parameterized version of mantle heterogeneity, ideally for well-sampled event populations where location effects are suppressed by coverage. In this case, the crossing coverage from multiple paths can build up the image of spatially varying velocity structure, although in almost every case, the amplitude of the actual heterogeneity will be intrinsically underestimated by the inversion model. This is the primary approach to imaging lower mantle heterogeneity on large and small scales; although the requirement of well-resolved source locations is seldom met in practice, approximations in ray tracing are commonly made, and iteration to attain self-consistent event locations and aspherical models is performed in only a minority of studies (e.g., Mégnin and Romanowicz, 2000). All results of lower mantle seismic tomography must thus be viewed as having limited resolution at this time, and there is significant inconsistency in small-scale structures between models. Even with these limitations, the implications of the current generation of models are profound.

One of the earliest fundamental contributions of global seismic tomography was the demonstration that coherent structure exists in the lower mantle on scale lengths of several thousand kilometers and that this unexpected configuration of large-scale deep heterogeneity can account for previously unexplained long-wavelength features in Earth's geoid (e.g., Clayton and Comer, 1983; Dziewonski, 1984; Dziewonski et al., 1977; Hager et al., 1985; Masters et al., 1982). Establishing this connection required both the development of global models and the improved understanding of how mantle heterogeneities induce flow and deflection of boundaries that affect the geoid (Hager, 1984; Richards and Hager, 1984). While the early low-resolution tomographic models for the lower mantle have relatively strong spherical harmonic components from degrees 2 to 5, and proved remarkably successful

in accounting for the long-wavelength geoid (see review by Hager and Richards, 1989), there has been continuing debate about the spectrum of lower mantle heterogeneity. Are the long-wavelength patterns the result of truly diffuse structures or are they in part due to smoothed sampling of smaller scale but very heterogeneous features such as slabs embedded in the lower mantle? If the latter is the case, the long-wavelength distribution of heterogeneity in the lower mantle is more a consequence of the last few hundred million years of surface tectonics and associated plate subduction than a very long-term aspect of the lower mantle convective regime (e.g., McNamara and Zhong, 2005). Similarly, if the long-wavelength patterns in surface hot spots reflect swarms of thermal plumes rising from the CMB, then the distribution of recent D″ boundary layer instabilities may contribute to the present long-wavelength structure of the deep mantle.

Imaging of deep mantle structure has advanced in resolution by steadily increasing the size and raypath coverage of the data sets and by using improved measurement and inversion approaches. There is significant convergence in large-scale structures in recent deep mantle tomographic shear velocity models (e.g., Antolik et al., 2003; Grand, 2002; Grand et al., 1997; Gu et al., 2001; Houser et al., 2008; Kustowski et al., 2008; Lekic et al., 2012; Li and Romanowicz, 1996; Liu and Dziewonski, 1998; Masters et al., 1996, 2000; Mégnin and Romanowicz, 2000; Panning and Romanowicz, 2006; Panning et al., 2010; Ritsema et al., 1999, 2011; Simmons et al., 2007, 2009, 2010; Takeuchi, 2007), all of which have dominant long-wavelength heterogeneities. The same is true for large-scale P velocity models, although there is still less agreement between models and somewhat less complete coverage of lower mantle regions (e.g., Antolik et al., 2003; Bijwaard and Spakman, 1999; Bijwaard et al., 1998; Boschi and Dziewonski, 1999, 2000; Fukao et al., 1992, 2001; Houser et al., 2008; Karáson and van der Hilst, 2001; Lei and Zhao, 2006; Li et al., 2008; Myers et al., 2011; Simmons et al., 2011, 2012; van der Hilst and Kárason, 1999; Vasco and Johnson, 1998; Widiyantoro and van der Hilst, 1996; Zhao, 2001).

As the resolution of large-scale lower mantle 3D structure has improved with each new generation of global tomographic models, it has become clear that there are significant intermediate-scale features in the lower mantle. This had previously been deduced for localized regions by array studies or by analyses of differential travel times for phase pairs sensitive to lower mantle structure (e.g., Jordan and Lynn, 1974; Lay, 1983), but the geometry and lateral extent of such features could not be resolved until large-scale tomographic models were produced. Recent high-resolution S-wave velocity (e.g., Grand, 2002; Simmons et al., 2010) and P-wave velocity (Ren et al., 2007; van der Hilst et al., 1997) models resolve a high-velocity quasitabular structure extending nearly vertically in the lower mantle beneath North America and South America and a similar elongate body beneath southern Eurasia, both of which extend to at least 1300–1600 km depth (**Figure 3**). The width of these features is not tightly resolved, but appears to be at least 500 km, and the anomalies are 1–2%, which is relatively high for this depth range in the mantle. These features are usually interpreted as relatively cold, sinking slab material that has penetrated into the lower mantle as the Americas moved westward and as the Tethys Sea closed, respectively. The aspherical seismic velocity structure in the mid-mantle near 1300 km depth is dominated by these elongate tabular high-velocity features, and it is likely that these contribute significantly to the strong long-wavelength patterns in spherical

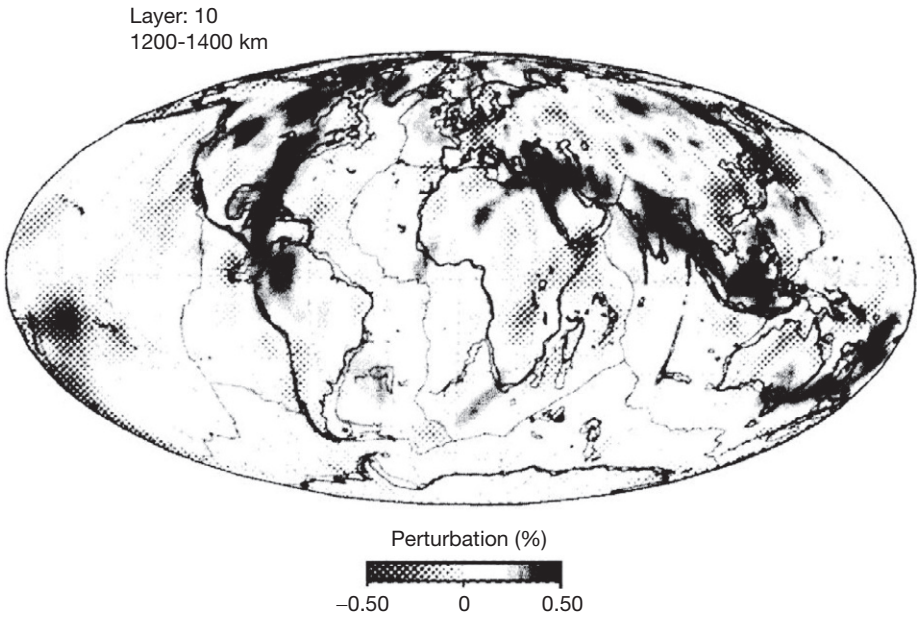

Figure 3 Horizontal section through a tomographic model of P-wave velocity structure near 1300 km deep in the lower mantle, obtained by inversion of ISC arrival times after careful processing for depth determination. Solid dark areas correspond to relatively high velocities, with two major coherent features that correspond to tabular structures extending semivertically below southern Asia and eastern North America. These are inferred to be subducted slab material that has penetrated into the lower mantle. Reproduced from van der Hilst RD, Widiyantoro S, and Engdahl ER (1997) Evidence for deep mantle circulation from global tomography. *Nature* 386: 578–584.

harmonic models that have lower resolution (see corresponding features in the early lower-resolution models discussed by Dziewonski et al., 1993). While there may be contributions to these structures from inadequately suppressed shallow mantle structures, particularly strong near-source slab anomalies, the high-velocity regions do appear in models with different data sets, different model parameterizations, and varying source–receiver geometries, so it is very difficult to dismiss them as artifacts.

Below about 1600 km depth, tomographic models show less coherence, relatively weak velocity anomalies, and tabular structures are not clearly imaged (e.g., Grand et al., 1997; Simmons et al., 2012). Instead, the models tend to become dominated by horizontally extensive regions of high and low velocity with strong degree 2 and 3 patterns in the lowermost mantle (Figure 4). The strength of the velocity heterogeneity increases in the lowermost 300–500 km of the mantle, particularly for shear waves (Figure 5). Lateral variations of ±4% in S-wave velocity and ±1.5% in P-wave velocity are observed. High shear velocities in the lowermost mantle are found beneath circum-Pacific margins, although only in a few places is there apparent continuity of high-velocity features from the mid-mantle all the way to the CMB. The aspherical S-wave velocity models all display two large low-shear-velocity provinces (LLSVPs) located below the central Pacific and the southern Atlantic/southern Africa/southern India Ocean region. The latter two low-velocity regions appear to extend upward above the D″ region, possibly as much as 800–1000 km. These features have sometimes been called 'superplumes,' given than their scale greatly exceeds that expected for isolated D″ boundary layer instabilities, and Dziewonski et al. (1993) called them the 'Equatorial Pacific Plume Group' and the 'Great African Plume,' respectively. Attributing dynamic significance to these features with the 'plume' label is complicated and very uncertain; low velocities may be caused by high temperatures or by chemical differences. It is preferable to use the dynamically neutral label of LLSVPs, as discussed later.

1.22.3.2 Dynamic Structures

While the geoid and some attributes of subduction zone morphology provide geodynamic constraints on lower mantle dynamics, most of what we know about dynamic processes in the deep Earth derives from interpretations of seismic tomography. This is not a trivial undertaking because there are limitations in the spatial resolution of the tomographic models and possible contributions from both thermal and chemical heterogeneities that are difficult to separate. Any

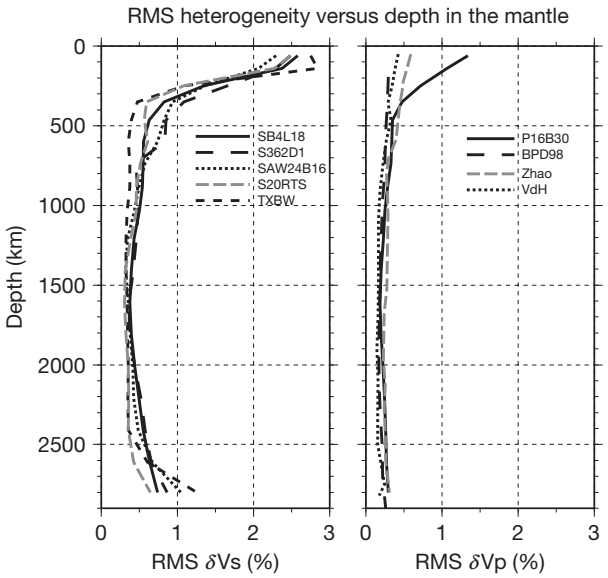

Figure 5 RMS velocity fluctuations at various depths in the mantle shear velocity models SB4L18 (Masters et al., 2000), S362D1 (Gu et al., 2001), SAW24B16 (Mégnin and Romanowicz, 2000), S20RTS (Ritsema and van Heijst, 2000), and TXBW (Grand, 2002) and in the mantle compressional velocity models P16B30 (Bolton, 1996), BPD98 (Boschi and Dziewonski, 1999), Zhao (Zhao, 2001), and VdH (Karáson and van der Hilst, 2001).

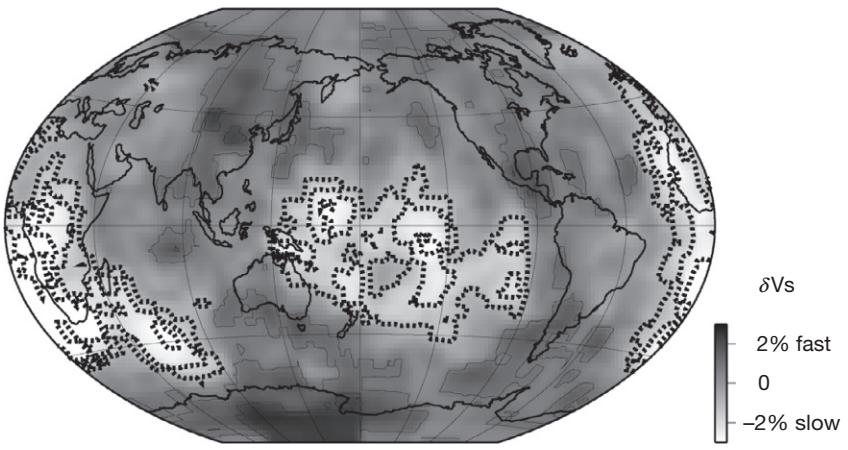

Figure 4 Representative large-scale mantle tomography for S-wave velocity structure (Grand, 2002) near the base of the mantle. Note the long-wavelength patterns of high velocities beneath the circum-Pacific and low velocities beneath the central Pacific and Africa. 1% contours are shown, with dotted lines highlighting the internal variations in the two large low-shear-velocity provinces. Variations of ±3% are imaged by this and other models with similar spatial patterns. Note the contrast in scale length of predominant heterogeneities with the mid-mantle pattern in Figure 3.

interpretation of tomography requires a foundation in mineral physics characterization of material property dependence on temperature and composition for the high-pressure conditions of the deep Earth. It also requires geodynamic analysis to assess the deformation processes taking place, guided by the seismological and mineral physics constraints on structure.

Seismological resolution of overall lower mantle structure has to be achieved by using different data types that provide distinct control on spatial and depth variations of structure. Overtones and multiple surface reflections provide sampling of structure near and below the transition zone, direct body-wave phases including core phases provide spatially nonuniform sampling of deep mantle corridors, diffracted waves extend coverage of structure near the CMB, and normal modes provide control on the large-scale even harmonics of the structure. One of the main challenges is that differences in how inversions of various data sets are regularized have large effects on how structural characterizations are interpolated and extrapolated in the various models (e.g., Boschi and Dziewonski, 1999). The very large-scale, degrees 2 and 3 patterns of heterogeneity are pronounced and well resolved now, and one of the key issues is whether weaker shorter-wavelength features are independent of or linked to the causes of the long-wavelength patterns.

While the lower mantle does not appear to have pronounced internal layering, it has been proposed that the downward transition in heterogeneity pattern from a mid-mantle dominated by slablike structures to a deep mantle dominated by large-scale high-velocity and low-velocity features is caused by compositional stratification. The stratification could be in a thin layer essentially confined to D″ (e.g., Davies and Gurnis, 1986) or in a much thicker layer. In the latter model (see Kellogg et al., 1999; van der Hilst and Kárason, 1999), the lowermost mantle is compositionally distinct, being composed of undifferentiated, possibly 'primordial' mantle material that is then invoked as the source of isotopic anomalies sampled by upwelling thermal plumes that produce distinctive surface hot spot volcanism. Downwelling slabs can depress the conjectured chemical boundary by hundreds of kilometers, deflecting it from a depth of around 2000 km. The chemical boundary is not expected to be a strong reflector and does not give rise to coherent features in the radially averaged mantle model. The density increase of the deep layer could be due to enrichment in iron or silica, which has competing effects on the velocity structure. This is a highly speculative model, but it can begin to reconcile the current observations of the deep mantle seismic structure with geochemical observations. An alternative to chemical layering is the presence of distinct blobs of chemically distinct mantle mixed into the lower mantle, in the so-called plum-pudding model (Davies, 1984). An intermediate scenario, motivated by recent seismic observations, of discrete piles of chemically distinct material in the LLSVP regions is discussed later.

Significant improvement of our understanding of the lower mantle will come with reliable determination of density heterogeneity directly from simultaneous inversion of normal modes and gravity observations. A first step in this direction has been presented by Ishii and Tromp (1999). While preliminary, that study found that high-density material may be piled up in the regions of low shear velocity, presumably hot material beneath the Pacific and Africa. A significant chemical heterogeneity density effect is needed to offset any thermal buoyancy of the upwellings. Until the models improve, it may thus be premature to associate the low shear velocities with upwellings, for chemical heterogeneity is likely to be important in the deep mantle.

The existence of large-scale lower mantle features enables the formulation of simultaneous or iterative inversions for dynamic features such as the geoid and dynamic topography, and this has emerged as a new area of research (e.g., Dziewonski et al., 1993; Forte and Mitrovica, 2001; Forte et al., 1993, 1994; Hager and Clayton, 1989; Hager et al., 1985; Mitrovica and Forte, 2004; Phipps Morgan and Shearer, 1993; Simmons et al., 2009, 2010; Soldati et al., 2012; Tackley, 2012). The primary additional parameter that is constrained in such geodynamic models is the viscosity structure, and it is generally found in geoid inversions and contemporary studies of glacial rebound processes that the viscosity of the lower mantle is one to two orders of magnitude higher on average than that of the average upper mantle (e.g., Mitrovica and Forte, 1997, 2004). This may be a consequence of lower mantle mineralogy, or it may represent the effect of devolatilization of the lower mantle during extensive melting early in Earth history. The simultaneous interpretation of thermal, chemical, and dynamic structures based on probabilistic tomographic velocity structures has been expanded to statistical approaches that recognize the uncertainties and correlations among thermal and compositional parameters (e.g., Cobden et al., 2009, 2012; Deschamps and Tackley, 2008; Deschamps and Trampert, 2003; Hernlund and Houser, 2008; Mosca et al., 2012; Trampert et al., 2004).

Resolving small-scale structures in the lower mantle by seismic imaging is a complementary approach to imaging the dynamic system. Essentially, seismologists look for the strong patterns expected to accompany mantle convection that is extensively driven by boundary layer flow. The primary elements of this are expected to be cold, sinking lithospheric slabs, which should have relatively high seismic velocities and tabular geometries, and hot, rising thermal plumes, which should have relatively low seismic velocities and cylindrical geometries. Extensive work has addressed lower mantle penetration by subducting oceanic lithosphere, which clearly penetrates down through at least the transition zone in some regions, given the occurrence of deep earthquakes in subduction zones. Jordan (1977) introduced a residual sphere modeling formalism for seeking patterns in travel time residuals from individual earthquakes in subduction zones, which was further developed by Creager and Jordan (1984, 1986a). These studies demonstrated the sensitivity of the method to both upper mantle and transition zone slab geometry and velocity heterogeneity, as well as to geometry of any steeply dipping slab extension into the lower mantle. Provocative results based on both P-wave modeling and S-wave modeling suggested that slab penetration to depths of at least 1000 km with little distortion other than steepening dip occurs in the Kuril, Marianas, and Japan arcs.

Additional applications of the residual sphere method were presented by Fischer et al. (1988, 1991), Zhou and Anderson (1989), Zhou et al. (1990), Boyd and Creager (1991), Ding and Grand (1994), and Pankow and Lay (1999). The method makes very explicit the limitations of arrival time data, as event location effects have a major effect on relative arrival time anomalies if the data coverage is limited (particularly true if

only teleseismic observations are used). As noted previously, tomographic methods are strongly biased by this unless the data coverage is such that residual patterns faithfully preserve the slab effects (which may be true when extensive upgoing and downgoing data are included, but not otherwise). Residual sphere modeling also makes clear the importance of deep mantle and receiver corrections, and early applications did not adequately address this issue. In fact, it has been shown that for S waves, much of what was initially attributed to near-source effects is eliminated when improved path corrections are applied (e.g., Deal and Nolet, 1999; Deal et al., 1999; Gaherty et al., 1991; Pankow and Lay, 1999; Schwartz et al., 1991). As global tomographic models improve further, this will become less of a problem. The analysis of differential residual spheres for events in the same slab, as first introduced by Toksöz et al. (1971), is one approach that has been pursued to suppress distant effects rather completely (e.g., Ding and Grand, 1994; Okano and Suetsugu, 1992; Pankow and Lay, 1999; Takei and Suetsugu, 1989). These studies indicate that in some cases, slabs may penetrate to depths of 800 km or more, but significant slab broadening may occur, as well as the reduction of velocity heterogeneity to on the order of 2%, much weaker than in early residual sphere studies and similar to the weak heterogeneity inferred when a priori slab structures are introduced into tomographic modeling. As regional and global tomography has advanced, there is a clear convergence with the results from the enhanced residual sphere modeling, with support for a few slabs directly penetrating into the lower mantle beneath Java and the Caribbean, but others such as the Izu and Japan slabs show strong deflections into large transition zone accumulations of slab material.

The analysis of upwelling regions is even more challenging, in that seismological imaging of low-velocity features is intrinsically difficult due to wave diffraction and wave front healing effects. Nonetheless, global tomography studies suggest that there are concentrated low-velocity regions beneath some of the major surface hot spots (e.g., Montelli et al., 2004; Schmerr et al., 2010; Sun et al., 2010; Takeuchi, 2009; Zhao, 2004), but the confidence in such features remains limited because the results appear to depend heavily on how inversions are parameterized and damped. While the evidence for lithospheric slab penetration into the upper portion of the lower mantle is relatively strong, the direct imaging of any plume upwellings remains in an early stage. Waveform healing effects and the intrinsic limitations of tomographic resolution for low-velocity regions require the evaluation of how tomography filters and smooths the images of specific deep mantle structures such as plumes (e.g., Boschi et al., 2007, 2008; Bull et al., 2009; Hwang et al., 2011; Ritsema et al., 2007; Styles et al., 2011). The complex structures near the base of the mantle that are described later include features attributed to plumelike instabilities from the thermochemical boundary layer above the CMB, but whether these features ascend to the surface or induce localized upwellings that do remains to be established.

1.22.4 D″ Region

The numerous efforts to image the detailed velocity structure below regions of subduction have been motivated as a test of the hypothesis of stratified versus whole-mantle convection, a key issue in mantle dynamics. Similarly, studying the structure of the D″ region is largely motivated by the notion that this region may play a critical role in mantle convection, especially if there is significant heating from below (e.g., Garnero et al., 2007a; Lay and Garnero, 2004). While most estimates of Earth's heat flow budget suggest that only 10–30% of the mantle's heat fluxes upward through the CMB (Lay et al., 2008; Zhong, 2006), this is still substantial heating that will give rise to a thermal boundary layer. Internal heating, resulting from radiogenic materials distributed in the mantle, is expected to contribute to large-scale flow without producing concentrated structures. In contrast, boundary layer-driven flow is expected to yield both localized upwellings and downwellings, which provide specific targets for seismic imaging. D″ structure is thus of particular interest as this region serves as the lower boundary layer of the mantle convection system. It is now generally appreciated that the lowermost mantle is also of great importance to convection in the core and the resulting geodynamo (e.g., Glatzmaier et al., 1999; Takahashi et al., 2008; Willis et al., 2007). The structure of D″ appears to be very complex, and efforts to elucidate this complexity underlie many approaches to understanding core and mantle dynamics.

1.22.4.1 Large-Scale Seismic Velocity Attributes

There are several important seismological probes of the large-scale elastic velocity structure in the D″ region. The large seismic velocity reductions across the CMB cause seismic wave energy to diffract into the geometric shadow zone at distances $>100^{\circ}$. Waves diffracted along the CMB are sensitive to the absolute velocities and the velocity gradients in the D″ region and have long been studied to constrain average and laterally varying structure (e.g., Alexander and Phinney, 1966; Bolt et al., 1970; Doornbos and Mondt, 1979; Mondt, 1977; Mula and Müller, 1980; Sacks, 1966; To and Romanowicz, 2009; To et al., 2011; Valenzuela and Wysession, 1998; Wysession, 1996; Wysession and Okal, 1989). These studies demonstrate that no single velocity structure sufficiently characterizes D″ everywhere and that in some cases, there are strong negative velocity gradients in D″, while in other places, there are near-zero or positive velocity gradients. There are also changes in the relative perturbation of P-wave and S-wave velocities that are likely due to mineralogical or textural origin (e.g., Wysession et al., 1999). Diffracted phases involve extensive lateral averaging of what appears to be a region rich in small-scale structure and therefore yield limited resolution, but they do provide important input into large-scale tomographic models for D″ because of their extensive spatial coverage (e.g., Bréger and Romanowicz, 1998; Castle et al., 2000; Kuo and Wu, 1997; Kuo et al., 2000).

The large-scale variations in D″ imaged by early global seismic wave travel time tomography studies were shown to have predominant degrees 2 and 3 spherical harmonic components (e.g., Dziewonski et al., 1996; Kuo and Wu, 1997; Kuo et al., 2000; Li and Romanowicz, 1996; Liu and Dziewonski, 1998; Masters et al., 1996; Su et al., 1994). These models established the presence of high shear velocities in D″ beneath the Pacific Ocean margins and low velocities beneath the central Pacific and the southeastern Atlantic and southern Africa

(Figure 4). This geometry results in a correlation between areas of slab subduction over the past several hundred million years (e.g., Lithgow-Bertelloni and Richards, 1998) and high-velocity regions of D″, which could result if slabs penetrate to the base of the mantle while retaining enough thermal anomaly to produce high seismic velocities. Similarly, the low-velocity regions of D″ are generally located below regions with hot spots at the surface, suggesting that D″ upwellings may penetrate all the way to Earth's surface.

1.22.4.2 Thermal Boundary Layer Aspect

To first order, the lower mantle appears to be a relatively uniform layer with properties varying radially largely due to self-compression and having most lateral heterogeneity concentrated in the D″ region above the CMB. The latter is consistent with the presence of a thermal boundary layer, as expected to result from heat fluxing out of the core into the mantle. The existence of a thermal boundary layer is strongly supported by the calculations of energetics of the geodynamo, which suggest that there must be some net flux of heat out of the core to sustain the core convective regime. The precise amount of heat flux is uncertain, with estimates ranging from 0.5 to 10 TW, and this amount must be added to heat conducted down the core adiabat (at least 2–5 TW) (e.g., Buffett, 2003). Thus, at least several TWs, and possibly as much as 15 TW of heat, are fluxing into the base of the mantle (about 44 TW flux through Earth's surface) (e.g., Kellogg et al., 1999; Lay et al., 2008; Zhong, 2006).

The CMB is a major compositional boundary; therefore, the heat flux from the core must conduct into the base of D″ with a superadiabatic temperature gradient (e.g., Stacey and Loper, 1983). Such a thermal boundary layer is likely to thicken over time and to build up instabilities that give rise to thermal plumes that carry excess temperatures from the boundary layer upward (e.g., Leng and Zhong, 2008, 2009). Time-dependent flow and uncertainty in material properties make dynamic calculations of CMB heat flux carried by thermal plumes very uncertain, but these probably provide a lower-bound estimate of total heat flux across the CMB (e.g., Glisovic et al., 2012; Manthilake et al., 2011; Mittelstaedt and Tackley, 2006; Monnereau and Yuen, 2010; Nakagawa and Tackley, 2008).

The very low viscosity of the core-side alloy ensures that the CMB is maintained at nearly isothermal conditions, temperature estimates of the CMB being in the range 2700–4200 °C (e.g., Williams, 1998). If there is no thermal boundary layer in the transition zone or mid-mantle, the overall temperature drop across the CMB thermal boundary layer must be on the order of 1000 ± 500 °C, comparable to that across the lithosphere. Lateral variations in temperature in the deep mantle will produce varying thermal gradients above the CMB resulting in a variable heat flux boundary condition on the core. In places where the mantle temperatures are relatively low, the heat flux will be higher than in places where the mantle temperature is relatively high. This heat flux variation is likely to exert a long-term influence of the mantle on the outer core convective regime (Buffett, 2003; Glatzmaier et al., 1999; Gubbins et al., 2007; Lay et al., 2004b; Sumita and Olson, 2000) and may influence the inner core as well (Sreenivasan and Gubbins, 2011).

The thickness of the boundary layer is quite uncertain due to significant pressure effects on material properties and questions about the existence of partial melting and chemical heterogeneity, but the general expectation is that the boundary layer may be as much as a few hundred kilometers thick (thicker than the lithospheric thermal boundary layer) mainly due to pressure effects suppressing the thermal expansion coefficient near the base of the mantle. In this case, the D″ region corresponds, at a minimum, to a thermal boundary layer with a rapid increase in temperature with depth. This is likely to be manifested as a reduction of seismic velocity gradients relative to the mid-mantle, given the inverse dependence of velocity on temperature. This may be a subtle effect in general due to the pressure effects on thermal expansion, but if the temperature increase approaches the eutectic melting point of the lower mantle or of some minor component in D″, very strong velocity reductions can occur for minor degrees of partial melting. The accurate determination of the velocity gradient above the CMB could thus potentially be used to constrain the thermal boundary layer properties (e.g., Doornbos et al., 1986; Lay and Helmberger, 1983a; Loper and Lay, 1995; Stacey and Loper, 1983), but this approach encounters the immediate challenge that the velocity gradient appears to vary laterally.

Like Earth's lithosphere, the thermal boundary layer at the base of the mantle is likely undergoing strong lateral and vertical flow, as upwellings produced by thermal boundary layer instabilities drain hot material from the boundary layer and downwellings replace it with cooler material. However, as a hot, low-viscosity boundary layer, there is probably much more small-scale structure in the D″ dynamic regime than is found in the cold, relatively stiff lithosphere. It is generally accepted that thermal heterogeneity within the boundary layer is partially responsible for the seismic inhomogeneity detected by Bullen (1949), and it likely contributes to the complexities described here, but it appears that more than just thermal heterogeneity is present.

As is true near Earth's surface, one cannot immediately attribute all variations in seismic velocities to the effects of temperature variations; chemistry may play an important or even the major part, especially given the inhibiting effects of great pressure on temperature derivatives for seismic velocities. The juxtaposition of the lowermost mantle boundary layer adjacent to the largest density contrast in Earth heightens the probability that there is also chemical heterogeneity in the D″ region. This may involve density-stratified residue from Earth's core formation process, ongoing chemical differentiation of the mantle, or even chemical reactions between the core and the mantle (e.g., Garnero and McNamara, 2008; Goarant et al., 1992; Hayden and Watson, 2007; Jeanloz, 1993; Knittle and Jeanloz, 1989; Lay, 1989; Manga and Jeanloz, 1996). The probability of both thermal and chemical heterogeneities existing within the lowermost mantle prompts the consideration of the region as a thermochemical boundary layer (e.g., Anderson, 1991; Lay, 1989; Lay et al., 2004b; Trønnes, 2009), much as Earth's lithosphere must be considered a thermochemical boundary layer due to large-scale chemical variations between oceanic and continental regions. The evidence for a thermochemical boundary layer is provided by several seismological attributes of the D″ region, as described in the next few sections.

1.22.5 D″ Discontinuities

Detailed studies of teleseismic waveforms indicate that P-wave and S-wave velocity structures both have a 0.5–3.0% velocity discontinuity at many locations near the top of the D″ region (the top of D″ is not precisely defined, and many researchers take it to correspond to either the depth at which there is a discontinuity or the onset of a change in velocity gradient, somewhere in the range from 50 to 350 km above the CMB). This feature is often called the D″ discontinuity (e.g., Wysession et al., 1998), and representative shear velocity structures obtained by waveform modeling are shown in Figure 6. These models, obtained for distinct regions of D″, involve a 2.5–3% shear velocity increase at depths from 130 to 300+ km above the CMB that is laterally extensive over intermediate-scale (500–1000 km) regions. Wysession et al. (1998) reviewed the many early studies of this structure, noting that there are substantial inferred variations in depth of the velocity discontinuity. Typically, S-wave velocity increases are larger than P-wave velocity increases, with the latter usually being 0.5–1.0%, though some models do propose 3% discontinuities (e.g., Weber and Davis, 1990; Wright et al., 1985). The increase in velocity at the top of D″ may be distributed over up to 30–50 km in depth, or it may be very sharp (e.g., Lay, 2008; Lay and Helmberger, 1983a; Lay and Young, 1989; Young and Lay, 1987a).

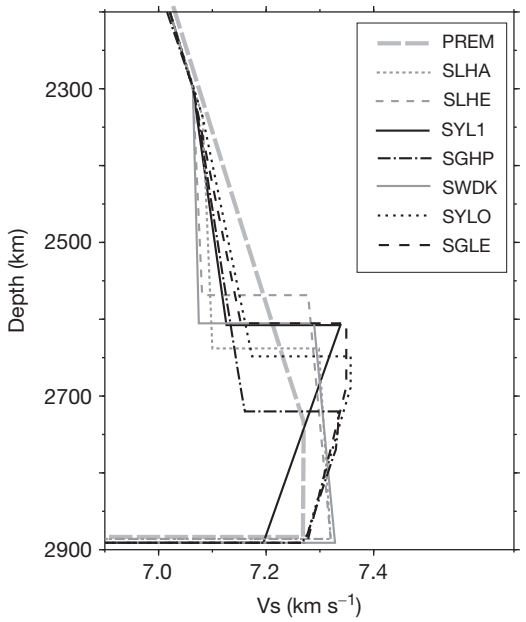

Figure 6 Radial profiles of S-wave velocity in the lowermost mantle: PREM (Dziewonski and Anderson, 1981), SLHE, SLHA (Lay and Helmberger, 1983a), SYL1 (Young and Lay, 1987a), SGHP (Garnero et al., 1988), SWDK (Weber and Davis, 1990), SYLO (Young and Lay, 1990), and SGLE (Gaherty and Lay, 1992). The discontinuity models represent localized structures, determined for spatially limited regions of the D″ layer, the locations of which are indicated in Figure 6.8(a). Shear velocity increases of 2.5–3.0% are found in regions under Eurasia (SWDK and SGLE), Alaska (SYLO), Central America (SLHA), the Indian Ocean (SYL1), and the central Pacific (SGHP). The velocity increase is typically modeled as a sharp discontinuity, but it may be distributed over up to 50 km in depth. Decreased velocity gradients above the discontinuity may exist but are artifacts of the modeling in most cases. The reduction of velocity below the discontinuity in more recent models (orange) may be real but may be an artifact of modeling a heterogeneous region with a one-dimensional model. The variations in depth of the discontinuity are uncertain due to the lack of constraint on velocity above and below the discontinuity, but some variation appears to exist.

1.22.5.1 Seismic Wave Triplications

The velocity increases at the top of D″ are primarily detected by reflections and triplications, which arrive ahead of the core-reflected PcP and ScS phases (e.g., Avants et al., 2006b; Chaloner et al., 2009; Ding and Helmberger, 1997; Gaherty and Lay, 1992; Houard and Nataf, 1993; Hutko et al., 2008, 2009; Kendall and Nangini, 1996; Kendall and Shearer, 1994; Kito and Krüger, 2001; Kito et al., 2004, 2007a,b; Kohler et al., 1997; Lay and Helmberger, 1983a; Lay et al., 2004a, 2006; Reasoner and Revenaugh, 1999; Sun and Helmberger, 2008; Sun et al., 2006, 2009; Takeuchi and Obara, 2010; Thomas and Weber, 1997; Thomas et al., 2002, 2004a,b; Thorne et al., 2007; Weber, 1993; Weber and Davis, 1990; Wright and Lyons, 1975; Wright et al., 1985; Young and Lay, 1987a, 1990). The clearest observations of deep mantle triplications are from distances of 65° to 95°, where the critical angle interaction with the velocity increase greatly enhances the amplitudes of the reflected signals relative to precritical distance ranges. Examples of the triplication arrival are shown in Figure 7, with broadband shear-wave data having a strong arrival between S and ScS phases that would not be predicted by a smooth velocity model such as PREM. The reflector that produces this extra arrival varies globally in depth by several

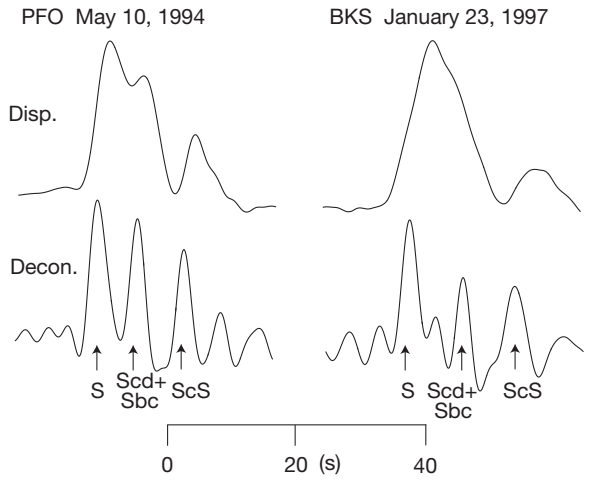

Figure 7 Examples of broadband SH displacements at stations PFO ($\Delta = 79.8°$) and BKS ($\Delta = 79.8°$) for two deep South American events. Instrument-corrected ground displacements (disp.) are shown in the top row. The first arrival is S, and about 15–20 s later, ScS, the reflection from the core–mantle boundary, arrives. Deconvolution by the event-averaged source wavelets and low-pass filtering below 0.3 Hz yields the spike trains below for each record (decon.). The intermediate arrival, Scd + Sbc (SdS), which is produced by triplication from a deep mantle velocity increase, is clearly isolated in the deconvolutions. Reproduced from Lay T, Garnero EJ, and Russell S (2004a) Lateral variation of the D″ discontinuity beneath the Cocos Plate. *Geophysical Research Letters* 31: L15612, http://dx.doi.org/10.1029/2004GL020300.

hundred kilometers (e.g., Kendall and Shearer, 1994) and appears to have regional-scale lateral variations of on the order of a hundred kilometers that may produce scattering rather than simple reflections (e.g., Emery et al., 1999; Freybourger et al., 1999; Hutko et al., 2006; Krüger et al., 1995; Lay et al., 1997, 2004a; Scherbaum et al., 1997; Thomas et al., 2004a,b; van der Hilst et al., 2007; Weber, 1993; Yamada and Nakanishi, 1998).

It has been argued that the D″ discontinuities are actually globally extensive, with lateral variations in depth and strength being the result of lateral temperature variations and interactions with upwelling and downwelling flow (e.g., Nataf and Houard, 1993; Sidorin et al., 1998, 1999). Many studies suggest that no reflections from a discontinuity are observed for certain regions (e.g., Wysession et al., 1998), but most of these fail to establish whether the data truly preclude the presence of some velocity increase. Others studies have questioned whether thee is a first-order discontinuity at all, preferring the notion that the extra seismic arrivals involve scattering from velocity gradients imaged in long-wavelength tomography models (e.g., Cormier, 1985; Haddon and Buchbinder, 1986; Liu et al., 1998; Schlittenhardt et al., 1985). The latter possibility requires large increases in the magnitude of the tomographic heterogeneities and/or sharpening of the velocity gradients, but there must be some relationship between the volumetric structure and the discontinuities (Ni et al., 2000). It has been demonstrated that scattering of SV energy into SH (Cormier, 1985) is not a likely explanation for the extra phases interpreted as triplication arrivals (Lay and Young, 1986). Young and Lay (1987b) showed that velocity decreases, as proposed by Haddon and Buchbinder (1986), cannot explain the data either. Thin high-velocity or low-velocity lamella models appear to fit some P-wave observations at least as well as first-order velocity discontinuity models (Freybourger et al., 1999; Thomas et al., 1998; Weber, 1994), but this has not been demonstrated convincingly for S-wave observations. An alternative is a transition in the heterogeneity spectrum with depth, possibly linking a gradient in anisotropy to the reflector (e.g., Cormier, 2000; Lay et al., 2004b).

One recent approach to determining the structure in the lowermost mantle with few assumptions about the nature of the structural complexity is waveform inversion, which uses large data sets and a complete calculation of waveform partial derivatives to structure for a set of basis functions. This approach has been applied to several areas where there had been previous forward modeling studies, allowing comparison of inferred structures. Applications have abounded (e.g., Fuji et al., 2010; He et al., 2010; Kawai and Geller, 2010b,c; Kawai et al., 2007a,b, 2009, 2010; Konishi et al., 2009, 2012). In general, there is fairly good agreement between forward modeling and waveform inversion studies for specific regions (Lay and Garnero, 2011), but it is clear that the resolution of velocity gradients and even depths of velocity increases and decreases is quite limited; details of all models, whether from forward modeling or inversion, must be interpreted with caution.

The regions with the strongest evidence for a shear-wave velocity discontinuity or strong velocity increase near the top of D″ are highlighted in **Figure 8(a)**. Wysession et al. (1998) showed individual data sampling in greater detail. Some of these areas also have evidence for a P-wave velocity discontinuity, but in some regions, such as under Alaska and Central America, any P-wave velocity discontinuity must be at or below the detection threshold of about 0.5% (Ding and Helmberger, 1997; Hutko et al., 2009; Reasoner and Revenaugh, 1999;

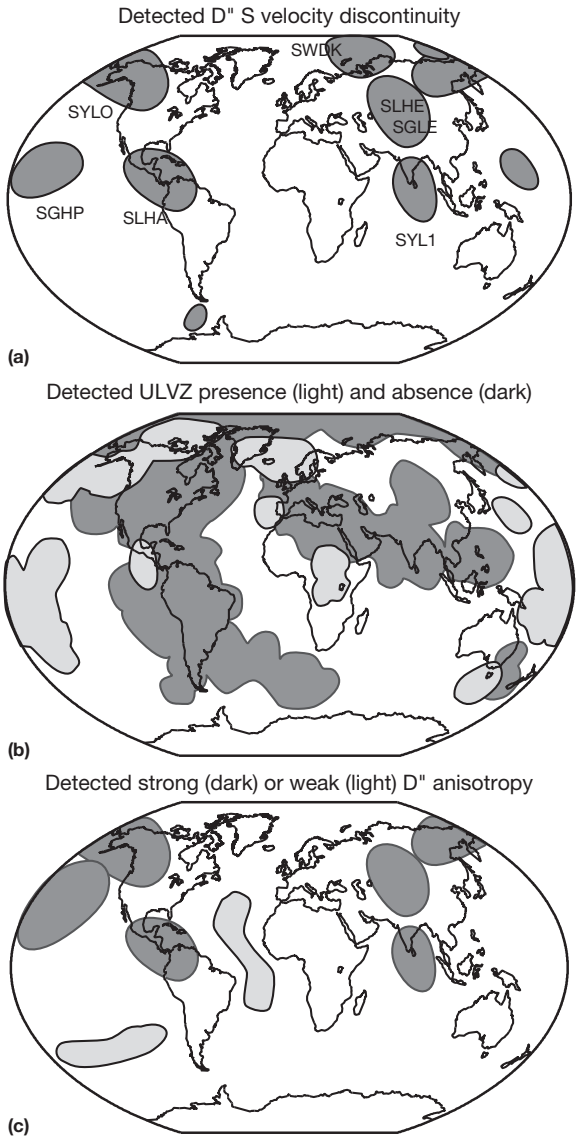

Figure 8 Maps summarizing spatial variations of seismic wave characteristics of D″. (a) Regions where regional shear velocity discontinuities have been observed in large numbers of data, typically with 2–3% increase in velocity at depths from 200 to 300 km above the CMB (see labeled models in **Figure 6**). (b) Regions where ULVZ structures at the CMB have been detected or not, primarily based on SPdiffKS observations and assuming a Fresnel zone appropriate for a horizontal layer. (c) Regions where regional studies of D″ shear-wave splitting have been conducted. Most areas exhibiting splitting have waveforms compatible with vertical transverse isotropy, with decoupling (or only weak coupling) of the transverse and longitudinal components of the S-wavefield, with 1–2% faster transverse components. Modified from Lay T, Garnero EJ, and Williams Q (2004b) Partial melting in a thermo-chemical boundary layer at the base of the mantle. *Physics of the Earth and Planetary Interiors* 146: 441–467.

Wright and Kuo, 2007; Young and Lay, 1989). Beneath Central America, there may be a small P-wave velocity reduction at the same depth as the S-wave velocity increase (Hutko et al., 2008). Stacking of array data is essential to detect such small discontinuities, and many 'non-observations' reported for individual seismograms must be viewed as inconclusive.

It is unlikely that long-period waveform inversion approaches will resolve the fine-scale structure reliably, so imaging methods will continue to play a major role in unveiling the structure. Several efforts have been made to apply industry-style migration methods to large data sets to image small-scale structures near the base of the mantle. Migrations of P-wave and S-wave data sets reveal both large-scale reflectors and localized, intermittent reflectors, with either velocity increases or decreases (e.g., Chambers and Woodhouse, 2006a,b; Hutko et al., 2006; Kito et al., 2007a,b; Ma et al., 2007; Rost and Thomas, 2010; van der Hilst et al., 2007; Wang et al., 2006, 2008). The complexity of structure in the deep mantle is approaching that of the lithosphere, and high-resolution imaging methods will be essential for making further progress.

The S-wave observations tend to be longer wavelength than the P-wave data used to look for the discontinuity, so it is viable that a transition zone several tens of kilometers thick may explain the absence of high-frequency precritical P-wave reflections. Most areas with strong evidence for an S-wave reflector are in the high-velocity regions beneath the circum-Pacific; the primary exception is under the central Pacific, where a variable S-wave velocity discontinuity is observed in a region having large-scale low D″ shear velocities (e.g., Avants et al., 2006b; Garnero et al., 1988; Kawai and Geller, 2010a; Lay et al., 2006; Russell et al., 2001). As the tomographic resolution of large-scale structure improves, the existence of strong lateral heterogeneities within both circum-Pacific and central Pacific regions is being recognized (Bréger and Romanowicz, 1998; Bréger et al., 2001; Fisher et al., 2003; Hung et al., 2005; Sun et al., 2007a, 2009; Wysession et al., 2001), so the bimodal characterization of the discontinuity structure is overly simplified.

It remains important to determine whether there is any density increase in D″ accompanying the seismic velocity increases, as this could help to resolve whether a chemical change or phase change is involved, either of which could strongly affect the dynamics of the boundary layer (e.g., Hansen and Yuen, 1988; Kellogg, 1997; Montague et al., 1998; Sleep, 1988; Tackley, 1998). Unfortunately, wide-angle triplication observations have very limited sensitivity to density contrasts, so this is an exceedingly difficult attribute to resolve, and normal modes have limited resolution of any small, laterally varying density increases in the relatively thin D″ region (e.g., Koelemeijer et al., 2012).

1.22.5.2 Phase Change in Perovskite

As noted in **Section 1.22.1.2**, the predominant lower mantle mineral, magnesium silicate $(Mg,Fe)SiO_3$ perovskite, is stable over a huge domain of lower mantle conditions spanning a several thousand kilometer depth range. However, high-pressure experiments conducted in Japan (Murakami et al., 2004; Oganov and Ono, 2004) first demonstrated that for pressures greater than about 120 GPA, corresponding to depths in the lowermost mantle within a few hundred kilometers of the CMB, magnesium silicate perovskite at a temperature near 2500 K undergoes a transition to a new mineral structure, called postperovskite. This phase transition is widely viewed as the probable explanation for the D″ discontinuity, as it can plausibly account for salient features of the seismic observations (Bower et al., 2013; Hirose, 2006, 2007; Lay and Garnero, 2007; Lay et al., 2005; Shim, 2008).

The phase transition from perovskite to postperovskite does not involve a change of mineral composition, but the postperovskite phase is about 1–1.2% denser and has higher shear modulus than perovskite. X-ray diffraction studies of experimental samples at high pressures established the existence and the change in volume of the postperovskite phase and provided constraints on the atomic lattice for theoretical modeling of the precise crystal structure of the mineral (Caracas and Cohen, 2006; Iitaka et al., 2004; Komabayashi et al., 2008; Martin and Parise, 2008; Murakami et al., 2004, 2005; Oganov and Ono, 2004; Ono and Oganov, 2005; Stackhouse et al., 2005b; Tsuchiya et al., 2004a; Wentzcovitch et al., 2006). Molecular dynamics modeling is required to predict the crystal structure of the postperovskite phase, and the theoretical calculations provide many important physical characteristics of postperovskite. This includes the prediction of the slope of the phase boundary in pressure–temperature (P–T) space, called the Clapeyron slope. The computed Clapeyron slope for the pure Mg end-member composition, $MgSiO_3$, is about 7.5 MPa K^{-1}, a rather large positive value typical of the postperovskite structure (Hirose and Fujita, 2005; Tsuchiya et al., 2004a). Experiments suggest the slope may be as large as 11.5 MPa K^{-1} (Hirose et al., 2006; Tateno et al., 2009). The positive value indicates that the phase boundary should occur at lower pressure (shallower in the mantle) in regions that are relatively lower temperature. Large variations in the depth of the phase transition could thus result from the strong thermal heterogeneity expected to exist in the vicinity of the thermal boundary layer in the lowermost mantle (Lay et al., 2005). Experiments also indicate high electrical conductivity for postperovskite, which may enhance electromagnetic coupling across the CMB (Ohta et al., 2008b), and it has been explored whether this is detectable (Velimsky et al., 2012).

Numerical calculations (e.g., Stackhouse and Brodholt, 2007; Tsuchiya and Tsuchiya, 2006; Tsuchiya et al., 2004b) and recent laboratory experiments (e.g., Guignot et al., 2007; Murakami et al., 2007b) also predict the crystal elasticity of postperovskite for lower mantle P–T conditions, providing estimates of the seismic P-wave and S-wave velocities. The P-wave velocity changes little relative to that for perovskite as a result of competing effects of increasing shear modulus, increasing density, and decreasing bulk modulus (Wookey et al., 2005b); however, the S-wave velocity is about 0.5–2% faster than for perovskite. If the transition from perovskite to postperovskite is confirmed to occur over a small pressure (depth) range, the resulting rapid increase in S-wave velocity is expected to produce a velocity increase that can reflect shear-wave energy. This could account for the shear velocity discontinuities shown in **Figure 6** (e.g., Kawai and Tsuchiya, 2009; Lay and Garnero, 2007; Tsuchiya et al., 2004b; Wookey et al., 2005b). The theoretical models of elasticity also predict

anisotropic properties of the postperovskite crystals. These differ significantly from those for perovskite in low-temperature calculations, with increasing temperature reducing the differences but still allowing a contrast in anisotropic properties under deep mantle conditions (e.g., Merkel et al., 2006; Oganov et al., 2005; Stackhouse et al., 2005b).

Numerous studies have used stable low-pressure mineral forms such as $CaIrO_3$, $MnGeO_3$, $MgGeO_3$, $CdGeO_3$, and $CaRuO_3$ and $NaCoF_3$, $NaMgF_3$, and $NaNiF_3$ as analogs for characterizing the postperovskite transition and deformational properties under relatively accessible (for both laboratory and computations) P–T conditions (e.g., Boffa Ballaran et al., 2007; Cheng et al., 2010, 2011; Dobson et al., 2011; Hirose et al., 2005b, 2010; Hunt et al., 2009; Hustoft et al., 2008a,b; Ito et al., 2010; Kojitani et al., 2007a,b; Kubo et al., 2006, 2008; Martin et al., 2006a,b, 2007a,b; Metsue et al., 2009; Miyagi et al., 2008; Miyajima et al., 2006, 2010; Niwa et al., 2007, 2011, 2012; Runge et al., 2006; Shim et al., 2007; Stolen and Tronnes, 2007; Tateno et al., 2006, 2010; Tsuchiya and Tsuchiya, 2007; Umemoto et al., 2006; Usui et al., 2010; Walte et al., 2007; Wu et al., 2011).

The pioneering experimental and theoretical work on postperovskite was performed for the pure magnesium ($MgSiO_3$) end-member and its analogs, but effects of the presence of iron (Fe) and aluminum (Al) have now been extensively explored experimentally and theoretically (Akber-Knutson et al., 2005; Andrault et al., 2010; Caracas, 2010a; Caracas and Cohen, 2007, 2008; Catalli et al., 2010a; Grocholski et al., 2012; Hirose et al., 2008; Jackson et al., 2009; Lee et al., 2009; Mao et al., 2004, 2005, 2006a,b, 2007; Metsue and Tsuchiya, 2011; Nishio-Hamane and Yagi, 2009; Nishio-Hamane et al., 2007; Sakai et al., 2009b; Shieh et al., 2011; Shim et al., 2008, 2009; Sinmyo et al., 2006, 2008a,b, 2011; Spera et al., 2006; Stackhouse et al., 2005a, 2006a; Tateno et al., 2005, 2007; Tschauner et al., 2008; Tsuchiya and Tsuchiya, 2008; Yamanaka et al., 2012; Zhang and Ogonov, 2007; Zhang et al., 2012). It is believed that lower mantle silicates probably contain at least 10–15% iron substitution for magnesium. Initial work suggested that having iron in the postperovskite mineral should reduce the pressure of the phase transition, such that it may occur hundreds of kilometers shallower in the mantle than for an iron-free mineral (Mao et al., 2004). These results have been contested in experiments that find less pressure effect due to the inclusion of Fe (Hirose et al., 2006). Theoretical predictions of the effects of Al substitution for both Mg and Si in the crystal lattice suggest that there may be a significant depth range (a few hundred kilometers) over which perovskite and postperovskite can coexist, which would reduce any velocity discontinuity, weakening seismic wave reflections from the transition (e.g., Akber-Knutson et al., 2005; Andrault et al., 2010; Catalli et al., 2009; Tateno et al., 2005). The compositional variations complicate any connection between seismic models and specific phase change properties, and there may be kinetic effects on the deep mantle phase change that have to be accounted for as well.

Lower mantle rocks, like all rocks in the Earth, will involve an assemblage of mineral phases, with variations in crystal size and rock fabric as a result of solid-state convection. While there has been some experimental work done on real rock samples at lower mantle pressures and temperatures with the postperovskite phase being observed (Murakami et al., 2005; Shieh et al., 2006), full assessment of coexisting multiphases is still in an early stage. For example, the properties of ferropericlase (Mg,Fe)O are important, especially the partitioning coefficient of iron between perovskite and ferropericlase (e.g., Kobayashi et al., 2005; Nakajima et al., 2012). The Fe spin transitions may also influence the postperovskite phase boundary, with iron partitioning affecting the postperovskite composition (Caracas, 2010b; Hsu et al., 2012; Li, 2007; Lin et al., 2008; Mao et al., 2010; Sturhahn et al., 2005; Yamanaka et al., 2010; Yu et al., 2012).

Subducted oceanic slab material could be relatively low temperature compared to surrounding ambient mantle, and if it penetrates to the base of the mantle, it may thus preferentially undergo transition to postperovskite, resulting in a reflecting surface at the phase change within slab material, even if the boundaries of the slab are not strong reflectors. Postperovskite may exist in large patches of lower mantle material cooled by recently subducted slab material, and as this heats up over time, the material may change back to perovskite. If the pattern of heterogeneity in **Figure 4** indicates relative temperatures (rather than a compositional change), low-velocity regions should be hotter, and therefore, any postperovskite phase transition may occur at greater depth or not at all in the low-shear-velocity regions (Helmberger et al., 2005). Seismologists are seeking to establish whether the low-shear-velocity regions have any S-wave velocity discontinuity, but there is so far limited evidence for this other than under the central Pacific (e.g., Avants et al., 2006b; Lay et al., 2006; Russell et al., 2001), and that may be for a region near the margin of the low-shear-velocity province. It is interesting to note that while the volumetric shear velocity in the central Pacific is relatively low, the discontinuity, while highly variable, is not located much deeper than in circum-Pacific regions, contrary to the predicted thermal effect. Compositional effects may compete with thermal effects on the phase transition in this region (Ohta et al., 2008a).

The CMB is likely to be at a temperature too high for postperovskite to be stable, so there may be a thin basal layer with rapidly increasing temperature below regions cooled by slab material, in which the minerals transform back to perovskite (Hernlund et al., 2005; Lay et al., 2006; van der Hilst et al., 2007). A deeper velocity discontinuity with a velocity decrease should be present if this is the case, but this is seismically much more difficult to observe than a velocity increase because there is no critical angle amplification (Flores and Lay, 2005). Waveform stacking and detailed modeling are essential for the confident identification of any small velocity decreases in D″. Stacking of ScS data traversing the high-velocity region under the Cocos plate does not reveal any negative velocity discontinuity below the positive velocity increase at the top of D″, but similar stacking for data traversing the central Pacific does show a sharp decrease about 60 km above the CMB (Avants et al., 2006a,b; Lay et al., 2006). If paired velocity increases and decreases can be confidently identified, they present the opportunity to directly estimate the temperature gradient, under the assumption that the structure does involve double intersection of the phase boundary. Coupled with an assumption of thermal conductivity, one can then estimate heat flux directly (Lay et al., 2006; van der Hilst et al., 2007), although the detailed

nature of the phase boundary in the thermal gradient is important to consider (Buffett, 2007; Hernlund, 2010; Hernlund and Labrosse, 2007). The importance of thermal conductivity in D″ has prompted a substantial experimental and theoretical research effort, complicated by the difficulty of reliably measuring thermal conductivity at extreme *P*–*T* conditions, the uncertain mineralogy Fe spin state, and uncertain relative contribution from phonon and radiative conductivity (e.g., Chen et al., 2012b; Goncharov et al., 2006, 2008, 2009, 2010; Haigis et al., 2012; Hofmeister, 2008; Keppler et al., 2007, 2008; Ohta et al., 2012; Stackhouse et al., 2010).

The large positive Clapeyron slope of the postperovskite phase boundary in the presence of lateral temperature differences at the base of the convecting mantle may influence the generation of boundary layer instabilities. Warmer regions of the boundary layer will have a thinner layer of dense postperovskite mineralogy, while colder regions of the boundary layer will have a thicker layer of the denser material. This thermally induced topography on the phase boundary is like that near the 410 km olivine/wadsleyite phase transition, and in both cases, the pattern promotes flow of material across the boundary layer (as the elevated dense material sinks, it pulls down overlying material that transforms to the denser phase). Because the Clapeyron slope for the deep mantle transition is about twice that of the upper mantle transition, the effect is enhanced, and convection models that include the postperovskite transition have quite unstable lower thermal boundary layers that tend to generate vigorous deep mantle flow (e.g., Cizkova et al., 2010; Kameyama and Yuen, 2006; Matyska and Yuen, 2004, 2006; Monnereau and Yuen, 2007; Nakagawa and Tackley, 2004, 2005, 2006; Tackley et al., 2007; Tosi et al., 2010; van den Berg et al., 2010; Yuen et al., 2007). Seismological mapping of the phase boundary can thus provide a probe of the thermal and dynamic processes in the lowermost mantle.

There are indications that D″ material may be very weak and have low viscosity (e.g., Ammann et al., 2010; Nakada and Karato, 2012; Nakada et al., 2012) due to both the high-temperature boundary layer effect on viscosity and efficient diffusion within the minerals. Such a low-viscosity layer has significant effect on boundary layer deformation and instabilities that may even influence the geoid (e.g., Cadek and Fleitout, 2006; Nakagawa and Tackley, 2011; Samuel and Tosi, 2012; Tosi et al., 2009).

1.22.6 Large Low-Shear-Velocity Provinces

The two large regions of low shear velocity in the lowermost mantle located beneath the south-central Pacific and southern Africa/southern Atlantic/southern Indian Ocean regions (**Figure 4**) are particularly unusual structures. Their lateral extent is far greater than might be expected for a hot upwelling plume from a thermal boundary layer, giving rise to the label 'superplumes.' However, attaching dynamic attributes to these regions based on the sign of their velocity anomaly may be misleading. For example, the continents have comparably large-scale regions of relatively high-shear-velocity material in the lithosphere, and one could thus infer that they are cold, sinking regions, whereas the reality is that they are chemically buoyant. The deep mantle anomalies have much stronger S-wave velocity reductions than P-wave velocity reductions, which suggests that some chemical change may be involved. The uncertain thermochemical nature of these LLSVPs warrants a dynamically neutral name.

There are also smaller-scale regions with low seismic velocities in the lower mantle that may be consistent with plumes rising from the thermal boundary layer (e.g., Montelli et al., 2004; Zhao, 2004), and it remains to be determined whether these are distinct from the LLSVPs. For example, while the tomographic model of Ritsema et al. (1999) does not have a low-shear-velocity zone in the lower mantle beneath Iceland, Bijwaard and Spakman (1999) presented a P-wave velocity image with low velocity under Iceland all the way to the CMB, and Helmberger et al. (1998) found very low S-wave velocities in D″ beneath Iceland. Goes et al. (1999) found a low P-wave velocity structure beneath Europe from 660 to 2000 km depth, which they invoke as the source of small plumes in the upper mantle associated with volcanism in Europe. Smaller-scale plume or slab features that are below the current resolution of global seismic tomography, but can be resolved in regional-scale inversions (e.g., Hung et al., 2005; Wysession et al., 2001), exist in the D″ region as well. Innovative scattering analysis or array imaging may prove to be the only means by which to constrain even smaller-scale structures (e.g., Ji and Nataf, 1998; Tibuleac and Herrin, 1999; Tilmann et al., 1998). The characterization of LLSVPs is rapidly improving and more detailed than for any of the smaller-scale structures, so this section will focus on them.

1.22.6.1 Seismic Velocity Properties

The existence of the LLSVPs was first indicated by mantle shear-wave velocity tomography models (e.g., Dziewonski et al., 1993), and as discussed earlier, there is fairly good consistency among recent global models for the large-scale structure (e.g., Lekic et al., 2012). The global distribution of sources and permanent seismic stations limits the resolution of velocity gradients and total extent of the LLSVPs under Africa (**Figure 9**) and the Pacific, so deployments of portable instruments have been important for detailed differential travel time analyses and waveform modeling used to improve the resolution of LLSVP structure.

Ritsema et al. (1998b) and Ni and Helmberger (2003a,b) found that low-shear-velocity structure under southern Africa involves 3% anomalies and strong lateral gradients, both of which are more pronounced than in tomographic models. The LLSVP model they advance extends upward about 800–1200 km from the CMB, so the anomalous material is not confined to D″. Even stronger anomalies are reported in the D″ region below the southeastern Atlantic and southern Indian Ocean, with 1–10% S-wave velocity reductions increasing with depth across a 300 km thick layer (Wang and Wen, 2004, 2007a; Wen, 2001, 2006; Wen et al., 2001). Intermediate estimates of shear velocity reductions (1–7%) under the south Pacific LLSVP have been reported (e.g., Ford et al., 2006; Tanaka, 2002; To et al., 2005), and the margins and internal structure of the Pacific LLSVP have been constrained by He et al. (2006), Takeuchi et al. (2008), Tanaka et al.

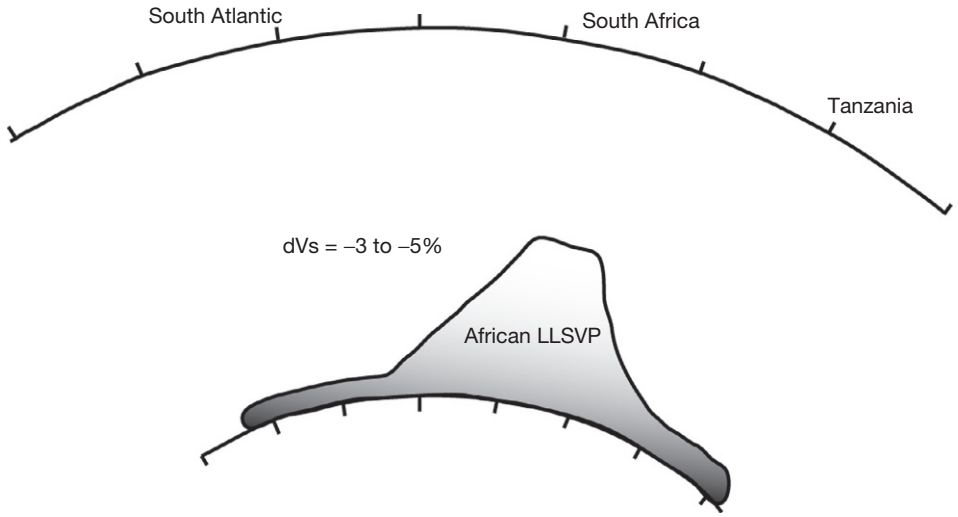

Figure 9 A cross section through the LLSVP beneath Africa and the southern Atlantic, indicating the region of anomalously low shear velocities. The tick marks are 10° increments along a great-circle arc trending from southwest (left) to northeast (right). The velocity anomaly is about −3% in the shallower part of the structure and may increase to about −5% in the D″ region. The geometry of the structure is constrained by S, ScS, and SKS raypaths from various azimuths recorded at mainly African stations. The structure has the appearance of an upswept pile that is about 4000 km wide at the base and extends 1300 km upward from the CMB. Modified from Wang Y and Wen L (2007a) Geometry and P and S velocity structures of the "African Anomaly." *Journal of Geophysical Research* 112: B05313, http://dx.doi.org/10.1029/2006JB004483.

(2009), To and Romanowicz (2009), He and Wen (2009, 2011, 2012), Koki et al. (2012), and Takeuchi (2012).

There are very strong lateral gradients in seismic velocity structure in D″ on the margins of the LLSVPs that seem incompatible with thermal variations alone, unless there is a superimposed chemical or melting effect (e.g., He and Wen, 2012; Ni et al., 2002, 2005; To et al., 2005; Wen et al., 2001). Even in the mid-mantle, the lateral gradients remain strong, which is difficult, if not impossible, to explain by simple thermal gradients (e.g., Ni et al., 2002). Given the reduction of the sensitivity of shear velocity to temperature at deep mantle pressures, lateral thermal changes of 500–1000° over ~100 km are needed to account for the observed velocity anomalies, which could lead to the onset of partial melting that can strongly reduce velocities (Lay et al., 2004b). But chemical variations appear to be important in LLSVPs, so the temperature contrasts may be far lower.

One of the key indications that LLSVPs involve chemical heterogeneity comes from comparisons of P-wave and S-wave velocities. Generally, global tomography models find good correlation between P-wave velocity and S-wave velocity structures in the lowermost mantle (e.g., Antolik et al., 2003; Houser et al., 2008; Masters et al., 2000); however, this correlation appears to break down in certain regions, such as beneath the northern Pacific, where P-wave velocity anomalies tend to be positive and S-wave velocity anomalies tend to be negative. A south-to-north decrease in the P-wave/S-wave velocity ratio has also been found using diffracted waves traversing D″ below the northern Pacific (Wysession et al., 1999). While the sampling of the lowermost mantle remains relatively poor for P waves (S-wave phases such as ScS and SKS greatly augment the deep mantle S-wave sampling), the LLSVPs do tend to have low-velocity expressions in global P-wave models. However, the relative strength of the anomalies is important to consider.

Shear velocity models show markedly stronger increases in RMS velocity heterogeneity in the lowermost 300 km of the mantle than do compressional velocity models, although the various models do differ in the extent to which shear velocity heterogeneity is concentrated toward the CMB (**Figure 5**). Even for well-correlated P-wave and S-wave velocity models (e.g., Houser et al., 2008; Masters et al., 2000), this raises the possibility of distinct behavior for P waves and S waves due to competing thermal and chemical variations, coupled with the possible presence of low degrees of partial melting (Lay et al., 2004b; Simmons and Grand, 2002). Indeed, the variability in velocity ratios and the occasional decorrelation of P-wave and S-wave anomalies provide strong evidence that thermal effects alone cannot explain all D″ seismic observations.

Simultaneous inversions of P-wave and S-wave data have been performed in attempts to isolate bulk sound velocity variations from shear velocity variations (e.g., Antolik et al., 2003; Houser et al., 2008; Kennett et al., 1998; Masters et al., 2000; Resovsky and Trampert, 2003; Robertson and Woodhouse, 1996; Su and Dziewonski, 1997; Trampert et al., 2004), but there are significant discrepancies between these models, perhaps as a consequence of incompatible resolution of P-wave and S-wave structures on a global basis. Della Mora et al. (2011) and Hernlund and Houser (2008) argued that resolution differences cannot account for the decorrelation overall. Direct comparisons of P-wave and S-wave travel time anomalies on specific paths support the possible decorrelation of these elastic velocities for localized regions within D″ (e.g., Lay et al., 2004b; Saltzer et al., 2001), as well as reaffirming the greater variations for S-wave velocities than P-wave velocities in LLSVPs (**Figure 10**; e.g., Simmons and Grand, 2002; Tkalcic and Romanowicz, 2002). The overall result is that LLSVPs have a bulk sound velocity anomaly that is anticorrelated with the S-wave velocity anomalies, and this dominates the pattern of

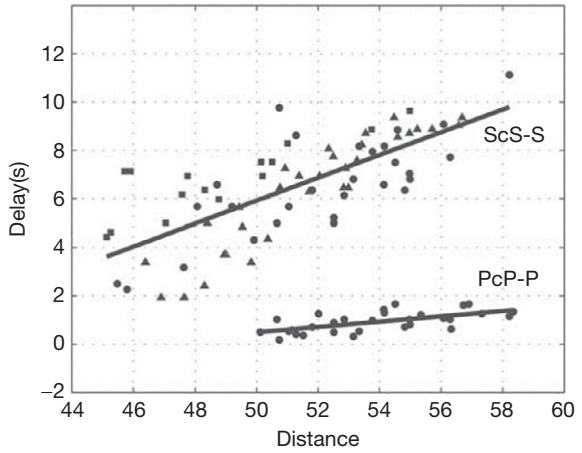

Figure 10 Differential travel times for ScS-S and PcP-P for paths sampling the southern margin of the African LLSVP. The S waves have much larger relative times, requiring shear velocity decreases 2–2.8 times stronger than the compressional velocity reductions depending on the depth extent of the anomalous region. This relative behavior is stronger than expected for a thermal variation in uniform lower mantle chemistry and requires either a compositional effect or a contribution from partial melting. Reproduced from Simmons NA and Grand SP (2002) Partial melting in the deepest mantle. *Geophysical Research Letters* 29, http://dx.doi.org/10.1029/2001GL013716.

the large-scale inversions for bulk sound velocity anomalies. This behavior requires an increase in incompressibility that contrasts with a decrease in rigidity in the LLSVPs. While this type of behavior is not necessarily unique to LLSVPs, it is generally accepted that at least part of (and possibly all of) their shear velocity anomaly is due to chemical anomaly, possibly involving enrichment in iron (Deschamps et al., 2011, 2012; Trampert et al., 2004). Some researchers have been reevaluating whether thermal effects alone dominate, using updated estimates of bulk chemistry and predicted elasticity, or whether the evidence for chemical heterogeneity in LLSVPs is truly compelling (e.g., Brodholt et al., 2007; Davies et al., 2012; Schuberth et al., 2009). This is clearly important to resolve.

There is also some indication that density heterogeneity exists at the base of the mantle based on the analysis of normal modes and that on a large scale, dominated by the two LLSVPs, it is anticorrelated with shear velocity (and, hence, positively correlated with bulk velocity models), favoring chemical heterogeneity (Ishii and Tromp, 1999; Trampert et al., 2004). Thus, LLSVPs may be denser than surrounding mantle and hence dynamically stabilized even if they are hotter than their surroundings, a situation inverse to that for continents. This remains a topic of much uncertainty (e.g., Kuo and Romanowicz, 2002; Romanowicz, 2001), and resolving the density structure is critical for assessing whether LLSVPs are buoyant or not.

1.22.6.2 Thermal–Chemical Interpretations

The very presence of the LLSVPs in the deep mantle at this stage of Earth evolution suggests that unless they are being replenished by some process, such as segregation of former oceanic crustal components, they are likely to be very long-lived and not particularly buoyant (e.g., Ni and Helmberger, 2003a). Their large vertical extent certainly could reflect some thermal buoyancy, perhaps in competition with chemical negative buoyancy, but the LLSVPs may also represent mounds of low-velocity chemical heterogeneities piled up under large-scale mantle upwellings (Garnero and McNamara, 2008; Garnero et al., 2007a; Maruyama et al., 2007; McNamara and Zhong, 2004, 2005). If the chemical anomaly in the LLSVP is primarily responsible for the sharp edges of these structures, which can be nearly vertical in the deep mantle, there are many ensuing implications. One is that it seems likely that LLSVPs will have thermal boundary layers developed along their discrete boundaries, with these boundary layers conducting heat out of (or into) the pile. If the LLSVPs are enriched in radiogenic materials, they may be relatively hot, and the enveloping thermal boundary layers might themselves become detached to rise as thermal plumes, perhaps entraining trace materials of the distinct chemistry of the LLSVP (Deschamps et al., 2012). The distinct material properties of LLSVPs associated with their chemistry (e.g., the relatively high incompressibility suggested by the Vp/Vs anomaly) have implications for the internal dynamics of the LLSVPs. High incompressibility can lead to a metastable condition for thermal upwellings that causes them to stall in the mid-mantle, producing the large mound of the LLSVP primarily by internal dynamics rather than external flow conditions (e.g., Sun et al., 2007b; Tan and Gurnis, 2005, 2007; Tan et al., 2011). Long-term oscillations of metastable plume may account for Pacific geoid anomalies (Cadio et al., 2011).

The general correlation of low-velocity regions in D″ with the surface distribution of hot spot volcanoes (e.g., Williams et al., 1998) has long been noted, but even stronger correlation is found between the margins of LLSVPs and hot spot volcanoes (Thorne et al., 2004), supporting the notion that boundary layer instabilities may shed from the edges of LLSVPs (Davaille, 1999; Jellinek and Manga, 2002), rather than the entire structure being a superplume. The present-day location of LLSVPs places their margins below many reconstructed locations of large igneous provinces produced over several hundred million years (e.g., Burke and Torsvik, 2004; Burke et al., 2008; Torsvik et al., 2006, 2008). This suggests the possibility of very long time stability of the thermochemical piles (Nebel et al., 2007) and their importance for generating boundary layer instabilities (e.g., Garnero et al., 2007a; Steinberger and Torsvik, 2012) that have affected Earth's surface profoundly throughout at least Cenozoic and Mesozoic time (Dziewonski et al., 2010). The notion that deep mantle heterogeneity, which displaces sluggishly relative to the upper mantle, may play a long-term role in surface geologic processes emphasizes the importance of resolving lower mantle structure and processes.

1.22.7 Ultralow-Velocity Zones

Another important aspect of D″ that has been inferred from seismic waveform investigations is the widespread existence of a layer from 5 to 40 km thick overlying the CMB with very strong P-wave and S-wave velocity reductions of up to −10% and −30%, respectively (see **Figure 8(b)**). Early observations of these ULVZs are summarized by Garnero et al. (1998) and Thorne and Garnero (2004). Extensive regions of ULVZ appear

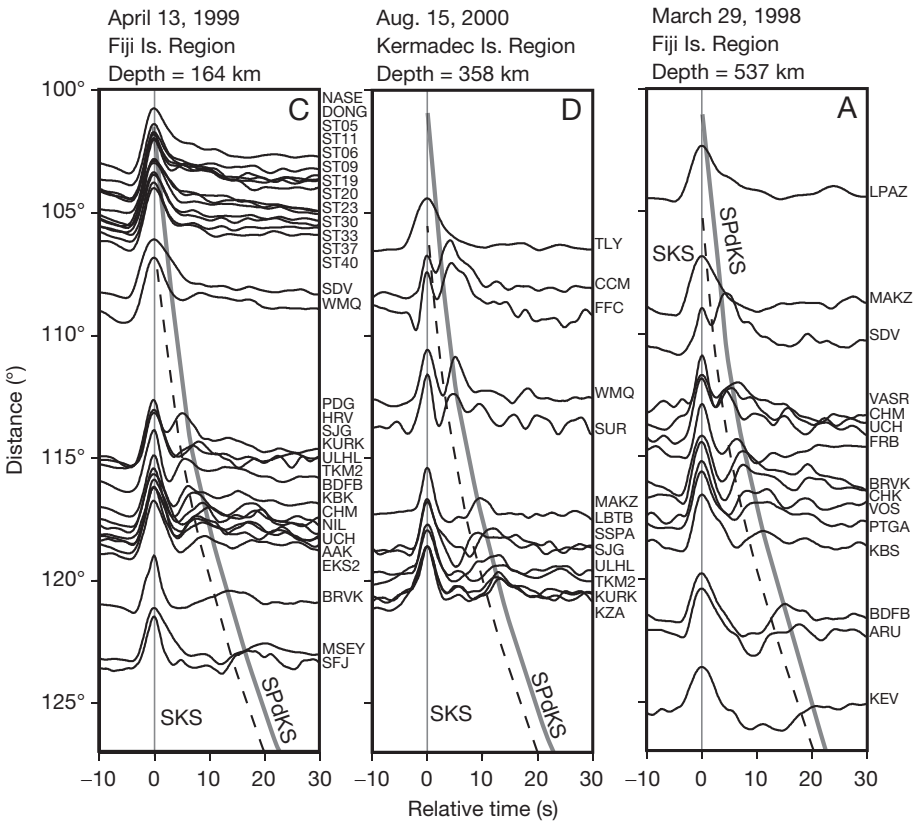

Figure 11 Waveforms with anomalously late SPdKS arrivals. The signals are aligned on SKS, with the dashed curves indicating the expected time for the peak of SPdKS based on the PREM structure. The observed arrivals are 2–3 s later than expected, which must be due to anomalously low P velocity right at the CMB where SPdKS diffracts along the boundary. Modeling indicates that about 5–10% low P velocity in a layer 5–10 km thick can match the data. This strong P velocity reduction defines the ULVZ. Courtesy of Ed Garnero.

to exist, although the actual lateral extent is uncertain because either broad horizontally stratified regions or localized three-dimensional domes and blobs may explain the data (Helmberger et al., 1998, 2000). In some cases, the ULVZ region appears to be enhanced to scales of 600–900 km lateral extent and several tens of kilometers of thickness, as under the central Pacific (Cottaar and Romanowicz, 2012) and below the region northeast of Tonga (Thorne et al., 2013). Similarly, the absence of seismically detectable ULVZ does not preclude the presence of a very thin (<5 km) layer that is not resolved by seismic probes of the CMB, and only upper bounds on thickness and velocity drop can be determined (Stutzmann et al., 2000). Nonetheless, there are regions where there is no evidence of complexity in structure right at the CMB in high-quality short-period data (e.g., Castle and van der Hilst, 2000; Persch et al., 2001) and other regions with evidence for rapid small-scale variations in ULVZ structure (e.g., Havens and Revenaugh, 2001; Rost and Revenaugh, 2003). Thus, there are certainly variations in ULVZ structure, so these structures are not globally represented by any one-dimensional model.

1.22.7.1 Seismic Phases Used for Detection

Evidence for a ULVZ at the base of the mantle was first presented by Garnero et al. (1993) and Silver and Bina (1993) based on the behavior of SKS phases that interact with the CMB. The primary evidence for the ULVZ involves delayed $SP_{diff}KS$ phases (**Figure 11**; e.g., Garnero and Helmberger, 1995, 1998; Helmberger et al., 1998; Rondenay and Fischer, 2003; Rondenay et al., 2010; Thorne et al., 2013), precursors to PcP reflections (e.g., Mori and Helmberger, 1995; Revenaugh and Meyer, 1997; Ross et al., 2004; Rost et al., 2006, 2010b), precursors to ScS reflections (**Figure 12**; Avants et al., 2006a), S-wave diffractions (Cottaar and Romanowicz, 2012; To et al., 2011), precursors/postcursors to ScP reflections (Garnero and Vidale, 1999; Idehara, 2011; Idehara et al., 2007; Reasoner and Revenaugh, 2000; Rost and Revenaugh, 2001, 2003; Rost et al., 2005, 2006, 2010a), and SKKS/SKS ratios (Zhang et al., 2009). Strong scattering of PKP and PKKP precursors has also been used to constrain ULVZ structure at the CMB (Rost and Garnero, 2006; Vidale and Hedlin, 1998; Wen, 2000; Wen and Helmberger, 1998; Xu and Koper, 2009; Zou et al., 2007). A variety of seismic wave probes of ULVZ structure are needed in order to characterize the P-wave, S-wave, and density structures, as each phase has sensitivity to more than one parameter. For some phases, there are strong trade-offs with structure on the core side of the CMB as well, with a thin layer of finite rigidity in the outermost core being an alternate possibility (e.g., Buffett et al., 2000; Garnero and Jeanloz, 2000; Rost and Revenaugh, 2001). This yields significant non-uniqueness in the models, but it does appear that the S-wave velocity reductions tend to be larger than the P-wave velocity

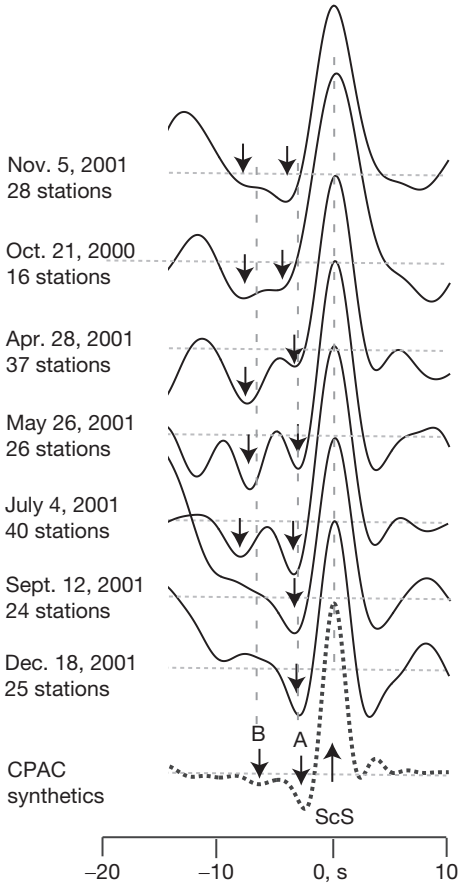

Figure 12 Stacks of the indicated number of deconvolved seismograms for several deep-focus events in the Tonga subduction zone, aligned on *ScS*, ordered by increasing event distance from California from top to bottom. Two stable negative amplitude peaks in the 10 s window before *ScS* are observed in the five closer events, with only one precursor being observed for the two more distant events. A stack of synthetics for a model CPAC with −1.1% and −3.8% discontinuities 70 and 30 km above the CMB, respectively. Direct S energy arrives 10–25 s before the windows shown. These data indicate that structure above the CMB is more complex than a single ULVZ. Reproduced from Avants M, Lay T, and Garnero EJ (2006a) A new probe of ULVZ S-wave velocity structure: Array stacking of ScS waveforms. *Geophysical Research Letters* 33: L07314, http://dx.doi.org/10.1029/2005GL024989.

reductions, and the density may increase by several to tens of percent.

1.22.7.2 Partial Melting and Chemical Anomalies

The strong velocity reductions in ULVZs are most easily explained by the presence of a melt component (Williams and Garnero, 1996), suggesting that either the mantle eutectic is exceeded at the hottest temperatures in the thermal boundary layer or there is infiltration of core material into the lowermost mantle. There is some correlation between locations of ULVZ patches and surface hot spots, which may further suggest a relationship between partial melting in D″ and large-scale upwellings (e.g., Garnero et al., 2007b; Lay et al., 2004b; Williams et al., 1998). Thermally induced rigidity variations can produce large shear velocity fluctuations relative to compressional velocities ($R = \mathrm{d}(\ln \mathrm{Vs})/\mathrm{d}(\ln \mathrm{Vp}) = 2.7$), whereas chemical variations tend to produce smaller values of $R \sim 1$–2. Partial melting can produce R-values of ~2.7–3.0 (e.g., Berryman, 2000; Williams and Garnero, 1996). The ratio of S-wave velocity anomaly to P-wave velocity anomaly in ULVZs has thus been of importance to assessing whether there is a significant chemical anomaly involved, even while partial melting appears to be the only way to approach the magnitude of the velocity decrements in ULVZs. Unfortunately, the ratio is very difficult to resolve given the many trade-offs in model parameters. Available results do favor a ratio closer to three than to one, but further analysis of P-wave velocity and S-wave velocity structure in the same spot using multiple seismic probes is needed to robustly resolve this issue. The observed ~10% P-wave velocity decrement associated with the ULVZ and the more poorly constrained ~30% S-wave velocity decrease imply melt fractions of between ~6% for 1:100 aspect ratio films of melt and ~30% for spherical melt inclusions (Berryman, 2000; Williams and Garnero, 1996).

The presence of a melt component in the ULVZ has important dynamic and chemical implications. Somehow the melt (if denser than the coexisting solids) does not simply percolate deeper to form a pure melt layer overlying the core. Alternatively, if the melt is buoyant, it would be expected either to rise to its depth of neutral buoyancy or to resolidify during adiabatic ascent (Hernlund and Jellinek, 2010; Hernlund and Tackley, 2007). This juxtaposition of solids and liquids thus implies that one of several possible effects occurs within the ULVZ: (1) the melt is not interconnected and thus is physically unable to efficiently drain from the surrounding solids; (2) the melt density closely matches that of the surrounding solids, so the buoyancy forces on the melt are insufficient to allow the melt to efficiently percolate; or (3) the average vertical convective velocity within the ULVZ is substantially greater than the velocity of melt percolation. Lay et al. (2004b) considered these scenarios, tending to favor the second or third as a means of developing a volumetrically extensive region with a melt component. Many ULVZ locations are on or within the margins of LLSVPs, suggesting some relationship to the thermal and dynamic processes in the LLSVPs. If the LLSVPs are dynamically configured by surrounding mantle flow and the ULVZs are configured by internal LLSVP dynamics, mapping of the structures provides first-order information on the location of deep mantle reservoirs (McNamara et al., 2010).

The presence of a melt component within the basal layer of the mantle is likely to have enhanced chemical interactions with the core through time and may be indicative of an enrichment of this zone in elements that are incompatible in mantle minerals near CMB pressures and temperatures. Thus, iron enrichment of D″ may have occurred through melt descent from above (e.g., Knittle, 1998), through subduction of iron-rich ancient oceanic crust (Dobson and Brodholt, 2005), or possibly through core interactions from below (e.g., Sakai et al., 2006). Recent work indicates that the core is undersaturated in Si and O, so the likelihood of significant diffusion of Fe into the mantle now appears low, and the lowermost mantle may instead be depleted in Fe (Ozawa et al., 2008). Mechanical mechanisms of core infiltration might still be plausible (e.g., Kanda and Stevenson, 2006; Otsuka and Karato, 2012). Labrosse et al. (2007) considered a model of ULVZ being

remnant of a much more extensive dense magma ocean above the CMB, which has cooled and solidified over time, concentrating partial melt into the ULVZ. Silicate melts in the deep mantle appear likely to be denser than surround material, allowing them to accumulate over time (e.g., Mosenfelder et al., 2009; Murakami and Bass, 2011; Thomas et al., 2012). The enrichment of radiogenic elements in D″ within the solidified basal magma ocean is generally consistent with a magmatic evolution for this boundary layer (Lay et al., 2004a,b): radiogenic element enrichment within the boundary layer has been suggested as a mechanism to reduce the required heat flux out of the outer core (Buffett, 2003).

A subsolidus mechanism to account for ULVZs involving postperovskite has been proposed by Mao et al. (2006a,b). Experiments indicate that postperovskite is tolerant of quite large amounts of Fe, up to 40% or higher, and that such large iron content has a dramatic effect on both S-wave and P-wave velocities. If postperovskite is stable at the hottest temperatures in the mantle at CMB pressures, this idea offers an alternative to having a dense melt component present. As noted earlier, there is large uncertainty in the absolute temperature in D″, and there is substantial uncertainty in the Clapeyron slope of the phase transition, so this possibility remains highly conjectural. Experimental measurements of sound velocities in $(Mg_{.16},Fe_{.84})O$ by Wicks et al. (2010) indicate that large uptake of Fe in magnesiowüstite results in pronounced seismic velocity reductions as well. Bower et al. (2011) proposed that iron-rich (Mg,Fe)O concentrations in localized patches account for the ULVZ. Further testing of these alternatives to partial melt fractions as an explanation for ULVZs is of high priority.

1.22.8 Lower Mantle Anisotropy

While the bulk of the lower mantle does not appear to have large-scale organized anisotropy, the D″ region has been shown to have extensive regions where shear-wave splitting occurs (see reviews by Kendall, 2000; Lay et al., 1998a,b; Moore et al., 2003; Nowacki et al., 2011). These observations have prompted increased consideration of the anisotropic crystallography of high-pressure phases likely to be present in the lower mantle along with what deformation mechanisms are likely to control the formation of fabrics (e.g., Karato, 1998; Stixrude, 1998). There remain substantial uncertainties in the nature of the anisotropy and its cause. Strong shear flows in the boundary layer may induce lattice-preferred orientation (LPO) of the anisotropic lower mantle minerals, but it is not immediately clear why this would not also hold for the overlying lower mantle. Sheared inclusions of chemical heterogeneities and pockets of partial melt may also play a role in generating the seismic anisotropy. The postperovskite phase transition may also be important. As observational and laboratory constraints improve, it is likely that modeling anisotropy in D″ will provide important constraints on the thermal and dynamic processes in the boundary layer, and impressive efforts in this direction have commenced (Walker et al., 2011).

1.22.8.1 Shear-Wave Splitting Observations

Observations of splitting for ScS phases have been made for several decades (e.g., Lay and Helmberger, 1983b; Mitchell and Helmberger, 1973; Rokosky et al., 2004), but observations of diffracted waves and wide-angle grazing S waves convincingly demonstrate that anisotropy is present in D″ (e.g., Ford et al., 2006; Garnero and Lay, 1997, 1999; Garnero et al., 2004a,b; Kendall and Silver, 1996; Lay and Young, 1991; Matzel et al., 1996; Maupin et al., 2005; Panning and Romanowicz, 2004; Ritsema, 2000; Ritsema et al., 1998a; Russell et al., 1998; Thomas and Kendall, 2002; Vinnik et al., 1989, 1995, 1998b). **Figure 8(c)** indicates the regions that have been studied in detail. All observations of D″ anisotropy are subject to uncertainties because of the limitations of the corrections for upper mantle anisotropy and the possibility of significant near-source anisotropy even for deep-focus earthquakes. Komatitsch et al. (2010) demonstrated that isotropic structure can produce apparent splitting for diffracted waves, so caution is required for diffracted data interpretations.

The large majority of observations involve horizontally polarized shear-wave components (SH) traveling faster through D″ than vertically polarized shear waves (SV) for grazing incidence or wide-angle reflections, with relatively large-scale regions of D″ displaying 0.5–1.5% anisotropy (e.g., Fouch et al., 2001; Garnero and Lay, 2003; Kendall and Silver, 1996; Ritsema, 2000; Rokosky et al., 2004; Thomas and Kendall, 2002; Thomas et al., 2007, 2011; Usui et al., 2005, 2008; Vinnik et al., 1998b; Walker et al., 2011; Wang and Wen, 2007b; Wookey and Kendall, 2008). While almost none of the studies have significant azimuthal raypath sampling, the observations are at least compatible with extensive vertical transverse isotropy, as may be caused by hexagonally symmetrical material with a vertical symmetry axis or fine-scale horizontal layering. The onset of shear-wave splitting appears to be linked to the S-wave velocity increase at the top of D″ in high-velocity regions (e.g., Garnero and Lay, 1997; Matzel et al., 1996), but the resolution of the depth extent of the anisotropy in the boundary layer remains very limited (Moore et al., 2003).

Localized observations of shear-wave splitting in D″ with SV velocities being higher than SH velocities have been reported, with localized upwellings in the boundary layer being invoked as one possible way to modify the symmetry axis for shape-preferred orientation (SPO) or LPO (e.g., Pulliam and Sen, 1998; Rokosky et al., 2004; Russell et al., 1998, 1999). Garnero et al. (2004a), Niu and Perez (2004), Maupin et al. (2005), Wookey et al. (2005a), Rokosky et al. (2006), Long (2009), and Nowacki et al. (2010) presented clear observations of azimuthal anisotropy from the analysis of S, SKS, and SKKS phases (**Figure 13**), with fast and slow waves mixed on the SH and SV components. Restivo and Helffrich (2006) did find that on the large scale, differential splitting of SKS and SKKS is relatively minor, with azimuthal anisotropy $< 2\%$ for extended regions.

1.22.8.2 Mineralogical/Dynamic Implications

Anisotropy compatible with the primary seismic observations of shear-wave splitting in D″ could be the result of LPO for a D″ mineral component or the result of SPO of chemical or partial melt components in a sheared boundary layer. A candidate major component of the lower mantle that may develop anisotropy with SH velocity faster than SV velocity in a horizontally sheared boundary layer is MgO or ferropericlase (e.g., Karato, 1998; Karki et al., 1999; Kendall, 2000; Long et al.,

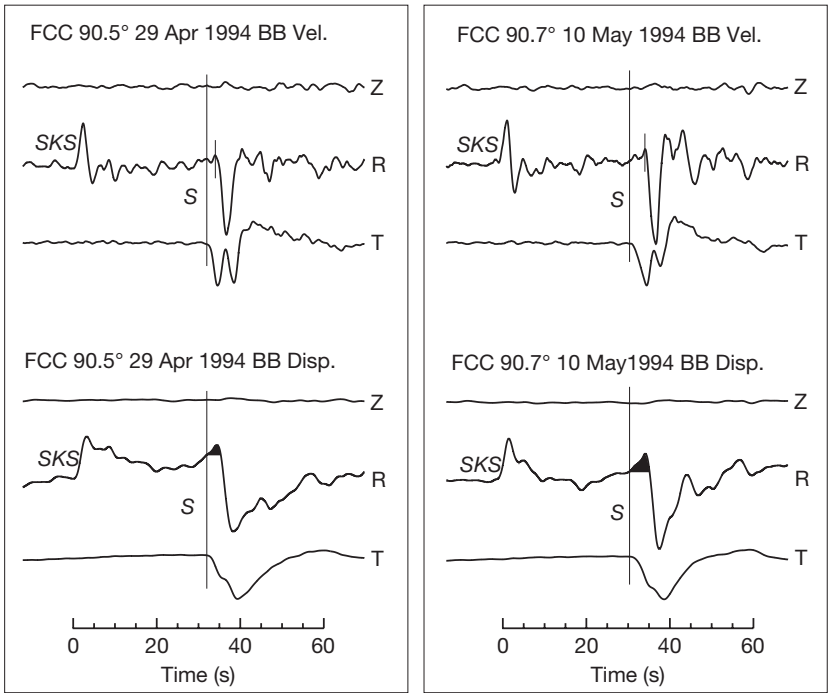

Figure 13 Three-component records from station FCC (Fort Churchill, Canada) for two deep South American earthquakes, showing ground velocity (upper plots) and ground displacement (lower plots) spanning the SKS and S arrivals. Corrections for receiver lithospheric anisotropy have been applied (note that no SKS energy is seen on the transverse component), and the Z and R rotations are to the wave front normal and wave front parallel directions for the SKS arrival, respectively. The arrival time of S is indicated by the vertical lines. The small reverse-polarity upswing at the beginning of the S wave on the radial components of the displacement seismograms is colored in black. This feature is easily missed in the velocity records, and one is tempted to pick a sharp correct-polarity negative arrival as the first SV arrival (small ticks). The reverse-polarity energy is produced by azimuthal anisotropy, either in D″ or possibly near the source, which couples the fast arrival to the R and T components. Reproduced from Maupin V, Garnero EJ, Lay T, and Fouch MJ (2005) Azimuthal anisotropy in the D″ layer beneath the Caribbean. *Journal of Geophysical Research* 110: B08301, http://dx.doi.org/10.1029/2004JB003506).

2006; Mainprice et al., 2000; Marquardt et al., 2009a; Stixrude, 1998; Yamazaki and Karato, 2002), whereas low-velocity lamellae composed of partially melted crust or other chemical heterogeneities are also possible causes of such anisotropy (e.g., Fouch et al., 2001; Kendall and Silver, 1998; Moore et al., 2003; Wysession et al., 1999). Anisotropy of perovskite has also been quantified (e.g., Mainprice et al., 2008). McNamara et al. (2001, 2002, 2003) used thermal convection models to compute variations in temperature and stress regime that might result in the localization of dislocation creep that favor LPO in some areas and diffusion-dominated deformation in others that would require SPO to account for any anisotropy. These dynamic calculations indicate that conditions favorable for mid-mantle anisotropy may exist in downwellings, but as yet, there is no clear evidence for anisotropy in the bulk of the mid-mantle (e.g., Kaneshima and Silver, 1995; Meade et al., 1995).

The anisotropic properties of postperovskite may further explain the strong association between regions with a lower mantle S-wave velocity discontinuity and regions with S-wave splitting that is stronger than observed in lower-velocity regions. Stackhouse et al. (2005b) computed the anisotropic properties of postperovskite and considered the propensity for developing LPO compatible with seismic observations. It appears that postperovskite has more favorable properties than perovskite for acquiring LPO in D″ (Nowacki et al., 2010, 2012; Wookey and Kendall, 2007). The deformation of postperovskite and analog materials also supports the notion that postperovskite may acquire anisotropic fabrics in the lowermost mantle (Carrez et al., 2007b; Merkel et al., 2006, 2007; Miyagi et al., 2010, 2011; Niwa et al., 2007, 2012; Okada et al., 2010; Walte et al., 2009; Wenk et al., 2011; Yamazaki and Karato, 2007; Yamazaki et al., 2006; Yoshino and Yamazaki, 2007; Zhan, 2011). The size of the D″ discontinuity may exceed the velocity increase for the postperovskite phase change on average, and anisotropic properties may be required to match the observations (Murakami et al., 2007b).

1.22.9 Small-Scale Heterogeneities

The emphasis in the foregoing sections has been on intermediate and large-scale structure, as this is most readily resolved by tomographic and waveform modeling procedures. However, as is true of the lithosphere, key dynamic and chemical structures exist in D″ on scales below the limit of deterministic resolution using seismic waves with wavelengths longer than 10 km or so. Very fine structure will scatter seismic energy, and statistical attributes of the structure can be constrained using various approaches.

1.22.9.1 Scattering in D″

Small-scale variations in D″, with about 1% heterogeneities on scale lengths of about 10 km, are revealed by scattered P-wave signals. This has been demonstrated by the analysis of short-period precursors to PKP phases (e.g., Bataille and Flatté, 1988; Bataille et al., 1990; Brana and Helffrich, 2004; Cao and Romanowicz, 2007; Cleary and Haddon, 1972; Cormier, 1999; Doornbos, 1976; Garcia et al., 2009; Haddon and Cleary, 1974; Hedlin and Shearer, 2000; Hedlin et al., 1997; Miller and Niu, 2008; Thomas et al., 2009) and P′P′ (Wu et al., 2012). The small-scale structure is also analyzed using diffracted coda waves (e.g., Bataille and Lund, 1996), PKKP reflections (e.g., Earle and Shearer, 1997; Rost and Earle, 2010), triplications (e.g., Kohler et al., 1997), and scatterer migrations (e.g., Thomas et al., 1999). Some studies purport to show evidence for thin layers of anomalous properties or lamellae in the boundary layer (e.g., Lay and Helmberger, 1983b; Thomas et al., 1998; Weber, 1994). The structural heterogeneities involve scale lengths of a few to tens of kilometers, with various estimates of velocity fluctuations of a few to 10%. It has generally been believed that the levels of heterogeneity increase in D″ relative to the overlying mantle, but there is evidence that small-scale structure in D″ is not distinctive from that throughout the mantle (e.g., Hedlin et al., 1997). Nonetheless, it is clear that some of the strongest scattering, involving much larger velocity heterogeneities, does arise within D″ (Vidale and Hedlin, 1998; Wen and Helmberger, 1998), and this is likely associated with the patchy ULVZ just above the CMB. The bandwidth of the signals used in scattering analyses controls the sensitivity to scatterers of different dimensions, and the analysis of broadband data indicates a rich spectrum of scattering scale lengths in D″.

Cormier (2000) had developed the perspective of D″ being a transition in the heterogeneity spectrum of the lowermost mantle, with a relatively 'red' spectrum, having substantial power at long wavelengths but still significant strength at short wavelengths. It is plausible that small-scale structure also exists on the core side of the CMB, concentrated in topographic highs (e.g., Buffett et al., 2000; Garnero and Jeanloz, 2000; Rost and Revenaugh, 2003).

1.22.9.2 Core–Mantle Boundary Topography

Given the complexity of structure at all scales in D″, it is not surprising that large uncertainty remains as to whether there is much topography on the CMB itself. Long-wavelength topography of the CMB was proposed by Creager and Jordan (1986b) and Morelli and Dziewonski (1987) based on studies of bulletin PcP and PKP arrival times, but it has been demonstrated that allowing for strong heterogeneity in D″ and the limited resolution of the available data make CMB topography models very uncertain (e.g., Doornbos and Hilton, 1989; Garcia and Souriau, 2000; Obayashi and Fukao, 1997; Pulliam and Stark, 1993; Rodgers and Wahr, 1993; Sze and van der Hilst, 2003). As models for the entire mantle improve, this may prove to be a solvable problem, and it is a critical one, for CMB topography plays a major role in estimating the extent of mechanical coupling between the core and the mantle. For imaging shorter-wavelength topography of the CMB, the primary approach has involved travel time fluctuations and precursors to underside reflections of internal core reverberations (PKKP). These phases provide an upper bound of about 100 m topography on 10 km scale lengths (e.g., Bataille and Flatté, 1988; Chang and Cleary, 1978; Doornbos, 1974, 1980; Earle and Shearer, 1997, 1998; Tanaka, 2010). Nutation data bounds very long-wavelength topography on the CMB to a few hundred meters (Defraigne et al., 1996). The calculations of topography induced by flow (e.g., Lassak et al., 2007; Yoshida, 2008; Youngs and Houseman, 2007) provide testable predictions that can be evaluated by using seismic observations (Lassak et al., 2010).

1.22.10 Conclusions

Any attempt to characterize the knowledge of the lower mantle and D″ region can only provide a snapshot of a rapidly evolving, even exploding topic. Interdisciplinary progress in mineral physics theory and experimentation, geodynamics, and geochemistry resonates with advances in seismological imaging, redefining conceptual models with remarkable rapidity. One decade's 'superplumes' become the next decade's 'superpiles,' with major shifts in perception of the roles played by seismically detected heterogeneities. This is both stimulating and unsettling, with our understanding of the mantle system acquiring more and more levels of complexity. The extensive citations provided here are intended to help the reader penetrate into the deluge of findings from multiple disciplines addressing lower mantle and D″ topics. This is an increasingly daunting task with a very distributed literature, and there is no slowing down of activity as yet.

So, what lies ahead? There continues to be great potential to make major advances in our understanding of the thermal regime in the lowermost mantle if the postperovskite phase transition is shown to be the correct explanation for the D″ discontinuity. This is because a phase transition can be calibrated in actual P–T space, greatly reducing the uncertainty in temperature estimates currently obtained by extrapolation over thousands of kilometers in depth. Parallel efforts in mineral physics and seismology can advance this topic much as they have advanced our understanding of transition zone conditions; however, it has become clear just how important the role of precise chemistry of each mineral phase is, compounded by the effects of iron spin transitions.

Increasing densification and accumulation of seismological data sets is enabling new approaches such as migration to be applied to deep mantle targets. While coverage is, and will remain, embarrassingly limited compared to exploration industry data sets, the advantage of generally parameterized migrations for rough structure has already been established and promises to reveal important structural characteristics in the lower mantle. Large data sets are also critical to one of the persistent challenges in deep Earth imaging, separating source, deep, and receiver contributions to the signals. Studies of lower mantle scattering, lower mantle anisotropy, and lower mantle stratification are all plagued by near-source and near-receiver signal-generated noise. Improved suppression of these effects by combining empirical filters and stacking approaches holds much promise for improving seismological resolution of deep structure. The large data sets enable full waveform inversion

approaches to some extent, although the problem in deep mantle applications is the severe limitation of azimuthal path sampling, so it is not clear yet whether there is any true gain to be had by waveform inversions over imaging methods. It is clear that expanding global coverage of seismic observations, particularly by increased long-term operation of ocean floor recording systems, is essential for better characterizing deep Earth structure globally. With new procedures such as noise correlation allowing deep structure to be probed between all pairs of stations (e.g., Lin et al., 2013), each new observation point provides extensive new probing of deep mantle structure below each station.

Seismological structures in the deep mantle LLSVPs have been shown to have lateral gradients as strong as radial gradients, and the search for steeply dipping interfaces using azimuthal data gathers has proved fruitful. Approaches to quantifying three-dimensional structures for poorly sampled wave fields require both efficient 3D computational tools and new strategies for modeling, and significant progress is being made in this arena. Approaches based on iterating from initial tomographic models have shown some success, but the wave field complexity often involves smaller scales than constrained by tomography. One cannot help but feel that we have still only scratched the surface of the complex regime that likely exists in the deep mantle. Much work remains.

Acknowledgment

T. Lay's research on lower mantle structure is supported by NSF Grant EAR1245717.

References

Adams DJ and Oganov AR (2006) Ab initio molecular dynamics study of $CaSiO_3$ perovskite at *P–T* conditions of Earth's lower mantle. *Physical Review B* 73: 184106.

Adams LH and Williamson ED (1923) The composition of the Earth's interior. Smithsonian Institute Annual Reports, 241–260.

Aizawa Y and Yoneda A (2006) *P–V–T* equation of state of $MgSiO_3$ perovskite and MgO periclase: Implications for lower mantle composition. *Physics of the Earth and Planetary Interiors* 155: 87–95. http://dx.doi.org/10.1016/j.pepi.2005.10.002.

Akber-Knutson S, Steinle-Neumann G, and Asimow PD (2005) Effect of Al on the sharpness of the $MgSiO_3$ perovskite to post-perovskite phase transition. *Geophysical Research Letters* 32: L14303. http://dx.doi.org/10.1029/2005GL023192.

Alexander SS and Phinney RA (1966) A study of the core–mantle boundary using P-waves diffracted by the Earth's core. *Journal of Geophysical Research* 71: 5943–5958.

Ammann MW, Brodholt JP, and Dobson DP (2011) Ferrous iron diffusion in ferro-periclase across the spin transition. *Earth and Planetary Science Letters* 302: 393–402.

Ammann MW, Brodholt JP, Wookey J, and Dobson DP (2010) First-principles constraints on diffusion in lower-mantle minerals and a weak D″ layer. *Nature* 465: 462–465. http://dx.doi.org/10.1038/nature09052.

Anderson DL (1967) The anelasticity of the mantle. *Geophysical Journal of the Royal Astronomical Society* 14: 135–164.

Anderson DL (1991) Chemical boundaries in the mantle. In: Sabadini R, Lambeck K, and Boschi E (eds.) *Glacial Isostasy, Sea-Level and Mantle Rheology*, pp. 379–401. The Netherlands: Kluwer.

Anderson DL (1998) The EDGES of the mantle. In: Gurnis M, Wysession ME, Knittle E, and Buffett BA (eds.) *The Core–Mantle Boundary Region*, pp. 255–271. Washington, DC: American Geophysical Union.

Anderson DL and Hart RS (1978) Q of the Earth. *Journal of Geophysical Research* 83: 5869–5882.

Anderson DL, Kanamori H, Hart RS, and Liu H-P (1977) The Earth as a seismic absorption band. *Science* 196: 1104–1106.

Andrault D, Bolfan-Casanova N, Bouhifd MA, Guignot N, and Kawamoto T (2007) The role of Al-defects on the equation of state of Al–$(Mg,Fe)SiO_3$ perovskite. *Earth and Planetary Science Letters* 263: 167–179.

Andrault D, Muñoz M, Bolfan-Casanova N, et al. (2010) Experimental evidence for perovskite and post-perovskite coexistence throughout the whole D″ region. *Earth and Planetary Science Letters* 293: 90–96.

Antolik M, Gu YJ, and Ekström G (2003) J362D28: A new joint model of compressional and shear velocity in the Earth's mantle. *Geophysical Journal International* 153: 443–466.

Antonangeli D, Siebert J, Aracne CM, et al. (2011) Spin crossover in ferropericlase at high pressure: A seismologically transparent transition? *Science* 331(6013): 64–67.

Auzende A-L, Badro J, Reyerson FJ, et al. (2008) Element partitioning between magnesium silicate perovskite and ferropericlase: New insights into bulk lower-mantle geochemistry. *Earth and Planetary Science Letters* 269: 164–174. http://dx.doi.org/10.1016/j.epsl.2008.02.001.

Avants M, Lay T, and Garnero EJ (2006) A new probe of ULVZ S-wave velocity structure: Array stacking of ScS waveforms. *Geophysical Research Letters* 33: L07314. http://dx.doi.org/10.1029/2005GL024989.

Avants M, Lay T, Russell SA, and Garnero EJ (2006) Shear velocity variation within the D″ region beneath the Central Pacific. *Journal of Geophysical Research* 111: B05305. http://dx.doi.org/10.1029/2004JB003270.

Badro J, Fiquet G, Guyot F, et al. (2003) Iron partitioning in Earth's mantle: Toward a deep lower mantle discontinuity. *Science* 300: 789–791.

Badro J, Rueff J-P, Vankó G, Monaco G, Fiquet G, and Guyot F (2004) Electronic transitions in perovskite: Possible nonconvecting layers in the lower mantle. *Science* 305: 383–386.

Bataille K and Flatté SM (1988) Inhomogeneities near the core–mantle boundary inferred from short-period scattered PKP-waves recorded at the global digital seismograph network. *Journal of Geophysical Research* 93: 15057–15064.

Bataille K and Lund F (1996) Strong scattering of short-period seismic waves by the core–mantle boundary and the P-diffracted wave. *Geophysical Research Letters* 18: 2413–2416.

Bataille K, Wu RS, and Flatté SM (1990) Inhomogeneities near the core–mantle boundary evidenced from scattered waves: A review. *Pure and Applied Geophysics* 132: 151–173.

Bengtson A, Li J, and Morgan D (2009) Mossbauer modeling to interpret the spin state of iron in $(Mg,Fe)SiO_3$ perovskite. *Geophysical Research Letters* 36: L15301. http://dx.doi.org/10.1029/2009GL038340.

Bengtson A, Persson K, and Morgan D (2008) Ab initio study of the composition dependence of the pressure-induced spin crossover in perovskite $(Mg_{1-x}, Fe_x)SiO_3$. *Earth and Planetary Science Letters* 265: 535–545.

Berryman JG (2000) Seismic velocity decrement ratios for regions of partial melt in the lower mantle. *Geophysical Research Letters* 27: 421–424.

Bijwaard H and Spakman W (1999) Tomographic evidence for a narrow whole mantle plume below Iceland. *Earth and Planetary Science Letters* 166: 121–126.

Bijwaard H, Spakman W, and Engdahl ER (1998) Closing the gap between regional and global travel time tomography. *Journal of Geophysical Research* 103: 30055–30078.

Boffa Ballaran T, Kurnosov A, Konstantin G, et al. (2012) Effect of chemistry on the compressibility of silicate perovskite in the lower mantle. *Earth and Planetary Science Letters* 333–334: 181–190.

Boffa Ballaran T, Trønnes RG, and Frost DJ (2007) Equations of state of $CaIrO_3$ perovskite and post-perovskite phases. *American Mineralogist* 92: 1760–1763.

Bolfan-Casanova N, Andrault D, Amiguet E, and Guignot N (2009) Equation of state and post-stishovite transformation of Al-bearing silica up to 100 GPa and 3000 K. *Physics of the Earth and Planetary Interiors* 174: 70–77.

Bolt BA, Niazi M, and Somerville MR (1970) Diffracted ScS and the shear velocity at the core boundary. *Geophysical Journal of the Royal Astronomical Society* 19: 299–305.

Bolton H (1996) Long Period Travel Times and the Structure of the Mantle. Ph.D. Thesis, University of California, San Diego, 204 pp.

Boschi L, Becker TW, and Steinberger B (2007) Mantle plumes: Dynamic models and seismic images. *Geochemistry, Geophysics, Geosystems* 8: Q10006. http://dx.doi.org/10.1029/2007GC001733.

Boschi L, Becker TW, and Steinberger B (2008) On the statistical significance of correlations between synthetic mantle plumes and tomographic models. *Physics of the Earth and Planetary Interiors* 167: 230–238.

Boschi L and Dziewonski AM (1999) High-and low-resolution images of the Earth's mantle: Implications of different approaches to tomographic modeling. *Journal of Geophysical Research* 104: 25567–25594.

Boschi L and Dziewonski AM (2000) Whole Earth tomography from delay times of P, PcP, and PKP phases: Lateral heterogeneities in the outer core or radial anisotropy in the mantle? *Journal of Geophysical Research* 105: 13675–13696.

Boulard E, Menguy N, Auzende AL, et al. (2012) Experimental investigation of the stability of Fe-rich carbonates in the lower mantle. *Journal of Geophysical Research* 117: B02208. http://dx.doi.org/10.1029/2011JB008733.

Bower DJ, Gurnis M, Jackson JM, and Sturhahn W (2009) Enhanced convection and fast plumes in the lower mantle induced by the spin transition in ferropericlase. *Geophysical Research Letters* 36: L10306. http://dx.doi.org/10.1029/2009GL037706.

Bower DJ, Gurnis M, and Sun D (2013) Dynamic origins of seismic wavespeed variation in D″. *Physics of the Earth and Planetary Interiors* 214: 74–86.

Bower DJ, Wicks JK, Gurnis M, and Jackson JM (2011) A geodynamic and mineral physics model of a solid-state ultralow-velocity zone. *Earth and Planetary Science Letters* 303: 193–202.

Boyd TM and Creager KC (1991) The geometry of Aleutian subduction: Three-dimensional seismic imaging. *Journal of Geophysical Research* 96: 2267–2291.

Brana L and Helffrich G (2004) A scattering region near the core–mantle boundary under the North Atlantic. *Geophysical Journal International* 153: 625–636. http://dx.doi.org/10.1111/j.1365-246X.2004.02306.x.

Bréger L and Romanowicz B (1998) Three-dimensional structure at the base of the mantle beneath the central Pacific. *Science* 282: 718–720.

Bréger L, Romanowicz B, and Ng C (2001) The Pacific plume as seen by S, ScS, and SKS. *Geophysical Research Letters* 28: 1859–1862.

Brodholt JP, Helffrich G, and Trampert J (2007) Chemical versus thermal heterogeneity in the lower mantle: The most likely role of anelasticity. *Earth and Planetary Science Letters* 262: 429–437. http://dx.doi.org/10.1016/j.epsl.2007.07.054.

Buffett BA (2003) The thermal state of Earth's core. *Science* 299: 1675–1677.

Buffett BA (2007) A bound on heat flow below a double crossing of the perovskite–postperovskite phase transition. *Geophysical Research Letters* 34: L17302. http://dx.doi.org/10.1029/2007GL030930.

Buffett BA, Garnero EJ, and Jeanloz R (2000) Sediments at the top of Earth's core. *Science* 290: 1338–1342.

Bull AL, McNamara AK, and Ritsema J (2009) Synthetic tomography of plume clusters and thermochemical piles. *Earth and Planetary Science Letters* 278: 152–162.

Bullen KE (1949) Compressibility-pressure hypothesis and the Earth's interior. *Monthly Notes of the Royal Astronomical Society. Geophysical Supplement* 5: 355–368.

Burdick LJ and Powell C (1980) Apparent velocity measurements for the lower mantle from a wide aperture array. *Journal of Geophysical Research* 85: 3845–3856.

Burke K, Steinberger B, Tosvik TH, and Smethurst MA (2008) Plume generation zones at the margins of large low shear velocity provinces on the core–mantle boundary. *Earth and Planetary Science Letters* 265: 49–60.

Burke K and Torsvik TH (2004) Derivation of large igneous provinces of the past 200 million years from long-term heterogeneities in the deep mantle. *Earth and Planetary Science Letters* 227: 531–538.

Cadek O and Fleitout L (2006) Effect of lateral viscosity variations in the core–mantle boundary region on predictions of the long-wavelength geoid. *Studia Geophysica et Geodaetica* 50: 217–232.

Cadio C, Panet I, Davaille A, Diament M, Métivier L, and de Viron O (2011) Pacific geoid anomalies revisited in light of thermochemical oscillating domes in the lower mantle. *Earth and Planetary Science Letters* 306: 123–135.

Cammarano F, Marquardt H, Speziale S, and Tackley PJ (2010) Role of iron–spin transition in ferropericlase on seismic interpretation: A broad thermochemical transition in the mid mantle? *Geophysical Research Letters* 37: L03308. http://dx.doi.org/10.1029/2009GL041583.

Cao A and Romanowicz B (2007) Locating scatterers in the mantle using array analysis of PKP precursors from an earthquake doublet. *Earth and Planetary Science Letters* 255: 22–31.

Caracas R (2010a) Elasticity of $AlFeO_3$ and $FeAlO_3$ perovskite and post-perovskite from first-principles calculations. *Geophysical Research Letters* 37: L20306. http://dx.doi.org/10.1029/2010GL044404.

Caracas R (2010b) Spin and structural transitions in $AlFeO_3$ and $FeAlO_3$ perovskite and post-perovskite. *Physics of the Earth and Planetary Interiors* 182: 10–17.

Caracas R and Cohen RE (2006) Theoretical determination of the Raman spectra of $MgSiO_3$ perovskite and post-perovskite at high pressure. *Geophysical Research Letters* 33: L12S05. http://dx.doi.org/10.1029/2006GL025736.

Caracas R and Cohen RE (2007) Effect of chemistry on the physical properties of perovskite and post-perovskite. In: Hirose K, et al. (eds.) *Post-Perovskite: The Last Mantle Phase Transition*. *Geophysical Monograph Series*, vol. 174, pp. 115–128. Washington, DC: AGU.

Caracas R and Cohen RE (2008) Ferrous iron in post-perovskite from first-principles calculations. *Physics of the Earth and Planetary Interiors* 168: 147–152.

Caracas R, Mainprice D, and Thomas C (2010) Is the spin transition in Fe^{2+}-bearing perovskite visible in seismology? *Geophysical Research Letters* 37: L13309. http://dx.doi.org/10.1029/2010GL043320.

Carrez P, Ferré D, and Cordier P (2007a) Implications for plastic flow in the deep mantle from modeling dislocations in $MgSiO_3$ minerals. *Nature* 446: 68–70.

Carrez P, Ferré D, and Cordier P (2007b) Peierls-Nabarro model for dislocations in $MgSiO_3$ post-perovskite calculated at 120 GPa from first principles. *Philosophical Magazine* 1–19. http://dx.doi.org/10.1080/14786430701268914.

Castle JC and Creager KC (1999) A steeply dipping discontinuity in the lower mantle beneath Izu-Bonin. *Journal of Geophysical Research* 104: 7279–7292.

Castle JC, Creager KC, Winchester JP, and van der Hilst RD (2000) Shear wave speeds at the base of the mantle. *Journal of Geophysical Research* 105: 21543–21557.

Castle JC and van der Hilst RD (2000) The core–mantle boundary under the Gulf of Alaska: No ULVZ for shear waves. *Earth and Planetary Science Letters* 176: 311–321.

Catalli K, Shim S-H, Dera P, et al. (2011) Effects of Fe^{3+} spin transition on the properties of aluminous perovskite—New insights for lower-mantle seismic heterogeneities. *Earth and Planetary Science Letters* 310: 293–302.

Catalli K, Shim S-H, and Prakapenka V (2009) Thickness and Clapeyron slope of the post-perovskite boundary. *Nature* 462: 782–785.

Catalli K, Shim S-H, Prakapenka V, Zhao J, and Sturhahn W (2010) x-Ray diffraction and Mossbauer spectroscopy of Fe^{3+}-bearing Mg-silicate post-perovskite at 128–138 GPa. *American Mineralogist* 95: 418–421.

Catalli K, Shim S-H, Prakapenka VB, et al. (2010) Spin state of ferric iron in $MgSiO_3$ perovskite and its effect on elastic properties. *Earth and Planetary Science Letters* 289: 68–75.

Chaloner J, Thomas C, and Rietbrock A (2009) P-and S-wave reflectors in D″ beneath southeast Asia. *Geophysical Journal International* 179: 1080–1092.

Chambers K and Woodhouse JH (2006a) Transient D″ discontinuity revealed by seismic migration. *Geophysical Research Letters* 33: L17312. http://dx.doi.org/10.1029/2006GL027043.

Chambers K and Woodhouse JH (2006b) Investigating the lowermost mantle using migrations of long-period S-ScS data. *Geophysical Journal International* 106: 667–678.

Chang AC and Cleary JR (1978) Precursors to PKKP. *Bulletin of the Seismological Society of America* 68: 1059–1079.

Chen Y, Chernatynskiy A, Brown D, Schelling PK, Artacho E, and Phillpot SR (2012a) Critical assessment of classical potentials for $MgSiO_3$ perovskite with application to thermal conductivity calculations. *Physics of the Earth and Planetary Interiors* 210–211: 75–89.

Chen B, Jackson JM, Sturhahn W, et al. (2012b) Spin crossover equation of state and sound velocities of $(Mg_{0.65}Fe_{0.35})O$ ferropericlase to 140 GPa. *Journal of Geophysical Research* 117: B08208.

Cheng J-G, Zhou JS, and Goodenough JB (2010) Stress-induced perovskite to postperovskite transition in $CaIrO_3$ at room temperature. *Physical Review B* 82: 132103.

Cheng J-G, Zhou JS, Goodenough JB, Sui Y, Ren Y, and Suchomel MR (2011) High-pressure synthesis and physical properties of perovskite and post-perovskite $Ca_{1-x}Sr_xIrO_3$. *Physical Review B* 83: 064401.

Chinnery MA and Toksöz MN (1967) P-wave velocities in the mantle below 700 km. *Bulletin of the Seismological Society of America* 57: 199–226.

Cizkova H, Cadek O, Matyska C, and Yuen DA (2010) Implications of post-perovskite transport properties for core–mantle dynamics. *Physics of the Earth and Planetary Interiors* 180: 235–243.

Clayton R and Comer R (1983) A tomographic analysis of mantle heterogeneities from body wave travel time data (abstract). *Eos, Transactions of the American Geophysical Union* 64: 776.

Cleary JR and Haddon RAW (1972) Seismic wave scattering near the core–mantle boundary: A new interpretation of precursors to PKP. *Nature* 240: 549–551.

Cobden L, Goes S, Ravenna M, et al. (2009) Thermochemical interpretation of 1-D seismic data for the lower mantle: The significance of nonadiabatic thermal gradients and compositional heterogeneity. *Journal of Geophysical Research* 114: B11309. http://dx.doi.org/10.1029/2008JB006262.

Cobden L, Mosca I, Trampert J, and Ritsema J (2012) On the likelihood of post-perovskite near the core–mantle boundary: A statistical interpretation of seismic observations. *Physics of the Earth and Planetary Interiors* 201–211: 21–35.

Cordier P, Ungár T, Zsoldos L, and Tichy G (2004) Dislocation creep in $MgSiO_3$ perovskites at conditions of Earth's uppermost lower mantle. *Nature* 428: 837–840. http://dx.doi.org/10.1038/nature02472.

Cormier VF (1985) Some problems with S, SKS, and ScS observations and implications for the structure of the base of the mantle and the outer core. *Journal of Geophysics* 57: 14–22.

Cormier VF (1999) Anisotropy of heterogeneity scale lengths in the lower mantle from PKIKP precursors. *Geophysical Journal International* 136: 373–384.
Cormier VF (2000) D″ as a transition in the heterogeneity spectrum of the lowermost mantle. *Journal of Geophysical Research* 105: 16193–16205.
Cottaar S and Romanowicz B (2012) An unusually large ULVZ at the base of the mantle near Hawaii. *Earth and Planetary Science Letters* 355–356: 213–222.
Courtier AM, Bagley B, and Revanaugh J (2007) Whole mantle discontinuity structure beneath Hawaii. *Geophysical Research Letters* 34: L17304. http://dx.doi.org/10.1029/2007GL031006.
Courtier AM and Revenaugh J (2008) Slabs and shear wave reflectors in the midmantle. *Journal of Geophysical Research* 113: B08312. http://dx.doi.org/10.1029/2007JB005261.
Creager KC and Jordan TH (1984) Slab penetration into the lower mantle. *Journal of Geophysical Research* 89: 3031–3049.
Creager KC and Jordan TH (1986a) Slab penetration into the lower mantle beneath the Mariana and other island arcs of the northwest Pacific. *Journal of Geophysical Research* 91: 3573–3589.
Creager KC and Jordan TH (1986b) Aspherical structure of the core–mantle boundary from PKP traveltimes. *Geophysical Research Letters* 13: 1497–1500.
Crowhurst J, Brown J, Goncharov A, and Jacobsen S (2008) Elasticity of (Mg,Fe)O through the spin transition of iron in the lower mantle. *Science* 319: 451–453. http://dx.doi.org/10.1126/science.1149606.
Datt R and Muirhead KJ (1976) Evidence for a sharp velocity increase near 770 km depth. *Physics of the Earth and Planetary Interiors* 13: 37–46.
Davaille A (1999) Simultaneous generation of hotspots and superswells by convection in a heterogeneous planetary mantle. *Nature* 402: 756–760.
Davies G (1984) Geophysical and isotopic constraints on mantle convection: An interim synthesis. *Journal of Geophysical Research* 89: 6017–6040.
Davies DR, Goes S, Davies JH, Schuberth BSA, Bunge H-P, and Ritsema J (2012) Reconciling dynamic and seismic models of Earth's lower mantle: The dominant role of thermal heterogeneity. *Earth and Planetary Science Letters* 353–354: 253–269.
Davies G and Gurnis M (1986) Interaction of mantle dregs with convection: Lateral heterogeneity at the core–mantle boundary. *Geophysical Research Letters* 13: 1517–1520.
de Koker N (2010) Thermal conductivity of MgO periclase at high pressure: Implications for the D″ region. *Earth and Planetary Science Letters* 292: 392–398.
de Koker N, Karki BB, and Stixrude L (2013) Thermodynamics of the MgO–SiO_2 liquid system in Earth's lowermost mantle from first principles. *Earth and Planetary Science Letters* 361: 58–63.
de Koker N and Stixrude L (2009) Self-consistent thermodynamic description of silicate liquids with application to shock melting of MgO periclase and $MgSiO_3$ perovskite. *Geophysical Journal International* 178: 162–179.
Deal MM and Nolet G (1999) Slab temperature and thickness from seismic tomography 2. Izu-Bonin, Japan, and Kuril subduction zones. *Journal of Geophysical Research* 104: 28803–28812.
Deal MM, Nolet G, and van der Hilst RD (1999) Slab temperature and thickness from seismic tomography. 1. Method and application to Tonga. *Journal of Geophysical Research* 104: 28789–28802.
Defraigne P, Dehant V, and Wahr J (1996) Internal loading of an inhomogeneous compressible earth with phase boundaries. *Geophysical Journal International* 125: 173–192.
Della Mora S, Boschi L, Tackley PJ, Nakagawa T, and Giardini D (2011) Low seismic resolution cannot explain S/P decorrelation in the lower mantle. *Geophysical Research Letters* 38: L12303. http://dx.doi.org/10.1029/2011GL047559.
Deng L, Gong Z, and Fei Y (2008) Direct shock wave loading of $MgSiO_3$ perovskite to lower mantle conditions and its equation of state. *Physics of the Earth and Planetary Interiors* 170: 210–214.
Deschamps F, Cobden L, and Tackley PJ (2012) The primitive nature of large low shear-wave velocity provinces. *Earth and Planetary Science Letters* 349–350: 198–208.
Deschamps F, Kaminski E, and Tackley PJ (2011) A deep mantle origin for the primitive signature of ocean island basalt. *Nature Geoscience* 4: 879–882.
Deschamps F and Tackley PJ (2008) Searching for models of thermo-chemical convection that explain probabilistic tomography. I. Principles and influence of rheological parameters. *Physics of the Earth and Planetary Interiors* 171: 357–373.
Deschamps F and Trampert J (2003) Mantle tomography and its relation to temperature and composition. *Physics of the Earth and Planetary Interiors* 140: 272–291.
Ding X-Y and Grand SP (1994) Seismic structure of the deep Kurile subduction zone. *Journal of Geophysical Research* 99: 23767–23786.
Ding X and Helmberger DV (1997) Modeling D″ structure beneath Central America with broadband seismic data. *Physics of the Earth and Planetary Interiors* 101: 245–270.
Dobson DP and Brodholt JP (2005) Subducted banded iron formations as a source of ultralow-velocity zones at the core–mantle boundary. *Nature* 434: 371–374.
Dobson DP, Hunt SA, Lindsay-Scott A, and Wood IG (2011) Towards better analogues for $MgSiO_3$ post-perovskite: $NaCoF_3$ and $NaNiF_3$, two new recoverable fluoride post-perovskites. *Physics of the Earth and Planetary Interiors* 189: 171–175.
Doornbos DJ (1974) Seismic wave scattering near caustics: Observations of PKKP precursors. *Nature* 247: 352–353.
Doornbos DJ (1976) Characteristics of lower mantle inhomogeneities from scattered waves. *Geophysical Journal of the Royal Astronomical Society* 44: 447–470.
Doornbos DJ (1980) The effect of a rough core–mantle boundary on PKKP. *Physics of the Earth and Planetary Interiors* 21: 351–358.
Doornbos DJ and Hilton T (1989) Models of the core–mantle boundary and the travel times of internally reflected core phases. *Journal of Geophysical Research* 94: 15741–15751.
Doornbos DJ and Mondt JC (1979) P and S-waves diffracted around the core and the velocity structure at the base of the mantle. *Geophysical Journal of the Royal Astronomical Society* 57: 381–395.
Doornbos DJ, Spiliopoulos S, and Stacey FD (1986) Seismological properties of D″ and the structure of a thermal boundary layer. *Physics of the Earth and Planetary Interiors* 41: 225–239.
Dorfman SM, Shieh SR, Meng Y, Prakapenka VB, and Duffy TS (2012) Synthesis and equation of state of perovskites in the $(Mg,Fe)_3Al_2Si_3O_{12}$ system to 177 GPa. *Earth and Planetary Science Letters* 357–358: 194–202.
Dziewonski AM (1984) Mapping the lower mantle: Determination of lateral heterogeneity in P velocity up to degree and order 6. *Journal of Geophysical Research* 89: 5929–5942.
Dziewonski AM and Anderson DL (1981) Preliminary reference Earth model. *Physics of the Earth and Planetary Interiors* 25: 297–356.
Dziewonski AM, Ekström G, and Liu X-F (1996) Structure at the top and bottom of the mantle. In: Husebye ES and Dainty AM (eds.) *Monitoring a Comprehensive Test Ban Treaty*, pp. 521–550. The Netherlands: Kluwer.
Dziewonski AM, Forte AM, Su W-J, and Woodward RL (1993) Seismic tomography and geodynamics. In: Aki K and Dmowska R (eds.) *Relating Geophysical Structures and Processes: The Jeffreys Volume*, pp. 67–105. Washington, DC: American Geophysical Union.
Dziewonski AM, Hager BH, and O'Connell RJ (1977) Large scale heterogeneity in the lower mantle. *Journal of Geophysical Research* 82: 239–255.
Dziewonski AM, Hales AL, and Lapwood ER (1975) Parametrically simple Earth models consistent with geophysical data. *Physics of the Earth and Planetary Interiors* 10: 12–48.
Dziewonski AM, Lekic V, and Romanowicz BA (2010) Mantle anchor structure: An argument for bottom up tectonics. *Earth and Planetary Science Letters* 299: 69–79. http://dx.doi.org/10.1016/j.epsl.2010.08.013.
Earle PS and Shearer PM (1997) Observations of PKKP precursors used to estimate small-scale topography on the core–mantle boundary. *Science* 277: 677–680.
Earle PS and Shearer PM (1998) Observations of high-frequency scattered energy associated with the core phase PKKP. *Geophysical Research Letters* 25: 405–408.
Emery V, Maupin V, and Nataf H-C (1999) Scattering of S-waves diffracted at the core–mantle boundary; forward modeling. *Geophysical Journal International* 139: 325–344.
Fang C and Ahuja R (2008) Local structure and electronic-spin transition of Fe-bearing $MgSiO_3$ perovskite under conditions of the Earth's lower mantle. *Physics of the Earth and Planetary Interiors* 16: 77–82.
Fei Y, Zhang L, Corgne A, et al. (2007) Spin transition and equations of state of (Mg,Fe)O solid solutions. *Geophysical Research Letters* 34: L17307. http://dx.doi.org/10.1029/2007GL030712.
Ferré D, Carrez P, and Cordier P (2007) First principles determination of dislocations properties of $MgSiO_3$ perovskite at 30 GPa based on the Peierls-Nabarro model. *Physics of the Earth and Planetary Interiors* 163: 283–291.
Fiquet G, Auzende AL, Siebert J, et al. (2010) Melting of peridotite to 140 Gigapascals. *Science* 329: 1516–1518.
Fiquet G, Dewaele A, Andrault D, Kunz M, and Le Bihan T (2000) Thermoelastic properties and crystal structure of $MgSiO_3$ perovskite at lower mantle pressure and temperature conditions. *Geophysical Research Letters* 27: 21–24.
Fischer KM, Creager KC, and Jordan TH (1991) Mapping the Tonga slab. *Journal of Geophysical Research* 96: 14403–14427.
Fischer KM, Jordan TH, and Creager KC (1988) Seismic constraints on the morphology of deep slabs. *Journal of Geophysical Research* 93: 4773–4783.
Fisher JL, Wysession ME, and Fischer KM (2003) Small-scale lateral variations in D″ attenuation and velocity structure. *Geophysical Research Letters* 30. http://dx.doi.org/10.1029/2002GL016179.
Flores C and Lay T (2005) The trouble with seeing double. *Geophysical Research Letters* 32: L24305. http://dx.doi.org/10.1029/2005GL024366.
Ford SR, Garnero EJ, and McNamara AK (2006) A strong lateral shear velocity gradient and anisotropy heterogeneity in the lowermost mantle beneath the southern Pacific.

Journal of Geophysical Research 111: B03306. http://dx.doi.org/10.1029/2004JB003574.

Ford SR, Garnero EJ, and Thorne MS (2012) Differential t* measurements via instantaneous frequency matching: Observations of lower mantle shear attenuation heterogeneity beneath western Central America. *Geophysical Journal International* 189: 513–523. http://dx.doi.org/10.1111/j.1365-246X.2011.05348.x.

Forte AM and Mitrovica JX (2001) Deep-mantle high-viscosity flow and thermochemical structure inferred from seismic and geodynamic data. *Nature* 410: 1049–1056.

Forte AM, Peltier WR, Dziewonski AM, and Woodward RL (1993) Dynamic surface topography: A new interpretation based upon mantle flow models derived from seismic tomography. *Geophysical Research Letters* 20: 225–228.

Forte AM, Woodward RL, and Dziewonski AM (1994) Joint inversions of seismic and geodynamic data for models of three-dimensional mantle heterogeneity. *Journal of Geophysical Research* 99: 21857–21877.

Fouch MJ, Fischer KM, and Wysession ME (2001) Lowermost mantle anisotropy beneath the Pacific: Imaging the source of the Hawaiian plume. *Earth and Planetary Science Letters* 190: 167–180.

Freybourger M, Krüger F, and Achauer U (1999) A 22° long seismic profile for the study of the top of D″. *Geophysical Research Letters* 26: 3409–3412.

Frost DJ, Liebske C, Langenhorst F, McCammon CA, Trannes RG, and Rubie DC (2004) Experimental evidence for the existence of iron-rich metal in the Earth's lower mantle. *Nature* 428: 409–412.

Fuji N, Kawai K, and Geller RJ (2010) A methodology for inversion of broadband seismic waveforms for elastic and anelastic structure and its application to the mantle transition zone beneath the Northwestern Pacific. *Physics of the Earth and Planetary Interiors* 180: 118–137.

Fujino K, Nishio-Hamane D, Seto Y, et al. (2012) Spin transition of ferric iron in Al-bearing Mg-perovskite up to 200 GPa and its implication for the lower mantle. *Earth and Planetary Science Letters* 317–318: 407–412.

Fukao Y, Obayashi M, Inoue H, and Nenbai M (1992) Subducting slabs stagnant in the mantle transition zone. *Journal of Geophysical Research* 97: 4809–4822.

Fukao Y, Widiyantori S, and Obayashi M (2001) Stagnant slabs in the upper and lower mantle transition region. *Reviews of Geophysics* 39: 291–323.

Fukui H, Tsuchiya T, and Baron AQR (2012) Lattice dynamics calculations for ferropericlase with internally consistent LDA+U method. *Journal of Geophysical Research* 117: B12202. http://dx.doi.org/10.1029/2012JB009591.

Gaherty JB and Lay T (1992) Investigation of laterally heterogeneous shear velocity structure in D″ beneath Eurasia. *Journal of Geophysical Research* 97: 417–435.

Gaherty JB, Lay T, and Vidale JE (1991) Investigation of deep slab structure using long period S-waves. *Journal of Geophysical Research* 96: 16349–16367.

Garcia RF, Chevrot S, and Calvet M (2009) Statistical study of seismic heterogeneities at the base of the mantle from PKP differential traveltimes. *Geophysical Journal International* 179: 1607–1616.

Garcia R and Souriau A (2000) Amplitude of the core–mantle boundary topography estimated by stochastic analysis of core phases. *Physics of the Earth and Planetary Interiors* 117: 345–359.

Garnero EJ (2000) Heterogeneity of the lowermost mantle. *Annual Reviews of the Earth and Planetary Sciences* 28: 509–537.

Garnero EJ, Grand SP, and Helmberger DV (1993) Low P-wave velocity at the base of the mantle. *Geophysical Research Letters* 20: 1843–1846.

Garnero EJ and Helmberger DV (1995) A very slow basal layer underlying large-scale low velocity anomalies in the lower mantle beneath the Pacific: Evidence from core phases. *Physics of the Earth and Planetary Interiors* 91: 161–176.

Garnero EJ and Helmberger DV (1998) Further structural constraints and uncertainties of a thin laterally varying ultralow-velocity layer at the base of the mantle. *Journal of Geophysical Research* 103: 12495–12509.

Garnero EJ, Helmberger DV, and Engen G (1988) Lateral variation near the core–mantle boundary. *Geophysical Research Letters* 20: 1843–1846.

Garnero EJ and Jeanloz R (2000) Fuzzy patches on the Earth's core–mantle boundary. *Geophysical Research Letters* 27: 2777–2780.

Garnero EJ and Lay T (1997) Lateral variations in the lowermost mantle shear wave anisotropy beneath the north Pacific and Alaska. *Journal of Geophysical Research* 102: 8121–8135.

Garnero EJ and Lay T (1999) Effects of D″ anisotropy on seismic velocity models of the outermost core. *Geophysical Research Letters* 25: 2341–2344.

Garnero EJ and Lay T (2003) D″ shear velocity heterogeneity, anisotropy and discontinuity structure beneath the Caribbean and Central America. *Physics of the Earth and Planetary Interiors* 140: 219–242.

Garnero EJ, Lay T, and McNamara AK (2007) Implications of lower-mantle structural heterogeneity for existence and nature of whole-mantle plumes. In: Foulger GR and Jurdy DM (eds.) *Plates, Plumes, and Planetary Processes*, pp. 79–109. Geological Society of America, Geological Society of America Special Paper 430, 2007.

Garnero EJ, Maupin V, Lay T, and Fouch MJ (2004) Variable azimuthal anisotropy in Earth's lowermost mantle. *Science* 306: 259–261.

Garnero EJ and McNamara AK (2008) Structure and dynamics of Earth's lower mantle. *Science* 320: 626–628.

Garnero EJ, McNamara A, Thorne M, and Rost S (2007) Fine-scale ultra-low velocity zone layering at the core–mantle boundary and superplumes. In: Yuen DA, et al. (eds.) *Superplumes: Beyond Plate Tectonics*, pp. 139–158. New York: Springer.

Garnero EJ, Moore MM, Lay T, and Fouch MJ (2004) Isotropy or weak vertical transverse isotropy in D″ beneath the Atlantic Ocean. *Journal of Geophysical Research* 109: B08308. http://dx.doi.org/10.1029/2004JB003004.

Garnero EJ, Revenaugh JS, Williams Q, Lay T, and Kellogg LH (1998) Ultralow velocity zone at the core–mantle boundary. In: Gurnis M, Wysession ME, Knittle E, and Buffett BA (eds.) *The Core–Mantle Boundary Region*, pp. 319–334. Washington, DC: American Geophysical Union.

Garnero EJ and Vidale JE (1999) ScP: A probe of ultralow velocity zones at the base of the mantle. *Geophysical Research Letters* 26: 377–380.

Gilbert F and Dziewonski AM (1975) An application of normal mode theory to the retrieval of structural parameters and source mechanisms from seismic spectra. *Philosophical Transactions of the Royal Society of London, Series A* 278: 187–269.

Glatzmaier GA, Coe RS, Hongre L, and Roberts PH (1999) The role of the Earth's mantle in controlling the frequency of geomagnetic reversals. *Nature* 401: 885–890.

Gleason AE, Marquardt H, Chen B, Speziale S, Wu J, and Jeanloz R (2011) Anomalous sound velocities in polycrystalline MgO under non-hydrostatic compression. *Geophysical Research Letters* 38: L03304. http://dx.doi.org/10.1029/2010GL045860.

Glisovic P, Forte AM, and Moucha R (2012) Time-dependent convection models of mantle thermal structure constrained by seismic tomography and geodynamics: Implications for mantle plume dynamics and CMB heat flux. *Geophysical Journal International* 190: 785–815.

Goarant F, Guyot F, Peyronneau J, and Poirier J-P (1992) High pressure and high temperature reactions between silicates and liquid iron alloys in the diamond anvil cell, studied by analytical electron microscopy. *Journal of Geophysical Research* 97: 4477–4487.

Goes S, Spakman W, and Bijwaard H (1999) A lower mantle source for Central European volcanism. *Science* 286: 1928–1931.

Goncharov AF, Beck P, Struzhkin VV, Haugen BD, and Jacobsen SD (2009) Thermal conductivity of lower-mantle minerals. *Physics of the Earth and Planetary Interiors* 174: 24–32.

Goncharov AF, Haugen BD, Struzhkin VV, Beck P, and Jacobsen SD (2008) Radiative conductivity in the Earth's lower mantle. *Nature* 456: 231–234. http://dx.doi.org/10.1038/nature07412.

Goncharov AF, Struzhkin VV, and Jacobsen SD (2006) Reduced radiative conductivity of low-spin (Mg,Fe)O in the lower mantle. *Science* 312(5777): 1205–1208.

Goncharov AF, Struzhkin VV, Montoya JA, et al. (2010) Effect of composition, structure and spin state on the thermal conductivity of the Earth's lower mantle. *Physics of the Earth and Planetary Interiors* 180: 148–153.

Gong Z, Fei Y, Dai F, Zhang L, and Jing F (2004) Equation of state and phase stability of mantle perovskite up to 140 GPa shock pressure and its geophysical implications. *Geophysical Research Letters* 31: L04614. http://dx.doi.org/10.1029/2003GL019132.

Grand SP (2002) Mantle shear-wave tomography and the fate of subducted slabs. *Philosophical Transactions of the Royal Society of London, Series A* 360: 2475–2491.

Grand SP, van der Hilst RD, and Widiyantoro S (1997) Global seismic tomography: A snapshot of convection in the Earth. *Geological Society of America Today* 7: 1–7.

Green DH and Falloon TJ (1998) Pyrolite: A Ringwood concept and its current expression. In: Jackson I (ed.) *The Earth's Mantle*, pp. 311–378. Cambridge: Cambridge University Press.

Grocholski B, Catalli K, Shim S-H, and Prakapenka V (2012) Mineralogical effects on the detectability of the postperovskite boundary. *Proceedings of the National Academy of Sciences of the United States of America* 109: 2275–2279.

Grocholski B, Shim S-H, Sturhahn W, Zhao J, Xiao Y, and Chow PC (2009) Spin and valence states of iron in $(Mg_{0.8}Fe_{0.2})SiO_3$ perovskite. *Geophysical Research Letters* 36: L24303.

Gu YJ, Dziewonski AM, Su W, and Ekström G (2001) Models of the mantle shear velocity and discontinuities in the pattern of lateral heterogeneities. *Journal of Geophysical Research* 106: 11169–11199.

Gubbins D, Willis AP, and Sreenivasan B (2007) Correlation of Earth's magnetic field with lower mantle thermal and seismic structure. *Physics of the Earth and Planetary Interiors* 162: 256–260.

Guignot N, Andrault D, Morard G, Bolfan-Casanova N, and Mezouar M (2007) Thermoelastic properties of post-perovskite phase $MgSiO_3$ determined

experimentally at core–mantle boundary *P–T* conditions. *Earth and Planetary Science Letters* 256: 162–168.
Haddon RA and Buchbinder GGR (1986) Wave propagation effects and the Earth's structure in the lower mantle. *Geophysical Research Letters* 13: 1489–1492.
Haddon RA and Cleary JR (1974) Evidence for scattering of seismic PKP-waves near the core–mantle boundary. *Physics of the Earth and Planetary Interiors* 8: 211–234.
Hager B (1984) Subducted slabs and the geoid: Constraints on mantle rheology and flow. *Journal of Geophysical Research* 89: 6003–6015.
Hager B and Clayton RW (1989) Constraints on the structure of mantle convection using seismic observations, flow models, and the geoid. In: Peltier WR (ed.) *Mantle Convection: Plate Tectonics and Global Dynamics*, pp. 657–763. Newark, NJ: Gordon and Breach.
Hager B, Clayton RW, Richards MA, Comer RP, and Dziewonski AM (1985) Lower mantle heterogeneity, dynamic topography and the geoid. *Nature* 313: 541–545.
Hager B and Richards MA (1989) Long-wavelength variations in the Earth's geoid: Physical models and dynamical implications. *Philosophical Transactions of the Royal Society of London, Series A* 328: 309–327.
Haigis V, Salanne M, and Jahn S (2012) Thermal conductivity of MgO, $MgSiO_3$ perovskite and post-perovskite in the Earth's deep mantle. *Earth and Planetary Science Letters* 355–356: 102–108.
Hales AL, Cleary JR, and Roberts JL (1968) Velocity distribution in the lower mantle. *Bulletin of the Seismological Society of America* 58: 1975–1989.
Hales AL and Roberts JL (1970) Shear velocities in the lower mantle and the radius of the core. *Bulletin of the Seismological Society of America* 60: 1427–1436.
Hansen U and Yuen DA (1988) Numerical simulations of thermal-chemical instabilities at the core–mantle boundary. *Nature* 334: 237–240.
Havens E and Revenaugh J (2001) A broadband study of the lowermost mantle beneath Mexico: Constraints on ultralow velocity zone elasticity and density. *Journal of Geophysical Research* 106: 30809–30820.
Hayden LA and Watson EB (2007) A diffusion mechanism for core–mantle interaction. *Nature* 450: 709–711.
He Y, Levander A, and Niu F (2010) A localized waveform inversion at teleseismic distances: An application to the D″ region beneath the Cocos plate. *Geophysical Journal International* 180: 1344–1352. http://dx.doi.org/10.1111/j.1365-246X.2009.04489.x.
He Y and Wen L (2009) Structural features and shear-velocity structure of the "Pacific Anomaly." *Journal of Geophysical Research* 114: B02309. http://dx.doi.org/10.1029/2008JB005814.
He Y and Wen L (2011) Seismic velocity structure and detailed features of the D″ discontinuity near the core–mantle boundary beneath eastern Eurasia. *Physics of the Earth and Planetary Interiors* 189: 176–184.
He Y and Wen L (2012) Geographic boundary of the "Pacific Anomaly" and its geometry and transitional structure in the north. *Journal of Geophysical Research* 117: B09308. http://dx.doi.org/10.1029/2012JB009436.
He Y, Wen L, and Zheng T (2006) Geographic boundary and shear wave velocity structure of the "Pacific anomaly" near the core–mantle boundary beneath western Pacific. *Earth and Planetary Science Letters* 244: 302–314.
Hedlin MAH and Shearer PM (2000) An analysis of large-scale variations in small-scale mantle heterogeneity using Global Seismographic Network recordings of precursors to PKP. *Journal of Geophysical Research* 105: 13655–13673.
Hedlin MAH, Shearer PM, and Earle PS (1997) Seismic evidence for small-scale heterogeneity throughout the Earth's mantle. *Nature* 387: 145–150.
Helmberger DV, Lay T, Ni S, and Gurnis M (2005) Deep mantle structure and the postperovskite phase transition. *Proceedings of the National Academy of Sciences of the United States of America* 102: 17257–17263. http://dx.doi.org/10.1073/pnas.0502504102.
Helmberger DV, Ni S, Wen L, and Ritsema J (2000) Seismic evidence for ultra-low velocity zones beneath Africa and eastern Atlantic. *Journal of Geophysical Research* 105: 23865–23878.
Helmberger DV, Wen L, and Ding X (1998) Seismic evidence that the source of the Iceland hotspot lies at the core–mantle boundary. *Nature* 396: 251–255.
Hernlund JW (2010) On the interaction of the geotherm with a post-perovskite phase transition in the deep mantle. *Physics of the Earth and Planetary Interiors* 180: 222–234.
Hernlund JW and Houser C (2008) On the statistical distribution of seismic velocities in Earth's deep mantle. *Earth and Planetary Science Letters* 265: 423–437.
Hernlund JW and Jellinek AM (2010) Dynamics and structure of a stirred partially molten ultralow-velocity zone. *Earth and Planetary Science Letters* 296: 1–8.
Hernlund JW and Labrosse S (2007) Geophysically consistent values of the perovskite to post-perovskite transition Clapeyron slope. *Geophysical Research Letters* 34: L05309. http://dx.doi.org/10.1029/2006GL028961.
Hernlund JW and Tackley PJ (2007) Some dynamical consequences of partial melting in Earth's deep mantle. *Physics of the Earth and Planetary Interiors* 162: 149–163.
Hernlund JW, Thomas C, and Tackley PJ (2005) A doubling of the post-perovskite phase boundary and structure of the Earth's lowermost mantle. *Nature* 434: 882–886.
Herrin E (1968) Introduction to "1968 Seismological Tables for P-phases". *Bulletin of the Seismological Society of America* 58: 1193–1195.
Hirose K (2006) Postperovskite phase transition and its geophysical implications. *Reviews of Geophysics* 44: RG3001. http://dx.doi.org/10.1029/2005RG000186.
Hirose K (2007) Discovery of post-perovskite phase transition and the nature of D″ layer. In: Hirose K, Brodholt J, Lay T, and Yuen DA (eds.) *Post-perovskite: The Last Mantle Phase Transition*, pp. 19–35. Washington, DC: American Geophysical Union.
Hirose K and Fujita Y (2005) Clapeyron slope of the post-perovskite phase transition in $CaIrO_3$. *Geophysical Research Letters* 32: L13313. http://dx.doi.org/10.1029/2005GL023219.
Hirose K, Kawamura K, Ohishi Y, Tateno S, and Sata N (2005) Stability and equation of state of $MgGeO_3$ post-perovskite phase. *American Mineralogy* 90: 262–265.
Hirose K, Nagaya Y, Merkel S, and Ohishi Y (2010) Deformation of $MnGeO_3$ post-perovskite at lower mantle pressure and temperature. *Geophysical Research Letters* 37: L20302. http://dx.doi.org/10.1029/2010GL044977.
Hirose K, Sinmyo R, Sata N, and Ohishi Y (2006) Determination of post-perovskite phase transition boundary in $MgSiO_3$ using Au and MgO pressure standards. *Geophysical Research Letters* 33: L01310. http://dx.doi.org/10.1029/2005GL024468.
Hirose K, Takafuji N, Fujino K, Shieh SR, and Duffy TS (2008) Iron partitioning between perovskite and post-perovskite: A transmission electron microscope study. *American Mineralogist* 93: 1678–1681. http://dx.doi.org/10.2138/am.2008.3001.
Hirose K, Takafuji N, Sata N, and Ohishi Y (2005) Phase transition and density of subducted MORB crust in the lower mantle. *Earth and Planetary Science Letters* 237: 239–251.
Hofmeister AM (2006) Is low-spin Fe^{2+} present in Earth's mantle? *Earth and Planetary Science Letters* 243: 44–52.
Hofmeister AM (2008) Inference of high thermal transport in the lower mantle from laser-flash experiments and the damped harmonic oscillator model. *Physics of the Earth and Planetary Interiors* 170: 201–206.
Houard S and Nataf HC (1993) Laterally varying reflector at the top of D″ beneath northern Siberia. *Geophysical Journal International* 115: 168–182.
Houser C, Masters G, Shearer P, and Laske G (2008) Shear and compressional velocity models of the mantle from cluster analysis of long-period waveforms. *Geophysical Journal International* 174: 195–212.
Hsu H, Blaha P, Cococcioni M, and Wentzcovitch RM (2011) Spin-state crossover and hyperfine interactions of ferric iron in $MgSiO_3$ perovskite. *Physical Review Letters* 106: 118501.
Hsu H, Umemoto K, Blaha P, and Wentzcovitch RM (2010) Spin states and hyperfine interactions of iron in $(Mg,Fe)SiO_3$ perovskite under pressure. *Earth and Planetary Science Letters* 294: 19–26.
Hsu H, Yu YG, and Wentzcovitch RM (2012) Spin crossover of iron in aluminous $MgSiO_3$ perovskite and post-perovskite. *Earth and Planetary Science Letters* 359–360: 34–39.
Hung S-H, Garnero EJ, Chiao L-Y, Kuo B-Y, and Lay T (2005) Finite-frequency tomography of D″ shear velocity heterogeneity beneath the Caribbean. *Journal of Geophysical Research* 110: B07305. http://dx.doi.org/10.1029/2004JB003373.
Hunt SA, Weidner DJ, Li L, et al. (2009) Weakening of calcium iridate during its transformation from perovskite to post-perovskite. *Nature Geosciences* 2: 794–797.
Hustoft J, Catalli K, Shim S-H, Kubo A, Prakapenka VB, and Kunz M (2008) Equation of state of $NaMgF_3$ postperovskite: Implication for the seismic velocity changes in the D″ region. *Geophysical Research Letters* 35: L10309. http://dx.doi.org/10.1029/2008GI034042.
Hustoft J, Shim S-H, Kubo A, and Nishiyama N (2008) Raman spectroscopy of $CaIrO_3$ postperovskite up to 30 GPa. *American Mineralogist* 93: 1654–1658.
Hutko A, Lay T, Garnero EJ, and Revenaugh JS (2006) Seismic detection of folded, subducted lithosphere at the core–mantle boundary. *Nature* 441: 333–336.
Hutko AR, Lay T, and Revenaugh J (2009) Localized double-array stacking analysis of PcP: D″ and ULVZ structure beneath the Cocos Plate, Mexico, central Pacific and north Pacific. *Physics of the Earth and Planetary Interiors* 173: 60–74.
Hutko A, Lay T, Revenaugh J, and Garnero EJ (2008) Anticorrelated seismic velocity anomalies from post-perovskite in the lowermost mantle. *Science* 320: 1070–1074.
Hwang YK and Ritsema J (2011) Radial structure of the lower mantle from teleseismic body-wave spectra. *Earth and Planetary Science Letters* 303: 369–375.
Hwang YK, Ritsema J, van Keken PE, Goes S, and Styles E (2011) Wavefront healing renders deep plumes seismically invisible. *Geophysical Journal International* 187: 273–277. http://dx.doi.org/10.1111/j.1365-246X.2011.05173.x.
Idehara K (2011) Structural heterogeneity of an ultra-low-velocity zone beneath the Philippine Islands: Implications for core–mantle chemical interactions induced by

massive partial melting at the bottom of the mantle. *Physics of the Earth and Planetary Interiors* 184: 80–90.
Idehara K, Yamada A, and Zhao D (2007) Seismological constraints on the ultralow velocity zones in the lowermost mantle from core-reflected waves. *Physics of the Earth and Planetary Interiors* 165: 25–46.
Iitaka T, Hirose K, Kawamura K, and Murakami M (2004) The elasticity of the $MgSiO_3$ post-perovskite phase in the Earth's lowermost mantle. *Nature* 430: 442–444.
Irifune T, Shinmei T, McCammon CA, Miyajima N, Rubie DC, and Frost DJ (2010) Iron partitioning and density changes of pyrolite in Earth's lower mantle. *Science* 327: 193–195.
Ishii M and Tromp J (1999) Normal-mode and free-air gravity constraints on lateral variations in velocity and density of Earth's mantle. *Science* 285: 1231–1236.
Ito E, Akaogi M, Topor L, and Navrotsky A (1990) Negative pressure–temperature slopes for reactions forming $MgSiO_3$ perovskite from calorimetry. *Science* 249: 1275–1278.
Ito E and Takahashi E (1989) Postspinel transforms in the system Mg_2SiO_4–Fe_2SiO_4 and some geophysical implications. *Journal of Geophysical Research* 94: 10637–10646.
Ito Y and Toriumi M (2010) Silicon self-diffusion of $MgSiO_3$ perovskite by molecular dynamics and its implication for lower mantle rheology. *Journal of Geophysical Research* 115: B12205. http://dx.doi.org/10.1029/2010JB000843.
Ito E, Yamazaki D, Yoshino T, et al. (2010) Pressure generation and investigation of the post-perovskite transformation in $MgGeO_3$ by squeezing the Kawai-cell equipped with sintered diamond anvils. *Earth and Planetary Science Letters* 293: 84–89.
Jackson I and Kung J (2008) Thermoelastic behavior of silicate perovskites: Insights from new high-temperature ultrasonic data for $ScAlO_3$. *Physics of the Earth and Planetary Interiors* 167: 195–204.
Jackson JM, Sinogeikin SV, Jacobsen SD, Reichmann HJ, Mackwell SJ, and Bass JD (2006) Single-crystal elasticity and sound velocities of $(Mg_{094}Fe_{006})O$ ferropericlase to 20 GPa. *Journal of Geophysical Research* 111: B09203. http://dx.doi.org/10.1029/2005JB004052.
Jackson JM, Sturhahn W, Shen G, et al. (2005) A synchrotron Mossbauer spectroscopy study of $(Mg,Fe)SiO_3$ perovskite up to 120 GPa. *American Mineralogist* 90: 199–205.
Jackson JM, Sturhahn W, Tschauner O, Lerche M, and Fei Y (2009) Behavior of iron in $(Mg,Fe)SiO_3$ post-perovskite assemblages at Mbar pressures. *Geophysical Research Letters* 36: L10301. http://dx.doi.org/10.1029/2009GL037815.
Jeanloz R (1993) Chemical reactions at Earth's core–mantle boundary: Summary of evidence and geomagnetic implications. In: Aki K and Dmowska R (eds.) *Relating Geophysical Structures and Processes: The Jeffreys Volume*. *Geophysical Monograph Series*, vol. 76, pp. 121–127. Washington, DC: American Geophysical Union.
Jellinek AM and Manga M (2002) The influence of a chemical boundary layer on the fixity, spacing and lifetime of mantle plumes. *Nature* 418: 760–763.
Ji Y and Nataf H-C (1998) Detection of mantle plumes in the lower mantle by diffraction tomography: Theory. *Earth and Planetary Science Letters* 159: 87–98.
Johnson LR (1969) Array measurements of P velocities in the lower mantle. *Bulletin of the Seismological Society of America* 59: 973–1008.
Jordan TH (1977) Lithospheric slab penetration into the lower mantle beneath the Sea of Okhotsk. *Journal of Geophysics* 43: 473–496.
Jordan TH and Anderson DL (1974) Earth structure from free oscillations and travel times. *Geophysical Journal of the Royal Astronomical Society* 36: 411–459.
Jordan TH and Lynn WS (1974) A velocity anomaly in the lower mantle. *Journal of Geophysical Research* 79: 2679–2685.
Jung DY and Oganov AR (2005) Ab initio study of the high-pressure behavior of $CaSiO_3$ perovskite. *Physics and Chemistry of Minerals* 32: 146–153.
Jung DY, Vinograd VL, Fabrichnaya OB, Oganov AR, Schmidt MW, and Winkler B (2010) Thermodynamics of mixing in the $MgSiO_3$–Al_2O_3 perovskite and ilmenite from ab initio calculations. *Earth and Planetary Science Letters* 295: 477–486.
Kameyama M and Yuen DA (2006) 3-D convection studies on the thermal state in the lower mantle with post-perovskite phase transition. *Geophysical Research Letters* 33: L12S10. http://dx.doi.org/10.1029/2006GL025744.
Kanamori H and Anderson DL (1977) Importance of physical dispersion in surface-wave and free oscillation problems, Review. *Reviews of Geophysics and Space Physics* 15: 105–112.
Kanda RVS and Stevenson DJ (2006) Suction mechanism for iron entrainment into the lower mantle. *Geophysical Research Letters* 33: L02310. http://dx.doi.org/10.1029/2005GL025009.
Kaneshima S (2009) Seismic scatterers at the shallowest lower mantle beneath subducted slabs. *Earth and Planetary Science Letters* 286: 304–315.
Kaneshima S and Helffrich G (1998) Detection of lower mantle scatterers northeast of the Mariana subduction zone using short-period array data. *Journal of Geophysical Research* 103: 4825–4838.
Kaneshima S and Helffrich G (2009) Lower mantle scattering profiles and fabric below Pacific subduction zones. *Earth and Planetary Science Letters* 282: 234–239.
Kaneshima S and Silver PG (1995) Anisotropic loci in the mantle beneath central Peru. *Physics of the Earth and Planetary Interiors* 88: 257–272.
Kantor I, Dubrovinsky LS, and McCammon CA (2006) Spin crossover in (Mg,Fe)O: A Mossbauer effect study with an alternative interpretation of x-ray emission spectroscopy data. *Physical Review B* 73: 100101.
Karáson H and van der Hilst RD (2001) Tomographic imaging of the lowermost mantle with differential times of refracted and diffracted core phases (PKP, Pdiff). *Journal of Geophysical Research* 106: 6569–6587.
Karato S-I (1998) Some remarks on the origin of seismic anisotropy in the D″ layer. *Earth, Planets and Space* 50: 1019–1028.
Karki BB, Wentzcovitch RM, de Gironcoli S, and Baroni S (1999) First-principles determination of elastic anisotropy and wave velocities of MgO at lower mantle conditions. *Science* 286: 1705–1709.
Katsura T, Yokoshi S, Kawabe K, et al. (2009) *P–V–T* relations of $MgSiO_3$ perovskite determined by in situ x-ray diffraction using a large-volume high-pressure apparatus. *Geophysical Research Letters* 36: L01305. http://dx.doi.org/10.1029/2008GL035658.
Kawai K and Geller RJ (2010a) Waveform inversion for localized seismic structure and an application to D″ structure beneath the Pacific. *Journal of Geophysical Research* 115: B01305. http://dx.doi.org/10.1029/2009JB006503.
Kawai K and Geller RJ (2010b) Inversion of seismic waveforms for shear wave velocity structure in the lowermost mantle beneath the Hawaiian hotspot. *Physics of the Earth and Planetary Interiors* 183: 136–142.
Kawai K and Geller RJ (2010c) The vertical flow in the lowermost mantle beneath the Pacific from inversion of seismic waveforms for anisotropic structure. *Earth and Planetary Science Letters* 297: 190–198.
Kawai K, Geller RJ, and Fuji N (2007) D″ beneath the Arctic from inversion of shear waveforms. *Geophysical Research Letters* 34: L21305. http://dx.doi.org/10.1029/2007GL031517.
Kawai K, Geller RJ, and Fuji N (2010) Waveform inversion for S-wave structure in the lowermost mantle beneath the Arctic: Implications for mineralogy and chemical composition. *Geophysical Research Letters* 37: L16301. http://dx.doi.org/10.1029/2010GL043654.
Kawai K, Sekine S, Fuji N, and Geller RJ (2009) Waveform inversion for D″ structure beneath northern Asia using Hi-net tiltmeter data. *Geophysical Research Letters* 36: L20314. http://dx.doi.org/10.1029/2009GL039651.
Kawai K, Takeuchi N, Geller RJ, and Fuji N (2007) Possible evidence for a double crossing phase transition in D″ beneath Central America from inversion of seismic waveforms. *Geophysical Research Letters* 34: L09314. http://dx.doi.org/10.1029/2007GL029642.
Kawai K and Tsuchiya T (2009) Temperature profile in the lowermost mantle from seismological and mineral physics joint modeling. *Proceedings of the National Academy of Sciences of the United States of America* 106: 22119–22123.
Kawakatsu H and Niu FL (1994) Seismic evidence for a 920-km discontinuity in the mantle. *Nature* 371: 301–305.
Kellogg LH (1997) Growing the Earth's D″ layer: Effect of density variations at the core–mantle boundary. *Geophysical Research Letters* 22: 2749–2752.
Kellogg LH, Hager BH, and van der Hilst RD (1999) Compositional stratification in the deep mantle. *Science* 283: 1881–1884.
Kendall JM (2000) Seismic anisotropy in the boundary layers of the mantle. In: Karato SI, Forte AM, Liebermann RC, Masters G, and Stixrude L (eds.) *Earth's Deep Interior: Mineral Physics and Tomography From the Atomic to the Global Scale*, pp. 133–159. Washington, DC: American Geophysical Union.
Kendall JM and Nangini C (1996) Lateral variations in D″ below the Caribbean. *Geophysical Research Letters* 23: 399–402.
Kendall JM and Shearer PM (1994) Lateral variations in D″ thickness from long-period shear wave data. *Journal of Geophysical Research* 99: 11575–11590.
Kendall JM and Silver PG (1996) Constraints from seismic anisotropy on the nature of the lowermost mantle. *Nature* 381: 409–412.
Kendall JM and Silver PG (1998) Investigating causes of D″ anisotropy. In: Gurnis M, Wysession ME, Knittle E, and Buffett BA (eds.) *The Core–Mantle Boundary Region*, pp. 97–118. Washington, DC: American Geophysical Union.
Kennett BLN and Engdahl ER (1991) Travel times for global earthquake location and phase identification. *Geophysical Journal International* 105: 429–465.
Kennett BLN, Engdahl ER, and Buland R (1995) Constraints on seismic velocities in the Earth from travel times. *Geophysical Journal International* 122: 108–124.
Kennett BLN, Widiyantoro S, and van der Hilst RD (1998) Joint seismic tomography for bulk sound and shear wave speed in the Earth's mantle. *Journal of Geophysical Research* 103: 12469–12493.

Keppler H, Dubrovinsky LS, Narygina O, and Kantor I (2008) Optical absorption and radiative thermal conductivity of silicate perovskite to 125 gigapascals. *Science* 322: 1529–1532. http://dx.doi.org/10.1126/science.1164609.

Keppler H, Kantor I, and Dubrovinsky L (2007) Optical absorption of ferropericlase to 84 GPa. *American Mineralogist* 92: 433–436.

Kito T and Krüger F (2001) Heterogeneities in D″ beneath the southwestern Pacific inferred from scattered and reflected P-waves. *Geophysical Research Letters* 28: 2545–2548.

Kito T, Krüger F, and Negishi H (2004) Seismic heterogeneous structure in the lowermost mantle beneath the southwestern Pacific. *Journal of Geophysical Research* 109: B09304. http://dx.doi.org/10.1029/20023JB002677.

Kito T, Rietbrock A, and Thomas C (2007) Slowness-backazimuth weighted migration: A new array approach to a high-resolution image. *Geophysical Journal International* 169: 1201–1209.

Kito T, Rost S, Thomas C, and Garnero EJ (2007) New insights into the P- and S-wave velocity structure of the D″ discontinuity beneath the Cocos plate. *Geophysical Journal International* 169: 631–645.

Kito T, Thomas C, Rietbrock A, Garnero EJ, Nippress SEJ, and Heath AE (2008) Seismic evidence for a sharp lithospheric base persisting to the lowermost mantle beneath the Caribbean. *Geophysical Journal International* 174: 1019–1028. http://dx.doi.org/10.1111/j.1365-246X.2008.03880.x.

Knittle E (1998) The solid/liquid partitioning of major and radiogenic elements at lower mantle pressures: Implications for the core–mantle boundary region. In: Gurnis M, Wysession ME, Knittle E, and Buffett BA (eds.) *The Core–Mantle Boundary Region*, pp. 119–130. Washington, DC: American Geophysical Union.

Knittle E and Jeanloz R (1987) Synthesis and equation of state of $(Mg,Fe)SiO_3$ perovskite to over 100 gigapascals. *Science* 235: 668–670.

Knittle E and Jeanloz R (1989) Simulating the core–mantle boundary: An experimental study of high pressure reactions between silicates and liquid iron. *Geophysical Research Letters* 16: 609–612.

Kobayashi Y, Kondo T, Ohtani E, et al. (2005) Fe–Mg partitioning between $(Mg,Fe)SiO_3$ post-perovskite, perovskite, and magnesiowüstite in the Earth's lower mantle. *Geophysical Research Letters* 32: L19301. http://dx.doi.org/10.1029/2005GL023257.

Koelemeijer PJ, Deuss A, and Trampert J (2012) Normal mode sensitivity to Earth's D″ layer and topography on the core–mantle boundary: What we can and cannot see. *Geophysical Journal International* 190: 553–568. http://dx.doi.org/10.1111/j.1365-246X.2012.05499.x.

Kohler MD, Vidale JE, and Davis PM (1997) Complex scattering within D″ observed on the very dense Los Angeles Region Seismic Experiment passive array. *Geophysical Research Letters* 24: 1855–1858.

Kojitani H, Furukawa A, and Akaogi M (2007) Thermochemistry and high-pressure equilibria of the post-perovskite phase transition in $CaIrO_3$. *American Mineralogist* 92: 229–232.

Kojitani H, Shirako Y, and Akaogi M (2007) Post-perovskite phase transition in $CaRuO_3$. *Physics of the Earth and Planetary Interiors* 165: 127–134.

Kojitani H, Wakabayashi Y, Tejima Y, Kato C, Haraguchi M, and Akaogi M (2009) High-pressure phase relations in Ca_2AlSiO_{55} and energetics of perovskite-related compounds with oxygen defects in the $Ca_2Si_2O_6$–$Ca_2Al_2O_5$ join. *Physics of the Earth and Planetary Interiors* 173: 349–353.

Koki I, Tanaka S, and Takeuchi N (2012) High velocity anomaly adjacent to the western edge of the Pacific low-velocity province. *Geophysical Journal International*. http://dx.doi.org/10.1093/gji/ggs002.

Komabayashi T, Hirose K, Nagaya Y, Sugimura E, and Ohishi Y (2010) High temperature compression of ferropericlase and the effect of temperature on iron spin transition. *Earth and Planetary Science Letters* 297: 691–699. http://dx.doi.org/10.1016/j.epsl.2010.07.025.

Komabayashi T, Hirose K, Sata N, Ohishi Y, and Dubrovinksy LS (2007) Phase transition in $CaSiO_3$ perovskite. *Earth and Planetary Science Letters* 260: 564–569.

Komabayashi T, Hirose K, Sugimura E, Sata N, Ohishi Y, and Dubrovinsky LS (2008) Simultaneous volume measurements of post-perovskite and perovskite in $MgSiO_3$ and their thermal equations of state. *Earth and Planetary Science Letters* 265: 515–524. http://dx.doi.org/10.1016/j.epsl.2007.10.036.

Komatitsch D, Vinnik LP, and Chevrot S (2010) SHdiff–SVdiff splitting in an isotropic Earth. *Journal of Geophysical Research* 115: B07312. http://dx.doi.org/10.1029/2009JB006795.

Konishi K, Kawai K, Geller RJ, and Fuji N (2009) MORB in the lowermost mantle beneath the western Pacific: Evidence from waveform inversion. *Earth and Planetary Science Letters* 278: 219–225.

Konishi K, Kawai K, Geller RJ, and Fuji N (2012) Waveform inversion of broad-band body wave data for the S-velocity structure in the lowermost mantle beneath the Indian subcontinent and Tibetan Plateau. *Geophysical Journal International* 191: 305–316. http://dx.doi.org/10.1111/j.1365-246X.2012.05614.x.

Kono Y, Higo Y, Ohfuji H, Inoue T, and Irifune T (2007) Elastic wave velocities of garnetite with a MORB composition up to 14 GPa. *Geophysical Research Letters* 34: L14308. http://dx.doi.org/10.1029/2007GL030312.

Krüger F, Weber M, Scherbaum F, and Schlittenhardt J (1995) Normal and inhomogeneous lowermost mantle and core–mantle boundary under the Arctic and Northern Canada. *Geophysical Journal International* 122: 637–658.

Kubo A, Kiefer B, Shen G, Prakapenka VB, Cava RJ, and Duffy TS (2006) Stability and equation of state of the post-perovskite phase in $MgGeO_3$ to 2 Mbar. *Geophysical Research Letters* 33: L12S12. http://dx.doi.org/10.1029/2006GL025686.

Kubo A, Kiefer B, Shim S-H, Shen GY, Prakapenka VB, and Duffy TS (2008) Rietveld structure refinement of $MgGeO_3$ post-perovskite phase to 1 Mbar. *American Mineralogist* 93: 965–976.

Kudo Y, Hirose K, Murakami M, et al. (2012) Sound velocity measurements of $CaSiO_3$ perovskite to 133 GPa and implications for lowermost mantle seismic anomalies. *Earth and Planetary Science Letters* 345–350: 1–7.

Kuo BY, Garnero EJ, and Lay T (2000) Tomographic inversion of S-SKS times for shear velocity heterogeneity in D″: Degree 12 and hybrid models. *Journal of Geophysical Research* 105: 28139–28157.

Kuo C and Romanowicz B (2002) On the resolution of density anomalies in the Earth's mantle using spectral fitting of normal-mode data. *Geophysical Journal International* 150: 162–179.

Kuo BY and Wu KY (1997) Global shear velocity heterogeneities in the D″ layer: Inversion from Sd-SKS differential travel times. *Journal of Geophysical Research* 102: 1177511788.

Kustowski B, Ekstrom G, and Dziewonski AM (2008) Anisotropic shear-wave velocity structure of the Earth's mantle: A global model. *Journal of Geophysical Research* 113: B06306. http://dx.doi.org/10.1029/2007JB005169.

Labrosse S, Hernlund JW, and Coltice N (2007) A crystallizing dense magma ocean at the base of the Earth's mantle. *Nature* 450: 866–869.

Lakshtanov DL, Sinogeikin SV, Litasov KD, et al. (2007) The post-stishovite phase transition in hydrous alumina-bearing SiO_2 in the lower mantle of the Earth. *Proceedings of the National Academy of Sciences of the United States of America* 104: 13588–13590.

Lassak TM, McNamara AK, Garnero EJ, and Zhong S (2010) Core–mantle boundary topography as a possible constraint on lower mantle chemistry and dynamics. *Earth and Planetary Science Letters* 289: 232–241.

Lassak TM, McNamara AK, and Zhong S (2007) Influence of thermochemical piles on topography at Earth's core–mantle boundary. *Earth and Planetary Science Letters* 261: 443–455.

Lavina B, Dera P, Downs RT, et al. (2009) Siderite at lower mantle conditions and the effects of the pressure-induced spin-pairing transition. *Geophysical Research Letters* 36: L23306. http://dx.doi.org/10.1029/2009GL039652.

Lavina B, Dera P, Downs RT, et al. (2010) Structure of siderite $FeCO_3$ to 56 GPa and hysteresis of its spin-pairing transition. *Physical Review B* 82: 064110. http://dx.doi.org/10.1103/PhysRevB.82.064110.

Lawrence JG and Wysession ME (2006) QLM9: A new radial quality factor ($Q^{\wedge}$) model for the lower mantle. *Earth and Planetary Science Letters* 241: 962–971.

Lay T (1983) Localized velocity anomalies in the lower mantle. *Geophysical Journal of the Royal Astronomical Society* 72: 483–516.

Lay T (1989) Structure of the core–mantle transition zone: A chemical and thermal boundary layer. *EoS, Transactions of the American Geophysical Union* 70: 49, 54–55, 58–59.

Lay T (2008) Sharpness of the D″ discontinuity beneath the Cocos Plate: Implications for the perovskite to post-perovskite phase transition. *Geophysical Research Letters* 35: L03304. http://dx.doi.org/10.1029/2007GL032465.

Lay T and Garnero EJ (2004) Core–mantle boundary structures and processes. In: Sparks RSJ and Hawkesworth CJ (eds.) *The State of the Planet: Frontiers and Challenges in Geophysics*, pp. 25–41. Washington, DC: American Geophysical Union.

Lay T and Garnero EJ (2007) Reconciling the post-perovskite phase with seismological observations of lowermost mantle structure. In: Hirose K, et al. (ed.) *Post-Perovskite: The Last Mantle Phase Transition*, pp. 129–153. Washington, DC: American Geophysical Union.

Lay T and Garnero EJ (2011) Deep mantle seismic modeling and imaging. *Annual Reviews of Earth and Planetary Sciences* 39: 91–123.

Lay T, Garnero EJ, and Russell S (2004a) Lateral variation of the D″ discontinuity beneath the Cocos Plate. *Geophysical Research Letters* 31: L15612. http://dx.doi.org/10.1029/2004GL020300.

Lay T, Garnero EJ, and Williams Q (2004b) Partial melting in a thermo-chemical boundary layer at the base of the mantle. *Physics of the Earth and Planetary Interiors* 146: 441–467.

Lay T, Garnero EJ, Young CJ, and Gaherty JB (1997) Scale-lengths of shear velocity heterogeneity at the base of the mantle from S-wave differential travel times. *Journal of Geophysical Research* 102: 9887–9910.

Lay T, Heinz D, Ishii M, et al. (2005) Multidisciplinary impact of the lower mantle perovskite phase transition. *EoS. Transactions of the American Geophysical Union* 86: 1–5.

Lay T and Helmberger DV (1983a) A lower mantle S-wave triplication and the velocity structure of D″. *Geophysical Journal of the Royal Astronomical Society* 75: 799–837.

Lay T and Helmberger DV (1983b) The shear wave velocity gradient at the base of the mantle. *Journal of Geophysical Research* 88: 8160–8170.

Lay T, Hernlund J, and Buffett BA (2008) Core–mantle boundary heat flow. *Nature Geoscience* 1: 25–32.

Lay T, Hernlund J, Garnero EJ, and Thorne MS (2006) A post-perovskite lens and D″ heat flux beneath the central Pacific. *Science* 314: 1272–1276.

Lay T and Wallace TC (1995) *Modern Global Seismology*. San Diego: Academic Press, 521 pp.

Lay T, Williams Q, and Garnero EJ (1998) The core–mantle boundary layer and deep earth dynamics. *Nature* 392: 461–468.

Lay T, Williams Q, Garnero EJ, Kellogg L, and Wysession ME (1998) Seismic wave anisotropy in the D″ region and its implications. In: Gurnis M, Wysession ME, Knittle E, and Buffett BA (eds.) *The Core–Mantle Boundary Region*, pp. 299–318. Washington, DC: American Geophysical Union.

Lay T and Young CJ (1986) The effect of SKS scattering on models of the shear velocity-structure of the D″ region. *Journal of Geophysics* 59: 11–15.

Lay T and Young CJ (1989) Waveform complexity in teleseismic broadband SH displacements: Slab diffractions or deep mantle reflections? *Geophysical Research Letters* 16: 605–608.

Lay T and Young CJ (1991) Analysis of seismic SV waves in the core's penumbra. *Geophysical Research Letters* 18: 1373–1376.

Lee RC and Johnson LR (1984) Extremal bounds on the seismic velocities in the Earth's mantle. *Geophysical Journal of the Royal Astronomical Society* 77: 667–681.

Lee KKM, Steinle-Neumann G, and Akber-Knutson S (2009) Ab initio predictions of potassium partitioning between Fe and Al-bearing $MgSiO_3$ perovskite and post-perovskite. *Physics of the Earth and Planetary Interiors* 174: 247–253.

Lei J and Zhao D (2006) Global P-wave tomography: On the effect of various mantle and core phases. *Physics of the Earth and Planetary Interiors* 154: 44–69.

Lekic V, Cottaar S, Dziewonski A, and Romanowicz B (2012) Cluster analysis of global lower mantle tomography: A new class of structure and implications for chemical heterogeneity. *Earth and Planetary Science Letters* 357–358: 68–77.

Leng W and Zhong S (2008) Controls on plume heat flux and plume excess temperature. *Journal of Geophysical Research* 113: B04408. http://dx.doi.org/10.1029/2007JB005155.

Leng W and Zhong S (2009) More constraints on internal heating rate of the Earth's mantle from plume observations. *Geophysical Research Letters* 36: L02306. http://dx.doi.org/10.1029/2008GL036449.

Li J (2007) Electronic transitions and spin states in perovskite and post-perovskite. In: Hirose K, et al. (eds.) *Post-Perovskite: The Last Mantle Phase Transition*. *Geophysical Monograph Series*, vol. 174, pp. 47–69. Washington, DC: AGU.

Li L, Brodholt JP, Stackhouse S, Weidner DJ, Alfredsson M, and Price GD (2005) Electronic spin state of ferric iron in Al-bearing perovskite in the lower mantle. *Geophysical Research Letters* 32: L17307. http://dx.doi.org/10.1029/2005GL023045.

Li X-D and Romanowicz B (1996) Global mantle shear velocity model developed using nonlinear asymptotic coupling theory. *Journal of Geophysical Research* 101: 2224522272.

Li J, Struzhkin VV, Mao HK, et al. (2004) Electronic spin state of iron in lower mantle perovskite. *Proceedings of the National Academy of Sciences of the United States of America* 101(39): 14027–14030. http://dx.doi.org/10.1073/pnas.0405804101.

Li J, Sturhahn W, Jackson JM, et al. (2006) Pressure effect on the electronic structure of iron in (Mg,Fe) $(Si,Al)O_3$ perovskite: A combined synchrotron Mossbauer and x-ray emission spectroscopy study up to 100 GPa. *Physics and Chemistry of Minerals* 33(8–9): 575–585. http://dx.doi.org/10.1007/s00269-006-0105-y.

Li C, van der Hilst RD, Engdahl ER, and Burdick W (2008) A new global model for P wave speed variations in Earth's mantle. *Geochemistry, Geophysics, Geosystems* 9: Q05018. http://dx.doi.org/10.1029/2007GC001806.

Li L, Weidner DJ, Brodholt J, et al. (2006a) Elasticity of $CaSiO_3$ perovskite at high pressure and high temperature. *Physics of the Earth and Planetary Interiors* 155: 249–259.

Li L, Weidner DJ, Brodholt J, et al. (2006b) Phase stability of $CaSiO_3$ perovskite at high pressure and temperature: Insights from ab initio molecular dynamics. *Physics of the Earth and Planetary Interiors* 155: 260–268.

Liebske C and Frost DJ (2012) Melting phase relations in the MgO–$MgSiO_3$ system between 16 and 26 GPa: Implications for melting in Earth's deep interior. *Earth and Planetary Science Letters* 345–348: 159–170.

Lin J-F, Gavriliuk AG, Struzhkin VV, et al. (2006) Pressure-induced electronic spin transition of iron in magnesiowustite-(Mg,Fe)O. *Physical Review B* 73: 113107.

Lin J-F, Jacobsen SD, Sturhahn W, Jackson JM, Zhao J, and Yoo C-S (2006) Sound velocities of ferropericlase in the Earth's lower mantle. *Geophysical Research Letters* 33: L22304. http://dx.doi.org/10.1029/2006GL028099.

Lin J-F, Struzhkin VV, Jacobsen SD, et al. (2005) Spin transition of iron in magnesiowustite in the Earth's lower mantle. *Nature* 436: 377–380.

Lin F-C, Tsai VC, Schmandt B, Duputel Z, and Zhan Z (2013) Extracting seismic core phases with array interferometry. *Geophysical Research Letters* 40. http://dx.doi.org/10.1002/grl.50237.

Lin J-F and Tsuchiya T (2008) Spin transition of iron in the Earth's lower mantle. *Physics of the Earth and Planetary Interiors* 170: 248–259.

Lin J-F, Vankó G, Jacobsen SD, et al. (2007) Spin transition zone in Earth's lower mantle. *Science* 317: 1740–1743.

Lin J-F, Watson H, Vankó G, et al. (2008) Intermediate-spin ferrous iron in lowermost mantle post-perovskite and perovskite. *Nature Geoscience* 1: 688–691.

Lin J-F, Weir ST, Jackson DD, et al. (2007) Electrical conductivity of the lower-mantle ferropericlase across the electronic spin transition. *Geophysical Research Letters* 34: L16305. http://dx.doi.org/10.1029/2007GL030523.

Litasov KD, Fei Y, Ohtani E, Kuribayashi T, and Funakoshi K (2008) Thermal equation of state of magnesite to 32 GPa and 2073 K. *Physics of the Earth and Planetary Interiors* 168: 191–203. http://dx.doi.org/10.1016/j.pepi.2008.06.018.

Lithgow-Bertelloni C and Richards MA (1998) The dynamics of Cenozoic and Mesozoic plate motions. *Reviews of Geophysics* 36: 27–78.

Liu L-G (1974) Silicate perovskite from phase transformation of pyrope-garnet at high pressure and temperature. *Geophysical Research Letters* 1: 277–280.

Liu H-P, Anderson DL, and Kanamori H (1976) Velocity dispersion due to anelasticity: Implications for seismology and mantle composition. *Geophysical Journal of the Royal Astronomical Society* 47: 41–58.

Liu X-F and Dziewonski AM (1998) Global analysis of shear wave velocity anomalies in the lowermost mantle. In: Gurnis M, Wysession ME, Knittle E, and Buffett BA (eds.) *The Core–Mantle Boundary Region*, pp. 21–36. Washington, DC: American Geophysical Union.

Liu X-F, Tromp J, and Dziewonski AM (1998) Is there a first-order discontinuity in the lowermost mantle? *Earth and Planetary Science Letters* 160: 343–351.

Long MD (2009) Complex anisotropy in D″ beneath the eastern Pacific from SKS-SKKS splitting discrepancies. *Earth and Planetary Science Letters* 283: 181–189.

Long MD, Xiao X, Jiang Z, Evans B, and Karato S-I (2006) Lattice preferred orientation in deformed polycrystalline (Mg, Fe)O and implications for seismic anisotropy in D″. *Physics of the Earth and Planetary Interiors* 156: 75–88.

Loper DE and Lay T (1995) The core–mantle boundary region. *Journal of Geophysical Research* 100: 6397–6420.

Lundin S, Catalli K, Santillân J, et al. (2008) Effect of Fe on the equation of state of mantle silicate perovskite over 1 Mbar. *Physics of the Earth and Planetary Interiors* 168: 97–102.

Ma P, Wang P, Tenorio L, de Hoop MV, and van der Hilst RD (2007) Imaging of structure at and near the core–mantle boundary using a generalized radon transform: 2. Statistical inference of singularities. *Journal of Geophysical Research* 112: B08303. http://dx.doi.org/10.1029/2006JB004513.

Mainprice D, Barruol G, and Ben Ismail W (2000) The seismic anisotropy of the Earth's mantle: From single crystal to polycrystal. In: Karato S-I, Forte AM, Liebermann RC, Masters G, and Sixrude L (eds.) *Earth's Deep Interior: Mineral Physics and Tomography From the Atomic to the Global Scale*, pp. 237–264. Washington, DC: American Geophysical Union.

Mainprice D, Tommasi A, Ferré D, Carrez P, and Cordier P (2008) Predicted glide systems and crystal preferred orientations of polycrystalline silicate Mg-Perovskite at high pressure: Implications for the seismic anisotropy in the lower mantle. *Earth and Planetary Science Letters* 271: 135–144.

Manga M and Jeanloz R (1996) Implications of a metal bearing chemical boundary layer in D″ for mantle dynamics. *Geophysical Research Letters* 23: 3091–3094.

Manthilake GM, de Koker N, Frost DJ, and McCammon CA (2011) Lattice thermal conductivity of lower mantle minerals and heat flux from Earth's core. *Proceedings of the National Academy of Sciences of the United States of America* 108: 17901–17904.

Mao Z, Armentrout M, Rainey E, et al. (2011a) Dolomite III: A new candidate lower mantle carbonate. *Geophysical Research Letters* 38: L22303. http://dx.doi.org/10.1029/2011GL049519.

Mao Z, Lin J-F, Liu J, and Prakapenka VB (2011b) Thermal equation of state of lower-mantle ferropericlase across the spin crossover. *Geophysical Research Letters* 38: L23308. http://dx.doi.org/10.1029/2011GL049915.

Mao WL, Campbell AJ, Prakapenka VB, Hemley RJ, and Mao H-K (2007) Effect of iron on the properties of post-perovskite silicate. In: Hirose K, et al. (ed.) *Post-Perovskite: The Last Mantle Phase Transition*. *Geophysical Monograph Series*, vol. 174, pp. 37–46. Washington, DC: AGU.

Mao Z, Lin JF, Jacobs C, et al. (2010) Electronic spin and valence states of Fe in $CaIrO_3$-type silicate post-perovskite in the Earth's lowermost mantle. *Geophysical Research Letters* 37: L22304. http://dx.doi.org/10.1029/2010GL045021.

Mao WL, Mao H-K, Prakapenka VB, Shu J, and Hemley RJ (2006a) The effect of pressure on the structure and volume of ferromagnesian postperovskite. *Geophysical Research Letters* 33: L12S02. http://dx.doi.org/10.1029/2006GL025770.

Mao WL, Mao H-K, Sturhahn W, et al. (2006b) Iron-rich post-perovskite and the origin of ultralow-velocity zones. *Science* 312: 564–565.

Mao WL, Meng Y, Shen G, et al. (2005) Iron-rich silicates in the Earth's D″ layer. *Proceedings of the National Academy of Sciences of the United States of America* 102: 9751–9753.

Mao WL, Shen G, Prakapenka VB, et al. (2004) Ferromagnesian postperovskite silicates in the D″ layer of the Earth. *Proceedings of the National Academy of Sciences of the United States of America* 101: 15867–15869.

Marquardt H, Speziale S, Reichmann HJ, Frost DJ, and Schilling FR (2009) Single-crystal elasticity of $(Mg_{0.9}Fe_{0.1})O$ to 81 GPa. *Earth and Planetary Science Letters* 287: 345–352.

Marquardt H, Speziale S, Reichmann HJ, Frost DJ, Schilling FR, and Garnero EJ (2009) Elastic shear anisotropy of ferropericlase in Earth's lower mantle. *Science* 324: 224–226.

Martin CD, Chapman KW, Chupas PJ, et al. (2007) Compression, thermal expansion, structure, and instability of $CaIrO_3$, the structure model of $MgSiO_3$ post-perovskite. *American Mineralogist* 92(7): 1048–1053.

Martin CD, Crichton WA, Liu HZ, Prakapenka VB, Chen J, and Parise JB (2006a) In-situ Rietveld structure refinement of perovskite and post-perovskite phases of $NaMgF_3$ (Neighborite) at high pressures. *American Mineralogist* 91(10): 1703–1706.

Martin CD, Crichton WA, Liu H, Prakapenka V, Chen J, and Parise JB (2006b) Phase transitions and compressibility of $NaMgF_3$ (Neighborite) in perovskite-and post-perovskite-related structures. *Geophysical Research Letters* 33: L11305. http://dx.doi.org/10.1029/2006GL026150.

Martin CD and Parise JB (2008) Structure constraints and instability leading to the postperovskite phase transition of $MgSiO_3$. *Earth and Planetary Science Letters* 265: 630–640.

Martin CD, Smith RI, Marshall WG, and Parise JB (2007) High pressure structure and bonding in $CaIrO_3$; the structure model of $MgSiO_3$ post-perovskite investigated with time-of-flight neutron powder diffraction. *American Mineralogist* 92(11–12): 1912–1918.

Maruyama S, Santosh M, and Zhao D (2007) Superplume, supercontinent, and post-perovskite: Mantle dynamics and anti-plate tectonics on the core–mantle boundary. *Gondwana Research* 11: 7–37. http://dx.doi.org/10.1016/j.gr.2006.06.003.

Masters G and Gilbert F (1983) Attenuation in the Earth at low frequencies. *Philosophical Transactions of the Royal Society of London, Series A* 308: 479–522.

Masters G, Johnson S, Laske G, and Bolton H (1996) A shear-velocity model of the mantle. *Philosophical Transactions of the Royal Society of London, Series A* 354: 1385–1411.

Masters G, Jordan TH, Silver PG, and Gilbert F (1982) Aspherical Earth structure from fundamental spheroidal mode data. *Nature* 298: 609–613.

Masters G, Laske G, Bolton H, and Dziewonski AM (2000) The relative behavior of shear velocity, bulk sound speed, and compressional velocity in the mantle: Implications for chemical and thermal structure. In: Karato S-I, Forte AM, Liebermann RC, Masters G, and Stixrude L (eds.) *Earth's Deep Interior: Mineral Physics and Tomography From the Atomic to the Global Scale*, pp. 63–87. Washington, DC: American Geophysical Union.

Masters G, Laske G, Dziewonski A, and Boschi L (1999) Towards a spherical reference Earth model. *EoS. Transactions of the American Geophysical Union* 80: F27.

Matas J, Bass J, Ricard Y, Mattern E, and Bukowinski MST (2007) On the bulk composition of the lower mantle: Predictions and limitations from generalized inversion of radial seismic profiles. *Geophysical Journal International* 170: 764–780. http://dx.doi.org/10.1111/j.1365-246X.2007.03454.x.

Matyska C and Yuen DA (2004) The importance of radiative heat transfer for superplumes with a deep mantle phase transition. *Earth and Planetary Science Letters* 125: 255–266.

Matyska C and Yuen DA (2006) Lower mantle dynamics with the post-perovskite phase change, radiative thermal conductivity, temperature-and depth-dependent viscosity. *Physics of the Earth and Planetary Interiors* 154: 196–207.

Matzel E, Sen MK, and Grand SP (1996) Evidence for anisotropy in the deep mantle beneath Alaska. *Geophysical Research Letters* 23: 2417–2420.

Maupin V, Garnero EJ, Lay T, and Fouch MJ (2005) Azimuthal anisotropy in the D″ layer beneath the Caribbean. *Journal of Geophysical Research* 110: B08301. http://dx.doi.org/10.1029/2004JB003506.

McCammon C, Dubrovinsky L, Narygina O, et al. (2010) Low-spin Fe^{2+} in silicate perovskite and a possible layer at the base of the lower mantle. *Physics of the Earth and Planetary Interiors* 180: 215–221.

McCammon C, Kantor I, Narygina O, et al. (2008) Stable intermediate-spin ferrous iron in lower-mantle perovskite. *Nature Geoscience* 1: 684–687.

McNamara AK, Garnero EJ, and Rost S (2010) Tracking deep mantle reservoirs with ultra-low velocity zones. *Earth and Planetary Science Letters* 299: 1–9. http://dx.doi.org/10.1016/j.epsl.2010.07.042.

McNamara AK, Karato S-I, and van Keken PE (2001) Localization of dislocation creep in the lower mantle: Implications for the origin of seismic anisotropy. *Earth and Planetary Science Letters* 191: 85–99.

McNamara AK, van Keken PE, and Karato S-I (2002) Development of anisotropic structure in the Earth's lower mantle by solid-state convection. *Nature* 416: 310–314.

McNamara AK, van Keken PE, and Karato S-I (2003) Development of finite strain in the convecting lower mantle and its implications for seismic anisotropy. *Journal of Geophysical Research* 108(B5): 2230. http://dx.doi.org/10.1029/2002JB001970.

McNamara AK and Zhong S (2004) Thermochemical structures within a spherical mantle: Superplumes or piles? *Journal of Geophysical Research* 109: B07402. http://dx.doi.org/10.1029/2003JB02847.

McNamara AK and Zhong S (2005) Thermochemical structures beneath Africa and the Pacific Ocean. *Nature* 437: 1136–1139. http://dx.doi.org/10.1038/nature04066.

Meade C, Silver PG, and Kaneshima S (1995) Laboratory and seismological observations of lower mantle isotropy. *Geophysical Research Letters* 22: 1293–1296.

Mégnin C and Romanowicz B (2000) The three-dimensional shear velocity structure of the mantle from the inversion of body, surface, and higher-mode waveform. *Geophysical Journal International* 143: 709–728.

Merkel S, Kubo A, Miyagi L, et al. (2006) Plastic deformation of $MgGeO_3$ post-perovskite at lower mantle pressures. *Science* 311: 644–646.

Merkel S, McNamara AK, Kubo A, et al. (2007) Deformation of $(Mg,Fe)SiO_3$ post-perovskite and D″ anisotropy. *Science* 316: 1729–1732. http://dx.doi.org/10.1126/science.1140609.

Metsue A, Carrez P, Mainprice D, and Cordier P (2009) Numerical modeling of dislocations and deformation mechanisms in $CaIrO_3$ and $MgGeO_3$ post-perovskites—Comparison with $MgSiO_3$ post-perovskite. *Physics of the Earth and Planetary Interiors* 174: 165–173. http://dx.doi.org/10.1016/j.pepi.2008.04.003.

Metsue A and Tsuchiya T (2011) Lattice dynamics and thermodynamic properties of $(Mg,Fe^{2+})SiO_3$ postperovskite. *Journal of Geophysical Research* 116: B08207. http://dx.doi.org/10.1029/2010JB008018.

Miller MS and Niu F (2008) Bulldozing the core–mantle boundary: Localized seismic scatterers beneath the Caribbean Sea. *Physics of the Earth and Planetary Interiors* 170: 89–94.

Minster JB (1980) Anelasticity and attenuation. In: Dziewonski AM and Boschi E (eds.) *Physics of the Earth's Interior*, pp. 152–212. Amsterdam: North-Holland.

Minster JB and Anderson DL (1981) A model of dislocation controlled rheology for the mantle. *Philosophical Transactions of the Royal Society of London* 299: 319–356.

Mitchell BJ and Helmberger DV (1973) Shear velocities at the base of the mantle from observations of S and ScS. *Journal of Geophysical Research* 78: 6009–6020.

Mitrovica JX and Forte AM (1997) Radial profile of mantle viscosity: Results from the joint inversion of convection and postglacial rebound observables. *Journal of Geophysical Research* 102: 2751–2769.

Mitrovica JX and Forte AM (2004) A new inference of mantle viscosity based upon joint inversion of convection and glacial isostatic adjustment data. *Earth and Planetary Science Letters* 225: 177–189.

Mittelstaedt E and Tackley PJ (2006) Plume heat flow is much lower than CMB heat flow. *Earth and Planetary Science Letters* 241: 202–210.

Miyagi L, Kanitpanyacharoen W, Kaercher P, Lee KKM, and Wenk H-R (2010) Slip systems in $MgSiO_3$ post-perovskite: Implications for D″ anisotropy. *Science* 329: 1639–1642.

Miyagi L, Kanitpanyacharoen W, Stackhouse S, Militzer B, and Wenk H-R (2011) The enigma of post-perovskite anisotropy: Deformation versus transformation textures. *Physical Chemistry of Minerals* 38: 665–678.

Miyagi L, Merkel S, Yagi T, Sata N, Ohishi Y, and Wenk HR (2006) Quantitative Rietveld texture analysis of $CaSiO_3$ perovskite deformed in a diamond anvil cell. *Journal of Physics: Condensed Matter* 18: S995–S1005.

Miyagi L, Merkel S, Yagi T, Sata N, Ohishi Y, and Wenk H-R (2009) Diamond anvil cell deformation of $CaSiO_3$ perovskite up to 49 GPa. *Physics of the Earth and Planetary Interiors* 174: 159–164.

Miyagi L, Nishiyama N, Wang Y, et al. (2008) Deformation and texture development in $CaIrO_3$ post-perovskite phase up to 6 GPa and 1300 K. *Earth and Planetary Science Letters* 268: 515–525. http://dx.doi.org/10.1016/j.epsl.2008.02.005.

Miyajima N, Niwa K, Heidelbach F, Yagi T, and Ohgushi K (2010) Deformation microtextures in $CaIrO_3$ post-perovskite under high stress conditions using a laser-heated diamond anvil cell. *Journal of Physics: Conference Series* 215: 012097.

Miyajima N, Ohgushi K, Ichihara M, and Yagi T (2006) Crystal morphology and dislocation microstructures of $CaIrO_3$: A TEM study of an analogue of the $MgSiO_3$ post-perovskite phase. *Geophysical Research Letters* 33: L12302. http://dx.doi.org/10.1029/2005GL025001.

Miyajima N, Yagi T, and Ichihara M (2009) Dislocation microstructures of $MgSiO_3$ perovskite at a high pressure and temperature condition. *Physics of the Earth and Planetary Interiors* 174: 153–158.

Mondt JC (1977) SH waves: Theory and observations for epicentral distances greater than 90 degrees. *Physics of the Earth and Planetary Interiors* 15: 46–59.

Monnereau M and Yuen DA (2007) Topology of the postperovskite phase transition and mantle dynamics. *Proceedings of the National Academy of Sciences of the United States of America* 104: 9156–9161.

Monnereau M and Yuen DA (2010) Seismic imaging of the D″ and constraints on the core heat flux. *Physics of the Earth and Planetary Interiors* 180: 258–270.

Montagner J-P and Kennett BLN (1996) How to reconcile body-wave and normal-mode reference Earth models. *Geophysical Journal International* 125: 229–248.

Montague NL, Kellogg LH, and Manga M (1998) High Rayleigh number thermo-chemical models of a dense boundary layer in D″. *Geophysical Research Letters* 25: 2345–2348.

Montelli R, Nolet G, Dahlen FA, Masters G, Engdahl ER, and Hung SH (2004) Finite-frequency tomography reveals a variety of plumes in the mantle. *Science* 303: 338–343.

Mookherjee M (2011) Mid-mantle anisotropy: Elasticity of aluminous phases in subducted MORB. *Geophysical Research Letters* 38: L14302. http://dx.doi.org/10.1029/2011GL047923.

Moore MM, Garnero EJ, Lay T, and Williams Q (2003) Shear wave splitting and waveform complexity for lowermost mantle structures with low-velocity lamellae and transverse isotropy. *Journal of Geophysical Research* 109: B02319. http://dx.doi.org/10.1029/2003JB002546.

Morelli A and Dziewonski AM (1987) Topography of the core–mantle boundary and lateral heterogeneity of the liquid core. *Nature* 325: 678–683.

Morelli A and Dziewonski AM (1993) Body wave travel times and a spherically symmetric P and S-wave velocity model. *Geophysical Journal International* 112: 178–194.

Mori J and Helmberger DV (1995) Localized boundary layer below the mid-Pacific velocity anomaly identified from a PcP precursor. *Journal of Geophysical Research* 100: 20359–20365.

Mosca I, Cobden L, Deuss A, Ritsema J, and Trampert J (2012) Seismic and mineralogical structures of the lower mantle from probabilistic tomography. *Journal of Geophysical Research* 117: B06304. http://dx.doi.org/10.1029/2011JB008851.

Mosenfelder JL, Asimow PD, and Ahrens TJ (2007) Thermodynamic properties of Mg_2SiO_4 liquid at ultra-high pressures for shock measurements to 200 GPa on forsterite and wadsleyite. *Journal of Geophysical Research* 112: B06208.

Mosenfelder JL, Asimow PD, Frost DJ, Rubie DC, and Ahrens TJ (2009) The $MgSiO_3$ system at high pressure: Thermodynamic properties of perovskite, postperovskite, and melt from global inversion of shock and static compression data. *Journal of Geophysical Research* 114: B01203. http://dx.doi.org/10.1029/2008JB005900.

Muirhead KJ and Hales AL (1980) Evidence for P-wave discontinuities at depths greater than 650 km in the mantle. *Physics of the Earth and Planetary Interiors* 23: 304–313.

Mula AH and Müller G (1980) Ray parameters of diffracted long period P and S-waves and the velocities at the base of the mantle. *Pure and Applied Geophysics* 188: 1270–1290.

Murakami M and Bass JD (2011) Evidence of denser $MgSiO_3$ glass above 133 gigapascal (GPa) and implications for remnants of ultradense silicate melt from a deep magma ocean. *Proceedings of the National Academy of Sciences of the United States of America* 108(42): 17286–17289.

Murakami M, Hirose K, Kawamura K, Sata N, and Ohishi Y (2004) Post-perovskite phase transition in $MgSiO_3$. *Science* 304: 855–858.

Murakami M, Hirose K, Sata N, and Ohishi Y (2005) Post-perovskite phase transition and mineral chemistry in the pyrolitic lowermost mantle. *Geophysical Research Letters* 32: L03304. http://dx.doi.org/10.1029/2004GL021956.

Murakami M, Ohishi Y, Hirao N, and Hirose K (2009) Elasticity of MgO to 130 GPa: Implications for lower mantle mineralogy. *Earth and Planetary Science Letters* 277(1–2): 123–129.

Murakami M, Ohishi Y, Hirao N, and Hrose K (2012) A perovskitic lower mantle inferred from high-pressure, high-temperature sound velocity data. *Nature* 485: 90–94.

Murakami M, Sinogeikin SV, Bass JD, Sata N, Ohishi Y, and Hirose K (2007) Sound velocity of $MgSiO_3$ post-perovskite phase: A constraint on the D″ discontinuity. *Earth and Planetary Science Letters* 259(1–2): 18–23.

Murakami M, Sinogeikin SV, Hellwig H, Bass JD, and Li J (2007) Sound velocity of $MgSiO_3$ perovskite to Mbar pressure. *Earth and Planetary Science Letters* 256(1–2): 47–54. http://dx.doi.org/10.1016/j.epsl.2007.01.011.

Myers SC, Johannesson G, and Simmons NA (2011) Global-scale P wave tomography optimized for prediction of teleseismic and regional travel times for Middle East events: 1. Data set development. *Journal of Geophysical Research* 116: B04304.

Nakada M, Iriguchi C, and Karato S-I (2012) The viscosity structure of the D″ layer of the Earth's mantle inferred from the analysis of Chandler wobble and tidal deformation. *Physics of the Earth and Planetary Interiors* 208–209: 11–24.

Nakada M and Karato S-I (2012) Low viscosity of the bottom of the Earth's mantle inferred from the analysis of Chandler wobble and tidal deformation. *Physics of the Earth and Planetary Interiors* 192–193: 68–80.

Nakagawa T and Tackley PJ (2004) Effects of a perovskite–post perovskite phase change near core–mantle boundary in compressible mantle convection. *Geophysical Research Letters* 31: L16611. http://dx.doi.org/10.1029/2004GL020648.

Nakagawa T and Tackley PJ (2005) The interaction between the post-perovskite phase change and thermo-chemical boundary layer near the core–mantle boundary. *Earth and Planetary Science Letters* 238: 204–216.

Nakagawa T and Tackley PJ (2006) Three-dimensional structures and dynamics in the deep mantle: Effects of post-perovskite phase change and deep mantle layering. *Geophysical Research Letters* 33: L12S11. http://dx.doi.org/10.1029/2006GL025719.

Nakagawa T and Tackley PJ (2008) Lateral variations in CMB heat flux and deep mantle seismic velocity caused by a thermal-chemical-phase boundary layer in 3D spherical convection. *Earth and Planetary Science Letters* 271: 348–358.

Nakagawa T and Tackley PJ (2011) Effects of low-viscosity post-perovskite on thermochemical mantle convection in a 3-D spherical shell. *Geophysical Research Letters* 38: L04309. http://dx.doi.org/10.1029/2010GL046494.

Nakajima Y, Frost DJ, and Rubie DC (2012) Ferrous iron partitioning between magnesium silicate perovskite and ferropericlase and the composition of perovskite in the Earth's lower mantle. *Journal of Geophysical Research* 117: B08201. http://dx.doi.org/10.1029/2012JB009151.

Narygina O, Dubrovinsky LS, Samuel H, et al. (2011) Chemically homogeneous spin transition zone in Earth's lower mantle. *Physics of the Earth and Planetary Interiors* 185: 107–111.

Nataf H-C and Houard S (1993) Seismic discontinuity at the top of D″: A world-wide feature? *Geophysical Research Letters* 20: 2371–2374.

Nebel O, Münker C, Nebel-Jacobsen YJ, Kleine T, Mezger K, and Mortimer N (2007) Hf–Nd–Pb isotope evidence from Permian arc rocks for the long-term presence of the Indian-Pacific mantle boundary in the SW Pacific. *Earth and Planetary Science Letters* 254: 377–392.

Ni S, Ding X, and Helmberger DV (2000) Constructing synthetics from deep earth tomographic models. *Geophysical Journal International* 140: 71–82.

Ni S and Helmberger DV (2003a) Seismological constraints on the South African superplume; could be the oldest distinct structure on earth. *Earth and Planetary Science Letters* 206: 119–131.

Ni S and Helmberger DV (2003b) Ridge-like lower mantle structure beneath South Africa. *Journal of Geophysical Research* 108(B2): 2094. http://dx.doi.org/10.1029/2001JB001545.

Ni S, Helmberger DV, and Tromp J (2005) Three-dimensional structure of the Africa superplume from waveform modeling. *Geophysical Journal International* 161: 283–294.

Ni S, Tan E, Gurnis M, and Helmberger DV (2002) Sharp sides to the African superplume. *Science* 296: 1850–1852.

Nishio-Hamane D, Fujino K, Seto Y, and Nagai T (2007) Effect of the incorporation of $FeAlO_3$ into $MgSiO_3$ perovskite on the post-perovskite transition. *Geophysical Research Letters* 34: L12307. http://dx.doi.org/10.1029/2007GL029991.

Nishio-Hamane D, Seto Y, Fujino K, and Nagai T (2008) Effect of $FeAlO_3$ incorporation into $MgSiO_3$ on the bulk modulus of perovskite. *Physics of the Earth and Planetary Interiors* 166: 219–225.

Nishio-Hamane D and Yagi T (2009) Equations of state for postperovskite phases in the $MgSiO_3$–$FeSiO_3$–$FeAlO_3$ system. *Physics of the Earth and Planetary Interiors* 175: 145–150.

Nishiyama N, Yagi T, Ono S, Gotou H, Harada T, and Kikegawa T (2007) Effect of incorporation of iron and aluminum on the thermoelastic properties of magnesium silicate perovskite. *Physical Chemistry of Minerals* 34: 131–143. http://dx.doi.org/10.1007/s00269-006-0134-6.

Niu F and Kawakatsu H (1997) Depth variation of the mid-mantle seismic discontinuity. *Geophysical Research Letters* 24: 429–432.

Niu F and Perez AM (2004) Seismic anisotropy in the lower mantel: A comparison of waveform splitting of SKS and SKKS. *Geophysical Research Letters* 31: L24612. http://dx.doi.org/10.1029/2004GL021196.

Niwa K, Miyajima N, Seto Y, Ohgushi K, Gotou H, and Yagi T (2012) In situ observation of shear stress-induced perovskite to post-perovskite phase transition in $CaIrO_3$ and

the development of its deformation texture in a diamond-anvil cell up to 30 GPa. *Physics of the Earth and Planetary Interiors* 194–195: 10–17.
Niwa K, Yagi T, and Ohgushi K (2011) Elasticity of $CaIrO_3$ with perovskite and postperovskite structure. *Physical Chemistry of Minerals* 38: 21–31.
Niwa K, Yagi T, Ohgushi K, Merkel S, Miyajima N, and Kikegawa T (2007) Lattice preferred orientation in $CaIrO_3$ perovskite and postperovskite formed by plastic deformation under pressure. *Physical Chemistry of Minerals* 34: 679–686. http://dx.doi.org/10.1007/s00269-007-0182-6.
Nomura R, Hirose K, Sata N, and Ohishi Y (2010) Precise determination of post-stishovite phase transition boundary and implications for seismic heterogeneities in the mid-lower mantle. *Physics of the Earth and Planetary Interiors* 183: 104–109.
Nomura R, Ozawa H, Tateno S, et al. (2011) Spin crossover and iron-rich silicate melt in the Earth's deep mantle. *Nature* 473: 199–202. http://dx.doi.org/10.1038/nature09940.
Nowacki A, Walker AM, Wookey J, and Kendall J-M (2012) Evaluating post-perovskite as a cause of D″ anisotropy in regions of paleosubduction. *Geophysical Journal International*. http://dx.doi.org/10.1093/gji/ggs068.
Nowacki A, Wookey J, and Kendall J-M (2010) Deformation of the lowermost mantle from seismic anisotropy. *Nature* 467: 1091–1094.
Nowacki A, Wookey J, and Kendall J-M (2011) New advances in using seismic anisotropy, mineral physics and geodynamics to understand deformation in the lower mantle. *Journal of Geodynamics* 52: 205–228.
Obayashi M and Fukao Y (1997) P and PcP travel time tomography for the core–mantle boundary. *Journal of Geophysical Research* 102: 17825–17841.
Oganov AR, Glass CW, and Ono S (2006) High-pressure phases of $CaCO_3$: Crystal structure prediction and experiment. *Earth and Planetary Science Letters* 241: 95–103. http://dx.doi.org/10.1016/j.epsl.2005.10.014.
Oganov AR, Martonak R, Laio A, Raiteri P, and Parrinello M (2005) Anisotropy of Earth's D″ layer and stacking faults in the $MgSiO_3$ post-perovskite phase. *Nature* 438: 1142–1144.
Oganov AR and Ono S (2004) Theoretical and experimental evidence for a post-perovskite phase of $MgSiO_3$ in Earth's D″ layer. *Nature* 430: 445–448.
Oganov AR, Ono S, Ma Y, Glass CW, and Garcia A (2008) Novel high-pressure structures of $MgCO_3$, $CaCO_3$ and CO_2 and their role in Earth's lower mantle. *Earth and Planetary Science Letters* 273: 38–47. http://dx.doi.org/10.1016/j.epsl.2008.06.005.
Ohta K, Hirose K, Ichiki M, Shimizu K, Sata N, and Ohishi Y (2010) Electrical conductivities of pyrolitic mantle and MORB materials up to the lowermost mantle conditions. *Earth and Planetary Science Letters* 289: 497–502. http://dx.doi.org/10.1016/j.epsl.2009.11.042.
Ohta K, Hirose K, Lay T, Sata N, and Ohishi Y (2008) Phase transitions in pyrolite and MORB at lowermost mantle conditions: Implications for a MORB-rich pile above the core–mantle boundary. *Earth and Planetary Science Letters* 267: 107–117.
Ohta K, Hirose K, Onoda S, and Shimizu K (2007) The effect of iron spin transition on electrical conductivity of (Mg,Fe)O magnesiowüstite. *Proceedings of the Japanese Academy, Series B* 83: 97–100.
Ohta K, Hirose K, Shimizu K, Sata N, and Ohishi Y (2010) The electrical resistance measurements of $(Mg,Fe)SiO_3$ perovskite at high pressures and implications for electronic spin transition of iron. *Physics of the Earth and Planetary Interiors* 180: 154–158.
Ohta K, Onoda S, Hirose K, et al. (2008) The electrical conductivity of post-perovskite in Earth's D″ layer. *Science* 320: 89–91.
Ohta K, Yagi T, Taketoshi N, et al. (2012) Lattice thermal conductivity of $MgSiO_3$ perovskite and post-perovskite at the core–mantle boundary. *Earth and Planetary Science Letters* 349–350: 109–115.
Okada T, Yagi T, Niwa K, and Kikegawa T (2010) Lattice-preferred orientations in post-perovskite-type $MgGeO_3$ formed by transformations from different pre-phases. *Physics of the Earth and Planetary Interiors* 180: 195–202. http://dx.doi.org/10.1016/j.pepi.2009.08.002.
Okano K and Suetsugu D (1992) Search for lower mantle high velocity zones beneath the deepest Kurile and Mariana earthquakes. *Geophysical Research Letters* 19: 745–748.
Ono S, Kikegawa T, and Ohishi Y (2006) Equation of state of $CaIrO_3$-type $MgSiO_3$ up to 144 GPa. *American Mineralogist* 91: 475–478. http://dx.doi.org/10.2138/am.2006.2118.
Ono S and Oganov AR (2005) In situ observations of phase transition between perovskite and $CaIrO_3$-type phase in $MgSiO_3$ and pyrolitic mantle composition. *Earth and Planetary Science Letters* 236: 914–931.
Ono S, Oganov AR, Koyama T, and Shimizu H (2006) Stability and compressibility of the high-pressure phases of Al_2O_3 up to 200 GPa: Implications for the electrical conductivity of the base of the lower mantle. *Earth and Planetary Science Letters* 246: 326–335.
Otsuka K and Karato S-I (2012) Deep penetration of molten iron into the mantle caused by a morphological instability. *Nature* 492: 243–246.
Ozawa H, Hirose K, Mitome M, Bando Y, Sata N, and Ohishi Y (2008) Chemical equilibrium between ferropericlase and molten iron to 134 GPa and implications for iron content at the bottom of the mantle. *Geophysical Research Letters* 35: L05308. http://dx.doi.org/10.1029/2007GL032648.
Panero WR, Akber-Knutson S, and Stixrude L (2006) Al_2O_3 incorporation in $MgSiO_3$ perovskite and ilmenite. *Earth and Planetary Science Letters* 252: 152–161.
Pankow KL and Lay T (1999) Constraints on the Kurile slab from shear wave residual sphere analysis. *Journal of Geophysical Research* 104: 7255–7278.
Panning MP, Lekić V, and Romanowicz BA (2010) Importance of crustal corrections in the development of a new global model of radial anisotropy. *Journal of Geophysical Research* 115: B12325. http://dx.doi.org/10.1029/2010JB007520.
Panning MP and Romanowicz B (2004) Inferences on flow at the base of Earth's mantle based on seismic anisotropy. *Science* 303: 351–353.
Panning M and Romanowicz B (2006) A three-dimensional radially anisotropic model of shear velocity in the whole mantle. *Geophysical Journal International* 167: 361–379. http://dx.doi.org/10.1111/j.1365-246X.2006.03100.x.
Persch ST, Vidale JE, and Earle PS (2001) Absence of short-period ULVZ precursors to PcP and ScP from two regions of the CMB. *Geophysical Research Letters* 28: 387–390.
Persson K, Bengtson A, Ceder G, and Morgan D (2006) *Ab initio* study of the composition dependence of the pressure-induced spin transition in the $(Mg_{1-x}Fe_x)O$ system. *Geophysical Research Letters* 33: L16306. http://dx.doi.org/10.1029/2006GL026621.
Phipps Morgan J and Shearer PM (1993) Seismic constraints on mantle flow and topography of the 660-km discontinuity: Evidence for whole mantle convection. *Nature* 365: 506–511.
Pulliam J and Sen MK (1998) Seismic anisotropy in the core–mantle transition zone. *Geophysical Journal International* 135: 113–128.
Pulliam J and Stark P (1993) Bumps on the core–mantle boundary: Are they facts or artifacts? *Journal of Geophysical Research* 98: 1943–1956.
Randall MJ (1971) A revised travel-time table for S. *Geophysical Journal of the Royal Astronomical Society* 22: 229–234.
Reasoner C and Revenaugh J (1999) Short-period P-wave constraints on D″ reflectivity. *Journal of Geophysical Research* 104: 955–961.
Reasoner C and Revenaugh J (2000) ScP constraints on ultralow-velocity zone density and gradient thickness beneath the Pacific. *Journal of Geophysical Research* 105: 28173–28182.
Ren Y, Stutzmann E, van der Hilst RD, and Besse J (2007) Understanding seismic heterogeneities in the lower mantle beneath the Americas from seismic tomography and plate tectonic history. *Journal of Geophysical Research* 112: B01302. http://dx.doi.org/10.1029/2005JB004154.
Resovsky J and Trampert J (2003) Using probabilistic seismic tomography to test mantle velocity–density relationships. *Earth and Planetary Science Letters* 215: 121–130.
Restivo A and Helffrich G (2006) Core–mantle boundary structure investigated using SKS and SKKS polarization anomalies. *Geophysical Journal International* 165: 288–302. http://dx.doi.org/10.1111/j.1365-246X.2006.02901.x.
Revenaugh JS and Jordan TH (1991) Mantle layering from *ScS* reverberations, 2. The transition zone. *Journal of Geophysical Research* 96: 19763–19780.
Revenaugh JS and Meyer R (1997) Seismic evidence of partial melt within a possibly ubiquitous low-velocity layer at the base of the mantle. *Science* 277: 670–673.
Richards MA and Hager BH (1984) Geoid anomalies in a dynamic Earth. *Journal of Geophysical Research* 89: 5987–6002.
Ricolleau A, Fei Y, Cottrell E, et al. (2009) Density profile of pyrolite under the lower mantle conditions. *Geophysical Research Letters* 36: L06302. http://dx.doi.org/10.1029/2008GL036759.
Ricolleau A, Perrillat J-P, Fiquet G, et al. (2010) Phase relations and equation of state of a natural MORB: Implications for the density profile of subducted oceanic crust in the Earth's lower mantle. *Journal of Geophysical Research* 115: B08202. http://dx.doi.org/10.1029/2009JB006709.
Ritsema J (2000) Evidence for shear wave anisotropy in the lowermost mantle beneath the Indian Ocean. *Geophysical Research Letters* 27: 1041–1044.
Ritsema J, Deuss A, van Heijst HJ, and Woodhouse JH (2011) S40RTS: A degree-40 shear-velocity model for the mantle from new Rayleigh wave dispersion, teleseismic traveltime and normal-mode splitting function measurements. *Geophysical Journal International* 184: 1223–1236. http://dx.doi.org/10.1111/j.1365-246X.2010.04884.x.
Ritsema J, Lay T, Garnero EJ, and Benz H (1998a) Seismic anisotropy in the lowermost mantle beneath the Pacific. *Geophysical Research Letters* 25: 1229–1232.
Ritsema J, Ni S, Helmberger DV, and Crotwell HP (1998b) Evidence for strong shear velocity reductions and velocity gradients in the lower mantle beneath Africa. *Geophysical Research Letters* 25: 4245–4248.

Ritsema J, McNamara AK, and Bull AL (2007) Tomographic filtering of geodynamical models. *Journal of Geophysical Research* 112: B01303. http://dx.doi.org/10.1029/2006JB004566.

Ritsema J and van Heijst HJ (2000) Seismic imaging of structural heterogeneity in Earth's mantle: Evidence for large-scale mantle flow. *Science Progress* 83: 243–259.

Ritsema J, van Heijst HJ, and Woodhouse JH (1999) Complex shear wave velocity structure imaged beneath Africa and Iceland. *Science* 286: 1925–1928.

Robertson GS and Woodhouse JH (1996) Ratio of relative *S* to *P* velocity heterogeneity in the lower mantle. *Journal of Geophysical Research* 101: 20041–20052.

Rodgers A and Wahr J (1993) Inference of core–mantle boundary topography from ISC PcP and PKP traveltimes. *Geophysical Journal International* 115: 991–1011.

Rokosky JM, Lay T, and Garnero EJ (2006) Small-scale lateral variations in azimuthally anisotropic D″ structure beneath the Cocos Plate. *Earth and Planetary Science Letters* 248: 411–425.

Rokosky JM, Lay T, Garnero EJ, and Russell SA (2004) High-resolution investigation of shear wave anisotropy in D″ beneath the Cocos Plate. *Geophysical Research Letters* 31: L07605. http://dx.doi.org/10.1029/2003GL018902.

Romanowicz B (2001) Can we resolve 3D density heterogeneity in the lower mantle? *Geophysical Research Letters* 28: 1107–1110.

Rondenay S, Cormier VF, and Van Ark EM (2010) SKS and SPdKS sensitivity to two-dimensional ultralow-velocity zones. *Journal of Geophysical Research* 115: B04311. http://dx.doi.org/10.1029/2009JB006733.

Rondenay S and Fischer KM (2003) Constraints on localized core–mantle boundary structure from multichannel, broadband SKS coda analysis. *Journal of Geophysical Research* 108: 2537. http://dx.doi.org/10.1029/2003JB002518.

Ross AR, Thybo H, and Solidilov LN (2004) Reflection seismic profiles of the core–mantle boundary. *Journal of Geophysical Research* 109: B08303. http://dx.doi.org/10.1029/2003JB002515.

Rost S and Earle PS (2010) Identifying regions of strong scattering at the core–mantle boundary from analysis of PKKP precursor energy. *Earth and Planetary Science Letters* 297: 616–626.

Rost S and Garnero EJ (2006) Detection of an ultralow velocity zone at the core–mantle boundary using diffracted PKKPab waves. *Journal of Geophysical Research* 111: B07309. http://dx.doi.org/10.1029/2005JB003850.

Rost S, Garnero EJ, and Stefan W (2010) Thin and intermittent ultralow-velocity zones. *Journal of Geophysical Research* 115: B06312. http://dx.doi.org/10.1029/2009JB006981.

Rost S, Garnero EJ, Thorne MS, and Hutko AR (2010) On the absence of an ultralow-velocity zone in the North Pacific. *Journal of Geophysical Research* 115: B04312. http://dx.doi.org/10.1029/2009JB006420.

Rost S, Garnero EJ, and Williams Q (2006) Fine-scale ultralow-velocity zone structure from high-frequency seismic array data. *Journal of Geophysical Research* 111: B09310. http://dx.doi.org/10.1029/2005JB004088.

Rost S, Garnero EJ, and Williams Q (2008) Seismic array detection of subducted oceanic crust in the lower mantle. *Journal of Geophysical Research* 113: B06303. http://dx.doi.org/10.1029/2007JB005263.

Rost S, Garnero EJ, Williams Q, and Manga M (2005) Seismological constraints on a possible plume root at the core–mantle boundary. *Nature* 435: 666–669.

Rost S and Revenaugh J (2001) Seismic detection of rigid zones at the top of the core. *Science* 294: 1911–1914.

Rost S and Revenaugh J (2003) Small-scale ultralow-velocity zone structure imaged by ScP. *Journal of Geophysical Research* 108: 2056. http://dx.doi.org/10.1029/2001JB001627.

Rost S and Thomas C (2010) High resolution CMB imaging from migration of short-period core reflected phases. *Physics of the Earth and Planetary Interiors* 183: 143–150.

Runge CE, Kubo A, Kiefer B, et al. (2006) Equation of state of $MgGeO_3$ perovskite to 65 GPa: Comparison with the post-perovskite phase. *Physical Chemistry of Minerals* 33: 699–709.

Russell SA, Lay T, and Garnero EJ (1998) Seismic evidence for small-scale dynamics in the lowermost mantle at the root of the Hawaiian hotspot. *Nature* 396: 255–258.

Russell SA, Lay T, and Garnero EJ (1999) Small-scale lateral shear velocity and anisotropy heterogeneity near the core–mantle boundary beneath the central Pacific imaged using broadband *ScS-waves*. *Journal of Geophysical Research* 104: 13183–13199.

Russell SA, Reasoner C, Lay T, and Revenaugh J (2001) Coexisting shear-and compressional-wave seismic velocity discontinuities beneath the central Pacific. *Geophysical Research Letters* 28: 2281–2284.

Sacks S (1966) Diffracted waves studies of the earth's core: 1. Amplitudes, core size, and rigidity. *Journal of Geophysical Research* 71: 1173–1181.

Saha S, Bengtson A, Crispin KL, VanOrman JA, and Morgan D (2011) Effects of spin transition on diffusion of Fe^{2+} in ferropericlase in Earth's lower mantle. *Physical Review B* 85: 184102.

Saha S, Bengtson A, and Morgan D (2013) Effect of anomalous compressibility on Fe diffusion in ferropericlase throughout the spin crossover in the lower mantle. *Earth and Planetary Science Letters* 326: 1–5.

Saikia A, Boffa Ballaran T, and Frost DJ (2009) The effect of Fe and Al substitution on the compressibility of $MgSiO_3$-perovskite determined through single-crystal x-ray diffraction. *Physics of the Earth and Planetary Interiors* 173: 153–161. http://dx.doi.org/10.1016/j.pepi.2008.11.006.

Sakai T, Kondo T, Ohtani E, et al. (2006) Interaction between iron and post-perovskite at core–mantle boundary and core signature in plume source region. *Geophysical Research Letters* 33: L15317. http://dx.doi.org/10.1029/2006GL026868.

Sakai T, Ohtani E, Terasaki H, et al. (2009a) Fe–Mg partitioning between perovskite and ferropericlase. *American Mineralogist* 94: 921–925. http://dx.doi.org/10.2138/am.2009.3123.

Sakai T, Ohtani E, Terasaki H, et al. (2009b) Fe–Mg partitioning between postperovskite and ferropericlase in the lowermost mantle. *Physical Chemistry of Minerals* 37(487–496): 1–10.

Saltzer RL, van der Hilst RD, and Kârason H (2001) Comparing P and S-wave heterogeneity in the mantle. *Geophysical Research Letters* 28: 1335–1338.

Samuel H and Tosi N (2012) The influence of post-perovskite strength on the Earth's mantle thermal and chemical evolution. *Earth and Planetary Science Letters* 323–324: 50–59.

Scherbaum F, Krüger F, and Weber M (1997) Double beam imaging: Mapping lower mantle heterogeneities using combinations of source and receiver arrays. *Journal of Geophysical Research* 102: 507–522.

Schlittenhardt J, Schweitzer J, and Müller G (1985) Evidence against a discontinuity at the top of D″. *Geophysical Journal of the Royal Astronomical Society* 81: 295–306.

Schmerr N, Garnero E, and McNamara A (2010) Deep mantle plumes and convective upwelling beneath the Pacific Ocean. *Earth and Planetary Science Letters* 294: 143–151.

Schuberth BSA, Bunge H-P, and Ritsema J (2009) Tomographic filtering of high-resolution mantle circulation models: Can seismic heterogeneity be explained by temperature alone? *Geochemistry, Geophysics, Geosystems* 10: Q05W03. http://dx.doi.org/10.1029/2009GC002401.

Schwartz SY, Lay T, and Grand SP (1991) Seismic imaging of subducted slabs: Trade-offs with deep path and near-receiver effects. *Geophysical Research Letters* 18: 1265–1268.

Seagle CT, Heinz DL, Campbell AJ, Prakapenka VB, and Wanless ST (2008) Melting and thermal expansion in the Fe–FeO system at high pressure. *Earth and Planetary Science Letters* 265: 655–665.

Sengupta MK and Julian BR (1978) Radial variation of compressional and shear velocities in the Earth's lower mantle. *Geophysical Journal of the Royal Astronomical Society* 54: 185–219.

Sengupta MK and Toksoz MN (1976) Three-dimensional model of seismic velocity variation in the Earth's mantle. *Geophysical Research Letters* 3: 84–86.

Shahnas MH, Peltier WR, Wu Z, and Wentzcovitch R (2011) The high-pressure electronic spin transition in iron: Potential impacts upon mantle mixing. *Journal of Geophysical Research* 116: B08205. http://dx.doi.org/10.1029/2010JB007965.

Shearer PM (1993) Global mapping of upper mantle reflectors from long-period *SS* precursors. *Geophysical Journal International* 115: 878–904.

Shieh SR, Dorfman SM, Kubo A, Prakapenka VB, and Duffy TS (2011) Synthesis and equation of state of post-perovskites in the $(Mg,Fe)_3Al_2Si_3O_{12}$ system. *Earth and Planetary Science Letters* 312: 422–428.

Shieh SR, Duffy TS, Kubo A, et al. (2006) Equation of state of the post-perovskite phase synthesized from a natural $(Mg,Fe)SiO_3$ orthopyroxene. *Proceedings of the National Academy of Sciences of the United States of America* 103: 3039–3043.

Shim SH (2008) The post-perovskite transition. *Annual Reviews of Earth and Planetary Sciences* 36: 569–599.

Shim S-H, Bengtson A, Morgan D, et al. (2009) Electronic and magnetic structures of the postperovskite-type Fe_2O_3—Implications for planetary magnetic records and deep interior transitions. *Proceedings of the National Academy of Sciences of the United States of America* 106: 5508–5512. http://dx.doi.org/10.1073/pnas.0808549106.

Shim S-H, Catalli K, Hustoft J, et al. (2008) Crystal structure and thermoelastic properties of $(Mg_{0.91}Fe_{0.09})SiO_3$ postperovskite up to 135 GPa and 2700 K. *Proceedings of the National Academy of Sciences of the United States of America* 105: 7382–7386.

Shim SH, Duffy TS, Jeanloz R, and Shen G (2004) Stability and crystal structure of $MgSiO_3$ perovskite to the core–mantle boundary. *Geophysical Research Letters* 31: L10603. http://dx.doi.org/10.1029/2004GL019639.

Shim SH, Duffy TH, and Shen GY (2001) Stability and structure of $MgSiO_3$ perovskite to 2300-kilometer depth in the Earth's mantle. *Science* 293: 2437–2440.
Shim S-H, Kubo A, and Duffy TS (2007) Raman spectroscopy of perovskite and post-perovskite phases of $MgGeO_3$ to 123 GPa. *Earth and Planetary Science Letters* 260: 166–178.
Sidorin I, Gurnis M, and Helmberger DV (1999) Evidence for a ubiquitous seismic discontinuity at the base of the mantle. *Science* 286: 1326–1331.
Sidorin I, Gurnis M, Helmberger DV, and Ding X (1998) Interpreting D″ seismic structure using synthetic waveforms computed from dynamic models. *Earth and Planetary Science Letters* 163: 31–41.
Silver PG and Bina CR (1993) An anomaly in the amplitude ratio of SKKS/SKS in the range 100–108° from portable teleseismic data. *Geophysical Research Letters* 20: 1135–1138.
Simmons NA, Forte AM, Boschi L, and Grand SP (2010) GyPSuM: A joint tomographic model of mantle density and seismic wave speeds. *Journal of Geophysical Research* 115: B12310. http://dx.doi.org/10.1029/2010JB007631.
Simmons NA, Forte AM, and Grand SP (2007) Thermochemical structure and dynamics of the African superplume. *Geophysical Research Letters* 34: L02301. http://dx.doi.org/10.1029/2006GL028009.
Simmons NA, Forte AM, and Grand SP (2009) Joint seismic, geodynamic and mineral physical constraints on three-dimensional mantle heterogeneity: Implications for the relative importance of thermal versus compositional heterogeneity. *Geophysical Journal International* 177: 1284–1304. http://dx.doi.org/10.1111/j.1365-246X.2009.04133.x.
Simmons NA and Grand SP (2002) Partial melting in the deepest mantle. *Geophysical Research Letters* 29. http://dx.doi.org/10.1029/2001GI013716.
Simmons NA, Myers SC, and Johannesson G (2011) Global-scale P wave tomography optimized for prediction of teleseismic and regional travel times for Middle East events: 2. Tomographic inversion. *Journal of Geophysical Research* 116: B04305. http://dx.doi.org/10.1029/2010JB007969.
Simmons NA, Myers SC, Johannesson G, and Matzel E (2012) LLNL-G3Dv3: Global P wave tomography model for improved regional and teleseismic travel time prediction. *Journal of Geophysical Research* 117: B10302. http://dx.doi.org/10.1029/2012JB009525.
Sinmyo R, Hirose K, Muto S, Ohishi Y, and Yasuhara A (2011) The valence state and partitioning of iron in the Earth's lowermost mantle. *Journal of Geophysical Research* 116: B07205. http://dx.doi.org/10.1029/2010JB008179.
Sinmyo R, Hirose K, Nishio-Hamane D, et al. (2008) Partitioning of iron between perovskite/postperovskite and ferropericlase in the lower mantle. *Journal of Geophysical Research* 113: B11204. http://dx.doi.org/10.1029/2008JB005730.
Sinmyo R, Hirose K, O-Neill HStC, and Okunishi E (2006) Ferric iron in Al-bearing post-perovskite. *Geophysical Research Letters* 33: L12S13. http://dx.doi.org/10.1029/2006GL025858.
Sinmyo R, Ozawa H, Hirose K, et al. (2008) Ferric iron content in $(Mg,Fe)SiO_3$ perovskite and post-perovskite at deep lower mantle conditions. *American Mineralogist* 93: 1899–1902.
Sleep NH (1988) Gradual entrainment of a chemical layer at the base of the mantle by overlying convection. *Geophysical Journal* 95: 437–447.
Soldati G, Boschi L, and Forte AM (2012) Tomography of core–mantle boundary and lowermost mantle coupled by geodynamics. *Geophysical Journal International* 189: 730–746. http://dx.doi.org/10.1111/j.1365-246X.2012.05413.x.
Spera FJ, Yuen DA, and Giles G (2006) Tradeoffs in chemical and thermal variations in the post-perovskite phase transition: Mixed phase regions in the deep lower mantle? *Physics of the Earth and Planetary Interiors* 159: 234–246. http://dx.doi.org/10.1016/j.pepi.2006.07.007.
Speziale S, Lee VE, Clark SM, Lin JF, Pasternak MP, and Jeanloz R (2007) Effects of Fe spin transition on the elasticity of (Mg,Fe)O magnesiowüstites and implications for the seismological properties of the Earth's lower mantle. *Journal of Geophysical Research* 112: B10212. http://dx.doi.org/10.1029/2006JB004730.
Speziale S, Milner A, Lee VE, Clark SM, Pasternak MP, and Jeanloz R (2005) Iron spin transition in Earth's mantle. *Proceedings of the National Academy of Sciences of the United States of America* 102(50): 17918–17922.
Speziale S, Zha C-S, Duffy TS, Hemley RJ, Mao HK, and Jeanloz R (2007) Quasihydrostatic compression of magnesium oxide to 52 GPa: Implications for the pressure–volume–temperature equation of state. *Journal of Geophysical Research* 106: 515–528.
Sreenivasan B and Gubbins D (2011) On mantle-induced heat flow variations at the inner core boundary. *Physics of the Earth and Planetary Interiors* 187: 336–341.
Stacey FD and Loper DE (1983) The thermal boundary layer interpretation of D″ and its role as a plume source. *Physics of the Earth and Planetary Interiors* 33: 45–55.
Stackhouse S and Brodholt JP (2007) High-temperature elasticity of $MgSiO_3$ postperovskite. In: Hirose K, Brodholt JP, Lay T, and Yuen D (eds.) *Post-perovskite: The Last Mantle Phase Transition*, pp. 99–113. Washington, DC: American Geophysical Union.
Stackhouse S, Brodholt J, Dobson D, and Price GD (2006) Electronic spin transitions and the seismic properties of ferrous iron-bearing $MgSiO_3$ post-perovskite. *Geophysical Research Letters* 33: L12S03. http://dx.doi.org/10.1029/2005GL025589.
Stackhouse S, Brodholt JP, and Price GD (2005) High temperature elastic anisotropy of the perovskite and post-perovskite polymorphs of AL_2O_3. *Geophysical Research Letters* 32: L132305. http://dx.doi.org/10.1029/2005GL0223163.
Stackhouse S, Brodholt JP, and Price GD (2006) Elastic anisotropy of $FeSiO_3$ end-members of the perovskite and post-perovskite phases. *Geophysical Research Letters* 33: L01304. http://dx.doi.org/10.1029/2006GL023887.
Stackhouse S, Brodholt J, and Price GD (2007) Electronic spin transitions in iron-bearing $MgSiO_3$ perovskite. *Earth and Planetary Science Letters* 253(1–2): 282–290. http://dx.doi.org/10.1016/j.epsl.2006.10.035.
Stackhouse S, Brodholt JP, Price GD, Wookey J, and Kendall JM (2005) The effect of temperature on the acoustic anisotropy of the perovskite and post-perovskite polymorphs of $MgSiO_3$. *Earth and Planetary Science Letters* 230: 1–10.
Stackhouse S, Stixrude L, and Karki BB (2010) Thermal conductivity of periclase (MgO) from first principles. *Physical Review Letters* 104: 208501.
Steinberger B and Torsvik T (2012) A geodynamic model of plumes from the margins of large low shear velocity provinces. *Geochemistry, Geophysics, Geosystems* 13: Q01W09.
Stixrude L (1998) Elastic constants and anisotropy of $MgSiO_3$ perovskite, periclase, and SiO_2 at high pressure. In: Gurnis M, Wysession ME, Knittle E, and Buffett BA (eds.) *The Core–Mantle Boundary Region*, pp. 83–86. Washington, DC: American Geophysical Union.
Stixrude L, de Koker N, Sun N, Mookherjee M, and Karki BB (2009) Thermodynamics of silicate liquids in the deep Earth. *Earth and Planetary Science Letters* 278: 226–232.
Stixrude L, Lithgow-Bertelloni C, Kiefer B, and Fumagalli P (2007) Phase stability and shear softening in $CaSiO_3$ perovskite at high pressure. *Physical Review B* 75: 024108.
Stolen S and Tronnes RG (2007) The perovskite to post-perovskite transition in $CaIrO_3$: Clapeyron slope and changes in bulk and shear moduli by density functional theory. *Physics of the Earth and Planetary Interiors* 164: 50–62.
Sturhahn W, Jackson JM, and Lin J-F (2005) The spin state of iron in minerals in Earth's lower mantle. *Geophysical Research Letters* 32: L12307. http://dx.doi.org/10.1029/2005GL022802.
Stutzmann E, Vinnik L, Ferreira A, and Singh S (2000) Constraint on the S-wave velocity at the base of the mantle. *Geophysical Research Letters* 27: 1571–1574.
Styles E, Goes S, van Keken PE, Ritsema J, and Smith H (2011) Synthetic images of dynamically predicted plumes and comparison with a global tomographic model. *Earth and Planetary Science Letters* 311: 351–363.
Su WJ and Dziewonski AM (1997) Simultaneous inversion for 3-D variations in shear and bulk velocity in the mantle. *Physics of the Earth and Planetary Interiors* 100: 135–156.
Su W, Woodward RL, and Dziewonski AM (1994) Degree 12 model of shear velocity heterogeneity in the mantle. *Journal of Geophysical Research* 99: 6945–6980.
Sueda Y, Irifune T, Yamada A, Inoue T, Liu X, and K-i Funakoshi (2006) The phase boundary between $CaSiO_3$ perovskite and $Ca_2SiO_4 + CaSi_2O_5$ determined by in situ x-ray observations. *Geophysical Research Letters* 33: L10307. http://dx.doi.org/10.1029/2006GL025772.
Sumita I and Olson P (2000) Thermal convection experiments in a rapidly rotating hemispherical shell. *Science* 286: 1547–1549.
Sun D and Helmberger D (2008) Lower mantle tomography and phase change mapping. *Journal of Geophysical Research* 113: B10305. http://dx.doi.org/10.1029/2007JB005289.
Sun D, Helmberger D, and Gurnis M (2010) A narrow, mid-mantle plume below southern Africa. *Geophysical Research Letters* 37: L09302. http://dx.doi.org/10.1029/2009GL042339.
Sun D, Helmberger D, Ni S, and Bower D (2009) Direct measures of lateral velocity variation in the deep Earth. *Journal of Geophysical Research* 114: B05303. http://dx.doi.org/10.1029/2008JB005873.
Sun D, Song AT-R, and Helmberger D (2006) Complexity of D″ in the presence of slab-debris and phase changes. *Geophysical Research Letters* 33: L12S07. http://dx.doi.org/10.1029/2005GL025384.
Sun D, Song X, Zheng S, and Helmberger DV (2007) Evidence for a chemical-thermal structure at base of mantle from sharp lateral P-wave variations beneath Central America. *Proceedings of the National Academy of Sciences of the United States of America* 104: 26–30.
Sun D, Tan E, Helmberger DV, and Gurnis M (2007) Seismological support for the metastable superplume model, sharp features, and phase changes within the lower

mantle. *Proceedings of the National Academy of Sciences of the United States of America* 104: 9151–9155.
Sze EKM and van der Hilst RD (2003) Core mantle boundary topography from short period *PcP*, *PKP*, and *PKKP* data. *Physics of the Earth and Planetary Interiors* 135: 27–46.
Tackley PJ (1998) Three-dimensional simulations of mantle convection with a thermo-chemical basal boundary layer: D″? In: Gurnis M, Wysession ME, Knittle E, and Buffett BA (eds.) *The Core–Mantle Boundary Region*, pp. 231–253. Washington, DC: American Geophysical Union.
Tackley PJ (2012) Dynamics and evolution of the deep mantle resulting from thermal, chemical, phase and melting effects. *Earth-Science Reviews* 110: 1–25.
Tackley PJ, Nakagawa T, and Hernlund JW (2007) Influence of the post-perovskite transition on thermal and thermo-chemical mantle convection. *Post-Perovskite: The Last Mantle Phase Transition*, *Geophysical Monograph Series*, vol. 174, 229–247.
Takahashi F, Tsunakawa H, Matsushima M, Mochizuki N, and Honkura Y (2008) Effects of thermally heterogeneous structure in the lowermost mantle on the geomagnetic field strength. *Earth and Planetary Science Letters* 272: 738–746.
Takei Y and Suetsugu D (1989) A high velocity zone in the lower mantle under the Japan subduction zone inferred from precise measurements of P-wave arrival times. *Journal of Physics of the Earth* 37: 225–231.
Takeuchi N (2007) Whole mantle SH velocity model constrained by waveform inversion based on three-dimensional Born kernels. *Geophysical Journal International* 169: 1153–1163.
Takeuchi N (2009) A low-velocity conduit throughout the mantle in the robust component of a tomography model. *Geophysical Research Letters* 36: L07306. http://dx.doi.org/10.1029/2009GL037590.
Takeuchi N (2012) Detection of ridge-like structures in the Pacific Large Low-Shear-Velocity Province. *Earth and Planetary Science Letters* 319–310: 55–64.
Takeuchi N, Morita Y, Xuyen ND, and Zung NQ (2008) Extent of the low-velocity region in the lowermost mantle beneath the western Pacific detected by the Vietnamese Broadband Seismograph Array. *Geophysical Research Letters* 35: L05307. http://dx.doi.org/10.1029/2008GL033197.
Takeuchi N and Obara K (2010) Fine-scale topography on the D″ discontinuity and its correlation to volumetric velocity fluctuations. *Physics of the Earth and Planetary Interiors* 183: 126–135.
Tan E and Gurnis M (2005) Metastable superplumes and mantle compressibility. *Geophysical Research Letters* 32: L20307. http://dx.doi.org/10.1029/2005GL024190.
Tan E and Gurnis M (2007) Compressible thermochemical convection and application to lower mantle structures. *Journal of Geophysical Research* 112: B06304. http://dx.doi.org/10.1029/2006JB004505.
Tan E, Leng W, and Zhong S (2011) On the location of plumes and lateral movement of thermochemical structures with high bulk modulus in the 3-d compressible mantle. *Geochemistry, Geophysics, Geosystems* 12: Q07005.
Tanaka S (2002) Very low shear wave velocity at the base of the mantle under the South Pacific superswell. *Earth and Planetary Science Letters* 203: 879–893.
Tanaka S (2010) Constraints on the core–mantle boundary topography from P4KP-PcP differential travel times. *Journal of Geophysical Research* 115: B04310. http://dx.doi.org/10.1029/2009JB006563.
Tanaka S, Suetsugu D, Shiobara H, et al. (2009) On the vertical extent of the large low shear velocity province beneath the South Pacific Superswell. *Geophysical Research Letters* 36: L07305. http://dx.doi.org/10.1029/2009GL037568.
Tange Y, Kuwayama Y, Irifune T, Funakoshi K-i, and Ohishi Y (2012) *P–V–T* equation of state of $MgSiO_3$ perovskite based on the MgO pressure scale: A comprehensive reference for mineralogy of the lower mantle. *Journal of Geophysical Research* 117: B06201. http://dx.doi.org/10.1029/2011JB008988.
Tange Y, Takahashi E, Nishihara Y, Funakoshi K, and Sata N (2009) Phase relations in the system MgO–FeO–SiO_2 to 50 GPa and 2000 °C: An application of experimental techniques using multianvil apparatus with sintered diamond anvils. *Journal of Geophysical Research* 114: B02214. http://dx.doi.org/10.1029/2008JB005891.
Tarits P and Mandéa M (2010) The heterogeneous electrical conductivity structure of the lower mantle. *Physics of the Earth and Planetary Interiors* 183: 115–125.
Tateno S, Hirose K, Sata N, and Ohishi Y (2005) Phase relations in $Mg_3Al_2Si_3O_{12}$ to 180 GPa: Effect of Al on post-perovskite phase transition. *Geophysical Research Letters* 32: L15306. http://dx.doi.org/10.1029/2005GL023309.
Tateno S, Hirose K, Sata N, and Ohishi Y (2006) High-pressure behavior of $MnGeO_3$ and $CdGeO_3$ and the post-perovskite phase transition. *Physical Chemistry of Minerals* 32: 721–725.
Tateno S, Hirose K, Sata N, and Ohishi Y (2007) Solubility of FeO in $(Mg,Fe)SiO_3$ perovskite and the post-perovskite phase transition. *Physics of the Earth and Planetary Interiors* 160: 319–325.
Tateno S, Hirose K, Sata N, and Ohishi Y (2009) Determination of post-perovskite phase transition boundary up to 4400 K and implications for thermal structure in D″ layer. *Earth and Planetary Science Letters* 277: 130–136.
Tateno S, Hirose K, Sata N, and Ohishi Y (2010) Structural distortion of $CaSnO_3$ perovskite under pressure and the quenchable post-perovskite phase as a low pressure analogue to $MgSiO_3$. *Physics of the Earth and Planetary Interiors* 181: 54–59.
Terasaki H, Frost DJ, Rubie DC, and Langenhorst F (2007) Interconnectivity of Fe–O–S liquid in polycrystalline silicate perovskite at lower mantle conditions. *Physics of the Earth and Planetary Interiors* 161: 170–176.
Thomas C, Garnero EJ, and Lay T (2004a) High-resolution image of lowermost mantle structure under the Cocos Plate. *Journal of Geophysical Research* 109: B08307. http://dx.doi.org/10.1029/2004JB003013.
Thomas C, Kendall J-M, and Lowman J (2004b) Lower-mantle seismic discontinuities and the thermal morphology of subducted slabs. *Earth and Planetary Science Letters* 225: 105–113.
Thomas C, Heesom T, and Kendall JM (2002) Investigating the heterogeneity of the D″ region beneath the northern Pacific using a seismic array. *Journal of Geophysical Research* 107(B11): 2274. http://dx.doi.org/10.1029/2000JB000021.
Thomas C and Kendall JM (2002) The lowermost mantle beneath northern Asia: (2) Evidence for D″ anisotropy. *Geophysical Journal International* 151: 296–308.
Thomas C, Kendall J-M, and Helffrich G (2009) Probing two low-velocity regions with PKP b-caustic amplitudes and scattering. *Geophysical Journal International* 178: 503–512.
Thomas CW, Liu Q, Agee CB, Asimow PD, and Lange RA (2012) Multi-technique equation of state for Fe_2SiO_4 melt and the density of Fe-bearing silicate melts from 0 to 161 GPa. *Journal of Geophysical Research* 117: B10206. http://dx.doi.org/10.1029/2012JB009403.
Thomas C and Weber M (1997) P velocity heterogeneities in the lower mantle determined with the German Regional Seismic Network: Improvement of previous models and results of 2D modeling. *Physics of the Earth and Planetary Interiors* 101: 105–117.
Thomas C, Weber M, Agnon A, and Hofstetter A (1998) A low velocity lamella in D″. *Geophysical Research Letters* 25: 2885–2888.
Thomas C, Weber M, Wicks CW, and Scherbaum F (1999) Small scatterers in the lower mantle observed at German broadband arrays. *Journal of Geophysical Research* 104: 15073–15088.
Thomas C, Wookey J, Brodholt J, and Fieseler T (2011) Anisotropy as cause for polarity reversals of D″ reflections. *Earth and Planetary Science Letters* 307: 369–376.
Thomas C, Wookey J, and Simpson M (2007) D″ anisotropy beneath Southeast Asia. *Geophysical Research Letters* 34: L04301. http://dx.doi.org/10.1029/2006GL028965.
Thorne MS and Garnero EJ (2004) Inferences on ultralow-velocity zone structure from a global analysis of SPdKS waves. *Journal of Geophysical Research* 109: B08301. http://dx.doi.org/10.1029/2004JB003010.
Thorne MS, Garnero EJ, and Grand SP (2004) Geographic correlation between hot spots and deep mantle lateral shear-wave velocity gradients. *Physics of the Earth and Planetary Interiors* 146: 47–63.
Thorne MS, Garnero EJ, Jahnke G, Igel H, and McNamara AK (2013) Mega ultra low velocity zone and mantle flow. *Earth and Planetary Science Letters* 364: 59–67. http://dx.doi.org/10.1016/j.epsl.2012.12.034.
Thorne MS, Lay T, Garnero EJ, Jahnke G, and Igel H (2007) Seismic imaging of the laterally varying D″ region beneath the Cocos Plate. *Geophysical Journal International* 170: 635–648. http://dx.doi.org/10.1111/j.1365-246X.2006.03279.x.
Tibuleac IM and Herrin E (1999) Lower mantle lateral heterogeneity beneath the Caribbean Sea. *Science* 285: 1711–1715.
Tilmann FJ, McKenzie D, and Priesley KF (1998) P and S-wave scattering from mantle plumes. *Journal of Geophysical Research* 103: 21145–21163.
Tkalcic H and Romanowicz B (2002) Short scale heterogeneity in the lowermost mantle: Insights form PcP-P and ScS-S data. *Earth and Planetary Science Letters* 201: 57–68.
To A, Fukao Y, and Tsuboi S (2011) Evidence for a thick and localized ultra low shear velocity zone at the base of the mantle beneath the central Pacific. *Physics of the Earth and Planetary Interiors* 184: 119–133.
To A and Romanowicz B (2009) Finite frequency effects on global S diffracted traveltimes. *Geophysical Journal International* 179: 1645–1657. http://dx.doi.org/10.1111/j.1365-246X.2009.04359.x.
To A, Romanowicz B, Capdeville Y, and Takeuchi N (2005) 3D effects of sharp boundaries at the borders of the African and Pacific Superplumes: Observation and modeling. *Earth and Planetary Science Letters* 233: 237–253.
Toksöz MN, Minear JW, and Julian BR (1971) Temperature field and geophysical effects of a downgoing slab. *Journal of Geophysical Research* 76: 1113–1138.
Torsvik TH, Smethurst MA, Burke K, and Steinberger B (2006) Large Igneous Provinces generated from the margins of the large low-velocity provinces in the deep mantle. *Geophysical Journal International* 167: 1447–1460. http://dx.doi.org/10.1111/j.1365-246X.2006.03158.x.

Torsvik T, Smethurst MA, Burke K, and Steinberger B (2008) Long term stability in deep mantle structure: Evidence from the 300 Ma Skagerrak-Centered Large Igneous Province (the SCLIP). *Earth and Planetary Science Letters* 267: 444–452.

Tosi N, Cadek O, Martinec Z, Yuen DA, and Kaufmann G (2009) Is the long-wavelength geoid sensitive to the presence of post-perovskite above the core–mantle boundary? *Geophysical Research Letters* 36: L05303. http://dx.doi.org/10.1029/2008GL036902.

Tosi N, Yuen DA, and Čadek O (2010) Dynamical consequences in the lower mantle with the post-perovskite phase change and strongly depth-dependent thermodynamic and transport properties. *Earth and Planetary Science Letters* 298: 229–243.

Trampert J, Deschamps F, Resovsky J, and Yuen D (2004) Probabilistic tomography maps chemical heterogeneities throughout the lower mantle. *Science* 306: 853–856.

Trønnes RG (2009) Structure, mineralogy and dynamics of the lowermost mantle. *Mineralogy and Petrology*, http://dx.doi.org/10.1007/s00710-009-0068-z.

Tschauner O, Kiefer B, Liu H, Sinogeikin S, Somayazulu M, and Luo S-N (2008) Possible structural polymorphism in Al-bearing magnesium silicate post-perovskite. *American Mineralogist* 93: 533–539.

Tsuchiya T (2011) Elasticity of subducted basaltic crust at the lower mantle pressures: Insights on the nature of deep mantle heterogeneity. *Physics of the Earth and Planetary Interiors* 188: 142–149.

Tsuchiya T and Tsuchiya J (2006) Effect of impurity on the elasticity of perovskite and post-perovskite: Velocity contrast across the post-perovskite transition in (Mg,Fe,Al)(Si,Al)O_3. *Geophysical Research Letters* 33: L12S04. http://dx.doi.org/10.1029/2006GL025706.

Tsuchiya T and Tsuchiya J (2007) High-pressure–high-temperature phase relations of $MgGeO_3$: First-principles calculations. *Physical Review B* 76: 092105. http://dx.doi.org/10.1103/PhysRevB.76.092105.

Tsuchiya J and Tsuchiya T (2008) Postperovskite phase equilibria in the $MgSiO_3$–Al_2O_3 system. *Proceedings of the National Academy of Sciences of the United States of America* 105: 19160–19164.

Tsuchiya T, Tsuchiya J, Umemoto K, and Wentzcovitch RM (2004a) Phase transition in $MgSiO_3$ perovskite in the Earth's lower mantle. *Earth and Planetary Science Letters* 224: 241–248.

Tsuchiya T, Tsuchiya J, Umemoto K, and Wentzcovitch RM (2004b) Elasticity of post-perovskite $MgSiO_3$. *Geophysical Research Letters* 31: L14603. http://dx.doi.org/10.1029/2004GL020278.

Tsuchiya T, Wentzcovitch RM, da Silva CRS, and de Gironcoli S (2006) Spin transition in magnesiowustite in Earth's lower mantle. *Physical Review Letters* 96(19): 198501–198504. http://dx.doi.org/10.1103/PhysRevLett.96.198501.

Tsuchiya T, Wentzcovitch RM, da Silva CRS, de Gironcoli S, and Tsuchiya J (2006) Pressure induced high spin to low spin transition in magnesiowüstite. *Physica Status Solidi* 243(9): 2111–2116. http://dx.doi.org/10.1002/pssb.200666814.

Tsujino N and Nishihara Y (2010) Effect of pressure on grain-growth kinetics of ferropericlase to lower mantle conditions. *Geophysical Research Letters* 37: L14304. http://dx.doi.org/10.1029/2010GL043491.

Uhrhammer R (1978) S-wave travel times for a spherically averaged earth. *Geophysical Journal of the Royal Astronomical Society* 55: 283–309.

Umemoto K, Hsu H, and Wentzcovitch RM (2010) Effect of site degeneracies on the spin crossovers in (Mg,Fe)SiO_3 perovskite. *Physics of the Earth and Planetary Interiors* 180: 209–214.

Umemoto K, Wentzcovitch RM, Weidner DJ, and Parise JB (2006) $NaMgF_3$: A low-pressure analog of $MgSiO_3$. *Geophysical Research Letters* 33: L15304. http://dx.doi.org/10.1029/2006GL026348.

Umemoto K, Wentzcovitch RM, Yu YG, and Requist R (2008) Spin transition in (Mg,Fe)SiO_3 perovskite under pressure. *Earth and Planetary Science Letters* 276(1–2): 198–206.

Usui Y, Hiramatsu Y, Furumoto M, and Kanao M (2005) Thick and anisotropic D″ layer beneath Antarctic Ocean. *Geophysical Research Letters* 32: L13311. http://dx.doi.org/10.1029/2005GL022622.

Usui Y, Hiramatsu Y, Furumoto M, and Kanao M (2008) Evidence of seismic anisotropy and a lower temperature condition in the D″ layer beneath Pacific Antarctic Ridge in the Antarctic Ocean. *Physics of the Earth and Planetary Interiors* 167: 205–216.

Usui Y, Tsuchiya J, and Tsuchiya T (2010) Elastic, vibrational, and thermodynamic properties of $MgGeO_3$ postperovskite investigated by first principles simulation. *Journal of Geophysical Research* 115: B03201. http://dx.doi.org/10.1029/2009JB006468.

Valenzuela R and Wysession ME (1998) Illuminating the base of the mantle with core-diffracted waves. In: Gurnis M, Wysession ME, Knittle E, and Buffett BA (eds.) *The Core–Mantle Boundary Region*, pp. 57–72. Washington, DC: American Geophysical Union.

van den Berg AP, de Hoop MV, Yuen DA, Duchkov A, van der Hilst RD, and Jacobs MHG (2010) Geodynamical modeling and multiscale seismic expression of thermo-chemical heterogeneity and phase transitions in the lowermost mantle. *Physics of the Earth and Planetary Interiors* 180: 244–257. http://dx.doi.org/10.1016/j.pepi.2010.02.008.

van der Hilst RD, de Hoop MV, Wang P, Shim SH, Ma P, and Tenoria L (2007) Seismostratigraphy and thermal structure of Earth's core–mantle boundary region. *Science* 315: 1813–1817.

van der Hilst RD and Kárason H (1999) Compositional heterogeneity in the bottom 1000 kilometers of Earth's mantle: Toward a hybrid convection model. *Science* 283: 1885–1888.

van der Hilst RD, Widiyantoro S, and Engdahl ER (1997) Evidence for deep mantle circulation from global tomography. *Nature* 386: 578–584.

Vanacore E, Niu F, and Kawakatsu H (2006) Observations of the mid-mantle discontinuity beneath Indonesia from S to P converted waveforms. *Geophysical Research Letters* 33: L04302. http://dx.doi.org/10.1029/2005GL025106.

Vanpeteghem CB, Angel RJ, Ross N, et al. (2006) Al, Fe substitution in the $MgSiO_3$ perovskite structure: A single-crystal x-ray diffraction study. *Physics of the Earth and Planetary Interiors* 155(1–2): 96–103.

Vanpeteghem CB, Zhao J, Angle RJ, Ross NL, and Bolfan-Casanova N (2006) Crystal structure and equation of state of $MgSiO_3$ perovskite. *Geophysical Research Letters* 33: L03306. http://dx.doi.org/10.1029/2005GL024955.

Vasco DW and Johnson LR (1998) Whole Earth structure estimated from seismic arrival times. *Journal of Geophysical Research* 103: 2633–2671.

Velimsky J (2010) Electrical conductivity in the lower mantle: Constraints from CHAMP satellite data by time-domain EM induction modeling. *Physics of the Earth and Planetary Interiors* 180: 111–117.

Velimsky J, Benesova N, and Cizkova H (2012) On the detectability of 3-D postperovskite distribution in D″ by electromagnetic induction. *Physics of the Earth and Planetary Interiors* 202–203: 71–77.

Vidale JE and Hedlin MAH (1998) Evidence for partial melt at the core–mantle boundary north of Tonga from the strong scattering of seismic waves. *Nature* 391: 628–684.

Vinnik LP, Breger L, and Romanowicz B (1998) Anisotropic structure at the base of the Earth's mantle. *Nature* 393: 564–567.

Vinnik LP, Farra V, and Romanowicz B (1989) Observational evidence for diffracted *SV* in the shadow of the Earth's core. *Geophysical Research Letters* 16: 519–522.

Vinnik LP, Niu F, and Kawakatsu H (1998) Broadband converted phases from midmantle discontinuities. *Earth, Planets and Space* 50: 987–997.

Vinnik LP, Oreshin SI, Speziale S, and Weber M (2010) Mid-mantle layering from SKS receiver functions. *Geophysical Research Letters* 37: L24302. http://dx.doi.org/10.1029/2010GL045323.

Vinnik L, Romanowicz B, LeStunff Y, and Makeyeva L (1995) Seismic anisotropy in the D″ layer. *Geophysical Research Letters* 22: 1657–1660.

Walker AM, Forte AM, Wookey J, Nowacki A, and Kendall J-M (2011) Elastic anisotropy of D″ predicted from global models of mantle flow. *Geochemistry, Geophysics, Geosystems* 12. http://dx.doi.org/10.1029/2011GC003732.

Walte N, Heidelbach F, Miyajima N, and Frost D (2007) Texture development and TEM analysis of deformed $CaIrO_3$: Implications for the D″ layer at the core–mantle boundary. *Geophysical Research Letters* 34: L08306. http://dx.doi.org/10.1029/2007GL029407.

Walte NP, Heidelbach F, Miyajima N, Frost DJ, Rubie DC, and Dobson DP (2009) Transformation textures in post-perovskite: Understanding mantle flow in the D″ layer of the Earth. *Geophysical Research Letters* 36: L04302. http://dx.doi.org/10.1029/2008GL036840.

Wang P, De Hoop MV, and van der Hilst RD (2008) Imaging of the lowermost mantle (D″) and the core–mantle boundary with SKKS coda waves. *Geophysical Journal International* 175: 103–115. http://dx.doi.org/10.1111/j.1365-246X.2008.03861.x.

Wang P, de Hoop MV, van der Hilst RD, Ma P, and Tenorio L (2006) Imaging of structure at and near the core–mantle boundary using a generalized radon transform: 1. Construction of image gathers. *Journal of Geophysical Research* 111: B12304.

Wang F, Tange Y, Irifune T, and Funakoshi K-i (2012) *P–V–T* equation of state of stishovite up to mid-lower mantle conditions. *Journal of Geophysical Research* 117: B06209. http://dx.doi.org/10.1029/2011JB009100.

Wang Y and Wen L (2004) Mapping the geometry and geographic distribution of a very low velocity province at the base of the Earth's mantle. *Journal of Geophysical Research* 109: B10305. http://dx.doi.org/10.1029/2003JB002674.

Wang Y and Wen L (2007a) Geometry and P and S velocity structures of the "African Anomaly" *Journal of Geophysical Research* 112: B05313. http://dx.doi.org/10.1029/2006JB004483.

Wang Y and Wen L (2007b) Complex seismic anisotropy at the border of a very low velocity province at the base of the Earth's mantle. *Journal of Geophysical Research* 112: B09305. http://dx.doi.org/10.1029/2006JB004719.

Weber M (1993) P and S-wave reflections from anomalies in the lowermost mantle. *Geophysical Journal International* 115: 183–210.

Weber M (1994) Lamellae in D″? An alternative model for lower mantle anomalies. *Geophysical Research Letters* 21: 2531–2534.

Weber M and Davis JP (1990) Evidence of a laterally variable lower mantle structure from P and S-waves. *Geophysical Journal International* 102: 231–255.

Wen L (2000) Intense seismic scattering near the Earth's core–mantle boundary beneath the Comoros hotspot. *Geophysical Research Letters* 27: 3627–3630.

Wen L (2001) Seismic evidence for a rapidly-varying compositional anomaly at the base of the Earth's mantle beneath Indian ocean. *Earth and Planetary Science Letters* 194: 83–95.

Wen L (2006) A compositional anomaly at the Earth's core–mantle boundary as an anchor to the relatively slowly moving surface hotspots and as source to the DUPAL anomaly. *Earth and Planetary Science Letters* 246: 138–148.

Wen L and Helmberger DV (1998) Ultra-low velocity zones near the core–mantle boundary from broadband PKP precursors. *Science* 279: 1701–1703.

Wen L, Silver P, James D, and Kuehnel R (2001) Seismic evidence for a thermo-chemical boundary layer at the base of the Earth's mantle. *Earth and Planetary Science Letters* 189: 141–153.

Wenk H-R, Cottaar S, Tomé CN, McNamara A, and Romanowicz B (2011) Deformation in the lowermost mantle: From polycrystal plasticity to seismic anisotropy. *Earth and Planetary Science Letters* 306: 33–45.

Wentzcovitch RM, Fusto J, Wu Z, da Silva C, Yuen D, and Kohlstedt D (2009) Anomalous compressibility of ferropericlase throughout the iron spin crossover. *Proceedings of the National Academy of Sciences of the United States of America* 106: 8447–8452.

Wentzcovitch RM, Karki BB, Cococcioni M, and de Gironcoli S (2004) Thermoelastic properties of $MgSiO_3$-perovskite: Insights on the nature of the Earth's lower mantle. *Physical Review Letters* 92: 018501-1–018501-4.

Wentzcovitch RM, Tsuchiya T, and Tsuchiya J (2006) $MgSiO_3$ postperovskite at D″ conditions. *Proceedings of the National Academy of Sciences of the United States of America* 103: 543–546.

Wicks JK, Jackson JM, and Sturhahn W (2010) Very low sound velocities in iron-rich (Mg,Fe)O: Implications for the core–mantle boundary region. *Geophysical Research Letters* 37: L15304. http://dx.doi.org/10.1029/2010GL043689.

Widiyantoro S and van der Hilst RD (1996) Mantle structure beneath Indonesia inferred from high-resolution tomographic imaging. *Geophysical Journal International* 130: 167–182.

Widmer R, Masters G, and Gilbert F (1991) Spherically symmetric attenuation within the Earth from normal mode data. *Geophysical Journal International* 104: 541–553.

Williams Q (1998) The temperature contrast across D″. In: Gurnis M, Wysession ME, Knittle E, and Buffett BA (eds.) *The Core–Mantle Boundary Region*, pp. 73–81. Washington, DC: American Geophysical Union.

Williams Q and Garnero EJ (1996) Seismic evidence for partial melt at the base of the Earth's mantle. *Science* 273: 1528–1530.

Williams Q, Revenaugh J, and Garnero EJ (1998) A correlation between ultra-low basal velocities in the mantle and hot spots. *Science* 281: 564–569.

Willis AP, Sreenivasan B, and Gubbins D (2007) Thermal core–mantle interaction: Exploring regimes for 'lockeD' dynamo action. *Physics of the Earth and Planetary Interiors* 165: 83–92.

Wookey J and Kendall J-M (2007) Seismic anisotropy of post-perovskite and the lowermost mantle. In: Hirose K, Brodholt J, Lay T, and Yuen D (eds.) *Post-Perovskite: The Last Mantle Phase Transition*. *Geophysical Monograph Series*, vol. 174, pp. 171–189. Washington, DC: AGU, 984.

Wookey J and Kendall J-M (2008) Constraints on lowermost mantle mineralogy and fabric beneath Siberia from seismic anisotropy. *Earth and Planetary Science Letters* 275: 32–42. http://dx.doi.org/10.1016/j.epsl.2008.07.049.

Wookey J, Kendall J-M, and Rümpker G (2005) Lowermost mantle anisotropy beneath the north Pacific from differential S-ScS splitting. *Geophysical Journal International* 161: 829–838.

Wookey J, Stackhouse S, Kendall J-M, Brodholt J, and Price GD (2005) Efficacy of the post-perovskite phase as an explanation for lowermost-mantle seismic properties. *Nature* 438: 1004–1007.

Wright C and Kuo B-Y (2007) The P-wavespeed structure in the lowermost 700 km of the mantle below the central part of the Indian Ocean. *Physics of the Earth and Planetary Interiors* 161: 243–266.

Wright C and Lyons JA (1975) Seismology, $dT/d\Delta$ and deep mantle convection. *Geophysical Journal of the Royal Astronomical Society* 40: 115–138.

Wright C, Muirhead KJ, and Dixon AE (1985) The P-wave velocity structure near the base of the mantle. *Journal of Geophysical Research* 90: 623–634.

Wu Z, Justo JF, da Silva CRS, de Gironcoli S, and Wentzcovitch RM (2009) Anomalous thermodynamic properties in ferropericlase throughout its spin crossover. *Physical Review B* 80: 014409. http://dx.doi.org/10.1103/PhysRevB.80.014409.

Wu W, Ni S, and Zeng X (2012) Evidence for P′P′ asymmetrical scattering at near podal distances. *Geophysical Research Letters* 39: L11306. http://dx.doi.org/10.1029/2012GL052179.

Wu X, Qin S, Gu T-T, Yang J, and Manthilake G (2011) Structural and elastic properties of $CaGeO_3$ perovskite at high pressures. *Physics of the Earth and Planetary Interiors* 189: 151–156.

Wu Z, Wentzcovitch RM, Umemoto K, Li B, Hirose K, and Zheng J-C (2008) Pressure–volume–temperature relations in MgO: An ultrahigh pressure–temperature scale for planetary sciences applications. *Journal of Geophysical Research* 113: B06204. http://dx.doi.org/10.1029/2007JB005275.

Wysession ME (1996) Large-scale structure at the core–mantle boundary from diffracted waves. *Nature* 382: 244–248.

Wysession ME, Fischer KM, Al-eqabi GI, Shore PJ, and Gurari I (2001) Using MOMA broadband array ScS-S data to image smaller-scale structures at the base of the mantle. *Geophysical Research Letters* 28: 867–870.

Wysession ME, Langenhorst A, Fouch MJ, et al. (1999) Lateral variations in compressional/shear velocities at the base of the mantle. *Science* 284: 120–125.

Wysession M, Lay T, Revenaugh J, et al. (1998) The D″ discontinuity and its implications. In: Gurnis M, Wysession ME, Knittle E, and Buffett BA (eds.) *The Core–Mantle Boundary Region*, pp. 273–298. Washington, DC: American Geophysical Union.

Wysession ME and Okal EA (1989) Regional analysis of D″ velocities from the ray parameters of diffracted P profiles. *Geophysical Research Letters* 16: 1417–1420.

Xu Y and Koper KD (2009) Detection of a ULVZ at the base of the mantle beneath the northwest Pacific. *Geophysical Research Letters* 36: L17301. http://dx.doi.org/10.1029/2009GL039387.

Xu J, Yamazaki D, Katsura T, et al. (2011) Silicon and magnesium diffusion in a single crystal of $MgSiO_3$ perovskite. *Journal of Geophysical Research* 116: B12205. http://dx.doi.org/10.1029/2011JB008444.

Yamada A and Nakanishi I (1998) Short-wavelength lateral variation of a D″ P-wave reflector beneath the southwestern Pacific. *Geophysical Research Letters* 25: 4545–4548.

Yamanaka T, Hirose K, Mao WL, et al. (2012) Crystal structures of $(Mg_{1-x}Fe_x)SiO_3$ postperovskite at high pressures. *Proceedings of the National Academy of Sciences of the United States of America* 109: 1035–1040.

Yamanaka T, Mao WL, Hemley RJ, and Shen G (2010) New structure and spin state of iron rich $MgFeSiO_3$ post-perovskite. *Journal of Physics: Conference Series* 215: 012100.

Yamazaki D and Karato S-I (2002) Fabric development in (Mg,O) during large strain shear deformation: Implications for seismic anisotropy in Earth's lower mantle. *Physics of the Earth and Planetary Interiors* 131: 251–267.

Yamazaki D and Karato S (2007) Lattice preferred orientation of lower mantle materials and seismic anisotropy in the D″ layer. In: Hirose K, Brodholt J, Lay T, and Yuen D (eds.) *Post-Perovskite: The Last Mantle Phase Transition*, *Geophysical Monograph Series*, vol. 174, pp. 69–78.

Yamazaki D, Yoshino T, Matsuzaki T, Katsura T, and Yoneda A (2009) Texture of $(Mg,Fe)SiO_3$ perovskite and ferro-periclase aggregate: Implications for rheology of the lower mantle. *Physics of the Earth and Planetary Interiors* 174: 138–144.

Yamazaki D, Yoshino T, Ohfuji H, Ando J, and Yoneda A (2006) Origin of seismic anisotropy in the D″ layer inferred from shear deformation experiments on post-perovskite phase. *Earth and Planetary Science Letters* 252: 372–378.

Yoshida M (2008) Core–mantle boundary topography estimated from numerical simulations of instantaneous flow. *Geochemistry, Geophysics, Geosystems* 9(7): Q07002. http://dx.doi.org/10.1029/2008GC002008.

Yoshino T, Ito E, Katsura T, et al. (2011) Effect of iron content on electrical conductivity of ferropericlase with implications for the spin transition pressure. *Journal of Geophysical Research* 116: B04202. http://dx.doi.org/10.1029/2010JB007801.

Yoshino T and Yamazaki D (2007) Grain growth kinetics of $CaIrO_3$ perovskite and postperovskite, with implications for rheology of D″ layer. *Earth and Planetary Science Letters* 255: 485–493.

Young CJ and Lay T (1987a) Evidence for a shear velocity discontinuity in the lower mantle beneath India and the Indian Ocean. *Physics of the Earth and Planetary Interiors* 49: 37–53.

Young CJ and Lay T (1987b) Comment on "Wave propagation effects and the Earth's structure in the lower mantle" *Geophysical Research Letters* 14: 562–565.

Young CJ and Lay T (1989) The core shadow zone boundary and lateral variations of the P velocity structure of the lowermost mantle. *Physics of the Earth and Planetary Interiors* 54: 64–81.

Young CJ and Lay T (1990) Multiple phase analysis of the shear velocity structure in the D″ region beneath Alaska. *Journal of Geophysical Research* 95: 17385–17402.

Youngs BAR and Houseman GA (2007) Topography on the D″ region from analysis of a thin dense layer beneath a convecting cell. *Physics of the Earth and Planetary Interiors* 160: 60–74.

Yu YG, Hsu H, Cococcioni M, and Wentzcovitch RM (2012) Spin states and hyperfine interactions of iron incorporated in $MgSiO_3$ post-perovskite. *Earth and Planetary Science Letters* 331–332: 1–7.

Yu YG, Wentzcovitch RM, Tsuchiya T, Umemoto K, and Weidner DJ (2007) First principles investigation of the postspinel transition in Mg_2SiO_4. *Geophysical Research Letters* 34: L10306. http://dx.doi.org/10.1029/2007GL029462.

Yuen DA, Matyska C, Cadek O, and Kameyama M (2007) The dynamical influences from physical properties in the lower mantle and post-perovskite phase transition. *Post-Perovskite: The Last Mantle Phase Transition*, *Geophysics Monograph Series*, 174, pp. 249–270.

Zhan D (2011) Shearing mechanism of $MgSiO_3$ at conditions of the Earth's D″ layer. *Geophysical Research Letters* 38: L16319. http://dx.doi.org/10.1029/2011GL048203.

Zhang L and Fei Y (2008) Melting behavior of (Mg,Fe)O solid solutions at high pressure. *Geophysical Research Letters* 35: L13302. http://dx.doi.org/10.1029/2008GL034585.

Zhang Y and Guo G (2009) Partitioning of Si and O between liquid iron and silicate melt: A two-phase ab-initio molecular dynamics study. *Geophysical Research Letters* 36: L18305. http://dx.doi.org/10.1029/2009GL039751.

Zhang L, Meng Y, and Mao WL (2012) Effect of pressure and composition on lattice parameters and unit-cell volume of $(Fe,Mg)SiO_3$ post-perovskite. *Earth and Planetary Science Letters* 317–318: 120–125.

Zhang F and Oganov AR (2006) Valence state and spin transitions of iron in Earth's mantle silicates. *Earth and Planetary Science Letters* 249(3–4): 436–443. http://dx.doi.org/10.1016/j.epsl.2006.07.023.

Zhang FW and Ogonov AR (2007) Mechanisms of Al^{3+} incorporation in $MgSiO_3$ post-perovskite at high pressures. *Earth and Planetary Science Letters* 248: 69–76.

Zhang Y, Ritsema J, and Thorne MS (2009) Modeling the ratios of SKKS and SKS amplitudes with ultra-low velocity zones at the core–mantle boundary. *Geophysical Research Letters* 36: L19303. http://dx.doi.org/10.1029/2009GL040030.

Zhao D (2001) Seismic structure and origin of hotspots and mantle plumes. *Earth and Planetary Science Letters* 192: 251–265.

Zhao D (2004) Global tomographic images of mantle plumes and subducting slabs: Insight into deep Earth dynamics. *Physics of the Earth and Planetary Interiors* 146: 3–34.

Zhong S (2006) Constraints on thermochemical convection of the mantle from plume heat flux, plume excess temperature, and upper mantle temperature. *Journal of Geophysical Research* 111: B04409. http://dx.doi.org/10.1029/2005JB003972.

Zhou H-W and Anderson DL (1989) Search for deep slabs in the northwest Pacific mantle. *Proceedings of the National Academy of Sciences of the United States of America* 86: 8602–8606.

Zhou H-W, Anderson DL, and Clayton RW (1990) Modeling of residual spheres for subduction zone earthquakes, 1: Apparent slab penetration signatures in the NW Pacific caused by deep diffuse mantle anomalies. *Journal of Geophysical Research* 95: 6799–6827.

Zou Z, Leyton F, and Koper KD (2007) Partial melt in the lowermost mantle near the base of a plume. *Geophysical Journal International* 168: 809–817. http://dx.doi.org/10.1111/j.1365-246X.2006.03266.x.

This page intentionally left blank

1.23 Deep Earth Structure: The Earth's Cores

A Souriau and M Calvet, CNRS and Université Paul Sabatier, Toulouse, France

© 2015 Elsevier B.V. All rights reserved.

This chapter is a revision of the previous edition chapter by A Souriau, Volume 1, pp. 655–693, © 2007, Elsevier B.V.

1.23.1	**Introduction**	725
1.23.2	**The Discovery of the Core**	726
1.23.2.1	Indirect Evidences for the Existence of a Core and Historical Controversies	726
1.23.2.2	The Seismological Detection of the Liquid Core and Inner Core	727
1.23.3	**Investigation Tools**	728
1.23.3.1	Body-Wave Seismology: The Core Phases	728
1.23.3.2	Normal Modes	729
1.23.3.3	High-Pressure Physics	729
1.23.4	**Radial Structure of the Core in Global Earth Models**	730
1.23.5	**The Major Discontinuities**	731
1.23.5.1	The Core–Mantle Boundary	731
1.23.5.1.1	The topography of the CMB	732
1.23.5.2	The Inner Core Boundary	732
1.23.5.2.1	The topography at ICB	733
1.23.5.2.2	The density jump at ICB and its implications	733
1.23.6	**The Liquid Outer Core**	733
1.23.6.1	The Main Questions Relative to Liquid Core Structure	733
1.23.6.2	The Stratification at the Base of the Liquid Core	734
1.23.6.3	The Stratification at the Top of the Liquid Core	734
1.23.6.4	Search for a Three-Dimensional Structure Inside the Liquid Core	735
1.23.6.5	The Attenuation in the Liquid Core	735
1.23.7	**The Inner Core: Seismic Velocities**	736
1.23.7.1	S-Waves and the Rigidity of the Inner Core	736
1.23.7.2	The Anisotropy in P-Wave Velocity	736
1.23.7.2.1	Evidence for anisotropy in P-wave velocity: early studies	736
1.23.7.2.2	Depth dependence of the anisotropy and hemispherical variations	737
1.23.7.2.3	The origin of anisotropy	740
1.23.7.3	Lateral Heterogeneities Inside the Inner Core and Scatterers	742
1.23.8	**The Inner Core: Seismic Attenuation**	742
1.23.8.1	P-Wave Attenuation: Depth Dependence and Hemispherical Variations	742
1.23.8.2	The Attenuation in Shear	744
1.23.8.3	The Anisotropy in Attenuation	744
1.23.8.4	Interpretation of Inner Core Attenuation	744
1.23.8.5	Origin of the Hemispherical Pattern in the Uppermost Inner Core	745
1.23.9	**Inner Core: Differential Rotation with Respect to the Mantle**	746
1.23.9.1	Tracking the Drift of a Heterogeneity Along a Stable Seismic Path	747
1.23.9.2	A Search for a Differential Rotation with a Worldwide Approach	749
1.23.9.3	Rotation or No Rotation? Implications	749
1.23.10	**Conclusion**	750
1.23.10.1	Summary of the Results	750
1.23.10.2	Open Questions and Future Challenges	751
References		752

1.23.1 Introduction

The Earth's core represents 16% of the volume of the Earth and more than 30% of its mass. It is composed of an iron alloy that incorporates light elements and nickel. At the center of this wide ocean of iron, the solid inner core, of about the size of the moon, represents only 4.3% of the volume of the core and $<1\%$ of the volume of the Earth. It results from the freezing of the liquid core during the cooling of the Earth, with a strong depletion in light elements. The core plays a very important role in Earth physics and chemistry. However, despite its impact on many physical processes such as magnetic field and the Earth's rotation, which have been investigated for centuries, the core has been detected very late, in 1906, when the seismological observation of the deep Earth became possible. Since then, important advances have been made, combining observations, laboratory experiments, and theoretical modeling. But the core remains enigmatic. If some of the core

properties are now firmly established, many others are still controversial. This chapter will attempt to give a survey of the present state of the art, trying to give a degree of confidence to the various results.

Before going through the details of the core structure, it is useful to recall some basic information concerning the core, which in addition shows its importance in the planet Earth system. The core is governed by complex systems of relations implying thermodynamics, hydrodynamics, geomagnetism, and geochemistry. Advances and results concerning these different disciplines may be found in other chapters of this treatise, in particular **Chapters 2.06**, **3.10**, **8.02**, **8.04–8.09**, **8.12**, **8.13**, **9.03**, and **9.08**.

The core forms very early in the history of our planet, as revealed by the analyses of lead and uranium mantle isotopes and other radionuclide chronometers and by the presence of a magnetic field in the oldest rocks of the Earth, 3.5 Ga old. It is generally accepted that the inner core formed by crystallization of the liquid core. Some thermodynamic arguments favor a rather young inner core, about 1 Ga old, but this is still open to discussion.

Convection in the liquid core is at the origin of the main part of the magnetic field. From this point of view, the core is essential to the life, as it protects the Earth from the solar wind. Numerical simulations of the Earth geodynamo show that the inner core has probably a stabilizing role for the magnetic field, as it prevents frequent geomagnetic reversals.

The boundary of the core with the silicate mantle, the core–mantle boundary (CMB), is a place of thermal, dynamic, and probably chemical exchanges. In particular, the exchange of angular momentum influences the Earth's rotation. At the inner core boundary (ICB), the freezing of the liquid iron alloy occurs with a depletion of the light elements that are present in the liquid core. The ICB is thus also an important place for chemical and energy exchanges. Heat sources linked to inner core growth, including latent heat and gravitational energy, are essential for powering the geodynamo and are important factors in the thermal history of the Earth.

In what follows, we will only consider the aspects relevant to the structure of the core, giving a particular importance to seismology, which has provided most of the results obtained today about its internal properties. After a brief historical review, we will present the most usual tools used in core seismology. The radial structure of the core will then be investigated, paying particular attention to the core boundaries. Then, a large section will concern the inner core, for which different properties will be considered: its rigidity; its anisotropy for both velocity and attenuation; its hemispherical dichotomy, which also concerns both velocity and attenuation; and its possible differential rotation or oscillation with respect to the mantle. We will end this chapter with the still open questions and future challenges.

1.23.2 The Discovery of the Core

Scientific arguments coming from astronomical and geological observations and theoretical developments concerning heat propagation, thermodynamics, geodesy, and mechanics led to the proposal that the Earth is stratified, with a silicate mantle and an iron core. But the specification of core properties is mostly derived from seismological observations. Combined with mineral physics, they have allowed us to obtain the present picture of the Earth, made of a silicate mantle, an iron liquid core, and a solid iron inner core, with a radius of 3480 km (0.55 ×Earth radius) for the CMB and a radius of 1220 km (0.19 ×Earth radius) for the ICB.

1.23.2.1 Indirect Evidences for the Existence of a Core and Historical Controversies

The fascination for the Earth's interior is present in the literature since the antiquities (see historical aspects in Brush, 1980; Bolt, 1982; Deparis and Legros, 2002). During the nineteenth century, it is generally accepted that the Earth has been fluid at its origin. This idea resulted mostly from the observation of the Earth flattening, an equilibrium figure supposed to be acquired during fluid stage, and from the identification of plutonic rocks. The question was raised of whether the Earth is still fluid in its interior, or solid as a result of its complete cooling, or partly solid. The geothermal gradient measured at the surface (about 30 °C km^{-1}) predicts a melting of the Earth silicates at about 80–100 km depth, an idea reinforced by the fluid lavas rejected by volcanoes. An argument against this model is given by Ampère (1775–1836), who noted that such a structure would not be able to support the high stresses induced by the lunar tides on the thin solid envelope. On the other hand, Poisson (1781–1840) noted that the melting temperature of rocks increases with pressure, opening the possibility of a completely solid Earth.

Two discoveries have allowed us to reconcile a solid Earth model with the high geothermal gradient: first, the idea that the internal heat is eliminated not only by conduction but also (and mostly) by convection and, second, the discovery of radioactivity as a source of internal heat, in addition to the initial heat. These two discoveries explain the impossibility of extrapolating the upper crust geothermal gradient downward. On the other hand, the comparison of the precession and nutations of the Earth observed from astronomy with those computed for different structures led Hopkins (1793–1866) to propose a solid envelope of at least 1000 km thickness, the fluid center being thus much too deep for being the feeding region of the volcanoes. More refined computations by Kelvin (1824–1907) gave a 2000–2500 km thickness for the solid envelope.

The mean density of the Earth, 5.52×10^3 kg m^{-3}, is much higher than that of the rocks (about 2.6×10^3 kg m^{-3} for granite), even at the temperature and pressure conditions present at 2500 km depth. Its moment of inertia, $I = 0.33\ Ma^2$, where M is the mass of the Earth and a its radius, is smaller than that of a homogeneous sphere ($I = 0.40\ Ma^2$), implying high densities at depth, thus a chemical differentiation. Geochemical arguments, in particular cosmic abundances and the existence of both silicate and iron meteorites, led to propose an iron core. Stony-iron meteorites such as pallasites may represent the CMB. At the end of the nineteenth century, a model with a silicate mantle above an iron core was widely accepted (e.g., Wiechert, 1896).

The effective detection of the core is, however, attached to seismology. In 1889, the first recording of a remote earthquake opened the possibility of sampling deep Earth structure with teleseismic data. This discovery stimulated the deployment of worldwide observatories and the international organization of seismology (see **Chapter 1.01**).

1.23.2.2 The Seismological Detection of the Liquid Core and Inner Core

Most of the teleseismic records exhibit two clear arrivals, a primary, compressional phase (P), and a secondary, shear phase (S). Oldham (1906) noted that the propagation time of the S-wave as a function of distance was delayed by about 10 min for angular distances larger than 130°. He ascribed this delay to the propagation through a core in which the velocity is smaller than in the mantle, due to a change in physical properties. Although the observed late phase was not S, but SS (an S phase reflected once beneath the surface), this observation led to consider that Oldham is the discoverer of the core. Gutenberg (1913) determined the depth of the CMB at 2900 km, a value that has not significantly changed later. The fluidity of the core was confirmed by Jeffreys (1926) thanks to the evaluation of the mean Earth rigidity deduced from Earth tides, which is lower than the mantle rigidity deduced from seismic wave propagation. The nature of this core, mostly made of fluid iron, was established by Birch (1952, 1964), a pioneer in high-pressure physics, who demonstrated that a silicate at pressure and temperature similar to core conditions could not reach the inferred mass density of about 10^4 kg m^{-3}.

The discovery of the inner core is due to Lehmann (1936), who detected a seismic phase arrival at a distance where no P-phase is supposed to arrive, in a distance range (about 110–140°) called the shadow zone of the core (**Figure 1(a)**). She

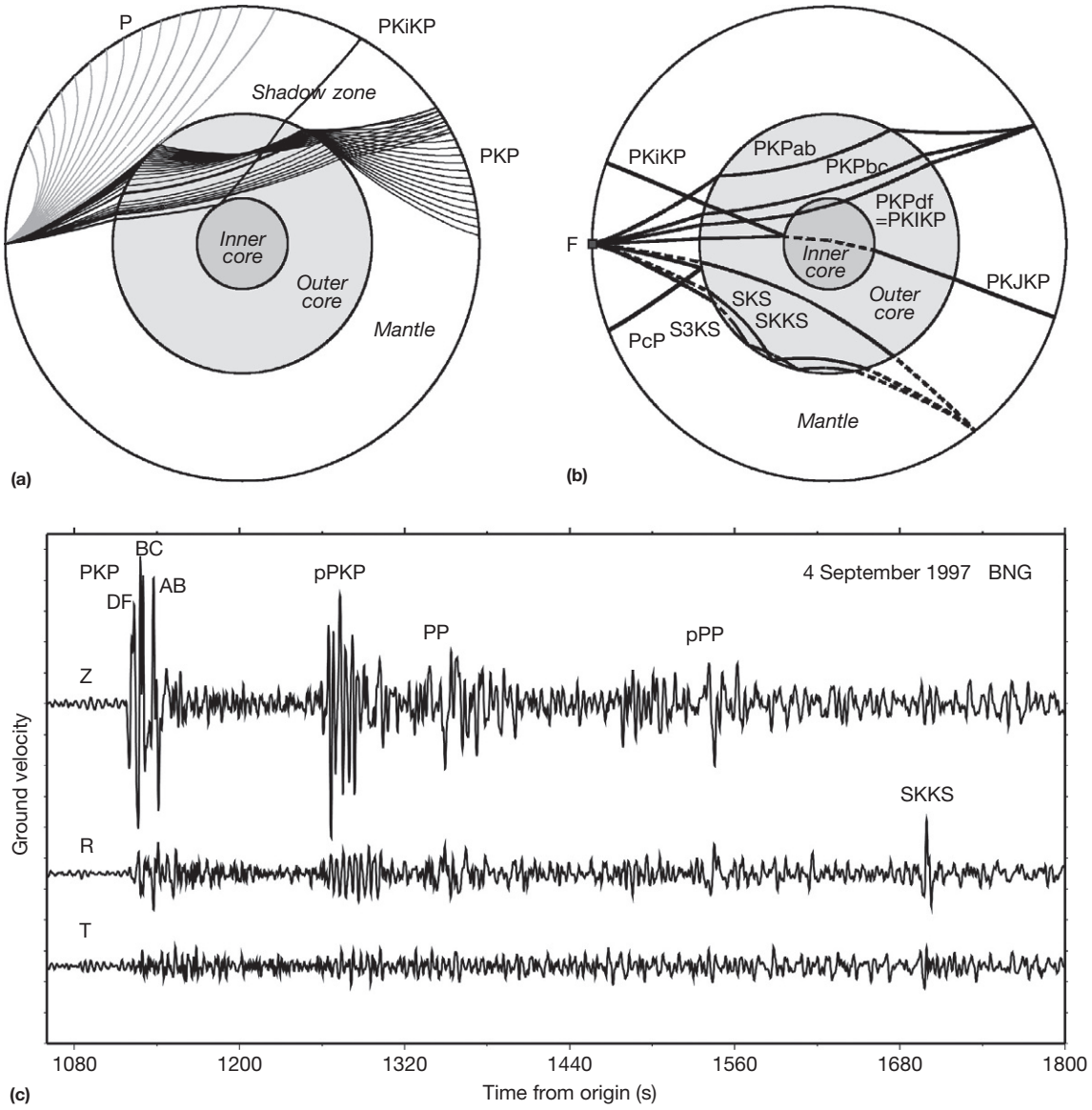

Figure 1 (a) Shadow zone of the core, due to the P-wave velocity decrease from the mantle to outer core, and PKiKP ray reflected at the inner core boundary, at the origin of the discovery of the inner core. (b) Paths of the main core phases inside the Earth propagating as P-waves (full lines) or S-waves (dashed lines). (c) Example of data: the first 11 min record of the Fiji islands, 04 September 1997 event (magnitude $M_b = 6.3$, depth = 621 km), at the Geoscope broadband station BNG (Bangui, Central African Republic), at distance 151°. Three components: Z-vertical, R-radial (in the ray direction), and T-transverse. Note the three phases of PKP on the vertical component, the pPKP phases first reflected at the Earth surface, and the SKKS phase on the radial component. The other phases are mantle phases. Courtesy of E. Stutzmann.

ascribed this phase to a P-wave reflected at an unknown discontinuity at a depth of about 5000 km, the ICB. A physical argument in favor of inner core rigidity is given by Jacobs (1953), who showed that the increase with pressure (thus with depth) of the melting point of iron must result in a phase change from liquid to solid at ICB conditions. An indirect proof of the inner core rigidity is given by the periods of the free oscillations of the Earth that are excited after large earthquakes and that are sensitive to the elastic properties of the deep Earth (Dziewonski and Gilbert, 1971).

Table 1 summarizes the main physical parameters of the core. Elastic parameters are taken from two global Earth models that are widely used as reference, PREM (Dziewonski and Anderson, 1981) and ak135 (Kennett et al., 1995). The temperature is the most poorly defined parameter, as it depends on the composition of the core, which is still debated. In particular, the presence of light elements may decrease the melting temperature of iron by 500–1000 °K (Poirier and Shankland, 1993), depending on their nature and concentration.

1.23.3 Investigation Tools

Among the various tools used to infer the core structure and properties, seismology is certainly the most powerful. Seismic waves allow us to obtain very precise values of the elastic parameters; to image lateral heterogeneities in velocities, anisotropy, and attenuation; and even to seek time variations, induced, for example, by a possible inner core rotation. However, the interpretation of the images obtained by seismology relies strongly on the results of mineral physics at high pressure and high temperature. Another important information is given by the Earth's rotation, in particular nutations and length of day, which are sensitive to the Earth's shape and stratification. The analysis of the magnetic field and its temporal variations give information on the convective motions in the liquid core, which will not be considered here (see Volume 8).

1.23.3.1 Body-Wave Seismology: The Core Phases

Core studies are based on travel times and amplitudes of the different phases sampling the core (compressional waves, shear waves, and combinations of both) and increasingly on whole waveform modeling (see Chapters 1.06 and 1.07). The worldwide digital broadband stations are the main source of waveform data. For travel times, values reported in the bulletins of the International Seismological Centre (ISC) or in derived improved catalogs (EHB file; Engdahl et al., 1998) are also used. For these data, the large amount of values collected since 1964, combined with statistical analyses, compensates for the uneven quality of single values. Finally, for some phases with a very low energy, stacking of records collected at arrays is necessary.

There are three particularities of core phases:

- S-waves, which is are shear waves, do not propagate inside the liquid core. Thus, the liquid core may be investigated only through P-waves.
- The waves sampling the core also travel twice through the mantle and crust, at station side and at source side. The crust and the base of the mantle, the so-called D″ layer, are highly heterogeneous, as well as the upper mantle in most of the source regions, because of the dipping slabs associated with subduction zones. Each time it is possible, it is thus convenient to use differential travel times between neighboring phases, which partly remove the perturbing contributions of the mantle and crust and mislocation and clock errors. In particular, the phase PKP(DF), also called PKIKP, which samples the inner core, is often compared to PKP (BC), a nearby phase that has its turning point at the base of the liquid core and has nearly the same waveform. It may also be compared to PKP(AB), which is more distant, more

Table 1 Main physical parameters for the Earth's core and the main discontinuities, from PREM at 1 s period (Dziewonski and Anderson, 1981), except for hydrostatic equilibrium ellipticity (Bullen and Haddon, 1973), and for temperatures

	Radius (km)	*Depth (km)*	V_P *(km s^{-1})*	V_S *(km s^{-1})*	*Density (g cm^{-3})*	*Pressure (GPa)*	*Temperature (°K)*	*Gravity (m s^{-2})*	*Ellipticity*
Crust and	6371	0	5.80	3.20	2.60	0	300	9.81	1/298.3
mantle	*6371*	*0*	*5.80*	*3.46*					
Silicates of Fe,	3480	2891	13.72	7.26	5.57	140	4100	10.7	1/392.7
Mg	*3479.5*	*2891.5*	*13.66*	*7.28*			(3700–4200)		
Core–mantle boundary (CMB)									
Liquid core	3480	2891	8.06	0	9.90	140	4100	10.7	1/392.7
Iron + light	*3479.5*	*2891.5*	*8.00*	*0*			(3700–4200)		
elements	1221.5	5149.5	10.36	0	12.17	330	5500	4.4	1/411
	1217.5	*5153.5*	*10.29*	*0*			(4600–5700)		
Inner core boundary (ICB)									
Inner core	1221.5	5149.5	11.03	3.50	12.76	330	5500	4.4	1/411
Almost pure	*1217.5*	*5153.5*	*11.04*	*3.50*			(4600–5700)		
iron	0	6371	11.26	3.67	13.09	360	5800	0	0
	0	*6371*	*11.26*	*3.67*			(5000–6000)		

Values in italics, velocity values for model ak135 (Kennett et al., 1995); temperatures from Chapter 9.08 and from Hirose K, Labrosse S, and Hernlund J (2013) Composition and state of the core. *Annual Review of Earth and Planetary Sciences* 41: 25.1–25.35.

affected by D″ heterogeneities, which differs from PKP(DF) by a Hilbert transform (Choy and Richards, 1975), but which is the simplest reference phase at large distance. These three PKP phases form a triplication in the PKP travel time curves as a function of distance.

– Because of their long path through the Earth, core phases have large Fresnel zones inside the core. For example, a PKP(DF) wave of 2 s period samples a tube about 500 km wide at its turning point, which is quite large compared to the inner core radius of 1220 km (Calvet et al., 2006; Figure 2). Thus, PKP(DF) returns a smeared image of the inner core.

A list of the main core phases and their use for core studies are given in Table 2. Their paths inside the Earth are shown in Figure 1(b), and an example of record is shown in Figure 1(c). Some of the paths are purely P-waves, with refractions or reflections at the core boundaries (PKP, PKKP, etc.); others are a combination of S- and P-waves, such as SKS, which propagates as S-wave in the mantle, or PKJKP, which propagates as S-wave inside the inner core.

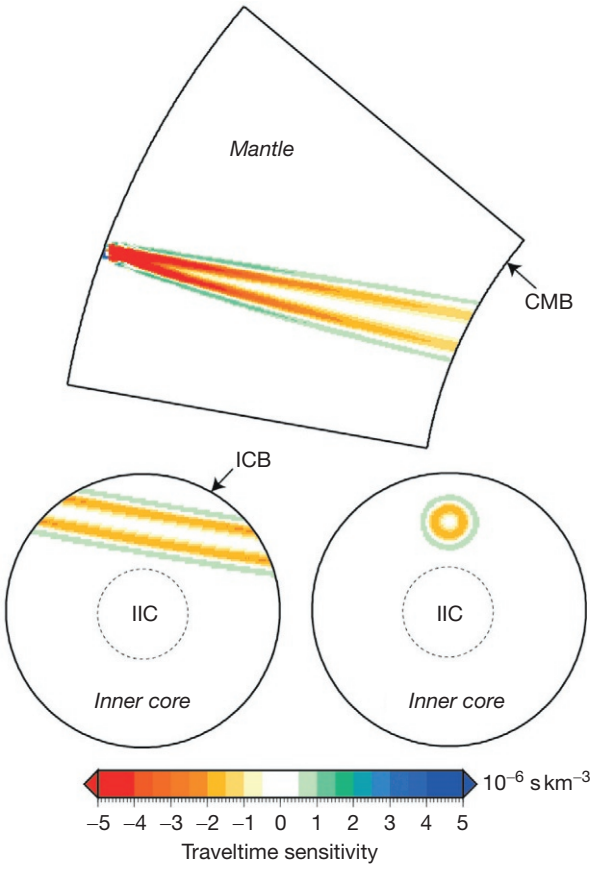

Figure 2 Travel time sensitivity kernel of PKP(DF) at 2 s period and 160° epicentral distance, giving the sensitivity of travel time to structure. (Top) Fresnel zone in the mantle along the ray. (Bottom) Fresnel zone in the inner core along the ray and perpendicular to the ray at its turning point. CMB, core–mantle boundary; ICB, inner core boundary; ICC, innermost inner core (see Section 1.23.7.2.2.3). Note the sensitivity of the PKP(DF) ray to the upper mantle structure and the large size of the Fresnel zone in the inner core, which will smear the images of small-scale heterogeneities or sharp discontinuities.

1.23.3.2 Normal Modes

The periods and amplitudes of free oscillations (or normal modes) allow us to retrieve the mean elastic parameters, density, and attenuation as a function of radius and their long wavelength heterogeneities (see Chapters 1.03 and 1.04). They avoid the problem of sparse sampling due to body waves. The splitting of the modes in multiplets gives information on the anisotropy, once the contributions of the Earth's rotation and ellipticity are corrected (e.g., Durek and Romanowicz, 1999; Dziewonski and Gilbert, 1971; Irving and Deuss, 2011a; Laske and Masters, 2003; Tromp, 1993). Modes are mostly sensitive to the even part of Earth structure. Thus, for example, a possible degree-one (hemispherical) pattern will be difficult to detect, unless mode coupling is considered (Irving et al., 2009). Moreover, only a limited number of modes have significant energy in the core, still fewer in the inner core, and mode energy decreases to zero at the Earth's center. Very large earthquakes are thus required to observe inner core-sensitive modes.

Normal modes are however crucial for core studies, as they allow us to obtain S-velocity and density (Kennett, 1998; Masters, 1979; Masters and Gubbins, 2003), which are very difficult to obtain from body waves. Moreover, they sample the low-frequency part of the spectrum, which is not accessible to body waves. Because of the fluidity of the core, only spheroidal modes are considered.

Figure 3 gives the energy in compression, shear, and density as a function of radius for various core-sensitive modes. The energy in the inner core remains small compared to that in the mantle and liquid core; it is thus necessary to combine data sensitive to different depths to reduce the influence of the mantle. The ability of modes to resolve sharp discontinuities remains however very poor.

1.23.3.3 High-Pressure Physics

High-pressure physics provides essential information for deriving the chemical, mineralogical, and textural structure of the Earth from seismic observations (see Volume 2). For example, the knowledge of the crystal structure of iron alloy is necessary for modeling seismic anisotropy in the inner core and for proposing models of core dynamics. Materials at core conditions may be explored either from laboratory experiments or from theoretical computations. Only few experiments in diamond anvil cells have reached the 360 GPa pressure present at the Earth's center. Core conditions are more easily reproduced by shock-wave experiments even if the temperature remains difficult to estimate. Computations based on first-principle molecular dynamics simulations, or ab initio computations, provide an alternative for simulating core conditions. These methods allow us to predict almost all the parameters of core materials (phase diagram of iron alloy, melting temperature, rheology, elasticity, etc.). However, the results depend on the approximations made and on the input parameters, for example, the nature and the amount of light elements included in the iron alloy.

Table 2 Main body waves sampling the core

Phase name	*Path*	*Use and peculiarities*
PKP(DF) = PKPdf = PKIKP	P propagating through the inner core	Inner core structure and anisotropy
PKP(BC) = PKPbc	P turning at the base of the liquid core	Liquid core structure Reference phase for PKP(DF) at distances 149–155°
PKP(AB) = PKPab	P turning in the middle of the liquid core	D″ structure Reference phase (poor) for PKP(DF) at large distance
PKKP = P2KP, P*n*KP	P with ($n-1$) underside reflections at CMB	Three branches (DF, BC, AB), difficult to observe CMB topography P*n*KP(BC): structure of the liquid core
PcP, ScS, PcS, ScP	P or S reflected as P or S at CMB (upperside reflection)	D″ structure CMB topography PcP: reference phase for PKiKP
PKiKP	P reflected at ICB (upperside reflection)	Topography and scatterers at ICB, density and S-velocity jump at ICB Difficult to observe at short distance
PKJKP	S through the inner core, P elsewhere	S-structure of the inner core Not directly observable
SKS, S*m*KS	S in the mantle, propagating as P in the liquid core ($m-1$) underside reflections at CMB	D″ structure Structure of the uppermost liquid core

CMB, core–mantle boundary; ICB, inner core boundary.

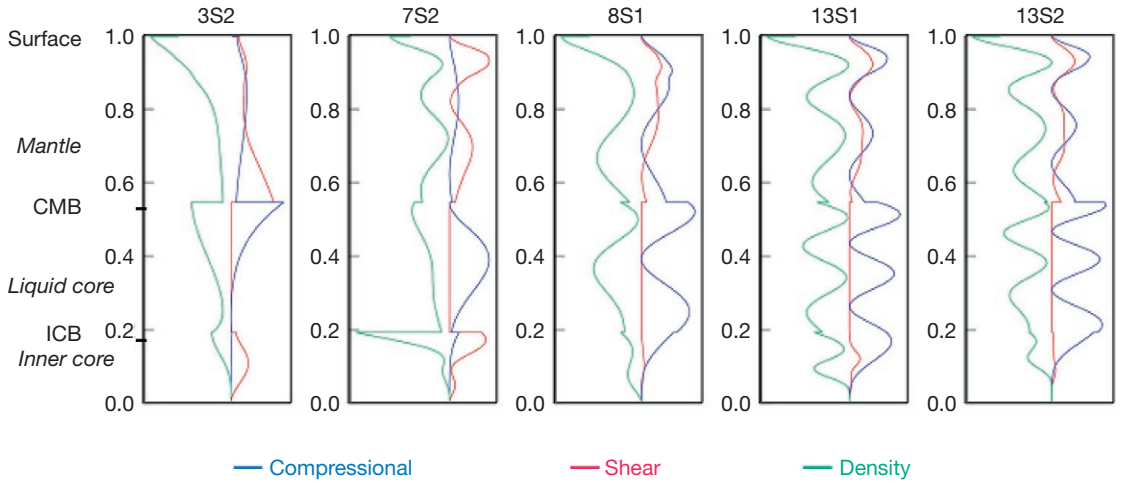

Figure 3 Sensitivity kernels for some core-sensitive modes as a function of radius, for a 1D Earth model (no lateral heterogeneity). Blue lines are for κ (compressional energy), red lines for μ (shear energy; note that it is zero in the fluid outer core), and green lines for density. CMB, core–mantle boundary; ICB, inner core boundary. Courtesy of G. Laske.

1.23.4 Radial Structure of the Core in Global Earth Models

The first accurate core models were derived from travel times and amplitudes of PKP and PKKP waves, from natural earthquakes, and also from nuclear explosions, which provide sources outside subduction zones. S*m*KS waves were used to constrain the upper part of the liquid core, where no PKP wave has its turning point. These models have given with a good precision the radii of the outer core and inner core and the mean velocity profiles and quality factors throughout the core (see references in Souriau and Poupinet, 1991). However, some of these models present artifacts, either because D″ heterogeneities were unmodeled or because PKP precursors, which are due to scatterers at the base of the mantle (Cleary and Haddon, 1972), were erroneously ascribed to a liquid core discontinuity (e.g., Bolt, 1962). This shows the importance of considering whole Earth inversion to obtain reliable reference core models (see **Chapter 1.01**). We will thus consider only the two global models, PREM (Dziewonski and Anderson, 1981) and ak135 (Kennett et al., 1995), which are the most commonly used (**Table 1**). Through this chapter, we will focus on the perturbations to these models inferred from the analyses of specific core phases and normal modes. Several other radial models are also convenient as reference models, for example, SP6 (Morelli and Dziewonski, 1993), IASP91 (Kennett and Engdahl, 1991), and ak135-f (Montagner and Kennett, 1995), derived from ak135 with the addition of density and

shear quality factor. They all exhibit nearly the same features and differ from each other by $<0.5\%$.

PREM (Dziewonski and Anderson, 1981; **Table 1**) was constructed using a combination of body waves and normal modes, thus allowing the authors to obtain a model not only in P- and S-velocities but also in density. The model is compatible with the mass and moment of inertia of the Earth. Moreover, a constraint on stable stratification was introduced a priori in the model before inversion, that is, the Adams–Williamson equation must be satisfied both in the liquid core and in the inner core, each of them assumed to be homogeneous. The final model does not depart significantly from this constraint, except perhaps at the very base of the liquid core. However, some models departing from this stability condition and compatible with normal mode data may also be found (Kennett, 1998).

Model ak135 (Kennett et al., 1995) is constructed from body-wave data only and is right now the best P-wave model inside the core. Its departure from PREM remains small (**Table 1**). ak135 has relatively low velocities at the top of the core but is slightly faster than PREM in the middle of the core. The main difference compared to PREM is a reduced velocity gradient at the base of the liquid core. The P-velocity jump at the ICB is larger in ak135 ($0.75\ \mathrm{km\ s^{-1}}$ instead of $0.67\ \mathrm{km\ s^{-1}}$), a value that may have implications for the percentage and nature of the light elements in the inner core. A comparison of the two models inside the core is shown in **Figure 4**.

It is important to draw attention on several particularities of the velocity profiles in the core. First, the upper part of the liquid core corresponds to a low P-velocity zone with respect to the mantle. This is at the origin of the refraction of P-wave to large distance when it encounters the CMB, giving the so-called shadow zone of the core (**Figure 1(a)** and **5**). The increase of P-velocity with depth bends the ray when its incidence angle decreases, leading to an emergence at shorter distance. This results in a triplication in the PKP travel time curve, each of the branches AB, BC, and DF sampling a different depth range in the core: AB corresponds to a turning point of the ray in the middle of the liquid core, BC at the base of the liquid core, and DF inside the inner core. The three PKP phases coexist in a small distance range between 145° and 155° (**Figure 5**). A second particularity of the velocity profile is that the S-velocity at the base of the mantle is nearly equal to the P-velocity at the top of the liquid core. Thus, the SKS wave (traveling as S in the mantle and P in the liquid core) is not strongly deflected at the CMB (**Figure 1(b)**) and may have its turning point in the uppermost liquid core. Finally, the velocity inside the inner core is nearly constant; thus, the rays are nearly straight. Note also the high Poisson's ratio in the inner core (0.44) compared to that of the mantle (0.26–0.30), which is a characteristic of metals.

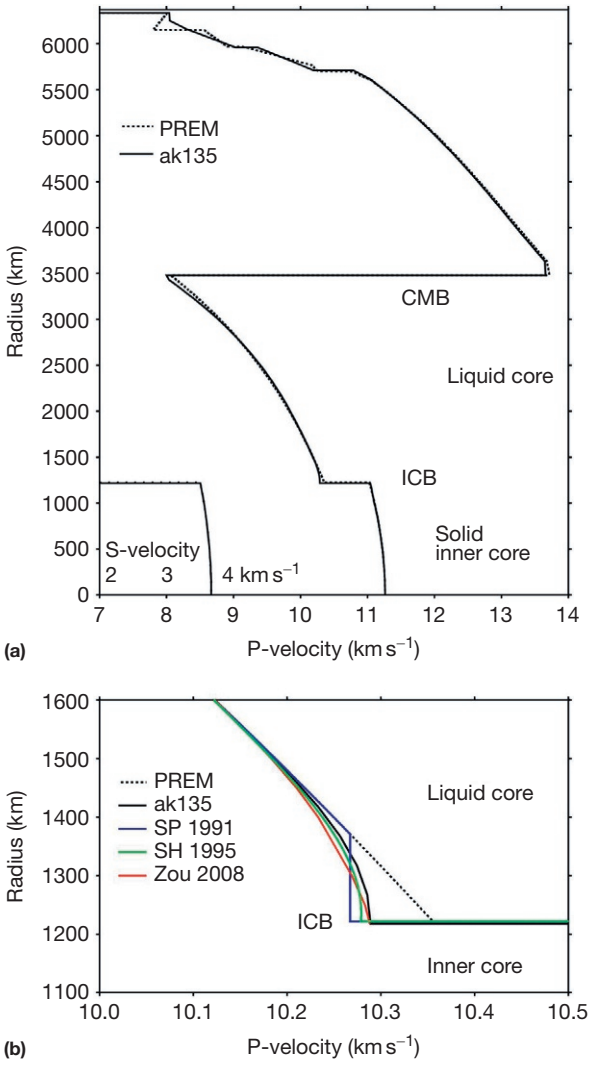

Figure 4 (a) Comparison of the P-velocities for the two global Earth models, PREM (Dziewonski and Anderson, 1981) and ak135 (Kennett et al., 1995). Also shown is the S-velocity model in the inner core (note the different scale). (b) Comparison of the velocity profiles at the base of the liquid core for PREM and ak135 and for three other specific models, Souriau and Poupinet (1991), Song and Helmberger (1995a), and Zou et al. (2008), showing the presence of a low velocity gradient.

1.23.5 The Major Discontinuities

1.23.5.1 The Core–Mantle Boundary

The CMB is the strongest discontinuity in the Earth, with a density jump of $4.3 \times 10^3\ \mathrm{kg\ m^{-3}}$, about 1.5 times larger than the density jump between the Earth's surface and atmosphere. This explains its very important role in Earth dynamics, in particular if a topography is present or if the liquid core has a high viscosity at CMB (see **Chapter 3.10**). The coupling between the core and mantle depends on amplitudes and wavelengths of the CMB topography and influences the Earth's rotation. This topography is induced by mantle dynamics, which is driven by both thermal and chemical heterogeneities (e.g., Defraigne et al., 1996; Forte et al., 1995; Greff-Lefftz and Legros, 1996; Lassak et al., 2010). Recent models predict that the amplitudes generally stay in the range ± 5 km, with a spectrum predominantly at long wavelengths (Lassak et al., 2010). The CMB is also a place where thermal, chemical, and electromagnetic interactions occur between the mantle and core (see **Chapters 7.11**, **8.08**, and **8.09**).

From the seismological point of view, the CMB appears as a first-order discontinuity. It is surrounded by the D″ layer, a

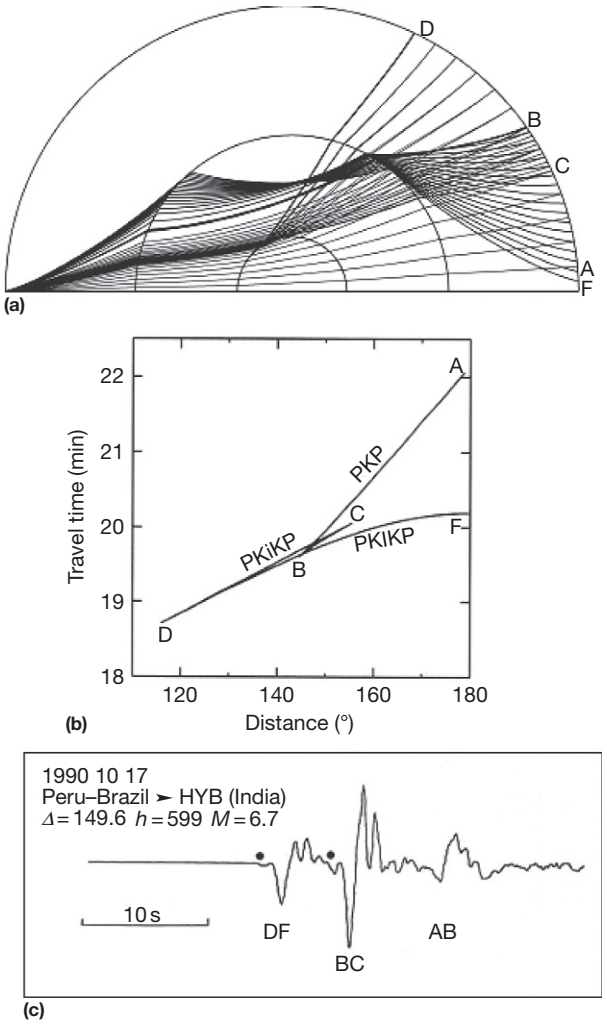

Figure 5 The PKP triplication. (a) Ray paths inside the Earth; (b) PKP travel time curve showing the triplication near 145° and the coexistence of the three PKP phases between 145° and 155°; (c) example of a deep Peru–Brazil event (depth = 599 km) recorded at the Geoscope broadband station HYB (Hyderabad, India), at distance 149.6°. Note the shape similarity between PKP(DF) and PKP(BC), whereas PKP(AB) is the Hilbert transform of PKP(BC).

very heterogeneous layer at the base of the mantle. Large low shear-wave velocity provinces corresponding to compositional heterogeneities are responsible for a strong degree two in the heterogeneity pattern of D″, but a high level of short wavelength heterogeneities is also present (see **Chapters 1.22** and **1.24**). This complex structure of D″ is the strongest difficulty to overcome for the seismological investigation of the CMB.

1.23.5.1.1 The topography of the CMB

The dynamic ellipticity may be obtained from the Earth nutations, which suggest an extra flattening (decrease of polar minus equatorial radius) of about 300–500 m, depending on the importance of the magnetic coupling at the CMB (Gwinn et al., 1986; Mathews et al., 2002). All the other results come either from modeling of mantle dynamics (see **Chapters 1.27** and **7.11**) or from seismology. Seismological results mostly rely on the analysis of travel times and amplitudes of waves reflected at the CMB or transmitted through the CMB (**Table 2**). The data are generally from bulletins. They lead to poorly consistent results, depending on the phases used and on the inverted parameters (Creager and Jordan, 1986; Morelli and Dziewonski, 1987; Rodgers and Wahr, 1993; Obayashi and Fukao, 1997; see references for other early studies in Sze and Van der Hilst, 2003). A major difficulty is the strong trade-off between D″ heterogeneities and CMB topography; it is thus important to include these two structures in the inversion of the data (e.g., Doornbos and Hilton, 1989). Even so, it is difficult to separate these two contributions. Mantle heterogeneities may also be accounted for by coupling mantle dynamics with seismological information (Soldati et al., 2012); this requires strong assumptions on the nature (thermal or chemical) of mantle heterogeneities and on mantle viscosity. Normal modes give an independent approach to the problem, but they allow us to resolve the even part of the topography only, and the trade-off with mantle heterogeneities is again strong (Koelemeijer et al., 2012; Li et al., 1991).

Studies to date propose topographic maps with amplitudes ranging from about 2 to 10 km, for wavelengths generally larger than 4000 km. They are very different from one model to the other. Normal modes give an upper limit of 5 km (Koelemeijer et al., 2012). For body-wave analyses, important biases may result from the existence of unsampled regions at the CMB surface (Pulliam and Stark, 1993). Moreover, simulations show the great difficulty to map both D″ heterogeneities and CMB topography with the presently available data (Garcia and Souriau, 2000a; Sze and Van der Hilst, 2003). A stochastic analysis of residuals of core phases shows that 95% of the CMB topography is in the range $\pm \sim 1.5$ km for characteristic lengths larger than 1200 km (Garcia and Souriau, 2000a). Similar values (± 1.75 km) are obtained in three regions around the Pacific (Koper et al., 2003). This is consistent with the most recent maps obtained at a worldwide scale (Sze and Van der Hilst, 2003), which found a peak-to-peak amplitude of about 3 km.

Short wavelength undulations responsible for wave scattering are also probably present (Rost and Revenaugh, 2004), but they must have very small amplitudes, because of the difficulty to support dynamically such heavy anomalies. They are difficult to quantify, because of the complicated signature they have in both travel times and amplitudes, as revealed by experimental and theoretical models (Emmerich, 1993; Kampfman and Müller, 1989; Menke, 1986; Rekdal and Doornbos, 1992). PcP amplitudes limit this topography to a few hundred meters in the wavelength range 2–50 km (Menke, 1986); PKKP precursors suggest topographic highs of the order of 300 m with correlation lengths of about 10 km (Earle and Shearer, 1997; Shearer et al., 1998) (see **Chapter 1.24**).

1.23.5.2 The Inner Core Boundary

This boundary is essential to understand the growing mechanism of the inner core and the thermal, chemical, and mechanical interactions between liquid and solid cores. Several models of growth are proposed, implying either a dendritic growth at the inner core surface (Bergman et al., 2003) or a slurry layer made of unconnected particles that crystallize above the ICB (Loper and Roberts, 1981; Shimizu et al., 2005). The prevailing mechanism will depend on the iron alloy present at the base of

the liquid core (Hirose et al., 2013) and on the thermodynamic conditions. Seismic data may help specify this mechanism. For example, the velocity and density contrasts at the ICB are key parameters for specifying the amount of light elements in the core and to detect partial melting at the ICB.

From the geodynamic point of view, the ICB has only a limited influence, as it corresponds to a weaker density contrast and to a smaller radius than the CMB. It has, however, an impact on the Slichter mode, a translation mode of the inner core inside the fluid whose period of about 5 h is very sensitive to the density contrast and liquid core viscosity at the ICB (Crossley et al., 1992; Rosat et al., 2006).

Seismic waveforms indicate that the ICB can generally be considered as a first-order discontinuity, <2 km thick (Cummins and Johnson, 1988a; Kawakatsu, 2006). This is consistent with thermodynamic considerations: although the uppermost inner core may incorporate fluid inclusions when it forms, it is likely to collapse under its own weight, the unconsolidated material having a thickness probably smaller than 1 km (Deguen et al., 2007).

1.23.5.2.1 The topography at ICB

The topography at ICB is certainly very weak and present at long wavelength only: first, because iron is at its melting point, thus freezing or melting will erase any topography as soon as the liquid core may transport latent heat, and, second, because the inner core has a low viscosity, probably in the range 10^{11}–10^{22} Pa s (Buffett, 1997; Deguen, 2012). Seismic waves reflected at different latitudes at the ICB show that the ellipticity is consistent with the equilibrium figure in a rotating Earth (Souriau and Souriau, 1989). An ICB topography could be induced by the gravimetric forcing of the mantle and inner core heterogeneities, with in addition the dynamic response to a possible convection inside the inner core. Mantle loading and inner core loading give each a stable topography of the order of 100 m peak to peak (Defraigne et al., 1996); thus, it could not be detected by seismological methods. However, local topographies of about 100 m to more than 10 km, with horizontal extension of a few kilometers, are reported from observations of waves reflected at the ICB by several authors (Cao et al., 2007; Dai et al., 2012; Song and Dai, 2008). If these observations are sound, they may indicate a high viscosity at the top of the inner core or the presence, at least at some places, of solid inclusions at the base of the liquid core forming a slurry boundary.

1.23.5.2.2 The density jump at ICB and its implications

At vertical incidence, the impedance contrast of a discontinuity depends primarily on its density contrast. Thus, the density jump at the ICB, $\Delta\rho_{ICB}$, may be directly obtained from the amplitude of the PKiKP waves reflected normally at the ICB. It is generally referred to the amplitude of the PcP waves reflected at the CMB, provided that the velocity and density contrasts at the CMB are known (Bolt and Qamar, 1970). As PKiKP has small amplitude at vertical incidence, stacking of several records is generally necessary to enhance the signal. Away from vertical incidence, there is a strong trade-off between density contrast, shear velocity contrast, and attenuation at the top of the inner core, as shown from waveform modeling of PKP (Cummins and Johnson, 1988b).

Density jump at the ICB ranging from 0.2 to 1.4 g cm^{-3} has been obtained from the amplitude ratios PKiKP/PcP (Figure 6) or PKiKP/P, assuming that the density contrast at the CMB has PREM's value (Cao and Romanowicz, 2004a; Koper and Dombrovskaya, 2005; Koper and Pyle, 2004; Shearer and Masters, 1990; Souriau and Souriau, 1989; Tkalčić et al., 2009). On the other hand, the data at large epicentral distances seem to require a low shear velocity jump at the ICB (2.0–2.5 km s^{-1}) compared to PREM (Cao and Romanowicz, 2004a; Koper and Pyle, 2004). These measurements are however very scattered, and this variability may reflect the sensitivity of the data to mantle structure and CMB topography, which induce wave focusing and defocusing (Leyton and Koper, 2007a). It could also reflect a variable density contrast at the CMB, which affects the reference phase PcP (Tkalčić et al., 2009), or lateral heterogeneities at the inner core surface (Krasnoshchekov et al., 2005).

Normal modes give mean values of $\Delta\rho_{ICB}$ of 0.6–1.0 g cm^{-3} (Kennett, 1998; Masters and Gubbins, 2003). Although these values correspond to a broader depth range than body waves on both ICB sides, due to mode resolution, they are globally compatible with the values obtained in the most recent body-wave studies.

The density contrast inferred from seismology is significantly too high to be explained solely by the change in volume due to a phase transition (Alfè et al., 2003). It requires chemical partitioning during crystallization, with a depletion of the inner core in light elements compared to the liquid core.

1.23.6 The Liquid Outer Core

1.23.6.1 The Main Questions Relative to Liquid Core Structure

The comparison of seismological results with high-pressure experiments and theoretical computations has shown that

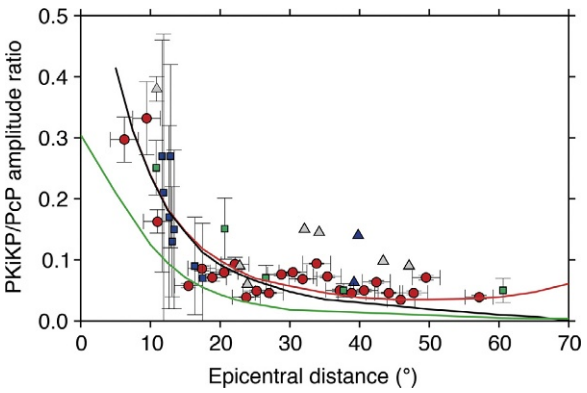

Figure 6 The amplitude ratio of the two phases PKiKP (reflected at inner core boundary ICB) and PcP (reflected at core–mantle boundary) as a function of distance, for the determination of the density contrast $\delta\rho$ and S-velocity contrast δv_S at ICB. Symbols are experimental values. Gray triangles, early results compiled by Souriau and Souriau (1989); blue triangles, Shearer and Masters (1990) (data with identified PKiKP phase); green squares, best data of Cao and Romanowicz (2004a); red dots, binned values of Koper and Pyle (2004) (horizontal bars correspond to the binning intervals); blue squares, Tkalčić et al. (2009). Curves, theoretical values; black, PREM ($\delta\rho = 0.6$ g cm^{-3}, $\delta v_S = 3.5$ km s^{-1}); green, same as PREM with $\delta\rho = 0$, showing the need for depletion in light elements during crystallization; red, same as PREM with $\delta v_S = 2.5$ km s^{-1}, suggesting a v_S decrease in the uppermost inner core.

the outer liquid core is less dense than the pure molten iron at the same conditions of temperature and pressure, indicating the presence of light elements in the core, in an amount of about 10% by weight (Birch, 1964; Jephcoat and Olson, 1987; Poirier, 1994). Many candidates are possible. Sulfur has a great solubility inside liquid iron at core conditions; it is thus a possible candidate, but other elements such as O, N, Si, and K are likely to be present (Alfè et al., 2003; Andrault et al., 2009; Badro et al., 2007; Hirose et al., 2013; Poirier, 1994). The radioactive isotope ^{40}K, if present in the core, will be an additional source of energy to power the Earth dynamo. The presence of Ni (which has a higher density than Fe) in a proportion of about 4% is far from compensating the density decrease due to light elements (see **Chapters 2.06** and **8.02** for more details about the chemical state of the outer core).

The main questions relative to the fluid core concern its possible radial inhomogeneity, due in particular to the presence of these light elements. They are released at the ICB when the liquid iron alloy crystallizes, may migrate upward, and form a distinct alloy layer beneath the CMB. A stratification or a distinct layer at the top of the core is thus possible; it is predicted by thermodynamic models of core evolution (Buffett and Seagle, 2010; Lister and Buffett, 1998). It may influence the core–mantle coupling with consequences for Earth dynamics, nutations, and length of day and for the magnetic field (see **Chapter 3.10**). It may also give constraints on the nature of the light elements (Helffrich and Kaneshima, 2004). On the other hand, a dense layer at the base of the liquid core, due to heavy alloys, could bring information on the crystallization process of the inner core. A stratification may also result in variations of the thermal conductivity with depth. It is thus important to go in more details in the radial core structure. The periods of free oscillations indicate that the outer core is not strongly stratified (Masters, 1979). This is confirmed by the velocity profiles in global Earth models, which indicate radial homogeneity, except close to the core boundaries. If stratification is present, it will thus concern primarily the boundaries.

Lateral heterogeneities inside the liquid core are less probable, as an active convection is made possible by the low viscosity of the liquid alloy, comparable to that of water at the Earth surface ($\eta = 6 \times 10^{-3}$ Pa s, Poirier, 1988), or possibly slightly higher at the core boundary (Koot et al., 2010; Palmer and Smylie, 2005; Smylie, 1999; see also the review in Cormier et al., 2011). However, fluid motions in a rotating fluid sphere are organized in cylinders with axis parallel to the Earth's rotation axis (ERA) (Busse, 1975). The structures inside the cylinder tangent to the inner core are thus partly insulated from the fluid outside this tangent cylinder, being perhaps able to carry material with distinct properties. Sedimentation of a different material beneath the polar caps or the equatorial bulge may also be favored by the rotation.

The following sections present the seismological approach to these questions.

1.23.6.2 The Stratification at the Base of the Liquid Core

The propagation time of the PKP(BC) wave, which becomes diffracted along the ICB at large distance (giving the PKP(C_{diff}) wave), gives direct information on the structure of the lowermost 150 km of the liquid core. The velocities appear significantly lower than those of PREM, which roughly correspond to the adiabatic gradient (Souriau and Poupinet, 1991). This has been confirmed from waveform modeling of short-period records (Song and Helmberger, 1992, 1995a) and from other PKP(C_{diff}) observations (Zou et al., 2008). The data are well explained by a low velocity gradient in the lower 100–150 km at the base of the liquid core, where the velocity becomes nearly constant (**Figure 4(b)**). This low velocity gradient layer is sometimes improperly called the F-layer, in reference to a denomination of Bullen (1940). The anomalously low-amplitude decay of the diffracted waves PKP(C_{diff}) with distance (Song and Helmberger, 1995a; Souriau and Roudil, 1995) is another argument in favor of this low velocity gradient, which acts as a guide for the diffracted waves. However, the amplitude ratios of PKP(C_{diff})/PKP(DF) are close to PREM's predictions (Zou et al., 2008), an observation interpreted as due to either small-scale topography at the ICB or a thin sub-layer of relatively low-quality factor at the very base of the outer core.

A hemispherical pattern has been proposed for the low velocity layer (Yu et al., 2005), but the inner core structure could be responsible for this pattern as well (Cormier et al., 2011). Such a heterogeneity could not be sustained by the liquid unless its viscosity is very high (Cormier et al., 2011). This is not completely excluded: This layer could be a zone of small, nonzero rigidity ($v_S = 0.1$–0.5 km s^{-1}), as revealed by both normal modes (Mochizuki and Ohminato, 1989) and PKiKP waves reflected at the ICB (Cormier, 2009); thus, it could also be a zone of increased viscosity. The free inner core nutations suggest a viscosity of $\sim 10^5$ Pa s (Koot et al., 2010). The Slichter mode would be sensitive to such a layer (Smylie, 1999), but its identification on superconducting gravimeter records is highly controversial (Rosat et al., 2006).

Gubbins et al. (2008) have clearly shown that this low-velocity, high-density layer must be of compositional origin. In a slurry model, freezing and melting occur in this layer, and the P-velocity gradient is caused by a compositional gradient with heavy elements at the bottom. Melting appears necessary to generate this layer. Two mechanisms, which may coexist, have been invoked to produce melting: an inner core translation in the equatorial plane (Alboussière et al., 2010; Monnereau et al., 2010) and the thermal forcing by outer core convection (Gubbins et al., 2011). Alboussière et al. (2010) argue that melting on the inner core hemisphere exposed to pressure decrease during translation will produce a dense iron-rich liquid that spreads at the surface of the inner core. Gubbins et al. (2011) propose that melting occurs in response to heat transport by the outer core flow. This flow is driven by the large lateral variations of heat extraction at the CMB; it induces a large area of melting at the ICB under the Pacific and freezing mainly located under Indonesia.

1.23.6.3 The Stratification at the Top of the Liquid Core

The uppermost third of the core is mostly investigated with the S*m*KS wave, which becomes a whispering wave beneath the CMB for large *m* (*m* up to five has been observed as a distinct phase). Unfortunately, its travel time is strongly affected by the heterogeneities in the D″ layer, an effect that is only imperfectly corrected by the use of differential travel times between successive S*m*KS phases. Waveform modeling of S*m*KS may also be

used (Choy, 1977). Normal modes that sample the CMB region also provide useful information but, as previously said, they have poor depth resolution.

The different results do not lead to a consensus. Several studies implying different methods have proposed the presence of a thin (50–100 km thick) layer with slightly lower velocities at the top of the liquid core, which could correspond to an iron alloy enriched in light elements (Garnero et al., 1993; Helffrich and Kaneshima, 2010; Lay and Young, 1990; Tanaka, 2007). However, some studies fail to identify a distinct layer (Alexandrakis and Eaton, 2010; Helffrich and Kaneshima, 2004), while others detect a layer with increased velocity (Eaton and Kendall, 2006) or large-scale heterogeneities (Tanaka and Hamaguchi, 1993). The resolution of the different methods is, however generally not sufficient to discard the influence of lower mantle heterogeneities. It turns out that a thin uppermost distinct fluid layer is generally not required by the data (Garnero and Lay, 1998; Kohler, 1997).

Finally, the presence of a very thin, conductive, and slightly rigid layer of silicate deposits at the top of the core has been proposed to explain the amplitudes of the Earth nutations (Buffett et al., 2010). Even though normal modes may be compatible with a small amount of shear at the top of the liquid core (Romanowicz and Bréger, 2000), its seismological detection is still questionable (Rost and Revenaugh, 2001).

1.23.6.4 Search for a Three-Dimensional Structure Inside the Liquid Core

Gravitational forcing from the heterogeneities located inside the mantle and inner core (Piersanti et al., 2001; Wahr and de Vries, 1989) and steady-state dynamics must result in a 3D structure inside the fluid core. However, as shown by Stevenson (1987), the liquid core is not able to sustain relative density heterogeneities $\delta\rho/\rho$ larger than 10^{-4}. Assuming that velocity heterogeneities in liquid iron are proportional to density heterogeneities with a proportionality factor of -1 (Stevenson, 1987), the heterogeneities will be much below the level of detection by seismological methods. Despite this theoretical limit, several seismological results propose an outer core structure, that is, a departure from spherical symmetry (after ellipticity correction).

A large-scale aspheric structure in the liquid core is suggested by the splitting of some normal modes, which are difficult to explain by inner core and mantle structure alone (Ritzwoller et al., 1986; Widmer et al., 1992). Pushing to the extreme, it would be possible to explain the splitting of most of the core modes by outer core structure only (Romanowicz and Bréger, 2000), although the favored interpretation, which is more physically acceptable, is inner core anisotropy, as will be seen later.

A search for cylindrical structures related to the magnetohydrodynamic models of the core, such as embedded cylinders parallel to the ERA, has been performed using travel times of SKS and PKP(BC) and normal modes. No evidence of heterogeneity could be firmly established. PKP(BC) shows that P-velocities are identical inside and outside the tangent cylinder (Ohtaki et al., 2012; Souriau et al., 2003b; Yu et al., 2005), a result confirmed by normal mode analyses (Ishii and Dziewonski, 2005). It has also not been possible to detect P-wave anomalies beneath the polar caps nor beneath the equatorial bulge (Souriau et al., 2003b).

1.23.6.5 The Attenuation in the Liquid Core

Measurements of attenuation in the liquid core at high frequency (~1 Hz) are based on the amplitude of the phases P*n*KP reflected $(n-1)$ times under the CMB, with n up to 7 (**Figure 7**). The quality factor for P-waves, Q_α, is larger than 5000–10 000 (Cormier and Richards, 1976; Qamar and Eisenberg, 1974). Slightly lower values ($Q_\alpha = 1600$–7000, depending on frequency) are given by Tanaka and Hamaguchi (1996). Q_α may thus be considered as close to infinity. Such large values are not found elsewhere inside the Earth. Very large values are also obtained from normal mode analyses ($Q_\alpha = 12\,000$, Widmer et al., 1991), suggesting that Q is not strongly frequency-dependent inside the liquid core.

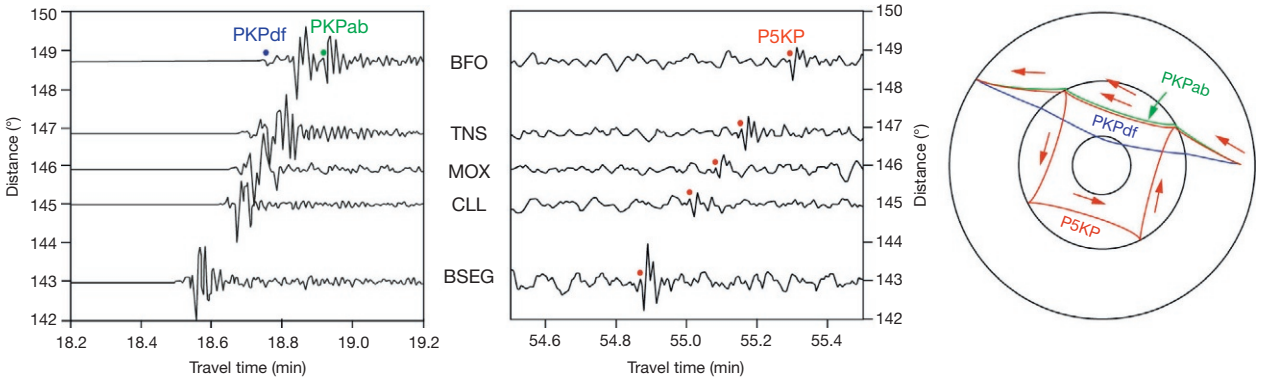

Figure 7 Right: Path of the P5KP wave inside the Earth (red), for a deep event of Fiji Island region (Dec. 18, 2000). The path of the PKP(AB) ray is superimposed (green); also shown is the PKP(DF) ray turning inside the inner core (blue). Left and middle: Waveforms of PKP and P5KP, respectively, recorded at different distances (station codes are between the two figures). The observation of P5KP on single records and its shape similarity with PKP(AB) are all together a proof of the lateral homogeneity of the liquid core, of its low attenuation, of the strong P-wave reflection coefficient underside the core–mantle boundary (which appears as a first-order discontinuity), and of the absence of significant topography at this boundary. Modified from Figure 11.71 of Bormann P, Klinge K, and Wendt S (2002) Chapter 11: Data analysis and seismogram interpretation. In: Bormann P (ed.) *IASPEI New Manual of Seismological Observatory Practice*, vol. 1, 102 pp. Potsdam: GeoForschungsZentrum; © IASPEI, with permission.

1.23.7 The Inner Core: Seismic Velocities

Seismic data have allowed us to establish the rigidity of the inner core, to specify its radial structure, and to detect long wavelength lateral variations. One of its most spectacular physical properties is its anisotropy, present in a large volume of the inner core: waves that propagate parallel to the ERA travel faster than those that propagate parallel to the equatorial plane. The anisotropy inside the inner core is however not uniform, with both radial and lateral variations. A hemispherical heterogeneity, which roughly distinguishes the Eastern and the western hemispheres defined with respect to the origin meridian, destroys the symmetry with respect to ERA. It is a very intriguing feature and a fundamental piece of information to understand how the inner core grows and how the anisotropy is generated.

1.23.7.1 S-Waves and the Rigidity of the Inner Core

Evidence of the rigidity of the inner core and v_S profiles inside the inner core have been mostly obtained by indirect observations. The observed periods of core-sensitive normal modes require rigidity (Dziewonski and Gilbert, 1971). They robustly constrain the mean value of the S-velocity to 3.5–3.6 km s^{-1} (Deuss, 2008; Dziewonski and Gilbert, 1971; Masters, 1979; Suda and Fukao, 1990), close to that of mean PREM. However, normal modes have no sensitivity at the Earth's center. The modeling of the PKP waveforms generally gives lower v_S values beneath the ICB, from nearly 0 (Choy and Cormier, 1983) to 2.5–4.0 km s^{-1} (Cummins and Johnson, 1988b; Häge, 1983; Müller, 1973). Amplitudes of the PKiKP reflected wave also favor a small v_S value at the ICB, of the order of 2–3 km s^{-1} (Cao and Romanowicz, 2004a; Koper and Dombrovskaya, 2005; Koper and Pyle, 2004; Shearer and Masters, 1990). Generally, these values are significantly lower than those given in global Earth models. Their compatibility with normal mode results implies the existence of a strong shear velocity gradient in the uppermost 200–300 km of the inner core (Cao and Romanowicz, 2004a; Choy and Cormier, 1983; Häge, 1983).

A direct evidence of the rigidity of the inner core relies on the detection of the phase PKJKP, which propagates as an S-wave inside the inner core and as a P-wave outside. Because of the very low amplitude of this phase, due to the strong shear-wave attenuation in the inner core, to the poor P- to S-wave conversion factor at the ICB, and to S-wave splitting due to anisotropy, there is no hope to observe PKJKP on single records. Stacking of several records is thus necessary to enhance the signal and even so is the success quite uncertain (Doornbos, 1974; Shearer et al., 2011). Optimal conditions are required for stacking, in particular, the appropriate phase velocity and distance and the appropriate frequency domain. This constitutes the major difficulty, because these conditions are poorly known. The distance at which PKJKP will have its maximum amplitude depends on the velocity and density contrasts at the ICB and on the S-velocity profile inside the inner core, which are not well known. In the worst case, if the S-velocity is close to zero at the top of the inner core (Choy and Cormier, 1983; Cormier et al., 2011), PKJKP will simply not exist. This may occur if a mushy zone is present at the top of the inner core. The frequency domain where PKJKP is observed is also unknown, although the strong attenuation inside the inner core suggests that it must be better detected on broadband records than on short-period records.

An identification of PKJKP on short-period records is proposed in three studies: Julian et al. (1972) proposed a very low S-velocity of 2.95 km s^{-1} in the inner core, whereas Okal and Cansi (1998) and Wookey and Helffrich (2008) found values close to those proposed in mean Earth models. Studies on broadband data have been conducted by Kawakatsu (1992), Deuss et al. (2000), Cao et al. (2005), and Shearer et al. (2011). Kawakatsu and Shearer et al. failed to observe PKJKP. Deuss et al. obtained a velocity of 3.6 km s^{-1} from the observation of a combination of two other parent phases (pPKJKP + SKJKP). Cao et al. obtained a clear phase arriving 9 s before PREM's predictions, implying that, if this phase is really PKJKP, v_S in the deep inner core must be about 1.5% larger than in PREM, where it is mostly constrained by normal modes sampling the outer part of the inner core. The two models may be reconciled if v_S increases with depth inside the inner core.

Most ab initio calculations on the elastic properties of iron crystals in the inner core display v_S values significantly higher than those inferred from seismology (Deuss, 2008; Vočadlo, 2007). This discrepancy has been used to support the presence of liquid in the inner core, resulting from dendritic solidification (Deguen et al., 2007; Singh et al., 2000; Vočadlo, 2007). Alternative explanations invoke the role of light elements and nickel, the presence of crystal defects that induces low rigidity (Belonoshko et al., 2007), or wave scattering by polycrystalline aggregates, in which wave velocity is decreased compared to that in single crystals (Calvet and Margerin, 2008).

1.23.7.2 The Anisotropy in P-Wave Velocity

The investigation of inner core anisotropy faces two major difficulties: (1) finding rays with various orientations turning in the same region at the same depth (from this point of view, the inner core sampling is very poor) and (2) getting rid of the perturbing contributions of the crust and mantle structures. Polar paths (i.e., paths parallel to ERA) are crucial, but they are rare, with an oversampling of the path from South Sandwich Island events to high-latitude stations, which often appear as anomalous (Tkalčić et al., 2002). In parallel, modeling relies on strong assumptions concerning the characteristics of anisotropy.

1.23.7.2.1 Evidence for anisotropy in P-wave velocity: early studies

The evidence of faster propagation along the polar axis than in the equatorial plane was first reported by Poupinet et al. (1983) from the analysis of the large amount of the PKP(DF) residuals collected by the ISC. This anomaly has been interpreted by Morelli et al. (1986) as due to inner core anisotropy. It is also well observed in the differential travel times of PKP(DF)–PKP(BC) and PKP(DF)–PKP(AB) (**Figure 8**). These observations confirm that the anomaly originates in the inner core, not in the liquid core or in the mantle (e.g., Creager, 1992; Shearer et al., 1988). On the other hand, the anomalous splitting of inner core-sensitive normal modes, which remains after correction for ellipticity and the Earth's rotation, is also well explained by anisotropy (Li et al., 1991; Tromp, 1993;

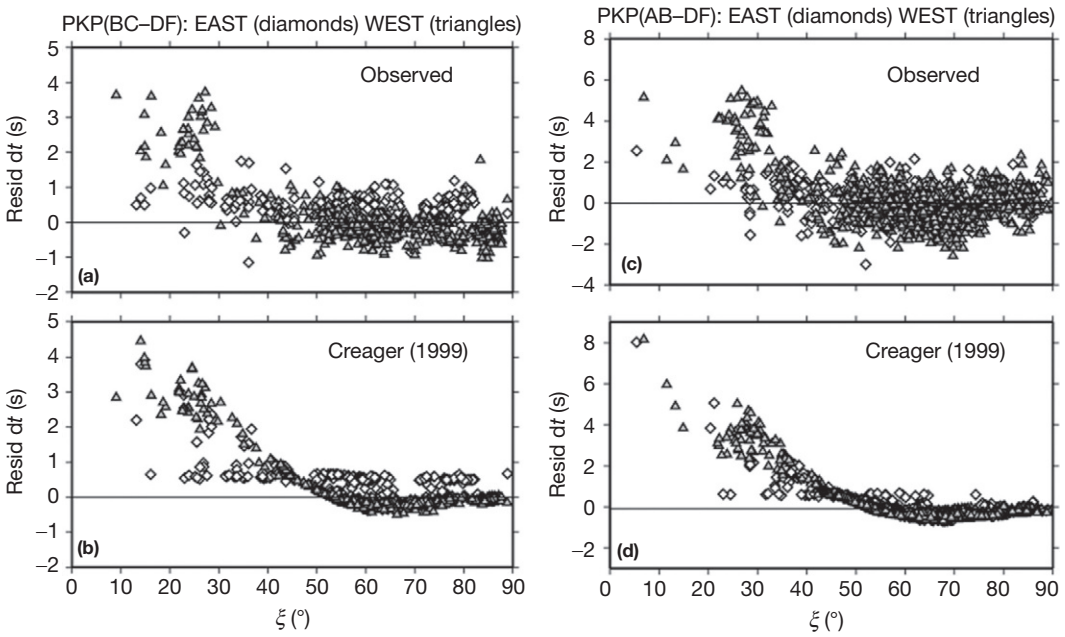

Figure 8 Evidence for anisotropy in the inner core. Differential travel time residuals for PKP(BC)–PKP(DF) (a) and for PKP(AB)–PKP(DF) (c) as a function of the angle ξ of the ray inside the inner core with respect to the Earth's rotation axis, distinguishing quasi-eastern (diamonds) and quasi-western (triangles) hemispheres (see **Section 1.23.7.2.2.2**). The high residuals at low ξ-values reveal that PKP(DF) polar paths are faster than equatorial paths. (b and d) Predictions of a cylindrical anisotropy model (transverse isotropy) by Creager (1999), with different coefficients for the two hemispheres. Reproduced from Romanowicz B, Tkalčić H, and Bréger L (2003) On the origin of complexity in PKP travel time data. In: Dehant V, et al. (eds.) *Core Dynamics*, *Structure and Rotation*. *Geophysical Monograph*, vol. 31, pp. 31–44. Washington, DC: American Geophysical Union.

Woodhouse et al., 1986). The travel time anomaly, after ellipticity correction, may reach up to 6 s for polar paths (Vinnik et al., 1994), compared to a total propagation time of about 1200 s through the Earth, of which about 220 s is through the inner core. Such a P-wave travel time anomaly is very large, compared to those observed for propagation through the mantle, which rarely exceed 2 s. A uniform cylindrical anisotropy (transverse isotropy), with a fast axis parallel to ERA and a level of anisotropy between 1.5% and 4%, explains the general features of the data (e.g., Creager, 1992; McSweeney et al., 1997; Morelli et al., 1986; Shearer, 1994; Song, 1996; Su and Dziewonski, 1995; Vinnik et al., 1994; see also a compilation of models in Ishii et al., 2002b). It is however insufficient to explain all the seismological observations, as a significant non-axisymmetric signal is also present (Su and Dziewonski, 1995) (see Tkalčić and Kennett, 2008, for a review of the first results).

One of the most commonly used expressions for representing inner core cylindrical anisotropy is (Su and Dziewonski, 1995)

$$\delta v_P/v_0 = a_0 + \varepsilon \cos^2\xi + \gamma \sin^2 2\xi \qquad [1]$$

where ξ is the angle between the ray inside the inner core and the symmetry axis. ε represents the P-wave anisotropy, that is, the difference between the P-velocity along the symmetry axis and the velocity perpendicular to it; γ is a mixed term that controls the P-wave propagation at intermediate angles; and a_0 represents a perturbation with respect to the P-velocity v_0 of the reference model. Many other equivalent expressions are also used in the literature (see equivalences in Calvet et al., 2006). The isotropic velocity is defined as the mean of the anisotropic velocity over the whole space (Creager, 1999), and its perturbation with respect to the reference model is given by

$$(\delta v_P/v_0)_{iso} = a_0 + \varepsilon/3 + (8/15)\gamma \qquad [2]$$

As will be seen hereafter, depth dependence and long wavelength variations are present in the anisotropy, thus, in the a_0, ε, γ parameters.

Some studies have proposed that the anisotropic symmetry axis could be slightly tilted with respect to ERA (Creager, 1992; Romanowicz et al., 1996; Su and Dziewonski, 1995). The data are well explained by such models, but the tilt is not required; it may result from the lack of data in some directions (Souriau et al., 1997). The question has also been raised whether the anisotropy could be an artifact due to mantle or liquid core heterogeneities that, because of their geographic distribution, may mimic a polar fast propagation (Bréger et al., 2000a,b; Ishii et al., 2002a; Romanowicz et al., 2003). Such a contribution is probable, but cannot fully explain the observations (Romanowicz and Bréger, 2000; Tkalčić et al., 2002). Anisotropy thus seems to provide the simplest explanation able to reconcile most of the seismological observations. We will specify hereafter its main characteristics.

1.23.7.2.2 Depth dependence of the anisotropy and hemispherical variations

The variation of anisotropy with depth is mostly deduced from the travel time anomalies of PKP(DF) as a function of epicentral distance for different ray orientations with respect to ERA. PKP(DF) is referred to the PKiKP reflected wave for sampling the uppermost 100 km, to PKP(BC) for the depth range 100–500 km, and to PKP(AB) at greater depths (**Figure 5(a)**).

1.23.7.2.2.1 The isotropic layer

There is a general agreement about a low level of P-wave anisotropy (<1%) in the uppermost 50–150 km of the inner core, with even perhaps no anisotropy at all (Creager, 1999, 2000; Garcia and Souriau, 2000b; McSweeney et al., 1997; Ouzounis and Creager, 2001; Shearer, 1994; Song and Helmberger, 1995b, 1998; Waszek and Deuss, 2011). Normal modes do not require this layer; they limit its mean thickness to 150–200 km (Durek and Romanowicz, 1999; Ishii et al., 2002a,b). Irving and Deuss (2011a) show that it is isotropic for both P- and S-waves. Some seismic observations favor a sharp discontinuity between the isotropic layer and the underlying anisotropic structure (Ouzounis and Creager, 2001; Song and Helmberger, 1998; Waszek and Deuss, 2011), but this is still controversial, as waves reflected at this discontinuity are not widely observed, and scattering from small-scale heterogeneities within the inner core may explain these observations as well (Leyton et al., 2005).

A hemispherical heterogeneity in this layer has been clearly identified by Niu and Wen (2001) from PKiKP and PKIKP records, the velocities in the quasi-eastern hemisphere (longitudes 40–180° E) being higher than in the Western one (**Figure 9**). This result reinforces previous sparse observations (Cormier and Choy, 1986; Kaneshima, 1996). It has been confirmed and refined by many other studies, which specify the level of heterogeneity in each hemisphere, the velocity gradient beneath the ICB, the depth to which the isotropic layer extends, and the longitudes of the transition between hemispheres (Cao and Romanowicz, 2004b; Garcia, 2002b; Waszek and Deuss, 2011; Wen and Niu, 2002; Yu and Wen, 2006a). For example, Yu and Wen (2006a) obtain a velocity gradient beneath the ICB that is larger in the quasi-western hemisphere than in the quasi-eastern hemisphere (5.0×10^{-4} and 0.4×10^{-4} (km s^{-1} km^{-1}, respectively), together with a smaller velocity jump at the ICB (0.65 and 0.75 km s^{-1}, respectively). There are significant variations among the different results: Irving and Deuss (2011b) give a difference in isotropic velocity of only 0.2% between the two hemispheres, Niu and Wen (2001) propose a value of 0.8%, Monnereau et al. (2010) obtain a value close to 0.5%, and Tanaka (2012) proposes 1.4% from equatorial paths. This hemispherical difference extends at least down 85 km beneath the ICB (Cao and Romanowicz, 2004b), possibly deeper (Tanaka, 2012; Yu and Wen, 2006a). The total thickness of the isotropic layer is also different for the two hemispheres, of the order of 100 km beneath the western hemisphere, extending deeper (400 km) beneath the Eastern one (Creager, 2000; Garcia and Souriau, 2000b). Monnereau et al. (2010) find a smooth transition between the two hemispheres, a result also supported by data sampling the high southern latitudes (Ohtaki et al., 2012). By contrast, Waszek and Deuss (2011) and Miller et al. (2013) propose sharp boundaries, but the same data may be as well explained by smooth variations in inner core texture from one hemisphere to the other (Geballe et al., 2013).

Heterogeneities in the isotropic layer are certainly present at other scale lengths. A broad, 3% low-velocity layer has been detected at the top 40 km of the inner core beneath equatorial Africa and the Indian Ocean (Stroujkova and Cormier, 2004). Local variations in the velocity at the ICB (Krasnoshchekov et al., 2005) or in the thickness of the isotropic layer (Yu and Wen, 2007) have also been proposed.

1.23.7.2.2.2 The anisotropy down to ~700 km depth

Beneath the isotropic layer, in the depth range 100–700 km for the quasi-western hemisphere and 400–700 km for the quasi-eastern one, anisotropy with fast axis parallel to ERA provides the simplest way to explain the dependence of P-wave velocity to ray angle ξ.

The difference between a strongly anisotropic quasi-western hemisphere and a weakly anisotropic quasi-eastern hemisphere is clearly pointed out by Tanaka and Hamaguchi (1997) from the differential travel times PKP(BC)–PKP(DF) (**Figure 10**). Creager (1999) found 2–4% anisotropy in the quasi-western hemisphere and only 0.5% in the quasi-eastern hemisphere. Other studies proposed an anisotropy level as high as 5% beneath the isotropic layer in the western hemisphere (Irving and Deuss, 2011b; Ouzounis and Creager, 2001). A mean value of 3% is generally accepted for the western hemisphere and 0.5–1% for the Eastern one.

The hemispherical pattern could partly be an artifact of the propagation through the lower mantle heterogeneities (Ishii et al., 2002a), but these heterogeneities fail to fully explain the observed pattern (Romanowicz et al., 2003). The South Sandwich Island events bias the polar path observations (Garcia et al., 2006; Tkalčić et al., 2002). Nevertheless, the hemispherical pattern in anisotropy seems to be a robust feature, and it is observed on both equatorial and polar data with opposite variations, as expected from relation [1] (Creager, 2000; Souriau et al., 2003a; Tanaka and Hamaguchi, 1997). In both hemispheres, the anisotropy is parallel to ERA. The isotropic velocity is nearly the same (Creager, 2000), which rules out an interpretation in terms of the difference in composition or fluid content. A variation in crystal alignment may explain the observations (Creager, 1999; Garcia, 2002b; Sun and Song, 2008). An alternative explanation invokes the difference in the thickness of the isotropic layer beneath the two hemispheres, which affects differently the PKP(DF) travel times so that it mimics variations in anisotropy (**Figure 10(c)**).

1.23.7.2.2.3 The innermost inner core

The presence of a different anisotropy in the central part of the core has been proposed to explain the travel time anomalies of PKP(DF) with nearly antipodal paths (Ishii and Dziewonski, 2002; Su and Dziewonski, 1995; **Figure 11**). A slow direction of propagation at about 45–55° from ERA is observed in the data sampling the innermost inner core (Calvet et al., 2006; Cao and Romanowicz, 2007; Ishii and Dziewonski, 2002, 2003; Niu and Chen, 2008; Sun and Song, 2008). Several studies have attempted to specify the anisotropy in this innermost inner core, with assumptions of transverse isotropy and symmetry axis parallel to ERA, but very different models have been obtained. Some models propose a fast axis parallel to ERA (Ishii and Dziewonski, 2003; Sun and Song, 2008) with a 3.5–3.7% anisotropy, higher than in the surrounding structures (**Figure 11(c)**, left). From a normal mode analysis, Beghein and Trampert (2003) propose a smooth model that favors a change in the sign of P-wave anisotropy in the central part of the inner core, thus an innermost inner core with a slow axis parallel to ERA (**Figure 11(c)**, right). An innermost inner core

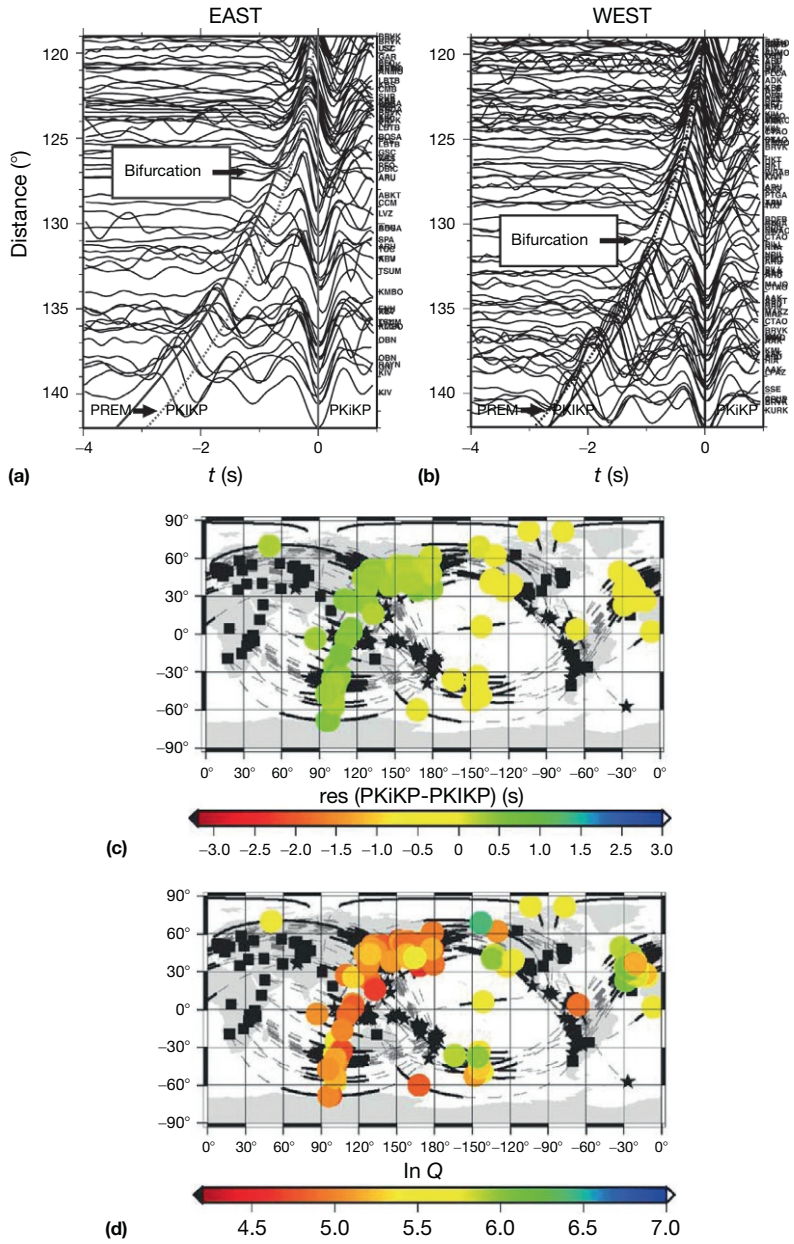

Figure 9 (a and b) Evidence for a hemispherical pattern in the uppermost inner core. Records of PKiKP and PKIKP phases sampling, respectively, the inner core boundary and the uppermost inner core beneath eastern and western hemispheres. The records are aligned on PKiKP, and the thick lines follow the phase maxima. Dashed line is the prediction for PREM. 'Bifurcation' corresponds to the separation of the two interfering phases. Note the difference between the two hemispheres for both differential travel times and PKIKP amplitudes, indicating a hemispherical heterogeneity in P-velocity and attenuation (reproduced from Wen L and Niu F (2002) Seismic velocity and attenuation structures in the top of the Earth's inner core. *Journal of Geophysical Research* 107 (B11): 2273). (c and d) Differential travel time residuals of PKiKP–PKIKP (in s) and quality factor (plotted in logarithmic scale) at the top of the inner core (depth 32–85 km below ICB, corresponding to distance 135–142°), showing that the eastern hemisphere is faster and more attenuating that the western hemisphere (reproduced from Cao A and Romanowicz B (2004) Hemispherical transition of seismic attenuation at the top of the earth's inner core. *Earth and Planetary Science Letters* 228: 243–253).

with P-wave anisotropy rate $\varepsilon = 0$ is obtained by Ishii et al. (2002a) (**Figure 11(c)**, middle). It turns out that, with the presently available data, the exact nature of the anisotropy in the innermost inner core is still hard to resolve and that the three families of models may be derived from the same PKP data, depending on data processing and assumptions used (Calvet et al., 2006). There is however some agreement about the mean radius of the innermost inner core, in the range 300–600 km for the most recent studies (Beghein and Trampert, 2003; Calvet et al., 2006; Cao and Romanowicz, 2007; Cormier and Li, 2002; Sun and Song, 2008). A sharp discontinuity at the top of the innermost inner core could not be detected (Cormier and Stroujkova, 2005; Garcia et al., 2006; Leyton et al., 2005; Niu and Chen, 2008). Cormier and

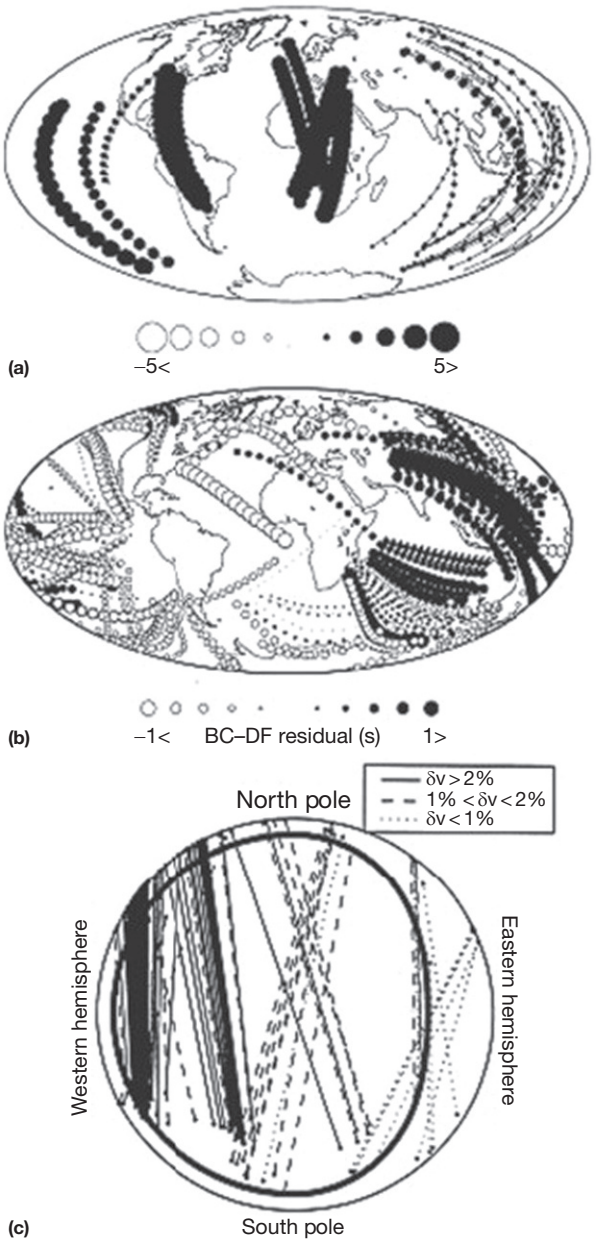

Figure 10 Evidence of a hemispherical pattern in the upper half of the inner core, as seen by PKP(BC)–PKP(DF) differential travel times. (a) Polar paths, the western hemisphere is faster than the eastern hemisphere; (b) the opposite is observed for East–West paths, but note the different scale (±5 s for (a), ±1 s for (b)) (reproduced from Tanaka S and Hamaguchi H (1997) Degree one heterogeneity and hemispherical variation of anisotropy in the inner core from PKP(BC)-PKP(DF) times. *Journal of Geophysical Research* 102: 2925–2938). (c) Interpretative cross section through the inner core looking from meridian 0°, showing the paths with their velocity anomalies, and a heavy line separating the isotropic asymmetric upper layer from the anisotropic structure (reproduced from Creager KC (2000) Inner core anisotropy and rotation. In: Dehant V, et al. (eds.) *Core Dynamics, Structure and Rotation*. *American Geodynamic Series*, vol. 31, pp. 89–114. Washington, DC: American Geophysical Union).

Stroujkova (2005) suggest the existence, between the two structures, of a broad, 50–100 km thick, transition zone at radius $r \sim 500$ km, which also coincides with a transition from low attenuation ($r < 500$ km) to high attenuation ($r > 500$ km) (Li and Cormier, 2002).

1.23.7.2.3 The origin of anisotropy

Seismic anisotropy in the inner core may be due to the preferred orientation of either anisotropic iron crystals, or elongated grains (each grain being an assemblage of crystals with similar orientations), or nonspherical fluid inclusions. In the first case, the seismic properties strongly depend on the elastic properties of the iron crystals and on their degree of alignment. In the second case, additional parameters are the orientation of crystals in each grain and the distribution of grain orientations in the medium. In the third case, the shape of inclusions and melt fraction are the key parameters.

The nature of iron or iron alloy at inner core conditions is a highly debated question. Details and references may be found in **Chapter 2.06**. The hexagonal closed-packed (hcp) structure of pure iron may be stable, but, because of the uncertainty on the temperature in the inner core, body-centered cubic (bcc), double hcp, and orthorhombic structures have also been proposed, on the basis of high-pressure experiments or theoretical computations. The presence of nickel or of light elements may stabilize the bcc or face-centered cubic phases. There is also no consensus on the elastic properties of the stable iron alloys and on the deformation slip system (Poirier and Price, 1999). Theoretical and experimental investigations on hcp iron have led to contradictory conclusions concerning the sign of P-wave anisotropy (fast or slow *c*-axis) depending on impurities and temperature, with even the possibility of a very low anisotropic rate. Iron in the bcc form, which is strongly anisotropic, provides an interesting alternative to hcp for explaining inner core anisotropy.

A degree of crystal alignment from 20% to 100% is necessary to explain the observed seismic anisotropy, depending on the elastic properties of the iron crystal. The distinct anisotropy in the innermost inner core suggests either the presence of a different iron phase (Kuwayama et al., 2008), or a different iron alloy, or some variation in the degree of crystal alignment. The reverse of the sign of the anisotropy at depth proposed by some seismic models may be explained by a variation with depth of the preferred orientation of a same form of iron.

A preferred orientation of ellipsoidal fluid inclusions is another possible mechanism to generate anisotropy (Singh et al., 2000). The presence of molten iron inclusions trapped in the iron lattice, at least in the upper half of the inner core, is proposed in support of the low S-velocity and high attenuation observed in that part of the inner core. The complex phase diagrams of iron alloys also favor a transition from solid to liquid with partial melting. A fluid volume fraction of 3–10%, present as oblate inclusions aligned in the equatorial plane, may explain the observed velocity anisotropy. However, as will be seen later, it fails to explain some characteristics of attenuation.

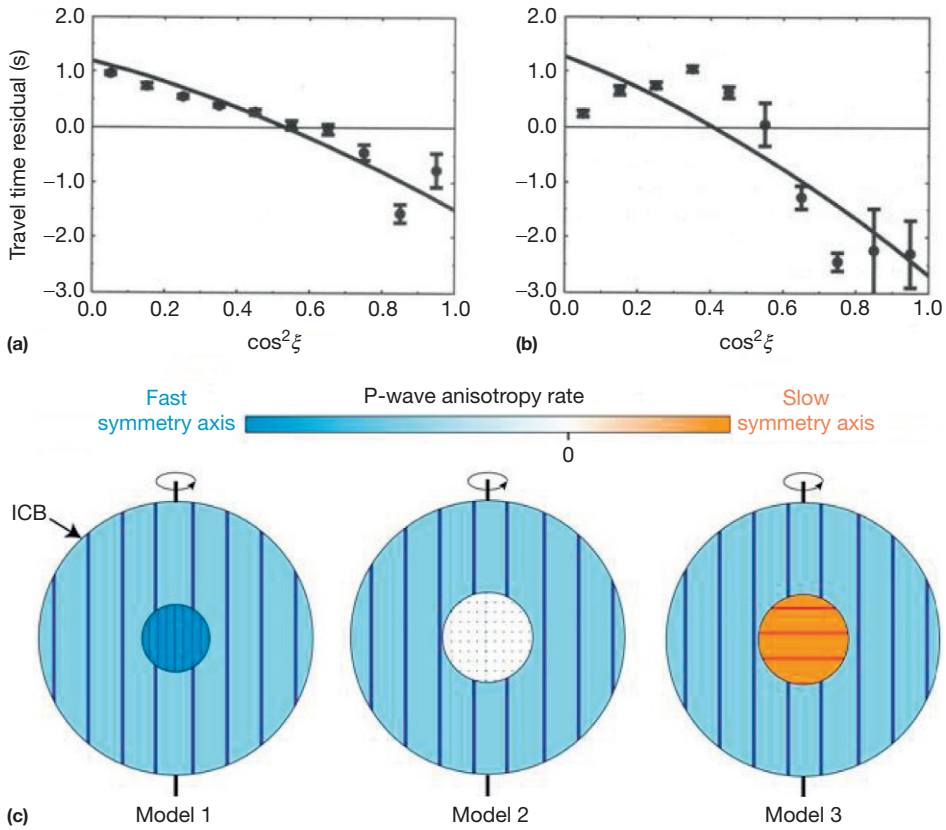

Figure 11 Evidence for a distinct anisotropy in the central part of the inner core. PKP(DF) residuals with respect to the reference model PREM, as a function of $\cos^2\xi$, where ξ is the ray angle with respect to the Earth's rotation axis inside the inner core (polar paths correspond to $\cos^2\xi = 1$). (a) Distance 153–155° (depth ~300 km beneath inner core boundary). (b) Distance 173–180° (turning point near the Earth's center). Black dots are the means of the observations with their error bars; thick lines are predictions for a uniform anisotropy model. Note on (b) the difference with the predictions for $\cos^2\xi \sim 0.35$ ($\xi \sim 55°$) ((a and b) reproduced from Ishii M and Dziewonski AM (2002) The innermost inner core of the Earth: Evidence for a change in anisotropic behaviour at the radius of about 300 km. *PNAS* 99: 14026–14030). (c) Cartoon showing the inner core with three possible innermost inner core structures that fit the data, with different P-wave anisotropy ((c) modified from Calvet M, Chevrot S, and Souriau A (2006) P-wave propagation in transversely isotropic media. II. Application to inner core anisotropy: Effects of data merging, parametrization and a priori information. *Physics of the Earth and Planetary Interiors* 156: 21–40).

The mechanism at the origin of a preferred alignment is also debated (see **Chapter 8.12** and Deguen, 2012, for reviews). The preferred orientation may be either acquired during the inner core growth (solidification texturing) or induced by deformation within the inner core. With solidification texturing, the internal structure is a record of inner core history since its formation, unless it has been erased by later processes. Solidification texturing may result from the growth of dendrites in the direction of heat extraction, thus in the radial direction with a cylindrical symmetry consistent with the convective pattern in the outer core (Bergman, 1997). Other texturing mechanisms able to generate anisotropy have been proposed, in particular alignment of iron crystal with the magnetic field (Karato, 1993) or compaction in the mushy zone at the ICB during inner core growth (Sumita et al., 1996).

Anisotropy may also result from inner core deformation. For example, it has been proposed that, because of the cylindrical pattern of the outer core flow that governs heat extraction, the inner core is expected to grow faster at the equator than near the poles. The adjustment of the inner core to its equilibrium figure is performed by a flow from the equator to poles (Yoshida et al., 1996), but the resulting deformation may be too weak to generate a substantial preferential orientation (Deguen, 2012). However, if the inner core has a compositional density stratification, the flow will be mostly concentrated in the upper layers, so that the central part of the core may keep the fossil texture of the primitive inner core (Deguen and Cardin, 2009).

Plastic deformation induced by convection inside the inner core may also produce anisotropy (Buffett, 2009; Cottaar and Buffett, 2012; Deguen and Cardin, 2011; Jeanloz and Wenk, 1988; Romanowicz et al., 1996; Weber and Machetel, 1992; Wenk et al., 2000). Convection may be driven by thermal or compositional instability in the inner core (Gubbins et al., 2013). The conditions required for triggering thermal convection are however not necessarily fulfilled, as they depend on debated parameters such as the thermal conductivity of iron, the amount of radioactive elements in the inner core, the conductivity profile of the outer core, and the heat flux at CMB (Buffett,

2000; Deguen, 2012; Hirose et al., 2013; Yukutake, 1998; see **Chapter 8.12**). Moreover, thermal convection hardly generates large-scale anisotropy, unless it is coupled with magnetic field (Buffett and Wenk, 2004; Karato, 1999).

1.23.7.3 Lateral Heterogeneities Inside the Inner Core and Scatterers

Lateral heterogeneities in the inner core may be due either to a change in isotropic velocity or to a change in anisotropy. In the first case (change in isotropic velocity), heterogeneities of thermal origin are ruled out, as the temperature is nearly uniform inside the inner core (Weber and Machetel, 1992). One may thus invoke either a chemical heterogeneity, a phase change, a change in the amount of partial melting, or a change in grain size of randomly oriented anisotropic grains. In the second case (change in anisotropy), the heterogeneity could be either an anisotropic domain with similar elastic properties but with different orientation or a domain with different anisotropic properties. Because of the poor geographic sampling, it is generally impossible to discriminate between bulk heterogeneities and anisotropy perturbations.

We have previously mentioned the existence of a hemispherical heterogeneity in isotropic velocity in the uppermost 85 km and a hemispherical variation in anisotropy in the depth range 100–700 km beneath ICB. We will later discuss the interpretation of this observation.

In the wavelength range 20–200 km, many studies have reported the possible existence of heterogeneities (Bréger et al., 1999; Collier and Helffrich, 2001; Creager, 1997; Kaneshima, 1996; Lindner et al., 2010; Song, 2000; Zhang et al., 2005). However, in none of these cases, it is possible to completely discard a mantle origin. A stochastic analysis of PKP(DF) at different distances shows that the heterogeneity in isotropic velocity does not exceed 0.3% for wavelengths 100–400 km (Garcia and Souriau, 2000b).

The existence of small-scale heterogeneities inside the uppermost inner core has been inferred from the observation of scattered energy in the coda of the PKiKP wave (Vidale and Earle, 2000). These scatterers raise great interest, because they may give information on the fine structure of the uppermost inner core, in particular on its possible dendritic growths and on the fate of grains and fluid inclusions with depth. They also contribute to the strong wave attenuation inside the inner core. The analysis of the PKiKP coda generally requires records from small aperture arrays (**Figure 12(a)**), in order to eliminate coda signal generated in the mantle or at the CMB. It is best observed in the frequency range 4–6 Hz (Koper et al., 2004; Poupinet and Kennett, 2004).

Two types of coda have been observed. In the first case, the signal may arrive emergently (**Figure 12(b)** and **12(c)**) with a spindle-shaped envelope lasting about 200 s after the theoretical arrival time of PKiKP, even if this phase is not observed (this is the case at distance ~70° because the reflection coefficient at the ICB is close to 0). This signal requires heterogeneities located in the uppermost 350 km of the inner core, with a size of the order of 1–10 km, and velocity contrast of 1–10%, or possibly more (Leyton and Koper, 2007a; Peng et al., 2008; Vidale and Earle, 2000). In the second case, the coda maximum is immediately after the PKiKP onset, with a rapid amplitude drop in the first seconds or tens of seconds, followed by a constant coda level during about 100–200 s (**Figure 12(d)**; Koper et al., 2004; Leyton and Koper, 2007b; Peng et al., 2008; Poupinet and Kennett, 2004; Vidale and Earle, 2000). Codas with sharp onsets may be better explained by scatterers at the ICB rather than in the inner core volume (Poupinet and Kennett, 2004; see **Chapter 1.24**).

Although the Earth sampling remains poor due to the limited number of small aperture arrays, the scatterer distribution appears uneven. The regions generating clear PKiKP coda are mostly beneath northern Pacific and eastern Asia, and the absence of coda is preferably observed beneath the Atlantic Ocean (Leyton and Koper, 2007b). This distribution may be related to the hemispherical pattern observed in the isotropic layer, even though additional observations are still necessary.

1.23.8 The Inner Core: Seismic Attenuation

The attenuation of seismic waves may give information on the physical nature of the inner core and on its texturing. In particular, if partial melting is present, a strong anelastic attenuation correlated with low S-velocities and low viscosity is expected. Energy loss may also be due to scattering induced by texture (anisotropic crystals with various orientations or shapes), by the presence of fluid pockets, or less likely by compositional heterogeneities. These two mechanisms induce wave dispersion thus PKP(DF) pulse broadening, but this effect is much more important for viscoelastic attenuation with flat relaxation spectrum than for forward scattering. The attenuation is usually quantified through the quality factor Q (attenuation is proportional to Q^{-1}). The total attenuation is expressed as the sum of anelastic (or intrinsic) attenuation Q_i^{-1} and scattering attenuation Q_s^{-1}:

$$Q^{-1} = Q_i^{-1} + Q_s^{-1} \quad [3]$$

(Sato et al., 2012).

P-wave attenuation Q_α^{-1} at high frequency is constrained by body waves, mostly by the amplitude of PKP(DF). For its anelastic contribution, Q_α depends on both the attenuation in bulk (Q_κ^{-1}) and in shear (Q_μ^{-1}), such as

$$Q_\alpha^{-1} = kQ_\mu^{-1} + (1-k)Q_\kappa^{-1} \quad [4]$$

where $k = 4/3 \times (v_S/v_P)^2$, v_P and v_S being the P- and S-velocities (see **Chapter 1.25**). Attenuation is also constrained by the normal modes, whose damping gives attenuation in the low-frequency part of the spectrum. Modes are mostly sensitive to the attenuation in shear and are insensitive to scattering by small-scale heterogeneities (<100 km). As for elastic parameters, they have a poor sensitivity to the central part of the core. A first difficulty in the interpretation of Q will thus result from the difference in the parameters and frequency bands sampled by body waves and normal modes. Another difficulty is to decipher the relative contributions of viscoelasticity and scattering.

1.23.8.1 P-Wave Attenuation: Depth Dependence and Hemispherical Variations

A comparison of the amplitude of PKP(DF) with the one of a nearby reference phase is often used to estimate the attenuation along the ray, using geometries that minimize source and mantle path contributions and assuming that Q is infinite in the liquid core. In the same way as for velocity models, the reference phase

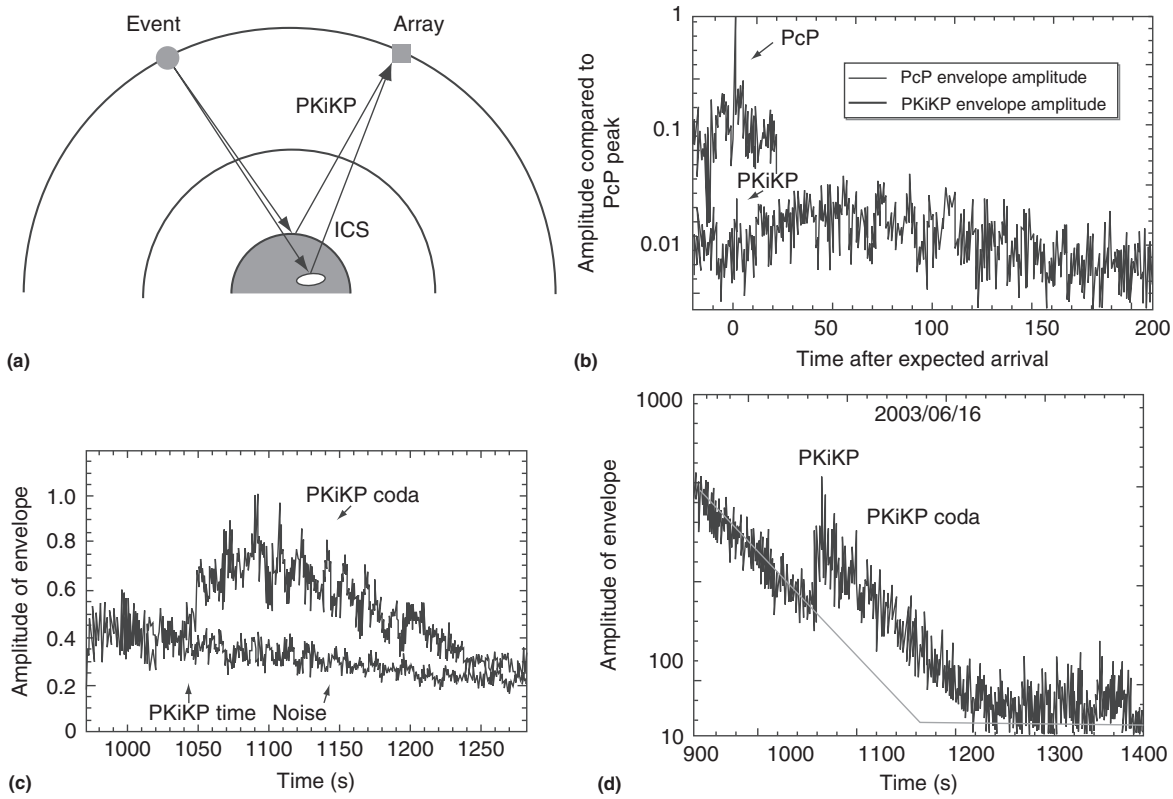

Figure 12 Detection of scatterers inside the inner core, from the coda of the PKiKP wave reflected at inner core boundary. (a) Principle of the method: energy arrival following PKiKP is detected at an array. (b) Comparison of the envelopes of the signal for the PcP wave reflected at core–mantle boundary and for the PKiKP wave, showing that the coda originates in the inner core, not in the mantle; the signals are stacks of two Novaya Zemlya nuclear tests. (c) Average of different PKiKP stacks for events at distances 60–70° from LASA in Montana, United States, compared to the noise ((a–c) reproduced from Vidale JE and Earle PS (2000) Fine-scale heterogeneity in the Earth's inner core. *Nature* 404: 273–275). (d) Same as (c) for an event at 74° from WRA array in Australia, showing a PKiKP coda with a different shape, an indication of variations in the scatterer properties inside the inner core ((d) reproduced from Poupinet G and Kennett BLN (2004) On the observation of high frequency PKiKP and its coda in Australia. *Physics of the Earth and Planetary Interiors* 146: 497–511).

is PKiKP in the uppermost 100 km and PKP(BC) for depths 100–300 km below the ICB with an extension down to 600 km using PKP(C_{diff}), but in this case, the amplitude of the reference phase becomes highly sensitive to the velocity gradient at the base of the liquid core. PKP(AB) is also sometimes used. The comparison of the two phases i and j is made either in the temporal domain, where the amplitude ratio A_i/A_j is measured on filtered traces, or in the spectral domain, taking advantage of the linearity of $\mathrm{Ln}(A_i/A_j)$ with frequency, if anelastic attenuation is dominant and not frequency-dependent. The intrinsic attenuation as a function of depth is then retrieved from the A_i/A_j ratio at different distances. A better approach uses waveform modeling, based on the comparison of the observed waveforms with the predictions of synthetic seismograms. It allows to sample any depth in the inner core, but it requires the knowledge of source and mantle structure (Li and Cormier, 2002; Tanaka, 2012).

The various studies come to a general agreement about a low Q_α in the uppermost inner core at frequency $f \sim 1$ Hz, with values ranging from 100 to 400 in the uppermost 200 km, increasing with depth up to 400–600 at 400 km beneath ICB (Bhattacharyya et al., 1993; Bolt, 1977; Cormier, 1981; Doornbos, 1974, 1983; Iritani et al., 2010; Ivan and Moloto-A-Kenguemba, 2007; Kazama et al., 2008; Niazi and Johnson, 1992; Ohtaki et al., 2012; Oreshin and Vinnik, 2004; Souriau and Roudil, 1995; Tanaka, 2012; Tseng et al., 2001; Yu and Wen, 2006a). These studies, which concern different regions, exhibit very different Q-profiles with depth. However, the error bars are large, and short wavelengths in mantle heterogeneities and CMB topography may strongly affect wave amplitudes (Bowers et al., 2000; Leyton and Koper, 2007a), which makes difficult the detection of regional variations, if any.

In the uppermost 50–100 km, a hemispherical pattern similar to the one observed for seismic velocities is clearly observed, the attenuation being stronger in the quasi-eastern hemisphere (40°–180° E) than in the quasi-western hemisphere (**Figure 9 (d)**). Q_α-values in the ranges 50–250 and 330–600 are reported for the eastern and western hemispheres, respectively (Cao and Romanowicz, 2004b; Garcia, 2002a; Monnereau et al., 2010; Tanaka, 2012; Wen and Niu, 2002; Yu and Wen, 2006a). Thus, high attenuation correlates with high velocity in the quasi-eastern hemisphere and low attenuation with low velocity in the quasi-western hemisphere. This correlation is opposite to that observed in the mantle, where it is ascribed to thermal effects. It is clearly detected down to 100 km but may be present deeper (Tanaka, 2012).

In the lowermost 500 km, waveform modeling of PKP at nearly antipodal distances reveals a Q-increase, together with a decrease in the scatter of the Q-values (Li and Cormier, 2002).

This central, high-Q zone approximately corresponds to the innermost inner core (**Figure 13**) and could correspond to a different fabric (Cormier and Stroujkova, 2005).

Studies based on spectral ratio analyses fail to detect a frequency dependence of Q_α in the narrow frequency range (0.2–2 Hz) sampled by body waves (e.g., Cormier, 1981; Souriau and Roudil, 1995), but waveform modeling, which takes into account the dispersive effect of viscoelasticity, suggests that such a frequency dependence is present (Cummins and Johnson, 1988b; Doornbos, 1983; Li and Cormier, 2002).

1.23.8.2 The Attenuation in Shear

The very strong attenuation in shear ($Q_\mu = 85$ in the PREM model) is mostly derived from the inversion of normal modes. Some specific studies of inner core-sensitive modes have proposed much larger Q-values, between 1500 and 4000 (Masters and Gilbert, 1981; Suda and Fukao, 1990), indicating that Q_μ must be high, about 3500. However, Widmer et al. (1991) have shown that these high Q_μ-values are possibly due to a misidentification of neighboring modes; they obtain $Q_\mu \sim 110$ for PKIKP-equivalent modes. On the other hand, Andrews et al. (2006) show that the Q-values may be affected by mode coupling and that Q_μ is low, so that the discrepancy between normal modes and body waves is small.

From waveform modeling of PKJKP, Cao and Romanowicz (2009) obtained a Q_μ-value of 315 ± 150. This is larger than the values given in PREM. As PKJKP better samples the Earth's center than modes, this discrepancy suggests that Q_μ increases with depth, as do Q_α and v_S.

The compatibility of modes and body waves has long been a subject of debate (see discussion in Romanowicz and Durek, 2000), because of the high Q_μ-values first proposed for inner core-sensitive modes. This seems no longer the case. However, the values of Q_α and Q_μ are not constrained well enough to infer the Q_κ value from relation [4], in particular to see if $Q_\kappa \gg Q_\mu$ as in the mantle. From the seismological results, it is also not possible to specify if several absorption bands are present in the inner core and what are the respective contributions of scattering and anelasticity.

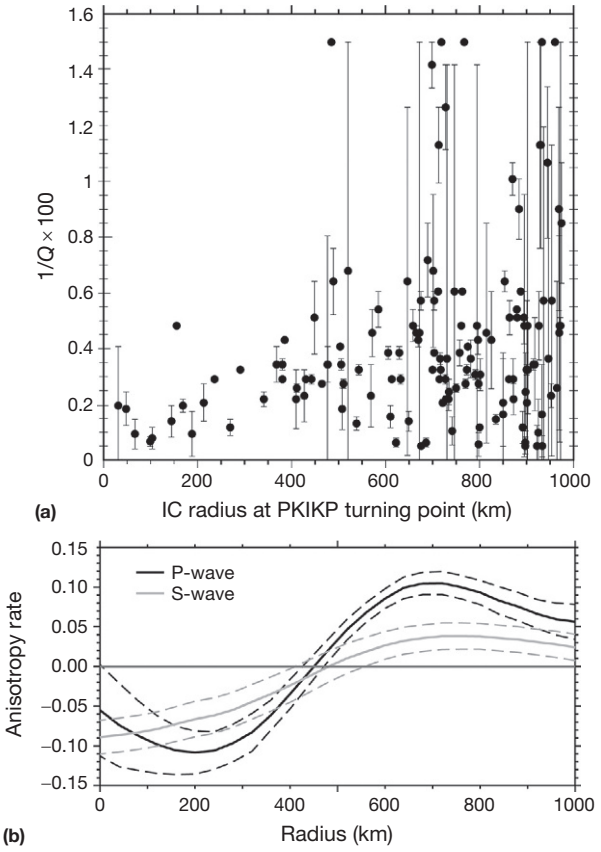

Figure 13 (a) Attenuation $1/Q_\alpha$ for PKP(DF) paths turning at different depths inside the inner core (Q_α is the P-wave quality factor) (reproduced from Cormier VF and Stroujkova A (2005) Waveform search for the innermost inner core. *Earth and Planetary Science Letters* 236: 96–105). (b) Two coefficients describing the anisotropy of P-wave velocity (black) and S-wave velocity (gray). Note the decrease of the attenuation and its smaller scatter inside the innermost inner core, where a different anisotropy is also observed (modified from Beghein C and Trampert J (2003) Robust normal mode constraints on inner core anisotropy from model space search. *Science* 299: 552–555).

1.23.8.3 The Anisotropy in Attenuation

A first direct evidence of anisotropy in P-wave attenuation is given by an analysis of PKP(DF) waves with turning points beneath the same region (Africa), but with various orientations with respect to ERA. Polar paths, which correspond to a faster propagation, also correspond to a stronger attenuation (Souriau and Romanowicz, 1996a; **Figure 14**). This result has been extended to the worldwide scale (Souriau and Romanowicz, 1996b) and to greater depth from waveform modeling of PKP at large distance (Cormier et al., 1998). Oreshin and Vinnik (2004) and Yu and Wen (2006b) confirm the dependence of attenuation with the ray angle with respect to ERA but show that it is observed in the western hemisphere only, where anisotropy in seismic velocity is the strongest one. Ray orientation also has an influence on the frequency dependence of attenuation and on dispersion (Souriau, 2009): For polar paths, the PKP(DF) wave is clearly dispersed and its amplitude decay is larger at high frequency than at low frequency, a frequency dependence that is not observed for equatorial paths.

From inner core-sensitive modes, Mäkinen and Deuss (2013) have identified a zonal pattern in anelasticity, suggesting that a cylindrical anisotropy in attenuation may also be present in shear, with again the high S-attenuation correlated to the high velocity.

1.23.8.4 Interpretation of Inner Core Attenuation

Two main mechanisms may contribute to attenuation: viscoelasticity (Cormier, 1981; Doornbos, 1974; Li and Cormier, 2002) and scattering (Calvet and Margerin, 2008; Cormier, 2007; Cormier and Li, 2002). They may be present simultaneously in the inner core.

A viscoelastic model with frequency-dependent attenuation is able to explain the main characteristics of attenuation in the body-wave domain (Li and Cormier, 2002), but the low dispersion of the data requires very particular conditions to be explained with this mechanism. Viscoelasticity could be

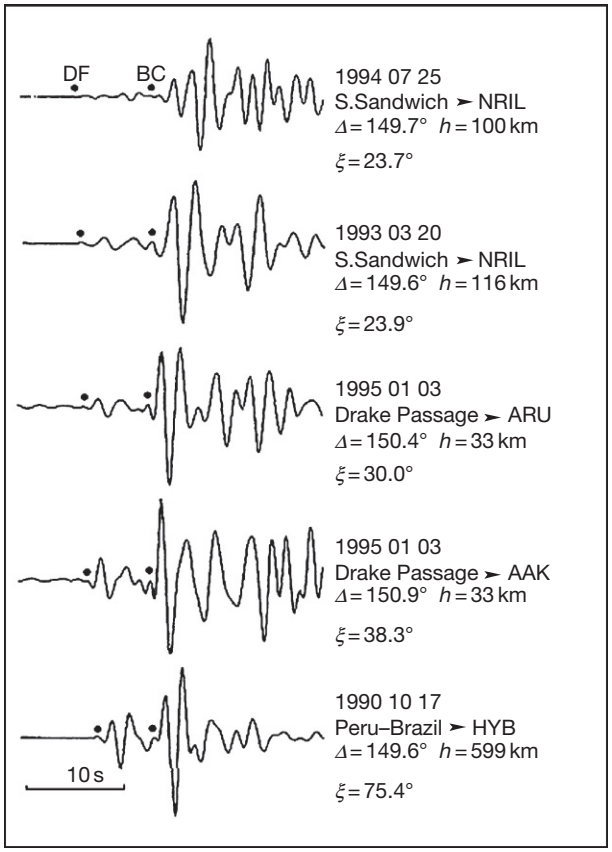

Figure 14 Evidence for anisotropy in attenuation correlated to the anisotropy in velocity, from records corresponding to paths turning in the inner core beneath Africa, with nearly the same distance Δ, but with different orientations ξ with respect to the Earth's rotation axis (h is the focal depth). PKP(BC) being the reference phase, note the fast propagation (large BC−DF time) and strong attenuation (small DF/BC amplitude) for nearly polar paths (small ξ). Data are band-pass filtered at 2 s. Reproduced from Souriau A and Romanowicz B (1996) Anisotropy in inner core attenuation: A new type of data to constrain the nature of the solid core. *Geophysical Research Letters* 23: 1–4.

present at the top of the inner core, because of a possible high proportion of fluid inclusions trapped in the iron lattice (Fearn et al., 1981; Loper and Roberts, 1981). However, the correlation of high (respectively low) attenuation with high (respectively low) velocity observed in the uppermost isotropic layer is opposite to model predictions (O'Connell and Budianski, 1977), which indicates that this mechanism is not predominant. From PKiKP coda analysis, Leyton and Koper (2007b) obtained a coda Q-value close to 500 and inferred that scattering attenuation must be at least comparable, or possibly larger, than anelastic attenuation in the uppermost inner core.

The difficulties met with the anelastic model are overcome with a scattering model Cormier (2002). The observation of PKiKP coda is a strong argument in favor of this mechanism. Scattering attenuation depends on the typical scale length of the heterogeneities and on the amplitude of velocity perturbations. The PKP(DF) attenuation may be explained by a heterogeneous random medium with P-wave velocity perturbations of ~8% and typical scale lengths 0.5–2 km (Cormier et al., 1998) or slightly larger, about 10 km (Cormier and Li, 2002). From the energy envelopes of PKiKP coda waves, Vidale and Earle (2000) found heterogeneities of about 2 km with velocity fluctuations of only 1.2% in the uppermost 300 km of the inner core. Cormier (2007) proposed that these coda waves are induced by reverberation on a platelike fabric developing at ICB under the shearing of the tangential outer core flow and obtained perturbations of 10%. Calvet and Margerin (2008) developed a scattering model in which the heterogeneities result from the random orientation of grains with similar anisotropy. They showed that iron grains of size ~400 m may easily explain Q_α-values in the range 300–600. The hemispherical variations may be due either to a variation of the preferred orientation in the texture (Cormier, 2007) or to a grain size difference between the two hemispheres (Monnereau et al., 2010). We will return to this point in the next section. On the other hand, from laboratory crystallization experiments and from geodynamic considerations, Bergman (1997, 1998) found a grain width around 200 m, which is in rather good agreement with seismological estimates.

The anisotropy in attenuation is too large to be explained by wave-front distortion due to velocity anisotropy. The correlation between anisotropy in velocity and anisotropy in attenuation, with the high attenuation axis corresponding to the fast axis parallel to ERA and low attenuation corresponding to slow propagation parallel to the equatorial plane, may give some indications about the mechanisms at the origin of anisotropy. If the velocity anisotropy were due to fluid inclusions, as proposed by Singh et al. (2000), the opposite correlation would be observed (Peacock and Hudson, 1990). The right correlation may be observed in anelastic anisotropic media characterized by complex stiffness tensor (Carcione and Cavallini, 1994). Again, scattering (by anisotropic crystals or elongated heterogeneities) appears to be the most plausible attenuation mechanism to explain the observed correlation for anisotropy. Following the dendritic model of Bergman (1997), Cormier (2007) proposed that radially oriented, elongated structures may explain both velocity and attenuation. The strong attenuation of paths parallel to ERA would be a consequence of the large number of grain boundaries crossed by the seismic rays.

Scattering is likely the predominant attenuation mechanism at high and intermediate frequencies (0.02–2 Hz) (Cormier and Li, 2002), but not in the normal mode frequency band (0.001–0.01 Hz) where viscoelasticity is favored. When scatterers cannot been directly detected from coda waves, deciphering the relative contributions of viscoelasticity and scattering relies on measurements of induced effects, such as pulse distortion or wave dispersion, which are difficult to observe (Cormier and Li, 2002; Li and Cormier, 2002).

1.23.8.5 Origin of the Hemispherical Pattern in the Uppermost Inner Core

The hemispherical pattern is certainly the most intriguing feature of the inner core. It appears at two levels: (1) in the uppermost isotropic layer, where the quasi-eastern hemisphere has high velocity and high attenuation compared to the Western one, and (2) in the depth range 100–700 km below ICB, where the western hemisphere has strong anisotropy in both velocity and attenuation with the fast axis and high

attenuation axis parallel to ERA, compared to the eastern hemisphere where anisotropy is weak for both velocity and attenuation. There is to date no satisfying explanation of these different observations. Scattering related to the iron crystal structure and diffusion related to fluid inclusions have both been invoked to explain the uppermost inner core dichotomy. Also, several geodynamic models are possible; some of them invoke simultaneous freezing and melting at ICB.

Cao and Romanowicz (2004b) argue that hemispherical variations of heat flow near ICB may induce variations in the melt fraction content and/or connectivity of liquid inclusions in a mushy zone. The liquid inclusions may be well isolated in the eastern hemisphere, while they may remain partly connected in the western hemisphere that may be colder and freezing more rapidly (Cao and Romanowicz, 2004b). The effect of the connectivity of fluids on the seismic properties is however highly complex (O'Connell and Budianski, 1977).

From laboratory experiments, it is inferred that textures acquired by solidification at the ICB may be closely coupled to heat extraction by the fluid flow at the base of the outer core (Bergman et al., 2002). Cormier (2007) proposes that, in actively crystallizing regions associated to outer core upwellings, the fabric is characterized by dendrites elongated in the radial direction with hcp iron c-axis perpendicular to the dendrite elongation (Bergman et al., 2002). This texture results in high velocity, strong PKP(DF) attenuation, and weak PKiKP coda (**Figure 15(a)**) and may represent the eastern hemisphere structure. By contrast, when the outer core flow is tangent to ICB, the longer scale lengths of the texture tend to be parallel to ICB, and the PKIKP attenuation is less efficient. Such a texture may develop in the western hemisphere where anisotropy is also observed. Lateral variations from strong to weak velocity and attenuation and from weak to strongly backscattered PKiKP coda may thus be explained by a textural variation from vertical- to horizontal-oriented platelike structures (Cormier, 2007). However, Cormier et al. (2011) argue that the long PKiKP codas observed by Peng et al. (2008) in the western hemisphere are better explained with an isotropic distribution of scale lengths (**Figure 15(b)**), together with viscoelastic dissipation.

Thermal heterogeneities may drastically affect fluid flow in the outer core, which in turn induces textural heterogeneity in the inner core (Sumita and Olson, 1999). Following this idea, Aubert et al. (2008) developed a model of thermochemical convection in the outer core, in which long-term cyclonic circulation beneath Asia causes fast freezing in the eastern hemisphere and slow freezing in the Western one where well-textured crystals develop (**Figure 16(a)**). The hemispherical texture and thermal conditions are thus opposite to those of Cormier et al. (2011) and Cao and Romanowicz (2004b). On the other hand, from geodynamo simulations, Gubbins et al. (2011) propose that melting and freezing may occur simultaneously at different places at the ICB, a broad melting zone being related to an outer core upwelling beneath the Pacific in the western hemisphere.

Thermal convection inside the inner core has also been proposed to explain the East–West seismic dichotomy. Convection with open boundaries (thus the possibility of freezing or melting at ICB) may induce a solid translation of the inner core (Alboussière et al., 2010; Monnereau et al., 2010). For large viscosity, the main convective mode is a global translation of

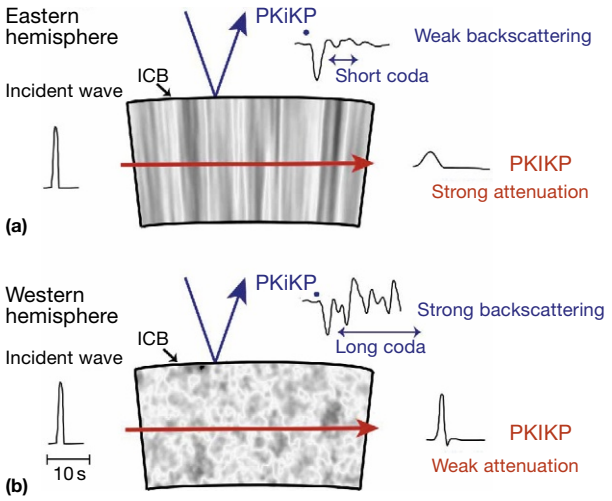

Figure 15 Possible textures explaining the hemispherical dichotomy in the uppermost inner core and their consequences for seismic waves. (a) Dendrites developing perpendicularly to inner core boundary (ICB), a possible model for the eastern hemisphere. The transmitted PKP(DF) wave (also noted PKIKP) is strongly dispersed and attenuated by the numerous boundaries encountered by the seismic ray (note the broadening of the signal), whereas the reflected PKiKP wave is almost undistorted. (b) Randomly distributed scatterers, a possible model for the western hemisphere. The strong backscattering is responsible for the long coda of transmitted waves. Modified from Cormier VF (2007) Texture of the uppermost inner core from forward- and backscattered seismic waves. *Earth and Planetary Science Letters* 258: 442–453.

the inner core with melting at the surface of one hemisphere and solidification at the other one (**Figure 16(b)**). Monnereau et al. (2010) suggest that grains grow during their transit from the crystallizing western hemisphere to the melting eastern hemisphere. Multiple scattering modeling of seismic waves in iron crystal aggregate explains the East–West dichotomy in both velocity and attenuation. The direction of translation and the resulting crystallizing hemisphere are however subjects of debate, as they depend on the forcing by thermal heterogeneities and on the liquid core flow; moreover, they may evolve with time (Aubert, 2013; Olson and Deguen, 2012).

The hemispherical pattern in anisotropy at depth is not fully explained by any models. For example, the translation mode does not produce any deformation. However, high-degree convective modes may develop for decreasing viscosity and induce texturing in the colder hemisphere (Mizzon and Monnereau, 2013). On the other hand, to explain the weak anisotropy in the eastern hemisphere, Bergman et al. (2010) suggest that the anisotropic solidification texture acquired in the western hemisphere is gradually lost during translation toward the melting side, as the result of thermal annealing.

1.23.9 Inner Core: Differential Rotation with Respect to the Mantle

A differential eastward rotation of the inner core with respect to the mantle (i.e., a faster rotation of the inner core) is predicted by some models of geodynamo (e.g., Aubert and Dumberry,

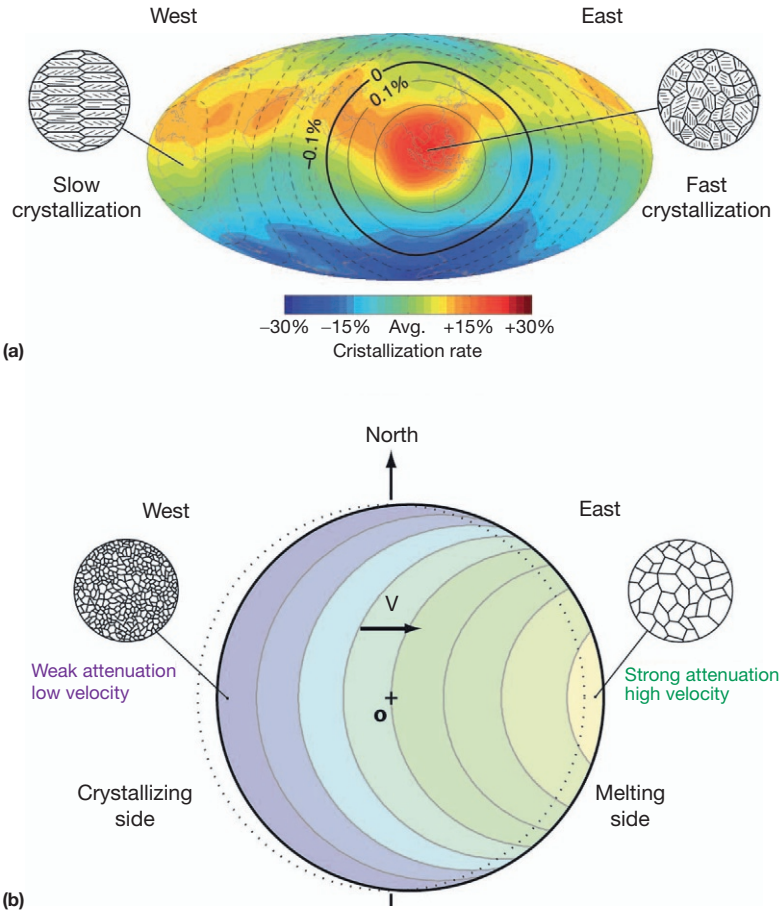

Figure 16 Cartoons illustrating two growth models at the origin of the seismic hemispherical pattern and possible resulting textures (grain size and orientation) in the uppermost inner core. (a) Relative crystallization rate (with respect to mean rate) at inner core surface resulting from heat extraction at ICB induced by the forcing of the thermal heterogeneities at CMB; superimposed is the seismic velocity degree one from Tanaka and Hamaguchi (1997) (modified from Aubert J, Amit H, Hulot G, and Olson P (2008) Thermochemical flows couple the Earth's inner core growth to mantle heterogeneity. *Nature* 454: 758–761). (b) Cross-section showing the age distribution in the inner core resulting from solid translation V (here from left to right, from dashed to plain positions). The age increases from the crystallizing side (blue) to the melting side (yellow) (reproduced from Monnereau M, Calvet M, Margerin L, and Souriau A (2010) Lopsided growth of Earth's inner core. *Science* 328: 1014–1017).

2011; Aurnou et al., 1996; Glatzmaier and Roberts, 1996; Gubbins, 1981; see Volume 8). The predicted rotation rate is as large as 2–3° year^{-1}; thus, time-dependent phenomenons induced by this rotation could possibly be detected by the propagation of seismic waves. At the same time, gravimetric coupling predicts that inner core heterogeneities and topography induced by mantle heterogeneities must be locked by the mantle gravity field, forcing the inner core to rotate at the same rate as the mantle (Buffett, 1997; see **Chapter 8.08**). Thus, the inner core rotation may give important constraints on the balance of these two antagonist effects and on their dynamic and structural consequences.

The basic idea for detecting inner core rotation is to track inner core heterogeneities during a long time, either along particular seismic paths that are unchanged during decades (**Figure 17(a)**) or at the worldwide scale. Seismological data are available since the 1950s, but high-quality digital data required for accurate analyses are available only since the 1980s. Before the 1970s, mechanical and optical limitations on recording systems made it hard to reach the accuracy level (< 0.1 s) required for such studies.

1.23.9.1 Tracking the Drift of a Heterogeneity Along a Stable Seismic Path

The heterogeneity could be either an identified small-scale heterogeneity inside the inner core (Creager, 1997; Lindner et al., 2010; Mäkinen and Deuss, 2011; Song, 2000), or the transition between the two inner core hemispheres (Souriau and Poupinet, 2003; Waszek et al., 2011), or scatterers (Vidale and Earle, 2005; Vidale et al., 2000), or the topography at ICB (Cao et al., 2007; Souriau, 1989; Wen, 2006).

Song and Richards (1996) proposed to use the apparent wobble of the tilted anisotropy symmetry axis, and, from the analysis of a 30-year data of South Sandwich Island events recorded at College Station (COL) in Alaska, they obtained a 1.1° year^{-1} eastward rotation rate. Soon after, another estimation at 3° year^{-1} was obtained from a worldwide analysis of

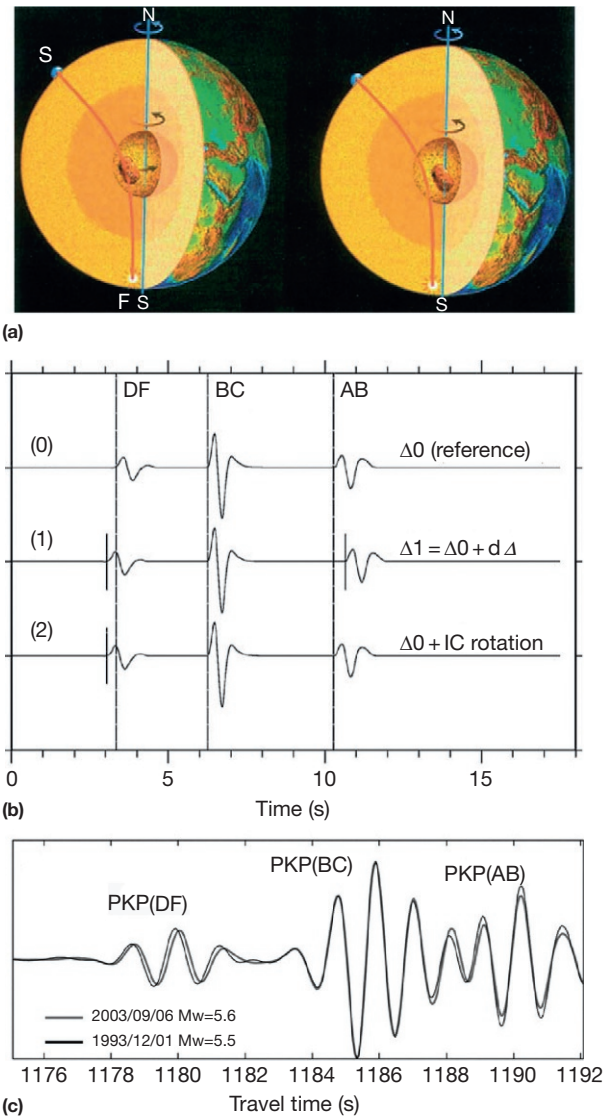

Figure 17 (a) Principle of the detection of an inner core differential rotation with respect to the mantle, from the drift of an inner core heterogeneity through a seismic ray. Figure on the right corresponds to a later stage than figure on the left, assuming an eastward (faster) rotation of the inner core. (b) Principle of doublets for discriminating between inner core rotation and earthquake mislocation, by the use of the three PKP phases (DF, BC, and AB). A small difference in location, giving a difference in epicentral distance $d\Delta$ with respect to the reference event at distance $\Delta 0$ (trace 0), results in a proportional variation of (BC−DF) and (AB−BC) (trace 1) compared to (0). Trace (2) corresponds to an event with same location as (0), but the DF time only is modified, due to the drift of an inner core heterogeneity along the DF ray ((b) reproduced from Souriau A, Garcia R, and Poupinet G (2003) The seismological picture of the inner core: Structure and rotation. *Compte-Rendus Geoscience* 335: 51–63). (c) Example of doublet of two South Sandwich Island events separated by 10 years (1993, 2003) recorded in Alaska. The DF time shift is interpreted as due to inner core rotation ((c) reproduced from Zhang J, Song X, Li Y, Richards PG, Sun X, and Waldhauser F (2005) Inner core differential motion confirmed by earthquake waveform doublets. *Science* 309: 1357–1360).

travel times (Su et al., 1996). These puzzling observations started an interesting debate that involved both observational and theoretical aspects, even though the interpretation in terms of tilt axis was criticized (Souriau et al., 1997). The data of South Sandwich Island events at COL were reinterpreted as due to the drift of a heterogeneity (Creager, 1997), leading to a rotation rate of 0–0.3° year^{-1}, depending on mantle heterogeneities. A difficulty arises from the perturbing signal of the subduction zones on both source and station sides. Paths that avoid subduction zones, for example, Novaya Zemlya nuclear tests recorded at Antarctic stations, led to time perturbations generally smaller than those observed for the path from South Sandwich Island to COL and sometimes of opposite sign (e.g., Isse and Nakanishi, 2002; Li and Richards, 2003b; Souriau, 1998). On the other hand, despite some attempts to retrieve simultaneously inner core structure and rotation, the existence of an inner core heterogeneity along the investigated path is generally difficult to assess (see Souriau and Poupinet, 2003; and Song, 2003, for reviews and discussions of the earlier results).

Another difficulty is to eliminate focal mislocations. Seismological networks have evolved with time, inducing systematic, time variable, location biases (Kennett and Engdahl, 1991) that could induce effects similar to those due to rotation. A way to circumvent this difficulty is to use doublets, that is, pairs of events with nearly the same focal location, recorded at the same station with similar waveforms (Poupinet et al., 1984). A difference in distance for the two events results in an apparent dilatation or contraction of one record with respect to the other (**Figure 17(b)**), whereas an inner core heterogeneity encountered along the path affects the PKP(DF) travel time only.

The doublet approach, first applied to the path from South Sandwich Island to COL (Poupinet et al., 2000), has been widely applied since. Despite the use of high-quality doublets, controversial results depending on the method refinement and on the paths considered have been obtained. In some cases, the same high-quality doublet (**Figure 17(c)**) recorded at different stations led to different interpretations involving either inner core rotation or variations in inner core radius (Cao et al., 2007; Wen, 2006; Zhang et al., 2005).

The results obtained along particular paths are globally inconsistent. Some of the paths give an eastward rotation, with rotation rates in the range 0.1–0.2° year^{-1} for most of them (Cao et al., 2007; Mäkinen and Deuss, 2011) and higher values (0.2 and 0.6° year^{-1}) for the paths from South Sandwich Island to Alaska (Lindner et al., 2010; Song, 2000; Tkalčić et al., 2013; Zhang et al., 2005). Some paths do not detect any variation (Collier and Helffrich, 2001; Isse and Nakanishi, 2002; Poupinet et al., 2000; Zhang et al., 2008) or a westward rotation (Mäkinen and Deuss, 2011). Nonmonotonic rotation (Lindner et al., 2010; Tkalčić et al., 2013) or inner core oscillations (Collier and Helffrich, 2001) have also been proposed. The incompatibility among the different paths led Mäkinen and Deuss (2011) to reject inner core rotation with rates exceeding 0.1° year^{-1}.

Scatterers inside the inner core may also be used. Their main advantage is the rapid modification of the diffraction

pattern when they move, thus the possibility to detect inner core rotation in a few years. Vidale et al. (2000) analyzed the scattered waves that follow PKiKP for two closely located Novaya Zemlya nuclear tests at 3-year interval and recorded at LASA (large aperture seismic array in Montana, United States). The change in the diffraction pattern may be explained by a $0.15^\circ\,\text{year}^{-1}$ faster rotation of the inner core. A similar analysis, carried out on seven Mururoa (Pacific Ocean) French nuclear tests recorded at NORSAR (Norway), gives a rotation rate of $0.05–0.10^\circ\,\text{year}^{-1}$ (Vidale and Earle, 2005). The location of the nuclear tests is however not known very accurately (within 5–10 km) so that systematic biases due to source location cannot be ruled out.

1.23.9.2 A Search for a Differential Rotation with a Worldwide Approach

Local or regional heterogeneities inside the inner core are difficult to identify; they may be hidden by mantle heterogeneities and are smeared by the PKP(DF) Fresnel zone. A way to avoid this problem is to solve inner core rotation at the worldwide scale.

Several studies are based on the data from the ISC catalog, using statistical approaches. The results are often poorly conclusive, either because of the uneven Earth sampling with time (Su et al., 1996) or because of the lack of resolution of the data (Souriau and Poupinet, 2003).

The most reliable results are obtained from the analysis of normal modes at two different epochs. They rely on the identification of long wavelength, even degree heterogeneities inside the inner core, after correction for mantle heterogeneities. Inner core heterogeneities are responsible for splitting of the resonance peaks, which are described by splitting functions whose time variations are analyzed. This method has the potential to estimate accurately the rotation rate, but a good Earth coverage and the use of a large number of modes are necessary. Sharrock and Woodhouse (1998) analyzed seven modes for the period 1977–96, and they obtained a westward rotation rate of $0.5–2.5^\circ\,\text{year}^{-1}$, depending on the mode considered. Laske and Masters (1999) analyzed a larger data set and found that the rotation rate is essentially zero over 20 years ($0 \pm 0.2^\circ\,\text{year}^{-1}$). A later study (Laske and Masters, 2003), with more modes and more events, shows that the results are consistent for different mantle corrections and again emphasizes the dependence of the result on the mode considered, with rotation rates either positive or negative (**Figure 18**). The mean eastward rotation rate is $0.13 \pm 0.11^\circ\,\text{year}^{-1}$, thus a rotation that is barely significant.

1.23.9.3 Rotation or No Rotation? Implications

After two decades of controversies, the absence of steady rotation now seems favored in the light of the most recent results, which show inconsistencies among the rotation rates obtained for different paths and for different normal modes. Note however that the resolution of the different methods hardly exceeds

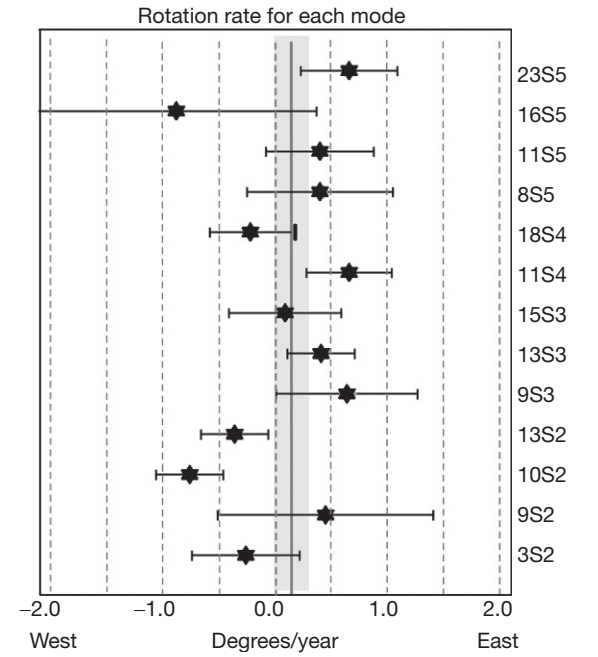

Figure 18 Inner core rotation rates obtained for various inner core-sensitive modes, after correction for mantle heterogeneities. The results vary with modes and are often compatible with a null rotation. Light gray area, least square fit of the rotation rate for all the modes. Modified from Laske G and Masters G (2003) The Earth's free oscillations and the differential rotation of the inner core. In: Dehant V, et al. (eds.) *Earth's Core, Dynamics, Structure, Rotation. Geodynamics Series*, vol. 31, pp. 5–22. Washington, DC: American Geophysical Union; Courtesy of G. Laske.

$0.05^\circ\,\text{year}^{-1}$, so that a rotation or oscillation rates lower than this value cannot be ruled out.

The largest rotation rates have been obtained for the paths from SSI to Alaska (time variations of $0.01\ \text{s year}^{-1}$ and rotation rates between 0.05 and $1.1^\circ\,\text{year}^{-1}$), which is the best sampled polar path. Unfortunately, it is also highly anomalous, as revealed by the large scatter of its PKP(DF) residuals (Bréger et al., 1999), and subject to criticism because of the difficulty to correct for mantle contributions and hypocentral mislocations. Moreover, PKP(DF) emerges barely from the noise, because of the strong attenuation in the polar direction (Li and Richards, 2003a). At the other end, the lower rotation rates are obtained from global studies, which are less dependent on the identification of a single heterogeneity. They are globally compatible with the absence of rotation. The analyses of reflected waves and scattered waves also lead to low rotation rates, $0.05–0.15^\circ\,\text{year}^{-1}$.

Whatever the path considered, and even for global Earth investigations, the main uncertainty concerns the heterogeneities that are used to quantify the differential rotation. The inner core sampling is generally too sparse to reliably map these heterogeneities. Only the quasi-hemispherical heterogeneity is robustly identified; temporal variations for this structure have been detected neither from body waves nor from normal modes (Souriau and Poupinet, 2003; Waszek et al., 2011).

The geodynamic consequences of an inner core rotation depend on the relative contributions of the gravitational, geomagnetic, and viscous couplings. These antagonistic effects may result in large ($\sim 0.1^\circ\,\text{year}^{-1}$) inner core oscillations with respect to the mantle about ERA, superimposed to a small steady rotation (Aubert and Dumberry, 2011; Buffett and Glatzmaier, 2000), but these results are strongly model-dependent. Some important parameters are the viscosity of the liquid core at the ICB and the viscosity of the inner core. The possible presence of a slurry layer above the ICB may contribute to increase the liquid core viscosity at the ICB. On the other hand, the inner core viscosity controls the ability of the inner core to deform in order to permanently adjust its shape to the mantle gravity field (Buffett, 1997).

If differential rotation is present, viscous deformation may concern the uppermost inner core only or the whole inner core, depending on the viscosity of the inner core. If the deformation is confined in an uppermost low viscosity layer, the strong shear induced by the viscous deformation would induce a preferred orientation of crystals or melt inclusions, in contradiction with the absence of anisotropy in the uppermost inner core. If the deformation involves the whole inner core, the inner core will be continuously mixed by the viscous flow, with relaxation times of the order of 3000 years. It will be hard in this context to maintain heterogeneities inside the inner core. Moreover, the readjustment flow will have a degree-two symmetry (Buffett, 1997); thus, it will induce a degree-four pattern in anisotropy, which is not observed. It is also difficult to reconcile a large rotation rate with the generation of a hemispherical pattern in the inner core, whose textural development requires a long-term coupling with the mantle, even though it is internally driven (see discussion in Deguen, 2012). A variation with depth of the hemispherical pattern, which could be a signature of the differential rotation during inner core growth (Waszek et al., 2011), may not easily be resolved with the seismological data because of the large Fresnel zone of the PKP waves. A large steady rotation thus seems unrealistic. This is consistent with dynamic models, which predict that the coupled effects of electromagnetic, viscous, and gravitational forces result in a mean rotation rate far below the detection threshold of seismological methods.

Inner core oscillations of the order of $0.1^\circ\,\text{year}^{-1}$ with typical period of 75 years are predicted from models taking into account the different torques acting on the inner core, although it must be noted that the fluctuations are far from being periodic (Aubert and Dumberry, 2011; Buffett and Glatzmaier, 2000). It has been suggested that the rotation observed in some studies could be part of an oscillation. This also seems unrealistic, because the different results relevant to a same time period do not give the same rotation rate (Mäkinen and Deuss, 2011).

The only way to reconcile the different observations is to imagine time-variable phenomena inside the inner core or at the ICB, which would have a local extension and which would be strong enough to give a seismological signature (Cao and Romanowicz, 2007; Mäkinen and Deuss, 2011; Sharrock and Woodhouse, 1998). It could be, for example, a modification in a slurry layer above ICB or in the mushy zone in the uppermost inner core. Alternatively, the source of variation could be outside the core. Finally, and more likely, the observations may still suffer from uncorrected mantle contributions and source location biases, even though doublet analyses remove most of them. In any case, more seismological and theoretical analyses are still necessary to make progress on this subject.

1.23.10 Conclusion

From the previous analyses, it may seem that the picture of the core is rather confused and that few characteristics meet a general agreement. This is true: the core is still a wide, almost virgin area of investigation compared to other structures in the Earth. Its deep location beneath heterogeneous layers (in particular D″ at the base of the mantle), together with the complexity of the physics of the core, let us anticipate that it will still long be a subject of controversy. At the same time, and for the same reasons, it is one of the most attractive objects for Earth scientists. We will attempt to summarize hereafter the seismological results that are considered as almost certain, those that are highly probable, and those that are still controversial or doubtful. We will then give some elements for future research.

1.23.10.1 Summary of the Results

The radii of the outer core and inner core are known with a good accuracy: 3480 ± 1 km for the CMB and 1215–1221 km for the ICB. These two boundaries are first-order discontinuities for the seismic waves (thickness < 2 km). The CMB has a small extra flattening (of < 500 m) with respect to its equilibrium figure and possibly a weak topography at different wavelengths, which may hardly exceed 4 km. The ICB has roughly the shape of its hydrostatic figure (thus is nearly spherical), with probably a long wavelength topography of no more than a few hundred meters, undetectable by seismology.

The liquid core is homogeneous from the seismological point of view, with neutral stratification except at the ICB, and perhaps at the CMB. Its density, well constrained by normal modes, shows a deficit with respect to molten iron that implies the presence of about 10% by weight of light elements. The base of the liquid core exhibits an ~ 150 km thick layer with low velocity gradient and increased density; it may correspond to an enrichment in iron. A repeated freezing and melting at the ICB is a possible mechanism to generate this layer. The liquid core has everywhere a nearly infinite quality factor. It is thus a transparent medium for seismic waves. It has a zero rigidity and a low viscosity; thus, it cannot sustain heterogeneities, except perhaps at the very base of the liquid core.

The ICB corresponds to an increase in P-velocity of about $0.7\ \text{m s}^{-1}$ and an increase in density of about $0.5–1.0 \times 10^3\ \text{kg m}^{-3}$, which indicate a strong depletion in light elements compared to the liquid core. The inner core is rigid, but the S-velocity profile inside the inner core is still poorly known. A lower shear velocity in the uppermost inner core suggests the presence of liquid inclusions. The P-wave quality factor Q_α is low (100–400) with scattered values in the uppermost 300 km. An increase of Q_α with depth is favored by most of the studies, and a rapid change in the characteristics of the attenuation seems to be present at radius ~ 500 km. The relative contributions of anelasticity and scattering in attenuation

are difficult to specify, and anelastic attenuation is probably present both in shear ($1/Q_\mu$) and in bulk ($1/Q_\kappa$).

The inner core is anisotropic in seismic velocities, with to the first approximation a cylindrical anisotropy (transverse isotropy) of 1–3% and a fast axis parallel to the ERA. The uppermost 100–150 km is almost isotropic. Anisotropy in attenuation is also present, with strong attenuation correlated with high velocities in the direction of the ERA. An innermost inner core with radius 300–600 km and an anisotropy different from that in the outer inner core have been detected, but the nature of the anisotropy inside this structure is still debated. It is also a zone of reduced attenuation.

A hemispherical pattern is present in the uppermost 600 km of the inner core, both for uppermost isotropic layer and for anisotropy. In the uppermost 80 km of the isotropic layer, the quasi-eastern hemisphere (40–180° E) has higher velocities and higher attenuation than the western hemisphere. In the depth range 100–600 km, the western hemisphere appears to be more anisotropic than the Eastern one for both P-velocity and attenuation. This dichotomy in anisotropy could be explained either by a variation in the degree of crystal alignment or by a difference in thickness of the isotropic layer, 400 km thick beneath the eastern hemisphere and only 100 km thick beneath the western hemisphere. The correlation between velocity and attenuation, opposite to that observed in the mantle, is best explained by scattering on iron anisotropic crystals or iron grains.

Small-scale lateral heterogeneities inside the inner core are hard to identify unambiguously. At very short wavelengths, scatterers of size 1–10 km have been identified inside the upper part of the inner core and at ICB from the coda of reflected waves. Their characteristics do not seem to be identical everywhere.

A search for a differential rotation of the inner core with respect to the mantle has led to very variable results, depending on the method and data used. Rotation rates from negative (westward rotation) up to more than $1^\circ\,\text{year}^{-1}$ (eastward rotation) have been obtained, large positive values being obtained along a few specific paths involving South Sandwich Island events and null rotation for worldwide analyses. Most of the recent results favor the absence of rotation or very small oscillations, in agreement with the predictions of geodynamic models.

Figure 19 summarizes the main results concerning the core.

1.23.10.2 Open Questions and Future Challenges

The distribution of inner core anisotropy with depth is an important issue. It could help specify the structure of iron in the inner core and how the anisotropy is generated. In parallel, the distribution of attenuation with depth and the S-velocity profile are important pieces of information to specify the texture and to detect partial melting.

The core boundaries are possible places of sedimentation, differentiation, and chemical exchanges that call for refined analyses. In particular, the ICB, which appears as a first-order discontinuity despite the possible presence of a mushy zone, remains to some extent enigmatic. An open question concerns the growing mechanism of the inner core, either from dendrites formed at the ICB or from a 'snow' of iron alloy formed in the lowermost liquid core. The relations between the uppermost inner core and the surrounding dense liquid layer have to be understood. Also, the possibility of liquid core layers with nonzero rigidity and increased viscosity at CMB and ICB deserve further exploration.

The East–West hemispherical pattern, which is a violation of the cylindrical symmetry imposed by the Earth's rotation, must be explained. Other degree-one structures exist in the Earth (e.g., the ocean–continent distribution). The existence of such a pattern in the uppermost inner core, without evidence of compositional heterogeneity, is a puzzling question. A model explaining simultaneously the hemispherical variations in the uppermost isotropic layer, those in anisotropy, and the presence of an innermost inner core has to be found, but a clear image of the inner core structure at depth is still missing.

The debate concerning inner core rotation with respect to the mantle is not completely closed. The origin of the highly varying rotation rates, depending on the method used and on the path considered, has to be understood. The numerous geodynamic problems related to a possible differential rotation or to inner core oscillations require that this question be definitively resolved.

Outside the field of seismology, many constraints are expected from the other domains of physics and chemistry. In particular, the improved performances of experimental and numerical simulations in high-pressure physics will hopefully give new constrains on the phase and texture present at the center of the Earth and on the light elements that could be incorporated in iron. Viscosity of the inner core is also an important parameter to specify, as it is related to thermal convection, deformation ability, and grain size, thus indirectly to anisotropy. On the other hand, geodynamo models including dynamic constraints will give new insights on inner core rotation or oscillations.

Through the different problems presented in this chapter, we have an appraisal of the numerous different fields of physics and chemistry involved in liquid core and inner core structure and dynamics. It seems now very important to favor strong interactions between the concerned scientific communities. This is particularly true for the modeling of the solid–fluid interactions and of the hemispherical pattern.

For seismology, improvements are expected in both observation and modeling. The numerical methods for computing synthetic seismograms in complex structures are important tools that could be more extensively used and that will still evolve. On the other hand, computation of scattered energy in complex media has still to be improved. From the experimental point of view, one of the most drastic problems remains the poor distribution of the data. This is particularly crucial for studying anisotropy, which requires a good sampling in all directions. The large unsampled provinces and the scarcity of polar paths illustrate the importance of maintaining observatories at high latitudes and of developing ocean-bottom observatories. A growing number of seismological studies process signals of very small amplitude, for which stacking is necessary. Permanent small aperture arrays, which are essential for such studies, are still missing at high southern latitudes. Finally, maintaining observatories for decades, despite the considerable effort it represents, is crucial to resolve inner core rotation and more generally to address time-dependent seismology.

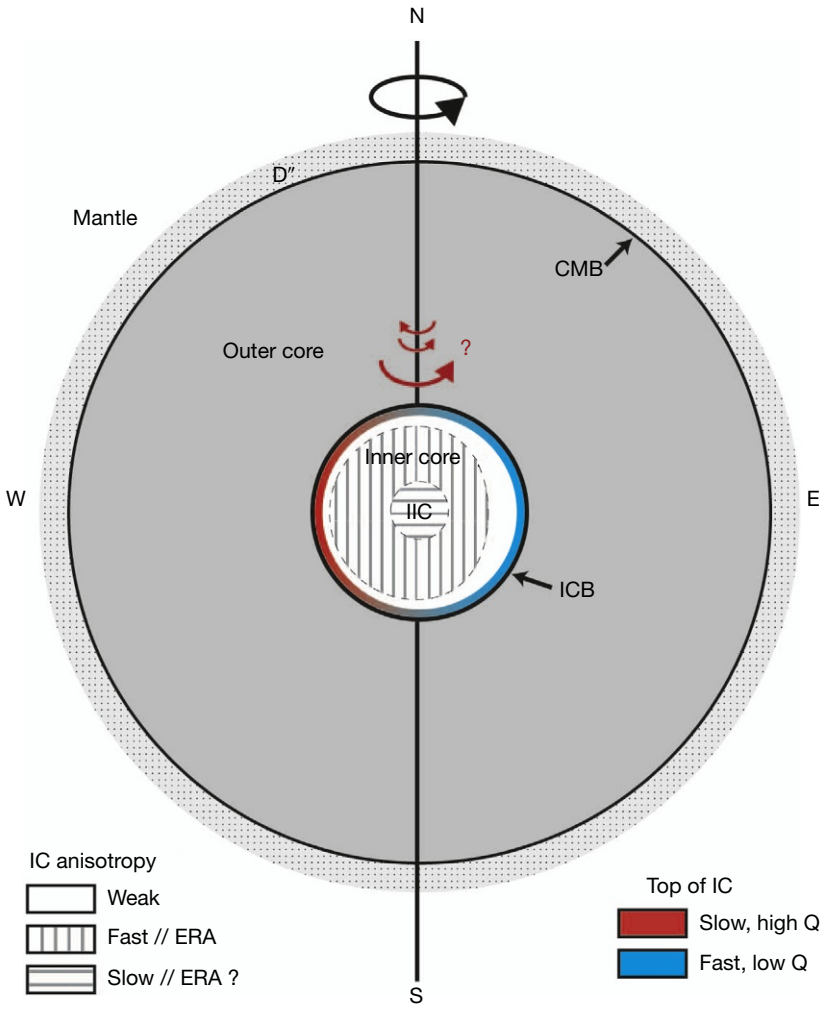

Figure 19 Cartoon of the structure of the core, summarizing the main seismological results: the absence of 3D structure in the liquid core, the existence of a nearly isotropic layer at the top of the inner core with a hemispherical pattern at the very top and a different thickness in each hemisphere, and anisotropy in the body of the inner core with fast axis parallel to the Earth's rotation axis. Still debated (or to specify) are the characteristics of the anisotropy in the innermost inner core and the differential rotation or oscillations of the inner core with respect to the mantle, although a null rotation rate seems now favored. IC, inner core; IIC, innermost inner core; ICB, inner core boundary; CMB, core–mantle boundary; ERA, Earth's rotation axis; Q, P-wave quality factor.

References

Alboussière T, Deguen R, and Melzani M (2010) Melting induced stratification above the Earth's inner core due to convective translation. *Nature* 466: 744–747.

Alexandrakis C and Eaton DW (2010) Precise seismic-wave velocity atop Earth's core: No evidence for outer-core stratification. *Physics of the Earth and Planetary Interiors* 180: 59–65.

Alfè D, Gillan M, and Price GD (2003) Thermodynamics from first principles: Temperature and composition of the Earth's core. *Mineralogical Magazine* 67: 113–123.

Andrault D, Bolfan-Casanova N, Ohtaka O, et al. (2009) Melting diagrams of Fe-rich alloys determined from synchrotron in situ measurements in the 15–23 GPa pressure range. *Physics of the Earth and Planetary Interiors* 174: 181–191.

Andrews J, Deuss A, and Woodhouse J (2006) Coupled normal-mode sensitivity to inner-core shear velocity and attenuation. *Geophysical Journal International* 167: 204–212.

Aubert J (2013) Flow throughout the Earth's core inverted from geomagnetic observations and numerical dynamo models. *Geophysical Journal International* 192: 537–556.

Aubert J, Amit H, Hulot G, and Olson P (2008) Thermochemical flows couple the Earth's inner core growth to mantle heterogeneity. *Nature* 454: 758–761.

Aubert J and Dumberry M (2011) Steady and fluctuating inner core rotation in numerical geodynamo models. *Geophysical Journal International* 184: 162–170.

Aurnou J, Brito D, and Olson P (1996) Mechanisms of inner core super-rotation. *Geophysical Research Letters* 23: 3401–3404.

Badro J, Fiquet G, Guyot F, et al. (2007) Effect of light elements on the sound velocities in solid iron: Implications for the composition of Earth's core. *Earth and Planetary Science Letters* 254: 233–238.

Beghein C and Trampert J (2003) Robust normal mode constraints on inner core anisotropy from model space search. *Science* 299: 552–555.

Belonoshko AB, Skorodumova NV, Davis S, Osiptsov AN, Rosengren A, and Johansson B (2007) Origin of the low rigidity of the Earth's inner core. *Science* 316: 1603–1605.

Bergman MI (1997) Measurements of elastic anisotropy due to solidification texturing and the implications for the Earth's inner core. *Nature* 389: 60–63.

Bergman MI (1998) Estimates of the Earth's inner core grain size. *Geophysical Research Letters* 25: 1593–1596.

Bergman MI, Agrawal S, Carter M, and Macleod-Silberstein M (2003) Transverse solidification textures in hexagonal close-packed alloys. *Journal of Crystal Growth* 255: 204–211.

Bergman MI, Cole DM, and Jones JR (2002) Preferred crystal orientations due to melt convection during directional solidification. *Journal of Geophysical Research* 107: ECV 6-1–6-8.

Bergman MI, Lewis DJ, Myint IH, Slivka L, Karato SI, and Abreu A (2010) Grain growth and loss of texture during annealing of alloys, and the translation of Earth's inner core. *Geophysical Research Letters* 37: L22313.
Bhattacharyya J, Shearer P, and Masters G (1993) Inner core attenuation from short-period PKP(BC) versus PKP(DF) waveforms. *Geophysical Journal International* 114: 1–11.
Birch F (1952) Elasticity and constitution of the Earth's interior. *Journal of Geophysical Research* 57: 227.
Birch F (1964) Density and composition of mantle and core. *Journal of Geophysical Research* 69: 4377–4388.
Bolt BA (1962) Gutenberg's PKP early observations. *Nature* 196: 122–124.
Bolt BA (1977) The detection of PKIIKP and damping in the inner core. *Annali di Geofisica* 30: 507–520.
Bolt BA (1982) *Inside the Earth*. San Francisco, CA: Freeman.
Bolt BA and Qamar A (1970) Upper bound to the density jump at the boundary of the Earth's inner core. *Nature* 228: 148–150.
Bormann P, Klinge K, and Wendt S (2002) Chapter 11: Data analysis and seismogram interpretation. In: Bormann P (ed.) *IASPEI New Manual of Seismological Observatory Practice*, vol. 1, p. 102. Potsdam: GeoForschungsZentrum.
Bowers D, McCormack DA, and Sharrock DS (2000) Observations of PKP(DF) and PKP(BC) across the United Kingdom: Implications for studies of attenuation in the earth's core. *Geophysical Journal International* 140: 374–384.
Bréger L, Romanowicz B, and Rousset S (2000a) New constraints on the structure of the inner core from P′P′. *Geophysical Research Letters* 17: 2781–2784.
Bréger L, Romanowicz B, and Tkalčić H (1999) PKP(BC-DF) travel time residuals and short scale heterogeneity in the deep Earth. *Geophysical Research Letters* 26: 3169–3172.
Bréger L, Tkalčić H, and Romanowicz B (2000b) The effect of D″ on PKP(AB-DF) travel time residuals and possible implications for inner core structure. *Earth and Planetary Science Letters* 175: 133–143.
Brush SG (1980) Discovery of the Earth's core. *American Journal of Physics* 48: 705–724.
Buffett BA (1997) Geodynamic estimates of the viscosity of the Earth's inner core. *Nature* 338: 571–573.
Buffett BA (2000) Dynamics of the Earth's core. In: *Earth's Deep Interior: Mineral Physics and Tomography from the Atomic to the Global Scale*. *AGU Geophysical Monograph*, vol. 117, pp. 37–62. Washington, DC: American Geophysical Union.
Buffett BA (2009) Onset and orientation of convection in the inner core. *Geophysical Journal International* 179: 711–719.
Buffett BA, Garnero EL, and Jeanloz R (2010) Sediments at the top of Earth's core. *Science* 290: 1338–1342.
Buffett BA and Glatzmaier GA (2000) Gravitational breaking of inner core rotation in geodynamo simulations. *Geophysical Research Letters* 27: 3125–3128.
Buffett BA and Seagle CT (2010) Stratification of the top of the core due to chemical interactions with the mantle. *Journal of Geophysical Research* 115: B04407.
Buffett BA and Wenk HR (2004) Texturing of the Earth's inner core by Maxwell stresses. *Nature* 413: 60–63.
Bullen K (1940) The problem of the Earth's density variation. *Bulletin of the Seismological Society of America* 30: 235–250.
Bullen KE and Haddon RAW (1973) The ellipticities of surfaces of equal density inside the Earth. *Physics of the Earth and Planetary Interiors* 7: 199–202.
Busse FH (1975) A model of the geodynamo. *Geophysical Journal of the Royal Astronomical Society* 42: 437–459.
Calvet M, Chevrot S, and Souriau A (2006) P-wave propagation in transversely isotropic media. II. Application to inner core anisotropy: Effects of data merging, parametrization and a priori information. *Physics of the Earth and Planetary Interiors* 156: 21–40.
Calvet M and Margerin L (2008) Constraints on the grain size and stable iron phases in the uppermost inner core from multiple scattering modeling of seismic velocity and attenuation. *Earth and Planetary Science Letters* 156: 21–40.
Cao A, Masson Y, and Romanowicz B (2007) Short wavelength topography on the inner core boundary. *PNAS* 104: 31–35.
Cao A and Romanowicz B (2004a) Constraints on density and shear velocity contrasts at the inner core boundary. *Geophysical Journal International* 157: 1–6.
Cao A and Romanowicz B (2004b) Hemispherical transition of seismic attenuation at the top of the earth's inner core. *Earth and Planetary Science Letters* 228: 243–253.
Cao A and Romanowicz B (2007) Test of the innermost inner core models using broadband PKIKP travel time residuals. *Geophysical Research Letters* 34: L08303.
Cao A and Romanowicz B (2009) Constraints on shear wave attenuation in the Earth's inner core from an observation of PKJKP. *Geophysical Research Letters* 36: L09301.
Cao A, Romanowicz B, and Takeuchi N (2005) An observation of PKJKP: Inferences on inner core shear properties. *Science* 308: 1453–1455.
Carcione JM and Cavallini F (1994) A rheological model for anelastic anisotropic media with applications to seismic wave propagation. *Geophysical Journal International* 119: 338–348.
Choy GL (1977) Theoretical seismograms of core phases calculated by frequency-dependent full wave theory, and their interpretation. *Geophysical Journal of the Royal Astronomical Society* 51: 275–312.
Choy GL and Cormier VF (1983) The structure of the inner core inferred from short-period and broadband GDSN data. *Geophysical Journal of the Royal Astronomical Society* 72: 1–21.
Choy GL and Richards PG (1975) Pulse distortion and Hilbert transformation in multiply reflected and refracted body waves. *Bulletin of the Seismological Society of America* 65: 55–70.
Cleary J and Haddon RAW (1972) Seismic wave scattering near the core-mantle boundary: A new interpretation of precursors of PKP. *Nature* 240: 549–551.
Collier JD and Helffrich G (2001) Estimate of inner core rotation rate from United Kingdom regional seismic network data and consequences for inner core dynamical behaviour. *Physics of the Earth and Planetary Interiors* 193: 523–537.
Cormier VF (1981) Short-period PKP phases and the anelastic mechanism of the inner core. *Physics of the Earth and Planetary Interiors* 24: 291–301.
Cormier VF (2007) Texture of the uppermost inner core from forward- and backscattered seismic waves. *Earth and Planetary Science Letters* 258: 442–453.
Cormier VF (2009) A glassy lowermost outer core. *Geophysical Journal International* 179: 374–380.
Cormier VF, Attanayake J, and He K (2011) Inner core freezing and melting: Constraints from seismic body waves. *Physics of the Earth and Planetary Interiors* 188: 163–172.
Cormier VF and Choy GL (1986) A search for lateral heterogeneity in the inner core from differential travel times near PKP-D and PKP-C. *Geophysical Research Letters* 13: 1553–1556.
Cormier VF and Li X (2002) Frequency-dependent seismic attenuation in the inner core. 2. A scattering and fabric interpretation. *Journal of Geophysical Research* 107(B12): 2362.
Cormier VF, Li X, and Choy GL (1998) Seismic attenuation of the inner core: Viscoelastic or stratigraphic? *Geophysical Research Letters* 25: 4019–4022.
Cormier VF and Richards PG (1976) Comments on "The damping of core waves" by Antony Qamar and Alfredo Eisenberg. *Journal of Geophysical Research* 81: 3066–3068.
Cormier VF and Stroujkova A (2005) Waveform search for the innermost inner core. *Earth and Planetary Science Letters* 236: 96–105.
Cottaar S and Buffett B (2012) Convection in the Earth's inner core. *Physics of the Earth and Planetary Interiors* 198: 67–78.
Creager KC (1992) Anisotropy in the inner core from differential travel times of the phases PKP and PKIKP. *Nature* 356: 309–314.
Creager KC (1997) Inner core rotation rate from small scale heterogeneity and time-varying travel times. *Science* 278: 1284–1288.
Creager KC (1999) Large-scale variations in inner core anisotropy. *Journal of Geophysical Research* 104: 23127–23139.
Creager KC (2000) Inner core anisotropy and rotation. In: Dehant V, et al. (eds.) *Core Dynamics, Structure and Rotation*. *American Geodynamic Series*, vol. 31, pp. 89–114. Washington, DC: American Geophysical Union.
Creager KC and Jordan TH (1986) Aspherical structure of the core–mantle boundary from PKP travel times. *Geophysical Research Letters* 13: 1497–1500.
Crossley DJ, Rochester M, and Peng Z (1992) Slichter modes and Love numbers. *Geophysical Research Letters* 19: 1679–1682.
Cummins P and Johnson L (1988a) Synthetic seismograms for an inner core transition of finite thickness. *Geophysical Journal* 94: 21–34.
Cummins P and Johnson L (1988b) Short-period body wave constraints on the properties of the Earth's inner core boundary. *Journal of Geophysical Research* 93: 9058–9074.
Dai Z, Wang W, and Wen L (2012) Irregular topography at the Earth's inner core boundary. *PNAS* 109: 7654–7658.
Defraigne P, Dehant V, and Wahr JM (1996) Internal loading of an inhomogeneous compressible earth with phase boundaries. *Geophysical Journal International* 125: 173–192.
Deguen R (2012) Structure and dynamics of Earth's inner core. *Earth and Planetary Science Letters* 333–334: 211–225.
Deguen R, Alboussière T, and Brito D (2007) On the presence and structure of a mush at the inner core boundary of the Earth. *Physics of the Earth and Planetary Interiors* 274: 1887–1891.
Deguen R and Cardin P (2009) Tectonic history of the Earth's inner core preserved in its seismic structure. *Nature Geoscience* 2: 419–422.
Deguen R and Cardin P (2011) Thermo-chemical convection in Earth's inner core. *Geophysical Journal International* 187: 1101–1118.

Deparis V and Legros H (2002) *Voyage à l'intérieur de la Terre*, 627 pp. Paris: CNRS Edition.

Deuss A (2008) Normal mode constraints on shear and compressional wave velocity of the Earth's inner core. *Earth and Planetary Science Letters* 268: 365–375.

Deuss A, Woodhouse JH, Paulssen H, and Trampert J (2000) The observation of inner core shear waves. *Geophysical Journal International* 142: 67–73.

Doornbos DJ (1974) The anelasticity of the inner core. *Geophysical Journal of the Royal Astronomical Society* 38: 397–415.

Doornbos DJ (1983) Observable effects of the seismic absorption band in the Earth. *Geophysical Journal of the Royal Astronomical Society* 75: 693–711.

Doornbos DJ and Hilton T (1989) Models of core–mantle boundary and the travel times of internally reflected core phases. *Journal of Geophysical Research* 94: 15741–15751.

Durek JJ and Romanowicz B (1999) Inner core anisotropy inferred by direct inversion of normal mode spectra. *Geophysical Journal International* 139: 599–622.

Dziewonski AM and Anderson DL (1981) Preliminary reference earth model. *Physics of the Earth and Planetary Interiors* 25: 297–356.

Dziewonski AM and Gilbert F (1971) Solidity of the inner core of the Earth inferred from normal mode oscillations. *Nature* 234: 465.

Earle PS and Shearer PM (1997) Observations of PKKP precursors used to estimate small-scale topography on the core-mantle boundary. *Science* 277: 667–670.

Eaton DW and Kendall JM (2006) Improving seismic resolution of outermost core structure by multichannel analysis and deconvolution of broadband SmKS phases. *Physics of the Earth and Planetary Interiors* 155: 104–119.

Emmerich H (1993) Theoretical study of the influence of CMB topography on the core reflections ScS. *Physics of the Earth and Planetary Interiors* 80: 125–134.

Engdahl ER, Van der Hilst R, and Buland RP (1998) Global teleseismic earthquake relocation with improved travel times and procedures for depth determination. *Bulletin of the Seismological Society of America* 88: 722–743.

Fearn DR, Loper DE, and Roberts PH (1981) Structure of the Earth's inner core. *Nature* 292: 232–233.

Forte AM, Mitrovica JX, and Woodward RL (1995) Seismic-geodynamic determination of the origin of excess ellipticity of the core–mantle boundary. *Geophysical Research Letters* 22: 1013–1016.

Garcia R (2002a) Constraints on upper inner core structure from waveform inversion of core phases. *Geophysical Journal International* 150: 651–664.

Garcia R (2002b) Seismological and mineral constraints on the inner core fabric. *Geophysical Research Letters* 29: 1958.

Garcia R and Souriau A (2000a) Amplitude of core–mantle boundary estimated by stochastic analysis of core phases. *Physics of the Earth and Planetary Interiors* 117: 345–359.

Garcia R and Souriau A (2000b) Inner core anisotropy and heterogeneity level. *Geophysical Research Letters* 27: 3121–3124; Correction (2001) *Geophysical Research Letters* 28: 85.

Garcia R, Tkalčić H, and Chevrot S (2006) A new global PKP data set to study Earth's core and deep mantle. *Physics of the Earth and Planetary Interiors* 159: 15–31.

Garnero EJ, Helmberger DV, and Grand SP (1993) Constraining outermost core velocity with SmKS waves. *Geophysical Research Letters* 25: 2341–3344.

Garnero EJ and Lay T (1998) Effects of D″ anisotropy on seismic velocity models of the outermost core. *Geophysical Research Letters* 20: 2463–2466.

Geballe ZM, Lasbleis M, Cormier VF, and Day EA (2013) Sharp hemisphere boundaries in a translating inner core. *Geophysical Research Letters* 40: 1719–1723. http://dx.doi.org/10.1002/grl.50372.

Glatzmaier GA and Roberts PH (1996) Rotation and magnetism of Earth's inner core. *Science* 274: 1887–1891.

Greff-Lefftz M and Legros H (1996) Viscoelastic mantle density heterogeneity and core–mantle boundary topography. *Geophysical Journal International* 125: 567–576.

Gubbins D (1981) Rotation of the inner core. *Journal of Geophysical Research* 86: 11695–11699.

Gubbins D, Alfè D, and Davies CJ (2013) Compositional instability of Earth's solid inner core. *Geophysical Research Letters* 40: 1–5.

Gubbins D, Masters G, and Nimmo F (2008) A thermochemical boundary layer at the base of the Earth's outer core and independent estimate of core heat flux. *Geophysical Journal International* 174: 1007–1018.

Gubbins D, Sreenivasan B, Bound J, and Rost S (2011) Melting of the Earth's inner core. *Nature* 473: 361–363.

Gutenberg B (1913) Uber die Konstitution des Erdinnern, erschlossen aus Erdbebenbeobachtungen. *Physikalische Zeitschrift* 14: 1217.

Gwinn CR, Herring TA, and Shapiro II (1986) Geodesy by radio interferometry: Studies of the forced nutations of the Earth: 2. Interpretation. *Journal of Geophysical Research* 91: 4755–4765.

Häge H (1983) Velocity constraints for the inner core inferred from long period PKP amplitudes. *Physics of the Earth and Planetary Interiors* 31: 171–185.

Helffrich G and Kaneshima S (2004) Seismological constraints on core composition from Fe–O–S liquid immiscibility. *Science* 306: 2239–2242.

Helffrich G and Kaneshima S (2010) Outer-core compositional stratification from observed core wave speed profile. *Nature* 468: 807–811.

Hirose K, Labrosse S, and Hernlund J (2013) Composition and state of the core. *Annual Review of Earth and Planetary Sciences* 41: 25.1–25.35.

Iritani R, Takeuchi N, and Kawakatsu H (2010) Seismic attenuation structure of the top half of the inner core beneath the northeastern Pacific. *Geophysical Research Letters* 37: L19303.

Irving JCE and Deuss A (2011a) Stratified anisotropic structure at the top of Earth's inner core: A normal mode study. *Physics of the Earth and Planetary Interiors* 186: 59–69.

Irving JCE and Deuss A (2011b) Hemispherical structure in inner core velocity anisotropy. *Journal of Geophysical Research* 116: B04307.

Irving JCE, Deuss A, and Woodhouse JH (2009) Normal mode coupling due to hemispherical anisotropic structure in Earth's inner core. *Geophysical Journal International* 178: 962–975.

Ishii M and Dziewonski AM (2002) The innermost inner core of the Earth: Evidence for a change in anisotropic behaviour at the radius of about 300 km. *PNAS* 99: 14026–14030.

Ishii M and Dziewonski AM (2003) Distinct seismic anisotropy at the centre of the Earth. *Physics of the Earth and Planetary Interiors* 140: 203–217.

Ishii M and Dziewonski AM (2005) Constraints on the outer core tangent cylinder using normal-mode splitting measurements. *Geophysical Journal International* 162: 787–792.

Ishii M, Dziewonski AM, Tromp J, and Ekström G (2002a) Joint inversion of normal mode and body wave data for inner core anisotropy 2. Possible complexities. *Journal of Geophysical Research* 107: 2380.

Ishii M, Tromp J, Dziewonski AM, and Ekström G (2002b) Joint inversion of normal mode and body wave data for inner core anisotropy 1. Laterally homogeneous anisotropy. *Journal of Geophysical Research* 107: 2379.

Isse T and Nakanishi I (2002) Inner-core anisotropy beneath Australia and differential rotation. *Geophysical Journal International* 151: 255–263.

Ivan M and Moloto-A-Kenguemba GR (2007) Attenuation in the uppermost inner core from PKP recordings at African seismological stations. *Studia Geophysica et Geodetica* 51: 221–230.

Jacobs JA (1953) The Earth's inner core. *Nature* 172: 297.

Jeanloz R and Wenk HR (1988) Convection and anisotropy of the inner core. *Geophysical Research Letters* 15: 72–75.

Jeffreys H (1926) The rigidity of the Earth's central core. *Monthly Notices of the Royal Astronomical Society* 1: 371.

Jephcoat A and Olson P (1987) Is the inner core of the Earth pure iron? *Nature* 325: 332–335.

Julian BR, Davies D, and Sheppard RM (1972) PKJKP. *Nature* 235: 317–318.

Kampfman W and Müller G (1989) PcP amplitude calculations for a core–mantle boundary with topography. *Geophysical Research Letters* 16: 653–656.

Kaneshima S (1996) Mapping heterogeneity of the uppermost inner core using two pairs of core phases. *Geophysical Research Letters* 23: 3075–3078.

Karato S (1993) Inner core anisotropy due to the magnetic field-induced preferred orientation of iron. *Science* 262: 1708–1710.

Karato S (1999) Maxwell stress-induced flow in the Earth's inner core: Implications for seismic anisotropy and geodynamo. *Nature* 402: 871–873.

Kawakatsu H (1992) Some attempt to observe PKJKP. *Central Core of the Earth* 2: 53–56 (in Japanese).

Kawakatsu H (2006) Sharp and seismically transparent inner core boundary region revealed by an entire network observation of near vertical PKiKP. *Earth, Planets and Space* 58: 855–863.

Kazama T, Kawakatsu H, and Takeuchi N (2008) Depth-dependent attenuation structure of the inner core inferred from short-period Hi-net data. *Physics of the Earth and Planetary Interiors* 167: 155–160.

Kennett BLN (1998) On the density distribution within the Earth. *Geophysical Journal International* 132: 374–382.

Kennett BLN and Engdahl ER (1991) Traveltimes for global earthquake location and phase identification. *Geophysical Journal International* 105: 429–465.

Kennett BLN, Engdahl ER, and Buland R (1995) Constraints on seismic velocities in the Earth from travel times. *Geophysical Journal International* 122: 108–124.

Koelemeijer PJ, Deuss A, and Trampert J (2012) Normal mode sensitivity to Earth's D″ layer and topography on the core-mantle boundary: What we can and cannot see. *Geophysical Journal International* 190: 553–568.
Kohler M (1997) Three-dimensional velocity structure and resolution of the core–mantle boundary region from whole mantle-inversion of body waves. *Physics of the Earth and Planetary Interiors* 101: 85–104.
Koot L, Dumberry M, Rivoldini A, de Viron O, and Dehant V (2010) Constraints on the coupling at the core–mantle and inner core boundaries inferred from nutation observations. *Geophysical Journal International* 182: 1279–1294.
Koper KD and Dombrovskaya M (2005) Seismic properties of the inner core boundary from PKiKP/P amplitude ratios. *Earth and Planetary Science Letters* 237: 680–694.
Koper KD, Franks JM, and Dombrovskaya M (2004) Evidence for small-scale heterogeneity in Earth's inner core from a global study of PKiKP coda waves. *Earth and Planetary Science Letters* 228: 227–241.
Koper KD and Pyle ML (2004) Observation of PKiKP/PcP amplitude ratios and implications for Earth structure at the boundaries of the liquid core? *Journal of Geophysical Research* 109: B03301.
Koper KD, Pyle ML, and Franks JM (2003) Constraints on aspherical core structure from PKiKP-PcP differential travel times. *Journal of Geophysical Research* 108: 2168–2180.
Krasnoshchekov DN, Kaaziz PB, and Ovtchinnikov VM (2005) Seismological evidence for mosaic structure of the surface of the Earth's inner core. *Nature* 435: 483–487.
Kuwayama Y, Hirose K, Sata N, and Oshihi Y (2008) Phase relation of iron and iron-nickel alloys up to 300 GPa: Implications for composition and structure of the Earth's inner core. *Earth and Planetary Science Letters* 273: 379–385.
Laske G and Masters G (1999) Limits on differential rotation of the inner core from an analysis of the Earth's free oscillations. *Nature* 402: 66–68.
Laske G and Masters G (2003) The Earth's free oscillations and the differential rotation of the inner core. In: Dehant V, et al. (eds.) *Earth's Core, Dynamics, Structure, Rotation*. *Geodynamics Series*, vol. 31, pp. 5–22. Washington, DC: American Geophysical Union.
Lassak TM, McNamara AK, Garnero EJ, and Zhong S (2010) Core–mantle boundary topography as a possible constraint on lower mantle chemistry and dynamics. *Earth and Planetary Science Letters* 289: 232–241.
Lay T and Young CJ (1990) The stably stratified outermost core revisited. *Geophysical Research Letters* 17: 2001–2004.
Lehmann I (1936) P′. *Bureau Central Seismologique International, Strasbourg, Travaux Scientifiques A* 14: 3–31.
Leyton F and Koper KD (2007a) Using PKiKP coda to determine inner core structure: 1. Synthesis of coda envelopes using single-scattering theories. *Journal of Geophysical Research* 112: B05316.
Leyton F and Koper KD (2007b) Using PKiKP coda to determine inner core structure: 2. Determination of Q_C. *Journal of Geophysical Research* 112: B05317.
Leyton F, Koper KD, Zhu L, and Dombrovskaya M (2005) On the lack of seismic discontinuities within the inner core. *Geophysical Journal International* 162: 779–786.
Li X and Cormier VF (2002) Frequency dependent seismic attenuation in the inner core. 1. A viscoelastic interpretation. *Journal of Geophysical Research* 107(B12): 2361.
Li X, Giardini D, and Woodhouse JH (1991) Large-scale three-dimensional even-degree structure of the Earth from splitting of long-period normal modes. *Journal of Geophysical Research* 96: 551–577.
Li A and Richards PG (2003a) Using earthquake doublets to study inner core rotation and seismicity catalog precision. *Geochemistry, Geophysics, Geosystems* 4: 1072.
Li A and Richards PG (2003b) Study of inner core structure and rotation using seismic records from Novaya Zemlya underground nuclear tests. In: Dehant V, et al. (eds.) *Earth's Core, Dynamics, Structure, Rotation*. *Geodynamics Series*, vol. 31, pp. 23–30. Washington, DC: American Geophysical Union.
Lindner D, Song X, Ma P, and Christensen DH (2010) Inner core rotation and its variability from nonparametric modeling. *Journal of Geophysical Research* 115: B04307.
Lister JR and Buffett BA (1998) Stratification of the outer core at the core–mantle boundary. *Physics of the Earth and Planetary Interiors* 105: 5–19.
Loper DE and Roberts PH (1981) A study of conditions at the inner core boundary of the Earth. *Physics of the Earth and Planetary Interiors* 24: 302–307.
Mäkinen A and Deuss A (2011) Global seismic body wave observations of temporal variations in the Earth's inner core, and implications for its differential rotation. *Geophysical Journal International* 187: 355–370.
Mäkinen A and Deuss A (2013) Normal mode splitting function measurements of anelasticity and attenuation in the Earth's inner core. *Geophysical Journal International* 194: 401–416. http://dx.doi.org/10.1093/gji/ggt092.
Masters G (1979) Observational constraints on the chemical and thermal structure of the earth's deep interior. *Geophysical Journal of the Royal Astronomical Society* 57: 507–534.
Masters G and Gilbert F (1981) Structure of the inner core inferred from observations of its spheroidal shear modes. *Geophysical Research Letters* 8: 569–571.
Masters G and Gubbins D (2003) On the resolution of density within the Earth. *Physics of the Earth and Planetary Interiors* 140: 159–167.
Mathews PM, Herring TA, and Buffett B (2002) Modeling of nutation and precession: New nutation series for nonrigid Earth and insights into the Earth's interior. *Journal of Geophysical Research* 107(B4): 2068.
McSweeney TJ, Creager KC, and Merrill RT (1997) Depth extent of inner-core seismic anisotropy and implications for geomagnetism. *Physics of the Earth and Planetary Interiors* 101: 131–156.
Menke W (1986) Few 2–50 km corrugation on the core–mantle boundary. *Geophysical Research Letters* 13: 1501–1504.
Miller MS, Niu F, and Vanacore EA (2013) Aspherical structure heterogeneity within the uppermost inner core: Insights into the hemispherical boundaries and core formation. *Physics of the Earth and Planetary Interiors* 223: 8–20.
Mizzon H and Monnereau M (2013) Implication of the lopsided growth for the viscosity of Earth's inner core. *Earth and Planetary Science Letters* 361: 391–401.
Mochizuki E and Ohminato T (1989) On the anomalous splitting of Earth's free oscillations. *Geophysical Research Letters* 16: 1415–1416.
Monnereau M, Calvet M, Margerin L, and Souriau A (2010) Lopsided growth of Earth's inner core. *Science* 328: 1014–1017.
Montagner J-P and Kennett BLN (1995) How to reconcile body-wave and normal mode reference Earth's models? *Geophysical Journal International* 125: 229–248.
Morelli A and Dziewonski AM (1987) Topography of the core–mantle boundary and lateral homogeneity of the liquid core. *Nature* 325: 678–683.
Morelli A and Dziewonski AM (1993) Body wave traveltimes and a spherically symmetric P- and S-wave velocity model. *Geophysical Journal* 112: 178–194.
Morelli A, Dziewonski AM, and Woodhouse JH (1986) Anisotropy of the inner core inferred from PKIKP travel times. *Geophysical Research Letters* 13: 1545–1548.
Müller G (1973) Amplitude studies of core phases. *Journal of Geophysical Research* 78: 3469–3490.
Niazi M and Johnson LR (1992) Q in the inner core. *Physics of the Earth and Planetary Interiors* 74: 55–62.
Niu F and Chen Q-F (2008) Seismic evidence for distinct anisotropy in the innermost inner core. *Nature Geoscience* 1: 692–696.
Niu F and Wen L (2001) Hemispherical variations in seismic velocity at the top of the Earth's inner core. *Nature* 410: 1081–1084.
O'Connell R and Budianski B (1977) Viscoelastic properties of fluid-saturated cracked solids. *Journal of Geophysical Research* 82: 5719–5735.
Obayashi M and Fukao Y (1997) P and PcP travel time tomography for the core–mantle boundary. *Journal of Geophysical Research* 102: 17825–17841.
Ohtaki T, Kaneshima S, and Kanjo K (2012) Seismic structure near the inner core boundary in the south polar region. *Journal of Geophysical Research* 117: B03312.
Okal E and Cansi Y (1998) Detection of PKJKP at intermediate periods by progressive multichannel correlation. *Earth and Planetary Science Letters* 164: 23–30.
Oldham RD (1906) The constitution of the interior of the Earth as revealed by earthquakes. *Quarterly Journal of the Geological Society of London* 62: 456.
Olson P and Deguen R (2012) Eccentricity of the geomagnetic dipole caused by lopsided inner core growth. *Nature Geoscience* 5: 565–569.
Oreshin SI and Vinnik LP (2004) Heterogeneity and anisotropy of seismic attenuation in the inner core. *Geophysical Research Letters* 31: L02613.
Ouzounis A and Creager KC (2001) Isotropy overlying anisotropy at the top of the inner core. *Geophysical Research Letters* 28: 4331–4334.
Palmer A and Smylie D (2005) VLBI observations of free core nutations and viscosity at the top of the core. *Physics of the Earth and Planetary Interiors* 148: 285–301.
Peacock S and Hudson JA (1990) Seismic properties of rocks with distribution of small cracks. *Geophysical Journal International* 102: 471–484.
Peng Z, Koper KD, Vidale JE, Leyton F, and Shearer P (2008) Inner-core fine-scale structure from scattered waves recorded by LASA. *Journal of Geophysical Research* 113: B09312.
Piersanti A, Boschi L, and Dziewonski AM (2001) Estimating lateral structure inside the Earth's outer core. *Geophysical Research Letters* 28: 1659–1662.
Poirier JP (1988) Transport properties of liquid metals and viscosity of the Earth's core. *Geophysical Journal International* 92: 99–105.
Poirier JP (1994) Light elements in the Earth's outer core – A critical review. *Physics of the Earth and Planetary Interiors* 85: 319–337.
Poirier JP and Price GD (1999) Primary slip system of ε-iron and anisotropy of the Earth's inner core. *Physics of the Earth and Planetary Interiors* 110: 147–156.

Poirier JP and Shankland TJ (1993) Dislocation melting of iron and the temperature of the inner core boundary, revisited. *Geophysical Journal International* 115: 147–151.

Poupinet G, Ellsworth WL, and Fréchet J (1984) Monitoring velocity variation in the crust using earthquake doublet: An application to the Calaveras fault, California. *Journal of Geophysical Research* 89: 5719–5731.

Poupinet G and Kennett BLN (2004) On the observation of high frequency PKiKP and its coda in Australia. *Physics of the Earth and Planetary Interiors* 146: 497–511.

Poupinet G, Pillet R, and Souriau A (1983) Possible heterogeneity in the Earth's core deduced from PKIKP travel times. *Nature* 305: 204–206.

Poupinet G, Souriau A, and Coutant O (2000) The existence of an inner core super-rotation questioned by teleseismic doublets. *Physics of the Earth and Planetary Interiors* 118: 77–88.

Pulliam RJ and Stark PB (1993) Bumps on the core–mantle boundary: Are they facts or artefacts? *Journal of Geophysical Research* 98: 1943–1955.

Qamar A and Eisenberg A (1974) The damping of core waves. *Journal of Geophysical Research* 79: 758–765.

Rekdal T and Doornbos DJ (1992) The times and amplitudes of core phases for a variable core–mantle boundary layer. *Geophysical Journal International* 108: 546–556.

Ritzwoller MH, Masters G, and Gilbert F (1986) Observations of anomalous splitting and their interpretation in terms of aspherical structure. *Journal of Geophysical Research* 91: 10203–10228.

Rodgers A and Wahr J (1993) Inference of core-mantle boundary topography from ISC PcP and PKP traveltimes. *Geophysical Journal International* 115: 991–1011.

Romanowicz B and Bréger L (2000) Anomalous splitting of free oscillations: A reevaluation of possible interpretations. *Journal of Geophysical Research* 105: 21559–21578.

Romanowicz B and Durek JJ (2000) Seismological constraints on attenuation in the Earth: A review. In: Karato S-I, et al. (ed.) *Earth's Deep Interior: Mineral Physics and Tomography from the Atomic to the Global Scale. AGU Geophysical Monograph*, vol. 117, pp. 161–180. Washington, DC: American Geophysical Union.

Romanowicz B, Li XD, and Durek JJ (1996) Anisotropy in the inner core: Could it be due to low-order convection? *Science* 274: 963–966.

Romanowicz B, Tkalčić H, and Bréger L (2003) On the origin of complexity in PKP travel time data. In: Dehant V, et al. (eds.) *Earth's Core Dynamics, Structure and Rotation. AGU Geodynamics Series*, vol. 31, pp. 31–44. Washington, DC: American Geophysical Union.

Rosat S, Rogister Y, Crossley D, and Hinderer J (2006) A search for the Slichter triplet with superconducting gravimeters: Impact of the density jump at the inner core boundary. *Journal of Geodynamics* 41: 296–306.

Rost S and Revenaugh J (2001) Seismic detection of rigid zones at the top of the core. *Science* 294: 1911–1914.

Rost S and Revenaugh J (2004) Small-scale changes of core–mantle boundary reflectivity studied using core reflected PcP. *Physics of the Earth and Planetary Interiors* 145: 19–36.

Sato S, Fehler MC, and Maeda T (2012) *Seismic Wave Propagation and Scattering in the Heterogeneous Earth*, 2nd edn. Berlin: Springer.

Sharrock DS and Woodhouse JH (1998) Investigation of time dependent inner core structure by the analysis of free-oscillation spectra. *Earth, Planets and Space* 50: 1013–1018.

Shearer P (1994) Constraints on inner core anisotropy from PKP(DF) travel times. *Journal of Geophysical Research* 99: 19647–19659.

Shearer P, Hedlin MAH, and Earle PS (1998) PKP and PKKP precursor observations: Implications for the small-scale structure of the deep mantle and core. In: *The Core Mantle Boundary Region. Geodynamics Series*, vol. 28, pp. 37–55. Washington, DC: American Geophysical Union.

Shearer P and Masters G (1990) The density and shear velocity contrast at the inner core boundary. *Geophysical Journal International* 102: 491–498.

Shearer PM, Rychert CA, and Liu Q (2011) On the visibility of the inner-core shear wave phase PKJKP at long periods. *Geophysical Journal International* 185: 1379–1383.

Shearer PM, Toy KM, and Orcutt JA (1988) Axi-symmetric Earth models and inner core anisotropy. *Nature* 333: 228–232.

Shimizu H, Poirier JP, and Le Mouël JL (2005) On crystallization at the inner core boundary. *Physics of the Earth and Planetary Interiors* 151: 37–51.

Singh S, Taylor MAJ, and Montagner JP (2000) On the presence of liquid in Earth's inner core. *Science* 287: 2471–2474.

Smylie DE (1999) Viscosity near Earth's solid inner core. *Science* 284: 461–463.

Soldati G, Boschi L, and Forte AM (2012) Tomography of core–mantle boundary and lowermost mantle coupled by geodynamics. *Geophysical Journal International* 180: 730–746.

Song X (1996) Anisotropy in central part of inner core. *Journal of Geophysical Research* 101: 16089–16097.

Song X (2000) Joint inversion for inner core rotation, inner core anisotropy, and mantle heterogeneity. *Journal of Geophysical Research* 105: 7931–7943.

Song X (2003) Three-dimensional structure and differential rotation of the inner core. In: Dehant V, et al. (eds.) *Earth's Core, Dynamics, Structure and Rotation. Geophysical Monograph Geodynamics Series*, vol. 31, pp. 45–63. Washington, DC: American Geophysical Union.

Song X and Dai W (2008) Topography of Earth's inner core boundary from high-quality waveform doublets. *Geophysical Journal International* 175: 386–399.

Song X and Helmberger DV (1992) Velocity structure near the inner core boundary from waveform modeling. *Journal of Geophysical Research* 97: 6573–6586.

Song X and Helmberger DV (1995a) A P wave velocity model of the Earth's core. *Journal of Geophysical Research* 100: 9817–9830.

Song X and Helmberger DV (1995b) Depth dependence of anisotropy of Earth's inner core. *Journal of Geophysical Research* 100: 9805–9816.

Song X and Helmberger DV (1998) Seismic evidence for an inner core transition zone. *Science* 282: 924.

Song X and Richards PG (1996) Seismological evidence for differential rotation of the Earth's inner core. *Nature* 382: 221–224.

Souriau A (1989) A search for time dependent phenomena inside the core from seismic data. In: *EGS Meeting Abstracts, Barcelona*.

Souriau A (1998) New seismological constraints on differential rotation of the inner core from Novaya Zemlya events recorded at DRV, Antarctica. *Geophysical Journal International* 134: F1–F5.

Souriau A (2009) Inner core structure: Constraints from frequency dependent seismic anisotropy. *Comptes Rendus Geoscience* 341: 439–445.

Souriau A, Garcia R, and Poupinet G (2003a) The seismological picture of the inner core: Structure and rotation. *Comptes Rendus Geoscience* 335: 51–63.

Souriau A and Poupinet G (1991) The velocity profile at the base of the liquid core from PKP(BC + C_{diff}) data: An argument in favor of radial inhomogeneity. *Geophysical Research Letters* 18: 2023–2026.

Souriau A and Poupinet G (2003) Inner core rotation: A critical appraisal. In: Dehant V, et al. (ed.) *Earth's Core, Dynamics, Structure and Rotation. Geophysical Monograph, Geodynamics Series*, vol. 31, pp. 65–82. Washington, DC: American Geophysical Union.

Souriau A and Romanowicz B (1996a) Anisotropy in inner core attenuation: A new type of data to constrain the nature of the solid core. *Geophysical Research Letters* 23: 1–4.

Souriau A and Romanowicz B (1996b) Anisotropy in the inner core: Relation between P-velocity and attenuation. *Physics of the Earth and Planetary Interiors* 101: 33–47.

Souriau A and Roudil P (1995) Attenuation in the uppermost inner core from broad-band GEOSCOPE PKP data. *Geophysical Journal International* 123: 572–587.

Souriau A, Roudil P, and Moynot B (1997) Inner core rotation: Facts and artefacts. *Geophysical Research Letters* 24: 2103–2106.

Souriau A and Souriau M (1989) Ellipticity and density at the inner core boundary from subcritical PKiKP and PcP data. *Geophysical Journal International* 98: 39–54.

Souriau A, Teste A, and Chevrot S (2003b) Is there any structure inside the liquid core? *Geophysical Research Letters* 30(11): 1567.

Stevenson DJ (1987) Limits on lateral density and velocity variations in the Earth's outer core. *Geophysical Journal of the Royal Astronomical Society* 88: 311–319.

Stroujkova A and Cormier VF (2004) Regional variations in the uppermost 100 km of the Earth's inner core. *Journal of Geophysical Research* 109: B10307.

Su WJ and Dziewonski AM (1995) Inner core anisotropy in three dimensions. *Journal of Geophysical Research* 100: 9831–9852.

Su W-J, Dziewonski AM, and Jeanloz R (1996) Planet within a planet: Rotation of the inner core of the Earth. *Science* 274: 1883–1887.

Suda N and Fukao Y (1990) Structure of the inner core inferred from observations of seismic core modes. *Geophysical Journal International* 103: 403–413.

Sumita I and Olson P (1999) A laboratory model for convection in Earth's core driven by a thermally heterogeneous mantle. *Science* 286: 1547–1549.

Sumita I, Yoshida S, Kumazawa M, and Hamano Y (1996) A model for sedimentary compaction of a viscous medium and its application to inner core growth. *Geophysical Journal International* 124: 502–524.

Sun X and Song X (2008) Tomographic inversion for the three-dimensional anisotropy of the Earth's inner core. *Physics of the Earth and Planetary Interiors* 167: 53–70.

Sze EKM and Van der Hilst RD (2003) Core mantle boundary topography from short period PcP, PKP and PKKP data. *Physics of the Earth and Planetary Interiors* 135: 27–46.

Tanaka S (2007) Possibility of a low P-wave velocity layer in the outermost core from global SmKS waveforms. *Earth and Planetary Science Letters* 259: 486–499.

Tanaka S (2012) Depth extent of hemispherical inner core from PKP(DF) and PKP (C_{diff}) for equatorial paths. *Physics of the Earth and Planetary Interiors* 210–211: 50–62.

Tanaka S and Hamaguchi H (1993) Degree one heterogeneity at the top of the earth's core, revealed by SmKS travel times. In: *Dynamics of Earth's Deep Interior and Earth's Rotation*. *IUGG/AGU Geophysical Monograph*, vol. 72, pp. 127–134. Washington, DC: IUGG/AGU.

Tanaka S and Hamaguchi H (1996) Frequency-dependent Q in the Earth's outer core from short period P4KP/PcP spectral ratio. *Journal of Physics of the Earth* 44: 745–759.

Tanaka S and Hamaguchi H (1997) Degree one heterogeneity and hemispherical variation of anisotropy in the inner core from PKP(BC)-PKP(DF) times. *Journal of Geophysical Research* 102: 2925–2938.

Tkalčić H and Kennett BLN (2008) Core structure and heterogeneity: Seismological perspective. *Australian Journal of Earth Sciences* 55: 419–431.

Tkalčić H, Kennett BLN, and Cormier VF (2009) On the inner–outer core density contrast from PKikP/PcP amplitude ratios and uncertainties caused by seismic noise. *Geophysical Journal International* 179: 425–443.

Tkalčić H, Romanowicz B, and Houy N (2002) Constraints on D″ structure using PKP (AB-DF), PKP(BC-DF) and PcP-P travel time data from broadband records. *Geophysical Journal International* 149: 599–616.

Tkalčić H, Young M, Bodin T, Ngo S, and Sambridge M (2013) The shuffling rotation of the Earth's inner core revealed by earthquake doublets. *Nature Geoscience* 6: 497–502.

Tromp J (1993) Support for anisotropy of the Earth's inner core from free oscillations. *Nature* 366: 678–681.

Tseng T-L, Huang B-S, and Chin B-H (2001) Depth-dependent attenuation in the uppermost inner core from the Taiwan short period seismic array PKP data. *Geophysical Research Letters* 29: 459–462.

Vidale JE, Dodge DA, and Earle PS (2000) Slow differential rotation of the Earth's inner core indicated by temporal changes in scattering. *Nature* 405: 445–448.

Vidale JE and Earle PS (2000) Fine-scale heterogeneity in the Earth's inner core. *Nature* 404: 273–275.

Vidale JE and Earle PS (2005) Evidence for inner-core rotation from possible changes with time in PKP coda. *Geophysical Research Letters* 32: L01309.

Vinnik L, Romanowicz B, and Bréger L (1994) Anisotropy in the center of the inner core. *Geophysical Research Letters* 21: 1671–1674.

Vočadlo L (2007) Ab initio calculations of the elasticity of iron and iron alloys at inner core conditions: Evidence for a partially molten inner core? *Earth and Planetary Science Letters* 254: 227–232.

Wahr J and de Vries D (1989) The possibility of lateral structure inside the core and its implications for nutations and Earth tide observations. *Geophysical Journal International* 99: 511–519.

Waszek L and Deuss A (2011) Distinct layering in the hemispherical seismic velocity structure of Earth's upper inner core. *Journal of Geophysical Research* 116: B12313, Correction (2012) *Journal of Geophysical Research* 117: B10304.

Waszek L, Irving J, and Deuss A (2011) Reconciling the hemispherical structure of Earth's inner core with its super-rotation. *Nature Geoscience* 4: 264–267.

Weber P and Machetel P (1992) Convection within the inner core and thermal implications. *Geophysical Research Letters* 19: 2107–2110.

Wen L (2006) Localized temporal change of the Earth's inner core boundary. *Science* 314: 967–970.

Wen L and Niu F (2002) Seismic velocity and attenuation structures in the top of the Earth's inner core. *Journal of Geophysical Research* 107(B11): 2273.

Wenk HR, Baumgardner JR, Lebensohn RA, and Tomé CN (2000) A convection model to explain anisotropy in the inner core. *Journal of Geophysical Research* 105: 5662–5677.

Widmer RG, Masters F, and Gilbert F (1991) Spherically symmetric attenuation within the Earth from normal mode data. *Geophysical Journal International* 104: 541–553.

Widmer RG, Masters F, and Gilbert F (1992) Observably split multiplets – Data analysis and interpretation in terms of large-scale aspherical structure. *Geophysical Journal International* 111: 559–576.

Wiechert E (1896) Uber die Beschaffenheit des Erdinneren. *Verhandlungen der Gesellschaft Deutscher Naturforscher und Ärzte* 2: 42.

Woodhouse JH, Giardini D, and Li X-D (1986) Evidence for inner core anisotropy from free oscillations. *Geophysical Research Letters* 13: 1549–1552.

Wookey J and Helffrich G (2008) Inner-core shear-wave anisotropy and texture from an observation of PKJKP. *Nature* 454: 873–877.

Yoshida S, Sumita I, and Kumazawa M (1996) Growth model of the inner core coupled with the outer core dynamics and the resulting elastic anisotropy. *Journal of Geophysical Research* 101: 28085–28103.

Yu W and Wen L (2006a) Seismic velocity and attenuation structures in the top 400 km of the earth's inner core along equatorial paths. *Journal of Geophysical Research* 11: B07308. http://dx.doi.org/10.1029/2005JB003995.

Yu W and Wen L (2006b) Inner core anisotropy in attenuation. *Earth and Planetary Science Letters* 245: 581–594.

Yu W and Wen L (2007) Complex seismic anisotropy in the top of the Earth's inner core beneath Africa. *Journal of Geophysical Research* 112: B08304.

Yu W, Wen L, and Niu F (2005) Seismic velocity structure in the Earth's outer core. *Journal of Geophysical Research* 110: B02302. http://dx.doi.org/10.1029/2003JB002928.

Yukutake T (1998) Implausibility of thermal convection in the Earth's solid inner core. *Physics of the Earth and Planetary Interiors* 108: 1–13.

Zhang J, Richards PG, and Schaff DP (2008) Wide-scale detection of earthquake waveform doublets and further evidence of inner core super-rotation. *Geophysical Journal International* 174: 993–1006.

Zhang J, Song X, Li Y, Richards PG, Sun X, and Waldhauser F (2005) Inner core differential motion confirmed by earthquake waveform doublets. *Science* 309: 1357–1360.

Zou Z, Koper K, and Cormier V (2008) The structure at the base of the outer core inferred from seismic waves diffracted around the inner core. *Journal of Geophysical Research* 113: B05314.

This page intentionally left blank

1.24 Deep Earth Structure: Seismic Scattering in the Deep Earth

PM Shearer, University of California, San Diego, La Jolla, CA, USA

© 2015 Elsevier B.V. All rights reserved.

1.24.1	**Introduction**	759
1.24.2	**Scattering Theory**	759
1.24.2.1	Single-Scattering Theory and Random Media	760
1.24.2.1.1	*Q* notation and definitions	761
1.24.2.2	Finite-Difference Calculations and the Energy-Flux Model	761
1.24.2.3	Multiple-Scattering Theories	763
1.24.2.4	Other Theoretical Methods	765
1.24.3	**Scattering Observations**	766
1.24.3.1	Local and Regional S Coda	767
1.24.3.2	P Coda	768
1.24.3.3	P_n Coda	771
1.24.3.4	P_{diff} Coda	771
1.24.3.5	PP and P′P′ Precursors	773
1.24.3.6	PKP Precursors	774
1.24.3.7	PKKP Precursors and $PKKP_X$	776
1.24.3.8	PKiKP and PKP Coda and Inner-Core Scattering	777
1.24.3.9	Other Phases	779
1.24.4	**Discussion**	780
Acknowledgments		781
References		781

1.24.1 Introduction

Most seismic analyses of Earth structure rely on observations of the travel times and waveforms of direct seismic waves that travel along ray paths determined by Earth's large-scale velocity structure. These observations permit inversions for radially averaged P-wave and S-wave velocity profiles as well as three-dimensional (3D) perturbations. However, smaller-scale velocity or density perturbations cause some fraction of the seismic energy to be scattered in other directions, usually arriving following the main phase as incoherent energy over an extended time interval. This later-arriving wave train is termed the coda of the direct phase. Given the number of different scattering events and the complexity of the scattered wavefield, it is generally impossible to resolve individual scatterers. Instead, coda-wave observations are modeled using random media theories that predict the average energy in the scattered waves as a function of scattering angle, given the statistical properties of the velocity and density perturbations. In this way, it is possible to characterize Earth's heterogeneity at much smaller scales than can be imaged using tomography or other methods.

The fact that direct seismic waves can be observed in the Earth indicates that this scattering must be relatively weak so that a significant fraction of the seismic energy remains in the primary arrivals. In contrast, scattering on the Moon is proportionally much stronger than in the Earth, preventing the easy observation of direct P and S waves at global distances (at least at the recorded frequencies of the available data) and complicating inversions for lunar structure. In addition to facilitating observations of direct arrivals, weak (as opposed to strong) scattering also can simplify modeling by permitting use of single-scattering theory (i.e., the Born approximation). However, it is now clear that accurate modeling of scattering in the lithosphere, and possibly deeper in the mantle as well, requires calculations based on multiple-scattering theories. Fortunately, increased computer power makes these calculations computationally feasible.

Although both body waves and surface waves exhibit scattering, my emphasis in this chapter is on observations and modeling of deep-Earth scattering, for which body waves provide the primary constraints. In addition, I also will give more attention to the mantle and core than the lithosphere, which has been the focus of the majority of coda studies to date. Finally, I will only briefly summarize the different scattering theories. For more details on these topics, the reader should consult the book by Sato and Fehler (1998, 2012), which provides an extensive review of scattering theory and analysis methods, as well as a comprehensive summary of crustal and lithospheric studies.

1.24.2 Scattering Theory

Wave scattering from random heterogeneities is a common phenomenon in many fields of science, and theoretical modeling approaches have been extensively developed in physics, acoustics, and seismology. Solving this problem for the full elastic wave equation (i.e., for both P and S waves) in the presence of strong perturbations in the elastic tensor and density is quite difficult, so various simplifying approximations are often applied. These include assuming an isotropic elastic tensor, using first-order perturbation theory in the case of weak

 http://dx.doi.org/10.1016/B978-0-444-53802-4.00018-X

scattering, using the diffusion equation for very strong scattering, and assuming correlations among the velocity and density perturbations.

1.24.2.1 Single-Scattering Theory and Random Media

For sufficiently weak velocity and density perturbations, most scattered energy will have experienced only one scattering event and can be adequately modeled using single-scattering theory. The mathematics in this case is greatly simplified if we assume that the primary waves are unchanged by their passage through the scattering region (the Born approximation). The total energy in the seismic wavefield therefore increases by the amount contained in the scattered waves, and energy conservation is not obeyed. Thus, this approximation is only valid when the scattered waves are much weaker than the primary waves, which is the case in the Earth when the velocity and density perturbations are relatively small (quantifying exactly how small depends upon the frequency of the waves and the source–receiver distance). Single-scattering theory is sometimes called Chernov theory after Chernov (1960). Detailed descriptions of Born scattering theory for elastic waves are contained in Wu and Aki (1985a,b), Wu (1989), and Sato and Fehler (1998, 2012). A review of the properties (elasticity, conductivity, and permeability) and statistics of random heterogeneous materials is given in the text by Torquato (2002).

Single-scattering theory provides equations that give the average scattered power as a function of the incident and scattered wave types (i.e., P or S), the power of the incident wave, the local volume of the scattering region, the bulk and statistical properties of the random medium, the scattering angle (the angle between the incident wave and the scattered wave), and the seismic wave number ($k = 2n/A$, where A is the wavelength). A general random medium could have separate perturbations in P velocity, S velocity, and density, but in practice, a common simplification is to assume a linear scaling relationship among the perturbations (e.g., Sato, 1990) and/or to assume zero density perturbations. However, as pointed out by Hong et al. (2004), density variations can have an important influence on scattering properties. Performing the actual calculation for a specific source–receiver geometry involves integrating the contributions of small volume elements over the scattering region of interest. Each volume element will have a specific scattering angle and geometric spreading factors for the source–scatterer and scatterer–receiver ray paths.

The nature of the scattering strongly depends upon the relative length scales of the heterogeneity and the seismic waves. The scale of perturbations in a random medium can be characterized by the autocorrelation function (ACF), with the correlation distance, a, providing a rough measure of the average size of the 'blobs' in many commonly assumed forms for the ACF (e.g., Gaussian, exponential, and van Karman). Figure 1 shows examples of random realizations of the Gaussian and exponential ACF models. If the heterogeneity is large compared to the seismic wavelength ($a \gg \Lambda$, ka is large), then forward scattering predominates and becomes increasingly concentrated near the direction of the incident wave as ka increases. In the limit of large ka, the energy remains along the primary ray path and scattering effects do not need to be taken into account. Alternatively, if the blobs are small compared to the seismic wavelength ($a \ll \Lambda$, ka is small), then the scattering is often approximated as isotropic and the scattered power scales as k^4a^3. In the limit of small ka, the scattering strength goes to zero and the medium behaves like a homogeneous solid. As discussed by Aki and Richards (1980, pp. 749–750), scattering effects are strongest when a and A are of comparable size (i.e., when $ka \sim 2\pi$).

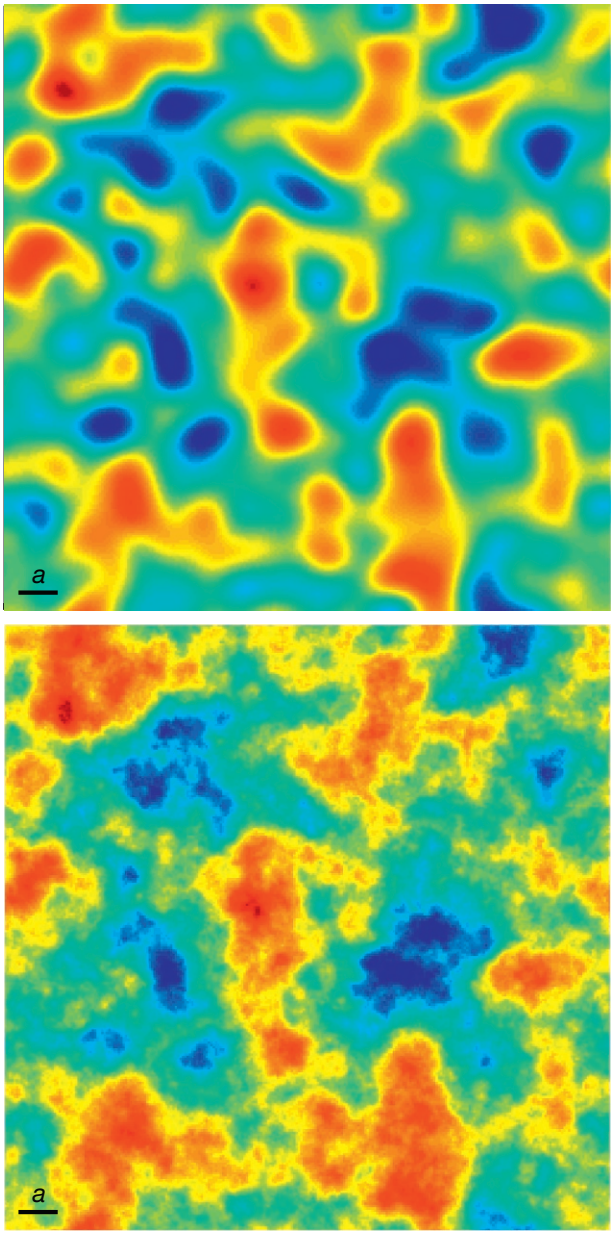

Figure 1 Examples of random media defined by a Gaussian autocorrelation function (top) and an exponential autocorrelation function (bottom). The correlation distance, a, is indicated in the lower left corner. The exponential medium has more structure at short wavelengths than the Gaussian medium.

Aki and Chouet (1975) presented an important application of single-scattering theory to predict coda decay rates for local earthquakes. For a colocated source and receiver and homogeneous body-wave scattering in 3D media, they obtained

$$A_C(t) \propto t^{-1} e^{-\omega t/2Q_C} \quad [1]$$

where A_C is the coda amplitude at time t (from the earthquake origin time) and angular frequency ω. Q_C is termed the coda Q, and there has been some uncertainty regarding its physical meaning, in particular whether it describes intrinsic attenuation, scattering attenuation, or some combination of both. I will discuss this more later in the context of more complete theories. Regardless of its interpretation, this formula has proven successful in fitting coda decay rates in a large number of studies.

Single-scattering theory has also been important for modeling deep-Earth scattering in terms of random heterogeneity models, including interpretation of PKP precursor observations (e.g., Doornbos, 1976; Haddon and Cleary, 1974), PP precursors (King et al., 1975), P′P′ precursors (Vinnik, 1981), P_{diff} coda (Earle and Shearer, 2001), and PKiKP coda (Vidale and Earle, 2000). Born theory has also been used to model expected travel-time variations in direct arrivals that travel through random velocity heterogeneity (e.g., Baig and Dahlen, 2004a,b; Baig et al., 2003; Spetzler and Snieder, 2001). Although my focus in this chapter is largely on incoherent scattering from random media, it should be noted that the Born approximation can also be used to model the effect of specific velocity structures, provided their perturbations are weak compared to the background velocity field. In this case, true synthetic seismograms can be computed, not just the envelope functions. For example, Dalkolmo and Friederich (2000) recently used this approach to model the effect of several different hypothesized velocity anomalies near the core–mantle boundary (CMB) on long-period P waves. In addition, Born theory forms the basis for computing sensitivity kernels in finite-frequency tomography methods (e.g., Dahlen et al., 2000; Nolet et al., 2005).

1.24.2.1.1 Q notation and definitions

Coda Q, intrinsic Q, and scattering Q will be termed Q_C, Q_I, and Q_{Sc}, respectively. P-wave and S-wave Q are termed ${}^{\alpha}Q$ and ${}^{\beta}Q$, respectively. These can be combined so that, for example, ${}^{\beta}Q_I$ is intrinsic S-wave Q. This convention eliminates any chance of confusing shear-wave Q and scattering Q (both have sometimes been termed Q_S). The transmission Q, Q_T, describes the total attenuation (both intrinsic and scattering) suffered by the direct wave

$$Q_T^{-1} = Q_I^{-1} + Q_{Sc}^{-1} \quad [2]$$

and the amplitude reduction of the transmitted pulse for a constant Q_T medium is

$$A(t) = A_0 e^{-\omega t/2Q_T} \quad [3]$$

where A_0 is the amplitude of the pulse at $t=0$ and we have ignored any geometric spreading.

The scattering coefficient, g, is defined as the scattering power per unit volume (e.g., Sato, 1977) and has units of reciprocal length. The total scattering coefficient, g_0, is defined as the average of g over all directions and can also be expressed as

$$g_0 = l^{-1} = Q_{Sc}^{-1} k \quad [4]$$

where l is the mean free path and k is the wave number. One common way to estimate g_0 for S waves has been to compare the energy in the S coda to the total radiated S energy. Finally, following Wu (1985), we define the seismic albedo as the ratio of scattering attenuation to total attenuation

$$B_0 = \frac{Q_{Sc}^{-1}}{Q_{Sc}^{-1} + Q_I^{-1}} = \frac{g_0}{g_0 + Q_I^{-1} k} \quad [5]$$

These definitions of Q, g_0, and B_0 are general and can be applied to the multiple-scattering theories discussed later in this chapter.

1.24.2.2 Finite-Difference Calculations and the Energy-Flux Model

Finite-difference methods provide a direct, albeit computationally intensive, solution to the seismic wave equation for media of arbitrary complexity, and they (together with the finite element method) have become one of the most widely used techniques in seismology. Their earliest applications to study scattering involved modeling surface-wave and body-to-surface-wave scattering from surface topography, sediment-filled basins, and other buried interfaces (e.g., Levander and Hill, 1985). Here, I will discuss only their use in modeling body-wave scattering in random media. Reviews of this topic are contained in Frankel (1990) and Sato and Fehler (1998, 2012).

As computing power has improved, finite-difference simulations have progressed from the 2D parabolic approximation, to 2D using the full wave equation, to full 3D synthetics. The parabolic approximation considers only forward scattering and is useful when the heterogeneity correlation length is large compared to the seismic wavelength. Complete finite-difference simulations in 2D random media have been performed by Frankel and Clayton (1984, 1986), McLaughlin et al. (1985), McLaughlin and Anderson (1987), Frankel and Wennerberg (1987), Gibson and Levander (1988), Roth and Korn (1993), and Saito et al. (2003). Frenje and Juhlin (2000) computed both 2D and 3D finite-difference simulations. Hong and Kennett (2003), Hong (2004), and Hong et al. (2005) used a wavelet-based numerical approach to compute 2D synthetics for random media and Hong and Wu (2005) computed 2D synthetics for anisotropic models.

The Frankel studies provided key results in formulating the influential energy-flux model (EFM) of seismic coda (Frankel and Wennerberg, 1987) so I will describe them in some detail. Frankel and Clayton (1986) modeled teleseismic P-wave travel-time variations with a ~1 Hz plane wavelet vertically incident on a layer 150 km wide by 55 km thick, with a finite-difference grid spacing of 500 m. They found that observed travel-time variations of about 0.2 s (RMS) among stations spaced 10–150 km apart could be explained with 5% RMS random P-velocity variations, provided the correlation length was 10 km or greater. Frankel and Clayton (1986) also modeled high-frequency coda from local earthquakes using a ~20 Hz explosive source at the bottom corner of a layer 8 km long by 2 km thick. They found that the amplitude of high-frequency coda depends strongly on the presence of high wave number velocity perturbations. Gaussian and exponential models with correlation lengths of 10 km or greater (required to fit observed teleseismic travel-time variations) do not have sufficient small-scale structure to produce observed levels of

high-frequency coda. In contrast, a self-similar random medium model with a correlation distance of at least 10 km and RMS velocity variations of 5% can account for both sets of observations.

By measuring peak amplitude versus distance in their synthetics, Frankel and Clayton (1986) estimated Q for their random medium. Because their finite-difference calculation did not contain any intrinsic attenuation, this represents a measure of scattering Q (Q_{Sc}). The predicted attenuation (Q^{-1}) peaks at ka values between 1 and 2 for Gaussian random media and between about 1 and 6 for exponential random media. This is consistent with the strongest scattering occurring when the seismic wavelength is comparable to the size of the scatterers. However, attenuation is constant with frequency for self-similar random media, as expected since the velocity fluctuations have equal amplitudes over a wide range of scales. Frankel and Clayton showed that these results were in rough agreement with those predicted by single-scattering theory in two dimensions (to match the geometry of the finite-difference simulations).

Frankel and Clayton (1986) also measured coda decay rates for finite-difference synthetics computed for sources within a 12 km by 12 km grid at 20 m spacing. They found that their observed coda decay rates were significantly less than those predicted by single-scattering theory in the case of moderate to large scattering attenuation ($Q_{Sc} \leq 200$), indicating that multiple scattering is contributing a substantial portion of the coda energy. This implies that in these cases, coda Q (Q_C) as determined from coda falloff and the single-scattering model of coda (e.g., Aki and Chouet, 1975) does not provide a reliable estimate of transmission Q.

Motivated by these finite-difference results and the limitations of the single-scattering model of coda generation, Frankel and Wennerberg (1987) introduced what they termed the EFM of coda. This phenomenological model is based on the idea that the coda energy behind the direct wave front can be approximated as homogeneous in space. This observation had previously been reported for microearthquake coda for lapse times more than twice the S-wave travel time (e.g., Aki, 1969; Rautian and Khalturin, 1978), and Frankel and Wennerberg (1987) showed that it also could be seen in finite-difference synthetics (see **Figure 2**). It implies that at sufficiently long times, the coda amplitude at all receivers is approximately the same (scaling only with the magnitude of the source), regardless of the source–receiver distance. The EFM permits the time decay of the coda amplitude to be modeled very simply and to separate the effects of scattering and intrinsic attenuation in the medium.

By considering the energy density of the coda uniformly distributed in an expanding volume behind the direct wave front, Frankel and Wennerberg derived an expression for the predicted time decay of the coda amplitude

$$A_C(t) \propto t^{-3/2} e^{-\omega t/2Q_I} \sqrt{1 - e^{-\omega t/Q_{Sc}}} \qquad [6]$$

where t is time, ω is angular frequency, Q_I^{-1} is intrinsic attenuation, and Q_{Sc}^{-1} is scattering attenuation. For short time and/or high Q_{Sc} (i.e., weak scattering, tQ_{Sc}^{-1} is very small), this equation reduces to

$$A_C(t) \propto t^{-1} e^{-\omega t/2Q_I} \qquad [7]$$

This is equivalent to the Aki and Chouet (1975) expression (eqn [1]) for the single-scattering model, assuming coda Q and intrinsic Q are equivalent ($Q_C = Q_I$). This agrees with the original interpretation of Q_C given by Aki and Chouet (1975) and contradicts the Aki (1980) statement that in the context of single-scattering theory, Q_C should be considered as an effective Q that includes both absorption and scattering effects. Frankel and Wennerberg (1987) showed that the EFM predicts the amplitude and coda decay observed in finite-difference synthetics for random media with a wide range of scattering Q and is more accurate than the single-scattering model for media with moderate to strong scattering attenuation ($Q_{Sc} \leq 150$). Finally, they used the EFM to estimate Q_{Sc} and Q_I from the coda of two $M \sim 3$ earthquakes near Anza, California.

There have been numerous other studies that have attempted to resolve Q_{Sc} and Q_I from local earthquake coda (e.g., Cirerone et al., 2011; Fehler et al., 1992; Jemberie and Nyblade, 2009; Mayeda et al., 1991; Padhy and Subhadra, 2010; Padhy et al., 2011; Toksöz et al., 1988; Wu and Aki, 1988). Notable are Mayeda et al. (1992), who analyzed S-wave coda from Hawaii, Long Valley, and central California. They found a complicated relationship between theoretical predictions and observed Q_C, Q_{Sc}, and Q_I and argued that models with depth-dependent scattering and intrinsic attenuation are necessary to explain their results.

The EFM was developed to explain local earthquake coda and finite-difference simulations of spherical wave fronts in media with uniform scattering. It is not directly applicable to modeling teleseismic coda because of the strong concentration of scattering in the crust and lithosphere compared to much weaker scattering deeper in the mantle. This has motivated the development of extended EFMs involving the response of one or more scattering layers to a wave incident from below (e.g., Korn, 1988, 1990, 1997; Langston, 1989).

The resulting formulas for the coda decay rate are more complicated than the simple EFM because they depend upon several additional parameters, including the travel time through the layer and the amount of leakage back into the half-space. Korn (1988) developed the theory for a spherical wave with a cone of energy incident upon a scattering zone

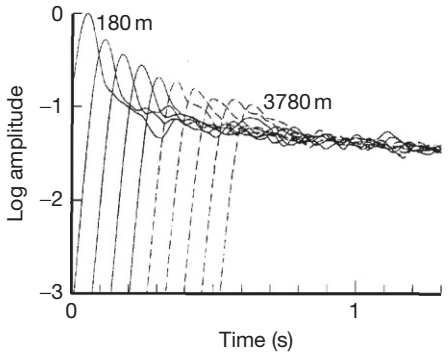

Figure 2 Envelopes of finite-difference synthetic seismograms for receivers at distances of 180–3780 m from the source as computed by Frankel and Wennerberg (1987) for a random medium with a correlation distance of 40 m. Note that the envelopes decay to a common level following the initial pulse, indicating spatial homogeneity of coda energy.

and used it to model regional earthquakes recorded by the Warramunga array in Australia. Langston (1989) developed a scattering layer-over-half-space model and showed that it was consistent with coda decay in teleseismic P waves recorded at two stations (named PAS and SCP) in the United States. Korn (1990) tested a scattering layer over homogenous half-space EFM using a 2D acoustic finite-difference code and found that it gave reliable results for both weak and strong scattering regimes. Korn (1997) further extended the EFM to explicitly include depth-dependent scattering and showed that it gave reliable results when compared to synthetics computed for a 2D elastic (P–SV) finite-difference code.

Wagner and Langston (1992a) computed 2D acoustic and elastic finite-difference synthetics for upcoming P waves incident on 150 different models of heterogeneous layers over a homogeneous half-space. These models varied in their layer thickness, random heterogeneity correlation length (different vertical and horizontal correlation lengths were allowed), and RMS velocity heterogeneity. They found that the scattering attenuation of the direct pulse depends upon ka and is strongest for spatially isotropic heterogeneity, in which case most of the coda energy was contained in low apparent velocity S waves and surface waves. In contrast, anisotropic models with horizontally elongated heterogeneities produce coda with mostly vertically propagating layer reverberations.

More recent finite-difference calculations for random media include the 2D whole-Earth pseudospectral calculations of Furumura et al. (1998) and Wang et al. (2001), Thomas et al. (2000) who computed 2D whole-Earth acoustic synthetics to model PKP precursors, Cormier (2000) who used a 2D elastic pseudospectral method to model the effects of D'' heterogeneity on the P and S wavefields, Korn and Sato (2005) who compared 2D finite-difference calculations with synthetics based on the Markov approximation, and Jahnke et al. (2008) who developed an axisymmetric finite-difference code suitable for parallel computers and showed how it can be used to model whole-mantle scattering at frequencies up to 0.4 Hz.

1.24.2.3 Multiple-Scattering Theories

If the energy in the scattered wavefield is a significant fraction of the energy in the direct wave, then the Born approximation is inaccurate and a higher-order theory should be used that takes into account the energy reduction in the primary wave and the fact that the scattered waves may experience more than one scattering event. These effects are all naturally accounted for using the finite-difference calculations discussed earlier, but these are computationally intensive and there is a need for faster approaches that also provide physical insight into the scattering process. In the case of very strong scattering, the diffusion equation can be applied by assuming a random walk process. Although this approach preserves energy, it violates causality by permitting some energy to arrive before the direct P wave. The first applications of the diffusion equation in seismology include the coda-wave analyses of Wesley (1965) and Aki and Chouet (1975) and the lunar seismogram studies of Nakamura (1977), Dainty and Toksöz (1977), and Dainty and Toksöz (1981).

At large times and small distances from the source, the diffusion equation predicts that the coda amplitude varies as

$$A(t) \propto t^{-3/4} e^{-\omega t/2Q_I} \quad [8]$$

where Q_I is the intrinsic attenuation. Notice that Q_{Sc} does not appear in this equation because the exact level of scattering is not important provided it is strong enough that the energy is obeying a random walk process. The diffusion equation can also be used to model the case of a strong scattering layer over a homogeneous half-space (e.g., Dainty et al., 1974; Margerin et al., 1998, 1999; Wegler, 2004), in which case an additional decay term exists to account for the energy leakage into the half-space.

Another approach to modeling multiple scattering is to sum higher-order scattered energy, and the predicted time dependence of scattered energy was obtained in this way for double-scattering (Kopnichev, 1977) and multiple scattering up to seventh order (Gao et al., 1983a,b). Hoshiba (1991) used a Monte Carlo approach (see the succeeding text) to correct and extend these results to tenth-order scattering. Richards and Menke (1983) performed numerical experiments on 1D structures with many fine layers to characterize the effects of scattering on the apparent attenuation of the transmitted pulse and the relative frequency content of the direct pulse and its coda.

Most current approaches to synthesizing multiple scattering use radiative transfer theory to model energy transport. Radiative transfer theory was first used in seismology by Wu (1985) and Wu and Aki (1988), and recent reviews of the theory are contained in Sato and Fehler (1998, 2012) and Margerin (2004). Other results are detailed in Shang and Gao (1988), Zeng et al. (1991), Sato (1993), and Sato et al. (1997). Sato and Nishino (2002) used radiative transfer theory to model multiple Rayleigh-wave scattering. Analytic solutions are possible for certain idealized cases (e.g., Sato, 1993; Wu, 1985; Zeng, 1991), but obtaining general results requires extensive computer calculations.

Two analytic results are of particular interest (and can be used as tests of numerical simulations). For the case of no intrinsic attenuation, Zeng (1991) showed the coda power converges to the diffusion solution at long lapse times

$$P_C(t) \propto t^{-3/2} \quad [9]$$

For elastic waves with no intrinsic attenuation, the equilibrium ratio of P and S energy density is given by (e.g., Papanicolaou et al., 1996; Ryzhik et al., 1996; Sato, 1994)

$$E_P/E_S = \frac{1}{2}(\beta/\alpha)^3 \quad [10]$$

Assuming a Poisson solid, this predicts about ten times more S energy than P energy at equilibrium, a result of the relatively low efficiency of S-to-P scattering compared to P-to-S scattering (e.g., Malin and Phinney, 1985; Zeng, 1993). For media with intrinsic attenuation, an equilibrium ratio also exists but will generally differ from the purely elastic case (Margerin et al., 2001a,b). Shapiro et al. (2000) showed that this ratio can be estimated from the divergence and curl of the displacement as measured with a small-aperture array and that its stability with time provides a test of whether the coda is in the diffusive regime.

Equation [10] is only valid for scattering within a uniform whole space and somewhat lower E_S/E_P ratios are expected at the surface of a uniform half-space. Margerin et al. (2009)

examined energy partitioning of seismic coda at Piñon Flat Observatory in California and obtained an average E_S/E_P ratio of about 2.8, over two times smaller than the expected value of 7.2 for equilibrium partitioning at the surface of a Poisson half-space. They explained their results by developing a theory of energy partitioning in a layered media and showed that E_S/E_P drops near the resonant frequency of a surface low-velocity layer. Thus, observations of equilibrium E_S/E_P ratios can provide information on local Earth structure. Margerin (2013) provided a theoretical treatment of multiple scattering and energy partitioning from randomly distributed point scatterers, which includes the effects of strong resonant scattering.

Wu (1985) used radiative transfer theory to address the problem of separating scattering from intrinsic attenuation. He showed that the coda energy density versus distance curves have different shapes depending upon the seismic albedo, B_0 (see eqn [5]), and thus, in principle, it is possible to separate scattering and intrinsic Q by measuring energy density distribution curves. Hoshiba (1991) pointed out that in practice, the use of finite window lengths for measuring coda will lead to underestimating the total energy (compared to the infinite lapse-time windows in Wu's theory), likely biasing the resulting estimates of seismic albedo. To deal with this problem, Fehler et al. (1992) introduced the multiple lapse-time window (MLTW) analysis, which measures the energy in consecutive time windows as a function of epicentral distance. The MLTW approach has been widely used in studies of S coda (see the succeeding text).

A powerful method for computing synthetic seismograms based on radiative transfer theory is to use a computer-based Monte Carlo approach to simulate the random walk of millions of seismic energy 'particles,' which are scattered with probabilities derived from random media theory. **Figure 3** illustrates a simple example of this method applied to 2D isotropic scattering. Variations on this basic technique are described by Gusev and Abubakirov (1987), Abubakirov and Gusev (1990), Hoshiba (1991, 1994, 1997), Margerin et al. (2000), Bal and Moscoso (2000), Yoshimoto (2000), Margerin and Nolet (2003a,b), and Shearer and Earle (2004). Because of the potential of the Monte Carlo method for modeling whole-Earth, high-frequency scattering, these results are now summarized in some detail.

Gusev and Abubakirov (1987) used the Monte Carlo method to model acoustic-wave scattering in a whole space and considered both isotropic scattering and forward scattering with a Gaussian angle distribution. They parameterized the scattering in terms of a uniform probability per unit volume, resulting in an exponential distribution of path lengths. Intrinsic attenuation was not included. They showed that their results agree with the diffusion model for large lapse times. Abubakirov and Gusev (1990) described in detail this method and its application to model S coda from Kamchatka earthquakes. They obtained an S-wave mean free path for the Kamchatka lithosphere of 110–150 km over a 1.5–6 Hz frequency range.

Hoshiba (1991) modeled the spherical radiation of S-wave energy in a constant velocity medium using a Monte Carlo simulation that included isotropic scattering with uniform probability. He showed that the results agreed with single-scattering theory for weak scattering (i.e., travel distances

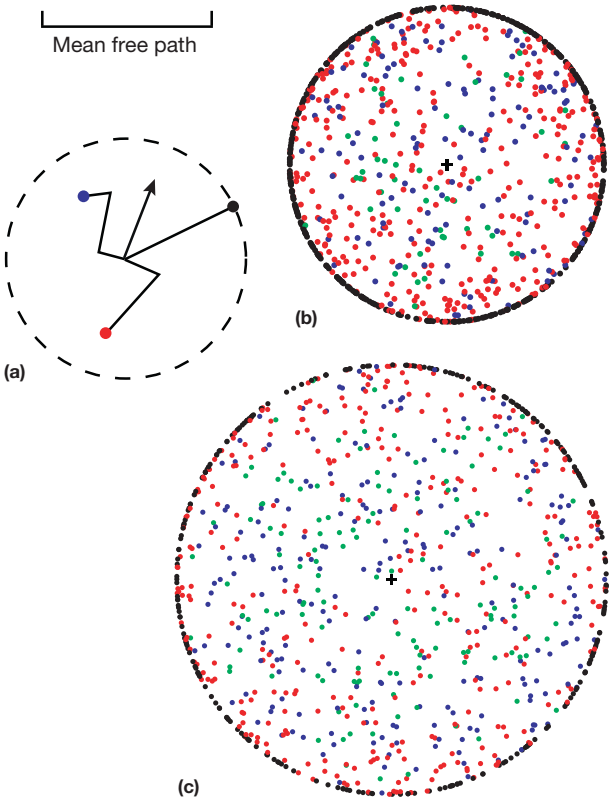

Figure 3 Example of a Monte Carlo computer simulation of random scattering of seismic energy particles, assuming 2D isotropic scattering in a uniform whole space. Particles are sprayed in all directions from the source with constant scattering probability defined by the indicated mean free path length, l. As indicated in (a), black dots show particles that have not been scattered, red dots show particles that have scattered once, blue dots show particles that have scattered twice, and green dots show particles scattered three or more times. (b) Results for 1000 particles after $t = 0.8/v$, where v is velocity. (c) Results for 1000 particles after $t = 1.25/v$. Note that the particle density is approximately constant for the scattered energy inside the circle defining the direct wave front, as predicted by the energy-flux model.

$<10\%$ of the mean free path) and agreed with the diffusion model for strong scattering (i.e., travel distances more than ten times longer than the mean free path). Hoshiba (1991) was able to use his Monte Carlo results to correct and extend the multiple-scattering terms of Gao et al. (1983a,b). He found that his simulations at long lapse times were consistent with the radiative transfer theory of Wu (1985) but that reliable estimates of seismic albedo are problematic from short time windows. Finally, Hoshiba (1991) showed that for multiple scattering, coda Q is much more sensitive to intrinsic Q than to scattering Q (as was argued by Frankel and Wennerberg, 1987, on the basis of the EFM).

Wennerberg (1993) considered the implications of lapse time-dependent observations of Q_C and methods for separating intrinsic and scattering attenuation with respect to the single-scattering model, Zeng's (1991) multiple-scattering model, Hoshiba's (1991) model, and Abubakirov and Gusev's (1990) results. Hoshiba (1994) extended his Monte Carlo method to consider depth-dependent scattering strength and intrinsic attenuation, and Hoshiba (1997) included the

effects of a layered velocity structure to model local earthquake coda at distances up to 50 km. Hoshiba simulated SH-wave reflection and transmission coefficients at layer interfaces as probabilities of reflection or transmission of particles in the Monte Carlo method but did not include P waves and the conversions between P and S waves. The results showed that coda amplitudes depend upon the source depth even late into the coda.

Margerin et al. (1998) applied the Monte Carlo approach to a layer over a half-space model, representing the crust and upper mantle, and included both surface- and Moho-reflected and transmitted phases. As in Hoshiba (1997), reflection and transmission coefficients are converted to probabilities for the individual particles. S waves only are modeled (using the scalar-wave approximation, i.e., no P-to-S conversions) and no intrinsic attenuation is included. Margerin et al. (1998) compared their numerical results in detail with solutions based on the diffusion equation and found good agreement for suitable mean free path lengths. They point out the importance of the crustal waveguide for trapping energy near the surface and that the possibility of energy leakage into the mantle should be taken into account in calculations of seismic albedo.

Bal and Moscoso (2000) explicitly included S-wave polarization and showed that S waves become depolarized under multiple scattering. Yoshimoto (2000) introduced the direct simulation Monte Carlo method, which uses a finite-difference scheme for ray tracing and can thus handle velocity models of arbitrary complexity, including lateral varying structures. However, intrinsic attenuation and directional scattering were not included. Yoshimoto showed that a velocity increase with depth strongly affects the shape of the coda envelope, compared with uniform velocity models, and that it is important to properly model energy that may be trapped at shallow depths.

Margerin et al. (2000) extended the Monte Carlo approach to elastic waves, taking into account P-to-S conversions and S-wave polarization. They considered scattering from randomly distributed spherical inclusions within a homogeneous background material, using the solutions of Wu and Aki (1985a). For both Rayleigh scatterers (spheres much smaller than the seismic wavelength) and Rayleigh–Gans scatterers (spheres comparable to the seismic wavelength), they found good agreement with single-scattering theory at short times and with the diffusion equation solution at long times. In addition, the P-to-S energy density ratio and the coda decay rate at long times converged to their theoretical expected values.

Margerin and Nolet (2003a,b) further extended the Monte Carlo approach to model whole-Earth wave propagation and scattering. They showed that their Monte Carlo synthetics for the PKP AB and BC branches produced energy versus distance results in good agreement with geometric ray theory. They computed scattering properties based on random media models characterized by velocity perturbations with an exponential correlation length. For whole-mantle scattering, they found that the Born approximation is only valid up to mean free paths of about 400 s, corresponding to 0.5% RMS velocity perturbations. They also applied their method to model PKP precursor observations; these results will be discussed later in this chapter.

Shearer and Earle (2004) implemented a particle-based Monte Carlo method for computing whole-Earth scattering. They included both P and S waves radiated from the source, mode conversions, S-wave polarizations, and intrinsic attenuation. For a simple whole-space model, they showed that their approach agreed with theoretical results for the S/P energy ratio and expected t^{-15} falloff in power at large times. For modeling the whole Earth, they included the effects of reflection and transmission coefficients at the free surface, Moho, CMB, and inner-core boundary (ICB). Scattering probabilities and scattering angles were computed assuming random velocity and density variations characterized by an exponential ACF. They applied this method to model the time and distance dependence of high-frequency P coda amplitudes (see **Section 1.24.3.2**).

Wegler et al. (2006), Przybilla et al. (2006), and Przybilla and Korn (2008) compared Monte Carlo solutions using the elastic radiative transfer equations to 3D finite-difference calculations and found good agreement in envelope shapes, including peak amplitudes, envelope broadening, and coda decay rates. However, Przybilla and Korn (2008) documented an interesting breakdown in radiative transfer results based on the Born scattering coefficients in the vicinity of a point source, where waveform modeling shows that even for a pure compressional source, there is some fraction of shear-wave energy generated by near-source scattering that is missed in Born approximation calculations.

All of these results suggest that body-wave scattering in the whole Earth can now be reasonably well modeled using ray theory and particle-based Monte Carlo methods. Although somewhat computationally intensive, continued improvements in computer speed make them practical to run on modest machines. They can handle multiple scattering over a range of scattering intensities, bridging the gap between the Born approximation for weak scattering and the diffusion equation for strong scattering. They also can include general depth-dependent or even 3D variations in scattering properties, including non-isotropic scattering, without a significant increase in computation time compared to simpler problems.

1.24.2.4 Other Theoretical Methods

Lerche and Menke (1986) presented an inversion method to separate intrinsic and scattering attenuation for a plane-layered medium. Gusev (1995) and Gusev and Abubakirov (1999a,b) developed a theory for reconstructing a vertical profile of scattering strength from pulse broadening and delay of the peak amplitude. Saito et al. (2002, 2003) modeled envelope broadening in S waves by applying the parabolic approximation to a von Karman random medium. Sato et al. (2004) extended this approach to develop a hybrid method for synthesizing whole-wave envelopes that uses the envelope obtained from the Markov approximation as a propagator in the radiative transfer integral and showed that the results agreed with finite-difference calculations. Takahashi (2012) also used the Markov approximation to model wide-angle scattering of S waves in northeastern Japan and the time delays in their maximum amplitudes.

The effect of anisotropic random media (where the scattering properties depend upon the angle of the incident wave)

was considered numerically by Wagner and Langston (1992a) and Roth and Korn (1993) and theoretically by Müller and Shapiro (2003), Hong and Wu (2005), and Margerin (2006). Recent work on using small-aperture seismic arrays on coda energy to constrain the directions of individual scatterers includes Schisselé et al. (2004) and Matsumoto (2005).

1.24.3 Scattering Observations

Seismic scattering within the Earth is mainly observed in the incoherent energy that arrives between the direct seismic phases, such as P, S, and PKP. In addition, occasionally specific scatterers can be imaged using seismic arrays. Scattering can also influence the direct phases through amplitude reduction and pulse broadening, effects characterized by the scattering attenuation parameter, Q_{Sc}^{-1}. In this way, studies of seismic attenuation are also resolving scattering, although they often do not attempt to separate intrinsic and scattering attenuation. The incoherent scattered seismic wavefield usually follows a direct seismic arrival and is termed the *coda* of that phase (e.g., P coda and S coda), but occasionally, the ray geometry is such that scattered energy can arrive before a direct phase (e.g., PKP precursors). These precursory arrivals are particularly valuable for studying deep-Earth scattering because they are less sensitive to the strong scattering in the lithosphere. Scattering is usually studied at relatively high frequencies (1 Hz or above) where coda is relatively strong and local earthquake records have their best signal-to-noise ratio.

S-wave coda from local and regional events has been the focus of many studies, has motivated much of the theoretical work, and continues to be an active field of research. Here, I will briefly review S coda studies and their implications for scattering in the crust and lithosphere but will devote more attention to other parts of the scattered seismic wavefield, which provide better constraints on deep-Earth structure. Previous review articles that discuss deep-Earth scattering include Bataille et al. (1990) and Shearer et al. (1998). **Figure 4** shows where much of the scattered energy arrives with respect to travel-time curves for the major seismic phases. In principle, any seismic phase that travels through the lower mantle or the CMB will be sensitive to deep-Earth scattering. Although separating deep scattering effects from crust and lithospheric scattering can be challenging, this is possible in some cases, either

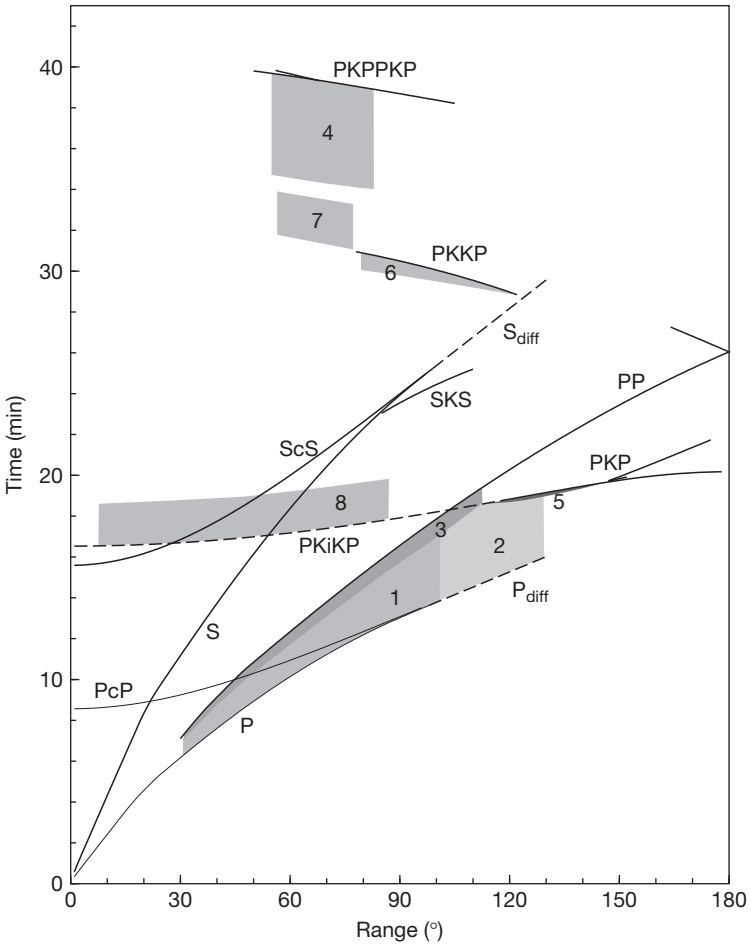

Figure 4 Travel-time curves for teleseismic body waves and some of the regions in the short-period wavefield that contain scattered arrivals. These include (1) P coda, (2) P_{diff} coda, (3) PP precursors, (4) P′P′ precursors, (5) PKP precursors, (6) PKKP precursors, (7) $PKKP_X$, and (8) PKiKP coda. The plotted boundaries are approximate.

from a fortunate ray geometry or by careful comparison of coda amplitudes at different distances or between different phases.

The picture that is emerging from these studies is that seismic scattering from small-scale velocity perturbations is present throughout the Earth, with the exception of the fluid outer core. However, the exact strength, scale length, depth dependence, and lateral variability of the scattering remain unresolved, particularly in the vicinity of the core–mantle and ICBs, where they may also be contributions from topographic irregularities or boundary layer structure.

1.24.3.1 Local and Regional S Coda

S coda measurements are of two main types: (1) those that simply fit the coda decay rate and estimate ${}^{\beta}Q_C$ without attempting to separate scattering and intrinsic attenuation and (2) those that measure energy density and estimate the scattering coefficient g_0 (or its reciprocal, the mean free path). The latter studies typically obtain a separate estimate for intrinsic attenuation and thus can compute the seismic albedo, B_0. The basic relationships among these parameters are given in eqns [4] and [5]. In both types of studies, frequency dependence can also be examined by filtering the data in different bands.

Coda Q studies include Rautian and Khalturin (1978), Roecker et al. (1982), Rodriguez et al. (1983), Singh and Herrmann (1983), Biswas and Aki (1984), Pulli (1984), Rhea (1984), Jin et al. (1985), Del Pezzo et al. (1985), Jin and Aki (1988), van Eck (1988), Kvamme and Havskov (1989), Matsumoto and Hasegawa (1989), Baskoutas and Sato (1989), Oancea et al. (1991), Tsuruga et al. (2003), Giampiccolo et al. (2004), and Goutbeek et al. (2004).

Reviews of Q_C measurements include Herraiz and Espinoa (1987), Matsumoto (1995), and Sato and Fehler (1998, 2012). In general, Q_C is frequency-dependent and increases from about 100 at 1 Hz to 1000 at 20 Hz (i.e., there is less attenuation at higher frequencies). However, there are regional variations of about a factor of ten and typically Q_C is lower in tectonically active areas and higher in stable regions, such as shields. As discussed previously, how to interpret Q_C in terms of Q_{Sc} and Q_I has been the subject of some debate, and it is becoming increasingly clear that depth-dependent calculations (which include variations in the background velocity, the scattering characteristics, and the intrinsic attenuation) are required in many cases to fully describe coda observations.

Some studies (e.g., Akamatsu, 1991; Gagnepain-Beyneix, 1987; Giampiccolo et al., 2004; Goutbeek et al., 2004; Gupta et al., 1998; Kosuga, 1992; Kvamme and Havskov, 1989; Rautian and Khalturin, 1978; Roecker et al., 1982; Singh et al., 2001) have observed that Q_C increases with increasing lapse time (i.e., eqn [1] does not fit the entire coda envelope), suggesting that the later part of the coda contains energy that propagated through less attenuating material than the early part of the coda. Gusev (1995) showed that an increase in Q_C with time in the coda is predicted from a single isotropic scattering model in which Q_{Sc} increases with depth. Margerin et al. (1998) applied radiative transfer theory to show that a model of scattering in the crust above much weaker scattering in the mantle predicts Q_C values that depend upon the reflection coefficient at the Moho, implying that energy leakage into the mantle has implications for the interpretation of coda Q.

Following Sato and Fehler (1998, 2012), we may divide scattering attenuation estimates into those obtained using the single-scattering model and those based on the MLTW analysis. Single-scattering studies include Sato (1978), Aki (1980), Pulli (1984), Dainty et al. (1987), Kosuga (1992), and Baskoutas (1996). Multiple lapse-time studies are summarized in **Figure 5** and include Fehler et al. (1992), Mayeda et al. (1992), Hoshiba (1993), Jin et al. (1994), Akinci et al. (1995), Canas et al. (1998), Ugalde et al. (1998, 2002), Hoshiba et al. (2001), Bianco et al. (2002, 2005), Vargas et al. (2004), Goutbeek et al. (2004), Mukhopadhyay and Tyagi (2008), Badi et al. (2009), Chung et al. (2010), Carcolé and Sato (2010), Lee et al. (2010), and Del Pezzo et al. (2011). Values of the coefficient go for S-to-S scattering range from about 0.002 to 0.05 km^{-1} (mean free paths of 20–500 km) for frequencies between 1 and 30 Hz. Some papers (e.g., Bianco et al., 2005; Goutbeek et al., 2004; Hoshiba, 1993; Jin et al., 1994; Mayeda et al., 1992) have found a frequency dependence in the seismic albedo and among different regions, but in general, this dependence is not as consistent as that seen in Q_C studies. Several recent papers noted the importance of considering depth-dependent velocity structure in computing scattering attenuation (e.g., Bianco et al., 2002, 2005; Hoshiba et al., 2001).

Lacombe et al. (2003) modeled S coda in France at epicentral distances between 100 and 900 km using acoustic radiative transfer theory applied to a two-layer model. They found that a model with scattering confined to the crust and uniform intrinsic attenuation could explain their data at 3 Hz but that the trade-off between scattering and intrinsic attenuation was too strong to reliably determine the relative contribution of each

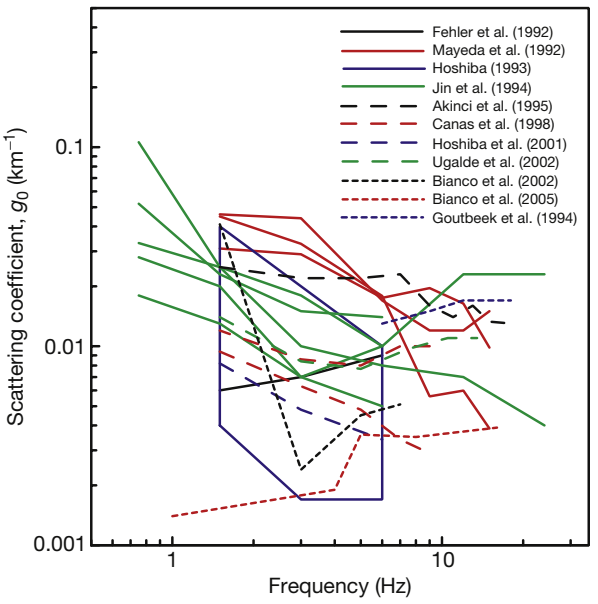

Figure 5 A summary of observations of the total scattering coefficient g_0 for S-wave scattering versus frequency, obtained using the multiple lapse-time window (MLTW) method. Results from various studies around the world are indicated with different colors.

parameter. At the regional epicentral distances of their model, the crustal waveguide had a dominating effect on the S coda.

Carcolé and Sato (2010) applied the MLTW analysis to the over 700 stations of the Japanese Hi-net seismic network to obtain high-resolution maps of both scattering and intrinsic attenuation, which show strong regional variations. In general, northeast Japan has stronger scattering than southwest Japan at 1–2 Hz, with the strongest scattering occurring near the volcanic arcs. In general, scattering and intrinsic attenuation variations are correlated and strong scattering and high intrinsic attenuation are often seen in areas where low seismic velocity anomalies have been observed in other studies. The Carcolé and Sato (2010) results agree reasonably well with the earlier work of Hoshiba (1993) for common stations, but the much greater Hi-net station density permits much more detailed mapping of scattering structure.

In addition to the S coda decay rates at relatively long lapse times used to determine coda Q, there are other aspects of the coda that provide additional constraints on scattering. The complete seismogram envelope can be studied, including the broadening of the direct S envelope and the delay in its peak amplitude (e.g., Obara and Sato, 1995; Sato, 1989, 1991; Scherbaum and Sato, 1991). Deviations from the average coda decay rate for a number of stations can be inverted to construct a 3D model of scattering intensity in the crust and upper mantle (e.g., Chen and Long, 2000; Nishigami, 1991, 1997; Obara, 1997; Taira and Yomogida, 2004). Similar methods were used by Revenaugh (1995, 1999, 2000) to back-project P coda recorded in southern California and by Hedlin and Shearer (2000) to invert PKP precursor amplitudes (see the succeeding text). Periodic rippling of SH coda envelopes in northeastern Japan was noted by Kosuga (1997) who suggested this may be caused by trapped waves within a low-velocity layer in the top part of the subducting slab.

Spudich and Bostwick (1987) showed how Green's function reciprocity can be used to obtain information about the ray takeoff directions from the earthquake source region, using a cluster of earthquakes as a virtual array. Applying this method to aftershocks of the 1984 Morgan Hill earthquake in California, they found that the early S coda was dominated by multiple scattering within 2 km of each seismic station. Scherbaum et al. (1991) used this approach to study two microearthquake clusters in northern Switzerland and found that the early S coda contained energy leaving the source at close to the same angle as the direct wave but that the later (at least 1.5–2 times the S travel time) coda contains energy from waves leaving the source in a variety of directions. Spudich and Miller (1990) and Spudich and Iida (1993) showed how an interpolation approach using distributed earthquake sources can be used to estimate scattering locations in the vicinity of the 1986 North Palm Springs earthquake in California.

Hong and Menke (2008) applied source-array analysis to regional recordings of nuclear explosions at the Balapan test site in Kazakhstan and identified coherent coda energy originating as *Rg* waves that lasts continuously to the end of the coda (more than 700 s) at 0.2–0.8 Hz. This suggests that *Rg*-to-*Rg* scattering is the main contributor to the low-frequency scattered wavefield. However, about 80% of the coda energy is composed of diffusive (multiplied scattered) waves.

1.24.3.2 P Coda

Local and many regional coda studies have mainly focused on the S-wave coda because of its higher amplitude and longer duration than P-wave coda (which is truncated by the S-wave arrival). However, at teleseismic distances, P waves and their coda are more prominent than S waves at high frequencies because of the severe effect of mantle attenuation on the shear waves. A number of studies both from single stations and arrays have attempted to resolve the origin of the scattered waves in the P coda and to distinguish between near-source scattering and near-receiver scattering.

Aki (1973) modeled scattering of P waves beneath the Montana Large Aperture Seismic Array (LASA) using Chernov single-scattering theory. At 0.5 Hz, he achieved a good fit to the data with a random heterogeneity model extending to 60 km depth beneath LASA, with RMS velocity fluctuations of 4% and a correlation distance of 10 km. Stronger scattering at higher frequencies exceeded the validity limits of the Born approximation.

Frankel and Clayton (1986) compared teleseismic travel-time anomalies observed across the LASA and NORSAR, as well as very high-frequency coda ($f \geq 30$ Hz) observed for microearthquakes, to synthetic seismograms for random media generated using a finite-difference method. They found that a random medium with self-similar velocity fluctuations ($a \geq 10$ km) of 5% within an $\sim$100 km thick layer could explain both types of observations.

Dainty (1990) reviewed array studies of teleseismic P coda, such as that recorded by the LASA and NORES arrays. He distinguished between 'coherent' coda, which has nearly the same slowness and back azimuth as direct P, and 'diffuse' coda, which is characterized by energy arriving from many different directions. He argued that coherent coda is generated by shallow, near-source scattering in the crust, rather than deeper in the mantle, because it is absent or weak for deep-focus earthquakes. In contrast, the diffuse coda is produced by near-receiver scattering and has power concentrated at slownesses typical of surface shear waves (Lg). Lay (1987) showed that the dispersive character of the first 15 s of the P coda from nuclear explosions was due to near-source effects.

Gupta and Blandford (1983) and Cessaro and Butler (1987) addressed the question as to how scattering can cause transversely polarized energy to appear in P and P coda, an issue relevant to discrimination methods between earthquakes and explosions. Their observations at different distances and frequency bands suggested that both near-source and near-receiver scattering must be present. Flatté and Wu (1988) performed a statistical analysis of phase and amplitude variations of teleseismic P waves recorded by the NORSAR array. They fitted their results with a two-overlapping-layer model of lithospheric and asthenospheric heterogeneity beneath NORSAR, consisting of the summed contributions from a 0 to 200 km layer with a flat power spectrum and a 15–250 km layer with a k^{-4} power spectrum (the deeper layer corresponds to an exponential autocorrelation model with scale larger than the array aperture of 110 km). The RMS P-velocity variations are 1–4%. This model has relatively more small-scale scatterers in the shallow crust (which the authors attribute to clustered cracks or intrusions) and relatively more large-scale scatterers in the

asthenosphere (which the authors suggest may be temperature or compositional heterogeneities).

Langston (1989) studied teleseismic P waves recorded at station PAS in California and SCP in Pennsylvania. He showed that the coda amplitude cannot be explained by horizontally layered structures of realistic velocity contrasts and that 3D scattering is required. He could explain the observed coda decay by adopting the EFM of Frankel and Wennerberg (1987) for the case of a scattering layer above a homogenous half-space. He found that scattering is more severe at PAS than SCP, as indicated by higher coda levels and a slower decay rate, obtaining a scattering Q estimate for PAS of 239 (2 s period) compared to 582 for SCP.

Korn (1988) examined the P coda from Indonesian earthquakes recorded at the Warramunga array in central Australia and found that the coda energy decreased with increasing source depth. He computed the power in the coda at different frequency bands between 0.75 and 6 Hz and fitted the results with the EFM of Frankel and Wennerberg (1987). The results indicated frequency dependence in both intrinsic attenuation and scattering attenuation ($Q_I = 300$ at 1 Hz, increasing almost linearly with frequency above 1 Hz; $Q_{Sc} = 340$ at 1 Hz, increasing as $f^{0.85}$). Assuming random velocity fluctuations with an exponential ACF, results from Sato (1984) can be used to estimate that RMS velocity variations of 5% at 5.5 km scale length are consistent with the observed Q_{Sc} below the Warramunga array. Korn (1990) extended the EFM to accommodate a scattering layer over a homogeneous half-space (a modeling approach similar to that used by Langston, 1989) and applied the method to the short-period Warramunga array data of Korn (1988) for deep earthquakes. With the new model, he found an average scattering Q of 640 at 1 Hz for the lithosphere below the array and higher values of intrinsic Q, implying that diffusion rather than anelasticity is the dominant factor controlling teleseismic coda decay rates. Korn (1993) further applied this approach to teleseismic *P* coda observations from nine stations around the Pacific. He found significant differences in scattering Q among the stations ($Q_{Sc} = 100$–500). The observed frequency dependence of Q_{Sc} is in approximate agreement with single-scattering theory for random heterogeneities and favors von Karman type ACFs over Gaussian or self-similar models.

Bannister et al. (1990) analyzed teleseismic P coda recorded at the NORES array using both array and three-component methods. They resolved both near-source and near-receiver scattering contributions to coda, with the bulk of receiver-side scattering resulting from P-to-*Rg* conversions from two nearby areas (10 and 30 km away) with significant topography. Gupta et al. (1990) performed frequency–wave number analysis on high-frequency NORES data and identified both near-receiver P-to-*Rg* scattering and near-source *Rg*-to-P scattering. Dainty and Toksöz (1990) examined scattering in regional seismograms recorded by the NORES, FINES, and ARCES arrays. P coda energy was concentrated in the on-azimuth direction but appeared at different phase velocities, suggesting different contribution mechanisms.

Wagner and Langston (1992b) applied frequency–wave number analysis to P′P′ (PKPPKP) waves recorded by the NORES arrays for deep earthquakes. Most of the coda was vertically propagating, but an arrival about 15 s after the direct wave can be identified as body-to-Rayleigh-wave scattering from a point 30 km west-southwest of the array (this scattering location was previously identified in P-wave coda by Bannister et al. (1990) and Gupta et al. (1990). Revenaugh (1995, 1999, 2000) applied a Kirchhoff migration approach to back-project P coda recorded in southern California to image lateral variations in scattering intensity within the crust and identified correlations between scattering strength and the locations of faults and other tectonic features. Frederiksen and Revenaugh (2004) applied Born scattering theory to teleseismic P coda to invert for variations in scattering strength near faults in southern California.

Neele and Snieder (1991) used the NARS and GRF arrays in Europe to study long-period teleseismic P coda and found it to be coherent with energy arriving from the source azimuth. They concluded that long-period P coda does not contain a significant amount of scattered energy and can be explained with spherically symmetrical models and is particularly sensitive to structure in upper-mantle low-velocity zones. Ritter et al. (1997, 1998) studied the frequency dependence of teleseismic P coda recorded in the French Massif Central, which they modeled as a 70 km thick layer with velocity fluctuations of 3–7% and heterogeneity scale lengths of 1–16 km. Rothert and Ritter (2000) studied P coda in intermediate-depth Hindu Kush earthquakes recorded at the GRF array in Germany about 44° away. They applied a method based on the theory of Shapiro and Kneig (1993) and Shapiro et al. (1996) and found that the observed wavefield fluctuations are consistent with random crustal heterogeneities of 3–7% and isotropic correlation lengths of 0.6–4.8 km. Ritter and Rothert (2000) used a similar approach on teleseismic P coda to infer differences in scattering strength beneath two local networks in Europe. Hock et al. (2000, 2004) used teleseismic P coda to characterize random lithospheric heterogeneities across Europe using the EFM. They obtained a range of different scale lengths and RMS velocity fluctuations on the order to 3–8%. Nishimura et al. (2002) analyzed transverse components in teleseismic P coda for stations in the western Pacific and noted stronger scattering for stations close to plate boundaries compared to those on stable continents.

In some cases, analysis of P coda can reveal individual scatterers and/or discontinuities at midmantle depths below subduction zone earthquakes (Castle and Creager, 1999; Kaneshima, 2003, 2009; Kaneshima and Helffrich, 1998, 1999, 2003, 2009, 2010; Krüger et al., 2001; Niu and Kawakatsu, 1994, 1997). Other individual scatterers (or regions of strong scattering) have been observed near the CMB from PcP precursors (Brana and Helffrich, 2004; Scherbaum et al., 1997; Weber and Davis, 1990; Weber and Kornig, 1990) and PKP precursors (Thomas et al., 1999; Vidale and Hedlin, 1998).

Shearer and Earle (2004) attempted to systematically characterize and model globally averaged short-period teleseismic P coda from both shallow and deep earthquakes. This was the first attempt to fit a global data set of P-wave amplitudes and coda energy levels with a comprehensive energy-preserving model that specified scattering and intrinsic attenuation throughout the Earth. Examining global seismic network (GSN) data between 1990 and 1999 at source–receiver distances between 10° and 100°, they identified high signal-to-noise records and stacked over 7500 traces from shallow

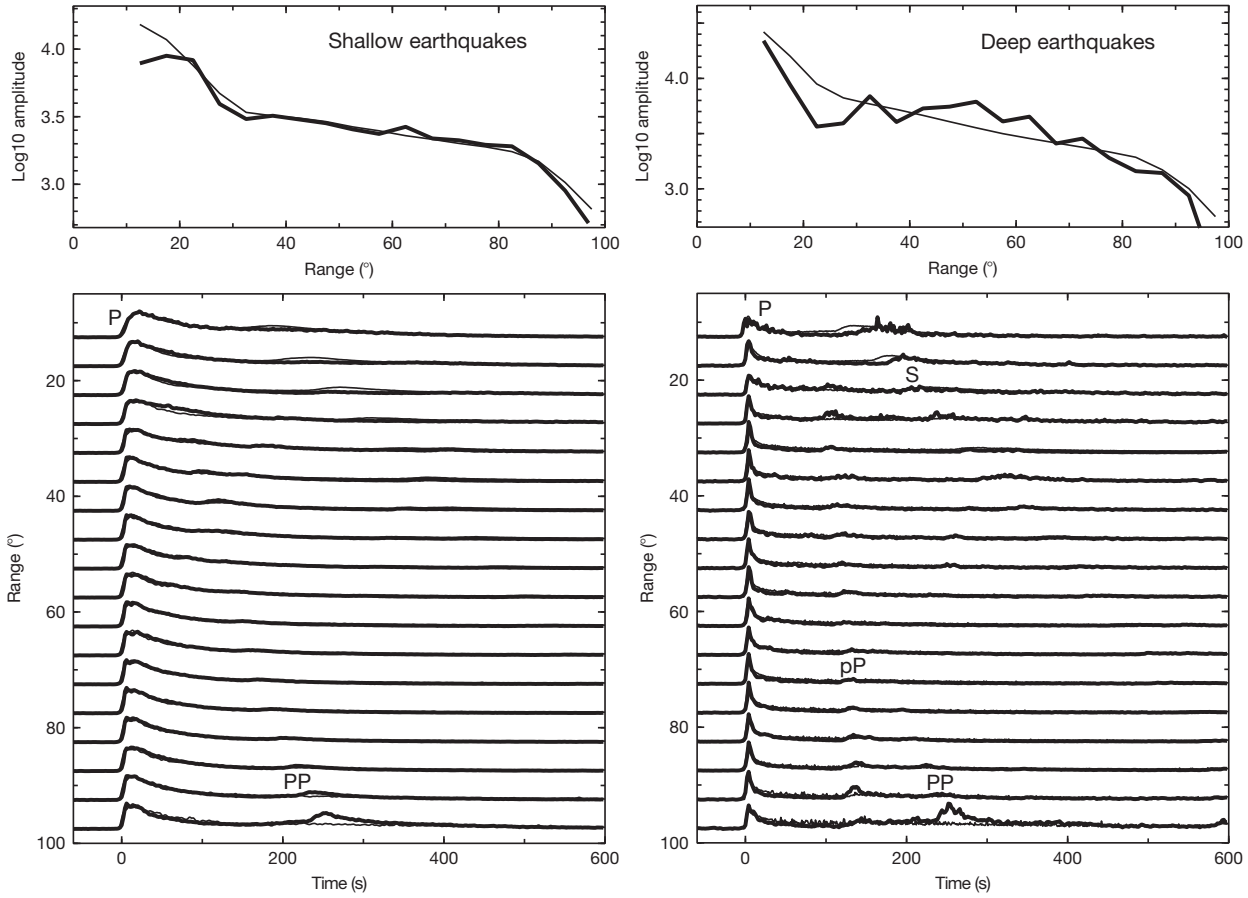

Figure 6 Comparisons between envelope function stacks of teleseismic P-wave arrivals (solid lines) with predictions of a Monte Carlo simulation for a whole-Earth scattering model (thin lines) as obtained by Shearer and Earle (2004). The left panels show results for shallow earthquakes ($\leq$50 km); the right panels are for deep earthquakes ($\geq$400 km). The top panels show peak P-wave amplitude versus epicentral distance. The bottom panels show coda envelopes in 5° distance bins plotted as a function of time from the direct P arrivals, with amplitudes normalized to the same energy in the first 30 s.

events (depth $\leq$ 50 km) and over 650 traces from deep events (depth $\geq$400 km). The stacking method involved summing envelope functions from 0.5 to 2.5 Hz band-pass-filtered traces, normalized to the maximum P amplitude. Peak P amplitudes were separately processed so that absolute P amplitude versus source–receiver distance information was preserved. The coda shape was markedly different between the shallow and deep-event stacks (see **Figure 6**). The shallow earthquake coda was much more energetic and long-lasting than the deep-event coda, indicating that the bulk of the teleseismic P coda from shallow events is caused by near-source scattering above 600 km depth.

Shearer and Earle modeled these observations using a Monte Carlo, particle-based approach (see above) in which millions of seismic phonons are randomly sprayed from the source and tracked through the Earth. They found that most scattering occurs in the lithosphere and upper mantle, as previous results had indicated, but that some lower-mantle scattering was also required to achieve the best fits to the data. Their preferred exponential autocorrelation random heterogeneity model contained 4% RMS velocity heterogeneity at 4 km scale length from the surface to 200 km depth, 3% heterogeneity at 4 km scale between 200 and 600 km, and 0.5% heterogeneity at 8 km scale length between 600 km and the CMB. They assumed equal and correlated P and S fractional velocity perturbations and a density/velocity scaling ratio of 0.8. Intrinsic attenuation was ${}^{\alpha}Q_I = 450$ above 200 km and ${}^{\alpha}Q_I = 2500$ below 200 km, with ${}^{\beta}Q_I = (4/9)\ {}^{\alpha}Q_I$ (an approximation that assumes all the attenuation is in shear). This model produced a reasonable overall fit, for both the shallow and deep-event observations, of the amplitude decay with epicentral distance of the peak P amplitude and the P coda amplitude and duration (see **Figure 6**). These numbers imply that for both P and S waves, the seismic albedo, B_0, is about 75–90% in the upper mantle above 600 km and about 25–35% in the lower mantle, consistent with the total attenuation being dominated by scattering in the upper mantle and by intrinsic energy loss in the lower mantle.

The 4% velocity perturbations for the uppermost layer in the Shearer and Earle (2004) model are in rough agreement with previous P coda analyses by Frankel and Clayton (1986), Flatté and Wu (1988), and Korn (1988); and the S-wave mean

free path of 50 km for the upper 200 km is within the range of mean free paths estimated from regional measurements of lithospheric scattering. However, limitations of the Shearer and Earle (2004) study include the restriction to single-station, vertical-component data (i.e., wave polarization, slowness, and azimuth constraints from three-component and/or array analyses are not used) and a single frequency band near 1 Hz. In addition, the ray theoretical approach cannot properly account for body-to-surface-wave-converted energy, which some array studies suggest are an important component of P coda. In addition, the Shearer and Earle (2004) models are for globally averaged P coda stacks. Later, Shearer and Earle (2008) showed that separating P coda stacks by source and receiver locations reveals significant variations, indicating lateral variations in scattering strength.

Resolving possible lower-mantle scattering using P coda is difficult because of the much stronger scattering from shallow structure. However, Shearer and Earle (2004) found that ~0.5% RMS velocity heterogeneity in the lower mantle was required to achieve the best fit to P coda amplitudes at epicentral distances beyond 50°. This value is substantially more than the estimates for lower-mantle velocity perturbations derived from PKP precursors of 0.1–0.2% from Margerin and Nolet (2003b) and 0.1% from Mancinelli and Shearer (2013).

1.24.3.3 P_n Coda

A prominent feature of long-range records of nuclear explosions across Eurasia is P_n and its coda, which can be observed to distances of more than 3000 km (e.g., Morozov et al., 1998; Ryberg et al., 1995, 2000). As discussed by Nielsen and Thybo (2003), there are two main models for upper-mantle structure that have been proposed to explain these observations: (1) Ryberg et al. (1995, 2000) and Tittgemeyer et al. (1996) proposed random velocity fluctuations between the Moho and about 140 km depth in which the vertical correlation length (0.5 km) is much smaller than the horizontal correlation length (20 km). These fluctuations cause multiple scattering that form a waveguide that can propagate high-frequency P_n to long distances. (2) Morozov et al. (1998), Morozov and Smithson (2000), Nielsen et al. (2003b), and Nielsen and Thybo (2006) favored a model in which P_n is a whispering gallery phase traveling as multiple underside reflections off the Moho, with the coda generated by crustal scattering. Nielsen and Thybo's (2003) preferred model has random crustal velocity perturbations between 15 and 40 km depth with a vertical correlation length of 0.6 km and a horizontal correlation length of 2.4 km. However, Nielsen et al. (2003a) found that the scattered arrivals seen at 800–1400 km distance for profile 'Kraton' required scattering within a layer between about 100 and 185 km depth and could be modeled with 2D finite-difference synthetics assuming 2% RMS velocity variations.

An important aspect of all these models is that their random velocity perturbations are horizontally elongated (i.e., anisotropic). At least for the lower crust, there is also some evidence for this from reflection seismic profiles (e.g., Holliger and Levander, 1992; Wenzel et al., 1987). This contrasts with most modeling of S and P coda, which typically assumes isotropic random heterogeneity.

1.24.3.4 P_{diff} Coda

Another phase particularly sensitive to deep-Earth scattering is P_{diff} and its coda. P_{diff} contains P energy diffracted around the CMB and is observed at distances >98°. The direct phase is seen most clearly at long periods, but high-frequency (~1 Hz) P_{diff} and its coda can be detected to beyond 130° (e.g., Earle and Shearer, 2001). P_{diff} coda is a typically emergent wave train that decays slowly enough that it can commonly be observed for several minutes until it is obscured by the PP and PKP arrivals. Husebye and Madariaga (1970) concluded that P_{diff} coda (which they termed P(diff) tail) could not be explained as simple P diffraction at the CMB or by reflections from the core and suggested that it originated from reflections or multiple paths in the upper mantle (similar to the proposed explanation for PP precursors given by Bolt et al., 1968). However, later work has shown this to be unlikely, given the large differences seen between observations of deep-turning direct P coda and P_{diff} coda. Bataille et al. (1990) reviewed previous studies of P_{diff} coda and suggested that it is caused by multiple scattering near the CMB, with propagation to long distances possibly enhanced by the presence of a low-velocity layer within D″.

Tono and Yomogida (1996) examined P_{diff} coda in 15 short-period records from deep earthquakes at distances of 103°–120° and found considerable variation in the appearance and duration of P_{diff} coda. Comparisons between P_{diff} and direct P waves at shorter distances, as well as particle motion analysis of P_{diff} coda, indicated that the coda was caused by deep-Earth scattering. Tono and Yomogida computed synthetics using the boundary integral method of Benites et al. (1992), applied to a simplified model of an incident wave grazing an irregular CMB. They were able to fit a subset of their observations in which the P_{diff} coda duration was relatively short (<50 s), with bumps on the CMB with minimum heights of 5–40 km. Such large CMB topography is unrealistic given PcP studies, which have indicated a relatively flat and smooth CMB (e.g., Kampfmann and Muüller, 1989; Vidale and Benz, 1992), and PKKP precursor observations that limit CMB RMS topography to <315 m at 10 km wavelength (Earle and Shearer, 1997, see in the succeeding text), but it is likely that volumetric heterogeneity within *D″* could produce similar scattering. Although the Tono and Yomogida (1996) model included multiple scattering, they could not fit the long tail (>50 s) of some of their P_{diff} observations, and they suggested that for such cases, a low-velocity zone just above the CMB is channeling the scattered energy. Strong heterogeneity and low-velocity zones of varying thicknesses have been observed above the CMB (e.g., see review by Garnero, 2000, and Lay, this volume), but it is not yet clear if these models can explain P_{diff} observations.

Bataille and Lund (1996) argued for a deep origin for P_{diff} coda by comparing coda shapes for P near 90° range and P_{diff} at 102°–105°. The P_{diff} coda is more emergent and lasts much longer than the direct P coda. This argues against a shallow source for the coda because this would produce roughly the same effect on both P and P_{diff}. Baitaille and Lund found that their observed coda decay rate for a single P_{diff} observation at 116° could be fitted with a model of multiple scattering within a 2D shell at the CMB. Tono and Yomogida (1997) examined P_{diff} in records of the 1994 Bolivian deep earthquake at

epicentral distances of 100°–122°. They analyzed both global broadband stations and short-period network stations from New Zealand. They found that short-period energy continued to arrive for over 100 s after P_{diff} itself, more than twice as long as the estimated source duration of the mainshock. Comparisons between the coda decay rate of P_{diff} with other phases, as well as polarization analysis, indicated a deep origin for P_{diff} coda.

Earle and Shearer (2001) stacked 924 high-quality, short-period seismograms from shallow events at source–receiver distances between 92.5° and 132.5° to obtain average P and P_{diff} coda shapes. The results confirm the Bataille and Lund (1996) observation that P coda changes in character near 100°. In particular, P_{diff} becomes increasingly extended and emergent at longer distances. Its peak amplitude also diminishes with increasing distance, but P_{diff} can still be observed in the stacks at 130°. Earle and Shearer also performed a polarization stack (Earle, 1999), which showed that the polarization of P_{diff} coda is similar to P_{diff} (see **Figure 7**). To model these results, Earle and Shearer (2001) applied single-scattering theory for

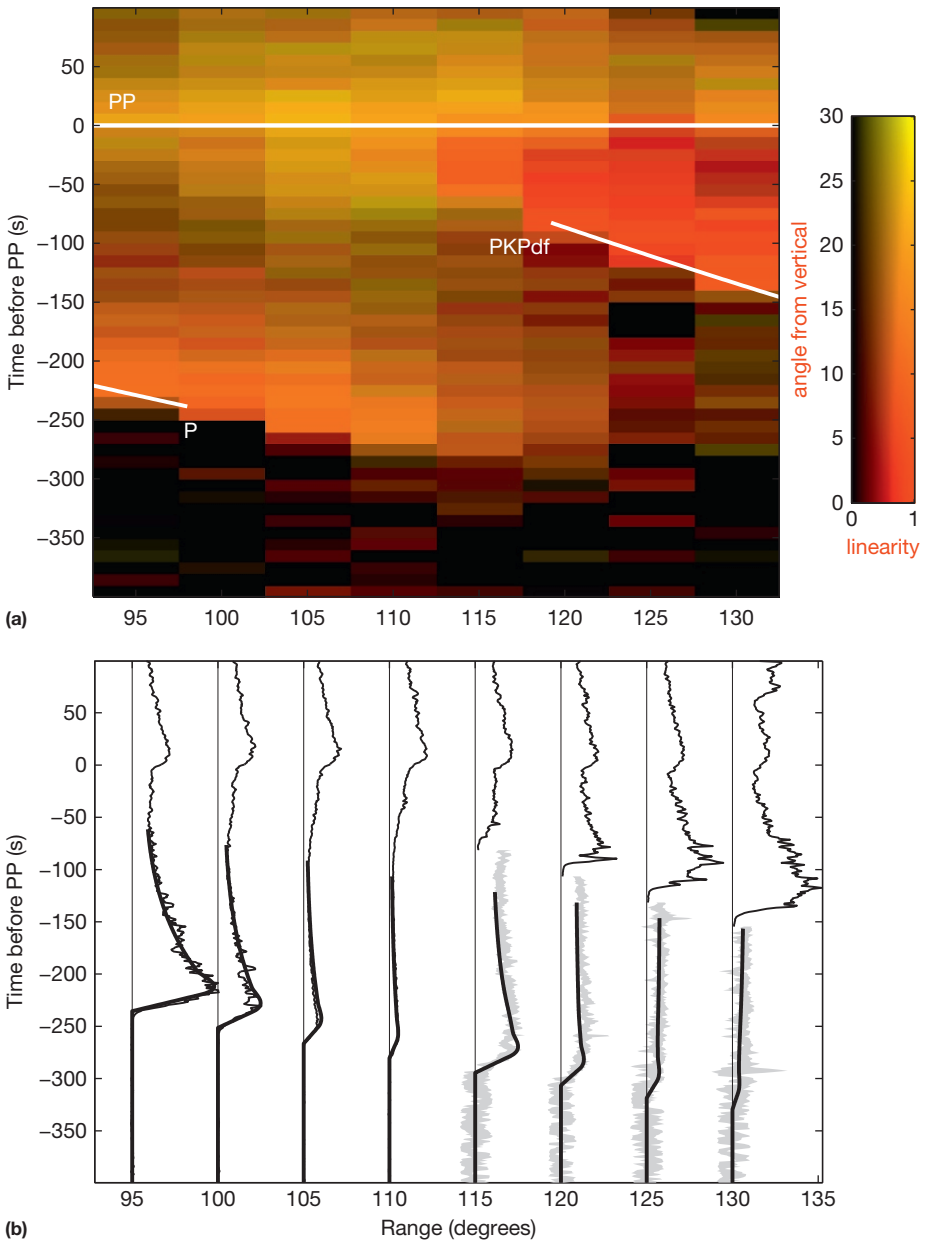

Figure 7 Global seismogram stacks and scattering model predictions for high-frequency P_{diff} from Earle and Shearer (2001). (a) A stacked image of P_{diff} polarization and linearity. Times are relative to the theoretical PP arrival times, and direct P and PKP(DF) are also shown. (b) An amplitude stack of P_{diff} envelopes (wiggly lines) compared to model predictions (smooth lines) for a uniform mantle scattering model. Amplitudes are normalized to the maximum PP amplitude. To better show the small-amplitude P_{diff} arrivals, the traces are magnified by 10 for times 20 s before PKP at distances $>112.5°$. The width of the magnified data traces is equal to the two-sigma error in the data stack, estimated using a bootstrap method.

evenly distributed scatterers throughout the mantle. The resulting synthetics included P-to-P, P_{diff}-to-P, and P-to-P_{diff} scattering paths. They applied a hybrid scheme that used reflectivity to compute deep-turning P and P_{diff} amplitudes and ray theory for the shallower turning rays. Scattering was computed assuming a random medium model with an exponential ACF. Synthetics generated for a scale length of 2 km and 1% RMS velocity variations achieved a good fit to the amplitude and shape of P and P_{diff} coda and a reasonable fit to the polarization angles. Thus, a fairly modest level of whole-mantle scattering appears sufficient to explain the main features in P_{diff} observations, although Earle and Shearer could not exclude the possibility that multiple-scattering models could achieve similar fits. More recently, Rost et al. (2006) stacked short-period seismograms from the GSNs and noticed that almost no short-period P_{diff} is detectable at distances larger than 108°. They suggested that this abrupt disappearance of high-frequency P_{diff} is caused by strong heterogeneity and scattering at the CMB.

1.24.3.5 PP and P′P′ Precursors

The decay in short-period coda amplitude with time following direct P and P_{diff} stops and amplitudes begin to increase some time before the surface-reflected PP phase at distances less than about 110° (at longer distances PKP intercedes). This energy is typically incoherent but sometimes forms distinct arrivals; both are termed PP precursors. Early explanations for PP precursor observations involved topside and bottomside reflections off discontinuities in the upper mantle (Bolt, 1970; Bolt et al., 1968; Gutowski and Kanasewich, 1974; Husebye and Madariaga, 1970; Nguyen-Hai, 1963). It is now recognized that such arrivals do exist and form globally coherent seismic phases that can readily be observed at long periods (e.g., Shearer, 1990, 1991). In particular, the 410 and 660 km discontinuities create discrete topside reflections that follow direct P by about 1.5–2.5 min and underside reflections that proceed PP by similar time offsets. However, the high-frequency PP precursor wavefield is much more continuous, and it is difficult to identify discrete arrivals from upper-mantle discontinuities, although Wajeman (1988) was able to identify underside P reflections from discontinuities at 300 and 670 km depth by stacking broadband data from the NARS array in Europe. Wright and Muirhead (1969) and Wright (1972) used array studies to show that PP precursors often have slownesses that are significantly less than or greater than that expected for underside reflections beneath the PP bouncepoint, which is consistent with asymmetrical reflections at distances near 20° from either the source or the receiver. However, this explanation does not explain the generally continuous nature of the PP precursor wavefield. The currently accepted explanation for the bulk of the PP precursor energy involves scattering from the near-surface and was first proposed by Cleary et al. (1975) and King et al. (1975). Cleary et al. (1975) proposed that PP precursors result from scattering by heterogeneities within and near the crust, as evidenced by travel-time and slowness observations of two Novaya Zemlya explosions recorded by the Warramunga array in Australia. King et al. (1975) modeled PP precursor observations from the Warramunga array and NORSAR using Born single-scattering theory. They assumed 1% RMS variations in elastic properties and a Gaussian autocorrelation model with a 12 km scale length within the uppermost 100 km of the crust and upper mantle. This model successfully predicted the onset times, duration, and slowness of the observed PP precursors but underpredicted the precursor amplitudes, suggesting that stronger scattering, perhaps too large for single-scattering theory, would be required to fully explain the observations. King et al. noted that the focusing of energy at 20° distance by the mantle transition zone could explain the high and low slowness observations of their study and of Wright (1972).

More recently, Rost et al. (2008) studied PP precursors recorded by the Yellowknife array in Canada and used both slowness, back azimuth, and travel-time information to locate mantle scatterers between the surface and about 1000 km depth. Scattering locations below Tonga and the Marianas are consistent with the positions of subducted slabs and the presence of small-scale velocity contrasts from the chemically distinct old oceanic crust penetrating well below 660 km depth.

A related discussion has concerned precursors to PKPPKP (or P′P′), for which the main phase also has an underside reflection near the midpoint between source and receiver. In this case, however, short-period reflections from the 410 and 660 km discontinuities are much easier to observe, and this has become one of the best constraints on the sharpness of these features (e.g., Benz and Vidale, 1993; Davis et al., 1989; Engdahl and Flinn, 1969; Richards, 1972; Xu et al., 2003). However, these reflections arrive 90–150 s before P′P′ and cannot explain the later parts of the precursor wave train. Whitcomb (1973) suggested they were asymmetrical reflections at sloping interfaces, a mechanism similar to that proposed by Wright and Muirhead (1969) and Wright (1972) for PP precursors. King and Cleary (1974) proposed that near-surface scattering near the P′P′ bouncepoint could explain the extended duration and emergent nature of P′P′ precursors. Vinnik (1981) used single-scattering theory to model globally averaged P′P′ precursor amplitudes at three different time intervals and obtained a good fit with a Gaussian ACF of 13 km scale length with RMS velocity perturbations in the lithosphere of about 1.6%.

More recently, Tkalčić et al. (2006) observed P′P′ precursors at epicentral distances $< 10°$, which they interpret as backscattering from small-scale heterogeneities at 150–220 km depth beneath the P′P′ bouncepoints because array studies show that the precursors have the same slowness as the direct phase. Earle et al. (2011) reported and studied P′P′ precursors at 1 Hz between 30° and 50° epicentral distance. Beamforming of data from the LASA array in Montana showed that the arrivals likely result from off-azimuth scattering of PKPbc to PKPbc in the crust and upper mantle. The Earle et al. LASA observations can be approximately fitted with scattering confined to the uppermost 200 km of the crust and mantle, but the scattering geometry should in principle be able to place bounds on scattering strength throughout the entire depth range of the mantle and thus provide a useful complement to PKP precursor studies, which are sensitive only to the lowermost mantle. Wu et al. (2012) also studied high-frequency P′P′ precursors, both using global seismic stations and the Yellowknife and Warramunga arrays, obtaining results that supported the Earle et al. (2011) model of asymmetrical scattering as being the main cause of the precursor energy.

1.24.3.6 PKP Precursors

Perhaps the most direct evidence for deep-Earth scattering comes from observations of precursors to the core phase PKP. They were first noted by Gutenberg and Richter (1934). The precursors are seen at source–receiver distances between about 120° and 145° and precede PKP by up to ~20 s. They are observed most readily at high frequencies and are usually emergent in character and stronger at longer distances. Older, and now discredited, hypotheses for their origin include refraction in the inner core (Gutenberg, 1957), diffraction of PKP from the CMB (Bullen and Burke-Gaffney, 1958; Doornbos and Husebye, 1972), and refraction or reflection of PKP at transition layers between the inner and outer cores (Bolt, 1962; Sacks and Saa, 1969). However, it is now understood that PKP precursors are not caused by radially symmetrical structures but result from scattering from small-scale heterogeneity at the CMB or within the lowermost mantle (Cleary and Haddon, 1972; Haddon, 1972). This scattering diverts energy from the primary PKP ray paths, permitting waves from the AB and BC branches to arrive at shorter source–receiver distances than the B caustic near 145° and earlier than the direct PKP(DF) phase. It should be noted that although the PKP precursors arrive in front of PKP(DF), they result from scattering from different PKP branches. Scattered energy from PKP(DF) itself contributes only to the coda following PKP(DF), not to the precursor wavefield. In addition, the scattering region must be deep to create the precursors. Scattering of PKP(BC) from the shallow mantle will not produce precursors at the observed times and distances. Thus, deep-Earth scattering can be observed uncontaminated by the stronger scattering that occurs in the crust and upper mantle. This unique ray geometry, which results from the velocity drop between the mantle and the outer core, makes PKP precursors invaluable for characterizing small-scale heterogeneity near the CMB.

The interpretation of PKP precursors in terms of scattering was first detailed by Haddon (1972) and Cleary and Haddon (1972). The primary evidence in favor of this model is the good agreement between the observed and theoretical onset times of the precursor wave train for scattering at the CMB. However, analyses from seismic arrays (e.g., Davies and Husebye, 1972; Doornbos, 1976; Doornbos and Husebye, 1972; Doornbos and Vlaar, 1973; Husebye et al., 1976; King et al., 1973, 1974) also showed that the travel times and incidence angles of the precursors were consistent with the scattering theory. Haddon and Cleary (1974) used Chernov scattering theory to show that the precursor amplitudes could be explained with 1% random velocity heterogeneity with a correlation length of 30 km in a 200 km thick layer in the lowermost mantle just above the CMB. In contrast, Doornbos and Vlaar (1973) and Doornbos (1976) argued that the scattering region extends to 600–900 km above the CMB and calculated (using the Knopoff and Hudson, 1964, single-scattering theory) that much larger velocity anomalies must be present. Later, however, Doornbos (1978) used perturbation theory to show that short-wavelength CMB topography could also explain the observations (see also Haddon, 1982), as had previously been suggested by Haddon and Cleary (1974). Bataille and Flatté (1988) concluded that their observations of 130 PKP precursor records could be explained equally well by 0.5–1% RMS velocity perturbations in a 200 km thick layer at the base of the mantle or by CMB topography with RMS height of ~300 m (see also Bataille et al., 1990).

One difficulty in comparing results among these older PKP precursor studies is that it is not clear how many of their differences are due to differences in observations (i.e., the selection of precursor waveforms they examine) compared to differences in theory or modeling assumptions. PKP precursor amplitudes are quite variable, and it is likely that studies that focus on the clearest observations will be biased (at least in terms of determining globally averaged Earth properties) by using many records with anomalously large amplitudes. To obtain a clearer global picture of average PKP precursor behavior, Hedlin et al. (1997) stacked envelope functions from 1600 high signal-to-noise PKP waveforms at distances between 118° and 145° (see **Figure 8**). They included all records, regardless of whether precursors could be observed, to avoid biasing their estimates of average precursor amplitudes. In this way, they obtained the first comprehensive image of the precursor wavefield and found that precursor amplitude grows with both distance and time. The growth in average precursor amplitude with time continues steadily until the direct PKP(DF) arrival; no maximum amplitude peak is seen prior to PKP(DF) as had been suggested by Doornbos and Husebye (1972). This is the fundamental observation that led Hedlin et al. (1997) to conclude that scattering is not confined to the immediate vicinity of the CMB but must extend for some distance into the mantle.

Hedlin et al. (1997) and Shearer et al. (1998) modeled these observations using single-scattering theory for a random medium characterized with an exponential ACF. They found that the best overall fit to the observations was provided with ~1% RMS velocity heterogeneity (this value was later found to be erroneously large owing to a programming bug, see below) at 8 km scale length extending throughout the lower mantle, although fits almost as good could be obtained for 4 and 12 km scale lengths. Similar fits could also be achieved with a Gaussian ACF using a slightly lower RMS velocity heterogeneity. To explain the steady increase in precursor amplitude with time, these models contained uniform heterogeneity throughout the lower mantle, and Hedlin et al. (1997) argued that the data require the scattering to extend at least 1000 km above the CMB and that there is no indication for a significant concentration of the scattering near the CMB. This conclusion was supported by Cormier (1999), who tested both isotropic and anisotropic distributions of scale lengths and found that the PKP precursor envelope shapes are consistent with dominantly isotropic 1% fluctuations in P velocity in the 0.05–0.5 km^{-1} wave number band (i.e., 12–120 km wavelengths).

Most modeling of PKP precursors has used single-scattering theory and the Born approximation. The validity of this approximation for mantle scattering was questioned by Hudson and Heritage (1981). However, Doornbos (1988) found similar results from single- versus multiple-scattering theory for CMB topography of several hundred meters (i.e., the amount proposed by Doornbos, 1978, to explain PKP precursor observations), and Cormier (1995) found the Born approximation to be valid for modeling distributed heterogeneity in the D'' region when compared to results from the higher-order theory of Korneev and Johnson (1993a,b). More recently,

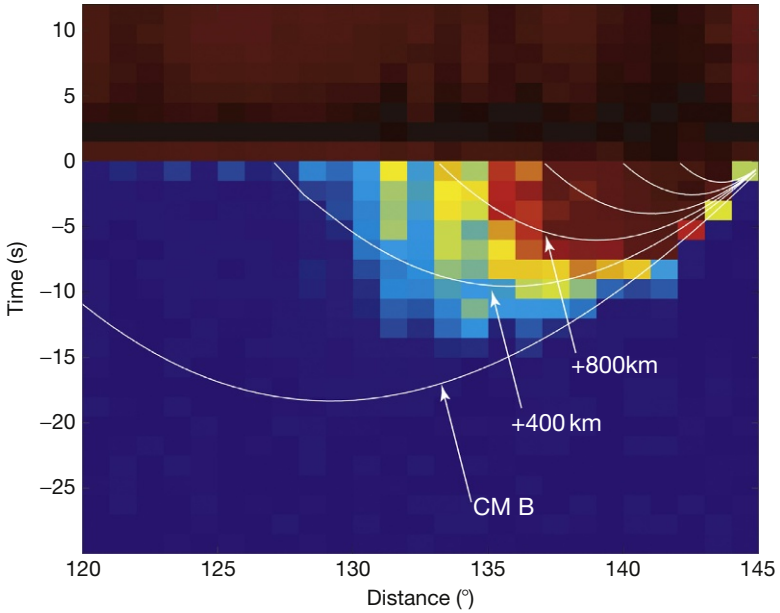

Figure 8 PKP precursors as imaged by stacking 1600 short-period seismograms by Hedlin et al. (1997). The colors indicate the strength of the precursors, ranging from dark blue (zero amplitude) to green, yellow, red, and brown (highest amplitudes). The onset of PKP(DF) is shown by the edge of the brown region at zero time. The precursors exhibit increasing amplitude with both distance and time. The white curves show the theoretical precursor onset times for scattering at 400 km depth intervals above the core–mantle boundary (CMB).

Margerin and Nolet (2003a,b) modeled PKP precursors using radiative transfer theory and a Monte Carlo method (see the preceding text). Their results supported Hedlin et al. (1997) and Shearer et al. (1998) in finding that whole-mantle scattering fit the data better than scattering restricted to near the CMB, but they obtained much smaller P-velocity perturbations of 0.1–0.2% versus the 1% originally proposed by Hedlin et al. The accuracy of the Margerin and Nolet result for the velocity perturbations was recently confirmed by Mancinelli and Shearer (2013), who used a multiple-scattering Monte Carlo method to show that updated PKP precursor stacks could be fit with 0.1% RMS velocity perturbations. They found that similar results could be obtained using Born theory and that the 1% value in the older Hedlin et al. work was due to a programming mistake. Margerin and Nolet showed that the Born approximation is accurate for whole-mantle scattering models only when the velocity heterogeneity is $< 0.5\%$. Finally, they concluded that exponential correlation length models do not fit the distance dependence in PKP precursor amplitudes as well as models containing more small-scale structure.

The steady increase in amplitude with time in PKP precursor stacks requires that globally averaged small-scale mantle heterogeneity extends above the lowermost few hundred kilometers of the mantle. However, determining exactly how far the scattering must extend above the CMB is a challenging problem because only a small fraction of the precursor wavefield is sensitive to scattering above 600 km from the CMB, and this fraction continues to shrink for shallower scattering depths. For example, at 1200 km above the CMB, precursors are produced only between 138° and 145° and arrive at most 3 s before PKP(DF) (see **Figure 8**). Separating the amplitude contribution from these arrivals from that produced by scattering at deeper depths in the mantle is very difficult, particularly when the pulse broadening caused by realistic source-time functions and shallow scattering and reverberations are taken into account. An alternative approach to constraining the strength of midmantle scattering is to examine the scattered PKP wavefield after the direct PKP(DF) arrival (Hedlin and Shearer, 2002). This is comprised of a sum of PKP(DF) coda and scattered PKP(AB) and PKP(BC) energy. In principle, if the contribution from the PKP(DF) coda could be removed, the remaining scattered wavefield would provide improved constraints on the strength of midmantle scattering. However, Hedlin and Shearer (2002) found that this approach did not provide improved depth resolution of mantle scattering compared to previous analyses of PKP precursors, owing at least in part to relatively large scatter in coda amplitudes as constrained by a data resampling analysis. Their results were, however, consistent with uniform mantle scattering with 1% RMS random velocity perturbations at 8 km scale length.

The preceding discussion considered only average PKP precursor properties and models with radial variations in scattering. However, PKP precursor amplitudes are quite variable, as noted by Bataille and Flatté (1988) and Bataille et al. (1990), suggesting lateral variations in scattering strength. Vidale and Hedlin (1998) identified anomalously strong PKP precursors for ray paths that indicated intense scattering at the CMB beneath Tonga. Wen and Helmberger (1998) observed broadband PKP precursors from near the same region, which they modeled as Gaussian-shaped ultra-low-velocity zones of 60–80 km height with P-velocity drops of 7% or more over 100–300 km (to account for the long-period part of the precursors), superimposed on smaller-scale anomalies to explain the high-frequency part of the precursors.

Array analyses can resolve the source–receiver ambiguity of PKP scattering and often permit location of individual

scatterers or regions of strong scattering in the lower mantle. Thomas et al. (1999) used German network and array records of PKP precursors to identify isolated scatterers in the lower mantle. Niu and Wen (2001) identified strong PKP precursors for South American earthquakes recorded by the Jarray in Japan, which they modeled with 6% velocity perturbations within a 100 km thick layer just above the CMB in a 200 km by 300 km area west of Mexico. Cao and Romanowicz (2007) used Canadian Yellowknife array records of an earthquake doublet to identify receiver-side scatterers at depths ranging from 0 to 600 km above the CMB and scattering angles between 16° and 46°. They found that the scatterer locations suggest they may be fragments of fossil slabs from ancient subduction under North America. Miller and Niu (2008) used data from Caribbean arrays to image strong scatterers near the CMB, which are surrounded by high-velocity anomalies associated with the Farallon slab, and suggested a segregation mechanism that could concentrate the scatterers into a localized region. Thomas et al. (2009) examined South Pacific earthquakes recorded by German and Ethiopian arrays and studied both PKP precursors (seen for both arrays) and the amplitude of diffractions from the PKP b caustic (anomalously large for the Ethiopian data). They found that low-velocity regions just above the CMB could act as waveguides to produce large PKP b-diffractions but that these low-velocity regions must also contain small-scale heterogeneities to explain the high-frequency scattering seen in the data. They proposed that melt inclusions could explain both the lower velocities seen at long wavelengths and produce the scattering observed at short wavelengths.

Hedlin and Shearer (2000) attempted to systematically map lateral variations in scattering strength using a global set of high-quality PKP precursor records. Their analysis was complicated by the limited volume sampled by each source–receiver pair, the ambiguity between source- and receiver-side scattering, and the sparse and uneven data coverage. However, they were able to identify some large-scale variations in scattering strength that were robust with respect to data resampling tests. These include stronger than average scattering beneath Central Africa, parts of North America, and just north of India and weaker than average scattering beneath South and Central America, eastern Europe, and Indonesia.

Finally, it should be noted that the earliest onset time of observed PKP precursors agrees closely with that predicted for scattering at the CMB (e.g., Cleary and Haddon, 1972; Shearer et al., 1998). If scattering existed in the outer core at significant depths below the CMB, this would cause arrivals at earlier times than are seen in the data. This suggests that no observable scattering originates from the outer core, although a quantitative upper limit on small-scale outer-core heterogeneity based on this constraint has not yet been established. Such a limit would be useful to test the recent hypothesis of Dai and Song (2008) that movement of outer-core heterogeneities could explain their observations of increased temporal variability in travel times for core seismic phases compared to mantle phases.

1.24.3.7 PKKP Precursors and $PKKP_X$

PKKP is another seismic core phase that provides information on deep-Earth scattering. Precursors to PKKP have been observed within two different distance intervals. PKKP(DF) precursors at source–receiver distances beyond the B caustic near 125° are analogous to the PKP precursors discussed in the previous section and result from scattering in the mantle. Doornbos (1974) detected these precursors in NORSAR (Norwegian Seismic Array) records of Solomon Islands earthquakes and showed that their observed slownesses were consistent with scattering from the deep mantle. At ranges $<125°$, PKKP(BC) precursors can result from scattering off short-wavelength CMB topography. Chang and Cleary (1978, 1981) observed these precursors from Novaya Zemlya explosions recorded by the LASA array in Montana at about 60° range. These observations were suggestive of CMB topography but had such large amplitudes that they were difficult to fit with realistic models. Doornbos (1980) obtained additional PKKP(BC) precursor observations from NORSAR records from a small number of events at source–receiver distances between 80° and 110°. He modeled these observations with CMB topography of 100–200 m at 10–20 km horizontal scale length. Motivated by PKKP precursor observations (see the succeeding text), Cleary (1981) suggested that some observations of P′P′ precursors (e.g., Adams, 1968; Haddon et al., 1977; Husebye et al., 1977; Whitcomb and Anderson, 1970) might be explained as CMB-scattered PKKKP precursors.

A comprehensive study of PKKP(BC) precursors was performed by Earle and Shearer (1997), who stacked 1856 high-quality PKKP seismograms, obtained from the GSN at distances between 80° and 120°. PKKP is most readily observed at high frequencies (to avoid interference from low-frequency S coda), so the records were band-pass-filtered to between 0.7 and 2.5 Hz. To avoid biasing the stacked amplitudes, no consideration was given to the visibility or lack of visibility of PKKP precursors on individual records. The resulting stacked image showed that energy arrives up to 60 s before direct PKKP(BC) and that average precursor amplitudes gradually increase with time. Earle and Shearer (1997) modeled these observations using Kirchhoff theory for small-scale CMB topography. Their best-fitting model had a horizontal scale length of 8 km and RMS amplitude of 300 m. However, they identified a systematic misfit between the observations and their synthetics in the dependence of precursor amplitude with source–receiver distance. In particular, the Kirchhoff synthetics predict that precursor amplitude should grow with range but this trend is not apparent in the data stack. Thus, the model underpredicts the precursor amplitudes at short ranges and overpredicts the amplitudes at long ranges. Earle and Shearer (1997) and Shearer et al. (1998) explored possible reasons for this discrepancy between PKKP(BC) precursor observations and predictions for CMB topography models. They were not able to identify a very satisfactory explanation but speculated that scattering from near the ICB might be involved because it could produce precursor onsets that agreed with the observations (see Figure 13 from Shearer et al., 1998). However, scattering angles of 90° or more are required and it is not clear, given the expected amplitude of the direct PKKP(DF) phase, that the scattered amplitudes would be large enough to explain the PKKP(BC) precursor observations. They concluded that strong inner-core scattering would be required, which could only be properly modeled with a multiple-scattering theory. Regardless of the possible presence of scattering from

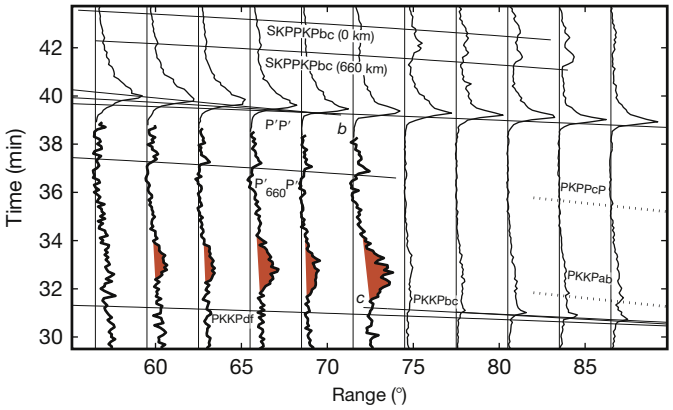

Figure 9 A stack of 994 seismograms from Earle and Shearer (1998), showing the $PKKP_X$ phase (red) in the high-frequency wavefield preceding P′P′. The stacked traces are normalized to the maximum P′P′ amplitude and are plotted with respect to the origin time of a zero depth earthquake. To better show the $PKKP_X$ arrival, amplitudes are magnified by eight for traces preceding P′P′ at epicentral distances $<73°$ (indicated by the heavy lines). Labels indicate observed phases and the position of the P′P′ b and PKKP c caustics.

sources outside the CMB, these PKKP(BC) precursor observations can place upper limits on the size of any CMB topography. Earle and Shearer (1997) concluded that the RMS topography could not exceed 315 m at 10 km wavelength.

Earle and Shearer (1998) stacked global seismograms using P′P′ as a reference phase and identified an emergent, long-duration, high-frequency wave train near PKKP (see **Figure 9**), which they named $PKKP_X$ because it lacked a clear explanation. $PKKP_X$ extends back from the PKKP(C) caustic at 72° to a distance of about 60°. Its 150 s long duration, apparent move-out, and proximity to PKKP suggest a deep scattering origin. However, Earle and Shearer were not able to match these observations with predictions of single-scattering theory for scattering in the lower mantle, CMB, or ICB. They speculated that some form of multiple-scattering model at the CMB might be able to explain the observations, perhaps involving a low-velocity zone just above the CMB to trap high-frequency energy, a model similar to that proposed to explain P_{diff} coda by Bataille et al. (1990), Tono and Yomogida (1996), and Bataille and Lund (1996). Earle (2002) further explored the origin of $PKKP_X$ and other scattered phases near PKKP by performing slant stacks on LASA data. His results suggested that, in addition to off-great-circle-path near-CMB scattering, near-surface P-to-PKP scattering is likely an important contributor to high-frequency energy around PKKP at distances between 50° and at least 116°. In particular, such scattering arrives at the same time as observations of PKKP precursors and $PKKP_X$, thus providing a possible explanation for why PKKP precursor amplitudes are hard to fit purely with CMB scattering models. However, quantitative modeling of P-to-PKP scattering has not yet been performed to test this hypothesis.

More recently, Rost and Earle (2010) examined PKKP precursors using small-aperture seismic arrays in Canada and India. Beamforming analysis showed regions of strong scattering near the CMB beneath the Caribbean, Patagonia, the Antarctic Peninsula, and southern Africa. The 1 Hz scattered energy suggests small-scale chemical heterogeneity, and Rost and Earle speculated that the scattering beneath Antarctica and the Americas is related to ancient subducted crust, whereas the southern Africa scattering may be related to partial melt associated with the edge of a large low shear velocity province just above the CMB in that region.

1.24.3.8 PKiKP and PKP Coda and Inner-Core Scattering

The ICB-reflected phase PKiKP is of relatively low amplitude and observations from single stations are fairly rare, particularly at source–receiver distances $<50°$. However, improved signal-to-noise ratio and more details can be obtained from analysis of short-period array data. Vidale and Earle (2000) examined 16 events at 58°–73° range recorded by the LASA in Montana between 1969 and 1975. As shown in **Figure 9**, a slowness versus time stack of the data (band-pass-filtered at 1 Hz) revealed a 200 s long wave train with an onset time and slowness in agreement with that predicted for PKiKP. They attributed this energy to scattering from the inner core because it arrived at a distinctly different slowness from late-arriving P coda and it was much more extended in time than LASA PcP records for the same events. The PKiKP wave train takes 50 s to reach its peak amplitude and averages only about 2% of the amplitude of PcP. Direct PKiKP is barely visible, with an amplitude close to its expected value, which is small because the ICB reflection coefficient has a node at distances near 72° (e.g., Shearer and Masters, 1990).

Vidale and Earle (2000) fitted their observations with synthetics computed using single-scattering theory applied to a model of random inner-core heterogeneity with 1.2% RMS variations in density and the Lamé parameters (λ and μ) and a correlation distance of 2 km, assuming an exponential autocorrelation model. They assumed ${}^{\alpha}Q_I = 360$ uniformly throughout the inner core, a value obtained from a study (Bhattacharyya et al., 1993) of pulse broadening of PKP(DF) compared to PKP(BC). They noted that without inner-core attenuation, the predicted scattered PKiKP wave train would take 100 s to attain its peak value and would last 350 s. The low value of ${}^{\alpha}Q_I$ resulted in only the shallow penetrating P waves retaining sufficient amplitude to be seen. Model-predicted scattering angles were near 90°, making the scattering most sensitive to variations in inner-core λ. Vidale and Earle (2000) found a trade-off between the various free parameters

in their model and picked their 2 km correlation length because it minimized the required RMS variation of 1.2% necessary to fit the observations. They computed a fractional energy loss of 10% from scattering in the top 300 km of the inner core, helping to justify the use of the Born single-scattering approximation. Vidale et al. (2000) examined LASA data for two nuclear explosions 3 years apart and separated by <1 km. They identified systematic time shifts in PKiKP coda, which they explained as resulting from differential inner-core rotation, as previously proposed by Song and Richards (1996). In contrast, much smaller time differences are observed in PKKP and PKPPKP arrivals, supporting the idea that the time dependence originates in the inner core. Vidale et al. (2000) estimated an inner-core rotation rate of 0.15° per year.

Cormier et al. (1998) measured pulse broadening in PKP(DF) waveforms and showed that they could be fitted either with intrinsic inner-core attenuation or with scattering caused by random layering (1D) with 8% P-velocity perturbations and 1.2 km scale length. Cormier and Li (2002) inverted 262 broadband PKP(DF) waveforms for a model of inner-core scattering attenuation based on the dynamic composite elastic medium theory of Kaelin and Johnson (1998) for a random distribution of spherical inclusions. They not only obtained a mean velocity perturbation of ~8% and a heterogeneity scale length of ~10 km but also observed path-dependent differences in these parameters, with both depth dependence and anisotropy in the size of the scattering attenuation. They suggested that scattering attenuation is the dominant mechanism of attenuation in the inner core in the 0.02–2 Hz frequency band. Cormier and Li (2002) argued that the large discrepancy in RMS velocity perturbation and scale length between their study (RMS = 8%, scale length = 10 km) and the model (RMS = 1.2%, scale length = 2 km) of Vidale and Earle (2002) may be due to the significant intrinsic attenuation assumed by Vidale and Earle and differences in depth sensitivity between the studies.

Poupinet and Kennett (2004) analyzed PKiKP recorded by Australian broadband stations and the Warramunga array for events at short distances ($<\sim45°$). They found that PKiKP could frequently be observed on single traces filtered at 1–5 Hz. In contrast to Vidale and Earle (2000), they found that PKiKP typically had an impulsive onset with a coda that decayed rapidly to a relatively small amplitude that persisted for more than 200 s. Although most of the Poupinet and Kennett results were for shorter source–receiver distances than the 58°–73° range of the Vidale and Earle study, they did analyze one event at 74° that exhibited similar behavior. Poupinet and Kennett suggested that the differences in the appearance of PKiKP coda between the studies may reflect different sampling latitudes at the ICB and different frequency filtering. They pointed to similarities in the appearance of PKiKP coda and P_{diff} coda (see the preceding text) and speculated that both result from their interaction with a major interface that may involve energy channeling to produce an extended wave train. Poupinet and Kennett (2004) argued that the high-frequency nature of PKiKP coda excludes an origin deep within the inner core where attenuation is high and suggested that multiple scattering near the ICB is a more likely mechanism.

Koper et al. (2004) analyzed PKiKP coda waves recorded by short-period seismic arrays of the International Monitoring System (IMS) at source–receiver distances ranging from 10° to 90°. Stacked beam envelopes for the 10°–50° data showed impulsive onsets for PcP, ScP, and PKiKP, but a markedly different coda for PKiKP, which maintained a nearly constant value that lasted for over 200 s. This is consistent with the Poupinet and Kennett (2004) results at similar distances and supports the idea that inner-core scattering is contributing to the PKiKP coda. At distances from 50° to 90°, Koper et al. (2004) found one event at 56° with a PKiKP coda that increased in amplitude with time, peaking nearly 50 s after the arrival of direct PKiKP, behavior very similar to the LASA observations of Vidale and Earle (2000). At 4 Hz, 13 out of 36 PKiKP observations had emergent codas that peaked at least 10 s into the wave train. However, more commonly, the peak coda amplitude occurred at the onset of PKiKP. Koper et al. (2004) found that the average PKiKP coda decay rate was roughly constant between stacks at short- and long-distance intervals, supporting the hypothesis of inner-core scattering. They argued that the best distance range to study inner-core scattering is 50°–75°, where the direct PKiKP amplitude is weak (because of a very small ICB reflection coefficient) so that scattering from the crust and mantle is unlikely to contribute as much to the observed coda as scattering from the inner core. However, they also discussed the possibility that CMB scattering could deflect a P wave into a PKiKP wave that could reflect from the ICB at an angle with a much higher reflection coefficient and contribute to the observed coda.

Leyton and Koper (2007a,b) applied single-scattering theory to model PKiKP coda observations and found that the emergent coda seen in previous observations (e.g., **Figure 10**) can only be produced by scattering in the uppermost 350 km of the inner core. They obtained an average Q_C of 500 for the inner core, but with a geographic dependence in which most PKiKP coda observations are from the Pacific Ocean and Asia and relatively few from the Atlantic. This implies that inner-core scattering has a hemispheric dependence, which has also been observed in other properties (e.g., anisotropy strength) of the outermost inner core. Peng et al. (2008) presented additional LASA records of PKiKP coda, which they forward modeled using the Monte Carlo seismic phonon code of Shearer and Earle (2004). Consistent with Leyton and Koper (2007a), they found that the general properties of the PKiKP coda could be explained with small-scale volumetric heterogeneities in the uppermost few hundred kilometers of the inner core. Cormier (2007) modeled both backscattered PKiKP and forward-scattering PKP(DF) waves at frequencies up to 1 Hz using a 2D pseudospectral finite-difference code and showed how an anisotropic texture with hemispheric variations could explain the observations. Cormier et al. (2011) further developed this model and related it to hypotheses for inner-core crystal growth. Calvet and Margerin (2008) proposed a model in which uppermost inner-core scattering and attenuation are explained with an aggregate of randomly oriented anisotropic blobs of aligned iron crystals.

$PKP(C)_{diff}$ is the P wave that diffracts around the ICB and is seen as an extension of the PKP(BC) branch to distances beyond 153°. Nakanishi (1990) analyzed Japanese records of $PKP(C)_{diff}$ coda from a deep earthquake in Argentina and suggested that scattering near the bottom of the upper mantle could explain its times and slowness. Tanaka (2005) examined $PKP(C)_{diff}$ coda from 28 deep earthquakes recorded using small-aperture short-period seismic arrays of the IMS at epicentral distances of 153°–160°. Beamforming at 1–4 Hz

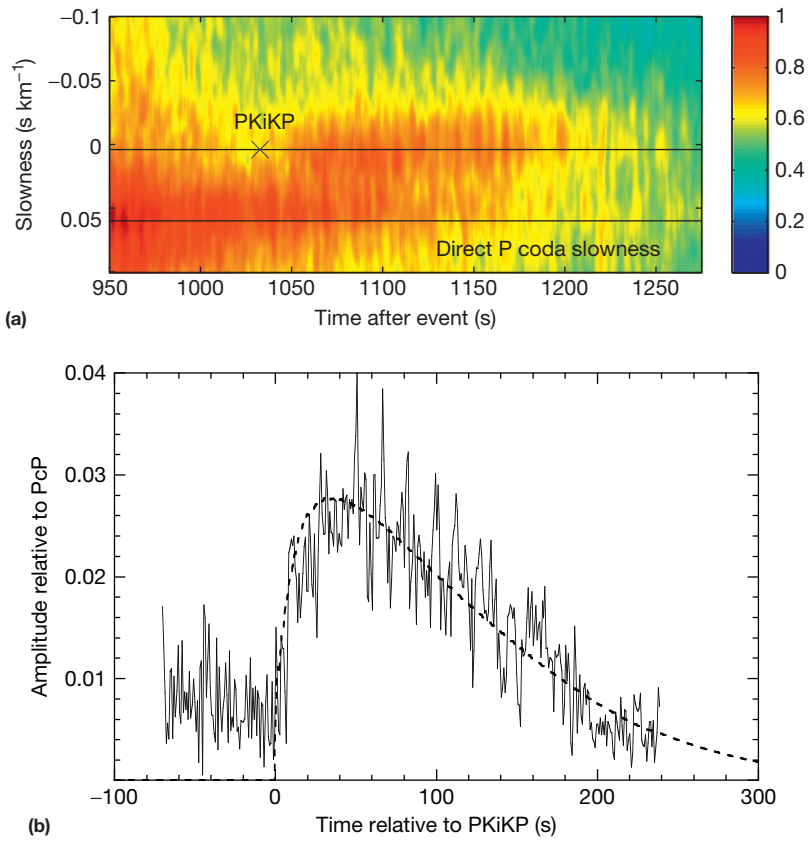

Figure 10 PKiKP coda as observed and modeled by Vidale and Earle (2000) for data from 12 earthquakes and four nuclear explosions recorded at the LASA in Montana. The top panel (Zhi-gang Peng, personal communication) shows a slowness versus time envelope function stack of energy arriving between 950 and 1270 s from the event origin times. The predicted direct PKiKP arrival is shown with the ×. Late P coda forms the stripe seen at a slowness near 0.5 s km^{-1}. PKiKP coda is the stripe seen near zero slowness. The bottom panel compares a PKiKP amplitude stack (wiggly line) to the predicted scattering envelope for an inner-core random heterogeneity model (dashed line).

resolved the slownesses and back azimuths of PKP(DF), PKP(C)$_{diff}$, and PKP(AB). The PKP(C)$_{diff}$ coda lasted longer than PKP(AB), but the wide slowness distribution of PKP(C)$_{diff}$ coda is difficult to explain as originating solely from the ICB, and Tanaka suggested that scattering near the CMB is an important contributor to PKP(C)$_{diff}$ coda.

Vidale and Earle (2005) studied PKP coda from seven Muruoa Island nuclear explosions over a 10-year period recorded by the NORSAR at an epicentral distance of 136°. They observed complicated arrivals lasting ∼10 s that were more extended than the relatively simple pulses observed for direct P waves from explosions recorded in the western United States. Vidale and Earle suggested that these complications likely arose from scattering at or near the ICB. They showed that small time shifts in the PKP coda were consistent with shifts predicted for point scatterers in an inner core that rotated at 0.05°–0.1° per year, although they could not entirely rule out systematic changes in source location.

1.24.3.9 Other Phases

Emery et al. (1999) computed the effect of different types of D'' heterogeneity on S_{diff}, using both the Langer and Born approximations. They found that their long-period S_{diff} observations are not particularly sensitive to the types of small-scale heterogeneities proposed to explain other data sets. Cormier (2000) used the coda power between P and PcP and S and ScS, together with limits on pulse broadening in PcP and ScS waveforms, to model D'' heterogeneity using a 2D pseudospectral calculation. He attempted to resolve the heterogeneity power spectrum over a wide range of scale lengths, to bridge the gaps among global tomography studies, D'' studies, and PKP precursor analyses.

Lee et al. (2003) noted an offset in S coda observations for Central Asian earthquakes (150–250 km deep) recorded about 750 km away at station AAK. The offset occurred near the ScS arrivals in coda envelopes at 10 and 15 s period. At shorter periods (1–4 s), a change in coda decay rate appeared associated with the ScS arrival. They simulated these observations with a Monte Carlo method based on radiative transfer theory and isotropic scattering. For a two-layer mantle model (separated at 670 km), their best-fitting synthetics at 4 s had a total scattering coefficient g_0 of about 1.3×10^{-3} km^{-1} and 6.0×10^{-4} km^{-1} for the upper and lower layers, respectively. Corresponding results at 10 s were about 4.7×10^{-4} km^{-1} and 2.6×10^{-4} km^{-1}. Lee et al. (2006) further studied S and ScS coda envelopes from deep earthquakes recorded at nine distributed global seismic stations and modeled the results with a Monte Carlo method with isotropic scattering and obtained estimates of both the frequency and depth dependence of

average mantle scattering. They also identified regions of stronger scattering, including beneath Central Asia and New Guinea, and argued that scattering attenuation is much stronger than intrinsic attenuation in the 4–10 s band for some regions.

1.24.4 Discussion

Scattering from small-scale irregularities has now been detected at all depths inside the Earth with the exception of the fluid outer core, although many details of this heterogeneity (power spectral density, depth dependence, etc.) remain poorly resolved, at least on a global scale. Scattering is the strongest near the surface, but significant scattering also occurs throughout the lower mantle (e.g., Cormier, 1999; Earle and Shearer, 2001; Hedlin et al., 1997; Margerin and Nolet, 2003b; Shearer and Earle, 2004; Shearer et al., 1998). Small-scale heterogeneity within the deep mantle is almost certainly compositional in origin because thermal anomalies would diffuse away over relatively short times (Hedlin et al., 1997; Helffrich and Wood, 2001) and supports models of incomplete mantle mixing (e.g., Allègre and Turcotte, 1986; Gurnis and Davies, 1986; Morgan and Morgan, 1999; Olson et al., 1984). Helffrich and Wood (2001) discussed the implications of small-scale mantle structure in terms of convective mixing models and suggested that the scatterers are most likely remnants of lithospheric slabs. Assuming subduction-induced heterogeneities are 11–16% of the volume of the mantle, they proposed that most of this heterogeneity occurs at scale lengths <4 km, where it would have little effect on typically observed seismic wavelengths. Meibom and Anderson (2003) discussed the implications of small-scale compositional heterogeneity in the upper mantle, where partial melting may also be an important factor.

There is a large gap between the smallest scale lengths resolved in global mantle tomography models and the ~10 km scale length of the random heterogeneity models proposed to explain scattering observations. Chevrot et al. (1998) showed that the amplitude of the heterogeneity in global and regional tomography models obeys a power law decay with wave number, that is, that most of the power is concentrated at low spherical harmonic degree, a result previously noted by Su and Dziewonski (1991) for global models. For the shallow mantle, this is probably caused in part by continent–ocean differences (G. Masters, personal communication, 2005), but a decay of order k^{-2}–k^{-3} is also predicted for heterogeneity caused by temperature variations in a convecting fluid (Cormier, 2000; Hill, 1978). However, this decay cannot be extrapolated to very small scales because it would predict heterogeneity much weaker than what is required to explain seismic scattering observations at ~10 km scale. As discussed by Cormier (2000), the most likely explanation is a change from thermal to compositionally dominated heterogeneity and that small-scale (<100 km) mantle perturbations are chemical in origin. Spherical heterogeneities of radii 38 km or smaller can be entrained in mantle flow, assuming a mantle viscosity of 10^{21} Pa s, a density contrast of 1 g cc^{-1}, and a convective velocity of 1 cm year^{-1} (Cormier, 2000). Because settling rate scales as the radius squared, smaller blobs will be entrained even at much smaller density contrasts.

The role of the core–mantle and ICBs in small-scale scattering is not yet clear. The D'' region has stronger heterogeneity than the midmantle in tomography models, and large velocity contrasts have been identified in specific regions, including ULVZs and strong individual PKP scatterers (e.g., Niu and Wen, 2001; Vidale and Hedlin, 1998; Wen and Helmberger, 1998). However, globally averaged PKP precursor studies do not find evidence for stronger scattering at the CMB than in the rest of the lower mantle (Hedlin et al., 1997; Margerin and Nolet, 2003b). CMB topography can also produce scattering and has been invoked by some authors to explain PKP and PKKP precursors but fails to predict globally averaged PKKP precursor amplitude versus distance behavior (Earle and Shearer, 1997). Vidale and Earle modeled PKiKP coda observations with bulk scattering within the inner core, while Poupinet and Kennett (2004) suggested that scattering from near the ICB, where several recent studies have found evidence for anomalous structures (e.g., Koper and Dombrovskaya, 2005; Krasnoshchekov et al., 2005), was more likely responsible for their PKiKP coda observations. Strong attenuation is observed in the inner core, but it is not yet clear how much of this is caused by intrinsic versus scattering attenuation. Inner-core scattering might be caused by small-scale textural anisotropy (Cormier et al., 1998, 2011; Vidale and Earle, 2000) or by compositionally induced variations in partial melt (Vidale and Earle, 2000).

At shallow depths, it is clear that there are both strong scattering and significant lateral variations in scattering strength, but the number and diversity of studies on lithospheric scattering make it difficult to draw general conclusions. There is a large literature on both the theory of seismic scattering and on coda observations, but there has been much less effort to integrate these studies into a comprehensive picture of scattering throughout Earth's interior. Review articles (e.g., Aki, 1982; Fehler and Sato, 2003; Herraiz and Espinoa, 1987; Matsumoto, 1995; Sato, 1991) and the book by Sato and Fehler (1998, 2012) are certainly helpful, but their summaries often involve comparisons among studies that differ in many key respects, such as their choice of seismic phase (P, S, etc.); their epicentral distance, frequency range, and time window; and their modeling assumptions (e.g., single scattering, MLTW, finite difference, and radiative transfer). It is not always clear whether models proposed to explain one type of data are supported or contradicted by other types of data. For example, models with horizontally elongated crust and/or upper-mantle heterogeneity appear necessary to explain long-range P_n propagation across Eurasia, and many models of lower crustal reflectors are anisotropic (e.g., Holliger and Levander, 1992; Wenzel et al., 1987). Tkalčić et al. (2010) proposed anisotropic scattering from near-receiver random heterogeneity to explain their observations of anticorrelated PcP and PKiKP amplitudes. Yet almost all modeling of local earthquake coda assumes isotropic random heterogeneity.

A promising development is the increasingly open availability at data centers of seismic records from local and regional networks, portable experiments, and the GSNs. This should enable future coda studies to be more comprehensive and analyze larger numbers of stations around the world using a standardized approach. This would help to establish a baseline of globally averaged scattering properties and maps of

lateral variations in scattering strength over large regions. Data from small-aperture seismic arrays are also very important, because they permit beamforming analysis that can pinpoint the locations of individual scatterers or scattering regions, as several recent studies have shown (e.g., Cao and Romanowicz, 2007; Miller and Niu, 2008; Rost and Earle, 2010; Rost et al., 2008; Thomas et al., 2009). Ultimately, more detailed information on lithospheric heterogeneity (amplitude, scale length, and anisotropy) will enable more detailed comparisons to geologic and petrologic constraints on rock chemistry (e.g., Levander et al., 1994; Ritter and Rothert, 2000).

Analyses of deep-Earth scattering have also used a variety of different phase types and modeling approaches. Even today, there are still fundamental features in the high-frequency wavefield, such as $PKKP_X$ (Earle, 2002), that lack definitive explanations and have never been quantitatively modeled. However, given recent improvements in modeling capabilities (e.g., Monte Carlo calculations based on radiative transfer theory and whole Earth finite-difference calculations), there is now a clear path toward creating 1D models of Earth's average scattering properties and resolving between scattering and intrinsic attenuation mechanisms. It appears that a substantial part of seismic attenuation at high frequencies is caused by scattering rather than intrinsic energy loss, but fully resolving trade-offs between Q_{Sc} and Q_I will require analysis of scattering observations at a wide range of frequencies and epicentral distances. An interesting comparison can be made with seismologist's efforts to map bulk seismic velocity variations. Regional velocity profiling of the upper mantle gave way in the 1980s to comprehensive velocity inversions (i.e., 'tomography') to image global 3D mantle structure. This required working with large data sets of body-wave travel-time and surface-wave phase-velocity measurements and developing and evaluating methods to invert large matrices. The earliest models were crude and controversial in their details, but rapid progress was made as different groups began comparing their results. We may be poised to make similar advances in resolving Earth scattering. But progress will require improved sharing of data from local and regional networks as well as greater testing and standardization of numerical simulation codes. As models of small-scale random heterogeneity become more precise, comparisons to geochemical and convection models will become increasingly relevant.

Acknowledgments

Barbara Romanowicz and Sebastian Rost provided helpful comments. This research was supported by National Science Foundation grants EAR-0229323, EAR-0710881, and EAR-1111111.

References

Abubakirov IR and Gusev AA (1990) Estimation of scattering properties of lithosphere of Kamchatka based on Monte-Carlo simulation of record envelope of a near earthquake. *Physics of the Earth and Planetary Interiors* 64: 52–67.

Adams RD (1968) Early reflections of PP as an indication of upper mantle structure. *Bulletin of Seismological Society of America* 58: 1933–1947.

Akamatsu J (1991) Coda attenuation in the Lützow-Holm Bay region, East Antarctica. *Physics of the Earth and Planetary Interiors* 67: 65–75.

Aki K (1969) Analysis of seismic coda of local earthquakes as scattered waves. *Journal of Geophysical Research* 74: 615–631.

Aki K (1973) Scattering of P waves under the Montana LASA. *Journal of Geophysical Research* 78: 1334–1346.

Aki K (1980) Scattering and attenuation of shear waves in the lithosphere. *Journal of Geophysical Research* 85: 6496–6504.

Aki K (1982) Scattering and attenuation. *Bulletin of Seismological Society of America* 72: 319–330.

Aki K and Chouet B (1975) Origin of coda waves: Source attenuation and scattering effects. *Journal of Geophysical Research* 80: 3322–3342.

Aki K and Richards PG (1980) *Quantitative Seismology*. vol. II: San Francisco, CA: W.H. Freeman.

Akinci A, Del Pezzo E, and Ibanez JM (1995) Separation of scattering and intrinsic attenuation in southern Spain and western Anatolia (Turkey). *Geophysical Journal International* 121: 337–353.

Allègre C and Turcotte DL (1986) Implications of a two-component marble-cake mantle. *Nature* 323: 123–127.

Badi G, Del Pezzo E, Ibanez JM, Bianco F, Sabbione N, and Araujo M (2009) Depth dependent seismic scattering in the Nuevo Cuyo region (south central Andes). *Geophysical Research Letters* 36. http://dx.doi.org/10.1029/2009GL041081.

Baig AM and Dahlen FA (2004a) Statistics of traveltimes and amplitudes in random media. *Geophysical Journal International* 158: 187–210.

Baig AM and Dahlen FA (2004b) Traveltime biases in random media and the *S*-wave discrepancy. *Geophysical Journal International* 158: 922–938.

Baig AM, Dahlen FA, and Hung S-H (2003) Traveltimes of waves in three-dimensional random media. *Geophysical Journal International* 153: 467–482.

Bal G and Moscoso M (2000) Polarization effects of seismic waves on the basis of radiative transport theory. *Geophysical Journal International* 142: 571–585.

Bannister SC, Husebye S, and Ruud BO (1990) Teleseismic P coda analyzed by three-component and array techniques: Deterministic location of topographic P-to-Rg scattering near the NORESS array. *Bulletin of Seismological Society of America* 80: 1969–1986.

Baskoutas I (1996) Dependence of coda attenuation on frequency and lapse time in central Greece. *Pure and Applied Geophysics* 147: 483–496.

Baskoutas I and Sato H (1989) Coda attenuation Qc^{-1} for 4 to 64 Hz signals in the shallow crust measured at Ashio, Japan. *Bollettin Della Geofisica Teoreticheskoi Applicata* 21: 277–283.

Bataille K and Flatté SM (1988) Inhomogeneities near the core-mantle boundary inferred from short-period scattered PKP waves recorded at the global digital seismograph network. *Journal of Geophysical Research* 93: 15057–15064.

Bataille K and Lund F (1996) Strong scattering of short-period seismic waves by the core-mantle boundary and the P-diffracted wave. *Geophysical Research Letters* 23: 2413–2416.

Bataille K, Wu RS, and Flatté SM (1990) Inhomogeneities near the core-mantle boundary evidenced from scattered waves: A review. *Pure and Applied Geophysics* 132: 151–173.

Benites R, Aki K, and Yomogida K (1992) Multiple scattering of SH waves in 2D-media with many cavities. *Pure and Applied Geophysics* 138: 353–390.

Benz HM and Vidale JE (1993) The sharpness of upper mantle discontinuities determined from high-frequency *P′P′* precursors. *Nature* 365: 147–150.

Bhattacharyya J, Shearer PM, and Masters TG (1993) Inner core attenuation from short-period PKP(BC) versus PKP(DF) waveforms. *Geophysical Journal International* 114: 1–11.

Bianco F, Del Pezzo E, Castellano M, Ibanez J, and Di Luccio F (2002) Separation of intrinsic and scattering attenuation in the southern Apennines, Italy. *Geophysical Journal International* 150: 10–22.

Bianco F, Del Pezzo E, Malagnini L, Di Luccio F, and Akinci A (2005) Separation of depth-dependent intrinsic and scattering seismic attenuation in the northeastern sector of the Italian peninsula. *Geophysical Journal International* 161: 130–142.

Biswas NN and Aki K (1984) Characteristics of coda waves: Central and southcentral Alaska. *Bulletin of Seismological Society of America* 74: 493–507.

Bolt BA (1962) Gutenberg's early PKP observations. *Nature* 196: 122–124.

Bolt BA (1970) PdP and PKiKP waves and diffracted PcP waves. *Geophysical Journal of the Royal Astronomical Society* 20: 367–382.

Bolt BA, ONeill M, and Qamar A (1968) Seismic waves near 110°: Is structure in core or upper mantle responsible? *Geophysical Journal of the Royal Astronomical Society* 16: 475–487.

Brana L and Helffrich G (2004) A scattering region near the core-mantle boundary under the North Atlantic. *Geophysical Journal International* 158: 625–636.

Bullen KE and Burke-Gaffney TN (1958) Diffracted seismic waves near the PKP caustic. *Geophysical Journal International* 1: 9–17.

Calvet M and Margerin L (2008) Constraints on grain size and stable iron phases in the uppermost inner core from multiple scattering modeling of seismic velocity and attenuation. *Earth and Planetary Science Letters* 267: 200–212. http://dx.doi.org/10.1016/j.epsl.2007.11.048.

Canas JA, Ugalde A, Pujades LG, Carracedo JC, Soler V, and Blanco MJ (1998) Intrinsic and scattering wave attenuation in the Canary Islands. *Journal of Geophysical Research* 103: 15037–15050.

Cao A and Romanowicz B (2007) Locating scatterers in the mantle using array analysis of PKP precursors from an earthquake doublet. *Earth and Planetary Science Letters* 255: 22–31. http://dx.doi.org/10.1016/j.epsl.2006.12.002.

Carcolé E and Sato H (2010) Spatial distribution of scattering loss and intrinsic absorption of short-period *S* waves in the lithosphere of Japan on the basis of the multiple lapse time window analysis of Hi-net data. *Geophysical Journal International* 180: 268–290. http://dx.doi.org/10.1111/j.1365-246X.2009.04394.x.

Castle JC and Creager KC (1999) A steeply dipping discontinuity in the lower mantle beneath Izu-Bonin. *Journal of Geophysical Research* 104: 7279–7292.

Cessaro RK and Butler R (1987) Observations of transverse energy for *P* waves recorded on a deep-ocean borehole seismometer located in the northwest Pacific. *Bulletin of Seismological Society of America* 77: 2163–2180.

Chang AC and Cleary JR (1978) Precursors to *PKKP*. *Bulletin of Seismological Society of America* 68: 1059–1079.

Chang AC and Cleary JR (1981) Scattered *PKKP*: Further evidence for scattering at a rough core-mantle boundary. *Physics of the Earth and Planetary Interiors* 24: 15–29.

Chen X and Long LT (2000) Spatial distribution of relative scattering coefficients determined from microearthquake coda. *Bulletin of Seismological Society of America* 90: 512–524.

Chernov LA (1960) *Wave Propagation in a Random Media*. New York: McGraw-Hill.

Chevrot S, Montagner JP, and Snieder R (1998) The spectrum of tomographic earth models. *Geophysical Journal International* 133: 783–788.

Chung TW, Yoshimoto K, and Yun S (2010) The separation of intrinsic and scattering seismic attenuation in South Korea. *Bulletin of Seismological Society of America* 100: 3183–3193. http://dx.doi.org/10.1785/0120100054.

Cirerone RD, Doll CG, and Toksoz MN (2011) Scattering and attenuation of seismic waves in northeastern North America. *Bulletin of Seismological Society of America* 101: 2897–2903. http://dx.doi.org/10.1785/0120090216.

Cleary J (1981) Seismic wave scattering on underside reflection at the core-mantle boundary. *Physics of the Earth and Planetary Interiors* 26: 266–267.

Cleary JR and Haddon RAW (1972) Seismic wave scattering near the core-mantle boundary: A new interpretation of precursors to PKP. *Nature* 240: 549–551.

Cleary JR, King DW, and Haddon RAW (1975) P-wave scattering in the Earth's crust and upper mantle. *Geophysical Journal of the Royal Astronomical Society* 43: 861–872.

Cormier VF (1995) Time-domain modelling of PKIKP precursors for constraints on the heterogeneity in the lowermost mantle. *Geophysical Journal International* 121: 725–736.

Cormier VF (1999) Anisotropy of heterogeneity scale lengths in the lower mantle from PKIKP precursors. *Geophysical Journal International* 136: 373–384.

Cormier VF (2000) *D″* as a transition in the heterogeneity spectrum of the lowermost mantle. *Journal of Geophysical Research* 105: 16193–16205.

Cormier VF (2007) Texture of the uppermost inner core from forward-and back-scattered seismic waves. *Earth and Planetary Science Letters* 258: 442–453. http://dx.doi.org/10.1016/j.epsl.2007.04.003.

Cormier VF, Attanayake J, and He K (2011) Inner core freezing and melting: Constraints from seismic body waves. *Physics of the Earth and Planetary Interiors* 188: 163–172. http://dx.doi.org/10.1016/j.pepi.2011.07.007.

Cormier VF and Li X (2002) Frequency-dependent seismic attenuation in the inner core 2. A scattering and fabric interpretation. *Journal of Geophysical Research* 107: B12.

Cormier VF, Xu L, and Choy GI (1998) Seismic attenuation in the inner core: Viscoelastic or stratigraphic? *Geophysical Research Letters* 21: 4019–4022.

Dahlen FA, Hung S-H, and Nolet G (2000) Fréchet kernels for finite-frequency traveltimes—I. Theory. *Geophysical Journal International* 141: 157–174.

Dai W and Song X (2008). Detection of Motion and Heterogeneity in Earth's Liquid Outer Core. *Geophysical Research Letters* 35, doi:10.1029/2008GL034895.

Dainty AM (1990) Studies of coda using array and three-component processing. *Pure and Applied Geophysics* 132: 221–244.

Dainty AM, Duckworth RM, and Tie A (1987) Attenuation and backscattering from local coda. *Bulletin of Seismological Society of America* 77: 1728–1747.

Dainty AM and Toksöz MN (1977) Elastic wave propagation in a highly scattering medium—A diffusion approach. *Journal of Geophysics* 43: 375–388.

Dainty AM and Toksöz MN (1981) Seismic codas on the earth and the moon: A comparison. *Physics of the Earth and Planetary Interiors* 26: 250–260.

Dainty AM and Toksöz MN (1990) Array analysis of seismic scattering. *Bulletin of Seismological Society of America* 80: 2242–2260.

Dainty AM, Toksöz MN, Anderson KR, Pines PJ, Nakamura Y, and Latham G (1974) Seismic scattering and shallow structure of the moon in Oceanus Procellarum. *Moon* 91: 11–29.

Dalkolmo J and Friederich W (2000) Born scattering of long-period body waves. *Geophysical Journal International* 142: 867–888.

Davies DJ and Husebye ES (1972) Array analysis of PKP phases and their precursors. *Nature Physical Sciences* 232: 8–13.

Davis JP, Kind R, and Sacks IS (1989) Precursors to *P′P′* re-examined using broad-band data. *Geophysical Journal International* 99: 595–604.

Del Pezzo E, Bianco F, Marzorati S, Augliera P, D'Alema E, and Massa M (2011) Depth-dependent intrinsic and scattering attenuation in north central Italy. *Geophysical Journal International* 186: 373–381. http://dx.doi.org/10.1111/j.1365-246X.2011.05053.x.

Del Pezzo E, De Natale G, Scarcella G, and Zollo A (1985) q_c of three component seismograms of volcanic microearthquakes at Campi Flegrei volcanic area – southern Italy. *Pure and Applied Geophysics* 123: 683–696.

Doornbos DJ (1974) Seismic wave scattering near caustics: Observations of *PKKP* precursors. *Nature* 247: 352–353.

Doornbos DJ (1976) Characteristics of lower mantle inhomogeneities from scattered waves. *Geophysical Journal of the Royal Astronomical Society* 44: 447–470.

Doornbos DJ (1978) On seismic wave scattering by a rough core-mantle boundary. *Geophysical Journal of the Royal Astronomical Society* 53: 643–662.

Doornbos DJ (1980) The effect of a rough core-mantle boundary on *PKKP*. *Physics of the Earth and Planetary Interiors* 21: 351–358.

Doornbos DJ (1988) Multiple scattering by topographic relief with application to the core-mantle boundary. *Geophysical Journal* 92: 465–478.

Doornbos DJ and Husebye ES (1972) Array analysis of PKP phases and their precursors. *Physics of the Earth and Planetary Interiors* 5: 387.

Doornbos DJ and Vlaar NJ (1973) Regions of seismic wave scattering in the Earth's mantle and precursors to PKP. *Nature Physical Science* 243: 58–61.

Earle PS (1999) Polarization of the Earth's teleseismic wavefield. *Geophysical Journal International* 139: 1–8.

Earle PS (2002) Origins of high-frequency scattered waves near PKKP from large aperture seismic array data. *Bulletin of Seismological Society of America* 92: 751–760.

Earle PS, Rost S, Shearer PM, and Thomas C (2011) Scattered *P′P′* waves observed at short distances. *Bulletin of Seismological Society of America* 101: 2843–2854. http://dx.doi.org/10.1785/0120110157.

Earle PS and Shearer PM (1997) Observations of *PKKP* precursors used to estimate small-scale topography on the core-mantle boundary. *Science* 277: 667–670.

Earle PS and Shearer PM (1998) Observations of high-frequency scattered energy associated with the core phase *PKKP*. *Geophysical Research Letters* 25: 405–408.

Earle PS and Shearer PM (2001) Distribution of fine-scale mantle heterogeneity from observations of P_{diff} coda. *Bulletin of Seismological Society of America* 91: 1875–1881.

Emery V, Maupin V, and Nataf H-C (1999) Scattering of *S* waves diffracted at the core-mantle boundary: Forward modelling. *Geophysical Journal International* 139: 325–344.

Engdahl ER and Flinn EA (1969) Seismic waves reflected from discontinuities within Earth's upper mantle. *Science* 163: 177–179.

Fehler M, Hoshiba M, Sato H, and Obara K (1992) Separation of scattering and intrinsic attenuation for the Kanto-Tokai region, Japan, using measurements of *S*-wave energy versus hypocentral distance. *Geophysical Journal International* 198: 787–800.

Fehler M and Sato H (2003) Coda. *Pure and Applied Geophysics* 160: 541–554.

Flatté SM and Wu R-S (1988) Small-scale structure in the lithosphere and asthenosphere deduced from arrival time and amplitude fluctuations at NORSAR. *Journal of Geophysical Research* 93: 6601–6614.

Frankel A (1990) A review of numerical experiments on seismic wave scattering. *Pure and Applied Geophysics* 131: 639–685.

Frankel A and Clayton RW (1984) A finite difference simulation of wave propagation in two-dimensional random media. *Bulletin of Seismological Society of America* 74: 2167–2186.

Frankel A and Clayton RW (1986) Finite difference simulations of seismic scattering: Implications for the propagation of short-period seismic waves in the crust and models of crustal heterogeneity. *Journal of Geophysical Research* 91: 6465–6489.

Frankel A and Wennerberg L (1987) Energy-flux model of seismic coda: Separation of scattering and intrinsic attenuation. *Bulletin of Seismological Society of America* 77: 1223–1251.

Frederiksen AW and Revenaugh J (2004) Lithospheric imaging via teleseismic scattering. *Geophysical Journal International* 159: 978–990.
Frenje L and Juhlin C (2000) Scattering attenuation: 2-D and 3-D finite difference simulations vs. theory. *Journal of Applied Geophysics* 44: 33–46.
Furumura T, Kennett BLN, and Furumura M (1998) Seismic wavefield calculation for laterally heterogeneous whole earth models using the pseudospectral method. *Geophysical Journal International* 135: 845–860.
Gagnepain-Beyneix J (1987) Evidence of spatial variations of attenuation in the western Pyrenean range. *Geophysical Journal of the Royal Astronomical Society* 89: 681–704.
Gao LS, Lee LC, Biswas NN, and Aki K (1983a) Effects of multiple scattering on coda waves in three dimensional medium. *Pure and Applied Geophysics* 121: 3–15.
Gao LS, Lee LC, Biswas NN, and Aki K (1983b) Comparison of the effects between single and multiple scattering on coda waves for local earthquakes. *Bulletin of Seismological Society of America* 73: 377–390.
Garnero EJ (2000) Heterogeneity of the lowermost mantle. *Annual Review of Earth and Planetary Sciences* 28: 509–537.
Giampiccolo E, Gresta A, and Rasconà F (2004) Intrinsic and scattering attenuation from observed seismic codas in south-eastern Sicily (Italy). *Physics of the Earth and Planetary Interiors* 145: 55–66.
Gibson BS and Levander AR (1988) Modeling and processing of scattered waves in seismic reflection surveys. *Geophysics* 53: 466–478.
Goutbeek FH, Dost B, and van Eck T (2004) Intrinsic absorption and scattering attenuation in the southern Netherlands. *Journal of Seismology* 8: 11–23.
Gupta IN and Blandford RR (1983) A mechanism for generation of short-period transverse motion from explosions. *Bulletin of Seismological Society of America* 73: 571–591.
Gupta IN, Lynnes CS, McElfresh TW, and Wagner RA (1990) F-K analysis of NORESS array and single station data to identify sources of near-receiver and near-source scattering. *Bulletin of Seismological Society of America* 80: 2227–2241.
Gupta SC, Teotia SS, Rai SS, and Gautam N (1998) Coda *Q* estimates in the Koyna region, India. *Pure and Applied Geophysics* 153: 713–731.
Gurnis M and Davies F (1986) Mixing in numerical models of mantle convection incorporating plate kinematics. *Journal of Geophysical Research* 91: 6375–6395.
Gusev AA (1995) Vertical profile of turbidity and coda Q. *Geophysical Journal International* 123: 665–672.
Gusev AA and Abubakirov IR (1987) Monte Carlo simulation of record envelope of a near earthquake. *Physics of the Earth and Planetary Interiors* 49: 30–36.
Gusev AA and Abubakirov IR (1999a) Vertical profile of effective turbidity reconstructed from broadening of incoherent body-wave pulses—I. General approach and the inversion procedure. *Geophysical Journal International* 136: 295–308.
Gusev AA and Abubakirov IR (1999b) Vertical profile of effective turbidity reconstructed from broadening of incoherent body-wave pulses—II. Application to Kamchatka data. *Geophysical Journal International* 136: 309–323.
Gutenberg B (1957) The boundary of the Earth's inner core. *Eos, Transactions American Geophysical Union* 38: 750–753.
Gutenberg B and Richter CF (1934) On seismic waves; I. *Gerlands Beitrage zur Geophysik* 43: 56–133.
Gutowski PR and Kanasewich ER (1974) Velocity spectral evidence of upper mantle discontinuities. *Geophysical Journal of the Royal Astronomical Society* 36: 21–32.
Haddon RAW (1972) Corrugations on the CMB or transition layers between the inner and outer cores? (abstract). *Eos, Transactions American Geophysical Union* 53: 600.
Haddon RAW (1982) Evidence for inhomogeneities near the core-mantle boundary. *Philosophical Transactions of the Royal Society London A* 306: 61–70.
Haddon RAW and Cleary JR (1974) Evidence for scattering of seismic PKP waves near the mantle-core boundary. *Physics of the Earth and Planetary Interiors* 8: 211–234.
Haddon RAW, Husebye ES, and King DW (1977) Origin of precursors to PP. *Physics of the Earth and Planetary Interiors* 14: 41–71.
Hedlin MAH and Shearer PM (2000) An analysis of large-scale variations in small-scale mantle heterogeneity using global Seismographic Network recordings of precursors to PKP. *Journal of Geophysical Research* 105: 13655–13673.
Hedlin MAH and Shearer PM (2002) Probing mid-mantle heterogeneity using PKP coda waves. *Physics of the Earth and Planetary Interiors* 130: 195–208.
Hedlin MAH, Shearer PM, and Earle PS (1997) Seismic evidence for small-scale heterogeneity throughout Earth's mantle. *Nature* 387: 145–150.
Helffrich GR and Wood BJ (2001) The Earth's mantle. *Nature* 412: 501–507.
Herraiz M and Espinoa AF (1987) Coda waves: A review. *Pure and Applied Geophysics* 125: 499–577.
Hill RJ (1978) Models of the scalar spectrum for turbulent advection. *Journal of Fluid Mechanics* 88: 541–562.
Hock S, Korn M, Ritter JRR, and Rothert E (2004) Mapping random lithospheric heterogeneities in northern and central Europe. *Geophysical Journal International* 157: 251–264.
Hock S, Korn M, and TOR Working Group (2000) Random heterogeneity of the lithosphere across the Trans-European Suture Zone. *Geophysical Journal International* 141: 57–70.
Holliger K and Levander AR (1992) A stochastic view of lower crustal fabric based on evidence from the Ivrea zone. *Journal of Geophysical Research* 19: 1153–1156.
Hong T-K (2004) Scattering attenuation ratios of *P* and *S* waves in elastic media. *Geophysical Journal International* 158: 211–224.
Hong T-K and Kennett BLN (2003) Scattering attenuation of 2-D elastic waves: Theory and numerical modelling using a wavelet-based method. *Bulletin of Seismological Society of America* 93: 922–938.
Hong T-K, Kennett BLN, and Wu R-S (2004) Effects of the density perturbation in scattering. *Geophysical Research Letters* 31. http://dx.doi.org/10.1029/2004GL019933.
Hong T-K and Menke W (2008) Constituent energy of regional seismic coda. *Bulletin of Seismological Society of America* 98: 454–462. http://dx.doi.org/10.1785/0120070121.
Hong T-K and Wu R-S (2005) Scattering of elastic waves in geometrically anisotropic random media and its implication to sounding of heterogeneity in the Earth's deep interior. *Geophysical Journal International* 163: 324–338.
Hong T-K, Wu R-S, and Kennett BLN (2005) Stochastic features of scattering. *Physics of the Earth and Planetary Interiors* 148: 131–148.
Hoshiba M (1991) Simulation of multiple scattered coda wave excitation based on the energy conservation law. *Physics of the Earth and Planetary Interiors* 67: 123–136.
Hoshiba M (1993) Separation of scattering attenuation and intrinsic absorption in Japan using the multiple lapse time window analysis of full seismogram envelope. *Journal of Geophysical Research* 98: 15809–15824.
Hoshiba M (1994) Simulation of coda wave envelope in depth dependent scattering and absorption structure. *Geophysical Research Letters* 21: 2853–2856.
Hoshiba M (1997) Seismic coda wave envelope in depth-dependent *S* wave velocity structure. *Physics of the Earth and Planetary Interiors* 104: 15–22.
Hoshiba M, Rietbrock A, Scherbaum F, Nakahara H, and Haberland C (2001) Scattering attenuation and intrinsic absorption using uniform and depth dependent model—Application to full seismogram envelope recorded in northern Chile. *Journal of Seismology* 5: 157–179.
Hudson JA and Heritage JR (1981) Use of the Born approximation in seismic scattering problems. *Geophysical Journal of the Royal Astronomical Society* 66: 221–240.
Husebye ES, Haddon RAW, and King DW (1977) Precursors to PP and upper mantle discontinuities. *Journal of Geophysical Research* 43: 535–543.
Husebye ES, King DW, and Haddon RAW (1976) Precursors to PKIKP and seismic wave scattering near the mantle-core boundary. *Journal of Geophysical Research* 81: 1870–1882.
Husebye E and Madariaga R (1970) The origin of precursors to core waves. *Bulletin of Seismological Society of America* 60: 939–952.
Jahnke G, Thorne MS, Cochard A, and Igel H (2008) Global SH-wave propagation using a parallel axisymmetric spherical finite-difference scheme: Application to whole mantle scattering. *Geophysical Journal International* 173: 815–826. http://dx.doi.org/10.1111/j/1365-246X.2008.03744.x.
Jemberie AL and Nyblade AA (2009) Intrinsic and scattering Q near 1 Ha across the East African Plateau. *Bulletin of Seismological Society of America* 99: 3516–3524. http://dx.doi.org/10.1785/0120090062.
Jin A and Aki K (1988) Spatial and temporal correlation between coda Q and seismicity in China. *Bulletin of Seismological Society of America* 78: 741–769.
Jin A, Cao T, and Aki K (1985) Regional change of coda Q in the oceanic lithosphere. *Journal of Geophysical Research* 90: 8651–8659.
Jin A, Mayeda K, Adams D, and Aki K (1994) Separation of intrinsic and scattering attenuation in southern California using TERRAscope data. *Journal of Geophysical Research* 99: 17835–17848.
Kaelin B and Johnson LR (1998) Dynamic composite elastic medium theory, 2, three-dimensional media. *Journal of Applied Physics* 84: 5458–5468.
Kampfmann W and Muüller G (1989) PcP amplitude calculations for a core-mantle boundary with topography. *Geophysical Research Letters* 16: 653–656.
Kaneshima S (2003) Small-scale heterogeneity at the top of the lower mantle around the Mariana slab. *Earth and Planetary Science Letters* 209: 85–101.
Kaneshima S (2009) Seismic scatterers at the shallowest lower mantle beneath sub ducted slabs. *Earth and Planetary Science Letters* 286: 304–315. http://dx.doi.org/10.1016/j.epsl.2009.06.044.
Kaneshima S and Helffrich G (1998) Detection of lower mantle scatterers northeast of the Mariana subduction zone using short-period array data. *Journal of Geophysical Research* 103: 4825–4838.
Kaneshima S and Helffrich G (1999) Dipping low-velocity layer in the mid-lower mantle: Evidence for geochemical heterogeneity. *Science* 283: 1888–1892.

Kaneshima S and Helffrich G (2003) Subparallel dipping heterogeneities in the mid-lower mantle. *Journal of Geophysical Research* 108. http://dx.doi.org/10.1029/2001JB001596.

Kaneshima S and Helffrich G (2009) Lower mantle scattering profiles and fabric below Pacific subduction zones. *Earth and Planetary Science Letters* 282: 234–239. http://dx.doi.org/10.1016/j.epsl.2009.03.024.

Kaneshima S and Helffrich G (2010) Small scale heterogeneity in the mid-lower mantle beneath the circum-Pacific area. *Physics of the Earth and Planetary Interiors* 183: 91–103. http://dx.doi.org/10.1016/j.pepi.2010.03.011.

King DW and Cleary JR (1974) A note on the interpretation of precursors to PKPPKP. *Bulletin of Seismological Society of America* 64: 721–723.

King DW, Haddon RAW, and Cleary JR (1973) Evidence for seismic wave scattering in the *D″* layer. *Earth and Planetary Science Letters* 20: 353–356.

King DW, Haddon RAW, and Cleary JR (1974) Array analysis of precursors to PKIKP in the distance range 128° to 142°. *Geophysical Journal of the Royal Astronomical Society* 37: 157–173.

King DW, Haddon RAW, and Husebye ES (1975) Precursors to PP. *Physics of the Earth and Planetary Interiors* 10: 103–127.

Knopoff L and Hudson JA (1964) Scattering of elastic waves by small inhomogeneities. *Journal of the Acoustical Society of America* 36: 338–343.

Koper KD and Dombrovskaya M (2005) Seismic properties of the inner core boundary from PKiKP/P amplitude ratios. *Earth and Planetary Science Letters* 237: 680–694.

Koper KD, Franks JM, and Dombrovskaya M (2004) Evidence for small-scale heterogeneity in Earth's inner core from a global study of PKiKP coda waves. *Earth and Planetary Science Letters* 228: 227–241.

Kopnichev YF (1977) The role of multiple scattering in the formulation of a seismogram's tail. *Izy. Acad. Nauk USSR (Engl. Trans. Physics of the Solid Earth)* 13: 394–398.

Korn M (1988) P-wave coda analysis of short-period array data and the scattering and absorptive properties of the lithosphere. *Geophysical Journal* 93: 437–449.

Korn M (1990) A modified energy flux model for lithospheric scattering of teleseismic body waves. *Geophysical Journal International* 102: 165–175.

Korn M (1993) Determination of site-dependent scattering Q from P-wave coda analysis with an energy flux model. *Geophysical Journal International* 113: 54–72.

Korn M (1997) Modelling the teleseismic P coda envelope: Depth dependent scattering and deterministic structure. *Physics of the Earth and Planetary Interiors* 104: 23–36.

Korn M and Sato H (2005) Synthesis of plane vector wave envelopes in two-dimensional random elastic media based on the Markov approximation and comparison with finite-difference synthetics. *Geophysical Journal International* 161: 839–848.

Korneev VA and Johnson LR (1993a) Scattering of elastic waves by a spherical inclusion—I. Theory and numerical results. *Geophysical Journal International* 115: 230–250.

Korneev VA and Johnson LR (1993b) Scattering of elastic waves by a spherical inclusion—II. Limitations of asymptotic solutions. *Geophysical Journal International* 115: 251–263.

Kosuga M (1992) Determination of coda *Q* on frequency and lapse time in the western Nagano region, Japan. *Journal of Physics of the Earth* 40: 421–445.

Kosuga M (1997) Periodic ripple of coda envelope observed in northeastern Japan. *Physics of the Earth and Planetary Interiors* 104: 91–108.

Krasnoshchekov DN, Kaazik PB, and Ovtchinnikov VM (2005) Seismological evidence for mosaic structure of the surface of the Earth's inner core. *Nature* 435: 483–487. http://dx.doi.org/10.1038/nature03613.

Krüger FK, Baumann M, Scherbaum F, and Weber M (2001) Mid mantle scatterers near the Mariana slab detected with a double array method. *Geophysical Research Letters* 28: 667–670.

Kvamme LB and Havskov J (1989) Q in southern Norway. *Bulletin of Seismological Society of America* 79: 1575–1588.

Lacombe C, Campillo M, Paul A, and Margerin L (2003) Separation of intrinsic absorption and scattering attenuation from Lg coda decay in central France using acoustic radiative transfer theory. *Geophysical Journal International* 154: 417–425.

Langston GA (1989) Scattering of teleseismic body waves under Pasadena, California. *Journal of Geophysical Research* 94: 1935–1951.

Lay T (1987) Analysis of near-source contributions to early *P*-wave coda for underground explosions. II. Frequency dependence. *Bulletin of Seismological Society of America* 77: 1252–1273.

Lee WS, Sato H, and Lee K (2003) Estimation of *S*-wave scattering coefficient in the mantle from envelope characteristics before and after the ScS arrival. *Geophysical Research Letters* 30: 24. http://dx.doi.org/10.1029/2003GL018413.

Lee WS, Sato H, and Lee K (2006) Scattering coefficients in the mantle revealed from the seismogram envelope analysis based on the multiple isotropic scattering model. *Earth and Planetary Science Letters* 2006: 888–900. http://dx.doi.org/10.1016/j/epsl.2005.10.035.

Lee WS, Yun S, and Do J-Y (2010) Scattering and intrinsic attenuation of short-period *S* waves in the Gyeongsang Basin, South Korea, revealed from S-wave seismogram envelopes based on the radiative transfer theory. *Bulletin of Seismological Society of America* 100: 833–840. http://dx.doi.org/10.1785/0120090149.

Lerche I and Menke W (1986) An inversion method for separating apparent and intrinsic attenuation in layered media. *Geophysical Journal of the Royal Astronomical Society* 87: 333–347.

Levander AR and Hill NR (1985) P-SV resonances in irregular low-velocity surface layers. *Bulletin of Seismological Society of America* 75: 847–864.

Levander A, Hobbs RW, Smith SK, England RW, Snyder DB, and Holliger K (1994) The crust as a heterogeneous "optical" medium, or "crocodiles in the mist". *Tectonophysics* 232: 281–297.

Leyton F and Koper KD (2007a) Using PKiKp coda to determine inner core structure: 1. Synthesis of coda envelopes using single scattering theories. *Journal of Geophysical Research* 112. http://dx.doi.org/10.1029/2006JB004369.

Leyton F and Koper KD (2007b) Using PKiKp coda to determine inner core structure: 2. Determination of Qc. *Journal of Geophysical Research* 112. http://dx.doi.org/10.1029/2006JB004370.

Malin PE and Phinney RA (1985) On the relative scattering of P and S waves. *Geophysical Journal of the Royal Astronomical Society* 80: 603–618.

Mancinelli NJ and Shearer PM (2013) Reconciling discrepancies among estimates of small-scale mantle heterogeneity from PKP precursors. *Geophysical Journal International* 195: 1721–1729. http://dx.doi.org/10.1093/gji/ggt319.

Margerin L (2004) Introduction to radiative transfer of seismic waves. *Seismic Data Analysis and Imaging with Global and Local Arrays. AGU Monograph Series.* Washington DC: American Geophysical Union.

Margerin L (2006) Attenuation, transport and diffusion of scalar waves in textured random media. *Tectonophysics* 416: 229–244. http://dx.doi.org/10.1016/j.tecto.2005.11.011.

Margerin L (2013) Diffusion approximation with polarization and resonance effects for the modeling of seismic waves in strongly scattering small-scale media. *Geophysical Journal International* http://dx.doi.org/10.1093/gji/ggs022.

Margerin L, Campillo M, Shapiro NM, and van Tiggelen BA (1999) Residence time of diffuse waves in the crust as a physical interpretation of coda Q: Application to seismograms recorded in Mexico. *Geophysical Journal International* 138: 343–352.

Margerin L, Campillo M, and van Tiggelen BA (1998) Radiative transfer and diffusion of waves in a layered medium: New insight into coda Q. *Geophysical Journal International* 134: 596–612.

Margerin L, Campillo M, and van Tiggelen B (2000) Monte Carlo simulation of multiple scattering of elastic waves. *Journal of Geophysical Research* 105: 7873–7892.

Margerin L, Campillo M, and van Tiggelen B (2001) Effect of absorption on energy partition of elastic waves. *Bulletin of Seismological Society of America* 91: 624–627.

Margerin L, Campillo M, van Tiggelen B, and Hennino R (2009) Energy partition of seismic coda waves in layered media: Theory and application to Pinyon Flats Observatory. *Geophysical Journal International* 177: 571–585. http://dx.doi.org/10.1111/j.1365-246X.2008.04068.x.

Margerin L and Nolet G (2003a) Multiple scattering of high-frequency seismic waves in the deep Earth: Modeling and numerical examples. *Journal of Geophysical Research* 108: B5. http://dx.doi.org/10.1029/2002JB001974.

Margerin L and Nolet G (2003b) Multiple scattering of high-frequency seismic waves in the deep Earth: PKP precursor analysis and inversion for mantle granularity. *Journal of Geophysical Research* 108: B11. http://dx.doi.org/10.1029/2003JB002455.

Margerin L, van Tiggelen B, and Campillo M (2001) Effect of absorption on energy partition of elastic waves in the seismic coda. *Bulletin of Seismological Society of America* 91: 624–627.

Matsumoto S (1995) Characteristics of coda waves and inhomogeneity of the earth. *Journal of Physics of the Earth* 43: 279–299.

Matsumoto S (2005) Scatterer density estimation in the crust by seismic array processing. *Geophysical Journal International* http://dx.doi.org/10.1111/j.1365-246X.2005.02773.x.

Matsumoto S and Hasegawa A (1989) Two-dimensional coda *Q* structure beneath Tohoku, NE Japan. *Geophysical Journal International* 99: 101–108.

Mayeda K, Koyanagi S, Hoshiba M, Aki K, and Zeng Y (1992) A comparative study of scattering, intrinsic, and coda Q^{-1} for Hawaii, Long Valley, and central California between 1.5 and 15.0 Hz. *Journal of Geophysical Research* 97: 6643–6659.

Mayeda K, Su F, and Aki K (1991) Seismic albedo from the total seismic energy dependence on hypocentral distances in southern California. *Physics of the Earth and Planetary Interiors* 67: 104–114.

McLaughlin KL and Anderson LM (1987) Stochastic dispersion of short-period *P*-waves due to scattering and multipathing. *Geophysical Journal of the Royal Astronomical Society* 89: 933–964.

McLaughlin KL, Anderson LM, and Der Z (1985) Investigation of seismic waves using 2-dimensional finite difference calculations. In: *Multiple Scattering of Seismic Waves in Random Media and Random Surfaces*, pp. 795–821. Pennsylvania State University.

Meibom A and Anderson DL (2003) The statistical upper mantle assemblage. *Earth and Planetary Science Letters* 217: 123–139.

Miller MS and Niu F (2008) Bulldozing the core-mantle boundary: Localized seismic scatterers beneath the Caribbean Sea. *Physics of the Earth and Planetary Interiors* 170: 89–94. http://dx.doi.org/10.1016/j.pepi.2008.07.044.

Morgan JP and Morgan WJ (1999) Two-stage melting and the geochemical evolution of the mantle: A recipe for mantle plum-pudding. *Earth and Planetary Science Letters* 170: 215–239.

Morozov IB, Morozova EA, Smithson SB, and Solodilov LN (1998) On the nature of the teleseismic Pn phase observed on the ultralong-range profile Quartz, Russia. *Bulletin of Seismological Society of America* 88: 62–73.

Morozov IB and Smithson SB (2000) Coda of long-range arrivals from nuclear explosions. *Bulletin of Seismological Society of America* 90: 929–939.

Mukhopadhyay S and Tyagi C (2008) Variation of intrinsic and scattering attenuation with depth in NW Himalayas. *Geophysical Journal International* 172: 1055–1065. http://dx.doi.org/10.1111/j/1365-246X.2007.03688.x.

Müller TM and Shapiro SA (2003) Amplitude fluctuations due to diffraction and reflection in anisotropic random media: Implications for seismic scattering attenuation estimates. *Geophysical Journal International* 155: 139–148.

Nakamura Y (1977) Seismic energy transmission in an intensively scattering environment. *Journal of Geophysical Research* 43: 389–399.

Nakanishi I (1990) High-frequency waves following PKP-Cdiff at distances greater than 155°. *Geophysical Research Letters* 17: 639–642.

Neele F and Snieder R (1991) Are long-period body wave coda caused by lateral heterogeneity? *Geophysical Journal International* 107: 131–153.

Nguyen-Hai (1963) Propagation des ondes longitudinales dans le noyau terrestre. *Annals of Geophysics* 15: 285–346.

Nielsen L and Thybo H (2003) The origin of teleseismic *Pn* waves: Multiple crustal scattering of upper mantle whispering gallery phases. *Journal of Geophysical Research* 108. http://dx.doi.org/10.1029/2003JB002487.

Nielsen L and Thybo H (2006) Identification of crustal and upper mantle heterogeneity by modeling of controlled source seismic data. *Tectonophysics* 416: 209–228. http://dx.doi.org/10.1016/j/tecto/2005.11.020.

Nielsen L, Thybo H, Levander A, and Solodilov LN (2003) Origin of upper-mantle seismic scattering – Evidence from Russian peaceful nuclear explosion data. *Geophysical Journal International* 154: 196–204.

Nielsen L, Thybo H, Morozov B, Smithson SB, and Solodilov L (2003) Teleseismic Pn arrivals: Influence of upper mantle velocity gradient and crustal scattering. *Geophysical Journal International* 153: F1–F7.

Nishigami K (1991) A new inversion method of coda waveforms to determine spatial distribution of coda scatterers in the crust and uppermost mantle. *Geophysical Research Letters* 18: 2225–2228.

Nishigami K (1997) Spatial distribution of coda scatterers in the crust around two active volcanoes and one active fault system in central Japan: Inversion analysis of coda envelope. *Physics of the Earth and Planetary Interiors* 104: 75–89.

Nishimura T, Yoshimoto K, Ohtaki T, Kanjo K, and Purwana I (2002) Spatial distribution of lateral heterogeneity in the upper mantle around the western Pacific region as inferred from analysis of transverse components of teleseismic P-coda. *Geophysical Research Letters* 29: 2137. http://dx.doi.org/10.1029/2002GL015606.

Niu F and Kawakatsu H (1994) Seismic evidence for a 920-km discontinuity in the mantle. *Nature* 371: 301–305.

Niu F and Kawakatsu H (1997) Depth variation of the mid-mantle discontinuity. *Geophysical Research Letters* 24: 429–432.

Niu F and Wen L (2001) Strong seismic scatterers near the core-mantle boundary west of Mexico. *Geophysical Research Letters* 28: 3557–3560.

Nolet G, Dahlen FA, Montelli R, Nolet G, Dahlen FA, and Montelli R (2005) Travel times and amplitudes of seismic waves: A re-assessment. In: *Seismic Earth: Analysis of Broadband Seismograms*, *AGU Monograph Series*, pp. 37–48.

Oancea V, Bazacliu O, and Mihalache G (1991) Estimation of the coda quality factor for the Romanian territory. *Physics of the Earth and Planetary Interiors* 67: 87–94.

Obara K (1997) Simulations of anomalous seismogram envelopes at coda portions. *Physics of the Earth and Planetary Interiors* 104: 109–125.

Obara K and Sato H (1995) Regional differences of random heterogeneities around the volcanic front in the Kanto-Tokai area, Japan revealed from the broadening of *S* wave seismogram envelopes. *Journal of Geophysical Research* 100: 2103–2121.

Olson P, Yuen DA, and Balsiger D (1984) Convective mixing and the fine structure of mantle heterogeneity. *Physics of the Earth and Planetary Interiors* 36: 291–304.

Padhy S and Subhadra N (2010) Attenuation of high-frequency seismic waves in northeastern India. *Geophysical Journal International* 181: 453–467. http://dx.doi.org/10.1111/j/1365-246X.2010.04502.x.

Padhy S, Subhadra N, and Kayal JR (2011) Frequency-dependent attenuation of body and coda waves in the Andaman Sea Basin. *Bulletin of Seismological Society of America* 101: 109–125. http://dx.doi.org/10.1785/0120100032.

Papanicolaou G, Ryshik L, and Keller J (1996) On the stability of the P to S energy ratio in the diffusive regime. *Bulletin of Seismological Society of America* 86: 1107–1115, see also erratum in, Bulletin of Seismological Society of America, 86, p. 1997.

Peng Z, Koper KD, Vidale JE, Leyton F, and Shearer P (2008) Inner-core fine-scale structure from scattered waves recorded by LASA. *Journal of Geophysical Research* 113. http://dx.doi.org/10.1029/2007JB005412.

Poupinet G and Kennett BLN (2004) On the observation of high frequency PKiKP and its coda in Australia. *Physics of the Earth and Planetary Interiors* 146: 497–511.

Przybilla J and Korn M (2008) Monte Carlo simulation of radiative energy transfer in continuous elastic random media – Three-component envelopes and numerical validation. *Geophysical Journal International* 173: 566–576. http://dx.doi.org/10.1111/j/1365-246.2008.03747.x.

Przybilla J, Korn M, and Wegler U (2006) Radiative transfer of elastic waves versus finite difference simulations in two-dimensional random media. *Journal of Geophysical Research* 111. http://dx.doi.org/10.1029/2005JB003952.

Pulli JJ (1984) Attenuation of coda waves in New England. *Bulletin of Seismological Society of America* 74: 1149–1166.

Rautian TG and Khalturin VI (1978) The use of coda for determination of the earthquake source spectrum. *Bulletin of Seismological Society of America* 68: 923–948.

Revenaugh J (1995) The contribution of topographic scattering to teleseismic coda in southern California. *Geophysical Research Letters* 22: 543–546.

Revenaugh J (1999) Geologic applications of seismic scattering. *Annual Review of Earth and Planetary Sciences* 27: 55–73.

Revenaugh J (2000) The relation of crustal scattering to seismicity in southern California. *Journal of Geophysical Research* 105: 25403–25422.

Rhea S (1984) Q determined from local earthquakes in the south Carolina coastal plain. *Bulletin of Seismological Society of America* 74: 2257–2268.

Richards PG (1972) Seismic waves reflected from velocity gradient anomalies within the Earth's mantle. *Zeitschrift für Geophysik* 38: 517–527.

Richards PG and Menke W (1983) The apparent attenuation of a scattering medium. *Bulletin of Seismological Society of America* 73: 1005–1022.

Ritter JRR, Mai PM, Stoll G, and Fuchs K (1997) Scattering of teleseismic waves in the lower crust observations in the Massif Central, France. *Physics of the Earth and Planetary Interiors* 104: 127–146.

Ritter JRR and Rothert E (2000) Variations of the lithospheric seismic scattering strength below the Massif Central, France and the Frankonian Jura, SE Germany. *Tectonophysics* 328: 297–305.

Ritter JRR, Shapiro SA, and Schechinger B (1998) Scattering parameters of the lithosphere below the Massif Central, France, from teleseismic wavefield records. *Geophysical Journal International* 134: 187–198.

Rodriguez M, Havskov J, and Singh SK (1983) Q from coda waves near Petatlán, Guerrero, Mexico. *Bulletin of Seismological Society of America* 73: 321–326.

Roecker SW, Tucker B, King J, and Hatzfeld D (1982) Estimates of Q in central Asia as a function of frequency and depth using the coda of locally recorded earthquakes. *Bulletin of Seismological Society of America* 72: 129–149.

Rost S and Earle PS (2010) Identifying regions of strong scattering at the core-mantle boundary from analysis of *PKKP* precursor energy. *Earth and Planetary Science Letters* 297: 616–626. http://dx.doi.org/10.1016/j.epsl.2010.07.014.

Rost S, Garnero EJ, and Williams Q (2008) Seismic array detection of subducted oceanic crust in the lower mantle. *Journal of Geophysical Research* 113. http://dx.doi.org/10.1029/2007JB005263.

Rost S, Thorne MS, and Garnero EJ (2006) Imaging global seismic phase arrivals by stacking array processed short-period data. *Seismological Research Letters* 77: 697–707.

Roth M and Korn M (1993) Single scattering theory versus numerical modelling in 2-D random media. *Geophysical Journal International* 112: 124–140.

Rothert E and Ritter JRR (2000) Small-scale heterogeneities below the Gräfenberg array, Germany from seismic wavefield fluctuations of Hindu Kish events. *Geophysical Journal International* 140: 175–184. http://dx.doi.org/10.1046/j.1365-246x.2000.00013.x.

Ryberg T, Fuchs K, Egorkin V, and Solodilov L (1995) Observation of high-frequency teleseismic Pn waves on the long-range Quartz profile across northern Eurasia. *Journal of Geophysical Research* 100: 18151–18163.

Ryberg T, Tittgemeyer M, and Wenzel F (2000) Finite difference modelling of *P*-wave scattering in the upper mantle. *Geophysical Journal International* 141: 787–800.

Ryzhik LV, Papanicolaou GC, and Keller JB (1996) Transport equations for elastics and other waves in random media. *Wave Motion* 24: 327–370.

Sacks IS and Saa G (1969) The structure of the transition zone between the inner core and the outer core. *Year Book*, vol. 69, pp. 419–426. Washington: Carnegie Inst.

Saito T, Sato H, Fehler M, and Ohtake M (2003) Simulating the envelope of scalar waves in 2D random media having power-law spectra of velocity fluctuation. *Bulletin of Seismological Society of America* 93: 240–252.

Saito T, Sato H, and Ohtake M (2002) Envelope broadening of spherically outgoing waves in three-dimensional random media having power law spectra. *Journal of Geophysical Research* 107. http://dx.doi.org/10.1029/2001JB000264.

Sato H (1977) Energy propagation including scattering effects, single isotropic scattering approximation. *Journal of Physics of the Earth* 25: 27–41.

Sato H (1978) Mean free path of *S*-waves under the Kanto district of Japan. *Journal of Physics of the Earth* 26: 185–198.

Sato H (1984) Attenuation and envelope formation of three-component seismograms of small local earthquakes in randomly inhomogeneous lithosphere. *Journal of Geophysical Research* 89: 1221–1241.

Sato H (1989) Broadening of seismogram envelopes in the randomly inhomogeneous lithosphere based on the parabolic approximation: Southeast Honshu, Japan. *Journal of Geophysical Research* 94: 17735–17747.

Sato H (1990) Unified approach to amplitude attenuation and coda excitation in the randomly inhomogeneous litho-sphere. *Pure and Applied Geophysics* 132: 93–121.

Sato H (1991) Study of seismogram envelopes based on scattering by random inhomogeneities in the lithosphere: A review. *Physics of the Earth and Planetary Interiors* 67: 4–19.

Sato H (1993) Energy transportation in one- and two-dimensional scattering media: Analytic solutions of the multiple isotropic scattering model. *Geophysical Journal International* 112: 141–146.

Sato H (1994) Multiple isotropic scattering model including P-S conversions for the seismogram envelope formulation. *Geophysical Journal International* 117: 487–494.

Sato H and Fehler MC (1998) *Seismic Wave Propagation and Scattering in the Heterogeneous Earth*. New York: Springer-Verlag.

Sato H, Fehler M, and Saito T (2004) Hybrid synthesis of scalar wave envelopes in two-dimensional random media having rich short-wavelength spectra. *Journal of Geophysical Research* 109. http://dx.doi.org/10.1029/2003JB002673.

Sato H, Nakahara H, and Ohtake M (1997) Synthesis of scattered energy density for nonspherical radiation from a point shear-dislocation source based on the radiative transfer theory. *Physics of the Earth and Planetary Interiors* 104: 1–13.

Sato H and Nishino M (2002) Multiple isotropic-scattering model on the spherical Earth for the synthesis of Rayleigh-wave envelopes. *Journal of Geophysical Research* 107: 2343. http://dx.doi.org/10.1029/2001JB000915.

Scherbaum F, Gilard D, and Deichmann N (1991) Slowness power analysis of the coda composition of two microearthquake clusters in northern Switzerland. *Physics of the Earth and Planetary Interiors* 67: 137–161.

Scherbaum F, Krüger F, and Wever M (1997) Double beam imaging: Mapping lower mantle heterogeneities using combinations of source and receiver arrays. *Journal of Geophysical Research* 102: 507–522.

Scherbaum F and Sato H (1991) Inversion of full seismogram envelopes based on the parabolic approximation: Estimation of randomness and attenuation in southeast Honshu, Japan. *Journal of Geophysical Research* 96: 2223–2232.

Schisselé E, Guilbert J, Gaffet S, and Cansi Y (2004) Accurate time-frequency-wavenumber analysis to study coda waves. *Geophysical Journal International* 158: 577–591.

Shang T and Gao L (1988) Transportation theory of multiple scattering and its application to seismic coda waves of impulsive source. *Scientia Sinica* 31: 1503–1514.

Shapiro NM, Campillo M, Margerin L, Singh SK, Kostoglodov V, and Pacheco J (2000) The energy partitioning and the diffusive character of the seismic coda. *Bulletin of Seismological Society of America* 90: 655–665.

Shapiro SA and Kneig G (1993) Seismic attenuation by scattering: Theory and numerical results. *Geophysical Journal International* 114: 373–391.

Shapiro SA, Schwarz R, and Gold N (1996) The effect of random isotropic inhomogeneities on the phase velocity of seismic waves. *Geophysical Journal International* 114: 373–391.

Shearer PM (1990) Seismic imaging of upper-mantle structure with new evidence for a 520-km discontinuity. *Nature* 344: 121–126.

Shearer PM (1991) Constraints on upper-mantle discontinuities from observations of long-period reflected and converted phases. *Journal of Geophysical Research* 96: 18147–18182.

Shearer PM and Earle PS (2004) The global short-period wavefield modelled with a Monte Carlo seismic phonon method. *Geophysical Journal International* 158: 1103–1117.

Shearer PM and Earle PS (2008) Observing and modeling elastic scattering in the deep Earth. *Advances in Geophysics* 150: 167–193. http://dx.doi.org/10.1016/S0065-2687(08)00006-X (Chapter 6).

Shearer PM, Hedlin MAH, and Earle PS (1998) PKP and PKKP precursor observations: Implications for the small-scale structure of the deep mantle and core. In: *The Core-Mantle Boundary Region*. *Geodynamics*, 28, pp. 37–55. American Geophysical Union.

Shearer PM and Masters TG (1990) The density and shear velocity contrast at the inner core boundary. *Geophysical Journal International* 102: 491–498.

Singh DD, Govoni A, and Bragato PL (2001) Coda Qc attenuation and source parameter analysis in Friuli (NE Italy) and its vicinity. *Pure and Applied Geophysics* 158: 1737–1761.

Singh S and Herrmann RB (1983) Regionalization of crustal coda Q in the continental Unites States. *Journal of Geophysical Research* 88: 527–538.

Song XD and Richards PG (1996) Seismological evidence for differential rotation of the Earth's inner core. *Nature* 382: 221–224.

Spetzler J and Snieder R (2001) The effect of small-scale heterogeneity on the arrival time of waves. *Geophysical Journal International* 145: 786–796.

Spudich P and Bostwick T (1987) Studies of the seismic coda using an earthquake cluster as a deeply buried seismography array. *Journal of Geophysical Research* 92: 10526–10546.

Spudich P and Iida M (1993) The seismic coda, site effects, and scattering in alluvial basins studied using aftershocks of the 1986 North Palm Springs, California, earthquake as source arrays. *Bulletin of Seismological Society of America* 83: 1721–1743.

Spudich P and Miller DP (1990) Seismic site effects and the spatial interpolation of earthquake seismograms: Results using aftershocks of the 1986 North Palm Springs, California, earthquake. *Bulletin of Seismological Society of America* 80: 1504–1532.

Su W-J and Dziewonski AM (1991) Predominance of long-wavelength heterogeneity in the mantle. *Nature* 352: 121–126.

Taira T and Yomogida K (2004) Imaging of three-dimensional small-scale heterogeneities in the Hidaka, Japan region: A coda spectral analysis. *Geophysical Journal International* 158: 998–1008.

Takahashi T (2012) Three-dimensional attenuation structure of intrinsic absorption and wide-angle scattering of *S* waves in northeastern Japan. *Geophysical Journal International* 189: 1667–1680. http://dx.doi.org/10.1111/j.1365-246X.2012.05438.x.

Tanaka S (2005) Characteristics of PKP-Cdiff coda revealed by small-aperture seismic arrays: Implications for the study of the inner core boundary. *Physics of the Earth and Planetary Interiors* 153: 49–60.

Thomas C, Igel H, Weber M, and Scherbaum F (2000) Acoustics simulation of *P*-wave propagation in a heterogeneous spherical earth; numerical method and application to precursor wave to PKP*df*. *Geophysical Journal International* 141: 307–320.

Thomas C, Kendall J-M, and Helffrich G (2009) Probing two low-velocity regions with PKP b-caustic amplitudes and scattering. *Geophysical Journal International* 178: 503–512. http://dx.doi.org/10.1111/j.1365-246X.2009.04189.x.

Thomas C, Weber M, Wicks CW, and Scherbaum F (1999) Small scatterers in the lower mantle observed at German broadband arrays. *Journal of Geophysical Research* 104: 15073–15088.

Tittgemeyer MF, Wenzel F, Fuchs K, and Ryberg T (1996) Wave propagation in a multiple-scattering upper mantle: Observations and modeling. *Geophysical Journal International* 127: 492–502.

Tkalčić H, Cormier VF, Kennett BLN, and He K (2010) Steep reflections from the earth's core reveal small-scale heterogeneity in the upper mantle. *Physics of the Earth and Planetary Interiors* 178: 80–91. http://dx.doi.org/10.1016/j.pepi.2009.08.004.

Tkalčić H, Flanagan M, and Cormier VF (2006) Observation of near-podal *P′P′* precursors: Evidence for back scattering from the 150–220 km zone in the Earth's upper mantle. *Geophysical Research Letters* 33. http://dx.doi.org/10.1029/2005GL024626.

Toksöz NM, Daity AM, Reiter E, and Wu RS (1988) A model for attenuation and scattering in the earth's crust. *Pure and Applied Geophysics* 128: 81–100.

Tono Y and Yomogida K (1996) Complex scattering at the core-mantle boundary observed in short-period diffracted P-waves. *Journal of Physics of the Earth* 44: 729–744.

Tono Y and Yomogida K (1997) Origin of short-period signals following P-diffracted waves: A case study of the 1994 Bolivian deep earthquake. *Physics of the Earth and Planetary Interiors* 103: 1–16.

Torquato S (2002) *Random Heterogeneous Materials: Microscopic and Macroscopic Properties*. New York: Springer.

Tsuruga K, Yomogida K, Ito H, and Nishigami K (2003) Detection of localized small-scale heterogeneities in the Hanshin-Awaji region, Japan, by anomalous amplification of coda level. *Bulletin of Seismological Society of America* 93: 1516–1530.

Ugalde A, Pujades LG, Canas JA, and Villasenor A (1998) Estimation of the intrinsic absorption and scattering attenuation in northeastern Venezuela (southern Caribbean) using coda waves. *Pure and Applied Geophysics* 153: 685–702.

Ugalde A, Vargas CA, Pujades LG, and Canas JA (2002) Seismic coda attenuation after the Mw = 6.2 Armenia (Columbia) earthquake of 25 January 1999. *Journal of Geophysical Research:* 107. http://dx.doi.org/10.1029/2001JB000197.

van Eck T (1988) Attenuation of coda waves in the dead sea region. *Bulletin of Seismological Society of America* 78: 770–779.

Vargas CA, Ugalde A, Pujades LG, and Canas JA (2004) Spatial variation of coda wave attenuation in northwestern Columbia. *Geophysical Journal International* 158: 609–624.

Vidale JE and Benz HM (1992) A sharp and flat section of the core-mantle boundary. *Nature* 359: 627–629.

Vidale JE, Dodge DA, and Earle PS (2000) Slow differential rotation of the Earth's inner core indicated by temporal changes in scattering. *Nature* 405: 445–448.

Vidale JE and Earle PS (2000) Fine-scale heterogeneity in the Earth's inner core. *Nature* 404: 273–275.

Vidale JE and Earle PS (2005) Evidence for inner-core rotation from possible changes with time in PKP coda. *Geophysical Research Letters* 32. http://dx.doi.org/10.1029/2004GL021240.

Vidale JE and Hedlin MAH (1998) Evidence for partial melt at the core-mantle boundary north of Tonga from the strong scattering of seismic waves. *Nature* 391: 682–685.

Vinnik LP (1981) Evaluation of the effective cross-section of scattering in the lithosphere. *Physics of the Earth and Planetary Interiors* 26: 268–284.

Wagner GS and Langston CA (1992a) A numerical investigation of scattering effects for teleseismic plane wave propagation in a heterogeneous layer over a homogeneous half-space. *Geophysical Journal International* 110: 486–500.

Wagner GS and Langston CA (1992b) Body-to-surface-wave scattered energy in teleseismic coda observed at the NORESS seismic array. *Bulletin of Seismological Society of America* 82: 2126–2138.

Wajeman N (1988) Detection of underside *P* reflections at mantle discontinuities by stacking broadband data. *Geophysical Research Letters* 15: 669–672.

Wang Y, Takenaka H, and Furumura T (2001) Modelling seismic wave propagation in a two-dimensional cylindrical whole-earth model using the pseudospectral method. *Geophysical Journal International* 145: 689–708.

Weber M and Davis JP (1990) Evidence of a laterally variable lower mantle structure from P- and S-waves. *Geophysical Journal International* 102: 231–255.

Weber M and Kornig M (1990) Lower mantle inhomogeneities inferred from PcP precursors. *Geophysical Research Letters* 17: 1993–1996.

Wegler U (2004) Diffusion of seismic waves in a thick layer: Theory and application to Vesuvius volcano. *Journal of Geophysical Research* 109. http://dx.doi.org/10.1029/2004JB003048.

Wegler U, Korn M, and Przybilla J (2006) Modeling full seismogram envelopes using radiative transfer theory with Born scattering coefficients. *Pure and Applied Geophysics* 163. http://dx.doi.org/10.1007/s00024-005-0027-5.

Wen L and Helmberger DV (1998) Ultra-low velocity zones near the core-mantle boundary from broadband PKP precursors. *Science* 279: 1701–1703.

Wennerberg L (1993) Multiple-scattering interpretations of coda-Q measurements. *Bulletin of Seismological Society of America* 83: 279–290.

Wenzel F, Sandmeier K-J, and Walde W (1987) Properties of the lower crust from modeling refraction and reflection data. *Journal of Geophysical Research* 92: 11575–11583.

Wesley JP (1965) Diffusion of seismic energy in the near range. *Journal of Geophysical Research* 70: 5099–5106.

Whitcomb JH (1973) Asymmetric PP: An alternative to PdP reflections in the uppermost mantle (0–100 km). *Bulletin of Seismological Society of America* 63: 133–143.

Whitcomb JH and Anderson DL (1970) Reflection of PP seismic waves from discontinuities in the mantle. *Journal of Geophysical Research* 75: 5713–5728.

Wright C (1972) Array studies of seismic waves arriving between P and PP in the distance range 90° to 115°. *Bulletin of Seismological Society of America* 62: 385–400.

Wright C and Muirhead KJ (1969) Longitudinal waves from the Novaya Zemlya nuclear explosion of October 27, 1966, recorded at the Warramunga seismic array. *Journal of Geophysical Research* 74: 2034–2047.

Wu R-S (1985) Multiple scattering and energy transfer of seismic waves separation of scattering effect from intrinsic attenuation I. Theoretical modelling. *Geophysical Journal of the Royal Astronomical Society* 82: 57–80.

Wu R-S (1989) The perturbation method in elastic wave scattering. *Pure and Applied Geophysics* 131: 605–637.

Wu R and Aki K (1985a) Scattering characteristics of elastic waves by an elastic heterogeneity. *Geophysics* 50: 582–595.

Wu R and Aki K (1985b) Elastic wave scattering by a random medium and the small-scale inhomogeneities in the lithosphere. *Journal of Geophysical Research* 90: 10261–10273.

Wu R-S and Aki K (1988) Multiple scattering and energy transfer of seismic waves separation of scattering effect from intrinsic attenuation II. Application of the theory to Hindu Kush region. *Pure and Applied Geophysics* 128: 49–80.

Wu W, Ni S, and Zeng X (2012) Evidence for P'P' asymmetrical scattering at near podal distances. *Geophysical Research Letters* 39. http://dx.doi.org/10.1029/2012GL052179.

Xu F, Vidale JE, and Earle PS (2003) Survey of precursors to *P'P'*: Fine structure of mantle discontinuities. *Journal of Geophysical Research* 108. http://dx.doi.org/10.1029/2001JB000817.

Yoshimoto K (2000) Monte Carlo simulation of seismogram envelopes in scattering media. *Journal of Geophysical Research* 105: 6153–6161.

Zeng Y (1991) Compact solutions for multiple scattered wave energy in the time domain. *Bulletin of Seismological Society of America* 81: 1022–1029.

Zeng Y (1993) Theory of scattered P- and S-wave energy in a random isotropic scattering medium. *Bulletin of Seismological Society of America* 83: 1264–1276.

Zeng Y, Su F, and Aki K (1991) Scattered wave energy propagation in a random isotropic scattering medium. *Journal of Geophysical Research* 96: 607–619.

This page intentionally left blank

1.25 Deep Earth Structure: *Q* of the Earth from Crust to Core

BA Romanowicz, University of California, Berkeley, CA, USA
BJ Mitchell, Saint Louis University, St. Louis, MO, USA

© 2015 Elsevier B.V. All rights reserved.

1.25.1	**Introduction**	789
1.25.2	**Early Studies**	790
1.25.3	**Frequency Dependence of *Q***	791
1.25.4	**1D Global Mantle *Q* Models**	793
1.25.4.1	Normal Mode and Surface-Wave-Based 1D *Q* Mantle Models	793
1.25.4.2	Body-Wave-Based 1D Mantle *Q* Models	794
1.25.5	***Q* in the Core**	796
1.25.5.1	The Outer Core	796
1.25.5.2	Attenuation in the Inner Core	796
1.25.5.2.1	Hemispheric variations	797
1.25.5.2.2	Anisotropic attenuation	798
1.25.6	**Global 3D Attenuation Structure in the Upper Mantle**	799
1.25.6.1	Normal Modes and Long-Period Surface Waves	799
1.25.6.1.1	Early studies	799
1.25.6.1.2	Anelasticity and focusing	799
1.25.6.1.3	Current status	800
1.25.6.2	Global Body-Wave Studies	803
1.25.6.3	Body-Wave Studies of Regional Extent	804
1.25.6.3.1	Multiple ScS studies	804
1.25.6.3.2	Body-wave attenuation studies in North America	805
1.25.6.3.3	Body-wave studies of upper mantle *Q* around subduction zones	805
1.25.6.3.4	Regional studies of upper mantle *Q* in mid-oceanic settings	807
1.25.7	**Regional *Q* Variations in the Crust and Uppermost Mantle**	807
1.25.7.1	Introduction	807
1.25.7.2	*Q* or Attenuation Determinations for Seismic Waves in the Crust	808
1.25.7.2.1	Spectral decay methods in which source effects cancel: regional phases	808
1.25.7.2.2	Spectral decay methods in which source effects cancel: fundamental-mode surface waves	809
1.25.7.2.3	Spectral decay methods in which source effects cancel: Lg coda	810
1.25.7.2.4	Spectral decay methods for which assumptions are made, or information can be learned, about the source spectrum: regional phases	811
1.25.7.2.5	Spectral decay methods for which assumptions are made about the source spectrum: fundamental-mode surface waves	812
1.25.7.3	Tomographic Mapping of Crustal *Q*	812
1.25.7.3.1	Q_{Lg}^{C}, Q_{Lg}, and Q_{μ} tomography in regions of Eurasia	814
1.25.7.3.2	Q_{Lg}^{C} tomography in Africa	815
1.25.7.3.3	Q_{Lg}^{C} and Q_{Lg} tomography in South America	815
1.25.7.3.4	Q_{Lg}^{C} tomography in Australia	815
1.25.7.3.5	Q_{Lg}^{C}, Q_{Lg}, and P/S tomography in North America	816
1.25.7.3.6	Q_{P} variation near ocean ridges	820
1.25.7.3.7	Variation of crustal *Q* with time	820
1.25.8	**Conclusions**	820
Acknowledgment		821
References		821

1.25.1 Introduction

Seismic waves have long been known to attenuate at a rate greater than that predicted by geometric spreading of their wave fronts. Knopoff (1964) pointed out more than four decades ago that much of that attenuation must occur because of the intrinsic anelastic properties of the Earth. Were it not for that fortunate circumstance, waves generated by all past earthquakes, as noted by Knopoff, would still be reverberating in the Earth today. Since it redistributes rather than absorbs wave energy, scattering would not have the same effect.

A commonly used measure of the efficiency of wave propagation is the quality factor Q or its inverse, the internal friction Q^{-1}. The latter quantity is most often defined by the expression

$$Q^{-1} = \Delta E / 2\pi E_{\max} \quad [1]$$

where ΔE is the elastic energy lost per cycle and $E_{\max}$ is the maximum elastic energy contained in a cycle. O'Connell and Budiansky (1978) proposed replacing maximum energy by average stored energy in eqn [1], a change that requires the integer 4 replace 2 in that equation. That form of the definition permits writing Q as the ratio of the real to imaginary part of the complex elastic modulus. However, most seismologists use eqn [1].

Because of its strong dependence on temperature, partial melting, and water content, mapping anelastic attenuation in the Earth has the potential to provide valuable information on Earth's three-dimensional (3D) structure and dynamics, in complement to what can be learned from mapping elastic velocities. A significant challenge is to separate the effects of anelastic (or intrinsic) attenuation from those of elastic scattering and focusing due to propagation in elastic 3D structure.

Practical aspects of seismic-wave attenuation include the need to account for it when determining earthquake magnitudes and when computing realistic synthetic seismograms. In addition, seismologists must know the attenuation structure in the Earth if they wish to determine dispersion that is produced by anelasticity (Jeffreys, 1967; Liu et al., 1976), which is needed, in particular, to interpret seismic models in the light of other observables such as the geoid (e.g., Romanowicz, 1990). The principle of causality requires that such velocity dispersion accompany intrinsic attenuation (Futterman, 1962; Lomnitz, 1957; Strick, 1967).

The following sections present a review of our current knowledge about seismic-wave attenuation from earliest studies to the present. It is a rapidly growing field for which measurements have only recently become sufficiently numerous and reliable to allow mapping at relatively small scales. It has consistently been observed that measurement errors are large, and it has recently become clear that systematic, rather than random, errors are the greatest cause of concern in Q determinations.

A major consideration is the frequency dependence of Q. After a brief review of earliest studies, we thus begin by describing the state of understanding of this issue. Next, we discuss 1D models of Q: Even now, only the average variation of Q with depth is reasonably constrained in the deep Earth, and frequency-dependent differences between the upper and lower mantle are emerging from the analysis of high-quality global data accumulated over the last 20 years. Following that, we discuss regional variations of Q in the upper mantle and in the crust, for which robust constraints are beginning to emerge. Earlier reviews on this topic can be found in Mitchell (1995) for the crust, Romanowicz (1998) for the mantle, and, most recently, Romanowicz and Durek (2000) for the whole Earth. This review is an updated version of Romanowicz and Mitchell (2007).

1.25.2 Early Studies

Although seismic-wave attenuation did not become a popular area of research until the 1970s, the first contributions appeared not long after global deployments of seismographs in the early 1900s. Here, we describe several important studies completed before 1970, which, in addition to providing the first estimates of Q for several phases, provided the first inklings of the difficulties associated with amplitude measurements.

Angenheister, working in Göttingen, Germany, in 1906, reported the first known measurements of the attenuation rate of a seismic wave. Instruments at that time were still primitive and surface waves consequently dominated most seismograms recorded by Göttingen's Wiechert seismometers. Angenheister (1906) used records from those instruments to measure the amplitude decay of 20 s surface waves for three different segments of the same great-circle path and found the decay rate to be about 0.00025 km^{-1}. For group velocities near 3 km s^{-1}, that rate corresponds to a Q value of about 200, a value implying that the measured attenuation coefficient lies within the range of commonly measured 20 s values today. He later published what was probably the first report of regional variations of surface-wave attenuation (Angenheister, 1921) in which he found that the decay of surface-wave amplitudes along oceanic paths was greater than that along continental paths. This result holds only for those cases where attenuation over relatively low-Q oceanic paths is compared to attenuation over high-Q continental paths (Mitchell, 1995).

Gutenberg also made some early determinations of Q using surface waves. He determined a Q value of 70 for Love waves at 100 s period (Gutenberg, 1924) and a value of 200 for Rayleigh waves at 20 s period (Gutenberg, 1945b). The latter value corresponds well with Angenheister's earlier measurement of Rayleigh-wave attenuation at that period. Gutenberg also determined Q for body phases, first finding a Q of 1300 for 4 s P and PKP waves (Gutenberg, 1945a). He then measured Q for three body-wave phases at different periods (Gutenberg, 1958), finding Qs of 2500 for P and PP at 2 s and 400 for P and PP at 12 s. In the same study, he also measured Q for S waves, finding values of 700 at 12 s and 400 at 24 s. Press (1956) also determined Q for S waves, finding it to be 500 or less.

Evernden (1955) studied the arrival directions of SV-, Rayleigh-, and Love-wave phases using a tripartite array in California and found that all of those phases deviated from great-circle paths between the events and the array. Although Evernden did not address Q, he brought attention to the fact that seismic waves may deviate from a great-circle path during propagation, a problem that continues, to this day, to plague determinations of Q from amplitude measurements.

The 1960s produced the first definitive evidence for lateral variations of body-wave Q even over relatively small distances. Asada and Takano (1963), in a study of the predominant periods of teleseismic phases recorded in Japan, found that those periods differed at two closely spaced stations and attributed that to differences in crustal Q. Ichikawa and Basham (1965) and Utsu (1967) studied spectral amplitudes at 0.5–3.0 Hz frequencies and concluded that P-wave absorption beneath a seismic station at Resolute, Canada, was greater than that beneath other stations in northern Canada.

Tryggvason (1965) devised a least-squares method for simultaneously obtaining Rayleigh-wave attenuation coefficients and source amplitudes using several stations located at varying distances from an explosive source. Since he assumed the source radiation pattern in this method to be circular, he had no need to determine that pattern or know the crustal velocity structure. In the same year, Anderson et al. (1965)

developed equations that allowed measured surface-wave attenuation to be inverted for models of Q_μ variation with depth and applied it to long-period surface waves that were sensitive to anelasticity at upper mantle depths.

Sutton et al. (1967) studied radiation patterns for Pg and Lg phases recorded at several stations in the United States and found that focusing and regional attenuation differences affected both waves. They concluded that the nature of the tectonic provinces traversed by the waves was more important than initial conditions at the source in determining the observed radiation patterns.

1.25.3 Frequency Dependence of *Q*

Determinations available in the 1960s from seismic observations and laboratory measurements suggested that Q was only weakly dependent on frequency (Knopoff, 1964). That conclusion, however, conflicted with the frequency dependence known for single relaxation mechanisms that exhibit rather narrowly peaked spectra for Q^{-1} centered at a characteristic frequency. Liu et al. (1976) reconciled those two observations by considering that, over the seismic frequency band in the Earth, Q^{-1} consists of a superposition of many thermally activated relaxation mechanisms for which maxima occurred at different frequencies. That superposition produces a continuous absorption band with a nearly frequency-independent Q^{-1} distribution in the seismic frequency band (**Figure 1**). The high- and low-frequency limits of the absorption band are described by relaxation times τ_1 and τ_2 and result in the following expression for the absorption band model (Kanamori and Anderson, 1977):

$$Q^{-1}(\omega) = (2/\pi)Q_m^{-1}\tan^{-1}\left[\omega(\tau_1 - \tau_2)/\left(1 + \omega^2\tau_1\tau_2\right)\right] \qquad [2]$$

where Q_m represents the maximum within the absorption band. A more realistic distribution of relaxation times yields a mild frequency dependence $Q \approx \omega^\alpha$ within the absorption band (Minster and Anderson, 1981; Mueller, 1986), with $Q^{-1} \sim \omega^{+1}$ at the higher end of the absorption band and $Q^{-1} \sim \omega^{-1}$ at the low end (Minster and Anderson, 1981). Measurements of attenuation of multiple ScS phases (Sipkin and Jordan, 1979) and other body waves (e.g., Der et al., 1982; Lundquist and Cormier, 1980; Sacks, 1980; Ulug and Berckhemer, 1984) have provided evidence that the high-frequency corner is located in the band 0.1–1 Hz. A later model (Anderson and Given, 1982) constructed to explain variations of Q for various depths in the Earth from the comparison of surface wave, free oscillation, and body-wave data obtained a single absorption band with $Q_\mu = 80$, $\alpha = 0.15$, and a width of five decades centered at different frequencies for different depths in the mantle, with a shift of the absorption band to longer periods at greater depth. Such a model could satisfy many of the known values of Q in the early 1980s. In particular, $\alpha = 0.15$ is compatible with a study of the damping of the Chandler wobble (Smith and Dahlen, 1981).

Many years of body-wave studies have since constrained the frequency dependence $Q \propto \omega^\alpha$ in the body-wave band to have $\alpha \sim 0.1$–1. Ulug and Berckhemer (1984) used spectral ratios of S/P waves in the frequency range 0.04–1.5 Hz and found

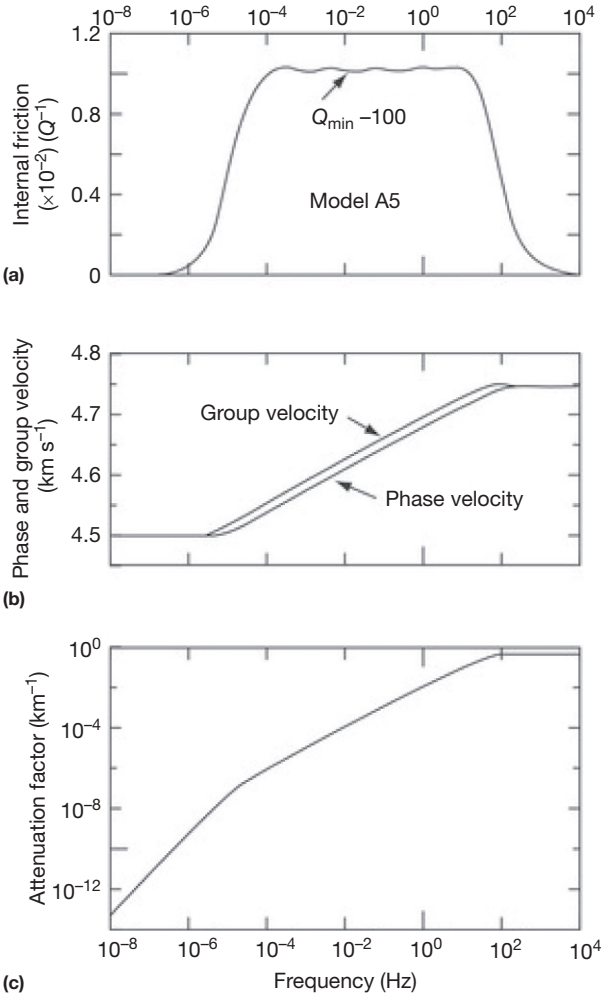

Figure 1 (a) Internal friction (Q^{-1}), (b) phase and group velocity dispersion, and (c) attenuation coefficient as functions of frequency. Reproduced from Liu HP, Anderson DL, and Kanamori H (1976) Velocity dispersion due to anelasticity: Implication for seismology and mantle composition. *Geophysical Journal of the Royal Astronomical Society* 47: 41–58, with permission from Blackwell Publishing.

$\alpha \sim 0.25$–0.6. This frequency range was extended to 6 Hz by Cheng and Kennett (2002), who found $\alpha \sim 0.2$–1 in Australia. Flanagan and Wiens (1998) found a factor of 2 difference in Q measured from sS/S and pP/P phase pairs in the Lau back-arc region, implying a strong frequency dependence in the 1–10 s period range, and inferred $\alpha \sim 0.1$–0.3.

More recently, Shito et al. (2004) used regional waveform data in western Pacific subduction zones to estimate α from P–P spectral ratios in the frequency range 0.08–8 Hz and found a range of $\alpha \sim 0.1$–0.4, which is in agreement with laboratory studies for solid olivine (e.g., Gueguen et al., 1989; Jackson, 2000) and seems to indicate that solid-state processes are the primary mechanism for the observed attenuation. Indeed, according to laboratory results, partial melting results in weak frequency dependence in a broad frequency range (e.g., Jackson et al., 2004), which is inconsistent with these observations.

In order to reconcile teleseismic S–P differential travel times measured by handpicking, on the one hand, and by

comparison of observed and synthetic seismograms, on the other, Oki et al. (2000) found that a frequency dependence with $\alpha \sim 0.04$ needs to be introduced in the reference preliminary reference Earth model (PREM) Q model (Dziewonski and Anderson, 1981), a value much smaller than in other studies.

More recently, Lekic et al. (2009) applied a Backus–Gilbert approach to globally averaged normal mode and surface-wave measurements in order to isolate the frequency dependence from that due to the frequency dependence reflecting the depth sensitivity of Q_μ. They found that α varies with frequency within the period range considered (80–3000 s), with $\alpha \sim 0.3$ at periods shorter than 200 s (compatible with most body-wave results), decreasing to ~0.1 between 300 and 800 s and possibly becoming negative at even longer periods (**Figure 2**). From most recent comparisons of global 1D Q models obtained from surface waves and free oscillations, on the one hand, and teleseismic P and S body waves, on the other, it appears that this frequency dependence is manifested primarily in the lower mantle (see **Section 1.25.4**).

At crustal depths, the frequency dependence of Q is usually described by the equation $Q = Q_0 f^{\zeta}$ where Q_0 is a reference frequency and ζ is the frequency dependence parameter. For shear-wave Q (Q_μ), it appears to be between about 0.0 and 1.0 and varies regionally, with depth in the crust and with frequency, as will be described in more detail in a later section.

An important consequence of the frequency dependence of Q in the Earth is the presence of velocity dispersion due to attenuation. Velocity dispersion was first recognized to be important when comparing global mantle elastic velocity models based on free oscillation and body-wave travel time data centered at 1 s. A dispersion correction of 0.5–1.5% helped reconcile these models (Kanamori and Anderson, 1977; Liu et al., 1976) and has been applied systematically in global seismology (e.g., Dziewonski and Anderson, 1981), although Montagner and Kennett (1996) showed that attenuation alone is insufficient to reconcile both types of data and suggested the need to perturb the density structure and introduce radial anisotropy in different parts of the mantle. In the presence of large lateral variations in Q in the upper mantle, which could be in excess of 100%, it is also necessary to account for velocity dispersion when interpreting global tomographic models in the light of other geophysical data, such as the geoid, as illustrated by Romanowicz (1990) in the case of very long wavelength structure. Karato (1993) estimated the contribution of anelasticity to the calculation of partial derivatives of elastic velocities with temperature and concluded that it should be important in the deep mantle, as anelastic effects might dominate anharmonic effects at high pressures, a conclusion confirmed by Karato and Karki (2001), who used an improved model for the calculation of anelastic effects, including the nonlinear dependence of attenuation on temperature.

In order to interpret seismologically derived 1D and 3D Q models in the Earth, it is necessary to confront them with laboratory experiments, which should provide constraints on (1) the physical mechanisms responsible for attenuation (i.e., grain boundary or dislocation processes (e.g., Jackson, 1993; Karato, 1998)) and the related frequency dependence and (2) the dependence of Q on temperature and pressure. Unfortunately, this has proven to be a major challenge, particularly for the deep mantle, due to the difficulties of reproducing in the laboratory both the high P and high T conditions, the low frequency range of seismic observations, and the location of the absorption band far from the frequency range of ultrasonic experiments, preventing ready extrapolation of seismic frequencies.

The variation of Q_μ with temperature can be expressed as (e.g., Jackson, 1993; Karato, 1993)

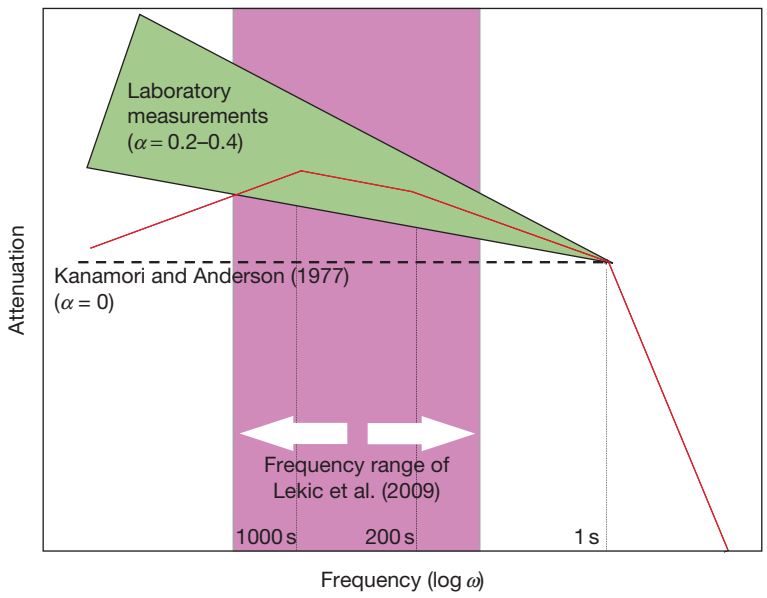

Figure 2 Frequency dependence of attenuation within the absorption band obtained from low-frequency data. A corner frequency is assumed at 1 Hz, beyond which $\alpha = 1$ (Sipkin and Jordan, 1979). Seismically inferred values (pink) are compared to those obtained from laboratory measurements (green) and the estimates assuming no frequency dependence (broken line). After Lekic V, Matas J, Panning M, and Romanowicz B (2009) Measurement and implications of frequency dependence of attenuation. *Earth and Planetary Science Letters* 282: 285–293.

$$Q^{-1} = A\omega^{-\alpha}\exp(-\alpha H/RT) \quad [3]$$

where $H = E^* + PV^*$ is the activation enthalpy, which depends on pressure through the activation volume V^*, a quantity that is not precisely known. One way to circumvent this is to parametrize this expression in terms of homologous temperature T_m/T (e.g., Cammarano et al., 2003; Karato, 1993; Sato et al., 1989):

$$Q^{-1} = A\omega^{-\alpha}\exp(-\alpha g T_m/T) \quad [4]$$

where g is a dimensionless factor, which depends on H, the melting temperature T_m, and the gas constant R. Such a parametrization removes the need for accurate knowledge of the activation volume and also allows the use of a simple scaling law to relate grain size to frequency (Sato et al., 1989). The pressure dependence is folded into T_m, which is easier to measure in the laboratory.

Much progress in the measurement of attenuation at seismically relevant frequencies has been achieved in the last 15 years (e.g., Faul et al., 2004; Getting et al., 1997; Jackson, 1993; Jackson and Faul, 2010; Karato and Spetzler, 1990). Recently, reliable results for olivine have become available at pressures and temperatures down to asthenospheric depths. There is some evidence that attenuation scales with diffusion creep viscosity (e.g., McCarthy and Takei, 2011), that hydration of mantle minerals causes significant increases in attenuation (Aizawa et al., 2008), and that water (Shito et al., 2006) and melt (Faul et al., 2004; McCarthy et al., 2011) can significantly increase attenuation. Research continues into the mechanism of attenuation, including grain boundary sliding (Morris and Jackson, 2009), diffusion creep (Sundberg and Cooper, 2010), and the effect of dislocations (Farla et al., 2012). These recent advances are described in more detail in **Chapter 2.21**.

While most physical mechanisms invoked consider volumetric contributions to attenuation in the Earth (e.g., Jackson, 2007), several authors have pointed out recently that solid–solid phase transitions may play a role in bulk dissipation of seismic energy, through the finite character of their kinetics. However, this process is clearly strongly frequency-dependent, and there is no agreement yet on the relevance of the attenuation band to seismically relevant frequencies (e.g., Durand et al., 2012; Li, 2010; Ricard et al., 2009). Nevertheless, global 1D mantle Q profiles are generally readily interpreted in terms of thermally activated, viscoelastic relaxation mechanisms (e.g., Faul and Jackson, 2005; see also **Chapter 2.21**).

1.25.4 1D Global Mantle *Q* Models

Our knowledge of the 1D Q structure of the Earth comes from two types of data spanning different ranges of frequencies: normal modes/surface waves, on the one hand, and body waves, on the other. Because of the suggestive evidence for frequency dependence of Q, with an upper frequency limit for the corresponding absorption band falling in the range of body-wave studies, it is important to consider these two types of models separately before comparing them. Another issue is that of lateral variations in Q and how representative the sampling might be in different types of studies: for example, normal mode data, by the nature of their global sampling, will likely provide models that are more representative of the true global average than multiple ScS data, which sample primarily subduction zone regions and their vicinities. A third issue is that some bulk attenuation appears to be needed to explain normal mode data, but different authors locate it in different parts of the mantle.

1.25.4.1 Normal Mode and Surface-Wave-Based 1D *Q* Mantle Models

As noted in a previous review of this topic (Romanowicz and Durek, 2000), early studies based on normal mode and surface-wave data developed measurement and inversion methodologies and established the main features of the variation of Q_μ with depth (e.g., Anderson and Archambeau, 1966; Buland and Gilbert, 1978; Deschamps, 1977; Geller and Stein, 1978; Gilbert and Dziewonski, 1975; Jobert and Roult, 1976; Kanamori, 1970; Roult, 1975; Sailor and Dziewonski, 1978). These studies found that

1. shear-wave attenuation is low in the lithosphere;
2. there is a high-attenuation zone roughly corresponding to the low-velocity zone generally associated with the asthenosphere;
3. below 200 km depth, Q_μ increases with depth with a sharp gradient across the transition zone; and
4. Q_μ is higher on average in the lower mantle than in the upper mantle.

In the last decades, an intriguing discrepancy has emerged between the measurements of fundamental mode Q_R obtained for spheroidal modes using a propagating wave approach (e.g., Durek and Ekström, 1996; Durek et al., 1993; Dziewonski and Steim, 1982; Romanowicz, 1990, 1994a) and those using a standing-wave approach (Roult and Clévédé, 2000; Smith and Masters, 1989; Widmer et al., 1991). In the period band 150–300 s, where measurements by the two methods overlap, Q_R estimates derived from standing-wave observations are systematically higher than those derived from surface waves by about 15–20%, which translates into higher Q_μ in the transition zone for models based on free oscillation data (**Figure 3**). The cause of this discrepancy was first investigated by Durek and Ekström (1997) who explored the influence of realistic background noise on normal mode-based measurements, which require the use of long time series. This issue is particularly relevant in the light of the discovery of continuously excited background free oscillations (e.g., Suda et al., 1998). While the background noise does contribute to a bias toward higher Q values, if measurements are done with care, the bias does not exceed about 5–10%, failing to explain the larger observed discrepancy. On the other hand, Masters and Laske (1997) questioned the accuracy of surface-wave Q measurements at very long periods, pointing out the difficulty in finding an appropriate time window isolating the fundamental mode in the presence of overlapping wave trains and overtones. A more recent study by Roult and Clévédé (2000) confirms the higher Q values obtained from mode-based measurements (**Figure 3**). These authors concluded that mode Q measurements are more reliable than measurements

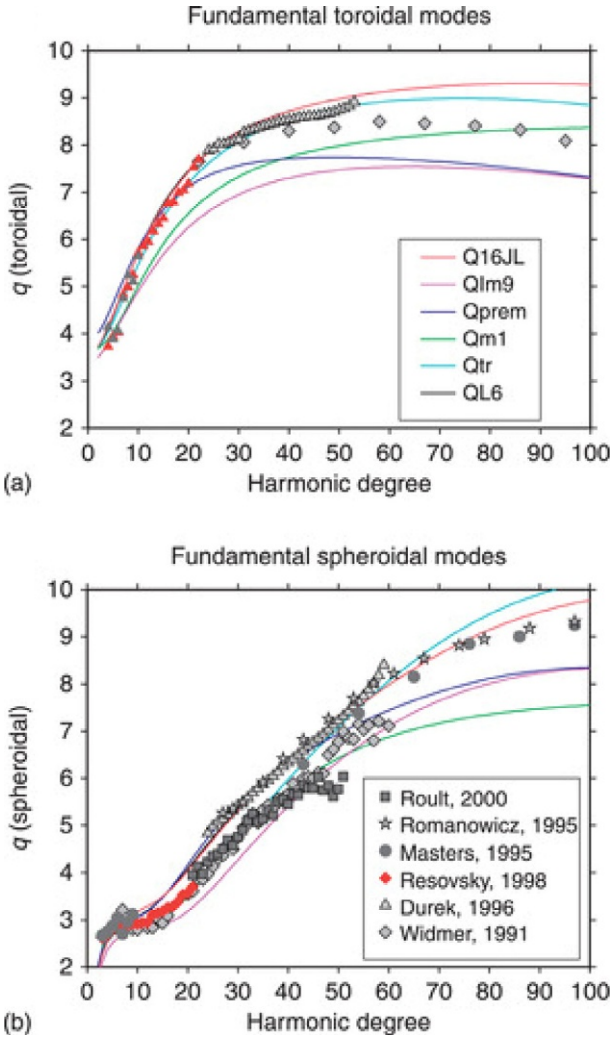

Figure 3 Fundamental-mode Q measurements obtained using either a standing mode approach (Masters and Laske, 1997; Roult and Clévédé, 2000; Widmer et al., 1991) or a propagating surface-wave approach (Durek and Ekström, 1996; Romanowicz, 1995). Note the discrepancy between the two approaches in the frequency band where both methods can be applied. Also shown are fits to the data for several models of Q_μ shown in Figure 3. (a) Toroidal modes and (b) spheroidal modes. Data are from the REM website.

based on great-circle surface-wave amplitude ratios, which they attribute to contamination by higher modes and to the relative deficiency in low frequencies of the first arriving R1 train. We note however that the QL6 model of Durek and Ekström (1996) was derived from traveling surface-wave data using a different method than tested by Roult and Clévédé (2000). QL6 (**Figures 3** and **4**) not only fits surface-wave data better than mode-based models such as QM1 (Widmer et al., 1991) but also fits toroidal mode Q data better than both QM1 and PREM (Dziewonski and Anderson, 1981). Therefore, it seems that the question of the mode/surface-wave discrepancy has not been resolved yet. A more recent study by Resovsky et al. (2005) revisited the construction of a 1D Q model of the Earth using a forward modeling approach based on the neighborhood algorithm and produced a family of acceptable models with robust error estimates. Their mode data set was augmented through recent measurements of the attenuation of low-angular-order modes (e.g., He and Tromp, 1996; Resovsky and Ritzwoller, 1998). They circumvented the mode/surface-wave discrepancy problem by including both fundamental-mode surface-wave and spheroidal mode measurements in the period range 150–300 s and attributing a low weight to these incompatible data. Their final family of models appears to be in good agreement, on average, with the surface-wave-based model QL6, in particular in the transition zone (**Figure 4**). While PREM and QL6 have constant Q_μ in the lower mantle, the Resovsky et al. (2005) study tentatively includes three layers in the lower mantle and confirms the presence of a mild Q_μ maximum in the mid-lower mantle (Qtr, **Figure 3**), as was found in earlier models (SL8, Anderson and Hart (1978); PAR2C, Okal and Jo (2002); QM1, Widmer et al. (1991); and Q7U15L, Durek and Ekström (1996); see the review by Romanowicz and Durek (2000)). What is perhaps not yet well constrained is the precise location of this maximum.

1.25.4.2 Body-Wave-Based 1D Mantle *Q* Models

Body-wave studies typically derive Q structure from the measurement of t^* ('t-star'), which is defined as follows:

$$t^* = \int \frac{ds}{Qv} \qquad [5]$$

where the integral is taken along the body-wave path and v is the wave velocity. See **Section 1.25.6.2** for more details on how t^* is measured.

Nearly vertically traveling multiple ScS waves provided early constraints on the average Q_μ in the whole mantle (e.g., Kovach and Anderson, 1964; Yoshida and Tsujiura, 1975) and confirmed the increase in Q_μ in the mid-mantle. Studies of amplitude ratios of body-wave phases interacting with the core–mantle boundary (CMB) provided early evidence for a possible lower Q_μ zone at the base of the mantle (e.g., Kuster, 1972; Mitchell and Helmberger, 1973).

More recently, Lawrence and Wysession (2006a) developed a Q_μ model based on a large global data set of differential ScS/S amplitude measurements, using a niching genetic algorithm to fit the variations of these amplitudes with distance. Because of the nature of their data, their model (QLM9, **Figure 4**) is best constrained in the lower mantle, so they chose to fix the top 400 km of the mantle to the PREM value. The resulting model also provides evidence for the existence of a Q_μ maximum in the lower mantle, in this case right above the D″ region. However, the high Q values that they obtain in the transition zone are incompatible with the fundamental-mode spheroidal and toroidal data (**Figure 3(a)**). Replacing their upper mantle with that of QL6 solves this problem (**Figure 3(b)**), and little adjustment is needed in the lower mantle to fit the ScS/S amplitude data (Lawrence, personal communication).

Most recently, Durand et al. (2013) applied a method based on instantaneous frequency measurements (Ford et al., 2012; Gao et al., 2011) to obtain differential t^*_{S-ScS} estimates in the northeast Pacific and under Central America with a strict data quality selection. These authors infer a 1D Q_μ profile of the mantle that is generally in good agreement with QLM9

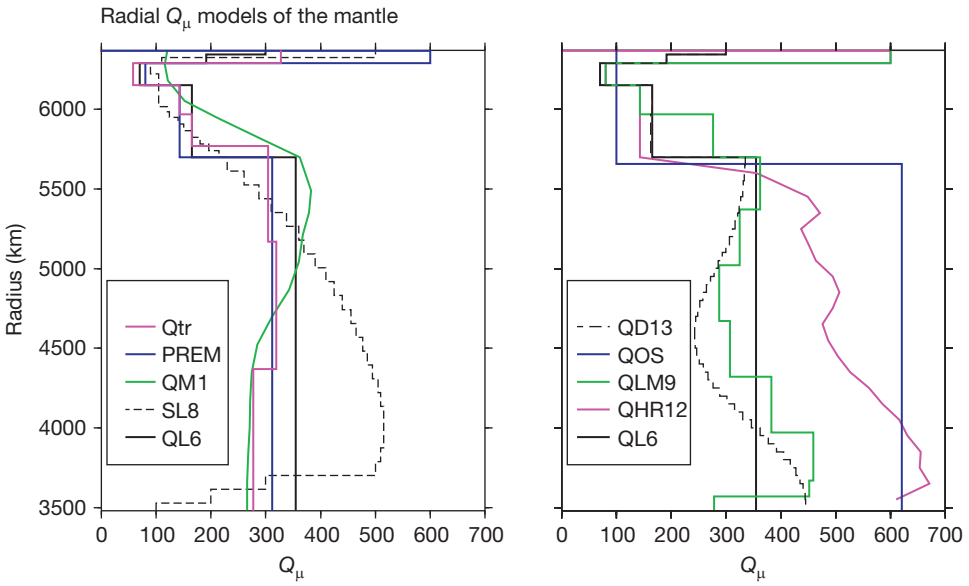

Figure 4 Radial models of Q_μ in the mantle. (Left panel) Free oscillation and surface-wave-based models. Models QM1 (Widmer et al., 1991); SL8 (Anderson and Hart, 1978); PREM (Dziewonski and Anderson, 1981); QL6 (Durek and Ekström, 1996); and Qtr (Resovsky et al., 2005). PREM and QL6 fit fundamental-mode Rayleigh-wave data, but only QL6 also fits fundamental-mode toroidal mode data. (Right panel) Body-wave-based models: QLM9 (Lawrence and Wysession, 2006a) from ScS/S amplitude data; QI6JL: a model that fits both ScS/S amplitude data and fundamental-mode surface-wave data (Lawrence, personal communication); QOS08 (Oki and Shearer, 2008); QHR12 (Hwang and Ritsema, 2011). The latter two models are based on teleseismic P and S waves.

(Figure 4). They suggest that differences can be attributed to a slight frequency dependence with $\alpha \sim 0.1$.

The typical frequency range of studies based on ScS and multiple ScS is about 0.02–0.2 Hz. Higher frequency studies have been based on a combination of P and S waves or P and PP waves. Warren and Shearer (2000) derived a series of 1D global Q_α models from stacked spectra of P and PP waves in the frequency band 0.16–0.86 Hz. While frequency dependence cannot be ignored in this frequency band, as discussed further in the following text, when assuming no frequency dependence, these authors find that the upper mantle is five times more attenuating than the lower mantle.

Recently, Oki and Shearer (2008) constructed a two-layered 1D Q_μ model for short-period body waves (3–10 s), using a large data set of measurements from teleseismic P and S waves from broadband seismograms and extracting differential t^*_{S-P} measurements. They obtained similar average Q_μ in the upper mantle as derived from long-period surface-wave/mode measurements but higher Q_μ (by a factor of 2) in the lower mantle, which they inferred to indicate stronger frequency dependence of Q_μ in the lower mantle. Hwang and Ritsema (2011) reexamined this question with an order of magnitude larger data set and confirmed the larger Q_μ in the lower mantle. Their proposed model (model HR11, Figure 4), which has a fixed upper mantle Q_μ profile equal to that of PREM (Dziewonski and Anderson, 1981), features increasing Q_μ from 360 at the top of the lower mantle to 670 in the lowermost mantle. The authors point out that this difference with depth is as large as lateral differences in Q_μ between tectonic and stable areas of the continents. The details of the lower mantle structure may change if the upper mantle model QL6 (Durek and Ekström, 1996) is used rather than PREM, as would be appropriate to fit long-period surface waves. However, the general trend of Q_μ increasing with depth in the lower mantle, which is the most robust feature of model HR11, would not change.

Clearly, the large differences between the Q values obtained from body waves, especially those including P waves in the analysis, and low-frequency surface waves and free oscillations suggest a frequency-dependent effect. Moreover, this effect may be different in the upper and lower mantle. To accommodate both normal mode and body-wave observations, Anderson and Hart (1976, 1978) proposed a model with a Q_μ maximum in the lower mantle, a feature that has successively appeared and disappeared in subsequent whole mantle models based on normal mode and surface-wave data (Giardini and Woodhouse, 1988; Li, 1990; Masters and Gilbert, 1983; Okal and Jo, 2002; Smith and Masters, 1989; Widmer et al., 1991). Anderson and Given (1982) proposed that the absorption band is shifted to lower frequencies in the lower mantle, compared to the upper mantle, resulting in a more prominent frequency dependence in the lower mantle. This is in agreement with the results of Oki and Shearer (2008). On average, the large differences between lower mantle Q values derived from low-frequency and high-frequency data can be accommodated with a frequency dependence with $\alpha \sim 0.1$, as also noted by Lekic et al. (2009) (Figure 2).

In these body-wave studies, it is generally assumed that bulk attenuation (Q_κ^{-1}) can be neglected. Using the relationship between Q_α, Q_β, and Q_κ (Anderson and Hart, 1978)

$$Q_\alpha^{-1} = \frac{4}{3}(V_S/V_P)^2 Q_\beta^{-1} + \left[1 - \frac{4}{3}(V_S/V_P)^2\right] Q_\kappa^{-1} \qquad [6]$$

this leads to the commonly used conversion between Q_α and Q_β, assuming a Poisson solid ($V_S = \sqrt{3}V_P$):

$$Q_\alpha = \frac{9}{4} Q_\beta$$

However, some regional studies in subduction zones suggest that bulk attenuation could be as large as 1/3 of attenuation in shear (e.g., Roth et al., 1999).

Bulk attenuation is necessary to simultaneously fit high-Q radial mode data and surface-wave data, and some models such as SL8 (Anderson and Hart, 1978) and the widely used PREM (Dziewonski and Anderson, 1981) locate it in the inner core, while others prefer to place it in the upper mantle (e.g., Sailor and Dziewonski, 1978), in the outer core (Anderson and Given, 1982; Widmer et al., 1991), and, more recently, in the asthenosphere (Durek and Ekström, 1995). Resovsky et al. (2005) also revisited this question and found bulk attenuation to be negligible in the inner core and preferentially located in the outer core and lower mantle. The issue of the location of bulk attenuation in the Earth is not resolved.

New constraints on average shear and bulk attenuation in the Earth and the core and their frequency dependence, from a combination of body-wave and normal mode analysis, may be forthcoming, owing to the high-quality digital data set assembled in the last 20 years on the global broadband seismic network and owing to the occurrence of several very large earthquakes, especially great earthquakes such as that in Sumatra on 26 December 2004 and Tohoku (Japan) on 12 March 2010. In particular, these data are providing an opportunity to revisit the Qs of the gravest modes of the Earth, in particular the radial mode ${}_0S_0$, and, for the first time, measure the Q of individual singlets of modes such as ${}_0S_2$ or ${}_2S_1$ (e.g., Rosat et al., 2005; Roult et al., 2006).

1.25.5 *Q* in the Core

1.25.5.1 The Outer Core

In the liquid outer core, Q is very high, and generally well approximated by $Q_\kappa \sim \infty$, to fit both free oscillation and body-wave data. Finite Q_κ is, however, required to explain some free oscillation data in the outer core, but the depth range where it is located is still the subject of debate (Anderson and Given, 1982; Durek and Ekström, 1996; Resovsky et al., 2005; Widmer et al., 1991) and, in general, the upper mantle and the inner core are preferred locations for finite Q_κ. Likewise, while some evidence for finite Q_κ from short-period core phases has been suggested, it is not clear that it is resolvable (Cormier and Richards, 1976). There is some indication for the existence of a thin layer of relatively low Q just above the inner core boundary (ICB) (Zou et al., 2008), which could be due to the presence of suspended solid particles in the F-layer (Jeffreys, 1939; Loper and Roberts, 1981).

1.25.5.2 Attenuation in the Inner Core

Attenuation in the inner core is investigated using inner core-sensitive modes, as well as spectral amplitude ratios of different core phases. Topics that have been the subject of recent work include

- the compatibility of normal mode and body-wave measurements and implications for the frequency dependence of Q in the inner core,
- variations with depth,
- anisotropy in Q_α, and
- hemispheric variations at the top of the inner core.

From early on, measurements of amplitude ratios of PKP(DF) (sampling the inner core) and PKP(BC) (sampling the outer core) constrained Q_α in the top 500 km of the inner core to be in the range 200–600 (e.g., Bhattacharyya et al., 1993; Bolt, 1977; Choy and Cormier, 1983; Cormier, 1981; Doornbos, 1974, 1983; Ivan et al., 2005; Niazi and Johnson, 1992; Sacks, 1969; Song and Helmberger, 1993; Tseng et al., 2001). Most studies have suggested an increase of Q_α with depth, although some find that Q_α is constant with depth (e.g., Bhattacharyya et al., 1993; Niazi and Johnson, 1992). In these studies, the sampling depth range was limited by the narrow distance range in which the phase PKP(BC) is observed. Extending the depth range sampled by previous studies to 600 km by including diffracted PKP(BC) phases, Souriau and Roudil (1995) proposed a two-layered model with $Q_\alpha \sim 200$ in the topmost 100 km of the inner core and $Q_\alpha \sim 440$ below. Cormier et al. (1998) designed a new approach that allowed them to investigate the variation of Q_α deeper in the inner core, by comparing observed and synthetic PKIKP waveforms in the distance range 150–180°. The synthetic waveforms are built using the source time history of each earthquake, determined from the analysis of P waveforms, and include the effects of mantle attenuation. In a recent improved implementation of this method, which takes into account surface reflections and reverberations near the source, Li and Cormier (2002) obtained a mean for the inner core of Q_α 307 ± 90 and much stronger attenuation in the top 300 km of the inner core. Testing the hypothesis of an innermost inner core, Cormier and Stroujkova (2005) found a rapid change in the magnitude and variance of seismic attenuation of PKIKP in the middle of the inner core, in the interval 400–600 km in Earth radius (**Figure 4**), which supports the existence of a distinct innermost inner core (e.g., Ishii and Dziewonski, 2002). Recently, Waszek and Deuss (2013) have suggested the presence of a high-Q_α layer in the top 30 km of the inner core.

While the analysis of core-sensitive PKP phases provides constraints on Q_α, normal modes primarily provide constraints on Q_μ. If there were no significant attenuation in bulk, and no frequency dependence, the inferred Q_μ from body-wave studies would be on the order of ~40. Confronting this value with measurements based on inner core-sensitive normal mode data has resulted in some puzzles. Early normal mode studies found very large values of Q_μ (1500–3500) based on the measurement of attenuation of spheroidal core modes (Buland and Gilbert, 1978; Masters and Gilbert, 1981), whereas most more recent models have much lower Q_μ, such as PREM ($Q_\mu = 85$; Dziewonski and Anderson, 1981) or QM1 ($Q_\mu = 110$; Widmer et al., 1991), which is also compatible with measurements of Giardini and Woodhouse (1988). On the other hand, applying the Sompi method, Kumazawa et al. (1990) and Suda and Fukao (1990) measured Q_μ of modes sensitive to shear in the top part of the inner core and found very large values and an increase with depth, with $Q_\mu = 1500$ in the top 200 km and $Q_\mu = 3800$ at greater depth. However, their identification of modes has been questioned, and, recently, Andrews et al. (2006) have shown that measurements of

inner core Q_μ could be biased by neglecting mode coupling. Through the comparison of observations and synthetic predictions including mode coupling effects, these authors found that models with very high Q_μ are incompatible with the observations, which favor moderate values of $Q_\mu \sim 80–100$. While such moderate values are now established in the top part of the inner core, where normal modes concentrate their sensitivity, a recent observation of PKJKP, which samples deep into the inner core (Cao et al., 2005), has provided the opportunity to estimate the average Q_μ in the inner core, which was found to be >150, possibly as large as 300 (Cao and Romanowicz, 2009), and which would imply an increase with depth, like that for Q_α. This result, however, needs to be confirmed by additional observations of PKJKP.

Even the lowest proposed values for Q_μ currently favored are incompatible with the Q_α results, unless one invokes either (1) significant bulk attenuation in the inner core, or (2) significant frequency dependence of Q, or (3) a significant scattering component. The rather low value for Q_α found is compatible with the existence of a mushy zone in the top part of the inner core, whose presence is related to the process of solidification of iron alloy (Fearn et al., 1981; Loper and Fearn, 1983; Loper and Roberts, 1981) involving a solid matrix and fluid inclusions. This would result primarily in compressional attenuation and could explain some of the observations of seismic anisotropy in the inner core (e.g., Singh et al., 2000). Bowers (2000) cautioned that the large scatter observed in Q_α measurements from PKP amplitude ratios could be due to the effects of lateral variations in structure near the CMB and in particular the presence of ultralow-velocity zones. On the other hand, Krasnoshchekov et al. (2005) suggested that variability in the amplitudes of ICB reflected PKiKP phases could be due to a mosaic of partially molten patches of scale length 10–100 km.

In a series of papers, Cormier and collaborators recently explored two different interpretations for the attenuation in the inner core, invoking a viscoelastic mechanism and a scattering mechanism, respectively (Cormier and Li, 2002; Cormier et al., 1998; Li and Cormier, 2002). In the viscoelastic interpretation, they considered the absorption band model of Cormier and Richards (1988) and, through a parameter search approach, sought to constrain the low-frequency corner τ_1, as well as the peak attenuation Q_m^{-1} and the attenuation at 1 Hz (Li and Cormier, 2002). While constraining τ_1 turned out to be problematic, they found that the data are consistent with frequency-dependent attenuation in the inner core and weak velocity dispersion in the seismic body-wave band. The existence of scattering, at least at the top of the inner core, was clearly documented by Vidale and Earle (2000) through the modeling of PKiKP coda and more recently by Leyton and Koper (2007). In the scattering interpretation, Cormier and Li (2002) investigated a model of inner core attenuation due to forward scattering by 3D fabric caused by solidification texturing, which could also be responsible for the observed depth-dependent inner core anisotropy. They found a mean scale length of heterogeneity of 9.8 ± 2.4 km and a mean velocity perturbation of $8.4 \pm 1.8\%$. They confirmed the depth dependence found in the viscoelastic interpretation but with a sharper transition between the highly attenuating upper part of the inner core and the lower attenuating center (e.g., Figure 13 in Souriau and Calvet, 2015). They suggested that scattering plays a dominant role in attenuating inner core traversing phases in the frequency band 0.02–2 Hz, as it can also explain elastic and anelastic anisotropy and their depth dependence and helps reconcile the body-wave and normal mode Q measurements. A synthesis of waveform and travel time observations led Cormier (2007) to propose a model of texture of the uppermost inner core that may reflect the solidification process of the inner core.

1.25.5.2.1 Hemispheric variations

Another observation in favor of the presence of a mushy transition zone at the top of the inner core is that of hemispheric differences, first observed in elastic velocity using differential travel time measurements of the pair of phases PKP(BC), PKP(DF) (Creager, 1999; Tanaka and Hamaguchi, 1997). A pair of useful phases for the study of hemispheric variations in attenuation is (PKiKP, PKIKP) in the distance range 120–144°. In this distance range, PKiKP is postcritically reflected at the ICB and PKIKP samples the top ~100 km of the inner core (Garcia, 2002; Niu and Wen, 2001). These phases have almost the same ray paths in the mantle and in the outer core, so the differences in travel times and amplitudes can be attributed to the vicinity of the ICB. Indeed, in a study covering the epicentral distance range 131–141°, the faster eastern hemisphere (40–180 °E) was also found to have lower Q_α than the slower western hemisphere (Wen and Niu, 2002). In order to better constrain the depth dependence of the hemispheric variations in Q_α, Cao and Romanowicz (2004) extended the epicentral distance range to 144° and found large differences in Q_α, with $Q_\alpha \sim 335$ in the western hemisphere and ~160 in the eastern hemisphere, which they interpreted as resulting from small lateral temperature variations at the top of the inner core. Such temperature variations could be imposed on the inner core by heterogeneities at the CMB (e.g., Sumita and Olson, 1999) and would influence the connectivity of fluid inclusions in the mushy zone. Below about 85 km depth, the hemispheric differences appeared to wane. However, several studies found evidence for persisting differences at greater depth. Oreshin and Vinnik (2004) measured spectral ratios of PKP(DF) and either PKP(AB) or PKP(BC) in the distance range 150–170° and found differences in Q_α between the hemispheres down to 600 km depth. Yu and Wen (2006a) combined observations of PKiKP/PKIKP in the distance range 120–141° and PKP(BC)/PKIKP in the distance range 146–160°, along equatorial paths, and proposed that they could resolve hemispheric differences in Q down to at least 200 km (**Figure 5**). However, in the distance range 149–155°, PKP(BC) interferes with PKiKP, causing large scatter in the data. On the other hand, Li and Cormier (2002) did not find evidence for such hemispheric variations in the deeper inner core using PKIKP data at larger distances.

Recently, depth-dependent attenuation structure was constrained in the inner core below the north East Pacific (western hemisphere), using PKP data from the dense short-period HiNet array in Japan (Iritani et al., 2010; Kazama et al., 2008). These authors found evidence for a peak in attenuation around 200–250 km depth, which may provide constraints on the mode of growth of the inner core. Most recently, lopsided growth of the inner core has been proposed to explain seismic

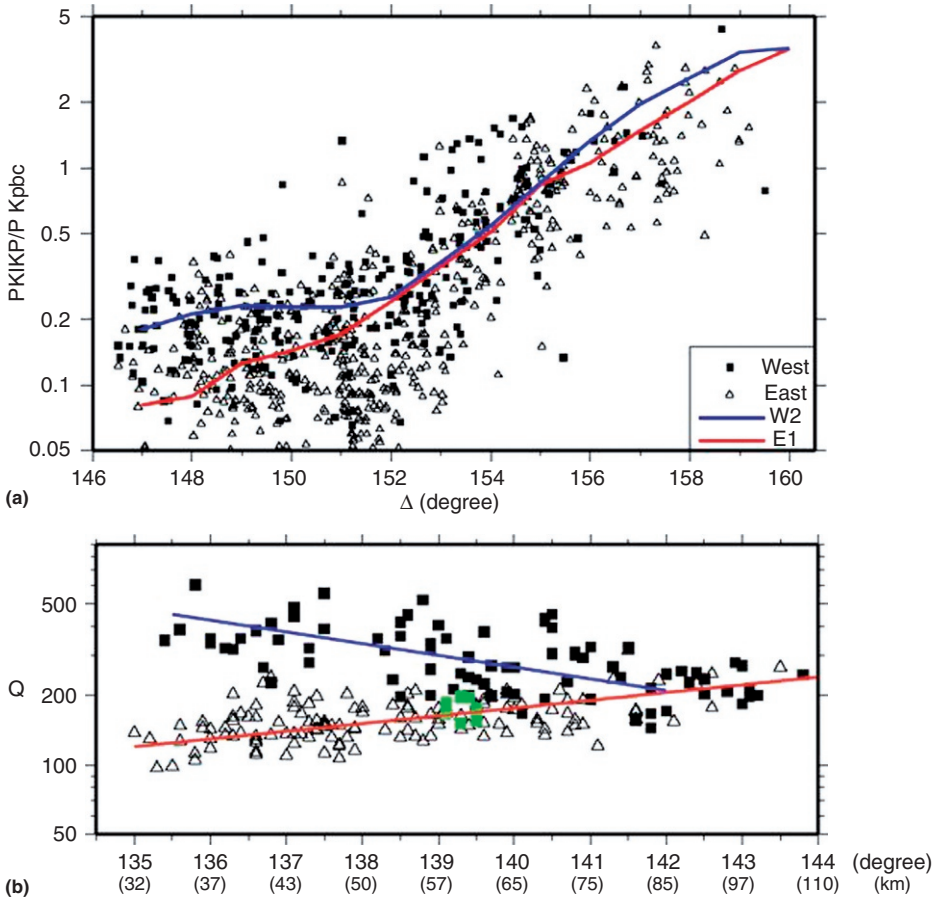

Figure 5 Hemispheric variations of *Q* in the inner core. (a) Variations of amplitude ratios of PKIKP/PKP(BC) as a function of distance and predictions of *Q* models for the western (W2) and eastern (E1) hemispheres. Adapted from Yu W and Wen L (2006a) Seismic velocity and attenuation structures in the top 400 km of the Earth's inner core along equatorial paths. *Journal of Geophysical Research* 111: http://dx.doi.org/10.1029/2005JB003995. (b) *Q* measurements as a function of distance from amplitude ratios of PKIKP/PKiKP showing differences between the western (triangles) and eastern (squares) hemispheres. Reproduced from Cao A and Romanowicz B (2004) Hemispherical transition of seismic attenuation at the top of the Earth's inner core. *Earth and Planetary Science Letters* 228: 243–253.

hemispheric variations in the inner core (Alboussière et al., 2010; Monnereau et al., 2010).

1.25.5.2.2 Anisotropic attenuation

The presence of velocity anisotropy is well documented for the inner core (e.g., Creager, 1992; Morelli et al., 1986; Shearer, 1994; Su and Dziewonski, 1990; Vinnik et al., 1994; Woodhouse and Wong, 1986). Theoretical studies indicate that anisotropy in attenuation should accompany anisotropy in velocity, and several authors have noted the stronger attenuation of PKP(DF) phases traveling along polar paths (Creager, 1992; Song and Helmberger, 1993). Anisotropy in attenuation was first proposed by Souriau and Romanowicz (1996), who examined a carefully selected data set of PKP(DF)/PKP(BC) amplitude ratios for paths whose turning points were located under western Africa and for which good azimuthal coverage was available. They found a significant correlation between high attenuation and high velocity and inferred that the origin of anisotropy in the top half of the inner core must be due to the orientation of iron crystals, which would produce this type of correlation (Carcione and Cavallini, 1995), rather than fluid inclusions, which would result in correlation of high velocity with low attenuation (Peacock and Hudson, 1990). These results were subsequently extended to a global data set (Souriau and Romanowicz, 1997) and to antipodal paths (Cormier et al., 1998). Using an effective medium theory, Singh et al. (2000) proposed that both velocity and attenuation anisotropy could be explained by a model of oblate fluid inclusions aligned in the equatorial plane. Li and Cormier (2002) suggested that anisotropy in attenuation also varies with depth and preferred a scattering interpretation. Oreshin and Vinnik (2004) confirmed the correlation of anisotropy in attenuation with that in velocity, which, however, may not be present at high latitudes (Helffrich et al., 2002). Yu and Wen (2006b) confirmed these global trends from measurements of amplitude ratios of PKIKP/PKiKP and PKIKP/PKPbc, finding an average Q_α for polar paths of 200–250, in contrast to 600 for equatorial paths in the top 200 km of the inner core. More recently, the need for attenuation anisotropy in the inner core was challenged by Waszek and Deuss (2013), who analyzed an extended data set of PKIKP/PKiKP amplitude ratios, confirming the hemispheric variations in Q_α. These

authors noted that most previous studies did not take into account hemispheric variations in velocity when interpreting amplitude ratios of core-sensitive phases and suggested that these velocity variations alone could account for apparent attenuation anisotropy.

For more details on inner core attenuation, see **Chapter 1.23**.

1.25.6 Global 3D Attenuation Structure in the Upper Mantle

1.25.6.1 Normal Modes and Long-Period Surface Waves

1.25.6.1.1 Early studies

In the 1970s, after the occurrence of the 1960 Great Chilean Earthquake (Mw 9.6), and with the accumulation of data from the World-Wide Standardized Seismographic Network, measurements of long-period surface-wave attenuation, then based on relatively few records, showed large disagreements (e.g., Ben-Menahem, 1965; Jobert and Roult, 1976; Mills and Hales, 1978; Smith, 1972). At that time, it was realized that (1) elastic effects were important in limiting the accuracy of Q measurements; (2) anelastic attenuation caused frequency dependence of elastic velocities, which needed to be taken into account (Akopyan et al., 1976; Kanamori and Anderson, 1977; Liu et al., 1976; Luh, 1974; Randall, 1976); and (3) large systematic lateral variations existed, correlated with those of phase velocities and suggesting significant differences in attenuation under different tectonic regions, with low attenuation under shields and high attenuation under oceans and tectonically active provinces (e.g., Dziewonski and Steim, 1982; Lee and Solomon, 1979; Nakanishi, 1978, 1979b, 1981; Roult, 1982).

Most global upper mantle 3D Q models up to now, as we will discuss in the succeeding text, have been on surface waveform or amplitude data. However, several authors attempted to measure lateral variations in Q from normal mode data, which in principle should provide sensitivity at greater depths in the mantle. Because the mode amplitude data set is very contaminated by elastic effects (e.g., Smith and Masters, 1989), it was possible to recover only the longest wavelengths in the even-degree structure (Romanowicz et al., 1987; Roult et al., 1984; Suda et al., 1991). The most important result of these early studies is the presence of a long wavelength, degree 2, structure in Q_μ in the transition zone, shifted toward the west with respect to the degree 2 in the shallower mantle, with lowest Q centered in the central Pacific Ocean and under Africa.

1.25.6.1.2 Anelasticity and focusing

One of the main issues limiting resolution in global mantle attenuation tomography is the contamination of amplitudes by elastic focusing effects. Numerous cases of such contamination in Earth circling mantle waves have been reported. For example, for moderate size earthquakes, for which the effect of source directivity can be ruled out, one expects successive Rayleigh-wave trains to gradually decrease in amplitude, due to the effects of attenuation and geometric spreading. However, it is sometimes observed that an R_{n+1} train has larger amplitude than R_n, where n is the orbit number of the Rayleigh wave (e.g., Lay and Kanamori, 1985; Romanowicz, 1987, 2002), and such observations can be qualitatively reproduced by including focusing effects in synthetic seismograms obtained by normal mode summation (e.g., Romanowicz, 1987). Also in the frequency domain, long-period surface-wave amplitude spectra are often irregular, with many 'holes' that cannot be attributed to intrinsic attenuation or source effects (e.g., Romanowicz, 1994a).

To first order, in the framework of single scattering and in the high-frequency approximation, analytic expressions have been obtained for the focusing effect, both in a propagating wave formalism (Woodhouse and Wong, 1986) and in a normal mode asymptotic formalism (Park, 1987; Romanowicz, 1987). Using asymptotic approximations in the framework of normal mode theory, it was shown that focusing effects depend on the transverse gradients of elastic structure, as expressed in terms of phase velocity perturbations, in the case of propagating waves, and of local frequency perturbations, in the case of normal modes. The expressions obtained in both approaches are equivalent (Romanowicz, 1987). In the propagating surface-wave case and in the frequency domain,

$$\ln \delta A_F(\omega) = \frac{1}{2}\operatorname{cosec}\Delta \int_0^\Delta \left[\sin(\Delta-\phi)\sin\phi\,\partial_\theta^2 - \cos(\Delta-2\phi)\partial_\phi\right]\frac{\delta c}{c_0}(\omega)\,\mathrm{d}\phi \qquad [7]$$

where Δ is epicentral distance, ϕ is the angular distance along the source-station great-circle path, $\delta c/c_0$ is the relative perturbation in phase velocity along the path, and $\delta A_F(\omega)$ is the contribution to the amplitude at frequency ω due to focusing.

In the standing-wave case and time domain, for an isotropic source,

$$\delta F_k(\Delta) = \frac{a\Delta}{U}\left(\frac{\hat{D}_k - \widetilde{D}_k}{2k} + \frac{\cot\Delta}{8k}\left(\delta\hat{\omega}_k - \delta\widetilde{\omega}_k\right)\right) \qquad [8]$$

where $F_k = (1+\delta F_k(\Delta))$ is the perturbation to the time domain amplitude of the seismogram for multiplet k and $\delta\hat{\omega}_k$ and $\delta\widetilde{\omega}_k$ are the perturbations to the great-circle average and minor are average local frequencies for that multiplet respectively, $k = l + 1/2$, where l is the angular order of the mode, and we have defined

$$\widetilde{D} = \frac{1}{\Delta}\int_0^\Delta \partial_\Gamma(\delta\omega_k(s))\,\mathrm{d}s$$
$$\hat{D} = \frac{1}{2\pi}\int_0^{2\pi} \partial_\Gamma(\delta\omega_k(s))\,\mathrm{d}s \qquad [9]$$

where ∂_Γ denotes the second transverse derivative along the great-circle path, which reduces to the integrand in eqn [7]. Accounting for the radiation pattern in eqn [8] is equivalent to using eqn [7] together with ray tracing.

Because the focusing effects are so strongly dependent on the transverse gradients of the elastic structure, and because those are not generally well constrained, compounded by the fact that these expressions are approximate and valid only to first order, it has been a difficult challenge, for the last decade, to properly account for focusing effects in surface-wave attenuation tomography. Indeed, if the corrections made on the basis of an existing elastic model are inaccurate, they can potentially introduce more biases than they can correct.

Noting that focusing effects and attenuation behave very differently as Rayleigh waves circle around the Earth, with the

sign of attenuation always the same, while focusing/defocusing depends on the direction of propagation along the great circle, Romanowicz (1990) and Durek et al. (1993) showed that, by using four consecutive Rayleigh-wave trains, one can eliminate, at least to first order, the effect of focusing, as well as uncertainties in the source amplitude. This resulted in the first, low-degree, even-degree global tomographic models of attenuation in the upper mantle, which confirmed the existence of a strong degree 2 in attenuation, as first suggested in studies based on normal modes. These models showed that attenuation in the uppermost mantle was correlated with seismic velocities, at least at the longest wavelengths (~4000 km). There are two drawbacks to this approach: First, only even-degree structure can be retrieved in this fashion, as only great-circle average attenuation can be measured, and second, elastic effects become increasingly more pronounced as distance increases, and the first-order approximation is not suitable for higher orbit trains, leading to a decrease in the ability to retrieve the intrinsic attenuation signal. Moreover, higher orbit trains are more dispersed, limiting the frequency range in which consecutive Rayleigh-wave trains do not interfere with each other and/or with overtones.

In order to be able to retrieve odd-degree structure while not explicitly correcting for unknown focusing effects, and avoiding the drawbacks of using multiple orbit wave trains, a different approach was proposed by Romanowicz (1995), using three consecutive Rayleigh-wave trains (R1, R2, and R3). She noted that the R1 and R2 trains are the least contaminated by focusing effects. However, their amplitudes also depend on uncertainties in the source amplitude. The source amplitude shift varies slowly with frequency and can be estimated by comparing the overall level of the amplitude spectrum computed in two different fashions: (1) directly from R1 (or R2) and (2) using a linear combination of R1, R2, and R3 (Romanowicz, 1994a). This approach, combined with a rigorous data selection in which all R1 and R2 amplitude spectra that were not smoothly varying with frequency were rejected, led to the first low-degree (equivalent to about degree 5) tomographic model of upper mantle shear attenuation, QR19 (Romanowicz, 1995). Even though this first model had very low resolution, it confirmed the correlation of lateral variations of Q with V_S in the top 250 km of the upper mantle and a shift to a different pattern in the transition zone, dominated by low Q in the central Pacific and Africa and correlated with hotspots. Romanowicz (1994b) showed that, in the transition zone, at least at the longest wavelengths, anelastic attenuation correlated with the hotspot distribution, whereas the velocity structure correlates better with the slab distribution, consistent with expectations that Q is more sensitive to high temperature regions. The desensitizing approach used, however, limited the lateral resolution of the model obtained, since a relatively small number of paths qualified for inclusion in the inversion.

The applicability of the linear asymptotic approximation to the computation of focusing (eqns [7]–[9]) has been tested by Selby and Woodhouse (2000) on a large data set of Rayleigh-wave amplitudes on minor and major arcs, in the period range 73–171 s. These authors derived maps of lateral variations of $q_R(\omega) = Q_R^{-1}(\omega)$ at different frequencies, assuming that the amplitude of a fundamental-mode Rayleigh wave observed at distance Δ and angular frequency ω can be written as

$$A(\omega, \Delta) = A_0(\omega)(1 + F(\omega))\exp[-\omega a \Delta \widetilde{q}_R(\omega)]/2U_0(\omega) \quad [10]$$

where U_0 is group velocity, a is the radius of the earth, $A_0(\omega)$ is source term, and $\widetilde{q}_R(\omega)$ is the average Rayleigh-wave attenuation along the source-station path:

$$\widetilde{q}_R(\omega) = \frac{1}{\Delta}\int_0^{\Delta} q_R(\omega, s)\mathrm{d}s \quad [11]$$

$F(\omega)$ represents the effect of focusing, which can be calculated from a reference elastic 3D model using expression [6]. Selby and Woodhouse (2000) compared the maps obtained by (1) inverting the observed amplitude data set for lateral variations in Q_R without correcting for focusing, (2) inverting synthetic maps of apparent attenuation obtained by assuming the amplitudes are only affected by focusing and using the elastic phase velocity model of Trampert and Woodhouse (1995), and (3) inverting the observed amplitude data set for Q_R after correcting for focusing. In these experiments, a degree-20 model of 3D apparent attenuation was obtained. They concluded that at the longer periods (e.g., 146 s), the amplitude signal is not severely affected by focusing, whereas at the shorter periods (e.g., 73 s), the contaminating effect is stronger. Also, Selby and Woodhouse (2000) found that low-degree attenuation structure (up to degree 8 in a spherical harmonics expansion) is not significantly affected by focusing in the entire period range considered. In a subsequent study, they inverted the maps of $Q_R(\omega)$ with and without corrections for focusing to obtain a series of models of lateral variations in attenuation in the upper mantle up to degree 8 (Selby and Woodhouse, 2002). In the latter study, they also considered the effect of uncertainties in the source term and found that a frequency-dependent correction factor is necessary to combine the $Q_R(\omega)$ maps into a successful depth-dependent model of attenuation. They concluded that the details of focusing and source corrections did not affect the robustness of their models up to degree 8, but would be more important at shorter wavelengths.

1.25.6.1.3 Current status

An important result of the Selby and Woodhouse studies was the confirmation that surface-wave amplitudes contained information not only on anelastic structure but also on elastic structure that could be exploited, as already suggested by Woodhouse and Wong (1986) and Wong (1989). At about the same time, Billien and Lévêque (2000) made the first attempt at inverting simultaneously Rayleigh-wave amplitude and phase data, for maps of phase velocity and Q_R between 40 and 150 s. The effects of focusing were included using eqn [7], which allowed them to consider shorter periods and shorter wavelengths. The maps obtained at short periods indicate significant correlation between phase velocity and attenuation, and therefore, tectonics and the even-degree part (degrees 2, 4, and 6) of their longer-period maps are compatible with those of other studies. However, their odd-degree part is dominated by degree 5, a feature not found in other studies.

In a recent study, Dalton and Ekström (2006a,b) considered a large global data set of Rayleigh-wave amplitudes in the period range 50–250 s. They inverted this data set, simultaneously, for maps of lateral variations in phase velocity up to spherical harmonics degree 20, attenuation up to degree 12, as well as source and receiver correction factors. As in previous

studies, the focusing effect is also included using expression [7]. A notable result of their study is the high-quality phase velocity maps that they were able to obtain by using only the amplitude constraints in their inversion (Dalton and Ekström, 2006b). Inclusion of the source and receiver correction factors was also found to improve the attenuation mapping. They constructed maps of Rayleigh-wave attenuation at different periods and also found a good correlation of the Q^{-1} distribution with tectonics for periods sensitive to the first 250 km of the upper mantle (Dalton and Ekström, 2006a).

The studies described so far considered only fundamental-mode surface waves, which, in practice, limits the resolution in depth to the top 300–400 km of the upper mantle, even though some attempts at interpreting deeper structure were shown. These studies also used a two-step approach, and often only the results of the first step, inverting for maps of lateral variations of $Q_R(\omega)$ at different periods, were presented (e.g., Billien and Lévêque, 2000; Dalton and Ekström, 2006a; Romanowicz, 1990). The more recent 3D attenuation models include both even and odd terms of lateral heterogeneity in Q_μ (Dalton et al., 2008; Romanowicz, 1995; Selby and Woodhouse, 2002) or in Q_R (Dalton and Ekström, 2006a). **Figure 6** compares maps of Q^{-1} at a depth of ~150 km obtained in different recent studies and shows that while details are still variable from model to model, the large-scale features, with high Q in shield areas low Q under ridges and back arcs, are quite consistent.

In order to improve the depth resolution in the transition zone, it is desirable to develop a methodology that includes information from surface-wave overtones, as well as Love waves. Because overtones are not easily separable due to their similar group velocities, a waveform methodology is desirable. Such a methodology uses a comparison of observed and synthetic seismograms in the time domain. The synthetics can be computed using normal mode theory, taking into account 3D effects at various degrees of approximation. However, to obtain accurate amplitude information from surface-wave data, it is necessary to employ an approach based on the measurement of envelopes or to first align the phase of waveforms before comparing observed and synthetic waveforms. Following these considerations, Gung and Romanowicz (2004) recently developed an iterative waveform inversion approach, in which a large global data set of three-component fundamental and overtone waveforms, filtered in the frequency range 80–250 s, is first inverted for elastic 3D structure, using the nonlinear asymptotic coupling theory approach developed by Li and Romanowicz (1995), up to spherical harmonics degree 24. Different elastic models are computed for Love and Rayleigh waves, to account for the strong radially anisotropic signal in the uppermost mantle (e.g., Ekström and Dziewonski, 1997; Gung et al., 2003; Montagner and Tanimoto, 1991). In a second step, the waveforms, corrected for the 3D elastic structure obtained in the previous step, are inverted for lateral variations of $Q_\mu(r)$ in the upper mantle, up to degree 8. In this process, the waveforms are directly inverted for depth dependence in elastic and anelastic structure.

Although Gung and Romanowicz (2004) did not include focusing effects in deriving their model QRLW8, subsequent tests indicated that the model was robust with respect to these effects, in agreement with the predictions of Selby and Woodhouse (2000). In particular, Gung and Romanowicz (2004) compared the degree-8 $Q_\mu(r)$ model obtained with and without focusing terms, the latter computed using expression [8] in the 3D elastic model obtained in the first step, and found no significant changes. Including focusing in the second step of the inversion justifies inverting for a higher-degree Q_μ model. **Figure 7** shows a comparison of the models obtained

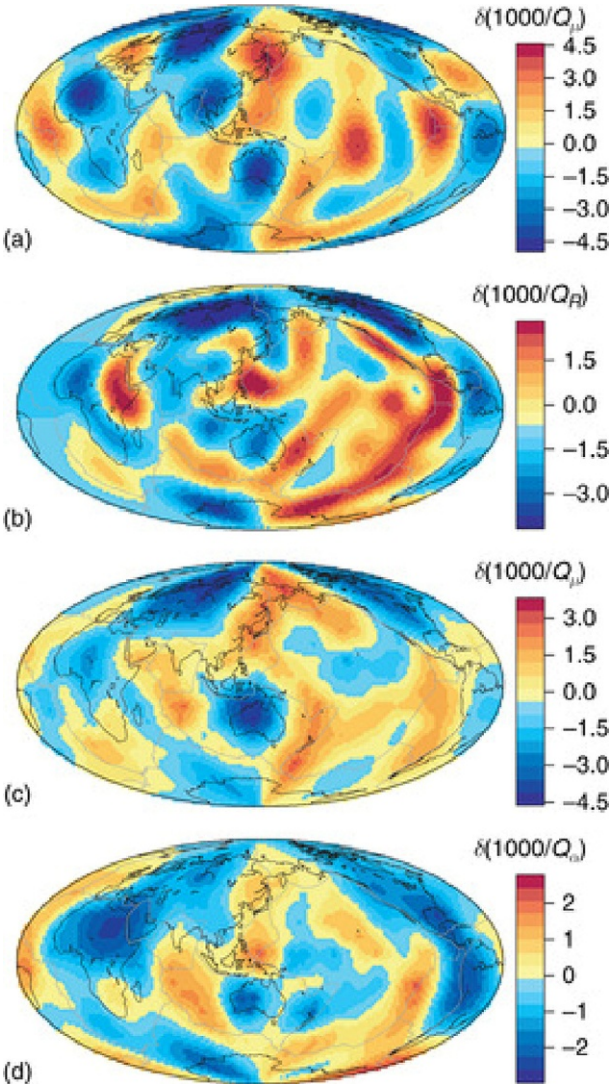

Figure 6 Comparison of global Q models in the uppermost mantle. (a) QRLW8 model (Gung and Romanowicz, 2004), from inversion of three-component surface-wave and overtone waveform data, presented is Q_μ at a depth of 160 km. (b) Map at 150 km of the Rayleigh-wave-based Q model QRFS12 of Dalton et al. (2008). (c) Average Q_μ in the depth range 0–250 km from Selby and Woodhouse (2002) and also from Rayleigh waves. (d) Average variations in Q_α in the first 250 km of the mantle from amplitude ratios of P and PP (Warren and Shearer, 2002). Some of the differences observed may be due to the different depth ranges sampled: in models (a), (c), and (d), the global ridge and back-arc systems all stand out as low Q_μ features, whereas the Atlantic ridge is not as prominent in model (b), while the Red Sea region lights up more strongly. This may be due to the fact that (b) has not been inverted with depth and therefore may include some effects of structure deeper than 250 km.

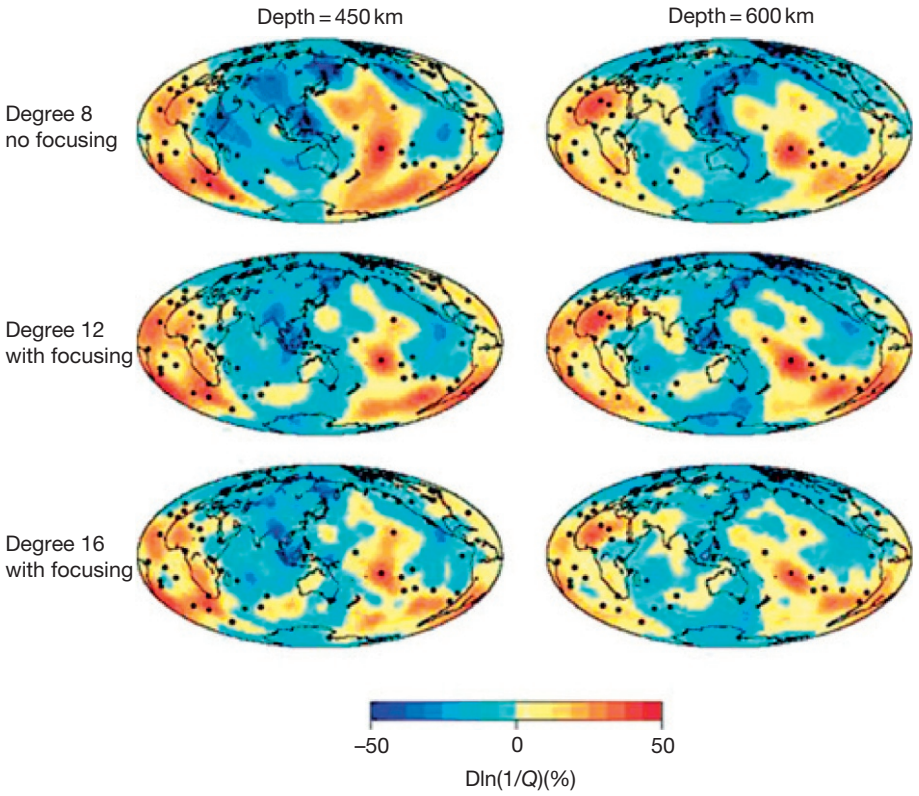

Figure 7 Lateral variations of Q_β in the upper mantle transition zone. (Top) Degree-8 model QRLW8 (Gung and Romanowicz, 2004). In this relatively low-degree model, no corrections for elastic focusing have been included. (Middle/bottom) Inversion of the same three-component long-period seismograms for a degree-12 model (middle) and a degree-16 model (bottom). In both cases, the waveforms have been corrected for focusing effects before inversion, using an asymptotic higher-order formalism (Romanowicz, 1987). The main features of these models, namely, strong low-*Q* anomalies in the South Pacific and under Africa, correlated with the hotspot distribution of Davies (1990) (black dots) and high-*Q* anomalies under the western Pacific, remain stable, but the low-*Q* features sharpen up in the higher-resolution models.

up to degrees 12 and 16, in the transition zone, when focusing terms are included. Clearly, the large-scale features remain stable among the models, with some variability in the details. They indicate that, in contrast to the upper 200–300 km of the mantle, the main features in Q_μ in the transition zone are two large low-Q regions in the south-central Pacific and under Africa, which correlate with the distribution of elastic velocities at the base of the mantle (Romanowicz and Gung, 2002), as well as the distribution of hotspots, confirming earlier results (Romanowicz, 1994b).

The most recent global 3D upper mantle model of Q_μ was developed by Dalton et al. (2008) based on fundamental-mode Rayleigh-wave data using the methodology of Dalton and Ekström (2006b). The resulting model (QRFSI12), expressed to degree 12 in spherical harmonics, takes into account source and station terms as well as focusing effects. It confirms the correlation of Q_μ^{-1} with surface tectonics in the first 200–250 km of the upper mantle (e.g., **Figure 6**) and a shift at greater depth to a structure dominated by high attenuation beneath the central Pacific and Africa and low attenuation in subduction zone regions. Dalton et al. (2009) found strong correlations between attenuation distribution (in model QRFSI12) and shear velocity in different tectonic regions and inferred that lateral variations in temperature of 150–200 °C can explain most of the observed variability in velocity and attenuation in the top 250 km of the upper mantle, except in cratonic regions where compositional differences may be required, in agreement with earlier studies. In particular, inversion of long-period seismic waveforms assuming only lateral variations in temperature results in temperatures in the cratonic upper mantle that are more than 100 °C colder than estimated from heat flow measurements and the analysis of xenoliths (e.g., Cammarano and Romanowicz, 2007). Dalton and Faul (2010) compared the seismological trends to experimental trends in dry olivine samples and concluded that in regions of the upper mantle where the relationship between attenuation and velocity cannot be explained by temperature variations alone, the discrepancies can be explained by a combination of the presence of partial melt (oceans at depths ~100 km) or compositional differences (cratons at depths <250 km), although the composition that would give rise to the observed mismatch in cratons remains elusive.

Some variability in the correlation between velocity and attenuation maps may be due to the effects of anelastic dispersion due to attenuation, as also investigated by Zhou (2009). Assuming a 3D Q model derived from an existing 3D shear velocity model under the assumption that all lateral variations of structure in the upper mantle are due to temperature

variations, Zhou (2009) calculated finite frequency kernels and found that dispersion corrections in the phase due to attenuation are important enough in the period range 50–200 s (up to 25% of the elastic effect) so that they cannot be neglected in global surface-wave tomography.

With the advent of accurate global 3D numerical computations of the seismic wavefield, it has become possible to evaluate more precisely the effects of 3D elastic structure on the amplitudes of long-period surface waveforms and, vice-versa, the effect of 3D Q variations on velocity modeling, through anelastic dispersion. Savage et al. (2010) incorporated attenuation into their spectral element code (Specfem, e.g., Komatitsch et al., 2002) and investigated competing effects on amplitudes due to elastic and anelastic 3D structure at the regional scale. Ruan and Zhou (2010) used the same spectral element method to quantify the effects of 3D Q structure on surface-wave phase delays and found that about 15–20% of the phase delays may be due to 3D Q structure through the mechanism of anelastic dispersion, especially in the period range 60–150 s, less so at longer periods. Using a similar approach, Ruan and Zhou (2012) confirmed, in turn, that the effects of elastic focusing and scattering on surface-wave amplitudes are as important as those of 3D Q and cannot be ignored, even at long periods. Such numerical techniques hold promise for advances in the resolution of Q structure at global and regional scales.

1.25.6.2 Global Body-Wave Studies

In the same way as differential travel times of teleseismic body-wave phases are used to obtain information on the distribution of upper mantle velocities, global-scale lateral variations in attenuation can be inferred from differential amplitude measurements (i.e., amplitude ratios). These measurements are difficult, however, as they are sensitive to the window chosen for each phase, as well as to contamination by complex structure near the source, receiver, and bounce points. Komatitsch et al. (2002) have called attention to the importance of considering the effects of focusing and scattering in the crust. **Chapter 1.06** provides details about the theoretical computation of the effects of attenuation on body waves.

Only three published studies to date have developed models of upper mantle Q based on differential body-wave measurements, two for Q_μ using S phases (Bhattacharyya et al., 1996; Reid et al., 2001) and one for Q_α (Warren and Shearer, 2002). Each of them used slightly different methods, but the basic principle remains the same.

The amplitude spectra of recorded body waves can be expressed as

$$A(\omega) = cS(\omega)R(\omega)I(\omega)A_c(\omega)F(\omega)\exp(-\omega t^*/2) \qquad [12]$$

where c is a constant expressing the radiation pattern and the geometric spreading, $S(\omega)$ is the source spectrum, $R(\omega)$ is the crustal response, $I(\omega)$ is the instrument response, A_c is the crustal layering/reflectivity at the bounce point for reflected waves, F is a hypothetical factor that includes possible effects of focusing, and t^* is defined in eqn [5]. In body-wave studies, the frequency dependence of Q needs to be taken into account, because the measurements are performed at higher frequency (typically 0.15–1 Hz for P waves and 0.05–0.1 Hz for S waves), closer to the high-frequency cutoff in the Earth's absorption band. The frequency dependence of Q is often expressed in terms of an absorption band model (eqn [2]). However, Warren and Shearer (2002) estimated the effect of frequency dependence on the attenuation of P waves around a period of 1 s and concluded that neglecting it did not significantly bias their measurements of lateral variations in Q_α. On the other hand, Reid et al. (2001) suggested that the frequency dependence might be absorbed in the source terms.

Pairs of phases (1,2) are selected so as to eliminate as many factors as possible from their spectral amplitude ratio. The differential δt^* can then be obtained by measuring the slope of the remaining spectral ratio as a function of frequency:

$$\ln(A_2/A_1) = -\omega/2(\delta t^*) + \varepsilon \qquad [13]$$

where $\delta t^* = t_2^* - t_1^*$ and ε is a constant containing the effects of differential radiation pattern, geometric spreading, and focusing for the two phases. The assumption of frequency independence needs to be verified even if dispersion corrections have been applied, and this is usually done by checking the linearity of the slope, as well as the constancy of the phase of the complex spectral ratio.

Because the lateral variations of Q in the lower mantle are thought to be much smaller than in the upper mantle, the differential t^* thus obtained is attributed to lateral variations of structure in the upper mantle under the bounce point of the reflected phase. Given the steep approach of the reflected rays at the bounce point and the relatively sparse global sampling, these measurements provide information about the average upper mantle lateral variations in Q but have little depth resolution.

This general principle of slope measurement was used by Bhattacharyya et al. (1996) and Warren and Shearer (2002). However, these authors used different approaches to correct for potential receiver and source biases. Bhattacharyya et al. (1996) considered the spectra of S and SS from the same records, in the distance range 40–120° and the period range 15–25 s, and then estimated the differential t^* by applying a multiple-record stacking technique, grouping the records by bounce point location, and assuming that effects of source, receiver, and path, outside of the common upper mantle path of the SS waves with common bounce location, would average out in the stacks. The bounce point location area over which the stacking was performed was caps of 5° radius, larger than the estimated Fresnel zones of the corresponding reflected waves. These authors used a frequency domain multitaper technique to minimize the effects of finite source duration and near-source or near-receiver structure complexity. They found a correspondence between the cap-averaged t^* and tectonic provinces, with, as expected, lowest attenuation under platforms and shields and highest attenuation under young oceans. In a second step, they inverted for a depth-dependent model of Q_μ in the upper mantle, expanded laterally up to degree 8 in spherical harmonics, and assuming three layers in depth (20–220, 220–400, and 400–670 km). Resolution experiments indicated that the best resolved layer was the deepest one, and the two shallower ones could not be distinguished uniquely.

Warren and Shearer (2002), on the other hand, considered independent data sets of P waveforms, in the distance range 40–80°, and PP waveforms in the distance range 80–160°.

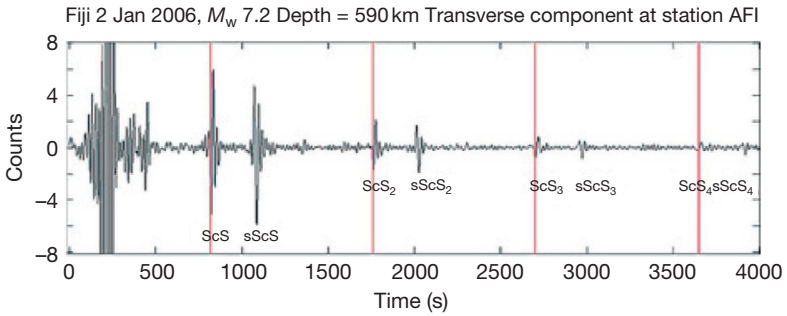

Figure 8 Example of multiple ScS record for a deep earthquake in the Fiji Islands, showing clear multiples out to ScS_4, as well as their depth phases. Courtesy of Ved Lekic.

Working in the frequency domain, they first determined source and receiver terms for the P data set, using an iterative stacking procedure over common sources and common receivers. Then they assumed that the same source and receiver terms could be applied to the PP phases, since the two phases have similar takeoff angles, path lengths, and turning depths, given the distance ranges considered. They thus corrected the PP amplitude spectra using the source and receiver terms determined from the P spectra and estimated the residual t^* attributed to the upper mantle beneath the bounce point. Finally, to reduce the scatter in the data, they estimated cap averages over nonoverlapping bounce point areas of 5° radius. They too found the highest Q_α (smallest t^*) under shields and platforms and the lowest Q_α (largest t^*) under young oceans (e.g., **Figure 6**). Unlike Bhattacharyya et al. (1996), these authors considered, however, that their measurements reflected the average structure over the top 220 km of the mantle and derived the corresponding Q_α averaged over that depth range.

Reid et al. (2001) developed a somewhat different method, based on waveform fitting, which they applied to a large data set of SS and S waveforms from seismograms collected in the distance range 50–105° and also to SSS and SS, in the distance range 90–179°. In the process, they included the effects of elastic structure on differential travel times of these phases. These authors considered that their data had sensitivity down to 400 km and inverted their t^* data set for a model of Q_μ expanded laterally to degree 8 and in depth, using a spline parametrization with six knots. However, their resolution tests indicated that the depth resolution was poor and that they could not attribute the lateral variations found to a particular depth.

The most recent attempt at using body-wave phases to constrain 3D Q_μ variations at the global scale is a study that includes differential attenuation measurements between S and a combination of upper and lower mantle-sensitive multiple phases (ScS, SS, and corresponding depth phases; Lawrence and Wysession, 2006b). These authors validate their model in the upper mantle against model QRLW8 (Gung and Romanowicz, 2004), arguing that the qualitative similarities imply robustness of their lower mantle model. The most striking feature of their lower mantle model is a large low-*Q* region in the depth range 700–1400 km beneath the subduction zones in eastern Asia, which they attribute to the presence of water. However, the authors do not evaluate or make any corrections for elastic contaminating effects in this highly heterogeneous region, which makes their model tentative until confirmed by future independent studies.

1.25.6.3 Body-Wave Studies of Regional Extent

1.25.6.3.1 Multiple ScS studies

Although they do not provide a complete global coverage, the most widely used shear-wave phases for large-scale regional mantle attenuation studies have been multiple ScS phases. Measurements of the attenuation of these near-vertical multiply reflected waves are relatively uncontaminated by source, instrument, and geometric spreading effects. They and their depth phases appear very clearly on transverse seismograms in the 'reverberative interval,' after the first arriving surface-wave train (**Figure 8**). In the absence of noise, the spectral domain transfer function relating ScS_n to ScS_{n+1} is

$$H(\omega) = \exp[-\omega T_0/2Q(\omega)]\cdot\exp[i\theta(\omega, T_0)] \qquad [14]$$

where T_0 is the differential travel time between the two phases, θ is a phase function, and $Q(\omega)$ is the quality factor, which is an estimate of the vertically averaged attenuation through the mantle. As in the case of other differential measurements, the estimate of Q_{ScS} is obtained by measuring the slope of the amplitude of the transfer function as a function of frequency. The stability of the phase spectrum is used as an additional indication of the quality of the measurement.

Early studies used spectral ratios measured on hand-digitized and hand-rotated transverse component seismograms and provided evidence for large amplitude lateral variations of Q_{ScS} in the mantle (e.g., Kovach and Anderson, 1964; Press, 1956; Sato and Espinosa, 1967; Yoshida and Tsujiura, 1975). Because of the analog records used, and the measurement methods employed, which did not take into consideration the biasing effects of noise, these early estimates are considered to be less accurate than more recent ones. They are also generally biased toward very high values of Q_{ScS}, compared to normal mode results, which has been attributed not only to the effects of noise but also, potentially, to the effect of frequency dependence of *Q*, as the instruments that produced the records had limited bandwidth. With the advent of digital long-period instrumentation, and the development of more sophisticated methods that were better suited for minimizing the effects of noise (e.g., Jordan and Sipkin, 1977; Nakanishi, 1979a), measurements became more accurate. For example, Jordan and Sipkin (1977) introduced a method of phase equalization, by computing cross correlation between successive ScS multiples, as well as stacking to reduce measurement scatter. Nakanishi (1979a) used a maximum likelihood method to reduce the

effects of noise. Most measurements are performed in the frequency band between 10 and 40–60 MHz, where frequency dependence of Q_{ScS} has been found to be negligible (e.g., Sipkin and Jordan, 1979). These studies have confirmed the existence of large lateral variations in Q_{ScS} (e.g., Chan and Der, 1988; Gomer and Okal, 2003; Lay and Wallace, 1983, 1988; Revenaugh and Jordan, 1989, 1991; Sipkin and Jordan, 1980; Sipkin and Revenaugh, 1994; Suetsugu, 2001). The derived average mantle values for $Q_\mu \sim 220$–240 are, in general, compatible with those obtained from normal modes.

Measurements under oceans and in the vicinity of subduction zones are more numerous, because of the availability of deep earthquakes and the relatively simple effects of the thin crust at the surface reflection points. Measurements under continents are more difficult, because the effect of crustal multiples at the surface reflection point needs to be taken into account (e.g., Isse and Nakanishi, 1997; Sipkin and Revenaugh, 1994). In order to expand the coverage under continents, it is also necessary to consider shallow earthquakes, for which the reverberation interval is more noisy because of the presence of strong multipathing surface waves.

These studies determined that, on average, Q_{ScS} is higher under continents than under ocean basins. Regional variability on relatively short scales has been found in subduction zone regions. In particular, low Q was estimated under the Sea of Japan (e.g., $Q_{ScS} \sim 160$; Nakanishi, 1979a) and under northern South America ($Q_{ScS} \sim 93$; Lay and Wallace, 1983), in regions sampling the upper mantle wedge and/or back-arc region behind subduction zones, which, if primarily attributed to the upper mantle, translates into very low Q. On the other hand, high Q values comparable to continental estimates were obtained on path sampling through slabs (e.g., $Q_{ScS} \sim 232$, in South America, Lay and Wallace (1983); $Q_{ScS} \sim 226$, under Japan/Kuriles, Nakanishi (1979a); and $Q_{ScS} \sim 266 \pm 57$ in Argentina, Sipkin and Jordan (1980)). These older measurements are generally in agreement with a more recent study by Chan and Der (1988), except in the southwest Pacific, where these authors found $Q_{ScS} \sim 214 \pm 42$ compared to the estimate of $Q_{ScS} \sim 157 \pm 17$ (Sipkin and Jordan, 1980). This may however be due to the way the latter averaged their measurements over an extended region where strong lateral variations in Q_{ScS} have since been confirmed (Gomer and Okal, 2003; Suetsugu, 2001). Using short epicentral distance data ($<20°$) filtered between 10 and 50 MHz, Suetsugu (2001) found very low Q under the South Pacific superswell ($Q_{ScS} \sim 70$–80), whereas Gomer and Okal (2003) found very high Q under the Ontong Java Plateau, also using short distances (10–20°) and a bandpass between 10 and 62.5 MHz.

The lateral variations found in Q_{ScS} are attributed primarily to the upper mantle, because of the much higher Q in the lower mantle, which reduces the effects on multiple ScS of any, even significant, lateral variations (e.g., Warren and Shearer, 2002) and the significant correlation of Q_{ScS} with tectonics. Furthermore, the correlation with travel time anomalies from the same multiple ScS phases suggests that they could be primarily related to lateral variations in temperature.

Caution must be exercised, of course, in attributing all of the Q_{ScS} signals to the upper mantle, in particular if there is a low-Q zone at the base of the mantle (e.g., Revenaugh and Jordan, 1991) and significant lateral variations of Q in D″. While attenuation in D″ and its variations have yet to be explored at the global scale, the presence of large variations in velocity implies that at least some lateral variations exist in Q as well. Recently, Fisher and Wysession (2003) showed evidence for the existence of an ~600 km wide high-attenuation, low-velocity region in D″ beneath Central America, using spectral ratios of S and ScS phases.

1.25.6.3.2 Body-wave attenuation studies in North America

A few recent studies have taken advantage of the large quantity of broadband data available over North America to estimate lateral variations in attenuation across the continent, using surface waves (Lawrence et al., 2006) or body waves (Hwang et al., 2009, 2011). In agreement with global studies and early studies (e.g., Der et al., 1982; Solomon and Toksöz, 1970), these studies generally find large-scale lateral variations correlated with tectonics. More such studies are forthcoming, with the growing database from the EarthScope USArray program.

1.25.6.3.3 Body-wave studies of upper mantle Q around subduction zones

High attenuation has been reported in the back of island arcs using other types of body waves (e.g., Wiens et al., 2008). Early estimates were very qualitative (e.g., Barazangi and Isaaks, 1971; Barazangi et al., 1975; Bowman, 1988). This was confirmed by several regional studies (e.g., Flanagan and Wiens, 1990, 1994; Roth et al., 1999, 2000) that utilized shear depth phases from deep earthquakes observed teleseismically or at regional arrays to obtain constraints on the attenuation in the upper mantle wedge above different subduction zones. Flanagan and Wiens (1990) measured differential attenuation between sS–S and sScS–ScS phase pairs beneath the Lau back-arc spreading center in the Fiji–Tonga region. Studying the variation of the estimated Q as a function of depth of the source, they found high attenuation in the first 200–300 km and decreasing attenuation at greater depth. They found very high attenuation ($Q \sim 20$–35) in the uppermost mantle beneath the spreading center and somewhat lower attenuation ($Q \sim 50$) beneath older parts of the Lau Basin. Flanagan and Wiens (1994) extended this approach to the study of several inactive back-arc basins in the western Pacific and confirmed the presence of high attenuation ($Q \sim 40$–50) in the uppermost mantle (depths <160 km), with even lower Qs (<40) in the vicinity of the volcanic centers. They also confirmed a systematic increase of Q with depth ($Q \sim 115$ between 160 and 430 km and $Q \sim 173$ in the transition zone). The frequency band of these two studies was 10–80 MHz.

Following the method of Teng (1968), Roth et al. (1999) assembled a data set of differential S–P and P–P attenuation measurements from a temporary local array of broadband land and ocean bottom stations in the Tonga–Fiji region. The data set they assembled allowed them higher resolution compared to teleseismic data because of the geometry of the source-station distribution, the short paths, and the small Fresnel zones compared to teleseismic phases. These authors measured δt from spectral ratios and obtained an estimate of the best fitting Q_α/Q_β ratio as part of the inversion for Q_α and Q_β, assuming that Q is not frequency-dependent in the

band-pass of their study (0.1–3.5 Hz), which seems to be verified by the data. They confirmed the high-attenuation values in the uppermost mantle found previously beneath the spreading center. In their model, the slab appears as a high-Q zone ($Q_\alpha > 900$) down to at least 400 km, below which it is indistinguishable from the surrounding mantle. An abrupt transition from the high-Q slab to the low-Q back-arc basin occurs approximately at the Tonga volcanic front. The lowest Q_α values (~ 90) are found directly under the Lau back-arc spreading center. There is also evidence for a north–south trend, with attenuation on average higher by 10% in the northern part of the region. This Q tomographic model correlates well with velocity models in the region. The best fitting Q_α/Q_β ratio is ~ 1.75, which is in agreement with a loss in bulk about 1/3 that of the loss in shear, assuming a Poisson solid (**Figure 9**).

A similar study under the northern Philippine Sea, this time using only S–P spectral ratios (Shito and Shibutan, 2003b), also found high Q in the Philippine and Izu–Bonin slabs and low Q under the spreading center in the Shikoku Basin. However, the lowest values of Q were found at larger depths (250 km) than in the Lau Basin. The authors attributed that to the older age of the Shikoku spreading center. Several other studies in the last decade have investigated different subduction zones and confirmed the presence of strong lateral variations in Q, with lowest values under volcanic centers (as low as $Q_\mu = 40$ at 1 Hz in some areas) and an order of magnitude higher in the slab. These studies have used local earthquake data in Japan (Nakajima and Hasegawa, 2003; Takanami et al., 2000; Tsumura et al., 2000), in New Zealand (Eberhart-Phillips and Chadwick, 2002), in the Andes (Haberland and Rietbrock, 2001; Myers et al., 1998; Schurr et al., 2003), in Alaska (Stachnik et al., 2004), and more recently in Central America (Rychert et al., 2008), and in the Marianas (Pozgay et al., 2009). The recent studies have investigated frequency dependence in Q and, in some cases, have attempted to constrain attenuation in bulk, from Q_P/Q_s ratios. Frequency dependence appears to be in agreement with laboratory measurements ($\alpha \sim 0.1$–0.3), while the amount of attenuation in bulk is not yet very well constrained, reaching 30% of the value of attenuation in shear in some cases (e.g., Roth et al., 2000), but not required at all in some other studies (e.g., Pozgay et al.,

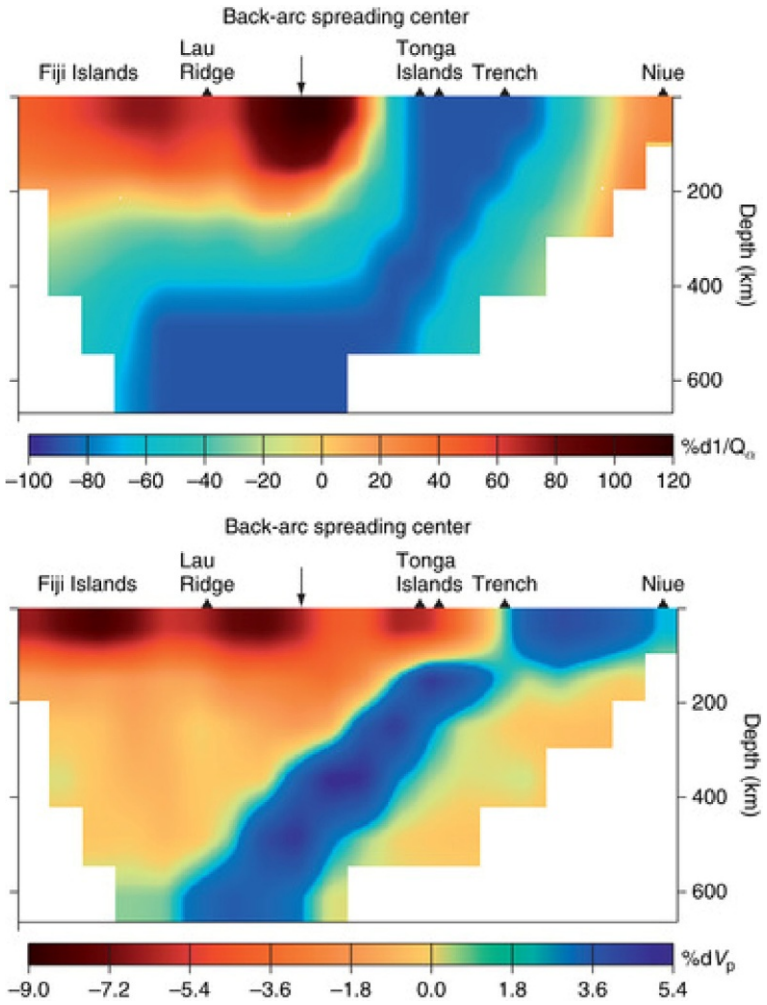

Figure 9 Cross section illustrating lateral variations of structure in the Lau back-arc basin. (Top) Attenuation. (Bottom) Velocity (V_p). Reproduced from Roth E, Wiens DA, and Zhao D (2000) An empirical relationship between seismic attenuation and velocity anomalies in the upper mantle. *Geophysical Research Letters* 27: 601–604.

2009). There may be a suggestion of the need for bulk attenuation only in the slab and not in the wedge (Stachnik et al., 2004). Further high-resolution studies are needed to more clearly separate the effect of frequency dependence from that of bulk attenuation.

1.25.6.3.4 Regional studies of upper mantle Q in mid-oceanic settings

Just as the upper mantle is found to be highly attenuating under back-arc spreading centers, other studies have investigated mid-ocean ridge systems and found very low *Q* (Ding and Grand, 1993; Molnar and Oliver, 1969; Sheehan and Solomon, 1992; Solomon, 1973). Sheehan and Solomon (1992) used the pair of teleseismic phases S and SS along the North Atlantic ridge and found that SS–S differential attenuation decreases with increasing age of the oceanic plate and that, in order for their measurements to be compatible with surface-wave studies, the high-attenuation region must extend into the asthenosphere. Ding and Grand (1993) performed waveform modeling of multiple S phases (up to S_4) at distances between 30° and 80° along the East Pacific Rise. Because their data have sensitivity to the deep mantle, they found that, in order for their measurements to be compatible with multiple ScS results, a significantly lower average *Q* in the lower mantle is needed than obtained from normal mode measurements, indicating that lateral variations in *Q* may also exist in the lower mantle. Note that Sipkin and Jordan attributed a lower *Q* in the Fiji–KIP corridor from multiple ScS measurements to frequency dependence. In the light of the Ding and Grand (1993) study, it seems more likely that the observations of Sipkin and Jordan (1979) could just be due to lower *Q*s in the lower mantle, especially as both studies sampled regions of the Pacific superplume. Strong lateral variations in the lower or lowermost mantle would need to be invoked to reconcile these results with the recent 1D mantle *Q* models constructed using body-wave data of similar frequencies, which exhibit high *Q*s in the lower mantle (e.g., **Figure 4**).

In the last decade, there have been increasing efforts to interpret tomographic models of the upper mantle at various scales in terms of temperature, degrees of partial melt, water content, and rock composition, using constraints from elastic and anelastic tomography, heat flow, gravity, and experimental data. Thus, Sobolev et al. (1996) found that the Massif Central in France is underlain by a hot mantle body with a potential temperature 100–200 °C higher than the upper mantle average. In an interpretation of velocity and *Q* tomography under the Philippine Sea, Shito and Shibutan (2003a) found that the deeper upper mantle (300–400 km depth) may contain 10–50 times more water than average. Boyd and Sheehan (2005) measured differential t^* of S-phase waveforms from the Rocky Mountain Front broadband network and found a north–south zone of very low Q_μ in the upper mantle beneath the Rocky Mountains. Combining attenuation and velocity data, they inferred that the Colorado Rocky Mountains are supported by low-density mantle and a thick crust. On the other hand, comparing their laboratory measurements of Q_μ with global seismological *Q* models, Faul and Jackson (2005) inferred that the upper mantle low-velocity zone could be explained by solid-state processes, without invoking partial melting. Lawrence et al. (2006) applied a waveform cross-correlation method and cluster analysis to the study of upper mantle P- and S-wave attenuation across the North American continent and found that the distribution of attenuation is in general correlated with that of velocity, implying higher temperatures beneath the western tectonic regions than under the more stable east, in agreement with both global and crustal continental-scale studies.

In general, t^* measurements and surface-wave attenuation measurements are interpreted in terms of anelastic attenuation; however, contributions from scattering can be important and need to be considered. For example, in a study of S-wave amplitude variations under Iceland, Allen et al. (1999) found that the low-velocity cylindrical-shaped plume acts as a lens, causing frequency-dependent focusing that dominates over anelastic effects on the amplitudes.

A somewhat puzzling result is that of Yang et al. (2007), who, for the first time, measured attenuation of surface waves in the vicinity of the East Pacific Rise, from a regional ocean bottom network. From a joint inversion for velocity and attenuation, taking into account elastic effects on the amplitudes to some degree, these authors found surprisingly lower attenuation than expected under the youngest ocean (Q_μ not less than 90, which is higher than the global average estimates), while elastic velocities are very low. These results are not compatible with a purely thermal model of attenuation (e.g., Faul and Jackson, 2005) nor with results from back-arc spreading centers in Mariana and Tonga/Lau (e.g., Pozgay et al., 2009). The authors suggest that the presence of water might be partially responsible for the drop in velocity, through the anelastic attenuation effect, and that some partial melting may be present beneath the youngest seafloor. However, this would require the absorption peak to be outside of the seismic frequency band. Reconciling these results with those in back arcs and global averages will necessitate further studies that more accurately take into account the elastic effects on amplitudes.

1.25.7 Regional *Q* Variations in the Crust and Uppermost Mantle

1.25.7.1 Introduction

One of the most interesting aspects of *Q* in the crystalline crust and upper mantle of the Earth is the large magnitude of its variation from region to region. Whereas broad-scale seismic velocities vary laterally at those depths by at most 10–15%, *Q* can vary by an order of magnitude or more. **Figure 10** illustrates the large effect that regional *Q* variations can have on phases that travel through both the upper mantle (P and S waves) and the crust (Lg) by comparing records for paths across the eastern and western United States. Since variations in *Q* can be so large, seismic-wave attenuation is often able to relate *Q* variations to variations in geologic and geophysical properties that are not easily detected by measurements of seismic velocities. Factors known to contribute to *Q* variations in the crust and upper mantle include temperature and interstitial fluids.

In this section, we will emphasize studies of *Q* variation conducted over regions sufficiently broad to contribute to our knowledge of crust and upper mantle structure and evolution. In so doing, we neglect many studies that have provided useful information on crustal *Q* over small regions.

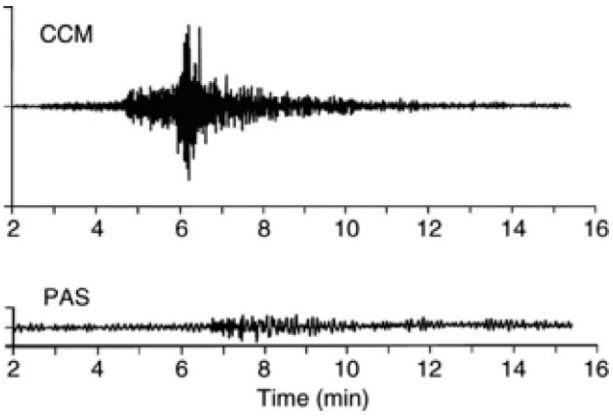

Figure 10 Seismograms recorded at stations CCM (Cathedral Cave, MO) and PAS (Pasadena, CA) for the m_b 4.5 event in southeastern New Mexico that occurred on 2 January 1992 at 11:45:35.6 UT. The epicentral distance to CCM (along a relatively high-*Q* path) is 1256 km and to PAS (along a relatively low-*Q* path) is 1417 km. Reproduced from Mitchell BJ (1995) Anelastic structure and evolution of the continental crust and upper mantle from seismic surface wave attenuation. *Reviews of Geophysics* 33: 441–462.

1.25.7.2 *Q* or Attenuation Determinations for Seismic Waves in the Crust

Investigators have employed different methods, phases, and frequency ranges to study the anelastic properties of the crust and upper mantle. At higher frequencies and shorter distances often employed for crustal studies, some researchers have emphasized determinations of intrinsic Q (Q_i), some have emphasized the scattering contribution (Q_s), and some have sought to determine the relative contributions of Q_i and Q_s. The importance of scattering became apparent from the groundbreaking work of Aki (1969) who first showed that the codae of various regional phases are composed of scattered waves. His work spawned a large literature on both theoretical and observational aspects of scattering that is discussed in Chapter 1.24.

The contributions of the intrinsic and scattering components to total attenuation, $1/Q_t$, can be described by

$$\frac{1}{Q_t} = \frac{1}{Q_i} + \frac{1}{Q_s} \qquad [15]$$

where Q_i and Q_s refer, respectively, to intrinsic Q and scattering Q (Dainty, 1981). Richards and Menke (1983) verified that the contributions of intrinsic and scattering attenuation are approximately additive as described by eqn [15]. Seismologists often wish to focus on Earth's intrinsic anelastic structure. To do so, they must select a phase or work in a frequency range such that the effect of scattering can either be determined or is small relative to the effect of intrinsic Q.

This chapter almost entirely addresses intrinsic Q, but we will discuss one type of scattered wave (Lg coda) quite extensively. Although Lg coda is thought to contain a large amount of scattered energy, some theoretical and computational studies (discussed later) of scattered S-wave energy suggest that measured Q values for that wave may largely reflect intrinsic properties of the crust.

All of the measurements that we discuss in this section can be placed in one of two major categories: (1) those in which seismic source effects cancel and (2) those in which assumptions are made about the seismic source spectrum. For category (1), the cancellation is most often achieved by using ratios of amplitudes recorded by two or more instruments. But it has also been achieved using ratios of amplitudes from different portions of a single time series. The primary application of the latter type of cancellation has been for the determination of Lg coda Q (Q_{Lg}^{C}). We divide this category into three parts that address regional phases, fundamental-mode surface waves, and Lg coda. Category (2) permits studies of Q using a single station but requires knowledge of the source depth, source mechanism, and velocity model for the source region. We divide this category into two parts, one addressing regional phases and the other fundamental-mode surface waves.

Seismologists have measured the dispersion of body waves due to anelasticity and have successfully used that dispersion to infer values for body-wave Q. We will not cover that topic because it has been the subject of relatively few studies and has been applied mainly to small regions.

The following subsections discuss methodology and present some representative results using the cited methods as applied to the crust. Because the number of studies for continents is overwhelmingly greater than for oceans, most of the discussion will pertain to continental regions. A few studies will, however, be described for oceanic regions.

1.25.7.2.1 Spectral decay methods in which source effects cancel: regional phases

Regional phases include P, S, and Lg phases recorded at distances less than about 1000 km. The early portion of this section mostly covers Q determinations for P and S phases, but in cases where researchers measured Q_{Lg}, as well as Q_P and Q_S, all results will be presented. The latter part of this subsection will discuss Lg exclusively since this phase has been widely used in recent years to study variations of Q over broad regions.

In order to cancel source effects, several methods utilize stations that lie on a common great-circle path with the seismic source, but other methods are able to dispense with the need for great-circle path propagation. All studies, however, need to first remove the effect of wave-front spreading before measuring amplitude changes due to attenuation. In this subsection, we will restrict our discussion to studies at frequencies that pertain totally or predominantly to the crust with occasional reference to the upper mantle for studies that include results for both the crust and upper mantle.

Regional and near-distance studies of P- and S-wave attenuation (or their respective quality factors Q_P and Q_S) often cancel the source by utilizing several stations at varying distances (e.g., Carpenter and Sanford, 1985; Nuttli, 1978, 1980; Thouvenot, 1983).

More recently, amplitude measurements in which both the source and sensor reside in boreholes beneath any sediments or weathered layers have provided much-improved estimates of Q_P and Q_S. Abercrombie (1997) used borehole recordings to determine spectral ratios of direct P to S waves and found that they are well modeled with a frequency-independent Q_P distribution in the borehole increasing from $Q_P \sim 26$–133 at depths between the upper 300 m and 1.5–3 km. Q_S increased

from 15 to 47 in the same depth range. Abercrombie (2000), in another borehole study near the San Andreas Fault, found that the rate of attenuation on the northeastern side of the fault is about twice that on the southwestern side.

Lg is very useful for Q studies because it both travels predominantly in the crustal waveguide, providing Q information for a known depth interval, and is a large and easily recognizable phase. Even relatively small earthquakes can generate useable records; thus, data in many regions are plentiful. Lg can be represented by a superposition of many higher-mode surface waves or by a composite of rays multiply reflected in the crust. It is usually assumed that Q_{Lg} follows a power-law frequency dependence, $Q = Q_0 f^{\eta}$, where Q_0 is the value of Q_{Lg} at a reference frequency and η is the frequency dependence parameter at that frequency. Lg travels through continental crust at velocities between about 3.2 and 3.6 km s^{-1} and is usually followed by a coda of variable duration. That coda is discussed in a later subsection. Since the Lg wave consists of many higher modes, it is often assumed that, even though the radiation patterns for individual modes differ from one another, the totality of modes combines to form a source radiation pattern that is approximately circular. If that assumption is correct, the source and stations need not necessarily line up along the same great-circle path to estimate Q.

Early determinations of Q_{Lg}, after correcting for wavefront spreading, compared observed attenuation with distance with theoretically predicted attenuation for the Lg phase and chose the theoretical curve (predicted by selected values of Q_0 and η), which agreed best with observations (e.g., Bollinger, 1979; Campillo et al., 1985; Chavez and Priestley, 1986; Chun et al., 1987; Hasegawa, 1985; Nuttli, 1973; Street, 1976).

Benz et al. (1997) studied four regions (southern California, the Basin and Range Province, the central United States, and the northeastern United States and southeastern Canada) of North America in the frequency range 0.5–14.0 Hz. They found that, at 1 Hz, Q_{Lg} varies from about 187 in southern California to 1052 in the northeastern United States and southeastern Canada and about 1291 in the central United States. They also found that the frequency dependence of Q also varies regionally, being relatively high ($\alpha \sim 0.55$–0.56) in southern California and the Basin and Range Province and smaller ($\alpha \sim 0$–0.22) in the other three regions.

Xie and Mitchell (1990a) applied a stacking method to many two-station measurements of Q_{Lg} at 1 Hz frequency in the Basin and Range Province. This method, first developed for single-station determinations of Lg coda Q (Q_{Lg}^{C}), will be discussed in the subsection on Lg coda. They found that $Q_{Lg} = (275 \pm 50) f^{(0.5 \pm 0.2)}$ and $Q_{Lg}^{C} = (268 \pm 50) f^{(0.5 \pm 0.2)}$.

Xie et al. (2004) extended the method to multiple pairs of stations in instrument arrays across the Tibetan Plateau. For an array in central Tibet (INDEPTH III), they found very low values for Q_0 (~ 90) that they attributed to very high temperatures and partial melt to the crust. An array in southern Tibet yielded even lower values, ~ 60, for Q_0 in the northern portion of the array but higher values (~ 100) in a central portion and much higher values (>300) in the southernmost portion. Xie et al. (2006) used a two-station method to obtain more than 5000 spectral ratios for 594 interstation paths and obtained Q_0 and η for those paths. They obtained tomographic maps of those values that are described in the subsection on tomographic mapping. With the purpose of obtaining attenuation information in the upper mantle, Xie (2007) studied Pn attenuation beneath the Tibetan Plateau. He obtained Q_0 and η and studied its regional variation across several regions. He found Q_0 to be highest (374, with η being 0.3) in easternmost Tibet and lowest (188 with η being 0.3) in northern Tibet. The high values for Q_0 are comparable to those reported earlier for central Asia. He found regional Pn attenuation varies inversely with Pn velocity.

1.25.7.2.2 Spectral decay methods in which source effects cancel: fundamental-mode surface waves

When using fundamental-mode surface waves to study lateral variations of crustal Q_{μ}, we need to measure the attenuation of relatively short-period (5–100 s) amplitudes. In continents, these waves may be biased by systematic errors associated with laterally varying elastic properties along the path of travel, as discussed earlier. Two-station studies of fundamental-mode surface waves are especially susceptible to these types of error because researchers might incorrectly assume great-circle propagation along a path through the source and the two stations. Non-great-circle propagation would mean that surface-wave energy arriving at two stations along different great-circle paths could originate at different portions of the source radiation pattern. If that pattern is not circular, the two-station method can produce attenuation coefficient values that are either too high or too low, depending on the points of the radiation pattern at which the waves originate.

To determine surface-wave attenuation, measurements for the situation in which a source and two stations lie approximately on the same great-circle path have often been used to determine surface-wave attenuation. The method was described by Tsai and Aki (1969) and determines the average surface-wave Q between the two stations after correcting for the different wavefront spreading factors at the two stations. They applied the method to many two-station paths from the Parkfield, California, earthquake on 28 June 1966 and, using the formulation of Anderson et al. (1965), obtained a frequency-independent model of intrinsic shear-wave Q (Q_{μ}) with a low-Q zone that coincided with the Gutenberg low-velocity zone in the upper mantle. Love-wave Q was greater than 800, and Rayleigh-wave Q was greater than 1000 in the period range 20–25 s.

Other studies using that method to obtain Q_{μ} models at crustal and uppermost mantle depths include Hwang and Mitchell (1987) for several stable and tectonically active regions of the world, Al-Khatib and Mitchell (1991) for the western United States, and Cong and Mitchell (1998) for the Middle East.

Models have also been obtained in which Q_{μ} varies with frequency. That frequency dependence is described by the relation $Q_{\mu} = Q_0 f^{\zeta}$ where ζ may vary with frequency (Mitchell, 1975) and/or with depth (Mitchell and Xie, 1994). The inversion process for Q_{μ} in those cases requires appropriate extensions of the Anderson et al. (1965) equations. The process requires both fundamental-mode surface-wave attenuation data and Q or attenuation information for either an individual higher mode or the combination of higher modes that form the Lg phase. The process proceeds by assuming a simple one- or two-layer distribution of ζ and inverting the

fundamental-mode data for a Q_μ model. ζ is adjusted until a Q_μ model is obtained that explains both the fundamental-mode and higher-mode attenuation data. Mitchell and Xie (1994) applied the method to the Basin and Range Province of the western United States. Example Q_μ models for which ζ varies with depth (Mitchell and Xie, 1994) appear in **Figure 11**.

Other surface-wave studies for which the source is canceled are those that use many stations at various distances and azimuths and simultaneously solve for surface-wave attenuation coefficient values and seismic moments for particular periods by linear least squares. Tryggvason (1965) first did this, as described in our section on early studies, using explosions and assuming circular radiation patterns. Tsai and Aki (1969) extended this method to use earthquake sources and applied it to surface waves generated by the 28 June 1966 Parkfield, California, earthquake. This process was later applied to the central United States (Herrmann and Mitchell, 1975; Mitchell, 1973) and the Basin and Range Province of the western United States (Patton and Taylor, 1989).

A nonlinear variation of the Tsai and Aki method (Mitchell, 1975) represents a nuclear explosion with strain release by a superposition of an explosion (with a circular radiation pattern) and a vertical strike-slip fault (represented by a horizontal double couple). Variations of the orientation of the double couple and its strength relative to the explosion produce a wide variety of radiation patterns. The inversion solves for the moment of the explosion, the orientation of the double couple, the strength of the double couple relative to the explosion, and an average attenuation coefficient value for each period of interest. Mitchell applied the method to two nuclear events in Colorado as recorded by stations throughout the United States and found that Q_μ in the upper crust of the eastern United States is about twice as high as it is in the western United States at surface-wave frequencies.

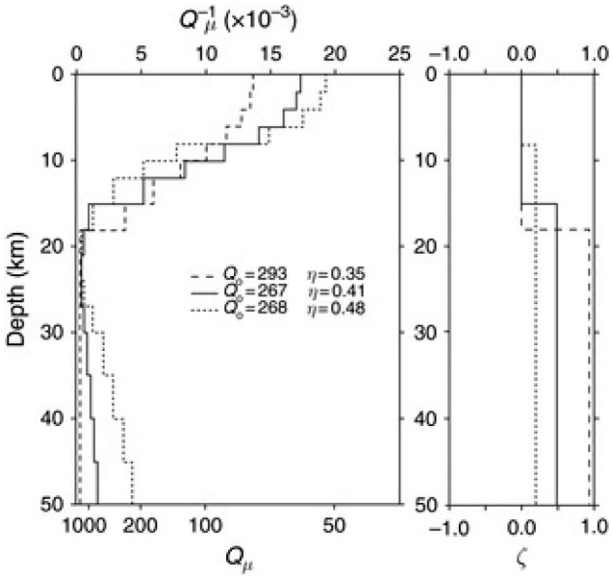

Figure 11 (Left) Three Q_μ models resulting from inversion of Rayleigh-wave attenuation coefficient data from the Basin and Range Province. The numbers refer to the value of Q_0 and η predicted by three models for Q_{Lg}. (Right) Three selected models for the variation of Q_μ frequency dependence with depth in the crust of the Basin and Range Province. Each of these depth distributions was fixed during inversions that produced Q_μ models. Reproduced from Mitchell BJ and Xie J (1994) Attenuation of multiphase surface waves in the Basin and Range province. Part III: Inversion for crustal anelasticity. *Geophysical Journal International* 116: 468–484, with permission from Blackwell Publishing.

The first attempts at mapping regional variations of attenuation or Q utilized crude regionalizations (two or three regions) based upon broad-scale geologic or geophysical information. Studies have produced models for Eurasia (Yacoub and Mitchell, 1977) using the method of Mitchell (1975) and for the Pacific (Canas and Mitchell, 1978) and Atlantic (Canas and Mitchell, 1981) using the two-station method.

1.25.7.2.3 Spectral decay methods in which source effects cancel: Lg coda

Lg coda, like direct Lg, is sensitive to properties through a known depth range (the crust) in which it travels and is a large amplitude phase for which data are plentiful. In addition, since the coda of Lg is comprised of scattered energy, it can continue to oscillate for several hundred seconds following the onset of the direct Lg phase, thus making it possible to stack spectral amplitudes for many pairs of time windows to make a Q estimate. Other positive aspects of using Lg coda for Q studies are that the averaging effect of scattering stabilizes Q_{Lg}^C determinations and, if stacking methods are utilized to determine Q for Lg coda, site effects cancel (Xie and Mitchell, 1990a).

Two methods have been applied to Lg coda to make Q determinations. The first of these was developed by Herrmann (1980) and applied by Singh and Herrmann (1983) to data in the United States. The method extended the coda theory of Aki (1969) utilizing the idea that coda dispersion is due to the combined effects of the instrument response and the Q filter of the Earth. The two studies provided new approximations for the relative variation of Q across the United States. Herrmann later realized, however, that his method did not take into consideration the broadband nature of the recorded signal and overestimates Q by about 30% (R. B. Herrmann, personal communication).

Xie and Nuttli (1988) introduced the stacked spectral ratio (SSR) method, which stacks spectra from several pairs of windows along the coda of Lg. That process leads to

$$R_k = f^{1-\eta}/Q_0 \qquad [16]$$

as the expression for the SSR, or in logarithmic form

$$\log R_k = (1-\eta)\log f_k - \log Q_0 + e \qquad [17]$$

from which Q_0 and η can be obtained by linear regression. f_k, Q_0, η, and e in these equations are, respectively, a discrete frequency, the value of Q at 1 Hz, the frequency dependence of Q at frequencies near 1 Hz, and an estimate for random error. This stacking process provides stable estimates of Q_0 and η with standard errors sufficiently low to allow tomographic mapping of those quantities. A detailed description of the SSR method appears in Xie and Nuttli (1988) and more briefly in Mitchell et al. (1997).

Figure 12 shows an example of Lg coda and its associated SSR for a relatively high-Q path in India, which can be fit over a

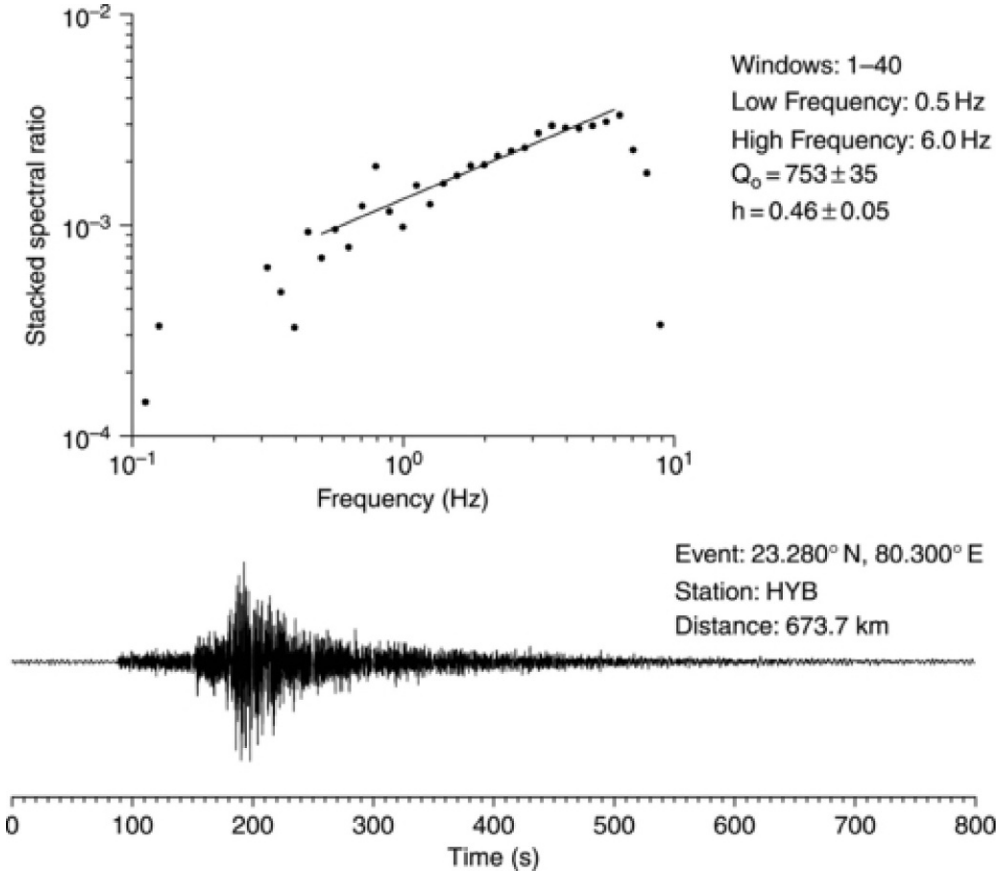

Figure 12 (Bottom) Seismogram. (Top) Stacked spectral ratio as a function of frequency for a relatively high-*Q* path in India.

broad frequency range with a straight line on a log–log plot. The value at 1 Hz provides an estimate of $1/Q$ at that frequency and the slope of the line gives an estimate for η. Inversions of sets of those values over a broad region can yield tomographic maps of those quantities.

Past studies have shown that several factors may contribute to reductions in Q_0; these include thick accumulations of young sediments (Mitchell and Hwang, 1987) and the presence of a velocity gradient rather than a sharp interface at the CMB (Bowman and Kennett, 1991; Mitchell et al., 1998). In addition, decreasing depth of the Moho in the direction of Lg travel or undulations of the Moho surface can be expected to decrease measured Q_{Lg} or Q_{Lg}^C, whereas increasing depth would produce larger values. To our knowledge, this effect has not been quantitatively studied and is expected to be small over large regions. These factors may cause determinations of correlation coefficients between Q_{Lg} or Q_{Lg}^C and various crustal or mantle properties to be relatively low whenever they are determined (e.g., Artemieva et al., 2004; Zhang and Lay, 1994).

1.25.7.2.4 Spectral decay methods for which assumptions are made, or information can be learned, about the source spectrum: regional phases

Hough et al. (1988) studied S waves traveling over relatively short distances near Anza, California, and defined the instrument-corrected acceleration spectrum at a station located a distance r from the source as

$$A(r,f) = A_0 e^{-\pi t^*} \quad [18]$$

where t^* is defined in eqn [12]. For crustal studies, it is common to assume that Q is constant along the path, in which case

$$t^* = \frac{t}{Q} \quad [19]$$

where t is the travel time.

Hough et al. (1988) defined A_0 as

$$A_0 = (2\pi f)^2 S(f) G(r,f) \quad [20]$$

where $S(f)$ is the source displacement spectrum and $G(r, f)$ is the geometric spreading factor, which, if we assume frequency-independent propagation in a homogeneous medium, is $1/r$ for body waves. At higher frequencies, these methods assume a spectral falloff rate (such as ω^{-2} or ω^{-3}) and attribute additional falloff to attenuation. Since a large body of data supports the ω^{-2}, or Brune, model (Brune, 1970), that is the one most commonly used. Taking the natural logarithm of eqn [18] leaves

$$\ln A(f) = \ln A_0 - \pi f t^* \quad [21]$$

For the frequency-independent case, this equation defines a straight line with an intercept of $\ln A_0$ and a slope of $-\pi t/Q_0$.

Anderson and Hough (1984) hypothesized that, to first order, the shape of the acceleration spectrum at high frequencies can be described by

$$\alpha(f) = A_0 e^{-\pi\kappa f} \quad f > f_E \qquad [22]$$

where f_E is the frequency above which the spectral shape is indistinguishable from spectral decay and A_0 depends on source properties and epicentral distance. They found that κ increased slowly with distance, an observation consistent with a Q model of the crust that increases with depth in its shallow layers and that it was systematically smaller on rock sites than at alluvial sites. Hough et al. (1988) studied κ as a function of hypocentral distance, as well as site and source characteristics, and found that $\kappa(0)$ differed for sites at Anza and the Imperial Valley in California but that $d\kappa/dr$ was similar for the two regions. Their interpretation was that $\kappa(0)$ was a component of attenuation that reflects Q_i in the shallow portion of the crust while $d\kappa/dr$ was due to regional structure at great depth. This method was applied to various regions in the world including the Canadian Shield (Hasegawa, 1974), the Pyrenees (Modiano and Hatzfeld, 1982), the New Madrid zone of the central United States (Al-Shukri et al., 1988), and eastern Asia (Phillips et al., 2000).

Shi et al. (1996) studied Q_{Lg} variation for five tectonically different regions of the northeastern United States. They used eight pairs of colocated earthquakes to determine accurate source spectrum corner frequencies by applying an empirical Green's function method to Pg and Lg or Sg phases. Based upon the corner frequencies, Sg or Lg displacement spectra were used to obtain values of Q and η values for 87 event–station paths at frequencies between 1 and 30 Hz. The 1 Hz Q_0 values for the five regions vary between 561 and 905 while η varies between 0.40 and 0.47.

1.25.7.2.5 Spectral decay methods for which assumptions are made about the source spectrum: fundamental-mode surface waves

A multimode spectral method has yielded simple crustal models (two or three layers) of shear-wave Q (Q_μ) in a few regions. The method assumes a flat source spectrum and tries to match theoretical amplitude spectra to two sets of observed spectral amplitude data, one corresponding to the fundamental mode and the other to the superposition of higher modes that forms the longer-period (3–10 s) component of the Lg phase. The higher modes travel faster than all but the longest-period fundamental-mode energy observed on records for relatively small events that are used with this method.

The first study using this method (Cheng and Mitchell, 1981) compared upper crustal Q_μ for three regions of North America and found values of 275 for the eastern United States, 160 for the Colorado Plateau, and 85 for the Basin and Range Province. Kijko and Mitchell (1983) applied the method to the Barents Shelf, a region of relatively high-Q crystalline crust overlain by low-Q sediments. They found the method to be sensitive to Q_μ in the sediments and upper crust but insensitive to Q_μ in the lower crust and to P-wave Q at all depths. Cong and Mitchell (1998) obtained models in which Q_μ is very low at all depths beneath the Iran/Turkish plateaus and somewhat higher but still much lower than expected beneath the Arabian Peninsula. Models they obtained using the multimode method agree well with those they obtained using the two-station method.

Jemberie and Mitchell (2004) applied the method to China and peripheral regions and obtained three-layer crustal models with low Q_μ and wide variation across China. Values decrease with depth beneath regions such as southeastern China and increase with depth beneath other regions such as the eastern Tibetan Plateau.

Seismologists have, in recent years, developed methods to measure the attenuation of regional phases (Pn, Pg, Sn, and Lg) in which the effects of source spectra are considered. One of those (Walter et al., 2007) used source spectra derived from the coda of those phases. It determined apparent Q by subtracting source spectra amplitudes from the observed amplitudes that were corrected for geometric spreading. They tested the method for several paths in Italy and found that they could determine path and recording site attenuation that satisfied the equation $Q(f) = Q_0 f^\eta$ well, for all phases, over the frequency range 0.5–8 Hz. Their measured values were also quite repeatable. Ford et al. (2008) compared several methods, including this one, for determining the attenuation of Lg in northern California. All methods returned similar values for Q_0 and η but with large 95% confidence regions ($Q_0 = 80 \pm 40$; $\eta = 0.65 \pm 0.35$). Another study of broadband Lg attenuation in the Middle East (Pasyanos et al., 2009) used the magnitude and distance amplitude correction developed by Walter and Taylor (2001). The method formulates the source term in terms of a corner frequency ω_c with an ω^{-2} falloff (Aki, 1967 and others) where the corner frequency and source term include constants that depend on medium properties as well as seismic moment. Their studies compared favorably with the results found by other studies in the region and, like those studies, showed a strong correlation with tectonics.

1.25.7.3 Tomographic Mapping of Crustal *Q*

Seismologists are currently attempting to map variations of Q and its frequency variation in the Earth in as much detail as possible. For continents, researchers have obtained tomographic maps for several broad regions using Lg coda, the direct Lg phase, and surface waves. Studies using P and S waves have yielded important results in regions where earthquakes and recording stations are plentiful. Studies of even smaller regions, such as volcanoes and geothermal areas, have utilized P and S waves (e.g., Hough et al., 1999). In this chapter, we restrict our discussion to more broad-scale studies.

An earlier section described three early regionalized studies of surface-wave attenuation in the late 1970s and early 1980s, one for continental paths and two for oceanic paths in which the Eurasian continent, the Pacific Ocean, and Atlantic Ocean were divided into two or three regions. Since then, tomographic mapping using Lg coda has made possible a much finer regionalization of crustal Q in continents. This section will discuss tomography results for continents and for one oceanic region using either direct Lg, fundamental-mode surface waves, or P and S waves.

We emphasize Lg coda since tomographic maps of Q_{Lg}^C, all obtained for the same frequency and using the same methodology, are available for all continents except Antarctica. This

commonality in phase, frequency, and method allows us to compare Q from one continent to that in others and also to various geophysical and geologic properties. These comparisons contribute to our understanding of the mechanisms for seismic-wave attenuation in the crust.

Earlier sections have indicated that Lg coda has several properties that make it useful for tomographic studies. First, it is usually a large amplitude phase making it easily available for study in most regions of the world. Second, it is a scattered wave and the averaging effect of that scattering makes Lg coda relatively insensitive to focusing. Third, the SSR method used to determine Q_0 and η tends to cancel site effects. Fourth, although it is a scattered wave, measurements of Q for seismic coda have been shown theoretically and computationally to yield measures of intrinsic Q (e.g., Frankel and Wennerberg, 1987; Mitchell, 1995; Sarker and Abers, 1999). If that is correct, researchers can interpret Q variation in terms of Earth structure and evolution. Other studies, however (e.g., Aki, 1980; Gusev and Abubakirov, 1996) attribute energy loss to scattering.

Akinci et al. (1995), employing the energy partition method of Frankel and Wennerberg (1987) for a Q study in western Turkey, found that shear-wave scattering predominated at low frequencies (1–4 Hz) and short hypocentral distances (0–80 km). Intrinsic anelasticity, however, became the dominant contributor to attenuation at greater distances. Cicerone et al. (2011) obtained a similar result for northeastern North America, while Sahin et al. (2013) also came to that conclusion when studying Lg attenuation in central Turkey. Those three studies suggest that for typical studies of Lg attenuation at large distances (about 200 km and more), Q values will largely reflect intrinsic properties of the Earth's crust.

Mitchell et al. (2014) proposed that the reason these path length-dependent differences occur can be understood by considering a supposition of rays taken to characterize Lg propagation. At very short lateral distances, most of the rays that comprise shear waves are reflected at angles smaller that the critical angle. For that reason, much of the wave energy at short distances is scattered into the mantle and quickly lost. At large lateral distances, waves that combine to form Lg reflect off the crust–mantle boundary (and other crustal boundaries) at angles that exceed the critical angle. That being the case, Lg and its coda will be largely constrained to travel in the crust, and relatively little energy is lost to the mantle.

As indicated earlier, Lg coda Q (Q_{Lg}^{C}) is typically assumed to follow a power-law frequency dependence, $Q_{Lg}^{C} = Q_0 f^{\eta}$, where Q_0 is the Q value at 1 Hz and η is the frequency dependence of Q near 1 Hz. Tomographic maps of the 1 Hz values of Q_{Lg}^{C} (Q_0 and η) with nearly continent-wide coverage are now available for Eurasia (Mitchell et al., 1997, 2008), Africa (Xie and Mitchell, 1990b), South America (DeSouza and Mitchell, 1998), and Australia (Mitchell et al., 1998). In North America, broad-scale determinations of Q_{Lg}^{C} are currently restricted to the United States (Baqer and Mitchell, 1998). These studies have shown a wide range of average Q_0 values for different continents and a very wide range within each continent. Average Q_0 tend to be highest in continents that contain the most old stable cratonic regions that have not undergone later tectonic or orogenic activity (e.g., Africa and South America).

Tomographic studies have also been completed for more restricted regions using the direct Lg phase in Eurasia, North America, and South America, and high-resolution tomographic maps of Q for P and S waves are available for southern California. For oceanic regions, tomographic mapping of Q variations, to our knowledge, is currently available only for P waves in one broad portion of the East Pacific Rise (Wilcock et al., 1995).

Sarker and Abers (1998) showed that, for comparative studies, it is important that researchers use the same phase and methodology in comparative Q studies. The Lg coda Q maps presented here adhere to that principle; thus, the continental-scale maps of Q_0 and η for Lg coda at 1 Hz that are available can be considered to provide the closest thing to global Q coverage at crustal depth that currently exists. The maps also present the possibility for comparisons of Q_0 variation patterns with variations in seismic velocity, temperature, plate subduction, seismicity, the surface velocity field, and tectonics when that information is available.

A discussion of the inversion method for mapping Q_0 and η appears, in detail, in Xie and Mitchell (1990b) and, more briefly, in Mitchell et al. (1997). The method assumes that the area occupied by the scattered energy of recorded Lg coda can be approximated by an ellipse with the source at one focus and the recording station at the other, as was shown theoretically by Malin (1978) to be the case for single scattering.

Xie and Mitchell (1990b) utilized a back-projection algorithm (Humphreys and Clayton, 1988) to develop a methodology for deriving tomographic images of Q_0 and η over broad regions using a number of Q_0 or η values determined from observed ground motion. **Figures 13–17(a)** show the ellipses that approximate data coverage for the event–station pairs used in Q_{Lg}^{C} studies of Eurasia, Africa, South America, Australia, and the United States. The inversion process assumes that each ellipse approximates the spatial coverage of scattered energy comprising late Lg coda. The areas of the ellipses grow larger with increasing lag time of the Lg coda components. The ellipses in the figure are plotted for maximum lag times used in the determination of Q_0 and η. Ideally, each inversion should utilize many ellipses that are oriented in various directions and exhibit considerable overlap in order to obtain the redundancy needed to obtain the best possible resolution for features of interest. Xie and Mitchell (1990b) discuss the procedure in detail, presenting methods for obtaining standard errors for Q_0 and η and for estimating spatial resolution.

Because Lg coda consists of scattered energy, it must be distributed, for each event–station pair, over an area surrounding the great-circle path between the source and receiver. Because of this areal coverage, our maps may not include effects of Lg blockage in regions where such blockage has been reported. We may have no data from blocked paths but are likely to have other paths, such as those subparallel to the blocking feature or for which the source or recording station, represented by one focus of the scattering ellipse, lies near the blocking feature. In both cases, portions of the scattering ellipses may overlap the blocking feature, but that feature will not substantially contribute to the values we obtain for Q_0 and η. A comparison of mapped Q_0 for all continents (**Figures 13–17(b)**) shows that it is typically highest in the stable portions of the continents and lowest in regions that are, or recently have been, tectonically active. Exceptions occur, however, especially for stable regions. For instance, the Arabian

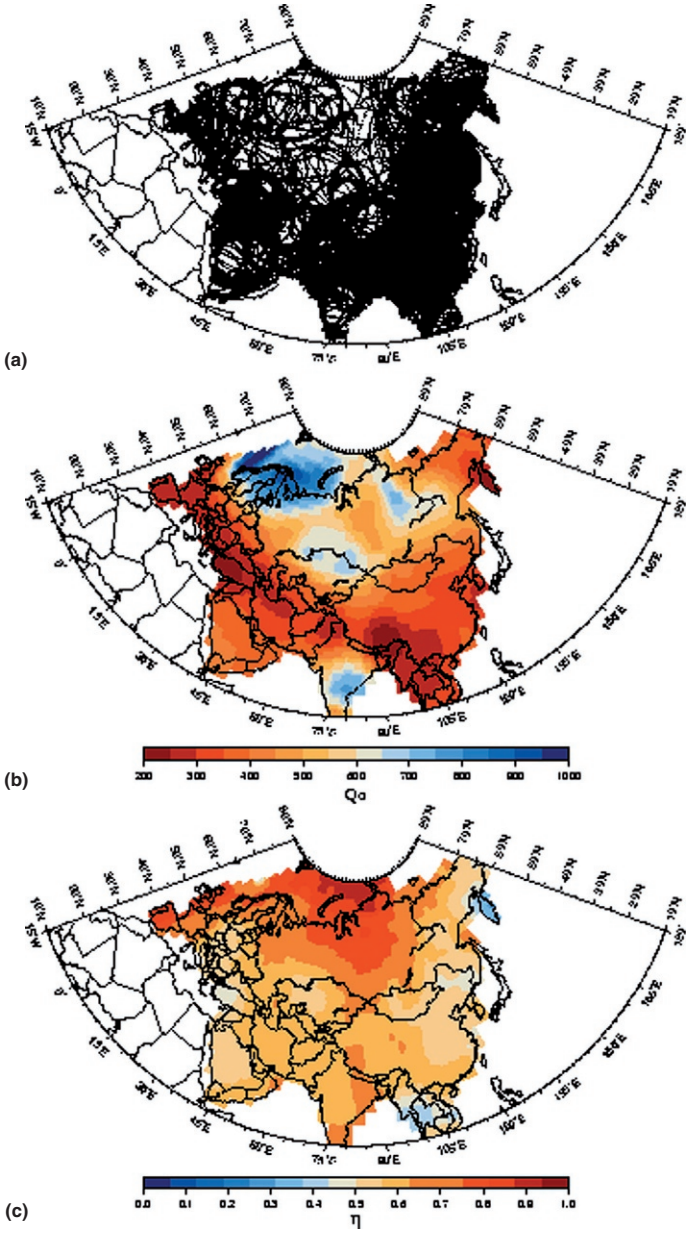

Figure 13 (a) A scattering ellipse map, (b) a Q_0 map, and (c) an η map for Eurasia. Adapted from Mitchell BJ, Cong L, and Ekström G. (2008) A continent-wide 1-Hz map of *Lg* coda *Q* variation across Eurasia and its implications for lithospheric evolution. *Journal of Geophysical Research* 113. http://dx.doi.org/10.1029/2007JB005065.

Peninsula, although being a stable platform, shows Q_0 variations between 300 and 450, values that are one-half or less of maximum values in other Eurasian platforms. Other regions showing lower than expected Q_0 include the Siberian Trap region of northern Siberia and the cratonic regions of Australia.

The frequency dependence values of $Q_{\mathrm{Lg}}^{\mathrm{C}}$ (η) in Figures 13–17(c) appear to show consistent relationships to Q_0 in some individual continents. For instance, in both Africa and South America, high-*Q* regions are typically regions of low η. That same relationship, however, does not occur consistently in Eurasia, Australia, or the United States. η is high, for instance, throughout much of the northern portions of Eurasia where Q_0 is mostly high but is low in California, Kamchatka, and a portion of southeast Asia where Q_0 is very low.

1.25.7.3.1 Q_{Lg}^{C}, Q_{Lg}, and Q_{μ} tomography in regions of Eurasia

Figure 13 shows maps of data coverage, Q_0, and η across most of Eurasia (Mitchell et al., 2008). These maps represent a major increase in data coverage for northeastern Siberia, southeastern Asia, India, and Spain, compared to those of an earlier study (Mitchell et al., 1997) and provide additional redundancy in regions where there was earlier coverage. As indicated in Figure 13(a), the data coverage is excellent for virtually all of

Eurasia. Low Q_0 values extend through the Tethysides belt that extends across southern Eurasia from western Europe to eastern China, and its southern portions appear to be related to subduction processes occurring at the present time. Q_0 is generally high in the platforms of northern Eurasia and India (600–950). It is, however, low in the Kamchatka Peninsula and regions directly north of there, which, like the Tethysides region, are seismically active. A conspicuous region of relatively low Q_0 lies in central Siberia and corresponds spatially to the Siberian Traps.

The four zones with lowest Q values lie in the Kamchatka Peninsula in northeastern Siberia, the southeastern portions of the Tibetan Plateau and Himalaya, and the Hindu Kush (just north of India) and western Turkey. All of these regions are also highly seismically active, a correspondence that suggests that low-Q regions are associated with regions of high crustal strain.

Other low-Q regions appear to be related to upper mantle processes. A comparison of **Figure 13(b)** with wave velocities at long periods (Ekström et al., 1997), which are not sensitive to crustal properties, shows a correspondence of low-Q regions with regions of low upper mantle velocities. This is most apparent for the broadband of low Q values throughout southern Eurasia but also occurs in the Siberian Trap region of Siberia. Both the low-Q and low-velocity regions largely coincide with high upper mantle temperatures (Artemieva and Mooney, 2001).

Patterns of frequency dependence (η) variation in **Figure 13(c)**, in contrast to those of Q_0 variation, show no clear-cut relationship to tectonics. They similarly show no relation to patterns of Q_0 variation. For instance, Kamchatka has low Q_0 and low η while Spain has low Q_0 and high η.

Seismologists have performed other tomographic studies for portions of Eurasia using Q_{Lg} and shear-wave Q (Q_μ). Xie et al. (2006) used a two-station version of the SSR method to determine more than 5000 spectral ratios over 594 paths in eastern Eurasia. They were able to obtain tomographic models for Q_0 and η with resolution ranging between 4° and 10° in which Q_0 varies between 100 and 900.

Using the single-station multimode method, Cheng and Mitchell (1981) and Jemberie and Mitchell (2004) obtained tomographic maps of shear-wave Q (Q_μ) for depth ranges of 0–10 and 10–30 km. Although large standard errors accompany those determinations, several features of their variation patterns, such as the low-Q regions in southern Tibet, resemble the map of Q_0 variations (**Figure 13(b)**). Q_μ varies between about 30 and 280 in the upper 10 km of the crust and between about 30 and 180 at 10–30 km depth.

1.25.7.3.2 Q^C_{Lg} tomography in Africa

Xie and Mitchell (1990b), in the first tomographic study of Lg coda, determined Q_0 and η for continental Africa. **Figure 14** shows maps of data coverage, Q_0 and η for that entire continent (Xie and Mitchell, 1990b). The feature in the Q_0 map (**Figure 14(b)**) that is most obviously related to tectonics is the low-Q region that broadly coincides with the East African Rift system. The three high-Q regions correspond to Precambrian cratons: the West African Craton in the northwest, the East Sahara Craton in the northeast, and the Kalahari Craton in the south. The Congo Craton, situated just to the north of the Kalahari Craton does not show up as a region of high Q, probably because waves are damped by a broad and deep basin of low-Q sedimentary rock in that region.

Low Q_0 values also occur in the Atlas Mountains (Cenozoic age) of northern Africa, the Cape Fold Belt (Permian–Triassic age) at the southern tip of Africa, and the Cameroon line (Miocene age), which is oriented in an NNE–SSW direction from the point where the western coast changes direction from east–west to north–south.

1.25.7.3.3 Q^C_{Lg} and Q_{Lg} tomography in South America

Figure 15 shows data coverage and values of Q_0 and η obtained for South America (DeSouza and Mitchell, 1998). The data coverage (**Figure 15(a)**) is excellent throughout western South America where seismicity is high but poor in eastern regions, especially the most easterly regions, where there are few earthquakes. **Figure 15(b)** shows that, as expected, the low-Q (250–450) portion of South America is associated with the tectonically active western coastal regions. The lowest Q_0 values occur along the coast between 15° and 25° S latitude where the level of intermediate-depth seismicity is highest in the continent. The slab in this region also dips steeply (>20°) and significant volcanism occurs (Chen et al., 2001). Davies (1999) had studied the role of hydraulic fractures and intermediate-depth earthquakes in generating subduction zone magmatism. He suggested that the level of intermediate-depth earthquakes was high because liberated fluids favored brittle fracture in response to stresses acting on the slab. Q levels may be low there because earthquake activity creates a degree of permeability that allows dehydrated fluids to be transported to the mantle wedge.

Ojeda and Ottemöller (2002) developed maps of Lg attenuation for most of Colombia at various frequencies in the 0.5–5.0 Hz range. They delineated regional variations of Q_{Lg} within that relatively small region.

1.25.7.3.4 Q^C_{Lg} tomography in Australia

Figure 16 shows the data coverage and values of Q_0 and η obtained for Australia (Mitchell et al., 1998). Data coverage (**Figure 16(a)**) there was the poorest of the five continents where $Q^{\mathrm{C}}_{\mathrm{Lg}}$ was mapped over continent-scale dimensions. Q_0 variation there is consistent, however, with the other studies, and, for all but peripheral regions where systematic measurement errors can be high, it displays a clear relationship with past tectonic activity. Q_0 in Australia (**Figure 16(b)**) is unusually low for a stable continental region, perhaps because a velocity gradient rather than a sharp interface separates the crust and mantle.

Highest values range between 550 and 600 in the southeastern corner of the continent (the Yilgarn Block) and along the southern coast (the Gawler Block). Values between 400 and 500 characterize much of the remaining cratonic crust. This compares with values of 800 and higher in most of the African and South American cratons. The youngest crust lies in eastern Australia where Q_0 is between 350 and 400. An orogeny occurred there during the Devonian Period, and another occurred in the eastern portion of that region during the Permian Period. Low Q_0 values in the most westerly point of the continent and along the northern coast are probably due to very poor data coverage there (**Figure 16(a)**) and are probably meaningless.

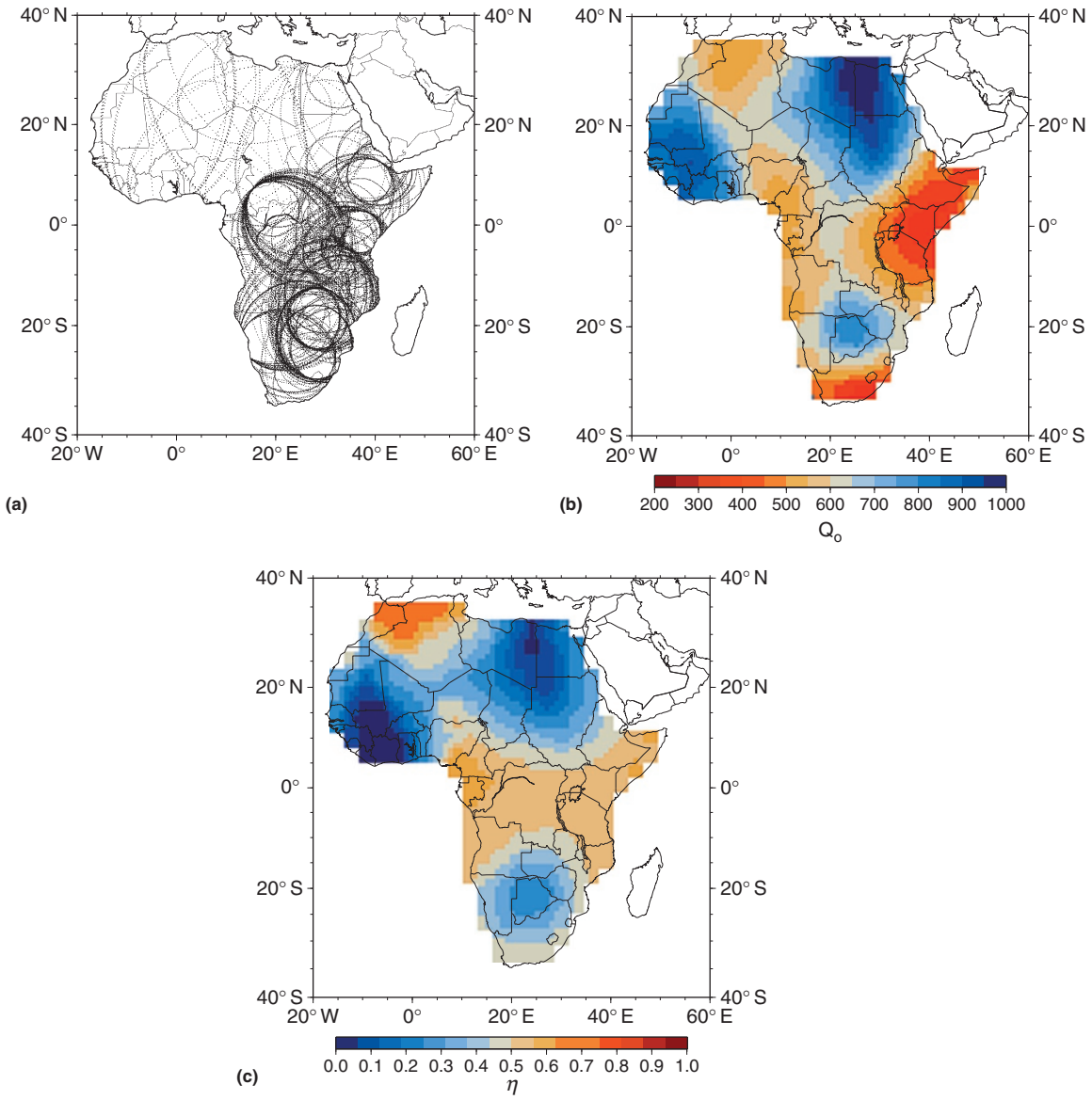

Figure 14 (a) A scattering ellipse map, (b) a Q_0 map, and (c) an η map for Africa. Adapted from Xie J and Mitchell BJ (1990b) A back-projection method for imaging large-scale lateral variations of *Lg* coda *Q* with application to continental Africa. *Geophysical Journal International* 100: 161–181.

1.25.7.3.5 Q^c_{Lg}, Q_{Lg}, and P/S tomography in North America

Figure 17(a) shows approximate data coverage and values of Q_0 and η for the first Lg coda *Q* study of the entire North American continent (Mitchell et al., 2014). This work utilized 1122 event–station pairs distributed across virtually all of North America, a number that represents a more than fivefold increase in data coverage over that of an earlier Lg coda *Q* study of the United States (Baqer and Mitchell, 1998). Data coverage is densest in the westernmost portion of North America where seismicity rates are high but coverage is also more than adequate for most of the rest of the continent. This is especially true for the south-central and northeastern portions of the United States, as well as for southeastern Canada. The ability to use relatively small earthquakes, even in central and north-central Canada where seismicity rates are low, allowed us to achieve quite good data coverage.

The Q_0 map (Figure 17(b)) reveals two major features that cover vast areas of North America. One is a region of high-*Q* values (700–1000) that covers much of the Canadian Shield with a southeastern arm that extends through southern New England and New York to the Atlantic coast. The other is a band of low-*Q* values (about 200–350) that runs continuously, with some variations in width (between about 20 and 500 km), from southern Alaska to southern Central America. The transition from the high-*Q* shield values to low values in western Canada is surprisingly sharp and suggests that the pattern of mapped Q_0 cannot be explained as being produced by temperature variations alone in the crust. One possibility that would nicely explain the sharp transition is a change from high levels of interstitial fluid content in the low-*Q* region compared to lower fluid levels in the high-*Q* region.

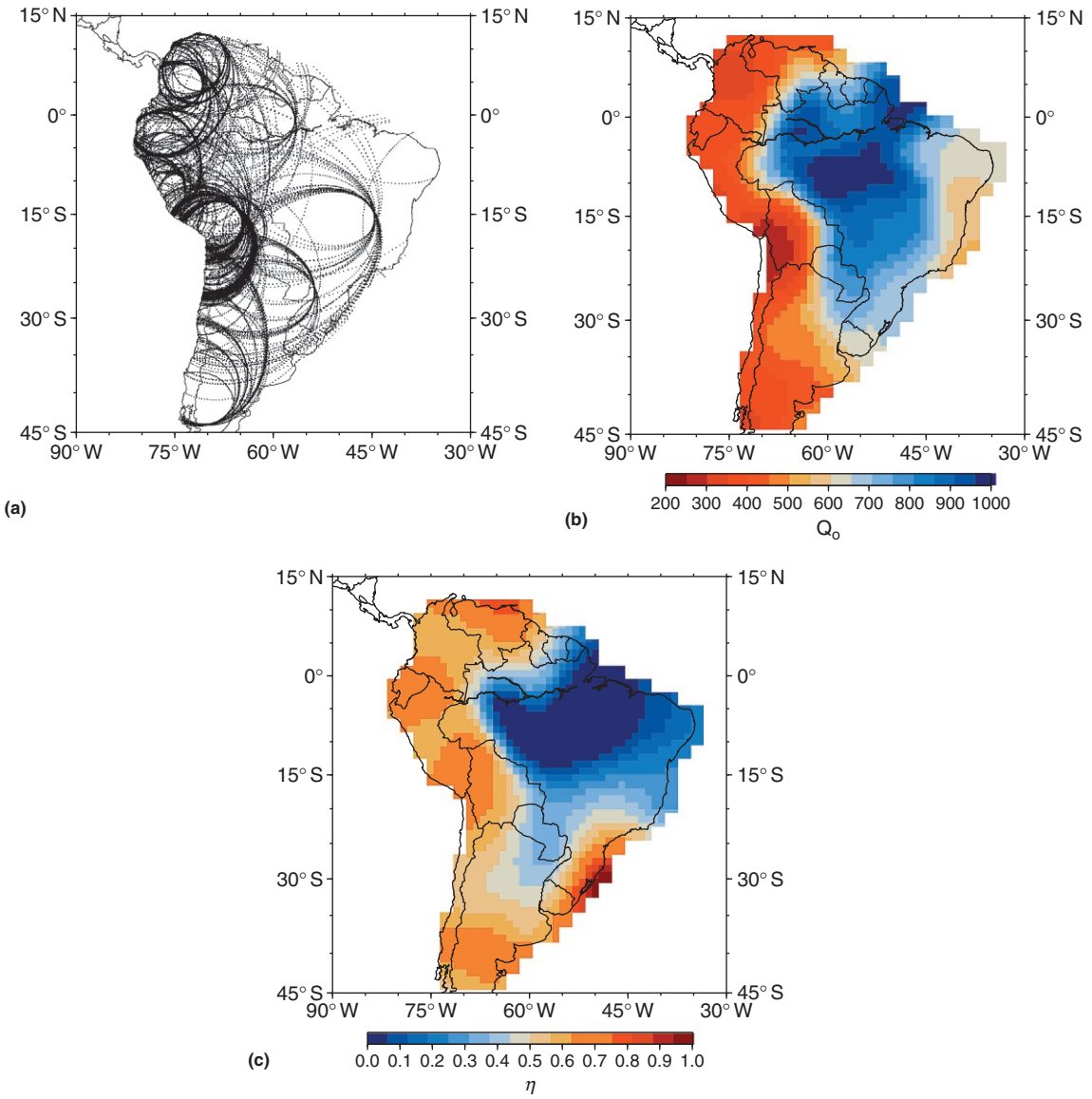

Figure 15 (a) A scattering ellipse map, (b) a Q_0 map, and (c) an η map for South America. Adapted from DeSouza JL and Mitchell BJ (1998) *Lg* coda *Q* variations across South America and their relation to crustal evolution. *Pure and Applied Geophysics* 153: 587–612.

A small but important feature on the map appears as a circular region of high Q_0 values (600–700) with a diameter of about 500–700 km in the central United States. It coincides well with the Ozark uplift of southern Missouri and northern Arkansas. The region of relatively high Q_0 includes the St. Francis Mountains, a region of Precambrian rock, which contains some of the oldest rock in North America.

One region of moderately low Q_0 values includes the east–west band that extends from the eastern edge of very low-Q_0 regions of southern California and northern Mexico through southern portions of the Gulf coast states and northward along the Atlantic coast to an extension of the high-Q_0 Canadian Shield. Another is the relatively low-Q_0 band from northeastern Canada through most of the continental shelf of northern Canada. All of these features are probably due to the accumulations of thick sediments known to occupy those regions.

Figure 17(c) shows the distribution of the frequency dependence parameter (η) for North America. The excellent coverage of this study makes possible a better understanding of the regional variation in η than has been previously possible. The most striking feature of the map is the high-η band stretching from northern Canada to the western coast of the Gulf of Mexico. The highest values stretch northward from Great Slave Lake to the coast and are associated with high errors for both Q_0 and η. This probably indicates that crustal complexity, not intrinsic rock properties, causes anomalous values for η. More moderate η values (0.6–0.8) extend southward from the Great Slave Lake anomaly to the Gulf of Mexico. Lower values (0.3–0.6) characterize four regions of North America: (1) the Canadian Shield, (2) the eastern United States, (3) the western United States, and (4) the region of northwestern Canada and southern Alaska. We have discussed the likelihood that the very

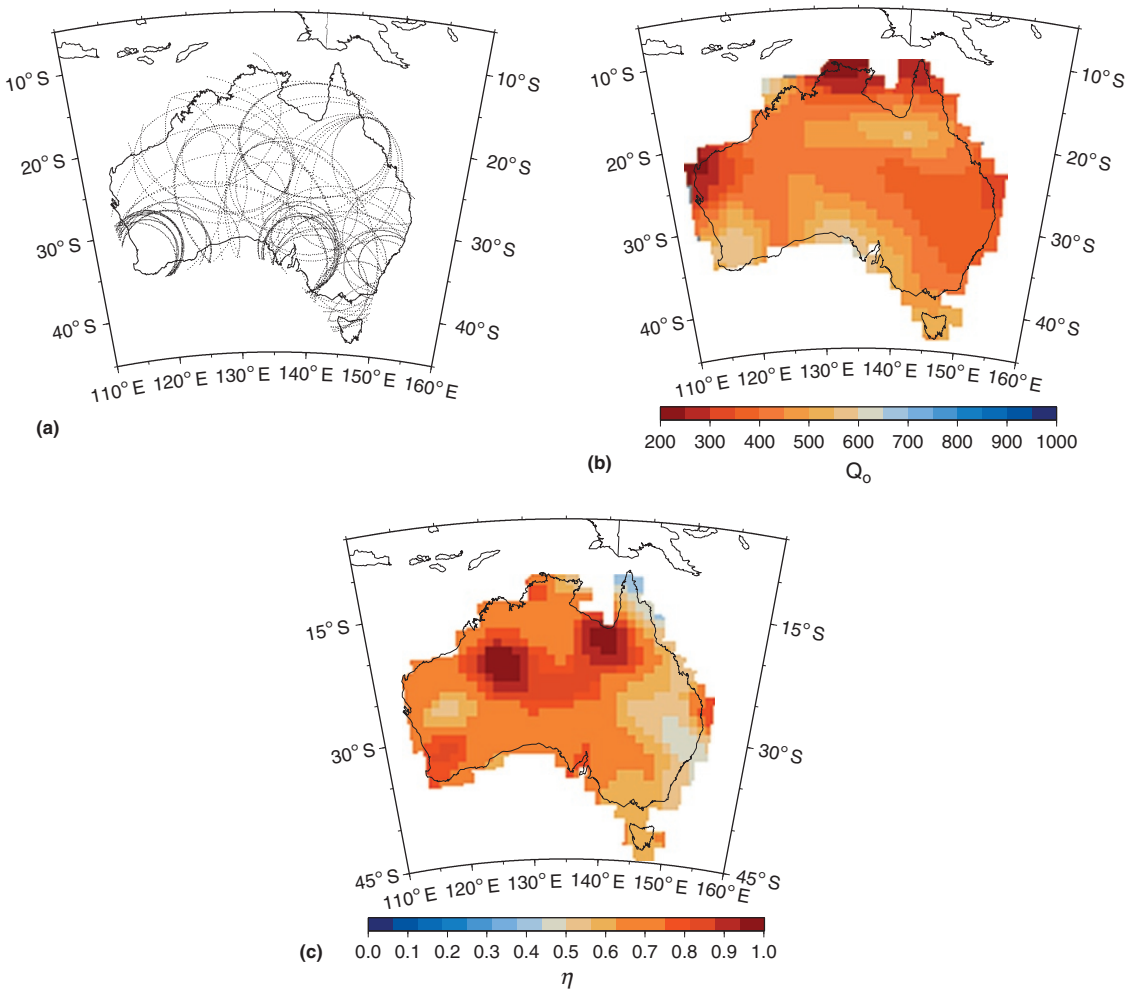

Figure 16 (a) A scattering ellipse map, (b) a Q_0 map, and (c) an η map of Q_{Lg}^{C} for Australia. Adapted from Mitchell BJ, Baqer S, Akinci A, and Cong L (1998) *Lg* coda *Q* in Australia and its relation to crustal structure and evolution. *Pure and Applied Geophysics* 153: 639–653.

high η values (0.8–1.0) in northern Canada are due to scattering causing the crustal complexity known to exist there. A broadband of high η values (0.6–0.8) extends southward from the concentration of highest values forming a long and broad high-η band extending from there to the Gulf of Mexico. That band lies between the Great Plains on its eastern side and the Rocky Mountains on its western side and may be caused by a transition zone with changing east–west crustal thickness.

Two research groups have studied the 3D structure of P-wave and S-wave attenuation in southern California. Schlotterbeck and Abers (2001) fit theoretical spectra to observed spectra using the least-square minimization method of Hough et al. (1988) and determined t^* for P and S waves at frequencies between 0.5 and 25 Hz. Their inversions showed that P and S results were in substantial agreement, and that Q varies spatially and correlates with regional tectonics.

The second California study (Hauksson, 2006) also determined t^* from P- and S-wave spectra. They assumed that t^* consists of the sum of the whole-path attenuation and the local site effect at each recording station and utilized an expression of Eberhart-Phillips and Chadwick (2002) for the velocity spectrum. The inversion, in addition to providing t^*, yields parameters defining the velocity amplitude spectra. They determined t^* for about 340 000 seismograms from more than 5000 events of t^* data to obtain 3D, frequency-independent crustal models for Q_P and Q_S in the crust and uppermost mantle in southern California. They found that both Q_P and Q_S generally increase with depth from values of 50 or less in surface sediments to 1000 and greater at midcrustal depths. Their models reflect major tectonic structures to a much greater extent than they reflect the thermal structure of the crust. Al-Eqabi and Wysession (2006) conducted a tomographic study of Q_{Lg} in the Basin and Range Province using a genetic algorithm technique. They found that Q_{Lg} increases (234–312) in a southwest–northeast direction across the Basin and Range Province in good agreement with the variation of Q_{Lg}^{C} reported by Baqer and Mitchell (1998). As part of a broader study of Lg wave propagation in southern Mexico, Ottemöller et al. (2002) used formal inversion methods to separately obtain tomographic maps of Q_{Lg} at three frequencies (0.5, 2.0, and 5.0 Hz) using 1° by 1° cells. Because of uneven path coverage in southern Mexico, they applied regularization conditions to their inversion equations. They found lower than average Q_{Lg} in the Gulf of Mexico coastal plain and the area east of 94° W,

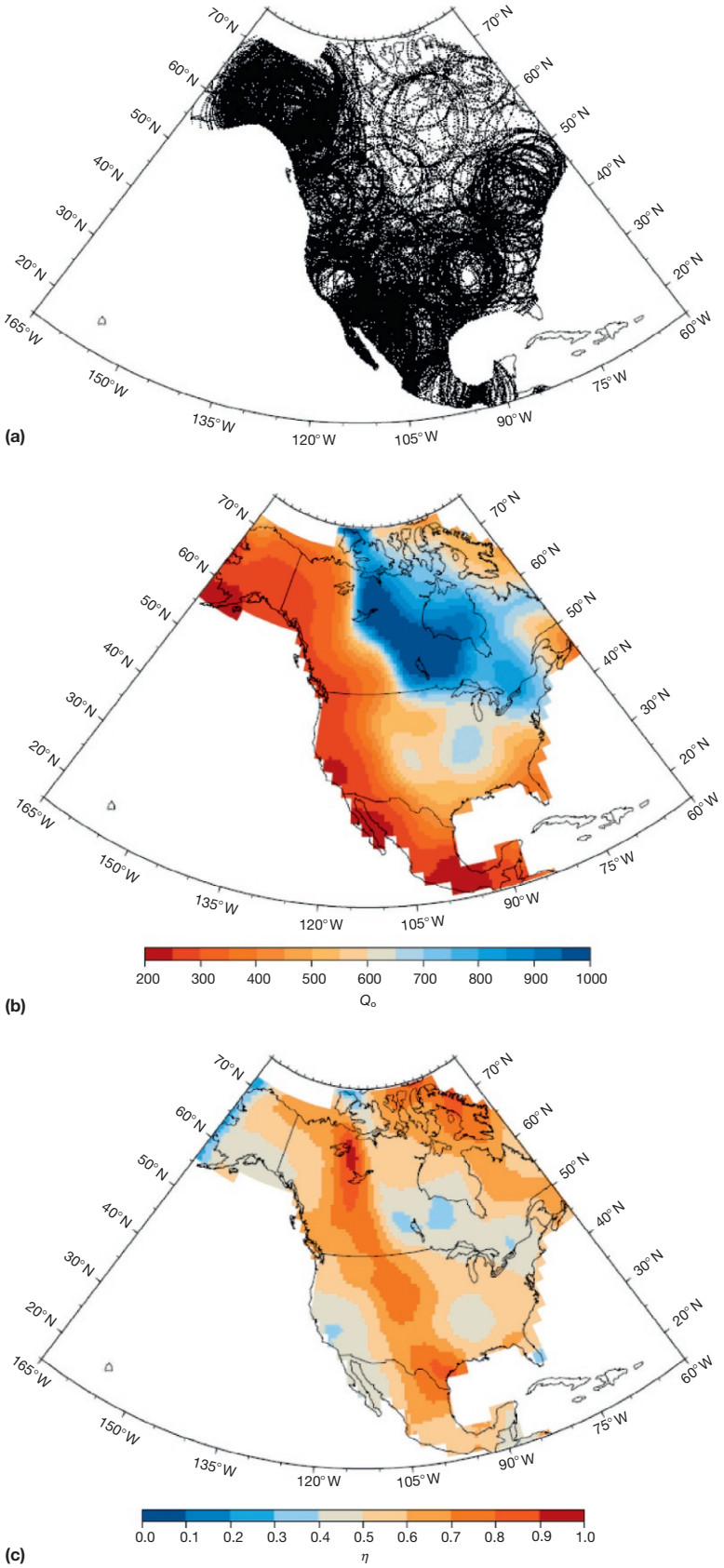

Figure 17 (a) A scattering ellipse map, (b) a Q_0 map, and (c) an η map of Q_{Lg}^{C} for North America. Adapted from Mitchell BJ, Cong L, and Jemberie A (2014) Continent-wide maps of *Lg* coda *Q* for North America and their relationship to crustal structure and evolution. *Bulletin of the Seismological Society of America*.

average values in the northern portion of the Pacific coastal region, and below average values in the southern portion.

1.25.7.3.6 Q_P variation near ocean ridges

Wilcock et al. (1995) developed a spectral technique by which they determined the attenuation of P waves in an active-source experiment centered at the East Pacific Rise at latitude 9°30′N. It is, to date, the only tomographic study of crustal Q variation in an oceanic region. They obtained over 3500 estimates of t^*, the path integral of the product of Q^{-1} and P-wave velocity where both quantities are variable along the path. Wilcock et al. display plots of both cross-axis and along-axis structures for upper crustal and lower crustal Q^{-1} structures. Within the ridge magma chamber, Q reaches minimum values of 20–50, which extend to the base of the crust. Off the ridge axis, they find that Q in the upper crust is 35–50 and at least 500–1000 at depths greater than 2–3 km.

1.25.7.3.7 Variation of crustal Q with time

Several investigators (e.g., Chouet, 1979; Jin and Aki, 1986) have reported temporal variations of Q over timescales of a few years. Although this observation has been reported several times, it continues to be controversial. Spatial patterns of Q variation and their apparent relation to time that has elapsed since the most recent episode of tectonic activity in any region, however, suggest that temporal variations of Q over very long periods of time can easily be detected. Mitchell and Cong (1998) found that variation for Q_{Lg}^{C} at 1 Hz extends between roughly 250, for broad regions that are currently tectonically active, and about 1000 for shields that have been devoid of tectonic activity for a billion years or more (Figure 18). Mitchell et al. (1997) explained those observations as being due to variable volumes of fluids in faulted, fractured, and permeable rock. Fluids may enhance the rate of attenuation of seismic waves either because the waves must expend energy to push those fluids through permeable rock as they propagate or because they may traverse a region of enhanced scattering that causes loss of wave energy into the mantle. Figure 18 points to an evolutionary process in which fluids are relatively abundant in tectonically active regions due to their generation by hydrothermal reactions at high temperatures. With time, fluids are gradually lost, either by migration to the Earth's surface or absorption due to retrograde metamorphism. This process causes low Q values early in the tectonic cycle and gradually increasing values at later times as the fluids dissipate.

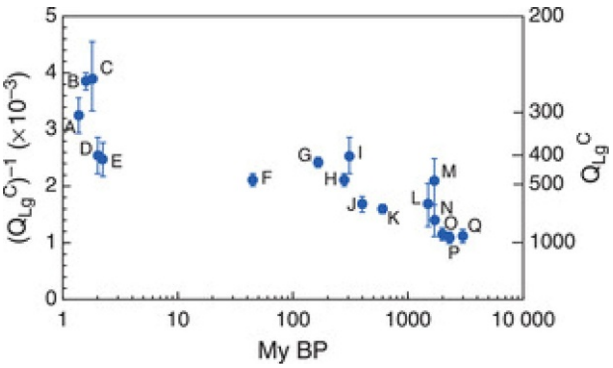

Figure 18 Q_0 for Q_{Lg}^{C} at 1 Hz versus time elapsed in selected regions since the most recent episode of tectonic or orogenic activity. A, the Andes; B, Basin and Range Province in the western United States; C, Tethys region of convergence between the Eurasian and African/Arabian/Indian plates; D, the Arabian Peninsula; E, the East African Rift; F, the Rocky Mountains; G, northeastern China; H, the eastern Altaids in Eurasia; I, the Tasman Province in Australia; J, the Atlantic Shield in South America; K, the African fold belts; L, the portion of the North American Craton in the United States; M, the Australian Craton; N, Eurasian cratons; O, African shields; P, the Brazilian shield; *Q*, the Indian shield. Adapted from Mitchell BJ and Cong L (1998) *Lg* coda *Q* and its relation to the structure and evolution of continents: A global perspective. *Pure and Applied Geophysics* 153: 655–663.

1.25.8 Conclusions

Much progress has been made in the last 15 years in characterizing the lateral variations in attenuation in the crust, especially under continents, and their relation to tectonics. Characterizing the nature and distribution of attenuation deeper in the Earth still remains a challenging subject, because of the persistent difficulties in separating anelastic and scattering effects and the nonuniform sampling achieved with available data.

Still, it is encouraging to see that there is now consistency in the large-scale features of lateral variations in Q in the upper 200 km of the mantle, correlated with tectonics, and that accounting for focusing effects using a single scattering approximation in present-day elastic 3D models is helpful, at least at the longest wavelengths. It is still important to consider that, when the inversion experiment is well designed, the unmodeled scattering effects can be minimized, or even utilized to constrain velocity models (e.g., Dalton and Ekström, 2006b), but the consequence is that significant damping needs to be applied in the inversion for lateral variations in Q. This results in large uncertainties (a factor of 2 or more) in the amplitudes of lateral variations of Q, so that physical interpretations of these models must remain tentative. On the other hand, the spatial distribution of low- and high-Q regions is, in general, more robust. Thus far, only one research group has produced models of lateral variations of Q_μ in the transition zone. While the results are consistent within this group using different methodologies (Gung and Romanowicz, 2004; Romanowicz, 1995) and point to an intriguing correlation with structure at the base of the mantle (Romanowicz and Gung, 2002), these results need to be confirmed by independent studies.

At the regional, uppermost mantle scale, consistent results have been obtained in subduction zones (high Qs) and back-arc regions (very low Qs), less so in oceanic settings. A promising trend, made possible by improved data and techniques, is to combine attenuation, velocity, and other geophysical parameters to better constrain lateral variations of temperature and composition. An ambitious goal would be to do the same at the global, and deeper, scale. Progress in laboratory experiments on Q at seismic frequencies is just starting to provide reliable mineral physics parameters on the behavior of Q at depths down to the upper mantle low-velocity zone, so that joint inversions of seismic waveform data for elastic and anelastic 3D structure can be envisaged (e.g., Cammarano and Romanowicz, 2007, 2008). The challenge

here is in the nonlinearities introduced by the exponential variation of Q with temperature, on the one hand, and the variation in the position of mineral phase changes depending on composition, on the other.

Important uncertainties remain in the characterization of the 1D profile of Q_μ in the mantle – first and foremost, explaining once and for all the discrepancy between free oscillations and surface-wave measurements, which has consequences for the value of Q_μ in the transition zone. Because there are still unexplained discrepancies between elastic models of the upper mantle, and particularly the transition zone, produced from seismic data, on the one hand, and from mineral physics data and computations, on the other (e.g., Cammarano et al., 2003), it is particularly important to apply accurate anelastic corrections when interpreting seismic velocity models in terms of composition. The evidence for a maximum in Q_μ in the lower mantle, and therefore lower Q_μ at the base of the mantle, is now clear; however, the location of this maximum is not well constrained. The confirmation of frequency dependence of Q in the mantle, with $\alpha \sim 0.3$, and a shift of the absorption band to lower frequencies in the lower mantle, seems to emerge from the comparison of 1D Q profiles derived from normal modes/surface-wave data, on the one hand, and body-wave data, on the other. The location in the Earth of the attenuation in bulk required to explain some normal mode data is still the subject of debate.

The presence of hemispheric variations in Q_α at the top of the inner core and the confirmation of increasing Q with depth and of anisotropy in Q_α correlated with anisotropy in velocity are exciting results that need further investigation, in particular in the light of recent studies by Li and Cormier (2002) favoring a scattering interpretation of attenuation in the inner core.

Finally, in the shallow Earth, it has been found over the past four decades that crustal Q, as manifested by regional studies of body waves, Lg and Lg coda, varies tremendously across continents, as well as in average values of different continents. Q_0 for Lg coda varies between about 150 and 1000 for features that can be resolved at 1 Hz frequency and the frequency dependence of Lg coda Q varies between about 0.0 and 1.0. Recent work on energy partitioning to learn the extent to which Lg attenuation is governed by intrinsic rock properties or by scattering shows that while scattering is predominant at short distances, intrinsic rock properties play the larger role at long distances. Most Q determinations at short periods in any region appear to be governed, most prominently, by the time that has elapsed since the most recent episode of tectonic or orogenic activity there.

Further advances in mapping the Q structure in the crust and mantle may come from the implementation of novel methodologies, such as the use of powerful numerical techniques for wavefield computations (e.g., Ruan and Zhou, 2012; Savage et al., 2010) and the use of noise correlation data (e.g., Lawrence and Prieto, 2011; Prieto et al., 2009; **Chapter 1.12**).

Acknowledgment

The research of BJM was partially supported by the Air Force Research Laboratory under Award FA 8718-04-C-0021.

References

Abercrombie RE (1997) Near-surface attenuation and site effects from comparison of surface and deep borehole recordings. *Bulletin of the Seismological Society of America* 87: 731–744.

Abercrombie RE (2000) Crustal attenuation and site effects at Parkfield, California. *Journal of Geophysical Research* 105: 6277–6286.

Aizawa Y, Barnhoorn A, Faul UH, Fitz Gerald JD, Jackson I, and Kovács I (2008) Seismic properties of Anita Bay dunite: An exploratory study of the influence of water. *Journal of Petrology* 49: 841–855. http://dx.doi.org/10.1093/petrology/egn007.

Aki K (1967) Scaling law of seismic spectrum. *Journal of Geophysical Research* 72: 729–740.

Aki K (1969) Analysis of the seismic coda of local earthquakes as scattered waves. *Journal of Geophysical Research* 74: 615–631.

Aki K (1980) Scattering and attenuation of shear waves in the lithosphere. *Journal of Geophysical Research* 85: 6496–6504.

Akinci A, Del Pezzo E, and Ibanez JM (1995) Separation of scattering and intrinsic attenuation in southern Spain and western Anatolia (Turkey). *Geophysical Journal International* 121: 337–353.

Akopyan ST, Zharkov VN, and Lyubimov VM (1976) Corrections to the eigenfrequencies of the Earth due to dynamic shear modulus. *Bulletin of the Seismological Society of America* 12: 625–630.

Alboussière T, Deguen R, and Melzani M (2010) Melting-induced stratification above the Earth's inner core due to convective translation. *Nature* 466: 744–747.

Al-Eqabi GI and Wysession ME (2006) Q_{Lg} distribution in the Basin and Range province of the western United States. *Bulletin of the Seismological Society of America* 96: 348–354.

Al-Khatib HH and Mitchell BJ (1991) Upper mantle anelasticity and tectonic evolution of the western United States from surface wave attenuation. *Journal of Geophysical Research* 96: 18129–18146.

Allen RM, Nolet G, Morgan WJ, et al. (1999) The thin hot plume beneath Iceland. *Geophysical Journal International* 137: 51–63.

Al-Shukri HJ, Mitchell BJ, and Ghalib HAA (1988) Attenuation of seismic waves in the New Madrid seismic zone. *Seismological Research Letters* 59: 133–140.

Anderson DL and Archambeau CB (1966) The anelasticity of the Earth. *Journal of Geophysical Research* 69: 2071–2084.

Anderson DL, Ben-Menahem A, and Archambeau CB (1965) Attenuation of seismic energy in the upper mantle. *Journal of Geophysical Research* 70: 1441–1448.

Anderson DL and Given JW (1982) Absorption band Q model for the Earth. *Journal of Geophysical Research* 87: 3893–3904.

Anderson DL and Hart RS (1976) An Earth model based on free oscillations and body waves. *Journal of Geophysical Research* 81: 1461–1475.

Anderson DL and Hart RS (1978) Q of the Earth. *Journal of Geophysical Research* 83: 5869–5882.

Anderson JG and Hough SE (1984) A model for the shape of Fourier amplitude spectrum of acceleration at high frequencies. In: 1984 *Annual Meeting 30 May–3 June, 1984* Anchorage, Alaska: Seismological Society of America.

Andrews J, Deuss A, and Woodhouse J (2006) Coupled normal mode sensitivity to inner-core shear velocity and attenuation. *Geophysical Journal International* 167: 204–212.

Angenheister GH (1906) Bestimmung der fortpflanzungsgeschwindigkeit und absorption von erdbebenwellen, die durch den gegenpunkt des Herdes gegangen sind. *Nachrichten von der Königlichen Gesellschaft der Wissenschaften zu Göttingen* 110–120.

Angenheister GH (1921) Beobachtungen an pazifischen beben. *Nachrichten von der Königlichen Gesellschaft der Wissenschaften zu Göttingen* 113–146.

Artemieva IM, Billien M, Lévêque JJ, and Mooney WD (2004) Shear-wave velocity, seismic attenuation, and thermal structure of the continental upper mantle. *Geophysical Journal International* 157: 607–628.

Artemieva IM and Mooney WD (2001) Thermal evolution of precambrian lithosphere: A global study. *Journal of Geophysical Research* 106: 16387–16414.

Asada T and Takano K (1963) Attenuation of short-period *P* waves in the mantle. *Journal of Physics of the Earth* 11: 25–34.

Baqer S and Mitchell BJ (1998) Regional variation of *Lg* coda *Q* in the continental United States and its relation to crustal structure and evolution. *Pure and Applied Geophysics* 153: 613–638.

Barazangi M and Isaaks B (1971) Lateral variations of seismic-wave attenuation in the upper mantle above the inclined earthquake zone of the Tonga Island Arc: Deep anomaly in the upper mantle. *Journal of Geophysical Research* 76: 8493–8516.

Barazangi M, Pennington W, and Isaaks B (1975) Global study of seismic wave attenuation in the upper mantle behind Island Arcs using P waves. *Journal of Geophysical Research* 80: 1079–1092.

Ben-Menahem A (1965) Observed attenuation and Q values of seismic surface waves in the upper mantle. *Journal of Geophysical Research* 70: 4641–4651.

Benz HM, Frankel A, and Boore DM (1997) Regional *Lg* attenuation for the continental United States. *Bulletin of the Seismological Society of America* 87: 606–619.

Bhattacharyya J, Masters G, and Shearer P (1996) Global lateral variations of shear wave attenuation in the upper mantle. *Journal of Geophysical Research* 101: 22273–22289.

Bhattacharyya J, Shearer P, and Masters G (1993) Inner core attenuation from short period *PKP*(*BC*) versus *PKP*(*DF*) waveforms. *Geophysical Journal International* 114: 1–11.

Billien M and Lévêque J (2000) Global maps of Rayleigh wave attenuation for periods between 40 and 150 seconds. *Geophysical Research Letters* 27: 3619–3622.

Bollinger GA (1979) Attenuation of the *Lg* phase and determination of m_b in the Southeastern United States. *Bulletin of the Seismological Society of America* 69: 45–63.

Bolt BA (1977) The detection of PKIIKP and damping in the inner core. *Annali di Geofisica* 30: 507–520.

Bowers RJ (2000) Observations of PKP(DF) and PKP(BC) across the United Kingdom: Implications for studies of attenuation in the Earth's core. *Geophysical Journal International* 140: 374–384.

Bowman JR (1988) Body wave attenuation structure in the Tonga subduction zone. *Journal of Geophysical Research* 93: 2125–2139.

Bowman JR and Kennett BLN (1991) Propagation of *Lg* waves in the North Australian craton: Influence of crustal velocity gradients. *Bulletin of the Seismological Society of America* 81: 592–610.

Boyd OS and Sheehan AF (2005) Attenuation tomography beneath the rocky mountain front: Implications for the physical state of the upper mantle. In: Karlstrom KE and Keler GR (eds.) *The Rocky Mountain Region: An evolving lithosphere*. *Geophysical Monograph Series*, vol. 154, pp. 361–377. Washington, DC: American Geophysical Union.

Brune JN (1970) Tectonic stress and the spectra of seismic shear waves from earthquakes. *Journal of Geophysical Research* 75: 4997–5009.

Buland R and Gilbert F (1978) Improved resolution of complex eigenfrequencies in analytically continued seismic spectra. *Geophysical Journal of the Royal Astronomical Society* 52: 457–470.

Cammarano F, Goes S, Vacher P, and Giardini D (2003) Inferring upper-mantle temperatures from seismic velocities. *Physics of the Earth and Planetary Interiors* 138: 197–222.

Cammarano F and Romanowicz B (2007) Insights into the nature of the transition zone from physically constrained inversion of long period seismic data. *Proceedings of the National Academy of Sciences of the United States of America* 104: 9139–9144. http://dx.doi.org/10.1073/pnas.0608075104.

Cammarano F and Romanowicz B (2008) Radial profiles of seismic attenuation in the upper mantle based on physical models. *Geophysical Journal International* 175: 116–134.

Campillo M, Plantet JL, and Bouchon M (1985) Frequency-dependent attenuation in the crust beneath central France from *Lg* waves: Data analysis and numerical modeling. *Bulletin of the Seismological Society of America* 75: 1395–1411.

Canas JA and Mitchell BJ (1978) Lateral variation of surface-wave anelastic attenuation across the Pacific. *Bulletin of the Seismological Society of America* 68: 1637–1650.

Canas JA and Mitchell BJ (1981) Rayleigh-wave attenuation and its variation across the Atlantic Ocean. *Geophysical Journal of the Royal Astronomical Society* 67: 159–176.

Cao A and Romanowicz B (2004) Hemispherical transition of seismic attenuation at the top of the Earth's inner core. *Earth and Planetary Science Letters* 228: 243–253.

Cao A and Romanowicz B (2009) Constraints on shear wave attenuation in the Earth's inner core from an observation of PKJKP. *Geophysical Research Letters* 36: L09301. http://dx.doi.org/10.1029/2009GL038342.

Cao A, Romanowicz B, and Takeuchi N (2005) An observation of *PKJKP*: Inferences on inner core shear properties. *Science* 308: 1453–1455.

Carcione JM and Cavallini F (1995) A rheological model for anelastic anisotropic media with applications to seismic wave propagation. *Geophysical Journal International* 119: 338–348.

Carpenter PJ and Sanford AR (1985) Apparent *Q* for upper crustal rocks of the central Rio Grande Rift. *Journal of Geophysical Research* 90: 8661–8674.

Chan WW and Der ZA (1988) Attenuation of multiple *ScS* in various parts of the world. *Geophysical Journal International* 92: 303–314.

Chavez D and Priestley KF (1986) Measurement of frequency dependent *Lg* attenuation in the Great Basin. *Geophysical Research Letters* 60: 551–554.

Chen PF, Bina CR, and Okal EA (2001) Variations in slab dip along the subducting Nazca plate, as related to stress patterns and moment release of intermediate-depth seismicity and to surface volcanism. *Geochemistry, Geophysics, Geosystems* 2. http://dx.doi.org/10.1029/2001GC000153.

Cheng HX and Kennett BLN (2002) Frequency dependence of seismic wave attenuation in the upper mantle in the Australian region. *Geophysical Journal International* 150: 45–47.

Cheng CC and Mitchell BJ (1981) Crustal *Q* structure in the United States from multi-mode surface waves. *Bulletin of the Seismological Society of America* 71: 161–181.

Chouet B (1979) Temporal variation in the attenuation of earthquake coda near Stone Canyon, California. *Geophysical Research Letters* 6: 143–146.

Choy G and Cormier VF (1983) The structure of the inner core inferred from short-period and broadband GDSN data. *Geophysical Journal International* 63: 457–470.

Chun KY, West GF, Kikoski RJ, and Samson C (1987) A novel technique for measuring *Lg* attenuation – Results from eastern Canada between 1-Hz and 10-Hz. *Bulletin of the Seismological Society of America* 77: 398–419.

Cicerone RD, Doll CG, and Toksöz MN (2011) Scattering and attenuation of seismic waves in northeastern North America. *Bulletin of the Seismological Society of America* 101: 2897–2903.

Cong L and Mitchell BJ (1998) Seismic velocity and *Q* structure of the Middle Eastern crust and upper mantle from surface-wave dispersion and attenuation. *Pure and Applied Geophysics* 153: 503–538.

Cormier VF (1981) Short period *PKP* phases and the anelastic mechanism of the inner core. *Physics of the Earth and Planetary Interiors* 24: 291–301.

Cormier VF (2007) Texture of the uppermost inner core from forward- and back-scattered seismic waves. *Earth and Planetary Science Letters* 258: 442–453.

Cormier VF and Li X (2002) Frequency-dependent seismic attenuation in the inner core. Part 2: A scattering and fabric interpretation. *Journal of Geophysical Research* 107. http://dx.doi.org/10.1029/2002JB001796.

Cormier VF and Richards P (1976) Comments on the damping of core waves by Anthony Qamar and Alfredo Eisenberg. *Journal of Geophysical Research* 81: 3066–3068.

Cormier VF and Richards P (1988) Spectral synthesis of body waves in Earth models specified by vertically varying layers. In: Doornbos D (ed.) *Seismological Algorithms*, pp. 3–45. San Diego, CA: Academic Press.

Cormier VF and Stroujkova A (2005) Waveform search for the innermost inner core. *Earth and Planetary Science Letters* 236: 96–105.

Cormier VF, Xu L, and Choy GL (1998) Seismic attenuation of the inner core: Viscoelastic or stratigraphic? *Geophysical Research Letters* 25: 4019–4022.

Creager KC (1992) Anisotropy of the inner core from differential travel times of the phases *PKP* and *PKIKP*. *Nature* 356: 309–314.

Creager KC (1999) Large-scale variations in inner core anisotropy. *Journal of Geophysical Research* 104: 23127–23139.

Dainty AM (1981) A scattering model to explain *Q* observations in the lithosphere between 1 and 30 Hz. *Geophysical Research Letters* 8: 1126–1128.

Dalton C and Ekström G (2006a) Constraints on global maps of phase velocity from surface-wave amplitudes. *Geophysical Journal International* 167: 820–826.

Dalton C and Ekström G (2006b) Global models of surface wave attenuation. *Journal of Geophysical Research* 111. http://dx.doi.org/10.1029/2005JB003997.

Dalton CA, Ekström G, and Dziewonski AM (2008) The global attenuation structure of the upper mantle. *Journal of Geophysical Research* 113. http://dx.doi.org/10.1029/2007JB005429.

Dalton CA, Ekström G, and Dziewonski AM (2009) Global seismological shear velocity and attenuation: A comparison with experimental observations. *Earth and Planetary Science Letters* 284: 65–75.

Dalton CA and Faul U (2010) The oceanic and cratonic upper mantle: Clues from joint interpretation of global velocity and attenuation models. *Lithos* 120: 160–172.

Davies JH (1990) Mantle plumes, mantle stirring and hotspot geometry. *Earth and Planetary Science Letters* 99: 94–109.

Davies JH (1999) The role of hydraulic fractures and intermediate-depth earthquakes in generating subduction-zone magmatism. *Nature* 398: 142–145.

Der ZA, McElfresh TW, and O'Donnell A (1982) An investigation of the regional variations and frequency dependence of anelastic attenuation in the mantle under the United States in the 0.5–4 Hz band. *Geophysical Journal of the Royal Astronomical Society* 69: 67–99.

Deschamps A (1977) Inversion of the attenuation data of free oscillations of the Earth (fundamental and first higher modes). *Geophysical Journal of the Royal Astronomical Society* 50: 699–722.

DeSouza JL and Mitchell BJ (1998) *Lg* coda *Q* variations across South America and their relation to crustal evolution. *Pure and Applied Geophysics* 153: 587–612.

Ding CY and Grand SP (1993) Upper mantle Q structure under the East Pacific Rise. *Journal of Geophysical Research* 98: 1973–1975.

Doornbos DJ (1974) The anelasticity of the inner core. *Geophysical Journal of the Royal Astronomical Society* 38: 397–415.

Doornbos DJ (1983) Observable effects of the seismic absorption band in the Earth. *Geophysical Journal of the Royal Astronomical Society* 57: 381–395.

Durand S, Chambat F, Matas J, and Ricard Y (2012) Constraining the kinetics of mantle phase changes with seismic data. *Geophysical Journal International* 189: 1557–1564.

Durand S, Matas J, Ford S, Ricard Y, Romanowicz B, and Montagner JP (2013) Insights from ScS–S measurements on deep mantle attenuation. *Geophysical Journal International* 374: 101–110.

Durek JJ and Ekström G (1995) Evidence for bulk attenuation in the asthenosphere from recordings of the Bolia earthquake. *Geophysical Research Letters* 22: 2309–2312.

Durek JJ and Ekström G (1996) A radial model of anelasticity consistent with long-period surface wave attenuation. *Bulletin of the Seismological Society of America* 86: 144–158.

Durek JJ and Ekström G (1997) Investigating discrepancies among measurements of traveling and standing wave attenuation. *Journal of Geophysical Research* 102: 24529–24544.

Durek JJ, Ritzwoller MH, and Woodhouse JH (1993) Constraining upper mantle anelasticity using surface wave amplitude anomalies. *Geophysical Journal International* 114: 249–272.

Dziewonski AM and Anderson DL (1981) Preliminary reference Earth model. *Physics of the Earth and Planetary Interiors* 25: 297–356.

Dziewonski AM and Steim JM (1982) Dispersion and attenuation of mantle waves through waveform inversion. *Geophysical Journal of the Royal Astronomical Society* 70: 503–527.

Eberhart-Phillips D and Chadwick M (2002) Three-dimensional attenuation model of the shallow Hikurangi subduction zone in the Raukumara Peninsula, New Zealand. *Journal of Geophysical Research* 107. http://dx.doi.org/10.1029/2000JB000; 046.

Ekström G and Dziewonski AM (1997) The unique anisotropy of the Pacific upper mantle. *Nature* 394: 168–172.

Ekström G, Tromp J, and Larson EWF (1997) Measurements and global models of surface wave propagation. *Journal of Geophysical Research* 102: 8137–8157.

Evernden JF (1955) Tripartite results for the Kamchatka earthquake of November 4, 1952. *Bulletin of the Seismological Society of America* 45: 167–178.

Farla RM, Jackson I, FitzGerald JD, Faul UH, and Zimmerman ME (2012) Dislocation damping and anisotropic seismic wave attenuation in earth's upper mantle. *Science* 336: 332–335.

Faul U, FitzGerald J, and Jackson I (2004) Shear wave attenuation and dispersion in melt-bearing olivine polycrystals. Part 2: Microstructural interpretation and seismological implications. *Journal of Geophysical Research* 109. http://dx.doi.org/10.1029/2003JB002407.

Faul U and Jackson I (2005) The seismological signature of temperature and grain size variations in the upper mantle. *Earth and Planetary Science Letters* 234: 119–134.

Fearn DR, Loper DE, and Roberts PH (1981) Structure of the Earth's inner core. *Nature* 292: 232–233.

Fisher JL and Wysession ME (2003) Small-scale lateral variations in D″ attenuation and velocity structure. *Geophysical Research Letters* 30. http://dx.doi.org/10.1029/2002GL016179.

Flanagan MP and Wiens DA (1990) Attenuation structure beneath the Lau back arc spreading center from teleseismic S phases. *Geophysical Research Letters* 17: 2117–2120.

Flanagan MP and Wiens DA (1994) Radial upper mantle structure of inactive back-arc basins from differential shear wave measurements. *Journal of Geophysical Research* 99: 15469–15485.

Flanagan MP and Wiens DA (1998) Attenuation of broadband P and S waves in Tonga: Observations of frequency dependent Q. *Pure and Applied Geophysics* 153: 345–375.

Ford SR, Dreger DS, Mayeda K, Walter WR, Malagnini L, and Phillips WS (2008) Regional attenuation in northern California: A comparison of five 1D Q methods. *Bulletin of the Seismological Society of America* 98: 2033–2046.

Ford SR, Garnero EJ, and Thorne MS (2012) Differential t* measurements via instantaneous frequency matching: Observations of lower mantle shear attenuation heterogeneity beneath western Central America. *Geophysical Journal International* 189: 513–523.

Frankel A and Wennerberg L (1987) Energy-flux model for seismic coda: Separation of scattering and intrinsic attenuation. *Bulletin of the Seismological Society of America* 77: 1223–1251.

Futterman A (1962) Dispersive body waves. *Journal of Geophysical Research* 67: 5279–5291.

Gao J, Yang S, Wang D, and Wu R (2011) Estimation of quality factor Q from the instantaneous frequency at the envelope peak of a seismic signal. *Journal of Computational Acoustics* 19: 155–179. http://dx.doi.org/10.1142/S0218396x11004390.

Garcia R (2002) Constraints on upper inner-core structure from waveform inversion of core phases. *Geophysical Journal International* 150: 651–664.

Geller RJ and Stein S (1978) Time domain measurements of attenuation of fundamental modes ($_0S_6$–$_0S_{28}$). *Bulletin of the Seismological Society of America* 69: 1671–1691.

Getting IC, Dutton SJ, Burnley PC, Karato SI, and Spetzler HA (1997) Shear attenuation and dispersion in MgO. *Physics of the Earth and Planetary Interiors* 99: 249–257.

Giardini DXDL and Woodhouse JH (1988) Splitting functions of long period normal modes of the Earth. *Journal of Geophysical Research* 93: 13716–13742.

Gilbert F and Dziewonski AM (1975) An application of normal mode theory to the retrieval of structural parameters and source mechanisms from seismic spectra. *Philosophical Transactions of the Royal Society of London, Series A* 278: 187–269.

Gomer BM and Okal EA (2003) Multiple-ScS probing of the Ontong-Java Plateau. *Physics of the Earth and Planetary Interiors* 138: 317–331.

Gueguen Y, Darot M, Mazot P, and Woirgard J (1989) Q^{-1} of forsterite single crystals. *Physics of the Earth and Planetary Interiors* 55: 254–258.

Gung Y, Panning M, and Romanowicz BA (2003) Anisotropy and thickness of the lithosphere. *Nature* 422: 707–711.

Gung Y and Romanowicz BA (2004) Q tomography of the upper mantle using three component long period waveforms. *Geophysical Journal International* 157: 813–830.

Gusev AA and Abubakirov IR (1996) Simulated envelopes of non-isotropically scattered body waves as compared to observed ones: Another manifestation of fractal inhomogeneity. *Geophysical Journal International* 127: 49–60.

Gutenberg B (1924) Dispersion und extinktion von seismischen oberflächenwellen und der aufbau der obersten erdschichten. *Physikalische Zeitschrift* 25: 377–381.

Gutenberg B (1945a) Amplitudes of *P*, *PP*, and *SS* and magnitude of shallow earthquakes. *Bulletin of the Seismological Society of America* 35: 57–69.

Gutenberg B (1945b) Amplitudes of surface waves and magnitudes of shallow earthquakes. *Bulletin of the Seismological Society of America* 35: 3–12.

Gutenberg B (1958) Attenuation of seismic waves in the Earth's mantle. *Bulletin of the Seismological Society of America* 48: 269–282.

Haberland C and Rietbrock A (2001) Attenuation tomography in the western central Andes: A detailed insight into the structure of a magmatic arc. *Journal of Geophysical Research* 106: 11151–11167.

Hasegawa HS (1974) Theoretical synthesis and analysis of strong motion spectra of earthquakes. *Canadian Geotechnical Journal* 11: 278–297.

Hasegawa HS (1985) Attenuation of *Lg* waves in the Canadian shield. *Bulletin of the Seismological Society of America* 75: 1569–1582.

Hauksson E (2006) Attenuation models (Q_P and Q_S) in three dimensions of the Southern California crust: Inferred fluid saturation at seismogenic depths. *Journal of Geophysical Research* 111(B05): 302. http://dx.doi.org/10.1029/2005JB003947.

He X and Tromp J (1996) Normal-mode constraints on the structure of the Earth. *Journal of Geophysical Research* 101: 20053–20082.

Helffrich G, Kaneshima S, and Kendall JM (2002) A local, crossing-path study of attenuation and anisotropy of the inner core. *Geophysical Research Letters* 29. http://dx.doi.org/10.1029/2001GL014059.

Herrmann RB (1980) *Q* estimates using the coda of local earthquakes. *Bulletin of the Seismological Society of America* 70: 447–468.

Herrmann RB and Mitchell BJ (1975) Statistical analysis and interpretation of surface-wave anelastic attenuation data for the stable interior of North America. *Bulletin of the Seismological Society of America* 65: 1115–1128.

Hough SE, Anderson JG, Brune J, et al. (1988) Attenuation near Anza, California. *Bulletin of the Seismological Society of America* 78: 672–691.

Hough SE, Lees JM, and Monastero F (1999) Attenuation and source properties at the Coso geothermal area, California. *Bulletin of the Seismological Society of America* 89: 1606–1619.

Humphreys E and Clayton RW (1988) Adaptation of back projection tomography to seismic travel time problems. *Journal of Geophysical Research* 93: 1073–1086.

Hwang HJ and Mitchell BJ (1987) Shear velocities, Q_β, and the frequency dependence of Q_β in stable and tectonically active regions from surface wave observations. *Geophysical Journal of the Royal Astronomical Society* 90: 575–613.

Hwang YK and Ritsema J (2011) Radial Q_β structure of the lower mantle from teleseismic body-wave spectra. *Earth and Planetary Science Letters* 303: 369–375.

Hwang YK, Ritsema J, and Goes S (2009) Spatial variations of P wave attenuation in the mantle beneath North America. *Journal of Geophysical Research* 114: B06312.

Hwang YK, Ritsema J, and Goes S (2011) Global variations of body-wave attenuation in the upper mantle from teleseismic P wave and S wave spectra. *Geophysical Research Letters* 38: L06308.

Ichikawa M and Basham PW (1965) Variations in short-period records from Canadian seismograph stations. *Canadian Journal of Earth Sciences* 2: 510–542.

Iritani R, Takeuchi N, and Kawakatsu H (2010) Seismic attenuation structure of the top half of the inner core beneath the northeastern Pacific. *Geophysical Research Letters* 37: L19303.

Ishii M and Dziewonski AM (2002) The innermost inner core of the earth: Evidence for a change in anisotropic behavior at the radius of about 300 km. *Proceedings of the National Academy of Sciences of the United States of America* 22: 14026–14030.

Isse T and Nakanishi I (1997) The effect of the crust on the estimation of mantle Q from spectral ratios of multiple ScS phases. *Bulletin of the Seismological Society of America* 87: 778–781.

Ivan M, Marza V, de Farias Caixeta D, and de Melo Arraes T (2005) Uppermost inner core attenuation from PKP data at South American seismological stations. *Geophysical Journal International* 164: 441–448.

Jackson I (1993) Progress in the experimental study of seismic wave attenuation. *Annual Review of Earth and Planetary Sciences* 21: 375–406.

Jackson I (2000) Laboratory measurement of seismic wave dispersion and attenuation: Recent progress. *Journal of Geophysical Research* 109. http://dx.doi.org/10.1029/2003JB002406.

Jackson I (2007) Properties of rocks and minerals – Physical origins of anelasticity and attenuation in rock. In: Romanowicz B and Dziewonski AM (eds.) *Treatise on Geophysics*, vol. 1, pp. 493–525. USA: Elsevier.

Jackson I and Faul UH (2010) Grainsize-sensitive viscoelastic relaxation in olivine: Towards a robust laboratory-based model for seismological application. *Physics of the Earth and Planetary Interiors* 183: 151–163. http://dx.doi.org/10.1016/j.pepi.2010.09.005.

Jackson I, Faul UH, Fitzgerald JD, and Tan BH (2004) Shear wave attenuation and dispersion in melt-bearing olivine polycrystals. Part 1: Specimen fabrication and mechanical testing. In: Karato S-I, Forte AM, Liebermann RC, Masters G, and Stixrude L (eds.) *Earth's Deep Interior: Mineral Physics and Tomography from the Atomic to the Global Scale*. *Geophysical Monograph Series*, vol. 117, pp. 265–289. Washington, DC: American Geophysical Union.

Jeffreys H (1939) The times of the core waves. *Monthly Notices of the Royal Astronomical Society of Geophysics* (supplement 4): 498.

Jeffreys H (1967) Radius of the Earth's core. *Nature* 215: 1365–1366.

Jemberie AL and Mitchell BJ (2004) Shear-wave *Q* structure and its lateral variation in the crust of China and surrounding regions. *Geophysical Journal International* 157: 363–380.

Jin A and Aki K (1986) Temporal change in coda *Q* before the Tangshan earthquake of 1976 and the Haicheng earthquake of 1975. *Journal of Geophysical Research* 91: 665–673.

Jobert N and Roult G (1976) Periods and damping of free oscillations observed in France after 16 earthquakes. *Geophysical Journal of the Royal Astronomical Society* 45: 155–176.

Jordan TH and Sipkin SS (1977) Estimation of the attenuation operator for multiple ScS waves. *Geophysical Research Letters* 4: 167–170.

Kanamori H (1970) Velocity and Q of mantle waves. *Physics of the Earth and Planetary Interiors* 2: 259–275.

Kanamori H and Anderson DL (1977) Importance of physical dispersion in surface-wave and free oscillation problems. *Reviews of Geophysics* 15: 105–112.

Karato SI (1993) Importance of anelasticity in the interpretation of seismic tomography. *Geophysical Research Letters* 20: 1623–1626.

Karato SI (1998) A dislocation model of seismic wave attenuation and micro-creep in the Earth: Harold Jeffreys and the rheology of the solid Earth. *Pure and Applied Geophysics* 153: 239–256.

Karato SI and Karki BB (2001) Origin of lateral variation of seismic wave velocities and density in the deep mantle. *Journal of Geophysical Research* 106: 21771–21783.

Karato SI and Spetzler H (1990) Defect microdynamics in minerals and solid state mechanisms of seismic wave attenuation and velocity dispersion in the mantle. *Reviews of Geophysics* 28: 399–421.

Kazama T, Kawakatsu H, and Takeuchi N (2008) Depth-dependent attenuation structure of the inner core inferred from short-period Hi-net data. *Physics of the Earth and Planetary Interiors* 167: 155–160.

Kijko A and Mitchell BJ (1983) Multimode Rayleigh wave attenuation and Q_β in the crust of the Barents shelf. *Journal of Geophysical Research* 88: 3315–3328.

Knopoff L (1964) Q. *Reviews of Geophysics* 2: 625–660.

Komatitsch D, Ritsema J, and Tromp J (2002) The spectral-element method, Beowulf computing, and global seismology. *Science* 298: 1737–1742.

Kovach RL and Anderson DL (1964) Attenuation of shear waves in the upper and lower mantle. *Bulletin of the Seismological Society of America* 54: 1855–1864.

Krasnoshchekov DN, Kaazik PB, and Ovtchinnikov VM (2005) Seismological evidence for mosaic structure of the surface of the Earth's inner core. *Nature* 435: 483–487.

Kumazawa M, Imanashi Y, Fukao Y, Furumoto M, and Yananoto A (1990) A theory of spectral analysis based on the characteristic property of a linear dynamical system. *Geophysical Journal International* 101: 613–630.

Kuster GT (1972) *Seismic Wave Propagation in Two-Phase Media and Its Application to the Earth's Interior*. PhD Dissertation, Cambridge, MA: MIT.

Lawrence JF and Prieto G (2011) Attenuation tomography of the western United States from ambient seismic noise. *Journal of Geophysical Research* 116: B06302. http://dx.doi.org/10.1029/2010JB007836.

Lawrence JF, Shearer P, and Masters G (2006) Mapping attenuation beneath North America using waveform cross-correlation and cluster analysis. *Geophysical Research Letters* 33. http://dx.doi.org/10.1029/2006GL025813.

Lawrence JF and Wysession ME (2006a) QLM9: A new radial quality factor (Q_{mu}) model for the lower mantle. *Earth and Planetary Science Letters* 241: 962–971.

Lawrence JF and Wysession ME (2006b) Seismic evidence for subduction-transported water in the lower mantle. In: *Earth's Deep Water Cycle*. *Geophysics Monograph Series*, vol. 168, p. 251. Washington, DC: American Geophysical Union.

Lay T and Kanamori H (1985) Geometric effects of global lateral heterogeneity on long-period surface wave propagation. *Journal of Geophysical Research* 90: 605–621.

Lay T and Wallace T (1983) Multiple ScS travel times and attenuation beneath Mexico and Central America. *Geophysical Research Letters* 10: 301–304.

Lay T and Wallace T (1988) Multiple ScS attenuation and travel times beneath Western North America. *Bulletin of the Seismological Society of America* 78: 2041–2061.

Lee WB and Solomon SC (1979) Simultaneous inversion of surface-wave phase velocity and attenuation: Rayleigh and Love waves over continental and oceanic paths. *Bulletin of the Seismological Society of America* 69: 65–95.

Lekic V, Matas J, Panning M, and Romanowicz B (2009) Measurement and implications of frequency dependence of attenuation. *Earth and Planetary Science Letters* 282: 285–293.

Leyton P and Koper KD (2007) Using PKiKP coda to determine inner core structure: 2. Determination of Q_C. *Journal of Geophysical Research* 112: B05317.

Li XD (1990) *Asphericity of the Earth from Free Oscillations*. PhD Dissertation, Cambridge, MA: Harvard University.

Li L (2010) Bulk attenuation in the earth's mantle due to phase transitions. *Physics of the Earth and Planetary Interiors* 183: 473–477.

Li X and Cormier VF (2002) Frequency-dependent seismic attenuation in the inner core. Part 1: A viscoelastic interpretation. *Journal of Geophysical Research* 107. http://dx.doi.org/10.1029/2002JB001795.

Li XD and Romanowicz B (1995) Comparison of global waveform inversions with and without considering cross branch coupling. *Geophysical Journal International* 121: 695–709.

Liu HP, Anderson DL, and Kanamori H (1976) Velocity dispersion due to anelasticity: Implication for seismology and mantle composition. *Geophysical Journal of the Royal Astronomical Society* 47: 41–58.

Lomnitz C (1957) Linear dissipation in solids. *Journal of Applied Physics* 28: 201–205.

Loper DE and Fearn DR (1983) A seismic model of a partially molten inner core. *Journal of Geophysical Research* 88: 1235–1242.

Loper DE and Roberts PH (1981) A study of conditions at the inner core boundary of the Earth. *Physics of the Earth and Planetary Interiors* 24: 302–307.

Luh P (1974) Normal modes of a rotating, self gravitating inhomogeneous Earth. *Geophysical Journal of the Royal Astronomical Society* 38: 187–224.

Lundquist GM and Cormier VC (1980) Constraints on the absorption band model of Q. *Journal of Geophysical Research* 85: 5244–5256.

Malin PE (1978) *A First Order Scattering Solution for Modeling Lunar and Terrestrial Seismic Coda*. PhD Dissertation, Princeton, NJ: Princeton University.

Masters G and Gilbert F (1981) Structure of the inner core inferred from observations of its spheroidal shear modes. *Geophysical Research Letters* 8: 569–571.

Masters G and Gilbert F (1983) Attenuation in the Earth at low frequencies. *Philosophical Transactions of the Royal Society of London, Series XI* 308: 479–522.

Masters G and Laske G (1997) On bias in surface wave and free oscillation attenuation measurements. *Eos Transactions of the American Geophysical Union* 78: F485.

McCarthy C and Takei Y (2011) Anelasticity and viscosity of partially molten rock analogue: Toward seismic detection of small quantities of melt. *Geophysical Research Letters* 38: L18306. http://dx.doi.org/10.1029/2011GL048776.

McCarthy C, Takei Y, and Hiraga T (2011) Experimental study of attenuation and dispersion over a broad frequency range: 2. The universal scaling of polycrystalline materials. *Journal of Geophysical Research* 116: B09207. http://dx.doi.org/10.1029/2011JB008384.

Mills J and Hales A (1978) Great circle Rayleigh wave attenuation and group velocity. Part III: Inversion of global average group velocity and attenuation coefficients. *Physics of the Earth and Planetary Interiors* 17: 307–322.

Minster B and Anderson DL (1981) A model of dislocation controlled rheology for the mantle. *Philosophical Transactions of the Royal Society of London, Series A* 299: 319–356.

Mitchell BJ (1973) Radiation and attenuation of Rayleigh waves from the Southeastern Missouri earthquake of October 21, 1965. *Journal of Geophysical Research* 78: 886–899.

Mitchell BJ (1975) Regional Rayleigh wave attenuation on North America. *Journal of Geophysical Research* 35: 4904–4916.

Mitchell BJ (1995) Anelastic structure and evolution of the continental crust and upper mantle from seismic surface wave attenuation. *Reviews of Geophysics* 33: 441–462.

Mitchell BJ, Baqer S, Akinci A, and Cong L (1998) *Lg* coda *Q* in Australia and its relation to crustal structure and evolution. *Pure and Applied Geophysics* 153: 639–653.

Mitchell BJ and Cong L (1998) *Lg* coda *Q* and its relation to the structure and evolution of continents: A global perspective. *Pure and Applied Geophysics* 153: 655–663.

Mitchell BJ, Cong L, and Ekström G (2008) A continent-wide 1-Hz map of Lg coda Q variation across Eurasia and its implications for lithospheric evolution. *Journal of Geophysical Research* 113. http://dx.doi.org/10.1029/2007JB005065.

Mitchell BJ and Helmberger DV (1973) Shear velocities at the base of the mantle from observations of *S* and *ScS*. *Journal of Geophysical Research* 78: 6009–6020.

Mitchell BJ and Hwang HJ (1987) The effect of low-*Q* sediments and crustal *Q* on *Lg* attenuation in the United States. *Bulletin of the Seismological Society of America* 77: 1197–1210.

Mitchell BJ, Pan Y, Xie J, and Cong L (1997) *Lg* coda *Q* across Eurasia and its relation to crustal evolution. *Journal of Geophysical Research* 102: 22767–22779.

Mitchell BJ and Xie J (1994) Attenuation of multiphase surface waves in the Basin and Range province. Part III: Inversion for crustal anelasticity. *Geophysical Journal International* 116: 468–484.

Mitchell BJ, Cong L, and Jemberie A (2014) Continent-wide maps of Lg coda Q for North America and their relationship to crustal structure and evolution. *Bulletin of the Seismological Society of America*. http://dx.doi.org/10.1785/0120130235.

Modiano T and Hatzfeld D (1982) Experimental study of the spectral content for shallow earthquakes. *Bulletin of the Seismological Society of America* 72: 1739–1758.

Molnar P and Oliver J (1969) Lateral variations in attenuation in the upper mantle and discontinuities in the lithosphere. *Journal of Geophysical Research* 74: 2648–2682.

Monnereau M, Calvet M, Margerin L, and Souriau A (2010) Lopsided growth of Earth's inner core. *Science* 328: 1014–1017.

Montagner JP and Kennett BLN (1996) How to reconcile body-wave and normal-mode reference Earth models. *Geophysical Journal International* 125: 229–248.

Montagner JP and Tanimoto T (1991) Global upper mantle tomography of seismic velocities and anisotropy. *Journal of Geophysical Research* 96: 20337–20351.

Morelli A, Dziewonski AM, and Woodhouse JH (1986) Anisotropy of the core inferred from PKIKP travel times. *Geophysical Research Letters* 13: 1545–1548.

Morris SJS and Jackson I (2009) Diffusionally-assisted grain-boundary sliding and viscoelasticity of polycrystals. *Journal of the Mechanics and Physics of Solids* 57: 744–761.

Mueller G (1986) Rheological properties and velocity dispersion of a medium with power law dependence of Q in frequency. *Journal of Geophysics* 54: 20–29.

Myers SC, Beck S, Zandt G, and Wallace T (1998) Lithospheric-scale structure across the Bolivian Andes from tomographic images of velocity and attenuation for P and S waves. *Journal of Geophysical Research* 103: 21233–21252.

Nakajima J and Hasegawa A (2003) Estimation of thermal structure in the mantle wedge of northeastern Japan from seismic attenuation data. *Geophysical Research Letters* 30(14): 1760. http://dx.doi.org/10.1029/2003GL017185.

Nakanishi I (1978) Regional differences in the phase velocity and the quality factor Q of mantle Rayleigh waves. *Science* 200: 1379–1381.

Nakanishi I (1979a) Attenuation of multiple ScS waves beneath the Japanese Arc. *Physics of the Earth and Planetary Interiors* 19: 337–347.

Nakanishi I (1979b) Phase velocity and Q of mantle Rayleigh waves. *Geophysical Journal of the Royal Astronomical Society* 58: 35–59.

Nakanishi I (1981) Shear velocity and shear attenuation models inverted from the worldwide and pure-path average data of mantle Rayleigh waves (${}_0S_{25}$ to ${}_0S_{80}$) and fundamental spheroidal modes (${}_0S_2$ to ${}_0S_{24}$). *Geophysical Journal of the Royal Astronomical Society* 66: 83–130.

Niazi M and Johnson LR (1992) Q in the inner core. *Physics of the Earth and Planetary Interiors* 74: 55–62.

Niu F and Wen L (2001) Hemispherical variations in seismic velocity at the top of the Earth's inner core. *Nature* 410: 1081–1084.

Nuttli OW (1973) Seismic wave attenuation and magnitude relations for Eastern North America. *Journal of Geophysical Research* 78: 876–885.

Nuttli OW (1978) A time-domain study of the attenuation of 10-Hz waves in the New Madrid seismic zone. *Bulletin of the Seismological Society of America* 68: 343–355.

Nuttli OW (1980) The excitation and attenuation of seismic crustal phases in Iran. *Bulletin of the Seismological Society of America* 70: 469–484.

O'Connell RJ and Budiansky B (1978) Measures of dissipation in viscoelastic media. *Geophysical Research Letters* 5: 5–8.

Ojeda A and Ottemöller L (2002) Q_{Lg} tomography in Colombia. *Physics of the Earth and Planetary Interiors* 130: 253–270.

Okal EA and Jo BG (2002) *Q* measurements for phase X overtones. *Pure and Applied Geophysics* 132: 331–362.

Oki S, Fukao Y, and Obayashi M (2000) Reference frequency of teleseismic body waves. *Journal of Geophysical Research* 109. http://dx.doi.org/10.1029/2003JB002821.

Oki S and Shearer PM (2008) Mantle Q structure from S–P differential attenuation measurements. *Journal of Geophysical Research* 113. http://dx.doi.org/10.1029/2007JB005567.

Oreshin SI and Vinnik LP (2004) Heterogeneity and anisotropy of seismic attenuation in the inner core. *Geophysical Research Letters* 31. http://dx.doi.org/10.1029/2003GL018591.

Ottemöller L, Shapiro NM, Singh SK, and Pacheco JF (2002) Lateral variation of *Lg* wave propagation in southern Mexico. *Journal of Geophysical Research* 107(B1): Art No. 2008. http://dx.doi.org/10.1029/2001JB000, 206.

Park J (1987) Asymptotic coupled-mode expressions for multiplet amplitude anomalies and frequency shift on a laterally heterogeneous Earth. *Geophysical Journal of the Royal Astronomical Society* 90: 129–170.

Pasyanos ME, Matzel EM, Walter WR, and Rodgers AJ (2009) Broad-band Lg attenuation modelling in the Middle East. *Geophysical Journal International* 177: 1166–1176.

Patton HJ and Taylor SR (1989) *Q* structure of the Basin and Range from surface waves. *Journal of Geophysical Research* 89: 6929–6940.

Peacock S and Hudson JA (1990) Seismic properties of rocks with distributions of small cracks. *Geophysical Journal International* 102: 471–484.

Phillips S, Hartse HE, Taylor SR, and Randall GE (2000) 1 Hz *Lg* Q tomography in central Asia. *Geophysical Research Letters* 27: 3425.

Pozgay SH, Wiens DA, Conder JA, Shiobara H, and Sugioka S (2009) Seismic attenuation tomography of the Mariana subduction system: Implications for thermal structure, volatile distribution, and slow spreading dynamics. *Geochemistry, Geophysics, Geosystems* 19: Q04X05.

Press F (1956) Rigidity of the Earth's core. *Science* 124: 1204.

Prieto GA, Lawrence JF, and Beroza GC (2009) Anelastic Earth structure from the coherency of the ambient seismic field. *Journal of Geophysical Research* 114: B07303. http://dx.doi.org/10.1029/2008JB006067.

Randall MJ (1976) Attenuative dispersion and frequency shifts of the Earth's free oscillations. *Physics of the Earth and Planetary Interiors* 12: P1–P4.

Reid FJL, Woodhouse JH, and van Heist H (2001) Upper mantle attenuation and velocity structure from measurements of differential S phases. *Geophysical Journal International* 145: 615–630.

Resovsky JS and Ritzwoller MH (1998) New and refined constraints on three-dimensional Earth structure from normal modes below 3 MHz. *Journal of Geophysical Research* 103: 783–810.

Resovsky JS, Trampert J, and van der Hilst RD (2005) Error bars for the global seismic Q profile. *Earth and Planetary Science Letters* 230: 413–423.

Revenaugh J and Jordan TH (1989) A study of mantle layering beneath the western Pacific. *Journal of Geophysical Research* 94: 5787–5813.

Revenaugh J and Jordan TH (1991) Mantle layering from ScS reverberations. Part 2: The transition zone. *Journal of Geophysical Research* 96: 19763–19780.

Ricard Y, Matas J, and Chambat F (2009) Seismic attenuation in a phase change coexistence loop. *Physics of the Earth and Planetary Interiors* 176(1–2): 124–131. http://dx.doi.org/10.1016/j.pepi.2009.04.007.

Richards PG and Menke W (1983) The apparent attenuation of a scattering medium. *Bulletin of the Seismological Society of America* 73: 1005–1021.

Romanowicz B (1987) Multiplet–multiplet coupling due to lateral heterogeneity: Asymptotic effects on the amplitude and frequency of the Earth's normal modes. *Geophysical Journal of the Royal Astronomical Society* 90: 75–100.

Romanowicz B (1990) The upper mantle degree. Part 2: Constraints and inferences on attenuation tomography from global mantle wave measurements. *Journal of Geophysical Research* 95: 11051–11071.

Romanowicz B (1994a) On the measurement of anelastic attenuation using amplitudes of low-frequency surface waves. *Physics of the Earth and Planetary Interiors* 84: 179–191.

Romanowicz B (1994b) Anelastic tomography: A new perspective on upper-mantle thermal structure. *Earth and Planetary Science Letters* 128: 113–121.

Romanowicz B (1995) A global tomographic model of shear attenuation in the upper mantle. *Journal of Geophysical Research* 100: 12375–12394.

Romanowicz B (1998) Attenuation tomography of the Earth's mantle: A review of current status. *Pure and Applied Geophysics* 153: 257–272.

Romanowicz B (2002) Inversion of surface waves: A review. In: Lee WHK (ed.) *Handbook of Earthquake and Engineering Seismology, IASPEI, Part A*, pp. 149–174. Amsterdam: Academic Press.

Romanowicz B and Durek J (2000) Seismological constraints on attenuation in the Earth: A review. In: Karato S-I, Forte AM, Liebermann RC, Masters G, and Stixrude L (eds.) *Earth's Deep Interior: Mineral Physics and Tomography from the Atomic to the Global Scale. Geophysical Monograph Series*, vol. 117, pp. 161–180. Washington, DC: American Geophysical Union.

Romanowicz B and Gung Y (2002) Superplumes from the core–mantle boundary to the lithosphere: Implications for heat-flux. *Science* 296: 513–516.

Romanowicz B and Mitchell BJ (2007) Deep earth structure: Q of the Earth from crust to core. In: Romanowicz B and Dziewonski AM (eds.) *Treatise on Geophysics*, vol. 1. chapter 1.21. USA: Elsevier.

Romanowicz B, Roult G, and Kohl T (1987) The upper mantle degree two pattern: Constraints from geoscope fundamental spheroidal model eigenfrequency and attenuation measurements. *Geophysical Research Letters* 14: 1219–1222.

Rosat S, Sato T, Imanishi Y, et al. (2005) High resolution analysis of the gravest seismic normal modes after the 2005 Mw = 9 Sumatra earthquake using superconducting gravimeter data. *Geophysical Research Letters* 32. http://dx.doi.org/10.1029/2005GL023128.

Roth E, Wiens DA, Dorman LM, Hildebrand J, and Webb SC (1999) Seismic attenuation tomography of the Tonga–Fiji region using phase pair methods. *Journal of Geophysical Research* 104: 4795–4809.

Roth E, Wiens DA, and Zhao D (2000) An empirical relationship between seismic attenuation and velocity anomalies in the upper mantle. *Geophysical Research Letters* 27: 601–604.

Roult G (1975) Attenuation of seismic waves of very low frequency. *Physics of the Earth and Planetary Interiors* 10: 159–166.

Roult G (1982) The effect of young oceanic regions on the periods and damping of free oscillation of the Earth. *Journal of Geophysical Research* 51: 38–43.

Roult G and Clévédé E (2000) New refinements in attenuation measurements from free oscillations and surface wave observations. *Physics of the Earth and Planetary Interiors* 121: 1–37.

Roult G, Romanowicz B, and Montagner JP (1984) 3D upper mantle shear velocity and attenuation from fundamental mode free oscillation data. *Geophysical Journal International* 101: 61–80.

Roult G, Rosat S, Clévédé E, Millot-Langet R, and Hinderer J (2006) New determination of Q quality factors eigenfrequencies for the whole set of singlets of Earth's normal modes ${}_0S_0$, ${}_0S_2$, ${}_0S_3$, and ${}_2S_1$, using superconducting Gravimeter data from the GGP network. *Journal of Geodynamics* 41: 345–357.

Ruan Y and Zhou Y (2010) The effects of 3-D anelasticity (Q) structure on surface wave phase delays. *Geophysical Journal International* 181: 479–492.

Ruan Y and Zhou Y (2012) The effects of 3-D anelasticity (Q) structure on surface wave amplitudes. *Geophysical Journal International* 189: 967–983.

Rychert CA, Fischer KM, Abers GA, and Plank T (2008) Strong along-arc variations in attenuation in the mantle wedge between Costa Rica and Nicaragua. *Geochemistry, Geophysics, Geosystems* 9: Q10S10.

Sacks IS (1969) Anelasticity of the inner core. *Annual Report of the Director of Department of Terrestrial Magnetism* 69: 416–419.

Sacks IS (1980) Q_s of the lower mantle – A body wave determination. *Annual Report of the Director of Department of Terrestrial Magnetism* 79: 508–512.

Sahin S, Xueyang B, Turkelli N, Sandvol E, Teoman U, and Kahraman M (2013) Lg wave attenuation in the Isparta Angle and Anatolian Plateau. *Pure and Applied Geophysics* 170: 337–351.

Sailor RV and Dziewonski AM (1978) Measurements and interpretation of normal mode attenuation. *Geophysical Journal of the Royal Astronomical Society* 53: 559–581.

Sarker G and Abers GA (1998) Comparison of seismic body wave and coda wave measures of Q. *Pure and Applied Geophysics* 153: 665–683.

Sarker G and Abers GA (1999) Lithospheric temperature estimates from seismic attenuation across range fronts in southern and central Eurasia. *Geology* 27: 427–430.

Sato R and Espinosa AF (1967) Dissipation in the Earth's mantle and rigidity and viscosity in the Earth's core determined from waves multiply-reflected from the mantle–core boundary. *Bulletin of the Seismological Society of America* 57: 829–856.

Sato H, Sacks IS, Murase T, Muncill G, and Fukuyama F (1989) Q_P-melting temperature relation in peridotite at high pressure and temperature: Attenuation mechanism and implications for the mechanical properties of the upper mantle. *Journal of Geophysical Research* 94: 10647–10661.

Savage B, Komatitsch D, and Tromp J (2010) Effects of 3D attenuation on seismic wave amplitude and phase measurements. *Bulletin of the Seismological Society of America* 100: 1241–1251.

Schlotterbeck BA and Abers GA (2001) Three-dimensional attenuation variations in Southern California. *Journal of Geophysical Research* 106: 30719–30735.

Schurr B, Asch G, Rietbrock A, Trumbull R, and Haberland C (2003) Complex patterns of fluid and melt transport in the central Andean subduction zone revealed by attenuation tomography. *Earth and Planetary Science Letters* 215(1–2): 105–119. http://dx.doi.org/10.1016/S0012-821X(03)00441-2.

Selby ND and Woodhouse JH (2000) Controls on Rayleigh wave amplitudes: Attenuation and focusing. *Geophysical Journal International* 142: 933–940.

Selby ND and Woodhouse JH (2002) The Q structure of the upper mantle: Constraints from Rayleigh wave amplitudes. *Journal of Geophysical Research* 107. http://dx.doi.org/10.1029/2001JB000,257.

Shearer P (1994) Constraints on inner core anisotropy from PKP(DF) travel times. *Journal of Geophysical Research* 99: 19647–19659.

Sheehan A and Solomon SC (1992) Differential shear wave attenuation and its lateral variation in the north Atlantic region. *Journal of Geophysical Research* 97: 15339–15350.

Shi J, Kim WY, and Richards PG (1996) Variability of crustal attenuation in the northeastern United States from *Lg* waves. *Journal of Geophysical Research* 101: 25231–25242.

Shito A, Karato S-I, Matsukage KN, and Nishibara Y (2006) Towards mapping the three-dimensional distribution of water in the upper mantle from velocity and attenuation tomography. In: Jacobsen SD and vanderLee S (eds.) *Earth's Deep Water Cycle. Geophysical Monograph Series*, vol. 168, pp. 225–236. Washington, DC: AGU.

Shito A, Karato S, and Park J (2004) Frequency dependence of Q in Earth's upper mantle inferred from continuous spectra of body waves. *Geophysical Research Letters* 31. http://dx.doi.org/10.1029/2004GL019582.

Shito A and Shibutan T (2003a) Anelastic structure of the upper mantle beneath the northern Philippine Sea. *Physics of the Earth and Planetary Interiors* 140: 319–329.

Shito A and Shibutan T (2003b) Nature of heterogeneity of the upper mantle beneath the northern Philippine Sea as inferred from attenuation and velocity tomography. *Physics of the Earth and Planetary Interiors* 140: 331–341. http://dx.doi.org/10.1016/j.pepi.2003.09.010.

Singh S and Herrmann RB (1983) Regionalization of crustal Q in the continental United States. *Journal of Geophysical Research* 88: 527–538.

Singh SC, Taylor MJ, and Montagner JP (2000) On the presence of liquid in the Earth's inner core. *Science* 287: 2471–2474.

Sipkin SA and Jordan TH (1979) Frequency dependence of Q_{ScS}. *Bulletin of the Seismological Society of America* 69: 1055–1079.

Sipkin SA and Jordan TH (1980) Regional variation of Q_{ScS} phases. *Bulletin of the Seismological Society of America* 70: 1071–1102.

Sipkin SA and Revenaugh J (1994) Regional variation of attenuation and travel times in China from analysis of multiple ScS phases. *Journal of Geophysical Research* 99: 2687–2699.

Smith S (1972) The anelasticity of the mantle. *Tectonophysics* 13: 601–622.

Smith ML and Dahlen FA (1981) The period and Q of the Chandler wobble. *Geophysical Journal of the Royal Astronomical Society* 64: 223–282.

Smith MF and Masters G (1989) Aspherical structure constraints from free oscillation frequency and attenuation measurements. *Journal of Geophysical Research* 94: 1953–1976.

Sobolev SV, Zeyen H, Soll G, Werling F, Altherr R, and Fuchs K (1996) Upper mantle temperatures from teleseismic tomography of French Massif Central including the effects of composition, mineral reactions, anharmonicity, anelasticity and partial melt. *Earth and Planetary Science Letters* 139: 147–163.

Solomon SC (1973) Seismic wave attenuation and melting beneath the mid-Atlantic Ridge. *Journal of Geophysical Research* 78: 6044–6059.

Solomon SC and Toksöz MN (1970) Lateral variation of attenuation of P and S waves beneath the United States. *Bulletin of the Seismological Society of America* 60: 819–838.

Song XD and Helmberger D (1993) Anisotropy of the Earth's inner core. *Geophysical Research Letters* 20: 285–288.

Souriau A and Calvet M (2015) The Earth's cores. *Treatise on Geophysics*, vol. 1. USA: Elsevier.

Souriau A and Romanowicz B (1996) Anisotropy in inner core attenuation: A new type of data to constrain the nature of the solid core. *Geophysical Research Letters* 23: 1–4.

Souriau A and Romanowicz B (1997) Anisotropy in the inner core: Relation between P-velocity and attenuation. *Physics of the Earth and Planetary Interiors* 101: 33–47.

Souriau A and Roudil P (1995) Attenuation in the uppermost inner core from broadband GEOSCOPE PKP data. *Geophysical Journal International* 123: 572–587.

Stachnik JC, Abers GA, and Christensen DH (2004) Seismic attenuation and mantle wedge temperatures in the Alaska subduction zone. *Journal of Geophysical Research* 109: B10304. http://dx.doi.org/10.1029/2004JB003018.

Street RL (1976) Scaling northeastern United States/southeastern Canadian earthquakes by the *Lg* waves. *Bulletin of the Seismological Society of America* 66: 1525–1537.

Strick E (1967) The determination of *Q*, dynamic viscosity and creep curves from wave propagation measurements. *Geophysical Journal of the Royal Astronomical Society* 13: 197–218.

Su WJ and Dziewonski AM (1990) Inner core anisotropy in three dimensions. *Journal of Geophysical Research* 100: 9831–9852.

Suda N and Fukao Y (1990) Structure of the inner core inferred from observations of seismic core modes. *Geophysical Journal International* 103: 403–413.

Suda N, Nawa K, and Fukao Y (1998) Earth's background free oscillations. *Science* 279: 2089–2091.

Suda N, Shibata N, and Fukao Y (1991) Degree 2 pattern of attenuation structure in the upper mantle from apparent complex frequency measurements of fundamental spheroidal modes. *Geophysical Research Letters* 18: 1119–1122.

Suetsugu D (2001) A low Q_{ScS} anomaly near the South Pacific Superswell. *Geophysical Research Letters* 28: 391–394.

Sumita I and Olson P (1999) A laboratory model for convection in Earth's core driven by a thermally heterogeneous mantle. *Geophysical Research Letters* 286: 1547–1549.

Sundberg M and Cooper RF (2010) A composite viscoelastic model for incorporating grain boundary sliding and transient diffusion creep; correlating creep and attenuation responses for materials with a fine grain size. *Philosophical Magazine* 90(20): 2817–2840. http://dx.doi.org/10.1080/14786431003746656.

Sutton GH, Mitronovas W, and Pomeroy PW (1967) Short-period seismic energy radiation patterns from underground explosions and small-magnitude earthquakes. *Bulletin of the Seismological Society of America* 57: 249–267.

Takanami T, Sacks S, and Hasegawa A (2000) Attenuation structure beneath the volcanic front in northeastern Japan from broad-band seismograms. *Physics of the Earth and Planetary Interiors* 121: 339–357.

Tanaka S and Hamaguchi H (1997) Degree one heterogeneity and hemispherical variation of anisotropy in the inner core from PKP(BC)-PKP(DF) times. *Journal of Geophysical Research* 102: 2925–2938.

Teng TL (1968) Attenuation of body waves and the Q structure of the mantle. *Journal of Geophysical Research* 73: 2195–2208.

Thouvenot F (1983) Frequency dependence of the quality factor in the upper crust: A deep seismic sounding approach. *Geophysical Journal of the Royal Astronomical Society* 73: 427–447.

Trampert J and Woodhouse JH (1995) Global phase velocity maps of Love and Rayleigh waves between 40 and 150 seconds. *Geophysical Journal International* 122: 675–690.

Tryggvason E (1965) Dissipation of Rayleigh-wave energy. *Journal of Geophysical Research* 70: 1449–1455.

Tsai YB and Aki K (1969) Simultaneous determination of the seismic moment and attenuation of seismic surface waves. *Bulletin of the Seismological Society of America* 59: 275–287.

Tseng TL, Huang BS, and Chin BH (2001) Depth-dependent attenuation in the uppermost inner core from the Taiwan short period PKP data. *Geophysical Research Letters* 28: 459–462.

Tsumura N, Matsumoto S, Horiuchi S, and Hasegawa A (2000) Three-dimensional attenuation structure beneath the northeastern Japan arc estimated from spectra of small earthquakes. *Tectonophysics* 319(4): 241–260. http://dx.doi.org/10.1016/S0040-1951(99)00297-8.

Ulug A and Berckhemer G (1984) Frequency dependence of Q for seismic body waves in the Earth's mantle. *Journal of Geophysics* 56: 9–19.

Utsu T (1967) Anomalies in seismic wave velocity and attenuation associated with a deep earthquake zone. *Journal of the Faculty of Science, Hokkaido University* 7: 1–25.

Vidale JE and Earle PS (2000) Fine-scale heterogeneity in the Earth's inner core. *Nature* 404: 273–275.

Vinnik LP, Romanowicz B, and Bréger L (1994) Anisotropy in the center of the inner core. *Geophysical Research Letters* 21: 1671–1674.

Walter WR, Mayeda K, Malagnini L, and Scognamiglio L (2007) Regional body-wave attenuation using a coda source normalization method: Application to MEDNET records of earthquakes in Italy. *Geophysical Research Letters* 34.

Walter WR and Taylor SR (2001) A revised magnitude and distance amplitude correction (MDAC2) procedure for regional seismic discriminants. *Theory and Testing at NTS Lawrence Livermore National Laboratory Technical Report*, UCRL-ID-146882.

Warren LM and Shearer PM (2000) Investigating the frequency dependence of mantle Q by stacking P and PP spectra. *Journal of Geophysical Research* 105: 25391–25402.

Warren LM and Shearer PM (2002) Mapping lateral variation in upper mantle attenuation by stacking *P* and *PP* spectra. *Journal of Geophysical Research* 107. http://dx.doi.org/10.1029/2001JB001195.

Waszek L and Deuss A (2013) A low attenuation layer in Earth's uppermost inner core. *Geophysical Journal International* 195: 2005–2015. http://dx.doi.org/10.1093/gji/ggt368.

Wen L and Niu F (2002) Seismic velocity and attenuation structures in the top of the Earth's inner core. *Journal of Geophysical Research* 107. http://dx.doi.org/10.1029/2001JB000170.

Widmer R, Masters G, and Gilbert F (1991) Spherically symmetric attenuation within the Earth from normal mode data. *Geophysical Journal International* 104: 541–553.

Wiens DA, Conder JA, and Faul UH (2008) The seismic structure and dynamics of the mantle wedge. *Annual Review of Earth and Planetary Sciences* 36: 421–455. http://dx.doi.org/10.1146/annurev.earth.33.092203.122633.

Wilcock WSD, Solomon SC, Purdy GM, and Toomey D-R (1995) Seismic attenuation structure of the East Pacific Rise near 9°30′N. *Journal of Geophysical Research* 100: 24147–24165.

Wong YK (1989) *Upper Mantle Heterogeneity from Phase and Amplitude Data of Mantle Waves*. PhD Dissertation, Cambridge, MA: Harvard University.

Woodhouse JH and Wong YK (1986) Amplitude, phase and path anomalies of mantle waves. *Geophysical Journal of the Royal Astronomical Society* 87: 753–773.

Xie J (2007) Pn attenuation beneath the Tibetan Plateau. *Bulletin of the Seismological Society of America* 97: 2040–2052.

Xie J, Gok R, Ni J, and Aoki Y (2004) Lateral variations of crustal seismic attenuation along the INDEPTH profiles in Tibet from *Lg Q* inversion. *Journal of Geophysical Research* 109(B10): 988. http://dx.doi.org/10.1029/2004JB002.

Xie J and Mitchell BJ (1990a) Attenuation of multiphase surface waves in the Basin and Range province. Part I: *Lg* and *Lg* coda. *Geophysical Journal International* 102: 121–127.

Xie J and Mitchell BJ (1990b) A back-projection method for imaging large-scale lateral variations of *Lg* coda *Q* with application to continental Africa. *Geophysical Journal International* 100: 161–181.

Xie J and Nuttli OW (1988) Interpretation of high-frequency coda at large distances: Stochastic modeling and method of inversion. *Geophysical Journal* 95: 579–595.

Xie J, Wu X, Liu R, Schaff D, Liu Y, and Liang J (2006) Tomographic regionalization of crustal *Lg Q* in eastern Eurasia. *Geophysical Research Letters* 33(L03). http://dx.doi.org/10.1029/2005GL024; 410.

Yacoub NK and Mitchell BJ (1977) Attenuation of Rayleigh wave amplitudes across Eurasia. *Bulletin of the Seismological Society of America* 67: 751–769.

Yang Y, Forsyth DW, and Weeraratne DS (2007) Seismic attenuation near the East Pacific Rise and the origin of the low-velocity zone, Earth planet. *Science Letters* 258: 260–268. http://dx.doi.org/10.1016/j.epsl.2007.03.040.

Yoshida M and Tsujiura M (1975) Spectrum and attenuation of multiply-reflected core phases. *Journal of Physics of the Earth* 23: 31–42.

Yu W and Wen L (2006a) Seismic velocity and attenuation structures in the top 400 km of the Earth's inner core along equatorial paths. *Journal of Geophysical Research* 111. http://dx.doi.org/10.1029/2005JB003995.

Yu W and Wen L (2006b) Inner core attenuation anisotropy. *Earth and Planetary Science Letters* 245: 581–594.

Zhang T and Lay T (1994) Analysis of short-period regional phase path effects associated with topography in Eurasia. *Bulletin of the Seismological Society of America* 84: 119–132.

Zhou Y (2009) Surface wave sensitivity to 3-D anelasticity. *Geophysical Journal International* 178: 1403–1410.

Zou Z, Koper KD, and Cormier VF (2008) The structure of the base of the outer core inferred from seismic waves diffracted around the inner core. *Journal of Geophysical Research* 113. http://dx.doi.org/10.1029/2007JB005316.

Relevant Websites

http://mahi.ucsd.edu/galai/rem.dir/rem.home.html – The Reference Earth Model.

This page intentionally left blank

1.26 Constraints on Seismic Models from Other Disciplines - Constraints from Mineral Physics on Seismological Models

L Stixrude, University College London, London, UK
R Jeanloz, University of California at Berkeley, Berkeley, CA, USA

© 2015 Elsevier B.V. All rights reserved.

1.26.1	**Introduction**	829
1.26.2	**Mineral Elasticity**	831
1.26.2.1	Overview	831
1.26.2.2	One-Dimensional Lattice Dynamics and the Continuum Limit	831
1.26.2.3	Experimental Methods	832
1.26.2.4	3D Lattice Dynamics: Polarization and Anisotropy	833
1.26.2.5	Nontrivial Crystal Structures, Optic Modes, and Thermodynamics	836
1.26.2.6	Influence of Pressure and Temperature on the Elastic Constants	839
1.26.3	**Rock Elasticity**	841
1.26.3.1	Overview	841
1.26.3.2	Composites Theory	841
1.26.3.3	Attenuation and Dispersion	843
1.26.4	**Seismological Elasticity and Anelasticity**	846
1.26.4.1	Scaling	846
1.26.4.2	Uncertainties	846
1.26.4.3	Implications for Inversions	848
1.26.5	**Conclusions and Outlook**	849
Acknowledgments		849
References		849

1.26.1 Introduction

Earth is unique among the planets as the only body for which we have a detailed picture of its internal structure. We may compare that part of seismology concerned with Earth structure to an experimental science concerned with a single, very large sample. The source of illumination is generated naturally, mainly in the form of earthquakes, many each year large enough to generate measurable ground accelerations at the antipodes. (There are typically more than ten major, magnitude 7–8; 100 large, magnitude 6–7; and 1000 damaging, magnitude 5–6 earthquakes each year. Prior to the current international moratorium, nuclear explosions have also provided seismic illumination of the Earth's deep interior: magnitudes of 5, 6, and 7 correspond roughly to yields of 32 kt, 1 Mt, and 32 Mt. In addition, storms, volcanic eruptions, bolide impact, and other phenomena create an ambient background field of 'seismic daylight.') The detectors are seismic recording stations, which now number in the hundreds of high quality (e.g., producing broadband, three-component digital records). The basic measurement is of the travel time from source to receiver, from which can be deduced the elastic-wave velocity along the path of propagation; the displacement versus time (waveform) shown by the seismic record also provides information about the spatial gradients of wave velocity at depth. Millions of crossing rays have illuminated every corner of the interior, leading to models of Earth structure in which the velocity is considered known to within 1%. In addition, the frequencies of the Earth's resonances (free oscillations or normal modes) excited by large earthquakes, typically determined to a part in 10^3 for hundreds of overtones, provide important information on the distribution of density at depth.

Such extraordinary precision rivals or exceeds our ability to measure elastic-wave velocities in the laboratory at conditions representative of most of the Earth's interior. In reality, the seismological determination of velocity is somewhat more limited than this comparison would suggest, primarily by spatial resolution: the smaller the region of interest, the larger the uncertainties (Gilbert et al., 1973).

Earth is unusual as an experimental sample in ways other than its large size. Pressure, temperature, and composition are all inhomogeneous, and the spatial variations of these quantities are due to processes internal to the planet, rather than being externally imposed. Temperature and compositional fields both show large radial and lateral variations that are the product of the Earth's origin, evolution, and dynamics. But how to determine these quantities? We have no *in situ* measurements of either temperature or composition below the crust, and seismology alone does not suffice: only the elastic-wave velocities and density are measured, not temperature or composition.

A central concern of mineral physics has been to uncover the nature of the Earth's internal temperature and composition, with a view toward placing critical observational constraints on the planet's history and geologic processes. For example, by recognizing the connection between the bulk-sound velocity determined seismologically and the compressibility ($1/K_S$), Williamson and Adams (1923) showed that much of Earth structure can be explained by adiabatic

self-compression of matter with depth. By comparing seismological models and experimental – mostly shock wave – data, Birch identified iron as the primary constituent of the Earth's core and the mean atomic mass of the mantle as being similar to that of certain xenoliths (rock fragments of the Earth's interior brought to the surface by volcanic processes) (Birch, 1952). Ringwood, Akimoto, and others showed that seismologically observed mantle discontinuities can be explained by phase transformations observed in laboratory experiments on samples of mantle-like composition (Akimoto and Fujisawa, 1968; Ringwood and Major, 1970). In each case, a key to our current view of the Earth's origin and state was established.

It may seem at first surprising that materials of such different size, from thousand kilometer structures in Earth to laboratory samples as small as a few microns – a range of 12 orders of magnitude – may be compared at all. (Though they are usually ignored for bulk samples, if one takes surface effects into account, the comparison can be extended down to the nanometer scale.) Actually, the basic approach is not unique to geophysics and forms the basis for understanding the structure and evolution of stars and other planets, including exoplanets (Kippenhahn et al., 2012; Valencia et al., 2006). The theoretical basis for spanning the range of length scales from atoms to planets lies at the heart of thermodynamics and statistical mechanics: the prediction that the bulk equilibrium properties of materials should not depend on the size of the sample. There are deep connections to seismology, as well: the analysis of the normal modes of vibration of an atomic lattice leads to concepts of dispersion and elastic-wave velocity that can be linked directly to analogous seismological problems. Relating the large to the small is essential for uncovering the temperature and composition throughout the Earth's interior. High-pressure devices and theoretical simulations figuratively transport us to the inaccessible interior, giving us a unique window into its nature.

From the point of view of materials theory, Earth is a particularly challenging object because it consists of solids and fluids (condensed matter) at moderate to high pressures. Unlike the gases that make up planetary atmospheres, the temperature-dependent constitutive relations between stress, strain, and strain rate (pressure, density, and deformation rate for a fluid) cannot be written down analytically. Much of the effort in mineral physics is devoted to discovering these constitutive relations, either by experimental measurement or by quantum mechanical theory.

The solid state is also complex in that elements organize themselves into multiple phases of different composition and crystal structure (i.e., geometric arrangement by which the atoms are packed together to form the crystal). Each phase has distinctive physical and chemical properties, and its behavior must be understood separately and in combination with other phases. The exploration of high pressure continues to be one of the frontiers of mineral physics, including the challenge of measuring physical properties in the laboratory at conditions of the Earth's interior and the ongoing discovery of new solid phases.

Perhaps, the most challenging aspect of the solidity of materials making up the mantle is that it imposes limitations on our ability to scale from the laboratory to the Earth. These limitations arise from the heterogeneity inherent even in the purest sample in the form of grain boundaries and the differences in size, shape, and orientation of the constituent grains. So, for example, it is not possible to uniquely compute the seismic velocity of a rock from the properties of its constituent single crystals, although rigorous bounds can be formulated if the grains are randomly oriented. An exact computation requires complete specification of the grain geometry. Although usually not the case for Earth materials, the bounds can be far apart in the presence of significant mechanical heterogeneities such as partial melts or cracks. More generally, some physical properties such as attenuation and scattering depend essentially on length scale and often in ways that are difficult to predict.

The significance of the length scale of heterogeneity is intimately linked to the timescale of deformation. All materials contain defects, such as dislocations, interstitial atoms, and vacancies. When deformed at very high ('infinite') frequency, the types and concentrations of defects are of little consequence, and the material deforms elastically because the defects are frozen in place. Seismic waves have much longer periods of deformation however: roughly 14 orders of magnitude greater than those of atomic vibrations. At these timescales, defects can move in response to deformation, leading to anelastic behavior with the absorption of mechanical energy and lowering of the elastic wave relative to the elastic limit. In the limit of much longer periods of deformation, such as those that characterize mantle convection, the deformation is entirely viscous and dominated by the motion of defects.

The nature and degree of anelasticity depends in detail on defect types (point defects, dislocation, and grain boundary), concentrations, and mobilities. Anelasticity is thus not necessarily a state function, in the usual thermodynamic sense, and can depend on the past history of the sample. This presents severe challenges to experimental control and characterization and to our ability to relate the results to the Earth where the deformation history that the materials have undergone may be very different from those prepared in the laboratory. On the other hand, the fact that anelasticity depends on so many more variables than the elastic-wave velocity presents the opportunity for further characterizing the nature of the Earth's interior in ways that are not possible through the analysis of the elastic limit alone. These comments apply to nonequilibrium properties more generally, such as thermal conductivity, chemical diffusivity, and effective viscosity, among others: properties that are important not only because they play crucial roles in controlling the Earth's evolution but also because they allow minerals to approach the condition of thermodynamic equilibrium on which we focus. Nonequilibrium properties of minerals and rocks are beyond the scope of this chapter.

Here, we highlight the relationship between mineral elasticity (and density) and Earth structure. Our approach will be that of the forward problem. We begin with the fundamentals of mineral elasticity, including the basic theory of lattice vibrations, dispersion and normal modes, and its relationship to the various experimental probes of elasticity, to the thermodynamic properties of minerals, and to the underlying quantum mechanics of bonding. The discussion of the elasticity of rocks includes an outline of the theory of composites as applied to the elastic constants and the essentials of anelasticity (i.e., at quasiequilibrium). Finally, we consider the issue of scaling in length and time, from the laboratory to the Earth. We end with

thoughts on the prospects for the inverse problem, that is, formally inverting seismological observations for quantities such as the temperature and compositional fields at depth via knowledge of the materials properties.

1.26.2 Mineral Elasticity

1.26.2.1 Overview

In the limit of ideal crystals and small deformations, the elasticity of solids is most usefully viewed in the context of the vibrational modes of crystalline structures. The theory of the dynamics of perfect crystals is our most powerful way of envisioning length scaling. It gives us a formally exact means of relating the elastic-wave velocity of samples ranging in size from sub-micrometer to – in principle – infinite size, limited only by considerations of surface effects at small scales and of self-gravitation (and, implicitly, strength) as we approach planetary size. The material can be treated as a continuum at large scales, and its properties derived from the consideration of the forces acting between atoms, that is, from a description at the smallest of scales. In particular, the seismic-wave velocities of a perfect crystal are determined by the crystal structure and interatomic forces.

The approach of lattice dynamics is also important in geophysics because it underlies our understanding of the influence of temperature on physical properties, including thermal expansion that drives convection of the mantle and core and seismic-wave velocities that provide images of our planet's interior. The theory of thermal conductivity also derives from concepts of phonons, which are the modes of oscillation of atoms in a crystal (analogous to the normal modes of the Earth). The theory of lattice dynamics is well developed, and there are many excellent texts covering the subject more deeply than we can here (Ashcroft and Mermin, 1976; Born and Huang, 1954; Dove, 1993). In addition to illustrating the connection between microscopic and macroscopic properties, our goals are to illustrate the relationship between experimental and geophysical measurements of elastic-wave velocities.

1.26.2.2 One-Dimensional Lattice Dynamics and the Continuum Limit

A good illustration of these concepts is provided by the one-dimensional (1D) normal modes of vibration of a linear chain of identical atoms of mass m separated by a distance a and connected with Hookean springs, for which the relationship between force F and displacement u is $F=Ku$, where K is the force constant (Figure 1). The potential energy is a quadratic function of the displacement of the atoms, and the equations of motion are

$$m\frac{\partial u_n^2}{\partial t^2} = K\left[(u_{n+1}-u_n)^2 + (u_{n-1}-u_n)^2\right] \qquad [1]$$

Here, u_n is the displacement of the nth atom from its ideal lattice site, located at the position na. Substituting a traveling-wave solution for u_n as a function of position and time, $u=A\exp[i(\omega t-kx)]$, we find the dispersion relation (Figure 1)

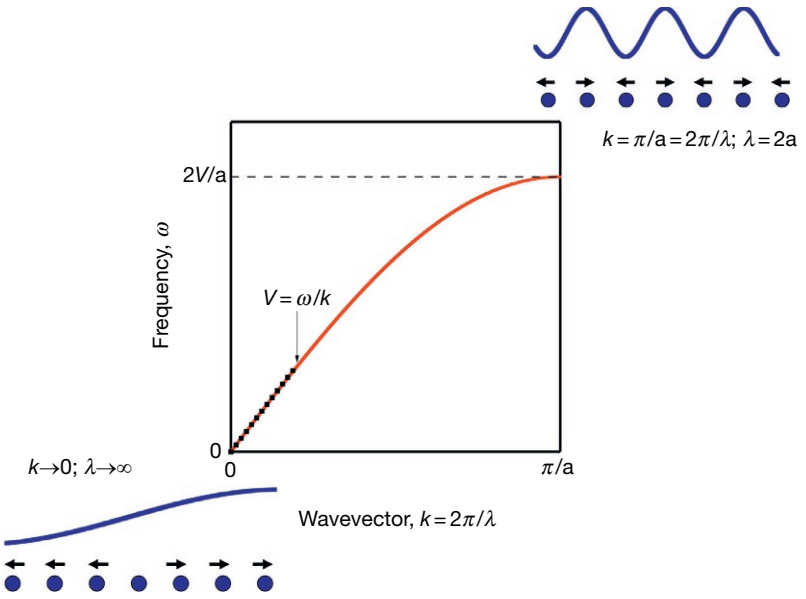

Figure 1 Phonon dispersion relation for the one-dimensional lattice (1D) (red line) indicating the relationship to the acoustic velocity as the slope at the origin (dashed black line). Schematically illustrated are vibrational modes, with arrows and blue curves indicating the sense of displacement of the atoms (blue circles) in the limits of long wavelengths (lower left) and of the shortest wavelengths (upper right). The group velocity (slope of the ω–k curve) vanishes at the Brillouin zone edge, $k=\pi/a$, because shorter wavelengths cannot be propagated across the discrete row of atoms; consequently, there is a standing wave with no wave-energy propagation for $\lambda=2a$. In detail, the ω–k curve (branch) is actually a collection of N distinct points, corresponding to the N normal modes (standing waves) of a 1D chain of N atoms; for N large enough (bulk sample), the set of points is indistinguishable from a continuous line. Reproduced from Stixrude L and Lithgow-Bertelloni C (2012) Geophysics of chemical heterogeneity in the mantle. *Annual Review of Earth and Planetary Sciences* 40: 569–595.

$$\omega = 2\sqrt{\frac{K}{m}}\left|\sin\left(\frac{ka}{2}\right)\right| \quad [2]$$

where ω is the frequency (in rad s^{-1}), $k=2\pi/\lambda$ is the wave number (in rad m^{-1}), and λ is the wavelength (in m $cycle^{-1}$) of the normal mode of vibration. (In 2D and 3D, the wave vector specifies propagation direction and its magnitude gives the wave number.) The phase velocity describing the propagation speed of a given wavelength is given by $V_\phi=\omega/k$, whereas the group velocity that describes the propagation speed of a wave packet (i.e., many different wavelengths and hence the wave energy) is $V_G=\partial\omega/\partial k$. In general, the linear monatomic chain is thus dispersive, with wavelength-dependent velocities and specifically $V_G<V_\phi$ (i.e., a low-pass filter; longer waves travel faster than shorter waves, thereby 'dispersing' an originally compact wave packet into a more extended displacement bundle).

At long wavelength, as $k\to 0$, the group and phase velocities are the same (which means there is no dispersion – i.e., spreading out of a wave packet):

$$V = a\sqrt{\frac{K}{m}} = \sqrt{\frac{M}{\rho}} \quad [3]$$

where the last equality emphasizes the relationship with the seismic-wave velocity expressed in terms of an elastic modulus $M=K/a$ and a density $\rho=m/a^3$. Here, M is the longitudinal modulus, since propagation and polarization are parallel for the present 1D example. The motion described by eqns [2] and [3], with $\omega\to 0$ as $k\to 0$, is referred to as an acoustic mode.

Equation [3] applies to the continuum limit, with wavelengths being much larger than interatomic spacings, as is the case for seismic waves. Indeed, it agrees with our intuitive notions about seismic-wave velocities. As we increase the strength of the interatomic forces, the velocity increases, for example, in the case of increasing pressure. Also, as we increase the mass of the atoms, the velocity decreases, for example, in the case of iron enrichment.

What do the normal modes look like in the limit of the wavelength approaching twice the interatomic spacing, $k\to\pi/a$? This is of interest because shorter wavelengths cannot be supported by the chain of discrete atoms; in fact, normal modes with wavelengths less than twice the interatomic spacing are indistinguishable from those within the wave number range $k=0$ to π/a. (This limitation is identical to the Nyquist theorem encountered in Fourier and signal theory, which specifies that at least two samples per wavelength are needed to characterize a wave, and also corresponds to the Heisenberg uncertainty principle in quantum mechanics.) This range of wave numbers defining the first Brillouin zone in reciprocal (wave number or Fourier transform) space contains complete information on all the normal modes that the chain of atoms can experience. At the Brillouin zone edge ($k=\pi/a$), the motion of each atom opposes its neighbors (**Figure 1**): each bond is stretched or compressed by the same amount, producing the maximum frequency $\omega = 2\sqrt{(K\ m^{-1})} = 2V/a$.

The particulate nature of matter thus produces velocity dispersion as wavelengths approach atomic (or unit cell) dimensions, well below the continuum range. This is reflected in the nonlinear form of eqn [2] and, for example, the difference between the Brillouin zone-edge frequency and the linear extrapolation of eqn [2] to the Brillouin zone edge $\omega=\pi V/a$. This type of dispersion is negligible in the usual geophysical context and, for ideal crystals, scaling from laboratory samples to geophysical length scales is essentially exact. From eqn [2], we find that even for length scales corresponding to very small grains (1 μm), the dispersion is only about one part in three thousand. This unity of length scales is modified by heterogeneity (e.g., grain boundaries, as well as variations in mineral phase abundances, compositions, and orientations) and anelasticity in real (nonideal) samples.

1.26.2.3 Experimental Methods

Experimental probes of the elastic-wave velocities have characteristic wavelengths that, while orders of magnitude smaller than those of seismic waves, lie well within the continuum, infinite-size limit of ideal crystals. Brillouin spectroscopy is most closely connected to the phonon spectrum (Duffy et al., 1995; Jackson et al., 2000; Marquardt et al., 2009; Murakami et al., 2009; Sinogeikin and Bass, 2000; Weidner et al., 1982). Here, one measures the normal-mode frequency of the acoustic branch at a small but finite value of the wave number related to the wavelength of the (generally visible) light used to probe the sample, with the ratio of frequency to wave number yielding the elastic-wave velocity. The wave number is given by the magnitude of the scattering vector (i.e., the projection of the light's wavelength onto the direction of acoustic-wave propagation in the crystal) through a formula analogous to Bragg's law for x-ray diffraction. The frequency is observed as a Doppler-like shift of the scattered relative to the incoming light, and Brillouin spectroscopy can be thought of as the acoustic-mode analog of Raman spectroscopy, the latter scattering off the optic modes to be described later. In impulsive stimulated scattering, a time-domain version of Brillouin spectroscopy, a phonon is excited by one laser and scatters light from a second laser, yielding information on elasticity as well as thermal conductivity (Abramson et al., 1999; Brown et al., 1989; Crowhurst et al., 2008; Zaug et al., 1993). Nuclear resonant inelastic x-ray scattering is also sensitive to phonon energies over a range of wave vectors, so can yield information about sound velocities (Fiquet et al., 2001; Mao et al., 2001).

Similarly, resonant ultrasound spectroscopy and ultrasonic interferometry determine the normal-mode frequencies of a macroscopic crystal (megahertz for typical experimental sample sizes) and are thus analogous to normal-mode studies of the Earth (Anderson and Isaak, 1995; Goto et al., 1976). Other ultrasonic methods are analogous to body-wave seismology: an acoustic pulse of frequency megahertz–gigahertz is generated via a transducer and the travel time across the sample measured; multiple reflections and interference are used to maximize precision (Chantel et al., 2012; Jackson and Niesler, 1982; Rigden et al., 1991; Spetzler, 1970; Yoneda, 1990). High frequencies are essential so that the acoustic wavelength (10 μm–1 mm) is much smaller than the size of the sample (~1 mm for *in situ* high-pressure measurements).

All of these methods involve small ('infinitesimal')-amplitude waves. In addition, two classes of finite-compression methods are available: dynamic (shock wave) and static. In the first, a large-amplitude deformation wave is generated by the

impact of a projectile or a laser pulse into the sample, which is then compressed on a timescale of *ns*. The velocity of the resulting shock wave is then approximately equal to the longitudinal-wave velocity at low pressures (below the dynamic yielding point) and to the bulk-sound velocity at higher pressures (thermal and other corrections can be made to obtain more exact results). Above the dynamic yielding point, the shock front moves at close to the high-pressure bulk-sound velocity (i.e., fluid-like response), but rarefaction waves – inevitably generated at all free surfaces of the sample – propagate into the shock-loaded state: this is measurable, with the decompression traveling at the longitudinal- (compressional-) wave velocity relative to the shocked material. The bulk-sound velocity (V_B) and longitudinal-wave velocity (V_P) can thus be probed dynamically, and the shear-wave velocity (V_S) is obtained from the relation (Brown and McQueen, 1986; Duffy and Ahrens, 1992; Nguyen and Holmes, 2004)

$$\frac{4}{3}V_S^2 = V_P^2 - V_B^2 \qquad [4]$$

The bulk-sound velocity can also be determined in static experiments from the equation of state (Duffy and Wang, 1998; Jeanloz and Thompson, 1983; Stixrude et al., 1992). Using a diamond anvil cell or other high-pressure device, one measures the volume (or density ρ) as a function of pressure via very slow (minutes–days) stepwise compression: x-ray diffraction is used to determine the compression, for example. The slope of the relationship yields the isothermal bulk modulus $K_T = (\partial P/\partial \ln \rho)_T$ that is related to V_B through

$$V_B = \sqrt{\frac{K_S}{\rho}} \qquad [5]$$

and the correction from the isothermal to the adiabatic (K_S) bulk modulus, which is small at room temperature.

One of the important conclusions to arise from these various probes of material elasticity is that frequency dependence is essentially undetectable over eight orders of magnitude: Shear- and longitudinal-wave velocities are indistinguishable from 100 THz (Brillouin) to 1 MHz (ultrasonic), and the bulk-sound velocity is invariant from 100 THz to the essentially zero-frequency (DC) measurements of static compression. In contrast, the Earth shows measurable frequency dependence of the shear-wave velocity over a much narrower range of lower frequencies (hertz to millihertz) (Dziewonski and Anderson, 1981). The comparison with laboratory studies suggests that the magnitude of shear-wave attenuation – and resulting dispersion – is larger at the low frequencies of seismic observations than at the higher frequencies of laboratory measurements; over yet longer timescales, the response of Earth materials to shear stresses merges into the viscous relaxation that controls tectonic motions. At the same time, changes in volume (e.g., due to pressure changes) create shear stresses and strains inside a composite medium (such as a polycrystalline or polymineralic rock), resulting in bulk attenuation due to the coupling with shear attenuation. The upshot is that both compressional and shear waves (and spheroidal and toroidal normal modes) can show evidence of attenuation and consequent dispersion at the low frequencies of seismic observations.

1.26.2.4 3D Lattice Dynamics: Polarization and Anisotropy

Only longitudinal elastic modes are possible in one dimension: shear elastic modes are higher-dimensional phenomena because the polarization (direction of atomic displacement) differs from that of propagation (wave vector). In three dimensions, there are three acoustic branches, one corresponding to the P-wave and two to the S-waves (Figure 2; the optic modes are discussed later). All solids support both longitudinal and shear waves. In the case of isotropic solids (glasses) and liquids, the two shear branches are indistinguishable (degenerate) despite corresponding to perpendicular polarizations. (Just as at low-enough deformation rates solids flow plastically, at high-enough frequencies, fluids transmit shear waves over finite distances.) For nonisotropic media (crystals and liquid crystals), the two shear branches are in general distinct, although they may be degenerate along certain high-symmetry directions (the two shear branches represent crystallographically orthogonal polarizations but, depending on crystal structure and propagation direction, do not in general represent exactly perpendicular displacements).

Anisotropy, the variation of elastic-wave velocity with propagation and polarization directions, is governed by the fourth-rank elastic-constant tensor, c_{ijkl} (Kosevich et al., 1986; Wallace, 1972). The polarizations and original slopes of the three acoustic branches for wave vector $\boldsymbol{k}$ are given by the Christoffel equation:

$$\rho V^2 = c_{ijkl}\hat{w}_i\hat{k}_j\hat{w}_k\hat{k}_l \qquad [6]$$

where w_i is the polarization vector and the carets indicate unit vectors. We have used the Einstein notation: summation over repeated subscripts, and each subscript takes on each of its values, $i = 1, 2, 3$ (e.g., x, y, and z directions). The symmetry of the elastic-constant tensor reflects that of the point group of the crystal (Nye, 1985). For an isotropic solid (glass), there are only two independent elastic constants, which may be taken as the bulk and shear moduli. For cubic crystals, there are three, c_{11}, c_{12}, and c_{44}, referred to as longitudinal, off-diagonal, and shear, respectively, and as many as 21 for the lowest-symmetry point group (triclinic crystals). Evaluating eqn [6] for pure P-wave propagation ($k = w$) in cubic symmetry,

$$\frac{\rho V_P^2}{c_{11}} = 1 + 2A\left(k_1^2k_2^2 + k_1^2k_3^2 + k_2^2k_3^2\right) \qquad [7]$$

where the anisotropy factor

$$A = \frac{2c_{44} - (c_{11} - c_{12})}{c_{11}} \qquad [8]$$

completely determines the P-wave anisotropy (Karki et al., 1997b). We have used the Voigt contraction for the indices of the elastic constants: $11 \to 1$, $22 \to 2$, $33 \to 3$, $12 \to 6$, $13 \to 5$, $23 \to 4$. One can show that A also determines the azimuthal and polarization shear anisotropy. The right side of eqn [7] gives $1 + 2/3A$, $1 + 2/9A$, and 1 for propagation along [1 1 1], [1 1 0], and [1 0 0], respectively.

We can evaluate the likely magnitude of single-crystal anisotropy if we assume that the interatomic forces are central and between nearest neighbors only and we neglect coupling between strain and vibrational modes. The elastic-constant tensor is then (Gieske and Barsch, 1968)

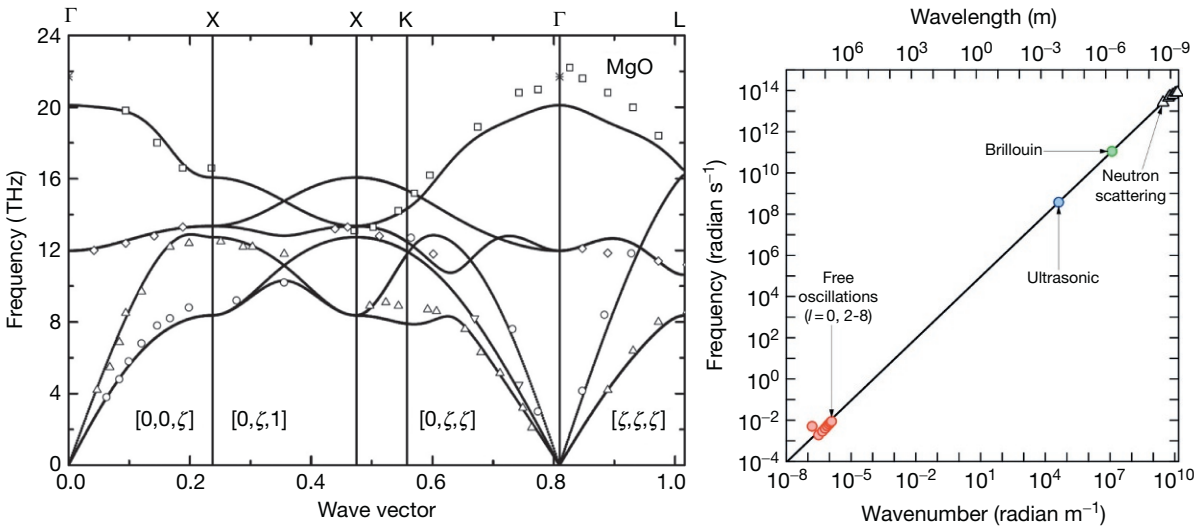

Figure 2 (left) Phonon dispersion curves of periclase (MgO) according to density-functional theory (lines) and experiment (symbols), showing the three acoustic modes with zero frequency at the Brillouin zone center (Γ point) and the three optic modes with finite frequency at Γ (some of the branches are degenerate – overlap – in all directions shown except for [0, ζ, ζ]). The direction of the wave vector is indicated in square brackets in each panel, the magnitude of the wave vector is given in units of $Å^{-1}$, and high-symmetry directions, defined in terms of the wave vector, are given conventional labels along the top (Lax, 1974). From Parlinski et al. (2000). (right) The longitudinal acoustic (LA, higher frequency) branch in the Γ–X direction plotted on a log–log scale: the black line and triangles have the same meaning as in the left-hand figure. Also shown are Brillouin spectroscopic measurements of the LA mode frequency at zero pressure plotted at the wave number of the laser probe (wavelength = 514.5 nm) and the observed frequency (green symbol) (Sinogeikin and Bass, 2000), the ultrasonic measurement of the P-wave velocity at zero pressure (blue symbol) (Jackson and Niesler, 1982), and the lowest-order spheroidal free oscillation modes of the Earth (red symbols) (Masters and Widmer, 1995). Reproduced from Stixrude L and Lithgow-Bertelloni C (2012) Geophysics of chemical heterogeneity in the mantle. *Annual Review of Earth and Planetary Sciences* 40: 569–595.

$$c_{ijkl} = (K - P)\frac{9}{z}\sum_{\alpha=1}^{z} \hat{r}_i^{\alpha}\hat{r}_j^{\alpha}\hat{r}_k^{\alpha}\hat{r}_l^{\alpha} \qquad [9]$$

where P is pressure, K is the bulk modulus, z is the coordination number, and $\hat{\mathbf{r}}^{\alpha}$ is the unit vector between an atom and its nearest neighbor α; the sum is over all nearest neighbors. For body-centered cubic (bcc) and face-centered cubic (fcc) crystal structures, eqn [9] yields positive values of A and therefore greater velocities along [1 1 1] and [1 1 0] than along [1 0 0]. The magnitude of the anisotropy is large: for fcc, $A = ½$, yielding peak-to-peak variations in the P-wave velocity of 30%. This simple model has been applied to oxides based on the argument that the elasticity is primarily governed by the oxygen sublattice and oxygen–oxygen repulsion, with the cations largely playing a passive, charge-balancing role.

The relative importance of central versus other interatomic forces can be deduced by comparing the elements of the elastic-constant tensor to the predictions of the Cauchy relations, which apply for purely central forces (**Figure 3**). (Angle-dependent and three-body forces are examples of noncentral interactions between atoms; Weiner (1983) showed more generally that for centrosymmetric crystals, the harmonic elastic moduli satisfy the Cauchy relations if the electron charge density follows the (homogeneous) deformation of the underlying lattice of nuclei.) For example, in a cubic material, the Cauchy relations predict

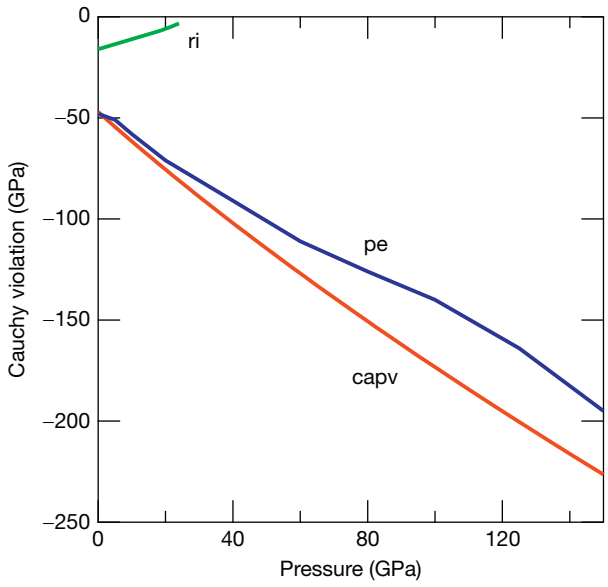

Figure 3 Violation of the Cauchy relation (eqn [10]) of three cubic minerals according to density-functional theory: spinel-structured Mg_2SiO_4, ringwoodite (ri); NaCl-structured MgO, periclase (pe); and perovskite-structured $CaSiO_3$ (capv) (Karki and Crain, 1998; Karki et al., 1997b; Kiefer et al., 1997). Reproduced from Stixrude L and Lithgow-Bertelloni C (2012) Geophysics of chemical heterogeneity in the mantle. *Annual Review of Earth and Planetary Sciences* 40: 569–595.

$$c_{12} - c_{44} = 2P \qquad [10]$$

In the case of MgO, often considered to be a prototypical ionic solid for which one expects central forces to be dominant, eqn [10] is increasingly violated with increasing pressure (Isaak et al., 1990; Karki et al., 1997b). This shows that the interatomic forces become increasingly noncentral with increasing pressure, as expected from comparisons of elastic moduli among several oxides of the same crystal structure. One consequence of this change in forces is that the sign of the elastic anisotropy changes with increasing pressure (Figure 4). Whereas at low pressure, A is large and positive, in accord with expectations based on eqn [9] and the fcc oxygen sublattice of MgO, at high pressure, A becomes negative, with a magnitude at the core–mantle boundary greater than that at ambient pressure. The change in sign of A corresponds to a change in the fastest and slowest directions: [1 1 1] is fastest for P-wave propagation at ambient pressure, whereas [1 0 0] is fastest at the core–mantle boundary. Other minerals also show strong pressure dependence of the magnitude and sense of the anisotropy (Karki et al., 2001).

Considerations of mechanical stability place constraints on the relative magnitude of the elastic constants of any material, whether single crystals or rocks. For isotropic symmetry, the stability condition is simply that the bulk and shear moduli be positive definite. For cubic symmetry, the conditions are

$$c_{44} > 0, \quad c_{11} > |c_{12}|, \quad c_{11} + 2c_{12} > 0 \qquad [11]$$

and for hexagonal symmetry,

$$c_{44} > 0, \quad c_{11} > |c_{12}|, \quad (c_{11} + c_{12})c_{33} > 2c_{13}^2 \qquad [12]$$

The more general statement from which stability conditions for arbitrary symmetry derive is that the principal minors of the elastic-constant matrix (Voigt notation) must be positive definite (Nye, 1985). Elastic instabilities place fundamental constraints on the phases that exist in the Earth. For example, it has been argued that the predicted elastic instability in the bcc phase of iron means that this phase cannot exist in the inner core, with important implications for the origin of anisotropy in this region (Stixrude et al., 1994). More recent experimental and theoretical work shows that there is no evidence of bcc Fe being stable at inner-core conditions (e.g., Ping et al., 2013).

One of the most fundamental conclusions from experimental and theoretical studies of minerals is that the elastic anisotropy of individual crystals is much larger than that observed seismologically in most parts of the Earth, albeit over much greater length scales ($\sim 10^3$–10^6 m) as compared with crystal dimensions ($\sim 10^{-3}$–10°m). Peak-to-peak azimuthal variation in velocities of 10% or more is typical in mantle and core minerals, as compared with a few percent in the Earth. The single-crystalline anisotropy of some minerals is sufficiently large to produce cusps in the group velocity envelope (Helbig, 1984) (Figure 5). Experimental measurement and prediction of the single-crystal anisotropy is essential because it forms the basis for estimating the anisotropy of rocks and places an upper bound on the observed elastic anisotropy that can be produced by lattice-preferred orientation. Most of the experimental methods discussed previously are capable of measuring the full elastic-constant tensor and therefore the velocity in all directions. These measurements must be made on single crystals. In the case of Brillouin or ultrasonic interferometry, several measurements are necessary, varying the direction of the impulse with respect to the crystallographic axes in order to sample different directions in reciprocal space.

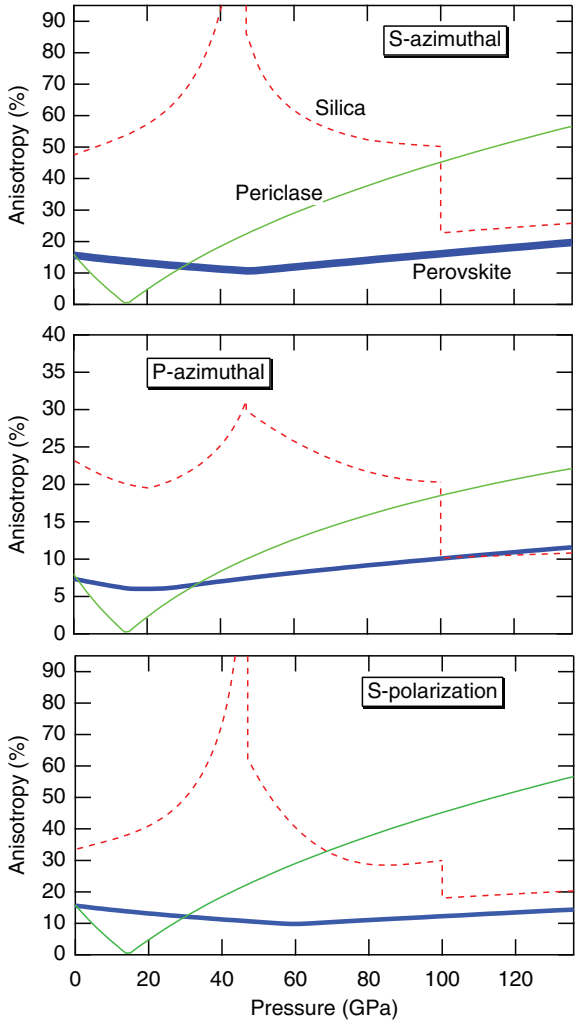

Figure 4 Elastic anisotropy of SiO_2 (red dashed curves), MgO periclase (light green solid), and $MgSiO_3$ perovskite (bold blue solid) according to density-functional theory. P-azimuthal anisotropy and S-azimuthal anisotropy are the differences between the maximum and the minimum P- and S-wave velocities, respectively, over all propagation and polarization directions, and the polarization anisotropy is the maximum difference in velocity between the two S-wave polarizations over all propagation directions. The discontinuous changes in the curve for SiO_2 are due to phase transformations from stishovite to the $CaCl_2$ structure at 47 GPa and to the α-PbO_2 structure at 100 GPa. Breaks in slope in the MgO and $MgSiO_3$ curves represent pressures at which the pattern of anisotropy changes. In the case of MgO, the break in slope near 15 GPa coincides with a vanishing of the anisotropy that is due to a change in sign of the anisotropy factor A (eqn [8]). Reproduced from Stixrude L (1998) Elastic constants and anisotropy of $MgSiO_3$ perovskite, periclase, and SiO_2 at high pressure. In: Gurnis M, et al. (eds.) *The Core-Mantle Boundary Region*, pp. 83–96. Washington, DC: American Geophysical Union.

What is the origin of anisotropy in the mantle and core? There are at least two possible explanations, shape-preferred orientation and lattice-preferred orientation. These two

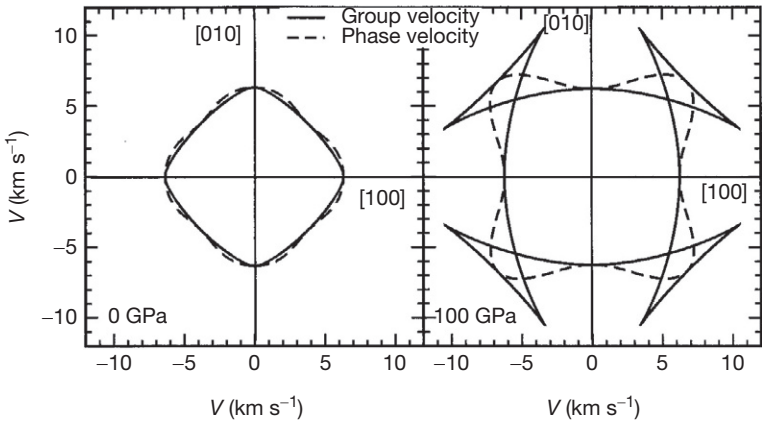

Figure 5 Group velocity (solid curves) and phase velocity (dashed curves) surfaces of S-waves in MgO in the (001) plane at two pressures. The two velocities are close to each other at zero pressure due to relatively weak anisotropy, but they differ substantially at 100 GPa due to relatively strong anisotropy. Reproduced from Kark BB, Stixrude L, and Wentzcovitch RM (2001) High-pressure elastic properties of major materials of Earth's mantle from first principles. *Reviews of Geophysics* 39: 507–534.

mechanisms for generating anisotropy in a polycrystalline aggregate arise in principle from very different sets of processes and so carry important implications for our understanding of mantle dynamics and evolution. In the case of lattice-preferred orientation, anisotropy originates in the elastic anisotropy of the constituent crystals and is in general present for single- as well as multiphase aggregates. Since the single-crystal anisotropy can be large, it is natural to consider lattice-preferred orientation as the primary explanation in many cases (Figure 4). Knowledge of the single-crystal elastic anisotropy is not sufficient to determine that of a polycrystalline aggregate, however. For this, one must also know the texture, that is, the orientations of all the crystals in the aggregate.

Shape-preferred orientation arises from an inhomogeneous distribution of phases with different elastic properties. Anisotropy due to shape-preferred orientation scales with the contrast in physical properties between the phases and therefore applies only to multiphase aggregates (composites). It can be large, for example, in cracked or partially molten rock. In the limit of large scales, variations of rock types (lithologic variations) can induce anisotropy that affects seismic waves.

Presumably, both shape-preferred orientation and lattice-preferred orientation cause seismic anisotropy within the Earth. That the observed anisotropy is quantitatively much smaller than could be expected based on laboratory and theoretical studies of individual minerals and mineral aggregates strongly suggests that the seismological information is spatially aliased. That is, the seismic wavelengths ($\sim 10^3$–10^6 m) are typically so much longer than the dimensions of crystals, or even lithologic variations, that they reflect only a broad spatial average of the true heterogeneity and anisotropy at depth.

1.26.2.5 Nontrivial Crystal Structures, Optic Modes, and Thermodynamics

Lattice vibrations are geophysically significant not only for their connection to elasticity but also because they govern most thermodynamic properties of Earth materials, including the magnitude of entropy and heat capacity as well as the temperature dependence of the elastic constants. Most of the temperature dependence of the energy of a crystal comes from the increasing energy of atomic vibrations with increasing temperature. The derivation of the internal energy due to lattice vibrations is outlined in the texts listed earlier. Here, we seek an intuitive understanding, simply quoting the result for the internal energy associated with atomic vibrations:

$$U_{\text{vib}} = \frac{1}{2}\sum_i \hbar\omega_i + k_{\text{B}}T\sum_i \frac{\hbar\omega_i/k_{\text{B}}T}{e^{\hbar\omega_i/k_{\text{B}}T} - 1} \qquad [13]$$

where $\hbar$ is Planck's constant divided by 2π, k_{B} is Boltzmann's constant, and the sums are over all $3N$ vibrational modes (in 3D) with N being the number of atoms in the crystal. The first term is due to zero-point motion and can be attributed to the Heisenberg uncertainty principle. The second term is the product of the energy of a particular vibrational mode ($\hbar\omega$) and the probability of excitation ('occupation') of that mode. The probability of occupation may appear unfamiliar because it is derived from the appropriate quantum (Bose–Einstein) statistics, but it does reduce to the Boltzmann factor $\exp(-\hbar\omega/kT)$ in the limit of high temperatures. The probability of occupation says that while very high-frequency modes (such as the stretching of the O—H bond) will barely be excited until one reaches mantle temperatures, the part of the acoustic branch near the Brillouin zone origin (i.e., wavelengths much larger than the interatomic spacing) is already fully excited even at room temperature.

Eventually, all vibrational modes are fully excited, and the second sum on the right-hand side approaches a constant, equal to the number of modes ($3N$). In this Dulong–Petit limit, the vibrational energy is linear in temperature, and the heat capacity at constant density approaches a constant value

$$C_\rho = \left(\frac{\partial U_{\text{vib}}}{\partial T}\right)_\rho \rightarrow 3Nk_{\text{B}} \qquad [14]$$

or 1188 J K^{-1} g^{-1} for a mean atomic mass typical of the mantle (21 g mol^{-1}). Vibrational frequencies of Earth materials are such that the Dulong–Petit limit is obeyed to within a few percent at temperatures typically reached beneath the crust.

A practical difficulty in using eqn [13] is that all the vibrational frequencies must be known, which is rarely the case for mantle phases, particularly at high pressure. By reformulating as a sum over energies rather than states, with the energy of a mode of frequency ω_ι being given by $\hbar\omega_\nu$ we reestablish the connection with the analysis of phonon dispersion outlined earlier and develop a useful starting point for approximating the sums. The vibrational energy can then be written as

$$U_{\text{vib}} = k_{\text{B}}T\int_0^\infty \left(\frac{1}{2}+\frac{1}{e^{\hbar\omega/k_{\text{B}}T}-1}\right)\frac{h\omega}{k_{\text{B}}T}g(\omega)\,\mathrm{d}\omega \qquad [15]$$

where the vibrational density of states $g(\omega)$ (see Figure 2) is normalized such that

$$3N = \int_0^\infty g(\omega)\,\mathrm{d}\omega \qquad [16]$$

The power of this reformulation is illustrated by one of the simplest approximations for $g(\omega)$, due to Debye:

$$g(\omega) = 9N\omega^2\omega_{\text{D}}^{-3} \qquad [17]$$

This is derived by treating the material as a homogeneous continuum: that is, ignoring optic modes (described later) and approximating the acoustic phonon branch as linear with slope equal to the acoustic velocity (see eqn [3]; for this case without dispersion, $\omega \propto k$, and because $g(\omega) \propto k^2$ in 3D, it is proportional to ω^2 as in eqn [17]). The quantity ω_{D} is the Debye frequency, obtained by linearly extrapolating the acoustic branch to the Brillouin zone edge and ensuring that eqn [16] is satisfied. (Ensuring that only $3N$ normal modes, i.e., $3N$ degrees of freedom, are present for a crystal of N atoms in 3D takes into account the atomic constituents of the medium. It was Debye's genius to realize that a self-inconsistent model of a homogeneous continuum with underlying atomic structure would lead to a physically sound result.) In three dimensions, the velocity is replaced by an appropriate average over all directions and polarizations and the bond length by the mean atomic spacing. The squared-frequency dependence arises from the assumptions that the density of vibrational states is uniform in reciprocal space and that the first Brillouin zone is a sphere. The Debye approximation captures much of the essential features of the heat capacity, including the observation that it vanishes at zero temperature as T^3 and approaches the Dulong–Petit limit at high temperature.

Simple approximations to the vibrational density of states, like the Debye approximation, do not explicitly account for the structural complexity characteristic of most Earth materials: in particular, several different atoms are typically present in each unit cell of the crystal structure (e.g., Mg and O in MgO). What influence do these complexities have on the normal modes of vibration? The essential features are captured by a linear chain but now with two different spring constants (see also Kieffer, 1979) (Figure 6). The broken symmetry doubles the unit cell (i.e., two atoms, one of each color in each unit cell vs. one atom per unit cell in the monatomic linear chain) and halves the first Brillouin zone. The relationship of the monatomic and diatomic unit cells in reciprocal space is one of folding the phonon branches so that the vibrational mode that appeared on the Brillouin zone edge in the monatomic case is now folded back to the Brillouin zone center. This is significant

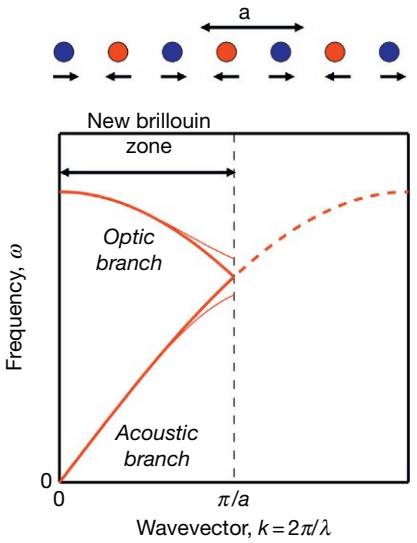

Figure 6 Phonon dispersion curve in a 1D lattice with two types of atoms. The unit cell dimension a is doubled compared with the monatomic case, which halves the size of the reciprocal-space Brillouin zone and folds the dispersion curve, producing an optic branch. The pattern of vibration of the optic mode at zero wave vector is illustrated (top); note that each unit cell has the identical pattern of vibration. The thin solid lines schematically illustrate the opening of an acoustic–optical gap that is produced if the lattice contains two different force constants or if the atoms have different masses. Reproduced from Stixrude L and Lithgow-Bertelloni C (2012) Geophysics of chemical heterogeneity in the mantle. *Annual Review of Earth and Planetary Sciences* 40: 569–595.

because now, we have a vibrational mode of finite frequency at the Brillouin zone center; as this can be observed with long-wavelength probes such as visible light, it is called an optic branch. In general, there are $3n$ mode frequencies at each wave number k in a 3D crystal structure having n atoms per unit cell. To be precise, we refer to the 'primitive' (smallest and irreducible) unit cell throughout this text. Other definitions of the crystallographic unit cell are often used for convenience.

Now, consider what happens when the difference in the two spring constants begins to grow or the masses of the two atoms in the unit cell are allowed to differ (Figure 6). The frequencies of the two normal modes at the Brillouin zone edge begin to separate, as is seen by considering the patterns of vibration. This zone-edge splitting appears whenever the material has bonds of different strength. So, for example, the contrast between the strong Si—O bond and the weaker inter-tetrahedral forces in quartz causes large zone-edge splittings and a clear separation of acoustic and optic modes. Periclase, for which the contrast in bond strengths is much less, shows almost no acoustic–optic gap (in detail, nonnearest neighbor and noncentral forces open a gap even in periclase along certain high-symmetry directions; electron-polarization effects can also play an important role in shifting longitudinal-relative to transverse-optic modes).

In any case, at a given wave vector, we always have three acoustic modes and $3n-3$ optic modes (n is the number of atoms in the unit cell), and all the branches have to have zero slope (standing waves) at the Brillouin zone edge, as is also the

case for optic modes at the zone center. It is also known that longer-range interactions add structure to the ω–k dispersion relation: essentially, each successive coordination shell adds a Fourier component to the mode branch (Gonze et al., 1994).

In the limit of no optical gap, the vibrational density of states may be reasonably approximated by the Debye relation (eqn [17]), regardless of how many atoms are in the unit cell, as the main modification of phonon dispersion is Brillouin zone folding. This realization has led to the concept of Debye-like solids, periclase and corundum being prototypical examples (Anderson, 1995). Materials like quartz and those containing hydrogen bonds are typical counterexamples, for which more elaborate models such as those due to Kieffer are more appropriate (Kieffer, 1980). Even when deviations from a Debye-like spectrum are large, the influence on thermochemical properties is not necessarily significant because these depend at high temperature only on low-order moments (weighted averages) of the vibrational density of states (Barron et al., 1957) (**Figure 7**). Deviations are likely to be largest for water-rich hydrous phases, because the stretching frequency for the O—H bond is so much larger than for any other bond thought to be important in the mantle (Williams, 1995). The essential relationship between acoustic and optic branches has also led to the idea of determining an average elastic-wave velocity from a measurement of the appropriate optic mode at the Brillouin zone center (Merkel et al., 2000).

Thermal expansion arises, in a first approximation, from the volume dependence of the vibrational frequencies (quasiharmonic model). This modification of the theory retains the normal-mode description of the frequencies but allows the frequency spectrum to shift with compression. Anharmonicity generally refers to time dependence of the normal modes (e.g., due to mode mixing) and accounts for physical effects such as temperature dependence of the vibrational frequencies at constant volume that are not explained by quasiharmonic theory (Gillet et al., 1996).

As the crystal compresses, bonds generally become stronger; the vibrational frequencies increase; and, from eqn [13], the vibrational energy decreases. The volume dependence of the vibrational energy produces a vibrational pressure that is positive and tends to expand the lattice. The vibrational or thermal pressure is

$$P_{\text{vib}} = \gamma \rho U_{\text{vib}} \qquad [18]$$

where the Grüneisen parameter is defined by

$$\gamma \equiv \frac{1}{\rho}\left(\frac{\partial P}{\partial U}\right)_{\rho} = \frac{\alpha K_{\text{T}}}{\rho C_{\rho}} = \left(\frac{\partial \ln T}{\partial \ln \rho}\right)_{\text{S}} \qquad [19]$$

and the second and third relations are thermodynamic identities. This makes explicit the relationship between thermal pressure and thermal expansivity α and also shows that the Grüneisen parameter controls the magnitude of the adiabatic temperature gradient (right-hand side of eqn [19]). For models of the vibrational density of states with a single characteristic frequency, such as the Debye or Einstein approximations or, more generally, under the Grüneisen approximation that the logarithmic density dependence of all vibrational frequencies is equal, the following relation also holds:

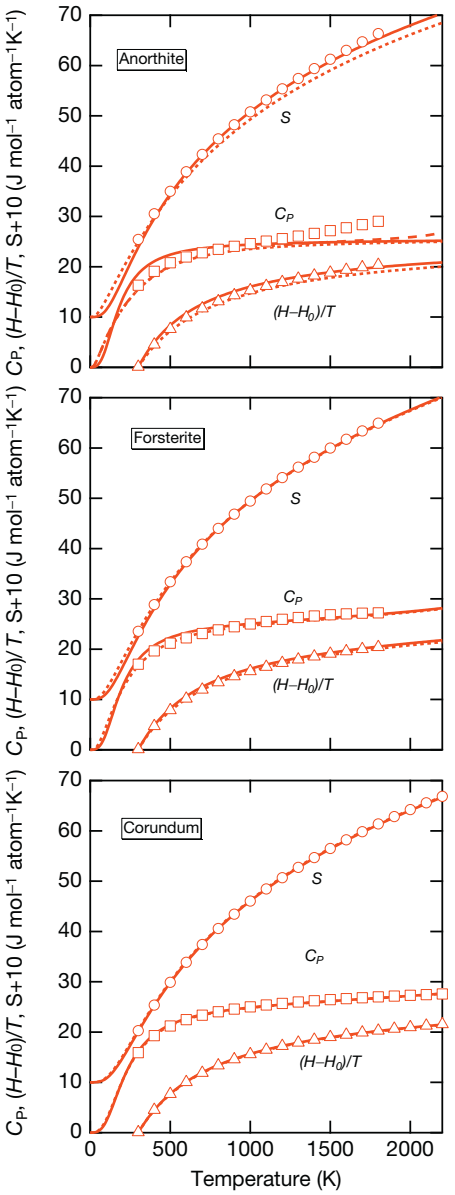

Figure 7 Experimentally derived (Robie and Hemingway, 1995) entropy (circles), heat capacity (squares), and enthalpy function (triangles) compared with (solid lines) Debye model with effective Debye temperature fit to the entropy at 1000 K and (short dashed) the model of Kieffer (1980). For anorthite, the long-dashed line shows the influence of cation disorder on the heat capacity according to the model of Holland and Powell (1998). The entropy is shifted upward for clarity. Reproduced from Stixrude L and Lithgow-Bertelloni C (2005) Thermodynamics of mantle minerals – I. Physical properties. *Geophysical Journal International* 162: 610–632.

$$\gamma = \frac{\partial \ln \omega}{\partial \ln \rho} \qquad [20]$$

establishing the link between quasiharmonic thermal properties such as thermal expansivity and the density dependency of the normal modes of the lattice. The Grüneisen parameter is dimensionless and empirically found to be about 1–3, so is a convenient way of capturing many related influences of

temperature on the physical properties of minerals inside a planet (Mcqueen et al., 1970; Stixrude and Lithgow-Bertelloni, 2005a, 2011; Wallace, 1972). In particular, the thermal expansivity is of geophysical interest because this is the property causing buoyancy, hence driving convection, inside a planet.

To introduce the influence of temperature on the elastic constants, consider the vibrational contribution to the bulk modulus. Taking the density derivative of eqn [18], we see that the temperature dependence of the elastic constants involves not only the Grüneisen parameter, which we assume to depend only on volume, but also the volume derivative

$$q = -\frac{\partial \ln \gamma}{\partial \ln \rho} \qquad [21]$$

where the parameter q is dimensionless and takes on values in the range 1–3 for most mantle phases (McQueen et al., 1967; Stixrude and Lithgow-Bertelloni, 2005a, 2011). The thermal pressure at temperatures above the Debye temperature can be approximated by

$$P_{\mathrm{TH}} \approx 3nRT\gamma\rho \qquad [22]$$

and the thermal contribution to the adiabatic bulk modulus along an isochore is then just the logarithmic density derivative of eqn [22] at conditions of constant entropy

$$K_{\mathrm{TH}} \approx 3nRT\rho\gamma(\gamma + 1 - q) \qquad [23]$$

An important consequence of the fact that $q \geq 1$ for most mantle materials is that the thermal pressure and other thermal effects tend to decrease with compression. For example, the thermal expansivity and the influence of temperature on the elastic-wave velocities decrease with depth, with important implications for mantle dynamics and the interpretation of seismic tomography (Chopelas and Boehler, 1989; Isaak et al., 1992).

Because the Grüneisen parameter plays such a central role in our understanding of the thermal state of the Earth, there has been a great deal of interest in determining its dependence on compression. Many experimental data are consistent with the assumption that q is constant without necessarily requiring it (McQueen et al., 1967). Experimental analyses and theoretical studies suggest that q tends to decrease with compression (Agnon and Bukowinski, 1990; McQueen et al., 1970; Speziale et al., 2001), and analytical forms that capture this behavior have been examined (Jeanloz, 1989; Oganov and Dorogokupets, 2003; Stixrude and Lithgow-Bertelloni, 2005a).

1.26.2.6 Influence of Pressure and Temperature on the Elastic Constants

An important feature of the Earth is that compressions are large – the characteristic pressure is a large fraction of typical zero-pressure values of mineral bulk moduli – and the characteristic temperature is larger than typical vibrational energies of Earth materials. This means that measurements of the pressure and temperature derivatives of the elastic constants near ambient conditions do not suffice to give us a full picture of the variation of these quantities over the conditions of the Earth's interior. Indeed, experimental measurements show that the bulk modulus varies by more than a factor of 2 over the pressure range of the mantle. Such large changes are seen in the density and other properties too and led Birch to apply the theory of Eulerian finite strain to understand the Earth's interior. The theory of finite strain has been generalized to encompass the elastic constants (Davies, 1974) and has recently been reformulated in a thermodynamically self-consistent manner (Stixrude and Lithgow-Bertelloni, 2005a). Only the final results are discussed here.

The variations of the bulk and shear moduli with volume and temperature are, respectively,

$$K = (1+2f)^{5/2}\left[K_0 + (3K_0K_0' - 5K_0)f + \frac{27}{2}\left(K_0K_0'' - 4K_0\right)f^2\right] + (\gamma + 1 - q)\gamma\rho\Delta U_{\mathrm{vib}} - \gamma^2\rho\Delta(C_{\mathrm{V}}T) \qquad [24]$$

$$G = (1+2f)^{5/2}\left[G_0 + (3K_0G_0' - 5G_0)f + \left(6K_0G_0' - 24K_0 - 14G_0 + \frac{9}{2}K_0K_0'\right)f^2\right] - \eta_{\mathrm{S}}\rho\Delta U_{\mathrm{vib}} \qquad [25]$$

where f is the Eulerian strain measure

$$f = \frac{1}{2}\left[\left(\frac{V}{V_0}\right)^{-2/3} - 1\right] \qquad [26]$$

and subscript 0 indicates the value of a quantity at the reference state (e.g., ambient conditions), primes indicate pressure derivatives, and Δ indicates the difference between the temperature of interest and the temperature of the reference state. The quantity η_{S} takes on positive values near unity for mantle phases and derives from the shear part of the fourth-rank tensor formed from the strain derivative of the tensorial generalization of γ, which we have assumed to be isotropic. Taking typical values of γ and q (1 and 2, respectively), the temperature-dependent terms show that both moduli decrease with increasing temperature at constant volume. The decrease with increasing temperature at constant pressure is greater than that at constant volume according to

$$\left(\frac{\partial M}{\partial T}\right)_{\mathrm{P}} = \left(\frac{\partial M}{\partial T}\right)_{\mathrm{V}} - \rho C_{\mathrm{V}}\gamma M_0' \qquad [27]$$

where M stands for either the bulk or the shear modulus.

Finite-strain theory suggests systematic relationships between the values of the pressure derivatives of the elastic constants and the moduli themselves (Karki et al., 2001). It has been known for some time that the Eulerian finite strain theory owes its success at least in part to that fact that it rapidly converges to experimentally measured equations of state with increasingly higher orders of the finite strain. In fact, for many materials, the lowest-order terms suffice. The term linear in f in the normalized equation of state vanishes when $K_0' = 4$, a value that is typical of mantle phases and many other materials as well. We may take the same approach in the case of eqns [24] and [25] and ask what relationships are implied by the vanishing of the term linear in f within the square brackets. In the case of the shear modulus, this yields a relationship between the pressure derivative of G and the ratio of shear modulus to bulk modulus, which is satisfied approximately for mantle phases (Stixrude and Lithgow-Bertelloni, 2005a). The temperature

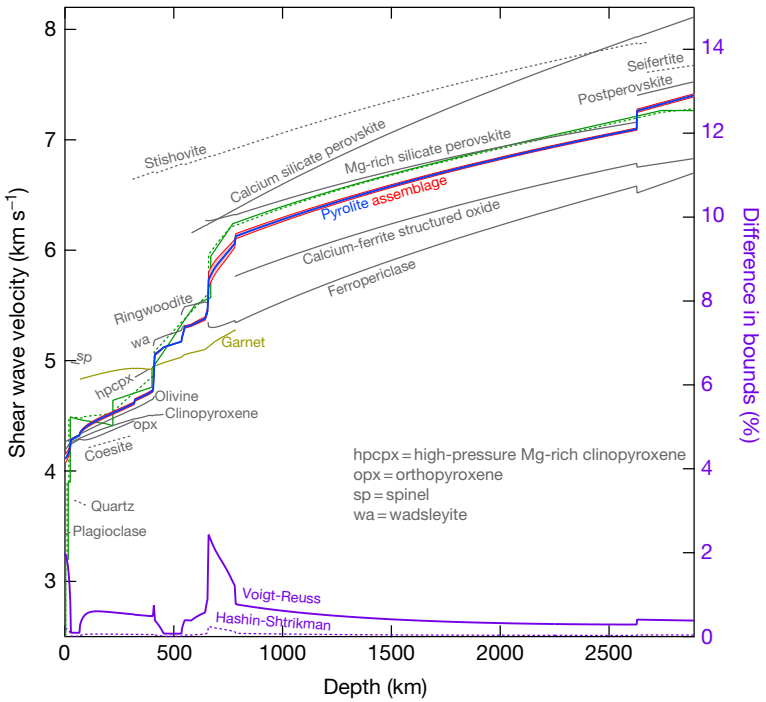

Figure 8 Velocities of mantle phases (gray lines), a pyrolite assemblage (blue with red envelope indicating Voigt–Reuss bounds), and the difference between Voigt–Reuss bounds (solid purple line) and Hashin–Shtrikman bounds (dashed purple line) on the velocity of the assemblage (purple, right-hand axis) along a self-consistently computed 1600 K isentrope. The velocity of phases is plotted over their pressure range of stability. Silica phases are not stable in pyrolite and are shown for comparison. Green lines are radial seismological models: (solid) PREM (Dziewonski and Anderson, 1981) (dashed) AK135 (Kennett and Engdahl, 1991). Computed with HeFESTo (Stixrude and Lithgow-Bertelloni, 2011). Reproduced from Stixrude L and Lithgow-Bertelloni C (2012) Geophysics of chemical heterogeneity in the mantle. *Annual Review of Earth and Planetary Sciences* 40: 569–595.

derivative of the shear modulus scales with the value of the shear modulus itself (Stixrude and Lithgow-Bertelloni, 2005a).

We can relate the elastic moduli of mantle phases to those found seismologically via a compilation of experimental and theoretical results for the parameters appearing in eqns [24] and [25] (**Figure 8**). Comparison with seismological observations tends to support the standard model of a homogeneous peridotite composition for the entire mantle. Peridotite is a rock primarily composed of the mineral olivine. Model mantle compositions, based on comparison with seismology, the genesis of magmas, and the analysis of mantle xenoliths, typically contain 50–60% olivine and lesser amounts of orthopyroxene, clinopyroxene, and garnet. Peridotites produce a series of phase transformations with increasing depth: the velocity of the upper mantle is spanned by that of olivine, orthopyroxene, clinopyroxene, and garnet; in the shallow transition zone (410–520 km), by clinopyroxene, majorite, and wadsleyite; and in the deep transition zone (500–660 km), by Ca-perovskite, ringwoodite, and majorite. Velocities in the lower mantle are spanned by those of Mg-perovskite, magnesiowüstite, and Ca-perovskite. In the upper mantle and transition zone, we find that the change in shear-wave velocity due to phase transformations exceeds the influence of pressure on the velocity of any one phase. This suggests the essential role that phase transformations play in producing the anomalous velocity gradient of the transition zone and emphasizes the importance of going beyond the elasticity of individual minerals in understanding mantle structure, as we will discuss further in the next section.

One of the most remarkable patterns in the temperature and compositional derivatives of the elastic moduli, aside from the large influence of compression discussed earlier, is the large difference between garnet–majorite and other phases (**Figure 9**). The compositional derivative for garnet and majorite (and clinopyroxene) is only a third those of olivine and orthopyroxene, while the temperature derivatives of garnet and majorite are approximately half those of olivine and orthopyroxene. The contrast in compositional derivatives can be traced directly to the shear modulus of Mg and Fe end-members of the phases: while the shear modulus of fayalite is 40% less than that of forsterite, that of almandine is actually slightly greater than that of pyrope, partially offsetting the effect of the greater density of almandine on V_S. The contrast in temperature derivatives can be related to experimental measurements of dG/dT of the dominant species: 8 and 9 MPa K^{-1} for pyrope and majorite, respectively, compared to 15 MPa K^{-1} for forsterite. One consequence of the unusual properties of garnet is that the influence of temperature and iron content is sensitive to bulk composition. Specifically, more garnet-rich compositions, such as basalt, are less sensitive to variations in temperature or iron content than garnet-poor bulk compositions such as harzburgite (Speziale et al., 2005). (Basalt is a rock primarily composed of pyroxene and plagioclase feldspar that makes up most of the oceanic crust and is produced by partial melting of the mantle. Harzburgite is a rock that is richer in olivine than the average mantle and is thought to be the residuum of partial melting of the mantle.)

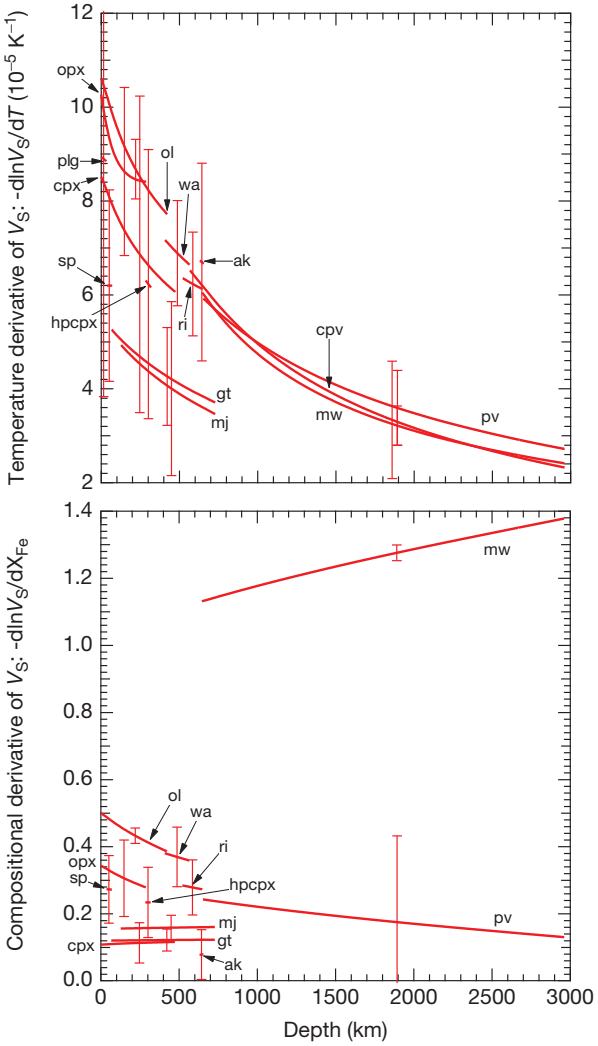

Figure 9 Variation of the shear-wave velocity with respect to (top) temperature and (bottom) composition. Reproduced from Stixrude L and Lithgow-Bertelloni C (2005) Thermodynamics of mantle minerals – I. Physical properties. *Geophysical Journal International* 162: 610–632.

1.26.3 Rock Elasticity

1.26.3.1 Overview

Knowledge of mineral elasticity is necessary for estimating the elastic properties of a rock, but it is not sufficient. There are two primary considerations. The first is that rocks are heterogeneous. In the mantle, this heterogeneity is most pronounced at the grain scale (1–10 mm): every part of the mantle is made of several different mineral phases, each with different elastic properties. The difference in elastic properties between coexisting minerals is generally larger than that between different mantle rock types. The second difficulty is that minerals tend to be preferentially aligned by deformation. The alignment is neither perfect, in which case the elasticity would reduce to that of a single crystal, nor negligible. Indeed, the detection of preferential alignment via the resulting anisotropic propagation of seismic waves is one of our most powerful potential probes of mantle flow.

In principle, one needs to know – in addition to the elastic-constant tensors of the constituent minerals – the location, size, shape, and orientation of each mineral grain in the assemblage. But such a detailed description is neither practical nor useful: a part of the Earth's mantle the size of a typical mantle body wave (100 km) contains on the order of 10^{21} individual mineral grains, assuming 1 cm grains! This is another statement of the spatial aliasing problem described earlier. Model statistical distributions of mineral geometry play an important role, in particular in the analysis of preferred orientation. Idealizations, in which either the preferred orientation or the spatial inhomogeneity, or both, is simplified and permits exact solutions or rigorous bounds, are also important.

Additional complications arise at finite frequency: Dissipative mechanisms exist in aggregates that are not present in single crystals, and these are thought to be important for producing attenuation and dispersion in the mantle, particularly at grain boundaries.

1.26.3.2 Composites Theory

Consider first a homogeneous isotropic medium, corresponding to a glass or a liquid. The elasticity is completely characterized by two elastic constants, which may be taken to be the bulk modulus, K, and shear modulus, G. The longitudinal and shear-wave velocities for all propagation and polarization directions are

$$V_P = \sqrt{\frac{K + 4/3G}{\rho}} \quad V_S = \sqrt{\frac{G}{\rho}} \qquad [28]$$

where ρ is the density and, in the case of a liquid deformed on a timescale long compared with its Maxell relaxation time, $G = 0$.

Consider an inhomogeneous system consisting of N isotropic phases with distinct elastic properties, such that phase α has bulk and shear moduli K^α and G^α and $\alpha = 1,\ldots,N$. Suppose that the only properties of the grain geometry we know are the volume fractions of the phases ϕ^α. The volume fraction is the only feature that is uniquely determined by the usual equilibrium thermodynamics and is thus independent of the history of the sample. The stress and strain tensors are now functions of position:

$$\sigma_{ij}(\mathbf{x}) = c_{ijkl}(\mathbf{x})\varepsilon_{kl}(\mathbf{x}) \qquad [29]$$

$$\varepsilon_{ij}(\mathbf{x}) = s_{ijkl}(\mathbf{x})\sigma_{kl}(\mathbf{x}) \qquad [30]$$

where the compliance tensor is the inverse of the elastic-constant tensor:

$$s_{ijkl} = c^{-1}_{ijkl} \qquad [31]$$

The volume average stress and strain of the rock are assumed related to that in each of the phases by

$$\bar{\sigma}_{ij} = \sum_\alpha \phi^\alpha \bar{\sigma}^\alpha_{ij} \qquad [32]$$

$$\bar{\varepsilon}_{ij} = \sum_\alpha \phi_\alpha \bar{\varepsilon}^\alpha_{ij} \qquad [33]$$

where the bars indicate volume averages. We define the effective elastic moduli of the composite as

$$\bar{\sigma}_{ij} = c^*_{ijkl}\bar{\varepsilon}_{kl} \qquad [34]$$

If we assume that the average stress and strain in each phase are a unique function of the average stress and strain, respectively, of the aggregate, then it is possible to show that the values of c^* are bounded such that

$$M^*_R = \left(\sum_\alpha \frac{\phi^\alpha}{M^\alpha}\right)^{-1} < M^* < \sum_\alpha \phi^\alpha M^\alpha = M^*_V \qquad [35]$$

where M refers to either K or G and the bounds M^*_R and M^*_V correspond, respectively, to the assumption that the stress (Reuss bound) and strain (Voigt bound) are homogeneous throughout the composite (Hill, 1963; Watt et al., 1976). Except in special geometries, neither of these approximations is correct: the assumption of constant stress requires the opening of gaps between grains, while the assumption of constant strain violates mechanical equilibrium. Indeed, the assumptions embedded in eqns [32] and [33] are in general not justifiable, and one of the complications of composites theory is that the stress tensor can no longer be treated as symmetric (e.g., Juanzemis, 1967).

Ignoring these complications, the Voigt and Reuss bounds limit the possible degree of anisotropy due to inhomogeneous arrangement of phases. This type of anisotropy is sometimes referred to as shape-preferred orientation. Plane layering is the classic example for which Voigt and Reuss bounds can be realized (Backus, 1962). The P-wave velocity for waves propagating normal to the layers is $\rho V_P^2 = K_R + 4/3G_R$, while that for propagation parallel to the layers is $\rho V_P^2 = K_V + 4/3G_V$. Thus, heterogeneity produces anisotropy. This relationship has been examined on the atomic level as well. There are several crystal structures in which layers of more compressible units, for example, Mg coordination polyhedrons, alternate with layers of stiffer units such as Si polyhedrons. Such alternation leads to the large anisotropy of the olivine structure (Hazen et al., 1996; Wentzcovitch and Stixrude, 1997).

For illustration, we compare the Voigt and Reuss bounds of a typical mantle lithology (peridotite) in **Figure 8**. The bounds are wide in the shallow mantle due to the extremely low velocity of plagioclase and in the vicinity of the 660 km discontinuity due to the much higher velocity of perovskite than garnet, whereas they are nearly coincident in the shallow transition zone where wadsleyite and garnet have similar velocities. In the lower mantle, the bounds differ by less than 2% and by less than 1% at the core–mantle boundary. These results suggest that shape-preferred orientation in subsolidus peridotites is unlikely to be the source of anisotropy in the D" layer at the base of the mantle, as has previously been proposed on the basis of the contrast in elastic properties between perovskite and periclase (Karato, 1998).

It is not possible to estimate more precisely the value of the effective elastic moduli without further information. It is common in the literature to quote the so-called Voigt–Reuss–Hill mean, which is simply the arithmetic mean of the Voigt and Reuss bounds (Hill, 1952). This value is not rigorously justified as a best estimate of the actual effective moduli.

With further assumptions about the distribution of the phases, it is possible to derive narrower bounds. The Hashin–Shtrikman analysis (Hashin and Shtrikman, 1963) assumes that the distribution of phases is statistically random and that the elastic properties of the aggregate are given as a solution to a variational problem. So, for example, regular arrangements such as layering are excluded. The Hashin–Shtrikman bounds, given in compact form by Berryman (1995), are narrower than the Voigt–Reuss bounds in most cases, including for the mantle (**Figure 8**). Watt et al. (1976) recommend that the Hashin–Shtrikman bounds should generally be used in reporting the elastic properties of multiphase materials, rather than the Voigt–Reuss bounds, or the VRH average. However, this may be misleading because the Hashin–Shtrikman bounds are based on a limiting assumption excluding geometries that are important in some parts of the Earth (e.g., layering).

In certain cases, the Voigt–Reuss and Hashin–Shtrikman bounds are too wide to yield useful estimates. This can occur when the moduli of the constituent phases differ significantly, as in the case of a porous solid or a partial melt. In such cases, the analysis of specific geometries may be useful. Typically, one assumes that one phase is the host (i.e., the solid rock) and the other is treated as an inclusion (air, water, or melt). Results for specific inclusion shapes have been derived, including spheres, needles, disks, and penny-shaped cracks (Berryman, 1995). For a given volume fraction of inclusions, the effective moduli are most similar to those of the host for spherical inclusions, whereas large-aspect-ratio disks or cracks have the largest influence on the shear modulus (**Figure 10**) (Williams and Garnero, 1996). It should be noted that very little is known concerning the actual form of melt inclusions in partial melts within the mantle. The relevant controlling parameters are many; include the pressure, temperature, bulk composition, and deformation history; and may be influenced by nonequilibrium effects (Bruhn et al., 2000; Hier-Majumder and Abbott, 2010).

An additional ambiguity in the computation of the effective elastic moduli of isotropic composites arises from the intrinsic anisotropy of crystals. Even in the case of a monophase aggregate, the effective elastic moduli are inherently uncertain unless the texture has been completely specified (Watt et al., 1976). Hill (1952) showed that rigorous bounds correspond to the

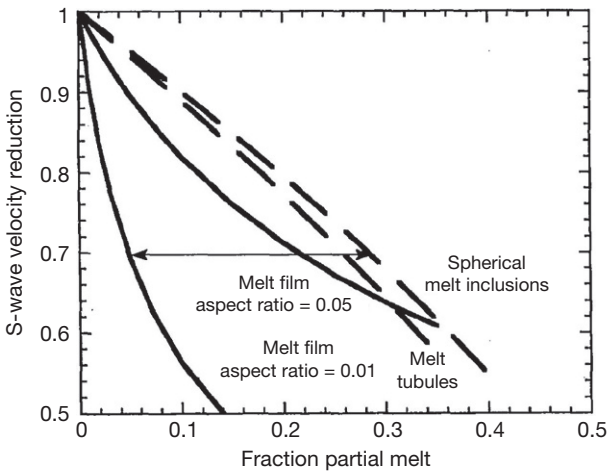

Figure 10 Ratio of the S-wave velocity of melt-bearing mantle to that of solid mantle for varying melt fractions and melt geometries. The arrow corresponds to the variation in melt fraction implied by the inferred P-wave velocity depression of 10% in the ultralow-velocity zone at the base of the mantle. Reproduced from Williams Q and Garnero EJ (1996) Seismic evidence for partial melt at the base of Earth's mantle. *Science* 273: 1528–1530.

assumption of, respectively, homogeneous strain and homogeneous stress. The Voigt (homogeneous strain) bounds are

$$K_V^* = \frac{1}{3}(A + 2B) \quad [36]$$

$$G_V^* = \frac{1}{5}(A - B + 3C) \quad [37]$$

where A, B, and C, are, respectively, the mean diagonal, off-diagonal, and shear elastic constants

$$\begin{aligned} A &= \frac{1}{3}(c_{11} + c_{22} + c_{33}) \\ B &= \frac{1}{3}(c_{12} + c_{13} + c_{23}) \\ C &= \frac{1}{3}(c_{44} + c_{55} + c_{66}) \end{aligned} \quad [38]$$

And the Reuss (homogeneous stress) bounds are

$$K_R^* = \frac{1}{3(a + 2b)} \quad [39]$$

$$G_R^* = \frac{5}{4a - 4b + 3c} \quad [40]$$

where a, b, and c are similar to A, B, and C but with the components of the compliance tensor replacing those of the elastic-constant tensor. The Hashin–Shtrikman bounds for the monophase aggregate are narrower (Hashin and Shtrikman, 1962). Expressions have been derived for cubic, tetragonal, orthorhombic, hexagonal, trigonal, and monoclinic Bravais lattices (Watt, 1988, and references therein). The difference between Voigt and Reuss bounds for the shear-wave velocity of olivine at ambient conditions is 2%. The difference tends to increase with increasing single-crystal anisotropy; in fact, the difference between Voigt and Reuss bounds has been proposed as the basis for a universal anisotropy index (Ranganathan and Ostoja-Starzewski, 2008). For materials with very large anisotropy, such as periclase at the core–mantle boundary (azimuthal shear anisotropy = 60%), Voigt and Reuss bounds on the shear modulus differ by 30% and the Hashin–Shtrikman bounds differ by 5% (Karki et al., 2001). Spinel is an example of a mineral that is extremely anisotropic at ambient conditions and for which bounds are wide (Yoneda, 1990).

Preferred orientation (preferential crystallographic alignment) of the constituent grains results in macroscopic anisotropy detectable by seismic waves. The preferred orientation is characterized by the orientation distribution function:

$$f(\mathbf{g})\mathrm{d}\mathbf{g} = \frac{\mathrm{d}V_\mathbf{g}}{V} \quad [41]$$

where $\mathbf{g}$ is the rotation matrix that relates the crystallographic axes to the spatial or laboratory reference frame and $\mathrm{d}V_\mathbf{g}/V$ is the volume fraction of crystals with orientation lying within the range $\mathrm{d}\mathbf{g}$. The effective elastic moduli of the aggregate may then be estimated by (Bunge et al., 2000)

$$c_{ijkl}^* = \int_g g_{im} g_{jn} g_{ko} g_{lp} c_{mnop} f(\mathbf{g})\,\mathrm{d}\mathbf{g} \quad [42]$$

where the effective elastic moduli are referred to the laboratory frame and the elastic-constant tensor in the integrand is referred to the crystallographic frame. This expression yields the Voigt bound on the effective elastic moduli; the Reuss bound involves the compliances. Two simple cases of orientation distribution functions are of special interest (Stixrude, 1998). If the texture is perfect, that is, all crystals identically aligned, then the effective elastic-constant tensor is identical to that of the single crystal rotated into the laboratory frame. Such a texture might be considered the asymptotic limit of lattice-preferred orientation produced by mantle flow. A transversely anisotropic aggregate is produced if deformation is dominated by an easy-glide plane. In this case, the effective elastic-constant tensor has hexagonal symmetry with the symmetry axis normal to the glide plane.

1.26.3.3 Attenuation and Dispersion

When deformed by small stresses over short timescales, the mantle behaves nearly elastically, propagating shear waves, whereas at long timescales, it behaves like a fluid, deforming viscously in mantle convection. (Though not relevant to the immediate discussion, rock also behaves as a fluid under the short but high-amplitude stresses of impact-induced shock.) The boundary between these two types of behavior is characterized by the Maxwell relaxation time:

$$\tau_M = \frac{\eta}{G} \quad [43]$$

where η is the viscosity. For the upper mantle, $\tau_M \sim 1000$ years and determined from glacial rebound.

At seismic periods, deformation is also not perfectly elastic. The relative amount of elastic energy lost per cycle, $\mathrm{d}E/E$, defines the quality factor Q, the inverse of which is referred to as the internal friction or attenuation:

$$Q^{-1} = \frac{\mathrm{d}E}{E} \quad [44]$$

Attenuation entails dispersion: the acoustic-wave velocity depends on the wavelength or frequency of the probe (Figure 11) (Jackson, 2000). This results from causality, the requirement that the

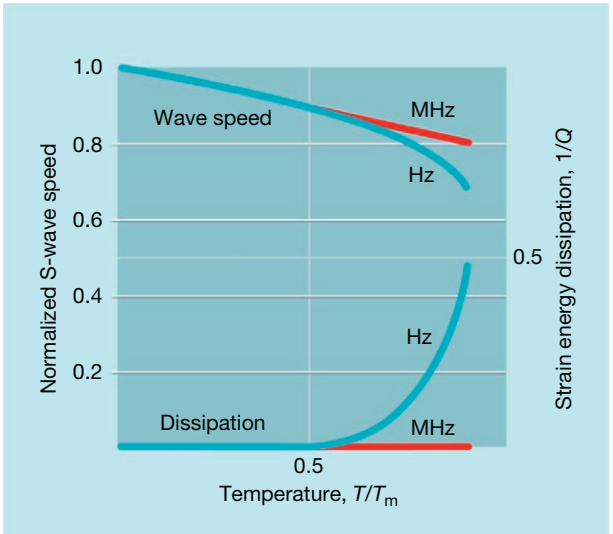

Figure 11 Schematic representation of the variation of acoustic-wave velocity (upper curves) and attenuation (Q^{-1}) (lower curves) with temperature at high frequencies (red) and lower frequencies within the seismic band (blue). Reproduced from Jackson I (2000) Geophysics – Taking the Earth's temperature. *Nature* 406: 470–471.

mechanical energy of the wave cannot propagate faster than the signal velocity, as encapsulated by the fact that the frequency-dependent elastic modulus and attenuation are not independent: they are Hilbert transform-related real and imaginary components of the complex modulus (eqn [47]) and therefore satisfy integral conditions (Kramers–Kronig relations) (Bracewell, 1999). This kind of dispersion – which involves nonequilibrium processes, with mechanical energy converted to heat – is distinct from the dispersion we encountered in the context of lattice dynamics of perfect crystals, which is an equilibrium phenomenon arising from the atomic nature of matter.

Simple models are useful for thinking about attenuation and dispersion, even when they do not correspond to geophysically relevant materials. The Maxwell model is the simplest, consisting of an elastic spring and a dashpot in series. The Voigt model has these two elements in parallel. At short periods, both of these simple models produce elastic behavior governed by the spring. At long periods, the behavior is very different. Whereas the Maxwell model produces a purely viscous, unrecoverable response, governed by the dashpot, the Voigt model shows anelastic behavior: time-dependent but fully recoverable. The so-called Kelvin or standard linear solid consists of a Voigt model in series with a spring. The simplest model that shows the full range of response, elastic, anelastic, and viscous, is the Burgers model, which can be thought of as a Maxwell solid and a Voigt solid in series. See, for example, Cooper (2002) for a recent discussion of these models.

These simple models make an important point. Viscous flow, which governs mantle convection, and anelastic deformation, which causes attenuation and dispersion in the seismic band, are considered as separate dashpots. While the connection to real materials is not obvious, it is likely that viscosity and attenuation are governed by separate microscopic deformation mechanisms if for no other reason than that the strain rates and total strains are so vastly different. Experimental measurements of viscosity, which are more numerous than measurements of seismic attenuation at relevant mantle conditions, are not necessarily a reliable guide to the dependence of attenuation on pressure, temperature, or composition.

Consider the response of these models to periodic loading

$$\sigma = \sigma_0 e^{i\omega t} \qquad [45]$$

which produces the strain response

$$\varepsilon = \varepsilon_0 e^{i\omega t+\delta} \qquad [46]$$

In most experiments, the attenuation is actually measured by the phase lag δ. The elastic modulus is complex and frequency-dependent:

$$M(\omega) = M_R + iM_I \qquad [47]$$

and the attenuation can also be written as the ratio of imaginary to real parts $Q^{-1} = M_I/M_R$. The acoustic-wave velocity is

$$V = \sqrt{\frac{M}{\rho}} \qquad [48]$$

where ρ is the density.

The simple models described all predict attenuation that depends strongly on frequency (**Figure 12**). For the Maxwell solid $Q^{-1} = 1/\omega\tau$, and for the Voigt solid, $Q^{-1} = \omega\tau$, where τ is the characteristic relaxation time. The standard linear solid shows Maxwell-like and Voigt-like behavior in the limit of zero and infinite frequency, respectively, with a peak attenuation centered at $\omega\tau = 1$:

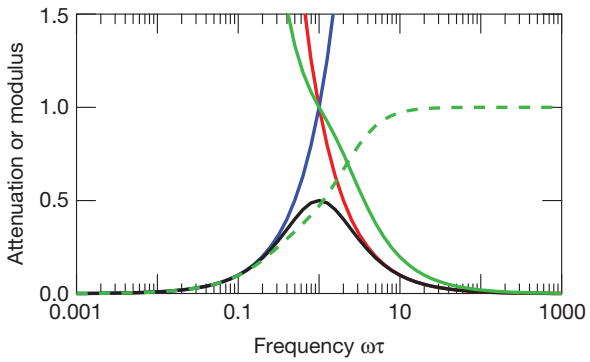

Figure 12 Frequency dependence of the attenuation (solid curves) and modulus (dashed curve for the Burgers model) for simple mechanical models: Maxwell (red), Voigt (blue), Kelvin (black), and Burgers (green). Reproduced from Stixrude L and Lithgow-Bertelloni C (2012) Geophysics of chemical heterogeneity in the mantle. *Annual Review of Earth and Planetary Sciences* 40: 569–595.

$$Q^{-1} = \frac{\omega\tau}{1+(\omega\tau)^2} \qquad [49]$$

and the velocity dispersion is

$$V(\omega) = V(0)\left(1 + Q^{-1}_{\max}\frac{(\omega\tau)^2}{1+(\omega\tau)^2}\right) \qquad [50]$$

For the Burgers model

$$Q^{-1} = \frac{1+2\omega^2\tau^2}{2\omega\tau+\omega^3\tau^3} \qquad [51]$$

there is a Maxwell-like decrease of attenuation with increasing frequency, interrupted by a region near $\omega\tau = 1$ where the dependence on frequency is much reduced. Depending on the details of how the Burgers model is parameterized, this shoulder may become a small peak.

Much of the literature on microscopic mechanisms of attenuation in solids has focused on those materials that show clear peaks in the attenuation spectrum. The dependence of the peak amplitude and frequency on temperature and material characteristics is essential for identifying the mechanism(s) responsible. Among the mechanisms that have been identified in this way are the migration of defects, the exchange of substituents in solid solution, dislocation motion, grain-boundary relaxation, and thermal currents (Jackson and Anderson, 1970; Nowick and Berry, 1972). Because so many mechanisms can contribute to the attenuation, it is often necessary to specially prepare the sample to have, for example, high purity or uniform grain size, in order to produce a spectrum with a single clear peak. Many silicate liquids show attenuation that is well described by a single characteristic relaxation time (Rivers and Carmichael, 1987).

Perhaps, the most important result from the studies of mantle-like materials is the absence of attenuation peaks (Jackson et al., 2002). Attenuation is found to vary slowly and monotonically with frequency over a broad spectrum. The reason for this behavior is not clear. It is possible that there exists a broad and nearly continuous spectrum of relaxation times. The behavior is similar to the so-called high-temperature background found in many materials (Nowick and Berry, 1972). Even those materials that show distinct peaks at low temperature may exhibit featureless attenuation spectra at high temperature.

In the case of attenuation dominated by elastically accommodated grain-boundary sliding, the featureless, nearly flat attenuation spectrum may be rationalized as follows (Jackson et al., 2002). The characteristic relaxation time is

$$\tau_{gb} = \gamma \frac{\eta_{gb} d}{G\delta} \qquad [52]$$

where d is the grain size, δ is the width of the grain-boundary region, γ (not the Grüneisen parameter, here) is of order 1, and η_{gb} is a grain-boundary viscosity (much less than the viscosity of the bulk). A spectrum of relaxation times might be produced by a distribution of grain sizes, grain-boundary widths, and grain-boundary viscosities. In particular, the effective grain-boundary viscosity could exhibit a wide range because of the variable presence of grain-boundary irregularities or impurities that would tend to inhibit sliding.

The following empirical expression represents the data of Jackson et al. (2002) within the seismic frequency band (~1–100 s periods) (**Figure 13**):

$$Q^{-1}(P,T,\omega) = Ad^{-m}\omega^{-\alpha}\exp\left(-\alpha\frac{E^* + PV^*}{RT}\right) \qquad [53]$$

$$V(P,T,\omega) = V(P,T,\infty)\left[1 - \frac{1}{2}\cot\left(\frac{\alpha\pi}{2}\right)Q^{-1}(P,T,\omega)\right] \qquad [54]$$

where ω is the frequency, d is the grain size, $m = 0.28$ is the grain size exponent, $\alpha = 0.26$ is the frequency exponent, $E^* = 430$ kJ mol^{-1} is the activation energy, V^* is the activation volume, and R is the gas constant. For the experimental value of α, the factor multiplying Q^{-1} in eqn [53] has the value 1.16. The activation volume is currently unconstrained, which means that the influence of pressure on attenuation is highly uncertain. The relationship between attenuation and dispersion is made explicit by eqn [54].

The experimental results can be compared with attenuation spectra proposed for the Earth. The absorption band model (Anderson and Given, 1982) consists of a broad frequency range over which Q^{-1} depends weakly on frequency, bounded by narrower low- and high-frequency ranges where Q^{-1} decreases to zero. The intermediate frequency range of this model, the absorption band, agrees well with experimental results. The estimates of the value of alpha based on seismological observations are consistent with those found experimentally at similar frequencies. But experimental support for the boundaries of the absorption band is lacking. At long periods, experiments show that the attenuation will continue to increase with increasing period and at a higher rate, with $\alpha = 1$ (Gribb and Cooper, 1998; Jackson et al., 2002). At the high-frequency end, there is no indication of a sharp transition

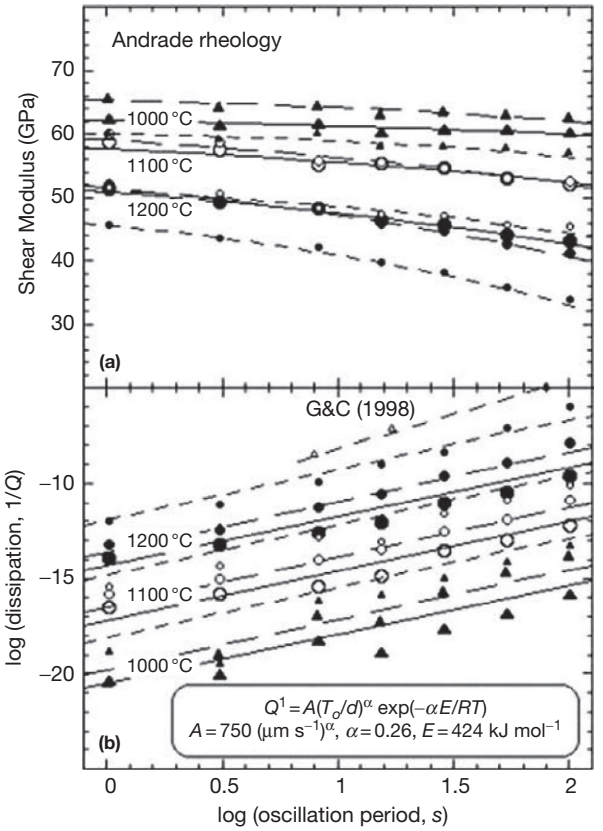

Figure 13 Grain size sensitivity of the high-temperature mechanical behavior of olivine polycrystals. Data for specimens 6261, 6365, and 6381 of average grain sizes 23.4, 12.4, and 2.9 mm are denoted by the large, medium, and small plotting symbols and by the solid, long-dashed, and short-dashed curves, respectively. Solid circles, open circles, and solid triangles denote data for 1200, 1100, and 1000 °C, respectively. (a) Shear modulus. Curves labeled with temperature indicate the modulus dispersion associated with Andrade models fitted simultaneously to $G(T_o)$ and $Q^{-1}(T_o)$, where $T_o = 2\pi/\omega$ is the oscillation period (cf. eqns [53] and [54]). (b) The log (dissipation, Q^{-1}). Lines represent the preferred fit (eqns [7] and [8]) to the entire 1000–1300 °C, 1–100 s data set for all four specimens, except for the uppermost line representing the results of Gribb and Cooper (1998) for a resynthesized dunite of 2.8 mm grain size at 1200 °C. Reproduced from Jackson I, Gerald JDF, Faul UH, et al. (2002) Grain-size-sensitive seismic wave attenuation in polycrystalline olivine. *Journal of Geophysical Research-Solid Earth* 107: 2360.

requiring a larger value of α. In fact, there is an indication in the data that the attenuation becomes less sensitive to frequency at high frequency (Cooper, 2002).

The influence of partial melt is generally to increase the attenuation (Faul et al., 2004; Jackson et al., 2004). The frequency dependence is also affected by partial melt. A broad absorption peak is superimposed on a high-temperature background. The origin of this peak appears not to be the melt squirt mechanism that has been widely discussed, but elastically accommodated grain-boundary sliding enhanced by partial melt. For probable mantle-grain sizes and attenuation in the seismic band, Q is nearly independent of frequency for 1% partial melt.

The influence of crystallographically bound hydrogen on the attenuation is currently not well constrained, although it is

known that viscosity decreases with increasing hydrogen concentration (Mei and Kohlstedt, 2000a,b).

The bulk attenuation – that is, the time dependence of volume compression due to a change in hydrostatic pressure – is much smaller than shear attenuation. Seismological observations require a small but finite value of the bulk attenuation in the Earth, the locus of which is difficult to resolve uniquely (Durek and Ekstrom, 1995). In the limit that bulk attenuation vanishes, the attenuation of longitudinal and shear waves is related by

$$Q_P^{-1} = \frac{4}{3}\left(\frac{V_S}{V_P}\right)^2 Q_S^{-1} \qquad [55]$$

Experimental measurements and theoretical analyses of possible mechanisms also find that bulk attenuation is much smaller than shear attenuation: proposed mechanisms for bulk attenuation involve the elastic heterogeneity of polyphase assemblages, coupling to the kinetics of first-order phase transformations, and compositional fluctuations in the liquid outer core (Anderson, 1980; Heinz et al., 1982; Li and Weidner, 2008; Ricard et al., 2009).

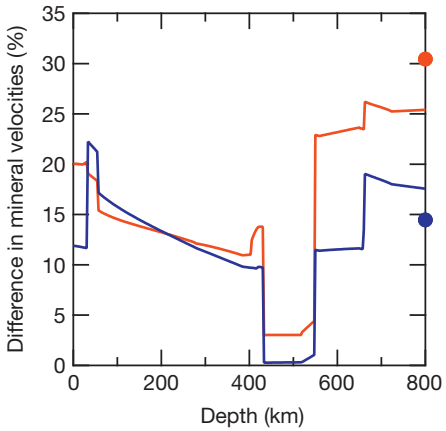

Figure 14 Maximum difference in the shear (red) and longitudinal (blue) velocities of coexisting phases in a model mantle composition to 800 km depth. Symbols represent the values at the core–mantle boundary (2900 km depth). Reproduced from Stixrude L and Lithgow-Bertelloni C (2012) Geophysics of chemical heterogeneity in the mantle. *Annual Review of Earth and Planetary Sciences* 40: 569–595.

1.26.4 Seismological Elasticity and Anelasticity

1.26.4.1 Scaling

When the scale length of heterogeneity is comparable to the seismic wavelength, there are two additional considerations. The first is dispersion due to structure. This is seen in observations of surface waves, the velocity of which depends on frequency. This frequency dependence is mostly due to the fact that larger wavelengths sample greater depths where the intrinsic acoustic velocity is greater.

Random heterogeneity can produce scattering of seismic waves (Frankel and Clayton, 1986). Consider a random medium with average velocity, v, characterized by heterogeneity of length scale a and velocity perturbation, d, and probed by acoustic waves with wavelength λ. On average, the first-arriving waves tend to select paths that preferentially sample the high-velocity heterogeneities; in this sense, the medium appears to have a wave velocity slightly greater than v. In addition, the velocity depends on wavelength, that is, heterogeneity causes dispersion. The direct wave is attenuated, as energy is redirected due to scattering, but this is essentially different from the intrinsic attenuation discussed earlier for which mechanical energy is dissipated by being converted to heat. The difficulty, however, is that scattering due to heterogeneity has many of the same characteristics as intrinsic attenuation and dispersion of seismic waves, so the two causes of seismic-wave attenuation as a function of distance along the wave path – scattering versus dissipation – are difficult if not impossible to disentangle. This means that any interpretation of attenuation in terms of the strong temperature dependence expected from intrinsic (dissipative) mechanisms, for example, needs to be treated with caution.

What is the scale of heterogeneity in the mantle? The magnitude of the heterogeneity is largest at the grain scale, with differences in shear-wave velocity between coexisting minerals being 10–30% throughout most of the outer mantle (except for the shallow transition zone) as well as near the core–mantle boundary (Figure 14). The ratio of the grain size typically observed in mantle xenoliths (1–10 mm) to teleseismic wavelengths is $d/\lambda \sim 10^{-7} \ll 1$ characteristic of Rayleigh scattering. In this long-wavelength limit, the apparent attenuation falls with increasing wavelength like $(d/\lambda)^3$ and is probably negligible as long as the heterogeneity is weak (say less than 1–10%). The grain-scale heterogeneity indicated in Figure 14 can plausibly be accommodated within the Rayleigh-scattering model, but it is less likely that the stronger heterogeneity associated with partial melt or major compositional variations (e.g., mixtures of core metal and mantle silicates) can also be considered in this weak-scattering limit. Moreover, the grain size of the mantle is still highly uncertain at great depth, particularly below the zone of magma genesis (Ave Lallemant et al., 1980).

Larger-scale heterogeneities, approaching or comparable to seismic wavelengths, are also likely in the mantle (Stixrude and Lithgow-Bertelloni, 2012). At the mid-ocean ridge, basalt and a depleted residuum, harzburgite, are generated, both of which have significantly different physical properties from undifferentiated mantle. The initial scale length of heterogeneity may be taken as the thickness of the oceanic crust (~7 km), which is likely to scatter seismic waves significantly. The magnitude of the velocity difference depends on depth (Figure 15). Basalt is slower than peridotite at shallow depths, reflecting the well-known difference in velocity between crust and mantle. Basalt then becomes much faster near 100 km depth because of the transition to eclogite (plagioclase and pyroxenes forming garnet under pressure) that increases velocities by approximately 10%. Velocity contrasts in the lower mantle are not as well constrained, but appear to be less than 10%. For comparison, one seismological study found that scattering of P-waves could be explained by heterogeneity with scale length 8 km and magnitude 1% uniformly distributed throughout the mantle, but this result may be biased by contamination from heterogeneity at the base of the mantle (Hedlin et al., 1997).

1.26.4.2 Uncertainties

The largest source of uncertainty in constructing isotropic models of radial upper-mantle and transition-zone structure is

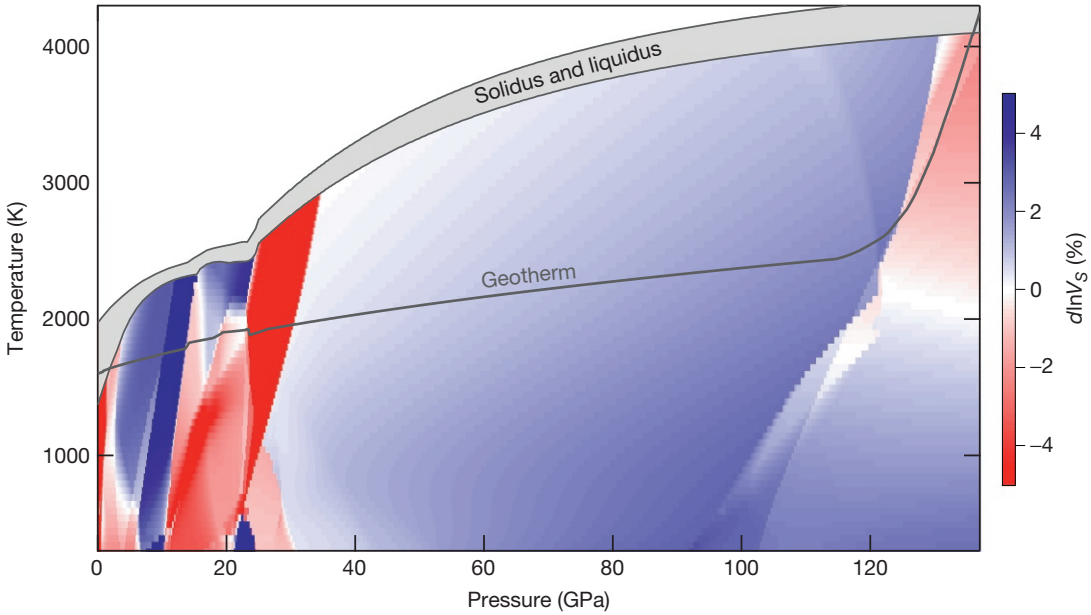

Figure 15 Difference in shear-wave velocity between basalt and harzburgite. The geotherm (thick gray line) and the melting interval (gray envelope) are from Stixrude et al. (2009). Computed with HeFESTo (Stixrude and Lithgow-Bertelloni, 2011). Reproduced from Stixrude L and Lithgow-Bertelloni C (2012) Geophysics of chemical heterogeneity in the mantle. *Annual Review of Earth and Planetary Sciences* 40: 569–595.

Table 1 Elastic properties of major mantle phases; after (Stixrude and Lithgow-Bertelloni, 2005a) and references therein

Phase	K_0	dK_0/dX	K_0'	dK/dT	G_0	dG/dX	G_0'	dG/dT
plg	84(5)	–	4.0(10)	*4*(1)	40(3)	–	*1.1*(5)	*6*(3)
sp	197(1)	12(2)	5.7(2)	29(3)	109(10)	−24(16)	0.4(5)	13(2)
ol	128(2)	7(2)	4.2(2)	18(1)	82(2)	−31(2)	1.4(1)	14(1)
wa	169(3)	0(13)	4.3(2)	22(6)	112(2)	−40(12)	1.4(2)	18(1)
ri	183(2)	16(7)	4.1(2)	23(2)	120(2)	−25(10)	1.3(1)	17(2)
opx	107(2)	−7(4)	7.0(4)	19(5)	77(1)	−25(5)	1.6(1)	13(2)
cpx	112(5)	7(6)	5.2(18)	18(9)	67(2)	−6(2)	*1.4*(5)	*11*(4)
hcpcx	121(1)	*0*(10)	5.5(3)	20(3)	90(1)	−19(10)	1.5(1)	17(2)
capv	236(4)	–	3.9(2)	22(13)	165(12)*	–	2.5(5)*	*26*(4)
ak	211(4)	*0*(10)	4.5(5)	*20*(6)	132(8)	*25*(12)	1.6(5)*	*21*(4)
gt	170(2) − 9Y	7(3)	4.1(3) + 0.1Y	16(2)	94(2)	4(3)	1.3(2) + 0.1Y	10(1) − 2Y
st	314(8)	–	4.4(2)	31(18)	220(12)	–	*1.6*(5)	*36*(5)
pv	251(3)	30(40)*	4.1(1)	23(4)	175(2)	−37(40)*	1.7(2)*	25(3)*
fp	161(3)	18(3)	3.9(2)	21(1)	130(3)	−83(3)	2.2(1)	26(1)

Symbols and units: K, adiabatic bulk modulus (GPa); G, shear modulus (GPa), $X = \mathrm{Fe}/(\mathrm{Mg}+\mathrm{Fe})$; $Y = mj/(py+mj)$; subscript indicates values at zero pressure, and primes indicate pressure derivatives; dK/dT and dG/dT in MPa/K. Italicized entries are unconstrained by experiment. Asterisk indicates values taken from density-functional theoretical calculations. Values in parentheses indicate estimated uncertainties.

the elastic constants of minerals at high pressure and temperature (Table 1). The propagated uncertainty in the elastic shear-wave velocity is approximately 1.3% or 0.06 km s^{-1} (Stixrude and Lithgow-Bertelloni, 2005b). This is somewhat larger than the difference between Voigt and Reuss bounds throughout most of this region and considerably more than the difference between the Hashin–Shtrikman bounds (Figure 8). Uncertainties in computed elastic properties arise mainly because of the need to extrapolate existing measurements taken over limited ranges of pressure and/or temperature to mantle conditions. For a few phases, large discrepancies exist in measured properties that cannot be reconciled at present. An important example is garnet–majorite, for which Brillouin spectroscopy yields a value for $G' = 1.3(2)$ (Sinogeikin and Bass, 2002), while ultrasonic studies yield a much higher value: 1.9 (Liu et al., 2000). We have followed the discussion of Jiang et al. (2004) in favoring the Brillouin value in this case but must emphasize that in this as in other instances of apparent discrepancy, there may be real differences between samples (as yet not recognized or controlled for) and that it is not a question of poor measurements.

These results highlight the importance of measuring elastic properties directly at mantle pressure–temperature conditions. The elastic properties of transition-zone and lower-mantle phases were recently measured at mantle pressure–temperature

conditions for the first time (Higo et al., 2008; Murakami et al., 2012).

Another kind of uncertainty comes from the linkage between velocity dispersion and attenuation, because there is virtually no constraint on the latter at mantle conditions based on laboratory experiments. Simple models, based on the Weertman law (scaling by the ratio of temperature to melting temperature) or a constant activation volume, apparently do not reproduce the qualitative features of seismological radial Q models (Faul and Jackson, 2005). While attenuation has a small effect on the velocity, the lateral variation of velocity in tomographic models is also small, so that intrinsic dispersion is a large part of the 3D structure (Brodholt et al., 2007; Karato, 1993; Matas and Bukowinski, 2007). Progress will come from experimental measurements of Q^{-1} in the seismic band at elevated pressure, an enormous challenge.

In the lower mantle, the reliability with which seismological observations can be interpreted is probably limited by our understanding of the relevant mineral-scale physics. For example, the recently discovered high-spin to low-spin transition (Badro et al., 2003, 2004; Pasternak et al., 1997) appears to have a significant influence on density and elasticity (Mao et al., 2011; Marquardt et al., 2009). While the transition appears to be well understood in ferropericlase, the nature and even existence of a high-spin to low-spin transition in silicate perovskite over the pressure regime of the mantle remains controversial (Hsu et al., 2010; McCammon et al., 2008; Stackhouse et al., 2007). It also remains to be understood how the transition in perovskite depends on compositional variables, such as Al content and ferric iron content (Catalli et al., 2011; Li et al., 2005). Valence transitions induced by pressure, for example, between ferric and ferrous iron also remain poorly understood (Frost et al., 2004), as does the phase diagram of the third most abundant lower-mantle constituent, calcium silicate perovskite. A temperature-induced transition from a low-temperature tetragonal phase to a high-temperature cubic phase has been predicted (Stixrude et al., 1996), and low-temperature structural distortions have been seen experimentally (Shim et al., 2002), but the details remain uncertain. This transition is accompanied by a large elastic anomaly (15% in shear-wave velocity) (Stixrude et al., 2007).

Constructing mineralogical models of anisotropic structure remains a considerable challenge (Nowacki et al., 2013). There has been substantial progress from experiment and theory in our knowledge of the full elastic-constant tensors of major mantle minerals (Karki et al., 2001). We still have a great deal to learn about deformation mechanisms and in particular dominant slip planes at mantle conditions and at relevant strains and strain rates. Experimental results and first-principles calculations now exist for many mantle minerals (Carrez et al., 2007; Cordier, 2002). For lower-mantle minerals, it is important to keep in mind that deformation mechanisms may change profoundly with increasing pressure, as suggested by the change in anisotropy of ferropericlase and magnesium silicate perovskite at high pressure (Karki et al., 1997a,b). Another important uncertainty lies in understanding how polycrystals respond to mantle flow at large finite strains (Blackman et al., 1996; Chastel et al., 1993; Ribe, 1989). This understanding is necessary for estimating the strength of the texture and the resulting magnitude of anisotropy.

Uncertainties related to composite effects are largest in the context of partial melts. The geometry of the melt phase, whether it exists as spheres, needles, or disks, has an enormous effect on the rock shear elasticity. What is required is an understanding of the relevant mineral–melt interface energetics that control this geometry (Hier-Majumder and Abbott, 2010). Melt geometry can be scale-dependent, as demonstrated by experiments in which the melt geometry changes fundamentally on deformation (Bruhn et al., 2000).

1.26.4.3 Implications for Inversions

There are essentially two approaches used for linking seismology and mineral physics, forward and inverse modeling. For the first, a mineralogical model based on an assumed bulk composition and potential temperature is compared with seismological observations (Duffy and Anderson, 1989; Ita and Stixrude, 1992; Stixrude and Lithgow-Bertelloni, 2005b). (For applications to adiabatic temperature profiles in the Earth, the 'potential temperature' refers to the adiabatic temperature at zero pressure.) In practice, mineralogical models are typically compared with seismological models, an approach that is fraught with difficulty because the seismological models are derivative of the data and nonunique. These difficulties are particularly prevalent in the upper mantle, where lateral variations, attenuation, and anisotropy are all large and radial models are prone to mislead.

A promising alternative to forward modeling is to compute the actual seismological observables (e.g., travel times or mode frequencies) directly from the mineralogical model (Cammarano et al., 2009). This permits a much more direct and certain comparison to the structure of the Earth. The uncertainties inherent in the forward model can in principle be assessed and propagated to uncertainties in predicted seismological observables.

An additional benefit of forward mineralogical models is that they might be used as a reference for seismic tomographic inversions. Tomographic models are usually determined as deviations from an assumed radial structure, and the radial model may bias the inversion. For example, in oceanic regions of the upper mantle, tomographic inversions based on preliminary reference earth model (PREM) (Dziewonski and Anderson, 1981) might be biased by the large Lehmann discontinuity in this radial model. PREM and other radial seismic models assume a parametrically simple radial structure. For example, the transition-zone gradient is assumed to be linear, which does not agree with expectations based on the phase transformations that take place in typical mantle lithologies. Advantages of using a mineralogical model would be that all anticipated structure from phase transitions would be included. Moreover, the reference state is one associated with a well-defined, if imprecise, physical meaning in terms of bulk composition and geotherm (Cammarano et al., 2003; Cobden et al., 2009). With ever-improving knowledge of mantle phase equilibriums and physical properties, one may envision substantial improvements in the construction of mineralogical models and our ability to interpret seismological observations in terms of radial and lateral variations in temperature and bulk composition.

An inverse model seeks to invert seismic observations directly for radial and lateral variations in bulk composition and

temperature. In practice, inverse models have been based on the intermediate step of a velocity model. Several studies have inverted radial or 3D velocity and density models for radial and lateral variations in temperature and bulk composition (Deschamps and Trampert, 2003; Goes et al., 2000; Matas et al., 2007; Shapiro and Ritzwoller, 2004; Stixrude et al., 1992; Trampert et al., 2001). Some caution is in order because of the uncertainty in the nonlinear and linked phenomena involved, particularly in the estimate of attenuation. Also important are systematic effects that have not been included in some of these inversions. There are three sources of lateral heterogeneity in the mantle, due to lateral variations of temperature, bulk composition, and phase. The quantities necessary to estimate the influence of phase on lateral structure are reasonably well known in the upper mantle and transition zone: phase equilibriums and physical properties of the minerals involved are experimentally documented and should continue to be included in future efforts (Stixrude and Lithgow-Bertelloni, 2007).

1.26.5 Conclusions and Outlook

The contact between mineral physics and seismology of the Earth's mantle has grown considerably richer and more sophisticated in recent years. Birch's vision of constraining the chemical and thermal state of the mantle on the basis of mineralogical properties and seismic observations is becoming a reality. In addition, mineral physics is beginning to provide the foundation required for inferring the dynamic state of the mantle, and some aspects of its geologic evolution, from the seismological observations.

Progress will come from continued expansion of our knowledge of the elastic properties of mantle minerals at *in situ* conditions of high pressure and high temperature. These data remain the basis for any discussion of mantle structure in terms of radial or lateral variations in temperature or bulk composition. Among recent experimental advances has been a dramatic increase in the pressure and temperature range over which measurements of the shear modulus can be made, to 1 Mbar (2300 km depth) and 2000 K (Murakami et al., 2012). At the same time, first-principles theory continues to make important strides, including in the computation of the elastic constants of important phases over the entire mantle pressure–temperature regime (Oganov et al., 2001; Wentzcovitch et al., 2004; Zhang et al., 2013).

Equally important is a better understanding of recently discovered physics and chemistry, including the postperovskite phase transition, the high-spin to low-spin transition of iron in oxides and silicates, and the possible role of valence state changes of iron at high pressure. Among physical properties that are still poorly understood is the attenuation (or its inverse, the quality factor Q). While recent experiments have laid an important foundation (Gribb and Cooper, 1998; Jackson et al., 2002, 2004; McCarthy et al., 2011), we still have little experimental data bearing on the influence of pressure or water content on attenuation. Also uncertain are the dominant deformation mechanisms in mantle minerals at high pressure and temperature, and these provide an additional link between experimental measurements of the elastic-constant tensor and seismically observed anisotropy. Recent experimental discoveries suggest that more surprises await (Mainprice et al., 2005; Miyagi et al., 2010).

Along with improved knowledge of the physical properties of individual phases will come increasing understanding of aggregate properties and the construction of mineralogical models of the mantle as a whole. An important advance will be closer contact between mineralogical models and seismological observations.

Acknowledgments

Research supported by the European Research Council under grant agreement no. 291432 "MoltenEarth" (FP7/2007–2013).

References

Abramson EH, Brown JM, and Slutsky LJ (1999) Applications of impulsive stimulated scattering in the earth and planetary sciences. *Annual Review of Physical Chemistry* 50: 279–313.

Agnon A and Bukowinski MST (1990) Delta-S at high-pressure and $DlnV_S/DlnV_P$ in the lower mantle. *Geophysical Research Letters* 17: 1149–1152.

Akimoto SI and Fujisawa H (1968) Olivine-spinel solid solution equilibria in system Mg_2SiO_4–Fe_2SiO_4. *Journal of Geophysical Research* 73: 1467–1479.

Anderson DL (1980) Bulk attenuation in the earth and viscosity of the core. *Nature* 285: 204–207.

Anderson OL (1995) *Equations of State of Solids for Geophysics and Ceramic Science*. Oxford: Oxford University Press.

Anderson DL and Given JW (1982) Absorption-band Q model for the Earth. *Journal of Geophysical Research* 87: 3893–3904.

Anderson OL and Isaak DG (1995) Elastic constants of mantle minerals at high temperature. In: Ahrens TJ (ed.) *Mineral Physics and Crystallography: A Handbook of Physical Constants*, pp. 64–97. Washington, DC: American Geophysical Union.

Ashcroft NW and Mermin ND (1976) *Solid State Physics*, 826 pp. New York: Holt Rinehart and Winston.

Ave Lallemant HG, Mercier JCC, Carter NL, and Ross JV (1980) Rheology of the upper mantle – Inferences from peridotite xenoliths. *Tectonophysics* 70: 85–113.

Backus GE (1962) Long-wave elastic anisotropy produced by horizontal layering. *Journal of Geophysical Research* 67: 4427–4440.

Badro J, Fiquet G, Guyot F, et al. (2003) Iron partitioning in Earth's mantle: Toward a deep lower mantle discontinuity. *Science* 300: 789–791.

Badro J, Rueff JP, Vanko G, Monaco G, Fiquet G, and Guyot F (2004) Electronic transitions in perovskite: Possible nonconvecting layers in the lower mantle. *Science* 305: 383–386.

Barron THK, Berg WT, and Morrison JA (1957) The thermal properties of alkali halide crystals. 2. Analysis of experimental results. *Proceedings of the Royal Society of London Series A-Mathematical and Physical Sciences* 242: 478–492.

Berryman JG (1995) In: Ahrens TJ (ed.) *Rock Physics and Phase Relations: A Handbook of Physical Constants*, pp. 205–228. Washington, DC: American Geophysical Union.

Birch F (1952) Elasticity and constitution of the Earth's interior. *Journal of Geophysical Research* 57: 227–286.

Blackman DK, Kendall JM, Dawson PR, Wenk HR, Boyce D, and Morgan JP (1996) Teleseismic imaging of subaxial flow at mid-ocean ridges: Traveltime effects of anisotropic mineral texture in the mantle. *Geophysical Journal International* 127: 415–426.

Born M and Huang K (1954) *Dynamical Theory of Crystal Lattices*. Oxford: Clarendon Press.

Bracewell RN (1999) *The Fourier Transform and Its Applications*, 3rd edn. New York: McGraw-Hill.

Brodholt JP, Helffrich G, and Trampert J (2007) Chemical versus thermal heterogeneity in the lower mantle: The most likely role of anelasticity. *Earth and Planetary Science Letters* 262: 429–437.

Brown JM and McQueen RG (1986) Phase transitions, Grüneisen parameter, and elasticity for shocked iron between 77 GPa and 400 GPa. *Journal of Geophysical Research* 91: 7485–7494.

Brown JM, Slutsky LJ, Nelson KA, and Cheng LT (1989) Single-crystal elastic-constants for San Carlos peridot – An application of impulsive stimulated

scattering. *Journal of Geophysical Research: Solid Earth and Planets* 94: 9485–9492.
Bruhn D, Groebner N, and Kohlstedt DL (2000) An interconnected network of core-forming melts produced by shear deformation. *Nature* 403: 883–886.
Bunge HJ, Kiewel R, Reinert T, and Fritsche L (2000) Elastic properties of polycrystals – Influence of texture and stereology. *Journal of the Mechanics and Physics of Solids* 48: 29–66.
Cammarano F, Goes S, Vacher P, and Giardini D (2003) Inferring upper-mantle temperatures from seismic velocities. *Physics of the Earth and Planetary Interiors* 138: 197–222.
Cammarano F, Romanowicz B, Stixrude L, Lithgow-Bertelloni C, and Xu WB (2009) Inferring the thermochemical structure of the upper mantle from seismic data. *Geophysical Journal International* 179: 1169–1185.
Carrez P, Ferre D, and Cordier P (2007) Implications for plastic flow in the deep mantle from modelling dislocations in $MgSiO_3$ minerals. *Nature* 446: 68–70.
Catalli K, et al. (2011) Effects of the Fe^{3+} spin transition on the properties of aluminous perovskite – New insights for lower-mantle seismic heterogeneities. *Earth and Planetary Science Letters* 310: 293–302.
Chantel J, Frost DJ, McCammon CA, Jing ZC, and Wang YB (2012) Acoustic velocities of pure and iron-bearing magnesium silicate perovskite measured to 25 GPa and 1200 K. *Geophysical Research Letters* 39: L19307.
Chastel YB, Dawson PR, Wenk HR, and Bennett K (1993) Anisotropic convection with implications for the upper-mantle. *Journal of Geophysical Research: Solid Earth* 98: 17757–17771.
Chopelas A and Boehler R (1989) Thermal-expansion measurements at very high-pressure, systematics, and a case for a chemically homogeneous mantle. *Geophysical Research Letters* 16: 1347–1350.
Cobden L, Goes S, Ravenna M, et al. (2009) Thermochemical interpretation of 1-D seismic data for the lower mantle: The significance of nonadiabatic thermal gradients and compositional heterogeneity. *Journal of Geophysical Research: Solid Earth* 114: B11309.
Cooper RF (2002) Seismic wave attenuation: Energy dissipation in viscoelastic crystalline solids. *Reviews in Mineralogy and Geochemistry: Plastic Deformation of Minerals and Rocks* 51: 253–290.
Cordier P (2002) Dislocations and slip systems of mantle minerals. *Reviews in Mineralogy and Geochemistry: Plastic Deformation of Minerals and Rocks* 51: 137–179.
Crowhurst JC, Brown JM, Goncharov AF, and Jacobsen SD (2008) Elasticity of (Mg, Fe)O through the spin transition of iron in the lower mantle. *Science* 319: 451–453.
Davies GF (1974) Effective elastic-moduli under hydrostatic stress. 1. Quasi-harmonic theory. *Journal of Physics and Chemistry of Solids* 35: 1513–1520.
Deschamps F and Trampert J (2003) Mantle tomography and its relation to temperature and composition. *Physics of the Earth and Planetary Interiors* 140: 277–291.
Dove MT (1993) *Introduction to Lattice Dynamics*. Cambridge: Cambridge University Press.
Duffy TS and Ahrens TJ (1992) Sound velocities at high-pressure and temperature and their geophysical implications. *Journal of Geophysical Research: Solid Earth* 97: 4503–4520.
Duffy TS and Anderson DL (1989) Seismic velocities in mantle minerals and the mineralogy of the upper mantle. *Journal of Geophysical Research: Solid Earth and Planets* 94: 1895–1912.
Duffy TS and Wang YB (1998) Pressure–volume–temperature equations of state. *Reviews in Mineralogy* 37: 425–457.
Duffy TS, Zha CS, Downs RT, Mao HK, and Hemley RJ (1995) Elasticity of forsterite to 16 GPa and the composition of the upper-mantle. *Nature* 378: 170–173.
Durek JJ and Ekstrom G (1995) Evidence of bulk attenuation in the asthenosphere from recordings of the Bolivia earthquake. *Geophysical Research Letters* 22: 2309–2312.
Dziewonski AM and Anderson DL (1981) Preliminary reference earth model. *Physics of the Earth and Planetary Interiors* 25: 297–356.
Faul UH, Gerald JDF, and Jackson I (2004) Shear wave attenuation and dispersion in melt-bearing olivine polycrystals: 2. Microstructural interpretation and seismological implications. *Journal of Geophysical Research: Solid Earth* 109: B06202.
Faul UH and Jackson I (2005) The seismological signature of temperature and grain size variations in the upper mantle. *Earth and Planetary Science Letters* 234: 119–134.
Fiquet G, Badro J, Guyot F, Requardt H, and Krisch M (2001) Sound velocities in iron to 110 gigapascals. *Science* 291: 468–471.
Frankel A and Clayton RW (1986) Finite-difference simulations of seismic scattering: Implications for the propagation of short-period seismic-waves in the crust and models of crustal heterogeneity. *Journal of Geophysical Research: Solid Earth and Planets* 91: 6465–6489.
Frost DJ, Liebske C, Langenhorst F, McCammon CA, Tronnes RG, and Rubie DC (2004) Experimental evidence for the existence of iron-rich metal in the Earth's lower mantle. *Nature* 428: 409–412.
Gieske JH and Barsch GR (1968) Pressure dependence of elastic constants of single crystalline aluminum oxide. *Physica Status Solidi* 29: 121–131.
Gilbert F, Dziewons A, and Brune J (1973) Informative solution to a seismological inverse problem – (Earth's interior structure mass moment of inertia). *Proceedings of the National Academy of Sciences of the United States of America* 70: 1410–1413.
Gillet P, Guyot F, and Wang YB (1996) Microscopic anharmonicity and equation of state of $MgSiO_3$-perovskite. *Geophysical Research Letters* 23: 3043–3046.
Goes S, Govers R, and Vacher P (2000) Shallow mantle temperatures under Europe from P and S wave tomography. *Journal of Geophysical Research: Solid Earth* 105: 11153–11169.
Gonze X, Charlier JC, Allan DC, and Teter MP (1994) Interatomic force-constants from first principles – The case of alpha-quartz. *Physical Review B* 50: 13035–13038.
Goto TI, Ohno I, and Sumino Y (1976) The determination of the elastic constants of natural almandine-pyrope garnet by rectangular parallelepiped resonance method. *Journal of Physics of the Earth* 24: 149–156.
Gribb TT and Cooper RF (1998) Low-frequency shear attenuation in polycrystalline olivine: Grain boundary diffusion and the physical significance of the Andrade model for viscoelastic rheology. *Journal of Geophysical Research: Solid Earth* 103: 27267–27279.
Hashin Z and Shtrikman S (1962) A variational approach to the theory of the elastic behavior of polycrystals. *Journal of the Mechanics and Physics of Solids* 10: 343–352.
Hashin Z and Shtrikman S (1963) A variational approach to the theory of the elastic behaviour of multiphase materials. *Journal of the Mechanics and Physics of Solids* 11: 127–140.
Hazen RM, Downs RT, and Finger LW (1996) High-pressure crystal chemistry of $LiScSiO_4$: An olivine with nearly isotropic compression. *American Mineralogist* 81: 327–334.
Hedlin MAH, Shearer PM, and Earle PS (1997) Seismic evidence for small-scale heterogeneity throughout the Earth's mantle. *Nature* 387: 145–150.
Heinz D, Jeanloz R, and O'Connell RJ (1982) Bulk attenuation in a polycrystalline Earth. *Journal of Geophysical Research* 87: 7772–7778.
Helbig K (1984) *Foundations of Anisotropy for Exploration Seismics*. New York: Pergamon.
Hier-Majumder S and Abbott ME (2010) Influence of dihedral angle on the seismic velocities in partially molten rocks. *Earth and Planetary Science Letters* 299: 23–32.
Higo Y, Inoue T, Irifune T, Funakoshi KI, and Li BS (2008) Elastic wave velocities of $(Mg_{0.91}Fe_{0.09})_2SiO_4$ ringwoodite under P-T conditions of the mantle transition region. *Physics of the Earth and Planetary Interiors* 166: 167–174.
Hill R (1952) The elastic behaviour of a crystalline aggregate. *Proceedings of the Physical Society of London, Section A* 65: 349–355.
Hill R (1963) Elastic properties of reinforced solids: Some theoretical principles. *Journal of the Mechanics and Physics of Solids* 11: 357–372.
Holland TJB and Powell R (1998) An internally consistent thermodynamic data set for phases of petrological interest. *Journal of Metamorphic Geology* 16: 309–343.
Hsu H, Umemoto K, Blaha P, and Wentzcovitch RM (2010) Spin states and hyperfine interactions of iron in (Mg, Fe)SiO_3 perovskite under pressure. *Earth and Planetary Science Letters* 294: 19–26.
Isaak DG, Anderson OL, and Cohen RE (1992) The relationship between shear and compressional velocities at high pressures: Reconciliation of seismic tomography and mineral physics. *Geophysical Research Letters* 19: 741–744.
Isaak DG, Cohen RE, and Mehl ME (1990) Calculated elastic constants and thermal properties of MgO at high pressures and temperatures. *Journal of Geophysical Research* 95: 7055–7067.
Ita J and Stixrude L (1992) Petrology, elasticity, and composition of the mantle transition zone. *Journal of Geophysical Research: Solid Earth* 97: 6849–6866.
Jackson I (2000) Geophysics – Taking the Earth's temperature. *Nature* 406: 470–471.
Jackson DD and Anderson DL (1970) Physical mechanisms of seismic-wave attenuation. *Reviews of Geophysics and Space Physics* 8: 1–63.
Jackson I, Faul UH, Gerald JDF, and Tan BH (2004) Shear wave attenuation and dispersion in melt-bearing olivine polycrystals: 1. Specimen fabrication and mechanical testing. *Journal of Geophysical Research: Solid Earth* 109: B06201.
Jackson I, Gerald JDF, Faul UH, and Tan BH (2002) Grain-size-sensitive seismic wave attenuation in polycrystalline olivine. *Journal of Geophysical Research: Solid Earth* 107: 2360.
Jackson I and Niesler H (1982) The elasticity of periclase to 3 GPa and some geophysical implications. In: Akimoto S and Manghnani MH (eds.) *High-Pressure Research in Geophysics*, pp. 93–133. Tokyo: Center for Academic Publications.

Jackson JM, Sinogeikin SV, and Bass JD (2000) Sound velocities and elastic properties of gamma-Mg_2SiO_4 to 873 K by Brillouin spectroscopy. *American Mineralogist* 85: 296–303.
Jeanloz R (1989) Shock-wave equation of state and finite strain theory. *Journal of Geophysical Research: Solid Earth and Planets* 94: 5873–5886.
Jeanloz R and Thompson AB (1983) Phase transitions and mantle discontinuities. *Reviews of Geophysics* 21: 51–74.
Jiang FM, Speziale S, and Duffy TS (2004) Single-crystal elasticity of grossular- and almandine-rich garnets to 11 GPa by Brillouin scattering. *Journal of Geophysical Research: Solid Earth* 109: B10210.
Juanzemis W (1967) *Continuum Mechanics*. New York: MacMillan.
Karato S (1993) Importance of anelasticity in the interpretation of seismic tomography. *Geophysical Research Letters* 20: 1623–1626.
Karato S-I (1998) Seismic anisotropy in the deep mantle, boundary layers and the geometry of mantle convection. *Pure and Applied Geophysics* 151: 565–587.
Karki BB and Crain J (1998) First-principles determination of elastic properties of $CaSiO_3$ perovskite at lower mantle pressures. *Geophysical Research Letters* 25: 2741–2744.
Karki BB, Stixrude L, Clark SJ, Warren MC, Ackland GJ, and Crain J (1997a) Elastic properties of orthorhombic $MgSiO_3$ perovskite at lower mantle pressures. *American Mineralogist* 82: 635–638.
Karki BB, Stixrude L, Clark SJ, Warren MC, Ackland GJ, and Crain J (1997b) Structure and elasticity of MgO at high pressure. *American Mineralogist* 82: 51–60.
Karki BB, Stixrude L, and Wentzcovitch RM (2001) High-pressure elastic properties of major materials of Earth's mantle from first principles. *Reviews of Geophysics* 39: 507–534.
Kennett BLN and Engdahl ER (1991) Traveltimes for global earthquake location and phase identification. *Geophysical Journal International* 105: 429–465.
Kiefer B, Stixrude L, and Wentzcovitch RM (1997) Elastic constants and anisotropy of Mg_2SiO_4 spinel at high pressure. *Geophysical Research Letters* 24: 2841–2844.
Kieffer SW (1979) Thermodynamics and lattice vibrations of minerals, I: Mineral heat capacities and their relationship to simple lattice vibrational modes. *Reviews of Geophysics and Space Physics* 17: 1–19.
Kieffer SW (1980) Thermodynamics and lattice-vibrations of minerals 4. Application to chain and sheet silicates and orthosilicates. *Reviews of Geophysics* 18: 862–886.
Kippenhahn R, Weigert A, and Weiss A (2012) *Stellar Structure and Evolution*, 2nd edn., 668 pp. New York: Springer.
Kosevich AM, Lifshitz LD, Landau LD, and Pitaevskii LP (1986) *Theory of Elasticity*, 3rd edn., 195 pp. Oxford, UK: Butterworth-Heinemann.
Lax M (1974) *Symmetry Principles in Solid State and Molecular Physics*, 499 pp. New York: John Wiley and Sons.
Li L, Brodholt JP, Stackhouse S, Weidner DJ, Alfredsson M, and Price GD (2005) Electronic spin state of ferric iron in Al-bearing perovskite in the lower mantle. *Geophysical Research Letters* 32: L17307.
Li L and Weidner DJ (2008) Effect of phase transitions on compressional-wave velocities in the Earth's mantle. *Nature* 454: 984–986.
Liu J, Chen GL, Gwanmesia GD, and Leibermann RC (2000) Elastic wave velocities of pyrope-majorite garnets ($Py_{62}Mj_{38}$ and $Py_{50}Mj_{50}$) to 9 GPa. *Physics of the Earth and Planetary Interiors* 120: 153–163.
Mainprice D, Tommasi A, Couvy H, Cordier P, and Frost DJ (2005) Pressure sensitivity of olivine slip systems and seismic anisotropy of Earth's upper mantle. *Nature* 433: 731–733.
Mao Z, Lin JF, Liu J, and Prakapenka VB (2011) Thermal equation of state of lower-mantle ferropericlase across the spin crossover. *Geophysical Research Letters* 38: L23308.
Mao HK, et al. (2001) Phonon density of states of iron up to 153 gigapascals. *Science* 292: 914–916.
Marquardt H, Speziale S, Reichmann HJ, Frost DJ, Schilling FR, and Garnero EJ (2009) Elastic shear anisotropy of ferropericlase in Earth's lower mantle. *Science* 324: 224–226.
Masters TG and Widmer R (1995) Free oscillations: Frequencies and attenuations. In: Ahrens TJ (ed.) *Global Earth Physics*, pp. 104–125. Washington, DC: American Geophysical Union.
Matas J, Bass J, Ricard Y, Mattern E, and Bukowinski MSI (2007) On the bulk composition of the lower mantle: Predictions and limitations from generalized inversion of radial seismic profiles. *Geophysical Journal International* 170: 764–780.
Matas J and Bukowinski MST (2007) On the anelastic contribution to the temperature dependence of lower mantle seismic velocities. *Earth and Planetary Science Letters* 259: 51–65.
McCammon C, Kantor I, Narygina O, et al. (2008) Stable intermediate-spin ferrous iron in lower-mantle perovskite. *Nature Geoscience* 1: 684–687.
McCarthy C, Takei Y, and Hiraga T (2011) Experimental study of attenuation and dispersion over a broad frequency range: 2. The universal scaling of polycrystalline materials. *Journal of Geophysical Research: Solid Earth* 116: B09207.
McQueen RG, Marsh SP, and Fritz JN (1967) Hugoniot equation of state of 12 rocks. *Journal of Geophysical Research* 72: 4999–5036.
McQueen RG, Marsh SP, Taylor JW, Fritz JN, and Carter WJ (1970) The equation of state of solids from shock wave studies. In: Kinslow R (ed.) *High-Velocity Impact Phenomena*, pp. 293–417. New York, NY: Academic Press.
Mei S and Kohlstedt DL (2000a) Influence of water on plastic deformation of olivine aggregates 2. Dislocation creep regime. *Journal of Geophysical Research: Solid Earth* 105: 21471–21481.
Mei S and Kohlstedt DL (2000b) Influence of water on plastic deformation of olivine aggregates 1. Diffusion creep regime. *Journal of Geophysical Research: Solid Earth* 105: 21457–21469.
Merkel S, Goncharov AF, Mao HK, Gillet P, and Hemley RJ (2000) Raman spectroscopy of iron to 152 gigapascals: Implications for Earth's inner core. *Science* 288: 1626–1629.
Miyagi L, Kanitpanyacharoen W, Kaercher P, Lee KKM, and Wenk HR (2010) Slip systems in $MgSiO_3$ post-perovskite: Implications for D" anisotropy. *Science* 329: 1639–1641.
Murakami M, Ohishi Y, Hirao N, and Hirose K (2009) Elasticity of MgO to 130 GPa: Implications for lower mantle mineralogy. *Earth and Planetary Science Letters* 277: 123–129.
Murakami M, Ohishi Y, Hirao N, and Hirose K (2012) A perovskitic lower mantle inferred from high-pressure, high-temperature sound velocity data. *Nature* 485: 90–95.
Nguyen JH and Holmes NC (2004) Melting of iron at the physical conditions of the Earth's core. *Nature* 427: 339–342.
Nowacki A, Walker AM, Wookey J, and Kendall JM (2013) Evaluating post-perovskite as a cause of D" anisotropy in regions of palaeosubduction. *Geophysical Journal International* 192: 1085–1090.
Nowick AS and Berry BS (1972) *Anelastic Relaxation in Crystalline Solids*. New York: Academic Press.
Nye JF (1985) *Physical Properties of Crystals: Their Representation by Tensors and Matrices*, 2nd edn. Oxford: Oxford, UK.
Oganov AR, Brodholt JP, and Price GD (2001) The elastic constants of $MgSiO_3$ perovskite at pressures and temperatures of the Earth's mantle. *Nature* 411: 934–937.
Oganov AR and Dorogokupets PI (2003) All-electron and pseudopotential study of MgO: Equation of state, anharmonicity, and stability. *Physical Review B* 67: 224110.
Parlinski K, Lazewski J, and Kawazoe Y (2000) Ab initio studies of phonons in MgO by the direct method including LO mode. *Journal of Physics and Chemistry of Solids* 61: 87–90.
Pasternak MP, Taylor RD, Jeanloz R, Li X, Nguyen JH, and McCammon CA (1997) High pressure collapse of magnetism in $Fe_{0.94}O$: Mossbauer spectroscopy beyond 100 GPa. *Physical Review Letters* 79: 5046–5049.
Ping Y, Coppar F, Hicks DG, et al. (2013) Solid iron compressed up to 560 GPa. *Physical Review Letters* 111: 065501.
Ranganathan SI and Ostoja-Starzewski M (2008) Universal elastic anisotropy index. *Physical Review Letters* 101: 055504.
Ribe NM (1989) Seismic anisotropy and mantle flow. *Journal of Geophysical Research: Solid Earth and Planets* 94: 4213–4223.
Ricard Y, Matas J, and Chambat F (2009) Seismic attenuation in a phase change coexistence loop. *Physics of the Earth and Planetary Interiors* 176: 124–131.
Rigden SM, Gwanmesia GD, Fitz Gerald JD, Jackson I, and Liebermann RC (1991) Spinel elasticity and seismic structure of the transition zone of the mantle. *Nature* 354: 143–145.
Ringwood AE and Major A (1970) The system Mg_2SiO_4–Fe_2SiO_4 at high pressures and temperatures. *Physics of the Earth and Planetary Interiors* 3: 89–108.
Rivers ML and Carmichael ISE (1987) Ultrasonic studies of silicate melts. *Journal of Geophysical Research: Solid Earth and Planets* 92: 9247–9270.
Robie RA and Hemingway BS (1995) *Thermodynamic Properties of Minerals and Related Substances at 298.15 K and 1 bar (10^5 Pascals) Pressure and at Higher Temperature*, 461 pp. Washington, DC: United States Geological Survey.
Shapiro NM and Ritzwoller MH (2004) Thermodynamic constraints on seismic inversions. *Geophysical Journal International* 157: 1175–1188.
Shim SH, Jeanloz R, and Duffy TS (2002) Tetragonal structure of $CaSiO_3$ perovskite above 20 GPa. *Geophysical Research Letters* 29: 2166.
Sinogeikin SV and Bass JD (2000) Single-crystal elasticity of pyrope and MgO to 20 GPa by Brillouin scattering in the diamond cell. *Physics of the Earth and Planetary Interiors* 120: 43–62.
Sinogeikin SV and Bass JD (2002) Elasticity of majorite and a majorite-pyrope solid solution to high pressure: Implications for the transition zone. *Geophysical Research Letters* 29: 1017.

Spetzler H (1970) Equation of state of polycrystalline and single-crystal MgO to 8 kilobars and 800 degrees K. *Journal of Geophysical Research* 75: 2073–2087.

Speziale S, Jiang F, and Duffy TS (2005) Compositional dependence of the elastic wave velocities of mantle minerals: Implications for seismic properties of mantle rocks. In: van der Hilst RD, et al. (eds.) *Earth's Deep Mantle: Structure, Composition, and Evolution*, pp. 301–320. Washington, DC: American Geophysical Union.

Speziale S, Zha CS, Duffy TS, Hemley RJ, and Mao HK (2001) Quasi-hydrostatic compression of magnesium oxide to 52 GPa: Implications for the pressure–volume–temperature equation of state. *Journal of Geophysical Research: Solid Earth* 106: 515–528.

Stackhouse S, Brodholt JP, and Price GD (2007) Electronic spin transitions in iron-bearing $MgSiO_3$ perovskite. *Earth and Planetary Science Letters* 253: 282–290.

Stixrude L (1998) Elastic constants and anisotropy of $MgSiO_3$ perovskite, periclase, and SiO_2 at high pressure. In: Gurnis M, et al. (eds.) *The Core–Mantle Boundary Region*, pp. 83–96. Washington, DC: American Geophysical Union.

Stixrude L, Cohen RE, and Singh DJ (1994) Iron at high pressure: Linearized augmented plane wave calculations in the generalized gradient approximation. *Physical Review B* 50: 6442–6445.

Stixrude L, Cohen RE, Yu RC, and Krakauer H (1996) Prediction of phase transition in $CaSiO_3$ perovskite and implications for lower mantle structure. *American Mineralogist* 81: 1293–1296.

Stixrude L, de Koker N, Sun N, Mookherjee M, and Karki BB (2009) Thermodynamics of silicate liquids in the deep Earth. *Earth and Planetary Science Letters* 278: 226–232.

Stixrude L, Hemley RJ, Fei Y, and Mao HK (1992) Thermoelasticity of silicate perovskite and magnesiowustite and stratification of the Earth's mantle. *Science* 257: 1099–1101.

Stixrude L and Lithgow-Bertelloni C (2005a) Thermodynamics of mantle minerals – I. Physical properties. *Geophysical Journal International* 162: 610–632.

Stixrude L and Lithgow-Bertelloni C (2005b) Mineralogy and elasticity of the oceanic upper mantle: Origin of the low-velocity zone. *Journal of Geophysical Research: Solid Earth* 110: B03204.

Stixrude L and Lithgow-Bertelloni C (2007) Influence of phase transformations on lateral heterogeneity and dynamics in Earth's mantle. *Earth and Planetary Science Letters* 263: 45–55.

Stixrude L and Lithgow-Bertelloni C (2011) Thermodynamics of mantle minerals – II. Phase equilibria. *Geophysical Journal International* 184: 1180–1213.

Stixrude L and Lithgow-Bertelloni C (2012) Geophysics of chemical heterogeneity in the mantle. *Annual Review of Earth and Planetary Sciences* 40: 569–595.

Stixrude L, Lithgow-Bertelloni C, Kiefer B, and Fumagalli P (2007) Phase stability and shear softening in $CaSiO_3$ perovskite at high pressure. *Physical Review B* 75: 024108.

Trampert J, Vacher P, and Vlaar N (2001) Sensitivities of seismic velocities to temperature, pressure and composition in the lower mantle. *Physics of the Earth and Planetary Interiors* 124: 255–267.

Valencia D, O'Connell RJ, and Sasselov D (2006) Internal structure of massive terrestrial planets. *Icarus* 181: 545–554.

Wallace DC (1972) *Thermodynamics of Crystals*, 1st edn. New York: John Wiley and Sons.

Watt JP (1988) Elastic properties of polycrystalline minerals – Comparison of theory and experiment. *Physics and Chemistry of Minerals* 15: 579–587.

Watt JP, Davies GF, and Connell RJO (1976) The elastic properties of composite materials. *Reviews of Geophysics and Space Physics* 14: 541–563.

Weidner DJ, Bass JD, Ringwood AE, and Sinclair W (1982) The single-crystal elastic moduli of stishovite. *Journal of Geophysical Research* 87: 4740–4746.

Weiner JH (1983) *Statistical Mechanics of Elasticity*, 439 pp. New York: Wiley.

Wentzcovitch RM, Karki BB, Cococcioni M, and de Gironcoli S (2004) Thermoelastic properties of $MgSiO_3$-perovskite: Insights on the nature of the Earth's lower mantle. *Physical Review Letters* 92: 018501.

Wentzcovitch RM and Stixrude L (1997) Crystal chemistry of forsterite: A first principles study. *American Mineralogist* 82: 663–671.

Williams Q (1995) Infrared, Raman and optical spectroscopy of Earth materials. In: Ahrens TJ (ed.) *Mineral Physics and Crystallography: A Handbook of Physical Constants*. Washington, DC: American Geophysical Union.

Williams Q and Garnero EJ (1996) Seismic evidence for partial melt at the base of Earth's mantle. *Science* 273: 1528–1530.

Williamson ED and Adams LH (1923) Density distribution in the Earth. *Journal of the Washington Academy of Sciences* 13: 413–428.

Yoneda A (1990) Pressure derivatives of elastic-constants of single-crystal MgO and $MgAl_2O_4$. *Journal of Physics of the Earth* 38: 19–55.

Zaug JM, Abramson EH, Brown JM, and Slutsky LJ (1993) Sound velocities in olivine at Earth mantle pressures. *Science* 260: 1487–1489.

Zhang Z, Stixrude L, and Brodholt J (2013) Elastic properties of $MgSiO_3$-perovskite under lower mantle conditions and the composition of the deep Earth. *Earth and Planetary Science Letters* 379: 1–12.

1.27 Constraints on Seismic Models from Other Disciplines - Constraints on 3-D Seismic Models from Global Geodynamic Observables: Implications for the Global Mantle Convective Flow

AM Forte, Université du Québec à Montréal, Montréal, QC, Canada
NA Simmons, Lawrence Livermore National Laboratory, Livermore, CA, USA
SP Grand, University of Texas, Austin, TX, USA

© 2015 Elsevier B.V. All rights reserved.

This chapter is a revision of the previous edition chapter by A M Forte, Volume 1, pp. 805–858, © 2007, Elsevier B.V.

1.27.1	**Introduction**	853
1.27.2	**Geodynamic Observables and Mantle Flow Theory**	854
1.27.2.1	Convection-Related Surface Observations	854
1.27.2.2	Evidence for Mantle Flow in Correlations between Internal Structure and Surface Gravity Anomalies	857
1.27.2.3	Fluid Mechanical Modeling of Viscous Mantle Flow	858
1.27.2.3.1	Governing equations	858
1.27.2.3.2	Spectral treatment of the mantle flow equations	860
1.27.2.3.3	Internal boundary conditions	861
1.27.2.3.4	Boundary conditions at Earth's solid surface	863
1.27.2.3.5	Boundary conditions at CMB	864
1.27.2.3.6	Determining viscous flow Green functions	865
1.27.2.3.7	Incorporating tectonic plates as a surface boundary condition	866
1.27.2.4	Geodynamic Response Functions for the Mantle	868
1.27.2.5	Depth Dependence of Mantle Viscosity	869
1.27.3	**Modeling Geodynamic Observables with Seismic Tomography**	872
1.27.3.1	Seismic Heterogeneity Models	872
1.27.3.2	Mantle Density Anomalies	874
1.27.3.3	Predicted Tectonic Plate Motions	876
1.27.3.4	Predicted Free-Air Gravity Anomalies	876
1.27.3.5	Predicted Dynamic Surface Topography	876
1.27.3.6	Predicted CMB Topography	885
1.27.4	**Joint Seismic–Geodynamic Inversions for 3-D Structure and Flow in the Mantle**	885
1.27.4.1	Deficiencies in Mantle Flow Models Based on Pure Seismic Tomography Inversions	886
1.27.4.2	Mantle Flow Modeling Based on Tomography Models Derived from Seismic Data Alone Is Insufficient	888
1.27.4.3	Simultaneous Inversions of Seismic, Geodynamic, and Mineral Physical Data	889
1.27.4.3.1	Geodynamic and seismic data sets	889
1.27.4.3.2	Joint inversion procedure	890
1.27.4.4	Relating Mantle Density and Seismic Velocity Anomalies	890
1.27.4.5	Joint Seismic–Geodynamic Mapping of Density Anomalies	894
1.27.4.6	Implications for Global Mantle Flow	897
1.27.5	**Concluding Remarks**	902
Acknowledgments		903
References		903

1.27.1 Introduction

The earliest tomography models (e.g., Clayton and Comer, 1983; Dziewonski et al., 1977; Dziewonski, 1984 – reported in Hager and Clayton, 1989; Woodhouse and Dziewonski, 1984) exhibited a large-scale three-dimensional (3-D) structure in Earth's mantle, which was reasonably well correlated to the major surface manifestations of mantle convection, namely, the large-scale nonhydrostatic geoid (Hager et al., 1985) and the large-scale tectonic plate motions (Forte and Peltier, 1987). These early models of mantle heterogeneity thus helped to show that seismic tomography can indeed resolve the lateral variations in mantle structure, which drive the convective flow responsible for the 'drift' of the continents and the large-scale perturbations in Earth's gravitational field.

Steady progress in global seismic tomographic imaging over the past 15 years has yielded models of 3-D mantle structure, which posses significantly improved resolution and reliability (e.g., Antolik et al., 2003; Boschi and Dziewonski, 2000; Ekström and Dziewonski, 1998; Grand, 2002; Kustowski et al., 2008; Li et al., 2008; Masters et al., 2000; Mégnin and Romanowicz, 2000; Ritsema et al., 1999, 2011; Simmons et al., 2010). These improvements are evident in the remarkable accord among the images of large-scale mantle structure

provided by these different models. Such agreement is encouraging, especially when we consider that these models are obtained on the basis of different data sets, different theoretical treatments of seismic wave propagation, and different algorithms for inverting the global seismic data. Helpful reviews of the methods, data sets, and current challenges in global seismic imaging may be found in Dziewonski and Romanowicz (2007) and Thurber and Ritsema (2007).

While the analyses and discussion presented in the preceding text will focus on how seismically inferred 3-D mantle structure may be used to explain geodynamic data and to model mantle flow dynamics, it is important to note that much effort has also been dedicated to the converse approach, namely, to infer 3-D mantle structure from geodynamic data. This inverse approach based on geodynamic constraints began at almost the same time as the earliest global tomography inversions. Hager (1984) proposed a mantle flow model based on estimated density anomalies associated with seismically active subducted slabs and used this model to obtain a good match to very long-wavelength geoid anomalies. Although subsequent studies, for example, by Ricard et al. (1989), attempted a more general inference of mantle heterogeneity using different geodynamic data, the subducted slab geodynamic models developed by Hager (1984) became prevalent. This led, for example, to a study by Forte and Peltier (1989), which constrained the distribution of subducted slab heterogeneity using other geodynamic observables such as tectonic plate motions and core–mantle boundary (CMB) topography. The latter study also attempted to use the geodynamic observables to infer the buoyancy forces associated with mantle plumes under mid-ocean ridges.

Tectonic plate motions and long-wavelength geoid anomalies have proved to be the most important constraints in developing geodynamic models of 3-D mantle heterogeneity in terms of subducted slabs. The geologic history of tectonic plate motions as derived from paleomagnetic data (e.g., Gordon and Jurdy, 1986) has been an especially important ingredient in developing models of both past and present-day subducted slab heterogeneities (e.g., Ricard et al., 1993; Richards and Engebretson, 1992). These models have been very useful for exploring time-dependent dynamics of the mantle (e.g., Lithgow-Bertelloni and Gurnis, 1997; Lithgow-Bertelloni and Richards, 1998). Direct comparisons between the long-wavelength pattern of subducted slab heterogeneity and the corresponding pattern of heterogeneity derived from seismic tomography have shown good correlations at the longest wavelengths (Richards and Engebretson, 1992). When all wavelengths are considered, however, the global correlations between the slab heterogeneity and different tomography models are relatively poor, with correlation coefficients <0.3 throughout the mantle (Figure 7 in Lithgow-Bertelloni and Richards, 1998).

There are various factors that might explain the less than satisfactory agreement between the seismic models of 3-D mantle structure and the reconstructions of mantle heterogeneity in terms of subducted slabs. Firstly, from a purely technical perspective, the evolution of the slab trajectories was not determined in a fluid mechanically consistent manner by numerically solving the advection–diffusion equations. Progress in this direction has been made by Bunge et al. (1998), McNamara and Zhong (2005), and Quéré and Forte (2006) by solving the full set of thermal convection equations with moving tectonic plates as a surface boundary condition. Secondly, the slab models assume that thermally generated heterogeneity dominates in the mantle and this may not be applicable in regions of the mantle with significant compositional heterogeneity (e.g., Forte and Mitrovica, 2001; McNamara and Zhong, 2005). Perhaps the most important deficiency in these efforts to explain mantle heterogeneity in terms of slab subduction alone is that they do not account for the presence and evolution of hot thermal plumes in the mantle, which have been consistently imaged in the global tomography models (e.g., Montelli et al., 2004; Nolet et al., 2006). A recent appraisal of the origin and importance of mantle plumes in convection models that incorporate 3-D mantle structure derived from seismic tomography may be found in Glisovic et al. (2012).

Seismic tomography continues to be the single most important technique for directly inferring the 3-D heterogeneity in the mantle, which is associated with the process of thermal convection. The significant advances in global seismic imaging over the past few years provide the underlying motivation for the detailed discussion of the geodynamic implications, which will be presented in the succeeding text. A recent detailed review by Becker and Boschi (2002) of the currently available tomography models focused on a quantitative analysis of similarities and differences between these models. The work presented in the succeeding text will further extend this previous analysis by carrying out calculations of the mantle flow predicted on the basis of these tomography models and examining in detail the extent to which the tomography-based flow models provide a satisfactory explanation for the main convection-related surface observables.

1.27.2 Geodynamic Observables and Mantle Flow Theory

In the following, the main global geophysical constraints on mantle structure will be presented. These constraints include the free-air gravity anomalies, the dynamic surface and CMB topography, and the tectonic plate motions. The theoretical relationship between these convection-related observables and the internal 3-D structure will be developed in terms of a fluid mechanical model of mantle dynamics.

1.27.2.1 Convection-Related Surface Observations

An understanding of thermal convection in the mantle is necessary for explaining a multitude of geophysical and geologic processes, which we can observe and measure at the surface of the Earth, such as continental drift, earthquakes, mountain building, volcanism, perturbations in Earth's gravitational field, variations in oceanic bathymetry and continental elevation, and long-term changes in global sea-level variations. The principal surface manifestations of mantle convection that have been employed to study the large-scale structure and dynamics of the solid Earth are illustrated schematically in **Figure 1**.

The observational constraints on 3-D mantle structure and dynamics, which will be considered in the succeeding text, are the global free-air gravity anomalies, the dynamic surface and

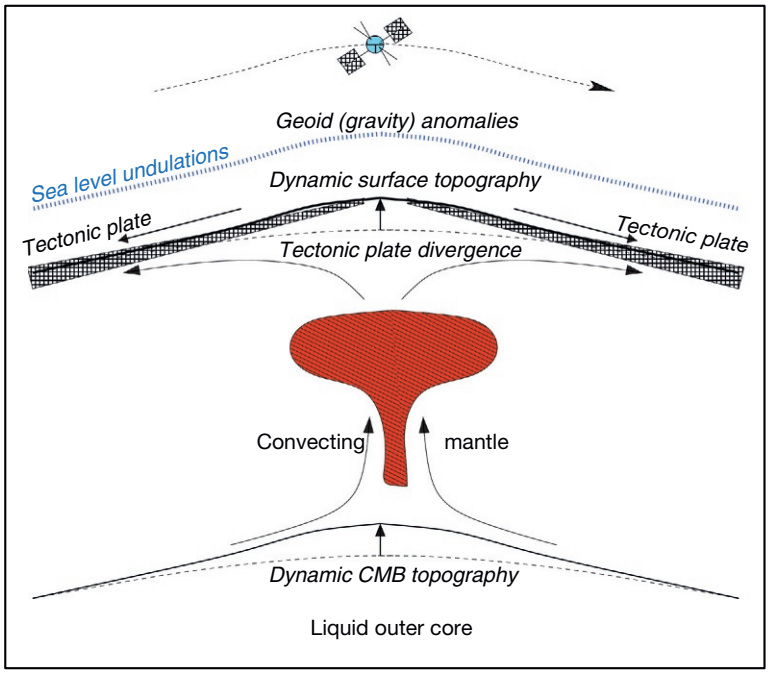

Figure 1 Convection-related surface observations. The most direct manifestations of thermal convection in the mantle (represented schematically by the upwelling plume colored in red) are the surface motions of tectonic plates – which may be summarized by their horizontal divergence field – and the flow-induced topography of the solid surface and the core–mantle boundary (CMB). The boundary undulations and the density anomalies in the mantle (due, e.g., to the hot upwelling plume) give rise to surface gravitational potential perturbations, which may be measured in terms of geoid or gravity anomalies.

CMB topography, and the horizontal divergence of the tectonic plate motions. The Earth's gravitational potential perturbations are usually represented in terms of geoid anomalies; however, as pointed out in Forte et al. (1994), a more detailed and evenly balanced representation (especially at long wavelengths) of the spectral content is provided by the free-air gravity anomalies shown in **Figure 2(a)**.

We will employ the term 'dynamic topography' to mean all contributions to Earth's surface topography, which arise from density anomalies in the convecting mantle – including the lithosphere. Observational constraints on dynamic topography therefore require an accurate model of crustal heterogeneity in order to remove all isostatic crustal contributions to Earth's measured surface topography. The topographic crustal correction, here based on model CRUST2.0 (Bassin et al., 2000), is described in detail by Perry et al. (2003), and the resulting dynamic topography is shown in **Figure 2(b)**.

The tectonic plate velocity field $\mathbf{v}$ may be conveniently summarized in terms of two complimentary scalar fields: the horizontal divergence $\nabla_H \cdot \mathbf{v}$ and the radial vorticity $\hat{\mathbf{r}} \cdot \nabla \times \mathbf{v}$ (Forte and Peltier, 1987). The constraint of plate rigidity imposes a linear dependence between these two scalar fields (Forte and Peltier, 1991), and hence, it suffices that we consider only the plate divergence, shown in **Figure 2(c)**. (A more detailed discussion of the implications of plate rigidity, in terms of allowed plate motions, is also presented in **Section 1.27.2.3.7**.)

The most robust global constraint on deep-mantle density heterogeneity and dynamics (Forte et al., 1995a,b) is currently provided by the dynamic ellipticity of the CMB shown in **Figure 2(d)**. The discrepancy between theoretical predictions of the free core nutation (FCN) period (Wahr, 1981) and the value determined from very long baseline interferometry (Herring et al., 1986) led Gwinn et al. (1986) to conclude that the CMB ellipticity is larger than that implied by theoretical calculations, which assumed a rotating Earth in hydrostatic equilibrium. This inference of an 'excess' ellipticity, in which the nonhydrostatic radius of the CMB at the poles is 400 m less than at the equator, is supported by recent analyses of the FCN period (Mathews et al., 2002).

The most appropriate mathematical basis functions for describing any bounded and continuous function on a spherical surface are the spherical harmonics $Y_\ell^m(\theta, \varphi)$, where position on the spherical surface is defined by colatitude θ and colongitude ϕ. We may therefore expand the geodynamic observables in **Figure 2** in terms of spherical harmonics as follows:

$$f(\theta, \varphi) = \sum_{\ell=0}^{\infty} \sum_{m=-\ell}^{+\ell} f_\ell^m \, Y_\ell^m(\theta, \varphi) \qquad [1]$$

where the function $f(\theta, \phi)$ represents any of the observables (gravity, topography, or plate divergence) and the indices ℓ, m, which characterize each spherical harmonic, are called the *harmonic degree* and *azimuthal order*, respectively. (A useful introduction to spherical harmonic functions may be found in Jackson, 1975.)

The spatial variation of the spherical harmonics is oscillatory in character; it may be characterized in terms of an equivalent horizontal wavelength. On a spherical surface of radius r,

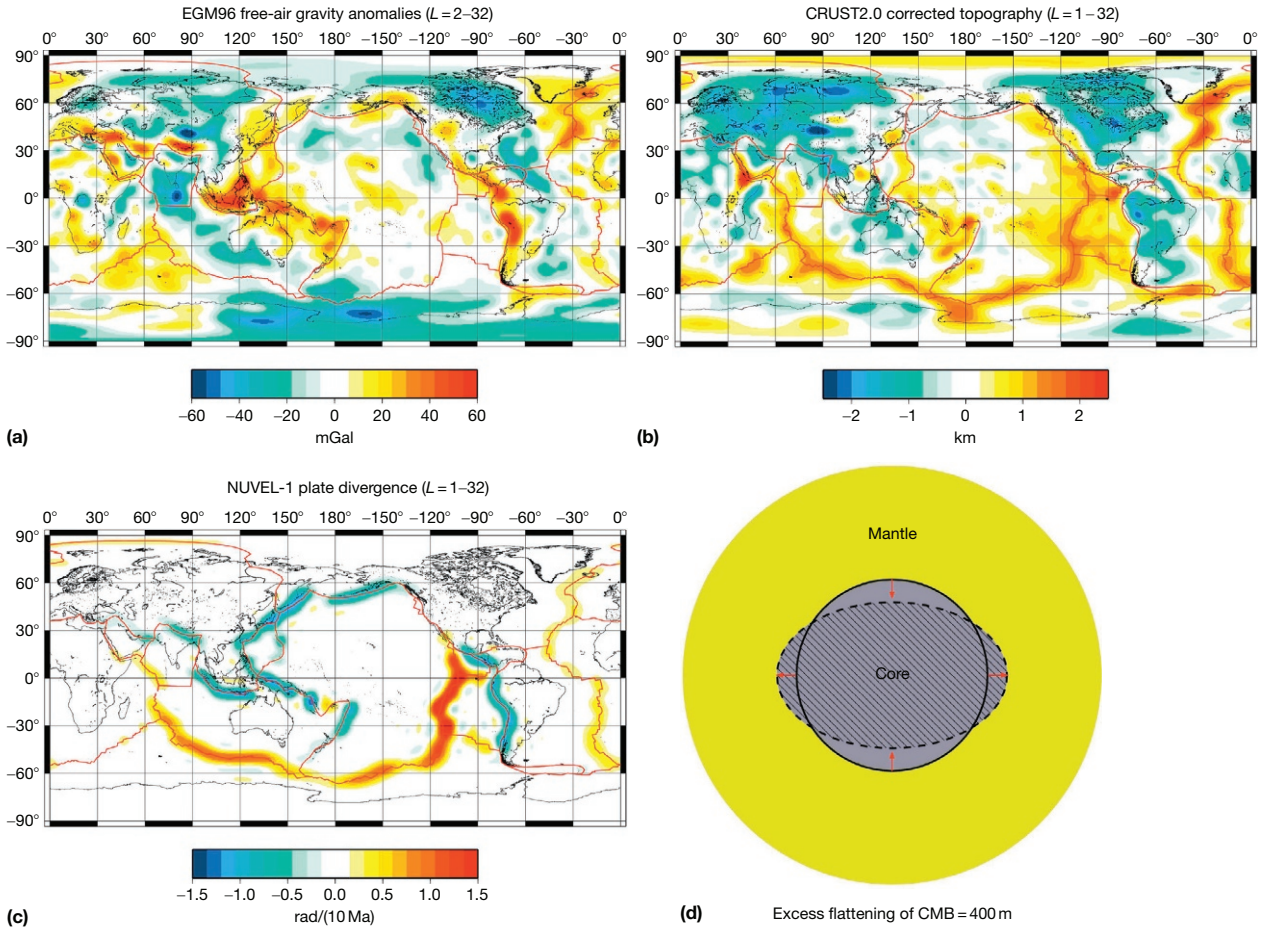

Figure 2 Geodynamic observables. (a) The free-air gravity anomalies derived from the joint geopotential model EGM96 (Lemoine et al., 1998). (b) The dynamic surface topography obtained by removing the topography due to isostatically compensated crustal heterogeneity from Earth's observed topography. The CRUST2.0 (Bassin et al., 2000) crustal heterogeneity model is employed here. (c) The horizontal divergence of the tectonic plate velocities given by the NUVEL-1 model (DeMets et al., 1990). (d) The excess or dynamic CMB ellipticity inferred from core nutation data (Mathews et al., 2002). All fields, with the exception of (d), have been expanded in spherical harmonics up to degree and order 32 (see eqn [1]).

a spherical harmonic $Y_\ell^m(\theta,\varphi)$ has a characteristic wavelength λ_ℓ given by the following expression:

$$\lambda_\ell = \frac{2\pi r}{\sqrt{\ell(\ell+1)}} \approx \frac{2\pi r}{\ell+\frac{1}{2}}, \text{valid for } \ell \gg 1 \qquad [2]$$

In practice, the infinite sum over degree ℓ in eqn [1] is truncated at some finite value ℓ_{max} and for the fields in Figure 2 it is $\ell_{max}=32$. At the Earth's surface ($r=6368$ km), this is equivalent to a minimum horizontal length scale (or half wavelength) of about 600 km.

Spherical harmonic representations of surface fields can be used to quantify their spectral content in terms of an amplitude spectrum. The amplitude spectrum measures the mean (globally averaged) amplitude of a field at a particular wavelength λ_ℓ [2], and it is defined in terms of a 'degree variance' σ_ℓ as follows:

$$\sigma_\ell = \sqrt{\sum_{m=-\ell}^{+\ell} f_\ell^{m^*} f_\ell^m} \qquad [3]$$

in which f_ℓ^m are the spherical harmonic coefficients of the surface field (see expression [1]) and * denotes complex conjugation.

A spectral description of the spatial correlation between two fields, as a function of harmonic degree or wavelength, is quantified in terms of 'degree correlation' r_ℓ, defined as follows:

$$r_\ell = \frac{\sum_{m=-\ell}^{+\ell} f_{1\ell}^{m*} f_{2\ell}^m}{\sqrt{\sum_{m=-\ell}^{+\ell} f_{1\ell}^{m*} f_{1\ell}^m}\sqrt{\sum_{m=-\ell}^{+\ell} f_{2\ell}^{m^*} f_{2\ell}^m}} \qquad [4]$$

in which $f_{1\ell}^m$ and $f_{2\ell}^m$ are the spherical harmonic coefficients of the two fields.

Degree variances and correlations are very useful spectral characterizations of the amplitude and spatial variation of globally defined surface fields (e.g., O'Connell, 1971), and would be used frequently in the discussions presented in the succeeding text.

1.27.2.2 Evidence for Mantle Flow in Correlations between Internal Structure and Surface Gravity Anomalies

The need for a dynamic interpretation of the surface observables (Figure 2) in terms of very deep-seated convective flow in the mantle is illustrated in Figure 3 in which long-wavelength gravity anomalies are directly compared to seismically inferred lateral heterogeneity in the lower mantle. The large-scale pattern of faster than average shear velocities, which lie below the periphery of the Pacific Ocean (blue-colored regions in Figure 3(b)), has long been interpreted in terms of accumulating lithospheric slabs, which have subducted below the margins of the Pacific Ocean since Mesozoic times (Chase, 1979; Chase and Sprowl, 1983; Richards and Engebretson, 1992). These seismic anomalies, which presumably represent positive density anomalies (i.e., cold subducted slabs), are closely correlated with a broad ringlike pattern of negative gravity anomalies around the periphery of the Pacific Ocean (red-colored regions in Figure 3(a)).

The correlation between long-wavelength seismic heterogeneity in the lower-mantle and surface gravity anomalies was first identified by Dziewonski et al. (1977), and they postulated that a dynamic interpretation in terms of mantle flow could explain the negative sign of the correlation. In a rigid or elastic mantle in which flow is absent, a positive correlation between internal density and surface gravity is expected. However, in a convecting mantle, the gravitational signal of internal density anomalies is opposed by the effect of flow-induced topography at the surface and at the CMB, and this dynamic balance can lead to the observed negative correlation (e.g., Parsons and Daly, 1983; Pekeris, 1935; Richards and Hager, 1984).

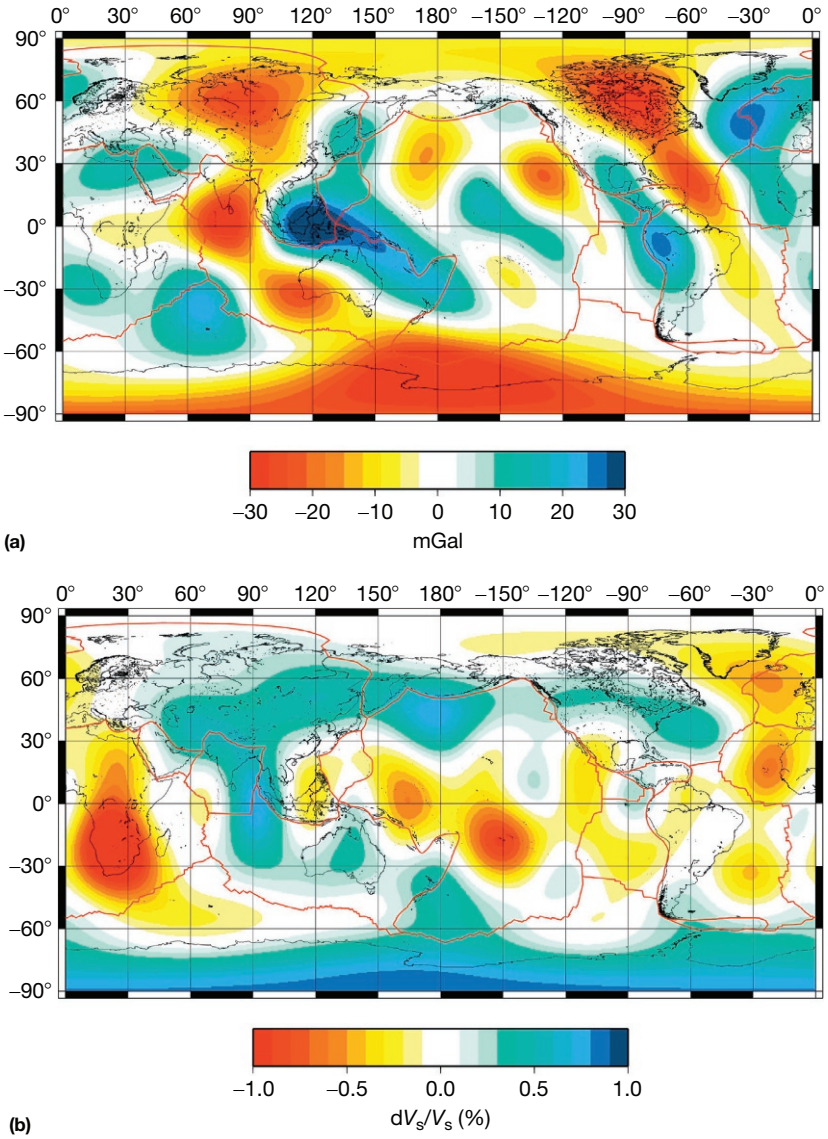

Figure 3 Surface gravity anomalies and deep-mantle heterogeneity. (a) Long-wavelength free-air gravity anomalies derived from the joint geopotential model EGM96 (Lemoine et al., 1998). (b) Long-wavelength seismic shear-velocity anomalies at a depth of 2100 km derived from the tomography model of Grand (2002). Both the gravity and seismic anomaly fields are synthesized from spherical harmonics in the degree range $\ell = 1 - 8$.

It is instructive to consider a more detailed spectral analysis of the correlation between surface gravity anomalies and seismically inferred lateral heterogeneity at different depths in the mantle. The degree correlations shown in Figure 4 indicate which depth ranges in the mantle may be important contributors to the different wavelengths of the surface gravitational field. The strongest positive correlations appear in the transition zone region of the mantle (from ~400 to ~800 km depth), and at the longest wavelength (degree 2), they extend down to about 1400 km depth. The positive sign of these correlations indicates that long-wavelength gravity highs overlie similarly large-scale seismically fast regions located at the base of the upper mantle. Negative degree correlations between long-wavelength seismic and gravity anomalies are found in the near-surface region, down to about 400 km depth and in lower mantle below 1400 km depth (as in Figure 3) where the strongest negative correlations are found. These depth-dependent degree correlations, obtained on the basis of long-wavelength tomography models derived more than a decade ago, are robust observations, which have been verified using the latest seismic tomographic inferences of 3-D mantle structure (Ricard et al., 2006).

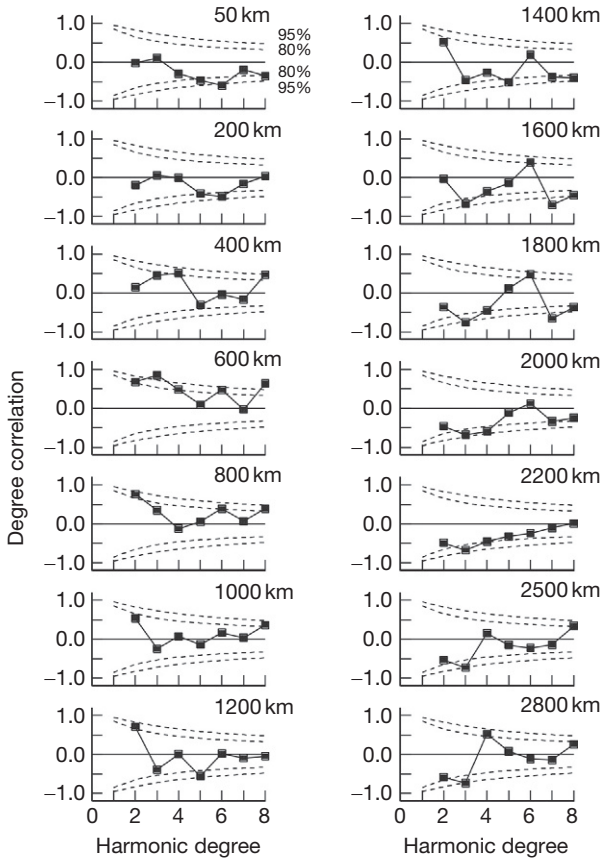

Figure 4 Depth-dependent correlations between 3-D mantle structure and gravity anomalies. Each frame shows the degree correlations between surface gravity anomalies and lateral variations in seismic shear velocity at a particular depth in the mantle. The seismic anomalies are derived from an earlier long-wavelength tomography model *SH8/U4L8* (Forte et al., 1993a). Adapted from Forte AM, Dziewonski AM, and Woodward RL (1993a) Aspherical structure of the mantle, tectonic plate motions, nonhydrostatic geoid, and topography of the core-mantle boundary. In: LeMouël J-L, Smylie DE, and Herring T (eds.) *Dynamics of the Earth's Deep Interior and Earth Rotation*. Geophysical Monograph Series, vol. 72, pp. 135–166, Washington, DC: American Geophysical Union.

The correlation between mantle heterogeneity and surface gravity anomalies in a convecting mantle has been shown to be a strong function of the depth dependence of the rheological properties of the mantle (e.g., Forte and Peltier, 1987; Hager, 1984; Hager et al., 1985; Ricard et al., 1984). In particular, as will be discussed further in the succeeding text, the change from positive correlations at the top of the lower mantle to negative correlations at the bottom of lower mantle (Figure 4) can be interpreted in terms of a significant increase in mean viscosity across the mantle. Other surface observables, such as the tectonic plate motions, also provide important constraints on the depth dependence of mantle rheology (e.g., Forte et al., 1991; Ricard and Vigny, 1989). The geodynamic surface observables also provide direct constraints on the 3-D distribution of density anomalies in the mantle, and hence, these observables provide a fundamentally important and independent means of evaluating the extent to which seismic tomography models successfully resolve the lateral heterogeneity in the mantle, which is associated with mantle convection.

In the next section, the dynamic link between lateral heterogeneity in the mantle and convection-related surface observables will be developed in the theoretical framework of a fluid mechanical model of viscous flow in the mantle. The reader wishing to skip over this detailed mathematical treatment of the mantle flow theory is encouraged to jump directly to Sections 1.27.2.4 and 1.27.2.5, where the viscous response of the mantle and current mantle viscosity inferences, respectively, are summarized.

1.27.2.3 Fluid Mechanical Modeling of Viscous Mantle Flow

1.27.2.3.1 Governing equations

Laboratory and geologic evidence of the ability of mantle rocks to creep indefinitely over geologic timescales is understood in terms of the existence of atomic-scale defects in the lattice of crystal grains (e.g., Nicolas and Poirier, 1976). If the ambient mantle temperature is sufficiently high, the imposition of nonhydrostatic stresses causes the lattice defects to propagate and thus allows the mantle rocks to creep or 'flow' slowly. This process may be characterized in terms of a single parameter, namely, an effective viscosity (e.g., Weertman, 1978; Weertman and Weertman, 1975).

The characterization of the long-term creep properties of the mantle in terms of an effective viscosity allows us to model the slow flow of the mantle with the conventional hydrodynamic field equations. The hydrodynamic field equations (Landau and Lifshitz, 1959), which express the principles of conservation of mass and momentum, are

$$\frac{\partial \rho}{\partial t} + \nabla \cdot (\rho \mathbf{u}) = 0 \qquad [5]$$

$$\rho \frac{\mathrm{d}\mathbf{u}}{\mathrm{d}t} = \nabla \cdot \boldsymbol{\sigma} + \rho \mathbf{g} \qquad [6]$$

in which $\mathbf{u}$ is the velocity field, $\mathrm{d}/\mathrm{d}t = \partial/\partial t + \mathbf{u}\cdot\nabla$ is the total (Lagrangian) time derivative, $\boldsymbol{\sigma}$ is the stress tensor, g is the gravitational acceleration, and ρ is the density.

We may represent the gravitational field $\mathbf{g}$ in terms of a gravitational potential:

$$\mathbf{g} = \nabla\phi \qquad [7]$$

Notice that the sign convention adopted here is opposite to that generally adopted in classical physics, where a *negative* gradient of the potential is used. With this sign convention, Poisson's equation for the relationship between the gravity potential and density is

$$\Delta\phi = -4\pi G\rho \quad (\Delta \equiv \nabla\cdot\nabla) \qquad [8]$$

An explicit expression for the stress tensor is given by

$$\sigma_{ij} = -P\delta_{ij} + \tau_{ij} \qquad [9]$$

$$\text{with } \tau_{ij} = \eta\left(u_{i,j} + u_{j,i} - \frac{2}{3}\delta_{ij}u_{k,k}\right) + \lambda\delta_{ij}u_{k,k} \qquad [10]$$

where τ_{ij} is the viscous stress tensor, δ_{ij} is the identity tensor, P is the total pressure, η and λ are the *isotropic* viscosity coefficients, and $u_{i,j} = \partial u_i/\partial x_j$ represents the derivative of the velocity components i with respect to the coordinate direction j.

A number of simplifications are possible when applying the earlier field equations to the problem of flow in the mantle:

- Since mantle rocks creep much slower than the acoustic velocity in the mantle, we can safely ignore the term $\partial\rho/\partial t$ in the conservation of mass (eqn [5]), and we thus have the following anelastic-liquid approximation:

$$\nabla\cdot(\rho\mathbf{u}) = 0 \qquad [11]$$

This simplification will explicitly rule out acoustic waves as solutions of the flow equations.

- The second viscosity coefficient λ in the viscous stress tensor τ_{ij} describes the dissipation associated with change in fluid volume (density). This volume dissipation may be neglected if the changes in fluid volume occur on timescales that are much longer than for molecular relaxation processes (Landau and Lifshitz, 1959), and this is certainly true for mantle flow. Therefore, the viscous stress tensor τ_{ij} will be purely deviatoric:

$$\tau_{ij} = \eta\left(u_{i,j} + u_{j,i} - \frac{2}{3}\delta_{ij}u_{k,k}\right) \qquad [12]$$

- We will further assume a Newtonian (i.e., linear) rheology, in which the mantle viscosity η is not a function of stress or strain rate. This assumption is not necessarily appropriate for the mantle (particularly in high-stress regions, such as subduction zones), but it will greatly simplify the mathematical resolution of the flow equations, which is presented in the succeeding text.
- A major simplification, from a purely mathematical standpoint, derives from the assumption that mantle viscosity varies only with radius. Although this assumption will significantly simplify the mathematical treatment of the flow theory, it may have important physical implications for the dynamics of buoyancy-induced flow in the mantle (e.g., Richards and Hager, 1989). These implications have been examined previously in the context of global-scale flow in 3-D spherical geometry (e.g., Čadek and Fleitout, 2003; Forte and Peltier, 1994; Martinec et al., 1993; Moucha et al., 2007; Ricard et al., 1988; Zhang and Christensen, 1993) and they will be discussed later.
- A fundamental physical simplification arises from the very large value of the effective viscosity in the mantle. We may nondimensionalize the conservation of momentum equation with the following variable transformations:

$$\left.\begin{aligned}(x, y, z) &= (\mathrm{d}x, \mathrm{d}y, \mathrm{d}z)\\ t &= \left(d^2/\kappa_o\right)t\\ \rho = \rho_o\rho;& g = g_o g; \eta = \eta_o\eta\end{aligned}\right\} \qquad [13]$$

where the original variables are on the left and the nondimensional ones are on the right. Quantities d, κ_o, ρ_o, η_o, g_o are characteristic scales for length, thermal diffusivity, density, viscosity, and gravitational acceleration, respectively, in the mantle. The use, in eqn [13], of a thermal diffusion timescale

$$t_\kappa = d^2/\kappa_o \qquad [14]$$

is appropriate since we are dealing with mantle flow arising from thermal convection. The stress tensor and pressure have the same physical units (see expression [9]), and hence, their nondimensional transformation is

$$P = (\rho_o g_o d)\, P \quad \text{and} \quad \boldsymbol{\tau} = (\rho_o g_o d)\boldsymbol{\tau} \qquad [15]$$

where, again, the original quantities are on the left and the nondimensional ones on the right. By virtue of the constitutive relation [12], and expression [15], we obtain the following nondimensional transformation for the flow variable:

$$\mathbf{u} = \frac{\rho_o g_o d^2}{\eta_o}\mathbf{u} \qquad [16]$$

or, equivalently,

$$\mathbf{u} = g_o t_v \mathbf{u} \qquad [17]$$

where $t_v = d^2/v_o$ is the timescale for viscous diffusion of momentum and $v_o = \eta_o/\rho_o$ is the kinematic viscosity. Finally, substitution of expressions [9] and [13]–[17] into [6] yields the following nondimensional momentum conservation equation:

$$\rho\left[\frac{1}{Pr}\frac{\partial\mathbf{u}}{\partial t} + \left(\frac{g_o}{d}\right)t_v^2\mathbf{u}\cdot\nabla\mathbf{u}\right] = \nabla\cdot\boldsymbol{\tau} - \nabla P + \rho\mathbf{g} \qquad [18]$$

in which $Pr = t_\kappa/t_v$ is the Prandtl number, which characterizes the ratio of temperature and momentum diffusion timescales.

To assess the importance of the terms on the left-hand side of eqn [18], we assume the following values for the scaling variables: $d = 3\times10^6$ m (for whole-mantle flow), $\rho_o = 3.3\times10^3$ kg m^{-3}, $g_o = 10$ m s^{-2}, $\kappa_o = 1.5\times10^{-6}$ m^2 s^{-1}, and $\eta_o = 10^{21}$ Pa s, and we thus obtain

$$\begin{aligned}&t_v = 3\times10^{-5}\,\mathrm{s};\ t_\kappa = 6\times10^{18}\,\mathrm{s};\ \frac{g_o}{d} = 3.3\times10^{-6}\,\mathrm{s}^{-2};\\ &Pr = 2\times10^{23}\end{aligned} \qquad [19]$$

The key quantity here is the characteristic time for momentum diffusion t_v, which is very small (i.e., mantle flow will

come to a complete halt in much less than a millisecond if all buoyancy forces are suddenly removed).

The vanishingly small momentum diffusion time, and hence the very large Prandtl number, implies that the inertial forces ($\rho \mathrm{d}\mathbf{u}/\mathrm{d}t$) in the momentum conservation equation are completely negligible. Therefore, using expression [7], the momentum conservation (eqn [6]) simplifies to

$$\nabla\cdot\boldsymbol{\tau} - \nabla P + \rho\nabla\phi = \mathbf{0} \qquad [20]$$

Equation [20] shows that in the absence of inertia, there must at all times be a balance between the buoyancy forces $\rho\mathbf{g}$ and the forces of viscous dissipation described by $\nabla\cdot\boldsymbol{\tau}$. In other words, any changes in internal buoyancy forces will instantly produce changes in fluid flow: this is a consequence of the essentially instantaneous diffusion of momentum in the mantle.

We may define an idealized hydrostatic reference state for the mantle, which corresponds to the absence of any internal flow or deformation (i.e., $\mathbf{u} = \mathbf{0}$). In this situation, the deviatoric stress field τ vanishes and the momentum conservation (eqn [6]) reduces to

$$-\nabla P_o + \rho_o \nabla\phi_o = 0 \qquad [21]$$

in which P_o, ρ_o, and ϕ_o are the pressure, density, and gravity potentials in the hydrostatic state. Poisson's eqn [8] for a hydrostatic planet is

$$\Delta\phi_o = -4\pi G\rho_o \qquad [22]$$

We assume that in a dynamic mantle, with a nonvanishing mantle flow $\mathbf{u}$, the pressure, density, and gravity potentials will be perturbed as follows:

$$P = P_o + P_1 \quad \rho = \rho_o + \rho_1 \quad \phi = \phi_o + \phi_1 \qquad [23]$$

in which all perturbations are assumed to be small, that is,

$$\left|\frac{P_1}{P_o}\right| \ll 1 \quad \left|\frac{\rho_1}{\rho_o}\right| \ll 1 \quad \left|\frac{\phi_1}{\phi_o}\right| \ll 1$$

If we now substitute the perturbed variables [23] into the equations of mass and momentum conservation ([11]–[20]) and Poisson's eqn [8] and then subtract out the hydrostatic reference (eqns [21] and [22]), we finally obtain the following set of first-order accurate, perturbed equations for mantle flow dynamics:

$$\text{mass conservation} \quad \nabla\cdot(\rho_o\mathbf{u}) = 0 \qquad [24]$$

$$\text{momentum conservation} \quad \nabla\cdot\boldsymbol{\tau} - \nabla P_1 + \rho_o\nabla\phi_1 + \rho_1\nabla\phi_o = \mathbf{0} \qquad [25]$$

$$\text{gravity} \quad \boldsymbol{\Delta}\phi_1 = -4\pi G\rho_1 \qquad [26]$$

Notice in eqn [25] that in addition to the driving buoyancy forces ($\rho_1\nabla\phi_o$), there also exist self-gravitational loads ($\rho_o\nabla\phi_1$) due to the perturbed gravitational field. The equations in the preceding text must be supplemented by the linear relationship [12] between stress and strain rate, which is valid for an isotropic rheology:

$$\text{Newtonian constitutive equation} \quad \boldsymbol{\tau} = \eta\left(\vec{\nabla}\mathbf{u} + \mathbf{u}\overleftarrow{\nabla} - \frac{2}{3}\,\mathbf{I}\,\nabla\cdot\mathbf{u}\right) \qquad [27]$$

1.27.2.3.2 Spectral treatment of the mantle flow equations

A classical technique for solving the dynamic flow equations in 3-D spherical geometry is the spectral Green function method, in which all flow variables are expressed in terms of spherical harmonic basis functions introduced in eqn [1] (e.g., Forte and Peltier, 1987, 1991; Hager and O'Connell, 1981; Ricard et al., 1984; Richards and Hager, 1984). The spectral Green functions provide a very convenient mathematical description of the instantaneous relationship between the mantle density anomalies and the viscous flow field, as well as all surface manifestations of the internal flow dynamics.

The spectral method is employed here for solving the coupled equations of mass, momentum, and gravity conservation (eqns [24]–[26]), supplemented by the viscous constitutive relation [27]. The method follows that initially developed by Forte and Peltier (1991) for gravitationally consistent compressible flow in spherical geometry. Other treatments of compressible mantle flow in spherical geometry have been presented by Corrieu et al. (1995), Panasyuk et al. (1996), and Defraigne (1997). An overview of the method is presented later, and we refer to Forte and Peltier (1991), Forte and Woodward (1997a), and Forte (2000) for complete details.

One begins by rewriting eqns [24]–[27], in the following Cartesian tensor form:

$$\left.\begin{aligned} u_{k,k} &= -\frac{\dot{\rho}_o}{\rho_o}u_r \\ \sigma_{ij,j} + \rho_o(\phi_1)_{,i} - \rho_1 g_o\hat{r} &= 0 \\ \sigma_{ij} &= -P_1\delta_{ij} + \eta\left(u_{i,j} + u_{j,i} - \frac{2}{3}\delta_{ij}u_{k,k}\right) \\ (\phi_1)_{,kk} &= -4\pi G\rho_1 \end{aligned}\right\} \qquad [28]$$

in which $\dot{\rho}_o = \mathrm{d}\rho_o/\mathrm{d}r$, $u_r = \hat{\mathbf{r}}\cdot\mathbf{u}$ and $(\phi_o)_{,i} = -g_o\hat{r}$. It should also be noted that in these equations, the total stress tensor $\boldsymbol{\sigma}$ is used, rather than the deviatoric stress $\boldsymbol{\tau}$ used in [25].

The determination of a solution to the system of tensor (eqn [28]) in spherical geometry may be greatly simplified by using an elegant mathematical technique described by Phinney and Burridge (1973). Following their technique, one introduces a new coordinate system defined by the following complex basis vectors in spherical geometry:

$$\left.\begin{aligned} \hat{\boldsymbol{e}}_- &= \frac{1}{\sqrt{2}}\left(\hat{\boldsymbol{\vartheta}} - \imath\,\hat{\boldsymbol{\varphi}}\right) \\ \hat{\boldsymbol{e}}_0 &= \hat{\boldsymbol{r}} \\ \hat{\boldsymbol{e}}_+ &= -\frac{1}{\sqrt{2}}\left(\hat{\boldsymbol{\vartheta}} + \imath\,\hat{\boldsymbol{\varphi}}\right) \end{aligned}\right\} \qquad [29]$$

in which $\imath = \sqrt{-1}$ and $\hat{\boldsymbol{r}}, \hat{\boldsymbol{\vartheta}}, \hat{\boldsymbol{\varphi}}$ are the unit basis vectors for the standard spherical polar coordinate system.

Following Phinney and Burridge (1973), all the tensors appearing in the original system [28] are rotated into the

coordinate system defined by [29], thereby yielding the following covariant tensor form of the dynamic equations:

$$\left.\begin{aligned} cu^{\alpha,\beta}e_{\alpha\beta} &= -\frac{\dot{\rho}_o}{\rho_o}u^0 \\ \sigma^{\alpha\beta,\gamma}e_{\beta\gamma} + \rho_o(\phi_1)^{,\alpha} - \rho_1 g_o \delta_0^\alpha &= 0 \\ \sigma^{\alpha\beta} = -P_1 e^{\alpha\beta} + \eta\left(u^{\alpha,\beta}+u^{\beta,\alpha}\right) - \frac{2}{3}\eta\left(u^{\delta,\gamma}e_{\delta\gamma}\right)e^{\alpha\beta} \\ (\phi_1)^{,\alpha\beta}e_{\alpha\beta} &= -4\pi G\rho_1 \end{aligned}\right\} \quad [30]$$

in which the Greek indices denote the coordinate directions in system [29] and therefore range over the values (−1, 0, and +1). The quantities $e^{\alpha\beta}$, $e_{\alpha\beta}$, and δ^α_β are the contravariant, covariant, and mixed tensor representations of the Cartesian identity tensor δ_{ij}.

The velocity (u^α) and stress ($\sigma^{\alpha\beta}$) components are expanded in terms of the generalized spherical functions Y_ℓ^{Nm} (Phinney and Burridge, 1973) such that

$$\begin{aligned} u^-(r,\theta,\phi) &= \sum_{\ell,m} U_\ell^{-m}(r)Y_\ell^{-1m}(\theta,\phi) \\ u^0(r,\theta,\phi) &= \sum_{\ell,m} U_\ell^{0m}(r)Y_\ell^{0m}(\theta,\phi) \\ u^+(r,\theta,\phi) &= \sum_{\ell,m} U_\ell^{+m}(r)Y_\ell^{+1m}(\theta,\phi) \end{aligned} \quad [31]$$

$$\sigma^{\alpha\beta}(r,\theta,\phi) = \sum_{\ell,m} T_\ell^{\alpha\beta m}(r)Y_\ell^{(\alpha+\beta)m}(\theta,\phi) \quad (\alpha,\beta=-1,0,+1) \quad [32]$$

All scalar fields involved in the governing eqn [30] are expanded in terms of ordinary spherical harmonics. For example,

$$\begin{aligned} \rho_1(r,\theta,\phi) &= \sum_{\ell,m}(\rho_1)_\ell^m(r)Y_\ell^m(\theta,\phi) \\ \phi_1(r,\theta,\phi) &= \sum_{\ell,m}(\phi_1)_\ell^m(r)Y_\ell^m(\theta,\phi) \end{aligned} \quad [33]$$

where $Y_\ell^m \equiv Y_\ell^{0m}$.

We can simplify subsequent numerical computations by nondimensionalizing all relevant physical variables using the following transformations:

$$\left.\begin{aligned} r = \mathrm{d}r,\ g_o(r) = g_o g(r),\ \ \eta(r) = \eta_o\eta(r),\ \ \rho_1 = (\Delta\rho)\rho_1, \\ T^{\alpha\beta} = (\Delta\rho g_o d)\ T^{\alpha\beta},\ \ U^\alpha = \left(\frac{\Delta\rho g_o d^2}{\eta_o}\right)U^\alpha,\ \ \phi_1 = \left(\frac{4\pi G R_o}{2\ell+1}\Delta\rho d\right)\phi_1 \end{aligned}\right\} \quad [34]$$

in which the original variables are on the left of each equation and the nondimensional variables are on the right. The scaling quantities we have used are defined as follows:

$d = 2888$ km	≡	radial thickness of mantle
$g_o = 9.82$ ms^{-2}	≡	mean surface gravitational acceleration
$\Delta\rho = 0.1$ Mgm^{-3}	≡	characteristic subducted slab density anomaly
$\eta_o = 10^{21}$ Pa s	≡	Haskell (1935) reference value
$R_o = 6371$ km	≡	mean surface radius of Earth

Substituting expressions [31]–[33] into the flow eqn [30], and using the nondimensionalization scheme [34] as well as the orthogonality properties of the generalized spherical harmonics (as in Phinney and Burridge, 1973), yields two independent systems of flow equations. The first system, governing a poloidal geometry of flow, consists of the following six coupled, first-order, ordinary differential equations:

$$\frac{\mathrm{d}}{\mathrm{d}r}\begin{pmatrix} U^0 \\ U^P \\ T^0 \\ T^P \\ \phi_1 \\ g_1 \end{pmatrix} = \begin{pmatrix} -\frac{[2+r(\dot{\rho}_o/\rho_o)]}{r} & \frac{\Omega_1}{r} & 0 & 0 & 0 & 0 \\ -\frac{2\Omega_1}{r} & \frac{1}{r} & 0 & \frac{\eta_o}{\eta} & 0 & 0 \\ \frac{4[3+r(\dot{\rho}_o/\rho_o)]}{r^2}\frac{\eta}{\eta_o} & -\frac{6\Omega_1}{r^2}\frac{\eta}{\eta_o} & 0 & \frac{\Omega_1}{r} & \frac{3}{2\ell+1}\frac{\dot{\rho}_o}{\overline{\rho}} & 0 \\ -\frac{4\Omega_1[3+r(\dot{\rho}_o/\rho_o)]}{r^2}\frac{\eta}{\eta_o} & \frac{2[\Omega_2^2+3\Omega_1^2]}{r^2}\frac{\eta}{\eta_o} & -\frac{2\Omega_1}{r} & -\frac{3}{r} & 0 & 0 \\ 0 & 0 & 0 & 0 & 0 & 1 \\ 0 & 0 & 0 & 0 & \frac{\ell(\ell+1)}{r^2} & -\frac{2}{r} \end{pmatrix} \begin{pmatrix} U^0 \\ U^P \\ T^0 \\ T^P \\ \phi_1 \\ g_1 \end{pmatrix} + \begin{pmatrix} 0 \\ 0 \\ g(r) \\ 0 \\ 0 \\ (-2\ell+1)\frac{d}{R_o} \end{pmatrix}\frac{\rho_1(r)}{\Delta\rho} \quad [35]$$

in which $\dot{\rho}_o = \mathrm{d}\rho_o/\mathrm{d}r$, $\Omega_1 = [\ell(\ell+1)/2]^{1/2}$, $\Omega_2 = [(\ell-1)(\ell+2)/2]^{1/2}$ and $\overline{\rho}$ is Earth's mean density (5.5143×10^3 kg m^{-3}).

The second system, governing a toroidal geometry of flow, consists of the following two coupled, first-order, ordinary differential equations:

$$\frac{\mathrm{d}}{\mathrm{d}r}\begin{pmatrix} U^T \\ T^T \end{pmatrix} = \begin{pmatrix} \frac{1}{r} & \frac{1}{\eta} \\ \frac{2\Omega_2^2\eta}{r^2} & -\frac{3}{r} \end{pmatrix}\begin{pmatrix} U^T \\ T^T \end{pmatrix} \quad [36]$$

The flow, stress, and gravity variables in the poloidal and toroidal-flow systems ([35], [36]) are all dependent on the same harmonic degree ℓ and order m (this dependence has been dropped for notational convenience). The dependence of these variables on the harmonic coefficients of flow [31], stress [32], and gravitational potential [33] is

$$\begin{aligned} U^P(r) &= U^+(r) + U^-(r) \\ U^T(r) &= U^+(r) - U^-(r) \\ T^0 = T^{00}(r) &+ \frac{3}{2\ell+1}\frac{\rho_0(r)}{\overline{\rho}}\phi_1(r) \\ T^P &= T^{0+}(r) + T^{0-}(r) \\ T^T &= T^{0+}(r) - T^{0-}(r) \end{aligned} \quad [37]$$

1.27.2.3.3 Internal boundary conditions

The determination of a unique solution of the system of flow (eqns [35] and [36]) derived in the preceding section requires the specification of appropriate boundary conditions at the top

and bottom surfaces of the mantle and internal matching conditions at all material interfaces within the mantle. We will consider the latter first since the surface boundary conditions can be obtained as a special case of the internal matching conditions.

The need for internal boundary conditions in solving for mantle flow is evident upon inspection of the depth variation of mantle density $\rho_o(r)$ (see **Figure 5**) given by the PREM seismic reference model (Dziewonski and Anderson, 1981). The PREM density profile is characterized by two major jumps at depths of 400 and 670 km. These density jumps have long been interpreted as manifestations of phase-change boundaries (e.g., Jeanloz and Thompson, 1983), which presumably also affect the depth variation of viscosity at these depths (e.g., Sammis et al., 1977).

We now derive the matching conditions that must be satisfied when characteristic properties of the mantle, in particular density, viscosity, and chemical composition, change very rapidly across phase-change or chemical horizons in the mantle. We will approximate such rapid changes as mathematical discontinuities. Denoting the mean (i.e., horizontally averaged) location of the internal material boundary as $r=r_i$, geographic variations in the radial location (i.e., deflections) of the boundary are then represented by

$$r = r_i + \delta r_i, \quad \text{where we assume } \left|\frac{\delta r_i}{r_i}\right| \ll 1 \qquad [38]$$

A discontinuous change in density across an internal boundary implies that

$$\left(\frac{\mathrm{d}\rho_o}{\mathrm{d}r}\right)_{r=r_i} = \left[\rho_o\left(r_i^+\right) - \rho_o\left(r_i^-\right)\right]\delta(r-r_i) \qquad [39]$$

By virtue of this last expression, the density perturbation due to the boundary deflection δr_i is given by the following sheet-mass anomaly:

$$\delta\rho_i = -\left(\frac{\mathrm{d}\rho_o}{\mathrm{d}r}\right)_{r=r_i}\delta r_i = -\left[\rho_o\left(r_i^+\right) - \rho_o\left(r_i^-\right)\right]\delta r_i\delta(r-r_i) \qquad [40]$$

This last expression shows that an internal boundary deflection gives rise to a mantle buoyancy source, which may be approximated by a delta-function load and the corresponding density perturbation is, in nondimensional terms:

$$\frac{\rho_1(r)}{\Delta\rho} = -\frac{\left[\rho_o\left(r_i^+\right) - \rho_o\left(r_i^-\right)\right]}{\Delta\rho}\frac{\delta r_i}{d}\delta(r-r_i) \qquad [41]$$

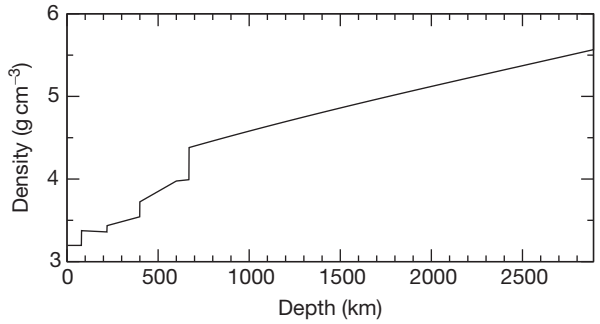

Figure 5 Depth-dependent mean density in the mantle from the PREM seismic reference model (Dziewonski and Anderson, 1981).

This expression shows that from a purely fluid mechanical perspective, the dynamic effect of a deformed phase-change boundary is indistinguishable from integrated buoyancy forces elsewhere in the mantle. If the material interface instead corresponds to a chemical discontinuity in the mantle, the fluid mechanical buoyancy effect is also the same. The main distinction between the deflection-induced buoyancy of phase-change and chemical discontinuities is that the former is controlled by thermodynamics (i.e., the Clapeyron slope), whereas the latter is due to the change in intrinsic chemical buoyancy across the interface.

The matching condition for the radial component of the flow field is obtained by integrating the first row in system [35] from $r_i^- = r_i - \epsilon$ to $r_i^+ = r_i + \epsilon$, taking the limit $\varepsilon \to 0$. In terms of the radial flow variable U^0, this yields the following mass conservation equation:

$$\rho_o\left(r_i^+\right)U^0\left(r_i^+\right) = \rho_o\left(r_i^-\right)U^0\left(r_i^-\right) \qquad [42]$$

where $\rho_o(r_i^+)$ and $\rho_o(r_i^-)$ are the mantle density immediately above and below the material boundary, respectively. If the internal boundary corresponds to a chemical discontinuity, then we must impose a zero radial velocity condition:

$$U^0\left(r_i^+\right) = 0 = U^0\left(r_i^-\right) \qquad [43]$$

The matching condition for the tangential mantle flow velocity is obtained by integrating the second equation in eqn [35], which yields the following continuity of the tangential flow variable U^P:

$$U^P\left(r_i^+\right) = U^P\left(r_i^+\right) \qquad [44]$$

This continuity of tangential flow also applies to the case of an internal chemical boundary.

The internal matching condition for the radial stress T^0 across a deformed material interface is obtained by integrating the third row in system [35], in which we substitute result [41] into the buoyancy force term $\rho_1/\Delta\rho$ in expression [35], thereby yielding

$$T^0\left(r_i^+\right) - T^0\left(r_i^-\right) = \Delta_u(r_i) + \frac{3}{2\ell+1}\left[\frac{\rho_o\left(r_i^+\right) - \rho_o\left(r_i^-\right)}{\bar{\rho}}\right]\phi_1(r_i) - \frac{\left[\rho_o\left(r_i^+\right) - \rho_o\left(r_i^-\right)\right]}{\Delta\rho}\frac{\delta r_i}{d}g(r_i) \qquad [45]$$

in which the term

$$\Delta_u(r_i) = -\frac{2}{r_i}\left(\frac{\eta\left(r_i^+\right) + \eta\left(r_i^-\right)}{\eta_o}\right)\left[U^0\left(r_i^+\right) - U^0\left(r_i^-\right)\right] \qquad [46]$$

arises from the discontinuous change in radial flow (see expression [42]) due to a density jump across an internal (phase-change) boundary. This term vanishes in the case of a chemical discontinuity since expression [43] then applies. The matching condition for the tangential stress T^P is obtained by integrating the fourth equation in eqn [35]:

$$T^P\left(r_i^+\right) - T^P\left(r_i^-\right) = -\Omega_1\Delta_u(r_i) \qquad [47]$$

The term Δ_u gives rise to an apparent discontinuity in tangential stress, and this is again a consequence of our

mathematical treatment of a discontinuous change in radial flow across a material interface. The significance of this apparent jump in tangential stress was first noted by Corrieu et al. (1995), and a subsequent analysis by Forte and Woodward (1997a) determined that the effect of this discontinuity was negligible. In the case of a chemical discontinuity, the term Δ_u vanishes and the tangential stress is then continuous across the interface.

Integration of the fifth row in [35] across the material interface located at mean radius r_i yields the following matching condition for the perturbed gravitational potential:

$$\phi_1(r_i^+) = \phi_1(r_i^-) \quad [48]$$

The matching condition for the perturbed gravitational acceleration is obtained by substituting expression [41] into the buoyancy force term $\rho_1/\Delta\rho$ in [35] and then integrating the sixth row of this system, yielding the following nondimensional expression:

$$g_1(r_i^+) - g_1(r_i^-) = (2\ell+1)\left(\frac{d}{R_o}\right)\frac{[\rho_o(r_i^+) - \rho_o(r_i^-)]}{\Delta\rho}\frac{\delta r_i}{d} \quad [49]$$

in which $g_1 = \mathrm{d}\phi_1/\mathrm{d}r$.

The internal matching conditions for the toroidal components of mantle flow are readily obtained following the same procedure employed for the poloidal flow. Integration of the first row in system [36] yields the following continuity of toroidal flow across any (phase-change or chemical) interface:

$$U^T(r_i^+) = U^T(r_i^-) \quad [50]$$

Similarly, an integration of the second row in [36] yields the following continuity of tangential stress across any internal material interface:

$$T^T(r_i^+) = T^T(r_i^-) \quad [51]$$

1.27.2.3.4 Boundary conditions at Earth's solid surface

It will be assumed that the spherically symmetrical, hydrostatic reference Earth model is overlain by a global ocean layer, which is 3 km thick, as in PREM (Dziewonski and Anderson, 1981). PREM's crust and seismic lithosphere are combined into a single mechanical layer containing the same total mass as the two PREM layers assuming, for simplicity, that both layers deform and move together in response to the buoyancy-driven flow in the mantle. The top surface of the combined crust–lithosphere is located at radius $r = 6368$ km and the base is located at radius 6291 km (i.e., at a depth of 80 km below the surface of the global ocean layer). This redefined lithosphere has mass density of 3.2 Mg m^{-3}.

In view of the very complicated mechanical and rheological properties of the crust and underlying lithosphere, in particular the tectonic plates, it is clear that the flow theory developed here with a purely depth-dependent viscosity cannot provide an adequate representation of the near-surface dynamics. An approximate treatment of the effect of surface tectonic plates is presented in Section 1.27.2.3.7. In the meantime, we will consider here two different boundary conditions of relevance at the solid surface: *free-slip* and *no-slip*.

Earth's bounding surface at $r = a = 6368$ km is a chemical (compositional) boundary across which there can be no flow and hence the matching condition [43] is applicable:

$$U^0(a^-) = 0, \quad \text{for both free-slip \& no-slip} \quad [52]$$

where a^- denotes the radial location $r = a - \varepsilon$. We can, to first-order accuracy, ignore surface deflections (i.e., topography) in specifying the boundary conditions on the flow.

The condition for the surface tangential flow $U^P(a^-)$ in the lithosphere is

$$U^P(a^-) = \begin{cases} U^P(a^-) & \text{to be determined, for free-slip} \\ 0 & \text{for no-slip} \end{cases} \quad [53]$$

In the case of the surface toroidal flow, the boundary condition is

$$U^T(a^-) = V^T \quad [54]$$

in which V^T is determined from the coupling of surface poloidal and toroidal flows due to the presence of rigid surface tectonic plates. The mathematical formulation of this coupling and an explicit expression for V^T are presented in Section 1.27.2.3.7.

We can apply the radial stress T^0 matching condition in [45] to the deformed surface boundary, which, by virtue of conditions [52], becomes

$$T^0(a^-) - T^0(a^+) = \frac{3}{2\ell+1}\left[\frac{\Delta\rho_a}{\bar{\rho}}\right]\phi_1(a^-) - \left[\frac{\Delta\rho_a}{\Delta\rho}\right]\frac{\delta a}{d}g(a) \quad [55]$$

where we have defined the density jump across the solid surface:

$$\Delta\rho_a = \rho_o(a^-) - \rho_o(a^+) = 3.2 - 1.0\ \mathrm{Mg\,m^{-3}} = 2.2\,\mathrm{Mg\,m^{-3}} \quad [56]$$

and where we have also invoked the universally valid condition [48] for the vertical continuity of the perturbed gravitational potential.

In expression [55], $T^0(a^+)$ corresponds to the radial stress in the global ocean layer. If we assume that the viscosity in the global ocean layer is negligible (i.e., $\eta/\eta_o \to 0$), then the second row in system [35] yields

$$T^P(r) = 0, \text{throughout the ocean layer} \quad [57]$$

and therefore, by virtue of this result, the fourth row in system [35] yields

$$T^0(r) = 0, \text{throughout the ocean layer} \quad [58]$$

Substituting result [58] into expression [55] yields the desired radial stress boundary condition at the surface:

$$T^0(a^-) = \frac{3}{2\ell+1}\left[\frac{\Delta\rho_a}{\bar{\rho}}\right]\phi_1(a^-) - \left[\frac{\Delta\rho_a}{\Delta\rho}\right]\frac{\delta a}{d}g(a) \text{ valid for free-slip \& no-slip} \quad [59]$$

in which δa is the flow-induced vertical deflection of the solid surface (i.e., dynamic surface topography).

The condition for the surface poloidal tangential stress $T^P(a^-)$ is as follows:

$$T^P(a^-) = \begin{cases} 0 & \text{for free-slip} \\ T^P(a^-) & \text{to be determined, for no-slip} \end{cases} \quad [60]$$

and the condition for the surface toroidal tangential stress is

$$T^T(a^-) = T^T(a^-) \text{ to be determined} \quad [61]$$

On the basis of the general result [48], and using result [49], the surface matching conditions for the perturbed gravitational potential and acceleration are

$$\phi_1(a^-) = \phi_1(a^+) \quad [62]$$

$$g_1(a^-) = g_1(a^+) + (2\ell+1)\left(\frac{d}{R_o}\right)\left[\frac{\Delta\rho_a}{\Delta\rho}\right]\frac{\delta a}{d} \quad [63]$$

The ocean-layer potential and gravitational fields $\phi_1(a^+)$ and $g_1(a^+)$, respectively, are not independent of each other, and as shown in Forte and Peltier (1991), they are both related to the perturbed potential at the surface of the global ocean layer, $\phi_1(r=R_o)$:

$$\phi_1(a^+) = P_\ell \phi_1(R_o) \quad [64]$$

$$g_1(a^+) = G_\ell \phi_1(R_o) \quad [65]$$

in which the ocean-layer response functions P_ℓ and G_ℓ are as follows:

$$P_\ell = \left(\frac{R_o}{a}\right)^{\ell+1} - \frac{3}{2\ell+1}\frac{\rho_w}{\overline{\rho}}\left[\left(\frac{R_o}{a}\right)^{\ell+2} - \left(\frac{a}{R_o}\right)^{\ell-1}\right] \quad [66]$$

$$G_\ell = -(\ell+1)\frac{d}{R_o}\left(\frac{R_o}{a}\right)^{\ell+2} + \frac{3}{2\ell+1}\frac{\rho_w}{\overline{\rho}}\frac{d}{R_o}\left[(\ell+1)\left(\frac{R_o}{a}\right)^{\ell+3} + \ell\left(\frac{a}{R_o}\right)^{\ell-2}\right] \quad [67]$$

in which $\rho_w \equiv \rho(a^+) = 1$ Mg m^{-3} is the density of the global ocean layer.

Substitution of results [64] and [65] into expressions [62] and [63] yields the complete surface boundary conditions for the gravitational variables:

$$\phi_1(a^-) = P_\ell \phi_1(R_o), \quad \text{valid for free-slip \& no-slip} \quad [68]$$

$$g_1(a^-) = G_\ell \phi_1(R_o) + (2\ell+1)\left(\frac{d}{R_o}\right)\left[\frac{\Delta\rho_a}{\Delta\rho}\right]\frac{\delta a}{d}, \quad \text{valid for free-slip \& no-slip} \quad [69]$$

It should be noted that expression [68] should also be substituted into the radial stress condition [59].

The complete set of free-slip and no-slip surface boundary conditions, in terms of the poloidal-flow vector $\mathbf{v}(r) = (U^0(r), U^P(r), T^0(r), T^P(r), \phi_1(r), g_1(r))^{Tr}$ (where Tr denotes transposition) employed in system [35], is as follows:

Free-slip:

$$\mathbf{v}(a^-) = U^P(a^-)\mathbf{y}_1 + \phi_1(R_o)\mathbf{y}_2 + \frac{\Delta\rho_a}{\Delta\rho}\frac{\delta a}{d}\mathbf{y}_3 \quad [70]$$

in which the surface basis vectors are

$$\mathbf{y}_1 = \begin{pmatrix} 0 \\ 1 \\ 0 \\ 0 \\ 0 \\ 0 \end{pmatrix} \quad \mathbf{y}_2 = \begin{pmatrix} 0 \\ 0 \\ \frac{3}{2\ell+1}\frac{\Delta\rho_a}{\overline{\rho}}P_\ell \\ 0 \\ P_\ell \\ G_\ell \end{pmatrix} \quad \mathbf{y}_3 = \begin{pmatrix} 0 \\ 0 \\ -g(a) \\ 0 \\ 0 \\ (2\ell+1)\left(\frac{d}{R_o}\right) \end{pmatrix} \quad [71]$$

No-slip:

$$\mathbf{v}(a^-) = T^P(a^-)\mathbf{y}_1' + \phi_1(R_o)\mathbf{y}_2 + \frac{\Delta\rho_a}{\Delta\rho}\frac{\delta a}{d}\mathbf{y}_3 \quad [72]$$

in which the surface basis vectors are

$$\mathbf{y}_1' = \begin{pmatrix} 0 \\ 0 \\ 0 \\ 1 \\ 0 \\ 0 \end{pmatrix} \text{ and } \mathbf{y}_2, \mathbf{y}_3 \text{ are defined in [71]} \quad [73]$$

The surface boundary conditions ([54], [61]) for the toroidal-flow vector $\mathbf{u}(r) = [U^T(r), T^T(r)]^{Tr}$, which is governed by system [36], are

$$\mathbf{u}(a^-) = V^T\mathbf{z}_1 + T^T(a^-)\mathbf{z}_2 \quad [74]$$

in which the two surface basis vectors are

$$\mathbf{z}_1 = \begin{pmatrix} 1 \\ 0 \end{pmatrix} \quad \mathbf{z}_2 = \begin{pmatrix} 0 \\ 1 \end{pmatrix} \quad [75]$$

1.27.2.3.5 Boundary conditions at CMB

The derivation of the boundary conditions that apply at the CMB, located at mean radius $r = b = 3480$ km, is almost identical to the derivation for the surface boundary conditions in the preceding section. The liquid outer core is regarded as having negligible viscosity relative to the mantle, and hence, the CMB is treated as a purely free-slip boundary. The only difference concerns the application of gravitational matching conditions at $r = b$, since we must now deal with the interaction between a deformed CMB and a compressible, hydrostatic core.

A detailed treatment of the gravitational perturbations maintained in a hydrostatic core is presented in Forte and Peltier (1991), where it is shown that perturbed gravitational acceleration at the top of the core (i.e., immediately below the CMB) is determined by the perturbed potential at the bottom of the mantle (i.e., immediately above the CMB), as follows:

$$g_1(b^-) = R_\ell \phi_1(b^+)$$

where b^- denotes the radial location $r = b - \varepsilon$ (i.e., bottom side of the CMB) and b^+ denotes $r = b + \varepsilon$ (i.e., topside of the CMB). R_ℓ is a numerically determined coefficient, which is obtained on the basis of the compressible density profile throughout the core (Forte and Peltier, 1991).

The complete set of free-slip CMB boundary conditions in terms of the poloidal-flow vector $\mathbf{v}(r) = [U^0(r), U^p(r), T^0(r), T^P(r), \phi_1(r), g_1(r)]^{Tr}$ in system [35] is

$$\mathbf{v}(b^+) = U^P(b^+)\mathbf{x}_1 + \phi_1(b^+)\mathbf{x}_2 + \frac{\Delta\rho_b}{\Delta\rho}\frac{\delta b}{d}\mathbf{x}_3 \quad [76]$$

in which the CMB basis vectors are

$$\mathbf{x}_1 = \begin{pmatrix} 0 \\ 1 \\ 0 \\ 0 \\ 0 \\ 0 \end{pmatrix} \quad \mathbf{x}_2 = \begin{pmatrix} 0 \\ 0 \\ \frac{3}{2\ell+1}\frac{\Delta\rho_b}{\overline{\rho}} \\ 0 \\ 1 \\ R_\ell \end{pmatrix} \quad \mathbf{x}_3 = \begin{pmatrix} 0 \\ 0 \\ -g(b) \\ 0 \\ 0 \\ (2\ell+1)\left(\frac{d}{R_o}\right) \end{pmatrix} \quad [77]$$

where $\Delta\rho_b = \rho_o(b^+) - \rho(b^-) = -4.434\ \text{Mg m}^{-3}$ is the density jump across the CMB and δb is the deflection (i.e., dynamic topography) of the CMB.

The free-slip CMB boundary condition for the toroidal-flow vector $\mathbf{u}(r) = [U^T(r),\ T^T(r)]^{Tr}$ in system [36] is

$$\mathbf{u}(b^+) = U^T(b^+)\mathbf{w}_1 \qquad [78]$$

in which the CMB basis vector is

$$\mathbf{w}_1 = \begin{pmatrix} 1 \\ 0 \end{pmatrix} \qquad [79]$$

1.27.2.3.6 Determining viscous flow Green functions

The solution to the system of flow (eqn [35]) may be expressed in terms of Green functions, which relate the poloidal-flow velocity and the stress tensor at an arbitrary radius $r = r_0$ to a delta-function density load $\rho_1(r) = \delta(r - r')$ at any other radius $r = r'$.

For arbitrarily complex density (e.g., as in PREM) and viscosity profiles, the poloidal-flow system of eqn [35] must be integrated numerically. When $r \neq r'$, this linear system of equations is homogeneous:

$$\frac{\mathrm{d}}{\mathrm{d}r}\mathbf{v}(r) = \mathbf{M}_P(r)\mathbf{v}(r),\ \text{(when } r \neq r') \qquad [80]$$

in which $\mathbf{M}_P(r)$ is the 6×6 matrix appearing in system [35]. We can propagate each of the surface boundary vectors $\mathbf{y}_i$ ($i = 1, 2, 3$) in [71] or [73], by numerically integrating [80] from the surface ($r = a^-$) downward to $r = r'$, stopping along the way at all internal material boundaries ($r = r_i$) where we apply the internal matching conditions described previously (Section 1.27.2.3.3). We can similarly propagate each of the CMB basis vectors $\mathbf{x}_i$ ($i = 1, 2, 3$) in [77] from the CMB ($r = b^+$) upward to $r = r'$. The basic procedure is summarized schematically in Figure 6.

At the location $r = r'$ of the delta-function load, we apply the matching conditions [42], [44], [45], and [47]–[49]. For each of these matching conditions, we employ the corresponding components of the poloidal-flow vectors $\mathbf{v}(r'_+)$ and $\mathbf{v}(r'_-)$, which are obtained from expressions [70], [72], and [76]:

$$\mathbf{v}(r'_+) = \begin{Bmatrix} U^P(a^-)\mathbf{y}_1(r'_+) \\ T^P(a^-)\mathbf{y}'_1(r'_+) \end{Bmatrix} + \phi_1(R_o)\mathbf{y}_2(r'_+) + \frac{\Delta\rho_a}{\Delta\rho}\frac{\delta a}{d}\mathbf{y}_3(r'_+) \qquad [81]$$

and

$$\mathbf{v}(r'_-) = U^P(b^+)\mathbf{x}_1(r'_-) + \phi_1(b^+)\mathbf{x}_2(r'_-) + \frac{\Delta\rho_b}{\Delta\rho}\frac{\delta b}{d}\mathbf{x}_3(r'_-) \qquad [82]$$

in which the surface and CMB basis vectors, $\mathbf{y}_i(r'_+)$ and $\mathbf{x}_i(r'_-)$, have been obtained by the numerical integration of [80], as outlined earlier. The application of the six matching conditions then yields the following system of equations:

$$\mathbf{A}\mathbf{p} = \boldsymbol{\delta}_p \qquad [83]$$

in which

$$\mathbf{p} = \begin{pmatrix} U^P(a^-)\ \text{or}\ T^P(a^-) \\ \phi_1(R_o) \\ \dfrac{\Delta\rho_a}{\Delta\rho}\dfrac{\delta a}{d} \\ U^P(b^+) \\ \phi_1(b^+) \\ \dfrac{\Delta\rho_b}{\Delta\rho}\dfrac{\delta b}{d} \end{pmatrix} \quad \text{and} \quad \boldsymbol{\delta}_p = \begin{pmatrix} 0 \\ 0 \\ g(r') \\ 0 \\ 0 \\ -(2\ell+1)\dfrac{d}{R_o} \end{pmatrix} \qquad [84]$$

Each column of the 6×6 matrix $\mathbf{A}$ in [83] involves the corresponding basis vectors $\mathbf{y}_i(r'_+)$ and $\mathbf{x}_i(r'_-)$ in [81] and [82].

For any given position $r = r'$ of the delta-function load, we obtain a system of equations given by [83], which can be simply solved to find the unknown vector $\mathbf{p}$. The elements of $\mathbf{p}$ define the poloidal-flow impulse response (kernel) functions of the mantle, which are discussed in Section 1.27.2.4.

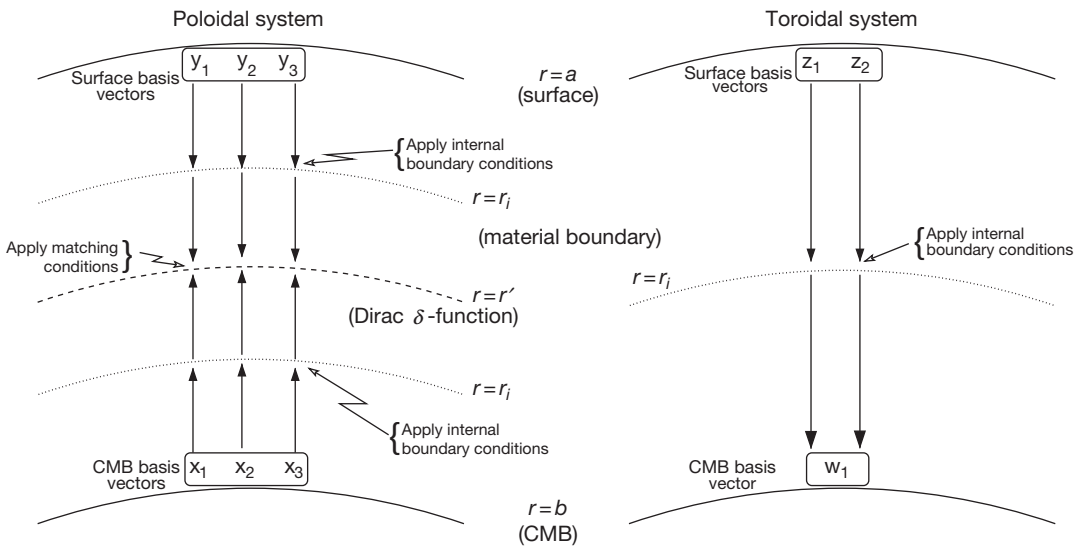

Figure 6 Numerical integration of poloidal-flow system of eqn [35] (left) and toroidal-flow system of eqn [36] (right). The poloidal-flow basis vectors $\mathbf{y}_i$ and $\mathbf{x}_i$ are defined in expressions [71], [73], and [77]. The toroidal-flow basis vectors are defined in expressions [75] and [79].

The toroidal-flow system [36] may be written as the following homogeneous equation:

$$\frac{\mathrm{d}}{\mathrm{d}r}\mathbf{u}(r) = \mathbf{M}_T(r)\mathbf{u}(r) \qquad [85]$$

in which $\mathbf{M}_T(r)$ is the 2×2 matrix appearing in system [36]. We can propagate each of the surface boundary vectors $\mathbf{z}_i$ $(i=1, 2)$ in [75], by numerically integrating [85] from the surface $(r=a^-)$ downward to $r=b^+$, stopping along the way at all internal material boundaries $(r=r_i)$ where we apply the internal matching conditions [50] and [51]. The basic procedure is summarized schematically in Figure 6. The resulting flow vector $\mathbf{u}(b^+)$ is

$$\mathbf{u}(b^+) = V^T\mathbf{z}_1(b^+) + T^T(a^-)\mathbf{z}_2(b^+) \qquad [86]$$

which must be matched to the toroidal flow in expression [79]

$$\mathbf{u}(b^+) = U^T(b^+)\mathbf{w}_1 \qquad [87]$$

We thereby obtain the following simple system:

$$\mathbf{B}\mathbf{t} = \boldsymbol{\delta}_t \qquad [88]$$

in which

$$\mathbf{t} = \begin{pmatrix} U^T(b^+) \\ T^T(a^-) \end{pmatrix} \quad \text{and} \quad \boldsymbol{\delta}_t = V^T\mathbf{z}_1(b^+) \qquad [89]$$

Each column of the 2×2 matrix $\mathbf{B}$ in [88] involves the corresponding basis vectors $\mathbf{w}_1$ and $-\mathbf{z}_2$ in [86] and [87]. Expression [88] shows that the toroidal flow throughout the mantle is 'driven' by the surface toroidal flow V^T generated by rotating tectonic plates, which are themselves driven by the buoyancy-induced poloidal flow in the mantle. This surface coupling of poloidal and toroidal flows, due to the presence of surface tectonic plates, is discussed in the next section.

1.27.2.3.7 Incorporating tectonic plates as a surface boundary condition

The boundary conditions at the top of the mantle are more complex because of the presence of tectonic plates. If the plates are assumed to be an integral part of the underlying mantle flow and they fully participate in the flow, then a simple free-slip surface boundary condition would be appropriate. This free-slip assumption has often been employed in tomography-based flow studies (e.g., Forte and Peltier, 1987; Hager and Richards, 1989; Hager et al., 1985; King and Masters, 1992). If, on the other hand, we recognize that the plates are mechanically and rheologically distinct from the underlying mantle, then a more realistic surface boundary condition that explicitly treats the effective rigidity of plates is required.

Essentially, rigid tectonic plates are a fundamental aspect of convection dynamics in the Earth, and although their treatment lies beyond classical fluid mechanics theory, their dynamic impact on thermal convection in the mantle must be considered. One approach for modeling the coupling of convection and plates, developed by Ricard and Vigny (1989) and Gable et al. (1991), is based on an explicit treatment of the net vertical torque (or horizontal force) acting on the base of each surface plate. This method is a direct extension of the torque-balance analysis originally employed by Hager and O'Connell (1981) in their modeling of dynamic plate motions. The fundamental underlying assumption in the method developed by Ricard and Vigny is that the plate boundaries are completely stress-free. This method has been employed in a number of mantle flow models over the past few years (e.g., Corrieu et al., 1994; Lithgow-Bertelloni and Richards, 1998).

An alternative method for coupling the motions of rigid surface plates to buoyancy-induced mantle flow was developed by Forte and Peltier (1991, 1994). Only the main aspects of this method will be summarized here. It may be shown that for a given geometry of surface plates, the internal density anomalies $\rho_1(r, \theta, \phi)$ are partitioned into two families:

$$\rho_1(r, \theta, \phi) = \hat{\rho}_1(r, \theta, \phi) + \overline{\rho}_1(r, \theta, \phi) \qquad [90]$$

where the density perturbations $\hat{\rho}_1(r, \theta, \phi)$ are obtained through a projection operator $\hat{P}$ as follows:

$$\hat{\rho}_{1s}^{\,t}(r) = \hat{P}_{s,t,l,m}(r)\rho_{1l}^{\,m}(r) \qquad [91]$$

The calculation of the projection operator $\hat{P}_{s,t,l,m}(r)$ is given in Forte and Peltier (1994) and it depends on the geometry of the surface plates. The other component of the density anomalies $\overline{\rho}_1(r, \theta, \phi)$ is simply given by the expression

$$\overline{\rho}_{1s}^{\,t}(r) = \rho_{1s}^{\,t}(r) - \hat{\rho}_{1s}^{\,t}(r) \qquad [92]$$

As Forte and Peltier (1994) showed, the poloidal mantle flow field produced by the component $\hat{\rho}_1$ is consistent with the geometry of possible rigid plate motions at the surface, whereas the one produced by $\overline{\rho}_1$ is orthogonal to any possible plate motion. In other words, the plates participate in the underlying flow driven by $\hat{\rho}_1$, while they resist the flow produced by $\overline{\rho}_1$. Hence, free-slip $(T^p(r_s)=0)$ and no-slip $(V^p(r_s)=0)$ surface boundary conditions are applied to model the internal flows driven by $\hat{\rho}_1$ and $\overline{\rho}_1$, respectively.

A simple application of the plate projection operator is illustrated in Figure 7, where we compare the buoyancy-driven plate motions predicted on the basis of two hypothetical hot thermal anomalies under the Pacific Plate, which differ only in their spatial relationship to the nearby East Pacific Ridge (EPR). Both 'plumes' are constructed in an ad hoc manner as rectangular-shaped, negative density anomalies with constant amplitude $-0.1\ \mathrm{g\,cm^{-3}}$ located in the depth range 400–750 km, equivalent to -2.6% relative density perturbation at 525 km depth. This amplitude is much greater than expected on the basis of the seismic tomography models (see Figure 12) and is only used here for the purpose of illustration. The predicted mantle flow field varies linearly with the amplitude of the driving density anomaly; therefore, a 'plume' anomaly that is ten times smaller $(-0.01\ \mathrm{g\,cm^{-3}})$ will produce surface motions ten times smaller than those shown in Figure 7.

In the absence of plates, both of the hypothetical plumes (Figure 7(a) and 7(b)) produce the same amplitude and pattern of horizontal flow divergence at the surface of the mantle (compare Figure 7(c) with 7(d)). The situation changes radically when the present-day configuration of rigid plates is imposed at the top of the mantle. The plume that is offset from the nearest plate boundary (Figure 7(a)), the EPR, drives a mantle flow field, which produces only a small fraction of the horizontal surface divergence obtained in the absence of plates (compare Figure 7(c) with 7(e)). The plate projection operator [91] maps most of the original plume density anomaly ρ_1 into

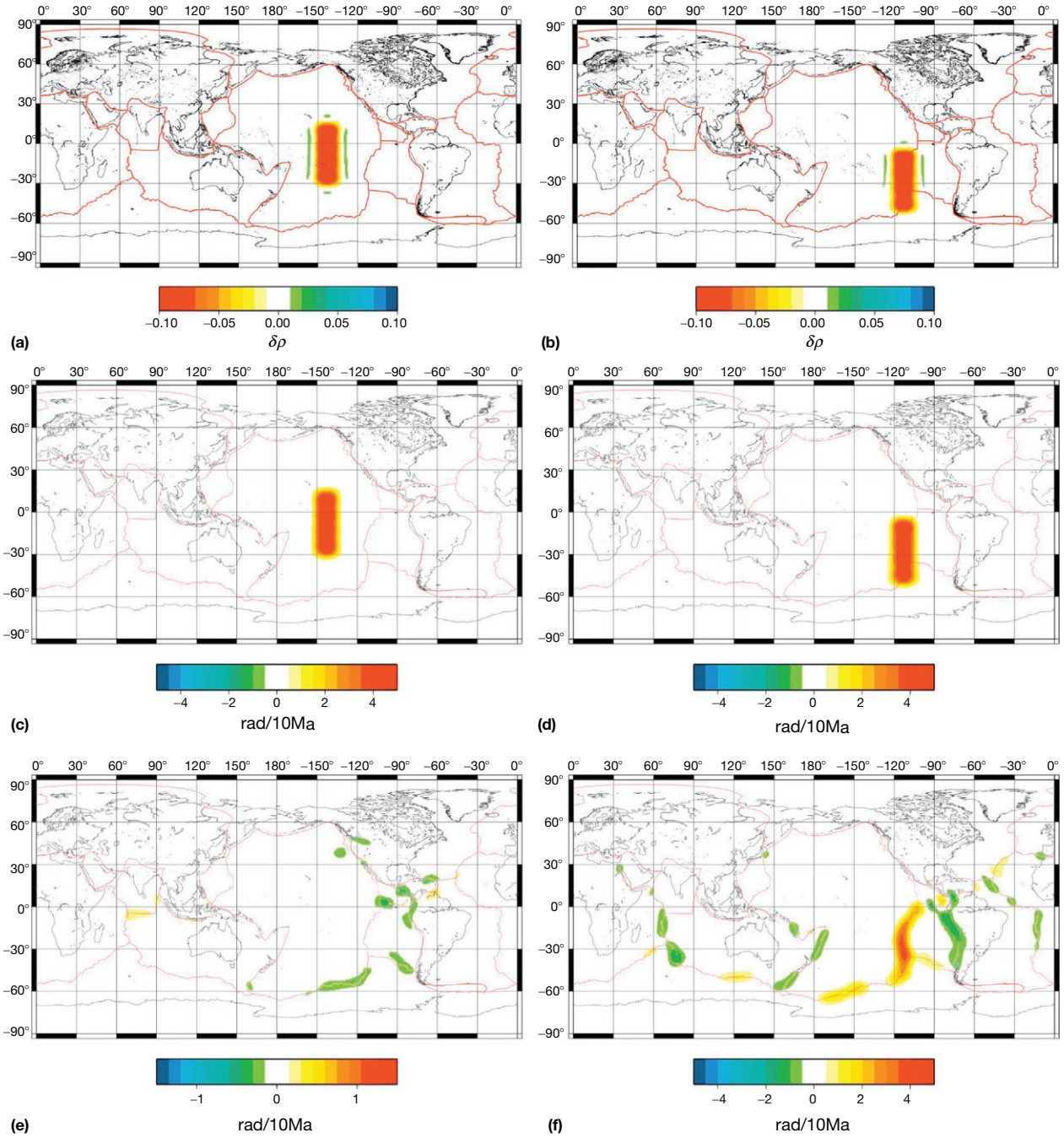

Figure 7 Interaction of hypothetical upwelling plumes with rigid surface plates. Maps (a) and (b) show two rectangular-shaped, negative density anomalies (the hypothetical 'plumes') with amplitude -0.1 g cm^{-3} assumed to be constant in the depth interval 400–750 km. Both plume anomalies have been expanded in terms of spherical harmonics up to degree and order 32. Maps (c) and (d) show the corresponding patterns of predicted horizontal surface divergence for a hypothetical mantle with a free-slip surface boundary (no plates) where the predicted motions are calculated up to harmonic degree 32. The mantle flow calculation was carried out assuming a depth-dependent viscosity variation shown in **Figure 9**. Maps (e) and (f) show the corresponding patterns of plate divergence (up to harmonic degree 32) when the present-day configuration of rigid tectonic plates is imposed as a surface boundary condition in the mantle flow calculation.

the no-slip family of density anomalies $\overline{\rho}_1$, which cannot produce observable plate motions. According to the alternative plate motion theory employed by Ricard and Vigny (1989), this hypothetical plume anomaly produces flow-induced driving torques on the overlying Pacific Plate, which nearly cancel because the center of the upwelling is too far away from the nearest plate boundary. In contrast, the plume located under the EPR (**Figure 7(b)**) produces horizontal divergence of the Pacific and Nazca Plates with an amplitude comparable with that obtained in the absence of plates (compare **Figure 7(d)**

with 7(f)). In this case, a substantial fraction of the original density anomaly ρ_1 was mapped into the free-slip family of density anomalies $\hat{\rho}_1$. It should be noted that mutual interactions among the plates will generate nonzero far-field plate divergence and convergence (Figure 7(f); e.g., in the Indian Ocean), which is a consequence of the assumed rigidity of the plates.

From the perspective of the tectonic plates, the existence of a null-space corresponding to the family of internal density anomalies $\hat{\rho}_1$ [92], which cannot drive observable motions (as in Figure 7(e)), constitutes a fundamental nonuniqueness in the interpretation of plate tectonics. The present-day plate motions (DeMets et al., 1990), or the geologic reconstructions of the history of plate motions (Gordon and Jurdy, 1986), therefore provide completely nonunique constraints on the mantle density anomalies generated by the thermal convection process. Other convection-related observables (e.g., global gravity anomalies) are required to constrain the density anomalies, which fall into the null-space $\hat{\rho}_1$. A further exploration of the implications of the nonunique interpretation of plate motions is presented by Forte and Peltier (1994).

The plate motions, which are driven by the buoyancy-induced (poloidal) mantle flow 30, will necessarily posses a toroidal component. This toroidal component is directly coupled to the poloidal component of the plate motions as follows:

$$(\hat{\mathbf{r}}\cdot\nabla\times\mathbf{v})_s^t = C_{s,t,l,m}(\nabla_H\cdot\mathbf{v})_l^m \qquad [93]$$

in which the spherical harmonic coefficients of the radial vorticity of the plate velocity field $\mathbf{v}$ are linearly dependent on the harmonic coefficients of the horizontal divergence of the plate motions. The vorticity and divergence fields are themselves directly dependent on the toroidal and poloidal scalar representations, respectively, of the plate velocity field (Forte and Peltier, 1987). It is important to note that expression [93] is only valid for toroidal harmonic degree $s \geq 2$ and that the coupling matrix $C_{s,t,l,m}$ is dependent only on the geometry of the plates (Forte and Peltier, 1994).

As discussed previously in Section 1.27.2.3.6, the viscous coupling between the plates and underlying mantle will result in the downward propagation of the surface toroidal flow into the mantle. The surface boundary condition [74] requires that the toroidal mantle flow match the toroidal component of plate motions, which is equivalent to their radial vorticity [93]:

$$V^T = U^T(a^-) = \frac{r_a}{\Omega_1}(\hat{\mathbf{r}}\cdot\nabla\times\mathbf{v})_l^m \qquad [94]$$

where $\imath = \sqrt{-1}$ and $r_a = a$ is the mean radius of the solid surface (6368 km).

The Green function solutions of the poloidal and toroidal-flow equations (see Section 1.27.2.3.6) may be used to describe the viscous response of the mantle to an arbitrary distribution of internal density anomalies ρ_1 as follows:

$$\begin{pmatrix} U_\ell^{\alpha m}(r) \\ T_\ell^{\alpha\beta m}(r) \end{pmatrix} = \int_b^a \begin{pmatrix} \mathsf{U}_\ell^{\alpha}(r,r') \\ \mathsf{T}_\ell^{\alpha\beta}(r,r') \end{pmatrix} \rho_1{}_\ell^m(r')\mathrm{d}r' \qquad [95]$$

where $U_\ell^{\alpha m}(r)$ and $T_\ell^{\alpha\beta m}(r)$ are the generalized spherical harmonic coefficients of the velocity and stress fields [31] and [32], respectively, and $\mathsf{U}_\ell^{\alpha}(r,r')$ and $\mathsf{T}_\ell^{\alpha\beta}(r,r')$ are the corresponding (poloidal) Green functions.

Tectonic plates may well represent the most extreme manifestation of lateral variations in rheology in the convecting mantle. The plate coupling procedure described earlier thus provides an explicit means of incorporating the dynamic impact of such extreme lateral heterogeneity in the flow calculations, which will be presented in the succeeding text. It is nonetheless true that eqns [35] and [36] governing flow in the mantle do not include lateral variations in viscosity and hence buoyancy forces will only directly excite a poloidal flow. In these calculations, toroidal mantle flow is excited passively from above, via the rotating surface plates.

A more general flow theory that models the effects of lateral viscosity variations (LVV) throughout the mantle (e.g., Forte and Peltier, 1994; Martinec et al., 1993) is required to describe the direct excitation of toroidal flow by mantle buoyancy forces. The dynamic implications of large-amplitude LVV throughout the mantle have been studied by Moucha et al. (2007). Despite the considerably more complex theory (relative to eqns [35] and [36]) needed to calculate flow in a 3-D viscosity field, Moucha et al. found the impact on predicted surface observables such as topography and geoid is relatively small. This finding provides important support for the modeling and interpretation of geodynamic observables using the plate-coupled flow theory with purely depth-dependent viscosity in the mantle. The results obtained on the basis of this simplified treatment of mantle dynamics will be presented in the sections that follow.

1.27.2.4 Geodynamic Response Functions for the Mantle

The theoretical relationship between the mantle density anomalies and the principal convection-related surface observables (i.e., geoid or gravity anomalies, dynamic surface and CMB topography, and plate motions) may be summarized in terms of geodynamic response or kernel functions (see Forte, 2000; Hager and Clayton, 1989, for reviews). These kernel functions are calculated in the spherical harmonic spectral domain using the viscous flow Green functions defined in expression [95]. The principal assumption we shall make in calculating these geodynamic kernels – in addition to the assumption of purely depth-dependent viscosity below the plates – is that the 670 km seismic discontinuity is not a barrier to radial mantle flow. This whole-mantle flow assumption has been recently subjected to a series of direct tests based on joint inversions of global seismic and geodynamic data sets (Simmons et al., 2006). It is found that the most satisfactory reconciliation of the global seismic and geodynamic constraints on 3-D mantle structure is obtained with whole-mantle flow and significantly poorer fits are obtained with flow models, which assume vertical flow barriers at 670 km depth or within the lower mantle (e.g., at 1800 km depth).

The geoid kernels $G_\ell(\eta; r)$ relate the spherical harmonic coefficients of the nonhydrostatic geoid field, δN_ℓ^m, to the spherical harmonic coefficients of the density perturbations $\delta\rho_\ell^m(r)$ as follows:

$$\delta N_\ell^m = \frac{3}{(2\ell+1)\overline{\rho}}\int_{r_{\mathrm{cmb}}}^{r_s} G_\ell(\eta; r)\delta\rho_\ell^m(r)\mathrm{d}r \qquad [96]$$

where $\overline{\rho} = 5.515\,\mathrm{Mg\,m^{-3}}$ is the mean density of the Earth, r_s is the mean radius of the solid surface, and r_{cmb} is the mean radius of the CMB. The geoid kernels are a functional of the nondimensional radial mantle viscosity profile $\eta(r)/\eta_o$. The free-air gravity anomaly coefficients δG_ℓ^m are related to the nonhydrostatic geoid coefficients δN_ℓ^m as follows:

$$\delta G_\ell^m = (\ell - 1)\frac{g_o}{R_o}\delta N_\ell^m \qquad [97]$$

where $g_o = 9.82\ \mathrm{m\ s^{-2}}$ (982 000 mGal) is the mean gravitational acceleration at Earth's surface and $R_o = 6371$ km is Earth's mean radius. Through the combination of eqns [96] and [97], we can relate the gravity anomaly coefficients to the internal density perturbations.

As discussed in the preceding section, a dynamic flow model that incorporates rigid plate motions must include mixed free-slip and no-slip surface boundary conditions. In the calculation of the flow-related observables, we must therefore determine the separate contributions provided by the density anomalies $\delta\hat{\rho}$ and $\delta\overline{\rho}$, which are convolved with kernel functions derived with free-slip and no-slip surface boundaries, respectively. For example, in the case of the nonhydrostatic geoid anomalies, we rewrite eqn [96] as follows:

$$\delta N_\ell^m = \frac{3}{(2\ell+1)\overline{\rho}}\int_{r_{cmb}}^{r_s}\left[\hat{G}_\ell(\eta; r)\delta\hat{\rho}_\ell^m(r) + \overline{G}_\ell(\eta; r)\delta\overline{\rho}_\ell^m(r)\right]\mathrm{d}r \qquad [98]$$

where the geoid kernels $\hat{G}_\ell(\eta; r)$ and $\overline{G}_\ell(\eta; r)$ are calculated with free-slip and no-slip surface boundaries, respectively. As shown in Forte and Peltier (1994), the density anomalies $\delta\hat{\rho}$ are spatially correlated with the positions of divergent or convergent plate boundaries. Subducting slabs and mid-ocean ridge heterogeneity are therefore resolved as part of the $\delta\hat{\rho}$ anomalies.

The surface topography kernel functions $T_\ell(\eta; r)$ relate the spherical harmonic coefficients of the flow-induced surface topography δa_ℓ^m to the spherical harmonic coefficients of the internal density anomalies as follows:

$$\delta a_\ell^m = \frac{1}{\Delta\rho_{mo}}\int_{r_{cmb}}^{r_s}\left[\hat{T}_\ell(\eta; r)\delta\hat{\rho}_\ell^m(r) + \overline{T}_\ell(\eta; r)\delta\overline{\rho}_\ell^m(r)\right]\mathrm{d}r \qquad [99]$$

where $\Delta\rho_{mo} = 2.2\ \mathrm{Mg\,m^{-3}}$ is the density jump across the mantle–ocean boundary and $\hat{T}_\ell(\eta; r)$ and $\overline{T}_\ell(\eta; r)$ are calculated with free-slip and no-slip surface boundaries, respectively.

Similarly, the spherical harmonic coefficients of the flow-induced CMB topography δb_ℓ^m may be expressed in terms of CMB topography kernels $B_\ell(\eta; r)$ as follows:

$$\delta b_\ell^m = \frac{1}{\Delta\rho_{cm}}\int_{r_{cmb}}^{r_s}\left[\hat{B}_\ell(\eta; r)\delta\hat{\rho}_\ell^m(r) + \overline{B}_\ell(\eta; r)\delta\overline{\rho}_\ell^m(r)\right]\mathrm{d}r \qquad [100]$$

where $\hat{B}_\ell(\eta; r)$ and $\overline{B}_\ell(\eta; r)$ are calculated with free-slip and no-slip surface boundaries, respectively, and $\Delta\rho_{cm} = -4.43\ \mathrm{Mg\,m^{-3}}$ is the density jump across the CMB. As in the case of the nonhydrostatic geoid in eqn [98], the dependence on viscosity of the predicted surface and CMB topography appears explicitly through the nondimensional profile $\eta(r)/\eta_o$.

Surface plate velocities $\mathbf{v}$ may be characterized by their horizontal divergence field $\nabla_H\cdot\mathbf{v}$ (Forte and Peltier, 1987). The horizontal divergence kernels $D_\ell(\eta; r)$ relate the spherical harmonic coefficients of the predicted plate divergence $(\nabla_H\cdot\mathbf{v})_\ell^m$ to the spherical harmonic coefficients of the density perturbations as follows:

$$(\nabla_H\cdot\mathbf{v})_\ell^m = \frac{g_o}{\eta_o}\int_{r_{cmb}}^{r_s} D_\ell(\eta; r)\delta\hat{\rho}_\ell^m(r)\mathrm{d}r \qquad [101]$$

in which the free-slip component of the mantle density anomalies $\delta\hat{\rho}$, defined in expression [91], is required to model the surface divergence of the plates. We also note the presence of the reference scaling value of viscosity η_o. This presence implies that plate motions, unlike the other observables in eqns [96]–[100], will be dependent on the absolute value of mantle viscosity.

1.27.2.5 Depth Dependence of Mantle Viscosity

Understanding the long timescale rheology of the mantle as represented by its effective viscosity is a central and enduring problem in global geophysics. The diverse methods and data sets that have been employed to constrain mantle viscosity have been a source of ongoing contention and debate. The importance and intensity of this debate are an apt reflection of the fundamental role of mantle viscosity in controlling a wide array of geodynamic processes. For example, millennial timescale glacial isostatic adjustment (GIA) processes such as Pleistocene and Holocene sea-level variations and related anomalies in Earth's gravitational field and rotational state are known to be strongly dependent on the depth dependence of mantle viscosity. On much longer, million- to hundred million-year timescales, viscosity exerts fundamental control on the dynamics of mantle convection and on the corresponding evolution of the thermal and chemical state of Earth's interior. The very long timescale implications of mantle viscosity also include fundamental surface geologic and geophysical processes, such as global-scale epeirogeny and associated sea-level changes, global geoid anomalies, and tectonic plate motions.

The spatial variation of viscosity in Earth's mantle can, in principle, be determined from a consideration of the microphysical properties, which control the steady-state creep of mantle rocks (e.g., Nicolas and Poirier, 1976; Sammis et al., 1977). In practice, however, the microphysical models of mantle viscosity depend on knowledge of a number of critical physical properties, such as grain size and activation volume and energy, which are poorly known in the mantle and hence require extrapolations of laboratory creep experiments, which greatly exceed the physical conditions (i.e., pressure, temperature, or creep rate) under which these experiments were originally performed. It is nonetheless possible to show, on the basis of microphysical considerations, that the global horizontal average viscosity may increase by up to three orders of magnitude across the mantle (e.g., Ranalli, 2001). More precise determinations of the radial viscosity profile require additional constraints from geophysical data sets, which are sensitive to the long-term rheology of the mantle.

The first and most influential geophysical contribution to our understanding of mantle viscosity is Haskell's (1935) study of Fennoscandian postglacial uplift, which was found to require an average viscosity of 10^{21} Pa s down to a depth approximately equal to the horizontal dimension of the surface load (about

1000–1500 km). McConnell's (1968) spectral analysis of the Fennoscandian uplift data led to the inference that mantle viscosity increased significantly with depth while at the same time still satisfying the Haskell average. The Haskell average value of viscosity over the upper 1000–1200 km of the mantle was also supported in subsequent work by O'Connell (1971). These initial studies that supported the compatibility between the Haskell constraint on viscosity and significant increases of viscosity in the lower mantle were displaced by subsequent analyses by Cathles (1975) and Peltier and Andrews (1976) who concluded that viscosity was nearly constant from the base of the lithosphere to the CMB. This view of mantle viscosity characterized by only moderate increases with depth was reinforced in later studies involving larger GIA data sets (e.g., Tushingham and Peltier, 1991; Wu and Peltier, 1983). A review of the GIA constraints on viscosity may be found in Mitrovica (1996).

The first inferences of the depth variation of mantle viscosity based on surface data sets associated with mantle convection (e.g., Hager, 1984; Richards and Hager, 1984; Ricard et al., 1984) disagreed strongly with the GIA inferences of mantle viscosity, which prevailed since the earliest studies by Cathles, Peltier, and collaborators. These convection-based analyses of viscosity, in particular the first study of Earth's global geoid anomalies by Hager (1984), suggested a large increase of viscosity in the sublithospheric mantle with an approximately factor of 30 increase in the average viscosity of the lower mantle relative to the upper mantle. This conclusion was supported by subsequent studies by Forte and Peltier (1987) and Forte et al. (1991) who extended the viscous flow modeling to include the plate velocities. The geodynamic inferences for significant (one to two orders of magnitude) increases in the average viscosity of the lower mantle relative to that of the upper mantle were reinforced by subsequent analyses carried out by Ricard et al. (1989), Ricard and Vigny (1989), Hager and Clayton (1989), Forte and Peltier (1991), Forte et al. (1993a, 1994), King and Masters (1992), Corrieu et al. (1994), and Thoraval and Richards (1997). A survey of some of the earliest viscosity inferences derived on the basis of global geoid anomalies is shown in **Figure 8**. Reviews of mantle viscosity inferences based on either convective flow or GIA data sets may be found in King (1995) and Kaufmann and Lambeck (2000).

Additional geodynamic considerations that suggest a substantial increase of viscosity with depth are based on a wide variety of analyses, which include the stability of the hot spot reference frame (e.g., Quéré and Forte, 2006; Richards, 1991), long-term rates of polar wander (e.g., Richards et al., 1997; Sabadini and Yuen, 1989; Spada et al., 1992; Steinberger and O'Connell, 1997), and the planform of mantle convection (e.g., Bunge et al., 1996; Forte and Mitrovica, 2001; Zhang and Yuen, 1995).

The inference of mantle viscosity from convection-related surface data, considered in the context of tomography-based mantle flow models, was initially carried out through an effectively trail-and-error fitting procedure (e.g., Forte and Peltier, 1987, 1991; Forte et al., 1993a,b,c; Hager and Clayton, 1989). Subsequently, a number of formal mathematical inversions of the geodynamic data were carried out (e.g., Corrieu et al., 1994; Forte, 2000; Forte and Mitrovica, 1996; Forte et al., 1991; Kido et al., 1998; King, 1995; King and Masters, 1992; Panasyuk and Hager, 2000; Ricard and Wuming, 1991). The viscosity profiles obtained by inverting geodynamic data sets (**Figure 8**) are all characterized by strong overall increases in viscosity with depth, but it is also clear that there are significant differences in the detailed character of these viscosity inferences. There are many factors that can contribute to these differences and they include, most notably, the use of different tomography-based inferences of mantle density anomalies, different combinations of geodynamic data (e.g., geoid only, geoid plus plate motions, geoid plus dynamic topography, and all of the preceding texts), and different inversion methods (e.g., Monte Carlo, Bayesian, genetic, and Occam algorithms). The formulation of the viscous flow models themselves can also play a critical role in explaining these differences, since it is known that the use of different surface boundary conditions (e.g., free-slip, no-slip, and freely rotating tectonic plates) will lead to rather different viscosity inferences (e.g., Thoraval and Richards, 1997). Finally, the limited resolving power of the geodynamic constraints precludes a direct interpretation of viscosity at any given depth in the mantle. For example, Forte and Mitrovica (2001) found that the combined constraints provided by global free-air gravity anomalies, tectonic plate motions, and excess ellipticity of the CMB could only resolve average values of viscosity in rather broad depth intervals.

The discordant viscosity inferences derived from either GIA or convection-related data sets were initially regarded as evidence for the transient nature of mantle viscosity over the timescales that separate these two processes (e.g., Peltier, 1985; Sabadini et al., 1985). The necessity for time-dependent viscosity in the mantle was later weakened by two independent analyses of the GIA data sets. The first argument against transient viscosity was provided by an analysis of differential Late Holocene sea-level high stands in the Australian region by Nakada and Lambeck (1989), who showed that these GIA data required a nearly two orders of magnitude increase of viscosity across the mantle. The second independent argument was provided by Mitrovica (1996), who showed that previous inferences of a nearly constant-viscosity mantle (e.g., Tushingham and Peltier, 1991; Wu and Peltier, 1983) were conditioned by a misinterpretation of the original Haskell (1935) constraint. The latter was erroneously assumed to apply only to the top 670 km of the mantle (i.e., the upper mantle), rather than to the average value of viscosity down to depths of about 1000–1500 km (Mitrovica, 1996).

The recognition that GIA data are not incompatible with large increases of mantle viscosity with depth spurred new efforts to reconcile GIA and convection data sets with a single profile of mantle viscosity. The first efforts were undertaken by Forte and Mitrovica (1996) and Mitrovica and Forte (1997). Despite the very different timescales and spatial scales over which these processes operate, these authors found that it was possible to simultaneously explain both decay times associated with the postglacial uplift of Hudson Bay and Fennoscandia and long-wavelength free-air gravity anomalies associated with mantle convection with a single viscosity profile characterized by an approximately two orders of magnitude increase with depth, which also satisfied the original Haskell constraint on mantle viscosity. These joint GIA–convection inversions culminated in the recent study by Mitrovica and Forte (2004) in which the

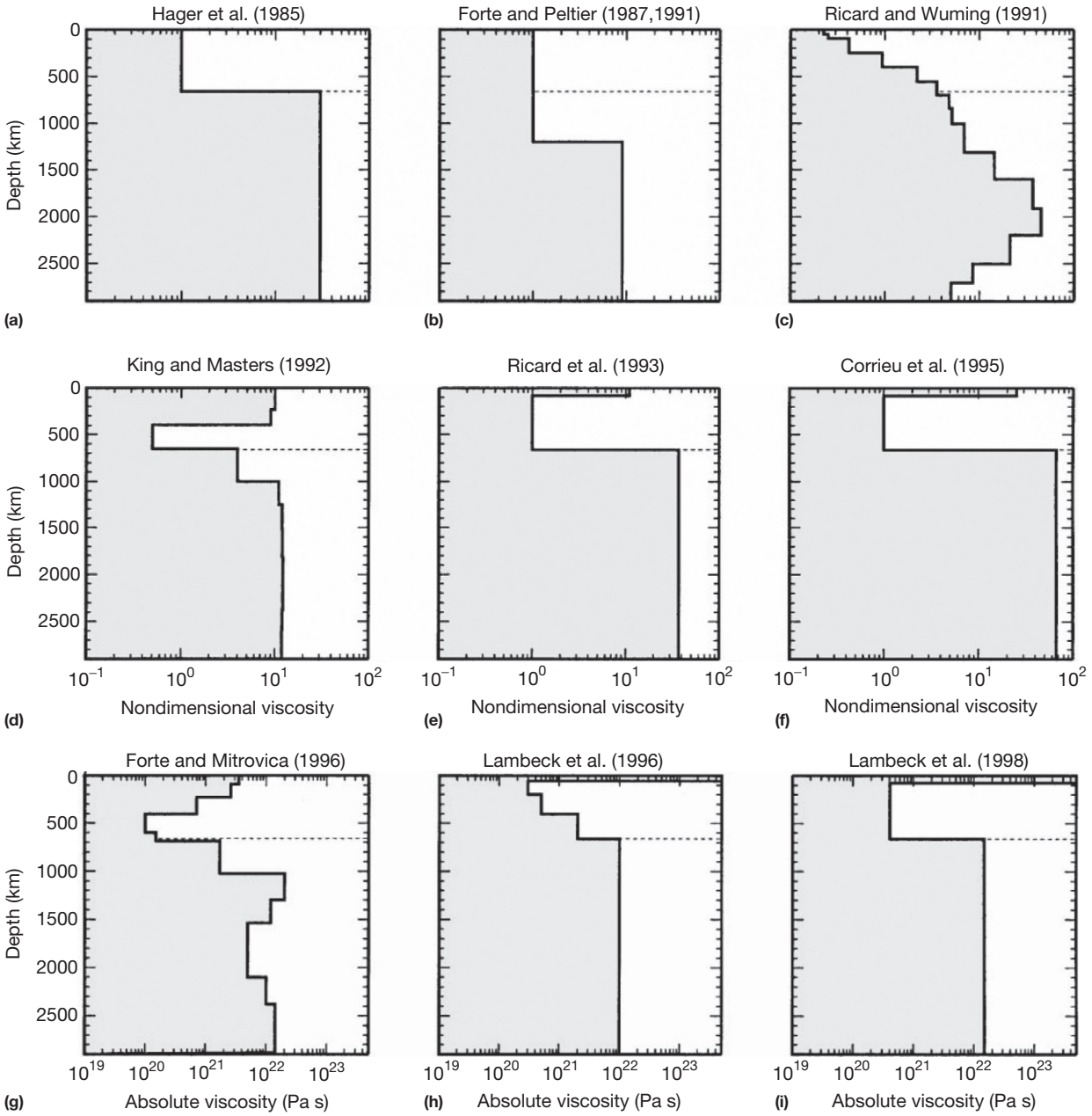

Figure 8 A survey of previous geodynamic inferences of depth-dependent mantle viscosity. Frames (a)–(f) show relative (nondimensional) variations of viscosity with depth derived on the basis of global long-wavelength geoid anomalies. Frames (g)–(i) show radial (absolute) viscosity profiles inferred on the basis of GIA data (in addition to geoid data in the case of frame (g)). The GIA data sets constrain the absolute value of viscosity, whereas the steady-state viscous flow modeling of the geoid data only constrains relative variations of viscosity with depth. Adapted from Kaufmann G and Lambeck K (2000) Mantle dynamics, postglacial rebound and the radial viscosity profile. *Physics of the Earth and Planetary Interiors* 121: 301–324.

range of viscosity profiles consistent with both families of surface data is summarized in Figure reffig-visc. The convection data employed in these viscosity inversions are shown in Figure 2. The GIA data include the Fennoscandian relaxation spectrum and a set of decay times determined from the postglacial sea-level history in Hudson Bay and Sweden.

The inverted viscosity profiles are characterized by a three orders of magnitude increase from the upper mantle (mean value of $\sim 4 \times 10^{20}$ Pa s) to a high-viscosity ($> 10^{23}$ Pa s) peak at 2000 km depth. Below 2000 km, the viscosity shows a significant, two to three orders of magnitude, reduction toward the CMB. Similar radial variations in lower-mantle viscosity have been inferred in other independent studies (e.g., Ricard and Wuming, 1991). The preferred viscosity profile (solid black line, Figure 9) provides an optimal fit to both (GIA and convection) families of data, and unless stated otherwise, this profile will be employed to calculate all convection-related surface observables presented in the succeeding text.

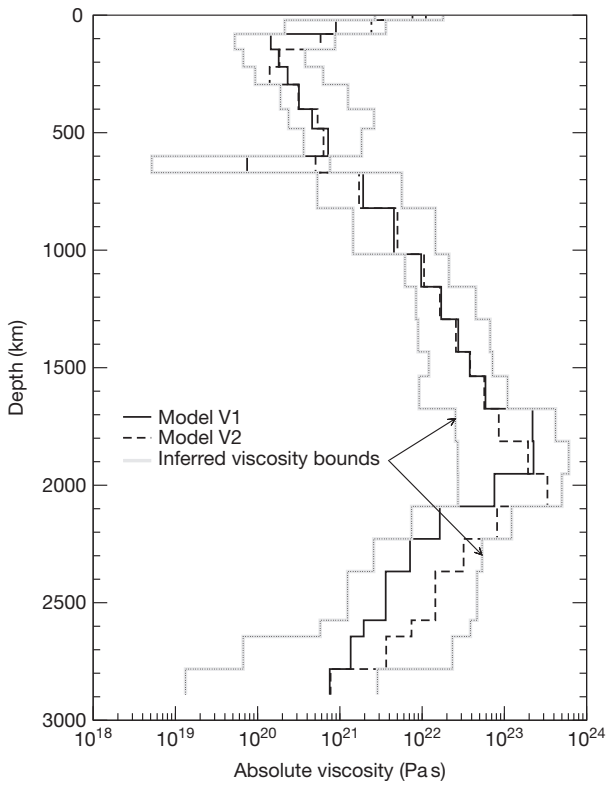

Figure 9 Results of inversions of the GIA and convection data sets. Full details of the inversions are presented in Mitrovica and Forte (2004). The convection data are interpreted in terms of a tomography-based mantle flow model in which the density anomalies are derived from the Grand (2002) tomography model (**Figure 3(b)**). The thick gray lines illustrate the range of allowable values of mantle viscosity, which are consistent with the joint GIA–convection constraints. The solid black line (model V1) is the preferred viscosity profile, on the basis of the Grand (2002) tomography model, which provides an optimal fit to the entire suite of geodynamic data. The dashed line (model V2) was inverted with strong smoothing constraints applied across the horizon separating upper and lower mantle and yields slightly lower fits to the combined GIA–convection data sets (Forte et al., 2010).

The geodynamic response or kernel functions calculated on the basis of the preferred mantle viscosity profile (model 'V1' in **Figure 9**) are illustrated in **Figure 10**. Comparing the free-slip and no-slip geoid kernels, we note that the largest contribution from density anomalies in the top half of the mantle is provided by those anomalies $\delta\hat{\rho}$ that are efficient in driving observable plate motions. These anomalies correspond to subducting slabs and upper-mantle plumes below the mid-ocean ridges. In the bottom half of the mantle, the density anomalies belonging to the $\delta\overline{\rho}$ family provide the largest contribution to the surface geoid or gravity anomalies. These $\delta\overline{\rho}$ anomalies produce no observable plate motions. At sufficiently short horizontal wavelengths (corresponding to harmonic degrees $\ell \geq 32$), we note that the distinction between $\delta\hat{\rho}$ and $\delta\overline{\rho}$ anomalies begins to disappear: both provide equal contributions to the surface geoid or gravity anomalies. The free-slip and no-slip surface topography kernels show that the density anomalies $\delta\overline{\rho}$ provide the strongest contribution to dynamic surface topography, especially at long horizontal wavelengths (corresponding to the degree range $\ell = 2-8$). At short horizontal wavelengths, the distinction between the two classes of density anomalies again ceases to be important.

1.27.3 Modeling Geodynamic Observables with Seismic Tomography

We will now consider the extent to which the 3-D mantle structure resolved in recent seismic tomographic models may be used to explain the global convection-related data sets shown in **Figure 2**. The geodynamic response functions obtained on the basis of the preferred radial viscosity profile (**Figure 10**) will be used to establish the connection between the seismically inferred heterogeneity in the mantle and the surface geodynamic observables. A broad selection of seismic shear-velocity models, obtained in independent studies using diverse and complementary seismic data and using different seismic modeling and inversion techniques, will be employed here. Seismic shear-velocity heterogeneity is the initial focus of this tomography-based modeling because it is expected that S-wave anomalies δV_S will be most sensitive to the temperature anomalies maintained by the mantle convection process (e.g., Forte and Perry, 2000; Forte et al., 2002; Röhm et al., 2000).

1.27.3.1 Seismic Heterogeneity Models

The S-wave tomography models employed here are, in chronological order, model *S20A* (isotropic version) from Ekström and Dziewonski (1998), model *S20RTS* from Ritsema et al. (1999), model *SAW24* from Mégnin and Romanowicz (2000), model *SB4_L18* from Masters et al. (2000), model *TX2002* from Grand (2002), and model *J362D28* from Antolik et al. (2003). The spatial variation of seismic heterogeneity in these S-wave models is parameterized in terms of a wide assortment of basis functions, ranging from B-splines to piecewise-discontinuous layers in the radial direction and spherical harmonics to equal-area cells in the horizontal direction.

To facilitate a direct comparison among these seismic heterogeneity models and the subsequent usage of the models in viscous flow calculations, all models have been projected onto a common set of radial and horizontal basis functions as follows:

$$\frac{\delta V_S}{V_S} = \sum_{k=0}^{32} \sum_{\ell=0}^{20} \sum_{m=-\ell}^{+\ell} {}_k c_\ell^m T_k(x) Y_\ell^m(\theta, \varphi) \qquad [102]$$

in which $T_k(x)$ are Chebyshev polynomials in the normalized radius $x = (2r - r_{sur\,f} - r_{cmb})/(r_{sur\,f} - r_{cmb})$ and Y_ℓ^m are ordinary spherical harmonics. Notice that all models are expanded up to order 32 in the radial Chebyshev polynomials and up to degree 20 in the surface spherical harmonics.

When each of the S-wave heterogeneity models is projected onto the representation [102], the depth variations of the root-mean-square (rms) amplitudes of the velocity anomalies are shown in **Figure 11**. Here, we note that, with the exception of the top 300 km in the mantle, the average amplitudes of the relative perturbations of seismic shear velocity $\delta V_S/V_S$ show significant differences in the mantle, especially in the transition zone region (400–1000 km depth) and at the base of the mantle (2500–2891 km depth).

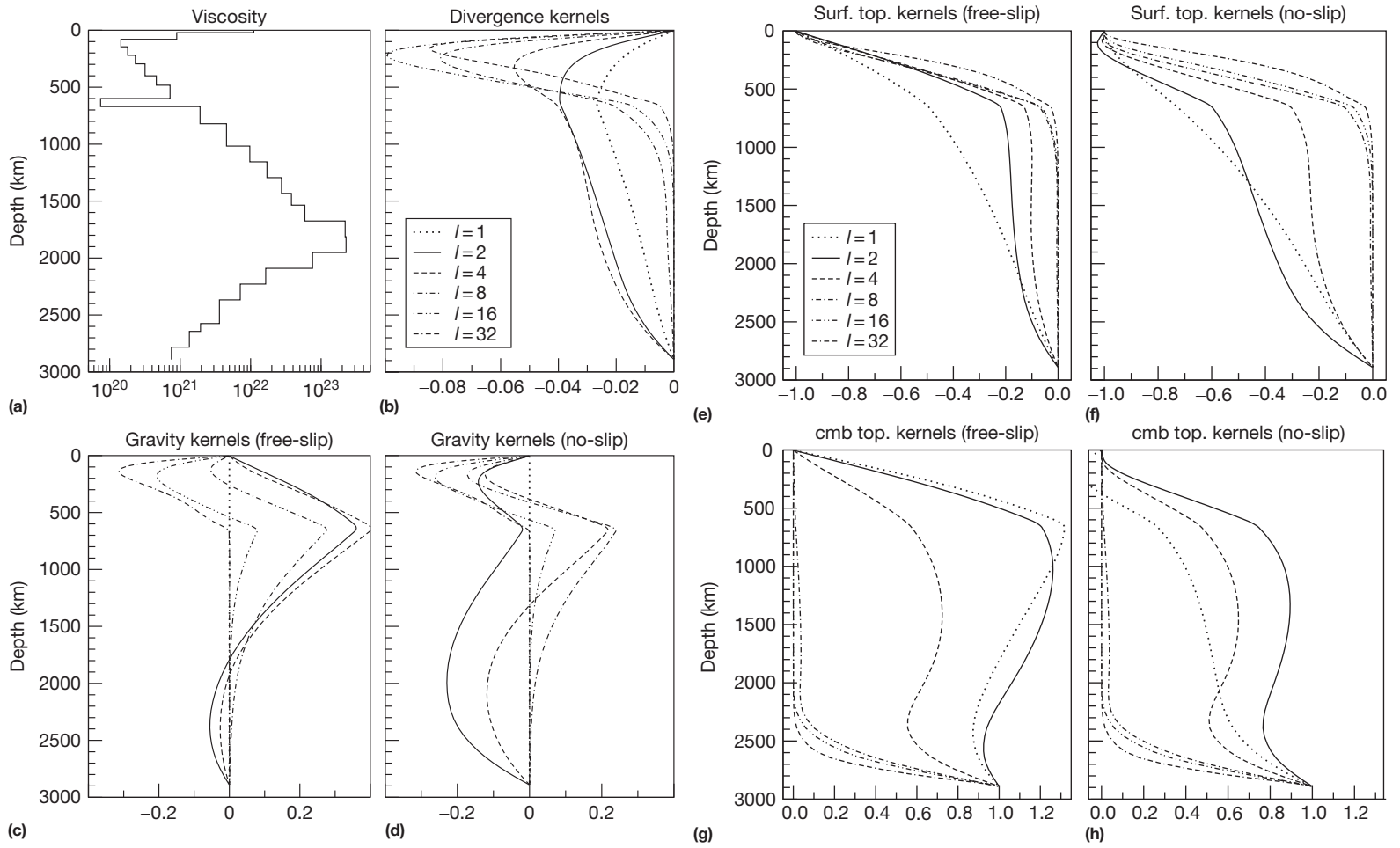

Figure 10 Geodynamic kernel functions. The geodynamic response functions shown here are calculated on the basis of the preferred GIA–convection-inferred viscosity profile shown in frame (a) (same as model 'V1' in **Figure 9**). The kernels corresponding to harmonic degrees $\ell = 1, 2, 4, 8, 16, 32$ are identified by the legend in frame (b) (repeated in frame (e)). The horizontal divergence kernels, defined in eqn [101], are shown in frame (b). The gravity kernels, defined in eqn [98], for free-slip and no-slip surface boundary conditions are shown in frames (c) and (d), respectively. The surface topography kernels, defined in eqn [99], for free-slip and no-slip conditions are shown in frames (e) and (f), respectively. The kernels for the dynamic CMB topography, defined in eqn [100], are shown in frame (g) and (h) for free-slip and no-slip conditions, respectively.

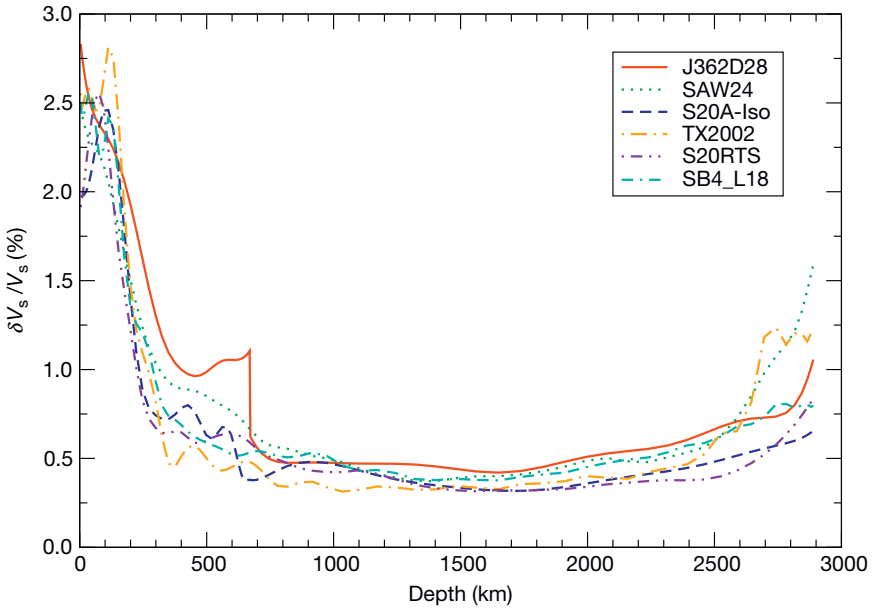

Figure 11 Amplitude of S-wave heterogeneity in the mantle. Plotted here is the root-mean-square (rms) amplitude of relative perturbations of seismic shear velocity obtained from the following tomography models: *J362D28* (Antolik et al., 2003), *SAW24* (Mégnin and Romanowicz, 2000), *S20A-Iso* (Ekström and Dziewonski, 1998), *TX2002* (Grand, 2002), *S20RTS* (Ritsema et al., 1999), and *SB4_L18* (Masters et al., 2000). All tomography models have been projected onto the spatial parameterization given by expression [102].

1.27.3.2 Mantle Density Anomalies

The mantle density anomalies required in modeling the convection-related surface observables may be derived from the seismic tomography models using experimental and theoretical results from mineral physics (e.g., Čadek et al., 1994; Jackson, 2001; Karato, 1993; Karato and Karki, 2001; Oganov et al., 2001a,b; Sobolev et al., 1997; Stacey, 1998; Stixrude and Lithgow-Bertelloni, 2001; Trampert et al., 2001; Wang and Weidner, 1996; Zhang and Weidner, 1999). This derivation would, however, require that the amplitudes of seismic velocity anomalies are well constrained and that all relevant mineralogical variables in the mantle (e.g., reference composition, temperature, and equation of state parameters) are sufficiently well known. To satisfy all these requirements at the same time is a great challenge, but efforts to simultaneously interpret mantle density and seismic velocity anomalies using mineral physics data are showing much promise (e.g., Forte and Woodward, 1997b; Forte et al., 1994; Simmons et al., 2007, 2009, 2010).

An alternative method for inferring mantle density anomalies is based on the direct inversion of the convection-related geophysical observables (e.g., Corrieu et al., 1994; Deschamps et al., 2001; Forte and Mitrovica, 2001; Forte and Perry, 2000; Forte et al., 1993a,b; Karpychev and Fleitout, 2000; Panasyuk and Hager, 2000; Pari, 2001). This approach is useful when contending with significant uncertainties in the amplitudes of the seismic anomalies, as is evident in **Figure 11**. This figure underscores a key concern, namely, that the use of mineral physics data to translate the seismic anomalies can lead to large variations in the estimated mantle density anomalies, depending on the choice of tomography model. To avoid this difficulty, it is preferable to carry out simultaneous inversions of all global geodynamic data (**Figure 2**) to determine an optimal velocity-to-density scaling factor $\mathrm{d}\ln\rho/\mathrm{d}\ln V_S$ (e.g., Forte and Mitrovica, 2001), such that

$$\frac{\delta\rho}{\rho} = \left(\frac{\mathrm{d}\ln\rho}{\mathrm{d}\ln V_S}\right)\frac{\delta V_S}{V_S} \qquad [103]$$

where $\delta V_S/V_S$ are shear-velocity anomalies obtained from a tomography model and $\delta\rho/\rho$ are the relative perturbations in density, which are constrained by the geodynamic data. This approach has also been employed in other tomography-based mantle flow models (e.g., Corrieu et al., 1994; Hager and Clayton, 1989; Panasyuk and Hager, 2000).

The geodynamic data provide direct, linear constraints on the density anomalies in the mantle (see eqns [98]–[100]), which may be generically expressed as follows:

$$\begin{aligned}\delta O_\ell^m &= f_\ell \int_b^a K_\ell(\eta; r')(\rho_1)_\ell^m(r')\mathrm{d}r' \\ &\approx f_\ell \sum_{i=1}^{N} K_\ell(\eta; r_i)(\rho_1)_\ell^m(r_i)w_i \end{aligned} \qquad [104]$$

in which δO_ℓ^m are the spherical harmonic coefficients of a geodynamic observable (e.g., geoid or free-air gravity anomalies), $K_\ell(\eta; r')$ is the corresponding kernel function, and f_ℓ is a factor that depends on the geodynamic observable (see, e.g., eqn [98]). The numerical calculation of integrals is usually carried out with equivalent finite sums, such as in [104], where w_i is a weighting term, which depends on the numerical summation algorithm (e.g., Gauss–Legendre quadrature). On the basis of expression [103], we may further rewrite eqn [104] as

$$\delta O_\ell^m = f_\ell \sum_{i=1}^{N} w_i K_\ell(\eta; r_i)\rho_o(r_i)\left(\frac{\delta V_S}{V_S}\right)_\ell^m(r_i)\left(\frac{\mathrm{d}\ln\rho}{\mathrm{d}\ln V_S}\right)(r_i) \qquad [105]$$

in which $\delta V_S/V_S$ are the shear-velocity anomalies in the mantle and $d \ln \rho / d \ln V_S$ is the corresponding velocity-to-density scaling, which is assumed to vary with depth in the mantle.

Expression [105] provides the basis for a discrete, linear inversion of the geodynamic data δO_ℓ^m to find an optimal velocity-to-density scaling profile $d \ln \rho / d \ln V_S$. A series of Occam inversions (Constable et al., 1987) of the geodynamic data (**Figure 2**) were carried out to find the smoothest family of $d \ln \rho / d \ln V_S$ profiles, which are consistent with the data. For each Occam inversion, a different seismic shear wave tomography model (**Figure 11**) was employed, and in each case, the same geodynamic kernel functions (**Figure 10**) were employed to relate the mantle heterogeneity to the geodynamic data. The results of these inversions are summarized in **Figure 12**, which shows the optimal profiles of $d \ln \rho / d \ln V_S$ and the resulting depth variation of the rms amplitude of the lateral density anomalies implied by expression [103].

Mineral physics estimates of the velocity-to-density scaling (**Figure 12**) show significant departures from the scaling profiles derived from the Occam inversions. As discussed earlier, this discrepancy may in part arise from the inadequate resolution of seismic heterogeneity in the mantle – especially in the midmantle region between 1000 and 2000 km depth – and it may also arise from inadequacy of the theoretical assumptions inherent in the mineral physics estimates. In the latter case, the chief assumption that may be deficient is the dominance of thermal effects on both the seismic and density anomalies in the mantle. Compositional effects, especially on mantle density heterogeneity, may be one important explanation for the deviations from theoretical mineral physics estimates based on temperature effects alone (e.g., Stacey, 1998). The relative importance of thermal and compositional contributions to mantle heterogeneity can be directly tested in the context of simultaneous inversions of seismic and geodynamic data (Simmons et al., 2007, 2009, 2010), and these will be discussed in the succeeding text.

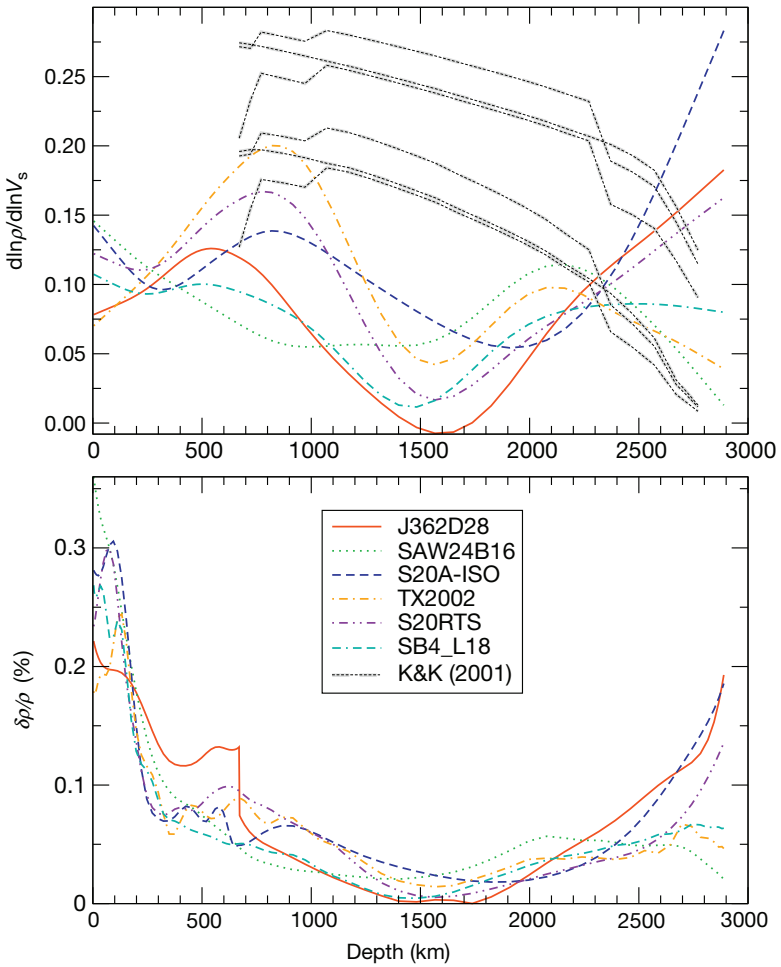

Figure 12 Occam inversions for mantle density anomalies. In the *top frame* are shown the optimal Occam-inferred velocity-to-density scaling profiles for each of the tomography models illustrated in **Figure 11**. The legend identifying the results is in the bottom frame. For comparison are shown (thick dashed gray lines) a series of theoretical estimates of the depth variation of $d \ln \rho / d \ln V_S$ in the lower mantle obtained by Karato and Karki (2001) on the basis of mineral physics data. These mineral physical estimates assume that both density and seismic anomalies are produced by temperature perturbations in the mantle. In the *bottom frame* are shown the resulting inferences of the depth variation of the rms density anomalies, which are calculated on the basis of the seismic shear-velocity anomalies using expression [103].

1.27.3.3 Predicted Tectonic Plate Motions

In this and the next few sections, we will consider the extent to which the tomography-based inferences of mantle density anomalies presented in Figure 12 provide a successful explanation of the convection-related surface observables (Figure 2). We begin here with a consideration of convection-induced tectonic plate motions. The predicted horizontal divergence of the plate motions, calculated on the basis of expression [101] and using the kernels in Figure 10(b), is presented in Figure 13 alongside the observed NUVEL-1 divergence of the plates. A detailed spectral comparison between the predicted and observed plate divergences is shown in Figure 14.

A quantitative summary of the overall agreement between the predicted and observed plate divergence, quantified in terms of total rms amplitude, total spatial correlation, and variance reduction, is provided in Table 1. The variance reduction is defined as follows:

$$\text{var.red.} = 100\% \times \left[1 - \frac{\sum_{\ell}\sum_{m=-\ell}^{+\ell}(O-P)_{\ell}^{m*}(O-P)_{\ell}^{m}}{\sum_{\ell}\sum_{m=-\ell}^{+\ell}O_{\ell}^{m*}O_{\ell}^{m}}\right] \quad [106]$$

where $(O-P)_{\ell}^{m}$ and O_{ℓ}^{m} are the harmonic coefficients of the difference between the observed and predicted fields and the observed fields, respectively.

An important characteristic of the predicted divergence fields shown in Figure 13, which is also confirmed in Table 1, is the subdued amplitude of the predicted fields relative to the data. As will be seen in the next few sections, all tomography-based predictions of geodynamic observables, which are calculated on the basis of the optimal Occam-inverted density-to-velocity scaling profiles (Figure 12), are systematically reduced in amplitude relative to the amplitude of the observed fields. This systematic bias to low predicted amplitudes is a natural consequence of the least-squares misfit criterion, which is employed in almost all inversion algorithms (including the Occam approach), which leads to significantly damped inferences of the $\mathrm{d}\ln\rho/\mathrm{d}\ln V_S$ scaling profiles.

It can be readily shown that the inherent damping of tomography-based inferences of $\mathrm{d}\ln\rho/\mathrm{d}\ln V_S$ arises as a consequence of poorly resolved 3-D seismic structure in geodynamically important regions of the mantle, such as the midmantle region (e.g., Forte et al., 1994). We can illustrate this in an inverse problem in which we seek, for the sake of simplicity, the best-fitting constant $\mathrm{d}\ln\rho/\mathrm{d}\ln V_S$ value. As shown in expression [104], the predicted convection-related observables are linearly dependent on the internal density perturbations in the mantle. By virtue of expression [105], we may write

$$d(\theta,\varphi) = \left(\frac{\mathrm{d}\ln\rho}{\mathrm{d}\ln V_S}\right) p(\theta,\varphi)$$

where $d(\theta, \phi)$ represent the surface data and $p(\theta, \phi)$ is the corresponding mantle flow prediction assuming $\mathrm{d}\ln\rho/\mathrm{d}\ln V_S = 1$. We can then show that the optimal $\mathrm{d}\ln\rho/\mathrm{d}\ln V_S$ value that minimizes the least-squares misfit between data and the predictions is given by the following expression:

$$\frac{\mathrm{d}\ln\rho}{\mathrm{d}\ln V_S} = \frac{\sigma_d}{\sigma_p}\, c(d,p), \quad [107]$$

where σ_d and σ_p are the rms amplitudes of the data and the predictions,

$$\sigma_d^2 = \frac{1}{4\pi}\int\int_{S_1} |d(\theta,\varphi)|^2 d^2S, \;\; \sigma_p^2 = \frac{1}{4\pi}\int\int_{S_1} |p(\theta,\varphi)|^2 d^2S,$$

and

$$c(d,p) = \frac{1}{4\pi}\int\int_{S_1} d(\theta,\varphi)p(\theta,\varphi)\, d^2S \quad [108]$$

where all integrals are defined over the surface of the unit sphere S_1. The quantity $c(d, p)$ defined in [108] is the cross correlation between the data and the predictions. Equation [107] thus shows that the inferences of $\mathrm{d}\ln\rho/\mathrm{d}\ln V_S$ will be directly proportional to the spatial correlation between the surface data and the corresponding geodynamic integral of the 3-D structure in the seismic tomography model. As previously shown by Forte et al. (1994), this correlation may be significantly degraded if the 3-D seismic structure is poorly resolved.

1.27.3.4 Predicted Free-Air Gravity Anomalies

Tomography-based mantle flow models of Earth's nonhydrostatic gravitational potential have almost exclusively been based on analyses of the equivalent geoid anomalies, beginning with the earliest studies by Richards and Hager (1984) and Hager et al. (1985) and continuing to recent studies (e.g., Panasyuk and Hager, 2000). Since the global geoid anomalies are strongly dominated by horizontal wavelengths corresponding to harmonic degrees $\ell = 2, 3$, they will effectively constrain only the longest wavelength components of 3-D mantle structure. To avoid this very long-wavelength bias, we consider here a representation of the nonhydrostatic geopotential in terms of equivalent global free-air gravity anomalies (see expression [97]). The free-air gravity anomalies contain a more evenly balanced representation of the different horizontal wavelengths in the nonhydrostatic geopotential (i.e., a 'flatter' amplitude spectrum).

The observed and predicted gravity anomaly fields, calculated on the basis of expressions [97] and [98] and using the kernels in Figure 10(c) and 10(d), are presented in Figure 15. A comparison of the predicted and observed gravity anomalies in the spectral domain is shown in Figure 16. In Table 2 is presented a detailed summary of the global agreement between the predicted and observed gravity anomalies. In contrast to the predicted plate divergence discussed in the preceding section, we note that the amplitudes of the predicted gravity anomaly fields are somewhat less muted (compare Tables 1 and 2). The overall agreement with the gravity data (in terms of variance reduction) is however poorer than the plate divergence fits because of the decreased spatial correlation between the predictions and the data.

1.27.3.5 Predicted Dynamic Surface Topography

The term 'dynamic topography' is here defined to include all contributions to the topography of Earth's solid surface which

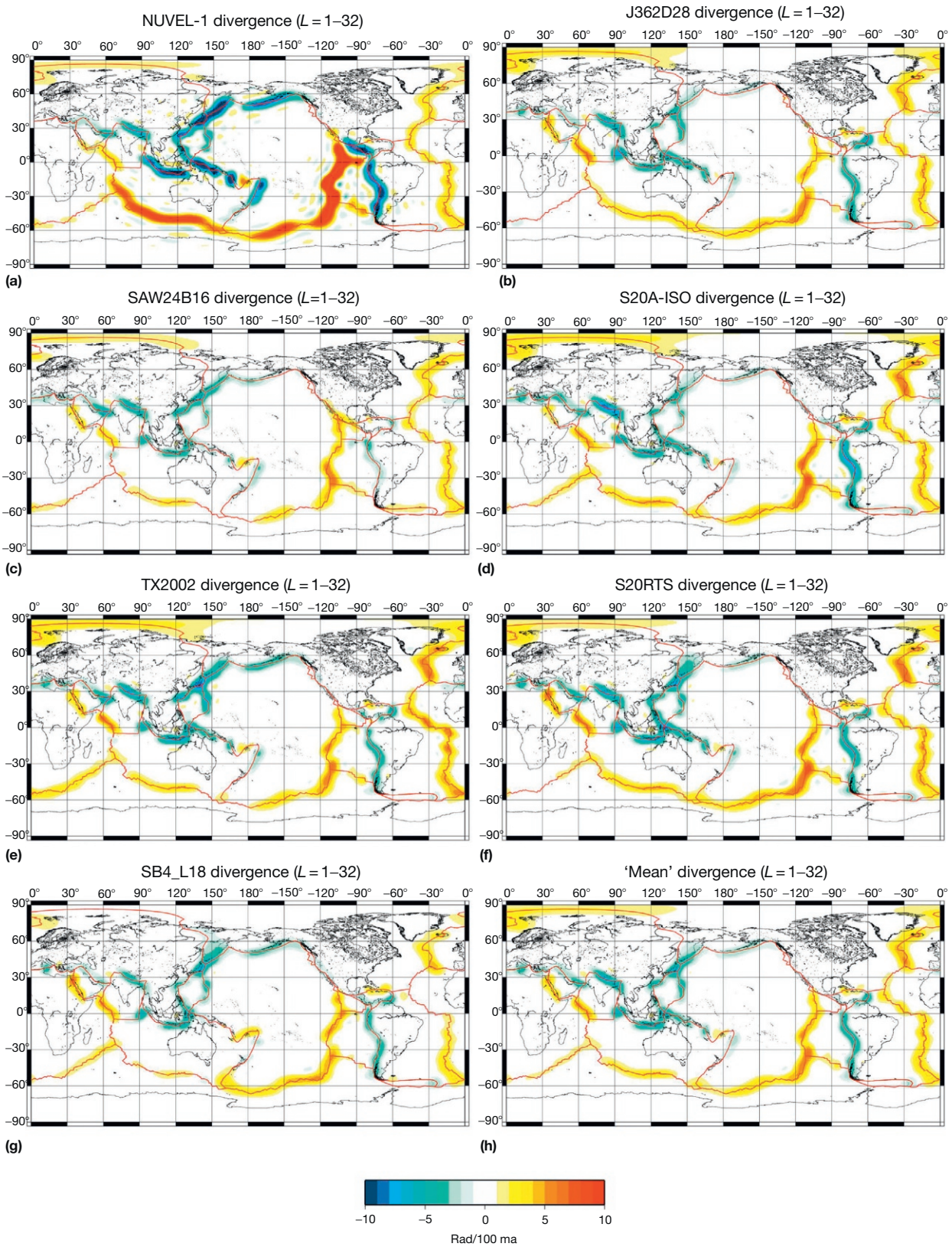

Figure 13 Tomography-based horizontal divergence of the tectonic plates. (a) Observed NUVEL-1 horizontal plate divergence (DeMets et al., 1990). (b)–(g) show the surface divergence predicted on the basis of tomography models *J362D28* (Antolik et al., 2003), *SAW24* (Mégnin and Romanowicz, 2000), *S20A-Iso* (Ekström and Dziewonski, 1998), *TX2002* (Grand, 2002), *S20RTS* (Ritsema et al., 1999), and *SB4_L18* (Masters et al., 2000), using the corresponding d ln ρ/d ln V_S scaling profiles in **Figure 12**. All shear-velocity heterogeneity models have been projected onto the common parameterization in expression [102] prior to calculating the predicted plate motions. (h) The 'mean' prediction of plate divergence obtained by calculating the statistical sample average of all the predictions (b)–(g). The observed and predicted plate motions shown here are all synthesized from spherical harmonics up to degree and order 32.

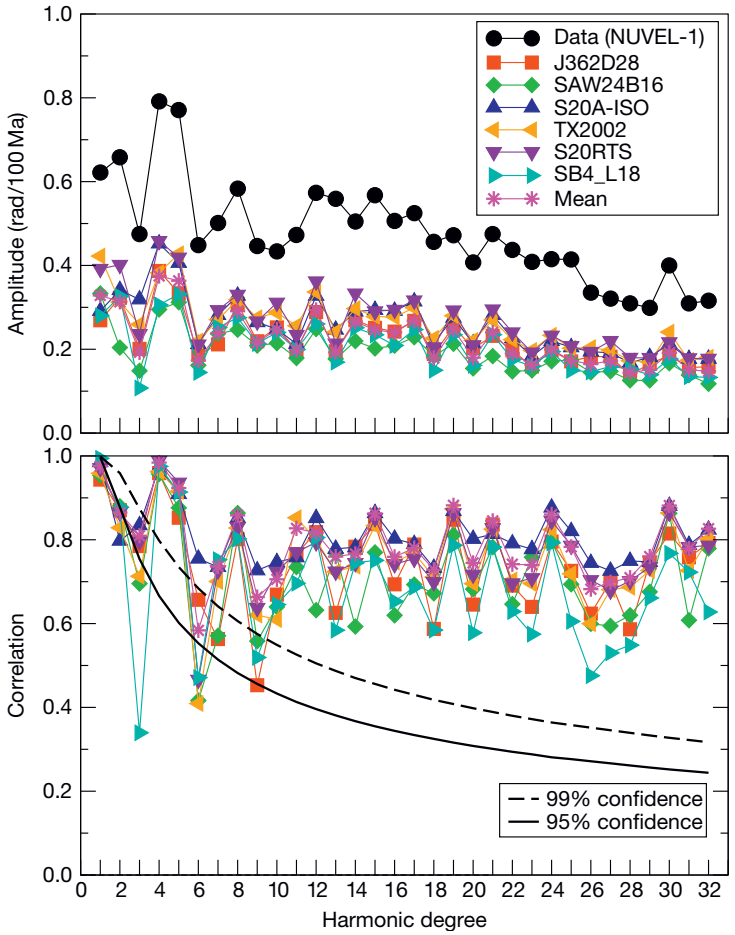

Figure 14 Spectral comparison of predicted and observed plate divergence. *Top frame* shows the degree variance, as defined in eqn [3], of the observed and predicted plate divergence fields shown in **Figure 13**. *Bottom frame* shows the degree correlations, as defined in eqn [4]. The black solid and dashed lines represent the 95% and 99% confidence levels, respectively.

Table 1 Comparison of observed[a] and predicted[b] horizontal plate divergence

Model	*NUVEL*[c]	J362D28	SAW24	S20A-Iso	TX2002	S20RTS	SB4_L18	*Mean*
rms	2.8	1.3	1.1	1.5	1.5	1.6	1.2	1.3
correl	–	0.77	0.74	0.83	0.78	0.80	0.74	0.82
var. red.	–	50%	44%	60%	56%	59%	45%	55%

Note: rms, root-mean-square amplitude, expressed here in units of 10^{-8} a^{-1}; correl, global cross correlation; var. red., variance reduction.
[a]Data and predictions (shown in **Figure 13**) are synthesized from spherical harmonics up to degree 32.
[b]Predictions employ the tomography model indicated at the top of each column and they use the corresponding velocity-to-density scalings in **Figure 12**.
[c]Horizontal divergence of the plates is derived from the NUVEL-1 (DeMets et al., 1990) description of present-day plate velocities.

arise from mantle convection. There has been some controversy as to origin and amplitude of Earth's dynamic topography, with some confusion as to how this dynamic topography should even be defined (e.g., Forte et al., 1993a,b; Gurnis, 1990; Gurnis, 1993). As will be discussed below, the interpretation of dynamic surface topography employed here, namely the topography arising from all density anomalies in the mantle (including those in the lithosphere), is not universally accepted. A detailed review and analysis of the opposing schools of thought in this debate has been presented by Pari (2001).

Numerous studies over the past three decades have focused exclusively on the topography of ocean floor, and the general conclusion is that this topography can be almost completely explained in terms of shallow, thermally induced density anomalies which arise from the age-dependent cooling of the oceanic lithosphere (e.g. Parsons and Sclater, 1977; Stein and Stein, 1992). The oceanic bathymetry is modeled in terms of isostatic compensation of density anomalies in the oceanic lithosphere and hence many studies have regarded this form of thermal isostasy as not being a 'dynamic' contribution to

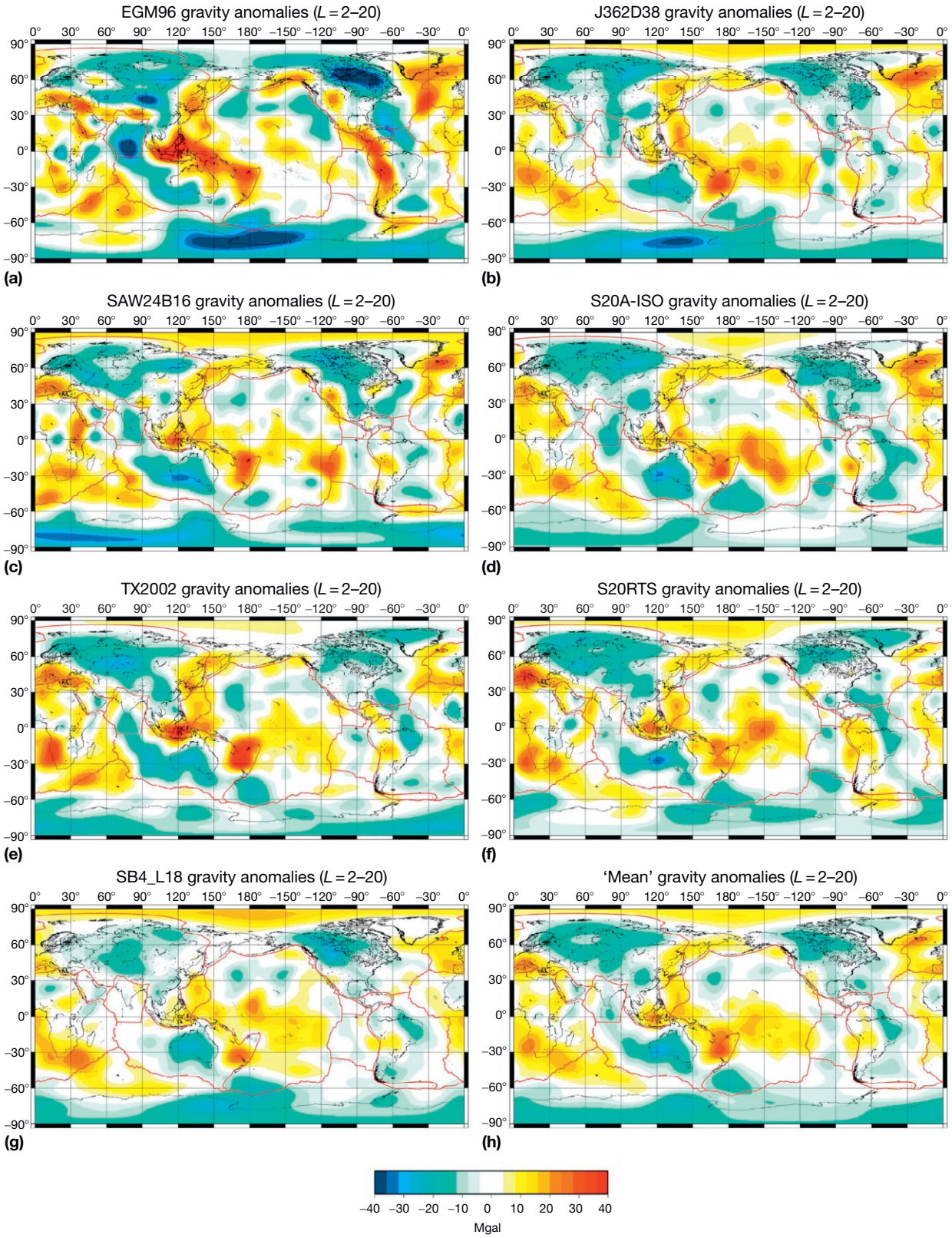

Figure 15 Tomography-based global free-air gravity anomalies. (a) Observed EGM96 anomalous free-air gravitational field (Lemoine et al., 1998). (b)–(g) show the free-air anomalies predicted on the basis of tomography models *J362D28* (Antolik et al., 2003), *SAW24* (Mégnin and Romanowicz, 2000), *S20A-Iso* (Ekström and Dziewonski, 1998), *TX2002* (Grand, 2002), *S20RTS* (Ritsema et al., 1999), and *SB4_L18* (Masters et al., 2000), using the corresponding d ln ρ/d ln V_S scaling profiles in **Figure 12**. All shear-velocity heterogeneity models have been projected onto the common parameterization in expression [102] prior to calculating the gravity anomalies. (h) The 'mean' free-air gravity anomaly field obtained by calculating the statistical sample average of all the predictions (b)–(g). The observed and predicted gravity anomalies shown here are all synthesized from spherical harmonics up to degree and order 20.

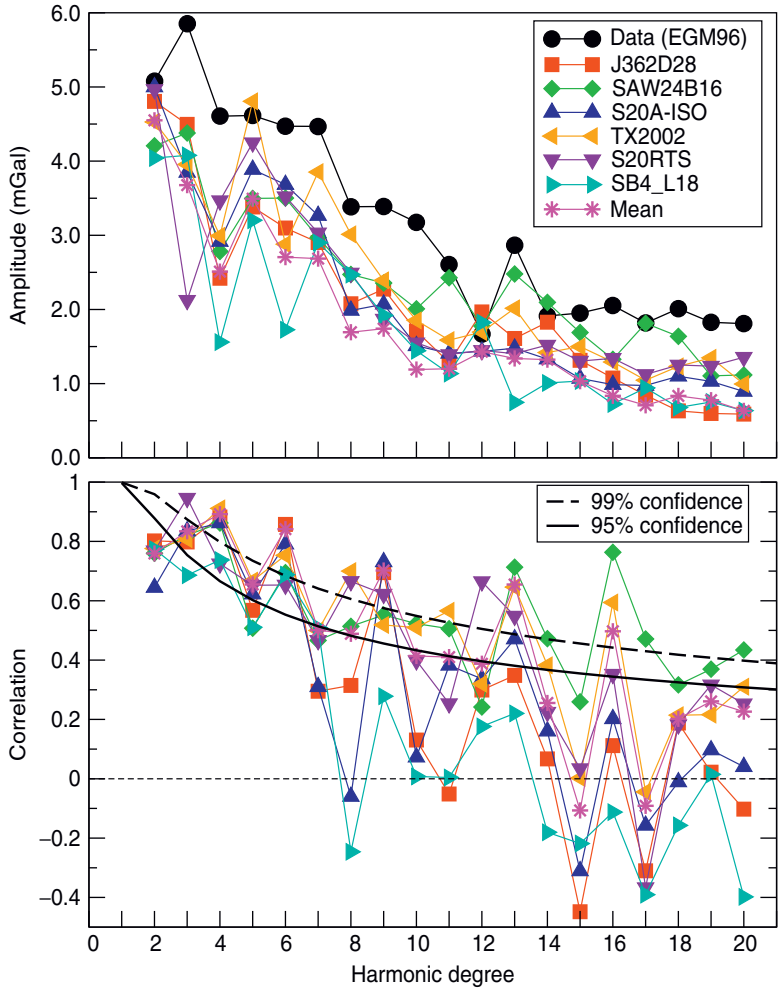

Figure 16 Spectral comparison of predicted and observed free-air gravity anomalies. *Top frame* shows the degree variance, as defined in eqn [3], of the observed and predicted gravity anomaly fields shown in **Figure 15**. *Bottom frame* shows the degree correlations, as defined in eqn [4]. The black solid and dashed lines represent the 95% and 99% confidence levels, respectively.

Table 2 Comparison of observed[a] and predicted[b] free-air gravity anomalies

Model	*EGM96*[c]	J362D28	SAW24	S20A-Iso	TX2002	S20RTS	SB4_L18	*Mean*
rms	14.8	10.4	11.2	10.6	11.4	10.5	8.9	9.3
correl	–	0.55	0.62	0.54	0.64	0.58	0.42	0.64
var. red.	–	28%	37%	26%	39%	33%	15%	41%

Note: rms, root-mean-square amplitude, expressed here in units of *mGal*; correl, global cross correlation; var. red., variance reduction.
[a]Data and predictions (shown in **Figure 15**) are synthesized from spherical harmonics up to degree 20.
[b]Predictions employ the tomography model indicated at the top of each column and they use the corresponding velocity-to-density scalings in **Figure 12**.
[c]The global free-air gravity anomalies are derived from the EGM96 geopotential model (Lemoine et al., 1998).

surface topography. An adequate review of the extensive literature dealing with this interpretation of seafloor topography is well beyond the scope of this chapter, but previous studies of age-dependent oceanic bathymetry, with extensive references to past analyses, may be found in Doin and Fleitout (2000) and in Crosby et al. (2006). Possible causes for the deviation of oceanic bathymetry from that predicted by a simple cooling lithosphere model have been analyzed by Zhong et al. (2007) and they considered 'reheating' of old lithosphere due to deeper mantle flow. More recent analyses by Adam and Vidal (2010, 2011) have explored the validity, or not (Croon et al., 2011), of a revised interpretation of ocean-floor subsidence due to lithospheric cooling by again appealing to the influence of mantle flow in the asthenosphere.

Whether or not the thermal isostatic signal in seafloor bathymetry may be regarded as 'static' or 'dynamic' depends on the temporal variability of the structure of the upper thermal boundary layer (i.e., the lithosphere in oceanic regions) due to time-dependent mantle convection. A purely mechanical interpretation of the instantaneous, present-day isostatic compensation of thermal anomalies in the lithosphere ignores this back-ground time-dependence. The lateral temperature

variations in the cooling lithosphere are essentially maintained by a balance between vertical heat conduction and horizontal heat advection (e.g., Parsons and McKenzie, 1978; Jarvis and Peltier, 1982) and the latter is clearly a dynamic effect. In the absence of convection, the upper thermal boundary layer and the corresponding variations in oceanic bathymetry will vanish. The importance of time-dependent changes in the structure of the lithosphere, and hence the corresponding changes in the contribution to surface topography, is highlighted by the significant changes in plate tectonic velocities and plate geometries in the Cenozoic (e.g., Lithgow-Bertelloni and Richards, 1998) which suggest significant departures from steady-state conditions.

In the absence of convection, the only contribution to surface topography arises from the isostatic compensation of lateral variations in crustal thickness and crustal density. Earth's present-day topography is therefore the superposition of the crustal isostatic topography and the dynamic topography – as defined here – due to density anomalies in the mantle which are maintained by mantle convection (Forte et al., 1993b). The crustal isostatic topography is large and it explains most of the observed present-day topography on Earth (e.g., Forte and Perry, 2000; Pari and Peltier, 2000). The dynamic topography is obtained by subtracting the crustal isostatic topography from the observed topography and this therefore requires an accurate model of crustal structure. This requirement presents a major challenge because of the uneven and incomplete seismic sampling of global crustal thickness and also because of the significant uncertainties in constraining the density of the crust.

Until recently (2013), the most complete compilation of global crustal heterogeneity was model CRUST2.0 (Bassin et al., 2000). This global compilation has been updated to include new seismological constraints on crustal structure, yielding a new model of crustal heterogeneity: CRUST1.0 (Laske et al., 2013). A comparison of the dynamic topography fields inferred using CRUST2.0 and CRUST1.0 is presented in **Figure 17**. The most obvious difference is the greater amplitude of the long-wavelength variations in dynamic topography derived from CRUST1.0 relative to CRUST2.0, where the former are on average about 40% larger than the latter. This amplitude difference is most strongly expressed at the longest horizontal wavelengths (see **Figure 17c**), such that the dynamic topography of continents inferred with CRUST1.0 is substantially more depressed than with CRUST2.0, implying that the dynamic height of the mid-ocean ridges is also increased as a consequence.

The origin of these long-wavelength differences in non-isostatic or dynamic topography derived from two global crustal compilations is not yet clear at this time, but it does serve to aptly highlight the important impact of uncertainties in crustal structure in applying topographic constraints on density anomalies in the mantle, especially those in the upper mantle (**Figure 10e,f**). In the following analysis, we

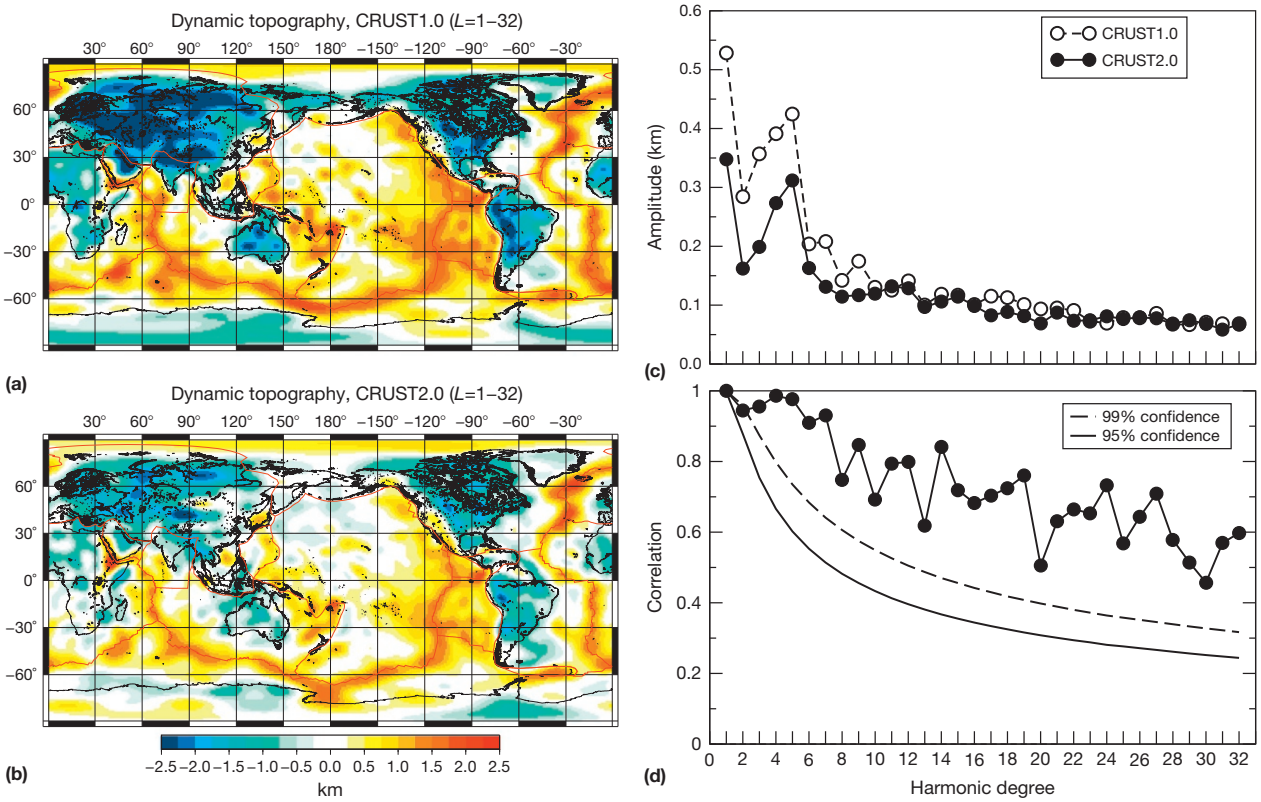

Figure 17 Long wavelength dynamic topography inferred from two crustal heterogeneity models. (a) Dynamic surface topography estimated by removing isostatically compensated crustal heterogeneity described by model CRUST1.0 (Laske et al., 2013) from the observed present-day surface topography. (b) Dynamic topography similarly inferred by removal of isostatically compensated CRUST2.0 (Bassin et al., 2000). (c) Comparison of spectral amplitudes (eqn [3]) from a spherical harmonic analysis of the inferred crustcorrected dynamic topography. (d) The degree correlations (eqn [4]) between the CRUST1.0and CRUST2.0 inferences of dynamic topography. The crust-corrected inferences of dynamic topography shown here are all synthesized from spherical harmonics up to degree and order 32.

employ the dynamic topography derived from the CRUST2.0 model (Figure 17b).

The observed and predicted dynamic topography fields, calculated on the basis of expressions (99) and using the kernels in Figure 10e,f, are presented in Figure 18. A quantitative spectral comparison of the predicted and observed dynamic topography is shown in Figure 19. In Table 3 is presented a detailed summary of the match between the predicted and observed topography fields. The topography kernels (Figure 10e,f) show that near-surface density anomalies provide the strongest contributions to the predicted surface topography (Figure 18) and that they will be in near-isostatic equilibrium, where perfect isostatic compensation corresponds to a kernel value of -1. We note that in the case of density anomalies which effectively see a no-slip surface boundary (given by expression 92), the condition of near-isostasy extends to depths of about 200 km (see Figure 10f).

In view of the debate (discussed above) concerning the magnitude of the thermal isostatic contributions to surface topography in oceanic regions, it is helpful to explore the relative importance of shallow (i.e. lithospheric) and deep-mantle (i.e. sub-lithospheric) buoyancy using the seismic tomography models. In this regard, it is useful to first evaluate the extent to which the tomography-based topography predictions incorporate the age-dependent cooling of the oceanic lithosphere. Tomography models employing seismic travel-time and/or surface wave data place strong constraints on lithospheric mantle heterogeneity and they contain a clear signature of the oceanic cooling history (e.g., Woodward and Masters, 1991; Su et al., 1992; Trampert and Woodhouse, 1996; Ritzwoller et al., 2004).

Here, we consider the global tomography models *SAW24* (Mégnin and Romanowicz, 2000) and *TX2002* (Grand, 2002), employed in Figure 18c and 18e, respectively. The age-dependent lateral temperature variations in the oceanic lithosphere were calculated using a simple halfspace cooling model with the same thermal parameters as the *GDH 1* plate-cooling model of Stein and Stein (1992). The seafloor age was determined using the Müller et al. (1997) digital isochrons. The global ocean basins were then sampled on a $1^\circ \times 1^\circ$ grid and for each grid cell the corresponding values of ocean age, shear velocity perturbation dV_S/V_S, and temperature perturbation ΔT were determined. These samples were then averaged into two million-year age bins and the resulting relationship between seismic shear velocity and temperature is plotted in Figure 20.

A linear regression analysis (solid lines in Figure 20) yields an excellent fit to the binned $V_S - T$ variation and the slopes of the regression lines provide estimates of the effective temperature derivative of S-velocity in the depth range 0–100 km. These estimated derivatives are $8.7 \times 10^{-5}\ \mathrm{K}^{-1}$ and $9.4 \times 10^{-5}\ \mathrm{K}^{-1}$ for models *SAW24* and *TX2002*, respectively. These effective thermal derivatives agree well with independent mineral physics values determined by Stixrude and Lithgow-Bertelloni (2005) which range between 8 and $9 \times 10^{-5}\ \mathrm{K}^{-1}$. These results confirm that the global tomography models considered in this study successfully resolve the pattern and amplitude of age-dependent cooling of the oceanic lithosphere.

The relative importance of surface topography due to lithospheric versus more deeply-seated density anomalies is illustrated in Figure 21. As expected, the topography contributions in oceanic regions from density anomalies in the upper 200 km of the mantle are dominated by the age-dependent cooling of the oceanic lithosphere. The accurate resolution of these shallow-mantle contributions to dynamic topography, which is dominated in the ocean basins by the cooling lithosphere signal, are important to obtaining good correlations (Table 3) to the crust-corrected inferences of global dynamic topography. Depressions in continental regions exceed observational estimates (Figure 18a) because the use of a purely depth dependent dln ρ/dln V_S scaling factor (Figure 12) does not resolve the intrinsic chemical buoyancy in the sub-continental mantle. This intrinsic buoyancy can be included in geodynamic models which allow for lateral variations of dln ρ/dln V_S in the shallow mantle (e.g., Forte and Perry, 2000; Deschamps et al., 2001).

The topography generated by sub-lithospheric buoyancy (Figure 21b), with rms amplitude equal to 410 m, is comparable to that generated by lithospheric density anomalies (Figure 21a) which has an rms amplitude equal 580 m. These sub-lithospheric contributions to topography in the central Pacific and Atlantic oceans, and in southern Africa, are surface expressions of deep-seated buoyancy with sources in the lower mantle (Figure 3). The depressions below the eastern and western margins of the Pacific (Figure 21b) may be interpreted in terms of present-day and Cenozoic subduction history (e.g. Lithgow-Bertelloni and Gurnis, 1997).

We note from Figure 18 that the amplitude of the predicted dynamic topography is somewhat larger than the crust-corrected estimate of the observed dynamic topography. Table 3 shows that the rms amplitude of the mean topography prediction is 25% larger than the observed topography. This discrepancy is in marked contrast to that of the predicted gravity and plate divergence fields (Tables 1 and 2) which are, on average, 40–50% smaller than the corresponding observed fields. The mismatched amplitudes of the predicted surface topography have motivated previous efforts (e.g., Le Stunff and Ricard, 1995, 1997) to introduce additional buoyancy forces in the mantle arising, for example, from undulations of the 670 km seismic discontinuity (e.g., Thoraval et al., 1995; Forte and Woodward, 1997b) which internally compensate the excess surface topography.

In assessing the significance of this discrepancy, in terms of mantle dynamics, it is important to recognize that the crustal correction employed in Figure 18a contains significant uncertainties which may in part be responsible for the mismatched amplitudes. Perhaps more important is the question of the validity of a purely depth-dependent velocity–density scaling (Figure 12) employed in the topography predictions. Such depth-dependence, which may be justified if one assumes that thermal effects on mantle heterogeneity dominate (e.g., Karato and Karki, 2001), is not a good approximation in the presence of large lateral variations in chemical composition. Such compositional heterogeneity is expected to be important in the shallow subcontinental mantle and it will oppose the local thermal buoyancy, implying significant reductions in the amplitude of continental surface topography (e.g., Forte and Perry, 2000).

To understand why the gravity (and plate motion) predictions, in contrast to the surface topography, have substantially smaller amplitudes than the observed fields, we must first appreciate that the global seismic data have difficulty resolving heterogeneity in the deep mantle, particularly in the southern

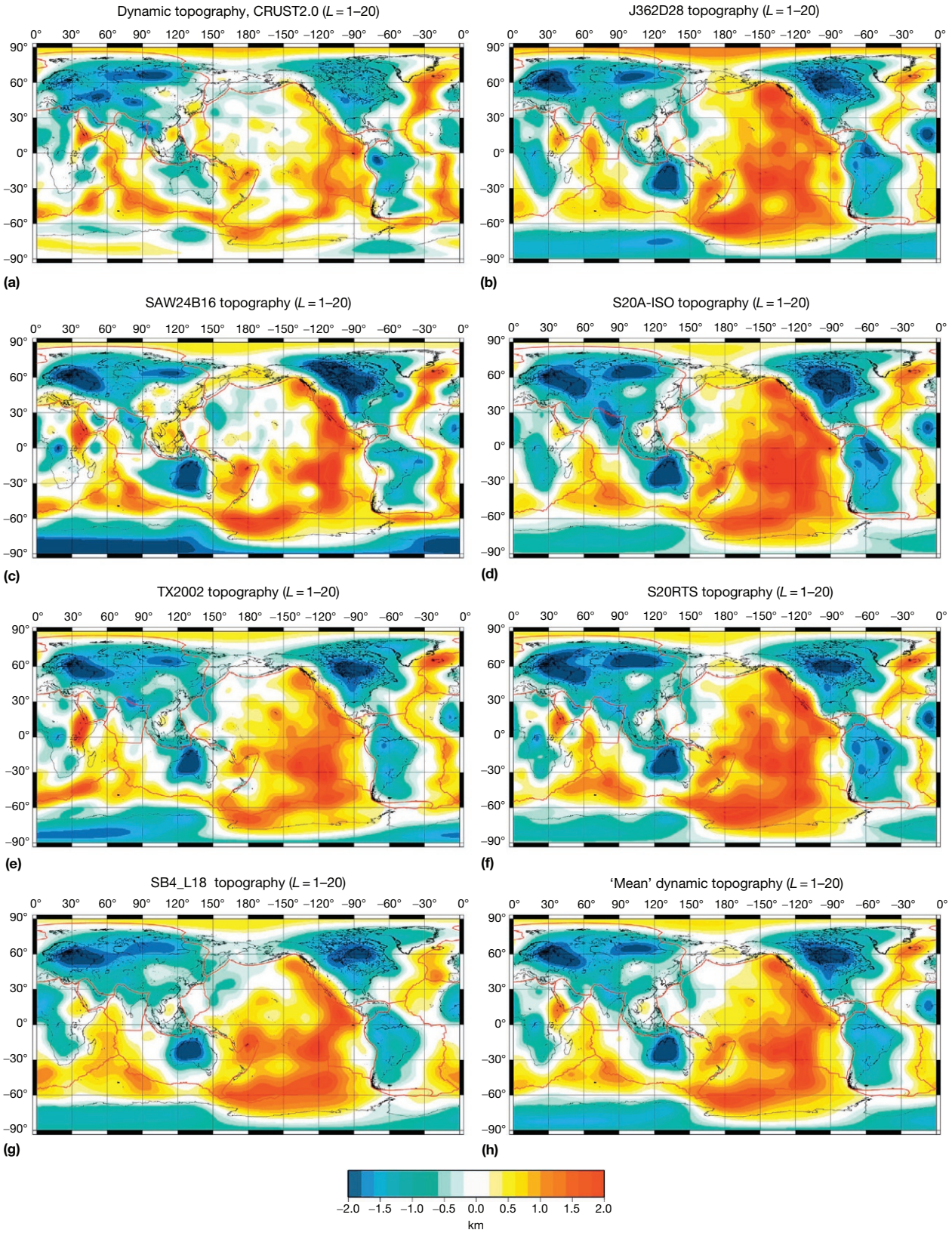

Figure 18 Tomography-based global dynamic surface topography. (a) Dynamic surface topography estimated by removing isostatically compensated crustal heterogeneity – described by model CRUST2.0 (Bassin et al., 2000) – from the observed present-day surface topography. (b)–(g) show the dynamic surface topography predicted on the basis of tomography models *J362D28* (Antolik et al., 2003), *SAW24* (Mégnin and Romanowicz, 2000), *S20A-Iso* (Ekström and Dziewonski, 1998), *TX2002* (Grand, 2002), *S20RTS* (Ritsema et al., 1999), and *SB4_L18* (Masters et al., 2000), using the corresponding d ln ρ/d ln V_S scaling profiles in **Figure 12**. All shear-velocity heterogeneity models have been projected onto the common parameterization in expression [102] prior to calculating the dynamic topography. (h) The 'mean' dynamic surface topography field obtained by calculating the statistical sample average of all the predictions (b)–(g). The crust-corrected and predicted dynamic topography shown here are all synthesized from spherical harmonics up to degree and order 20.

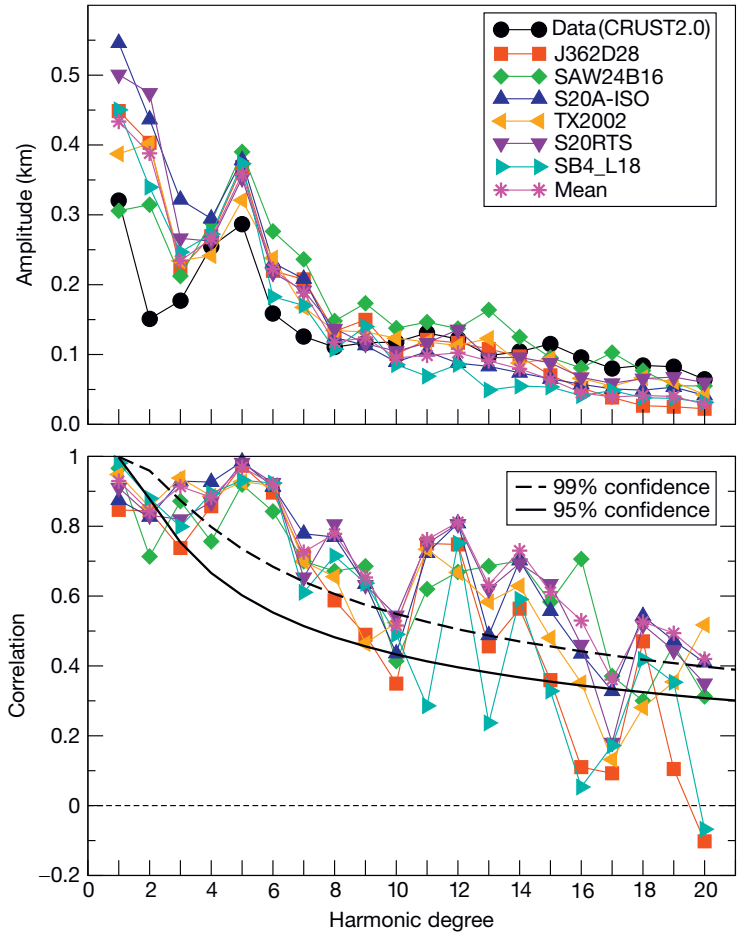

Figure 19 Spectral comparison of predicted and observed (crust-corrected) dynamic surface topography. *Top frame* shows the degree variance, as defined in eqn [3], of the observed and predicted topography fields shown in **Figure 18**. *Bottom frame* shows the degree correlations, as defined in eqn [4]. The black solid and dashed lines represent the 95% and 99% confidence levels, respectively.

Table 3 Comparison of observed[a] and predicted[b] dynamic surface topography

Model	*CRUST*[c]	J362D28	SAW24	S20A-Iso	TX2002	S20RTS	SB4_L18	*Mean*
rms	696	908	893	1002	860	972	849	873
correl	–	0.75	0.76	0.80	0.78	0.78	0.79	0.87
var. red.	–	25%	30%	22%	41%	24%	44%	47%

Note: rms, root-mean-square amplitude, expressed here in units of *m*; correl, global cross correlation; var. red., variance reduction.
[a]Data and predictions (shown in **Figure 18**) are synthesized from spherical harmonics up to degree 20.
[b]Predictions employ the tomography model indicated at the top of each column and they use the corresponding velocity-to-density scalings in **Figure 12**.
[c]The global dynamic surface topography obtained by subtracting CRUST2.0 (Bassin et al., 2000) isostatic crust from the observed topography.

hemisphere (e.g., Forte et al., 1994; Simmons et al., 2006). This difficulty does not apply to the shallow mantle where, as shown above (**Figure 20**), the tomography models are able to successfully resolve the cooling oceanic lithosphere. The predicted surface topography is dominated by the density anomalies located in the upper mantle, whereas the gravity predictions contain significant contributions from lower-mantle density anomalies (**Figure 10**). Joint inversions of global seismic and convection-related data sets have shown that increased amplitudes of the predicted gravity anomalies and substantially improved fits to the global gravity data can be achieved by modifying deep-mantle heterogeneity in a way that is consistent with both the seismic and geodynamic constraints (e.g., Forte et al., 1994; Simmons et al., 2006, 2007, 2009, 2010). Such modifications to lower-mantle heterogeneity have little impact on the amplitude of the predicted surface topography. These basic observations suggest that current mismatches between the amplitudes of the predicted and observed dynamic topography are not more significant, or fundamentally different, from the mismatch between the other predictions (i.e., gravity and plate motions) and their corresponding observables.

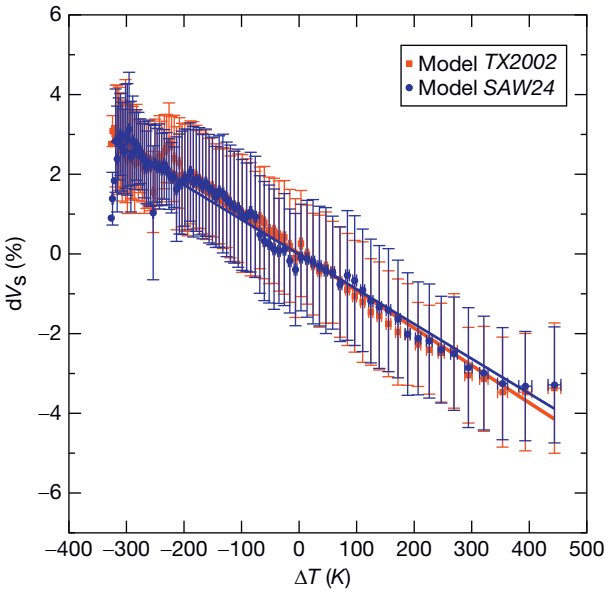

Figure 20 Comparison of seismic shear-velocity and temperature anomalies in the oceanic lithosphere. Seismic shear-velocity anomalies, vertically averaged in the depth interval 0–100 km, are derived from tomography models *SAW24* (Mégnin and Romanowicz, 2000) and *TX2002* (Grand, 2002). The S-velocity anomalies, measured relative to the global oceanic mean value, were averaged into 2 Ma age bins using the global ocean-age compilation of Müller et al. (1997). The age-dependent temperature variations in the oceanic lithosphere were determined using a simple half-space cooling model with the same thermal parameters as the *GDH*1 plate model of Stein and Stein (1992). These temperature variations were vertically averaged down to 100 km depth and subsequently averaged into 2 Ma age bins. The temperature anomalies are measured relative to the global oceanic mean value. The vertical and horizontal error bars represent one standard deviation relative to the average shear velocity and temperature, respectively, in each age bin. The solid blue and red lines are the best-fitting linear regression lines for models *SAW24* and *TX2002*, respectively.

1.27.3.6 Predicted CMB Topography

Tomography-based studies of the flow-induced deformations of the CMB have been rather limited (e.g., Forte et al., 1993a, 1995a,b; Hager et al., 1985) relative to the much greater number of studies that have focused on the surface geoid or topography. This is in large part a consequence of the uncertain and often contrasting inferences of the CMB topography, which have been derived from inversions of seismic phases, which are sensitive to this topography (e.g., Boschi and Dziewonski, 2000; Garcia and Souriau, 2000; Morelli and Dziewonski, 1987; Obayashi and Fukao, 1997; Rodgers and Wahr, 1993; Sze and van der Hilst, 2003). A detailed discussion of the seismological uncertainties and difficulties in obtaining reliable global images of the CMB topography may be found in Garcia and Souriau (2000).

The most accurate constraint on the topographic undulations of the CMB is derived from space-geodetic analyses of Earth's nutations. A brief review of these constraints was presented in **Section 1.27.2.1**. Unfortunately, these geodetic analyses can only constrain the excess flattening or dynamic ellipticity of the CMB – albeit with high precision – and this corresponds to only one coefficient ($\ell=2, m=0$) in a full spherical harmonic expansion (expression [1]) of the spatially varying CMB topography field. This constraint on excess CMB flattening is included in all the Occam-inferred $\mathrm{d}\ln\rho/\mathrm{d}\ln V_S$ scaling profiles in **Figure 12**.

For the purpose of comparison, we consider a relatively recent seismological inference of the CMB topography (**Figure 22(a)**) obtained by Boschi and Dziewonski (2000) (henceforth referred to as 'BD2000') on the basis of seismic PcP and PKP travel-time delays. The flow-induced CMB topography predicted on the basis of the Occam-inferred $\mathrm{d}\ln\rho/\mathrm{d}\ln V_S$ profiles (**Figure 12**) and, using the kernels in **Figure 10(g)** and **10(h)**, is presented in **Figure 22**. All predictions of CMB topography shown here exactly reproduce the geodetically constrained 400 m excess CMB ellipticity. A quantitative spectral analysis (**Figure 23**) of the predicted CMB topography fields shows that they are strongly dominated by the horizontal wavelengths corresponding to harmonic degrees $\ell=2,3$. In **Table 4** is presented a detailed summary of the match between the predicted and observed CMB topography fields.

The overall spatial correlation between the predicted maps of flow-induced CMB topography and the BD2002 model (**Figure 22**) is quite good; however, it is quite clear that there is a significant difference in the overall amplitude. The CMB topography obtained on the basis of the tomography-based flow calculations is approximately a factor of three to four times smaller than that in BD2002. Although, as noted earlier (**Section 1.27.3.3**), there likely exists an inherent damping in the flow predictions, it is not possible to increase the amplitude of the predicted CMB topography (by increasing, e.g., the magnitude of the $\mathrm{d}\ln\rho/\mathrm{d}\ln V_S$ scaling) without at the same time significantly degrading the fit to the other geodynamic observables. The ±1.5 km-scale undulations in the predicted, flow-induced CMB topography are in the range estimated by Garcia and Souriau (2000) for horizontal wavelengths in excess of 1200 km.

1.27.4 Joint Seismic–Geodynamic Inversions for 3-D Structure and Flow in the Mantle

In the preceding sections, all interpretations of the 3-D structure and flow in the mantle, and the predicted surface geodynamic observables associated with this flow, have been entirely based on purely seismic inversions for 3-D lateral heterogeneity in the mantle. This approach, in which previously published seismic tomography models are converted a posteriori into an equivalent mapping of 3-D density anomalies, as described in **Section 1.27.3.2**, is followed in essentially all analyses of tomography-based mantle convection that have been published since the advent of the first global tomography models in the mid-1980s (e.g., Forte and Peltier, 1987) up to the present (e.g., Alisic et al., 2012; Becker and Faccenna, 2011; Conrad et al., 2011).

In the following, we will instead consider how the seismic constraints on global heterogeneity in the mantle may be simultaneously inverted with independent constraints on 3-D structure from geodynamic and mineral physical data to obtain a new generation of mantle tomography models that successfully reconcile all these constraints, thereby providing new insights in the structure and dynamics of the mantle convective flow.

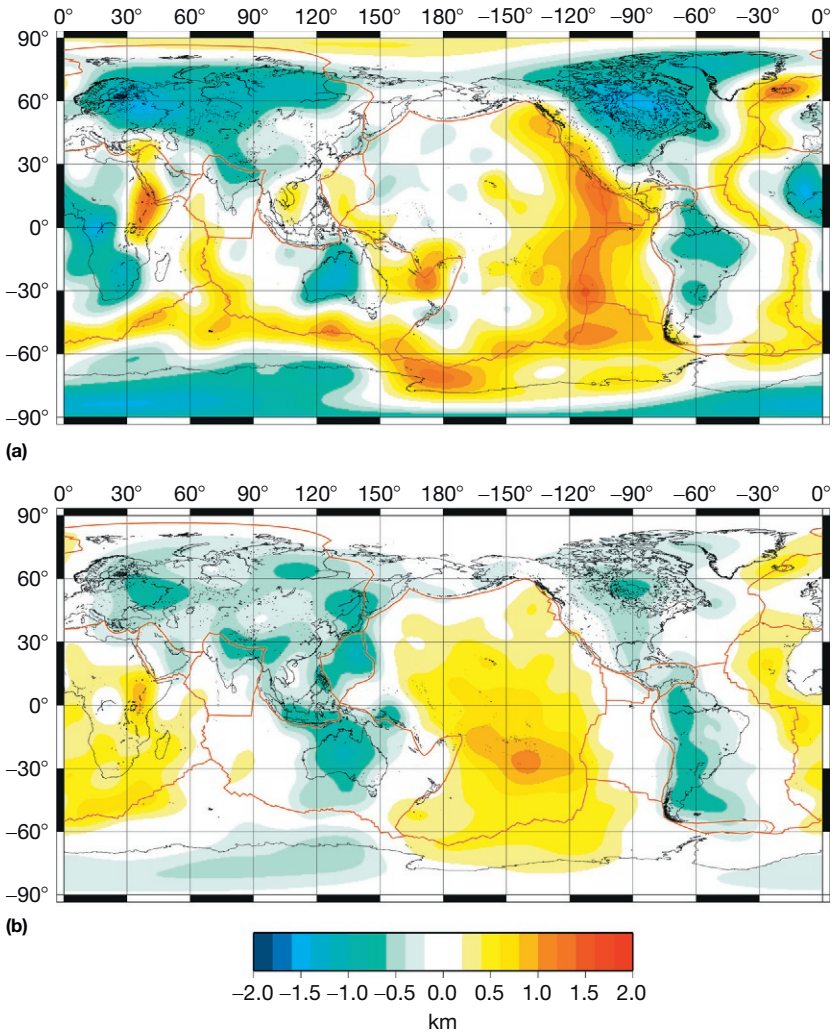

Figure 21 Shallow versus deep-mantle contributions to surface topography. (a) Surface topography predicted on the basis of tomography-derived density anomalies in the upper 200 km of the mantle. (b) Surface topography predicted on the basis of all density anomalies below 200 km depth. In both cases, the density anomalies are derived from tomography model *TX2002* (Grand, 2002) and using the corresponding d ln ρ/d ln V_S scaling profiles in **Figure 12**. The summation of the topography fields in maps (a) and (b) yields the total field shown in **Figure 18(e)**. All fields are synthesized from spherical harmonics up to degree and order 20.

1.27.4.1 Deficiencies in Mantle Flow Models Based on Pure Seismic Tomography Inversions

While the a posteriori scaling of mantle tomography models, derived purely from seismic data, into equivalent density heterogeneity models has provided reasonably good fits to the global convection-related data sets, there remain significant unexplained misfits to these surface geodynamic constraints. More specifically, the variance reductions achieved in fitting long-wavelength global plate motions, gravity, and dynamic topography anomalies are 55%, 41%, and 47%, respectively. These misfits characterize the summary or '*mean*' predictions in the final column of **Tables 1–3**. These results, obtained with optimized depth-dependent velocity-to-density scaling factors, suggest that, on average, about 50% of the power in convection-related data cannot be explained by the a posteriori scaling of the currently available seismic tomography models.

In assessing the origin of the outstanding misfit between the tomography-based predictions of the convection-related observables and the corresponding data, a number of possible deficiencies in the mantle flow calculations should be considered. As discussed in **Section 1.27.2.3.1**, a major simplification in the mantle flow modeling is the assumption that the sublithospheric viscosity of the mantle varies with depth only. We should note, however, that these flow models incorporate the effect of what is arguably the greatest-amplitude lateral heterogeneity of rheology in the solid Earth: the tectonic plates. All flow predictions presented in the preceding sections are carried out with surface tectonic plates coupled to the mantle flow and driven by this flow. The outstanding question is therefore whether LVV in the underlying mantle can account for a significant fraction of the current misfit to the geodynamic data.

In addressing the impact of LVV on global convection-related surface data, Moucha et al. (2007) found that global-

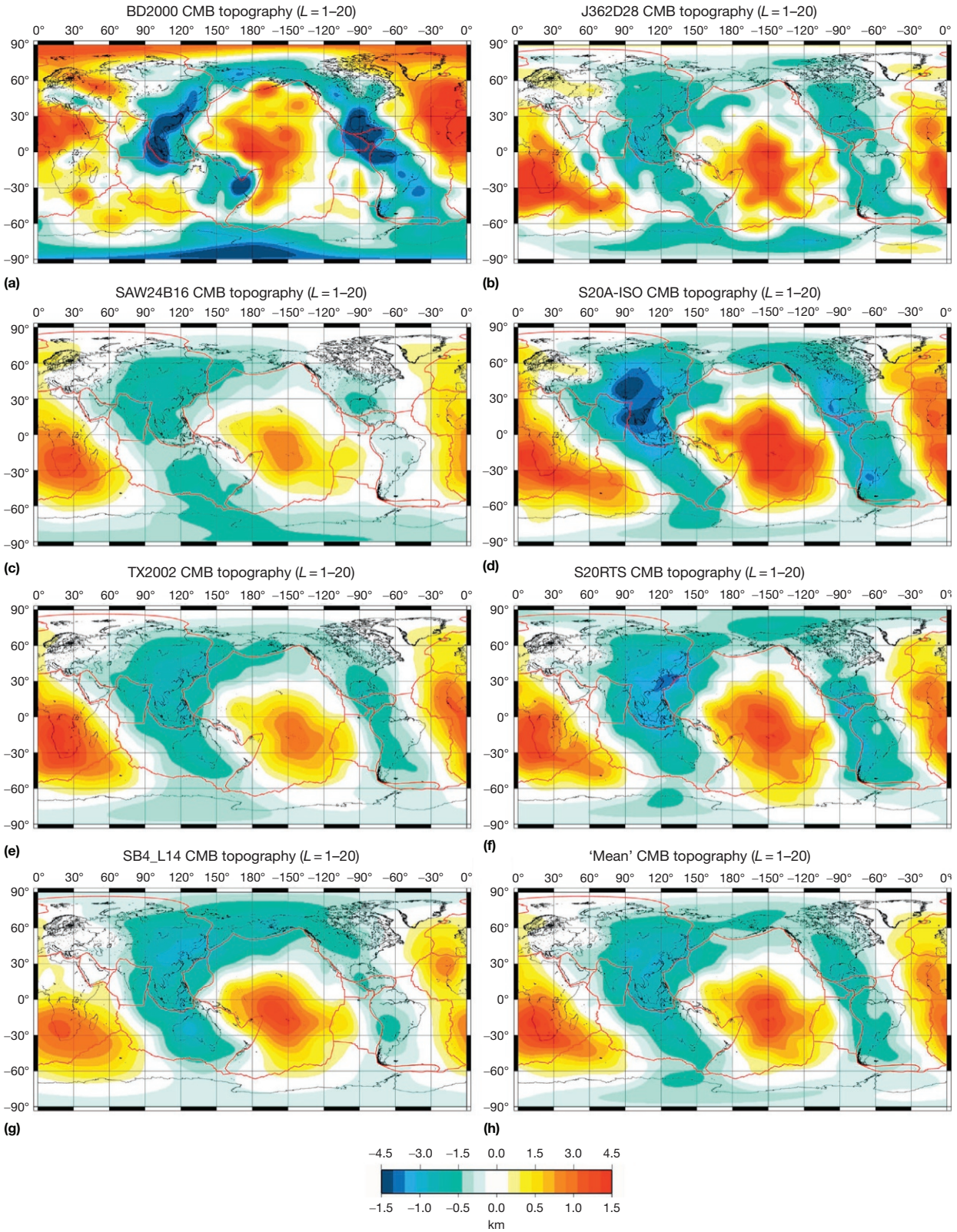
BD2000 CMB topography (L = 1–20)
J362D28 CMB topography (L = 1–20)
(a)
(b)
SAW24B16 CMB topography (L = 1–20)
S20A-ISO CMB topography (L = 1–20)
(c)
(d)
TX2002 CMB topography (L = 1–20)
S20RTS CMB topography (L = 1–20)
(e)
(f)
SB4_L14 CMB topography (L = 1–20)
'Mean' CMB topography (L = 1–20)
(g)
(h)
0° 30° 60° 90° 120° 150° 180° –150° –120° –90° –60° –30° 0°
90° 60° 30° 0° –30° –60° –90°
–4.5 –3.0 –1.5 0.0 1.5 3.0 4.5
–1.5 –1.0 –0.5 0.0 0.5 1.0 1.5
km

Figure 22 Tomography-based global CMB topography. (a) Seismically inferred CMB topography derived by Boschi and Dziewonski (2000). The amplitudes correspond to the top values (±4.5 km) in the bottom scale bar. (b)–(g) show the CMB topography predicted on the basis of tomography models *J362D28* (Antolik et al., 2003), *SAW24* (Mégnin and Romanowicz, 2000), *S20A-Iso* (Ekström and Dziewonski, 1998), *TX2002* (Grand, 2002), *S20RTS* (Ritsema et al., 1999), and *SB4_L18* (Masters et al., 2000), using the corresponding d ln ρ/d ln V_S scaling profiles in **Figure 12**. All shear-velocity heterogeneity models have been projected onto the common parameterization in expression [102] prior to calculating the CMB topography. (h) The 'mean' CMB topography field obtained by calculating the statistical sample average of all the predictions (b)–(g). The amplitudes for (b)–(h) correspond to the bottom values (±1.5 km) in the bottom scale bar. The observed and predicted CMB topography shown here are all synthesized from spherical harmonics up to degree and order 20.

scale heterogeneity in viscosity, in which the amplitude of the LVV is equivalent to the variations in the mean depth-dependent viscosity (up to three orders of magnitude), yields predictions that differ by about 20% from those obtained by neglecting LVV. These differences were also found to be substantially smaller than the differences obtained using two different global tomography models. These results suggest that LVV in the mantle are not likely to be the principal source of the outstanding 50% misfit between the current tomography-based flow predictions and the surface geodynamic observables.

Another, possibly major, source of misfit may be due to the neglect of lateral variations in the scaling between seismic velocity and density, as would be the case in the presence of significant compositional heterogeneity in the mantle. The predicted geodynamic observables presented in Section 1.27.3 are obtained using a purely depth-dependent scaling, as expected if thermal contributions to mantle heterogeneity are assumed dominant (see, e.g., Figure 12).

A detailed exploration of the amplitude and distribution of chemical heterogeneity inferred on the basis of previously published tomography models, to achieve maximum agreement with the surface geodynamic data, was carried out by Forte (2007). This analysis allowed for explicit lateral variations in the velocity-to-density scaling by inverting for different scaling factors in regions of the mantle characterized by anomalously hot material (e.g., rising plumes) and anomalously cold material (e.g., subducting lithosphere in the lower mantle and deep subcontinental roots in the upper mantle). This parameterization of chemical heterogeneity is analogous to that advocated by Xu et al. (2008), in which the composition of the mantle is assumed to be a mechanical mixture of basalt and harzburgite generated by a long-term history of partial melting at mid-ocean ridges and subsequent transport into the deep mantle by subducting lithosphere. The inversions by Forte (2007) for a laterally variable scaling, associated with 'hot' and 'cold' regions of the mantle, yielded an improved fit to the surface convection-related data sets, but the improvement of about 10% is largely insufficient to account for the outstanding 50% misfit to these data.

We refer the interested reader to Forte (2007) for a detailed discussion of the geodynamic and mineral physical interpretation of global tomography models, derived solely from seismic data, in terms of compositional heterogeneity in the mantle. An alternative view of compositional heterogeneity in the mantle, based on 'probabilistic' (purely seismic) inversions for 3-D mantle structure, is presented in Mosca et al. (2012).

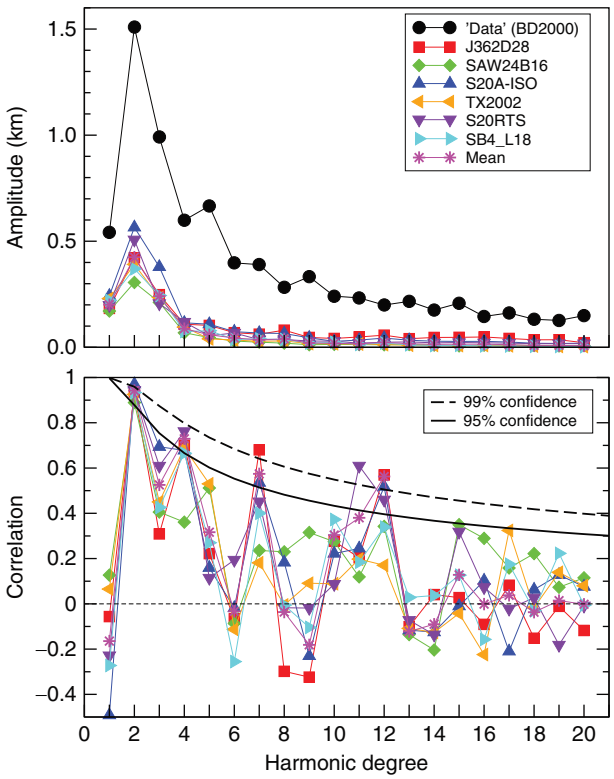

Figure 23 Spectral comparison of predicted and observed CMB topography. *Top frame* shows the degree variance, as defined in eqn [3], of the observed and predicted CMB topography fields shown in Figure 22. *Bottom frame* shows the degree correlations, as defined in eqn [4]. The black solid and dashed lines represent the 95% and 99% confidence levels, respectively.

1.27.4.2 Mantle Flow Modeling Based on Tomography Models Derived from Seismic Data Alone Is Insufficient

The considerations presented in the previous section suggest that the origin of the outstanding (nearly 50%) misfit between the tomography-based predictions of the convection-related observables and corresponding data is not likely to be resolved by the introduction of additional complexity in the mantle flow theory, such as LVV or lateral heterogeneity in major element mantle composition.

The main reason for the substantial misfit of the tomography-based geodynamic predictions is most likely due to a basic limitation inherent in published tomography models derived solely from global seismic data. This limitation arises

Table 4 Comparison of seismically observed[a] and predicted[b] CMB topography

Model	*BD2000*[c]	J362D28	SAW24	S20A-Iso	TX2002	S20RTS	SB4_L18	*Mean*
rms	2.3	0.58	0.42	0.76	0.53	0.61	0.51	0.55
correl	–	0.56	0.56	0.64	0.59	0.65	0.55	0.62
var. red.	–	22%	18%	31%	22%	27%	20%	24%

Note: rms, root-mean-square amplitude, expressed here in units of km; correl, global cross correlation; var. red., variance reduction.
[a]Seismic observations and predictions (shown in Figure 22) are synthesized from spherical harmonics up to degree 20.
[b]Predictions employ the tomography model indicated at the top of each column and they use the corresponding velocity-to-density scalings in Figure 12.
[c]CMB topography derived by Boschi and Dziewonski (2000) from global tomographic inversion of seismic delay times.

because the data sets employed in the derivation of these tomography models do not provide unique constraints on lateral heterogeneity throughout the mantle. It has long been understood that the amplitude of seismically inferred heterogeneity is poorly constrained over a large depth interval in the mid and lower mantle and that direct comparisons between different models published in the literature yield ambiguous information (e.g., deWit et al., 2012; Masters et al., 2000). This ambiguity or nonuniqueness is the direct consequence of the existence of a large null-space in the seismic data constraints on lateral heterogeneity in the mantle (e.g., deWit et al., 2012).

The relatively weak global seismic constraints in the mid-mantle region were explicitly shown in Forte et al. (1994) where it was also demonstrated that the seismic sampling of heterogeneity in the Southern Hemisphere portion of the deep mantle was weak. This limited sampling of mantle heterogeneity in the Southern Hemisphere is especially marked in tomography models derived predominantly from direct arriving seismic waves (e.g., Li et al., 2008). A clear illustration of the outstanding difficulty in resolving mantle heterogeneity in the depth interval 600–2000 km is provided by the comparison of recently published tomography models presented by Ritsema et al. (2011, see Figures 1 and 11 in their paper).

The mid-mantle region is of great importance in geodynamic modeling because the mantle flow excited by buoyancy forces in this region explains a significant fraction of the convection-related surface data such as the long-wavelength free-air gravity anomalies (see **Figure 10(c)** and **10(d)**) and the tectonic plate motions (see **Figure 10(b)**). An accurate resolution of mid-mantle buoyancy forces, over a large depth interval (from about 400 to 2000 km depth), is also crucial for understanding the amplitude and spatial pattern of flow across the entire mantle, with direct implications for the extent to which the flow is vertically stratified (e.g., Forte, 2000; Forte and Woodward, 1997a,b; Simmons et al., 2006).

Currently published seismic tomography models do not represent the full range of models that are compatible with the global seismic data sets (e.g., deWit et al., 2012). Although the tomographic inversions may contain far more data than the parameters used to represent the 3-D models (e.g., Boschi and Dziewonski, 2000; Kustowski et al., 2008; Li et al., 2008; Ritsema et al., 2011), the data nonetheless provide limited and nonuniform sampling of deep-mantle heterogeneity. This limitation arises in large part from the geographically restricted distribution of seismic stations and earthquake sources. Smoothness and amplitude-damping constraints are therefore used to regularize the tomographic inversions in order to stabilize the heterogeneity in those portions of the mantle that are poorly sampled by the seismic data. If these regularization conditions are changed, then so are the tomography models that result from the inversions. Furthermore, the result of any seismic inversion will be dependent on a number of other factors that include model parameterization, data weighting, and seismic wave theory employed in the data interpretation. Changes in any one of these ingredients will result in different 3-D seismic models that will yield different and, in some cases, conflicting geodynamic interpretations of mantle heterogeneity.

Since any individual seismic tomography model is only a single realization out of the infinitely large space of models that are compatible with the global seismic data, it is not sufficient to test mantle flow hypotheses, or to evaluate the significance of predicted geodynamic surface observables, on the basis of the published tomography models. As initially shown by Forte et al. (1994) and subsequently by Simmons et al. (2006, 2007, 2009, 2010), a robust test of different mantle flow scenarios, and the degree to which mantle heterogeneity is controlled by lateral temperature variations, is to check the plausibility of these scenarios directly against the widest range of available seismic and geodynamic data. This testing can be effectively accomplished by simultaneously inverting all data constraints in a single large-scale inversion. These joint inversions will immediately reveal the extent to which these different constraints on mantle structure, composition, and flow can be simultaneously and successfully reconciled by at least one model of 3-D mantle heterogeneity.

1.27.4.3 Simultaneous Inversions of Seismic, Geodynamic, and Mineral Physical Data

In essence, a joint tomographic inversion of multiple and distinct classes of geophysical data involves the search for (a) 3-D mantle heterogeneity model(s) that can simultaneously satisfy all these data. This was the approach developed by Forte et al. (1994) and Forte and Woodward (1997a,b), who implemented a method for jointly inverting global seismic and geodynamic data. The key feature of these joint inversions, which sets them apart from classical tomography inversions of seismic data alone, is the inclusion of constraints directly relating to buoyancy-induced mantle flow, in particular the relationship between this flow and convection-related surface data. These joint inversions are thus able to directly test to what extent the seismic constraints on mantle heterogeneity are compatible with entirely independent geodynamic constraints on the same structure (e.g., Simmons et al., 2006). This joint inversion procedure also allows a direct test of the degree to which mantle heterogeneity is controlled by the thermal anomalies maintained by the mantle convection process (e.g., Forte and Woodward, 1997a,b; Simmons et al., 2009).

1.27.4.3.1 Geodynamic and seismic data sets

The principal geodynamic surface observables that can be used to effectively constrain the 3-D structure and dynamics of the convecting mantle were described previously in **Section 1.27.2.1**, and they include the global free-air gravity anomalies, the crust-corrected dynamic topography, the present-day tectonic plate velocities, and the excess 'flattening' or ellipticity of the CMB (all fields are shown in **Figure 2**).

The theoretical, linear-integral relationship between the spherical harmonic coefficients of any one of these observable geodynamic fields and the corresponding harmonic coefficients of the internal density perturbations in the mantle is provided by geodynamic kernel or 'response' functions, as shown in eqn [104]. In the recent series of joint seismic–geodynamic tomography inversions carried out by Simmons et al. (2007, 2009, 2010), the geodynamic response functions have been calculated on the basis of the radial viscosity profile, shown in **Figure 9**, derived from the simultaneous inversions of GIA and convection data by Mitrovica and Forte (2004). The depth-dependent geodynamic kernel functions that are derived on the basis of

this geodynamically inferred viscosity profile are presented in Figure 10. These kernels will be employed in the joint tomography inversions described in the succeeding text.

The seismic data employed in the joint seismic–geodynamic tomography inversions consist of over 46 000 travel times of shear body waves (S waves) that were measured by Simmons (2007) and Grand (2002) through cross correlation of synthetic waveforms (for 1-D reference Earth model) and observed waveforms. These travel-time measurements were made mainly on teleseismic, horizontally polarized (SH) shear waves, including reflected multiple phases: Sn and ScSn, where n is the number of surface reflections and c denotes a reflection from the CMB. The data set also contains vertically polarized (SV) teleseismic shear phases: SKS and SKKS. An additional, critically important component of the global data set consists of regional, shallow-turning SH phases and surface-reflected multiples that are triplicated due to sharp velocity increases in the upper-mantle transition zone (Grand, 1994). These shallow phases provide increased lateral resolution of strongly varying upper-mantle structures that teleseismic body waves do not provide. A thorough discussion of the seismic data measurement and modeling procedure is provided by Simmons (2007), with a detailed summary to be found in Simmons et al. (2006).

1.27.4.3.2 Joint inversion procedure

The joint inversion of the seismic and geodynamic data sets described in the preceding section is carried out by first parameterizing the heterogeneity in the mantle in terms of individual blocks, in each of which the heterogeneity is assumed to be constant. This block representation of 3-D mantle structure is accomplished by dividing the mantle into 22 layers, from the surface down to the CMB, where the layer thickness varies between 75 (in the upper mantle) and 150 km (in the lower mantle). The lowermost mantle layer (layer 22), representing the heterogeneity in the seismic D″ region, has a thickness of 240 km. Each layer is then divided into rectangular voxels whose sides have a horizontal dimension of 275 km. This parameterization of mantle structure yields nearly 99 000 blocks.

The suite of convection-related geodynamic observables (Figure 2) are combined with the global seismic data into a single linear system, yielding an inverse problem that simultaneously constrains seismic velocity and density heterogeneity as follows:

$$\begin{pmatrix} \mathbf{L} \\ \lambda_G \mathbf{G}(R_{\rho/s}) \\ \lambda_{cmb} c(R_{\rho/s}) \\ \lambda_R \mathbf{R} \end{pmatrix} \mathbf{m} = \begin{pmatrix} \mathbf{r} \\ \lambda_G \mathbf{s} \\ \lambda_{cmb} e \\ \mathbf{0} \end{pmatrix} \qquad [109]$$

in which the heterogeneity in the mantle, denoted here by the column vector $\mathbf{m}$ with ~99 000 components, is expressed in terms of seismic slowness perturbations. The seismic constraints on mantle heterogeneity are incorporated via $\mathbf{L}$, a sparse matrix of ray path lengths (seismic sensitivities), and $\mathbf{r}$, the shear wave travel-time residuals. $\mathbf{L}$ has a row dimension of ~46 000, corresponding to the total number of seismic travel times. The geodynamic constraints are incorporated through $\mathbf{G}$, a fully populated matrix containing the viscous flow sensitivity kernels (Figure 10), where each row corresponds to a specific spherical harmonic component of the free-air gravity, plate divergence, and dynamic topography constraints. Since each of these fields is expressed by truncated spherical harmonic expansions up to a maximum harmonic degree $\ell = 16$, there are a total of 861 rows in $\mathbf{G}$. Each component of the column vector $\mathbf{s}$ contains the spherical harmonic coefficients of the geodynamic observables (Figure 2(a)–2(c)) normalized by their estimated standard error. The row vector c is the viscous flow response function (i.e., kernel) for the $\ell = 2$ zonal harmonic coefficient describing the excess ellipticity of the CMB (Figure 2(d)), contained in the data component e.

The inversion is stabilized through the introduction of a regularization or smoothing operator represented by the matrix $\mathbf{R}$, designed to yield a second-order smoothing in both the vertical (layers) and horizontal (blocks) directions (Simmons, 2007). The λ terms in eqn [109] are scalar quantities that determine the relative weights applied to the seismic, geodynamic, and smoothing constraints.

Since the geodynamic data are strictly related to density perturbations rather than the seismic heterogeneity (see Section 1.27.3.2), we must also incorporate a relationship between perturbations of density (ρ) and shear wave velocity (V_S). In eqn [109], the density-to-velocity relationship is identified by $R_{\rho/s}$, which is defined by

$$R_{\rho/s} = \frac{d \ln \rho}{d \ln V_S} \qquad [110]$$

The selection of appropriate density-to-velocity scaling is clearly important in ensuring that the independent constraints on mantle heterogeneity provided by the seismic and geodynamic data can be fully reconciled. This reconciliation also bears on the extent to which this heterogeneity is dominated, or not, by the thermal structure maintained by the convecting mantle. These considerations are discussed in the next section.

Finally, the joint linear system in [109] is inverted using an iterative LSQR inversion technique (Paige and Saunders, 1982). Special attention is required to ensure successful convergence of the iterations, owing to the mixed (i.e., sparse and fully populated) character of the joint matrix on the left-hand side of expression [109]. A modified LSQR scheme was therefore implemented by Simmons (2007). This modified scheme also permits an independent specification of the density-to-velocity scaling in eqn [110] such that it is fully decoupled from the geodynamic kernels in expression [105]. In a further modification introduced by Simmons et al. (2010), the LSQR iterations are embedded in a very fast simulated annealing process that ensures maximum consistency between the seismic and geodynamic constraints on 3-D mantle structure.

1.27.4.4 Relating Mantle Density and Seismic Velocity Anomalies

The principal hypothesis employed in previous joint inversions of global seismic and geodynamic data sets (Forte and Woodward, 1997b; Forte et al., 1994; Simmons et al., 2007, 2009, 2010) is that the lateral temperature variations maintained by the process of thermal convection are the dominant source of lateral heterogeneity in the mantle. The most notable and generally accepted exception to this thermal dominance is the

heterogeneity associated with the so-called tectosphere (e.g., Jordan, 1981), namely, the deep lithospheric roots below ancient continental shields, wherein geodynamic data consistently show that significant compositional heterogeneity occurs and that it almost completely offsets the negative buoyancy of thermally generated density anomalies (e.g., Forte and Perry, 2000).

The other, more speculative exception concerns the possible dominance of large-scale thermochemical 'piles' at the very bottom of the mantle (e.g., McNamara and Zhong, 2005), which could be interpreted as the consequence of long-term accumulation of subducted MORB-derived heterogeneity in the seismic D″ layer (e.g., Nakagawa and Tackley, 2008). The dominant signature of these chemical piles is less generally accepted because mantle convection modeling has shown that most of the seismic (shear-velocity) heterogeneity in the lower mantle can be explained quantitatively in terms of lateral temperature variations (e.g., Quéré and Forte, 2006; Schuberth et al., 2009). The possibility that lateral temperature variations maintained by the convecting mantle are the dominant source of 3-D mantle heterogeneity is further supported by recent seismic modeling of mantle structure generated by theoretical convection models (Schuberth et al., 2012).

Whether or not compositional heterogeneity is a dominant contributor to 3-D seismically inferred structure in the lithospheric mantle below continents, or in the seismic D″ layer, the main driving force for the convective flow is due to buoyancy forces in the bulk of the mantle that are generated by hot thermal plumes and cold subducting lithosphere. This fundamental fluid mechanical property of thermal convection, in which the global circulation is mainly driven by the buoyancy associated with thermal anomalies in the interior of the convecting layer (i.e., outside the thermal boundary layers at the top and bottom of the layer), has been understood and established long ago (e.g., Jarvis and Peltier, 1982; Turcotte and Oxburgh, 1967). It is therefore clear that constraining the amplitude and spatial distribution of thermal anomalies in the bulk of the mantle holds the key to understanding the dynamics of the convecting mantle.

In view of the preceding considerations, the natural starting assumption to employ in the simultaneous tomographic inversion of global seismic and geodynamic data sets is an a priori relationship between seismic shear-velocity and density anomalies, $R_{\rho/s}$, defined in eqn [110] that is expressed in terms of lateral temperature variations and is accordingly quantified in terms of mineral physics data. In the recent series of inversions carried out by Simmons et al. (2007, 2009, 2010), the iterative determination of lateral heterogeneity in the mantle that simultaneously explains seismic and geodynamic data was commenced with a depth-dependent $R_{\rho/s}$ based on the mineral physical results of Cammarano et al. (2003) for the upper mantle and Karato and Karki (2001) for the lower mantle. The optimal 1-D $R_{\rho/s}$ profile that was determined on the basis of these mineral physics studies is represented by the red curve in **Figure 24** (explicit values are provided in Table 3 in Simmons et al., 2009).

The joint tomography model derived on the basis of this 1-D density-to-velocity scaling (red curve in **Figure 24**) provides an excellent match to the global seismic data (93% variance reduction) that is essentially identical to a pure seismic model obtained in an inversion without geodynamic constraints (Simmons et al., 2009). The joint tomography model also yields a reasonably good match to the global geodynamic constraints: variance reductions of 71%, 96%, and −9% to the free-air gravity anomalies, plate motions (expressed in terms of their horizontal divergence), and crust-corrected dynamic topography, respectively. Although the fits to the gravity anomalies and plate motions are now a great improvement over those obtained with pure seismic tomography models (see **Tables 1** and **2**), it is also clear that a purely thermal interpretation of mantle heterogeneity is not compatible with the dynamic topography data. The principal source of topography misfit in continental regions is the neglect of compositional heterogeneity under ancient cratons, as discussed in the preceding text, and the nonlinear thermal effects associated with temperature-dependent seismic attenuation and partial melting in the shallow mantle, under oceanic (especially mid-ocean ridges) and tectonically active regions (Simmons et al., 2009).

To account for the impact of this upper-mantle compositional heterogeneity under cratons and for nonlinear thermal effects, Simmons et al. (2009, 2010) introduced an effectively 1.5-D or 'corrected' $R_{\rho/s}$ scaling relationship, defined as follows:

$$R_{\rho/s}^{\text{corrected}} = R_{\rho/s}^{\text{1D}} + \kappa\delta \ln V_S, \quad \text{where } \kappa = \left(\frac{\partial R_{\rho/s}}{\partial \ln V_S}\right) \qquad [111]$$

The partial derivative κ adjusts or corrects the density-to-velocity scaling $R_{\rho/s}$ according to the seismic heterogeneity model, $\delta \ln V_S$, obtained in the preceding joint inversion assuming the radially symmetrical $R_{\rho/s}^{\text{1D}}$ model (red curve in **Figure 24**).

Simmons et al. (2009) conducted a search for optimal values of κ in expression [111] by first identifying three distinct regions in the upper mantle: (1) cratonic lithospheric roots, from 25 to 250 km depth; (2) noncratonic shallow mantle, from 25 to 250 km depth; and (3) deep upper mantle, from 250 to 650 km. The values of κ in regions (2) and (3) model the impact of nonlinear, purely thermal effects in the upper mantle. The value of κ in region (1) models the impact of the compositional heterogeneity in the cratonic upper-mantle associated with the continental tectosphere. Simmons et al. (2010) further refined this regionalization of the shallow mantle by searching for separate κ values in the depth intervals 25–100 and 100–250 km.

The κ values in eqn [111] that provide an optimal reconciliation of the joint seismic and geodynamic (especially dynamic topography) constraints on mantle heterogeneity are summarized in **Table 3** in Simmons et al. (2009) and in **Table 4** in Simmons et al. (2010). On the basis of this effectively 1.5-D parameterization of $R_{\rho/s}$, the variance reductions to the geodynamic data reported by Simmons et al. (2009) are 75% for free-air gravity, 98% for horizontal plate divergence, and 41% for dynamic topography. In the joint inversions of Simmons et al. (2010), the variance reductions for 1.5-D $R_{\rho/s}$ are 73% for free-air gravity, 97% for horizontal plate divergence, and 32% for dynamic topography. The fit (variance reduction) to the global seismic shear-velocity data is 93% for Simmons et al. (2009) and 90% for Simmons et al. (2010), where the latter inversion is also constrained to satisfy global P-wave traveltime residuals.

These upper-mantle corrections to the purely 1-D, thermal $R_{\rho/s}$ scaling profile, in particular under continental cratons,

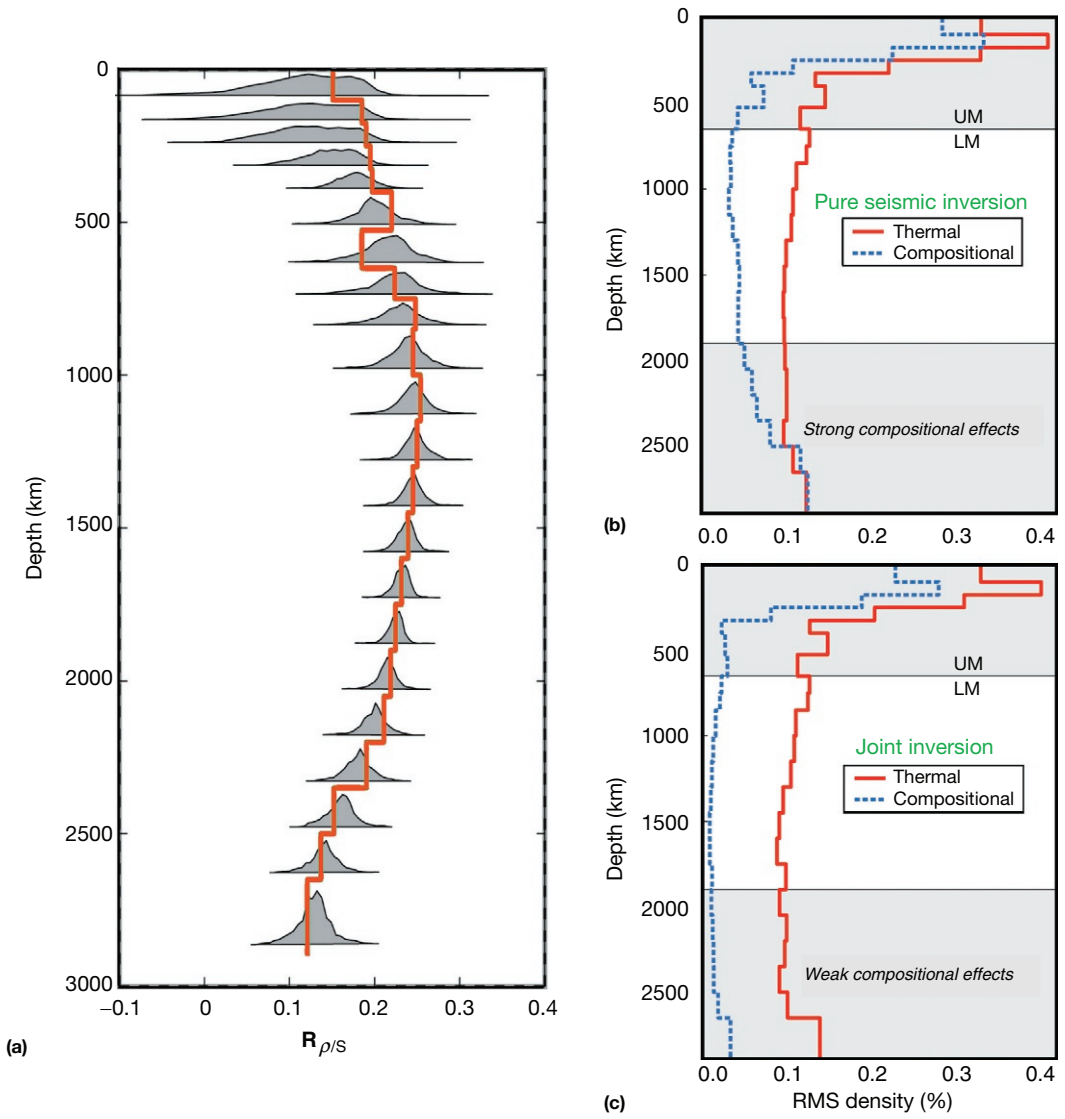

Figure 24 Implications of joint seismic-geodynamic-mineral physical constraints for thermal and nonthermal contributions to mantle heterogeneity. (a) The red curve represents the optimal 1-D density-velocity scaling $R_{\rho/s}$ derived from mineral physical data assuming that thermal contributions to heterogeneity are dominant (see text for details). The shaded histograms at each depth represent the normalized distribution of the 3-D density-to-velocity scaling $R^{3D}_{\rho/s}$ derived from the joint seismic–geodynamic inversions (Simmons et al., 2009). (b) The red curve represents the thermal contributions to mantle heterogeneity when a seismic tomography model, *TX*2008*s* derived by Simmons et al., 2009 from seismic data alone, is scaled to density using the 1-D thermal $R_{\rho/s}$ profile shown in (a). The subsequent inversion for a 3-D density-to-velocity scaling $R^{3D}_{\rho/s}$ that provides a fit to the geodynamic data yields the compositional (nonthermal) contributions to mantle density shown by the blue dashed curve. (c) When the seismic and geodynamic constraints are simultaneously inverted, in an iterative inversion that is initiated with the thermal $R_{\rho/s}$ profile shown by the red curve in panel (a), the thermal and compositional contributions to mantle heterogeneity in tomography model *TX*2008 (Simmons et al., 2009) are shown by the red and blue dashed curves, respectively. Adapted and modified from Simmons NA, Forte AM, and Grand SP (2009) Joint seismic, geodynamic and mineral physical constraints on three-dimensional mantle heterogeneity: Implications for the relative importance of thermal versus compositional heterogeneity. *Geophysical Journal International* 177(3): 1284–1304.

yield a substantially improved fit to the dynamic topography, but it is still clear that this geodynamic observable is not reproduced as well as the gravity or plate motion data. One possible explanation for this deficiency is that the 1.5-D corrections, as modeled in expression [111], do not accurately reproduce a number of mineral physical effects, which include (1) additional compositional heterogeneity in the cratonic roots not explained in terms of the simplified velocity-based correction, (2) compositional heterogeneity elsewhere in the mantle, and (3) partial melting and strongly nonlinear (e.g., seismic *Q*-dependent) effects that cannot be simply explained by the velocity-based correction.

The more complex, compositional, or nonthermal effects not accounted for in the corrected 1.5-D density-to-velocity scaling in expression [111] can be determined by solving for a fully 3-D $R^{3D}_{\rho/s}$ scaling relationship between seismic shear-velocity and density anomalies. The determination of this completely general density-to-velocity scaling relationship is an intrinsically

nonlinear problem that is based on the linear system in eqn [109] that defines the joint tomography model, and it yields $R_{\rho/s}^{3D}$ by iteratively solving the following linear system:

$$\begin{pmatrix} \lambda_G \mathbf{G}(\mathbf{m}^k) \\ \lambda_{CMB} c(\mathbf{m}^k) \\ \lambda_R \mathbf{R} \end{pmatrix} \mathbf{R}_{\rho/\mathbf{s}}^{3D,k+1} = \begin{pmatrix} \lambda_G \mathbf{s} \\ \lambda_{CMB} e \\ \mathbf{0} \end{pmatrix} \quad [112]$$

where $\mathbf{m}^k$ is the seismic slowness model obtained by joint inversion of system [109] assuming a density-to-velocity scaling $R_{\rho/s}^{3D,k}$ obtained in a previous cycle of the iterative process. System [112] is solved via an LSQR inversion, as the original system [109], except that the unknowns are the block representation of the density-to-velocity scaling $\mathbf{R}_{\rho/\mathbf{s}}^{3D,k+1}$, for a fixed or given seismic heterogeneity model. At the very outset, for $k=0$, the iterations are initiated with the corrected 1.5-D scaling defined in expression [111]. The next iterative update of the density-to-velocity scaling, $R_{\rho/s}^{3D,k+1}$, is then found by inverting expression [112] and the cycles continue until convergence.

In Simmons et al. (2009), only the first $k=0$ cycle was solved in eqn [109], where the final seismic shear heterogeneity model was determined on the basis of the 1.5-D-corrected density-to-velocity scaling [111] and the final 3-D scaling was found by solving eqn [112] once. **Figure 24(a)** provides a graphical summary of the lateral variability of the 3-D density-to-velocity scaling $R_{\rho/s}^{3D}$ relative to the 1-D thermally derived scaling. The large scatter in the top 300 km of the mantle, extending to negative values, represents strong compositional contributions in the subcratonic mantle under ancient continental shields. In the upper-mantle transition zone, the modes of the histograms representing the lateral variability are displaced relative to the 1-D thermal profile, suggesting that some revision to the depth-dependent mineral physical estimates may be warranted. This may be due to compositional or mineralogical (phase change-dependent) complexity that is not modeled with the thermally derived background scaling. In the lower mantle, below 2000 km depth, there is also similar evidence of displaced modal values relative to the thermal scaling. Nonetheless, the outstanding characteristic of the laterally variable $R_{\rho/s}^{3D}$ in the lower mantle is the close grouping of the scaling values around the a priori mineral physical estimates, and this demonstrates that a dominantly thermal origin for heterogeneity in the mantle is fully compatible with the combined seismic and geodynamic constraints on the 3-D mantle structure.

Simmons et al. (2010) iteratively inverted the combined system of eqns [109] and [112] through about 60 cycles to achieve convergence. In each cycle, the initial, thermally based 1-D scaling relationship (red curve in **Figure 24(a)**) and the nonlinear thermal effects, as modeled by eqn [111], were also corrected and revised. The final, optimal 1-D scaling is shown by the red curve in **Figure 25(a)**, and the distribution

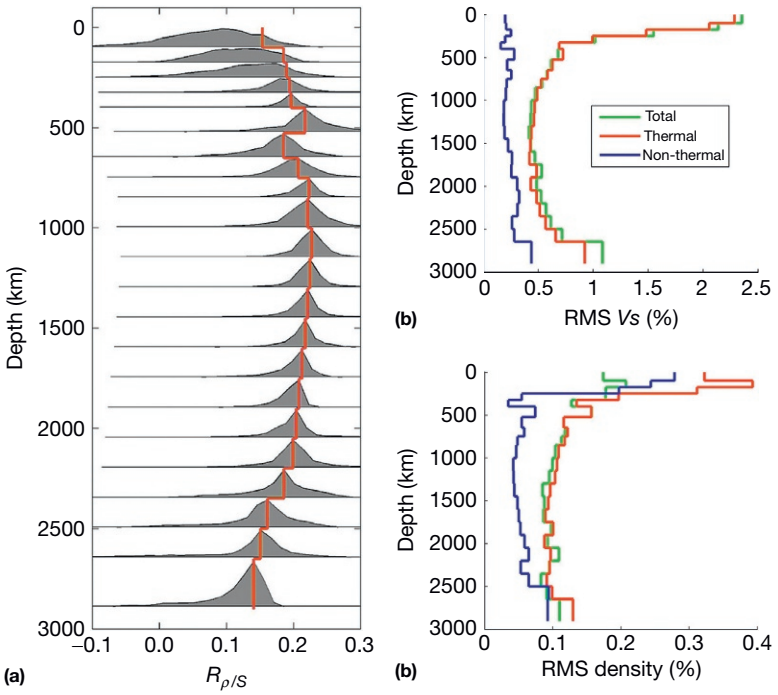

Figure 25 Importance of thermal and compositional heterogeneity from multiparameter joint seismic-geodynamic-mineral physical inversions for V_s, V_p, and ρ anomalies in the mantle. (a) The red curve represents the 1-D density-velocity scaling $R_{\rho/s}$ derived from an iterative, simulated annealing optimization that was initiated with the purely thermal scaling profile based on mineral physics data (red curve in **Figure 24(a)**). The gray, filled regions represent the normalized distribution of the 3-D density-velocity scaling $R_{\rho/s}^{3D}$ derived from the joint seismic-geodynamic inversions (Simmons et al., 2010). (b) The green curve represents the total (rms) amplitude of mantle V_s anomalies in seismic tomography model *GyPSuM* derived from joint inversion of seismic, geodynamic and mineral physical data (Simmons et al., 2010). The red and blue curves represent the thermal and compositional (nonthermal) contributions, respectively. (c) As in panel (b), except that mantle density anomalies in model *GyPSuM* are represented. Adapted and modified from Simmons NA, Forte AM, Boschi L, and Grand SP (2010) GyPSuM: A joint tomographic model of mantle density and seismic wave speeds. *Journal of Geophysical Research* 115, doi:10.1029/2010JB007631.

of laterally variable 3-D scaling at each depth in the model, inferred by solving system [112], is represented by the shaded histograms. In the upper 300 km of the mantle, we again note the strongly elongated distribution, extending to negative values, that is needed to characterize the subcontinental mantle under cratons and strongly nonlinear effects (e.g., partial melting) under oceans. In the deeper mantle, the modes of the 3-D scaling distribution are all centered on the background 1-D scaling values (red curve) that have been adjusted relative to the initial thermally derived 1-D scaling. In the bottom 500 km of the lower mantle, the scaling distribution extends to zero values, and these characterize the compositional, intrinsically dense interiors of the 'superplume' structures under the African and Pacific Plates (see next section).

1.27.4.5 Joint Seismic–Geodynamic Mapping of Density Anomalies

The joint seismic–geodynamic tomography inversion for mantle density anomalies is accomplished by solving expression [109], which is characterized by a nonlinear coupling of the seismic shear-velocity heterogeneity $\delta \ln V_S$ and the density-to-velocity scaling $R_{\rho/s}$. As discussed in the preceding section, the solution is obtained through the iterative inversion of the coupled system of linear eqns [109] and [112]. The final iteration of this coupled system yields a mapping of the total density perturbation field $\delta \ln \rho^{\text{total}}$ that includes both thermal and nonthermal compositional effects:

$$\delta \ln \rho^{\text{total}} = R^{3D}_{\rho/s} \delta \ln V_S^{\text{final}} \qquad [113]$$

in which $R^{3D}_{\rho/s}$ and $\delta \ln V_S^{\text{final}}$ are the final 3-D density-to-velocity scaling and seismic shear heterogeneity, respectively, derived from the iterative inversion process.

The purely thermal contributions to the mantle density anomalies can be estimated using the following expression:

$$\delta \ln \rho^{\text{thermal}} = R^{\text{thermal}}_{\rho/s} \delta \ln V_S^{\text{final}} \qquad [114]$$

in which the thermal density-to-velocity scaling $R^{\text{thermal}}_{\rho/s}$ is obtained from expression [111], in which the 1-D profile $R^{1D}_{\rho/s}$ is derived from mineral physical data for thermal effects and the parameterization of the nonlinear thermal effects in the upper mantle is accounted for by the κ term. In the latter case, we exclude the use of κ values estimated for the cratonic upper mantle, since these model compositional effects. Explicit values for these thermal terms may be found in **Tables 3** and 4 of Simmons et al. (2009) and Simmons et al. (2010), respectively.

Finally, the compositional or nonthermal contributions to the mantle density anomalies may be simply estimated by subtracting expressions [113] and [114]:

$$\delta \ln \rho^{\text{non-thermal}} = \delta \ln \rho^{\text{total}} - \delta \ln \rho^{\text{thermal}} \qquad [115]$$

This definition of nonthermal contributions can also include effects not directly modeled by the assumed thermal scaling in [111], such as possible higher-order nonlinear behavior due to Q dependence of seismic shear velocity or partial melting.

Current efforts to constrain the magnitude of compositional contributions to mantle density perturbations, in particular the hypothesized lower-mantle chemical 'piles,' are important to understanding the thermal and chemical evolution of the convecting mantle (e.g., Davies et al., 2012; Nakagawa et al., 2010). These analyses must contend with the likelihood of bias introduced by a posteriori conversion of published tomography models, derived from seismic data alone, into equivalent maps of density anomalies. The possibility of this bias was demonstrated in an experiment conducted by Simmons et al. (2009), in which they determined a 3-D density-to-velocity scaling by inverting system [112], in which the seismic heterogeneity model $\mathbf{m}$ is independently derived from a classical inversion involving seismic data alone. The amplitudes of the thermal and compositional density anomalies, calculated according to expressions [114] and [115], are shown in **Figure 24(b)** where we note this a posteriori analysis of a pure seismic heterogeneity model yields the inference of strong compositional heterogeneity in the lower mantle. In contrast, when the density and seismic shear-velocity anomalies are simultaneously determined in a joint inversion that is initially constrained by mineral physical data (red curve in **Figure 24(a)**), the inferred amplitude of compositional heterogeneity in the lower mantle is much weaker (**Figure 24(c)**).

The most recent effort at constraining the thermal and compositional heterogeneity in the mantle, via simultaneous inversion of seismic, geodynamic, and mineral physics data, was carried out by Simmons et al. (2010). In contrast to the previous joint inversions by Simmons et al. (2007, 2009), the seismic shear-velocity data were augmented to include a very large set of global P-wave travel times. The joint inversions were therefore designed to simultaneously map lateral variations in ρ, V_S, and V_P throughout the mantle. The relative amplitudes of thermal and compositional contributions to the seismic shear-velocity heterogeneity, where the former is determined in an inversion based on the thermally dependent version of the 1.5-D scaling in eqn [111], are summarized in **Figure 25(b)**. A substantially different illustration of the relative importance of thermal and compositional contributions is provided by the amplitudes of the density anomalies shown in **Figure 25(c)**, where we observe that nonthermal and thermal contributions (obtained via eqns [114] and [115]) are of similar magnitude in the top 250 and bottom 500 km of the mantle. This contrasts with the clear dominance of thermal effects at all depths in the case of the seismic shear-velocity heterogeneity. The latter result lends further support to the conclusion reached by Forte and Mitrovica (2001) that seismic shear-velocity anomalies, in particular in the deep lower mantle, provide a reliable mapping of the lateral temperature variations maintained by the mantle convective circulation.

The field of total density anomalies in the mantle as defined by expression [113] and obtained in the joint inversions by Simmons et al. (2009) is referred to as model *TX*2008. The corresponding model of total density anomalies obtained in the joint inversions by Simmons et al. (2010) is referred to as model *GyPSuM*. Model *TX*2007 is an earlier density heterogeneity model, essentially a precursor to *TX*2008 but with weaker smoothing constraints, that was obtained by Simmons et al. (2007). Maps of all three models at selected depths in the upper and lower mantle are provided in **Figures 26** and **27**, respectively.

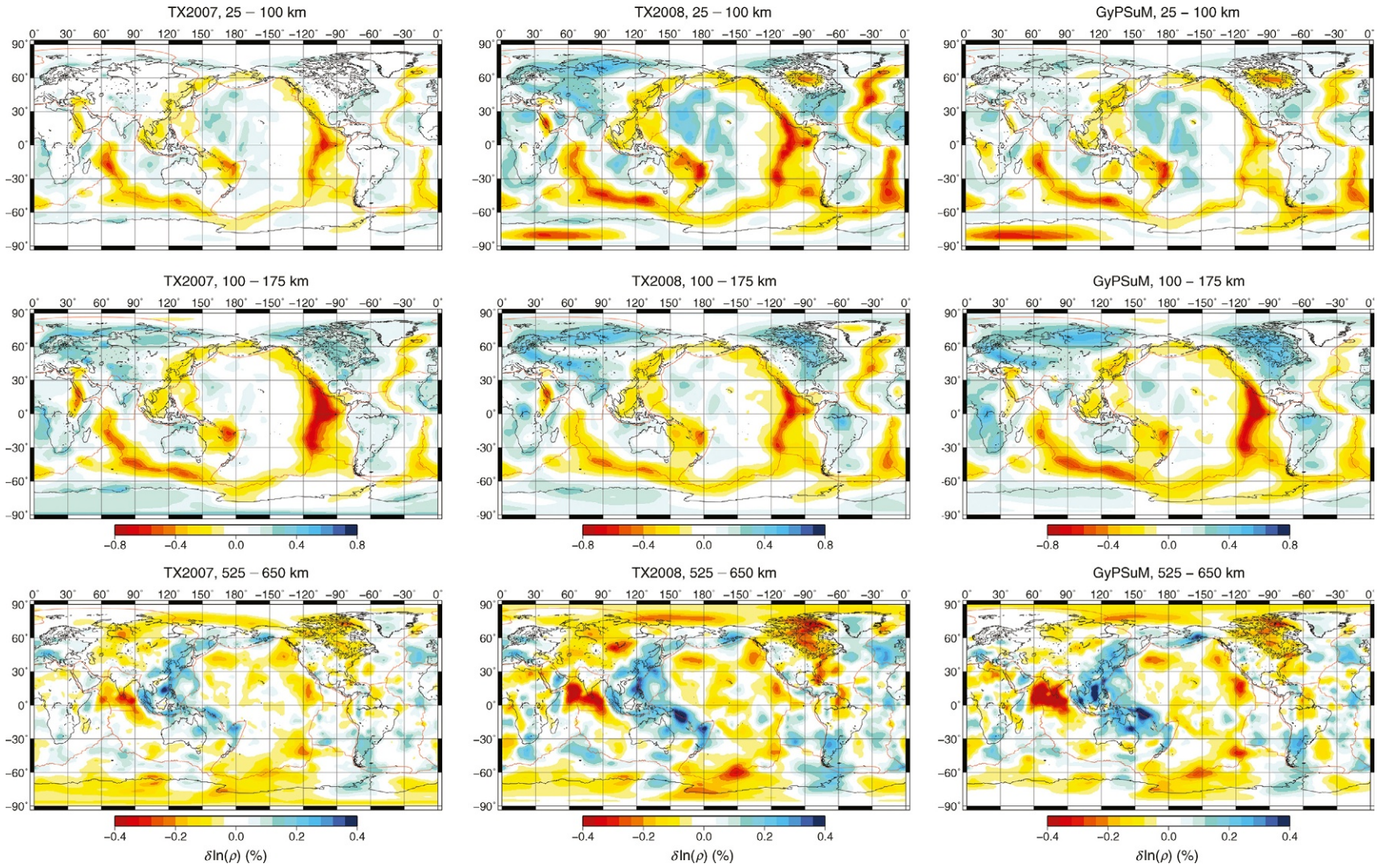

Figure 26 Global maps of lateral density variations in the upper mantle. (Left column) Model *TX*2007 derived by Simmons et al. (2007). (Middle column) Model *TX*2008 derived by Simmons et al. (2009). (Right column) Model *GyPSuM* derived by Simmons et al. (2010). A different color scale is used for the depth interval 25–175 km than for 525–625 km. The density anomalies are represented by a spherical harmonic expansion, as in eqn [1], truncated at degree $\ell = 72$, or a minimum half wavelength of ~275 km equivalent to the lateral block dimension employed in the tomography inversions.

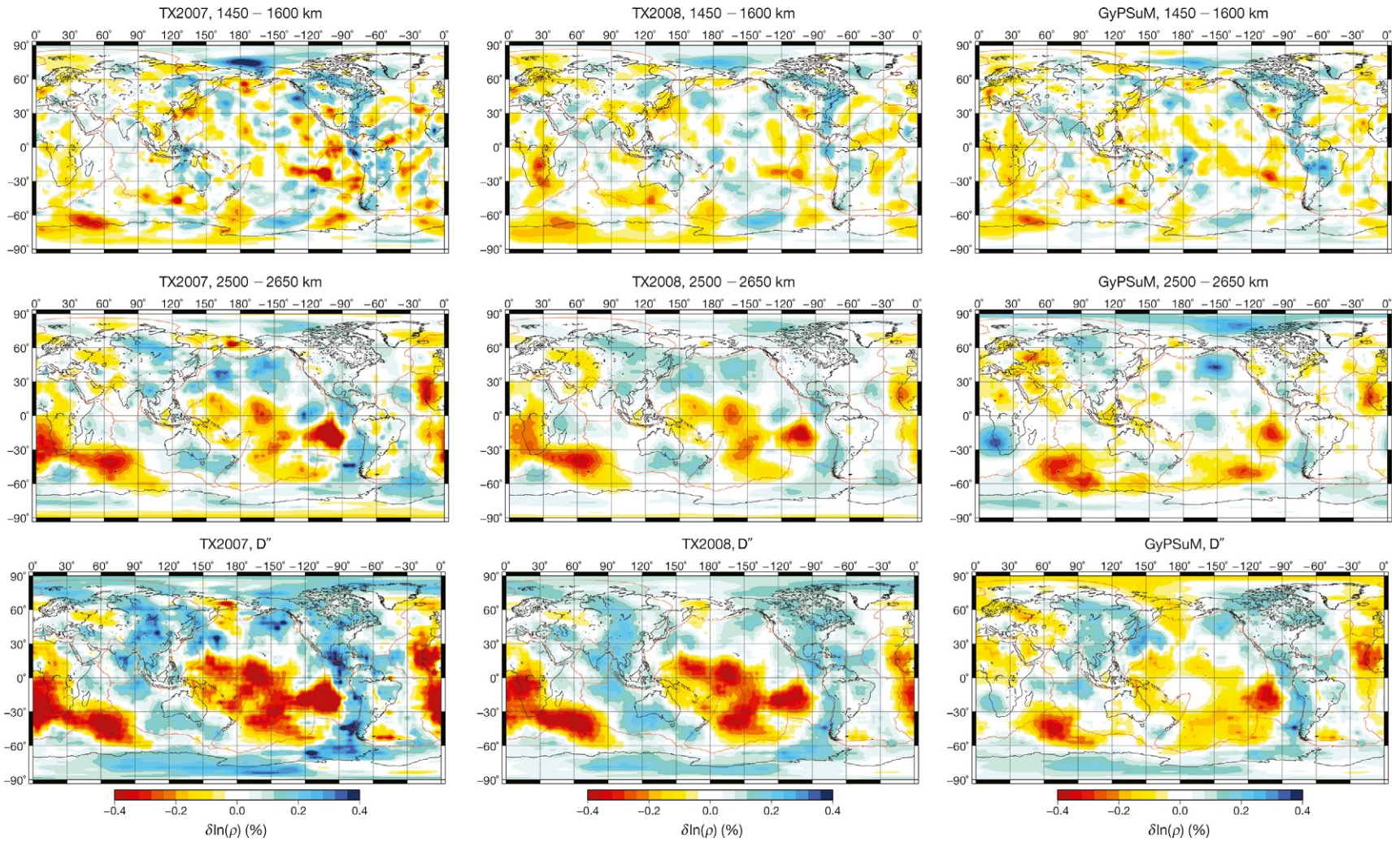

Figure 27 Global maps of lateral density variations in the lower mantle. (Left column) Model *TX*2007 derived by Simmons et al. (2007). (Middle column) Model *TX*2008 derived by Simmons et al. (2009). (Right column) Model *GyPSuM* derived by Simmons et al. (2010). As in **Figure 26**, the density anomalies are represented by a spherical harmonic expansion truncated at degree $\ell = 72$.

The amplitudes of the upper-mantle density anomalies (Figure 26) generally do not exceed a value of about 0.5%. For example, under the Western Pacific subduction zone, in the transition zone (depth interval 525–650 km), the maximum amplitude of the positive density anomalies that correspond to subducted slabs is +0.5%. We can understand the plausibility of this value by considering an idealized descending lithospheric slab with average temperature contrast relative to adiabatic mantle of about 700° and having an average width of about 100 km. If we further assume that this signal is 'smoothed' over a horizontal distance of 275 km, corresponding to the lateral dimension of a single block in the tomography model, then we predict a relative density perturbation +0.5% for this block, assuming a thermal expansion coefficient of $2 \times 10^{-5}\ \mathrm{K}^{-1}$.

These density anomalies in the upper-mantle transition zone provide important driving forces for the mantle-wide convective flow, especially for surface plate motions (see the divergence kernels in Figure 10(b)). Notice, however, that there are other important sources of upper-mantle buoyancy that are not related to subducted slab heterogeneity, in particular the plume-related anomalies under the Eastern Pacific oceanic ridge system that will also provide a strong contribution to the mantle convective flow and the associated surface plate motions.

The maps of lower-mantle density anomalies (Figure 27) reveal long-wavelength structures that have been long resolved in numerous purely seismic tomography models (e.g., Dziewonski, 1984; Grand, 2002; Romanowicz, 2003). The most noteworthy features in these density maps are the elongated structures of positive buoyancy located deep under the Eastern Pacific oceanic ridge system, as found in the upper mantle (Figure 26), especially under the East Pacific Rise (EPR). The implications of this buoyancy will become evident in the discussion of mantle flow presented in the next section. We also note, especially in the *GyPSuM* model, the occurrence of compositionally dense material in the core of the hot superplume structures under the Central Pacific Ocean and under Southern Africa. The effect of this negative, compositional buoyancy in the Central Pacific is the further enhancement of the importance of the flow driven by the buoyant hot material associated with plumes under the Eastern and Southwestern Pacific Ocean.

The excellent fits to the combined seismic and geodynamic data sets provided by the three joint tomography models is summarized in Table 5. Even a cursory comparison of these fits with those obtained on the basis of previously published, purely seismic tomography models (see Tables 1–4), reveals the power of the joint inversion method in achieving a very satisfactory reconciliation of the independent constraints on mantle heterogeneity provided by the global seismic and geodynamic data sets. It is of course important to underline that this reconciliation is accomplished in the context of a dominantly thermal origin for the lateral heterogeneity in the mantle.

1.27.4.6 Implications for Global Mantle Flow

In developing a successful or 'realistic' model of the present-day thermal convective flow in the mantle, it is clearly essential that such a model be capable of providing a satisfactory fit to a diverse suite of surface geodynamic observables, as summarized in Table 5 in the preceding section. This necessary condition follows from the recognition that these observables provide robust constraints on density anomalies across the entire mantle, as shown by the geodynamic kernel functions in Figure 10. The density anomalies that are constrained by these surface observables are, of course, those that also drive the mantle-wide convective circulation.

The relationship between the mantle convective flow and the internal density anomalies can be explicitly quantified in terms of Green functions that characterize the viscous flow impulse response of the mantle to point density loads (e.g., Forte and Peltier, 1987; Parsons and Daly, 1983). The derivation of these Green functions for a compressible, self-gravitating mantle with a complex depth dependence of density and viscosity was presented in Section 1.27.2.3. We recall from Section 1.27.2.3.7, in particular expression [95], that the viscous flow Green functions relate the 3-D mantle flow field to the internal density perturbations via the following convolution integral:

$$U_\ell^{xm}(r) = \int_b^a \mathbf{U}_\ell^x(r, r')\rho_\ell^m(r')\mathrm{d}r' \qquad [116]$$

in which $\rho_\ell^m(r')$ is the spherical harmonic coefficient of the mantle density perturbations, $U_\ell^x m(r)$ is the generalized spherical harmonic coefficient of the velocity field (see eqn [31]), and $U_\ell^x(r, r')$ is the corresponding Green function.

The Green functions for the vertical component of flow, calculated on the basis of the 'V2' viscosity profile (Figure 9), are plotted at four target depths in Figure 28. The average amplitudes of the Green functions for depths <1000 km are

Table 5 Global data fits by joint seismic–geodynamic tomography models

Tomography model	*Data fits*[a]				
	Seismic (%)	*Gravity*[b] *(%)*	*Divergence*[b] *(%)*	*Topography*[b] *(%)*	*CMB*[b] *(m)*
*TX*2007	95	89 (69)	94 (92)	73 (62)	400
*TX*2008	93	91 (68)	99 (99)	80 (66)	400
GyPSuM	93	88 (65)	99 (99)	72 (60)	400

[a]With the exception of the excess CMB ellipticity (last column), all data fits are expressed as percent (%) variance reductions.

[b]The geodynamic data include the global free-air gravity anomalies, horizontal divergence of present-day plate motions, the crust-corrected dynamic topography, and the excess CMB ellipticity ('observed' value = 400 m), all shown in Figure 2. With the exception of the CMB, the fits cited are for flow predictions and geodynamic observables truncated at spherical harmonic degree $\ell = 16$. The values in parentheses () are fits for predictions and observables truncated at spherical harmonic degree $\ell = 32$. In all cases, the geodynamic predictions are obtained on the basis of a flow calculation using the 'V1' viscosity profile in Figure 9.

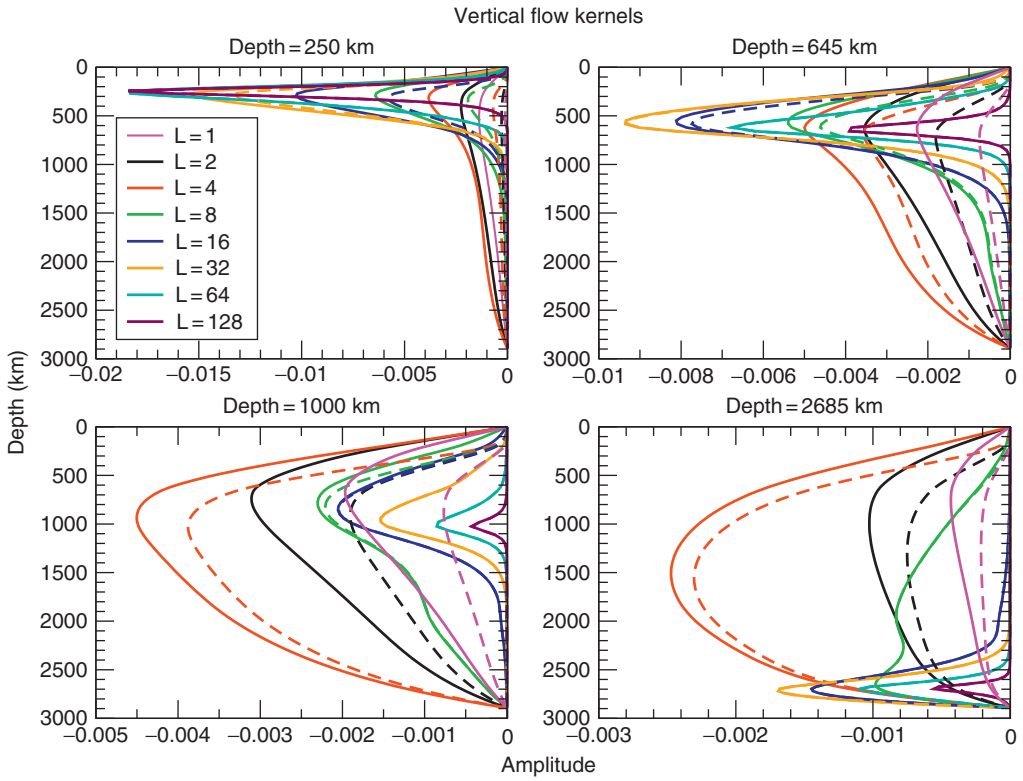

Figure 28 Green functions $U_\ell^0(r,r')$ for the vertical component, $U_\ell^{Pm}(r)$ (see eqn [31]), of the mantle flow field. The Green functions are plotted for four different depths in the mantle: (top-left) 250 km, in the mantle asthenosphere; (top-right) 645 km, at the bottom of the transition zone; (bottom-left) 1000 km, in the top half of the lower mantle; and (bottom-right) 2685 km, at the top of the seismic D″ layer. The kernels are color-coded according to the spherical harmonic degree of the flow (legend in the top-left panel). The solid lines represent kernels calculated for a free-slip surface boundary and the dashed lines represent kernels for a no-slip (rigid) surface. The kernels are calculated for the 'V2' mantle viscosity profile (**Figure 9**) and for the depth-dependent density given by PREM (**Figure 5**).

significantly greater than those for the deeper mantle, owing to the significantly lower viscosity in upper mantle. At shallow depths, in the low-viscosity asthenosphere region, flows characterized by shorter horizontal wavelengths (in the degree range $\ell > 8$) are excited most efficiently. This characteristic persists to bottom of the upper mantle, in the transition zone, although it is now the intermediate wavelengths (in the range $8 < \ell < 64$) that are more strongly excited. The shorter horizontal wavelengths are more sensitive to the higher-magnitude local viscosity in the transition zone and hence are more attenuated. In the lower mantle, a completely different situation arises, where the longest horizontal wavelengths of flow (in the range $\ell < 8$) are excited with the greatest amplitude, because of the very high viscosity in the deep mantle. It is especially noteworthy that these long-wavelength components of the lower-mantle flow field are providing an integrated response to density anomalies across the entire depth of the mantle.

It is instructive to note, as a general rule, that at sufficiently short horizontal wavelengths, for $\ell \gg 1$, the vertical flow at a given target radius r_o in the mantle is sensitive to density anomalies located in a vertical interval $r_o - \Delta r/2 < r_o < r_o + \Delta r/2$, where $\Delta r \approx 2\pi r_0/\ell$. Hence, even at shallow depths, for example, in the low-viscosity asthenosphere where intermediate to shorter wavelengths are excited strongly, the flow is sensitive to the integral of density anomalies across the entire upper mantle (see top-left panel in **Figure 28**). It is therefore difficult to make robust inferences of shallow mantle flow, for example, under continents, by only considering 3-D images recovered from regional tomography studies that describe lateral heterogeneity in the top 200 or 300 km of the mantle (e.g., Levander et al., 2011), especially when the tomography models are derived from short-period seismic surface waves or ambient noise techniques (e.g., Shen et al., 2013). Shallow flow driven by sources of buoyancy located in the transition zone region of the upper mantle will be important and their contribution must be included in flow modeling.

There are two distinct contributions to the horizontal component of mantle flow, the poloidal contribution $U_\ell^{Pm}(r)$ (defined in eqn [37]) that is directly driven by mantle density anomalies according to expression [116] and the independent toroidal contribution $U_\ell^{Tm}(r)$ (defined in eqn [37]) that is viscously coupled to the radial vorticity of the tectonic plates, whose motions are generated by the buoyancy-driven (poloidal) mantle flow (see eqn [94]).

The Green functions for horizontal poloidal flow are plotted in **Figure 29** at the same four target depths as for the vertical flow kernels (**Figure 28**). The horizontal flow kernels provide a sensitivity to mantle density anomalies that is markedly different from that of the vertical flow. Indeed, it is quite clear that at sufficiently short horizontal wavelengths ($\ell > 8$), the horizontal flow kernels are effectively a radial derivative of the vertical flow kernels. This is expected on theoretical grounds (see eqn

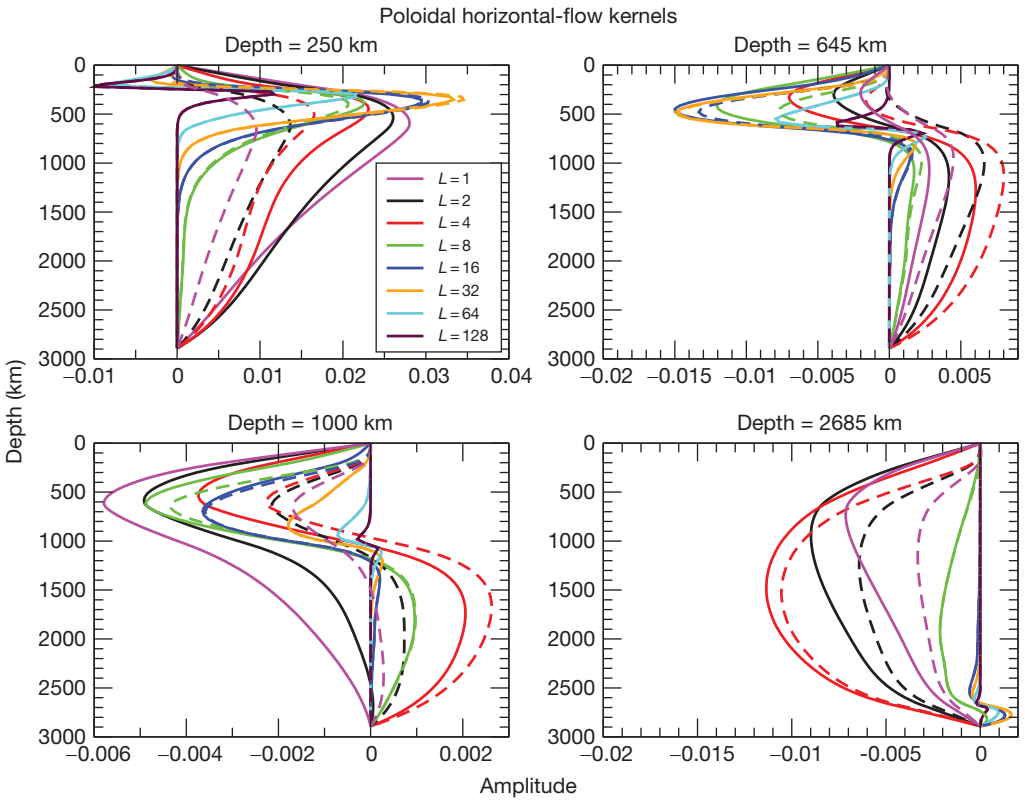

Figure 29 Green functions $U_\ell^P(r,r')$ for the horizontal component, $U_\ell^{Pm}(r)$ (see eqn [37]), of the poloidal mantle flow field. All calculations and details are as in **Figure 28**.

[119] in Forte and Peltier, 1994). Horizontal flow will therefore be particularly sensitive to depth-dependent changes in the distribution of the mantle density anomalies. In the deep interior of the mantle (e.g., at depths of 645 and 1000 km – see **Figure 29**), this vertical sensitivity is also apparent at the longest horizontal wavelengths. In the deep lower mantle, we again note, owing to the high viscosity of this region, that only the longest horizontal wavelengths (corresponding to $\ell < 8$) of horizontal flow are efficiently excited and they will provide an integrated response to density anomalies across the entire mantle.

The viscous excitation function for toroidal flow is defined by the following extension to eqn [94]:

$$U_l^{Tm}(r) = F_\ell^T(r)\frac{lr_a}{\Omega_1}(\hat{\mathbf{r}}\cdot\nabla\times\mathbf{v})_l^m \qquad [117]$$

where $F_\ell^T(r)$ is the depth-dependent toroidal-flow response, determined by the downward propagation of the surface vector defined in eqn [74]. This downward propagation is described in **Section 1.27.2.3.6**. A plot of the toroidal-flow excitation function $F_\ell^T(r)$ is presented in **Figure 30**. We note here that excitation of toroidal flow, through viscous coupling with the overlying plate motions, is most efficient in the upper mantle and very little extends into the lower mantle. The only apparent exception is the degree-1 toroidal flow, which has significant amplitude at all depths in the mantle. This is, however, an entirely degenerate solution of the toroidal-flow equations (see eqn [36]) when viscosity varies only with depth and has no dynamic significance.

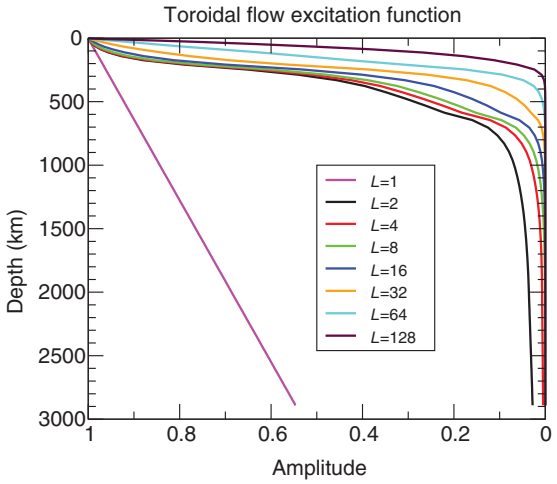

Figure 30 Excitation functions $F_\ell^T(r)$ for the horizontal component, $U_\ell^{Tm}(r)$ (see eqn [37]), of the toroidal mantle flow field. These excitation functions are calculated for the 'V2' mantle viscosity profile (**Figure 9**).

The numerical solution for the $\ell = 1$ excitation function presented in **Figure 30** is mathematically identical to the simple function $F_{\ell=1}^T(r) = (r/r_a)$ and hence is independent of the mantle viscosity structure. It is possible to show (e.g., Forte and Peltier, 1994) that this function yields a horizontal flow in the mantle that is everywhere mathematically identical to a simple rigid-body rotation of the entire mantle:

$$\mathbf{u}_{\ell=1}^{\text{toroidal}}(r) = \boldsymbol{\Omega} \times \boldsymbol{r} \qquad [118]$$

where the angular rotation $\boldsymbol{\Omega}$ is identical to the global net rotation of the tectonic plate motions. This rigid-body rotation is associated with a state of zero stress in the mantle, and therefore, it cannot be generated in a dynamically consistent treatment where the viscosity varies with depth only. LVV variations are required to generate degree-1 toroidal flow (e.g., Forte and Peltier, 1994). The degree-1 degeneracy that arises with radially symmetrical viscosity is eliminated by calculating flow in reference frame with zero net rotation. The latter is dynamically equivalent to the rotating frame described by expression [118] because all flow-induced stresses in the mantle are identical in the two reference frames. For this reason, all mantle flow predictions presented in the succeeding text (Figures 31 and 32) employ a global no-net-rotation frame for the mantle.

Given the excellent geodynamic fits provided by the joint seismic–geodynamic tomography density models, it is of interest to explore the implications of these models for the global convective flow in the mantle. Figures 31 and 31 show the predicted convective flow at selected depths in the upper and lower mantle, respectively, obtained on the basis of the *TX*2008 and *GyPSuM* tomography models. The predicted flow at the top of the lithosphere (top row in Figure 31)

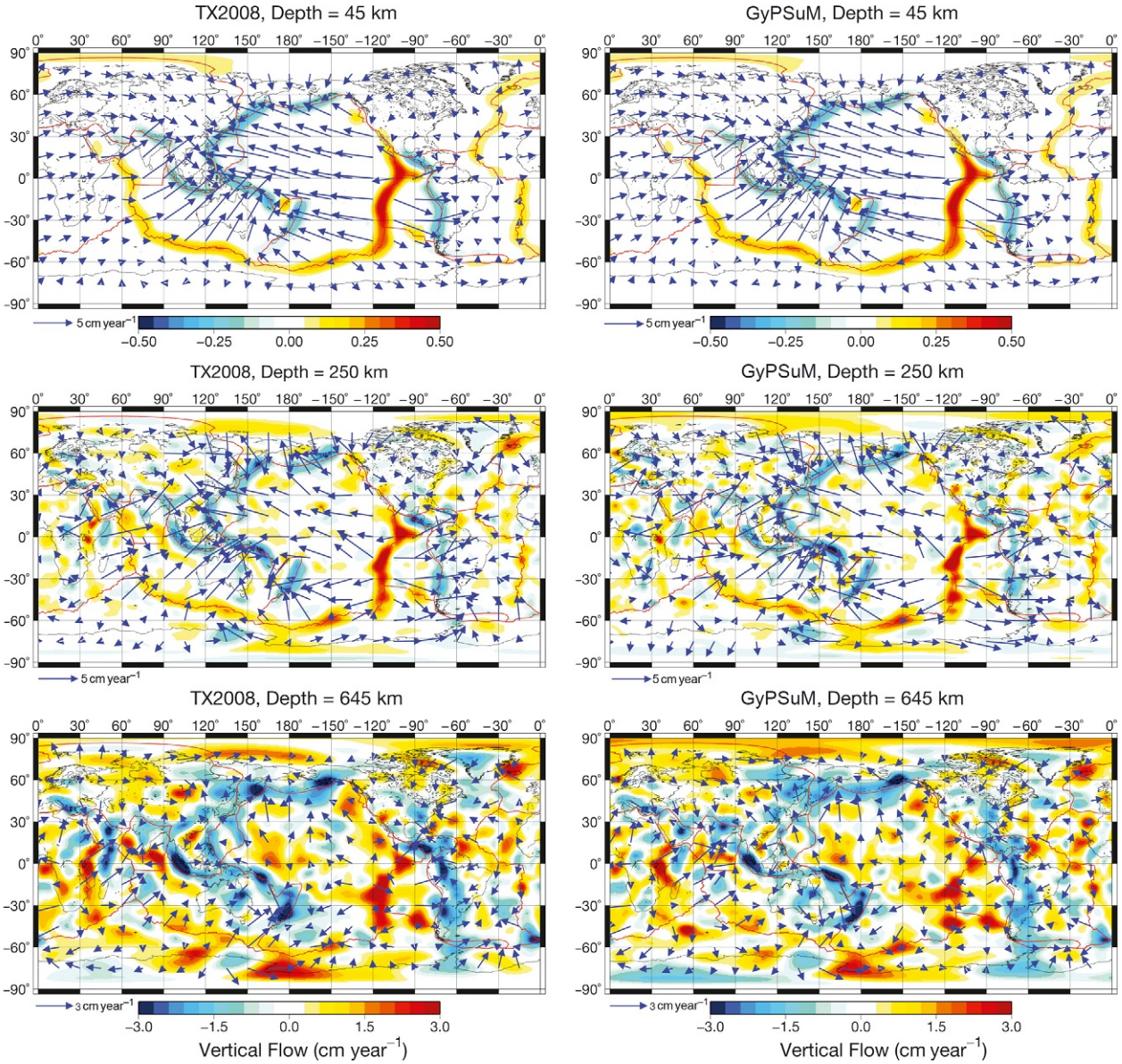
TX2008, Depth = 45 km
GyPSuM, Depth = 45 km
TX2008, Depth = 250 km
GyPSuM, Depth = 250 km
TX2008, Depth = 645 km
GyPSuM, Depth = 645 km
5 cm year−1
3 cm year−1
−0.50 −0.25 0.00 0.25 0.50
−3.0 −1.5 0.0 1.5 3.0
Vertical Flow (cm year−1)

Figure 31 Predicted mantle flow at three different depths in the upper mantle: lithosphere (top row), asthenosphere (middle row), and base of the transition zone (bottom row). The buoyancy forces are derived from two joint seismic–geodynamic inversions for mantle density anomalies: models *TX*2008 (Simmons et al., 2009) and *GyPSuM* (Simmons et al., 2010) in the *left* and *right* columns, respectively. The viscous flow kernels are calculated on the basis of the 'V2' viscosity profile, derived from the joint GIA–convection inversions, shown in Figure 9. The flow fields are all represented in terms of a spherical harmonic expansion truncated at degree $\ell = 72$. All flow predictions are in a mantle reference frame with zero global (net) rotation.

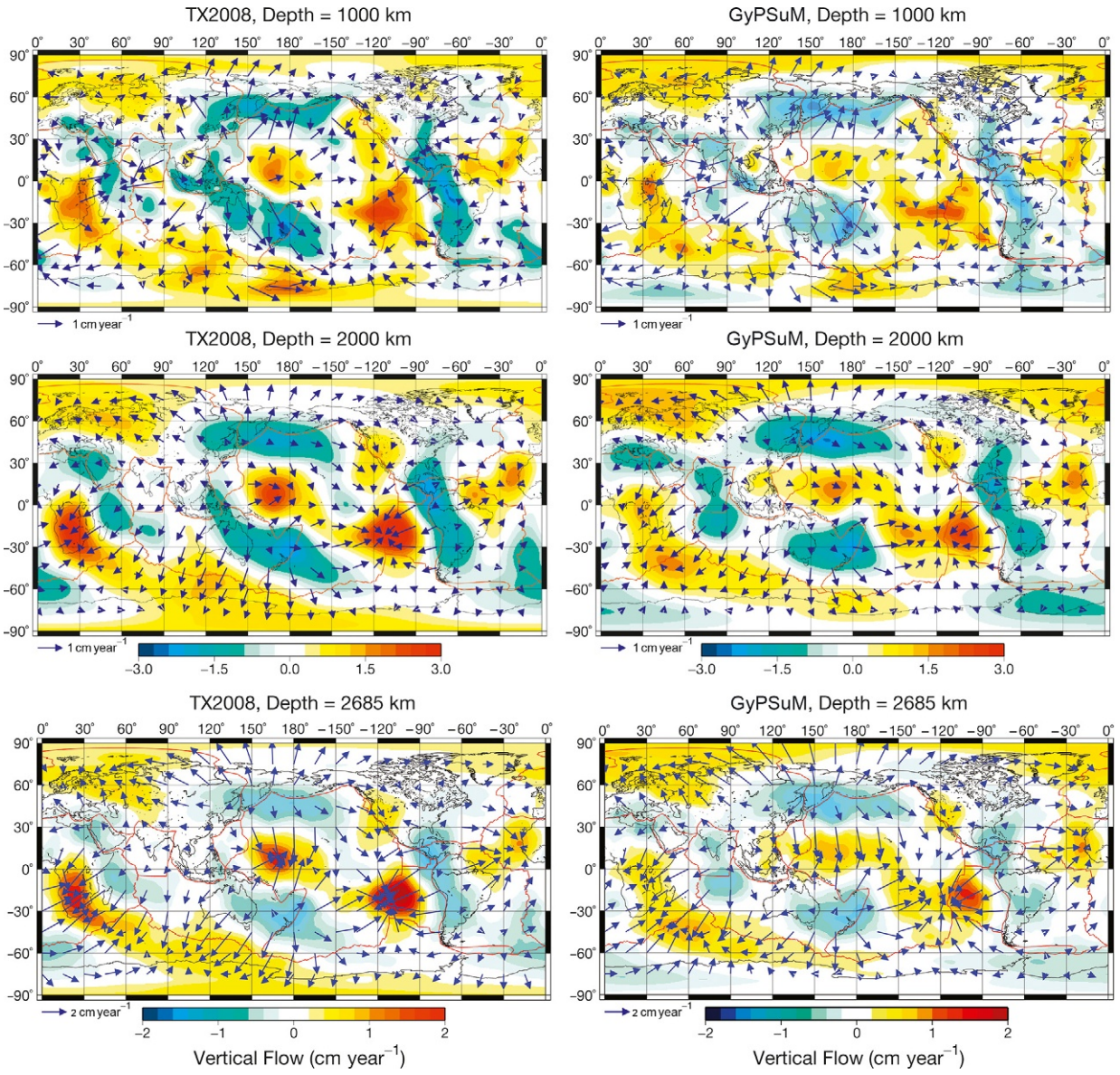
TX2008, Depth = 1000 km
GyPSuM, Depth = 1000 km
TX2008, Depth = 2000 km
GyPSuM, Depth = 2000 km
TX2008, Depth = 2685 km
GyPSuM, Depth = 2685 km
1 cm year−1
2 cm year−1
−3.0 −1.5 0.0 1.5 3.0
−2 −1 0 1 2
Vertical Flow (cm year−1)

Figure 32 Predicted mantle flow at three different depths in the lower mantle: 1000 km (top row), 2000 km (middle row), and 2685 km, corresponding to the top of the seismic D″ layer (bottom row). The flow calculation for input density anomalies from models *TX*2008 (Simmons et al., 2009) and *GyPSuM* (Simmons et al., 2010) is identical to that in **Figure 31**.

provides an excellent match to the (no-net-rotation) NUVEL-1 plate velocity field. This is not unexpected since the joint seismic–geodynamic tomography models were inverted with the divergence of the surface plate motions as a constraint (see **Table 5**). This prediction mainly serves as an explicit demonstration that the density anomalies in the mantle, integrated with the kernels in **Figures 29** and **30**, have been properly resolved by the tomographic inversion procedure.

In the low-viscosity asthenosphere (middle row in **Figure 31**), the large-scale pattern of vertical flow is similar to that in the lithosphere, with upwellings and downwellings under the oceanic ridges and subduction zones, respectively. The pattern of horizontal flow, however, deviates significantly from the lithospheric pattern in many locations and can even be anticorrelated, for example, under the Western United States. There is an additional complexity that is represented by the striking, 'mottled' pattern of shorter wavelength upwellings that is ubiquitous. For example, local plume-related upwellings under Hawaii, Iceland, and the numerous volcanic swells of the African Plate (e.g., Azores, Canaries, Cape Verde, Hoggar Massif, and East African Rift) are clearly evident. In addition, and less generally recognized, are the upwellings under the interiors of the Eurasian and North American Plates and the many local upwellings under the Pacific Plate. The quasilinear pattern of upwellings that extends from the Caribbean to Eastern Canada, along the Atlantic Coast of the United States, and the clearly resolved upwelling under Bermuda has achieved considerable prominence in recent work that reveals the importance of these upwellings in driving variable topographic uplift of the US East Coast (Rowley et al., 2013).

The predicted flow at the bottom of the upper mantle, in the transition zone region (bottom row in Figure 31), strongly reinforces the pattern of (plume-related) upwelling and (subducted slab) downwelling found at shallower depths. Focused plume-related upwellings under Hawaii, Iceland, Crozet, Kerguelen, Caroline, Canary, and Cape Verde Islands are all evident. A deep, linear upwelling under the southern margin of the Indian Plate contributes to strong north–northeast-directed horizontal flow (see flow at 250 km) that clearly represents a source of strong (viscous shear) forcing for the continued motion and collision of the overlying Indian Plate. Most striking, however, is the intensified pattern of deep upwelling under the EPR system. The deep-seated, buoyancy-driven flow under the EPR, in particular, is found to be an important driver of the Pacific Plate motion, such that time-dependent changes in this buoyancy have been directly linked to the geologically recent deceleration of this plate (Forte et al., 2009).

The lower mantle is a region of very high viscosity (see Figure 9), and as anticipated on the basis of the flow kernels (Figures 28 and 29), the predicted flow (see Figure 32) is dominated by the longest horizontal wavelengths. The long-lived history of lithospheric subduction under the Northern and Southwestern Pacific is clearly imprinted in the pattern of lower-mantle downwellings, as is the history of subduction under the Tethys and Farallon convergence zones. The predicted flow field in the deep lower mantle (middle and bottom row of Figure 32) reveals several distinct centers of active, buoyancy-driven upwellings, or 'superplumes.' The most prominent superplumes in the model *TX*2008 prediction are located under Southern Africa and Southwest Indian Ocean, under the Southwestern Pacific (under the Caroline Islands), and under the EPR (centered under Easter Island). Additional prominent, but lower-amplitude, upwellings are located under western Siberia, under Cape Verde, and under the Southwestern United States. The upwelling under Siberia is of particular interest because it is correlated with the proposed location of the eruption of the Siberian Traps (Smirnov and Tarduno, 2010). As shown by the mantle convection modeling of Glisovic et al. (2012), the lateral stability and activity of this 'Siberian plume' are predicted to be long-lived, extending over several hundred million years. In general, the amplitudes of the predicted upwellings are greater, and also more spatially focused, than the more diffuse downwellings. These results are closely matched by the flow predictions obtained using the density anomalies in model *GyPSuM* (Figure 32).

The robustness and dynamic significance of the predicted lower-mantle superplumes may first be appreciated by noting that this long-wavelength pattern of upwellings is produced by an integral of the density anomalies across the entire depth of the mantle (see the kernels in Figures 28 and 29). This pattern of lower-mantle flow is therefore very well constrained by the joint seismic–geodynamic tomography inversions, particularly because they also include additional effects from lower-mantle compositional heterogeneity that acts to locally oppose or cancel thermally generated buoyancy. The dynamic significance of these lower-mantle superplumes, in terms of the long-term thermal evolution of the mantle, has been explored in detail by Glisovic et al. (2012). They carried out mantle convection simulations that were initiated with the present-day density heterogeneity in joint tomography model *TX*2008, and the thermal evolution of the 3-D structure in the mantle was integrated forward over many hundred million years (in excess of 2 billion years, in total). These very long time convection simulations revealed the extraordinary stability and longevity of the present-day superplumes shown in Figure 32, requiring a strong flux ($>13TW$) of heat entering the mantle from the core.

Arguably, the most striking feature of the flow predictions shown in the upper and lower mantle (Figures 31 and 32) is the strong, vertically coherent superplume-related upwelling under the EPR. This active upwelling, driven by the integrated buoyancy across the entire mantle, is clearly evident at all depths in the mantle. The EPR is thus the only oceanic ridge that sits above an upwelling that extends down to the CMB. This result has not been found in previous tomography-based simulations of mantle dynamics because, until now, they employed purely seismic 3-D mantle models that have been converted a posteriori to density with simple scaling factors. The longevity and lateral stability of the EPR superplume, possibly over several hundred million years as shown in Glisovic et al. (2012), should have a major impact on the long-term evolution of plate tectonics in the Pacific Ocean and for the overall thermal evolution of the mantle.

1.27.5 Concluding Remarks

Tomography models of 3-D mantle structure, derived solely by inverting global seismic data, provide reasonably good fits to a wide variety of surface geodynamic observables related to mantle convection. The previous tomography-based models of mantle dynamics thus demonstrated that global seismic data can indeed be used to recover images of lateral heterogeneity that are produced by the thermal convection process in Earth's mantle. The tabulated summaries of the predicted convection results (Tables 1–4) show, however, that the fits leave considerable room for improvement and this raises the fundamental question as to what aspects of the previous tomography models, or indeed the mantle flow calculations, may be deficient or inadequate.

A major development that goes far in addressing this outstanding question is the technique for the joint or simultaneous inversion of global seismic and geodynamic data sets that also incorporates mineral physical constraints on the thermal contributions to mantle heterogeneity (e.g., Forte et al., 1994; Forte and Woodward, 1997; Simmons et al., 2006, 2007, 2009, 2010). These joint seismic–geodynamic inversions show that it is possible to obtain greatly improved fits to the global convection-related data (see Table 5) using the mantle flow theory which was presented and discussed in detail in Section 1.27.2.3. The improved fits are found to be the result of relatively small adjustments (mainly in amplitude) to the seismically inferred heterogeneity in the mantle, especially the mid-mantle region, in order to satisfy the independent constraints on 3-D mantle structure imposed by the geodynamic data. Moreover, it is found that this reconciliation of seismic and geodynamic constraints can be achieved in the context of a dominantly thermal origin for mantle heterogeneity. The joint seismic–geodynamic inversions thus provide strong support

for the hypothesis that most of the heterogeneity in the mantle is thermal in origin and that it is maintained by the process of thermal convection.

The improved resolution of 3-D mantle structure provided by the recent tomography inversions is yielding important new insights on the connections between the convective flow in the mantle and the surface geological evolution of our planet (e.g., Forte et al., 2010). A number of efforts to explicitly map the time-dependence of these connections, using tomography-based, time-reversed convection simulations (e.g., Conrad and Gurnis, 2003; Müller et al., 2008; Moucha et al., 2008; Glišović and Forte, 2014) are providing new perspectives on the evolution of 3-D mantle structure in the geological past and how this evolution controls changes in the surface topography of the Earth. A recent review of the methods employed in time-reversed convection modeling, with more extensive references to previous studies, may be found in Glišović and Forte (2014).

The use of joint seismic–geodynamic tomography models as a starting point for time-reversed convection modeling is showing much promise, helping to further clarify a range of geological problems that include the evolution of African topography (e.g., Moucha and Forte, 2011) and recent sea level change along the East Coast of the U.S. (e.g., Rowley et al., 2013). The latter issue has generated considerable debate, with one group of convection models predicting long-term subsidence of the East Coast during the Cenzoic (e.g., Müller et al., 2008; Spasojevic et al., 2008), while another group of models predict uplift (e.g., Moucha et al., 2008; Rowley et al., 2013). These diametrically opposed predictions of topography changes arise from differences in the assumed distribution of mantle buoyancy where, on the one hand, this buoyancy is derived by *a posteriori* conversion of previously published tomography models into equivalent density models (e.g., Spasojevic et al., 2008) and, on the other hand, the buoyancy is directly constrained through the joint seismic–geodynamic tomography inversions (e.g., Moucha et al., 2008).

The recent interpretation of variably uplifted Pliocene shorelines along the U.S. East Coast (Rowley et al., 2013) shows that previous predictions of continuous subsidence along the Atlantic margin (e.g., Müller et al., 2008; Spasojevic et al., 2008) are not in accord with the geological data. Moreover, recent analyses of river channels that drain the central Appalachians also reveal the occurrence of significance rock uplift along the eastern seaboard of North America over the past 15 million years (e.g., Miller et al., 2013). The predictions of convection-driven uplift along the eastern U.S. seaboard (e.g., Moucha et al., 2008; Rowley et al., 2013) are achieved because the joint seismic–geodynamic tomography inversions successfully resolve positive buoyancy in the upper mantle below the eastern margin of North America.

The key ingredient that contributes to the reliability and realism of the time-reversed convection simulations is the use of density anomalies, coupled with appropriately constrained mantle viscosity (e.g., Figure 9), derived from the joint seismic-geodyamic inversions. The use of geodynamically consistent tomography models ensures that the present-day mantle flow (see Figures 31 and 32) is as realistic as possible. This is a fundamental issue, because the present-day mantle flow determines the critically important starting trajectory for the highly nonlinear time-reversed convection simulations.

There remain a number of challenges in mapping the 3-D buoyancy distribution in the mantle via the simultaneous inversion of global seismic and geodynamic data sets. As noted above, one important challenge is the derivation of geodynamic response functions (i.e., kernels) using a mantle flow theory that explicitly includes the effect of lateral viscosity variations (LVV) throughout the mantle (e.g., Petrunin et al., 2013, and references therein). These response functions are important because they represent the dynamical connection between the convection-related geodynamic data and the internal distribution of density anomalies in the mantle. The joint inversions would provide a robust method for testing whether the amplitude and pattern of the LVV assumed in the mantle flow models allow a successful reconciliation of the independent seismic and geodynamic constraints on 3-D mantle structure. Another challenge is the incorporation of updated mineral physical constraints on the temperature dependence of seismic wave speeds that also include the nonlinear dependence on temperature arising from seismic attenuation in the mantle (e.g., Cammarano et al., 2003). The explicit representation of localized buoyancy associated with undulations of the major phase-change boundaries in the mantle is another outstanding issue.

Acknowledgments

I am indebted to a number of colleagues who have closely worked with me on many of the topics covered by this chapter. Their invaluable contributions are gratefully acknowledged: Petar Glisovic, Jerry Mitrovica, Robert Moucha, Sandrine Quéré, and David Rowley. Work by NAS is performed under the auspices of Lawrence Livermore National Laboratory, operated by Lawrence Livermore National Security, LLC, for the US Department of Energy, National Nuclear Security Administration under Contract DE-AC52-07NA27344. SPG acknowledges support from the National Science Foundation, grant EAR0309189. Work by AMF has been made possible thanks to support provided by the Canadian Institute for Advanced Research and the Canadian National Science and Engineering Research Council.

References

Adam C and Vidal V (2010) Mantle flow drives the subsidence of oceanic plates. *Science* 328: 83–85.

Adam C and Vidal V (2011) Response to comment on "Mantle flow drives the subsidence of oceanic plates" *Science* 331: 1011.

Alisic L, Gurnis M, Stadler G, Burstedde C, and Ghattas O (2012) Multi-scale dynamics and rheology of mantle flow with plates. *Journal of Geophysical Research* 117: 1–27. http://dx.doi.org/10.1029/2012JB009234, B10402.

Antolik M, Gu YJ, Ekström G, and Dziewonski AM (2003) J362D28: A new joint model of compressional and shear velocity in the Earth's mantle. *Geophysical Journal International* 153: 443–466.

Bassin C, Laske G, and Masters G (2000) The current limits of resolution for surface wave tomography in North America. *Eos, Transactions American Geophysical Union* 81(48): 897.

Becker TW and Boschi L (2002) A comparison of tomographic and geodynamic mantle models. *Geochemistry, Geophysics, Geosystems* 3. http://dx.doi.org/10.1029/2001GC000168.

Becker TW and Faccenna C (2011) Mantle conveyor beneath the Tethyan collisional belt. *Earth and Planetary Science Letters* 310: 453–461.

Boschi L and Dziewonski AM (2000) Whole Earth tomography from delay times of P, PcP, and PKP phases: Lateral heterogeneities in the outer core or radial anisotropy in the mantle? *Journal of Geophysical Research* 105: 13675–13696.

Bunge H-P, Richards MA, and Baumgardner JR (1996) Effect of depth-dependent viscosity on the planform of mantle convection. *Nature* 379: 436–438.

Bunge H-P, Richards MA, Lithgow-Bertelloni C, Baumgardner JR, Grand SP, and Romanowicz BA (1998) Time scales and heterogeneous structure in geodynamic Earth models. *Science* 280: 91–95.

Čadek O and Fleitout L (2003) Effect of lateral viscosity variations in the top 300 km on the geoid and dynamic topography. *Geophysical Journal International* 152: 566–580.

Čadek O, Yuen DA, Steinbach V, Chopelas A, and Matyska C (1994) Lower mantle thermal structure deduced from seismic tomography, mineral physics and numerical modelling. *Earth and Planetary Science Letters* 121: 385–402.

Cammarano F, Goes S, Vacher P, and Giardini D (2003) Inferring upper-mantle temperatures from seismic velocities. *Physics of the Earth and Planetary Interiors* 138: 197–222.

Cathles LM (1975) *The Viscosity of the Earth's Mantle*. Princeton, NJ: Princeton University Press.

Chase CG (1979) Subduction, the geoid, and lower mantle convection. *Nature* 282: 464–468.

Chase CG and Sprowl DR (1983) The modern geoid and ancient plate boundaries. *Earth and Planetary Science Letters* 62: 314–320.

Clayton RW and Comer RP (1983) A tomographic analysis of mantle heterogeneities from body wave travel times. *Eos, Transactions American Geophysical Union* 64(45): 776.

Conrad CP, Bianco TA, Smith EI, and Wessel P (2011) Patterns of intraplate volcanism controlled by asthenospheric shear. *Nature Geoscience* 4: 317–321.

Constable SC, Parker RL, and Constable CG (1987) Occam's inversion: A practical algorithm for generating smooth models from electromagnetic sounding data. *Geophysics* 52: 289–300.

Corrieu V, Ricard Y, and Froidevaux C (1994) Converting mantle tomography into mass anomalies to predict the Earth's radial viscosity. *Physics of the Earth and Planetary Interiors* 84: 3–13.

Corrieu V, Thoraval C, and Ricard Y (1995) Mantle dynamics and geoid Green functions. *Geophysical Journal International* 120: 516–523.

Croon MB, Hillier JK, and Sclater JG (2011) Comment on "Mantle flow drives the subsidence of oceanic plates" *Science* 331: 1011.

Crosby AG, McKenzie D, and Sclater JG (2006) The relationship between depth, age and gravity in the oceans. *Geophysical Journal International* 166: 553–573.

Davies DR, Goes S, Davies JH, Schuberth BSA, Bunge H-P, and Ritsema J (2012) Reconciling dynamic and seismic models of Earth's lower mantle: The dominant role of thermal heterogeneity. *Earth and Planetary Science Letters* 353–354: 253–269.

Defraigne P (1997) Internal loading of a compressible Earth: Effect of a solid lithosphere. *Physics of the Earth and Planetary Interiors* 101: 303–313.

DeMets CR, Gordon RG, Argus DF, and Stein S (1990) Current plate motions. *Geophysical Journal International* 101: 425–478.

Deschamps F, Snieder R, and Trampert J (2001) The relative density-to-shear velocity scaling in the uppermost mantle. *Physics of the Earth and Planetary Interiors* 124: 193–212.

deWit RWL, Trampert J, and van der Hilst RD (2012) Toward quantifying uncertainty in travel time tomography using the null-space shuttle. *Journal of Geophysical Research* 117. http://dx.doi.org/10.1029/2011JB008754, B03301.

Doin M-P and Fleitout L (2000) Flattening of the oceanic topography and geoid: Thermal versus dynamic origin. *Geophysical Journal International* 143: 582–594.

Dziewonski AM (1984) Mapping the lower mantle: Determination of lateral heterogeneity in *P* velocity up to degree and order 6. *Journal of Geophysical Research* 89: 5929–5952.

Dziewonski AM and Anderson DL (1981) Preliminary reference Earth model. *Physics of the Earth and Planetary Interiors* 25: 297–356.

Dziewonski AM, Hager BH, and O'Connell RJ (1977) Large scale heterogeneity in the lower mantle. *Journal of Geophysical Research* 82: 239–255.

Dziewonski AM and Romanowicz BA (2007) Overview. In: Romanowicz BA and Dziewonski AM (eds.) *Treatise of Geophysics*, vol. 1, pp. 1–29. Amsterdam: Elsevier.

Ekström G and Dziewonski AM (1998) The unique anisotropy of the Pacific upper mantle. *Nature* 394: 168–172.

Forte AM (2000) Seismic-geodynamic constraints on mantle flow: Implications for layered convection, mantle viscosity, and seismic anisotropy in the deep mantle. In: Karato S-i, et al. (eds.) *Earth's Deep Interior: Mineral Physics and Tomography from the Atomic to the Global Scale*. *Geophysical Monograph Series*, 117: pp. 3–36. Washington, DC: American Geophysical Union.

Forte AM (2007) Constraints on seismic models from other disciplines – Implications for mantle dynamics and composition. In: Romanowicz B and Dziewonski AM (eds.) *Treatise of Geophysics*, vol. 1, pp. 805–858. Amsterdam: Elsevier.

Forte AM, Dziewonski AM, and O'Connell RJ (1995) Continent-ocean chemical heterogeneity in the mantle based on seismic tomography. *Science* 268: 386–388.

Forte AM, Dziewonski AM, and Woodward RL (1993) Aspherical structure of the mantle, tectonic plate motions, nonhydrostatic geoid, and topography of the core–mantle boundary. In: LeMouël J-L, Smylie DE, and Herring T (eds.) *Dynamics of the Earth's Deep Interior and Earth Rotation*. *Geophysical Monograph Series*, 72: pp. 135–166. Washington, DC: American Geophysical Union.

Forte AM and Mitrovica JX (1996) New inferences of mantle viscosity from joint inversion of long-wavelength mantle convection and post–glacial rebound data. *Geophysical Research Letters* 23: 1147–1150.

Forte AM and Mitrovica JX (2001) Deep-mantle high-viscosity flow and thermochemical structure inferred from seismic and geodynamic data. *Nature* 410: 1049–1056.

Forte AM, Mitrovica JX, and Espesset A (2002) Geodynamic and seismic constraints on the thermochemical structure and dynamics of convection in the deep mantle. *Philosophical Transactions of the Royal Society of London A* 360: 2521–2543.

Forte AM, Mitrovica JX, and Woodward RL (1995) Seismic-geodynamic determination of the origin of excess ellipticity of the core–mantle boundary. *Geophysical Research Letters* 22: 1013–1016.

Forte AM, Moucha R, Rowley DB, et al. (2009) Recent tectonic plate decelerations driven by mantle convection. *Geophysical Research Letters* 36. http://dx.doi.org/10.1029/2009GL040224, L23301.

Forte AM and Peltier WR (1987) Plate tectonics and aspherical Earth structure: The importance of poloidal–toroidal coupling. *Journal of Geophysical Research* 92: 3645–3679.

Forte AM and Peltier WR (1989) Core–mantle boundary topography and whole-mantle convection. *Geophysical Research Letters* 16: 621–624.

Forte AM and Peltier WR (1991) Viscous flow models of global geophysical observables, 1. Forward problems. *Journal of Geophysical Research* 96: 20131–20159.

Forte AM and Peltier WR (1994) The kinematics and dynamics of poloidal–toroidal coupling in mantle flow: The importance of surface plates and lateral viscosity variations. *Advances in Geophysics* 36: 1–119.

Forte AM, Peltier WR, and Dziewonski AM (1991) Inferences of mantle viscosity from tectonic plate velocities. *Geophysical Research Letters* 18: 1747–1750.

Forte AM, Peltier WR, Dziewonski AM, and Woodward RL (1993a) Dynamic surface topography: A new interpretation based upon mantle flow models derived from seismic tomography. *Geophysical Research Letters* 20: 225–228.

Forte AM, Peltier WR, Dziewonski AM, and Woodward RL (1993b) Reply to comment by M. Gurnis. *Geophysical Research Letters* 20: 1665–1666.

Forte AM and Perry HKC (2000) Geodynamic evidence for a chemically depleted continental tectosphere. *Science* 290: 1940–1944.

Forte AM, Quéré S, Moucha R, et al. (2010) Joint seismic-geodynamic-mineral physical modelling of African geodynamics: A reconciliation of deep-mantle convection with surface geophysical constraints. *Earth and Planetary Science Letters* 295: 329–341.

Forte AM and Woodward RL (1997a) Seismic-geodynamic constraints on vertical flow between the upper and lower mantle: The dynamics of the 670 km seismic discontinuity. In: Crossley D (eds.) *The Fluid Dynamics of Astrophysics and Geophysics*. *Earth's Deep Interior*, vol. 7, pp. 337–404. Newark, NJ: Gordon and Breach.

Forte AM and Woodward RL (1997b) Seismic-geodynamic constraints on three-dimensional structure, vertical flow, and heat transfer in the mantle. *Journal of Geophysical Research* 102: 17981–17994.

Forte AM, Woodward RL, and Dziewonski AM (1994) Joint inversions of seismic and geodynamic data for models of three-dimensional mantle heterogeneity. *Journal of Geophysical Research* 99: 21857–21877.

Gable CW, O'Connell RJ, and Travis BJ (1991) Convection in three dimensions with surface plates. *Journal of Geophysical Research* 96: 8391–8405.

Garcia R and Souriau A (2000) Amplitude of the core–mantle boundary topography estimated by stochastic analysis of core phases. *Physics of the Earth and Planetary Interiors* 117: 345–359.

Glisovic P, Forte AM, and Moucha R (2012) Time-dependent convection models of mantle thermal structure constrained by seismic tomography and geodynamics: Implications for mantle plume dynamics and CMB heat flux. *Geophysical Journal International* 190: 785–815.

Gordon RG and Jurdy DM (1986) Cenozoic global plate motions. *Journal of Geophysical Research* 91: 12389–12406.

Grand SP (1994) Mantle shear structure beneath the Americas and surrounding oceans. *Journal of Geophysical Research* 99: 11591–11621.
Grand SP (2002) Mantle shear-wave tomography and the fate of subducted slabs. *Philosophical Transactions of the Royal Society A* 360: 2475–2491.
Gurnis M (1990) Bounds on global dynamic topography from Phanerozoic flooding of continental platforms. *Nature* 344: 754–756.
Gurnis M (1993) Comment. *Geophysical Research Letters* 20: 1663–1664.
Gwinn CR, Herring TA, and Shapiro II (1986) Geodesy by radio interferometry; studies of the forced nutations of the Earth; 2. Interpretation. *Journal of Geophysical Research* 91: 4755–4766.
Hager BH (1984) Subducted slabs and the geoid: Constraints on mantle rheology and flow. *Journal of Geophysical Research* 89: 6003–6015.
Hager BH and Clayton RW (1989) Constraints on the structure of mantle convection using seismic observations, flow models, and the geoid. In: Peltier WR (eds.) *Mantle Convection: Plate Tectonics and Global Dynamics*, pp. 657–763. New York: Gordon and Breach.
Hager BH, Clayton RW, Richards MA, Comer RP, and Dziewonski AM (1985) Lower mantle heterogeneity, dynamic topography and the geoid. *Nature* 313: 541–545.
Hager BH and O'Connell RJ (1981) A simple global model of plate dynamics and mantle convection. *Journal of Geophysical Research* 86: 4843–4867.
Hager BH and Richards MA (1989) Long-wavelength variations in the Earth's geoid: Physical models and dynamical implications. *Philosophical Transactions of the Royal Society of London A* 328: 309–327.
Haskell NA (1935) The motion of a viscous fluid under a surface load. *Journal of Applied Physics* 6: 265–269.
Herring TA, Gwinn CR, and Shapiro II (1986) Geodesy by radio interferometry; studies of the forced nutations of the Earth; 1. Data analysis. *Journal of Geophysical Research* 91: 4745–4754.
Jackson JD (1975) *Classical Electrodynamics*. New York: J. Wiley & Sons Inc.
Jackson I (2001) Chemical composition and temperature of the lower mantle from seismological models: Residual uncertainties. In: *Integrated Models of Earth Structure and Evolution*, *AGU Virtual Meeting – 2001 Spring Meeting, 20 June* [online].
Jarvis GT and Peltier WR (1982) Mantle convection as a boundary layer phenomenon. *Geophysical Journal of the Royal Astronomical Society* 68: 385–424.
Jeanloz R and Thompson AB (1983) Phase transitions and mantle discontinuities. *Reviews of Geophysics and Space Physics* 21: 51–74.
Jordan TH (1981) Continents as a chemical boundary layer. *Philosophical Transactions of the Royal Society of London A* 301: 359–373.
Karato S-i (1993) Importance of anelasticity in the interpretation of seismic tomography. *Geophysical Research Letters* 20: 1623–1626.
Karato S-I and Karki BB (2001) Origin of lateral variation of seismic wave velocities and density in the deep mantle. *Journal of Geophysical Research* 106: 21771–21784.
Karpychev M and Fleitout L (2000) Long-wavelength geoid: The effect of continental roots and lithosphere thickness variations. *Geophysical Journal International* 143: 945–963.
Kaufmann G and Lambeck K (2000) Mantle dynamics, postglacial rebound and the radial viscosity profile. *Physics of the Earth and Planetary Interiors* 121: 301–324.
Kido M, Yuen DA, Čadek O, and Nakakuki T (1998) Mantle viscosity derived by genetic algorithm using oceanic geoid and seismic tomography for whole-mantle versus blocked-flow situations. *Physics of the Earth and Planetary Interiors* 107: 307–326.
King SD (1995) Models of mantle viscosity. In: Ahrens TJ (eds.) *A Handbook of Physical Constants: Mineral Physics and Crystallography*. *AGU Reference Shelf Series*, vol. 2, pp. 227–236. Washington, DC: American Geophysical Union.
King S and Masters G (1992) An inversion for the radial viscosity structure using seismic tomography. *Geophysical Research Letters* 19: 1551–1554.
Kustowski B, Ekström G, and Dziewonski AM (2008) Anisotropic shear-wave velocity structure of the Earth's mantle: A global model. *Journal of Geophysical Research* 113. http://dx.doi.org/10.1029/2007JB005169, B06306.
Lambeck K, Johnston P, Smither C, and Nakada M (1996) Glacial rebound of the British Isles. III. Constraints on mantle viscosity. *Geophysical Journal International* 125: 340–354.
Lambeck K, Smither C, and Johnston P (1998) Sea-level change, glacial rebound and mantle viscosity for northern Europe. *Geophysical Journal International* 134: 102–144.
Landau LD and Lifshitz EM (1959) *Fluid Mechanics*, vol. 6. New York: Pergamon.
Laske G, Masters G, Ma Z, and Pasyanos M (2013) Update on crust1. 0-a 1-degree global model of earths crust. *EGU General Assembly Conference Abstracts* 15: 2658.
Le Stunff Y and Ricard Y (1995) Topography and geoid due to lithospheric mass anomalies. *Geophysical Journal International* 122: 982–990.
Le Stunff Y and Ricard Y (1997) Partial advection of equidensity surfaces; a solution for the dynamic topography problem? *Journal of Geophysical Research* 102: 24655–24667.
Lemoine F, Pavlis N, Kenyon S, Rapp R, Pavlis E, and Chao B (1998) New high-resolution model developed for earth's gravitational field. *Eos, Transactions American Geophysical Union* 79(9): 113.
Levander A, Schmandt B, Miller MS, et al. (2011) Continuing Colorado plateau uplift by delamination-style convective lithospheric downwelling. *Nature* 472: 461–465.
Li C, van der Hilst RD, Engdahl ER, and Burdick S (2008) A new global model for P wave speed variations in Earth's mantle. *Geochemistry, Geophysics, Geosystems* 9. http://dx.doi.org/10.1029/2007GC001806, Q05018.
Lithgow-Bertelloni C and Gurnis M (1997) Cenozoic subsidence and uplift of continents from time-varying dynamic topography. *Geology* 25: 735–738.
Lithgow-Bertelloni C and Richards MA (1998) The dynamics of Cenozoic and Mesozoic plate motions. *Reviews of Geophysics* 36: 27–78.
Martinec Z, Matyska C, Cadek O, and Hrdina P (1993) The Stokes problem with 3-D Newtonian rheology in a spherical shell. *Computer Physics Communication* 76: 63–79.
Masters G, Laske G, Bolton H, and Dziewonski AM (2000) The relative behaviour of shear velocity, bulk sound speed, and compressional velocity in the mantle: Implications for chemical and thermal structure. In: Karato S-I, et al. (eds.) *Earth's Deep Interior: Mineral Physics and Tomography From the Atomic to the Global Scale*. *Geophysical Monograph Series*, vol. 117, pp. 63–87. Washington, DC: American Geophysical Union.
Mathews PM, Herring TA, and Buffett BA (2002) Modeling of nutation and precession: New nutation series for nonrigid Earth and insights into the Earth's interior. *Journal of Geophysical Research* 107: 2068. http://dx.doi.org/10.1029/2001JB000390.
McConnell RK (1968) Viscosity of the mantle from relaxation time spectra of isostatic adjustment. *Journal of Geophysical Research* 73: 7089–7105.
McNamara AK and Zhong S-J (2005) Thermochemical structures beneath Africa and the Pacific Ocean. *Nature* 437: 1136–1139.
Mégnin C and Romanowicz B (2000) The three-dimensional shear velocity structure of the mantle from the inversion of body, surface and higher-mode waveforms. *Geophysical Journal International* 143: 709–728.
Mitrovica JX (1996) Haskell [1935] revisited. *Journal of Geophysical Research* 101: 555–569.
Mitrovica JX and Forte AM (1997) Radial profile of mantle viscosity: Results from the joint inversion of convection and post-glacial rebound observables. *Journal of Geophysical Research* 102: 2751–2769.
Mitrovica JX and Forte AM (2004) A new inference of mantle viscosity based upon joint inversion of convection and glacial isostatic adjustment data. *Earth and Planetary Science Letters* 225: 177–189.
Montelli R, Nolet G, Dahlen FA, Masters G, Engdahl ER, and Hung SH (2004) Finite-frequency tomography reveals a variety of plumes in the mantle. *Science* 303: 338–343.
Morelli A and Dziewonski AM (1987) Topography of the core–mantle boundary and lateral homogeneity of the liquid core. *Nature* 325: 678–683.
Mosca I, Cobden L, Deuss A, Ritsema J, and Trampert J (2012) Seismic and mineralogical structures of the lower mantle from probabilistic tomography. *Journal of Geophysical Research* 117. http://dx.doi.org/10.1029/2011JB008851, B06304.
Moucha R and Forte AM (2011) Changes in African topography driven by mantle convection. *Nature Geoscience* 4: 707–712.
Moucha R, Forte AM, Mitrovica JX, and Daradich A (2007) Geodynamic implications of lateral variations in mantle rheology on convection related observables and inferred viscosity models. *Geophysical Journal International* 169: 113–135.
Moucha R, Forte AM, Mitrovica JX, et al. (2008) Dynamic topography and long-term sea-level variations: There is no such thing as a stable continental platform. *Earth and Planetary Science Letters* 271: 101–108.
Müller RD, Roest WR, Royer J-Y, Gahagan LM, and Sclater JG (1997) Digital isochrons of the world's ocean floor. *Journal of Geophysical Research* 102: 3211–3214.
Nakada M and Lambeck K (1989) Late Pleistocene and Holocene sea-level change in the Australian region and mantle rheology. *Geophysical Journal International* 96: 497–517.
Nakagawa T and Tackley PJ (2008) Lateral variations in CMB heat flux and deep mantle seismic velocity caused by a thermal? Chemical-phase boundary layer in 3D spherical convection. *Earth and Planetary Science Letters* 271: 348–358.
Nakagawa T, Tackley PJ, Deschamps F, and Connolly JAD (2010) The influence of MORB and Harzburgite composition on thermo-chemical mantle convection in a 3D spherical shell with self-consistently calculated mineral physics. *Earth and Planetary Science Letters* 296: 403–412.
Nicolas A and Poirier J-P (1976) *Crystalline Plasticity and Solid State Flow in Metamorphic Rocks*. London: Wiley 444 pp.
Nolet G, Karato S-I, and Montelli R (2006) Plume fluxes from seismic tomography. *Earth and Planetary Science Letters* 248: 685–699.

Obayashi M and Fukao Y (1997) P and PcP travel time tomography for the core–mantle boundary. *Journal of Geophysical Research* 102: 17825–17841.
O'Connell RJ (1971) Pleistocene glaciation and viscosity of the lower mantle. *Geophysical Journal of the Royal Astronomical Society* 23: 299–327.
Oganov AR, Brodholt JP, and Price GD (2001a) *Ab initio* elasticity and thermal equation of state of $MgSiO_3$ perovskite. *Earth and Planetary Science Letters* 184: 555–560.
Oganov AR, Brodholt JP, and Price GD (2001b) The elastic constants of $MgSiO_3$ perovskite at pressures and temperatures of the Earth's mantle. *Nature* 411: 934–937.
Paige CC and Saunders MA (1982) LSQR: An algorithm for sparse linear equations and sparse least squares. *ACM Transactions on Mathematical Software* 8: 43–71.
Panasyuk SV and Hager BH (2000) Inversion for mantle viscosity profiles constrained by dynamic topography and the geoid, and their estimated errors. *Geophysical Journal International* 143: 821–836.
Panasyuk SV, Hager BH, and Forte AM (1996) Understanding the effects of mantle compressibility on geoid kernels. *Geophysical Journal International* 124: 121–133.
Pari G (2001) Crust 5.1-based inference of the Earth's dynamic surface topography: Geodynamic implications. *Geophysical Journal International* 144: 501–516.
Pari G and Peltier WR (2000) Subcontinental mantle dynamics; a further analysis based on the joint constraints of dynamic surface topography and free-air gravity. *Journal of Geophysical Research* 105: 5635–5662.
Parsons B and Daly S (1983) The relationship between surface topography, gravity anomalies, and temperature structure of convection. *Journal of Geophysical Research* 88: 1129–1144.
Parsons B and McKenzie D (1978) Mantle convection and the thermal structure of the plates. *Journal of Geophysical Research* 83: 4485–4496.
Parsons B and Sclater JG (1977) An analysis of the variation of ocean floor bathymetry and heat flow with age. *Journal of Geophysical Research* 82: 803–827.
Pekeris CL (1935) Thermal convection in the interior of the Earth. *Monthly Notices of the Royal Astronomical Society Geophysical Supplements* 3: 343–367.
Peltier WR (1985) New constraint on transient lower mantle rheology and internal mantle buoyancy from glacial rebound data. *Nature* 318: 614–617.
Peltier WR and Andrews JT (1976) Glacial isostatic adjustment, I. The forward problem. *Geophysical Journal of the Royal Astronomical Society* 46: 605–646.
Perry HKC, Forte AM, and Eaton DWS (2003) Upper-mantle thermochemical structure below North America from seismic–geodynamic flow models. *Geophysical Journal International* 154: 279–299.
Phinney RA and Burridge R (1973) Representation of the elastic-gravitational excitation of a spherical Earth model by generalized spherical harmonics. *Geophysical Journal of the Royal Astronomical Society* 34: 451–487.
Quéré S and Forte AM (2006) Influence of past and present-day plate motions on spherical models of mantle convection: Implications for mantle plumes and hotspots. *Geophysical Journal International* 165: 1041–1057.
Ranalli G (2001) Mantle rheology: Radial and lateral viscosity variations inferred from microphysical creep laws. *Journal of Geodynamics* 32: 425–444.
Ricard Y, Chambat F, and Lithgow-Bertelloni C (2006) Gravity observations and 3D structure of the Earth. *Comptes Rendus Geoscience* 338: 992–1001.
Ricard Y, Fleitout L, and Froidevaux C (1984) Geoid heights and lithospheric stresses for a dynamic Earth. *Annals of Geophysics* 2: 267–286.
Ricard Y, Froidevaux C, and Fleitout L (1988) Global plate motion and the geoid: A physical model. *Geophysical Journal International* 93: 477–484.
Ricard Y, Richards M, Lithgow-Bertelloni C, and Le Stunff Y (1993) A geodynamic model of mantle density heterogeneity. *Journal of Geophysical Research* 98: 21895–21909.
Ricard Y and Vigny C (1989) Mantle dynamics with induced plate tectonics. *Journal of Geophysical Research* 94: 17543–17559.
Ricard Y, Vigny C, and Froidevaux C (1989) Mantle heterogeneities, geoid, and plane motion – A Monte Carlo inversion. *Journal of Geophysical Research* 94: 13739–13754.
Ricard Y and Wuming B (1991) Inferring viscosity and the 3-D density structure of the mantle from geoid, topography and plate velocities. *Geophysical Journal International* 105: 561–572.
Richards MA (1991) Hot spots and the case for a high viscosity lower mantle. In: Sabadini R, Lambeck K, and Boschi E (eds.) *Glacial Isostasy, Sea-Level and Mantle Rheology. NATO ASI Series C*, vol. 334, pp. 571–588. Norwell, MA: Kluwer Academic.
Richards MA and Engebretson DC (1992) Large-scale mantle convection and the history of subduction. *Nature* 355: 437–440.
Richards MA and Hager BH (1984) Geoid anomalies in a dynamic Earth. *Journal of Geophysical Research* 89: 5987–6002.
Richards MA and Hager BH (1989) Effects of lateral viscosity variations on long-wavelength geoid anomalies and topography. *Journal of Geophysical Research* 94: 10299–10313.
Richards MA, Ricard Y, Lithgow-Bertelloni C, Spada G, and Sabadini R (1997) An explanation for the long-term stability of Earth's rotation axis. *Science* 275: 372–375.
Ritsema J, Deuss A, van Heijst HJ, and Woodhouse JH (2011) S40RTS: A degree-40 shear-velocity model for the mantle from new Rayleigh wave dispersion, teleseismic traveltime and normal-mode splitting function measurements. *Geophysical Journal International* 184: 1223–1236.
Ritsema J, van Heijst HJ, and Woodhouse JH (1999) Complex shear velocity structure imaged beneath Africa and Iceland. *Science* 286: 1925–1928.
Ritzwoller MH, Shapiro NM, and Zhong S-J (2004) Cooling history of the Pacific lithosphere. *Earth and Planetary Science Letters* 226: 69–84.
Rodgers A and Wahr J (1993) Inference of core–mantle boundary topography from ISC PcP and PKP traveltimes. *Geophysical Journal International* 115: 991–1011.
Röhm AHE, Snieder R, Goes S, and Trampert J (2000) Thermal structure of continental upper mantle inferred from S-wave velocity and surface heat flow. *Earth and Planetary Science Letters* 181: 395–407.
Romanowicz B (2003) Global mantle tomography: Progress status in the past 10 years. *Annual Review of Earth and Planetary Sciences* 31: 303–328.
Rowley DB, Forte AM, Moucha R, Mitrovica JX, Simmons NA, and Grand SP (2013) Dynamic topography change of the Eastern U.S. Since 3 million years ago. *Science* 340: 1560–1563.
Sabadini R and Yuen DA (1989) Mantle stratification and long-term polar wander. *Nature* 339: 373–375.
Sabadini R, Yuen DA, and Gasperini P (1985) The effects of transient rheology on the interpretation of lower mantle rheology. *Geophysical Research Letters* 12: 361–365.
Sammis CG, Smith JC, Schubert G, and Yuen DA (1977) Viscosity-depth profile of the earth's mantle: Effects of polymorphic phase transitions. *Journal of Geophysical Research* 82: 3747–3761.
Schuberth BSA, Bunge H-P, and Ritsema J (2009) Tomographic filtering of high-resolution mantle circulation models: Can seismic heterogeneity be explained by temperature alone? *Geochemistry, Geophysics, Geosystems* 10. http://dx.doi.org/10.1029/2009GC002401, Q05W03.
Schuberth BSA, Zaroli C, and Nolet G (2012) Synthetic seismograms for a synthetic Earth: Long-period P- and S-wave traveltime variations can be explained by temperature alone. *Geophysical Journal International* 188: 1393–1412.
Shen W, Ritzwoller MH, and Schulte-Pelkum V (2013) A 3-D model of the crust and uppermost mantle beneath the Central and Western US by joint inversion of receiver functions and surface wave dispersion. *Journal of Geophysical Research* 118: 262–276. http://dx.doi.org/10.1029/2012JB009602.
Simmons NA (2007) *Mantle Heterogeneity and Flow from Seismic and Geodynamic Constraints*. Doctoral Dissertation, University of Texas at Austin.
Simmons NA, Forte AM, Boschi L, and Grand SP (2010) GyPSuM: A joint tomographic model of mantle density and seismic wave speeds. *Journal of Geophysical Research* 115. http://dx.doi.org/10.1029/2010JB007631.
Simmons NA, Forte AM, and Grand SP (2006) Constraining modes of mantle flow with seismic and geodynamic data: A joint approach. *Earth and Planetary Science Letters* 246: 109–124.
Simmons NA, Forte AM, and Grand SP (2007) Thermochemical structure and dynamics of the African superplume. *Geophysical Research Letters* 34. http://dx.doi.org/10.1029/2006GL028009, L02301.
Simmons NA, Forte AM, and Grand SP (2009) Joint seismic, geodynamic and mineral physical constraints on three-dimensional mantle heterogeneity: Implications for the relative importance of thermal versus compositional heterogeneity. *Geophysical Journal International* 177(3): 1284–1304.
Smirnov AV and Tarduno JA (2010) Co-location of eruption sites of the Siberian Traps and North Atlantic Igneous Province: Implications for the nature of hotspots and mantle plumes. *Earth and Planetary Science Letters* 297(3–4): 687–690.
Sobolev SV, Zeyen H, Granet M, et al. (1997) Upper mantle temperatures and lithosphere–asthenosphere system beneath the French Massif Central constrained by seismic, gravity, petrologic and thermal observations. *Tectonophysics* 275: 143–164.
Spada G, Ricard Y, and Sabadini R (1992) Excitation of true polar wander by subduction. *Nature* 360: 452–454.
Stacey FD (1998) Thermoelasticity of a mineral composite and a reconsideration of lower mantle properties. *Physics of the Earth and Planetary Interiors* 106: 219–236.
Stein CA and Stein S (1992) A model for the global variation in oceanic depth and heat flow with lithospheric age. *Nature* 359: 123–129.

Steinberger B and O'Connell RJ (1997) Change of the Earth's rotation axis inferred from the advection of mantle density heterogeneities. *Nature* 387: 169–173.

Stixrude L and Lithgow-Bertelloni C (2001) The origin of lateral heterogeneity in the mantle. In: *Integrated Models of Earth Structure and Evolution*, *AGU Virtual Meeting – 2001 Spring Meeting, 20 June* .

Stixrude L and Lithgow-Bertelloni C (2005) Mineralogy and elasticity of the oceanic upper mantle: Origin of the low-velocity zone. *Journal of Geophysical Research* 110. http://dx.doi.org/10.1029/2004JB002965, B03204.

Su W-J, Woodward RL, and Dziewonski AM (1992) Deep origin of mid-ocean ridge seismic velocity anomalies. *Nature* 360: 149–152.

Sze EKM and van der Hilst RD (2003) Core mantle boundary topography from short period PcP, PKP, and PKKP data. *Physics of the Earth and Planetary Interiors* 135: 27–46.

Thoraval C, Machetel P, and Cazenave A (1995) Locally layered convection inferred from dynamic models of the Earth's mantle. *Nature* 375: 777–780.

Thoraval C and Richards MA (1997) The geoid constraint in global geodynamics: Viscosity structure, mantle heterogeneity models, and boundary conditions. *Geophysical Journal International* 131: 1–8.

Thurber C and Ritsema J (2007) Theory and observations – Seismic tomography and inverse methods. In: Romanowicz BA and Dziewonski AM (eds.) *Treatise of Geophysics*, vol. 1, pp. 323–360. Amsterdam: Elsevier.

Trampert J, Vacher P, and Vlaar N (2001) Sensitivities of seismic velocities to temperature, pressure and composition in the lower mantle. *Physics of the Earth and Planetary Interiors* 124: 255–267.

Trampert J and Woodhouse JH (1996) High resolution global phase velocity distributions. *Geophysical Research Letters* 23: 21–24.

Turcotte DL and Oxburgh ER (1967) Finite amplitude convective cells and continental drift. *Journal of Fluid Mechanics* 28(1): 29–42.

Tushingham AM and Peltier WR (1991) ICE-3G: A new global model of late Pleistocene deglaciation based upon geophysical predictions of postglacial relative sea level change. *Journal of Geophysical Research* 96: 4497–4523.

Wahr J (1981) The forced mutations of an elliptical, rotating elastic and oceanless Earth. *Geophysical Journal of the Royal Astronomical Society* 64: 705–727.

Wang Y and Weidner DJ (1996) $(\partial\mu/\partial T)_P$ of the lower mantle. *Pure and Applied Geophysics* 146: 533–549.

Weertman J (1978) Creep laws for the mantle of the Earth. *Philosophical Transactions of the Royal Society of London A* 288: 9–26.

Weertman J and Weertman JR (1975) High temperature creep of rock and mantle viscosity. *Annual Review of Earth and Planetary Sciences* 3: 293–315.

Woodhouse JH and Dziewonski AM (1984) Mapping the upper mantle: Three-dimensional modeling of earth structure by inversion of seismic waveforms. *Journal of Geophysical Research* 89: 5953–5986.

Woodward RL and Masters G (1991) Global upper mantle structure from long-period differential travel times. *Journal of Geophysical Research* 96: 6351–6377.

Wu P and Peltier WR (1983) Glacial isostatic adjustment and the free air gravity anomaly as a constraint on deep mantle viscosity. *Geophysical Journal of the Royal Astronomical Society* 74: 377–449.

Xu W, Lithgow-Bertelloni C, Stixrude L, and Ritsema J (2008) The effect of bulk composition and temperature on mantle seismic structure. *Earth and Planetary Science Letters* 275: 70–79.

Zhang S and Christensen U (1993) Some effects of lateral viscosity variations on geoid and surface velocities induced by density anomalies in the mantle. *Geophysical Journal International* 114: 531–547.

Zhang J and Weidner DJ (1999) Thermal equation of state of aluminum-enriched silicate perovskite. *Science* 284: 782–784.

Zhang S and Yuen DA (1995) The influences of lower mantle viscosity stratification on 3D spherical-shell mantle convection. *Earth and Planetary Science Letters* 132: 157–166.

Zhong S, Ritzwoller M, Shapiro N, Landuyt W, Huang J, and Wessel P (2007) Bathymetry of the Pacific plate and its implications for thermal evolution of lithosphere and mantle dynamics. *Journal of Geophysical Research* 112(B6). http://dx.doi.org/10.1029/2006JB004628, B06412.